



High-energy emission from a magnetar giant flare in the Sculptor galaxy

The Fermi-LAT Collaboration*

Magnetars are the most highly magnetized neutron stars in the cosmos (with magnetic field 10^{13} – 10^{15} G). Giant flares from magnetars are rare, short-duration (about 0.1 s) bursts of hard X-rays and soft γ rays^{1,2}. Owing to the limited sensitivity and energy coverage of previous telescopes, no magnetar giant flare has been detected at gigaelectronvolt (GeV) energies. Here, we report the discovery of GeV emission from a magnetar giant flare on 15 April 2020 (refs. ^{3,4} and A. J. Castro-Tirado et al., manuscript in preparation). The Large Area Telescope (LAT) on board the Fermi Gamma-ray Space Telescope detected GeV γ rays from 19 s until 284 s after the initial detection of a signal in the megaelectronvolt (MeV) band. Our analysis shows that these γ rays are spatially associated with the nearby (3.5 megaparsecs) Sculptor galaxy and are unlikely to originate from a cosmological γ -ray burst. Thus, we infer that the γ rays originated with the magnetar giant flare in Sculptor. We suggest that the GeV signal is generated by an ultra-relativistic outflow that first radiates the prompt MeV-band photons, and then deposits its energy far from the stellar magnetosphere. After a propagation delay, the outflow interacts with environmental gas and produces shock waves that accelerate electrons to very high energies; these electrons then emit GeV γ rays as optically thin synchrotron radiation. This observation implies that a relativistic outflow is associated with the magnetar giant flare, and suggests the possibility that magnetars can power some short γ -ray bursts.

On 15 April 2020, the Fermi Gamma-ray Burst Monitor (GBM) triggered and located γ -ray burst (GRB) 200415A⁴, which was initially classified as a short (duration <2 s) γ -ray burst (SGRB). The Interplanetary Network of γ -ray detectors (IPN, <http://ssl.berkeley.edu/ipn3/index.html>) reduced the uncertainty on the GBM position to 20 square arcmin, suggesting that the GRB originated from the nearby Sculptor galaxy³, located at a distance of about 3.5 megaparsecs⁵. This, with the resemblance of the GBM sub-MeV light curve (E. Burns, manuscript in preparation) to the extragalactic soft gamma repeater (SGR) giant flare candidates GRB 051103^{3,6} and GRB 070201⁷, and the detection of quasi-periodic oscillations by the Atmosphere–Space Interaction Monitor (A. J. Castro-Tirado et al., manuscript in preparation), led to the identification of GRB 200415A as a magnetar giant flare (MGF) in Sculptor. GRB 200415A was 43° from the LAT boresight at the GBM trigger time T_0 (08:48:05.563746 UTC) and remained well within the LAT field of view (FOV) until 500 seconds after T_0 . Three γ rays were detected by the LAT, allowing the localization of GRB 200415A at high energies (>100 MeV); this detection of high-energy γ -ray emission from an MGF suggests that magnetars can power the relativistic outflows observed in some SGRBs.

To study the localization of the γ -ray signal observed by the LAT we perform a likelihood analysis and compute a test statistic (TS)

for the presence of the source at different positions. The best position is obtained from the maximum of the TS ($TS_{\max}=29$, corresponding to a detection significance close to 5σ ; see the Methods and Extended Data Fig. 1 for the numerical value of the best-fit model). Then, the variation of the TS around this position provides the map of localization contours shown in Fig. 1. The iso-contours in red encompass localization probabilities of 68% and 90%.

Four galaxies (IC 1576, IC 1578, IC 1582 and NGC 253) from the NGC 2000 catalogue⁸ are located within a circular region of radius r_{99} , whose area is equivalent to the 99% confidence level, and which is centred on the maximum of the TS map at right ascension (RA) = 11.13° and declination (dec.) = -24.97° (J2000). NGC 253, also known as the Sculptor galaxy, has already been detected as a steady source in γ rays^{9,10} with a flux integrated between 100 MeV and 100 GeV of $(1.3 \pm 0.2) \times 10^{-8} \text{ cm}^{-2} \text{ s}^{-1}$. The γ -ray emission is powered by cosmic rays accelerated by supernova remnants interacting with the interstellar gas, and the enhanced massive star-formation activity in the galaxy also favours the presence of stellar remnants like magnetars. The centre of the galaxy lies on the contour containing a localization probability of 72%.

We apply the likelihood ratio (LR) method¹¹ to quantify the reliability of a possible association of the γ -ray source with Sculptor. This method can distinguish between two situations: the true counterpart associated with a γ -ray emitter, which appears to lie a certain distance away owing to localization uncertainties; or a background object which, by chance, happens to lie close to the γ -ray position. Our analysis takes into account the angular size of the counterpart candidate and the elongated shape of the LAT localization contours shown in Fig. 1. Since the LR method takes into account the magnitude of the galaxy, we find that the Sculptor galaxy is the most likely host galaxy of the source detected by the LAT with a LR value approximately 60 times larger than the values for other galaxies. To evaluate the statistical significance of this association, we compare the LR values obtained in these analyses with the same analyses repeated over a sample of random locations in the sky. The P values range from 3.2×10^{-4} to 2.9×10^{-3} depending on the particular analysis (see details in the Methods and Extended Data Figs. 3 and 4). Both analyses suggest a positional association between Sculptor and the LAT γ -ray detection. Assuming that the emission detected by the LAT is from an SGRB, our calculation of the false alarm rates (FARs) ranges from $5.4 \times 10^{-4} \text{ yr}^{-1}$ to $4.7 \times 10^{-3} \text{ yr}^{-1}$.

We perform a detailed maximum likelihood spectral analysis of the LAT emission by modelling GRB 200415A as a point source with a power-law spectrum. As part of our analysis we estimate the probability that each photon detected by the LAT is associated with the point source, as opposed to any of the other model components. The list of events is shown in Extended Data Fig. 2. Three events are associated with the source with a probability greater than 90%. The arrival times (after T_0) of these events are 19 s, 180 s and 284 s, with

*A list of authors and their affiliations appears at the end of the paper.

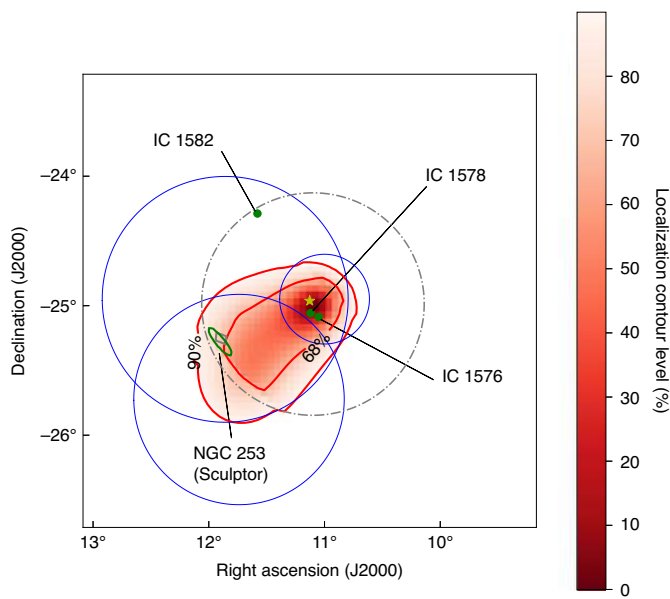


Fig. 1 | Map of the localization contour probability. The contours encompassing a probability of 68% and 90% are displayed in red, while the yellow star marks the location of the TS maximum. Galaxies from the NGC 2000 catalogue are shown as green disks, except for NGC 253 (Sculptor galaxy), which is shown as an extended source. The grey box indicates the localization provided by the IPN³. The circle whose area is equivalent to the 99% confidence level is displayed with a grey dashed-dotted line, while the blue circles indicate the 68% containment of the point spread function (PSF) for the three γ rays probably associated with the flare.

energies 480 MeV, 1.3 GeV and 1.7 GeV, respectively. The reconstructed directions of these events are shown in Fig. 1 as circles with a radius equal to the PSF of the instrument at their respective energies. To estimate the significance of this cluster of three events (triplet) and the probability that it is due to a background fluctuation, we look at a region of 1° radius around the location of Sculptor using the entire LAT dataset available (more than 12 years of data). Two different analyses, applying that of Li and Ma¹² and Bayesian blocks (BB) methods^{13,14}, result respectively in P values of $P_{\text{Li\&Ma}} = 8.3 \times 10^{-7}$ and $P_{\text{BB}} = 2.3 \times 10^{-3}$. See Methods for details, as well as Extended Data Figs. 5 and 6. Finally, we calculate the rate of chance coincidence between a LAT triplet signal and a GBM SGRB in the same region of Sculptor within a given time window. The FARs for the two analyses are $1.6 \times 10^{-7} \text{ yr}^{-1}$ and $6.3 \times 10^{-8} \text{ yr}^{-1}$ respectively.

To summarize, the FAR of detecting high-energy emission from an SGRB spatially associated by chance to Sculptor is one event in approximately 200–1,800 years, depending on the analysis method, while the FAR of the event also being temporally coincident with a GBM SGRB is of the order of one event every 10^6 – 10^7 yr. Accordingly, we conclude that the LAT signal is associated with an MGF event in Sculptor.

The intense GBM emission below 1 MeV defines the so-called ‘initial spike’ of the MGF and must come from a relativistic wind⁴. The three local magnetars that have displayed MGFS (two in the Milky Way and one in the Large Magellanic Cloud) each had pulsating late-time emission of effective temperature 10–25 keV, emitting about 10^{44} erg of energy over a few hundred seconds. The LAT signal cannot come from this region ($R \lesssim 3 \times 10^7$ cm) owing to the high opacity¹⁵ to $\gamma \rightarrow e^+e^-$ pair creation in the magnetar’s enormous magnetic field. The long ($t_{\text{del}} = 19$ s) delay between the initial spike and first LAT photon detection suggests that the GeV emission must take place well outside the light cylinder radius $Pc/2\pi \approx 10^{10}$ – 10^{11} cm

for magnetars of rotation periods $P \approx 2$ –12 s. Thus, the scenario we propose is that the GeV emission arises from dissipation associated with the collision between an ultra-relativistic outflow from the MGF and an external shell of swept-up material. The huge energy release, approximately 10^{47} erg, within about 0.14 s (ref. ⁴), probably from magnetically induced crustal fracturing of the magnetar surface¹⁶ or from the deformation of the magnetosphere^{17,18}, creates a very hot plasma. Initially, the radiation is trapped inside this magnetized plasma rich in electron–positron pairs and vastly fewer baryons. The plasma accelerates under its own radiation pressure and becomes optically transparent to electron scattering at distances $R > 10^8$ cm from the magnetar. The emission of radiation from a range of radii and with a range of effective temperatures $\lesssim 300$ keV constitutes a Comptonized spectrum peaking at about 1 MeV, as observed by the GBM. The accompanying plasma continues its outward flow with a bulk Lorentz factor $\Gamma_{\text{ej}} \approx 100$ and kinetic energy of about 3×10^{46} erg (refs. ^{19,20}). Such a high Lorentz factor is in contrast to the MGFS observed in the Milky Way that powered only mildly relativistic outflows observed as radio nebulae^{21,22} expanding at about $0.7c$, where the much lower expansion velocity can be attributed to entrainment of a larger baryon mass. The inferred kinetic energy of the outflow from the MGF in Sculptor is, however, comparable with the total radiated energy in the initial spike, as was also inferred for the previous local MGFS.

In its quiescent state, the magnetar putatively emits a pulsar-type ultra-relativistic magnetohydrodynamic wind powered by its spin-down energy. The continual wind sweeps up interstellar gas, and stalls at a bow shock, forming a shell at a distance $R_{\text{bs}} \approx 8 \times 10^{15}$ cm. The MGF outflow, which itself becomes a thin shell over time, therefore propagates essentially inside an evacuated cavity until it collides with the bow-shock shell. The time of collision is approximately $R_{\text{bs}}/2\Gamma_{\text{ej}}^2 c \approx 10$ s, which is similar to the time t_{del} . After collision, a forward shock propagates inside the bow-shock shell and a reverse shock propagates inside the MGF shell. Electrons are accelerated at the shocks to relativistic energies and emit synchrotron radiation up to GeV energies in shock-generated magnetic fields. The duration of the peak emission is approximately $R_{\text{bs}}/2\Gamma_{\text{sh}}^2 c \approx 400$ s, where $\Gamma_{\text{sh}} \approx 20$ is the bulk Lorentz factor of the forward shock. This is the timescale over which the LAT detected synchrotron photons with energies of up to a few GeV (Methods).

GRB 200415A is an MGF detected at $\gtrsim 100$ MeV energies, noting that similarities between the MGFS and cosmological GRBs have been pointed out in the past^{2,23,24}. Previous searches in LAT data for persistent hard γ -ray emission from several Galactic magnetars resulted in stringent upper limits^{25,26}. The 10–500 seconds (from T_0) LAT spectrum of GRB 200415A, with a photon index $\Gamma = -1.7 \pm 0.3$ and a flux of $(4.1 \pm 2.2) \times 10^{-6} \text{ cm}^{-2} \text{ s}^{-1}$ (two orders of magnitude brighter than the non-variable flux of Sculptor), is typical of an SGRB detected by the LAT. What makes GRB 200415A different from other LAT-detected SGRBs is the long delay of about 19 s compared to typical values of $\lesssim 1$ s between the GBM trigger time and the LAT detection²⁷ (Methods). Among the 17 SGRBs detected by the LAT in the first 10 years, GRB 200415A shows the longest delay between the end of the GBM-detected emission and the beginning of the high-energy emission, and only two SGRBs were detected by the LAT for a duration comparable to that of GRB 200415A (see Extended Data Fig. 7). Although these peculiarities by themselves do not rule out GRB 200415A being a cosmological SGRB, its association with Sculptor, its very flat GBM spectrum below 1 MeV (ref. ⁴), and the quasi-periodic oscillation detection by the Atmosphere–Space Interaction Monitor (A. J. Castro-Tirado et al., manuscript in preparation) all strongly point toward an MGF origin.

We suggest that an ultra-relativistic outflow with energy similar to the prompt γ -ray energy emanated from the MGF in Sculptor and that this outflow hit a dense shell of material surrounding the magnetar. Shock-heated material accelerated electrons to relativistic

energies, which emitted synchrotron radiation in the presence of a magnetic field generated in the shocks. The GRB 200415A detected by the LAT is thus the high-energy component of the spectrum of an MGE.

Methods

The LAT. The Fermi Gamma-Ray Space Telescope was placed in a low-Earth orbit on June 11, 2008. Its two scientific instruments, the LAT²⁸ and the GBM²⁹, together provide the capability of probing emission over several decades in energy. The LAT is a pair production telescope sensitive to γ rays in the energy range from about 30 MeV to more than 300 GeV. Whether or not a γ ray is detected by the LAT is primarily defined by two angles: the angle ζ with respect to the spacecraft zenith, and the viewing angle θ from the LAT boresight. In the analysis performed in this paper, we do not make any explicit cuts on the angle θ ; however, the exposure drops very quickly for θ greater than about 75°. When we calculate the exposure and the live time, on the other hand, we only include time intervals when the entire region of interest (ROI) has $\zeta < 100^\circ$ and $\theta < 80^\circ$. The wide FOV (about 2.4 sr at 1 GeV) of the LAT, its high observing efficiency (scanning the entire sky every 3 h), its broad energy range, its large effective area, its low dead time per event (about 27 μ s), its efficient background rejection, and its good angular resolution (the 68% containment radius of the PSF is about 0.8° at 1 GeV) are all much better than those of previous instruments. With respect to those instruments, the LAT provides more GRB detections, higher statistics per detection, and more accurate localization. From the second LAT GRB catalogue (2FLGC)²⁷, the average detection rates for the LAT are 1.7 short GRBs and 17 long GRBs per year.

Detection and localization of the LAT signal. We perform an unbinned maximum likelihood analysis, using LAT P8_TRANSIENT020E events within a ROI with a radius of 12° (initially centred on the GBM final ground position³⁰). We select a time interval of 10–500 s after the GBM trigger time T_0 , which contains all the γ rays detected by the LAT before the GRB exited its FOV. We also select the events with energies between 100 MeV and 10 GeV, and with a zenith angle $< 100^\circ$ to limit the contribution from the bright Earth limb. The GRB photon spectrum is modelled with a power law $dN/dE = AE^{\Gamma}$. The main background component consists of charged particles that are mis-classified as γ rays. It is included in the analysis using the iso_P8R2_TRANSIENT020_V6_v06.txt template. Although the contribution from the Galactic diffuse emissions is very small because of the high Galactic latitude of the GRB, it is accounted for by using the gll_iem_v07.fits template. Both templates are available at the Fermi Science Support Center (<https://fermi.gsfc.nasa.gov/ssc/>). No source from the fourth LAT GRB catalogue (4FGL) is bright enough to be considered in the model of the ROI.

To localize the GRB and estimate its signal significance in the LAT, we perform a likelihood ratio test for the presence of the source at different positions³¹. Using the gttsmap tool, we evaluate TS to be twice the increment of the logarithm of the likelihood by fitting the data with and without the GRB component added to the background components in the model. The maximum value, $TS_{\max} = 29$, is found at a location of RA = 11.13°, dec. = −24.97° (J2000), consistent with what was first reported by Omodei et al.³². This TS_{\max} value corresponds to a detection significance of 4.4 σ or 5.0 σ (one-sided) if the TS distribution follows $(1/2)\chi^2_4$ or $(1/2)\chi^2_2$, respectively. As explained in the first LAT GRB catalogue³³, the two coordinates of the source are considered to be unknown and are left free to vary in the former case (namely, 4 degrees of freedom including the two spectral parameters), while the latter case is more suitable when an external position is used as an input to the analysis (for example, the GBM initial position here).

We compute the error contours of the source localization from the variation of the TS values around the best position, namely TS_{\max} . In each pixel i of the map displayed in Fig. 1, we first compute the difference in TS as $\Delta TS_i = TS_{\max} - TS_i$. Then, we convert it to a probability contour level assuming that the ΔTS_i is distributed as a χ^2 with 2 degrees of freedom (the two coordinates)^{31,33}:

$$P_i = \int_0^{\Delta TS_i} \chi^2_2(t) dt. \quad (1)$$

The iso-contours containing localization probabilities of 68% and 90% are highlighted in Fig. 1. The best-fit spectral parameters obtained at the position of TS_{\max} are summarized in Extended Data Fig. 1. We also calculate the isotropic energy (E_{iso}) and luminosity (L_{iso}) assuming the distance of the Sculptor galaxy to be about 3.5 megaparsecs³⁴. Finally, we use the gtsrcprob tool to compute the probability for each LAT γ ray to be associated with the LAT-detected source. The first γ ray exceeding a probability of 90% arrives at $T_0 + 19.18$ s, with an energy of 480 MeV. A 1.3-GeV photon is detected at $T_0 + 180.22$ s, while the highest-energy γ ray is a 1.7-GeV photon at $T_0 + 284.05$ s. All of these γ rays belong to the SOURCE class (or to a cleaner event class), which results from a tight event classification that drastically reduces the residual background rate. Extended Data Fig. 2 shows all the γ rays detected within the 12° ROI with their probability of being associated with the GRB. The three γ rays with the highest association probability ($> 90\%$) are displayed in Fig. 1 with circles of radius equal to the 68% containment radius of the LAT PSF^{34,35}.

Spatial association of the high-energy emission with the Sculptor galaxy. Four galaxies from the NGC2000 catalogue³⁶ (IC 1576, IC 1578, IC 1582 and NGC 253) are located within the ROI centred at the position of the LAT source with radius r_{99} , and many more fainter galaxies are certainly located inside the region. Adding more galaxies from catalogues with a greater limiting magnitude (more fainter galaxies) would vastly increase the number of counterpart candidates. To take this consideration into account, we adopt the LR method^{36–44}, applied in several studies for counterpart searches in different catalogues^{36–44}. This approach allows us to obtain and quantify the reliability of a possible γ -ray association, using the counterparts' local surface density: in this sense the LR can be used to calculate the probability that a suggested association is the true counterpart of a source. If we define $r_{\alpha\beta}$ as the angular distance d between the γ -ray localization α and the counterpart candidate β , scaled by the γ -ray location uncertainty (at the 68% confidence level) r_{68} , then it is given by

$$r_{\alpha\beta} = \frac{d}{r_{68}}. \quad (2)$$

The probability that a counterpart β lies at a distance $r_{\alpha\beta}$ from the γ -ray localization α is distributed as a Rayleigh distribution ($r_{\alpha\beta} e^{-r_{\alpha\beta}^2/2}$), while the probability that β is a background source that, by chance, happens to lie close to the position α follows a linear distribution ($\propto r_{\alpha\beta}$). The LR can thus be computed as:

$$LR = \frac{p}{N(\leq m_\beta)A}, \quad (3)$$

where $p = e^{-r_{\alpha\beta}^2/2}$, $N(\leq m_\beta)$ is the surface density of sources brighter than the counterpart candidate β (of magnitude m_β) and A is the solid angle spanned by r_{99} . To evaluate the surface density $N(\leq m_\beta)$, we count the galaxies brighter than the candidate β in a region of 20° around the γ -ray source. At the position of the LAT-detected source, the values of the LR for the four galaxies are LR = 2.1 (IC 1576), 2.9 (IC 1578), 0.3 (IC 1582), and 60 (NGC 253). Although two NGC galaxies (IC 1576 and IC 1578) are closer to the LAT best position, the LR favours the most luminous NGC 253 (the Sculptor galaxy). To take into account the extension of the counterpart galaxy, expressed by its radial angular extent in optical r_{ext} , we modified equation (3) for the LR by adding in quadrature r_{ext} to r_{68} . We can write the new equation for LR in a convenient form as:

$$LR_{\text{ext}} = \frac{p^\xi}{N(\leq m_\beta)A}, \quad (4)$$

where the exponent ξ is simply defined as:

$$\xi = \frac{1}{1 + \left(\frac{r_{\text{ext}}}{r_{68}}\right)^2}. \quad (5)$$

To quantify the significance of the LR and LR_{ext} values we perform a set of 10⁵ simulations by randomizing the position over the sky of the LAT excess, and repeating the procedure described above. For every random position we select the maximum of the LR and LR_{ext} , which corresponds to the galaxy with greatest association probability within the ROI, and we fill a histogram with these values. The LR method can also be applied using the probability map illustrated in Fig. 1. From this map we can directly evaluate $1 - p_i$ with p_i from equation (1), and use it as the numerator in the LR formula. In this way, we consider the shape of the TS map and we abandon the hypothesis implicit in the Rayleigh distribution that the two spatial coordinates are independently normally distributed. As in the previous case, we generate 10⁵ observations, choosing the position of the TS map randomly on the celestial sphere. For each location, we compute the LR values for the NGC galaxies in the ROI, considering them as point-like or extended sources. The P values quantify the potential association between the Sculptor galaxy and the LAT γ -ray source. They are defined as the number of cases where the LR is greater than that obtained for the Sculptor galaxy divided by the total number of simulated cases. They can thus be obtained from the normalized cumulative distributions, displayed in Extended Data Fig. 3. The two distributions (point-like versus extended source) are similar and yield comparable association probabilities. For the Rayleigh case, P values range from 1.7×10^{-3} to 2.9×10^{-3} , whereas using the TS map to compute the LR gives lower P values, 3.2×10^{-4} for point-like sources and 3.6×10^{-4} for extended sources. Lower P values are expected from this second analysis given the elongation of the TS map toward the Sculptor galaxy, with a smaller value for the extended case because of the large extension of the Sculptor galaxy (around 25 arcmin). Assuming that the emission detected at high energies is from a SGRB, we can calculate the FAR by multiplying the P values by the rate of SGRBs observed by the LAT. Values range from $5.4 \times 10^{-4} \text{ yr}^{-1}$ to $4.7 \times 10^{-3} \text{ yr}^{-1}$ as summarized in the first part of Extended Data Fig. 4. Both the analyses suggest a strong likelihood of positional association between the Sculptor galaxy and the LAT γ -ray source.

Significance of the temporal coincidence. From Extended Data Fig. 2, we can see that three γ rays with energies 0.5 GeV, 1.3 GeV and 1.7 GeV are reconstructed within 1° of Sculptor, and they arrive within a time span of approximately 300 s.

We calculate the significance of the LAT triplet by selecting all the SOURCE events (between 100 MeV and 300 GeV) received by the LAT in 12 years of data within a radius of 1° from the centre of the Sculptor galaxy (RA = 11.89°, dec. = -25.29°, J2000). The total live time of the selected ROI is about 2.98 yr. To compute the probability that three photons cluster by chance, owing to statistical fluctuations of the background, in the 10–500 s interval after T_0 , we apply the LR method of ref. ¹². The maximum likelihood ratio, testing the presence of a new source, is defined as:

$$\lambda = \left[\frac{\alpha}{1+\alpha} \left(1 + \frac{N_B}{N_S} \right) \right]^{N_S} \left[\frac{1}{1+\alpha} \left(1 + \frac{N_S}{N_B} \right) \right]^{N_B}, \quad (6)$$

where $N_S = 3$ and $N_B = 5361$ are respectively the number of LAT photons observed during and outside the analysis time window and α is the ratio between the analysed time interval (490 s) and the total live time (about 2.98 yr). The significance S of the LAT triplet signal can thus be calculated as:

$$S \approx \sqrt{-2\ln\lambda} = 5.3\sigma, \quad (7)$$

corresponding to a P value of 8.3×10^{-7} . To estimate whether such a cluster of three events is common for the analysed ROI, we use again the entire LAT dataset of the Sculptor galaxy region to compute the time intervals Δt_i for each triplet i formed by three consecutive events:

$$\Delta t_i = t_{i+2} - t_i. \quad (8)$$

Thus, the resulting intervals are used to create the dashed red histogram of Extended Data Fig. 5, in which the blue line corresponds to the Fermi orbit period and the yellow line shows the Δt of the triplet of photons observed for the LAT-detected source. This simple analysis does not consider that the ROI periodically enters and exits the LAT FOV, potentially splitting some triplets into different time windows. To take this effect into account, we perform a second and more conservative analysis subtracting from each Δt_i the duration of the time intervals during which the ROI is not observable (bad time intervals). As expected, the bulk of the distribution moves toward shorter time intervals (green histogram in Extended Data Fig. 5) but no significant new entries appear at the tail of the distribution. This corrected histogram is in agreement with the theoretical curve expected in the case of independent events (black dashed line in Extended Data Fig. 5). For a Poisson distribution of γ ray arrival times from a steady source, indeed, the probability density P of observing a triplet with time interval Δt given the mean rate R is:

$$P(\Delta t) = R^2 \Delta t e^{-R\Delta t}. \quad (9)$$

with a rate $R \approx 5.7 \times 10^{-5}$ Hz, this results in a probability of 1.4×10^{-4} for an interval shorter than $\Delta t \approx 300$ s.

We find that three events clustered in a time window shorter than the one related to the LAT source on only one occasion over 12 years (within an interval of 240 s starting at 2017 November 21 at 03:07:33 UTC), but the likelihood analysis of this triplet resulted in a low detection significance ($TS_{\max} = 16$).

We compute the FAR (in units of hertz) for the temporal coincidence of the LAT-detected source with GRB 200415A as:

$$FAR = A \times R_{\text{triplet}} \times R_{\text{GRB}} \times \delta t \quad (10)$$

where $A = \pi \text{ deg}^2$ is the area of the circular region under consideration, $R_{\text{GRB}} = 3.7 \times 10^{-11} \text{ s}^{-1} \text{ deg}^{-2}$ is the rate of SGRBs detected by the GBM, obtained from the online catalogue of GBM GRBs¹⁵ and scaled by the GBM FOV, and $\delta t = 500$ s is the coincidence time window after the SGRB prompt emission during which we expect a signal in the LAT data. R_{triplet} is the mean rate of triplets having a Δt smaller than a fixed threshold and, for a value of 500 s, we count only eight triplets over 2.98 yr of live time (see Extended Data Fig. 5). The resulting FAR is $1.6 \times 10^{-7} \text{ yr}^{-1}$. Considering only events with energies greater than 480 MeV (the energy of the least-energetic photon within the cluster associated with the GRB), we find only the triplet related to the MGF and the FAR accordingly decreases to $2 \times 10^{-8} \text{ yr}^{-1}$.

We also apply the Bayesian blocks (BB) algorithm^{13,14} to the dataset with the bad time intervals removed. We used BB to detect and characterize statistically significant variations in rates of LAT γ rays, such as the photon time tags analysed here. It provides optimal, maximum goodness of fit, segmentation of the observed time series, from among all possible partitions of the observation interval. The arrival times of the photons are binned using the BB edges, and a rate for each block is obtained by dividing its number of included photons by its width in time. The only free parameter describes the prior for the distribution of the number of blocks. Within a range suggested by calibrations based on limiting the false positive rate for single change-point detection¹⁴, this penalty constant can be adjusted in the same spirit as with a smoothing parameter. Extended Data Fig. 6 shows the results of this analysis for a selected value of the penalty constant, together with daily and weekly count rates. We also display the weekly average exposures. Three epochs are shaded in yellow, corresponding to three distinct observing profiles. The first, at the beginning of the mission, coincides with the period in which Fermi had a 35° rocking angle. This represents the angle between the zenith and the pointing

direction of the LAT and was gradually increased until it reached 55° in September 2009. Between December 2013 and July 2015, instead, Fermi spent most of its time pointing at the Galactic Centre: this corresponds to the second highlighted interval, which is consequently characterized, on average, by a decrease of exposure in the direction of the Sculptor galaxy. The third highlighted period starts with the occurrence of the solar panel drive anomaly of the Fermi spacecraft (https://fermi.gsfc.nasa.gov/ssc/observations/types/post_anomaly/), in March 2018 and ends when a new optimized observing profile was adopted to mitigate the effect of this issue in February 2019. Spikes and dips in the exposure are the effect of occasional pointed observations (called targets of opportunity). However, at the time of GRB 200415A no particular features are evident in the time dependence of the accumulation of exposure. The clear spike of γ -ray rate at T_0 corresponds to the cluster of the events arriving within about 300 s. In particular, there are three events in the bin with the highest rate (and a width of 810 s). From simple Poisson statistics, considering the average rate of γ rays detected from the direction of Sculptor in the remaining time history, the probability of this rate being a fluctuation is 2.3×10^{-3} .

Finally, to estimate the FAR we use a formula similar to equation (10), with $\delta t = 810$ s (the width of the time block) and R_{triplet} replaced by R_{block} , namely, the average detection rate of blocks exceeding a threshold of 10^{-3} Hz. With just two such blocks in 2.98 yr of total live time (see Extended Data Fig. 6), the corresponding FAR is $6.3 \times 10^{-8} \text{ yr}^{-1}$. These results are summarized in the second part of Extended Data Fig. 4.

Comparison with other LAT SGRBs. Here we compare GRB 200415A with the population of GRBs detected by the LAT. The spectrum of GRB 200415A is typical for short bursts detected by the LAT, with a photon index $\Gamma = -1.7 \pm 0.3$ consistent with the distribution of photon indices $\Gamma_{\text{ext}} = -2.03 \pm 0.4$ (at 90% confidence level) of the 2FLGC. In that catalogue, the subscript ‘ext’ indicates that the integration window that is used to compute the photon index is restricted to the duration of the temporally extended emission detected by the LAT, which is the most appropriate in the comparison with the photon index of GRB 200415A. The flux and fluence measured for GRB 200415A are also typical, being on the low end of the distributions. What is quite peculiar about the LAT emission from GRB 200415A is its delay and duration.

The left-hand panel of Extended Data Fig. 7, from the 2FLGC, shows the arrival time of the first LAT γ ray with probability >0.9 of association with the GRB, which marks the beginning of the high-energy emission, as a function of the GBM T_{95} , which marks the end of the prompt emission observed by the GBM¹. For a short burst, GRB 200415A has an exceptionally delayed high-energy emission with respect to the end of the prompt phase. Two other short bursts in the 2FLGC show comparable delays: GRB 160702A was detected by Konus-Wind, INTEGRAL (SPI-ACS), Mars-Odyssey (HEND), and Swift (BAT)⁴⁶. Fermi was in the South Atlantic Anomaly at the time of the trigger, precluding a search for high-energy emission during (or immediately after) the prompt emission. Similarly, GRB 170127 was outside the FOV of the LAT, with a boresight angle of 142° at the time of the GBM trigger. An autonomous re-pointing request was issued by the GBM, and the LAT detected high-energy emission once the burst entered its FOV. GRB 200415A is the only LAT SGRB that was within the FOV at the time of trigger, and additionally its high-energy emission started much later than the end of the GBM prompt emission. The right-hand panel of Extended Data Fig. 7 shows that GRB 200415A has a relatively long duration at high energies for a SGRB. Again, only the same two other SGRBs mentioned above have similar durations.

GeV γ -ray flare from ultra-relativistic debris from a magnetar colliding with an outlying shell. An MGF is a catastrophic event in the life-cycle of a magnetar, releasing a sizeable fraction of its approximately 10^{48} erg magnetic energy^{16,47}. Different trigger mechanisms have been proposed for an MGF, for example, a rupture of the solid crust due to magnetic stress at the core-cusp boundary¹⁶, or a deformation of the magnetosphere^{17,18}. Such a process releases a huge amount of energy within a very short period of time in a small volume near the magnetar with radius $r_0 = 10^6 r_{0.6}$ cm. This produces copious e^+e^- pairs and an optically thick fireball^{16,49}. A qualitative description of this fireball and its evolution^{19,20} depends on its total luminosity $L_0 = L_{\gamma, \text{iso}}/\xi_\gamma \approx 3 \times 10^{47} \xi_\gamma^{-1} L_{\gamma, 47} \text{ erg s}^{-1}$. Here $L_{\gamma, \text{iso}} = 10^{47} L_{\gamma, 47} \text{ erg s}^{-1}$ is the average isotropic-equivalent γ -ray luminosity during the prompt duration containing 90% of the fluence $T_{90} = 0.141 \text{ s period}^4$, and $\xi_\gamma = 0.3 \xi_{\gamma, 0.5}$ is the assumed fraction of the total luminosity in γ rays, which includes the magnetic energy and kinetic energy carried by the baryons in the fireball. The initial effective temperature of the fireball is $T_0 = (L_0/4\pi r_0^2 c a)^{1/4} \approx 275 \xi_\gamma^{-1/4} L_{\gamma, 47}^{1/4} r_{0.6}^{-1/2} \text{ keV}$; note that the luminosity is lower than that indicative of full thermalization⁴. Here $a = \pi^2 k^4/15 h^3 c^3 = 7.6 \times 10^{-15} \text{ erg cm}^{-3} \text{ K}^{-4}$ is the radiation density constant. A key finding for GRB 200415A is that the total energy in the LAT emission, $E_{\text{LAT, iso}} = 3.6 \times 10^{45} \text{ erg}$, is much less than the prompt GBM energy of $1.5 \times 10^{46} \text{ erg}^4$. This implies that the fireball is ultra-relativistic and the kinetic outflow attains a terminal bulk Lorentz factor similar to a critical value obtained from the Thomson opacity argument as^{19,20} $\eta_* = (L_0 \sigma_T/4\pi m_p c^3 r_0)^{1/4} \approx 140 \xi_\gamma^{-1/4} L_{\gamma, 47}^{1/4} r_{0.6}^{-1/4}$. Here

σ_T is the Thomson cross-section and m_p is the mass of the proton. The total isotropic-equivalent energy of the kinetic outflow (ejecta), after decoupling from the radiation, is $E_{k,iso} = 3 \times 10^{46} E_{k,46.5}$ erg with a bulk Lorentz factor $\Gamma_{ej} = 10^2 \Gamma_{ej,2}$, where the parameters $E_{k,46.5} \approx \Gamma_{ej,2} \approx 1$. These numbers may change somewhat if the influence of field line flaring in modifying the outflow dynamics is fully taken into account. As we discuss next and in contrast to the previously modelled radio nebula from the 2004 MGF of SGR 1806-20 with an outflow velocity of about $0.7c$ (refs. 21,22), this ultra-relativistic kinetic outflow is critical for our interpretation of the LAT observation.

Absent an intermediate electron acceleration site, for example a magnetic reconnection zone in the MHD wind outside the light cylinder, no relevant emission is produced from the outflow before it interacts with an external shell. The external shell is naturally produced as the spindown-powered relativistic pulsar-type MHD wind emanating from the magnetar sweeps up the surrounding interstellar medium (ISM) and creates a bow shock. The radial distance of the shell is found from balancing in the rest frame of the magnetar (and of the head of the bow shock) the ram pressure of the incoming ISM with that of the MHD wind. For nominal values of the spin-down luminosity $L_{sd} = 10^{34} \text{ erg s}^{-1}$, the proper motion velocity of the magnetar $v = 10^3 v_3 \text{ km s}^{-1}$ and the ISM density $n = 10^{-1.6} n_{-1.6} \text{ cm}^{-3}$, the radius of the bow shock is $R_{bs} = (L_{sd}/4\pi n m_p v^2 c)^{1/2} = 8 \times 10^{15} L_{sd,34}^{1/2} n_{-1.6}^{-1/2} v_3^{-1} \text{ cm}$. The bow-shock shell has an inner part of shocked MHD wind and an outer part of shocked ISM, the two being separated by a contact discontinuity.

The observed collision time between the outflow, which propagates essentially in vacuum, and the bow-shock shell is given by $t_{coll} = R_{bs}/2\Gamma_{ej}^2 c \approx 10 \text{ s}$, where we identify t_{coll} with the arrival time of the first photons to the observer from the head of the outflow along the line of sight. The duration of LAT emission, however, depends on the angular time scale over which emission arrives from the shocked outflow and bow-shock shell. This time scale is $t_\theta = R_{bs}/2\Gamma_{sh}^2 c$, where Γ_{sh} is the bulk Lorentz factor of the forward shock propagating in the outer part of the shell with shocked ISM (the inner part with shocked wind offers negligible resistance). For a strong shock the density contrast between the outflow and bow-shock shell is $f \equiv n_{ej}/n_{bs} \approx 30 L_{sd,34}^{-3/2} E_{k,46.5} n_{-1.6}^{1/2} v_3^3$, after calculating the outflow ejecta density $n_{ej} = E_{k,iso}/4\pi R_{bs}^3 m_p c^2 \approx 3 L_{sd,34}^{-3/2} E_{k,46.5} n_{-1.6}^{3/2} v_3^3 \text{ cm}^{-3}$ and $n_{bs} \approx 4n \approx 0.1 n_{-1.6} \text{ cm}^{-3}$. As a result⁵⁰, $\Gamma_{sh} = f^{1/4} (\Gamma_{ej}/2)^{1/2} \approx 20 L_{sd,34}^{-1/4} t_{coll,1}^{-1/4} E_{k,46.5}^{1/4} v_3^{1/2}$ and $t_\theta \approx 400 L_{sd,34}^{1/2} E_{k,46.5}^{-1/2} n_{-1.6}^{1/2} v_3^{-2} \text{ s}$ is sufficiently long to account for the duration of the LAT emission of about 300 s.

The LAT emission is produced by the shock-accelerated electrons in the material behind the forward shock that is propagating into the bow shock. The radiation efficiency $E_{LAT,iso}/E_{k,iso} \approx 0.1$ is typical of GRB afterglow emission. The maximum synchrotron photon energy emitted by these electrons is limited by their acceleration and cooling times to⁵¹ $E_{syn,max} = \Gamma_{sh} \kappa (m_e c^2 / \alpha_F) \approx 1.4 \kappa L_{sd,34}^{-1/4} t_{coll,1}^{1/4} E_{k,46.5}^{1/4} v_3^{1/2} \text{ GeV}$, where $\alpha_F = e^2/\hbar c \approx 1/137$ is the fine-structure constant. The factor κ is of order unity⁵² and can be different for differing assumptions about electron acceleration rates and diffusion in a shock layer. Therefore, the synchrotron photon energy can explain the highest-energy LAT γ ray observed from GRB 200415A if $\Gamma_{sh} \gtrsim 20$.

Data availability

The Fermi-LAT data are publicly available at the Fermi Science Support Center website: <https://fermi.gsfc.nasa.gov/ssc/>. Filtered data supporting the findings of this study are available at https://www-glast.stanford.edu/pub_data/1801/.

Code availability

In this study we use the Fermi-LAT Science Tools, publicly available at the Fermi Science Support Center website: <https://fermi.gsfc.nasa.gov/ssc/>. The code required to reproduce each figure of the paper is available from the corresponding authors upon request.

Received: 20 October 2020; Accepted: 1 December 2020;

Published online: 13 January 2021

References

- Frail, D. A., Kulkarni, S. R. & Bloom, J. S. An outburst of relativistic particles from the soft γ -ray repeater SGR1900+14. *Nature* **398**, 127–129 (1999).
- Hurley, K. et al. An exceptionally bright flare from SGR 1806-20 and the origins of short-duration γ -ray bursts. *Nature* **434**, 1098–1103 (2005).
- Svinkin, D. & the IPN Team. Bright twin γ -ray flares in two nearby galaxies as giant magnetar flares. *Nature* <https://doi.org/10.1038/s41586-020-03076-9> (2021).
- Roberts, O. J. & the GBM and Swift Teams. Rapid spectral variability of a giant flare from an extragalactic magnetar. *Nature* <https://doi.org/10.1038/s41586-020-03077-8> (2021).
- Rekola, R. et al. Distance to NGC 253 based on the planetary nebula luminosity function. *Mon. Not. R. Astron. Soc.* **361**, 330–336 (2005).
- Frederiks, D. D. et al. On the possibility of identifying the short hard burst GRB 051103 with a giant flare from a soft gamma repeater in the M81 group of galaxies. *Astron. Lett.* **33**, 19–24 (2007).
- Mazets, E. P. et al. A giant flare from a soft gamma repeater in the Andromeda galaxy (M31). *Astrophys. J.* **680**, 545–549 (2008).
- VizieR Online Data Catalog NGC 2000.0 VII/118 (Sky Publishing, 1988); <http://go.nature.com/3bsaO6o>
- Abdollahi, S. et al. Fermi Large Area Telescope fourth source catalog. *Astrophys. J. Suppl.* **247**, 33 (2020).
- Ackermann, M. et al. GeV observations of star-forming galaxies with the Fermi Large Area Telescope. *Astrophys. J.* **755**, 164 (2012).
- de Ruiter, H. R., Willis, A. G. & Arp, H. C. A Westerbork 1415 MHz survey of background radio sources. II. Optical identifications with deep IIIa-J plates. *Astron. Astrophys. Suppl.* **28**, 211–293 (1977).
- Li, T. P. & Ma, Y. Q. Analysis methods for results in gamma-ray astronomy. *Astrophys. J.* **272**, 317–324 (1983).
- Scargle, J. D. Studies in astronomical time series analysis. V. Bayesian blocks, a new method to analyze structure in photon counting data. *Astrophys. J.* **504**, 405 (1998).
- Scargle, J. D., Norris, J. P., Jackson, B. & Chiang, J. Studies in astronomical time series analysis. VI. Bayesian block representations. *Astrophys. J.* **764**, 167 (2013).
- Story, S. A. & Baring, M. G. Magnetic pair creation transparency in gamma-ray pulsars. *Astrophys. J.* **790**, 61 (2014).
- Thompson, C. & Duncan, R. C. The soft gamma repeaters as very strongly magnetized neutron stars—I. Radiative mechanism for outbursts. *Mon. Not. R. Astron. Soc.* **275**, 255–300 (1995).
- Lyutikov, M. Mass-loading of pulsar winds. *Mon. Not. R. Astron. Soc.* **339**, 623–632 (2003).
- Gill, R. & Heyl, J. S. On the trigger mechanisms for soft gamma-ray repeater giant flares. *Mon. Not. R. Astron. Soc.* **407**, 1926–1932 (2010).
- Ioka, K., Razzaque, S., Kobayashi, S. & Mészáros, P. TeV-PeV neutrinos from giant flares of magnetars and the case of SGR 1806-20. *Astrophys. J.* **633**, 1013–1017 (2005).
- Nakar, E., Piran, T. & Sari, R. Pure and loaded fireballs in soft gamma-ray repeater giant flares. *Astrophys. J.* **635**, 516–521 (2005).
- Gelfand, J. D. et al. A rebrightening of the radio nebula associated with the 2004 December 27 giant flare from SGR 1806-20. *Astrophys. J. Lett.* **634**, L89–L92 (2005).
- Granot, J. et al. Diagnosing the outflow from the SGR 1806-20 giant flare with radio observations. *Astrophys. J.* **638**, 391–396 (2006).
- Cheng, K. S. & Wang, X. Y. The radio afterglow from the giant flare of SGR 1900+14: the same mechanism as afterglows from classic gamma-ray bursts? *Astrophys. J. Lett.* **593**, L85–L88 (2003).
- Hurley, K. The short gamma-ray burst—SGR giant flare connection. *Adv. Space Res.* **47**, 1337–1340 (2011).
- Abdo, A. A. et al. Search for gamma-ray emission from magnetars with the Fermi Large Area Telescope. *Astrophys. J. Lett.* **725**, L73–L78 (2010).
- Li, J., Rea, N., Torres, D. F. & de Oña-Wilhelmi, E. Gamma-ray upper limits on magnetars with six years of Fermi-LAT observations. *Astrophys. J.* **835**, 30 (2017).
- Ajello, M. et al. A decade of gamma-ray bursts observed by Fermi-LAT: the second GRB catalog. *Astrophys. J.* **878**, 52 (2019).
- Atwood, W. B. et al. The Large Area Telescope on the Fermi Gamma-Ray Space Telescope Mission. *Astrophys. J.* **697**, 1071–1102 (2009).
- Meegan, C. et al. The Fermi Gamma-ray Burst Monitor. *Astrophys. J.* **702**, 791 (2009).
- Bissaldi, E. et al. GRB 200415A: Fermi GBM observation. *GRB Coord. Netw. No.* 27587 (2020).
- Matttox, J. R. et al. The likelihood analysis of EGRET data. *Astrophys. J.* **461**, 396 (1996).
- Omodei, N. et al. GRB 200415A: Fermi-LAT localization update. *GRB Coord. Netw. No.* 27597 (2020).
- Ackermann, M. et al. The first Fermi-LAT gamma-ray burst catalog. *Astrophys. J. Suppl.* **209**, 11 (2013).
- Abdo, A. A. et al. The on-orbit calibration of the Fermi Large Area Telescope. *Astropart. Phys.* **32**, 193–219 (2009).
- Atwood, W. et al. Pass 8: toward the full realization of the Fermi-LAT scientific potential. Preprint at <https://arxiv.org/abs/1303.3514> (2013).
- Sutherland, W. & Saunders, W. On the likelihood ratio for source identification. *Mon. Not. R. Astron. Soc.* **259**, 413–420 (1992).
- Masci, F. J. et al. A new complete sample of submillijansky radio sources: an optical and near-infrared study. *Publ. Astron. Soc. Pac.* **113**, 10–28 (2001).
- Cileigi, P. et al. A deep VLA survey at 6 cm in the Lockman Hole. *Astron. Astrophys.* **398**, 901–918 (2003).
- Ackermann, M. et al. The second catalog of active galactic nuclei detected by the Fermi Large Area Telescope. *Astrophys. J.* **743**, 171 (2011).
- Ackermann, M. et al. The first Fermi-LAT catalog of sources above 10 GeV. *Astrophys. J. Suppl.* **209**, 34 (2013).

41. McAlpine, K., Jarvis, M. J. & Bonfield, D. G. Evolution of faint radio sources in the VIDEO-XMM3 field. *Mon. Not. R. Astron. Soc.* **436**, 1084–1095 (2013).
42. Ackermann, M. et al. The third catalog of active galactic nuclei detected by the Fermi Large Area Telescope. *Astrophys. J.* **810**, 14 (2015).
43. Ajello, M. et al. The fourth catalog of active galactic nuclei detected by the Fermi Large Area Telescope. *Astrophys. J.* **892**, 105 (2020).
44. de Menezes, R., D'Abrusco, R., Massaro, F., Gasparrini, D. & Nemmen, R. On the physical association of Fermi-LAT blazars with their low-energy counterparts. *Astrophys. J. Suppl.* **248**, 23 (2020).
45. von Kienlin, A. et al. The fourth Fermi-GBM gamma-ray burst catalog: a decade of data. *Astrophys. J.* **893**, 46 (2020).
46. Hurley, K. et al. IPN triangulation of GRB 160702A (short/hard). *GRB Coord. Netw.* No. 19666 (2016).
47. Kaspi, V. M. & Beloborodov, A. M. Magnetars. *Annu. Rev. Astron. Astrophys.* **55**, 261–301 (2017).
48. Paczynski, B. Gamma-ray bursters at cosmological distances. *Astrophys. J. Lett.* **308**, L43–L46 (1986).
49. Goodman, J. Are gamma-ray bursts optically thick? *Astrophys. J. Lett.* **308**, L47 (1986).
50. Sari, R. & Piran, T. Hydrodynamic timescales and temporal structure of gamma-ray bursts. *Astrophys. J. Lett.* **455**, 143 (1995).
51. Razzaque, S., Dermer, C. D. & Finke, J. D. Synchrotron radiation from ultra-high energy protons and the Fermi observations of GRB 080916C. *Open Astron. J.* **3**, 150–155 (2010).
52. De Jager, O. et al. Gamma-ray observations of the Crab nebula: a study of the synchro-compton spectrum. *Astrophys. J.* **457**, 253 (1996).

Acknowledgements

The Fermi-LAT Collaboration acknowledges support for LAT development, operation and data analysis from NASA and the Department of Energy (United States), CEA/Irfu and IN2P3/CNRS (France), ASI and INFN (Italy), MEXT, KEK and JAXA (Japan), and

the K. A. Wallenberg Foundation, the Swedish Research Council and the National Space Board (Sweden). Science analysis support in the operations phase from INAF (Italy) and CNES (France) is also gratefully acknowledged. This work was performed in part under Department of Energy contract DE-AC02-76SF00515. E. Burns is a NASA Postdoctoral Program Fellow.

Author contributions

The Fermi-LAT was designed and constructed by the Fermi-LAT Collaboration. The operation, data processing, calibration, Monte Carlo simulations of the detector and of theoretical models, and data analyses were performed by the members of the Fermi-LAT Collaboration. All Fermi-LAT collaborators that signed this paper contributed to the editing of and comments on the final version of the manuscript. A.B., N. Di Lalla, N.O. and F.P. contributed to the analysis and the writing of the manuscript and S. Razzaque provided the interpretation and contributed to the writing of the paper.

Competing interests

The authors declare no competing financial interests.

Additional information

Extended data is available for this paper at <https://doi.org/10.1038/s41550-020-01287-8>.

Correspondence and requests for materials should be addressed to A.B., N.D.L., N.O., F.P. or S.R.

Peer review information *Nature Astronomy* thanks the anonymous reviewers for their contribution to the peer review of this work.

Reprints and permissions information is available at www.nature.com/reprints.

Publisher's note Springer Nature remains neutral with regard to jurisdictional claims in published maps and institutional affiliations.

© The Author(s), under exclusive licence to Springer Nature Limited 2021

The Fermi-LAT Collaboration

M. Ajello¹, W. B. Atwood², M. Axelsson^{3,4}, L. Baldini⁵, G. Barbiellini^{6,7}, M. G. Baring⁸, D. Bastieri^{9,10}, R. Bellazzini¹¹, A. Berretta¹²✉, E. Bissaldi^{13,14}, R. D. Blandford¹⁵, R. Bonino^{16,17}, J. Bregeon¹⁸, P. Bruel¹⁹, R. Buehler²⁰, E. Burns^{21,22}, S. Buson²³, R. A. Cameron¹⁵, P. A. Caraveo²⁴, E. Cavazzuti²⁵, S. Chen^{9,26}, C. C. Cheung²⁷, G. Chiaro²⁴, S. Ciprini^{28,29}, D. Costantin³⁰, M. Crnogorčević³¹, S. Cutini³², F. D'Ammando³³, P. de la Torre Luque¹³, F. de Palma¹⁶, S. W. Digel¹⁵, N. Di Lalla¹⁵✉, L. Di Venere^{13,14}, F. Fana Dirirsa³⁴, Y. Fukazawa³⁵, S. Funk³⁶, P. Fusco^{13,14}, F. Gargano¹⁴, N. Giglietto^{13,14}, R. Gill^{37,38}, F. Giordano^{13,14}, M. Giroletti³³, J. Granot³⁸, D. Green³⁹, I. A. Grenier⁴⁰, S. Griffin²², S. Guiriec^{22,37}, E. Hays²², D. Horan¹⁹, G. Jóhannesson^{41,42}, M. Kerr²⁷, M. Kovačević³², M. Kuss¹¹, S. Larsson^{4,43,44}, L. Latronico¹⁶, J. Li²⁰, F. Longo^{6,7}, F. Loparco^{13,14}, M. N. Lovellette²⁷, P. Lubrano³², S. Maldera¹⁶, A. Manfreda⁵, G. Martí-Devesa⁴⁵, M. N. Mazziotta¹⁴, J. E. McEnery^{22,31}, I. Mereu^{12,32}, P. F. Michelson¹⁵, T. Mizuno⁴⁶, M. E. Monzani¹⁵, A. Morselli²⁸, I. V. Moskalenko¹⁵, M. Negro^{47,48}, N. Omodei¹⁵✉, M. Orienti³³, E. Orlando^{15,49}, V. S. Paliya²⁰, D. Paneque³⁹, Z. Pei¹⁰, M. Pesce-Rollins¹¹, F. Piron¹⁸✉, H. Poon³⁵, T. A. Porter¹⁵, G. Principe³³, J. L. Racusin²², S. Rainò^{13,14}, R. Rando^{9,26,50}, B. Rani^{22,51}, S. Razzaque⁵²✉, A. Reimer^{15,45}, O. Reimer⁴⁵, P. M. Saz Parkinson^{2,53,54}, J. D. Scargle⁵⁵, L. Scotton¹⁸, D. Serini¹³, C. Sgrò¹¹, E. J. Siskind⁵⁶, G. Spandre¹¹, P. Spinelli^{13,14}, H. Tajima^{15,57}, M. N. Takahashi³⁹, D. Tak^{22,58}, D. F. Torres^{59,60}, G. Tosti^{12,32}, E. Troja^{22,31}, Z. Wadiasingh²², K. Wood⁶¹, M. Yassine^{6,7}, A. Yusafzai³⁶ and G. Zaharijas^{49,62}

¹Department of Physics and Astronomy, Clemson University, Kinard Lab of Physics, Clemson, SC, USA. ²Santa Cruz Institute for Particle Physics, Department of Physics and Department of Astronomy and Astrophysics, University of California at Santa Cruz, Santa Cruz, CA, USA. ³Department of Physics, Stockholm University, Stockholm, Sweden. ⁴Department of Physics, KTH Royal Institute of Technology, Stockholm, Sweden. ⁵Università di Pisa and Istituto Nazionale di Fisica Nucleare, Pisa, Italy. ⁶Istituto Nazionale di Fisica Nucleare, Trieste, Italy. ⁷Dipartimento di Fisica, Università di Trieste, Trieste, Italy. ⁸Department of Physics and Astronomy, Rice University, Houston, TX, USA. ⁹Istituto Nazionale di Fisica Nucleare, Padua, Italy. ¹⁰Dipartimento di Fisica e Astronomia "Galileo Galilei", Università di Padova, Padua, Italy. ¹¹Istituto Nazionale di Fisica Nucleare, Pisa, Italy. ¹²Dipartimento di Fisica, Università degli Studi di Perugia, Perugia, Italy. ¹³Dipartimento di Fisica, "M. Merlin" dell'Università e del Politecnico di Bari, Bari, Italy.

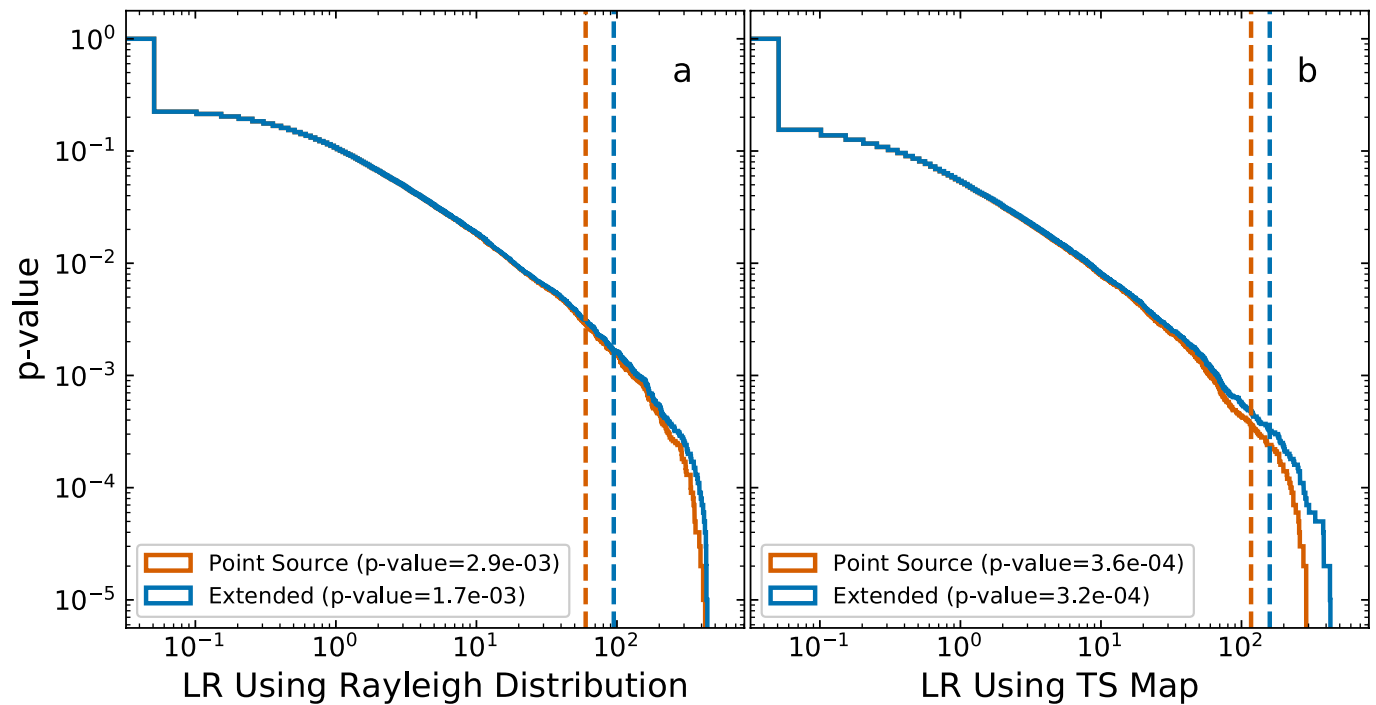
¹⁴Istituto Nazionale di Fisica Nucleare, Bari, Italy. ¹⁵W. W. Hansen Experimental Physics Laboratory, Kavli Institute for Particle Astrophysics and Cosmology, Department of Physics and SLAC National Accelerator Laboratory, Stanford University, Stanford, CA, USA. ¹⁶Istituto Nazionale di Fisica Nucleare, Turin, Italy. ¹⁷Dipartimento di Fisica, Università degli Studi di Torino, Turin, Italy. ¹⁸Laboratoire Univers et Particules de Montpellier, Université Montpellier, CNRS/IN2P3, Montpellier, France. ¹⁹Laboratoire Leprince-Ringuet, École polytechnique, CNRS/IN2P3, Palaiseau, France. ²⁰Deutsches Elektronen Synchrotron (DESY), Zeuthen, Germany. ²¹Department of Physics and Astronomy, Louisiana State University, Baton Rouge, LA, USA. ²²NASA Goddard Space Flight Center, Greenbelt, MD, USA. ²³Institut für Theoretische Physik und Astrophysik, Universität Würzburg, Würzburg, Germany. ²⁴INAF-Istituto di Astrofisica Spaziale e Fisica Cosmica Milano, Milan, Italy. ²⁵Italian Space Agency, Rome, Italy. ²⁶Department of Physics and Astronomy, University of Padova, Padua, Italy. ²⁷Space Science Division, Naval Research Laboratory, Washington, DC, USA. ²⁸Istituto Nazionale di Fisica Nucleare, Rome, Italy. ²⁹Space Science Data Center - Agenzia Spaziale Italiana, Rome, Italy. ³⁰Department of Statistical Science, University of Padua, Padua, Italy. ³¹Department of Astronomy, University of Maryland, College Park, MD, USA. ³²Istituto Nazionale di Fisica Nucleare, Perugia, Italy. ³³INAF Istituto di Radioastronomia, Bologna, Italy. ³⁴Department of Physics, University of Johannesburg, Johannesburg, South Africa. ³⁵Department of Physical Sciences, Hiroshima University, Hiroshima, Japan. ³⁶Friedrich-Alexander Universität Erlangen-Nürnberg, Erlangen Centre for Astroparticle Physics, Erlangen, Germany. ³⁷Department of Physics, The George Washington University, Washington, DC, USA. ³⁸Department of Natural Sciences, Open University of Israel, Ra'anana, Israel. ³⁹Max-Planck-Institut für Physik, Munich, Germany. ⁴⁰AIM, CEA, CNRS, Université Paris-Saclay, Université Paris Diderot, Gif-sur-Yvette, France. ⁴¹Science Institute, University of Iceland, Reykjavik, Iceland. ⁴²Nordita, Royal Institute of Technology and Stockholm University, Stockholm, Sweden. ⁴³The Oskar Klein Centre for Cosmoparticle Physics, Stockholm, Sweden. ⁴⁴School of Education, Health and Social Studies, Natural Science, Dalarna University, Falun, Sweden. ⁴⁵Institut für Astro- und Teilchenphysik, Leopold-Franzens-Universität Innsbruck, Innsbruck, Austria. ⁴⁶Hiroshima Astrophysical Science Center, Hiroshima University, Hiroshima, Japan. ⁴⁷Center for Research and Exploration in Space Science and Technology (CREST) and NASA Goddard Space Flight Center, Greenbelt, MD, USA. ⁴⁸Department of Physics and Center for Space Sciences and Technology, University of Maryland, Baltimore, MD, USA. ⁴⁹Istituto Nazionale di Fisica Nucleare, and Università di Trieste, Trieste, Italy. ⁵⁰Center for Space Studies and Activities “G. Colombo”, University of Padova, Padua, Italy. ⁵¹Korea Astronomy and Space Science Institute, Daejeon, Korea. ⁵²Centre for Astro-Particle Physics (CAPP) and Department of Physics, University of Johannesburg, Johannesburg, South Africa. ⁵³Department of Physics, The University of Hong Kong, Hong Kong, China. ⁵⁴Laboratory for Space Research, The University of Hong Kong, Hong Kong, China. ⁵⁵Space Sciences Division, NASA Ames Research Center, Moffett Field, CA, USA. ⁵⁶NYCB Real-Time Computing Inc., Lattingtown, NY, USA. ⁵⁷Solar-Terrestrial Environment Laboratory, Nagoya University, Nagoya, Japan. ⁵⁸Department of Physics, University of Maryland, College Park, MD, USA. ⁵⁹Institute of Space Sciences (CSICIEEC), Barcelona, Spain. ⁶⁰Institució Catalana de Recerca i Estudis Avançats (ICREA), Barcelona, Spain. ⁶¹Praxis Inc., Alexandria, VA, USA; resident at Naval Research Laboratory, Washington, DC, USA. ⁶²Center for Astrophysics and Cosmology, University of Nova Gorica, Nova Gorica, Slovenia. ⁶³e-mail: alessandra.berretta@pg.infn.it; niccolo.dilalla@stanford.edu; nicola.omodei@stanford.edu; piron@in2p3.fr; srazzaque@uj.ac.za

Source	Parameter	Value	Units	T.S.
LAT source	Index (Γ)	-1.7 ± 0.3		29
	Energy Flux	$(4.8 \pm 2.7) \times 10^{-9}$	$\text{erg cm}^{-2} \text{s}^{-1}$	
	Flux	$(4.1 \pm 2.2) \times 10^{-6}$	$\text{cm}^{-2} \text{s}^{-1}$	
	L_{iso}	$(7.4 \pm 4.2) \times 10^{42}$	erg s^{-1}	
	E_{iso}	$(3.6 \pm 2.1) \times 10^{45}$	erg	
GalacticTemplate	Const	1 (fixed)		1
IsotropicTemplate	Const	1.0 ± 0.8		3

Extended Data Fig. 1 | Best-fit parameters from the LAT unbinned likelihood analysis. All fluxes are calculated in the 100 MeV to 10 GeV energy range.

Time since T_0 (s)	Energy (MeV)	R.A. ($^{\circ}$)	Dec ($^{\circ}$)	Prob.	Dist. _{NGC253} ($^{\circ}$)	σ_{68} ($^{\circ}$)
19.18	480	11.8	−25.0	0.990	0.3	1.0
130.21	110	359.2	−26.4	0.13	11.4	6.7
135.92	410	19.9	−25.7	0.13	7.3	2.3
157.96	131	5.9	−28.9	0.26	6.4	2.9
180.22	1300	11.7	−25.7	0.988	0.5	0.9
221.92	310	7.1	−26.8	0.50	4.5	1.5
262.17	350	16.3	−25.9	0.31	4.1	1.3
276.87	530	12.8	−27.2	0.73	2.1	1.0
284.05	1700	11.0	−25.0	0.999	0.9	0.4
357.32	350	17.5	−30.9	0.14	7.5	2.6
471.16	140	10.1	−21.5	0.75	4.2	2.8

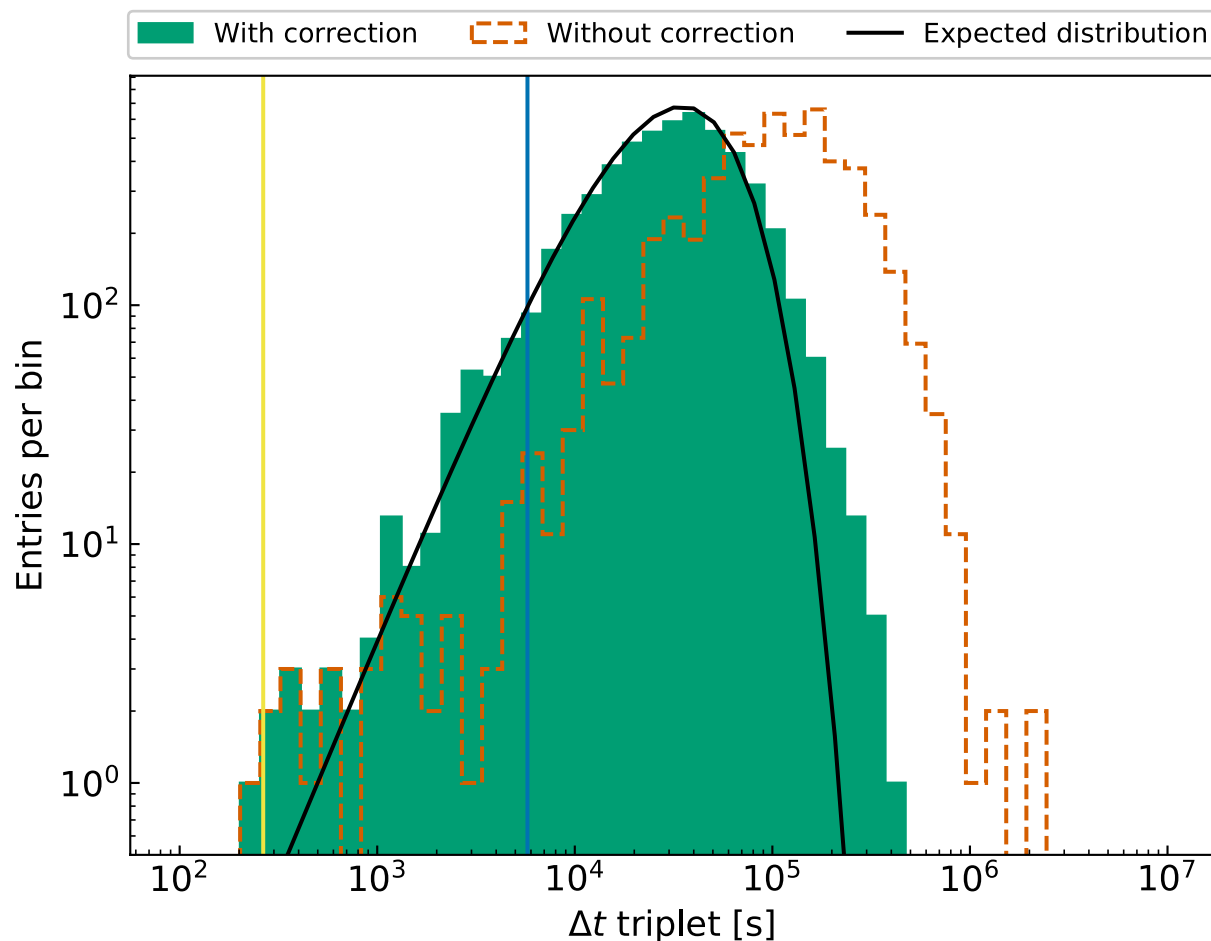
Extended Data Fig. 2 | List of selected events. We highlight those with high probability ($>90\%$) to be associated with the LAT-detected source, according to the likelihood analysis. The uncertainty on the estimated γ -ray energies is of the order of 10%. The last two columns show the angular distance to the centre of NGC 253 (the Sculptor galaxy) and the 68% containment radius of the PSF.



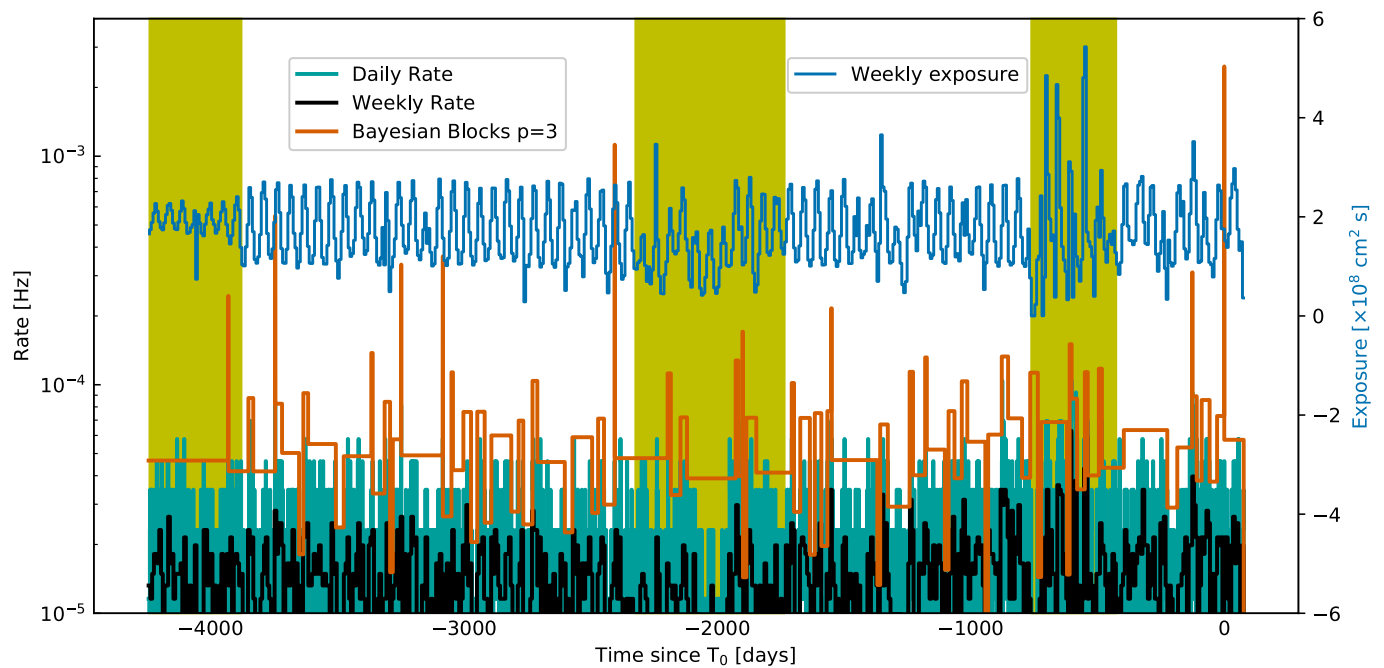
Extended Data Fig. 3 | Distribution of likelihood ratio (LR) values. LR values for 10^5 simulated ROIs using the standard Rayleigh formula (a) and using the TS map to compute the probability (b). The red distributions correspond to the point source hypothesis, while the blue distributions take into account of the galaxy extension. The step in the distributions at low LR is due to many low-LR trials occupying the first bin. The values of the LRs associated with the Sculptor galaxy are highlighted by red and blue vertical dashed lines for the two cases.

Analysis	p-value	FAR (yr ⁻¹)
Spatial Association with the Sculptor galaxy		
LR (Rayleigh)	2.9×10^{-3}	4.7×10^{-3}
LR _{ext} (Rayleigh)	1.7×10^{-3}	2.9×10^{-3}
LR (TS Map)	3.6×10^{-4}	6.0×10^{-4}
LR _{ext} (TS Map)	3.2×10^{-4}	5.4×10^{-4}
Temporal Association with GRB 200415A		
Triplet Analysis	8.3×10^{-7} (Li & Ma)	1.6×10^{-7}
Bayesian Blocks	2.3×10^{-3} (Poisson)	6.3×10^{-8}

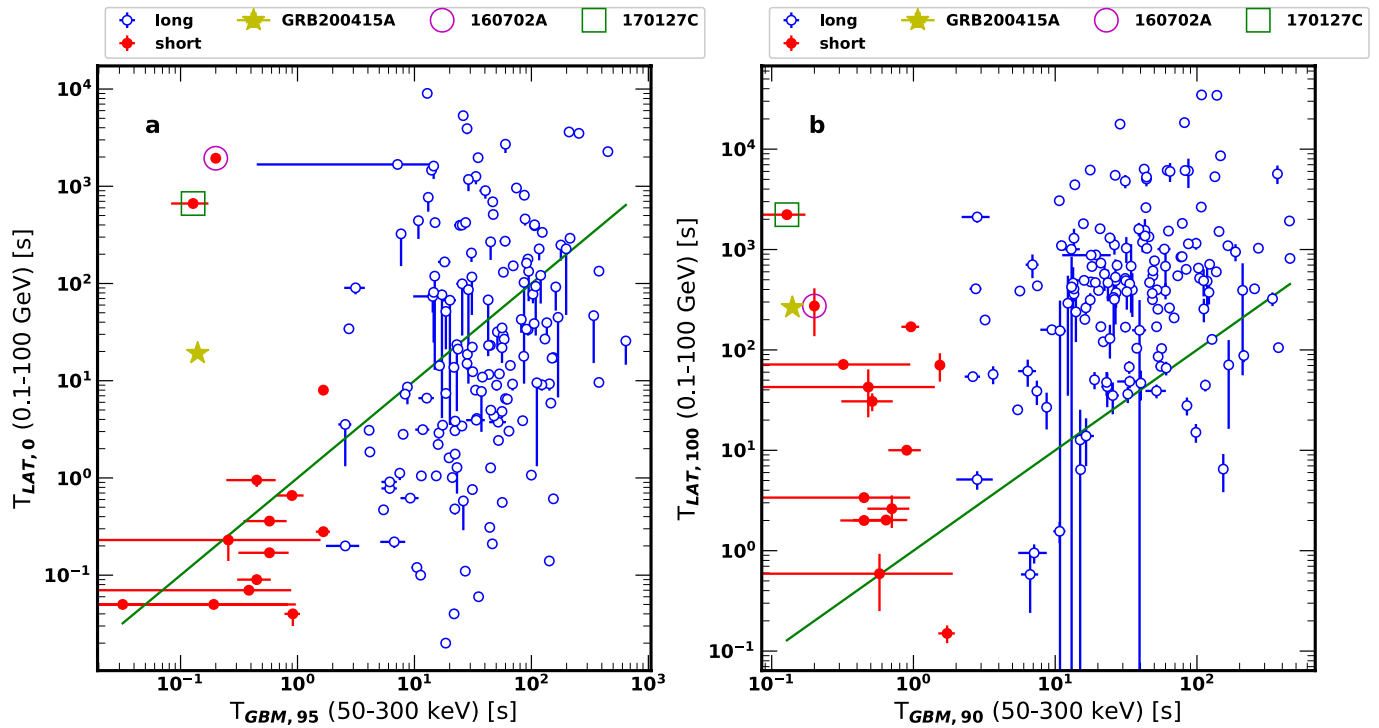
Extended Data Fig. 4 | Association probability and false alarm rate. Summary of the probability for a random association with the Sculptor galaxy and with the GRB 200415A.



Extended Data Fig. 5 | Triplet distribution. Distribution of the time intervals Δt for triplets formed by three consecutive photons with (green) and without (dashed red) taking into account the correction for the effects of the LAT orbit and FOV. The expected distribution in case of independent events is represented as a solid black line. The vertical line in blue shows the period of the Fermi orbit (5,790 s), while the yellow vertical line indicates $\Delta t = 264.87$ s corresponding to the photon triplet detected by the LAT after GBM detected emission from GRB 200415A.



Extended Data Fig. 6 | Rate and exposure as a function of time. Bayesian blocks representation of the arrival times of the γ rays with the prior parameter $p=3$ (red). Light green and dark gray are the daily and weekly count rates, while the blue curve shows the weekly-averaged exposure (between 100 MeV and 300 GeV, assuming a power-law photon index of -2) for a 1° -radius ROI in the direction of Sculptor for the entire time of the mission. Values of the exposure, in units of $10^8 \text{ cm}^2 \text{ s}$, can be read from the right y-axis. The three yellow bands highlight three characteristic observing profiles: 35° rocking angle, at the beginning of the mission, an observation strategy favouring the Galactic Centre region, in the middle, and, lastly, the period between the start of the solar drive anomaly and the implementation of a reoptimized survey strategy.



Extended Data Fig. 7 | Comparison with the second Fermi-LAT GRB catalogue. a, Onset times ($T_{\text{LAT},0}$) in the 100 MeV–100 GeV band versus the end of the GRB as detected by GBM in the 50–300 keV energy range ($T_{\text{GBM},95}$). **b,** Durations ($T_{\text{LAT},100}$) calculated in the 100 MeV–100 GeV energy range versus the same quantities calculated in the 50–300 keV energy range ($T_{\text{GBM},90}$). The solid line denotes where the two values are equal. Empty Blue and filled red circles represent long and short GRBs, respectively (data from 2FLGC²⁷). GRB 200415A is added and marked with a yellow star. The two SGRBs 160702A and GRB 170127C from 2FLGC, which exhibit similar durations, are highlighted with a magenta circle and green square, respectively.



First Fermi-LAT Solar Flare Catalog

M. Ajello¹, L. Baldini², D. Bastieri^{3,4}, R. Bellazzini⁵, A. Berretta⁶, E. Bissaldi^{7,8}, R. D. Blandford⁹, R. Bonino^{10,11}, P. Bruel¹², S. Buson¹³, R. A. Cameron⁹, R. Caputo¹⁴, E. Cavazzuti¹⁵, C. C. Cheung¹⁶, G. Chiaro¹⁷, D. Costantin¹⁸, S. Cutini¹⁹, F. D'Ammando²⁰, F. de Palma¹⁰, R. Desiante¹⁰, N. Di Lalla⁹, L. Di Venere^{7,8}, F. Fana Dirisa²¹, S. J. Fegan¹², Y. Fukazawa²², S. Funk²³, P. Fusco^{7,8}, F. Gargano⁸, D. Gasparri^{24,25}, F. Giordano^{7,8}, M. Giroletti²⁰, D. Green²⁶, S. Guiriec^{14,27}, E. Hays¹⁴, J. W. Hewitt²⁸, D. Horan¹², G. Jóhannesson^{29,30}, M. Kovac'evic¹⁹, M. Kuss⁵, S. Larsson^{31,32,33}, L. Latronico¹⁰, J. Li³⁴, F. Longo^{35,36}, M. N. Lovellette¹⁶, P. Lubrano¹⁹, S. Maldera¹⁰, A. Manfreda², G. Martí-Devesa³⁷, M. N. Mazziotta⁸, I. Mereu^{6,19}, P. F. Michelson⁹, T. Mizuno³⁸, M. E. Monzani⁹, A. Morselli²⁴, I. V. Moskalenko⁹, M. Negro^{39,40}, N. Omodei⁹, M. Orienti²⁰, E. Orlando^{9,41}, D. Paneque²⁶, Z. Pei⁴, M. Persic^{35,42}, M. Pesce-Rollins⁵, V. Petrosian⁹, F. Piron⁴³, T. A. Porter⁹, G. Principe²⁰, J. L. Racusin¹⁴, S. Rainò^{7,8}, R. Rando^{3,44,45}, B. Rani^{14,46}, M. Razzano^{5,52}, S. Razzaque²¹, A. Reimer^{9,37}, O. Reimer³⁷, D. Serini⁷, C. Sgrò⁵, E. J. Siskind⁴⁷, G. Spandre⁵, P. Spinelli^{7,8}, D. Tak^{14,48}, E. Troja^{14,49}, J. Valverde¹², K. Wood⁵⁰, and G. Zaharijas^{41,51}

¹ Department of Physics and Astronomy, Clemson University, Kinard Lab of Physics, Clemson, SC 29634-0978, USA

² Università di Pisa and Istituto Nazionale di Fisica Nucleare, Sezione di Pisa I-56127 Pisa, Italy

³ Istituto Nazionale di Fisica Nucleare, Sezione di Padova, I-35131 Padova, Italy

⁴ Dipartimento di Fisica e Astronomia "G. Galilei," Università di Padova, I-35131 Padova, Italy

⁵ Istituto Nazionale di Fisica Nucleare, Sezione di Pisa, I-56127 Pisa, Italy; melissa.pesce.rollins@pi.infn.it

⁶ Dipartimento di Fisica, Università degli Studi di Perugia, I-06123 Perugia, Italy

⁷ Dipartimento di Fisica "M. Merlin" dell'Università e del Politecnico di Bari, via Amendola 173, I-70126 Bari, Italy

⁸ Istituto Nazionale di Fisica Nucleare, Sezione di Bari, I-70126 Bari, Italy

⁹ W. W. Hansen Experimental Physics Laboratory, Kavli Institute for Particle Astrophysics and Cosmology, Department of Physics and SLAC National Accelerator Laboratory, Stanford University, Stanford, CA 94305, USA; nicola.omodei@stanford.edu, vahep@stanford.edu

¹⁰ Istituto Nazionale di Fisica Nucleare, Sezione di Torino, I-10125 Torino, Italy

¹¹ Dipartimento di Fisica, Università degli Studi di Torino, I-10125 Torino, Italy

¹² Laboratoire Leprince-Ringuet, École polytechnique, CNRS/IN2P3, F-91128 Palaiseau, France

¹³ Institut für Theoretische Physik und Astrophysik, Universität Würzburg, Campus Hubland Nord, Emil-Fischer-Str. 31, D-97074 Würzburg, Germany

¹⁴ NASA Goddard Space Flight Center, Greenbelt, MD 20771, USA

¹⁵ Italian Space Agency, Via del Politecnico snc, I-00133 Roma, Italy

¹⁶ Space Science Division, Naval Research Laboratory, Washington, DC 20375-5352, USA

¹⁷ INFN-Istituto di Astrofisica Spaziale e Fisica Cosmica Milano, via E. Bassini 15, I-20133 Milano, Italy

¹⁸ University of Padua, Department of Statistical Science, Via 8 Febbraio, 2, 35122 Padova, Italy

¹⁹ Istituto Nazionale di Fisica Nucleare, Sezione di Perugia, I-06123 Perugia, Italy

²⁰ INFN Istituto di Radioastronomia, I-40129 Bologna, Italy

²¹ Department of Physics, University of Johannesburg, PO Box 524, Auckland Park 2006, South Africa

²² Department of Physical Sciences, Hiroshima University, Higashi-Hiroshima, Hiroshima 739-8526, Japan

²³ Friedrich-Alexander Universität Erlangen-Nürnberg, Erlangen Centre for Astroparticle Physics, Erwin-Rommel-Str. 1, D-91058 Erlangen, Germany

²⁴ Istituto Nazionale di Fisica Nucleare, Sezione di Roma "Tor Vergata," I-00133 Roma, Italy

²⁵ Space Science Data Center - Agenzia Spaziale Italiana, Via del Politecnico, snc, I-00133, Roma, Italy

²⁶ Max-Planck-Institut für Physik, D-80805 München, Germany

²⁷ The George Washington University, Department of Physics, 725 21st St NW, Washington, DC 20052, USA

²⁸ University of North Florida, Department of Physics, 1 UNF Drive, Jacksonville, FL 32224, USA

²⁹ Science Institute, University of Iceland, IS-107 Reykjavik, Iceland

³⁰ Nordita, Royal Institute of Technology and Stockholm University, Roslagstullsbacken 23, SE-106 91 Stockholm, Sweden

³¹ Department of Physics, KTH Royal Institute of Technology, AlbaNova, SE-106 91 Stockholm, Sweden

³² The Oskar Klein Centre for Cosmoparticle Physics, AlbaNova, SE-106 91 Stockholm, Sweden

³³ School of Education, Health and Social Studies, Natural Science, Dalarna University, SE-791 88 Falun, Sweden

³⁴ Deutsches Elektronen Synchrotron DESY, D-15738 Zeuthen, Germany

³⁵ Istituto Nazionale di Fisica Nucleare, Sezione di Trieste, I-34127 Trieste, Italy; francesco.longo@trieste.infn.it

³⁶ Dipartimento di Fisica, Università di Trieste, I-34127 Trieste, Italy

³⁷ Institut für Astro- und Teilchenphysik, Leopold-Franzens-Universität Innsbruck, A-6020 Innsbruck, Austria

³⁸ Hiroshima Astrophysical Science Center, Hiroshima University, Higashi-Hiroshima, Hiroshima 739-8526, Japan

³⁹ Center for Research and Exploration in Space Science and Technology (CRESST) and NASA Goddard Space Flight Center, Greenbelt, MD 20771, USA

⁴⁰ Department of Physics and Center for Space Sciences and Technology, University of Maryland Baltimore County, Baltimore, MD 21250, USA

⁴¹ Istituto Nazionale di Fisica Nucleare, Sezione di Trieste, and Università di Trieste, I-34127 Trieste, Italy

⁴² Osservatorio Astronomico di Trieste, Istituto Nazionale di Astrofisica, I-34143 Trieste, Italy

⁴³ Laboratoire Univers et Particules de Montpellier, Université Montpellier, CNRS/IN2P3, F-34095 Montpellier, France

⁴⁴ Department of Physics and Astronomy, University of Padova, Vicolo Osservatorio 3, I-35122 Padova, Italy

⁴⁵ Center for Space Studies and Activities "G. Colombo," University of Padova, Via Venezia 15, I-35131 Padova, Italy

⁴⁶ Korea Astronomy and Space Science Institute, 776 Daedeokdae-ro, Yuseong-gu, Daejeon 30455, Korea

⁴⁷ NYCB Real-Time Computing Inc., Lattigtown, NY 11560-1025, USA

⁴⁸ Department of Physics, University of Maryland, College Park, MD 20742, USA

⁴⁹ Department of Astronomy, University of Maryland, College Park, MD 20742, USA

⁵⁰ Praxis Inc., Alexandria, VA 22303, USA

⁵¹ Center for Astrophysics and Cosmology, University of Nova Gorica, Nova Gorica, Slovenia

Received 2020 July 23; revised 2020 November 30; accepted 2020 December 6; published 2021 January 20

⁵² Funded by contract FIRB-2012-RBFR12PM1F from the Italian Ministry of Education, University and Research (MIUR).

⁵³ Resident at Naval Research Laboratory, Washington, DC 20375, USA.

Abstract

We present the first Fermi-Large Area Telescope (LAT) solar flare catalog covering the 24th solar cycle. This catalog contains 45 Fermi-LAT solar flares (FLSFs) with emission in the γ -ray energy band (30 MeV–10 GeV) detected with a significance of $\geq 5\sigma$ over the years 2010–2018. A subsample containing 37 of these flares exhibits delayed emission beyond the prompt-impulsive hard X-ray phase, with 21 flares showing delayed emission lasting more than two hours. No prompt-impulsive emission is detected in four of these flares. We also present in this catalog observations of GeV emission from three flares originating from active regions located behind the limb of the visible solar disk. We report the lightcurves, spectra, best proton index, and localization (when possible) for all FLSFs. The γ -ray spectra are consistent with the decay of pions produced by >300 MeV protons. This work contains the largest sample of high-energy γ -ray flares ever reported and provides a unique opportunity to perform population studies on the different phases of the flare and thus allowing a new window in solar physics to be opened.

Unified Astronomy Thesaurus concepts: [Solar flares \(1496\)](#); [Solar gamma-ray emission \(1497\)](#); [Gamma-ray sources \(633\)](#); [Gamma-ray telescopes \(634\)](#); [Catalogs \(205\)](#)

1. Introduction

It is generally accepted that the magnetic energy released through reconnection during solar flares is capable of accelerating electrons and ions to relativistic energies on timescales as short as a few seconds. Much is known of the electron acceleration during these explosive phenomena thanks to the observations made in hard X-rays (10 keV–1 MeV; HXRs; see, e.g., Vilmer 1987; Dennis 1988; Lin & Team 2003) and microwaves (see, e.g., Trottet et al. 1998). The observed impulsive-phase radiation in solar flares is dominated by electron emission; however, a fair fraction of stronger flares, with longer impulsive phase, show even higher-energy emission at γ -ray energies ($E > 3$ MeV) by accelerated protons and other ions in the form of nuclear de-excitation lines and by ~ 3 –50 MeV ions, and >100 MeV continuum due to the decay of pions produced by >300 MeV ions (see, e.g., Vilmer et al. 2011). The first reported observation of γ -rays with energies above 10 MeV was made in 1981 with the Solar Maximum Mission (SMM) spectrometer (Chupp et al. 1982) and throughout the 1980s, several other observations were made (see, e.g., Forrest et al. 1985, 1986), providing evidence of pion-decay emission and revealing multiple phases in the flares.

The first detection of GeV γ -rays was made by the Energetic Gamma-Ray Experiment Telescope (EGRET) on board the Compton Gamma-Ray Observatory (CGRO; see, e.g., Kanbach et al. 1993; Vilmer et al. 2003). The majority of the flares observed from 50 MeV to 2 GeV by EGRET had durations lasting tens of minutes but up to several hours in two flares, leading to a new class of flares initially known as long-duration gamma-ray flares (Ryan 2000; Chupp & Ryan 2009). This new class of flares presented a challenge to the classical magnetic reconnection theory for particle acceleration during flares because the γ -ray emission persisted beyond any other flare emissions, therefore suggesting the need for an additional mechanism and site for acceleration of protons and other ions. However, with only two such detections, the search for an additional acceleration mechanism and site was very challenging.

Additional cases suggesting the need for a new source of ion acceleration came with the observations of γ -ray emission, up to only 100 MeV, from three flares whose host active regions (ARs) were located behind the limb (BTL) of the visible solar disk (Vestrand & Forrest 1993; Barat et al. 1994; Vilmer et al. 1999). It is generally believed that lower-energy γ -rays are produced at the dense footpoints of flare loops by ions accelerated at the reconnection regions near the top of these loops. Thus,

observations of BTL flares pose interesting questions regarding the acceleration site and mechanism of the ions and about their transport to the high-density photospheric regions on the visible disk. Although there were some scenarios put forth (Cliver et al. 1993), no convincing explanations were given for the acceleration and transport sites and mechanisms of particles responsible for these observations.

Prior to the launch of the Fermi Gamma-ray Space Telescope in 2008, the understanding of these emission mechanisms was severely limited because of the limited amount of high-energy γ -ray flares detected.

The Fermi-Large Area Telescope (LAT; Atwood et al. 2009) observations of the flaring Sun over its first 12 years in orbit have revealed an extremely rich and diverse sample of events, spanning from short prompt-impulsive flares (Ackermann et al. 2012b) to the gradual-delayed long-duration phases (Ackermann et al. 2014), including the longest extended emission ever detected (~ 20 hr) from the SOL2012 March 7, a Geostationary Operational Environmental Satellite (GOES) X-class flare (Ajello et al. 2014).⁵⁴ The LAT, thanks to its large field of view (FoV) of 2.4 sr, monitors the entire sky every two orbits as an excellent general-purpose γ -ray astrophysics observatory, but in doing so, it keeps the Sun in the FoV 40% of the time.

Nonetheless, thanks to its technology improvements with respect to previous γ -ray space-based missions, the Fermi-LAT has increased the total number of >30 MeV detected solar flares by almost a factor of 10. More importantly, the LAT with its higher spatial resolution than EGRET can localize the centroids of the γ -ray emissions on the photosphere, which is particularly important for the interpretation of the BTL flares.

In this Fermi-LAT Solar Flare (FLSF) catalog, we present the observations of 45 flares with >30 MeV emission in the period 2010 January–2018 January (covering most of the 24th solar cycle). From these observations, we now know that >100 MeV γ -ray emission from even moderate GOES-class flares is fairly common (roughly half of the FLSFs in our catalog are associated with M-class flares) and that this high-energy emission is not correlated with the intensity of the X-ray flare, as one might expect. Our spectral analysis indicates that the >100 MeV emission is due to accelerated ions as opposed to HXR and microwave producing electrons. Based on the timing evolution of the γ -ray emission, we find that there are

⁵⁴ Solar flares observed by the GOES are classified, on the basis of their peak flux in the soft X-ray range of 0.5–10 keV, as X, M, C, and A class with peak fluxes greater than 10^{-4} , 10^{-5} , 10^{-6} , and 10^{-7} Watt m⁻², respectively.

two main populations of γ -ray flares: impulsive prompt (prompt hereafter) and gradual delayed (delayed hereafter). The prompt flares are those whose emission evolution is similar to that of the HXRs, indicating common acceleration sites and mechanism of electrons and ions. The emission of delayed FLSFs, which are always (with the exception of FLSF 2012 October 23 and FLSF 2012 November 27) associated with fast coronal mass ejections (CMEs), rises at the end of the impulsive HXR phase and, like solar energetic particles (SEPs), extends well beyond the end of the HXR emission (for up to tens of hours). This and other observations suggest a different acceleration site and mechanism.

In Section 2, we describe the analysis methods and procedures used in this work, which includes the description of an automated pipeline (Section 2.1), the LAT Low Energy (LLE) analysis (Section 2.2), spectral analysis (Section 2.3), how we perform our localization of the γ -ray emission (Section 2.4), and the search for spatial extension in the γ -ray emission of the brightest flares (Section 2.5). Here we also describe the methods used to calculate the total emission, fluence, and the total number of accelerated >500 MeV protons needed to produce the observed emission (Section 2.6). In Section 3, we describe how solar flares are classified based on the evolution of their γ -ray emission. In Section 4, we present the results of the catalog. In Section 5, we discuss the main findings of this work and the theoretical implications of our results. The tables and figures for each individual flare in this catalog are reported at doi:[10.5281/zenodo.4311156](https://doi.org/10.5281/zenodo.4311156).

2. Analysis Methods and Procedures

The LAT is sensitive to γ -rays in the energy range between 30 MeV and >300 GeV (Atwood et al. 2013). The LAT registers energy, direction, and time information for each detected particle. Each such “event” is classified by on-ground processing as a photon or other particle based on the consistency of its interaction with that expected from energetic γ rays.

Event classes correspond to different levels of purity tolerance of the γ -ray sample appropriate for use in different types of analyses. For each event class, there is a corresponding set of Instrument Response Functions (IRFs) describing the performance of the instrument. The standard analysis and software are described at the Fermi Science Support Center (FSSC) website⁵⁵ and, in great detail, in Ackermann et al. (2012a).

For the FLSF catalog, we developed two analysis chains, the first one, which we call *standard*, uses data with energies between 60 MeV and 10 GeV from two sets of event classes, P8R3_SOURCE and the solar flare Transient class P8R3_TRANSIENT015s (S15).⁵⁶ The P8R3_SOURCE (Bruehl et al. 2018) class is the event class recommended for the standard Fermi-LAT source analysis, while the S15 class was specifically developed to be insensitive to the potential pulse pile-up in the anti-coincidence detector (ACD) scintillators of the LAT resulting from the intense flux of X-rays during the prompt phase of solar flares. Pile-up of X-rays during the readout integration time of the ACD coincident with the entry of a γ ray into the LAT can cause the otherwise good γ ray to be misidentified as a charged particle by the instrument flight software or event-classification ground software and thereby

mistakenly vetoed. The Fermi-LAT instrument team closely monitors this effect and tags time intervals with particularly high activity in the sunward ACD tiles as “bad time intervals” (BTI) in the public data archive.⁵⁷ The S15 event class is robust against these spurious vetoes because it is defined using selections that exclude variables associated with the ACD and are therefore less susceptible to X-ray pile-up activity which can occur during the impulsive phase of solar flares; thus, all analysis in this catalog during a BTI used the S15 event class.

Additionally, a subset of results on short-duration prompt solar flares was obtained using the second chain based on LLE analysis methods. The LLE technique is an analysis method designed to study bright transient phenomena, such as gamma-ray bursts and solar flares, in the 30 MeV–1 GeV energy range. The LAT collaboration developed this analysis using a different approach from that used in the standard photon analysis. The idea behind LLE is to maximize the effective area below ~ 1 GeV by relaxing the standard analysis requirement on background rejection; see Ajello et al. (2014) for a full description of the LLE method. The LAT collaboration has already used the LLE technique to analyze solar flares, in particular FLSF 2010 June 12 (the first flare detected by the LAT; see Ackermann et al. 2012b) and the prompt phase of the FLSF 2012 March 7 flares (Ajello et al. 2014). In this FLSF catalog, we used the LLE selection to study the short prompt phase of 14 solar flares.

These two approaches are complementary: the LLE method suffers from large background contamination and is effective only for short transients but, because it is much less restrictive than the P8R3_SOURCE event class, the LLE class has a much larger effective area and has significantly greater sensitivity at high incidence angles.

Indeed, the FLSF 2010 June 12 was detected with the LLE approach when the Sun was more than 75° off-axis (Ackermann et al. 2012b).

2.1. The Fermi-LAT SunMonitor

We have created an automated data analysis pipeline, the Fermi-LAT SunMonitor, to monitor the high-energy γ -ray flux from the Sun throughout the Fermi mission.⁵⁸ The time intervals during which we run the analysis are when the Sun is $<70^\circ$ from the LAT boresight.

The effective area of the LAT decreases significantly for sources at incidence angles larger than 60° , so only very bright transients are detectable past this limit. Selecting a maximum off-axis angle of 70° extends the window of continuous Sun exposure for the brightest flares. The duration of these windows varies (ranging from 5 to 80 minutes, with an average duration of 30 minutes, as is shown in Figure 1) as the Sun advances along the ecliptic and as the orbit of Fermi precesses. Contamination from γ rays produced by cosmic-ray interactions with Earth’s atmosphere is reduced by selecting only events arriving within 100° of the zenith.⁵⁹

Each interval is analyzed using an RoI of 10° radius, centered on the position of the Sun at the central time of the

⁵⁷ <http://fermi.gsfc.nasa.gov/ssc/data/access/>

⁵⁸ Results from this pipeline are available online at https://hesperia.gsfc.nasa.gov/fermi_solar/.

⁵⁹ We used the `gtmkttime` filter `cut=(DATA_QUAL>0||DATA_QUAL==1) LAT_CONFIG==1 angsep(R.A._ZENITH, decl._ZENITH, R.A., decl.) < (zmax-rad)`, where R.A. and decl. are those of the position of the Sun at the time of the flare, `zmax = 100°` and `rad` is the radius of the region of interest (RoI) used for the analysis.

⁵⁵ <http://fermi.gsfc.nasa.gov/ssc/>

⁵⁶ Events belonging to the P8R3_TRANSIENT015s class are available in the extended photon data through the Fermi Science Support Center.

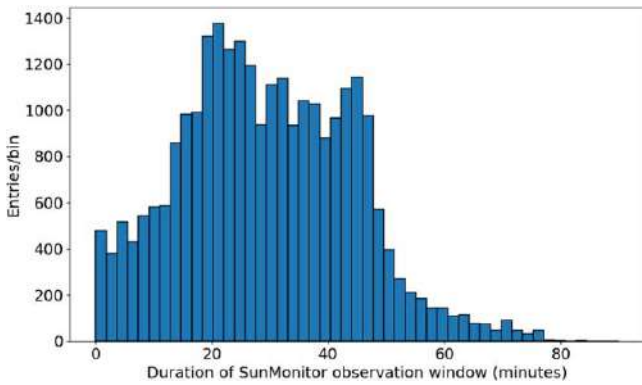


Figure 1. Duration of the Fermi SunMonitor observation windows. The duration varies from 5 to 80 minutes with an average duration of 30 minutes.

interval. On average, the duration of a SunMonitor interval is 30 minutes. During this time, the maximum deviation of the true position of the Sun from the RoI center due to its apparent motion is $\sim 0.02^\circ$. This is smaller than the typical angular resolution of the instrument: the 68% containment angle of the reconstructed incoming γ -ray direction for normal incidence at 1 GeV is 0.8° and at 100 MeV is 5° . Furthermore, the statistical uncertainty on the measured centroid of the >100 MeV emission is always larger than 0.03° , even for the brightest solar flares. It is therefore not necessary to apply a correction to account for the motion of the Sun from the center of the RoI. In each SunMonitor interval, we perform an unbinned maximum likelihood analysis using the tools in the Fermi ScienceTools software package.⁶⁰ The unbinned analysis computes the log-likelihood of the data using the reconstructed direction and energy of each individual γ -ray and the assumed sky model folded through the instrument response functions corresponding to the selected event class.

The likelihood analysis consists of maximizing the probability of obtaining the data given an input model as well as deriving error estimates. The RoI is modeled with a solar component and two templates for diffuse γ -ray background emission: a galactic component produced by the interaction of cosmic rays with the gas and interstellar radiation fields of the Milky Way, and an isotropic component that includes both the contribution of the extragalactic diffuse emission and the residual cosmic rays that passed the γ -ray classification.⁶¹ We fix the normalization of the galactic component but leave the normalization of the isotropic background as a free parameter to account for variable fluxes of residual cosmic rays.

When the Sun is not flaring, it is a steady, faint source of γ rays. This emission consists of two components: a disk emission originating from hadronic cosmic-ray cascades in the solar atmosphere and a spatially extended emission from the inverse Compton scattering of cosmic-ray electrons on solar photons in the heliosphere. The disk emission was first mentioned by Dolan & Fazio (1965) and Seckel et al. (1991), and the existence of an additional, spatially extended component was not realized until recently (Moskalenko et al. 2006; Orlando & Strong 2007; Linden et al. 2018; Mazziotta et al. 2020). The quiet Sun was detected for the first time in γ rays in the EGRET data (Orlando & Strong 2008). We also include the

quiet Sun emission disk component as a point source in our RoI; however, we did not include the extended inverse Compton (IC) component described in Abdo et al. (2011) because it is too faint to be detected during these time intervals. The >100 MeV flux of the solar disk component used in the FLSF catalog, obtained during the first 18 months of Fermi-LAT observations (Abdo et al. 2011), is $4.6 (\pm 0.2^{\text{stat}} \pm 1.0^{\text{syst}}) \times 10^{-7} \text{ ph cm}^{-2} \text{ s}^{-1}$.

We rely on the likelihood ratio test and the associated test statistic (TS; Mattox et al. 1996) to estimate the significance of the detection. Here we define TS as twice the increment of the logarithm of the likelihood obtained by fitting the data with the source and background model component simultaneously with respect to a fit with only the background. Note that the significance in σ for the 68% confidence interval can be roughly approximated as $\sqrt{\text{TS}}$.

With a pipeline testing for detection in so many time windows (33,511 total over the period of this work), we need to account for the trials factor to understand the statistical significance of a γ -ray source detected in the SunMonitor with a particular value of TS.

Assuming each window is independent, a TS of 20, which would otherwise correspond to a confidence of about 4.5σ , corresponds to 1.38σ post trials. In order to have a detection significance of $\geq 5\sigma$, we must impose a cut on the TS with a minimum of 30. This corresponds to a selection of 133 time windows, some of them consecutive in time for solar flares lasting more than an hour. Following this systematic sweep with SunMonitor, a detailed analysis is performed on those windows with a TS above 30.

From 2010 January to the end of 2018 January, we applied the SunMonitor pipeline analysis to 33,511 intervals of duration longer than 5 minutes. The cases when the duration is less than 5 minutes are likely due to the RoI being close to the maximum zenith angle or cut short by a passage of the satellite into the South Atlantic Anomaly (SAA). These are generally not long enough to yield a reliable point-source likelihood detection and constrain the background. Overall, the Sun was observable for an average duty cycle of 28% for the entire timespan of the FLSF catalog.

Note that outside the time interval considered here, since 2018 April, the LAT has been operating with a modified observing profile due to a failure of one of the solar array drive assemblies that reduce its exposure to the Sun.⁶² This change in observing strategy results in an average 45% reduction in solar exposure for the standard event classes (22% reduction for LLE) and consequently in the potential for solar physics science with the LAT.

2.2. LAT Low-energy Spectral Analysis

The LLE technique is designed to study bright transient phenomena, such as solar flares, in the 30 MeV–1 GeV energy range. In this catalog, we used the LLE selection to study the prompt phase of 14 solar FLSFs. To obtain the LLE spectral data, we used the *gtburst* package, available in the FermiTools distribution from the FSSC. The LLE data are divided by *gtburst* in 50 logarithmically spaced energy bins from 10 MeV to 10 GeV. For the spectral analysis, we used only the bins in the energy range optimized for the LLE selection.

⁶⁰ We used version 2011 May 3 available at <http://fermi.gsfc.nasa.gov/ssc/>.

⁶¹ The models used for this analysis, *gll_iem_v07.fits* and *iso_P8R3_SOURCE_V2_v1.txt*, are available at <http://fermi.gsfc.nasa.gov/ssc/data/access/lat/BackgroundModels.html>.

⁶² See https://fermi.gsfc.nasa.gov/ssc/observations/types/post_anomaly/ for more information.

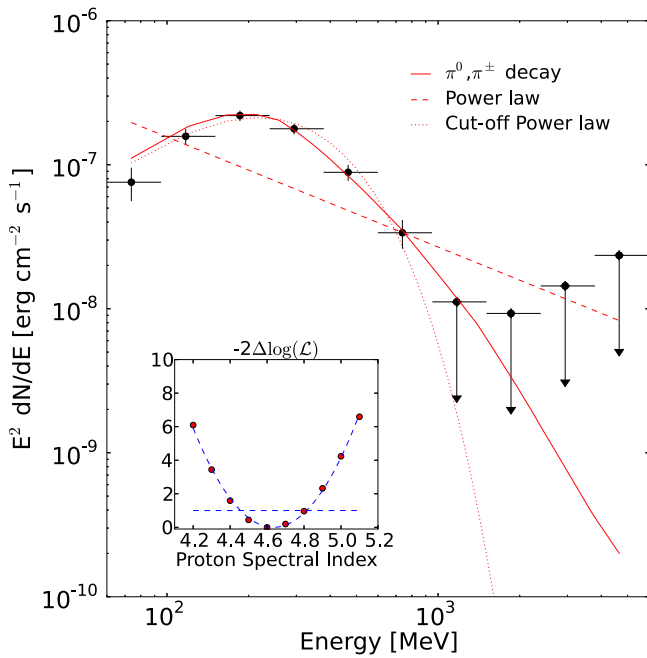


Figure 2. Example γ -ray spectra for SOL2012 March 7. The data were fit with three models (PL, PLEXP, and pion templates) and when the curved model (PLEXP) is preferred to the PL model, we perform a scan over the pion templates to search for the best proton index. In the insert, we show the fit to the log-likelihood values with a parabola, and the 68% confidence level is indicated by the straight line at $-2\Delta\log(\mathcal{L}_{\min}) + 1$.

A spectral fit was then performed using the *XSPEC* (Arnaud 1996) package following an approach similar to the one previously adopted for the analysis of the prompt phase of SOL2012 March 7 (Ajello et al. 2014). The results of the joint analysis with the Fermi Gamma-ray Burst Monitor (GBM) Bismuth-Germanate (BGO) data (300 keV–20 MeV) will be reported in a forthcoming publication.

2.3. Spectral Analysis

We fit three models to the Fermi-LAT γ -ray solar spectral data. The first two, a simple power law (PL) and a power-law with an exponential cutoff (PLEXP), are phenomenological functions that may describe bremsstrahlung emission from relativistic electrons. The parameters of these models are varied to obtain the best fit to the data. When the PLEXP provides a significantly better fit than the PL, we also fit the data with a third model consisting of pion-decay emission templates.⁶³ This third model uses a series of γ -ray spectral templates derived from a detailed study of γ rays from the decay of pions produced by interactions of accelerated protons and ions with background protons and ions. The accelerated particles are assumed to have a power-law energy spectrum ($dN/dE \propto E^{-\beta}$), where E is the kinetic energy of the protons with index β and an isotropic pitch angle distribution, injected into a thick target with a coronal composition (Reames 1995) taking $\text{He}/\text{H} = 0.1$ (updated from Murphy et al. 1987).

When the PLEXP provides a significantly better fit than the PL, we fit the data with the pion templates to determine the proton index that best fits the data. To do this, we calculate the variation of the log-likelihood with the proton spectral index

and fit it with a parabola. We run the likelihood analysis for each of the 41 proton spectral indices available from our templates (2.0–6.0 in steps of 0.1). The minimum of this distribution (\mathcal{L}_{\min}) gives the best-fit spectral index and the corresponding value s_0 as the maximum likelihood. Figure 2 shows an example of a spectral energy distribution of SOL2012 March 7 obtained following this procedure.

Once we have found the proton index corresponding to the best fit and the value of the observed γ -ray emission, we can estimate the total number of >500 MeV accelerated protons (N500 hereafter) needed to produce the observed γ -ray emission over a given time following the prescription of Murphy et al. (1987).

To compute the photon spectral energy distribution, we divide the data into 10 energy bins (in the energy range 60 MeV–10 GeV) and determine the source flux using the unbinned maximum likelihood algorithm *gtlike*, keeping the normalization of the background constant at the best-fit value and assuming that the spectrum of the point source is an E^{-2} power law. For nondetections ($\text{TS} < 9$), we compute 95% CL upper limits.

2.4. Localizing the Emission from Fermi-LAT Solar Flares

The standard tool for studying the localization of γ -ray sources with an unbinned likelihood analysis is the *gtfindsrc* algorithm from ScienceTools.⁶⁴ The likelihood analysis is based on sky models with background sources at fixed spatial positions and the best spectral fit for the source of interest. *gtfindsrc* uses a multidimensional minimization of the unbinned likelihood for a grid of positions around an initial guess until the convergence tolerance for a positional fit is reached. However, the Sun is in the FoV of the LAT for relatively short timescales, which can result in inhomogeneous exposure across the FoV. For this reason, we relied on the *gttmap* algorithm to study the localization for the FLSFs of the catalog. The TS maps are created by moving a putative point source through a grid of locations on the sky and maximizing $-\log(\text{likelihood})$ at each grid point, with any other well-identified sources within the RoI included in each fit. The solar flare source is then identified at the local maximum of the TS map. The 68% containment radius (or 1σ statistical localization error) on the position corresponds to a drop in the TS value of 2.30 (4.61 and 9.21 correspond to 2σ and 3σ , respectively). See Figure 3 for an example TS map of FLSF 2017 September 10.

When performing the localization of the Fermi-LAT data of the Sun it is necessary to also take into account the fish-eye effect. The fish-eye effect is a selection bias in the LAT trigger and reconstruction algorithms. At low energies and high incidence angles, particles that scatter toward the LAT boresight (having a smaller apparent incidence angle) are reconstructed with higher efficiency than particles that scatter away from the LAT boresight (having a larger apparent incidence angle). The reconstructed position of the source is biased and ends up appearing closer to the boresight axis than its true position.

The fish-eye effect can be quantified on an event-by-event basis using Monte Carlo simulations. The correction depends both on the true incidence angle and the energy of the particle. The correction becomes dramatic at energies below 100 MeV

⁶³ We are using only pion-production emission, ignoring other (minor) components that contribute to the γ -ray emission.

⁶⁴ Available at <http://fermi.gsfc.nasa.gov/ssc/data/analysis/software/>.

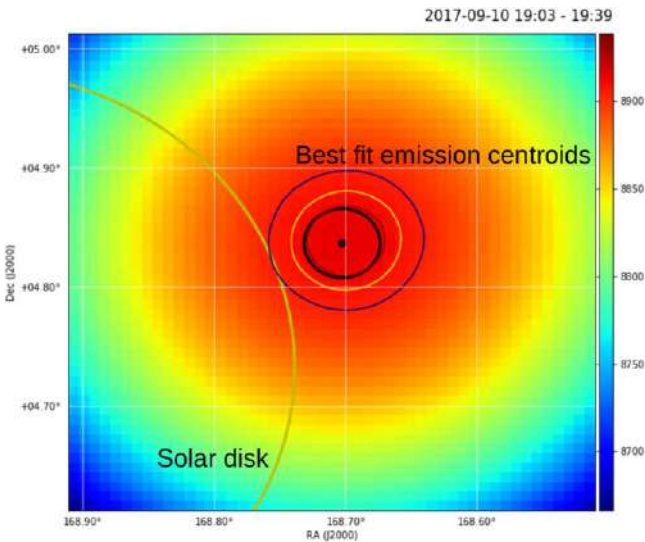


Figure 3. TS map for the observation of FLSF 2017 September 10 in the time interval of 19:03–19:39 UT. The large yellow circle represents the solar disk, the solid black circle represents the 68% statistical error. The thin red, yellow, and blue lines track the 1σ , 2σ , and 3σ contours on the TS map. These are not always perfectly circular, but a circular error containment region (black circle) provides a good approximation.

and incidence angle greater than 70° , reaching several degrees shift (see Ackermann et al. 2012a for a detailed description of the fish-eye effect).

The correction of the fish-eye effect is crucial particularly for bright flares, when the statistical error on the position becomes smaller than 0.1° and the uncertainty becomes dominated by systematics. We investigated the effect of the fish-eye correction on two bright solar flares (FLSF 2012 March 7 and FLSF 2017 September 10). We varied the value of the minimum energy threshold to quantify the amplitude of the correction and the systematic error it induces. The amplitude of the fish-eye correction decreases with energy so we expect the distance between the corrected and uncorrected positions to decrease with energy. This is indeed what we observe in Figure 4: the correction is largest above a 60 MeV minimum energy, and above 300 MeV, the two positions are consistent.

Solar flares generally have soft γ -ray spectra, cutting off at energies just above 100 MeV, so that the localization error (statistical) does not really improve as the threshold energy is increased, as can be seen in an example in Figure 4, where the statistical error on the localization above 300 MeV (green) is larger than the one above 60 MeV (red). Due to this, we use only photons with measured energies above 100 MeV when performing the localization study. Note that, although the localization uncertainties at 60 and 100 MeV are very similar, the fish-eye correction that we had to apply to the events between 60 and 100 MeV is larger than the one for the events above 100 MeV; therefore, in order to minimize the systematic uncertainty, we use only events with energy >100 MeV to estimate the localization of the emission.

2.4.1. Localization of BTL FLSF 2014 September 1

The emission centroid for the other FLSFs previously published all remained within the 68% error radius with the new analysis tool; the FLSF 2014 September 1 is the only exception that we found during the analysis performed for this work.

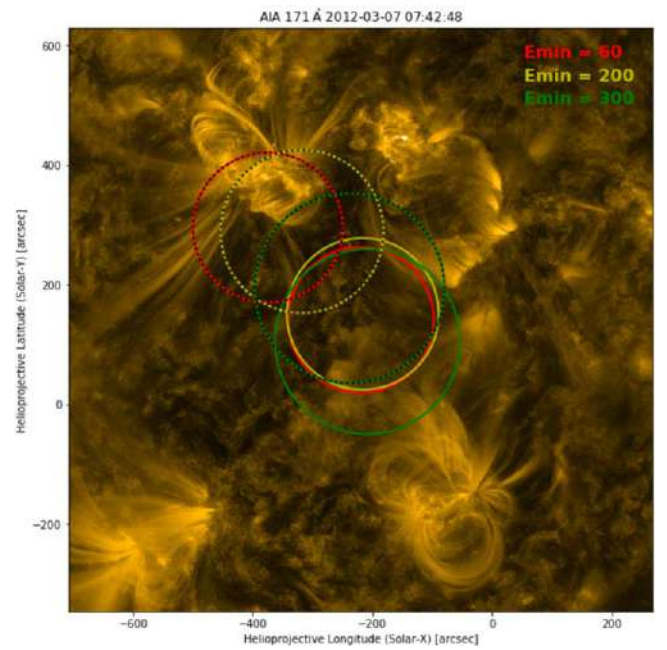


Figure 4. Comparison of the localization of the bright FLSF 2012 March 7 between fish-eye corrected (solid line) and not corrected (dashed line) with 60 (red), 200 (yellow), and 300 (green) MeV energy thresholds. Each circle marks the 68% statistical containment radius. The background is an Atmospheric Imaging Assembly (AIA) 171 Å image taken on 2012 March 7 07:42:48 UT by the Solar Dynamics Observatory (SDO).

As mentioned in Section 2.4, the tool used to perform localization studies for the FLSF catalog to compensate for the potential systematic errors tied to inhomogeneous exposures across the FoV for short detections is `gttsmap` and no longer the `gtfindsrc` tool. We also reported (in Section 2.4) the study performed to quantify the impact on the localization results due to the fish-eye effect and showed that it depends on the energy and incidence angle of the source. For this reason, in the FLSF catalog, we have decided to perform localization studies using `gttsmap` on bright flares with exposure times longer than 20 minutes, with incidence angles smaller than 60° and with energies greater than 100 MeV in order to avoid potentially large systematic effects in the resulting emission centroids.

The first detection window of the BTL FLSF 2014 September 1 unfortunately occurred when the Sun was at an angle of 67° from the LAT boresight and lasted for only 16 minutes and the emission centroid published in Ackermann et al. (2017) was obtained using the `gtfindsrc` tool. After a careful reanalysis of this flare with the new localization tool and the knowledge obtained from the fish-eye systematic study, we find that the emission centroid for FLSF 2014 September 1 has moved with respect to the previously published value as can be seen in Figure 5.

2.5. Test for Spatial Extension

We test the possibility of measuring spatial extension in the localization results of the bright FLSF 2012 March 7 and FLSF 2017 September 10 by using `fermipy` (Wood et al. 2017). This tool has been used in several Fermi-LAT publications (Abeysekara et al. 2018; Ackermann et al. 2018; Di Mauro et al. 2018; Ahnen et al. 2019). It is based on a binned likelihood analysis and, although not optimal for low

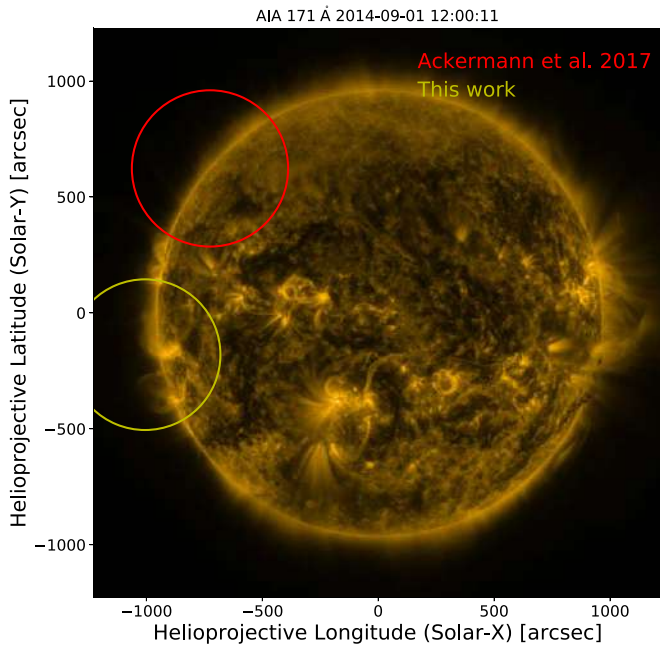


Figure 5. Emission centroid for FLSF 2014 September 1 for energies greater than 100 MeV with a 95% uncertainty error radius using the `gttmap` tool and the fish-eye correction in yellow and the previously published position is shown in red (with the 95% uncertainty error radius). The new position is centered at helioprojective coordinates $X, Y = [-1105'', -128'']$ with a 95% uncertainty error radius of $643''$.

counting statistics,⁶⁵ presents the advantage of being very fast and allows the extension of γ -ray emission to be studied by comparing a model with a source with a radial extension (uniform disk or Gaussian) with the data, and profiling the value of $\log(\mathcal{L})$ by varying the extension radius.

For FLSF 2012 March 7, we use the same time window used in Ajello et al. (2014), namely from 2012 March 7 02:27:00 UT to 2012 March 7 10:14:32 UT, thus avoiding the time interval affected by ACD pile-up. For FLSF 2017 September 10, we use the time window from 2017 September 10 15:56:55 UT to 2017 September 11 02:00:21 UT and SOURCE class events with energies greater than 100 MeV. The RoI is 10° wide. In this analysis the spectra of the FLSFs are described by a power law with exponential cutoff, and the model is reoptimized during the fit procedure. For convenience, we use `ThreeML` (Vianello et al. 2015) as an interface to `fermipy`. It allows us to perform the fit to the LAT data using the `fermipy` plugin, providing, at the same time, an easy interface to download the data and build the model to be fitted. In Figure 6, we show the radial profile of a point-source model compared to the data, for the best-fit model. The model (which is convolved with the IRFs of the instrument), matches very well the radial profile of the counts in both directions, and no residual counts that could suggest the presence of a spatially extended emission are visible. Note that in our analysis we first optimize the localization of the source (hence the offset in Figure 6) and then we test for an extension. The optimized locations are at helioprojective coordinates $X, Y = [-400'', 400'']$ with a 68% uncertainty error radius of $100''$ for FLSF 2012 March 7, and $X, Y = [600'', -60'']$ with an uncertainty of $70''$ for FLSF 2017 September 10.

⁶⁵ Both FLSF 2012 March 7 and FLSF 2017 September 10 are very bright and a binned likelihood analysis is appropriate.

Finally, in Figure 7, we show the profile of the likelihood as a function of the radial extension for two different spatial templates, for the two flares. The improvement with respect to the point-source hypothesis is very small ($\Delta TS < 1.5$ in both cases), and only an upper limit of the radius can be placed. The 95% confidence level upper limits (corresponding to a $-\Delta \log(\mathcal{L}) \approx 1.35$) are $0^\circ.18$ for the Gaussian disk and $0^\circ.14$ for the radial disk for FLSF 2012 March 7, and $0^\circ.23$ (Gaussian) and $0^\circ.17$ (radial) for FLSF 2017 September 10. These two events are the only two flares detected by the LAT that are bright enough to allow a dedicated spatial extension analysis. Even so, we can only set an upper limit on the extension that is smaller than the solar radius.

2.6. Total Emission Duration, Fluence, and Total Number of Protons Greater than 500 MeV

With the Sun being observable by the LAT for only 20–40 minutes every 1.5–3 hr, it can be challenging to reconstruct the complete lightcurve and to estimate the true duration of the γ -ray emission. In order to overcome the issues caused by the observational gaps, we are forced to make some assumptions on the behavior of the emission when the Sun is outside of the FoV of the LAT. To identify the start of the FLSF, we rely on the timing of the associated GOES X-ray flare. For example, when the GOES X-ray flare occurs during an LAT data gap and the start of the LAT detection window (t_{start}) occurs after the end of the GOES X-ray flare, we take the end of the GOES X-ray flare as the start of the γ -ray emission. For the cases where the GOES X-ray flare occurs within the detection window and the LAT statistics are not sufficient to perform a fine time binning analysis, we take t_{start} to be the start of the detection window. The end time of the FLSF (t_{stop}) is taken as the midpoint between the end of the last detection window and the start of the following observational window (with an upper limit on the γ -ray emission from the Sun). The total duration of the FLSF is then simply $\Delta t = t_{\text{stop}} - t_{\text{start}}$. These assumptions on the start and stop of the FLSF are not needed for the short prompt FLSF flares where the true start/stop of the γ -ray emission can be identified within the observational window.

Once we have estimated the start and stop of the FLSF, we can build a functional shape⁶⁶ to describe the lightcurve of the FLSF even in the cases where we only have one detection point (see Figure 8). Having a full description of the lightcurve of the FLSF emission, it is possible to evaluate the total γ -ray fluence by simply integrating the lightcurve over the estimated duration of the flare. When integrating, we assume that the flux values at the start and end of the FLSF are equal to $4.6 \times 10^{-7} \text{ ph cm}^{-2} \text{ s}^{-1}$, which corresponds to the >100 MeV quiet Sun emission.

For every FLSF that is best described by the pion template model, we provide an estimate of N500 needed to produce the γ -ray emission detected in the observational time window. However, if we want to know the total N500 needed to produce the total γ -ray emission over the full duration, then we need to build a functional form (just as was done for the lightcurve) also for the temporal evolution of N500. The start and stop of the FLSF remain the same as described above; the main challenge lies in estimating the value for N500 at t_{start} and t_{stop} . The value of N500 depends on two parameters, the normalization of the spectral function used to fit the data and the best

⁶⁶ We use `scipy` splines to build the functional shape of the γ -ray lightcurve.

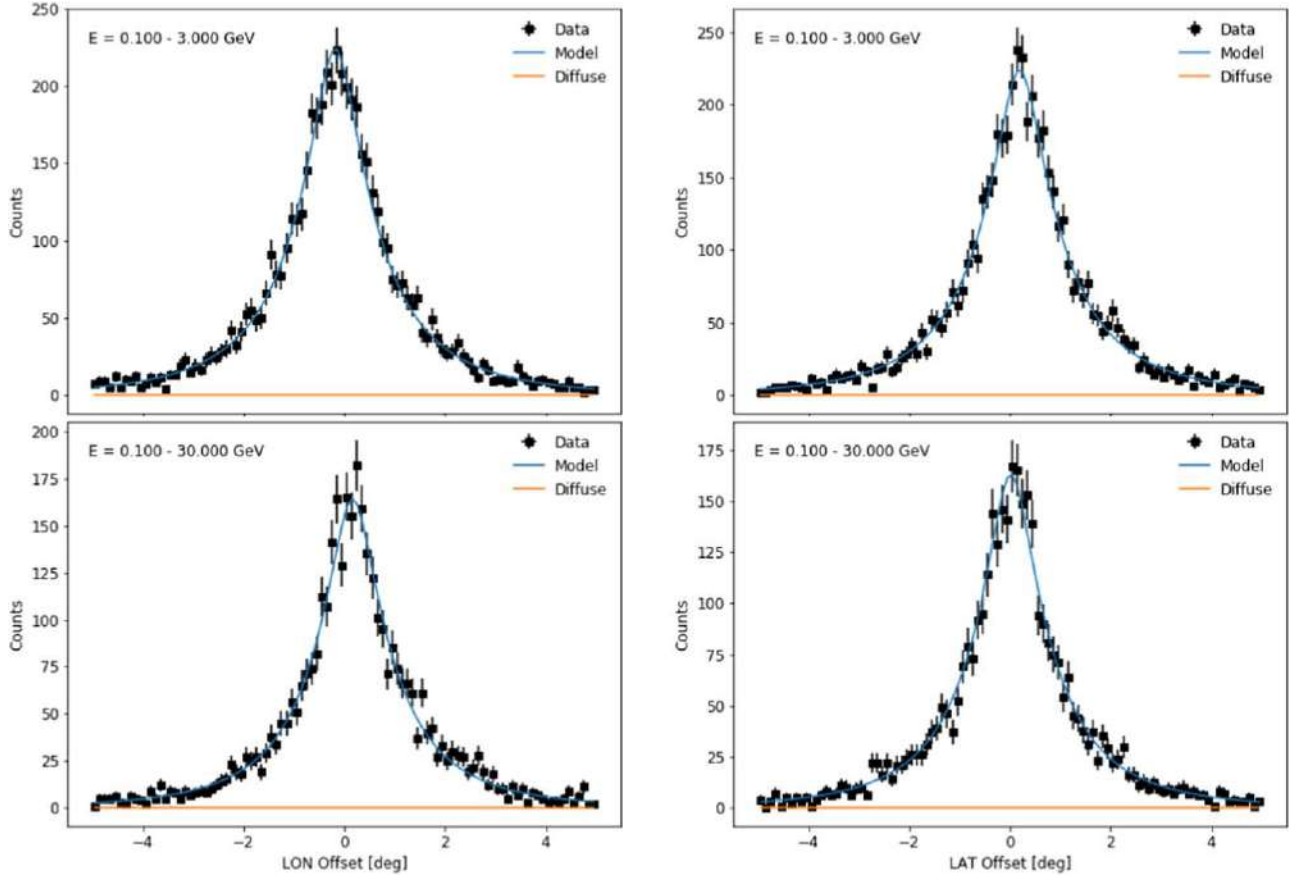


Figure 6. Longitude (left) and latitude (right) radial profile for FLSF 2012 March 7 (top row) and for FLSF 2017 September 10 (bottom row). The x -axis shows the offset with respect to the optimized localization.

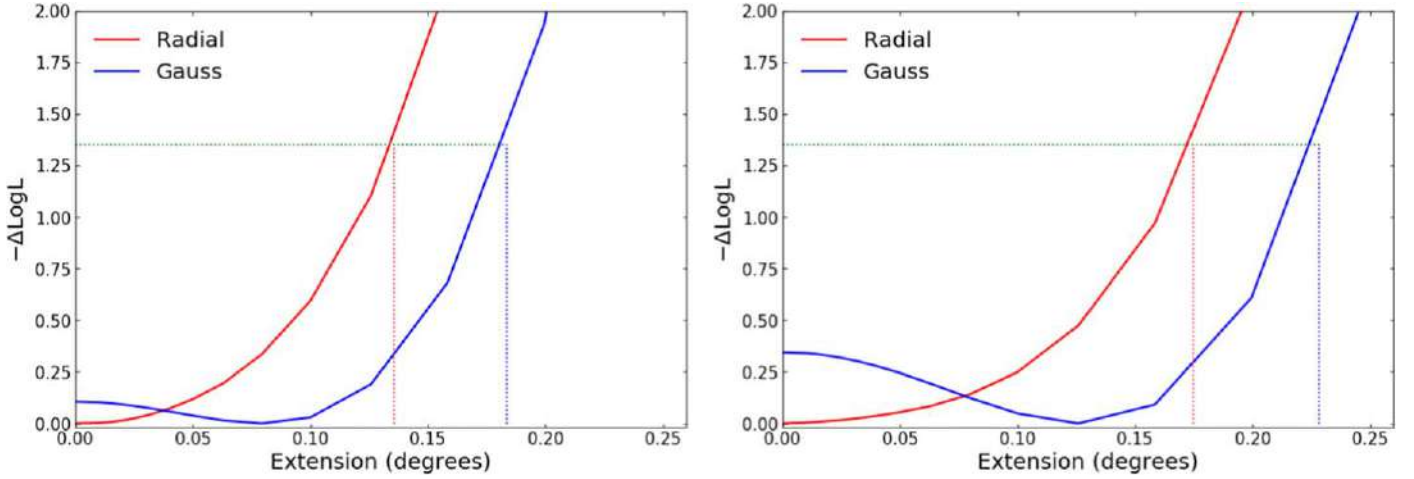


Figure 7. Likelihood profile of FLSF 2012 March 7 (left) and FLSF 2017 September 10 (right) as a function of a spatial profile for a Gaussian profile (Gauss) and a radial profile (Radial). The horizontal green dotted lines show the increment of $-\Delta \log(L) \approx 1.35$, corresponding to a C.L. of 95%. The blue and red dotted lines are the estimated values for the upper limits on the radius.

proton index resulting from the spectral analysis (as described in 2.3). We therefore find the best value for the N500 corresponding to the quiet Sun flux level by performing a scan over all the possible proton indices (ranging from 2 to 6, with the same gradation as used during the likelihood analysis) and used the average value of 6×10^{22} . Finally, as in the case of the fluence, we integrate the functional form to find the N500 needed to produce the total emission of the FLSF. The values

for the total fluence and total N500 with their associated uncertainties for all of the FLSFs in the catalog are listed in Table 1.

The main uncertainties on the fluence and total N500 are due to the values of t_1 and t_2 , where t_1 is defined as the duration between the assumed start of the emission (t_{start}) and the start of the detection window and t_2 is the duration between the end of the detection window and the assumed end of the emission

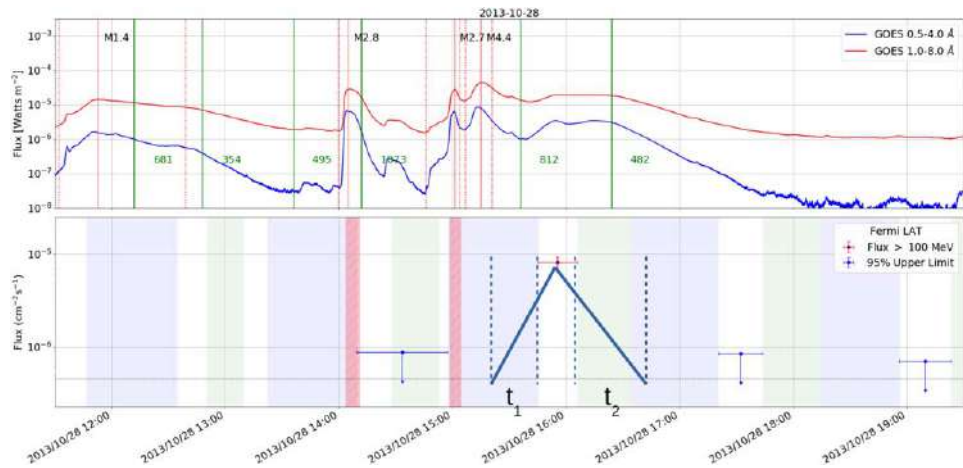


Figure 8. Lightcurve of the >100 MeV emission from FLSF 2013 October 28 with multiple flaring episodes prior to the start of the γ rays. The M2.7 and M4.4 and 812 km s^{-1} CMEs, all from the same active region (AR), are likely associated with the γ ray emission, although it is possible that the activity from another AR (M2.8 flare and 1073 km s^{-1} CME) may contribute to the γ rays. The solid green lines represent the first appearance of the Large Angle and Spectrometric Coronagraph (LASCO) CME C2; the linear speed value is annotated next to the line (also in green). The dashed/solid red lines represent the start (stop)/peak of the GOES X-ray flare; the GOES class is also annotated next to the solid red line. In the lower panel, the vertical dashed lines denote the t_1 and t_2 quantities, where t_1 is defined as the time between the assumed start of the emission and the start of the detection window and t_2 is the time between the end of the detection window and the assumed end of the emission. For further details on how we use the t_1 and t_2 quantities to determine the uncertainties on the total fluence and total N500, see Section 2.6. The solid triangle represents the assumed lightcurve for this flare. The light-green bands indicate when the Fermi satellite was in the South Atlantic Anomaly (SAA), the blue bands indicate when the Sun was outside of the FoV of the LAT, and the pink bands indicate the presence of potential pile-up in the data.

(t_{stop}). See Figure 8 for an illustration of t_1 and t_2 for the case of the single point detection of FLSF 2013 October 28. To estimate this uncertainty, we vary the value of t_1 and t_2 by $\pm 50\%$ and repeat the integral over the flux and N500, the error is then found by taking the difference between this value and the nominal one.

3. FLSF Classification

We associate each significant detection of γ -ray emission from solar flares with solar events as seen by other instruments. For most cases, the association of the γ -ray emission to a specific GOES flare or CME is straightforward: linking the FLSF to a single flare or CME within an hour of the start of the γ -rays. In some cases, however, the association with a single GOES flare or a single CME is not obvious when several events happen within a short time frame. In these cases, we tend to pick the GOES flare or the CME closest in time to the γ -ray emission. For example, in the FLSF 2013 October 28 (shown in Figure 8), a series of three M-class flares occurred, accompanied by two CMEs, all prior to the γ -ray detection. In this case, the γ -ray emission is likely associated with the pair of flares M2.7 and M4.4 (both of which started within an hour of the start of the FLSF) from the same AR and the associated CME with speed 812 km s^{-1} (LASCO first appearance occurred ≈ 15 minutes prior to the start of the FLSF).

In the cases of the BTL FLSFs, the soft X-ray emission detected by GOES is either absent or biased toward lower fluxes than would have been the case if it were a disk flare. For those, the STEREO satellites provide the direct extreme ultraviolet (EUV) observation of the flare, which allows us to estimate the peak soft X-ray flux (for a detailed description of this procedure, see Ackermann et al. 2017).

Once we have found a GOES X-ray flare associated with the FLSF, then we can begin to classify the flares in the catalog. In the attempt to better characterize the features present in each of the FLSFs and hopefully to also understand the underlying acceleration mechanisms at work during the flares in the FLSF

catalog, we compare the γ -ray timing evolution with that in hard X-Rays. This is because HXR emission traces the high-energy electron population accelerated during the flare energy release and γ -ray signatures of protons accelerated by the same processes and on the same timescales have been observed in the past by SMM and EGRET (Thompson et al. 1993).

The Fermi-GBM (Meegan et al. 2009) on board the Fermi satellite consists of 12 Na sci detectors and two BGO detectors covering the energy range 8 keV–40 MeV. Thanks to the fact that the Fermi-GBM continuously monitors the nonocculted sky, it provides excellent HXR coverage of the FLSFs in this catalog. For each FLSF in the catalog with a time window coincident with the prompt phase of an X-ray solar flare, we compare the HXR evolution observed by the two instruments of the Fermi-GBM to a finely time-resolved γ -ray lightcurve as shown in Figure 9 for the FLSF 2011 September 6. If we find that the γ -ray emission evolution is synchronous with the HXR evolution, we classify it as a prompt flare.

When performing these finely time-resolved lightcurves, different patterns emerge, revealing a more complex picture of the γ -ray solar flares. This can be seen again for FLSF 2011 September 6 (Figure 9). A prompt component coincident with the bright HXR peak appears in γ -rays and is immediately followed by a second phase lasting for more than 20 minutes after the start of the flare. This phase consists of a second, less bright peak with a longer rise and fall timescales, but there is no sign of such behavior in the HXRs. The Sun passed in the FoV two hours later and no γ -rays were detected. Cases such as FLSF 2011 September 6 are classified as prompt short-delayed.

A flare is prompt only if the γ -ray emission does not extend beyond the HXR duration, as was the case for the flare detected on 2010 June 12 (Ackermann et al. 2012b). All flares detected through the LLE method are associated with prompt emission, but some exhibit delayed emission as well. The fine time-resolved lightcurves for all FLSFs classified as prompt are reported at doi:10.5281/zenodo.4311156.

A large number of solar flares observed by Fermi-LAT do not fall in the prompt category: γ -ray emission is detected

Table 1
FLSF Catalog for Flares Detected with the Fermi-LAT SunMonitor and Their Likely GOES X-Ray Flare Associations

Name	GOES Class	GOES Start-Stop	Detection duration (hr)	Total Duration (hr)	Peak Flux ($10^{-5}\text{cm}^{-2}\text{s}^{-1}$)	Fluence >100 MeV (cm^{-2})	Flare Type	Total Protons >500 MeV (10^{27})
FLSF 2011 Mar 7	M3.7 ^c	19:43–20:58	13.5	15.8 ± 3.1	3.23 ± 0.22	1.076 ± 0.029	Delayed	64.4 ± 1.8
FLSF 2011 Jun 7	M2.5	06:16–06:59	3.8	6.0 ± 2.2	3.18 ± 0.20	0.295 ± 0.030	Delayed	19.5 ± 2.0
FLSF 2011 Aug 4	M9.3	03:41–04:04	0.7	2.3 ± 0.7	2.30 ± 0.18	0.13 ± 0.05	Delayed	9 ± 4
FLSF 2011 Aug 9	X6.9	07:48–08:08	0.5	0.87 ± 0.34	2.29 ± 0.23	0.037 ± 0.018	Prompt Short-Delayed ^a	2.7 ± 1.3
FLSF 2011 Sep 6	X2.1	22:12–22:24	0.6	2.0 ± 1.4	22.8 ± 0.4	0.87 ± 0.17	LLE-Prompt Short-Delayed ^a	58 ± 12
FLSF 2011 Sep 7	X1.8	22:32–22:44	0.8	2.02 ± 0.35	0.77 ± 0.08	0.041 ± 0.014	Delayed	2.3 ± 0.7
FLSF 2011 Sep 24	X1.9	09:21–09:48	0.5	1.2 ± 0.7	0.50 ± 0.10	0.014 ± 0.007	LLE-Prompt Short-Delayed ^a	...
FLSF 2012 Jan 23	M8.7	03:38–04:34	5.3	5.9 ± 1.0	1.99 ± 0.12	0.340 ± 0.014	Delayed	24.7 ± 1.0
FLSF 2012 Jan 27	X1.7	17:37–18:56	5.3	6.8 ± 1.5	3.3 ± 0.5	0.248 ± 0.025	Delayed	17.2 ± 1.8
FLSF 2012 Mar 5	X1.1	02:30–04:43	3.8	4.4 ± 1.2	0.63 ± 0.07	0.085 ± 0.007	Delayed	6.1 ± 0.5
FLSF 2012 Mar 7	X5.4 ^c	00:02–00:40	19.6	20.3 ± 0.8	233 ± 8	33.996 ± 0.030	Delayed	1844.7 ± 1.3
FLSF 2012 Mar 9	M6.3	03:22–04:18	5.5	7.2 ± 1.7	0.96 ± 0.12	0.148 ± 0.007	No-Prompt Delayed	9.29 ± 0.23
FLSF 2012 Mar 10	M8.4	17:15–18:30	2.3	6 ± 4	0.23 ± 0.06	0.042 ± 0.012	Delayed	2.3 ± 0.6
FLSF 2012 May 17	M5.1	01:25–02:14	2.1	2.6 ± 0.5	1.19 ± 0.19	0.0572 ± 0.0026	Delayed	2.29 ± 0.09
FLSF 2012 Jun 3	M3.3	17:48–17:57	0.4	1.9 ± 1.5	3.06 ± 0.25	0.117 ± 0.031	LLE-Prompt Short-Delayed ^a	7.7 ± 2.0
FLSF 2012 Jul 6	X1.1	23:01–23:14	0.8	1.27 ± 0.35	3.06 ± 0.15	0.100 ± 0.021	Delayed	7.5 ± 1.6
FLSF 2012 Oct 23	X1.8	03:13–03:21	0.5	1.9 ± 0.5	0.73 ± 0.18	0.047 ± 0.018	LLE-Prompt Delayed ^a	...
FLSF 2012 Nov 13	M6.0	01:58–02:04	0.7	0.041 ± 0.006	0.46 ± 0.09	0.006 ± 0.022	Prompt	...
FLSF 2012 Nov 27	M1.6	15:52–16:03	0.8	0.166 ± 0.025	0.27 ± 0.07	0.005 ± 0.030	Prompt Short-Delayed	...
FLSF 2013 Apr 11	M6.5	06:55–07:29	0.7	0.38 ± 0.27	5.71 ± 0.24	0.099 ± 0.016	No-Prompt Short-Delayed	6 ± 6
FLSF 2013 May 13a	X1.7	01:53–02:32	0.7	4.0 ± 1.3	0.96 ± 0.11	0.11 ± 0.06	Delayed	8 ± 5
FLSF 2013 May 13b	X2.8	15:48–16:16	3.9	6.1 ± 2.2	2.41 ± 0.21	0.35 ± 0.04	Delayed	19.7 ± 2.3
FLSF 2013 May 14	X3.2	00:00–01:20	5.6	5.9 ± 0.5	3.30 ± 0.15	0.401 ± 0.004	No-Prompt Delayed	27.82 ± 0.28
FLSF 2013 May 15	X1.2	01:25–01:58	0.8	3.5 ± 0.5	0.36 ± 0.07	0.052 ± 0.023	No-Prompt Delayed	...
FLSF 2013 Oct 11	M4.9 [*]	07:01–07:45	0.7	0.38 ± 0.32	12.5 ± 0.4	0.262 ± 0.013	BTL Short-Delayed	9 ± 9
FLSF 2013 Oct 25a	X1.7	07:53–08:09	0.7	1.4 ± 0.5	1.15 ± 0.12	0.042 ± 0.013	Delayed	3.3 ± 1.0
FLSF 2013 Oct 28 c	M2.7 ^c	14:46–15:04	0.3	1.6 ± 0.6	0.81 ± 0.12	0.036 ± 0.014	Delayed	...
FLSF 2014 Jan 06	X3.5 [*]	07:40–08:08	0.6	0.27 ± 0.04	0.42 ± 0.09	0.0061 ± 0.0028	BTL Short-Delayed	0.31 ± 0.31
FLSF 2014 Jan 07	X1.2	18:04–18:58	0.8	1.05 ± 0.26	0.29 ± 0.07	0.0081 ± 0.0020	Delayed	...
FLSF 2014 February 25	X4.9	00:39–01:03	6.7	8.4 ± 1.8	169.6 ± 2.0	13.95 ± 0.18	LLE-Prompt Delayed ^a	719 ± 8
FLSF 2014 Jun 10	X1.5	12:36–13:03	0.4	1.9 ± 0.6	1.17 ± 0.26	0.064 ± 0.026	LLE-Prompt Delayed ^a	...
FLSF 2014 Jun 11	X1.0	08:59–09:10	0.4	0.23 ± 0.17	0.99 ± 0.26	0.007 ± 0.005	Short-Delayed	...
FLSF 2014 Sep 1	X2.4 [*]	10:58–11:40	1.9	2.5 ± 1.2	379 ± 7	12.1 ± 2.3	BTL Delayed	$(7.4 \pm 1.4) \times 10^2$
FLSF 2014 Sep 10	X1.6	17:21–18:20	0.3	0.30 ± 0.06	7.4 ± 0.5	0.172 ± 0.012	Short-Delayed	5 ± 5
FLSF 2015 Jun 21	M2.7 ^c	02:04–03:15	10.1	11.5 ± 2.5	1.26 ± 0.15	0.296 ± 0.011	Prompt Delayed	16.7 ± 0.7
FLSF 2015 Jun 25	M7.9	08:02–09:05	0.7	2.4 ± 1.3	0.40 ± 0.08	0.030 ± 0.004	Delayed	2.28 ± 0.29
FLSF 2017 Sep 6a	X2.2	08:57–09:17	0.5	0.169 ± 0.025	1.31 ± 0.16	0.020 ± 0.007	Prompt	0.6 ± 0.6
FLSF 2017 Sep 6b	X9.3 ^c	11:53–12:10	13.0	13.33 ± 0.32	3.6 ± 0.5	1.0700 ± 0.0022	Delayed	79.41 ± 0.13
FLSF 2017 Sep 10	X8.2	15:35–16:31	13.3	13.9 ± 1.2	291.0 ± 2.1	22.2 ± 1.6	Prompt Delayed ^a	$(9.5 \pm 0.7) \times 10^2$

Note. In the GOES-class column, entries with an * identify the BTL flares, whose class is estimated based on the STEREO observation, and ^a indicates that there is also an LLE detection of the flare. The analysis results for the LLE flares are shown in Table 3.

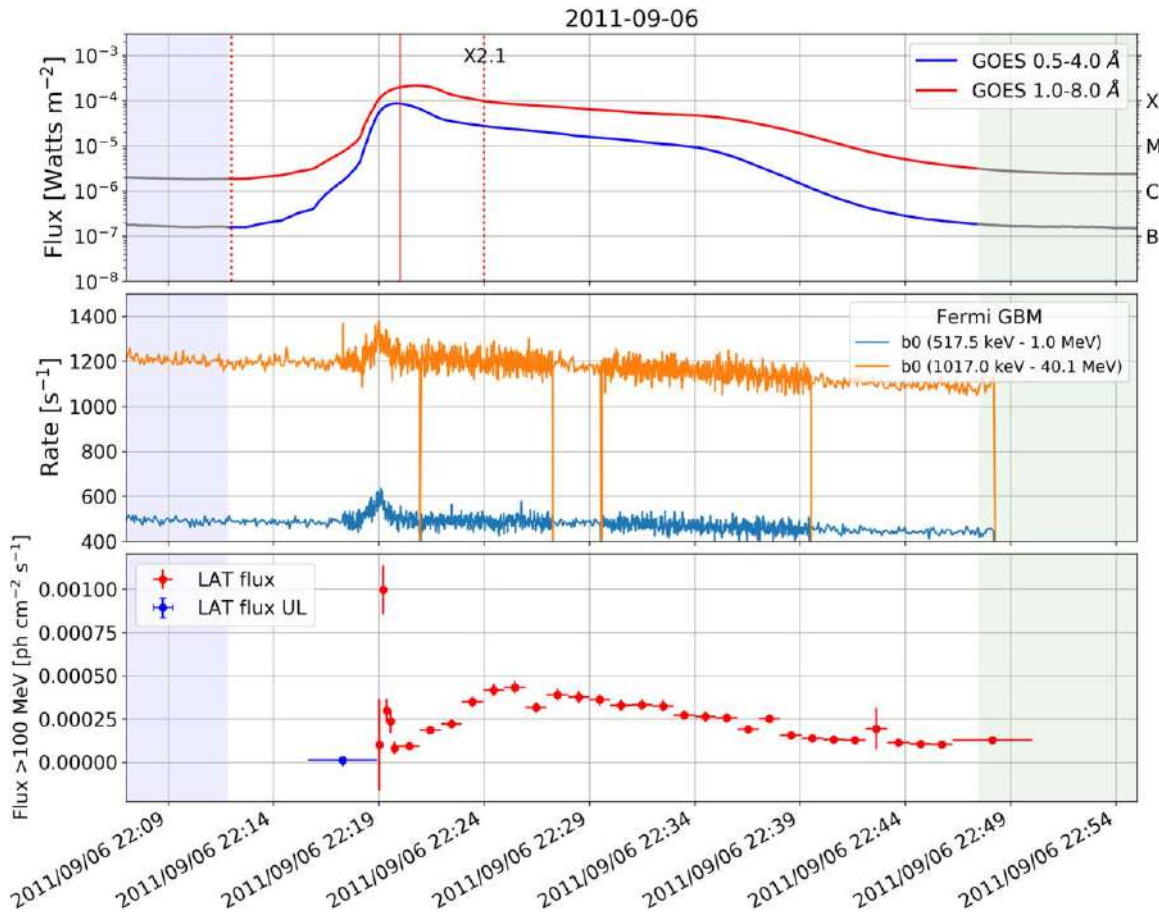


Figure 9. Example of a flare with a prompt component coincident with the bright HXR peak followed by a γ -ray delayed emission; that occurred on 2011 September 6. From top to bottom, the GOES X-ray flux in two energy bands, the Fermi-GBM X-ray lightcurve, and the Fermi-LAT >100 MeV flux using the standard likelihood analysis with a fine time binning to reveal the prompt component. The dashed/solid red lines represent the start (stop)/peak of the GOES X-ray flare; the GOES class is also annotated next to the solid red line.

beyond the end of the HXR emission and even the end of the SXR seen by GOES. We refer to that general category as delayed emission. The subset of flares classified as delayed also exhibit a wide variety of behaviors. For example, there are cases where no significant γ -rays are detected during the prompt phase of the flare in X-rays, but γ -ray emission seen rising and falling later on. We refer to these flares as being delayed only.

One of the most interesting results of the Fermi-LAT observations of solar flares is events with detectable emission lasting several hours. As already discussed in Section 1, the LAT has the Sun in its FoV on average only 40% of its orbit, greatly limiting the coverage of these delayed γ -ray flares. As a result, it is difficult to study the time profiles of these flares throughout the entire duration of the emission.

This is the case for the FLSF 2012 March 9, which is associated with a GOES M6.3 flare with HXR extending up to the GBM Na sci 100–300 KeV channel. Most of the prompt phase was observable by the Fermi-LAT and the bright SXR affected the instrument response (BTI in red in Figure 10). No γ -ray emission was detected during the peak of the prompt phase using the S15 event class or the LLE analysis method. Yet γ -ray emission was detected when the Sun came back in the FoV, almost two hours after the start of the flare in X-rays, and lasted for four orbits. It followed a rise and fall pattern,

reaching its peak after 4 hr and ending 7 hr after the start of the flare in X-rays.

Similarly, the FLSF 2013 May 15 had no significant emission detected during either the impulsive phase or in the first time window following the flare, but significant emission detected in the following time window (Figure 11). In itself, it might not be a new type of behavior, as it can be seen as a rise-and-fall pattern with the starting flux being just below the Fermi-LAT sensitivity but the peak flux being high enough to be detected.

These behaviors highlight the possibility that high-energy emission above 100 MeV can arise at later times, even if the prompt phase itself did not show a strong nonthermal component (almost no HXR above 300 keV and no γ -rays below 30 MeV). Although these cases are rare (only four cases in the catalog), they are particularly interesting for understanding whether the acceleration of high-energy particles is solely due to the prompt phase of solar flares or due to a separate mechanism entirely.

There are also FLSFs with both a clear prompt and a long-duration delayed component present; these flares are classified as prompt-delayed. An example of this class of flares is the FLSF 2017 September 10 (Omodei et al. 2018) that exhibited a very bright prompt phase and almost 14 hr of delayed γ -ray emission. In the FLSF catalog, we were able to classify the flares into six different categories: prompt, prompt only,

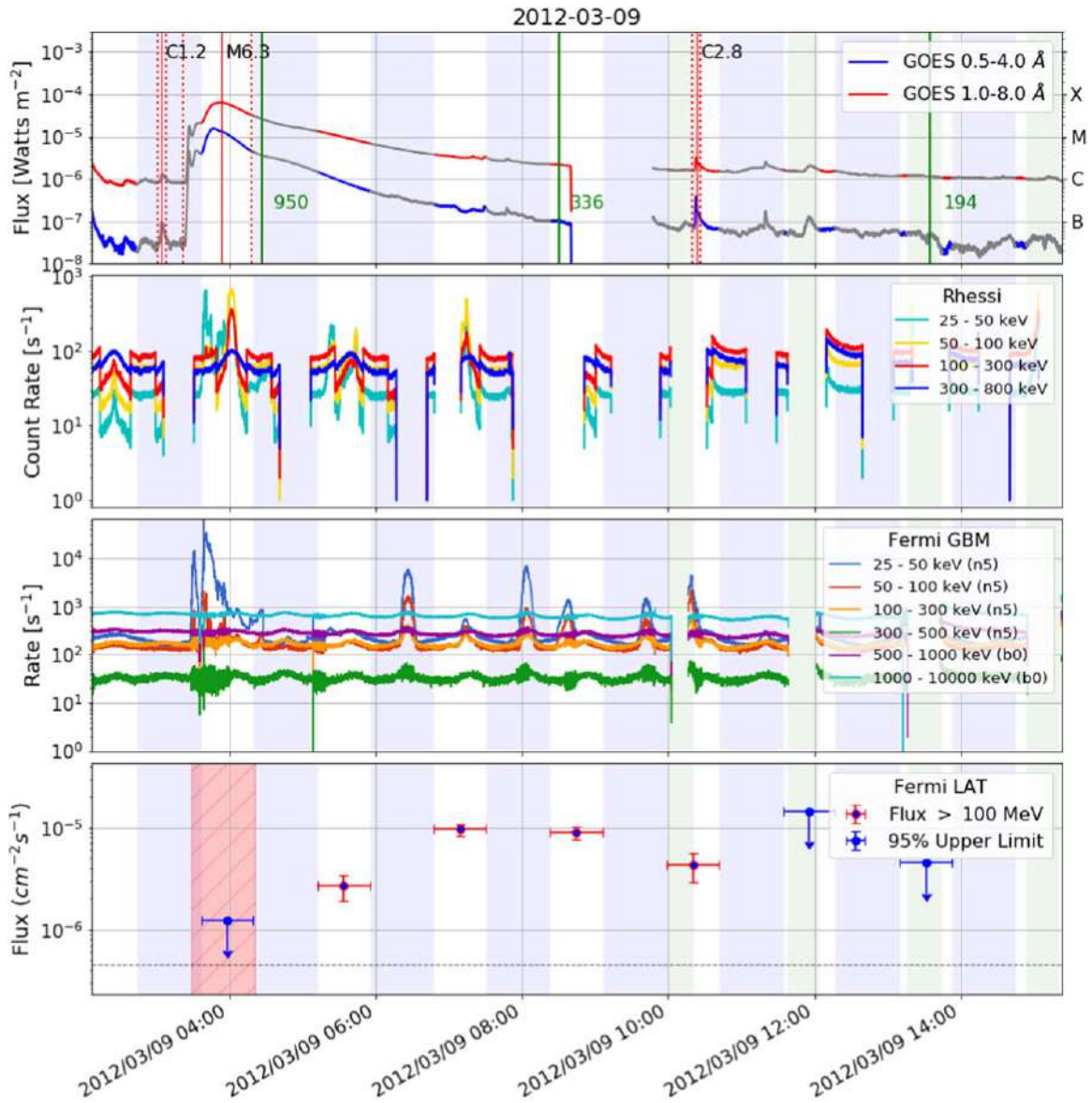


Figure 10. Lightcurve of the >100 MeV emission from FLSF 2012 March 9 lasting more than 6 hr but with no detectable high-energy γ -ray emission in the impulsive phase, classified as delayed only. The four panels report the lightcurve measured by GOES, RHESSI, Fermi/GBM, and Fermi/LAT in various energy ranges. The solid green lines represent the first appearance of the LASCO CME C2; the linear speed value is annotated next to the line (also in green). The dashed/solid red lines represent the start (stop)/peak of the GOES X-ray flare; the GOES class is also annotated next to the solid red line. The light-green bands indicate when the Fermi satellite was in the SAA, and the blue bands indicate when the Sun was outside of the FoV of the LAT. The pink bands indicate the time interval over which potential pile-up effects could be present.

delayed, delayed only, prompt short-delayed, prompt-delayed. All of the lightcurves and categories of FLSFs are reported at doi:[10.5281/zenodo.4311156](https://doi.org/10.5281/zenodo.4311156).

4. Results

Continuous monitoring of the Sun has led to the high-confidence ($TS \geq 30$) detection of 45 solar flares with γ -ray emission above 60 MeV. For 39 of these flares, γ -ray emission was significant in 92 SunMonitor time windows. The remaining six flares were detected with LLE analysis only. Of these 45 flares, 6 are classified as prompt only, 4 are classified as delayed only, and for 10 flares both the prompt and delayed emission were clearly observed by Fermi-LAT. For the remaining cases, we cannot exclude the presence of a prompt emission because the Sun was not in the FoV of the LAT during the HXR activity. Because of the

observing strategy of the Fermi-LAT, more than half of the solar flares detected are only detected in a single time window, whereas 16 are detected in more than one window. Of the 16 flares detected in multiple time windows, 5 are detected in only 2 time windows, and 11 are detected in 3 or more (up to 11) time windows well beyond the HXR signatures of the high-energy electrons. Seven flares in the latter group show a well-defined pattern of rise and decay phases after the end of the HXR and 2 show a decay phase only. All five flares detected in two time windows show a decay between the two points. Some of these may represent a rise and fall case with a peak occurring in between the two time windows. However, this is unlikely because statistically, one would expect two or three of these flares showing rise instead of decay, and because this would imply a faster rise and fall than seen in the flares with more than three windows of observation.

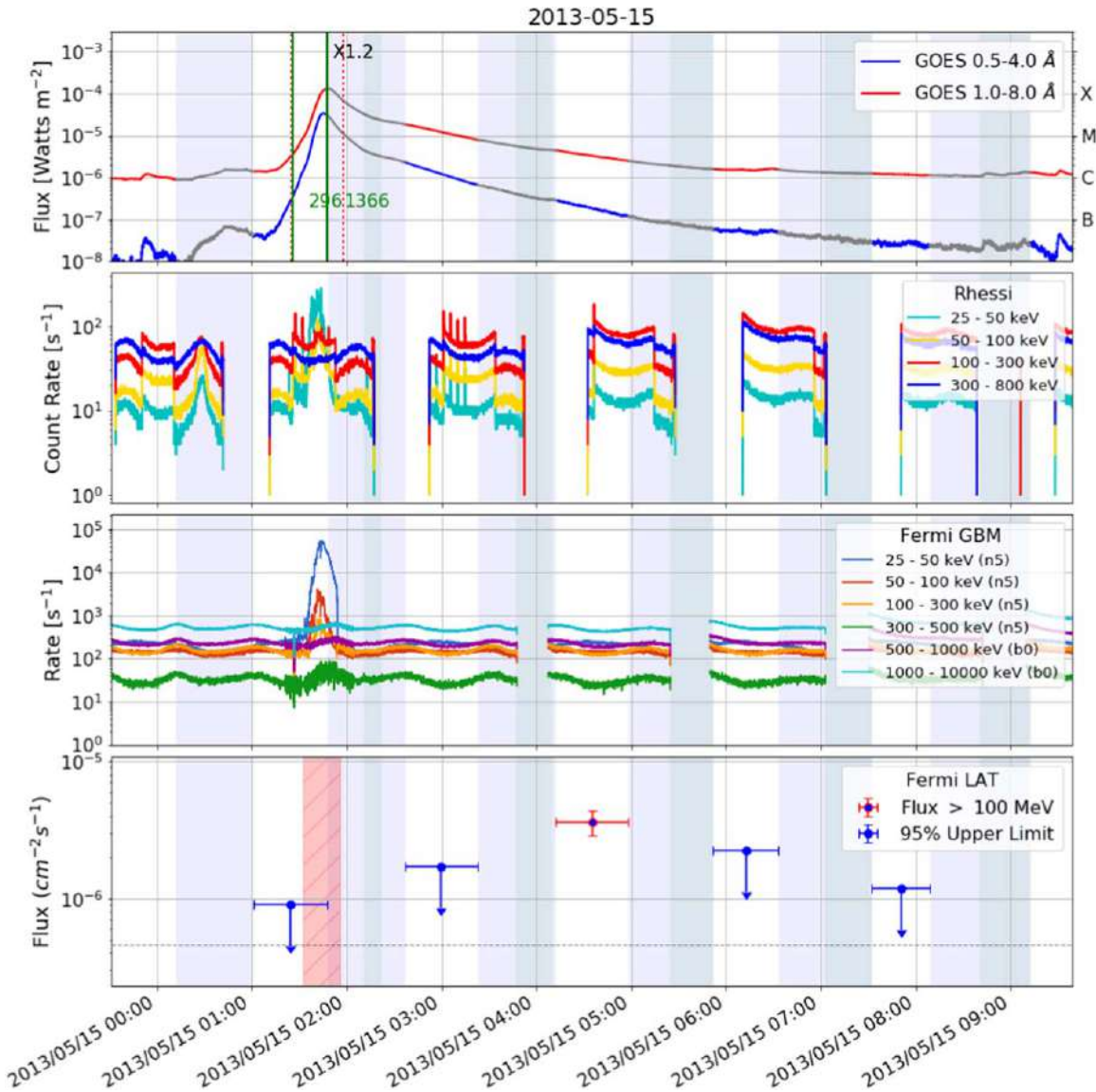


Figure 11. The delayed-only lightcurve of the >100 MeV emission from the FLSF 2013 May 15 flare with no detectable high-energy γ -ray emission in the impulsive phase or the following time window. The four panels report the same quantities as those in Figure 10.

In Table 1, we show the time-integrated results for the FLSFs detected with the SunMonitor. The columns report the LAT detection start date and time, the GOES soft X-ray start and end times, the LAT detection duration, the total duration of the FLSF,⁶⁷ the fluence, namely the time-integrated flux over the total duration, the FLSF flare type, and the total number of accelerated >500 MeV protons (N500). The GOES classes for the three BTL flares (identified by an *) are estimated based on STEREO UV fluxes as described in Pesce-Rollins et al. (2015).

The characteristics of the γ -ray emission in each SunMonitor time window are listed in Table 2. Results from flares detected in more than one time window are listed together. The columns of Table 2 are the time of each detection window, the duration of the window, the >100 MeV flux, TS, and the spectral parameters (power-law indices and cutoff energies) of

the best-fitting photon model. For the cases where the $\Delta TS > 9$, we give the proton index based on the pion-decay model in the last column. The fluxes are given in 10^{-5} $\text{ph cm}^{-2} \text{s}^{-1}$ and calculated for the emission between 100 MeV and 10 GeV. The LAT emission in all SunMonitor time windows with TS larger than 70 shows significant spectral curvature and can be well described with the exponential cutoff model. This does not mean that all fainter γ -ray flares are only consistent with a power-law model, but rather that the lower statistics make it impossible to distinguish between the two.⁶⁸

We retract the LAT detection of the C-class flare on 2011 June 2 reported in Ackermann et al. (2014), because during the month of June, the Sun passes through the Galactic plane, and a higher background flux of photons enters into the RoI around the Sun relative to other periods in the year. After careful reanalysis of this event, we found that the reported detection was not statistically significant.

⁶⁷ The detection duration is simply the sum of the SunMonitor detection windows duration while the total duration is that found using the approach described in Section 2.6.

⁶⁸ The FLSF of 2013 October 28 is the only exception, having a TS of 120 and the exponential cutoff model is not preferred ($\Delta TS = 8$).

Table 2
Maximum Likelihood Results for Each SunMonitor Observing Time Window Associated with a Solar Flare Detected by the Fermi-LAT

Date and Time (UTC)	Exposure (minutes)	Flux (10^{-5} ph cm $^{-2}$ s $^{-1}$)	TS	Δ TS	Model	Photon Index	Cutoff Energy (MeV)	Proton index
2011 Mar 7 20:10–20:39	29	2.06 ± 0.19	317	27	Exp	-0.76 ± 0.45	172 ± 55	4.3 ± 0.4
2011 Mar 7 23:21–00:05	44	3.04 ± 0.20	710	70	Exp	-0.31 ± 0.36	138 ± 27	4.13 ± 0.26
2011 Mar 8 02:33–03:16	43	3.23 ± 0.22	621	66	Exp	-0.15 ± 0.41	110 ± 22	4.70 ± 0.32
2011 Mar 8 05:44–06:27	44	1.40 ± 0.15	219	32	Exp	0.67 ± 0.99	63 ± 22	>6
2011 Mar 8 09:13–09:39	26	0.48 ± 0.11	46	-0.1	PL	-2.55 ± 0.25
2011 Jun 7 07:47–08:23	36	3.18 ± 0.20	740	76	Exp	-0.13 ± 0.37	104 ± 19	4.97 ± 0.33
2011 Jun 7 11:16–11:34	19	0.32 ± 0.10	19	5	PL	-2.70 ± 0.35
2011 Aug 4 04:55–05:37	42	2.30 ± 0.18	413	49	Exp	-0.09 ± 0.50	95 ± 21	5.4 ± 0.4
2011 Aug 9 07:37–08:09	32	$2.29 \pm 0.23^*$	186	26	Exp	-0.04 ± 0.87	91 ± 37	5.4 ± 0.6
2011 Sep 6 22:11–22:47	36	$22.8 \pm 0.4^*$	8197	437	Exp	-0.89 ± 0.09	161 ± 11	4.89 ± 0.11
2011 Sep 7 23:35–00:23	48	0.77 ± 0.08	270	30	Exp	-0.10 ± 0.69	114 ± 40	4.4 ± 0.5
2011 Sep 24 09:18–09:47	30	$0.50 \pm 0.10^*$	50	5	PL	-2.51 ± 0.22
2012 Jan 23 04:06–04:46	40	1.12 ± 0.11	258	26	Exp	0.12 ± 1.09	81 ± 40	5.5 ± 0.6
2012 Jan 23 05:33–06:21	48	1.99 ± 0.12	796	92	Exp	0.25 ± 0.41	80 ± 13	5.6 ± 0.4
2012 Jan 23 07:20–07:47	27	1.97 ± 0.31	93	12	Exp	-0.25 ± 1.05	100 ± 49	5.5 ± 0.9
2012 Jan 23 08:58–09:26	28	1.63 ± 0.23	116	27	Exp	1.81 ± 1.41	51 ± 18	5.6 ± 0.8
2012 Jan 27 19:37–19:55	18	3.3 ± 0.5	102	14	Exp	0.31 ± 1.43	65 ± 33	>6
2012 Jan 27 21:08–21:36	28	0.72 ± 0.14	66	8	PL	-2.53 ± 0.20
2012 Jan 28 00:19–00:55	36	0.25 ± 0.09	19	1	PL	-2.60 ± 0.39
2012 Mar 5 04:07–04:49	42	0.58 ± 0.09	100	11	Exp	0.34 ± 1.33	63 ± 31	>6
2012 Mar 5 05:36–06:24	48	0.63 ± 0.07	175	16	Exp	-0.20 ± 0.85	79 ± 31	>6
2012 Mar 5 07:18–07:54	36	0.55 ± 0.11	53	6	PL	-2.52 ± 0.21
2012 Mar 7 00:40–01:20	40	$233 \pm 8^*$	75611	-254574	Exp	-0.65 ± 0.03	182 ± 4	3.875 ± 0.025
2012 Mar 7 02:26–02:45	18	75.1 ± 2.6	2377	117	Exp	-1.45 ± 0.13	355 ± 47	3.77 ± 0.10
2012 Mar 7 03:51–04:31	40	95.1 ± 1.2	21100	1459	Exp	-0.84 ± 0.05	199 ± 8	4.01 ± 0.05
2012 Mar 7 05:38–05:55	18	97.3 ± 3.2	2675	249	Exp	-0.59 ± 0.17	147 ± 14	4.51 ± 0.13
2012 Mar 7 07:02–07:42	40	62.8 ± 1.0	12829	1210	Exp	-0.30 ± 0.08	120 ± 5	4.71 ± 0.07
2012 Mar 7 08:49–09:06	17	49.8 ± 2.5	1181	123	Exp	-0.17 ± 0.32	102 ± 14	5.17 ± 0.24
2012 Mar 7 10:14–10:54	25	26.8 ± 0.9	2803	344	Exp	0.27 ± 0.21	84 ± 7	5.28 ± 0.17
2012 Mar 7 13:24–14:04	13	8.6 ± 0.9	258	31	Exp	0.30 ± 0.75	78 ± 22	5.7 ± 0.6
2012 Mar 7 16:35–16:48	13	1.54 ± 0.32	49	10	Exp	1.41 ± 1.91	46 ± 23	>6
2012 Mar 7 18:23–18:32	9	2.2 ± 0.7	25	8	PL	-2.91 ± 0.41
2012 Mar 7 19:46–20:15	29	0.26 ± 0.08	22	3	PL	-2.37 ± 0.30
2012 Mar 9 05:12–05:55	43	0.27 ± 0.08	32	-0.2	PL	-2.24 ± 0.25
2012 Mar 9 06:47–07:30	43	0.96 ± 0.12	139	20	Exp	0.09 ± 0.92	87 ± 34	5.5 ± 0.7
2012 Mar 9 08:22–09:05	43	0.89 ± 0.12	140	28	Exp	1.78 ± 1.21	50 ± 15	5.6 ± 0.8
2012 Mar 9 09:58–10:41	22	0.43 ± 0.13	25	0.3	PL	-2.51 ± 0.32
2012 Mar 10 21:00–21:34	34	0.23 ± 0.06	25	2	PL	-2.50 ± 0.30
2012 Mar 10 22:35–23:15	40	0.19 ± 0.06	18	3	PL	-3.04 ± 0.40
2012 May 17 02:12–02:44	32	1.19 ± 0.19	100	10	Exp	-0.72 ± 0.77	207 ± 117	3.7 ± 0.5
2012 May 17 03:49–04:18	30	0.44 ± 0.13	29	7	PL	-2.30 ± 0.28
2012 Jun 3 17:38–18:02	24	3.06 ± 0.25	395	39	Exp	-0.19 ± 0.63	104 ± 34	5.0 ± 0.4
2012 Jul 6 23:20–00:08	48	3.06 ± 0.15	1173	143	Exp	0.40 ± 0.35	74 ± 10	5.75 ± 0.29
2012 Oct 23 04:13–04:43	30	0.73 ± 0.18	39	9	PL	-2.73 ± 0.27
2012 Nov 13 01:34–02:14	40	$0.46 \pm 0.09^*$	60	7	PL	-2.61 ± 0.21
2012 Nov 27 15:48–16:34	46	0.27 ± 0.07	44	2	PL	-2.22 ± 0.21
2013 Apr 11 07:00–07:39	39	$5.71 \pm 0.24^*$	1422	120	Exp	-0.43 ± 0.27	105 ± 15	5.67 ± 0.27
2013 May 13 17:15–17:58	30	2.41 ± 0.21	371	43	Exp	-0.24 ± 0.48	142 ± 38	3.91 ± 0.31
2013 May 13 20:26–21:09	43	1.72 ± 0.14	371	43	Exp	0.21 ± 0.73	80 ± 25	5.5 ± 0.5

Table 2
(Continued)

Date and Time (UTC)	Exposure (minutes)	Flux (10^{-5} ph cm $^{-2}$ s $^{-1}$)	TS	Δ TS	Model	Photon Index	Cutoff Energy (MeV)	Proton index
2013 May 13 04:31–05:14	43	0.96 ± 0.11	188	36	Exp	3.00 ± 0.14	31 ± 2	>6
2013 May 14 01:08–01:55	47	$1.02 \pm 0.09^*$	292	46	Exp	0.55 ± 0.67	65 ± 15	>6
2013 May 14 02:43–03:31	47	3.30 ± 0.15	1518	193	Exp	0.62 ± 0.32	77 ± 9	4.95 ± 0.24
2013 May 14 04:19–05:06	47	2.32 ± 0.16	546	87	Exp	1.26 ± 0.61	54 ± 9	5.9 ± 0.4
2013 May 14 05:59–06:42	42	0.59 ± 0.09	105	19	Exp	1.05 ± 1.43	54 ± 24	>6
2013 May 15 04:12–04:58	46	0.36 ± 0.07	51	9	PL	-2.62 ± 0.22
2013 Oct 11 06:56–07:39	42	12.5 ± 0.4	3949	317	Exp	-0.34 ± 0.16	131 ± 12	4.33 ± 0.12
2013 Oct 25 08:15–08:57	42	$1.15 \pm 0.12^*$	211	21	Exp	0.07 ± 0.88	79 ± 30	6 ± 4
2013 Oct 28 15:45–16:05	21	0.81 ± 0.12	120	8	PL	-2.32 ± 0.15
2014 Jan 06 07:55–08:30	34	0.42 ± 0.09	52	13	Exp	1.84 ± 2.16	49 ± 26	5.8 ± 1.9
2014 Jan 07 18:41–19:29	48	0.29 ± 0.07	32	5	PL	-2.68 ± 0.27
2014 Feb 25 01:09–01:29	20	$169.6 \pm 2.0^*$	24030	2121	Exp	-0.33 ± 0.06	154 ± 5	3.78 ± 0.04
2014 Feb 25 04:20–04:40	20	28.3 ± 0.9	2707	370	Exp	1.17 ± 0.28	47 ± 4	>6
2014 Feb 25 07:30–07:51	21	0.87 ± 0.17	74	11	Exp	2.39 ± 2.53	29 ± 14	>6
2014 Jun 10 14:00–14:26	25	1.17 ± 0.26	49	5	PL	-2.47 ± 0.22
2014 Jun 11 09:06–09:30	24	$0.99 \pm 0.26^*$	30	3	PL	-2.77 ± 0.30
2014 Sep 1 11:02–11:18	16	379 ± 7	41620	-5590	Exp	-1.03 ± 0.09	177 ± 10	4.70 ± 0.07
2014 Sep 1 12:25–12:57	32	2.98 ± 0.22	545	31	Exp	-1.16 ± 0.29	290 ± 82	3.72 ± 0.24
2014 Sep 10 17:35–17:53	18	$7.4 \pm 0.5^*$	559	66	Exp	0.35 ± 0.54	86 ± 20	4.66 ± 0.34
2015 Jun 21 02:09–02:42	33	0.25 ± 0.08	23	5	PL	-3.05 ± 0.39
2015 Jun 21 05:19–05:53	33	1.26 ± 0.15	162	16	Exp	-0.18 ± 0.74	118 ± 44	4.3 ± 0.6
2015 Jun 21 08:30–09:03	33	0.81 ± 0.13	101	12	Exp	0.03 ± 1.14	110 ± 57	4.2 ± 0.7
2015 Jun 21 11:40–12:14	33	0.38 ± 0.10	31	10	Exp	2.05 ± 2.61	49 ± 29	>6
2015 Jun 25 09:24–10:09	45	0.40 ± 0.08	48	6	PL	-2.72 ± 0.22
2017 Sep 6 12:10–12:35	25	$0.96 \pm 0.11^*$	156	17	Exp	0.05 ± 1.06	58 ± 23	>6
2017 Sep 6 13:23–14:10	26	$2.63 \pm 0.17^*$	604	66	Exp	0.39 ± 0.55	60 ± 12	>6
2017 Sep 6 15:03–15:40	18	2.9 ± 0.4	137	24	Exp	1.20 ± 1.29	59 ± 23	5.6 ± 0.8
2017 Sep 6 16:45–17:09	19	3.6 ± 0.5	130	24	Exp	1.24 ± 1.24	64 ± 22	5.2 ± 0.7
2017 Sep 6 18:14–18:50	36	2.73 ± 0.24	337	49	Exp	0.67 ± 0.68	71 ± 17	5.4 ± 0.5
2017 Sep 6 19:55–20:20	25	2.27 ± 0.35	96	17	Exp	0.74 ± 1.33	65 ± 27	>6
2017 Sep 6 21:25–22:00	35	2.56 ± 0.24	318	36	Exp	0.11 ± 0.67	84 ± 24	5.5 ± 0.5
2017 Sep 6 23:05–23:31	26	0.96 ± 0.22	43	4	PL	-3.06 ± 0.30
2017 Sep 7 00:36–01:11	35	0.62 ± 0.13	52	4	PL	-2.63 ± 0.22
2017 Sep 6 08:51–09:19	28	$1.31 \pm 0.16^*$	130	21	Exp	0.59 ± 1.05	60 ± 22	>6
2017 Sep 10 15:52–16:28	35	$291.0 \pm 2.1^*$	61725	4429	Exp	-0.67 ± 0.03	195 ± 4	3.737 ± 0.026
2017 Sep 10 17:33–17:58	24	76.4 ± 1.9	6112	469	Exp	-0.70 ± 0.30	248 ± 49	3.30 ± 0.06
2017 Sep 10 19:03–19:39	36	88.3 ± 1.3	16954	1819	Exp	-0.02 ± 0.07	140 ± 5	3.70 ± 0.05
2017 Sep 10 20:44–21:08	24	35.8 ± 1.3	2311	276	Exp	0.07 ± 0.22	117 ± 11	4.18 ± 0.14
2017 Sep 10 22:13–22:49	36	15.0 ± 0.5	2559	315	Exp	0.35 ± 0.22	91 ± 8	4.67 ± 0.16
2017 Sep 10 23:54–00:18	24	5.6 ± 0.5	310	68	Exp	2.03 ± 0.84	55 ± 11	4.9 ± 0.4
2017 Sep 11 01:23–02:00	36	2.38 ± 0.22	284	55	Exp	1.69 ± 0.83	48 ± 10	6.0 ± 0.5
2017 Sep 11 03:05–03:29	24	1.39 ± 0.28	59	12	Exp	1.00 ± 1.58	70 ± 34	5.0 ± 1.0
2017 Sep 11 04:34–05:11	37	0.49 ± 0.11	43	2	PL	-2.65 ± 0.24

Note. Some flares are detected in more than one time window. The horizontal lines separate the flares. The columns are the start date and time of the observing window (reported in UTC), the exposure of the time window, the flux >100 MeV integrated over the observing time window, the TS value for the simple power-law model fit, the Δ TS between the power-law and the power-law with exponential cutoff fit, the model with higher TS value, the photon index from the best-fit model, the cutoff energy value (for the cases where the exponential cutoff model best fits the data), best proton index (from fit to the data with pion templates) for the cases where the curved model best describes the data.

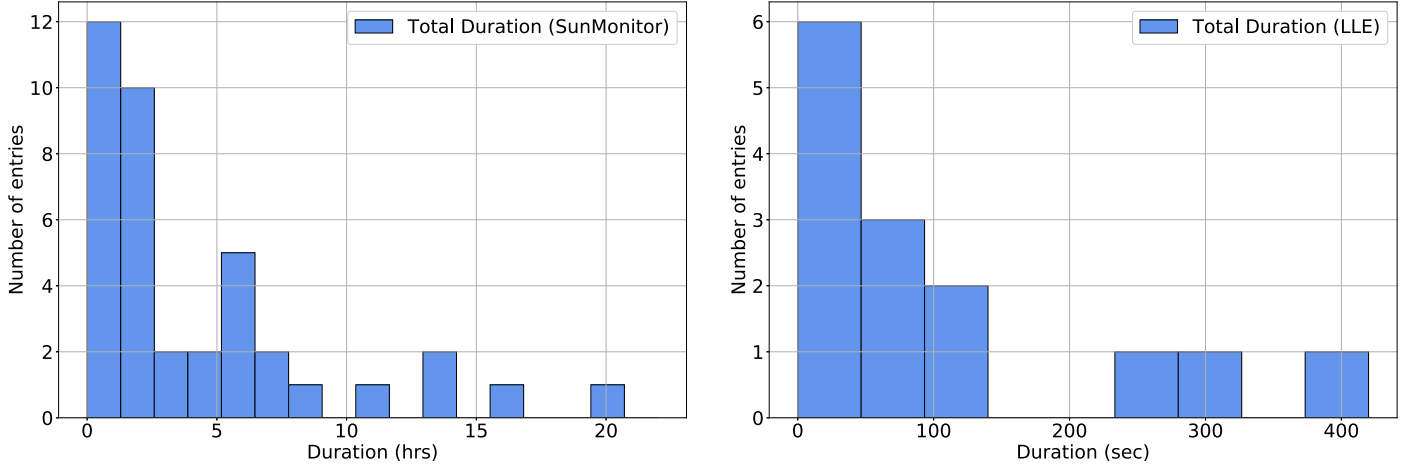


Figure 12. Distribution of the total duration for all of the *SunMonitor* detected flares (in hours, left panel) and the LLE detected flares (in seconds, right panel) in the FLSF catalog.

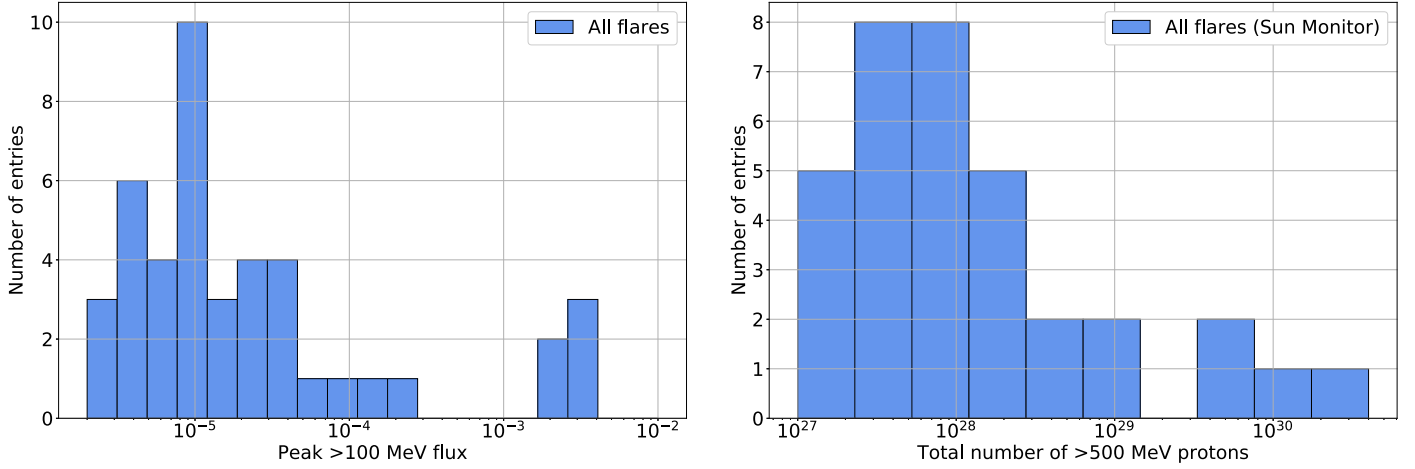


Figure 13. Distributions of the peak >100 MeV flux (in $\text{ph cm}^{-2} \text{s}^{-1}$; left panel) for all FLSFs in the catalog and the total number of accelerated >500 MeV protons needed to produce the detected γ -ray emission for each of the *SunMonitor* detected FLSFs (right panel).

Table 3
LLE FLSF Catalog Results with Associated GOES X-Ray Flare

Name	Start (UTC)	Duration (s)	Flux (30 MeV–10 GeV)	Flux (100 MeV–10 GeV)	Proton Index	GOES Class	<i>SunMonitor</i> Detected
FLSF 2010 Jun 12	2010 Jun 12 00:55:49	30	446 ± 35	191 ± 12	6.0 ± 0.4	M2.0	NO
FLSF 2011 Aug 9	2011 Aug 9 08:01:51	250	31.20 ± 0.24	13.02 ± 0.22	5.68 ± 0.13	X6.9	YES
FLSF 2011 Sep 6	2011 Sep 6 22:18:07	100	54.0 ± 1.4	16.6 ± 1.1	3.2 ± 0.4	X2.1	YES
FLSF 2011 Sep 24	2011 Sep 24 09:35:53	100	65.2 ± 1.7	0.43 ± 0.07	3.2 ± 0.4	X1.9	YES
FLSF 2012 Jun 3	2012 Jun 3 17:53:20	20	111 ± 5	50 ± 5	6.0 ± 1.5	M3.3	YES
FLSF 2012 Aug 6	2012 Aug 6 04:36:01	30	205 ± 5	1.79 ± 0.12	6.0 ± 1.5	M1.6	NO
FLSF 2012 Oct 23	2012 Oct 23 03:15:33	20	$(3.08 \pm 0.27) \times 10^3$	105 ± 20	6.0 ± 1.5	X1.8	YES
FLSF 2013 Oct 25b	2013 Oct 25 20:56:52	10	38.9 ± 1.0	1.13 ± 0.09	6.0 ± 1.5	M1.9	NO
FLSF 2013 Oct 28a	2013 Oct 28 01:59:15	70	0.450 ± 0.035	$<3 \times 10^{-3}$	6.0 ± 1.5	X1.0	NO
FLSF 2013 Oct 28b	2013 Oct 28 04:37:48	50	25.9 ± 1.3	0.0029 ± 0.0016	6.0 ± 1.5	M5.1	NO
FLSF 2013 Oct 28d	2013 Oct 28 20:54:47	50	9.8 ± 0.6	0.33 ± 0.05	6.0 ± 1.5	M1.5	NO
FLSF 2014 Feb 25	2014 Feb 25 00:44:47	400	1407 ± 25	631 ± 26	6.0 ± 0.7	X4.9	YES
FLSF 2014 Jun 10	2014 Jun 10 12:47:18	25	6.7 ± 1.3	2.9 ± 1.1	2.2 ± 1.4	X1.5	YES
FLSF 2017 Sep 10	2017 Sep 10 15:57:47	325	1060 ± 9	601 ± 7	3.01 ± 0.04	X8.2	YES

Note. For the cases where the curved spectrum is preferred, we also list the best inferred proton index. The *SunMonitor* detected column indicates whether the flare was detected by the *SunMonitor* automatic pipeline. The fluxes are in units of $10^{-5} \text{ ph s}^{-1} \text{ cm}^{-2}$.

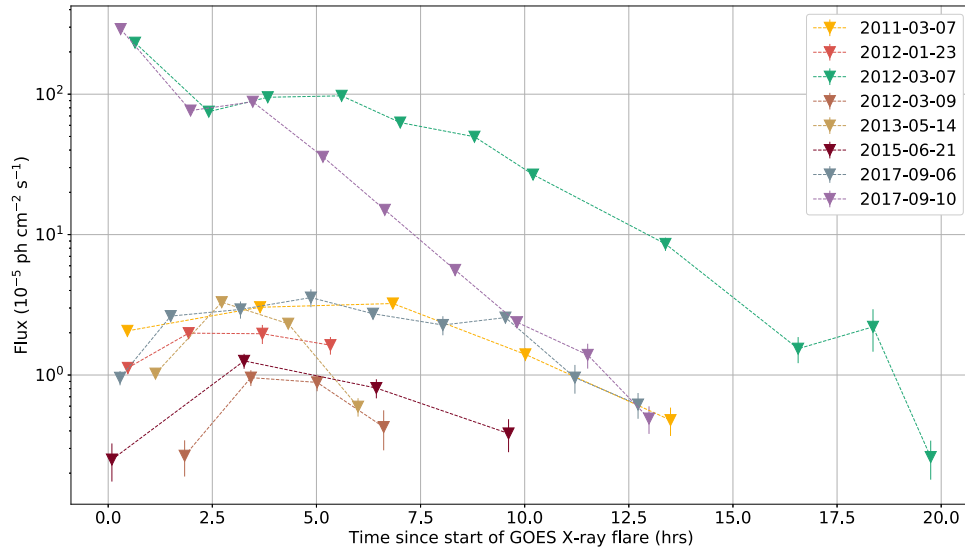


Figure 14. The time profiles of flux between 0.1 and 10 GeV for each FLSF lasting two or more hours vs. the time since the start of the GOES X-ray flare. The typical rise and fall behavior of the γ -ray emission during the delayed phase is most evident for the cases where no prompt emission was present during the detection.

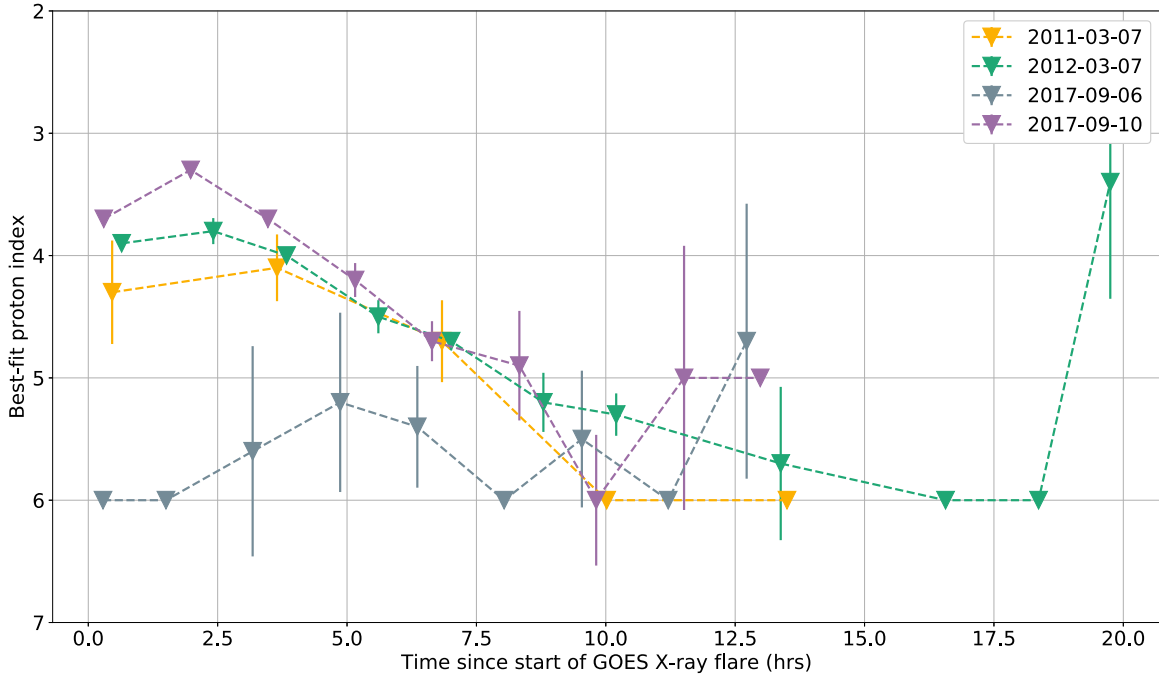


Figure 15. Variation with time (since the start of the GOES X-ray flare) of the best-fit proton spectral index for the four FLSFs for which a statistically meaningful measurement can be made.

The FLSF LLE catalog results are reported in Table 3. Three of the flares detected with LLE were outside the nominal LAT FoV. For the 11 flares in the FoV, five were not detected above 60 MeV by the SunMonitor analysis, and an upper limit was obtained for the time window when the flare happened. For the six flares detected with both analyses in the same time window, the >100 MeV fluxes reported in the SunMonitor results (Table 1) are the average over the time window, and the >100 MeV fluxes obtained through the LLE approach are listed in Table 3.

The durations for the flares detected with the SunMonitor range from 0.6 to 20.3 hr, whereas the LLE detected flares have durations ranging from 10 to 400 s (see Figure 12). Both the >100 MeV peak γ -ray fluxes and the total number of

>500 MeV protons needed to produce the observed γ -ray emission for all of the FLSFs in the catalog span over four orders of magnitude (see Figure 13).

Eight of the 45 FLSFs have durations of two hours or more. Their >100 MeV fluxes as a function of time (since the start of the associated GOES X-ray flare) are shown in Figure 14. The time profiles of all these delayed FLSFs follow a rise-and-fall behavior. However, the rise times to reach the peak flux and the fall times vary significantly from flare to flare. For example, the FLSF 2017 September 10 has a rise time of ≈ 1.5 hr while the FLSF 2017 September 6 takes ≈ 4.5 hr to reach its peak. The peak flux values also vary from flare to flare by up to two orders of magnitude, emphasizing the wide variety of these

Table 4
Multiwavelength Associations for All of the FLSFs in This Work

Name	Total Duration (hr)	Flare Type	GOES Start (UT)	GOES Class	CME Speed (km s ⁻¹)	CME First C2 app. (UT)	SEP Emax (MeV)	HXR Emax (keV)
FLSF 2010 Jun 12	30*	LLE-Prompt ^a	2010 Jun 12 00:30	M2.0	486	2010 Jun 12 01:31	10	1000
FLSF 2011 Mar 7	15.8 ± 3.1	Delayed	2011 Mar 7 19:43	M3.7 ^c	2125	2011 Mar 7 20:00	50	>100
FLSF 2011 Jun 7	6.0 ± 2.2	Delayed	2011 Jun 7 06:16	M2.5	1255	2011 Jun 7 06:49	100	100
FLSF 2011 Aug 4	2.3 ± 0.7	Delayed	2011 Aug 4 03:41	M9.3	1315	2011 Aug 4 04:12	100	300
FLSF 2011 Aug 9	0.87 ± 0.34	Prompt Short-Delayed ^a	2011 Aug 9 07:48	X6.9	1610	2011 Aug 9 08:12	100	300
FLSF 2011 Sep 6	2.0 ± 1.4	LLE-Prompt Short-Delayed ^a	2011 Sep 6 22:12	X2.1	575	2011 Sep 6 23:05	100	1000
FLSF 2011 Sep 7	2.02 ± 0.35	Delayed	2011 Sep 7 22:32	X1.8	792	2011 Sep 7 23:05	50 ^d	500
FLSF 2011 Sep 24	1.2 ± 0.7	LLE-Prompt Short-Delayed ^a	2011 Sep 24 09:21	X1.9	1936	2011 Sep 24 09:48	50 ^d	1000
FLSF 2012 Jan 23	5.9 ± 1.0	Delayed	2012 Jan 23 03:38	M8.7	2175	2012 Jan 23 04:00	100	>100
FLSF 2012 Jan 27	6.8 ± 1.5	Delayed	2012 Jan 27 17:37	X1.7	2508	2012 Jan 27 18:27	605	>100
FLSF 2012 Mar 5	4.4 ± 1.2	Delayed	2012 Mar 5 02:30	X1.1	1531	2012 Mar 5 04:00	40 ^d	>100
FLSF 2012 Mar 7	20.3 ± 0.8	Delayed	2012 Mar 7 00:02	X5.4 ^c	2684 ^b	2012 Mar 7 00:24	605	1000
FLSF 2012 Mar 9	7.2 ± 1.7	No-Prompt Delayed	2012 Mar 9 03:22	M6.3	950	2012 Mar 9 04:26	100 ^d	>100
FLSF 2012 Mar 10	6 ± 4	Delayed	2012 Mar 10 17:15	M8.4	1296	2012 Mar 10 18:00	100 ^d	>50
FLSF 2012 May 17	2.6 ± 0.5	Delayed	2012 May 17 01:25	M5.1	1582	2012 May 17 01:48	605	>100
FLSF 2012 Jun 3	1.9 ± 1.5	LLE-Prompt Short-Delayed ^a	2012 Jun 3 17:48	M3.3	605	2012 Jun 3 18:12	...	100
FLSF 2012 Jul 6	1.27 ± 0.35	Delayed	2012 Jul 6 23:01	X1.1	1828	2012 Jul 6 23:24	100	...
FLSF 2012 Aug 6	30*	LLE-Prompt ^a	2012 Aug 6 04:33	M1.6	198	2012 Aug 6 05:12	...	100
FLSF 2012 Oct 23	1.9 ± 0.5	LLE-Prompt Delayed ^a	2012 Oct 23 03:13	X1.8	1000
FLSF 2012 Nov 13	0.041 ± 0.006	Prompt	2012 Nov 13 01:58	M6.0	851	2012 Nov 13 02:24	...	100
FLSF 2012 Nov 27	0.166 ± 0.025	Prompt Short-Delayed	2012 Nov 27 15:52	M1.6	500
FLSF 2013 Apr 11	0.38 ± 0.27	No-Prompt Short-Delayed	2013 Apr 11 06:55	M6.5	861	2013 Apr 11 07:24	100	100
FLSF 2013 May 13a	4.0 ± 1.3	Delayed	2013 May 13 01:53	X1.7	1270	2013 May 13 02:00	60	>300
FLSF 2013 May 13b	6.1 ± 2.2	Delayed	2013 May 13 15:48	X2.8	1850	2013 May 13 16:07	60	800
FLSF 2013 May 14	5.9 ± 0.5	No-Prompt Delayed	2013 May 14 00:00	X3.2	2625	2013 May 14 01:25	60	500
FLSF 2013 May 15	3.5 ± 0.5	No-Prompt Delayed	2013 May 15 01:25	X1.2	1366	2013 May 15 01:48	50	100
FLSF 2013 Oct 11	0.38 ± 0.32	BTL Short-Delayed	2013 Oct 11 07:01	M4.9*	1200	2013 Oct 11 07:24	60	10
FLSF 2013 Oct 25a	1.4 ± 0.5	Delayed	2013 Oct 25 07:53	X1.7	587	2013 Oct 25 08:12	60	300
FLSF 2013 Oct 25b	10*	LLE-Prompt ^a	2013 Oct 25 20:54	M1.9	60 ^d	100
FLSF 2013 Oct 28a	70*	LLE-Prompt ^a	2013 Oct 28 01:41	X1.0	695	2013 Oct 28 02:24	...	1000
FLSF 2013 Oct 28b	50*	LLE-Prompt ^a	2013 Oct 28 04:32	M5.1	1201	2013 Oct 28 04:48	...	1000
FLSF 2013 Oct 28 c	1.6 ± 0.6	Delayed	2013 Oct 28 14:46	M2.7 ^c	812	2013 Oct 28 15:36	60	50
FLSF 2013 Oct 28d	50*	LLE-Prompt ^a	2013 Oct 28 20:48	M1.5	771	2013 Oct 28 21:25	100 ^d	100
FLSF 2014 Jan 06	0.27 ± 0.04	BTL Short-Delayed	2014 Jan 06 07:40	X3.5*	1402	2014 Jan 06 08:00	605	6
FLSF 2014 Jan 07	1.05 ± 0.26	Delayed	2014 Jan 07 18:04	X1.2	1830	2014 Jan 07 18:24	100	>20
FLSF 2014 Feb 25	8.4 ± 1.8	LLE-Prompt Delayed ^a	2014 Feb 25 00:39	X4.9	2147	2014 Feb 25 01:25	100	7000
FLSF 2014 Jun 10	1.9 ± 0.6	LLE-Prompt Delayed ^a	2014 Jun 10 12:36	X1.5	1469	2014 Jun 10 13:30	60	1000
FLSF 2014 Jun 11	0.23 ± 0.17	Short-Delayed	2014 Jun 11 08:59	X1.0	829	2014 Jun 11 09:24	...	1000
FLSF 2014 Sep 1	2.5 ± 1.2	BTL Delayed	2014 Sep 1 10:58	X2.4*	1901	2014 Sep 1 11:12	100	100
FLSF 2014 Sep 10	0.30 ± 0.06	Short-Delayed	2014 Sep 10 17:21	X1.6	1071 ^b	2014 Sep 10 17:24	100	100
FLSF 2015 Jun 21	11.5 ± 2.5	Prompt Delayed	2015 Jun 21 02:04	M2.7 ^c	1366	2015 Jun 21 02:36	10	>50
FLSF 2015 Jun 25	2.4 ± 1.3	Delayed	2015 Jun 25 08:02	M7.9	1627	2015 Jun 25 08:36	10	1000

Table 4
(Continued)

Name	Total Duration (hr)	Flare Type	GOES Start (UT)	GOES Class	CME Speed (km s ⁻¹)	CME First C2 app. (UT)	SEP Emax (MeV)	HXR Emax (keV)
FLSF 2017 Sep 6a	0.169 ± 0.025	Prompt	2017 Sep 6 08:57	X2.2	391	2017 Sep 6 09:48	...	300
FLSF 2017 Sep 6b	13.33 ± 0.32	Delayed	2017 Sep 6 11:53	X9.3 ^c	1571	2017 Sep 6 12:24	100	>300
FLSF 2017 Sep 10	13.9 ± 1.2	Prompt Delayed ^a	2017 Sep 10 15:35	X8.2	3163	2017 Sep 10 16:00	605	3000

Note. Entries with an * indicate that the duration is in seconds and not in hours because these are LLE-only flare detections, ^a indicates that there is also an LLE detection of the flare but the total duration refers to the standard analysis, ^b indicates cases with two CMEs and the CME width is marked H for halo CMEs, which corresponds to a width of 360°, ^c indicates cases where multiple GOES flares were present, and ^d indicates that an increase in the SEP energy channel was present.

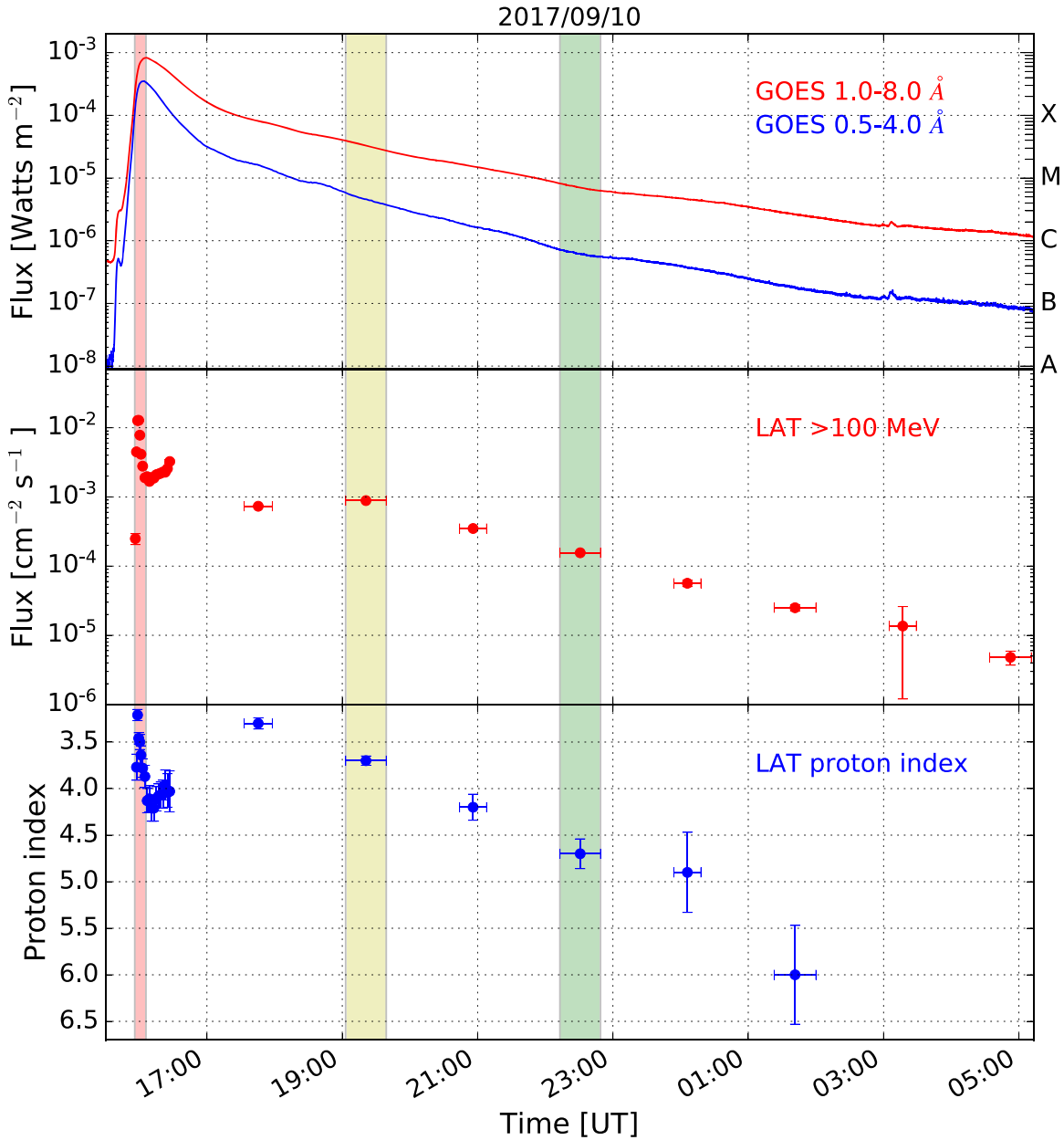


Figure 16. Composite lightcurve for the FLSF 2017 September 10 with data from GOES X-rays, Fermi-LAT >100 MeV flux, and the best proton index inferred from the LAT γ -ray data. The figure is taken from Omodei et al. (2018). The evolution of the proton index shows three distinct phases, a softening during the prompt-impulsive phase, a plateau, and another softening during the decay phase. The three color bands represent the time windows over which we performed the localization of the emission.

delayed flares. The two brightest flares in Figure 14 were coincident with very strong SEP events; Ground Level Enhancement (GLE)#72 in the case of the FLSF 2017 September 10 and a sub-GLE event in the case of the FLSF 2012 March 7.⁶⁹ Coincidentally, the γ -ray fluxes for these two flares are more than an order of magnitude higher than the other events. In Table 4, we list some multiwavelength associations with the FLSFs presented in this work. In particular, we include GOES X-ray flares, CMEs, SEPs, and HXR counterparts to the gamma-ray flares.

⁶⁹ GLEs are sudden increases in the cosmic-ray intensity recorded by ground-based detectors. The number following the GLE indicates the number of GLEs that have been observed since 1956; see the GLE database <http://gle.oulu.fi> for more details.

For the FLSFs with more than four SunMonitor detection windows, it is possible to study the variation of the proton index with time. In Figure 15, we show the accelerated proton spectral index as a function of time since the start of the GOES X-ray flare (assuming that the γ -ray emission is due to pion decay). The statistical uncertainties limit the amount of information available from the time variation of the proton indices. However, the data suggest that the proton spectra tend to gradually steepen (get softer), following a trend similar to the γ -ray fluxes for these delayed flares.

For the extremely bright FLSF 2017 September 10, both the prompt and delayed phases were well observed by the LAT, and we are not limited by statistics. The data from this flare show three phases in the evolution of the proton index over the almost two hours of γ -ray emission (see Figure 16). This flare

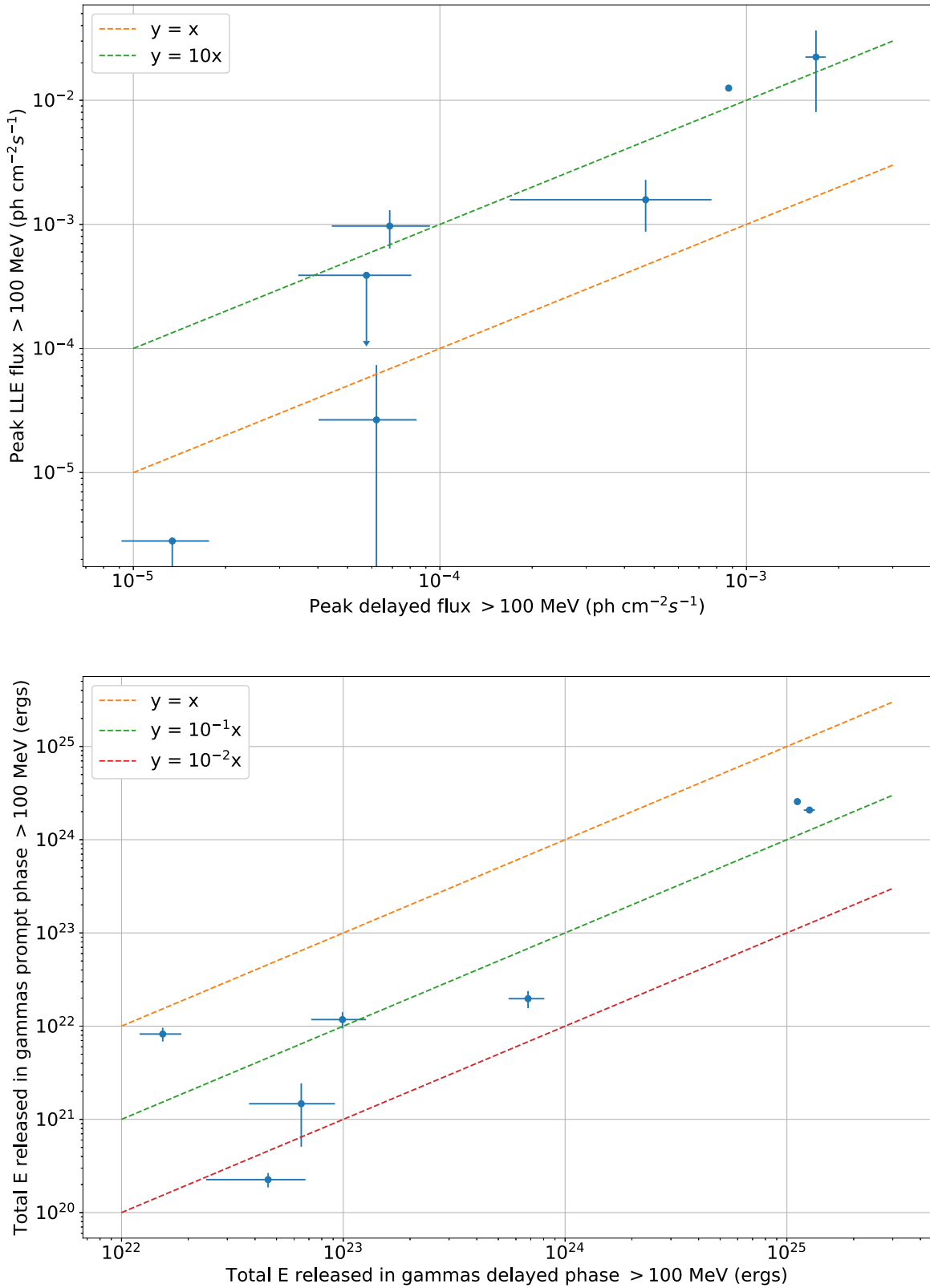


Figure 17. Scatter plot of the peak flux during the prompt phase vs. the peak flux during the delayed phase for the seven FLSFs with both the prompt and delayed phases observed fully. The prompt peak fluxes tend to be higher than those during the delayed phase, in some cases up to more than 10 times. Bottom panel: scatter plot of the total energy released in γ -rays above 100 MeV during the prompt and delayed phases. The total energy released during the delayed phase is on average about 10 times larger than the prompt phase.

was also associated with GLE #72, and Kocharov et al. (2020) show that these phases correspond to separate components of the GLE.

Solar cycle 24 has been particularly poor in GLE events. Only two have been firmly identified: GLE #71 and #72, which occurred on 2012 May 17 and 2017 September 10. Both

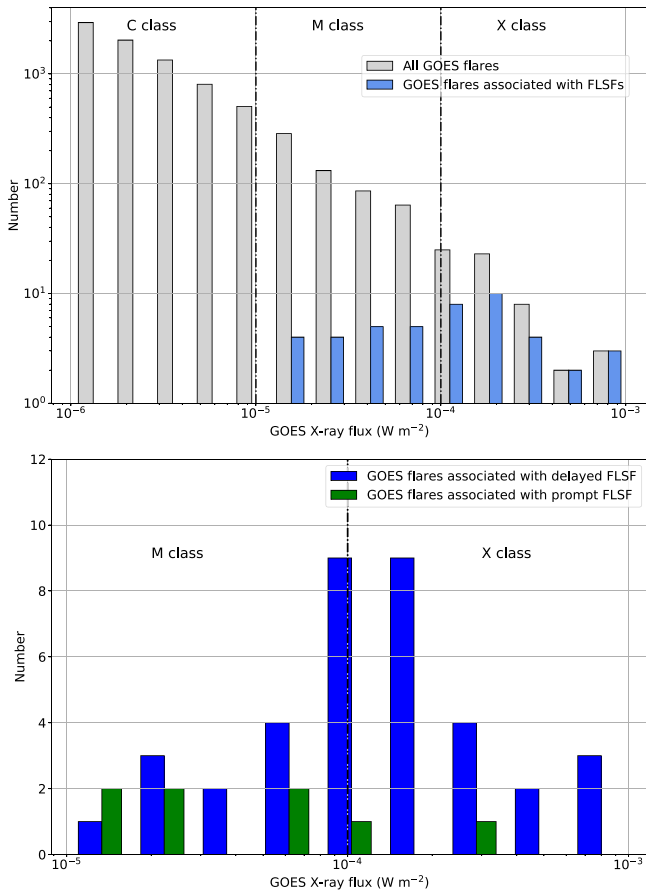


Figure 18. Top panel: distribution of the GOES class for all of the X-ray flares of solar cycle 24 (in gray) and for the FLSFs (light blue). Bottom panel: distribution of the GOES class for the FLSFs separated by type delayed (blue) and prompt flares (green).

events were detected with the Fermi-LAT. In addition to GLEs, five “sub-GLE” events have been identified. Sub-GLE events are those detected only by high-elevation neutron monitors and correspond to less energetic events, extending to a few hundred MeV (Poliunov et al. 2017). They occurred on 2012 January 27, 2012 March 7, 2014 January 06, 2015 June 7, and 2015 October 29 at levels of relative increase in neutron flux of 5%, 5%, 4%, 8%, and 7%, respectively (smaller than the relative increase of 17% for GLE#71). The first three correspond to flares in the FLSF catalog, but no emission was detected for the last two.

Flares with both the LLE-prompt and delayed phases detected by the LAT allow a comparison of the prompt and delayed emission characteristics within the same flare. Seven flares in the catalog (2011 September 6, 2011 September 24, 2012 June 3, 2012 October 23, 2014 February 25, 2014 June 10, and 2017 September 10) satisfy this criterion. For these flares, we found the peak flux value for the prompt phase by fitting the LLE data at the peak of the lightcurve with two models: a simple power law or a power law with an exponential cutoff using the *xspec* analysis package.⁷⁰ The correlation between the peak fluxes of the prompt and delayed phases is shown in the top panel of Figure 17 illustrating that, on average, the prompt peak flux is up to 10 times higher than the peak of the delayed emission. The bottom panel of this figure

⁷⁰ *xspec* model *pegpwlw* and *pegpwlw*highcut*

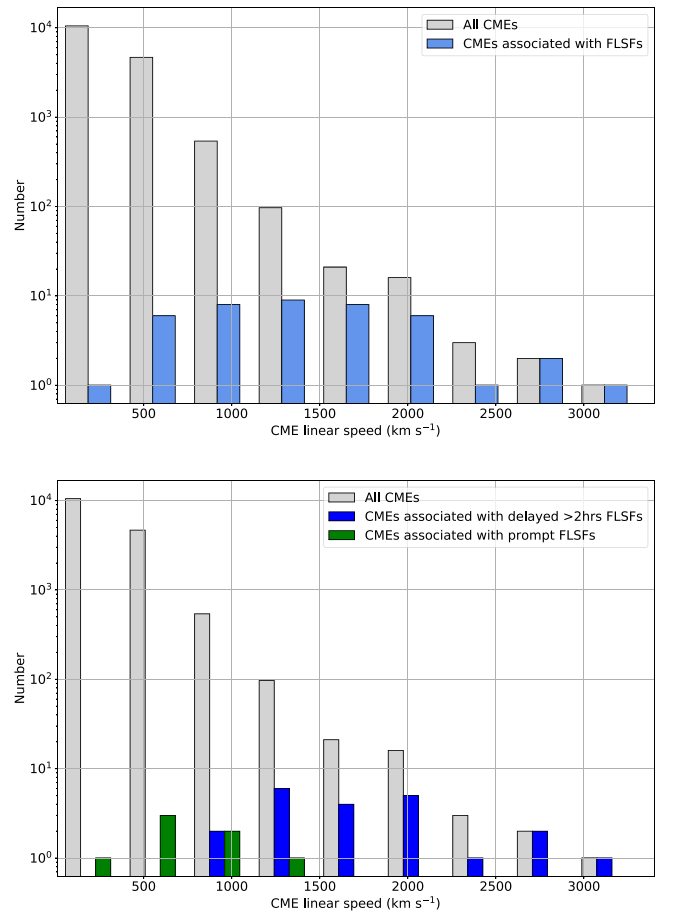


Figure 19. Top panel: distribution of the CME linear speed for all of solar cycle 24 (in gray) and for all the FLSFs in this work (light blue). Bottom panel: distribution of the CME linear speed for FLSFs classified as delayed (blue) and FLSFs classified as prompt (green). The mean speed for the delayed flares is 1535 km s^{-1} and for the prompt flares is 656 km s^{-1} . As in the top panel, the gray histogram represents the CME linear speed for all of the CMEs of solar cycle 24 (whose mean speed is 342 km s^{-1}).

shows the correlation between the total γ -ray energies ($>100 \text{ MeV}$), showing a larger dispersion and a total energy released during the delayed phase that, on average, is about 10 times larger than that in the prompt phase.

The FLSFs in the catalog are almost evenly distributed between GOES M- and X-class flares (in the 0.5–10 keV energy range), with 25 flares associated with the X class and 20 associated with the M class (see top panel of Figure 18, where the gray distribution represents all of the M- and X-class GOES flares that occurred during the time period considered in this paper). As can be seen in the bottom panel of Figure 18, the FLSFs of delayed type are evenly distributed between the M- and X-class flares while the prompt-type flares are mostly associated with M GOES-class flares (75% of the flares are M class). These distributions also illustrate how the increase in sensitivity of the LAT with respect to the previous γ -ray detectors has allowed $>100 \text{ MeV}$ emission to be detected over a wider range of GOES X-ray flares. Furthermore, when combining the information from Figures 18 and 19, it appears that the presence of a fast CME is more relevant for the delayed-type flares than the brightness of the associated X-ray flare.

During Cycle 24, the number of GOES M-class and X-class flares in the period covered by this catalog (2010 January–2018

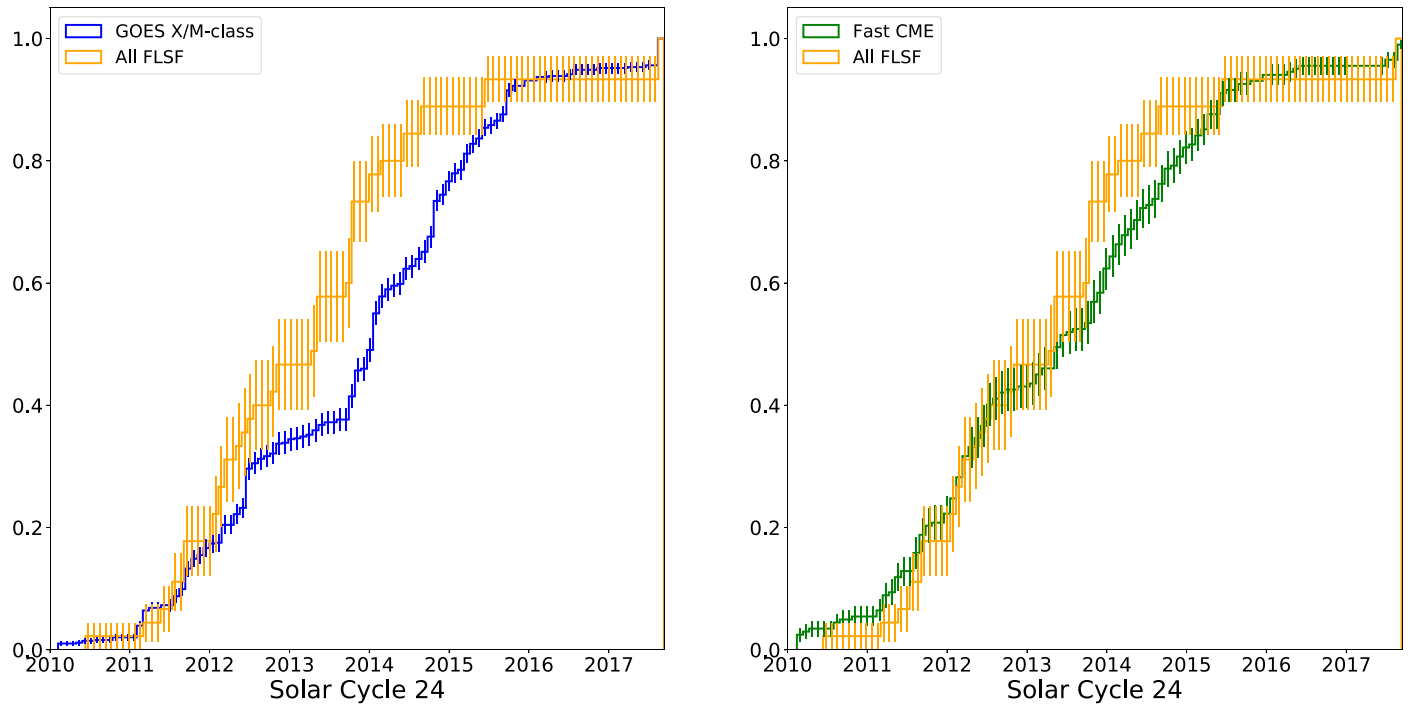


Figure 20. Cumulative number of FLSFs as a function of time compared with the distribution for M-/X-class GOES flares (left) and fast CME (linear speed $>1000 \text{ km s}^{-1}$) events (right).

January) was approximately the same in the first half as in the second (384 and 389, respectively), while the majority of fast CME events (those with speed $>1200 \text{ km s}^{-1}$) happened in the earlier half (2010 January–2014 January, 61 versus 35). A similar behavior was observed for major SEP events (30 in the first half and 12 in the second half of the cycle). Interestingly, the number of FLSFs is also larger in the first half of the cycle, with 33 flares, while only 12 occurred in the second half. To quantify this behavior, we show in Figure 20 the cumulative distributions of XRT flares and fast CME (linear speed $>1000 \text{ km s}^{-1}$) events compared with the distribution of FLSFs. The latter seems to be in much better agreement with the distribution of fast CME events, with a Kolmogorov–Smirnov test p value of 0.15, while the comparison of XRT flares with FLSFs gives a p value of 4.6×10^{-4} . This result is also suggesting that high-energy solar flares have a stronger association with fast CMEs rather than with bright X-ray flares.

4.1. FLSF Active Region Positions

The positions on the solar surface of the ARs associated with the FLSFs are plotted together with the M-/X-class flares detected by Hinodes’s XRT (Sakurai 2008) in Figure 21. Three BTL flares, whose position was inferred from STEREO, appear with longitudes smaller or greater than -90° and $+90^\circ$. The distribution in longitude is rather uniform, with the same number of flares in positive and negative longitudes between -90° and $+90^\circ$. However, there is an asymmetry in the distributions in latitude, with a preponderance of FLSFs ($\sim 65\%$) in the northern hemisphere, while the opposite is true for the XRT flares. This asymmetry is also evident in Figure 22, where we plot the positions of FLSF ARs as a function of time, illustrating the so-called butterfly pattern, with ARs migrating toward the equator as the solar cycle evolves.

4.2. Flare Series

A notable feature of the FLSF population is that more than half (25 out of 45) are part of a cluster of flares originating from the same AR (see Table 5). It is common for an AR to be the source of several flares, but the high fraction of such clusters in the FLSF catalog might indicate that some ARs have the right conditions to be associated with the production of γ -rays. The most notable series happened from 2012 March 5 to 2012 March 10 and 2013 March 13 to 2013 March 15, each with four FLSFs. All of these flares were associated with fast CMEs, and both series produced strong and long-lasting SEP events. They all yielded delayed FLSF γ -ray emission lasting more than three hours. In addition, three of the eight flares were identified as having no $>100 \text{ MeV}$ γ -rays detected during the prompt phase; only delayed emission was detected. Only one additional flare behaved this way, FLSF 2013 April 11, which was found to have a short delayed emission and no prompt emission. This could indicate that the presence of previous SEP events and multiple fast CMEs is more important for the production of long-lasting γ -ray emission than the presence of impulsive HXRs produced by high-energy electrons.

4.3. Gamma-Ray Localization

The Fermi-LAT is the first telescope capable of determining the centroid of $>100 \text{ MeV}$ emission from solar flares. The position of the emission centroid on the solar disk can yield valuable information on where on the photosphere the precipitating ions produce the high-energy γ -rays.

For the majority of the FLSFs in the catalog, the 68% error on the emission centroid is larger than $500''$, and therefore, it becomes difficult to distinguish a specific region on the solar disk from which the emission is originating. For eight of the FLSFs, the 68% error radius is $\leq 365''$ (roughly a third of the solar disk), providing meaningful constraints on the location of

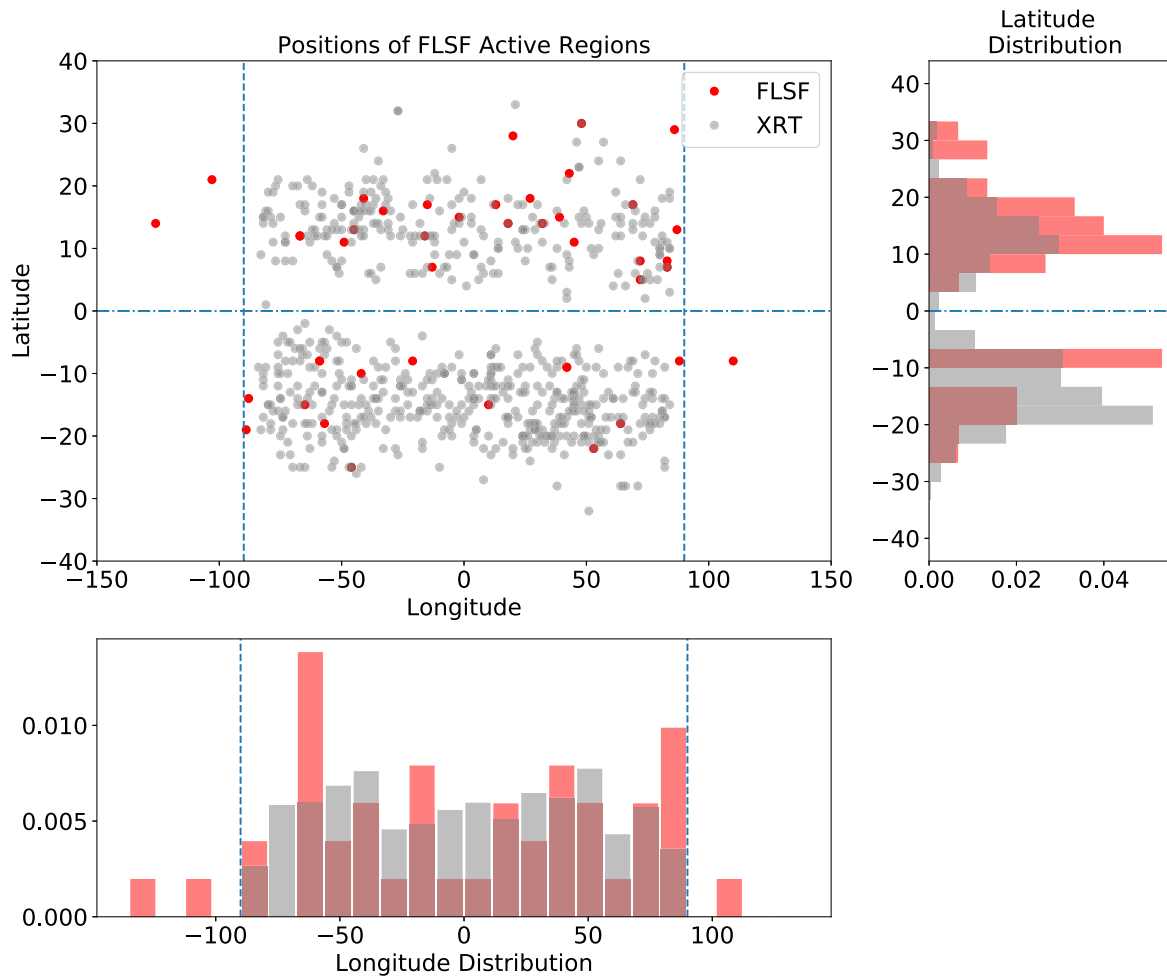


Figure 21. Positions of active regions associated with FLSFs (red) and M-/X-class XRT flares (gray). Longitudes beyond -90° and $+90^\circ$ correspond to BTL flares. The right-hand panel shows the latitude distribution of the AR positions, illustrating the asymmetry in the population. 64% of the ARs from which the FLSFs originate are located in the northern heliosphere whereas 62% of the ARs from which the XRT flares originate are located in the southern heliosphere.

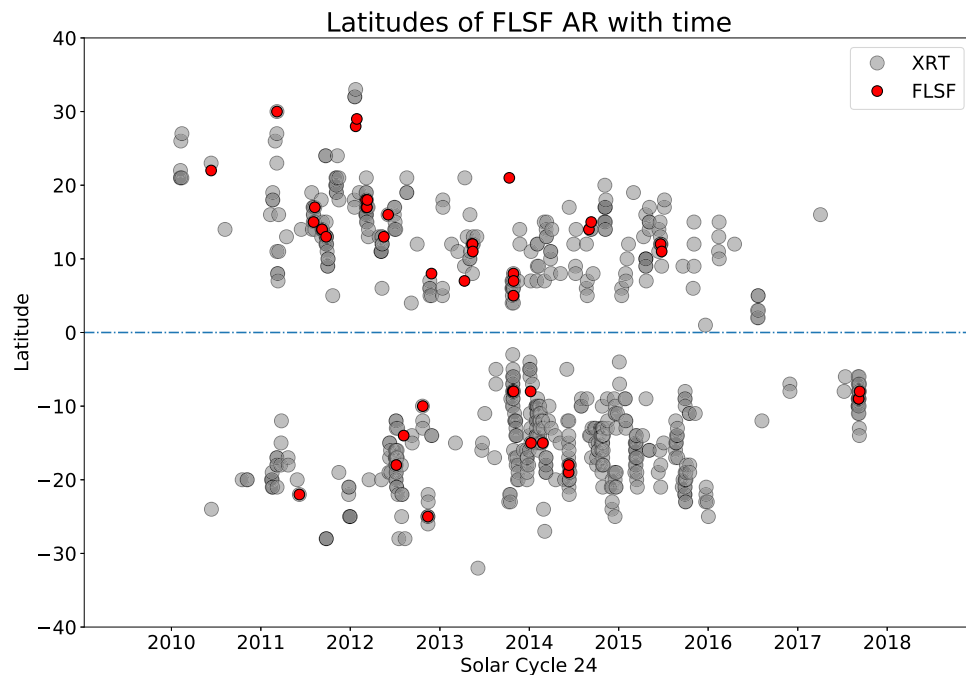


Figure 22. Positions of ARs associated with FLSF (red) and M-/X-class GOES flare (gray) as a function of time. The distribution of positions follows the so-called butterfly pattern, i.e., at the beginning of a new solar cycle, sunspots tend to form at high latitudes, but as the cycle reaches its maximum the sunspots tend to form at lower latitudes.

Table 5
List of FLSFs from Similar Active Regions

Name	Flare Type	Duration (hr)	CME Speed (km s ⁻¹)	Width	GOES Class	SEP Emax (MeV)	HXR Emax (keV)	AR	AR pos
FLSF 2011 Sep 6	Prompt Delayed	0.6	575	H	X2.1	100	1000	11283	N14W18
FLSF 2011 Sep 7	Delayed	1.9	792	290	X1.8	50‡	500	11283	N14W32
FLSF 2012 Jan 23	Delayed	5.8	2175	H	M8.7	100	>100	11402	N28W20
FLSF 2012 Jan 27	Delayed	7.3	2508	H	X1.7	605	>100	11402	N29W86
FLSF 2012 Mar 5	Delayed	5.4	1531	H	X1.1	40‡	>100	11429	N18E41
FLSF 2012 Mar 7	Delayed	20.2	2684*	H	X5.4*	605	1000	11429	N17E15
FLSF 2012 Mar 9	Delayed only	7.3	950	H	M6.3	100‡	>100	11429	N17W13
FLSF 2012 Mar 10	Delayed	6.0	1296	H	M8.4	100‡	>50	11429	N18W27
FLSF 2013 May 13	Delayed	3.4	1270	H	X1.7	60	>300	11748	N12E67
FLSF 2013 May 13	Delayed	5.4	1850	H	X2.8	60	800	11748	N12E67
FLSF 2013 May 14	Delayed only	6.7	2625	H	X3.2	60	500	11748	N12E67
FLSF 2013 May 15	Delayed only	3.6	1366	H	X1.2	50	100	11748	N11E49
FLSF 2013 Oct 25	Delayed	1.1	587	H	X1.7	60	300	11882	S08E59
FLSF 2013 Oct 25	Prompt	0.1	...		M1.9	60‡	100	11882	S08E59
FLSF 2013 Oct 28	Delayed	1.3	812	H	M2.7*	60	50	11882	S08E21
FLSF 2013 Oct 28	Prompt	0.3	695	H	X1.0	0	1000	11875	N05W72
FLSF 2013 Oct 28	Prompt	0.1	1201	315	M5.1	0	1000	11875	N08W72
FLSF 2013 Oct 28	Prompt	0.1	771	284	M1.5	100‡	100	11875	N07W83
FLSF 2014 Jun 10	Prompt Delayed	1.8	1469	H	X1.5	60	1000	12087	S19E89
FLSF 2014 Jun 11	Delayed	0.5	829	130	X1.0	0	1000	12087	S18E57
FLSF 2015 Jun 21	Prompt Delayed	10.2	1366	H	M2.7*	10	>50	12371	N12E16
FLSF 2015 Jun 25	Delayed	2.1	1627	H	M7.9	10	1000	12371	N11W45
FLSF 2017 Sep 6	Prompt	0.3	391	245	X2.2	0	300	12673	S09W42
FLSF 2017 Sep 6	Delayed	13.3	1571	H	X9.3*	100	>300	12673	S09W42
FLSF 2017 Sep 10	Prompt Delayed	13.6	3163	H	X8.2	605	3000	12673	S08W88

Note. * indicates several X-ray classes or CMEs during the duration of the γ -ray emission. ‡ indicates the previous presence of SEPs, without this event being an SEP event.

the emission centroid that can then be compared with the lower-energy flare emission sites. The localization results for these eight flares are given in Table 6. The first eight columns of Table 6 report the date and time window of the detection, position of the centroid of the >100 MeV emission in helioprojective coordinates (X , Y), the 68% and 95% uncertainty on the emission centroid, the AR number and position, and the angular distance and relative distance of the emission centroid from the AR.⁷¹ The last column shows the ratio of this distance to the 95% error radius. We emphasize that the position and the confidence intervals in the table are derived by modeling the high-energy emission as a point source, i.e., with no geometric extent on the solar surface.

Three of the eight flares (FLSF 2012 March 7, FLSF 2014 February 25, and FLSF 2017 September 10) were sufficiently bright and long lasting to be localized in multiple SunMonitor time windows. The FLSF 2012 March 7 was an exceptional γ -ray flare in terms of both duration and brightness. The error radius was smaller than $300''$ in four detection windows, and the emission centroid moved progressively across the solar disk over the ~ 10 hr of γ -ray emission, as shown in Figure 23. This flare was the first for which this behavior in >100 MeV γ rays could be observed, and it was interpreted as supporting evidence for the CME-driven shock scenario as the particle accelerator

(Ajello et al. 2014). For FLSF 2014 February 25, the statistics were sufficient to provide meaningful localization in only two time intervals, and the emission centroid remained consistent with the AR position over three hours, as shown in Figure 24. Finally, FLSF 2017 September 10 was also an exceptionally bright flare, but, because the AR was located at the very edge of the western limb, it was impossible to observe any progressive motion of the γ -ray source. Throughout the 7 hr detection, the source centroid remained consistent with the AR position, as shown in Figure 25.

Two out of these eight flares originated from ARs whose position was located behind the visible solar disk, highlighting how bright these flares were regardless of the position of the AR. All eight FLSFs were classified as GOES X-class flares, with the exception of the BTL FLSF 2013 October 11 whose GOES classification of M4.9 is most likely an underestimation (Nitta et al. 2013; Pesce-Rollins et al. 2015). The peak γ -ray fluxes were all greater than 3×10^{-5} ph cm⁻² s⁻¹ and exposure times were all greater than 20 minutes, indicating that they are not impulsive flares. Five of the FLSFs originated from ARs from the eastern quadrant and three from the western quadrant of the solar disk.

4.4. GOES X-class Flares Not Detected by the LAT

In an attempt to characterize the solar flares associated with γ -ray detections, we can also examine the population of solar flares not detected by the Fermi-LAT above 30 MeV. During

⁷¹ The position of the AR at the time of the GOES X-ray flare.

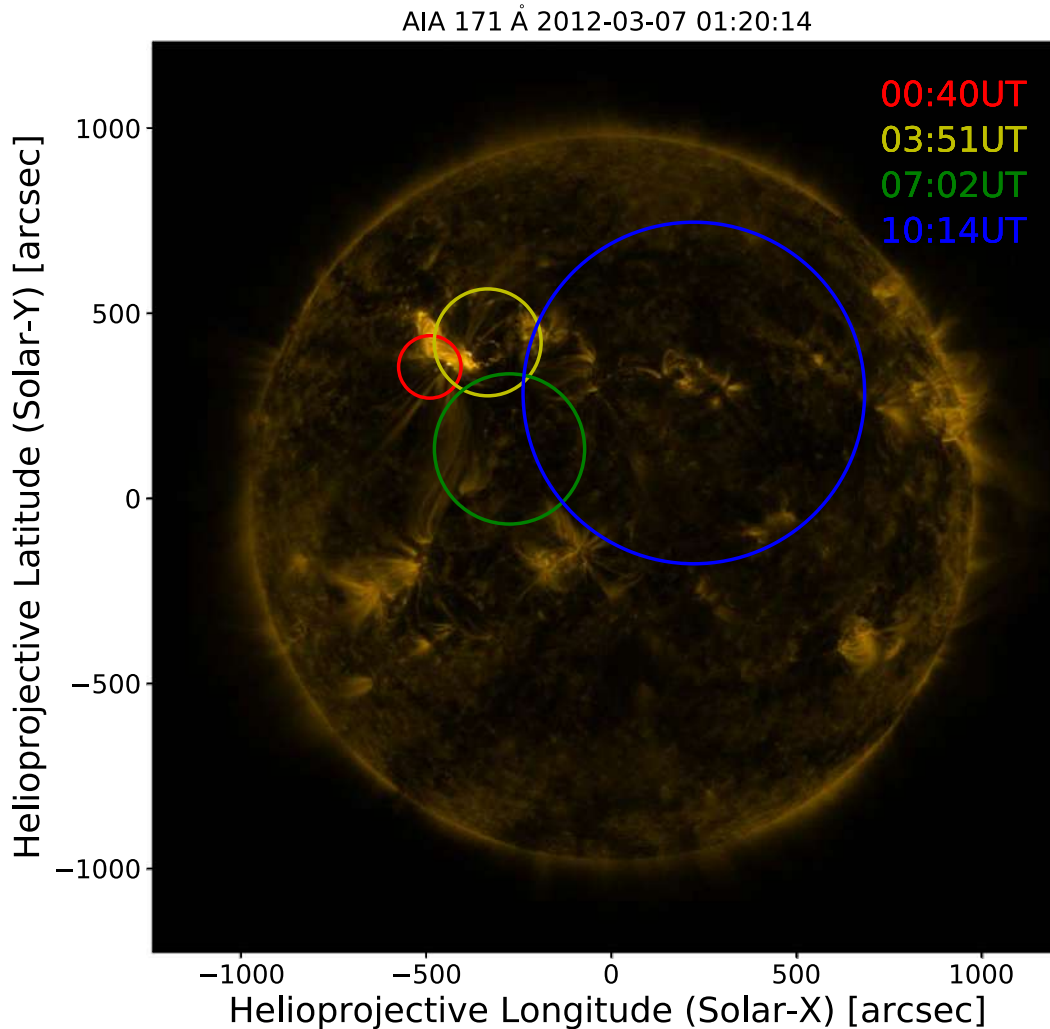


Figure 23. Fermi-LAT localization of the >100 MeV data in multiple time windows from the FLSF 2012 March 7. The error radii correspond to the 95% confidence region. The start of the time windows is annotated in the upper-right corner of the figure. The localization centroid is overplotted on the AIA 171 Å image of the Sun at the time of the flare.

the time period considered in this paper, there were a total of 772 M- and X-class flares (49 were X-class flares and 24 of these were associated with FLSFs).⁷² In Table 7, we list only the 25 X-class flares not associated with a γ -ray detection and their possible associations with CMEs and SEP events. Figure 26 shows a scatter plot of CME speed versus GOES flux for all FLSFs and all the M-/X-class flares not detected by the LAT. We have labeled the four quadrants (I–IV) that indicate the population of flares classified as M/X class and whether they were associated with a CME with linear speed $>/<1000 \text{ km s}^{-1}$. We report the fraction of LAT-detected flares over the total number of flares that fall within the quadrant. From this figure, it is possible to see that the most favorable condition for the LAT to detect γ -ray emission is for the flare to be of X class and be associated with a CME with linear speed greater than 1000 km s^{-1} (86% of the flares detected by the LAT) and that the least favorable condition (1% of the flares detected by the LAT) is diagonally opposite (i.e.,

M class and slow CME speed). The conditions in the off-diagonal quadrants appear to be equally favorable. Out of the three flares not detected by the LAT and in quadrant IV, the SunMonitor picked up a marginal detection in the three following observing windows (with a $\sigma = 4.5, 4.0, 4.0$) for the flare of 2011 September 22 that was associated with a halo CME with a linear speed of 1905 km s^{-1} .

5. Summary and Discussion

Continuous monitoring of the Sun by Fermi-LAT has led to high-confidence detection of 45 solar flares with γ -ray emission above 60 MeV. With such a relatively sizable sample of flares, it is now possible to perform population studies of γ -ray solar flares. Based on the temporal characteristics and associations with multiwavelength flaring activity, we have found that there are at least two distinct types of γ -ray emission in solar flares: prompt-impulsive and delayed-gradual. Within these two broad classes, we find a rich and diverse sample of events with a wide variety of characteristics. Of the 45 FLSFs discussed in this work, six have been detected only with a prompt-impulsive emission correlated with HXR emission (classified as prompt only), four have no γ -ray emission detected during the

⁷² Here we include FLSF 2012 March 7; we associate the γ -ray emission with the X5.4 X-ray flare and with the CME with a linear speed of 2684 km s^{-1} . Two of the three BTL flares have an estimated GOES class of X3.5 and X2.4, but are not considered in this comparison because we do not have a catalog of X-class flares occurring BTL.

Table 6
Localization Results for the FLSFs with 68% Error Radius < 0.1

Date and Time	Helio X ($''$)	Helio Y ($''$)	ERR 68 ($''$)	ERR 95 ($''$)	AR Number	AR Position	Angular Dist. ($''$)	Relative Dist. (95)
2011 Sep 6 22:11–22:47	219	533	139	220	11283	N14W18	382	1.7
2012 Mar 7 00:40–01:20	−562	231	56	84	11429	N17E15	45	0.5
2012 Mar 7 03:51–04:31	−300	342	84	144	11429	N17E15	143	1.0
2012 Mar 7 07:02–07:42	−320	20	126	203	11429	N17E15	331	1.6
2012 Mar 7 10:14–10:54	207	245	291	462	11429	N17E15	707	1.5
2012 Jul 6 23:20–00:08	530	−432	362	586	11515	S18W64	122	0.2
2013 May 14 02:43–03:31	−1137	333	314	504	11748	N12E67	279	0.6
2013 Oct 11 06:56–07:39	−930	311	151	263	BTL	N21E103
2014 Feb 25 01:09–01:29	−933	−347	92	147	11990	S15E65	63	0.4
2014 Feb 25 04:20–04:40	−982	−213	358	574	11990	S15E65	109	0.2
2014 Sep 1 11:02–11:18	−1126	−182	202	322	BTL	N14E126
2017 Sep 10 15:52–16:28	847	−207	59	95	12673	S08W88	72	0.8
2017 Sep 10 19:03–19:39	1034	−131	104	166	12673	S08W88	168	1.0
2017 Sep 10 22:13–22:49	1139	137	271	443	12673	S08W88	336	0.8

Note. We report the date and detection time window start and stop, LAT > 100 MeV emission centroid position in Helio X and Y coordinates, the 68% and 95% error radius (in arcseconds), the AR number and position, the distance of the centroid from the active region, and the ratio of this distance to the 95% error radius.

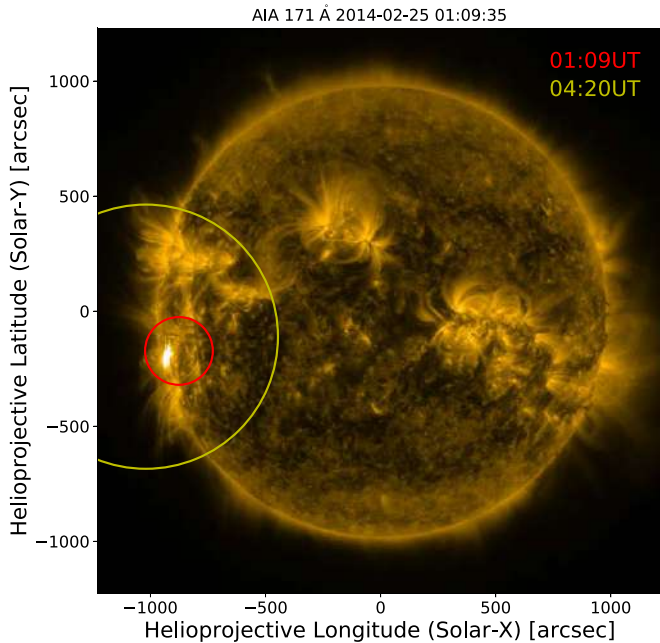


Figure 24. Fermi-LAT localization of the > 100 MeV data in multiple time windows from the FLSF 2014 February 25. The error radii correspond to the 95% confidence region. The start of the time windows is annotated in the upper-right corner of the figure. The localization centroid is overplotted on the AIA 171 Å image of the Sun at the time of the flare.

impulsive HXR emission but were significantly bright after all other flare emission activities had ceased (classified as delayed only), and 10 have both prompt and delayed emission. For the remaining 25 flares with delayed emission, we cannot exclude the presence of *prompt* emission because the Sun was not in the FoV of the LAT during the impulsive HXR activity phase.

The most significant results presented in this work can be summarized as follows:

1. Emission above 60 MeV could be due to bremsstrahlung radiation produced by electrons of Lorentz factor $\gamma_e > 100$ with a relatively hard spectrum is most probably an unlikely scenario. This is because the acceleration of electrons to such energies is difficult due to high synchrotron losses. We find that emission due to the decay of pions (π^0 , π^\pm) produced by > 300 MeV protons and ions, with a power-law spectrum of index ~ 4 – 5 , extending up to 10s of GeV, produces a very good fit to all observed γ rays.
2. All of the FLSFs with LLE prompt emission (produced by > 300 MeV ions) reach their peak within seconds of the 100–300 keV emission peak (produced by > 100 keV electrons) observed with Fermi-GBM, implying that these ions and electrons are accelerated, transported, and interact with the ambient medium at the same time. Similar conclusions for the acceleration of lower-energy (1–30 MeV) ions were reached by Chupp (1987) and Hurford et al. (2006) based on the RHESSI imaging of the 2.223 MeV neutron-capture γ -ray line, and by Shih et al. (2009) who reported a tight correlation between the 2.223 MeV line fluence and the > 300 keV electron bremsstrahlung fluence.
3. All but three of the flares in the FLSF catalog are associated with CMEs. The delayed-type flares are associated with faster CMEs (mean speed of 1535 km s^{-1}), whereas the prompt-type FLSFs are associated with slower CMEs (mean speed of 656 km s^{-1}).
4. One of the most important contributions of Fermi-LAT has been its ability to localize the centroids of high-energy γ -ray emission on the Sun. In most such cases, the initial centroid position is at or near the AR where the flare originated. In several long-lasting strong flares, there are clear indications of change of the centroid position with time, often away from the AR. This change is best observed in the strong, long-lasting FLSF 2012 March 7, where the centroid of > 100 MeV emission gradually

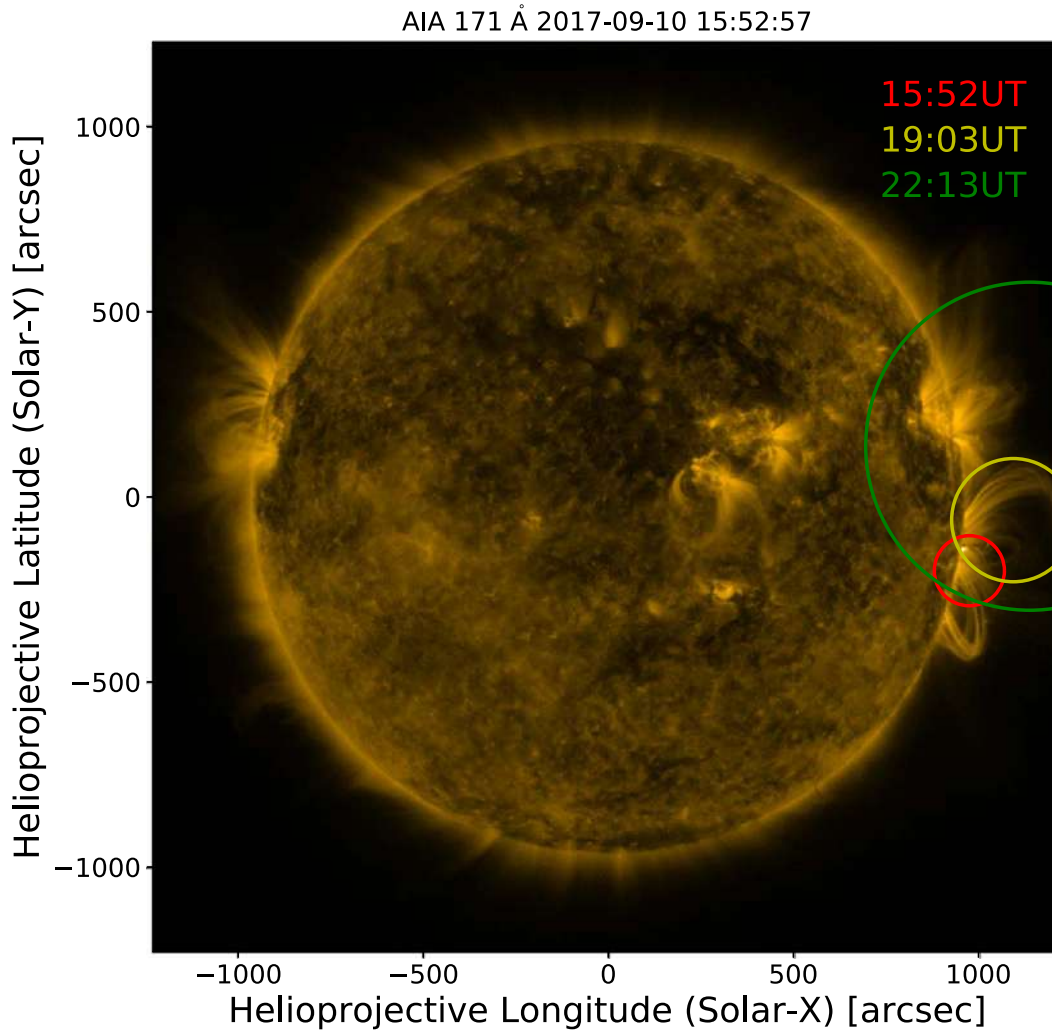


Figure 25. Fermi-LAT localization of the 100 MeV data in multiple time windows from the FLSF 2017 September 10. The error radii correspond to the 95% containment, the start of the time windows is annotated in the upper left-hand corner of the figure. The localization centroid is overplotted on the AIA 171 Å image of the Sun at the time of the flare.

migrates away from the AR up to tens of degrees. This indicates that the acceleration site of the γ -ray-producing high-energy ions is magnetically connected to regions on the photosphere far away from the initial AR.

5. Further evidence for this scenario comes from, for the first time, Fermi observation of GeV emission from three BTL flares including two-hour emission from FLSF 2014 September 1 originating 40° BTL. Localization of the γ -ray emission from two of these flares indicates that the emission occurred on the visible disk, again necessitating a way for the ions from the acceleration site to access regions on the visible disk (more than 40° away from the AR) to interact and to produce the observed γ -rays. Similar conclusions were also reached by Cliver et al. (1993) and Vestrland & Forrest (1993) for the observations with CGRO-EGRET of BTL flares with emission up to 100 MeV.
6. There is an asymmetry in the latitude distribution of the ARs from which the FLSFs originate, with 65% of the flares coming from the northern heliosphere. The opposite is true for the M-/X-class XRT flares detected during the same time interval. Shrivastava & Singh (2005) found that

CMEs associated with Forbush decreases also come predominately from the northern heliosphere.

7. More than half of the FLSFs in this catalog are part of a series of flare clusters. The most notable clusters happened from 2012 March 5 to 2012 March 10 and from 2013 May 13 to 2013 May 15, with each consisting of four FLSFs. All of these flares were associated with fast CMEs, and both series produced strong and long-lasting SEP events. They all yielded delayed FLSF γ -ray emission lasting more than three hours. In addition, three of these eight flares showed no impulsive-phase γ -ray emission (only one other nonseries FLSF was found with similar properties). This could suggest that the presence of previous SEP events and multiple fast CMEs is more important for the production of long-lasting γ -ray emission than the presence of impulsive HXRs produced by high-energy electrons.
8. Seven FLSFs in the catalog are detected with both LLE-prompt and delayed phases, with the average peak flux of the prompt phase 10 times higher than that of the delayed phase. However, the total energy released during the delayed phase is 10–100 times larger than that during the prompt phase.

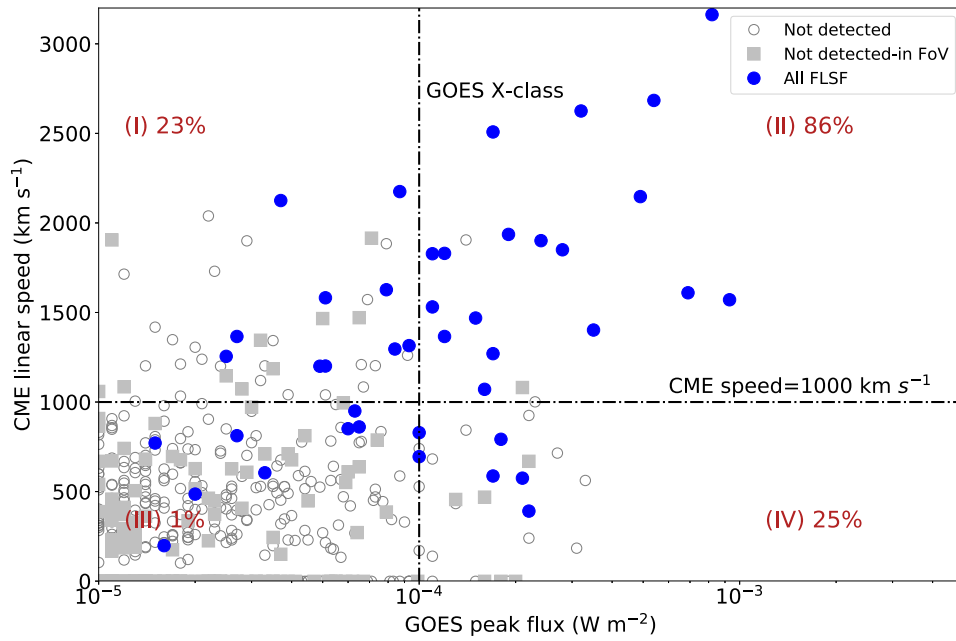


Figure 26. CME linear speed vs. GOES peak flux for all the FLSFs (blue points), M-/X-class flares not detected by the Fermi-LAT outside the LAT FoV (gray empty circles) and in the FoV (gray filled square) at the time of the GOES X-ray flare. The vertical dashed line indicates the border between M- and X-class GOES flares. The horizontal dashed line indicates a 1000 km s^{-1} CME speed. In each of the four quadrants (labeled I–IV), we indicate the fraction of flares detected by the LAT in that quadrant.

Table 7
X-class GOES Flares Not Associated with Any γ -Ray Emission above 30 MeV

GOES Start–Stop	GOES Class	CME First Appear. (UT)	CME Speed (km s^{-1})	CME Width (deg)	LAT Observable	SEP Event
2011 Feb 15 01:44–02:06	X2.2	2011 Feb 15 02:24	669	Halo	X	...
2011 Mar 9 23:13–23:29	X1.5	X	...
2011 Sep 22 10:29–11:44	X1.4	2011 Sep 22 10:48	1905	Halo	...	SEP
2011 Nov 3 20:16–20:32	X1.9	—
2012 Jul 12 15:37–17:30	X1.4	2012 Jul 12 16:24	843	76	X	SEP
2013 Oct 25 14:51–15:12	X2.1	2013 Oct 25 15:12	1081	Halo
2013 Oct 29 21:42–22:01	X2.3	2013 Oct 29 22:00	1001	Halo
2013 Nov 5 22:07–22:15	X3.3	2013 Nov 5 22:36	562	195
2013 Nov 8 04:20–04:29	X1.1
2013 Nov 10 05:08–05:18	X1.1	2013 Nov 10 05:36	682	262
2013 Nov 19 10:14–10:34	X1.0	2013 Nov 19 10:36	740	Halo
2014 Mar 29 17:35–17:54	X1.0	2014 Mar 29 18:12	528	Halo
2014 Apr 25 00:17–00:38	X1.3	2014 Apr 25 00:48	456	296	X	...
2014 Jun 10 11:36–11:44	X2.2	2014 Jun 10 11:48	925	111
2014 Oct 19 04:17–05:48	X1.1	2014 Oct 19 06:12	170	43
2014 Oct 22 14:02–14:50	X1.6	X	...
2014 Oct 24 21:07–22:13	X3.1	2014 Oct 24 21:48	184	35
2014 Oct 25 16:55–18:11	X1.0	2014 Oct 25 17:36	171	49
2014 Oct 26 10:04–11:18	X2.0	X	...
2014 Oct 27 14:12–15:09	X2.0	2014 Oct 27 15:12	170	55
2014 Nov 7 16:53–17:34	X1.6	2014 Nov 7 17:12	469	87
2014 Dec 20 00:11–00:55	X1.8	X	...
2015 Mar 11 16:11–16:29	X2.2	2015 Mar 11 17:00	240	74
2015 May 5 22:05–22:15	X2.7	2015 May 5 22:24	715	Halo
2017 Sep 7 14:20–14:55	X1.3	2017 Mar 9 12:36	223	7

Note. The Fermi-LAT observable column indicates whether the prompt phase of the X-ray flare occurred within a SunMonitor time window. The SEP event column indicates the presence of this flare in the Major SEP Event list.

Solar eruptive events involve two distinct but related phenomena: (1) acceleration of electrons and ions at the reconnection regions in coronal loops that produce the impulsive nonthermal radiation observed from microwaves to

γ rays, lasting several minutes, and are observed as impulsive-prompt SEPs, often with substantial enhanced abundances of ^3He and heavier ions. (2) Production of a supersonic CME which drives a shock, where particles are accelerated, resulting

in long-duration SEPs with normal ionic abundances, with only one radiative signature of type II radio emission produced by less numerous SEP electrons. As summarized above, the Fermi-LAT observations show both prompt-impulsive γ -ray emission having lightcurves similar to those of the HXRs, and long-duration delayed emission with temporal behavior similar to SEPs, and like gradual SEPs, associated with fast CMEs. These similarities between gradual SEPs and >60 MeV gradual-delayed emission, plus the observed drifting of the centroid of γ -ray emission from the original active region, which is accentuated by the observations of BTL flares, indicate that the site and mechanism of the acceleration of ions responsible for the long-duration γ rays is different from that of particles producing the impulsive nonthermal flare radiation and suggest that long-duration γ rays are another radiative signature of acceleration in CME shocks. However, unlike the type II radiation, they are produced by ions (accelerated in the CME-driven shock) and not in the low-density environment of the CME. While SEPs are particles escaping the upstream of the shock, the γ rays must be produced by ions escaping from the downstream region of the shock back to the high-density photosphere of the Sun, and because of the complex and changing magnetic connection between the CME and the Sun, sometimes to regions far from the AR from which the eruptions originated. The recent reconstruction of these magnetic connections by Jin et al. (2018) provides support for this scenario.

Alternative scenarios for explaining the gradual-delayed emission observed by Fermi have been put forth by authors such as De Nolfo et al. (2019) in their comparison between the characteristics of high-energy SEPs observed by PAMELA and those of the delayed-type emission γ -ray flares. One such scenario is that particles are accelerated via the second-order Fermi mechanism and trapped locally within extended coronal loops. These accelerated particles would then diffuse to the denser photosphere to radiate (Ryan & Lee 1991). With this approach, it is possible to decouple the acceleration of the particles producing γ rays from the acceleration and transport of the SEPs, allowing for different energetic particle productivities.

Thanks to the increase in sensitivity of the Fermi-LAT the sample of >100 MeV γ -ray flares has increased by almost a factor of 10 thus allowing us to perform population studies on these events for the first time. The observations presented in this work suggest that the particles producing the prompt-type emission and those producing the delayed-type emission are accelerated via different mechanisms. However, further multi-wavelength observations and in-depth simulations are needed in order to come to a definitive answer to which acceleration mechanism is driving the delayed-type γ -ray emission of solar flares.


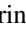



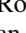
The Fermi-LAT Collaboration acknowledges generous ongoing support from a number of agencies and institutes that have supported both the development and the operation of the LAT as well as scientific data analysis. These include the National Aeronautics and Space Administration and the Department of Energy in the United States, the Commissariat à l’Energie Atomique and the Centre National de la Recherche Scientifique/Institut National de Physique Nucléaire et de Physique des Particules in France, the Agenzia Spaziale Italiana and the Istituto Nazionale di Fisica Nucleare in Italy,

the Ministry of Education, Culture, Sports, Science and Technology (MEXT), High Energy Accelerator Research Organization (KEK) and Japan Aerospace Exploration Agency (JAXA) in Japan, and the K. A. Wallenberg Foundation, the Swedish Research Council, and the Swedish National Space Board in Sweden.

Additional support for science analysis during the operations phase is gratefully acknowledged from the Istituto Nazionale di Astrofisica in Italy and the Centre National d’Études Spatiales in France. This work performed in part under DOE contract DE-AC02-76SF00515.

M.P.R. and N.O. acknowledge relevant and helpful discussions with members of the ISSI International Team on Energetic Ions: The Elusive Component of Solar Flares and with participants in the Lorentz Center Workshop on Solar Sources of GeV Gamma-rays, 2018 February 26–March 2.

ORCID iDs

M. Ajello  <https://orcid.org/0000-0002-6584-1703>
 L. Baldini  <https://orcid.org/0000-0002-9785-7726>
 D. Bastieri  <https://orcid.org/0000-0002-6954-8862>
 R. Bellazzini  <https://orcid.org/0000-0002-2469-7063>
 E. Bissaldi  <https://orcid.org/0000-0001-9935-8106>
 R. D. Blandford  <https://orcid.org/0000-0002-1854-5506>
 C. C. Cheung  <https://orcid.org/0000-0002-4377-0174>
 F. D’Ammando  <https://orcid.org/0000-0001-7618-7527>
 Y. Fukazawa  <https://orcid.org/0000-0002-0921-8837>
 S. Funk  <https://orcid.org/0000-0002-2012-0080>
 P. Fusco  <https://orcid.org/0000-0002-9383-2425>
 F. Gargano  <https://orcid.org/0000-0002-5055-6395>
 D. Gasparrini  <https://orcid.org/0000-0002-5064-9495>
 M. Giroletti  <https://orcid.org/0000-0002-8657-8852>
 S. Guiriec  <https://orcid.org/0000-0001-5780-8770>
 E. Hays  <https://orcid.org/0000-0002-8172-593X>
 J. W. Hewitt  <https://orcid.org/0000-0001-5254-2248>
 M. Kuss  <https://orcid.org/0000-0003-1212-9998>
 S. Larsson  <https://orcid.org/0000-0003-0716-107X>
 F. Longo  <https://orcid.org/0000-0003-2501-2270>
 P. Lubrano  <https://orcid.org/0000-0003-0221-4806>
 S. Maldera  <https://orcid.org/0000-0002-0698-4421>
 A. Manfreda  <https://orcid.org/0000-0002-0998-4953>
 M. N. Mazziotta  <https://orcid.org/0000-0001-9325-4672>
 T. Mizuno  <https://orcid.org/0000-0001-7263-0296>
 M. E. Monzani  <https://orcid.org/0000-0002-8254-5308>
 A. Morselli  <https://orcid.org/0000-0002-7704-9553>
 I. V. Moskalenko  <https://orcid.org/0000-0001-6141-458X>
 N. Omodei  <https://orcid.org/0000-0002-5448-7577>
 M. Pesce-Rollins  <https://orcid.org/0000-0003-1790-8018>
 V. Petrosian  <https://orcid.org/0000-0002-2670-8942>
 J. L. Racusin  <https://orcid.org/0000-0002-4744-9898>
 R. Rando  <https://orcid.org/0000-0001-6992-818X>
 B. Rani  <https://orcid.org/0000-0001-5711-084X>
 M. Razzano  <https://orcid.org/0000-0003-4825-1629>
 S. Razzaque  <https://orcid.org/0000-0002-0130-2460>
 A. Reimer  <https://orcid.org/0000-0001-8604-7077>
 O. Reimer  <https://orcid.org/0000-0001-6953-1385>
 E. Troja  <https://orcid.org/0000-0002-1869-7817>

References

- Abdo, A. A., Ackermann, M., Ajello, M., et al. 2011, *ApJ*, 734, 116
 Abeyssekara, A. U., Archer, A., Benbow, W., et al. 2018, *ApJ*, 866, 24
 Ackermann, M., Ajello, M., Albert, A., et al. 2012a, *ApJS*, 203, 4

- Ackermann, M., Ajello, M., Albert, A., et al. 2014, [ApJ](#), **787**, 15
- Ackermann, M., Ajello, M., Allafort, A., et al. 2012b, [ApJ](#), **745**, 144
- Ackermann, M., Ajello, M., Baldini, L., et al. 2018, [ApJS](#), **237**, 32
- Ackermann, M., Allafort, A., Baldini, L., et al. 2017, [ApJ](#), **835**, 219
- Ahnen, M. L., Ansoldi, S., Antonelli, L. A., et al. 2019, [MNRAS](#), **485**, 356
- Ajello, M., Albert, A., Allafort, A., et al. 2014, [ApJ](#), **789**, 20
- Arnaud, K. A. 1996, in ASP Conf. Ser. 101, *Astronomical Data Analysis Software and Systems V*, ed. G. H. Jacoby & J. Barnes (San Francisco, CA: ASP), 17
- Atwood, W., Albert, A., Baldini, L., et al. 2013, arXiv:1303.3514
- Atwood, W. B., Abdo, A. A., Ackermann, M., et al. 2009, [ApJ](#), **697**, 1071
- Barat, C., Trotter, G., Vilmer, N., et al. 1994, [ApJL](#), **425**, L109
- Bruel, P., Burnett, T. H., Digel, S. W., et al. 2018, arXiv:1810.11394
- Chupp, E. L. 1987, [PhST](#), **18**, 5
- Chupp, E. L., Forrest, D. J., Ryan, J. M., et al. 1982, [ApJL](#), **263**, L95
- Chupp, E. L., & Ryan, J. M. 2009, [RAA](#), **9**, 11
- Cliver, E. W., Kahler, S. W., & Vestrand, W. T. 1993, ICRC (Calgary), **23**, 91
- De Nolfo, G., Bruno, A., Ryan, J., et al. 2019, [ApJ](#), **879**, 90
- Dennis, B. R. 1988, [SoPh](#), **118**, 49
- Di Mauro, M., Manconi, S., Zechlin, H. S., et al. 2018, [ApJ](#), **856**, 106
- Dolan, J. F., & Fazio, G. G. 1965, [RvGeo](#), **3**, 319
- Forrest, D. J., Vestrand, W. T., Chupp, E. L., et al. 1985, ICRC (La Jolla), **19**, 146
- Forrest, D. J., Vestrand, W. T., Chupp, E. L., Rieger, E., & Cooper, J. 1986, [AdSpR](#), **6**, 115
- Hurford, G. J., Krucker, S., Lin, R. P., et al. 2006, [ApJL](#), **644**, L93
- Jin, M., Petrosian, V., Liu, W., et al. 2018, [ApJ](#), **867**, 122
- Kanbach, G., Bertsch, D. L., Fichtel, C. E., et al. 1993, *A&AS*, **97**, 349
- Kocharov, L., Pesce-Rollins, M., Laitinen, T., et al. 2020, [ApJ](#), **890**, 13
- Lin, R. P., & Team, Rhessi 2003, [AdSpR](#), **32**, 1001
- Linden, T., Zhou, B., Beacom, J. F., et al. 2018, [PhRvL](#), **121**, 131103
- Mattox, J. R., Bertsch, D. L., Chiang, J., et al. 1996, [ApJ](#), **461**, 396
- Mazziotta, M. N., Luque, P. D. L. T., Di Venere, L., et al. 2020, [PhRvD](#), **101**, 083011
- Meegan, C., Lichti, G., Bhat, P. N., et al. 2009, [ApJ](#), **702**, 791
- Moskalenko, I. V., Porter, T. A., & Digel, S. W. 2006, [ApJL](#), **652**, L65
- Murphy, R. J., Dermer, C. D., & Ramaty, R. 1987, [ApJS](#), **63**, 721
- Nitta, N. V., Aschwanden, M. J., Boerner, P. F., et al. 2013, [SoPh](#), **288**, 241
- Omodei, N., Pesce-Rollins, M., Longo, F., Allafort, A., & Krucker, S. 2018, [ApJL](#), **865**, L7
- Orlando, E., & Strong, A. W. 2007, [Ap&SS](#), **309**, 359
- Orlando, E., & Strong, A. W. 2008, [A&A](#), **480**, 847
- Pesce-Rollins, M., Omodei, N., Petrosian, V., et al. 2015, [ApJL](#), **805**, L15
- Poluianov, S. V., Usoskin, I. G., Mishev, A. L., Shea, M. A., & Smart, D. F. 2017, [SoPh](#), **292**, 176
- Reames, D. V. 1995, [AdSpR](#), **15**, 41
- Ryan, J. M. 2000, [SSRv](#), **93**, 581
- Ryan, J. M., & Lee, M. A. 1991, [ApJ](#), **368**, 316
- Sakurai, T. 2008, *The Hinode Mission* (Berlin: Springer)
- Seckel, D., Stanev, T., & Gaisser, T. K. 1991, [ApJ](#), **382**, 652
- Shih, A. Y., Lin, R. P., & Smith, D. M. 2009, [ApJL](#), **698**, L152
- Shrivastava, P. K., & Singh, N. 2005, [ChJAA](#), **5**, 198
- Thompson, D. J., Bertsch, D. L., Fichtel, C. E., et al. 1993, [ApJS](#), **86**, 629
- Trotter, G., Vilmer, N., Barat, C., et al. 1998, *A&A*, **334**, 1099
- Vestrand, W. T., & Forrest, D. J. 1993, [ApJL](#), **409**, L69
- Vianello, G., Lauer, R. J., Younk, P., et al. 2015, arXiv:1507.08343
- Vilmer, N. 1987, *Hard X-ray Emission Processes in Solar Flares* (Springer Netherlands: Dordrecht), 207
- Vilmer, N., MacKinnon, A. L., & Hurford, G. J. 2011, [SSRv](#), **159**, 167
- Vilmer, N., MacKinnon, A. L., Trotter, G., & Barat, C. 2003, [A&A](#), **412**, 865
- Vilmer, N., Trotter, G., Barat, C., et al. 1999, *A&A*, **342**, 575
- Wood, M., Caputo, R., Charles, E., et al. 2017, ICRC (Busan), **35**, 824



Erratum: First Fermi-LAT Solar Flare Catalog (2021, ApJS, 252, 13)

M. Ajello¹, L. Baldini², D. Bastieri^{3,4}, R. Bellazzini⁵, A. Berretta⁶, E. Bissaldi^{7,8}, R. D. Blandford⁹, R. Bonino^{10,11}, P. Bruel¹², S. Buson¹³, R. A. Cameron⁹, R. Caputo¹⁴, E. Cavazzuti¹⁵, C. C. Cheung¹⁶, G. Chiaro¹⁷, D. Costantin¹⁸, S. Cutini¹⁹, F. D'Ammando²⁰, F. de Palma¹⁰, R. Desiante¹⁰, N. Di Lalla⁹, L. Di Venere^{7,8}, F. Fana Dirisa²¹, S. J. Fegan¹², Y. Fukazawa²², S. Funk²³, P. Fusco^{7,8}, F. Gargano⁸, D. Gasparrini^{24,25}, F. Giordano^{7,8}, M. Giroletti²⁰, D. Green²⁶, S. Guiriec^{14,27}, E. Hays¹⁴, J. W. Hewitt²⁸, D. Horan¹², G. Jóhannesson^{29,30}, M. Kovac'evic¹⁹, M. Kuss⁵, S. Larsson^{31,32,33}, L. Latronico¹⁰, J. Li³⁴, F. Longo^{35,36}, M. N. Lovellette¹⁶, P. Lubrano¹⁹, S. Maldera¹⁰, A. Manfreda², G. Martí-Devesa³⁷, M. N. Mazziotta⁸, I. Mereu^{6,19}, P. F. Michelson⁹, T. Mizuno³⁸, M. E. Monzani⁹, A. Morselli²⁴, I. V. Moskalenko⁹, M. Negro^{39,40}, N. Omodei⁹, M. Orienti²⁰, E. Orlando^{9,41}, D. Paneque²⁶, Z. Pei⁴, M. Persic^{35,42}, M. Pesce-Rollins⁵, V. Petrosian⁹, F. Piron⁴³, T. A. Porter⁹, G. Principe²⁰, J. L. Racusin¹⁴, S. Rainò^{7,8}, R. Rando^{3,44,45}, B. Rani^{14,46}, M. Razzano^{5,52}, S. Razzaque²¹, A. Reimer^{9,37}, O. Reimer³⁷, D. Serini⁷, C. Sgrò⁵, E. J. Siskind⁴⁷, G. Spandre⁵, P. Spinelli^{7,8}, D. Tak^{14,48}, E. Troja^{14,49}, J. Valverde¹², K. Wood^{50,53}, and G. Zaharijas^{41,51}

¹ Department of Physics and Astronomy, Clemson University, Kinard Lab of Physics, Clemson, SC 29634-0978, USA

² Università di Pisa and Istituto Nazionale di Fisica Nucleare, Sezione di Pisa, I-56127 Pisa, Italy

³ Istituto Nazionale di Fisica Nucleare, Sezione di Padova, I-35131 Padova, Italy

⁴ Dipartimento di Fisica e Astronomia "G. Galilei," Università di Padova, I-35131 Padova, Italy

⁵ Istituto Nazionale di Fisica Nucleare, Sezione di Pisa, I-56127 Pisa, Italy; melissa.pesce.rollins@pi.infn.it

⁶ Dipartimento di Fisica, Università degli Studi di Perugia, I-06123 Perugia, Italy

⁷ Dipartimento di Fisica "M. Merlin" dell'Università e del Politecnico di Bari, via Amendola 173, I-70126 Bari, Italy

⁸ Istituto Nazionale di Fisica Nucleare, Sezione di Bari, I-70126 Bari, Italy

⁹ W. W. Hansen Experimental Physics Laboratory, Kavli Institute for Particle Astrophysics and Cosmology, Department of Physics and SLAC National Accelerator Laboratory, Stanford University, Stanford, CA 94305, USA; nicola.omodei@stanford.edu, vahep@stanford.edu

¹⁰ Istituto Nazionale di Fisica Nucleare, Sezione di Torino, I-10125 Torino, Italy

¹¹ Dipartimento di Fisica, Università degli Studi di Torino, I-10125 Torino, Italy

¹² Laboratoire Leprince-Ringuet, École polytechnique, CNRS/IN2P3, F-91128 Palaiseau, France

¹³ Institut für Theoretische Physik und Astrophysik, Universität Würzburg, Campus Hubland Nord, Emil-Fischer-Str. 31, D-97074 Würzburg, Germany

¹⁴ NASA Goddard Space Flight Center, Greenbelt, MD 20771, USA

¹⁵ Italian Space Agency, Via del Politecnico snc, I-00133 Roma, Italy

¹⁶ Space Science Division, Naval Research Laboratory, Washington, DC 20375-5352, USA

¹⁷ INFN-Istituto di Astrofisica Spaziale e Fisica Cosmica Milano, via E. Bassini 15, I-20133 Milano, Italy

¹⁸ University of Padua, Department of Statistical Science, Via 8 Febbraio, 2, 35122 Padova, Italy

¹⁹ Istituto Nazionale di Fisica Nucleare, Sezione di Perugia, I-06123 Perugia, Italy

²⁰ INFN Istituto di Radioastronomia, I-40129 Bologna, Italy

²¹ Department of Physics, University of Johannesburg, P.O. Box 524, Auckland Park 2006, South Africa

²² Department of Physical Sciences, Hiroshima University, Higashi-Hiroshima, Hiroshima 739-8526, Japan

²³ Friedrich-Alexander Universität Erlangen-Nürnberg, Erlangen Centre for Astroparticle Physics, Erwin-Rommel-Str. 1, D-91058 Erlangen, Germany

²⁴ Istituto Nazionale di Fisica Nucleare, Sezione di Roma "Tor Vergata," I-00133 Roma, Italy

²⁵ Space Science Data Center—Agenzia Spaziale Italiana, Via del Politecnico, snc, I-00133, Roma, Italy

²⁶ Max-Planck-Institut für Physik, D-80805 München, Germany

²⁷ The George Washington University, Department of Physics, 725 21st St NW, Washington, DC 20052, USA

²⁸ University of North Florida, Department of Physics, 1 UNF Drive, Jacksonville, FL 32224, USA

²⁹ Science Institute, University of Iceland, IS-107 Reykjavik, Iceland

³⁰ Nordita, Royal Institute of Technology and Stockholm University, Roslagstullsbacken 23, SE-106 91 Stockholm, Sweden

³¹ Department of Physics, KTH Royal Institute of Technology, AlbaNova, SE-106 91 Stockholm, Sweden

³² The Oskar Klein Centre for Cosmoparticle Physics, AlbaNova, SE-106 91 Stockholm, Sweden

³³ School of Education, Health and Social Studies, Natural Science, Dalarna University, SE-791 88 Falun, Sweden

³⁴ Deutsches Elektronen Synchrotron DESY, D-15738 Zeuthen, Germany

³⁵ Istituto Nazionale di Fisica Nucleare, Sezione di Trieste, I-34127 Trieste, Italy; francesco.longo@trieste.infn.it

³⁶ Dipartimento di Fisica, Università di Trieste, I-34127 Trieste, Italy

³⁷ Institut für Astro- und Teilchenphysik, Leopold-Franzens-Universität Innsbruck, A-6020 Innsbruck, Austria

³⁸ Hiroshima Astrophysical Science Center, Hiroshima University, Higashi-Hiroshima, Hiroshima 739-8526, Japan

³⁹ Center for Research and Exploration in Space Science and Technology (CRESST) and NASA Goddard Space Flight Center, Greenbelt, MD 20771, USA

⁴⁰ Department of Physics and Center for Space Sciences and Technology, University of Maryland Baltimore County, Baltimore, MD 21250, USA

⁴¹ Istituto Nazionale di Fisica Nucleare, Sezione di Trieste, and Università di Trieste, I-34127 Trieste, Italy

⁴² Osservatorio Astronomico di Trieste, Istituto Nazionale di Astrofisica, I-34143 Trieste, Italy

⁴³ Laboratoire Univers et Particules de Montpellier, Université Montpellier, CNRS/IN2P3, F-34095 Montpellier, France

⁴⁴ Department of Physics and Astronomy, University of Padova, Vicolo Osservatorio 3, I-35122 Padova, Italy

⁴⁵ Center for Space Studies and Activities "G. Colombo," University of Padova, Via Venezia 15, I-35131 Padova, Italy

⁴⁶ Korea Astronomy and Space Science Institute, 776 Daedeokdae-ro, Yuseong-gu, Daejeon 30455, Republic of Korea

⁴⁷ NYCB Real-Time Computing Inc., Lattingtown, NY 11560-1025, USA

⁴⁸ Department of Physics, University of Maryland, College Park, MD 20742, USA

⁴⁹ Department of Astronomy, University of Maryland, College Park, MD 20742, USA⁵⁰ Praxis Inc., Alexandria, VA 22303, USA⁵¹ Center for Astrophysics and Cosmology, University of Nova Gorica, Nova Gorica, Slovenia






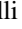
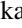





Received 2021 August 23; published 2021 September 17

In the published article, several references were accidentally left out of the text. The papers that we would like to cite are the following:

1. In the *Introduction* section, on page 2 the first sentence of the seventh paragraph should be: In this Fermi-LAT Solar Flare (FLSF) catalog we present the observations of 45 flares with >30 MeV emission in the period 2010–2018 January (covering most of the 24th solar cycle), extending on the work done by Share et al. (2018).
2. In the *Results* section, page 20 at the end of the first paragraph: All CME information was obtained from the CME online catalog of Gopalswamy et al. (2009, 2010).
3. In the *Results* section, page 23 at the end of the first paragraph: Winter et al. (2018) also reported that nearly all fast CMEs are associated with long-duration gamma-ray solar flares.
4. In subsection 4.2, *Flare Series*, on page 23 at the end of the paragraph: Similar results on the connection of long-lasting gamma-ray emission with SEPs were also reported by Gopalswamy et al. (2019).
5. In the *Summary and Discussion* section, end of list item 7: as first suggested by Gopalswamy et al. (2019).
6. In the *Summary and Discussion* section, after the second sentence on page 30: Fermi-LAT gamma-ray duration has been found to be correlated with the type II burst duration indicating the shock origin of the underlying electrons and ions (Gopalswamy et al. 2018).
7. In the *Summary and Discussion* section, at the end of the first paragraph on page 30: Further support for the CME-shock scenario has been reported by Gopalswamy et al. (2018, 2019, 2020, 2021), Kouloumvakos et al. (2020), Plotnikov et al. (2017), and Share et al. (2018).
8. In the *Summary and Discussion* section, at the end of the second sentence of the second paragraph on page 30, Ryan (2000) should be cited.
9. In the *Summary and Discussion* section, at the end of the second paragraph on page 30: Intriguing support for this scenario has been reported by Gary et al. (2018) and Grechnev et al. (2018).

ORCID iDs

M. Ajello  <https://orcid.org/0000-0002-6584-1703>
 L. Baldini  <https://orcid.org/0000-0002-9785-7726>
 D. Bastieri  <https://orcid.org/0000-0002-6954-8862>
 R. Bellazzini  <https://orcid.org/0000-0002-2469-7063>
 E. Bissaldi  <https://orcid.org/0000-0001-9935-8106>
 R. D. Blandford  <https://orcid.org/0000-0002-1854-5506>
 R. Bonino  <https://orcid.org/0000-0002-4264-1215>
 R. A. Cameron  <https://orcid.org/0000-0003-0942-2747>
 R. Caputo  <https://orcid.org/0000-0001-7150-9638>
 E. Cavazzuti  <https://orcid.org/0000-0001-7150-9638>
 C. C. Cheung  <https://orcid.org/0000-0002-4377-0174>
 S. Cutini  <https://orcid.org/0000-0002-1271-2924>
 F. D’Ammando  <https://orcid.org/0000-0001-7618-7527>
 N. Di Lalla  <https://orcid.org/0000-0002-7574-1298>
 L. Di Venere  <https://orcid.org/0000-0003-0703-824X>
 Y. Fukazawa  <https://orcid.org/0000-0002-0921-8837>
 S. Funk  <https://orcid.org/0000-0002-2012-0080>
 P. Fusco  <https://orcid.org/0000-0002-9383-2425>
 F. Gargano  <https://orcid.org/0000-0002-5055-6395>
 D. Gasparri  <https://orcid.org/0000-0002-5064-9495>
 M. Giroletti  <https://orcid.org/0000-0002-8657-8852>
 D. Green  <https://orcid.org/0000-0003-0768-2203>
 S. Guiriec  <https://orcid.org/0000-0001-5780-8770>
 E. Hays  <https://orcid.org/0000-0002-8172-593X>
 J. W. Hewitt  <https://orcid.org/0000-0001-5254-2248>
 G. Jóhannesson  <https://orcid.org/0000-0003-1458-7036>
 M. Kuss  <https://orcid.org/0000-0003-1212-9998>

S. Larsson  <https://orcid.org/0000-0003-0716-107X>
 L. Latronico  <https://orcid.org/0000-0002-0984-1856>
 F. Longo  <https://orcid.org/0000-0003-2501-2270>
 P. Lubrano  <https://orcid.org/0000-0003-0221-4806>
 S. Maldera  <https://orcid.org/0000-0002-0698-4421>
 A. Manfreda  <https://orcid.org/0000-0002-0998-4953>
 M. N. Mazziotta  <https://orcid.org/0000-0001-9325-4672>
 I. Mereu  <https://orcid.org/0000-0003-0219-4534>
 T. Mizuno  <https://orcid.org/0000-0001-7263-0296>
 M. E. Monzani  <https://orcid.org/0000-0002-8254-5308>
 A. Morselli  <https://orcid.org/0000-0002-7704-9553>
 I. V. Moskalenko  <https://orcid.org/0000-0001-6141-458X>
 M. Negro  <https://orcid.org/0000-0002-6548-5622>
 N. Omodei  <https://orcid.org/0000-0002-5448-7577>
 M. Persic  <https://orcid.org/0000-0003-1853-4900>
 M. Pesce-Rollins  <https://orcid.org/0000-0003-1790-8018>
 V. Petrosian  <https://orcid.org/0000-0002-2670-8942>
 F. Piron  <https://orcid.org/0000-0001-6885-7156>
 T. A. Porter  <https://orcid.org/0000-0002-2621-4440>
 J. L. Racusin  <https://orcid.org/0000-0002-4744-9898>
 S. Rainò  <https://orcid.org/0000-0002-9181-0345>
 R. Rando  <https://orcid.org/0000-0001-6992-818X>
 B. Rani  <https://orcid.org/0000-0001-5711-084X>
 M. Razzano  <https://orcid.org/0000-0003-4825-1629>
 S. Razzaque  <https://orcid.org/0000-0002-0130-2460>
 A. Reimer  <https://orcid.org/0000-0001-8604-7077>
 O. Reimer  <https://orcid.org/0000-0001-6953-1385>
 D. Serini  <https://orcid.org/0000-0002-9754-6530>
 C. Sgrò  <https://orcid.org/0000-0001-5676-6214>
 E. Troja  <https://orcid.org/0000-0002-1869-7817>

⁵² Funded by contract FIRB-2012-RBFR12PM1F from the Italian Ministry of Education, University and Research (MIUR), Italy.

⁵³ Resident at Naval Research Laboratory, Washington, DC 20375, USA.

References

- Gary, D. E., Chen, B., Dennis, B. R., et al. 2018, [ApJ](#), **863**, 83
- Gopalswamy, N., Mäkelä, P., Yashiro, S., et al. 2018, [ApJL](#), **868**, L19
- Gopalswamy, N., Mäkelä, P., Yashiro, S., et al. 2019, [JPhCS](#), **1332**, 012004
- Gopalswamy, N., Mäkelä, P., Yashiro, S., et al. 2020, [SoPh](#), **295**, 18
- Gopalswamy, N., Yashiro, S., Mäkelä, P., Xie, H., & Akiyama, S. 2021, [ApJ](#), **915**, 82
- Gopalswamy, N., Yashiro, S., Michalek, G., et al. 2009, [EM&P](#), **104**, 295
- Gopalswamy, N., Yashiro, S., Michalek, G., et al. 2010, [SunGe](#), **5**, 7
- Grechnev, V. V., Kiselev, V. I., Kashapova, L. K., et al. 2018, [SoPh](#), **293**, 133
- Kouloumvakos, A., Rouillard, A. P., Share, G. H., et al. 2020, [ApJ](#), **893**, 76
- Plotnikov, I., Rouillard, A. P., & Share, G. H. 2017, [A&A](#), **608**, A43
- Ryan, J. M. 2000, [SSRv](#), **93**, 581
- Share, G. H., Murphy, R. J., White, S. M., et al. 2018, [ApJ](#), **869**, 182
- Winter, L. M., Bernstein, V., Omodei, N., & Pesce-Rollins, M. 2018, [ApJ](#), **864**, 39



Fermi Large Area Telescope Fourth Source Catalog

S. Abdollahi¹, F. Acero², M. Ackermann³, M. Ajello⁴, W. B. Atwood⁵, M. Axelsson^{6,7}, L. Baldini⁸, J. Ballet², G. Barbiellini^{9,10}, D. Bastieri^{11,12}, J. Becerra Gonzalez^{13,14,15}, R. Bellazzini¹⁶, A. Berretta¹⁷, E. Bissaldi^{18,19}, R. D. Blandford²⁰, E. D. Bloom²⁰, R. Bonino^{21,22}, E. Bottacini^{20,23}, T. J. Brandt¹⁴, J. Bregeon²⁴, P. Bruel²⁵, R. Buehler³, T. H. Burnett²⁶, S. Buson²⁷, R. A. Cameron²⁰, R. Caputo¹⁴, P. A. Caraveo²⁸, J. M. Casandjian², D. Castro^{14,29}, E. Cavazzuti³⁰, E. Charles²⁰, S. Chaty², S. Chen^{11,23}, C. C. Cheung³¹, G. Chiaro²⁸, S. Ciprini^{32,33}, J. Cohen-Tanugi²⁴, L. R. Cominsky³⁴, J. Coronado-Blázquez^{35,36}, D. Costantin³⁷, A. Cuoco^{21,38}, S. Cutini³⁹, F. D'Ammando⁴⁰, M. DeKlotz⁴¹, P. de la Torre Luque¹⁸, F. de Palma²¹, A. Desai⁴, S. W. Digel²⁰, N. Di Lalla⁸, M. Di Mauro¹⁴, L. Di Venere^{18,19}, A. Domínguez⁴², D. Dumora⁴³, F. Fana Dirisa⁴⁴, S. J. Fegan²⁵, E. C. Ferrara¹⁴, A. Franckowiak³, Y. Fukazawa¹, S. Funk⁴⁵, P. Fusco^{18,19}, F. Gargano¹⁹, D. Gasparrini^{32,33}, N. Giglietto^{18,19}, P. Giommi³³, F. Giordano^{18,19}, M. Giroletti⁴⁰, T. Glanzman²⁰, D. Green⁴⁶, I. A. Grenier², S. Griffin¹⁴, M.-H. Grondin⁴³, J. E. Grove³¹, S. Guiriec^{14,47}, A. K. Harding¹⁴, K. Hayashi⁴⁸, E. Hays¹⁴, J. W. Hewitt⁴⁹, D. Horan²⁵, G. Jóhannesson^{50,51}, T. J. Johnson⁵², T. Kamae⁵³, M. Kerr³¹, D. Kocevski¹⁴, M. Kovac'evic³⁹, M. Kuss¹⁶, D. Landriu², S. Larsson^{7,54,55}, L. Latronico²¹, M. Lemoine-Goumard⁴³, J. Li³, I. Liodakis²⁰, F. Longo^{9,10}, F. Loparco^{18,19}, B. Lott⁴³, M. N. Lovellette³¹, P. Lubrano³⁹, G. M. Madejski²⁰, S. Maldera²¹, D. Malyshev⁴⁵, A. Manfreda⁸, E. J. Marchesini²², L. Marcotulli⁴, G. Martí-Devesa⁵⁶, P. Martin⁵⁷, F. Massaro^{21,22,58}, M. N. Mazziotta¹⁹, J. E. McEnery^{14,15}, I. Mereu^{17,39}, M. Meyer²⁰, P. F. Michelson²⁰, N. Mirabal^{14,59}, T. Mizuno⁶⁰, M. E. Monzani²⁰, A. Morselli³², I. V. Moskalenko²⁰, M. Negro^{21,22}, E. Nuss²⁴, R. Ojha¹⁴, N. Omodei²⁰, M. Orienti⁴⁰, E. Orlando^{20,61}, J. F. Ormes⁶², M. Palatiello^{9,10}, V. S. Paliya³, D. Paneque⁴⁶, Z. Pei¹², H. Peña-Herazo^{21,22,58,63}, J. S. Perkins¹⁴, M. Persic^{9,64}, M. Pesce-Rollins¹⁶, V. Petrosian²⁰, L. Petrov¹⁴, F. Piron²⁴, H. Poon¹, T. A. Porter²⁰, G. Principe⁴⁰, S. Rainò^{18,19}, R. Rando^{11,12}, M. Razzano^{16,82}, S. Razzaque⁴⁴, A. Reimer^{20,56}, O. Reimer⁵⁶, Q. Remy²⁴, T. Reposeur⁴³, R. W. Romani²⁰, P. M. Saz Parkinson^{5,65,66}, F. K. Schinzel^{67,68}, D. Serini¹⁸, C. Sgrò¹⁶, E. J. Siskind⁶⁹, D. A. Smith⁴³, G. Spandre¹⁶, P. Spinelli^{18,19}, A. W. Strong⁷⁰, D. J. Suson⁷¹, H. Tajima^{20,72}, M. N. Takahashi⁴⁶, D. Tak^{14,73}, J. B. Thayer²⁰, D. J. Thompson¹⁴, L. Tibaldo⁵⁷, D. F. Torres^{74,75}, E. Torresi⁷⁶, J. Valverde²⁵, B. Van Klaveren²⁰, P. van Zyl^{77,78,79}, K. Wood⁸⁰, M. Yassine^{9,10}, and G. Zaharijas^{61,81}

¹ Department of Physical Sciences, Hiroshima University, Higashi-Hiroshima, Hiroshima 739-8526, Japan

² AIM, CEA, CNRS, Université Paris-Saclay, Université Paris Diderot, Sorbonne Paris Cité, F-91191 Gif-sur-Yvette, France; jean.ballet@cea.fr

³ Deutsches Elektronen Synchrotron DESY, D-15738 Zeuthen, Germany

⁴ Department of Physics and Astronomy, Clemson University, Kinard Lab of Physics, Clemson, SC 29634-0978, USA

⁵ Santa Cruz Institute for Particle Physics, Department of Physics and Department of Astronomy and Astrophysics, University of California at Santa Cruz, Santa Cruz, CA 95064, USA

⁶ Department of Physics, Stockholm University, AlbaNova, SE-106 91 Stockholm, Sweden

⁷ Department of Physics, KTH Royal Institute of Technology, AlbaNova, SE-106 91 Stockholm, Sweden

⁸ Università di Pisa and Istituto Nazionale di Fisica Nucleare, Sezione di Pisa I-56127 Pisa, Italy

⁹ Istituto Nazionale di Fisica Nucleare, Sezione di Trieste, I-34127 Trieste, Italy

¹⁰ Dipartimento di Fisica, Università di Trieste, I-34127 Trieste, Italy

¹¹ Istituto Nazionale di Fisica Nucleare, Sezione di Padova, I-35131 Padova, Italy

¹² Dipartimento di Fisica e Astronomia "G. Galilei," Università di Padova, I-35131 Padova, Italy

¹³ Instituto de Astrofísica de Canarias, Observatorio del Teide, C/Via Lactea, s/n, E38205, La Laguna, Tenerife, Spain

¹⁴ NASA Goddard Space Flight Center, Greenbelt, MD 20771, USA

¹⁵ Department of Astronomy, University of Maryland, College Park, MD 20742, USA

¹⁶ Istituto Nazionale di Fisica Nucleare, Sezione di Pisa, I-56127 Pisa, Italy

¹⁷ Dipartimento di Fisica, Università degli Studi di Perugia, I-06123 Perugia, Italy

¹⁸ Dipartimento di Fisica "M. Merlin" dell'Università e del Politecnico di Bari, I-70126 Bari, Italy

¹⁹ Istituto Nazionale di Fisica Nucleare, Sezione di Bari, I-70126 Bari, Italy

²⁰ W.W. Hansen Experimental Physics Laboratory, Kavli Institute for Particle Astrophysics and Cosmology, Department of Physics and SLAC National Accelerator Laboratory, Stanford University, Stanford, CA 94305, USA; digel@stanford.edu

²¹ Istituto Nazionale di Fisica Nucleare, Sezione di Torino, I-10125 Torino, Italy

²² Dipartimento di Fisica, Università degli Studi di Torino, I-10125 Torino, Italy

²³ Department of Physics and Astronomy, University of Padova, Vicolo Osservatorio 3, I-35122 Padova, Italy

²⁴ Laboratoire Univers et Particules de Montpellier, Université Montpellier, CNRS/IN2P3, F-34095 Montpellier, France

²⁵ Laboratoire Leprince-Ringuet, École polytechnique, CNRS/IN2P3, F-91128 Palaiseau, France

²⁶ Department of Physics, University of Washington, Seattle, WA 98195-1560, USA; tburnett@u.washington.edu

²⁷ Institut für Theoretische Physik and Astrophysik, Universität Würzburg, D-97074 Würzburg, Germany

²⁸ INFN-Istituto di Astrofisica Spaziale e Fisica Cosmica Milano, via E. Bassini 15, I-20133 Milano, Italy

²⁹ Harvard-Smithsonian Center for Astrophysics, Cambridge, MA 02138, USA

³⁰ Italian Space Agency, Via del Politecnico snc, I-00133 Roma, Italy

³¹ Space Science Division, Naval Research Laboratory, Washington, DC 20375-5352, USA

³² Istituto Nazionale di Fisica Nucleare, Sezione di Roma "Tor Vergata," I-00133 Roma, Italy

³³ Space Science Data Center—Agenzia Spaziale Italiana, Via del Politecnico, snc, I-00133, Roma, Italy

³⁴ Department of Physics and Astronomy, Sonoma State University, Rohnert Park, CA 94928-3609, USA

³⁵ Instituto de Física Teórica UAM/CSIC, Universidad Autónoma de Madrid, E-28049, Madrid, Spain

³⁶ Departamento de Física Teórica, Universidad Autónoma de Madrid, E-28049 Madrid, Spain

³⁷ University of Padua, Department of Statistical Science, Via 8 Febbraio, 2, I-35122 Padova, Italy

³⁸ RWTH Aachen University, Institute for Theoretical Particle Physics and Cosmology, (TTK), D-52056 Aachen, Germany

³⁹ Istituto Nazionale di Fisica Nucleare, Sezione di Perugia, I-06123 Perugia, Italy

- ⁴⁰ INAF Istituto di Radioastronomia, I-40129 Bologna, Italy
⁴¹ Stellar Solutions Inc., 250 Cambridge Avenue, Suite 204, Palo Alto, CA 94306, USA
⁴² Grupo de Altas Energías, Universidad Complutense de Madrid, E-28040 Madrid, Spain
⁴³ Centre d'Études Nucléaires de Bordeaux Gradignan, IN2P3/CNRS, Université Bordeaux 1, BP120, F-33175 Gradignan Cedex, France; lott@cenbg.in2p3.fr
⁴⁴ Department of Physics, University of Johannesburg, P.O. Box 524, Auckland Park 2006, South Africa
⁴⁵ Friedrich-Alexander Universität Erlangen-Nürnberg, Erlangen Centre for Astroparticle Physics, Erwin-Rommel-Str. 1, D-91058 Erlangen, Germany
⁴⁶ Max-Planck-Institut für Physik, D-80805 München, Germany
⁴⁷ The George Washington University, Department of Physics, 725 21st St, NW, Washington, DC 20052, USA
⁴⁸ Department of Physics and Astrophysics, Nagoya University, Chikusa-ku Nagoya 464-8602, Japan
⁴⁹ University of North Florida, Department of Physics, 1 UNF Drive, Jacksonville, FL 32224, USA
⁵⁰ Science Institute, University of Iceland, IS-107 Reykjavik, Iceland
⁵¹ Nordita, Royal Institute of Technology and Stockholm University, Roslagstullsbacken 23, SE-106 91 Stockholm, Sweden
⁵² College of Science, George Mason University, Fairfax, VA 22030, resident at Naval Research Laboratory, Washington, DC 20375, USA
⁵³ Department of Physics, Graduate School of Science, University of Tokyo, 7-3-1 Hongo, Bunkyo-ku, Tokyo 113-0033, Japan
⁵⁴ The Oskar Klein Centre for Cosmoparticle Physics, AlbaNova, SE-106 91 Stockholm, Sweden
⁵⁵ School of Education, Health and Social Studies, Natural Science, Dalarna University, SE-791 88 Falun, Sweden
⁵⁶ Institut für Astro- und Teilchenphysik, Leopold-Franzens-Universität Innsbruck, A-6020 Innsbruck, Austria
⁵⁷ IRAP, Université de Toulouse, CNRS, UPS, CNES, F-31028 Toulouse, France
⁵⁸ Istituto Nazionale di Astrofisica-Osservatorio Astrofisico di Torino, via Osservatorio 20, I-10025 Pino Torinese, Italy
⁵⁹ Department of Physics and Center for Space Sciences and Technology, University of Maryland Baltimore County, Baltimore, MD 21250, USA
⁶⁰ Hiroshima Astrophysical Science Center, Hiroshima University, Higashi-Hiroshima, Hiroshima 739-8526, Japan
⁶¹ Istituto Nazionale di Fisica Nucleare, Sezione di Trieste, and Università di Trieste, I-34127 Trieste, Italy
⁶² Department of Physics and Astronomy, University of Denver, Denver, CO 80208, USA
⁶³ Instituto Nacional de Astrofísica, Óptica y Electrónica, Tonantzintla, Puebla 72840, Mexico
⁶⁴ Osservatorio Astronomico di Trieste, Istituto Nazionale di Astrofisica, I-34143 Trieste, Italy
⁶⁵ Department of Physics, The University of Hong Kong, Pokfulam Road, Hong Kong, People's Republic of China
⁶⁶ Laboratory for Space Research, The University of Hong Kong, Hong Kong, People's Republic of China
⁶⁷ National Radio Astronomy Observatory, 1003 Lopezville Road, Socorro, NM 87801, USA
⁶⁸ University of New Mexico, MSC07 4220, Albuquerque, NM 87131, USA
⁶⁹ NYCB Real-Time Computing Inc., Lattingtown, NY 11560-1025, USA
⁷⁰ Max-Planck Institut für extraterrestrische Physik, D-85748 Garching, Germany
⁷¹ Purdue University Northwest, Hammond, IN 46323, USA
⁷² Solar-Terrestrial Environment Laboratory, Nagoya University, Nagoya 464-8601, Japan
⁷³ Department of Physics, University of Maryland, College Park, MD 20742, USA
⁷⁴ Institute of Space Sciences (CSICIEEC), Campus UAB, Carrer de Magrans s/n, E-08193 Barcelona, Spain
⁷⁵ Institució Catalana de Recerca i Estudis Avançats (ICREA), E-08010 Barcelona, Spain
⁷⁶ INAF-Istituto di Astrofisica Spaziale e Fisica Cosmica Bologna, via P. Gobetti 101, I-40129 Bologna, Italy
⁷⁷ Hartebeesthoek Radio Astronomy Observatory, P.O. Box 443, Krugersdorp 1740, South Africa
⁷⁸ School of Physics, University of the Witwatersrand, Private Bag 3, WITS-2050, Johannesburg, South Africa
⁷⁹ Square Kilometre Array South Africa, Pinelands, 7405, South Africa
⁸⁰ Praxis Inc., Alexandria, VA 22303, resident at Naval Research Laboratory, Washington, DC 20375, USA
⁸¹ Center for Astrophysics and Cosmology, University of Nova Gorica, Nova Gorica, Slovenia
Received 2019 September 26; revised 2020 January 7; accepted 2020 January 13; published 2020 March 10

Abstract

We present the fourth *Fermi* Large Area Telescope catalog (4FGL) of γ -ray sources. Based on the first eight years of science data from the *Fermi* Gamma-ray Space Telescope mission in the energy range from 50 MeV to 1 TeV, it is the deepest yet in this energy range. Relative to the 3FGL catalog, the 4FGL catalog has twice as much exposure as well as a number of analysis improvements, including an updated model for the Galactic diffuse γ -ray emission, and two sets of light curves (one-year and two-month intervals). The 4FGL catalog includes 5064 sources above 4σ significance, for which we provide localization and spectral properties. Seventy-five sources are modeled explicitly as spatially extended, and overall, 358 sources are considered as identified based on angular extent, periodicity, or correlated variability observed at other wavelengths. For 1336 sources, we have not found plausible counterparts at other wavelengths. More than 3130 of the identified or associated sources are active galaxies of the blazar class, and 239 are pulsars.

Unified Astronomy Thesaurus concepts: [Catalogs \(205\)](#); [Gamma-ray astronomy \(628\)](#); [Sky surveys \(1464\)](#)

1. Introduction

The *Fermi* Gamma-ray Space Telescope was launched in 2008 June, and the Large Area Telescope (LAT) on board has been continually surveying the sky in the GeV energy range since then. Integrating the data over many years, the *Fermi*-LAT collaboration produced several generations of high-energy γ -ray source catalogs (Table 1). The previous all-purpose catalog (3FGL, Acero et al. 2015) contained 3033 sources, mostly active

galactic nuclei (AGNs) and pulsars, but also a variety of other types of extragalactic and Galactic sources.

This paper presents the fourth catalog of sources, abbreviated as 4FGL (for *Fermi* Gamma-ray LAT) detected in the first eight years of the mission. As in previous catalogs, sources are included based on the statistical significance of their detection considered over the entire time period of the analysis. For this reason, the 4FGL catalog does not contain transient γ -ray sources, which are detectable only over a short duration, including Gamma-ray Bursts (GRBs; Ajello et al. 2019), solar flares (Ackermann et al. 2014b), and most novae (Ackermann et al. 2014a).

⁸² Funded by contract FIRB-2012-RBFR12PM1F from the Italian Ministry of Education, University and Research (MIUR).

Table 1
Previous *Fermi*-LAT Catalogs

Acronym	IRFs/Diffuse Model	Energy Range/Duration	Sources	Analysis/Reference
1FGL	P6_V3_DIFFUSE gll_iem_v02	0.1–100 GeV 11 months	1451 (P)	Unbinned, F/B Abdo et al. (2010e)
2FGL	P7SOURCE_V6 gal_2yearp7v6_v0	0.1–100 GeV 2 yr	1873 (P)	Binned, F/B Nolan et al. (2012)
3FGL	P7REP_SOURCE_V15 gll_iem_v06	0.1–300 GeV 4 yr	3033 (P)	Binned, F/B Acero et al. (2015)
FGES	P8R2_SOURCE_V6 gll_iem_v06	10 GeV–2 TeV 6 yr	46 (E)	Binned, PSF, $ b < 7^\circ$ Ackermann et al. (2017b)
3FHL	P8R2_SOURCE_V6 gll_iem_v06	10 GeV–2 TeV 7 yr	1556 (P)	Unbinned, PSF Ajello et al. (2017)
FHES	P8R2_SOURCE_V6 gll_iem_v06	1 GeV–1 TeV 7.5 yr	24 (E)	Binned, PSF, $ b > 5^\circ$ Ackermann et al. (2018)
4FGL	P8R3_SOURCE_V2 gll_iem_v07 (Section 2.4.1)	0.05 GeV–1 TeV 8 yr	5064 (P)	Binned, PSF this work

Notes. In the Analysis column, F/B stands for *Front/Back*, and PSF for PSF event types^a. In the Sources column, we write (P) when the catalog’s objective is to look for point-like sources, (E) when it looks for extended sources.

^a See https://fermi.gsfc.nasa.gov/ssc/data/analysis/LAT_essentials.html.

The 4FGL catalog benefits from a number of improvements with respect to the 3FGL, besides the twice longer exposure:

1. We used Pass 8 data⁸³ (Section 2.2). The principal difference relative to the P7REP data used for 3FGL is improved angular resolution above 3 GeV and about 20% larger acceptance at all energies, reaching 2.5 m² sr between 2 and 300 GeV. The acceptance is defined here as the integral of the effective area over the field of view. It is the most relevant quantity for a survey mission such as *Fermi*-LAT.
2. We developed a new model of the underlying diffuse Galactic emission (Section 2.4).
3. We introduced weights in the maximum likelihood analysis (Section 3.2) to mitigate the effect of systematic errors due to our imperfect knowledge of the Galactic diffuse emission.
4. We accounted for the effect of energy dispersion (reconstructed event energy not equal to the true energy of the incoming γ -ray). This is a small correction (Section 4.2.2) and was neglected in previous *Fermi*-LAT catalogs because the energy resolution (measured as the 68% containment half width) is better than 15% over most of the LAT energy range and the γ -ray spectra have no sharp features.
5. We tested all sources with three spectral models (power law, log normal, and power law with subexponential cutoff, Section 3.3).
6. We explicitly modeled 75 sources as extended emission regions (Section 3.4), up from 25 in 3FGL.
7. We built light curves and tested variability using two different time bins (one year and two months, Section 3.6).
8. To study the associations of LAT sources with counterparts at other wavelengths, we updated several of the counterpart catalogs, and correspondingly recalibrated the association procedure.

A preliminary version of this catalog (FL8Y⁸⁴) was built from the same data and the same software, but using the previous interstellar emission model (gll_iem_v06) as background, starting at 100 MeV and switching to curved spectra at $TS_{\text{curv}} > 16$ (see Section 3.3 for definition). We use it as a starting point for source detection and localization, and to estimate the impact of changing the underlying diffuse model. The result of a dedicated effort for studying the AGN population in the 4FGL catalog is published in the accompanying fourth LAT AGN catalog (4LAC; *Fermi*-LAT collaboration 2019) paper.

Section 2 describes the LAT, the data, and the models for the diffuse backgrounds, celestial and otherwise. Section 3 describes the construction of the catalog, with emphasis on what has changed since the analysis for the 3FGL catalog. Section 4 describes the catalog itself, Section 5 explains the association and identification procedure, and Section 6 details the association results. We conclude in Section 7. We provide appendices with technical details of the analysis and of the format of the electronic version of the catalog.

2. Instrument and Background

2.1. The Large Area Telescope

The LAT detects γ -rays in the energy range from 20 MeV to more than 1 TeV, measuring their arrival times, energies, and directions. The field of view of the LAT is ~ 2.7 sr at 1 GeV and above. The per-photon angular resolution (point-spread function, PSF; 68% containment radius) is $\sim 5^\circ$ at 100 MeV, improving to 0.8° at 1 GeV (averaged over the acceptance of the LAT), varying with energy approximately as $E^{-0.8}$ and asymptoting at $\sim 0.1^\circ$ above 20 GeV (Figure 1). The tracking section of the LAT has 36 layers of silicon strip detectors interleaved with 16 layers of tungsten foil (12 thin layers, 0.03 radiation length, at the top or *Front* of the instrument, followed by four thick layers, 0.18 radiation lengths, in the *Back* section). The silicon strips track charged particles, and the tungsten foils facilitate conversion of γ -rays to positron-

⁸³ See https://fermi.gsfc.nasa.gov/ssc/data/analysis/documentation/Pass8_usage.html.

⁸⁴ See <https://fermi.gsfc.nasa.gov/ssc/data/access/lat/fl8y/>.

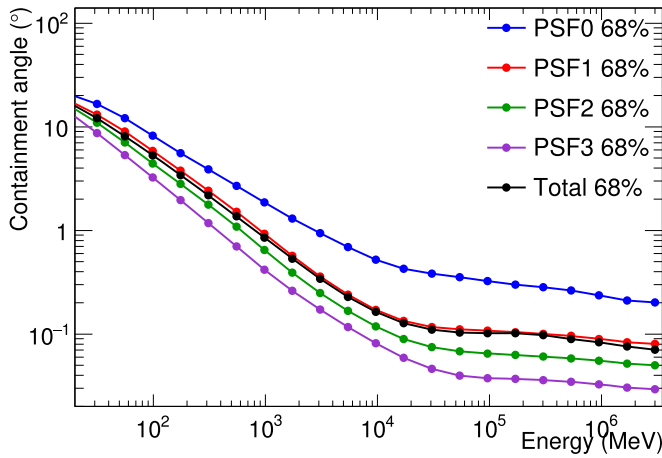


Figure 1. Containment angle (68%) of the *Fermi*-LAT PSF as a function of energy, averaged over off-axis angle. The black line is the average over all data, whereas the colored lines illustrate the difference between the four categories of events ranked by PSF quality from worst (PSF0) to best (PSF3).

electron pairs. Beneath the tracker is a calorimeter composed of an eight-layer array of CsI crystals (~ 8.5 total radiation lengths) to determine the γ -ray energy. More information about the LAT is provided in Atwood et al. (2009), and the in-flight calibration of the LAT is described in Abdo et al. (2009d) and Ackermann et al. (2012a, 2012c).

The LAT is also an efficient detector of the intense background of charged particles from cosmic rays and trapped radiation at the orbit of the *Fermi* satellite. A segmented charged-particle anticoincidence detector (plastic scintillators read out by photomultiplier tubes) around the tracker is used to reject charged-particle background events. Accounting for γ -rays lost in filtering charged particles from the data, the effective collecting area at normal incidence (for the P8R3_SOURCE_V2 event selection used here; see below)⁸⁵ exceeds 0.3 m^2 at 0.1 GeV , 0.8 m^2 at 1 GeV , and remains nearly constant at $\sim 0.9 \text{ m}^2$ from 2 to 500 GeV . The live time is nearly 76%, limited primarily by interruptions of data taking when *Fermi* is passing through the South Atlantic Anomaly (SAA, $\sim 15\%$) and readout dead-time fraction ($\sim 9\%$).

2.2. The LAT Data

The data for the 4FGL catalog were taken during the period 2008 August 4 (15:43 UTC) to 2016 August 2 (05:44 UTC) covering eight years. During most of this time, *Fermi* was operated in sky-scanning survey mode (viewing direction rocking north and south of the zenith on alternate orbits). As in 3FGL, intervals around solar flares and bright GRBs were excised. Overall, about two days were excised due to solar flares, and 39 ks due to 30 GRBs. The precise time intervals corresponding to selected events are recorded in the GTI extension of the FITS file (Appendix A). The maximum exposure ($4.5 \times 10^{11} \text{ cm}^2 \text{ s}$ at 1 GeV) is reached at the North celestial pole. The minimum exposure ($2.7 \times 10^{11} \text{ cm}^2 \text{ s}$ at 1 GeV) is reached at the celestial equator.

The current version of the LAT data is Pass 8 P8R3 (Atwood et al. 2013; Bruel et al. 2018). It offers 20% more acceptance than P7REP (Bregeson et al. 2013) and a narrower PSF at high energies. Both aspects are very useful for source detection and

localization (Ajello et al. 2017). We used the Source class event selection, with the Instrument Response Functions (IRFs) P8R3_SOURCE_V2. Pass 8 introduced a new partition of the events, called PSF event types, based on the quality of the angular reconstruction (Figure 1), with approximately equal effective area in each event type at all energies. The angular resolution is critical to distinguish point sources from the background, so we split the data into those four categories to avoid diluting high-quality events (PSF3) with poorly localized ones (PSF0). We split the data further into 6 energy intervals (also used for the spectral energy distributions in Section 3.5) because the extraction regions must extend further at low energy (broad PSF) than at high energy, but the pixel size can be larger. After applying the zenith angle selection (Section 2.3), we were left with the 15 components described in Table 2. The log-likelihood is computed for each component separately, then they are summed for the SummedLikelihood maximization (Section 3.2).

The lower bound of the energy range was set to 50 MeV , down from 100 MeV in 3FGL, to constrain the spectra better at low energy. It does not help detecting or localizing sources because of the very broad PSF below 100 MeV . The upper bound was raised from 300 GeV in 3FGL to 1 TeV . This is because as the source-to-background ratio decreases, the sensitivity curve (Figure 18 of Abdo et al. 2010e, 1FGL) shifts to higher energies. The 3FHL catalog (Ajello et al. 2017) went up to 2 TeV , but only 566 events exceed 1 TeV over 8 yr (to be compared to 714,000 above 10 GeV).

2.3. Zenith Angle Selection

The zenith angle cut was set such that the contribution of the Earth limb at that zenith angle was less than 10% of the total (Galactic + isotropic) background. Integrated over all zenith angles, the residual Earth limb contamination is less than 1%. We kept PSF3 event types with zenith angles less than 80° between 50 and 100 MeV , PSF2 and PSF3 event types with zenith angles less than 90° between 100 and 300 MeV , and PSF1, PSF2, and PSF3 event types with zenith angles less than 100° between 300 MeV and 1 GeV . Above 1 GeV , we kept all events with zenith angles less than 105° (Table 2).

The resulting integrated exposure over 8 yr is shown in Figure 2. The dependence on decl. is due to the combination of the inclination of the orbit (25.6°), the rocking angle, the zenith angle selection, and the off-axis effective area. The north-south asymmetry is due to the SAA, over which no scientific data is taken. Because of the regular precession of the orbit every 53 days, the dependence on R.A. is small when averaged over long periods of time. The main dependence on energy is due to the increase of the effective area up to 1 GeV , and the addition of new event types at 100 MeV , 300 MeV , and 1 GeV . The off-axis effective area depends somewhat on energy and event type. This, together with the different zenith angle selections, introduces a slight dependence of the shape of the curve on energy.

Selecting on zenith angle applies a kind of time selection (which depends on direction in the sky). This means that the effective time selection at low energy is not exactly the same as at high energy. The periods of time during which a source is at zenith angle $< 105^\circ$ but (for example) $> 90^\circ$ last typically a few minutes every orbit. This is shorter than the main variability timescales of astrophysical sources in 4FGL and is, therefore, not a concern. There remains however the modulation due to

⁸⁵ See http://www.slac.stanford.edu/exp/glast/groups/canda/lat_Performance.htm.

Table 2
4FGL Summed Likelihood Components

Energy Interval (GeV)	NBins	ZMax (deg)	Ring Width (deg)	Pixel Size (deg)				
				PSF0	PSF1	PSF2	PSF3	All
0.05–0.1	3	80	7	0.6	...
0.1–0.3	5	90	7	0.6	0.6	...
0.3–1	6	100	5	...	0.4	0.3	0.2	...
1–3	5	105	4	0.4	0.15	0.1	0.1	...
3–10	6	105	3	0.25	0.1	0.05	0.04	...
10–1000	10	105	2	0.04

Note. We used 15 components (all in binned mode) in the 4FGL Summed Likelihood approach (Section 3.2). Components in a given energy interval share the same number of energy bins, the same zenith angle selection and the same RoI size but have different pixel sizes in order to adapt to the PSF width (Figure 1). Each filled entry under Pixel size corresponds to one component of the summed log-likelihood. NBins is the number of energy bins in the interval, ZMax is the zenith angle cut, Ring width refers to the difference between the RoI core and the extraction region, as explained in item 5 of Section 3.2.

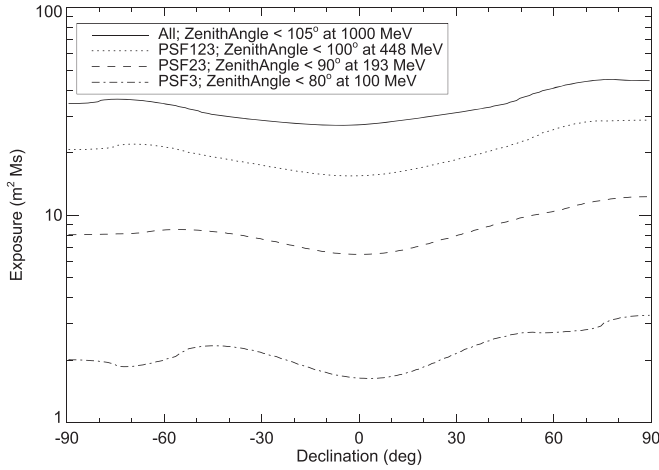


Figure 2. Exposure as a function of decl. and energy, averaged over R.A., summed over all relevant event types as indicated in the figure legend.

the precession of the spacecraft orbit on longer timescales over which blazars can vary. This is not a problem for a catalog (it can at most appear as a spectral effect and should average out when considering statistical properties), but it should be kept in mind when extracting spectral parameters of individual variable sources. We used the same zenith angle cut for all event types in a given energy interval, to reduce systematics due to that time selection.

Because the data are limited by systematics at low energies everywhere in the sky (Appendix B), rejecting half of the events below 300 MeV and 75% of them below 100 MeV does not impact the sensitivity (if we had kept these events, the weights would have been lower).

2.4. Model for the Diffuse Gamma-Ray Background

2.4.1. Diffuse Emission of the Milky Way

We extensively updated the model of the Galactic diffuse emission for the 4FGL analysis, using the same P8R3 data selections (PSF types, energy ranges, and zenith angle limits). The development of the model is described in greater detail (including illustrations of the templates and residuals) online⁸⁶. Here, we summarize the primary differences from the model developed for the 3FGL catalog (Acero et al. 2016a). In both

cases, the model is based on linear combinations of templates representing components of the Galactic diffuse emission. For 4FGL, we updated all of the templates, and added a new one as described below.

We have adopted the new, all-sky high-resolution, 21 cm spectral line HI4PI survey (HI4PI Collaboration et al. 2016) as our tracer of H I, and extensively refined the procedure for partitioning the H I and H₂ (traced by the 2.6 mm CO line) into separate ranges of Galactocentric distance (“rings”), by decomposing the spectra into individual line profiles, so the broad velocity dispersion of massive interstellar clouds does not effectively distribute their emission very broadly along the line of sight. We also updated the rotation curve and adopted a new procedure for interpolating the rings across the Galactic center and anticenter, now incorporating a general model for the surface density distribution of the interstellar medium to inform the interpolation, and defining separate rings for the Central Molecular Zone (within ~ 150 pc of the Galactic center and between 150 and 600 pc of the center). With this approach, the Galaxy is divided into ten concentric rings.

The template for the inverse-Compton emission is still based on a model interstellar radiation field and cosmic-ray electron distribution (calculated in GALPROP v56, described in Porter et al. 2017)⁸⁷, but now we formally subdivide the model into rings (with the same Galactocentric radius ranges as for the gas templates), which are fit separately in the analysis, to allow for some spatial freedom relative to the static all-sky inverse-Compton model.

We have also updated the template of the “dark gas” component (Grenier et al. 2005), representing interstellar gas that is not traced by the H I and CO line surveys, by comparison with the *Planck* dust optical depth map.⁸⁸ The dark gas is inferred as the residual component after the best-fitting linear combination of total $N(\text{H I})$ and W_{CO} (the integrated intensity of the CO line) is subtracted, i.e., as the component not correlated with the atomic and molecular gas spectral line tracers, in a procedure similar to that used in Acero et al. (2016a). In particular, as before we retained the negative residuals as a “column density correction map.”

New to the 4FGL model, we incorporated a template representing the contribution of unresolved Galactic sources. This was derived from the model spatial distribution and luminosity function developed based on the distribution of

⁸⁶ https://fermi.gsfc.nasa.gov/ssc/data/analysis/software/aux/4fgl/Galactic_Diffuse_Emission_Model_for_the_4FGL_Catalog_Analysis.pdf

⁸⁷ <http://galprop.stanford.edu>

⁸⁸ COM_Map_Dust-GNILC-Model-Opacity_2048_R2.01.fits, Planck Collaboration et al. (2016).

Galactic sources in Acero et al. (2015) and an analytical evaluation of the flux limit for source detection as a function of direction on the sky.

As for the 3FGL model, we iteratively determined and re-fit a model component that represents non-template diffuse γ -ray emission, primarily Loop I and the *Fermi* bubbles. To avoid overfitting the residuals, and possibly suppressing faint Galactic sources, we spectrally and spatially smoothed the residual template.

The model fitting was performed using Gardian (Ackermann et al. 2012e), as a summed log-likelihood analysis. This procedure involves transforming the ring maps described above into spatial-spectral templates evaluated in GALPROP. We used model $^5L^Z6R30^T150^C2$ from Ackermann et al. (2012e). The model is a linear combination of these templates, with free scaling functions of various forms for the individual templates. For components with the largest contributions, a piecewise continuous function, linear in the logarithm of energy, with nine degrees of freedom was used. Other components had a similar scaling function with five degrees of freedom, or power-law scaling, or overall scale factors, chosen to give the model adequate freedom while reducing the overall number of free parameters. The model also required a template for the point and small-extended sources in the sky. We iterated the fitting using preliminary versions of the 4FGL catalog. This template was also given spectral degrees of freedom. Other diffuse templates, described below and not related to Galactic emission, were included in the model fitting.

2.4.2. Isotropic Background

The isotropic diffuse background was derived over 45 energy bins covering the energy range 30 MeV to 1 TeV, from the eight-year data set excluding the Galactic plane ($|b| > 15^\circ$). To avoid the Earth limb emission (more conspicuous around the celestial poles), we applied a zenith angle cut at 80° and also excluded declinations higher than 60° below 300 MeV. The isotropic background was obtained as the residual between the spatially averaged data and the sum of the Galactic diffuse emission model described above, a preliminary version of the 4FGL catalog and the solar and lunar templates (Section 2.4.3), so it includes charged particles misclassified as γ -rays. We implicitly assume that the acceptance for these residual charged particles is the same as for γ -rays in treating these diffuse background components together. To obtain a continuous model, the final spectral template was obtained by fitting the residuals in the 45 energy bins to a multiply broken power law with 18 breaks. For the analysis, we derived the contributions to the isotropic background separately for each event type.

2.4.3. Solar and Lunar Template

The quiescent Sun and the Moon are fairly bright γ -ray sources. The Sun moves in the ecliptic but the solar γ -ray emission is extended because of cosmic-ray interactions with the solar radiation field; detectable emission from inverse-Compton scattering of cosmic-ray electrons on the radiation field of the Sun extends several degrees from the Sun (Orlando & Strong 2008; Abdo et al. 2011). The Moon is not an extended source in this way but the lunar orbit is inclined somewhat relative to the ecliptic and the Moon moves through a larger fraction of the sky than the Sun. Averaged over time, the γ -ray emission from the Sun and Moon trace a region

around the ecliptic. Without any correction, this can seriously affect the spectra and light curves, so starting with 3FGL we model that emission.

The Sun and Moon emission are modulated by the solar magnetic field, which deflects cosmic rays more (and therefore reduces γ -ray emission) when the Sun is at maximum activity. For that reason, the model used in 3FGL (based on the first 18 months of data when the Sun was near minimum) was not adequate for 8 yr. We used the improved model of the lunar emission (Ackermann et al. 2016a) and a data-based model of the solar disk and inverse-Compton scattering on the solar light (S. Raino 2019, private communication).

We combined those models with calculations of their motions and of the exposure of the observations by the LAT to make templates for the equivalent diffuse component over 8 yr using *gtsuntemp* (Johannesson et al. 2013). For 4FGL, we used two different templates: one for the inverse-Compton emission on the solar light (pixel size 0.25°) and one for the sum of the solar and lunar disks. For the latter, we reduced the pixel size to 0.125° to describe the disks accurately, and computed a specific template for each event type/maximum zenith angle combination of Table 2 (because their exposure maps are not identical). As in 3FGL, those components have no free parameter.

2.4.4. Residual Earth Limb Template

For 3FGL, we reduced the low-energy Earth limb emission by selecting zenith angles less than 100° , and modeled the residual contamination approximately. For 4FGL, we chose to cut harder on zenith angle at low energies and select event types with the best PSF (Section 2.3). That procedure eliminates the need for a specific Earth limb component in the model.

3. Construction of the Catalog

The procedure used to construct the 4FGL catalog has a number of improvements relative to that of the 3FGL catalog. In this section, we review the procedure, emphasizing what was done differently. The significances (Section 3.2) and spectral parameters (Section 3.3) of all catalog sources were obtained using the standard *pyLikelihood* framework (Python analog of *glike*) in the LAT Science Tools⁸⁹ (version v11r7p0). The localization procedure (Section 3.1), which relies on *pointlike* (Kerr 2010), provided the source positions, the starting point for the spectral fitting in Section 3.2, and a comparison for estimating the reliability of the results (Section 3.7.2).

Throughout the text, we denote as RoIs, for Regions of Interest, the regions in which we extract the data. We use the Test Statistic $TS = 2 \log(\mathcal{L}/\mathcal{L}_0)$ (Mattox et al. 1996) to quantify how significantly a source emerges from the background, comparing the maximum value of the likelihood function \mathcal{L} over the RoI including the source in the model with \mathcal{L}_0 , the value without the source. Here and everywhere else in the text, “log” denotes the natural logarithm. The names of executables and libraries of the Science Tools are written in italics.

⁸⁹ See <http://fermi.gsfc.nasa.gov/ssc/data/analysis/documentation/Cicerone/>.

3.1. Detection and Localization

This section describes the generation of a list of candidate sources, with locations and initial spectral fits. This initial stage uses *pointlike*. Compared with the *gtlike*-based analysis described in Sections 3.2–3.7, it uses the same time range and IRFs, but the partitioning of the sky, the weights, the computation of the likelihood function, and its optimization are independent. The zenith angle cut is set to 100° . Energy dispersion is neglected for the sources (we show in Section 4.2.2 that it is a small effect). Events below 100 MeV are not useful for source detection and localization, and are ignored at this stage.

3.1.1. Detection Settings

The process started with an initial set of sources, from the 8 yr FL8Y analysis, including the 75 spatially extended sources listed in Section 3.4, and the three-component representation of the Crab (Section 3.3). The same spectral models were considered for each source as in Section 3.3, but the favored model (power law, curved, or pulsar-like) was not necessarily the same. The point-source locations were also re-optimized.

The generation of a candidate list of additional sources, with locations and initial spectral fits, is substantially the same as for 3FGL. The sky was partitioned using HEALPix⁹⁰ (Górski et al. 2005) with $N_{\text{side}} = 12$, resulting in 1728 tiles of $\sim 24 \text{ deg}^2$ area. (Note: references to N_{side} in the following refer to HEALPix.) The RoIs included events in cones of 5° radius about the center of the tiles. The data were binned according to energy, 16 energy bands from 100 MeV to 1 TeV (up from 14 bands to 316 GeV in 3FGL), *Front* or *Back* event types, and angular position using HEALPix, but with N_{side} varying from 64 to 4096 according to the PSF. Only *Front* events were used for the two bands below 316 MeV, to avoid the poor PSF and contribution of the Earth limb. Thus, the log-likelihood calculation, for each RoI, is a sum over the contributions of 30 energy and event-type bands.

All point sources within the RoI and those nearby, such that the contribution to the RoI was at least 1% (out to 11° for the lowest energy band), were included. Only the spectral model parameters for sources within the central tile were allowed to vary to optimize the likelihood. To account for correlations with fixed nearby sources, and a factor of three overlap for the data (each photon contributes to ~ 3 RoIs), the following iteration process was followed. All 1728 RoIs were optimized independently. Then the process was repeated, until convergence, for all RoIs for which the log-likelihood had changed by more than 10. Their nearest neighbors (presumably affected by the modified sources) were iterated as well.

Another difference from 3FGL was that the diffuse contributions were adjusted globally. We fixed the isotropic diffuse source to be actually constant over the sky but globally refit its spectrum up to 10 GeV, since point-source fits are insensitive to diffuse emission above this energy. The Galactic diffuse emission component also was treated quite differently. Starting with a version of the Galactic diffuse model (Section 2.4.1) without its non-template diffuse γ -ray emission, we derived an alternative adjustment by optimizing the Galactic diffuse normalization for each RoI and the eight bands below 10 GeV. These values were turned into an 8-layer

map, which was smoothed and then applied to the PSF-convolved diffuse model predictions for each band. Next, the corrections were remeasured. This process converged after two iterations, such that no further corrections were needed. The advantage of the procedure, compared to fitting the diffuse spectral parameters in each RoI (Section 3.2), is that the effective predictions do not vary abruptly from an RoI to its neighbors and are unique for each point. Also, it does not constrain the spectral adjustment to be a power law.

After a set of iterations had converged, the localization procedure was applied, and source positions were updated for a new set of iterations. At this stage, new sources were occasionally added using the residual TS procedure described in Section 3.1.2. The detection and localization process resulted in 7841 candidate point sources with $TS > 10$, of which 3179 were new. The fit validation and likelihood weighting were done as in 3FGL, except that, due to the improved representation of the Galactic diffuse, the effect of the weighting factor was less severe.

The *pointlike* unweighting scheme is slightly different from that described in the 3FGL paper (Section 3.1.2). A measure of the sensitivity to the Galactic diffuse component is the average count density for the RoI divided by the peak value of the PSF, N_{diff} , which represents a measure of the diffuse background under the point source. For the RoI at the Galactic center, and the lowest energy band, this is 4.15×10^4 counts. We unweight the likelihood for all energy bands by effectively limiting this implied precision to 2%, corresponding to 2500 counts. As before, we divide the log-likelihood contribution from this energy band by $\max(1, N_{\text{diff}}/2500)$. For the aforementioned case, this value is 16.6. A consequence is to increase the spectral fit uncertainty for the lowest energy bins for every source in the RoI. The value for this unweighting factor was determined by examining the distribution of the deviations between fluxes fitted in individual energy bins and the global spectral fit (similar to what is done in Section 3.5). The 2% precision was set such that the rms for the distribution of positive deviations in the most sensitive lowest energy band was near the statistical expectation. (Negative deviations are distorted by the positivity constraint, resulting in an asymmetry of the distribution).

An important validation criterion is the all-sky counts residual map. Since the source overlaps and diffuse uncertainties are most severe at the lowest energy, we present, in Figure 3, the distribution of normalized residuals per pixel, binned with $N_{\text{side}} = 64$, in the 100–177 MeV *Front* energy band. There are 49,920 such pixels, with data counts varying from 92 to 1.7×10^4 . For $|b| > 10^\circ$, the agreement with the expected Gaussian distribution is very good, while it is clear that there are issues along the plane. These are of two types. First, around very strong sources, such as Vela, the discrepancies are perhaps a result of inadequacies of the simple spectral models used, but the (small) effect of energy dispersion and the limited accuracy of the IRFs may contribute. Regions along the Galactic ridge are also evident, a result of the difficulty modeling the emission precisely, the reason we unweight contributions to the likelihood.

3.1.2. Detection of Additional Sources

As in 3FGL, the same implementation of the likelihood used for optimizing source parameters was used to test for the presence of additional point sources. This is inherently

⁹⁰ <http://healpix.sourceforge.net>

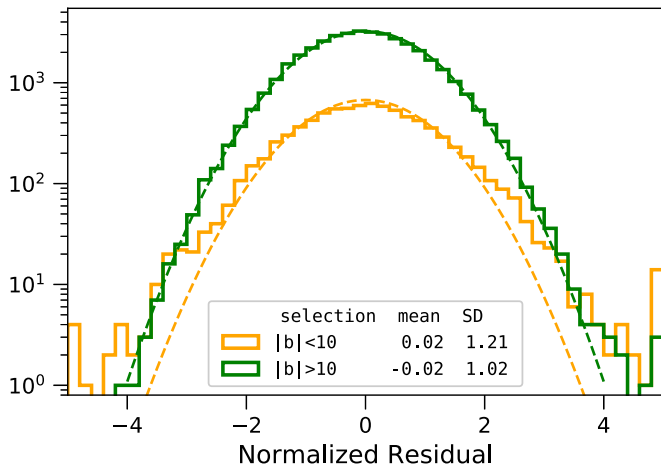


Figure 3. Photon count residuals with respect to the model per $N_{\text{side}} = 64$ bin, for energies 100–177 MeV, normalized by the Poisson uncertainty, that is, $(N_{\text{data}} - N_{\text{model}})/\sqrt{N_{\text{model}}}$. Histograms are shown for the values at high latitude ($|b| > 10^\circ$) and low latitude ($|b| < 10^\circ$) (capped at $\pm 5\sigma$). The dashed lines are the Gaussian expectations for the same number of sources. The legend shows the mean and standard deviation for the two subsets.

iterative, in that the likelihood is valid to the extent that the model used to calculate it is a fair representation of the data. Thus, the detection of the faintest sources depends on accurate modeling of all nearby brighter sources and the diffuse contributions.

The FL8Y source list from which this started represented several such additions from the 4 yr 3FGL. As before, an iteration starts with choosing a HEALPix $N_{\text{side}} = 512$ grid, 3.1 M points with average separation 0.15 degrees. But now, instead of testing a single power-law spectrum, we try five spectral shapes; three are power laws with different indices, two with significant curvature. Table 3 lists the spectral shapes used for the templates. They are shown in Figure 4.

For each trial position, and each of the five templates, the normalizations were optimized, and the resulting TS associated with the pixel. Then, as before, but independently for each template, a cluster analysis selected groups of pixels with $\text{TS} > 16$, as compared to $\text{TS} > 10$ for 3FGL. Each cluster defined a seed, with a position determined by weighting the TS values. Finally, the five sets of potential seeds were compared and, for those within 1° , the seed with the largest TS was selected for inclusion.

Each candidate was added to its respective RoI, then fully optimized, including localization, during a full likelihood optimization including all RoIs. The combined results of two iterations of this procedure, starting from a *pointlike* model including only sources imported from the FL8Y source list, are summarized in Table 3, which shows the number for each template that was successfully added to the *pointlike* model, and the number finally included in 4FGL. The reduction is mostly due to the $\text{TS} > 25$ requirement in 4FGL, as applied to the *gtlike* calculation (Section 3.2), which uses different data and smaller weights. The selection is even stricter ($\text{TS} > 34$, Section 3.3) for sources with curved spectra. Several candidates at high significance were not accepted because they were too close to even brighter sources, or inside extended sources, and thus unlikely to be independent point sources.

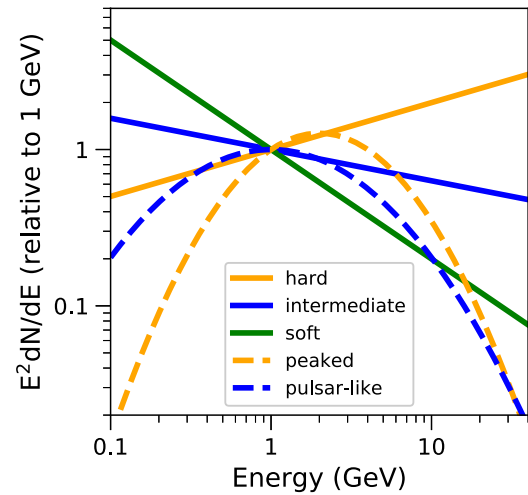


Figure 4. Spectral shape templates used in source finding.

Table 3
Spectral Shapes for Source Search

α	β	E_0 (GeV)	Template	Generated	Accepted
1.7	0.0	50.00	Hard	471	101
2.2	0.0	1.00	Intermediate	889	177
2.7	0.0	0.25	Soft	476	84
2.0	0.5	2.00	Peaked	686	151
2.0	0.3	1.00	Pulsar-like	476	84

Note. The spectral parameters α , β , and E_0 refer to the LogParabola spectral shape (Equation (2)). The last two columns show the number, for each shape, that were successfully added to the *pointlike* model, and the number accepted for the final 4FGL list.

3.1.3. Localization

The position of each source was determined by maximizing the likelihood with respect to its position only. That is, all other parameters are kept fixed. The possibility that a shifted position would affect the spectral models or positions of nearby sources is accounted for by iteration. In the ideal limit of large statistics, the log-likelihood is a quadratic form in any pair of orthogonal angular variables, assuming small angular offsets. We define Localization Test Statistic (LTS) to be twice the log of the likelihood ratio of any position with respect to the maximum; the LTS evaluated for a grid of positions is called an LTS map. We fit the distribution of LTS to a quadratic form to determine the uncertainty ellipse (position, major and minor axes, and orientation). The fitting procedure starts with a prediction of the LTS distribution from the current elliptical parameters. From this, it evaluates the LTS for eight positions in a circle of a radius corresponding to twice the geometric mean of the two Gaussian sigmas. We define a measure, the localization quality (LQ), of how well the actual LTS distribution matches this expectation as the sum of squares of differences at those eight positions. The fitting procedure determines a new set of elliptical parameters from the eight values. In the ideal case, this is a linear problem and one iteration is sufficient from any starting point. To account for finite statistics or distortions due to inadequacies of the model, we iterate until changes are small. The procedure effectively minimizes LQ.

We flagged apparently significant sources that do not have good localization fits ($LQ > 8$) with Flag 9 (Section 3.7.3), and for them, we estimated the position and uncertainty by performing a moment analysis of an LTS map instead of fitting a quadratic form. Some sources that did not have a well-defined peak in the likelihood were discarded by hand, on the consideration that they were most likely related to residual diffuse emission. Another possibility is that two adjacent sources produce a dumbbell-like shape; for a few of these cases, we added a new source by hand.

As in 3FGL, we checked the sources spatially associated with 984 AGN counterparts, comparing their locations with the well-measured positions of the counterparts. Better statistics allowed examination of the distributions of the differences separately for bright, dim, and moderate-brightness sources. From this, we estimate the absolute precision Δ_{abs} (at the 95% confidence level) more accurately at $\sim 0^\circ.0068$, up from $\sim 0^\circ.005$ in 3FGL. The systematic factor f_{rel} was 1.06, slightly up from 1.05 in 3FGL. Equation (1) shows how the statistical errors Δ_{stat} are transformed into total errors Δ_{tot} :

$$\Delta_{\text{tot}}^2 = (f_{\text{rel}} \Delta_{\text{stat}})^2 + \Delta_{\text{abs}}^2, \quad (1)$$

which is applied to both ellipse axes.

3.2. Significance and Thresholding

The framework for this stage of the analysis is inherited from the 3FGL catalog. It splits the sky into RoIs, varying typically half a dozen sources near the center of the RoI at the same time. Each source is entered into the fit with the spectral shape and parameters obtained by *pointlike* (Section 3.1), the brightest sources first. Soft sources from *pointlike* within $0^\circ.2$ of bright ones were intentionally deleted. They appear because the simple spectral models we use are not sufficient to account for the spectra of bright sources, but including them would bias the spectral parameters. There are 1748 RoIs for 4FGL, listed in the *ROIIs* extension of the catalog (Appendix A). The global best fit is reached iteratively, injecting the spectra of sources in the outer parts of the RoI from the previous step or iteration. In this approach, the diffuse emission model (Section 2.4) is taken from the global templates (including the spectrum, unlike what is done with *pointlike* in Section 3.1), but it is modulated in each RoI by three parameters: normalization (at 1 GeV) and small corrective slope of the Galactic component, and normalization of the isotropic component.

Among the more than 8000 seeds coming from the localization stage, we keep only sources with $TS > 25$, corresponding to a significance of just over 4σ evaluated from the χ^2 distribution with four degrees of freedom (position and spectral parameters of a power-law source; Mattox et al. 1996). The model for the current RoI is readjusted after removing each seed below threshold. The low-energy flux of the seeds below threshold (a fraction of which are real sources) can be absorbed by neighboring sources closer than the PSF radius. As in 3FGL, we manually added known LAT pulsars that could not be localized by the automatic procedure without phase selection. However, none of those reached $TS > 25$ in 4FGL.

We introduced a number of improvements with respect to 3FGL (by decreasing order of importance):

1. In 3FGL, we had already noted that systematic errors due to an imperfect modeling of diffuse emission were larger than statistical errors in the Galactic plane and were at the

same level over the entire sky. With twice as much exposure and an improved effective area at low energy with Pass 8, the effect now dominates. The approach adopted in 3FGL (comparing runs with different diffuse models) allowed us to characterize the effect globally and flag the worst offenders but left purely statistical errors on source parameters. In 4FGL, we introduce weights in the maximum likelihood approach (Appendix B). This allows obtaining directly (although in an approximate way) smaller TS and larger parameter errors, reflecting the level of systematic uncertainties. We estimated the relative spatial and spectral residuals in the Galactic plane where the diffuse emission is strongest. The resulting systematic level $\epsilon \sim 3\%$ was used to compute the weights. This is by far the most important improvement, which avoids reporting many dubious soft sources.

2. The automatic iteration procedure at the next-to-last step of the process was improved. There are now two iteration levels. In a standard iteration, the sources and source models are fixed and only the parameters are free. An RoI and all its neighbors are run again until $\log \mathcal{L}$ does not change by more than 10 from the previous iteration. Around that, we introduce another iteration level (superiterations). At the first iteration of a given superiteration, we reenter all seeds and remove (one by one) those with $TS < 16$. We also systematically check a curved spectral shape versus a power-law fit to each source at this first iteration and keep the curved spectral shape if the fit is significantly better (Section 3.3). At the end of a superiteration, an RoI (and its neighbors) enters the next superiteration until $\log \mathcal{L}$ does not change by more than 10 from the last iteration of the previous superiteration. This procedure stabilizes the spectral shapes, particularly in the Galactic plane. Seven superiterations were required to reach full convergence.
3. The fits are now performed from 50 MeV to 1 TeV, and the overall significances (*Signif_Avg*) as well as the spectral parameters refer to the full band. The total energy flux, on the other hand, is still reported between 100 MeV and 100 GeV. For hard sources with photon index less than 2, integrating up to 1 TeV would result in much larger uncertainties. The same is true for soft sources with photon indices larger than 2.5 when integrating down to 50 MeV.
4. We considered the effect of energy dispersion in the approximate way implemented in the Science Tools. The effect of energy dispersion is calculated globally for each source and applied to the whole 3D model of that source, rather than accounting for energy dispersion separately in each pixel. This approximate rescaling captures the main effect (which is only a small correction, see Section 4.2.2) at a very minor computational cost. In evaluating the likelihood function, the effects of energy dispersion were not applied to the isotropic background and the Sun/Moon components whose spectra were obtained from the data without considering energy dispersion.
5. We used smaller RoIs at higher energy because we are interested in the core region only, which contains the sources whose parameters come from that RoI (sources in the outer parts of the RoI are entered only as background). The core region is the same for all energy intervals, and the RoI is obtained by adding a ring to that core region, whose

width adapts to the PSF and therefore decreases with energy (Table 2). This does not significantly affect the result, because the outer parts of the RoI would not have been correlated to the inner sources at high energy anyway, but this saves memory and CPU time.

- At the last step of the fitting procedure, we tested all spectral shapes described in Section 3.3 (including log-normal for pulsars and cutoff power law for other sources), readjusting the parameters (but not the spectral shapes) of neighboring sources.

We used only binned likelihood analysis in 4FGL because unbinned mode is much more CPU intensive and does not support weights or energy dispersion. We split the data into fifteen components, selected according to PSF event type and described in Table 2. As explained in Section 2.4.4, at low energy, we kept only the event types with the best PSF. Each event type selection has its own isotropic diffuse template (because it includes residual charged-particle background, which depends on event type). A single component is used above 10 GeV to save memory and CPU time: at high energy, the background under the PSF is small, so keeping the event types separate does not markedly improve significance; it would help for localization, but this is done separately (Section 3.1.3).

A known inconsistency in acceptance exists between Pass 8 PSF event types. It is easy to see on bright sources or the entire RoI spectrum and peaks at the level of 10% between PSF0 (positive residuals, underestimated effective area) and PSF3 (negative residuals, overestimated effective area) at a few GeV. In that range, all event types were considered, so the effect on source spectra average out. Below 1 GeV, the PSF0 event type was discarded but the discrepancy is lower at low energy. We checked by comparing with preliminary corrected IRFs that the energy fluxes indeed tend to be underestimated, but by only 3%. The bias on power-law index is less than 0.01.

3.3. Spectral Shapes

The spectral representation of sources largely follows what was done in 3FGL, considering three spectral models (power law, power law with subexponential cutoff, and log-normal). We changed two important aspects of how we parameterize the cutoff power law:

- The cutoff energy was replaced by an exponential factor (a in Equation (4)), which is allowed to be positive. This makes the simple power law a special case of the cutoff power law and allows for fitting of that model to all sources, even those with negligible curvature.
- We set the exponential index (b in Equation (4)) to $2/3$ (instead of 1) for all pulsars that are too faint for it to be left free. This recognizes the fact that $b < 1$ (subexponential) in all six bright pulsars that have b free in 4FGL. Three have $b \sim 0.55$ and three have $b \sim 0.75$. We chose $2/3$ as a simple intermediate value.

For all three spectral representations in 4FGL, the normalization (flux density K) is defined at a reference energy E_0 chosen such that the error on K is minimal. E_0 appears as `Pivot_Energy` in the FITS table version of the catalog (Appendix A). The 4FGL spectral forms are thus:

- A log-normal representation (`LogParabola` under `SpectrumType` in the FITS table) for all significantly curved spectra except pulsars, 3C 454.3 and the Small

Magellanic Cloud (SMC):

$$\frac{dN}{dE} = K \left(\frac{E}{E_0} \right)^{-\alpha - \beta \log(E/E_0)} \quad (2)$$

The parameters K , α (spectral slope at E_0), and the curvature β appear as `LP_Flux_Density`, `LP_Index` and `LP_beta` in the FITS table, respectively. No significantly negative β (spectrum curved upwards) was found. The maximum allowed β was set to 1 as in 3FGL. Those parameters were used for fitting because they allow for the minimization of the correlation between K and the other parameters. However, a more natural representation would use the peak energy E_{peak} at which the spectrum is maximum (in νF_ν representation)

$$E_{\text{peak}} = E_0 \exp \left(\frac{2 - \alpha}{2\beta} \right). \quad (3)$$

- A subexponentially cutoff power law for all significantly curved pulsars (`PLSuperExpCutoff` under `SpectrumType` in the FITS table):

$$\frac{dN}{dE} = K \left(\frac{E}{E_0} \right)^{-\Gamma} \exp(a(E_0^b - E^b)) \quad (4)$$

where E_0 and E in the exponential are expressed in MeV. The parameters K , Γ (low-energy spectral slope), a (exponential factor in MeV^{-b}), and b (exponential index) appear as `PLEC_Flux_Density`, `PLEC_Index`, `PLEC_Expfactor` and `PLEC_Exp_Index` in the FITS table, respectively. Note that in the Science Tools that spectral shape is called `PLSuperExpCutoff2` and no E_0^b term appears in the exponential, so the error on K (`Unc_PLEC_Flux_Density` in the FITS table) was obtained from the covariance matrix. The minimum Γ was set to 0 (in 3FGL it was set to 0.5, but a smaller b results in a smaller Γ). No significantly negative a (spectrum curved upwards) was found.

- A simple power-law form (Equation (4) without the exponential term) for all sources not significantly curved. For those parameters K and Γ appear as `PL_Flux_Density` and `PL_Index` in the FITS table.

The power law is a mathematical model that is rarely sustained by astrophysical sources over as broad a band as 50 MeV to 1 TeV. All bright sources in 4FGL are actually significantly curved downwards. Another drawback of the power-law model is that it tends to exceed the data at both ends of the spectrum, where constraints are weak. It is not a worry at high energy, but at low energy (broad PSF), the collection of faint sources modeled as power laws generates an effectively diffuse excess in the model, which will make the curved sources more curved than they should be. Using a `LogParabola` spectral shape for all sources would be physically reasonable, but the very large correlation between sources at low energy due to the broad PSF makes that unstable.

We use the curved representation in the global model (used to fit neighboring sources) if $\text{TS}_{\text{curv}} > 9$ (3σ significance) where $\text{TS}_{\text{curv}} = 2 \log(\mathcal{L}(\text{curved spectrum})/\mathcal{L}(\text{power-law}))$. This is a step down from 3FGL or FL8Y, where the threshold was at 16, or 4σ , while preserving stability. The curvature significance is reported as `LP_SigCurv` or `PLEC_SigCurv`, replacing the former unique `Signif_Curve` column of 3FGL. Both values were derived from TS_{curv} and corrected

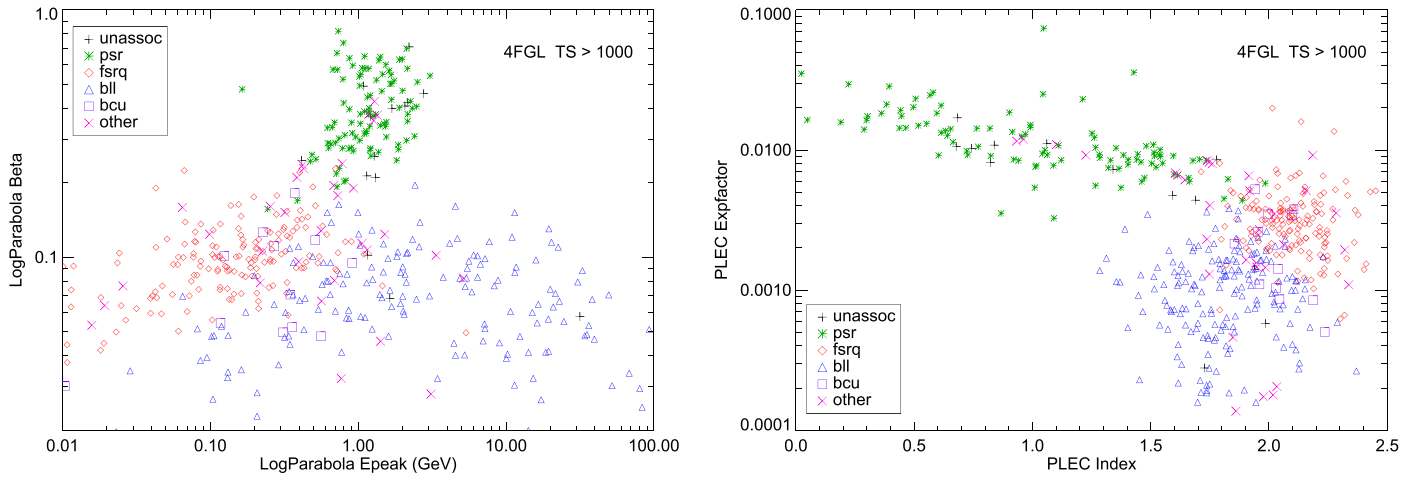


Figure 5. Spectral parameters of all bright sources ($TS > 1000$). The different source classes (Section 6) are depicted by different symbols and colors. Left panel: log-normal shape parameters E_{peak} (Equation (3)) and β . Right panel: subexponentially cutoff power-law shape parameters Γ and a (Equation (4)).

for systematic uncertainties on the effective area following Equation (3) of 3FGL. As a result, 51 LogParabola sources (with $TS_{\text{curv}} > 9$) have $LP_SigCurv$ less than 3.

Sources with curved spectra are considered significant whenever $TS > 25 + 9 = 34$. This is similar to the 3FGL criterion, which requested $TS > 25$ in the power-law representation, but accepts a few more strongly curved faint sources (pulsar-like).

One more pulsar (PSR J1057–5226) was fit with a free exponential index, besides the six sources modeled in this way in 3FGL. The Crab was modeled with three spectral components, as in 3FGL, but the inverse-Compton emission of the nebula (now an extended source, Section 3.4) was represented as a log-normal instead of a simple power law. The parameters of that component were fixed to $\alpha = 1.75$, $\beta = 0.08$, $K = 5.5 \times 10^{-13}$ ph cm $^{-2}$ MeV $^{-1}$ s $^{-1}$ at 10 GeV, mimicking the broken power law fit by Buehler et al. (2012). They were unstable (too much correlation with the pulsar) without phase selection. Four extended sources had fixed parameters in 3FGL. The parameters in these sources (Vela X, MSH 15–52, γ Cygni, and the Cygnus X cocoon) were freed in 4FGL.

Overall in 4FGL, seven sources (the six brightest pulsars and 3C 454.3) were fit as PLSuperExpCutoff with free b (Equation (4)), 214 pulsars were fit as PLSuperExpCutoff with $b = 2/3$, the SMC was fit as PLSuperExpCutoff with $b = 1$, 1302 sources were fit as LogParabola (including the fixed inverse-Compton component of the Crab and 38 other extended sources), and the rest were represented as power laws. The larger fraction of curved spectra compared to 3FGL is due to the lower TS_{curv} threshold.

The way the parameters are reported has changed as well:

1. The spectral shape parameters are now explicitly associated with the spectral model they come from. They are reported as Shape_Param where Shape is one of PL (PowerLaw), PLEC (PLSuperExpCutoff), or LP (LogParabola) and Param is the parameter name. Columns Shape_Index replace Spectral_Index, which was ambiguous.
2. All sources were fit with the three spectral shapes, so all fields are filled. The curvature significance is calculated twice by comparing power law with both log-normal and exponentially cutoff power law (although only one is

actually used to switch to the curved shape in the global model, depending on whether the source is a pulsar or not). There are also three Shape_Flux_Density columns referring to the same Pivot_Energy. The preferred spectral shape (reported as SpectrumType) remains what is used in the global model, when the source is part of the background (i.e., when fitting the other sources). It is also what is used to derive the fluxes, their uncertainties, and the significance.

This additional information allows us to compare unassociated sources with either pulsars or blazars using the same spectral shape. This is illustrated in Figure 5. Pulsar spectra are more curved than AGNs, and among AGNs, flat-spectrum radio quasars (FSRQs) peak at lower energy than BL Lacs (BLL). It is clear that when the error bars are small (bright sources), any of those plots is very discriminant for classifying sources. They complement the variability versus curvature plot (Figure 8 of the 1FGL paper). We expect most of the (few) bright remaining unassociated sources (black plus signs) to be pulsars, from their location on those plots. The same reasoning implies that most of the unclassified blazars (bcu) should be FSRQs, although the distinction with BL Lacs is less clear-cut than with pulsars. Unfortunately, most unassociated sources are faint ($TS < 100$) and for those, the same plots are very confused, because the error bars become comparable to the ranges of parameters.

3.4. Extended Sources

As in the 3FGL catalog, we explicitly model as spatially extended those LAT sources that have been shown in dedicated analyses to be spatially resolved by the LAT. The catalog process does not involve looking for new extended sources, testing possible extension of sources detected as point-like, nor refitting the spatial shapes of known extended sources.

Most templates are geometrical, so they are not perfect matches to the data and the source detection often finds residuals on top of extended sources, which are then converted into additional point sources. As in 3FGL, those additional point sources were intentionally deleted from the model, except if they met two of the following criteria: associated with a plausible counterpart known at other wavelengths, much harder than the extended source (Pivot_Energy larger by a factor e or more) or very significant ($TS > 100$). Contrary to 3FGL,

Table 4
Extended Sources Modeled in the 4FGL Analysis

4FGL Name	Extended Source	Origin	Spatial Form	Extent [deg]	Reference
J0058.0–7245e	SMC Galaxy	Updated	Map	1.5	Caputo et al. (2016)
J0221.4+6241e	HB 3	New	Disk	0.8	Katagiri et al. (2016b)
J0222.4+6156e	W 3	New	Map	0.6	Katagiri et al. (2016b)
J0322.6–3712e	Fornax A	3FHL	Map	0.35	Ackermann et al. (2016c)
J0427.2+5533e	SNR G150.3+4.5	3FHL	Disk	1.515	Ackermann et al. (2017b)
J0500.3+4639e	HB 9	New	Map	1.0	Araya (2014)
J0500.9–6945e	LMC FarWest	3FHL	Map ^a	0.9	Ackermann et al. (2016d)
J0519.9–6845e	LMC Galaxy	New	Map ^a	3.0	Ackermann et al. (2016d)
J0530.0–6900e	LMC 30DorWest	3FHL	Map ^a	0.9	Ackermann et al. (2016d)
J0531.8–6639e	LMC North	3FHL	Map ^a	0.6	Ackermann et al. (2016d)
J0534.5+2201e	Crab Nebula IC	New	Gaussian	0.03	Ackermann et al. (2018)
J0540.3+2756e	S 147	3FGL	Disk	1.5	Katsuta et al. (2012)
J0617.2+2234e	IC 443	2FGL	Gaussian	0.27	Abdo et al. (2010j)
J0634.2+0436e	Rosette	New	Map	(1.5, 0.875)	Katagiri et al. (2016a)
J0639.4+0655e	Monoceros	New	Gaussian	3.47	Katagiri et al. (2016a)
J0822.1–4253e	Puppis A	3FHL	Disk	0.443	Ackermann et al. (2017b)
J0833.1–4511e	Vela X	2FGL	Disk	0.91	Abdo et al. (2010h)
J0851.9–4620e	Vela Junior	3FHL	Disk	0.978	Ackermann et al. (2017b)
J1023.3–5747e	Westerlund 2	3FHL	Disk	0.278	Ackermann et al. (2017b)
J1036.3–5833e	FGES J1036.3–5833	3FHL	Disk	2.465	Ackermann et al. (2017b)
J1109.4–6115e	FGES J1109.4–6115	3FHL	Disk	1.267	Ackermann et al. (2017b)
J1208.5–5243e	SNR G296.5+10.0	3FHL	Disk	0.76	Ajero et al. (2016b)
J1213.3–6240e	FGES J1213.3–6240	3FHL	Disk	0.332	Ackermann et al. (2017b)
J1303.0–6312e	HESS J1303–631	3FGL	Gaussian	0.24	Aharonian et al. (2005)
J1324.0–4330e	Centaurus A (lobes)	2FGL	Map	(2.5, 1.0)	Abdo et al. (2010d)
J1355.1–6420e	HESS J1356–645	3FHL	Disk	0.405	Ackermann et al. (2017b)
J1409.1–6121e	FGES J1409.1–6121	3FHL	Disk	0.733	Ackermann et al. (2017b)
J1420.3–6046e	HESS J1420–607	3FHL	Disk	0.123	Ackermann et al. (2017b)
J1443.0–6227e	RCW 86	3FHL	Map	0.3	Ajello et al. (2016)
J1501.0–6310e	FHES J1501.0–6310	New	Gaussian	1.29	Ackermann et al. (2018)
J1507.9–6228e	HESS J1507–622	3FHL	Disk	0.362	Ackermann et al. (2017b)
J1514.2–5909e	MSH 15–52	3FHL	Disk	0.243	Ackermann et al. (2017b)
J1533.9–5712e	HESS J1534–571	New	Disk	0.4	Araya (2017)
J1552.4–5612e	MSH 15–56 PWN	New	Map	0.08	Devin et al. (2018)
J1552.9–5607e	MSH 15–56 SNR	New	Map	0.3	Devin et al. (2018)
J1553.8–5325e	FGES J1553.8–5325	3FHL	Disk	0.523	Ackermann et al. (2017b)
J1615.3–5146e	HESS J1614–518	3FGL	Disk	0.42	Lande et al. (2012)
J1616.2–5054e	HESS J1616–508	3FGL	Disk	0.32	Lande et al. (2012)
J1626.9–2431e	FHES J1626.9–2431	New	Gaussian	0.29	Ackermann et al. (2018)
J1631.6–4756e	FGES J1631.6–4756	3FHL	Disk	0.256	Ackermann et al. (2017b)
J1633.0–4746e	FGES J1633.0–4746	3FHL	Disk	0.61	Ackermann et al. (2017b)
J1636.3–4731e	SNR G337.0–0.1	3FHL	Disk	0.139	Ackermann et al. (2017b)
J1642.1–5428e	FHES J1642.1–5428	New	Disk	0.696	Ackermann et al. (2018)
J1652.2–4633e	FGES J1652.2–4633	3FHL	Disk	0.718	Ackermann et al. (2017b)
J1655.5–4737e	FGES J1655.5–4737	3FHL	Disk	0.334	Ackermann et al. (2017b)
J1713.5–3945e	RX J1713.7–3946	3FHL	Map	0.56	H.E.S.S. Collaboration et al. (2018a)
J1723.5–0501e	FHES J1723.5–0501	New	Gaussian	0.73	Ackermann et al. (2018)
J1741.6–3917e	FHES J1741.6–3917	New	Disk	1.65	Ackermann et al. (2018)
J1745.8–3028e	FGES J1745.8–3028	3FHL	Disk	0.528	Ackermann et al. (2017b)
J1801.3–2326e	W 28	2FGL	Disk	0.39	Abdo et al. (2010g)
J1804.7–2144e	HESS J1804–216	3FHL	Disk	0.378	Ackermann et al. (2017b)
J1805.6–2136e	W 30	2FGL	Disk	0.37	Ajello et al. (2012)
J1808.2–2028e	HESS J1808–204	New	Disk	0.65	Yeung et al. (2016)
J1810.3–1925e	HESS J1809–193	New	Disk	0.5	Araya (2018b)
J1813.1–1737e	HESS J1813–178	New	Disk	0.6	Araya (2018b)
J1824.5–1351e	HESS J1825–137	2FGL	Gaussian	0.75	Grondin et al. (2011)
J1834.1–0706e	SNR G24.7+0.6	3FHL	Disk	0.214	Ackermann et al. (2017b)
J1834.5–0846e	W 41	3FHL	Gaussian	0.23	Abramowski et al. (2015)
J1836.5–0651e	FGES J1836.5–0651	3FHL	Disk	0.535	Ackermann et al. (2017b)
J1838.9–0704e	FGES J1838.9–0704	3FHL	Disk	0.523	Ackermann et al. (2017b)
J1840.8–0453e	Kes 73	New	Disk	0.32	Li et al. (2017a)
J1840.9–0532e	HESS J1841–055	3FGL	2D Gaussian	(0.62, 0.38)	Aharonian et al. (2008)
J1852.4+0037e	Kes 79	New	Disk	0.63	Li et al. (2017a)
J1855.9+0121e	W 44	2FGL	2D Ring	(0.30, 0.19)	Abdo et al. (2010i)

Table 4
(Continued)

4FGL Name	Extended Source	Origin	Spatial Form	Extent [deg]	Reference
J1857.7+0246e	HESS J1857+026	3FHL	Disk	0.613	Ackermann et al. (2017b)
J1908.6+0915e	SNR G42.8+0.6	New	Disk	0.6	Li et al. (2017a)
J1923.2+1408e	W 51C	2FGL	2D Disk	(0.375, 0.26)	Abdo et al. (2009a)
J2021.0+4031e	γ Cygni	3FGL	Disk	0.63	Lande et al. (2012)
J2028.6+4110e	Cygnus X cocoon	3FGL	Gaussian	3.0	Ackermann et al. (2011a)
J2045.2+5026e	HB 21	3FGL	Disk	1.19	Pivato et al. (2013)
J2051.0+3040e	Cygnus Loop	2FGL	Ring	1.65	Katagiri et al. (2011)
J2129.9+5833e	FHES J2129.9+5833	New	Gaussian	1.09	Ackermann et al. (2018)
J2208.4+6443e	FHES J2208.4+6443	New	Gaussian	0.93	Ackermann et al. (2018)
J2301.9+5855e	CTB 109	3FHL	Disk	0.249	Ackermann et al. (2017b)
J2304.0+5406e	FHES J2304.0+5406	New	Gaussian	1.58	Ackermann et al. (2018)

Notes. List of all sources that have been modeled as spatially extended. The Origin column gives the name of the *Fermi*-LAT catalog in which that spatial template was introduced. The Extent column indicates the radius for Disk (flat disk) sources, the 68% containment radius for Gaussian sources, the outer radius for Ring (flat annulus) sources, and an approximate radius for Map (external template) sources. The 2D shapes are elliptical; each pair of parameters (a , b) represents the semimajor (a) and semiminor (b) axes.

^a Emissivity model.

that procedure was applied inside the Cygnus X cocoon as well.

The latest compilation of extended *Fermi*-LAT sources prior to this work consists of the 55 extended sources entered in the 3FHL catalog of sources above 10 GeV (Ajello et al. 2017). This includes the result of the systematic search for new extended sources in the Galactic plane ($|b| < 7^\circ$) above 10 GeV (FGES; Ackermann et al. 2017b). Two of those were not propagated to 4FGL:

1. FGES J1800.5–2343 was replaced by the W 28 template from 3FGL, and the nearby excesses (Hanabata et al. 2014) were left to be modeled as point sources.
2. FGES J0537.6+2751 was replaced by the radio template of S 147 used in 3FGL, which fits better than the disk used in the FGES paper (S 147 is a soft source, so it was barely detected above 10 GeV).

The supernova remnant (SNR) MSH 15-56 was replaced by two morphologically distinct components, following Devin et al. (2018): one for the SNR (SNR mask in the paper) and the other one for the pulsar wind nebula (PWN) inside it (radio template). We added back the W 30 SNR on top of FGES J1804.7–2144 (coincident with HESS J1804–216). The two overlap but the best localization clearly moves with energy from W 30 to HESS J1804–216.

Eighteen sources were added, resulting in 75 extended sources in 4FGL:

1. The Rosette nebula and Monoceros SNR (too soft to be detected above 10 GeV) were characterized by Katagiri et al. (2016a). We used the same templates.
2. The systematic search for extended sources outside the Galactic plane above 1 GeV (FHES, Ackermann et al. 2018) found sixteen reliable extended sources. Three of them were already known as extended sources. Two were extensions of the Cen A lobes, which appear larger in γ -rays than the *WMAP* template that we use following Abdo et al. (2010d). We did not consider them, waiting for a new morphological analysis of the full lobes. We ignored two others: M31 (extension only marginally significant, both in FHES and Ackermann et al. 2017a)

and CalTech A (CTA) 1 (SNR G119.5+10.2) around PSR J0007+7303 (not significant without phase gating). We introduced the nine remaining FHES sources, including the inverse-Compton component of the Crab Nebula and the ρ Oph star-forming region (= FHES J1626.9–2431). One of them (FHES J1741.6–3917) was reported by Araya (2018a) as well, with similar extension.

3. Four H.E.S.S. sources were found to be extended sources in the *Fermi*-LAT range as well: HESS J1534–571 (Araya 2017), HESS J1808–204 (Yeung et al. 2016), HESS J1809–193, and HESS J1813–178 (Araya 2018b).
4. Three extended sources were discovered in the search for GeV emission from magnetars (Li et al. 2017a). They contain SNRs (Kes 73, Kes 79, and G42.8+0.6) but are much bigger than the radio SNRs. One of them (around Kes 73) was also noted by Yeung et al. (2017).

Table 4 lists the source name, origin, spatial template, and the reference for the dedicated analysis. These sources are tabulated with the point sources, with the only distinction being that no position uncertainties are reported and their names end in e (see Appendix A). Unidentified point sources inside extended ones are indicated as “xxx field” in the ASSOC2 column of the catalog.

3.5. Flux Determination

Thanks to the improved statistics, the source photon fluxes in 4FGL are reported in seven energy bands (1: 50–100 MeV; 2: 100–300 MeV; 3: 300 MeV–1 GeV; 4: 1–3 GeV; 5: 3–10 GeV; 6: 10–30 GeV; 7: 30–300 GeV) extending both below and above the range (100 MeV–100 GeV) covered in 3FGL. Up to 10 GeV, the data files were exactly the same as in the global fit (Table 2). To get the best sensitivity in band 6 (10–30 GeV), we split the data into four components per event type, using pixel size $0^\circ.04$ for PSF3, $0^\circ.05$ for PSF2, $0^\circ.1$ for PSF1 and $0^\circ.2$ for PSF0. Above 30 GeV (band 7), we used unbinned likelihood, which is as precise while using much smaller files. It does not allow us to correct for energy dispersion, but this is not an important issue in that band. The fluxes were obtained by freezing the power-law index to that obtained in the fit over

Table 5
Definitions of the Analysis Flags

Flag ^a	N_{sources}	Meaning
1	215	Source with TS > 35 which went to TS < 25 when changing the diffuse model (Section 3.7.1) or the analysis method (Section 3.7.2). Sources with TS ≤ 35 are not flagged with this bit because normal statistical fluctuations can push them to TS < 25.
2	215	Moved beyond its 95% error ellipse when changing the diffuse model.
3	342	Flux (>1 GeV) or energy flux (>100 MeV) changed by more than 3σ when changing the diffuse model or the analysis method. Requires also that the flux change by more than 35% (to not flag strong sources).
4	212	Source-to-background ratio less than 10% in highest band in which TS > 25. Background is integrated over πr_{68}^2 or 1 square degree, whichever is smaller.
5	398	Closer than θ_{ref} ^b from a brighter neighbor.
6	92	On top of an interstellar gas clump or small-scale defect in the model of diffuse emission; equivalent to the c designator in the source name (Section 3.7.1).
7	...	Not used.
8	...	Not used.
9	136	Localization Quality > 8 in <i>pointlike</i> (Section 3.1) or long axis of 95% ellipse > 0.25.
10	27	$\sum_i S_i^2 > 20.5$ or $S_i^2 > 9$ in any band (Equation (5)).
11	...	Not used.
12	103	Highly curved spectrum; LP_beta fixed to 1 or PLEC_Index fixed to 0 (see Section 3.3).

Notes.

^a In the FITS version (see Appendix A), the values are encoded as individual bits in a single column, with Flag n having value $2^{(n-1)}$.

^b θ_{ref} is defined in the highest band in which source TS > 25, or the band with highest TS if all are < 25. θ_{ref} is set to 3.77 below 100 MeV, 1.68 between 100 and 300 MeV (FWHM), 1.03 between 300 MeV and 1 GeV, 0.76 between 1 and 3 GeV (in-between FWHM and $2 r_{68}$), 0.49 between 3 and 10 GeV and 0.25 above 10 GeV ($2 r_{68}$).

the full range and adjusting the normalization in each spectral band. For the curved spectra (Section 3.3), the photon index in a band was set to the local spectral slope at the logarithmic mid-point of the band $\sqrt{E_n E_{n+1}}$, restricted to be in the interval [0,5].

In each band, the analysis was conducted in the same way as for the 3FGL catalog. To adapt more easily to new band definitions, the results (photon fluxes and uncertainties, νF_ν differential fluxes, and significances) are reported in a set of four vector columns (Appendix A: Flux_Band, Unc_Flux_Band, nuFnu_Band, Sqrt_TS_Band) instead of a set of four columns per band as in previous FGL catalogs.

The spectral fit quality is computed in a more precise way than in 3FGL from twice the sum of log-likelihood differences, as we did for the variability index (Section 3.6 of the 2FGL paper). The contribution from each band S_i^2 also accounts for systematic uncertainties on effective area via

$$S_i^2 = \frac{2\sigma_i^2}{\sigma_i^2 + (f_i^{\text{rel}} F_i^{\text{fit}})^2} \log [\mathcal{L}_i(F_i^{\text{best}}) / \mathcal{L}_i(F_i^{\text{fit}})] \quad (5)$$

where i runs over all bands, F_i^{fit} is the flux predicted by the global model, F_i^{best} is the flux fitted to band i alone, σ_i is the statistical error (upper error if $F_i^{\text{best}} \leq F_i^{\text{fit}}$, lower error if $F_i^{\text{best}} > F_i^{\text{fit}}$) and the spectral fit quality is simply $\sum_i S_i^2$. The systematic uncertainties⁹¹ f_i^{rel} are set to 0.15 in the first band, 0.1 in the second and the last bands, and 0.05 in bands 3–6. The uncertainty is larger in the first band because only PSF3 events are used.

Too large values of spectral fit quality are flagged (Flag 10 in Table 5). Since there are seven bands and (for most sources, which are fit with the power-law model) two free parameters,

the flag is set when $\sum_i S_i^2 > 20.5$ (probability 10^{-3} for a χ^2 distribution with five degrees of freedom). Only six sources trigger this. We also set the same flag whenever any individual band is off by more than 3σ ($S_i^2 > 9$). This occurs in 26 sources. Among the 27 sources flagged with Flag 10 (examples in Figure 6), the Vela and Geminga pulsars are very bright sources for which our spectral representation is not good enough. A few show signs of a real second component in the spectrum, such as Cen A (H.E.S.S. Collaboration et al. 2018b). Several would be better fit by a different spectral model: the Large Magellanic Cloud (LMC) probably decreases at high energy as a power law like our own Galaxy, and 4FGL J0336.0+7502 is better fit by a PLSuperExpCutoff model. The latter is an unassociated source at 15° latitude, which has a strongly curved spectrum and is not variable: it is a good candidate for a millisecond pulsar. Other sources show deviations at low energy and are in confused regions or close to a brighter neighbor, such as the Cygnus X cocoon. This extended source contains many point sources inside it, and the PSF below 300 MeV is too broad to provide a reliable separation.

The fluxes in the 50–100 MeV band are very hard to estimate because of the enormous confusion. The average distance between sources (1.7°) is about equal to the half width at half maximum of PSF3 events in that band, so it is nearly always possible to set a source to 0 and compensate by a suitable combination of flux adjustments in its neighbors. This is why only 34 sources have TS > 25 in that band (all are bright sources with global TS > 700). This is far fewer than the 198 low-energy (30–100 MeV) *Fermi*-LAT sources reported by Principe et al. (2018, 1FLE). The reason for this is that in 4FGL, we consider that even faint sources in the catalog can have strong low-energy emission, so the total source flux is distributed over 5000 sources, whereas 1FLE focused on finding individual peaks.

⁹¹ See https://fermi.gsfc.nasa.gov/ssc/data/analysis/LAT_caveats.html.

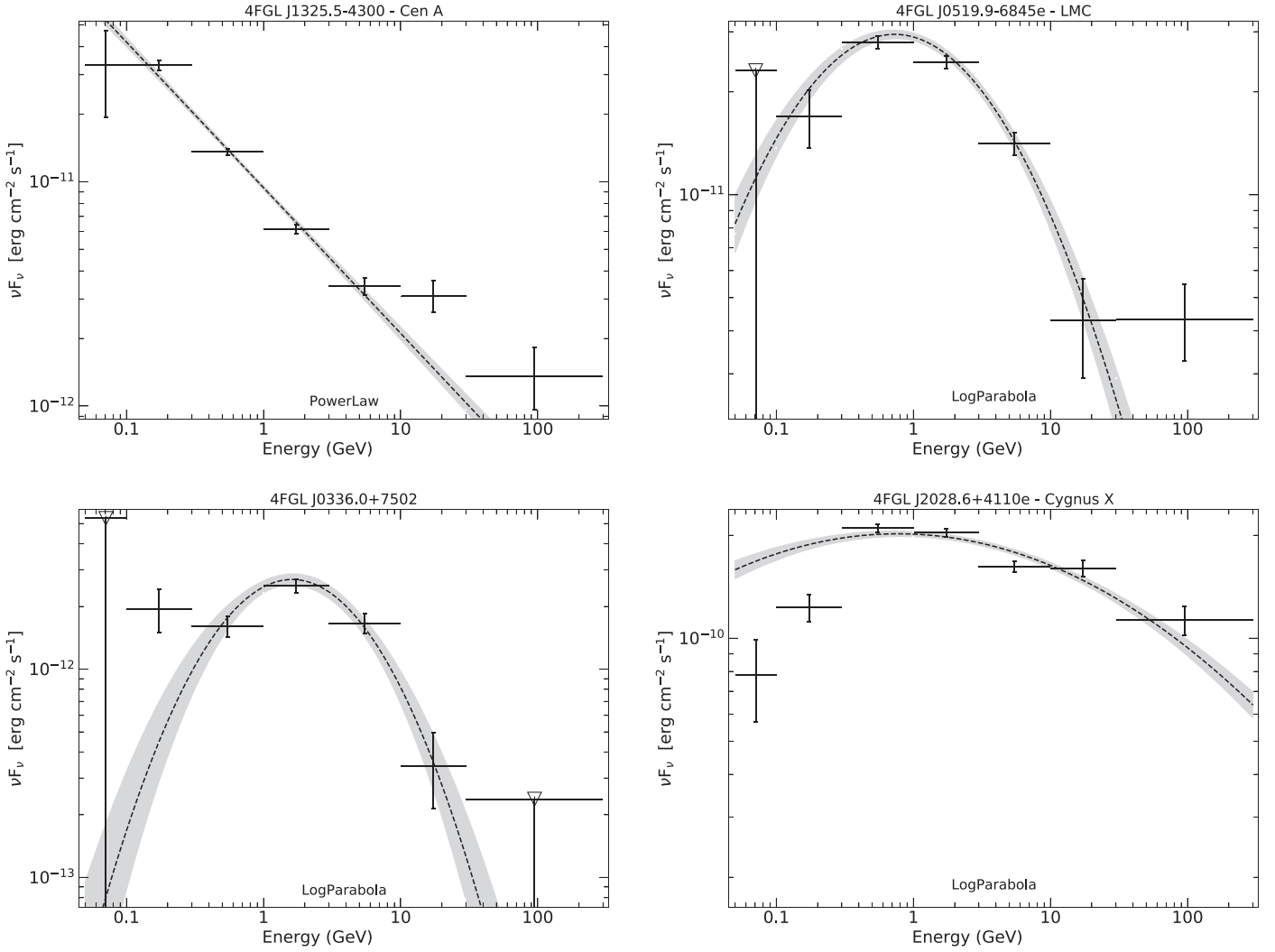


Figure 6. Spectral energy distributions of four sources flagged with bad spectral fit quality (Flag 10 in Table 5). On all plots, the dashed line is the best fit from the analysis over the full energy range, and the gray shaded area shows the uncertainty obtained from the covariance matrix on the spectral parameters. Downward triangles indicate upper limits at 95% confidence level. The vertical scale is not the same in all plots. Top left panel: the Cen A radio galaxy (4FGL J1325.5–4300) fit by a power law with $\Gamma = 2.65$. It is a good representation up to 10 GeV, but the last two points deviate from the power-law fit. Top right panel: the Large Magellanic Cloud (4FGL J0519.9–6845e). The fitted LogParabola spectrum appears to drop too fast at high energy. Bottom left panel: the unassociated source 4FGL J0336.0+7502. The low-energy points deviate from the LogParabola fit. Bottom right panel: the Cygnus X cocoon (4FGL J2028.6+4110e). The deviation from the LogParabola fit at the first two points is probably spurious, due to source confusion.

At the other extreme, 618 sources have $TS > 25$ in the 30 to 300 GeV band, which is entirely limited by photon counting ($TS > 25$ in that band corresponds to about five events). Only 13 of those are not associated with a 3FHL or FHES source. The brightest of them (at $TS = 54$ in that band) is a hard source associated with 1RXS J224123.5+294244, mostly significant in the last year, after the 3FHL time range.

As in past FGL catalogs, the photon fluxes between 1 and 100 GeV as well as the energy fluxes between 100 MeV and 100 GeV were derived from the full-band analysis assuming the best spectral shape, and their uncertainties come from the covariance matrix. Even though the full analysis is carried out down to 50 MeV and up to 1 TeV in 4FGL, we have not changed the energy range over which we quote fluxes so that they can be easily compared with fluxes in past catalogs. The photon fluxes above 100 GeV are negligible except in the very hardest power-law sources, and the energy fluxes below 100 MeV and above 100 GeV are not precisely measured (even for soft and hard sources, respectively).

3.6. Variability

3.6.1. One-year Intervals

We started by computing light curves over 1 yr intervals. This is much faster and more stable than fitting smaller time intervals, and provides a good variability assessment already. We used binned likelihood and the same data as in the main run up to 10 GeV (Table 2), but to save disk space and CPU time, we merged event types together. Above 10 GeV, we used unbinned likelihood (more efficient when there are few events). We ignored events above 100 GeV (unimportant for variability).

As in 3FGL, the fluxes in each interval were obtained by freezing the spectral parameters to those obtained in the fit over the full range and adjusting the normalization. As in previous FGL catalogs, the fluxes in each interval are reported as photon fluxes between 0.1 and 100 GeV.

The weights appropriate for one year were computed using the procedure explained in Appendix B, entering the same data

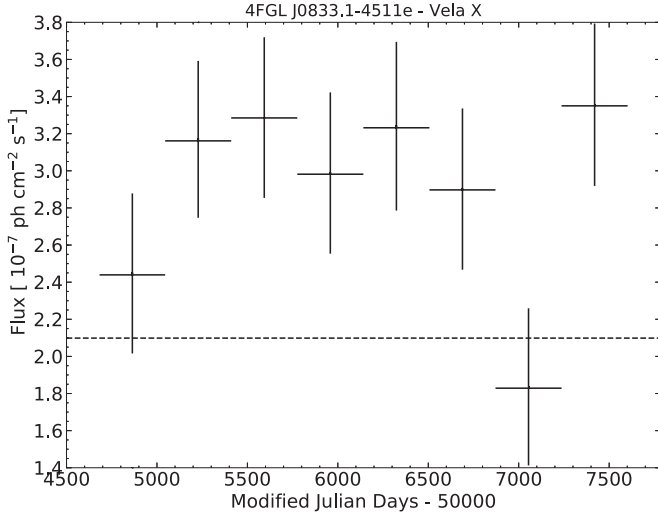


Figure 7. Light curve of Vela X (4FGL J0833.1–4511e) in the 0.1 to 100 GeV band. It is an extended source that should not be variable. Indeed the yearly fluxes are compatible with a constant (the average flux is $2.9 \times 10^{-7} \text{ ph cm}^{-2} \text{ s}^{-1}$) but not with the flux extracted over the full eight years (dashed line, too low). That inconsistency is due to differences in the data analysis settings between the global fit and the fits per year (the weights in particular). Vela X is very close to the very bright Vela pulsar, so it is strongly attenuated by the weights. For most sources, the average flux is much closer to the global flux.

cube divided by eight (we use the same weights in each year), and ignoring the last steps specific to splitting event types. The weights are of course much larger than those for 8 yr, but remain a significant correction (the weights are less than 0.2 in the Galactic Ridge up to 300 MeV). We used the same Sun/Moon model for each year. This amounts to neglecting the modulation of their intrinsic flux along the 11 yr solar cycle.

Because of the different weights between the full analysis and that in 1 yr intervals, the average flux from the light curve F_{av} can differ somewhat from the flux in the total analysis F_{glob} (low energies are less attenuated in the analysis over 1 yr intervals). This is illustrated in Figure 7. In 4FGL, we compute the variability index TS_{var} (reported as `Variability_Index` in the FITS file) as

$$\text{TS}_{\text{var}} = 2 \sum_i \log \left[\frac{\mathcal{L}_i(F_i)}{\mathcal{L}_i(F_{\text{glob}})} \right] - \max(\chi^2(F_{\text{glob}}) - \chi^2(F_{\text{av}}), 0) \quad (6)$$

$$\chi^2(F) = \sum_i \frac{(F_i - F)^2}{\sigma_i^2} \quad (7)$$

where F_i are the individual flux values, $\mathcal{L}_i(F)$ is the likelihood in the interval i assuming flux F , and σ_i are the errors on F_i (upper error if $F_i \leq F$, lower error if $F_i > F$). The first term in Equation (6) is the same as Equation (4) of 2FGL. The second term corrects (in the Gaussian limit) for the difference between F_{glob} and F_{av} (since the average flux is known only at the very end, it could not be entered when computing $\mathcal{L}_i(F)$). We subtract the second term only when it is positive (it is not necessarily positive because the best χ^2 is reached at the average weighted by σ_i^{-2} , not the straight average). On the other hand, we did not correct the variability index for the relative systematic error, which is already accounted for in the weighting procedure.

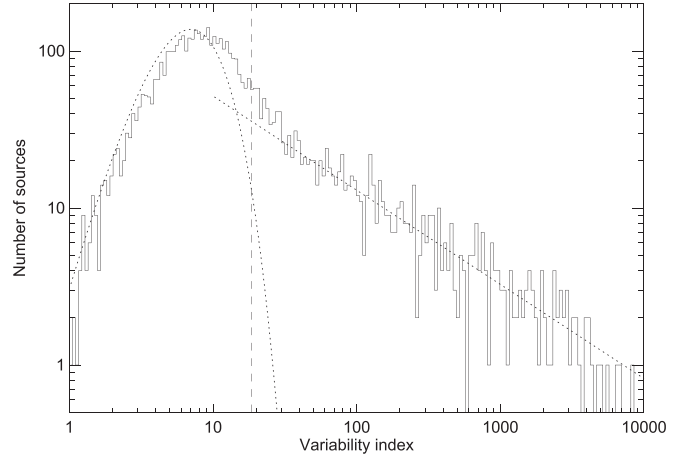


Figure 8. Distribution of the variability index (Equation (6)) over one-year intervals. The dotted line at left is the χ^2 distribution for seven degrees of freedom, expected for a set of non-variable sources. The dotted line at right is a power law decreasing as $\text{TS}_{\text{var}}^{-0.6}$. The vertical dashed line is the threshold above which we consider that a source is likely variable.

The distribution of observed TS_{var} is shown in Figure 8. It looks like a composite of a power-law distribution and a $\chi^2(7)$ distribution with $N_{\text{int}} - 1 = 7$ degrees of freedom, where N_{int} is the number of intervals. The left branch corresponds both to constant sources (such as most pulsars) and sources too faint to have measurable variability. There are many blazars among them, which are most likely just as variable as brighter blazars. This contribution of real variability to TS_{var} is the reason why the histogram is a little offset to the right of the $\chi^2(7)$ distribution (that offset is absent in the Galactic plane, and stronger off the plane).

Variability is considered probable when $\text{TS}_{\text{var}} > 18.48$, corresponding to 99% confidence in a $\chi^2(7)$ distribution. We find 1327 variable sources with that criterion. After the χ^2 -based correction of Equation (6), Vela X remains below that threshold. One extended source still exceeds the variability threshold. This is HESS J1420–607 (Figure 9), confused with its parent pulsar PSR J1420–6048. A similar flux transfer occurred in the third year between the Crab pulsar and the Crab Nebula. This can be understood because the synchrotron emission of the nebula becomes much harder during flares, while our pipeline assumes the soft power-law fit over the full interval applies throughout. None of those variabilities are real.

Besides the Crab and the known variable pulsars PSR J1227–4853 (Johnson et al. 2015) and PSR J2021+4026 (Allafort et al. 2013), three other pulsars are above the variability threshold. Two are just above it and could be chance occurrences (there are more than 200 pulsars, so we expect two above the 1% threshold). The last one is PSR J2043+2740 (Figure 10), which looks like a case of genuine variability (secular flux decrease by a factor of three).

In 4FGL, we report the fractional variability of the sources in the FITS file as `Frac_Variability`. It is defined for each source from the excess variance on top of the statistical and systematic fluctuations:

$$\text{Var} = \frac{1}{N_{\text{int}} - 1} \sum_i (F_i - F_{\text{av}})^2 \quad (8)$$

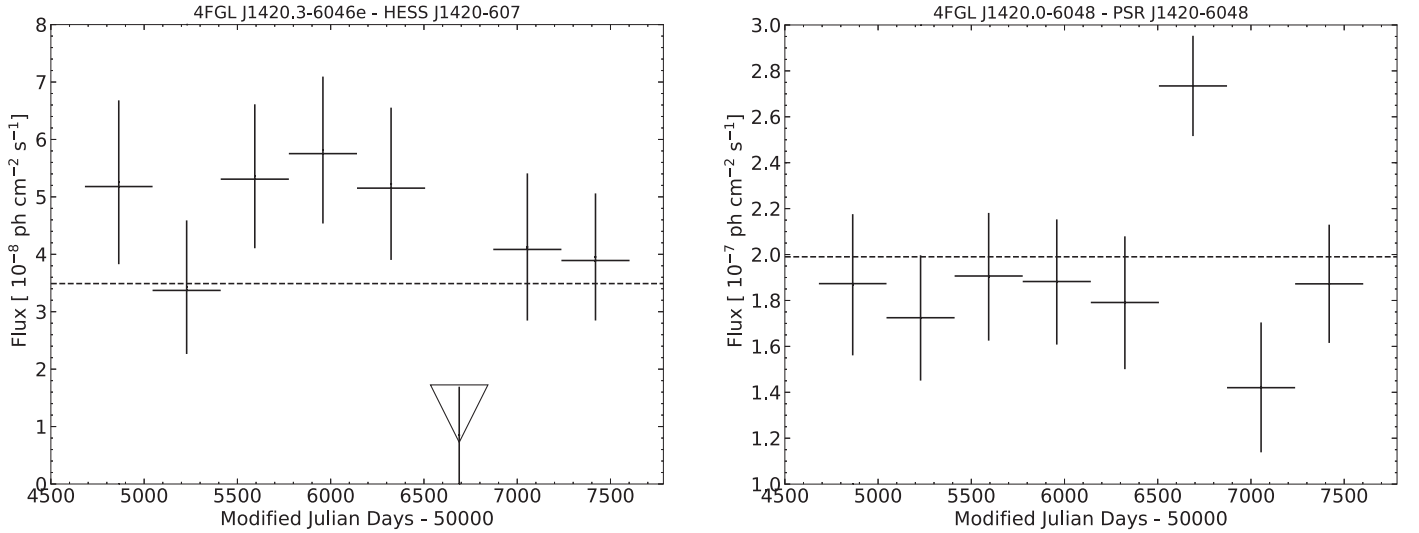


Figure 9. Light curves of the pulsar wind nebula HESS J1420–607 (4FGL J1420.3–6046e) at $TS_{\text{var}} = 23.4$ over one-year intervals and its parent pulsar PSR J1420–6048 (4FGL J1420.0–6048). The apparent variability of HESS J1420–607 is due to the low point in the sixth year (the downward triangle is an upper limit at 95% confidence level), which corresponds to a high point in the light curve of PSR J1420–6048. This is clearly a case of incorrect flux transfer due to the strong spatial confusion (the nebula is only $0^{\circ}12$ in radius), despite the spectral difference between the two sources. The perturbation of the pulsar (brighter than the nebula) is not enough to exceed the variability threshold.

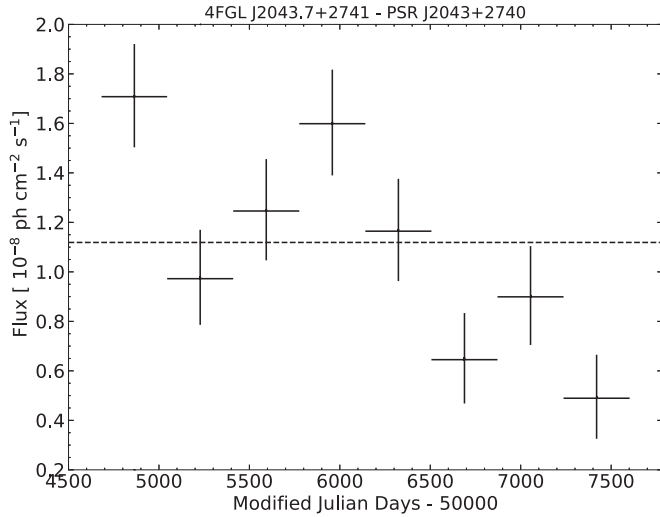


Figure 10. Light curve of the pulsar PSR J2043+2740 (4FGL J2043.7+2741), at $TS_{\text{var}} = 33$ over one-year intervals. The flux of this pulsar appears to be decreasing secularly.

$$\delta F = \sqrt{\max\left(\text{Var} - \frac{\sum_i \sigma_i^2}{N_{\text{int}}}, 0\right)} \quad (9)$$

$$\frac{\sigma_F}{F} = \max\left(\frac{1}{\sqrt{2(N_{\text{int}} - 1)}} \frac{V_i}{F_{\text{av}} \delta F}, 10\right) \quad (10)$$

where the fractional variability itself is simply $\delta F/F_{\text{av}}$. This is similar to Equation (3) of 1FGL, except we omit the systematic error term because it is now incorporated in the σ_i^2 via the weights. The error σ_F/F is estimated from the expected scatter on the sample variance Var , which is the dominant source of uncertainty. We cap it at 10 to avoid reporting meaningless high uncertainties. Figure 11 can be compared to Figure 8 of Abdo et al. (2009c), which was based on one-week intervals (and contained many fewer sources, of course). The fractional

variability is similar in the two figures, going up to 1, reflecting the absence of a preferred variability timescale in blazars. The criterion we use is not sensitive to relative variations smaller than 50% at $TS = 100$, so only bright sources can populate the lower part of the plot. There is no indication that fainter sources are less variable than brighter ones, but we simply cannot measure their variability.

3.6.2. Two-month Intervals

To characterize variability, it is of course useful to have information on shorter timescales than one year. Rather than use monthly bins as in 3FGL (which would have resulted in many upper limits), we have chosen to keep the same number of intervals and build light curves over 48 two-month bins. Because the analysis is not limited by systematics at low energy over two months, we tried to optimize the data selection differently. We used binned likelihood up to 3 GeV and the same zenith angle cuts as in Table 2, but included PSF2 events between 50 and 100 MeV (not only PSF3), and added PSF1 events between 100 and 300 MeV to our standard PSF2+3 selection. This improves the average source significance over one bin, and the Earth limb contamination remains minor. Similarly to the one-year analyses, to save disk space and CPU time we merged event types together in the binned data sets. We used unbinned likelihood above 3 GeV and again ignored events above 100 GeV (unimportant for variability).

The weights appropriate for two months were computed using the same procedure (Appendix B), entering the total data cube divided by 48 (same weights in each interval). The weights are of course larger than those for one year but remain a significant correction in the Galactic plane. Up to 100 MeV the weights range from 0.2 in the Galactic Ridge to 0.85 at high latitude. At 300 MeV, they increase to 0.55 in the Galactic Ridge and 0.99 at high latitude. We used a different Sun/Moon model for each interval (the Sun averages out only over one year) but, again, assuming constant flux.

Variability is considered probable when $TS_{\text{var}} > 72.44$, corresponding to 99% confidence in a χ^2 distribution with

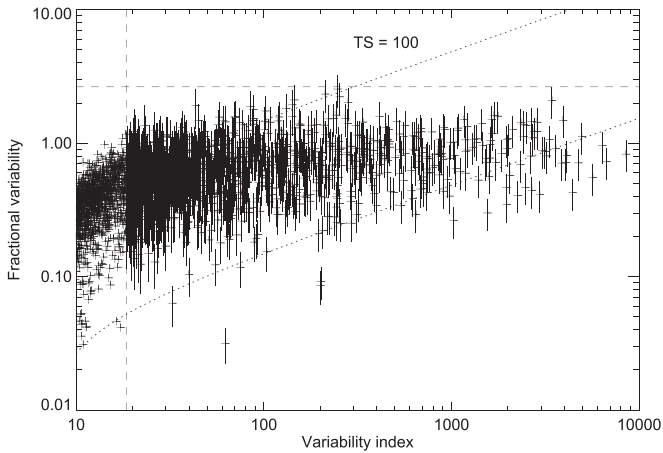


Figure 11. Fractional variability of all sources plotted as a function of variability index, over one-year intervals. The vertical dashed line (below which the points have no error bar) is the variability threshold. The horizontal dashed line is the maximum fractional variability that can be reached ($\sqrt{N_{\text{int}} - 1}$). The dotted lines show how the variability index depends on $\delta F/F$ at $TS = 100$ and at $TS = 10,000$. At a given TS threshold, the lower right part of the diagram is not accessible. The error bars are omitted below the variability threshold for clarity.

$N_{\text{int}} - 1 = 47$ degrees of freedom. We find 1173 variable sources with that criterion, 1057 of which were also considered variable with one-year intervals. Among the 116 sources considered variable only with two-month light curves, 37 (1% of 3738) would be expected by chance, so more than two-thirds must be truly variable. Similarly, 270 sources are considered variable only with one-year intervals (39 expected by chance).

Two extended sources exceed the two-month variability threshold. They are the Monoceros SNR and the Cen A lobes. Both are very extended (several degrees). It is likely that their variability is due to a flaring background source that was missed by the global source detection over eight years. Indeed, the peak in the light curve of the Monoceros SNR is in 2012 June–July, at the time of Nova V959 Mon 2012 (Ackermann et al. 2014a). Another unexpected variable source is the Geminga pulsar. We think that its variability is not real but due to the direct pointings triggered toward the Crab when it was flaring (Geminga is 15° away), combined with details of the effective area or PSF dependence on off-axis angle and azimuthal, that normally average out in scanning mode.

Because the source fluxes are not allowed to be negative, the distribution of fluxes for a given source is truncated at 0. For faint sources, this results in a slight overestimate of the average flux (of no consequence) but also an underestimate of the sample variance (Equation (8)). As a result, the fractional variability (Equation (9)) is underestimated for faint sources and is often zero for weakly variable sources (below threshold). This even happens for two sources considered variable (just above threshold).

More sources are found to be variable using one-year intervals than using two-month intervals. The reason is illustrated in Figure 12, which shows the variability indices divided by $N_{\text{int}} - 1$ (so that they become directly comparable). If the sources behaved like white noise (as the statistical errors) then the correlation would be expected to follow the diagonal. But blazars behave as red noise (more variability on longer timescales) so the correlation is shifted to the right, and it is more advantageous to use longer intervals to detect variability

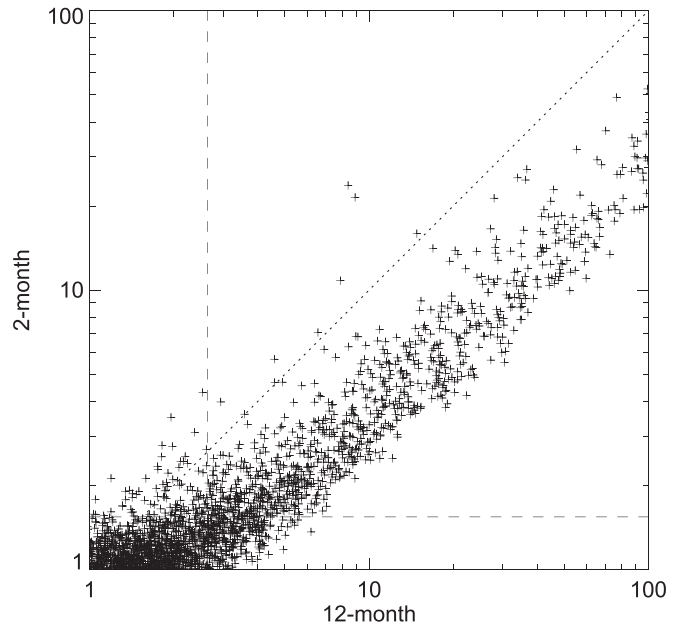


Figure 12. Comparison of the reduced variability index (divided by $N_{\text{int}} - 1$) from two-month intervals with that for one-year intervals. This illustrates that, for the majority of sources (AGNs characterized by red noise), using longer intervals detects variability better. The dotted line is the diagonal (expected for white noise). The dashed lines show the two variability thresholds.

with that criterion, because statistical errors decrease more than intrinsic variability.

Extending this relation to even shorter intervals, the 2FAV catalog of *Fermi*-LAT flaring sources (Abdollahi et al. 2017), which used one-week intervals, found 518 significantly varying sources. The methodology was completely different (it did not start from a catalog over many years), and the duration was a little shorter (7.4 yr). However, the same trend remains to find fewer variable sources on shorter intervals. Not all sources are dominated by red noise though, and a fraction are above the diagonal in Figure 12. An example is provided in Figure 13 (left panel). In all cases, the variability is of course much better characterized with smaller intervals. An extreme example is provided in Figure 13 (right panel).

3.7. Limitations and Systematic Uncertainties

3.7.1. Diffuse Emission Model

The model of diffuse emission is the main source of uncertainties for faint sources. Contrary to the effective area, it does not affect all sources equally: its effects are smaller outside the Galactic plane where the diffuse emission is fainter and varying on larger angular scales. It is also less of a concern at high energy (>3 GeV) where the core of the PSF is narrow enough that the sources dominate the background under the PSF. But it is a serious concern inside the Galactic plane at low energy (<1 GeV) and particularly inside the Galactic ridge ($|l| < 60^\circ$) where the diffuse emission is strongest and very structured, following the molecular cloud distribution. It is not easy to assess precisely how large the uncertainties are, because they relate to uncertainties in the distributions of interstellar gas, the interstellar radiation field, and cosmic rays, which depend in detail on position on the sky.

We estimate, from the residuals over the entire Galactic plane, that the systematics are at the 3% level. This is already

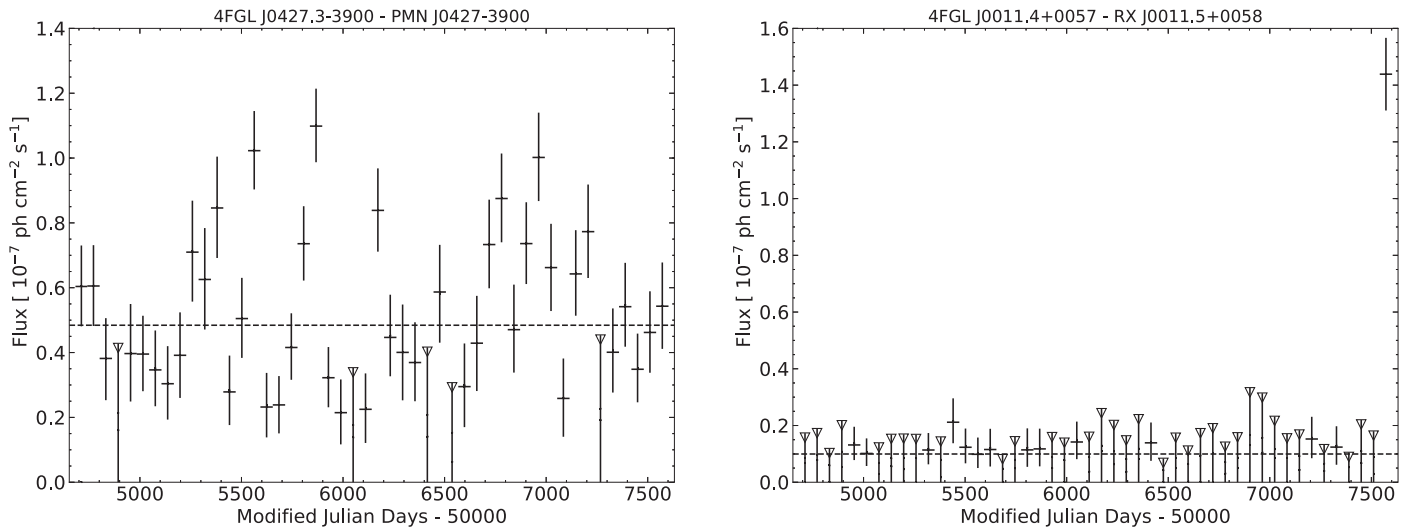


Figure 13. Light curves over two-month intervals of two blazars showing fast variability. Downward triangles indicate upper limits at the 95% confidence level. Left panel: unclassified blazar PMN J0427–3900 (4FGL J0427.3–3900) at $TS_{\text{var}} = 202$. This is the highest TS_{var} among sources considered non-variable over one-year intervals ($TS_{\text{var}} = 17.8$). Its variability is very fast (more like white noise than red noise) and averages out over one-year intervals. Right panel: flat-spectrum radio quasar RX J0011.5+0058 (4FGL J0011.4+0057) at $TS_{\text{var}} = 278$, showing a single flare in the last two-month bin. This source was detected as variable with one-year intervals ($TS_{\text{var}} = 79$).

an achievement, but the statistical Poisson errors corresponding to the diffuse emission integrated over the PSF (as described in Appendix B) are much smaller than this. Integrating energies up to twice the current one in the Galactic ridge, the statistical precision is 0.2%, 0.4%, 1%, 2%, and 5% above 100, 200, 500 MeV, and 1 and 2 GeV, respectively.

The weights are able to mitigate the systematic effects globally, but cannot correct the model locally. In particular, underestimating the mass of an interstellar cloud will always tend to create spurious sources on top of it, and overestimating diffuse emission at a particular place tends to make the sources on top of it harder than they should be (because the model creates negative residuals there, and those are felt mostly at low energy). For an approximate local assessment, we have compared the 4FGL catalog with a version of the FL8Y source list (which used the 3FGL Galactic diffuse model `gll_iem_v06`) obtained with the same setup as 4FGL (see Section 4.2.2). Flags 1, 2, and 3 in Table 5 reflect that.

As we did for the 2FGL and 3FGL catalogs, we have checked which unidentified, non-variable sources with detection $TS < 150$ can be biased by large uncertainties in the modeling of the underlying Galactic interstellar emission. As described in greater detail in the 2FGL paper, we have flagged sources that are potentially confused with complex small-scale structures in the interstellar emission. Their positions, fluxes, and spectral characteristics may not be reliable because of the uncertain contributions of the different gas components in their direction. Most flagged sources have $TS < 100$, but a large TS value does not guarantee their reliability, since a deficit in the bright interstellar background is necessarily compensated by one bright, statistically significant, point source (or several of them). Most of the flagged sources have power-law indices above 2.2, but nine of them are harder. This is possible if the interstellar deficit is at sub-degree angular scales. The diffuse model can adapt spectrally up to the energy at which the PSF is at the same angular scale as the interstellar deficit, leaving only a high-energy excess. Those sources are assigned Flag 6 in the

catalog (Table 5). We also append *c* to the source names (except the extended ones). Most (64, $\sim 70\%$) of those suspect sources have no association with a counterpart at other wavelengths, 10 have class UNK and 7 have class SPP (Section 5).

3.7.2. Analysis Method

As in 3FGL, we use the *pointlike*-based method described in Section 3.1 to estimate systematic errors due to the way the main *gtlike*-based method (Section 3.2) is set up in detail. Many aspects differ between the two methods: the code, the weights implementation, the RoIs, and the diffuse model adjustments. The *pointlike*-based method does not remove faint sources (with $TS < 25$) from the model. Even the data differ, since the *pointlike*-based method uses *Front* and *Back* event types whereas the *gtlike*-based method uses PSF event types with a different zenith angle cut. Both methods reject a fraction of the events below 1 GeV, but not the same one.

Because of all those differences, we expect that comparing the results of the two methods source by source can provide an estimate of the sensitivity of the source list to details of the analysis. In particular, we use it to flag sources whose spectral characterization differs strongly with the two methods (Flags 1 and 3 in Table 5).

3.7.3. Analysis Flags

As in 3FGL, we identified a number of conditions that should be considered cautionary regarding the reality of a source or the magnitude of the systematic uncertainties of its measured properties. They are described in Table 5, together with the number of sources flagged for each reason. Flags 1, 2, and 3 alert us to a different result with *pointlike* or the previous diffuse model. Flag 4 indicates a low source-to-background ratio. Flag 5 alerts us to confusion, Flag 6 to a possible contamination by diffuse emission, Flag 9 to a bad localization, Flag 10 to a bad spectral representation, and Flag 12 to a very

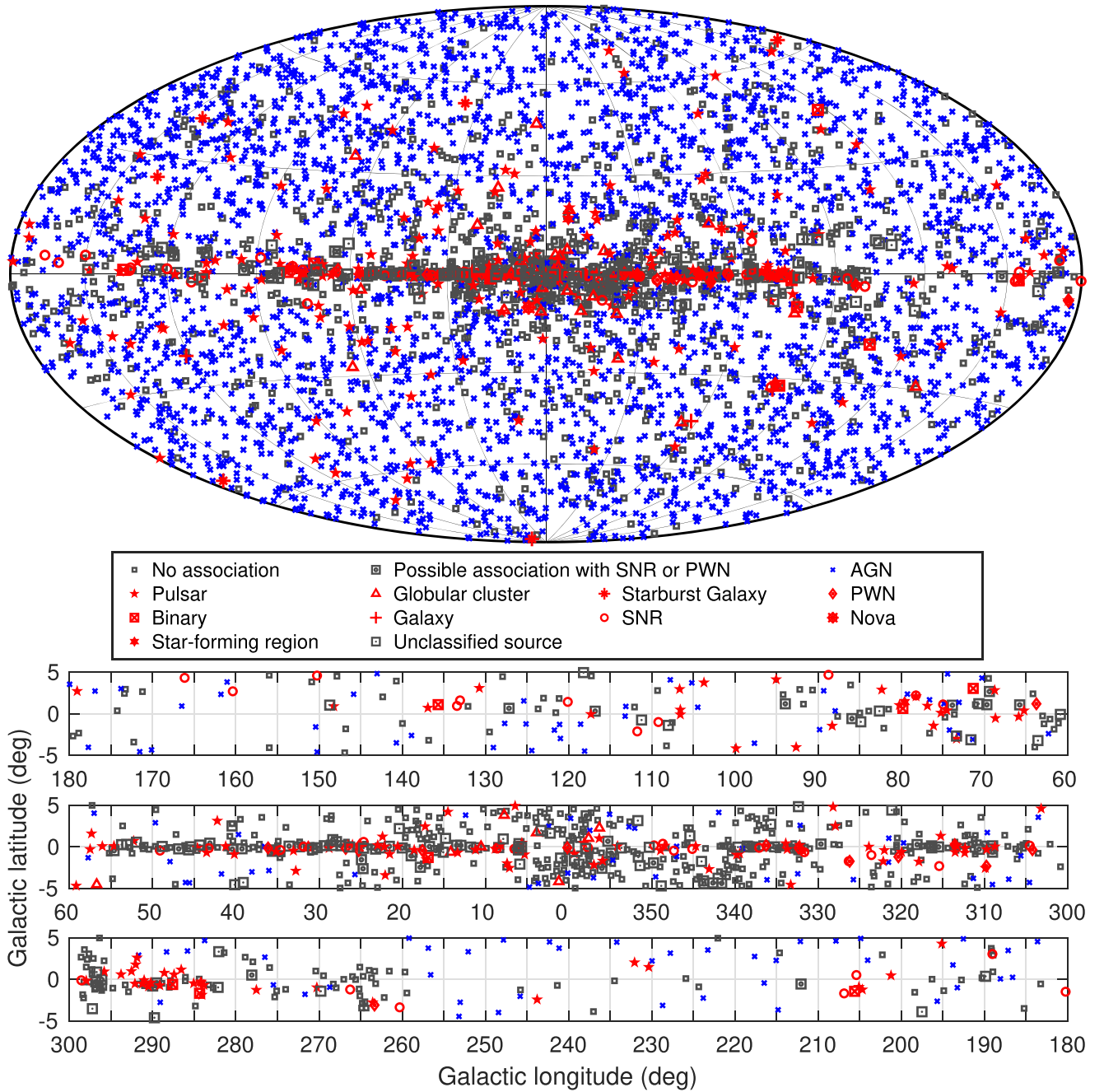


Figure 14. Full sky map (top panel) and blow-up of the Galactic plane split into three longitude bands (bottom panel) showing sources by source class (see Section 6, no distinction is made between associations and identifications). All AGN classes are plotted with the same blue symbol for simplicity. Other associations to a well-defined class are plotted in red. Unassociated sources and sources associated to counterparts of unknown nature are plotted in black.

highly curved spectrum. We have slightly changed the definition of Flag 5 on the conservative side. For any source, we define its best band k_0 as before (i.e., the highest-energy band in which it has $TS > 25$, or the band with highest TS if none reaches 25). Defining TS_0 as the TS of the source in that band, we now consider that a neighbor is brighter whenever it has $TS > TS_0$ in band k_0 or in any higher-energy band. This catches soft sources close to a harder neighbor only somewhat more significant. The localization check with *gtfindsrc* (Flag 7 in 3FGL) was not done because unbinned likelihood is very slow and does not support energy dispersion nor weights. The Sun check (Flag 11 in 3FGL) is no longer necessary since we now have a good model of the solar emission.

In total, 1164 sources are flagged in 4FGL (about 23%, similar to 3FGL). Only 15% of the sources with power-law index $\Gamma < 2.5$ are flagged, but 47% of the soft sources with $\Gamma \geq 2.5$. This attests to the exacerbated sensitivity of soft sources to the underlying background emission and nearby sources. For the same reason, and also because of more confusion, 52% of sources close to the Galactic plane (latitude less than 10°) are flagged while only 12% outside that region are. Only 15% of associated sources are flagged but 45% of the non-associated ones are flagged. This is in part because the associated sources tend to be brighter, therefore more robust, and also because many flagged sources are close to the Galactic plane where the association rate is low.

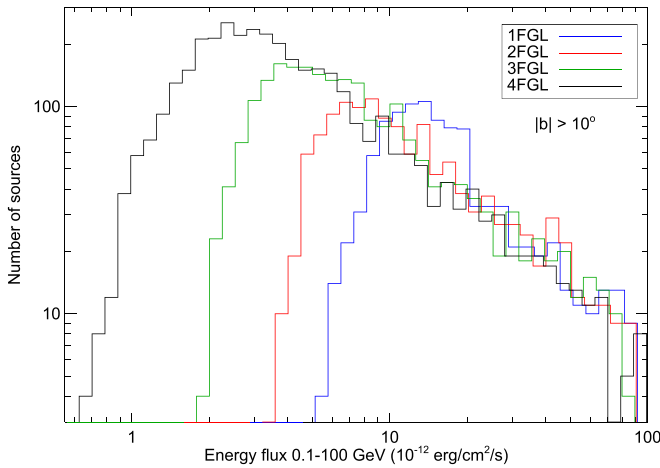


Figure 15. Distributions of the energy flux for the high-latitude sources ($|b| > 10^\circ$) in the 1FGL (1043 sources, blue), 2FGL (1319 sources, red), 3FGL (2193 sources, green), and 4FGL (3646 sources, black) catalogs, illustrating the approximate detection threshold.

4. The 4FGL Catalog

4.1. Catalog Description

The catalog is available online,⁹² together with associated products. It contains 5064 sources.⁹³ The source designation is 4FGL JHHMM.m+DDMM where the 4 indicates that this is the fourth LAT catalog, and FGL represents *Fermi* Gamma-ray LAT. Sources confused with interstellar cloud complexes are singled out by a c appended to their names, where the c indicates that caution should be used in interpreting or analyzing these sources. The 75 sources that were modeled as extended for 4FGL (Section 3.4) are singled out by an e appended to their names. The catalog columns are described in Appendix A. Figure 14 illustrates the distribution of the 4FGL sources over the sky, separately for AGN (blue) and other (red) classes.

4.2. Comparison with 3FGL and Earlier

4.2.1. General Comparison

Figure 15 shows the energy flux distribution in 1FGL, 2FGL, 3FGL, and 4FGL outside the Galactic plane. Comparing the current flux threshold with those published in previous LAT Catalog papers, we see that in 4FGL, the threshold is down to $\approx 2 \times 10^{-12}$ erg cm⁻² s⁻¹. This is about a factor of two better than 3FGL. In the background-limited regime (up to a few GeV), doubling the exposure time would lead only to a factor $\sqrt{2}$. The remaining factor is due to the increased acceptance, the better PSF, and splitting the data into the PSF event types (Section 2.2). The weights (Appendix B) do not limit the general detection at high latitudes. Above 10^{-11} erg cm⁻² s⁻¹, the 2FGL and 3FGL distributions are entirely compatible with 4FGL. The 1FGL distribution shows a distinct bump between 1 and 2×10^{-11} erg cm⁻² s⁻¹. That accumulation of fluxes was clearly incorrect. We attribute it primarily to overestimating significances and fluxes due to the unbinned likelihood bias in the 1FGL analysis, and also to the

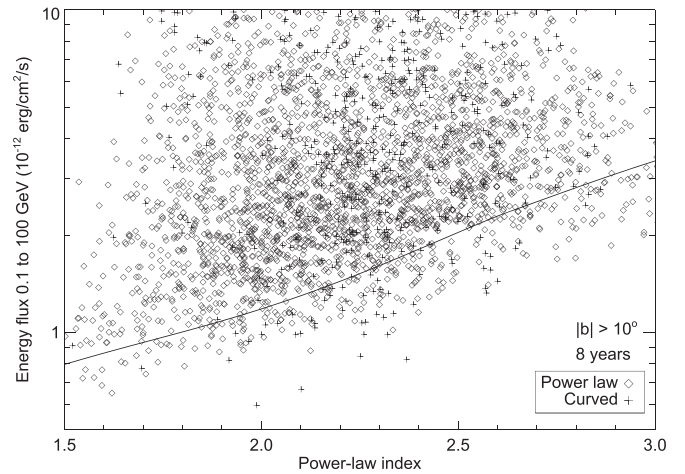


Figure 16. Energy flux and power-law index of all sources outside the Galactic plane ($|b| > 10^\circ$). The solid line shows the expected detection threshold for a power-law spectrum. It is consistent with the fluxes of detected power-law sources (diamonds). The four sources furthest below the line are all curved (+ signs). Indeed, the detection threshold (in terms of energy flux from 0.1 to 100 GeV) is lower for curved sources.

less accurate procedure then used to extract source flux (see discussion in the 2FGL paper).

The threshold at low flux is less sharp in 4FGL than it was in 2FGL or 3FGL. This reflects a larger dependence of the detection threshold on the power-law index (Figure 16). The expected detection threshold is computed from Equation A1 of Abdo et al. (2010e). The systematic limitation ϵ (entered in the weighted log-likelihood as described in Appendix B) is accounted for approximately by limiting the integral over angles to $\theta_{\max}(E)$ such that $g(\theta_{\max}, E) = \epsilon$, since $g(\theta_{\max}, E)$ in that equation is exactly the source to background ratio. The detection threshold for soft sources decreases only slowly with exposure due to that. On the other hand, the detection threshold improves in nearly inverse proportion to exposure for hard sources because energies above 10 GeV are still photon-limited (not background-limited).

The power-law index Γ provides a way to compare all sources over all catalog generations, ignoring the complexities of the curved models. Figure 17 shows that the four distributions of the power-law indices of the sources at high Galactic latitude are very similar. Their averages and dispersions are $\Gamma_{1\text{FGL}} = 2.22 \pm 0.33$, $\Gamma_{2\text{FGL}} = 2.17 \pm 0.30$, $\Gamma_{3\text{FGL}} = 2.22 \pm 0.31$ and $\Gamma_{4\text{FGL}} = 2.23 \pm 0.30$.

Small differences in the power-law index distributions could be related to slightly different systematic uncertainties in the effective area between the IRFs used, respectively, for 4FGL, 3FGL, 2FGL, and 1FGL (Table 1). There is actually no reason why the distribution should remain the same, since the detection threshold depends on the index and the log N -log S of FSRQs, which are soft *Fermi*-LAT sources, differs from that of BL Lacs, whose spectra are hard in the LAT band (Ackermann et al. 2015, Figure 7). The apparent constancy may largely be the result of competing effects.

We have compared the distribution of error radii (defined as the geometric mean of the semimajor and semiminor axes of the 95% confidence error ellipse) of the 1FGL, 2FGL, 3FGL, and 4FGL sources at high Galactic latitude. Overall, the source localization improves with time as more photons are added to previously detected sources. We concentrate instead on what happens specifically for faint sources. Figure 18 shows the

⁹² See https://fermi.gsfc.nasa.gov/ssc/data/access/lat/8yr_catalog/.

⁹³ The file has 5065 entries because the Crab PWN is represented by two components (Section 3.3).

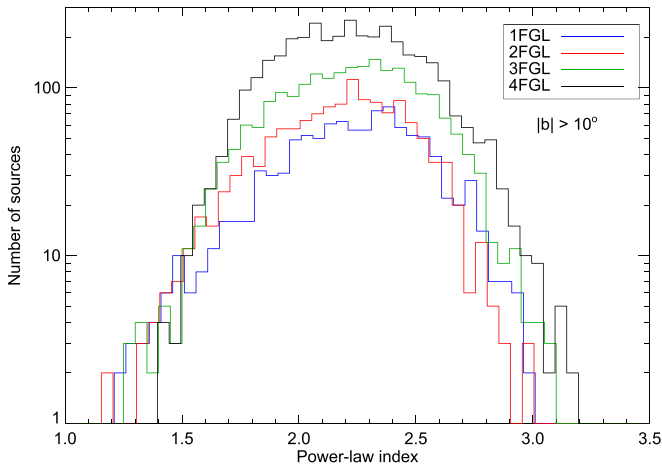


Figure 17. Distributions of the power-law index for the high-latitude sources in the 1FGL (blue), 2FGL (red), 3FGL (green), and 4FGL (black) catalogs. The sources are the same as in Figure 15.

distribution of 95% confidence error radii for those sources with $25 < TS < 100$ in any of the catalogs. The improvement at a given TS level is partly due to the event-level analysis (from Pass 6 to 7 and 8, see Table 1) and partly to the fact that, at a given significance level and for a given spectrum, fainter sources over longer exposures are detected with more photons. This improvement is key to preserving a high rate of source associations (Section 6), even though the source density increases.

4.2.2. Step-by-step from 3FGL to 4FGL

To understand the improvements of the 4FGL analysis with respect to 3FGL, we have considered the effects of changing the analysis and the data set without changing the time range (i.e., leaving it as four years). To that end, we started with the same seeds as the 3FGL catalog, changed each element in sequence (in the order of the list below), and compared each intermediate result with the previous one. The effect of introducing energy dispersion was described in Section 3.2.

1. We first switched from P7REP to Pass 8 (P8R3), eliminating the Earth limb by cutting zenith angles $>90^\circ$ at 100–300 MeV and $>97.5^\circ$ at 300 MeV–1 GeV for Front, $>80^\circ$ at 100–300 MeV and $>95^\circ$ at 300 MeV–1 GeV for Back. The resulting TS increased by 27%, in keeping with the effective area increase (the number of sources at $TS > 25$ did not rise, for lack of seeds). The energy flux decreased by 7% in faint sources. In the Galactic plane, source spectra tended to soften, with power-law indices increasing by 0.04 on average. Both effects appear to be due to the diffuse emission modeling, because they are absent in the bright sources. The isotropic spectrum was recomputed, and even though the Galactic diffuse model was the same, its effects differed because the effective-area increase with Pass 8 is stronger at low energy. Those offsets are accompanied by a large scatter: only 72% of P7REP γ -rays are still in P8R3, and even for those, the reconstructed direction differs.
2. Accounting for energy dispersion increased energy flux on average by 2.4%. The effect was larger for soft sources (3% at $\Gamma > 2.1$). The average power-law index did not change, but hard sources got a little softer and soft

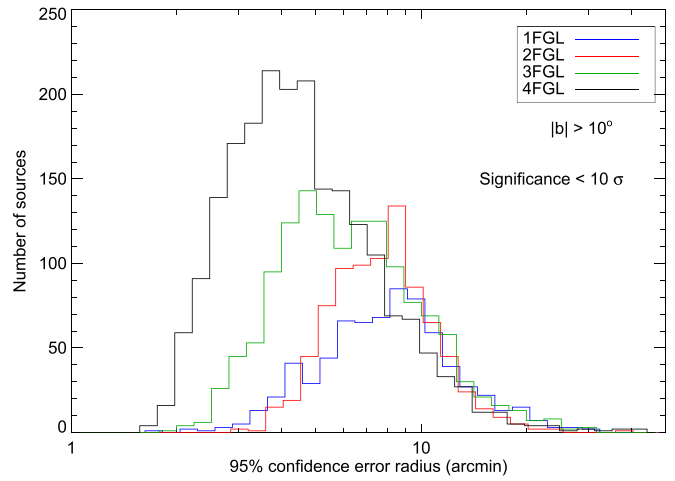


Figure 18. Distributions of the 95% confidence error radii for high-latitude sources with significance $< 10\sigma$ in 1FGL (713 sources, blue), 2FGL (843 sources, red), 3FGL (1387 sources, green), and 4FGL (2090 sources, black), illustrating the improvement of localizations for sources of equivalent detection significances.

sources a little harder (with shifts no larger than 0.02), reducing the width of the power-law index distribution. Spectra became more curved as expected (energy dispersion can only broaden the spectra): the curvature β increased by 0.014 on average. None of these trends depend on Galactic latitude. The logLikelihood improved, but only by a few tens.

3. Switching from Front/Back to PSF event types increased TS by 10% (140 more sources). This was the intended effect (not diluting good events with bad ones should increase significance). No systematic effect was noted on energy flux. Soft sources got somewhat softer with PSF event types (power-law indices larger than 2.7 increased by 0.1 on average), but the bias averaged over all sources was only +0.01. The number of curved sources decreased by 50 and the curvature β by 0.025 (this is the same effect: low energies moved up, so spectra got closer to a power law).
4. Applying the weights results in a general decrease of TS and increase of errors, as expected. However, because source detection is dominated by energies above 1 GeV even without weights, the effect is modest (the number of sources decreased by only 40). The difference is of course largest for soft sources and in the Galactic plane, where the background is larger and the weights are smaller. There are a few other side effects. The number of curved sources decreased by 30. This is because the lever arm decreases as the low-energy γ -rays are unweighted. The pivot energy tended to increase for the same reason, and this resulted in a softening of the power-law index of curved sources (not exceeding 0.1). Overall, in the Galactic ridge, the power-law index increased by 0.025.

We evaluated the other two changes on eight years of data:

1. Changing the energy range to start at 50 MeV did not improve TS, as expected (the PSF is too broad below 100 MeV to contribute to the overall significance). The energy flux (defined in the same 100 MeV to 100 GeV band) tended to decrease in the Galactic plane (by as much as -10% in the Galactic ridge), and the power-law

index tended to become harder (by as much as -0.05 in the Galactic ridge). This is because the low-energy information tends to stabilize artificially soft sources. Neither effect was noticeable outside of the Galactic plane. The other consequence was to increase the number of significantly curved sources by 80, because the broader energy range made it easier to detect curvature (this was true everywhere in the sky).

2. Changing the Galactic diffuse emission model from `gll_iem_v06` used in 3FGL to that used here (Section 2.4), without changing the analysis or the data, had a noticeable effect. The flags in Section 3.7.3 are based on the comparison to a version of the FL8Y source list (using `gll_iem_v06`) extending the energy range to start at 50 MeV, and using the same extended sources and TS_{curv} threshold as 4FGL. The source significance is lower in 4FGL by 0.1σ , on average, and the number of sources decreased by 10%. The energy flux is lower in 4FGL by 2%, the power-law index is smaller (harder) by 0.02, and there are more curved sources than in FL8Y. This is all because the intensity of the new diffuse model is somewhat higher below 100 MeV. Because this is a background-related effect, it affects primarily the faint sources. The strong overprediction west of Carina in `gll_iem_v06` is gone, but overall, the residuals are at a similar level.

In conclusion, in the first order, the resulting net changes are not very large, consistent with the general comparison between 4FGL and 3FGL in Section 4.2.1. Systematic effects are collectively visible but within calibration errors, and within statistical errors of individual sources.

5. Automated Source Associations

We use two complementary methods in the association task. The Bayesian method is based only on spatial coincidence between the gamma-ray sources and their potential counterparts. This method does not require any additional information (like an available $\log N$ – $\log S$) for the considered catalogs. It is of general use and applicable to many counterpart catalogs. However, it is inappropriate when considering large surveys (e.g., in the radio or X-ray bands), because of their high source densities. The Likelihood Ratio method, on the other hand, can be applied to these surveys, owing to the use of their $\log N$ – $\log S$. This method allows us to retrieve some associations with relatively bright counterparts that were missed with the Bayesian method. The mitigation of the effect of large effective counterpart densities is not perfect. The resulting association probabilities are typically lower than for the Bayesian method.

The Bayesian source association method (Abdo et al. 2010e) for the *Fermi*-LAT, implemented with the `gtsrcid` tool,⁹⁴ was developed following the prescription devised by Mattox et al. (1997) for EGRET. It relies on the fact that the angular distance between a LAT source and a candidate counterpart is driven by (i) the position uncertainty in the case of a real association and (ii) the counterpart density in the case of a false (random) association. In addition to the angular-distance probability density functions for real and false associations, the posterior probability depends on a prior. This prior is calibrated via Monte Carlo simulations so that the number of false

associations, N_{false} is equal to the sum of the association-probability complements. For a given counterpart catalog, the so-obtained prior is found to be close to $N_{\text{assoc}}/N_{\text{tot}}$, where N_{assoc} is the number of associations from this catalog and N_{tot} is the number of catalog sources. The sum of the association probabilities over all pairs (γ -ray source, potential counterpart) gives the total number of real associations for a particular catalog, allowing the number of subthreshold associations to be estimated. The total numbers of associations are reported in Section 6 for the various classes, where the overlap between associations from different catalogs is taken into account. A uniform threshold of $P \geq 0.8$ is applied to the posterior probability for the association to be retained. The reliability of the Bayesian associations is assessed by verifying that the distribution of the angular offset between γ -ray source and counterpart well matches the expected one in the case of a true association, i.e., a Rayleigh function with its width parameter given by the sources' positional uncertainties.

The counterpart catalogs (Table 6) include known γ -ray-emitting source classes: AGNs (Ackermann et al. 2015), galaxies (Abdo et al. 2010b), pulsars (Abdo et al. 2013), PWNe (Ackermann et al. 2011c), SNRs (Acero et al. 2016b), globular clusters (GLCs; Abdo et al. 2010a), low- and high-mass X-ray binaries (Abdo et al. 2009b, 2010f) or surveys of candidate blazars at other frequencies (radio, IR, X-rays). The reported source classes are derived in the same way as in 3FGL. For non-AGN sources, this classification is based on the nature of the association catalogs. For AGNs, the subclasses as FSRQs, BL Lac-type objects (BLLs), blazar candidates of uncertain type (BCUs), radio galaxies (RDGs), narrow-line Seyfert 1 (NLSY1s), steep spectrum radio quasars (SSRQs), Seyfert galaxies (SEYs), or simply AGNs (if no other particular subclass can be assigned), have been selected according to the counterpart properties at other wavelengths. Please note that we did not use the blazar classes from the Simbad database⁹⁵ since some of them correspond to predictions based on the *WISE*-strip approach (D'Abrusco et al. 2014) and not to assessment with the measured strengths of the emission lines.

Complementing the Bayesian method, the Likelihood Ratio (LR) method (Ackermann et al. 2011b, 2015), following de Ruiter et al. (1977) provides supplementary associations with blazar candidates based on large radio and X-ray surveys: NVSS (Condon et al. 1998), SUMSS (Mauch et al. 2003), *ROSAT* (Voges et al. 1999, 2000), and AT20G (Murphy et al. 2010). This method is similar in essence to the Bayesian method, but the false-association rate is derived from the density of objects brighter than the considered candidate, assessed from the survey $\log N$ – $\log S$ distribution. While the LR method is able to handle large surveys, its fraction of false associations is notably larger than for the Bayesian method (typically 10% versus 2%). The overlap between the results of the Bayesian and LR methods is about 75% for blazars. Because the surveys include a large number of Galactic sources at low Galactic latitudes, the class of $|b| < 10^\circ$ sources associated solely via the LR-method has been set to “UNK” (standing for unknown) as opposed to the BCU class used by default for sources at higher latitudes.

Firm identifications are based on periodic variability for LAT-detected pulsars or X-ray binaries, correlated variability at

⁹⁴ <https://fermi.gsfc.nasa.gov/ssc/data/analysis/scitools/overview.html>

⁹⁵ <http://simbad.u-strasbg.fr/simbad/>

Table 6
Catalogs Used for the Automatic Source Association Methods

Name	Objects ^a	References
High \dot{E}/d^2 pulsars	313	Manchester et al. (2005) ^b
Other normal pulsars	2248	Manchester et al. (2005) ^b
Millisecond pulsars	240	Manchester et al. (2005) ^b
Pulsar wind nebulae	69	Collaboration internal
High-mass X-ray binaries	137	Garcia et al. (2019)
Low-mass X-ray binaries	187	Liu et al. (2007)
Point-like SNR	158	Green (2014) ^c
Extended SNR ^d	295	Green (2014) ^c
Globular clusters	160	Harris (1996)
Dwarf galaxies ^d	100	McConnachie (2012)
Nearby galaxies	276	Schmidt et al. (1993)
IRAS bright galaxies	82	Sanders et al. (2003)
BZCAT (Blazars)	3561	Massaro et al. (2009)
BL Lac	1371	Véron-Cetty & Véron (2010)
AGN	10066	Véron-Cetty & Véron (2010)
QSO	129,853	Véron-Cetty & Véron (2010)
Seyfert galaxies	27651	Véron-Cetty & Véron (2010)
Narrow-line Seyfert galaxies	18	Berton et al. (2015)
Narrow-line Seyfert galaxies	556	Rakshit et al. (2017)
FRICAT (Radio galaxies)	233	Capetti et al. (2017a)
FRIICAT (Radio galaxies)	123	Capetti et al. (2017b)
Giant Radio Source	349	Kuźmiec et al. (2018)
2WHSP	1691	Chang et al. (2017)
WISE blazar catalog	12319	D’Abrusco et al. (2014)
Radio Fundamental Catalog (2019a)	15740	http://astrogeo.org/rfc
CGRaBS	1625	Healey et al. (2008)
CRATES	11499	Healey et al. (2007)
ATCA 20 GHz southern sky survey	5890	Murphy et al. (2010)
105 month <i>Swift</i> /BAT catalog	1632	Oh et al. (2018)
4th IBIS catalog	939	Bird et al. (2016)
2nd <i>AGILE</i> catalog ^e	175	Bulgarelli et al. (2019)
3rd EGRET catalog ^e	271	Hartman et al. (1999)
EGR catalog ^e	189	Casandjian & Grenier (2008)
0FGL list ^e	205	(Abdo et al. 2009c, 0FGL)
1FGL catalog ^e	1451	(Abdo et al. 2010e, 1FGL)
2FGL catalog ^e	1873	(Nolan et al. 2012, 2FGL)
3FGL catalog ^e	3033	(Acero et al. 2015, 3FGL)
1FHL catalog ^e	514	(Ackermann et al. 2013, 1FHL)
2FHL catalog ^e	360	(Ackermann et al. 2016b, 1FHL)
3FHL catalog ^e	1556	(Ajello et al. 2017, 1FHL)
TeV point-like source catalog ^{d,e}	108	http://tevcat.uchicago.edu/
TeV extended source catalog ^f	72	http://tevcat.uchicago.edu/
LAT pulsars	234	Collaboration internal ^g
LAT identified	145	Collaboration internal

Notes.

^a Number of objects in the catalog.

^b Version 1.56, <http://www.atnf.csiro.au/research/pulsar/psrcat>

^c Green D. A., 2017, “A Catalogue of Galactic Supernova Remnants (2017 June version),” Cavendish Laboratory, Cambridge, United Kingdom (available at <http://www.mrao.cam.ac.uk/surveys/snrs/>)

^d Version of 2018 November 30.

^e For these catalogs, the association is performed according to Equation (11).

^f For these catalogs of extended sources, the association is performed by requiring that the separation from the 4FGL sources is less than the quadratic sum of the 95% confidence error radii.

^g <https://confluence.slac.stanford.edu/display/GLAMCOG/Public+List+of+LAT+Detected+Gamma-Ray+Pulsars>.

other wavelengths for AGNs, or spatial morphology related to that found in another band for extended sources.

The association and classification procedures greatly benefited from data of recent intensive follow-up programs, motivated by the study of the unidentified/unassociated γ -ray sources. This study was recognized as one of the major scientific goals of the *Fermi* mission. Many groups carried out follow-up observations and/or applied statistical procedures to investigate and discern the nature of the unassociated sources from their gamma-ray properties (see, e.g., Ackermann et al. 2012b; Hassan et al. 2013; Doert & Errando 2014). In particular, follow-up campaigns were carried out at different wavelengths with both ground-based and space telescopes above GHz frequencies (see, e.g., Kovalev 2009; Petrov et al. 2011, 2013; Hovatta et al. 2012, 2014; Schinzel et al. 2015, 2017) and below (see, e.g., Massaro et al. 2013; Nori et al. 2014; Giroletti et al. 2016), or using submillimeter (see, e.g., Giommi et al. 2012; López-Caniego et al. 2013) and infrared observations (see, e.g., Massaro et al. 2011, 2012a, 2012b; D’Abrusco et al. 2014; Arsioli et al. 2015; Massaro & D’Abrusco 2016) up to the X-rays with *Swift* (e.g., Mirabal & Halpern 2009; Acero et al. 2013; Paggi et al. 2013; Stroh & Falcone 2013; Takeuchi et al. 2013; Landi et al. 2015; Paiano et al. 2017b) as well as with *Chandra* and *Suzaku* (e.g., Maeda et al. 2011; Cheung et al. 2012; Kataoka et al. 2012; Takahashi et al. 2012; Takeuchi et al. 2013). Over the years, these observations have allowed additions to the lists of potential counterparts, which were then used with the methods previously described. In addition, to assess the real nature and classify all newly associated sources, it has been crucial to perform additional spectroscopic optical observations, which, for extragalactic objects, were also able to provide estimates of their cosmological distances (see, e.g., Shaw et al. 2013a, 2013b; Paggi et al. 2014; Landoni et al. 2015a, 2015b; Massaro et al. 2015a, 2015b; Ricci et al. 2015; Álvarez Crespo et al. 2016a, 2016c; Chiaro et al. 2016; Paiano et al. 2017a, 2017c, 2017d; Peña-Herazo et al. 2017; Landoni et al. 2018; Marchesi et al. 2018; Marchesini et al. 2019). These campaigns are continuously updated including searches in the optical databases of the major surveys (see, e.g., Cowperthwaite et al. 2013; Massaro et al. 2014, 2016; Maselli et al. 2015; Álvarez Crespo et al. 2016b; de Menezes et al. 2019).

The false-association rate is difficult to estimate for the new associations resulting from these follow-up observations, preventing them from being treated on the same footing as those obtained as described above. The most recent Radio Fundamental Catalog⁹⁶ (RFC) includes many new entries that came from dedicated follow-up observations. Applying the Bayesian method to the whole catalog and retaining associations with $P \geq 0.8$, the association probability attached to the recent additions (181 sources) are reported as NULL to distinguish them from the others.

6. Association Summary

The association summary is given in Table 7. Out of 5064 LAT sources in 4FGL, 1336 are unassociated (26.4%). Some 92 others are classified as UNKs, and 78 as SPPs (sources of unknown nature but overlapping with known SNRs or PWNe and thus candidates to these classes), representing 3.3% in

⁹⁶ Available at <http://astrogeo.org/rfc>.

Table 7
LAT 4FGL Source Classes

Description	Identified		Associated	
	Designator	Number	Designator	Number
Pulsar, identified by pulsations	PSR	232
Pulsar, no pulsations seen in LAT yet	psr	7
Pulsar wind nebula	PWN	11	pwn	6
Supernova remnant	SNR	24	snr	16
Supernova remnant/Pulsar wind nebula	SPP	0	spp	78
Globular cluster	GLC	0	glc	30
Star-forming region	SFR	3	sfr	0
High-mass binary	HMB	5	hmb	3
Low-mass binary	LMB	1	lmb	1
Binary	BIN	1	bin	0
Nova	NOV	1	nov	0
BL Lac type of blazar	BLL	22	bll	1109
FSRQ type of blazar	FSRQ	43	fsrq	651
Radio galaxy	RDG	6	rdg	36
Non-blazar active galaxy	AGN	1	agn	10
Steep spectrum radio quasar	SSRQ	0	ssrq	2
Compact Steep Spectrum radio source	CSS	0	css	5
Blazar candidate of uncertain type	BCU	2	bcu	1310
Narrow-line Seyfert 1	NLSY1	4	nlsy1	5
Seyfert galaxy	SEY	0	sey	1
Starburst galaxy	SBG	0	sbg	7
Normal galaxy (or part)	GAL	2	gal	1
Unknown	UNK	0	unk	92
Total	...	358	...	3370
Unassociated	1336

Note. The designation “spp” indicates potential association with SNR or PWN. Designations shown in capital letters are firm identifications; lower case letters indicate associations.

total. Some 3463 sources are associated with the Bayesian method (1069 associations from this method only, overall $N_{\text{false}} = 36.6$) and 2604 sources with the LR method (210 associations from this method only, $N_{\text{false}} = 22.2$ for the latter). The overall association fraction, 70%, is similar to that obtained in previous LAT catalogs. The association fraction is lower for fainter sources (essentially all $\text{TS} > 500$ sources are associated), in particular due to their larger error regions. This fraction also decreases as sources lie closer to the Galactic plane, as illustrated in Figure 19. It decreases from about 85% at high Galactic latitudes to $\simeq 40\%$ close to the Galactic plane. The reason for such an effect is twofold. We are not able to associate many of the Galactic sources with high confidence. In addition, the association of background extragalactic sources is impeded by the larger flux limits of some extragalactic-counterpart catalogs due to absorption effects for the X-ray band through the Galactic plane. The properties of the unassociated sources are discussed below.

Sources reported as new below were not in previous FGL catalogs, although their detections may have been reported in other works (e.g., Zhang et al. 2016; Arsioli & Polenta 2018) or

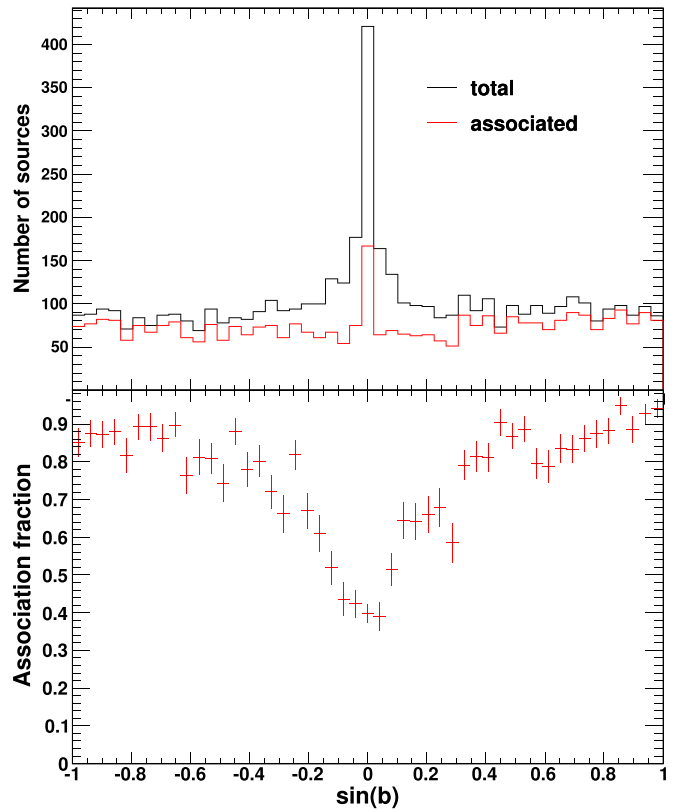


Figure 19. Upper panel: distributions in Galactic latitude b of 4FGL sources (black histogram) and associated sources (red histogram). Lower panel: association fraction as a function of Galactic latitude.

in specialized LAT catalogs. Table 8 lists the 12 3FGL sources that have different counterparts in 4FGL. Pulsations have been detected for five sources previously classified as SPPs. As discussed below, the association of 4FGL J0647.7–4418 with RX J0648.0–4418 instead of SUMSS J064744–441946 remains uncertain.

6.1. Extragalactic Sources

6.1.1. Active Galactic Nuclei

The largest source population in 4FGL is that of AGNs, with 3137 blazars, 42 radio galaxies, and 28 other AGNs. The blazar sample comprises 694 FSRQs, 1131 BLLs, and 1312 BCUs. The detailed properties of the 4FGL AGNs, including redshifts and fitted synchrotron-peak positions, will be the subject of the 4LAC companion catalog. We note here that the separation in γ -ray spectral hardness between FSRQs and BL Lacs that was already reported in previous LAC AGN catalogs is confirmed: 93% of FSRQs and 81% of BL Lacs have power-law photon indices greater and lower than 2.2, respectively. Among the 70 non-blazar AGNs, 35 were present in 3FGL. Note that the location of the γ -ray source associated with Cen B is not coincident with that of the radio-galaxy core but points to the southern radio jet. Twenty-three radio galaxies, listed in Table 9, are new. Four 3FGL sources have changed classes to radio galaxies: three former BCU (IC 1531, TXS 0149+710, PKS 1304–215) and one former BLL (B3 1009+427). The 28 other AGNs include five compact steep spectrum radio sources (CSS, three are new: 3C 138, 3C 216, 3C 309.1), two SSRQs (new is 3C 212), nine narrow-line Seyferts 1 (NLSY1), one

Table 8
3FGL Sources with Different Counterparts in 4FGL

3FGL Name	3FGL Counterpart	3FGL Class	4FGL Name	4FGL Counterpart	4FGL Class
J0500.3+5237	...	spp	J0500.2+5237	GB6 J0500+5238	bcu
J0618.0+7819	1REX J061757+7816.1	fsrq	J0618.1+7819	NGC 2146	sbg
J0647.1-4415	SUMSS J064648-441929	bcu	J0647.7-4418	RX J0648.0-4418	hmb
J0941.6+2727	MG2 J094148+2728	fsrq	J0941.9+2724	GB6 J0941+2721	bll
J1048.6+2338	NVSS J104900+233821	bll	J1048.6+2340	PSR J1048+2339	PSR
J1111.9-6038	...	spp	J1111.8-6039	PSR J1111-6039	PSR
J1132.8+1015	4C +10.33	fsrq	J1130.8+1016	2MASS J11303636+1018245	bcu
J1741.1-3053	MSH 17-39	snr	J1741.4-3046	NVSS J174122-304712	unk
J1811.3-1927c	...	spp	J1811.5-1925	PSR J1811-1925	psr
J1817.2-1739	...	spp	J1817.1-1742	PSR J1817-1742	PSR
J2022.2+3840	...	spp	J2022.3+3840	PSR J2022+3842	PSR
J2224.6-1122	PKS 2221-116	bll	J2225.5-1114	PKS 2223-114	bll

Table 9
New Radio Galaxies in 4FGL

4FGL Name	4FGL Counterpart
J0038.7-0204	3C 17
J0057.7+3023	NGC 315
J0237.7+0206	PKS 0235+017
J0312.9+4119	B3 0309+411B
J0433.0+0522	3C 120
J0708.9+4839	NGC 2329
J0931.9+6737	NGC 2892
J1116.6+2915	B2 1113+29
J1149.0+5924	NGC 3894
J1236.9-7232	PKS 1234-723
J1306.3+1113	TXS 1303+114
J1449.5+2746	B2 1447+27
J1516.5+0015	PKS 1514+00
J1518.6+0614	TXS 1516+064
J1521.1+0421	PKS B1518+045
J1724.2-6501	NGC 6328
J1843.4-4835	PKS 1839-48
J2156.0-6942	PKS 2153-69
J2227.9-3031	PKS 2225-308
J2302.8-1841	PKS 2300-18
J2326.9-0201	PKS 2324-02
J2329.7-2118	PKS 2327-215
J2341.8-2917	PKS 2338-295

Seyfert galaxy (the Circinus galaxy, SEY), and 11 AGNs of other types (AGN). Three NLSY1 are new: IERS B1303+515, B3 1441+476, and TXS 2116-077.

6.1.2. Other Galaxies

No other nearby galaxies, besides the SMC, LMC, and M 31, are detected. Seven starburst galaxies in the *IRAS* catalog (Sanders et al. 2003) are associated with 4FGL sources. Two sources, Arp 220 (Griffin et al. 2016; Peng et al. 2016; Yoast-Hull et al. 2017) and NGC 2146 (Tang et al. 2014), have been reported as LAT detections since the 3FGL release. Yoast-Hull et al. (2017) found an excess of γ -rays over the expected starburst contribution in Arp 220, similar to the case of the Circinus galaxy (Hayashida et al. 2013). NGC 2146, being close ($0^\circ.1$) to the FSRQ 1REX J061757+7816.1, the association is ambiguous. We favor the NGC 2146 association as no evidence for variability is found, and the 4FGL photon index (2.17 ± 0.17) is somewhat low for an FSRQ. Another

source, NGC 3424, was not present in 3FGL. The *IRAS* source UGC 11041, which could have been classified as sbg, shows significant variability in the LAT band, so the γ -ray emission most likely arises from an AGN (there is a flat-spectrum radio source, MG2 J175448+3442 at a distance of $2^\circ.4$), and it is classified as such. In addition to these seven associations, the Bayesian method predicts that three more 4FGL sources should be starburst galaxies (corresponding to the subthreshold associations mentioned in Section 5). Some 4FGL sources are positionally consistent with known galaxy clusters, but these clusters host radio galaxies, which are the most likely emitters. No dwarf galaxies have been detected.

6.2. Galactic Sources

The Galactic sources include:

1. 239 pulsars (PSR). The public list of LAT-detected pulsars is regularly updated.⁹⁷ Some 232 pulsars in this list are included in 4FGL (68 would have been missed by the association pipeline using the ATNF catalog), while six are absent because they did not pass the $TS > 25$ criterion. These pulsars represent by far the largest population of identified sources in 4FGL. Another seven pulsars from the ATNF database are associated with 4FGL sources with high-confidence via the Bayesian method that we consider γ -ray pulsar candidates. This method predicts that about 30 other 4FGL sources are ATNF pulsars. Note that out of the 24 pulsar candidates presented in 3FGL, pulsations have now been detected for 19 of them. The other five are not associated with pulsars in 4FGL.
2. 40 SNRs. Out of them, 24 are extended and thus firmly identified. The other 16 are not resolved. SNR G150.3+4.5 has a log-normal spectral shape with a very hard photon index Γ of 1.6, which indicates that the emission is most likely leptonic and makes this source an excellent candidate for the Cerenkov Telescope Array (CTA). In contrast, the softer spectrum of the LMC SNR N 132D (photon index = 2.07) makes the hypothesis of a dominant hadronic emission likely. The significant spectral curvature seen in Puppis A is consistent with its non-detection in the TeV domain.

⁹⁷ See <https://confluence.slac.stanford.edu/display/GLAMCOG/Public+List+of+LAT-Detected+Gamma-Ray+Pulsars>.

3. 17 PWNe, 15 of them being extended. New associations are N 157B, PWN G63.7+1.1, HESS J1356–645, FGES J1631.6–4756, FGES J1836.5–0651, FGES J1838.9–0704, HESS J1857+026. The median photon index of the 4FGL PWNe is 2.31. N 157B, located in the LMC, has a photon index of 2.0, hinting at an additional contribution from a (yet-undetected) pulsar at low energy on top of the PWN.
4. 78 unassociated sources overlapping with known PWNe or SNRs (SPP). Estimation of missed associations of SNR, PWN and SPP sources is made difficult by the intrinsic spatial extension of the sources; no attempts have thus been made along this line.
5. 30 globular clusters (GLC). Missing relative to 3FGL is 2MS–GC01. The 16 new associations are NGC 362, NGC 1904, NGC 5286, NGC 5904, NGC 6139, NGC 6218, NGC 6304, NGC 6341, NGC 6397, NGC 6402, NGC 6838, NGC 7078, Terzan 1, Terzan 2, GLIMPSE C01, GLIMPSE C02. Only two other 4FGL sources are estimated to be GLCs.
6. Six high-mass X-ray binaries (HMB). The three new sources are HESS J0632+057, which has a reported LAT detection after 3FGL (Li et al. 2017b), Cyg X-1, an archetypical black hole binary reported after the 3FGL (Zanin et al. 2016; Zdziarski et al. 2017), and RX J0648.0–4418/HD 49798, which is a peculiar X-ray binary (Mereghetti et al. 2011; Popov et al. 2018). The association probability of RX J0648.0–4418/HD 49798 is just barely larger (0.85 versus 0.80) than that of the blazar candidate SUMSS J064744–441946. Three other 4FGL sources are estimated to be HMBs according to the Bayesian method.
7. Three star-forming regions; new since 3FGL is the association of the extended source FHES J1626.9–2431 (Section 3.4) with the ρ Ophiuchi star-forming region. Positional coincidences between 4FGL sources and two of the brightest extended H II regions present in the catalog of Paladini et al. (2003) have been found. They are reported here as candidate associations: one region corresponds to NGC 6618 in M17, whose extension of 6' at 2.7 GHz encompasses 4FGL J1820.4–1609; the second one corresponds to NGC 4603, which has a similar extension of 6' at 2.7 GHz and encompasses 4FGL J1115.1–6118.
8. Two low-mass X-ray binaries (LMB). PSR J1023+0038 is a known binary millisecond pulsar/LMB transition system, with a change in γ -ray flux detected (Stappers et al. 2014) simultaneously with a state change, and was previously detected as 2FGL J1023.6+0040 (but not detected in 3FGL). The LMB 2S 0921–630 (V395 Car) is a well-studied binary involving a neutron star and a K0 III star with an orbital period of 9 days (Shahbaz & Watson 2007) and is a new LAT detection.
9. One binary star system (BIN), η Carinae (Abdo et al. 2010f; Reiterberger et al. 2015).
10. One nova (NOV), V5668 Sagittarii (Cheung et al. 2016). Other novae detected by the LAT are missing. Novae have short durations, and most are below the significance threshold because their signal is diluted over the eight years of 4FGL data. As discussed in Section 3.6.2, Nova V959 Mon 2012 is confused with the SNR Monoceros.

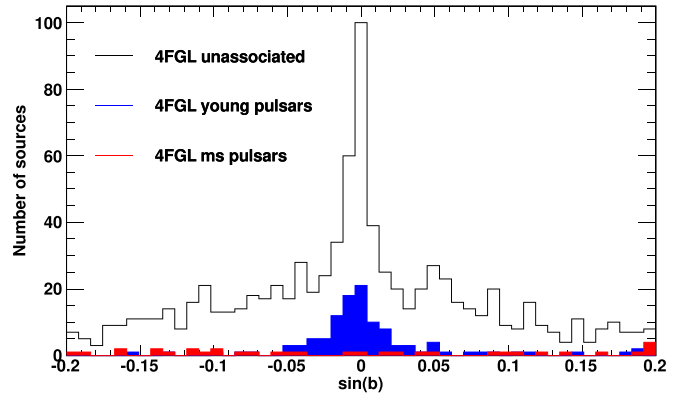


Figure 20. Distributions in Galactic latitude b of 4FGL low-latitude, unassociated sources (black histogram), compared to those of LAT-detected pulsars (young pulsars: blue histogram, millisecond pulsars (MSP): red histogram).

6.3. Low-probability Associations

As a new feature relative to previous catalogs, the most probable counterpart to a 4FGL unassociated source is given in a separate column of the FITS table, along with the corresponding association probability (applying a threshold of 0.1 on that probability). This additional information, to be used with care given its low confidence, is meant to foster further investigations regarding the nature of these 4FGL sources and to help clarify why detections claimed in other works are sometimes missing in 4FGL. We report 124 low-confidence ($0.1 < P < 0.8$) associations with the Bayesian method. Note that the relative distances between γ -ray and counterpart sources remain quite small (53 are within r_{95} and all within $1.85 r_{95}$). This notably small number of low-confidence associations illustrates how quickly the Bayesian association probability drops with increasing relative distance in the case of 4FGL. Except for rare exceptions, the other 1199 4FGL sources (having not even low-confidence associations) will not get associated with any of the tested sources (i.e., belonging to the catalogs listed in Table 6) in a future LAT catalog. We also report 42 matches (classified as UNK) with sources from the *Planck* surveys (with $0.1 < P \leq 1$) to guide future investigations.

6.4. Unassociated Sources

Out of the 1336 sources unassociated in 4FGL, 368 already present in 3FGL had no associations there. Another 27 sources previously associated in 3FGL have now lost their associations because of a shift in their locations relative to 3FGL.

About half of the unassociated sources are located less than 10° away from the Galactic plane. Their wide latitude extension is hard to reconcile with those of known classes of Galactic γ -ray sources. For instance, Figure 20 compares this latitude distribution with that of LAT pulsars. In addition to nearby millisecond pulsars, which have a quasi-isotropic distribution, the LAT detects only young isolated pulsars (age $< 10^6$ yr), which are by nature clustered close to the plane. Older pulsars, which have had time to drift further off the plane, show a wider Galactic-latitude distribution, more compatible with the observed distribution of the unassociated sources, but these pulsars have crossed the “ γ -ray death line” (see Abdo et al. 2013) and are hence undetectable. Attempts to spatially cross correlate the unassociated population with other

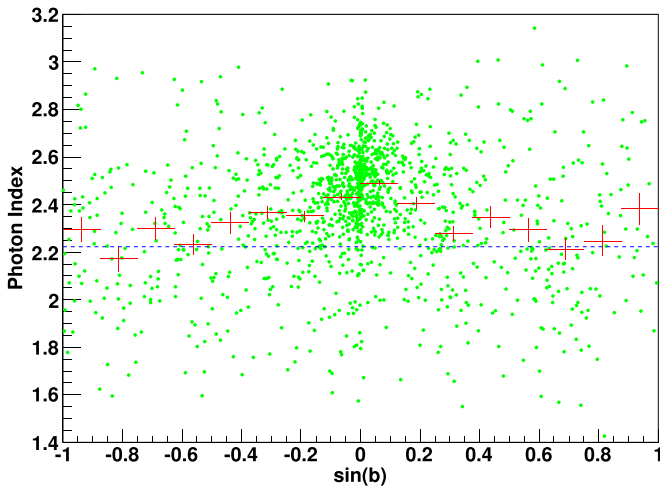


Figure 21. Green symbols: power-law photon index vs. Galactic latitude, b , for the unassociated 4FGL sources. Red bars: average photon index for different bins in b . Dashed blue line: average photon index of 4FGL BCU blazars.

potential classes, e.g., LMBs (Liu et al. 2007), O stars,⁹⁸ and Be stars⁹⁹ have been unsuccessful. The observed clustering of these unassociated sources in high-density “hot spots” may be a clue that they actually correspond to yet-to-be identified, relatively nearby extended sources. The Galactic latitude distribution near the plane is clearly non-Gaussian as visible in Figure 20, which may indicate the presence of several components.

The spectral properties of these sources can also provide insight into their nature, as illustrated in Figure 21, which shows the latitude distribution of their spectral indices. The change in spectral hardness with sky location demonstrates the composite nature of the unassociated population. The high-latitude sources have an average photon index compatible with that of blazars of unknown type ($\Gamma = 2.24$), a hint that these sources could be predominantly blazars. Unassociated sources lying closer to the Galactic plane have softer spectra, closer to that expected for young pulsars ($\Gamma = 2.42$). Another interesting possibility is that some of these unassociated sources actually correspond to WIMP dark matter annihilating in Galactic subhalos (Ackermann et al. 2012d; Coronado-Blázquez et al. 2019). Indeed, Λ CDM cosmology predicts the existence of thousands of subhalos below $\sim 10^7 M_\odot$, i.e., not massive enough to retain gas or stars at all. As a result, they are not expected to emit at other wavelengths, and therefore, they would not possess astrophysical counterparts. Annihilation of particle dark matter may yield a pulsar-like spectrum (Baltz et al. 2007).

6.5. Sources Missing from Previous Fermi Catalogs

The correspondence of 4FGL sources with previous *Fermi*-LAT catalogs (reported in the ASSOC_FGL and ASSOC_FHL columns) was based, as in 3FGL, on error-circle overlap at the 95% confidence level, amounting to

$$\Delta \leq d_{x,a} = \sqrt{\theta_{x,a}^2 + \theta_{x,4FGL}^2} \quad (11)$$

where Δ is the angular distance between a 4FGL source and a source in catalog a , and the θ_x are derived from the

Conf_95_SemiMajor columns in the two catalogs at the $x\%$ confidence level (assuming a 2D normal distribution). We also considered that a previous LAT source corresponds to a 4FGL source whenever they have the same association (the associations can have offsets greater than θ_{95} , depending on the density of sources in the catalogs of counterparts at other wavelengths).

We checked all sources that did not have an obvious counterpart in 4FGL inside d_{95} , nor a common association. The procedure is described in detail in Section 4.2.3 of the 3FGL paper. The result is provided in one FITS file per catalog,¹⁰⁰ reporting the same information as Table 11 of the 3FGL paper: counterparts up to 1° , whether they are inside $d_{99.9}$ ($= 1.52 d_{95}$) or not, and specific conditions (flagged, c source, close to an extended source, split into several sources). The number of missed sources and their nature are provided in Table 10.

We have looked at the most recent catalogs, 3FGL and 3FHL, in more detail. Because the first four years are in common, we expect the 3FGL and 4FGL positions to be correlated. That correlation is however less than one might think because the data have changed (from Pass 7 to Pass 8, Section 2.2). We found that the distribution of $\Delta/d_{95,3FGL}$ (when it is less than 1) is narrower by a factor 0.83 than the Rayleigh distribution. This means that, by cutting at $d_{95,3FGL}$, we expect only 1.3% misses by chance (about 40 sources). With 3FHL, the correlation is larger because it used Pass 8 already, the overlap is 7 yr, and for the hard sources present in 3FHL, the lower-energy photons do not contribute markedly to the localization. The distribution of $\Delta/d_{95,3FHL}$ is narrowed by a factor 0.62, and the number of chance misses by cutting at $d_{95,3FHL}$ should be only 0.04% (about 1 source). The correlation is similarly large with 2FHL (6 yr of Pass 8 data). That correlation effect is less for earlier catalogs, so for them, the fraction of true counterparts that are found outside the combined 95% error circle is closer to 5%. Most of those true sources are expected to have a 4FGL counterpart at the 99.9% level in the FITS files.

Out of 3033 3FGL sources, 469 are missing in 4FGL for various reasons, including the change of diffuse emission model, point sources being absorbed into new extended ones, or variability effects. Most of these missing sources had low significance in 3FGL. Only 72 sources were associated. The majority are blazars (35 BCUs, 17 FSRQs, one BLL, and one SSRQ) plus one AGN. While BLLs are 36% more numerous relative to FSRQs in 3FGL, only one has gone away in 4FGL, an effect possibly related to the larger variability of FSRQs relative to BLLs observed in the LAT energy band (Ackermann et al. 2015). Other missing sources include 11 SPPs, 3 PSRs, one SNR, and one PWN. The nova V407 Cyg is now missing as it no longer fulfills the average-significance criterion.

Two LAT pulsars are considered lost. PSR J1513–5908 ($=$ 3FGL J1513.9–5908) inside the PWN MSH 15–52 is a pulsar peaking at MeV energies (Kuiper et al. 1999), very soft in the LAT band (Pellizzoni et al. 2009; Abdo et al. 2010c), which has gone below threshold after applying the weights. PSR J1112–6103 ($=$ 3FGL J1111.9–6058) was split into two 4FGL sources. One is still associated with the pulsar, but it is not the one closest to the 3FGL position. The third missing pulsar association was between 3FGL J1632.4–4820 and the

⁹⁸ Galactic O-star catalog (GOSC) <https://gosc.cab.inta-csic.es/>.

⁹⁹ Be Star Spectra (BeSS) <http://basebe.obspm.fr/basebe/>.

¹⁰⁰ The files are available at https://www-glast.stanford.edu/pub_data/1626/.

Table 10
Statistics of Previous *Fermi* Sources Missing in 4FGL

	0FGL	1FGL	2FGL	3FGL	1FHL	2FHL	3FHL
All	16	283	311	469	23	34	33
With flags ^a	...	117	229	262
Name-FGL \subset ^b	...	83	97	52
Split into several 4FGL sources ^c	13	58	68	65	3	3	5
Within 1° of a 4FGL e^d	11	45	65	93	4	6	5
AGN	1	8	17	55	1	2	10
PSR	0	1	2	3	0	0	0
spp	4	7	19	11	2	0	0
Other class-type	0	1	2	3	0	1	3
Unassociated	11	266	271	397	20	31	20
Present in 0FGL	...	6	2	6	1	1	0
Present in 1FGL	8	...	56	35	4	3	3
Present in 2FGL	4	74	...	78	4	6	1
Present in 3FGL	7	52	91	...	6	4	4
Present in 1FHL	0	12	7	2	...	8	2
Present in 2FHL	1	3	0	2	5	...	1
Present in 3FHL	0	8	4	4	2	4	...
Not in any other <i>Fermi</i> -LAT catalog	4	186	188	369	12	21	27

Notes.

^a Those are flagged as F in the FITS files.

^b \subset indicates that based on the region of the sky, the source is considered to be potentially confused with Galactic diffuse emission.

^c Those are flagged as S in the FITS files.

^d e indicates a source that was modeled as spatially extended. Those are flagged as E in the FITS files.

non-LAT PSR J1632–4818, in a confused region now covered by the extended source 4FGL J1633.0–4746e. Among the five most significant lost 3FGL sources ($>20\sigma$), the brightest one (3FGL J1714.5–3832 = CTB 37A) was split into two 4FGL sources, the brighter of which is associated instead with the newly discovered pulsar PSR J1714–3830 (Saz Parkinson et al. 2018) inside the CTB 37A SNR and, hence, was not recognized as a common association. Two others (3FGL J1906.6+0720 and 3FGL J0536.4–3347) were also split, and now both members of each pair are associated. This is definitely an improvement. The last two (3FGL J1745.3–2903c and 3FGL J1747.0–2828) were within 0°6 of the Galactic center, a region of the sky where changing the diffuse model had a strong impact. They have no 4FGL counterpart at all.

Concerning sources missing from 3FHL, established with Pass 8 data as 4FGL, they amount to 33, with 17 unassociated, nine blazars (four BLLs and five BCUs), one AGN, one SNR, four UNKs, and the transient HMB PSR B1259–63 (diluted over 8 yr). All of these sources had a TS close to the TS = 25 significance threshold.

6.6. TeV Sources

The synergy between the LAT and the Cerenkov telescopes operating in the TeV energy domain has proven extremely fruitful, in particular by bringing out promising TeV candidates in the LAT catalogs. This approach, further motivated by the upcoming deployment of the CTA, has justified the release of LAT source catalogs above 10 GeV, like the 3FHL (Ajello et al. 2017) based on 7 yr of data. The associations of 4FGL sources with extended sources listed in TeVCat¹⁰¹ are presented in Table 11. Relative to 3FHL, nine new extended

TeV sources are associated with 4FGL extended sources (TeV sources: HESS J1534–571, HESS J1808–204, HESS J1809–193, see Section 3.4), or (sometimes multiple) 4FGL point sources (TeV sources: HESS J1718–385, HESS J1729–345, HESS J1848–018, HESS J1858+020, MGRO J1908+06, HESS J1912+101). All TeV blazars have 4FGL counterparts. The median value of Γ for 4FGL point sources associated with TeV point sources is 1.95, indicating hard spectra as expected. In associations with extended TeV sources, the median Γ changes from 2.09 to 2.38 depending on whether the 4FGL sources are extended or not. This fairly large difference favors the interpretation that most associations between extended TeV sources and non-extended 4FGL sources are accidental.

6.7. Counterpart Positions

Whenever a high-confidence association with a point-like counterpart is obtained, we provide the most accurate counterpart position available and its uncertainty. In particular, 2775 4FGL AGNs have Very Long Baseline Interferometry (VLBI) counterparts. VLBI, i.e., radio interferometry with baseline lengths of >1000 km, is sensitive to radio emission from compact regions of AGNs that are smaller than 20 milli-arcsecond (mas), which corresponds to parsec scales. Such observations allow for the determination of positions of the AGN jet base with mas-level accuracy. We used the RFC catalog based on the dedicated ongoing observing program (Schinzel et al. 2015, 2017) with the Very Long Baseline Array (Napier et al. 1994), as well as VLBI data under other programs. The association between γ -ray source and VLBI counterpart was evaluated along a similar, but distinct, scheme as that presented in Section 5. This scheme (see Petrov et al. 2013, for more details) is based on the strong connection between the γ -ray emission and radio emission at parsec scales and on the sky density of bright compact radio sources being

¹⁰¹ <http://tevcat.uchicago.edu/>

Table 11
Associations of 4FGL with Extended TeV Sources

TeVcat Name ^a	4FGL Name
Boomerang	J2229.0+6114
CTA 1	J0007.0+7303
CTB 37A	J1714.4–3830
CTB 37B	J1714.1–3811
Crab	J0534.5+2201e
G318.2+00.1	J1453.4–5858
Geminga	J0633.9+1746
HESS J1018–589B	J1016.3–5857
HESS J1026–582	J1028.5–5819
HESS J1303–631	J1303.0–6312e
HESS J1356–645	J1355.2–6420e
HESS J1420–607	J1420.3–6046e
HESS J1427–608	J1427.8–6051
HESS J1458–608	J1456.7–6050, J1459.5–6053
HESS J1507–622	J1507.9–6228e
HESS J1534–571	J1533.9–5712e
HESS J1614–518	J1615.3–5146e
HESS J1616–508	J1616.2–5054e
HESS J1632–478	J1633.0–4746e
HESS J1640–465	J1640.6–4632
HESS J1702–420	J1705.7–4124
HESS J1718–385	J1718.2–3825
HESS J1729–345	J1730.1–3422
HESS J1745–303	J1745.8–3028e
HESS J1800–240A	J1801.8–2358
HESS J1800–240B	J1800.2–2403, J1800.7–2355, J1800.9–2407
HESS J1804–216	J1804.7–2144e
HESS J1808–204	J1808.2–2028e
HESS J1809–193	J1810.3–1925e
HESS J1813–126	J1813.4–1246
HESS J1813–178	J1813.1–1737e
HESS J1825–137	J1824.5–1351e
HESS J1826–130	J1826.1–1256
HESS J1834–087	J1834.5–0846e
HESS J1841–055	J1840.9–0532e
HESS J1848–018	J1847.2–0141, J1848.6–0202, J1848.7–0129
HESS J1857+026	J1857.7+0246e
HESS J1858+020	J1858.3+0209
HESS J1912+101	J1911.7+1014, J1912.7+0957, J1913.3+1019
IC 443	J0617.2+2234e
Kookaburra (Rabbit)	J1417.7–6057, J1418.7–6057
Kookaburra PWN	J1420.0–6048
MGRO J1908+06	J1906.2+0631, J1907.9+0602
MGRO J2031+41	J2028.6+4110e
MSH 15–52	J1514.2–5909e
RCW 86	J1443.0–6227e
RX J0852.0–4622	J0851.9–4620e
RX J1713.7–3946	J1713.5–3945e
SNR G292.2–00.5	J1119.1–6127
TeV J1626–490	J1628.2–4848
Terzan 5	J1748.0–2446
VER J2019+407	J2021.0+4031e
Vela X	J0833.1–4511e
W 28	J1801.3–2326e
W 51	J1923.2+1408e
Westerlund 1	J1645.8–4533, J1648.4–4611, J1649.2–4513, J1650.3–4600, J1652.2–4516
Westerlund 2	J1023.3–5747e

Note.

^a From <http://tevcat.uchicago.edu>.

relatively low. The chance of finding a bright background, unrelated compact radio source within the LAT positional error ellipse is low enough to establish an association. The likelihood

ratio (with a somewhat different definition from that implemented in the LR-method) was required to be greater than 8 to claim an association, with an estimated false-association fraction of 1%.

For AGNs without VLBI counterparts, the position uncertainties were set to typical values of 20'' for sources associated from the RASS survey and 10'' otherwise. For identified pulsars, the position uncertainties come from the rotation ephemeris used to find γ -ray pulsations, many of which were obtained from radio observations (Smith et al. 2019). If the ephemeris does not include the uncertainties and for pulsar candidates, we use the ATNF psrcat values. If neither of those exist, we use the 0.1 uncertainties from the list maintained by the West Virginia University Astrophysics group.¹⁰² Ephemeris position uncertainties are often underestimated, so we arbitrarily apply a minimum uncertainty of 1 mas. For GLC, from Harris (1996),¹⁰³ the position uncertainties were assigned a typical value of 2''.

7. Conclusions

The fourth *Fermi* LAT source catalog is the deepest yet in the GeV energy range. The increased sensitivity relative to the 3FGL catalog is due to both the longer time interval (8 yr versus 4 yr) and the use of Pass 8 data, which provides greater acceptance over the entire energy range and a narrower PSF at high energy. The 4FGL catalog also benefits from higher-level improvements in the analysis, including an improved model for Galactic diffuse emission, a weighted log-likelihood method to mitigate the systematic effects due to that diffuse emission model, and systematic testing of three spectral representations, useful to classify unassociated sources.

The 4FGL catalog includes 5064 sources. The sources are detected ($TS > 25$) based on their average fluxes in the 8 yr data set; 1327 of the sources are found to be significantly variable on one-year timescales, and 1173 on two-month timescales. We mark 92 (1.8%) of the sources as potentially related to imperfections in the model for Galactic diffuse emission; the character *c* is appended to their names (except those already marked as *e* for extended). An additional 1072 (21.2%) are flagged in the catalog for less serious concerns, e.g., for the spectral model having a poor fit or for being close to a brighter source. Of the 5064 sources in the catalog, 358 (7.1%) are considered identified, based on pulsations, correlated variability, or correlated angular sizes with observations at other wavelengths. We find likely lower-energy counterparts for 3370 other sources (66.5%). The remaining 1336 sources (26.4%) are unassociated.

The identified and associated sources in the 4FGL catalog include many Galactic and extragalactic source classes. The largest Galactic source class continues to be pulsars, with 232 known γ -ray pulsars and seven associations with non-LAT pulsars. Other Galactic source classes have continued to grow; 30 globular clusters, 40 SNRs, and 17 PWNe are now associated with LAT sources. Blazars remain the largest class of extragalactic sources, with more than 1800 identified or associated with BL Lac or FSRQ active galaxies. Non-blazar classes of active galaxies are also found, including nine narrow-line Seyfert galaxies, five compact steep spectrum radio sources, and 42 radio galaxies. The populations of active

¹⁰² <http://astro.phys.wvu.edu/GalacticMSPs/GalacticMSPs.txt>

¹⁰³ <https://heasarc.gsfc.nasa.gov/w3browse/all/globclust.html>

galaxies in 4FGL are considered in greater detail in the companion 4LAC catalog.

The *Fermi* LAT Collaboration acknowledges generous ongoing support from a number of agencies and institutes that have supported both the development and the operation of the LAT as well as scientific data analysis. These include the National Aeronautics and Space Administration and the Department of Energy in the United States, the Commissariat à l’Energie Atomique and the Centre National de la Recherche Scientifique/Institut National de Physique Nucléaire et de Physique des Particules in France, the Agenzia Spaziale Italiana and the Istituto Nazionale di Fisica Nucleare in Italy, the Ministry of Education, Culture, Sports, Science and Technology (MEXT), High Energy Accelerator Research Organization (KEK) and Japan Aerospace Exploration Agency (JAXA) in Japan, and the K. A. Wallenberg Foundation, the Swedish Research Council and the Swedish National Space Board in Sweden.

Additional support for scientific analysis during the operations phase is gratefully acknowledged from the Istituto Nazionale di Astrofisica in Italy and the Centre National d’Études Spatiales in France. This work performed in part under DOE Contract DE-AC02-76SF00515 and MIUR contract FIRB-2012-RBFR12PM1F.

This work made extensive use of the ATNF pulsar catalog¹⁰⁴ (Manchester et al. 2005). This research has made use of the NASA/IPAC Extragalactic Database (NED), which is operated by the Jet Propulsion Laboratory, California Institute of Technology, under contract with the National Aeronautics and Space Administration, and of archival data, software and online services provided by the ASI Science Data Center (ASDC) operated by the Italian Space Agency. We used the Manitoba SNR catalog (Ferrand & Safi-Harb 2012) to check recently published extended sources.

Facility: *Fermi*-LAT.

Software: Gardian (Ackermann et al. 2012e), GALPROP¹⁰⁵ (Porter et al. 2017), HEALPix¹⁰⁶ (Górski et al. 2005), Aladin,¹⁰⁷ TOPCAT¹⁰⁸ (Taylor 2005), XSPEC.¹⁰⁹

Appendix A

Description of the FITS Version of the 4FGL Catalog

The FITS format version of the second release of the 4FGL catalog has eight binary table extensions. The extension `LAT_Point_Source_Catalog` Extension has all of the information about the sources. Its format is described in

Table 12. The table has 5065 rows for 5064 sources, because the Crab Nebula is described by two entries (the synchrotron component and the inverse-Compton component) but counted as only one source. The Crab pulsar is another entry and counted as a separate source.

The extension `GTI` is a standard Good-Time Interval listing the precise time intervals (start and stop in Mission Elapsed Time, MET) included in the data analysis. The number of intervals is fairly large because on most orbits (~95 minutes), *Fermi* passes through the SAA, and science data taking is stopped during these times. In addition, data taking is briefly interrupted on each non-SAA-crossing orbit, as *Fermi* crosses the ascending node. Filtering of time intervals with large rocking angles, GRBs, solar flares, data gaps, or operation in non-standard configurations introduces some more entries. The `GTI` is provided for reference and is useful, e.g., for reconstructing the precise data set that was used for the analysis.

The extension `ExtendedSources` (format unchanged since 2FGL) contains information about the 75 spatially extended sources that are modeled in the 4FGL source list (Section 3.4), including locations and shapes. The extended sources are indicated by an `e` appended to their names in the main table.

The extension `ROIs` contains information about the 1748 ROIs over which the analysis ran. In particular, it reports the best-fit diffuse parameters. Its format is very close to that in 3FGL, with one exception. The `RADIUS` column is replaced by `CoreRadius`, which reports the radius of the ROI core (in which the sources that belong to the ROI are located). The ROI radius (half-width in binned mode) depends on the component and is given by the core radius plus `RingWidth`, where the latter is given in the `Components` extension.

The extension `Components` is new to 4FGL. It reports the settings of each individual component (15 in all) whose sum forms the entire data set for the SummedLikelihood approach, as described in Table 2. Its format is given by Table 13.

The extension `EnergyBounds` is new to 4FGL. It contains the definitions of the bands in which the fluxes reported in the `xx_Band` columns of the main extension were computed, and the settings of the analysis. Its format is the same as that of the `Components` extension, plus one more column (`SysRel`) reporting the systematic uncertainty on effective area used to flag the sources with Flag 10 (Table 5). When several components were used in one band, several lines appear with the same `LowerEnergy` and `UpperEnergy`.

¹⁰⁴ <http://www.atnf.csiro.au/research/pulsar/psrcat>

¹⁰⁵ <http://galprop.stanford.edu>

¹⁰⁶ <http://healpix.jpl.nasa.gov/>

¹⁰⁷ <http://aladin.u-strasbg.fr/>

¹⁰⁸ <http://www.star.bristol.ac.uk/~mbt/topcat/>

¹⁰⁹ <https://heasarc.gsfc.nasa.gov/xanadu/xspec/>

Table 12
LAT 4FGL FITS Format: LAT_Point_Source_Catalog Extension

Column	Format	Unit	Description
Source_Name	18A	...	Source name 4FGL JHHMM.m+DDMMa ^a
RAJ2000	E	deg	Right ascension
DEJ2000	E	deg	Declination
GLON	E	deg	Galactic Longitude
GLAT	E	deg	Galactic Latitude
Conf_68_SemiMajor	E	deg	Long radius of error ellipse at 68% confidence ^b
Conf_68_SemiMinor	E	deg	Short radius of error ellipse at 68% confidence ^b
Conf_68_PosAng	E	deg	Position angle of the 68% ellipse ^b
Conf_95_SemiMajor	E	deg	Long radius of error ellipse at 95% confidence
Conf_95_SemiMinor	E	deg	Short radius of error ellipse at 95% confidence
Conf_95_PosAng	E	deg	Position angle (eastward) of the long axis from celestial North
ROI_num	I	...	RoI number (cross-reference to ROIs extension)
Extended_Source_Name	18A	...	Cross-reference to the ExtendedSources extension
Signif_Avg	E	...	Source significance in σ units over the 100 MeV to 1 TeV band
Pivot_Energy	E	MeV	Energy at which error on differential flux is minimal
Flux1000	E	$\text{cm}^{-2} \text{s}^{-1}$	Integral photon flux from 1 to 100 GeV
Unc_Flux1000	E	$\text{cm}^{-2} \text{s}^{-1}$	1σ error on integral photon flux from 1 to 100 GeV
Energy_Flux100	E	$\text{erg cm}^{-2} \text{s}^{-1}$	Energy flux from 100 MeV to 100 GeV obtained by spectral fitting
Unc_Energy_Flux100	E	$\text{erg cm}^{-2} \text{s}^{-1}$	1σ error on energy flux from 100 MeV to 100 GeV
SpectrumType	18A	...	Spectral type in the global model (PowerLaw, LogParabola, PLSuperExpCutoff)
PL_Flux_Density	E	$\text{cm}^{-2} \text{MeV}^{-1} \text{s}^{-1}$	Differential flux at Pivot_Energy in PowerLaw fit
Unc_PL_Flux_Density	E	$\text{cm}^{-2} \text{MeV}^{-1} \text{s}^{-1}$	1σ error on PL_Flux_Density
PL_Index	E	...	Photon index when fitting with PowerLaw
Unc_PL_Index	E	...	1σ error on PL_Index
LP_Flux_Density	E	$\text{cm}^{-2} \text{MeV}^{-1} \text{s}^{-1}$	Differential flux at Pivot_Energy in LogParabola fit
Unc_LP_Flux_Density	E	$\text{cm}^{-2} \text{MeV}^{-1} \text{s}^{-1}$	1σ error on LP_Flux_Density
LP_Index	E	...	Photon index at Pivot_Energy (α of Equation (2)) when fitting with LogParabola
Unc_LP_Index	E	...	1σ error on LP_Index
LP_beta	E	...	Curvature parameter (β of Equation (2)) when fitting with LogParabola
Unc_LP_beta	E	...	1σ error on LP_beta
LP_SigCurv	E	...	Significance (in σ units) of the fit improvement between PowerLaw and LogParabola. A value greater than 4 indicates significant curvature
PLEC_Flux_Density	E	$\text{cm}^{-2} \text{MeV}^{-1} \text{s}^{-1}$	Differential flux at Pivot_Energy in PLSuperExpCutoff fit
Unc_PLEC_Flux_Density	E	$\text{cm}^{-2} \text{MeV}^{-1} \text{s}^{-1}$	1σ error on PLEC_Flux_Density
PLEC_Index	E	...	Low-energy photon index (Γ of Equation (4)) when fitting with PLSuperExpCutoff
Unc_PLEC_Index	E	...	1σ error on PLEC_Index
PLEC_Expfactor	E	...	Exponential factor (a of Equation (4)) when fitting with PLSuperExpCutoff
Unc_PLEC_Expfactor	E	...	1σ error on PLEC_Expfactor
PLEC_Exp_Index	E	...	Exponential index (b of Equation (4)) when fitting with PLSuperExpCutoff
Unc_PLEC_Exp_Index	E	...	1σ error on PLEC_Exp_Index
PLEC_SigCurv	E	...	Same as LP_SigCurv for PLSuperExpCutoff model
Npred	E	...	Predicted number of events in the model
Flux_Band	7E	$\text{cm}^{-2} \text{s}^{-1}$	Integral photon flux in each spectral band
Unc_Flux_Band	$2 \times 7E$	$\text{cm}^{-2} \text{s}^{-1}$	1σ lower and upper error on Flux_Band ^c
nuFnu_Band	7E	$\text{erg cm}^{-2} \text{s}^{-1}$	Spectral energy distribution over each spectral band
Sqrt_TS_Band	7E	...	Square root of the Test Statistic in each spectral band
Variability_Index	E	...	Sum of $2 \times \log(\text{Likelihood})$ difference between the flux fitted in each time interval and the average flux over the full catalog interval; a value greater than 18.48 over 12 intervals indicates $<1\%$ chance of being a steady source
Frac_Variability	E	...	Fractional variability computed from the fluxes in each year
Unc_Frac_Variability	E	...	1σ error on fractional variability
Signif_Peak	E	...	Source significance in peak interval in σ units
Flux_Peak	E	$\text{cm}^{-2} \text{s}^{-1}$	Peak integral photon flux from 100 MeV to 100 GeV
Unc_Flux_Peak	E	$\text{cm}^{-2} \text{s}^{-1}$	1σ error on peak integral photon flux
Time_Peak	D	s (MET)	Time of center of interval in which peak flux was measured
Peak_Interval	E	s	Length of interval in which peak flux was measured
Flux_History	12E	$\text{cm}^{-2} \text{s}^{-1}$	Integral photon flux from 100 MeV to 100 GeV in each year (best fit from likelihood analysis with spectral shape fixed to that obtained over full interval)
Unc_Flux_History	$2 \times 12E$	$\text{cm}^{-2} \text{s}^{-1}$	1σ lower and upper error on integral photon flux in each year ^c
Sqrt_TS_History	12E	...	Square root of the Test Statistic in each year
Variability2_Index	E	...	Variability_Index over two-month intervals; a value greater than 72.44 over 48 intervals indicates $<1\%$ chance of being a steady source
Frac2_Variability	E	...	Fractional variability computed from the fluxes every two months
Unc_Frac2_Variability	E	...	1σ error on Frac2_Variability

Table 12
(Continued)

Column	Format	Unit	Description
Signif2_Peak	E	...	Source significance in peak interval in σ units
Flux2_Peak	E	$\text{cm}^{-2} \text{s}^{-1}$	Peak integral photon flux from 100 MeV to 100 GeV
Unc_Flux2_Peak	E	$\text{cm}^{-2} \text{s}^{-1}$	1σ error on peak integral photon flux
Time2_Peak	D	s (MET)	Time of center of interval in which peak flux was measured
Peak2_Interval	E	s	Length of interval in which peak flux was measured
Flux2_History	48E	$\text{cm}^{-2} \text{s}^{-1}$	Integral photon flux from 100 MeV to 100 GeV in each two-month interval
Unc_Flux2_History	$2 \times 48\text{E}$	$\text{cm}^{-2} \text{s}^{-1}$	1σ lower and upper error on Flux2_History ^c
Sqrt_TS2_History	48E	...	Square root of the Test Statistic in each two-month interval
ASSOC_FGL	18A	...	Most recent correspondence to previous FGL source catalogs, if any
ASSOC_FHL	18A	...	Most recent correspondence to previous FHL source catalogs, if any
ASSOC_GAM1	18A	...	Name of likely corresponding 2AGL source, if any
ASSOC_GAM2	18A	...	Name of likely corresponding 3EG source, if any
ASSOC_GAM3	18A	...	Name of likely corresponding EGR source, if any
TEVCAT_FLAG	A	...	P if positional association with non-extended source in TeVCat E if associated with an extended source in TeVCat, N if no TeV association
ASSOC_TEV	24A	...	Name of likely corresponding TeV source from TeVCat, if any
CLASS1	5A	...	Class designation for associated source; see Table 7
CLASS2	5A	...	Class designation for low-confidence association
ASSOC1	28A	...	Name of identified or likely associated source
ASSOC2	26A	...	Name of low-confidence association or of enclosing extended source
ASSOC_PROB_BAY	E	...	Probability of association according to the Bayesian method ^d
ASSOC_PROB_LR	E	...	Probability of association according to the Likelihood Ratio method ^e
RA_Counterpart	D	deg	R.A. of the counterpart ASSOC1
DEC_Counterpart	D	deg	decl. of the counterpart ASSOC1
Unc_Counterpart	E	deg	95% precision of the counterpart localization ^f
Flags	I	...	Source flags (binary coding as in Table 5) ^g

Notes.

^a The coordinates are rounded, following the IAU convention. The letter at the end can be c (coincident with interstellar clump), e (extended source), i (for Crab Nebula inverse Compton), or s (for Crab Nebula synchrotron).

^b From the 95% ellipse, assuming a Gaussian distribution.

^c Separate 1σ errors are computed from the likelihood profile toward lower and larger fluxes. The lower error is set equal to NULL and the upper error is derived from a Bayesian upper limit if the 1σ interval contains 0 (TS < 1).

^d NaN in this column when ASSOC1 is defined means that the probability could not be computed, either because the source is extended or because the counterpart is the result of dedicated follow-up.

^e Probabilities < 0.8 are formally set to 0.

^f For extended counterparts, this reports their extension radius.

^g Each condition is indicated by one bit among the 16 bits forming *Flags*. The bit is raised (set to 1) in the dubious case, so that sources without any warning sign have *Flags* = 0.

Table 13
LAT 4FGL FITS Format: Components Extension

Column	Format	Unit	Description
LowerEnergy	E	MeV	Lower bound of component's energy interval
UpperEnergy	E	MeV	Upper bound of component's energy interval
ENumBins	I	...	Number of bins inside energy interval
EvType	I	...	Event type selection for this component
ZenithCut	E	deg	Maximum zenith angle for this component
RingWidth	E	deg	Difference between RoI radius and core radius
PixelSize	E	deg	Pixel size for this component (of exposure map in unbinned mode)
BinnedMode	I	...	0 = Unbinned, 1 = Binned
Weighted	I	...	1 if weights were applied to this component

Appendix B
Weighted log-likelihood

The extension *Hist_Start* (format unchanged since 1FGL) contains the definitions of the time intervals used to build the light curves. The new extension *Hist2_Start* (same format) describes the time intervals used to build the second series of light curves.

In 3FGL, we introduced a first attempt at accounting for systematic errors in the maximum likelihood process itself, at the source detection level. It was not used in the source

characterization, however, for lack of a suitable framework. The standard way to account for systematic errors (for example in XSPEC¹¹⁰) is to define them as a fraction ϵ of the signal and add them to the statistical errors in quadrature, in a χ^2 formalism. This can be adapted to the maximum likelihood framework by introducing weights $w_i < 1$ (Hu & Zidek 2002) as

$$\log \mathcal{L} = \sum_i w_i (n_i \log M_i - M_i) \quad (12)$$

where M_i and n_i are the model and observed counts in each bin, and the sum runs over all bins in space and energy. The source significance can then be quantified in the same way, via the Test Statistic $TS = 2 \log(\mathcal{L}/\mathcal{L}_0)$ in which \mathcal{L} and \mathcal{L}_0 are the (weighted) log-likelihood with and without the source of interest, respectively.

Since the statistical variance in Poisson statistics is the signal itself, a first guess for the weights could be

$$w_i = \frac{M_i}{M_i + (\epsilon M_i)^2} = \frac{1}{1 + \epsilon^2 M_i}. \quad (13)$$

However, that formulation has a serious flaw, which is that it is not stable to rebinning. If one splits the bins in half, then M_i is split in half while ϵ stays the same (it is defined externally). In the limit of very small bins, obviously the weights will all tend to 1 and the log \mathcal{L} formula will tend to the unweighted one, even though nothing has changed in the underlying data or the model.

The solution we propose, originally presented in Ballet & Fermi LAT Collaboration (2015), is to define a suitable integral over energy (E) and space (\mathbf{r}) $N(\mathbf{r}, E)$, which does not depend on binning. M_i in the weight formula is then replaced by $N(\mathbf{r}_i, E_i)$ taken at the event's coordinates. For the integral over space, since the catalog mostly deals with point sources, the logical solution is to integrate the background under the PSF, i.e., to convolve the model with the PSF $P(\mathbf{r}, E)$, normalized to 1 at the peak (this is equivalent, for a flat diffuse emission, to multiplying by the PSF solid angle). Note that the model already contains the PSF, so this amounts to applying a double convolution to the sky model.

For the energy integral, the choice is less obvious. The source spectrum is not a narrow line, so convolving with the energy dispersion (similar to what is done for space) is not justified. An integral over the full energy range would give the same weight to all energies, which is clearly not what we want (there is no reason to downplay the few high-energy events). The option we adopt here is to start the integration at the current energy:

$$w_i = \frac{1}{1 + \epsilon^2 N(\mathbf{r}_i, E_i)} \quad (14)$$

$$N(\mathbf{r}_i, E_i) = \int_{E_i}^{E_{\max}} S(\mathbf{r}_i, E) dE \quad (15)$$

$$S(\mathbf{r}, E) = \frac{dM}{dE}(\mathbf{r}, E) * P(\mathbf{r}, E) \quad (16)$$

where dM/dE is the differential model. As energy increases, the spectra (in counts) decrease and the LAT PSF gets narrower so the convolution makes S even steeper than dM/dE . As a result, the integral giving N is nearly always dominated by the lowest energies, so the exact upper bound E_{\max} is not critical.

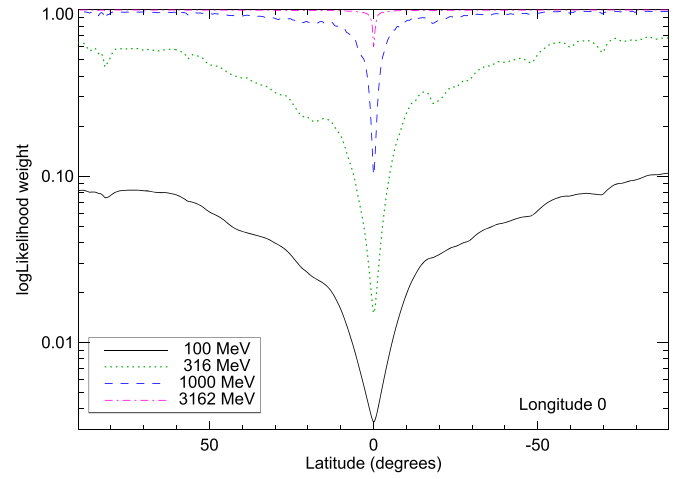


Figure 22. Data-based log-likelihood weights as a function of latitude across the Galactic Center, at 100 MeV, 300 MeV, 1 GeV, and 3 GeV, assuming all events are used throughout, and the same zenith cut at 105° . The dips at some latitudes are point sources, which are included in the data-based weights. Those weights were not used in 4FGL (which uses separate event types), they are shown here only for illustration.

The only spectral region where it is important is the very lowest energies (< 100 MeV) where the effective area rises steeply. In order not to penalize the lowest energies too much, we set $E_{\max} = 2E_i$ in Equation (15).

There are two possibilities to define dM/dE . Since the main origin of the systematic error is the diffuse emission, we can restrict dM/dE to the diffuse emission model only (we call the result model-based weights). On the other hand, there are also systematic uncertainties on sources due to PSF calibration and our imperfect spectral representation, so another option is to enter the full model (or the data themselves) into dM/dE (we call the result data-based weights). That second choice limits spurious sources next to bright sources. There is of course no reason why the level of systematics ϵ should be the same for the diffuse emission model and the sources, but in practice, it is a reasonable approximation.

Another important point, for the procedure to be stable, is that the weights should not change with the model parameters. So dM/dE must be defined beforehand (for example from a previous fit). In this work, we use data-based weights computed from the data themselves, with a common ϵ . The data are not as smooth as the model, but this is not a problem in the regime of large counts where weights play a role.

We assume here that ϵ is a true constant (it depends neither on space nor on energy). For a given ϵ , the weights are close to 1 at high energy and decrease toward low energy. At a given energy, the weights are smallest where the data is largest (in the Galactic ridge). We illustrate that behavior in Figure 22, merging all event types together (not what we do in 4FGL), for 8 yr and $\epsilon = 3\%$. The width of the trough in the Galactic Ridge gets narrower at high energy, as the PSF improves. At 100 MeV, the weights are everywhere less than 12%. They reach 50% at high latitude at 250 MeV, and 90% at 500 MeV. This justifies our choice of discarding 75% of the events below 100 MeV and 50% below 300 MeV (Table 2). The entire sky is limited by systematic effects below 300 MeV. On average, in the Galactic ridge (a little better than the very center shown in Figure 22), the weights are 0.5% at 100 MeV, 1.5% at 250 MeV, 5% at 500 MeV, 20% at 1 GeV, 60% at 2 GeV, and reach 90% at 4.5 GeV.

¹¹⁰ <https://heasarc.gsfc.nasa.gov/xanadu/xspec/>

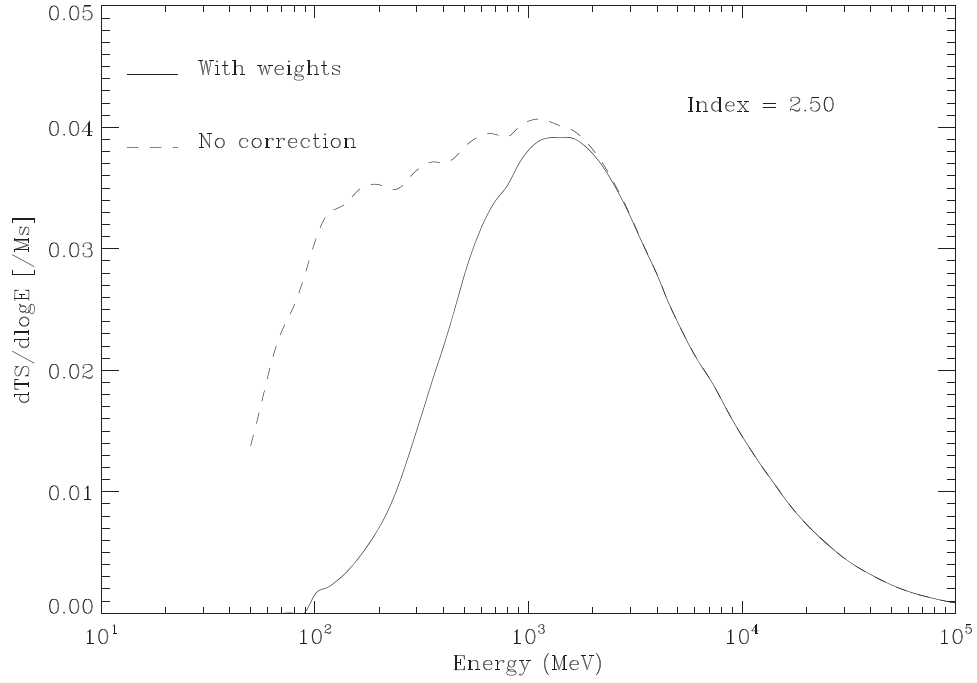


Figure 23. Contribution to TS as a function of energy for a power-law source with $\Gamma = 2.5$ at high latitude, with and without weights. This assumes all events are used throughout (and with the same zenith cut at 105°), as in Figure 22.

Another way to illustrate the effect of the weights is shown in Figure 23 (similar to Figure 18 of the 1FGL paper). It shows the contribution to TS of all energies, for a rather soft source at high latitude (the background and exposure are averaged over all latitudes larger than 10°), with and without weights. Energies below 300 MeV contribute very little when the weights are applied. This remains true with the actual data selection used in 4FGL.

A specific difficulty remains, because at a given energy, we split the data into several components, each corresponding to a particular event type (with a different PSF). Since the systematics act in the same way on all components, the weights must be computed globally (i.e., weights must be lower when using PSF2 and PSF3 events than when using PSF3 alone). On the other hand, the resulting uncertainties with two components should be smaller than those with a single component (adding a second one adds information). In this work, we started by computing weights w_k individually for each component k (the dependence on E and \mathbf{r} is left implicit). Then, we assumed that the final weights are simply proportional to the original ones, with a factor $\alpha < 1$ (α depends on E and \mathbf{r} as well). A reasonable solution is then

$$N_{\min} = \min_k N_k \quad (17)$$

$$K_{\text{tot}} = \sum_k \left(\frac{N_{\min}}{N_k} \right)^2 \quad (18)$$

$$\alpha = \frac{1 + \epsilon^2 N_{\min}}{1 + \epsilon^2 N_{\min} K_{\text{tot}}} \quad (19)$$

$$w_k = \frac{\alpha}{1 + \epsilon^2 N_k} \quad (20)$$

K_{tot} and α are 1 if one component dominates over the others, and K_{tot} is the number of components if they are all similar. The effect of this procedure is depicted in Figure 24 at 1 GeV, the lowest energy at which we use all event types. It illustrates

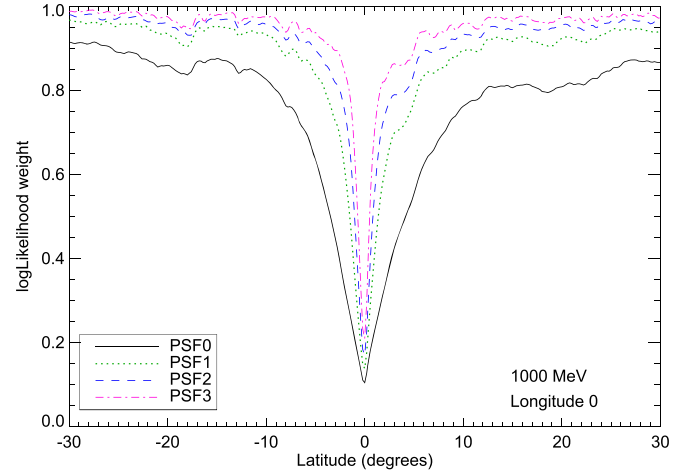













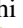
















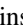











Figure 24. Data-based weights at 1 GeV for ZMax = 105° as a function of latitude (for the interesting $[-30^\circ, 30^\circ]$ region) across the Galactic Center, for different PSF event types, computed according to Equation (20). These weights were actually used in 4FGL. The average (over event types) weight is larger than the weight using all events together at the same 1 GeV energy (blue dashed line in Figure 22). This is because keeping event types separate is more favorable than merging them and losing the event type information.

quantitatively how the PSF0 events are unweighted at low latitudes, compared to better event types.

ORCID iDs

- M. Ajello <https://orcid.org/0000-0002-6584-1703>
M. Axelsson <https://orcid.org/0000-0003-4378-8785>
L. Baldini <https://orcid.org/0000-0002-9785-7726>
J. Ballet <https://orcid.org/0000-0002-8784-2977>
D. Bastieri <https://orcid.org/0000-0002-6954-8862>
J. Becerra Gonzalez <https://orcid.org/0000-0002-6729-9022>
R. Bellazzini <https://orcid.org/0000-0002-2469-7063>
E. Bissaldi <https://orcid.org/0000-0001-9935-8106>

E. Charles  <https://orcid.org/0000-0002-3925-7802>
 C. C. Cheung  <https://orcid.org/0000-0002-4377-0174>
 F. D'Ammando  <https://orcid.org/0000-0001-7618-7527>
 A. Desai  <https://orcid.org/0000-0001-7405-9994>
 A. Domínguez  <https://orcid.org/0000-0002-3433-4610>
 A. Franckowiak  <https://orcid.org/0000-0002-5605-2219>
 Y. Fukazawa  <https://orcid.org/0000-0002-0921-8837>
 S. Funk  <https://orcid.org/0000-0002-2012-0080>
 P. Fusco  <https://orcid.org/0000-0002-9383-2425>
 D. Gargano  <https://orcid.org/0000-0002-5055-6395>
 F. Gasparrini  <https://orcid.org/0000-0002-5064-9495>
 M. Giroletti  <https://orcid.org/0000-0002-8657-8852>
 T. Glanzman  <https://orcid.org/0000-0001-9649-3871>
 S. Guiriec  <https://orcid.org/0000-0001-5780-8770>
 A. K. Harding  <https://orcid.org/0000-0001-6119-859X>
 K. Hayashi  <https://orcid.org/0000-0001-6922-6583>
 M. Kerr  <https://orcid.org/0000-0002-0893-4073>
 M. Kuss  <https://orcid.org/0000-0003-1212-9998>
 S. Larsson  <https://orcid.org/0000-0003-0716-107X>
 M. Lemoine-Goumard  <https://orcid.org/0000-0002-4462-3686>
 J. Li  <https://orcid.org/0000-0003-1720-9727>
 I. Liodakis  <https://orcid.org/0000-0001-9200-4006>
 F. Loparco  <https://orcid.org/0000-0002-1173-5673>
 B. Lott  <https://orcid.org/0000-0003-2186-9242>
 P. Lubrano  <https://orcid.org/0000-0003-0221-4806>
 S. Maldera  <https://orcid.org/0000-0002-0698-4421>
 A. Manfreda  <https://orcid.org/0000-0002-0998-4953>
 L. Marcotulli  <https://orcid.org/0000-0002-8472-3649>
 M. N. Mazziotta  <https://orcid.org/0000-0001-9325-4672>
 M. Meyer  <https://orcid.org/0000-0002-0738-7581>
 N. Mirabal  <https://orcid.org/0000-0002-7021-5838>
 T. Mizuno  <https://orcid.org/0000-0001-7263-0296>
 M. E. Monzani  <https://orcid.org/0000-0002-8254-5308>
 A. Morselli  <https://orcid.org/0000-0002-7704-9553>
 I. V. Moskalenko  <https://orcid.org/0000-0001-6141-458X>
 V. S. Paliya  <https://orcid.org/0000-0001-7774-5308>
 M. Pesce-Rollins  <https://orcid.org/0000-0003-1790-8018>
 V. Petrosian  <https://orcid.org/0000-0002-2670-8942>
 T. A. Porter  <https://orcid.org/0000-0002-2621-4440>
 S. Rainò  <https://orcid.org/0000-0002-9181-0345>
 R. Rando  <https://orcid.org/0000-0001-6992-818X>
 M. Razzano  <https://orcid.org/0000-0003-4825-1629>
 S. Razzaque  <https://orcid.org/0000-0002-0130-2460>
 O. Reimer  <https://orcid.org/0000-0001-6953-1385>
 R. W. Romani  <https://orcid.org/0000-0001-6711-3286>
 F. K. Schinzel  <https://orcid.org/0000-0001-6672-128X>
 C. Sgrò  <https://orcid.org/0000-0001-5676-6214>
 D. A. Smith  <https://orcid.org/0000-0002-7833-0275>
 D. J. Thompson  <https://orcid.org/0000-0001-5217-9135>
 L. Tibaldo  <https://orcid.org/0000-0001-7523-570X>
 D. F. Torres  <https://orcid.org/0000-0002-1522-9065>

References

- Abdo, A. A., Ackermann, M., Ajello, M., et al. 2009a, *ApJL*, **706**, L1, (W51C)
 Abdo, A. A., Ackermann, M., Ajello, M., et al. 2009b, *ApJL*, **701**, L123, (LS I +61 303)
 Abdo, A. A., Ackermann, M., Ajello, M., et al. 2009c, *ApJS*, **183**, 46, (0FGL)
 Abdo, A. A., Ackermann, M., Ajello, M., et al. 2009d, *Aph*, **32**, 193, (On-orbit calibration)
 Abdo, A. A., Ackermann, M., Ajello, M., et al. 2010a, *A&A*, **524**, A75
 Abdo, A. A., Ackermann, M., Ajello, M., et al. 2010b, *ApJL*, **709**, L152
 Abdo, A. A., Ackermann, M., Ajello, M., et al. 2010c, *ApJ*, **714**, 927, (PSR B1509)
 Abdo, A. A., Ackermann, M., Ajello, M., et al. 2010d, *Sci*, **328**, 725, (Cen A lobes)
 Abdo, A. A., Ackermann, M., Ajello, M., et al. 2010e, *ApJS*, **188**, 405, (1FGL)
 Abdo, A. A., Ackermann, M., Ajello, M., et al. 2010f, *ApJ*, **723**, 649
 Abdo, A. A., Ackermann, M., Ajello, M., et al. 2010g, *ApJ*, **718**, 348, (W28)
 Abdo, A. A., Ackermann, M., Ajello, M., et al. 2010h, *ApJ*, **713**, 146, (Vela X)
 Abdo, A. A., Ackermann, M., Ajello, M., et al. 2010i, *Sci*, **327**, 1103, (W44)
 Abdo, A. A., Ackermann, M., Ajello, M., et al. 2010j, *ApJ*, **712**, 459, (IC 443)
 Abdo, A. A., Ackermann, M., Ajello, M., et al. 2011, *ApJ*, **734**, 116, (Sun)
 Abdo, A. A., Ajello, M., Allafort, A., et al. 2013, *ApJS*, **208**, 17, (2PC)
 Abdollahi, S., Ackermann, M., Ajello, M., et al. 2017, *ApJ*, **846**, 34
 Abramowski, A., Aharonian, F., Ait Benkhali, F., et al. 2015, *A&A*, **574**, A27
 Acero, F., Ackermann, M., Ajello, M., et al. 2015, *ApJS*, **218**, 23, (3FGL)
 Acero, F., Ackermann, M., Ajello, M., et al. 2016a, *ApJS*, **223**, 26, (Diffuse model)
 Acero, F., Ackermann, M., Ajello, M., et al. 2016b, *ApJS*, **224**, 8, (SNRCat)
 Acero, F., Donato, D., Ojha, R., et al. 2013, *ApJ*, **779**, 133
 Ackermann, M., Ajello, M., Albert, A., et al. 2012a, *ApJS*, **203**, 4, (Pass7)
 Ackermann, M., Ajello, M., Albert, A., et al. 2014a, *Sci*, **345**, 554
 Ackermann, M., Ajello, M., Albert, A., et al. 2014b, *ApJ*, **787**, 15
 Ackermann, M., Ajello, M., Albert, A., et al. 2016a, *PhRvD*, **93**, 082001 (Moon)
 Ackermann, M., Ajello, M., Albert, A., et al. 2017a, *ApJ*, **836**, 208
 Ackermann, M., Ajello, M., Allafort, A., et al. 2011a, *Sci*, **334**, 1103, (Cygnus X)
 Ackermann, M., Ajello, M., Allafort, A., et al. 2011b, *ApJ*, **743**, 171, (2LAC)
 Ackermann, M., Ajello, M., Allafort, A., et al. 2012b, *ApJ*, **753**, 83
 Ackermann, M., Ajello, M., Allafort, A., et al. 2012c, *Aph*, **35**, 346, (Energy scale)
 Ackermann, M., Ajello, M., Allafort, A., et al. 2013, *ApJS*, **209**, 34, (1FHL)
 Ackermann, M., Ajello, M., Atwood, W. B., et al. 2012d, *ApJ*, **761**, 91
 Ackermann, M., Ajello, M., Atwood, W. B., et al. 2012e, *ApJ*, **750**, 3
 Ackermann, M., Ajello, M., Atwood, W. B., et al. 2015, *ApJ*, **810**, 14, (3LAC)
 Ackermann, M., Ajello, M., Atwood, W. B., et al. 2016b, *ApJS*, **222**, 5, (2FHL)
 Ackermann, M., Ajello, M., Baldini, L., et al. 2011c, *ApJ*, **726**, 35
 Ackermann, M., Ajello, M., Baldini, L., et al. 2016c, *ApJ*, **826**, 1, (Fornax A)
 Ackermann, M., Ajello, M., Baldini, L., et al. 2017b, *ApJ*, **843**, 139, (FGES)
 Ackermann, M., Ajello, M., Baldini, L., et al. 2018, *ApJS*, **237**, 32, (FHES)
 Ackermann, M., Albert, A., Atwood, W. B., et al. 2016d, *A&A*, **586**, A71, (LMC)
 Aharonian, F., Akhperjanian, A. G., Aye, K.-M., et al. 2005, *A&A*, **439**, 1013
 Aharonian, F., Akhperjanian, A. G., Barres de Almeida, U., et al. 2008, *A&A*, **477**, 353
 Ajello, M., Allafort, A., Baldini, L., et al. 2012, *ApJ*, **744**, 80, (W30)
 Ajello, M., Arimoto, M., Axelsson, M., et al. 2019, *ApJ*, **878**, 52
 Ajello, M., Atwood, W. B., Baldini, L., et al. 2017, *ApJS*, **232**, 18, (3FHL)
 Ajello, M., Baldini, L., Barbiellini, G., et al. 2016, *ApJ*, **819**, 98, (RCW 86)
 Allafort, A., Baldini, L., Ballet, J., et al. 2013, *ApJL*, **777**, L2
 Álvarez Crespo, N., Masetti, N., Ricci, F., et al. 2016a, *AJ*, **151**, 32
 Álvarez Crespo, N., Massaro, F., D'Abusco, R., et al. 2016b, *Ap&SS*, **361**, 316
 Álvarez Crespo, N., Massaro, F., Milisavljevic, D., et al. 2016c, *AJ*, **151**, 95
 Araya, M. 2014, *MNRAS*, **444**, 860
 Araya, M. 2017, *ApJ*, **843**, 12
 Araya, M. 2018a, *MNRAS*, **474**, 102
 Araya, M. 2018b, *ApJ*, **859**, 69
 Arsioli, B., Fraga, B., Giommi, P., Padovani, P., & Marrese, P. M. 2015, *A&A*, **579**, A34
 Arsioli, B., & Polenta, G. 2018, *A&A*, **616**, A20
 Atwood, W. B., Abdo, A. A., Ackermann, M., et al. 2009, *ApJ*, **697**, 1071, (LAT)
 Atwood, W. B., Albert, A., Baldini, L., et al. 2013, arXiv:1303.3514, (Pass 8)
 Ballet, J. & Fermi LAT Collaboration 2015, Proc. ICRC, **34**, 848
 Baltz, E. A., Taylor, J. E., & Wai, L. L. 2007, *ApJL*, **659**, L125
 Berton, M., Foschini, L., Ciroi, S., et al. 2015, *A&A*, **578**, A28
 Bird, A. J., Bazzano, A., Malizia, A., et al. 2016, *ApJS*, **223**, 15
 Bregeon, J., Charles, E., & Wood, M. 2013, arXiv:1304.5456
 Bruehl, R., Burnett, T. H., Digel, S. W., et al. 2018, arXiv:1810.11394, (P305)
 Buehler, R., Scargle, J. D., Blandford, R. D., et al. 2012, *ApJ*, **749**, 26
 Bulgarelli, A., Fioretti, V., Parmiggiani, N., et al. 2019, *A&A*, **627**, A13
 Capetti, A., Massaro, F., & Baldi, R. D. 2017a, *A&A*, **598**, A49
 Capetti, A., Massaro, F., & Baldi, R. D. 2017b, *A&A*, **601**, A81
 Caputo, R., Buckley, M. R., Martin, P., et al. 2016, *PhRvD*, **93**, 062004
 Casandjian, J.-M., & Grenier, I. A. 2008, *A&A*, **489**, 849
 Chang, Y.-L., Arsioli, B., Giommi, P., & Padovani, P. 2017, *A&A*, **598**, A17
 Cheung, C. C., Donato, D., Gehrels, N., Sokolovsky, K. V., & Giroletti, M. 2012, *ApJ*, **756**, 33

- Cheung, C. C., Jean, P., Shore, S. N., et al. 2016, *ApJ*, **826**, 142
- Chiaro, G., Salvetti, D., La Mura, G., et al. 2016, *MNRAS*, **462**, 3180
- Condon, J. J., Cotton, W. D., Greisen, E. W., et al. 1998, *AJ*, **115**, 1693
- Coronado-Blázquez, J., Sánchez-Conde, M. A., Domínguez, A., et al. 2019, *JCAP*, **2019**, 020
- Cowperthwaite, P. S., Massaro, F., D'Abrusco, R., et al. 2013, *AJ*, **146**, 110
- D'Abrusco, R., Massaro, F., Paggi, A., et al. 2014, *ApJS*, **215**, 14
- de Menezes, R., Peña-Herazo, H. A., Marchesini, E. J., et al. 2019, *A&A*, **630**, A55
- de Ruiter, H. R., Willis, A. G., & Arp, H. C. 1977, *A&AS*, **28**, 211
- Devin, J., Acero, F., Ballet, J., & Schmid, J. 2018, *A&A*, **617**, A5
- Doert, M., & Errando, M. 2014, *ApJ*, **782**, 41
- Fermi-LAT collaboration 2019, arXiv:1905.10771, (4LAC)
- Ferrand, G., & Safi-Harb, S. 2012, *AdSpR*, **49**, 1313
- Garcia, F., Chaty, S., & Fortin, F. 2019, *A&A*, submitted
- Giommi, P., Polenta, G., Lähteenmäki, A., et al. 2012, *A&A*, **541**, A160
- Giroletti, M., Massaro, F., D'Abrusco, R., et al. 2016, *A&A*, **588**, A141
- Górski, K. M., Hivon, E., Banday, A. J., et al. 2005, *ApJ*, **622**, 759
- Green, D. A. 2014, *BASI*, **42**, 47
- Grenier, I. A., Casandjian, J.-M., & Terrier, R. 2005, *Sci*, **307**, 1292
- Griffin, R. D., Dai, X., & Thompson, T. A. 2016, *ApJL*, **823**, L17
- Grondin, M.-H., Funk, S., Lemoine-Goumard, M., et al. 2011, *ApJ*, **738**, 42
- Hanabata, Y., Katagiri, H., Hewitt, J. W., et al. 2014, *ApJ*, **786**, 145
- Harris, W. E. 1996, *AJ*, **112**, 1487
- Hartman, R. C., Bertsch, D. L., Bloom, S. D., et al. 1999, *ApJS*, **123**, 79
- Hassan, T., Mirabal, N., Contreras, J. L., & Oya, I. 2013, *MNRAS*, **428**, 220
- Hayashida, M., Stawarz, L., Cheung, C. C., et al. 2013, *ApJ*, **779**, 131
- Healey, S. E., Romani, R. W., Cotter, G., et al. 2008, *ApJS*, **175**, 97
- Healey, S. E., Romani, R. W., Taylor, G. B., et al. 2007, *ApJS*, **171**, 61
- H.E.S.S. Collaboration, Abdalla, H., Abramowski, A., et al. 2018a, *A&A*, **612**, A6
- H.E.S.S. Collaboration, Abdalla, H., Abramowski, A., et al. 2018b, *A&A*, **619**, A71
- H4PI Collaboration, Ben Bekhti, N., Flöer, L., et al. 2016, *A&A*, **594**, A116
- Hovatta, T., Aller, M. F., Aller, H. D., et al. 2014, *AJ*, **147**, 143
- Hovatta, T., Lister, M. L., Aller, M. F., et al. 2012, *AJ*, **144**, 105
- Hu, F., & Zidek, J. V. 2002, *Canad. J. Statist.*, **30**, 347
- Johannesson, G., Orlando, E. & the Fermi-LAT collaboration 2013, *Proc. ICRC*, **33**, 3106
- Johnson, T. J., Ray, P. S., Roy, J., et al. 2015, *ApJ*, **806**, 91
- Katagiri, H., Sugiyama, S., Ackermann, M., et al. 2016a, *ApJ*, **831**, 106
- Katagiri, H., Tibaldo, L., Ballet, J., et al. 2011, *ApJ*, **741**, 44
- Katagiri, H., Yoshida, K., Ballet, J., et al. 2016b, *ApJ*, **818**, 114
- Kataoka, J., Yatsu, Y., Kawai, N., et al. 2012, *ApJ*, **757**, 176
- Katsuta, J., Uchiyama, Y., Tanaka, T., et al. 2012, *ApJ*, **752**, 135
- Kerr, M. 2010, PhD thesis, Univ. Washington
- Kovalev, Y. Y. 2009, *ApJL*, **707**, L56
- Kuiper, L., Hermsen, W., Krijger, J. M., et al. 1999, *A&A*, **351**, 119
- Kuzmicz, A., Jamroz, M., Bronarska, K., Janda-Boczar, K., & Saikia, D. J. 2018, *ApJS*, **238**, 9
- Lande, J., Ackermann, M., Allafort, A., et al. 2012, *ApJ*, **756**, 5
- Landi, R., Bassani, L., Stephen, J. B., et al. 2015, *A&A*, **581**, A57
- Landoni, M., Falomo, R., Treves, A., Scarpa, R., & Reverte Payá, D. 2015a, *AJ*, **150**, 181
- Landoni, M., Massaro, F., Paggi, A., et al. 2015b, *AJ*, **149**, 163
- Landoni, M., Paiano, S., Falomo, R., Scarpa, R., & Treves, A. 2018, *ApJ*, **861**, 130
- Li, J., Rea, N., Torres, D. F., & de Oña-Wilhelmi, E. 2017a, *ApJ*, **835**, 30
- Li, J., Torres, D. F., Cheng, K. S., et al. 2017b, *ApJ*, **846**, 169
- Liu, Q. Z., van Paradijs, J., & van den Heuvel, E. P. J. 2007, *yCat*, **346**, 90807
- López-Cañiego, M., González-Nuevo, J., Massardi, M., et al. 2013, *MNRAS*, **430**, 1566
- Maeda, K., Kataoka, J., Nakamori, T., et al. 2011, *ApJ*, **729**, 103
- Manchester, R. N., Hobbs, G. B., Teoh, A., & Hobbs, M. 2005, *AJ*, **129**, 1993
- Marchesi, S., Kaur, A., & Ajello, M. 2018, *AJ*, **156**, 212
- Marchesini, E. J., Peña-Herazo, H. A., Álvarez Crespo, N., et al. 2019, *Ap&SS*, **364**, 5
- Maselli, A., Massaro, F., D'Abrusco, R., et al. 2015, *Ap&SS*, **357**, 141
- Massaro, E., Giommi, P., Leto, C., et al. 2009, *A&A*, **495**, 691
- Massaro, F., Álvarez Crespo, N., D'Abrusco, R., et al. 2016, *Ap&SS*, **361**, 337
- Massaro, F., & D'Abrusco, R. 2016, *ApJ*, **827**, 67
- Massaro, F., D'Abrusco, R., Ajello, M., Grindlay, J. E., & Smith, H. A. 2011, *ApJL*, **740**, L48
- Massaro, F., D'Abrusco, R., Giroletti, M., et al. 2013, *ApJS*, **207**, 4
- Massaro, F., D'Abrusco, R., Landoni, M., et al. 2015a, *ApJS*, **217**, 2
- Massaro, F., D'Abrusco, R., Tosti, G., et al. 2012a, *ApJ*, **750**, 138
- Massaro, F., D'Abrusco, R., Tosti, G., et al. 2012b, *ApJ*, **752**, 61
- Massaro, F., Landoni, M., D'Abrusco, R., et al. 2015b, *A&A*, **575**, A124
- Massaro, F., Masetti, N., D'Abrusco, R., Paggi, A., & Funk, S. 2014, *AJ*, **148**, 66
- Mattox, J. R., Bertsch, D. L., Chiang, J., et al. 1996, *ApJ*, **461**, 396
- Mattox, J. R., Wagner, S. J., Malkan, M., et al. 1997, *ApJ*, **476**, 692
- Mauch, T., Murphy, T., Buttery, H. J., et al. 2003, *MNRAS*, **342**, 1117
- McConnachie, A. W. 2012, *AJ*, **144**, 4
- Mereghetti, S., Palombara, N. L., Tiengo, A., et al. 2011, *ApJ*, **737**, 51
- Mirabal, N., & Halpern, J. P. 2009, *ApJL*, **701**, L129
- Murphy, T., Sadler, E. M., Ekers, R. D., et al. 2010, *MNRAS*, **402**, 2403
- Napier, P. J., Bagri, D. S., Clark, B. G., et al. 1994, *IEEEP*, **82**, 658
- Nolan, P. L., Abdo, A. A., Ackermann, M., et al. 2012, *ApJS*, **199**, 31, (2FGL)
- Nori, M., Giroletti, M., Massaro, F., et al. 2014, *ApJS*, **212**, 3
- Oh, K., Koss, M., Markwardt, C. B., et al. 2018, *ApJS*, **235**, 4
- Orlando, E., & Strong, A. W. 2008, *A&A*, **480**, 847
- Paggi, A., Massaro, F., D'Abrusco, R., et al. 2013, *ApJS*, **209**, 9
- Paggi, A., Milisavljevic, D., Masetti, N., et al. 2014, *AJ*, **147**, 112
- Paiano, S., Falomo, R., Franceschini, A., Treves, A., & Scarpa, R. 2017a, *ApJ*, **851**, 135
- Paiano, S., Franceschini, A., & Stamerra, A. 2017b, *MNRAS*, **468**, 4902
- Paiano, S., Landoni, M., Falomo, R., et al. 2017d, *ApJ*, **837**, 144
- Paiano, S., Landoni, M., Falomo, R., Treves, A., & Scarpa, R. 2017c, *ApJ*, **844**, 120
- Paladini, R., Burigana, C., Davies, R. D., et al. 2003, *A&A*, **397**, 213
- Pellizzoni, A., Pilia, M., Possenti, A., et al. 2009, *ApJL*, **695**, L115
- Peña-Herazo, H. A., Marchesini, E. J., Álvarez Crespo, N., et al. 2017, *Ap&SS*, **362**, 228
- Peng, F.-K., Wang, X.-Y., Liu, R.-Y., Tang, Q.-W., & Wang, J.-F. 2016, *ApJL*, **821**, L20
- Petrov, L., Mahony, E. K., Edwards, P. G., et al. 2013, *MNRAS*, **432**, 1294
- Petrov, L., Phillips, C., Bertarini, A., Murphy, T., & Sadler, E. M. 2011, *MNRAS*, **414**, 2528
- Pivato, G., Hewitt, J. W., Tibaldo, L., et al. 2013, *ApJ*, **779**, 179
- Planck Collaboration, Aghanim, N., Ashdown, M., et al. 2016, *A&A*, **596**, A109
- Popov, S. B., Mereghetti, S., Blinnikov, S. I., Kuranov, A. G., & Yungelson, L. R. 2018, *MNRAS*, **474**, 2750
- Porter, T. A., Jóhannesson, G., & Moskalenko, I. V. 2017, *ApJ*, **846**, 67
- Principe, G., Malyshev, D., Ballet, J., & Funk, S. 2018, *A&A*, **618**, A22, (IFLE)
- Rakshit, S., Stalín, C. S., Chand, H., & Zhang, X.-G. 2017, *ApJS*, **229**, 39
- Reithberger, K., Reimer, A., Reimer, O., & Takahashi, H. 2015, *A&A*, **577**, A100
- Ricci, F., Massaro, F., Landoni, M., et al. 2015, *AJ*, **149**, 160
- Sanders, D. B., Mazzarella, J. M., Kim, D.-C., Surace, J. A., & Soifer, B. T. 2003, *AJ*, **126**, 1607
- Saz Parkinson, P., Limyansky, B., Clark, C., Marelli, M., & Abdollahi, S. 2018, in *Proc. 8th Int. Fermi Symp. (Greenbelt, MD: NASA)*, https://fermi.gsfc.nasa.gov/science/mtgs/symposia/2018/program/wed/Pablo_Saz_Parkinson.pdf
- Schinzell, F. K., Petrov, L., Taylor, G. B., et al. 2015, *ApJS*, **217**, 4
- Schinzell, F. K., Petrov, L., Taylor, G. B., & Edwards, P. G. 2017, *ApJ*, **838**, 139
- Schmidt, K., Priebe, A., & Boller, T. 1993, *AN*, **314**, 371
- Shahbaz, T., & Watson, C. A. 2007, *A&A*, **474**, 969
- Shaw, M. S., Filippenko, A. V., Romani, R. W., Cenko, S. B., & Li, W. 2013a, *AJ*, **146**, 127
- Shaw, M. S., Romani, R. W., Cotter, G., et al. 2013b, *ApJ*, **764**, 135
- Smith, D. A., Bruel, P., Cognard, I., et al. 2019, *ApJ*, **871**, 78
- Stappers, B. W., Archibald, A. M., Hessels, J. W. T., et al. 2014, *ApJ*, **790**, 39
- Stroh, M. C., & Falcone, A. D. 2013, *ApJS*, **207**, 28
- Takahashi, Y., Kataoka, J., Nakamori, T., et al. 2012, *ApJ*, **747**, 64
- Takeuchi, Y., Kataoka, J., Maeda, K., et al. 2013, *ApJS*, **208**, 25
- Tang, Q.-W., Wang, X.-Y., & Tam, P.-H. T. 2014, *ApJ*, **794**, 26
- Taylor, M. B. 2005, in *ASP Conf. Ser. 347, Astronomical Data Analysis Software and Systems XIV*, ed. P. Shopbell, M. Britton, & R. Ebert (San Francisco, CA: ASP), **29**
- Véron-Cetty, M.-P., & Véron, P. 2010, *A&A*, **518**, A10
- Voges, W., Aschenbach, B., Boller, T., et al. 1999, *A&A*, **349**, 389
- Voges, W., Aschenbach, B., Boller, T., et al. 2000, *yCat*, **9029**
- Yeung, P. K. H., Kong, A. K. H., Tam, P. H. T., et al. 2016, *ApJ*, **827**, 41
- Yeung, P. K. H., Kong, A. K. H., Tam, P. H. T., et al. 2017, *ApJ*, **837**, 69
- Yost-Hull, T. M., Gallagher, John. S. I., Aalto, S., & Varenius, E. 2017, *MNRAS*, **469**, L89
- Zanin, R., Fernández-Barral, A., de Oña Wilhelmi, E., et al. 2016, *A&A*, **596**, A55
- Zdziarski, A. A., Malyshev, D., Chernyakova, M., & Pooley, G. G. 2017, *MNRAS*, **471**, 3657
- Zhang, P. F., Xin, Y. L., Fu, L., et al. 2016, *MNRAS*, **459**, 99



Bright Gamma-Ray Flares Observed in GRB 131108A

M. Ajello¹, M. Arimoto², K. Asano³, M. Axelsson^{4,5}, L. Baldini⁶, G. Barbiellini^{7,8}, D. Bastieri^{9,10}, R. Bellazzini¹¹, A. Berretta¹², E. Bissaldi^{13,14}, R. D. Blandford¹⁵, R. Bonino^{16,17}, E. Bottacini^{15,18}, J. Bregeon¹⁹, P. Bruel²⁰, R. Buehler²¹, S. Buson²², R. A. Cameron¹⁵, R. Caputo²³, P. A. Caraveo²⁴, E. Cavazzuti²⁵, S. Chen^{9,18}, G. Chiaro²⁴, S. Ciprini^{26,27}, D. Costantin²⁸, S. Cutini²⁹, F. D'Ammando³⁰, P. de la Torre Luque¹³, F. de Palma¹⁶, N. Di Lalla⁶, L. Di Venere^{13,14}, F. Fana Dirirsa³¹, S. J. Fegan²⁰, A. Franckowiak²¹, Y. Fukazawa³², P. Fusco^{13,14}, F. Gargano¹⁴, D. Gasparrini^{26,27}, N. Giglietto^{13,14}, F. Giordano^{13,14}, M. Giroletti³⁰, D. Green³³, I. A. Grenier³⁴, M.-H. Grondin³⁵, S. Guiriec^{23,36}, E. Hays²³, D. Horan²⁰, G. Jóhannesson^{37,38}, D. Kocevski²³, M. Kovac'evic²⁹, M. Kuss¹¹, S. Larsson^{5,39,40}, L. Latronico¹⁶, J. Li²¹, I. Liodakis¹⁵, F. Longo^{7,8}, F. Loparco^{13,14}, M. N. Lovellette⁴¹, P. Lubrano²⁹, S. Maldera¹⁶, A. Manfreda⁶, G. Martí-Devesa⁴², M. N. Mazziotta¹⁴, J. E. McEnery^{23,43}, I. Mereu^{12,29}, P. F. Michelson¹⁵, T. Mizuno⁴⁴, M. E. Monzani¹⁵, E. Moretti⁴⁵, A. Morselli²⁶, I. V. Moskalenko¹⁵, M. Negro^{16,17}, E. Nuss¹⁹, M. Ohno⁴⁶, N. Omodei¹⁵, M. Orienti³⁰, E. Orlando^{15,47}, M. Palatiello^{7,8}, V. S. Paliya²¹, D. Paneque³³, Z. Pei¹⁰, M. Persic^{7,48}, M. Pesce-Rollins¹¹, V. Petrosian¹⁵, F. Piron¹⁹, H. Poon³², T. A. Porter¹⁵, G. Principe³⁰, J. L. Racusin²³, S. Rainò^{13,14}, R. Rando^{9,10}, B. Rani²³, M. Razzano^{11,59}, A. Reimer^{15,42}, O. Reimer⁴², D. Serini¹³, C. Sgrò¹¹, E. J. Siskind⁴⁹, G. Spandre¹¹, P. Spinelli^{13,14}, H. Tajima^{15,50}, K. Takagi³², D. Tak^{51,23}, D. F. Torres^{52,53}, J. Valverde²⁰, K. Wood⁵⁴, R. Yamazaki⁵⁵, M. Yassine^{7,8}, S. Zhu⁵⁶, Z. Lucas Uhm⁵⁷, and Bing Zhang⁵⁸

¹ Department of Physics and Astronomy, Clemson University, Kinard Lab of Physics, Clemson, SC 29634-0978, USA

² Faculty of Mathematics and Physics, Institute of Science and Engineering, Kanazawa University, Kakuma, Kanazawa, Ishikawa 920-1192, Japan

³ Institute for Cosmic-Ray Research, University of Tokyo, 5-1-5 Kashiwanoha, Kashiwa, Chiba, 277-8582, Japan

⁴ Department of Physics, Stockholm University, AlbaNova, SE-106 91 Stockholm, Sweden

⁵ Department of Physics, KTH Royal Institute of Technology, AlbaNova, SE-106 91 Stockholm, Sweden

⁶ Università di Pisa and Istituto Nazionale di Fisica Nucleare, Sezione di Pisa I-56127 Pisa, Italy

⁷ Istituto Nazionale di Fisica Nucleare, Sezione di Trieste, I-34127 Trieste, Italy

⁸ Dipartimento di Fisica, Università di Trieste, I-34127 Trieste, Italy

⁹ Istituto Nazionale di Fisica Nucleare, Sezione di Padova, I-35131 Padova, Italy

¹⁰ Dipartimento di Fisica e Astronomia "G. Galilei," Università di Padova, I-35131 Padova, Italy

¹¹ Istituto Nazionale di Fisica Nucleare, Sezione di Pisa, I-56127 Pisa, Italy

¹² Dipartimento di Fisica, Università degli Studi di Perugia, I-06123 Perugia, Italy

¹³ Dipartimento di Fisica "M. Merlin" dell'Università e del Politecnico di Bari, I-70126 Bari, Italy

¹⁴ Istituto Nazionale di Fisica Nucleare, Sezione di Bari, I-70126 Bari, Italy

¹⁵ W.W. Hansen Experimental Physics Laboratory, Kavli Institute for Particle Astrophysics and Cosmology, Department of Physics and SLAC National Accelerator Laboratory, Stanford University, Stanford, CA 94305, USA

¹⁶ Istituto Nazionale di Fisica Nucleare, Sezione di Torino, I-10125 Torino, Italy

¹⁷ Dipartimento di Fisica, Università degli Studi di Torino, I-10125 Torino, Italy

¹⁸ Department of Physics and Astronomy, University of Padova, Vicolo Osservatorio 3, I-35122 Padova, Italy

¹⁹ Laboratoire Univers et Particules de Montpellier, Université Montpellier, CNRS/IN2P3, F-34095 Montpellier, France

²⁰ Laboratoire Leprince-Ringuet, École polytechnique, CNRS/IN2P3, F-91128 Palaiseau, France

²¹ Deutsches Elektronen Synchrotron DESY, D-15738 Zeuthen, Germany

²² Institut für Theoretische Physik und Astrophysik, Universität Würzburg, D-97074 Würzburg, Germany

²³ NASA Goddard Space Flight Center, Greenbelt, MD 20771, USA

²⁴ INFN-Istituto di Astrofisica Spaziale e Fisica Cosmica Milano, via E. Bassini 15, I-20133 Milano, Italy

²⁵ Italian Space Agency, Via del Politecnico snc, I-00133 Roma, Italy

²⁶ Istituto Nazionale di Fisica Nucleare, Sezione di Roma "Tor Vergata," I-00133 Roma, Italy

²⁷ Space Science Data Center—Agenzia Spaziale Italiana, Via del Politecnico, snc, I-00133, Roma, Italy

²⁸ University of Padua, Department of Statistical Science, Via 8 Febbraio, 2, I-35122, Padova, Italy

²⁹ Istituto Nazionale di Fisica Nucleare, Sezione di Perugia, I-06123 Perugia, Italy

³⁰ INFN Istituto di Radioastronomia, I-40129 Bologna, Italy

³¹ Department of Physics, University of Johannesburg, P.O. Box 524, Auckland Park 2006, South Africa

³² Department of Physical Sciences, Hiroshima University, Higashi-Hiroshima, Hiroshima 739-8526, Japan

³³ Max-Planck-Institut für Physik, D-80805 München, Germany

³⁴ AIM, CEA, CNRS, Université Paris-Saclay, Université Paris Diderot, Sorbonne Paris Cité, F-91191 Gif-sur-Yvette, France

³⁵ Centre d'Études Nucléaires de Bordeaux Gradignan, IN2P3/CNRS, Université Bordeaux 1, BP120, F-33175 Gradignan Cedex, France

³⁶ The George Washington University, Department of Physics, 725 21st St., NW, Washington, DC 20052, USA

³⁷ Science Institute, University of Iceland, IS-107 Reykjavik, Iceland

³⁸ Nordita, Royal Institute of Technology and Stockholm University, Roslagstullsbacken 23, SE-106 91 Stockholm, Sweden

³⁹ The Oskar Klein Centre for Cosmoparticle Physics, AlbaNova, SE-106 91 Stockholm, Sweden

⁴⁰ School of Education, Health and Social Studies, Natural Science, Dalarna University, SE-791 88 Falun, Sweden

⁴¹ Space Science Division, Naval Research Laboratory, Washington, DC 20375-5352, USA

⁴² Institut für Astro- und Teilchenphysik, Leopold-Franzens-Universität Innsbruck, A-6020 Innsbruck, Austria

⁴³ Department of Astronomy, University of Maryland, College Park, MD 20742, USA

⁴⁴ Hiroshima Astrophysical Science Center, Hiroshima University, Higashi-Hiroshima, Hiroshima 739-8526, Japan

⁴⁵ Institut de Física d'Altes Energies (IFAE), Edifici Cn, Universitat Autònoma de Barcelona (UAB), E-08193 Bellaterra (Barcelona), Spain

⁴⁶ MPA Research Group for Physical Geodesy and Geodynamics, H-1585 Budapest, Hungary

⁴⁷ Istituto Nazionale di Fisica Nucleare, Sezione di Trieste, and Università di Trieste, I-34127 Trieste, Italy

⁴⁸ Osservatorio Astronomico di Trieste, Istituto Nazionale di Astrofisica, I-34143 Trieste, Italy

⁴⁹ NYCB Real-Time Computing Inc., Lattingtown, NY 11560-1025, USA

⁵⁰ Solar-Terrestrial Environment Laboratory, Nagoya University, Nagoya 464-8601, Japan

⁵¹ Department of Physics, University of Maryland, College Park, MD 20742, USA; donggeun.tak@gmail.com

⁵² Institute of Space Sciences (CSICIEEC), Campus UAB, Carrer de Magrans s/n, E-08193 Barcelona, Spain

⁵³ Institució Catalana de Recerca i Estudis Avançats (ICREA), E-08010 Barcelona, Spain⁵⁴ Praxis Inc., Alexandria, VA 22303, Resident at Naval Research Laboratory, Washington, DC 20375, USA⁵⁵ Department of Physics and Mathematics, Aoyama Gakuin University, Sagamihara, Kanagawa, 252-5258, Japan⁵⁶ Albert-Einstein-Institut, Max-Planck-Institut für Gravitationsphysik, D-30167 Hannover, Germany⁵⁷ Korea Astronomy and Space Science Institute, Daejeon 34055, Republic of Korea⁵⁸ Department of Physics and Astronomy, University of Nevada, Las Vegas, NV 89154, USA

Received 2019 September 25; revised 2019 November 11; accepted 2019 November 11; published 2019 November 27

Abstract

GRB 131108A is a bright long gamma-ray burst (GRB) detected by the Large Area Telescope and the Gamma-ray Burst Monitor on board the *Fermi Gamma-ray Space Telescope*. Dedicated temporal and spectral analyses reveal three γ -ray flares dominating above 100 MeV, which are not directly related to the prompt emission in the Gamma-ray Burst Monitor band (10 keV–10 MeV). The high-energy light curve of GRB 131108A (100 MeV–10 GeV) shows an unusual evolution: a steep decay, followed by three flares with an underlying emission, and then a long-lasting decay phase. The detailed analysis of the γ -ray flares finds that the three flares are 6–20 times brighter than the underlying emission and are similar to each other. The fluence of each flare, $(1.6 \sim 2.0) \times 10^{-6}$ erg cm $^{-2}$, is comparable to that of emission during the steep decay phase, 1.7×10^{-6} erg cm $^{-2}$. The total fluence from three γ -ray flares is 5.3×10^{-6} erg cm $^{-2}$. The three γ -ray flares show properties similar to the usual X-ray flares that are sharp flux increases, occurring in $\sim 50\%$ of afterglows, in some cases well after the prompt emission. Also, the temporal and spectral indices during the early steep decay phase and the decaying phase of each flare show the consistency with a relation of the curvature effect ($\hat{\alpha} = 2 + \hat{\beta}$), which is the first observational evidence of the high-latitude emission in the GeV energy band.

Unified Astronomy Thesaurus concepts: [Gamma-ray bursts \(629\)](#)

1. Introduction

Gamma-ray bursts (GRBs), the most luminous electromagnetic events in the universe, show two emission phases: the prompt emission and the afterglow. The prompt emission, short and spiky pulses, dominates in the keV–MeV energy range with multiple spectral components (Guiriec et al. 2015, and references therein). On the other hand, the light curve and spectrum of the afterglow, emission from the interaction between an outgoing blast wave from the central engine and a circumburst medium (Mészáros & Rees 1997; Sari et al. 1998), are characterized by a series of broken power laws, sometimes accompanying bright flares (Nousek et al. 2006; Zhang et al. 2006). The afterglow is observed in a broad energy band from radio to γ -ray. The flares are commonly observed in the X-ray band (e.g., Romano et al. 2006), but rarely in the optical band (e.g., Roming et al. 2006). The X-ray flares have been explained as a result of the late-time activities of the central engine (e.g., Fan & Wei 2005; Falcone et al. 2006, 2007; Zhang et al. 2006; Chincarini et al. 2007; Galli & Piro 2007; Lazzati & Perna 2007).

Due to the curvature effect of a spherical, relativistic jet producing an X-ray flare, the decay phase of the X-ray flare evolves in a certain way. This effect was first discussed by Fenimore et al. (1996), and Kumar & Panaitescu (2000) characterized the evolution of the temporal decaying index of the X-ray flare ($\hat{\alpha}$) as a function of corresponding spectral index ($\hat{\beta}$), $\hat{\alpha} = 2 + \hat{\beta}$ in convention of $F_\nu \propto t^{-\hat{\alpha}} \nu^{-\hat{\beta}}$. This relation has been identified in many X-ray flares (e.g., Liang et al. 2006; Chincarini et al. 2007; Jia et al. 2016; Uhm & Zhang 2016).

The *Fermi Gamma-ray Space Telescope* (*Fermi*) has observed numerous GRBs and helped to uncover the exotic high-energy evolution of GRBs. The high-energy emission (>100 MeV) of GRBs observed by the Large Area Telescope (LAT) on board *Fermi* shares common features: delayed onset

and lasting longer compared to keV–MeV emission, requiring additional spectral components, and a power-law decaying light curve (Ackermann et al. 2013; Ajello et al. 2019). These GeV features can be interpreted as the early afterglow emission (e.g., Ghisellini et al. 2010; Kumar & Barniol Duran 2010; Tak et al. 2019). Abdo et al. (2011) reported the GeV emission during vigorous X-ray flaring activities, but a flare above the underlying afterglow emission in the GeV energy band has not been reported before this work.

In this work, we first report the three bright γ -ray flares observed in GRB 131108A, which are ~ 6 –20 times brighter than the underlying light curve (Figure 1). We will compare spectral and temporal properties of three γ -ray flares and the X-ray flares. The broadband spectral analysis and the correlation test between the low- and high-energy bands will be described.

2. Observations

At 20:41:55.76 UTC on 2013 November 8 (T_0), LAT triggered on a bright high-energy emission from GRB 131108A (Racusin et al. 2013), which is simultaneously observed by the Gamma-ray Burst Monitor (GBM) on board *Fermi* (Younes 2013). The duration of the burst (T_{90}^{60}), is 18.2 s, but the high-energy emission lasts $\sim T_0 + 600$ s. With the observation of the bright afterglow of GRB 131108A by various instruments such as *Swift* (Chester & Stroh 2013; Stroh & Kennea 2013), *AGILE* (Giuliani et al. 2013), the accurate location and redshift of GRB 131108A were reported as (R.A., decl.) = (156.50, 9.66) with an uncertainty of $3''.6$ in radius (Stroh & Kennea 2013) and $z \sim 2.40$ (de Ugarte Postigo et al. 2013), respectively. *Swift*/XRT started to observe the afterglow of GRB 131108A 3.9 ks (~ 1 hr) after the GBM trigger, where the X-ray light curve decays smoothly in time (Stroh & Kennea 2013).

We perform a time-resolved analysis of LAT data in energy range of 100 MeV–10 GeV with the *Fermi Science Tools*

⁵⁹ Funded by contract FIRB-2012-RBFR12PM1F from the Italian Ministry of Education, University and Research (MIUR).

⁶⁰ A duration where a GRB emits from 5% of its total counts to 95%.

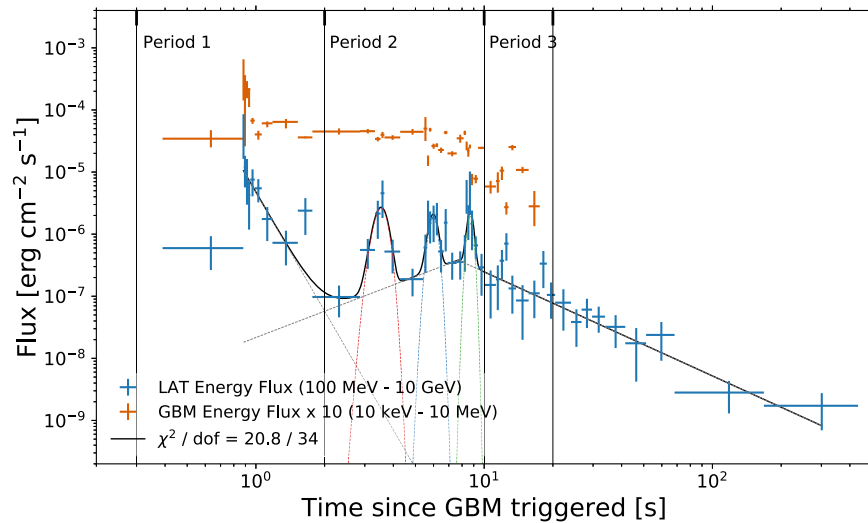


Figure 1. GBM and LAT light curves of GRB 131108A. The energy fluxes in the LAT energy band (100 MeV to 10 GeV) and in the GBM energy band (10 keV–1 MeV) are plotted in blue and orange, respectively. They are calculated from the best-fit model for each time interval in the spectral analysis with each instrument. The solid black line shows the fit of the LAT light curve consisting of five components: a simple power law (dotted gray line), a broken power law (dotted green line), and three Gaussian functions (dotted red, green, and blue lines).

(*v11r5p3*). We use “*Transient020E*” class events with the standard cuts. Photons from within the 15° region of interest around GRB 131108A are considered, and the maximum zenith angle is set to 100° . We fit a background rate from 3FGL sources (Acero et al. 2015), the galactic diffuse emission (*gll_iem_v06*), and the isotropic diffuse emission (*iso_P8R2_TRANSIENT020_V6_v06*).⁶¹ The LAT events observed in GRB 131108A are binned. For four sequential LAT events, we perform an unbinned likelihood analysis, and compute a test statistic (TS)⁶² for the burst. If the resultant TS is lower than 9 (equivalent to 3σ), we add the next event to the bin and compute the TS again. Once we have the bin with the $TS \geq 9$, we collect the following four events, and repeat this procedure. As a result, each bin contains at least four LAT events, resulting in a $TS \geq 9$. For each of these bins, we perform an unbinned maximum likelihood fit on the energy spectrum with a simple power-law (PL) model.

The high-energy light curve of GRB 131108A shows an unusual evolution compared to other bright LAT GRBs (Figure 1); rather, it resembles the canonical X-ray early afterglow light curve though compressed to earlier and shorter timescales (seconds to tens of seconds compared to hundreds to thousands of seconds; Nousek et al. 2006; Zhang et al. 2006). We find the best description of the LAT light curve by fitting several models and their parameters with the maximum likelihood method. The light curve is well-fitted with five components ($\chi^2/\text{dof} = 20.8/34$): a simple power law, a broken power law, and three Gaussian functions for the three bright pulses above an underlying emission. Note that single-component models such as a simple power law ($\chi^2/\text{dof} = 130.8/47$) or a broken power law ($\chi^2/\text{dof} = 90.8/45$) are not a good model for this light curve. The model of each pulse can be replaced with the Norris function (Norris et al. 1996) ($\chi^2/\text{dof} = 20.5/31$), a broken power law ($\chi^2/\text{dof} = 20.2/31$), or a smoothly broken power law (Liang et al. 2006) ($\chi^2/\text{dof} = 19.4/28$). However, the Gaussian function is the best-fit model considering its statistics and the number of free parameters. The best-fit parameters for the three Gaussian

Table 1

The Physical Properties of Three Flares

	Peak Flux ^a ($\times 10^{-6}$ erg cm $^{-2}$ s $^{-1}$)	Peak Time (s)	FWHM ^b (s)	Fluence ^a ($\times 10^{-6}$ erg cm $^{-2}$)
Flare 1	2.6 ± 1.3	3.5 ± 0.1	0.8 ± 0.2	2.0 ± 0.9
Flare 2	1.4 ± 0.6	6.0 ± 0.1	0.9 ± 0.2	1.6 ± 0.6
Flare 3	2.4 ± 1.0	8.5 ± 0.1	0.9 ± 0.2	1.6 ± 0.6

Notes.

^a In 100 MeV–10 GeV.

^b Full width at half maximum.

functions are listed in Table 1. Note that there are hints of more than three flares but other fluctuations are insignificant, which are composed of one or two flux point. The fluence of each pulse is (2.0 ± 0.8) , (1.6 ± 0.6) , and $(1.7 \pm 0.7) \times 10^{-6}$ erg cm $^{-2}$, totally $(5.3 \pm 1.2) \times 10^{-6}$ erg cm $^{-2}$. The fluence of each pulse is comparable to that of emission during the early steep decay phase, $(1.7 \pm 0.4) \times 10^{-6}$ erg cm $^{-2}$. The decaying index of the later segment of the broken power law is 1.6 ± 0.2 , consistent with other Fermi-LAT GRBs (Ajello et al. 2019).

Considering the LAT light curve and its best-fit model, we define three time periods (Figure 2): the early steep decay period (time period 1; $T_0 + 0.3$ s– $T_0 + 2$ s), the three γ -ray unusual pulses with the underlying emission period (time period 2; $T_0 + 2$ s– $T_0 + 10$ s), and the long-lasting shallow decay period (time period 3; $T_0 + 10$ s– $T_0 + 20$ s). Note that the third time period can be extended until the end of the LAT emission, but stops at the end of the prompt emission for the joint-fit purpose. The evolution of the first and last periods is commonly seen in the LAT GRBs, but the phenomena of the second time period are noteworthy.

For the three time periods, we perform a broadband spectral analysis with GBM and LAT data in energy band from 10 keV to 10 GeV. Of the 12 NaI and 2 BGO detectors that make up GBM, 4 NaI detectors (0, 3, 6, and 7; 10 keV–1 MeV), and 2 BGO detectors (0 and 1; 200 keV–40 MeV) show a considerably high count rate above the background level, so that we

⁶¹ <https://fermi.gsfc.nasa.gov/ssc/data/access/lat/BackgroundModels.html>

⁶² The detection significance of the source above the background.

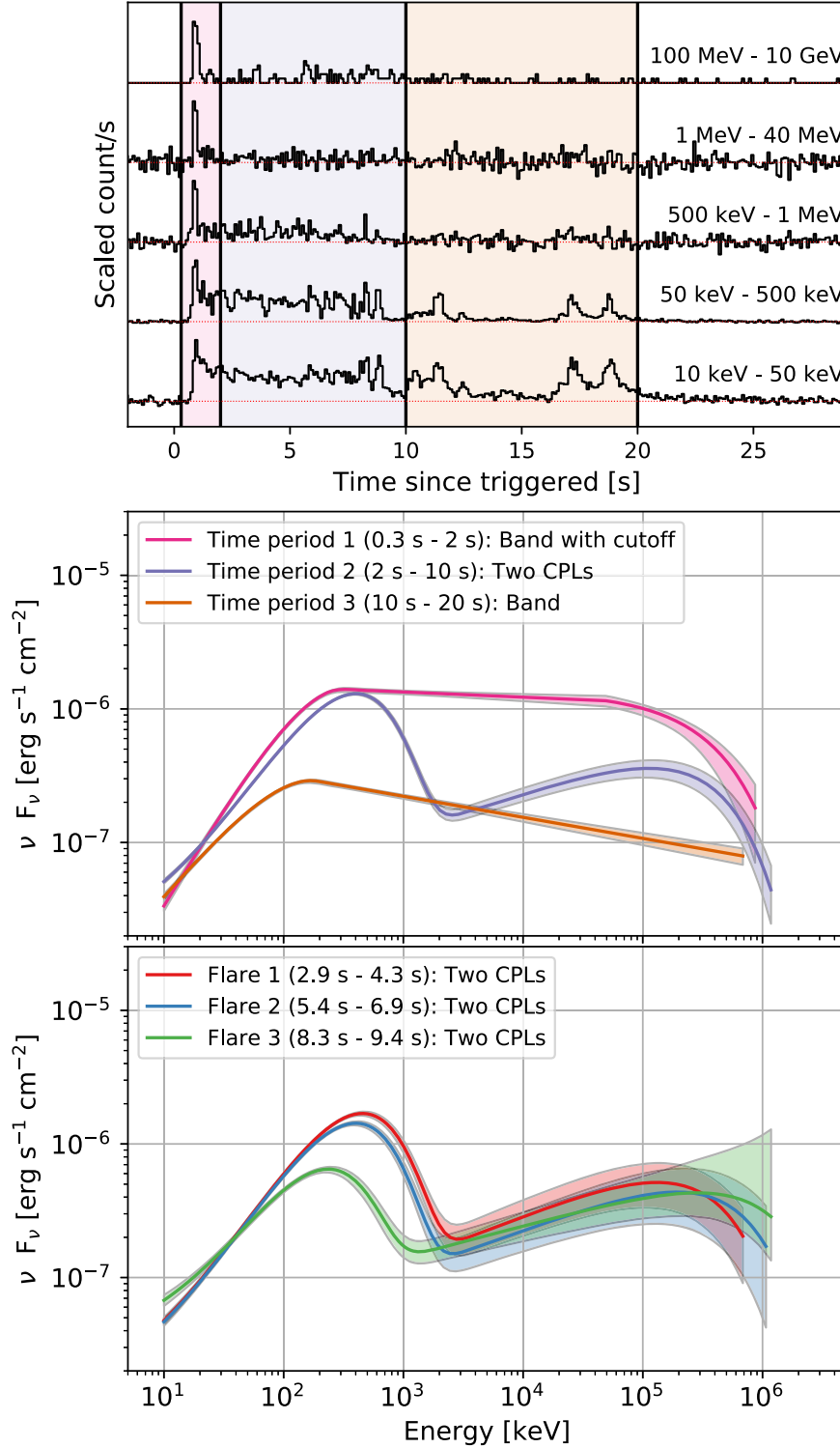


Figure 2. Count-rate curves and spectral energy distributions (SEDs). The top panel shows the scaled count-rate curves in different energy bands. The lower two panels show the joint-fit SEDs in energy band from 10 keV to 10 GeV. The color coding of the shaded region in the top panel and the spectrum in the middle panel indicates three time periods: pink (time period 1; 0.3–2 s), violet (time period 2; 2–10 s), and orange (time period 3; 10–20 s). The bottom panel shows SEDs for three GeV flares (red, blue, and green). Each solid curve represents the best-fit spectral shape (thick) with 1 confidence level contour (shaded region) derived from the errors on the fit parameters.

constitute a set of data from these detectors. In addition to the GBM data, LAT Low Energy (LLE; 30 MeV–100 MeV) and LAT (*Transient020E*; 100 MeV–10 GeV) data are used. The background rate of GBM and LLE data is estimated by making use of the analysis package, *RMfit* (*version43pr2*), by fitting a time interval combined before and after the prompt emission

phase of the burst with a polynomial function. The LAT background is estimated with “gtbkg”⁶³ provided by the *Fermi*

⁶³ This tool generates a background spectrum file, which contains the total background rate from 3FGL sources, the galactic diffuse source, and the isotropic diffuse source.

Table 2
Joint-fit Spectral Analysis Parameters

Time Period	Model	α	β	Γ	$E_{p,low}$ (keV)	$E_{p,high}$ (MeV)	E_f (MeV)	PG-stat	dof	BIC
1	Band	$-0.50^{+0.06}_{-0.06}$	$-2.07^{+0.02}_{-0.02}$		$320.6^{+22.3}_{-20.1}$			745	695	771
(0.3–2 s)	Band with highcut ^a	$-0.48^{+0.07}_{-0.06}$	$-2.01^{+0.02}_{-0.02}$		$305.3^{+21.5}_{-19.8}$		$350.3^{+143.1}_{-87.6}$	722	694	754
2	Band	$-0.73^{+0.02}_{-0.02}$	$-2.24^{+0.01}_{-0.01}$		$389.7^{+14.2}_{-13.4}$			880	695	906
(2–10 s)	CPL + CPL	$-0.50^{+0.07}_{-0.07}$		$1.69^{+0.02}_{-0.03}$	$394.2^{+13.3}_{-12.4}$	$126.2^{+25.6}_{-19.5}$		821	693	860
3	Band	$-0.94^{+0.05}_{-0.05}$	$-2.15^{+0.02}_{-0.02}$		$168.0^{+12.5}_{-11.2}$			741	695	767
(10–20 s)	CPL + CPL	$-0.92^{+0.13}_{-0.09}$		$1.68^{+0.07}_{-0.11}$	$198.9^{+13.7}_{-12.0}$	$68.7^{+21.5}_{-15.5}$		742	693	781
Flare 1	CPL + CPL	-0.5^{fixed} ^b		$1.64^{+0.04}_{-0.04}$	$447.9^{+19.9}_{-18.7}$	$131.3^{+63.3}_{-35.7}$		819	692 ^c	852
Flare 2	CPL + CPL	-0.5^{fixed} ^b		$1.67^{+0.04}_{-0.04}$	$396.0^{+18.1}_{-16.9}$	$193.1^{+126.7}_{-62.0}$		763	692 ^c	796
Flare 3	CPL + CPL	-0.5^{fixed} ^b		$1.76^{+0.03}_{-0.03}$	$229.0^{+17.5}_{-15.7}$	$284.9^{+419.4}_{-124.4}$		716	692 ^c	749

Notes.

^a The cutoff energy E_c is fixed to 50 MeV.

^b The photon index for the low-energy CPL component is fixed to -0.5 , which is the photon index of the best-fit model in the second time interval.

^c Note that the change in the dof results from decrease in the number of the energy bin of LAT data.

Science Tools. The energy spectrum of each time period is fitted with various models by using the maximum likelihood method with *Xspec* (12.9.1) (Arnaud 1996). We use a Poisson data with Gaussian background statistic (PG-stat) for the parameter estimation, and then use the Bayesian information criterion (BIC; Schwarz 1978) for comparing the likelihood of fit and selecting the best-fit model. The best-fit model is a model with the lowest BIC value.

In the first time period characterized by the short bright emission commonly observed in the broad energy band from 10 keV to 10 GeV, the best-fit model for this time period is the Band function (Band et al. 1993) with a high-energy cutoff⁶⁴ (Table 2). The decrease in BIC as a result of adding the high-energy cutoff to the Band function is ~ 17 units, implying that the high-energy cutoff is strongly required. One alternative model is a combination of two spectral components, Band and a power law with an exponential cutoff (CPL).⁶⁵ This Band + CPL model describes the data slightly better (lower PG-stat), but the statistical improvement is not high enough to compensate the increase of a free parameter, making BIC higher than the best-fit model.

The second time interval where we found the unusual pulses shows a high count rate only in the low- (10 keV–1 MeV) and high-energy regimes (100 MeV–10 GeV) (upper panel in Figure 2). The observed data is best explained by a two-component model, CPL + CPL⁶⁶ (orange in Figure 2), which is preferred over a single-component model such as Band (Table 2). The two CPLs have distinct peak energies, $E_{p,low} \sim 400$ keV and $E_{p,high} \sim 130$ MeV, respectively (Table 2).

When any one of the CPL components is replaced with the Band function, β becomes very soft so that the high-energy segment of Band is indistinguishable from the exponential cutoff. Therefore, the combination of Band and CPL is not necessary. The two-component scenario for GRB 131108A is also reported by Giuliani et al. (2014), who analyzed the *AGILE* (350 keV–30 GeV) data and reached the conclusion that the extrapolation of the low-energy spectral component could not explain the high-energy emission, and an additional spectral component with a peak energy at few MeV is required. The CPL dominating in the low-energy band has $\alpha \simeq -0.5$ consistent with that of the best-fit model in the first time period (Table 2), implying that the low-energy emission of the first and second time periods may be continuous. Given the best-fit model, the LAT emission is described by the high-energy CPL component. In addition, we perform a time-resolved spectral analysis for time intervals during the three high-energy pulses, and two distinct spectral components are again observed (Table 2 and Figure 2). The fluence of this high-energy component during the second time period is $5.9^{+0.5}_{-0.8} \times 10^{-6}$ erg cm⁻², comparable to the sum of fluence from three γ -ray pulses, $(5.2 \pm 1.2) \times 10^{-6}$ erg cm⁻² (Table 1). Most of the LAT emission during the second time period can be dominated by the three γ -ray pulses, and thus the high-energy CPL component may represent the spectral shape of the three γ -ray pulses.

During the third time period, short-soft pulses in the low-energy band (< 500 keV) are observed. The best-fit model in this time period is the Band function (green in Figure 2). A CPL + CPL model does not give a better result, which requires two more parameters but resulting in the similar statistics (Table 2). After $T_0 + 20$ s, the LAT spectrum is well-described by a power law with a photon index $\Gamma = 2.8 \pm 0.3$.

Figure 1 and the upper panel of Figure 2 show that the low- (keV to few MeV) and high-energy (100 MeV–10 GeV) light curves evolve differently, and the broadband spectral analysis reveals the presence of the two spectral components. We check the correlation between the low- and high-energy light curves with the discrete correlation function (Edelson & Krolik 1988), which compares the variability of two light curves and estimates the time lag and the respective cross-correlation coefficient (e.g., Rani et al. 2009). For this purpose, we performed a time-resolved spectral analysis for the time bin

64

$$\frac{dN}{dE} = \begin{cases} N_0 \left(\frac{E}{100 \text{ keV}} \right)^\alpha \exp \left(-\frac{E(\alpha+2)}{E_p} \right) & \text{if } E \leq \frac{\alpha-\beta}{2+\alpha} E_p \\ N_0 \left(\frac{E}{100 \text{ keV}} \right)^\beta \left(\frac{E_p}{100 \text{ keV}} \right)^{\alpha-\beta} \exp(\beta-\alpha) & \text{if } \frac{\alpha-\beta}{2+\alpha} E_p < E \leq E_c \\ N_0 \left(\frac{E}{100 \text{ keV}} \right)^\beta \left(\frac{E_p}{100 \text{ keV}} \right)^{\alpha-\beta} \exp(\beta-\alpha) \exp \left(\frac{E_c-E}{E_f} \right) & \text{if } E > E_c \end{cases} \quad (1)$$

where α and β are the low- and high-energy photon indices, respectively, E_p is the peak energy of the Band function, E_c is the cutoff energy which is fixed to 50 MeV, and E_f is the e-folding energy for the high-energy cutoff.

$$^{65} \frac{dN}{dE} = N_0 \left(\frac{E}{100 \text{ keV}} \right)^\alpha \exp \left(-\frac{E(\alpha+2)}{E_p} \right).$$

$$^{66} \frac{dN}{dE} = N_{0,low} \left(\frac{E}{100 \text{ keV}} \right)^\alpha \exp \left(-\frac{E(\alpha+2)}{E_{p,low}} \right) + N_{0,high} \left(\frac{E}{100 \text{ keV}} \right)^{-\Gamma} \exp \left(-\frac{E(-\Gamma+2)}{E_{p,high}} \right).$$

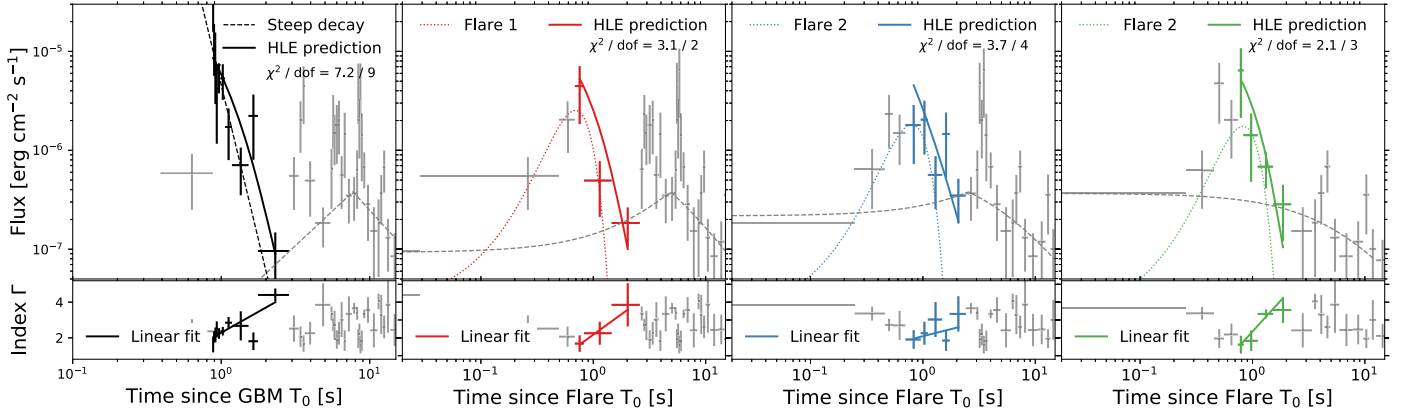


Figure 3. Test of the curvature effect for early steep decay emission and three γ -ray flares. The upper panels show the light curve of the early steep decay emission and the three γ -ray flares separately after removing the t_0 effect. The lower panel shows the evolution of the photon index. The data points corresponding to the decay phase of each flare are in red, blue, and green. The early steep decay phase is marked in black. The solid lines in the upper panels show the expected light curve derived from the relation of the curvature effect, $\hat{\alpha} = 2 + \hat{\beta}$. These theoretical light curves are computed from the linear fit of the photon indices of the decay phase (solid line in the lower panel).

used for the LAT light curve (Figure 1) with the GBM data, and computed flux in the range of 10 keV–10 MeV with the best-fit model for each time interval (orange points in Figure 1). When the entire interval is considered, the correlation between the two light curves, 10 keV–10 MeV and 100 MeV–10 GeV, is evident (correlation coefficient peak = 0.8 ± 0.1). However, if only the light curves in the second time period is considered, the correlation analysis does not suggest any correlation between the two light curves (correlation coefficient peak ~ 0.1).

Considering the temporal and spectral features, the γ -ray pulses invoke a distinct origin from the prompt emission of the low-energy band as well as the LAT extended emission. From now on, the individual γ -ray pulse is called a “ γ -ray flare.”

3. Discussion

First of all, we compare and test the well-known properties of X-ray flares to the observation of the γ -ray flares in GRB 131108A.

A flux variation of the X-ray flares, a flux ratio of a flare to an underlying emission ($\delta F_\nu / F_\nu$), ranges from 6 (e.g., GRB 050406; Romano et al. 2006) to higher than 100 (e.g., GRB 050202B; Burrows et al. 2005). The γ -ray flares are about 6–20 times brighter than the underlying emission, which slowly changes in time, $F_\nu \sim 2.7 \times 10^{-7}$ erg cm $^{-2}$ s $^{-1}$ on average (see Figure 1), and thus the flux variation of the γ -ray flares is subnormal, compared to X-ray flares (Chincarini et al. 2007). The duration of the X-ray flares varies from few hours to a day (Chincarini et al. 2007; Swenson & Roming 2014), and there is an empirical relation between the onset time and the duration of the X-ray flares, $\delta t / t \sim 0.1$ (e.g., Chincarini et al. 2007, 2010; Swenson & Roming 2014). In case of the γ -ray flares, they last only a few seconds (Table 1), much shorter than the X-ray flares (Chincarini et al. 2007). Also, the γ -ray flares are observed in $< T_0 + 10$ s, which is earlier than any X-ray flares (Chincarini et al. 2007). Combining these two unusual features, surprisingly, the temporal characteristics of the γ -ray flares are not in conflict with the empirical relation. A comparison between the flux variability and the temporal variability of the γ -ray flares ($\delta F_\nu / F_\nu$ versus $\delta t / t$) shows that the γ -ray flares are consistent with X-ray flares (Chincarini et al. 2007). Furthermore, this comparison implies that the γ -ray flares are not

related to the fluctuations of the external shock as previously discussed for the X-ray flares (Ioka et al. 2005; Zhang et al. 2006).

The steep decay of the X-ray flares is regarded as a result of the curvature effect, which is identified by testing the relation, $\hat{\alpha} = 2 + \hat{\beta}$ (e.g., Liang et al. 2006; Chincarini et al. 2007; Jia et al. 2016; Uhm & Zhang 2016). It is possible that the decay phase of the γ -ray flares also show evidence of the curvature effect. Before testing the relation, we should remove the so-called t_0 effect (Zhang et al. 2006; Kobayashi & Zhang 2007). Each flare is attributed to the late-time activity of the central engine and thus has its own onset time (t_0). Since the shape of a light curve in the logarithmic space is very sensitive to the choice of t_0 , the intrinsic light curve of the flare can only be provided if the light curve is shifted to the true t_0 . Due to the underlying emission, however, the true onset of the γ -ray flares is ambiguous. Therefore, we properly choose the onset of each flare as the time when the flux of the flare is 1/100 of its peak. Figure 3 shows the γ -ray flares after shifting them to the proper t_0 for each flare. For these light curves, we test the curvature effect relation. After selecting the data points corresponding to the decaying phase, we fit the measured photon indices (Γ) with a linear function, $\Gamma = f(t - t_0)$ (solid line in lower panel of Figure 3). Next, the photon index is converted to the spectral index, $\hat{\beta} = \Gamma - 1$. We then apply the HLE relation and get the temporal index as a function of time, $\hat{\alpha} = f(t - t_0) + 1$. Finally, the light curve expected by the curvature effect is described by a function of time, $F_\nu = F_{\nu,0} (t - t_0)^{f(t-t_0)+1}$ (solid line in upper panel of Figure 3). We fit this function with the observed, shifted flux points and conclude that the decay phases of all three γ -ray flares are consistent with the expectation by the curvature effect (Figure 3). Also, we find the spectral softening during the decay phase of the flares, which is the well-known phenomenon identified in the X-ray flares (Chincarini et al. 2007; Falcone et al. 2007).

The X-ray flares are likely attributed to internal shocks, where accelerated electrons at the shocks radiate via the synchrotron process. On the other hand, the γ -ray flares with $E_p \sim 130$ MeV may originate from the synchrotron self-Compton (SSC) process from the same population of electrons that might have produced X-ray flares. In principle, there could be two possible cases for the inverse Compton process: SSC from the

internal emission region and the external inverse Compton (EIC) from the external shock region (Wang et al. 2006; Fan et al. 2008). The observation of the high-latitude emission in the flares disfavors the EIC origin and supports the SSC origin. Assuming the typical electron Lorentz factor, $\gamma_e \gtrsim 10^3$, the peak energy of the seed photon should be $\lesssim 0.13$ keV, which is far below the GBM energy band. Another possibility for the origin of the γ -ray flares is the residual collision in the internal dissipation process (Li & Waxman 2008). In this case, the γ -ray flares can be interpreted as the SSC counterpart of the optical emission produced by the residual collision at large radii. Note that there were no X-ray and optical observations during the prompt emission phase of this burst, so that these hypotheses cannot be tested.

The very first steep decay emission in the first time period corresponds to the tail of the first bright broadband pulse. This decay emission is also consistent with the curvature effect (the first panel in Figure 3).

The underlying emission in the second time period can be interpreted as the emission during the development of the forward shock (e.g., Maxham et al. 2011), and the long-lasting decay emission (the third time period) can be the continuous emission from the fully developed forward shock when the total energy is not noticeably increased by the additional energy injection (e.g., Mészáros & Rees 1997; Sari et al. 1998).

The observation of GRB 131108A uncovers a new phenomenon in the high-energy GRB light curve. Even though the three γ -ray flares were observed in the prompt phase of the burst, they showed the temporal and spectral properties similar to those of the X-ray flares. Also, we found the evidence of the curvature effect in the GeV energy band for the first time.

The *Fermi*-LAT Collaboration acknowledges support for LAT development, operation, and data analysis from NASA and DOE (United States), CEA/Irfu and IN2P3/CNRS (France), ASI and INFN (Italy), MEXT, KEK, and JAXA (Japan), and the K.A. Wallenberg Foundation, the Swedish Research Council and the National Space Board (Sweden). Science analysis support in the operations phase from INAF (Italy) and CNES (France) is also gratefully acknowledged. This work performed in part under DOE Contract DE-AC02-76SF00515.

Software: XSPEC (v12.9.1; Arnaud 1996), Fermi Science Tools (v11r5p3).

ORCID iDs

M. Ajello  <https://orcid.org/0000-0002-6584-1703>
M. Arimoto  <https://orcid.org/0000-0003-1250-7872>
M. Axelsson  <https://orcid.org/0000-0003-4378-8785>
F. D’Ammando  <https://orcid.org/0000-0001-7618-7527>
A. Franckowiak  <https://orcid.org/0000-0002-5605-2219>
M. Kuss  <https://orcid.org/0000-0003-1212-9998>

S. Larsson  <https://orcid.org/0000-0003-0716-107X>
F. Longo  <https://orcid.org/0000-0003-2501-2270>
S. Maldera  <https://orcid.org/0000-0002-0698-4421>
T. Mizuno  <https://orcid.org/0000-0001-7263-0296>
I. V. Moskalenko  <https://orcid.org/0000-0001-6141-458X>
V. S. Paliya  <https://orcid.org/0000-0001-7774-5308>
J. L. Racusin  <https://orcid.org/0000-0002-4744-9898>
R. Yamazaki  <https://orcid.org/0000-0002-1251-7889>

References

- Abdo, A. A., Ackermann, M., Ajello, M., et al. 2011, *ApJL*, 734, L27
Acero, F., Ackermann, M., Ajello, M., et al. 2015, *ApJS*, 218, 23
Ackermann, M., Ajello, M., Asano, K., et al. 2013, *ApJS*, 209, 11
Ajello, M., Arimoto, M., Axelsson, M., et al. 2019, *ApJ*, 878, 52
Arnaud, K. A. 1996, in ASP Conf. Ser. 101, Astronomical Data Analysis Software and Systems V, ed. V. Systems, G. H. Jacoby, & J. Barnes (San Francisco, CA: ASP), 17
Band, D., Mateson, J., Ford, L., et al. 1993, *ApJ*, 413, 281
Burrows, D. N., Romano, P., Falcone, A., et al. 2005, *Sci*, 309, 1833
Chester, M. M., & Strohm, M. C. 2013, GCN, 1, 15476
Chincarini, G., Mao, J., Margutti, R., et al. 2010, *MNRAS*, 406, 2113
Chincarini, G., Moretti, A., Romano, P., et al. 2007, *ApJ*, 671, 1903
de Ugarte Postigo, A., Thoene, C. C., Gorosabel, J., et al. 2013, GCN, 15470, 1
Edelson, R. A., & Krolik, J. H. 1988, *ApJ*, 333, 646
Falcone, A. D., Burrows, D. N., Lazzati, D., et al. 2006, *ApJ*, 641, 1010
Falcone, A. D., Morris, D., Racusin, J., et al. 2007, *ApJ*, 671, 1921
Fan, Y.-Z., Piran, T., Narayan, R., & Wei, D.-M. 2008, *MNRAS*, 384, 1483
Fan, Y. Z., & Wei, D. M. 2005, *MNRAS*, 364, L42
Fenimore, E. E., Madras, C. D., & Nayakshin, S. 1996, *ApJ*, 473, 998
Galli, A., & Piro, L. 2007, *A&A*, 475, 421
Ghisellini, G., Ghirlanda, G., Nava, L., & Celotti, A. 2010, *MNRAS*, 403, 926
Giuliani, A., Longo, F., Verrecchia, F., et al. 2013, GCN, 1, 15479
Giuliani, A., Mereghetti, S., Marisaldi, M., et al. 2014, arXiv:1407.0238
Guiriec, S., Kouveliotou, C., Daigne, F., et al. 2015, *ApJ*, 807, 148
Ioka, K., Kobayashi, S., & Zhang, B. 2005, *ApJ*, 631, 429
Jia, L.-W., Uhm, Z. L., & Zhang, B. 2016, *ApJS*, 225, 17
Kobayashi, S., & Zhang, B. 2007, *ApJ*, 655, 973
Kumar, P., & Barniol Duran, R. 2010, *MNRAS*, 409, 226
Kumar, P., & Panaitescu, A. 2000, *ApJL*, 541, L51
Lazzati, D., & Perna, R. 2007, *MNRAS*, 375, L46
Li, Z., & Waxman, E. 2008, *ApJL*, 674, L65
Liang, E. W., Zhang, B., O’Brien, P. T., et al. 2006, *ApJ*, 646, 351
Maxham, A., Zhang, B.-B., & Zhang, B. 2011, *MNRAS*, 415, 77
Mészáros, P., & Rees, M. J. 1997, *ApJ*, 476, 232
Norris, J. P., Nemiroff, R. J., Bonnell, J. T., et al. 1996, *ApJ*, 459, 393
Nousek, J. A., Kouveliotou, C., Grupe, D., et al. 2006, *ApJ*, 642, 389
Racusin, J. L., Zhu, S., Kocevski, D., et al. 2013, GCN, 1, 15464
Rani, B., Wiita, P. J., & Gupta, A. C. 2009, *ApJ*, 696, 2170
Romano, P., Moretti, A., Banat, P. L., et al. 2006, *A&A*, 450, 59
Roming, P. W. A., Vanden Berk, D., Pal’shin, V., et al. 2006, *ApJ*, 651, 985
Sari, R., Piran, T., & Narayan, R. 1998, *ApJL*, 497, L17
Schwarz, G. 1978, *AnSta*, 6, 461
Strohm, M. C., & Kennea, J. A. 2013, GCN, 1, 15474
Swenson, C. A., & Roming, P. W. A. 2014, *ApJ*, 788, 30
Tak, D., Omodei, N., Uhm, Z. L., et al. 2019, *ApJ*, 883, 134
Uhm, Z. L., & Zhang, B. 2016, *ApJL*, 824, L16
Wang, X.-Y., Li, Z., & Mészáros, P. 2006, *ApJL*, 641, L89
Younes, G. 2013, GCN, 1, 15477
Zhang, B., Fan, Y. Z., Dyks, J., et al. 2006, *ApJ*, 642, 354

Exploring X-ray variability with unsupervised machine learning

I. Self-organizing maps applied to *XMM-Newton* data[★]

M. Kovačević¹, M. Pasquato^{2,3,4,5,1}, M. Marelli¹, A. De Luca^{1,6}, R. Salvaterra¹, and A. Belfiore¹

¹ Istituto di Astrofisica Spaziale e Fisica Cosmica (INAF IASF-MI), 20133 Milano, Italy
e-mail: milos.kovacevic@inaf.it; milosh.kovacevic@gmail.com

² Center for Astro, Particle and Planetary Physics (CAP³), New York University, Abu Dhabi, UAE
e-mail: mp5757@nyu.edu

³ Physics and Astronomy Department Galileo Galilei, University of Padova, Vicolo dell'Osservatorio 3, 35122, Padova, Italy

⁴ Département de Physique, Université de Montréal, Montréal, Québec H3T 1J4, Canada

⁵ Istituto Nazionale di Fisica Nucleare - Sezione di Padova, Via Marzolo 8, 35131 Padova, Italy

⁶ INFN, Sezione di Pavia, via A. Bassi 6, 27100 Pavia, Italy

Received 14 October 2021 / Accepted 26 January 2022

ABSTRACT

Context. *XMM-Newton* provides unprecedented insight into the X-ray Universe, recording variability information for hundreds of thousands of sources. Manually searching for interesting patterns in light curves is impractical, requiring an automated data-mining approach for the characterization of sources.

Aims. Straightforward fitting of temporal models to light curves is not a sure way to identify them, especially with noisy data. We used unsupervised machine learning to distill a large data set of light-curve parameters, revealing its clustering structure in preparation for anomaly detection and subsequent searches for specific source behaviors (e.g., flares, eclipses).

Methods. Self-organizing maps (SOMs) achieve dimensionality reduction and clustering within a single framework. They are a type of artificial neural network trained to approximate the data with a two-dimensional grid of discrete interconnected units, which can later be visualized on the plane. We trained our SOM on temporal-only parameters computed from $\gtrsim 10^5$ detections from the Exploring the X-ray Transient and variable Sky catalog.

Results. The resulting map reveals that the ≈ 2500 most variable sources are clustered based on temporal characteristics. We find distinctive regions of the SOM map associated with flares, eclipses, dips, linear light curves, and others. Each group contains sources that appear similar by eye. We single out a handful of interesting sources for further study.

Conclusions. The condensed view of our dataset provided by SOMs allowed us to identify groups of similar sources, speeding up manual characterization by orders of magnitude. Our method also highlights problems with fitting simple temporal models to light curves and can be used to mitigate them to an extent. This will be crucial for fully exploiting the high data volume expected from upcoming X-ray surveys, and may also help with interpreting supervised classification models.

Key words. methods: statistical – methods: miscellaneous – catalogs – astronomical databases: miscellaneous – X-rays: general – methods: data analysis

1. Introduction

X-ray astronomy probes highly diverse phenomena related to the most extreme physical conditions observable in the Universe: very strong gravitational and/or electromagnetic fields, very high temperatures, and populations of particles moving close to the speed of light. Variability as a function of time is the rule in the X-rays, and studying the temporal properties of the sources is crucial to understanding their physics. The current generation of space-based X-ray observatories, by performing single-photon spectral imaging over a relatively large field of view, collect an enormous amount of information on hundreds of new serendipitous sources and their variability each day.

The European Photon Imaging Camera (EPIC) on board the European Space Agency (ESA) X-ray Multi-Mirror Mission (*XMM-Newton*) spacecraft (Jansen et al. 2001), consisting of two MOS¹ cameras (Turner et al. 2001) and one pn detector

(Strüder et al. 2001), is the most powerful tool currently available with which to study the soft X-ray sky thanks to the unprecedented combination of a large field of view, high sensitivity to point sources, and good time resolution. More than 20 years since its launch, it is still fully operative. Based on its serendipitous data, a very rich catalog of X-ray sources has been produced, including more than half a million unique sources. The long time actively spent in orbit (exposure time of ~ 300 million seconds up to now, with the prospect of further years of observations) guarantees unprecedented sky coverage for an X-ray telescope and the possibility of discovering relatively rare events.

All available temporal domain information were extracted for serendipitous *XMM-Newton* sources within the EU-FP7 EXTrAS project (Exploring the X-ray Transient and variable Sky; De Luca et al. 2021). We characterized the aperiodic, short, and long-term variability (on timescales ranging from the EPIC time resolution² to years) and searched for periodicity in more than 300 000 unique sources; we also searched for fast transients in

[★] The movie associated to Fig. 12 is available at <https://www.aanda.org>

¹ Metal Oxide Semi-conductor.

² The pn detector has the time resolution of 73 ms.

all observations. All EXTraS results are available in the EXTraS Public Archive. These include short-term and long-term light curves, power spectra, and a database of synthetic parameters (several hundred for each source, quantifying and describing all aspects of temporal variability). The potential of these results for science is very large for all classes of X-ray sources – from the detection of a superflare from a nearby ultracool L dwarf star (De Luca et al. 2020), to the observation of a supernova shock breakout in a distant galaxy at $z \approx 0.1$ (Novara et al. 2020), to the discovery of pulsations in ultraluminous X-ray sources (Israel et al. 2017a,b).

The EXTraS project is an example of astronomy entering into the big data era. There are at least two ways in which a data set can be considered “big”: because it contains many objects, such as stars or galaxies, and because for each of these objects a large number of attributes has been measured. Imagined as a table, the first case corresponds to a large number of rows, and the second to a large number of columns, resulting in a high-dimensional data set. While, traditionally, authors have had to deal with the problem of having too little data, the era of big data poses a set of new, complementary problems. Condensing a data set by reducing its size becomes useful and even necessary (see e.g., Bien & Tibshirani 2011). Many unsupervised methods in machine learning focus on this exact task: “clustering” attempts to reduce the number of rows, extracting or synthesizing a limited number of representative instances; variable selection and “dimensionality reduction” on the other hand attempt to reduce the number of columns by either selecting few relevant variables, or by combining several variables into new ones.

In this paper, we make use of a technique that accomplishes both dimensionality reduction and clustering at the same time: self-organizing maps (SOM; Kohonen 1982, 2001). This technique identifies groups of sources with shared characteristics, mapping them out onto a plane. This allows us to optimize visual inspection of the sources, revealing groups that share astrophysically relevant behavior (e.g., flares, eclipses) despite the fact that the method is agnostic with respect to the underlying physics.

While this approach is very well suited to our data, a broad variety of machine learning techniques, both unsupervised and supervised, is being increasingly applied to astronomy. The former are concerned with extracting patterns from a data set without direct guidance in the form of labeled data, while the latter focus on learning a function from labeled examples to carry out classification or regression. Examples of the former are anomaly detection (Protopapas et al. 2006; Baron & Poznanski 2017; Giles & Walkowicz 2020), clustering (e.g., Pasquato & Chung 2019), dimensionality reduction (e.g., Reis et al. 2018), and even integrated approaches including interactive visualization (Reis et al. 2021). While we do not discuss supervised methods in the following (nor even unsupervised methods except for SOM), we point the interested reader to two relevant reviews: Ball & Brunner (2010) and the more recent Baron (2019).

The paper is organized as follows. In Sect. 2, we give a detailed explanation of our unsupervised learning approach, in Sect. 3 we described our dataset, in Sect. 4 we present our results, and in Sect. 5 we draw conclusions.

2. Self-organizing maps

2.1. General information

A SOM is a type of artificial neural network (ANN), but despite this classification, SOMs work quite differently from typical

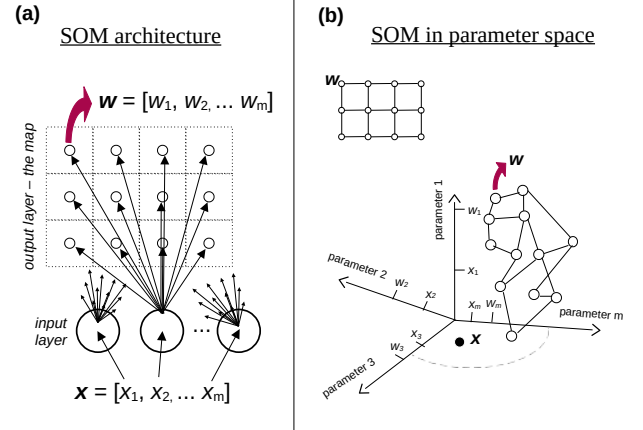


Fig. 1. SOM schematics. *Panel a:* SOM architecture. The bottom circles represent input neurons while the upper smaller circles represent the output neurons which build up the flat 2D map. The input neurons receive the values of the object parameters and are connected to all the output neurons as indicated through arrows. The dashed squares centered on the output neurons are the pixels used to visualize the map. For the sake of clarity, only one input neuron shows arrows going all the way to each output neuron. Also weights \mathbf{w} of only one output neuron are explicitly shown. *Panel b:* SOM in m -dimensional parameter space. The position of the output neurons on the flat 2D map grid is visualized with lines connecting them. The same map is shown below, immersed in the input parameter space, where each axis represents one parameter. The coordinates of one neuron \mathbf{w} and one object \mathbf{x} are explicitly shown on the axes.

ANNs such as feed-forward neural networks and related architectures³. Also, unlike most ANNs, SOMs are designed for unsupervised learning tasks, performing dimensionality reduction and clustering for data visualization.

Self-organizing maps have already found wide application in astronomy, especially when dealing with large multidimensional data sets. They have been applied: to light curves of variable stars (Brett et al. 2004; Armstrong et al. 2016); as an aid in the context of photometric redshift estimation (Geach 2012; Masters et al. 2015); to cluster gamma-ray bursts (Rajaniemi & Mähönen 2002); for morphological classification of galaxies (Naim et al. 1997); to find star clusters or otherwise coherent structures in Gaia data (Yuan et al. 2018, 2020; Pang et al. 2020); to find anomalous data in SDSS spectra (Fustes et al. 2013; Meusinger & Balafkan 2014); to find variable active galactic nuclei (Faisst et al. 2019), and so on.

The SOM architecture is simple, consisting of an input layer and an output layer (Fig. 1; panel a). The input layer consists of m neurons, where m is the number of input parameters (one neuron per parameter). Each neuron in the input layer is connected to all the neurons in the output layer. The output layer is typically a 1D, 2D, or 3D⁴ network of neurons connected to each other in the form of a grid.

The output layer is the place where visualization, dimensionality reduction, clustering, and so on is observed and presents the actual map. Typically, a flat 2D map is used and the shape is usually rectangular (four edges)⁵. The output of these neurons

³ For example, convolutional neural networks, etc.

⁴ For visualization purposes, the output layer has a maximum of three dimensions. However, as a dimension reduction algorithm, the SOM output layer can have any number of $\leq m$ dimensions.

⁵ It can also be cylindrical (two edges), or closed, as in a sphere, an ellipsoid, or a torus surface.

indicates the number of objects placed on them. It is visualized as a map consisting of pixels where each pixel corresponds to a neuron. The shape of a pixel is typically square or hexagonal.

Each neuron in the output layer (the flat 2D map) has a unique set of m weights associated to it: $\mathbf{w} = [w_1, w_2, \dots, w_m]$ (Fig. 1; panel a). The number of weights m is the same as the number of input parameters describing each object $\mathbf{x} = [x_1, x_2, \dots, x_m]$. When a certain object with parameters \mathbf{x} is presented to the input layer, that object is placed on the neuron whose weights \mathbf{w} are most similar to the input parameters \mathbf{x} . The most commonly used metric for this purpose is the Euclidean distance:

$$d = \|\mathbf{w} - \mathbf{x}\| = \sqrt{(w_1 - x_1)^2 + (w_2 - x_2)^2 + \dots + (w_m - x_m)^2}. \quad (1)$$

The object is placed on the neuron with the smallest d . This neuron is commonly referred to as the “best matching unit” (BMU). When all n objects in the sample are presented to the SOM, they are distributed across the map depending on the weights of each neuron.

Another way to think about assigning objects to neurons is to imagine an Euclidean m -dimensional parameter space (Fig. 1; panel b). The objects parameters \mathbf{x} are then coordinates in this space and all objects populate this space. The neuron map coordinates in this space are their weights \mathbf{w} . The map grid, that is, positions of neighboring and other neurons on the flat 2D map, can be seen as the lines connecting them. This map is a curved discrete 2D surface embedded in the m -dimensional parameter space. Each object is assigned to its closest neuron according to the Euclidean distance metric d .

Assigning objects to neurons in the map represents a dimensionality reduction. Each object with m parameters associated to it has only two discrete parameters on the 2D map (the map grid coordinates of its BMU).

SOMs are designed to detect patterns, clusters, and so on of objects based on their parameters and to preserve the topology of their m -dimensional distribution when placing them on the map. Objects that are similar to each other (nearby in parameter space) should be close to each other on the map. If there are distinct groups of objects, it should show up on the map as 2D groups. If the map weights are random, the objects will be randomly distributed on the map, and so the map needs to be trained, that is, its weights adjusted according to the parameters of the objects. In this sense, the SOM algorithm is similar to other ANN algorithms which also need to be trained. However, objects used for training the SOM are not labeled. The objects do not necessarily need to be divided into training and testing (and validation) samples, and there is no loss or cost function that needs to be minimized until it converges to a global minimum. It is possible to define a certain cost function for a SOM and monitor its reduction as training progresses, but the minimization of that function is not behind the training algorithm.

The way the SOM algorithm works is by introducing objects, finding their BMU, adjusting the weights of the BMU to more closely match the parameter values of the object, then doing the same to the weights of the surrounding neurons, but to a lesser degree the further they are on the flat 2D map grid. The last part is essential for the self-organizing property of the map and enables similar objects to be placed on nearby pixels on the trained map. It also means that the positions of neurons on the flat 2D map grid with respect to each other is important when training the map. Another important factor is that with each iteration (presentation of object(s) to the algorithm) the weight adjustment and the radius around the BMU are reduced. This

allows the map to settle to the final position after a sufficient number of iterations. Finally, the weight adjustment depends linearly on the difference between weights and respective object parameter values, ensuring that the update of weights towards parameter values is larger when the difference between them is larger. The dependence of weight adjustments on the (flat 2D map) distance from the BMU, l , is described by a “neighboring function”, h . Typically h is a 2D symmetric Gaussian function centered on the BMU:

$$h = \exp\left(-\frac{l^2}{2\sigma_i^2}\right). \quad (2)$$

The σ_i factor controls the width (standard deviation) of the neighboring function h which reduces with each iteration i , typically in an exponential manner. The formula (in vector form) for updating the weight \mathbf{w} of a neuron at a distance l from the BMU is:

$$\mathbf{w}(i+1) = \mathbf{w}(i) + \alpha(i) \times h(l, \sigma(i)) \times [\mathbf{x} - \mathbf{w}(i)]. \quad (3)$$

At each iteration i , the object \mathbf{x} is different⁶ until all n objects from the sample are passed. This completes one epoch of training. The total number of iterations i_{\max} is then $i_{\max} = n \times n_{\text{ep}}$ where n_{ep} is the number of epochs. The term $\alpha(i)$ is chosen such that, at $i=0$, it starts from a certain maximal value and decreases to a certain minimal value at $i=i_{\max}$ which is usually significantly smaller than the starting value. The term $\sigma(i)$ typically starts from a value similar to the size of the map at $i=0$ and decreases to encompass just one neuron (the BMU) at $i=i_{\max}$.

Some conclusions can be drawn from the above algorithm, which is referred to as the “online algorithm”. As mentioned before, objects are not labeled and there is no cost function minimization behind this algorithm. The number of iterations is predetermined and does not depend on the cost function converging to a minimum. The way $\alpha(i)$ and $\sigma(i)$ are defined ensures the convergence of the map. However, it is important that the number of epochs is large enough for the map to converge smoothly to its optimal stage. Even starting from the same initial weight values, the final map will be different if the order of introducing objects in the sample is changed. In this case the final map should still show the same groups and patterns, but these will be located in different places on the map. Each iteration can only be performed after the previous one is completed. Therefore, the algorithm is one large loop and the process cannot be parallelized and remains relatively slow.

A similar form of algorithm also exists, called the “batch algorithm”, which processes all objects in the sample at the same time for each epoch. The formula that regulates how weights are updated is:

$$\mathbf{w}(i) = \frac{\sum_{j=1}^{j=n} h(l_j, \sigma(i)) \times \mathbf{x}_j}{\sum_{j=1}^{j=n} h(l_j, \sigma(i))}. \quad (4)$$

In this case, each iteration i represents one epoch, meaning that the total number of iterations is the number of epochs $i_{\max} = n_{\text{ep}}$. The summation is over all n objects in the sample. The factor $\sigma(i)$ changes only between epochs and there is no term $\alpha(i)$ as in the online algorithm. Within the summation, the term l_j depends on the object \mathbf{x}_j and its BMU.

⁶ Therefore, the distance from the BMU on the flat 2D map l also depends indirectly on the iteration i because a new object \mathbf{x} mainly corresponds to a different BMU.

Again, some conclusions can be drawn. As in the online algorithm, there are no labeled objects and no cost function minimization; the map converges to the final position on its own, and simply needs enough epochs to converge to an optimal state. If the initial weight values are the same, the final map will be the same regardless of the order of the objects in the summation. The summation part can be parallelized and the only serial loop is over the epochs. This can make the batch algorithm faster and saves time, which can make a significant difference if there are many objects n in the sample.

Equation (4) can be made more algorithmically concise by grouping objects with the same BMU together and summing over each pixel:

$$\mathbf{w}(i) = \frac{\sum_{k=1}^{n_{\text{pix}}} n_k^{\text{bmu}} \times h(l_k, \sigma(i)) \times \bar{\mathbf{x}}_k}{\sum_{k=1}^{n_{\text{pix}}} n_k^{\text{bmu}} \times h(l_k, \sigma(i))}. \quad (5)$$

Here the n_{pix} is the number of pixels, n_k^{bmu} is the number of objects whose BMU is pixel k . The term l_k remains the same for all objects with the same BMU. The term $\bar{\mathbf{x}}_k$ is an average vector value of all objects with the same BMU. This can further speed up the algorithm.

2.2. The algorithm

In this work, we used SOMPY⁷ (Moosavi et al. 2014) for the SOM implementation. It is written in Python⁸, uses batch training (Eqs. (4) and (5)), and is relatively fast. The algorithm characteristics and options are as follows, along with the settings chosen for this paper. It uses a flat 2D rectangular map with either square or hexagonal pixels: we chose square pixels for simplicity. We fixed the number of output pixels to the default value of $5 \times \sqrt{n}$ (n is the number of objects). This is a common rule of thumb regarding the map size. The map proportions were set to the default value, which was obtained from the proportional length of the two largest PCA⁹ vectors for the data set, which is another common rule of thumb for the map. The neighborhood function h can either be Gaussian (Eq. (2)) or “bubble”¹⁰. Gaussian function was chosen because it is typically used as a neighborhood function. The algorithm splits training in two parts: “rough” and “fine”, each with its own number of iterations. This is related to the value of the average width σ_i (Eq. (2)). During rough training, it starts from a value somewhat smaller than the map length and ends up with a value several times smaller. During fine training, it starts from the previous value and ends at a value close to ≈ 1 , which is the distance between a BMU and its neighboring pixels¹¹. In both cases, σ_i decreases linearly with each batch iteration i . By dividing the training phase into two parts with given starting and ending values for σ_i , it approximates exponential decay. Weight initialization can be random or defined by PCA. The second case initializes weights in such a way that the map forms a grid on a plane defined by the two largest PCA components in parameter space, and is centered on the data. This method was chosen because it gives a good starting position for the map even if the data are not intrinsically two-dimensional and linear. There are various options for normalizing the data, but a custom normalization was used, which

is explained in the following section. The number of training epochs for both rough and fine training were chosen such that the final map does not change significantly and that the average “quantization error” does not change by more than 1% when doubling the number of epochs. The quantization error is the difference between parameter values of an object and the weights of its BMU defined as d^2 (Eq. (1)). The average quantization error is the average d^2 over all n objects.

3. Data selection

Among the several results released by the EXTras collaboration¹², we explored the catalog reporting the short-term aperiodic variability analysis. For each detection, several short-term (within the time-span of one orbital period ≤ 160 ks) light curves are extracted and statistical parameters computed, where a detection is defined as an observation of a unique source within a unique *XMM-Newton* observation period¹³ with a unique camera¹⁴ and within a unique exposure time during the observation period¹⁵. There are four types of light-curve binning, six temporal models fitted to the light curves, and four energy bands. All of these combinations coupled with various other parameters extracted from light curves resulted in several hundred parameters for each detection.

The short-term variability EXTras catalog comprises 872 075 detections, each described through 754 parameters¹⁶. Parameters were chosen such that they: were derived from light curves with one set of time-bin definitions; only contain variability (and not spectral) information; and do not have many “null” values. We excluded the count rate or any proxy for the count rate, and other parameters¹⁷.

Starting from all of the 754 parameters, the selection criteria reduced their number in the following way. We only accepted parameters that were derived from light curves with uniform time bins of 500 s (down to 147 parameters). We selected light curves encompassing the full energy range, not any of the three subranges (down to 84 parameters). All the parameters related to the “exponential decay”, “flare”, and “eclipse” models were excluded because they contain many null values (down to 53 parameters). The parameter “relative excess variance” and its error were excluded for the same reason (down to 51 parameters). The parameter “average count rate” and its proxies¹⁸ were excluded (down to 47). Finally, excluding other parameters related to identification and so on leaves $m = 31$ parameters. The final selection of these parameters and their description is presented in Table A.1.

The 872 075 detections in the catalog were filtered through flags and quality checks, requiring at least 20 time bins, non-negative count rate, and non-null values for all the 31 parameters. By combining all these constraints, we are left with $n = 128\,925$ detections.

The astrophysical type is unknown for a large number of *XMM-Newton* sources. Our $n = 128\,925$ detections correspond

¹² <http://www.extras-fp7.eu/index.php/archive>

¹³ Period during which the telescope spends pointing in one direction.

¹⁴ There are three cameras in total: pn, MOS1, MOS2.

¹⁵ There can be several exposure times for a single camera during one *XMM-Newton* observation period.

¹⁶ See the help pages of the EXTras short-term variability archive for a complete list and description of the parameters.

¹⁷ Information related to identification, duration of observation, errors, redundant instrumental and statistical information, etc.

¹⁸ Median count rate and the first coefficients in the “constant”, “linear”, and “quadratic” models.

⁷ <https://github.com/sevamoo/SOMPY>

⁸ <https://www.python.org>

⁹ Principal component analysis.

¹⁰ A radial 2D function with a constant value that drops to zero at a given radius.

¹¹ Up, down, left, and right, not the four diagonal.

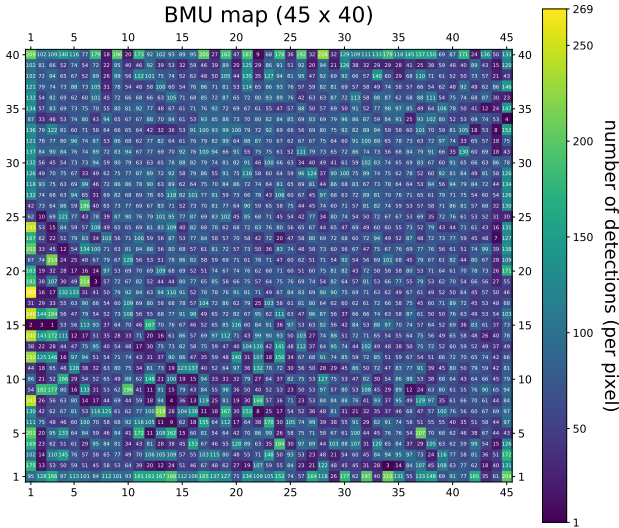


Fig. 2. BMU map. This BMU map corresponds to all $n = 128\,925$ detections. The color bar measures the number of detections placed on each pixel. This value is also indicated as a number on top of each pixel. The coordinates of the pixels within the grid start from the lower-left corner and are indicated on all sides of the map.

to about 43 000 unique sources, of which approximately 6000 reside in the Galactic plane $|b| \leq 2^\circ$ ($\sim 11\,000$ within $|b| \leq 10^\circ$). Given that most stars are within the Galactic plane while AGNs are above it, this can give an approximate idea of the composition of our sources. For a more quantitative description, a recent classification of *XMM-Newton* sources using a supervised method (Tranin et al. 2022) found that about 80% of the sources are AGNs, $\sim 20\%$ are stars, and few per cent are X-ray binaries and cataclysmic variables. These proportions should be similar with our sources.

The normalization of the $m = 31$ parameters and their mutual correlation is nontrivial and is explained in detail in Appendix A. With the data set of $n = 128\,925$ detections (samples) and adopting the configuration options explained in Sect. 2.2, the SOM algorithm settings in this case are: a map size of 45×40 ; 80 training epochs for both rough and fine tune training; σ_i (Eq. (2)) decreasing linearly from 6 to 1.5 during rough training and from 1.5 to 1 during fine training. With the batch implementation of the algorithm it took only about 5–10 minutes to train the algorithm on $n = 128\,925$ detections (samples) with $m = 31$ parameters (features) over 160 epochs (iterations) on an average CPU (one CPU at 2.6–3.5 GHz with four cores).

4. Results

4.1. SOM applied to the EXTrAS data

As explained in detail in Sect. 2, SOM performs dimensionality reduction starting from n objects described by m parameters resulting in a 2D map (BMU map) populated by n objects. At the same time, it performs clustering, such that objects which are similar end up close to each other on the BMU map forming a group.

As reported in Sect. 3, we applied SOM on $n = 128\,925$ *XMM-Newton* detections described by $m = 31$ variability parameters. The resulting BMU map is shown in Fig. 2. The numbering of pixels starting from the bottom left was introduced for guidance. The center of the map is mainly uniform while the lower-left part, which has a triangular shape, is highly fractured

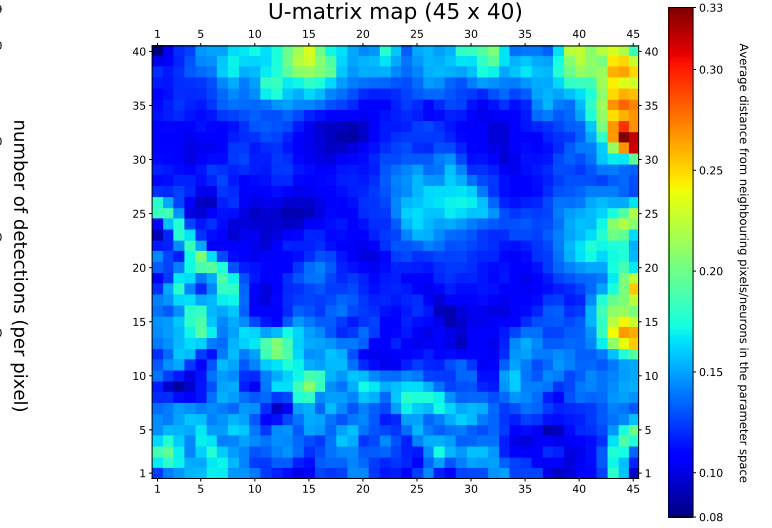


Fig. 3. U-matrix map. The color bar indicates the average distance of each pixel-neuron to its neighboring pixels-neurons in the normalized parameter space. Further details are in the text.

and seems to form a separate part. This suggests that the majority of detections in the broad map center form a single group in the normalized $m = 31$ dimensional parameter space. The lower-left part of the map suggests that detections placed here form many small groups.

In Fig. 3, the U-matrix plot is shown, which allows us to identify the clustering structure of our data by displaying the distance of each neuron from its four nearest neighbors in the normalized parameter space. Groups of similar (nearby) neurons representing points in our normalized parameter space, whose dimension is $m = 31$, can thus be visualized as regions of nearby neurons in the plane. These appear as contiguous dark blue structures in Fig. 3. Lighter colors, from sky blue to red, correspond instead to regions of lower density that divide groups (e.g., groups in the lower-left triangle; their division is seen as lines on the U-matrix map) or lie at the edges (e.g., groups on the U-matrix map at the up and right edges). The second case represents groups of outliers, that is, points that for whatever reason are different from the typical object in our data set. Clearly, objects that are systematically different may represent astrophysically interesting sources worthy of further study.

Figure 4 reveals how each of the $m = 31$ parameters map out onto this plane. Technically, these are the weights of the SOM neurons being shown over a grid of 1800 (40×45) neurons. Even though there are $45 \times 40 = 1800$ neurons in total and each of them has 31 weights for each parameter (corresponding to the relevant m coordinates in parameter space), Fig. 4 shows that they can be easily visualized as a 45×40 map for each parameter (i.e., each coordinate in the parameter space).

These maps can be visually compared to Fig. 3 to reveal the characteristics associated to each data subgroup; for example it can be readily checked that the upper-right corner of the map (corresponding mostly to outliers according to Fig. 3) has distinct variability properties. The combination of Figs. 3 and 4 thus acts as a look-up table guiding direct visual inspection of the sources.

4.2. Analysis of variable sources

In order to examine potentially interesting detections more closely, we focused on variable sources. Variability was defined

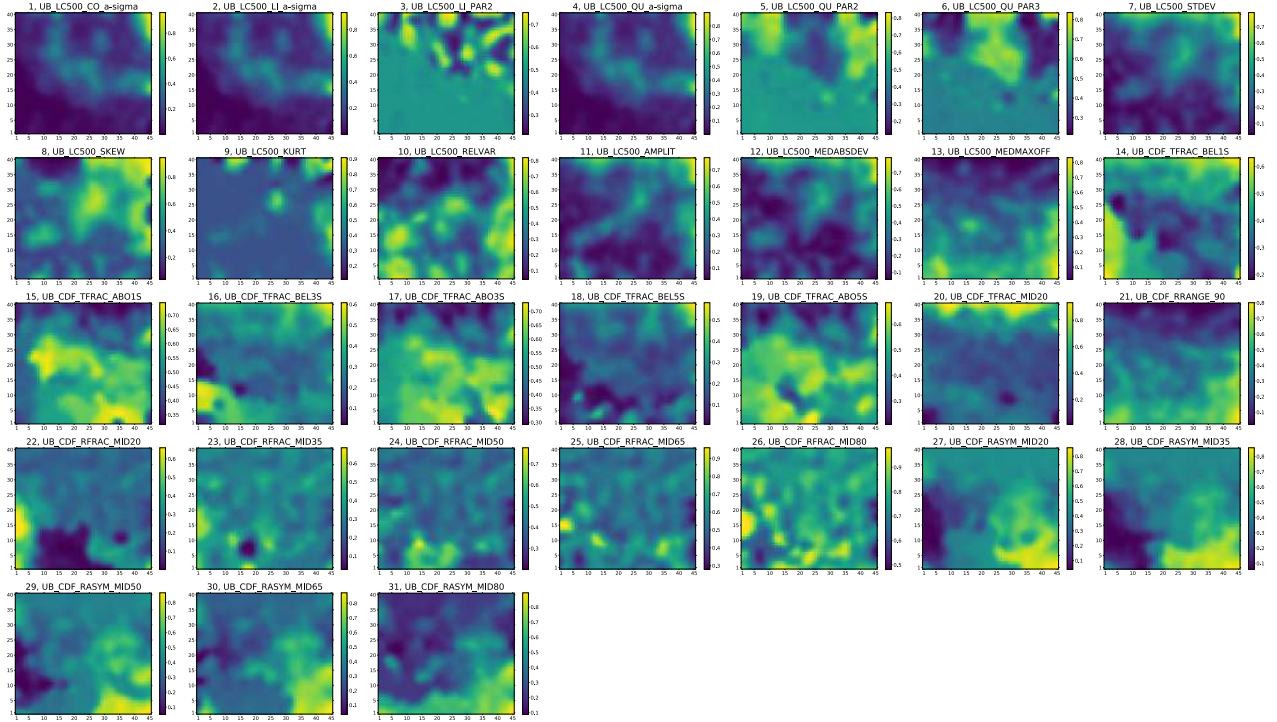


Fig. 4. SOM weights. SOM weights for each parameter are presented as maps of the same dimension as the main BMU map. The color bar represents the value of the weight for each pixel. The numbering of the parameters is the same as in Table A.1.

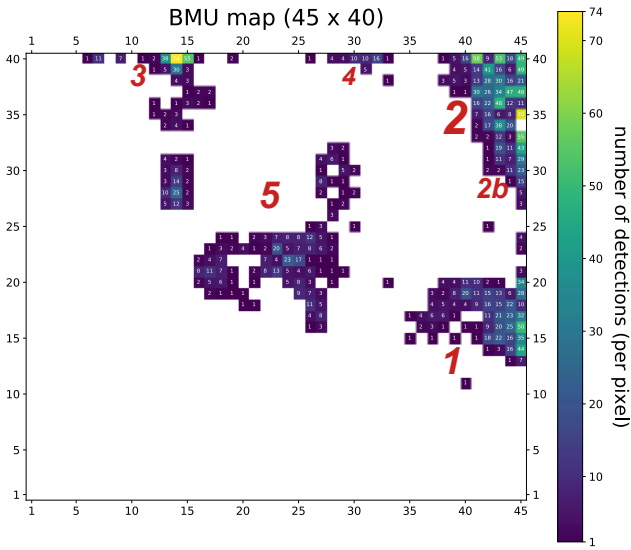


Fig. 5. BMU map. Same map as in Fig. 2 but showing only the most variable $n_{\text{var}} = 2654$ pn detections. White pixels correspond to zero detections. Red numbers correspond to numbering of “blobs” (more in the text) and their size is illustrative of the number of detections in each one.

such that the fit of the 500 s time bin light curve with a constant model is unacceptable ($>5\sigma$). Also, we only took the most sensitive pn camera light curves into account so as to ensure a sample with all the unique detections (unique source within unique time frame). The number of detections fulfilling these requirements is $n_{\text{var}} = 2654$. Their placement on the main BMU map (which was trained on all $n = 128\,925$ detections) is shown in Fig. 5.

It is apparent that variable sources form distinct groups, “blobs”, separated from each other. Most groups take the same

form as the core where the majority of detections are found, with the number of detections decreasing to zero as the distance from the core increases. Also, some groups show some substructure. In Fig. 3, pixels with the highest value mostly correspond to pixels containing groups of variable detections. The high value in the U-matrix map means that these neurons are far away from the neighboring neurons in the parameter space.

Figure 6 shows that 1800 SOM neurons follow the distribution of all the $n = 128\,925$ detections rather well¹⁹ for each of the $m = 31$ parameters. The distribution of the variable $n_{\text{var}} = 2654$ detections is more “stretched” towards the edges than that of all detections²⁰. For most parameters at the very edges (near zero and one), the two distributions practically overlap. This means that variable detections tend to lie towards the edges of the parameter space. This can be interpreted as variable detections belonging to several quasi-outlier groups; this interpretation is confirmed by looking at the U-matrix map (Fig. 3).

Based on a visual inspection of the BMU map of variable sources (Fig. 5), we can define some clear blobs as: *Blob 1* is in the lower-right corner with coordinates $X \geq 35, Y \geq 10, Y \leq 20$. The number of detections in this group is about 600. *Blob 2* is in the upper-right corner with coordinates $X \geq 35, Y \geq 20$. The number of detections in this group is about 1200. This group shows a substructure in its lower part (blob 2b), with a separation at coordinates $X \geq 40, Y < 35$, containing about 250 detections. *Blob 3* is in the upper-left corner with coordinates $X \geq 5, X \leq 20, Y \geq 33$. The number of detections in this group is about 250. *Blob 4* is in the upper center with coordinates $X \geq 25, X \leq 35, Y \geq 35$ and the second one below at $X \geq 25, X \leq 30, Y \geq 25, Y \leq 35$. This latter contains about 50 detections. *Blob 5* is made out of the central group at $X \geq 15, X \leq 32, Y \geq 12, Y \leq 32$, and contains about 550 detections.

¹⁹ The y -axis is in logarithmic scale.

²⁰ This might be intuitively expected for the most variable detections.

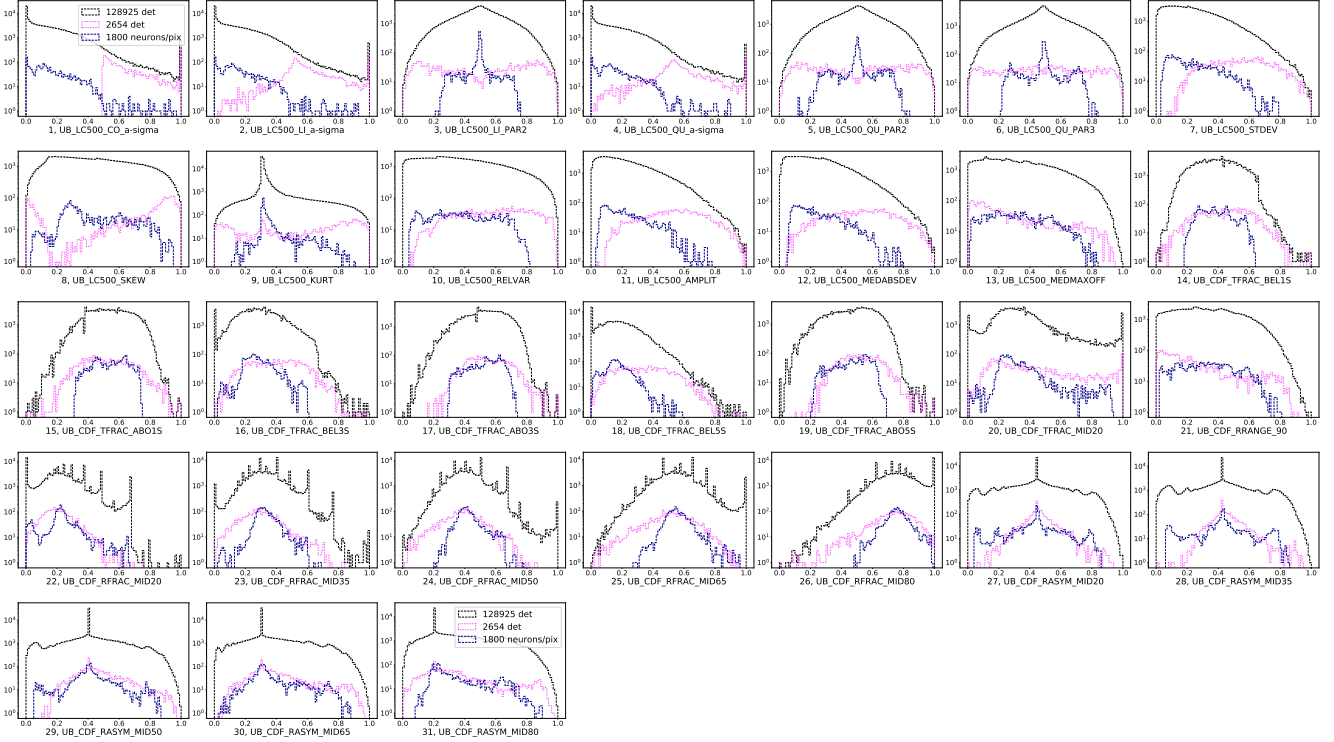


Fig. 6. Distributions of values for each of the $m = 31$ parameters. Comparison between the distribution of the whole dataset (black) and that of the SOM neurons (blue) is shown. We additionally visualize the distribution of variable sources (pink). The numbering of the parameters follows Table A.1.

The $n_{\text{var}} = 2654$ detections have, on average, an order of magnitude higher signal to noise ratio (S/N)²¹ than $n = 128\,925$ detections. This might be expected. Detections that are too faint to not cross the threshold of variability definition even if, intrinsically, they might be variable.

Training the SOM on just $n_{\text{var}} = 2654$ detections produces a uniform map without clearly separated blobs. It can be interpreted that one of the SOM results is finding and grouping interesting detections, and these detections mostly have a high S/N in order to be possible to distinguish their interesting features. In order for SOM or any other machine-learning algorithm to potentially “see” intrinsic features in faint sources (even if, for example, an astronomer with all the “ordinary” statistical tools would not be able to), instrumental and background effects would have to be input into the algorithm. Such an analysis is outside the scope of this paper.

4.3. Classification of different groups

4.3.1. Quick look at all the blobs

In order to roughly examine each blob, we randomly chose a quarter of the $n_{\text{var}} = 2654$ detections and visually inspected their light curve to search for characteristic patterns. We divided the light curves into classes on the basis of their main shape: flares, bumps, multiple flares, multiple bumps, dips-eclipses, linear, and random.

We classify any intense increase in flux followed by a fading to the quiescent level as flares and bumps, but, more specifically, flares follow a fast rise, exponential decay (FRED) time profile, while bumps have a more symmetrical shape (the same goes for

multiple flares and multiple bumps). Although flares and bumps may originate from similar mechanisms (e.g., Pye et al. 2015 show that coronal flares from stars may have comparable rise and decay times in a large fraction of cases), we decided to keep these two phenomenological classes of light curves separate. Dips and eclipses are in a single class featuring any curve with one or more sudden and significant decrease in flux followed by a recovery to the upper level; the few cases of apparent dips and eclipses partially covered by the observation were treated case by case. The Random class includes light curves that do not show a distinct type of variability. We built a map that shows the most numerous class in each pixel (Fig. 7).

It is apparent that certain classes of light curves are predominantly concentrated in certain areas. For example, single flares are highly concentrated in the core of blob 1 (lower-right). Blob 2 (upper-right), the largest group, is composed of a variety of classes but dominated by multiple features; its substructure (the bottom part) is instead dominated by dips and eclipses. Blob 3 (upper-left) is mainly composed of dips and eclipses. Blob 4 (upper-center) is mainly composed of linear curves. The random curves are concentrated in blob 5 (central).

The SOM algorithm successfully extracted and grouped variable sources with the same variability behavior. Among the different blobs, the most intriguing from an astrophysical point of view are the ones dominated by flares, dips, and eclipses. For those groups, we extended our visual analysis.

4.3.2. Single flares

From the analysis in Sect. 4.3.1, we find that almost all of the flares are distributed over blob 1 and blob 2 with FRED-like flares being mostly present in the former. In blob 1, flares seem to be concentrated in the core, while in blob 2 their distribution

²¹ Defined as the parameter PN_8_DET_ML (maximum likelihood) in the 3XMM-DR4 Catalog.

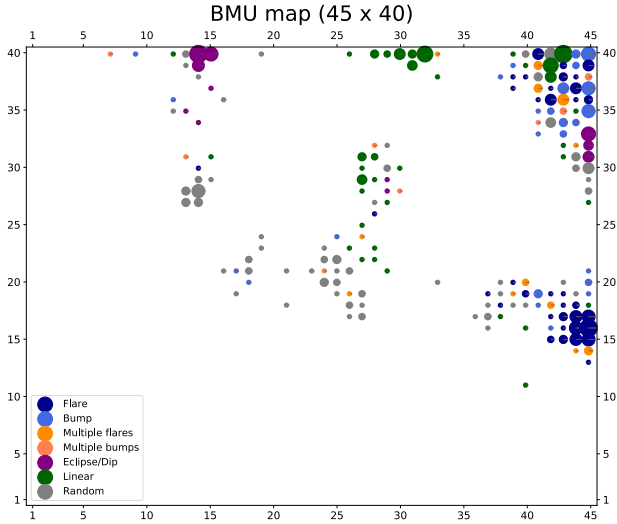


Fig. 7. Classes of visually inspected variable detections. A quarter of $n_{\text{var}} = 2654$ was inspected and classes are presented as colored disks for each pixel. The most populated class at each pixel is shown. Flares are in dark blue, bumps in light blue, multiple flares in dark orange, multiple bumps in light orange, eclipses and dips in purple, linear in green, and random in gray. The size (area) of the disk corresponds to the number of detections belonging to the most populated class in a given BMU pixel.

is more complex and many other types of sources contribute to this blob.

Because of the large concentration of FRED-like flares, we examined blob 1 in detail. Due to the relatively large number of elements in blob 1, we visually examined only half of the approximately 650 detections, with focus on phenomena that are likely to be related to an astrophysical flare.

We defined three main classes of light curves: (i) *Single flare* – the largest fraction are “textbook” flares with a FRED time profile fully within the observation period. Some are only partly within an observation period (e.g., with partial decay) and/or have a different time profile (e.g., “bumps” with similar rise and decay time). (ii) *Uncertain* – including all light curves showing some feature that could be related to an astrophysical flare (e.g., an exponential decay; a fast rise close to the end of the observation, etc.) but a different explanation could not be excluded. (iii) *Nonflares* – including all light curves that did not have any relevant feature reminiscent of a flare. Examples of single flares, uncertain flares, and nonflares are shown in Fig. 8.

Figure 9 shows the distributions of all classes. Single flares, uncertain flares, and nonflares are shown in the right, middle, and left panels, respectively.

As can be seen, the concentration of clear flares is highest in the core of the blob, and gets diluted towards the blob edges. To crudely quantify this structure, the blob was divided into three parts: core, corona, and tail.

The concentration of single flares and other detections can be described as follows: The core is defined as pixels with coordinates $X \approx [15, 18]$, $Y = [44, 45]$. The core contains about 200 detections of which 100 were visually inspected. Of these, 85 are single flares of which only five are bumps, 59 are FRED-like flares, and the rest are FRED-like flares not fully covered by observations. There are also 8 uncertain flares. The corona is defined as pixels with coordinates $X \approx [13, 20]$, $Y \geq 42$ excluding the core pixels. The corona contains about 300 detections of which 150 were visually inspected. Of these, 59 (39%) are single flares of which ten are bumps, 23 are FRED-like flares, and

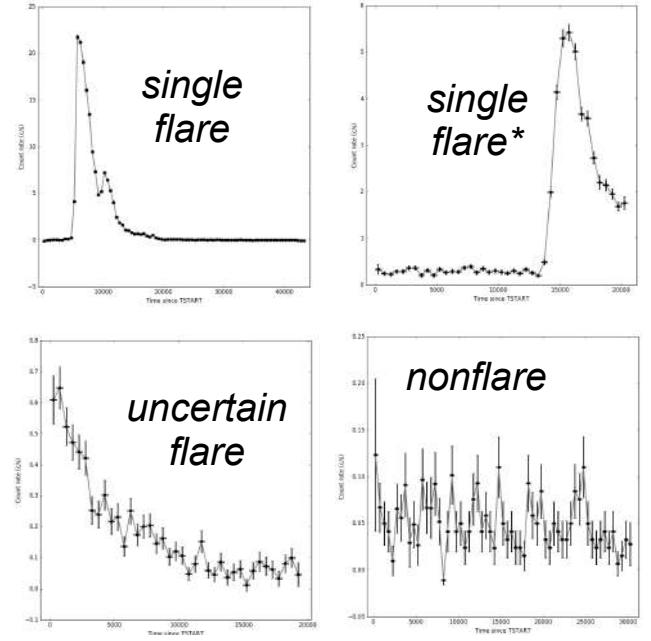


Fig. 8. Examples of flares. The light curves are binned with 500 s time bins in one short-term exposure window; the vertical axis shows background-subtracted count rate. *Upper-left:* Example of a bright flare: this detection is marked in the 3XMM-DR4 catalog as obs.id. 0604820301, src. 1. It is located at the BMU pixel $X=45$, $Y=16$. *Upper-right:* Example of a flare not fully covered by observations. This detection is marked in the 3XMM-DR4 catalog as: obs.id. 0134531601, src. 2. It is located at the BMU pixel $X=45$, $Y=15$. *Bottom-left:* Example of an uncertain flare. It shows exponential decay only, which could be the decaying part of the flare. This detection is marked in the 3XMM-DR4 catalog as: obs.id. 0302970201, src. 2. It is located at the BMU pixel $X=45$, $Y=14$. *Bottom-right:* Example of a nonflare. It shows a flickering behavior. This detection is marked in the 3XMM-DR4 catalog as: obs.id. 0302340101, src. 1. It is located at the BMU pixel $X=39$, $Y=19$.

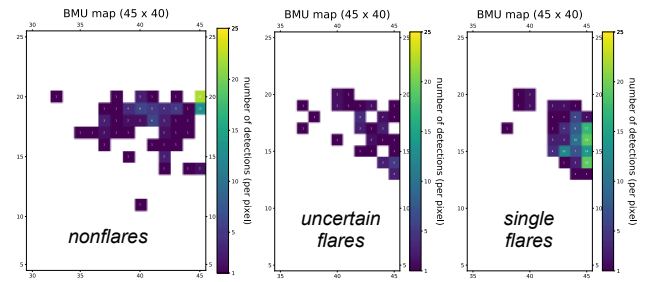


Fig. 9. Distribution of visually inspected detections in blob 1. Single flares, uncertain flares, and nonflares are in the *right*, *center*, and *left* panels, respectively. All three panels have the same upper limit in the color bar for the purpose of direct comparison.

the rest are FRED-like flares that were not fully observed. There are also 27 (18%) uncertain flares. The tail is defined as pixels with coordinates $X \approx [13, 20]$, $Y \leq 41$. The tail contains about 130 detections, of which 65 were visually inspected. Of these, six (9%) are single flares (two bumps and four faint FRED-like) and ten (15%) are uncertain flares.

It is interesting to compare results of SOM with the results of the fit statistics from the flare model²² from EXTrAS. We selected 566 detections (out of $n_{\text{var}} = 2654$) with a good flare model fit

²² The flare model in EXTrAS catalog is defined as a constant plus fast rise and exponential decay (FRED).

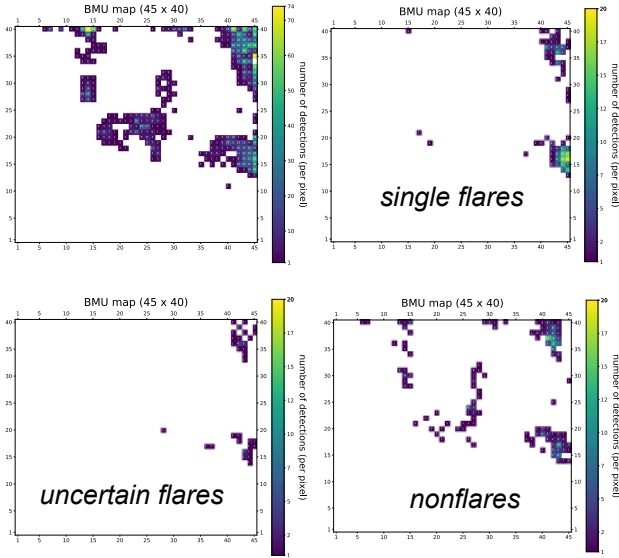


Fig. 10. Visually inspected detections which have a good flare fit statistics. Anticlockwise from the upper-right, the panels show all $n_{\text{var}} = 2654$ variable detections, single flares (251 detections), uncertain flares (42), and nonflares (273).

statistic²³: these were visually inspected and classified into single flares, uncertain flares, and nonflares. Single flares make up 251 detections, uncertain flares 42, and non-flares 273: roughly half of the 566 detections selected based on a good flare model fit are not actually flares (e.g., the light curve has some random pattern that the automatic analysis managed to fit with the model). Thus, using an approach based on a model fitting, half of the flares are not genuine flares; with SOM, on the other hand, 93% of the elements in the core of blob 1 are flares (or uncertain flares).

In Fig. 10, we show the three classes in the BMU map. About 90% of the well-fitted, visually inspected flares fall into blob 1 and blob 2 (in a ratio of $\sim 2:1$), in agreement with the findings of SOM (Figs. 7, 9). While flares are concentrated in the core in blob 1, they form a corona around the core in blob 2.

On the other hand, only about 60% of real single flares from the total visual inspection are well-fitted by the EXTras flare model, either because the real flare is not a perfect FRED, the flare is superimposed on some other minor variations, or the fit fails.

We conclude that SOM was able to extract 97% of the light curves with a “real” single flare and group them into two different groups (blob 1 and blob 2 with a ratio of $\sim 2:1$). Within blob 1, flares compose up to 93% of the core and up to 57% of the corona; within blob 2, flares are concentrated in the corona. For comparison, through a classical model fitting analysis we are able to extract 60% of the real single flares, and only 52% of the well-fitted light curves contain a real single flare.

Most of the visually inspected flares are likely emitted by coronally active stars; this is either confirmed by the association of the flaring sources with stars in the Simbad database, or suggested by the soft spectrum of the X-ray sources and by their positional coincidence with cataloged optical/near-infrared objects. Peculiar phenomena of nonstellar origin can also be found in the sample: for instance, in the core of blob 1, we find the puzzling case of XMMU J134736.6+173403. This source is

²³ (a) the null hypothesis of the flare model is $<5\sigma$ and (b) an f -test confirms the statistical improvement by using the flare model instead of a constant at $>5\sigma$.

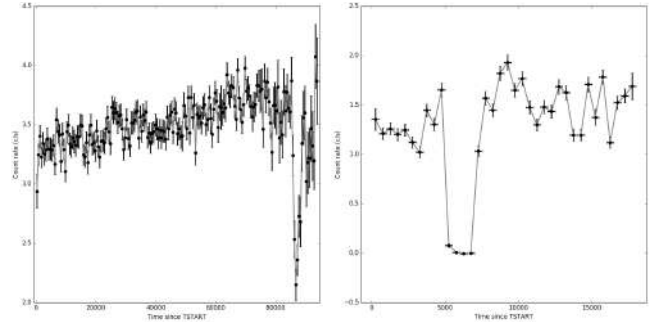


Fig. 11. Example of a dip (left) and an eclipse (right). The light curves are binned with 500 s time bins in one short-term exposure window. The vertical axis shows the background-subtracted count rate. The detection with the dip is marked in the 3XMM-DR4 catalog as obs.id. 0200470101, src. 1. It is located at the BMU pixel $X = 14$, $Y = 40$. The detection with the eclipse is marked in the 3XMM-DR4 catalog as obs.id. 0110660101, src. 1. It is located at the BMU pixel $X = 45$, $Y = 32$.

associated with a low-mass AGN and displays a sudden factor 6.5 decrease in flux occurring in about 1 hour²⁴. As discussed by Carpano et al. (2008) and Carpano & Jin (2018), this unusual drop in flux defies any easy explanation.

4.3.3. Dips and eclipses

From a quick visual inspection of blobs (Sect. 4.3.1), we find two distinct structures in the BMU map in which dips and eclipses are dominant: blob 3 and blob 2b (Fig. 5). These contain 38% and 22%, respectively, of the dips and eclipses found through the quick visual inspection; most of the remaining dips and eclipses are in the rest of blob 2 (23%). The upper-left blob core is composed of pixels (14,40) and (15,40) and contains 129 light curves; it is surrounded by a corona of 87 light curves and a tail of 20 curves. The blob 2b core is composed of pixels (45,31), (45,32), and (45,33) just below, but separated from, the main structure of blob 2; it contains 127 light curves.

Here, we examined blob 3 and blob 2b in detail. We visually inspected all the light curves in these regions in detail, focusing on phenomena that are likely to be related to a dip or an eclipse. We divided the sources into three classes: random, dip, and eclipse. Random light curves do not show any apparent fall-rise behavior (even if they can show any other behavior described in Sect. 4.3.1). We classified the remaining light curves as “dip” or “eclipse” based on the literature for associated sources. If there was no association with a dipping or eclipsing source, classification was based on the shape of the fall and rise: dips are short (less than 5 bins) with a clear decrease and increase (typically a “V” shape), while eclipses are longer and/or characterized by a constant, low flux level (typically a “U” shape). An example of a dip and an eclipse is shown in Fig. 11.

We find that, in the core of blob 3, 90% of the light curves are dips or eclipses, while in the corona this percentage is 45%, and in the tail these represent 20%. Most of them (97% in the core, 80% in the corona, and 83% in the tail) are dips. While some of the dips are instrumental errors occurring at the beginning or the end of the observation, we find many well-known dipping sources, for example: 2XMM J125048.6+410743 (Lin et al. 2013) and 3XMM J004232.1+411314 (Marelli et al. 2017).

²⁴ The overall shape of the light curve, featuring a “high state” lasting about 5 h, the sudden flux drop, and a “low state” lasting more than 10 h can be seen as a bump starting before the beginning of the observation.

In the core of blob 2b, 60% of the light curves are dips or eclipses, of which 60% are eclipses and the remaining dips are usually longer than those in blob 3 and/or their statistics are poorer. Among them, we find many well-known eclipsing sources, for example: V* V1727 Cyg (Bozzo et al. 2007) and V* XY Ari (Norton & Mukai 2007). We investigated the existence of a corona in the lower-left part of blob2, but only 8 of 105 light curves show a clear eclipse or dip.

The SOM algorithm was therefore able to extract 83% of the light curves that show one or more dip or eclipse and to group them into blob 3 and blob 2 (quick visual analysis in Sect. 4.3.1). From the detailed visual analysis, we find that, within blob 3, dips vastly dominate over eclipses and dips and eclipses compose 90% of the blob core and 45% of its corona. Blob 2b is dominated by dips and eclipses of which 60% are single or multiple eclipses while most of the dips are wider than the ones in blob 3. In the core of this blob, 60% of the light curves show one or more dips or eclipses.

In order to confirm and compare the results based on the visual inspection, we cannot rely on the eclipse model from EXTraS as we did for flares (Sect. 4.3.2). The eclipse model is indeed quite simple, with a perfect U shape, and thus it cannot describe more complex light curves (e.g., with a rise and decay time), dips, or periodic features; moreover, the eclipse model usually fits most of the random increases or decreases of a low-statistics light curve well. A rough comparison comes from the sample used for the quick visual analysis in Sect. 4.3.1: the number of well-fitted eclipses²⁵ is more than twice the number expected from the visual inspection, while only half of the dips and eclipses from visual inspection are well fitted by the eclipse model. Instead, we randomly selected a number of X-ray eclipsing-like sources observed by *XMM-Newton* from the literature. Our random selection comprises different types of objects, with one or more observations, and with one or more features in the same exposure. We selected 12 sources for a total of 22 detections (see Table B.1). Of the 22 detections, 16(+1) fall in the core (corona) of blob 2b. Four detections fall in the remaining part of blob 2, but always at X=45. One detection falls in blob 3. It is also interesting to note that different exposures of the same source usually fall in the same or the adjacent pixel.

4.4. Interesting sources

Dips and eclipses are quite rare and are interesting from an astrophysical point of view because they usually indicate binary systems and/or imply the presence of an accretion disk or blobs of dust. In this case, the SOM is particularly useful for the discovery of single, interesting systems. Therefore, we searched our sample for unpublished features and obtained eight sources. In the following, we report a brief description of them, including their *XMM-Newton* names, source numbers, and coordinates (all of which come from the 3XMM-DR4 catalog).

3XMM J063736.4+053932. (obs.id. 0655560101, src. 1, BMU pixel 14,39) is located at RA(J2000) 06:37:36.48, Dec(J2000) +05:39:32.59. The EXTraS pn light curve shows a total eclipse in the last 2 ks (over a 26 ks exposure) not covered by the MOS cameras. The positional coincidence with the 8.5 V magnitude star HD 47179 suggests this source is a stellar binary system.

3XMM J081928.9+704219. (obs.id. 0200470101, src. 1, BMU pixel 14,40) is located at RA(J2000) 08:19:29.00

Dec(J2000) +70:42:19.17. The EXTraS pn light curve clearly shows a dip that halves the X-ray count rate (5 ks over a 83 ks exposure). It falls during a very high-background period but the dip shape does not seem to be correlated with the background. This source is associated with the well-studied ultraluminous X-ray source Holmberg II X-1. Goad et al. (2006) analyzed this detection, but the time of the dip was discarded because of the high background. Although EXTraS tools are well suited to deal with high background (De Luca et al. 2021), a dedicated analysis is required to confirm this feature.

3XMM J133000.9+471343. (obs.id. 0303420201, src. 2, BMU pixel 14,40) is located at RA(J2000) 13:30:00.96 Dec(J2000) +47:13:43.65. The EXTraS pn light curve shows a peculiar flickering pattern, possibly quasi-periodic, with a timescale of ~20 min. Light curves from MOS cameras confirm this peculiar variability. Interestingly, the source is M51 ULX-7, a pulsating (~2.8 s) ultraluminous X-ray source with an orbital period of ~2 days and a possible super-orbital modulation of ~38.9 days (Rodríguez Castillo et al. 2020; Vasilopoulos et al. 2021).

3XMM J031822.1-663603. (obs.id. 0405090101, src. 2, BMU pixel 14,40) is located at RA(J2000) 03:18:22.17 Dec(J2000) -66:36:03.4. The EXTraS pn light curve shows a random variability with an eclipse-like sudden drop (~40% of the average count rate) during the last 3 ks of the observation. This drop is confirmed by both MOS cameras. This source is associated with the pulsating (~1.5 s) ultraluminous X-ray source NGC1313 X-2 (Sathyaprakash et al. 2019; Robba et al. 2021).

3XMM J080945.3-472110. (obs.id. 0112670501, src. 4, BMU pixel 45,32) is located at RA(J2000) 08:09:45.35 Dec(J2000) -47:21:10.16. The EXTraS pn light curve starts in a constant, low state that lasts for 3 ks (over a 28 ks exposure) and then suddenly rises by a factor of ~10 in count rate. It can be interpreted as either an eclipse or a FRED flare with a very long characteristic decay time (~30 ks). Data from MOS cameras are not available. We note that the only other *XMM-Newton* observation (55 ks exposure) of this source shows a count rate compatible with the low state. This source is positionally consistent with the young stellar object candidate 2MASS J08094536-4721101.

3XMM J063045.4-603113. (obs.id. 0679381201, src. 1, BMU pixel 45,32) is located at RA(J2000) 06:30:45.42 Dec(J2000) -60:31:13.15. The EXTraS light curve shows an eclipse or a series of dips in the last 3 ks of the observation (over a 13 ks exposure), with a drop of ~75% of the count rate. This behavior is confirmed by both MOS cameras. The source is associated with XMMSL1 J063045.9-603110, a peculiar transient source (Read et al. 2011) proposed to be a tidal disruption event (Mainetti et al. 2016), but later spectroscopically classified as a nova (Oliveira et al. 2017).

3XMM J182422.8-301833. (obs.id. 0551340201, src. 52, BMU pixel 45,32) is located at RA(J2000) 18:24:22.82 Dec(J2000) -30:18:33.2. The EXTraS pn light curve clearly shows a periodic, possibly sinusoidal (or, a series of dips) pattern. Indeed, the search for periodic sources performed within EXTraS reveals a significant coherent signal at 2919 s (a complete analysis will be presented in the EXTraS pulsators catalog (Israel et al., in prep.)). The X-ray source has a few possible optical counterparts and is also positionally consistent with a WISE

²⁵ We use the same definition as in Sect. 4.3.2.

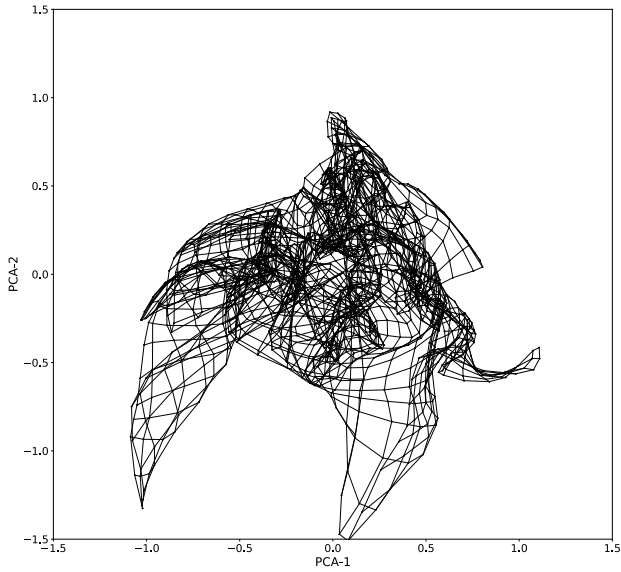


Fig. 12. SOM map projected on a plane formed by the two largest PCA vectors. Dots represent SOM neurons while lines are connections between neighboring neurons. The evolution of the SOM map projection during training is available as an [online movie](#) ‘fig_s5_som_pca12_movie’. One can see how the map goes from its starting position as a rectangle, changes during rough training (1–80 epoch), and converges to its final position during fine training (81–160 epoch).

source. It could be a low-mass X-ray binary, but a dedicated analysis is needed to confirm this hypothesis.

3XMM J053427.3-052420. (obs.id. 0403200101, src. 5, BMU pixel 45,33) is located at RA(J2000) 05:34:27.37 Dec(J2000) –05:24:20.92. The EXTras pn light curve starts in a constant, low state that lasts for 20 ks (over a 90 ks exposure) and then suddenly rises by a factor of ~ 2 in count rate. This should be interpreted as an eclipse – a FRED flare would have a very long characteristic decay time (~ 90 ks). Data from MOS cameras confirm the variability pattern. Other *XMM-Newton* observations see the source – which is usually variable – in different states. This source is positionally consistent with the 12.4 V magnitude variable star of Orion type V* V1961 Ori.

4.5. Caveats and robustness checks

In general, a SOM is not guaranteed to correctly represent all the relevant structure of a data set. A simple check of whether the training process led to an acceptable result is to consider the distribution of each variable from the initial high-dimensional space: is it the same on the SOM neurons as in the original data? As the aim of training a SOM is for the neurons to behave like representative data points or prototypes, this is clearly a minimum requirement. If the neurons have a very different distribution with respect to the original data then training did not work as expected, perhaps having to few iterations. In Fig. 6 we show all 31 normalized parameters, distinguishing all the 128 925 detections, the 2654 variable detections, and the 1800 SOM neurons. It is clear that our SOM neurons generally follow the distribution of the original data on each parameter.

Another test with a similar goal is to compare the results of our SOM to those of other, simpler dimensionality-reduction approaches. The simplest is PCA, which is a linear procedure building a set of orthogonal variance-maximizing linear combinations of the (standardized) original coordinates. Retaining

only the first two PCA coordinates – which explain the most variance in the data set – allows visualization on a plane. However, the linear nature of PCA makes it hard for it to correctly represent nonlinear structure. In Fig. 12, our SOM map is projected from the original 31-dimensional parameter space on to a plane formed by the first two PCA coordinates. Our map can clearly be seen to generally cover this PCA plane, even though it is twisted in a nontrivial way. This suggests that the original parameters are related in complex nonlinear ways, justifying the need for a SOM, or for nonlinear dimensionality reduction in general, as opposed to PCA. A possible cause for concern is that the SOM may have a complex shape (Fig. 12) because it is trying to compensate for the difference between the intrinsic dimension of the data set and the map intrinsic dimension of $D = 2$. Increasing the dimensionality of our SOM by arranging its neurons on a lattice in three-dimensional space would address this issue but make visualization more cumbersome. We therefore chose not to explore this option in the current paper, even though it may be worth investigating in a subsequent one.

5. Conclusions

The *XMM-Newton* telescope greatly advanced our knowledge of the X-ray sky, with the EXTras project detecting and characterizing the time variability of over 300 000 sources. The resulting data set poses the typical challenges of big data, serving as a clear illustration that X-ray astronomy is transitioning into this regime. In this context, traditional approaches (e.g., human visual inspection) do not allow us to take full advantage of the opportunities offered by the data.

In this paper, we applied a machine learning approach with the goal of automatically organizing data to maximize the effectiveness of direct human inspection. To this end, we selected a subset of parameters – from the originally large number provided by EXTras – that characterize the variability of each source, and applied dimensionality reduction to the resulting data set. This was achieved using the SOM algorithm, which represents the data on a plane, attempting to respect the topology of the original high-dimensional space. By construction, the SOM builds a grid of representative points that summarize the original data, and lays them out grouped together based on the similarity of their characteristics. It thus clusters the data while reducing its dimension to a plane for visualization purposes. This is something that would not be achieved by a linear approach such as PCA, which would miss most of the intrinsically nonlinear structure of our data set that SOM is able to capture, as shown in Fig. 12.

Despite being a time-tested algorithm which has already been used in astronomy, this is the first time²⁶ SOM is applied in this context (large X-ray data set). As a result, we streamlined a process of source recognition that would otherwise have been driven by serendipitous discovery, finding flares, dips, eclipses, and other source types, all arranged into contiguous clumps in the SOM plane. Used in this way, SOM allows an astronomer to concentrate on inspecting regions of data space that appear scientifically promising.

We highlighted the problem of straightforward temporal model fitting to light curves and its use to characterize them, especially when data are noisy, and showed that the SOM algorithm can overcome this problem to an extent by utilizing parameters derived from the light curves.

With the introduction of this new tool, we were able to explore the EXTras data set, focusing on variable sources,

²⁶ As far as we can tell.

quickly selecting a number of objects that have interesting properties that warrant further investigation, including different kinds of binary systems (from binary stars to ULXs) as well as more peculiar sources. While some of these objects were already investigated and described in the literature, for example the most luminous dipper known 3XMM J004232.2+411314 (Marelli et al. 2017), the peculiar transient 3XMM J063045.4-603113 (Mainetti et al. 2016), and the poorly understood, low-mass AGN XMMU J134736.6+173403 (Carpano et al. 2008), we also extracted some new interesting sources (Sect. 4.4). It should be noted that this data set, based on observations collected until 2012, was widely analyzed by the astronomical community for years before this work.

Summarizing data becomes more and more valuable as data sets grow. Our approach is therefore promising, especially in the light of the upcoming new EXTraS data, not to mention future space missions that may yield much richer and sensitive data than *XMM-Newton*, such as the ESA ATHENA observatory. Furthermore, our results pave the way for upcoming work focused on supervised learning, where the goal is to look for specific objects (e.g., “FRED” flare-like events or eclipses) armed with a good understanding of the parameter space. This will allow us, for instance, to visualize the predicted classification of a supervised learner on the SOM plane, which is an effective interpretability technique (see e.g., Molnar 2019).

acknowledgement. M.K. acknowledges financial support from the Italian Space Agency (ASI) under the ASI-INAF agreement 2017-14-H.0. M.P. acknowledges financial support from the European Union’s Horizon 2020 research and innovation program under the Marie Skłodowska-Curie grant agreement no. 896248. All the authors acknowledge comments and suggestions from the referee that led to the improvement of this work.

References

- Armstrong, D. J., Kirk, J., Lam, K. W. F., et al. 2016, *MNRAS*, **456**, 2260
- Ball, N. M., & Brunner, R. J. 2010, *Int. J. Mod. Phys. D*, **19**, 1049
- Baron, D. 2019, ArXiv e-prints [arXiv:1904.07248]
- Baron, D., & Poznanski, D. 2017, *MNRAS*, **465**, 4530
- Bien, J., & Tibshirani, R. 2011, *Ann. Appl. Stat.*, **2403**
- Boirin, L., Méndez, M., Díaz Trigo, M., Parmar, A. N., & Kaastra, J. S. 2005, *A&A*, **436**, 195
- Bonnet-Bidaud, J. M., & Haberl, F. 2004, *Mem. Soc. Astron. It.*, **75**, 484
- Bozzo, E., Falanga, M., Papitto, A., et al. 2007, *A&A*, **476**, 301
- Brett, D. R., West, R. G., & Wheatley, P. J. 2004, *MNRAS*, **353**, 369
- Carpano, S., & Jin, C. 2018, *MNRAS*, **477**, 3178
- Carpano, S., Altieri, B., King, A. R., Nucita, A., & Leisy, P. 2008, *A&A*, **480**, 807
- De Luca, A., Stelzer, B., Burgasser, A. J., et al. 2020, *A&A*, **634**, L13
- De Luca, A., Salvaterra, R., Belfiore, A., et al. 2021, *A&A*, **650**, A167
- Faisst, A. L., Prakash, A., Capak, P. L., & Lee, B. 2019, *ApJ*, **881**, L9
- Fustes, D., Manteiga, M., Dafonte, C., et al. 2013, *A&A*, **559**, A7
- Geach, J. E. 2012, *MNRAS*, **419**, 2633
- Giles, D. K., & Walkowicz, L. 2020, *MNRAS*, **499**, 524
- Goad, M. R., Roberts, T. P., Reeves, J. N., & Uttley, P. 2006, *MNRAS*, **365**, 191
- Israel, G. L., Belfiore, A., Stella, L., et al. 2017a, *Science*, **355**, 817
- Israel, G. L., Papitto, A., Esposito, P., et al. 2017b, *MNRAS*, **466**, L48
- Jansen, F., Lumb, D., Altieri, B., et al. 2001, *A&A*, **365**, L1
- Jin, C., Ponti, G., Haberl, F., Smith, R., & Valencic, L. 2018, *MNRAS*, **477**, 3480
- Kohonen, T. 1982, *Biol. Cybernet.*, **43**, 59
- Kohonen, T. 2001, *Learning Vector Quantization* (Berlin, Heidelberg: Springer Berlin Heidelberg), 245
- Lin, D., Irwin, J. A., Webb, N. A., Barret, D., & Remillard, R. A. 2013, *ApJ*, **779**, 149
- Mainetti, D., Campana, S., & Colpi, M. 2016, *A&A*, **592**, A41
- Marelli, M., Tiengo, A., De Luca, A., et al. 2017, *ApJ*, **851**, L27
- Masters, D., Capak, P., Stern, D., et al. 2015, *ApJ*, **813**, 53
- Meusinger, H., & Balafkan, N. 2014, *A&A*, **568**, A114
- Molnar, C. 2019, *Interpretable Machine Learning* (<https://christophm.github.io/>)
- Moosavi, V., Packmann, S., & Vallés, I. 2014, SOMPY: A Python Library for Self Organizing Map (SOM). Available: <https://github.com/sevamoo/SOMPY>
- Naim, A., Ratnatunga, K. U., & Griffiths, R. E. 1997, *ApJS*, **111**, 357
- Norton, A. J., & Mukai, K. 2007, *A&A*, **472**, 225
- Novara, G., Esposito, P., Tiengo, A., et al. 2020, *ApJ*, **898**, 37
- Oliveira, A. S., Rodrigues, C. V., Cieslinski, D., et al. 2017, *AJ*, **153**, 144
- Pang, X., Li, Y., Tang, S.-Y., Pasquato, M., & Kouwenhoven, M. B. N. 2020, *ApJ*, **900**, L4
- Pasquato, M., & Chung, C. 2019, *MNRAS*, **490**, 3392
- Pietsch, W., Haberl, F., & Vogler, A. 2003, *A&A*, **402**, 457
- Protopapas, P., Giammarco, J. M., Faccioli, L., et al. 2006, *MNRAS*, **369**, 677
- Pye, J. P., Rosen, S., Fyfe, D., & Schröder, A. C. 2015, *A&A*, **581**, A28
- Qiu, Y., Soria, R., Wang, S., et al. 2019, *ApJ*, **877**, 57
- Rajaniemi, H. J., & Mähönen, P. 2002, *ApJ*, **566**, 202
- Ramsay, G., & Cropper, M. 2007, *MNRAS*, **379**, 1209
- Ramsay, G., Bridge, C. M., Cropper, M., et al. 2004, *MNRAS*, **354**, 773
- Read, A. M., Saxton, R. D., & Esquej, P. 2011, *ATel*, **3811**, 1
- Reis, I., Poznanski, D., Baron, D., Zasowski, G., & Shahaf, S. 2018, *MNRAS*, **476**, 2117
- Reis, I., Rotman, M., Poznanski, D., Prochaska, J. X., & Wolf, L. 2021, *Astron. Comput.*, **34**, 100437
- Ribeiro, T., Lopes de Oliveira, R., & Borges, B. W. 2014, *ApJ*, **792**, 20
- Robba, A., Pinto, C., Walton, D. J., et al. 2021, *A&A*, **652**, A118
- Rodríguez Castillo, G. A., Israel, G. L., Belfiore, A., et al. 2020, *ApJ*, **895**, 60
- Sathyaprakash, R., Roberts, T. P., Walton, D. J., et al. 2019, *MNRAS*, **488**, L35
- Strüder, L., Briel, U., Dennerl, K., et al. 2001, *A&A*, **365**, L18
- Tranin, H., Godet, O., Webb, N., & Primorac, D. 2022, *A&A*, **657**, A138
- Turner, M. J. L., Abbey, A., Arnaud, M., et al. 2001, *A&A*, **365**, L27
- Vasilopoulos, G., Haberl, F., Brightman, M., et al. 2021, in *Am. Astron. Soc. Meeting Abstracts*, **53**, 225.02
- Vogel, J., Byckling, K., Schwöpe, A., et al. 2008, *A&A*, **485**, 787
- Younes, G., Boirin, L., & Sabra, B. 2009, *A&A*, **502**, 905
- Yuan, Z., Chang, J., Banerjee, P., et al. 2018, *ApJ*, **863**, 26
- Yuan, Z., Myeong, G. C., Beers, T. C., et al. 2020, *ApJ*, **891**, 39

Appendix A: Data selection, normalization, and correlation

Appendix A.1: Data normalization

The distribution of the values of each one of the 31 parameters we selected is presented in Fig. A.3. Most of the parameters are distributed with very narrow cores centered on zero and long tails either in both positive and negative directions or in the positive direction only. For some parameters, such as kurtosis and skewness, their distribution is highly asymmetric. In such cases histograms were binned in a symmetric logarithmic scale centered on zero and a linear scale around zero in order to have a clearer idea of their distribution. The parameter groups CDF_TFRAC_* and CDF_RFRAC_* span between zero and one, and their distribution does not have such a narrow core compared to the tail. They were plotted with linear time bins. All the parameters have exactly the same number of values. This is necessary for the SOM algorithm to work, that is, each detection in the parameter space has all its 31 coordinates defined.

All three p-values (histograms 1, 2, and 4 in Fig. A.3) were recalculated with higher precision and converted into one-sided sigma values in such a way that higher sigma corresponds to a poorer fit of the model. In this way, sigma is a proxy for variability against the three models. Another reason to transform p-values is that the vast majority of them are concentrated towards zero and one, and are hardly distinguishable in a linear scale; however they correspond to very different levels of goodness of fit to their models. Even with this higher precision recalculation, many values are capped at $\sim 37 \sigma$ and so they fall in the final bin.

Parameters in the group CDF_RFRAC_* show spikes on top of a smooth distribution. The reason for this is that they are defined as percentage of time the source spends in a certain state, and as there is always a finite number of time bins, this introduces a form of discretization.

The SOM algorithm typically relies on Euclidean distance in parameter space to quantify the dissimilarity between data points. To avoid over- or under-weighting parameters based on their units of measure, their values have to be normalized on a similar scale in order to give each of them similar influence in guiding the SOM training process.

Simply normalizing to a fixed range by linearly rescaling has several drawbacks in the presence of long tails and/or outliers. This prevents us from simply assigning the minimum and the maximum of each variable for instance to $[0, 1]$, as most values would end up concentrated around zero. Similar concerns also prevent us from normalizing by setting the sample standard deviation to unity.

We quantify the importance of parameter distribution core, tail and outliers by taking the ratio of the standard deviation to median absolute deviation, r_{nrw} (third column in Table A.1). The median absolute deviation is robust to long tails and outliers, while the standard deviation is not, and so large values of r_{nrw} imply the presence of long tails and/or outliers. About half of parameters have $r_{nrw} \gg 1$ with skewness and kurtosis having $r_{nrw} \sim 10^7$ and $r_{nrw} \sim 10^{10}$. The other half have $r_{nrw} > 1$, $r_{nrw} \gtrsim 1$ or $r_{nrw} \lesssim 1$.

To solve this issue we relied on a power transform of the affected variables. A power-law exponent p_{nrw} was defined as $p_{nrw} = \frac{1}{\log(10 \times r_{nrw})}$. The idea is that p_{nrw} decreases slowly from 1 with increasing r_{nrw} and when $r_{nrw} = 1$, $p_{nrw} = 1$ (p_{nrw} was set

to 1 also when $r_{nrw} \lesssim 1$). Therefore for all parameters $p_{nrw} \leq 1$ (and positive).

For each set of parameter values, the distance between two successive values Δx was transformed as $(\Delta x)^{p_{nrw}}$. This has the effect of increasing the distance between values which are too close and decreasing the distance between values which are too distant. Also, the effect of increasing or decreasing distance is larger (lower p_{nrw}) if the parameter has higher r_{nrw} . Crudely speaking, this process stretches the cores and squeezes the tails with an intensity depending on the initial distribution. This preserves the ordering (ranking) of values. Finally, all transformed parameters were rescaled linearly to the range $[0, 1]$.

The normalized distribution of each parameter is shown in Fig. A.4. All histograms are binned linearly between zero and one. The normalized values of the parameters are filling up the same range of $[0, 1]$, and are much more evenly distributed than the original values, while maintaining the general shape of the original distribution. Parameters with $r_{nrw} \lesssim 1$ ($p_{nrw} = 1$) have an identical distribution before and after normalization; parameters with $r_{nrw} > 1$ ($p_{nrw} \lesssim 1$) have a similar distribution in the two cases; the distribution of parameters with $r_{nrw} \gg 1$ ($p_{nrw} < 1$) is the most affected by normalization (in the sense of core stretching and tail squeezing). The extreme values (i.e., potential outliers) are still at the edges of their distribution, but are not too far from the majority of values.

Appendix A.2: Data correlation

As can be seen from histograms (Figs. A.3, A.4) several parameters appear to share a similar distribution. We quantified their pairwise correlations by calculating the "Pearson r" correlation coefficient, which measures the linear correlation between parameters.

The correlation matrix for our 31 normalized parameters is shown in Fig. A.1. As the distribution of parameter values is featured, "Kendall rank τ " and "Spearman rank ρ " correlation coefficients²⁷ were checked. They are similar to Pearson r coefficients.

As can be seen from Fig. A.1 there are many parameters with a large $|r| > 0.5$ association between each other. As expected some parameters form groups with high (anti)correlation such as the three UB_CDF_TFRAC_ABO*S parameters, the two UB_LC500_QU_PAR*, both standard deviations (UB_LC500_STDEV and UB_LC500_MEDABSDEV), the five UB_CDF_RASYM_MID* and others.

The Pearson r correlation coefficient cannot accurately describe complicated nonlinear dependencies. Some of the more obvious examples are shown in Fig. A.2. In the upper panel is a scatter plot of linear coefficient for linear and quadratic model (UB_LC500_LI_PAR2 and UB_LC500_QU_PAR2). Their correlation coefficient is almost zero, but there is a clear X-shaped dependence between these two parameters (the center corresponds to zero values of the original parameters). Two diagonal correlations have very similar absolute values but opposite signs, and cancel each other out producing a global coefficient close to zero. In the lower panel is a scatter plot between skewness and kurtosis. Their correlation coefficient is

²⁷ Rank correlation coefficients compare two distributions based on the ordering of their values (from smallest to largest), not on the values themselves. As long as ordering is the same, the distribution of values is not important.

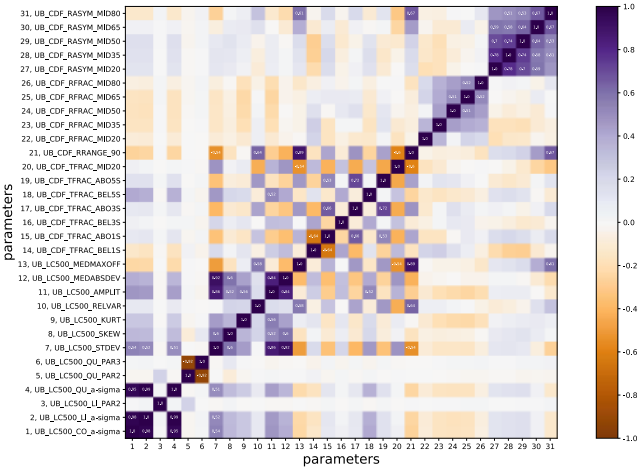


Fig. A.1. Pearson r correlation matrix of all $m=31$ normalized parameter values. Positive (purple) values correspond to positive correlation while negative (brown) values to negative correlation. Correlation coefficients with absolute value less than 0.5 are not explicitly written.

is more stable and faster with fewer parameters, and how each parameter affects the learning process is easier to interpret.

The redundant parameters are typically those with high correlation to a given parameter. In this case, the correlation between parameters is highly complicated and it is not straightforward to exclude them based on a simple criterion. In some cases, high correlation is the result of very high positive correlation and a small negative correlation. If only one parameter were to be chosen, information would be lost from the negatively correlated part. The SOM algorithm used in this work is relatively fast with this data set and there is no particular need to increase its speed efficiency by excluding parameters.

Redundancy to a given parameter increases the dimensionality of the parameter space but does not contribute significantly to the information that the given parameter carries. As SOM is a dimensionality-reduction algorithm, it takes care of this naturally. The issue is that if there are more parameters in a group of correlated parameters, then the influence of the information from that group on the SOM learning process is increased. This is because the SOM "sees" the data in parameter space based on Euclidean distance. Therefore, this effect is approximately proportional to the square root of the number of redundant parameters, which is why it is not drastically important. Based on all of the above, we decided to train the SOM with all the $m=31$ normalized parameters.

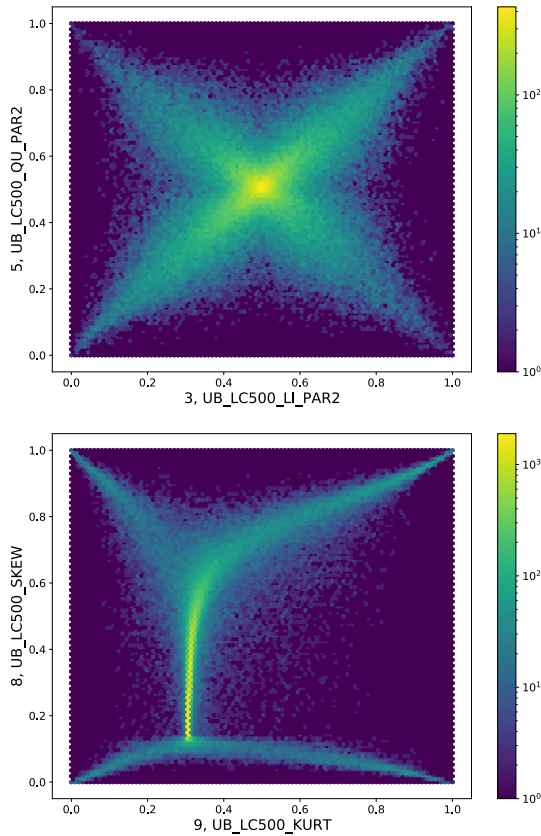


Fig. A.2. Two scatter plots illustrating nonlinear dependencies between parameters. As there are $n=128\,925$ detections, the scatter plot is presented as a density plot. The values covered by the color bar, in logarithmic scale, present the number of detections in a given discrete area of the plot. Further explanation of the parameter correlations is given in the text.

≈ 0.35 , but there is a clear dependence, similarly to the previous case, but with several groups instead of a symmetric "X."

It is common to exclude redundant parameters in the machine learning process for several reasons, such as: the algorithm

Table A.1. Selected parameters.

Parameter designation	Parameter description	Narrowness
UB_LC500_CO_PVAL ^a	Tail probability for a constant model.	3.77
UB_LC500_LI_PVAL ^a	Tail probability for a linear model.	3.71
UB_LC500_LI_PAR2	Best-fit value of parameter 2 (the linear coefficient) for a linear model.	85.5
UB_LC500_QU_PVAL ^a	Tail probability for a quadratic model.	3.70
UB_LC500_QU_PAR2	Best-fit value of parameter 2 (the linear coefficient) for a quadratic model.	58.9
UB_LC500_QU_PAR3	Best-fit value of parameter 3 (the quadratic coefficient) for a quadratic model.	118
UB_LC500_STDEV	Weighted standard deviation on the distribution of the rate.	24.7
UB_LC500_SKEW	Weighted skewness on the distribution of the rate.	1.98×10^7
UB_LC500_KURT	Weighted reduced kurtosis on the distribution of the rate.	3.68×10^{10}
UB_LC500_RELVAR	Relative variance (variance/average) on the distribution of the rate.	1.16×10^3
UB_LC500_AMPLIT	Amplitude of rate excursion ((max(rate)-min(rate))/2).	17.7
UB_LC500_MEDABSDEV	Median absolute deviation of the distribution of the rate.	24.6
UB_LC500_MEDMAXOFF	Maximum relative offset from the median (max(rate-median)/median) of the distribution of the rate.	37.2
UB_CDF_TFRAC_BEL1S	Fraction of time spent more than 1 sigma below the average rate.	0.89
UB_CDF_TFRAC_ABO1S	Fraction of time spent more than 1 sigma above the average rate.	0.88
UB_CDF_TFRAC_BEL3S	Fraction of time spent more than 3 sigma below the average rate.	1.01
UB_CDF_TFRAC_ABO3S	Fraction of time spent more than 3 sigma above the average rate.	0.93
UB_CDF_TFRAC_BEL5S	Fraction of time spent more than 5 sigma below the average rate.	0.97
UB_CDF_TFRAC_ABO5S	Fraction of time spent more than 5 sigma above the average rate.	0.90
UB_CDF_TFRAC_MID20	Fraction of time spent within 10 percent of the median rate.	1.62
UB_CDF_RRANGE_90	Width of the range of rates in which the source spends 90 percent of its time.	18.6
UB_CDF_RFRAC_MID20	Fraction of UB_CDF_RRANGE_90 in which the source spends 20 percent of its time.	1.27
UB_CDF_RFRAC_MID35	... 35 percent of its time.	1.23
UB_CDF_RFRAC_MID50	... 50 percent of its time.	1.04
UB_CDF_RFRAC_MID65	... 65 percent of its time.	1.08
UB_CDF_RFRAC_MID80	... 80 percent of its time.	1.06
UB_CDF_RASYM_MID20	Asymmetry of the rate distribution in which the source spends 20 percent of its time.	46.0
UB_CDF_RASYM_MID35	... 35 percent of its time.	41.6
UB_CDF_RASYM_MID50	... 50 percent of its time.	70.4
UB_CDF_RASYM_MID65	... 65 percent of its time.	73.7
UB_CDF_RASYM_MID80	... 80 percent of its time.	72.5

Notes. Parameters used in training. All parameters were derived from light curves with 500 s uniform time bins. First column is a designation of the parameter in the WP2 catalog. Second column is the description of the parameter. Third column is the ratio of standard deviation to median absolute deviation.

^(a)Tail probabilities (p-values) were recalculated with higher precision and transformed into one-sided sigma values such that higher sigma corresponds to a poorer model fit.

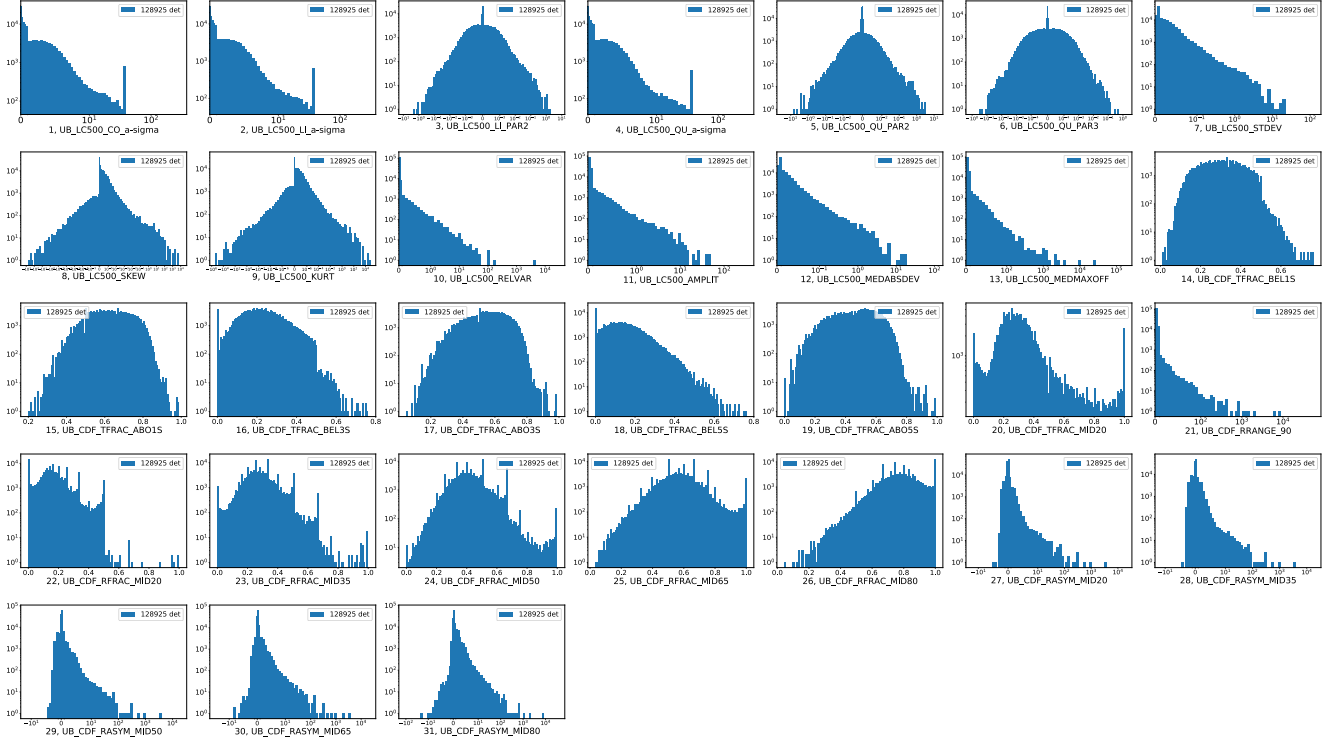


Fig. A.3. Histograms of the $m = 31$ parameter distributions. Each parameter is numbered corresponding to the order in Table A.1. The number of detections is the same for each parameter and is shown in the legend in every histogram. Histogram binning adaptively switches between linear (around zero) and logarithmic (in the distribution tails) in most cases to best present the distribution of each parameter. Number labels were omitted from ticks near zero for clarity. The vertical axes are in logarithmic scale.

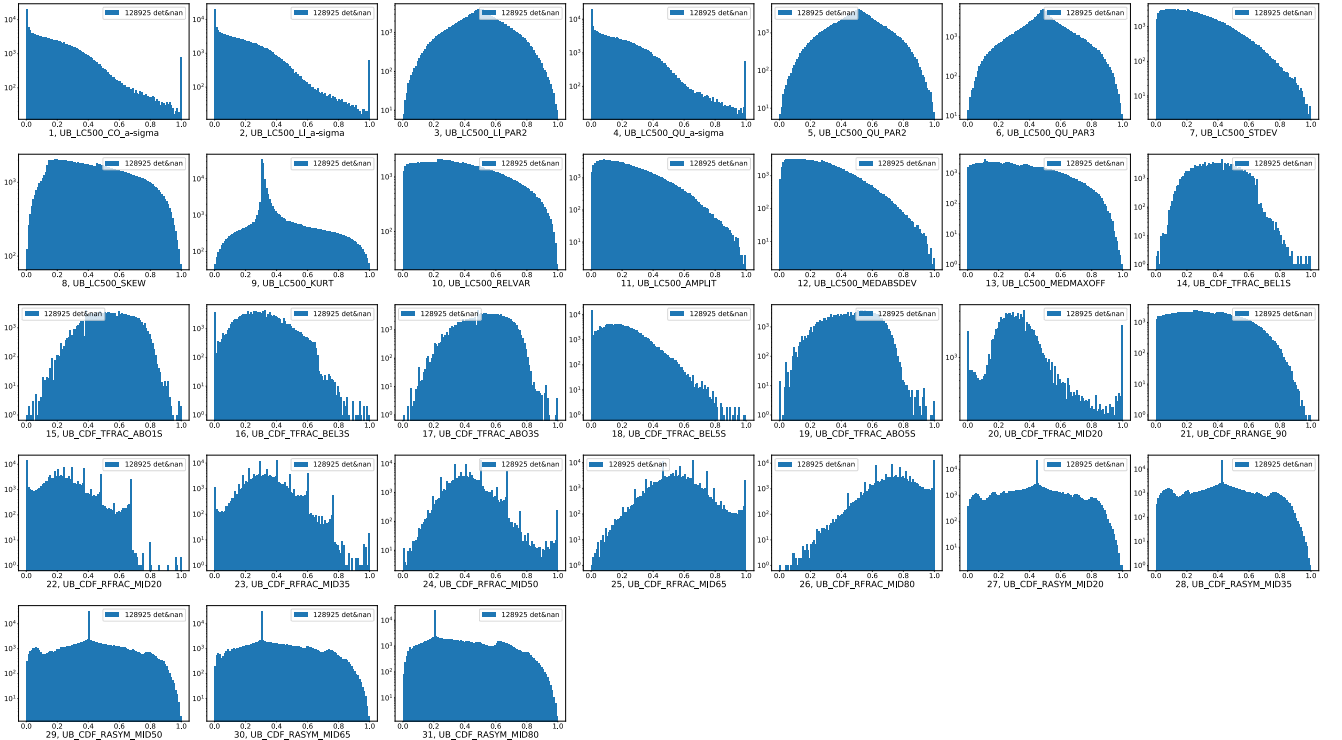


Fig. A.4. Histograms of $m = 31$ normalized parameter distributions. Each parameter is numbered corresponding to the order in Table A.1 and Fig. A.3. The number of detections is the same for each parameter and is shown in the legend in every histogram. All histograms are binned in linear scale ranging from zero to one. The vertical axes are in logarithmic scale, as in Fig. A.3.

Appendix B: Eclipsing sources from literature

Table B.1 contains eclipsing-like sources from the literature mentioned in Sect. 4.3.3.

Table B.1. Eclipsing-like sources from the literature.

Name	Reference	Obs. id	Src. num. ^a	Pixel
RX J0047174-251811	1	0110900101	7	45,28
EP Dra	2	0109464501	1	45,37
V* UY vol	3	0560180701	1	45,32
		0605560401	1	45,32
		0651690101	1	45,32
		0651690101	1	15,40
4U 1323-62	4	0109100201	1	45,40
V2301 Oph	5	0109465301	1	45,38
4U 2129+47	6	0502460101	1	45,31
		0502460201	1	45,31
		0502460301	1	45,31
		0502460401	1	45,31
2XMMp J131223.4+173659	7	0200000101	1	45,36
XTE J1710-281	8	0206990401	1	45,33
NGC 4736 ULX1	9	0094360601	1 ^b	45,32
		0094360601	2 ^b	45,31
CAL 87	10	0153250101	1	45,33
AX J1745.6-2901	11	0402430301	5	45,33
		0402430401	5	45,32
		0402430701	5	45,32
		0505670101	4	45,32
ULX CG X-1	12	0111240101	1	45,33

Notes. List of eclipsing-like sources randomly selected from the literature observed by *XMM-Newton*. We report the name, reference, observation and source number, and pixel coordinates in the BMU map (Fig. 5). Several detections may belong to the same source.

^(a)Source number refers to 3XMM-DR4 notation. ^(b)Here the same source is detected as two different point-like sources in 3XMM-DR4.

References. (1) Pietsch et al. (2003); (2) Ramsay et al. (2004); (3) Bonnet-Bidaud & Haberl (2004); (4) Boirin et al. (2005); (5) Ramsay & Cropper (2007); (6) Bozzo et al. (2007); (7) Vogel et al. (2008); (8) Younes et al. (2009); (9) Lin et al. (2013); (10) Ribeiro et al. (2014); (11) Jin et al. (2018); (12) Qiu et al. (2019).

Classification of blazar candidates of uncertain type from the Fermi LAT 8-yr source catalogue with an artificial neural network

M. Kovačević,¹★ G. Chiaro,² S. Cutini¹ and G. Tosti³

¹INFN – Istituto Nazionale di Fisica Nucleare Sez. Perugia, I-06123 Perugia, Italy

²INAF – Istituto di Astrofisica Spaziale e Fisica Cosmica, I-20133 Milano, Italy

³Dipartimento di Fisica e Geologia, Univ. degli Studi di Perugia, I-06123 Perugia, Italy

Accepted 2020 February 3. Received 2020 February 2; in original form 2020 January 7

ABSTRACT

The *Fermi* Large Area Telescope (LAT) has detected more than 5000 γ -ray sources in its first 8 yr of operation. More than 3000 of them are blazars. About 60 per cent of the *Fermi*-LAT blazars are classified as BL Lacertae objects (BL Lacs) or Flat Spectrum Radio Quasars (FSRQs), while the rest remain of uncertain type. The goal of this study was to classify those blazars of uncertain type, using a supervised machine learning method based on an artificial neural network, by comparing their properties to those of known γ -ray sources. Probabilities for each of 1329 uncertain blazars to be a BL Lac or FSRQ are obtained. Using 90 per cent precision metric, 801 can be classified as BL Lacs and 406 as FSRQs while 122 still remain unclassified. This approach is of interest because it gives a fast preliminary classification of uncertain blazars. We also explored how different selections of training and testing samples affect the classification and discuss the meaning of network outputs.

Key words: methods: statistical – galaxies: active – BL Lacertae objects: general – gamma-rays: galaxies.

1 INTRODUCTION

Blazars are active galactic nuclei (AGNs) with a radio-loud behaviour and a relativistic jet pointing towards the observer (Abdo et al. 2010b; Massaro et al. 2015). These sources are divided into two main classes: BL Lacertae objects (BL Lacs) and Flat Spectrum Radio Quasars (FSRQs), which show very different optical spectra. FSRQs have strong, broad emission lines, while BL Lacs show mostly weak or no emission lines. Compact radio cores, flat radio spectra, high brightness temperatures, superluminal motion, high polarization, and strong and rapid variability are also commonly found in BL Lacs and FSRQs. Blazars emit variable, non-thermal radiation across the whole electromagnetic spectrum, featuring components forming two broad humps in a νf_ν representation, where ν is the observing frequency and f_ν the spectral energy density. The low-energy hump is attributed to synchrotron radiation, and the high-energy one is usually thought to be due to inverse Compton radiation (Ghisellini 2013).

The *Fermi* Large Area Telescope (LAT) has been continuously observing the γ -ray sky since 2008 August in the 100 MeV–300 GeV energy range. The latest *Fermi*-LAT catalogue is the LAT 8-yr Source Catalogue 4FGL (The *Fermi*-LAT collaboration 2019a), which lists 5066 γ -ray sources, about 2000 more than the previous 3FGL catalogue (Acero et al. 2015), which was based

on four years of data. Out of the 5066 4FGL sources, 3131 are blazars: 1116 BL Lacs, 686 FSRQs, and 1329 blazar candidates of uncertain type (BCUs). If we compare the 4FGL with previous LAT catalogues we can see the significant increase of the number of unclassified sources. The percentage of BCUs increased from 14 per cent in 1FGL (Abdo et al. 2010a) to 42 per cent in 4FGL. In Table 1 we show the growth of the number of blazar sources detected by *Fermi*-LAT. The increased difficulty to have sufficiently extensive optical observation campaigns for rigorous classification of BCUs emphasizes the importance of finding alternative ways to classify blazars.

Since more than 1300 γ -ray sources in the 4FGL remain unassociated with any plausible source class, the full nature of almost half the sources in the 4FGL catalogue remains undetermined. Classifying BCUs remains a strategic goal not only to enlarge the number of detected BL Lacs and FSRQs but also to confirm the extragalactic background light absorption of high energy photons that will be strategic in the next Cherenkov Telescope Array (CTA) extragalactic survey, which will investigate the physics of high-energy emission from relativistic AGN jets. For this reason, studies and methods for hunting and characterizing BCUs are very useful for the scientific community. When optical spectra or multiwavelength information needed for a rigorous classification are not available, a statistical approach to the problem, including machine learning, can be very useful for classification of BCUs.

Machine learning is a method of recognizing patterns within data in order to achieve goals such as classification. In a type of

★ E-mail: milos.kovacevic@pg.infn.it

Table 1. Blazar class distribution in *Fermi*-LAT catalogues.

Class	1FGL	2FGL	3FGL	4FGL
BL Lac	295 (44 per cent)	436 (41 per cent)	660 (38 per cent)	1116 (36 per cent)
FSRQ	278 (42 per cent)	370 (35 per cent)	484 (28 per cent)	686 (22 per cent)
BCU	92 (14 per cent)	257 (24 per cent)	573 (34 per cent)	1329 (42 per cent)
Total	665	1063	1717	3131

machine learning called *supervised* machine learning, an algorithm classifies unknown objects by comparing their characteristics with characteristics of known objects.

Machine learning has been applied by Ackermann et al. (2012), Lee et al. (2012), Hassan et al. (2013), Doert & Errando (2014), Chiaro et al. (2016), Einecke (2016), Mirabal et al. (2016), Saz Parkinson et al. (2016), Yi et al. (2017), Lefaucheur & Pita (2017), Salvetti et al. (2017), Kang et al. (2019), Kovačević et al. (2019), Kaur et al. (2019) and other studies in order to classify unassociated sources and/or BCUs from the LAT catalogues. Some of the most commonly used machine learning techniques in the above cited works, and astrophysics in general, include: Random Forest (Breiman 2001), Artificial Neural Network (ANN) (Bishop 1995), Support Vector Machines (Cortes & Vapnik 1995; Vapnik 1995), and Boosted Decision Trees (Friedman, Hastie & Tibshirani 2000).

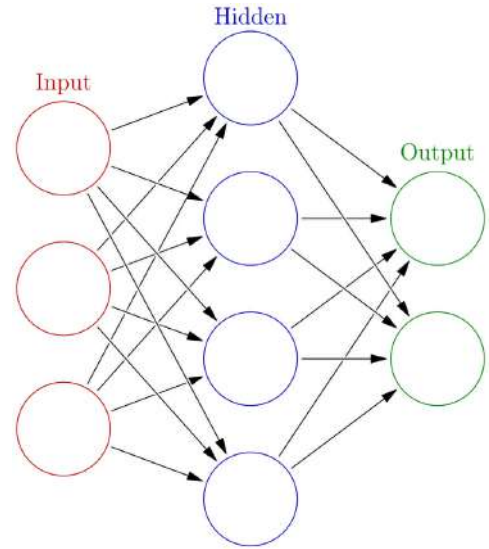
Following Chiaro et al. (2016), Salvetti et al. (2017), Kovačević et al. (2019) (hereinafter *C16*, *S17*, *K19*) in which ANN was used to classify BCUs and BCU candidates from 3FGL catalogue, here we used ANN in order to classify BCUs from the 4FGL catalogue. For input parameters to the network we used γ -ray parameters present in the 4FGL catalogue¹ which is publicly available. For ANN we used TENSORFLOW² (Abadi et al. 2016) which was implemented in PYTHON.³

The paper is organized as follows: in Section 2 we present the ANN method used. In Section 3 we discuss the network outputs and caveats. In Sections 4 and 5 we present and validate the results.

2 THE ANN METHOD

The ANN technique is modelled by the way biological neural systems in the brain work. The schematic view of a simple ANN is presented in Fig. 1. The information enters the input layer and is sent to neurons in hidden layer(s) where it is processed. Finally it exits the output layer producing a desired outcome (classification of objects, for example).

Basically, ANN is a mathematical function over an N -dimensional space, where N is the number of input parameters to the network. Input parameters are values which describe an object (blazars in our case). ANN produces a likelihood for the object to belong to a certain class (when ANN is used for classification). The network is trained on already classified objects (known BL Lacs and FSRQs in our case). Training the network involves adjusting the very large number of ANN parameters in order to find a function which best separates objects belonging to different classes. The network is then tested on classified objects which were not used in training in order to evaluate the trained network. After that the

**Figure 1.** Schematic view of a simple feedforward ANN with one hidden layer. Circles represent neurons where information is processed and arrows represent travel direction of information through the network.

trained network can be used to classify unknown objects (BCUs in our case).

More detailed information on general characteristics of ANN, and particularly ANN for classifying BCUs, is present in *C16*, *S17*, *K19*. The following method mostly follows the ones from the three cited works (particularly *K19*). Spectra and variability (obtained from the light curve) are two main features by which BL Lacs and FSRQs are distinguished in gamma-ray band (The Fermi-LAT collaboration 2019a, b). Therefore, for input parameters we used γ -ray light curves and spectra present in the 4FGL catalogue. More precisely we used eight energy-integrated fluxes corresponding to 1-yr observation periods sorted by increasing value, and time-integrated flux values in seven different energy bands. This produced a set of $N = 15$ input parameters to the network for each source.

2.1 Gamma-ray light curves

We use the γ -ray light curves with sorted flux values from lowest to highest for each source, which is in line with an Empirical cumulative distribution function. In the 3FGL catalogue, time bins had a duration of one month. This created a set of (12 months \times 4 yr) 48 sorted monthly flux values for each source, which were used in previous studies. The 4FGL catalogue contains light curves with a bin duration of 1 yr. This created a set of (1 yr \times 8 yr) eight sorted annual flux values for each source. While the light curves in the 4FGL catalogue have smaller time resolution, each flux value is obtained from a 12 times longer observational period; therefore they are more precisely determined. Consequently, there are no

¹https://fermi.gsfc.nasa.gov/ssc/data/access/lat/8yr_catalog/.

²<https://www.tensorflow.org>. TensorFlow is an open source library for machine learning. It is relatively fast, easy to use, and transparent.

³<https://www.python.org/>

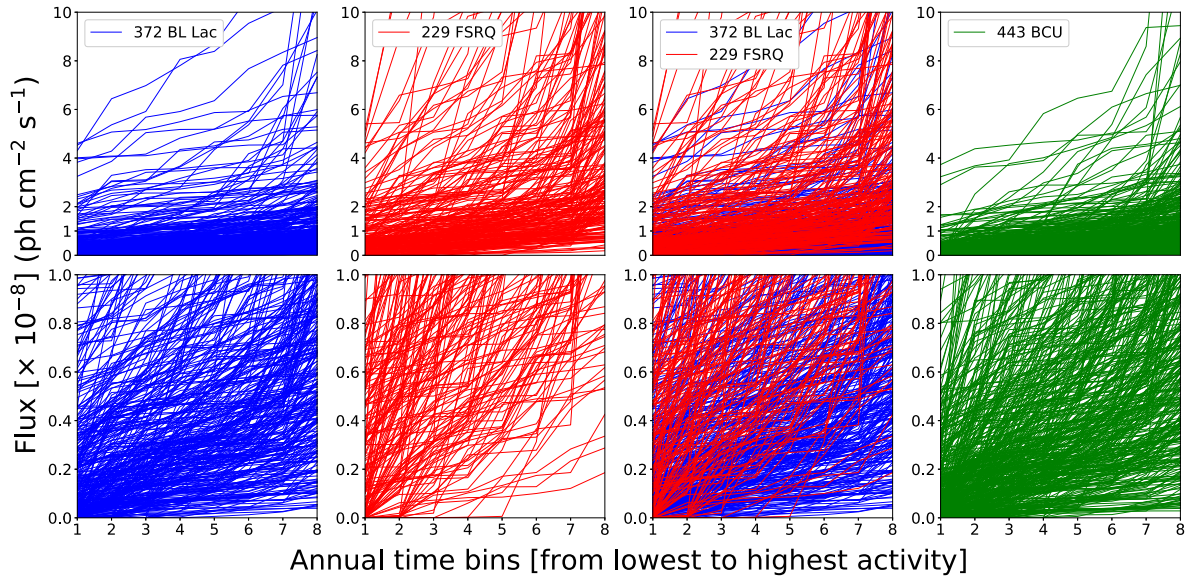


Figure 2. The annual fluxes of 4FGL blazars sorted from lowest to highest values. Each curve represents a single source. Vertical axes present annual flux values for the energy range 0.1–100 GeV. The lower and upper plots correspond to flux ranges of $0\text{--}1 \times 10^{-8} \text{ ph cm}^{-2} \text{ s}^{-1}$ and $0\text{--}10 \times 10^{-8} \text{ ph cm}^{-2} \text{ s}^{-1}$. Horizontal axes present eight annual time bins. For each source the curve is made by sorting annual flux values from lowest (1st time bin) to highest (8th time bin). Therefore, lower time bins correspond to years of lower activity while higher to years of higher activity for each source. BL Lacs are in the first plot column (left-hand panel), FSRQs in the second, both are in the third and BCUs are in the fourth (right-hand panel). For clarity only one third of sources for each class are plotted.

undetermined fluxes with only upper limits in the 4FGL light curves as was the case with the 3FGL light curves. Also, the twice as long observational period allows us to better capture true characteristics of blazar light curves. Although the 4FGL also has two-month-long light curves, we choose to focus on the longer duration time bins for the reasons described above.

Sorting the flux values from lowest to highest is one way of making blazar activities comparable. The eight annual time bins corresponding to 8 yr of *Fermi*-LAT observations are random time intervals in the life of each blazar. Fluxes in the same observational time bin go into the same input node of the network, but there is no physical meaning for this. By sorting the flux values, we are directly comparing fluxes of dimmest, average, and brightest periods for each blazar and relationships between them.

The corresponding curves are presented in Fig. 2. Most of the sources occupy the range of flux values in the $0\text{--}10 \times 10^{-8} \text{ ph cm}^{-2} \text{ s}^{-1}$ interval (upper plots). In order to capture characteristics at lower flux values, the range $0\text{--}1 \times 10^{-8} \text{ ph cm}^{-2} \text{ s}^{-1}$ has been plotted separately below.

The curves contain information on average brightness, maximum annual-averaged activity, variability of sources, flaring patterns, etc. BL Lacs are on average dimmer than FSRQs in the *Fermi*-LAT energy range. Their activity tends to be more continuous over time than that of FSRQs. Quick comparison between BL Lacs and FSRQs shows several features. In the lower right part of the plots there is an area where mostly BL Lacs are found. Sources passing through this area are ones which have lower flux ($\lesssim 1 \times 10^{-8} \text{ ph cm}^{-2} \text{ s}^{-1}$) during their brightest years. Both dimmer and brighter BL Lacs, on average, have more *horizontal* curves with respect to FSRQs (of similar average flux), which reflects their more continuous emission over time and lower variability.

Similar behaviour was present with 3FGL blazars with a few differences. In general the resolution is higher (time bins smaller) for 3FGL blazars, so the differences between BL Lacs and FSRQs

are more obvious. For example, the area of lower flux values during brightest periods where mostly BL Lacs can be found is more clear for 3FGL BL Lacs ($\lesssim 2 \times 10^{-8} \text{ ph cm}^{-2} \text{ s}^{-1}$) than for 4FGL BL Lacs. 3FGL BL Lacs and especially BCUs have large numbers of time bins, during dimmer periods, with only upper limits while 4FGL BL Lacs and BCUs have relatively small but defined flux values thanks to the larger time bins of 4FGL blazars.

2.2 Gamma-ray spectra

We used spectral information in addition to light curves with sorted flux values. The 4FGL catalogue contains time-integrated fluxes in seven energy bands: 0.05–0.1, 0.1–0.3, 0.3–1, 1–3, 3–10, 10–30, 30–300 GeV (Fig. 3). This is a wider energy range (0.05–300 GeV) than the one from the 3FGL catalogue (0.1–100 GeV), which contained five energy bands. Energy bins 2, 3, 4, 5 (0.1–0.3–1–3–10 GeV) for 4FGL blazars are the same as energy bins 1, 2, 3, 4 for the 3FGL ones. Energy bin 1 (0.05–0.1 GeV) covers a new energy range in 4FGL while bins 6 and 7 (10–30–300 GeV) correspond partly to bin 5 in 3FGL (10–100 GeV). The improvement is due to longer observation period, i.e. better statistics and improvements in analysis techniques (The *Fermi*-LAT collaboration 2019a). This set of parameters contains information of average spectral index, spectral curvature, spectral breaks, hardness ratios, and other spectral information.

In the previous case fluxes were sorted in ascending order so that, among other reasons, there would be physical meaning for comparing fluxes (and relationships between them) that go into the same network input node. Here the fluxes of blazars in the same energy band go into the same network input node so the physical meaning is already there.

Quick comparison between BL Lacs and FSRQs shows several features: there is a difference in slope, i.e. average power-law index, with BL Lacs having a lower one; BL Lacs on average have higher

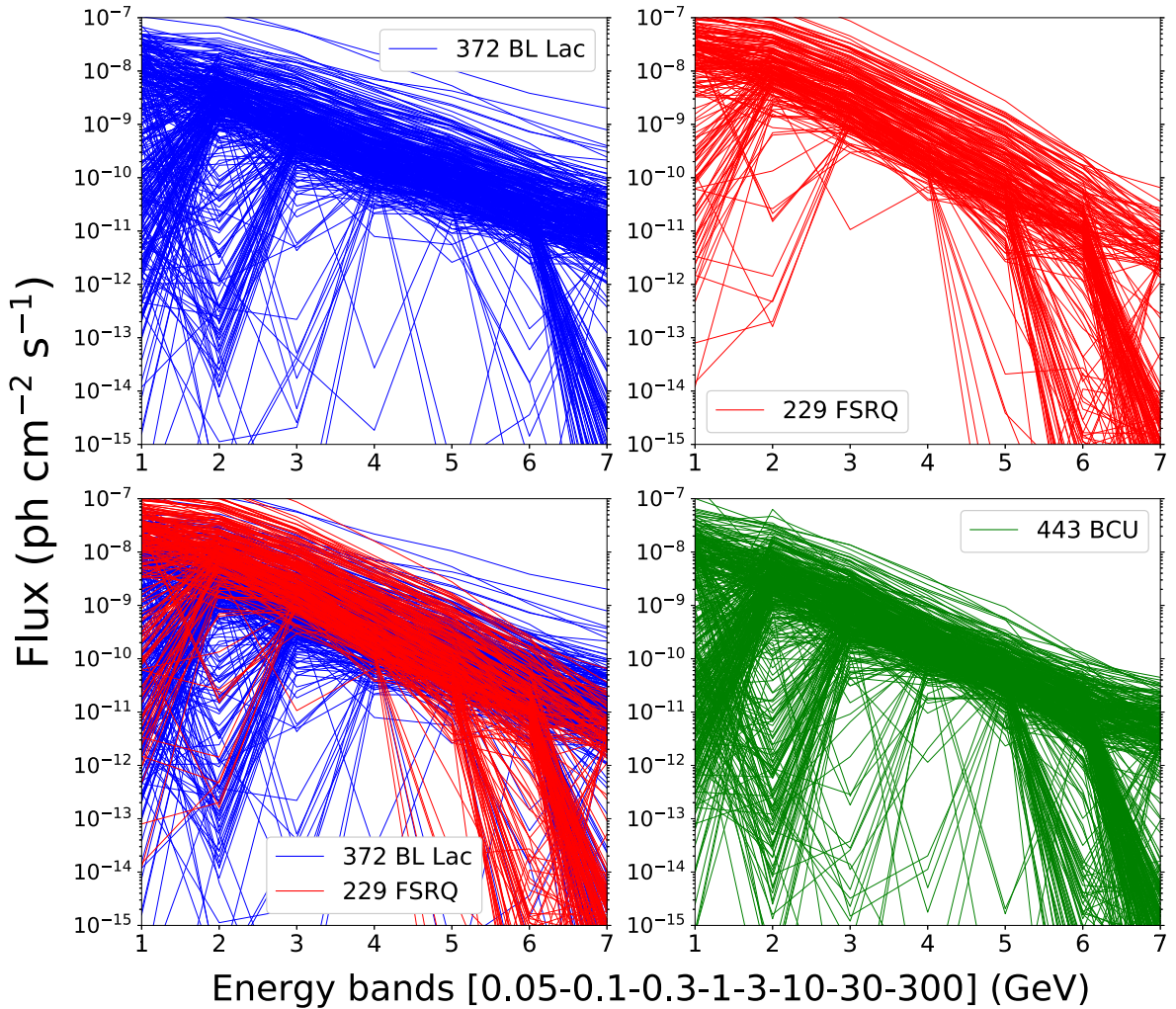


Figure 3. Time-integrated fluxes in seven energy bands: Band 1: 0.05–0.1 GeV; Band 2: 0.1–0.3 GeV; Band 3: 0.3–1 GeV; Band 4: 1–3 GeV; Band 5: 3–10 GeV; Band 6: 10–30 GeV; Band 7: 30–300 GeV. Each curve represents a single source. BL Lacs (blue) are in the top-left, FSRQs (red) in the top-right, both are in the lower left and BCUs (green) are in the lower right. For clarity only one third of sources for each class are plotted.

flux values than FSRQs in the highest energy band and vice versa for lowest; some blazars show sharp breaks in slopes at lower and/or higher energy bands, and this behaviour is mostly different for BL Lacs and FSRQs.

Comparing the spectral relationship of 4FGL BL Lacs to FSRQs with their relationship in 3FGL, it is mostly similar with several differences mainly related to spectral breaks thanks to the widening of the energy range. For example bin 1 in 4FGL (0.05–0.1 GeV) covers a new energy range and shows that some blazars peak in the energy range 0.1–0.3 GeV, which was not clear before. These blazars seem to be BL Lacs and FSRQs in similar proportion as the rest of the two classes. It also shows that some blazars (mainly BL Lacs) have a sharp decrease in flux from bin 1 to bin 2, and then sharp increase in bin 3, with the second feature also being present in 3FGL blazars.

2.3 The network

Here we briefly describe the network architecture and the training strategy. They mostly follow the architecture and training strategy

in *K19* and are explained in more detail there, particularly how overfitting was handled.

We used eight annual fluxes sorted in ascending order and seven flux values in different energy bands as input parameters. This produces a $N = 15$ dimensional parameter space in which each blazar occupies a certain position. We noted some obvious differences between BL Lacs and FSRQs when comparing their annual fluxes (Section 2.1) and spectra (Section 2.2). The purpose of the ANN algorithm is to fully determine the differences and to quantify them. It does so not just for sorted light curves and spectra separately but also taking into account relationships between them by examining the whole 15D parameter space.

The number of input neurons was 15 (8 for 8 annual sorted fluxes plus 7 for 7 fluxes in energy bands). The hidden layer had 40 neurons. The output layer had two neurons. The two output neurons produce likelihood that a source is BL Lac L_B or an FSRQ L_F such that $L_B + L_F = 1$ for each source. The larger the L_B , more likely that the source is a BL Lac and vice-versa. The Loss/Cost function used was the mean squared error. The number of ANN parameters, which are adjusted during network training, for this architecture is on the order of ~ 700 .

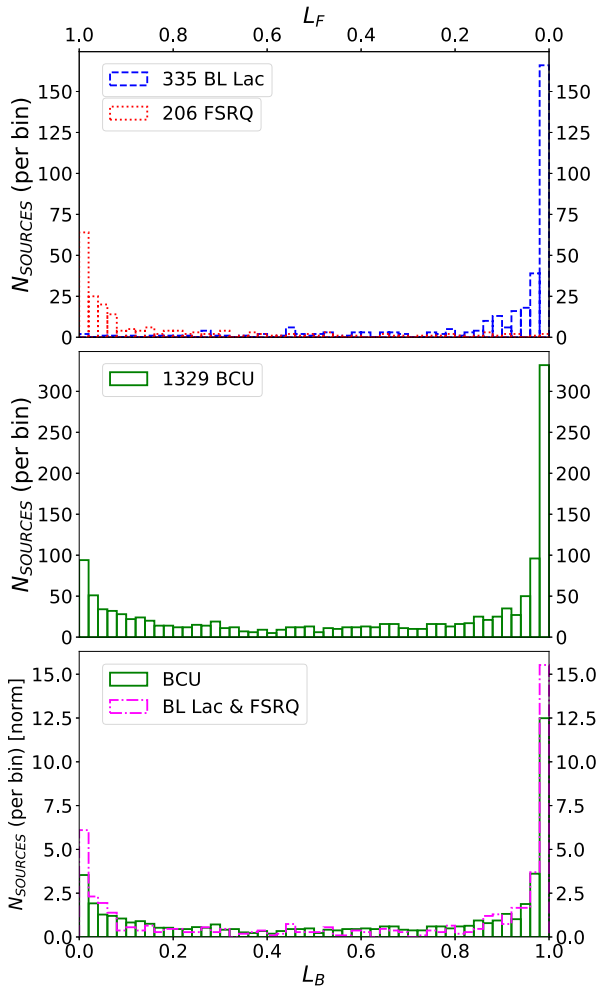


Figure 4. *Top:* Histogram of L_B for BL Lac (blue) and FSRQ (red) sources from the test sample obtained from inputting test sample source parameters into the trained network. *Middle:* Histogram of L_B for BCUs obtained from inputting BCU parameters into the trained network. *Bottom:* Histogram of BCUs (green) and sum of BL Lacs and FSRQs from the test sample (purple). Both histograms are normalized such that surface of each equals 1 (the number of sources in both is the same).

The training set consisted of 70 percent and the test set of 30 percent of the 4FGL classified blazars. The process of training the network and results from testing the network may depend on which sources were selected for the training sample and which for the testing sample. For this reason, we performed training and testing the network on 300 different combinations of training and testing samples and compared the results.

3 NETWORK OUTPUTS

3.1 Test sample sources versus BCUs

In order to better present the results of the full analysis, we show here results from a single train and test sample which is representative of the full analysis. The histogram of L_B for BL Lacs and FSRQs from the test sample is shown in the upper plot in Fig. 4. It is obtained by inputting parameters of sources from test sample (which the network never ‘saw’) into the trained network. As expected, BL Lacs concentrate towards $L_B \rightarrow 1$ while FSRQs $L_B \rightarrow 0$. The number of BL Lacs and FSRQs is 30 percent of the total sample

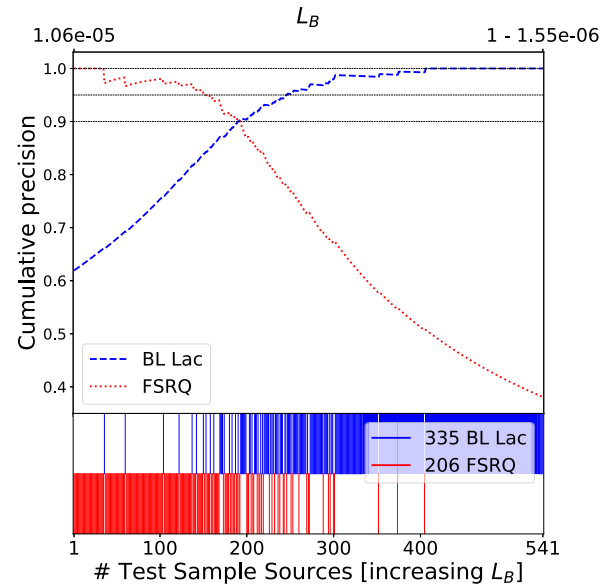


Figure 5. *Lower bar:* 335 BL Lacs (blue; vertical lines in upper half of the bar) and 206 FSRQs (red; vertical lines in lower half of the bar) from the test sample sorted by increasing L_B and at equal horizontal distance from each other. The L_B does not increase linearly in the plot. The lowest (left) and highest (right) obtained L_B are shown in the upper plot. *Upper plot:* change of cumulative precision with the L_B for BL Lacs (blue) and FSRQs (red).

and the ratio of BL Lacs to FSRQs is the same as the ratio in the total sample.

In Fig. 5 the cumulative precision versus L_B is shown. Sources from the test sample are sorted by their L_B . The two curves practically meet at 90 percent precision value, meaning that almost all sources from the test sample can be separated with 90 percent precision.

Inputting BCUs into the trained network produces a histogram (middle plot in Fig. 4) with peaks towards $L_B \rightarrow 1$ and $L_B \rightarrow 0$, imitating the distribution of BL Lacs and FSRQs from the test sample (upper plot in Fig. 4). This is expected since the large majority of BCUs are either BL Lacs or FSRQs. We can expect that BCUs with large L_B are mostly BL Lacs and vice versa.

In order to construct the same precision versus L_B relation (Fig. 5) to BCUs, the BCU distribution with respect to L_B should be as similar as possible to the combined distribution of BL Lacs and FSRQs from the test sample with respect to L_B . This is not entirely the case. In the bottom plot in Fig. 4, the histograms of BCUs and test sample sources are compared. Both histograms are normalized to the number of sources. While the peak at $L_B \rightarrow 1$ on histogram from the test sample sources and BCUs is very similar, the peak at $L_B \rightarrow 0$ is less pronounced for BCUs. In the middle range $0.2 \gtrsim L_B \gtrsim 0.8$ there are more sources with respect to both peaks for BCUs than for the test sample sources. In order to quantify these differences we use differential precision.

In Fig. 6 the differential precision, obtained from the test sample, is compared to L_B of BCUs. The lower bar is the same as in Fig. 5 and presents test sample BL Lacs and FSRQs sorted by increasing L_B . The middle plot shows the differential precision P_B . It is obtained by binning sources from the lower bar in equal bins of 20 (the last bin has 21 sources). Then, P_B is calculated for each bin as the ratio of BL Lacs to the number of sources and vice versa for FSRQs. This produces a set of P_B (a step function) for BL Lacs (blue line) and

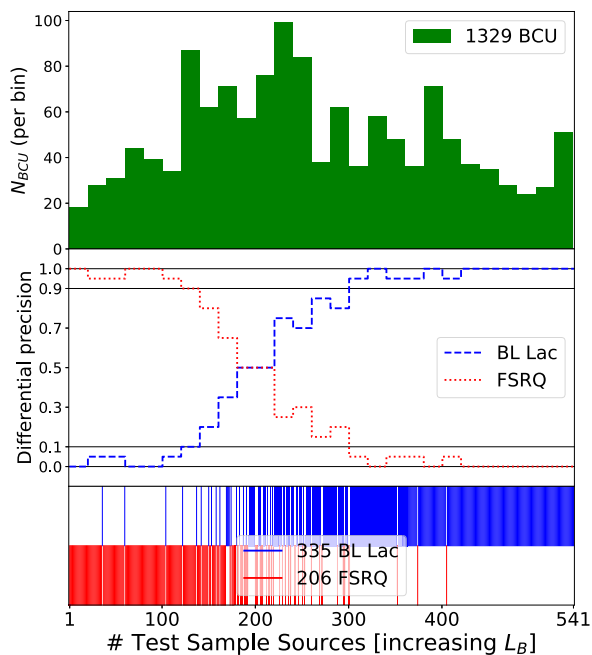


Figure 6. *Lower bar:* 335 BL Lacs (blue; vertical lines in upper half of the bar) and 206 FSRQs (red; vertical lines in lower half of the bar) from the test sample sorted by increasing L_B and at equal horizontal distance from each other. The L_B does not increase linearly. *Middle:* differential precision for each bin which contains 20 test sample sources (last bin has 21). Differential precision is ratio of BL Lacs to all sources in each bin and vice-versa for FSRQs. *Top:* number of BCUs in each bin. Each BCU is assigned to a bin such that its L_B is in between L_B of the bin edges.

FSRQs (red line) with resolution of 0.05 (1/20) such that their sum is 1 for each bin. Then the BCUs are sorted in each bin based on their L_B (upper plot) and a value of P_B (middle plot) is assigned to each BCU (upper plot). In this way P_B of BCUs can be considered as a probability that the given BCU is BL Lac or FSRQ.

Examining Fig. 6, the BCU distribution is not uniform across bins, meaning that the BCU distribution with respect to L_B is not the same as that of the combined BL Lacs and FSRQs from the test sample, which number 20 in each bin. A larger than average number of BCUs are in the range where P_B for either class is less than 90 per cent.

To overcome peculiarities of a single train and test sample and resolution lost to binning, the same process of training and testing the network was repeated for 300 different train-test samples. The final differential precision for each BCU \bar{P}_B is then calculated as the average of 300 P_B values. The value \bar{P}_B can then be considered a probability of a given BCU to be BL Lac (or $\bar{P}_F = 1 - \bar{P}_B$ to be FSRQ) taking into account fluctuations due to train-test sample selections.

Lower and upper values of the error interval are 2 values corresponding to ≈ 16 th and ≈ 84 th percentile of 300 P_B sorted from lowest to highest.⁴ The interval in between these values can then be considered 1σ errors due to differences in train-test sample selections.

We used differential precision to obtain probabilities for BCUs and classify them instead of thresholds obtained from test sample

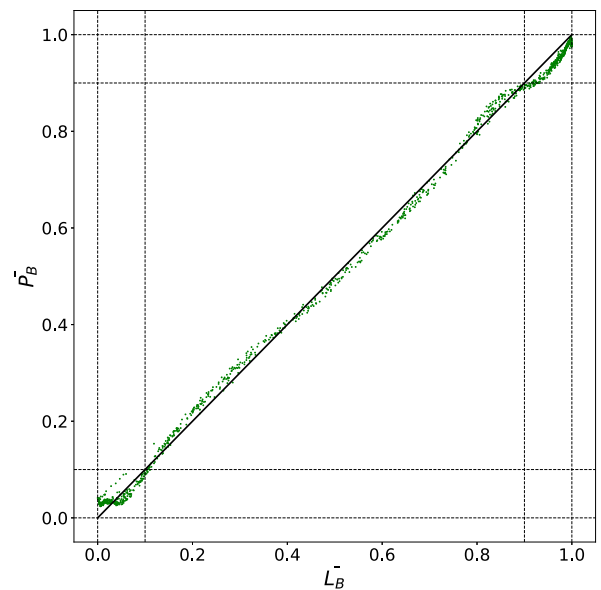


Figure 7. Average differential precision of 1329 BCUs to be BL Lac \bar{P}_B with respect to average network output to be BL Lac \bar{L}_B .

cumulative precision. Therefore we did not apply any cut to the test sample BL Lacs and FSRQs which occupy same parts of the parameter space (which makes them hardly distinguishable) in which BCUs are hardly present.

3.2 Differential precision versus Likelihood

When using mean squared error (MSE) (Gish 1990; Richard & Lippman 1991) or cross-entropy (Richard & Lippman 1991) for Loss/Cost function, the network output L_B can be considered an approximation to class probabilities. The accuracy of approximation depends on characteristics of the network architecture and training data (Richard & Lippman 1991). Since we used MSE, we also calculate \bar{L}_B as an average of 300 L_B and lower and upper limits as ≈ 16 th and ≈ 84 th percentile of 300 sorted L_B . The \bar{L}_F value is just $\bar{L}_F = 1 - \bar{L}_B$. The comparison of \bar{P}_B and \bar{L}_B is shown in Fig. 7. Both quantities for all 1329 BCUs are very close in value. There are obviously some small systematic differences, but they do not change the overall results by much. The differences are probably due to resolution lost to binning for \bar{P}_B and the above-mentioned approximation accuracy for \bar{L}_B . When experimenting with Loss/Cost functions which are not MSE or cross-entropy, the separation of test sample sources (Fig 5) and \bar{P}_B of BCUs remain similar while \bar{L}_B of test sample sources and BCUs may change significantly. In these cases \bar{L}_B cannot be considered in absolute terms as direct probability; instead it can be used in relative terms to compare sources to each other.

Showing equivalence between \bar{P}_B and \bar{L}_B in this case, from here on out we will use \bar{L}_B , since its interpretation as direct network output is more obvious and it gives more precisely defined errors (which are additionally affected by binning for \bar{P}_B).

3.3 Caveats

Here we note some caveats in the supervised learning approach. The issues have to do with how the parameters of known sources (known BL Lacs and FSRQs) compare to parameters of unknown (BL

⁴Since all 300 values have resolution of 0.05, the same values were linearly extrapolated in $[-0.025, +0.025]$ range.

Table 2. Example of seven classified BCU sources. The full list is available in electronic format. Columns: 4FGL name, Galactic latitude, Galactic longitude, \bar{L}_B , lower value of error interval \bar{L}_B^{low} , upper value of error interval \bar{L}_B^{up} .

Name	b (deg)	l (deg)	\bar{L}_B	\bar{L}_B^{low}	\bar{L}_B^{up}
4FGL J1224.7–8313	−20.397	302.096	0.039	0.031	0.048
4FGL J0804.5+0414	18.180	217.568	0.105	0.089	0.124
4FGL J0914.1–0202	30.177	233.058	0.431	0.327	0.540
4FGL J0709.0+4304	21.177	174.289	0.830	0.769	0.893
4FGL J1514.6–2044	30.895	342.539	0.920	0.898	0.942
4FGL J0538.2–3910	−30.297	244.438	0.977	0.969	0.986
4FGL J2251.7–43208	−63.607	14.738	0.997	0.995	0.999

Lacs and FSRQs among BCUs), and this is related to astronomical observations.

As a simple example, known LAT BL Lacs are 44 per cent more present in the northern Galactic hemisphere than in the southern one because larger and better optical spectroscopic data, required to identify BL Lacs so that LAT blazars can be associated to them, are more available for the Northern hemisphere (The Fermi-LAT collaboration 2019b). The *Fermi*-LAT sweeps the whole γ -ray sky continually, and there is no reason to think that the fraction of LAT BL Lacs is larger for the Northern hemisphere. If the Galactic latitude was used as a parameter, the machine learning algorithms would wrongly assume that BCUs in the Northern hemisphere are more likely to be BL Lacs.

Regarding the parameters used in this work, one of the obvious differences is that BCUs have lower flux values compared to known BL Lacs and FSRQs. This means that BCU population density in the parameter space is different than that of combined known BL Lacs and FSRQs. However this is not an issue since the ANN function is defined for each part of the parameter space. It just means that \bar{L}_B of BCUs will be differently distributed than those of combined known BL Lacs and FSRQs, but they will still be accurate. What is important is that the fraction of unknown BL Lacs and FSRQs among BCUs is similar to the fraction of known BL Lacs and FSRQs in each part of the parameter space, and that is a potential caveat.

Another important factor is the redshift/distance. The parameters in the 4FGL catalogue are observational parameters. A different redshift for the same source would change its flux values, observational time bin intervals, and energy bin intervals. It would, of course, be more accurate to take into account these effects in the analysis, but the majority of BCUs do not have measured redshift. In any case the difference in observational parameters does exist for BL Lacs and FSRQs. What is important is that unknown BL Lacs and FSRQs among BCUs have a similar redshift distribution as known BL Lacs and FSRQs. This is part of the previous requirement that the fraction of unknown BL Lacs and FSRQs among BCUs is similar to that of known BL Lacs and FSRQs throughout parameter space.

4 RESULTS

In Table 2 an example of seven classified BCU sources is shown. The complete list of 1329 BCUs is available in electronic format. The table contains Galactic coordinates, \bar{L}_B and upper and lower values of the error interval.

4.1 Classification

In Fig. 8 \bar{L}_B of 1329 BCUs is shown along with the error. The quantities \bar{L}_B and \bar{L}_F ($1 - \bar{L}_B$) are probabilities for a BCU to be a

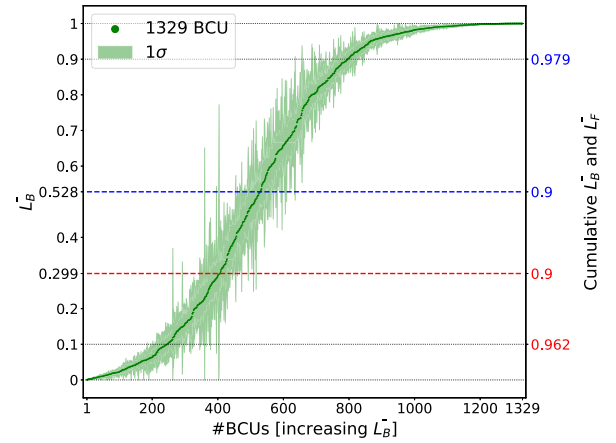


Figure 8. BL Lac probability \bar{L}_B ($1 - \bar{L}_F$) of 1329 BCUs. Each BCU is presented by a green dot. The right-hand vertical axis shows the corresponding cumulative \bar{L}_B (blue) and \bar{L}_F (red). Values where cumulative \bar{L}_B and \bar{L}_F reaches 0.9 are marked by two horizontal blue and red dashed lines. Cumulative \bar{L}_B and \bar{L}_F values where $\bar{L}_B \geq 0.9$ and $\bar{L}_F \geq 0.9$ (high probable candidates) are also shown. The light green area corresponds to 1σ error due to differences in train-test sample selections.

BL Lac or a FSRQ. In order to present results as number of sources classified by precision metric, cumulative \bar{L}_B (\bar{L}_{Bc}) and \bar{L}_F (\bar{L}_{Fc}) are calculated as average \bar{L}_B of all BCUs which have the same or higher \bar{L}_B and vice-versa for cumulative \bar{L}_F . Cumulative values are shown on the right-hand vertical axis in Fig. 8.

Selecting BL Lac and FSRQ candidates with a 90 per cent precision metric ($\bar{L}_{Bc} \geq 0.9$ and $\bar{L}_{Fc} \geq 0.9$; $\bar{L}_B \geq 0.528$ and $\bar{L}_F \geq 0.701$), 801 BCUs are classified as BL Lacs and 406 as FSRQs, leaving 122 unclassified. If only highly probable candidates are selected ($\bar{L}_B \geq 0.9$ and $\bar{L}_F \geq 0.9$; $\bar{L}_{Bc} \geq 0.979$ and $\bar{L}_{Fc} \geq 0.962$), then 534 BCUs are classified as BL Lacs and 245 as FSRQs. The second classification corresponds to 98 per cent precision for BL Lacs and 96 per cent for FSRQ.

The ratio of BL Lac to FSRQ candidates is about 2. For 90 per cent precision candidates it is 1.7, and for high probability candidates 2.2. Looking at Table 1, it is clear that the ratio of known BL Lacs to FSRQs has steadily increased (1FGL: 1.1; 2FGL: 1.2; 3FGL: 1.4; 4FGL: 1.6). Since BL Lacs are on average dimmer in γ -rays than FSRQs, at first they were hard to detect but as *Fermi*-LAT sensitivity increased due to its longer observational period, more BL Lacs started to be discovered with respect to FSRQs. For this reason, it is reasonable to assume that the true ratio among BCUs is larger than the current ratio of known BL Lacs to FSRQs.

Looking at Fig. 8, the network can classify many more BCUs as almost certain BL Lacs ($\bar{L}_B \rightarrow 1$) than FSRQs ($\bar{L}_F \rightarrow 1$). This is because some BL Lacs occupy parts of parameter space where there are no FSRQs, i.e. certain group of BL Lacs are easily distinguishable from FSRQs.

The error is naturally small for sources with high \bar{L}_B or \bar{L}_F and the network classified them as probable BL Lac/FSRQ irrespective of train-test sample selection. For sources with intermediate \bar{L}_B , errors are larger. This is expected because classification of BCUs with properties (input parameters to the network) not clearly corresponding to either class will be more affected by fluctuation due to train-test sample selection.

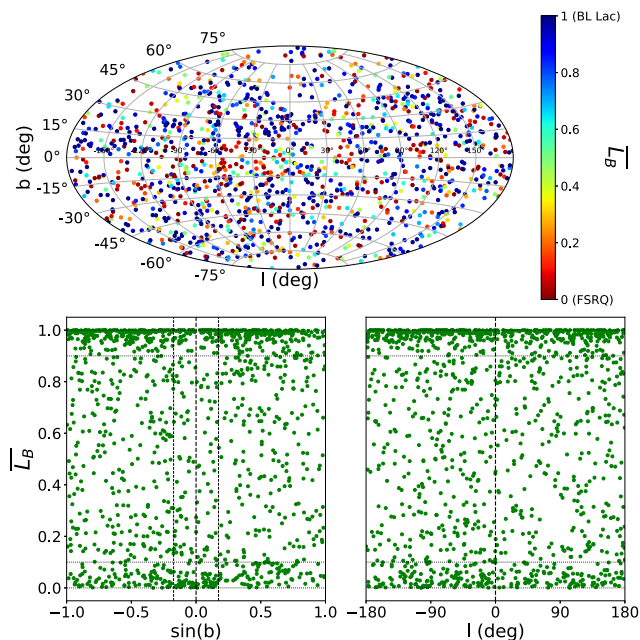


Figure 9. *Upper plot:* sky distribution in Galactic coordinates of 1329 BCUs from the 4FGL catalogue. Colours correspond to \bar{L}_B . *Bottom plots:* \bar{L}_B versus Galactic longitude (left-hand panel) and latitude (right-hand panel). *Bottom-left plot:* the two black dashed vertical lines around $b = 0^\circ$ correspond to $|b| = 10^\circ$.

4.2 Classification versus galactic latitude

The number of known BL Lacs and FSRQs within the Galactic plane region $|b| < 10^\circ$ is about 5 percent. The number of BCUs within the $|b| < 10^\circ$ region is 18 percent. The optical spectroscopy which is required to fully classify blazars is harder to do for sources near the Galactic plane.

In Fig. 9, the sky distribution in Galactic coordinates of 1329 BCUs is shown together with their classification \bar{L}_B . Galactic diffuse γ -ray emission from the Galactic disc and many point and extended sources inside it make it more difficult to detect γ -ray blazars and measure their flux. Here we look at differences in classification between sources inside the Galactic diffuse emission area ($|b| < 10^\circ$) and those outside ($|b| > 10^\circ$).

The threshold of $\bar{L}_B \approx 0.42$ corresponds to a precision of about 87 percent at which all BCUs can be classified (865 BL Lacs and 464 FSRQs). Then MSE is defined as $\sum (1 - \bar{L}_B)^2 / N$ for BL Lac candidates ($\bar{L}_B > 0.42$) and $\sum (0 - \bar{L}_B)^2 / N$ for FSRQ candidates ($\bar{L}_B < 0.42$). This quantity is an average measure of uncertainty of BCUs classification, i.e. how far away \bar{L}_B of BCUs is from the peaks at $\bar{L}_B = \{0, 1\}$. We found that this value is not bigger for BCUs at $|b| < 10^\circ$ than the ones at $|b| > 10^\circ$, meaning that BCUs near the Galactic plane are not classified with less certainty by the network.

The average integrated (in time and energy) flux value of BL Lac and FSRQ candidates near the plane region is about two times larger than for candidates outside it. The same is true for known BL Lacs and FSRQs. This is expected since the γ -ray emission from the disc makes it harder to detect sources with lower flux. Known FSRQs have on average larger flux than known BL Lacs and the same is true for FSRQ and BL Lac candidates. For this reason, the fraction of FSRQ candidates inside the region ($112: 464 \approx 0.24$) is larger than the fraction of BL Lacs ($125: 865 \approx 0.14$). Considering only highly probable candidates ($\bar{L}_B > 0.9$ and $\bar{L}_F > 0.9$) the difference

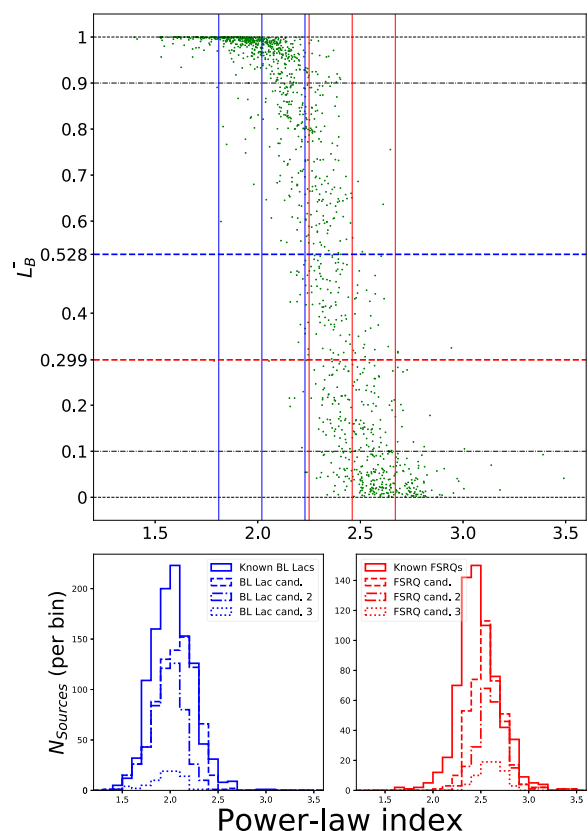


Figure 10. Comparison of BCU classifications with power-law (PL) indexes. The higher the probability of a BCU to be a BL Lac \bar{L}_B , the lower the PL index and vice-versa. The distribution of PL indexes of BL Lac and FSRQ candidates is in agreement with distribution of PL indexes of known BL Lacs and FSRQs. *Upper plot:* \bar{L}_B of 1329 BCUs with respect to their PL indexes. The blue and red vertical lines are mean values of PL indexes of known BL Lacs (2.02) and FSRQs (2.47) and their 1σ distribution widths which in both cases is 0.21. Horizontal blue and red dashed lines correspond to BL Lac and FSRQ candidates with 90 percent precision metric. *Bottom plots:* Histograms of PL indexes for BL Lacs (left-hand panel) and FSRQs (right-hand panel). BL Lac and FSRQ candidates are selected such that precision value is 90 percent. Candidates number 2 are highly probable candidates ($\bar{L}_B > 0.9$ for BL Lacs and $\bar{L}_F > 0.9$ for FSRQs). Candidates number 3 are highly probable candidates which are confined to Galactic plane region $|b| < 10^\circ$.

increases to 0.28:0.14. Therefore BCUs near the Galactic plane are made of a larger fraction of FSRQs when compared to BCUs outside of it. While the ratio of BL Lac to FSRQ candidates is about 2 for the whole sky, it is about 1 for the Galactic plane.

5 VALIDATION

It was discovered that BL Lacs and FSRQs are characterized by different γ -ray spectral properties. Usually BL Lacs show harder spectra than FSRQs (Ackermann et al. 2015; The Fermi-LAT collaboration 2019b). Fitting 4FGL blazars, assuming a power-law (PL) spectral model, it was observed that the best-fitting photon spectral index distribution is rather dissimilar for the two subclasses, making this observable an important γ -ray parameter to distinguish the two blazar classes. Since we did not include this parameter in our

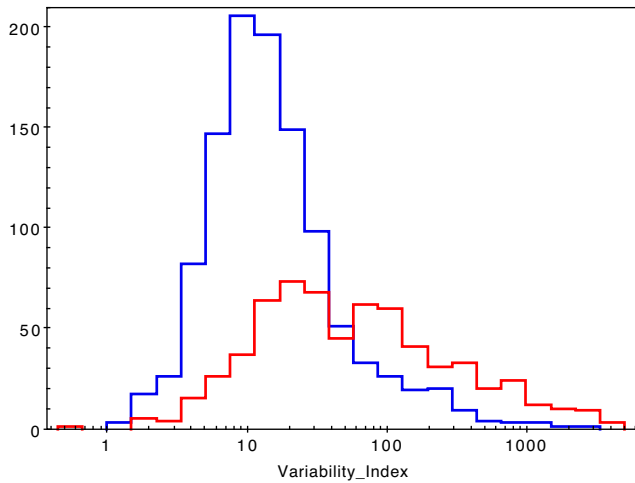


Figure 11. Variability index distribution for the known 4FGL blazars: BL Lacs (blue histogram) and FSRQs (red histogram). The evident overlap of the histograms show it to be inefficient at distinguishing blazar subclasses.

algorithm,⁵ in order to validate the performance of our algorithm (as a sanity check), we compared the PL index distribution of BCUs versus their \bar{L}_B together with the PL distribution of known BL Lacs and FSRQs.

A clear correlation between \bar{L}_B and PL index of BCUs exists (upper plot in Fig. 10) such that higher \bar{L}_B corresponds to lower PL index, i.e. harder spectrum, which is expected. Mean values and 1σ spread for known BL Lacs and FSRQs is also shown. In the bottom plots in Fig. 10, the same correlation is shown in the form of histograms. BL Lac and FSRQ candidates follow the PL index distribution of known BL Lacs and FSRQs. High probability BL Lac candidates have even lower PL index and vice-versa for FSRQs, which is expected. Finally, high probability candidates within the Galactic plane region $|b| < 10^\circ$ follow the same distribution as high probability candidates in total, showing that correctness of classification is no different for the Galactic plane even though there are differences when it comes to integrated flux values of blazars.

The good agreement of the PL index distribution for our candidates with the PL index distribution for known blazars confirms the correctness of the algorithm. We also plot the Variability Index distributions for known BL Lacs and FSRQs (Fig. 11). This parameter, unlike the PL index, is not as efficient at distinguishing blazar subclasses, so we did not use it for validation.

6 CONCLUSION

In this study we used a neural network method for the classification of uncertain blazars. We studied effects of selecting different training and testing samples, differences in test sample and BCU sample and discussed the meaning of network outputs. In the end, classification probabilities for each of 1329 BCUs are obtained along with error due to train-test sample selection. In terms of number of classified sources, 1207 BCU are classified compared to 1329 original BCUs, classifying 91 percent of the sample

with 90 percent precision. Ratio of BL Lac candidates to FSRQ candidates is about 2:1 for the whole sky, and 1:1 for the Galactic plane. This result confirms that machine learning techniques are powerful methods to classify uncertain astrophysical objects and particularly blazars.

In this work we used sets of γ -ray parameters that present spectra and light curves since these two features are known to be different for BL Lacs and FSRQs. It is, of course, possible to use other γ -ray parameters from the 4FGL catalogue (including the PL index⁶) as well as multiwavelength data, such as X-ray and radio flux⁷ present in the upcoming Fourth Catalogue of Active Galactic Nuclei *4LAC* (The Fermi-LAT collaboration 2019b) or other catalogues. This can be addressed in a future appendix to this paper.

Due to the increasing number of uncertain blazars during the *Fermi*-LAT mission, the ANN technique could be a very worthwhile opportunity for the scientific community to quickly select promising targets for multiwavelength rigorous classification and related studies at different energy ranges, mainly at very high energies by the present generation of Cherenkov telescopes and the forthcoming Cherenkov Telescope Array⁸ (CTA Consortium & Ong 2019).

ACKNOWLEDGEMENTS

The authors would like to thank David J. Thompson (NASA Goddard Space Flight Center, Greenbelt, MD, USA) for review of the paper. For science analysis during the operation phase, we acknowledge the Fermi-LAT collaboration for making the results available in such a useful form. The authors also acknowledge their institutions for providing opportunity to carry out research. We thank the anonymous reviewer for suggestions leading to improvement of this work.

REFERENCES

- Abadi M. et al., 2016, *OSDI*, 16, 265
- Abdo A. A. et al., 2010a, *ApJS*, 188, 405
- Abdo A. A. et al., 2010b, *ApJ*, 716, 30
- Acero M. et al., 2015, *ApJS*, 218, 23
- Ackermann M. et al., 2012, *ApJ*, 753, 83
- Ackermann M. et al., 2015, *ApJ*, 810, 14
- Bishop C. M., 1995, *Neural Networks for Pattern Recognition*. Oxford Univ. Press, New York
- Breiman L., 2001, *Mach. Learn.*, 45, 5
- Chiaro G. Salvetti D., La Mura G., Giroletti M., Thompson D. J., Bastieri D., 2016, *MNRAS*, 462, 3180 (C16)
- Cortes C., Vapnik V., 1995, *Mach. Learn.*, 20, 273
- CTA Consortium, Ong R. A., 2019, *EPJ Web Conf.*, 209, 01038
- Doert M., Errando M., 2014, *ApJ*, 782, 41
- Einecke S., 2016, *Galaxies*, 4, 14
- Friedman J., Hastie T., Tibshirani R., 2000, *Ann. Stat.*, 28, 337
- Ghisellini G., 2013, *EPJ Web Conf.*, 61, 05001
- Gish H., 1990, *Proc. Acoust. Speech Signal Process.*, 3, 1361
- Hassan T., Mirabal N., Contreras J. L., Oya I., 2013, *MNRAS*, 428, 220

⁶Information on PL index is already contained in seven fluxes in energy bands so it is not expected to bring new information. However the PL index is obtained from the likelihood fit over whole energy interval and it might be different for some blazars than PL index that would be obtained from seven fluxes in energy bands.

⁷It is possible to use radio and X-ray flux even if they are present for only a subset of LAT blazars (K19).

⁸www.cta-observatory.org.

⁵We did use fluxes in different energy bands which contain information on average power-law index, but the power-law index per se was never used as an input parameter.

- Kang S.-J., Fan J.-H., Mao W., Wu Q., Feng J., Yin Y., 2019, *ApJ*, 872, 189
- Kaur A., Falcone D. A., Stroh M. D., Kennea J. A., Ferrara E. C., 2019, *ApJ*, 887, 18
- Kovačević M., Chiaro G., Cutini S., Tosti G., 2019, *MNRAS*, 490, 4770 (K19)
- Lee K. J., Guillemot L., Yue Y. L., Kramer M., Champion D. J., 2012, *MNRAS*, 424, 2832
- Lefaucheur J., Pita S., 2017, *A&A*, 602, 86
- Massaro F., Landoni M., D'Abrusco R., Milisavljevic D., Paggi A., Masetti N., Smith H. A., Tosti G., 2015, *A&A*, 575, 124
- Mirabal N., Charles E., Ferrara E. C., Gonthier P. L., Harding A. K., Sánchez-Conde M. A., Thompson D. J., 2016, *ApJ*, 825, 69
- Richard M. P., Lippman R. P., 1991, *Neural Comp.*, 3, 461
- Salvetti D., Chiaro G., La Mura G., Thompson D. J., 2017, *MNRAS*, 470, 1291 (S17)
- Saz Parkinson P. M., Xu H., Yu P. L. H., Salvetti D., Marelli M., Falcone A. D., 2016, *ApJ*, 820, 8
- The Fermi-LAT collaboration, 2019a, preprint ([arXiv:1902.10045](https://arxiv.org/abs/1902.10045))

- The Fermi-LAT collaboration, 2019b, preprint ([arXiv:1905.10771](https://arxiv.org/abs/1905.10771))
- Vapnik V. N., 1995, *The Nature of Statistical Learning Theory*. Springer, New York
- Yi T.-F., Zhang J., Lu R.-J., Huang R., Liang E.-W., 2017, *ApJ*, 838, 34

SUPPORTING INFORMATION

Supplementary data are available at *MNRAS* online.

Table 2. Example of seven classified BCU sources.

Please note: Oxford University Press is not responsible for the content or functionality of any supporting materials supplied by the authors. Any queries (other than missing material) should be directed to the corresponding author for the article.

This paper has been typeset from a \LaTeX file prepared by the author.

Optimizing neural network techniques in classifying *Fermi*-LAT gamma-ray sources

M. Kovačević,^{1★} G. Chiaro,^{2★} S. Cutini¹ and G. Tosti³

¹INFN – Istituto Nazionale di Fisica Nucleare Sez. Perugia, Via A. Pascoli snc, I-06123 Perugia, Italy

²INAF – Istituto di Astrofisica Spaziale e Fisica Cosmica, Via A. Corti, I-20133 Milano, Italy

³Dipartimento di Fisica e Geologia, Univ. degli Studi di Perugia, Via A. Pascoli snc, I-06123 Perugia, Italy

Accepted 2019 October 14. Received 2019 October 10; in original form 2019 May 27

ABSTRACT

Machine learning is an automatic technique that is revolutionizing scientific research, with innovative applications and wide use in astrophysics. The aim of this study was to develop an optimized version of an Artificial Neural Network machine learning method for classifying blazar candidates of uncertain type detected by the *Fermi* Large Area Telescope γ -ray instrument. The final result of this study increased the classification performance by about 80 per cent with respect to previous method, leaving only 15 unclassified blazars out of 573 blazar candidates of uncertain type listed in the LAT 4-year Source Catalog.

Key words: methods: statistical – galaxies: active – BL Lacertae objects: general – gamma-rays: galaxies.

1 INTRODUCTION

Since August 2008 the *Fermi* Large Area Telescope (LAT) provides the most comprehensive view of the γ -ray sky in the 100 MeV to 300 GeV energy range (Atwood et al. 2009). The LAT 4-year Source Catalog 3FGL (Acero et al. 2015) listed 3033 γ -ray sources of which 1717 were blazars, including 573 blazar candidates of uncertain type (BCU). In addition 1010 of the detected sources had not even a tentative association with a likely γ -ray emitting source. As a result, the nature of about half the γ -ray sources is still not completely known even if, because blazars are the most numerous γ -ray source class, it could be reasonable to expect that a large fraction of unassociated sources might belong to the BL Lacertae (BL Lac) or Flat Spectrum Radio Quasar (FSRQ) class. When rigorous classification analyses are not available, machine learning techniques (MLTs) represent powerful tools that enable identification of uncertain objects based on their expected classification. Machine learning is a data analytics technique that teaches computers to do what comes naturally to humans and animals: learn from experience. Traditional computer programs do not consider the output of their tasks, and therefore they are unable to improve their efficiency. MLT addresses this exact problem and involves the creation of an algorithm that is able to learn and therefore improve its performances by gathering more data and experience. MLT uses identified objects to teach the algorithm to distinguish each source class on the basis of parameters that describe its intrinsic features. The algorithm adaptively improves its performance as the number of samples available for learning increases. The algorithm generates an

output that can be interpreted as a Bayesian a posteriori probability modelling the likelihood of membership class on the basis of input parameters (Gish 1990; Richard & Lippman 1991). In this work we explore the possibility to improve the performance of a machine learning algorithm Chiaro et al. (2016) based on the variability of blazars, applying new physical parameters that characterize the nature of those sources and some statistical adjustments in order to increase the accuracy of the algorithm, making it more efficient and effective.

The expected result should be an optimized algorithm that is able to estimate, with more precision than in the past, the number of uncertain blazars that could belong to the BL Lac or FSRQ class in the *Fermi*-LAT Source Catalogs.

The paper is organized as follows: in Section 2, we provide a brief description of the main features of the most frequently used MLTs in astrophysics. In Section 3, we present our optimization of an Artificial Neural Network (ANN) method. In Section 4, we compare the performance of the optimized algorithm against the original one and comment on the results testing the performance of the new algorithm on a sample of uncertain or unassociated γ -ray sources. We discuss predictions and implication of our results in Section 5.

2 MACHINE LEARNING TECHNIQUES

In previous studies, Ackermann et al. (2012), Lee et al. (2012), Hassan et al. (2013), Doert & Errando (2014), Chiaro et al. (2016), Mirabal et al. (2016), Saz Parkinson et al. (2016), Lefaucheur & Pita (2017), Salvetti et al. (2017), and other authors have explored the application of MLT classifying undetermined γ -ray sources in *Fermi*-LAT γ -ray source catalogues. The first study was applied to

* E-mail: milos.kovacevic@pg.infn.it (MK); graziano.chiaro@inaf.it (GC)

the 1-year Source Catalog *1FGL* (Abdo et al. 2010a), the next three studies to the 2-year Source Catalog *2FGL* (Nolan et al. 2012) and the rest were applied to the 4-year Source Catalog *3FGL* (Acero et al. 2015). Here we briefly introduce the general features of the most frequently used MLTs in astrophysics for such cases.

(i) **The Random Forest.** The Random Forest (RF) method (Beimann 1973) is an ensemble learning method that uses decision trees as building blocks for classification, regression, and other tasks. By aggregating the predictions based on a large number of decision trees, RF generally improves the overall predictive performance while reducing the natural tendency of standard decision trees to overfit the training set. The RF package also computes the proximity measure, which, for each pair of elements (i, j) , represents the fraction of trees in which elements i and j fall in the same terminal node. This can be used to calculate the *outlyingness* of a source, as the reciprocal of the sum of squared proximities between that source and all other sources in the same class, normalized by subtracting the median and dividing by the median absolute deviation, within each class. Liaw & Wiener (2002), Doert & Errando (2014), Hassan et al. (2013), Saz Parkinson et al. (2016), and Mirabal et al. (2016) used the RF algorithms in order to classify unassociated sources and uncertain active galactic nuclei (AGNs) from the *Fermi* γ -ray source catalogues.

(ii) **The Support Vector Machines.** The Support Vector Machine (SVM) (Cortes et al. 1995; Vapnik 1995) is a discriminative classifier formally defined by a separating hyperplane. In other words, given labelled training data (supervised learning), the algorithm outputs an optimal hyperplane which categorizes new examples. In two-dimensional space this hyperplane is a line dividing a plane in two parts where each class lies on either side. The method maximizes the separation between different classes, which can then be used in classification or regression analysis. In Hassan et al. (2013) the authors used an SVM algorithm and the RF algorithm building a classifier that can distinguish between two AGN classes: BL Lac and FSRQ based on observed γ -ray spectral properties. Combining both methods they managed to classify 235 out of 269 uncertain AGNs from the 2FGL catalogue into BL Lacs and FSRQs with 85 per cent accuracy.

(iii) **The Boosted Decision Trees.** The Boosted Decision Tree (BDT; Freud et al. 1999) is based on the decision trees, a classifier structured on repeated *yes/no* decisions designed to separate *positive* and *negative* classes of events. Thereby, the phase space of the discriminant parameters is split into two different regions and generates a forest of weak decision trees and combines them to provide a final strong decision. At each step, misclassified events are given an increasing weight. Lefaucheur & Pita (2017) used BDT together with ANN in order to classify unassociated sources and uncertain blazars (BCU) in the 3FGL catalogue. Selecting 486 unflagged BCUs, the authors classified 295 of them as BL Lacs with 13 predicted false associations, and 146 as FSRQs with 39 predicted false associations. Both MLT methods were found to perform similarly.

(iv) **The Artificial Neural Network.** The ANN (Bishop 1995) is probably the most used MLT in astrophysics. Regarding *Fermi*-LAT sources, ANN algorithms were used in Chiaro et al. (2016) and Salvetti et al. (2017) for classifying uncertain blazars and were also used in the above-mentioned work of Doert & Errando (2014) and Lefaucheur & Pita (2017) for classifying unassociated sources and uncertain blazars.

Basic units of neural networks are *neurons* which are organized into *layers* and are connected to each other. Neurons, layers, and lines

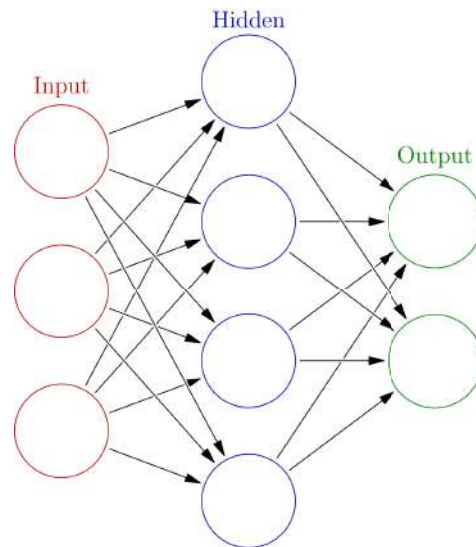


Figure 1. Schematic view of a 2LP, the ANN architecture. Each circle represents a single neuron. Each arrow represents association between output values of neurons to the weights of neurons in the successive layer. Outputs of neurons in the *Input layer* are just values of parameters describing an astronomical source. Data enter the 2LP through the nodes in the input layer. The information travels from left to right across the links and is processed in the nodes through an activation function. Each node in the output layer returns the likelihood of a source to be a specific class.

connecting them are abstract mathematical concepts that help to visualize how the input values (describing an astronomical source in our case) to the network are transformed in order to obtain classification for that source. A standard neural network consists of an input layer, one or more hidden layers and an output layer. In Fig. 1 the schematic view of the basic architecture of an ANN algorithm is shown. Neurons in the input layer are just values of input parameters from a single source (flux values in different time bins for example). Each neuron in the first hidden layer has a set of *weights* (numerical values) which are associated with input parameters. The number of weights in each neuron equals the number of input parameters. The association between weights and input parameters is presented by arrows connecting all input neurons to all neurons in the hidden layer. For each neuron in the hidden layer, the sum of products between each weight and input parameter¹ is then used in an *activation/transfer function* to create a single output. The outputs of neurons in the hidden layer are then used as input values for all neurons in the successive layer (which is also presented by arrows). Neurons in the output layer produce the final result.

When classification is the goal, the number of neurons in the output layer usually equals the number of classes. The sum of outputs from these neurons (for a single astronomical source) equals 1 and the output value from each neuron is interpreted as the probability of that source belonging to a given class.

Training the network with known/labelled sources involves setting the weights of all neurons in the network so that difference between given outputs and desired outputs (for many sources combined), quantified by a *Loss/Cost function*, is minimized. The sample of sources used in training the network typically contains

¹A single value *bias* can be added.

50–80 per cent of all known sources. The rest are divided into two independent samples – *validation sample* and *test sample*, which are used to avoid overfitting and to evaluate the network on sources it has not seen during training.

The original ANN algorithm that we considered in this study was used for the first time in Chiaro et al. (2016) (hereinafter *C16*) and subsequently in Salvetti et al. (2017) (hereinafter *S17*). The algorithm compared the γ -ray light-curve of the source under investigation with a template of classified blazar class light curves, then measured the difference in a proper metric. The authors of both papers used a simple neural model known as Two Layer Perceptron (2LP), rather similar to the method used by Lefaucheur et al. (2017) but with a simpler architecture.

In this work we explored possibilities to improve the efficiency of the original algorithm used in *C16* and subsequently in *S17*. Even if the original ANN algorithm was very effective, the number of sources with uncertain classification in *C16* and *S17* remained consistent. In *C16* analysing 573 BCUs, 77 sources remained with uncertain classification. Also in *S17* classifying with the same algorithm the AGN-like sources, 103 of 559 sources remained with uncertain blazar classification.

In order to optimize the performance, we decided to use additional parameters describing blazars and test different network architectures. Since we expected to perform the process of training the network many times, we decided to use *TensorFlow*.²

3 THE METHOD

3.1 Gamma-ray variability (ECDF)

In *C16* the Empirical Cumulative Distribution Function (ECDF) of the monthly bins of the 3FGL BCU γ -ray light curves was applied to the ANN as an estimator able to classify BCUs into BL Lacs and FSRQs. The monthly fluxes are in the energy range of 100 MeV to 100 GeV. The ECDF of a source is obtained by sorting monthly flux values (obtained from the 3FGL catalogue) from lowest to highest for that source. This produces a set of (12 months \times 4 yr) 48 sorted flux values. The ECDF contains information on flaring patterns, along with the monthly averaged brightest flares and variability of the sources. The distinctiveness of 3FGL BL Lacs and FSRQs sorted by ECDF is shown in Fig. 2. BL Lacs tend to be dimmer than FSRQs. Their emission also tends to be more continuous over time than that of FSRQs, which show more variability. This can be seen in the lower-left plot of Fig. 2. In the lower-right part of the plot there is an area where mostly BL Lacs are found. Sources passing through this area are ones that have lower flux ($\lesssim 2 \times 10^{-8}$ ph cm $^{-2}$ s $^{-1}$) during their brightest months. Both dimmer and brighter BL Lacs tend to have more ‘horizontal’ ECDFs that reflect their lower variability. This result convinced the authors in *C16* to use the ECDF as the sole ANN parameter to compute the likelihood of their sample of uncertain sources to be BL Lac or FSRQ. Quick comparison *looking by eyes* of blazar classes in Fig. 2 suggests that BCU ECDFs are closer to BL Lac ones and that the larger part of BCUs could be BL Lacs.

²<https://www.tensorflow.org>. TensorFlow is an open source library for machine learning. It is relatively easy to use, provides details on the process of training and options for different network architectures, and is built to be fast – network can be trained on an ordinary computer in relatively short time.

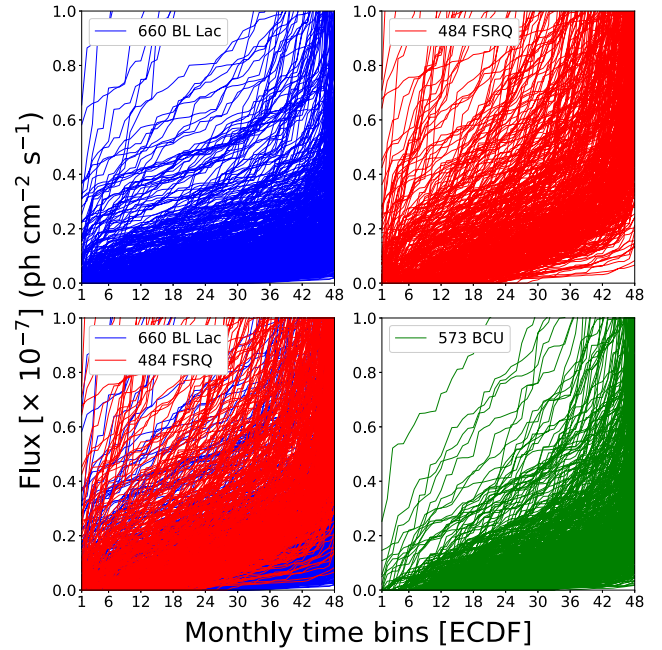


Figure 2. ECDFs of 3FGL blazars (4 yr of data). Fluxes are in the energy range of 100 MeV to 100 GeV. Each curve represents a single source. Vertical axes present monthly flux values. Horizontal axes present 48 monthly time bins. For each source, the N th monthly time bin corresponds to the month of observation when the N th lowest monthly flux was observed. Therefore, lower numbers correspond to months of lower activity for each source while higher numbers to months of higher activity. BL Lacs are in the top-left, FSRQs in the top-right, both are in the lower-left and BCUs are in the lower-right. ECDFs for some sources extend beyond the plot limit of 10^{-7} ph cm $^{-2}$ s $^{-1}$. Figure reproduced from Chiaro et al. (2016).

Since ECDF curves represent the only set of parameters originally used in *C16*, it was interesting to test if some statistical methods could improve the final performance of the network. While distinctiveness of BL Lacs and FSRQs is obvious for flux values $\lesssim 2 \times 10^{-8}$ ph cm $^{-2}$ s $^{-1}$ during the brightest months, they are much more intertwined and similar for sources which have higher flux value during dimmer months (upper-left part of the plots). Removing some of these sources would help the network make a better separation. One way to proceed is to identify sources that have a flux value above a detection threshold for the dimmest month (monthly bin number 1 on the plots in Fig. 3), and then to remove them. Applying this constraint, the number of BL Lacs fell from 660 to 589 (–10 per cent) and FSRQs from 484 to 433 (–10 per cent). The reduction of source number did not affect training and testing the network. The number of BCUs fell from 573 to 567, so only six sources were lost for classification (Fig. 3).

3.2 Gamma-ray spectrum

In order to further improve performance we use spectral information in addition to ECDF. In the 3FGL catalogue there are time-integrated flux values in five different energy bands: 0.1–0.3, 0.3–1, 1–3, 3–10, 10–100 GeV (Fig. 4). This set of parameters contains information of average spectral index, hardness and flux ratios, peak energy, and others. Hassan et al. (2013) and Lefaucheur & Pita (2017) used various spectral parameters obtained from fluxes in different energy bands in order to classify BCUs into BL Lacs and FSRQs, showing the value of using spectral information.

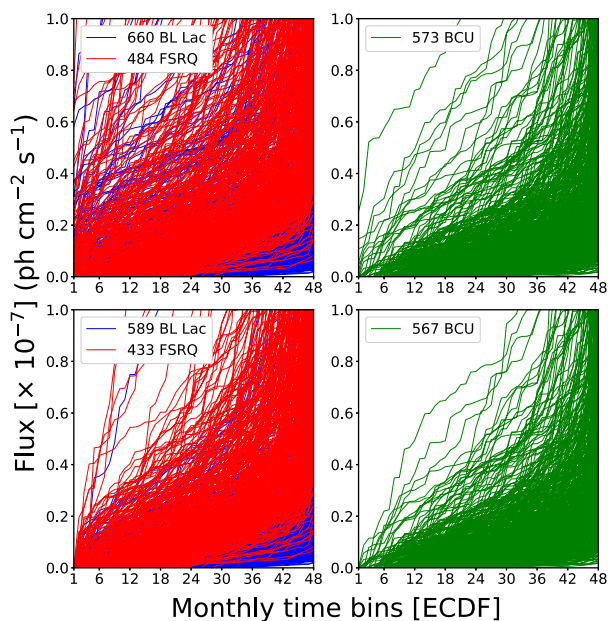


Figure 3. ECDF: The upper two plots contain all the 3FGL blazars while the two plots at the bottom contain 3FGL blazars after applying the flux threshold cut. The number of sources for each class is written on the plots before and after the cut. Blue curves correspond to BL Lacs, red to FSRQs, and green to BCUs. The sources affected by the cut have flux values above 0 for monthly bin number 1 (the dimmest month). After applying the cut, the upper-left part of the ECDF plot for BL Lacs and FSRQs becomes more clear. For BCUs, the same part of the ECDF plot remains similar after the cut because there were not many sources passing through it (only six sources are removed by the cut).

In the range of flux values $\sim 10^{-10}$ $\text{ph cm}^{-2} \text{s}^{-1}$ and energy bands from 0.1–0.3 up to 1–3 GeV, mostly BL Lacs are present, while for the energy band 10–100 GeV FSRQs are more numerous for the lower values of fluxes (around $\sim 10^{-10}$ $\text{ph cm}^{-2} \text{s}^{-1}$). The majority of BL Lacs and FSRQs also have different slopes, which is in part a reflection of different average power-law indices. As in the case of ECDFs, BCUs tend to behave more like BL Lacs, which would suggest that a larger number of them could belong to that class.

3.3 Radio and X-ray fluxes

Looking beyond γ -ray features of blazars, interesting information can be obtained from a multiwavelength study of the sources and particularly from X-ray and radio flux. In this study we tested the possibility to use those two parameters to improve the performance of the network. We did not consider any optical spectroscopy data because when considering uncertain sources, optical spectra are very often not available or not sufficiently descriptive of the nature of the source.

A particularly interesting parameter seems to be the ratio of radio (Sr) flux to the X-ray flux. In Fig. 5 (three plots on the left) the radio and X-ray flux histograms are shown. When the parameters are considered separately the contamination is not negligible (histogram on top-left and in the middle-left), but when the ratio Sr/X is considered it is possible to distinguish a clean area for BL Lacs where values are lower than 4×10^{13} (13.6 in the plot). Unfortunately not all the known and uncertain blazars have both radio and X-ray flux data. However the final result is still appreciable because considering 3FGL blazars, 322 BL Lacs out of

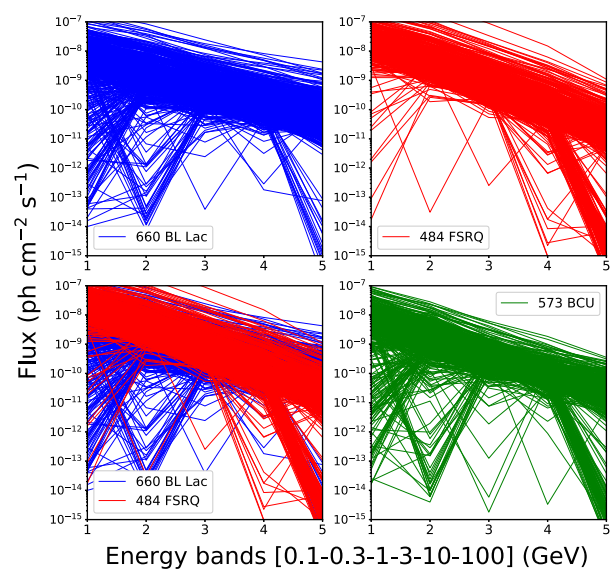


Figure 4. Time-integrated fluxes in five different energy bands. Band 1: 0.1–0.3 GeV; Band 2: 0.3–1 GeV; Band 3: 1–3 GeV; Band 4: 3–10 GeV; Band 5: 10–100 GeV. Each curve represents a single source. BL Lacs (blue) are in the top-left, FSRQs (red) in the top-right, both are in the lower-left, and BCUs (green) are in the lower-right.

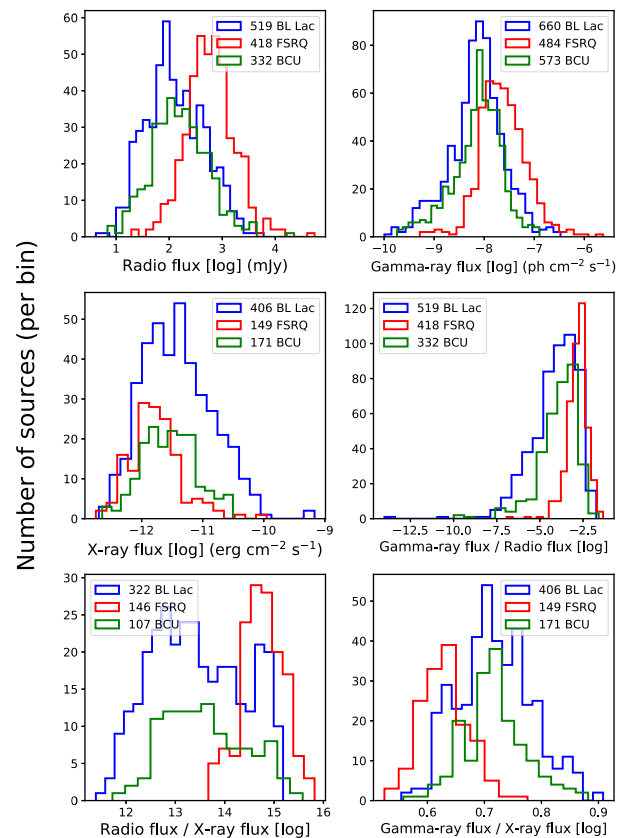


Figure 5. Top-left: 3FGL BL Lac, FSRQ, and BCU radio flux histogram. Middle-left: X-ray flux histogram. Bottom-left: radio flux / X-ray flux histogram. A BL Lac clean area is distinguished by ratio of radio to X-ray values lower than 4×10^{13} (13.6 in the plot). Top-right: 3FGL BL Lac, FSRQ, and BCU gamma-ray flux histogram. Middle-right: Ratio of gamma-ray flux to radio flux. Bottom-right: Ratio of gamma-ray flux to X-ray flux.

660 have both radio and X-ray measurements and for 188 sources (28 per cent) the value of Sr/X ratio is lower than 4×10^{13} . Out of 484 FSRQs, 146 FSRQs have both radio and X-ray data and the value of Sr/X ratio is above 4×10^{13} for all of them. Finally, out of 573 3FGL BCUs, 107 sources have both measurements while 57 show a value of the Sr/X ratio lower than 4×10^{13} . This means that the Sr/X ratio, although an overlap of data in higher values is not negligible, could be considered as a *smoking gun* area where a good separation for BL Lacs is possible.

For completeness we also consider time-integrated γ -ray flux (0.1–100 GeV band), and its ratios to radio and X-ray fluxes. The γ -ray flux was obtained by adding five time-integrated fluxes in five bands (Section 3.2). In Fig. 5, the three plots to the right show histograms of γ -ray flux (top-right), its ratio to radio (middle-right), and ratio to X-ray (lower-right). In the first two cases overlap is significant, while for the third the peaks are well separated but there is still significant overlap. Therefore, we decided to consider only ratios of radio and X-ray flux.

Radio and X-ray data were obtained from the *Fermi*-LAT 4-year AGN Catalog 3LAC (Ackermann et al. 2015). Radio fluxes used were measured at frequencies of 1.4 and 0.8 GHz; the X-ray fluxes were measured in the 0.1–2.4 keV range (Ackermann et al. 2015).

Numbers on the plots in Fig. 5 show how many sources have a given measurement and a flux value. In the case of ratios, numbers present how many sources have both given measurements and flux values.

3.4 Data input

If parameter values (for an input neuron) vary over several orders of magnitude, it is common practice to use the logarithm of those values. However this strategy may not always improve the performance of the network since all input neurons are treated together in training of the network. Combinations with both original values and their logarithms were checked. The results are reported in Section 4.1.

The input data were normalized by subtracting their average value and dividing by their standard deviation so most of the input values fell between -1 and $+1$ for each input neuron.

The majority of sources do not have monthly γ -ray flux values above the detection threshold for all monthly time bins. Additionally the radio and X-ray data are missing for many sources. One way to deal with missing input data to a neural network is to set the inputs to zero. In this way, zero input acts as if there is no input neuron. Since the *Fermi*-LAT detector sweeps the sky continuously, the non-detection of γ -ray flux is due to low value of photon flux during the month and not observational constraints. The missing radio and X-ray data are due to low flux and/or observational constraints.

In our tests, the input radio and X-ray parameters for sources which do not have these values were set to zero. These zero values were not used in normalization and remained zero after normalization. The same is true if the logarithm of radio and X-ray flux was taken.

The input data for missing monthly γ -ray flux is set to zero in the 3FGL catalogue. These values were used in normalization after which they still had the lowest, but non-zero values. In case the logarithm was taken, these values were set to minimal value of monthly detected flux of $4 \times 10^{-11} \text{ cm}^{-2} \text{ s}^{-1}$ (of any source) before the logarithm was taken. After applying the logarithm, values were normalized as in the previous case.

3.5 Network architecture

What follows is the architecture of the optimized network used in this work.

The number of neurons in input layer is equal to the number of input parameters: 48 neurons for 48 monthly γ -ray fluxes (ECDF), 5 for time-integrated γ -ray fluxes in 5 different energy bands, 1 for ratio of radio to X-ray flux. In total that is 54 neurons in input layer.

The hidden layer consisted of 100 neurons. The choice was made by experimenting with single example for fixed number of training epochs. It was found that number of neurons should be higher than the number of input parameters (about 50 in our case) but after that the performance did not change noticeably with further increase. The output layer consisted of two neurons. The activation function used in the hidden layer was hyperbolic tangent while for output neurons softmax (equation 1) function was applied which insured that sum of output neurons equals 1. In equation (1) σ_i is the output of the i -th neuron, z_i is the input value to the activation function for the i -th neuron, j is the summation index over neurons in the given layer.

$$\sigma_i = \frac{e^{z_i}}{\sum_j e^{z_j}}. \quad (1)$$

The batch size was set to number of sources in training sample which insured smooth convergence. We tried three different Loss functions: mean squared error (used in C16), mean absolute error, and binary cross-entropy (equation 2) which is typically used in binary classification. In equation (2), y_1 and y_2 are desired values of two output neurons and can take values $\{0, 1\}$ or $\{1, 0\}$, p_1 and p_2 are obtained values of two output neurons. Summation is performed over all sources in the batch sample.

$$\text{Loss} = - \sum_{\text{batch}} (y_1 \log p_1 + y_2 \log p_2). \quad (2)$$

The minimization algorithm used was adam-optimizer,³ a method for efficient stochastic optimization (Kingma et al. 2014), which converged quicker and gave better results in our case than classical stochastic gradient descent.

3.6 Training strategy

Typically samples/sources for the training set and other sets are chosen randomly. The fluctuation in performance depending on which sources are taken might be important. In our case there are about 1000 labelled sources (BL Lacs and FSRQs), and it was found that the number of unclassified BCUs may vary significantly depending how training and other sets are chosen. In Lefaucheur & Pita (2017) the same problem was noted, and we decided to test the strategy suggested by the authors, by training the network for 100 different training and testing samples and then selecting the set which is closest to the average results. The training set consisted of 70 per cent and the test set of 30 per cent of the 3FGL classified blazars.

Aside from training the network on 100 different train and test samples, to avoid introduction of a second independent sample (with a yet smaller number of sources in it), an alternate strategy was used: the number of epochs was fixed for all combinations of input parameters and selections of training and testing samples, and the network was evaluated at the end; regularization was used to

³https://www.tensorflow.org/api_docs/python/tf/train/AdamOptimizer

avoid overfitting. The value for regularization was chosen so that it allowed the network to get close to the lowest test Loss function and to have it smoothly converge by the final epoch.

The desired outcome for training sample sources was set to $\{1, 0\}$ and $\{0, 1\}$ for BL Lacs and FSRQs, respectively. In this way the output neurons returned the likelihood of a source belonging to either class. Inputting parameters from known/labelled sources from the testing sample into the trained network enables network evaluation. The two output neurons produce likelihood of a source being a BL Lac $L_{\text{BL Lac}}$ or a FSRQ L_{FSRQ} such that $L_{\text{BL Lac}} + L_{\text{FSRQ}} = 1$ for each source.

Network performance was evaluated by how many BCUs are left unclassified, applying a 90 per cent precision threshold *C16*.

4 VALIDATION

4.1 Results

The set of input parameters to the new network (Section 3.5) were: (a) 48 monthly γ -ray flux values sorted from lowest to highest (ECDFs, Section 3.1), (b) the 5 time-integrated γ -ray flux values in five energy bands (Section 3.2), (c) the radio to X-ray flux ratio described in Section 3.3. Additionally some sources were excluded by applying the cut as described in Section 3.1. All three types of Loss functions gave similar results, however the best was obtained with mean absolute error. The application of the logarithm to any of the parameters did not improve the final results.

Applying the new input parameters to the new network, we improved the performance by decreasing the number of unclassified BCUs to 30 instead of 77 as reported in *C16*.

When radio (Sr) and X-ray flux values were input separately instead of only the Sr/X ratio, the number further falls to 15. This result is due to the fact that more BCUs have Sr and/or X values than both Sr and X. Out of a total of 573 BCUs in the 3FGL catalogue, 332 have Sr values, 171 have X, and out of these 107 have both Sr and X (three left-hand plots in Fig. 5). Therefore, number of BCUs which have Sr and/or X is 396. If the ratio of Sr/X is added as additional input parameter to Sr and X alone, the performance remains the same. If integrated γ -ray flux (100 MeV to 100 GeV) and its ratios to Sr and X (three plots to the right in Fig. 5) are added as input parameters, the performance remains the same. These three parameters and Sr/X are combinations of parameters already used in the network and therefore they contain no true new information.

All the numbers of unclassified BCUs mentioned above are average values of unclassified BCU from 300 different selections for training and testing samples.

In Fig. 6 the histogram of $L_{\text{BL Lac}}$ for BL Lacs and FSRQs from a representative test sample is presented. As expected BL Lacs concentrate towards $L_{\text{BL Lac}} \rightarrow 1$ while FSRQs $L_{\text{BL Lac}} \rightarrow 0$. The numbers of BL Lacs and FSRQs in test sample are 177 and 130, respectively. The sources for the test sample were chosen randomly but with two constraints: the numbers are 30 per cent of the total sample after application of the cut; the ratio of BL Lacs to FSRQs in the test sample ($177:130 \approx 1.36$) was kept the same as the ratio in total sample ($589:433 \approx 1.36$).

The precision of the optimized neural network algorithm considering a threshold of 0.9 can be seen in Fig. 7. Sources from the test sample are sorted by their $L_{\text{BL Lac}}$ (as in Fig. 6), but sources are at equal distance from each other and $L_{\text{BL Lac}}$ does not increase linearly. The threshold where precision reaches 0.9 for BL Lacs and FSRQs is $L_{\text{BL Lac}} = 0.545$ and $L_{\text{BL Lac}} = 0.396$, respectively (blue and red vertical lines). The threshold for BL Lacs is lower

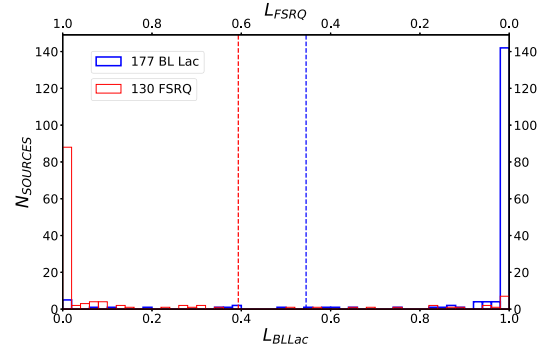


Figure 6. Histogram of $L_{\text{BL Lac}}$ for BL Lacs and FSRQs from the testing sample. The blue and red vertical lines (at $L_{\text{BL Lac}} = 0.545$ and $L_{\text{BL Lac}} = 0.396$, respectively) present thresholds for BL Lacs and FSRQs such that precision of 90 per cent is obtained.

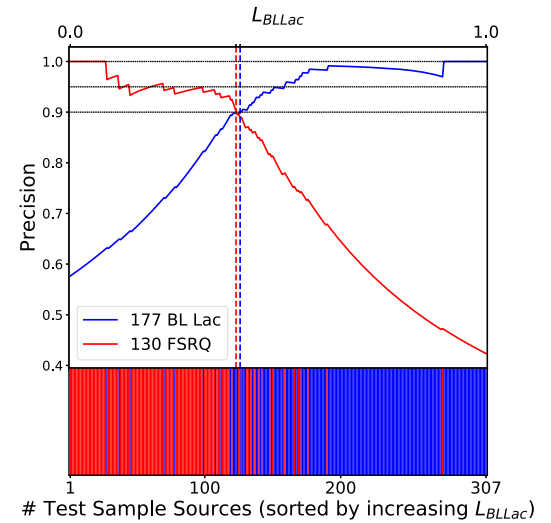


Figure 7. Lower bar: BL Lacs (blue) and FSRQs (red) sources from the test sample sorted by increasing $L_{\text{BL Lac}}$ and at equal distance from each other. The $L_{\text{BL Lac}}$ does not increase linearly in the plot. The upper plot presents the change of precision with the $L_{\text{BL Lac}}$ threshold for BL Lacs and FSRQs. The threshold where precision reaches 0.9 for BL Lacs and FSRQs is $L_{\text{BL Lac}} = 0.545$ and $L_{\text{BL Lac}} = 0.396$, respectively (blue and red vertical lines). Precision is on average a monotonically increasing/decreasing function with $L_{\text{BL Lac}}$ for BL Lac/FSRQ. The zig-zag oscillations in precision are due to the finite and relatively small number of sources in the testing sample.

(more easily achieved) because BL Lacs are more numerous than FSRQs.

Inputting BCU parameters into the trained network and applying the threshold values of $L_{\text{BL Lac}} = 0.545$ and $L_{\text{BL Lac}} = 0.396$ (Fig. 8), as described above, the neural network leaves 15 BCUs unclassified ($0.396 > L_{\text{BL Lac}} > 0.545$), 378 classified as BL Lacs ($L_{\text{BL Lac}} > 0.545$) and 174 as FSRQs ($L_{\text{BL Lac}} < 0.396$).

4.2 Properties of classified BCUs

In Table 1 an example of 10 classified BCU sources is shown. The complete list of 567 classified BCUs is available in electronic format in which sources are sorted by increasing $L_{\text{BL Lac}}$. The classification is based on the 0.9 precision threshold obtained by comparing BCUs $L_{\text{BL Lac}}$ with dependence of precision on $L_{\text{BL Lac}}$ (Fig. 7). Note that BL Lac and FSRQ precision versus $L_{\text{BL Lac}}$ are cumulative functions.

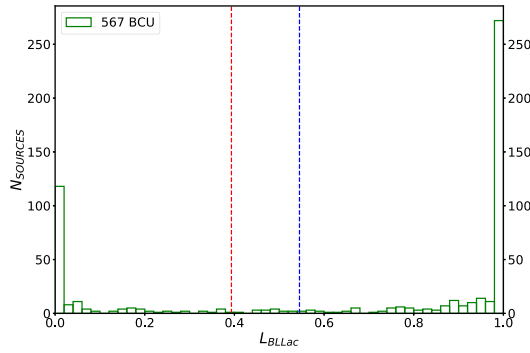


Figure 8. Trained network applied to 567 BCU sources. Applying the threshold values of $L_{\text{BLLac}} = 0.545$ and $L_{\text{BLLac}} = 0.396$ (blue and red vertical lines) leaves 15 BCU unclassified, 378 classified as BL Lacs and 174 as FSRQs.

Therefore a precision value listed for a source corresponds to precision for all sources which have higher or lower L_{BLLac} than a given source.

In Fig. 9 the sky distribution in Galactic coordinates of 567 BCUs used in the classification is shown. The 15 BCUs that are left unclassified show no dependence on latitude or longitude, i.e. position with respect to the Galactic plane or Galactic centre where γ -ray sources are more difficult to observe. The same can be noted for BCUs which are classified, but with less certainty (L_{BLLac} closer to threshold values). In order to quantify this we use a threshold $L_{\text{BLLac}} = 0.445$ corresponding to precision of about 89 per cent at which all BCUs can be classified. Then we use mean absolute error defined here as $\sum |1 - L_{\text{BLLac}}|/N$ for BL Lac candidates ($L_{\text{BLLac}} > 0.445$) and $\sum |0 - L_{\text{BLLac}}|/N$ for FSRQs candidates ($L_{\text{BLLac}} < 0.445$). This quantity is an average measure of uncertainty of BCUs classification. We found that this value is not bigger for BCUs at $|b| < 10^\circ$ than the ones at $|b| > 10^\circ$ meaning that BCUs near galactic plane are not classified with less certainty. The same result is obtained by using mean squared error.

4.3 Comparison with *C16* work

The last two columns in Table 1 present L_{BLLac} and BCU classification obtained in *C16*.

In Fig. 10 567 BCUs used for classification in this work are shown. The horizontal axis is L_{BLLac} obtained from this work while vertical is L_{BLLac} obtained from *C16*. Blue and red lines present BL

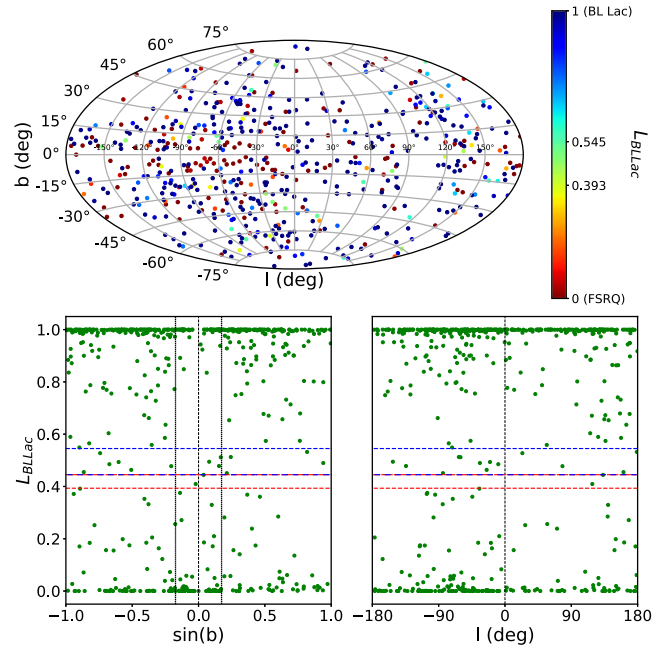


Figure 9. Upper plot: Sky distribution in Galactic coordinates of 567 BCUs used in classification. Colours correspond to L_{BLLac} . Thresholds of 0.545 and 0.396 for BL Lacs and FSRQs are shown in the colour bar. Bottom plots: L_{BLLac} of 567 BCUs versus Galactic longitude (left) and latitude (right). Blue and red horizontal lines correspond to the two thresholds. Blue-red line at $L_{\text{BLLac}} = 0.445$ is a threshold corresponding to precision of about 89 per cent at which all BCUs can be classified. Bottom-left plot: two black dashed vertical lines around $b = 0^\circ$ correspond to $|b| = 10^\circ$.

Lac and FSRQ 0.9 precision thresholds for new and *C16* network. There is substantial overlap between the network classifications. 328 BCUs are classified as BL Lacs by both networks (upper-right area), 137 BCUs are classified as FSRQs by both networks (lower-left). Out of 75 unclassified BCUs (from 567 used in this work) by the *C16* network, 38 are now classified as BL Lacs (middle-right) and 29 as FSRQs (middle-left) by the new network, while 8 (middle) are left unclassified by both networks. Out of 15 unclassified BCUs from the new network, 5 were classified as BL Lac (upper-middle) and 2 as FSRQs (lower-middle) by the *C16* network, while 8 are unclassified by both as mentioned. Finally, 12 BCUs are classified as BL Lacs by new network and as FSRQs by the *C16* one (lower-right); 8 BCUs are classified as FSRQs by new network and as BL Lacs

Table 1. An example of 10 classified BCU sources is shown. The full list is available in electronic format. Columns: 3FGL name, Galactic latitude, Galactic longitude, L_{BLLac} (this work), precision value for BL Lac, precision value for FSRQ, BCU classification (this work), L_{BLLac}^* (*C16*), and BCU classification (*C16*).

Name	b (deg)	l (deg)	L_{BLLac}	P_{BLLac}	P_{FSRQ}	Class	L_{BLLac}^*	Class*
3FGL J1532.7–1319	33.719	352.143	0.000		1.000	FSRQ	0.000	FSRQ
3FGL J1419.5–0836	48.376	336.849	0.003		0.947	FSRQ	0.011	FSRQ
3FGL J0939.2–1732	25.464	251.174	0.175		0.929	FSRQ	0.155	FSRQ
3FGL J2114.7+3130	–11.884	77.994	0.482			BCU	0.514	BCU
3FGL J0133.3+4324	–18.815	130.957	0.731	0.909		BL Lac	0.676	BL Lac
3FGL J1344.5–3655	24.739	314.585	0.942	0.938		BL Lac	0.825	BL Lac
3FGL J2049.0–6801	–35.896	326.659	0.995	0.977		BL Lac	0.919	BL Lac
3FGL J1434.6+6640	47.385	108.193	1.000	0.989		BL Lac	0.995	BL Lac
3FGL J0620.4+2644	5.632	185.708	1.000	0.986		BL Lac	0.987	BL Lac
3FGL J0649.6–3138	–14.196	241.507	1.000	1.000		BL Lac	0.978	BL Lac

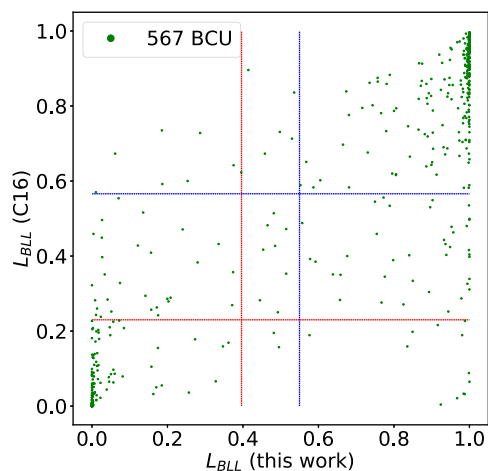


Figure 10. 567 BCUs used for classification in this work. Horizontal axis: L_{BLLac} obtained in this work. Vertical axis: L_{BLLac} obtained from the *C16* paper. Blue and red lines present BL Lac and FSRQ 0.9 precision thresholds for new ($L_{\text{BLLac}} = 0.545$ and $L_{\text{BLLac}} = 0.396$) and *C16* network ($L_{\text{BLLac}} = 0.566$ and $L_{\text{BLLac}} = 0.230$).

by the *C16* one (upper-left). In most cases, discrepancies between classifications are for sources which lie closer to threshold values with respect to majority of other sources, i.e. for sources which are classified with less certainty by both networks. Overall, it can be concluded that there is significant overlap between classifications, with the new network leaving fewer BCUs left unclassified using the same precision threshold as in *C16*.

5 CONCLUSION

In this study, we explored the possibilities to increase the performance of a neural network method previously used for the classification of uncertain blazars. We considered the improvement of performance applying new parameters both from the physical features of the sources, and also from statistic adjustment of the algorithm input. We developed an optimized version of the original algorithm improving the selecting performance of about 80 per cent. The final result of this study left 15 uncertain blazar sources instead of 77 in Chiaro et al. (2016). This result confirms the MLTs as powerful methods to classify uncertain astrophysical objects and particularly blazars. The ANN technique could be a very worthwhile opportunity for the scientific community to select promising targets for multiwavelength rigorous classification and related studies at different energy ranges, mainly at very high energies by the present generation of Cherenkov telescopes and the forthcoming Cherenkov Telescope Array.⁴

We plan to use techniques described in this paper for classifying BCUs from the forthcoming 8-year LAT Source Catalog. The new catalogue will have more than 1000 BCUs obtained from twice as long observation period.

ACKNOWLEDGEMENTS

Support for science analysis during the operation phase is gratefully acknowledged from the *Fermi*-LAT collaboration for making the

Fermi-LAT results available in such a useful form, the Institute of Space Astrophysics and Cosmic Physics in Milano – Italy (IASF), the Department of Physics and Geology of the University of Perugia – Italy, National Institute for Astrophysics (INAF) Rome – Italy, and National Institute for Nuclear Physics (INFN) Rome – Italy. The authors would like to thank David J. Thompson (NASA Goddard Space Flight Center, Greenbelt, MD, USA) for review of the paper and anonymous referee for discussion and suggestions leading to the improvement of this work.

REFERENCES

- Abdo A. A. et al., 2010a, *ApJS*, 188, 405
 Acero M. et al., 2015, *ApJS*, 218, 23
 Ackermann M. et al., 2012, *ApJ*, 753, 83
 Ackermann M. et al., 2015, *ApJ*, 810, 14
 Atwood W. B. et al., 2009, *ApJ*, 697, 1071
 Beiman L., 1973, Statistics. With a View Toward Applications. Houghton Mifflin Co., Boston
 Bishop C. M., 1995, Neural Networks for Pattern Recognition, Oxford University Press, New York, USA
 Chiaro G., Salvetti D., La Mura G., Giroletti M., Thompson D. J., Bastieri D., 2016, *MNRAS*, 462, 3180 (C16)
 Cortes C. et al., 1995, *Mach. Learn.*, 20, 273
 Doert M., Errando M., 2014, *ApJ*, 782, 41
 Freud Y. et al., 1999, 14, 771
 Gish H., 1990, Proceeding on Acoustic Speech and Signal Processing, IEEE (Institute of Electrical and Electronics Engineers), Piscataway, New Jersey, US, p. 1361
 Hassan T., Mirabal N., Contreras J. L., Oya I., 2013, *MNRAS*, 428, 220
 Kingma D. P., Ba J., 2014, preprint ([arXiv:1412.6980](https://arxiv.org/abs/1412.6980))
 Lee K. J., Guillemot L., Yue Y. L., Kramer M., Champion D. J., 2012, *MNRAS*, 424, 2832
 Leflaucheur J., Pita S., 2017, *A&A*, 602, 86
 Liaw A., Wiener M., 2002, *R News*, 2, 18
 Mirabal N., Charles E., Ferrara E. C., Gonthier P. L., Harding A. K., Sánchez-Conde M. A., Thompson D. J., 2016, *ApJ*, 825, 69
 Nolan P. L. et al., 2012, *ApJS*, 199, 31
 Richard M. P., Lippman R. P., 1991, *Neural Comput.*, 3, 461
 Salvetti D., Chiaro G., La Mura G., Thompson D. J., 2017, *MNRAS*, 470, 1291 (S17)
 Saz Parkinson P. M. et al., 2016, *ApJ*, 820, 2
 Vapnik V., 1995, The Nature of Statistical Learning Theory. Springer, New York, p. 138

SUPPORTING INFORMATION

Supplementary data are available at *MNRAS* online.

Table 1. An example of 10 classified BCU sources is shown.

Please note: Oxford University Press is not responsible for the content or functionality of any supporting materials supplied by the authors. Any queries (other than missing material) should be directed to the corresponding author for the article.

⁴www.cta-observatory.org



4FGLzoo. Classifying *Fermi*-LAT uncertain gamma-ray sources by machine learning analysis

Graziano Chiaro^a, Milos Kovacevic^a, Giovanni La Mura^b

^a Istituto di Fisica Cosmica e Astrofisica Spaziale IASF / INAF, Via A. Corti 12, 20133 Milano, Italy

^b Lab. de Instrumentação e Física Experimental de Partículas LIP, Av. Prof. Gama Pinto 2, 1649-003 Lisboa, Portugal

ARTICLE INFO

Article history:

Received 24 November 2020

Accepted 24 November 2020

Keywords:

Active galaxy

Blazar

Neural network

ABSTRACT

Since 2008 August the Fermi Large Area Telescope (LAT) has provided a continuous coverage of the gamma-ray sky yielding more than 5000 γ -ray sources, but 54% of the detected sources remain unidentified or with no certain association with a low energy counterpart. Rigorous determination of class type for a γ -ray source requires the optical spectrum of the correct counterpart but optical observations are demanding and time-consuming, then machine learning techniques can be a powerful alternative for screening and ranking. We use machine learning techniques to select blazar candidates among uncertain sources characterized by γ -ray properties very similar to those of Active Galactic Nuclei. Consequently, the percentage of sources of uncertain type drops from 54% to less than 12% predicting a new zoo for the Fermi γ -ray sources. The result of this study opens up new considerations on the population of the gamma energy sky, and it will facilitate the planning of significant samples for rigorous analysis and multi-wavelength observational campaigns.

© 2020 Elsevier B.V. All rights reserved.

1. Introduction

Since the beginning of its mission, the Fermi Large Area Telescope (Atwood et al., 2009) detected more than 5000 γ -ray sources in the 100 MeV - 300 GeV energy range. Referring to 10 years of monitoring (Ballet et al., 2020) in the fourth Fermi Large Area Telescope catalog (4FGL) the two largest classes of sources are Active Galactic Nuclei (AGN) and pulsars (PRS). Approximately 95% of AGNs can be classified as blazar objects subdivided in BL Lacertae (BLL) and Flat Spectrum Radio Quasars (FSRQ) or uncertain sources positionally coincident with an object showing distinctive broad-band blazar characteristics (BCU), but lacking reliable optical spectrum measurements. BCUs represent 43% of the blazar class. Also, 28% of the Fermi-LAT sources have not even a tentative association with a likely γ -ray emitting object and are referred to as Unassociated Gamma-ray Sources (UGS). As a result, the nature of $\sim 54\%$ of the γ -ray sources is not yet completely known.

However, since blazars are the most numerous γ -ray source class, we expect that a large fraction of the uncertain or unassociated sources might belong to one of the blazar subclasses, BLL or FSRQ.

FSRQs show strong, broad emission lines at optical wavelengths, while BLL spectra are more challenging since they show at most weak emission lines, but they are often featureless or can display absorption features (Abdo et al., 2010). Unfortunately optical observations are demanding and time-consuming. Machine learning techniques (ML) can be a powerful tool for screening and ranking gamma sources according to their classification. We tested the power of ML methods by applying a ML algorithm to the first release of the Fermi Large Area Telescope Fourth Source Catalog (Abdollahi et al., 2020). This paper is a continuation of a series of studies that use machine learning to classify Fermi Large Area Telescope gamma-ray sources that are likely active galactic nuclei (Chiaro et al., 2016; Salvetti et al., 2017).

In this study, we use an improved release of an original Artificial Neural Network (ANN) algorithm first applied in Chiaro et al. (2016) and based on the variation of the Empirical Cumulative Distribution Function (ECDF, Kolmogorov, 1933) extracted from the γ -ray light curves of the sources. A detailed description of the algorithm that we use and of its performance dealing with the BCU population in the 3FGL data set is described in Kovacevic et al. (2019). This paper is organized as follows: in Sect. 2 we provide a brief description of the machine learning technique. In that section, we also discuss the result of the ANN analysis. In Sect. 3 we validate the predictions by optical spectral observations of a number of targets, finally we discuss the 4FGL zoo in Sect. 4.

E-mail address: graziano.chiaro@inaf.it (G. Chiaro).

2. Machine learning technique

In previous studies, machine learning techniques, mainly ANN, have been applied to classifying uncertain γ -ray sources (see, e.g., Ackermann et al., 2012; Lee et al., 2012; Hassan et al., 2013; Doert et al., 2014; Chiaro et al., 2016; Mirabal et al., 2016; Saz Parkinson et al., 2016; Lefaucheur et al., 2017; Salvetti et al., 2017, and others).

The basic building block of an ANN algorithm is the neuron. Information is passed as inputs to the *neuron*, which produces an output (Gish, 1990; Richard et al., 1991). The output is typically determined as a mathematical function of the inputs and can be interpreted as a Bayesian a posteriori probability that models the likelihood of classification based on input parameters. The power of a ANN algorithm comes from assembling many neurons into a network. The network can model very complex behavior from input to output.

Here we apply the same ANN algorithm described in Kovacevic et al. (2019) to the data set available at the time of the 4FGL catalog publication (Abdollahi et al., 2020) which covered 8 years of observations. The improvement over the previous study is due to the use of a longer observing period, including the first eight years of operations, to better statistics on the measurements of the source parameters, and a wider database of multi-wavelength information. The only relevant change in the process consists in the use of the 7 energy bands for the measurements of energy-dependent properties in 4FGL (0.05–0.1, 0.1–0.3, 0.3–1, 1–3, 3–10, 10–30, 30–300 GeV), with respect to the 5 bands used in 3FGL.

2.1. Analysis of γ -ray sources

In Kovacevic et al. (2020), the authors analyzed 1329 BCUs and the algorithm selected 801 BLL candidates, 406 FSRQ candidates, while 122 sources remained with uncertain classification. Zhu et al. (2020) used a combination of Random Forest (RF) and ANN classification approaches to study 1336 UGS sources. As result 583 sources were classified as AGN-like, 115 as pulsars, and 154 as sources belonging to other classes of known gamma-ray emitters while 484 sources remained of uncertain classification.

Since the algorithm used in our study is specific for blazar classes selection we further extended the classification of these UGS sources, by providing a blazar classification likelihood for the ones identified as AGN candidates.

Machine learning techniques always consider the algorithm reliable efficiency to produce classification likelihoods if it achieves a precision of 90%.¹ In Fig. 1 the BL Lac likelihood L_B for each of the 583 sources in our sample is shown. Each source is presented by a green dot. On the left-hand vertical axis, the final value of L_B is an average of 300 L_B obtained by selecting different training and testing samples. On the right-hand side of the plot are the cumulative values. The cumulative value for each source is obtained by summing all the L_B values (from the left-hand vertical axis) above a given L_B for that source and dividing by the number of sources whose L_B is above the given L_B . If we consider all the sources with a cumulative value above 0.9, we expect 90% of them to be genuine BLLac with a 10% contamination of genuine FSRQ. The cumulative values for FSRQs can be obtained in a similar way.

The light green area corresponds to 1σ error due to differences in train-test sample selections. With 90% precision the algorithm identified 294 BLL candidates ($L_B \geq 0.639$) and 164 FSRQs ($L_B \leq 0.254$) while 125 sources remained of uncertain classification.

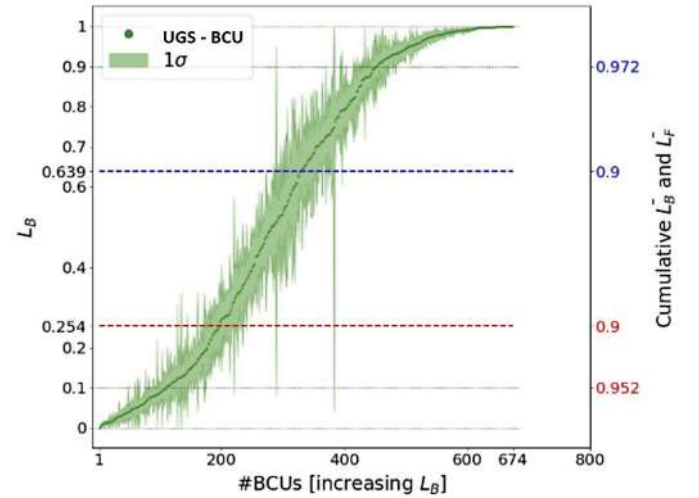


Fig. 1. BL Lac probability $L_B (= 1 - L_F)$ of 583 UGS_{BCU}. Each source is presented by a green dot. The right-hand vertical axis shows the corresponding cumulative L_B (blue) and L_F (red). The light green area corresponds to 1σ error due to differences in train-test sample selections. (For interpretation of the colors in the figures, the reader is referred to the web version of this article.)

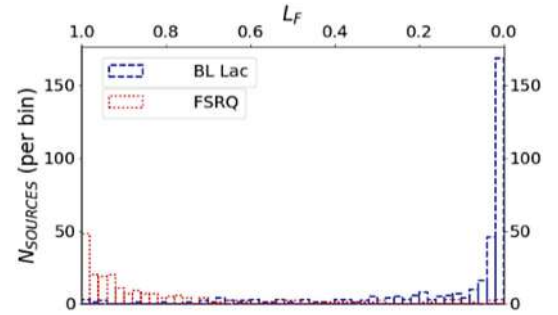


Fig. 2. Top: Histogram of the likelihood BL Lac (blue bar) and FSRQ (red bar) of the UGS_{BCU} sample. Two opposite and separate peaks differentiate the two classes of blazar.

Fig. 2 presents the histogram of classification likelihoods. Two distinct and opposite peaks for BL Lac (blue) and FSRQ (red), the former at $L_{BLL} \sim 1$, while the latter at $L_B \sim 0$ are visible.

3. Validation

Since optical observations represent the most rigorous and reliable test for the classification of uncertain γ -ray sources, to validate our ANN analysis, we compared the results with the source classes inferred by Pena-Herazo et al. (2020) optical spectroscopic observations. In that study, the authors produced optical spectra for 130 4FGL BCUs and 50 unassociated γ -ray sources. The majority of the observed sources are found to be BL Lacs since they show a featureless optical spectrum. Our ANN predictions show an excellent agreement with the optical results. Only 9 predictions out of 180 observed sources misclassify the targets. The misclassification relates to particularly weak and unusually soft BL Lac sources erroneously classified as FSRQ by the ANN algorithm. For completeness, we also considered the 103 3FGL sources that remained uncertain in Salvetti et al. (2017). In 4FGL catalog 78 of those sources are classified as blazar, but 25 still remained as BCUs. Applying our ANN algorithm we classified 13 of them, obtaining 11 BL Lac and 2 FSRQ, while 12 sources remained BCUs. The optical spectra in Pena-Herazo et al. (2020) confirm the ANN classifications also for the latter sources showing that our ANN algorithm provides a reliable method to classify uncertain or unidentified gamma-ray sources also without optical observations.

¹ Precision is a threshold based on the optimization of the positive association rate defined as the fraction of true positives over the objects classified as positive, of $\sim 90\%$.

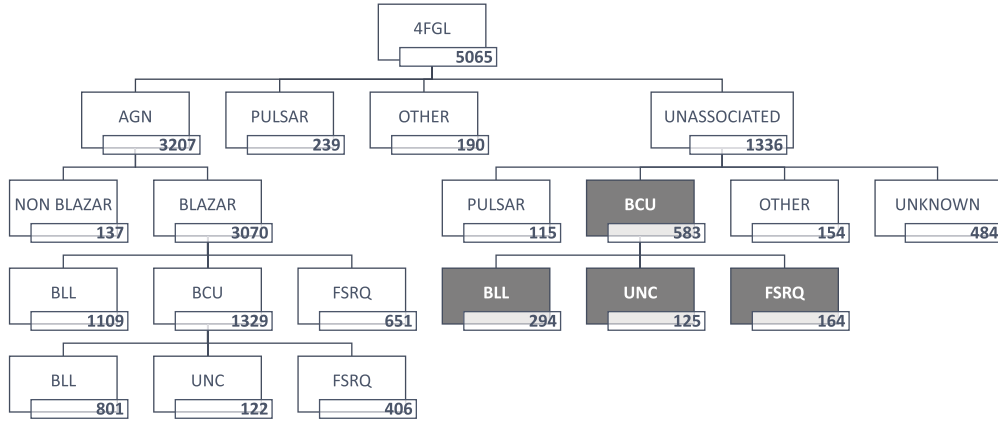


Fig. 3. The 4FGLzoo. The ANN results of this study are highlighted as cells with a gray background.

Table 1

Example of our classification for 10 4FGL UGS_{BCU} sources. The full list is available in electronic format. Columns: 4FGL name, Galactic latitude, Galactic longitude, L_B , lower value of error interval L_B low, upper value of error interval L_B up.

4FGL name	b(deg)	l(deg)	L_B	L_B low	L_B up
4FGLJ0000.3-7355	-42.73	307.709	0.882	0.844	0.92
4FGLJ0003.3+2511	-36.411	109.382	0.947	0.93	0.963
4FGLJ0004.0+5715	-5.023	116.526	0.097	0.061	0.137
4FGLJ0004.4-4001	-73.845	336.991	0.627	0.578	0.679
4FGLJ0006.6+4618	-15.87	114.92	0.39	0.335	0.442
4FGLJ0008.4+6926	6.886	119.148	0.335	0.207	0.466
4FGLJ0008.9+2509	-36.725	110.915	0.016	0.002	0.039
4FGLJ0009.1-5012	-65.545	319.395	0.236	0.171	0.297
4FGLJ0009.2+1745	-43.965	108.909	0.23	0.15	0.312
4FGLJ0009.7-1418	-73.912	83.706	0.37	0.285	0.454

Table 2

The classification of the blazar source classes in 4FGLzoo against the 3FGL zoo after ANN analysis.

Class	3FGLzoo	4FGLzoo
Blazar	2279	3672
- BL Lac	1276 (56%)	2204 (60%)
- FSRQ	823 (36%)	1221 (33%)
- BCU	180 (8%)	247 (7%)

4. 4FGLzoo

Improving the results of the previous studies (Kovacevic et al., 2020; Zhu et al., 2020; Kovacevic et al., 2019) with our UGS_{BCU} analysis we predict a new classification (for the 4FGL γ -ray population 4FGLzoo) with 1095 BL Lacs candidates and 570 FSRQs candidates while the fraction of the 4FGL uncertain sources decreases from 54% to 17% (Fig. 3). In Table 1 we give a partial list of classified UGS_{BCU} sources while the full list is available in the electronic format attached to this paper. It is also interesting to see, as shown in Table 2, how the relative contribution of the two blazar classes remains almost the same in both the eight years 4FGL catalog and in the four years 3FGL. By decreasing the uncertainty and increasing the sources class prediction the ANN could be useful to the gamma-ray science community as a valid discriminant of best targets for future follow-up multi-wavelength obser-

vations. The full list of classified 4FGL BCUs sources, analyzed in Kovacevic et al. (2020), is available in electronic format at <https://cdsarc.unistra.fr/viz-bin/cat/J/MNRAS/493/1926>.

Declaration of competing interest

The authors declare that they have no known competing financial interests or personal relationships that could have appeared to influence the work reported in this paper.

Acknowledgments

Support for science analysis during the operation phase is gratefully acknowledged from the Fermi-LAT Collaboration for making the LAT results available in such a useful form. The authors gratefully thank Francesco Massaro, Dept. of Physics, Università degli Studi, Torino, Italy and his collaborators for sharing optical spectroscopic material and Kerui Zhu, Dept. of Physics, Yunnan Normal University, ROC for sharing ML UGS results. The authors would like to thank the anonymous referee for discussion and suggestions leading to the improvement of this work.

References

- Abdo, A.A., et al., 2010. *Astrophys. J.* 716, 1.
- Abdollahi, S., et al., 2020. *Astrophys. J. Suppl. Ser.* 247, 33.
- Ackermann, M., et al., 2012. *Astrophys. J.* 753, 83.
- Atwood, W.B., et al., 2009. *Astrophys. J.* 697, 1071.
- Ballet, J., et al., 2020. *arXiv:2005.11208v3*.
- Chiaro, et al., 2016. *Mon. Not. R. Astron. Soc.* 462, 3180.
- Doert, M., et al., 2014. *Astrophys. J.* 782, 41.
- Gish, H., 1990. *Proc. Acoust. Speech Signal Process.* 3, 1361.
- Hassan, T., et al., 2013. *Mon. Not. R. Astron. Soc.* 428, 220.
- Kolmogorov, A., 1933. *G. Ist. Ital. Attuariale* (4) 83, 91.
- Kovacevic, M., et al., 2019. *Mon. Not. R. Astron. Soc.* 490, 477.
- Kovacevic, M., et al., 2020. *Mon. Not. R. Astron. Soc.* 493, 1926.
- Lee, K.J., et al., 2012. *Mon. Not. R. Astron. Soc.* 424, 2832.
- Lefaucheur, J., et al., 2017. *Astron. Astrophys.* 602, 86.
- Mirabal, N., et al., 2016. *Astrophys. J.* 825, 69.
- Pena-Herazo, H.A., et al., 2020. *arXiv:2009.07905*.
- Richard, M.P., et al., 1991. *Neural Comput.* 3, 461.
- Salvetti, D., et al., 2017. *Mon. Not. R. Astron. Soc.* 470, 1291.
- Saz Parkinson, P.M., et al., 2016. *Astrophys. J.* 820, 8.
- Zhu, K., et al., 2020. *arXiv:2001.06010*.



Gamma Rays from Fast Black-hole Winds

M. Ajello¹, L. Baldini², J. Ballet³, G. Barbiellini^{4,5}, D. Bastieri^{6,7}, R. Bellazzini⁸, A. Berretta⁹, E. Bissaldi^{10,11}, R. D. Blandford¹², E. D. Bloom¹², R. Bonino^{13,14}, P. Bruel¹⁵, S. Buson¹⁶, R. A. Cameron¹², D. Caprioli¹⁷, R. Caputo¹⁸, E. Cavazzuti¹⁹, G. Chartas²⁰, S. Chen^{6,21}, C. C. Cheung²², G. Chiaro²³, D. Costantin²⁴, S. Cutini²⁵, F. D’Ammando²⁶, P. de la Torre Luque¹⁰, F. de Palma^{27,28}, A. Desai²⁹, R. Diesing¹⁷, N. Di Lalla¹², F. Dirirsa³⁰, L. Di Venere^{10,11}, A. Domínguez³¹, S. J. Fegan¹⁵, A. Franckowiak³², Y. Fukazawa³³, S. Funk³⁴, P. Fusco^{10,11}, F. Gargano¹¹, D. Gasparrini^{35,36}, N. Giglietto^{10,11}, F. Giordano^{10,11}, M. Giroletti²⁶, D. Green³⁷, I. A. Grenier³, S. Guiriec^{18,38}, D. Hartmann¹, D. Horan¹⁵, G. Jóhannesson^{39,40}, C. Karwin¹, M. Kerr²², M. Kovačević²⁵, M. Kuss⁸, S. Larsson^{41,42,43}, L. Latronico¹³, M. Lemoine-Goumard⁴⁴, J. Li⁴⁵, I. Liodakis⁴⁶, F. Longo^{4,5}, F. Loparco^{10,11}, M. N. Lovellette²², P. Lubrano²⁵, S. Maldera¹³, A. Manfreda², S. Marchesi⁴⁷, L. Marcotulli¹, G. Martí-Devesa⁴⁸, M. N. Mazziotta¹¹, I. Mereu^{9,25}, P. F. Michelson¹², T. Mizuno⁴⁹, M. E. Monzani¹², A. Morselli³⁵, I. V. Moskalenko¹², M. Negro^{50,51}, N. Omodei¹², M. Orienti²⁶, E. Orlando^{12,52}, V. Paliya^{53,54}, D. Paneque³⁷, Z. Pei⁷, M. Persic^{4,55}, M. Pesce-Rollins⁸, T. A. Porter¹², G. Principe^{4,5,26}, J. L. Racusin¹⁸, S. Rainò^{10,11}, R. Rando^{6,21,56}, B. Rani^{18,57,58}, M. Razzano^{8,72}, A. Reimer^{12,48}, O. Reimer⁴⁸, P. M. Saz Parkinson^{59,60,61}, D. Serini¹⁰, C. Sgrò⁸, E. J. Siskind⁶², G. Spandre⁸, P. Spinelli^{10,11}, D. J. Suson⁶³, D. Tak^{18,64}, D. F. Torres^{65,66,67}, E. Troja^{18,68}, K. Wood^{69,70}, G. Zaharijas^{52,71}, and J. Zrake¹

¹ Department of Physics and Astronomy, Clemson University, Kinard Lab of Physics, Clemson, SC 29634-0978, USA; majello@clemson.edu, ckarwin@clemson.edu

² Università di Pisa and Istituto Nazionale di Fisica Nucleare, Sezione di Pisa I-56127 Pisa, Italy

³ AIM, CEA, CNRS, Université Paris-Saclay, Université de Paris, F-91191 Gif-sur-Yvette, France

⁴ Istituto Nazionale di Fisica Nucleare, Sezione di Trieste, I-34127 Trieste, Italy

⁵ Dipartimento di Fisica, Università di Trieste, I-34127 Trieste, Italy

⁶ Istituto Nazionale di Fisica Nucleare, Sezione di Padova, I-35131 Padova, Italy

⁷ Dipartimento di Fisica e Astronomia “G. Galilei”, Università di Padova, I-35131 Padova, Italy

⁸ Istituto Nazionale di Fisica Nucleare, Sezione di Pisa, I-56127 Pisa, Italy

⁹ Dipartimento di Fisica, Università degli Studi di Perugia, I-06123 Perugia, Italy

¹⁰ Dipartimento di Fisica “M. Merlin” dell’Università e del Politecnico di Bari, via Amendola 173, I-70126 Bari, Italy

¹¹ Istituto Nazionale di Fisica Nucleare, Sezione di Bari, I-70126 Bari, Italy

¹² W.W. Hansen Experimental Physics Laboratory, Kavli Institute for Particle Astrophysics and Cosmology, Department of Physics and SLAC National Accelerator Laboratory, Stanford University, Stanford, CA 94305, USA

¹³ Istituto Nazionale di Fisica Nucleare, Sezione di Torino, I-10125 Torino, Italy

¹⁴ Dipartimento di Fisica, Università degli Studi di Torino, I-10125 Torino, Italy

¹⁵ Laboratoire Leprince-Ringuet, École polytechnique, CNRS/IN2P3, F-91128 Palaiseau, France

¹⁶ Institut für Theoretische Physik und Astrophysik, Universität Würzburg, D-97074 Würzburg, Germany

¹⁷ Department of Astronomy and Astrophysics, University of Chicago, Chicago, IL 60637, USA; caprioli@uchicago.edu, rdiesing@uchicago.edu

¹⁸ NASA Goddard Space Flight Center, Greenbelt, MD 20771, USA

¹⁹ Italian Space Agency, Via del Politecnico snc, I-00133 Roma, Italy

²⁰ Department of Physics and Astronomy of the College of Charleston, Charleston, SC 29424, USA; chartasg@cofc.edu

²¹ Department of Physics and Astronomy, University of Padova, Vicolo Osservatorio 3, I-35122 Padova, Italy

²² Space Science Division, Naval Research Laboratory, Washington, DC 20375-5352, USA

²³ INFN-Istituto di Astrofisica Spaziale e Fisica Cosmica Milano, via E. Bassini 15, I-20133 Milano, Italy

²⁴ University of Padua, Department of Statistical Science, Via 8 Febbraio, 2, I-35122 Padova, Italy

²⁵ Istituto Nazionale di Fisica Nucleare, Sezione di Perugia, I-06123 Perugia, Italy

²⁶ INFN Istituto di Radioastronomia, I-40129 Bologna, Italy

²⁷ Dipartimento di Matematica e Fisica “E. De Giorgi”, Università del Salento, Lecce, Italy

²⁸ Istituto Nazionale di Fisica Nucleare, Sezione di Lecce, I-73100 Lecce, Italy

²⁹ Department of Physics, University of Wisconsin-Madison, Madison, WI 53706, USA

³⁰ Laboratoire d’Annecy-le-Vieux de Physique des Particules, Université de Savoie, CNRS/IN2P3, F-74941 Annecy-le-Vieux, France

³¹ Grupo de Altas Energías, Universidad Complutense de Madrid, E-28040 Madrid, Spain

³² Ruhr University Bochum, Faculty of Physics and Astronomy, Astronomical Institute (AIRUB), D-44780 Bochum, Germany

³³ Department of Physical Sciences, Hiroshima University, Higashi-Hiroshima, Hiroshima 739-8526, Japan

³⁴ Friedrich-Alexander Universität Erlangen-Nürnberg, Erlangen Centre for Astroparticle Physics, Erwin-Rommel-Str. 1, D-91058 Erlangen, Germany

³⁵ Istituto Nazionale di Fisica Nucleare, Sezione di Roma “Tor Vergata”, I-00133 Roma, Italy

³⁶ Space Science Data Center—Agenzia Spaziale Italiana, Via del Politecnico, snc, I-00133, Roma, Italy

³⁷ Max-Planck-Institut für Physik, D-80805 München, Germany

³⁸ The George Washington University, Department of Physics, 725 21st St, NW, Washington, DC 20052, USA

³⁹ Science Institute, University of Iceland, IS-107 Reykjavik, Iceland

⁴⁰ Nordita, Royal Institute of Technology and Stockholm University, Roslagstullsbacken 23, SE-106 91 Stockholm, Sweden

⁴¹ Department of Physics, KTH Royal Institute of Technology, AlbaNova, SE-106 91 Stockholm, Sweden

⁴² The Oskar Klein Centre for Cosmoparticle Physics, AlbaNova, SE-106 91 Stockholm, Sweden

⁴³ School of Education, Health and Social Studies, Natural Science, Dalarna University, SE-791 88 Falun, Sweden

⁴⁴ Centre d’Études Nucléaires de Bordeaux Gradignan, IN2P3/CNRS, Université Bordeaux 1, BP120, F-33175 Gradignan Cedex, France

⁴⁵ Department of Astronomy, School of Physical Sciences, University of Science and Technology of China, Hefei, Anhui 230026, People’s Republic of China

⁴⁶ Finnish Centre for Astronomy with ESO (FINCA), University of Turku, FI-21500 Piikkiö, Finland

⁴⁷ INFN—Osservatorio di Astrofisica e Scienza dello Spazio di Bologna, Via Piero Gobetti, 93/3, I-40129, Bologna, Italy

⁴⁸ Institut für Astro- und Teilchenphysik, Leopold-Franzens-Universität Innsbruck, A-6020 Innsbruck, Austria

⁴⁹ Hiroshima Astrophysical Science Center, Hiroshima University, Higashi-Hiroshima, Hiroshima 739-8526, Japan

⁵⁰ Center for Research and Exploration in Space Science and Technology (CRESST) and NASA Goddard Space Flight Center, Greenbelt, MD 20771, USA

- ⁵¹ Department of Physics and Center for Space Sciences and Technology, University of Maryland Baltimore County, Baltimore, MD 21250, USA
- ⁵² Istituto Nazionale di Fisica Nucleare, Sezione di Trieste, and Università di Trieste, I-34127 Trieste, Italy
- ⁵³ Aryabhata Research Institute of Observational Sciences (ARIES), Manora Peak, Nainital-263 129, Uttarakhand, India
- ⁵⁴ Deutsches Elektronen Synchrotron DESY, D-15738 Zeuthen, Germany
- ⁵⁵ Osservatorio Astronomico di Trieste, Istituto Nazionale di Astrofisica, I-34143 Trieste, Italy
- ⁵⁶ Center for Space Studies and Activities “G. Colombo”, University of Padova, Via Venezia 15, I-35131 Padova, Italy
- ⁵⁷ Korea Astronomy and Space Science Institute, 776 Daedeokdae-ro, Yuseong-gu, Daejeon 30455, Republic of Korea
- ⁵⁸ Department of Physics, American University, Washington, DC 20016, USA
- ⁵⁹ Santa Cruz Institute for Particle Physics, Department of Physics and Department of Astronomy and Astrophysics, University of California at Santa Cruz, Santa Cruz, CA 95064, USA
- ⁶⁰ Department of Physics, The University of Hong Kong, Pokfulam Road, Hong Kong, People’s Republic of China
- ⁶¹ Laboratory for Space Research, The University of Hong Kong, Hong Kong, People’s Republic of China
- ⁶² NYCB Real-Time Computing Inc., Lattingtown, NY 11560-1025, USA
- ⁶³ Purdue University Northwest, Hammond, IN 46323, USA
- ⁶⁴ Department of Physics, University of Maryland, College Park, MD 20742, USA
- ⁶⁵ Institute of Space Sciences (ICE, CSIC), Campus UAB, Carrer de Magrans s/n, E-08193 Barcelona, Spain
- ⁶⁶ Institut d’Estudis Espacials de Catalunya (IEEC), E-08034 Barcelona, Spain
- ⁶⁷ Institució Catalana de Recerca i Estudis Avançats (ICREA), E-08010 Barcelona, Spain
- ⁶⁸ Department of Astronomy, University of Maryland, College Park, MD 20742, USA
- ⁶⁹ Praxis Inc., Alexandria, VA 22303, USA
- ⁷⁰ Naval Research Laboratory, Washington, DC 20375, USA
- ⁷¹ Center for Astrophysics and Cosmology, University of Nova Gorica, Nova Gorica, Slovenia
- Received 2021 May 6; revised 2021 July 1; accepted 2021 August 5; published 2021 November 10

Abstract

Massive black holes at the centers of galaxies can launch powerful wide-angle winds that, if sustained over time, can unbind the gas from the stellar bulges of galaxies. These winds may be responsible for the observed scaling relation between the masses of the central black holes and the velocity dispersion of stars in galactic bulges. Propagating through the galaxy, the wind should interact with the interstellar medium creating a strong shock, similar to those observed in supernovae explosions, which is able to accelerate charged particles to high energies. In this work we use data from the Fermi Large Area Telescope to search for the γ -ray emission from galaxies with an ultrafast outflow (UFO): a fast ($v \sim 0.1 c$), highly ionized outflow, detected in absorption at hard X-rays in several nearby active galactic nuclei (AGN). Adopting a sensitive stacking analysis we are able to detect the average γ -ray emission from these galaxies and exclude that it is due to processes other than UFOs. Moreover, our analysis shows that the γ -ray luminosity scales with the AGN bolometric luminosity and that these outflows transfer $\sim 0.04\%$ of their mechanical power to γ -rays. Interpreting the observed γ -ray emission as produced by cosmic rays (CRs) accelerated at the shock front, we find that the γ -ray emission may attest to the onset of the wind–host interaction and that these outflows can energize charged particles up to the transition region between galactic and extragalactic CRs.

Unified Astronomy Thesaurus concepts: Active galactic nuclei (16); Galactic winds (572); Gamma-rays (637)

1. Introduction

Accreting supermassive black holes (SMBHs) at the centers of galaxies, often called active galactic nuclei (AGN), have been observed to launch and power outflows, which can have a dramatic impact on the host galaxies themselves, the intergalactic medium, and the intracluster medium (Silk & Rees 1998; McNamara & Nulsen 2007; Somerville et al. 2008; Hopkins & Elvis 2010; McCarthy et al. 2010). One spectacular, well-observed, type of outflow are relativistic jets, where particles are accelerated to near the speed of light in narrow collimated beams (often with an opening angle of $\sim 1^\circ$), which can extend up to megaparsec scales. These relativistic jets shine at all wavelengths, but are easily studied in radio, X-rays, and γ -rays when the jet axis is not far from our line of sight. Black-hole winds (King & Pounds 2015), on the other hand, are AGN outflows that are not collimated and are generally more difficult to detect, although no less important. Indeed, AGN winds have been proposed as the mechanism able to regulate the coevolution of the galaxy and its central SMBH, which is observed in the scaling of the black-hole mass and the bulge velocity dispersion (Gebhardt et al. 2000; Ferrarese & Ford 2005; Kormendy & Ho 2013). AGN

winds that are powerful enough can heat up and eject the gas from the galaxy, regulating the growth of both the galaxy itself and the black hole.

The most powerful AGN winds can reach velocities of $\sim 0.1\text{--}0.3c$ (Chartas et al. 2002; Pounds et al. 2003; Reeves et al. 2003; Tombesi et al. 2010b) and can carry enough energy to unbind the gas of the stellar bulge (King & Pounds 2015). Some of these winds have been identified in nearby AGN through X-ray observations of blueshifted Fe K-shell absorption lines (Reeves et al. 2003; Tombesi et al. 2010b, 2010a, 2012; Gofford et al. 2013).

These winds, which have been dubbed ultrafast outflows (UFOs), are made of highly ionized gas and are likely launched from near the SMBH (King & Pounds 2003). Their wide solid angle [$\Omega/2\pi \approx 0.4$, (Gofford et al. 2015)] and fast velocity allow UFOs to transfer a significant amount of kinetic energy from the AGN to the host galaxy. They are also believed to be common in nearby AGN (King & Pounds 2015).

UFOs, while traveling outward, interact and shock the interstellar medium (ISM; King 2010), producing a reverse shock and a forward shock. The reverse shock decelerates the wind itself while the forward shock travels through the galaxy with a velocity in the $\sim 200\text{--}1000 \text{ km s}^{-1}$ range and leads to the formation of a bubble of hot, tenuous gas, see, e.g., Zubovas & King (2012).

⁷² Funded by contract FIRB-2012-RBF12PM1F from the Italian Ministry of Education, University and Research (MIUR).

Because of the cooling, the phase and velocity of the outflow should change, eventually leading to the formation of low-velocity molecular outflows, commonly observed in many ultraluminous infrared (IR) galaxies (see e.g., Ciccone et al. 2014; Feruglio et al. 2015). Indeed, there are a handful of objects like IRAS 17020+4544 (Longinotti et al. 2018) and Mrk 231 (Feruglio et al. 2015) where both a UFO and molecular outflow have been detected and found in agreement with the prediction of the energy-conserving outflow model, which is the basis of AGN feedback (Fabian 2012).

UFOs have velocities comparable to (or even larger than) those of the ejecta launched in supernova explosions, which are known to shock the ISM and accelerate cosmic rays (CRs). Gamma-ray emission is a signature of the interaction of relativistic charged particles with ambient gas and photon fields and has been observed in many cases in supernova remnants (Acero et al. 2016). Given the similarity, in this work we search for the γ -ray emission from UFOs using the Large Area Telescope (LAT; Atwood et al. 2009) on board the Fermi Gamma-ray Space Telescope (Atwood et al. 2009).

Models of the γ -ray emission from AGN outflows (Wang & Loeb 2016a; Lamastra et al. 2017) show them to be weak emitters, with γ -ray luminosities of $\approx 10^{40}$ erg s $^{-1}$, which explains why UFOs have not yet been detected by the LAT.⁷³ Here, we adopt a different strategy and search for the collective γ -ray emission from a sample of UFOs using a stacking technique.

The paper is organized as follows. In Sections 2 and 3, we describe the sample selection and the data analysis. Results are presented in Section 4, with additional tests discussed in Section 5. Section 6 reports the theoretical interpretation of the observed γ -ray emission, while a discussion is given in Section 7. Finally, Section 8 gives our conclusions.

2. Sample Selection

We start from a sample of 35 sources that have been identified as UFOs through X-ray observations (Reeves et al. 2003; Tombesi et al. 2010b, 2010a, 2012; Gofford et al. 2013). We have verified that none of the objects are positionally coincident with any known γ -ray sources reported in the Fourth Fermi Large Area Telescope (4FGL) source catalog (Abdollahi et al. 2020). From the initial sample we make the following cuts. First, we only keep the radio-quiet sources (as specified in the original references) to avoid contamination of the signal from the relativistic jet. Furthermore, we only select sources that are nearby ($z < 0.1$) with a mildly relativistic wind velocity ($v > 0.1c$). The former cut is motivated by the expected low luminosity of the UFO emission (Wang & Loeb 2016a), and the latter cut is motivated by the fact that the γ -ray emission is predicted to scale with the kinetic power of the outflow (Wang & Loeb 2016a; Lamastra et al. 2017). After making these cuts we are left with 11 sources, which we use as our benchmark sample. The details of these sources are reported in Table 1.

Table 2 reports additional properties of our sample of UFOs, including the bulge velocity dispersion, 1.4 GHz radio flux and total (8–1000 μ m) IR luminosity. Figure 1 shows that the UFOs considered here obey the M – σ relation well (Gültekin et al. 2009; Woo et al. 2010), strengthening the evidence that these outflows operated in the energy-conserving phase in the past (King & Pounds 2015). Finally, the origin of the radio emission

in radio-quiet AGN is not very clear and it is likely due to a number of phenomena, including AGN winds, star formation, free-free emission from photoionized gas, and AGN coronal activity (Panessa et al. 2019). For these reasons, the radio fluxes reported in Table 2 are interpreted as upper limits to the synchrotron emission from accelerated electrons, as discussed in Section 6.

We note that there are alternative models explaining the absorption features as produced not by an outflowing wind, but as resonant absorption by highly ionized iron in the accretion disk (Gallo & Fabian 2011). However, this model has difficulties explaining several of the observed properties of the UFO features like the presence of P Cygni profiles (Nardini et al. 2015; Chartas et al. 2016), or the correlation between outflow velocity and the AGN bolometric luminosity (Saez & Chartas 2011; Matzeu et al. 2017).

3. Data Analysis

3.1. Data

We analyze data collected by Fermi-LAT between 2008 August 4 and 2019 September 10 (11.1 yr). The events have energies in the range of 1–800 GeV and are binned in eight bins per decade. The pixel size is 0.08°. To reduce contamination from the Earth’s limb, we use a maximum zenith angle of 105°. We define a 10° × 10° region of interest (ROI) centered at the position of each UFO source. We use the standard data filters: DATA_QUAL > 0 and LAT_CONFIG==1. The analysis is performed using Fermipy (v0.18.0),⁷⁴ which utilizes the underlying FermiTools (v1.2.23).

We select photons corresponding to the P8R3_SOURCE_V2 class (Atwood et al. 2013). In order to optimize the sensitivity of our stacking technique we implement a joint likelihood analysis with the four point-spread function (PSF) event types available in the Pass 8 data set.⁷⁵ The data is divided into quartiles corresponding to the quality of the reconstructed direction, from the lowest quality quartile (PSF0) to the best quality quartile (PSF3). Each sub-selection has its own binned likelihood instance that is combined in a global likelihood function for the ROI. This is easily implemented in Fermipy by specifying the components section in the configuration file. Each PSF type also has its own corresponding isotropic spectrum, namely, iso_P8R3_SOURCE_V2_PSF $_i$ _v1, for i ranging from 0–3. The Galactic diffuse emission is modeled using the standard component (gll_iem_v07), and the point-source emission is modeled using the 4FGL catalog (gll_psc_v20). In order to account for photon leakage from sources outside of the ROI due to the PSF of the detector, the model includes all 4FGL sources within a 15° × 15° region. The energy dispersion correction (edisp_bins=–1) is enabled for all sources except the isotropic component.

3.2. Analysis

In the Local Universe ($z < 0.1$) UFOs are predicted to have a γ -ray luminosity of $\sim 10^{40}$ erg s $^{-1}$ (Wang & Loeb 2016a), making them too faint to be detected individually by Fermi-LAT. Indeed, adopting the average photon index in the 4FGL

⁷³ No γ -ray source from the 4FGL catalog (Abdollahi et al. 2020) is associated with a UFO.

⁷⁴ Available at <https://fermipy.readthedocs.io/en/latest/>.

⁷⁵ For more information on the different PSF types see https://fermi.gsfc.nasa.gov/ssc/data/analysis/documentation/Cicerone/Cicerone_Data/LAT_DP.html.

Table 1
UFO Source Sample

Name	R.A. (deg) [J2000]	Decl. (deg) [J2000]	Type	Redshift [z]	Velocity [v/c]	$\log M_{\text{BH}}$ [M_{\odot}]	$\log \dot{E}_K^{\text{Min}}$ [erg s^{-1}]	$\log \dot{E}_K^{\text{Max}}$ [erg s^{-1}]	$\log L_{\text{Bol}}$ [erg s^{-1}]	95% UL ($\times 10^{-11}$) [$\text{ph cm}^{-2} \text{s}^{-1}$]
(1)	(2)	(3)	(4)	(5)	(6)	(7)	(8)	(9)	(10)	(11)
Ark 120 ^{a,c}	79.05	−0.15	Sy1	0.033	0.27	8.2 ± 0.1	>43.1	46.2 ± 1.3	45.0 ^f 44.2 ^b 44.6	7.5
MCG-5-23-16 ^{a,c}	146.92	−30.95	Sy2	0.0084	0.12	7.6 ± 1.0	42.7 ± 1.0	44.3 ± 0.2	44.1 ^l	4.3
NGC 4151 ^{a,c}	182.64	39.41	Sy1	0.0033	0.105	7.1 ± 0.2	>41.9	43.1 ± 0.5	44.1 ^g 42.9 ^h 43.9 ⁱ 42.9 ^j 43.2 ^k 43.4	10.6
PG 1211+143 ^{a,c}	183.57	14.05	Sy1	0.081	0.13	8.2 ± 0.2	43.7 ± 0.2	46.9 ± 0.1	45.7 ^f 44.8 ^h 44.7 ^j 45.0 ^k 45.1	3.7
NGC 4507 ^{a,c}	188.90	−39.91	Sy2	0.012	0.18	6.4 ± 0.5	>41.2	44.6 ± 1.1	44.3 ^e	3.4
NGC 5506 ^{b,d}	213.31	−3.21	Sy1.9	0.006	0.25	7.3 ± 0.7	43.3 ± 0.1	44.7 ± 0.5	44.3 ^e	6.4
Mrk 290 ^{a,c}	233.97	57.90	Sy1	0.030	0.14	7.7 ± 0.5	43.4 ± 0.9	45.3 ± 1.2	44.4 ^e	4.5
Mrk 509 ^{a,c}	311.04	−10.72	Sy1	0.034	0.17	8.1 ± 0.1	>43.2	45.2 ± 1.0	45.2 ^e 44.3 ^h 45.3 ⁱ 44.3 ^j 44.5 ^k 44.7	9.5
SWIFT J2127.4 +5654 ^{b,d}	321.94	56.94	Sy1	0.014	0.23	~ 7.2	42.8 ± 0.1	45.6 ± 0.5	44.5 ^d	9.1
MR 2251-178 ^{b,d}	343.52	−17.58	Sy1	0.064	0.14	8.7 ± 0.1	43.3 ± 0.1	46.7 ± 0.7	45.8 ^f	7.4
NGC 7582 ^{a,c}	349.60	−42.37	Sy2	0.0052	0.26	7.1 ± 1.0	43.4 ± 1.1	44.9 ± 0.4	43.3 ^e	4.7

Notes. Our sample comprises 11 sources with $z < 0.1$ and $v > 0.1c$. The first superscript on the source name indicates the reference for the detection, and the second superscript indicates the reference for the UFO parameters (Columns 6–9), where \dot{E}_K^{min} and \dot{E}_K^{max} are the minimum and maximum kinetic powers. Values for the bolometric luminosity (L_{Bol}) are taken from the literature, with the reference indicated by the superscript. For sources with numerous determinations we also give the mean value in boldface text. The γ -ray flux (1–800 GeV) upper limit (UL) is calculated at the 95% confidence level, using a photon index of -2.0 .

^a Tombesi et al. (2010a).

^b Gofford et al. (2013).

^c Tombesi et al. (2012).

^d Gofford et al. (2015).

^e Vasudevan et al. (2010).

^f Vasudevan & Fabian (2007).

^g Vasudevan & Fabian (2009).

^h Peterson et al. (2004).

ⁱ Crenshaw & Kraemer (2012).

^j (Kaspi et al. 2005, 5100 Å flux density).

^k (Kaspi et al. 2005, 1450 Å flux density).

^l Alonso-Herrero et al. (2011).

catalog of $\Gamma = -2.2$ we derive a > 1 GeV flux of $3.3 \times 10^{-12} \text{ ph cm}^{-2} \text{ s}^{-1}$, for a source with a luminosity of $10^{40} \text{ erg s}^{-1}$ at $z = 0.014$ (the median redshift of our sample). This flux is ~ 2.5 times fainter than the weakest source reported in the 4FGL catalog. We therefore analyze our source sample using a stacking technique. This technique has been developed previously and has been successfully employed for multiple studies, i.e., upper limits on dark matter interactions (Ackermann et al. 2011), detection of the extragalactic background light (Abdollahi et al. 2018), extreme blazars (Paliya et al. 2019), and star-forming galaxies (Ajello et al. 2020a).

The main assumption that we make for the stacking technique is that the sample of UFOs we are considering can be characterized by average quantities like the average flux and

the average photon index (when we model their spectra with a power law). There are then two steps to the method. In the first step, the model components are optimized for each ROI using a maximum likelihood fit. We evaluate the significance of each source in the ROI using the test statistic (TS), which is defined as

$$\text{TS} = -2 \log(L_0/L), \quad (1)$$

where L_0 is the likelihood for the null hypothesis, and L is the likelihood for the alternative hypothesis.⁷⁶ For the first iteration

⁷⁶ For a more complete explanation of the TS resulting from a likelihood fit see Mattox et al. (1996) and https://fermi.gsfc.nasa.gov/ssc/data/analysis/documentation/Cicerone/Cicerone_Likelihood/.

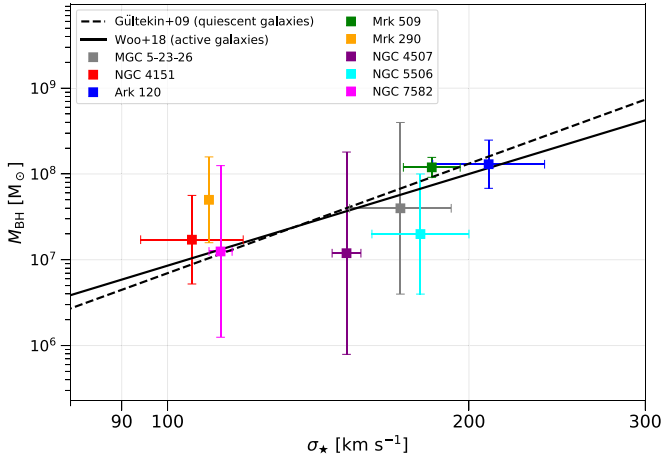


Figure 1. Bulge stellar velocity dispersion vs. black-hole mass for our UFO sample, with values taken from the literature. Measurements were found for 8/11 sources. The error bars are statistical plus systematic, where the systematic uncertainty comes from different independent estimates. Information for the velocity dispersion measurements is provided in Table 2. To quantify the systematic uncertainty in the black-hole mass, we use minimum and maximum values from the different references provided in Table 2, as well as the values given in Table 1. The solid and dashed lines show the scaling relations for active and quiescent galaxies, from Woo et al. (2010) and Gültekin et al. (2009), respectively.

Table 2
Additional UFO Properties

Name	Velocity Dispersion [km s ⁻¹]	1.4 GHz Radio Flux ^h [mJy]	IR Lum. ⁱ [log(L _⊙)]
(1)	(2)	(3)	(4)
Ark 120	184, 238 ^{b,c}	12.4	11.0
MCG-5-23-16	152, 192 ^{b,d}	14.3	9.6
NGC 4151	94, 119 ^{b,d}	347.6	10.2
PG 1211+143	...	4.3	...
NGC 4507 ^a	146, 156 ^e	67.4	10.5
NGC 5506	160, 200 ^e	355	10.5
Mrk 290	109, 111 ^f	5.32	<10.3
Mrk 509	172, 196 ^e	19.2	10.5
SWIFT J2127.4 +5654	...	6.4	10.4
MR 2251-178	...	16	<10.5
NGC 7582	110, 116 ^e	270	10.6

Notes. The second column gives velocity dispersion measurements taken from the literature, with the references indicated by the superscripts. Measurements were found for 8/11 sources, and we provide minimum and maximum values (separated by a comma). For sources with just one reference, the range is due to statistical error only, and for sources with two references, the range also includes the systematic error due to the different estimates.

^a Note that most published estimates of the black-hole mass for NGC 4507 are based on velocity dispersion and [O III] line widths, and thus they are not independent measures. In quantifying the uncertainty in Figure 1, we also use black-hole mass values from Bian & Gu (2007); Beifiori et al. (2012); Nicastro et al. (2003).

^b Woo et al. (2010).

^c Grier et al. (2013).

^d Onken et al. (2014).

^e Marinucci et al. (2012).

^f Bennert et al. (2015).

^g Hyperleada.

^h NVSS (Condon et al. 1998).

ⁱ IRAS (Kleinmann et al. 1986; Moshir et al. 1990).

of the fit, the spectral parameters of the Galactic diffuse component (index and normalization) and the isotropic component are freed. In addition, we free the normalizations of all 4FGL sources with $TS \geq 25$ that are within 5° of the ROI center, as well as sources with $TS \geq 500$ and within 7° . Lastly, the UFO source is fit with a power-law spectral model, and the spectral parameters (normalization and index) are also freed. In the first step, we also find new point sources using the Fermipy function *find_sources*, which generates TS maps and identifies new sources based on peaks in the TS. The TS maps are generated using a power-law spectral model with an index of -2.0 . The minimum separation between two point sources is set to 0.5° , and the minimum TS for including a source in the model is set to 16.

In the second step, 2D TS profiles are generated for the spectral parameters of each UFO source, where the TS is defined as in Equation (1). We scan photon indices from -1 to -3.3 with a spacing of 0.1 and total integrated photon flux (between 1 and 800 GeV) from 10^{-13} – 10^{-9} ph cm⁻² s⁻¹ with 40 logarithmically spaced bins, freeing just the parameters of the diffuse components. For this step, the power-law spectra of the UFOs are defined in terms of the total flux (F_{tot}), integrated between the minimum energy (E_{min}) and the maximum energy (E_{max}):

$$\frac{dN}{dE} = \frac{F_{\text{tot}}(\Gamma + 1)E^\Gamma}{E_{\text{max}}^{\Gamma+1} - E_{\text{min}}^{\Gamma+1}} \quad (2)$$

Note that the likelihood value for the null hypothesis is calculated at the end of the first step by removing the UFO source from the model. Since we perform a joint likelihood in the different PSF event types (PSF0–PSF3), the total profile for each source is obtained by adding the profiles from each of the four event types. Lastly, the TS profiles for all sources are added to obtain the stacked profile. The TS is an additive quantity, and so the stacked profile gives the statistical significance for the combined signal.

We validated the stacking method relying on a set of Monte Carlo simulations that reproduce the Fermi-LAT observations. In these tests, the simulations include the isotropic and Galactic emission, as well as an isotropic population of point sources resembling blazars, which account for the vast majority of sources detected by Fermi-LAT. Faint, below-threshold *blazars* are included in the synthetic sky following the models of Ajello et al. (2015). Using this setup, two different tests were performed. The stacking analysis was performed at 60 random *empty* positions, i.e., positions away from bright detected sources. This analysis yielded no detection, confirming that the technique does not generate spurious detections. The second set of tests was aimed at characterizing the detected signal. The stacking was performed for 60 simulated sources whose flux was extracted from a power-law distribution with index -2.5 and minimum and median flux of, respectively, 4×10^{-10} and 6.4×10^{-10} ph cm⁻² s⁻¹. The photon indices were extracted from a Gaussian distribution with average -2.21 and dispersion of 0.2 . The values derived from the stacking analysis (flux = $7.0^{+0.6}_{-0.7} \times 10^{-10}$ ph cm⁻² s⁻¹ and index of -2.24 ± 0.05) are in agreement with the inputs, showing that our analysis successfully retrieves the average quantities of a population of sources. Moreover, the likelihood profile would

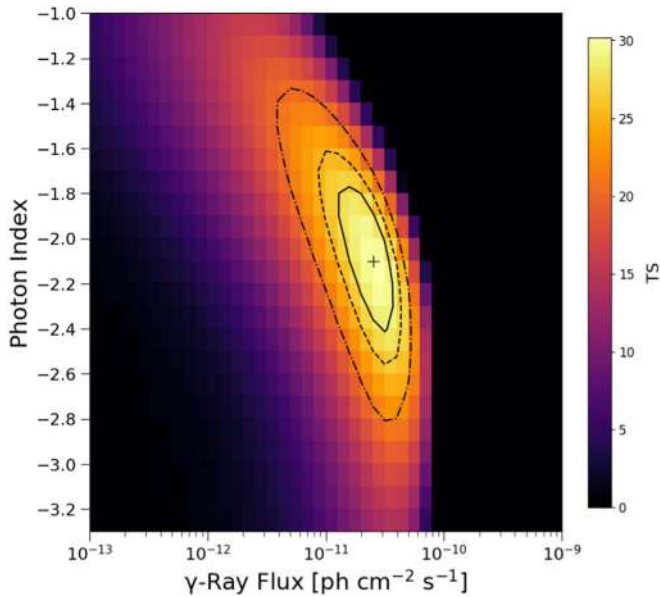


Figure 2. Stacked TS profile for the sample of UFOs. The color scale indicates the TS, and the plus sign indicates the location of the maximum value, with a TS = 30.1 (5.1σ). Significance contours (for 2 degrees of freedom (dof)) are overlaid on the plot showing the 68%, 90%, and 99% confidence levels, corresponding to Δ TS = 2.30, 4.61, and 9.21, respectively.

not show a significant peak if those average quantities were not representative of the population.

4. Results

4.1. Stacked TS Profile for the Benchmark Sample

The log-likelihoods (i.e., $\log L$) are maximized with the optimizer MINUIT (James & Roos 1975), and we have verified that each fit converges properly, as indicated by the MINUIT outputs of quality = 3 and status = 0. The 95% flux upper limits from the preprocessing step are reported in Table 1.

The stacked profile for our UFO sample is shown in Figure 2. The maximum TS is 30.1 (5.1σ)⁷⁷ corresponding to a best-fit index of -2.1 ± 0.3 and a best-fit photon flux (1–800 GeV) of $2.5^{+1.5}_{-0.9} \times 10^{-11}$ ph cm $^{-2}$ s $^{-1}$. The 68%, 90%, and 99% significance contours are overlaid on the map, and as can be seen the spectral parameters are well constrained. The source with the overall highest individual TS is NGC 4151, having a maximum value of 21.2 (4.2σ), corresponding to a best-fit index of $-1.9^{+0.5}_{-0.3}$ and a best-fit flux of $6.3^{+3.7}_{-3.8} \times 10^{-11}$ ph cm $^{-2}$ s $^{-1}$. The stacking analysis excluding NGC 4151 yields a maximum TS of 15.1 (3.5σ), corresponding to a best-fit index of -2.2 ± 0.4 and a best-fit flux of $2.0^{+2.0}_{-1.0} \times 10^{-11}$ ph cm $^{-2}$ s $^{-1}$.

4.2. Spectral Energy Distribution (SED) of UFOs

The best-fit SED for our UFO sample is shown in Figure 3. The butterfly plot is constructed by sampling the range of parameter values that are within the 68% confidence contour of the stacked profile. In addition, we calculate the SED flux in three logarithmically spaced bins between 1 and 800 GeV. In

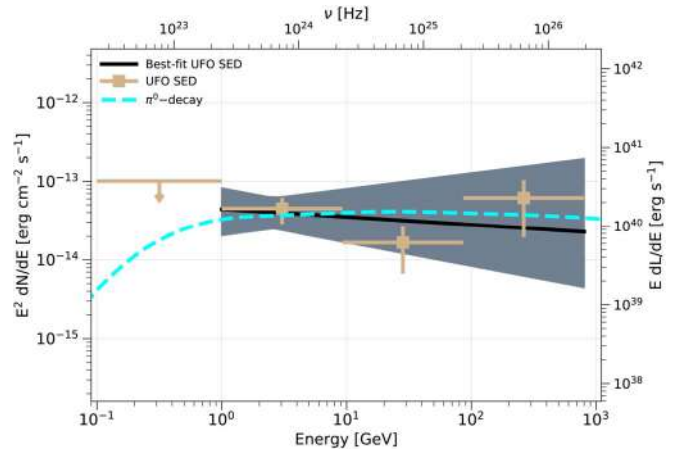


Figure 3. Best-fit UFO SED (black solid line) with 1σ uncertainty envelope (gray band). The tan data points show the UFO energy flux calculated in four different energy bins. The dashed cyan line shows our hadronic model (see Section 6), corresponding to an outflow that has propagated to ~ 20 pc. The effective redshift $z = 0.013$ was used to convert the γ -ray flux into luminosity.

every bin, we fix the power-law index of the UFOs to -2.0 and leave all other parameters free to vary. As can be seen, these data points are in agreement with the best-fit SED model. To characterize the UFO spectrum at low energy we repeat the stacking analysis in the energy range 0.1–1 GeV, which yields a 95% flux upper limit ($\Delta \log L = 2.71/2$) of 5.7×10^{-10} ph cm $^{-2}$ s $^{-1}$. We also overlay our best-fit hadronic model presented in Section 6.

4.3. Bins of Bolometric Luminosity and Kinetic Power

We test whether the γ -ray emission from UFOs scales with AGN bolometric luminosity and outflow kinetic power. To properly take the distance of each source into account, we stack in the luminosity-index space. We take estimates of the bolometric luminosity from the literature, as reported in Table 1. Such estimates can be obtained by applying a correction factor to a certain flux, typically the 5100 Å optical emission, the 1450 Å UV emission, or the 2–10 keV X-ray emission. Alternatively, the bolometric luminosity can be determined by fitting an SED to the broadband emission. In any case, the absorption from the host galaxy must be corrected for, which has a large dependence on the viewing angle of the source, and can introduce a rather significant uncertainty. In addition, the contribution from the host galaxy emission also needs to be corrected for (i.e., UV/IR/optical emission from the galactic disk). Most of the AGN emission is observed in the optical/UV, while $<10\%$ is emitted in the X-ray, and thus a broadband SED fitting ensures a more accurate determination of the bolometric luminosity. We therefore search the literature for the most reliable estimates of the bolometric luminosity, and rely on the X-ray determination for only two sources (MCG-5-23-16 and SWIFT J2127.4+5654) for which no other estimates could be found. For sources with multiple estimates we take the geometric mean. The mean of the bolometric luminosity of our sample is 2.5×10^{44} erg s $^{-1}$, and we create two bins around this value.

The stacked profiles for the two bins are shown in Figure 4. The first bin has five sources, with a mean redshift of 0.007. The maximum TS is 28.5 (5.0σ), corresponding to a best-fit index of $-1.9^{+0.3}_{-0.4}$ and a best-fit luminosity of $1.6^{+0.9}_{-0.8} \times 10^{40}$ erg s $^{-1}$. The second bin has six sources, with a mean redshift of 0.04. The maximum TS is 9.9 (2.7σ), corresponding to a best-fit index of

⁷⁷ The conversion from TS to σ has been performed on the assumption that the TS behaves asymptotically as a χ^2 distribution with 2 dof (Mattox et al. 1996). Additionally, the Akaike information criterion test also shows the null hypothesis to be highly disfavored with a relative likelihood of 2×10^{-6} .

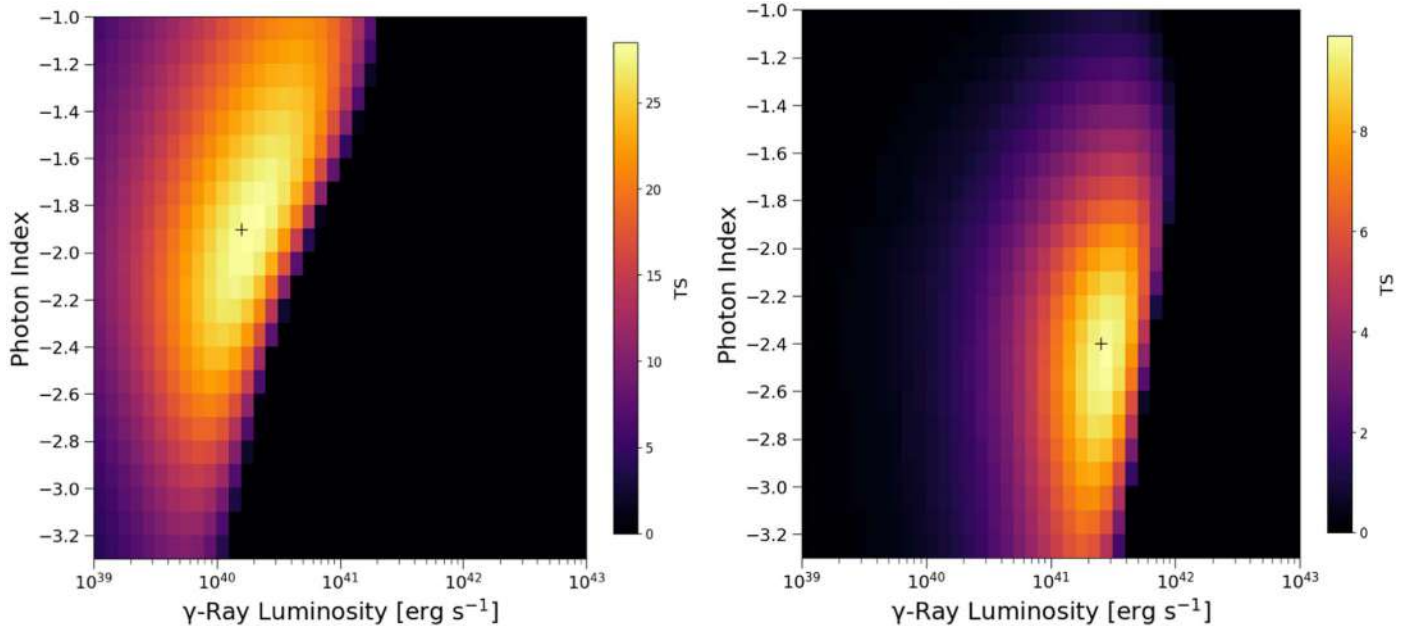


Figure 4. Stacked profiles for bins of bolometric luminosity (the mean kinetic power bins are also the same). The left and right panels show the stacking for sources with bolometric luminosity (or kinetic power) below and above the average, respectively. The color scale indicates the TS and is set to the maximum value for each bin. The black plus sign gives the best-fit parameters. The first bin consists of five sources, with a maximum TS of 28.5 (5.0σ); and the second bin consists of six sources, with a maximum TS of 9.9 (2.7σ).

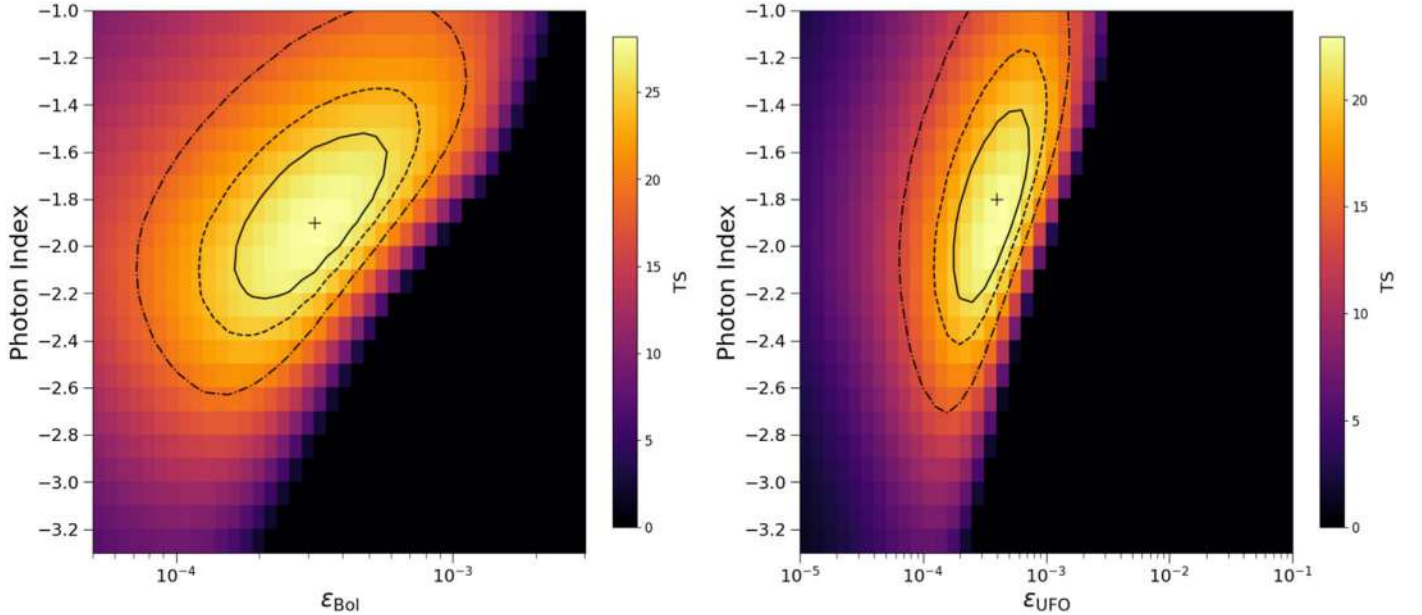


Figure 5. Stacked profiles for bolometric efficiency (left) and kinetic power efficiency (right). The color scale indicates the TS and is set to the maximum value. The black plus sign gives the best-fit parameters. Significance contours (for 2 dof) are overlaid on the plot showing the 68%, 90%, and 99% confidence levels, corresponding to $\Delta TS = 2.30, 4.61$, and 9.21 , respectively.

$-2.4^{+0.6}_{-0.5}$ and a best-fit luminosity of $2.5^{+1.5}_{-1.5} \times 10^{41} \text{ erg s}^{-1}$. The total TS (bin 1 + bin 2) for the stacking in bins is 38.4, compared to 30.1 for the full stack.

We also stack the γ -ray luminosity in bins of kinetic power. In general the kinetic power as determined from X-ray observations has a large uncertainty, as can be seen in Table 1. Minimum and maximum values are typically reported, corresponding to minimum and maximum radii of the outflow. We use the geometric mean of the minimum and maximum estimates for our calculations (also incorporating statistical

uncertainties in the range). We create two bins around the mean kinetic power, which has a value of $1.8 \times 10^{44} \text{ erg s}^{-1}$. The stacked profiles for the two bins turn out to be the same as those of the bolometric bins, as shown in Figure 4.

To further verify the relations found above for the stacking in bins, we perform the stacking analysis using both bolometric efficiency ($\epsilon_{\text{Bol}} = L_{\gamma}/L_{\text{Bol}}$) and kinetic power efficiency ($\epsilon_{\dot{E}_K} = L_{\gamma}/\dot{E}_K$). This is done by evaluating for each source the TS of a given ϵ_{Bol} (or $\epsilon_{\dot{E}_K}$) and using that efficiency value, the bolometric luminosity (or kinetic power), and the distance

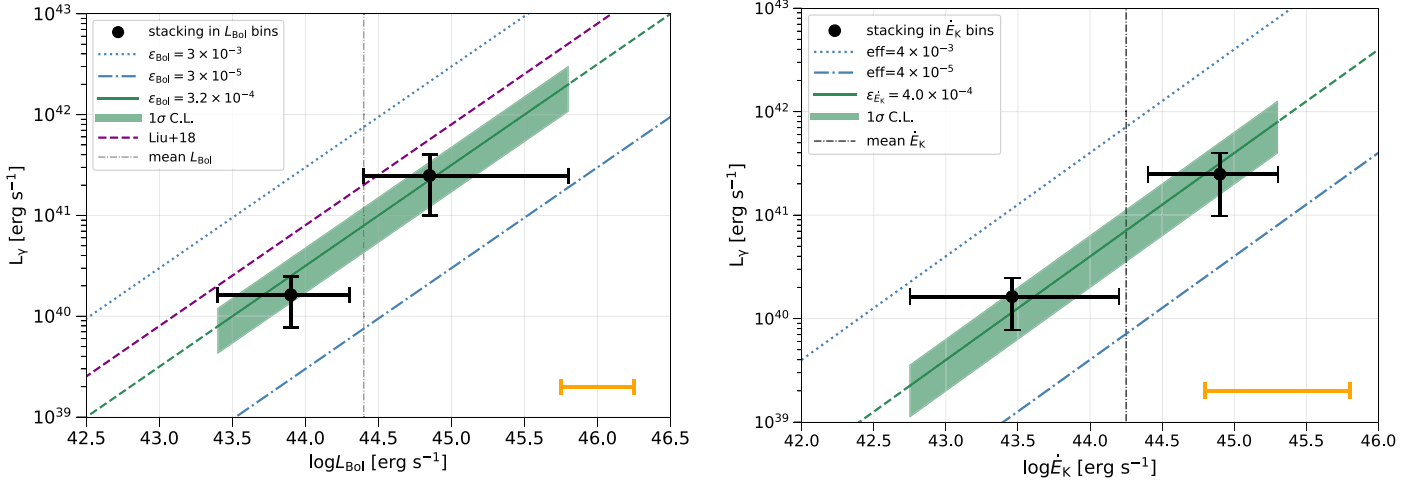


Figure 6. γ -ray luminosity vs. bolometric luminosity (left) and kinetic power (right). The black data points result from stacking in γ -ray luminosity, and the uncertainty in the x-axis corresponds to the bin widths. The gray dashed-dotted vertical lines show the value used to divide the bins. The solid green line shows the best fit resulting from stacking in efficiency, with the green band showing the 1σ confidence level. For reference, the blue lines show a range of efficiencies within roughly an order of magnitude of the best fit. The orange bar in both plots shows the average one-sided uncertainty in individual measurements of AGN bolometric luminosity (left) and kinetic power (right). In the left panel we also overlay the predicted efficiency derived from (Liu et al. 2018, dashed purple line). See the text for more details.

of the source to transform to γ -ray flux (for a given photon index). Results for these fits are shown in Figure 5. The left panel shows the bolometric efficiency, with a best-fit value of $3.2^{+1.6}_{-1.5} \times 10^{-4}$, corresponding to a best-fit index of $-1.9^{+0.3}_{-0.4}$, and a maximum TS of 28.2 (5σ). The right panel of Figure 5 shows the kinetic power efficiency, with a best-fit value of $4.0^{+2.3}_{-2.0} \times 10^{-4}$, corresponding to a best-fit index of $-1.8^{+0.3}_{-0.4}$, and a maximum TS of 23.0 (4.4σ). We note that the best-fit index from the efficiency analysis is slightly harder than the one found by the flux-index stacking, but compatible within 1σ uncertainties. The small shift observed in the best-fit index value is due to how the TS profiles are weighted differently when stacking in efficiency with respect to flux.

The result for stacking in bolometric luminosity and kinetic power are summarized in Figure 6. The left panel shows the γ -ray luminosity versus bolometric luminosity, and the right panel shows the γ -ray luminosity versus UFO kinetic power. The black data points are for stacking in bins, and the corresponding best-fit efficiency, along with the 1σ confidence interval, is plotted with the green band. Also plotted are lines for different efficiencies under the assumption of a linear scaling. As can be seen, the results on the efficiencies are in very good agreement with the stacking in bins.

In the left panel of Figure 6 we also overlay the predicted scaling of L_γ with L_{Bol} from Liu et al. (2018).⁷⁸ As can be seen, Liu et al. (2018) predict a nearly linear scaling between the logarithms of the two luminosities (over their $L_{\text{Bol}}(\text{erg s}^{-1}) = 10^{42} - 10^{45}$ range) with an efficiency of $\sim 8 \times 10^{-4}$, which is in reasonably good agreement with the one measured here.

4.4. Representative Luminosity of the Sample

Because the 11 UFO galaxies are detected at fairly different distances, we adopt a weighting scheme to compute the representative luminosity of the sample. In this framework

$\overline{L_\gamma} = \frac{\sum_{i=1}^{11} L_{\gamma,i} \times \text{TS}_i}{\text{TS}_{\text{tot}}}$, where $L_{\gamma,i}$ and TS_i are the luminosity and the TS for the i th galaxy at the global best-fit position (1–800 GeV flux of $2.5 \times 10^{-11} \text{ ph cm}^{-2} \text{ s}^{-1}$ and photon index of -2.1) and $\text{TS}_{\text{tot}} = 30.1$. The representative luminosity is found to be $\overline{L_\gamma} = 7.9^{+5.1}_{-2.9} \times 10^{40} \text{ erg s}^{-1}$ and would correspond to an effective redshift of $z = 0.013$ (adopting the above best-fit parameters). This luminosity is in very good agreement with the one obtained scaling the average bolometric luminosity $L_{\text{Bol}} = 2.5 \times 10^{44} \text{ erg s}^{-1}$ by the best-fit efficiency ($\epsilon_{\text{Bol}} = 3.2 \times 10^{-4}$). The effective redshift is also very close to the median redshift of the sample ($z = 0.013$ versus $z = 0.014$) making the TS-weighted luminosity compatible with the median γ -ray luminosity of the sample.

4.5. Simulations

The results presented here are validated using Monte Carlo simulations. We simulate the fields of the 11 UFOs considering the Galactic and isotropic emission (modeled as `gll_iem_v07` and `iso_P8R3_SOURCE_V2_v1`, respectively), background sources from the 4FGL catalog, and our test source at the position of the UFO in each ROI. The UFO spectral parameters are set to be the same as the best-fit values from the data, i.e., index $= -2.1$ and flux $= 2.5 \times 10^{-11} \text{ ph cm}^{-2} \text{ s}^{-1}$. For simplicity we use the standard event type (`evtype = 3`), i.e., we do not use the four different PSF event types. The data is simulated using the `simulate_roi` function from Fermipy. The simulation is created by generating an array of Poisson random numbers, where the expectation values are drawn from the model cube.⁷⁹ Finally, we run our stacking pipeline on the simulated data. We recover the input values, with a best-fit index of $-2.2^{+0.4}_{-0.2}$, a best-fit flux of $3.2^{+1.8}_{-1.6} \times 10^{-11} \text{ ph cm}^{-2} \text{ s}^{-1}$, and a maximum TS of 21.2 (4.2σ). The stacked profile is shown in Figure 7. Overall, the results from the simulation are consistent with the real data.

⁷⁸ Our derivation is made converting the peak 1 GeV luminosities (reported in their Figure 5) to the 1–800 GeV energy range using the best-fit spectral index of -2.1 .

⁷⁹ More information on generating the simulations is available at <https://fermipy.readthedocs.io/en/latest/fermipy.html>.

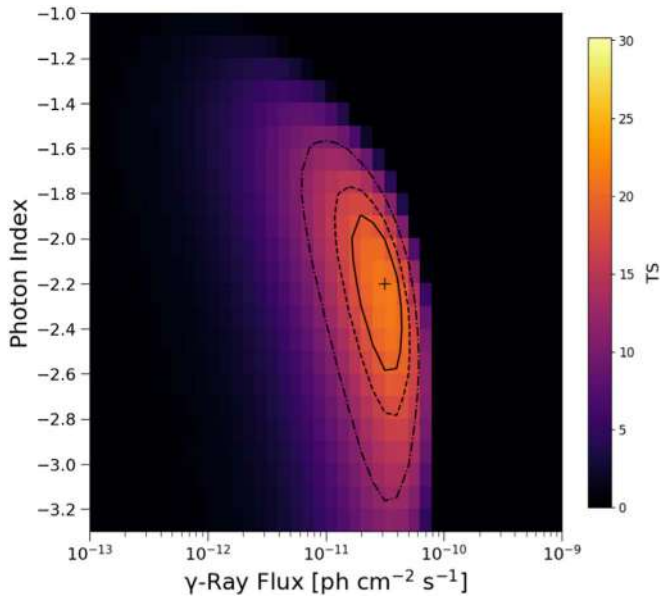


Figure 7. Stacked profile for our simulation run, in which the UFO sources are simulated with an index of -2.1 and a flux of $2.5 \times 10^{-11} \text{ ph cm}^{-2} \text{ s}^{-1}$. The color scale indicates the TS, and the plus sign indicates the location of the maximum value, with a $\text{TS} = 21.2$ (4.2σ). Significance contours (for 2 dof) are overlaid on the plot showing the 68%, 90%, and 99% confidence levels, corresponding to $\Delta\text{TS} = 2.30, 4.61$, and 9.21 , respectively. The maximum TS of the color scale is set to 30.1 (the maximum value from Figure 2).

5. Additional Tests

5.1. Control Sample

We repeat the analysis with a sample of 20 low redshift ($z < 0.1$) radio-quiet AGN that do not have UFOs. The sources were selected from the samples of Tombesi et al. (2010a) and Igo et al. (2020) for which no UFO was found. The sample of Tombesi et al. (2010a) is based on absorption features, while the sample of Igo et al. (2020) uses the excess variance method. Of the 20 sources in our control sample, there are 10 sources in common between the two studies, four additional sources from Tombesi et al. (2010a), and six additional sources from Igo et al. (2020). For reference, the list of sources in the control sample is given in Table 3. Figure 8 shows that the benchmark and control samples are well matched in X-ray luminosity and redshift.

Results for the stacked profile are shown in Figure 9. No signal is detected, with a maximum TS of 1.1. Using the profile likelihood method and a photon index of -2.0 , the upper limit on the flux (1–800 GeV) at the 95% confidence level is $8.8 \times 10^{-12} \text{ ph cm}^{-2} \text{ s}^{-1}$. This supports the interpretation of the γ -ray emission being due to the outflow rather than other processes in AGN.

5.2. Alternative UFO Samples

The fractional excess variance method was recently used in Igo et al. (2020) to search for UFOs in the samples of Tombesi et al. (2010a) and Kara et al. (2016). Overall, the results are in agreement with the past literature, finding that UFOs are a relatively widely observed phenomena in nearby AGN. However, there are differences with respect to previous studies in regards to which sources are classified as UFOs, and the corresponding UFO parameters.

Table 3
Control Sample

Name	R.A.	Decl.	Redshift	IR Lumin. [$\log(L_{\odot})$]	1.4 GHz flux [mJy]
(1)	(2)	(3)	(4)	(5)	(6)
ESO 198-G024	39.58	−52.19	0.046
Fairall 9	20.94	−58.81	0.047
H 0557-385	89.51	−38.33	0.034
MCG+8-11-11	88.72	46.44	0.020	11.1	286
Mrk 590	33.64	−0.77	0.026
Mrk 704	139.61	16.31	0.029
NGC 526A	20.98	−35.07	0.019	10.5	13.9
NGC 5548	214.50	25.14	0.017
NGC 7172	330.51	−31.87	0.0090	10.4	37.6
NGC 7469	345.82	8.874	0.016	11.6	181
ESO 113-G010	16.32	−58.44	0.027
ESO 362-G18	79.90	−32.66	0.012
IRAS 17020+4544	255.88	45.68	0.060	11.6	129
MS22549-3712	344.41	−36.94	0.039
NGC 1365	53.40	−36.14	0.0055	10.9	534
NGC 4748	193.05	−13.41	0.015	10.4	14.3
Mrk 110	141.30	52.29	0.035
IRAS 05078+1626	77.69	16.50	0.018	10.8	6.3
ESO 511-G30	214.84	−26.64	0.022
NGC 2110	88.05	−7.46	0.0078	10.3	300

Note. See Tombesi et al. (2010a) and Igo et al. (2020) for further details of the sources. The IR luminosity is reported in the 8–1000 μm range and derived from IRAS (Kleinmann et al. 1986; Moshir et al. 1990). The radio fluxes are derived from NVSS (Condon et al. 1998).

As the authors mention in Igo et al. (2020), their method relies on the variability of the strength of the emission (or absorption) features and is less sensitive in detecting cases where these features may vary in energy. The excess variance method is well suited for detecting UFOs in objects that show small changes in the energy of the UFO, but large changes of the equivalent width for the same energy. This is one reason why the excess variance method can potentially miss objects that were detected in spectral-timing analyses that model individual spectra in single epochs.

As an additional a posteriori test we perform our stacking analysis with the UFO sample determined in Igo et al. (2020), relying on sources classified as either likely outflows or possible outflows therein. Additionally, we use the same selection criterion as for our benchmark sample, i.e., $z < 0.1$ and $v > 0.1c$. This gives a sample of 18 sources. The maximum TS is 13.0 (3.2σ), corresponding to a best-fit flux of $\sim 2.0 \times 10^{-11} \text{ ph cm}^{-2} \text{ s}^{-1}$ and a best-fit index of ~ -2.4 . These results, although less significant, are in good agreement with those from our benchmark sample and show that there is γ -ray emission associated with UFOs independently of how these sources were selected.

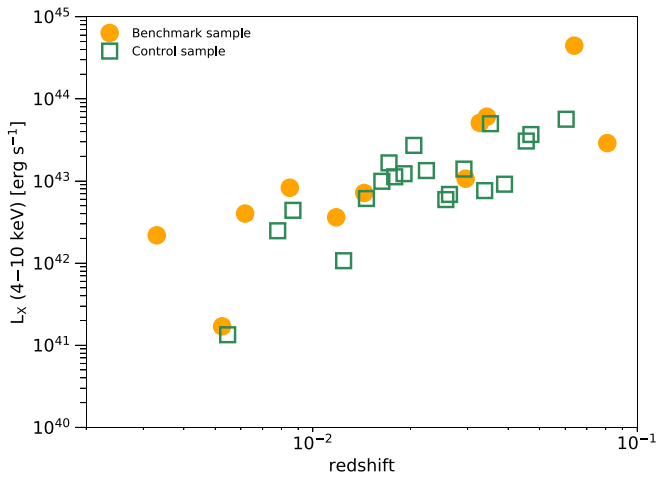


Figure 8. Comparison of redshift and X-ray luminosity (4–10 keV) for the control sample and benchmark sample, as indicated in the legend.

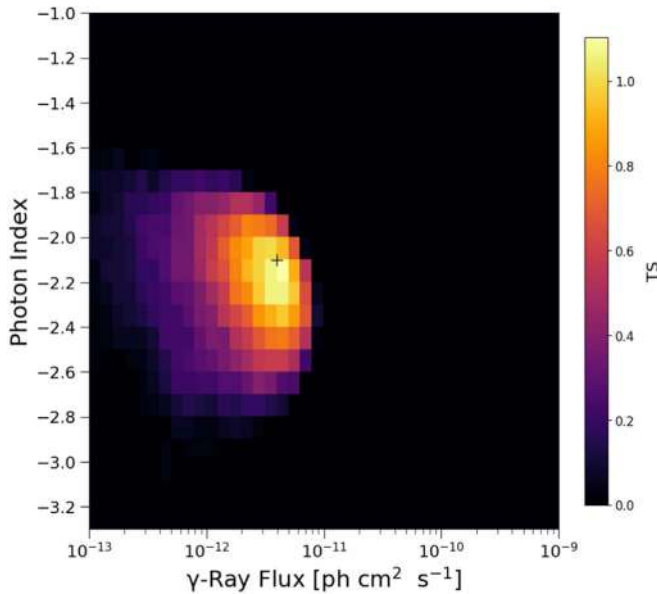


Figure 9. Stacked profile for our control sample consisting of 20 nearby ($z < 0.1$) radio-quiet AGN with no UFOs (i.e., a UFO has been searched for but none has been detected). No signal is detected, with a maximum TS of 1.1.

5.3. Emission from Star Formation Activity

Star-forming galaxies are known γ -ray emitters because of their CR population, which is accelerated at the shock fronts of supernova remnants and pulsar wind nebulae (Ajello et al. 2020a). The ensuing γ -ray emission is known to correlate well with the total IR luminosity (8–1000 μm), which is a tracer of star formation.

We find that the average total IR luminosity is $\log(L_{\odot}) = 10.4$ (see Table 2). According to the correlation reported in Ajello et al. (2020a), this implies an average γ -ray luminosity (>1 GeV) of $2.2 \times 10^{39} \text{ erg s}^{-1}$. This is about 40 times smaller than the observed luminosity and implies that the contamination due to star formation activity to the signal observed in the UFO sample is negligible.

As an additional test we searched for IR fluxes for the galaxies in the control sample (see Table 3). We could find data for nine galaxies with an average total IR luminosity of $\log(L_{\odot}) = 10.8$ (compared to 10.4 for the benchmark sample).

The stacking of this subset of galaxies in the control sample yields no detection (TS = 0.04 and 95% flux UL = $1.1 \times 10^{-11} \text{ ph cm}^{-2} \text{ s}^{-1}$) confirming that the contamination of the signal due to star formation is negligible.

5.4. Emission from Potential Jets in Radio-quiet AGN

The vast majority of the γ -ray sources detected by the LAT are powered by relativistic jets closely aligned to the line of sight (Ajello et al. 2020b). Some of the sources in our sample, particularly NGC 4151, may have a jet. However, there are several reasons why the γ -ray emission that we observe is unlikely to be produced by the jets, which may be present in these radio-quiet AGN. The best-studied system⁸⁰ is NGC 4151, for which an elongated series of knots, possibly associated with a jet, have been detected in radio (Johnston et al. 1982; Wilson & Ulvestad 1982). This jet has an angle of $\approx 40^\circ$ with respect to the line of sight and a speed $\approx 0.04c$ (Williams et al. 2017). This is among the lowest speeds measured for a jet and indicates nonrelativistic motion, likely due to thermal plasma (Ulvestad et al. 2005). NGC 4151’s jet lies on the opposite end of the spectrum of jets detected by the LAT, which are aligned often within 1° – 2° (Pushkarev et al. 2017), highly relativistic (Lister et al. 2016), dominated by nonthermal emission, and found only in radio-loud AGN (Ajello et al. 2020b).

Moreover, the emission from jets is not expected to correlate with the bolometric luminosity of radio-quiet AGN or the outflow kinetic power. It should also be noted that the sources in our sample follow the $L_{22 \text{ GHz}}/L_{14-195 \text{ keV}} \sim 10^{-5}$ trend, indicating a contribution to the radio luminosity from the hot AGN corona (Smith et al. 2020). Finally, the analysis of winds and jets in a sample of radio-loud AGN provides evidence for a wind-jet bimodality, where winds are the strongest when jets are the weakest (as measured by the radio-loudness parameter in Mehdipour & Costantini 2019).

More importantly, the same nine galaxies in the control sample for which we could find IR data also have 1.4 GHz fluxes (see Table 3). This sample is well matched in terms of radio fluxes and redshift to our benchmark sample and as reported above yields no γ -ray detection.

6. SED Modeling

We assume, as in Wang & Loeb (2016a) and Lamastra et al. (2017), that the γ -ray emission is dominated by hadronic processes resulting from diffusive shock acceleration (DSA). In order to model these processes in detail, we first calculate proton distributions using the Cosmic Ray Analytical Fast Tool (CRAFT), a code that uses a semi-analytical formalism for DSA described in Blasi (2002), Amato & Blasi (2006), Caprioli et al. (2010), and references therein. CRAFT self-consistently solves the diffusion-convection equation (e.g., Skilling 1975) for the transport of nonthermal particles in a quasi-parallel, nonrelativistic shock, including the dynamical effects of both accelerated particles and the magnetic turbulence they generate Caprioli (2011, 2012). CRAFT also uses microphysical information (particle injection, diffusion, magnetic field amplification) tuned on self-consistent kinetic plasma simulations of nonrelativistic shocks

⁸⁰ Other sources like NGC 5506 and NGC 7582 do not have resolved radio jets down to $0.1''$, while MCG-5-23-16 has a resolved morphology suggesting the presence of a jet (Orienti & Prieto 2010).

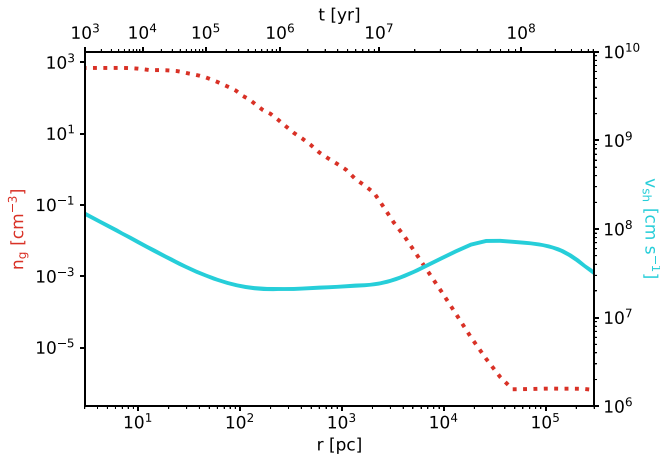


Figure 10. Ambient gas density (red dotted line) and velocity (blue solid line) profiles used in our UFO model. Both profiles come from the models calculated in Liu et al. (2018), for an AGN bolometric luminosity of $L_{\text{Bol}} = 2.5 \times 10^{44}$ erg s $^{-1}$.

(Caprioli & Spitkovsky 2014a, 2014b, 2014c; Caprioli et al. 2015; Haggerty & Caprioli 2019). Thus, given basic information about UFO shock hydrodynamics (age, velocity, and ambient density), CRAFT self-consistently predicts an instantaneous proton distribution.

To model the cumulative photon distribution of a UFO, we use the hydrodynamic model for the forward shock evolution calculated in Liu et al. (2018) and shown in Figure 10. More specifically, Liu et al. (2018) calculate the forward shock evolution (as in Lamastra et al. 2017; Wang & Loeb 2016a, 2016b, and elsewhere in the literature) using the thin-shell approximation, in which a spherically symmetric shell of negligible thickness expands due to the pressure of a hot bubble inside it. Liu et al. (2018) adopt a broken power-law density profile for the ambient gas, $\propto R^{-2}$, inside the disk radius and $\propto R^{-3.95}$ outside the disk. However, Liu et al. (2018) also include a flat core in the inner 100 pc of the galaxy to prevent high central densities that are inconsistent with observations, as well as a constant density beyond the virial radius of the galaxy to account for the presence of the intergalactic medium. This profile reproduces well the stellar velocity dispersion in the bulge of the galaxies in our sample (see Figure 1). Both the forward shock evolution and density profile apply to the case of an AGN with a bolometric luminosity of $L_{\text{Bol}} = 2.5 \times 10^{44}$ erg s $^{-1}$ (consistent with our measurement) and are both shown in Figure 10. Of course, the use of a 1D model has limitations; it cannot account for a more complex ambient medium, meaning that inferred values such as the forward shock age and radius are only approximate. However, given that the model in Liu et al. (2018) yields γ -ray spectra in good agreement with observations, this calculation demonstrates that the γ -ray emission reported in this work can be explained by a population of UFOs with reasonable parameters.

After using CRAFT to calculate the proton distribution produced at each time step of the shock evolution (see Figure 10), the resulting instantaneous distributions are weighted and shifted in energy to account for adiabatic losses as in Diesing & Caprioli (2019). Energy losses due to proton–proton collisions—which are eventually responsible for the UFO’s γ -ray emission—are also taken into account by calculating the collision rate for each distribution at each time step, assuming a target proton density given by the

adiabatically expanded postshock density of a given shell. We further assume that a proton loses half its energy in a single collision (i.e., we assume an inelasticity $\kappa = 0.5$, as in Liu et al. 2018). In other words, the accelerated proton population is treated as a series of adiabatically expanding shells, with the outermost shell located at the forward shock. Each of these shells experience proton–proton collisions—and by extension—produce γ -rays at every time step. Thus, to calculate a UFO’s γ -ray spectrum at a given time, we simply take these weighted proton distributions and convert them to photon spectra using the radiative processes code *naima* (Zabalza 2015). We then add these photon spectra together to produce a cumulative SED. Note that Coulomb losses are neglected in this calculation, as they are subdominant for protons with energies $\gtrsim 1$ GeV (Mannheim & Schlickeiser 1994).

The result is an estimate of a UFO’s SED at every stage of its evolution, as shown in the left panel of Figure 11. We obtain γ -ray luminosities consistent with those calculated in Liu et al. (2018) and find that the observed γ -ray emission can be explained by a forward shock that has traveled a distance between 0.02 and 0.3 kpc from the SMBH (age of $t = (0.3 - 10) \times 10^5$ yr). The modeled CR and γ -ray light curves of the UFO are also shown in the right panel of Figure 11. It is worth noting that the total energy in CRs—and thus the UFO’s γ -ray luminosity—naturally cuts off after roughly 10 Myr due to the fact that the ambient density in the reference galaxy decreases substantially with radius, thereby reducing the available energy flux across the shock.

We also estimate instantaneous electron distributions from our instantaneous proton distributions by using the formalism in Zirakashvili & Aharonian (2007) and accounting for the effects of both adiabatic and synchrotron losses in our weighting (see Diesing & Caprioli 2019). To confirm that the UFO’s synchrotron emission remains below the average radio upper limit from Table 2, the relative normalization of these electron distributions is taken to be a factor of a few larger than that needed to fit observations of Tycho’s supernova remnant (Morlino & Caprioli 2012). Again using *naima*, we then calculate the leptonic emission of a typical UFO from the weighted electron distributions, adding together the contribution of each shell to produce a cumulative SED at a given time step. As shown in Figure 11, the resulting synchrotron emission always falls below the measured average radio emission of the galaxies and the inverse-Compton and bremsstrahlung emissions are a factor >25 fainter than the π_0 emission. Note that the inverse-Compton emission is estimated by assuming that electrons scatter off the cosmic microwave background and starlight approximated by a blackbody with temperature $T = 3000$ K. This emission remains a factor >10 below the π_0 one even with an artificially enhanced stellar radiation field of energy density 100 eV cm^{-3} . We also model the inverse-Compton emission assuming electrons scatter off the AGN photon field described in Sazonov et al. (2004), normalized to the bolometric luminosity of the AGN sample, and find that this emission remains a factor >3 below that produced by π_0 decay (and with a much softer spectrum above 30 GeV).

Proton–proton interactions produce γ -rays with energy $E_\gamma \approx E_p/10$ (Kelner et al. 2006), and thus the observed γ -ray SED indicates a firm detection of CR protons with energies reaching at least as high as $\approx 10^{12-13}$ eV. Within our hadronic emission model we derive that the maximum energy of protons accelerated at the forward shock is $\approx 10^{17}$ eV. This makes AGN

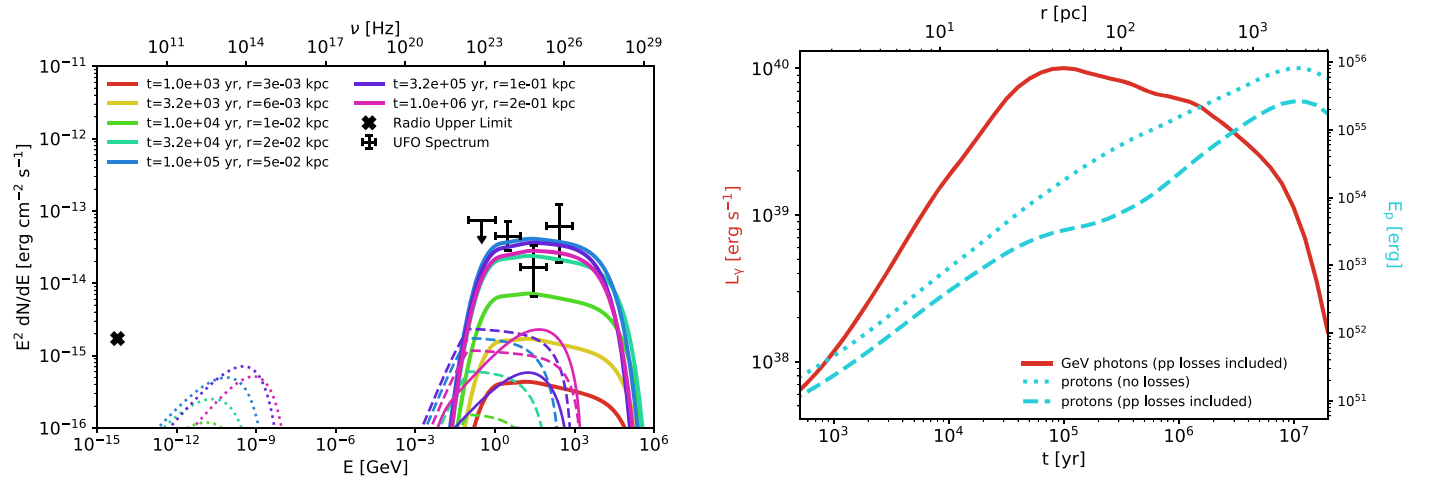


Figure 11. Left: predicted multiwavelength SED of the UFO’s nonthermal emission as a function of time. Synchrotron emission (dotted curves), bremsstrahlung emission (dashed curves), inverse-Compton emission (thin solid curves), and emission from π^0 decay (thick solid curves) are shown. The inverse-Compton emission remains subdominant despite assuming an artificially enhanced stellar radiation field of energy density 100 eV cm^{-3} . Also overlaid is the observed γ -ray flux as shown in Figure 3 and the average radio upper limit from Table 2. Note that the leptonic emission produced at early times often does not appear as it falls below the plot range. Right: light curve of a UFO-powered forward shock moving through a representative galaxy. The total energy in CRs is shown before and after proton–proton losses are included (blue dotted and dashed lines, respectively), as is the γ -ray luminosity at 1 GeV (red solid line).

winds a potential source of CRs with energies beyond the *knee* of the CR spectrum (i.e., $3 \times 10^{15} \text{ eV}$) and also likely contributors to the IceCube neutrino flux (Aartsen et al. 2013).

7. Discussion

This work has provided evidence for the existence of a new population of γ -ray emitters produced by AGN-driven outflows, which in the interaction with the ISM can create strong shocks able to energize charged particles potentially up to the transition region between Galactic and extragalactic CRs. These charged particles produce the observed γ -rays in the interaction with the ISM. According to our and other available models (Liu et al. 2018), the observed emission can be explained by a forward shock that has traveled $\gtrsim 20 \text{ pc}$ from the central SMBH. As such, the γ -ray emission from UFOs may signal the onset of the wind-host interaction. We caution the reader, however, that our model relies on a one-dimensional description of a galaxy and that it does not include the complex environment in the immediate vicinity of the SMBH. Nevertheless, our results are found to be in reasonably good agreement with previous predictions (Lamastra et al. 2016; Liu et al. 2018).

Most of the outflow energy is deposited in the bubble of hot gas rather than CRs. More precisely, this energy is a factor of ~ 10 larger than what is transferred to accelerated CRs, which is reported in the right panel of Figure 11. For an AGN with $\log L_{\text{Bol}} (\text{erg s}^{-1}) = 44.4$ the timescale to transfer 10^{56} erg of energy to the bubble is about 3 Myr. This timescale would grow slightly for less powerful AGN. Sgr A*, the SMBH in the center of the Milky Way, has an estimated mass of $4 \times 10^6 M_{\odot}$ (Abuter et al. 2019), and was very likely in an active state up to a few hundred years ago (Sunyaev et al. 1993; Koyama et al. 1996). Adopting a bolometric luminosity of $\log L_{\text{Bol}} (\text{erg s}^{-1}) = 42.7$ (about 1% of its Eddington luminosity), we find that the timescale to deposit an energy of 10^{56} erg to the thermal gas is $\approx 10 \text{ Myr}$. At that point in time, its γ -ray luminosity would be $\log L_{\gamma} (\text{erg s}^{-1}) \approx 38$ and would decline modestly in a few hundred years after the end of the AGN activity (see also Liu et al. 2018). This is in reasonable

agreement with the luminosity of the bubbles discovered by Fermi in our galaxy ($\log L_{\gamma} = 37.6 \text{ erg s}^{-1}$ Su et al. 2010) and the energetics of the thermal gas contained in the larger bubbles ($\sim 10^{56} \text{ erg}$) recently discovered by the Extended Roentgen Survey with an Imaging Telescope Array (eROSITA; Predehl et al. 2020). Thus, the Fermi and eROSITA bubbles may be the remnant of past UFO-like activity from the SMBH in the center of our galaxy.

It is important to note that the physical implications that can be inferred from the γ -ray detection are limited by the incompleteness of the current sample of UFOs, as well as the inherent uncertainty relating to the time variability of the UFOs. Indeed, detection of UFOs is limited to $\lesssim 50$ AGN (Tombesi et al. 2010b; Kara et al. 2016; Igo et al. 2020), which is by far not a complete sample. Moreover, UFOs have been found in these AGN to vary with time and energy and this has been interpreted as a series of expanding shells (see, e.g., King & Pounds 2015) rather than a continuous outflow like we have assumed here. Although we consider it unlikely, the variability may also impact the selection of a control sample as those AGN may not show a UFO precisely at the time when they were observed, but otherwise have an active UFO. A solution to these issues will be provided with the more sensitive observations that the X-ray Imaging and Spectroscopy Mission (XRISM; XRISM Science Team 2020) and the Advanced Telescope for High-Energy Astrophysics (Athena⁸¹) will provide.

8. Summary and Conclusion

To search for the collective UFO emission, a stacking technique that has been used with success in the past (Abdollahi et al. 2018; Paliya et al. 2019; Ajello et al. 2020a) is adopted. Our sample consists of all radio-quiet UFOs with $z < 0.1$ and $\nu > 0.1c$, which gives 11 sources in total. We model the UFO (γ -ray) spectrum with a power law, and we assume that the population can be characterized by an average flux and photon index. A fit to all the regions then optimizes

⁸¹ <https://www.the-athena-x-ray-observatory.eu>

these parameters. We find a TS of 30.1, which corresponds to a detection significance for the UFO emission of 5.1σ (2 dof). The best-fit parameters are measured to be $\Gamma = -2.1 \pm 0.3$ and flux (1–800 GeV) = $2.5^{+1.5}_{-0.9} \times 10^{-11}$ ph cm $^{-2}$ s $^{-1}$.

We performed several tests to confirm that the γ -ray emission is truly related to the presence of UFOs in this sample of galaxies. We employed a control sample of AGN with similar properties to those of the 11 galaxies used above, but lacking UFOs. This sample yields no detectable γ -ray emission with a (1–800 GeV) flux upper limit of 8.8×10^{-12} ph cm $^{-2}$ s $^{-1}$. We also use a sample of UFOs selected in a different way (Igo et al. 2020) than our benchmark sample. These galaxies show a γ -ray signal whose parameters are in good agreement with those reported above. Moreover, adopting a control sample matched in X-ray flux, IR luminosity, radio flux, and redshifts we can exclude that the observed γ -ray emission arises from star formation activity or the presence of a weak jet. These tests allow us to conclude that the observed emission is associated to the presence of UFOs in these galaxies.

Observations of AGN winds have shown that AGN transfer a small fraction ($\sim 1\%$ – 5%) of their bolometric luminosity to the winds. As our analysis indicates, a portion of this transferred luminosity in turn accelerates CRs and produces γ -rays. We find that AGN convert $\approx 3 \times 10^{-4}$ of their bolometric luminosity into γ rays. We also find that $\approx 4 \times 10^{-4}$ of the wind mechanical power is transferred to γ -rays. For comparison, in the Milky Way galaxy, supernova explosions transfer $\approx 2 \times 10^{-4}$ of their mechanical energy to γ -rays. This shows that AGN winds, if sustained for a few million years, can energize a large fraction of the CR population within a galaxy.

The physical model for the UFO SED is calculated by assuming that the γ -ray emission is dominated by hadronic processes resulting from DSA. For typical UFO shock velocities and densities, a leptonic origin of the γ -ray emission is disfavored, in that inverse-Compton scattering and bremsstrahlung of relativistic electrons would produce steeper γ -ray spectra with a lower normalization. The observed γ -ray SED indicates a firm detection of CR protons with energies reaching at least as high as $\approx 10^{12-13}$ eV.

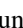
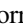
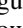


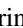





Within our hadronic emission model we derive that on average the forward shock has traveled ~ 20 – 300 pc (~ 65 – 980 lt-yr) away from the SMBH and that the maximum energy of protons accelerated at the forward shock is $\approx 10^{17}$ eV. This makes AGN winds a potential source of CRs with energies beyond the knee of the CR spectrum (i.e., 3×10^{15} eV) and also likely contributors to the IceCube neutrino flux (Aartsen et al. 2013; Padovani et al. 2018). Lastly, our results support the hypothesis that the Fermi and eROSITA bubbles may be the remnant of past UFO-like activity from the SMBH in the center of our galaxy.






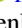
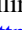







M.A. and C.K. acknowledge support from NSF and NASA through grants AST-1715256, 80NSSC21K1915, and 80NSSC18K1718. R.D. and D.C. acknowledge the Eugene & Niesje Parker Fellowship Fund, NASA (grants NNX17AG30G, 80NSSC18K1218, and 80NSSC18K1726) and the NSF (grants AST-1714658, AST-1909778). G.C. acknowledges financial support from NASA grants 80NSSC20K0438 and 80NSSC19K095.

The Fermi-LAT Collaboration acknowledges generous ongoing support from a number of agencies and institutes that

have supported both the development and the operation of the LAT as well as scientific data analysis. These include the National Aeronautics and Space Administration and the Department of Energy in the United States, the Commissariat à l’Energie Atomique and the Centre National de la Recherche Scientifique/Institut National de Physique Nucléaire et de Physique des Particules in France, the Agenzia Spaziale Italiana and the Istituto Nazionale di Fisica Nucleare in Italy, the Ministry of Education, Culture, Sports, Science and Technology (MEXT), High Energy Accelerator Research Organization (KEK) and Japan Aerospace Exploration Agency (JAXA) in Japan, and the K. A. Wallenberg Foundation, the Swedish Research Council and the Swedish National Space Board in Sweden. Additional support for science analysis during the operations phase is gratefully acknowledged from the Istituto Nazionale di Astrofisica in Italy and the Centre National d’Études Spatiales in France. This work performed in part under DOE Contract DE-AC02-76SF00515. Work at NRL is supported by NASA.

ORCID iDs

M. Ajello  <https://orcid.org/0000-0002-6584-1703>
 L. Baldini  <https://orcid.org/0000-0002-9785-7726>
 J. Ballet  <https://orcid.org/0000-0002-8784-2977>
 D. Bastieri  <https://orcid.org/0000-0002-6954-8862>
 R. Bellazzini  <https://orcid.org/0000-0002-2469-7063>
 E. Bissaldi  <https://orcid.org/0000-0001-9935-8106>
 R. Bonino  <https://orcid.org/0000-0002-4264-1215>
 D. Caprioli  <https://orcid.org/0000-0003-0939-8775>
 G. Chartas  <https://orcid.org/0000-0003-1697-6596>
 C. C. Cheung  <https://orcid.org/0000-0002-4377-0174>
 F. D’Ammando  <https://orcid.org/0000-0001-7618-7527>
 P. de la Torre Luque  <https://orcid.org/0000-0002-4150-2539>
 A. Desai  <https://orcid.org/0000-0001-7405-9994>
 R. Diesing  <https://orcid.org/0000-0002-6679-0012>
 N. Di Lalla  <https://orcid.org/0000-0002-7574-1298>
 L. Di Venere  <https://orcid.org/0000-0003-0703-824X>
 A. Domínguez  <https://orcid.org/0000-0002-3433-4610>
 A. Franckowiak  <https://orcid.org/0000-0002-5605-2219>
 Y. Fukazawa  <https://orcid.org/0000-0002-0921-8837>
 S. Funk  <https://orcid.org/0000-0002-2012-0080>
 P. Fusco  <https://orcid.org/0000-0002-9383-2425>
 F. Gargano  <https://orcid.org/0000-0002-5055-6395>
 D. Gasparri  <https://orcid.org/0000-0002-5064-9495>
 N. Giglietto  <https://orcid.org/0000-0002-9021-2888>
 M. Giroletti  <https://orcid.org/0000-0002-8657-8852>
 S. Guiriec  <https://orcid.org/0000-0001-5780-8770>
 D. Hartmann  <https://orcid.org/0000-0002-8028-0991>
 G. Jóhannesson  <https://orcid.org/0000-0003-1458-7036>
 C. Karwin  <https://orcid.org/0000-0002-6774-3111>
 M. Kerr  <https://orcid.org/0000-0002-0893-4073>
 M. Kovačević  <https://orcid.org/0000-0003-4928-4510>
 M. Kuss  <https://orcid.org/0000-0003-1212-9998>
 S. Larsson  <https://orcid.org/0000-0003-0716-107X>
 L. Latronico  <https://orcid.org/0000-0002-0984-1856>
 M. Lemoine-Goumard  <https://orcid.org/0000-0002-4462-3686>
 F. Longo  <https://orcid.org/0000-0003-2501-2270>
 F. Loparco  <https://orcid.org/0000-0002-1173-5673>
 P. Lubrano  <https://orcid.org/0000-0003-0221-4806>
 S. Maldera  <https://orcid.org/0000-0002-0698-4421>

A. Manfreda  <https://orcid.org/0000-0002-0998-4953>
 S. Marchesi  <https://orcid.org/0000-0001-5544-0749>
 L. Marcotulli  <https://orcid.org/0000-0002-8472-3649>
 M. N. Mazziotta  <https://orcid.org/0000-0001-9325-4672>
 I. Mereu  <https://orcid.org/0000-0003-0219-4534>
 T. Mizuno  <https://orcid.org/0000-0001-7263-0296>
 M. E. Monzani  <https://orcid.org/0000-0002-8254-5308>
 A. Morselli  <https://orcid.org/0000-0002-7704-9553>
 I. V. Moskalenko  <https://orcid.org/0000-0001-6141-458X>
 N. Omodei  <https://orcid.org/0000-0002-5448-7577>
 V. Paliya  <https://orcid.org/0000-0001-7774-5308>
 M. Persic  <https://orcid.org/0000-0003-1853-4900>
 M. Pesce-Rollins  <https://orcid.org/0000-0003-1790-8018>
 S. Rainò  <https://orcid.org/0000-0002-9181-0345>
 R. Rando  <https://orcid.org/0000-0001-6992-818X>
 B. Rani  <https://orcid.org/0000-0001-5711-084X>
 M. Razzano  <https://orcid.org/0000-0003-4825-1629>
 A. Reimer  <https://orcid.org/0000-0001-8604-7077>
 O. Reimer  <https://orcid.org/0000-0001-6953-1385>
 D. Serini  <https://orcid.org/0000-0002-9754-6530>
 C. Sgrò  <https://orcid.org/0000-0001-5676-6214>
 D. Tak  <https://orcid.org/0000-0002-9852-2469>
 D. F. Torres  <https://orcid.org/0000-0002-1522-9065>
 E. Troja  <https://orcid.org/0000-0002-1869-7817>

References

- Aartsen, M. G., Abbasi, R., Abdou, Y., et al. 2013, *Sci*, **342**, 1242856
 Abdollahi, S., Acero, F., Ackermann, M., et al. 2020, *ApJS*, **247**, 33
 Abdollahi, S., Ackermann, M., Ajello, M., et al. 2018, *Sci*, **362**, 1031
 Abuter, R., Amorim, A., Bauböck, M., et al. 2019, *A&A*, **625**, L10
 Acero, F., Ackermann, M., Ajello, M., et al. 2016, *ApJS*, **224**, 8
 Ackermann, M., Ajello, M., Albert, A., et al. 2011, *PhRvL*, **107**, 241302
 Ajello, M., Angioni, R., Axelsson, M., et al. 2020b, *ApJ*, **892**, 105
 Ajello, M., Di Mauro, M., Paliya, V. S., & Garrappa, S. 2020a, *ApJ*, **894**, 88
 Ajello, M., Gasparrini, D., Sanchez-Conde, M., et al. 2015, *ApJL*, **800**, L27
 Alonso-Herrero, A., Almeida, C. R., Mason, R., et al. 2011, *ApJ*, **736**, 82
 Amato, E., & Blasi, P. 2006, *MNRAS*, **371**, 1251
 Atwood, W. B., Abdo, A. A., Ackermann, M., et al. 2009, *ApJ*, **697**, 1071
 Atwood, W. B., Atwood, W. B., Baldini, L., et al. 2013, *ApJ*, **774**, 76
 Beifiori, A., Courteau, S., Corsini, E., & Zhu, Y. 2012, *MNRAS*, **419**, 2497
 Bennert, V. N., Treu, T., Auger, M. W., et al. 2015, *ApJ*, **809**, 20
 Bian, W., & Gu, Q. 2007, *ApJ*, **657**, 159
 Blasi, P. 2002, *Aph*, **16**, 429
 Caprioli, D. 2011, *JCAP*, **05**, 026
 Caprioli, D. 2012, *JCAP*, **7**, 38
 Caprioli, D., Amato, E., & Blasi, P. 2010, *Aph*, **33**, 307
 Caprioli, D., Pop, A., & Spitkovsky, A. 2015, *ApJ*, **798**, 28
 Caprioli, D., & Spitkovsky, A. 2014a, *ApJ*, **783**, 91
 Caprioli, D., & Spitkovsky, A. 2014b, *ApJ*, **794**, 46
 Caprioli, D., & Spitkovsky, A. 2014c, *ApJ*, **794**, 47
 Chartas, G., Brandt, W. N., Gallagher, S. C., & Garmire, G. P. 2002, *ApJ*, **579**, 169
 Chartas, G., Cappi, M., Hamann, F., et al. 2016, *ApJ*, **824**, 53
 Ciccone, C., Maiolino, R., Sturm, E., et al. 2014, *A&A*, **562**, A21
 Condon, J. J., Cotton, W. D., Greisen, E. W., et al. 1998, *AJ*, **115**, 1693
 Crenshaw, D. M., & Kraemer, S. B. 2012, *ApJ*, **753**, 75
 Diesing, R., & Caprioli, D. 2019, *PhRvL*, **123**, 071101
 Fabian, A. C. 2012, *ARA&A*, **50**, 455
 Ferrarese, L., & Ford, H. 2005, *SSRv*, **116**, 523
 Feruglio, C., Fiore, F., Carniani, S., et al. 2015, *A&A*, **583**, A99
 Gallo, L. C., & Fabian, A. C. 2011, *MNRAS*, **418**, L59
 Gebhardt, K., Bender, R., Bower, G., et al. 2000, *ApJL*, **539**, L13
 Gofford, J., Reeves, J., McLaughlin, D., et al. 2015, *MNRAS*, **451**, 4169
 Gofford, J., Reeves, J. N., Tombesi, F., et al. 2013, *MNRAS*, **430**, 60
 Grier, C., Martini, P., Watson, G., et al. 2013, *ApJ*, **773**, 90
 Gültekin, K., Richstone, D. O., Gebhardt, K., et al. 2009, *ApJ*, **698**, 198
 Haggerty, C. C., & Caprioli, D. 2019, *ApJ*, **887**, 165
 Hopkins, P. F., & Elvis, M. 2010, *MNRAS*, **401**, 7
 Igo, Z., Parker, M. L., Matzeu, G. A., et al. 2020, *MNRAS*, **493**, 1088
 James, F., & Roos, M. 1975, *CoPhC*, **10**, 343
 Johnston, K. J., Elvis, M., Kjer, D., & Shen, B. S. P. 1982, *ApJ*, **262**, 61
 Kara, E., Alston, W. N., Fabian, A. C., et al. 2016, *MNRAS*, **462**, 511
 Kaspi, S., Maoz, D., Netzer, H., et al. 2005, *ApJ*, **629**, 61
 Kelner, S. R., Aharonian, F. A., & Bugayov, V. V. 2006, *PhRvD*, **74**, 034018
 King, A., & Pounds, K. 2015, *ARA&A*, **53**, 115
 King, A. R. 2010, *MNRAS*, **402**, 1516
 King, A. R., & Pounds, K. A. 2003, *MNRAS*, **345**, 657
 Kleinmann, S. G., Cutri, R. M., Young, E. T., Low, F. J., & Gillett, F. C. 1986, *yCat*, **II/126**
 Kormendy, J., & Ho, L. C. 2013, *ARA&A*, **51**, 511
 Koyama, K., Maeda, Y., Sonobe, T., et al. 1996, *PASJ*, **48**, 249
 Lamastra, A., Fiore, F., Guetta, D., et al. 2016, *A&A*, **596**, A68
 Lamastra, A., Menci, N., Fiore, F., et al. 2017, *A&A*, **607**, A18
 Lister, M. L., Aller, M. F., Aller, H. D., et al. 2016, *AJ*, **152**, 12
 Liu, R.-Y., Murase, K., Inoue, S., Ge, C., & Wang, X.-Y. 2018, *ApJ*, **858**, 9
 Longinotti, A., Vega, O., Krongold, Y., et al. 2018, *ApJL*, **867**, L11
 Mannheim, K., & Schlickeiser, R. 1994, *A&A*, **286**, 983
 Marinucci, A., Bianchi, S., Nicastro, F., Matt, G., & Goulding, A. D. 2012, *ApJ*, **748**, 130
 Mattox, J. R., Bertsch, D. L., Chiang, J., et al. 1996, *ApJ*, **461**, 396
 Matzeu, G. A., Reeves, J. N., Braitto, V., et al. 2017, *MNRAS*, **472**, L15
 McCarthy, I. G., Schaye, J., Ponman, T. J., et al. 2010, *MNRAS*, **406**, 822
 McNamara, B. R., & Nulsen, P. E. J. 2007, *ARA&A*, **45**, 117
 Mehdipour, M., & Costantini, E. 2019, *A&A*, **625**, A25
 Morlino, G., & Caprioli, D. 2012, *A&A*, **538**, A81
 Moshir, M., Copan, G., Conrow, T., et al. 1990, *yCat*, **II/156A**
 Nardini, E., Reeves, J. N., Gofford, J., et al. 2015, *Sci*, **347**, 860
 Nicastro, F., Martocchia, A., & Matt, G. 2003, *ApJL*, **589**, L13
 Onken, C. A., Valluri, M., Brown, J. S., et al. 2014, *ApJ*, **791**, 37
 Orienti, M., & Prieto, M. A. 2010, *MNRAS*, **401**, 2599
 Padovani, P., Turcati, A., & Resconi, E. 2018, *MNRAS*, **477**, 3469
 Paliya, V. S., Dominguez, A., Ajello, M., Franckowiak, A., & Hartmann, D. 2019, *ApJL*, **882**, L3
 Panessa, F., Baldi, R. D., Laor, A., et al. 2019, *NatAs*, **3**, 387
 Peterson, B. M., Ferrarese, L., Gilbert, K. M., et al. 2004, *ApJ*, **613**, 682
 Pounds, K. A., Reeves, J. N., King, A. R., et al. 2003, *MNRAS*, **345**, 705
 Predehl, P., Sunyaev, R. A., Becker, W., et al. 2020, *Natur*, **588**, 227
 Pushkarev, A. B., Kovalev, Y. Y., Lister, M. L., & Savolainen, T. 2017, *MNRAS*, **468**, 4992
 Reeves, J., O'Brien, P. T., & Ward, M. 2003, *ApJL*, **593**, L65
 Saez, C., & Chartas, G. 2011, *ApJ*, **737**, 91
 Sazonov, S. Y., Ostriker, J. P., & Sunyaev, R. A. 2004, *MNRAS*, **347**, 144
 Silk, J., & Rees, M. J. 1998, *A&A*, **331**, L1
 Skilling, J. 1975, *MNRAS*, **172**, 557
 Smith, K. L., Mushotzky, R. F., Koss, M., et al. 2020, *MNRAS*, **492**, 4216
 Somerville, R. S., Hopkins, P. F., Cox, T. J., Robertson, B. E., & Hernquist, L. 2008, *MNRAS*, **391**, 481
 Su, M., Slatyer, T. R., & Finkbeiner, D. P. 2010, *ApJ*, **724**, 1044
 Sunyaev, R. A., Markevitch, M., & Pavlinsky, M. 1993, *ApJ*, **407**, 606
 Tombesi, F., Cappi, M., Reeves, J., & Braitto, V. 2012, *MNRAS*, **422**, L1
 Tombesi, F., Cappi, M., Reeves, J., et al. 2010a, *A&A*, **521**, A57
 Tombesi, F., Sambruna, R., Reeves, J., et al. 2010b, *ApJ*, **719**, 700
 Ulvestad, J. S., Wong, D. S., Taylor, G. B., Gallimore, J. F., & Mundell, C. G. 2005, *AJ*, **130**, 936
 Vasudevan, R., Fabian, A., Gandhi, P., Winter, L., & Mushotzky, R. 2010, *MNRAS*, **402**, 1081
 Vasudevan, R. V., & Fabian, A. C. 2007, *MNRAS*, **381**, 1235
 Vasudevan, R. V., & Fabian, A. C. 2009, *MNRAS*, **392**, 1124
 Wang, X., & Loeb, A. 2016a, *NatPh*, **12**, 1116
 Wang, X., & Loeb, A. 2016b, *JCAP*, **2016**, 012
 Williams, D. R. A., McHardy, I. M., Baldi, R. D., et al. 2017, *MNRAS*, **472**, 3842
 Wilson, A. S., & Ulvestad, J. S. 1982, *ApJ*, **263**, 576
 Woo, J.-H., Treu, T., Barth, A. J., et al. 2010, *ApJ*, **716**, 269
 XRISM Science Team 2020, arXiv:2003.04962
 Zabalza, V. 2015, Proc. ICRC (The Hague), **34**, 922
 Zirakashvili, V. N., & Aharonian, F. 2007, *A&A*, **465**, 695
 Zubovas, K., & King, A. R. 2012, *MNRAS*, **426**, 2751



The Fourth Catalog of Active Galactic Nuclei Detected by the *Fermi* Large Area Telescope

M. Ajello¹, R. Angioni^{2,3}, M. Axelsson^{4,5}, J. Ballet⁶, G. Barbiellini^{7,8}, D. Bastieri^{9,10}, J. Becerra Gonzalez¹¹, R. Bellazzini¹², E. Bissaldi^{13,14}, E. D. Bloom¹⁵, R. Bonino^{16,17}, E. Bottacini^{15,18}, P. Bruel¹⁹, S. Buson²⁰, F. Cafardo²¹, R. A. Cameron¹⁵, E. Cavazzuti²², S. Chen^{9,18}, C. C. Cheung²³, S. Ciprini^{3,2}, D. Costantin²⁴, S. Cutini²⁵, F. D'Ammando²⁶, P. de la Torre Luque¹³, R. de Menezes^{17,21}, F. de Palma¹⁶, A. Desai¹, N. Di Lalla¹⁵, L. Di Venere^{13,14}, A. Domínguez²⁷, F. Fana Dirirsa²⁸, E. C. Ferrara²⁹, J. Finke²³, A. Franckowiak³⁰, Y. Fukazawa³¹, S. Funk³², P. Fusco^{13,14}, F. Gargano¹⁴, S. Garrappa³⁰, D. Gasparrini^{2,3}, N. Giglietto^{13,14}, F. Giordano^{13,14}, M. Giroletti²⁶, D. Green³³, I. A. Grenier⁶, S. Guiriec^{29,34}, S. Harita³⁵, E. Hays²⁹, D. Horan¹⁹, R. Itoh³⁶, G. Jóhannesson^{37,38}, M. Kovac'evic²⁵, F. Krauss³⁹, M. Kreter^{20,40}, M. Kuss¹², S. Larsson^{5,41,42}, C. Leto², J. Li³⁰, I. Liodakis¹⁵, F. Longo^{7,8}, F. Loparco^{13,14}, B. Lott⁴³, M. N. Lovellette²³, P. Lubrano²⁵, G. M. Madejski¹⁵, S. Maldera¹⁶, A. Manfreda⁴⁴, G. Martí-Devesa⁴⁵, F. Massaro^{16,17,46}, M. N. Mazziotta¹⁴, I. Mereu^{25,47}, M. Meyer³², G. Migliori^{48,49}, N. Mirabal^{29,50}, T. Mizuno⁵¹, M. E. Monzani¹⁵, A. Morcelli³, I. V. Moskalenko¹⁵, M. Negro^{50,52}, R. Nemmen²¹, E. Nuss⁵³, L. S. Ojha²⁹, R. Ojha²⁹, N. Omodei¹⁵, M. Orienti²⁶, E. Orlando^{15,54}, J. F. Ormes⁵⁵, V. S. Paliya³⁰, Z. Pei¹⁰, H. Peña-Herazo^{16,17,46,56}, M. Persic^{7,57}, M. Pesce-Rollins¹², L. Petrov²⁹, F. Piron⁵³, H. Poon³¹, G. Principe²⁶, S. Rainò^{13,14}, R. Rando^{9,18,58}, B. Rani^{29,59}, M. Razzano^{12,71}, S. Razzaque²⁸, A. Reimer^{15,45}, O. Reimer⁴⁵, F. K. Schinzel^{60,61}, D. Serini¹³, C. Sgrò¹², E. J. Siskind⁶², G. Spandre¹², P. Spinelli^{13,14}, D. J. Suson⁶³, Y. Tachibana³⁵, D. J. Thompson²⁹, D. F. Torres^{64,65}, E. Torresi⁶⁶, E. Troja^{29,67}, J. Valverde¹⁹, P. van Zyl^{68,69,70}, and M. Yassine⁷⁸

¹ Department of Physics and Astronomy, Clemson University, Kinard Lab of Physics, Clemson, SC 29634-0978, USA

² Space Science Data Center—Agenzia Spaziale Italiana, Via del Politecnico, snc, I-00133, Roma, Italy; stefano.ciprini.asdc@gmail.com

³ Istituto Nazionale di Fisica Nucleare, Sezione di Roma “Tor Vergata,” I-00133 Roma, Italy; dario.gasparrini@ssdc.asi.it

⁴ Department of Physics, Stockholm University, AlbaNova, SE-106 91 Stockholm, Sweden

⁵ Department of Physics, KTH Royal Institute of Technology, AlbaNova, SE-106 91 Stockholm, Sweden

⁶ AIM, CEA, CNRS, Université Paris-Saclay, Université Paris Diderot, Sorbonne Paris Cité, F-91191 Gif-sur-Yvette, France

⁷ Istituto Nazionale di Fisica Nucleare, Sezione di Trieste, I-34127 Trieste, Italy

⁸ Dipartimento di Fisica, Università di Trieste, I-34127 Trieste, Italy

⁹ Istituto Nazionale di Fisica Nucleare, Sezione di Padova, I-35131 Padova, Italy

¹⁰ Dipartimento di Fisica e Astronomia “G. Galilei,” Università di Padova, I-35131 Padova, Italy

¹¹ Instituto de Astrofísica de Canarias, Observatorio del Teide, C/Via Lactea, s/n, E-38205, La Laguna, Tenerife, Spain

¹² Istituto Nazionale di Fisica Nucleare, Sezione di Pisa, I-56127 Pisa, Italy

¹³ Dipartimento di Fisica “M. Merlin” dell’Università e del Politecnico di Bari, via Amendola 173, I-70126 Bari, Italy

¹⁴ Istituto Nazionale di Fisica Nucleare, Sezione di Bari, I-70126 Bari, Italy

¹⁵ W. W. Hansen Experimental Physics Laboratory, Kavli Institute for Particle Astrophysics and Cosmology, Department of Physics and SLAC National Accelerator Laboratory, Stanford University, Stanford, CA 94305, USA

¹⁶ Istituto Nazionale di Fisica Nucleare, Sezione di Torino, I-10125 Torino, Italy

¹⁷ Dipartimento di Fisica, Università degli Studi di Torino, I-10125 Torino, Italy

¹⁸ Department of Physics and Astronomy, University of Padova, Vicolo Osservatorio 3, I-35122 Padova, Italy

¹⁹ Laboratoire Leprince-Ringuet, École polytechnique, CNRS/IN2P3, F-91128 Palaiseau, France

²⁰ Institut für Theoretische Physik und Astrophysik, Universität Würzburg, D-97074 Würzburg, Germany

²¹ Instituto de Astronomia, Geofísica e Ciências Atmosféricas, Universidade de São Paulo, Rua do Matão, 1226, São Paulo—SP 05508-090, Brazil

²² Italian Space Agency, Via del Politecnico snc, I-00133 Roma, Italy

²³ Space Science Division, Naval Research Laboratory, Washington, DC 20375-5352, USA

²⁴ University of Padua, Department of Statistical Science, Via 8 Febbraio, 2, I-35122, Padova, Italy

²⁵ Istituto Nazionale di Fisica Nucleare, Sezione di Perugia, I-06123 Perugia, Italy

²⁶ INAF Istituto di Radioastronomia, I-40129 Bologna, Italy

²⁷ Grupo de Altas Energías, Universidad Complutense de Madrid, E-28040 Madrid, Spain

²⁸ Department of Physics, University of Johannesburg, P.O. Box 524, Auckland Park 2006, South Africa

²⁹ NASA Goddard Space Flight Center, Greenbelt, MD 20771, USA

³⁰ Deutsches Elektronen Synchrotron DESY, D-15738 Zeuthen, Germany

³¹ Department of Physical Sciences, Hiroshima University, Higashi-Hiroshima, Hiroshima 739-8526, Japan

³² Friedrich-Alexander Universität Erlangen-Nürnberg, Erlangen Centre for Astroparticle Physics, Erwin-Rommel-Str. 1, D-91058 Erlangen, Germany

³³ Max-Planck-Institut für Physik, D-80805 München, Germany

³⁴ The George Washington University, Department of Physics, 725 21st St, NW, Washington, DC 20052, USA

³⁵ Department of Physics, Tokyo Institute of Technology, Meguro City, Tokyo 152-8551, Japan

³⁶ Bisei Astronomical Observatory, 1723-70 Ookura, Bisei-cho, Ibara, Okayama 714-1411, Japan

³⁷ Science Institute, University of Iceland, IS-107 Reykjavik, Iceland

³⁸ Nordita, Royal Institute of Technology and Stockholm University, Roslagstullsbacken 23, SE-106 91 Stockholm, Sweden

³⁹ Department of Astronomy and Astrophysics, Pennsylvania State University, University Park, PA 16802, USA

⁴⁰ Centre for Space Research, North-West University, Potchefstroom Campus, Private Bag X6001, Potchefstroom 2520, South Africa

⁴¹ The Oskar Klein Centre for Cosmoparticle Physics, AlbaNova, SE-106 91 Stockholm, Sweden

⁴² School of Education, Health and Social Studies, Natural Science, Dalarna University, SE-791 88 Falun, Sweden

⁴³ Centre d’Études Nucléaires de Bordeaux Gradignan, Université de Bordeaux, IN2P3/CNRS, F-33175 Gradignan Cedex, France; lott@cenbg.in2p3.fr

⁴⁴ Università di Pisa and Istituto Nazionale di Fisica Nucleare, Sezione di Pisa I-56127 Pisa, Italy

⁴⁵ Institut für Astro- und Teilchenphysik, Leopold-Franzens-Universität Innsbruck, A-6020 Innsbruck, Austria

⁴⁶ Istituto Nazionale di Astrofisica-Osservatorio Astrofisico di Torino, via Osservatorio 20, I-10025 Pino Torinese, Italy

⁴⁷ Dipartimento di Fisica, Università degli Studi di Perugia, I-06123 Perugia, Italy

⁴⁸ Dipartimento di Astronomia, Università di Bologna, I-40127 Bologna, Italy⁴⁹ Università di Bologna, I-40126 Bologna, Italy⁵⁰ Department of Physics and Center for Space Sciences and Technology, University of Maryland Baltimore County, Baltimore, MD 21250, USA⁵¹ Hiroshima Astrophysical Science Center, Hiroshima University, Higashi-Hiroshima, Hiroshima 739-8526, Japan⁵² Center for Research and Exploration in Space Science and Technology (CREST) and NASA Goddard Space Flight Center, Greenbelt, MD 20771, USA⁵³ Laboratoire Univers et Particules de Montpellier, Université Montpellier, CNRS/IN2P3, F-34095 Montpellier, France⁵⁴ Istituto Nazionale di Fisica Nucleare, Sezione di Trieste, and Università di Trieste, I-34127 Trieste, Italy⁵⁵ Department of Physics and Astronomy, University of Denver, Denver, CO 80208, USA⁵⁶ Instituto Nacional de Astrofísica, Óptica y Electrónica, Tonantzintla, Puebla 72840, Mexico; harold.penah@gmail.com⁵⁷ Osservatorio Astronomico di Trieste, Istituto Nazionale di Astrofisica, I-34143 Trieste, Italy⁵⁸ Center for Space Studies and Activities “G. Colombo,” University of Padova, Via Venezia 15, I-35131 Padova, Italy⁵⁹ Korea Astronomy and Space Science Institute, 776 Daedeokdae-ro, Yuseong-gu, Daejeon 305-348, Republic of Korea⁶⁰ National Radio Astronomy Observatory, 1003 Lopezville Road, Socorro, NM 87801, USA⁶¹ University of New Mexico, MSC07 4220, Albuquerque, NM 87131, USA⁶² NYCB Real-Time Computing Inc., Lattingtown, NY 11560-1025, USA⁶³ Purdue University Northwest, Hammond, IN 46323, USA⁶⁴ Institute of Space Sciences (CSICIEEC), Campus UAB, Carrer de Magrans s/n, E-08193 Barcelona, Spain⁶⁵ Institució Catalana de Recerca i Estudis Avançats (ICREA), E-08010 Barcelona, Spain⁶⁶ INAF-Istituto di Astrofisica Spaziale e Fisica Cosmica Bologna, via P. Gobetti 101, I-40129 Bologna, Italy⁶⁷ Department of Astronomy, University of Maryland, College Park, MD 20742, USA⁶⁸ Hartebeesthoek Radio Astronomy Observatory, P.O. Box 443, Krugersdorp 1740, South Africa⁶⁹ School of Physics, University of the Witwatersrand, Private Bag 3, WITS-2050, Johannesburg, South Africa⁷⁰ Square Kilometre Array South Africa, Pinelands, 7405, South Africa

Received 2020 January 9; revised 2020 February 15; accepted 2020 February 17; published 2020 April 2

Abstract

The fourth catalog of active galactic nuclei (AGNs) detected by the *Fermi* Gamma-ray Space Telescope Large Area Telescope (4LAC) between 2008 August 4 and 2016 August 2 contains 2863 objects located at high Galactic latitudes ($|b| > 10^\circ$). It includes 85% more sources than the previous 3LAC catalog based on 4 yr of data. AGNs represent at least 79% of the high-latitude sources in the fourth *Fermi*-Large Area Telescope Source Catalog (4FGL), which covers the energy range from 50 MeV to 1 TeV. In addition, 344 gamma-ray AGNs are found at low Galactic latitudes. Most of the 4LAC AGNs are blazars (98%), while the remainder are other types of AGNs. The blazar population consists of 24% Flat Spectrum Radio Quasars (FSRQs), 38% BL Lac-type objects, and 38% blazar candidates of unknown types (BCUs). On average, FSRQs display softer spectra and stronger variability in the gamma-ray band than BL Lacs do, confirming previous findings. All AGNs detected by ground-based atmospheric Cerenkov telescopes are also found in the 4LAC.

Unified Astronomy Thesaurus concepts: Active galactic nuclei (16); Blazars (164); Gamma-ray sources (633); Relativistic jets (1390); Quasars (1319); BL Lacertae objects (158)

Supporting material: machine-readable tables

1. Introduction

Thanks to its broad energy range, excellent sensitivity, and all-sky monitoring capabilities, the *Fermi* Gamma-ray Space Telescope Large Area Telescope (LAT) has revolutionized our view of the gamma-ray sky. The fourth *Fermi*-LAT source catalog (4FGL, The *Fermi*-LAT collaboration 2020), based on the first 8 yr of data from the mission, contains 5064 sources in the energy range 50 MeV to 1 TeV.

The fourth catalog of active galactic nuclei (AGNs) detected by the LAT (4LAC), presented here, is derived from the 4FGL catalog. At high Galactic latitudes, AGNs represent by far the dominant class of gamma-ray sources in the 4FGL. The vast majority of these AGNs are of the blazar type, which are characterized by having relativistic jets closely aligned with our line of sight. The two main classes of blazars are Flat Spectrum Radio Quasars (FSRQs) and BL Lac-type objects (BL Lacs), distinguished according to the strength of their optical emission lines. FSRQs have strong, broad emission lines, while BL Lacs have weak, narrow, or no such lines. In addition to the improvements of the 4FGL relative to previous gamma-ray catalogs, the 4LAC has benefited from updated methods of associating gamma-ray AGNs

with those known at other wavelengths. The 4LAC supersedes the third catalog of AGNs detected by the LAT (3LAC; Ackermann et al. 2015), which was based on 4 yr of data.

Gamma-ray AGN catalogs constitute unique resources for a broad range of astrophysics research. Recent applications include: population studies probing the BL Lac-FSRQ dichotomy (e.g., Ghisellini et al. 2017; Nalewajko & Gupta 2017); works on individual sources investigating the connections between gamma-ray loudness and brightness/polarization at other observational bands (e.g., Angelakis et al. 2016; Lico et al. 2017; Massaro et al. 2017; Fan & Wu 2018; Zargaryan et al. 2018); timing correlations between activity in the gamma-ray band and other wavelengths (e.g., Fuhrmann et al. 2016; Itoh et al. 2016); and tests of the possible link between gamma-ray AGNs and sources of ultra high-energy cosmic rays (e.g., Kagaya et al. 2017) or high-energy neutrinos (e.g., Padovani et al. 2016; Aartsen et al. 2017; Garrappa et al. 2019). These catalogs also enable probes of the extragalactic background light (EBL; e.g., Abdollahi et al. 2018) and the intergalactic magnetic field (e.g., Ackermann et al. 2018; Broderick et al. 2018), along with a measurement of the AGN contribution to the extragalactic diffuse gamma-ray background (e.g., Fornasa et al. 2016; Di Mauro et al. 2018).

The paper is organized as follows. Section 2 briefly describes the observations by the LAT and the analysis employed to

⁷¹ Funded by contract FIRB-2012-RBF12PM1F from the Italian Ministry of Education, University and Research (MIUR).

produce the eight-year catalog. In Section 3, we present the methods for associating gamma-ray sources with AGN counterparts and the different schemes for classifying them. Section 4 describes the contents of the 4LAC fits table and gives the statistics of the blazar and nonblazar populations. This section also includes a brief presentation of low-latitude ($|b| < 10^\circ$) AGNs, which do not formally belong to the 4LAC. Some of the basic properties of the catalog sources are given in S5, along with a discussion of the overlap with the AGNs detected at very high energies (VHE; energies above 100 GeV) by atmospheric Cerenkov telescopes. Section 6 summarizes our findings.

In the following, we use a Λ CDM cosmology with values from the *Planck* results (Planck Collaboration et al. 2014); in particular, we use $h = 0.67$, $\Omega_m = 0.32$, and $\Omega_\Lambda = 0.68$, where the Hubble constant $H_0 = 100h \text{ km s}^{-1} \text{ Mpc}^{-1}$.

2. Observations with the Large Area Telescope—Analysis Procedures

The 4LAC analysis was performed in the context of the 4FGL catalog, which is briefly summarized here. We refer the reader to the parent paper describing the 4FGL catalog for details (The Fermi-LAT collaboration 2020). The data were collected over the first 8 yr of the mission, from 2008 August 4 (MJD 54682) to 2016 August 2 (MJD 57602). The reprocessed P8R3_SOURCE_V2 event class (Bruehl et al. 2018) data were used, with photon energies between 50 MeV and 1 TeV, broadening the energy interval with respect to the 100 MeV–300 GeV range of 3FGL (Acero et al. 2015). The increase in acceptance relative to the P7REP class used in 3FGL is 20% at high energies, accompanied by a better point-spread function (PSF). These improvements are beneficial to the source detection and localization, and hence to the counterpart association. A dedicated diffuse emission model was developed for analyses using the new event class. Weights penalizing photons with low energies and/or having directions close to the Galactic plane were introduced in the 4FGL likelihood to better account for systematic uncertainties. More details are available in Table 2 of the 4FGL paper. Different spectral models (power-law, log-parabola, power-law with superexponential cutoff) were tested, and the results are systematically reported in 4FGL. Sources with a maximum likelihood Test Statistic (TS) greater than 25 were retained in 4FGL, corresponding to a significance just over 4σ evaluated for the χ^2 distribution with four degrees of freedom. Variability was assessed via both 1 yr and 2 month light curves.

3. Source Association and Classification

The associations of 4FGL gamma-ray sources are based on positional coincidence with potential counterparts that display AGN-type spectral characteristics in the radio, infrared, optical, or X-ray bands. A conservative policy adopted early in the mission by the *Fermi*-LAT Collaboration is that firm identification is only claimed when correlated variability with a counterpart detected at lower energy has been reported. So far, only 78 AGNs have met this condition (see Table 7 of 4FGL). For the other sources, we use statistical approaches for finding associations between LAT sources and AGNs. The two approaches used here, the Bayesian method and the likelihood-ratio method, have been extensively described in previous

Table 1
Catalogs Used for the Bayesian Association Method

Name	Objects ^a	References
BZCAT (Blazars)	3561	Massaro et al. (2015)
BL Lac	1371	Véron-Cetty & Véron (2010)
AGN	10066	Véron-Cetty & Véron (2010)
QSO	129,853	Véron-Cetty & Véron (2010)
Seyfert galaxies	27651	Véron-Cetty & Véron (2010)
Narrow-line Seyfert galaxies	18	Berton et al. (2015)
Narrow-line Seyfert galaxies	556	Rakshit et al. (2017)
FRICAT (radio galaxies)	233	Capetti et al. (2017a)
FRIICAT (radio galaxies)	123	Capetti et al. (2017b)
Giant Radio Source	349	Kuźmierz et al. (2018)
2WHSP	1691	Chang et al. (2017)
WISE blazar catalog	12319	D’Abrusco et al. (2014)
Radio Fundamental Catalog (2019a)	15740	http://astrogeo.org/rfc
CGRaBS	1625	Healey et al. (2008)
CRATES	11499	Healey et al. (2007)
ATCA 20 GHz southern sky survey	5890	Murphy et al. (2010)

Note.

^a Number of objects in the catalog.

catalogs (Abdo et al. 2010b; Ackermann et al. 2011, 2015) and are briefly summarized below.

3.1. Source Association

3.1.1. The Bayesian Association Method

The Bayesian method was adapted for the *Fermi*-LAT catalogs following the work of Mattox et al. (1997) developed for the Energetic Gamma Ray Experiment Telescope (EGRET) on the *Compton Gamma Ray Observatory*. This method is described in Abdo et al. (2010b) and implemented with the *gtsrcid* tool.⁷² The angular distance between a LAT source and a candidate counterpart corresponds to the position uncertainty in the case of a real association, while it is driven by the counterpart density in the case of a false (random) association. The prior distribution is fully characterized by a single number, which is the *a priori* probability that a given source of a catalog is the true counterpart of a gamma-ray source. This probability (referred to as the prior in the following) is assumed to be constant for a given catalog and is calibrated via Monte Carlo simulations so that the number of false associations, N_{false} , is equal to the sum of the association-probability complements. For a given counterpart catalog, the prior is found to be close to $N_{\text{assoc}}/N_{\text{tot}}$, where N_{assoc} is the number of associations from this catalog and N_{tot} is the number of catalog sources. A uniform threshold of 0.80 is applied to the posterior probability for the association to be retained.

The list of catalogs used for the AGN associations with 4FGL sources is given in Table 1. With respect to 3LAC (Ackermann et al. 2015), updates of counterpart catalogs, e.g., BZCAT (Massaro et al. 2015), have been used when available. An important addition to the set of catalogs is the Radio

⁷² <https://fermi.gsfc.nasa.gov/ssc/data/analysis/scitools/overview.html>

Fundamental Catalog⁷³ (RFC; Petrov et al. 2019), with 2720 associations with 4FGL sources (representing 85% of all AGNs). The high efficiency of association with VLBI catalogs that are sensitive to parsec-scale emission at 4–8 GHz is attributed to two factors: (1) the fact that γ -ray emission and parsec scale radio emission which originate from contemporary AGN activity are related, (2) the scarcity of radio sources with parsec scale emission at 4–8 GHz. The RFC includes many new entries that came from dedicated follow-up observations (Petrov et al. 2013; Schinzel et al. 2015, 2017) of unassociated gamma-ray sources, triggered by the publication of previous *Fermi*-LAT catalogs. Applying the Bayesian method to the whole catalog and retaining associations with $P \geq 0.80$, the association probability attached to the recent additions (181 sources) are reported as NULL to distinguish them for the others.

3.1.2. The Likelihood Ratio Association Method

The Likelihood Ratio (LR; e.g., de Ruiter et al. 1977; Cash 1979; Prestage & Peacock 1983; Sutherland & Saunders 1992; Lonsdale et al. 1998; Masci et al. 2001; Ackermann et al. 2011) method developed in the *Fermi*-LAT context makes use of large, relatively uniform surveys in the radio and in X-ray bands. These surveys enable us to search for possible counterparts among the faint radio and X-ray sources. The LR method is similar in nature to the Bayesian method, but the false association rate is computed from the density of objects brighter than the considered candidate, assessed from the survey log N –log S distribution. The method for computing the probability that a candidate is the “true” counterpart (called the reliability in this context) is described in detail in Section 3.2 of the 3LAC paper (Ackermann et al. 2015). A source is considered as a high-confidence counterpart of a given gamma-ray source if its reliability is greater than 0.80 for at least one survey.

For the LR approach, we analyzed the NRAO VLA Sky Survey (NVSS; Condon et al. 1998), the Sydney University Molonglo Sky Survey (SUMSS; Mauch et al. 2003), the Australia Telescope 20 GHz radio source catalog (Murphy et al. 2010), and the *ROSAT* All Sky Survey (RASS) Bright and Faint Source Catalogs (Voges et al. 1999, 2000). We also explored the second RASS catalog (Boller et al. 2016), but this attempt did not lead to further associations.

3.2. Association Results

The threshold adopted for the association probability is 0.80 in either method. This value represents a compromise between association efficiency and purity. The fraction of sources associated by both methods is 73% (2082/2863), with 684 and 97 sources being solely associated with the Bayesian and LR methods, respectively. The overall false-positive rate is 1.6%, where N_{false} is calculated as described in Section 3.1.1. The estimated number of false positives among the 1353 sources not previously reported in 3LAC is 35.6.

As in previous LAT AGN catalogs, we define a Clean Sample as those 4LAC sources that did not have any cautionary analysis flags, as described in Section 3.7.3 of the 4FGL paper (The *Fermi*-LAT collaboration 2020). The most frequent flags are flag 5 (source close to a brighter neighbor), flag 3 (large flux

variation when changing diffuse emission model), and flag 2 (large position shift when changing diffuse emission model). Table 2 compares the performance of the two methods in terms of total number of associations N_{assoc} , estimated number of false associations N_{false} , and number of sources associated solely via a given method, N_s , for the full and Clean samples.

3.3. Source Classification

The classification of a source as an AGN primarily relies on its optical spectrum. Other characteristics, like the radio loudness, the presence of a flat/steep radio spectrum between 1.4 and 5 GHz, the broadband emission, the core compactness or the level of radio extended emission, the detection of variability, and the degree of polarization observed in different bands are used as ancillary information. If available, earlier classifications reported in the literature have been checked.

3.3.1. Optical Classification

The different resources used in the 4LAC for the optical classification are, in decreasing order of precedence:

1. Optical spectra from recent intensive follow-up programs (e.g., Shaw et al. 2013a, 2013b; Massaro et al. 2014, 2015a, 2015b, 2015c; Paggi et al. 2014; Landoni et al. 2015; Ricci et al. 2015; Álvarez Crespo et al. 2016a, 2016b, 2016c; Chiaro et al. 2016; Paiano et al. 2017a, 2017b, 2017c, 2019; Peña-Herazo et al. 2017; Landoni et al. 2018; Marchesi et al. 2018; de Menezes et al. 2019; Marchesini et al. 2019); these data are especially valuable for blazar candidates of previous LAT AGN catalogs that had never been observed.
2. The optical classification published in the BZCAT list, which is a compilation of sources classified as blazars (Massaro et al. 2015).
3. Spectra available in the literature or from online databases, e.g., the Sloan Digital Sky Survey (SDSS; Ahn et al. 2012; Massaro et al. 2014), 6dF Galaxy Survey (Jones et al. 2009), when more recent than the latest version of BZCAT (Massaro et al. 2015). The latter information was used only if the spectrum was published.

The relevant references are reported in the electronic table of the catalog. We did not use the blazar classes from the Simbad database,⁷⁴ since some of them correspond to predictions based on the *Wide-field Infrared Survey Explorer* (WISE)-strip approach (D’Abrusco et al. 2014) and were not obtained from spectral observations.

In the 4LAC, we classify the AGN-like gamma-ray detected objects adopting the following terminology:

1. Confirmed classifications:
 - (a) FSRQ, BL Lac, radio galaxy, steep-spectrum radio quasar (SSRQ), compact steep spectrum radio source (CSS), Seyfert galaxy, and Narrow-line Seyfert 1 galaxy (NLSy1)—these are sources with a well-established classification in the literature and/or an optical spectrum with clear evidence for or lack of emission lines.
2. Tentative classifications:
 - (a) BCU, blazar candidates of uncertain type: these are considered candidate blazars because the association

⁷³ Available at <http://astrogeo.org/rfc>.

⁷⁴ <http://simbad.u-strasbg.fr/simbad/>

Table 2

Comparison of Association Methods in Terms of Total Number of Associations, N_{assoc} , Estimated Number of False Associations, N_{false} , and Number of Sources Associated Only via a Given Method, N_S

Sample	All Methods		Bayesian Method			LR Method		
	N_{assoc}	N_{false}	N_{assoc}	N_{false}	N_S	N_{assoc}	N_{false}	N_S
Full Sample	2863	44.4	2766	34.8	684	2179	143.1	97
Clean Sample	2614	36.5	2529	27.9	596	2018	130.9	85

methods (see Sections 3.1.1 and 3.1.2) select a candidate counterpart that satisfies at least one of the following conditions:

- i. a BZU object (blazars of uncertain/transitional type) in the BZCAT list;
- ii. a source with multiwavelength data in one or more of the *WISE*, AT20G, RFC (Petrov et al. 2019), CRATES (Healey et al. 2007), PMN-CA (Griffith & Wright 1993), CRATES-Gaps (Healey et al. 2009), or CLASS (Caccianiga et al. 2002) lists that indicates a flat radio spectrum and shows a typical two-humped, blazar-like spectral energy distribution (SED);
- iii. a source included in radio and X-ray catalogs not listed above and for which we found a typical two-humped, blazar-like SED (see Böttcher 2007).

The scheme followed in 3LAC whereby BCUs were further divided in three subclasses according to the quality or availability of their optical spectra has not been reconducted in 4LAC. The large number of new BCU sources would have made this task excessively manpower-intensive.

- (b) AGN—for these candidate counterparts, the existing data do not allow an unambiguous determination of the AGN type and do not meet any of the criteria to be classified as BCU. Their SEDs display properties typical of radio-loud compact core objects, but the literature information is either incomplete or conflicting for different epochs or wavelengths.

At low Galactic latitudes, the surveys include a large number of Galactic sources; therefore, the 4FGL class of $|b| < 10^\circ$ sources associated solely via the LR-method has been set to the “unknown” class as opposed to the “BCU” class used by default for sources at larger latitudes. These sources are thus not considered here.

3.3.2. Classification Based on the Broadband Spectral Energy Distribution

Blazars and more generally radio-loud AGNs can also be classified according to the peak photon frequency $\nu_{s,\text{peak}}$ of the synchrotron part of their broadband SEDs. As a large number of 4LAC sources do not have a measured redshift (see Section 5.2), the frequency in the observer frame was used. The SEDs of all 4LAC AGNs were generated using the SED data archive and SED(t)-Builder interactive web-tool available at the Italian Space Agency (ASI) Space Science Data Center (SSDC).⁷⁵ Inspection of the error ellipse and the position of the counterpart was first performed using the Sky Data Explorer at SSDC. Two different approaches were followed to enable a cross-check. The first was the parametric procedure used in

Abdo et al. (2010a) and Ackermann et al. (2011), which is based on the broadband spectral indices α_{ro} (between 5 GHz and 5000 Å) and α_{ox} (between 5000 Å and 1 keV). The list of surveys and catalogs providing the broadband flux density data is given in Abdo et al. (2010a). The second method, already used in 3LAC and favored here, consisted of fitting the SED synchrotron hump with a third-degree polynomial fit in the log-log plane. This fit was carried out manually on a source-by-source basis after carefully discarding outlying data (e.g., taken during flaring episodes) and those dominated by the thermal emission of the accretion disk or of the host galaxy. This methodology allowed us to assign a $\nu_{s,\text{peak}}$ value to more objects, since a measured X-ray flux is not required, provided the SED curvature is sufficiently pronounced in the IR-optical band. This fit also provided the νF_ν value at the peak position. Limitations arose from possible human errors, the use of nonsimultaneous broadband synchrotron data, and remaining contamination of thermal emission. This contamination may result in an overestimation of the $\nu_{s,\text{peak}}$ values for FSRQs, while the near-IR-optical contribution of the host galaxy may bias $\nu_{s,\text{peak}}$ low in BL Lacs. Comparing the results of the two procedures indicated that the fitting method led to an average shift of -0.23 (rms: 0.53) and -0.22 (rms: 0.80) in $\log \nu_{s,\text{peak}}$ relative to the initial method for FSRQs and BL Lacs, respectively. We identify these shifts as systematic uncertainties. Relative to 3LAC, a more conservative approach was followed when little data were available, leading to a lower fraction of classified sources. The mean differences in $\log \nu_{s,\text{peak}}$ between 4LAC and 3LAC are -0.14 (rms: 0.37) and -0.11 (rms: 0.65) for FSRQs and BL Lacs, respectively.

Following Abdo et al. (2010a), the value of the observed $\nu_{s,\text{peak}}$ was used to classify the source as either a low-synchrotron-peaked blazar (LSP, for sources with $\nu_{s,\text{peak}} < 10^{14}$ Hz), an intermediate-synchrotron-peaked blazar (ISP, for 10^{14} Hz $< \nu_{s,\text{peak}} < 10^{15}$ Hz), or a high-synchrotron-peaked blazar (HSP, if $\nu_{s,\text{peak}} > 10^{15}$ Hz). To obtain the rest-frame value of $\nu_{s,\text{peak}}$, a correction by a $(1 + z)$ factor is needed, where z is the redshift.

4. The Fourth LAT AGN Catalog (4LAC)

Figure 1 displays the loci of the 4LAC sources in Galactic and J2000 equatorial coordinates. As already noted in previous LAC catalogs, it is clear from this figure that sources of different classes are not uniformly distributed over the sky. This anisotropy is demonstrated in Figure 2, showing the Galactic-latitude distributions for all 4LAC sources as well as for FSRQs, BL Lacs, and BCUs separately. The anisotropy is most noticeable for BL Lacs, which are 42% more abundant in the northern Galactic hemisphere than in the southern one. BCUs show the opposite pattern and somewhat offset the overall anisotropy as seen in the total distribution of sources, which is close to being uniform. The observed anisotropies stem from the larger and better spectroscopic data available in the literature for

⁷⁵ <http://tools.ssdsc.asi.it/SED/>

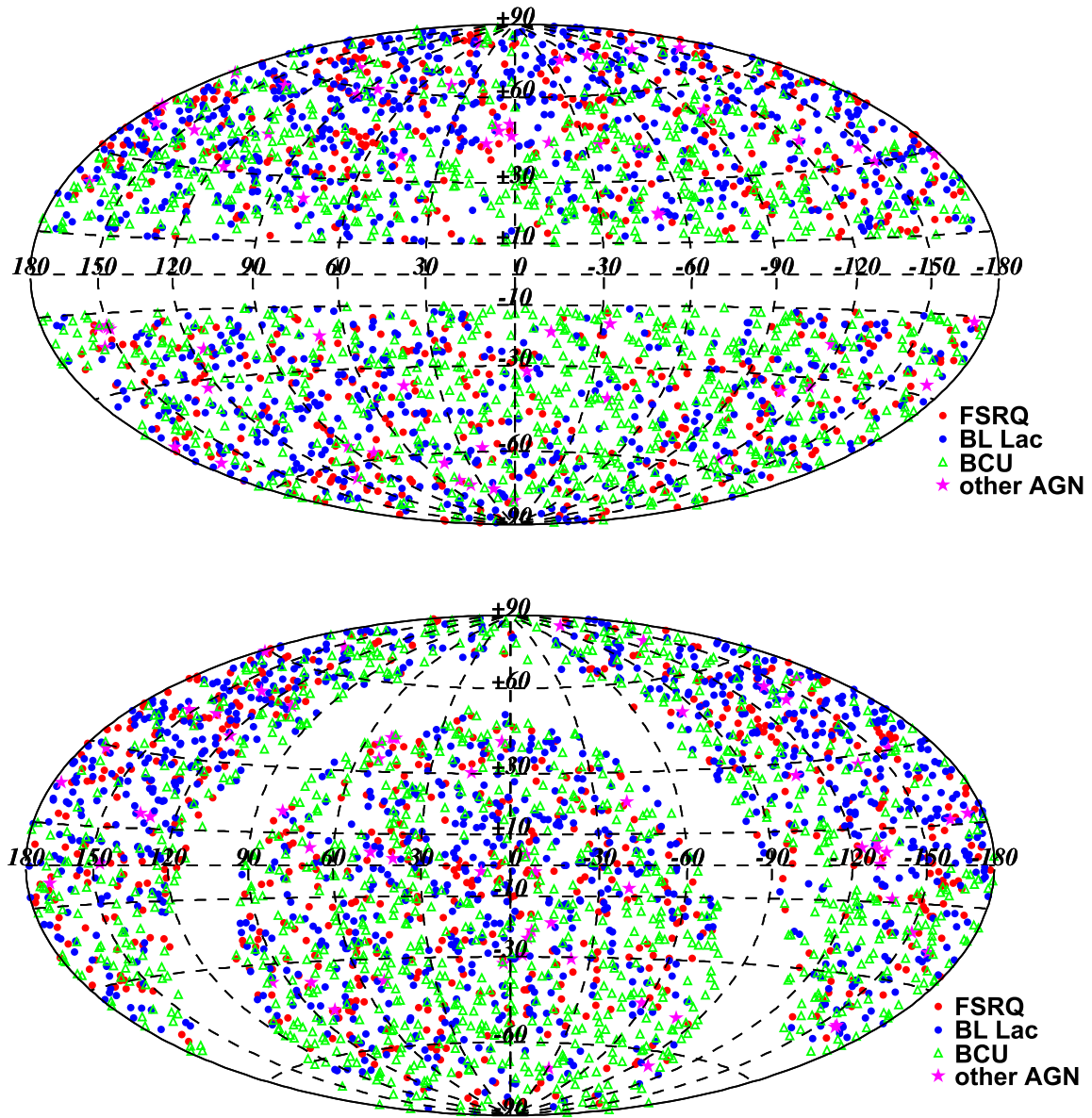


Figure 1. Locations of the sources in the Clean Sample in Galactic (top) and J2000 equatorial (bottom) coordinates and Hammer–Aitoff projection.

the northern hemisphere relative to the southern one. Better spectroscopic data are required to assess the BL Lac nature of an object relative to a FSRQ, because of the weaker optical emission lines in the spectrum of a BL Lac object.

The format of the 4LAC fits table is described in Table 3. In addition to relevant parameters⁷⁶ from the 4FGL fits file,⁷⁷ we report the optical and SED-based classes, redshifts, observer-frame synchrotron-peak frequencies, and νF_ν at the synchrotron-peak frequencies. When available, we also provide the VLBI and *Gaia* counterparts as given in the RFC. The median position accuracy of VLBI counterparts is 0.8 mas. Therefore, establishing association with VLBI immediately allows us to propagate the associations to the optical range using *Gaia* and

IR using *WISE*. Following this route, we obtain *Gaia* associations with 2134 gamma-ray blazars (74%).

4.1. Census

Table 4 summarizes the 4LAC statistics. The 4LAC includes 2863 sources, with 655 FSRQs, 1067 BL Lacs, 1077 BCUs, and 64 other AGNs. A total of 1353 sources were not reported in the previous 3LAC catalog, although some of these have been reported elsewhere, e.g., Arsioli & Chang (2017) and Arsioli & Polenta (2018). The new sources include 204 FSRQs, 290 BL Lacs, 822 BCUs, and 36 nonblazar AGNs. The Clean Sample contains 2614 sources, with 591 FSRQs, 1027 BL Lacs, 941 BCUs, and 55 other AGNs. The figures shown in the following only include Clean Sample sources, unless specified otherwise.

The SED-based scheme was able to classify 92% of the FSRQs and 85% of the BL Lacs in 4FGL. These values are lower than in 3LAC (99% and 97% for FSRQs and BL Lacs, respectively) due to the more conservative classification procedure used here. The classified fraction decreases to 60%

⁷⁶ The FSRQ 3C 454.3 is the only AGN whose preferred spectral shape is a power law with subexponential cutoff. The corresponding parameters can be found in the 4FGL fits file.

⁷⁷ https://fermi.gsfc.nasa.gov/ssc/data/access/lat/8yr_catalog/gll_psc_v20.fit

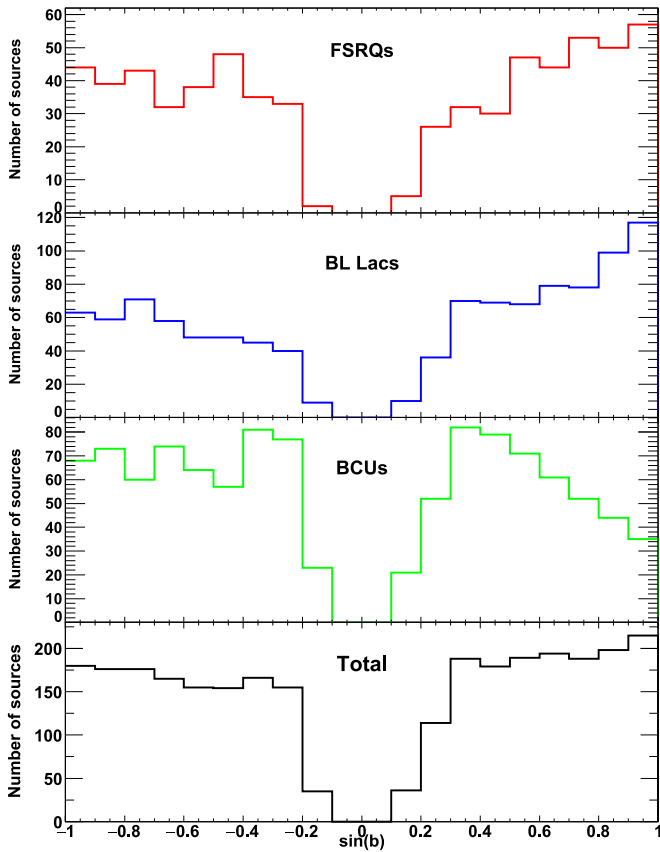


Figure 2. Distributions of Galactic latitudes for the different blazar classes.

for BCUs, for which fewer broadband archival data are available. Figure 3 shows the $\nu_{s,peak}$ distributions for the different classes. FSRQs are overwhelmingly of the LSP class; therefore, no distinction based on SED-based classes is made for them in figures and tallies. In addition to leaving more sources unclassified, the new procedure has produced a decrease in the share of ISPs and HSPs among FSRQs, from 10% to 2%. Of the five HSP FSRQs, all located at $z < 0.63$, two are new: B3 0038 + 377 and PKS 1555–140.

BL Lacs are fairly evenly distributed among the LSP, ISP, and HSP subclasses. The 4LAC $\nu_{s,peak}$ distribution differs substantially from the 3LAC one, where HSPs were the most abundant subclass. The new classification procedure caused 15% of the AGN previously classified as HSP to be reclassified as ISP.

As a testimony to the substantial follow-up observational efforts already mentioned, 144 sources reported as BCUs in the 3LAC paper (either at high or low Galactic latitudes) are now classified as BL Lacs and 17 as FSRQs. Three BCUs have been reclassified as radio galaxies (IC 1531, TXS 0149+710, PKS 1304–215). Eight sources have changed from a FSRQ to a BL Lac (RGB J0250+172, NVSS J040324–242946, GB6 J0941+2721, 2MASS J11303636+1018245, PKS 1144–379, 4C +15.54, TXS 1951–115, PKS 2233–173) and three more from a BL Lac to a FSRQ (PMN J0709–0255, B2 2234+28A, TXS 2241+406).

The 3LAC sources that are not present in 4LAC are listed in Table 5, along with the various reasons for this situation. Fifty-five 3LAC sources have not been detected in 4FGL. Nineteen 3LAC sources were duplicate associations for which the smaller 4FGL error boxes relative to 3FGL have enabled the association ambiguity to be lifted. Fifteen sources reported in

3LAC have lost their associations (becoming unassociated), while three others are now associated with non-AGN counterparts, all due to improved localizations.

4.2. Nonblazar AGNs and Misaligned AGNs

Table 6 lists the 70 nonblazar AGNs included in the 4FGL, 64 of which belong to the 4LAC and 6 are part of the low-latitude sample. Nonblazar sources represent about 2% of the total number of AGNs in the 4FGL, a fraction that is basically identical to that found in the 3LAC. Nonblazar sources are further separated into six different classes: 41 radio galaxies,⁷⁸ 9 NLSy1s, 5 CSSs, 2 SSRQs, 1 Seyfert galaxy, and 11 other AGNs.

A total of 36 new nonblazar AGNs are reported in the 4LAC, 22 of which are radio galaxies. The median 1.4 GHz radio luminosity of the newly detected radio galaxies is about $10^{24.4}$ W Hz⁻¹, with the distribution ranging over more than 4 decades (from below 10^{22} W Hz⁻¹, for NGC 2892, to above 10^{26} W Hz⁻¹, for PKS 2324–02). The detection of the FR I radio galaxy 3C 120 in gamma-rays was first reported by Abdo et al. (2010c) using 15 months of LAT data, but it is reported in a LAT catalog for the first time. Its absence from previous catalogs can be attributed to periods of flaring interspersed with long periods of low activity (Tanaka et al. 2015). TXS 1303 +114 and TXS 1516+064 are members of the FRICAT (Capetti et al. 2017a), although they were earlier proposed as candidate low-power BL Lacs in Capetti & Raiteri (2015) based on their mid-infrared and optical emission. Among the sources already present in previous LAT catalogs, Fornax A stands out because it is, for the first time, detected as an extended source (see Ackermann et al. 2016). Three 3FGL sources have changed class from BCU to radio galaxy (IC 1531, TXS 0149+710, and PKS 1304–215). We associate 4FGL J1346.3–6026 with Cen B, although its location is not coincident with that of the radio-galaxy core but points to the southern radio jet. Similarly, we associate 4FGL J1516.5 +0015 with the radio galaxy 4C +00.56 (PKS 1514+00, $z = 0.0525$) while the gamma-ray position is closer to the lobes than to the core of the radio galaxy.

The only new SSRQ is 3C 212, for which X-ray emission associated with both lobes was detected by *Chandra* (Aldcroft et al. 2003). Three new CSSs are reported in the 4LAC: 3C 138, 3C 216, and 3C 309.1. These new CSSs are hosted in quasars. At the pc scale, they show a core-jet structure with apparent superluminal motion, indicating Doppler effects and small viewing angles (Paragi et al. 2000; Shen et al. 2001; Lister et al. 2019). While the CSSs all have very high radio luminosity, at the opposite end of the radio luminosity distribution are two other new LAT sources, NGC 3894 and NGC 6328. Based on the small extent of their radio emission, two-sided parsec scale morphology (Taylor et al. 1998; Tingay & de Kool 2003), and low radio luminosity, these sources are excellent candidates for being young radio galaxies (see also Migliori et al. 2016; Principe et al. 2019).

The classification of a source as an NLSy1 relies on three criteria, as reported in Osterbrock & Pogge (1985), Goodrich (1989), and Pogge (2000): (i) a full width half maximum (FWHM) of the H_{β} line < 2000 km s⁻¹; (ii) a $[O III]\lambda 5007/H_{\beta}$ ratio < 3 ; and (iii) unusually strong Fe II lines. Nine NLSy1 are reported in the 4LAC. Four of them are new with respect to

⁷⁸ Two different gamma-ray sources are associated with the core and lobes of Cen A.

Table 3
4LAC FITS Format

Column	Format	Unit	Description
Source_Name	18A	...	Source name 4FGL JHHMM.m+DDMMa ^a
RAJ2000	E	deg	R.A.
DEJ2000	E	deg	Decl.
GLON	E	deg	Galactic Longitude
GLAT	E	deg	Galactic Latitude
Signif_Avg	E	...	Source significance in σ units over the 50 MeV–1 TeV band
Flux1000	E	$\text{cm}^{-2} \text{s}^{-1}$	Integral photon flux from 1 to 100 GeV
Unc_Flux1000	E	$\text{cm}^{-2} \text{s}^{-1}$	1σ error on integral photon flux from 1 to 100 GeV
Energy_Flux100	E	$\text{erg cm}^{-2} \text{s}^{-1}$	Energy flux from 100 MeV to 100 GeV obtained by spectral fitting
Unc_Energy_Flux100	E	$\text{erg cm}^{-2} \text{s}^{-1}$	1σ error on energy flux from 100 MeV to 100 GeV
SpectrumType	17A	...	Spectral type in the global model (PowerLaw, LogParabola, PLSuperExpCutoff)
PL_Index	E	...	Photon index when fitting with PowerLaw
Unc_PL_Index	E	...	1σ error on PL_Index
Pivot_Energy	E	MeV	Pivot Energy
LP_Index	E	...	Photon index at Pivot_Energy (α) when fitting with LogParabola
Unc_LP_Index	E	...	1σ error on LP_Index
LP_beta	E	...	Curvature parameter (β) when fitting with LogParabola
Unc_LP_beta	E	...	1σ error on LP_beta
Flags	I	...	Analysis flags
CLASS	6A	...	Class designation for associated source
ASSOC1	30A	...	Name of identified or likely associated source
ASSOC_PROB_BAY	E	...	Probability of association according to the Bayesian method
ASSOC_PROB_LR	E	...	Probability of association according to the Likelihood Ratio method
Counterpart_Catalog	10A	...	Counterpart catalog driving the association
RA_Counterpart	D	deg	R.A. of the counterpart ASSOC1
DEC_Counterpart	D	deg	Decl. of the counterpart ASSOC1
Unc_Counterpart	E	deg	95% precision of the counterpart localization
VLBI_Counterpart	14A	...	Name of the VLBI counterpart
Gaia_Counterpart	29A	...	Name of the <i>Gaia</i> counterpart established via the VLBI position
Gaia_G_Magnitude	E	...	Gaia Magnitude at the <i>G</i> band
Redshift	E	...	Redshift
SED_class	6A	...	SED-based class
nu_syn	E	Hz	Synchrotron-peak frequency in observer frame
nuFnu_syn	E	$\text{erg cm}^{-2} \text{s}^{-1}$	Spectral energy distribution at synchrotron-peak frequency
Variability_Index	E	...	Variability index
Frac_Variability	E	...	Fractional variability
Unc_Frac_Variability	E	...	1σ error on fractional variability
Highest_energy	E	GeV	Energy of the highest-energy ULTRACLEANVETO photon with association probability $P > 0.95$

Note.

^a The coordinates are rounded, following the IAU convention.

(This table is available in its entirety in machine-readable form.)

the 3LAC: 1ERS B1303+515, B3 1441+476, MG2 J164443+2618, and TXS 2116–077. B3 1441+476, MG2 J164443+2618, and TXS 2116–077 were previously reported by D’Ammando et al. (2015a) and Paliya et al. (2018), respectively. The Circinus galaxy (Hayashida et al. 2013) remains the only radio-quiet Seyfert galaxy detected by the LAT.

Among other AGNs, there are two remarkable cases. One is PKS 0521–36, previously classified as BCU in the 3LAC, which shows a knotty VLBA radio structure similar to misaligned AGN. Based on the broad emission lines in the optical and ultraviolet bands and the steep radio spectrum, a possible classification as an intermediate object between broad-line radio galaxies and SSRQ has been suggested by D’Ammando et al. (2015b). The new source PKS 2331–240 was the subject of a multiwavelength

study revealing features of a giant radio galaxy restarted as a blazar (Hernández-García et al. 2017).

Finally, 10 nonblazar AGNs reported in the 3LAC are not confirmed in the 4LAC. Five of them had a double association in the 3LAC and are now firmly associated with the other counterpart; two have changed associations (formerly with 3C 221 and 3C 275.1); one has been reclassified as a BCU (GB 1310+487); while two 3FGL nonblazar AGNs are missing in 4FGL (TXS 0348+013, PKS 1617–251).

4.3. Low-latitude AGNs

In addition to high-latitude ($|b| > 10^\circ$) 4LAC sources, we present a low-latitude sample. This sample is less complete than the 4LAC because the LAT detection flux limit is higher

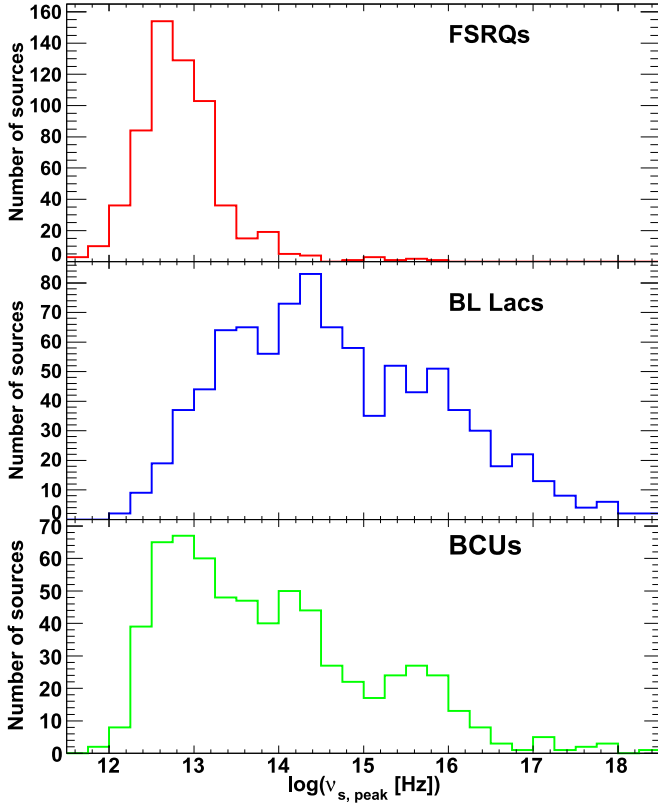


Figure 3. Distributions of the synchrotron peak frequency $\nu_{s,\text{peak}}$ for the different blazar classes.

Table 4
Census of Sources

AGN type	Entire 4LAC	4LAC Clean Sample ^a	Low-latitude Sample
All	2863	2614	344
FSRQ	655	591	36
LSP	587	540	34
ISP	11	9	0
HSP	5	4	0
No SED classification	52	38	2
BL Lac	1067	1027	64
LSP	297	288	15
ISP	280	270	7
HSP	326	316	25
No SED classification	164	153	17
Blazar of unknown type	1077	941	238
LSP	382	327	57
ISP	142	128	9
HSP	128	126	12
No SED classification	425	360	160
Nonblazar AGN	64	55	6
NLSy1	9	9	0
RG	38	31	4
CSS	5	5	0
SSRQ	2	2	0
SEY	0	0	1
Other AGN	10	8	1

Note.

^a Sources with single counterparts and without analysis flags. See Section 3.2 for the definitions of this sample.

Table 5
The 3LAC Sources Not Present in 4LAC

3FGL Name	Counterpart	Class	4FGL ^a
J0127.9+2551	4C +25.05	fsrq	M
J0135.0+6927	TXS 0130+691	bcu	M
J0211.7+5402	TXS 0207+538	bcu	M
J0216.1-7016	PMN J0215-7014	bcu	M
J0217.3+6209	TXS 0213+619	bcu	M
J0223.5+6313	TXS 0219+628	bcu	M
J0228.5+6703	GB6 J0229+6706	bcu	M
J0302.0+5335	GB6 J0302+5331	bcu	M
J0336.9-1304	PKS 0334-131	fsrq	M
J0351.1+0128	TXS 0348+013	ssrq	M
J0512.2+2918	B2 0509+29	bcu	M
J0514.4+5603	TXS 0510+559	fsrq	M
J0517.4+4540	4C +45.08	fsrq	M
J0528.3+1815	1RXS J052829.6+181657	bcu	M
J0618.9-1138	TXS 0616-116	bcu	M
J0627.9-1517	NVSS J062753-152003	bcu	M
J0730.3+6720	GB6 J0731+6718	fsrq	M
J0742.4-8133	SUMSS J074220-813139	bcu	M
J0744.1-3804	PMN J0743-3804	bcu	M
J0904.9+2739	GB6 J0905+2748A	fsrq	M
J0928.7+7300	GB6 J0929+7304	bcu	M
J0956.7-6441	AT20G J095612-643928	bcu	M
J1005.0-4959	PMN J1006-5018	bcu	M
J1016.0-0635	NVSS J101626-063624	bcu	M
J1024.8+0105	PMN J1024+0056	bcu	M
J1037.4-3742	PKS 1034-374	fsrq	M
J1123.2-6415	AT20G J112319-641735	bcu	M
J1205.4+0412	MG1 J120448+0408	fsrq	M
J1218.5+6912	NVSS J122044+690522	bcu	M
J1326.1+2931	TXS 1323+298	bl	M
J1330.0-3818	Tol 1326-379	fsrq	M
J1356.3-4029	SUMSS J135625-402820	bcu	M
J1415.0-1001	PKS B1412-096	fsrq	M
J1509.9-2951	TXS 1507-296	bcu	M
J1513.1-1014	PKS 1511-100	fsrq	M
J1514.1+2940	MG2 J151421+2930	fsrq	M
J1536.6+8331	NVSS J153556+832614	bcu	M
J1541.8+1105	MG1 J154207+1110	fsrq	M
J1621.1-2331	PKS 1617-235	agn	M
J1645.2-5747	AT20G J164513-575122	bcu	M
J1648.5-4829	PMN J1648-4826	bcu	M
J1723.5-5609	PMN J1723-5614	bcu	M
J1747.1+0139	PMN J1746+0141	bcu	M
J1757.4+6536	7C 1757+6536	bcu	M
J1804.1+0341	TXS 1801+036	fsrq	M
J1819.1+4259	NVSS J181927+425800	bcu	M
J1822.1-7051	PMN J1823-7056	bcu	M
J1949.4-6140	PMN J1949-6137	bcu	M
J2107.7-4822	PMN J2107-4827	bcu	M
J2151.6-2744	PMN J2151-2742	fsrq	M
J2203.7+3143	4C +31.63	fsrq	M
J2236.2-5049	SUMSSJ223605-505521	bcu	M
J2246.2+1547	NVSS J224604+154437	bcu	M
J2305.3-4219	SUMSS J230512-421859	bcu	M
J2343.6+1551	MG1 J234342+1542	fsrq	M
J0003.8-1151	PKS 0001-121	bcu	D
J0009.1+0630	GB6 J0009+0625	bl	D
J0059.1-5701	PKS 0056-572	bcu	L
J0203.6+3043	B2 0200+30	fsrq	D
J0426.6+0459	4C +04.15	bcu	L
J0442.6-0017	1RXS J044229.8-001823	bl	D
J0447.8-2119	PKS 0446-212	fsrq	L

Table 5
(Continued)

3FGL Name	Counterpart	Class	4FGL ^a
J0515.3-4557	PMN J0514-4554	bcu	D
J0526.0+4253	NVSS J052520+425520	bcu	C
J0542.2-8737	SUMSS J054923-874001	bcu	L
J0618.0+7819	1REX J061757+7816.1	fsrq	C
J0647.1-4415	SUMSS J064648-441929	bcu	C
J0712.2-6436	MRC 0712-643	bcu	L
J0744.8-4028	PMN J0744-4032	bcu	L
J0807.9+4946	SDSS J080754.50+494627.6	fsrq	D
J0824.9+3916	4C +39.23B	css	D
J0825.4-0213	PMN J0825-0204	bcu	L
J0934.1+3933	3C 221	rdg	D
J1007.4-3334	TXS 1005-333	bcu	D
J1010.8-0158	NVSS J101051-020227	fsrq	D
J1018.1+1904	MG1 J101810+1903	bcu	D
J1048.6+2338	NVSS J104900+233821	bll	C
J1101.5+4106	B3 1058+413	bcu	D
J1146.8+3958	NVSS J114653+395751	bcu	D
J1207.6-4537	PMN J1207-4531	bcu	L
J1244.1+1615	3C 275.1	ssrq	D
J1256.7+5328	TXS 1254+538	bcu	L
J1300.2+1416	NVSS J130041+141728	bcu	D
J1322.8-0938	PMN J1323-0943	bcu	D
J1451.2+6355	TXS 1450+641	bcu	D
J1514.8+4446	NVSS J151436+445003	fsrq	L
J1554.4+2010	1ES 1552+203	bll	L
J1617.3-2519	TXS 1613-251	agn	D
J1625.9+4125	4C +41.32	fsrq	D
J1908.8-0130	NVSS J190836-012642	bcu	L
J2036.8-2830	PMN J2036-2830	fsrq	L
J2110.3+3540	B2 2107+35A	bcu	L
J2348.4-5100	SUMSS J234852-510311	bcu	L

Note.

^a M: missing gamma-ray source in 4FGL. L: 3FGL source present in 4FGL but now unassociated. C: 3FGL source present in 4FGL but now associated with a non-AGN counterpart. D: duplicate counterpart in 3LAC now missing in 4LAC.

(This table is available in machine-readable form.)

in this region (by factors of a few) and the counterpart catalogs suffer from Galactic extinction. Because a large contamination of Galactic sources is present in the radio and X-ray surveys used in the LR association method, the classes of the resulting associations are highly uncertain. Consequently, these associations were not considered here. The census of the low-latitude sample is given in the last column of Table 4. The fraction of BCUs (62%) is overwhelming, as expected from the observational hindrance mentioned above.

5. Properties of the 4LAC Clean Sample Sources

5.1. Flux and Spectral Properties

Although many 4FGL/4LAC sources show significant spectral curvature in the gamma-ray band (The Fermi-LAT collaboration 2020), the gamma-ray power-law photon index, Γ , represents a convenient way to compare the spectral hardness of different sources across various classes and flux values. This index is plotted versus the 8 yr average energy flux above 100 MeV, S_{25} , in Figure 4. The flux detection limit ranges from $(1-4) \times 10^{-12}$ erg cm⁻² s⁻¹ (i.e., close to 1 eV

cm⁻² s⁻¹), with a slight dependence on the spectral hardness. This dependence is stronger than in 3LAC due to the introduction of weights in the 4FGL likelihood to better account for systematic uncertainties. BCUs are rare among the brightest sources (i.e., with $S_{25} > 10^{-11}$ erg cm⁻² s⁻¹), while they are dominant close to the flux limit.

Figure 5 displays the photon index distributions for the different optical blazar classes, for 4LAC sources already present in 3LAC and the new ones. Newly detected gamma-ray FSRQs, i.e., not reported in previous LAT AGN catalogs, have somewhat softer spectra (difference in median $\Gamma \simeq 0.08$) than the previously reported ones, possibly indicating the emergence of sources with SED peaking at lower energy. The difference between the FSRQ and BL Lac distributions is striking. The Γ medians and rms are 2.44 ± 0.20 and 2.02 ± 0.21 for FSRQs and BL Lacs respectively. The relative separation in gamma-ray spectral hardness between FSRQs and BL Lacs already reported in previous LAT catalogs is confirmed: 89% of FSRQs and 86% of BL Lacs have Γ greater and lower than 2.25, respectively. This feature by itself carries significant discrimination power between the two classes. The photon index varies among the BL Lac subclasses, with medians and rms in Γ of 2.17 ± 0.16 , 2.05 ± 0.19 , and 1.88 ± 0.14 for LSPs, ISPs, and HSPs, respectively. The BCU index distribution straddles that of the two classes and extends to $\Gamma = 3$. The expectation that both the BCU photon-index and $\nu_{s,\text{peak}}$ distributions correspond to linear combinations of the observed FSRQ and BL Lac distributions is tested in Figure 6. Composite distributions were built assuming the same fractions of FSRQs and BL Lacs as in the observed sample for the photon index distributions. For the $\nu_{s,\text{peak}}$ distribution, a slight correction (a factor of 0.92) in the normalization was introduced in disfavor of FSRQ to account for the difference in efficiency for fitting the SEDs successfully, due to better broadband data for FSRQs (see Section 4.1). The reasonable agreement between the composite and BCU distributions for both photon index and $\nu_{s,\text{peak}}$ seen in Figure 6 supports the idea that the sample of unclassified blazars (i.e., BCUs) is of a composition similar to that of the classified sample in 4LAC.

Figure 7 displays the photon index as a function of the observed synchrotron peak frequency. Even though $\nu_{s,\text{peak}}$ should be corrected by a factor $1+z$ to obtain the rest-frame value and make the correlation more physical, the fairly strong correlation already noted in previous catalogs is clearly visible. The correlation obtained in 3LAC was reproduced theoretically by Dermer et al. (2015) using an equipartition blazar model with a log-parabola description of the electron energy distribution. In the region of $\nu_{s,\text{peak}}$ where BL Lac LSPs and FSRQs overlap, their photon index distributions are very similar. This is the expected region for objects that might be transitioning between being FSRQs and BL Lacs. Ruan et al. (2014) found six such transitioning objects. Five of them, all of the LSP subclass, are present in 4LAC: OJ 451 (4FGL J0833.9+4223, FSRQ, $\Gamma = 2.44 \pm 0.07$), TXS 1013+054 (4FGL J1016.0+0512, FSRQ, $\Gamma = 2.18 \pm 0.04$), PKS 1247+025 (4FGL J1250.6+0217, BLL, $\Gamma = 2.00 \pm 0.10$), 5C 12.291 (4FGL J1308.5+3547, FSRQ, $\Gamma = 2.29 \pm 0.06$), and PMN J2206-0031 (4FGL J2206.8-0032, BLL, $\Gamma = 2.25 \pm 0.05$). Three of these sources have Γ very close to the $\Gamma = 2.25$ limit outlined above. The four HSP FSRQs in the Clean Sample all have $\Gamma < 2.02$, as expected from the class of “HFSRQs,” which is not fitting with the “blazar sequence” (see, e.g., Padovani 2007).

Table 6
Nonblazar Objects and Misaligned AGNs

4FGL Name	Name	Type	Photon Index	Redshift/Distance (Mpc)
J0009.7-3217	IC 1531	rdg	2.2 ± 0.14	93.4 ^a
J0013.6+4051	4C +40.01	agn	2.21 ± 0.14	0.255
J0038.7-0204	3C 17	rdg	2.81 ± 0.11	0.22
J0057.7+3023	NGC 315	rdg	2.35 ± 0.11	0.016
J0237.7+0206	PKS 0235+017	rdg	2.17 ± 0.18	0.022
J0308.4+0407	NGC 1218	rdg	2.0 ± 0.06	0.029
J0312.9+4119	B3 0309+411B	rdg	2.47 ± 0.19	0.136
J0316.8+4120	IC 310	rdg	1.78 ± 0.18	0.019
J0319.8+4130	NGC 1275	rdg	2.12 ± 0.01	0.69 ^a
J0322.6-3712e	Fornax A	rdg	2.05 ± 0.07	17.8 ^a
J0324.8+3412	1H 0323+342	nlsy1	2.82 ± 0.04	0.061
J0334.3+3920	4C +39.12	rdg	1.9 ± 0.13	0.021
J0433.0+0522	3C 120	rdg	2.72 ± 0.05	0.033
J0519.6-4544	Pictor A	rdg	2.46 ± 0.13	0.035
J0521.2+1637	3C 138	css	2.37 ± 0.13	0.759
J0522.9-3628	PKS 0521-36	agn	2.45 ± 0.01	0.056
J0627.0-3529	PKS 0625-35	rdg	1.9 ± 0.04	0.055
J0708.9+4839	NGC 2329	rdg	1.95 ± 0.18	0.019
J0758.7+3746	NGC 2484	rdg	2.01 ± 0.16	171 ^a
J0840.8+1317	3C 207	ssrq	2.48 ± 0.1	0.681
J0850.0+5108	SBS 0846+513	nlsy1	2.27 ± 0.02	0.583
J0858.1+1405	3C 212	ssrq	2.52 ± 0.15	1.048
J0910.0+4257	3C 216	css	2.52 ± 0.11	0.67
J0931.9+6737	NGC 2892	rdg	2.23 ± 0.06	0.023
J0948.9+0022	PMN J0948+0022	nlsy1	2.64 ± 0.02	0.585
J1012.7+4228	B3 1009+427	agn	1.76 ± 0.09	0.365
J1116.6+2915	B2 1113+29	rdg	1.44 ± 0.24	0.047
J1118.2-0415	PMN J1118-0413	agn	2.64 ± 0.08	...
J1144.9+1937	3C 264	rdg	1.94 ± 0.1	0.022
J1149.0+5924	NGC 3894	rdg	2.06 ± 0.12	46.9 ^a
J1230.8+1223	M87	rdg	2.06 ± 0.04	16.5 ^a
J1305.3+5118	IERS B1303+515	nlsy1	2.85 ± 0.17	0.788
J1306.3+1113	TXS 1303+114	rdg	1.95 ± 0.18	0.086
J1306.7-2148	PKS 1304-215	rdg	2.13 ± 0.09	0.126
J1325.5-4300	Cen A	rdg	2.65 ± 0.02	3.8 ^a
J1331.0+3032	3C 286	css	2.41 ± 0.14	0.85
J1356.2-1726	PKS B1353-171	agn	2.08 ± 0.15	0.075
J1443.1+5201	3C 303	rdg	1.98 ± 0.15	0.141
J1443.1+4728	B3 1441+476	nlsy1	2.56 ± 0.11	0.705
J1449.5+2746	B2 1447+27	rdg	1.54 ± 0.18	0.031
J1449.7-0910	1RXS J144942.2-091018	agn	2.04 ± 0.18	...
J1459.0+7140	3C 309.1	css	2.45 ± 0.09	0.91
J1505.0+0326	PKS 1502+036	nlsy1	2.59 ± 0.04	0.409
J1516.5+0015	PKS 1514+00	rdg	2.59 ± 0.11	0.052
J1518.6+0614	TXS 1516+064	rdg	1.86 ± 0.17	0.102
J1521.1+0421	PKS B1518+045	rdg	2.06 ± 0.15	0.052
J1543.6+0452	CGCG 050-083	agn	1.87 ± 0.08	0.04
J1630.6+8234	NGC 6251	rdg	2.35 ± 0.03	98.2 ^a
J1644.9+2620	MG2 J164443+2618	nlsy1	2.78 ± 0.1	0.144
J1724.2-6501	NGC 6328	rdg	2.49 ± 0.18	0.014
J1829.5+4845	3C 380	css	2.43 ± 0.03	0.695
J1843.4-4835	PKS 1839-48	rdg	1.99 ± 0.17	0.111
J2007.9-4432	PKS 2004-447	nlsy1	2.6 ± 0.05	0.24
J2114.8+2026	TXS 2112+202	agn	2.13 ± 0.16	...
J2118.8-0723	TXS 2116-077	nlsy1	2.83 ± 0.15	0.26
J2156.0-6942	PKS 2153-69	rdg	2.83 ± 0.11	0.028
J2227.9-3031	PKS 2225-308	rdg	1.99 ± 0.17	0.056
J2302.8-1841	PKS 2300-18	rdg	2.17 ± 0.15	0.129
J2326.9-0201	PKS 2324-02	rdg	2.44 ± 0.14	0.188
J2329.7-2118	PKS 2327-215	rdg	2.45 ± 0.16	0.031
J2334.9-2346	PKS 2331-240	agn	2.42 ± 0.12	0.048
J2338.1+0325	PKS 2335+03	agn	2.36 ± 0.15	0.27
J2341.8-2917	PKS 2338-295	rdg	2.24 ± 0.15	0.052

Table 6
(Continued)

4FGL Name	Name	Type	Photon Index	Redshift/Distance (Mpc)
J0153.4+7114	TXS 0149+710	rdg	1.9 ± 0.11	0.022
J0418.2+3807	3C 111	rdg	2.71 ± 0.06	0.05
J1236.9-7232	PKS 1234-723	rdg	2.36 ± 0.14	0.024
J1346.3-6026	Cen B	rdg	2.4 ± 0.05	0.013
J1413.1-6519	Circinus galaxy	sey	2.25 ± 0.1	4.0 ^a
J1824.7-3243	PKS 1821-327	agn	2.23 ± 0.12	0.355

Note. The table includes the nonblazar objects and MAGNs at high latitudes (top) and low latitudes (bottom) associated with 4FGL sources (Cen A Core and Cen A Lobes constitute a single object).

^a Indicates that the value is the distance in Mpc.

(This table is available in machine-readable form.)

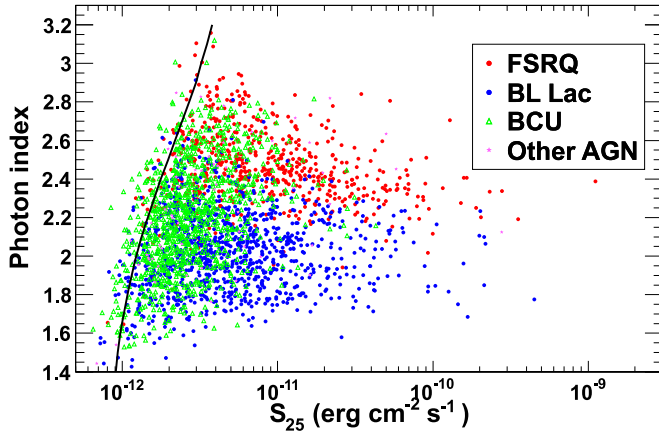


Figure 4. Photon index as a function of energy flux above 100 MeV. Curve represents the approximate detection limit. Error bars have been omitted for clarity. Mean photon-index uncertainties are 0.08, 0.10, and 0.14 for FSRQs, BL Lacs, and BCUs, respectively.

Some blazars have undergone statistically significant spectral changes since 3LAC: PKS 1349–439 (BL Lac, $\Delta\Gamma \equiv \Gamma_{4\text{FGL}} - \Gamma_{3\text{FGL}} = -0.37 \pm 0.12$), RX J1415.5+4830 (BL Lac, $\Delta\Gamma = -0.70 \pm 0.16$), PKS 1532+01 (FSRQ, $\Delta\Gamma = -0.41 \pm 0.12$), and S4 1800+44 (FSRQ, $\Delta\Gamma = -0.33 \pm 0.09$). The changes in photon index are all such that $\Gamma_{4\text{FGL}}$ is closer to the median of the class than was $\Gamma_{3\text{FGL}}$. Inspection of the light curves reveals that all four sources show enhanced activity in the last 4 yr of the 4LAC period relative to that of 3LAC, which may be correlated with the observed spectral hardening. Fourteen other sources have experienced spectral variations greater than 3σ but of lower amplitudes than these four.

As noted above, many FSRQs and BL Lacs show significant spectral curvature. The comparison of the TS distributions of sources with significantly curved spectra to those of the whole sample of FSRQs and BL Lacs (Figure 8) demonstrates that essentially all bright blazars have curved spectra in the LAT energy range. A total of 212 FSRQs, 172 BL Lacs, and 70 BCUs have significantly curved spectra. To enable comparison, if we apply the more stringent threshold on the curvature significance (i.e., approximately 4σ instead of 3σ) used in 3LAC, these numbers become 146 FSRQs, 112 BL Lacs, and 26 BCUs. In 3LAC, the comparable numbers were 57, 32, and 8, respectively. It is therefore likely that fainter blazars have curved spectra as well, but the current data do not allow their curvature to be established with high confidence.

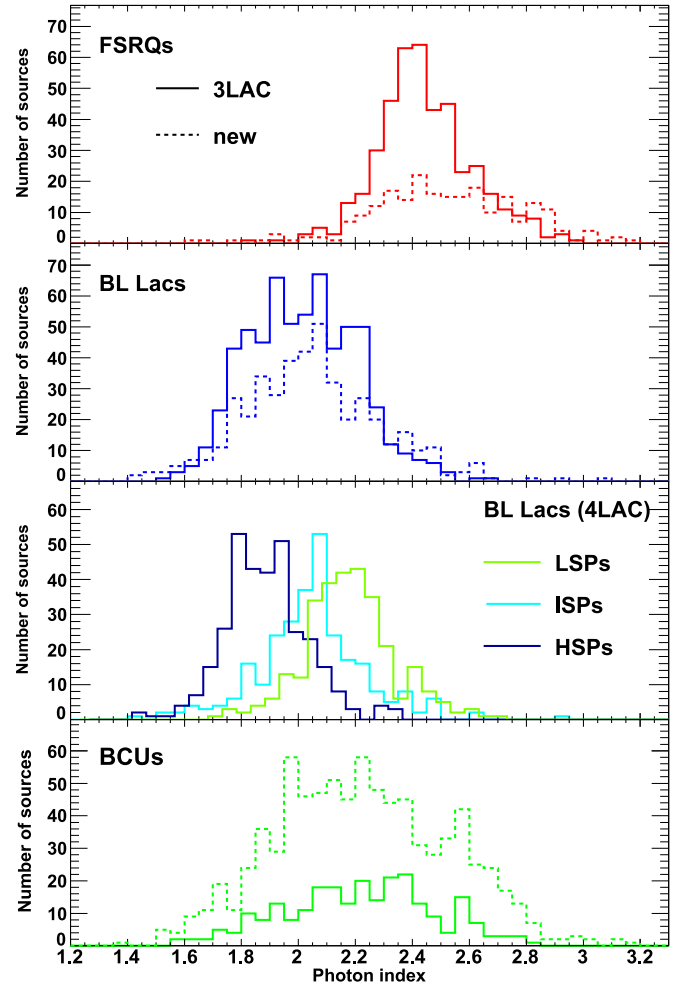


Figure 5. Photon index distributions for the different blazar classes and subclasses. In the top, second from top, and bottom panels, the solid histograms represent the 4LAC sources already present in 3LAC and the dashed histograms the new 4LAC sources.

5.2. Redshifts

We conducted a literature search for spectroscopic redshifts. Well-established redshifts (999) came from BZCAT or the optical campaigns mentioned in Section 3.3.1. For the other sources (656), remaining contamination from photometric values or from bad signal-to-noise ratio optical spectra cannot be excluded. We found redshifts for all the FSRQs, but were unable to find those for 36% of the BL Lacs in our sample.

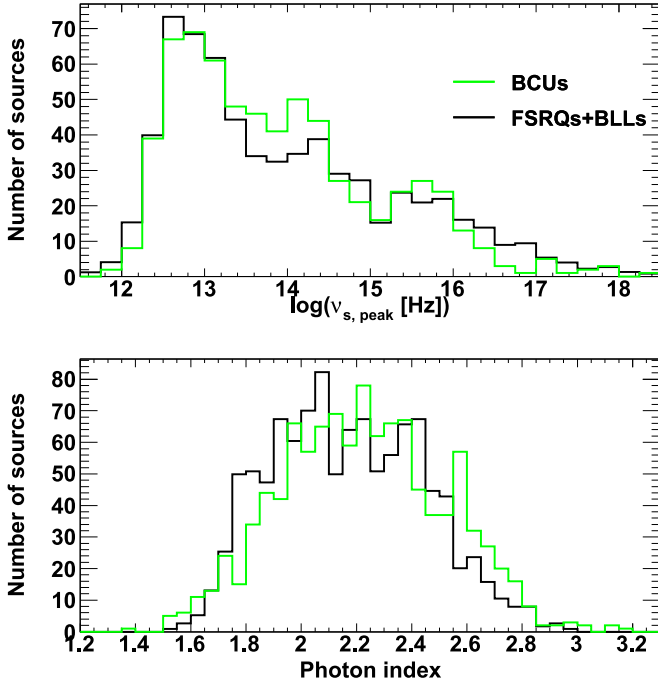


Figure 6. Comparison between the $\nu_{s, \text{peak}}$ (top) and photon index (bottom) distributions of BCUs (green) and the (normalized) distributions obtained by adding up the FSRQ and BL Lac distributions (black). See text for details.

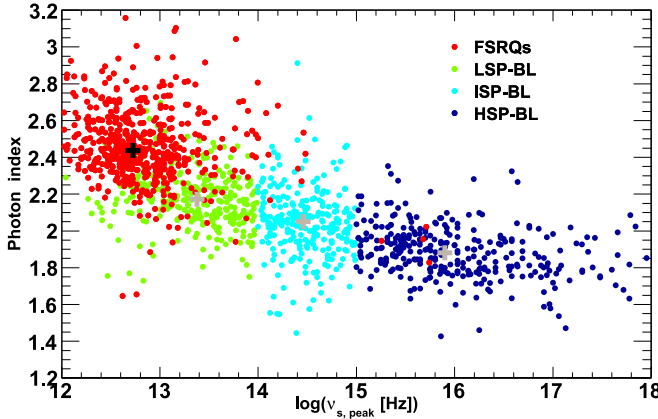


Figure 7. Photon index vs. frequency of the synchrotron peak $\nu_{s, \text{peak}}$ in the observer frame. Error bars have been omitted for clarity. The mean photon-index uncertainties are 0.08 and 0.10 for FSRQs and BL Lacs, respectively. Black cross depicts the FSRQ median photon index, while gray crosses depict those for the three BL Lac subclasses.

(compared to 50% of the BL Lacs without redshifts in 3LAC). This clear improvement has been primarily achieved thanks to follow-up observations of 3LAC blazars (see Section 3.3.1 for references). The fraction without redshifts is similar for the three BL Lac subclasses (41%, 42%, and 28% for LSPs, ISPs, and HSPs, respectively).

The redshift distributions are displayed in Figure 9 for FSRQs and BL Lacs. The FSRQ distribution shows a broad peak around $z = 1$. This trend confirms the conclusion that the number density of FSRQs grows dramatically up to redshift ≈ 0.5 – 2.0 and declines thereafter (Ajello et al. 2012). For BL Lacs, the overall peak lies at $z \approx 0.3$. For the sake of comparison, the distributions for previously and newly reported AGNs are plotted separately. The redshifts of the 3LAC and newly detected blazars are similar, with respective medians and

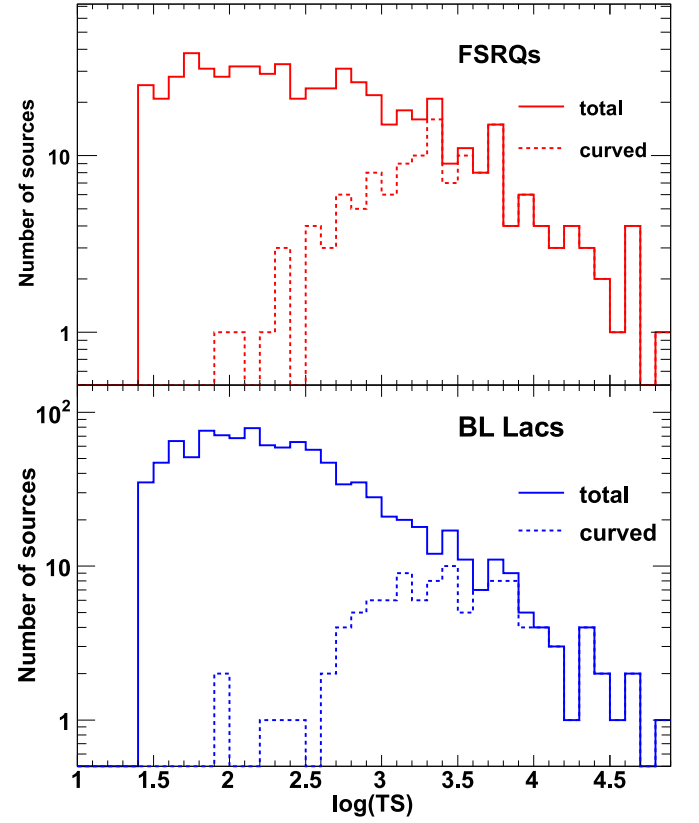


Figure 8. TS distributions of FSRQs (top) and BL Lacs (bottom) for curved-spectra sources and the whole sample.

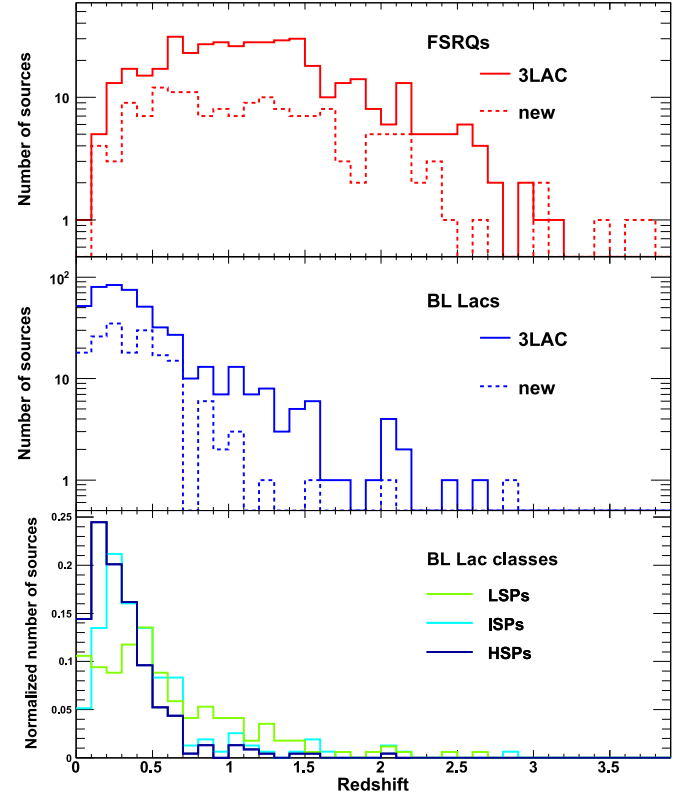


Figure 9. Redshift distributions, where solid lines indicate 4LAC sources also in 3LAC and dashed lines signify new 4LAC sources, for FSRQs (top) and BL Lacs (bottom).

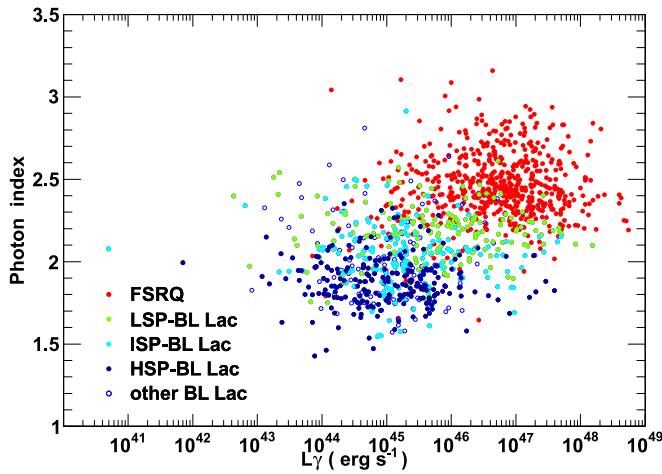


Figure 10. Photon index vs. gamma-ray luminosity for the different blazar classes and subclasses. Error bars have been omitted for clarity. Mean photon-index uncertainties are 0.08 and 0.10 for FSRQs and BL Lacs, respectively.

widths of 1.14 ± 0.62 and 1.09 ± 0.68 for FSRQs, and of 0.34 ± 0.42 and 0.36 ± 0.34 for BL Lacs. The median redshifts decrease between BL Lac LSPs, ISPs, and HSPs from 0.47 to 0.36 to 0.25, respectively. While the maximum redshift for an FSRQ was 3.1 in earlier LAC catalogs, five counterparts to 4LAC sources have higher redshifts: GB 1508+5714 ($z = 4.31$), PKS 1351–018 ($z = 3.72$), PKS 0335–122 ($z = 3.44$), MG3 J163554+3629 ($z = 3.65$), and PMN J0833–0454 ($z = 3.45$). GB 1508+5714 and PKS 0335–122 are not present in the Clean Sample, however, due to analysis flags. The detections of three of these sources (PKS 1351–018, GB 1508+5714, MG3 J163554+3629) were reported earlier in Ackermann et al. (2017). Two other high- z sources (NVSS J064632+445116 and NVSS J212912–153841), whose detections were also announced in Ackermann et al. (2017), are absent in the 4FGL/4LAC, possibly due to variability effects.

Figure 10 displays the photon index versus the gamma-ray luminosity for the different blazar classes. The trend of softer spectra with higher luminosity observed in earlier catalogs is confirmed. We reiterate the word of caution expressed in 3LAC: this trend is only significant when considering the whole sample of 4LAC blazars. It is not significant when considering the different blazar classes/subclasses individually. Figure 11 shows the corresponding plot for the nonblazar sources. Radio galaxies show a large scatter in photon index, while sources of the other classes have fairly soft spectra akin to those of FSRQs.

5.3. Variability

Variability is a key property of blazars and is known to depend on the energy band considered (e.g., Aleksić et al. 2015). This feature can be naturally explained as emitting electrons (assuming a leptonic scenario) of different energies, and thus different acceleration/cooling times contribute preferentially to the distinct bands. The assessment of variability in 4FGL does not only depend on intrinsic variability, but also on the overall significance of the source detection. Two different values of the variability index⁷⁹ are provided in 4FGL, derived

⁷⁹ The variability index is defined as twice the sum of the $\log(\text{Likelihood})$ difference between the flux fitted in each time interval and the average flux over the full catalog interval.

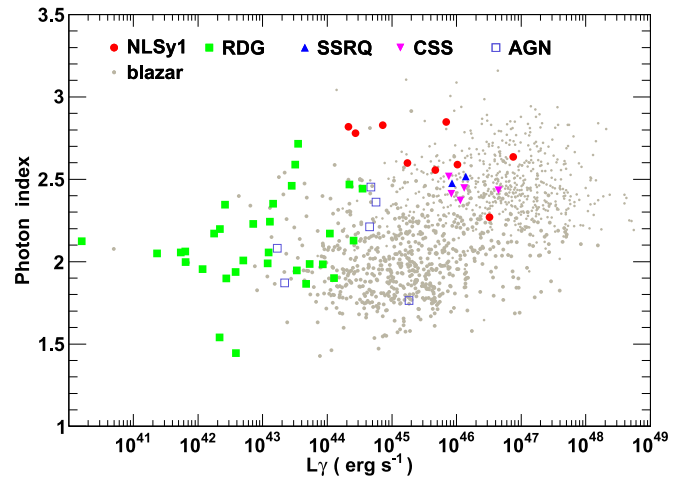


Figure 11. Photon index vs. gamma-ray luminosity for the different nonblazar classes. Blazars are included for comparison and depicted in gray regardless of their classes. Error bars have been omitted for clarity. Mean photon-index uncertainty is 0.11 for the nonblazar AGNs.

from the sets of 1 yr and 2 month light curves. The 1 yr light curves allow the variability of fainter sources to be established compared to the monthly light curves used in early FGL catalogs. Because the variability indices are distributed as χ^2 functions with N_{dof} degrees of freedom, a source is defined as variable if at least one of the variability indices is greater than the 99% confidence limit of 18.48 and 72.44 for the 1 yr ($N_{\text{dof}} = 7$) and 2 month ($N_{\text{dof}} = 47$) light curves, respectively.

Figure 12 displays the TS distributions of variable sources compared to those of the whole sets of FSRQs and BL Lacs. All bright blazars are found to be variable. The fraction of variable sources goes down from 79% (464/591) for FSRQs to 35% for BL Lacs (362/1027). A monotonic trend is observed for the BL Lac subclasses, with fractions of 49% (140/288), 36% (98/270), and 31% (98/316) for LSPs, ISPs, and HSPs, respectively. Only 17% (157/941) of the BCUs show variability, as expected from the fact that these sources tend to be fainter (Section 5.1). The median fractional variability amplitude is 0.63 for FSRQs and 0.27 for BL Lacs. More extended studies about variability of the LAT-detected blazars can be found in the 3LAC paper.

Among the radio galaxies, IC 310, NGC 1275, 3C 120, NCG 1218, 3C 111, NGC 2892, and IC 4516 are found to be variable, hinting at a blazar-like behavior for these sources. All NLSy1s show significant variability, except for IERS B1303+515, B3 1441+476, TXS 2116–077. Three out of five CSS sources are variable (3C 138, 3C 309.1, 3C 380), as well as one SSRQ (3C 207). The three variable sources of the AGN class are: PKS 0521–36, PMN J1118–0413, and CGCG 050–083.

5.4. Potential Transiently Detected AGNs Missing in 4LAC

Some *Fermi*-LAT sources show blazar-like flaring activity during limited time intervals but do not meet the detection significance criterion to be included in the 4FGL, which is based on a summed 8 yr data set. We present here information about some of these transient sources spatially consistent with AGNs.

When undergoing periods of enhanced activity in 6 hr and 1 day time intervals, some sources can be caught in near-real time by the *Fermi*-LAT Flare Advocate Gamma-ray Sky Watcher (FAGSW) service (Ciprini & *Fermi*-LAT Collaboration 2012;

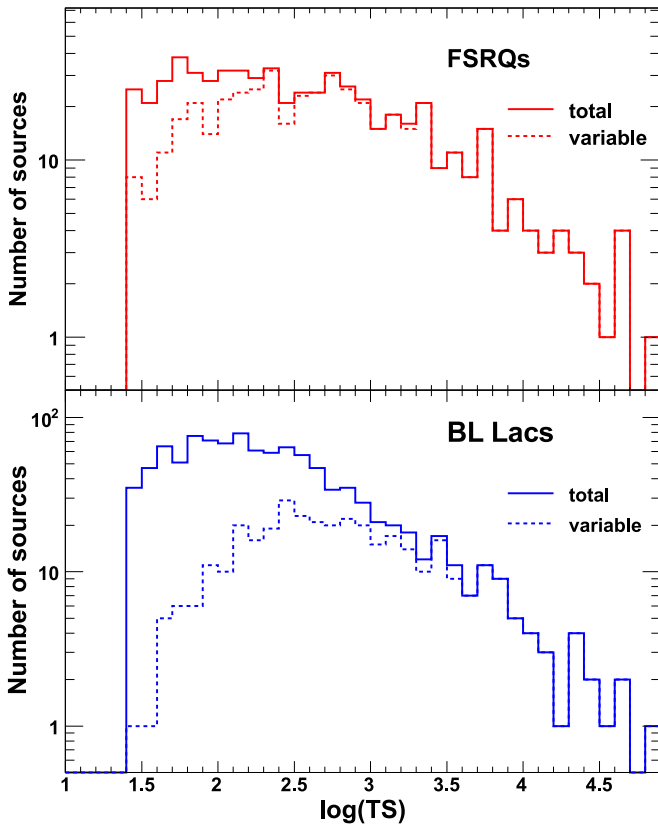


Figure 12. TS distributions of FSRQs (top) and BL Lacs (bottom) for variable sources and the whole sample.

Thompson et al. 2015, and references therein). The brightest sources are often reported to the community in Astronomer’s Telegrams (ATels). A total of 371 ATels (plus three errata) were posted on behalf of the LAT Collaboration in the 8 yr period considered in the 4FGL/4LAC (2008 August 4 to 2016 August 2), and a total of 472 ATels were published from 2008 July 24 (ATel 1628) to 2019 August 15 (ATel 13032). At the time of writing, announced transient sources that were positionally consistent with blazars or other AGNs include: NVSS J104516+275136 (ATel 12906); S5 0532+82 (ATel 12902; PKS 2247–131 (ATels 9285, 9620, 11141); PKS 1915–458 ($z = 2.47$, ATels 2666, 2679, and already reported as missing in the 3FGL/3LAC catalogs); TXS 0135+291 (ATel 12888); 2MASX J15441967–0649156 ($z \simeq 0.04$, ATel 10482); PKS 1251–71 (ATel 8215), PMN J0508–5628 (ATel 6658); PMN J2010–2524 ($z = 0.825$, ATel 6553); TXS 1731+152A (ATel 6395, 6410); PKS 2136–642 (ATel 5695); and PKS 1510–319 ($z = 1.71$, ATel 2528).

Sources detected on a one-week timescale were reported in the Second *Fermi*-LAT All-sky Variability Analysis (FAVA) Catalog (2FAV, Abdollahi et al. 2017), based on the first 7.4 yr of *Fermi*-LAT mission data. In the FAVA catalog,⁸⁰ the analysis was run in 100–800 MeV and 0.8–300 GeV energy bands, leading to the identification of 518 flaring gamma-ray sources. Among these sources, 13 were associated with established blazars or blazar candidates that are included in neither 4LAC nor 3LAC: PMN J0231–4746, 2MASS J06164292–4021527, TXS 0723+220, 4C +38.28 (B2 0913

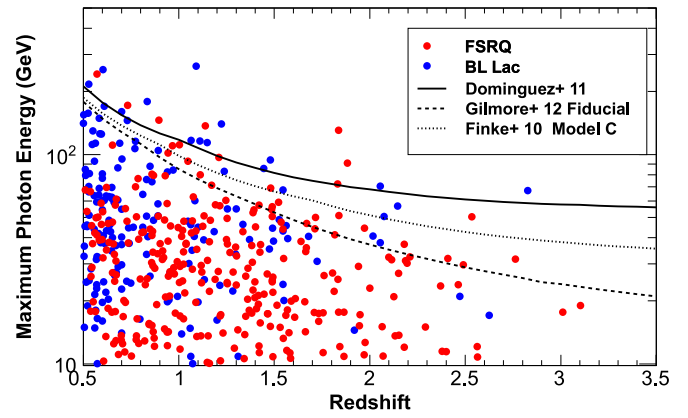


Figure 13. Energy of the highest-energy photon vs. redshift. Curves display the energies corresponding to an optical depth of 1 as predicted by different models.

+39), PKS 1200–051, PMN J1322–8419, PKS 1354–17, RX J1410.5+6100, PKS 1510–319, TXS 1534+378, TXS 1731+152A, PKS 1824–582, 1RXS J235018.0–055928.

For longer timescales, the first catalog of gamma-ray transient sources (1FLT, The *Fermi* LAT Collaboration in preparation) reports detections on monthly time intervals during the first 96 months of *Fermi*-LAT operation. This catalog contains 64 new gamma-ray sources not present in 4LAC/4FGL or earlier LAT catalogs. Their mean photon spectral index Γ of 2.6 indicates softer spectra than exhibited by the 4LAC sources (mean $\Gamma \sim 2.2$). These new sources include 24 BCUs (e.g., PKS 1649–031, TXS 0209+168, TXS 1601+160, PKS 2108–326 and others), 20 FSRQs (e.g., PKS 1524–13, TXS 1226+046, PKS 1200–051, PMN J2010–2524, PKS 1706+006 and others), one BL Lac object (1RXS J12100.6+014515), one NLSy1 (Mkn 1501), and two radio galaxies (S5 1733+71 and PKS 2236–364).

5.5. Highest-energy Photons

The highest-energy photons detected for each source were selected within the purest—i.e., with the lowest instrumental background—class (P8R3_ULTRACLEANVETO_V2). Based on the energy-dependent PSF, we required a probability⁸¹ greater than 0.95 for the photons to belong to the source being considered. Blazar gamma-ray spectra provide insight into the density of the EBL via the effect of photon-photon absorption, often defined in terms of an optical depth $\tau = 1$, where a photon has only a $1/e$ probability of reaching the observer (e.g., Abdollahi et al. 2018). A comparison between the energy of the highest-energy photon measured for a given source with the energy computed for $\tau = 1$ at that redshift by theoretical models of the EBL provides a simple and direct test of these models. Figure 13 compares the 4LAC highest-energy photons with the optical depth predictions of Finke et al. (2010), Domínguez et al. (2011), and Gilmore et al. (2012). Only a few photons exceed the $\tau = 1$ mark, thus remaining compatible with the predictions of these models.

⁸⁰ <https://fermi.gsfc.nasa.gov/ssc/data/access/lat/FAVA/>

⁸¹ This probability is derived via the source-to-background ratio defined in appendix A of the 1FGL paper (Abdo et al. 2010b) and implemented in the adaptive-binning package available at <https://fermi.gsfc.nasa.gov/ssc/data/analysis/user/>.

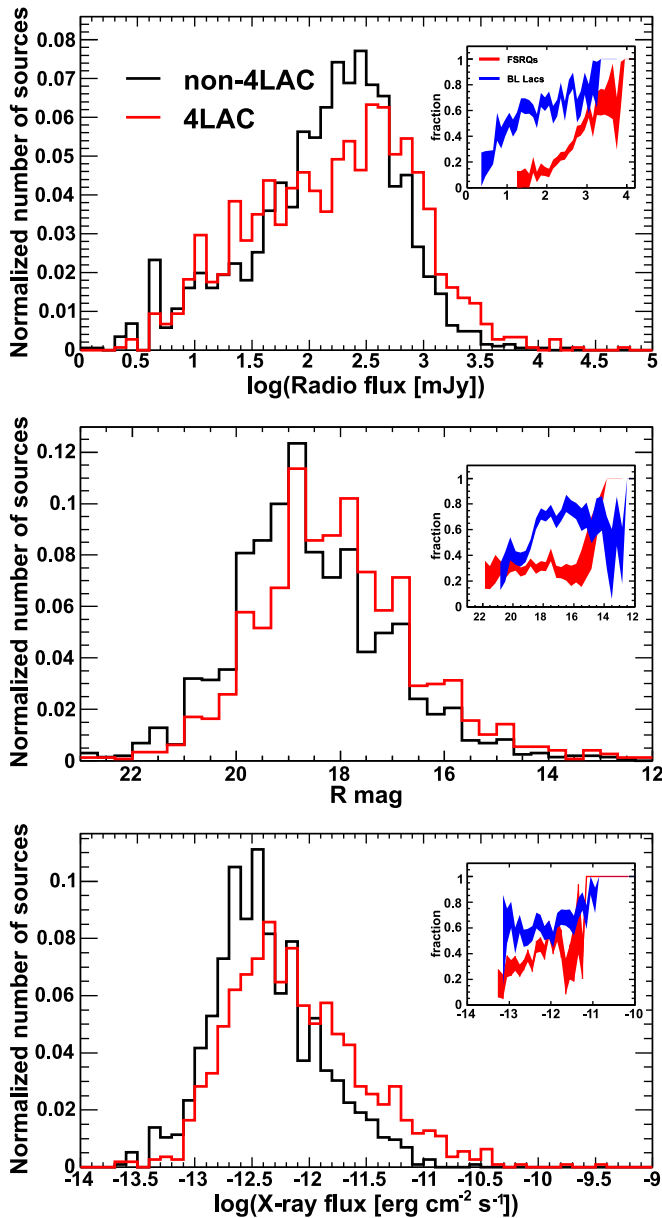


Figure 14. From top to bottom: radio flux density at 1.4 GHz, optical R magnitude, X-ray flux (0.1–2.4 keV) distributions for 4LAC (red) and non-4LAC (black) BZCAT sources. Insets show the fraction of 4LAC sources relative to the total for a given flux. Error bars have been omitted for clarity.

5.6. Gamma-Ray-detected versus Nondetected Blazars

The blazars detected in gamma-rays after 8 yr of LAT operation represent a sizable fraction of the whole population of known blazars as listed in BZCAT. This catalog represents an exhaustive list of all sources ever classified as blazars, but is by no means complete. Although a comparison between the gamma-ray-detected and nondetected blazars within that sample has no strong statistical meaning in terms of relative weights, it is nevertheless useful to look for general trends.

In total, the 4LAC includes 29% (562/1909), 66% (764/1151), and 38% (88/227) of the BZCAT (Massaro et al. 2015) FSRQs, BL Lacs, and BCUs, respectively. Out of the 1353 new 4FGL sources, 405 are present in BZCAT. Figure 14 compares the distributions of radio flux at 1.4 GHz, optical R -band magnitude, and X-ray (0.1–2.4 keV) fluxes for the gamma-ray-detected and nondetected BZCAT blazars, as

well as the fraction of gamma-ray-detected blazars relative to the total as a function of the different fluxes. The gamma-ray-detected blazars are somewhat brighter on average in all bands, confirming previous findings (Lister et al. 2011; Böck et al. 2016; Paliya et al. 2017). The fraction of 4LAC blazars in the total population of BZCAT blazars remains non-negligible even at the faint ends of the radio, optical, and X-ray flux distributions, in particular for BL Lacs. This observation is a clue that even the faintest known blazars could eventually shine in gamma-rays at LAT-detection levels.

5.7. Sources Detected at Very High Energies

Table 7 shows the list of 78 AGNs detected by ground-based Cerenkov telescopes, as listed in TeVCat.⁸² All are present in 4LAC, and the table shows their optical and SED-based classes, redshifts, and 4LAC photon indices. The 3LAC catalog included 55 of the 56 VHE AGNs with detections published or announced at that time; only HESS J1943+213 was missing. The overall mean of the 4LAC photon indices for these VHE AGNs is 1.91 ± 0.20 . For the most numerous subclass, the HSP BL Lacs, we find the mean index to be 1.81 ± 0.08 , i.e., a very hard gamma-ray spectrum. Of the 78, 56 4LAC AGNs are variable at a significance greater than 99%.

5.8. Miscellaneous Notes About Individual Sources

In the course of the 4LAC analysis, we found a number of individual sources that have changed classification or have unclear associations. We include this information about them for completeness. In case of conflicting associations, we only retained the most probable one in the 4LAC catalog.

1. 4FGL J0140.6–0758 is associated with the BL Lac RX J0140.7–0758. Another object, SDSS J014040.63–075857.2, is located $9''$ away (i.e., $0.04r_{95}$, where r_{95} is the 95% confidence radius), at a redshift of 2.674 coming from a broad-line SDSS optical spectrum. This source has no reported radio emission.
2. 4FGL J0242.3+5216 has two possible high-confidence associations: with GB6 J0242+5209 and TXS 0239+520, which have similar brightness in the radio band.
3. 4FGL J0337.8–1157 is associated with PKS 0335–122, a distant FSRQ at $z = 3.442$ that has a damped Ly α absorption system at $z = 3.180$ along the line of sight (Kanekar & Chengalur 2003).
4. 4FGL J0618.1+7819 is associated with the starburst galaxy NGC 2146 ($z = 0.002975$), but the FSRQ 6C 060948+781625 ($z = 1.43$) has a similar association probability.
5. 4FGL J0647.7–4418 is associated with the high-mass X-ray binary RX J0648.0–4418 in 4FGL, but the blazar candidate SUMSS J064744–441946 has a just barely lower association probability (0.80 versus 0.85).
6. 4FGL J0720.0–6237 is associated with the FSRQ PMN J0716–6240, but another FSRQ, PMN J0719–6218, lies just outside the 95% confidence region and might contribute to the gamma-ray emission.
7. 4FGL J0814.4+2941 is associated with the BL Lac EXO 0811.2+2949, but a broad-line quasar, SDSS J081425.89+294115.6, also lies within the 95% confidence region.

⁸² <http://tevcat.uchicago.edu/>, as of 2019 March.

Table 7
Properties of the 4LAC VHE AGNs

4FGL Name	Name	Source Class	SED Type	Redshift	Photon Index	Variability Index ^a
J0013.9-1854	RBS 0030	bll	HSP	0.09	1.97 ± 0.1	2.61
J0033.5-1921	KUV 00311-1938	bll	HSP	0.61	1.77 ± 0.02	27.17
J0035.9+5950	1ES 0033+595 ^b	bll	HSP	...	1.75 ± 0.02	149.76
J0112.1+2245	S2 0109+22	bll	LSP	0.26	2.07 ± 0.01	313.15
J0136.5+3906	B3 0133+388	bll	HSP	...	1.71 ± 0.02	51.08
J0152.6+0147	PMN J0152+0146	bll	HSP	0.08	1.96 ± 0.06	15.23
J0214.3+5145	TXS 0210+515 ^b	bll	HSP	0.05	1.88 ± 0.09	11.2
J0221.1+3556	B2 0218+357	fsrq	LSP	0.94	2.29 ± 0.01	3327.03
J0222.6+4302	3C 66A	bll	ISP	0.44	1.96 ± 0.01	976.11
J0232.8+2018	1ES 0229+200	bll	HSP	0.14	1.78 ± 0.11	4.36
J0238.4-3116	1RXS J023832.6-311658	bll	HSP	0.23	1.8 ± 0.04	33.44
J0303.4-2407	PKS 0301-243	bll	HSP	0.27	1.9 ± 0.02	253.95
J0316.8+4120	IC 310	rdg	ISP	0.02	1.78 ± 0.18	19.86
J0319.8+4130	NGC 1275	rdg	LSP	0.02	2.12 ± 0.01	1970.98
J0319.8+1845	1E 0317.0+1835	bll	HSP	0.19	1.67 ± 0.07	32.33
J0349.4-1159	1ES 0347-121	bll	HSP	0.19	1.76 ± 0.1	10.0
J0416.9+0105	1ES 0414+009	bll	HSP	0.29	1.89 ± 0.07	9.76
J0449.4-4350	PKS 0447-439	bll	HSP	0.2	1.85 ± 0.01	55.2
J0507.9+6737	1ES 0502+675	bll	HSP	0.42	1.58 ± 0.03	39.18
J0509.4+0542	TXS 0506+056	bll	ISP	0.34	2.08 ± 0.02	245.91
J0521.7+2112	TXS 0518+211 ^b	bll	HSP	0.11	1.92 ± 0.01	682.16
J0550.5-3216	PKS 0548-322	bll	HSP	0.07	1.89 ± 0.1	5.98
J0627.0-3529	PKS 0625-35	rdg	HSP	0.05	1.9 ± 0.04	11.56
J0648.7+1516	RX J0648.7+1516 ^b	bll	HSP	0.18	1.7 ± 0.04	3.2
J0650.7+2503	1ES 0647+250	bll	HSP	0.2	1.74 ± 0.02	117.43
J0710.4+5908	1H 0658+595	bll	HSP	0.13	1.68 ± 0.05	26.55
J0721.9+7120	S5 0716+71	bll	ISP	0.13	2.06 ± 0.01	1554.68
J0733.4+5152	NVSS J073326+515355	bcu	HSP	0.06	1.8 ± 0.1	14.97
J0739.2+0137	PKS 0736+01	fsrq	LSP	0.19	2.41 ± 0.02	1983.59
J0809.8+5218	1ES 0806+524	bll	HSP	0.14	1.88 ± 0.02	290.4
J0847.2+1134	RX J0847.1+1133	bll	ISP	0.2	1.72 ± 0.08	8.47
J0854.8+2006	OJ 287	bll	LSP	0.31	2.23 ± 0.01	611.67
J0958.7+6534	S4 0954+65	bll	LSP	0.37	2.21 ± 0.02	2012.73
J1010.2-3119	1RXS J101015.9-311909	bll	HSP	0.14	1.75 ± 0.07	34.16
J1015.0+4926	1H 1013+498	bll	HSP	0.21	1.84 ± 0.01	195.6
J1103.6-2329	1ES 1101-232	bll	HSP	0.19	1.73 ± 0.08	10.7
J1104.4+3812	Mkn 421	bll	HSP	0.03	1.78 ± 0.01	1028.05
J1136.4+6736	RX J1136.5+6737	bll	HSP	0.14	1.75 ± 0.05	23.5
J1136.4+7009	Mkn 180	bll	HSP	0.05	1.8 ± 0.03	20.39
J1144.9+1937	3C 264	rdg	HSP	0.02	1.94 ± 0.1	4.15
J1159.5+2914	Ton 599	fsrq	LSP	0.73	2.26 ± 0.01	1391.63
J1217.9+3007	B2 1215+30	bll	HSP	0.13	1.95 ± 0.01	396.98
J1221.3+3010	PG 1218+304	bll	HSP	0.18	1.71 ± 0.02	44.28
J1221.5+2814	W Comae	bll	ISP	0.1	2.16 ± 0.02	243.32
J1224.4+2436	MS 1221.8+2452	bll	HSP	0.22	1.89 ± 0.04	148.48
J1224.9+2122	4C +21.35	fsrq	LSP	0.43	2.33 ± 0.01	17566.6
J1230.2+2517	ON 246	bll	ISP	0.14	2.09 ± 0.02	1651.75
J1230.8+1223	M87	rdg	ISP	0.01	2.06 ± 0.04	16.98
J1256.1-0547	3C 279	fsrq	LSP	0.54	2.34 ± 0.01	5667.24
J1315.0-4236	MS 13121-4221	bll	HSP	0.1	1.72 ± 0.1	6.61
J1325.5-4300	Cen A	rdg	LSP	0.01	2.65 ± 0.02	8.25
J1427.0+2348	PKS 1424+240	bll	HSP	0.6	1.82 ± 0.01	205.42
J1428.5+4240	H 1426+428	bll	HSP	0.13	1.66 ± 0.05	14.91
J1442.7+1200	1ES 1440+122	bll	HSP	0.16	1.8 ± 0.07	10.06
J1443.9-3908	PKS 1440-389	bll	HSP	0.07	1.82 ± 0.02	22.05
J1443.9+2501	PKS 1441+25	fsrq	LSP	0.94	2.08 ± 0.02	2858.38
J1512.8-0906	PKS 1510-089	fsrq	LSP	0.36	2.38 ± 0.01	4421.04
J1517.7-2422	AP Librae	bll	LSP	0.05	2.12 ± 0.02	90.89
J1518.0-2731	TXS 1515-273	bll	HSP	...	2.06 ± 0.05	57.84
J1555.7+1111	PG 1553+113	bll	HSP	0.36	1.68 ± 0.01	74.97
J1653.8+3945	Mkn 501	bll	HSP	0.03	1.75 ± 0.01	292.85
J1725.0+1152	1H 1720+117	bll	HSP	0.18	1.86 ± 0.02	13.33
J1728.3+5013	I Zw 187	bll	HSP	0.05	1.78 ± 0.03	164.28

Table 7
(Continued)

4FGL Name	Name	Source Class	SED Type	Redshift	Photon Index	Variability Index ^a
J1744.0+1935	S3 1741+19	bll	HSP	0.08	1.93 ± 0.05	10.72
J1751.5+0938	OT 081	bll	LSP	0.32	2.26 ± 0.02	884.58
J1944.0+2117	MG2 J194359+2118 ^b	bcu	1.53 ± 0.09	15.42
J2000.0+6508	IES 1959+650	bll	HSP	0.05	1.82 ± 0.01	1052.41
J2001.2+4353	MG4 J200112+4352 ^b	bll	HSP	...	1.95 ± 0.02	1027.21
J2009.4+4849	PKS 2005-489	bll	HSP	0.07	1.83 ± 0.02	135.08
J2039.5+5218	IES 2037+521 ^b	bll	HSP	0.05	1.88 ± 0.09	4.58
J2056.7+4939	RGB J2056+496 ^b	bcu	HSP	...	1.85 ± 0.04	23.86
J2158.8-3013	PKS 2155-304	bll	HSP	0.12	1.85 ± 0.01	646.95
J2202.7+4216	BL Lac	bll	LSP	0.07	2.23 ± 0.01	2474.03
J2243.9+2021	RGB J2243+203	bll	HSP	...	1.86 ± 0.02	116.39
J2250.0+3825	B3 2247+381	bll	HSP	0.12	1.72 ± 0.06	24.53
J2324.7-4041	IES 2322-409	bll	HSP	0.17	1.78 ± 0.05	49.44
J2347.0+5141	IES 2344+514 ^b	bll	HSP	0.04	1.81 ± 0.02	56.97
J2359.0-3038	H 2356-309	bll	HSP	0.17	1.93 ± 0.07	1.77

Notes.

^a A variability index greater than 18.47 indicates that the source is variable at a significance greater than 99%.

^b Refers to low-latitude sources (not in 4LAC).

(This table is available in machine-readable form.)

8. 4FGL J0941.9+2724 may have a double association with the BL Lac 5BZBJ0941+2722 and the FSRQ MG2 J094148+2728, which was an association in 3FGL.
9. 4FGL J1300.4+1416 (3FGL J1300.2+1416) is associated with OW 197 (PKS 1257+145, $z = 1.1085$), as it was in 3LAC. At about 5' distance from OW 197, a blazar candidate NVSS J130041+141728 lies in both the 3FGL and 4FGL 95% confidence ellipses, despite a reduction in size of the ellipse by a factor of 4. The 4FGL source position is about midway between OW 197 and NVSS J130041+141728.
10. 4FGL J1625.7+4134 may have a double association, with 4C +41.32 and B3 1624+414.

6. Summary

The 4LAC, derived from the 4FGL catalog, based on 8 yr of *Fermi*-LAT data, includes 1353 (85%) more AGNs than the 3LAC. At high Galactic latitudes, AGNs represent at least 79% of the 4FGL sources. Unassociated sources lying in this sky region share common spectral features with BCUs (see Figure 22 of the 4FGL paper), suggesting that most of them are AGNs as well. BL Lacs and FSRQs represent 38% and 24% of the blazar population, respectively. The increase of the fraction of BCUs in the sample from 29% in 3LAC to 38% in 4LAC emphasizes the value of the spectroscopic endeavor carried out by several groups. From their photon index and $\nu_{s,peak}$ distributions, BCUs probably contain similar fractions of (still unclassified) FSRQs and BL Lacs as observed in the classified population.

Fits of the synchrotron-peak positions have been performed manually for all 4LAC sources, leading to an SED-based classification for 75% of the 4LAC blazars. The number of nonblazar AGNs has almost doubled relative to 3LAC, from 32 to 64, including 22 new radio galaxies. The overall properties of the 4LAC AGNs are similar to those found in 3LAC. A fairly clear separation in spectral hardness between BL Lacs and FSRQs is observed, with a transition around $\Gamma = 2.25$.

Five HSP FSRQs, which do not fit with the “blazar sequence” picture, are present in 4LAC. They all show spectra harder than average for the FSRQ class. Significant spectral curvature is observed for essentially all the brightest ($TS > 3000$) blazars. The redshift distributions of newly detected blazars resemble those found for 3LAC. Five new FSRQs have redshifts greater than the highest 3LAC redshift ($z = 3.1$), reaching $z = 4.31$. The correlation between photon index and gamma-ray luminosity is strong overall for blazars, but much weaker if the different classes are taken separately. Analysis of 1 yr and 2 month light curves shows that 79% of the FSRQs and 35% of the BL Lacs are variable, along with seven radio galaxies and 16 other AGNs. The highest-energy photons show compatibility with the EBL γ - γ attenuation predicted by some recent models. About 30% of the new blazars are present in BZCAT. Although the 4LAC blazars are predominantly associated with higher-than-average radio, optical, and X-ray fluxes in BZCAT, they remain non-negligible even at the faint ends of these flux distributions, in particular for BL Lacs. All 78 known VHE blazars are detected by the LAT, with 56 of them being variable in the GeV range.

The *Fermi* LAT Collaboration acknowledges generous ongoing support from a number of agencies and institutes that have supported both the development and the operation of the LAT as well as scientific data analysis. These include: the National Aeronautics and Space Administration and the Department of Energy in the United States; the Commissariat à l’Energie Atomique and the Centre National de la Recherche Scientifique/Institut National de Physique Nucléaire et de Physique des Particules in France; the Agenzia Spaziale Italiana and the Istituto Nazionale di Fisica Nucleare in Italy; the Ministry of Education, Culture, Sports, Science, and Technology (MEXT), High Energy Accelerator Research Organization (KEK), and Japan Aerospace Exploration Agency (JAXA) in Japan; and the K. A. Wallenberg Foundation, the Swedish Research Council, and the Swedish National Space Board in Sweden. Additional support for science analysis

during the operations phase is gratefully acknowledged from the Istituto Nazionale di Astrofisica in Italy and the Centre National d'Études Spatiales in France. This work was performed in part under DOE Contract DE-AC02-76SF00515.

This research has made use of data obtained from the high-energy Astrophysics Science Archive Research Center (HEASARC) provided by NASA's Goddard Space Flight Center; the SIMBAD database operated at CDS, Strasbourg, France; and the NASA/IPAC Extragalactic Database (NED) operated by the Jet Propulsion Laboratory, California Institute of Technology, under contract with the National Aeronautics and Space Administration. This research has made use of data archives, catalogs and software tools from the ASDC, a facility managed by the Italian Space Agency (ASI). Part of this work is based on the NVSS (NRAO VLA Sky Survey). The National Radio Astronomy Observatory is operated by Associated Universities, Inc., under contract with the National Science Foundation. This publication makes use of data products from the Two Micron All Sky Survey, which is a joint project of the University of Massachusetts and the Infrared Processing and Analysis Center/California Institute of Technology, funded by the National Aeronautics and Space Administration and the National Science Foundation. This publication makes use of data products from the *Wide-field Infrared Survey Explorer*, which is a joint project of the University of California, Los Angeles, and the Jet Propulsion Laboratory/California Institute of Technology, funded by the National Aeronautics and Space Administration. Funding for the SDSS and SDSS-II has been provided by the Alfred P. Sloan Foundation, the Participating Institutions, the National Science Foundation, the U.S. Department of Energy, the National Aeronautics and Space Administration, the Japanese Monbukagakusho, the Max Planck Society, and the Higher Education Funding Council for England. The SDSS Web Site is <http://www.sdss.org/>. The SDSS is managed by the Astrophysical Research Consortium for the Participating Institutions. The Participating Institutions are the American Museum of Natural History, Astrophysical Institute Potsdam, University of Basel, University of Cambridge, Case Western Reserve University, University of Chicago, Drexel University, Fermilab, the Institute for Advanced Study, the Japan Participation Group, Johns Hopkins University, the Joint Institute for Nuclear Astrophysics, the Kavli Institute for Particle Astrophysics and Cosmology, the Korean Scientist Group, the Chinese Academy of Sciences (LAMOST), Los Alamos National Laboratory, the Max-Planck-Institute for Astronomy (MPIA), the Max-Planck-Institute for Astrophysics (MPA), New Mexico State University, Ohio State University, University of Pittsburgh, University of Portsmouth, Princeton University, the United States Naval Observatory, and the University of Washington.

Appendix

Chronological Convention for Source Association Naming

In 3LAC and 4LAC, an approximate chronological scheme is adopted for the proper names of the radio/IR/optical/X-ray counterparts. For greater convenience and clarity, a time-ordered list of the source catalogs used here is given in Table 8. The proper names follow approximately the initial (discovery) names from radio, IR, optical, and X-ray surveys, catalogs and observations. These names have been checked to be recognized by the strict “name resolver” in the NASA-IPAC Extragalactic

Database (and therefore by many other web databases like HEASARC derived from it).

Radio galaxies, quasars, blazars, and other AGNs were first discovered as optical non-starlike nebulae objects (i.e., galaxies) listed in the C. Messier catalog in year 1791, and the NGC (J.L.E. Dreyer) and IC catalogs published between the years 1781 and 1905. Examples of sources in 4LAC are the radio galaxies M87, NGC 315, NGC 1275 (also known as Per A or 3C 84), and the starburst galaxies M82, NGC 253, and NGC 1068. Other AGNs were initially considered as optical variable stars (Argelander, e.g., BL Lac, W Com, AP Lib, and BW Tau, known as 3C 120). Some blazars and AGNs were discovered as unusual optically blue starlike objects (Ton, PHL, Mkn catalogs, about 1957–1974; for example, Ton 599, Mkn 180, Mkn 421, Mkn 501, PHL 1389) or in optical galaxy catalogs (CGCG, MCG, CGPG, ARP, UGC, Ark, Zw/I-V, Tol, during the period 1961–1976; for example, CGCG 050-083, UGC 773, I Zw 187, V Zw 326). Subsequent optically selected objects and quasar catalogs provide some names of 4LAC associations (for example, PG, PB, US, SBS, PGC, LEDA, HS, SDSS).

In parallel, the largest fraction of radio galaxies and AGNs were discovered during the early era of radio astronomy, with objects like Vir A, Cen A, Cen B, Per A appearing already in the first half of the 1950s, and the well-known point radio source catalogs 3C, CTA, PKS, 4C, O[+letter], VRO, NRAO, AO, DA, B2, GC, and S1/S2/S3 all published between about 1959 and 1974. The PKS (Parkes Radio Catalog, Australia) is the source name preferred for southern celestial radio AGNs, while northern radio AGNs were likely first reported in Cambridge catalogs (especially 3C, 4C) and the Ohio State University Radio Survey Catalog (Ohio Big Ear radio-antenna, O(x) catalog prefix), or in the CTA, NRAO, DA, B2, TXS, S1-5, or MG1-4 catalogs. Examples in the 4LAC are Cen A (already known as NGC 5128, but better known with its original radio name), Per A, Vir A (M87). Other radio catalogs published between about 1974 and the mid-1980s include TXS, 5C, S4/S5, MRC, and B3, while from the end of the 1980s until the end of 1990s, we have MG1/MG2/MG4, 87GB, 6C/7C, JVAS, PMN, EF, CJ2, FIRST, Cul, GB6, FBQS, WN, NVSS, CLASS, IERS, SUMSS, and CRATES. Some catalogs at IR or UV frequencies are also considered here (KUV, *EUVE*, 2MASSi, 2MASS). Further blazars and other AGNs, fainter in the radio band, were discovered directly thanks to the observations made by the first X-ray satellites (2A, 4U, XRS, EXO, H/1H, MS, 1E, 1ES, 2E, RX catalogs published from about 1978 to the mid-1990s). Later came the *ROSAT* survey catalogs from reanalysis and cross-matches, such as RGB, RBS, RHS, 1RXS, XSS.

Table 8 reports catalog and survey prefixes in an approximate chronological order that was adopted for the association names of the 4LAC catalog. The order is only approximate, due to the lack of precise information for each catalog as well as the need to follow, in some cases, the criterion of the most-used name in the literature and published papers for a source (even if this latter choice is rather arbitrary and subject to opinion).

The most frequent source association names in 4LAC come from the 3C, 4C, PKS, O[+letter], B2, S2/S3/S5, TXS, MG1/MG2, PMN, GB6, SDSS, 1ES, RX, RBS, 1RXS, NVSS, and 2MASS catalogs. Some 4LAC counterpart proper names may be somewhat inadequate because of the radio extension of the

Table 8
Historical Catalogs Reference for Naming of 4LAC Associations

Waveband	Publ. Year(s)/Range	Prefix	Catalog Name
Optical	1781	M	Charles Messier catalog of nebulae and non-starlike objects from M1 to M110.
Optical	1844–1915	xy+const.	Argelander convention for first-discovered variable stars in each constellations.
Optical	1848	GC	General Catalog
Optical	1888	NGC	New General Catalog
Optical	1896, 1905	IC	IC Index Catalogs (IC I and IC II, expansions of the NGC Catalog).
Radio	1947–1949	const.+letter	Constellation + Arabic letter (first radio sources ever discovered).
Optical	1952, 1963	PLX	Yale General Catalog of Trigonometric Stellar Parallaxes
Radio	1955	2C	Second Cambridge Radio Catalog at 178 MHz
Optical	1957–1959	Ton	Tonantzintla (Mexico) Catalog of Blue Stars
Radio	1959–1962	3C	Third Cambridge Radio Catalog at 178 MHz (3C, 3CR)
Radio	1960	CTA	Caltech Radio Survey List A
Optical	1961–1968	CGCG	Catalog of Galaxies and of Clusters of Galaxies
Optical	1962	PHL	Palomar-Haro-Luyten Blue Stellar Objects list
Optical	1962–1974	MCG	Morphological Catalog of Galaxies
Radio	1964–1967	Kes	Kesteven catalog of galactic radio sources
Radio	1964–1968, 1971–1975	PKS	Parkes catalog of radio sources
Radio	1965–1969	4C	Fourth Cambridge Radio Catalog
Radio	1965–1971	O(x) (Ohio (x))	Big Ear Ohio State University Radio Survey Catalog (O + R.A.hour letter)
Radio	1965–1971	VRO	Vermillion Radio Observatory survey catalog
Radio	1966	NRAO	National Radio Astron. Obs. Positions and Flux Densities of Radio Sources
Optical	1966	ARP	Arp Peculiar Galaxies catalog
Radio	1967–1970	AO	Arecibo Occultation Radio Sources
Optical	1967–1974	Mkn (Mrk)	Markaryan blue object list (Galaxies with an ultraviolet continuum)
Radio	1968	DA	Dominion Radio Observatory Survey, List A
Radio	1970–1974	B2	Second Bologna Catalog of radio sources
Radio	1971–1972	GC	Green Bank Radio Survey List C
Radio	1971–1972	S1/S2/S3	First/Second/Third “Strong” (radio) Source survey
Radio	1971–1972	GB (GB1)	Green Bank Radio Survey
Radio	1971–1978	GB2	Green Bank Radio Survey 2
Optical	1971	CGPG	Catalog of Selected Compact Galaxies and of Post-Eruptive Galaxies
Optical	1973	UGC	Uppsala General Catalog of Galaxies
Radio	1974–1983	TXS	Texas Survey of Radio Sources
Optical	1974	UGCA	Uppsala General Catalog Appendix
Radio	1975	5C	Fifth Cambridge Survey of Radio Sources
Optical	1975	Ark	Arakelian Emission Line Objects
Optical	1975	I-V Zw	First/Second/Third/Fourth/Fifth Zwicky list of compact galaxies
Optical	1976	Tol	Tololo List of Emission Line Galaxies
Optical	1976, 1983, 1986	PG	Palomar-Green Bright Quasar Catalog
Optical	1977–1984	PB	Palomar-Berger Faint Blue Stars Catalog
Radio	1978	S4	Fourth “Strong” (radio) Source survey
X-ray	1978	2A	Second ARIEL V survey catalog
X-ray	1978	4U	Fourth Uhuru Catalog of X-ray Sources
Radio	1978–1995	GRA (GR)	Grakovo Radio Decametric Survey
X-ray	1979	XRS	X-Ray Source catalog from rockets, balloons, satellites of 1964–1977
Ultraviolet	1980–1984	KUV	KisoUltraviolet Excess Objects catalogs
Optical	1980–1993	USNO (IDS)	U.S. Naval Observatory parallaxes catalog
Radio	1981	S5	Fifth “Strong” (radio) Source survey
X-ray	1981	3A	Third ARIEL V survey catalog
Gamma-ray	1981	2CG	Second COS-B catalog of high-energy gamma-ray sources
Optical	1981–1984	US	Usher Faint Blue Stars
Radio	1981, 1991	MRC	Molonglo Reference Catalog of Radio Sources
Radio	1981, 1994	1 Jy	Extragalactic radio sources with flux densities >1 Jy at 5 GHz catalog
Optical	1983–2000	SBS	Second Byurakan Survey of Emission Line Objects
X-ray	1983–1986	EXO	EXOSAT X-Ray Source Catalog
X-ray	1984	H (1H)	The HEAO A-1 X-Ray Source Catalog
X-ray	1984	EXO	EXOSAT XRay Source Catalog
Radio	1985	B3	Third Bologna Catalog of radio sources
Radio	1985–1993	6C	Sixth Cambridge Radio Catalog
Radio	1986	MG1	First MIT-Green Bank 5 GHz Survey
Optical	1987	AM	Arp and Madore Southern Peculiar Galaxies and Associations catalog
Infrared	1988	IRAS	Infrared Astronomy Satellite Point Source Catalog
Infrared	1990	IRAS F	Infrared Astronomy Satellite Faint Source Catalog
Optical	1989	PGC	Principal Galaxy Catalog

Table 8
(Continued)

Waveband	Publ. Year(s)/Range	Prefix	Catalog Name
Optical	1989	LEDA	Lyon-Meudon Extragalactic Database catalog
Optical	1989	[HB89]	Hewitt and Burbidge QSO compilation (mute prefix)
Optical	1989–1996	CTS	Calan-Tololo Survey of galaxies and quasars
Radio	1990	MG2	Second MIT-Green Bank 5 GHz Survey
Radio	1990	MG3	Third MIT-Green Bank 5 GHz Survey
Optical	1990	GSC	Hubble Guide Star Catalog
Radio	1990–1998	7C	Seventh Cambridge Survey of Radio Sources
X-ray	1990	1E	The Einstein Observatory (<i>HEAO 2</i>) catalog of IPC X-ray sources.
Radio	1991	MG4	Fourth MIT-Green Bank 5 GHz Survey
Radio	1991	87 GB	The 1987 Green Bank Radio Survey
Optical	1991–2007	HS (HE)	Hamburg/ESO QSO Survey
X-ray	1991	MS	Einstein (<i>HEAO-2</i>) Medium Sensitivity Survey
X-ray	1991	1ES	1st Einstein (<i>HEAO-2</i>) Slew Survey Source Catalog
Radio	1992	ZS	Zelenchuk Survey
Gamma-ray	1992–2000	GRO	Compton Gamma Ray Observatory source
Radio	1992–2002	JVAS	Jodrell Bank-VLA Astrometric Survey
Optical	1993	HIP	Hipparcos Catalog
Radio	1994	PMN	Parkes-MIT-NRAO Radio Survey catalog
Radio	1994	EF	Effelsberg Radio Sources catalog
Radio	1994	CJ2	Second Caltech-Jodrell Bank VLBI Survey catalog
Ultraviolet	1994	<i>EUVE</i>	Extreme UltraViolet Explorer Bright Source List
X-ray	1994	RX	First <i>ROSAT</i> Source Catalog of pointed observations with the PSPC
X-ray	1994	2E	Second Einstein (<i>HEAO-2</i>) Observatory catalog of IPC X-ray sources
Radio	1995–1997	FIRST	Faint Images of the Radio Sky at Twenty Centimeters
Radio	1995	Cul	Culgoora Radio Sources catalog
X-ray	1995	1WGA	First White Giommi Angelini <i>ROSAT</i> X-Ray sources list
Radio	1996	GB6	Green Bank 6 cm Radio Survey
Radio	1996	CJF	Caltech-Jodrell bank Flat spectrum survey
Ultraviolet	1996	2EUVE	2nd Extreme Ultraviolet Explorer source catalog
Radio	1996–2001	FBQS	FIRST Bright QSO Survey
Radio	1997, 2008	WN	WENSS North radio survey
X-ray	1997	RGB	<i>ROSAT</i> -Green Bank source catalog
X-ray	1997	EXSS	Einstein (<i>HEAO-2</i>) Extended X-Ray Sources
Radio	1998	NVSS	NRAO VLA Sky Survey
Radio	1998–2002	CLASS	Cosmic Lens All-Sky Survey catalog
Radio	1998–2010	IERS	International Earth Rotation Service
Radio	1998–2010	ICRF	International Celestial Reference Frame
Infrared	1998–2000	2MASSi	2 Micron All Sky Survey point sources Incremental release
X-ray	1998–2000	RBS	<i>ROSAT</i> Bright Survey catalog
X-ray	1998–2000	RHS	<i>ROSAT</i> Hard X-ray Spectra source catalog
Gamma-ray	1999	3EG	Third EGRET Catalog of High-Energy Gamma-Ray Sources
Optical	1999	MRSS	Muenster Red Sky Survey
Optical	1999–2008	SDSS	Sloan Digital Sky Survey Catalogs
X-ray	1999–2000, 2006, 2009	1RXS	<i>ROSAT</i> All-Sky Survey Bright Source Catalog
Radio	2000	VSOP	VLBI Space Observatory Programme
X-ray	2001, 2005	1AXG	1st ASCA X-ray survey from GIS experiment
Radio	2003, 2008	SUMSS	Sydney University Molonglo Sky Survey catalog
Radio	2003–2009	WMAP	WMAP Foreground Source Catalogs
Infrared	2003–2006	2MASS	2 Micron All Sky Survey Point objects Final Release
X-ray	2004	XSS	<i>RXTE</i> XTE Slew Survey catalog
X-ray	2004–2008	IGR	<i>INTEGRAL</i> Gamma Ray source
Ultraviolet	2005–2015	GALEXASC	GALaxy Evolution eXplorer All-Sky Survey Source Catalog
X-ray	2005	SHBL	Sedentary High energy peaked BL Lacs
X-ray	2005–2015	SWIFT	Swift source list
Gamma-ray	2006–...	HESS	High Energy Stereoscopic System observatory source list
Radio	2007	CRATES	Combined Radio All-Sky Targeted Eight GHz Survey
Radio	2007	VIPS	VLBA Imaging and Polarimetry Survey
Radio	2007	VERA	VLBI Exploration of Radio Astrometry
Radio	2007–2008	VLSS	VLA Low-frequency Sky Survey
X-ray	2007	SAXWFC	Beppo-SAX X-Ray Satellite Wide Field Camera catalog
X-ray	2007–2010	1XMM	1st <i>XMM-Newton</i> Serendipitous Source Catalog
X-ray	2007–2010	2XMM	2nd <i>XMM-Newton</i> Serendipitous Source Catalog
Radio	2008	CGRaBS	Candidate Gamma-Ray Blazar Survey

Table 8
(Continued)

Waveband	Publ. Year(s)/Range	Prefix	Catalog Name
Gamma-ray	2008	EGR	Revised catalog of gamma-ray sources detected by EGRET
Radio	2008–2010	AT20G	Australia Telescope 20 GHz Survey catalog
Gamma-ray	2008–...	VER	VERITAS gamma-ray source list
Gamma-ray	2009	1AGL	First AGILE GRID Catalog of High Confidence Gamma-Ray Sources
Multifrequency	2009–2018	BZ(x) (2-5BZ(x))	Roma Blazar catalog (the last published has prefix 5BZ+(letter))
Infrared	2010	AKARI-IRC-V1	AKARI/IRC Point Source Catalog Version 1
X-ray	2010	2PBC	Second Palermo <i>Swift</i> -BAT hard X-ray catalog
Infrared	2011	WISE	<i>Wide-field Infrared Survey Explorer</i> catalog
X-ray	2012	CXO	Chandra Source Catalog Release 1.1
Optical	2012, 2014	LQAC	Large Quasar Astrometric Catalog
Infrared	2013	SSTSL2	Spitzer Space Telescope Source List—version 4.2
X-ray	2013	2MAXI	Monitor of All-sky X-ray Image 37 month catalog
Millimeter	2013	PLCKERC0(nn)	Planck Early Release Compact Source Catalog at (nn)GHz
Radio	2014	WB (WIBRaLS)	WISE Blazar-like Radio-loud Sources
Ultraviolet	2016	UVQS	UV-bright Quasar Survey
Radio	2016	NVGRC	NVSS Giant Radio Sources Catalog
Gamma-ray	2016	MGRO	Milagro Gamma-Ray Observatory source list
Optical	2016– ...	Gaia DR(n)	<i>Gaia</i> Data Release (n) source
Gamma-ray	2017	2HWC	HAWC Observatory first catalog

AGN/radio galaxy. In some cases, the gamma-ray position may relate to the radio emission of the jet or lobe of an AGN, while the name refers to the radio core, which could be offset by a few arcseconds. This is manifest in the two different gamma-ray point-source components of Cen A (designed as Cen A core and Cen A lobe in the 4FGL). Another example is 4FGL J1758.7–1621 associated with AT20G J175841–161703 (also known as NVSS J175841–161705). This steep-spectrum AT20G radio source has a brighter neighbor (23.9 Jy at 160 MHz), PMN J1758–1616 (not included in the 3C catalog, because it lies 4° off the Galactic plane) at about 10'' offset. The radio structure map reveals that PMN J1758–1616 is an FR-II radio galaxy, while AT20G J175841–161703 corresponds to its radio lobe.

ORCID iDs

M. Axelsson <https://orcid.org/0000-0003-4378-8785>
J. Ballet <https://orcid.org/0000-0002-8784-2977>
G. Barbiellini <https://orcid.org/0000-0003-1720-9727>
D. Bastieri <https://orcid.org/0000-0002-6954-8862>
J. Becerra Gonzalez <https://orcid.org/0000-0002-6729-9022>
R. Bellazzini <https://orcid.org/0000-0002-2469-7063>
E. Bissaldi <https://orcid.org/0000-0001-9935-8106>
F. Cafardo <https://orcid.org/0000-0002-7910-2282>
C. C. Cheung <https://orcid.org/0000-0002-4377-0174>
F. D'Ammando <https://orcid.org/0000-0001-7618-7527>
R. de Menezes <https://orcid.org/0000-0001-5489-4925>
A. Desai <https://orcid.org/0000-0001-7405-9994>
A. Domínguez <https://orcid.org/0000-0002-3433-4610>
J. Finke <https://orcid.org/0000-0001-5941-7933>
A. Franckowiak <https://orcid.org/0000-0002-5605-2219>
Y. Fukazawa <https://orcid.org/0000-0002-0921-8837>
S. Funk <https://orcid.org/0000-0002-2012-0080>
P. Fusco <https://orcid.org/0000-0002-9383-2425>
F. Gargano <https://orcid.org/0000-0002-5055-6395>
S. Garrappa <https://orcid.org/0000-0003-2403-4582>
D. Gasparrini <https://orcid.org/0000-0002-5064-9495>
M. Giroletti <https://orcid.org/0000-0002-8657-8852>
S. Guiriec <https://orcid.org/0000-0001-5780-8770>

F. Krauss <https://orcid.org/0000-0001-6191-1244>
M. Kuss <https://orcid.org/0000-0003-1212-9998>
S. Larsson <https://orcid.org/0000-0003-0716-107X>
J. Li <https://orcid.org/0000-0003-1720-9727>
I. Liodakis <https://orcid.org/0000-0001-9200-4006>
F. Longo <https://orcid.org/0000-0003-2501-2270>
F. Loparco <https://orcid.org/0000-0002-1173-5673>
B. Lott <https://orcid.org/0000-0003-2186-9242>
P. Lubrano <https://orcid.org/0000-0003-0221-4806>
S. Maldera <https://orcid.org/0000-0002-0698-4421>
A. Manfreda <https://orcid.org/0000-0002-0998-4953>
F. Massaro <https://orcid.org/0000-0002-1704-9850>
M. N. Mazziotta <https://orcid.org/0000-0001-9325-4672>
N. Mirabal <https://orcid.org/0000-0002-7021-5838>
T. Mizuno <https://orcid.org/0000-0001-7263-0296>
M. E. Monzani <https://orcid.org/0000-0002-8254-5308>
A. Morselli <https://orcid.org/0000-0002-7704-9553>
I. V. Moskalenko <https://orcid.org/0000-0001-6141-458X>
R. Nemmen <https://orcid.org/0000-0003-3956-0331>
V. S. Paliya <https://orcid.org/0000-0001-7774-5308>
M. Pesce-Rollins <https://orcid.org/0000-0003-1790-8018>
S. Rainò <https://orcid.org/0000-0002-9181-0345>
M. Razzano <https://orcid.org/0000-0003-4825-1629>
O. Reimer <https://orcid.org/0000-0001-6953-1385>
F. K. Schinzel <https://orcid.org/0000-0001-6672-128X>
C. Sgrò <https://orcid.org/0000-0001-5676-6214>
D. J. Thompson <https://orcid.org/0000-0001-5217-9135>

References

- Aartsen, M. G., Abraham, K., Ackermann, M., et al. 2017, *ApJ*, 835, 45
Abdo, A. A., Ackermann, M., Agudo, I., et al. 2010a, *ApJ*, 716, 30
Abdo, A. A., Ackermann, M., Ajello, M., et al. 2010b, *ApJS*, 188, 405, (1FGL)
Abdo, A. A., Ackermann, M., Ajello, M., et al. 2010c, *ApJ*, 720, 912
Abdollahi, S., Ackermann, M., Ajello, M., et al. 2017, *ApJ*, 846, 34
Abdollahi, S., Ackermann, M., Ajello, M., et al. 2018, *Sci*, 362, 1031
Aceró, F., Ackermann, M., Ajello, M., et al. 2015, *ApJS*, 218, 23
Ackermann, M., Ajello, M., Allafort, A., et al. 2011, *ApJ*, 743, 171
Ackermann, M., Ajello, M., Atwood, W. B., et al. 2015, *ApJ*, 810, 14
Ackermann, M., Ajello, M., Baldini, L., et al. 2016, *ApJ*, 826, 1
Ackermann, M., Ajello, M., Baldini, L., et al. 2017, *ApJL*, 837, L5
Ackermann, M., Ajello, M., Baldini, L., et al. 2018, *ApJS*, 237, 32

- Ahn, C. P., Alexandroff, R., Allende Prieto, C., et al. 2012, *ApJS*, **203**, 21
- Ajello, M., Shaw, M. S., Romani, R. W., et al. 2012, *ApJ*, **751**, 108
- Aldcroft, T. L., Siemiginowska, A., Elvis, M., et al. 2003, *ApJ*, **597**, 751
- Aleksić, J., Ansoldi, S., Antonelli, L. A., et al. 2015, *A&A*, **576**, A126
- Álvarez Crespo, N., Masetti, N., Ricci, F., et al. 2016a, *AJ*, **151**, 32
- Álvarez Crespo, N., Massaro, F., D'Abrusco, R., et al. 2016b, *Ap&SS*, **361**, 316
- Álvarez Crespo, N., Massaro, F., Milisavljevic, D., et al. 2016c, *AJ*, **151**, 95
- Angelakis, E., Hovatta, T., Blinov, D., et al. 2016, *MNRAS*, **463**, 3365
- Arsioli, B., & Chang, Y. L. 2017, *A&A*, **598**, A134
- Arsioli, B., & Polenta, G. 2018, *A&A*, **616**, A20
- Berton, M., Foschini, L., Ciroi, S., et al. 2015, *A&A*, **578**, A28
- Böck, M., Kadler, M., Müller, C., et al. 2016, *A&A*, **590**, A40
- Boller, T., Freyberg, M. J., Trümper, J., et al. 2016, *A&A*, **588**, A103
- Böttcher, M. 2007, *Ap&SS*, **309**, 95
- Broderick, A. E., Tiede, P., Chang, P., et al. 2018, *ApJ*, **868**, 87
- Bruel, P., Burnett, T. H., Digel, S. W., et al. 2018, arXiv:1810.11394
- Caccianiga, A., Marchã, M. J., Antón, S., Mack, K., & Neeser, M. J. 2002, *MNRAS*, **329**, 877
- Capetti, A., Massaro, F., & Baldi, R. D. 2017a, *A&A*, **598**, A49
- Capetti, A., Massaro, F., & Baldi, R. D. 2017b, *A&A*, **601**, A81
- Capetti, A., & Raiteri, C. M. 2015, *A&A*, **580**, A73
- Cash, W. 1979, *ApJ*, **228**, 939
- Chang, Y.-L., Arsioli, B., Giommi, P., & Padovani, P. 2017, *A&A*, **598**, A17
- Chiaro, G., Salvetti, D., La Mura, G., et al. 2016, *MNRAS*, **462**, 3180
- Ciprini, S. & Fermi-LAT Collaboration 2012, in AIP Conf. Ser. 1505, 5th International Meeting on High Energy Gamma-Ray Astronomy, ed. F. A. Aharonian, W. Hofmann, & F. M. Rieger (Melville, NY: AIP), 697
- Condon, J. J., Cotton, W. D., Greisen, E. W., et al. 1998, *AJ*, **115**, 1693
- D'Abrusco, R., Massaro, F., Paggi, A., et al. 2014, *ApJS*, **215**, 14
- D'Ammando, F., Orienti, M., Larsson, J., & Giroletti, M. 2015a, *MNRAS*, **452**, 520
- D'Ammando, F., Orienti, M., Tavecchio, F., et al. 2015b, *MNRAS*, **450**, 3975
- de Menezes, R., Peña-Herazo, H. A., Marchesini, E. J., et al. 2019, *A&A*, **630**, A55
- de Ruiter, H. R., Arp, H. C., & Willis, A. G. 1977, *A&AS*, **28**, 211
- Dermer, C. D., Yan, D., Zhang, L., Finke, J. D., & Lott, B. 2015, *ApJ*, **809**, 174
- Di Mauro, M., Manconi, S., Zechlin, H.-S., et al. 2018, *ApJ*, **856**, 106
- Dominguez, A., Primack, J. R., Rosario, D. J., et al. 2011, *MNRAS*, **410**, 2556
- Fan, X.-L., & Wu, Q. 2018, *ApJ*, **869**, 133
- Finke, J. D., Razzaque, S., & Dermer, C. D. 2010, *ApJ*, **712**, 238
- Fornasa, M., Cuoco, A., Zavala, J., et al. 2016, *PhRvD*, **94**, 123005
- Fuhrmann, L., Angelakis, E., Zensus, J. A., et al. 2016, *A&A*, **596**, A45
- Garrappa, S., Buson, S., Franckowiak, A., et al. 2019, *ApJ*, **880**, 103
- Ghisellini, G., Righi, C., Costamante, L., & Tavecchio, F. 2017, *MNRAS*, **469**, 255
- Gilmore, R. C., Somerville, R. S., Primack, J. R., & Dominguez, A. 2012, *MNRAS*, **422**, 3189
- Goodrich, R. W. 1989, *ApJ*, **342**, 224
- Griffith, M. R., & Wright, A. E. 1993, *AJ*, **105**, 1666
- Hayashida, M., Stawarz, L., Cheung, C. C., et al. 2013, *ApJ*, **779**, 131
- Healey, S. E., Fuhrmann, L., Taylor, G. B., Romani, R. W., & Readhead, A. C. S. 2009, *AJ*, **138**, 1032
- Healey, S. E., Romani, R. W., Cotter, G., et al. 2008, *ApJS*, **175**, 97
- Healey, S. E., Romani, R. W., Taylor, G. B., et al. 2007, *ApJS*, **171**, 61
- Hernández-García, L., Panessa, F., Giroletti, M., et al. 2017, *A&A*, **603**, A131
- Itoh, R., Nalewajko, K., Fukazawa, Y., et al. 2016, *ApJ*, **833**, 77
- Jones, D. H., Read, M. A., Saunders, W., et al. 2009, *MNRAS*, **399**, 683
- Kagaya, M., Katagiri, H., Yoshida, T., & Fukuda, A. 2017, *ApJ*, **850**, 33
- Kanekar, N., & Chengalur, J. N. 2003, *A&A*, **399**, 857
- Kuźmicz, A., Jamroz, M., Bronarska, K., Janda-Boczar, K., & Saikia, D. J. 2018, *ApJS*, **238**, 9
- Landoni, M., Massaro, F., Paggi, A., et al. 2015, *AJ*, **149**, 163
- Landoni, M., Paiano, S., Falomo, R., Scarpa, R., & Treves, A. 2018, *ApJ*, **861**, 130
- Lico, R., Giroletti, M., Orienti, M., et al. 2017, *A&A*, **606**, A138
- Lister, M. L., Aller, M., Aller, H., et al. 2011, *ApJ*, **742**, 27
- Lister, M. L., Homan, D. C., Hovatta, T., et al. 2019, *ApJ*, **874**, 43
- Lonsdale, C., Conrow, T., Evans, T., et al. 1998, in IAU Symp. 179, New Horizons from Multi-Wavelength Sky Surveys, ed. B. J. McLean et al. (Dordrecht: Kluwer), 450
- Marchesi, S., Kaur, A., & Ajello, M. 2018, *AJ*, **156**, 212
- Marchesini, E. J., Peña-Herazo, H. A., Álvarez Crespo, N., et al. 2019, *Ap&SS*, **364**, 5
- Masci, F. J., Condon, J. J., Barlow, T. A., et al. 2001, *PASP*, **113**, 10
- Massaro, E., Maselli, A., Leto, C., et al. 2015, *Ap&SS*, **357**, 75
- Massaro, F., D'Abrusco, R., Landoni, M., et al. 2015a, *ApJS*, **217**, 2
- Massaro, F., Landoni, M., D'Abrusco, R., et al. 2015b, *A&A*, **575**, A124
- Massaro, F., Marchesini, E. J., D'Abrusco, R., et al. 2017, *ApJ*, **834**, 113
- Massaro, F., Masetti, N., D'Abrusco, R., Paggi, A., & Funk, S. 2014, *AJ*, **148**, 66
- Massaro, F., Thompson, D. J., & Ferrara, E. C. 2015c, *A&Arv*, **24**, 2
- Mattox, J. R., Wagner, S. J., Malkan, M., et al. 1997, *ApJ*, **476**, 692
- Mauch, T., Murphy, T., Buttery, H. J., et al. 2003, *MNRAS*, **342**, 1117
- Migliori, G., Siemiginowska, A., Sobolewska, M., et al. 2016, *ApJL*, **821**, L31
- Murphy, T., Sadler, E. M., Ekers, R. D., et al. 2010, *MNRAS*, **402**, 2403
- Nalewajko, K., & Gupta, M. 2017, *A&A*, **606**, A44
- Osterbrock, D. E., & Pogge, R. W. 1985, *ApJ*, **297**, 166
- Padovani, P. 2007, *Ap&SS*, **309**, 63
- Padovani, P., Resconi, E., Giommi, P., Arsioli, B., & Chang, Y. L. 2016, *MNRAS*, **457**, 3582
- Paggi, A., Milisavljevic, D., Masetti, N., et al. 2014, *AJ*, **147**, 112
- Paiano, S., Falomo, R., Franceschini, A., Treves, A., & Scarpa, R. 2017a, *ApJ*, **851**, 135
- Paiano, S., Falomo, R., Treves, A., Franceschini, A., & Scarpa, R. 2019, *ApJ*, **871**, 162
- Paiano, S., Landoni, M., Falomo, R., et al. 2017b, *ApJ*, **837**, 144
- Paiano, S., Landoni, M., Falomo, R., Treves, A., & Scarpa, R. 2017c, *ApJ*, **844**, 120
- Paliya, V. S., Ajello, M., Rakshit, S., et al. 2018, *ApJL*, **853**, L2
- Paliya, V. S., Marcotulli, L., Ajello, M., et al. 2017, *ApJ*, **851**, 33
- Paragi, Z., Frey, S., Fejes, I., et al. 2000, *PASJ*, **52**, 983
- Peña-Herazo, H. A., Marchesini, E. J., Álvarez Crespo, N., et al. 2017, *Ap&SS*, **362**, 228
- Petrov, L., de Witt, A., Sadler, E. M., Phillips, C., & Horiuchi, S. 2019, *MNRAS*, **485**, 88
- Petrov, L., Mahony, E. K., Edwards, P. G., et al. 2013, *MNRAS*, **432**, 1294
- Planck Collaboration, Ade, N., Aghanim, P. A. R., et al. 2014, *A&A*, **571**, A16
- Pogge, R. W. 2000, *NewAR*, **44**, 381
- Prestage, R. M., & Peacock, J. A. 1983, *MNRAS*, **204**, 355
- Principe, G., Migliori, G., Johnson, T. J., et al. 2019, *A&A*, in press
- Rakshit, S., Stalin, C. S., Chand, H., & Zhang, X.-G. 2017, *ApJS*, **229**, 39
- Ricci, F., Massaro, F., Landoni, M., et al. 2015, *AJ*, **149**, 160
- Ruan, J. J., Anderson, S. F., Plotkin, R. M., et al. 2014, *ApJ*, **797**, 19
- Schinzell, F. K., Petrov, L., Taylor, G. B., et al. 2015, *ApJS*, **217**, 4
- Schinzell, F. K., Petrov, L., Taylor, G. B., & Edwards, P. G. 2017, *ApJ*, **838**, 139
- Shaw, M. S., Filippenko, A. V., Romani, R. W., Cenko, S. B., & Li, W. 2013a, *AJ*, **146**, 127
- Shaw, M. S., Romani, R. W., Cotter, G., et al. 2013b, *ApJ*, **764**, 135
- Shen, Z.-Q., Jiang, D. R., Kameno, S., & Chen, Y. J. 2001, *A&A*, **370**, 65
- Sutherland, W., & Saunders, W. 1992, *MNRAS*, **259**, 413
- Tanaka, Y. T., Doi, A., Inoue, Y., et al. 2015, *ApJL*, **799**, L18
- Taylor, G. B., Wrobel, J. M., & Vermeulen, R. C. 1998, *ApJ*, **498**, 619
- The Fermi-LAT collaboration 2020, *ApJS*, **247**, 33
- Thompson, D. J., Ciprini, S., & Gasparri, D. 2015, AAS Meeting, **225**, 144.41
- Tingay, S. J., & de Kool, M. 2003, *AJ*, **126**, 723
- Véron-Cetty, M.-P., & Véron, P. 2010, *A&A*, **518**, A10
- Voges, W., Aschenbach, B., Boller, T., et al. 1999, *A&A*, **349**, 389
- Voges, W., Aschenbach, B., Boller, T., et al. 2000, *yCat*, **9029**, 0
- Zargaryan, D., Sahakyan, N., & Harutyunian, H. 2018, *IJMPD*, **27**, 1844022



Fermi and Swift Observations of GRB 190114C: Tracing the Evolution of High-energy Emission from Prompt to Afterglow

M. Ajello¹, M. Arimoto², M. Axelsson^{3,4}, L. Baldini⁵, G. Barbiellini^{6,7}, D. Bastieri^{8,9}, R. Bellazzini¹⁰, A. Berretta¹¹, E. Bissaldi^{12,13}, R. D. Blandford¹⁴, R. Bonino^{15,16}, E. Bottacini^{14,17}, J. Bregeon¹⁸, P. Bruel¹⁹, R. Buehler²⁰, E. Burns^{21,24}, S. Buson²², R. A. Cameron¹⁴, R. Caputo²³, P. A. Caraveo²³, E. Cavazzuti²⁴, S. Chen^{8,17}, G. Chiaro²³, S. Ciprini^{25,26}, J. Cohen-Tanugi¹⁸, D. Costantin²⁷, S. Cutini²⁸, F. D'Ammando²⁹, M. DeKlotz³⁰, P. de la Torre Luque¹², F. de Palma¹⁵, A. Desai¹, N. Di Lalla⁵, L. Di Venere^{12,13}, F. Fana Dirirsa³¹, S. J. Fegan¹⁹, A. Franckowiak²⁰, Y. Fukazawa³², S. Funk³³, P. Fusco^{12,13}, F. Gargano¹³, D. Gasparrini^{25,26}, N. Giglietto^{12,13}, R. Gill³⁴, F. Giordano^{12,13}, M. Giroletti²⁹, J. Granot³⁴, D. Green³⁵, I. A. Grenier³⁶, M.-H. Grondin³⁷, S. Guiriec^{21,38}, E. Hays²¹, D. Horan¹⁹, G. Jóhannesson^{39,40}, D. Kocevski⁴¹, M. Kovac'evic²⁸, M. Kuss¹⁰, S. Larsson^{4,42,43}, L. Latronico¹⁵, M. Lemoine-Goumard³⁷, J. Li²⁰, I. Liodakis¹⁴, F. Longo^{6,7}, F. Loparco^{12,13}, M. N. Lovellette⁴⁴, P. Lubrano²⁸, S. Maldera¹⁵, D. Malyshev³³, A. Manfreda⁵, G. Martí-Devesa⁴⁵, M. N. Mazziotta¹³, J. E. McEnery^{21,46}, I. Mereu^{11,28}, M. Meyer^{14,33}, P. F. Michelson¹⁴, W. Mitthumsiri⁴⁷, T. Mizuno⁴⁸, M. E. Monzani¹⁴, E. Moretti⁴⁹, A. Morselli²⁵, I. V. Moskalenko¹⁴, M. Negro^{15,16}, E. Nuss¹⁸, N. Omodei¹⁴, M. Orienti²⁹, E. Orlando^{14,50}, M. Palatiello^{6,7}, V. S. Paliya²⁰, D. Paneque³⁵, Z. Pei⁹, M. Persic^{6,51}, M. Pesce-Rollins¹⁴, V. Petrosian¹⁴, F. Piron¹⁸, H. Poon³², T. A. Porter¹⁴, G. Principe²⁹, J. L. Racusin²¹, S. Rainò^{12,13}, R. Rando^{8,9}, B. Rani²¹, M. Razzano^{10,85}, S. Razzaque³¹, A. Reimer⁴⁵, O. Reimer^{4,42}, F. Ryde^{4,42}, P. M. Saz Parkinson^{52,53,54}, D. Serini¹², C. Sgrò¹⁰, E. J. Siskind⁵⁵, G. Spandre¹⁰, P. Spinelli^{12,13}, H. Tajima^{14,56}, K. Takagi³², M. N. Takahashi³⁵, D. Tak^{21,57}, J. B. Thayer¹⁴, D. J. Thompson²¹, D. F. Torres^{58,59}, E. Troja^{21,46}, J. Valverde¹⁹, B. Van Klaveren¹⁴, K. Wood^{60,86}, M. Yassine^{6,7}, G. Zaharijas⁵⁰, B. Mailyan⁶¹, P. N. Bhat⁶¹, M. S. Briggs⁶¹, W. Cleveland⁶², M. Giles⁶³, A. Goldstein⁶⁴, M. Hui⁶⁵, Christian Malacaria^{66,67,87}, R. Preece⁶¹, O. J. Roberts⁶⁴, P. Veres⁶¹, C. Wilson-Hodge⁶⁵, A. von Kienlin⁶⁸, S. B. Cenko^{69,70}, P. O'Brien⁷¹, A. P. Beardmore⁷¹, A. Lien^{72,73}, J. P. Osborne⁷⁴, A. Tohuvavohu⁷⁴, V. D'Elia^{75,76}, A. D'Ai⁷⁷, M. Perri^{75,76}, J. Gropp⁷⁸, N. Klingler⁷⁸, M. Capalbi⁷⁹, G. Tagliaferri⁸⁰, M. Stamatikos^{21,81,82}, and M. De Pasquale⁸³

¹ Department of Physics and Astronomy, Clemson University, Kinard Lab of Physics, Clemson, SC 29634-0978, USA

² Faculty of Mathematics and Physics, Institute of Science and Engineering, Kanazawa University, Kakuma, Kanazawa, Ishikawa 920-1192, Japan
arimoto@se.kanazawa-u.ac.jp

³ Department of Physics, Stockholm University, AlbaNova, SE-106 91 Stockholm, Sweden

⁴ Department of Physics, KTH Royal Institute of Technology, AlbaNova, SE-106 91 Stockholm, Sweden

⁵ Università di Pisa and Istituto Nazionale di Fisica Nucleare, Sezione di Pisa I-56127 Pisa, Italy

⁶ Istituto Nazionale di Fisica Nucleare, Sezione di Trieste, I-34127 Trieste, Italy

⁷ Dipartimento di Fisica, Università di Trieste, I-34127 Trieste, Italy

⁸ Istituto Nazionale di Fisica Nucleare, Sezione di Padova, I-35131 Padova, Italy

⁹ Dipartimento di Fisica e Astronomia "G. Galilei", Università di Padova, I-35131 Padova, Italy

¹⁰ Istituto Nazionale di Fisica Nucleare, Sezione di Pisa, I-56127 Pisa, Italy

¹¹ Dipartimento di Fisica, Università degli Studi di Perugia, I-06123 Perugia, Italy

¹² Dipartimento di Fisica "M. Merlin" dell'Università e del Politecnico di Bari, I-70126 Bari, Italy

¹³ Istituto Nazionale di Fisica Nucleare, Sezione di Bari, I-70126 Bari, Italy

¹⁴ W.W. Hansen Experimental Physics Laboratory, Kavli Institute for Particle Astrophysics and Cosmology, Department of Physics and SLAC National Accelerator Laboratory, Stanford University, Stanford, CA 94305, USA; nicola.omodei@stanford.edu

¹⁵ Istituto Nazionale di Fisica Nucleare, Sezione di Torino, I-10125 Torino, Italy

¹⁶ Dipartimento di Fisica, Università degli Studi di Torino, I-10125 Torino, Italy

¹⁷ Department of Physics and Astronomy, University of Padova, Vicolo Osservatorio 3, I-35122 Padova, Italy

¹⁸ Laboratoire Univers et Particules de Montpellier, Université Montpellier, CNRS/IN2P3, F-34095 Montpellier, France

¹⁹ Laboratoire Leprince-Ringuet, École polytechnique, CNRS/IN2P3, F-91128 Palaiseau, France

²⁰ Deutsches Elektronen Synchrotron DESY, D-15738 Zeuthen, Germany

²¹ NASA Goddard Space Flight Center, Greenbelt, MD 20771, USA; donggeun.tak@gmail.com

²² Institut für Theoretische Physik und Astrophysik, Universität Würzburg, D-97074 Würzburg, Germany

²³ INFN-Istituto di Astrofisica Spaziale e Fisica Cosmica Milano, via E. Bassini 15, I-20133 Milano, Italy

²⁴ Italian Space Agency, Via del Politecnico snc, I-00133 Roma, Italy

²⁵ Istituto Nazionale di Fisica Nucleare, Sezione di Roma "Tor Vergata," I-00133 Roma, Italy

²⁶ Space Science Data Center - Agenzia Spaziale Italiana, Via del Politecnico, snc, I-00133, Roma, Italy

²⁷ University of Padua, Department of Statistical Science, Via 8 Febbraio, 2, 35122 Padova, Italy

²⁸ Istituto Nazionale di Fisica Nucleare, Sezione di Perugia, I-06123 Perugia, Italy

²⁹ INFN Istituto di Radioastronomia, I-40129 Bologna, Italy

³⁰ Stellar Solutions Inc., 250 Cambridge Avenue, Suite 204, Palo Alto, CA 94306, USA

³¹ Department of Physics, University of Johannesburg, P.O. Box 524, Auckland Park 2006, South Africa

³² Department of Physical Sciences, Hiroshima University, Higashi-Hiroshima, Hiroshima 739-8526, Japan

³³ Friedrich-Alexander Universität Erlangen-Nürnberg, Erlangen Centre for Astroparticle Physics, Erwin-Rommel-Str. 1, D-91058 Erlangen, Germany

³⁴ Department of Natural Sciences, Open University of Israel, 1 University Road, POB 808, Ra'anana 43537, Israel; rsigill.rg@gmail.com

³⁵ Max-Planck-Institut für Physik, D-80805 München, Germany

³⁶ AIM, CEA, CNRS, Université Paris-Saclay, Université Paris Diderot, Sorbonne Paris Cité, F-91191 Gif-sur-Yvette, France

³⁷ Centre d'Études Nucléaires de Bordeaux Gradignan, IN2P3/CNRS, Université Bordeaux 1, BP120, F-33175 Gradignan Cedex, France

³⁸ The George Washington University, Department of Physics, 725 21st Street, NW, Washington, DC 20052, USA

³⁹ Science Institute, University of Iceland, IS-107 Reykjavik, Iceland

⁴⁰ Nordita, Royal Institute of Technology and Stockholm University, Roslagstullsbacken 23, SE-106 91 Stockholm, Sweden

⁴¹ NASA Marshall Space Flight Center, Huntsville, AL 35808, USA; daniel.kocevski@nasa.gov

- ⁴² The Oskar Klein Centre for Cosmoparticle Physics, AlbaNova, SE-106 91 Stockholm, Sweden
- ⁴³ School of Education, Health and Social Studies, Natural Science, Dalarna University, SE-791 88 Falun, Sweden
- ⁴⁴ Space Science Division, Naval Research Laboratory, Washington, DC 20375-5352, USA
- ⁴⁵ Institut für Astro- und Teilchenphysik, Leopold-Franzens-Universität Innsbruck, A-6020 Innsbruck, Austria
- ⁴⁶ Department of Astronomy, University of Maryland, College Park, MD 20742, USA
- ⁴⁷ Department of Physics, Faculty of Science, Mahidol University, Bangkok 10400, Thailand
- ⁴⁸ Hiroshima Astrophysical Science Center, Hiroshima University, Higashi-Hiroshima, Hiroshima 739-8526, Japan
- ⁴⁹ Institut de Física d'Altes Energies (IFAE), Edifici Cn, Universitat Autònoma de Barcelona (UAB), E-08193 Bellaterra (Barcelona), Spain
- ⁵⁰ Istituto Nazionale di Fisica Nucleare, Sezione di Trieste, and Università di Trieste, I-34127 Trieste, Italy
- ⁵¹ Osservatorio Astronomico di Trieste, Istituto Nazionale di Astrofisica, I-34143 Trieste, Italy
- ⁵² Santa Cruz Institute for Particle Physics, Department of Physics and Department of Astronomy and Astrophysics, University of California at Santa Cruz, Santa Cruz, CA 95064, USA
- ⁵³ Department of Physics, The University of Hong Kong, Pokfulam Road, Hong Kong, People's Republic of China
- ⁵⁴ Laboratory for Space Research, The University of Hong Kong, Hong Kong, People's Republic of China
- ⁵⁵ NYCB Real-Time Computing Inc., Lattingtown, NY 11560-1025, USA
- ⁵⁶ Solar-Terrestrial Environment Laboratory, Nagoya University, Nagoya 464-8601, Japan
- ⁵⁷ Department of Physics, University of Maryland, College Park, MD 20742, USA
- ⁵⁸ Institute of Space Sciences (CSICIEEC), Campus UAB, Carrer de Magrans s/n, E-08193 Barcelona, Spain
- ⁵⁹ Institució Catalana de Recerca i Estudis Avançats (ICREA), E-08010 Barcelona, Spain
- ⁶⁰ Praxis Inc., Alexandria, VA 22303 USA
- ⁶¹ Center for Space Plasma and Aeronomic Research (CSPAR), University of Alabama in Huntsville, Huntsville, AL 35899, USA; peter.veres@uah.edu
- ⁶² Universities Space Research Association (USRA), Columbia, MD 21044, USA
- ⁶³ Jacobs Technology, Huntsville, AL 35806, USA
- ⁶⁴ Science and Technology Institute, Universities Space Research Association, Huntsville, AL 35805, USA
- ⁶⁵ NASA Marshall Space Flight Center, Huntsville, AL 35812, USA
- ⁶⁶ NASA Marshall Space Flight Center, NSSTC, 320 Sparkman Drive, Huntsville, AL 35805, USA
- ⁶⁷ Universities Space Research Association, NSSTC, 320 Sparkman Drive, Huntsville, AL 35805, USA
- ⁶⁸ Max-Planck Institut für extraterrestrische Physik, D-85748 Garching, Germany
- ⁶⁹ Astrophysics Science Division, NASA Goddard Space Flight Center, 8800 Greenbelt Road, Greenbelt, MD 20771, USA
- ⁷⁰ Joint Space-Science Institute, University of Maryland, College Park, MD 20742, USA
- ⁷¹ School of Physics and Astronomy, University of Leicester, University Road, Leicester, LE1 7RH, UK
- ⁷² Center for Research and Exploration in Space Science and Technology (CRESST) and NASA Goddard Space Flight Center, Greenbelt, MD 20771, USA
- ⁷³ Department of Physics, University of Maryland, Baltimore County, 1000 Hilltop Circle, Baltimore, MD 21250, USA
- ⁷⁴ Department of Astronomy and Astrophysics, University of Toronto, 50 St. George Street, Toronto, Ontario, M5S 3H4 Canada
- ⁷⁵ ASI Space Science Data Center, via del Politecnico snc, I-00133, Rome Italy
- ⁷⁶ INAF-Osservatorio Astronomico di Roma, via Frascati 33, I-00040 Monte Porzio Catone, Italy
- ⁷⁷ INAF-IAAF Palermo, via Ugo La Malfa 156, I-90123 Palermo, Italy
- ⁷⁸ Department of Astronomy and Astrophysics, 525 Davey Lab, The Pennsylvania State University, University Park, PA 16802, USA
- ⁷⁹ INAF-Istituto di Astrofisica Spaziale e Fisica Cosmica di Palermo, Via Ugo La Malfa 153, I-90146 Palermo, Italy
- ⁸⁰ INAF-Osservatorio Astronomico di Brera, via Bianchi 46, I-23807 Merate (LC), Italy
- ⁸¹ Department of Physics and Center for Cosmology and Astro-Particle Physics, Ohio State University, Columbus, OH 43210, USA
- ⁸² Department of Astronomy, Ohio State University, Columbus, OH 43210, USA
- ⁸³ Department of Astronomy and Space Sciences, Istanbul University, Fatih, 34119, Istanbul, Turkey

Received 2019 September 18; revised 2019 November 19; accepted 2019 November 22; published 2020 February 6

Abstract

We report on the observations of gamma-ray burst (GRB) 190114C by the *Fermi* Gamma-ray Space Telescope and the *Neil Gehrels Swift Observatory*. The prompt gamma-ray emission was detected by the *Fermi* GRB Monitor (GBM), the *Fermi* Large Area Telescope (LAT), and the *Swift* Burst Alert Telescope (BAT) and the long-lived afterglow emission was subsequently observed by the GBM, LAT, *Swift* X-ray Telescope (XRT), and *Swift* UV Optical Telescope. The early-time observations reveal multiple emission components that evolve independently, with a delayed power-law component that exhibits significant spectral attenuation above 40 MeV in the first few seconds of the burst. This power-law component transitions to a harder spectrum that is consistent with the afterglow emission observed by the XRT at later times. This afterglow component is clearly identifiable in the GBM and BAT light curves as a slowly fading emission component on which the rest of the prompt emission is superimposed. As a result, we are able to observe the transition from internal-shock- to external-shock-dominated emission. We find that the temporal and spectral evolution of the broadband afterglow emission can be well modeled as synchrotron emission from a forward shock propagating into a wind-like circumstellar environment. We estimate the initial bulk Lorentz factor using the observed high-energy spectral cutoff. Considering the onset of the afterglow component, we constrain the deceleration radius at which this forward shock begins to radiate in

⁸⁴ NASA Postdoctoral Program Fellow, USA.

⁸⁵ Funded by contract FIRB-2012-RBF12PM1F from the Italian Ministry of Education, University and Research (MIUR), Italy.

⁸⁶ Resident at Naval Research Laboratory, Washington, DC 20375, USA.

⁸⁷ NASA Postdoctoral Fellow.



order to estimate the maximum synchrotron energy as a function of time. We find that even in the LAT energy range, there exist high-energy photons that are in tension with the theoretical maximum energy that can be achieved through synchrotron emission from a shock. These violations of the maximum synchrotron energy are further compounded by the detection of very high-energy (VHE) emission above 300 GeV by MAGIC concurrent with our observations. We conclude that the observations of VHE photons from GRB 190114C necessitates either an additional emission mechanism at very high energies that is hidden in the synchrotron component in the LAT energy range, an acceleration mechanism that imparts energy to the particles at a rate that is faster than the electron synchrotron energy-loss rate, or revisions of the fundamental assumptions used in estimating the maximum photon energy attainable through the synchrotron process.

Unified Astronomy Thesaurus concepts: [Gamma-ray bursts \(629\)](#)

1. Introduction

Long gamma-ray bursts (GRBs) are thought to represent a specific subset of supernovae in which high-mass progenitors manage to retain a significant amount of angular momentum such that they launch a relativistic jet along their rotation axis at the point of stellar collapse (Woosley 1993). The highly variable emission of gamma-rays is thought to be produced by shocks internal to this expanding and collimated outflow (Goodman 1986; Paczynski 1986; Rees & Meszaros 1994), resulting in the most energetic bursts of electromagnetic emission in the universe. This prompt emission is followed by long-lived broadband afterglow emission that is thought to arise from the interaction of the expanding jet with the circumstellar environment (Rees & Meszaros 1992; Meszaros & Rees 1993).

Over 10 years of joint observations by the *Fermi Gamma-ray Space Telescope* and the *Neil Gehrels Swift Observatory* have dramatically expanded our understanding of the broadband properties of both the prompt and afterglow components of GRBs. The *Fermi* GRB Monitor (GBM) has detected over 2300 GRBs in the 11 years since the start of the mission (Bhat et al. 2016; Ajello et al. 2019), with approximately 8% of these bursts also detected by the *Fermi* Large Area Telescope (LAT). These observations have shown a complex relationship between the emission observed by the GBM in the keV to MeV energy range and that observed by the LAT above 100 MeV. The LAT-detected emission is typically, although not always, delayed with respect to the start of the prompt emission observed at lower energies and has been observed to last considerably longer, fading with a characteristic power-law decay for thousands of seconds in some cases (Abdo et al. 2009b; Ackermann et al. 2013a); see also the Second LAT GRB catalog (2FLGC, Ajello et al. 2019). Spectral analysis of the GBM- and LAT-observed emission has shown that it is typically not well fit by a single spectral component, but rather requires an additional power-law component to explain the emergence of the emission above 100 MeV (Abdo et al. 2009a; Ackermann et al. 2011, 2013b, 2014; Arimoto et al. 2016).

Simultaneous observations by the X-ray Telescope (XRT) on *Swift* of a small subset of LAT-detected bursts have revealed that the delayed power-law component observed above 100 MeV is largely consistent with an afterglow origin (e.g., Ackermann et al. 2013b). This component is commonly observed at X-ray, optical, and radio frequencies, but the extension of the afterglow spectrum to higher energies shows that it is also capable of producing significant emission at MeV and GeV energies. The observation of such a component in the LAT has significantly constrained the onset of the afterglow, allowing for estimates of the time at which the relativistic outflow begins to convert its internal energy into observable radiation.

In both the prompt and afterglow phases, nonthermal synchrotron emission has long been suggested as the radiation mechanism by which energetic particles accelerated in these outflows radiate their energy to produce the observed gamma-ray emission (see Piran 1999, 2004, for reviews). Evidence for synchrotron emission, typically attributed to shock-accelerated electrons, has been well established through multiwavelength observations of long-lived afterglow emission (Gehrels et al. 2009). Analysis of GBM observations has also shown that many of the long-standing challenges to attributing the prompt emission to the synchrotron process can be overcome (Burgess et al. 2011; Guiriec et al. 2011; Beniamini & Piran 2013). Synchrotron emission from shock-accelerated electrons should, in many scenarios, be accompanied by synchrotron self-Compton (SSC) emission, in which some fraction of the accelerated particles transfer their energy to the newly created gamma-rays before they escape the emitting region (e.g., Sari & Esin 2001; Fan & Piran 2008). The result is a spectral component that mirrors the primary synchrotron spectrum, but boosted in energy by the typical Lorentz factor of the accelerated electrons.

Despite the predicted ubiquity of an SSC component accompanying synchrotron emission from accelerated charged particles, no unambiguous evidence has been found for its existence in either prompt or afterglow spectra (although see Wei & Fan 2007; Fan et al. 2013; Tam et al. 2013; Wang et al. 2013). The LAT detection of only 8% of 2357 GRBs detected by the GBM (2FLGC) disfavors the ubiquity of bright SSC components in the 0.1–100 GeV energy range during the prompt emission. When there is detectable emission in the LAT, its delayed emergence, as well as low-energy excesses observed in the GBM data, have likewise disfavored an SSC origin of the prompt high-energy emission above 100 MeV (Abdo et al. 2009a; Ackermann et al. 2011, 2013b). Likewise, a recent study by Ajello et al. (2018) has also shown that simultaneous detections of GRB afterglows by *Swift* XRT and LAT could be sufficiently well modeled as the high-energy extension of the synchrotron spectrum, with no need for an extra SSC component to explain the late-time LAT-detected emission.

At the same time, there is a maximum energy beyond which synchrotron emission produced by shock-accelerated charged particles becomes inefficient. This occurs when the shock acceleration timescale approaches the radiative loss timescale, resulting in charged particles that lose their energy faster than they can regain it. This maximum photon energy has been shown to be violated by high-energy photons detected by the LAT from GRB 130427A (Ackermann et al. 2014), including a 95 GeV photon (128 GeV in its rest frame) a few minutes after the burst and a 32 GeV photon (43 GeV in the rest frame)

observed after 9 hr. These apparent violations of the maximum synchrotron energy would require an emission component in addition to the shock-accelerated synchrotron emission typically used to model LAT-detected bursts. SSC and/or inverse-Compton (IC) emission from the afterglow’s forward shock are both expected at TeV energies during the prompt emission, although a spectral hardening and/or a flattening of the LAT light curves is expected as a distinct SSC or IC component passes through the LAT energy range, neither of which was observed in GRB 130427A. In addition, late-time observations by *NuSTAR* provide further support for a single spectral component ranging from keV to GeV energies in GRB 130427A almost a day after the event (Kouveliotou et al. 2013). Synchrotron emission could still be a viable explanation for these observations, but only for an acceleration mechanism that imparts energy to the radiating particles faster than the electron synchrotron energy-loss rate, such as through magnetic reconnection.

Here we report on the high-energy detection of GRB 190114C by the *Fermi* GBM and LAT and the *Swift* Burst Alert Telescope (BAT), XRT, and UV Optical Telescope (UVOT). The early-time observations show a delayed high-energy emission above 40 MeV in the first few seconds of the burst, before a transition to a harder spectrum that is consistent with the afterglow emission observed by the XRT and GBM. We find that the temporal and spectral evolution of the broadband afterglow emission can be well modeled as synchrotron emission from a forward shock propagating into a wind-like circumstellar environment. We estimate the initial bulk Lorentz factor using the observed high-energy spectral cutoff. Considering the onset of the afterglow component, we constrain the deceleration radius in order to estimate the maximum synchrotron energy, which is in tension with high-energy photons observed by the LAT. The violation of the maximum synchrotron energy is further compounded by the detection of very high-energy (VHE) emission above 300 GeV by MAGIC from this burst (Mirzoyan 2019). We find that the detection of high-energy photons from GRB 190114C requires either an additional emission mechanism at high energies, a particle acceleration mechanism, or revisions to the fundamental assumptions used in estimating the maximum photon energy attainable through the synchrotron process.

The paper is organized as follows. We present an overview of the *Fermi* and *Swift* instruments in Section 2, and a summary of our observations in Section 3. The results of our temporal and spectral analyses are described in Section 4, and we use those results to model the high-energy afterglow in Section 5. We summarize our findings and discuss their implications for future VHE detections in Section 6. Throughout the paper, we assume a standard Λ CDM cosmology with $\Omega_\Lambda = 0.7$ and $\Omega_M = 0.3$, $H_0 = 0.7$. All errors quoted in the paper correspond to a 1σ confidence region, unless otherwise noted.

2. Overview of Instruments

2.1. Fermi GBM and LAT

The *Fermi* Gamma-ray Space Telescope consists of two scientific instruments, the GBM and the LAT. The GBM comprises 14 scintillation detectors designed to study the gamma-ray sky in the ~ 8 keV to 40 MeV energy range (Meegan et al. 2009). Twelve of the detectors are

semidirectional sodium iodide (NaI) detectors, which cover an energy range of 8–1000 keV, and are configured to view the entire sky unocculted by Earth. The other two detectors are bismuth germanate (BGO) crystals, sensitive in the energy range 200 keV to 40 MeV, and are placed on opposite sides of the spacecraft. Incident gamma-rays interact with the NaI and BGO crystals, creating scintillation photons, which are collected by attached photomultiplier tubes and converted into electronic signals. The signal amplitudes in the NaI detectors have an approximately cosine response relative to the angle of incidence θ , and relative rates between the various detectors are used to reconstruct source locations.

The LAT is a pair-conversion telescope comprising a 4×4 array of silicon strip trackers and cesium iodide (CsI) calorimeters covered by a segmented anti-coincidence detector to reject charged-particle background events. The LAT detects gamma-rays in the energy range from 20 MeV to more than 300 GeV with a field of view (FoV) of ~ 2.4 sr, observing the entire sky every two orbits (~ 3 hr) while in normal survey mode. The deadtime per event of the LAT is nominally 26 μ s, the shortness of which is crucial for observations of high-intensity transient events such as GRBs. The LAT triggers on many more background events than celestial gamma-rays; therefore, onboard background rejection is supplemented on the ground using event class selections that are designed to facilitate the study of a broad range of sources of interest (Atwood et al. 2009).

2.2. Swift BAT, XRT, and UVOT

The *Neil Gehrels Swift Observatory* (Gehrels et al. 2005) consists of the BAT (Barthelmy et al. 2005), the XRT (Burrows et al. 2005), and the UVOT (Roming et al. 2005). The BAT is a wide-field, coded mask gamma-ray telescope, covering an FoV of 1.4 sr with partial coding fraction cutoff choice of 50%, and an imaging energy range of 15–150 keV. The instrument’s coded mask allows for positional accuracy of $1'–4'$ within seconds of the burst trigger. The XRT is a grazing-incidence focusing XRT covering the energy range 0.3–10 keV and providing a typical localization accuracy of $\sim 1''–3''$. The UVOT is a telescope covering the wavelength range 170–650 nm with 11 filters and determines the location of a GRB afterglow with subarcsecond precision.

Swift operates autonomously in response to BAT triggers on new GRBs, automatically slewing to point the XRT and the UVOT at a new source within 1–2 minutes. Data are promptly downloaded, and localizations are made available from the narrow-field instruments within minutes (if detected). *Swift* then continues to follow-up GRBs as they are viewable within the observing constraints and if the observatory is not in the South Atlantic Anomaly, for at least several hours after each burst, sometimes continuing for days, weeks, or even months if the burst is bright and of particular interest for follow-up.

3. Observations

On 2019 January 14 at 20:57:02.63 UT (T_0), GBM triggered and localized GRB 190114C. The burst occurred 68° from the LAT boresight and 90° from the Zenith at the time of the GBM trigger. The burst was especially bright for the GBM (Hamburg et al. 2019), producing over $\sim 30,000$ counts per second above background in the most illuminated NaI detector. The LAT

detected a gamma-ray counterpart at R.A. (J2000), decl.(J2000) = $03^{\text{h}}38^{\text{m}}17^{\text{s}}$, $-26^{\circ}59'24''$ with an error radius of $3''$ (Kocevski et al. 2019). Such a high GBM count rate would normally trigger an Autonomous Repoint Request (ARR), in which the spacecraft slews to keep the burst within the LAT FoV. Unfortunately, ARR maneuvers have been disabled since 2018 March 16, due to Sun-pointing constraints as a result of an anomaly with one of the two Solar Drive Assemblies that articulate the pointing of the spacecraft’s solar panels.⁸⁸ As a result, the burst left the LAT FoV at $T_0 + 180$ s and the GBM FoV at $T_0 + 260$ s when it was occulted by Earth. The burst reemerged from Earth occultation at $T_0 + 2500$ s, but remained outside the LAT FOV for an additional orbit, reentering the LAT FoV at $T_0 + 8600$ s.

GRB 190114C triggered the *Swift* BAT at 20:57:03 UT and the spacecraft immediately slewed to the onboard burst localization (Gropp et al. 2019). The XRT began observing the field at 20:58:07.1 UT, 64.63 s after the GBM trigger, with settled observations beginning at $T_0 + 68.27$ s. UVOT began observing the field at $T_0 + 73.63$ s with a 150 s finding chart exposure using a White filter. The XRT and UVOT detected X-ray and optical counterparts, respectively, with a consistent location, with a UVOT position of R.A. (J2000), decl.(J2000) = $03^{\text{h}}38^{\text{m}}01^{\text{s}}16$, $-26^{\circ}56'46''9$ with an uncertainty of $0''.42$ (Osborne et al. 2019; Siegel & Gropp 2019), which is also consistent with the LAT position. Both the XRT and the UVOT continued observing the burst location throughout the following two weeks, with the last observation occurring 13.86 days post-trigger. The XRT light curve is taken from the XRT GRB light-curve repository (Evans et al. 2007, 2009). However, the lower energy limit was raised from the default of 0.3 keV–0.7 keV in order to avoid an apparent increase in the low-energy background caused by additional events created by the effects of trailing charge on the Windowed Timing (WT) readout mode data (see Section 4.2.2 and www.swift.ac.uk/analysis/xrt/digest_cal.php#trail).

The burst was also detected at high energies by the MCAL on *AGILE* (Ursi et al. 2019), SPI-ACS on *INTEGRAL* (Minaev & Pozanenko 2019), and Insight-HXMT (Xiao et al. 2019). Most notably, the MAGIC Cerenkov telescopes (Mirzoyan et al. 2019) also detected the burst, which reported a significant detection of high-energy photons above 300 GeV. The MAGIC observations mark the first announcement of a significant detection of VHE emission from a GRB by a ground-based Cerenkov telescope.

A host galaxy was identified in Pan-STARRS archival imaging observations by de Ugarte Postigo et al. (2019) and subsequent spectroscopic observations by Selsing et al. (2019) with the Nordic Optical Telescope found absorption lines in the afterglow spectrum, yielding a redshift of $z = 0.42$. The source was also detected in radio and submillimeter (Alexander et al. 2019; Cherukuri et al. 2019; Giroletti et al. 2019; Schulze et al. 2019; Tremou et al. 2019). The VLA location of the afterglow as reported by Alexander et al. (2019) was R.A. (J2000), decl.(J2000) = $03^{\text{h}}38^{\text{m}}01^{\text{s}}191 \pm 0''.04$, $-26^{\circ}56'46''.73 \pm 0''.02$, a distance of 4.36 and 0.01 from the LAT and UVOT locations, respectively. We adopt this location for the analysis carried out throughout the rest of the paper.

4. Analysis

4.1. Temporal Characteristics

Figure 1 shows the BAT, GBM, and LAT light curves for GRB 190114C in several different energy ranges. The BAT and GBM light curves can be characterized by highly variable prompt emission episodes, separated by a quiescent period lasting approximately ~ 7 s. A strong energy dependence of the light curves is clearly evident, with pulse widths being narrower at higher energies, a feature commonly attributed to hard-to-soft spectral evolution within an emission episode. This trend can be seen to extend up to the LAT Low Energy (LLE) data below 100 MeV (Pelassa et al. 2010), although the LAT emission above 100 MeV does not appear to be significantly correlated with the emission at lower energies. Photons with energies > 100 MeV are first observed at $T_0 + 2.4$ s, consistent with a delayed onset of the high-energy emission seen in other LAT-detected bursts (Ajello et al. 2019). Photons with energies > 1 GeV are first observed at $T_0 + 4.0$ s, and the highest-energy photon was detected at $T_0 + 20.9$ s with an energy of 21.0 GeV.

The prompt emission appears superimposed on a smoothly varying emission component that is present during the quiescent period and extends beyond the cessation of the highly variable emission. The T_{90} and T_{50} durations, defined as time intervals within which 90% and 50% of the GRB flux was collected, reveal that significant GBM emission above background exists longer than the prompt emission seen within the first 25 s of the burst. We estimate the T_{90} and T_{50} durations, in the 50–300 keV energy range, to be 116.4 ± 2.6 s and 6.9 ± 0.3 s, respectively. We also estimate the shortest coherent variation in the light curve, also called the minimum variability time, to be $t_{\text{min}} = 5.41 \pm 0.13$ ms in the NaI detectors, 6.49 ± 0.38 ms in the BGO detectors, and 30.00 ± 4.74 ms in the LLE band (20–200 MeV) of the LAT detector (Bhat 2013).

4.2. Spectral Characteristics

4.2.1. GBM–LAT Joint Spectral Analysis

We examined the underlying spectral characteristics of the prompt emission from GRB 190114C by performing joint time-resolved spectral analysis using the GBM and LAT data from T_0 to the start of the settled XRT observations at $T_0 + 68.27$ s. For GBM, we used the Time-Tagged Event data for two NaI detectors (n4 and n7) from 10 keV to 1 MeV and one BGO detector (b0) from 250 keV to 40 MeV, after considering the spacecraft geometry and viewing angles of the instruments to the burst location. We also include the LLE data, covering an energy range of 30 MeV–100 MeV. For both the GBM and LLE data, the background rate for each energy channel was estimated by fitting a second-order polynomial to data before and after GRB 190114C, taking care to exclude a weak soft precursor emission and any extended emission during the power-law decay observed in the GBM.

For the LAT data, we selected P8R3Transient010 class events in the 100 MeV–100 GeV energy range from a region of interest (ROI) of 12° radius centered on the burst location. We applied a maximum zenith angle cut of 105° to prevent contamination from gamma-rays from the Earth limb produced through interactions of cosmic rays with Earth’s atmosphere.

The LAT flux estimates were obtained by performing an unbinned likelihood analysis using *gtlike* from the standard

⁸⁸ https://fermi.gsfc.nasa.gov/ssc/observations/types/post_anomaly/

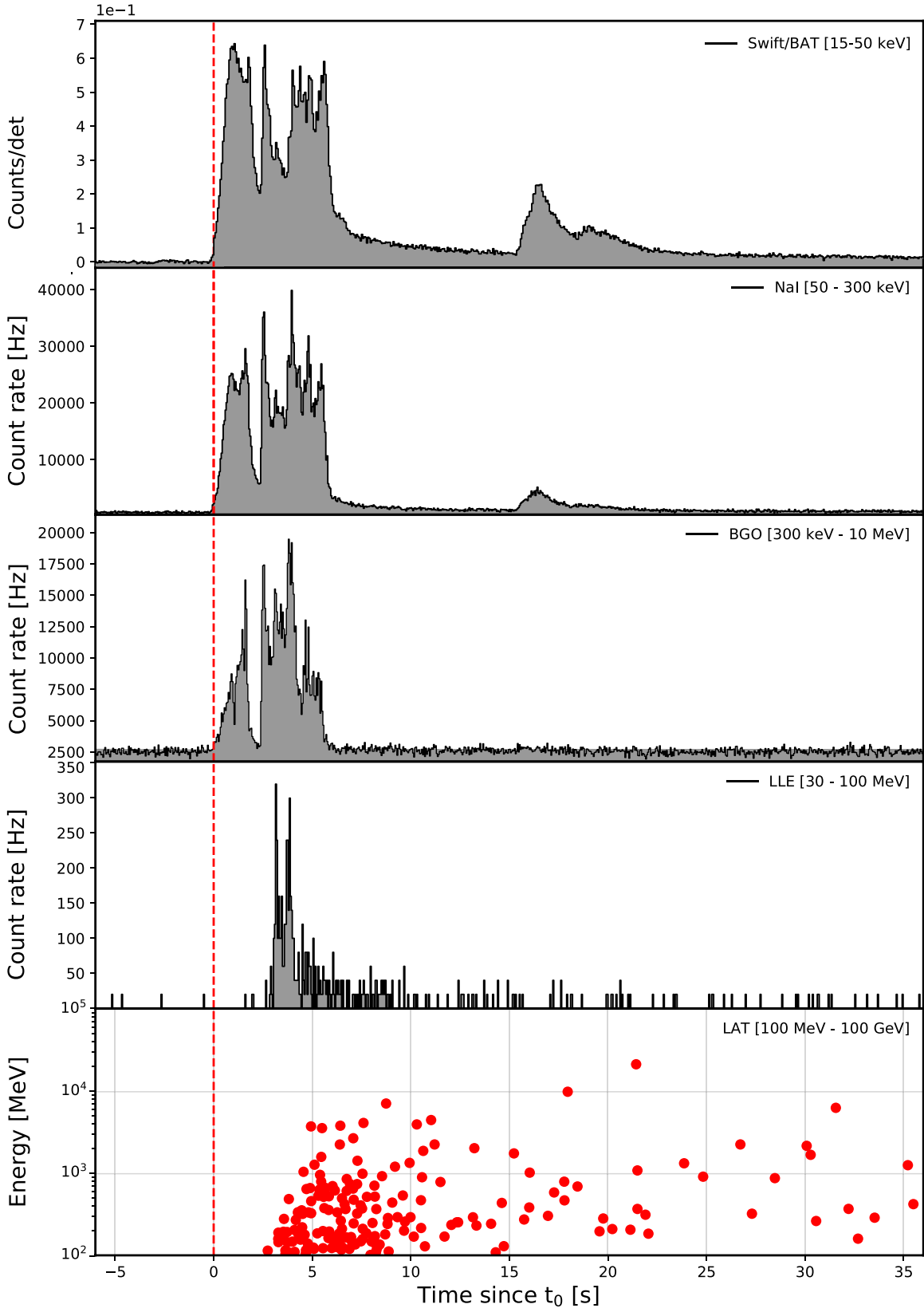


Figure 1. Composite light curve for GRB 190114C: the first panel displays the flux in the 15–50 keV energy range as measured with *Swift*/BAT. The second and third panels show the light curves for the most brightly illuminated GBM detectors, NaI (4, 7) and BGO (0) in the 50–300 keV and 0.3–10 MeV energy ranges, respectively. The bottom two panels show the LAT data for the LAT Low Energy (LLE) and P8R3Transient010 class events in the 30–100 MeV and >100 MeV energy ranges, respectively. In the last panel, we show the arrival times and energies of the individual LAT photons with probabilities $p > 0.9$ to be associated with the GRB. The red vertical dashed line is the GBM trigger time.

ScienceTools (version v11r5p3).⁸⁹ In unbinned likelihood fitting of individual sources, the observed distribution of counts from the burst is modeled as a point source using an energy-dependent LAT PSF and a power-law source spectrum with a normalization and photon index that are left as free parameters. In addition to the point source, we draw cataloged point sources from the 3FGL catalog, and we use the publicly available.⁹⁰ isotropic (gll_iem_v06) and Galactic diffuse (iso_P8R2_TRANSIENT020_V6_v06) templates.⁹¹ The free parameters of the model are then varied to maximize the likelihood of observing the data given the model. Additional details of the likelihood analysis employed for GRB analysis can be found in Abdo et al. (2009c).

We then use `gtbin` to generate the counts spectrum of the modeled burst and `gtbkg` to extract the associated background by computing the predicted counts from cataloged point sources and diffuse emission components in the ROI. The LAT instrument response for the each analysis interval was computed using `gtrspgen`.

The spectral fits were performed using the *XSPEC* software package (version 12.9.1u; Arnaud 1996), in which we minimize the PG_{stat} statistic for Poisson data with a Gaussian background (Arnaud et al. 2011). The best-fit model is selected by minimizing the Bayesian information criterion (BIC; Schwarz 1978). For each time interval, we test a variety of spectral models, including a power law (PL), a power law with an exponential cutoff (CPL), the Band function (Band; Band et al. 1993), a blackbody (BB), and combinations thereof.

The time interval from T_0 to $T_0 + 25$ s was subdivided into seven intervals after considering the temporal characteristics shown in Figure 2. Figure 2 also shows the best-fit model for each time interval. The spectrum of the first pulse phase ($T_0 + 0$ –2.3 s) is best fitted with the Band + BB model. The addition of the BB component to the Band component is weakly preferred ($\Delta\text{BIC} \sim 2$). The peak energy (E_{pk}) for the Band component is 586 ± 14 keV, and the temperature of the BB component is 44 ± 5 keV. The temperature of the BB component is consistent with similar components seen in other bright GRBs (Guiriec et al. 2011, 2013; Axelsson et al. 2012).

The main spectral component during the brightest emission episode observed from $T_0 + 2.3$ s to $T_0 + 7.0$ s is characterized by many short and overlapping pulses and is best fit by either a CPL or Band function. During this phase, the low-energy spectral index is very hard, ranging between -0.4 and 0.0 (see Table 1). The peak energy (E_{pk}) reaches a maximum value of $E_{\text{pk}} \sim 815$ keV from $T_0 + 2.8$ s to $T_0 + 3.8$ s, before decreasing in time (see Table 1).

An additional PL or CPL component begins to appear during the $T_0 + 2.3$ s to $T_0 + 2.8$ s time interval and lasts throughout the prompt emission phase. Arrival of the first LAT events above 100 MeV associated with the source begins at $T_0 + \sim 2.7$ s, consistent with the emergence of this spectral component. In the third ($T_0 + 2.8$ s to $T_0 + 3.8$ s) and fourth ($T_0 + 3.8$ s to $T_0 + 4.8$ s) time intervals, this additional component increases in brightness and exhibits a high-energy cutoff which increases in energy with time, ranging from 26–52 MeV (see Table 1). The high-energy cutoff is strongly required in both time intervals compared to the models without

the high-energy cutoff ($\Delta\text{BIC} \gg 10$). After ~ 4.8 s, the high-energy cutoff in this additional component disappears, and the high-energy emission is well described by a PL with a photon index ($dN/dE \propto E^{\Gamma_{\text{ph}}}$) of $\Gamma_{\text{ph,PL}} = -1.86 \pm 0.01$ or correspondingly an energy index ($F_{\nu} \propto \nu^{\beta}$) of $\beta_{\text{PL}} = -0.86 \pm 0.01$.

After the bright emission phase, the long-lived extended emission observed by the LAT is best described by a PL with an almost-constant photon index of $\Gamma_{\text{ph,PL}} \sim -2$, as shown in Figure 3. Figure 3 also shows that the energy flux of this extended emission phase (100 MeV–1 GeV) shows a power-law decay in time ($F_{\nu} \propto t^{\alpha}$), with an exponent of $\alpha_{\text{LAT}} = -1.09 \pm 0.02$. Extrapolation of this extended emission back into the earlier bright emission phase reveals that the flux from the additional spectral component in the prompt emission evolves similarly to the extended emission. This implies that the emission from the additional component and the extended emission may be from the same region. Because the power-law spectral and temporal characteristics of this broadband emission resemble the representative features of GRB afterglows, the end of the bright emission phase at about ~ 7 s represents the transition from the prompt to afterglow-dominated emission.

In addition to the extended emission, a weaker, short-duration pulse, with soft emission primarily below $\lesssim 100$ keV, is observed from $T_0 + 15$ s to $T_0 + 25$ s. This weak pulse, along with the long-lasting extended emission, is well described by the CPL + PL model. For these periods, we fix the photon index of the PL component to -2.0 , assuming that the photon index of the energy spectrum of the extended emission is unchanged in time.

4.2.2. Fermi–Swift Joint Spectral Analysis

We continue the time-resolved spectral analysis from $T_0 + 68.27$ s to $T_0 + 627.14$ s, but now include *Swift* data. For GBM, we prepared the data using the same process as described in Section 4.2.1, although for this time interval we excluded channels below 50 keV because of apparent attenuation due to partial blockage of the source by the spacecraft that is not accounted for in the GBM response. For LAT, we decreased the ROI radius to 10° and increased the maximum zenith angle cut to 110° . Both changes are made in order to reduce the loss of exposure that occurs when the ROI crosses the zenith angle cut and begins to overlap Earth’s limb. This increase in exposure, though, comes at the expense of increased background during intervals when Earth’s limb is approaching the burst position. The rest of the process is the same as described in Section 4.2.1.

We retrieve *Swift* data from the HEASARC archive. The BAT spectra are generated using the event-by-event data collected from $T_{0,\text{BAT}} - 239$ s to $T_{0,\text{BAT}} + 963$ s, with the standard BAT software (HEASOFT 6.25⁹²) and the latest calibration database (CALDB⁹³). The burst left the BAT FoV at $\sim T_{0,\text{BAT}} + 720$ s and was not reobserved until $\sim T_{0,\text{BAT}} + 3800$ s. For the intervals that include spacecraft slews, an average response file is generated by summing several short-interval (5 s) response files, weighted by the counts in each interval (see Lien et al. 2016, for a more detailed description).

⁸⁹ <http://fermi.gsfc.nasa.gov/ssc/>

⁹⁰ <http://fermi.gsfc.nasa.gov/ssc/data/access/lat/BackgroundModels.html>

⁹¹ The difference between the P8R2 and P8R3 isotropic spectra are small and do not affect the results of this analysis.

⁹² <http://heasarc.nasa.gov/lheasoft/>

⁹³ <http://heasarc.gsfc.nasa.gov/docs/heasarc/caldb/swift/>

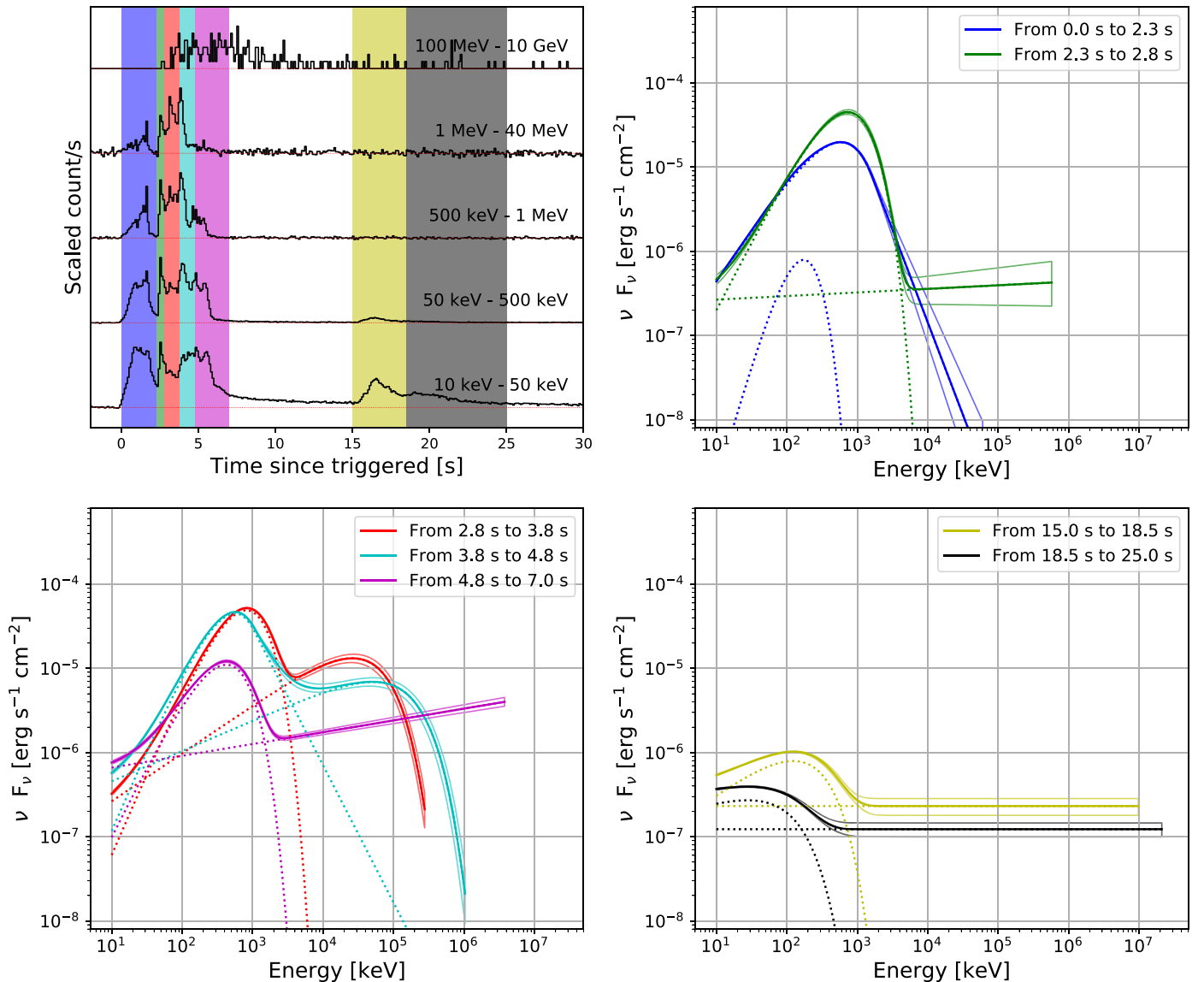


Figure 2. The scaled light curves and the νF_ν model spectra (and $\pm 1\sigma$ error contours) for each of the time intervals described in Section 4.2.1. Each SED extends up to the energy of the highest-energy photon detected by LAT. The color-coding used in the shading of time intervals in the top-left panel is carried over to the energy spectra in the other three panels. The dotted lines represent the components of the model spectra. The best-fit model and its parameters are listed in Table 1.

The XRT acquired the source at $T_0 + 64.63$ s and started taking WT data at $T_0 + 68.27$ s. In the analysis that follows, the XRT data were initially processed by the XRT data analysis software tools available in HEASOFT version 6.25, using the gain calibration files released on 2018 July 10. Prior to extracting spectra, we processed the WT event data using an updated, but as yet unreleased, version of the XRT science data analysis task XRTWTCORR (version 0.2.4), which includes a new algorithm for identifying unwanted events caused by the delayed emission of charge from deep charge traps that have accumulated in the CCD due to radiation damage from the harsh environment of space. Such trailing charge appears as additional low-energy events and can cause significant spectral distortion at low energies, especially for a relatively absorbed extragalactic X-ray source, like GRB 190114C. Once identified, the trailing charge events were removed from the event list, resulting in clean WT spectra that are usable below 0.7 keV. The XRT spectral extraction then proceeded using standard *Swift* analysis software included in HEASOFT

software (version 6.25). Grade 0 events were selected to help mitigate pileup and appropriately sized annular extraction regions were used, when necessary, to exclude pileup from the core of the WT point-spread function (PSF) profile when the source count rate was greater than ~ 100 cts s $^{-1}$. PSF and exposure-corrected ancillary response files were created to ensure correct recovery of the source flux during spectral fitting.

We tested three models in the joint spectral fits, a PL, a broken power law (BKNPL), and a smoothly broken power law (SBKNPL). Each model was multiplied by two photoelectric absorption models, one for Galactic absorption (“TBabs”) and another for the intrinsic host absorption (“zTBabs”). For the Galactic photoelectric absorption model, an equivalent hydrogen column density is fixed to 7.54×10^{19} atoms cm $^{-2}$ (Willingale et al. 2013). We let the equivalent hydrogen column density for the intrinsic host absorption model be a free parameter in the fit, but fixed the redshift to $z = 0.42$.

Table 1
Spectral Fitting to GBM + LLE + LAT data (10 keV–100 GeV) for Various Time Intervals

From (s)	To (s)	Model ^a	Main component				Additional component				$PG_{\text{stat}}/\text{dof}$	BIC
			Norm. ^b	$\Gamma_{\text{ph,low}}$	$\Gamma_{\text{ph,high}}$	E_{pk} (keV)	Norm. ^b	$\Gamma_{\text{ph,PL}}$	E_{pk} (MeV)	kT (keV)		
0.0	2.3	Band	$0.518^{+0.005}_{-0.005}$	$-0.73^{+0.01}_{-0.01}$	$-4.00^{+0.27}_{-0.42}$	$548.6^{+7.7}_{-7.6}$	$11.54^{+5.46}_{-4.30}$			$44.2^{+4.9}_{-4.7}$	518/353	542
		Band+BB	$0.481^{+0.011}_{-0.011}$	$-0.77^{+0.01}_{-0.01}$	$-4.20^{+0.31}_{-0.46}$	$585.4^{+14.2}_{-13.6}$					505/351	540
2.3	2.8	CPL+PL	$0.555^{+0.009}_{-0.009}$	$-0.36^{+0.03}_{-0.03}$		$730.0^{+16.2}_{-15.5}$	$0.018^{+0.004}_{-0.003}$	$-1.96^{+0.05}_{-0.06}$			425/352	454
2.8	3.8	CPL+PL	$0.374^{+0.006}_{-0.006}$	$-0.09^{+0.03}_{-0.03}$		$840.8^{+13.1}_{-12.9}$	$0.040^{+0.002}_{-0.002}$	$-1.68^{+0.01}_{-0.01}$			769/352	799
		CPL+CPL	$0.355^{+0.007}_{-0.007}$	$-0.04^{+0.03}_{-0.03}$		$814.9^{+13.4}_{-13.0}$	$0.061^{+0.004}_{-0.004}$	$-1.43^{+0.02}_{-0.02}$	$26.1^{+2.6}_{-2.3}$		477/351	512
3.8	4.8	Band+PL	$0.706^{+0.011}_{-0.011}$	$-0.05^{+0.03}_{-0.03}$	$-3.60^{+0.19}_{-0.28}$	$562.8^{+9.6}_{-9.2}$	$0.050^{+0.003}_{-0.003}$	$-1.64^{+0.02}_{-0.02}$			577/351	612
		Band+CPL	$0.675^{+0.010}_{-0.010}$	$-0.05^{+0.03}_{-0.03}$	$-3.63^{+0.21}_{-0.26}$	$563.1^{+8.8}_{-9.6}$	$0.065^{+0.004}_{-0.004}$	$-1.64^{+0.02}_{-0.02}$	$51.5^{+9.8}_{-7.4}$		519/350	560
4.8	7.0	CPL+PL	$0.322^{+0.006}_{-0.006}$	$-0.30^{+0.04}_{-0.04}$		$425.4^{+7.7}_{-7.4}$	$0.057^{+0.002}_{-0.002}$	$-1.86^{+0.01}_{-0.01}$			467/352	494
15	18.5	CPL+PL	$0.080^{+0.005}_{-0.005}$	$-1.41^{+0.08}_{-0.06}$		$122.9^{+7.5}_{-6.7}$	$0.014^{+0.003}_{-0.003}$	-2.00 fixed			407/353	430
18.5	25	CPL+PL	$0.030^{+0.005}_{-0.004}$	$-1.74^{+0.09}_{-0.08}$		$27.7^{+3.3}_{-4.1}$	$0.008^{+0.001}_{-0.001}$	-2.00 fixed			454/353	478

Notes. Errors correspond to a 1σ confidence region.

^a For the PL, CPL, and Band models, the pivot energy is fixed to 100 keV.

^b Photons $\text{cm}^{-2} \text{s}^{-1} \text{keV}^{-1}$.

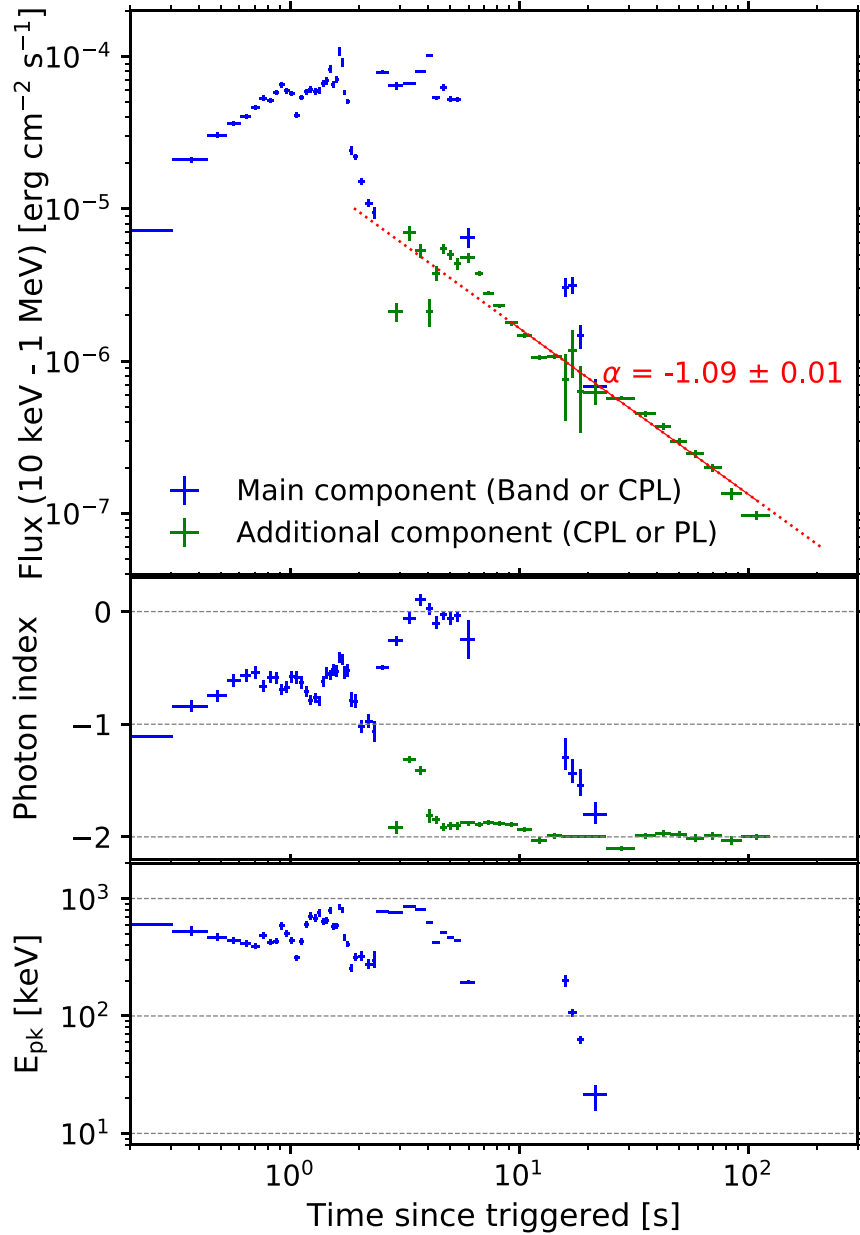


Figure 3. Temporal and spectral evolution of each spectral component. Top panel: energy flux in the 10 keV–1 MeV (blue) and 100 MeV–1 GeV (green) energy ranges. Middle panel: photon index (for the Band function, we refer to the low-energy photon index). Bottom panel: E_{pk} , where we use the trigger time T_0

We divided the extended emission phase, $T_0 + 68.27$ s to $T_0 + 627.14$ s, into four time intervals covering 68.27–110 s, 110–180 s, 180–380 s, and 380–627.18 s. The fit results for all four time intervals are listed in Table 2. For the first two time intervals, we fit the XRT, BAT, GBM, and LAT data simultaneously by using different fit statistics for each data type: C_{stat} (Poisson data with Poisson background) for the XRT, χ^2 for the BAT data, and PG_{stat} for GBM and LAT. These statistics are reported independently for each data set in Table 2. As shown in Table 2 and Figure 4, a BKNPL function is statistically preferred over the PL and SBKNPL functions in both time intervals, where Figure 4 also includes the spectral fitting results using each individual instrument. When the smoothness parameter s in the SBKNPL model is left free to vary, a sharp break with $s > 10$ is obtained, at which point an SBKNPL resembles a traditional BKNPL model. The low- and high-energy photon indices in the BKNPL model are consistent

in both time intervals, yielding $\Gamma_{\text{ph,low}} \sim -1.6$ and $\Gamma_{\text{ph,high}} \sim -2.1$, respectively, with break energies of $4.22^{+0.31}_{-0.67}$ keV and $5.11^{+0.42}_{-0.37}$ keV. We note that the high-energy photon index is consistent with the values in the additional component seen in the prompt phase. This result implies that BAT, GBM, and LAT are observing emission from the same side of the break in the energy spectrum from 10 keV to 100 GeV, which starts to appear during the prompt emission phase in the form of an additional spectral component, whereas the low-energy channels of the XRT are measuring the energy spectrum below this break.

Because the burst is outside the LAT FoV during the last two time intervals, we limit the joint fit during these intervals to XRT and BAT data. We again simultaneously fit the data to PL and BKNPL models, using again different fit statistics for each data type, χ^2 for the BAT data and C_{stat} for the XRT. Again,

Table 2
Spectral Fitting to *Fermi* and *Swift* data (1 keV–100 GeV) for Various Time Intervals

From (s)	To (s)	Model ^{a,b}	$\Gamma_{\text{ph,low}}$	$\Gamma_{\text{ph,high}}$	E_{break} (keV)	p	$N(\text{H})$ (10^{22} atoms cm^{-2})	PG_{stat}	C_{stat}	χ^2	dof	BIC
68.27	110	PL	$-2.09^{+0.01}_{-0.01}$				$10.55^{+0.27}_{-0.26}$	504	655	52	1086	1239
		BKNPL	$-1.55^{+0.12}_{-0.12}$	$-2.11^{+0.02}_{-0.02}$	$4.72^{+1.20}_{-0.37}$		$8.22^{+0.54}_{-0.52}$	502	625	56	1084	1225
		SBKNPL _{ISM} ^c	$-(p+1)/2$	$-(p+2)/2$	$4.63^{+3.38}_{-3.28}$	$2.46^{+0.08}_{-0.11}$	$9.91^{+0.27}_{-0.26}$	504	642	55	1085	1236
		SBKNPL _{wind} ^d	$-(p+1)/2$	$-(p+2)/2$	$7.46^{+72.89}_{-6.63}$	$2.54^{+0.15}_{-0.16}$	$10.06^{+0.27}_{-0.26}$	504	644	54	1085	1238
110	180	PL	$-2.00^{+0.02}_{-0.02}$				$10.42^{+0.23}_{-0.23}$	616	671	50	1087	1364
		BKNPL	$-1.57^{+0.08}_{-0.08}$	$-2.06^{+0.02}_{-0.02}$	$5.60^{+0.76}_{-0.46}$		$8.30^{+0.40}_{-0.39}$	616	627	51	1085	1336
		SBKNPL _{ISM}	$-(p+1)/2$	$-(p+2)/2$	$2.56^{+4.20}_{-1.54}$	$2.24^{+0.10}_{-0.08}$	$9.74^{+0.23}_{-0.23}$	621	653	50	1087	1358
		SBKNPL _{wind}	$-(p+1)/2$	$-(p+2)/2$	$1.69^{+4.63}_{-0.69}$	$2.26^{+0.10}_{-0.10}$	$9.89^{+0.23}_{-0.23}$	621	656	50	1086	1362
180	380	PL	$-1.90^{+0.01}_{-0.01}$				$9.57^{+0.17}_{-0.15}$		774	66	810	866
		BKNPL	$-1.54^{+0.06}_{-0.06}$	$-1.99^{+0.05}_{-0.05}$	$5.18^{+0.46}_{-0.36}$		$7.93^{+0.29}_{-0.28}$		727	63	808	830
		SBKNPL _{ISM}	$-(p+1)/2$	$-(p+2)/2$	$5.60^{+0.145}_{-1.512}$	$2.20^{+0.10}_{-0.02}$	$9.07^{+0.15}_{-0.14}$		756	64	809	854
		SBKNPL _{wind}	$-(p+1)/2$	$-(p+2)/2$	$6.88^{+0.35}_{-0.44}$	$2.25^{+0.16}_{-0.02}$	$9.21^{+0.16}_{-0.15}$		761	64	809	858
380	627.14	PL	$-1.86^{+0.01}_{-0.01}$				$9.09^{+0.13}_{-0.14}$		700	47	839	775
		BKNPL	$-1.71^{+0.05}_{-0.05}$	$-2.11^{+0.08}_{-0.09}$	$5.52^{+0.72}_{-0.38}$		$8.43^{+0.24}_{-0.23}$		686	42	837	768
		SBKNPL _{ISM}	$-(p+1)/2$	$-(p+2)/2$	$8.67^{+37.30}_{-6.78}$	$2.18^{+0.20}_{-0.16}$	$8.67^{+0.20}_{-0.11}$		694	44	838	772
		SBKNPL _{wind}	$-(p+1)/2$	$-(p+2)/2$	$9.16^{+36.96}_{-4.91}$	$2.20^{+0.19}_{-0.10}$	$8.77^{+0.18}_{-0.09}$		695	45	838	774

Notes. Errors correspond to the 1σ confidence region.

^a Because the XRT data are included, a model is multiplied by the photoelectric absorption models, TBabs with fixed hydrogen column density of $7.54 \times 10^{19} \text{ cm}^{-2}$ and zTBabs with fixed redshift of 0.4245.

^b Note that a “constant” factor is included in the model, which accounts for the potential of relative calibration uncertainties in the recovered flux (i.e., normalization) between BAT and GBM. The factor ranges from 0.8 to 1.3, which is acceptable.

^c Smoothness parameter $s = 1.15\text{--}0.06p$ (Granot et al. 2002).

^d Smoothness parameter $s = 0.80\text{--}0.03p$ (Granot et al. 2002).

the BKNPL model is statistically preferred over the simpler PL model. For the time interval from $T_0 + 180$ s to 380 s, the low- and high-energy photon indices, as well as the break energy, in the BKNPL model are consistent with those found during the earlier intervals. For the last time interval from $T_0 + 380$ s to 627.14 s, the low-energy photon index is slightly softer than previous intervals, with $\Gamma_{\text{ph,low}} = -1.71 \pm 0.05$, and the break energy is almost consistent with previous intervals.

4.3. Multiwavelength Afterglow Light Curves

Figure 5 shows light curves of GRB 190114C for the XRT, BAT, GBM, and LAT data. The selection for the GBM and LAT data is described in Section 4.2.1, and the flux is calculated from the best-fit function for each time interval in the spectral analysis with each individual instrument. The XRT (0.7 keV–10 keV), and BAT (15 keV–50 keV) light curves are obtained from the UK *Swift* Science Data Centre. The UVOT (2–5 eV for the white band) light curve is obtained by `uvotproduct` of the HEASoft package. The BAT, GBM, and LAT light curves show an obvious transition from the highly variable prompt emission to a smoothly decaying afterglow component ($\alpha_{\text{BAT}} = -1.00 \pm 0.01$, $\alpha_{\text{GBM}} = -1.10 \pm 0.01$, and $\alpha_{\text{LAT}} = -1.22 \pm 0.11$). At later times, all three light curves decay in time with consistent decay indices, $\alpha \sim -1$, implying that they originate from the same emitting region.

The XRT light curve is well described by a broken power law with temporal indices α_{XRT} of -1.30 ± 0.01 and -1.49 ± 0.02 with the break occurring at approximately $t_{\text{break}} \sim T_0 + \sim 19.8 \times 10^3$ s (~ 5.5 hr) (see inset in Figure 5). The prebreak decay index of the XRT light curve differs from the indices measured for the BAT, GBM and LAT data. This difference in

decay slopes indicates that the XRT is probing a different portion of the afterglow spectrum, a conclusion that is consistent with the observed spectral breaks in the *Swift* and *Fermi* joint-fit spectral analysis (Section 4.2.2).

On the other hand, the UVOT light curve exhibits decay slopes and a temporal break that are distinct from the XRT and BAT data. The temporal break occurs at ~ 400 s, with temporal indices α_{UVOT} before and after the break of -1.62 ± 0.04 and -0.84 ± 0.02 , respectively. These decay indices are steeper than the decay observed in the XRT before the break in the UVOT data and shallower than the XRT decay afterwards. This implies that the UVOT is observing yet another distinct portion of the afterglow spectrum. These observations can be interpreted as the contribution of an optically bright reverse shock that becomes subdominant to the forward-shock emission at the time of the observed temporal break. In such a scenario, the postbreak decay index seen in the UVOT would then reflect a distinct portion of the afterglow spectrum below the X-ray regime.

5. Discussion

5.1. Prompt Emission

The prompt emission observed in GRB 190114C resembles the complex relationship between multiple emission components commonly seen in LAT-detected GRBs. The emission observed in the first ~ 2 s is best characterized as a Band function spectrum with a possible subdominant BB component, which combined produce no detectable emission in the LAT energy range. The energy fluxes of the thermal and nonthermal components in the energy band from 10 keV to 1 MeV are

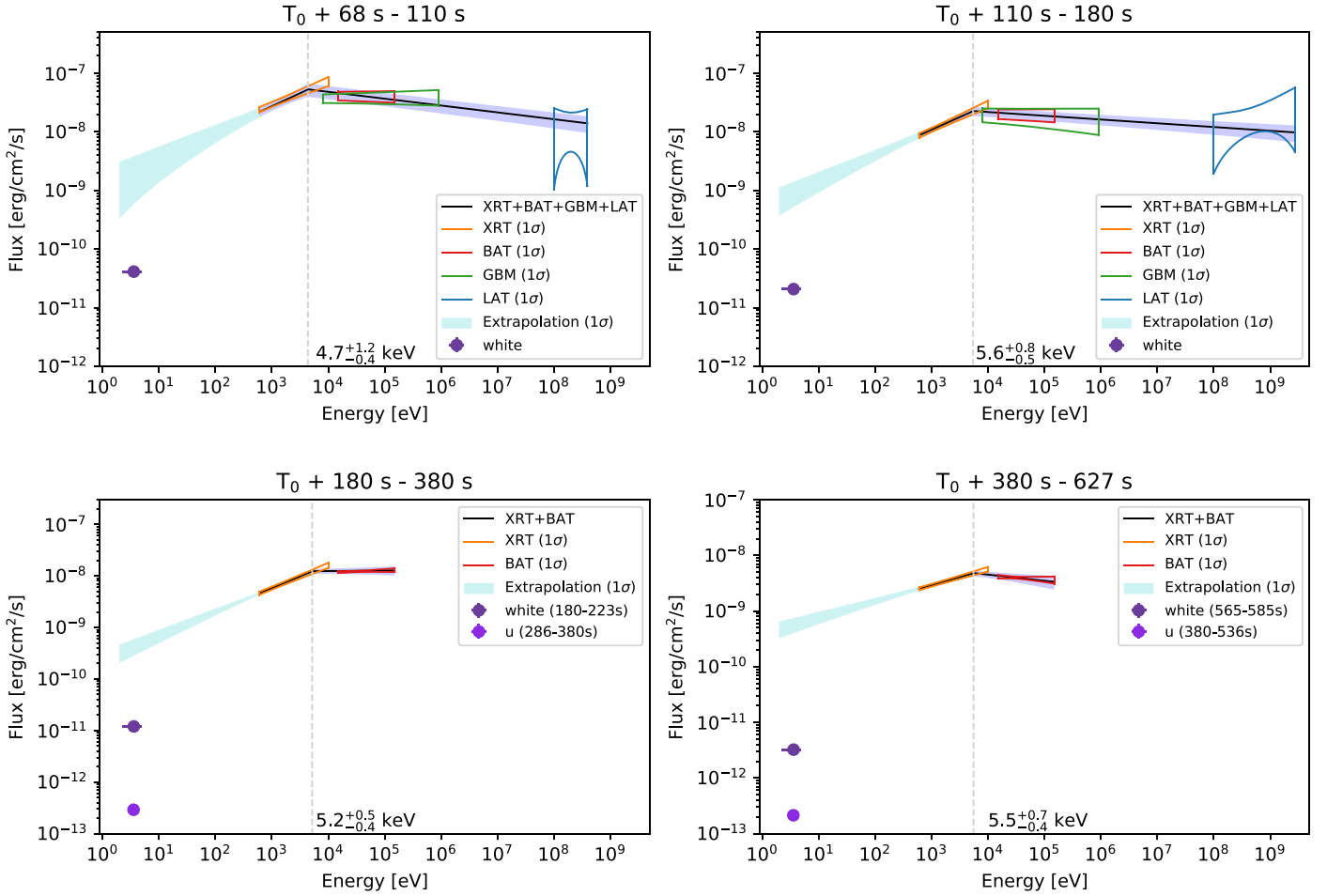


Figure 4. Spectral energy distributions from optical to gamma-ray energies for the four time intervals ($T_0 + 68.27$ s to 110 s, $T_0 + 110$ s to 180 s, $T_0 + 180$ s to 380 s, and $T_0 + 380$ s to 627 s) described in Section 4.2.2. The solid black lines represent the best-fitting broken power-law function. Each filled region corresponds to the 1σ error contour of the best-fit power-law function to the data from each individual instrument. The cyan regions are an extrapolation from the best-fitting broken power-law function. The dotted line denotes the best-fit break energy E_{break} . The simultaneous UVOT white- and u -band observations taken during the $T_0 + 180$ s to 380 s and $T_0 + 380$ s to 627 s intervals are also shown but are not included in the joint spectral fit. Note that the UVOT observations are uncorrected for Galactic or host absorption and as such serve as lower limits to the UV and optical flux.

$\sim 1.1 \times 10^{-6}$ and $\sim 3.9 \times 10^{-5} \text{ erg cm}^{-2} \text{ s}^{-1}$, respectively. We estimate the ratio of the thermal to nonthermal emission during this period to be approximately 3%.

The delay in the onset of the LAT-detected emission is related to the emergence of a hard PL component superimposed on the highly variable Band+BB component seen in the GBM. Furthermore, the PL component is initially attenuated at energies greater than ~ 100 MeV, and we interpret this spectral turnover as due to opacity to electron–positron pair production ($\gamma\gamma \rightarrow e^+e^-$) within the source. The cutoff energy associated with this turnover is observed to increase with time before disappearing entirely at later times. Similar behavior has been observed in other LAT-detected bursts (e.g., GRB 090926A; Ackermann et al. 2011) and has been attributed to the expansion of the emitting region, as the pair production opacity is expected to scale as $\tau_{\gamma\gamma} \propto R^{-1}$ for a fixed mean flux, where R is the distance from the central engine.

As has also been noted for other LAT-detected GRBs, e.g., GRBs 081024B (Abdo et al. 2010), 090510 (Ackermann et al. 2010), 090902B (Abdo et al. 2009a), 090926A (Ackermann et al. 2011), 110731A (Ackermann et al. 2013b), and 141207A (Arimoto et al. 2016), the existence of the extra PL component can be seen as a low-energy excess in the GBM data. This

observation disfavors SSC or IC emission from the prompt emission as the origin of the extra PL component, as SSC emission cannot produce a broad power-law spectrum that extends below the synchrotron spectral peak. Instead, we identify this component as the emergence of the early afterglow over which the rest of the prompt emission is superimposed. Similar conclusions have been drawn by Ravasio et al. (2019) as to the origin of the PL component seen in the GBM data.

5.2. Afterglow Emission

The *Swift* and *Fermi* data reveal that the power-law spectral component observed during the prompt emission transitions to a canonical afterglow component, which fades smoothly as a power law in time. In the standard forward-shock model of GRB afterglows (Sari et al. 1998), specific relationships between the temporal decay and spectral indices, the so-called “closure relations,” can be used to constrain the physical properties of the forward shock as well as the type of environment in which the blast wave is propagating.

Our broadband fits to the simultaneous XRT, GBM, BAT, and LAT data show evidence for a spectral break in the hard X-ray band (5–10 keV). In the context of the forward-shock model, this spectral break could represent either the frequency

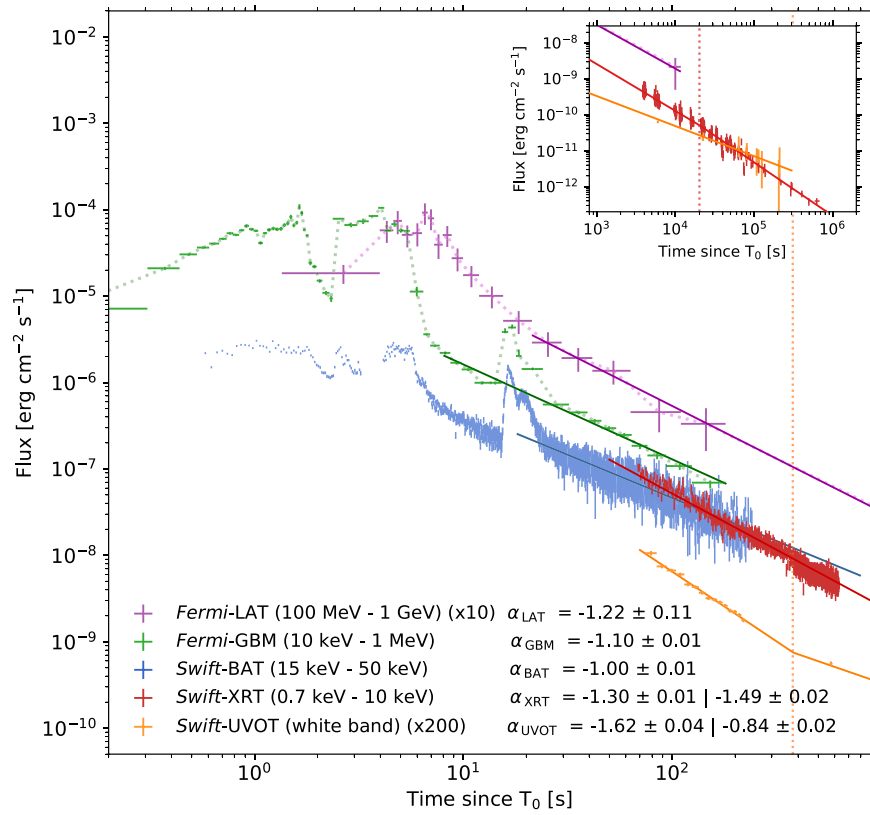


Figure 5. Multiwavelength afterglow light curves for the UVOT (yellow), XRT (red), BAT (blue), GBM (green), and LAT (purple) data from GRB 190114C. The flux for the GBM (10 keV–1 MeV) and LAT (100 MeV–1 GeV) data is calculated from the best-fit model for each time interval in the spectral analysis with each instrument. The BAT, GBM, and LAT emission show a transition after $\sim T_0 + 10$ s to an extended emission component decaying smoothly as a power law in time (solid lines). Both the XRT and the UVOT light curves are well described by a broken power law, respectively (solid lines), and their break times are 19.8×10^3 s (~ 5.5 hr) and 377 s, respectively (dotted lines). The inset shows the light curves of the LAT, XRT, and UVOT up to $\sim T_0 + 23$ days.

of the synchrotron emission electrons with a minimum Lorentz factor ν_m or the cooling frequency of the synchrotron emission ν_c . Because there are no additional spectral breaks observed up to and through the LAT energy range, if we assume the observed spectral break is either ν_m or ν_c , then we naturally hypothesize that $\nu_c < \nu_m$ or $\nu_m < \nu_c$, respectively. In the case where the spectral break is ν_m , the low-energy and high-energy photon indices are expected to be $\nu^{-1.5}$ for $\nu < \nu_m$ and $\nu^{-(p+2)/2} \sim \nu^{-2.1}$ for $\nu > \nu_m$, when assuming an electron spectral index of $p \sim 2.1$, a characteristic value obtained in previous studies (e.g., Waxman 1997; Bednarz & Ostrowski 1998; Freedman & Waxman 2001; Curran et al. 2010; Wang et al. 2015). These values are consistent with the observed photon indices, although the expected temporal index when $\nu < \nu_m$ is expected to be $\propto t^{-1/4}$, which is inconsistent with the XRT decay index of $\propto t^{-1.32 \pm 0.01}$ for either a constant-density (ISM) or wind-like (wind) circumstellar environment. Therefore, this scenario in which the break is due to ν_m is disfavored.

In the case where the spectral break is ν_c , the low-energy and high-energy photon indices are expected to be $\nu^{-(p+1)/2} \sim \nu^{-1.6}$ for $\nu < \nu_c$ and $\nu^{-(p+2)/2} \sim \nu^{-2.1}$ for $\nu > \nu_c$, again assuming $p \sim 2.1$, again consistent with the observed values. The expected temporal behavior when $\nu > \nu_c$ in both the ISM and wind cases is $\propto t^{(2-3p)/4} \sim t^{-1.1}$, which is consistent with the temporal decay measured in the BAT, GBM, and LAT energy ranges. For $\nu < \nu_c$, the expected temporal behavior significantly depends on the density profile of the circumstellar environment. In the ISM case, the temporal index is expected to be $\propto t^{3(1-p)/4} \sim t^{-0.8}$, inconsistent with the decay observed

in the XRT, whereas for the wind case, the expected temporal index is $\propto t^{(1-3p)/4} \sim t^{-1.3}$, matching the decay seen in X-rays.

If we are indeed observing an afterglow spectrum in which the XRT data are below ν_c , then we can follow the formalism established in Sari & Mészáros (2000) and van Eerten & Wijers (2009) to estimate an arbitrary circumstellar density profile index k , for $n(r) \propto R^{-k}$, to be $k = (12\beta - 8\alpha)/(1 + 3\beta - 2\alpha) = 1.92 \pm 0.07$, which also supports a wind profile ($k = 2$) scenario.

Figure 6 shows the observed evolution of E_{break} in the four time intervals we analyzed, along with the expected evolution of the cooling break $\nu_c \propto t^{+1/2}$ in a wind-like environment. Despite an initial increase in the break energy between the first two intervals, the break energy is consistent with remaining constant after $T_0 > 150$ s. This behavior is similar to that observed for GRB 130427A, in which the broadband modeling preferred a wind-like environment (Perley et al. 2014), but for which ν_c was nonetheless observed to remain constant through the late-time observations (Kouveliotou et al. 2013). Kouveliotou et al. (2013) concluded that GRB 130427A may have occurred in an intermediate environment, possibly produced through a stellar eruption late in the life of the progenitor which altered the circumstellar density profile (Fryer et al. 2006). Nonetheless, a wind-like environment for GRB 190114C matches conclusions drawn by Cenko et al. (2011), Ackermann et al. (2013b), and Ajello et al. (2018) from a growing number of bursts for a possible preference for LAT-detected bursts to occur in stratified environments, despite the observation that the majority of long GRB afterglows are

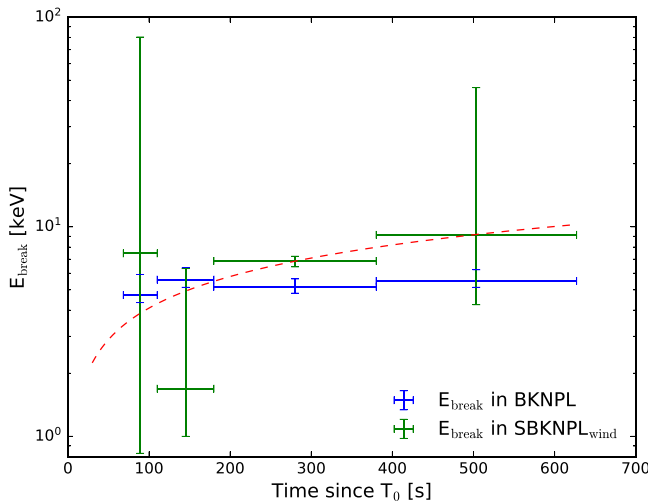


Figure 6. Observed spectral break energy vs. time. The blue and green points represent the break energy (E_{break}) in the BKNPL and SBKNPL_{wind} models in the four time intervals, respectively. The dashed line represents the cooling frequency with time ($\nu_c \propto t^{1/2}$) expected from the afterglow parameters. Despite an initial increase in the break energy between the first two intervals, the break energy is consistent with remaining constant after $T_0 + \sim 150$ s.

otherwise consistent with occurring in environments that exhibit uniform density profiles (Schulze et al. 2011).

The temporal decay of the UVOT data, although uncorrected for either Galactic or host-galaxy extinction, can provide additional constraints on the location of ν_m . The UVOT emission decays as a broken power-law function, starting with $t^{-1.62 \pm 0.06}$ from 70 to 400 s, before transitioning to a slower decay of $t^{-0.84 \pm 0.03}$ for 400–10⁵ s. The prebreak emission can be interpreted as the contribution from a reverse shock, which is expected to exhibit a temporal index of $\propto t^{-(73p+21)/96} \sim t^{-1.82}$, assuming $p = 2.1$ (Kobayashi 2000), roughly consistent with observations. If the UVOT-observed emission after $T_0 + \sim 400$ s is due to the forward-shock component in which the UVOT data are above ν_m but below ν_c , then the temporal decay is expected to be $\propto t^{(1-3p)/4} \sim t^{-1.3}$ for $p = 2.1$, which is too steep with respect to the observed postbreak UVOT decay ($t^{-0.84 \pm 0.03}$). On the other hand, if the UVOT data are below both ν_m and ν_c , the temporal decay is expected to be flat, $\propto t^0$. Without a clear preference for either of the two scenarios, we conjecture that the UVOT-detected emission may have a different origin or emission site than the X-ray and gamma-ray emission.⁹⁴

5.3. Energetics

GRB 190114C was exceptionally bright in the observer frame. The one-second peak photon flux measured by GBM is 247 ± 1 photons $\text{s}^{-1} \text{cm}^{-2}$, with a total fluence of $(4.433 \pm 0.005) \times 10^{-4}$ erg cm^{-2} , both in the 10–1000 keV band. This makes GRB 190114C the fourth brightest in peak flux and the fifth most fluent GRB detected by GBM, placing it in the top 0.3 percentile of GRBs in the third GBM catalog (Bhat et al. 2016).

⁹⁴ Although Laskar et al. (2019) suggested that the system is in fast cooling to explain the temporal and spectral behaviors in the optical and XRT bands, the fast-cooling scenario may face difficulty in reproducing different temporal behaviors between the XRT and BAT bands (i.e., $\alpha_{\text{XRT}} \sim -1.3$ and $\alpha_{\text{BAT}} \sim -1.0$).

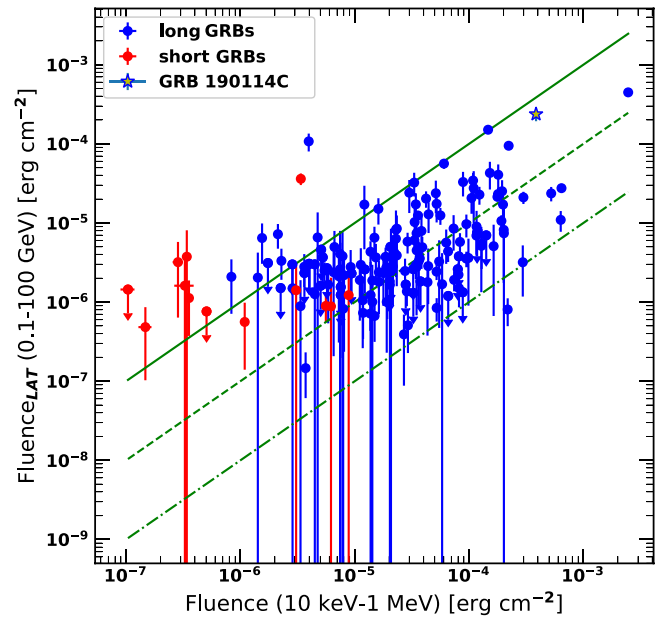


Figure 7. Fluence in the energy range of 0.1–100 GeV vs. 10 keV–1 MeV for GRB 190114C (star) compared with the sample of 186 LAT-detected GRBs from the 2FLGC. Red points are for short GRBs while blue points are for long GRBs.

The fluence in the 100 MeV–100 GeV energy band measured by the LAT, including the prompt and extended emission, is $(2.4 \pm 0.4) \times 10^{-5}$ erg cm^{-2} , which sets GRB 190114C as the second most fluent GRB detected by the LAT. Figure 7 shows the 10–1000 keV fluence versus the 0.1–100 GeV fluence for GRB 190114C in comparison with the sample of GRBs detected by the LAT from the 2FLGC. The fluence measured by the LAT is only slightly smaller than that of GRB 130427A, currently the most fluent GRB detected by the LAT.

At a redshift of $z = 0.42$ ($d_L = 2390$ Mpc), the total isotropic-equivalent energies E_{iso} released in the rest-frame GBM (1 keV–10 MeV), LAT (100 MeV–10 GeV), and combined (1 keV–10 GeV) energy ranges are $(2.5 \pm 0.1) \times 10^{53}$ erg, $(6.9 \pm 0.7) \times 10^{52}$ erg, and $(3.5 \pm 0.1) \times 10^{53}$ erg, respectively. We also estimate a one-second isotropic-equivalent luminosity of $L_{\gamma, \text{iso}} = (1.07 \pm 0.01) \times 10^{53}$ erg s^{-1} in the 1–10,000 keV energy range.

Figure 8 shows E_{iso} estimated in the 100 MeV–10 GeV rest frame along with the sample of the 34 LAT-detected GRBs with known redshift in the 2FLGC. We note that GRB 190114C is among the most luminous LAT-detected GRBs below $z < 1$, with an E_{iso} just below GRB 130427A, which also exhibited the highest-energy photons detected by the LAT from a GRB, including a 95 GeV photon emitted at 128 GeV in the rest frame of the burst.

5.4. Bulk Lorentz Factor

GRBs are intense sources of gamma-rays. If the emission originated in a nonrelativistic source, it would render gamma-ray photons with energies at the νF_ν peak energy and above susceptible to e^\pm -pair production ($\gamma\gamma \rightarrow e^\pm$) due to high optical depths ($\tau_\gamma(\Gamma_{\text{bulk}}, E) \gg 1$) for $\gamma\gamma$ -annihilation. This is the so-called “compactness problem,” which can be resolved if the emission region is moving ultrarelativistically, with $\Gamma_{\text{bulk}} \gtrsim 100$, toward the observer (Baring & Harding 1997; Lithwick & Sari 2001; Granot et al. 2008; Hascoët et al. 2012). In this case, the attenuation of flux, which either appears as an exponential

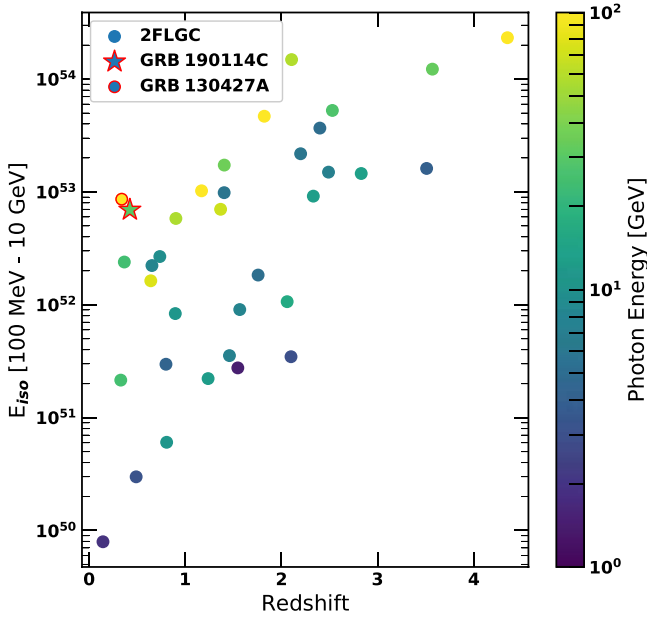


Figure 8. Scatter plot of E_{iso} (100 MeV–10 GeV) vs. redshift for various GRBs including GRB 190114C (star). Colors indicate the energy of the highest-energy photon for each GRB with an association probability $>90\%$.

cutoff or a smoothly broken power law (Granot et al. 2008, hereafter G08), due to $\gamma\gamma$ -annihilation occurs at much higher photon energies above the peak of the νF_ν spectrum where $\tau_{\gamma\gamma}(\Gamma_{\text{bulk}}, E > E_{\text{cut}}) > 1$. Such spectral cutoffs have now been observed in several GRBs, e.g., GRB 090926A (Ackermann et al. 2011), and GRBs 100724B and 160509A (Vianello et al. 2018); also see Tang et al. (2015) for additional sources. Under the assumption that these cutoffs indeed result from $\gamma\gamma$ -annihilation, they have been used to obtain a direct estimate of the bulk Lorentz factor of the emission region. When no spectral cutoff is observed, the highest-energy observed photon is often used to obtain a lower limit on Γ_{bulk} instead. In many cases, a simple one-zone estimate of $\tau_{\gamma\gamma}$ was employed, which makes the assumption that both the test photon, with energy E , and the annihilating photon, with energy $\gtrsim \Gamma_{\text{bulk}}^2 (m_e c^2)^2 / E(1+z)^2$, were produced in the same region of the flow (e.g., Lithwick & Sari 2001; Abdo et al. 2009b). Such models yield estimates of Γ_{bulk} that are typically larger by a factor ~ 2 than that obtained from more detailed models of $\tau_{\gamma\gamma}$. The latter either feature two distinct emission regions (a two-zone model; Zou et al. 2011) or account for the spatial, directional, and temporal dependence of the interacting photons (G08; Hascoët et al. 2012). Here we use the analytic model of G08, which assumes an expanding ultrarelativistic spherical thin shell and calculates $\tau_{\gamma\gamma}$ along the trajectory of each test photon that reaches the observer. The results of this model have been independently confirmed with numerical simulations (Gill & Granot 2018), which show that it yields an accurate estimate of Γ_{bulk} from observations of spectral cutoffs if the emission region remains optically thin to Thomson scattering due to the produced e^\pm pairs. In this case, the initial bulk Lorentz factor of the outflow $\Gamma_{\text{bulk},0}$ is estimated using

$$\Gamma_{\text{bulk},0} = 100 \left[\frac{396.9}{C_2(1+z)\Gamma_{\text{ph}}} \left(\frac{L_0}{10^{52} \text{ erg s}^{-1}} \right) \times \left(\frac{5.11 \text{ GeV}}{E_{\text{cut}}} \right)^{1+\Gamma_{\text{ph}}} \left(\frac{-\Gamma_{\text{ph}}}{2} \right)^{-5/3} \frac{33.4 \text{ ms}}{t_v} \right]^{1/(2-2\Gamma_{\text{ph}})} \quad (1)$$

Here, t_v is the variability timescale, Γ_{ph} is the photon index of the PL component, and $L_0 = 4\pi d_L^2(1+z)^{-\Gamma_{\text{ph}}-2}F_0$, where d_L is the luminosity distance of the burst, F_0 is the (unabsorbed) energy flux (νF_ν) obtained at 511 keV from the PL component of the spectrum. The parameter $C_2 \approx 1$ is constrained from observations of spectral cutoffs in other GRBs (Vianello et al. 2018). The estimate of the bulk Lorentz factor in Equation (1) should be compared with $\Gamma_{\text{bulk,max}} = (1+z)E_{\text{cut}}/m_e c^2$, which corresponds to the maximum bulk Lorentz factor for a given observed cutoff energy and for which the cutoff energy in the comoving frame is at the self-annihilation threshold, $E'_{\text{cut}} = (1+z)E_{\text{cut}}/\Gamma_{\text{bulk}} = m_e c^2$ (however, see, e.g., Gill & Granot 2018, where it was shown that the comoving cutoff energy can be lower than $m_e c^2$ due to Compton scattering by e^\pm pairs). The true bulk Lorentz factor is then the minimum of the two estimates.

In GRB 190114C, the additional PL component detected by the LAT exhibits a significant spectral cutoff at $E_{\text{cut}} \sim 140$ MeV (where $E_{\text{cut}} = E_{\text{pk}}/(2 + \Gamma_{\text{ph}})$) in the time period from $T_0 + 3.8$ s to $T_0 + 4.8$ s. Using the variability timescale in the GBM band of $t_v \sim 6$ ms, where we assume that the GBM and LAT emissions are cospatial, we obtain the bulk Lorentz factor $\Gamma_{\text{bulk},0} \sim 210$ from Equation (1), which is lower than $\Gamma_{\text{bulk,max}} \approx 400$ and is therefore adopted as the initial bulk Lorentz factor of the outflow.

5.5. Forward-shock Parameters

The timescale on which the forward shock sweeps up enough material to begin to decelerate and convert its internal energy into observable radiation depends on the density of the material into which it is propagating A , the total kinetic energy of the outflow ($E_{\text{iso}}/\eta \sim 1.8 \times 10^{54}$ erg, where $E_{\text{iso}} = 3.5 \times 10^{53}$ erg $\sim 10^{53.5}$ erg and $\eta = 0.2$ is the conversion efficiency of total shock energy into the observed gamma-ray emission), and its initial bulk Lorentz factor $\Gamma_{\text{bulk},0}$. Here, in a wind environment, we define a timescale t_γ on which the accumulated wind mass is $1/\Gamma_{\text{bulk},0}$ of the ejecta mass as

$$t_\gamma = \frac{E_{\text{iso}}(1+z)}{16\pi A m_p c^3 \eta \Gamma_{\text{bulk},0}^4} \sim 2 \text{ s } A_\star^{-1} \times \left(\frac{E_{\text{iso}}}{10^{53.5} \text{ ergs}} \right) \left(\frac{\eta}{0.2} \right)^{-1} \left(\frac{\Gamma_{\text{bulk},0}}{200} \right)^{-4}, \quad (2)$$

where $A = 3 \times 10^{35} A_\star \text{ cm}^{-1}$ with a mass-loss rate $10^{-5} M_\odot \text{ yr}^{-1}$ in the wind velocity of 10^3 km s^{-1} for $A_\star = 1$. If the reverse shock is Newtonian, or at least mildly relativistic (i.e., the thin-shell limit; Sari & Piran 1995; Zhang et al. 2003), t_γ is the deceleration time t_{dec} . In the thin-shell case, to obtain the observed temporal onset at $T_0 + \sim 10$ s, $A_\star = 0.2$ is needed. If the reverse shock is relativistic (thick-shell limit), one has $t_{\text{dec}} \sim t_{\text{GRB}} > t_\gamma$ (t_{GRB} is the burst duration), which approximately gives $A_\star > 0.2$.

Having constrained the location of the synchrotron break energies and the likely environment into which the blast wave is propagating, we can invert the equations governing the energies of these breaks to estimate the physical properties of the forward shock. These include the microphysical parameters describing the partition of energy within the shock, the total energy of the shock $E_K (=E_{\text{iso}}/\eta)$, and the circumstellar density normalization A_\star . The equations governing the location of ν_m ,

ν_c , and the flux at which the cooling break occurs, $F_\nu(\nu_c)$, in the case of only synchrotron radiation can be expressed as (Granot & Sari 2002)

$$\nu_c = 9.1 \times 10^{11} \epsilon_B^{-3/2} \left(\frac{A_*}{0.2}\right)^{-2} \left(\frac{t}{90 \text{ s}}\right)^{1/2} \times \left(\frac{E_{\text{iso}}}{10^{53.5} \text{ ergs}}\right)^{1/2} \left(\frac{\eta}{0.2}\right)^{-1/2} \text{ Hz} \quad (3)$$

$$F_\nu(\nu_c) = 4.2 \times 10^8 \epsilon_e^{p-1} \epsilon_B^{p-1/2} \left(\frac{A_*}{0.2}\right)^p \times \left(\frac{t}{90 \text{ s}}\right)^{1/2-p} \left(\frac{E_{\text{iso}}}{10^{53.5} \text{ ergs}}\right)^{1/2} \left(\frac{\eta}{0.2}\right)^{-1/2} \text{ mJy} \quad (4)$$

$$\nu_m = 2.1 \times 10^{19} \epsilon_e^2 \epsilon_B^{1/2} \left(\frac{t}{90 \text{ s}}\right)^{-3/2} \times \left(\frac{E_{\text{iso}}}{10^{53.5} \text{ ergs}}\right)^{1/2} \left(\frac{\eta}{0.2}\right)^{-1/2} \text{ Hz.} \quad (5)$$

Combining the observed constraints of $\nu_c \sim 4 \text{ keV}$ or $9.7 \times 10^{17} \text{ Hz}$ and $F_\nu(\nu_c) \sim 5 \text{ mJy}$ at $T_0 + 90 \text{ s}$, and the estimated $A_* = 0.2$ assuming the thin-shell case, we estimate the fraction of energy in the magnetic fields ϵ_B to be 9.9×10^{-5} , the fraction of energy in the accelerated electrons ϵ_e to be 4.0×10^{-2} , and ν_m to be $\sim 4 \times 10^{14} \text{ Hz}$ ($\sim 2 \text{ eV}$), which approximately corresponds to the white band of the UVOT. Note that these estimates are derived without taking into account the effect of SSC emission. These parameters allow us to calculate the expected evolution of the synchrotron cooling frequency with time, which is shown in Figure 6, roughly matching the temporal evolution of the observed spectral break in the broadband data. In the thick-shell case with $A_* > 0.2$, if we use fiducial values as $A_* = 1\text{--}10$, we obtain $\epsilon_e = (4.2\text{--}4.5) \times 10^{-2}$, $\epsilon_B = (120\text{--}5) \times 10^{-7}$, and $\nu_m = (1.3\text{--}0.3) \times 10^{14} \text{ Hz}$, respectively.

5.6. Maximum Synchrotron Energy

The analysis of our broadband data has shown that the observed spectral and temporal characteristics of the early afterglow emission from GRB 190114C are in good agreement with predictions from synchrotron radiation due to electrons accelerated in an external shock. The existence of late-time high-energy photons detected by the LAT, though, poses a direct challenge to this interpretation. The electrons in this scenario are accelerated via the Fermi process, in which they gain energy as they traverse from one side of the shock front to the other. The maximum photon energy that can be produced by such electrons is set by equating the electron energy-loss timescale due to synchrotron radiation to the Larmor timescale for an electron to execute a single gyration (i.e., the shortest route an electron can take across the shock front) and is considered to be roughly $\nu_{\text{max,rest}} = 2^{3/2} 27 m_e c^2 / (16 \pi h \alpha_f) \sim 100 \text{ MeV}$ in the comoving frame, where h and α_f are the Planck and the fine-structure constants, respectively, independent of the magnetic field strength (Ackermann et al. 2014). In the observer frame, this limit is boosted by the bulk Lorentz factor and becomes $\Gamma_{\text{bulk}} \nu_{\text{max,rest}} / (1 + z)$.

We estimated the bulk Lorentz factor at the transition from the coasting to deceleration phases in the previous section. After this transition, the outflow begins to transfer its internal

energy to the circumstellar medium and the Γ_{bulk} of the forward shock decreases with distance from the central engine as $\Gamma_{\text{bulk}} \propto R^{-(3-k)/2}$ (Sari 1997). As a result, the maximum synchrotron energy decreases with time as the external shock expands. Using the formalism described in the supplementary material in Ackermann et al. (2014), we calculate the evolution of $\Gamma_{\text{bulk}}(t)$ and use it to estimate the evolution of the maximum synchrotron energy $\nu_{\text{max}}(t)$. Figure 9 shows the expected maximum synchrotron energy as a function of time along with the observed LAT photons above 1 GeV. Several high-energy photons exceed the expected maximum synchrotron energy at the time of their arrival, including an 18.9 GeV photon arriving approximately 8900 s after T_0 , almost an order of magnitude higher in energy than our estimate for ν_{max} at this time. Given the arrival direction of this photon, we estimate its association probability with GRB 190114C to be approximately 99.8%, providing one of the most stringent violations of ν_{max} observed by the LAT. It is clear that these high-energy detections either necessitate an additional emission mechanism at higher energies or a revision of the fundamental assumptions used to calculate ν_{max} .

The SSC and IC mechanisms could both produce significant emission above ν_{max} . Synchrotron emission from shock-accelerated electrons should be accompanied by SSC emission, in which the newly created gamma-rays gain energy by scattering off energetic electrons before they escape the emitting region. The result is a spectral component that mirrors the primary synchrotron spectrum, but one that is boosted in energy. In particular, as discussed in Section 5.5, for both thin- and thick-shell cases, the observed afterglow parameters indicate a Compton Y -parameter of $\epsilon_e/\epsilon_B \sim Y \gg 1$, in which contributions from the effect of inverse-Compton scattering (Panaitescu & Kumar 2000; Sari & Esin 2001) would be expected. For a bulk Lorentz factor > 100 , the peak of the SSC component is expected to be at TeV energies, although as the blast wave decelerates, this peak is expected to evolve into the LAT energy range. The emergence of such a component should result in a hardening of the LAT spectrum and/or be apparent as deviations in the observed light curve, neither of which has ever been observed in any LAT-detected GRB during their smoothly decaying extended emission.

One possible solution would require an SSC component to remain subdominant to the forward-shock synchrotron emission throughout the evolution of the LAT-observed emission. Such a scenario could occur when the local energy density of the synchrotron photons is lower than the energy density of the local magnetic field (e.g., $Y < 1$). Furthermore a detailed numerical simulation of the SSC emission considering the evolution of the external-shock emission by Fukushima et al. (2017) showed that the expected SSC emission could remain weaker than the primary synchrotron emission even if the Compton Y -parameter were large. This effect could prevent a significant contribution to the LAT light curve and spectra, while still producing high-energy photons that exceed the maximum synchrotron limit.

Alternatively, a strong Klein–Nishina (KN) effect could also significantly constrain SSC emission at high energies. This occurs when the energy of the seed photon in the rest frame of the electrons exceeds $m_e c^2$, i.e. $\gamma_e E'_{\text{seed}} > m_e c^2$, where γ_e and E'_{seed} are the electron Lorentz factor and the energy of the seed photon in the comoving frame, respectively, beyond which SSC emission becomes increasingly inefficient. This results in

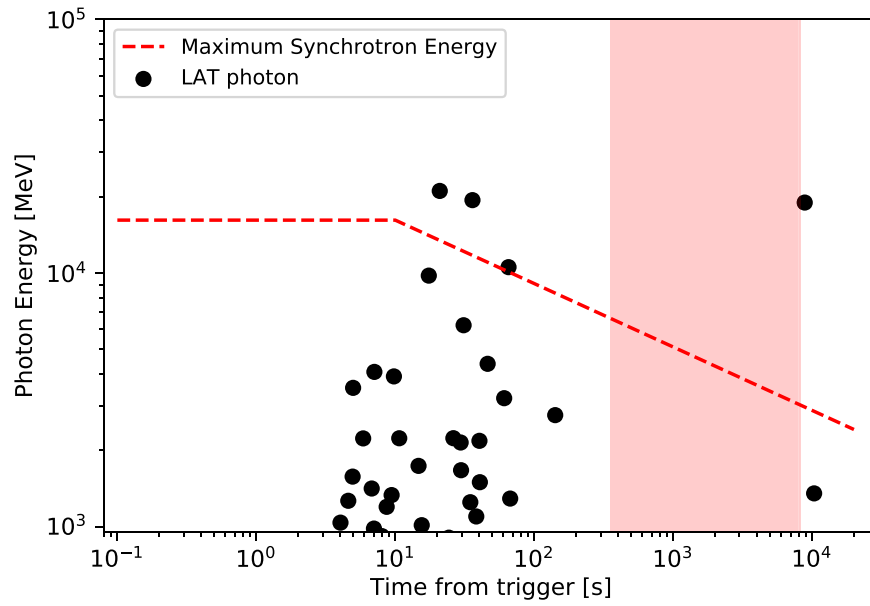


Figure 9. Photon energy vs. time. Photons with energies >1 GeV and $>90\%$ probability of association with GRB 190114C are indicated with black dots. Dashed line represents the maximum synchrotron limit for the adiabatic jet with the wind case. Here we use the estimated bulk Lorentz factor $\Gamma_{\text{bulk}} = 213$, $E_{\text{iso}} = 3.5 \times 10^{53}$ erg, and the efficiency of the total shock energy in converting into the gamma-ray emission $\eta = 0.2$. The deceleration time for the wind case is calculated with $A_* = 0.2$. The red shaded region represents a non-observable period for GRB 190114C due to Earth occultation.

the suppression of high-energy photons, yielding a cutoff in the SSC spectrum. We can estimate the energy at which this cutoff should manifest by reconsidering the forward-shock parameter discussed in Section 5.5 and taking into account SSC and KN effects. Following Granot & Sari (2002), both ν_c from Equation (3) and $F_\nu(\nu_c)$ from Equation (4) are multiplied by the factors of $(1 + Y)^{-2}$ and $(1 + Y)^{p-1}$. If we consider a case with no KN effect, we find that there are no self-consistent solutions for ϵ_e and ϵ_B ⁹⁵, emphasizing the need to account for the KN effect when considering the effect of SSC emission. If we assume that the observed ν_c is in the KN regime (e.g., the observed synchrotron spectrum is unaffected by significant IC losses), then $Y \ll 1$. Such a scenario would require that the Lorentz factor above which electrons are cooled efficiently, γ_c , to already be above the Lorentz factor $\hat{\gamma}_c$ at which photons cannot be efficiently upscattered by electrons because they are above the KN limit, where $\hat{\gamma}_c$ is given by $m_e c^2 \Gamma_{\text{bulk}} / h\nu_{\text{syn}}(\gamma_c)$ (Nakar et al. 2009). We estimate Γ_{bulk} to be ~ 100 at $T_0 + 90$ s and $h\nu_{\text{syn}}(\gamma_c)$ to be ~ 4 keV, which yields $\gamma_c > 10^4$. When $\gamma_m < \gamma_c$ and $\hat{\gamma}_c < \gamma_c$, high-energy SSC photons are not expected to be strongly damped above energies of $> \Gamma_{\text{bulk}} \gamma_c m_e c^2 \sim 0.5$ TeV. Therefore, the LAT-detected photons are not expected to be significantly affected by KN suppression, although the VHE spectrum observed by MAGIC could exhibit curvature, due to this effect.

Revisions to fundamental assumptions about collisionless shock physics have also been put forth to explain apparent violations of the maximum synchrotron energy. Kumar et al. (2012) showed that the upper limit for synchrotron emission could be raised substantially by relaxing the assumption of a uniform magnetic field in the emitting region. The authors argue that a magnetic field that decays ahead of the shock front could raise ν_{max} substantially, but only if the magnetic field

gradient varied on a length scale smaller than the distance traveled by the most energetic electrons. This solution could result in a value of ν_{max} that is orders of magnitude above the canonical estimate and help explain many of the LAT-detected bursts with late-time high-energy photons.

Finally, synchrotron emission above our estimated ν_{max} could still be possible through contributions from a high-energy hadronic component (Razzaque 2010), or if the electrons were accelerated through a process other than shock acceleration, such as magnetic reconnection, which could act on timescales faster than the Fermi process (Thompson 1994; Spruit et al. 2001; Lyutikov et al. 2003; Giannios & Spruit 2007; Lyubarsky 2010; Kagan et al. 2015). The latter scenario can occur in an outflow with a random magnetic field, for example through relativistic turbulence, such that magnetic field dissipation and jet acceleration can occur on a timescale much shorter than the diffusion time (Lyutikov et al. 2003; Kumar & Narayan 2009; Lazar et al. 2009; Granot 2016).

6. Conclusions

The joint observations of GRB 190114C by *Fermi* and *Swift* provide a rich data set with which to examine the complex relationship between prompt and afterglow-dominated emission often observed in LAT-detected GRBs. GRB 190114C is among the most luminous GRBs detected by GBM and LAT below $z < 1$, and exceeded only by GRB 130427A in isotropic-equivalent energy above 100 MeV. Our analysis of the prompt emission shows evidence for both thermal (BB) and nonthermal (CPL or Band) spectral components commonly seen in GRB spectra, in addition to the emergence of an additional PL component extending to high energies that explains the delayed onset of the LAT-detected emission. This additional PL component shows strong evidence for spectral attenuation above 40 MeV in the first few seconds of the burst, before transitioning to a harder spectrum that is consistent with the afterglow emission observed by the XRT and BAT at later times. We attribute the spectral attenuation of this component

⁹⁵ When including the effects of SSC, one finds self-consistent solutions for ϵ_e and ϵ_B only when adopting $A_* \sim 10^{-3}$: $\epsilon_e = 1.9 \times 10^{-1}$, $\epsilon_B = 4.5 \times 10^{-3}$, and $Y = 4.9$ for $A_* = 1.3 \times 10^{-3}$. However, such a very low A_* is not likely for this GRB as discussed in Section 5.5.

to opacity to electron–positron pair production and its evolution to the expansion of the emitting region. We find that the presence of this extra PL component is also evident as a low-energy excess in the GBM data throughout its evolution, disfavoring SSC or external IC emission from the CPL or Band components as the origin of the extra PL component.

The long-lived afterglow component is clearly identifiable in the GBM light curve as a slowly fading emission component over which the rest of the prompt emission is superimposed. This allows us to constrain the transitions from internal-shock-to external-shock-dominated emission in both the GBM and the LAT. The subsequent broadband *Fermi* and *Swift* data allow us to model the temporal and spectral evolution of the afterglow emission, which is in good agreement with predictions from synchrotron emission, due to a forward shock propagating into a wind-like circumstellar environment. We use the onset of the afterglow component to constrain the deceleration radius and initial Lorentz factor of the forward shock in order to estimate the maximum photon energy attainable through the synchrotron process for shock-accelerated electrons. We find that even in the LAT energy range, there exist high-energy photons that are in tension with the theoretical maximum photon energy that can be achieved through shock-accelerated synchrotron emission. The detection of VHE emission above 300 GeV by MAGIC concurrent with our observations further compounds this issue and challenges our understanding of the origin of the highest-energy photons detected from GRBs. The SSC and IC mechanisms could both produce significant emission above ν_{max} , although as was the case with GRB 130427A, a single power law from X-ray to the LAT energy range is capable of adequately fitting the broadband data, and no significant deviations from a simple power-law decay are evident in the late-time LAT light curve. We conclude that the detection of high-energy photons from GRB 190114C necessitates either an additional emission mechanism in the LAT energy range that is difficult to separate from the synchrotron component, or revisions to the fundamental assumptions used in estimating the maximum photon energy attainable through the synchrotron process. The detection of VHE emission from GRBs will be crucial for distinguishing between these two possibilities.

The *Fermi* LAT Collaboration acknowledges generous ongoing support from a number of agencies and institutes that have supported both the development and the operation of the LAT as well as scientific data analysis. These include the National Aeronautics and Space Administration and the Department of Energy in the United States, the Commissariat à l’Energie Atomique, and the Centre National de la Recherche Scientifique/Institut National de Physique Nucléaire et de Physique des Particules in France, the Agenzia Spaziale Italiana and the Istituto Nazionale di Fisica Nucleare in Italy, the Ministry of Education, Culture, Sports, Science and Technology (MEXT), High Energy Accelerator Research Organization (KEK), and Japan Aerospace Exploration Agency (JAXA) in Japan, and the K. A. Wallenberg Foundation, the Swedish Research Council, and the Swedish National Space Board in Sweden. Additional support for science analysis during the operations phase is gratefully acknowledged from the Istituto Nazionale di Astrofisica in Italy and the Centre National d’Études Spatiales in France.

The USRA coauthors gratefully acknowledge NASA funding through contract NNM13AA43C. The UAH coauthors
























gratefully acknowledge NASA funding from cooperative agreement NNM11AA01A and that this work was made possible in part by a grant of high performance computing resources and technical support from the Alabama Supercomputer Authority. E.B. is supported by an appointment to the NASA Postdoctoral Program at the Goddard Space Flight Center, and C.M. is supported by an appointment to the NASA Postdoctoral Program at the Marshall Space Flight Center, administered by Universities Space Research Association under contract with NASA. C.M.H. and C.A.W.-H. gratefully acknowledge NASA funding through the Fermi GBM project. R.G. and J.G. are supported by the Israel Science Foundation under grant No. 719/14. Support for the German contribution to GBM was provided by the Bundesministerium für Bildung und Forschung (BMBF) via the Deutsches Zentrum für Luft und Raumfahrt (DLR) under contract number 50 QV 0301.

This work was performed in part under DOE Contract DE-AC02-76SF00515 and support by JSPS KAKENHI grant No. JP17H06362, the JSPS Leading Initiative for Excellent Young Researchers program, and Sakigake 2018 Project of Kanazawa University (M.A.).

This work made use of data supplied by the UK Swift Science Data Centre at the University of Leicester.

Software: XSPEC (v12.9.1u; Arnaud 1996), HEASoft (v6.25; <http://heasarc.nasa.gov/lheasoft/>), Fermi ScienceTools (v11r5p3; <http://fermi.gsfc.nasa.gov/ssc/>).

ORCID iDs

M. Ajello  <https://orcid.org/0000-0002-6584-1703>
M. Arimoto  <https://orcid.org/0000-0003-1250-7872>
M. Axelsson  <https://orcid.org/0000-0003-4378-8785>
F. D’Ammando  <https://orcid.org/0000-0001-7618-7527>
A. Franckowiak  <https://orcid.org/0000-0002-5605-2219>
J. Granot  <https://orcid.org/0000-0001-8530-8941>
M. Kuss  <https://orcid.org/0000-0003-1212-9998>
S. Larsson  <https://orcid.org/0000-0003-0716-107X>
F. Longo  <https://orcid.org/0000-0003-2501-2270>
S. Maldera  <https://orcid.org/0000-0002-0698-4421>
T. Mizuno  <https://orcid.org/0000-0001-7263-0296>
A. Morselli  <https://orcid.org/0000-0002-7704-9553>
I. V. Moskalenko  <https://orcid.org/0000-0001-6141-458X>
V. S. Paliya  <https://orcid.org/0000-0001-7774-5308>
J. L. Racusin  <https://orcid.org/0000-0002-4744-9898>
D. F. Torres  <https://orcid.org/0000-0002-1522-9065>
E. Troja  <https://orcid.org/0000-0002-1869-7817>
M. Hui  <https://orcid.org/0000-0001-9067-7477>
Christian Malacaria  <https://orcid.org/0000-0002-0380-0041>
O. J. Roberts  <https://orcid.org/0000-0002-7150-9061>
S. B. Cenko  <https://orcid.org/0000-0003-1673-970X>
N. Klingler  <https://orcid.org/0000-0002-7465-0941>
G. Tagliaferri  <https://orcid.org/0000-0003-0121-0723>

References

- Abdo, A. A., Ackermann, M., Ajello, M., et al. 2009a, *ApJL*, 706, L138
- Abdo, A. A., Ackermann, M., Ajello, M., et al. 2010, *ApJ*, 712, 558
- Abdo, A. A., Ackermann, M., Arimoto, M., et al. 2009b, *Sci*, 323, 1688
- Abdo, A. A., Ackermann, M., Asano, K., et al. 2009c, *ApJ*, 707, 580
- Ackermann, M., Ajello, M., Asano, K., et al. 2011, *ApJ*, 729, 114
- Ackermann, M., Ajello, M., Asano, K., et al. 2013a, *ApJS*, 209, 11
- Ackermann, M., Ajello, M., Asano, K., et al. 2013b, *ApJ*, 763, 71
- Ackermann, M., Ajello, M., Asano, K., et al. 2014, *Sci*, 343, 42
- Ackermann, M., Asano, K., Atwood, W. B., et al. 2010, *ApJ*, 716, 1178
- Ajello, M., Arimoto, M., Axelsson, M., et al. 2019, *ApJ*, 878, 52

- Ajello, M., Baldini, L., Barbiellini, G., et al. 2018, *ApJ*, **863**, 138
- Alexander, K. D., Laskar, T., Berger, E., Mundell, C. G., & Margutti, R. 2019, *GCN*, **23726**, 1
- Arimoto, M., Asano, K., Ohno, M., et al. 2016, *ApJ*, **833**, 139
- Arnaud, K., Smith, R., & Siemiginowska, A. 2011, *Handbook of X-ray Astronomy* (Cambridge: Cambridge Univ. Press)
- Arnaud, K. A. 1996, in *ASP Conf. Ser. 101, Astronomical Data Analysis Software and Systems V*, ed. G. H. Jacoby & J. Barnes (San Francisco, CA: ASP), **17**
- Atwood, W. B., Abdo, A. A., Ackermann, M., et al. 2009, *ApJ*, **697**, 1071
- Axelsson, M., Baldini, L., Barbiellini, G., et al. 2012, *ApJL*, **757**, L31
- Band, D., Matteson, J., Ford, L., et al. 1993, *ApJ*, **413**, 281
- Baring, M. G., & Harding, A. K. 1997, *ApJ*, **491**, 663
- Barthelmy, S. D., Barbier, L. M., Cummings, J. R., et al. 2005, *SSRv*, **120**, 143
- Bednarz, J., & Ostrowski, M. 1998, *PhRvL*, **80**, 3911
- Beniamini, P., & Piran, T. 2013, *ApJ*, **769**, 69
- Bhat, P. N. 2013, arXiv:1307.7618
- Bhat, P. N., Meegan, C. A., von Kienlin, A., et al. 2016, *ApJS*, **223**, 28
- Burgess, J. M., Preece, R. D., Baring, M. G., et al. 2011, *ApJ*, **741**, 24
- Burrows, D. N., Hill, J. E., Nousek, J. A., et al. 2005, *SSRv*, **120**, 165
- Cenko, S. B., Frail, D. A., Harrison, F. A., et al. 2011, *ApJ*, **732**, 29
- Cherukuri, S. V., Jaiswal, V., Misra, K., et al. 2019, *GCN*, **23762**, 1
- Curran, P. A., Evans, P. A., de Pasquale, M., Page, M. J., & van der Horst, A. J. 2010, *ApJL*, **716**, L135
- de Ugarte Postigo, A., Kann, D. A., Thoene, C. C., & Izzo, L. 2019, *GCN*, **23692**, 1
- Evans, P. A., Beardmore, A. P., Page, K. L., et al. 2007, *A&A*, **469**, 379
- Evans, P. A., Beardmore, A. P., Page, K. L., et al. 2009, *MNRAS*, **397**, 1177
- Fan, Y.-Z., & Piran, T. 2008, *FrPhC*, **3**, 306
- Fan, Y.-Z., Tam, P. H. T., Zhang, F.-W., et al. 2013, *ApJ*, **776**, 95
- Freedman, D. L., & Waxman, E. 2001, *ApJ*, **547**, 922
- Fryer, C. L., Rockefeller, G., & Young, P. A. 2006, *ApJ*, **647**, 1269
- Fukushima, T., To, S., Asano, K., & Fujita, Y. 2017, *ApJ*, **844**, 92
- Gehrels, N., Chincarini, G., Giommi, P., et al. 2005, *ApJ*, **621**, 558
- Gehrels, N., Ramirez-Ruiz, E., & Fox, D. B. 2009, *ARA&A*, **47**, 567
- Giannios, D., & Spruit, H. C. 2007, *A&A*, **469**, 1
- Gill, R., & Granot, J. 2018, *MNRAS*, **475**, L1
- Giroletti, M., Orienti, M., Ghirlanda, G., et al. 2019, *GCN*, **24766**, 1
- Goodman, J. 1986, *ApJL*, **308**, L47
- Granot, J. 2016, *ApJL*, **816**, L20
- Granot, J., Cohen-Tanugi, J., & Silva, E. d. C. e. 2008, *ApJ*, **677**, 92
- Granot, J., Panaitescu, A., Kumar, P., & Woosley, S. E. 2002, *ApJL*, **570**, L61
- Granot, J., & Sari, R. 2002, *ApJ*, **568**, 820
- Gropp, J. D., Kennea, J. A., Klingler, N. J., et al. 2019, *GCN*, **23688**, 1
- Guiriec, S., Connaughton, V., Briggs, M. S., et al. 2011, *ApJL*, **727**, L33
- Guiriec, S., Daigne, F., Hascoët, R., et al. 2013, *ApJ*, **770**, 32
- Hamburg, R., Veres, P., Meegan, C., et al. 2019, *GCN*, **23707**, 1
- Hascoët, R., Daigne, F., Mochkovitch, R., & Vennin, V. 2012, *MNRAS*, **421**, 525
- Kagan, D., Sironi, L., Cerutti, B., & Giannios, D. 2015, *SSRv*, **191**, 545
- Kobayashi, S. 2000, *ApJ*, **545**, 807
- Kocevski, D., Omodei, N., Axelsson, M., et al. 2019, *GCN*, **23709**, 1
- Kouveliotou, C., Granot, J., Racusin, J. L., et al. 2013, *ApJL*, **779**, L1
- Kumar, P., Hernández, R. A., Bošnjak, Ž., & Barniol Duran, R. 2012, *MNRAS*, **427**, L40
- Kumar, P., & Narayan, R. 2009, *MNRAS*, **395**, 472
- Laskar, T., Alexander, K. D., Gill, R., et al. 2019, *ApJL*, **878**, L26
- Lazar, A., Nakar, E., & Piran, T. 2009, *ApJL*, **695**, L10
- Lien, A., Sakamoto, T., Barthelmy, S. D., et al. 2016, *ApJ*, **829**, 7
- Lithwick, Y., & Sari, R. 2001, *ApJ*, **555**, 540
- Lyubarsky, Y. 2010, *ApJL*, **725**, L234
- Lytikov, M., Pariev, V. I., & Blandford, R. D. 2003, *ApJ*, **597**, 998
- Meegan, C., Lichti, G., Bhat, P. N., et al. 2009, *ApJ*, **702**, 791
- Meszaros, P., & Rees, M. J. 1993, *ApJL*, **418**, L59
- Minaev, P., & Pozanenko, A. 2019, *GCN*, **23714**, 1
- Mirzoyan, R. 2019, *ATel*, **12390**, 1
- Mirzoyan, R., Noda, K., Moretti, E., et al. 2019, *GCN*, **23701**, 1
- Nakar, E., Ando, S., & Sari, R. 2009, *ApJ*, **703**, 675
- Osborne, J. P., Beardmore, A. P., Evans, P. A., & Goad, M. R. 2019, *GCN*, **23704**, 1
- Paczynski, B. 1986, *ApJL*, **308**, L43
- Panaitescu, A., & Kumar, P. 2000, *ApJ*, **543**, 66
- Pelassa, V., Preece, R., Piron, F., et al. 2010, arXiv:1002.2617
- Perley, D. A., Cenko, S. B., Corsi, A., et al. 2014, *ApJ*, **781**, 37
- Piran, T. 1999, *PhR*, **314**, 575
- Piran, T. 2004, *RvMP*, **76**, 1143
- Ravasio, M. E., Oganessian, G., Salafia, O. S., et al. 2019, *A&A*, **626**, A12
- Razzaque, S. 2010, *ApJL*, **724**, L109
- Rees, M. J., & Meszaros, P. 1992, *MNRAS*, **258**, 41
- Rees, M. J., & Meszaros, P. 1994, *ApJL*, **430**, L93
- Roming, P. W. A., Kennedy, T. E., Mason, K. O., et al. 2005, *SSRv*, **120**, 95
- Sari, R. 1997, *ApJL*, **489**, L37
- Sari, R., & Esin, A. A. 2001, *ApJ*, **548**, 787
- Sari, R., & Mészáros, P. 2000, *ApJL*, **535**, L33
- Sari, R., & Piran, T. 1995, *ApJL*, **455**, L143
- Sari, R., Piran, T., & Narayan, R. 1998, *ApJL*, **497**, L17
- Schulze, S., Anderson, G., Moin, A., et al. 2019, *GCN*, **23745**, 1
- Schulze, S., Klose, S., Björnsson, G., et al. 2011, *A&A*, **526**, A23
- Schwarz, G. 1978, *Ann. Statist.*, **6**, 461
- Selsing, J., Fynbo, J. P. U., Heintz, K. E., & Watson, D. 2019, *GCN*, **23695**, 1
- Siegel, M. H., & Gropp, J. D. 2019, *GCN*, **23725**, 1
- Spruit, H. C., Daigne, F., & Drenkhahn, G. 2001, *A&A*, **369**, 694
- Tam, P.-H. T., Tang, Q.-W., Hou, S.-J., Liu, R.-Y., & Wang, X.-Y. 2013, *ApJL*, **771**, L13
- Tang, Q.-W., Peng, F.-K., Wang, X.-Y., & Tam, P.-H. T. 2015, *ApJ*, **806**, 194
- Thompson, C. 1994, *MNRAS*, **270**, 480
- Tremou, L., Heywood, I., Vergani, S. D., et al. 2019, *GCN*, **23760**, 1
- Ursi, A., Tavani, M., Marisaldi, M., et al. 2019, *GCN*, **23712**, 1
- van Eerten, H. J., & Wijers, R. A. M. J. 2009, *MNRAS*, **394**, 2164
- Vianello, G., Gill, R., Granot, J., et al. 2018, *ApJ*, **864**, 163
- Wang, X.-G., Zhang, B., Liang, E.-W., et al. 2015, *ApJS*, **219**, 9
- Wang, X.-Y., Liu, R.-Y., & Lemoine, M. 2013, *ApJL*, **771**, L33
- Waxman, E. 1997, *ApJL*, **485**, L5
- Wei, D.-M., & Fan, Y.-Z. 2007, *ChJAA*, **7**, 509
- Willingale, R., Starling, R. L. C., Beardmore, A. P., Tanvir, N. R., & O'Brien, P. T. 2013, *MNRAS*, **431**, 394
- Woosley, S. E. 1993, *ApJ*, **405**, 273
- Xiao, S., Li, C. K., Li, X. B., et al. 2019, *GCN*, **23716**, 1
- Zhang, B., Kobayashi, S., & Mészáros, P. 2003, *ApJ*, **595**, 950
- Zou, Y.-C., Fan, Y.-Z., & Piran, T. 2011, *ApJL*, **726**, L2

A search for *Fermi* bursts associated with supernovae and their frequency of occurrence

M. Kovacevic^{1,2}, L. Izzo^{1,3}, Y. Wang¹, M. Muccino^{1,3}, M. Della Valle^{3,4}, L. Amati⁵, C. Barbarino^{1,4}, M. Enderli^{1,2}, G. B. Pisani^{1,2}, and L. Li^{6,7,8}

¹ Dip. di Fisica and ICRA, Sapienza Università di Roma, Piazzale Aldo Moro 5, 00185 Rome, Italy
 e-mail: [milosh.kovacevic; luca.izzo]@gmail.com, wangyu@me.com

² Université de Nice Sophia Antipolis, Cedex 2, Grand Château Parc Valrose, Nice, France

³ ICRA-Net-Pescara, Piazza della Repubblica 10, 65122 Pescara, Italy

⁴ INAF–Napoli, Osservatorio Astronomico di Capodimonte, Salita Moiariello 16, 80131 Napoli, Italy

⁵ INAF, Istituto di Astrofisica Spaziale e Fisica Cosmica, Bologna, via Gobetti 101, 40129 Bologna, Italy

⁶ Department of Physics, KTH Royal Institute of Technology, AlbaNova University Center, 106 91 Stockholm, Sweden

⁷ The Oskar Klein Centre for Cosmoparticle Physics, AlbaNova, 106 91 Stockholm, Sweden

⁸ Department of Physics, Stockholm University, AlbaNova, 106 91 Stockholm, Sweden

Received 29 July 2014 / Accepted 25 August 2014

ABSTRACT

Context. Observations suggest that most long duration gamma-ray bursts (GRBs) are connected with broad-line supernovae Ib/c, (SNe-Ibc). The presence of GRB-SNe is revealed by rebrightenings emerging from the optical GRB afterglow 10–15 days, in the rest-frame of the source, after the prompt GRB emission.

Aims. *Fermi*/GBM has a field of view (FoV) about 6.5 times larger than the FoV of *Swift*, therefore we expect that a number of GRB-SN connections have been missed because of lack of optical and X-ray instruments on board of *Fermi*, which are essential for revealing SNe associated with GRBs. This has motivated our search in the *Fermi* catalog for possible GRB-SN events.

Methods. The search for possible GRB-SN associations follows two requirements: (1) SNe should fall inside the *Fermi*/GBM error box of the considered long GRB, and (2) this GRB should occur within 20 days before the SN event.

Results. We have found five cases within $z < 0.2$ fulfilling the above reported requirements. One of them, GRB 130702A-SN 2013dx, was already known to have a GRB-SN association. We have analyzed the remaining four cases and we have concluded that three of them are, very likely, just random coincidences due to the *Fermi*/GBM large error box associated with each GRB detection. We found one GRB possibly associated with a SN 1998bw-like source, GRB 120121B/SN 2012ba.

Conclusions. The very low redshift of GRB 120121B/SN 2012ba ($z = 0.017$) implies a low isotropic energy of this burst ($E_{\text{iso}} = 1.39 \times 10^{48}$ erg). We then compute the rate of *Fermi* low-luminosity GRBs connected with SNe to be $\rho_{0,b} \leq 770 \text{ Gpc}^{-3} \text{ yr}^{-1}$. We estimate that *Fermi*/GBM could detect 1–4 GRBs-SNe within $z \leq 0.2$ in the next 4 years.

Key words. gamma-ray burst: general – supernovae: general

1. Introduction

Gamma-ray bursts (GRBs) are the most powerful stellar explosions in the universe (see Piran 2005; Gehrels & Mészáros 2012; Zhang 2014, for a review), with a total isotropic energy release of $E_{\text{iso}} = 10^{48-54}$ erg. Their origin is associated with the final collapse of very massive stars or with the merging of two compact objects. This first taxonomy was inferred from the existence of two observed classes for GRBs, based on their T_{90} duration (Klebesadel et al. 1982; Dezalay et al. 1992; Kouveliotou et al. 1993; Tavani 1998): GRBs with $T_{90} < 2$ s are named short GRBs; otherwise they are named long GRBs. All GRBs associated with supernovae (SNe) have been confirmed to be long bursts, although the opposite might not be true (Della Valle 2006; Fynbo et al. 2006; Gal-Yam et al. 2006). Observations carried out in the last decade suggest that long GRBs are associated with SNe Ib/c, which are believed to originate from the collapse of single very massive stars (Heger et al. 2003) or from moderate mass Wolf-Rayet stars in interacting binaries (Smartt 2009). To date, 35 GRB-SN associations have been confirmed on spectroscopic and/or photometric grounds (see Table 1). The

SN lightcurve peaks at 10–15 days after the GRB trigger (in the source rest-frame) powered by the radioactive decay of ^{56}Ni , and whose half-life time is about 6 days (Arnett 1996). Recently, it was proposed that GRB-SNe have the potential to be considered also as standardizable candles (Cano et al. 2014).

With the launch of satellites dedicated to GRBs studies, such as the *Swift* mission (Gehrels et al. 2009) and the *Fermi* spacecraft (Meegan et al. 2009), we have taken a step towards the understanding of GRB emission in the energy range between 0.3 keV and ~ 10 MeV. On the other hand, the Burst Alert Telescope (BAT, Barthelmy et al. 2005) on board *Swift*, is able to observe only a fraction of the sky that is 6.5 times smaller than that covered by the *Fermi* Gamma-ray Burst Monitor (GBM) detectors (Meegan et al. 2009). This implies that there could be long bursts, possibly connected with SNe, which have been detected by *Fermi*/GBM without soft X-rays and optical follow up, which are essential in order to reveal the presence of a SN in the GRB afterglow (Mangano et al. 2007). We can make a first order estimate of the expected number of *Fermi* long bursts connected with SNe as follows. If we restrict, for reasons of completeness, our analysis to GRB-SNe within $z \leq 0.2$, we have that *Swift*/BAT

Table 1. The sample of the 35 confirmed GRB-SN connections updated to 31 May 2014.

GRB	E_{iso} (erg)	Discovered by	z	SN identification	SN name	Refs.
970228	1.86×10^{52}	BATSE/SAX	0.695	bump		(Reichart 1997)
980326	5.60×10^{51}	BATSE/SAX	1(?)	bump		(Bloom et al. 1999)
980425	6.38×10^{47}	BATSE	0.0085	spec.	SN1998bw	(Galama et al. 1998)
990712	7.80×10^{51}	SAX	0.434	bump		(Frontera et al. 2009; Zeh et al. 2004)
991208	2.59×10^{53}	SAX	0.706	bump		(Frontera et al. 2009; Zeh et al. 2004)
000911	7.80×10^{53}	Konus-WIND	1.058	bump		(Lazzati et al. 2001; Hurley et al. 2000)
010921	1.10×10^{52}	HETE	0.45	bump		(Zeh et al. 2004)
011121	9.90×10^{52}	Ulysses	0.36	bump	SN 2001ke	(Bloom et al. 2002; Hurley et al. 2001; Greiner et al. 2003)
020305	$0.7\text{--}4.6 \times 10^{51}$	Ulysses	0.2-0.5	bump		(Gorosabel et al. 2005; Hurley et al. 2002b)
020405	1.28×10^{53}	Ulysses	0.695	bump		(Masetti et al. 2003; Hurley et al. 2002a)
020410	2.20×10^{52}	Konus-WIND	~ 0.5	bump		(Nicastrro et al. 2004; Levan et al. 2005)
021211	1.30×10^{52}	HETE	1.006	spec.	SN 2002lt	(Della Valle et al. 2003; Vreeswijk et al. 2003; Crew et al. 2002)
030329	1.70×10^{52}	Konus-WIND	0.168	spec.	SN 2003dh	(Golenetskii et al. 2003; Kawabata et al. 2003; Stanek et al. 2003)
030723	$<1.60 \times 10^{53}$	HETE	<1	bump		(Fynbo et al. 2003)
031203	9.99×10^{49}	INTEGRAL	0.105	spec.	SN 2003lw	(Soderberg et al. 2003; Tagliaferri et al. 2004)
040924	1.10×10^{52}	HETE	0.86	bump		(Fenimore et al. 2004; Soderberg et al. 2006c)
041006	3.50×10^{52}	HETE	0.716	bump		(Galassi et al. 2004; Bikmaev et al. 2004; Soderberg et al. 2006c)
050525A	3.39×10^{52}	Konus-WIND	0.606	spec.	SN 2005nc	(Della Valle et al. 2006)
060218	1.66×10^{49}	Swift	0.033	spec.	SN 2006aj	(Campana et al. 2006; Soderberg et al. 2006a)
060729	1.60×10^{52}	Swift	0.54	bump		(Cano et al. 2011; Parsons et al. 2006)
070419	7.90×10^{51}	Swift	0.97	bump		(Hill et al. 2007)
080319B	1.30×10^{54}	Swift	0.937	bump		(Perley et al. 2008; Kann et al. 2008; Cummings et al. 2008)
081007	2.50×10^{51}	Swift	0.5295	bump	SN2008hw	(Soderberg et al. 2008; Markwardt et al. 2008)
090618	2.90×10^{53}	Fermi/GBM	0.54	bump		(Izzo et al. 2012; Cano et al. 2011; McBreen 2009)
091127	1.60×10^{52}	Fermi/GBM	0.49	bump	SN 2009nz	(Cobb et al. 2010; Wilson-Hodge & Preece 2009)
100316D	9.81×10^{48}	Swift	0.059	spec.	SN 2010bh	(Bufano et al. 2012; Chornock et al. 2010; Sakamoto et al. 2010)
101219B	4.39×10^{51}	Fermi/GBM	0.55	spec.	SN 2010ma	(Sparre et al. 2011; van der Horst 2010)
111228A	7.52×10^{52}	Fermi/GBM	0.714	bump		(D'Avanzo et al. 2012; Briggs & Younes 2011)
120422A	1.28×10^{51}	Swift	0.283	spec.	SN 2012bz	(Melandri et al. 2012; Barthelmy et al. 2012)
120714B	4.51×10^{51}	Swift	0.3984	spec.	SN 2012eb	(Cummings et al. 2012; Klose et al. 2012)
120729A	2.30×10^{52}	Swift	0.80	bump		(Cano et al. 2014; Ukwatta et al. 2012)
130215A	3.10×10^{52}	Fermi/GBM	0.597	spec.	SN 2013ez	(de Ugarte Postigo et al. 2013; Younes & Bhat 2013)
130427A	9.57×10^{53}	Fermi/GBM	0.3399	spec.	SN 2013cq	(Melandri et al. 2014; Xu et al. 2013; von Kienlin 2013)
130702A	7.80×10^{50}	Fermi/GBM	0.145	spec.	SN 2013dx	(Cenko et al. 2013; Collazzi & Connaughton 2013; Singer et al. 2013)
130831A	4.56×10^{51}	Konus-WIND	0.4791	spec.	SN 2013fu	(Klose et al. 2013; Golenetskii et al. 2013)

has detected, to date, two such events, GRB 060218 (Campana et al. 2006) and GRB 100316D (Starling et al. 2011). Therefore, *Fermi*/GBM should have discovered $2_{-1.3}^{+2.6} \times \rho_{\text{GBM}}/\rho_{\text{BAT}} \times 0.6 = 2\text{--}11 \times 0.6 \sim 1\text{--}7$ GRB-SNe within $z \leq 0.2$. The ratio $\rho_{\text{GBM}}/\rho_{\text{BAT}}$ ($\rho_{\text{GBM}} = 238$ GRBs yr $^{-1}$, von Kienlin et al. 2014; $\rho_{\text{BAT}} = 95$ GRBs yr $^{-1}$, Sakamoto et al. 2011) takes into account the different sky coverage of both detectors and their different sensitivities (Band 2003), while the scale factor 0.6 accounts for the fact that *Fermi* has been monitoring the sky for 6 years, while *Swift* for 10 years. The attached 1σ Poissonian uncertainty at the rate of 2 GRB-SNe yr $^{-1}$, within $z \leq 0.2$, has been derived from Gehrels (1986).

We present in Sect. 2 the strategy that we have used to identify GRB-SN candidates. In Sect. 3 we discuss the 11 GRB-SN coincidences pinpointed by our code. In Sect. 4 we discuss our results and in Sect. 5 we present our conclusions.

2. Methodology and statistical analysis

Our code compares the positions of the Harvard catalog of SNe¹ and the Asiago SN catalog (Barbon et al. 2010) with the positions of 1147 long GRBs detected up to 31 May 2014, and reported in the *Fermi*/GBM catalog² with the attached error

¹ <http://www.cbat.eps.harvard.edu/lists/Supernovae.html>

² <http://heasarc.gsfc.nasa.gov/db-perl/W3Browse>

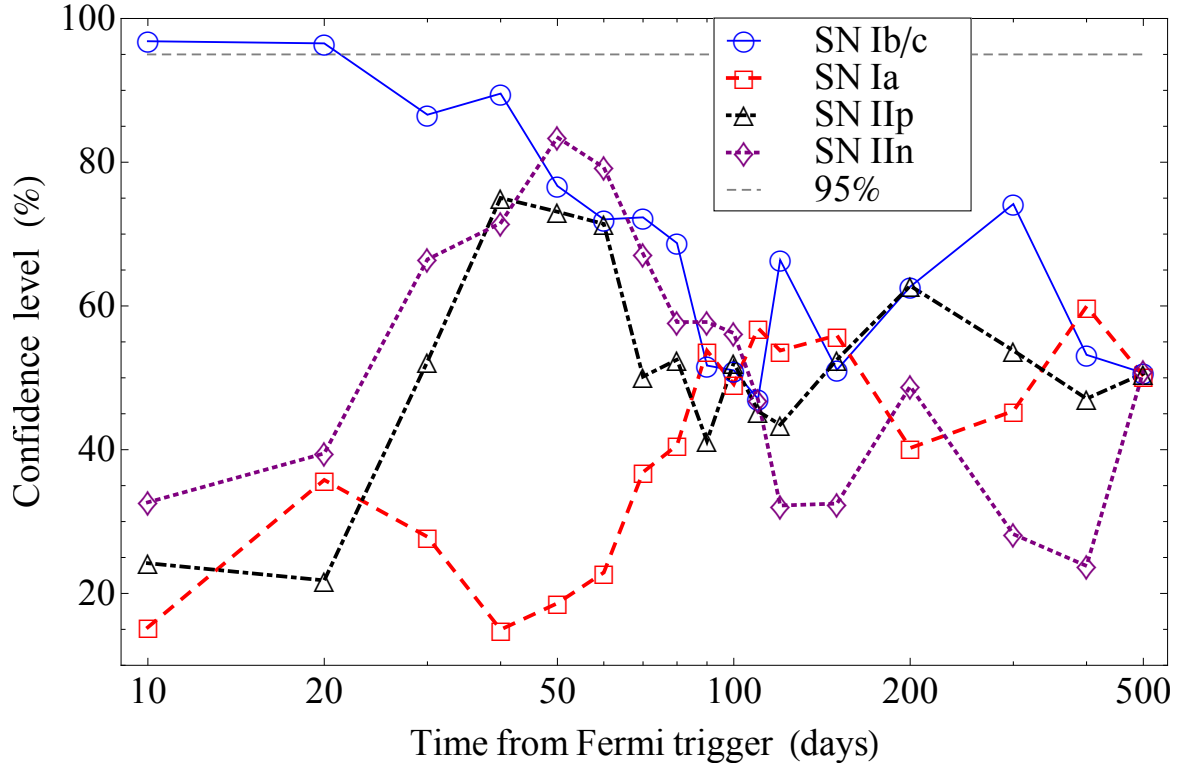
boxes. Subsequently, we considered only GRBs that were detected within Δt days before the occurrence of the SN. The exact value of Δt days was computed after taking into account several factors: the rise time of the SN (typically 10–15 days), the assumption that GRB and SN are simultaneous (Campana et al. 2006), and also the possibility that the SN was discovered after its maximum light. To discern physical GRB-SN associations by random spatial and temporal GRB-SN coincidences due to the large error box associated with GRB detections or uncertainties on the epoch of SN maximum, we also computed the statistical significance of GRB-SN associations for SN types for which we know a priori are not associated with GRBs, like SNe-Ia and Type II (see Valenti et al. 2005). In the first row of Table 2 we list the assumed Δt (in days) after the GRB trigger. In the following rows we list the cumulative number of possible associations, within Δt , for each type of SN, respectively, $N_{\text{Ib/c}}(\Delta t)$, $N_{\text{Ia}}(\Delta t)$, $N_{\text{IIp}}(\Delta t)$, and $N_{\text{IIc}}(\Delta t)$; and in the last row for all types, $N_{\text{tot}}(\Delta t)$. In the last column the percentage of the total number of each SN type over the total sample is also shown.

If we assume a random distribution of SNe in the sky, the spatial GRB-SN association follows the Poisson statistic, $e^{-\lambda} \lambda^n / n!$, where n is the number of observed associations and λ is the expected number of positive events in a chosen temporal window Δt . The expected number of positive events can be evaluated from $N_{\text{tot}}(\Delta t)$ (see last row in Table 2) times the percentage of each SN in the considered sample (see last column in Table 2). Therefore we have that $\lambda = N_{\text{tot}}(\Delta t) r_x$, where

Table 2. Cumulative number of each SN type associated within the error radius of *Fermi*-GRBs at different time intervals after the trigger time.

Δt (days)	10	20	30	40	50	60	70	80	90	100	110	120	150	200	300	400	500	r_x (%)
$N_{\text{Ib/c}}(\Delta t)$	8	9	9	13	13	15	17	18	18	20	21	26	30	42	68	81	96	12
$N_{\text{Ia}}(\Delta t)$	10	23	30	42	51	64	77	85	98	108	118	131	164	213	338	440	519	66
$N_{\text{IIp}}(\Delta t)$	2	4	8	14	16	19	19	21	22	26	27	30	39	54	82	103	124	16
$N_{\text{IIIn}}(\Delta t)$	1	2	4	6	8	9	9	9	10	11	11	11	14	21	30	38	51	6
$N_{\text{tot}}(\Delta t)$	31	67	98	136	166	209	240	260	288	314	338	378	471	627	893	1139	1399	100

Notes. In the first row the considered time intervals (in days) are listed. In the following rows the number of possible associations for each type of SN, respectively, Ib/c, Ia, IIp, and IIIn, and the total number of SNe, for each considered time interval, are listed. In the last column the percentage r_x of the total number of each SN type over the total sample is shown.

**Fig. 1.** Statistical significance of the GRB-SN occurrence as a function of the temporal window. This plot shows the significance of the deviation of SNe Ib/c in the time interval $(T_0, T_0 + 20)$ days from the expected number of events assuming the relative proportion seen in the total SN sample.

$x = \{\text{Ib/c, Ia, IIp, IIIn}\}$. We then compared it with the observations $N_x(\Delta t)$, and evaluated the corresponding confidence levels. The results of the computation are shown in Fig. 1. A simple comparison of significance tracks reported in Fig. 1 between SNe Ib/c and other SN types shows that, as expected, only SNe Ib/c within ~ 30 – 40 days after the GRB triggers are suggestive of the existence of physical associations with GRBs. From a simple application of Poissonian statistics in a regime of small numbers (Gehrels 1986), we derive a threshold of $\geq 95\%$ confidence level, which corresponds to $\Delta t = 20$ days. In the following we will conservatively consider only associations between GRBs and SNe within 20 days of the GRB trigger.

3. The sample of GRBs-SNe Ib/c

The list of GRB-SN Ib/c associations that our code has pinpointed is shown in Table 3, together with observational properties of the bursts and possibly related SNe. We found five cases. One of them, GRB 130702A – SN 2013dx, is already known

(Singer et al. 2013)³. For all SNe the redshift is determined from spectral observations of the host galaxy.

The values of E_{iso} given in Table 4 are derived from the spectral analysis of *Fermi*/GBM data of GRBs, using a Band function (Band et al. 1993) as spectral model (see also Amati et al. 2008). We have considered time-tagged events (TTE) *Fermi*/GBM spectra which combine a high time resolution (up to $2 \mu\text{s}$) with a good resolution in the spectral range. We fitted these spectra with the RMfit package⁴. The value of E_{iso} in the last column of the table shows that all events are low-luminosity GRBs, unlike those events from so-called cosmological GRBs, characterized by $E_{\text{iso}} \sim 10^{51}$ – 10^{54} erg.

³ If we relax the $z \leq 0.2$ constraint, our code detects three more well-known GRB-SN associations, specifically GRB 091127 – SN 2009nz (Troja et al. 2012), GRB 101219B – SN 2010ma (Sparre et al. 2011), and GRB 130427A – SN 2013cq (Xu et al. 2013; Melandri et al. 2014).

⁴ http://Fermi.gsfc.nasa.gov/ssc/data/analysis/rmfit/vc_rmfit_tutorial.pdf

Table 3. Main parameters of the *Fermi* GRB sample presented in this work and of the supernovae associated with these bursts.

GRB	RA GBM (deg)	Dec GBM (deg)	Error radius (deg)	T_{90} (s)	Fluence (0.01–1) MeV (erg cm ⁻²)	Peak flux (0.01–1) MeV (photon cm ⁻²)	SN	Date discovery	RA SN (deg)	Dec SN (deg)	z
090320B	183.4	49.8	9.5	29.2	1.67×10^{-6}	4.35 ± 0.25	2009di	2009 03 21	174.2411	45.0141	0.13
090426B	17.6	-19.2	18.1	16.1	6.77×10^{-7}	2.03 ± 0.18	2009em	2009 05 05	8.6855	-8.3993	0.006
110911A	258.58	-66.98	50.0*	8.96	5.94×10^{-7}	2.38 ± 0.41	2011gw	2011 09 15	112.0709	-62.3552	0.01
120121B	235.67	-39.34	7.9	18.4	1.95×10^{-6}	2.66 ± 0.21	2012ba	2012 01 21	230.6047	-38.2012	0.017
130702A	228.15	16.58	13.02	59	6.3×10^{-6}	7.03 ± 0.86	2013dx	2013 07 08	217.3116	15.7740	0.145

Notes. We also report the already known GRB-SN connection that we have found with our code in the last row of the table. (*) Nominal maximum value for the error radius of bursts detected by a single GBM detector.

Table 4. Results of the spectral fits of *Fermi*/GBM observations for the four GRBs with evidence of association with a SN Ic.

GRB	α	β	E_{peak} (keV)	E_{iso} (erg)
090320B	-0.65 ± 0.35	-2.42 ± 0.30	62.6 ± 12.0	9.13×10^{49}
090426B	-0.50 ± 3.12	-1.65 ± 0.15	39.9 ± 76.9	1.94×10^{47}
110911A	-0.47 ± 0.50	-1.36 ± 0.18	44.8 ± 20.1	6.22×10^{47}
120121B	-0.73 ± 0.21	-2.95 ± 0.89	92.2 ± 12.2	1.39×10^{48}

3.1. GRB 090320B – SN 2009di

GRB 090320B was detected by the *Fermi*/GBM detectors numbers 10 and 11 and also by Konus-WIND. The T_{90} duration reported by *Fermi* is 29.2 s, while unfortunately we do not have further information from Konus-WIND for this trigger. The possibly associated SN is SN 2009di, which was discovered on 21 March 2009, just one day after the detection by *Fermi*, by the CRTS (Drake et al. 2009). At the moment of the discovery, the unfiltered magnitude of the SN was 18.6. Spectroscopy made with the 5.1 m Palomar *Hale* telescope identified SN 2009di as a Type Ic SN. The redshift of the SN was reported to be $z = 0.13$. The distance between the SN and *Fermi* positions one is 7.8 degrees, while the *Fermi* error radius is about 9.5 degrees.

3.2. GRB 090426B – SN 2009em

GRB 090426B was observed by detectors 3 and 5 of *Fermi*/GBM, with a T_{90} duration of 16.1 s. SN 2009em, associated with this GRB, was discovered by Monard (2009) on 5 May 2009. Follow-up observations made 6 days later confirmed the presence of an unfiltered magnitude 16.6 supernova. Further spectroscopic observations (Navasardyan & Benetti 2009; Folatelli & Morrell 2009) made around May 19 confirmed the Ic nature of this SN, which corresponds to several known SNe Ic observed about one month from the maximum light, which plays against an association with GRB 090426B. The distance from the *Fermi* position is 13.8 degrees, to be compared with an error radius of 18 degrees. The redshift of this source was measured to be $z = 0.006$, which corresponds to a comoving distance of 25.31 Mpc.

3.3. GRB 110911A – SN 2011gw

This GRB triggered the *Fermi* detectors numbers 2 and 10. However, the signal from detector number 2 was dominated by noise, so we have considered only the flux detected by number 10. This GRB was characterized by $T_{90} = 8.96$ s. SN 2011gw

was discovered on 15 September by different observers as an object of magnitude approximately 17.4 (Pignata et al. 2011). A spectrum obtained one month later, on 20 October, at the NTT telescope revealed the Ib/c nature of this supernova, and a cross-check with the GELATO library found a match with other SNe at about two months post maximum. The redshift of this SN was reported to be 0.01 while the distance between the center of *Fermi*/GBM detectors and the SN was 48 degrees, with an error radius of 50 degrees. This large error box is due to the combination of two detectors that are located on the opposite sides of the *Fermi* spacecraft and that increase the probability of a casual association for this GRB-SN event.

3.4. GRB 120121B – SN 2012ba

GRB 120121B was detected by the *Fermi* detectors numbers 3 and 5. The T_{90} duration was of 18.4 s. The best fit of the integrated spectrum of the GRB is a Band function with an intrinsic peak energy of $E_{\text{peak},i} = (92.2 \pm 12.2)$ keV. The SN associated with this GRB may be SN 2012ba. It was discovered on 21 January, the same day of the GRB trigger, as an object of unfiltered magnitude 16.6 (Pignata et al. 2012), still in rising phase. A spectrum obtained on 2 March (40 days after the discovery) with the 6.5 m *Magellan II Clay* telescope and then cross-correlated with the SNID libraries of SN spectra, showed a match with a Type Ic SN more than 15 days after maximum. The redshift of the SN, $z = 0.017$ associated with the observed peak magnitude of 15.9, eleven days after the SN discovery (Pignata et al. 2012), implied an absolute magnitude at maximum of -18.5 , which is an upper limit to the intrinsic luminosity, considering the correction for dust extinction. This result suggests that SN 2012ba is a very luminous SN Ic, with an absolute magnitude similar to that of SN 2010bh, $R_{\text{abs}} \approx -18.5$ (Bufano et al. 2012), or even brighter, similarly to SN 1998bw $R_{\text{abs}} \approx -19$ (Patat et al. 2001). The distance between the SN position and the *Fermi* center was of 4.1 degrees, inside the *Fermi* error radius of 7.9 degrees.

4. Discussions

Our analysis discovered five GRB-SN coincidences within $z \leq 0.2$, and one of them was already known to be a physical association between GRB and SN (GRB 130702A-SN 2013dx; Singer et al. 2013). We note that the afterglow of GRB 130702A has been found by the authors of the above cited work upon searching 71 deg² surrounding the *Fermi*/GBM localization. This result further strengthens the reliability of the adopted methodology.

After discussion of the data, we found that SN 2012ba is the only bona fide candidate for being physical associated with a GRB (120121B). SN 2012ba was of Type Ic and quickly

reached a very bright maximum magnitude $R_{\text{abs}} \simeq -19$ about 11 days after the GRB trigger (Kryachko et al. 2012), which is very similar to the typical rising time of SNe associated with GRBs (Bufano et al. 2012). To date there are only two other SNe associated with GRBs and classified as Ic (rather than broad lines Ic or Hypernovae): SN 2002lt, associated with GRB 021211 (Della Valle et al. 2003), and SN 2013ez, associated with GRB 130215A (Cano et al. 2014). However, these observations do not imply that GRBs may be associated with standard Type Ic SNe. We note that in all three cases, 2012ba, 2002lt, and 2013ez, SN spectra were secured 20–40 days past maximum; therefore, even if the pre-maximum spectra showed significantly broader lines than observed in the post-maximum spectra, this difference shortly vanished after maximum (if the SN ejecta carry little mass) such that it is not easy to distinguish between the two types of SNe. The isotropic energy of this *Fermi* GRB-SN candidate is $E_{\text{iso}} = 1.39 \times 10^{48}$ erg, which implies that this burst belongs to the low-luminosity subclass of GRBs (Guetta & Della Valle 2007; Piran et al. 2013; Tsutsui & Shigeyama 2014). Now, we are in the position to independently estimate, admittedly on the very scanty statistic of one single object, the rate ρ_0 of local low-energetic long GRBs–Type Ic SNe. Following Soderberg et al. (2006b) and Guetta & Della Valle (2007), we have computed the photon peak flux f_p in the energy band 1–1000 keV and the corresponding threshold peak flux, following the analysis of Band (2003) for GRB 120121B. In this way we have evaluated the maximum redshift z_{max} at which this burst would have detected, $z = 0.0206$, and then the corresponding maximum comoving volume V_{max} .

The empirical rate can then be written as

$$\rho_0 = \frac{N_{\text{LE}}}{V_{\text{max}} f_p T}, \quad (1)$$

where $N_{\text{LE}} = 1$ is the number of found physical connections, $f_p \approx 0.76$ the average ratio of *Fermi* solid angle over the total, and $T = 6$ years the *Fermi* observational period. We infer a local rate for this GRB–SN Ic events of $\rho_0 = 77^{+289}_{-73} \text{ Gpc}^{-3} \text{ yr}^{-1}$, where the errors are determined from the 95% confidence level of the Poisson statistic (Gehrels 1986). There is growing body of evidence that low-luminosity GRBs are less beamed than high luminosity GRBs, indeed f_b^{-1} is on the order of 10, or less (see, e.g., Guetta & Della Valle 2007). After taking into account this correction we derive $\rho_{0,b} \leq 770 \text{ Gpc}^{-3} \text{ yr}^{-1}$, which is consistent with $\rho_0 = 380^{+620}_{-225} \text{ Gpc}^{-3} \text{ yr}^{-1}$ in Guetta & Della Valle (2007), $325^{+352}_{-177} \text{ Gpc}^{-3} \text{ yr}^{-1}$ in Liang et al. (2007), and $230^{+490}_{-190} \text{ Gpc}^{-3} \text{ yr}^{-1}$ in Soderberg et al. (2006b).

This analysis confirms the existence of a class of more frequent low-energetic GRBs–SNe Ic, whose rate is larger than the one obtained extrapolating at low redshifts the rate for high-energetic bursts, i.e., $\rho = 1.3^{+0.7}_{-0.6} \text{ Gpc}^{-3} \text{ yr}^{-1}$ (Wanderman & Piran 2010).

5. Conclusions

This paper presents the results of an analysis dedicated to finding possible connections between long GRBs listed in the *Fermi*/GBM catalog and SNe. Our analysis was motivated by the fact that we expected, on a statistical basis, to find in the *Fermi* catalog between one and seven GRB–SN connections within $z < 0.2$. From our analysis the following results emerge:

- we have found a total number of five possible connections at $z \leq 0.2$. One of them was already known as having physical GRB–SN associations. After discussing the remaining

four cases, we found that only GRB 120121B is very likely physically connected with SN 2012ba. This result of two observed GRBs–SNe is fully consistent with our initial estimate of 1–7 low- z events being found in the *Fermi* catalog;

- the very low redshift at which GRB 120121B/SN 2012b is observed implies a small isotropic energy emitted during the GRB, $E_{\text{iso}} = 1.39 \times 10^{48}$ erg. From this single connection, we compute the rate of *Fermi* low-luminosity GRBs connected with SNe to be $\rho_0 = 77^{+289}_{-73} \text{ Gpc}^{-3} \text{ yr}^{-1}$. If we consider an additional correction, due to a beaming in the low-luminosity GRB emission, f_b^{-1} on the order of 10 (Guetta & Della Valle 2007), we obtain for the *Fermi* rate $\rho_{0,b} \leq 770 \text{ Gpc}^{-3} \text{ yr}^{-1}$, which is consistent with $\rho_0 = 380^{+620}_{-225} \text{ Gpc}^{-3} \text{ yr}^{-1}$ in Guetta & Della Valle (2007), $325^{+352}_{-177} \text{ Gpc}^{-3} \text{ yr}^{-1}$ in Liang et al. (2007), and $230^{+490}_{-190} \text{ Gpc}^{-3} \text{ yr}^{-1}$ in Soderberg et al. (2006b);
- if we consider a continuous time coverage, including previous analysis from *Beppo*/SAX (7 years, 1 connection – GRB 980425, Galama et al. 1998) and *Swift* (9 years, 2 connections – GRB 060218, Campana et al. 2006; and GRB 100316D, Bufano et al. 2012), we obtain a comprehensive rate of $\rho_0^{\text{tot}} = 31^{+40}_{-20} \text{ Gpc}^{-3} \text{ yr}^{-1}$, which becomes $\rho_{0,b}^{\text{tot}} = 310^{+400}_{-200} \text{ Gpc}^{-3} \text{ yr}^{-1}$, assuming f_b^{-1} on the order of 10;
- on the basis of the annual rate of *Fermi* GRBs (238 GRBs/year), and of the expected number of *Fermi*/GBM bursts associated with low- z SNe (1–7 GRBs) in 6 years of observations, we estimate that in the next 4 years *Fermi*/GBM could detect ~ 1 –4 GRBs–SNe within $z \leq 0.2$.

Acknowledgements. We are grateful to Remo Ruffini, who provided support for the final outcome of this work. M.K., M.E., G.B.P. and L.L. are supported by the Erasmus Mundus Joint Doctorate Program by grant Nos. 2013-1471, 2012-1710, 2011-1640, and 2013-1471, respectively, from the EACEA of the European Commission.

References

- Arnett, D. 1996, *Supernovae and Nucleosynthesis* (Princeton University Press)
- Band, D. L. 2003, *ApJ*, 588, 945
- Band, D., Matteson, J., Ford, L., et al. 1993, *ApJ*, 413, 281
- Barbon, R., Buondi, V., Cappellaro, E., & Turatto, M. 2010, *VizieR Online Data Catalog*: II/24
- Barthelmy, S. D., Barbier, L. M., Cummings, J. R., et al. 2005, *Space Sci. Rev.*, 120, 143
- Barthelmy, S. D., Baumgartner, W. H., Cummings, J. R., et al. 2012, *GRB Coordinates Network*, 13246, 1
- Bikmaev, I., Sakhibullin, N., Alpar, M. A., et al. 2004, *GRB Coordinates Network*, 2826, 1
- Bloom, J. S., Kulkarni, S. R., Djorgovski, S. G., et al. 1999, *Nature*, 401, 453
- Bloom, J. S., Kulkarni, S. R., Price, P. A., et al. 2002, *ApJ*, 572, L45
- Briggs, M. S., & Younes, G. 2011, *GRB Coordinates Network*, 12744, 1
- Bufano, F., Pian, E., Sollerman, J., et al. 2012, *ApJ*, 753, 67
- Campana, S., Mangano, V., Blustin, A. J., et al. 2006, *Nature*, 442, 1008
- Cano, Z. 2014, *ApJ*, submitted [[arXiv:1407.2589](https://arxiv.org/abs/1407.2589)]
- Cano, Z., Bersier, D., Guidorzi, C., et al. 2011, *MNRAS*, 413, 669
- Cano, Z., de Ugarte Postigo, A., Pozenenko, A., et al. 2014, *A&A*, 568, A19
- Cenko, S. B., Gal-Yam, A., Kasliwal, M. M., et al. 2013, *GRB Coordinates Network*, 14998, 1
- Chornock, R., Berger, E., Levesque, E. M., et al. 2010 [[arXiv:1004.2262](https://arxiv.org/abs/1004.2262)]
- Cobb, B. E., Bloom, J. S., Perley, D. A., et al. 2010, *ApJ*, 718, L150
- Collazzi, A. C., & Connaughton, V. 2013, *GRB Coordinates Network*, 14972, 1
- Crew, G., Villasenor, J., Vanderspek, R., et al. 2002, *GRB Coordinates Network*, 1734, 1
- Cummings, J., Barthelmy, S. D., Fenimore, E., et al. 2008, *GRB Coordinates Network*, 7462, 1
- Cummings, J. R., Barthelmy, S. D., Baumgartner, W. H., et al. 2012, *GRB Coordinates Network*, 13481, 1
- D’Avanzo, P., Melandri, A., Palazzi, E., et al. 2012, *GRB Coordinates Network*, 13069, 1
- de Ugarte Postigo, A., Thoene, C. C., Gorosabel, J., et al. 2013, *GRB Coordinates Network*, 14303, 1

- Della Valle, M. 2006, in *Gamma-Ray Bursts in the Swift Era*, eds. S. S. Holt, N. Gehrels, & J. A. Nousek, AIP Conf. Ser., 836, 367
- Della Valle, M., Malesani, D., Benetti, S., et al. 2003, A&A, 406, L33
- Della Valle, M., Chincarini, G., Panagia, N., et al. 2006, *Nature*, 444, 1050
- Dezalay, J.-P., Barat, C., Talon, R., et al. 1992, in AIP Conf. Ser. 265, eds. W. S. Paciesas, & G. J. Fishman, 304
- Drake, A. J., Djorgovski, S. G., Mahabal, A., et al. 2009, *Central Bureau Electronic Telegrams*, 1766, 1
- Fenimore, E. E., Ricker, G., Atteia, J.-L., et al. 2004, *GRB Coordinates Network*, 2735, 1
- Folatelli, G., & Morrell, N. 2009, *Central Bureau Electronic Telegrams*, 1807, 1
- Frontera, F., Guidorzi, C., Montanari, E., et al. 2009, *ApJS*, 180, 192
- Fynbo, J. P. U., Hjorth, J., Gorosabel, J., et al. 2003, *GRB Coordinates Network*, 2345, 1
- Fynbo, J. P. U., Watson, D., Thöne, C. C., et al. 2006, *Nature*, 444, 1047
- Galama, T. J., Vreeswijk, P. M., van Paradijs, J., et al. 1998, *Nature*, 395, 670
- Galassi, M., Ricker, G., Atteia, J.-L., et al. 2004, *GRB Coordinates Network*, 2770, 1
- Gal-Yam, A., Fox, D. B., Price, P. A., et al. 2006, *Nature*, 444, 1053
- Gehrels, N. 1986, *ApJ*, 303, 336
- Gehrels, N., & Mészáros, P. 2012, *Science*, 337, 932
- Gehrels, N., Ramirez-Ruiz, E., & Fox, D. B. 2009, ARA&A, 47, 567
- Golenetskii, S., Mazets, E., Pal'Shin, V., Frederiks, D., & Cline, T. 2003, *GRB Coordinates Network*, 2026, 1
- Golenetskii, S., Aptekar, R., Frederiks, D., et al. 2013, *GRB Coordinates Network*, 15145, 1
- Gorosabel, J., Fynbo, J. P. U., Fruchter, A., et al. 2005, A&A, 437, 411
- Greiner, J., Klose, S., Salvato, M., et al. 2003, *ApJ*, 599, 1223
- Guetta, D., & Della Valle, M. 2007, *ApJ*, 657, L73
- Heger, A., Fryer, C. L., Woosley, S. E., Langer, N., & Hartmann, D. H. 2003, *ApJ*, 591, 288
- Hill, J., Garnavich, P., Kuhn, O., et al. 2007, *GRB Coordinates Network*, 6486, 1
- Hurley, K., Cline, T., Mazets, E., & Golenetskii, S. 2000, *GRB Coordinates Network*, 791, 1
- Hurley, K., Cline, T., Guidorzi, C., et al. 2001, *GRB Coordinates Network*, 1148, 1
- Hurley, K., Cline, T., Frontera, F., et al. 2002a, *GRB Coordinates Network*, 1325, 1
- Hurley, K., Cline, T., Ricker, G., et al. 2002b, *GRB Coordinates Network*, 1263, 1
- Izzo, L., Ruffini, R., Penacchioni, A. V., et al. 2012, A&A, 543, A10
- Kann, D. A., Schulze, S., & Updike, A. C. 2008, *GRB Coordinates Network*, 7627, 1
- Kawabata, K. S., Kosugi, G., Iye, M., et al. 2003, *IAU Circ.*, 8133, 2
- Klebesadel, R., Evans, W. D., Laros, J. G., et al. 1982, *ApJ*, 259, L51
- Klose, S., Greiner, J., Fynbo, J., et al. 2012, *Central Bureau Electronic Telegrams*, 3200, 1
- Klose, S., Nicuesa Guelbenzu, A., Kruehler, T., et al. 2013, *GRB Coordinates Network*, 15320, 1
- Kouveliotou, C., Meegan, C. A., Fishman, G. J., et al. 1993, *ApJ*, 413, L101
- Kryachko, T., Korotkiy, S., Satovskiy, B., et al. 2012, *Central Bureau Electronic Telegrams*, 3025, 1
- Lazzati, D., Covino, S., Ghisellini, G., et al. 2001, A&A, 378, 996
- Levan, A., Nugent, P., Fruchter, A., et al. 2005, *ApJ*, 624, 880
- Liang, E., Zhang, B., Virgili, F., & Dai, Z. G. 2007, *ApJ*, 662, 1111
- Mangano, V., Holland, S. T., Malesani, D., et al. 2007, A&A, 470, 105
- Markwardt, C. M., Barthelmy, S. D., Baumgartner, W. H., et al. 2008, *GRB Coordinates Network*, 8338, 1
- Masetti, N., Palazzi, E., Pian, E., et al. 2003, A&A, 404, 465
- McBreen, S. 2009, *GRB Coordinates Network*, 9535, 1
- Meegan, C., Lichti, G., Bhat, P. N., et al. 2009, *ApJ*, 702, 791
- Melandri, A., Pian, E., Ferrero, P., et al. 2012, A&A, 547, A82
- Melandri, A., Pian, E., D'Elia, V., et al. 2014, A&A, 567, A29
- Monard, L. A. G. 2009, *Central Bureau Electronic Telegrams*, 1798, 1
- Navasardyan, H., & Benetti, S. 2009, *Central Bureau Electronic Telegrams*, 1806, 1
- Nicastro, L., in't Zand, J. J. M., Heise, J., et al. 2004, in *Gamma-Ray Bursts in the Afterglow Era*, eds. M. Feroci, F. Frontera, N. Masetti, & L. Piro, ASP Conf. Ser., 312, 185
- Parsons, A., Barbier, L., Barthelmy, S. D., et al. 2006, *GRB Coordinates Network*, 5370, 1
- Patat, F., Cappellaro, E., Danziger, J., et al. 2001, *ApJ*, 555, 900
- Perley, D. A., Bloom, J. S., & Chen, H.-W. 2008, *GRB Coordinates Network*, 7535, 1
- Pignata, G., Cifuentes, M., Maza, J., et al. 2011, *Central Bureau Electronic Telegrams*, 2869, 1
- Pignata, G., Cifuentes, M., Apostolovski, Y., et al. 2012, *Central Bureau Electronic Telegrams*, 3058, 1
- Piran, T. 2005, *Rev. Mod. Phys.*, 76, 1143
- Piran, T., Bromberg, O., Nakar, E., & Sari, R. 2013, *Roy. Soc. Lond. Philosoph. Trans. Ser. A*, 371, 20273
- Reichart, D. E. 1997, *ApJ*, 485, L57
- Sakamoto, T., Barthelmy, S. D., Baumgartner, W. H., et al. 2010, *GRB Coordinates Network*, 10511, 1
- Sakamoto, T., Barthelmy, S. D., Baumgartner, W. H., et al. 2011, *ApJS*, 195, 2
- Singer, L. P., Cenko, S. B., Kasliwal, M. M., et al. 2013, *ApJ*, 776, L34
- Smartt, S. J. 2009, ARA&A, 47, 63
- Soderberg, A. M., Kulkarni, S. R., & Frail, D. A. 2003, *GRB Coordinates Network*, 2483, 1
- Soderberg, A., Berger, E., & Schmidt, B. 2006a, *IAU Circ.*, 8674, 2
- Soderberg, A. M., Kulkarni, S. R., Nakar, E., et al. 2006b, *Nature*, 442, 1014
- Soderberg, A. M., Kulkarni, S. R., Price, P. A., et al. 2006c, *ApJ*, 636, 391
- Soderberg, A., Berger, E., & Fox, D. 2008, *GRB Coordinates Network*, 8662, 1
- Sparre, M., Sollerman, J., Fynbo, J. P. U., et al. 2011, *ApJ*, 735, L24
- Stanek, K. Z., Matheson, T., Garnavich, P. M., et al. 2003, *ApJ*, 591, L17
- Starling, R. L. C., Wiersema, K., Levan, A. J., et al. 2011, *MNRAS*, 411, 2792
- Tagliaferri, G., Malesani, D., Chincarini, G., et al. 2004, *GRB Coordinates Network*, 2545, 1
- Tavani, M. 1998, *ApJ*, 497, L21
- Troja, E., Sakamoto, T., Guidorzi, C., et al. 2012, *ApJ*, 761, 50
- Tsutsui, R., & Shigeyama, T. 2014, *PASJ*
- Ukwatta, T. N., Burrows, D. N., Chester, M. M., et al. 2012, *GRB Coordinates Network*, 13530, 1
- Valenti, S., Cappellaro, E., Della Valle, M., et al. 2005, *Nuovo Cimento C Geophysics Space Physics C*, 28, 633
- van der Horst, A. J. 2010, *GRB Coordinates Network*, 11477, 1
- von Kienlin, A. 2013, *GRB Coordinates Network*, 14473, 1
- von Kienlin, A., Meegan, C. A., Paciesas, W. S., et al. 2014, *ApJS*, 211, 13
- Vreeswijk, P., Fruchter, A., Hjorth, J., & Kouveliotou, C. 2003, *GRB Coordinates Network*, 1785, 1
- Wanderman, D., & Piran, T. 2010, *MNRAS*, 406, 1944
- Wilson-Hodge, C. A., & Preece, R. D. 2009, *GRB Coordinates Network*, 10204, 1
- Xu, D., de Ugarte Postigo, A., Leloudas, G., et al. 2013, *ApJ*, 776, 98
- Younes, G., & Bhat, P. N. 2013, *GRB Coordinates Network*, 14219, 1
- Zeh, A., Klose, S., & Hartmann, D. H. 2004, *ApJ*, 609, 952
- Zhang, B. 2014, *Int. J. Mod. Phys. D*, 23, 30002



On the Ultra-relativistic Prompt Emission, the Hard and Soft X-Ray Flares, and the Extended Thermal Emission in GRB 151027A

R. Ruffini^{1,2,3,4}, L. Becerra^{1,2}, C. L. Bianco^{1,2} , Y. C. Chen^{1,2}, M. Karlica^{1,2,3}, M. Kovačević^{1,2,3}, J. D. Melon Fuksman^{1,2}, R. Moradi^{1,2}, M. Muccino^{1,2} , G. B. Pisani^{1,2} , D. Primorac^{1,2}, J. A. Rueda^{1,2,4}, G. V. Vereshchagin^{1,2}, Y. Wang^{1,2}, and S. S. Xue^{1,2}

¹ ICRA and Dipartimento di Fisica, Sapienza Università di Roma, P.le Aldo Moro 5, I-00185 Rome, Italy

² ICRANet, P.zza della Repubblica 10, I-65122 Pescara, Italy

³ Université de Nice Sophia Antipolis, CEDEX 2, Grand Château Parc Valrose, Nice, France

⁴ ICRANet-Rio, Centro Brasileiro de Pesquisas Físicas, Rua Dr. Xavier Sigaud 150, 22290-180 Rio de Janeiro, Brazil; ruffini@icra.it

Received 2017 December 13; revised 2018 November 2; accepted 2018 November 3; published 2018 December 20

Abstract

We analyze GRB 151027A within the binary-driven hypernova approach, with a progenitor of a carbon–oxygen core on the verge of a supernova (SN) explosion and a binary companion neutron star (NS). The hypercritical accretion of the SN ejecta onto the NS leads to its gravitational collapse into a black hole (BH), to the emission of the gamma-ray burst (GRB), and to a copious e^+e^- plasma. The impact of this e^+e^- plasma on the SN ejecta explains the early soft X-ray flare observed in long GRBs. Here, we apply this approach to the ultra-relativistic prompt emission (UPE) and to the hard X-ray flares. We use GRB 151027A as a prototype. From the time-integrated and the time-resolved analysis, we identify a double component in the UPE and confirm its ultra-relativistic nature. We confirm the mildly relativistic nature of the soft X-ray flare, of the hard X-ray flare, and of the extended thermal emission (ETE). We show that the ETE identifies the transition from an SN to a hypernova (HN). We then address the theoretical justification of these observations by integrating the hydrodynamical propagation equations of the e^+e^- into the SN ejecta, with the latter independently obtained from 3D smoothed particle hydrodynamics simulations. We conclude that the UPE, the hard X-ray flare, and the soft X-ray flare do not form a causally connected sequence. Within our model, they are the manifestation of the same physical process of the BH formation as seen through different viewing angles, implied by the morphology and the ~ 300 s rotation period of the HN ejecta.

Key words: binaries: general – black hole physics – gamma-ray burst: general – hydrodynamics – stars: neutron – supernovae: general

1. Introduction

Gamma-ray bursts (GRBs) are traditionally classified in short GRBs with a total duration of $\lesssim 2$ s, and as long GRBs lasting $\gtrsim 2$ s (Mazets et al. 1981; Dezalay et al. 1992; Klebesadel 1992; Kouveliotou et al. 1993; Tavani 1998). A large majority of long bursts are spatially correlated with bright star-forming regions in their host galaxies (Fruchter et al. 2006; Svensson et al. 2010). For this reason, the long GRBs have been traditionally associated with the collapse of the core of a single massive star to a black hole (BH), surrounded by a thick massive accretion disk: the collapsar (Woosley 1993; Paczyński 1998; MacFadyen & Woosley 1999; Piran 2004; Bromberg et al. 2013). In this traditional picture, the GRB dynamics follows the “fireball” model, which assumes the existence of a single ultra-relativistic collimated jet (see e.g., Blandford & McKee 1976; Shemi & Piran 1990; Meszaros et al. 1993; Piran et al. 1993; Mao & Yi 1994). The structures of long GRBs were described either by internal or external shocks (see Rees & Meszaros 1992, 1994). The emission processes were linked to the occurrence of a synchrotron and/or inverse-Compton radiation coming from the single ultra-relativistic jetted structure, characterized by Lorentz factors $\Gamma \sim 10^2\text{--}10^3$.

Such a collapsar model does not address some observational facts: (1) most massive stars are found in binary systems (Smith 2014), (2) most SNe Ib/c occur in binary systems (Smith et al. 2011), and (3) the SNe associated with long GRBs are indeed of type Ib/c (Della Valle 2011). These facts motivated us to develop the binary-driven hypernova (BdHN) model.

Recently, we have found evidence for multiple components in long GRB emissions, indicating the presence of a sequence of astrophysical processes (Izzo et al. 2012; Penacchioni et al. 2012), which have led us to formulate, in precise terms, the sequence of events in the Induced Gravitational Collapse (IGC) paradigm (Ruffini et al. 2001a, 2007a; Rueda & Ruffini 2012; Fryer et al. 2014), making explicit the role of binary systems as progenitors of the long GRBs.

Within the IGC scenario, the long bursts originate in tight binary systems composed of a carbon–oxygen core (CO_{core}) undergoing an SN explosion and a companion neutron star (NS; Becerra et al. 2015, 2016, 2018). The SN explosion triggers a hypercritical accretion process onto the companion NS; photons are trapped in the infalling material, and the gravitational energy gained by accretion is carried out through an efficient neutrino emission (Zel’dovich et al. 1972; Ruffini & Wilson 1973; Fryer et al. 2014). Depending on the CO_{core} –NS binary separation/period, two outcomes may occur. For widely separated ($a \gtrsim 10^{11}$ cm) CO_{core} –NS binaries, the hypercritical accretion rate is $< 10^{-2} M_{\odot} \text{ s}^{-1}$, and it is insufficient to induce the gravitational collapse of the NS to a BH. Instead, the NS just increases its mass, becoming a massive NS. This process leads to the emission of the so-called X-ray flashes (XRFs) with a typical X-ray emission of $\lesssim 10^{52}$ erg.

For more tightly bound ($a \lesssim 10^{11}$ cm) CO_{core} –NS binaries, the hypercritical accretion rate of the SN ejecta can be as large as $\gtrsim 10^{-2}\text{--}10^{-1} M_{\odot} \text{ s}^{-1}$, leading the companion NS to collapse into a BH. This process leads to the occurrence of the BdHN,

which exhibits a more complex structure than XRFs and an emission of $\gtrsim 10^{52}$ erg (Ruffini et al. 2016b).

The opportunity of introducing the BdHN model, based on binary progenitors, which exhibits a large number of new physical process and admits a theoretical treatment by detailed equations whose corresponding solutions are in agreement with the observations, has been presented in a large number of publications and was recently summarized in Ruffini et al. (2018c). There, we performed an extensive analysis using 421 BdHN, all with measured redshift and observed until the end of 2016, and described in their cosmological rest frame (Pisani et al. 2016).

The large variety of spectra and light curves has allowed the introduction of seven different GRBs subclasses (see e.g., Ruffini et al. 2016b, 2018b).

We recalled that since 2001, we fit the ultra-relativistic prompt emission (UPE) light curve and spectra, solving the equations of the dynamics of the e^+e^- baryon plasma and of its slowing down due to the interaction with the circumburst medium (CBM; see e.g., Ruffini et al. 1999, 2000, 2002). This treatment allows us to evaluate the ultra-relativistic gamma factor of the UPE exhibited in hundreds of short and long GRBs. Some under-luminous GRBs may well have a non-ultrarelativistic prompt emission (J. A. Rueda et al. 2018, in preparation).

Attention was then directed to examine the flare plateau afterglow (FPA) phase following the UPE.

Among the BdHNs, we identified all of the ones with a soft X-ray flare in the 0.3–10 keV rest-frame energy range in the FPA phase. In view of the excellent data and complete light curves, we could identify a thermal component in them (see Figure 32 and Table 7 in Ruffini et al. 2018c), which is essential in measuring the mildly relativistic expansion velocity of $v = c\beta \sim 0.8c$ (see Section 9 in Ruffini et al. 2018c).

In addition we then followed, through a hydrodynamical description, the propagation and the slowing down inside the SN ejecta of the e^+e^- plasma generated in the BH formation, in order to explain the mildly relativistic nature of the soft X-ray flares expansion velocity (see Section 10 in Ruffini et al. 2018c).

Obviously, these considerations cannot be repeated here.

We only recall a few points of the conclusions of Ruffini et al. (2018c); e.g., (a) the data of the soft X-ray flare have determined its mildly relativistic expansion velocity already ~ 100 s after the UPE, in contrast to the traditional approach; (b) the role of the interaction of the e^+e^- GRB emission in SN ejecta in order to explain the astrophysical origin of soft X-ray flare; (c) the determination of the density profile of the SN ejecta derived from the simulation of the IGC paradigm.

In this article, we apply our model to study a multiple component in the UPE phase observed in the range of 10–1000 keV as well as the hard X-ray flares observed in the range of 0.3–150 keV, the extended thermal emission (ETE), and finally the soft X-ray flare observed in the range of 0.3–10 keV using GRB 151027A as a prototype. The aim is to identify the crucial role of the SN and of its binary NS companion in the BdHN model, to analyze the interaction of the e^+e^- plasma generating the GRB with the SN ejecta via 3D simulations, and to compare and contrast the observational support of the BdHN model with the other traditional approaches. To facilitate the reader, we have made a special effort in referencing to the current works, in indicating new

developments and their observational verifications, and finally in giving references for the technical details in the text.

In Section 2, we outline the new results motivating our paper: (1) three thermal emissions processes in GRBs, compared and contrasted. The relativistic treatment that relates the velocity of expansion of the hard X-ray flare, of the soft X-ray flare and of the ETE to the observed fluxes and temperatures is particularly relevant for our work. (2) The 3D simulations of the hypercritical accretion in a BdHN, which are essential for obtaining the density profiles of the SN ejecta recently submitted for publication in Becerra et al. (2018). (3) The generalization of the spacetime representation of the BdHN. These are some useful conceptual tools needed to create a viable GRB model.

In Section 3, we refer to GRB 151027A as a prototype example of high-quality data, enabling the detailed time-resolved analysis for the UPE phase, with its thermal component, as well as the first high-quality data for studying the hard X-ray flare and especially for the clear evolution of the ETE. We perform the time-integrated analysis for the UPE, further analyze the two ultra-relativistic gamma-ray spikes in the UPE, and apply the fireshell model to the first spike. We identify the proper GRB (P-GRB), the baryon load $B = (1.92 \pm 0.35) \times 10^{-3}$; and an average CBM density of $(7.46 \pm 1.2) \text{ cm}^{-3}$, which are consistent with our numerical simulation presented in Section 6. We determine an initial Lorentz factor of the UPE $\Gamma_0 = 503 \pm 76$, confirming the clearly observed ultra-relativistic nature of the UPE.

In Section 4, we perform the time-resolved analysis for the hard X-ray flare and the soft X-ray flare, comparing and contrasting our results with the ones in the literature by Nappo et al. (2017). The hard X-ray flare is divided into eight time intervals, and we find a high significant thermal component existing in all time intervals (see Figure 8). We report the results of our time-resolved spectral analysis in the first five columns of Table 2. Using the best-fit model for a nonthermal component in the time interval 95–130 s, we determine a Lorentz factor $\Gamma = 3.28 \pm 0.84$ for the hard X-ray flare duration. The soft X-ray flare is analyzed in 4 time intervals, in which spectra are best fitted by a single power-law (PL).

In Section 5, we turn to the thermal component evolving across the hard X-ray flare by adopting the description in the GRB laboratory frame. Following our recent works (Ruffini et al. 2018c), we determine the expansion velocity evidencing the transition from an initial velocity $\approx 0.38c$ and increasing up to $0.98c$ in the late part; see column 6 of Table 2. This is the first relativistic treatment of the hard X-ray flare and its associated thermal emission clearly evidences the transition from an SN to an HN, which was first identified in GRB 151027A. We compare and contrast our results with the current ones in the literature.

In Section 6, we proceed to the hard X-ray flare and the soft X-ray flare theoretical explanation from the analysis of the e^+e^- plasma propagating and slowing down within the SN ejecta. The simulated velocity and radius of the hard X-ray flare and the soft X-ray flare are consistent with the observations. We visualize all these results by direct comparison of the observational data by *Swift*, the *International Gamma-ray Astrophysics Laboratory (INTEGRAL)*, *Fermi*, and *Agile*, in addition to the optical observations, with the theoretical understanding of the 3D dynamics of the SN recently jointly performed by our group in collaboration with the Los Alamos National Laboratory (Becerra et al. 2018). This visualization is

particularly helpful in order to appreciate the novel results made possible by the BdHN paradigm and also by allowing the visualization of a phenomena observed today but occurred 10 billion light years away in our past light cone. The impact of the e^+e^- plasma on the entire SN ejecta gives origin to the thermal emission from the external surface of the SN ejecta and, equally, we can therefore conclude that the UPE, the hard X-ray flare, and the soft X-ray flare are not a causally connected sequence (see Figures 14–17 and Table 2). Within our model, they are the manifestation of the same physical process of the BH formation as seen through different viewing angles, implied by the morphology and by the ~ 300 s rotation period of the HN ejecta.

In Section 7, we proceed to the summary, discussion, and conclusions:

1. In the summary, we have recalled the derived Lorentz gamma factor and the detailed time-resolved analysis of the light curves and spectra of UPE, hard X-ray flare, ETE, and soft X-ray flare. We mention a double spike structure in the UPE and in the FPA, which promises to be directly linked to the process of the BH formation. We have equally recalled our relativistic treatment of the ETE, which, for the first time, has allowed us to observe the transition of an SN into an HN—the main result of this paper.
2. WE have recalled in the discussions, using specific examples in this article, that our data analysis is performed within a consistent relativistic field-theoretical treatment. In order to be astrophysically significant, it needs the identification of the observed astrophysical components, including: the binary nature of the progenitor system, the presence of an SN component, and it also needs a 3D simulation of the process of hypercritical accretion in the binary progenitors. We have also recalled the special role of the rotation by which phenomena, traditionally considered different, are actually the same phenomenon as seen from different viewing angles.
3. Looking forward in the conclusions, three main implications follow from the BdHN model, which are now open to further scrutiny: (1) only 10% of the BdHNe whose line of sight lies in the equatorial plane of the progenitor binary system are actually detectable; in the other 90%, the UPE is not detectable due to the morphology of the SN ejecta (see Figure 2) and therefore the *Fermi* and *Swift* instruments are not triggered; (2) the E_{iso} , traditionally based on a spherically symmetric equivalent emission, has to be replaced by an E_{tot} , duly taking into account the contributions of the UPE, hard X-ray flare, ETE, and soft X-ray flare; (3) when the BdHNe are observed normally to the orbital plane, the GeV emission from the newly formed BH becomes observable, and this additional energy should also be accounted for.

We summarize in Table 1 the list of acronyms introduced in the present paper.

2. Recent Progress on BdHNe

We address three progresses obtained in the last year in the theory of BdHNe: (1) the identification of three different thermal emission processes, (2) the visualization of the IGC paradigm, and (3) an extended spacetime diagram of the BdHN

Table 1
Alphabetic Ordered List of the Acronyms Used in This Work

Extended Wording	Acronym
Binary-driven hypernova	BdHN
Black hole	BH
Carbon–oxygen core	CO _{core}
Circumburst medium	CBM
Extended thermal emission	ETE
Flare plateau afterglow	FPA
Gamma-ray burst	GRB
Gamma-ray flash	GRF
Induced gravitational collapse	IGC
Massive neutron star	MNS
Neutron star	NS
New neutron star	ι NS
Ultra-relativistic prompt emission	UPE
Proper gamma-ray burst	P-GRB
Short gamma-ray burst	S-GRB
Short gamma-ray flash	S-GRF
Supernova	SN
Ultrashort gamma-ray burst	U-GRB
White dwarf	WD
X-ray flash	XRF

with a viewing angle in the equatorial plane of the binary progenitors.

One of the first examples of a thermal emission has been identified in the early seconds after the trigger of some long GRBs (Ryde 2004; Ryde et al. 2006; Ryde & Pe’er 2009). This emission has been later identified in the BdHN model with the soft X-ray emission occurring in the photosphere of convective outflows in the hypercritical accretion process from the newly born SN into the NS binary companion. Additional examples have been given in BdHNe (Fryer et al. 2014) and in XRFs (Becerra et al. 2016). These process are practically Newtonian in character with the velocity of expansions of the order of 10^8 – 10^9 cm s^{−1} (see e.g., Izzo et al. 2012, for the case of GRB 090618).

A second thermal emission process has been identified in the acceleration process of GRBs, when the self-accelerating optically thick e^+e^- plasma reaches transparency and a thermal emission with very high Lorentz factor $\Gamma \sim 10^2$ – 10^3 is observed. This has been computed both in the fireball model (Piran 1999; Daigne & Mochkovitch 2002; Pe’er et al. 2007) and in the fireshell model (Ruffini 1999; Ruffini et al. 2000). The difference consists in the description of the equations of motion of the fireball assumed in the literature and instead is explicitly evaluated in the fireshell model from the integration of classical and quantum magnetohydrodynamic process (see also Ruffini et al. 2007b, and references therein). The moment of transparency leads to a thermal emission whose relativistic effect has been evaluated, leading to the concept of the equitemporal surface (EQTS; Bianco & Ruffini 2005a). This derivation has also been successfully applied to short GRBs (Ruffini et al. 2015, 2016a; Aimuratonov et al. 2017) and is here applied in Section 3 to the UPE.

There is finally a third additional ETE observed in BdHNe and in the X-ray flares (Ruffini et al. 2018c). This ETE has allowed the determination of the velocity of expansion and the Lorentz gamma factor of the thermal emission based on the variation in time of the observed radius and temperature of the thermal emission (see the equation in Figure 1) under the assumption of uncollimated emission and considering only the radiation coming

$$\frac{C\beta^5}{4[\ln(1+\beta) - (1-\beta)\beta]^2} \left(\frac{1+\beta}{1-\beta}\right)^{1/2} = \frac{D_L(z)}{1+z} \frac{1}{t_{a,2}^d - t_{a,1}^d} \left(\sqrt{\frac{F_{\text{bb,obs}}(t_{a,2}^d)}{\sigma T_{\text{obs}}^4(t_{a,2}^d)}} - \sqrt{\frac{F_{\text{bb,obs}}(t_{a,1}^d)}{\sigma T_{\text{obs}}^4(t_{a,1}^d)}} \right)$$

Derived Velocity Parameter Observable

Figure 1. Equation to compute the velocity from the thermal component. This equation is summarized from Ruffini et al. (2018c). The left-hand side term is only a function of velocity β , and the right-hand side term is only of the observables. $D_L(z)$ is the luminosity distance for redshift z . From the observed thermal flux, $F_{\text{bb,obs}}$, and the temperature, T_{obs} , at arrival times of the detector $t_{a,1}^d$ and $t_{a,2}^d$, the velocity and the corresponding Lorentz factor can be computed. This equation assumes uncollimated emission and considers only the radiation coming from the line of sight. The computed velocity is instantaneous, and there is no reliance on the expansion history.

from the line of sight. The left-hand side term is only a function of the velocity, β , the right-hand side term is only function of the observables, and $D_L(z)$ is the luminosity distance for redshift z . Therefore, from the observed thermal flux, $F_{\text{bb,obs}}$, and the temperature, T_{obs} , at times t_1 and t_2 , we can compute the velocity, β . This highly nonlinear equation is not straightforwardly solvable analytically, so in the present paper, we solve it numerically after verifying the monotonically increasing behavior of the left-hand side term as a function of β (see, e.g., C. L. Bianco et al. 2018, in preparation).

The second progress has been presented in Becerra et al. (2016) and more recently in Becerra et al. (2018). The first 3D smoothed particle hydrodynamics (SPH) simulations of the IGC leading to a BdHN are there presented. We simulate the SN explosion of a CO_{core} forming a binary system with a NS companion. We follow the evolution of the SN ejecta, including their morphological structure, subjected to the gravitational field of both the new NS (νNS), formed at the center of the SN, and the one of the NS companion. We compute the accretion rate of the SN ejecta onto the NS companion as well as onto the νNS from SN matter fallback. We determine the fate of the binary system for a wide parameter space, including different CO_{core} masses, orbital periods (~ 300 s), and SN explosion geometry and energies. We evaluate, for selected NS equations of state, if the accretion process leads the NS either to the mass-shedding limit or to the secular asymmetric instability for the gravitational collapse to a BH or to a more massive, fast rotating but stable NS. We also assess whether the binary keeps or is not gravitationally bound after the SN explosion, hence exploring the space of the binary and SN explosion parameters leading to the formation of νNS –NS or νNS –BH binaries. The consequences of our results for the modeling of GRBs via the IGC scenario are discussed in Becerra et al. (2018). The relevance of these simulations for GRB 151027A, which is subject of this paper, will be illustrated below (see Figure 2).

Finally, we present an update of the BdHN spacetime diagram (see Figure 3) that clearly evidences the large number of episodes and physical processes, each with observationally computed time-varying Lorentz Γ factors, which require the systematic use of the four different time coordinates, as already indicated in Ruffini et al. (2001a). The diagram illustrates departures from the traditional collapsar-fireball description of a GRB. The diagram shows how the sequence of events of the UPE, of the hard X-ray flare, and of the soft X-ray flare occur in a sequence only when parameterized in the arrival time and when they are not, in fact, causally related.

We recall that, within our model, the line of sight of the prototypical GRB 151027A lies in the equatorial plane of the progenitor binary system. The more general case of an arbitrary viewing angle has been explored in Ruffini et al. (2018a), and some specific additional characteristic features common to the collapsar model have been manifested in this more general case.

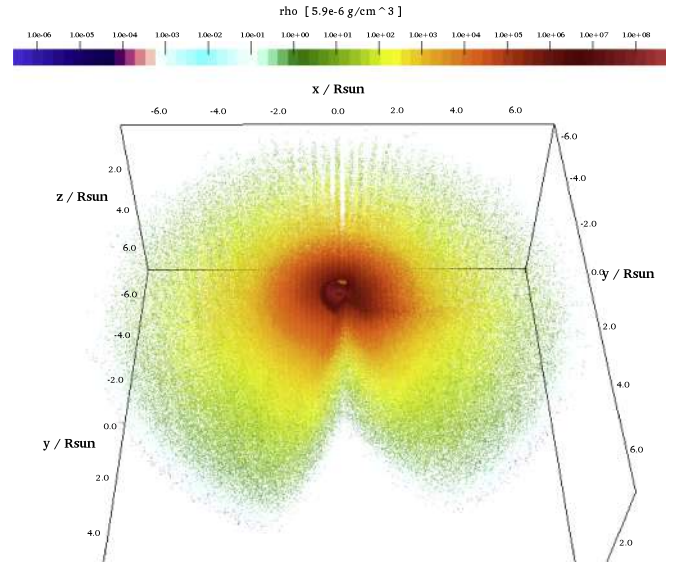


Figure 2. A 3D, half-hemisphere view of the density distribution of the SN ejecta at the moment of BH formation in a BdHN. The simulation is performed with an SPH code that follows the SN ejecta expansion under the influence of the gravitational field of both the νNS formed at the center of the SN and of the NS companion. It includes the effects of the orbital motion and the changes in the NS gravitational mass by the hypercritical accretion process (see Becerra et al. 2016, for additional details). The binary parameters of this simulation are: the NS companion has an initial mass of $2.0 M_{\odot}$; the CO_{core} , obtained from a progenitor with ZAMS mass, $M_{\text{ZAMS}} = 30 M_{\odot}$, which leads to a total ejecta mass of $7.94 M_{\odot}$ and to a $1.5 M_{\odot}$ νNS , and the orbital period is $P \approx 5$ min (binary separation $a \approx 1.5 \times 10^{10}$ cm). Only the sources, whose ultra-relativistic emission lies within the allowed cone of $\sim 10^\circ$ with low baryon contamination, will trigger the gamma-ray instrument (e.g., *Fermi*/GBM or *Swift*/BAT).

3. UPE

GRB 151027A was detected and located by the *Swift* Burst Alert Telescope (BAT; Maselli et al. 2015). It was also detected by the *Fermi* Gamma-ray Burst Monitor (GBM; Toelge et al. 2015), Monitor of All-sky X-ray Image (MAXI; Masumitsu et al. 2015), and by *Konus-Wind* (Golenetskii et al. 2015). The *Swift* X-Ray Telescope (XRT) started its observation 87 s after the burst trigger (Goad et al. 2015). The redshift of the source, measured through the Mg II doublet in absorption from the Keck/High Resolution Echelle Spectrometer (HIRES) spectrum, is $z = 0.81$ (Perley et al. 2015). The Large Area Telescope (LAT) boresight of the source was 10° at the time of the trigger, there are no associated high-energy photons; an upper limit of observed count flux is computed as 9.24×10^{-6} photons $\text{cm}^{-2} \text{s}^{-1}$ following the standard *Fermi*-LAT likelihood analysis. The BAT light curve shows a complex peaked structure lasting at least 83 s. XRT began observing the field 48 s after the BAT trigger. The GBM light curve consists of various pulses with a duration of about 68 s in the 50–300 keV

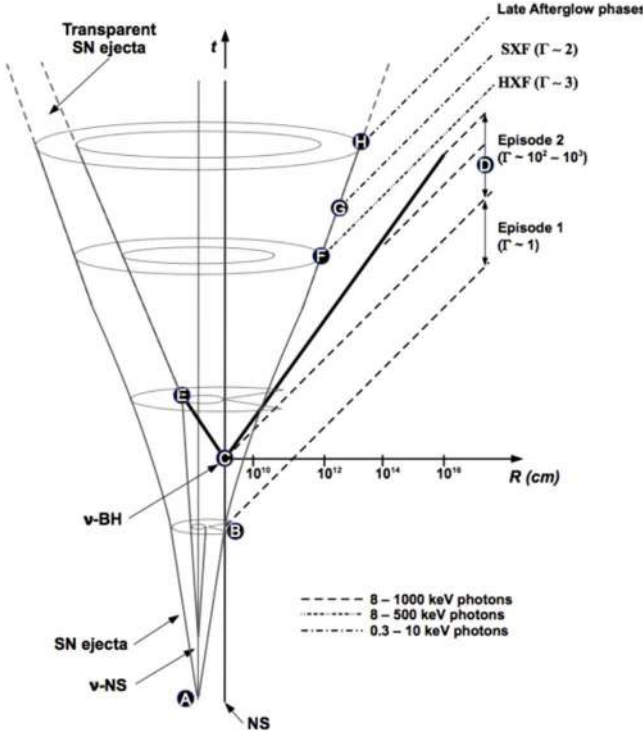


Figure 3. Spacetime diagram (not in scale) of BdHNe. The CO_{core} explodes as an SN at point A and forms a ν NS. The companion NS (bottom right line) accretes the SN ejecta starting from point B, giving rise to the nonrelativistic Episode 1 emission (with Lorentz factor $\Gamma \approx 1$). At point C, the NS companion collapses into a BH, and an e^+e^- plasma—the dyadosphere—is formed (Ruffini 1999). The following self-acceleration process occurs in a spherically symmetric manner (thick black lines). A large portion of plasma propagates in the direction of the line of sight, where the environment is cleaned up by the previous accretion into the NS companion, finding a baryon load of $B \lesssim 10^{-2}$ and leading to the GRB UPE gamma-ray spikes (Episode 2, point D) with $\Gamma \sim 10^2$ – 10^3 . The remaining part of the plasma impacts with the high-density portion of the SN ejecta (point E), propagates inside the ejecta encountering a baryon load of $B \sim 10^1$ – 10^2 , and finally reaches transparency, leading to the hard X-ray flare emission (point F) in gamma-rays with an effective Lorentz factor of $\Gamma \lesssim 10$ and to soft X-ray flare emission (point G) with an effective $\Gamma \lesssim 4$, which are then followed by the late afterglow phases (point H). For simplicity, this diagram is 2D and static and does not attempt to show the 3D rotation of the ejecta.

band. The *Konus-Wind* light curve consists of various pulses with a total duration of ~ 66 s. The MAXI detection is not significant, but the flux is consistent with the interpolation from the *Swift*/XRT light curve. The first 25 s (rest frame 14 s) corresponds to the UPE. It encompasses two spikes of duration of ≈ 8.5 s and ≈ 7.5 s, respectively, with a separation between two peaks of ≈ 17 s (see Figure 4 (a)). The rest-frame 1 – 10^4 keV isotropic equivalent energies computed from the time-integrated spectra of these two spikes (see Figures 4 (b) and (c)) are $E_{\text{iso},1} = (7.26 \pm 0.36) \times 10^{51}$ erg and $E_{\text{iso},2} = (4.99 \pm 0.60) \times 10^{51}$ erg, respectively.

A similar analysis was performed by Nappo et al. (2017). They describe the two spikes of the UPE by a single light curve with a “Fast Rise and Exponential Decay” (FRED) shape.

We analyze the first spike (see Figure 5) as the traditional UPE of a long GRB within the fireshell model (see, e.g., Ruffini et al. 2003, for a review).

Thanks to the wide energy range of the *Fermi*-GBM instrument (8–1000 keV), it has been possible to perform a time-resolved analysis within the UPE phase to search for the typical P-GRB emission at the transparency of the e^+e^- -baryon

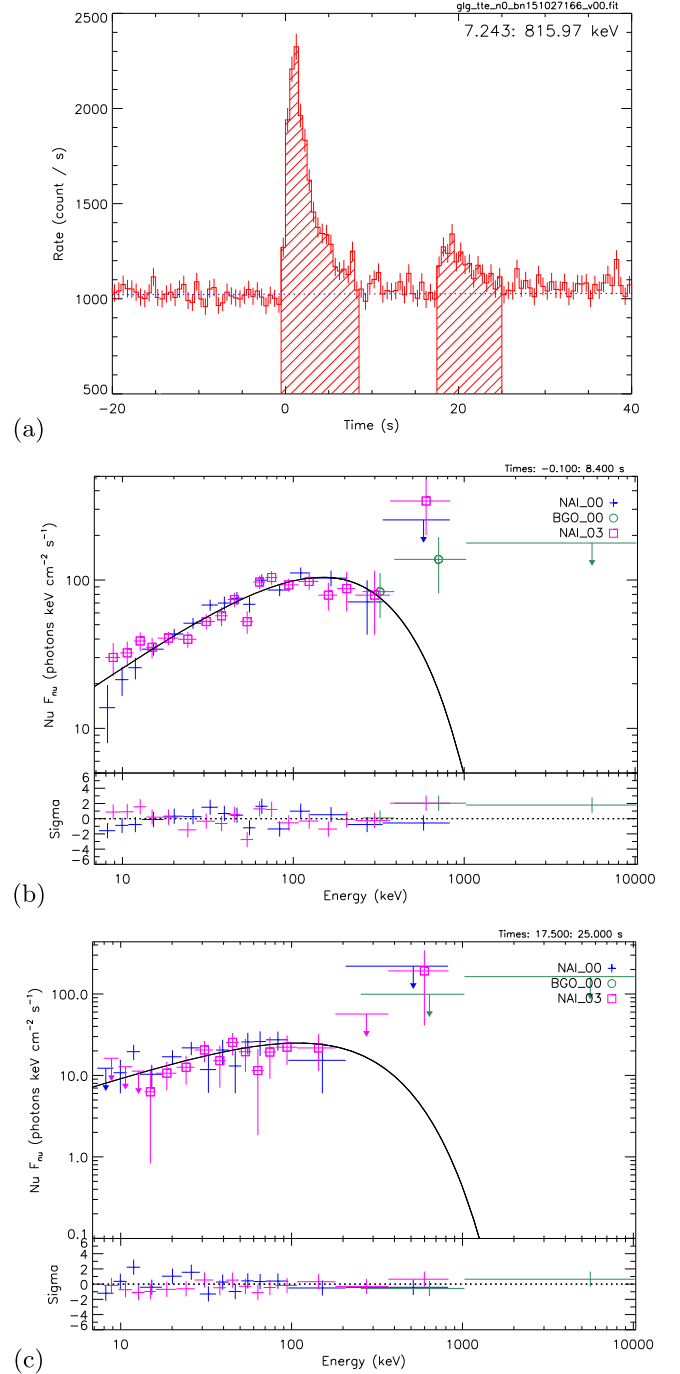


Figure 4. (a) *Fermi*-GBM light curve from the Na I-n0 detector (≈ 8 – 800 keV) of the UPE of GRB 151027A. The dotted horizontal line corresponds to the γ -ray background. (b) Time-integrated νF_ν spectrum of the first spike. (c) Time-integrated νF_ν spectrum of the second spike.

plasma (Ruffini 1999; Ruffini et al. 2000, 2001b). Indeed, we find this thermal spectral feature in the time interval $T_0 - 0.1$ – $T_0 + 0.9$ s (with respect to the *Fermi*-GBM trigger time T_0). The best-fit model of this emission is a composition of a blackbody (BB) spectrum and a cutoff power-law model (CPL, see Figure 5(a)). The BB component has an observed temperature of $kT = (36.6 \pm 5.2)$ keV and an energy of $E_{\text{BB}} = (0.074 \pm 0.038) \times E_{\text{iso},1} = (5.3 \pm 2.7) \times 10^{50}$ erg. These values are in agreement with an initial e^+e^- plasma of energy, $E_{\text{iso},1}$, with a baryon load of $B = (1.92 \pm 0.35) \times 10^{-3}$, and a Lorentz factor

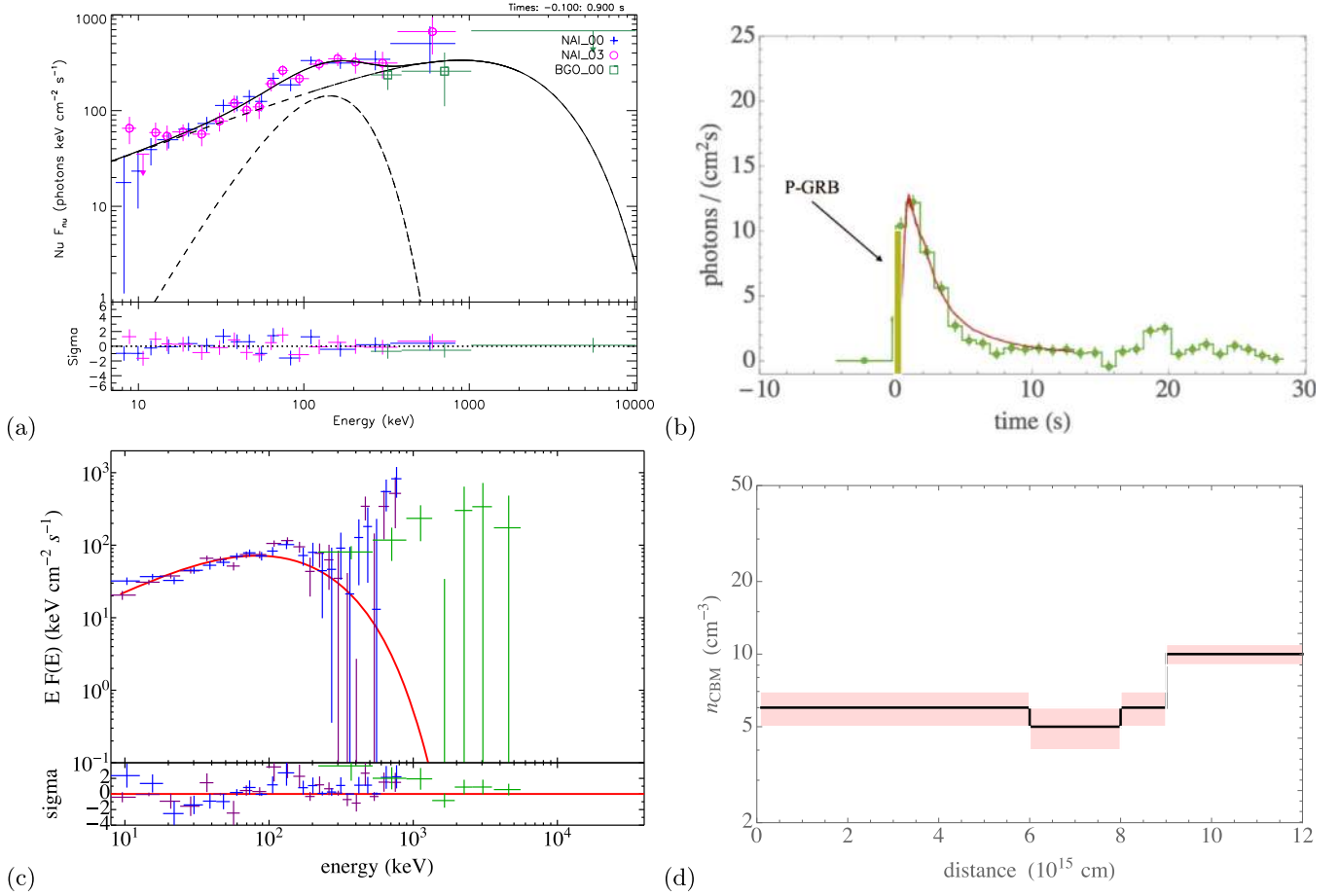


Figure 5. Ultra-relativistic prompt emission (UPE). (a) The combined Na I-n0, n3+BGO-b0 νF_ν spectrum of the P-GRB in the time interval $T_0 - 0.1$ – $T_0 + 0.9$ s. The best-fit model is CPL+BB. (b) The comparison between the background subtracted 10–1000 keV *Fermi*-GBM light curve (green) and the simulation with the fireshell model (red curve) in the time interval $T_0 + 0.9$ – $T_0 + 9.6$ s. (c) The comparison between the Na I-n0 (purple squares), n3 (blue diamonds), and the BGO-b0 (green circles) νF_ν data in the time interval, $T_0 + 0.9$ – $T_0 + 9.6$ s, and the simulated fireshell spectrum (red curve). (d) The radial density of the CBM clouds used for the above UPE light curve and spectrum simulations.

and a radius at the transparency condition of $\Gamma_0 = 503 \pm 76$ and $r_{tr} = (1.92 \pm 0.17) \times 10^{13}$ cm, respectively.

We turn now to the simulation of the remaining part of the first spike of the UPE (from $T_0 + 0.9$ s to $T_0 + 9.6$ s). In the fireshell model, this emission occurs after the P-GRB, and results from the slowing down of the accelerated baryons are due to their interaction with the CBM (Ruffini et al. 2002, 2006; Patricelli et al. 2012). To simulate the UPE light curve and its corresponding spectrum, we need to derive the number density of the CBM clouds surrounding the burst site. The agreement between the observations and the simulated light curve (see Figure 5(b)) and the corresponding spectrum (see Figure 5(c)) is obtained for an average CBM density of $(7.46 \pm 1.2) cm^{-3}$ (see Figure 5(d)), consistent with the typical value of the long-burst host galaxies at radii $\approx 10^{16}$ cm. By contrast, the second spike of the UPE appears to be featureless.

The general conclusion of the UPE is the following: from the morphological 3D simulation, the SN ejecta is distorted by the binary accretion. A cone of very low baryon contamination is formed along the direction from the SN center pointing to the newly born BH (see Figure 2). A portion of e^+e^- plasma generated from the BH formation propagates through this cone and engulfs a low baryon load of $B = (1.92 \pm 0.35) \times 10^{-3}$ and reaches a Lorentz gamma factor of $\Gamma_0 = 503 \pm 76$. The

e^+e^- plasma self-accelerates and expands ultra-relativistically until reaching transparency (Ruffini 1998; Aksenov et al. 2007; Ruffini et al. 2010), when a short-duration (< 1 s) thermal emission occurs: the P-GRB. The ultra-relativistic associated baryons then interact with the CBM clouds. The dynamics of the plasma has been integrated by the classical hydrodynamics equations and by the equation of annihilation-creation rate (Bianco et al. 2001; Bianco & Ruffini 2004, 2005a, 2005b, 2006). It enables us to simulate the structure of spikes in the prompt emission, and it has been applied to the case of BdHNe (see, e.g., Ruffini et al. 2002, 2016a; Bernardini et al. 2005; Izzo et al. 2012; Penacchioni et al. 2012, 2013). For a typical baryon load for the cone direction, $10^{-4} \lesssim B \lesssim 10^{-2}$, a Lorentz factor of $\Gamma \approx 10^2$ – 10^3 , characteristic of the prompt emission occurs in a distance $\approx 10^{15}$ – 10^{17} cm from the BH (Ruffini et al. 2016b).

1. A double emission is clearly manifested by presence of the two spikes at the time interval of the 17 s (rest frame 9 s). We are currently examining the possibility that this double emission is an imprinting of the process of the BH formation.
2. When we take into account the rotation period of the binary ~ 300 s, we see that UPE occurs in a cone centered in the BH of 10° .

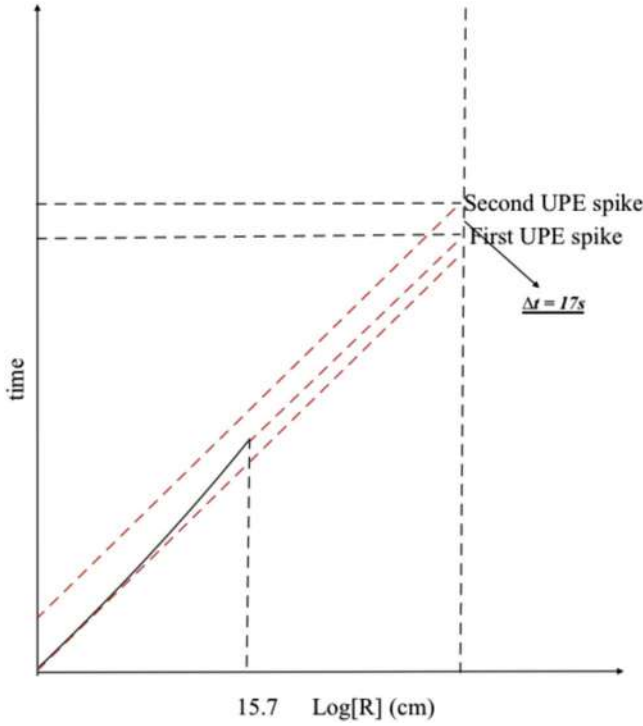


Figure 6. Spacetime diagram of the UPE. The initial e^+e^- plasma self-accelerates in the small-density cone until it reaches transparency (curved black line), producing the first of the two ultra-relativistic UPE spikes (bottom solid red line). The second one is produced by a latter emission from the BH formation, with a difference in the observed time of ~ 17 s (rest frame of ~ 9.4 s, top solid red line).

3. This conical region is endowed with a very low density determined by the P-GRB and the inferred CBM medium density of $(7.46 \pm 1.2) \text{ cm}^{-3}$ up to 10^{16} cm from BH along the cone (see Figure 5(d)).

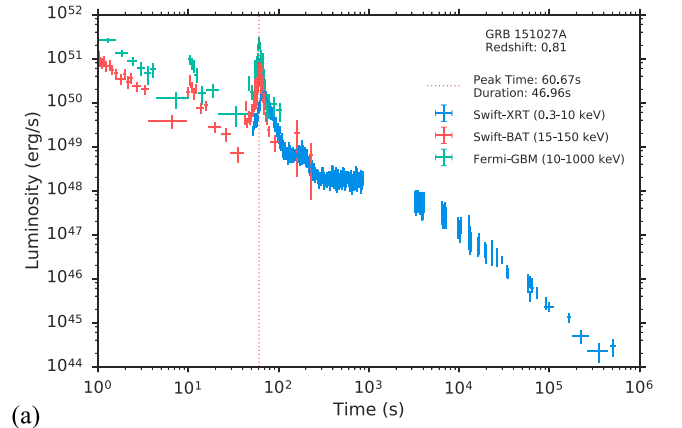
This conceptual framework can, in principle, explain the featureless nature of the second spike, which propagates along the region that has already been swept by the first spike (see Figure 6).

4. Hard and Soft X-Ray Flare

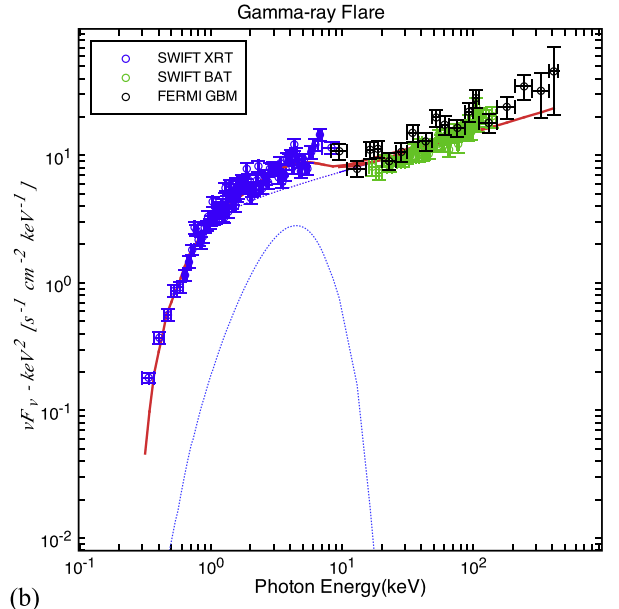
4.1. Hard X-Ray Flare

We turn now to the hard X-ray flare and the soft X-ray flare. The hard X-ray flare is observed in the time interval 94–180 s (corresponding to the rest-frame time interval 52–99 s; see Figure 7(a)). The luminosity light curves in the rest-frame energy bands of 10–1000 keV for *Fermi*-GBM (green), 15–150 keV for *Swift*-BAT (red), and 0.3–10 keV for *Swift*-XRT (blue) are displayed. The total isotropic energy of the hard X-ray flare is $E_\gamma = (3.28 \pm 0.13) \times 10^{52} \text{ erg}$. The overall spectrum is best fit by a superposition of a PL function with an index of -1.69 ± 0.01 and a BB model with a temperature of $kT = 1.13 \pm 0.08 \text{ keV}$ (see Figure 7(b)).

We perform a more detailed analysis by dividing the whole hard X-ray flare duration (94–180 s) into eight intervals (indicated with Δt_a^d in Table 2). Among these time intervals, the first six have both BAT and XRT data (total energy range 0.3–150 keV), while the last two fits involve XRT data only (an energy range of 0.3–10 keV). The XRT data were extremely piled up, and corrections have been performed in a conservative



(a)



(b)

Figure 7. (a) Luminosity light curves in the rest-frame energy bands: 10–1000 keV for *Fermi*-GBM (green), 15–150 keV for *Swift*-BAT (red), and 0.3–10 keV for *Swift*-XRT (blue). The red dotted line marks the position of the hard X-ray flare. (b) Time-integrated νF_ν spectrum of the hard X-ray flare and the PL+BB model (solid red curve) that best fit the data.

way to ascertain that the BB is not due to pileup effects (Romano et al. 2006). The absorption of the spectrum below 2 keV has been also taken into due account. Here, we use the following spectral energy distributions to fit the data: power law (PL), cutoff power law (CPL), PL+BB, and CPL+BB, PL+BB, and CPL+BB. An extra BB component is always preferred to the simple PL models and, only in the sixth interval, to the CPL model whose cutoff energy may be constrained within a 90% significance. The results of the time-resolved analysis are shown in Figure 8 and summarized in Table 2. The BB parameters and errors in Table 2 correspond, respectively, to the main values and the 90% probability interval errors with respect to the central values, both obtained from the Markov Chain-Monte Carlo method applied in *XSpec* with 10^5 steps (excluding first 10^4). The values are in line with the ones corresponding to minimum χ^2 and with errors to the ones corresponding to intervals obtained from the difference $\Delta\chi^2 = 2.706$ from the minimum χ^2 value. The only exception is the first time bin where χ_{\min}^2 value is almost two times lower than the main value. It is useful to infer the bulk Lorentz factor of the hard X-ray flare emission

Table 2
Hard X-Ray Flare: Parameters of the Time-resolved Spectral Analysis

Δt_a^d (s)	Model	α	E_p (keV)	kT_{obs} (keV)	A_{BB} (ph cm $^{-2}$ s $^{-1}$)	ϕ_0 (10 12 cm)	β	Γ	R (10 12 cm)
94–100	BB+PL	$1.349^{+0.024}_{-0.036}$		$2.2^{+1.1}_{-1.1}$	$0.052^{+0.043}_{-0.034}$	$0.065^{+0.070}_{-0.064}$	$0.38^{+0.19}_{-0.31}$	$1.079^{+0.138}_{-0.077}$	$0.10^{+0.11}_{-0.10}$
100–110	BB+PL	$1.293^{+0.029}_{-0.031}$		$2.57^{+0.43}_{-0.50}$	$0.206^{+0.083}_{-0.084}$	$0.094^{+0.037}_{-0.041}$	$0.606^{+0.042}_{-0.049}$	$1.257^{+0.057}_{-0.053}$	$0.194^{+0.077}_{-0.086}$
110–120	BB+PL	$1.392^{+0.028}_{-0.033}$		$2.17^{+0.22}_{-0.26}$	$0.62^{+0.14}_{-0.15}$	$0.229^{+0.053}_{-0.062}$	$0.852^{+0.035}_{-0.052}$	$1.91^{+0.26}_{-0.24}$	$0.80^{+0.21}_{-0.25}$
120–130	BB+PL	$1.732^{+0.049}_{-0.057}$		$1.10^{+0.14}_{-0.12}$	$0.592^{+0.077}_{-0.073}$	$0.87^{+0.23}_{-0.20}$	$0.957^{+0.014}_{-0.028}$	$3.46^{+0.78}_{-0.76}$	$5.7^{+1.8}_{-2.3}$
130–140	BB+PL	$1.82^{+0.11}_{-0.14}$		$0.617^{+0.046}_{-0.043}$	$0.247^{+0.037}_{-0.038}$	$1.79^{+0.30}_{-0.28}$	$0.983^{+0.0046}_{-0.0079}$	$5.6^{+1.0}_{-1.0}$	$19.1^{+4.2}_{-5.6}$
140–150	CPL+PL	$1.65^{+0.15}_{-0.16}$	$7.3^{+66.3}_{-4.6}$	$0.469^{+0.065}_{-0.064}$	$0.102^{+0.028}_{-0.027}$	$1.99^{+0.61}_{-0.61}$	$0.919^{+0.054}_{-0.560}$	$2.5^{+1.8}_{-1.5}$	$9.5^{+4.4}_{-9.5}$
150–160	BB+PL	$2.40^{+0.45}_{-0.34}$		$0.386^{+0.061}_{-0.061}$	$0.046^{+0.016}_{-0.015}$	$1.97^{+0.71}_{-0.70}$	$0.935^{+0.048}_{-0.934}$	$2.8^{+2.7}_{-1.8}$	$10.5^{+5.5}_{-10.5}$
160–180	BB+PL	$2.15^{+0.29}_{-0.34}$		$0.193^{+0.032}_{-0.030}$	$0.020^{+0.011}_{-0.013}$	$5.2^{+2.3}_{-2.3}$	$0.953^{+0.042}_{-0.952}$	$3.3^{+7.0}_{-2.3}$	32^{+21}_{-32}

Note. Columns list, respectively, the time interval of the spectral analysis; the PL or CPL Index α ; the CPL peak energy E_p when present; the BB observed temperature, kT_{obs} ; and normalization A_{BB} , fitted from Section 4. The quantity, ϕ_0 ; the expansion velocity, β ; the Lorentz factor, Γ ; and the effective thermal emitter radius in the laboratory frame, R , inferred from Section 5.

from the nonthermal component of the spectrum. Using the *Fermi* data, the best-fit model for this nonthermal component in the time interval 95–130 s is a CPL with a spectral cutoff energy, $E_c = 926 \pm 238$ keV. Such a cutoff can be caused by $\gamma\gamma$ absorption, for which the target photon's energy is comparable to E_c , i.e., $E_c \gtrsim [\Gamma m_e c^2 / (1+z)]^2 / E_c$ and, therefore, the Lorentz factor can be deduced by

$$\Gamma \approx \frac{E_c}{m_e c^2} (1+z), \quad (1)$$

where m_e is the electron mass. From the above value of E_c , we infer $\Gamma = 3.28 \pm 0.84$, which represents an average over the hard X-ray flare duration. It is in the range of the ones observed in thermal component (see the first five columns of the Table 2), coinciding in turn with the numerical simulation of the interaction of the e^+e^- plasma with the SN ejecta described in the Section 6.

4.2. Soft X-Ray Flare

The soft X-ray flare, which has been discussed in Ruffini et al. (2018c), peaks at a rest-frame time of $t_p = (184 \pm 16)$ s, has a duration of $\Delta t = (164 \pm 30)$ s, a peak luminosity of $L_p = (7.1 \pm 1.8) \times 10^{48}$ erg s $^{-1}$, and a total energy in the rest-frame 0.3–10 keV energy range of $E_X = (4.4 \pm 2.9) \times 10^{51}$ erg. The overall spectrum within its duration, Δt , is best-fit by a PL model with a PL index of -2.24 ± 0.03 (see Figure 9).

Here, we also perform a time-resolved analysis of the soft X-ray flare. We divide the total interval Δt into four subintervals, i.e., 235–300 s, 300–365 s, 365–435 s, and 435–500 s in the observer frame (see Figure 10). The best-fits of each of these four time intervals are PL models with indexes ranging from -2.3 to -2.1 , which are consistent with the typical values inferred in Ruffini et al. (2018c).

The complete spacetime diagram, showing UPE, hard X-ray flare, and soft X-ray flare, is represented in Figure 11.

5. Evolution of Thermal Component around the Hard X-Ray Flare

Following Figure 1, it is possible to infer the expansion velocity β (i.e., the velocity in units of the velocity of light c). We assume that the blackbody emitter has spherical symmetry and expands with a constant Lorentz gamma factor. Therefore,

the expansion velocity β is also constant during the emission. The relations between the comoving time, t_{com} ; the laboratory time, t ; the arrival time, t_a ; and the arrival time, t_a^d , at the detector (see Bianco et al. 2001; Ruffini et al. 2001c, 2002; Bianco & Ruffini 2005a) in this case become:

$$t_a^d = t_a(1+z) = t(1-\beta \cos \vartheta)(1+z) = \Gamma t_{\text{com}}(1-\beta \cos \vartheta)(1+z). \quad (2)$$

We can infer an effective radius R of the blackbody emitter from: (1) the observed blackbody temperature, T_{obs} , which comes from the spectral fit of the data; (2) the observed bolometric blackbody flux, $F_{\text{bb,obs}}$, computed from T_{obs} and the normalization of the blackbody spectral fit; and (3) the cosmological redshift z of the source (see also Izzo et al. 2012). We recall that $F_{\text{bb,obs}}$, by definition, is given by

$$F_{\text{bb,obs}} = \frac{L}{4\pi D_L(z)^2}, \quad (3)$$

where $D_L(z)$ is the luminosity distance of the source, which in turn is a function of the cosmological redshift z , and L is the source bolometric luminosity (i.e., the total emitted energy per unit time). L is Lorentz invariant, so we can compute it in the comoving frame of the emitter using the usual blackbody expression:

$$L = 4\pi R_{\text{com}}^2 \sigma T_{\text{com}}^4, \quad (4)$$

where R_{com} and T_{com} are the comoving radius and the comoving temperature of the emitter, respectively, and σ is the Stefan–Boltzmann constant. We recall that T_{com} is constant over the entire shell due to our assumption of spherical symmetry. From Equations (3) to (4), we then have

$$F_{\text{bb,obs}} = \frac{R_{\text{com}}^2 \sigma T_{\text{com}}^4}{D_L(z)^2}. \quad (5)$$

We now need the relation between T_{com} and the observed blackbody temperature, T_{obs} . Considering both the cosmological redshift and the Doppler effect due to the velocity of the emitting surface, we have:

$$T_{\text{obs}}(T_{\text{com}}, z, \Gamma, \cos \vartheta) = \frac{T_{\text{com}}}{(1+z)\Gamma(1-\beta \cos \vartheta)} = \frac{T_{\text{com}} \mathcal{D}(\cos \vartheta)}{1+z}, \quad (6)$$

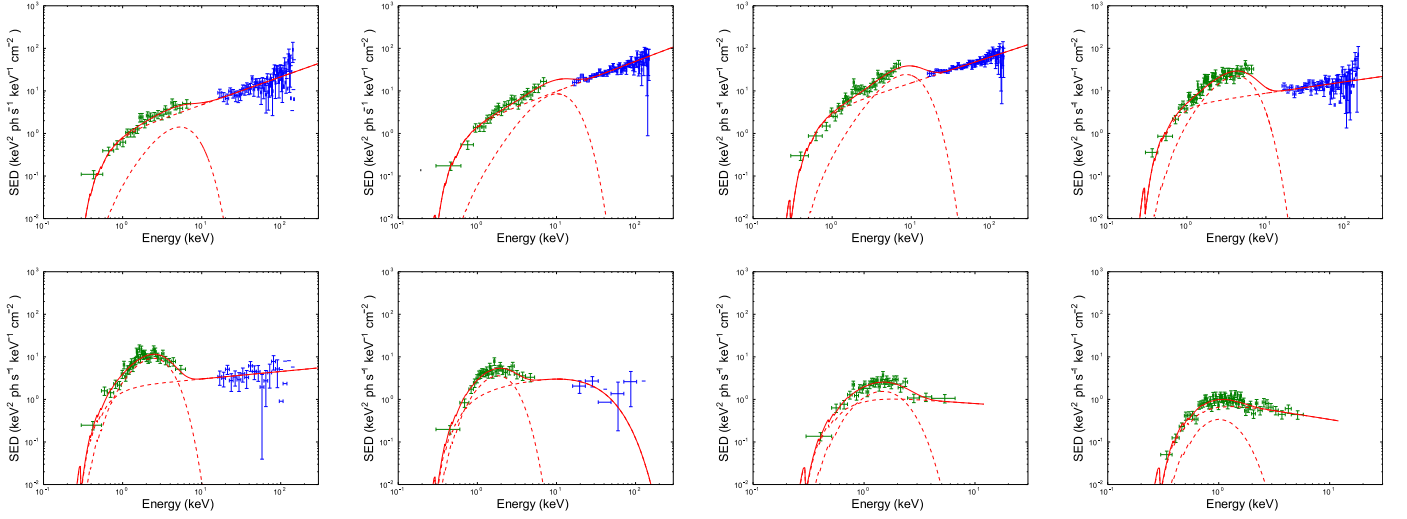


Figure 8. Hard X-ray flare: time-resolved νF_ν spectra of the eight time intervals in Table 2 (from the top left to the right, and from the bottom left to the right). XRT data are displayed in green and BAT data are in blue; BAT data points with no vertical lines corresponds to upper limits. Plots correspond to parameters obtained from minimum χ^2 fit.

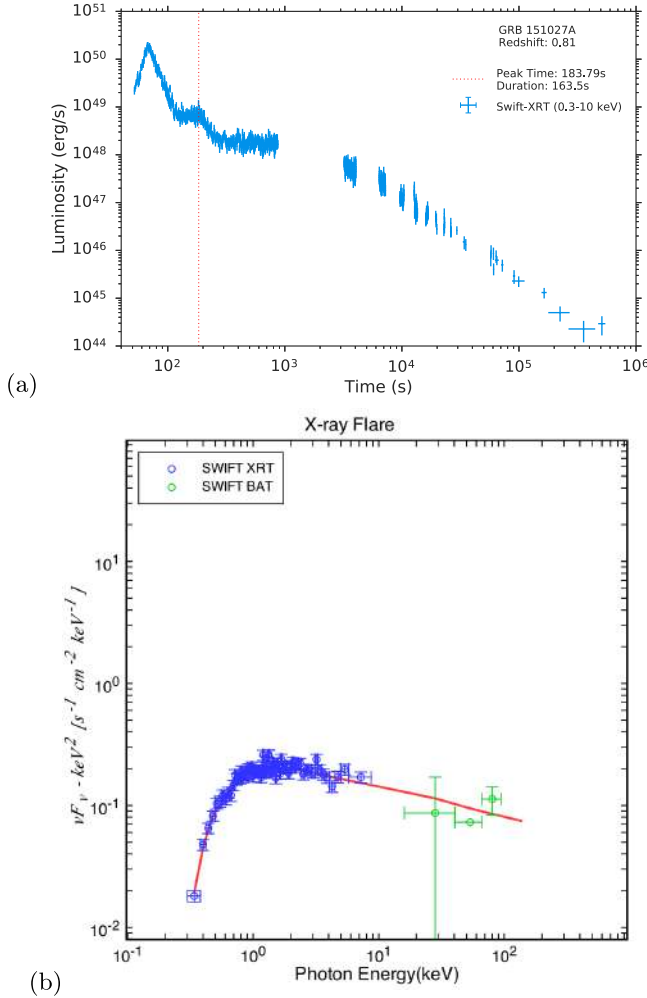


Figure 9. (a) Rest-frame 0.3–10 keV luminosity light curve of GRB 151027A. The red dotted line marks the position of the soft X-ray flare. (b) Time-integrated νF_ν spectrum of the X-ray flare and the PL model (solid red curve) that best fits the data.

where we have defined the Doppler factor $\mathcal{D}(\cos \vartheta)$ as

$$\mathcal{D}(\cos \vartheta) \equiv \frac{1}{\Gamma(1 - \beta \cos \vartheta)}. \quad (7)$$

Equation (6) gives us the observed blackbody temperature of the radiation coming from different points of the emitter surface, corresponding to different values of $\cos \vartheta$. However, since the emitter is at a cosmological distance, we are not able to resolve spatially the source with our detectors. Therefore, the temperature that we actually observe corresponds to an average of Equation (6) computed over the emitter surface:

$$\begin{aligned} T_{\text{obs}}(T_{\text{com}}, z, \Gamma) &= \frac{1}{1+z} \frac{\int_{\beta}^1 \mathcal{D}(\cos \vartheta) T_{\text{com}} \cos \vartheta d \cos \vartheta}{\int_{\beta}^1 \cos \vartheta d \cos \vartheta} \\ &= \frac{2}{1+z} \frac{\beta(\beta-1) + \ln(1+\beta)}{\Gamma \beta^2 (1-\beta^2)} T_{\text{com}} \\ &= \Theta(\beta) \frac{\Gamma}{1+z} T_{\text{com}}, \end{aligned} \quad (8)$$

where we defined

$$\Theta(\beta) \equiv 2 \frac{\beta(\beta-1) + \ln(1+\beta)}{\beta^2}. \quad (9)$$

We have used the fact that due to relativistic beaming, we observe only a portion of the surface of the emitter defined by

$$\beta \leq \cos \vartheta \leq 1, \quad (10)$$

and we used the definition of Γ given above. Therefore, inverting Equation (8), the comoving blackbody temperature, T_{com} , can be computed from the observed blackbody temperature, T_{obs} , the source cosmological redshift, z , and the emitter Lorentz gamma factor in the following way:

$$T_{\text{com}}(T_{\text{obs}}, z, \Gamma) = \frac{1+z}{\Theta(\beta)\Gamma} T_{\text{obs}}. \quad (11)$$

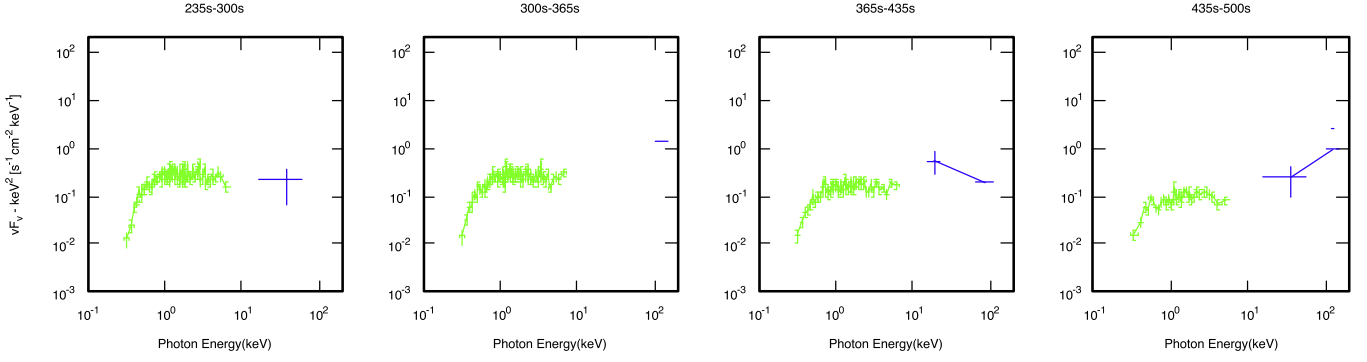


Figure 10. Soft X-ray flare: time-resolved BAT (blue) and XRT (green) νF_ν spectra of the soft X-ray flare in the indicated time intervals.

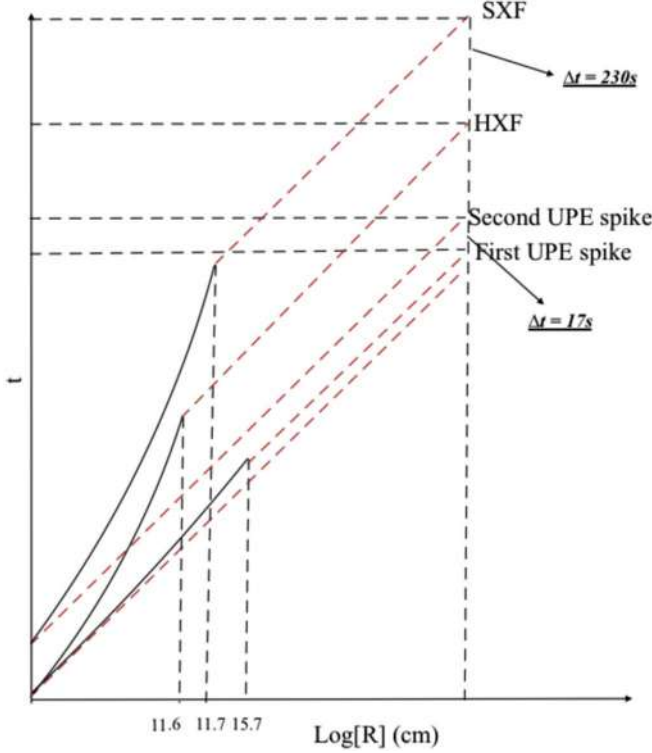


Figure 11. Same as Figure 6, but also showing the position of the plasma shock within the SN ejecta (dashed black lines) for each of the components of the UPE, until the breakout. The first spike originates as the hard X-ray flare, and the second spike originates as the soft X-ray flare. The photon worldlines (solid red lines) of the hard X-ray flare and the soft X-ray flare are observed with a time difference of ~ 230 s (rest frame of ~ 130 s) due to the differential deceleration of the two UPE components within the SN ejecta.

We can now insert Equation (11) into Equation (5) to obtain

$$F_{\text{bb,obs}} = \frac{R_{\text{com}}^2}{D_L(z)^2} \sigma T_{\text{com}}^4 = \frac{R_{\text{com}}^2}{D_L(z)^2} \sigma \left[\frac{1+z}{\Theta(\beta)\Gamma} T_{\text{obs}} \right]^4. \quad (12)$$

Since the radius, R , of the emitter in the laboratory frame is related to R_{com} by

$$R_{\text{com}} = \Gamma R, \quad (13)$$

we can insert Equation (13) into Equation (12) and obtain

$$F_{\text{bb,obs}} = \frac{(1+z)^4}{\Gamma^2} \left(\frac{R}{D_L(z)} \right)^2 \sigma \left[\frac{T_{\text{obs}}}{\Theta(\beta)} \right]^4. \quad (14)$$

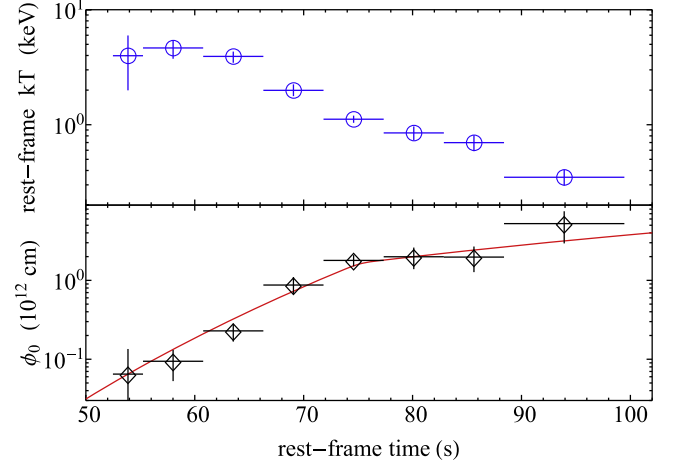


Figure 12. Cosmological rest-frame evolution of kT (top panel) and ϕ_0 (bottom panel) of the thermal emitter in the hard X-ray flare of GRB 151027A. The ϕ_0 interpolation (red line) is obtained using two smoothly joined PL segments.

Solving Equation (14) for R , we finally obtain the thermal emitter effective radius in the laboratory frame:

$$R = \Theta(\beta)^2 \Gamma \frac{D_L(z)}{(1+z)^2} \sqrt{\frac{F_{\text{bb,obs}}}{\sigma T_{\text{obs}}^4}} = \Theta(\beta)^2 \Gamma \phi_0, \quad (15)$$

where we have defined ϕ_0 as

$$\phi_0 \equiv \frac{D_L(z)}{(1+z)^2} \sqrt{\frac{F_{\text{bb,obs}}}{\sigma T_{\text{obs}}^4}}. \quad (16)$$

The evolutions of the rest-frame temperature and ϕ_0 are shown in Figure 12. In astronomy, the quantity ϕ_0 is usually identified with the radius of the emitter. However, in relativistic astrophysics, this identity cannot be straightforwardly applied, because the estimate of the effective emitter radius R in Equation (15) crucially depends on the knowledge of its expansion velocity β (and, correspondingly, of Γ).

It must be noted that Equation (15) above gives the correct value of R for all values of $0 \leq \beta \leq 1$ by taking all of the relativistic transformations properly into account. In the nonrelativistic limit ($\beta \rightarrow 0$), we have, respectively:

$$\Theta \xrightarrow{\beta \rightarrow 0} 1, \quad \Theta^2 \xrightarrow{\beta \rightarrow 0} 1, \quad (17)$$

$$T_{\text{com}} \xrightarrow{\beta \rightarrow 0} T_{\text{obs}}(1+z), \quad R \xrightarrow{\beta \rightarrow 0} \phi_0, \quad (18)$$

as expected. Analogously, in the ultra-relativistic limit ($\beta \rightarrow 1$), we have

$$\Theta \xrightarrow{\beta \rightarrow 1} 1.39, \quad \Theta^2 \xrightarrow{\beta \rightarrow 1} 1.92, \quad (19)$$

$$T_{\text{com}} \xrightarrow{\beta \rightarrow 1} \frac{0.72}{\Gamma} T_{\text{obs}}(1+z), \quad R \xrightarrow{\beta \rightarrow 1} 1.92\Gamma\phi_0. \quad (20)$$

It must also be noted that the numerical coefficient in Equation (15) is computed as a function of β using Equation (9) above, and it is different from the constant values proposed by Pe'er et al. (2007) and by Ghirlanda et al. (2013).

An estimate of the expansion velocity, β , can be deduced from the ratio between the variation of the emitter effective radius, ΔR , and the emission duration in laboratory frame, Δt , i.e.,

$$\beta = \frac{\Delta R}{c\Delta t} = \Theta(\beta)^2\Gamma(1 - \beta \cos \vartheta)(1+z) \frac{\Delta\phi_0}{c\Delta t_a^d}, \quad (21)$$

where we used Equation (15), the relation between Δt and Δt_a^d given in Equation (2), we used the definition of Γ given above, and ϑ is the displacement angle of the considered photon emission point on the surface from the line of sight. In the following, we only consider the case $\cos \vartheta = 1$. In this case, using Equation (9), Equation (21) assumes the form presented in Figure 1. It allows us to estimate the expansion velocity, β , of the emitter using only the observed blackbody flux, temperature, photon arrival time, and cosmological redshift, assuming uncollimated emission and only considering the radiation coming from the line of sight. We can explain the observed blackbody emission in GRB 151027A without introducing the “reborn fireball” scenario (see Ghisellini et al. 2007; Nappo et al. 2017).

To infer β , we fit the evolution of ϕ_0 (see Figure 12 and Table 2) using two smoothly joined PL segments. It allows us to estimate the ratio $\Delta\phi_0/(c\Delta t_a^d)$ in Equation (21) and, therefore, the values of β and Γ , assuming that they are constant in each time interval (see Figure 13, top and middle panels). Consequently, we can estimate the evolution of the radius, R , of the emitter in the laboratory frame by taking into account the relativistic transformations described in Equations (2), (15), and (16) (see bottom panel of Figure 13). The results are also summarized in Table 2.

6. On the Nature of the Hard X-Ray Flare and the Soft X-Ray Flare

Following the procedure described in Section 10 of Ruffini et al. (2018c), we interpret the thermal emission observed in the hard X-ray flare as the observational feature arising from the early interaction between the expanding SN ejecta and the e^+e^- plasma. In order to test the consistency of this model with the data, we have performed a series of numerical simulations, whose details we summarize as follows.

(a) Our treatment of the problem is based on an implementation of the 1D relativistic hydrodynamical module included in the PLUTO code⁵ (Mignone et al. 2011). In the spherically symmetric case considered, only the radial coordinate is used, and consequently the code integrates a system of partial differential equations in only two coordinates:

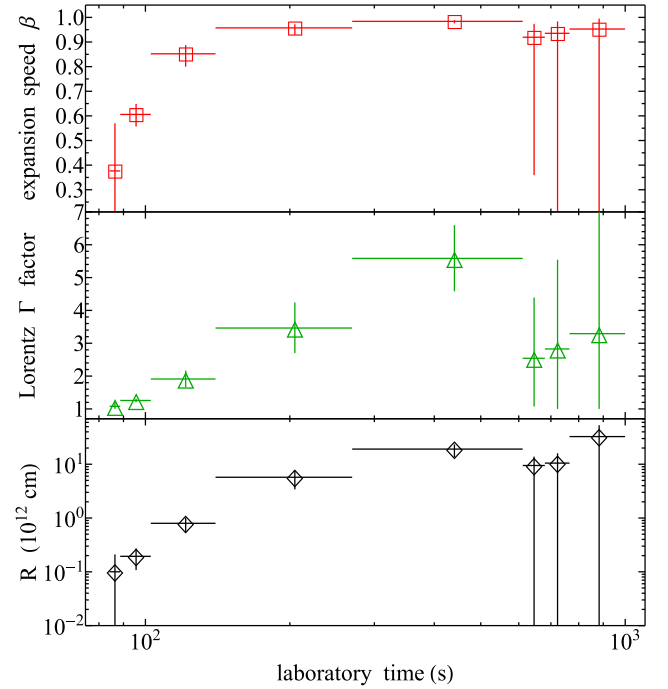


Figure 13. Evolution in the laboratory frame of β , Γ , and R of the thermal emitter from the time intervals in Table 2.

the radius and the time. This permits the study of the evolution of the plasma along one selected radial direction at a time. The aforementioned equations are those of an ideal relativistic fluid, which can be written as follows:

$$\frac{\partial(\rho\Gamma)}{\partial t} + \nabla \cdot (\rho\Gamma\mathbf{v}) = 0, \quad (22)$$

$$\frac{\partial m_r}{\partial t} + \nabla \cdot (m_r\mathbf{v}) + \frac{\partial p}{\partial r} = 0, \quad (23)$$

$$\frac{\partial \mathcal{E}}{\partial t} + \nabla \cdot (\mathbf{m} - \rho\Gamma\mathbf{v}) = 0, \quad (24)$$

where ρ and p are the comoving fluid density and pressure, \mathbf{v} is the coordinate velocity in natural units ($c = 1$), $\Gamma = (1 - \mathbf{v}^2)^{-\frac{1}{2}}$ is the Lorentz gamma factor, $\mathbf{m} = h\Gamma^2\mathbf{v}$ is the fluid momentum, m_r is the radial component, \mathcal{E} is the internal energy density measured in the comoving frame, and h is the comoving enthalpy density, which is defined by $h = \rho + \epsilon + p$. We define \mathcal{E} as follows:

$$\mathcal{E} = h\Gamma^2 - p - \rho\Gamma. \quad (25)$$

The first two terms on the right-hand side of this equation coincide with the T^{00} component of the fluid energy-momentum, and the last one is the mass density in the laboratory frame.

Under the conditions discussed in Ruffini et al. (2018c), the plasma satisfies the equation of state of an ideal relativistic gas, which can be expressed in terms of its enthalpy as

$$h = \rho + \frac{\gamma p}{\gamma - 1}, \quad (26)$$

with $\gamma = 4/3$. Imposing this equation of state closes and completely defines the system of equations, leaving as the only remaining freedom the choice as the matter density profile and the boundary conditions. To compute the evolution of these

⁵ <http://plutocode.ph.unito.it/>

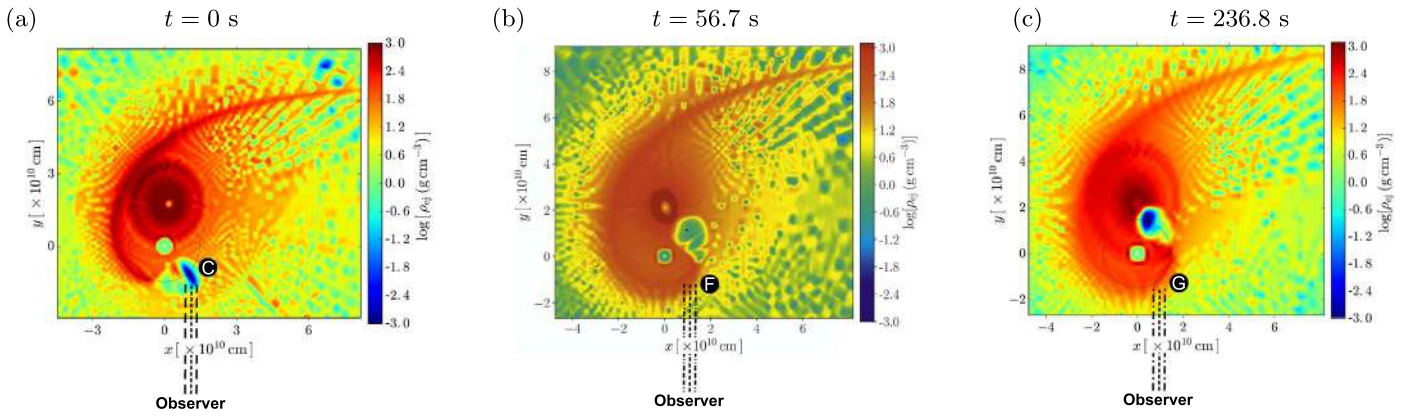


Figure 14. Three snapshots of the density distribution of the SN ejecta in the equatorial plane of the progenitor binary system. The time $t = 0$ indicates the instant when the NS companion reaches, by accretion, the critical mass and leads to the formation of a BH (black dot). As evidenced in panel (a), the location of the black hole formation is widely separated from the central position represented by the SN explosion, it is actually located in the white conical region in Figure 2. The binary parameters of this simulations are: the NS companion has an initial mass of $2.0 M_{\odot}$; the CO_{core} , obtained from a progenitor with a ZAMS mass of $M_{\text{ZAMS}} = 30 M_{\odot}$, leads to a total ejecta mass of $7.94 M_{\odot}$ and to a $1.5 M_{\odot}$ νNS (white dot); and the orbital period is $P \approx 5$ minutes, i.e., a binary separation of $a \approx 1.5 \times 10^{10}$ cm.

quantities in the chosen setup, the code uses the HLLC Riemann solver for relativistic fluids (see Mignone et al. 2011). The time evolution is performed by means of a second-order Runge–Kutta integration, and a second-order total variation diminishing scheme is used for the spatial interpolation. An adaptive mesh refinement algorithm is implemented as well, provided by the CHOMBO library (Colella et al. 2003). We turn now to the determination of the SN ejecta.

(b) The initially ultra-relativistic e^+e^- plasma expands through the SN ejecta matter, slowing down to mildly relativistic velocities. The SN density and velocity profiles are taken from the 3D SPH simulation of the SN ejecta expansion under the influence of the νNS and the NS companion gravitational field. In our simulations, we include the NS orbital motion and the NS gravitational-mass changes due to the accretion process modeled with the Bondi–Hoyle formalism (see Becerra et al. 2016, for more details). We set the SN ejecta initial conditions, adopting a homologous velocity distribution in free expansion, and the SN matter was modeled with 16 million point-like particles. Each SN layer is initially populated following a PL density profile of the CO_{core} , as obtained from low-metallicity progenitors evolved with the *Kepler* stellar evolution code (Woosley et al. 2002). Here, we take the simulation of an initial binary system formed by a $2.0 M_{\odot}$ NS and a CO_{core} produced by an $M_{\text{ZAMS}} = 30 M_{\odot}$ progenitor as a reference model. This leads to a total ejecta with a mass of $7.94 M_{\odot}$ and a νNS of $1.5 M_{\odot}$. The orbital period of the binary is $P \approx 5$ minutes, i.e., a binary separation of $a \approx 1.5 \times 10^{10}$ cm. The density profile exhibiting the evolution of the SN ejecta and the companion star is shown in Figure 14. Figure 15 shows the SN ejecta mass enclosed within a cone of 5° of the semi-aperture angle with the vertex at the position of the BH at the moment of its formation. The cone axis stands along the θ direction measured counterclockwise with respect to the line of sight. We simulate the interaction of the e^+e^- plasma with such ejecta from a radius $\approx 10^{10}$ cm all the way to $\approx 10^{12}$ cm where transparency is reached. We have recently run new 3D SPH simulations of this process in Becerra et al. (2018) using the SNSPH code (Fryer et al. 2006). These new simulations have allowed for a wide exploration of the binary parameter space and have confirmed the results and the physical picture presented in Becerra et al. (2016). On the basis

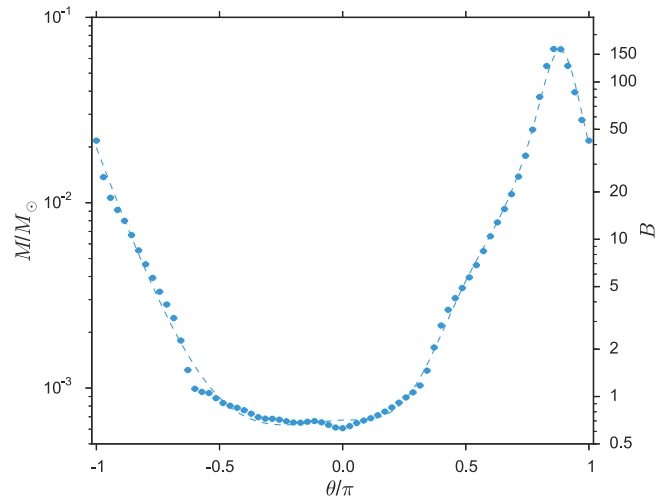


Figure 15. SN ejecta mass enclosed within a cone of 5° of semi-aperture angle and vertex centered on the SN and positioned to an angle θ , measured counterclockwise, with respect to the line of sight (which passes through the νNS and BH at the moment of its formation; see Conclusions). The binary parameters of this simulations are: the NS has an initial mass of $2.0 M_{\odot}$; the CO_{core} obtained from a progenitor with ZAMS mass $M_{\text{ZAMS}} = 30 M_{\odot}$, leads to a total ejecta mass $7.94 M_{\odot}$, the orbital period is $P \approx 5$ min, i.e., a binary separation $a \approx 1.5 \times 10^{10}$ cm. The right-side vertical axis gives, as an example, the corresponding value of the baryon load, B , assuming a plasma energy of $E_{e^+e^-} = 1 \times 10^{53}$ erg. It is appropriate to mention that the above values of the baryon load are computed using an averaging procedure, which is performed centered on the SN explosion and produces larger values than the one centered around the BH with a specific value of the baryon load $B \sim 1.9 \times 10^{-3}$ (see Figure 14(a)).

of these new simulations, we have determined the value of the baryon loads both for the hard X-ray flares and the soft X-ray flares.

(c) For the simulation of the hard X-ray flare, we set a total energy of the plasma equal to that of the hard X-ray flare, i.e., $E_{\gamma} = 3.28 \times 10^{52}$ erg, and a baryon load of $B = 79$, corresponding to a baryonic mass of $M_B = 1.45 M_{\odot}$. We obtain a radius of the transparency $R_{\text{ph}} = 4.26 \times 10^{11}$ cm, a Lorentz factor at transparency $\Gamma = 2.86$, and an arrival time of the corresponding radiation in the cosmological rest frame $t_a = 56.7$ s (see Figure 16). This time is in agreement with

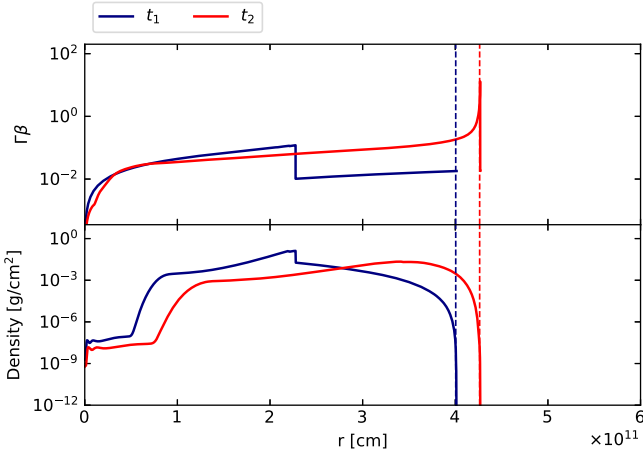


Figure 16. Numerical simulation of the hard X-ray flare. We set a total energy of the plasma as $E_\gamma = 3.28 \times 10^{52}$ erg and a baryon load as $B = 79$, corresponding to a baryonic mass of $M_B = 1.45 M_\odot$. Top: distribution of the velocity inside the SN ejecta at the two fixed values of the laboratory time t_1 (before the plasma reaches the external surface of the ejecta) and t_2 (the moment at which the plasma, after crossing the entire SN ejecta, reaches the external surface). We plotted the quantity $\Gamma\beta$, recalling that we have $\Gamma\beta \sim \beta$ when $\beta < 1$ and $\Gamma\beta \sim \Gamma$ when $\beta \sim 1$. Bottom: corresponding distribution of the mass density of the SN ejecta in the laboratory frame ρ_{lab} . We obtain a radius of the transparency of $R_{\text{ph}} = 4.26 \times 10^{11}$ cm, a Lorentz factor at transparency $\Gamma = 2.86$, and an arrival time of the corresponding radiation in the cosmological rest frame of $t_a = 56.7$ s.

the starting time of the hard X-ray flare in the source rest frame (see Section 3).

For the simulation of the soft X-ray flare, we set the energy $E_X = 4.39 \times 10^{51}$ erg as the total energy of the plasma and a baryon load as $B = 207$, which corresponds to a baryonic mass of $M_B = 0.51 M_\odot$. We obtain a radius of the transparency of $R_{\text{ph}} = 1.01 \times 10^{12}$ cm, a Lorentz gamma factor at transparency $\Gamma = 1.15$, and an arrival time of the corresponding radiation in the cosmological rest frame of $t_a = 236.8$ s (see Figure 17). This time is in agreement with the above time t_p at which the soft X-ray flare peaks in the rest frame.

7. Summary, Discussion, and Conclusions

7.1. Summary

It is by now clear that seven different subclass of GRBs with different progenitors exist (Ruffini et al. 2016b). Each GRB subclass is itself composed of different episodes, each one characterized by specific observational data that make their firm identification possible (see e.g., Ruffini et al. 2018c, and references therein). Here, we evidence how, within the BdHN subclass, a further differentiation follows by selecting special viewing angles. We have applied our recent treatment (Ruffini et al. 2018c) to the UPE phase and the hard X-ray flare using the specific case of GRB 151027A as a prototype in view of the excellent available data.

We recall three results:

1. We have confirmed the ultra-relativistic nature of the UPE, which appears to be composed of a double spike (see Figures 4(a) and 5(b)). This double spike structure appears to be also present in other systems, such as GRB 140206A and GRB 160509A (R. Ruffini et al. 2018, in preparation). From the analysis of the P-GRB of the first spike, we derived an ultra-relativistic Lorentz factor of $\Gamma_0 = 503 \pm 76$, a baryon load of

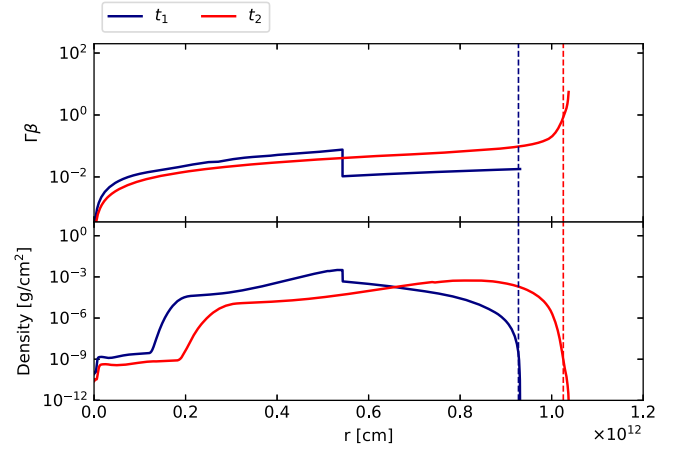


Figure 17. Numerical simulation of the soft X-ray flare. We set a total energy of the plasma as $E_X = 4.39 \times 10^{51}$ erg and a baryon load as $B = 207$, corresponding to a baryonic mass of $M_B = 0.51 M_\odot$. The plotted quantities are the same as in Figure 16. We obtain a radius of the transparency of $R_{\text{ph}} = 1.01 \times 10^{12}$ cm, a Lorentz factor at transparency $\Gamma = 1.15$, and an arrival time of the corresponding radiation in the cosmological rest frame of $t_a = 236.8$ s.

$B = (1.92 \pm 0.35) \times 10^{-3}$, and a structure in the CBM with the density $(7.46 \pm 1.2) \text{ cm}^{-3}$ extending to dimensions of 10^{16} cm (see Figure 5(d)). The second spike of energy, $E_{\text{iso},2} = (4.99 \pm 0.60) \times 10^{51}$ erg, after a cosmological rest-frame time of 9 s following the first spike of energy, $E_{\text{iso},1} = (7.26 \pm 0.36) \times 10^{51}$ erg (see Figures 4(b) and (c)), appear to be featureless. We are currently examining the possibility that the nature of these two spikes and their morphology could be directly connected to the formation process of the BH.

2. A double spikes appears to occur also in the FPA phase (see Figure 7(a)); the first component is the hard X-ray flare, and the second is the soft X-ray flare. The energy of the hard X-ray flare is $E_\gamma = (3.28 \pm 0.13) \times 10^{52}$ erg (Figure 7), and the energy of the soft X-ray flare is $E_X = (4.4 \pm 2.9) \times 10^{51}$ erg (Figure 9). We have analyzed both flares with our usual approach of the hydrodynamical equations describing the interaction of the e^+e^- plasma with the SN ejecta (see Figure 16 for the hard X-ray flare and Figure 17 for the soft X-ray flare). The baryon loads of the two flares are different: $B = 79$ for the hard X-ray flare, and $B = 207$ for the soft X-ray flare. This is visualized in Figure 11 as well as in our 3D simulations (see the three snapshots shown in Figure 14). Both the hard X-ray flare and the soft X-ray flare show mildly relativistic regimes, as already observed in Ruffini et al. (2018c), namely a Lorentz factor at transparency of $\Gamma \sim 5$ for the hard X-ray flare and a Lorentz factor of $\Gamma \sim 2$ for the soft X-ray flare.
3. We studied the ETE associated to the hard X-ray flare. We have measured its expansion velocity derived from the relativistic treatment described in Section 5, following the formula in Figure 1 (see also Ruffini et al. 2018c). We have identified the transition from an SN, with an initial computed velocity of $0.38c$, to an HN, with a computed velocity of $0.98c$ (see Figure 13 and Table 2). These results are in good agreement with observations of both SNe and HNe (see e.g., Table 3 and Figure 20 in Nicholl et al. 2015).

Table 3

Parameters of the Sequence of Astrophysical Processes that Characterize the BdHNe: The Columns List, Respectively, the Name of Each Process, the Radius of Transparency, the Lorentz Gamma Factor (Γ) and the Baryon Load, Starting Time of the Process, the Duration, and, Finally, the Best-fit Model of the Spectrum

	Name	Radius(cm)	Γ	Baryon Load	$t_{\text{start}}(s)$	Duration(s)	Spectrum
UPE	First spike (P-GRB)	$\sim 10^{13}$	$\sim 10^2 - 10^3$	$\sim 10^{-4} - 10^{-2}$	$\sim T_0$	~ 1	CPL+BB
	First spike (rest)	$\sim 10^{15} - 10^{17}$	$\sim 10^2 - 10^3$	$\sim 10^{-4} - 10^{-2}$	$\sim T_0 + 1$	~ 5	Band
	Second spike	$\sim 10^{15} - 10^{17}$	$\gtrsim 10^3$	$\lesssim 10^{-4}$	$\sim T_0 + 15$	~ 5	Band
	hard X-ray flare	$\sim 10^{11} - 10^{12}$	$\lesssim 10$	$\sim 10^2$	$\sim T_0 + 50$	$\sim 10^2$	PL+BB
	soft X-ray flare	$\sim 10^{12} - 10^{13}$	$\lesssim 4$	$\sim 10^3$	$\sim T_0 + 10^2$	~ 150	PL(+BB)
	Late afterglow	$\gtrsim 10^{13}$	$\lesssim 2$	—	$\gtrsim T_0 + 10^2$	$\gtrsim 10^6$	PL
	SN optical emission	$\sim 10^{15}$	~ 1	—	$\sim T_0 + 10^6$	$\gtrsim 10^6$	PL
	GeV emission	—	—	—	$\sim T_0 + 1$	$\sim 10^4$	PL

Note. T_0 is the *Fermi*-GBM trigger time.

The above observational analysis, as already presented in Pisani et al. (2013, 2016), set the ensemble of the data that any viable model of GRBs has to conform. In the last 30 years, the enormous number of high-quality data obtained (e.g., by *Beppo-SAX*, *Swift*, *Agile*, and *Fermi*) further extended by specific optical, radio, and ultrahigh-energy data offered the possibility to test the viable models that conform to these data. We have shown that the BdHN model can explain the above observational features.

7.2. Discussion

1. By adopting the BdHN approach, we discovered the existence of four different process: a double feature in the UPE phase, the hard X-ray flares, the soft X-ray flares, and the ETE phase. Each one of these processes is generated by a different e^+e^- injection occurring in a different baryon load medium. Using the binary nature of the progenitor system in BDHN, especially the presence of an incipient SN and a companion NS, together with an appropriate theoretical treatment and an ample program of numerical simulations (Becerra et al. 2018), we have been able to determine the nature of these processes. Clear observational predictions have followed, including (the major one) the coincidence of the numerical value of the velocity of expansion at the end of the ETE phase with the observed expansion velocity of the HN, confirmed in additional BdHN and currently being observationally addressed in additional cases. A clear temporal sequence in the occurrence of these processes, as well as the specific sequence in the values of the Lorentz gamma factors, has been established.
2. For the first time, the rotation of the binary system, of the order of 400 s, has been essential in order to untangle the sequence of events discovered and explained in this article, recognizing their a-causal nature and their modulation by the rotation of the progenitor binary system.
3. The above different processes, including the double spiky structure of the UPE phase, the hard and soft X-ray flares, and the ETE phase are actually different appearances of the same physical process: the black hole formation, as seen from different viewing angles due to the rotation of the SN ejecta in the binary system (see Figure 14) and the consequent angular dependence of the baryon load (see Figure 15).

7.3. Conclusions

1. A clear prediction that will soon be submitted, following our paper, is that of all of the BdHNe occurring with a line of sight in the orbital plane of the binary, with only a fraction of approximately 10% being actually detectable. They correspond to the sources whose ultra-relativistic emission lies within the allowed cone of $\sim 10^\circ$ of low baryon contamination (see Figure 2 and Figure 15). They are the only ones able to trigger the gamma-ray instruments (e.g., the *Fermi*/GBM or *Swift*/BAT detectors). The remaining 90% will not be detectable by current satellites and will possibly need a new mission operating in soft X-rays (like e.g., THESEUS; see Amati et al. 2018).
2. The E_{iso} , traditionally defined using an underlying assumption of isotropy of the BH emission, has to be modified by considering an anisotropic emission process. A total energy, E_{tot} , summing the energies of the UPE, of the hard X-ray flare, of the ETE, and of the soft X-ray flare, has to be considered for sources seen in the equatorial plane. It is not surprising that the energy of the hard X-ray flare in GRB 151027A is larger than the one of the UPE, pointing to an anisotropic emission from the BH.
3. When the inclination of the viewing angle is less than 60° from the normal to the plane of the binary system, the GeV radiation becomes detectable, and its energy, which has been related to the BH rotational energy, will need to be taken into account (Ruffini et al. 2018a).

We acknowledge the referee's comments, which have significantly helped us in formulating a clearer, logically motivated and well-balanced presentation of our results.

Software: PLUTO (Mignone et al. 2011), CHOMBO (Colella et al. 2003), SNSPH (Fryer et al. 2006).

ORCID iDs

C. L. Bianco  <https://orcid.org/0000-0001-7749-4078>
M. Muccino  <https://orcid.org/0000-0002-2234-9225>
G. B. Pisani  <https://orcid.org/0000-0003-3452-2491>

References

- Aimuratov, Y., Ruffini, R., Muccino, M., et al. 2017, *ApJ*, **844**, 83
Aksenov, A. G., Ruffini, R., & Vereshchagin, G. V. 2007, *PhRvL*, **99**, 125003

- Amati, L., O'Brien, P., Goetz, D., et al. 2018, *AdSpR*, **62**, 191
- Becerra, L., Bianco, C. L., Fryer, C. L., Rueda, J. A., & Ruffini, R. 2016, *ApJ*, **833**, 107
- Becerra, L., Cipolletta, F., Fryer, C. L., Rueda, J. A., & Ruffini, R. 2015, *ApJ*, **812**, 100
- Becerra, L., Ellinger, C. L., Fryer, C. L., Rueda, J. A., & Ruffini, R. 2018, *ApJ*, in press (arXiv:1803.04356)
- Bernardini, M. G., Bianco, C. L., Chardonnet, P., et al. 2005, *ApJL*, **634**, L29
- Bianco, C. L., & Ruffini, R. 2004, *ApJL*, **605**, L1
- Bianco, C. L., & Ruffini, R. 2005a, *ApJL*, **620**, L23
- Bianco, C. L., & Ruffini, R. 2005b, *ApJL*, **633**, L13
- Bianco, C. L., & Ruffini, R. 2006, *ApJL*, **644**, L105
- Bianco, C. L., Ruffini, R., & Xue, S.-S. 2001, *A&A*, **368**, 377
- Blandford, R. D., & McKee, C. F. 1976, *PhFI*, **19**, 1130
- Bromberg, O., Nakar, E., Piran, T., & Sari, R. 2013, *ApJ*, **764**, 179
- Colella, P., Graves, D. T., Johnson, J. N., et al. 2003, Chombo Software Package for AMR Applications Design Document Tech. Rep. LBNL-6615E
- Daigne, F., & Mochkovitch, R. 2002, *MNRAS*, **336**, 1271
- Della Valle, M. 2011, *IMPD*, **20**, 1745
- Dezalay, J.-P., Barat, C., Talon, R., et al. 1992, in AIP Conf. Ser. 265, Gamma-ray bursts, ed. W. S. Paciesas & G. J. Fishman (Melville, NY: AIP), 304
- Fruchter, A. S., Levan, A. J., Strolger, L., et al. 2006, *Natur*, **441**, 463
- Fryer, C. L., Rockefeller, G., & Warren, M. S. 2006, *ApJ*, **643**, 292
- Fryer, C. L., Rueda, J. A., & Ruffini, R. 2014, *ApJL*, **793**, L36
- Ghirlanda, G., Pescalli, A., & Ghisellini, G. 2013, *MNRAS*, **432**, 3237
- Ghisellini, G., Celotti, A., Ghirlanda, G., Firmani, C., & Nava, L. 2007, *MNRAS*, **382**, L72
- Goad, M. R., Osborne, J. P., Beardmore, A. P., & Evans, P. A. 2015, *GCN*, 18482
- Golenetskii, S., Aptekar, R., Frederiks, D., et al. 2015, *GCN*, 18516
- Izzo, L., Ruffini, R., Penacchioni, A. V., et al. 2012, *A&A*, **543**, A10
- Klebesadel, R. W. 1992, in The Durations of Gamma-ray Bursts, ed. C. Ho, R. I. Epstein, & E. E. Fenimore (Cambridge: Cambridge Univ. Press), 161
- Kouveliotou, C., Meegan, C. A., Fishman, G. J., et al. 1993, *ApJL*, **413**, L101
- MacFadyen, A. I., & Woosley, S. E. 1999, *ApJ*, **524**, 262
- Mao, S., & Yi, I. 1994, *ApJL*, **424**, L131
- Maselli, A., D'Ai, A., Lien, A. Y., et al. 2015, *GCN*, 18478
- Masumitsu, T., Negoro, H., Kawai, N., et al. 2015, *GCN*, 18525
- Mazets, E. P., Golenetskii, S. V., Ilinskii, V. N., et al. 1981, *Ap&SS*, **80**, 3
- Meszaros, P., Laguna, P., & Rees, M. J. 1993, *ApJ*, **415**, 181
- Mignone, A., Zanni, C., Tzeferacos, P., et al. 2011, *ApJS*, **198**, 7
- Nappo, F., Pescalli, A., Oganessyan, G., et al. 2017, *A&A*, **598**, A23
- Nicholl, M., Smartt, S. J., Jerkstrand, A., et al. 2015, *MNRAS*, **452**, 3869
- Paczynski, B. 1998, *ApJL*, **494**, L45
- Patricelli, B., Bernardini, M. G., Bianco, C. L., et al. 2012, *ApJ*, **756**, 16
- Pe'er, A., Ryde, F., Wijers, R. A. M. J., Mészáros, P., & Rees, M. J. 2007, *ApJL*, **664**, L1
- Penacchioni, A. V., Ruffini, R., Bianco, C. L., et al. 2013, *A&A*, **551**, A133
- Penacchioni, A. V., Ruffini, R., Izzo, L., et al. 2012, *A&A*, **538**, A58
- Perley, D. A., Hillenbrand, L., & Prochaska, J. X. 2015, *GCN*, 18487
- Piran, T. 1999, *PhR*, **314**, 575
- Piran, T. 2004, *RvMP*, **76**, 1143
- Piran, T., Shemi, A., & Narayan, R. 1993, *MNRAS*, **263**, 861
- Pisani, G. B., Izzo, L., Ruffini, R., et al. 2013, *A&A*, **552**, L5
- Pisani, G. B., Ruffini, R., Aimuratov, Y., et al. 2016, *ApJ*, **833**, 159
- Rees, M. J., & Meszaros, P. 1992, *MNRAS*, **258**, 41P
- Rees, M. J., & Meszaros, P. 1994, *ApJL*, **430**, L93
- Romano, P., Campana, S., Chincarini, G., et al. 2006, *A&A*, **456**, 917
- Rueda, J. A., & Ruffini, R. 2012, *ApJL*, **758**, L7
- Ruffini, R. 1998, in Frontiers Science Series 23, Black Holes and High Energy Astrophysics, ed. H. Sato & N. Sugiyama (Kyoto: Universal Academic Press), 167
- Ruffini, R. 1999, *A&A*, **138**, 513
- Ruffini, R., Bernardini, M. G., Bianco, C. L., et al. 2006, in AIP Conf. Ser. 836, Gamma-Ray Bursts in the Swift Era, ed. S. S. Holt, N. Gehrels, & J. A. Nousek (Melville, NY: AIP), 103
- Ruffini, R., Bernardini, M. G., Bianco, C. L., et al. 2007a, in ESA Spec. Publ. 622, The Obscured Universe, ed. S. Grebenev, R. Sunyaev, & C. Winkler (Noordwijk: ESA), 561
- Ruffini, R., Bianco, C. L., Chardonnet, P., Frascchetti, F., & Xue, S.-S. 2002, *ApJL*, **581**, L19
- Ruffini, R., Bianco, C. L., Frascchetti, F., Xue, S.-S., & Chardonnet, P. 2001a, *ApJL*, **555**, L117
- Ruffini, R., Bianco, C. L., Frascchetti, F., Xue, S.-S., & Chardonnet, P. 2001b, *ApJL*, **555**, L113
- Ruffini, R., Bianco, C. L., Frascchetti, F., Xue, S.-S., & Chardonnet, P. 2001c, *ApJL*, **555**, L107
- Ruffini, R., Bianco, C. L., Vereshchagin, G., & Xue, S.-S. 2007b, in Proc. Relativistic Astrophysics Legacy and Cosmology Conf., Einstein's Legacy, ed. B. Aschenbach et al. (Berlin: Springer), 402
- Ruffini, R., Moradi, R., Wang, Y., et al. 2018a, *ApJ*, submitted (arXiv:1803.05476)
- Ruffini, R., Muccino, M., Aimuratov, Y., et al. 2016a, *ApJ*, **831**, 178
- Ruffini, R., Muccino, M., Kovacevic, M., et al. 2015, *ApJ*, **808**, 190
- Ruffini, R., Rodriguez, J., Muccino, M., et al. 2018b, *ApJ*, **859**, 30
- Ruffini, R., Rueda, J. A., Muccino, M., et al. 2016b, *ApJ*, **832**, 136
- Ruffini, R., Salmonson, J. D., Wilson, J. R., & Xue, S.-S. 1999, *A&A*, **350**, 334
- Ruffini, R., Salmonson, J. D., Wilson, J. R., & Xue, S.-S. 2000, *A&A*, **359**, 855
- Ruffini, R., Vereshchagin, G., & Xue, S. 2010, *PhR*, **487**, 1
- Ruffini, R., Vitagliano, L., & Xue, S. 2003, *PhLB*, **573**, 33
- Ruffini, R., Wang, Y., Aimuratov, Y., et al. 2018c, *ApJ*, **852**, 53
- Ruffini, R., & Wilson, J. 1973, *PhRvL*, **31**, 1362
- Ryde, F. 2004, *ApJ*, **614**, 827
- Ryde, F., Björnsson, C.-I., Kaneko, Y., et al. 2006, *ApJ*, **652**, 1400
- Ryde, F., & Pe'er, A. 2009, *ApJ*, **702**, 1211
- Shemi, A., & Piran, T. 1990, *ApJL*, **365**, L55
- Smith, N. 2014, *ARA&A*, **52**, 487
- Smith, N., Li, W., Filippenko, A. V., & Chornock, R. 2011, *MNRAS*, **412**, 1522
- Svensson, K. M., Levan, A. J., Tanvir, N. R., Fruchter, A. S., & Strolger, L.-G. 2010, *MNRAS*, **405**, 57
- Tavani, M. 1998, *ApJL*, **497**, L21
- Toelge, K., Yu, H.-F., & Meegan, C. A. 2015, *GCN*, 18492
- Woosley, S. E. 1993, *ApJ*, **405**, 273
- Woosley, S. E., Heger, A., & Weaver, T. A. 2002, *RvMP*, **74**, 1015
- Zel'dovich, Y. B., Ivanova, L. N., & Nadezhin, D. K. 1972, *SvA*, **16**, 209



On the Rate and on the Gravitational Wave Emission of Short and Long GRBs

R. Ruffini^{1,2,3,4}, J. Rodriguez^{1,2}, M. Muccino^{1,2} , J. A. Rueda^{1,2,4} , Y. Aimuratov^{1,2}, U. Barres de Almeida^{4,5}, L. Becerra^{1,2}, C. L. Bianco^{1,2} , C. Cherubini^{6,7}, S. Filippi^{6,7}, D. Gizzi¹, M. Kovacevic^{1,2,3} , R. Moradi^{1,2}, F. G. Oliveira^{1,2,3}, G. B. Pisani^{1,2} , and Y. Wang^{1,2}

¹ Dipartimento di Fisica and ICRA, Sapienza Università di Roma, P.le Aldo Moro 5, I-00185 Rome, Italy

² ICRANet, P.zza della Repubblica 10, I-65122 Pescara, Italy

³ Université de Nice Sophia Antipolis, CEDEX 2, Grand Château Parc Valrose, Nice, France

⁴ ICRANet-Rio, Centro Brasileiro de Pesquisas Físicas, Rua Dr. Xavier Sigaud 150, 22290-180 Rio de Janeiro, Brazil

⁵ Centro Brasileiro de Pesquisas Físicas, Rua Dr. Xavier Sigaud 150, 22290-180 Rio de Janeiro, Brazil

⁶ Unit of Nonlinear Physics and Mathematical Modeling, Università Campus Bio-Medico di Roma, Via A. del Portillo 21, I-00128 Rome, Italy

⁷ ICRA, Università Campus Bio-Medico di Roma, Via A. del Portillo 21, I-00128 Rome, Italy

Received 2016 October 25; revised 2018 April 6; accepted 2018 April 15; published 2018 May 18

Abstract

On the ground of the large number of gamma-ray bursts (GRBs) detected with cosmological redshift, we classified GRBs in seven subclasses, all with binary progenitors which emit gravitational waves (GWs). Each binary is composed of combinations of carbon–oxygen cores (CO_{core}), neutron stars (NSs), black holes (BHs), and white dwarfs (WDs). The long bursts, traditionally assumed to originate from a BH with an ultrarelativistic jetted emission, not emitting GWs, have been subclassified as (I) X-ray flashes (XRFs), (II) binary-driven hypernovae (BdHNe), and (III) BH–supernovae (BH–SNe). They are framed within the induced gravitational collapse paradigm with a progenitor CO_{core}–NS/BH binary. The SN explosion of the CO_{core} triggers an accretion process onto the NS/BH. If the accretion does not lead the NS to its critical mass, an XRF occurs, while when the BH is present or formed by accretion, a BdHN occurs. When the binaries are not disrupted, XRFs lead to NS–NS and BdHNe lead to NS–BH. The short bursts, originating in NS–NS, are subclassified as (IV) short gamma-ray flashes (S-GRFs) and (V) short GRBs (S-GRBs), the latter when a BH is formed. There are (VI) ultrashort GRBs (U-GRBs) and (VII) gamma-ray flashes (GRFs) formed in NS–BH and NS–WD, respectively. We use the occurrence rate and GW emission of these subclasses to assess their detectability by Advanced LIGO–Virgo, eLISA, and resonant bars. We discuss the consequences of our results in view of the announcement of the LIGO/Virgo Collaboration of the source GW 170817 as being originated by an NS–NS.

Key words: binaries: general – black hole physics – gamma-ray burst: general – gravitational waves – stars: neutron – white dwarfs

1. Introduction

Thanks to the extensive observations carried out by γ -ray telescopes, such as AGILE, BATSE, *BeppoSAX*, *Fermi*, *HETE-II*, *INTEGRAL*, *Konus/WIND*, and *Swift*, our understanding of “long” and “short” gamma-ray burst (GRB) progenitor systems has greatly improved. This has led also to a vast literature devoted to the estimate of their relative occurrence rates, all in general agreement. For long bursts see, e.g., Soderberg et al. (2006b), Guetta & Della Valle (2007), Liang et al. (2007), Virgili et al. (2009), Rangel Lemos et al. (2010), Wanderman & Piran (2010), Guetta et al. (2011), and Kovacevic et al. (2014); for short bursts see, e.g., Virgili et al. (2011) and Wanderman & Piran (2015); and for both long and short bursts see, e.g., Sun et al. (2015) and Ruffini et al. (2016b). The rates of gravitational wave (GW) emission from GRBs have been calculated in the literature at a time in which short GRBs were considered to originate in neutron star–neutron star (NS–NS) binaries, while long GRBs were considered to originate in single events,⁸ e.g., *collapsars* (Woosley 1993; MacFadyen & Woosley 1999; MacFadyen et al. 2001; Woosley & Bloom 2006; see, however, Ruffini et al. 2018b) and *magnetars* (Usov 1992; Dai & Lu 1998a, 1998b; Kluźniak & Ruderman 1998; Zhang & Mészáros 2001; see, however, Ruffini et al.

2016b). Thus, only short GRBs have been up to now considered to estimate the simultaneous detection rate of GWs and GRBs. For instance, Wanderman & Piran (2015) used the luminosity function of short GRBs observed by *Swift*; Yonetoku et al. (2014), by BATSE; Patricelli et al. (2016), by *Fermi*; and Ghirlanda et al. (2016), by *Swift* and *Fermi*.

In our recent works (see Ruffini et al. 2016b, and references therein) we have introduced a new classification in which all GRBs, namely, both long and short, originate from merging and/or accreting binary systems, each composed of a different combination of carbon–oxygen cores (CO_{core}), NSs, black holes (BHs), and white dwarfs (WDs). For each system the initial state and the final state are here referred to as “in-state” and “out-state,” respectively. This opens an ample new scenario for the role of GWs both as detectable sources and as a determining factor in the coalescence process of the GRB progenitors.

We interpret the traditional long GRBs within the induced gravitational collapse (IGC) paradigm (Ruffini et al. 2006, 2007, 2008, 2015b; Izzo et al. 2012a; Rueda & Ruffini 2012; Fryer et al. 2014) that proposes as in-state a tight binary system composed of a CO_{core} undergoing a supernova (SN) explosion and a companion compact object, e.g., an NS (or a BH). The SN explosion triggers a hypercritical accretion onto the NS companion, whose details have been studied, simulated, and presented in several publications (see, e.g., Fryer et al. 2014, 2015b; Becerra et al. 2015, 2016, and references therein;

⁸ With the exception of the binary progenitors proposed in Fryer & Woosley (1998), Fryer et al. (1999a, 1999b), and Belczynski et al. (2002).

Appendix A). Depending on the binary parameters, the hypercritical accretion can lead to three very different outcomes:

- I. X-ray flashes (XRFs) with isotropic energy $E_{\text{iso}} \lesssim 10^{52}$ erg and rest-frame spectral peak energy $E_{p,i} \lesssim 200$ keV. This class occurs in CO_{core}-NS binaries when the hypercritical accretion onto the NS companion is not enough to induce gravitational collapse into a BH (Becerra et al. 2015, 2016). Following this definition, Ruffini et al. (2016b) estimated for the XRF a local observed rate of $\rho_{\text{XRF}} = 100^{+45}_{-34} \text{ Gpc}^{-3} \text{ yr}^{-1}$ (Ruffini et al. 2016b). This rate is in agreement with that of low-luminosity long GRBs, e.g., $325^{+352}_{-177} \text{ Gpc}^{-3} \text{ yr}^{-1}$ (Liang et al. 2007), $\sim 200 \text{ Gpc}^{-3} \text{ yr}^{-1}$ (Virgili et al. 2009), and $164^{+98}_{-65} \text{ Gpc}^{-3} \text{ yr}^{-1}$ (Sun et al. 2015). After the SN explosion, the binary can either get disrupted or remain bound depending on the mass loss and/or natal kick imparted to the system (see Postnov & Yungelson 2014, references therein; Appendix A.5). In the former case the XRF leads to two runaway NSs, while in the latter one the out-states of XRFs are binaries composed of a newly formed $\sim 1.4\text{--}1.5 M_{\odot}$ NS (hereafter νNS) born in the SN explosion and a massive NS (MNS) that accreted matter from the SN ejecta. Typical periods of these binaries are $P_{\text{orb}} \gtrsim 30$ minutes (Becerra et al. 2016).
- II. Binary-driven hypernovae (BdHNe) with $E_{\text{iso}} \gtrsim 10^{52}$ erg and $E_{p,i} \gtrsim 200$ keV. BdHNe occur in more compact CO_{core}-NS binaries, which leads to a more massive hypercritical accretion onto the NS, hence leading to BH formation. Following this definition, Ruffini et al. (2016b) estimated for the BdHNe a local observed rate $\rho_{\text{BdHN}} = 0.77^{+0.09}_{-0.08} \text{ Gpc}^{-3} \text{ yr}^{-1}$ (Ruffini et al. 2016b). This rate is in agreement with that for high-luminosity long GRBs, e.g., $1.3^{+0.6}_{-0.7} \text{ Gpc}^{-3} \text{ yr}^{-1}$ (Wanderman & Piran 2010) and $0.8^{+0.1}_{-0.1} \text{ Gpc}^{-3} \text{ yr}^{-1}$ (Sun et al. 2015). As in the case of XRFs, the SN explosion can disrupt the binary depending on the mass loss and/or natal kick. In the case when the system remains bound, the out-states of BdHNe are νNS -BH binaries (see Fryer et al. 2015b; Appendix A.5). Typical periods of these binaries are 5 minutes $\lesssim P_{\text{orb}} \lesssim 30$ minutes (Becerra et al. 2016).
- III. BH-SNe with $E_{\text{iso}} \gtrsim 10^{54}$ erg and $E_{p,i} \gtrsim 2$ MeV. BH-SNe occur in close CO_{core} (or helium or Wolf-Rayet star)-BH binaries (Ruffini et al. 2001) in which the hypercritical accretion occurs onto a previously formed BH. Such BH-SN systems correspond to the late evolutionary stages of X-ray binaries such as Cyg X-1 (Giacconi & Ruffini 1978; Belczynski et al. 2011) or microquasars (Mirabel & Rodríguez 1998). These systems might be also formed following the binary evolutionary patch leading to scenario XI in Fryer et al. (1999a). Since the estimated rate of BdHNe covers systems with the above E_{iso} and $E_{p,i}$ range, we can adopt the rate of BdHNe as an upper limit to the rate of BH-SNe, i.e., $\rho_{\text{BH-SN}} \lesssim \rho_{\text{BdHN}} = 0.77^{+0.09}_{-0.08} \text{ Gpc}^{-3} \text{ yr}^{-1}$ (Ruffini et al. 2016b). As in the above cases of XRFs and BdHNe, the SN explosion may disrupt the binary. If the binary survives, then the out-states of BH-SNe can be a νNS -BH or a BH-BH if the SN central remnant directly collapses to a BH. However, the latter scenario is currently ruled out by the observations of pre-SN cores

that appear to have masses $\lesssim 18 M_{\odot}$, very low to lead to direct BH formation (see, e.g., Smartt 2009, 2015, for details).

In the current literature such a difference between an XRF, a BdHN, and a BH-SN in the evaluation of GWs, here implemented, is still missing.

We turn now to the short bursts. Although their progenitors are still under debate, there is an ample consensus in the scientific community that they originate from NS-NS and/or NS-BH merging binaries (see, e.g., Goodman 1986; Paczynski 1986; Eichler et al. 1989; Narayan et al. 1991; Meszaros & Rees 1997; Rosswog et al. 2003; Lee et al. 2004; Berger 2014). By adopting the same in-states as in the above traditional models, namely, NS-NS and/or NS-BH mergers, they can be divided into three subclasses (Fryer et al. 2015b; Ruffini et al. 2015a, 2016b):

Short gamma-ray flashes (S-GRFs), with $E_{\text{iso}} \lesssim 10^{52}$ erg and $E_{p,i} \lesssim 2$ MeV, occur when no BH is formed in the NS-NS merger, i.e., they lead to an MNS. Following this definition, Ruffini et al. (2016b) estimated for the S-GRFs a local observed rate $\rho_{\text{S-GRF}} = 3.6^{+1.4}_{-1.0} \text{ Gpc}^{-3} \text{ yr}^{-1}$.

Authentic short GRBs (S-GRBs), with $E_{\text{iso}} \gtrsim 10^{52}$ erg and $E_{p,i} \gtrsim 2$ MeV, occur when a BH is formed in the NS-NS merger (Muccino et al. 2013; Ruffini et al. 2015a, 2016a). Following this definition, Ruffini et al. (2016b) estimated for the S-GRBs a local observed rate $\rho_{\text{S-GRB}} = (1.9^{+1.8}_{-1.1}) \times 10^{-3} \text{ Gpc}^{-3} \text{ yr}^{-1}$ (Ruffini et al. 2016b).

Ultrashort GRBs (U-GRBs), a new subclass of short bursts originating from νNS -BH merging binaries. They can originate from BdHNe (see subclass II above) or from BH-SN events (see subclass III above). Since in Fryer et al. (2015b) it was shown that the majority of BdHN out-states remain bound, we can assume as an upper limit of their local density rate $\rho_{\text{U-GRB}} \approx \rho_{\text{BdHN}} = 0.77^{+0.09}_{-0.08} \text{ Gpc}^{-3} \text{ yr}^{-1}$ (Ruffini et al. 2016b). U-GRBs are yet unobserved/unidentified and present a great challenge not only in the case of high energy but also possibly in the radio band, where they could manifest themselves, prior to the merger phase, as pulsar-BH binaries (see, e.g., Tauris et al. 2015a, and references therein).

It is important to mention that the sum of the occurrence rates of the above short burst subclasses IV–VI is in agreement with the estimates obtained from the whole short burst population reported in the literature (see, e.g., Sun et al. 2015; Wanderman & Piran 2015). It is then clear that what in the current literature are indicated as short GRBs are actually just S-GRFs.

In addition to the above three subclasses of long bursts and three subclasses of short bursts, we recall the existence of a class of bursts occurring in a low-density circumburst medium (CBM), e.g., $n_{\text{CBM}} \sim 10^{-3} \text{ cm}^{-3}$, which show hybrid properties between short and long bursts in γ -rays. These bursts are not associated with SNe, even at low redshift, where the SN detection would not be precluded (Della Valle et al. 2006). We have called such bursts gamma-ray flashes (GRFs; Ruffini et al. 2016b).

GRFs have $10^{51} \text{ erg} \lesssim E_{\text{iso}} \lesssim 10^{52} \text{ erg}$ and $0.2 \text{ MeV} \lesssim E_{p,i} \lesssim 2 \text{ MeV}$. These bursts, which show an extended and softer emission, are thought to originate in NS-WD mergers (Ruffini et al. 2016b). NS-WD binaries are notoriously

common astrophysical systems (Cadelano et al. 2015), and possible evolutionary scenarios leading to such mergers have been envisaged (see, e.g., Fryer et al. 1999b; Tauris et al. 2000; Lazarus et al. 2014).⁹ GRFs form an MNS and not a BH (see Ruffini et al. 2016b, for details). Following this definition, Ruffini et al. (2016b) estimated for the GRFs a local observed rate $\rho_{\text{GRF}} = 1.02^{+0.71}_{-0.46} \text{ Gpc}^{-3} \text{ yr}^{-1}$ (Ruffini et al. 2016b). This density rate appears to be low with respect to the current number of known NS–WD binaries in the Galaxy (see, e.g., Cadelano et al. 2015). From the GRB side, we note that indeed only one NS–WD merger has been identified (see analysis of GRB 060614 in Caito et al. 2009). The above implies that, very likely, the majority of the expected mergers are under the threshold of the existing X-ray and gamma-ray detectors.

The aforementioned density rates for all GRB subclasses have been estimated in Ruffini et al. (2016b) assuming no beaming. The presence of beaming would require the observation of achromatic jet breaks in the afterglow light curve. In the present case of short bursts such clear achromatic jet breaks have never been observed. Fong et al. (2015) reported four measured jet breaks in a sample of 11 short bursts: GRB 051221A, GRB 090426A, GRB 111020A, and GRB 130603B (see Table 5 there). However:

(1) GRB 051221A: The break is inferred only from the X-ray light curve, while the contemporary optical and radio data do not support such an interpretation (see Soderberg et al. 2006a).

(2) GRB 090426A: The break is inferred from the optical band only, and there are no contemporary observations in other bands (see Nicuesa Guelbenzu et al. 2011).

(3) GRB 111020A: The break is inferred only from the X-ray light curve, but this interpretation is based on a single upper limit by *Chandra* and no data points (see Fong et al. 2012).

(4) GRB 130603B: The break is inferred from the optical band and is compatible with the radio data. However, contemporary X-ray observations are clearly contradicting this interpretation and present no break at all. In fact, the authors invoke the presence of an extra source to justify what they call “late time X-ray excess” (see Fong et al. 2014).

In addition, Aimuratsv et al. (2017a) and Ruffini et al. (2018a) have shown that, in all the identified S-GRBs, the GeV emission has been always observed when the source was within the *Fermi*-LAT field of view. This result points as well to no significant presence of beaming in the GeV emission of S-GRBs.

Therefore, all the above points imply that there is still no evidence for the need to assume beaming.

We show in Table 1 a summary of the astrophysical aspects related to the GRB subclasses and their observational properties.

The aim of this article is to use the rate of occurrence of the above GRB subclasses to assess the detectability of their associated GW emission by the ground-based interferometers

Advanced LIGO and Advanced Virgo, by the space-based interferometer eLISA, and by the resonant bars, for completeness.

We show in Table 2 a summary of acronyms used in this work.

2. Relevance of the NS Structure and Critical Mass

Having introduced the above seven subclasses of GRBs, the relevance of the NS physics becomes clear, in particular the NS critical mass value, in the definition of subclasses I–II and IV–V.

First, we recall that in our previous works we have adopted an NS critical mass within the range $2.2\text{--}3.4 M_{\odot}$, depending on the equation of state (EOS) and on the NS angular momentum (Belvedere et al. 2014; Becerra et al. 2015; Cipolletta et al. 2015). These quoted values are for EOSs based on relativistic nuclear mean-field models (in this case the NL3, TM1, and GM1 models) and for an NS angular momentum from $J=0$ up to $J_{\text{max}} \approx 0.7 GM^2/c$ (Cipolletta et al. 2015). Hereafter, we adopt the stiffest model, namely, the NL3 EOS, which leads to the largest NS critical mass: from $M_{\text{crit}} \approx 2.7 M_{\odot}$ at $J=0$, which, as expected, is lower than the nonrotating critical mass upper limit of $3.2 M_{\odot}$ established by Rhoades & Ruffini (1974), to $M_{\text{crit}} \approx 3.4 M_{\odot}$ at J_{max} (Cipolletta et al. 2015). Our choice of relativistic mean-field theory models is based on the fact that they satisfy important properties such as Lorentz covariance, relativistic self-consistency (hence they do not violate causality), intrinsic inclusion of spin, and a simple mechanism of nuclear matter saturation (see, e.g., Dutra et al. 2014, 2016, for further details on these kinds of models). The above three representative EOSs that we have explored satisfy in addition the astrophysical constraint of leading to an NS critical mass larger than the heaviest massive NS observed, PSR J0348+0432, with $M = 2.01 \pm 0.04 M_{\odot}$ (Antoniadis et al. 2013).

As discussed in Ruffini et al. (2016b), the separatrix energy value of $\approx 10^{52}$ erg between subclasses I and II appears as a theoretical estimate of the upper limit to the energy emitted in the hypercritical accretion process onto a $\sim 1.4 M_{\odot}$ NS (see, e.g., Becerra et al. 2016) and the aforementioned adopted critical mass. This has been shown to be in agreement with the observations of 20 XRFs and 233 BdHNe (up to the end of 2014). In fact, observationally, the current upper limit for XRFs is $(7.3 \pm 0.7) \times 10^{51}$ erg, and the lower limit for BdHNe is $(9.2 \pm 1.3) \times 10^{51}$ erg (see Ruffini et al. 2016b, for further details). It is clear that the separatrix energy should have some dependence on the initial NS mass undergoing accretion and on the precise value of the nonrotating critical mass. Although the precise value of the latter is yet unknown, it is constrained within the range $2.0\text{--}3.2 M_{\odot}$, where the lower value is the mass of PSR J0348+0432 and the upper value is the well-established absolute maximum NS mass of Rhoades & Ruffini (1974).

It is clear that similar arguments apply also to the case of subclasses IV and V (Ruffini et al. 2015a), namely, the amount of energy emitted during the NS–NS merger leading to a BH should be $\gtrsim 10^{52}$ erg. Observationally, the current upper limit for S-GRFs is $(7.8 \pm 1.0) \times 10^{51}$ erg, and the lower limit for BdHNe is $(2.44 \pm 0.22) \times 10^{52}$ erg (see Ruffini et al. 2016b, for further details).

The above subclassification is further supported by the fact that GeV emission, expected in the presence of a rotating BH, is indeed observed only in BdHNe (e.g., Ruffini et al. 2015b) and in S-GRBs (e.g., Muccino et al. 2013; Ruffini et al. 2015a,

⁹ An additional (but less likely) scenario leading to merging NS–WD systems might occur in an NS–NS approaching the merger phase (Ruffini et al. 2016b). According to Bildsten & Cutler (1992) and Clark & Eardley (1977) (see also references therein), in a very close, NS–NS binary with unequal-mass components, stable mass transfer from the less massive to the more massive NS might occur for appropriate mass ratios in such a way that the donor NS moves outward in the mass-loss process until it reaches the beta-decay instability becoming a low-mass WD.

Table 1
Summary of the Astrophysical Aspects of the Different GRB Subclasses and of Their Observational Properties

	Subclass	In-state	Out-state	$E_{p,i}$ (MeV)	E_{iso} (erg)	$E_{iso,X}$ (erg)	$E_{iso,GeV}$ (erg)	z_{max}	ρ_{GRB} (Gpc ⁻³ yr ⁻¹)
I	XRFs	CO _{core} -NS	ν NS-NS	$\lesssim 0.2$	$\sim 10^{48}-10^{52}$	$\sim 10^{48}-10^{51}$...	1.096	100^{+45}_{-34}
II	BdHNe	CO _{core} -NS	ν NS-BH	$\sim 0.2-2$	$\sim 10^{52}-10^{54}$	$\sim 10^{51}-10^{52}$	$\lesssim 10^{53}$	9.3	$0.77^{+0.09}_{-0.08}$
III	BH-SN	CO _{core} -BH	ν NS-BH	$\gtrsim 2$	$> 10^{54}$	$\sim 10^{51}-10^{52}$	$\gtrsim 10^{53}$	9.3	$\lesssim 0.77^{+0.09}_{-0.08}$
IV	S-GRFs	NS-NS	MNS	$\lesssim 2$	$\sim 10^{49}-10^{52}$	$\sim 10^{49}-10^{51}$...	2.609	$3.6^{+1.4}_{-1.0}$
V	S-GRBs	NS-NS	BH	$\gtrsim 2$	$\sim 10^{52}-10^{53}$	$\lesssim 10^{51}$	$\sim 10^{52}-10^{53}$	5.52	$(1.9^{+1.8}_{-1.1}) \times 10^{-3}$
VI	U-GRBs	ν NS-BH	BH	$\gtrsim 2$	$> 10^{52}$	$\gtrsim 0.77^{+0.09}_{-0.08}$
VII	GRFs	NS-WD	MNS	$\sim 0.2-2$	$\sim 10^{51}-10^{52}$	$\sim 10^{49}-10^{50}$...	2.31	$1.02^{+0.71}_{-0.46}$

Note. In the first four columns we indicate the GRB subclasses and their corresponding in-states and out-states. In the fifth through eighth columns we list the ranges of $E_{p,i}$ and E_{iso} (rest-frame 1–10⁴ keV), $E_{iso,X}$ (rest-frame 0.3–10 keV), and $E_{iso,GeV}$ (rest-frame 0.1–100 GeV). The ninth and tenth columns list, for each GRB subclass, the maximum observed redshift and the local observed rate ρ_{GRB} obtained in Ruffini et al. (2016b). We refer the reader to Appendix B for details on the method used to calculate ρ_{GRB} .

Table 2
Acronyms Used in This Work in Alphabetic Order

Extended Wording	Acronym
Binary-driven hypervnova	BdHN
Black hole	BH
Carbon-oxygen core	CO _{core}
Gamma-ray burst	GRB
Gamma-ray flash	GRF
Induced gravitational collapse	IGC
Massive neutron star	MNS
Neutron star	NS
New neutron star created in the SN explosion	ν NS
Short gamma-ray burst	S-GRB
Short gamma-ray flash	S-GRF
Supernova	SN
Ultrashort gamma-ray burst	U-GRB
White dwarf	WD
X-ray flash	XRF

2016a; Aimuratov et al. 2017b) and absent in XRFs and S-GRFs where no BH is formed (see Figure 10 and the Appendix in Ruffini et al. 2016b, for more details).

Therefore, the direct observation of the separatrix energy between XRFs and BdHNe, as well as between S-GRFs and S-GRBs, and their precise occurrence rate ratio give crucial information on the actual NS critical mass value.

3. Ingredient Setup for the Computation of the GW Emission and Its Detectability

We have recalled in Section 1 that the evolution of the binary progenitors of both short and long GRBs leads to compact binaries that will eventually merge in a characteristic timescale and emit GWs. We turn in the following sections to assessing the detectability of the GW emission by these merging binaries by Advanced LIGO.

In order to do this, we make the following drastic simplified assumptions:

1. Although it is manifest that the release of gravitational energy of the system in the merger phase is dominated by the X-ray, gamma-ray, and GeV emission (see Table 1), we assume that the binary dynamics is only driven by the GW emission.

2. Consistent with the above GW emission dominance assumption, we further assume that the GW waveform is known and thus one can use the matched filtering technique to estimate the signal-to-noise ratio. The actual GW waveform under the realistic conditions of electromagnetic emission dominance is still unknown.
3. To estimate the maximum distance of GW detectability, we adopt optimally oriented sources with respect to the detector.

The above assumptions are made with the only aim of establishing an absolute upper limit to the GW emission and its putative detectability under the most optimistic conditions. Similarly, we assume that the binarity of the system does not compromise the interior structure of the NS (see Section 2).

The minimum GW frequency detectable by the broadband Advanced LIGO interferometer is $f_{min}^{aLIGO} \approx 10$ Hz (LIGO Scientific Collaboration et al. 2015). Since during the binary inspiral the GW frequency is twice the orbital one, the above implies that a binary is inside the Advanced LIGO band for orbital periods $P_{orb} \lesssim 0.2$ s.

3.1. Systems to Be Analyzed

The CO_{core}-NS binaries, in-states of XRFs and BdHNe, and CO_{core}-BH binaries, in-states of BH-SNe, are not detectable by Advanced LIGO since they have orbital periods $P_{orb} \gtrsim 5$ minutes $\gg 0.2$ s (Becerra et al. 2016). After their corresponding hypercritical accretion processes, it is clear that the out-states of both XRFs and BdHNe can become the in-states of short GRBs, as follows (Becerra et al. 2015; Fryer et al. 2015b; Ruffini et al. 2016b).

First, let us discuss the out-states of XRFs. We have mentioned that XRFs can either get disrupted by the SNe and lead to runaway NSs or, in the case in which the binary remains bound, lead to a ν NS-NS system. Since $\rho_{XRF} > \rho_{S-GRF} + \rho_{S-GRB}$, such ν NS-NS binaries, out-states of XRFs, could be the in-states of S-GRFs (NS-NS mergers leading to an MNS) and/or S-GRBs (NS-NS mergers leading to a BH). By denoting the total rate of short bursts as $\rho_{short} \equiv \rho_{S-GRF} + \rho_{S-GRB}$, our estimated rates would imply that the fraction of systems that appear to remain bound as ν NS-NS is $(\rho_{short}/\rho_{XRF}) \approx 2\%-8\%$, while 92%–98% of XRFs are disrupted by the SN explosion. Interestingly, this is consistent with the fraction of bound NS-NS obtained in population synthesis analyses (see, e.g., Dominik et al. 2012, 2015; Postnov & Yungelson 2014; Fryer et al. 2015a; Belczynski

et al. 2016, and references therein; Appendix A.4 and A.5). Therefore, these merging ν NS–NS binaries are clearly included in the S-GRF and S-GRB population. Such binaries are at birth undetectable by Advanced LIGO since they have initially $P_{\text{orb}} \gtrsim 5$ minutes $\gg 0.2$ s, but their merging can become detectable.

We have already recalled in the Introduction that in Fryer et al. (2015b) it was shown that, contrary to the case of XRFs, most BdHNe are expected to remain bound after the SN explosion in view of their short orbital periods and more massive accretion process. We have argued that those mergers would lead to the new class of short bursts, the U-GRBs (Fryer et al. 2015b), which, however, have still to be electromagnetically identified. The same applies to the ν NS–BH systems produced by BH–SN systems, with the only difference being the mass of the BH, which, by definition of this subclass, can be larger than the NS critical mass since this BH is formed from direct collapse of a massive star. All the above merging ν NS–BH binaries are, by definition, the U-GRB population. Such binaries are at birth undetectable by Advanced LIGO because their initial orbital periods $P_{\text{orb}} \gtrsim 5$ minutes $\gg 0.2$ s, but their merger can become detectable.

In the case of NS–WD binaries, the WD large radius and its very likely tidal disruption by the NS make their GW emission hard to detect (see, e.g., Paschalidis et al. 2009). Thus, we do not consider NS–WD binaries in the following GW discussion.

To summarize, we are going to analyze below the GW emission and detectability of S-GRF and S-GRB, the mergers of ν NS–NS produced by XRFs, as well as of U-GRBs, which are the mergers of the ν NS–BH produced by BdHNe and BH–SNe.

3.2. Binary Component Masses

For S-GRFs, we consider the simple case of nonspinning, equal-mass NS–NS merging binaries, i.e., $m_1 = m_2 = m$. The precise value of the merging NS masses leading to a BH is still poorly known; thus, we have chosen as an upper limit roughly half the maximum NS critical mass (see Section 2). Thus, we shall explore mass values $m \approx 1\text{--}1.7 M_\odot$.

For S-GRBs, we also consider nonspinning, equal-mass NS–NS merging binaries. For self-consistency, we choose a range of component masses starting from the upper edge of the S-GRF one, i.e., $m \approx 1.7 M_\odot$, up to the maximum nonrotating stable mass, i.e., $m \approx 2.8 M_\odot$.

For U-GRBs, we adopt in the case of out-states of BdHNe $m_1 = 1.5 M_\odot$ for the ν NS and $m_{\text{BH}} = 2.7\text{--}3.4 M_\odot$ for the BH (see Section 2). In the case of out-states of BH–SNe, we adopt $m_1 = 1.5 M_\odot$ for the ν NS and $m_{\text{BH}} = 3.4\text{--}10 M_\odot$ for the BH, consistent with the assumption that the BH in this subclass has been previously formed in the binary evolution and therefore it can have a mass larger than the NS critical mass.

3.3. Signal-to-noise Ratio

We first recall the main ingredients needed to estimate the detectability of the aforementioned merging binaries associated with the different GRB classes. The signal $h(t)$ induced in the detector is

$$h(t) = F_+(\theta, \phi, \psi)h_+(t, \iota, \beta) + F_\times(\theta, \phi, \psi)h_\times(t, \iota, \beta), \quad (1)$$

where h_+ and h_\times are the two polarizations of the GW; ι and β are the polar and azimuthal angles of the unit vector from the

source to the detector, relative to a coordinate system centered in the source. The detector pattern functions F_+ and F_\times depend on the localization of the source with respect to the detector, i.e., they depend on the spherical polar angles θ and ϕ of the source relative to a coordinate system centered in the detector. The pattern functions also depend on the polarization angle ψ .

Since the GW signal might be deep inside the noise, the signal-to-noise ratio, denoted hereafter by ρ , is usually computed using the matched filter technique, i.e. (Flanagan & Hughes 1998),

$$\rho^2 = 4 \int_0^\infty \frac{|\tilde{h}(f)|^2}{S_n(f)} df, \quad (2)$$

where f is the GW frequency in the detector's frame, $\tilde{h}(f)$ is the Fourier transform of $h(t)$, and $\sqrt{S_n(f)}$ is the one-sided amplitude spectral density (ASD) of the Advanced LIGO noise. We recall that in the detector's frame the GW frequency is redshifted by a factor of $1 + z$ with respect to the one in the source's frame, f_s , i.e., $f = f_s/(1 + z)$.

The exact position of the binary relative to the detector and the orientation of the binary rotation plane are usually unknown; thus, it is a common practice to estimate the signal-to-noise ratio averaging over all the possible locations and orientations, i.e.,

$$\langle \rho^2 \rangle = 4 \int_0^\infty \frac{\langle |\tilde{h}(f)|^2 \rangle}{S_n(f)} df = 4 \int_0^\infty \frac{h_c^2(f)}{f^2 S_n(f)} df, \quad (3)$$

with $h_c(f)$ the characteristic strain (Flanagan & Hughes 1998)

$$h_c = \frac{(1 + z)}{\pi d_l} \sqrt{\frac{\langle F_+^2 \rangle}{2} \frac{G}{c^3} \frac{dE}{df_s} [(1 + z)f]}, \quad (4)$$

where

$$d_l = \frac{(1 + z)c}{H_0} \int_0^z [\Omega_M(1 + x)^3 + \Omega_\Lambda]^{-1/2} dx \quad (5)$$

is the source luminosity distance and we have used the fact that $\langle F_+^2 \rangle = \langle F_\times^2 \rangle$ and $\langle F_+ F_\times \rangle = 0$. We recall that $\langle F_+^2 \rangle = 1/5$ for an interferometer and $\langle F_+^2 \rangle = 4/15$ for a resonant bar (see, e.g., Maggiore 2007). We adopt a Λ CDM cosmology with $H_0 = 71 \text{ km s}^{-1} \text{ Mpc}^{-1}$, $\Omega_M = 0.27$, and $\Omega_\Lambda = 0.73$ (Rigault et al. 2015). It is important to recall that, as we have mentioned, we are interested in estimating the GW detectability under the most optimistic conditions. Thus, to estimate the maximum distance of GW detectability, we adopt in Section 3 the ansatz of optimally oriented sources with respect to the detector. The above averaging procedure is here used with the only aim of giving an estimate of the GW strain amplitude, h_c , compared and contrasted below in Section 5 with the detector's strain noise.

4. GW Energy Spectrum

In general, a GW-driven binary system evolves in time through two regimes: the first is the *inspiral regime*, and the second, which we refer hereafter to as the *merger regime*, is composed in the most general case of the final plunge, the merger, and the ringdown (oscillations) of the newly formed object.

4.1. Inspiral Regime

During the inspiral regime, the system evolves describing quasi-circular orbits, and it is well described by the traditional point-like quadrupole approximation (Peters & Mathews 1963; Peters 1964; Rees et al. 1974; Landau & Lifshitz 1975). The GW frequency is twice the orbital frequency ($f_s = 2f_{\text{orb}}$) and grows monotonically. The energy spectrum during the inspiral regime is

$$\frac{dE}{df_s} = \frac{1}{3}(\pi G)^{2/3} M_c^{5/3} f_s^{-1/3}, \quad (6)$$

where $M_c = \mu^{3/5} M^{2/5} = \nu^{3/5} M$ is the called *chirp mass*, $M = m_1 + m_2$ is the total binary mass, $\mu = m_1 m_2 / M$ is the reduced mass, and $\nu \equiv \mu / M$ is the symmetric mass-ratio parameter. A symmetric binary ($m_1 = m_2$) corresponds to $\nu = 1/4$, and the test-particle limit is $\nu \rightarrow 0$. The total energy emitted during this regime can be estimated as the difference of the energy of the binary between infinity and the one at the last circular orbit (LCO). For a test particle in the Schwarzschild background the LCO is located at $r_{\text{LCO}} = 6GM/c^2$, its energy is $\sqrt{8/9} \mu c^2$, and then

$$\Delta E_{\text{insp}} = (1 - \sqrt{8/9}) \mu c^2. \quad (7)$$

4.2. Merger Regime

The GW spectrum of the merger regime is characterized by a GW burst (see, e.g., Davis et al. 1971; Shibata & Taniguchi 2011; Bernuzzi et al. 2015). Thus, to estimate whether this part of the signal contributes to the signal-to-noise ratio, it is sufficient to estimate the location of the GW burst in the frequency domain and its energy content. We recall that, in general, the merger regime is composed of plunge+merger+ringdown. The frequency range spanned by the GW burst is $\Delta f = f_{\text{qnm}} - f_{\text{merger}}$, where f_{merger} is the frequency at which the merger starts and f_{qnm} is the frequency of the ringing modes of the newly formed object after the merger, and the energy emitted is ΔE_{merger} . With these quantities defined, we can estimate the typical value of the merger regime spectrum as

$$\left(\frac{dE}{df_s} \right)_{\text{merger}} \sim \frac{\Delta E_{\text{merger}}}{\Delta f}. \quad (8)$$

Numerical relativity simulations (e.g., Shibata & Taniguchi 2011; Bernuzzi et al. 2015) show that finite size effects might end the inspiral regime before the LCO. After this point, the GW spectrum damps exponentially. For the case of NS–NS the merger starts in an orbit larger than the LCO, and for the case of an NS–BH, as we will see below, the merger can occur below the LCO, making the spectrum similar to a BH–BH merger. When the merger occurs well before the LCO, there is no plunge. Therefore, the emitted energy will be less than the case when the plunge is present. We can therefore obtain an upper limit to ΔE_{merger} by adopting the energy emitted during the plunge-merger-ringdown of a BH–BH merger (Detweiler & Szedenits 1979)

$$\Delta E_{\text{merger}} \approx 0.5 \nu^2 M c^2. \quad (9)$$

To complete the estimate of the merger regime spectrum, we have to estimate the value of Δf in the different cases of interest.

4.2.1. NS–NS Merger

The approach to the merger point, $r = r_{\text{merger}}$, depends on the nature of the binary system. Typically, the merger is assumed to start at the point of maximum GW strain (see, e.g., Bernuzzi et al. 2015, and references therein). However, since the transition from a binary system to a single merged object is not sharply definable, different definitions of the merger point in the literature can be found (see, e.g., Kawaguchi et al. 2015). For our purpose it is sufficient to estimate the frequency at “contact,” namely, the frequency at a binary separation $r_{\text{contact}} \approx r_1 + r_2$, where r_i is the radius of the i -component. This certainly sets a lower limit to the frequency at maximum strain at merger, i.e., $r_{\text{contact}} \gtrsim r_{\text{merger}}$. Thus, we adopt for these systems

$$f_{\text{merger}}^{\text{NS–NS}} \approx f_{\text{contact}}^{\text{NS–NS}} = \frac{1}{\pi} \frac{c^3}{GM} \left[\frac{C_1 C_2 (1+q)}{C_1 + q C_2} \right]^{3/2}, \quad (10)$$

where $q = m_2/m_1$ is the mass ratio, which is related to the symmetric mass-ratio parameter by $\nu = q/(1+q)^2$, and $C_i \equiv G m_i / c^2 r_i$ is the compactness of the i -component.

For a mass-symmetric NS–NS binary, we have that $f_{\text{contact}}^{\text{NS–NS}} \approx (1/\pi)(c^3/G) C_{\text{NS}}^{3/2} / M$, where $C_{\text{NS}} \equiv C_1 = C_2$ is the compactness parameter of the initial NS. For example, for the NL3 EOS, the NS compactness lies in the range $C_{\text{NS}} \approx 0.14$ – 0.3 for an NS mass 1.4 – $2.8 M_{\odot}$ (see, e.g., Cipolletta et al. 2015). Thus, using the same EOS, we have, for an $M = (1.4 + 1.4) M_{\odot} = 2.8 M_{\odot}$ binary, $f_{\text{contact}}^{\text{NS–NS}} \approx 1.34$ kHz and, for an $M = (2.0 + 2.0) M_{\odot} = 4.0 M_{\odot}$ binary, $f_{\text{contact}}^{\text{NS–NS}} \approx 1.43$ kHz.

In the merger regime either a BH or an MNS can be formed. If the merger does not lead to a BH, the merger frequency is dominated by the frequency of the quasi-normal modes of the MNS formed. This frequency is of the order of

$$f_{\text{qnm}}^{\text{MNS}} \approx \frac{1}{\pi} \left(\frac{GM}{R^3} \right)^{1/2} = \frac{1}{\pi} \left(\frac{c^3}{G} \right) \frac{C_{\text{MNS}}^{3/2}}{M}, \quad (11)$$

where R is the radius of the MNS and $C_{\text{MNS}} \equiv GM/(c^2 R)$ is its compactness. Thus, in the case of S-GRFs the value of Δf is

$$\begin{aligned} \Delta f_{\text{S-GRF}} &\equiv f_{\text{qnm}}^{\text{MNS}} - f_{\text{contact}}^{\text{NS–NS}} \\ &\approx (C_{\text{MNS}}^{3/2} - C_{\text{NS}}^{3/2}) \frac{c^3}{\pi GM}. \end{aligned} \quad (12)$$

If the merger forms a BH, the merger frequency is dominated by the frequency of the quasi-normal modes of the BH formed, namely, the GW-burst spectrum peaks at the frequency (Davis et al. 1971, 1972)

$$f_{\text{qnm}}^{\text{BH}} \approx \frac{0.32}{2\pi} \frac{c^3}{GM}, \quad (13)$$

i.e., $f_{\text{qnm}} \approx 3.4$ kHz for a Schwarzschild BH of $3 M_{\odot}$. In the case of a rotating BH, namely, a Kerr BH, the peak frequency shifts to higher values (Detweiler 1980). Thus, the value of $f_{\text{qnm}}^{\text{BH}}$ given by Equation (13) can be considered as a lower bound to the actual peak frequency. Thus, in the case of

S-GRBs the value of Δf is

$$\begin{aligned}\Delta f_{\text{S-GRB}} &\equiv f_{\text{qnm}}^{\text{BH}} - f_{\text{contact}}^{\text{NS-NS}} \\ &\approx (0.16 - \mathcal{C}_{\text{NS}}^{3/2}) \frac{c^3}{\pi GM}.\end{aligned}\quad (14)$$

In either case of BH or MNS formation, $f_{\text{qnm}} > f_{\text{contact}}$ is satisfied. It can be checked that the above frequency estimates are consistent with values obtained from full numerical relativity simulations (see, e.g., Anninos et al. 1995; Bernuzzi et al. 2015).

4.2.2. NS–BH Merger

For an NS–BH merger, the approach to merger is different since general relativistic effects avoid the objects to go all the way to the “contact” point following circular orbits. For example, let us assume $m_1 = m_{\text{BH}} \approx 3 M_{\odot}$ and $m_2 = M_{\text{NS}} \approx 1.5 M_{\odot}$, so that $M = 1.5 + 3.0 M_{\odot} = 4.5 M_{\odot}$. In this case $r_1 = 2Gm_{\text{BH}}/c^2$ (for a Schwarzschild BH) and $r_2 = Gm_2/(c^2\mathcal{C}_2)$, so $r_{\text{contact}} \approx 3.3GM/c^2$. Within the test-particle limit, the LCO around a Schwarzschild BH occurs at $r_{\text{LCO}} = 6Gm_{\text{BH}}/c^2 \approx 6GM/c^2 > r_{\text{contact}}$. Thus, we have that $r_{\text{contact}} < r_{\text{LCO}}$, which suggests that an NS–BH binary, similar to the case of a BH–BH one, can pass from the inspiral regime, to the plunge from $r_{\text{plunge}} = r_{\text{LCO}}$ to merger at $r_{\text{merger}} \approx r_{\text{contact}}$, to the ringing of the newly formed BH. At r_{plunge} , the GW frequency is

$$f_{\text{plunge}}^{\text{NS-BH}} \approx \frac{1}{\pi} \left(\frac{GM}{r_{\text{LCO}}^3} \right)^{1/2} = \frac{1}{\pi 6^{3/2}} \left(\frac{c^3}{GM} \right), \quad (15)$$

and as in the previous case of BH formation from an NS–NS merger, the NS–BH post-merger GW spectrum will be dominated by frequencies given by Equation (13). Namely, for the present example $f_{\text{plunge}}^{\text{NS-BH}} \approx 980$ Hz and $f_{\text{qnm}}^{\text{BH}} \approx 2.3$ kHz.

Thus, in the case of NS–BH merger (U-GRB subclass), the value of Δf is

$$\Delta f_{\text{U-GRB}} \equiv f_{\text{qnm}}^{\text{BH}} - f_{\text{plunge}}^{\text{NS-BH}} \approx 0.092 \frac{c^3}{\pi GM}. \quad (16)$$

In the above analysis we have neglected the possibility that the NS can be tidally disrupted by the BH before it reaches $r = r_{\text{LCO}}$. The NS is disrupted by the BH if $r_{\text{LCO}} < r_{\text{id}}$, where r_{id} is the tidal disruption radius. The value of r_{LCO} and r_{id} for an NS–BH system depends both on the binary mass ratio $q \equiv m_2/m_1 \leq 1$ and on the NS compactness \mathcal{C}_{NS} , which depends, in turn, on the NS mass and EOS. Numerical simulations of NS–BH binary mergers adopting a polytropic EOS for the NS matter suggest $r_{\text{id}} \approx 2.4q^{-1/3}R_{\text{NS}}$ and $r_{\text{LCO}} \approx 6GM/c^2[1 - 0.44q^{1/4}(1 - 3.54\mathcal{C}_{\text{NS}})^{-2/3}]$ (see Shibata & Taniguchi 2011, and references therein). The ratio $r_{\text{id}}/r_{\text{LCO}}$ is a decreasing function of the BH mass for given NS mass (but always close to unity). If we extrapolate these results to BH masses in the range of $3\text{--}10 M_{\odot}$ and an NS of $1.5 M_{\odot}$ obeying the NL3 EOS, we have $r_{\text{LCO}} < r_{\text{id}}$ for $m_{\text{BH}} \lesssim 6 M_{\odot}$ and $r_{\text{LCO}} > r_{\text{id}}$ otherwise. It is clear that the specific range of NS and BH masses for which there is tidal disruption is highly sensitive to the compactness of the NS and hence to the nuclear EOS, and thus more simulations using a wide set of updated nuclear EOSs are needed to assess this issue. If tidal disruption

occurs, the inspiral regime will cut off at a GW frequency

$$f_{\text{id}}^{\text{NS-BH}} \approx \frac{1}{\pi} \left(\frac{GM}{r_{\text{id}}^3} \right)^{1/2}. \quad (17)$$

Since r_{id} is near r_{LCO} for our systems, and to not introduce further uncertainties in our estimates, we shall adopt that the inspiral regime of our NS–BH systems ends at the GW frequency given by Equation (15).

5. Characteristic Strain and Detector Sensitivity

From Equations (6) and (8) and with the knowledge of the energy released in GWs (Equation (9)) and the spanned frequencies in the merger regime (see Table 3), we can estimate the characteristic strain given by Equation (4), which can be compared and contrasted with the strain noise of GW detectors.

Figure 1 shows the GW signal ASD produced by S-GRFs, S-GRBs, and U-GRBs, obtained with the aid of Equation (4). In this figure we adopt a $(1.4+1.4) M_{\odot}$ ν NS–NS merger for S-GRFs, a $(2.0+2.0) M_{\odot}$ ν NS–NS merger for S-GRBs, a $(1.5+3.0) M_{\odot}$ ν NS–BH merger for U-GRBs produced by out-states of BdHNe, and a $(1.5+10.0) M_{\odot}$ ν NS–BH merger for U-GRBs produced by out-states of BH–SNe. We have assumed in this plot that these sources are located at the closest luminosity distance d_l at which each subclass has been observed (see Table 3 for details). We show the noise ASD of Advanced LIGO in the current run (O1) and in the expected 2022+ run (Abbott et al. 2016); the expected noise ASD of Advanced Virgo (BNS-optimized; Abbott et al. 2016); the expected noise ASD of the space-based interferometer eLISA for the N2A1, N2A2, and N2A5 configurations (see, e.g., Klein et al. 2016); and the noise ASD of the NAUTILUS bar detector for a 1 ms GW burst (Astone et al. 2006, 2008). Narrowband resonant bar detectors (such as ALLEGRO, AURIGA, EXPLORER, NAUTILUS, and NIOBE) are sensitive within a bandwidth of $\sim 1\text{--}10$ Hz around the resonant frequency, which is typically $f_0 \sim 1$ kHz (see, e.g., Table 2 in Camp & Cornish 2004, for a summary of the properties of the bar detectors). The bar detector with the wider bandwidth is NAUTILUS, with a minimum strain spectral noise $\sqrt{S_n} = 10^{-21} \text{ Hz}^{-1/2}$ at $f_0 = 935$ Hz and $\sqrt{S_n} \leq 10^{-20} \text{ Hz}^{-1/2}$ in a bandwidth of ~ 30 Hz around f_0 (Astone et al. 2008). This implies that a 1 ms GW burst would be detected by this instrument if it has a strain amplitude $h \gtrsim 3 \times 10^{-19}$ (Astone et al. 2006, 2008).

From this figure we can conclude the following for the NS–NS and NS–BH binaries associated with S-GRFs, S-GRBs, and U-GRBs:

1. *Before merging*: they transit, during their inspiral regime which spans the frequency range $f < f_{\text{merger}}/(1+z)$ (see in Table 3 the frequencies and redshift), first the eLISA frequency band and then enter the Advanced LIGO–Virgo ones in the final orbits prior to the merging process (when $P_{\text{orb}} < 0.2$ s). The narrow bandwidth of the bar detectors does not cover these frequencies. For the adopted distances we see that the characteristic strain generated by all these sources is below the sensitivity of eLISA. S-GRFs are below the sensitivity of Advanced LIGO (O1), Advanced Virgo, and NAUTILUS, but inside the sensitivity of Advanced LIGO (2022+). S-GRBs are below the sensitivity of Advanced LIGO (all runs),

Table 3
Properties of the GW Emission of S-GRFs, S-GRBs, and U-GRBs

	ΔE_{insp} (erg)	ΔE_{merger} (erg)	f_{merger} (kHz)	f_{qnm} (kHz)	$z_{\text{min}}^{\text{obs}}$	d_{min} (Mpc)	d_{GW} (Mpc)		2022+
							O1	O2	
S-GRF	7.17×10^{52}	1.60×10^{53}	1.20	3.84	0.111	508.70	90.51–181.02	181.02–271.52	452.54
S-GRB	1.02×10^{53}	2.28×10^{53}	1.43	2.59	0.903	5841.80	121.84–243.67	243.67–365.51	609.18
U-GRB	1.02×10^{53}	2.03×10^{52}	0.98	2.30	0.169	804.57	126.71–253.43	253.43–380.14	633.57
U-GRB (BH–SN)	1.34×10^{53}	1.35×10^{53}	0.38	0.90	0.169	804.57	197.86–395.71	395.71–593.57	989.28

Note. We have made the Drastic simplified assumption that the binary evolution is only driven by GW emission, although it is manifest that the gravitational energy of the system in the merger phase is dominated by the radio, optical, X-ray, gamma-ray, and GeV emission (see Table 1). This assumption is made with the only aim of establishing an absolute upper limit to the GW emission and its detectability under the most optimistic conditions. Column (1): GRB subclass. Column (2): energy emitted in GWs during the inspiral regime ΔE_{insp} given by Equation (7). Column (3): energy emitted in GWs during the merger regime (plunge+merger+ringdown) ΔE_{merger} given by Equation (9). Column (4): GW frequency at merger. Column (5): GW frequency of the ringdown regime. Column (6): lowest cosmological redshift value $z_{\text{min}}^{\text{obs}}$ at which each subclass has been observed. Column (7): luminosity distance corresponding to $z_{\text{min}}^{\text{obs}}$, d_{min} , estimated from Equation (5). Columns (8)–(10): GW horizon calculated with the sensitivity of advanced LIGO during the O1 and O2 runs and with the expected final sensitivity including LIGO-India (2022+), respectively. It can be seen that the current GW horizon is much smaller than the observed distances of GRBs, impeding a positive detection by advanced LIGO. Only in the case of U-GRB (BH–SN) is a possible detection foreseen during the run 2022+. See also Table 4. We have used for S-GRFs $(1.4+1.4) M_{\odot}$, for S-GRBs $(2.0+2.0) M_{\odot}$, and for U-GRBs $(1.5+3.0) M_{\odot}$ and $(1.5+10.0) M_{\odot}$ for the out-states of BdHNe and of BH–SNe, respectively. Even if no U-GRB has yet been identified, we use here the values of $z_{\text{min}}^{\text{obs}}$ and d_{min} corresponding to the closest BdHN observed.

Advanced Virgo, and NAUTILUS. U-GRBs from out-states of BdHNe are below the sensitivity of Advanced LIGO (O1), Advanced Virgo, and NAUTILUS, but inside the sensitivity of Advanced LIGO (2022+). U-GRBs from out-states of BH–SNe are below the sensitivity of Advanced LIGO (O1) and NAUTILUS, inside the sensitivity of Advanced LIGO (2022+), and marginally inside the sensitivity of Advanced Virgo.

2. *Merging*: the merging regime, which expands frequencies from $f_{\text{contact}}/(1+z)$ to $f_{\text{qnm}}/(1+z)$ (see in Table 3 the frequencies and redshift), is outside the eLISA frequency band but inside the Advanced LIGO-Virgo and bar detector ones. The characteristic strain in this final merger phase $h \sim 10^{-24}$ to 10^{-23} is, unfortunately, well below the sensitivity of all of them (see also Kobayashi & Mészáros 2003, for similar conclusions for Advanced LIGO).

From the above it can be seen that the most interesting instrument for the possible detection of the GW emission from binaries associated with GRBs is Advanced LIGO. Therefore, we estimate in the next section the expected detection rates by Advanced LIGO-Virgo (see Figure 2 and Table 4).

6. GW Detection Rate

We assume a threshold for the Advanced LIGO-Virgo single detector $\rho_0 = 8$ (Abbott et al. 2016). This minimum ρ_0 defines a maximum detection distance or GW horizon distance, which is denoted as d_{GW} . This horizon corresponds to the most optimistic case when the binary is just above the detector and the binary plane is parallel to the detector plane, i.e., $\theta = \phi = \iota = 0$ (Allen et al. 2012):

$$d_{\text{GW}} = \frac{2A}{\rho_0} \left(\int_0^\infty \frac{f^{-7/3}}{S_n(f)} df \right)^{1/2}, \quad (18)$$

where $A = 5/(24\pi^{4/3})^{1/2} (GM_c/c^3)^{5/6} c$. Since not all the sources are optimally aligned with the detector, the number of detected sources inside a sphere of radius d_{GW} will be a fraction \mathcal{F}^3 of the total. This fraction determines the so-called “range” of the detector, $\mathcal{R} = \mathcal{F} d_{\text{GW}}$, where $\mathcal{F}^{-1} = 2.2627$ (see

Finn & Chernoff 1993, for details). In order to give an estimate of the annual number of detectable binaries associated with GRBs, we use the *search volume* as computed in Abbott et al. (2016), $\mathcal{V}_s = V_{\text{max}}^{\text{GW}} \mathcal{T}$, where $V_{\text{max}}^{\text{GW}} = (4\pi/3) \mathcal{R}^3$ and \mathcal{T} is the observing time accounting for the detector’s duty cycles. We use here the lower and upper values of \mathcal{R} and \mathcal{V}_s for a $(1.4+1.4) M_{\odot}$ NS binary for the different observational campaigns reported in Abbott et al. (2016): 2015/2016 (O1) with $\mathcal{R} = 40\text{--}80$ Mpc, $\mathcal{T} = 3$ months, $\mathcal{V}_s = (0.5\text{--}(4) \times 10^5 \text{ Mpc}^3 \text{ yr})$; 2016/2017 (O2) with $\mathcal{R} = 80\text{--}120$ Mpc, $\mathcal{T} = 6$ months, $\mathcal{V}_s = (0.6\text{--}2) \times 10^6 \text{ Mpc}^3 \text{ yr}$; 2017/2018 (O3) with $\mathcal{R} = 120\text{--}170$ Mpc, $\mathcal{T} = 9$ months, $\mathcal{V}_s = (3\text{--}10) \times 10^6 \text{ Mpc}^3 \text{ yr}$; and the one by the entire network including LIGO-India at design sensitivity (2022+) with $\mathcal{R} = 200$ Mpc, $\mathcal{T} = 1$ year, $\mathcal{V}_s = 4 \times 10^7 \text{ Mpc}^3 \text{ yr}$. We can use the above information for a $(1.4+1.4) M_{\odot}$ binary and extrapolate it to other binaries with different masses using the property that d_{GW} scales with the chirp mass as $M_c^{5/6}$ (see Equation (18)). We show in Table 3 the GW horizon for a specific value of the binary component masses expected for S-GRFs, S-GRBs, and U-GRBs (see Section 3.2).

From the inferred occurrence rates ρ_{GRB} (not to be confused with signal-to-noise ratio ρ) summarized in Table 1, we show in Figure 2 the expected number of GW detections by Advanced LIGO-Virgo for each observational campaign

$$\dot{N}_{\text{GW}} = \rho_{\text{GRB}} \mathcal{V}_s \quad (19)$$

for S-GRFs, S-GRBs, and U-GRBs as a function of the binary component masses (see Section 3.2).

We compare and contrast the following in Table 4 for the GRB subclasses: the expected GW detection rate by Advanced LIGO-Virgo given by Equation (19), \dot{N}_{GW} ; the inferred occurrence rate of GRBs, \dot{N}_{GRB} ; and the observed GRB rate from γ -ray telescopes (AGILE, BATSE, *BeppoSAX*, *Fermi*, *HETE-II*, *INTEGRAL*, *Konus/WIND*, and *Swift*), simply estimated as $\dot{N}_{\text{GRB}}^{\text{obs}} = N_{\text{GRB}}^{\text{obs}}/T_{\text{obs}}$, where $N_{\text{GRB}}^{\text{obs}}$ is the number of GRBs detected in the observing time T_{obs} . The rate \dot{N}_{GRB} is obtained from the GRB specific rate through the reconstruction of the GRB luminosity function and the study of its evolution with redshift (for details see Ruffini et al. 2016b; Appendix B).

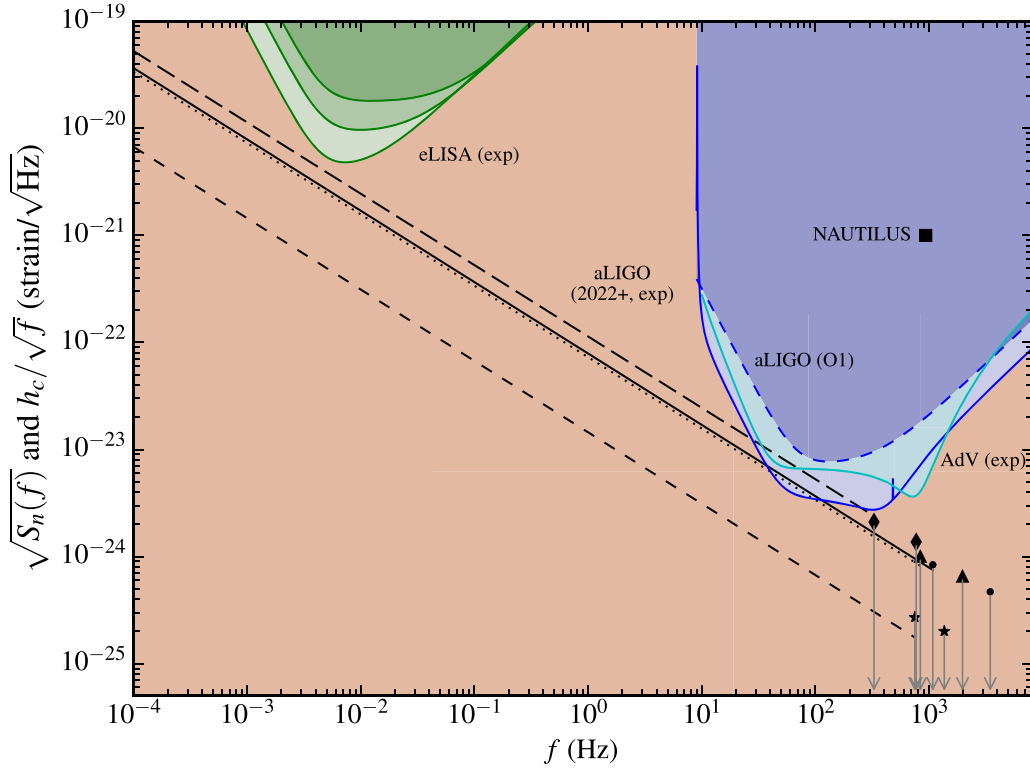


Figure 1. Comparison of the signal’s ASD h_c/\sqrt{f} of S-GRFs, S-GRBs, and U-GRBs with the noise’s ASD $\sqrt{S_n(f)}$, where S_n is the power spectrum density of the detector’s noise of eLISA, of Advanced LIGO (aLIGO), and of the bar detector NAUTILUS. The red lines, from top to bottom, are the expected noise’s ASD of the N2A1, N2A2, and N2A5 configurations of eLISA (Klein et al. 2016). The dashed and solid red lines correspond to the noise’s ASD of the Advanced LIGO O1 run (2015/2016) and of the expected Advanced LIGO 2022+ run (Abbott et al. 2016), respectively, and the cyan line is the expected noise’s ASD of Advanced Virgo (AdV) BNS-optimized (Abbott et al. 2016). The filled square indicates the noise’s ASD of the NAUTILUS resonant bar for a 1 ms GW burst (Astone et al. 2006, 2008). The red filled area indicates the region of undetectability by any of the above instruments. We recall that in this plot the GW frequency is redshifted by a factor of $1+z$ with respect to the source frame value, i.e., $f = f_s/(1+z)$, for which we use the cosmological redshift and corresponding luminosity distance of the closest observed source of each subclass (see Table 3). The following three curves correspond to the inspiral regime of the coalescence: S-GRFs with $(1.4+1.4) M_\odot$ (solid curve), S-GRBs with $(2.0+2.0) M_\odot$ (short-dashed curve), U-GRB with $(1.5+3.0) M_\odot$ (dotted curve) from out-states of BdHNe, and U-GRB with $(1.5+10.0) M_\odot$ (long-dashed curve) from out-states of BH-SNe. The circle, star, triangle, and diamond correspond to h_c in the merger regime for S-GRFs, S-GRBs, U-GRBs from out-states of BdHNe, and U-GRBs from out-states of BH-SNe, respectively. The first point is located at $f_{\text{merger}}/(1+z)$ and the second at $f_{\text{qnm}}/(1+z)$ (see Table 3). The downward-pointing arrows indicate that these estimates have to be considered as upper limits since we have assumed that all the energy released in the system goes in GWs, which clearly overestimates the GW energy output in view of the dominance of the electromagnetic emission (see Table 4). We have also overestimated the GW energy in the merger regime by using Equation (9), which is the expected GW energy emitted in the plunge+merger+ringdown phases of a BH–BH merger. For binary mergers involving NSs, as we have discussed in Section 4, the energy released in GWs must be necessarily lower than this value.

This estimate, therefore, is larger than $\dot{N}_{\text{GRB}}^{\text{obs}}$, which is limited to those events beyond the detector sensitivity threshold, falling inside its field of view and within its operational time.

7. Conclusions

Short and long GRBs have been divided into seven subclasses according to their binary nature (Ruffini et al. 2016b). We summarize in Table 1 their main physical properties characterizing the outcome of X-rays, gamma-rays, and high-energy and ultra-high-energy detectors, as well as their occurrence rate. Particularly important for the present work is the specification of the in-states and out-states of the GRB progenitors.

With the knowledge of the nature of the compact-object binaries associated with each GRB subclass and the relevance of the NS structure and critical mass in Section 2, we introduce in Section 3 the main ingredients for the computation of the GW emission and detectability for such systems. We describe in Section 4 the general properties of the GW emission during the inspiral and merger regimes of these binaries. We argue that S-GRFs, S-GRBs, and U-GRBs are the GRB subclasses relevant

for the GW analysis. It is manifest that the release of the gravitational energy of the system in the merger phase is dominated by the X-rays, gamma-rays, and GeV emission (see Table 1). In order to evaluate the GW emission, we have made in this work the drastic simplified assumption that the binary evolution is only driven by GW emission. This assumption is of interest, with the only aim of establishing an absolute upper limit and checking the detectability of the GW emission under this most optimistic condition. We compare and contrast in Section 5 the GW characteristic strain amplitude produced by the inspiral and merger regimes with the strain noise of the broadband detectors eLISA and Advanced LIGO-Virgo and of the narrowband resonant bar NAUTILUS. In order to do this, we use the cosmological redshift and corresponding luminosity distance of the closest observed source of each subclass (see Table 3). We show that the inspiral regime is possibly detectable only by Advanced LIGO (see Table 3 and Figure 1) and the merger regime is undetectable by any of these instruments.

Therefore, in Section 6 we assess quantitatively the GW detectability of the inspiral regime of S-GRFs, S-GRBs, and U-GRBs only by Advanced LIGO. We recall that, following

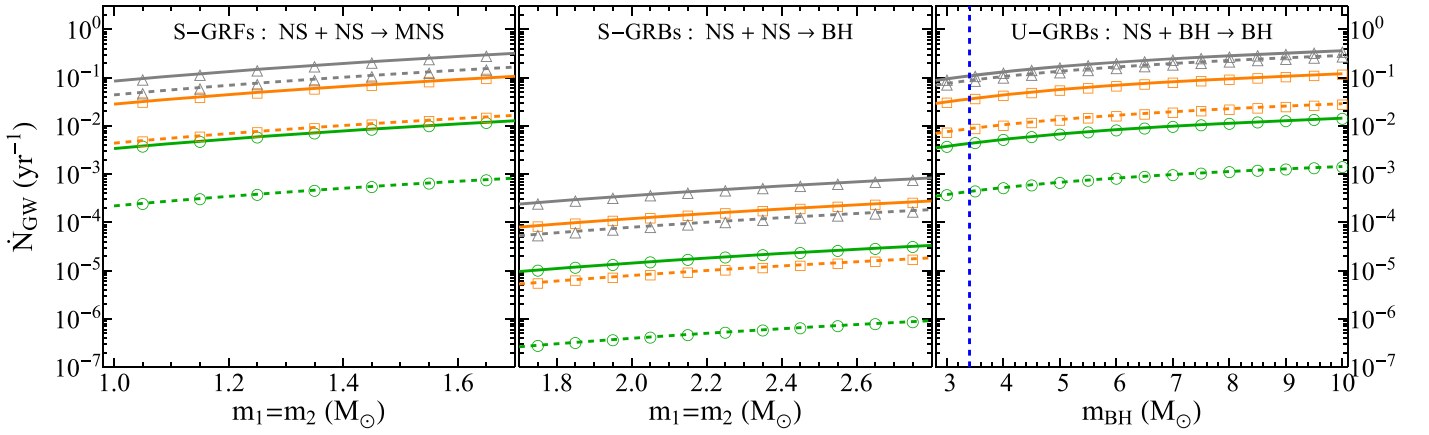


Figure 2. Expected annual GW upper and lower bounds (solid and dashed lines, respectively) for the detections expected from S-GRFs (left panel), S-GRBs (middle panel), and U-GRBs (right panel), for three selected observational campaigns: 2015/2016 (O1; red curves with circles), 2017/2018 (O3; orange curve with squares), and 2022+ (gray curve with triangles). The vertical red dashed line in the plot of U-GRBs separates ν NS–BH binaries produced by BdHNe (BH masses equal to the NS critical mass) and BH–SNe (BH masses larger than the NS critical mass).

Table 4

Inferred and Observed Number of GRBs Per Year, and the Corresponding Expected Rate of GW Detections for Each GRB Subclass

GRB Subclass	\dot{N}_{GRB} (yr^{-1})	$\dot{N}_{\text{GRB}}^{\text{obs}}$ (yr^{-1})	\dot{N}_{GW} (yr^{-1})
XRFs	144–733	1 (1997–2014)	Undetectable
BdHNe	662–1120	14 (1997–2014)	Undetectable
BH–SNe	$\lesssim 662$ –1120	$\lesssim 14$ (1997–2014)	Undetectable
S-GRFs	58–248	3 (2005–2014)	O1: 0.0001–0.002 O2: 0.002–0.01 O3: 0.008–0.05 2022+: 0.1–0.2
S-GRBs	2–8	1 (2006–2014)	O1: $(0.1\text{--}3.1) \times 10^{-6}$ O2: $(0.1\text{--}1.6) \times 10^{-5}$ O3: $(0.6\text{--}7.8) \times 10^{-5}$ 2022+: $(0.78\text{--}3.12) \times 10^{-4}$
U-GRBs	662–1120	...	O1: $(0.9\text{--}9) \times 10^{-4}$ O2: 0.001–0.005 O3: 0.006–0.024 2022+: 0.076–0.094
U-GRBs (BH–SN)	$\lesssim 662$ –1120	...	O1: $\lesssim 0.00036$ –0.0036 O2: $\lesssim 0.004$ –0.018 O3: $\lesssim 0.02$ –0.09 2022+: $\lesssim 0.29$ –0.36
GRFs	29–153	1 (2005–2014)	Undetectable

Note. Column (1): GRB subclass. Column (2): inferred number of GRBs per year in the entire universe, \dot{N}_{GRB} , for each GRB subclass (see also Figure 6 in Ruffini et al. 2016b). Column (3): number of GRBs observed per year, $\dot{N}_{\text{GRB}}^{\text{obs}}$, obtained from the observations of γ -ray telescopes such as AGILE, BATSE, BeppoSAX, Fermi, HETE-II, INTEGRAL, Konus/WIND, and Swift, in the indicated years of observations (see also Tables 2–6 in Ruffini et al. 2016b). Column (4): expected rate of GW detections by advanced LIGO of all the GRB subclasses, computed for three selected observational campaigns, 2015/2016 (O1), 2016/2017 (O2), and 2017/2018 (O3), and the one by the entire network at design sensitivity including LIGO-India (2022+). The binary component masses used here are the same as in Table 3.

Abbott et al. (2016), we adopt as the threshold for detectability a signal-to-noise ratio equal to 8. We present in Figure 2 and Table 4 the expected detection rate of the GW emission. Four observational campaigns of Advanced LIGO are analyzed: O1 (2015/2016), O2 (2016/2017), O3 (2017/2018), and 2022+, namely the one by the entire network at design sensitivity including LIGO-India. In Table 4 we compare and contrast this rate with the occurrence rate of the GRB subclasses and their rate of observations by γ -ray telescopes.

Keeping the above in mind, we conclude the following for each GRB subclass:

- I. XRFs: their ν NS–NS out-states transit, during the inspiral regime, which spans the frequency range $f < f_{\text{merger}}/(1+z)$ (see Table 3), first the eLISA frequency band and then enter the Advanced LIGO–Virgo ones in the final orbits prior to the merging process (i.e., when $P_{\text{orb}} < 0.2$ s). Resonant bar detectors are not sensitive in this inspiral regime frequency range. The characteristic strain generated by these sources in the inspiral regime is below the sensitivity of eLISA. The merger regime, which expands frequencies from $f_{\text{contact}}/(1+z)$ to $f_{\text{qnm}}/(1+z)$ (see Table 3), is outside the eLISA frequency band but inside the frequency band of Advanced LIGO–Virgo and bar detectors. See Figure 1 for details. These ν NS–NS mergers can lead to either S-GRFs or S-GRBs (see in IV and V below the conclusion about their GW detectability).
- II. BdHNe: their ν NS–BH out-states transit, during the inspiral regime, which spans the frequency range $f < f_{\text{merger}}/(1+z)$ (see Table 3), first the eLISA frequency band and then enter the Advanced LIGO–Virgo ones in the final orbits prior to the merging process (i.e., when $P_{\text{orb}} < 0.2$ s). Resonant bar detectors are not sensitive in this inspiral regime frequency range. The characteristic strain generated by these sources in the inspiral regime is below the sensitivity of eLISA. The merger regime, which expands frequencies from $f_{\text{contact}}/(1+z)$ to $f_{\text{qnm}}/(1+z)$ (see Table 3), is outside the eLISA frequency band but inside the frequency band of Advanced LIGO–Virgo and bar detectors. See Figure 1

- for details. These ν NS–BH mergers lead to U-GRBs (see in VI below the conclusion about their GW detectability).
- III. BH–SN: their ν NS–BH out-states transit, during the inspiral regime, which spans the frequency range $f < f_{\text{merger}} / (1 + z)$ (see Table 3), first the eLISA frequency band and then enter the Advanced LIGO–Virgo ones in the final orbits prior to the merging process (i.e., when $P_{\text{orb}} < 0.2$ s). Resonant bar detectors are not sensitive in this inspiral regime frequency range. The characteristic strain generated by these sources in the inspiral regime is below the sensitivity of eLISA. The merger regime, which expands frequencies from $f_{\text{contact}} / (1 + z)$ to $f_{\text{qnm}} / (1 + z)$ (see Table 3), is outside the eLISA frequency band but inside the frequency band of Advanced LIGO–Virgo and bar detectors. See Figure 1 for details. These ν NS–BH mergers lead to U-GRBs (see in VI below the conclusion about their GW detectability).
- IV. S-GRFs: the final orbits of the inspiral regime (when $P_{\text{orb}} < 0.2$ s) fall inside the frequency band of Advanced LIGO–Virgo and bar detectors. However, the GW energy output in the merger regime leads to a characteristic strain that is not sufficient to be detectable either by any of them. See Figure 1 for details. The inspiral regime is detectable for sources located at distances smaller than 181 Mpc for the O1 Advanced LIGO run and smaller than 452 Mpc for the 2022+ run (see Table 3). The closest S-GRF observed up to now is, however, located at 509 Mpc. See Table 4 for the expected GW detection rate.
- V. S-GRBs: the final orbits of the inspiral regime (when $P_{\text{orb}} < 0.2$ s) fall inside the frequency band of Advanced LIGO–Virgo and bar detectors. However, the GW energy output in the merger regime leads to a characteristic strain that is not sufficient to be detectable either by any of them. See Figure 1 for details. The inspiral regime is detectable for sources located at distances smaller than 244 Mpc for the O1 Advanced LIGO run and smaller than 609 Mpc for the 2022+ run (see Table 3). The closest S-GRB observed up to now is, however, located at 5842 Mpc. See Table 4 for the expected GW detection rate.
- VI. U-GRBs: the final orbits of the inspiral regime (when $P_{\text{orb}} < 0.2$ s) fall inside the frequency band of Advanced LIGO–Virgo and bar detectors. However, the GW energy output in the merger regime leads to a characteristic strain that is not sufficient to be detectable either by any of them. See Figure 1 for details. In the case of U-GRBs originating from the BdHN out-states, the inspiral regime is detectable for sources located at distances smaller than 253 Mpc for the O1 Advanced LIGO run and smaller than 634 Mpc for the 2022+ run (see Table 3). In the case of U-GRBs originating from the BH–SN out-states, the inspiral regime is detectable for sources at distances smaller than 396 Mpc for the O1 Advanced LIGO run and smaller than 989 Mpc for the 2022+ run (see Table 3). No U-GRB has yet been electromagnetically identified. The closest distance at which its possible progenitor, namely, a BdHN, is located is 805 Mpc. See Table 4 for the expected GW detection rate.
- VII. GRFs: The tidal disruption of the WD by the NS produces an undetectable GW emission (see, e.g., Paschalidis et al. 2009).

We recalled in the Introduction that the simultaneous detection rates of GWs and GRBs have been estimated up to now in the literature only in the case of S-GRFs, in which no BH is formed but instead the merger of the two NSs leads to an MNS. Indeed, it can be seen that the recent GW detection rate estimated by Patricelli et al. (2016) of short bursts at Advanced LIGO design sensitivity (see Table 1 there), $0.04\text{--}15\text{ yr}^{-1}$, is consistent with the one of S-GRFs estimated in this work, $\dot{N}_{\text{GW}} = 0.1\text{--}0.2\text{ yr}^{-1}$ (see Table 4). This represents the most favorable case for the possible GW detection by Advanced LIGO–Virgo of NS–NS merger, which, however, does not lead to a BH formation but to an MNS.

We have given in this article, for the first time, a rate for the formation of BHs in both short and long bursts, and this is of clear astrophysical relevance. Among such bursts producing a BH, the most favorable cases for GW detection are those from U-GRBs from BdHNe with $\dot{N}_{\text{GW}} = 0.08\text{--}0.09\text{ yr}^{-1}$ and those from BH–SNe with $\dot{N}_{\text{GW}} = 0.3\text{--}0.4\text{ yr}^{-1}$ (see Table 4). These NS–BH merging binaries were unknown in the literature, and thus their occurrence and GW detection rates are a definite prediction of this work.

Any detection by Advanced LIGO–Virgo of an NS–NS merger or an NS–BH merger will imply a drastic increase of the occurrence rate of events shown here and an examination of the consistency with GRB observations.

We have already given evidence on the unsuitability of the *collapsar* model to explain the GRB observations in Ruffini et al. (2018b). We have published a classification on the ground of the current observations of 480 sources with known redshift (Ruffini et al. 2016b, 2018b), which is both necessary and sufficient, as of today, to cover all GRBs observed. As the number of sources will increase, it is conceivable that the discovery of different systems will be observed, and in that case we will be ready for their inclusion in additional subclasses within our classification scheme.

As we have mentioned, the above are estimates based on the most favorable conditions for GW emission, and realistic \dot{N}_{GW} values will need the assessment of the ratio of GW to electromagnetic energy, which is necessarily smaller than unity from energy conservation.

After the submission of this work, the LIGO–Virgo Collaboration announced the detection of the signal GW 170817 and interpreted it as due to an NS–NS merger (Abbott et al. 2017b). As we have mentioned above, any possible GW detection of an NS–NS merger would imply a revision of its consistency with the inferences from GRB observations. It may then appear that our above conclusions of poor chance of detectability of NS–NS mergers by the Advanced LIGO–Virgo detector network are in tension with the detection of GW 170817 during the O2 run. The association of GW 170817 with GRB 170817A, a weak, short-duration GRB observed by the Gamma-ray Burst Monitor (GBM) on board the *Fermi* satellite (Abbott et al. 2017a; Goldstein et al. 2017) and followed-up in the optical bands (e.g., Cowperthwaite et al. 2017), in the X-rays (e.g., Haggard et al. 2017), and by further gamma-ray facilities (e.g., Savchenko et al. 2017), allows us in the following to make an assessment on this issue.

First, we recall that GRB 170817A, with its isotropic energy emitted in gamma rays of $E_{\text{iso}} \approx 5 \times 10^{46}$ erg (Goldstein et al. 2017) and peak luminosity of $(1.7 \pm 0.1) \times 10^{47} \text{ erg s}^{-1}$ (Zhang et al. 2017), would belong to the S-GRF subclass if we assume that it is produced in an NS–NS merger. On the

other hand, we recall that our estimates of the local density rate of the GRB subclasses (see Table 1), obtained from Ruffini et al. (2016b), are reliable for GRBs with luminosities higher than the lowest GRB luminosity in the subclass sample (see Appendix B for details). In the case of S-GRFs, we had identified GRB 050509B as the source with the lowest energetics, $E_{\text{iso}} \approx 8.5 \times 10^{48}$ erg (see Table 4 in Ruffini et al. 2016b), and a peak luminosity of $(1.1 \pm 0.5) \times 10^{51}$ erg s $^{-1}$ (Fox et al. 2005). This implies that our predicted detection rates for the Advanced LIGO-Virgo detectors for S-GRFs are valid for sources with electromagnetic emission over the above values. Even a single observation of a close and underluminous source, such as GRB 170817A, would lead to an increase of the local density rate of this GRB subclass. Indeed, Zhang et al. (2017) have recently estimated the increase in the local density rate when GRB 170817A is included in the sample of short bursts. Following a similar method to the one described in Appendix B, they found that their previously estimated isotropic local density rate of $3.2\text{--}5.5$ Gpc $^{-3}$ yr $^{-1}$, obtained for sources with peak luminosities above 7×10^{49} erg s $^{-1}$,¹⁰ increases to a lower limit of $30\text{--}630$ Gpc $^{-3}$ yr $^{-1}$, for sources with peak luminosities above 1.7×10^{47} erg s $^{-1}$, i.e., when GW 170817 is included in the sample. The above range implies an increase of the local density rate by a factor of $\sim 10\text{--}100$. It is then easy to check, using Table 4, that an increase of such a factor in the S-GRF density rate would imply a detection rate of $0.01\text{--}1$ yr $^{-1}$ for the O2 observational run, in agreement with the detection of GW 170817.

In fact, the above isotropic density rate inferred by Zhang et al. (2017) is consistent with the NS–NS observed merger rate of $320\text{--}4740$ Gpc $^{-3}$ yr $^{-1}$, inferred by the LIGO Collaboration with the detection of GW 170817 (see Section 5 in Abbott et al. 2017b, for details). This result implies that S-GRFs (or in general all short bursts) are not beamed or, if a beaming is assumed, the jet half-opening angle should be at least as large as $25^\circ\text{--}30^\circ$.

We thank the referee for suggestions that improved the presentation of our results. M.K. acknowledges the support given by the International Relativistic Astrophysics Erasmus Mundus Joint Doctorate Program under grants 2013–1471, from EACEA of the European Commission. M.M. and J.A.R. acknowledge the partial support of project no. 3101/GF4 IPC-11 and target program F.0679 of the Ministry of Education and Science of the Republic of Kazakhstan. C.C. and S.F. acknowledge INdAM-GNFM for support.

Appendix A

IGC, Hypercritical Accretion, and Long GRBs

We give in this appendix details of the accretion process within the IGC scenario following Fryer et al. (2014, 2015b) and Becerra et al. (2015, 2016).

There are two main physical conditions for which hypercritical (i.e., highly super-Eddington) accretion onto the NS occurs in XRFs and BdHNe. The first is that the photons are trapped within the inflowing material, and the second is that the shocked atmosphere on top of the NS becomes sufficiently hot ($T \sim 10^{10}$ K) and dense ($\rho \gtrsim 10^6$ g cm $^{-3}$) to produce a very

efficient neutrino–antineutrino ($\nu\bar{\nu}$) cooling emission. In this way the neutrinos become the main source responsible for releasing the energy gained by accretion, allowing hypercritical accretion to continue.

The first IGC simulations were performed in Fryer et al. (2014), including (1) realistic SN explosions of the CO $_{\text{core}}$, (2) the hydrodynamics within the accretion region, and (3) the simulated evolution of the SN ejecta up to their accretion onto the NS. Becerra et al. (2015) then estimated the amount of angular momentum carried by the SN ejecta and how much is transferred to the NS companion by accretion. They showed that the SN ejecta can circularize for a short time and form a disk-like structure surrounding the NS before being accreted. The evolution of the NS central density and rotation angular velocity (the NS is spun up by accretion) was computed from full numerical solutions of the axisymmetric Einstein equations. The unstable limits of the NS are set by the mass-shedding (or Keplerian) limit and the critical point of gravitational collapse given by the secular axisymmetric instability (see, e.g., Becerra et al. 2015, for details).

The accretion rate of the SN ejecta onto the NS is given by

$$\begin{aligned} \dot{M}_B(t) &= \pi \rho_{\text{ej}} R_{\text{cap}}^2 \sqrt{v_{\text{rel}}^2 + c_{\text{s, ej}}^2}, \\ R_{\text{cap}}(t) &= \frac{2GM_{\text{NS}}(t)}{v_{\text{rel}}^2 + c_{\text{s, ej}}^2}, \end{aligned} \quad (20)$$

where G is the gravitational constant, ρ_{ej} and $c_{\text{s, ej}}$ are the density and sound speed of the ejecta, respectively, R_{cap} and M_{NS} are the NS gravitational capture radius (Bondi–Hoyle radius) and gravitational mass, respectively, and v_{rel} is the ejecta velocity relative to the NS, $v_{\text{rel}} = v_{\text{orb}} - v_{\text{ej}}$, where $|v_{\text{orb}}| = \sqrt{G(M_{\text{core}} + M_{\text{NS}})/a}$ and v_{ej} is the velocity of the SN ejecta (see Figure 3).

Numerical simulations of the SN explosions suggest the adopted homologous expansion of the SN, i.e., $v_{\text{ej}}(r, t) = nr/t$, where r is the position of each layer from the SN center and n is the expansion parameter. The density evolves as

$$\rho_{\text{ej}}(r, t) = \rho_{\text{ej}}^0(r/R_{\text{star}}(t), t_0) \frac{M_{\text{env}}(t)}{M_{\text{env}}(0)} \left(\frac{R_{\text{star}}(0)}{R_{\text{star}}(t)} \right)^3, \quad (21)$$

where $M_{\text{env}}(t)$ is the mass of the CO $_{\text{core}}$ envelope, $R_{\text{star}}(t)$ is the radius of the outermost layer, and ρ_{ej}^0 is the pre-SN CO $_{\text{core}}$ density profile, $\rho_{\text{ej}}(r, t_0) = \rho_{\text{core}}(R_{\text{core}}/r)^m$, where ρ_{core} , R_{core} , and m are the profile parameters obtained from numerical simulations. Typical parameters of the CO $_{\text{core}}$ mass are $3.5\text{--}9.5 M_{\odot}$, corresponding to $15\text{--}30 M_{\odot}$ zero-age main-sequence progenitors (see Fryer et al. 2014; Becerra et al. 2015, for details). The binary period is limited from below by the request of having no Roche lobe overflow by the CO $_{\text{core}}$ before the SN explosion (Fryer et al. 2014). For instance, for a CO $_{\text{core}}$ of $9.5 M_{\odot}$ forming a binary system with a $2 M_{\odot}$ NS, the minimum orbital period allowed by this condition is $P_{\text{min}} \approx 5$ minutes. For these typical binary and pre-SN parameters, Equation (20) gives accretion rates of 10^{-4} to $10^{-2} M_{\odot}$ s $^{-1}$.

We adopt an initially nonrotating NS companion so that its exterior spacetime at time $t = 0$ is described by the Schwarzschild metric. The SN ejecta approach the NS with specific

¹⁰ This rate is consistent with the local density rate $\rho_{\text{S-GRFs}} + \rho_{\text{S-GRBs}} \approx \rho_{\text{S-GRFs}} = (2.6\text{--}5.0)$ Gpc $^{-3}$ yr $^{-1}$ used in the present work; see Table 1 and Ruffini et al. (2016b).

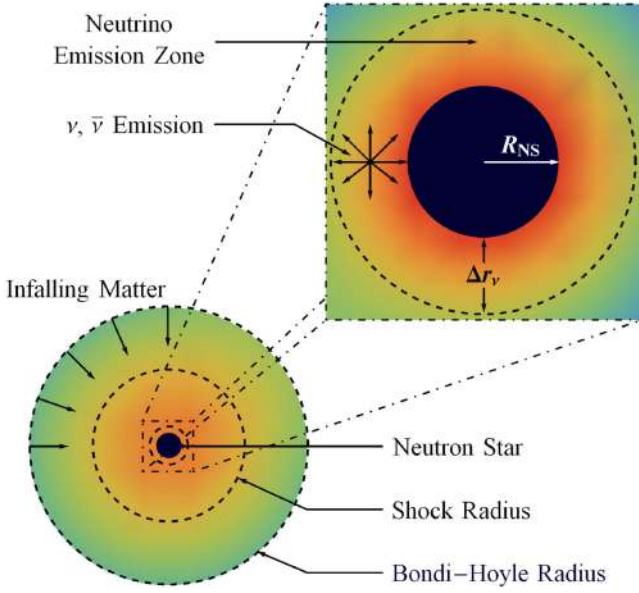


Figure 3. Scheme of the IGC scenario: the CO_{core} undergoes SN explosion, and the NS accretes part of the SN ejecta and then reaches the critical mass for gravitational collapse to a BH, with consequent emission of a GRB. The SN ejecta reach the NS Bondi-Hoyle radius and fall toward the NS surface. The material shocks and decelerates while it piles over the NS surface. At the neutrino emission zone, neutrinos take away most of the gravitational energy gained by the matter infall. The neutrinos are emitted above the NS surface in a region of thickness Δr_ν , about half the NS radius, which allows the material to reduce its entropy to be finally incorporated into the NS. For further details and numerical simulations of the above process see Fryer et al. (2014) and Becerra et al. (2015, 2016).

angular momentum, $l_{\text{acc}} = \dot{L}_{\text{cap}}/\dot{M}_B$, circularizing at a radius $r_{\text{circ}} \geq r_{\text{lco}}$ if $l_{\text{acc}} \geq l_{\text{lco}}$, with r_{lco} the radius of the LCO. For a nonrotating NS $r_{\text{lco}} = 6GM_{\text{NS}}/c^2$ and $l_{\text{lco}} = 2\sqrt{3}GM_{\text{NS}}/c$. For typical parameters, $r_{\text{circ}}/r_{\text{lco}} \sim 10\text{--}10^3$.

The accretion onto the NS proceeds from the radius r_{in} . The NS mass and angular momentum evolve as (Becerra et al. 2015; Cipolletta et al. 2017)

$$\dot{M}_{\text{NS}} = \left(\frac{\partial M_{\text{NS}}}{\partial M_b} \right)_{J_{\text{NS}}} \dot{M}_b + \left(\frac{\partial M_{\text{NS}}}{\partial J_{\text{NS}}} \right)_{M_b} \dot{J}_{\text{NS}}, \quad \dot{J}_{\text{NS}} = \xi l(r_{\text{in}}) \dot{M}_B, \quad (22)$$

where M_b is the NS baryonic mass; $l(r_{\text{in}})$ is the specific angular momentum of the accreted material at r_{in} , which corresponds to the angular momentum of the LCO; and $\xi \leq 1$ is a parameter that measures the efficiency of angular momentum transfer. In this picture we have $\dot{M}_b = \dot{M}_B$.

For the integration of Equations (20) and (22) we have to supply the values of the two partial derivatives in Equation (22). They are obtained from the relation of the NS gravitational mass, M_{NS} , with M_b and J_{NS} , namely, from the knowledge of the NS binding energy. For this we use the general relativistic calculations of rotating NSs presented in Cipolletta et al. (2015). They show that, independent of the nuclear EOS, the following analytical formula represents the numerical results with sufficient accuracy (error $< 2\%$):

$$\frac{M_b}{M_\odot} = \frac{M_{\text{NS}}}{M_\odot} + \frac{13}{200} \left(\frac{M_{\text{NS}}}{M_\odot} \right)^2 \left(1 - \frac{1}{137} j_{\text{NS}}^{1.7} \right), \quad (23)$$

where $j_{\text{NS}} \equiv cJ_{\text{NS}}/(GM_\odot^2)$.

Table 5

Critical NS Mass in the Nonrotating Case and Constants k and p Needed to Compute the NS Critical Mass in the Nonrotating Case Given by Equation (25)

EOS	$M_{\text{crit}}^{J=0} (M_\odot)$	p	k
NL3	2.81	1.68	0.006
GM1	2.39	1.69	0.011
TM1	2.20	1.61	0.017

Note. The values are given for the NL3, GM1, and TM1 EOS.

In the accretion process the NS gains angular momentum and therefore spin-up. To evaluate the amount of angular momentum transferred to the NS at any time, we include the dependence of the LCO specific angular momentum as a function of M_{NS} and J_{NS} . For corotating orbits the following relation is valid for the NL3, TM1, and GM1 EOS (Becerra et al. 2015; Cipolletta et al. 2017):

$$l_{\text{lco}} = \frac{GM_{\text{NS}}}{c} \left[2\sqrt{3} - 0.37 \left(\frac{j_{\text{NS}}}{M_{\text{NS}}/M_\odot} \right)^{0.85} \right]. \quad (24)$$

The NS continues to accrete until an instability limit is reached or up to when all the SN ejecta overcome the NS Bondi-Hoyle region. We take into account the two main instability limits for rotating NSs: the mass-shedding or Keplerian limit and the secular axisymmetric instability limit. The latter defines critical NS mass. For the aforementioned nuclear EOS, the critical mass is approximately given by (Cipolletta et al. 2015)

$$M_{\text{NS}}^{\text{crit}} = M_{\text{NS}}^{J=0} (1 + k j_{\text{NS}}^p), \quad (25)$$

where k and p are EOS-dependent parameters (see Table 5). These formulae fit the numerical results with a maximum error of 0.45%.

A.1. Most Recent Simulations of the IGC Process

Additional details and improvements of the hypercritical accretion process leading to XRFs and BdHNe were presented in Becerra et al. (2016). Specifically:

1. The density profile included finite size/thickness effects, and additional CO_{core} progenitors leading to different SN ejecta masses were considered.
2. In Becerra et al. (2015) the maximum orbital period, P_{max} , over which the accretion onto NS companion is not sufficient to bring it to the critical mass, was inferred. Thus, binaries with $P > P_{\text{max}}$ lead to XRFs, while the ones with $P \lesssim P_{\text{max}}$ lead to BdHNe. Becerra et al. (2016) extended the determination of P_{max} for all the possible initial values of the NS mass. They also examined the outcomes for different values of the angular momentum transfer efficiency parameter.
3. The expected luminosity during the process of hypercritical accretion for a wide range of binary periods covering both XRFs and BdHNe was estimated.
4. It was shown that the presence of the NS companion originates asymmetries in the SN ejecta (see, e.g., Figure 6 in Becerra et al. 2016). The signatures of such asymmetries in the X-ray emission were there shown in the specific example of XRF 060218.

A.2. Hydrodynamics and Neutrino Emission in the Accretion Region

The accretion rate onto the NS can be as high as $\sim 10^{-2}$ to $10^{-1} M_\odot \text{ s}^{-1}$. For such accretion rates:

1. The magnetic pressure is much smaller than the random pressure of the infalling material; therefore, the magnetic field effects on the accretion process are negligible (Fryer et al. 1996; Rueda & Ruffini 2012).
2. The photons are trapped within the infalling matter; hence, the Eddington limit does not apply and hypercritical accretion occurs. The trapping radius is defined by Chevalier (1989): $r_{\text{trapping}} = \min\{\dot{M}_B \kappa / (4\pi c), R_{\text{cap}}\}$, where κ is the opacity. Fryer et al. (2014) estimated a Rosseland mean opacity of $\approx 5 \times 10^3 \text{ cm}^2 \text{ g}^{-1}$ for the CO_{cores} . This, together with our typical accretion rates, leads to $\dot{M}_B \kappa / (4\pi c) \sim 10^{13} - 10^{19} \text{ cm}$. This radius is much bigger than the Bondi–Hoyle radius.
3. The above condition, as well as the temperature–density values reached on top of the NS surface, leads to an efficient neutrino cooling that radiates away the gain of gravitational energy of the infalling material (Zel’dovich et al. 1972; Ruffini & Wilson 1973; Fryer et al. 1996, 2014; Rueda & Ruffini 2012).

A.2.1. Convective Instabilities

The accretion shock moves outward as the material piles onto the NS. Since the post-shock entropy is inversely proportional to the shock radius position, the NS atmosphere is unstable with respect to Rayleigh–Taylor convection at the beginning of the accretion process. Such instabilities might drive high-velocity outflows from the accreting NS (Fryer et al. 2006; Fryer 2009). The entropy at the base of the atmosphere is (Fryer et al. 1996)

$$S_{\text{bubble}} \approx 16 \left(\frac{1.4 M_\odot}{M_{\text{NS}}} \right)^{-7/8} \left(\frac{M_\odot \text{ s}^{-1}}{\dot{M}_B} \right)^{1/4} \times \left(\frac{10^6 \text{ cm}}{r} \right)^{3/8} k_B / \text{nucleon}. \quad (26)$$

The material expands and cools down adiabatically, i.e., $T^3/\rho = \text{constant}$. In the case of a spherically symmetric expansion, $\rho \propto 1/r^3$ and $k_B T_{\text{bubble}} = 195 S_{\text{bubble}}^{-1} (10^6 \text{ cm}/r) \text{ MeV}$. In the more likely case that the material expands laterally, we have (Fryer 2009) $\rho \propto 1/r^2$, i.e., $T_{\text{bubble}} = T_0(S_{\text{bubble}})(r_0/r)^{2/3}$, where $T_0(S_{\text{bubble}})$ is obtained from the above equation at $r = r_0 \approx R_{\text{NS}}$. This implies a bolometric blackbody flux at the source from the rising bubbles:

$$F_{\text{bubble}} \approx 2 \times 10^{40} \left(\frac{M_{\text{NS}}}{1.4 M_\odot} \right)^{-7/2} \left(\frac{\dot{M}_B}{M_\odot \text{ s}^{-1}} \right) \times \left(\frac{R_{\text{NS}}}{10^6 \text{ cm}} \right)^{3/2} \left(\frac{r_0}{r} \right)^{8/3} \text{ erg s}^{-1} \text{ cm}^{-2}, \quad (27)$$

where σ is the Stefan–Boltzmann constant.

The above thermal emission has been shown (Fryer et al. 2014) to be a plausible explanation of the early ($t \lesssim 50 \text{ s}$) X-ray emission observed in some GRBs. In the specific example of GRB 090618 (Izzo et al. 2012a, 2012b), adopting an accretion rate of $10^{-2} M_\odot \text{ s}^{-1}$, the bubble temperature drops

from 50 to 15 keV while expanding from $r \approx 10^9 \text{ cm}$ to $6 \times 10^9 \text{ cm}$.

A.2.2. Neutrino Emission and Effective Accretion Rate

Temperatures $k_B T \sim 1\text{--}10 \text{ MeV}$ and densities $\rho \gtrsim 10^6 \text{ g cm}^{-3}$ develop near the NS surface during the accretion process. Under these conditions, e^+e^- annihilation into $\nu\bar{\nu}$ pairs becomes the dominant neutrino emission process in the accretion region (see Becerra et al. 2016, for details). The effective accretion rate onto the NS can be estimated as (e.g., Fryer et al. 1996) $\dot{M}_{\text{eff}} \approx \Delta M_\nu (L_\nu / E_\nu)$, where ΔM_ν and L_ν are the mass and neutrino luminosity in the emission region, respectively, and E_ν is half the gravitational potential energy gained by the material falling from infinity to a distance Δr_ν from the NS surface. Δr_ν is the thickness of the neutrino emitting region, which is approximately given by the temperature scale height ($\Delta r_\nu \approx 0.6 R_{\text{NS}}$). Since $L_\nu \approx 2\pi R_{\text{NS}}^2 \Delta r_\nu \epsilon_{e^-e^+}$, with $\epsilon_{e^-e^+}$ the e^+e^- pair annihilation process emissivity, and $E_\nu = (1/2) G M_{\text{NS}} \Delta M_\nu / (R_{\text{NS}} + \Delta r_\nu)$, for $M_{\text{NS}} = 1.4 M_\odot$ one obtains $\dot{M}_{\text{eff}} \approx 10^{-9}$ to $10^{-1} M_\odot \text{ s}^{-1}$ for $k_B T = 1\text{--}10 \text{ MeV}$.

A.3. Accretion Luminosity

The energy release in a time interval dt , when an amount of mass dM_b with angular momentum $l\dot{M}_b$ is accreted, is

$$L_{\text{acc}} = (\dot{M}_b - \dot{M}_{\text{NS}}) c^2 = \dot{M}_b c^2 \times \left[1 - \left(\frac{\partial M_{\text{NS}}}{\partial J_{\text{NS}}} \right)_{M_b} l - \left(\frac{\partial M_{\text{NS}}}{\partial M_b} \right)_{J_{\text{NS}}} \right]. \quad (28)$$

This is the amount of gravitational energy gained by the matter by infalling to the NS surface that is not spent in NS gravitational binding energy. The total energy release in the time interval from t to $t+dt$, $\Delta E_{\text{acc}} \equiv \int L_{\text{acc}} dt$, is given by the NS binding energy difference between its initial and final state. The typical luminosity is $L_{\text{acc}} \approx \Delta E_{\text{acc}} / \Delta t_{\text{acc}}$, where Δt_{acc} is the duration of the accretion process.

The value of Δt_{acc} is approximately given by the flow time of the slowest layers of the SN ejecta to the NS companion position. If we denote the velocity of these layers by v_{inner} , we have $\Delta t_{\text{acc}} \sim a/v_{\text{inner}}$, where a is the binary separation. For $a \sim 10^{11} \text{ cm}$ and $v_{\text{inner}} \sim 10^8 \text{ cm s}^{-1}$, $\Delta t_{\text{acc}} \sim 10^3 \text{ s}$. For shorter separations, e.g., $a \sim 10^{10} \text{ cm}$ ($P \sim 5 \text{ minutes}$), $\Delta t_{\text{acc}} \sim 10^2 \text{ s}$. For a binary with $P = 5 \text{ minutes}$, the NS accretes $\approx 1 M_\odot$ in $\Delta t_{\text{acc}} \approx 100 \text{ s}$. From Equation (23) one obtains that the binding energy difference of a $2 M_\odot$ and a $3 M_\odot$ NS is $\Delta E_{\text{acc}} \approx 13/200(3^2 - 2^2) M_\odot c^2 \approx 0.32 M_\odot c^2$. This leads to $L_{\text{acc}} \approx 3 \times 10^{-3} M_\odot c^2 \approx 0.1 \dot{M}_b c^2$. The accretion power can be as high as $L_{\text{acc}} \sim 0.1 \dot{M}_b c^2 \sim 10^{47} - 10^{51} \text{ erg s}^{-1}$ for accretion rates in the range $\dot{M}_b \sim 10^{-6}$ to $10^{-2} M_\odot \text{ s}^{-1}$.

A.4. Possible Evolutionary Scenario for CO_{core} –NS Binary Formation

Two independent communities have introduced a new evolutionary scenario for the formation of compact-object binaries (NS–NS or NS–BH). After the collapse of the primary star forming an NS, the binary undergoes mass-transfer episodes, finally leading to the ejection of both the hydrogen and helium shells of the secondary star. These processes lead naturally to a binary composed of a CO_{core} and an NS companion. In the X-ray binary and SN communities these

systems are called “ultra-stripped” binaries (see, e.g., Tauris et al. 2015b). These systems are expected to compose 0.1%–1% of the total SNe (Tauris et al. 2013).

In the above studies most of the binaries have orbital periods in the range of 3×10^3 – 3×10^5 s, which are longer than the periods expected in the BdHN scenario. The formation of the CO_{core}–NS binaries leading to BdHNe might be a subset of the ultra-stripped binaries. In such a subset the conditions of the initial orbital separation and CO_{core} mass must be such as to lead to final orbital periods in the range of 100–1000 s. Assuming an SN rate of $2 \times 10^4 \text{ Gpc}^{-3} \text{ yr}^{-1}$ (Guetta & Della Valle 2007), the ultra-stripped binaries would have a rate of 20–200 $\text{Gpc}^{-3} \text{ yr}^{-1}$, and thus BdHNe, with a rate of $\sim 1 \text{ Gpc}^{-3} \text{ yr}^{-1}$ (see Table 1 and Ruffini et al. 2016b), might be produced by the 0.5%–5% of the ultra-stripped binary population.

A.5. Post-explosion Orbits and NS–BH Binary Formation

The SN explosion leaves as a central remnant the ν NS, while the NS companion might lead, for sufficient accretion rates, to the formation of a BH. We examined in Fryer et al. (2015b) the question whether BdHNe can indeed form NS–BH binaries or, on the contrary, they are disrupted by the SN explosion.

Most of the typical binaries become unbound during an SN explosion owing to the amount of mass loss and momentum imparted (kick) to the ν NS in the explosion. Assuming an instantaneous explosion, the binary is disrupted if half of the binary mass is lost. For this reason the fraction of massive binaries that can produce double compact-object binaries might be as low as $\sim 0.001\%$ –1% (Fryer et al. 1999a; Dominik et al. 2012; Postnov & Yungelson 2014). Indeed, this is consistent with our estimated GRB local observed rates: we have shown in Section 3.1 that the NS–NS population leading to short bursts can be explained as being descendant from the CO_{core}–NS if $\sim 1\%$ of them remain bound after the SN explosion.

Assuming instantaneous mass loss, the post-explosion semimajor axis is (Hills 1983)

$$\frac{a}{a_0} = \frac{M_0 - \Delta M}{M_0 - 2a_0 \Delta M / r}, \quad (29)$$

where a_0 and a are the initial and final semimajor axes, respectively, M_0 is the (initial) binary mass, ΔM is the change of mass (in this case the amount of mass loss), and r is the orbital separation before the explosion. For circular orbits, the system is unbound if it loses half of its mass. For the very tight BdHNe, however, additional effects have to be taken into account to determine the fate of the binary.

The shock front in an SN moves at roughly 10^4 km s^{-1} , but the denser, lower-velocity ejecta can move at velocities as low as 10^2 – 10^3 km s^{-1} (Fryer et al. 2014). This implies that the SN ejecta overcomes an NS companion in a time 10–1000 s. For wide binaries this time is a small fraction of the orbital period and the “instantaneous” mass-loss assumption is perfectly valid. BdHNe have instead orbital periods as short as 100–1000 s; hence, the instantaneous mass-loss approximation breaks down.

We recall the specific examples studied in Fryer et al. (2015b): close binaries in an initial circular orbit of radius $7 \times 10^9 \text{ cm}$, CO_{core} radii of $(1\text{--}4) \times 10^9 \text{ cm}$ with a $2.0 M_\odot$ NS companion. The CO_{core} leaves a central $1.5 M_\odot$ NS, ejecting the rest of the core. The NS leads to a BH with a mass equal to the NS critical mass. For these parameters it was there obtained that even if 70% of the mass is lost, the binary remains bound

provided that the explosion time is of the order of the orbital period ($P = 180 \text{ s}$) with semimajor axes of less than 10^{11} cm .

The tight ν NS–BH binaries produced by BdHNe will, in due time, merge owing to the emission of GWs. For the above typical parameters the merger time is of the order of 10^4 yr , or even less. We expect little baryonic contamination around such a merger site since this region has been cleaned up by the BdHN. These conditions lead to a new family of sources that we have called ultrashort GRBs, U-GRBs.

Appendix B

Local Density Rate of GRB Subclasses

We recall now the method used in Ruffini et al. (2016b) to estimate, for each GRB subclass, the local observed density rates that we use in this work. This is defined by the convolution of the luminosity function, which tells us the fraction of bursts with isotropic equivalent luminosities in the interval $\log L$ and $\log L + d \log L$, and the cosmic GRB occurrence rate, which tells us the number of sources at different redshifts. These functions depend on a priori assumptions, and some investigations have been carried out in the literature: for long bursts (e.g., Soderberg et al. 2006b; Guetta & Della Valle 2007; Liang et al. 2007; Virgili et al. 2009; Rangel Lemos et al. 2010; Wanderman & Piran 2010; Guetta et al. 2011; Kovacevic et al. 2014), for short bursts (e.g., Virgili et al. 2011; Wanderman & Piran 2015), and for both long and short bursts (e.g., Sun et al. 2015). Additional properties that introduce further uncertainties are the instrumental sensitivity threshold, the field of view Ω_i , and the operational time T_i of the i -detector.

Hereafter we neglect the possible redshift evolution of the luminosity function. For ΔN_i events detected by various detectors in a finite logarithmic luminosity bin from $\log L$ to $\log L + \Delta \log L$, the total local event rate density between observed minimum (L_{\min}) and maximum (L_{\max}) luminosities is (e.g., Sun et al. 2015)

$$\rho_0 \simeq \sum_i \sum_{\log L_{\min}}^{\log L_{\max}} \frac{4\pi}{\Omega_i T_i} \frac{1}{\ln 10} \frac{1}{g(L)} \frac{\Delta N_i}{\Delta \log L} \frac{\Delta L}{L}, \quad (30)$$

where

$$g(L) = \int_0^{z_{\max}(L)} \frac{f(z)}{1+z} \frac{dV(z)}{dz} dz, \quad (31)$$

and the comoving volume is

$$\frac{dV(z)}{dz} = \frac{c}{H_0} \frac{4\pi d_L^2}{(1+z)^2 [\Omega_M(1+z)^3 + \Omega_\Lambda]^{1/2}}, \quad (32)$$

where d_L is the luminosity distance. We set $f(z) = 1$, namely, we do not assume any redshift dependence of the GRB cosmic event rate density. The maximum volume within which the event of luminosity L can be detected is defined by the maximum redshift $z_{\max}(L)$. The latter is computed, following Schaefer (2007), from the 1 s bolometric peak luminosity L , k -corrected from the observed detector energy band into the burst cosmological rest-frame energy band 1– 10^4 keV , and the corresponding 1 s threshold peak flux f_{th} . This is the limiting peak flux for the burst detection (Band 2003). With this, z_{\max} can be defined from

(see, e.g., Zhang et al. 2009; Ruffini et al. 2014)

$$f_{\text{th}} = \frac{L}{4\pi d_L^2(z_{\text{max}})k}. \quad (33)$$

The possible evolution with the redshift of the GRB density rates has been analyzed in Ruffini et al. (2016b) by separating the bursts into several redshift bins, following the method suggested in Sun et al. (2015). In each redshift interval $z_j \leq z \leq z_{j+1}$, the integration limits of Equation (31) are replaced by z_j and $\min[z_{j+1}, z_{\text{max},j}(L)]$, where $z_{\text{max},j}(L)$ is the maximum redshift for the j th redshift bin. Finally, from Equation (30) an event rate ρ_0^z in each redshift bin around z is obtained.

We adopt the fields of view and operational times for the detectors: *BeppoSAX*, $\Omega_{\text{BS}} = 0.25$ sr, $T_{\text{BS}} = 7$ yr; *BATSE*, $\Omega_{\text{B}} = \pi$ sr, $T_{\text{B}} = 10$ yr, *HETE-2*, $\Omega_{\text{H}} = 0.8$ sr, $T_{\text{H}} = 7$ yr; *Swift-BAT*, $\Omega_{\text{S}} = 1.33$ sr, $T_{\text{S}} = 10$ yr; *Fermi-GBM*, $\Omega_{\text{F}} = 9.6$ sr, $T_{\text{F}} = 7$ yr. We adopt no beaming correction.

ORCID iDs

M. Muccino  <https://orcid.org/0000-0002-2234-9225>
 J. A. Rueda  <https://orcid.org/0000-0002-3455-3063>
 C. L. Bianco  <https://orcid.org/0000-0001-7749-4078>
 M. Kovacevic  <https://orcid.org/0000-0003-4928-4510>
 G. B. Pisani  <https://orcid.org/0000-0003-3452-2491>

References

- Abbott, B. P., Abbott, R., Abbott, T. D., et al. 2016, *LRR*, 19, 1
 Abbott, B. P., Abbott, R., Abbott, T. D., et al. 2017a, *ApJL*, 848, L13
 Abbott, B. P., Abbott, R., Abbott, T. D., et al. 2017b, *PhRvL*, 119, 161101
 Aimuratov, Y., Ruffini, R., Muccino, M., et al. 2017a, *ApJ*, 844, 83
 Aimuratov, Y., Ruffini, R., Muccino, M., et al. 2017b, *arXiv:1704.08179*
 Allen, B., Anderson, W. G., Brady, P. R., Brown, D. A., & Creighton, J. D. E. 2012, *PhRvD*, 85, 122006
 Anninos, P., Hobill, D., Seidel, E., Smarr, L., & Suen, W.-M. 1995, *PhRvD*, 52, 2044
 Antoniadis, J., Freire, P. C. C., Wex, N., et al. 2013, *Sci*, 340, 448
 Astone, P., Ballantini, R., Babusci, D., et al. 2006, *CQGra*, 23, S57
 Astone, P., Ballantini, R., Babusci, D., et al. 2008, *CQGra*, 25, 114048
 Band, D. L. 2003, *ApJ*, 588, 945
 Becerra, L., Bianco, C. L., Fryer, C. L., Rueda, J. A., & Ruffini, R. 2016, *ApJ*, 833, 107
 Becerra, L., Cipolletta, F., Fryer, C. L., Rueda, J. A., & Ruffini, R. 2015, *ApJ*, 812, 100
 Belczynski, K., Bulik, T., & Bailyn, C. 2011, *ApJL*, 742, L2
 Belczynski, K., Bulik, T., & Rudak, B. 2002, *ApJ*, 571, 394
 Belczynski, K., Repetto, S., Holz, D. E., et al. 2016, *ApJ*, 819, 108
 Belvedere, R., Boshkayev, K., Rueda, J. A., & Ruffini, R. 2014, *NuPhA*, 921, 33
 Berger, E. 2014, *ARA&A*, 52, 43
 Bernuzzi, S., Dietrich, T., & Nagar, A. 2015, *PhRvL*, 115, 091101
 Bildsten, L., & Cutler, C. 1992, *ApJ*, 400, 175
 Cadelano, M., Pallanca, C., Ferraro, F. R., et al. 2015, *ApJ*, 812, 63
 Caito, L., Bernardini, M. G., Bianco, C. L., et al. 2009, *A&A*, 498, 501
 Camp, J. B., & Cornish, N. J. 2004, *ARNPS*, 54, 525
 Chevalier, R. A. 1989, *ApJ*, 346, 847
 Cipolletta, F., Cherubini, C., Filippi, S., Rueda, J. A., & Ruffini, R. 2015, *PhRvD*, 92, 023007
 Cipolletta, F., Cherubini, C., Filippi, S., Rueda, J. A., & Ruffini, R. 2017, *PhRvD*, 96, 024046
 Clark, J. P. A., & Eardley, D. M. 1977, *ApJ*, 215, 311
 Cowperthwaite, P. S., Berger, E., Villar, V. A., et al. 2017, *ApJL*, 848, L17
 Dai, Z. G., & Lu, T. 1998a, *A&A*, 333, L87
 Dai, Z. G., & Lu, T. 1998b, *PhRvL*, 81, 4301
 Davis, M., Ruffini, R., Press, W. H., & Price, R. H. 1971, *PhRvL*, 27, 1466
 Davis, M., Ruffini, R., & Tiomno, J. 1972, *PhRvD*, 5, 2932
 Della Valle, M., Chincarini, G., Panagia, N., et al. 2006, *Natur*, 444, 1050
 Detweiler, S. 1980, *ApJ*, 239, 292
 Detweiler, S. L., & Szedenis, E., Jr. 1979, *ApJ*, 231, 211
 Dominik, M., Belczynski, K., Fryer, C., et al. 2012, *ApJ*, 759, 52
 Dominik, M., Berti, E., O'Shaughnessy, R., et al. 2015, *ApJ*, 806, 263
 Dutra, M., Lourenço, O., Avancini, S. S., et al. 2014, *PhRvC*, 90, 055203
 Dutra, M., Lourenço, O., & Menezes, D. P. 2016, *PhRvC*, 93, 025806
 Eichler, D., Livio, M., Piran, T., & Schramm, D. N. 1989, *Natur*, 340, 126
 Finn, L. S., & Chernoff, D. F. 1993, *PhRvD*, 47, 2198
 Flanagan, É. É., & Hughes, S. A. 1998, *PhRvD*, 57, 4535
 Fong, W., Berger, E., Margutti, R., et al. 2012, *ApJ*, 756, 189
 Fong, W., Berger, E., Margutti, R., & Zauderer, B. A. 2015, *ApJ*, 815, 102
 Fong, W., Berger, E., Metzger, B. D., et al. 2014, *ApJ*, 780, 118
 Fox, D. B., Frail, D. A., Price, P. A., et al. 2005, *Natur*, 437, 845
 Fryer, C. L. 2009, *ApJ*, 699, 409
 Fryer, C. L., Belczynski, K., Ramirez-Ruiz, E., et al. 2015a, *ApJ*, 812, 24
 Fryer, C. L., Benz, W., & Herant, M. 1996, *ApJ*, 460, 801
 Fryer, C. L., Herwig, F., Hungerford, A., & Timmes, F. X. 2006, *ApJL*, 646, L131
 Fryer, C. L., Oliveira, F. G., Rueda, J. A., & Ruffini, R. 2015b, *PhRvL*, 115, 231102
 Fryer, C. L., Rueda, J. A., & Ruffini, R. 2014, *ApJ*, 793, L36
 Fryer, C. L., & Woosley, S. E. 1998, *ApJL*, 502, L9
 Fryer, C. L., Woosley, S. E., & Hartmann, D. H. 1999a, *ApJ*, 526, 152
 Fryer, C. L., Woosley, S. E., Herant, M., & Davies, M. B. 1999b, *ApJ*, 520, 650
 Ghirlanda, G., Salafia, O. S., Pescalli, A., et al. 2016, *A&A*, 594, A84
 Giacconi, R., & Ruffini, R. (ed.) 1978, *Physics and Astrophysics of Neutron Stars and Black Holes* (Amsterdam: North Holland Publishing Co.)
 Goldstein, A., Veres, P., Burns, E., et al. 2017, *ApJL*, 848, L14
 Goodman, J. 1986, *ApJL*, 308, L47
 Guetta, D., & Della Valle, M. 2007, *ApJL*, 657, L73
 Guetta, D., Pian, E., & Waxman, E. 2011, *A&A*, 525, A53
 Haggard, D., Nynka, M., Ruan, J. J., et al. 2017, *ApJL*, 848, L25
 Hills, J. G. 1983, *ApJ*, 267, 322
 Izzo, L., Rueda, J. A., & Ruffini, R. 2012a, *A&A*, 548, L5
 Izzo, L., Ruffini, R., Penacchioni, A. V., et al. 2012b, *A&A*, 543, A10
 Kawaguchi, K., Kyutoku, K., Nakano, H., et al. 2015, *PhRvD*, 92, 024014
 Klein, A., Barausse, E., Sesana, A., et al. 2016, *PhRvD*, 93, 024003
 Kluźniak, W., & Ruderman, M. 1998, *ApJL*, 505, L113
 Kobayashi, S., & Mészáros, P. 2003, *ApJ*, 589, 861
 Kovacevic, M., Izzo, L., Wang, Y., et al. 2014, *A&A*, 569, A108
 Landau, L. D., & Lifshitz, E. M. 1975, *The Classical Theory of Fields*, Vol. 2 (Oxford: Pergamon)
 Lazarus, P., Tauris, T. M., Knispel, B., et al. 2014, *MNRAS*, 437, 1485
 Lee, W. H., Ramirez-Ruiz, E., & Page, D. 2004, *ApJL*, 608, L5
 Liang, E., Zhang, B., Virgili, F., & Dai, Z. G. 2007, *ApJ*, 662, 1111
 LIGO Scientific Collaboration, Aasi, J., Abbott, B. P., et al. 2015, *CQGra*, 32, 074001
 MacFadyen, A. I., & Woosley, S. E. 1999, *ApJ*, 524, 262
 MacFadyen, A. I., Woosley, S. E., & Heger, A. 2001, *ApJ*, 550, 410
 Maggiore, M. 2007, *Gravitational Waves, Vol 1: Theory and Experiments* (Oxford: Oxford Univ. Press)
 Meszaros, P., & Rees, M. J. 1997, *ApJL*, 482, L29
 Mirabel, I. F., & Rodríguez, L. F. 1998, *Natur*, 392, 673
 Muccino, M., Ruffini, R., Bianco, C. L., Izzo, L., & Penacchioni, A. V. 2013, *ApJ*, 763, 125
 Narayan, R., Piran, T., & Shemi, A. 1991, *ApJL*, 379, L17
 Nicuesa Guelbenzu, A., Klose, S., Rossi, A., et al. 2011, *A&A*, 531, L6
 Paczynski, B. 1986, *ApJL*, 308, L43
 Paschalidis, V., MacLeod, M., Baumgarte, T. W., & Shapiro, S. L. 2009, *PhRvD*, 80, 024006
 Patricelli, B., Razzano, M., Cella, G., et al. 2016, *JCAP*, 11, 056
 Peters, P. C. 1964, *PhRv*, 136, 1224
 Peters, P. C., & Mathews, J. 1963, *PhRv*, 131, 435
 Postnov, K. A., & Yungelson, L. R. 2014, *LRR*, 17, 3
 Rangel Lemos, L. J., Bianco, C. L., Mosquera Cuesta, H. J., Rueda, J. A., & Ruffini, R. 2010, in 25th Texas Symp. Relativistic Astrophysics, ed. F. M. Rieger, C. van Eldik, & W. Hofmann (Triste: SISSA), 204
 Rees, M., Ruffini, R., & Wheeler, J. A. 1974, *Black Holes, Gravitational Waves and Cosmology* (New York: Gordon and Breach Science Publishers Inc.)
 Rhoades, C. E., & Ruffini, R. 1974, *PhRvL*, 32, 324
 Rigault, M., Aldering, G., Kowalski, M., et al. 2015, *ApJ*, 802, 20
 Rosswog, S., Ramirez-Ruiz, E., & Davies, M. B. 2003, *MNRAS*, 345, 1077

- Rueda, J. A., & Ruffini, R. 2012, [ApJL](#), **758**, L7
- Ruffini, R., Bernardini, M. G., Bianco, C. L., et al. 2006, in *The Tenth Marcel Grossmann Meeting*, ed. M. Novello, S. Perez Bergliaffa, & R. Ruffini (Singapore: World Scientific), 369
- Ruffini, R., Bernardini, M. G., Bianco, C. L., et al. 2007, in *Proc. of the VI INTEGRAL Workshop, The Obscured Universe*, ed. S. Grebenev, R. Sunyaev, & C. Winkler (Noordwijk: ESA), 561
- Ruffini, R., Bernardini, M. G., Bianco, C. L., et al. 2008, in *Proc. of the MG11 Meeting on General Relativity, The Eleventh Marcel Grossmann Meeting On Recent Developments in Theoretical and Experimental General Relativity, Gravitation and Relativistic Field Theories*, ed. H. Kleinert, R. T. Jantzen, & R. Ruffini (Singapore: World Scientific), 368
- Ruffini, R., Bianco, C. L., Frascchetti, F., Xue, S.-S., & Chardonnet, P. 2001, [ApJL](#), **555**, L117
- Ruffini, R., Izzo, L., Muccino, M., et al. 2014, [A&A](#), **569**, A39
- Ruffini, R., Muccino, M., Aimuratov, Y., et al. 2016a, [ApJ](#), **831**, 178
- Ruffini, R., Muccino, M., Aimuratov, Y., et al. 2018a, [arXiv:1802.07552](#)
- Ruffini, R., Muccino, M., Kovacevic, M., et al. 2015a, [ApJ](#), **808**, 190
- Ruffini, R., Rueda, J. A., Muccino, M., et al. 2016b, [ApJ](#), **832**, 136
- Ruffini, R., Wang, Y., Aimuratov, Y., et al. 2018b, [ApJ](#), **852**, 53
- Ruffini, R., Wang, Y., Enderli, M., et al. 2015b, [ApJ](#), **798**, 10
- Ruffini, R., & Wilson, J. 1973, [PhRvL](#), **31**, 1362
- Savchenko, V., Ferrigno, C., Kuulkers, E., et al. 2017, [ApJL](#), **848**, L15
- Schaefer, B. E. 2007, [ApJ](#), **660**, 16
- Shibata, M., & Taniguchi, K. 2011, [LRR](#), **14**, 6
- Smartt, S. J. 2009, [ARA&A](#), **47**, 63
- Smartt, S. J. 2015, [PASA](#), **32**, e016
- Soderberg, A. M., Berger, E., Kasliwal, M., et al. 2006a, [ApJ](#), **650**, 261
- Soderberg, A. M., Kulkarni, S. R., Nakar, E., et al. 2006b, [Natur](#), **442**, 1014
- Sun, H., Zhang, B., & Li, Z. 2015, [ApJ](#), **812**, 33
- Tauris, T. M., Kaspi, V. M., Breton, R. P., et al. 2015a, in *Proc. of Advancing Astrophysics with the Square Kilometre Array (AASKA14), Understanding the Neutron Star Population with the SKA (Triste: SISSA)*, 39
- Tauris, T. M., Langer, N., Moriya, T. J., et al. 2013, [ApJL](#), **778**, L23
- Tauris, T. M., Langer, N., & Podsiadlowski, P. 2015b, [MNRAS](#), **451**, 2123
- Tauris, T. M., van den Heuvel, E. P. J., & Savonije, G. J. 2000, [ApJL](#), **530**, L93
- Usov, V. V. 1992, [Natur](#), **357**, 472
- Virgili, F. J., Liang, E.-W., & Zhang, B. 2009, [MNRAS](#), **392**, 91
- Virgili, F. J., Zhang, B., O'Brien, P., & Troja, E. 2011, [ApJ](#), **727**, 109
- Wanderman, D., & Piran, T. 2010, [MNRAS](#), **406**, 1944
- Wanderman, D., & Piran, T. 2015, [MNRAS](#), **448**, 3026
- Woosley, S. E. 1993, [ApJ](#), **405**, 273
- Woosley, S. E., & Bloom, J. S. 2006, [ARA&A](#), **44**, 507
- Yonetoku, D., Nakamura, T., Sawano, T., Takahashi, K., & Toyano, A. 2014, [ApJ](#), **789**, 65
- Zel'dovich, Y. B., Ivanova, L. N., & Nadezhin, D. K. 1972, [SvA](#), **16**, 209
- Zhang, B., & Mészáros, P. 2001, [ApJL](#), **552**, L35
- Zhang, B., Zhang, B., Virgili, F. J., et al. 2009, [ApJ](#), **703**, 1696
- Zhang, B.-B., Zhang, B., Sun, H., et al. 2017, [arXiv:1710.05851](#)



Early X-Ray Flares in GRBs

R. Ruffini^{1,2,3,4}, Y. Wang^{1,2}, Y. Aimuravov^{3,1,2}, U. Barres de Almeida⁴, L. Becerra^{1,2}, C. L. Bianco^{1,2}, Y. C. Chen^{1,2}, M. Karlica^{1,2,3}, M. Kovacevic^{1,2,3}, L. Li^{2,5}, J. D. Melon Fuksman^{1,2}, R. Moradi^{1,2}, M. Muccino^{1,2}, A. V. Penacchioni^{2,6,7}, G. B. Pisani^{1,2}, D. Primorac^{1,2}, J. A. Rueda^{1,2,4}, S. Shakeri^{2,8}, G. V. Vereshchagin^{1,2}, and S.-S. Xue^{1,2}

¹ICRA and Dipartimento di Fisica, Sapienza Università di Roma, Piazzale Aldo Moro 5, I-00185 Rome, Italy

²ICRANet, Piazza della Repubblica 10, I-65122 Pescara, Italy; yu.wang@icranet.org

³Université de Nice Sophia Antipolis, CEDEX 2, Grand Château Parc Valrose, Nice, France

⁴ICRANet-Rio, Centro Brasileiro de Pesquisas Físicas, Rua Dr. Xavier Sigaud 150, 22290-180 Rio de Janeiro, Brazil

⁵Department of Physics, Stockholm University, SE-106 91 Stockholm, Sweden

⁶ASI Science Data Center, Via del Politecnico s.n.c., I-00133 Rome, Italy

⁷Dept. of Physical Sciences, Earth and Environment, University of Siena, Via Roma 56, I-53100 Siena, Italy

⁸Department of Physics, Isfahan University of Technology, 84156-83111, Iran

Received 2017 April 8; revised 2017 November 8; accepted 2017 November 23; published 2018 January 5

Abstract

We analyze the early X-ray flares in the GRB “flare–plateau–afterglow” (FPA) phase observed by *Swift*-XRT. The FPA occurs only in one of the seven GRB subclasses: the binary-driven hypernovae (BdHNe). This subclass consists of long GRBs with a carbon–oxygen core and a neutron star (NS) binary companion as progenitors. The hypercritical accretion of the supernova (SN) ejecta onto the NS can lead to the gravitational collapse of the NS into a black hole. Consequently, one can observe a GRB emission with isotropic energy $E_{\text{iso}} \gtrsim 10^{52}$ erg, as well as the associated GeV emission and the FPA phase. Previous work had shown that gamma-ray spikes in the prompt emission occur at $\sim 10^{15}$ – 10^{17} cm with Lorentz Gamma factors $\Gamma \sim 10^2$ – 10^3 . Using a novel data analysis, we show that the time of occurrence, duration, luminosity, and total energy of the X-ray flares correlate with E_{iso} . A crucial feature is the observation of thermal emission in the X-ray flares that we show occurs at radii $\sim 10^{12}$ cm with $\Gamma \lesssim 4$. These model-independent observations cannot be explained by the “fireball” model, which postulates synchrotron and inverse-Compton radiation from a single ultrarelativistic jetted emission extending from the prompt to the late afterglow and GeV emission phases. We show that in BdHNe a collision between the GRB and the SN ejecta occurs at $\sim 10^{10}$ cm, reaching transparency at $\sim 10^{12}$ cm with $\Gamma \lesssim 4$. The agreement between the thermal emission observations and these theoretically derived values validates our model and opens the possibility of testing each BdHN episode with the corresponding Lorentz Gamma factor.

Key words: binaries: general – black hole physics – gamma-ray burst: general – hydrodynamics – stars: neutron – supernovae: general

Supporting material: machine-readable table

1. Introduction

Following the discovery of the gamma-ray bursts (GRBs) by the *Vela* satellites (Klebesadel et al. 1973) and the observations by the BATSE detectors on board the *Compton Gamma-Ray Observatory* (CGRO; Gehrels et al. 1993), a theoretical framework for the interpretation of GRBs was established. This materialized into the “traditional” model of GRBs developed in a large number of papers by various groups. They all agree in their general aspects: short GRBs are assumed to originate from the merging of binary neutron stars (NSs; see, e.g., Goodman 1986; Paczynski 1986; Eichler et al. 1989; Narayan et al. 1991, 1992; Mészáros & Rees 1997), and long GRBs are assumed to originate from a “collapsar” (Woosley 1993; Paczyński 1998; MacFadyen & Woosley 1999; Bromberg et al. 2013), which, in turn, originates from the collapse of the core of a single massive star to a black hole (BH) surrounded by a thick massive accretion disk (Piran 2004). In this traditional picture, the GRB dynamics follows the “fireball” model, which assumes the existence of an ultrarelativistic collimated jet (see, e.g., Shemi & Piran 1990; Meszaros et al. 1993; Piran et al. 1993; Mao & Yi 1994). The structures of long GRBs were described by either internal or external shocks (see Rees & Meszaros 1992, 1994). The emission processes were linked to the occurrence of synchrotron and/or inverse-Compton radiation coming from the

jetted structure, characterized by Lorentz factors $\Gamma \sim 10^2$ – 10^3 , in what later will become known as the “prompt emission” phase (see Section 3).

The joint X-ray, gamma-ray, and optical observations heralded by *BeppoSAX* and later extended by *Swift* discovered the X-ray “afterglow,” which allowed the optical identification and the determination of the GRBs’ cosmological distance. The first evidence for the coincidence of a GRB and a supernova (SN; GRB 980425/SN 1998bw) was also announced as well as the first observation of an early X-ray flare (XRT), later greatly extended in number and spectral data by the *Swift* satellite, the subjects of this paper. The launch of the *Fermi* and *AGILE* satellites led to the equally fundamental discovery of GeV emission both in long and short GRBs (see Section 2).

The traditional model was modified in light of these new basic information by extending the description of the “collapsar” model, adopted for the prompt emission, to both the afterglow and GeV emission. This approach, based on the gravitational collapse of a single massive star, which was initially inspired by analogies with the astrophysics of active galactic nuclei, has been adopted with the aim to identify a “standard model” for all long GRBs and vastly accepted by concordance (see, e.g., Piran 1999, 2004; Mészáros 2002, 2006; Gehrels et al. 2009; Berger 2014; Kumar & Zhang 2015).

Attempts to incorporate the occurrence of an SN in the collapsar by considering nickel production in the accretion process around the BH were also proposed (MacFadyen & Woosley 1999). In 1999, a pioneering work by Fryer et al. (1999b) introduced considerations based on population synthesis computations and emphasized the possible relevance of binary progenitors in GRBs.

Since 2001, we have been developing an alternative GRB model based on the concept of induced gravitational collapse (IGC) paradigm, which involves, as progenitors, a binary system with standard components: an evolved carbon–oxygen core (CO_{core}) and a binary companion NS. The CO_{core} undergoes a traditional SN Ic explosion, which produces a new NS (νNS) and a large amount of ejecta. There is a multitude of new physical processes, occurring in selected episodes, associated with this process. The “first episode” (see Section 3) of the binary-driven hypernova (BdHN) is dominated by the hypercritical accretion process of the SN ejecta onto the companion NS. This topic has been developed in, e.g., Ruffini et al. (2001c), Rueda & Ruffini (2012), Fryer et al. (2014), and Becerra et al. (2015, 2016). These processes are not considered in the collapsar model. Our SN is a traditional Type Ic, the creation of the νNS follows standard procedure occurring in pulsar physics (see, e.g., Negreiros et al. 2012), the companion NS is a standard one regularly observed in binaries (see e.g., Rueda & Ruffini 2012; Rueda et al. 2017), and the physics of hypercritical accretion has been developed by us in a series of recent articles (see Section 3.4).

In a BdHN, the BH and a vast amount of e^+e^- plasma are formed only after the accreting NS reaches the critical mass and the “second episode” starts (see Section 3.5). The main new aspect of our model addresses the interaction of the e^+e^- plasma with the SN ejecta. We apply the fireshell model, which makes use of a general relativistic correct spacetime parametrization of the GRBs as well as a new set of relativistic hydrodynamics equation for the dynamics of the e^+e^- plasma. Selected values of the baryon loads are adopted in correspondence with the different time-varying density distributions of the SN ejecta.

In the “third episode” (see Section 3.6), we also mention the perspectives, utilizing the experience gained from both data analysis and theory for the specific understanding of X-ray flares, to further address in forthcoming publications the more comprehensive case of gamma-ray flares, the consistent treatment of the afterglow, and finally the implication of the GeV radiation.

As the model evolved, we soon realized that the discovery of new sources was not leading to a “standard model” of long GRBs but, on the contrary, they were revealing a number of new GRB subclasses with distinct properties characterizing their light curves, spectra, and energetics (see Ruffini et al. 2016b). Moreover, these seven subclasses did not necessarily contain a BH. We soon came to the conclusion that only in the subclass of BdHNe, with an E_{iso} larger than 10^{52} erg, does the hypercritical accretion from the SN onto the NS lead to the creation of a newly born BH with the associated signatures in the long GRB emission (see, e.g., Becerra et al. 2015, 2016).

While our alternative model was progressing, we were supported by new astrophysical observations: the great majority of GRBs are related to SNe Ic, which have no trace of hydrogen and helium in their optical spectra and are spatially

correlated with bright star-forming regions in their host galaxies (Fruchter et al. 2006; Svensson et al. 2010). Most massive stars are found in binary systems (Smith 2014) where most SNe Ic occur and which favor the deployment of hydrogen and helium from the SN progenitors (Smith et al. 2011), and the SNe associated with long GRBs are indeed of Type Ic (Della Valle 2011). In addition, these SNe associated with long bursts are broad-lined Ic SNe (hypernovae) showing the occurrence of some energy injection leading to a kinetic energy larger than that of traditional SNe Ic (Lyman et al. 2016).

The present paper addresses the fundamental role of X-ray flares as a separatrix between the two alternative GRB models and leads to the following main results, two obtained by data analysis and one obtained from the comparison of the alternative models:

- (1) The discovery of precise correlations between the X-ray flares and the GRB E_{iso} .
- (2) The radius of the occurrence of X-ray flares ($\sim 10^{12}$ cm) and the Lorentz Gamma factor ~ 2 .
- (3) The occurrence of a sharp break between the prompt emission phase and the flare–plateau–afterglow (FPA) phase, not envisaged in the current GRB literature. This transition is evidence of a contradiction in using the ultrarelativistic jetted emission to explain the X-ray flares, the plateau, and the afterglow.

In Section 2, we recall, following the gamma-ray observations by the *Vela* satellites and the *CGRO*, the essential role of *BeppoSAX* and the *Swift* satellite. These satellites provided X-ray observations specifically of the X-ray flares, to which our new data analysis techniques and paradigms have been applied. We also recall that the *Fermi* and *AGILE* satellites announced the existence of GeV emission, which has become essential for establishing the division of GRBs into different subclasses.

In Section 3, we update our classification of GRBs with known redshift into seven different subclasses (see Table 2). For each subclass, we indicate the progenitor “in-states” and the corresponding “out-states.” We update the list of BdHNe (see Appendix A): long GRBs with $E_{\text{iso}} \gtrsim 10^{52}$ erg, with an associated GeV emission and with the occurrence of the FPA phase. We also recall the role of appropriate time parametrization for GRBs, which properly distinguishes the four time variables that enter into their analysis. Finally, we recall the essential theoretical background needed for the description of the dynamics of BdHNe, the role of neutrino emission in the process of hypercritical accretion of the SN ejecta onto the binary companion NS, the description of the dynamics of the e^+e^- –baryon plasma, and the prompt emission phase endowed with gamma-ray spikes. We then briefly address the new perspectives opened up by the present work, to be further extended to the analysis of gamma-ray flares, to the afterglow, and the essential role of each BdHN component, including the νNS . Having established the essential observational and theoretical backgrounds in Sections 2 and 3, we proceed to the data analysis of the X-ray flares.

In Section 4, we address the procedure used to compare and contrast GRBs at different redshifts, including the description in their cosmological rest frame as well as the consequent K corrections. This procedure has been ignored in the current GRB literature (see, e.g., Chincarini et al. 2010 and references therein

as well as Section 11 of this paper). We then identify BdHNe as the only sources where early-time X-ray flares are identifiable. We recall that X-ray flares have neither been found in X-ray flashes nor in short GRBs. We also show that a claim of the existence of X-ray flares in short bursts has been superseded. We recall our 345 classified BdHNe (through the end of 2016). Their T_{90} ,⁹ properly evaluated in the source rest frame, corresponds to the duration of their prompt emission phase, mostly shorter than 100 s. Particular attention has been given to distinguishing X-ray flares from gamma-ray flares and spikes, each characterized by distinct spectral distributions and specific Lorentz Gamma factors. The gamma-ray flares are generally more energetic and with specific spectral signatures (see, e.g., the significant example of GRB 140206A in Section 5 below). In this article we focus on the methodology of studying X-ray flares: we plan to apply this knowledge to the case of the early gamma-ray flares. Out of the 345 BdHNe, there are 211 that have complete *Swift*-*XRT* observations, and among them, there are 16 BdHNe with a well-determined early X-ray flare structure. They cover a wide range of redshifts as well as the typical range of BdHN isotropic energies ($\sim 10^{52}$ – 10^{54} erg). The sample includes all identifiable X-ray flares.

In Section 5, we give the X-ray luminosity light curves of the 16 BdHNe in our sample and, when available, the corresponding optical observations. As usual, these quantities have been K -corrected to their rest frame (see Figures 9–24 and Section 4). In order to estimate the global properties of these sources, we also examine data from the *Swift*, *Konus-Wind*, and *Fermi* satellites. The global results of this large statistical analysis are given in Table 3, where the cosmological redshift z , the GRB isotropic energy E_{iso} , the flare peak time t_p , peak luminosity L_p , duration Δt , and the corresponding E_f are reproduced. This lengthy analysis has been carried out over the past years, and only the final results are summarized in Table 3.

In Section 6, we present the correlations between t_p , L_p , Δt , E_f , and E_{iso} and give the corresponding parameters in Table 4. In this analysis, we applied the Markov Chain Monte Carlo (MCMC) method, and we also have made public the corresponding numerical codes in <https://github.com/YWangScience/AstroNeuron> and <https://github.com/YWangScience/MCCC>.

In Section 7, we discuss the correlations between the energy of the prompt emission, the energy of the FPA phase, and E_{iso} (see Tables 5–6 and Figures 29–31).

In Section 8, we analyze the thermal emission observed during the X-ray flares (see Table 7). We derive, in an appropriate relativistic formalism, the relations between the observed temperature and flux and the corresponding temperature and radius of the thermal emitter in its comoving frame.

In Section 9, we use the results of Section 8 to infer the expansion speed of the thermal emitter associated with the thermal components observed during the flares (see Figure 32 and Table 8). We find that the observational data imply a Lorentz factor $\Gamma \lesssim 4$ and a radius of $\sim 10^{12}$ cm for such a thermal emitter.

In Section 10, we present a theoretical treatment using a new relativistic hydrodynamical code to simulate the interaction of the e^+e^- -baryon plasma with the high-density regions of the SN ejecta. We first test the code in the same low-density domain of validity describing the prompt emission phase, and then we apply it in the high-density regime of the propagation

Table 1
Alphabetic Ordered List of the Acronyms Used in this Work

Extended Wording	Acronym
Binary-driven hypernova	BdHN
Black hole	BH
Carbon–oxygen core	CO _{core}
Circumburst medium	CBM
Flare–Plateau–Afterglow	FPA
Gamma-ray burst	GRB
Gamma-ray flash	GRF
Induced gravitational collapse	IGC
Massive neutron star	MNS
Neutron star	NS
New neutron star	ν NS
Proper gamma-ray burst	P-GRB
Short gamma-ray burst	S-GRB
Short gamma-ray flash	S-GRF
Supernova	SN
Ultrashort gamma-ray burst	U-GRB
White dwarf	WD
X-ray flash	XRF

of the plasma inside the SN ejecta, which we use for the theoretical interpretation of the X-ray flares. Most remarkably, the theoretical code leads to a thermal emitter with a Lorentz factor $\Gamma \lesssim 4$ and a radius of $\sim 10^{12}$ cm at transparency. The agreement between these theoretically derived values and the ones obtained from the observed thermal emission validates the model and the binary nature of the BdHN progenitors, in clear contrast with the traditional ultrarelativistic jetted models.

In Section 11, we present our conclusions. We first show how the traditional model, describing GRBs as a single system with ultrarelativistic jetted emission extending from the prompt emission all the way to the final phases of the afterglow and of the GeV emission, is in conflict with the X-ray flare observations. We also present three new main results that illustrate the new perspectives opened up by our alternative approach based on BdHNe.

A standard flat Λ CDM cosmological model with $\Omega_M = 0.27$, $\Omega_\Lambda = 0.73$, and $H_0 = 71 \text{ km s}^{-1} \text{ Mpc}^{-1}$ is adopted throughout the paper, while Table 1 summarizes the acronyms we have used.

2. Background for the Observational Identification of the X-Ray Flares

The discovery of GRBs by the *Vela* satellites (Klebesadel et al. 1973) was presented at the AAAS meeting in February 1974 in San Francisco (Gursky & Ruffini 1975). The *Vela* satellites were operating in gamma-rays in the 150–750 keV energy range and only marginally in X-rays (3–12 keV; Cline et al. 1979). Soon after it was hypothesized from first principles that GRBs may originate from an e^+e^- plasma in the gravitational collapse to a Kerr–Newman BH, implying an energy $\sim 10^{54} M_{\text{BH}}/M_\odot$ erg (Damour & Ruffini 1975; see also Ruffini 1998).

Since 1991, the BATSE detectors on the *CGRO* (see Gehrels et al. 1993) have been leading to the classification of GRBs on the basis of their spectral hardness and of their observed T_{90} duration in the 50–300 keV energy band into short/hard bursts ($T_{90} < 2$ s) and long/soft bursts ($T_{90} > 2$ s) (Mazets et al. 1981; Dezalay et al. 1992; Klebesadel 1992; Kouveliotou et al. 1993; Tavani 1998). Such an emission was later called the GRB

⁹ T_{90} is the duration of the interval starting (ending) when 5% (95%) of the total energy of the event in gamma-rays has been emitted.

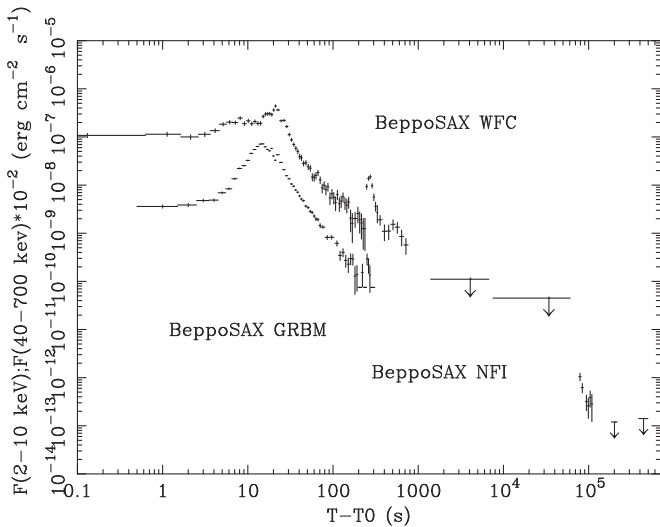


Figure 1. First X-ray flare observed by *BeppoSAX* in GRB 011121. Reproduced from Piro et al. (2005).

“prompt emission.” In a first attempt, it was proposed that short GRBs originate from merging binary NSs (see, e.g., Goodman 1986; Paczynski 1986; Eichler et al. 1989; Narayan et al. 1991, 1992; Mészáros & Rees 1997) and long GRBs originate from a single source with ultrarelativistic jetted emission (Woosley 1993; Paczyński 1998; MacFadyen & Woosley 1999; Bromberg et al. 2013).

The *BeppoSAX* satellite, operating since 1996, joined the expertise of the X-ray and gamma-ray communities. Its gamma-ray burst monitor (GRBM) operating in the 40–700 keV energy band determined the trigger of the GRB, and two wide-field cameras operating in the 2–30 keV X-ray energy band allowed the localization of the source within an arcminute resolution. This enabled a follow-up with the narrow-field instruments (NFI) in the 2–10 keV energy band. *BeppoSAX* discovered the X-ray afterglow (Costa et al. 1997), characterized by an X-ray luminosity decreasing with a constant index of ~ -1.3 (see de Pasquale et al. 2006 as well as Pisani et al. 2016). This emission was detected after an “8 hr gap” following the prompt emission identified by BATSE. The consequent determination of the accurate positions by the NFI, transmitted to the optical (van Paradijs et al. 1997) and radio telescopes (Frail et al. 1997), allowed the determination of the GRB cosmological redshifts (Metzger et al. 1997). The derived distances of ≈ 5 –10 Gpc confirmed their cosmological origin and their unprecedented energetics, $\approx 10^{50}$ – 10^{54} erg, thus validating our hypothesis derived from first principles (Damour & Ruffini 1975; Ruffini 1998).

To *BeppoSAX* goes the credit of the discovery of the temporal and spatial coincidence of GRB 980425 with SN 1998bw (Galama et al. 1998), which suggested the connection between GRBs and SNe, soon supported by many additional events (see, e.g., Woosley & Bloom 2006; Della Valle 2011; Hjorth & Bloom 2012). *BeppoSAX* also discovered the first “X-ray flare” in GRB 011121 closely following the prompt emission (Piro et al. 2005); see Figure 1. Our goal in this paper is to show how the X-ray flares, thanks to the observational campaign of the *Swift* satellite, have become the crucial test for

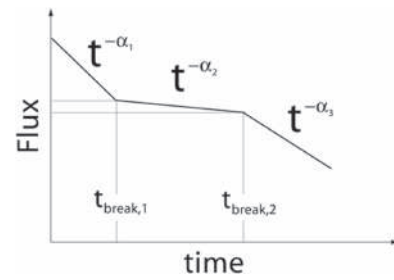


Figure 2. Schematic diagram of the X-ray light curve composed of three power-law segments with different slopes ($3 \lesssim \alpha_1 \lesssim 5$, $0.5 \lesssim \alpha_2 \lesssim 1.0$, $1 \lesssim \alpha_3 \lesssim 1.5$). Figure taken from Nousek et al. (2006).

understanding the astrophysical nature of the GRB–SN connection.

The *Swift* Burst Alert Telescope (BAT), operating in the 15–150 keV energy band, can detect GRB prompt emissions and accurately determine their position in the sky within 3 arcmin. Within 90 s, *Swift* can re-point the narrow-field X-ray telescope (XRT), operating in the 0.3–10 keV energy range, and relay the burst position to the ground. This overcomes the “8 hr gap” in the *BeppoSAX* data.

Thanks to the *Swift* satellite, the number of detected GRBs increased rapidly to 480 sources with known redshifts. By analyzing the light curve of some long GRBs, including the data in the “8 hr gap” of *BeppoSAX*, Nousek et al. (2006) and Zhang et al. (2006) discovered three power-law segments in the XRT flux light curves of some long GRBs. We refer to these as the “Nousek–Zhang power laws” (see Figure 2). The nature of this feature has been the subject of a long debates, still ongoing, and is finally resolved in this article.

We have used *Swift*–XRT data in differentiating two distinct subclasses of long GRBs: XRFs with $E_{\text{iso}} \lesssim 10^{52}$ erg and BdHNe with $E_{\text{iso}} \gtrsim 10^{52}$ erg (see Section 3). An additional striking difference appears between the XRT luminosities of these two subclasses when measured in their cosmological rest frames: in the case of BdHNe, the light curves follow a specific behavior that conforms to the Nousek–Zhang power law (see, e.g., Penacchioni et al. 2012, 2013; Pisani et al. 2013, 2016; Ruffini et al. 2014). None of these features are present in the case of XRFs (see Figure 3).

Finally, the *Fermi* satellite (Atwood et al. 2009), launched in 2008, detects ultrahigh energy photons from 20 MeV to 300 GeV with the Large Area Telescope (LAT) and detects photons from 8 keV to 30 MeV with the Gamma-ray Burst Monitor (GBM). For the purposes of this article addressing long GRBs, the *Fermi* observations have been prominent in further distinguishing between XRFs and BdHNe: the *Fermi*–LAT GeV emission has been observed only in BdHNe and never in XRFs.

3. Background for the Theoretical Interpretation of X-Ray Flares and Their Dynamics

3.1. The Classification of GRBs

The very extensive set of observations carried out by the above satellites in coordination with the largest optical and radio telescopes over a period of almost 40 years has led to an impressive set of data on 480 GRBs, all characterized by spectral, luminosity, and time variability information, and each one with a well-established cosmological redshift. By

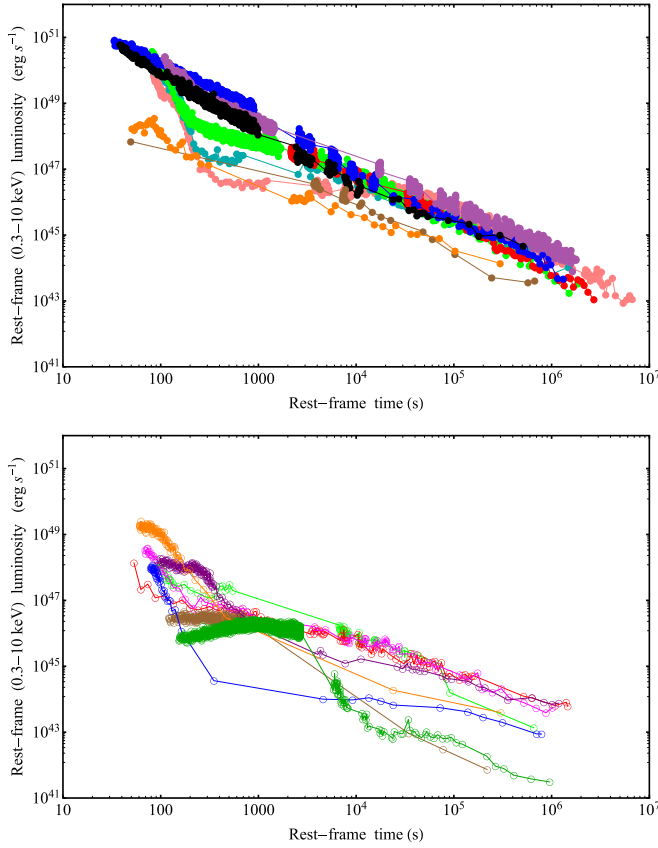


Figure 3. X-ray light curves of long GRBs observed by *Swift*. Top panel: BdHNe 050525 (brown), 060729 (pink), 061007 (black), 080319B (blue), 090618 (green), 091127 (red), 100816A (orange), 111228A (light blue), and 130427A (purple). Bottom panel: XRFs 050416A (red), 060218 (dark green), 070419A (orange), 081007 (magenta), 100316D (brown), 101219B (purple), and 130831A (green). XRFs have generally lower and more scattered light curves. All of these GRBs have known redshifts, and the light curves have been transformed to their cosmological rest frames.

classifying both the commonalities and the differences among all GRBs, it has been possible to create “equivalence relations” and divide GRBs into a number of subclasses, each one identified by a necessary and sufficient number of observables. We recall in Table 2 and Figure 4 the binary nature of all GRB progenitors and their classification into seven different subclasses (see, e.g., Ruffini et al. 2016b). In Table 2, we indicate the number of sources in each subclass, the nature of their progenitors and final outcomes of their evolution, their rest-frame T_{90} , their rest-frame spectral peak energy $E_{p,i}$ and E_{iso} as well as the isotropic energy in X-rays $E_{iso,X}$ and in GeV emission $E_{iso,GeV}$, and finally their local observed number density rate. In Figure 4, we mention the $E_{p,i}$ – E_{iso} relations for these sources, including the Amati one for BdHNe and the MuRuWaZha one for the short bursts (see Ruffini et al. 2016a, 2016b), comprising short gamma-ray flashes (S-GRFs) with $E_{iso} \lesssim 10^{52}$ erg, authentic short GRBs (S-GRBs) with $E_{iso} \gtrsim 10^{52}$ erg, and gamma-ray flashes (GRFs), sources with hybrid short/long burst properties in their gamma-ray light curves, i.e., an initial spike-like harder emission followed by a prolonged softer emission observed up to ~ 100 s, originating from NS–white dwarf binaries (Caito et al. 2009, 2010; Ruffini et al. 2016b). We have no evidence for an $E_{p,i}$ and E_{iso} relation in the XRFs (see Figure 4). The Amati and the MuRuWaZha

relations have not yet been theoretically understood, and as such they have no predictive power.

3.2. The Role of Time Parametrization in GRBs

Precise general relativistic rules in the spacetime parametrization of GRBs are needed (Ruffini et al. 2001a). Indeed, there are four time variables entering this discussion, which have to be properly distinguished one from another: (1) the comoving time t_{com} , which is the time used to compute the evolution of the thermodynamical quantities (density, pressure, temperature); (2) the laboratory time $t = \Gamma t_{com}$, where as usual the Lorentz Gamma factor is $\Gamma = (1 - \beta^2)^{-1/2}$ and $\beta = v/c$ is the expansion velocity of the source; (3) the arrival time t_a at which each photon emitted by the source reaches an observer in the cosmological rest frame of the source, given by (see also Bianco et al. 2001; Ruffini et al. 2002; Bianco & Ruffini 2005a)

$$t_a = t - \frac{r(t)}{c} \cos \vartheta, \quad (1)$$

where $r(t)$ is the radius of the expanding source in the laboratory frame and ϑ is the displacement angle of the normal to the emission surface from the line of sight; and (4) the arrival time at the detector on the Earth, $t_a^d = t_a(1 + z)$, corrected for cosmological effects, where z is the source redshift needed in order to compare GRBs at different redshifts z . As emphasized in Ruffini et al. (2001a, p. L108), “the bookkeeping of these four different times and the corresponding space variables must be done carefully in order to keep the correct causal relation in the time sequence of the events involved.” The chain of relations between these four times is given by (see e.g., Bianco et al. 2001; Ruffini et al. 2001a, 2002; Bianco & Ruffini 2005a, and see also Sections 8 and 9 for the dynamics of the flares)

$$\begin{aligned} t_a^d &= (1 + z)t_a = (1 + z) \left(t - \frac{r(t)}{c} \cos \vartheta \right) \\ &= (1 + z) \left(\Gamma t_{com} - \frac{r(\Gamma t_{com})}{c} \cos \vartheta \right). \end{aligned} \quad (2)$$

The proper use of these four time variables is mandatory in modeling GRB sources, especially when we are dealing with a model not based on a single component but on multiple components, each characterized by a different world line and a different Lorentz Gamma factor, as is the case for BdHNe (see Sections 4 and 5).

3.3. The Role of the GRBs’ Cosmological Rest Frame

In addition to all of the above, in order to compare the luminosities of different GRBs at different redshifts we need to express the observational data in the cosmological rest frames of each source (where the arrival time is t_a), and correspondingly apply the K correction to luminosities and spectra (see Section 4). This formalism is at the very foundation of the treatment presented in this paper and has been systematically neglected in the great majority of current GRB models.

3.4. Episode 1: The Hypercritical Accretion Process

In order to describe the dynamics of BdHNe, a number of different episodes involving different physical conditions have

Table 2
Summary of the Seven GRB Subclasses (XRFs, BdHNe, BH-SN, Short Gamma-ray Flashes (S-GRFs), Authentic Short GRBs (S-GRBs), Ultrashort GRBs (U-GRB), and GRFs) and Their Observational Properties

	Subclass	Number	In-state (Progenitor)	Out-state (Final outcome)	T_{90} (s)	$E_{p,i}$ (MeV)	E_{iso} (erg)	$E_{iso,X}$ (erg)	$E_{iso,GeV}$ (erg)	ρ_{GRB} (Gpc $^{-3}$ yr $^{-1}$)
I	XRFs	82	CO $_{core}$ -NS	ν NS-NS	$\sim 2-10^3$	$\lesssim 0.2$	$\sim 10^{48}-10^{52}$	$\sim 10^{48}-10^{51}$...	100^{+45}_{-34}
II	BdHNe	345	CO $_{core}$ -NS	ν NS-BH	$\sim 2-10^2$	$\sim 0.2-2$	$\sim 10^{52}-10^{54}$	$\sim 10^{51}-10^{52}$	$\lesssim 10^{53}$	$0.77^{+0.09}_{-0.08}$
III	BH-SN	...	CO $_{core}$ -BH	ν NS-BH	$\sim 2-10^2$	$\gtrsim 2$	$> 10^{54}$	$\sim 10^{51}-10^{52}$	$\gtrsim 10^{53}$	$\lesssim 0.77^{+0.09}_{-0.08}$
IV	S-GRFs	33	NS-NS	MNS	$\lesssim 2$	$\lesssim 2$	$\sim 10^{49}-10^{52}$	$\sim 10^{49}-10^{51}$...	$3.6^{+1.4}_{-1.0}$
V	S-GRBs	7	NS-NS	BH	$\lesssim 2$	$\gtrsim 2$	$\sim 10^{52}-10^{53}$	$\lesssim 10^{51}$	$\sim 10^{52}-10^{53}$	$(1.9^{+1.8}_{-1.1}) \times 10^{-3}$
VI	U-GRBs	...	ν NS-BH	BH	$\ll 2$	$\gtrsim 2$	$> 10^{52}$	$\gtrsim 0.77^{+0.09}_{-0.08}$
VII	GRFs	13	NS-WD	MNS	$\sim 2-10^2$	$\sim 0.2-2$	$\sim 10^{51}-10^{52}$	$\sim 10^{49}-10^{50}$...	$1.02^{+0.71}_{-0.46}$

Note. In the first five columns, we indicate the GRB subclasses and their corresponding number of sources with measured z , in-states, and out-states. In the following columns, we list the ranges of T_{90} in the rest frame, the rest-frame spectral peak energies $E_{p,i}$ and E_{iso} (rest frame 1–10⁴ keV), the isotropic energy of the X-ray data $E_{iso,X}$ (rest frame 0.3–10 keV), and the isotropic energy of the GeV emission $E_{iso,GeV}$ (rest frame 0.1–100 GeV). In the last column, we list, for each GRB subclass, the local observed number density rate ρ_{GRB} obtained in Ruffini et al. (2016b). For details, see Ruffini et al. (2014, 2015b, 2015c), Fryer et al. (2015), Ruffini et al. (2016a, 2016b), and Becerra et al. (2016).

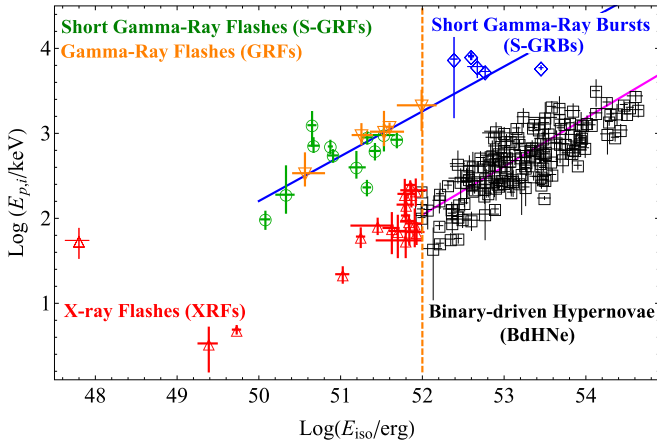


Figure 4. Updated $E_{p,i}$ – E_{iso} plane for the subclasses defined in Ruffini et al. (2016b): XRF (red triangles) cluster in the region defined by $E_{p,i} \lesssim 200$ keV and $E_{iso} \lesssim 10^{52}$ erg. BdHN (black squares) cluster in the region defined by $E_{p,i} \gtrsim 200$ keV and $E_{iso} \gtrsim 10^{52}$ erg and fulfilling the Amati relation (solid magenta line with slope $\alpha = 0.57 \pm 0.06$ and extra scatter $\sigma = 0.25$; see, e.g., Amati & Della Valle 2013; Calderone et al. 2015). S-GRFs (green circles) and the initial spike-like emission of the GRFs (orange reverse triangles) are concentrated in the region defined by $E_{p,i} \lesssim 2$ MeV and $E_{iso} \lesssim 10^{52}$ erg, while S-GRBs (blue diamonds) are concentrated in the region defined by $E_{p,i} \gtrsim 2$ MeV and $E_{iso} \gtrsim 10^{52}$ erg. Short bursts and GRFs fulfill the MuRuWaZha relation (blue solid line with slope $\alpha = 0.53 \pm 0.07$ and extra scatter $\sigma = 0.24$; see, e.g., Zhang et al. 2012; Calderone et al. 2015; Ruffini et al. 2015b, 2016a). The BH-SN and U-GRB subclasses (see Table 2 in Ruffini et al. 2016b for details) are not in the plot since their observational identifications are still pending. The crucial difference between BdHNe and XRFs, and S-GRBs and S-GRFs, is that BdHNe and S-GRBs form a BH, their energy is $\gtrsim 10^{52}$ erg, and they exhibit GeV emission.

to be described. Episode 1 is dominated by the IGC paradigm: the hypercritical accretion of an SN ejecta onto the companion binary NS (see, e.g., Fryer et al. 2014, 2015; Becerra et al. 2015, 2016). Weak interactions and neutrinos (see, e.g., Fermi 1934), which play a fundamental role in SNe through the URCA process (Gamow & Schoenberg 1940, 1941), are also needed in the case of hypercritical accretion processes onto an NS in an SN fallback (Colgate 1971; Zel’dovich et al. 1972; Ruffini & Wilson 1973). They are especially relevant in the case of BdHNe where the accretion rate onto the NS companion from CO $_{core}$ can reach up to $\dot{M} = 0.1 M_{\odot} \text{ s}^{-1}$

(Rueda & Ruffini 2012; Fryer et al. 2014; Becerra et al. 2015, 2016). Due to weak interactions, e^+e^- pairs annihilate to $\nu\bar{\nu}$ pairs with a cross-section $\sigma \sim G_F \langle E_e \rangle^2$ (Munakata et al. 1985; Itoh et al. 1989). In the thermal system of e^+e^- pairs at large temperature $kT > m_e c^2$ and density $n_e \sim T^3$, the neutrino emissivity of the e^+e^- annihilation is $\epsilon_{e^+e^-} \sim n_e^2 \langle \sigma \nu_e \rangle \langle E_e \rangle \sim 10^{25} (kT/\text{MeV})^9 \text{ erg s}^{-1} \text{ cm}^{-3}$, leading to neutrino luminosities $L_{\nu} \sim R_{NS}^3 \epsilon_{e^+e^-} \sim 10^{52} \text{ erg s}^{-1}$, which dominate over other microscopic processes for cooling (Becerra et al. 2016). Thus, e^+e^- pair annihilation to $\nu\bar{\nu}$ is the main process for cooling, allowing the process of hypercritical accretion to convert gravitational energy into thermal energy, to build up high temperature, and consequently to form an e^+e^- plasma. Only at the end of Episode 1, as the critical mass of the companion NS is reached, is a BH formed with the additional e^+e^- pairs linked to the BH electrodynamic process (Damour & Ruffini 1975; Cherubini et al. 2009).

3.5. Episode 2: e^+e^- Pairs Colliding with the SN Ejecta

Episode 2 is dominated by the new phenomenon of the impact of e^+e^- pairs generated in the GRB on the SN ejecta. We describe this process within the fireshell model. Two main differences exist between the fireshell and the fireball models. In the fireshell model, the e^+e^- plasma is initially in thermal equilibrium and undergoes ultrarelativistic expansion, keeping this condition of thermal equilibrium all the way to reaching transparency (Ruffini 1998; see also Aksenov et al. 2007; Ruffini et al. 2010 and references therein), while in the fireball model (Cavallo & Rees 1978), the e^+e^- pairs undergo an initial annihilation process that produces the photons driving the fireball. An additional basic difference is that the evolution of the e^+e^- plasma is not imposed by a given asymptotic solution but integrated following the relativistic fluid dynamics equations. The plasma, with energy $E_{e^+e^-}$, first goes through an initial acceleration phase (Ruffini et al. 1999). After colliding with the baryons (of total mass M_B), characterized by the baryon load parameter $B = M_B c^2 / E_{e^+e^-}$, the optically thick plasma keeps accelerating until it reaches transparency and emits a proper gamma-ray burst (P-GRB; see Ruffini et al. 2000). The accelerated baryons then interact with the circumburst medium (CBM) clouds (Ruffini et al. 2001b); the equation of motion of the plasma has been integrated, leading to results that differ from

the ones in Blandford & McKee’s (1976) self-similar solution (see Bianco & Ruffini 2004, 2005a, 2005b, 2006). By using Equation (2), which defines “equitemporal surfaces” (see Bianco et al. 2001; Bianco & Ruffini 2004, 2005a, 2005b, 2006), it has been possible to infer the structure of the gamma-ray spikes in the prompt emission, which for the most part has been applied to the case of BdHNe (see, e.g., Ruffini et al. 2002, 2016a; Bernardini et al. 2005; Izzo et al. 2012; Patricelli et al. 2012; Penacchioni et al. 2012, 2013). For typical baryon loads of $10^{-4} \lesssim B \lesssim 10^{-2}$ leading to Lorentz Gamma factors $\Gamma \approx 10^2\text{--}10^3$ at transparency for the e^+e^- -baryon plasma, characteristic distances from the BH of $\approx 10^{15}\text{--}10^{17}$ cm have been derived (see, e.g., Ruffini et al. 2016b and references therein). Those procedures are further generalized in this paper to compute the propagation of e^+e^- through the SN ejecta (see Section 10), after computing their density profiles (see Figure 35) and the corresponding baryon load (see Figure 34). The equations have been integrated all the way up to the condition of transparency (see Figures 36 and 37).

3.6. Episode 3: Ongoing Research on the Gamma-Ray Flares, Afterglow, and GeV Emission

We have exemplified the necessary steps in the analysis of each episode, which include determining the physical nature of each episode and the corresponding world line with the specific time-dependent Lorentz Gamma factor and so determining, using Equation (2), the arrival time at the detector, which has to agree, for consistency, with the one obtained from the observations. This program is applied in this article specifically for the analysis of early X-ray flares (see Sections 8 and 9). We will follow the same procedures for (1) the more complex analysis of gamma-ray flares, (2) the analysis of the afterglow consistent with the constraints on the X-ray flares observations, and (3) the properties of the GeV emission, common to BdHNe and S-GRBs (Ruffini et al. 2015c, 2016a). Having established the essential observational and theoretical background in Sections 2 and 3, we proceed to the data analysis of the early X-ray flares (see Sections 4–10).

4. The Early Flares and Sample Selection

With the increase in the number of observed GRBs, an attempt was made to analyze the X-ray flares and other processes considered to be similar in the observer reference frame, independent of the nature of the GRB type and of the value of their cosmological redshift or the absence of such a value. The goal of this attempt was to identify their “standard” properties, following a statistical analysis methodology often applied in classical astronomy (see Chincarini et al. 2007; Falcone et al. 2007; Margutti et al. 2010 as well as the review articles by Piran 1999, 2004; Mészáros 2002, 2006; Berger 2014; Kumar & Zhang 2015). We now summarize our alternative approach, having already given in the introduction and in Sections 2 and 3 the background for the observational identification and the theoretical interpretation of the X-ray flares.

As a first step, we only consider GRBs with an observed cosmological redshift. Having ourselves proposed the classification of all GRBs into seven different subclasses (see Section 3), we have given preliminary attention to verifying whether X-ray flares actually occur preferentially in some of these subclasses and if so, identifying the physical reasons

determining such a correlation. We have analyzed all X-ray flares and found, a posteriori, that X-ray flares only occur in BdHNe. No X-ray flare has been identified in any other GRB subclass, either long or short. A claim of their existence in short bursts (Barthelmy et al. 2005; Fan et al. 2005; Dai et al. 2006) has been superseded: GRB 050724 with $T_{90} \sim 100$ s is not a short GRB, but actually a GRF, expected to originate in the merging of an NS and a white dwarf (see Figure 4); the X-ray data for this source from XRT are sufficient to assert that there is no evidence of an X-ray flare as defined in this section. GRB 050709 is indeed a short burst. It has been classified as an S-GRF (Aimuratov et al. 2017) and has been observed by *HETE* with very sparse X-ray data (Butler et al. 2005), and no presence of an X-ray flare can be inferred; the *Swift* satellite pointed at this source too late, 38.5 hr after the *HETE* trigger (Morgan et al. 2005).

As a second step, since all GRBs have a different redshift z , in order to compare them we need a description of each of them in its own cosmological rest frame. The luminosities have to be estimated after doing the necessary K corrections and the time coordinate in the observer frame has to be corrected by the cosmological redshift $t_a^d = (1+z)t_a$. This also affects the determination of the T_{90} of each source (see, e.g., Figure 38 in Section 11 where the traditional approach by Kouveliotou et al. 1993 and Bromberg et al. 2013 has been superseded by ours).

As a third step, we recall an equally important distinction from the traditional fireball approach with a single ultrarelativistic jetted emission. Our GRB analysis envisages the existence of different episodes within each GRB, each one characterized by a different physical process and needing the definition of its own world line and corresponding Gamma factors, essential for estimating the time parametrization in the rest frame of the observer (see Section 2).

These three steps are applied in the present article, which specifically addresses the study of early X-ray flares and their fundamental role in establishing the physical and astrophysical nature of BdHNe and in distinguishing our binary model from the traditional one.

Before proceeding, let us recall the basic point of the K correction. All of the observed GRBs have a different redshift. In order to compare them, it is necessary to refer to each of them in its cosmological rest frame. This step has often been ignored in the current literature (Chincarini et al. 2007; Falcone et al. 2007; Margutti et al. 2010). Similarly, for the flux observed by the above satellites in Section 2, each instrument is characterized by its fixed energy window $[\epsilon_{\text{obs},1}; \epsilon_{\text{obs},2}]$. The observed flux f_{obs} , defined as the energy per unit area and time in a fixed instrumental energy window $[\epsilon_{\text{obs},1}; \epsilon_{\text{obs},2}]$, is expressed in terms of the observed photon number spectrum n_{obs} (i.e., the number of observed photons per unit energy, area, and time) as

$$f_{\text{obs},[\epsilon_{\text{obs},1}; \epsilon_{\text{obs},2}]} = \int_{\epsilon_{\text{obs},1}}^{\epsilon_{\text{obs},2}} \epsilon n_{\text{obs}}(\epsilon) d\epsilon. \quad (3)$$

It then follows that the luminosity L of the source (i.e., the total emitted energy per unit time in a given bandwidth), expressed by definition in the source cosmological rest frame, is related to f_{obs} through the luminosity distance $D_L(z)$:

$$L_{[\epsilon_{\text{obs},1}(1+z); \epsilon_{\text{obs},2}(1+z)]} = 4\pi D_L^2(z) f_{\text{obs},[\epsilon_{\text{obs},1}; \epsilon_{\text{obs},2}]} \quad (4)$$

The above Equation (4) gives the luminosities in different cosmological rest-frame energy bands, depending on the source

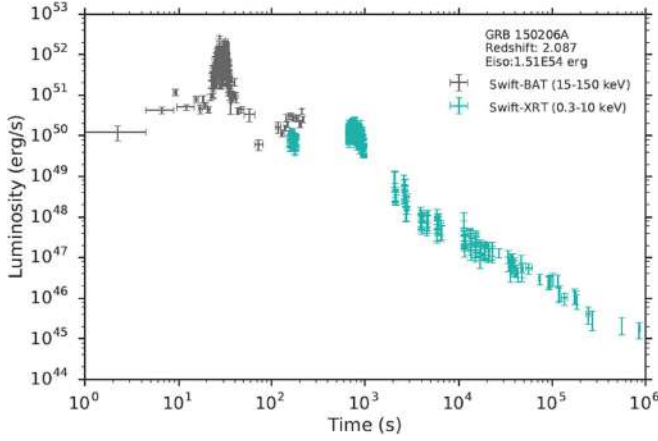


Figure 5. GRB 150206A is an example of a GRB with incomplete data, which therefore must be excluded. It only has 30 s *Swift-XRT* observations in the early 300 s. Flare determination is not possible under these conditions.

redshift. To express the luminosity L in a fixed cosmological rest-frame energy band, e.g., $[E_1; E_2]$, common to all sources, we can rewrite Equation (4) as

$$L_{[E_1; E_2]} = 4\pi D_L^2 f_{\text{obs}, [E_1; E_2]} \\ = 4\pi D_L^2 k[\epsilon_{\text{obs},1}; \epsilon_{\text{obs},2}; E_1; E_2; z] f_{\text{obs}, [\epsilon_{\text{obs},1}; \epsilon_{\text{obs},2}]}, \quad (5)$$

where we have defined the K -correction factor:

$$k[\epsilon_{\text{obs},1}; \epsilon_{\text{obs},2}; E_1; E_2; z] = \frac{f_{\text{obs}, [E_1; E_2]}}{f_{\text{obs}, [\epsilon_{\text{obs},1}; \epsilon_{\text{obs},2}]}} \\ = \frac{\int_{E_1/(1+z)}^{E_2/(1+z)} \epsilon n_{\text{obs}}(\epsilon) d\epsilon}{\int_{\epsilon_{\text{obs},1}}^{\epsilon_{\text{obs},2}} \epsilon n_{\text{obs}}(\epsilon) d\epsilon}. \quad (6)$$

If the energy range $[\frac{E_1}{1+z}; \frac{E_2}{1+z}]$ is not fully inside the instrumental energy band $[\epsilon_{\text{obs},1}; \epsilon_{\text{obs},2}]$, it may well happen that we will need to extrapolate n_{obs} within the integration boundaries $[\frac{E_1}{1+z}; \frac{E_2}{1+z}]$.

Finally, we express each luminosity in a rest-frame energy band that coincides with the energy window of each specific instrument.

We turn now to the selection procedure for early X-ray flares. We take the soft X-ray flux light curves of each source with known redshift from the *Swift-XRT* repository (Evans et al. 2007, 2009). We then apply the above K correction to obtain the corresponding luminosity light curves in the rest frame 0.3–10 keV energy band. Starting from 421 *Swift-XRT* light curves, we found in 50 sources X-ray flare structures in the early 200 s. Remarkably, all of them are in BdHNe. We further filter our sample by applying the following criteria:

1. We exclude GRBs with flares having a low (<20) signal-to-noise ratio or with an incomplete data coverage of the early X-ray light curve—14 GRBs are excluded (see e.g., Figure 5).
2. We consider only X-ray flares and do not address here the gamma-ray flares, which will be studied in a forthcoming article—eight GRBs having only gamma-ray flares are temporarily excluded (see, e.g., Figure 6). In Figure 7, we

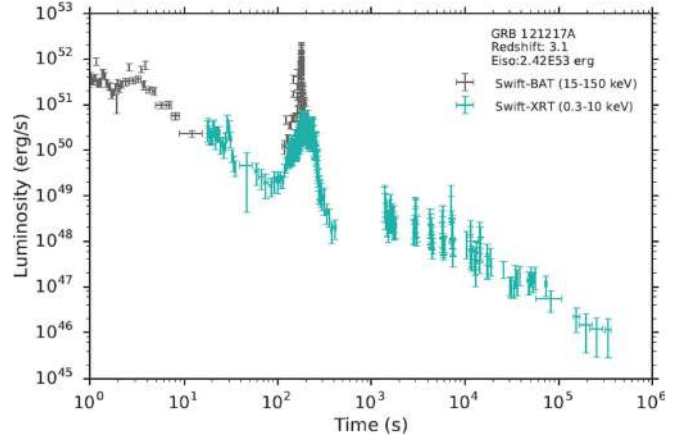


Figure 6. GRB 121217A clearly shows a gamma-ray flare observed by *Swift-BAT*, which coincides with a soft X-ray component observed by *Swift-XRT*. From the spectral analysis, it has a soft power-law photon index, and most of the energy is deposited in high-energy gamma-rays. This is an indication that the soft X-ray component is likely the low-energy part of a gamma-ray flare. For these reasons, we exclude it from our sample.

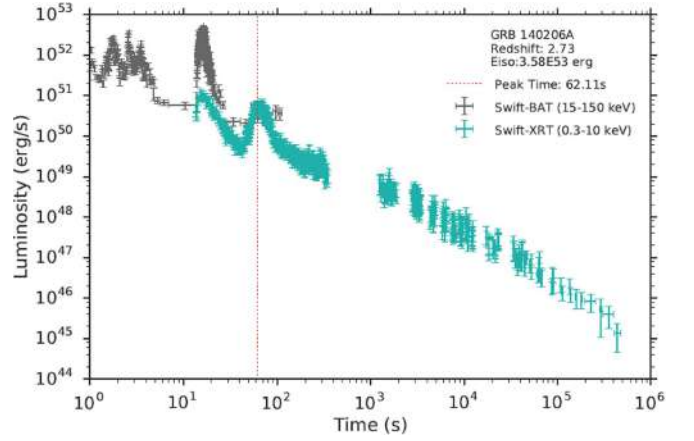


Figure 7. GRB 140206A has two flares. A gamma-ray flare coincides with the first flare while it is dim in the second one. The spectral analysis, using both *Swift-XRT* and *Swift-BAT* data, indicates a power-law index -0.88 ± 0.03 for the first flare. While the second flare requires an additional blackbody component; its power-law index is -1.73 ± 0.06 and its blackbody temperature is 0.54 ± 0.07 keV. Clearly, the energy of the first flare is contributed mainly by gamma-ray photons—it is a gamma-ray flare, and the second flare is an X-ray flare that we consider in this article.

show an illustrative example of the possible co-existence of an X-ray flare and a gamma-ray flare, and a way to distinguish them.

3. We also ignore here the late X-ray flare, including the ultralong GRB, which will be discussed in a forthcoming paper—six GRBs are consequently excluded.
4. We ignore the GRBs for which the soft X-ray energy observed by *Swift-XRT* (0.3–10 keV) before the plateau phase is higher than the gamma-ray energy observed by *Swift-BAT* (15–150 keV) during the entire valid *Swift-BAT* observation. This *Swift-BAT* anomaly points to an incomplete coverage of the prompt emission—six GRBs are excluded (see, e.g., Figure 8).

Finally, we have found 16 BdHNe satisfying all of the criteria to be included in our sample. Among them, seven

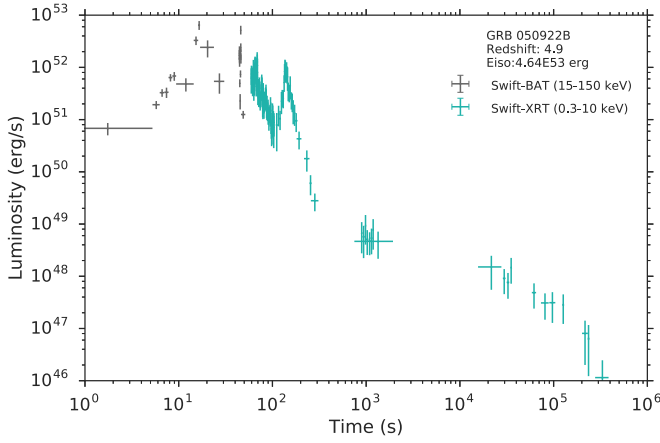


Figure 8. The *Swift*-BAT data of GRB 050922B has poor resolution—it cannot provide valid information after 50 s. The energy observed in its energy band, 15–150 keV, during this 50 s duration is 1.19×10^{53} erg. The energy observed by *Swift*-XRT is higher; the energy of the flares (60–200 s) in the *Swift*-XRT band 0.3–10 keV is 3.90×10^{53} erg. These results imply that the *Swift*-BAT observations may not cover the entire prompt emission phase; the isotropic energy computed from the *Swift*-BAT data is not reliable, and consequently the *Swift*-XRT observed partial prompt emission, which brings complexity to the X-ray light curve, makes the identification of the authentic X-ray flare more difficult.

BdHNe show a single flare. The other nine BdHNe contain two flares: generally, we exclude the first one, which appears to be a component from the gamma-ray spike or gamma-ray flare, and therefore select the second one for analysis (see, e.g., Figure 7).

These 16 selected BdHNe cover a wide range of redshifts. The closest one is GRB 070318 with redshift $z = 0.84$, and the farthest one is GRB 090516A with redshift $z = 4.11$. Their isotropic energy is also distributed over a large range: five GRBs have energies of the order of 10^{52} erg, nine GRBs of the order of 10^{53} erg, and two GRBs have extremely high isotropic energies $E_{\text{iso}} > 10^{54}$ erg. Therefore, this sample is well-constructed although the total number is limited.

5. The XRT Luminosity Light Curves of the 16 BdHN Sample

We now turn to the light curves of each of these 16 GRBs composing our sample (see Figures 9–24). The blue curves represent the X-rays observed by *Swift*-XRT, and the green curves are the corresponding optical observations when available. All of the values are in the rest frame and the X-ray luminosities have been K -corrected. The red vertical lines indicate the peak time of the X-ray flares. The rest-frame luminosity light curves of some GRBs show different flare structures compared to the observed count flux light curves. An obvious example is GRB 090516A, which follows from comparing Figure 18 in this paper with Figure 1 in Troja et al. (2015). The details of the FPA, as well as their correlations or the absence of correlation with E_{iso} , are given in the next section.

We then conclude that in our sample, there are *Swift* data for all GRBs: *Konus-Wind* observed GRBs 080607, 080810, 090516A, 131030A, 140419A, 141221A, and 151027A, while *Fermi* detected GRBs 090516A, 140206, 141221A, and 151027A. The energy coverage of the available satellites is limited, as mentioned in Section 2: *Fermi* detects the widest photon energy band, from 8 keV to 300 GeV, *Konus-Wind*

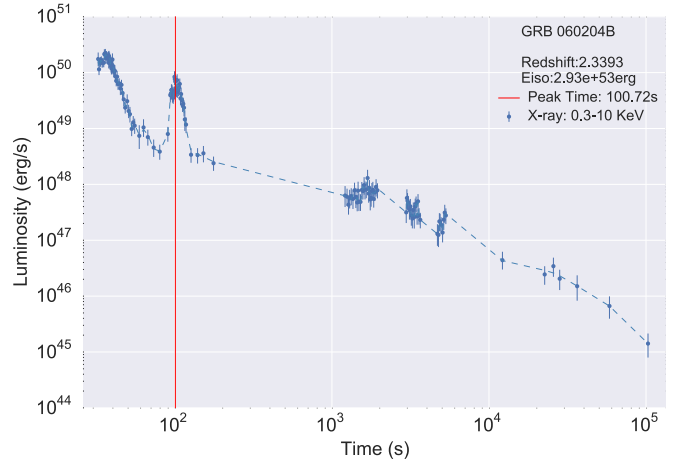


Figure 9. 060204B: this GRB triggered *Swift*-BAT (Falcone et al. 2006); *Swift*-XRT began observing 28.29 s after the BAT trigger. There is no observation from the *Fermi* satellite. X-shooter found its redshift at 2.3393 based on the host galaxy (Perley et al. 2016). The isotropic energy of this GRB reaches 2.93×10^{53} erg, computed from *Swift*-BAT data.

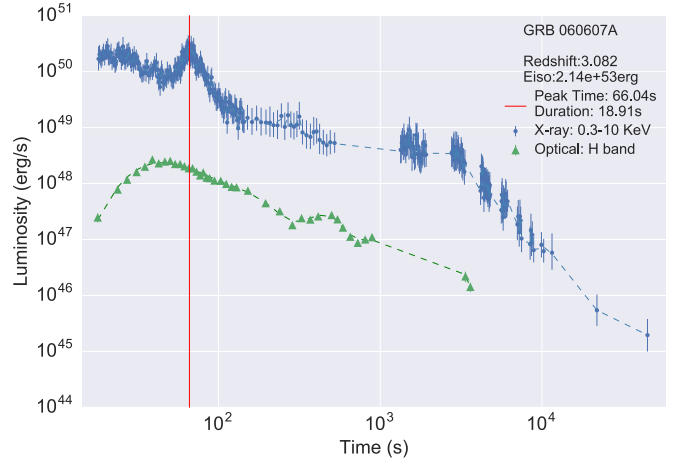


Figure 10. 060607A: this source was detected by the *Swift* satellite (Ziaepour et al. 2006). It has a bright optical counterpart (Ziaepour et al. 2006). It is located at a redshift $z = 3.082$ (Ledoux et al. 2006). The prompt light curve presents a doubled-peaked emission that lasts around 10 s, plus a second emission at ~ 25 s of 2.5 s duration. The isotropic energy is $E_{\text{iso}} = 2.14 \times 10^{53}$ erg. Optical data are from Nysewander et al. (2009).

observes from 20 keV to 15 MeV, and *Swift*-BAT has a narrow coverage from 15 keV to 150 keV. No GeV photons were observed, though GRB 090516A and 151027 were in the *Fermi*-LAT field of view. This contrasts with the observations of S-GRBs for which, in all of the sources so far identified and within the *Fermi*-LAT field of view, GeV photons were always observed (Ruffini et al. 2016a, 2016b) and can always freely reach a distant observer. These observational facts suggest that NS–NS (or NS–BH) mergers leading to the formation of a BH leave the surrounding environment poorly contaminated with the material ejected in the merging process ($\lesssim 10^{-2}$ – $10^{-3} M_{\odot}$) and therefore the GeV emission, originating from the accretion on the BH formed in the merger process (Ruffini et al. 2016a) can be observed. On the other hand, BdHNe originate in CO_{core} –NS binaries in which the material ejected from the CO_{core} explosion ($\approx M_{\odot}$) greatly pollutes the environment where the GeV emission has to propagate to reach the observer (see Section 3). This, together with the asymmetries of the SN

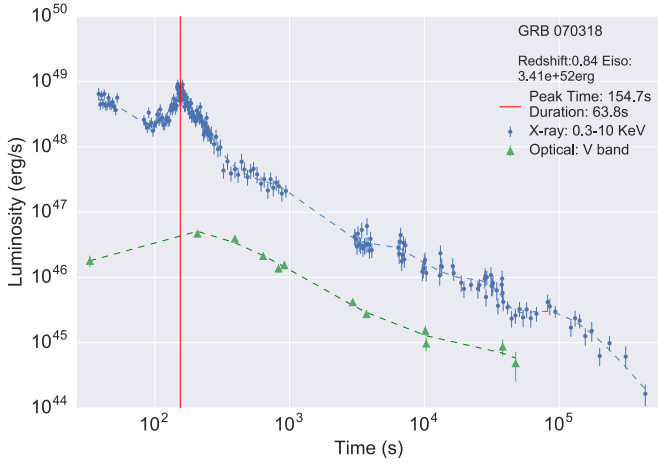


Figure 11. 070318: this source was detected by the *Swift* satellite (Cummings et al. 2007). It has a spectroscopic redshift of $z = 0.836$ (Jaunsen et al. 2007). The prompt light curve shows a peak with a typical fast-rise exponential-decay (FRED) behavior lasting about 55 s. XRT began observing the field 35 s after the BAT trigger. The isotropic energy is $E_{\text{iso}} = 3.64 \times 10^{52}$ erg. From the optical observation at ~ 20 days, no source or host galaxy is detected at the position of the optical afterglow, indicating that the decay rate of the afterglow must have steepened after some hours (Cobb 2007). Its optical data are from Chester et al. (2008).

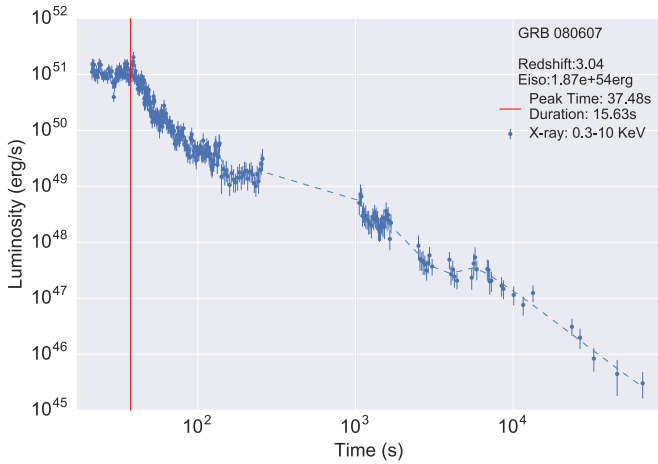


Figure 12. 080607: this source has been observed by *AGILE* (Marisaldi et al. 2008), *Konus-Wind* (Golenetskii et al. 2008), and *Swift* (Mangano et al. 2008). UVOT detected only a faint afterglow, since the source is located at a redshift $z = 3.04$. The isotropic energy is $E_{\text{iso}} = 1.87 \times 10^{54}$ erg. The BAT prompt light curve shows a very pronounced peak that lasts ~ 10 s, followed by several shallow peaks until 25 s. The *Swift* localization is at about 113° off-axis with respect to the *AGILE* pointing, so well out of the field of view of the *AGILE* gamma-ray imaging detector (GRID), which does not show any detection. The *Konus-Wind* light curve in the 50–200 keV range shows a multiple-peak emission lasting 15 s.

ejecta (see Section 3 and Becerra et al. 2016), lead to the possibility that the GeV emission in BdHNe can be “obsured” by the material of the SN ejecta, explaining the absence of GeV photons in the above cases of GRBs 090516A and 151027.

We derive the isotropic energy E_{iso} by assuming the prompt emission to be isotropic and by integrating the prompt photons in the rest-frame energy range from 1 keV to 10 MeV (Bloom et al. 2001). None of the satellites is able to cover the entire energy band of E_{iso} , so we need to fit the spectrum and find the best-fit function, then extrapolate the integration of energy by using this function. This method is relatively safe for GRBs observed by *Fermi* and *Konus-Wind*, but six GRBs in our

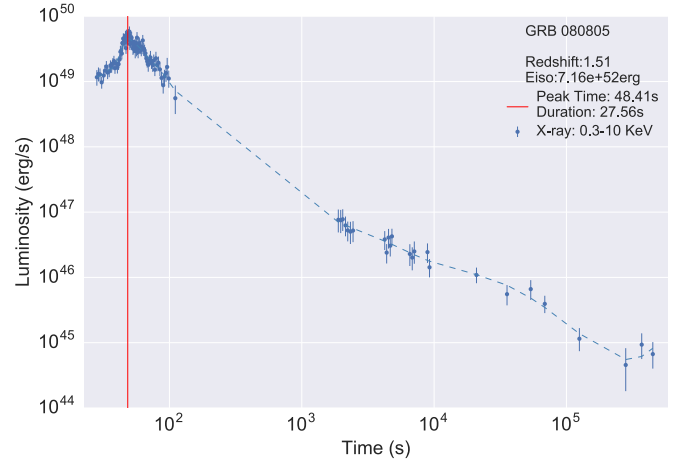


Figure 13. 080805: this source was detected by *Swift* (Pagani et al. 2008). The prompt light curve shows a peak with a FRED behavior lasting about 32 s. The redshift is $z = 1.51$, as reported by VLT (Jakobsson et al. 2008), and the isotropic energy is $E_{\text{iso}} = 7.16 \times 10^{52}$ erg.

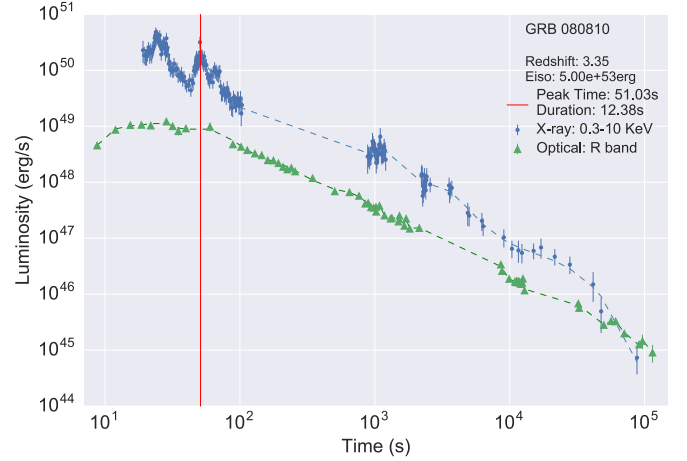


Figure 14. 080810: this source was detected by *Swift* (Golenetskii et al. 2008). The BAT light curve shows a multiple-peaked structure lasting about 23 s. XRT began observing the field 76 s after the BAT trigger. The source is located at a redshift of $z = 3.35$ and has an isotropic energy $E_{\text{iso}} = 3.55 \times 10^{53}$ erg. Optical data are taken from Page et al. (2009).

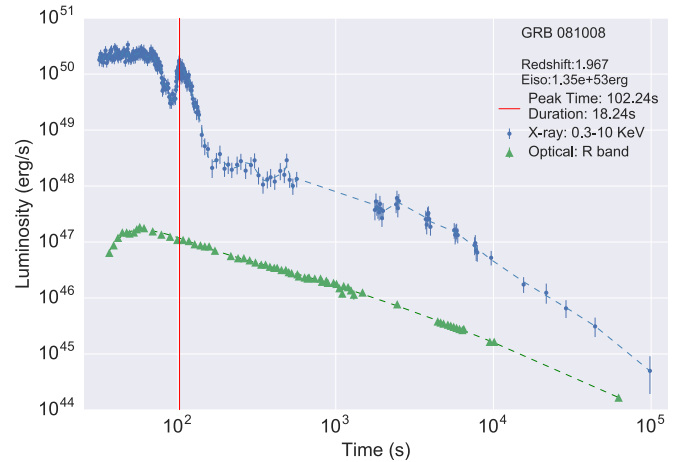


Figure 15. 081008: this source was detected by *Swift* (Racusin et al. 2008). The prompt emission lasts about 60 s and shows two peaks separated by 13 s. It is located at $z = 1.967$, as reported by VLT (D’Avanzo et al. 2008), and has an isotropic energy $E_{\text{iso}} = 1.07 \times 10^{53}$ erg. Optical data are from Yuan et al. (2010).

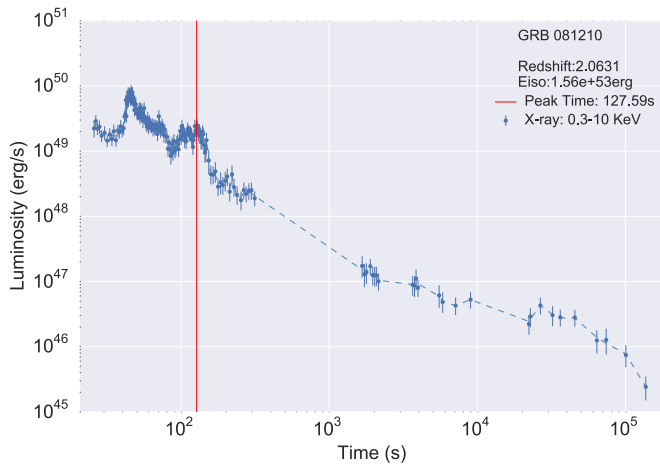


Figure 16. 081210: this GRB was detected by *Swift*-BAT (Krimm et al. 2008), *Swift*-XRT began observing 23.49 s after the BAT trigger. The BAT light curve begins with two spikes with a total duration of about 10 s and an additional spike at 45.75 s. There is no observation from the *Fermi* satellite. X-shooter found its redshift to be 2.0631 (Perley et al. 2016). The isotropic energy of this GRB is 1.56×10^{53} erg.

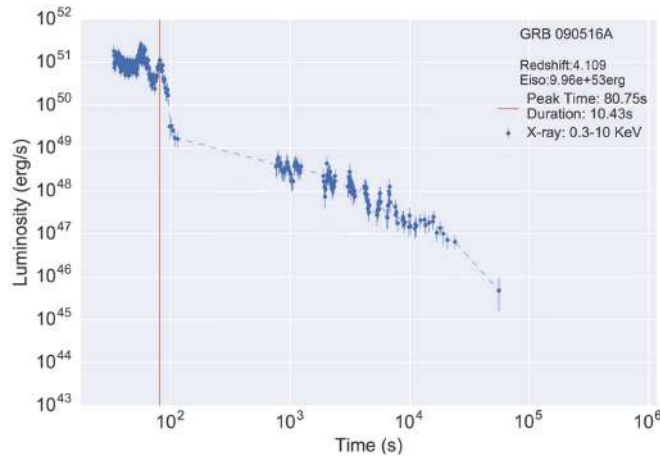


Figure 17. 090516A: this source was detected by *Swift* (Rowlinson et al. 2009), *Konus-Wind*, and *Fermi*/GBM (McBreen 2009). The BAT prompt light curve is composed of two episodes, the first starting 2 s before the trigger and lasting up to 10 s after the trigger, while the second episode starts at 17 s and lasts approximately 2 s. The GBM light curve consists of about five overlapping pulses from $T_{F,0} - 10$ s to $T_{F,0} + 21$ s (where $T_{F,0}$ is the trigger time of the *Fermi*/GBM). *Konus-Wind* observed this GRB in the waiting mode. VLT identified the redshift of the afterglow as $z = 4.109$ (de Ugarte Postigo et al. 2012), in agreement with the photometric redshift obtained with GROND (Rossi et al. 2009). *Fermi*-LAT was inside the field of view, following the standard *Fermi*-LAT likelihood analysis in https://fermi.gsfc.nasa.gov/ssc/data/analysis/scitools/likelihood_tutorial.html, the upper limit of the observed count flux is 4.76×10^{-6} photons $\text{cm}^{-2} \text{s}^{-1}$, and no GeV photon was found for this high redshift and low observed fluence GRB. The isotropic energy is $E_{\text{iso}} = 6.5 \times 10^{53}$ erg.

sample have been observed only by *Swift*, so we uniformly fit and extrapolate these six GRBs by power laws and cutoff power laws; we then take the average value as E_{iso} . In general, our priority in computing E_{iso} is *Fermi*, *Konus-Wind*, then *Swift*. In order to take into account the expansion of the universe, all of our computations consider the K correction. The formula of K correction for E_{iso} varies depending on the best-fit function. The energy in the X-ray afterglow is computed in the cosmological rest-frame energy band from 0.3 to 10 keV. We smoothly fit the luminosity light curve using an algorithm named locally weighted regression (Cleveland & Devlin 1988),

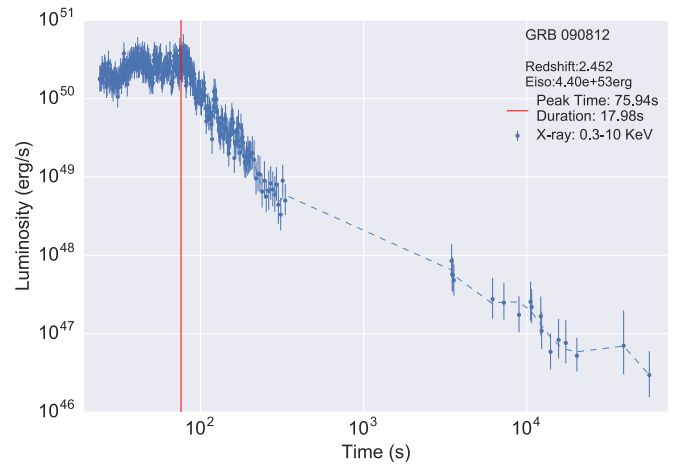


Figure 18. 090812: this source was detected by *Swift* (Stamatikos et al. 2009). It has a redshift $z = 2.452$ as confirmed by VLT (de Ugarte Postigo et al. 2012) and an isotropic energy $E_{\text{iso}} = 4.75 \times 10^{53}$ erg. The BAT light curve shows three successive bumps lasting ~ 20 s in total. XRT began observing the field 22 s after the BAT trigger (Stamatikos et al. 2009). The BAT light curve shows a simple power-law behavior.

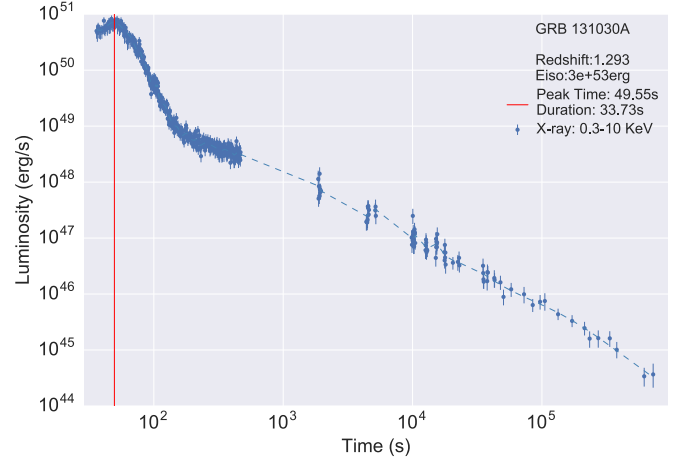


Figure 19. 131030A: this source was observed by *Swift* (Troja et al. 2013) and *Konus-Wind* (Golenetskii et al. 2013). The BAT light curve shows two overlapping peaks starting, with respect to the *Swift*-BAT trigger $T_{B,0}$, at $\sim T_{B,0} - 3.5$ s and peaking at $\sim T_{B,0} + 4.4$ s (Barthelmy et al. 2013). The duration is 18 s in the 15–350 keV band. The *Konus-Wind* light curve shows a multi-peaked pulse from $\sim T_{KW,0} - 1.3$ s until $\sim T_{KW,0} + 11$ s (where $T_{KW,0}$ is the *Konus-Wind* trigger time). The redshift of this source is $z = 1.293$, as determined by NOT (Xu et al. 2013). The isotropic energy is $E_{\text{iso}} = 3 \times 10^{53}$ erg.

which provides a sequence of power-law functions. The corresponding energy in a fixed time interval is obtained by summing up all of the integrals of the power laws within it. This method is applied to estimate the energy of the flare E_f as well as the energy of the FPA phase up to 10^9 s, E_{FPA} . An interesting alternative procedure was used in Swenson & Roming (2014) to fit the light curve and determine the flaring structure with a Bayesian Information method. On this specific aspect, the two treatments are equally valid and give compatible results.

Table 3 contains the relevant energy and time information of the 16 BdHNe of the sample: the cosmological redshift z , E_{iso} , the flare peak time t_p , the corresponding peak luminosity L_p , the flare duration Δt , and the energy of the flare E_f . To determine t_p , we apply a locally weighted regression, which results in a

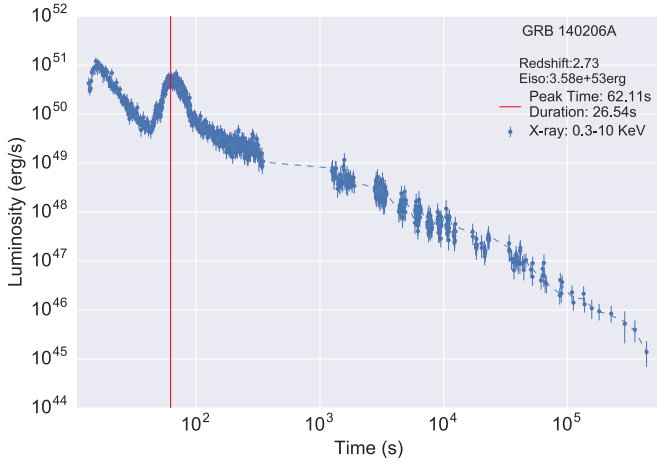


Figure 20. 140206A: this source was detected by all instruments on board *Swift* (Lien et al. 2014) and by *Fermi*/GBM (von Kienlin & Bhat 2014). The GBM light curve shows a single pulse with a duration of ~ 7 s (50–300 keV). The source was outside the field of view, 123° from the LAT boresight at the time of the trigger. The BAT light curve shows a multi-peaked structure with roughly three main pulses (Sakamoto et al. 2014). The source duration in the 15–350 keV band is 25 s. The redshift, as observed by NOT (Malesani et al. 2014), is $z = 2.73$, and the isotropic energy is $E_{\text{iso}} = 4.3 \times 10^{53}$ erg.

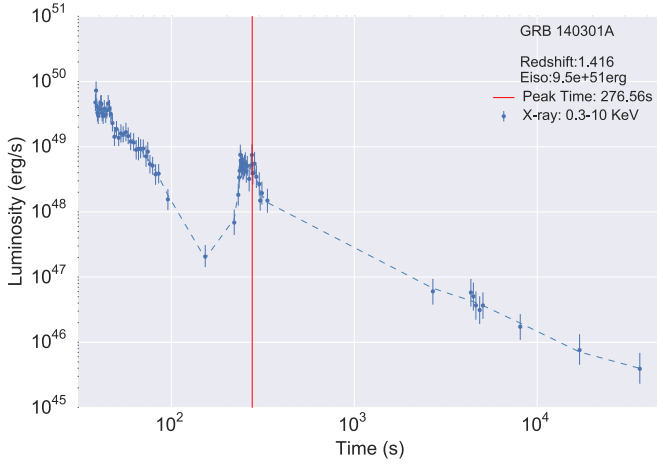


Figure 21. 140301A: this GRB triggered *Swift*-BAT (Page et al. 2014); the BAT light curve has a single spike with a duration of about 4 s. XRT started to observe 35.63 s after the BAT trigger. There is no observation from the *Fermi* satellite. From the X-shooter spectrum analysis, the redshift was revealed at 1.416 (Kruehler et al. 2014). The isotropic energy of this GRB is 9.5×10^{51} erg.

smoothed light curve composed of power-law functions: the flare peak is localized where the power-law index is zero. Therefore, t_p is defined as the time interval between the flare peak and the trigger time of *Swift*-BAT.¹⁰ Correspondingly, we find the peak luminosity L_p at t_p and its duration Δt , which is defined as the time interval between a start time and an end time where the luminosity is half of L_p . We have made public the entire details including the codes online.¹¹

¹⁰ In reality, the GRB occurs earlier than the trigger time, since there is a short period when the flux intensity is lower than the satellite trigger threshold (Fenimore et al. 2003).

¹¹ <https://github.com/YWangScience/AstroNeuron>

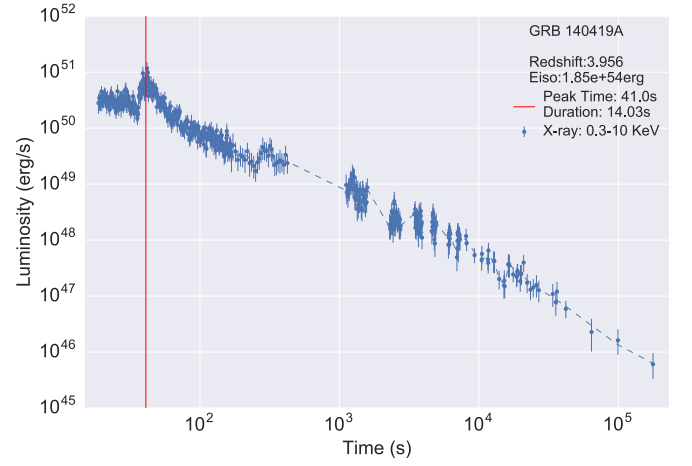


Figure 22. 140419A: this source was detected by Konus-Wind (Golenetskii et al. 2014) and *Swift* (Marshall et al. 2014). The Konus-Wind light curve shows a broad pulse from $\sim T_{\text{KW},0} - 2$ s to $\sim T_{\text{KW},0} + 8$ s, followed by softer pulses around $\sim T_{\text{KW},0} + 10$ s. The total duration of the burst is ~ 16 s. The BAT light curve shows two slightly overlapping clusters of peaks, starting at $\sim T_{\text{B},0} - 2$ s, peaking at $\sim T_{\text{B},0} + 2$ s and $\sim T_{\text{B},0} + 10$ s, and ending at $\sim T_{\text{B},0} + 44$ s (Baumgartner et al. 2014). The total duration (in 15–350 keV) is 19 s. The redshift of this source, as determined by Gemini, is $z = 3.956$ (Tanvir et al. 2014), and its isotropic energy is $E_{\text{iso}} = 1.85 \times 10^{54}$ erg.

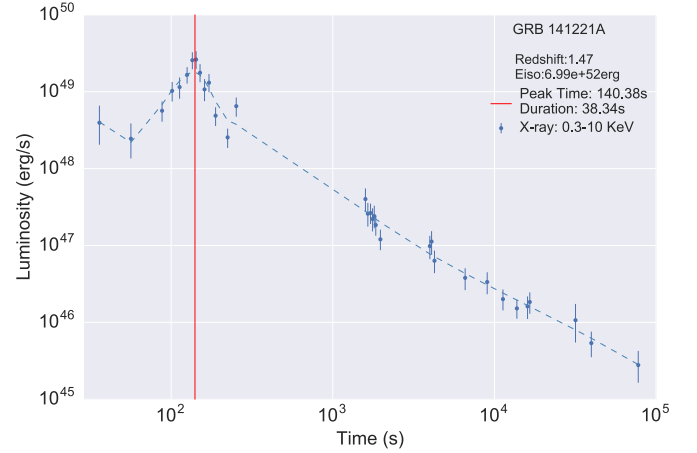


Figure 23. 141221A: this source is located at a spectroscopic redshift $z = 1.47$, as determined by Keck (Perley et al. 2014). Its isotropic energy is $E_{\text{iso}} = 1.91 \times 10^{52}$ erg. The emission was detected by all of the instruments on board *Swift* (Sonbas et al. 2014) and by *Fermi*/GBM (Yu 2014). The GBM light curve consists of two pulses with a duration of about 10 s (50–300 keV). The source was 76° from the LAT boresight at the time of the trigger, out of the field of view. The BAT light curve showed a double-peaked structure with a duration of about 8 s. XRT began observing the field 32 s after the BAT trigger.

6. Statistical Correlation

We then establish correlations between the above quantities characterizing each luminosity light curve of the sample with the E_{iso} of the corresponding BdHN. We have relied heavily on the MCMC method and iterated 10^5 times to obtain the best fit of the power law and their correlation coefficient. The main results are summarized in Figures 25–28. All of the codes are publicly available online.¹² We conclude that the peak time and

¹² <https://github.com/YWangScience/MCCC>

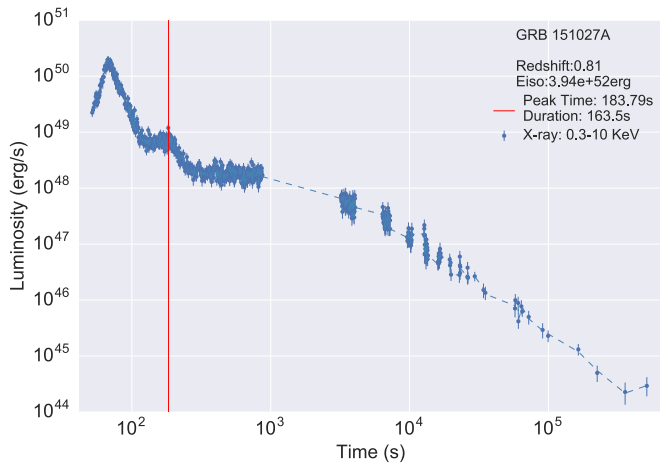


Figure 24. 151027A: this source was detected by MAXI (Masumitsu et al. 2015), Konus-Wind (Golenetskii et al. 2015), *Swift* (Maselli et al. 2015), and *Fermi*/GBM (Toelge et al. 2015). It is located at a redshift $z = 0.81$, as determined by Keck/HIRES (Perley et al. 2015), and the isotropic energy is $E_{\text{iso}} = 3.94 \times 10^{52}$ erg. The LAT boresight of the source was 10° at the time of the trigger, and there are no clear associated high-energy photons; an upper limit of the observed count flux is computed to be 9.24×10^{-6} photons $\text{cm}^{-2} \text{s}^{-1}$ following the standard *Fermi*-LAT likelihood analysis. The BAT light curve showed a complex peaked structure lasting at least 83 s. XRT began observing the field 48 s after the BAT trigger. The GBM light curve consists of three pulses with a duration of about 68 s in the 50–300 keV band. The Konus-Wind light curve consists of at least three pulses with a total duration of ~ 66 s. The MAXI detection is not significant, but the flux is consistent with the interpolation from the *Swift*/XRT light curve.

the duration of the flare, as well as the peak luminosity and the total energy of flare, are highly correlated with E_{iso} , with correlation coefficients larger than 0.6 (or smaller than -0.6). The average values and the 1σ uncertainties are shown in Table 4.

7. The Partition of the Electron–Positron Plasma Energy Between the Prompt Emission and the FPA

The energy of the prompt emission is proportional to E_{iso} if and only if spherical symmetry is assumed: this clearly follows from the prompt emission time-integrated luminosity. We are now confronted with a new situation: the total energy of the FPA emission up to 10^9 s (E_{FPA}) is also proportional to E_{iso} , following the correlation given in Tables 5 and 6, and Figure 29. What is clear is that there are two very different components where the energy of the dyadosphere $E_{e^+e^-}$ is utilized: the energy E_{prompt} of the prompt emission and the energy E_{FPA} of the FPA, i.e., $E_{e^+e^-} = E_{\text{iso}} = E_{\text{prompt}} + E_{\text{FPA}}$. Figures 30 and 31 show the distribution of $E_{e^+e^-} = E_{\text{iso}}$ between these two components.

As a consequence of the above, in view of the presence of the companion SN remnant ejecta (see Becerra et al. 2016 for more details), we assume here that the spherical symmetry of the prompt emission is broken. Part of the energy due to the impact of the e^+e^- plasma on the SN is captured by the SN ejecta, and gives rise to the FPA emission as originally proposed by Ruffini (2015). We shall return to the study of the impact between the plasma and the SN ejecta in Section 10 after studying the motion of the matter composing the FPA in the next few sections.

It can also be seen that the relative partition between E_{prompt} and E_{FPA} strongly depends on the value of $E_{e^+e^-}$: the lower the GRB

energy, the higher the FPA energy percentage, and consequently the lower the prompt energy percentage (see Figure 31).

In Becerra et al. (2016), we indicate that both the value of $E_{e^+e^-}$ and the relative ratio of the above two components can in principle be explained in terms of the geometry of the binary nature of the system: the smaller the distance is between the CO_{core} and the companion NS, the shorter the binary period of the system, and the larger the value of $E_{e^+e^-}$.

8. On the Flare Thermal Emission, Its Temperature, and Dynamics

We discuss now the profound difference between the prompt emission, which we recall is emitted at distances of the order of 10^{16} cm away from the newly born BH with $\Gamma \approx 10^2$ – 10^3 , and the FPA phase. We focus on a further fundamental set of data, which originates from a thermal emission associated with the flares.¹³ Only in some cases is this emission so clear and prominent that it allows the estimation of the flare expansion speed and the determination of its mildly relativistic Lorentz factor $\Gamma \lesssim 4$, which creates a drastic separatrix both in the energy and in the Gamma factor between the astrophysical nature of the prompt emission and of the flares.

Following the standard data reduction procedure of *Swift*-XRT (Romano et al. 2006; Evans et al. 2007, 2009), X-ray data within the duration of flare are retrieved from the United Kingdom *Swift* Science Data Centre (UKSSDC)¹⁴ and analyzed by Heasoft.¹⁵ Table 7 shows the fit of the spectrum within the duration Δt of the flare for each BdHN of the sample. As a first approximation, in computing the radius, we have assumed a constant expansion velocity of $0.8c$ indicated for some BdHNe, such as GRB 090618 (Ruffini et al. 2014) and GRB 130427A (Ruffini et al. 2015c). Out of 16 sources, seven BdHNe have highly confident thermal components (significance > 0.95 ; see boldfaced entries in Table 7), which means that the addition of a blackbody spectrum improves a single power-law fit (which is, conversely, excluded at the 2σ confidence level). These blackbodies have fluxes in a range from 1% to 30% of the total flux and share a similar order of magnitude radii, i.e., $\sim 10^{11}$ – 10^{12} cm. In order to have a highly significant thermal component, the blackbody radiation itself should be prominent as well as its ratio to the nonthermal part. Another critical reason is that the observable temperature must be compatible with the satellite bandpass. For example, *Swift*-XRT observes in the 0.3–10 keV photon energy band, but the hydrogen absorption affects the lower energy part (~ 0.5 keV), and data are not always adequate beyond 5 keV, due to the low effective area of satellite for high-energy photons. The reliable temperature only ranges from 0.15 keV to 1.5 keV (since the peak photon energy is equal to the temperature times 2.82), so the remaining nine GRBs may contain a thermal component in the flare but outside the satellite bandpass.

We now attempt to perform a more refined analysis to infer the value of β from the observations. We assume that during the flare, the blackbody emitter has spherical symmetry and expands with a constant Lorentz Gamma factor. Therefore, the expansion velocity β is also constant during the flare. The relations between the comoving time t_{com} , the laboratory time t ,

¹³ The late afterglow phases have been already discussed in Pisani et al. (2013, 2016).

¹⁴ <http://www.swift.ac.uk>

¹⁵ <http://heasarc.gsfc.nasa.gov/lheasoft/>

Table 3
GRB Sample Properties of the Prompt and Flare Phases

GRB	z	T_{90} (s)	E_{iso} (erg)	t_p (s)	L_p (erg s $^{-1}$)	Δt (s)	E_f (erg)	α_f
060204B	2.3393	40.12	$2.93(\pm 0.60) \times 10^{53}$	100.72 ± 6.31	$7.35(\pm 2.05) \times 10^{49}$	17.34 ± 6.83	$8.56(\pm 0.82) \times 10^{50}$	2.73
060607A	3.082	24.49	$2.14(\pm 1.19) \times 10^{53}$	66.04 ± 4.98	$2.28(\pm 0.48) \times 10^{50}$	18.91 ± 3.84	$3.33(\pm 0.32) \times 10^{51}$	1.72
070318	0.84	28.80	$3.41(\pm 2.14) \times 10^{52}$	154.7 ± 12.80	$6.28(\pm 1.30) \times 10^{48}$	63.80 ± 19.82	$3.17(\pm 0.37) \times 10^{50}$	1.84
080607	3.04	21.04	$1.87(\pm 0.11) \times 10^{54}$	37.48 ± 3.60	$1.14(\pm 0.27) \times 10^{51}$	15.63 ± 4.32	$1.54(\pm 0.24) \times 10^{52}$	2.08
080805	1.51	31.08	$7.16(\pm 1.90) \times 10^{52}$	48.41 ± 5.46	$4.66(\pm 0.59) \times 10^{49}$	27.56 ± 9.33	$9.68(\pm 1.24) \times 10^{50}$	1.25
080810	3.35	18.25	$5.00(\pm 0.44) \times 10^{53}$	51.03 ± 6.49	$1.85(\pm 0.53) \times 10^{50}$	12.38 ± 4.00	$1.80(\pm 0.17) \times 10^{51}$	2.37
081008	1.967	62.52	$1.35(\pm 0.66) \times 10^{53}$	102.24 ± 5.66	$1.36(\pm 0.33) \times 10^{50}$	18.24 ± 3.63	$1.93(\pm 0.16) \times 10^{51}$	2.46
081210	2.0631	47.66	$1.56(\pm 0.54) \times 10^{53}$	127.59 ± 13.68	$2.23(\pm 0.21) \times 10^{49}$	49.05 ± 6.49	$8.86(\pm 0.54) \times 10^{50}$	2.28
090516A	4.109	68.51	$9.96(\pm 1.67) \times 10^{53}$	80.75 ± 2.20	$9.10(\pm 2.26) \times 10^{50}$	10.43 ± 2.44	$7.74(\pm 0.63) \times 10^{51}$	3.66
090812	2.452	18.77	$4.40(\pm 0.65) \times 10^{53}$	77.43 ± 16.6	$3.13(\pm 1.38) \times 10^{50}$	17.98 ± 4.51	$5.18(\pm 0.61) \times 10^{51}$	2.20
131030A	1.293	12.21	$3.00(\pm 0.20) \times 10^{53}$	49.55 ± 7.88	$6.63(\pm 1.12) \times 10^{50}$	33.73 ± 6.55	$3.15(\pm 0.57) \times 10^{52}$	2.22
140206A	2.73	7.24	$3.58(\pm 0.79) \times 10^{53}$	62.11 ± 12.26	$4.62(\pm 0.99) \times 10^{50}$	26.54 ± 4.31	$1.04(\pm 0.59) \times 10^{51}$	1.73
140301A	1.416	12.83	$9.50(\pm 1.75) \times 10^{51}$	276.56 ± 15.50	$5.14(\pm 1.84) \times 10^{48}$	64.52 ± 10.94	$3.08(\pm 0.22) \times 10^{50}$	2.30
140419A	3.956	16.14	$1.85(\pm 0.77) \times 10^{54}$	41.00 ± 4.68	$6.23(\pm 1.45) \times 10^{50}$	14.03 ± 5.74	$7.22(\pm 0.88) \times 10^{51}$	2.32
141221A	1.47	9.64	$6.99(\pm 1.98) \times 10^{52}$	140.38 ± 5.64	$2.60(\pm 0.64) \times 10^{49}$	38.34 ± 9.26	$7.70(\pm 0.78) \times 10^{50}$	1.79
151027A	0.81	68.51	$3.94(\pm 1.33) \times 10^{52}$	183.79 ± 16.43	$7.10(\pm 1.75) \times 10^{48}$	163.5 ± 30.39	$4.39(\pm 2.91) \times 10^{51}$	2.26

Note. This table contains the redshift z , the T_{90} in the rest frame, the isotropic energy E_{iso} , the flare peak time t_p in the rest frame, the flare peak luminosity L_p , the flare duration where the starting and ending time correspond to half of the peak luminosity Δt , the flare energy E_f within the time interval Δt , and α_f the power-law index from the fitting of the flare's spectrum.

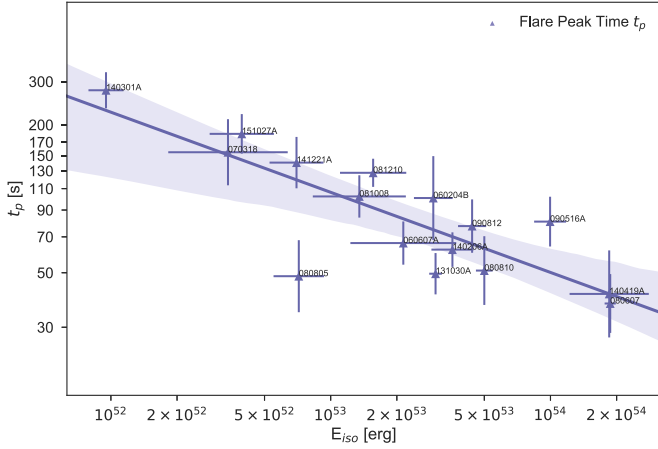


Figure 25. Relation between E_{iso} and t_p fit by a power law. The shaded area indicates the 95% confidence level.

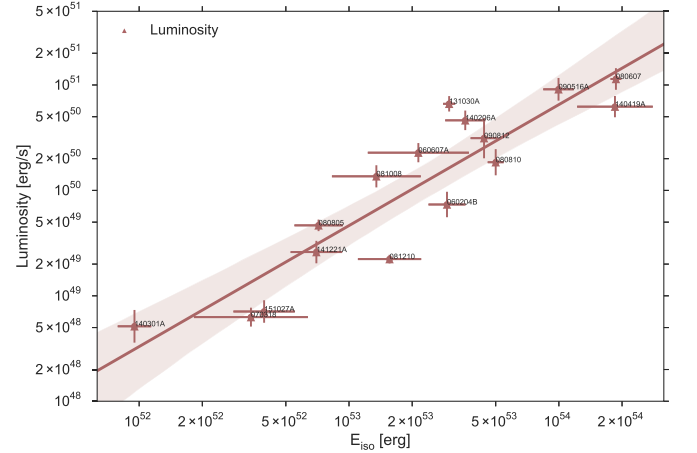


Figure 27. Relation between E_{iso} and L_p fit by a power law. The shaded area indicates the 95% confidence level.

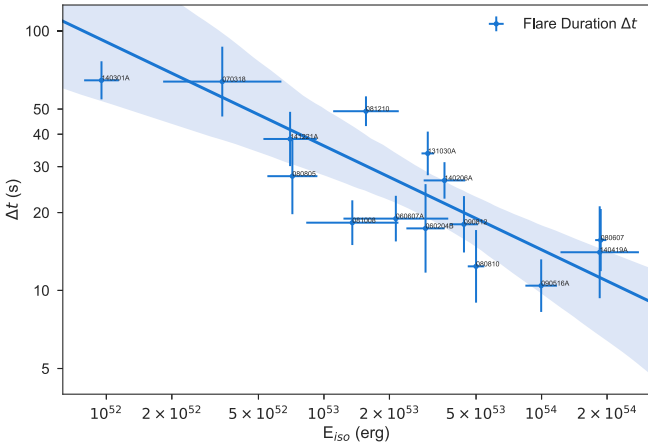


Figure 26. Relation between E_{iso} and Δt fit by a power law. The shaded area indicates the 95% confidence level.

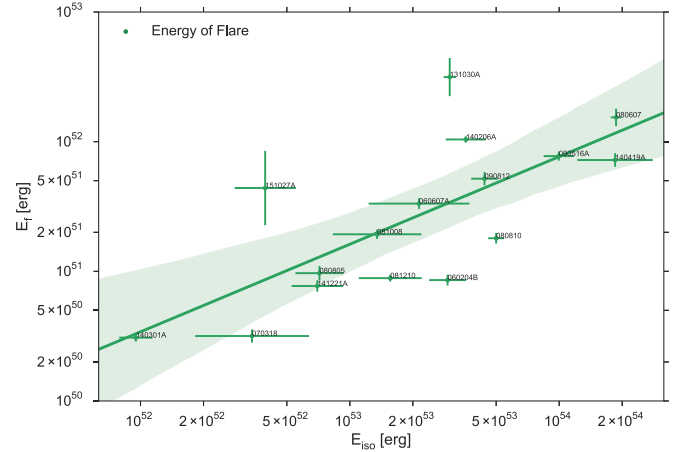


Figure 28. Relation between E_{iso} and E_f fit by a power law. The shaded area indicates the 95% confidence level.

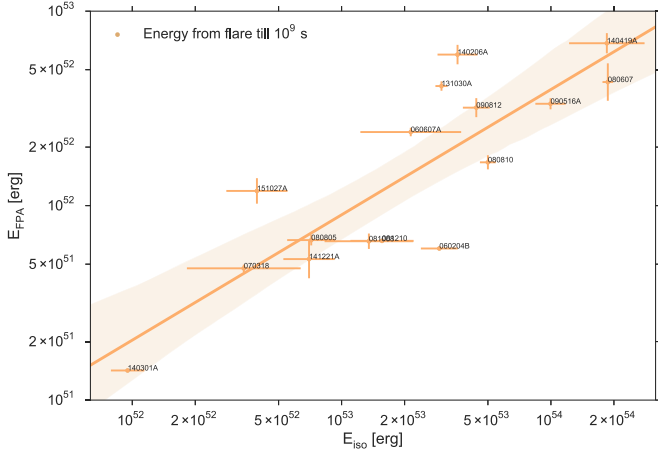


Figure 29. Relation between E_{iso} and E_{FPA} fit by a power law. The shaded area indicates the 95% confidence level.

Table 4
Power-law Correlations Among the Quantities in Table 3

Correlation	Power-law Index	Coefficient
$E_{\text{iso}} - t_p$	$-0.290(\pm 0.010)$	$-0.764(\pm 0.123)$
$E_{\text{iso}} - \Delta t$	$-0.461(\pm 0.042)$	$-0.760(\pm 0.138)$
$E_{\text{iso}} - L_p$	$1.186(\pm 0.037)$	$0.883(\pm 0.070)$
$E_{\text{iso}} - E_f$	$0.631(\pm 0.117)$	$0.699(\pm 0.145)$

Note. The values and uncertainties (at the 1σ confidence level) of the power-law index and of the correlation coefficient are obtained from 10^5 MCMC iterations. All relations are highly correlated.

Table 5
GRB Sample Properties of the Prompt and FPA Phases

GRB	z	E_{iso} (erg)	E_{FPA} (erg)
060204B	2.3393	$2.93(\pm 0.60) \times 10^{53}$	$6.02(\pm 0.20) \times 10^{51}$
060607A	3.082	$2.14(\pm 1.19) \times 10^{53}$	$2.39(\pm 0.12) \times 10^{52}$
070318	0.84	$3.41(\pm 2.14) \times 10^{52}$	$4.76(\pm 0.21) \times 10^{51}$
080607	3.04	$1.87(\pm 0.11) \times 10^{54}$	$4.32(\pm 0.96) \times 10^{52}$
080805	1.51	$7.16(\pm 1.90) \times 10^{52}$	$6.65(\pm 0.42) \times 10^{51}$
080810	3.35	$5.00(\pm 0.44) \times 10^{53}$	$1.67(\pm 0.14) \times 10^{52}$
081008	1.967	$1.35(\pm 0.66) \times 10^{53}$	$6.56(\pm 0.60) \times 10^{51}$
081210	2.0631	$1.56(\pm 0.54) \times 10^{53}$	$6.59(\pm 0.60) \times 10^{51}$
090516A	4.109	$9.96(\pm 1.67) \times 10^{53}$	$3.34(\pm 0.22) \times 10^{52}$
090812	2.452	$4.40(\pm 0.65) \times 10^{53}$	$3.19(\pm 0.36) \times 10^{52}$
131030A	1.293	$3.00(\pm 0.20) \times 10^{53}$	$4.12(\pm 0.23) \times 10^{52}$
140206A	2.73	$3.58(\pm 0.79) \times 10^{53}$	$5.98(\pm 0.69) \times 10^{52}$
140301A	1.416	$9.50(\pm 1.75) \times 10^{51}$	$1.42(\pm 0.14) \times 10^{50}$
140419A	3.956	$1.85(\pm 0.77) \times 10^{54}$	$6.84(\pm 0.82) \times 10^{52}$
141221A	1.47	$6.99(\pm 1.98) \times 10^{52}$	$5.31(\pm 1.21) \times 10^{51}$
151027A	0.81	$3.94(\pm 1.33) \times 10^{52}$	$1.19(\pm 0.18) \times 10^{52}$

Note. This table lists z , E_{iso} , and the FPA energy E_{FPA} from the flare until 10^9 s.

the arrival time t_a , and the arrival time t_a^d at the detector, given in Equation (2), in this case become

$$\begin{aligned} t_a^d &= t_a(1+z) = t(1-\beta \cos \vartheta)(1+z) \\ &= \Gamma t_{\text{com}}(1-\beta \cos \vartheta)(1+z). \end{aligned} \quad (7)$$

We can infer an effective radius R of the blackbody emitter from (1) the observed blackbody temperature T_{obs} , which

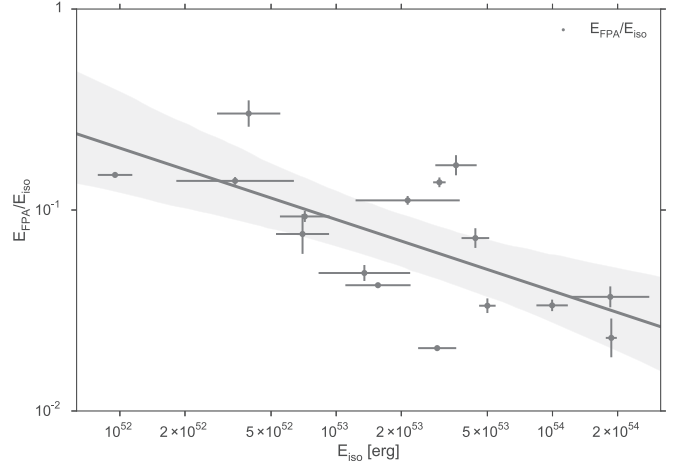


Figure 30. Relation between the percentage of $E_{e^+e^-}$ going to the SN ejecta and accounting for the energy in FPA, i.e., $E_{\text{FPA}}/E_{\text{iso}} \times 100\%$, and E_{iso} fit by a power law. The shaded area indicates the 95% confidence level.

Table 6
Power-law Correlations Among the Quantities in Table 5

Correlation	Power-law Index	Coefficient
$E_{\text{iso}} - E_{\text{FPA}}$	$0.613(\pm 0.041)$	$0.791(\pm 0.103)$
$E_{\text{iso}} - E_{\text{FPA}}/E_{\text{iso}}$	$-0.005(\pm 0.002)$	$0.572(\pm 0.178)$

Note. The statistical considerations of Table 4 are valid here as well.

comes from the spectral fit of the data during the flare; (2) the observed bolometric blackbody flux $F_{\text{bb,obs}}$, computed from T_{obs} and the normalization of the blackbody spectral fit; and (3) the cosmological redshift z of the source (see also Izzo et al. 2012). We recall that $F_{\text{bb,obs}}$ by definition is given by

$$F_{\text{bb,obs}} = \frac{L}{4\pi D_L(z)^2}, \quad (8)$$

where $D_L(z)$ is the luminosity distance of the source, which in turn is a function of the cosmological redshift z , and L is the source bolometric luminosity (i.e., the total emitted energy per unit time). L is Lorentz invariant, so we can compute it in the comoving frame of the emitter using the usual blackbody expression,

$$L = 4\pi R_{\text{com}}^2 \sigma T_{\text{com}}^4, \quad (9)$$

where R_{com} and T_{com} are the comoving radius and the comoving temperature of the emitter, respectively, and σ is the Stefan–Boltzmann constant. We recall that T_{com} is constant over the entire shell due to our assumption of spherical symmetry. From Equations (8) and (9), we then have

$$F_{\text{bb,obs}} = \frac{R_{\text{com}}^2 \sigma T_{\text{com}}^4}{D_L(z)^2}. \quad (10)$$

We now need the relation between T_{com} and the observed blackbody temperature T_{obs} . Considering both the cosmological redshift and the Doppler effect due to the velocity of the



Figure 31. Distribution of the GRB total energy $E_{e^+e^-} = E_{\text{iso}}$ into prompt and FPA energies. The percentage of $E_{e^+e^-}$ going to the SN ejecta accounting for the energy in the FPA phase appears in red, i.e., $E_{\text{FPA}}/E_{\text{iso}} \times 100\%$. The green part is therefore the percentage of $E_{e^+e^-}$ used in the prompt emission, i.e., $E_{\text{prompt}}/E_{\text{iso}} \times 100\%$. It can be seen that the lower the GRB energy $E_{e^+e^-} = E_{\text{iso}}$, the higher the FPA energy percentage, and consequently the lower the prompt energy percentage.

emitting surface, we have

$$T_{\text{obs}}(T_{\text{com}}, z, \Gamma, \cos \vartheta) = \frac{T_{\text{com}}}{(1+z)\Gamma(1-\beta \cos \vartheta)} = \frac{T_{\text{com}} \mathcal{D}(\cos \vartheta)}{1+z}, \quad (11)$$

where we have defined the Doppler factor $\mathcal{D}(\cos \vartheta)$ as

$$\mathcal{D}(\cos \vartheta) \equiv \frac{1}{\Gamma(1-\beta \cos \vartheta)}. \quad (12)$$

Equation (11) gives us the observed blackbody temperature of the radiation coming from different points of the emitter surface, corresponding to different values of $\cos \vartheta$. However, since the emitter is at a cosmological distance, we are not able to resolve spatially the source with our detectors. Therefore, the temperature that we actually observe corresponds to an average of Equation (11) computed over the emitter surface:¹⁶

$$\begin{aligned} T_{\text{obs}}(T_{\text{com}}, z, \Gamma) &= \frac{1}{1+z} \frac{\int_{\beta}^1 \mathcal{D}(\cos \vartheta) T_{\text{com}} \cos \vartheta d \cos \vartheta}{\int_{\beta}^1 \cos \vartheta d \cos \vartheta} \\ &= \frac{2}{1+z} \frac{\beta(\beta-1) + \ln(1+\beta)}{\Gamma \beta^2 (1-\beta^2)} T_{\text{com}} \\ &= \Theta(\beta) \frac{\Gamma}{1+z} T_{\text{com}}, \end{aligned} \quad (13)$$

where we defined

$$\Theta(\beta) \equiv 2 \frac{\beta(\beta-1) + \ln(1+\beta)}{\beta^2}. \quad (14)$$

¹⁶ From the point of view of the observer, the spectrum is not a perfect blackbody, coming from a convolution of blackbody spectra at different temperatures. The blackbody component we obtain from the spectral fit of the observed data is an effective blackbody of temperature T_{obs} , analogous to other cases of effective temperatures in cosmology (see, e.g., Ruffini et al. 1983).

Table 7
Radii and Temperatures of the Thermal Components Detected Within the Flare Duration Δt

GRB	Radius (cm)	kT_{obs} (keV)	Significance
060204B	$1.80(\pm 1.11) \times 10^{11}$	$0.60(\pm 0.15)$	0.986
060607A	$1.67(\pm 1.01) \times 10^{11}$	$0.92(\pm 0.24)$	0.991
070318	<i>unconstrained</i>	$1.79(\pm 1.14)$	0.651
080607	$1.52(\pm 0.72) \times 10^{12}$	$0.49(\pm 0.10)$	0.998
080805	$1.12(\pm 1.34) \times 10^{11}$	$1.31(\pm 0.59)$	0.809
080810	$2.34(\pm 4.84) \times 10^{11}$	$0.61(\pm 0.57)$	0.999
081008	$1.84(\pm 0.68) \times 10^{12}$	$0.32(\pm 0.03)$	0.999
081210	<i>unconstrained</i>	$0.80(\pm 0.51)$	0.295
090516A	<i>unconstrained</i>	$1.30(\pm 1.30)$	0.663
090812	$1.66(\pm 1.84) \times 10^{12}$	$0.24(\pm 0.12)$	0.503
131030A	$3.67(\pm 1.02) \times 10^{12}$	$0.55(\pm 0.06)$	0.999
140206A	$9.02(\pm 2.84) \times 10^{11}$	$0.54(\pm 0.07)$	0.999
140301A	<i>unconstrained</i>	<i>unconstrained</i>	0.00
140419A	$1.85(\pm 1.17) \times 10^{12}$	$0.23(\pm 0.05)$	0.88
141221A	$1.34(\pm 2.82) \times 10^{12}$	$0.24(\pm 0.24)$	0.141
151027A	$1.18(\pm 0.67) \times 10^{12}$	$0.29(\pm 0.06)$	0.941

Note. The observed temperatures kT_{obs} are inferred from fitting with a power-law plus blackbody spectral model. The significance of a blackbody is computed by the maximum likelihood ratio for comparing nested models and its addition improves a fit when the significance is >0.95 . The radii are calculated assuming mildly relativistic motion ($\beta = 0.8$) and isotropic radiation. The GRBs listed in boldface have prominent blackbodies, with radii of the order of $\sim 10^{11}$ – 10^{12} cm. Uncertainties are given at the 1σ confidence level.

We have used the fact that due to relativistic beaming, we observe only a portion of the surface of the emitter defined by

$$\beta \leq \cos \vartheta \leq 1, \quad (15)$$

and we used the definition of Γ given in Section 3. Therefore, inverting Equation (13), the comoving blackbody temperature T_{com} can be computed from the observed blackbody temperature T_{obs} , the source cosmological redshift z , and the emitter Lorentz Gamma factor as follows:

$$T_{\text{com}}(T_{\text{obs}}, z, \Gamma) = \frac{1+z}{\Theta(\beta)\Gamma} T_{\text{obs}}. \quad (16)$$

We can now insert Equation (16) into Equation (10) to obtain

$$F_{\text{bb,obs}} = \frac{R_{\text{com}}^2}{D_L(z)^2} \sigma T_{\text{com}}^4 = \frac{R_{\text{com}}^2}{D_L(z)^2} \sigma \left[\frac{1+z}{\Theta(\beta)\Gamma} T_{\text{obs}} \right]^4. \quad (17)$$

Since the radius R_{lab} of the emitter in the laboratory frame is related to R_{com} by

$$R_{\text{com}} = \Gamma R_{\text{lab}}, \quad (18)$$

we can insert Equation (18) into Equation (17) and obtain

$$F_{\text{bb,obs}} = \frac{(1+z)^4}{\Gamma^2} \left(\frac{R_{\text{lab}}}{D_L(z)} \right)^2 \sigma \left[\frac{T_{\text{obs}}}{\Theta(\beta)} \right]^4. \quad (19)$$

Solving Equation (19) for R_{lab} , we finally obtain the thermal emitter's effective radius in the laboratory frame:

$$R_{\text{lab}} = \Theta(\beta)^2 \Gamma \frac{D_L(z)}{(1+z)^2} \sqrt{\frac{F_{\text{bb,obs}}}{\sigma T_{\text{obs}}^4}} = \Theta(\beta)^2 \Gamma \phi_0, \quad (20)$$

where we have defined ϕ_0 ,

$$\phi_0 \equiv \frac{D_L(z)}{(1+z)^2} \sqrt{\frac{F_{\text{bb,obs}}}{\sigma T_{\text{obs}}^4}}. \quad (21)$$

In astronomy, the quantity ϕ_0 is usually identified with the radius of the emitter. However, in relativistic astrophysics, this identity cannot be straightforwardly applied, because the estimate of the effective emitter radius R_{lab} in Equation (20) crucially depends on the knowledge of its expansion velocity β (and, correspondingly, of Γ).

It must be noted that Equation (20) above gives the correct value of R_{lab} for all values of $0 \leq \beta \leq 1$ by taking all of the relativistic transformations properly into account. In the non-relativistic limit ($\beta \rightarrow 0$, $\Gamma \rightarrow 1$), we have, respectively:

$$\Theta \xrightarrow{\beta \rightarrow 0} 1, \quad \Theta^2 \xrightarrow{\beta \rightarrow 0} 1, \quad (22)$$

$$T_{\text{com}} \xrightarrow{\beta \rightarrow 0} T_{\text{obs}}(1+z), \quad R_{\text{lab}} \xrightarrow{\beta \rightarrow 0} \phi_0, \quad (23)$$

as expected.

9. Implications on the Dynamics of the Flares from Their Thermal Emission

An estimate of the expansion velocity β can be deduced from the ratio between the variation of the emitter effective radius ΔR_{lab} and the emission duration in laboratory frame Δt , i.e.,

$$\beta = \frac{\Delta R_{\text{lab}}}{c \Delta t} = \Theta(\beta)^2 \Gamma (1 - \beta \cos \vartheta) (1+z) \frac{\Delta \phi_0}{c \Delta t_a^d}, \quad (24)$$

where we have used Equation (20) and the relation between Δt and Δt_a^d given in Equation (7). We then have

$$\beta = \Theta(\beta)^2 \frac{1 - \beta \cos \vartheta}{\sqrt{1 - \beta^2}} (1+z) \frac{\Delta \phi_0}{c \Delta t_a^d}, \quad (25)$$

where we used the definition of Γ given in Section 3.

For example, in GRB 081008, we observe a temperature of $T_{\text{obs}} = (0.44 \pm 0.12)$ keV between $t_a^d = 280$ s and $t_a^d = 300$ s (i.e., 20 s before the flare peak time), and a temperature of $T_{\text{obs}} = (0.31 \pm 0.05)$ keV between $t_a^d = 300$ s and $t_a^d = 320$ s

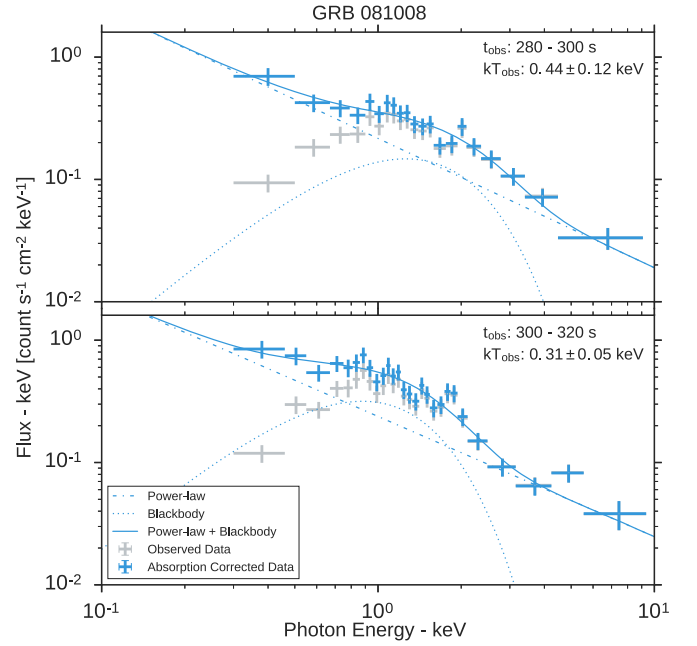


Figure 32. Thermal evolution of GRB 081008 ($z = 1.967$) in the observer frame. The X-ray flare of this GRB peaks at $304(\pm 17)$ s. Upper panel: *Swift*-XRT spectrum from 280 s to 300 s. Lower panel: *Swift*-XRT spectrum from 300 to 320 s. The gray points are the observed data markedly absorbed at low energies, while the blue points are absorption-corrected ones. The data are fit with a combination of power-law (dotted-dashed lines) and blackbody (dotted lines) spectra. The power-law + blackbody spectra are shown as solid curves. Clearly, the temperature decreases with time from ~ 0.44 keV to ~ 0.31 keV, but the ratio of the thermal component goes up from $\sim 20\%$ to $\sim 30\%$. This is a remarkably high percentage of our sample.

Table 8
List of the Physical Quantities Inferred from the Thermal Components Observed During the Flare of GRB 081008

Time Interval	$280 \text{ s} \leq t_a^d \leq 300 \text{ s}$	$300 \text{ s} \leq t_a^d \leq 320 \text{ s}$
T_{obs} (keV)	0.44 ± 0.12	0.31 ± 0.05
ϕ_0 (cm)	$(5.6 \pm 3.2) \times 10^{11}$	$(1.44 \pm 0.48) \times 10^{12}$
$\langle \beta \rangle_{(\cos \vartheta=1)}$	$0.19^{+0.10}_{-0.11}$	$0.42^{+0.10}_{-0.12}$
$\langle \Gamma \rangle$	$1.02^{+0.03}_{-0.02}$	$1.10^{+0.07}_{-0.05}$
R_{lab} (cm)	$(7.1 \pm 4.1) \times 10^{11}$	$(2.34 \pm 0.78) \times 10^{12}$

Note. For each time interval, we summarize the observed temperature T_{obs} , ϕ_0 , the average expansion speed $\langle \beta \rangle$ computed from the beginning up to the upper bound of the considered time interval, and the corresponding average Lorentz factor $\langle \Gamma \rangle$ and laboratory radius R_{lab} .

(i.e., 20 s after the flare peak time, see the corresponding spectra in Figure 32). In these two time intervals, we can infer ϕ_0 , and by solving Equation (25) and taking the errors of $\langle \beta \rangle$ corresponding to the average expansion speed of the emitter from the beginning of its expansion up to the upper bound of the time interval considered. The results so obtained are listed in Table 8. Moreover, we can also compute the value of $\langle \beta \rangle$ between the two time intervals considered above. For $\cos \vartheta = 1$, namely along the line of sight, we obtain $\langle \beta \rangle = 0.90^{+0.06}_{-0.31}$ and $\langle \Gamma \rangle = 2.34^{+1.29}_{-1.10}$. In conclusion, no matter what the details of the approximation adopted, the Lorentz Gamma factor is always moderate, i.e., $\Gamma \lesssim 4$.

10. The Electron–Positron Plasma as the Common Origin of the Prompt Emission and the X-Ray Flares

10.1. Necessity for a New Hydrodynamic Code for $10 \leq B \leq 10^2$

As stated above, there are many different components of BdHNe: following episode 1 of the hypercritical accretion of the SN ejecta onto the NS, the prompt emission occurs with $\Gamma \approx 10^2\text{--}10^3$, which represents the most energetic component accelerated by the e^+e^- plasma; a third component, which encompasses the X-ray flare with $\Gamma \lesssim 4$ and represents only a fraction of $E_{e^+e^-}$ ranging from 2% to 20% (see Figure 31); finally, there are in addition the gamma-ray flare and the late X-ray flares, which will be addressed in a forthcoming publication, as well as the late afterglow phases, which have been already addressed in Pisani et al. (2013, 2016) but whose dynamics will be discussed elsewhere. As already mentioned, for definiteness, we address here the case of X-ray flares.

In Section 3.5, we showed that our model successfully explains the entire prompt emission as originating from the transparency of an initially optically thick e^+e^- plasma with a baryon load $B < 10^{-2}$ reaching $\Gamma \approx 10^2\text{--}10^3$ and the accelerated baryons interacting with the clouds of the CBM. The fundamental equations describing the dynamics of the optically thick plasma, its self-acceleration to ultrarelativistic velocities, and its interaction with the baryon load have been described in Ruffini et al. (1999, 2000). A semi-analytic approximate numerical code was developed, which assumed that the plasma expanded as a shell with a constant thickness in the laboratory frame (the so-called “slab” approximation; see Ruffini et al. 1999). This semi-analytic approximate code was validated by comparing its results with the ones obtained by numerically integrating the complete system of equations for selected values of the initial conditions. It turns out that the semi-analytic code is an excellent approximation to the complete system of equations for $B < 10^{-2}$, which is the relevant regime for the prompt emission, but this approximation is not valid beyond this limit (see Ruffini et al. 1999, 2000 for details).

We examine here the possibility that the energy of the X-ray flare component also originates from a fraction of the e^+e^- plasma energy (see Figure 31) interacting with the much denser medium of the SN ejecta with $10 \lesssim B \lesssim 10^2$. The above-mentioned semi-analytic approximate code cannot be used for this purpose, since it is valid only for $B < 10^{-2}$, and therefore, thanks to the more powerful computers we have at present, we move on here to a new numerical code to integrate the complete system of equations.

We investigate if indeed the dynamics to be expected from an initially pure e^+e^- plasma with a negligible baryon load relativistically expanding in the fireshell model, with an initial Lorentz factor $\Gamma \sim 100$, and then impacting such an SN ejecta can lead, reaching transparency, to the Lorentz factor $\Gamma \lesssim 4$ inferred from the thermal emission observed in the flares (see Tables 7 and 8, and Figure 32).

We have performed hydrodynamical simulations of such a process using the one-dimensional relativistic hydrodynamical (RHD) module included in the freely available PLUTO¹⁷ code (Mignone et al. 2011). In the spherically symmetric case considered here, only the radial coordinate is used and the code integrates partial differential equations with two variables:

radius and time. This permits the study of the evolution of the plasma along one selected radial direction at a time. The code integrates the equations of an ideal relativistic fluid in the absence of gravity, which can be written as follows:

$$\frac{\partial(\rho\Gamma)}{\partial t} + \nabla \cdot (\rho\Gamma\mathbf{v}) = 0, \quad (26)$$

$$\frac{\partial m_r}{\partial t} + \nabla \cdot (m_r\mathbf{v}) + \frac{\partial p}{\partial r} = 0, \quad (27)$$

$$\frac{\partial \mathcal{E}}{\partial t} + \nabla \cdot (\mathbf{m} - \rho\Gamma\mathbf{v}) = 0, \quad (28)$$

where ρ and p are, respectively, the comoving fluid density and pressure, \mathbf{v} is the coordinate velocity in natural units ($c = 1$), $\Gamma = (1 - v^2)^{-\frac{1}{2}}$ is the Lorentz Gamma factor, $\mathbf{m} = h\Gamma^2\mathbf{v}$ is the fluid momentum, m_r its radial component, \mathcal{E} is the internal energy density, and h is the comoving enthalpy density, which is defined by $h = \rho + \epsilon + p$. In this last definition, ϵ is equal to \mathcal{E} measured in the comoving frame. We define \mathcal{E} as follows:

$$\mathcal{E} = h\Gamma^2 - p - \rho\Gamma. \quad (29)$$

The first two terms on the right-hand side of this equation coincide with the T^{00} component of the fluid energy–momentum tensor $T^{\mu\nu}$, and the last one is the mass density in the laboratory frame.

Under the conditions discussed in Appendix B, the plasma satisfies the equation of state of an ideal relativistic gas, which can be expressed in terms of its enthalpy as

$$h = \rho + \frac{\gamma p}{\gamma - 1}, \quad (30)$$

with $\gamma = 4/3$. Fixing this equation of state completely defines the system, leaving the choice of the boundary conditions as the only remaining freedom. To compute the evolution of these quantities in the chosen setup, the code uses the Harten–Lax–van Leer-contact Riemann solver. Time integration is performed by means of a second-order Runge–Kutta algorithm, and a second-order total variation diminishing scheme is used for spatial reconstruction (Mignone et al. 2011). Before each integration step, the grid is updated according to an adaptive mesh refinement algorithm, provided by the CHOMBO library (Colella et al. 2003).

It must be emphasized that the above equations are equivalent (although written in a different form) to the complete system of equations used in Ruffini et al. (1999, 2000). To validate this new numerical code, we compare its results with the ones obtained with the old semi-analytic “slab” approximate code in the domain of its validity (i.e., for $B < 10^{-2}$), finding excellent agreement. As an example, in Figure 33 we show the comparison between the Lorentz Gamma factors computed with the two codes for one particular value of $E_{e^+e^-}$ and B .

We can then conclude that for $B < 10^{-2}$, the new RHD code is consistent with the old semi-analytic “slab” approximate one, which in turn is consistent with the treatment done in Ruffini et al. (1999, 2000). This is not surprising, since we already stated that the above system of equations is equivalent to the one considered in Ruffini et al. (1999, 2000).

Having validated the new RHD code in the region of parameter space where the old semi-analytic one can also be

¹⁷ <http://plutocode.ph.unito.it/>

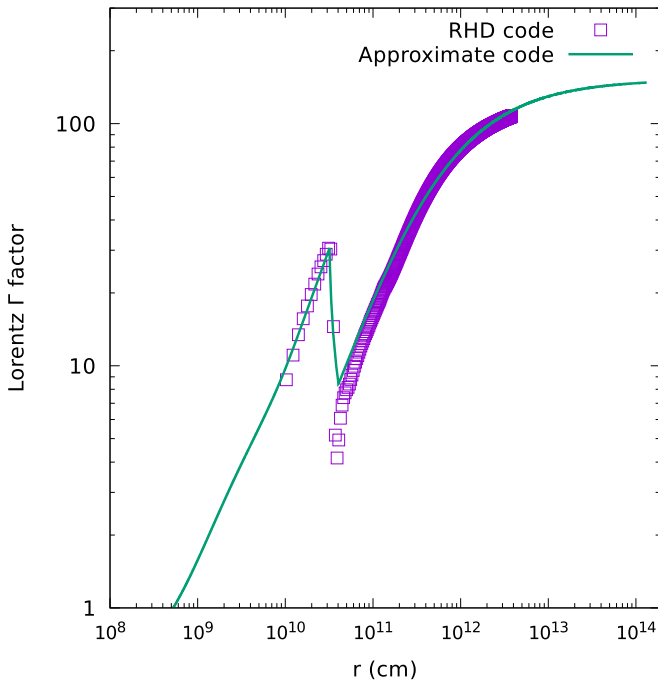


Figure 33. Lorentz Gamma factor computed with the new RHD code compared with the one computed with the old semi-analytic approximate code. This plot is for $E_{e^+e^-} = 1.0 \times 10^{53}$ erg and $B = 6.61 \times 10^{-3}$. Similar agreement is found for other values of $E_{e^+e^-}$ and B as long as $B < 10^{-2}$.

used, we now explore the region of $B > 10^{-2}$, which is relevant for the interaction of the plasma with the SN ejecta.

10.2. Inference from the IGC Scenario for the Ejecta Mass Profile

We start with the shape of the SN ejecta, following the results of the numerical simulations in Becerra et al. (2016).

The first simulations of the IGC process were presented in Fryer et al. (2014) including (1) detailed SN explosions of the CO_{core} obtained from a 1D core-collapse SN code of Los Alamos (Fryer et al. 1999a); (2) the hydrodynamic details of the hypercritical accretion process; and (3) the evolution of the SN ejecta material entering the Bondi–Hoyle region all the way up to its incorporation into the NS in a spherically symmetric approximation. Then, in Becerra et al. (2015), estimates of the angular momentum carried by the SN ejecta and transferred to the NS via accretion were presented. The effects of such angular momentum transfer on the evolution and fate of the system were examined there. These calculations followed the following procedure: first, the accretion rate onto the NS is computed by adopting a homologous expansion of the SN ejecta and introducing the pre-SN density profile of the CO_{core} envelope from numerical simulations. Then, the angular momentum that the SN material might transfer to the NS is estimated: it turns out that the ejecta have enough angular momentum to circularize for a short time and form a disk-like structure around the NS. Then, the evolution of the NS central density and rotation angular velocity is followed by computing the equilibrium configurations from the numerical solution of the axisymmetric Einstein equations in full rotation, until the critical point of collapse of the NS to a BH is reached, accounting for the stability limits given by mass shedding and the secular axisymmetric instability. In Becerra et al. (2016), an

improved simulation of all of the above processes leading to a BdHN was recently presented. In particular:

1. The accretion rate estimate includes the effects of the finite size/thickness of the ejecta density profile.
2. Different CO_{core} progenitors leading to different SN ejecta masses were also considered.
3. The maximum orbital period, P_{max} , up to which the accretion onto the NS companion is high enough to bring it to the critical mass for gravitational collapse to a BH, first estimated in Becerra et al. (2015), was computed for all possible initial values of the mass of the NS companion. Various values of the angular momentum transfer efficiency parameter were also explored there.
4. It was shown there how the presence of the NS companion gives rise to large asymmetries in the SN ejecta. As we show here, such a density of the SN ejecta modified by the presence of the NS companion plays a crucial role in the physical explanation for the occurrence of X-ray flares.
5. The evolution of the SN material and its consequent accretion onto the NS companion is followed via a smoothed-particle-hydrodynamic-like code in which point-like particles describe the SN ejecta. The trajectory of each particle is computed by solving the Newtonian equations of motion including the effects of the gravitational field of the NS on the SN ejecta, including the orbital motion as well as the changes in the NS gravitational mass owing to the accretion process via the Bondi–Hoyle formalism. The initial conditions of the SN are obtained from the Los Alamos core-collapse SN code (Fryer et al. 1999a). The initial power-law density profile of the CO envelope is simulated by populating the inner layers with more particles. The particles crossing the Bondi–Hoyle radius are captured and accreted by the NS so we remove them from the system. We adopted a total number of 16 million particles in this simulation.

For further details, we refer the reader to Becerra et al. (2016) and references therein.

10.3. The Density Profile of the Ejecta and the Reaching of Transparency

We now use the results of a simulation with the following binary parameters: the NS has an initial mass of $2.0 M_{\odot}$; the CO_{core} obtained from a progenitor with a zero-age main-sequence mass $M_{\text{ZAMS}} = 30 M_{\odot}$ leads to a total ejecta mass of $7.94 M_{\odot}$ and follows an approximate power-law profile $\rho_{\text{ej}}^0 \approx 3.1 \times 10^8 (8.3 \times 10^7 / r)^{2.8} \text{ g cm}^{-3}$. The orbital period is $P \approx 5$ minutes, i.e., a binary separation $a \approx 1.5 \times 10^{10} \text{ cm}$. For these parameters, the NS reaches the critical mass and collapses to form a BH.

Figure 34 shows the SN ejecta mass that is enclosed within a cone of 5° of the semi-aperture angle, whose vertex is at the position of the BH at the moment of its formation (see the lower-left panel of Figure 6 in Becerra et al. 2016), and whose axis is along various directions measured counterclockwise with respect to the line of sight. Figure 35 shows instead the cumulative radial mass profiles within a selected number of the aforementioned cones. We can see from these plots how the e^+e^- plasma engulfs different amounts of baryonic mass

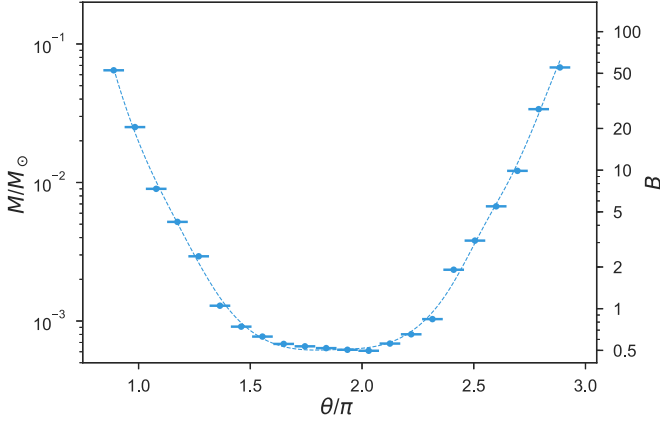


Figure 34. SN ejecta mass enclosed within a cone of 5° of semi-aperture angle, whose vertex is at the position of the BH at the moment of its formation (see the lower-left panel of Figure 6 in Becerra et al. 2016), and whose axis is along various directions measured counterclockwise with respect to the line of sight. The binary parameters of these simulations are the following: the NS has an initial mass of $2.0 M_\odot$; the CO_{core} obtained from a progenitor with a zero-age main-sequence mass $M_{\text{ZAMS}} = 30 M_\odot$ leads to a total ejecta mass $7.94 M_\odot$, and the orbital period is $P \approx 5$ minutes, i.e., a binary separation $a \approx 1.5 \times 10^{10}$ cm. The vertical axis on the right side gives, as an example, the corresponding value of the baryon loading B assuming a plasma energy of $E_{e^+e^-} = 3.16 \times 10^{53}$ erg.

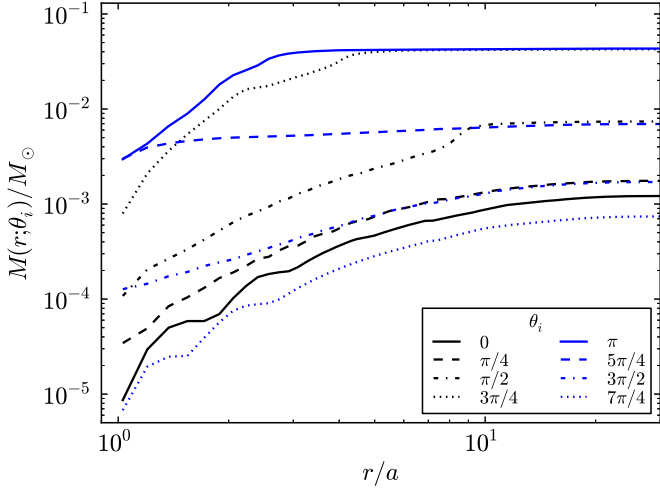


Figure 35. Cumulative radial mass profiles within selected cones among the ones used in Figure 34. We note that the final value for the cumulative mass reached at the end of each direction, namely the value when each curve flattens, is consistent with the total integrated mass value of the corresponding direction shown in Figure 34. The binary parameters of these simulations are the following: the NS has an initial mass of $2.0 M_\odot$; the CO_{core} obtained from a progenitor with a zero-age main-sequence mass $M_{\text{ZAMS}} = 30 M_\odot$ leads to a total ejecta mass $7.94 M_\odot$, and the orbital period is $P \approx 5$ minutes, i.e., a binary separation $a \approx 1.5 \times 10^{10}$ cm.

along different directions due to the asymmetry of the SN ejecta created by the presence of the NS binary companion and the accretion process onto it (see Becerra et al. 2016).

In these calculations, we have chosen initial conditions consistent with those of the BdHNe. At the initial time, the e^+e^- plasma has $E_{e^+e^-} = 3.16 \times 10^{53}$ erg, a negligible baryon load, and is distributed homogeneously within a region of radii on the order of 10^8 – 10^9 cm. The surrounding SN ejecta, whose pressure has been assumed to be negligible, has a mass density

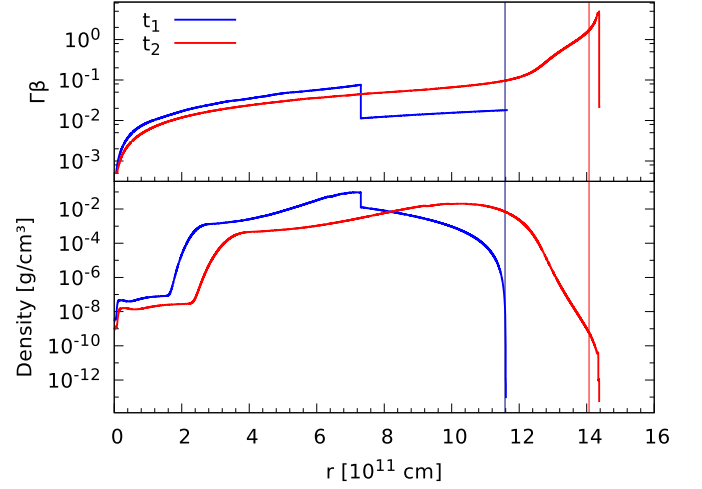


Figure 36. Top panel: distribution of the velocity inside the SN ejecta at the two fixed values of the laboratory times t_1 (before the plasma reaches the external surface of the ejecta) and t_2 (the moment at which the plasma, after having crossed the entire SN ejecta, reaches the external surface). We plotted the quantity $\Gamma\beta$, recalling that we have $\Gamma\beta \sim \beta$ when $\beta < 1$, and $\Gamma\beta \sim \Gamma$ when $\beta \sim 1$. Bottom panel: corresponding distribution of the mass density of the SN ejecta in the laboratory frame ρ_{lab} . These particular profiles are made using a baryon load $B = 200$. The dashed vertical lines corresponds to the two values of the transparency radius R_{ph} ; see Figure 37 and Equation (32). In particular, we see that at t_1 , the shock front has not yet reached R_{ph} and the system is optically thick.

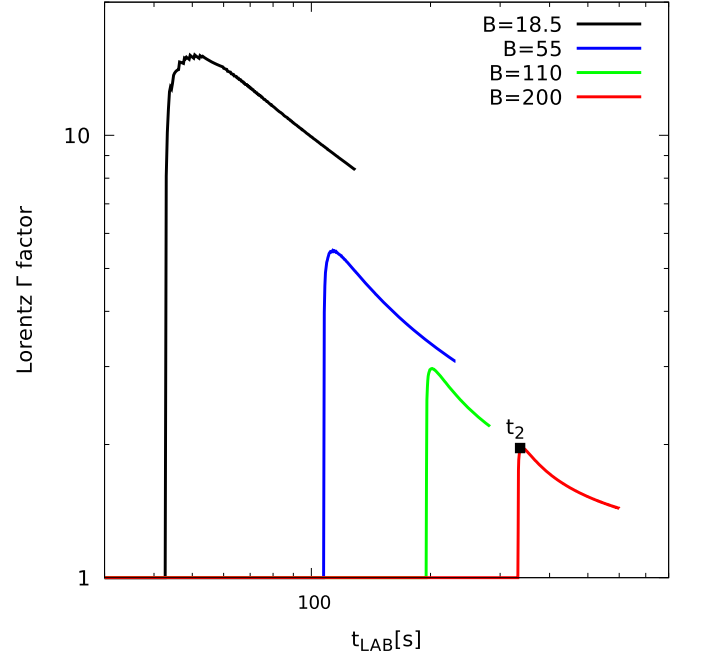


Figure 37. Lorentz Γ factor at the transparency radius R_{ph} as a function of the laboratory time for $E_{e^+e^-} = 3.16 \times 10^{53}$ erg and various selected values of the B parameter. Such B values correspond to the expansion of the e^+e^- plasma along various selected directions inside the remnant (see Figures 34 and 35). Along the red curve, corresponding to $B = 200$, the laboratory time instant t_2 represented in Figure 36 (at t_1 the plasma has not yet reached R_{ph}) is marked. We see that these results are in agreement with the Lorentz Gamma factor $\Gamma \lesssim 4$ inferred from the thermal emission observed in the flare (see Section 9).

radial profile given by

$$\rho \propto (R_0 - r)^\alpha, \quad (31)$$

where the parameters R_0 and α , with $2 < \alpha < 3$, as well as the normalization constant, are chosen to fit the profiles obtained in

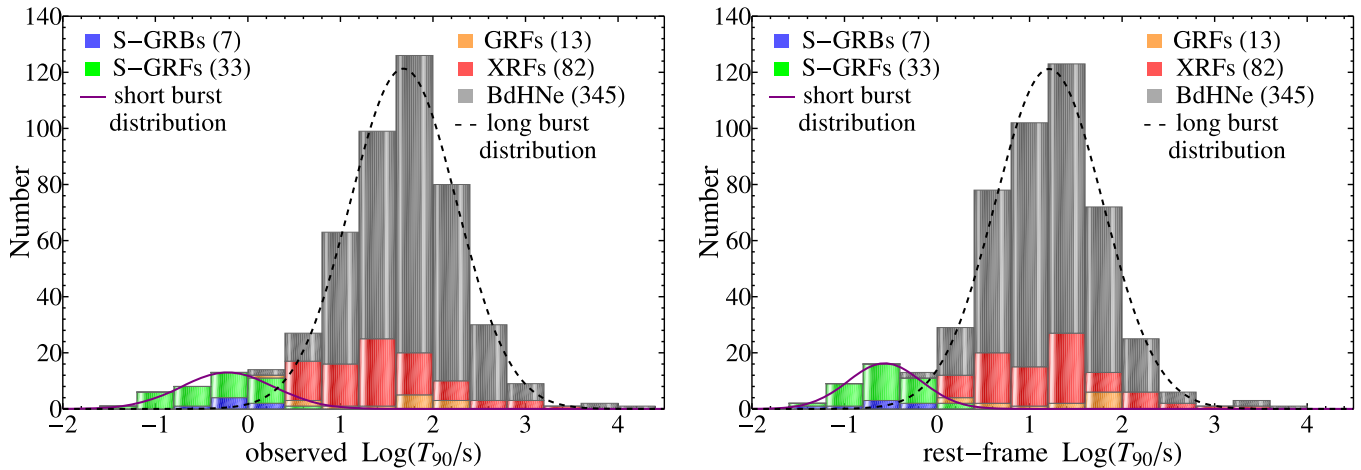


Figure 38. Histograms of T_{90} distributions in the (left panel) observer frame (which is the traditional treatment widely adopted in many previous articles; left panel; see, e.g., Kouveliotou et al. 1993; Bromberg et al. 2013, and references therein) and (right panel) in the cosmological rest frame (which is the approach adopted in the present paper). Both histograms are built using the total number of GRBs with known redshift. The contribution to the total distributions and the number of sources of each subclass are highlighted in the legend (the choice of colors is the same as in Figure 4). The short burst (solid purple curve) and the long burst (dashed black curve) distributions are also shown. In the observer frame, we obtain $T_{90}^{\text{short}} = 0.60_{-0.41}^{+1.31}$ s and $T_{90}^{\text{long}} = 48_{-35}^{+133}$ s; in the cosmological rest frame, we have $T_{90}^{\text{short}} = 0.27_{-0.16}^{+0.41}$ s and $T_{90}^{\text{long}} = 16_{-12}^{+46}$ s. The T_{90} value discriminating between short and long bursts shifts from ≈ 2 s in the observer frame to ≈ 0.75 s in the cosmological rest frame. The existence of BdHNe with $T_{90} \gtrsim 10^2$ s indicates the origin of the possible contamination between the prompt emission spikes and the X-ray flares, which is indeed observed in some cases (see Section 4 for details).

Becerra et al. (2016) and represented in Figure 35. The initial radial velocity is taken to be $v_r \propto r$ in order to reproduce the homologous expansion of the SN ejecta before its interaction with the plasma. Every choice of these parameters corresponds to studying the evolution along a single given direction.

The evolution from these initial conditions leads to the formation of a shock and to its subsequent expansion until reaching the outermost part of the SN. In Figure 36, we show the radial distribution profiles of the velocity and mass density ρ_{lab} in the laboratory frame inside the SN ejecta as a function of r for $B = 200$ at two selected values of the laboratory time. The velocity distribution peaks at the shock front (with a Lorentz Gamma factor $\Gamma \lesssim 4$), and behind the front it forms a broad tail of accelerated material with $0.1 \lesssim \beta \lesssim 1$.

Figure 37 shows the Lorentz Γ factor at the transparency radius R_{ph} , namely the radius at which the optical depth τ , calculated from the observer’s line of sight, is equal to 1. If we assume a constant cross-section, τ becomes Lorentz invariant, and therefore we can compute it in laboratory coordinates in the following way:

$$\tau = \int_{R_{\text{ph}}}^{\infty} dr \sigma_T n_e(r), \quad (32)$$

where $\sigma_T = 6.65 \times 10^{-25} \text{ cm}^2$ is the Thomson cross-section, and the electron density is related to the baryon mass density by means of the formula $n_e = \rho \Gamma / m_p$, where m_p is the proton mass, the mass of the electrons and positrons is considered to be negligible with respect to that of the baryons, and we have assumed one electron per nucleon on average. The values of Γ at $r = R_{\text{ph}}$ computed in this way are shown in Figure 37, as a function of the time measured in the laboratory frame, for several values of $B > 10^{-2}$ corresponding to the expansion of the e^+e^- plasma along several different directions inside the SN ejecta (see Figures 34 and 35).

We conclude that the relativistic expansion of an initially pure e^+e^- plasma (see Figure 33), interacting with an SN ejecta

with the above-described induced asymmetries (see Figures 39–40), leads to the formation of a shock that reaches the outermost part of the ejecta with Lorentz Gamma factors at the transparency radius $\Gamma(R_{\text{ph}}) \lesssim 4$. This is in striking agreement with the one inferred from the thermal component observed in the flares (see Section 9). The spacetime diagram of the global scenario is represented in Figure 39. Clearly in this approach neither ultrarelativistic jetted emission nor synchrotron or inverse-Compton processes play any role.

11. Summary, Conclusions and Perspectives

11.1. Summary

In the last 25 years, the number of observed GRBs has exponentially increased, thanks to unprecedented technological developments in all ranges of wavelengths, going from the X-ray to the gamma-ray, to GeV radiation as well as to the radio and the optical. In spite of this progress, the traditional GRB approach has continued to follow the paradigm of a single system (the “collapsar” paradigm; see Woosley 1993), where accretion onto an already formed BH occurs (see, e.g., Piran 2004 and references therein). Following the fireball model, synchrotron and inverse-Compton emission processes, related to an ultrarelativistic jetted emission described by the Blandford & McKee (1976) solution, have been assumed to occur (see, e.g., Troja et al. 2015 for one of the latest example where this approach is further extended to the GeV emission component). The quest for a “standard” GRB model has been pursued even recently (see, e.g., Chincarini et al. 2007; Margutti et al. 2010), ignoring differences among GRB subclasses and/or neglecting all relativistic corrections in the time parameterizations presented in Section 3. Under these conditions, it is not surprising that the correlations we have found here have been missed.

It is appropriate to recall that a “standard” GRB energy of 10^{51} erg (Frail et al. 2001) was considered, assuming the collimation of GRBs and the existence of a light-curve break in

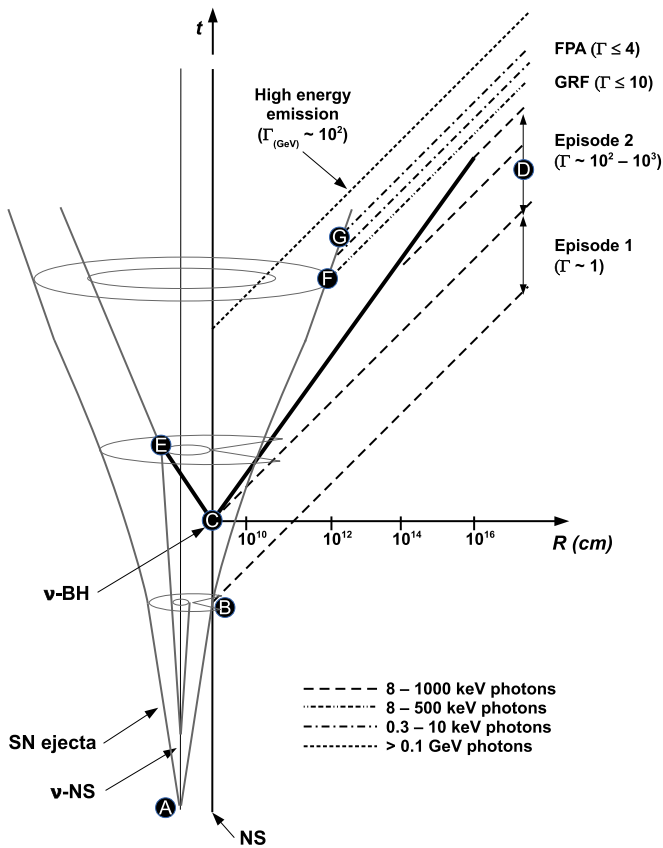


Figure 39. Spacetime diagram (not to scale) of a BdHN. The CO_{core} explodes as an SN at point A and forms a new NS (νNS). The companion NS (bottom-right line) accretes the SN ejecta starting from point B, giving rise to the non-relativistic episode 1 emission (with Lorentz factor $\Gamma \approx 1$). At point C, the NS companion collapses into a BH, and an e^+e^- plasma—the dyadosphere—is formed (Ruffini et al. 1999). The following self-acceleration process occurs in a spherically symmetric manner (thick black lines). A large portion of plasma propagates in the direction of the line of sight, where the environment is cleared by the previous accretion into the NS companion, finding a baryon load $B \lesssim 10^{-2}$ and leading to the GRB prompt gamma-ray spikes (GRSs; episode 2, point D) with $\Gamma \sim 10^2\text{--}10^3$. The remaining part of the plasma impacts the high-density portion of the SN ejecta (point E), propagates inside the ejecta encountering a baryon load $B \sim 10^1\text{--}10^2$, and finally reaches transparency, leading to the gamma-ray flare emission (point F) in gamma-rays with an effective Lorentz factor $\Gamma \lesssim 10$ and to the FPA emission (point G) corresponding to the X-ray flares with an effective $\Gamma \lesssim 4$ (see Sections 9 and 10). In the meantime, accretion over the newly formed BH produces the high-energy GeV emission with $\Gamma \sim 10^2$. For simplicity, this diagram is 2D and static and does not attempt to show the 3D rotation of the ejecta.

the GRB afterglows. This possibility followed from the traditional approach expecting the ultrarelativistic component to extend all the way from the prompt emission to the last phases of the afterglow (Mao & Yi 1994; Panaitescu & Mészáros 1999; Sari et al. 1999). This “traditional” approach to GRBs has appeared in a large number of papers over recent decades and is well summarized in a series of review papers (see, e.g., Piran 1999, 2004; Mészáros 2002, 2006; Berger 2014; Kumar & Zhang 2015), which are disproved by the data presented here in which the upper limit for the Lorentz factor $\Gamma \lesssim 4$ is established in the FPA phase.

Since 2001, we have followed an alternative approach, introducing three paradigms: the spacetime parametrization of GRBs (Ruffini et al. 2001a), the field equations of the prompt emission phase (Ruffini et al. 2002), and the IGC paradigm

(Rueda & Ruffini 2012; Penacchioni et al. 2013; Ruffini et al. 2015c); see Section 3. Since then,

(a) we have demonstrated that all GRBs originate in binary systems: the short GRBs in binary NSs or in binaries composed of an NS and a BH (Fryer et al. 2015; Ruffini et al. 2016b); the long GRBs in binary systems composed of CO_{core} and a NS, or alternatively a BH and a CO_{core} , or also a white dwarf and an NS;

(b) we have divided GRBs into seven different subclasses (Ruffini et al. 2016b), each characterized by specific signatures in their spectra and luminosities in the various energy bands;

(c) we have addressed the new physical and astrophysical processes in the ultrarelativistic regimes made possible by the vast amount of gravitational and rotational energies in such binaries.

As we recalled in Sections 1–3, we have confirmed the binary nature of the GRB progenitors (see, e.g., Fryer et al. 2014, 2015; Becerra et al. 2015, 2016; Ruffini et al. 2016a; Aimuratov et al. 2017). We have obtained the first evidence of the formation of a BH in the hypercritical accretion process of the SN ejecta onto the binary NS companion: the BdHN (Ruffini et al. 2014, 2015c, 2016b), which is clearly different from the single-star collapsar model. Finally, in this paper, we have addressed the interaction that occurs in a BdHN of the GRB on the SN ejecta considered as the origin of the X-ray flares. We use this process and the mildly relativistic region in which it occurs as a discriminant between the traditional approach and our binary system approach: we use the X-ray flare properties as a discriminant between our BdHN and the “fireball” GRB models.

11.2. Conclusions

We have reached three major results.

(1) We have searched X-ray flares in all GRBs and identified 16 of them with excellent data. After examining the seven GRB subclasses (Ruffini et al. 2016b), we conclude that they all occur in BdHNe, and no X-ray flares are observed in other GRB sources. This indicates a link between the occurrence of the flare and the formation of a black hole in long GRBs. In Section 4, we have shown how the previously proposed association of X-ray flares with the short GRBs 050724 and 050709 has been superseded.

By a statistical analysis, we correlate the time of occurrence of their peak luminosity in the cosmological rest frame, their duration, their energy, and their X-ray luminosity to the corresponding GRB E_{iso} . We also correlate the energy of the FPA phase, E_{FPA} , as well as the relative ratio $E_{\text{FPA}}/E_{\text{iso}}$, to E_{iso} .

(2) Using the data from the associated thermal emission, the relativistic relation between the comoving time, the arrival time at the detector, and the cosmological and Doppler corrections, we determine the thermal emitter effective radii as a function of the rest-frame time. We determine the expansion velocity of the emitter β as the ratio between the variation of the emitter effective radius ΔR_{lab} and the emission duration in laboratory time; see Equation (25). We obtain a radius of 10^{12} cm for the effective radius of the emitter, moving with $\Gamma \lesssim 4$ at a time ~ 100 s in the rest frame (see Table 8). These results show the clear rupture between the processes in the prompt emission phase, occurring prior to the flares at radii of the order of 10^{16} cm and $\Gamma = 10^2\text{--}10^3$, and the ones in the X-ray flares.

(3) We have modeled the X-ray flares by considering the impact of the GRB on the SN ejecta, introducing a new set of

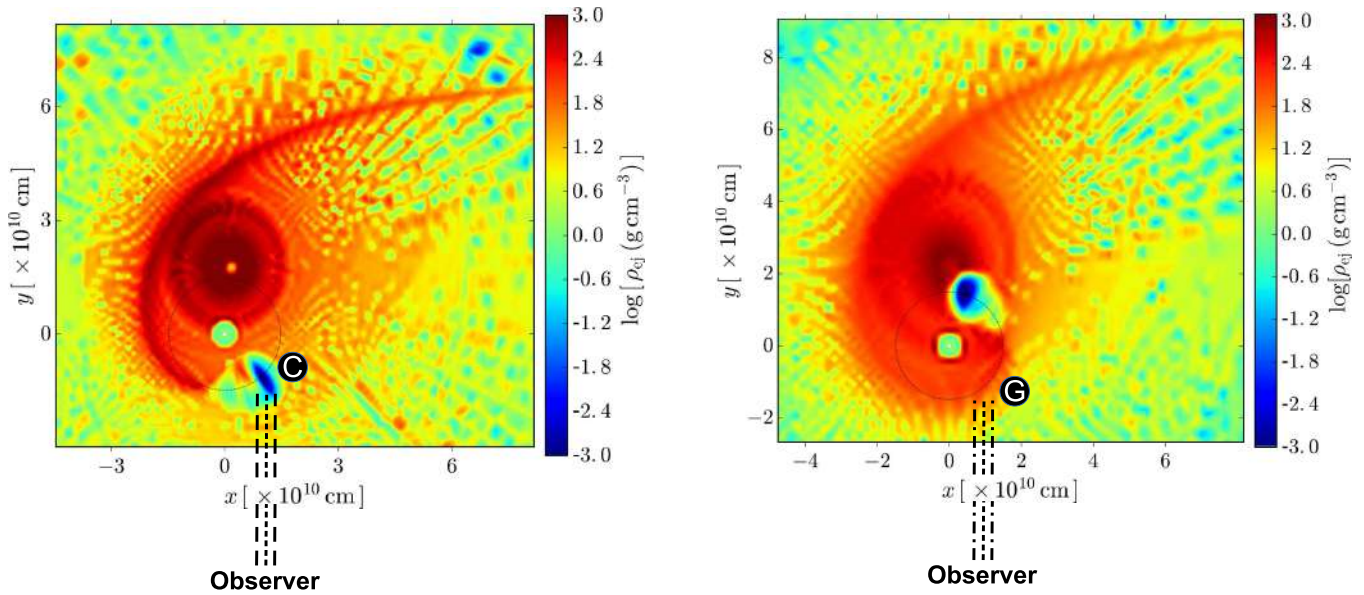


Figure 40. Two snapshots of the distribution of matter in the equatorial plane of the progenitor’s binary system. The one on the right side corresponds to point C, when the BH is formed and a large portion of the e^+e^- plasma starts to self-accelerate in a low-density environment ($B \lesssim 10^{-2}$) toward the observer producing the GRB prompt emission. The one on the left side corresponds to point G, when the remaining part of the plasma, after propagating inside the high-density SN ejecta ($B \sim 10^2\text{--}10^3$), reaches transparency and produces the FPA emission in the X-rays, which is directed toward the observer due to the rotation of the ejecta in the equatorial plane. The simulations of the matter distributions in the three snapshots are from Becerra et al. (2016).

relativistic hydrodynamic equations for the expansion of the optically thick e^+e^- plasma into a medium with baryon load in the range $10\text{--}10^2$. The matter density and velocity profiles of the ejecta are obtained from the 1D core-collapse code developed at Los Alamos (Fryer et al. 1999a). With this we generate the initial conditions for our smoothed-particle-hydrodynamics-like simulation (Becerra et al. 2016), which follows the evolution of the ejecta matter and the accretion rate at the position of the Bondi–Hoyle surface of the NS binary companion. In our simulations, we have adopted 16 million particles (see Section 10 for further details). We start the simulation of the interaction of the e^+e^- plasma with such ejecta at 10^{10} cm and continue all the way to 10^{12} cm, where transparency is reached. We found full agreement between the radius of the emitter at transparency and the one derived from the observations, as well as between the time of the peak energy emission and the observed time of arrival of the flare, derived following Equation (2) using the computed Lorentz Γ factor of the world line of the process.

We can now conclude the following.

The existence of such mildly relativistic Lorentz Gamma factors in the FPA phase rules out the traditional GRB model, including the claims of the existence of GRB beaming, collimation, and break in the luminosity (see, e.g., Piran 1999, 2004; Frail et al. 2001; Mészáros 2002, 2006; Berger 2014; Kumar & Zhang 2015). In these models, the common underlying assumption is the existence of a single ultrarelativistic component extending from the prompt radiation, through the FPA phase, all the way to the late afterglow and to the GeV emission, assuming a common dynamics solely described by the Blandford & McKee (1976) solution; see, however, Bianco & Ruffini (2005b, 2006). These assumptions were made without ever looking for observational support. It is not surprising that all GRB models in the current literature purport the existence of an ultrarelativistic Lorentz Gamma factor extending into the afterglow, among many others; see, e.g., Jin et al. (2010) and Yi et al. (2015). All these claims have

been disproven by the present article, where a drastic break from ultrarelativistic physics with $\Gamma \sim 10^2\text{--}10^3$, occurring in the prompt emission, is already indicated at times ~ 100 s, when the Lorentz Gamma factor is limited to $\Gamma \lesssim 4$.

In our approach, a multi-episode structure for each GRB is necessary. Each episode, being characterized by a different physical process, leads to a different world line with a specific Lorentz Gamma factor at each event. The knowledge of the world line is essential, following Equation (2) in Section 3, to compute the arrival time of the signals in the observer frame and to compare it with the observations. This procedure, previously routinely adopted in the prompt emission phase of a BdHN, has for the first time been introduced here for X-ray flares. As a byproduct, we have confirmed both the binarity and the nature of the progenitors of the BdHNe, composed of a CO_{core} undergoing an SN explosion and accreting onto a close-by binary NS, and the impact of the GRB on the hypernova ejecta.

11.3. Perspectives

Far from representing solely a criticism of the traditional approach, in this paper, (1) we exemplify new procedures in data analysis—see Sections 4 to 7, (2) we open up the topic to an alternative style of conceptual analysis which adopts procedures well-tested in high-energy physics and not yet appreciated in the astrophysical community—see Sections 8–10, and (3) we introduce new tools for simulation techniques affordable with present-day large computer facilities—see figures in Section 11, which, if properly guided by a correct theoretical understanding, can be particularly helpful in the visualization of these phenomena.

We give three specific examples of our new approach and indicate as well, when necessary, some disagreements with current approaches:

- (A) The first step in any research on GRBs is to represent the histogram of T_{90} for the GRB subclasses. We report in

Figure 38 the T_{90} values for all of the GRB subclasses we have introduced (see Ruffini et al. 2016b). The values reported are both in the observer frame (left panel; see, e.g., Kouveliotou et al. 1993; Bromberg et al. 2013) and properly converted to the cosmological rest frame of the sources (right panel). The large majority of papers on GRBs have been neglecting the cosmological corrections and subdivision in the subclasses, making impossible the comparison of T_{90} among different GRBs (see, e.g., Falcone et al. 2007; Chincarini et al. 2010).

- (B) For the first time, we present a simplified spacetime diagram of BdHNe (see Figure 39). This spacetime diagram emphasizes the many different emission episodes, each one with distinct corresponding Lorentz Gamma factors and consequently leading through Equation (2) to a specific value of their distinct times of occurrence in the cosmological rest frame of the GRB (see Figure 39). In all episodes we analyzed for the X-ray flares, and more generally for the entire FPA phase, there is no need for collapsar-related concepts. Nevertheless, in view of the richness of the new scenario in Figure 39, we have been examining the possibility that such concepts can play a role in additional episodes, either in BdHNe or in any of the additional six GRB subclasses, e.g., in S-GRBs. These results are being submitted for publication. The use of spacetime diagrams in the description of GRBs is indeed essential in order to illustrate the causal relation between the source in each episode, the place of occurrence, and the time at detection. Those procedures have been introduced long ago in the study of high-energy particle physics processes and codified in textbooks. Our group, since the basic papers (Ruffini et al. 2001a, 2001b, 2001c), has widely shared these spacetime formulations (see, e.g., in Taylor & Wheeler 1992) and also extended the concept of the quantum S-Matrix (Wheeler 1937; Heisenberg 1943) to the classic astrophysical regime of the many components of a BdHN, introducing the concept of the cosmic matrix (Ruffini et al. 2015c). The majority of astrophysicists today make wide use of the results of nuclear physics in the study of stellar evolution (Bethe 1991) and also of Fermi statistics in general relativity (Oppenheimer & Volkoff 1939). They have not yet been ready, however, to approach these additional concepts more typical of relativistic astrophysics and relativistic field theories, which are necessary for the study of GRBs and active galactic nuclei.
- (C) The visual representation of our result (see Figure 40) has been made possible thanks to the simulations of SN explosions with the core-collapse SN code developed at Los Alamos (see, e.g., Fryer et al. 1999a, 2014; Frey et al. 2013), the smoothed-particle-hydrodynamics-like simulations of the evolution of the SN ejecta accounting for the presence of an NS companion (Ruffini et al. 2016b), and the possibility of varying the parameters of the NS, of the SN, and of the distance between the two to explore all possibilities (Becerra et al. 2015; Ruffini et al. 2016b). We recall that these signals occur in each galaxy every \sim hundred million years, but with their luminosity of $\sim 10^{54}$ erg, they can be detected in all 10^9 galaxies. The product of these two factors gives the “once per day” rate. They are not visualizable in any other way, but analyzing

the spectra and time of arrival of the photons now, and simulating these data on the computer, we see that they indeed already occurred billions of years ago in our past light cone, and they are revived by scientific procedures today.

We are happy to acknowledge fruitful discussions with Fulvio Melia, Tsvi Piran, and Bing Zhang in our attempt to make these new results clearer for a broader audience, and with Roy Kerr on the implication of the GRB GeV emission for the Kerr–Newman solution. We also thank the second referee for important suggestions. We acknowledge the continuous support of the MAECI. This work made use of data supplied by the UK *Swift* Science Data Center at the University of Leicester. M.Ka. and Y.A. are supported by the Erasmus Mundus Joint Doctorate Program Grant N. 2014–0707 from EACEA of the European Commission. M.M. and J.A.R. acknowledge the partial support of the project N 3101/GF4 IPC-11 and the target program F.0679 0073-6/PTsF of the Ministry of Education and Science of the Republic of Kazakhstan.

Appendix A The Complete List of BdHNe

We present here in Table 9 the complete list of the 345 BdHNe observed through the end of 2016, which includes the 161 BdHNe already presented in Pisani et al. (2016).

Appendix B Parameters of the Equation of State

We give here details concerning the determination of the value of the index γ and verify the accuracy of our assumption $\gamma = 4/3$ adopted in the equation of state of the plasma (30). This index is defined as

$$\gamma \equiv 1 + \frac{p}{\epsilon}. \quad (33)$$

The total internal energy density and pressure are computed as

$$\epsilon = \epsilon_{e^-} + \epsilon_{e^+} + \epsilon_{\gamma} + \epsilon_B \quad (34)$$

$$p = p_{e^-} + p_{e^+} + p_{\gamma} + p_B, \quad (35)$$

where the subscript B indicates the contributions of the baryons in the fluid. The number and energy densities, as well as the pressure of the different particles, can be computed in natural units ($c = \hbar = k_B = 1$) using the following expressions (see, e.g., Landau & Lifshitz 1980):

$$n_{e^-} = A T^3 \int_0^\infty f(z, T, m_e, \mu_{e^-}) z^2 dz \quad (36)$$

$$n_{e^+} = A T^3 \int_0^\infty f(z, T, m_e, \mu_{e^+}) z^2 dz \quad (37)$$

$$\begin{aligned} \epsilon_{e^-} = A T^4 \int_0^\infty f(z, T, m_e, \mu_{e^-}) \\ \times \sqrt{z^2 + (m_e/T)^2} z^2 dz - m_e n_{e^-} \end{aligned} \quad (38)$$

$$\begin{aligned} \epsilon_{e^+} = A T^4 \int_0^\infty f(z, T, m_e, \mu_{e^+}) \\ \times \sqrt{z^2 + (m_e/T)^2} z^2 dz - m_e n_{e^+} \end{aligned} \quad (39)$$

Table 9
List of the BdHNe Considered in This Work

GRB	z	E_{iso}^a	LX ^b	Early Flare ^c	UL ^d	T_{90}^e	Instrument ^f	Reference ^g
970228	0.695	1.65 ± 0.16				80	B-SAX	(1)
970828	0.958	30.4 ± 3.6				90	BATSE	(2)
971214	3.42	22.1 ± 2.7				40	BATSE	IAUC 6789
980329	3.5	267 ± 53				54	B-SAX	(3)
980703	0.966	7.42 ± 0.74				400	BATSE	GCN 143
990123	1.6	241 ± 39				63.3	BATSE	GCN 224
990506	1.3	98.1 ± 9.9				131.33	BATSE	GCN 306
990510	1.619	18.1 ± 2.7				75	BATSE	GCN 322
990705	0.842	18.7 ± 2.7				42	B-SAX	(4)
991208	0.706	23.0 ± 2.3				68	Ulysses	(5)

Notes. It is composed of 345 sources spanning 12 years of *Swift*/XRT observation activity. In the table, we report important observational features: the redshift z , the isotropic energy E_{iso} , the observing instrument in the gamma-ray band, and the corresponding reference from which we take the gamma-ray spectral parameters in order to estimate E_{iso} .

^a In units of 10^{52} erg.

^b “LX” marks the sources with *Swift*/XRT data observed up to times larger than 10^4 s in the rest frame after the initial explosion.

^c “C” and “E” mark the sources showing an early flare in *Swift*/XRT, and they stand for “confirmed” and “excluded,” respectively. The 16 “C” sources compose the sample considered in the present paper.

^d “UL” stands for ultralong, indicating sources with $T_{90} \gtrsim 1000$ s.

^e Observed T_{90} (s).

^f “B-SAX” stands for *BeppoSAX*/GRBM; “BATSE” stands for *Compton-GRO*/BATSE; “Ulysses” stands for *Ulysses*/GRB; “KW” stands for *Konus/WIND*; “HETE” stands for *HETE-2*/FREGATE; “*Swift*” stands for *Swift*/BAT; “*Fermi*” stands for *Fermi*/GBM.

^g (1) Frontera et al. (1998), (2) Ruffini et al. (2015a), (3) in ’t Zand et al. (1998), (4) Amati et al. (2000), (5) Hurley et al. (2000), (6) in ’t Zand et al. (2001), (7) Barraud et al. (2003), (8) Shirasaki et al. (2008), (9) Cenko et al. (2006).

(This table is available in its entirety in machine-readable form.)

$$p_{e^-} = A \frac{T^4}{3} \int_0^\infty f(z, T, m_e, \mu_{e^-}) \frac{z^4}{\sqrt{z^2 + (m_e/T)^2}} dz \quad (40)$$

$$p_{e^+} = A \frac{T^4}{3} \int_0^\infty f(z, T, m_e, \mu_{e^+}) \frac{z^4}{\sqrt{z^2 + (m_e/T)^2}} dz \quad (41)$$

$$\epsilon_\gamma = a T^4 \quad (42)$$

$$p_\gamma = \frac{a T^4}{3} \quad (43)$$

$$\epsilon_B = \frac{3}{2} n_N T \quad (44)$$

$$p_B = n_N T, \quad (45)$$

where

$$f(z, T, m, \mu) = \frac{1}{e^{\sqrt{z^2 + (m/T)^2} - \mu/T} + 1} \quad (46)$$

is the Fermi–Dirac distribution, m_e is the electron mass, n_N the nuclei number density, $a = 8\pi^5 k_B^4 / 15h^3 c^3 = 7.5657 \times 10^{-15}$ erg cm⁻³ K⁻⁴ the radiation constant, and $A = 15a/\pi^4$. If the pair annihilation rate is zero, i.e., if the reaction $e^- + e^+ \rightleftharpoons 2\gamma$ is in equilibrium, then the equality $\mu_{e^-} = -\mu_{e^+} \equiv \mu$ holds, since the equilibrium photons have zero chemical potential. Besides, charge neutrality implies that the difference in the number of electrons and positrons is equal to the number of protons in the baryonic matter, which can be expressed as

$$n_{e^-}(\mu, T) - n_{e^+}(\mu, T) = Z n_B, \quad (47)$$

where n_B is the baryon number density and $1/2 < Z < 1$ is the average number of electrons per nucleon. The number density

n_B is related to the other quantities as

$$\rho = m_p n_B + m_e (n_{e^-} + n_{e^+}), \quad (48)$$










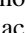
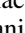
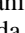
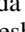
where m_p is the proton mass. If the baryons are only protons, then $Z = 1$ and $n_N = n_B$. Together with Equation (47), this completely defines the mass density as a function of (μ, T) . The equation of state that relates the pressure with the mass and internal energy densities is thus defined implicitly as the parametric surface

$$\{(\rho(\mu, T), \epsilon(\mu, T), p(\mu, T)) : T > 0, \mu \geq 0\} \quad (49)$$

that satisfies all of the above relations.

In the cases relevant for the simulations performed in Section 10, we indeed have that the index γ in the equation of state of the plasma, Equation (30), satisfies $\gamma = 4/3$ with a maximum error of 0.2%.

ORCID iDs

R. Ruffini  <https://orcid.org/0000-0003-0829-8318>
Y. Wang  <https://orcid.org/0000-0001-7959-3387>
Y. Aimuratov  <https://orcid.org/0000-0001-5717-6523>
U. Barres de Almeida  <https://orcid.org/0000-0001-7909-588X>
C. L. Bianco  <https://orcid.org/0000-0001-7749-4078>
Y. C. Chen  <https://orcid.org/0000-0002-7543-2727>
M. Kovacevic  <https://orcid.org/0000-0003-4928-4510>
R. Moradi  <https://orcid.org/0000-0002-2516-5894>
M. Muccino  <https://orcid.org/0000-0002-2234-9225>
A. V. Penacchioni  <https://orcid.org/0000-0001-7816-3668>
G. B. Pisani  <https://orcid.org/0000-0003-3452-2491>
J. A. Rueda  <https://orcid.org/0000-0003-4904-0014>
G. V. Vereshchagin  <https://orcid.org/0000-0002-1623-3576>

References

Aimuratov, Y., Ruffini, R., Muccino, M., et al. 2017, *ApJ*, **844**, 83
Aksenov, A. G., Ruffini, R., & Vereshchagin, G. V. 2007, *PhRvL*, **99**, 125003

- Amati, L., & Della Valle, M. 2013, *IJMPD*, **22**, 30028
- Amati, L., Frontera, F., Vietri, M., et al. 2000, *Sci*, **290**, 953
- Atwood, W. B., Abdo, A. A., Ackermann, M., et al. 2009, *ApJ*, **697**, 1071
- Barraud, C., Olive, J.-F., Lestrade, J. P., et al. 2003, *A&A*, **400**, 1021
- Barthelmy, S. D., Baumgartner, W. H., Cummings, J. R., et al. 2013, GCN, **15456**, 1
- Barthelmy, S. D., Chincarini, G., Burrows, D. N., et al. 2005, *Natur*, **438**, 994
- Baumgartner, W. H., Barthelmy, S. D., Cummings, J. R., et al. 2014, GCN, **16127**, 1
- Becerra, L., Bianco, C. L., Fryer, C. L., Rueda, J. A., & Ruffini, R. 2016, *ApJ*, **833**, 107
- Becerra, L., Cipolletta, F., Fryer, C. L., Rueda, J. A., & Ruffini, R. 2015, *ApJ*, **812**, 100
- Berger, E. 2014, *ARA&A*, **52**, 43
- Bernardini, M. G., Bianco, C. L., Chardonnet, P., et al. 2005, *ApJL*, **634**, L29
- Bethe, H. A. 1991, *The Road from LOS Alamos* (Melville, NY: AIP)
- Bianco, C. L., & Ruffini, R. 2004, *ApJL*, **605**, L1
- Bianco, C. L., & Ruffini, R. 2005a, *ApJL*, **620**, L23
- Bianco, C. L., & Ruffini, R. 2005b, *ApJL*, **633**, L13
- Bianco, C. L., & Ruffini, R. 2006, *ApJL*, **644**, L105
- Bianco, C. L., Ruffini, R., & Xue, S.-S. 2001, *A&A*, **368**, 377
- Blandford, R. D., & McKee, C. F. 1976, *PhFl*, **19**, 1130
- Bloom, J. S., Frail, D. A., & Sari, R. 2001, *AJ*, **121**, 2879
- Bromberg, O., Nakar, E., Piran, T., & Sari, R. 2013, *ApJ*, **764**, 179
- Butler, N., Ricker, G., Atteia, J.-L., et al. 2005, GCN, **3570**, 1
- Caito, L., Amati, L., Bernardini, M. G., et al. 2010, *A&A*, **521**, A80
- Caito, L., Bernardini, M. G., Bianco, C. L., et al. 2009, *A&A*, **498**, 501
- Calderone, G., Ghirlanda, G., Ghisellini, G., et al. 2015, *MNRAS*, **448**, 403
- Cavallaro, G., & Rees, M. J. 1978, *MNRAS*, **183**, 359
- Cenko, S. B., Kasliwal, M., Harrison, F. A., et al. 2006, *ApJ*, **652**, 490
- Cherubini, C., Giralico, A., Rueda, H. J. A., & Ruffini, R. 2009, *PhRvD*, **79**, 124002
- Chester, M. M., Wang, X. Y., Cummings, J. R., et al. 2008, in AIP Conf. Ser. 1000, *Gamma-Ray Bursts 2007*, ed. M. Galassi, D. Palmer, & E. Fenimore (Melville, NY: AIP), **421**
- Chincarini, G., Mao, J., Margutti, R., et al. 2010, *MNRAS*, **406**, 2113
- Chincarini, G., Moretti, A., Romano, P., et al. 2007, *ApJ*, **671**, 1903
- Cleveland, W., & Devlin, S. 1988, *J. Am. Stat. Assoc.*, **83**, 596
- Cline, T. L., Desai, U. D., Trainor, J., et al. 1979, *ApJL*, **229**, L47
- Cobb, B. E. 2007, GCN, **6296**, 1
- Colaella, P., Graves, D. T., Johnson, J. N., et al. 2003, Chombo Software Package for AMR Applications Design Document, Tech. Rep. LBNL-6615E
- Colgate, S. A. 1971, *ApJ*, **163**, 221
- Costa, E., Frontera, F., Heise, J., et al. 1997, *Natur*, **387**, 783
- Cummings, J. R., Barthelmy, S. D., Burrows, D. N., et al. 2007, GCN, **6210**, 1
- Dai, Z. G., Wang, X. Y., Wu, X. F., & Zhang, B. 2006, *Sci*, **311**, 1127
- Damour, T., & Ruffini, R. 1975, *PhRvL*, **35**, 463
- D'Avanzo, P., D'Elia, V., & Covino, S. 2008, GCN, **8350**, 1
- de Pasquale, M., Piro, L., Gendre, B., et al. 2006, *A&A*, **455**, 813
- de Ugarte Postigo, A., Fynbo, J. P. U., Thöne, C. C., et al. 2012, *A&A*, **548**, A11
- Della Valle, M. 2011, *IJMPD*, **20**, 1745
- Dezalay, J.-P., Barat, C., Talon, R., et al. 1992, in AIP Conf. Ser. 265, *Gamma-Ray Bursts*, ed. W. S. Paciesas & G. J. Fishman (Melville, NY: AIP), **304**
- Eichler, D., Livio, M., Piran, T., & Schramm, D. N. 1989, *Natur*, **340**, 126
- Evans, P. A., Beardmore, A. P., Page, K. L., et al. 2007, *A&A*, **469**, 379
- Evans, P. A., Beardmore, A. P., Page, K. L., et al. 2009, *MNRAS*, **397**, 1177
- Falcone, A., Barbier, L., Barthelmy, S., et al. 2006, GCN, **4655**, 1
- Falcone, A. D., Morris, D., Racusin, J., et al. 2007, *ApJ*, **671**, 1921
- Fan, Y. Z., Zhang, B., & Proga, D. 2005, *ApJL*, **635**, L129
- Fenimore, E. E., Palmer, D., Galassi, M., et al. 2003, in AIP Conf. Ser. 662, *Gamma-Ray Burst and Afterglow Astronomy 2001: A Workshop Celebrating the First Year of the HETE Mission*, ed. G. R. Ricker & R. K. Vanderspek (Melville, NY: AIP), **491**
- Fermi, E. 1934, *NCim*, **11**, 1
- Frail, D. A., Kulkarni, S. R., Nicastro, L., Feroci, M., & Taylor, G. B. 1997, *Natur*, **389**, 261
- Frail, D. A., Kulkarni, S. R., Sari, R., et al. 2001, *ApJL*, **562**, L55
- Frey, L. H., Fryer, C. L., & Young, P. A. 2013, *ApJL*, **773**, L7
- Frontera, F., Costa, E., Piro, L., et al. 1998, *ApJL*, **493**, L67
- Fruchter, A. S., Levan, A. J., Strolger, L., et al. 2006, *Natur*, **441**, 463
- Fryer, C., Benz, W., Herant, M., & Colgate, S. A. 1999a, *ApJ*, **516**, 892
- Fryer, C. L., Oliveira, F. G., Rueda, J. A., & Ruffini, R. 2015, *PhRvL*, **115**, 231102
- Fryer, C. L., Rueda, J. A., & Ruffini, R. 2014, *ApJL*, **793**, L36
- Fryer, C. L., Woosley, S. E., & Hartmann, D. H. 1999b, *ApJ*, **526**, 152
- Galama, T. J., Vreeswijk, P. M., van Paradijs, J., et al. 1998, *Natur*, **395**, 670
- Gamow, G., & Schoenberg, M. 1940, *PhRv*, **58**, 1117
- Gamow, G., & Schoenberg, M. 1941, *PhRv*, **59**, 539
- Gehrels, N., Chipman, E., & Kniffen, D. A. 1993, *A&AS*, **97**, 5
- Gehrels, N., Ramirez-Ruiz, E., & Fox, D. B. 2009, *ARA&A*, **47**, 567
- Golenetskii, S., Aptekar, R., Frederiks, D., et al. 2013, GCN, **15413**, 1
- Golenetskii, S., Aptekar, R., Frederiks, D., et al. 2014, GCN, **16134**, 1
- Golenetskii, S., Aptekar, R., Frederiks, D., et al. 2015, GCN, **18516**, 1
- Golenetskii, S., Aptekar, R., Mazets, E., et al. 2008, GCN, **7862**, 1
- Goodman, J. 1986, *ApJL*, **308**, L47
- Gursky, H., & Ruffini, R. (ed.) 1975, in Proc. Annual Meeting, Astrophysics and Space Science Library, Vol. 48, *Neutron Stars, Black Holes and Binary X-ray Sources* (Dordrecht: Reidel), **454**
- Heisenberg, W. 1943, *ZPhy*, **120**, 513
- Hjorth, J., & Bloom, J. S. 2012, in *Gamma-Ray Bursts*, ed. C. Kouveliotou, R. A. M. J. Wijers, & S. Woosley (Cambridge: Cambridge Univ. Press), **169**
- Hurley, K., Cline, T., Mazets, E., et al. 2000, *ApJL*, **534**, L23
- in 't Zand, J. J. M., Amati, L., Antonelli, L. A., et al. 1998, *ApJL*, **505**, L119
- in 't Zand, J. J. M., Kuiper, L., Amati, L., et al. 2001, *ApJ*, **559**, 710
- Itoh, N., Adachi, T., Nakagawa, M., Kohyama, Y., & Munakata, H. 1989, *ApJ*, **339**, 354
- Izzo, L., Ruffini, R., Penacchioni, A. V., et al. 2012, *A&A*, **543**, A10
- Jakobsson, P., Fynbo, J. P. U., Vreeswijk, P. M., & de Ugarte Postigo, A. 2008, GCN, **8077**, 1
- Jaunsen, A. O., Fynbo, J. P. U., Andersen, M. I., & Vreeswijk, P. 2007, GCN, **6216**, 1
- Jin, Z.-P., Fan, Y.-Z., & Wei, D.-M. 2010, *ApJ*, **724**, 861
- Klebesadel, R. W. 1992, in *Gamma-Ray Bursts—Observations, Analyses and Theories*, ed. C. Ho, R. I. Epstein, & E. E. Fenimore (Cambridge: Cambridge Univ. Press), **161**
- Klebesadel, R. W., Strong, I. B., & Olson, R. A. 1973, *ApJL*, **182**, L85
- Kouveliotou, C., Meegan, C. A., Fishman, G. J., et al. 1993, *ApJL*, **413**, L101
- Krimm, H. A., Beardmore, A. P., Brown, P. J., et al. 2008, GCN, **8648**, 1
- Kruehler, T., Tanvir, N. R., Malesani, D., Xu, D., & Fynbo, J. P. U. 2014, GCN, **15900**, 1
- Kumar, P., & Zhang, B. 2015, *PhR*, **561**, 1
- Landau, L. D., & Lifshitz, E. M. 1980, *Statistical Physics. Pt.1* (3rd ed.; Portsmouth, NH: Butterworth-Heinemann)
- Ledoux, C., Vreeswijk, P., Smette, A., Jaunsen, A., & Kaufer, A. 2006, GCN, **5237**, 1
- Lien, A. Y., Barthelmy, S. D., Chester, M. M., et al. 2014, GCN, **15784**, 1
- Lyman, J. D., Bersier, D., James, P. A., et al. 2016, *MNRAS*, **457**, 328
- MacFadyen, A., & Woosley, S. E. 1999, *ApJ*, **524**, 262
- Malesani, D., Xu, D., Fynbo, J. P. U., et al. 2014, GCN, **15800**, 1
- Mangano, V., Cummings, J. R., Cusumano, G., et al. 2008, GCN, **7847**, 1
- Mao, S., & Yi, I. 1994, *ApJL*, **424**, L131
- Margutti, R., Guidorzi, C., Chincarini, G., et al. 2010, *MNRAS*, **406**, 2149
- Marisaldi, M., Fuschino, F., Galli, M., et al. 2008, GCN, **7866**, 1
- Marshall, F. E., Cummings, J. R., Gronwall, C., et al. 2014, GCN, **16118**, 1
- Maselli, A., D'Ai, A., Lien, A. Y., et al. 2015, GCN, **18478**, 1
- Masumitsu, T., Negoro, H., Kawai, N., et al. 2015, GCN, **18525**, 1
- Mazets, E. P., Golenetskii, S. V., Ilinskii, V. N., et al. 1981, *Ap&SS*, **80**, 3
- McBreen, S. 2009, GCN, **9415**, 1
- Mészáros, P. 2002, *ARA&A*, **40**, 137
- Mészáros, P. 2006, *RPPH*, **69**, 2259
- Mészáros, P., Laguna, P., & Rees, M. J. 1993, *ApJ*, **415**, 181
- Mészáros, P., & Rees, M. J. 1997, *ApJL*, **482**, L29
- Metzger, M. R., Djorgovski, S. G., Kulkarni, S. R., et al. 1997, *Natur*, **387**, 878
- Mignone, A., Zanni, C., Tzeferacos, P., et al. 2011, *ApJS*, **198**, 7
- Morgan, A., Grupe, D., Gronwall, C., et al. 2005, GCN, **3577**, 1
- Munakata, H., Kohyama, Y., & Itoh, N. 1985, *ApJ*, **296**, 197
- Narayan, R., Paczynski, B., & Piran, T. 1992, *ApJL*, **395**, L83
- Narayan, R., Piran, T., & Shemi, A. 1991, *ApJL*, **379**, L17
- Negreiros, R., Ruffini, R., Bianco, C. L., & Rueda, J. A. 2012, *A&A*, **540**, A12
- Nousek, J. A., Kouveliotou, C., Grupe, D., et al. 2006, *ApJ*, **642**, 389
- Nysewander, M., Reichart, D. E., Crain, J. A., et al. 2009, *ApJ*, **693**, 1417
- Oppenheimer, J. R., & Volkoff, G. M. 1939, *PhRv*, **55**, 374
- Paczynski, B. 1986, *ApJL*, **308**, L43
- Paczynski, B. 1998, *ApJL*, **494**, L45
- Pagani, C., Baumgartner, W. H., Chester, M. M., et al. 2008, GCN, **8059**, 1
- Page, K. L., Barthelmy, S. D., Baumgartner, W. H., et al. 2014, GCNR, **460**, 1
- Page, K. L., Willingale, R., Bissaldi, E., et al. 2009, *MNRAS*, **400**, 134
- Panaiteescu, A., & Mészáros, P. 1999, *ApJ*, **526**, 707
- Patricelli, B., Bernardini, M. G., Bianco, C. L., et al. 2012, *ApJ*, **756**, 16

- Penacchioni, A. V., Ruffini, R., Bianco, C. L., et al. 2013, *A&A*, **551**, A133
- Penacchioni, A. V., Ruffini, R., Izzo, L., et al. 2012, *A&A*, **538**, A58
- Perley, D. A., Cao, Y., & Cenko, S. B. 2014, GCN, **17228**, 1
- Perley, D. A., Hillenbrand, L., & Prochaska, J. X. 2015, GCN, **18487**, 1
- Perley, D. A., Krühler, T., Schulze, S., et al. 2016, *ApJ*, **817**, 7
- Piran, T. 1999, *PhR*, **314**, 575
- Piran, T. 2004, *RvMP*, **76**, 1143
- Piran, T., Shemi, A., & Narayan, R. 1993, *MNRAS*, **263**, 861
- Piro, L., De Pasquale, M., Soffitta, P., et al. 2005, *ApJ*, **623**, 314
- Pisani, G. B., Izzo, L., Ruffini, R., et al. 2013, *A&A*, **552**, L5
- Pisani, G. B., Ruffini, R., Aimuratov, Y., et al. 2016, *ApJ*, **833**, 159
- Racusin, J. L., Baumgartner, W. H., Brown, P. J., et al. 2008, GCN, **8344**, 1
- Rees, M. J., & Meszaros, P. 1992, *MNRAS*, **258**, 41P
- Rees, M. J., & Meszaros, P. 1994, *ApJL*, **430**, L93
- Romano, P., Campana, S., Chincarini, G., et al. 2006, *A&A*, **456**, 917
- Rossi, A., Afonso, P., & Greiner, J. 2009, GCN, **9382**, 1
- Rowlinson, B. A., Beardmore, A. P., Evans, P. A., et al. 2009, GCN, **9374**, 1
- Rueda, J. A., Aimuratov, Y., de Almeida, U. B., et al. 2017, *IJMPD*, **26**, 1730016
- Rueda, J. A., & Ruffini, R. 2012, *ApJL*, **758**, L7
- Ruffini, R. 1998, in *Frontiers Science Series 23, Black Holes and High Energy Astrophysics*, ed. H. Sato & N. Sugiyama (Tokyo: Universal Academic Press), **167**
- Ruffini, R. 2015, in *Thirteenth Marcel Grossmann Meeting: On Recent Developments in Theoretical and Experimental General Relativity, Astrophysics and Relativistic Field Theories*, ed. K. Rosquist (Singapore: World Scientific), **242**
- Ruffini, R., Bianco, C. L., Chardonnet, P., Frascchetti, F., & Xue, S.-S. 2002, *ApJL*, **581**, L19
- Ruffini, R., Bianco, C. L., Frascchetti, F., Xue, S.-S., & Chardonnet, P. 2001a, *ApJL*, **555**, L107
- Ruffini, R., Bianco, C. L., Frascchetti, F., Xue, S.-S., & Chardonnet, P. 2001b, *ApJL*, **555**, L113
- Ruffini, R., Bianco, C. L., Frascchetti, F., Xue, S.-S., & Chardonnet, P. 2001c, *ApJL*, **555**, L117
- Ruffini, R., Izzo, L., Bianco, C. L., et al. 2015a, *ARep*, **59**, 626
- Ruffini, R., Muccino, M., Aimuratov, Y., et al. 2016a, *ApJ*, **831**, 178
- Ruffini, R., Muccino, M., Bianco, C. L., et al. 2014, *A&A*, **565**, L10
- Ruffini, R., Muccino, M., Kovacevic, M., et al. 2015b, *ApJ*, **808**, 190
- Ruffini, R., Rueda, J. A., Muccino, M., et al. 2016b, *ApJ*, **832**, 136
- Ruffini, R., Salmonson, J. D., Wilson, J. R., & Xue, S. 2000, *A&A*, **359**, 855
- Ruffini, R., Salmonson, J. D., Wilson, J. R., & Xue, S.-S. 1999, *A&A*, **350**, 334
- Ruffini, R., Song, D. J., & Stella, L. 1983, *A&A*, **125**, 265
- Ruffini, R., Vereshchagin, G., & Xue, S. 2010, *PhR*, **487**, 1
- Ruffini, R., Wang, Y., Enderli, M., et al. 2015c, *ApJ*, **798**, 10
- Ruffini, R., & Wilson, J. 1973, *PhRvL*, **31**, 1362
- Sakamoto, T., Barthelmy, S. D., Baumgartner, W. H., et al. 2014, GCN, **15805**, 1
- Sari, R., Piran, T., & Halpern, J. P. 1999, *ApJL*, **519**, L17
- Shemi, A., & Piran, T. 1990, *ApJL*, **365**, L55
- Shirasaki, Y., Yoshida, A., Kawai, N., et al. 2008, *PASJ*, **60**, 919
- Smith, N. 2014, *ARA&A*, **52**, 487
- Smith, N., Li, W., Filippenko, A. V., & Chornock, R. 2011, *MNRAS*, **412**, 1522
- Sonbas, E., Cummings, J. R., D'Elia, V., et al. 2014, GCN, **17206**, 1
- Stamatikos, M., Cummings, J. R., Evans, P. A., et al. 2009, GCN, **9768**, 1
- Svensson, K. M., Levan, A. J., Tanvir, N. R., Fruchter, A. S., & Strolger, L.-G. 2010, *MNRAS*, **405**, 57
- Swenson, C. A., & Roming, P. W. A. 2014, *ApJ*, **788**, 30
- Tanvir, N. R., Levan, A. J., Cucchiara, A., Perley, D., & Cenko, S. B. 2014, GCN, **16125**, 1
- Tavani, M. 1998, *ApJL*, **497**, L21
- Taylor, E. F., & Wheeler, J. A. 1992, *Spacetime Physics—Introduction to Special Relativity* (2nd ed.; New York: W. H. Freeman & Co.)
- Toelge, K., Yu, H. F., & Meegan, C. A. 2015, GCN, **18492**, 1
- Troja, E., Barthelmy, S. D., Baumgartner, W. H., et al. 2013, GCN, **15402**, 1
- Troja, E., Piro, L., Vasileiou, V., et al. 2015, *ApJ*, **803**, 10
- van Paradijs, J., Groot, P. J., Galama, T., et al. 1997, *Natur*, **386**, 686
- von Kienlin, A., & Bhat, P. N. 2014, GCN, **15796**, 1
- Wheeler, J. A. 1937, *PhRv*, **52**, 1107
- Woosley, S. E. 1993, *ApJ*, **405**, 273
- Woosley, S. E., & Bloom, J. S. 2006, *ARA&A*, **44**, 507
- Xu, D., Fynbo, J. P. U., Jakobsson, P., et al. 2013, GCN, **15407**, 1
- Yi, S.-X., Wu, X.-F., Wang, F.-Y., & Dai, Z.-G. 2015, *ApJ*, **807**, 92
- Yu, H.-F. 2014, GCN, **17216**, 1
- Yuan, F., Schady, P., Racusin, J. L., et al. 2010, *ApJ*, **711**, 870
- Zel'dovich, Y. B., Ivanova, L. N., & Nadezhin, D. K. 1972, *SvA*, **16**, 209
- Zhang, B., Fan, Y. Z., Dyks, J., et al. 2006, *ApJ*, **642**, 354
- Zhang, F.-W., Shao, L., Yan, J.-Z., & Wei, D.-M. 2012, *ApJ*, **750**, 88
- Ziaeeepour, H. Z., Barthelmy, S. D., Gehrels, N., et al. 2006, GCN, **5233**, 1



ON THE UNIVERSAL LATE X-RAY EMISSION OF BINARY-DRIVEN HYPERNOVAE AND ITS POSSIBLE COLLIMATION

G. B. PISANI^{1,2}, R. RUFFINI^{1,2,3,4}, Y. AIMURATOV^{1,3}, C. L. BIANCO^{1,2}, M. KOVACEVIC^{1,3}, R. MORADI^{1,2}, M. MUCCINO^{1,2},
A. V. PENACCHIONI^{5,6}, J. A. RUEDA^{1,2,4}, S. SHAKERI^{2,7}, AND Y. WANG^{1,2}

¹ Dipartimento di Fisica, Sapienza Università di Roma and ICRA, Piazzale Aldo Moro 5, I-00185 Roma, Italy

² ICRANet, Piazza della Repubblica 10, I-65122 Pescara, Italy

³ Université de Nice Sophia-Antipolis, Grand Château Parc Valrose, Nice, CEDEX 2, France

⁴ CRANet-Rio, Centro Brasileiro de Pesquisas Físicas, Rua Dr. Xavier Sigaud 150, Rio de Janeiro, RJ, 22290-180, Brazil

⁵ University of Siena, Department of Physical Sciences, Earth and Environment, Via Roma 56, I-53100 Siena, Italy

⁶ ASI Science Data Center, via del Politecnico s.n.c., I-00133 Rome, Italy

⁷ Department of Physics, Isfahan University of Technology, Isfahan 84156-83111, Iran

Received 2016 August 5; revised 2016 October 4; accepted 2016 October 12; published 2016 December 14

ABSTRACT

It has previously been discovered that there is a universal power-law behavior exhibited by the late X-ray emission (LXRE) of a “golden sample” of six long energetic GRBs, when observed in the rest frame of the source. This remarkable feature, independent of the different isotropic energy (E_{iso}) of each GRB, has been used to estimate the cosmological redshift of some long GRBs. This analysis is extended here to a new class of 161 long GRBs, all with $E_{\text{iso}} > 10^{52}$ erg. These GRBs are indicated as binary-driven hypernovae (BdHNe) in view of their progenitors: a tight binary system composed of a carbon–oxygen core (CO_{core}) and a neutron star undergoing an induced gravitational collapse (IGC) to a black hole triggered by the CO_{core} explosion as a supernova (SN). We confirm the universal behavior of the LXRE for the “enlarged sample” (ES) of 161 BdHNe observed up to the end of 2015, assuming a double-cone emitting region. We obtain a distribution of half-opening angles peaking at $\theta = 17.62^\circ$, with a mean value of 30.05° , and a standard deviation of 19.65° . This, in turn, leads to the possible establishment of a new cosmological candle. Within the IGC model, such universal LXRE behavior is only indirectly related to the GRB and originates from the SN ejecta, of a standard constant mass, being shocked by the GRB emission. The fulfillment of the universal relation in the LXRE and its independence of the prompt emission, further confirmed in this article, establishes a crucial test for any viable GRB model.

Key words: binaries: general – gamma-ray burst: general – stars: neutron – supernovae: general

1. INTRODUCTION

The initial observations by the BATSE instrument on board the Compton γ -ray Observatory satellite have evidenced what has later become known as the prompt radiation of GRBs. On the basis of their hardness as well as their duration, GRBs were initially classified into short and long at a time when their cosmological nature was still being disputed (Dezalay et al. 1992, pp. 161–168; Klebesadel 1992; Kouveliotou et al. 1993; Mazets et al. 1981; Tavani 1998).

The advent of the *BeppoSAX* satellite (Boella et al. 1997) introduced a novel approach to GRBs by introducing joint observations in the X-rays and γ -rays thanks to its instruments: the Gamma-ray Burst Monitor (40–700 keV), the Wide Field Cameras (2–26 keV), and the Narrow Field Instruments (2–10 keV). The unexpected and welcome discovery of the existence of a well separate component in the GRB soon appeared: the afterglow radiation lasting up to 10^5 – 10^6 s after the emission of the prompt radiation (see Costa et al. 1997b, 1997a; Frontera et al. 1998, 2000; de Pasquale et al. 2006). *BeppoSAX* clearly indicated the existence of a power-law behavior in the late X-ray emission (LXRE; see Figure 1).

The coming of the *Swift* satellite (Gehrels et al. 2004; Evans et al. 2007, 2010), significantly extending the observation in the X-ray band thanks to its X-ray Telescope (XRT band: 0.3–10 keV), has allowed us for the first time to cover the unexplored region between the end of the prompt radiation and the power-law late X-ray behavior discovered by *BeppoSAX*: in some long GRBs a steep decay phase was observed followed

by a plateau leading then to a typical LXRE power-law behavior (Evans et al. 2007, 2010).

Already, Pisani et al. (2013) noticed the unexpected result that the LXREs of a “golden sample” (GS) of six long, closeby ($z \lesssim 1$), energetic ($E_{\text{iso}} > 10^{52}$ erg) GRBs, when measured in the rest-frame of the sources, were showing a common power-law behavior (see Figure 2), independently from the isotropic energy E_{iso} coming from the prompt radiation (see Figure 3). More surprising was the fact that the plateau phase luminosity and duration before merging in the common LXRE power-law behavior were clearly functions of the E_{iso} (see Figure 3, and Ruffini et al. 2014c), while the late power law remains independent from the energetic of the prompt radiation (see Figures 2–3, and Pisani et al. 2013; Ruffini et al. 2014c). For this reason, this remarkable scaling law has been used as a standard candle to independently estimate the cosmological redshift of some long GRBs by requiring the overlap of their LXRE (see, e.g., Penacchioni et al. 2012, 2013; Ruffini et al. 2013b, 2013c, 2014a), and also to predict, 10 days in advance, the emergence of the typical optical signature of the supernova SN 2013cq, associated with GRB 130427A (de Ugarte Postigo et al. 2013; Levan et al. 2013; Ruffini et al. 2015, 2013a).

The current analysis is based on the paradigms introduced in Ruffini et al. (2001a) for the spacetime parametrization of the GRBs, in Ruffini et al. (2001b) for the interpretation of the structure of the GRB prompt emission, and in Ruffini et al. (2001c) for the induced gravitational collapse (IGC) process, further evolved in Ruffini et al. (2007), Rueda & Ruffini

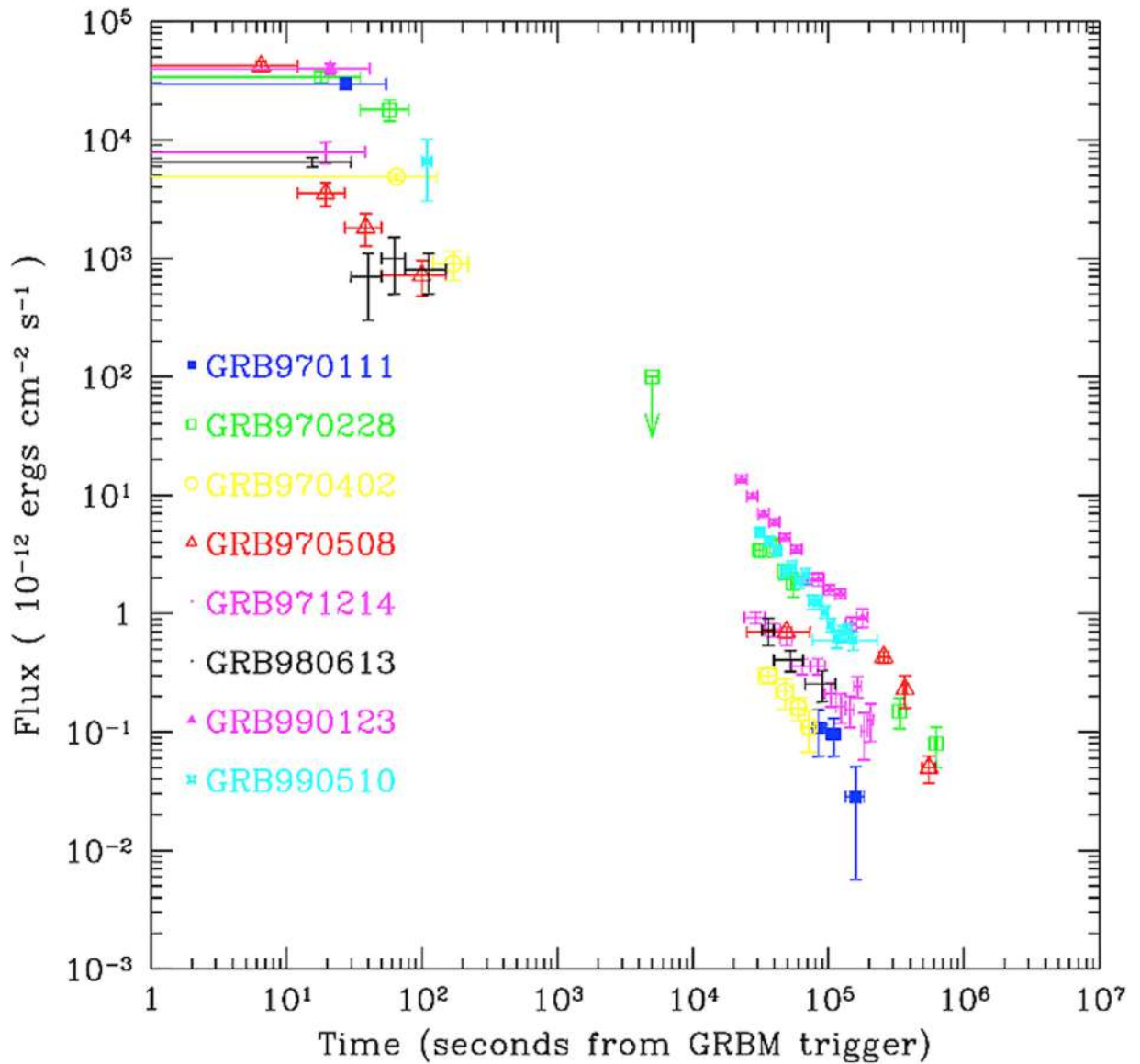


Figure 1. Collection of X-ray afterglow light curves observed by the Italian–Dutch satellite *BeppoSAX*.

(2012), Fryer et al. (2014), and Ruffini et al. (2016). In the present case, the phenomenon points to an IGC occurring when a tight binary system composed of a carbon–oxygen core (CO_{core}) undergoes a supernova (SN) explosion in the presence of a binary NS companion (Ruffini et al. 2001b, 2007; Izzo et al. 2012a; Rueda & Ruffini 2012; Fryer et al. 2014; Ruffini et al. 2015). When the IGC leads the NS to accrete enough matter and therefore to collapse to a black hole (BH), the overall observed phenomenon is called binary-driven hypernova (BdHN; Fryer et al. 2014; Ruffini et al. 2015, 2016).

A crucial further step has been the identification as a BdHN of GRB 090423 (Ruffini et al. 2014b) at the extreme redshift of $z = 8.2$ (Salvaterra et al. 2009; Tanvir et al. 2009). On top of that, the LXRE of GRB 090423 overlaps perfectly with the ones of the GS (see Figure 4), extending such a scaling law up to extreme cosmological distances. This result led to the necessity of checking such an universal behavior of the LXREs in BdHNe at redshifts larger than $z \sim 1$ (see the sample list in Table 2).

It is clear by now that the afterglow analysis is much more articulated than previously expected and contains new specific signatures. When theoretically examined within our framework, these new signatures lead to specific information on the astrophysical nature of the progenitor systems (Ruffini et al. 2016). In the present paper, we start by analyzing the signatures contained in the LXREs at $t_{\text{rf}} \gtrsim 10^4$ s, where t_{rf} is the rest-frame time after the initial GRB trigger. In particular, we probe a further improvement for the existence of such an LXRE universal behavior of BdHNe by the introduction of a collimation correction.

In Section 2, we present an “enlarged sample” (ES) of 161 BdHNe observed up to the end of 2015. In particular, we express for each BdHN: (1) redshift; (2) E_{iso} ; and (3) the LXRE power-law properties. We probe the universality of the LXRE power-law behavior as well as the absence of correlation with the prompt radiation phase of the GRB. In Section 3, we introduce the collimation correction for the LXRE of BdHNe. This, in turn, will aim to the possible establishment of a new cosmological candle, up to $z \gtrsim 8$. In Section 4, we present the

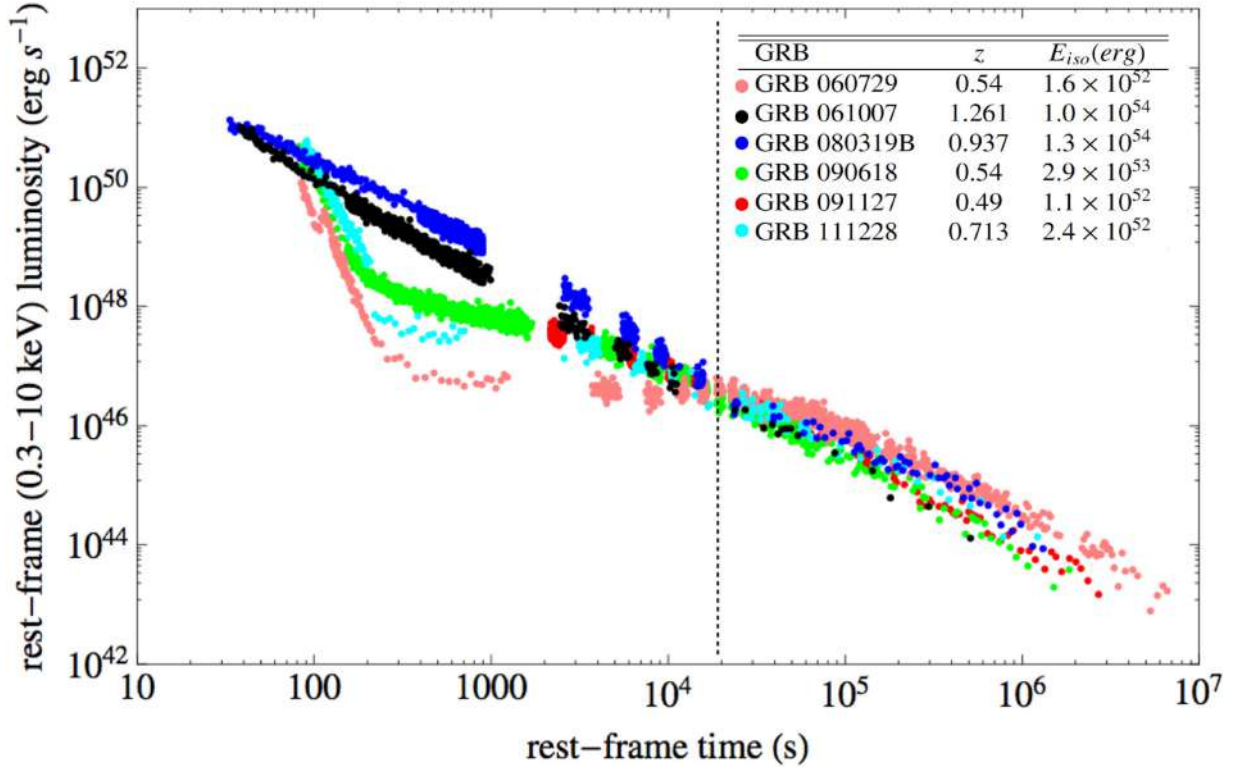


Figure 2. Scaling law found in the isotropic X-ray late times luminosity within the GS by Pisani et al. (2013). Despite the different early behavior, the different light curves join all together the same power law after a rest-frame time of $t_{\text{tr}} \sim 2 \times 10^4$ s.

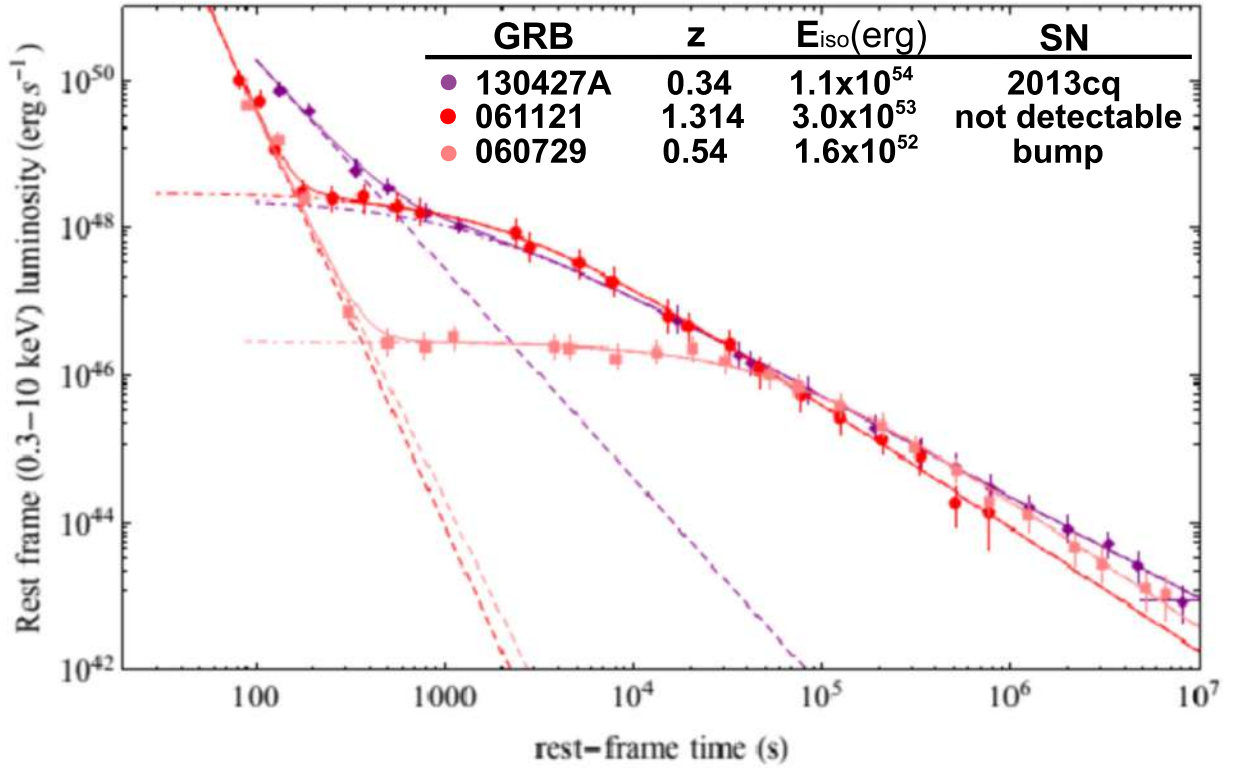


Figure 3. Nested structure of the isotropic X-ray luminosity of the BdHNe. This includes the previously mentioned scaling law of the late power-law and leads to an inverse proportionality between the luminosity of the plateau and the rest-frame time delimiting its end and the beginning of the late power-law decay Ruffini et al. (2014c).

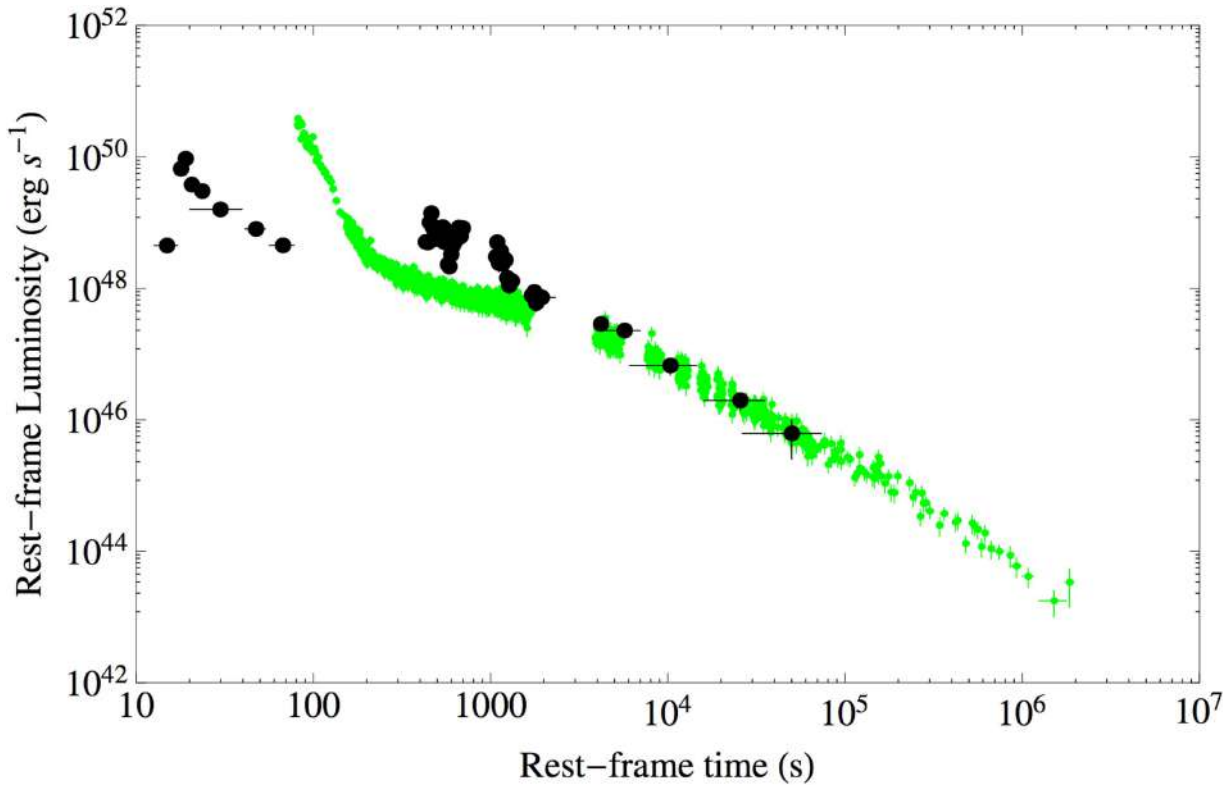


Figure 4. X-ray luminosity of GRB 090423 (black points) compared with the one of GRB 090618 (green points), the prototype BdHN, by Ruffini et al. (2014b).

inferences for the understading of the afterglow structure, and, in Section 5, we draw our conclusions.

2. THE BDHNE ENLARGED SAMPLE

We have built a new sample of BdHNe, which we name “enlarged sample” (ES), under the following selection criteria:

1. measured redshift z ;
2. GRB rest-frame duration larger than 2 s;
3. isotropic energy E_{iso} larger than 10^{52} erg; and
4. presence of associated *Swift*/XRT data lasting at least up to $t_{\text{rf}} = 10^4$ s.

We collected 161 sources, which satisfy our criteria, covering 11 years of *Swift*/XRT observations, up to the end of 2015, see Table 2. The E_{iso} of each source has been estimated using the measured redshift z together with the best-fit parameters of the γ -ray spectrum published in the GCN circular archive.⁸ The majority of the ES sources, 102 out of 161, have γ -ray data provided by *Fermi*/GBM and Konus-WIND, which, with their typical energy bands being 10–1000 keV and 20–2000 keV, respectively, lead to a reliable estimate of the E_{iso} , computed in the “bolometric” 1– 10^4 keV band (Bloom et al. 2001). The remaining sources of the ES have had their γ -ray emission observed by *Swift*/BAT only, with the sole exception of one source observed by *HETE*. The energy bands of these last two detectors, being 15–150 keV and 8–400 keV, respectively, lead to a standard estimate of E_{iso} by extrapolation in the “bolometric” 1– 10^4 keV band (Bloom et al. 2001).

We compare the *Swift*/XRT isotropic luminosity light curve $L_{\text{rf}}^{\text{iso}}$ for 161 GRBs of the ES in the common rest-frame energy range of 0.3–10 keV. We initially convert the observed *Swift*/XRT flux f_{obs} as if it had been observed in the 0.3–10 keV rest-frame energy range. In the detector frame, the 0.3–10 keV rest-frame energy range becomes $[0.3/(1+z)]$ – $[10/(1+z)]$ keV, where z is the redshift of the GRB. We assume a simple power-law function as the best fit for the spectral energy distribution of the *Swift*/XRT data⁹:

$$\frac{dN}{dA dt dE} \propto E^{-\gamma}. \quad (1)$$

Therefore, we can compute the flux light curve in the 0.3–10 keV rest-frame energy range, f_{rf} , multiplying the observed one, f_{obs} , by the k -correction factor:

$$f_{\text{rf}} = f_{\text{obs}} \frac{\int_{0.3/(1+z)}^{10/(1+z)} E^{1-\gamma} dE}{\int_{0.3 \text{ keV}}^{10 \text{ keV}} E^{1-\gamma} dE} = f_{\text{obs}} (1+z)^{\gamma-2}. \quad (2)$$

Then, to compute the isotropic X-ray luminosity L_{iso} , we have to multiply f_{rf} by the spherical surface having the luminosity distance as radius

$$L_{\text{iso}} = 4 \pi d_L^2(z) f_{\text{rf}}, \quad (3)$$

where we assume a standard cosmological Λ CDM model with $\Omega_m = 0.27$ and $\Omega_\Lambda = 0.73$. Finally, we convert the observed

⁸ http://gcnc.gsfc.nasa.gov/gcn3_archive.html

⁹ <http://www.swift.ac.uk/>

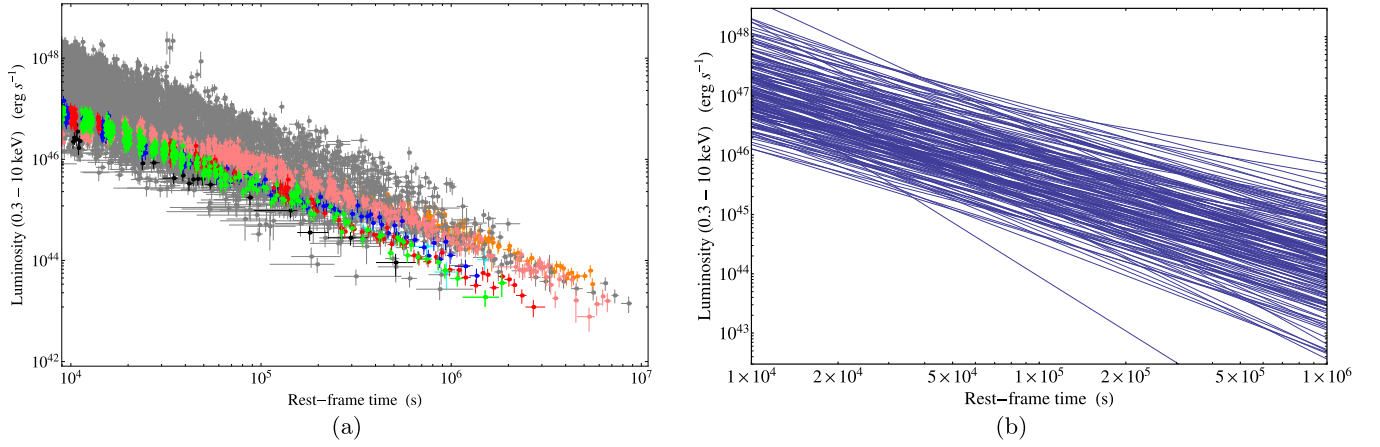


Figure 5. Panel (a): LXRE luminosity light curves of all 161 sources of the ES (gray) compared with the ones of the GS: GRB 060729 (pink), GRB 061007 (black), GRB 080913B (blue), GRB 090618 (green), GRB 091127 (red), and GRB 111228 (cyan), plus GRB 130427A (orange; Pisani et al. 2013; Ruffini et al. 2015). Panel (b): power laws that best fit the luminosity light curves of the X-ray emissions of all 161 sources of the ES.

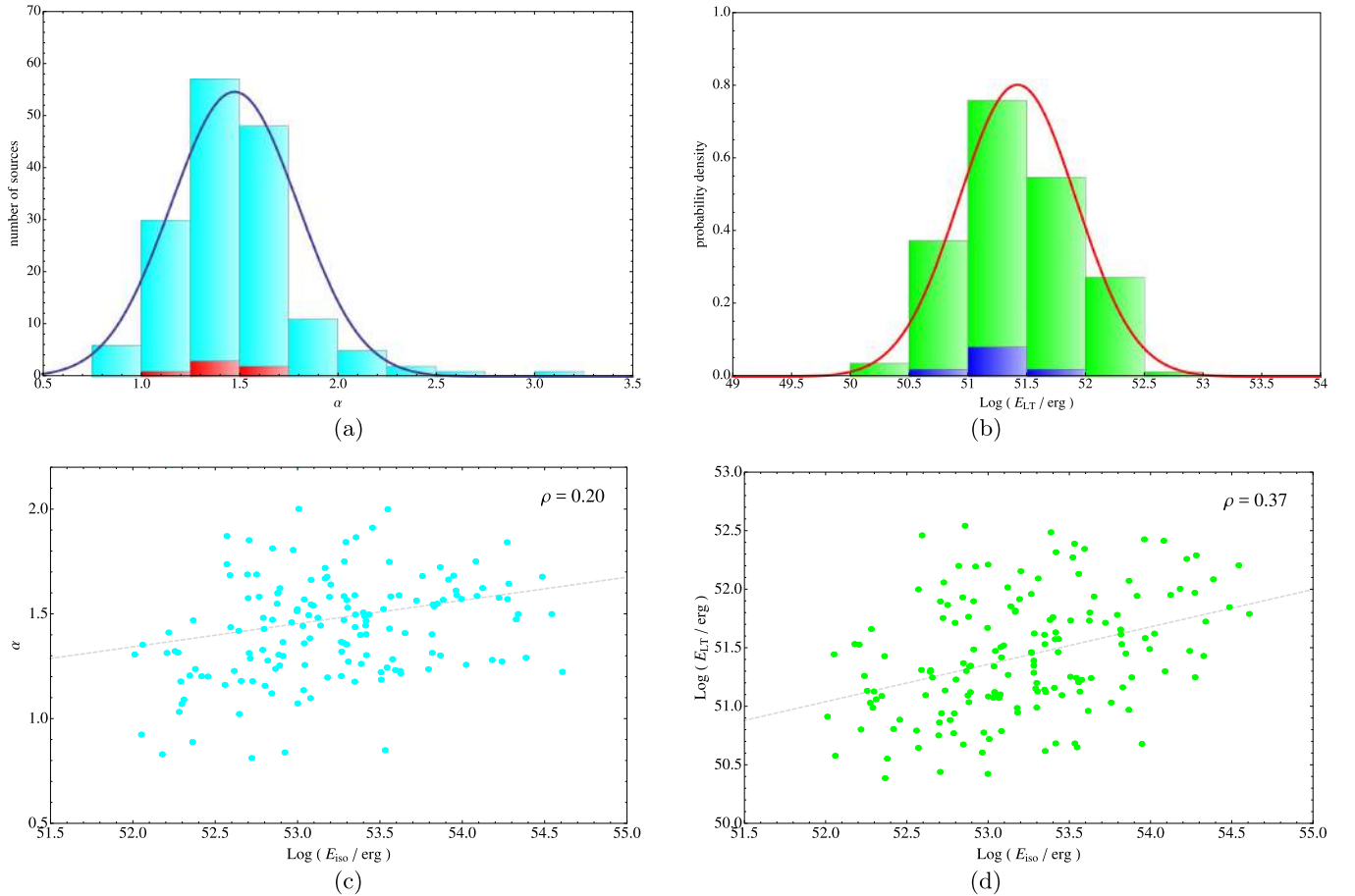


Figure 6. Panel (a): distribution of the LXRE power-law indexes α within the ES (cyan) compared to one of the GS (red). Such a distribution Gaussian behavior (blue line) with a mean value of $\mu_\alpha = 1.48$ and a standard deviation of $\sigma_\alpha = 0.32$ follows. Panel (b): probability distribution of the LXRE integrated energies within the time interval 10^4 – 10^6 s in the rest-frame after the initial GRB trigger for all the sources of the ES (in green) compared with the GS (in blue). The solid red line represents the Gaussian function, which best fits the ES data in logarithmic scale. Its mean value is $\mu_{\text{Log}_{10}(E_{LT})} = 51.40$, while its standard deviation is $\sigma_{\text{Log}_{10}(E_{LT})} = 0.47$. Panel (c): scatter plot of α vs. E_{iso} (cyan points) in logarithmic scale. The dashed gray line is the best linear fit on such points. If we look at the correlation coefficient of these data points, $\rho = 0.20$, we conclude that there is no evidence for correlation between the two quantities. Panel (d): scatter plot of E_{LT} vs. E_{iso} (green points) in logarithmic scale. The dashed gray line is the best linear fit on such points. If we look at the correlation coefficient of these data points, $\rho = 0.37$, we conclude that there is no evidence for correlation between the two quantities.

times into rest-frame times t_{rf} :

$$t_{\text{rf}} = \frac{t_{\text{obs}}}{1+z}. \quad (4)$$

We then fit the whole isotropic luminosity light-curve late phase with a decaying power-law function defined as:

$$L_{\text{iso}}(t_{\text{rf}}) = L_0 t_{\text{rf}}^{-\alpha}, \quad (5)$$

where α , the power-law index, is a positive number, and L_0 is the luminosity at an arbitrary time $t_{\text{rf}} = t_0$ after the GRB trigger in the rest-frame of the source. All the power laws are shown in Figure 5(b). Figure 6(a) shows the distribution of the α indexes within the ES. Such a distribution follows a Gaussian behavior with a mean value of $\mu_\alpha = 1.48$ and a standard deviation of $\sigma_\alpha = 0.32$ follows. The LXRE luminosity light curves of the ES in the 0.3–10 keV rest-frame energy band are plotted in Figure 5(a), compared to the curves of the GS. Figure 5(a) shows that the power laws within the ES span around two orders of magnitude in luminosity. The spread of the LXRE light curves in the ES is better displayed by Figure 6(b), which shows the distribution within the ES of the LXRE integrated energies E_{LT} defined as:

$$E_{\text{LT}} \equiv \int_{10^4 \text{ s}}^{10^6 \text{ s}} L_{\text{iso}}(t_{\text{rf}}) dt_{\text{rf}}. \quad (6)$$

We choose to represent the spread of the LXRE luminosity light curves with the late integrated energy E_{LT} at late times ($t_{\text{rf}} = 10^4$ – 10^6 s) instead of the luminosity L_{iso} at a particular time for two reasons: (1) there is no evidence for a particular time in which to compute L_{iso} and (2) we want to have a measurement of the spread as independent as possible from the slopes, whose dispersion causes the mixing of part of the light curves over time (see Figure 5(b)). The integration time interval $t_{\text{rf}} = 10^4$ – 10^6 reasonably contains most of the data in the late power-law behavior. In fact, the lower limit $t_{\text{rf}} = 10^4$ s is basically the average of the initial time for our linear fits on the data (more precisely $t_{\text{rf}}^{\text{start}} = 9167.13$ s), while the upper limit $t_{\text{rf}} = 10^6$ has been chosen because only 14% of the ES have X-ray data over such rest-frame time.

The solid red line in Figure 6(b) represents the Gaussian function that best fits the late integrated energies E_{LT} in logarithmic scale. Its mean value is $\mu_{\text{Log}_{10}(E_{\text{LT}})} = 51.40$, while its standard deviation is $\sigma_{\text{Log}_{10}(E_{\text{LT}})} = 0.47$.

The LXRE power-law spread, given roughly by $2\sigma_{\text{Log}_{10}(E_{\text{LT}})} = 0.94$, is larger in respect to the previous work of Pisani et al. (2013), which results as $2\sigma_{\text{Log}_{10}(E_{\text{LT}})} = 0.56$. This is clearly due to the significant growth of the number of BdHNe composing the ES (161) in respect to the ones of the GS (6).

Furthermore, Figures 6(c)–(d) show the scatter plots of the values of α and E_{LT} , respectively, versus the values of the E_{iso} for all the sources of the ES. In both cases the correlation factors, $\rho = 0.20$ and $\rho = 0.37$, respectively, are low, confirming that there is no evidence for a correlation between the LXRE power-law behavior and the isotropic energy emitted by the source during the prompt radiation.

These results address a different aspect than the ones by Margutti et al. (2013). There, the authors, after correctly noticing the difficulties of the traditional afterglow model (Meszaros & Rees 1997; Sari et al. 1998), attempt to find a model-independent correlation between the X-ray light curve

observed in both short and long GRBs with their prompt emission. In their work, Margutti et al. (2013) have considered the integrated X-ray emission over the entire light curve observed by XRT, following ~ 300 s after the GRB trigger both for short and long GRBs. Such an emission is clearly dominated by the contribution at $t_{\text{rf}} < 10^4$ s, where a dependence from the E_{iso} is self-evident from the above Figures 2 and 3. Our approach instead solely applies to the BdHNe: (1) long GRBs, and (2) $E_{\text{iso}} > 10^{52}$ erg. This restricts the possible sources in the Margutti et al. (2013) sample to 70 GRBs: in the present article, we consider a larger sample of 161 BdHNe. Moreover, (3) our temporal window starts at $t_{\text{rf}} \gtrsim 10^4$ s. Under these three conditions, our result of the universal LXRE behavior has been found.

3. COLLIMATION

We here propose reducing the spread of the LXRE power laws within the ES by introducing a collimation effect in the emission process. In fact, if the emission is not isotropic, Figures 5(a)–(b) should actually show overestimations of the intrinsic LXRE luminosities. By introducing a collimation effect, namely assuming that the LXREs are not emitted isotropically but within a double-cone region having half-opening angle θ , we can convert the isotropic $L_{\text{iso}}(t_{\text{rf}})$ to the intrinsic LXRE luminosity $L^{\text{intr}}(t_{\text{rf}})$ as:

$$L^{\text{intr}}(t_{\text{rf}}) = L_{\text{iso}}(t_{\text{rf}}) (1 - \cos \theta). \quad (7)$$

From Equation (7), an angle θ can be inferred for each source of the ES if an intrinsic universal LXRE light curve $L^{\text{intr}}(t_{\text{rf}})$ is assumed. For example, assuming an intrinsic standard luminosity L_0^{intr} , at an arbitrary time $t_{\text{rf}} = t_0$, Equation (7) becomes $L_0^{\text{intr}} = L_0 (1 - \cos \theta)$, which, in principle, could be used to infer θ for each source. On the other hand, for the same reasons expressed in the previous section, we choose to estimate the angles θ using the LXRE integrated energy E_{LT} instead of the L_{iso} at a particular time. Therefore, we simply integrate Equation (7) in the rest-frame time interval 10^4 – 10^6 s:

$$\int_{10^4 \text{ s}}^{10^6 \text{ s}} L^{\text{intr}}(t_{\text{rf}}) dt_{\text{rf}} = \int_{10^4 \text{ s}}^{10^6 \text{ s}} L_{\text{iso}}(t_{\text{rf}}) (1 - \cos \theta) dt_{\text{rf}}, \quad (8)$$

obtaining, consequentially

$$E_{\text{LT}}^{\text{intr}} = E_{\text{LT}} (1 - \cos \theta). \quad (9)$$

By assuming a universal $E_{\text{LT}}^{\text{intr}}$ for all BdHNe, it is possible to infer θ for each source of the ES. We assume GRB 050525A, having the lowest E_{LT} within the ES, as our unique “isotropic” source, namely, in which we can impose $E_{\text{LT}}^{\text{intr}} = E_{\text{LT}}$, which automatically gives $\theta = 90^\circ$, which means that the LXRE luminosity is emitted over all the isotropic sphere. On top of having the weakest LXRE over 11 years of *Swift*/XRT observations, GRB 050525A: (a) has been observed by Konus-WIND in the γ -rays (Golenetskii et al. 2005), then its E_{iso} estimate is reliable; (b) has a reliable late X-ray slope given by a complete *Swift*/XRT light curve (showing a late power-law behavior from 4000 to 7×10^5 s in the rest frame); (c) has an associated supernova (Della Valle et al. 2006a, 2006b). An instrumental selection effect cannot affect this choice since *Swift*/XRT can easily detect and follow X-ray emissions weaker than that of GRB 050525A. Some examples are the two X-ray luminosity light curves shown of GRB 060218 and GRB 101219B in Figure 8(a). Furthermore, in the case of a future observation of a BdHN

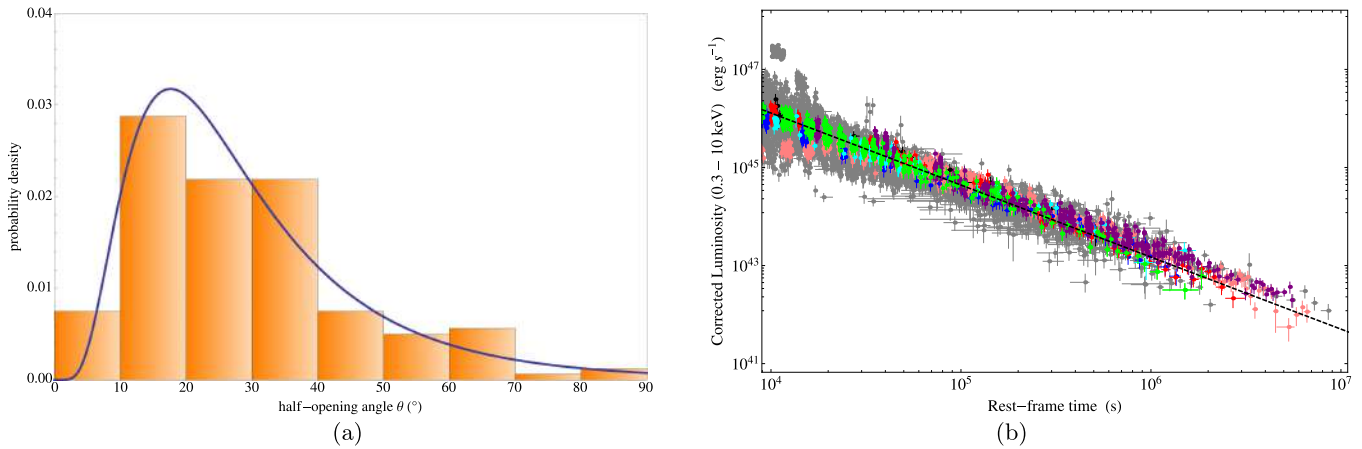


Figure 7. Left panel (a): probability distribution of the half-opening angle θ within the ES. The blue solid line represents a logarithmic normal distribution, which best fits the data. This distribution has a mode of $\text{Mo}_\theta = 17.62^\circ$, a mean of $\mu_\theta = 30.05^\circ$, a median of $\text{Me}_\theta = 25.15^\circ$, and a standard deviation of $\sigma_\theta = 19.65^\circ$. Right panel (b): corrected LXRE luminosity light curves of all 161 sources of the ES (gray) compared to the ones of the GS: GRB 060729 (pink), GRB 061007 (black), GRB 080913B (blue), GRB 090618 (green), GRB 091127 (red), and GRB 111228 (cyan), plus GRB 130427A (purple; Pisani et al. 2013; Ruffini et al. 2015). The black dotted line represents the universal LXRE power law, namely the linear fit of the late emission of GRB 050525A.

showing a E_{LT} weaker than the one of GRB 050525A, a renormalization of the angle distribution of Figure 7(a) down to lower angle values with respect to the new minimum one would be required, leaving the overall angle distribution unaltered. All of these facts make GRB 050525A a robust “isotropic” BdHN candidate. With $E_{\text{LT}}^{\text{intr}} = E_{\text{LT}}^{050525A} = 2.43 \times 10^{50}$ now fixed, a half-opening angle θ is inferred for each source of the ES using Equation (9). The values of θ are listed in Table 2. Figure 7(a) shows the probability distribution of the half-opening angle θ within the ES. The blue solid line represents a logarithmic normal distribution, which best fits the data. This distribution has a mode of $\text{Mo}_\theta = 17.62^\circ$, a mean of $\mu_\theta = 30.05^\circ$, a median of $\text{Me}_\theta = 25.15^\circ$, and a standard deviation of $\sigma_\theta = 19.65^\circ$. Moreover, it is possible to verify that, by correcting the $L_{\text{tr}}^{\text{iso}}$ light curve of each ES source for its corresponding θ , an overlap of the LXRE luminosity light curves as good as the one seen in the GS by Pisani et al. (2013) shown in Figure 2 is obtained. Since the LXRE follows a power-law behavior, we can quantify the tightness of the LXREs overlap looking at the correlation coefficient ρ between all the luminosity light-curve data points of the ES sources in a log–log scale. Considering the data points of the LXRE power laws within the 10^4 – 10^6 s time interval (where we have defined E_{LT}), we obtain $\rho = -0.94$ for the GS, $\rho = -0.84$ for the ES before the collimation correction, and $\rho = -0.97$ after the correction. Therefore, the collimation correction not only reduces the spread of the LXREs within the ES, but makes the LXREs overlap even tighter than the one previously found in the GS.

Finally, in order to test the robustness of our results, we do the same analysis excluding, by the ES, the sources seen only by *Swift*/BAT or *HETE* and not by *Fermi*/GBM or Konus-WIND, under the hypothesis that their E_{iso} estimates are unreliable. The results obtained using this new sample called ES2, namely the typical value and the dispersion of α , E_{LT} , and θ are summarized in Table 1. There is no significant difference between the results obtained from the two samples. Therefore, we conclude that a possible wrong estimate of E_{iso} for the sources observed by only *Swift*/BAT or *HETE* and not by *Fermi*/GBM or Konus-WIND does not bias our results.

Table 1

Summary of the Results of This Work Obtained By the Complete ES Sample in Comparison with the Ones Arising Using the Sample ES2, Namely the ES Deprived By the Sources Seen by *Swift*/BAT or *HETE* Only

Sample	ES	ES2
Sources Number	161	102
α	1.48 ± 0.32	1.45 ± 0.24
$\text{Log}_{10}(E_{\text{LT}}/\text{erg})$	51.40 ± 0.47	51.47 ± 0.48
θ ($^\circ$)	30.05 ± 19.65	28.26 ± 17.85
θ mode ($^\circ$)	17.62	17.08
θ median ($^\circ$)	25.15	23.90

4. INFERENCES FOR THE UNDERSTANDING OF THE X-RAY AFTERGLOW STRUCTURE

In the last 25 years we have seen in the GRB community a dominance of the fireball model, which sees the GRB as a single astrophysical system, the “Collapsar,” originating from an ultra-relativistic jetted emission described by the synchrotron/self-synchrotron Compton (SSC) and traditional afterglow models (see, e.g., Rees & Meszaros 1992; Woosley 1993; Piran 2005; Gehrels et al. 2009; Kumar & Zhang 2015, and references therein). Such methods have been systematically adopted to different types of GRBs like, for example, the short, hard GRB 090510 (Ackermann et al. 2010), the high energetic long GRB 130427A (Perley et al. 2014), the low energetic short GRB 051221A (Soderberg et al. 2006a), and the low energetic long GRB 060218 (Campana et al. 2006; Soderberg et al. 2006b), independently from the nature of their progenitors.

In the recent four years, substantial differences among seven distinct kinds of GRBs have been indicated, presenting different spectral and photometrical properties on different timescales (Ruffini et al. 2016). The discovery of several long GRBs showing multiple components and evidencing the presence of a precise sequence of different astrophysical processes during the GRB phenomenon (e.g., Izzo et al. 2012b; Penacchioni et al. 2012), led to the introduction of a novel paradigm expliciting the role of binary sources as progenitors of the long GRB-SN connection. This has led to the formulation of the IGC paradigm (Ruffini et al. 2001b, 2007,

Table 2
List of the the ES of BdHNe Considered in this Work

GRB	z	α	E_{LT}^{a}	θ ($^{\circ}$)	$E_{\text{iso}}^{\text{b}}$	Instrument ^c	GCN
050315A	1.95	0.838	15.6	10.1	8.32	<i>Swift</i>	3099
050318A	1.44	1.74	0.442	63.3	3.70	<i>Swift</i>	3134
050319A	3.24	1.27	12.3	11.4	20.2	<i>Swift</i>	3119
050401A	2.9	1.59	3.82	20.6	92.0	KW	3179
050408A	1.24	1.14	2.19	27.2	10.8	<i>HETE</i>	3188
050505A	4.27	1.41	8.66	13.6	44.6	<i>Swift</i>	3364
050525A	0.606	1.47	0.243	90.0	2.31	KW	3474
050730A	3.97	2.42	1.74	30.7	42.8	<i>Swift</i>	3715
050802A	1.71	1.55	1.24	36.5	7.46	<i>Swift</i>	3737
050814A	5.3	2.23	2.90	23.6	26.8	<i>Swift</i>	3803
050820A	2.61	1.23	22.1	8.51	39.0	KW	3852
050922C	2.2	1.57	0.974	41.4	19.8	KW	4030
051109A	2.35	1.20	9.09	13.3	18.3	KW	4238
060108A	2.03	0.830	3.40	21.8	1.50	<i>Swift</i>	4445
060115A	3.53	1.58	2.23	27.0	19.0	<i>Swift</i>	4518
060124A	2.296	1.30	20.7	8.79	26.0	KW	4599
060202A	0.783	1.03	4.57	18.8	1.90	<i>Swift</i>	4635
060206A	4.05	1.44	28.8	7.45	3.90	<i>Swift</i>	4697
060210A	3.91	1.75	25.9	7.86	120.	<i>Swift</i>	4734
060418A	1.49	1.54	0.614	52.9	12.0	KW	4989
060502A	1.51	1.26	2.96	23.4	11.0	<i>Swift</i>	5053
060510B	4.9	1.54	3.39	21.8	66.0	<i>Swift</i>	5107
060512A	2.1	1.24	0.356	71.5	2.38	<i>Swift</i>	5124
060526A	3.21	2.27	1.36	34.7	5.40	<i>Swift</i>	5174
060605A	3.8	2.00	0.524	57.6	10.1	<i>Swift</i>	5231
060607A	3.082	3.04	0.481	60.4	34.0	<i>Swift</i>	5242
060707A	3.43	1.18	11.4	11.8	5.30	<i>Swift</i>	5289
060708A	1.92	1.21	1.22	36.8	2.20	<i>Swift</i>	5295
060714A	2.71	1.47	1.93	29.0	19.0	<i>Swift</i>	5334
060729A	0.54	1.31	3.36	21.9	1.60	<i>Swift</i>	5370
060814A	0.84	1.16	1.69	31.1	6.30	KW	5460
060906A	3.685	1.47	0.482	60.3	25.9	<i>Swift</i>	5534
061007A	1.261	1.68	0.477	60.6	88.0	KW	5722
061121A	1.314	1.50	3.75	20.7	27.0	KW	5837
061126A	1.159	1.30	3.06	23.0	8.10	<i>Swift</i>	5860
061222A	2.088	1.52	18.7	9.25	33.0	KW	5984
070110A	2.35	1.10	3.20	22.5	11.9	<i>Swift</i>	6007
070306A	1.5	1.58	8.22	14.0	15.5	<i>Swift</i>	6173
070318A	0.84	1.42	1.97	28.8	4.37	<i>Swift</i>	6212
070508A	0.82	1.60	1.08	39.1	7.57	KW	6403
070529A	2.5	1.22	1.79	30.2	31.9	<i>Swift</i>	6468
070802A	2.45	1.41	0.633	52.0	1.64	<i>Swift</i>	6699
071003A	1.6	1.75	1.61	31.9	35.8	KW	6849
080210A	2.64	1.38	1.26	36.2	11.8	<i>Swift</i>	7289
080310A	2.43	1.53	1.34	35.1	20.0	<i>Swift</i>	7402
080319B	0.94	1.59	1.99	28.6	122.	KW	7482
080319C	1.95	1.72	6.40	15.8	14.6	KW	7487
080605A	1.64	1.59	1.39	34.5	22.1	KW	7854
080607A	3.04	1.57	1.77	30.4	187.	KW	7862
080721A	2.6	1.62	8.93	13.4	132.	KW	7995
080804A	2.2	1.68	1.08	39.3	56.9	<i>Swift</i>	8067
080805A	1.51	1.07	1.21	36.9	9.96	<i>Swift</i>	8068
080810A	3.35	1.57	1.77	30.4	76.1	KW+Swift	8101
080905B	2.37	1.51	4.67	18.6	9.85	<i>Fermi</i>	8205
080916C	4.35	1.29	12.1	11.5	242.	<i>Fermi</i>	8278
080928A	1.69	1.69	0.564	55.3	4.93	<i>Fermi</i>	8316
081008A	1.97	1.80	0.596	53.7	9.34	<i>Swift</i>	8351
081028A	3.04	1.66	2.62	24.9	12.0	<i>Swift</i>	8428
081109A	0.98	1.32	1.07	39.4	1.87	<i>Fermi</i>	8505
081121A	2.51	1.51	5.77	16.7	24.9	<i>Fermi</i>	8546
081203A	2.1	2.00	0.446	63.0	35.1	<i>Swift</i>	8595
081221A	2.26	0.849	24.5	8.09	33.8	<i>Fermi</i>	8704
081222A	2.77	1.40	4.28	19.4	25.9	<i>Fermi</i>	8715
090102A	1.55	1.35	1.58	32.2	19.8	KW	8776

Table 2
(Continued)

GRB	z	α	E_{LT}^a	θ ($^\circ$)	E_{iso}^b	Instrument ^c	GCN
090313A	3.38	2.72	10.4	12.4	13.1	<i>Swift</i>	8986
090328A	0.736	1.84	1.42	34.0	19.5	<i>Fermi</i>	9056
090418A	1.61	1.68	0.967	41.5	15.0	KW	9171
090423A	8.2	1.57	1.29	35.7	10.9	<i>Fermi</i>	9229
090424A	0.544	1.18	1.76	30.5	4.51	<i>Fermi</i>	9230
090516A	3.9	1.40	4.52	18.9	65.0	<i>Fermi</i>	9413
090618A	0.54	1.49	1.44	33.8	25.4	<i>Fermi</i>	9535
090715B	3.	1.18	4.08	19.9	22.1	KW	9679
090809A	2.74	1.57	0.727	48.3	4.98	<i>Swift</i>	9756
090812A	2.45	1.23	5.39	17.3	41.7	KW+ <i>Swift</i>	9821
090902B	1.82	1.22	6.15	16.2	403.	<i>Fermi</i>	9866
090926A	2.11	1.50	5.29	17.4	217.	<i>Fermi</i>	9933
091003A	0.9	1.36	1.32	35.3	10.9	<i>Fermi</i>	9983
091020A	1.71	1.30	2.19	27.3	7.63	<i>Fermi</i>	10095
091029A	2.75	1.60	5.81	16.6	7.52	<i>Swift</i>	10103
091127A	0.49	1.32	1.36	34.9	1.79	<i>Fermi</i>	10204
091208B	1.06	1.09	1.15	38.0	2.03	<i>Fermi</i>	10266
100302A	4.81	0.812	5.67	16.8	5.24	<i>Swift</i>	10462
100425A	1.75	1.20	0.767	46.9	2.84	<i>Swift</i>	10685
100513A	4.77	1.44	3.74	20.8	25.7	<i>Swift</i>	10753
100621A	0.542	1.12	8.52	13.7	6.93	KW	10882
100814A	1.44	1.64	14.3	10.6	15.8	<i>Fermi</i>	11099
100901A	1.41	1.36	7.89	14.3	8.09	<i>Swift</i>	11169
100906A	1.73	1.87	1.32	35.3	22.5	<i>Fermi</i>	11248
110128A	2.339	1.16	0.620	52.6	3.60	<i>Fermi</i>	11628
110205A	2.22	1.59	0.913	42.8	41.0	KW	11659
110213A	1.46	1.81	2.33	26.4	7.00	<i>Fermi</i>	11727
110422A	1.77	1.24	6.03	16.3	62.0	KW	11971
110503A	1.613	1.36	2.45	25.7	19.0	KW	12008
110715A	0.82	1.69	7.33	14.8	5.60	KW	12166
110731A	2.83	1.22	6.31	16.0	42.0	<i>Fermi</i>	12221
110808A	1.348	1.33	0.588	54.1	6.10	<i>Swift</i>	12262
110918A	0.982	1.64	19.5	9.07	190.	KW	12362
111008A	4.9898	1.66	8.76	13.5	82.0	KW	12433
111123A	3.1516	1.55	2.82	24.0	70.0	<i>Swift</i>	12598
111209A	0.67	1.54	1.45	33.6	67.0	KW	12663
111228A	0.716	1.23	1.24	36.4	4.10	<i>Fermi</i>	12744
120119A	1.73	1.28	1.68	31.2	37.5	<i>Fermi</i>	12874
120326A	1.8	1.87	9.97	12.7	3.70	<i>Fermi</i>	13145
120327A	2.81	1.58	1.33	35.1	36.5	<i>Swift</i>	13137
120711A	1.41	1.58	18.1	9.40	166.	<i>Fermi</i>	13437
120712A	4.17	1.37	2.90	23.7	18.3	<i>Fermi</i>	13469
120909A	3.93	1.30	11.8	11.7	73.2	<i>Fermi</i>	13737
120922A	3.1	1.19	5.41	17.3	32.0	<i>Fermi</i>	13809
121024A	2.3	1.44	1.18	37.4	10.7	<i>Swift</i>	13899
121027A	1.77	1.28	15.8	10.1	6.55	<i>Swift</i>	13910
121128A	2.2	1.48	1.85	29.7	13.2	<i>Fermi</i>	14012
121217A	3	1.26	30.6	7.23	24.2	<i>Fermi</i>	14094
130418A	1.218	1.52	0.265	85.4	9.90	KW	14417
130420A	1.297	1.25	1.32	35.4	7.74	<i>Fermi</i>	14429
130427A	0.338	1.26	4.17	19.7	105.	<i>Fermi</i>	14473
130427B	2.78	1.85	0.275	83.4	5.04	<i>Swift</i>	14469
130505A	2.27	1.50	16.0	10.0	347.	KW	14575
130514A	3.6	1.56	5.16	17.7	52.4	KW+ <i>Swift</i>	14702
130528A	1.25	1.02	2.03	28.3	4.40	<i>Fermi</i>	14729
130606A	5.91	1.91	1.24	36.4	28.3	KW	14808
130610A	2.092	1.47	0.472	61.0	6.99	<i>Fermi</i>	14858
130701A	1.155	1.20	0.639	51.7	2.60	KW	14958
130907A	1.238	1.68	7.02	15.1	304.	KW	15203
130925A	0.347	1.32	2.85	23.8	18.4	<i>Fermi</i>	15255
131030A	1.293	1.27	2.97	23.4	173.	KW	15413
131105A	1.686	1.24	1.75	30.6	34.7	<i>Fermi</i>	15455
131108A	2.4	1.72	0.932	42.3	73.0	<i>Fermi</i>	15477
131117A	4.042	1.31	0.816	45.4	1.02	<i>Swift</i>	15499

Table 2
(Continued)

GRB	z	α	E_{LT}^a	θ ($^\circ$)	E_{iso}^b	Instrument ^c	GCN
131231A	0.642	1.44	3.39	21.8	22.2	<i>Fermi</i>	15644
140206A	2.74	1.43	13.5	10.9	35.9	<i>Fermi</i>	15796
140213A	1.2076	2.21	16.2	9.94	9.93	<i>Fermi</i>	15833
140226A	1.98	1.58	0.762	47.1	5.80	KW	15889
140304A	5.283	1.44	7.14	15.0	13.7	<i>Fermi</i>	15923
140311A	4.954	1.49	1.18	37.5	11.6	<i>Swift</i>	15962
140419A	3.956	1.84	9.32	13.1	186.	KW	16134
140423A	3.26	1.31	4.11	19.8	65.3	<i>Fermi</i>	16152
140506A	0.889	0.924	2.78	24.2	1.12	<i>Fermi</i>	16220
140508A	1.027	1.40	5.46	17.2	23.9	<i>Fermi</i>	16224
140509A	2.4	1.46	0.402	66.7	9.14	<i>Swift</i>	16240
140512A	0.725	1.62	2.22	27.1	7.76	<i>Fermi</i>	16262
140614A	4.233	1.24	2.00	28.5	7.30	<i>Swift</i>	16402
140620A	2.04	1.43	5.16	17.7	6.22	<i>Fermi</i>	16426
140629A	2.275	1.48	0.868	44.0	6.15	KW	16495
140703A	3.14	2.21	1.82	30.0	1.72	<i>Fermi</i>	16512
140907A	1.21	0.888	2.68	24.6	2.29	<i>Fermi</i>	16798
141026A	3.35	2.24	34.8	6.78	7.17	<i>Swift</i>	16960
141109A	2.993	1.31	7.85	14.3	5.05	KW	17055
141121A	1.47	1.67	6.56	15.6	14.6	KW	17108
141221A	1.452	1.18	0.970	41.5	1.94	<i>Fermi</i>	17216
150206A	2.087	1.28	10.1	12.6	151.	KW	17427
150314A	1.758	1.57	3.08	22.9	98.1	<i>Fermi</i>	17579
150403A	2.06	1.61	26.7	7.74	91.0	<i>Fermi</i>	17674
150514A	0.807	1.35	0.378	69.1	1.14	<i>Fermi</i>	17819
150821A	0.755	1.20	0.884	43.5	15.1	<i>Fermi</i>	18190
150910A	1.36	1.50	0.415	65.6	22.3	<i>Swift</i>	18268
151021A	2.33	1.47	2.69	24.6	211.	KW	18433
151027A	0.81	1.69	2.04	28.3	3.86	<i>Fermi</i>	18492
151027B	4.063	1.75	4.19	19.6	19.1	<i>Swift</i>	18514
151111A	3.5	1.29	0.871	43.9	5.13	<i>Fermi</i>	18582
151112A	4.1	1.54	3.31	22.1	12.4	<i>Swift</i>	18593
151215A	2.59	1.07	1.34	35.1	1.97	<i>Swift</i>	18699

Notes. It is composed by 161 sources spanning 11 years of *Swift*/XRT observation activity. In the table, we report important observational features: the redshift z , our estimates of the LXRE power-law slope α , the late-time energy E_{LT} , the collimation half-opening angle θ , the isotropic energy E_{iso} of the GRB, the observing instrument in the γ -ray band, and the correspondent circular (GCN) from which we take the γ -ray spectral parameters in order to estimate the E_{iso} of the GRB source.

^a In units of 10^{51} erg.

^b In units of 10^{52} erg.

^c “*Swift*” stands for *Swift*/BAT; “*Fermi*” stands for *Fermi*/GBM; “KW” stands for Konus-WIND.

2015; Izzo et al. 2012a; Rueda & Ruffini 2012; Fryer et al. 2014). Within the IGC paradigm, a tight binary system composed of a carbon–oxygen core (CO_{core}) undergoing a supernova (SN) explosion in the presence of a binary NS companion has been suggested as the progenitor for long gamma-ray bursts. Different scenarios occur depending on the distance between the CO_{core} and the NS binary companion (Becerra et al. 2015). Correspondingly two different sub-classes of long bursts have been shown to exist (for details, see Ruffini et al. 2015, 2016). A first long burst sub-class occurs when the CO_{core} –NS binary separation a is so large (typically $a > 10^{11}$ cm, see, e.g., Becerra et al. 2015) that the accretion of the SN ejecta onto the NS is not sufficient to have the NS reach its critical mass, M_{crit} , for gravitational collapse to a BH to occur. The hypercritical accretion of the SN ejecta onto the NS binary companion occurs in this case at rates below 10^{-2} solar masses per second and is characterized by a large associated neutrino emission (Zel’dovich et al. 1972; Ruffini & Wilson 1973; Rueda & Ruffini 2012; Fryer et al. 2014). We refer to such systems as X-ray flashes (XRFs). A second long burst sub-class occurs when the CO_{core} –NS binary is more tightly

bound ($a < 10^{11}$ cm, see, e.g., Becerra et al. 2015). The larger accretion rate of the SN ejecta, e.g., 10^{-2} – 10^{-1} solar masses per second, leads the companion NS to easily reach its critical mass M_{crit} (Rueda & Ruffini 2012; Fryer et al. 2014; Becerra et al. 2015), leading to the formation of a BH. We refer to such systems as binary-driven hypernovae (BdHNe, see, e.g., Ruffini et al. 2014c, 2015). A main observational feature, which allows us to differentiate BdHNe from XRFs is the isotropic γ -ray energy E_{iso} being larger than 10^{52} erg. Such a separation energy value is intimately linked to the binary separation a of the binary progenitor and the consequent birth or not of the BH (for details, see Ruffini et al. 2016).

Thanks to the XRT instrument on board the *Swift* satellite (Gehrels et al. 2004; Evans et al. 2007, 2010), we can compare and contrast the X-ray afterglow emissions of BdHNe and XRFs (see Figure 8). The typical X-ray afterglows of XRFs can be divided into two main parts: an initial bump with rapid decay, followed by an emerging slight decaying power law (see Figure 8). The typical X-ray afterglow light curve of BdHNe can be divided into three different parts: (1) an initial spike followed by an early steep power-law decay; (2) a plateau

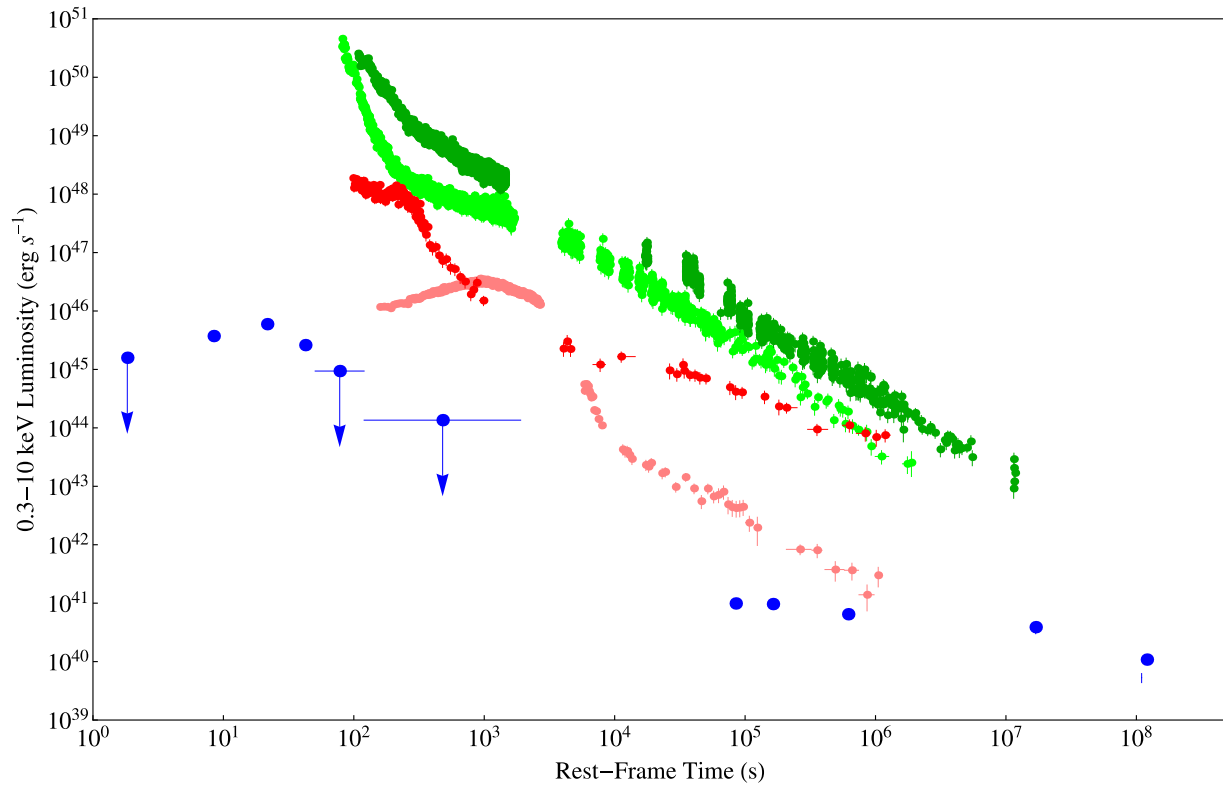


Figure 8. Comparison between rest-frame luminosity light curves of proto-typical BdHNe and XRFs sources. The BdHNe shown are GRB 130427A (dark green) and GRB 090618 (light green); while the XRF shown are GRB 101219B (red), GRB 060218 (pink), and GRB 980425 (blue).

phase; and (3) a late power-law decay, the LXRE, which is the presented in this work (Nousek et al. 2006; Ruffini et al. 2015). The treatment of the first parts of the X-ray afterglow of BdHNe, namely the spike, the initial steep decay, and the plateau phase, indeed fundamental within the BdHN picture, is beyond the scope of this article and it will be extensively shown in forthcoming works (R. Ruffini et al. 2016a, in preparation; R. Ruffini et al. 2016b, in preparation).

The universalities of the LXRE outlined in this article are then explained within the IGC paradigm, originating from the interaction of the GRB with the SN ejecta. The constancy of the late power-law luminosity in the rest frame is now explained in terms of the constancy in mass of the SN ejecta, which is standard in a BdHN (Rueda & Ruffini 2012; Fryer et al. 2014; Becerra et al. 2015).

It is appropriate to point out that no achromatic “Jet-break” effect has been observed in any of the 161 sources of our ES. We recall that the achromatic “Jet-break” effect is a consequence of relativistic jet pictures (Lorentz factor $\Gamma \sim 100$ –200), in which a change of slope is expected in the late X-ray light curve (see e.g., Rees & Meszaros 1992; Woosley 1993; Piran 2005; Gehrels et al. 2009; Kumar & Zhang 2015, and references therein), which clearly does not apply in the case of the BdHN following the IGC model. In this scenario, a velocity of expansion $v \sim 0.8c$ (Lorentz factor $\Gamma \sim 2$) is found, indicating that the collimation of the SN ejecta originates in a mildly relativistic regime (Ruffini et al. 2014c, 2015). This cannot be related to the ultra-relativistic jet emission recalled above, considered in the early work of Frail et al. (2001) and continued all the way to the more recent results presented by Ghirlanda et al. (2013). These authors attempted to explain all GRBs as originating from a single

object with an intrinsic energy approximately of 10^{50} erg (Frail et al. 2001) or 10^{48} erg (Ghirlanda et al. 2013): the different energetics and structures of all the GRBs were intended to be explained by the beaming effect with different ultra-relativistic Lorentz factors $\Gamma \sim 100$ –200. Indeed, it is by now clear (see Ruffini et al. 2015, 2016) that at least seven different classes of GRBs exist, each with different progenitors, different energies, and different spectra. In no way can these distinct classes can be explained by a single common progenitor, using simply relativistic beaming effects.

5. CONCLUSIONS

In this work, we give new statistical evidence for the existence of a universal behavior for the LXREs of BdHNe, introducing the presence of a collimation effect in such emission, and presenting the common LXRE energy $E_{LT}^{intr} = E_{LT}^{050525A} = 2.43 \times 10^{50}$ as a standard candle. We build an “enlarged sample” (ES) of 161 BdHNe, and focus on their LXREs and then we introduce a collimation effect. These analyses lead us to the following results.

- (1) We find for the ES an increased variability in the decaying LXRE power-law behavior in respect to the result previously deduced by Pisani et al. (2013). The typical slope of the power-law characterizing the LXRE is $\alpha = 1.48 \pm 0.32$ (GS: $\alpha = 1.44 \pm 0.18$), while the late-time integrated luminosity between 10^4 and 10^6 s in the rest frame is $\text{Log}_{10}(E_{LT}/\text{erg}) = 51.40 \pm 0.47$ (GS: $\text{Log}_{10}(E_{LT}/\text{erg}) = 51.15 \pm 0.28$).
- (2) The introduction of a collimation in the LXRE recovers a universal behavior. Assuming a double-cone shape for the LXRE region, we obtain a distribution of half-

opening angles peaking at $\theta = 17.62^\circ$, with a mean value of 30.05° , and a standard deviation of 19.65° , see Figure 7(a).

- (3) The application of the collimation effect to the LXREs of the ES indeed reduces the scattering of the power-law behavior found under the common assumption of isotropy; see Figures 5(a)–(b). The power-law scattering of the LXREs, after being corrected by the collimation factor, results in being even lower than the one found in the GS; see Figure 7(b).

The fact that these extreme conditions neither were conceived nor are explained within the traditional ultra-relativistic jetted SSC model (see, e.g., Rees & Meszaros 1992; Woosley 1993; Piran 2005; Gehrels et al. 2009; Kumar & Zhang 2015, and references therein), in view also of the clear success of the IGC paradigm in explaining the above features, comes as a clear support to a model for GRBs strongly influenced by the binary nature of their progenitors, involving a definite succession of selected astrophysical processes for a complete description of the BdHNe.

These intrinsic signatures in the LXREs of BdHNe, independent from the energetics of the GRB prompt emission, open the perspective for a standard candle up to $z \gtrsim 8$.

It is remarkable that the universal behavior occurs in the rest-frame time interval 10^4 – 10^6 s, which precisely corresponds to the temporal window of the early observations of Beppo-SAX at the time of the afterglow discovery (see Figure 1).

We thank both the editor and the referee for the fruitful correspondence that improved the presentation of our results. This work made use of data supplied by the UK Swift Science Data Center at the University of Leicester. M.K. and Y.A. are supported by the Erasmus Mundus Joint Doctorate Program by Grant Nummbers 2013-1471 and 2014-0707, respectively, from the EACEA of the European Commission.

REFERENCES

- Ackermann, M., Asano, K., Atwood, W. B., et al. 2010, *ApJ*, **716**, 1178
- Becerra, L., Cipolletta, F., Fryer, C. L., Rueda, J. A., & Ruffini, R. 2015, *ApJ*, **812**, 100
- Bloom, J. S., Frail, D. A., & Sari, R. 2001, *AJ*, **121**, 2879
- Boella, G., Butler, R. C., Perola, G. C., et al. 1997, *A&AS*, **122**, 299
- Campana, S., Mangano, V., Blustin, A. J., et al. 2006, *Natur*, **442**, 1008
- Costa, E., Feroci, M., Piro, L., et al. 1997a, *IAUC*, **6576**, 1
- Costa, E., Frontera, F., Heise, J., et al. 1997b, *Natur*, **387**, 783
- Della Valle, M., Malesani, D., Benetti, S., et al. 2006a, *IAUC*, **8696**, 1
- Della Valle, M., Malesani, D., Bloom, J. S., et al. 2006b, *ApJL*, **642**, L103
- de Pasquale, M., Piro, L., Gendre, B., et al. 2006, *A&A*, **455**, 813
- de Ugarte Postigo, A., Xu, D., Leloudas, G., et al. 2013, *GCN Circ.*, **14646**, 1
- Dezalay, J.-P., Barat, C., Talon, R., et al. 1992, in *AIP Conf. Ser.* 265, *Gamma-ray Bursts*, ed. W. S. Paciesas & G. J. Fishman, **304**
- Evans, P. A., Beardmore, A. P., Page, K. L., et al. 2007, *A&A*, **469**, 379
- Evans, P. A., Willingale, R., Osborne, J. P., et al. 2010, *A&A*, **519**, A102
- Frail, D. A., Kulkarni, S. R., Sari, R., et al. 2001, *ApJL*, **562**, L55
- Frontera, F., Amati, L., Costa, E., et al. 2000, *ApJSS*, **127**, 59
- Frontera, F., Costa, E., Piro, L., et al. 1998, *ApJL*, **493**, L67
- Fryer, C. L., Rueda, J. A., & Ruffini, R. 2014, *ApJL*, **793**, L36
- Gehrels, N., Chincarini, G., Giommi, P., et al. 2004, *ApJ*, **611**, 1005
- Gehrels, N., Ramirez-Ruiz, E., & Fox, D. B. 2009, *ARA&A*, **47**, 567
- Ghirlandi, G., Ghisellini, G., Salvaterra, R., et al. 2013, *MNRAS*, **428**, 1410
- Golenetskii, S., Aptekar, R., Mazets, E., et al. 2005, *GCN*, **3474**, 1
- Izzo, L., Rueda, J. A., & Ruffini, R. 2012a, *A&A*, **548**, L5
- Izzo, L., Ruffini, R., Penacchioni, A. V., et al. 2012b, *A&A*, **543**, A10
- Klebesadel, R. W. 1992, in *Gamma-Ray Bursts—Observations, Analyses and Theories*, ed. C. Ho, R. I. Epstein, & E. E. Fenimore (Cambridge: Cambridge Univ. Press)
- Kouveliotou, C., Meegan, C. A., Fishman, G. J., et al. 1993, *ApJL*, **413**, L101
- Kumar, P., & Zhang, B. 2015, *PhR*, **561**, 1
- Levan, A. J., Fruchter, A. S., Graham, J., et al. 2013, *GCN Circ.*, **14686**, 1
- Margutti, R., Zaninoni, E., Bernardini, M. G., et al. 2013, *MNRAS*, **428**, 729
- Mazets, E. P., Golenetskii, S. V., Ilinskii, V. N., et al. 1981, *Ap&SS*, **80**, 3
- Meszaros, P., & Rees, M. J. 1997, *ApJ*, **476**, 232
- Nousek, J. A., Kouveliotou, C., Grupe, D., et al. 2006, *ApJ*, **642**, 389
- Penacchioni, A. V., Ruffini, R., Bianco, C. L., et al. 2013, *A&A*, **551**, A133
- Penacchioni, A. V., Ruffini, R., Izzo, L., et al. 2012, *A&A*, **538**, A58
- Perley, D. A., Cenko, S. B., Corsi, A., et al. 2014, *ApJ*, **781**, 37
- Piran, T. 2005, *RvMP*, **76**, 1143
- Pisani, G. B., Izzo, L., Ruffini, R., et al. 2013, *A&A*, **552**, L5
- Rees, M. J., & Meszaros, P. 1992, *MNRAS*, **258**, 41
- Rueda, J. A., & Ruffini, R. 2012, *ApJL*, **758**, L7
- Ruffini, R., Bernardini, M. G., Bianco, C. L., et al. 2007, *ESA SP*, **622**, 561
- Ruffini, R., Bianco, C. L., Chardonnet, P., Frascchetti, F., & Xue, S.-S. 2001a, *ApJL*, **555**, L107
- Ruffini, R., Bianco, C. L., Chardonnet, P., Frascchetti, F., & Xue, S.-S. 2001b, *ApJL*, **555**, L113
- Ruffini, R., Bianco, C. L., Chardonnet, P., Frascchetti, F., & Xue, S.-S. 2001c, *ApJL*, **555**, L117
- Ruffini, R., Bianco, C. L., Enderli, M., et al. 2013a, *GCN Circ.*, **14526**, 1
- Ruffini, R., Bianco, C. L., Enderli, M., et al. 2013b, *GCN Circ.*, **14888**, 1
- Ruffini, R., Bianco, C. L., Enderli, M., et al. 2013c, *GCN Circ.*, **15576**, 1
- Ruffini, R., Bianco, C. L., Enderli, M., et al. 2014a, *GCN Circ.*, **15707**, 1
- Ruffini, R., Izzo, L., Muccino, M., et al. 2014b, *A&A*, **569**, A39
- Ruffini, R., Muccino, M., Bianco, C. L., et al. 2014c, *A&A*, **565**, L10
- Ruffini, R., Rueda, J. A., Muccino, M., et al. 2016, *ApJ*, **832**, 136
- Ruffini, R., Wang, Y., Enderli, M., et al. 2015, *ApJ*, **798**, 10
- Ruffini, R., & Wilson, J. 1973, *PhRvL*, **31**, 1362
- Salvaterra, R., Della Valle, M., Campana, S., et al. 2009, *Natur*, **461**, 1258
- Sari, R., Piran, T., & Narayan, R. 1998, *ApJL*, **497**, L17
- Soderberg, A. M., Berger, E., Kasliwal, M., et al. 2006a, *ApJ*, **650**, 261
- Soderberg, A. M., Kulkarni, S. R., Nakar, E., et al. 2006b, *Natur*, **442**, 1014
- Tanvir, N. R., Fox, D. B., Levan, A. J., et al. 2009, *Natur*, **461**, 1254
- Tavani, M. 1998, *ApJL*, **497**, L21
- Woosley, S. E. 1993, *ApJ*, **405**, 273
- Zel'dovich, Y. B., Ivanova, L. N., & Nadezhin, D. K. 1972, *SvA*, **16**, 209



ON THE CLASSIFICATION OF GRBs AND THEIR OCCURRENCE RATES

R. RUFFINI^{1,2,3,4}, J. A. RUEDA^{1,2,4}, M. MUCCINO^{1,2}, Y. AIMURATOV^{1,2}, L. M. BECERRA^{1,2}, C. L. BIANCO^{1,2}, M. KOVACEVIC^{1,2,3},
R. MORADI^{1,2}, F. G. OLIVEIRA^{1,2,3}, G. B. PISANI^{1,2}, AND Y. WANG^{1,2}

¹ Dipartimento di Fisica and ICRA, Sapienza Università di Roma, Piazzale Aldo Moro 5, I-00185 Rome, Italy

² ICRANet, Piazza della Repubblica 10, I-65122 Pescara, Italy

³ Université de Nice Sophia Antipolis, CEDEX 2, Grand Château Parc Valrose, Nice, France

⁴ ICRANet-Rio, Centro Brasileiro de Pesquisas Físicas, Rua Dr. Xavier Sigaud 150, 22290-180 Rio de Janeiro, Brazil

Received 2015 December 21; revised 2016 September 6; accepted 2016 September 7; published 2016 November 23

ABSTRACT

There is mounting evidence for the binary nature of the progenitors of gamma-ray bursts (GRBs). For a long GRB, the induced gravitational collapse paradigm proposes as progenitor, or “in-state,” a tight binary system composed of a carbon–oxygen core (CO_{core}) undergoing a supernova explosion that triggers hypercritical accretion onto a neutron star (NS) companion. For a short GRB (S-GRB), an NS–NS merger is traditionally adopted as the progenitor. We divide long and S-GRBs into two subclasses, depending on whether or not a black hole (BH) is formed in the merger or in the hypercritical accretion process exceeding the NS critical mass. For long bursts, when no BH is formed, we have the subclass of X-ray flashes (XRFs), with isotropic energy $E_{\text{iso}} \lesssim 10^{52}$ erg and rest-frame spectral peak energy $E_{p,i} \lesssim 200$ keV. When a BH is formed, we have the subclass of binary-driven hypernovae (BdHNe), with $E_{\text{iso}} \gtrsim 10^{52}$ erg and $E_{p,i} \gtrsim 200$ keV. In analogy, short bursts are similarly divided into two subclasses. When no BH is formed, short gamma-ray flashes (S-GRFs) occur, with $E_{\text{iso}} \lesssim 10^{52}$ erg and $E_{p,i} \lesssim 2$ MeV. When a BH is formed, the authentic S-GRBs occur, with $E_{\text{iso}} \gtrsim 10^{52}$ erg and $E_{p,i} \gtrsim 2$ MeV. We give examples and observational signatures of these four subclasses and their rate of occurrence. From their respective rates it is possible that “in-states” of S-GRFs and S-GRBs originate from the “out-states” of XRFs. We indicate two additional progenitor systems: white dwarf–NS and BH–NS. These systems have hybrid features between long and short bursts. In the case of S-GRBs and BdHNe evidence is given of the coincidence of the onset of the high-energy GeV emission with the birth of a Kerr BH.

Key words: binaries: general – black hole physics – gamma-ray burst: general – stars: neutron – supernovae: general – white dwarfs

1. INTRODUCTION

On 1974 February, at the same AAAS meeting in San Francisco where the discovery of gamma-ray bursts (GRBs) by the Vela satellites was publicly announced (Strong et al. 1975), the possible relation of GRBs to the “moment of gravitational collapse” leading to a black hole (BH) formation was advanced (see Gursky & Ruffini 1975). Damour & Ruffini (1975) considered, for definiteness, the vacuum polarization process occurring in an overcritical Kerr–Newman BH (KNBH). Evidence was given for (a) the formation of a vast amount of e^+e^- -baryon plasma; (b) the energetics of GRBs of the order of $E_{\text{max}} \approx 10^{54} M_{\text{BH}}/M_{\odot}$ erg, where M_{BH} is the BH mass, implying their cosmological origin; and (c) ultra-high-energy cosmic rays with energy up to $\sim 10^{20}$ eV originating from such an extreme electrodynamical process. Soon after, the role of an e^+e^- plasma for the origin of GRBs was also considered by Cavallo & Rees (1978). It took almost 30 yr to clarify some of the analogies and differences between these two processes of e^+e^- -pair creation leading, respectively, to the alternative concepts of “fireball” and “fireshell” (Aksenov et al. 2007, 2009).

Already in 1989, well before the establishment of the GRB cosmological nature and energetics, Eichler et al. (1989) gave support to the cosmological interpretation of GRBs and indicated in merging neutron star (NS) binaries their possible origin. They also pointed out the relevance of such NS–NS mergers for the occurrence of r -process, as well as for the emission of gravitational radiation, indicating the uncertainty in the determination of their rate of occurrence.

Following the launch of the *Compton Gamma Ray Observatory* and the observations by the BATSE detector (Meegan et al. 1992), a phenomenological classification based on the prompt T_{90} duration was advanced: GRBs were classified into long GRBs (L-GRBs) for $T_{90} > 2$ s and short GRBs (S-GRBs) for $T_{90} < 2$ s (Dezalay et al. 1992; Klebesadel 1992, pp. 161–68; Kouveliotou et al. 1993; Tavani 1998).

Shortly after, Narayan et al. (1992) indicated the possible cosmological origin of S-GRBs originating in binary NS mergers. They also introduced the clear indication of the role of $\nu\bar{\nu}$ annihilation leading to the formation of an e^+e^- plasma. This paper was followed by a large number of theoretical works including the gravitational wave emission in Newtonian, post-Newtonian, and general relativistic treatments (see, e.g., Rasio & Shapiro 1999), as well as the $\nu\bar{\nu}$ annihilation leading to an e^+e^- plasma (see, e.g., Salmonson & Wilson 2002 and Rosswog et al. 2003 and references therein).

Soon after the paper by Narayan et al. (1992), Woosley (1993) also supported the cosmological origin of GRBs and introduced the concept of BH accretion disks, produced by the collapse of a very massive star. Such a system was indicated by its author as a *collapsar* and was assumed to be the origin of ultrarelativistic jets expected to occur by the same author in L-GRBs. For a recent review see MacFadyen & Woosley (1999), MacFadyen et al. (2001), and Woosley & Bloom (2006).

After the determination of the cosmological nature of GRBs (Costa et al. 1997; Metzger et al. 1997; van Paradijs et al. 1997) and the confirmation of their outstanding energy ($\approx 10^{54}$ erg), we returned to our GRB scenario (Damour & Ruffini 1975). In

a period of 4 yr, from 1997 to 2001, we developed a fully relativistic GRB theoretical model examining, as well, the dynamics of the e^+e^- plasma originating the GRB emission (the fireshell model; see, e.g., Preparata et al. 1998; Ruffini et al. 1999, 2000, 2001a, 2001b, 2001c; see also Section 2). The fireshell model applies to both S-GRBs and L-GRBs.

The origin of S-GRBs from NS–NS (or NS–BH) binaries as “in-states” has been confirmed by strong observational and theoretical evidence (see, e.g., Goodman 1986; Paczynski 1986; Eichler et al. 1989; Narayan et al. 1991, 1992; Meszaros & Rees 1997; Rosswog et al. 2003; Lee et al. 2004; Berger 2014). In this article we address specifically some of the latest results within the fireshell model (Muccino et al. 2013; Ruffini et al. 2015b) on the possible presence or absence of a BH formation in NS–NS mergers; the consequent classification of short bursts into short gamma-ray flashes (S-GRFs), when no BH is formed (see Section 6), and S-GRBs, when a BH is formed (see Section 7); and the computation of their occurrence rate (see Section 10).

The application of the fireshell model to the case of L-GRBs followed a longer path for reaching a proper understanding of the overall phenomenon. The first application of our model to an L-GRB was implemented on GRB 991216 (Ruffini et al. 2001a, 2001b, 2001c, 2002, 2004, 2006a). In these papers a clear difference between the thermal component observed at the transparency of the e^+e^- plasma, the proper GRB (P-GRB) emission (Ruffini et al. 1999, 2000), and the nonthermal remaining part, later called prompt emission (Ruffini et al. 2001b), was evidenced. This fully relativistic approach was not readily accepted by the GRB community, also in view of its objective technical complexity and novelties in the theoretical physics scenario. Some authors attempted to describe the GRB phenomenon by simplified Newtonian approaches, e.g., those based on the concept of *magnetars* (Usov 1992; Dai & Lu 1998a, 1998b; Kluźniak & Ruderman 1998; Zhang & Mészáros 2001). As detailed observations of the X-ray afterglow by *Swift*-XRT (Evans et al. 2007) were obtained, as well as high-energy emission by *Fermi*-LAT (Atwood et al. 2009), our model has correspondingly evolved, pointing out the precise common power-law behavior of the rest-frame 0.3–10 keV X-ray luminosity light curves (Pisani et al. 2013), as well as the nesting properties (Ruffini et al. 2014b). As pointed out in the present article, the concept of L-GRBs has evolved into X-ray flashes (XRFs) and binary-driven hypernovae (BdHNe), depending on the possible presence or absence of a BH in their formation process (see also Ruffini et al. 2015c).

It is appropriate to recall that the quest for having progenitors for the collapsar hypothesized by Woosley (1993) led to an interesting direction of research dealing with a binary system composed of two very massive stars of $\approx 50 M_\odot$ each. The large masses involved in these systems were introduced in order to form a BH at the end of their evolution. Similarly, the large amount of angular momentum of the system would guarantee the formation of an accretion disk needed in the collapsar model (Fryer et al. 1999). Up to six different scenarios were there envisaged leading to a *collapsar*, as well as a few leading, alternatively, to a variety of binary compact systems. The need for choosing low-metallicity massive stars followed from the expectation of the formation of large BHs in their evolution (Fryer et al. 1999). The elimination of H from metal-rich massive stars would follow naturally, but the formation of a BH

was not expected in their final stage of evolution (Woosley 1993).

The spatial and temporal coincidence of an L-GRB explosion with an optical supernova (SN), first observed in the association between GRB 980425 and SN 1998bw, created a profound conceptual turmoil in the GRB community. Woosley and collaborators postulated the birth of an SN out of a collapsar (see, e.g., Woosley & Bloom 2006, and references therein).

In our approach, GRBs were supposed to originate from the BH formation, while SNe were expected to lead only to NSs (see, e.g., Ruffini 2015, and references therein). We consequently introduced a new paradigm to explain the coincidence of these two qualitative and quantitative different astrophysical events in space and time: the birth of an SN and the occurrence of a GRB. The induced gravitational collapse (IGC) paradigm was then introduced (see, e.g., Ruffini et al. 2001c, 2006b, 2007, 2008; Izzo et al. 2012b; Rueda & Ruffini 2012; Fryer et al. 2014). This approach differs from alternative descriptions of the GRB–SN coincidences occurring, e.g., in the *magnetars* and the *collapsar* models, where the two events are coming from a single progenitor star, and takes full advantage of the recent observations of SNe Ibc in interacting binary systems (Smartt 2009).

In a first formulation we considered a finely tuned process: the GRB triggering the explosion of a binary companion star very close to the onset of the SN (Ruffini et al. 2001c). This scenario soon led to the alternative IGC paradigm in which a CO_{core} undergoes an SN explosion in the presence of an NS companion in a tight binary system. This is also by itself an unlikely event that, in order to occur, needs a fine-tuning of the initial conditions of the binary system. This scenario was shown to be consistent with population synthesis analysis (Fryer et al. 1999, 2015). The SN explosion induces a hypercritical accretion of its ejecta onto the companion NS, leading to the formation of a more massive NS (MNS), when the NS critical mass M_{crit} is not reached, or to the formation of a BH with the associated GRB emission in the opposite case (see, e.g., Rueda & Ruffini 2012; Fryer et al. 2014). The IGC scenario was first tested and verified in GRB 090618 (Izzo et al. 2012b, 2012c). It soon became clear that the occurrence of a GRB is far from being a single event, but it is part of an authentic laboratory composed of a variety of astrophysical relativistic phenomena preceeding and following the prompt GRB emission.

We adopted as progenitor of our CO_{core}–NS binary system the massive binaries independently considered in Fryer et al. (1999) and Nomoto et al. (1994, 1995). In our case, the late evolution of such massive binary systems does not lead to a collapsar, nor to a hypernova, but to a much richer and vast number of possibilities, made possible by our IGC paradigm. Consistently with the considerations by Sakamoto et al. (2005), indicating that XRFs, X-ray-rich bursts, and all L-GRBs are part of the same population, which we show to originate in the hypercritical accretion process of the SN ejecta onto a binary companion NS.

In agreement with the considerations by Soderberg et al. (2006), Guetta & Della Valle (2007), and Liang et al. (2007) for a subclassification of long bursts into low-luminosity and high-luminosity GRBs, we have divided the long bursts into two different scenarios depending on the distance between the CO_{core} and the NS binary companion (Becerra et al. 2015).

Correspondingly, two different subclasses of long bursts, both originating in the hypercritical accretion process of the IGC scenario, have been shown to exist (Becerra et al. 2015; Ruffini et al. 2015c): the XRFs, which clearly include low-luminosity GRBs, such as GRB 060218 (Campana et al. 2006), when no BH is formed (see Section 4), and the BdHNe, such as GRB 130427A (Ruffini et al. 2015c), when a BH is formed (see Section 5). Their occurrence rates have been computed (see Section 10). Instead of proposing just a new classification, we also give the description of its underlying physical origin: the hypercritical accretion process of the SN ejecta onto a binary companion NS, with the full associated theoretical treatments at the basis of the IGC paradigm.

To the above four subclasses of long and short bursts, we have recently added a new hybrid subclass of ultrashort GRBs (U-GRBs), which, as recently pointed out in Fryer et al. (2015), can originate during the further evolution of the BdHNe out-states. Indeed, nearly 100% of the NS–BH binaries that are the outcome of BdHNe remain bound. Their orbital velocities are high, and even large kicks are unlikely to unbind these systems. They represent a new family of NS–BH binaries unaccounted for in current standard population synthesis analyses (see, e.g., Fryer et al. 2015 and Section 8).

The above considerations based on the IGC paradigm and the NS–NS paradigm as progenitors encompass and classify into subclasses most of the known astrophysical systems related to GRBs. We finally recall the existence of a class of L-GRBs occurring in a low-density circumburst medium (CBM) with density $\sim 10^{-3} \text{ cm}^{-3}$, with hybrid short/long burst properties in their γ -ray light curves: (1) an initial spike-like harder emission and (2) a prolonged softer emission observed for up to 100 s. These bursts do not have an associated SN, even though in the case of a low value of the cosmological redshift its detection would not be precluded. The prototype of such systems is GRB 060614 (Della Valle et al. 2006). The progenitor for this class of long bursts has been identified in a binary system composed of an NS and a white dwarf (WD) (Caito et al. 2009). Their merger leads to an MNS with additional orbiting material, but not to an authentic GRB. We refer to these systems, historically addressed as disguised S-GRBs, as gamma-ray flashes (GRFs; see, e.g., GRB 060614, Caito et al. 2009; and GRB 071227, Caito et al. 2010).

In the following we adopt the term *burst* only for those systems leading to BH formation, namely, S-GRBs, U-GRBs, and BdHNe. We refer to the term *flash*, instead, only for those systems not leading to BH formation, namely, S-GRFs, GRFs, and XRFs.

The main topic addressed in the present article is to estimate the rates of occurrence of the XRFs, BdHNe, S-GRFs, S-GRBs, U-GRBs, and GRFs and to give a general description of these GRB subclasses. In Section 2 we present a short summary on the fireshell model. In Section 3 we discuss the 10^{52} erg lower limit in binary systems leading to BH formation. After describing the observational properties of the above subclasses, their interpretation within the IGC paradigm, the NS–NS merger scenario, and the fireshell scenario, we present some prototypes (see Sections 4, 5, 6, 7, 8, and 9, respectively). We then proceed in Section 10 to estimate their observed occurrence rates and to compare and contrast our results with those outlined in the literature (see, e.g., Soderberg et al. 2006; Guetta & Della Valle 2007; Liang et al. 2007; Virgili et al. 2009, 2011; Rangel Lemos et al. 2010; Wanderman &

Table 1
Alphabetic Ordered List of the Acronyms Used in This Work

Extended wording	Acronym
Binary-driven hypernova	BdHN
black hole	BH
Carbon–oxygen core	CO _{core}
Circumburst medium	CBM
Equitemporal surfaces	EQTS
Gamma-ray burst	GRB
Gamma-ray flash	GRF
Induced gravitational collapse	IGC
Kerr–Newman black hole	KNBH
Massive neutron star	MNS
Neutron star	NS
New neutron star	ν NS
Proper gamma-ray burst	P-GRB
Short gamma-ray burst	S-GRB
Short gamma-ray flash	S-GRF
Supernova	SN
Ultrashort gamma-ray burst	U-GRB
White dwarf	WD
X-ray flash	XRF

Piran 2010, 2015; Kovacevic et al. 2014; Sun et al. 2015). We then draw some general conclusions in Section 11.

A standard flat Λ CDM cosmological model with $\Omega_M = 0.27$, $\Omega_\Lambda = 0.73$, and $H_0 = 71 \text{ km s}^{-1} \text{ Mpc}^{-1}$ is adopted throughout the paper. A summary of acronyms used throughout the paper is shown in Table 1.

2. SUMMARY OF THE FIRESHELL MODEL

The fireshell model for GRBs (see, e.g., Ruffini et al. 2001a, 2001b, 2001c) has been introduced to explain the GRB phenomenon as originating in the gravitational collapse leading to the formation of a BH (Damour & Ruffini 1975). The GRB emission results by taking into proper account relativistic magnetohydrodynamical effects, quantum electrodynamical processes, and relativistic spacetime transformations.

The role of the relativistic magnetohydrodynamical effects arising in the gravitational collapse of a globally neutral magnetized plasma has been first considered in Ruffini & Wilson (1975), where the occurrence of a local charge separation, during a globally neutral accretion process, led to the development of overcritical electric fields at the onset of a KNBH formation.⁵ These overcritical fields and, consequently, the vacuum polarization process leading to the creation of an e^+e^- plasma have been considered in Damour & Ruffini (1975), for the sake of definiteness in a KNBH, as the energy source of GRBs:⁶ the pair creation process is fully reversible, and as a result, a highly efficient energy extraction mechanism occurs, which may deliver as much as $E_{\text{max}} \approx 10^{54} M_{\text{BH}}/M_\odot \text{ erg}$.

Later on, the concept of *dyadotorus* for a KNBH (Cherubini et al. 2009; Ruffini 2009) was introduced to describe the region where pair creation occurs, leading to the formation of a BH. The dynamics of an optically thick *fireshell* of e^+e^- plasma of

⁵ Overcritical electric fields are defined as larger than the critical value $E_c = m_e^2 c^3 / (\hbar e)$, where m_e is the electron mass, c the speed of light in the vacuum, \hbar the reduced Planck constant, and e the electron charge.

⁶ The role of an e^+e^- plasma for the origin of GRBs was also considered independently by Cavallo & Rees (1978).

total energy $E_{e^+e^-}^{\text{tot}}$, i.e., its expansion and self-acceleration due to its own internal pressure, has been described in Ruffini et al. (1999). The effect of baryonic contamination, i.e., the remnant of the collapsed object, on the dynamics of the fireshell was then considered in Ruffini et al. (2000), where it was shown that even after the engulfment of a baryonic mass M_B , quantified by the baryon load $B = M_B c^2 / E_{e^+e^-}^{\text{tot}}$, the fireshell remains still optically thick and continues its self-acceleration up to ultrarelativistic velocities (Aksenov et al. 2007, 2009). When the fireshell reaches the transparency condition, a flash of thermal radiation termed P-GRB is emitted (Ruffini et al. 1999, 2000). The dynamics of the fireshell up to the transparency condition is fully described by $E_{e^+e^-}^{\text{tot}}$ and B : solutions with $B \leq 10^{-2}$ are characterized by regular relativistic expansion; for $B > 10^{-2}$ turbulence and instabilities occur (Ruffini et al. 2000).

The P-GRB emission is followed by the prompt emission (Ruffini et al. 2001b). The prompt emission originates in the collisions of the accelerated baryons left over after transparency, moving at Lorentz factor $\Gamma \approx 100$ –1000, with interstellar clouds of the CBM (Ruffini et al. 2002, 2004, 2005). These interactions give rise to a modified blackbody spectrum in the comoving frame (Patricelli et al. 2012). The resulting observed spectral shape, once the constant arrival time effect is taken into account in the equitemporal surfaces (EQTs; see Bianco & Ruffini 2005a, 2005b), is in general nonthermal, as a result of the convolution of a large number of modified thermal spectra with different Lorentz factors and temperatures. To reproduce the prompt emission light curve and spectra, three additional parameters, all related to the properties of the CBM, are required: the CBM density profile n_{CBM} , the filling factor \mathcal{R} that accounts for the size of the effective emitting area, and a low-energy power-law index α of the modified blackbody spectrum (Patricelli et al. 2012). These parameters are obtained by running a trial-and-error simulation of the observed prompt emission light curves and spectra.

To describe the dynamics of such an e^+e^- -baryon plasma from the vicinity of a BH all the way up to ultrarelativistic velocities at infinity, both in the P-GRB and in the prompt emission, the appropriate relative spacetime transformation paradigm was discussed in Ruffini et al. (2001a). It relates the observed GRB signal to its past light cone, defining the events on the worldline of the source that is essential for the interpretation of the data. Particular attention has been there given to the explicit equations relating the comoving time, the laboratory time, the arrival time, and the arrival time at the detector corrected by the cosmological effects, consistently with the equation of motion of the system (see also Bianco & Ruffini 2004, 2005a, 2005b, 2006), compared and contrasted with the corresponding treatments in the literature (see, e.g., Sari 1997, 1998; Waxman 1997; Panaitescu & Meszaros 1998; Rees & Meszaros 1998; Chiang & Dermer 1999; Granot et al. 1999; Panaitescu & Mészáros 1999).

As recalled above, the evolution of a baryon-loaded pair plasma is generally described in terms of $E_{e^+e^-}^{\text{tot}}$ and B , and it is independent of the way the pair plasma is created. Given this generality, in addition to the specific case of the dyadotorus mentioned above, these concepts can be applied as well in the case of a pair plasma created via the $\nu\bar{\nu} \leftrightarrow e^+e^-$ mechanism in an NS merger as described in Narayan et al. (1992), Salmonson & Wilson (2002), and Rosswog et al. (2003), or in the hyperaccretion disks around BHs as described in Woosley

(1993) and Zalamea & Beloborodov (2011), assuming that the created pair plasma is optically thick. The relative role of neutrino and weak interactions versus the electromagnetic interactions in building the dyadotorus is currently the topic of intense research.

In conclusion, the deeper understanding of the GRB phenomenon, occurring under very different initial conditions, has highlighted the possibility of using the general description of the dyadosphere (dyadotorus) for any source of an optically thick baryon-loaded e^+e^- plasma and, consequently, of applying the above fireshell treatment in total generality.

The generality of the fireshell approach clearly differs from alternative treatments purporting late activity from a central engine (see, e.g., the *collapsar* model in Woosley 1993; Popham et al. 1999; Woosley & Bloom 2006 and references therein; and the Newtonian *magnetar* model in Zhang & Mészáros 2001; Dai et al. 2006; Metzger et al. 2011; Bucciantini et al. 2012; Giacomazzo & Perna 2013; Lü & Zhang 2014, and references therein) and proposes a different explanation for the afterglow observations in L-GRBs (see Pisani et al. 2013; Y. Aimuratov et al. 2016, in preparation).

3. ON THE 10^{52} ERG LOWER LIMIT IN BINARY SYSTEMS LEADING TO BH FORMATION

During the hypercritical accretion process onto the NS, the total energy available to be released, e.g., in the form of neutrinos and photons, is given by the gain of gravitational potential energy of the matter being accreted by the NS (Zel'dovich et al. 1972; Ruffini & Wilson 1973; Rueda & Ruffini 2012; Fryer et al. 2014). The total energy released in the star in a time interval dt during the accretion of an amount of mass dM_b with angular momentum $l\dot{M}_b$ is given by (see, e.g., Sibgatullin & Sunyaev 2000; Becerra et al. 2015)

$$L_{\text{acc}} = (\dot{M}_b - \dot{M}_{\text{NS}})c^2 = \dot{M}_b c^2 \left[1 - \left(\frac{\partial M_{\text{NS}}}{\partial J_{\text{NS}}} \right)_{M_b} \times l - \left(\frac{\partial M_{\text{NS}}}{\partial M_b} \right)_{J_{\text{NS}}} \right], \quad (1)$$

where J is the NS angular momentum. The last two terms of the above equation take into due account the change of binding energy of the NS while accreting both matter and angular momentum. We assume, as a norm, a typical NS mass of $\approx 1.4 M_\odot$, a value observed in galactic NS binaries (Zhang et al. 2011; Antoniadis 2015) and characteristic of the XRFs (Becerra et al. 2016). We also assume an NS critical mass M_{crit} in the range from 2.2 up to $3.4 M_\odot$ depending on the equations of state and angular momentum (see Cipolletta et al. 2015; Becerra et al. 2016, 2015, for details). L_{acc} is clearly a function of both the NS mass and M_{crit} .

Since $L_{\text{acc}} \propto \dot{M}_b$, it evolves with time similarly to \dot{M}_b . We have shown that the accretion luminosity can be as high as $L_{\text{acc}} \sim 0.1 \dot{M}_b c^2 \sim 10^{47}$ – 10^{51} erg s^{-1} for accretion rates $\dot{M}_b \sim 10^{-6}$ – $10^{-2} M_\odot \text{s}^{-1}$ (see Becerra et al. 2015, 2016, for details). The duration of the accretion process is given approximately by the flow time of the slowest layers of the SN ejecta to the NS companion. If the velocity of these layers is v_{inner} , then $\Delta t_{\text{acc}} \sim a/v_{\text{inner}}$, where a is the binary separation. For $a \sim 10^{11}$ cm and $v_{\text{inner}} \sim 10^8$ cm s^{-1} we obtain $\Delta t_{\text{acc}} \sim 10^3$ s, while for shorter binary separation,

Table 2
List of the XRFs Considered in This Work up to the End of 2014

GRB	z	$E_{\text{iso}}/(10^{50} \text{ erg})$	GRB	z	$E_{\text{iso}}/(10^{50} \text{ erg})$
970508	0.835	65 ± 13	081007	0.5295	17 ± 2
980425	0.0085	0.0064 ± 0.0016	100316D	0.059	0.59 ± 0.05
980613	1.096	50 ± 10	100816A	0.8049	71 ± 9
990712	0.434	69 ± 13	101219B	0.55	63 ± 6
020819B	0.41	69 ± 18	110106B	0.618	$73 \pm$
020903	0.251	0.24 ± 0.06	120121B	0.017	0.0139 ± 0.0002
031203	0.105	0.99 ± 0.10	120422A	0.283	2.4 ± 0.8
050416A	0.6528	11 ± 2	120714B	0.3984	8.0 ± 2.0
060218	0.033	0.54 ± 0.05	130702A	0.145	6.5 ± 1.0
070419	0.97	24 ± 10	130831A	0.4791	46 ± 2

Note. For each source (first and fourth columns) the values of z and $E_{\text{iso}} \lesssim 10^{52}$ erg (second, third, fifth, and sixth columns) are listed.

e.g., $a \sim 10^{10}$ cm ($P \sim 5$ minutes), $\Delta t_{\text{acc}} \sim 10^2$ s. These estimates are validated by our numerical simulations (see, e.g., Becerra et al. 2015, 2016; Fryer et al. 2015, 2014). From the above results we obtain that for systems with the above short orbital periods the NS collapses to a BH, namely, BdHNe (Becerra et al. 2016), and a total energy larger than the separatrix energy of $\approx 10^{52}$ erg is released during the hypercritical accretion process. For systems with larger separations, in which the hypercritical accretion is not sufficient to induce the collapse of the NS into a BH, namely, the XRFs (Becerra et al. 2016), the value of $\approx 10^{52}$ erg represents a theoretical estimate of the upper limit to the energy emitted by norm in the hypercritical accretion process. These considerations are derived from theoretical expectations based on the above-mentioned masses for the accreting NSs and M_{crit} . Indeed, they are in satisfactory agreement with the observations of 20 XRFs and 233 BdHNe (considered up to the end of 2014), which we have used in our sample (see Tables 2 and 3, respectively). The upper limit for the XRFs is $(7.3 \pm 0.7) \times 10^{51}$ erg (see Section 4.1), while the lower limit for the BdHNe is $(9.2 \pm 1.3) \times 10^{51}$ erg (see Section 5.1).

The same arguments apply to the fusion process of two NSs in a binary NS merger (Ruffini et al. 2015b). Therefore, from these general arguments, we can conclude that the energy emitted during the merger process leading to the formation of a BH should be larger than $\approx 10^{52}$ erg. Indeed, we find an upper limit for the S-GRFs of $(7.8 \pm 1.0) \times 10^{51}$ erg (see Section 6.1) and a lower limit for the S-GRBs of $(2.44 \pm 0.22) \times 10^{52}$ erg (see Section 7.1).

Such a separatrix energy is clearly a function of the initial NS mass undergoing accretion, by norm assumed to be $\approx 1.4 M_{\odot}$. It is also a function of the yet unknown precise value of M_{crit} , for which only an absolute upper limit of $3.2 M_{\odot}$ has been established for the nonrotating case (Rhoades & Ruffini 1974). As already pointed out in Ruffini et al. (2015b) for the case of binary NS mergers, the direct observation of the separatrix energy between S-GRFs and S-GRBs, and also (in this case) between BdHNe and XRFs, gives fundamental information for the determination of the actual value of M_{crit} , for the minimum mass of the newly formed BH, and for the mass of the accreting NS. It is appropriate to notice that a value of the mass of the accreting NS binary larger than $\approx 1.4 M_{\odot}$ is a priori possible and would give interesting observational properties: an exceptional accreting NS with mass close to M_{crit} would lead to a BdHN with a value of the energy lower than the theoretical separatrix

of $\approx 10^{52}$ erg. Conversely, the accretion on an NS with mass smaller than $\approx 1.4 M_{\odot}$ should lead to an XRF with energy larger than $\approx 10^{52}$ erg. These rare possibilities will be precious in further probing the implications of the IGC paradigm, in estimating the NS masses, and in deriving more stringent limits on M_{crit} directly from observations.

Our theory of the hypercritical accretion, applied in the GRB analysis through the IGC paradigm in binary systems, introduces substantial differences with respect to the traditional ones. To appreciate these differences and gain familiarity in this novel approach, we recommend the reading of all the references quoted in this section.

4. THE X-RAY FLASHES

4.1. General Properties

The observational features of long bursts with energy below $\approx 10^{52}$ erg are listed below and summarized in Figure 2. These bursts are interpreted within the theoretical framework of the IGC as a new class that we indicate as XRFs.

The upper limit on the energetics of the XRFs is $(7.3 \pm 0.7) \times 10^{51}$ erg, as measured in GRB 110106B.

The isotropic energies are in the range $(6.4 \pm 1.6) \times 10^{47}$ erg $\lesssim E_{\text{iso}} \lesssim (7.3 \pm 0.7) \times 10^{51}$ erg (see Figure 1 and Amati & Della Valle 2013; Ruffini et al. 2015c).

The spectral peak energies are in the range $4 \lesssim E_{\text{p,i}} \lesssim 200$ keV (see Figure 1 and Amati & Della Valle 2013; Ruffini et al. 2015c) and increase monotonically with E_{iso} .

The cosmological redshifts are in the range $0.0085 \leq z \leq 1.096$, with an average value of ≈ 0.43 (see Table 2).

The prompt emission phase has a duration ranging between $\sim 10^2$ and 10^4 s (see Figure 2(a)) with a spectrum generally characterized by a thermal component and power-law component. The radii of the thermal emitter are in the range of 10^{10} – 10^{12} cm, and the temperatures vary in the range of 0.1–2 keV (see, e.g., Campana et al. 2006, and Figure 2(c)), depending on the values of the binary period and separation of the progenitor systems.

The long-lasting X-ray afterglow does not exhibit any specific common late power-law behavior (see Figure 2(a)).

For all XRFs at $z \lesssim 1$, an optical SN with a luminosity similar to the one of SN 2010bh (Bufano et al. 2012) occurs after 10–15 days in the cosmological rest frame.

No high-energy emission has ever been observed.

Table 3
List of the BdHNe Considered in This Work up to the End of 2014

GRB	z	$E_{\text{iso}}/(10^{52} \text{ erg})$	GRB	z	$E_{\text{iso}}/(10^{52} \text{ erg})$
970228	0.695	1.65 ± 0.16	081008	1.969	10.0 ± 1.0
970828	0.958	30.4 ± 3.6	081028	3.038	18.3 ± 1.8
971214	3.42	22.1 ± 2.7	081029	3.8479	12.1 ± 1.4
980329	3.5	267 ± 53	081109	0.9787	1.81 ± 0.12
980703	0.966	7.42 ± 0.74	081118	2.58	12.2 ± 1.2
990123	1.6	241 ± 39	081121	2.512	32.4 ± 3.7
990506	1.3	98.1 ± 9.9	081203A	2.05	32 ± 12
990510	1.619	18.1 ± 2.7	081221	2.26	31.9 ± 3.2
990705	0.842	18.7 ± 2.7	081222	2.77	27.4 ± 2.7
991208	0.706	23.0 ± 2.3	090102	1.547	22.6 ± 2.7
991216	1.02	69.8 ± 7.2	090205	4.6497	1.12 ± 0.16
000131	4.5	184 ± 32	090313	3.375	4.42 ± 0.79
000210	0.846	15.4 ± 1.7	090323	3.57	438 ± 53
000418	1.12	9.5 ± 1.8	090328	0.736	14.2 ± 1.4
000911	1.06	70 ± 14	090418A	1.608	17.2 ± 2.7
000926	2.07	28.6 ± 6.2	090423	8.1	8.8 ± 2.1
010222	1.48	84.9 ± 9.0	090424	0.544	4.07 ± 0.41
010921	0.45	0.97 ± 0.10	090429B	9.3	6.7 ± 1.3
011121	0.36	8.0 ± 2.2	090516	4.109	72 ± 14
011211	2.14	5.74 ± 0.64	090519	3.85	24.7 ± 2.8
020124	3.2	28.5 ± 2.8	090529	2.625	2.56 ± 0.30
020127	1.9	3.73 ± 0.37	090530	1.266	1.73 ± 0.19
020405	0.69	10.6 ± 1.1	090618	0.54	28.6 ± 2.9
020813	1.25	68 ± 17	090715B	3.0	23.8 ± 3.7
021004	2.3	3.47 ± 0.46	090809	2.737	1.88 ± 0.26
021211	1.01	1.16 ± 0.13	090812	2.452	47.5 ± 8.2
030226	1.98	12.7 ± 1.4	090902B	1.822	292 ± 29.2
030323	3.37	2.94 ± 0.92	090926	2.106	228 ± 23
030328	1.52	38.9 ± 3.9	090926B	1.24	4.14 ± 0.45
030329	0.169	1.62 ± 0.16	091003	0.897	10.7 ± 1.8
030429	2.65	2.29 ± 0.27	091020	1.71	8.4 ± 1.1
030528	0.78	2.22 ± 0.27	091024	1.092	18.4 ± 2.0
040912	1.563	1.36 ± 0.36	091029	2.752	7.97 ± 0.82
040924	0.859	0.98 ± 0.10	091109A	3.076	10.6 ± 1.4
041006	0.716	3.11 ± 0.89	091127	0.49	1.64 ± 0.18
050126	1.29	2.47 ± 0.25	091208B	1.063	2.06 ± 0.21
050315	1.95	6.15 ± 0.30	100219A	4.6667	3.93 ± 0.61
050318	1.444	2.30 ± 0.23	100302A	4.813	1.33 ± 0.17
050319	3.243	4.63 ± 0.56	100414A	1.368	55.0 ± 5.5
050401	2.898	37.6 ± 7.3	100513A	4.8	6.75 ± 0.53
050502B	5.2	2.66 ± 0.22	100621A	0.542	2.82 ± 0.35
050505	4.27	16.0 ± 1.1	100728A	1.567	86.8 ± 8.7
050525A	0.606	2.30 ± 0.49	100728B	2.106	3.55 ± 0.36
050603	2.821	64.1 ± 6.4	100814A	1.44	15.3 ± 1.8
050730	3.969	11.8 ± 0.8	100901A	1.408	4.22 ± 0.50
050802	1.71	5.66 ± 0.47	100906A	1.727	29.9 ± 2.9
050814	5.3	9.9 ± 1.1	101213A	0.414	2.72 ± 0.53
050820	2.615	103 ± 10	110128A	2.339	1.58 ± 0.21
050904	6.295	133 ± 14	110205A	2.22	48.3 ± 6.4
050908	3.347	1.54 ± 0.16	110213A	1.46	5.78 ± 0.81
0509220	2.199	5.6 ± 1.8	110213B	1.083	8.3 ± 1.3
051022	0.8	56.0 ± 5.6	110422A	1.77	79.8 ± 8.2
051109A	2.346	6.85 ± 0.73	110503A	1.613	20.8 ± 2.1
051111	1.55	15.4 ± 1.9	110715A	0.82	4.36 ± 0.45
060115	3.533	5.9 ± 3.8	110731A	2.83	49.5 ± 4.9
060124	2.296	43.8 ± 6.4	110801A	1.858	10.9 ± 2.7
060202	0.785	1.20 ± 0.09	110818A	3.36	26.6 ± 2.8
060206	4.056	4.1 ± 1.9	111008A	4.9898	24.7 ± 1.2
060210	3.91	32.2 ± 3.2	111107A	2.893	3.76 ± 0.55
060306	3.5	7.6 ± 1.0	111209A	0.677	5.14 ± 0.62
060418	1.489	13.5 ± 2.7	111228A	0.716	2.75 ± 0.28
060510B	4.9	19.1 ± 0.8	120119A	1.728	27.2 ± 3.6
060522	5.11	6.47 ± 0.63	120326A	1.798	3.27 ± 0.33
060526	3.22	2.75 ± 0.37	120327A	2.813	14.42 ± 0.46

Table 3
(Continued)

GRB	z	$E_{\text{iso}}/(10^{52} \text{ erg})$	GRB	z	$E_{\text{iso}}/(10^{52} \text{ erg})$
060605	3.773	4.23 ± 0.61	120404A	2.876	4.18 ± 0.34
060607A	3.075	11.9 ± 2.8	120624B	2.197	319 ± 32
060707	3.424	4.3 ± 1.1	120711A	1.405	180 ± 18
060708	1.92	1.06 ± 0.08	120712A	4.175	21.2 ± 2.1
060714	2.7108	7.67 ± 0.44	120716A	2.486	30.2 ± 3.0
060814	1.923	56.7 ± 5.7	120802A	3.796	12.9 ± 2.8
060906	3.6856	7.81 ± 0.51	120811C	2.671	6.41 ± 0.64
060908	1.884	7.2 ± 1.9	120815A	2.358	1.65 ± 0.27
060926	3.2086	2.29 ± 0.37	120909A	3.93	87 ± 10
060927	5.46	12.0 ± 2.8	121024A	2.298	4.61 ± 0.55
061007	1.262	90.0 ± 9.0	121027A	1.773	3.29 ± 0.17
061110B	3.4344	17.9 ± 1.6	121128A	2.2	8.66 ± 0.87
061121	1.314	23.5 ± 2.7	121201A	3.385	2.52 ± 0.34
061126	1.1588	31.4 ± 3.6	121229A	2.707	3.7 ± 1.1
061222A	2.088	30.0 ± 6.4	130408A	3.758	35.0 ± 6.4
070110	2.3521	4.98 ± 0.30	130418A	1.218	9.9 ± 1.6
070125	1.547	84.1 ± 8.4	130420A	1.297	7.74 ± 0.77
070306	1.4959	8.26 ± 0.41	130427A	0.334	92 ± 13
070318	0.84	3.64 ± 0.17	130427B	2.78	5.04 ± 0.48
070411	2.954	8.31 ± 0.45	130505A	2.27	347 ± 35
070508	0.82	7.74 ± 0.29	130514A	3.6	52.4 ± 9.2
070521	1.35	10.8 ± 1.8	130518A	2.488	193 ± 19
070529	2.4996	12.8 ± 1.1	130606A	5.91	28.3 ± 5.1
070611	2.0394	0.92 ± 0.13	130610A	2.092	6.99 ± 0.46
070721B	3.6298	24.2 ± 1.4	130701A	1.155	2.60 ± 0.09
071003	1.604	38.3 ± 4.5	130907A	1.238	304 ± 19
071010B	0.947	2.32 ± 0.40	130925A	0.347	18.41 ± 0.37
071020	2.145	10.0 ± 4.6	131105A	1.686	34.7 ± 1.2
071031	2.6918	4.99 ± 0.97	131117A	4.042	1.02 ± 0.16
071117	1.331	5.86 ± 2.7	140206A	2.74	35.93 ± 0.73
080207	2.0858	16.4 ± 1.8	140213A	1.2076	9.93 ± 0.15
080210	2.6419	4.77 ± 0.29	140226A	1.98	5.8 ± 1.1
080310	2.4274	8.58 ± 0.90	140304A	5.283	13.7 ± 1.1
080319B	0.937	118 ± 12	140311A	4.954	11.6 ± 1.5
080319C	1.95	14.9 ± 3.0	140419A	3.956	186 ± 77
080325	1.78	9.55 ± 0.84	140423A	3.26	65.3 ± 3.3
080411	1.03	16.2 ± 1.6	140428A	4.7	1.88 ± 0.31
080413A	2.433	8.6 ± 2.1	140430A	1.6	1.54 ± 0.23
080413B	1.1	1.61 ± 0.27	140506A	0.889	1.12 ± 0.06
080514B	1.8	18.1 ± 3.6	140508A	1.027	23.24 ± 0.26
080603B	2.69	6.0 ± 3.1	140509A	2.4	3.77 ± 0.44
080604	1.4171	1.05 ± 0.12	140512A	0.725	7.76 ± 0.18
080605	1.64	28 ± 14	140515A	6.32	5.41 ± 0.55
080607	3.036	200 ± 20	140518A	4.707	5.89 ± 0.59
080710	0.8454	1.68 ± 0.22	140614A	4.233	7.3 ± 2.1
080721	2.591	134 ± 23	140629A	2.275	6.15 ± 0.90
080804	2.205	12.0 ± 1.2	140703A	3.14	1.72 ± 0.09
080805	1.5042	5.05 ± 0.22	140801A	1.32	5.69 ± 0.05
080810	3.35	47.8 ± 5.5	140808A	3.29	11.93 ± 0.75
080905B	2.3739	4.55 ± 0.37	140907A	1.21	2.29 ± 0.08
080913	6.695	9.2 ± 2.7	141026A	3.35	7.17 ± 0.90
080916A	0.689	0.98 ± 0.10			
080916C	4.35	407 ± 86			
080928	1.692	3.99 ± 0.91			

Note. For each source (first and fourth columns) the values of z and E_{iso} (second, third, fifth, and sixth columns) are listed.

In view of the observed values of $E_{p,i}$ that occur in the X-ray domain and also because of the low values of their $E_{\text{iso}} < 10^{52} \text{ erg}$, we adopted the name XRFs for these soft and less energetic long bursts, a terminology already used in the literature on purely morphological grounds (see, e.g., Heise 2003; Amati et al. 2004; Soderberg et al. 2006).

4.2. Theoretical Interpretation of XRFs within the IGC Paradigm

In the IGC paradigm an XRF occurs when the CO_{core}–NS binary separation a is so large (typically $a > 10^{11} \text{ cm}$; see, e.g., Becerra et al. 2015) that the accretion of the SN ejecta onto the NS is not sufficient for the NS to reach M_{crit} . Correspondingly,

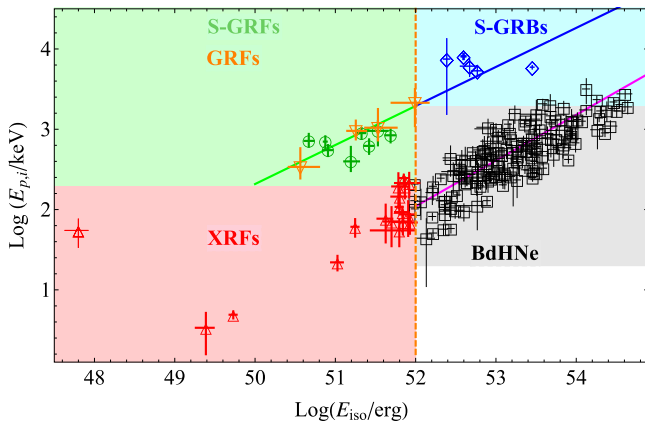


Figure 1. $E_{p,i}$ – E_{iso} plane for XRFs, BdHNe, S-GRBs, S-GRFs, and the initial spike-like emission of the GRFs. The XRFs (red triangles) cluster in the red shaded region ($E_{p,i} \lesssim 200$ keV and $E_{iso} \lesssim 10^{52}$ erg), while the BdHNe (black squares) cluster in the gray shaded one ($E_{p,i} \gtrsim 200$ keV and $E_{iso} \gtrsim 10^{52}$ erg); the Amati relation (Amati & Della Valle 2013) fulfilled by the BdHNe is plotted with a magenta solid line. The S-GRFs (green circles) and the initial spike-like emission of the GRFs (orange downward-pointing triangles) cluster in the green shaded region ($E_{p,i} \lesssim 2$ MeV and $E_{iso} \lesssim 10^{52}$ erg), while the S-GRBs (blue diamonds) cluster in the blue shaded one ($E_{p,i} \gtrsim 2$ MeV and $E_{iso} \gtrsim 10^{52}$ erg); the relation for short bursts (Zhang et al. 2012; Calderone et al. 2015; Ruffini et al. 2015b) is plotted with a green solid line for the S-GRFs and the GRFs, and in blue for the S-GRBs.

there is a critical or maximum value of the orbital period P_{\max} (e.g., $P_{\max} \approx 28$ minutes for an NS with initial mass of $1.4 M_{\odot}$) for which the NS collapses to a BH, namely, for $P > P_{\max}$ the accretion rate is not sufficient to induce the gravitational collapse of the companion NS into a BH (see Figures 2(d)).

The hypercritical accretion of the SN ejecta onto the NS binary companion occurs at rates $< 10^{-2} M_{\odot} \text{ s}^{-1}$ and can last from several hundreds of seconds all the way up to $\sim 10^4$ s, until the whole SN ejecta flies beyond the NS binary orbit (see Figure 2(a)). The photons are trapped in the accreting material, and the accretion energy is lost through a large associated neutrino emission (see, e.g., Zel’dovich et al. 1972; Ruffini & Wilson 1973; Rueda & Ruffini 2012; Fryer et al. 2014, and references therein). The upper limit of 10^{52} erg for these sources is explainable by estimating the gravitational energy of the matter accreted onto the NS reaching a mass below M_{crit} at the end of the accretion process (see Section 3).

The resulting emission, dubbed Episode 1, exhibits a spectrum composed of a thermal component, possibly originating from the outflow within the NS atmosphere driven out by Rayleigh–Taylor convection instabilities, and a power-law component. The shorter the binary period, the larger the accretion rate (see Figure 2(f)) and the values of E_{iso} and $E_{p,i}$, and correspondingly the shorter the prompt emission duration (see Figure 2(a)). The excess of angular momentum of the system necessarily leads to a jetted emission, manifested in the power-law spectral component (Becerra et al. 2015). Indeed, in the IGC simulations the typical radii inferred from the evolving thermal component coincide with the observed ones of 10^{10} – 10^{12} cm.

In the IGC paradigm the in-state is represented by an exploding CO_{core} and a companion NS. The out-state is a multiple system composed of an MNS, resulting from the accretion of part of the SN ejecta onto the binary companion NS, a ν NS, originating from the SN event, and the remaining

part of the SN ejecta shocked by the hypercritical accretion emission of the XRF. This energy injection into the SN ejecta leads to the occurrence of a broad-lined SN Ic (*hypernova*; see, e.g., Maeda & Nomoto 2003) with a kinetic energy larger than that of the traditional SNe Ic. The presence of ^{56}Ni in the SN ejecta leads to the observed SN emission after ≈ 10 – 15 days in the cosmological rest frame, which is observable for sources at $z \lesssim 1$.

Clearly the absence of hard γ -ray and GeV emissions is implicit in the nature of the hypercritical accretion process not leading to a BH and the corresponding rate of neutrino emission (see also the Appendix).

4.3. Prototypes

In Figure 2(a) we reproduce the rest-frame 0.3–10 keV luminosity light curves of four selected XRFs: GRB 980425 (Pian et al. 2000; Kouveliotou et al. 2004; Pian et al. 2004), associated with SN 1998bw (Galama et al. 1998), GRB 060218 associated with SN 2006aj (Campana et al. 2006; Soderberg et al. 2006), GRB 070419A (Evans et al. 2007, 2009) with an optical SN bump (Hill et al. 2007), and GRB 101219B (Evans et al. 2007, 2009) associated with SN 2010ma (Sparre et al. 2011). Their prompt emissions are represented by the above-mentioned Episode 1. In Figure 2(c) we plot the evolution of both temperature and radius inferred from the thermal component observed in the Episode 1 emission of GRB 060218. The increasing radius and almost constant temperature are obtained from the thermal component observed in GRB 060218 (Campana et al. 2006). Details will appear in forthcoming publications (Pisani et al. 2016; Becerra et al. 2016). A complete list of XRFs is shown in Table 2.

5. THE BINARY-DRIVEN HYPERNOVAE

5.1. General Properties

The observational features of long bursts with energy above $\approx 10^{52}$ erg are listed below and summarized in Figure 3. These bursts are interpreted within the theoretical framework of the IGC as a new class that we indicate as BdHNe.

The lower limit on the energetics of the BdHNe is $(9.2 \pm 1.3) \times 10^{51}$ erg as measured in GRB 070611.

The observed isotropic energies are in the range $(9.2 \pm 1.3) \times 10^{51} \text{ erg} \lesssim E_{iso} \lesssim (4.07 \pm 0.86) \times 10^{54} \text{ erg}$ (see Figure 1 and Amati & Della Valle 2013; Ruffini et al. 2015c) and are in principle dependent on the NS mass, which we have assumed, as an example, to be $\approx 1.4 M_{\odot}$ (see Section 3).

The spectral peak energies are in the range $0.2 \lesssim E_{p,i} \lesssim 2 \text{ MeV}$ (see Figure 1 and Amati & Della Valle 2013; Ruffini et al. 2015c) and increase monotonically with E_{iso} .

The cosmological redshifts are in the range $0.169 \leq z \leq 9.3$, with an average value of ≈ 2.42 (see Table 3).

The prompt emission phase of BdHNe exhibits a more complex structure than that of XRFs. Indeed, three different regimes are found:

- (a) A thermal emission with a decreasing temperature following a broken power-law behavior and an additional nonthermal spectral component (a power law) dominate the early emission in selected BdHNe (see, e.g., Izzo et al. 2012c, and Figure 3(a)). The existence of this

thermal component was first identified in the GRB BATSE data by Ryde (2004, 2005). It was then shown to occur in the case of BdHNe as GRB 090618 (Izzo et al. 2012c, and Figure 3(a)), GRB 101023 (Penacchioni et al. 2012), GRB 110709B (Penacchioni et al. 2013), and GRB 970828 (Ruffini et al. 2015a). The characteristic radii inferred from the cooling thermal component are of the order of 10^9 – 10^{10} cm, and the average expansion speed is $\sim 10^8$ – 10^9 cm s $^{-1}$ (Izzo et al. 2012c; Penacchioni et al. 2012, 2013; Ruffini et al. 2015a).

- (b) This early emission is followed by the characteristic GRB emission (see Figure 3(d)), encompassing a thermal precursor, the P-GRB (Ruffini et al. 1999, 2000), followed by the prompt emission (Ruffini et al. 2002, 2004, 2005).
- (c) The prompt emission is followed by a steep decay, then by a plateau and a late power-law decay. These features have been first reported in Nousek et al. (2006) and Zhang et al. (2006).

The late decay has typical slopes of $-1.7 \lesssim \alpha_X \lesssim -1.3$ (Pisani et al. 2013) and shows a characteristic power-law behavior both in the optical and in X-rays. When computed in the source cosmological rest frame, the late power-law decay in X-rays exhibits new features: overlapping and nesting (see Figure 3(c)). Overlapping has been proven in a sample of six BdHNe: GRBs 060729, 061007, 080319B, 090618, 091127, and 111228 (Izzo et al. 2012a; Pisani et al. 2013). The nested property of the BdHNe has been discussed in Ruffini et al. (2014b), where it has been shown that the duration (the luminosity) of the plateau phase is inversely (directly) proportional to the energy of the GRB emission: the more energetic the source, the smaller (higher) the duration (the luminosity) of the plateau.

For all BdHNe at $z \lesssim 1$, an optical SN with a luminosity similar to the one of SN 1998bw (Galama et al. 1998) occurs after 10–15 days in the cosmological rest frame.

A distinctive high-energy emission observed up to 100 GeV shows a luminosity light curve following a precise power-law behavior with index ≈ -1.2 (Figure 3(d) and Nava et al. 2014). The turn-on of this GeV emission occurs after the P-GRB emission and during the prompt emission phase.

5.2. Theoretical Interpretation of BdHNe within the IGC Paradigm

In the IGC paradigm a BdHN occurs when the CO_{core}–NS binary is more tightly bound ($a \lesssim 10^{11}$ cm; see, e.g., Becerra et al. 2015). The larger accretion rate of the SN ejecta, e.g., $\gtrsim 10^{-2}$ – $10^{-1} M_\odot$ s $^{-1}$, leads the companion NS to easily reach its critical mass M_{crit} (Rueda & Ruffini 2012; Fryer et al. 2014; Becerra et al. 2015), leading to the formation of a BH. The electrodynamic conditions encountered in the final accretion phase explain the existence of a vacuum polarization process leading to the creation of an e^+e^- plasma and to the formation of a KNBH with a large variety of new astrophysical phenomena. For the sake of clarity and independence on the physical regime encountered, in the IGC paradigm we have divided the activities of the BdHNe in a numbered set of distinct episodes.

Episode 1 of BdHNe originates in the same hypercritical accretion process as the corresponding one of XRFs. The corresponding spectrum again exhibits an expanding thermal

component and a power-law function (Izzo et al. 2012c; Ruffini et al. 2015a). The typical radii inferred from the thermal component are of the order of 10^9 – 10^{10} cm, and the average expansion speed is $\sim 10^8$ – 10^9 cm s $^{-1}$ (see Figure 3(a) and Izzo et al. 2012c; Ruffini et al. 2015a).

Episode 2 corresponds to the authentic L-GRB emission (see Figure 3(b)), stemming from the collapse of the companion NS to a BH. For its theoretical description we adopt the traditional fireshell model (see Ruffini et al. 2001a, 2001b, 2001c, and Section 2). The GRB emission occurs at a Lorentz factor at the transparency of $\Gamma = 10^2$ – 10^3 (Izzo et al. 2012c; Ruffini et al. 2015a), and the spatial extension of the interaction of the fireshell with the CBM goes all the way up to $\sim 10^{16}$ – 10^{17} cm, reached at the end of Episode 2 (Izzo et al. 2012c). The BdHNe have $E_{\text{iso}} \gtrsim 10^{52}$ erg, and their $E_{p,i} \gtrsim 200$ keV is in the hard γ -ray domain.

Episode 3 in BdHNe originates from the SN ejecta (Ruffini et al. 2015c). In this case an extra energy injection is delivered by the interaction of the GRB outflow with the SN ejecta, resulting in an isotropic energy emission of 10^{51} – 10^{52} erg. This interaction produces a flare at the beginning of Episode 3 (typically at a rest-frame time of $\sim 10^2$ s) with the typical signature of an expanding thermal component in its spectrum. The radii inferred from this thermal component are $\sim 10^{12}$ – 10^{13} cm, and their evolution reveals a mildly relativistic expansion at $\Gamma \approx 2$ (Ruffini et al. 2014b, 2015c). The rest-frame 0.3–10 keV luminosity light is then followed by a plateau phase and a late power-law decay. The late decay has been shown to exhibit a common power-law behavior and a nested structure (see, e.g., Pisani et al. 2013; Ruffini et al. 2014b, and Figure 3(c)). The possibility of using the late X-ray emission as a distance indicator has been explored by inferring the redshifts of GRBs 101023 and 110709B (Penacchioni et al. 2012, 2013) and has been applied to predict the occurrence of the SN associated with GRB 130427A after ~ 10 –15 days in the cosmological rest frame before its discovery (Ruffini et al. 2013), later confirmed by the observations (de Ugarte Postigo et al. 2013; Levan et al. 2013; Watson et al. 2013; Xu et al. 2013).

Episode 4, as predicted in the IGC paradigm and in analogy to XRFs, corresponds to the optical SN emission observable in all BdHNe at $z \lesssim 1$ after ~ 10 –15 days in the cosmological rest frame. It is remarkable that these SNe have a standard luminosity, like the one of SN 1998bw (see, e.g., Melandri et al. 2014).

A new Episode 5, here introduced, is identified with the long-lived GeV emission. This emission is conceptually distinct in its underlying physical process from that of Episode 3. When LAT data are available, the majority of BdHNe observed by the *Fermi* satellite (Atwood et al. 2009) exhibit such an emission, similar to the one observed in S-GRBs (see Section 6). In Ruffini et al. (2015c) the further accretion of matter onto the newly formed BH has been indicated as the origin of this GeV emission. An outstanding exception is GRB 151027A (M. Kovacevic et al. 2016, in preparation).

Also for BdHNe the in-state is composed of an exploding CO_{core} and a companion NS. The out-state is again a multiple system. First, there is a GRB composed of the P-GRB and its prompt emission. Then there is a newly formed BH, produced by the hypercritical accretion of part of the SN ejecta onto the binary companion NS reaching M_{crit} . Again, there is a ν NS originating from the SN explosion. Finally, there is the

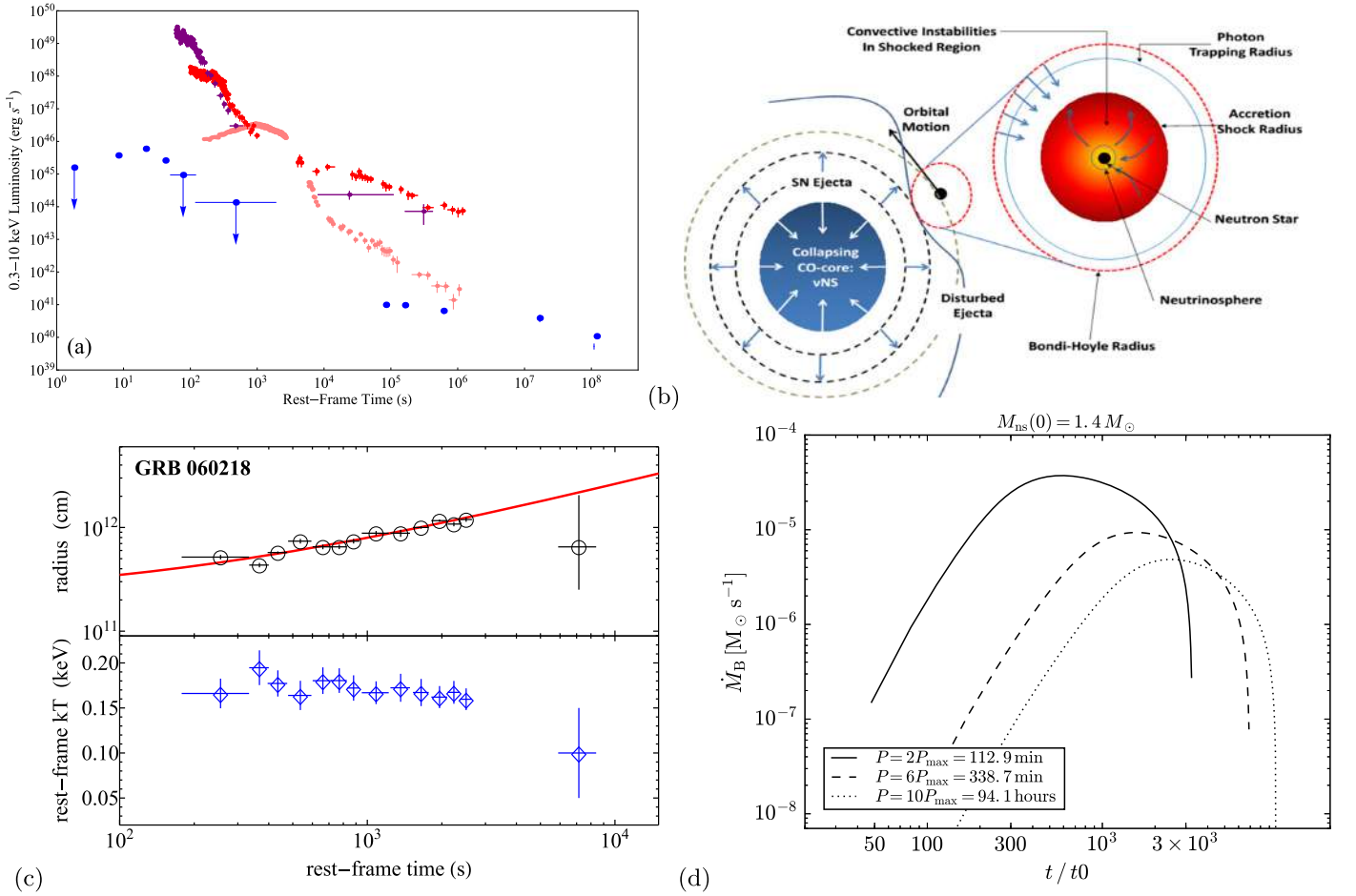


Figure 2. (a) Rest-frame 0.3–10 keV luminosity light curves of four selected XRFs: GRB 980425 (blue), GRB 060218 (pink), GRB 070419A (purple), and GRB 101219B (red). (b) Sketch of the CO_{core}-NS binary progenitor and the hypercritical accretion process in the IGC scenario (reproduced from Fryer et al. 2014). (c) Upper panel: evolution of the radius of the thermal component detected in GRB 060218 (black circles) and its linear fit (solid red curve). Lower panel: decay of the corresponding rest-frame temperature (blue diamonds). Reproduced from Campana et al. (2006). (d) Mass accretion rate \dot{M}_B of the SN ejecta onto an NS companion of initial mass $1.4 M_{\odot}$, as a function of time. Three cases are plotted for various selected orbital periods $P > P_{\text{max}}$ (see legend).

remaining part of the SN ejecta shocked by the GRB emission. The energy injection into the SN ejecta from both the hypercritical accretion phase and the GRB emission leads also in this case to the occurrence of a broad-lined SN Ic (*hypernova*; see, e.g., Maeda & Nomoto 2003) with a kinetic energy larger than that of the traditional SNe Ic.

5.3. Prototypes

In the following selected prototypes of BdHNe are given and illustrated in Figure 3.

The first systematic time-resolved spectral analysis of an Episode 1 of a BdHN has been performed for GRB 090618 (Izzo et al. 2012c). In this source the typical radii inferred from the cooling thermal component are of the order of 10^9 – 10^{10} cm and the average expansion speed is $\sim 10^8$ – 10^9 cm s⁻¹ (see Figure 3(a)). Similar results have been obtained for GRB 101023 (Penacchioni et al. 2012), GRB 110907B (Penacchioni et al. 2013), and GRB 980828 (Ruffini et al. 2015a).

The selected prototypes of Episode 2 emission have isotropic energies ranging from $E_{\text{iso}} = 1.60 \times 10^{53}$ erg in GRB 970828 (Ruffini et al. 2015a) to $E_{\text{iso}} = 1.32 \times 10^{54}$ erg in GRB 080319B (Patricelli et al. 2012). The amount of baryonic matter loaded before the P-GRB emission, the baryon load

$B \equiv \dot{M}_B c^2 / E_{e^+e^-}^{\text{tot}}$, where $E_{e^+e^-}^{\text{tot}}$ is the pair plasma energy and \dot{M}_B the engulfed baryon mass, is in the range from $B = 1.98 \times 10^{-3}$ for GRB 090618 (Izzo et al. 2012c) to $B = 7.0 \times 10^{-3}$ for GRB 970828 (Ruffini et al. 2015a). Correspondingly, their transparency emission occurs at Lorentz factors at the transparency ranging from $\Gamma = 143$ in GRB 970828 (Ruffini et al. 2015a) to $\Gamma = 490$ in GRB 090618 (Izzo et al. 2012c). The average density of the CBM in these prototypes, inferred from description of the interaction with the fireshell after its transparency (Ruffini et al. 2002, 2004, 2005), varies from 0.6 cm^{-3} in GRB 090618 (Izzo et al. 2012c) to $\sim 10^3 \text{ cm}^{-3}$ in GRB 970828 (Ruffini et al. 2015a). The size of the corresponding emitting region, $\sim 10^{16}$ – 10^{17} cm, is clearly incompatible with the radii inferred from Episodes 1 and 3. This points to the different origins in the emission mechanisms of the above three episodes.

The radii inferred from the expanding thermal components observed in the spectra of the flares at the beginning of Episode 3 are typically $\sim 10^{12}$ – 10^{13} cm. This has been found in the cases of GRB 090618 (see, e.g., Starling et al. 2010; Ruffini et al. 2014b) and GRB 130427A (Ruffini et al. 2015c). In both these sources, the expansion of the thermal emitter of Episode 3 proceeds at $\Gamma \approx 2$ (Ruffini et al. 2014b, 2015c). After the initial emission in the spike of Episode 3, the rest-frame

0.3–10 keV luminosity light curve is then followed by a plateau phase and a late power-law decay. The overlapping of the late power-law decay and the nested structure is reproduced in Figure 3(c) for selected sources: GRB 060729, GRB 061007, GRB 080319B, GRB 090618, GRB 091127B, and GRB 111228A (considered in Pisani et al. 2013), GRB 061121 and GRB 130427A (considered in Ruffini et al. 2014b, 2015c), GRB 090423 (Ruffini et al. 2014a), and GRB 140512A (introduced here).

Episode 4 has been spectroscopically identified for the two closest BdHNe, e.g., GRB 091127–SN 2009 nz (Cobb et al. 2010) and GRB 130427A–SN 2013cq (Xu et al. 2013). In the cases of GRB 060729 (Cano et al. 2011), GRB 080319B (Kann et al. 2008), GRB 090618 (Cano et al. 2011), and GRB 111228A (D’Avanzo et al. 2012), at $z \lesssim 1$, the identification was possible through the detection of bumps in their Episode 3 optical light curves.

Turning now to Episode 5 of BdHNe, the GeV emission has been studied in detail in the case of GRB 130427A (Ruffini et al. 2015c), as well as in other selected BdHNe (see Figure 3(d) and Ackermann et al. 2013). The turn-on has been identified as the onset of the emission from the newly formed BH (Ruffini et al. 2015c).

A complete list of BdHNe is shown in Table 3.

The ultralong GRBs (Levan et al. 2014; Boër et al. 2015) are certainly BdHNe on the ground of their late X-ray rest-frame luminosity (Pisani et al., 2016).

6. THE SHORT GAMMA-RAY FLASHES

6.1. General Properties

The observational features of short bursts with energy below $\approx 10^{52}$ erg are listed below and summarized in Figure 4. These bursts are interpreted within the theoretical framework of the NS–NS merger paradigm in the fireshell model as a new class that we indicate as S-GRFs.

The upper limit on the energetics of the S-GRFs is $(7.8 \pm 1.0) \times 10^{51}$ erg, as measured in GRB 100117A.

The isotropic energies are in the range $(8.5 \pm 2.2) \times 10^{48}$ erg $\lesssim E_{\text{iso}} \lesssim (7.8 \pm 1.0) \times 10^{51}$ erg (see Figure 1 and Zhang et al. 2012; Calderone et al. 2015; Ruffini et al. 2015b).

The spectral peak energies are in the range $0.2 \lesssim E_{p,i} \lesssim 2$ MeV (see Figure 1 and Zhang et al. 2012; Calderone et al. 2015; Ruffini et al. 2015b) and increase monotonically with E_{iso} .

The cosmological redshifts are in the range $0.111 \leq z \leq 2.609$, with an average value of ≈ 0.71 (see Table 4).

The prompt emission phase has a duration of a few seconds and is expected to crucially be a function of the masses of the binary NSs.

The long-lasting X-ray afterglow does not exhibit any specific common late power-law behavior (see Figure 4(a)).

For all S-GRFs no SN association is expected, nor observed.

No high-energy GeV emission is expected or observed in absence of BH formation.

6.2. Theoretical Interpretation of S-GRFs within the NS–NS Merger Paradigm in the Fireshell Model

As noted in the Introduction, current paradigms indicate mergers of NS–NS or NS–BH binaries as progenitors.

The extension of the IGC paradigm considerations to NS–NS mergers has led to a new classification of short bursts into two subclasses depending on the mass of the merged core, namely, whether or not a BH is formed out of the merger (see Figure 4(d) and Ruffini et al. 2015b). This, in turn, depends on the NS equation of state and on the adoption of a global neutrality model, as opposed to the case of absence of electromagnetic structures when local charge neutrality is imposed (see, e.g., Belvedere et al. 2012, and references therein; see also Figure 4(c)). Also relevant is the very different density distribution in the crust and in the core between these two treatments, which could play an important role in the NS–NS mergers (see Figure 4(d) and Oliveira et al. 2014).

S-GRFs originate from NS–NS mergers with initial total mass $m_1 + m_2$ leading to a merged core with mass smaller than M_{crit} ; therefore, their outcomes are an MNS with additional orbiting material, or even a binary NS or WD companion (see, e.g., Bildsten & Cutler 1992, and references therein), due to the energy and momentum conservation laws (Ruffini et al. 2015b). As discussed in Section 2, even though a BH is not formed out of the merger, also for these systems the general description of the fireshell model can be applied. A viable mechanism for S-GRFs can be the creation of a pair plasma via $\nu\bar{\nu} \leftarrow e^+e^-$ in an NS–NS merger (see, e.g., Narayan et al. 1992; Salmonson & Wilson 2002; Rosswog et al. 2003), where the maximum energy attainable in the process is $\approx 10^{52}$ erg, which represents indeed the upper limit to the energetics of these systems. Their energies are very similar to those emitted in XRFs. However, S-GRFs have $E_{p,i}$ as high as ~ 2 MeV (see, e.g., Zhang et al. 2012; Calderone et al. 2015; Ruffini et al. 2015b); therefore, in view of the hardness of their spectra, we adopted the name of S-GRFs to distinguish them from the corresponding XRFs.

S-GRFs coincide with the majority of the systems extensively discussed in Berger (2014). All S-GRFs have an extended X-ray afterglow (Berger 2014; Ruffini et al. 2015b). Similarly to XRFs, the rest-frame 0.3–10 keV luminosity light curve does not exhibit either a late common power-law behavior or the nesting discovered in the BdHNe (see Figure 4(a)). At the moment, there are still a large number of possible candidates for the description of the origin of the late X-ray afterglow emission: (a) the interaction of the MNS with orbiting material or with a less massive binary NS or WD companion, (b) the accelerated baryons interacting with the CBM after the P-GRB emission, or (c) the possible radioactive decay of heavy elements synthesized in the ejecta of a compact binary merger (Li & Paczyński 1998). In this light we recall the possibility of a *macronova* emission, a near-infrared/optical transient (a bump) in the late afterglow (see the case of GRB 130603B in Berger et al. 2013; Tanvir et al. 2013).

As a general conclusion, in Ruffini et al. (2015b) the necessary absence of an SN was indicated. It has been predicted there that, since no BH is produced in the merger, S-GRFs should never exhibit high-energy GeV emission, which is expected to originate in the newly born BH (Ruffini et al. 2015b). No counterexample has been found as of today. In Ruffini et al. (2016) it has been shown that the absence of detection of GeV emission, necessary within the fireshell model, is indeed supported by the observations. The entire Section 6.5 of that paper is dedicated to the GeV emission of S-GRFs and S-GRBs. As evidenced there, it is concluded that S-GRFs, due to the upper limits of the LAT observations, have,

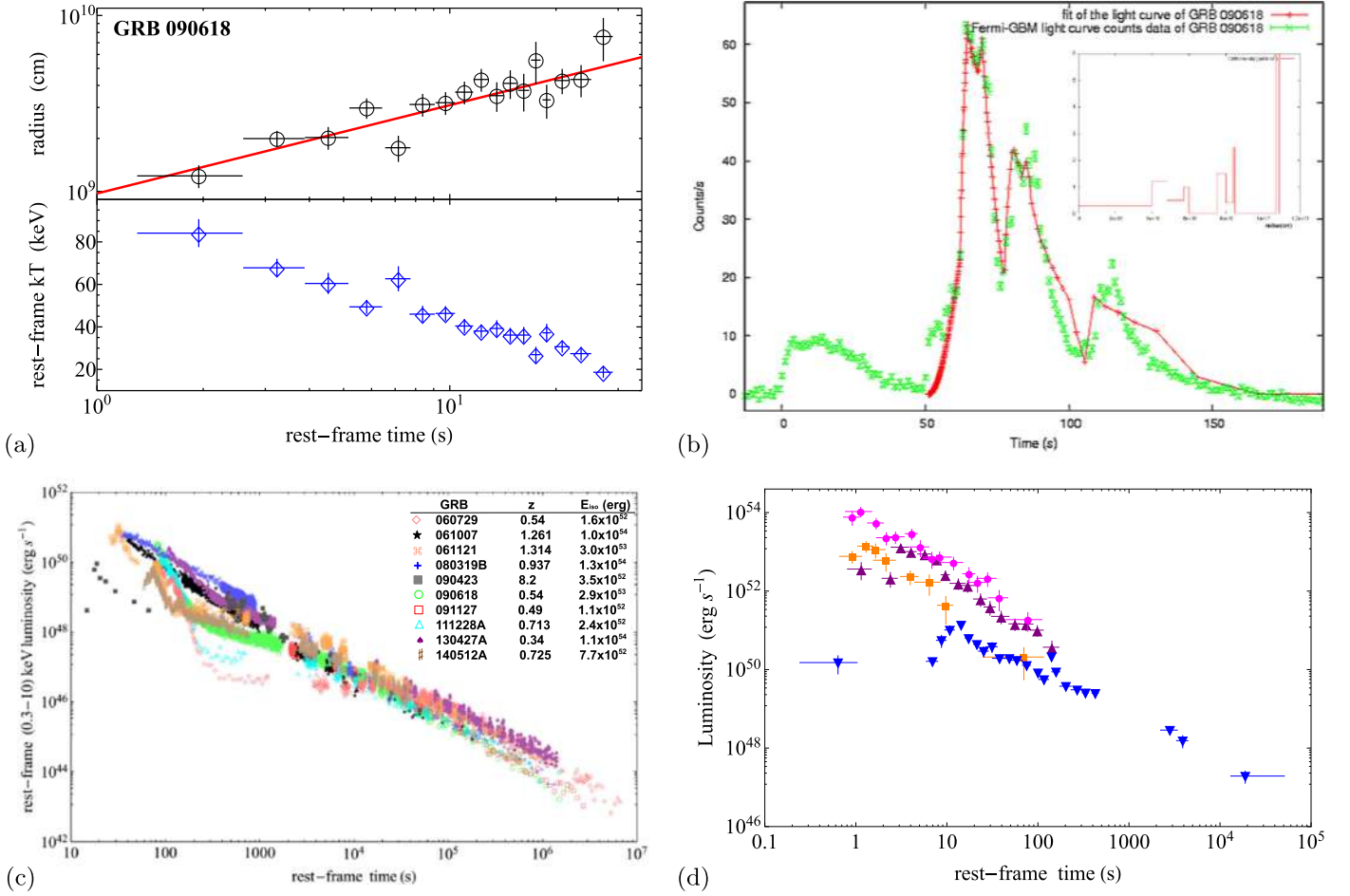


Figure 3. (a) Upper panel: evolution of the radius of the thermal component detected in Episode 1 of GRB 090618 (black circles) and its linear fit (solid red curve). Lower panel: decay of the corresponding rest-frame temperature (blue diamonds). Reproduced from Izzo et al. (2012c). (b) Fireshell simulation (red line) of the light curve of Episode 2 of the prototype GRB 090618 (green data). The small inset reproduces the CBM profile required for the simulation. Reproduced from Izzo et al. (2012c). (c) Rest-frame 0.3–10 keV luminosity light curves of selected BdHNe. All these sources exhibit the overlapping of the late power-law decay, outlined in Pisani et al. (2013), and a nested structure, as outlined in Ruffini et al. (2014b). (d) Rest-frame 0.1–100 GeV luminosity light curves of selected BdHNe (reproduced from Ackermann et al. 2013): GRB 080916C (magenta circles), GRB 090902B (purple triangles), GRB 110731A (orange squares), GRB 130427A (blue downward-pointing triangles).

if any, GeV fluxes necessarily 10^5 – 10^6 times weaker than those of S-GRBs, although their E_{iso} is only a factor of 10^2 smaller (see also the Appendix).

6.3. Prototypes

In Table 4 we indicate the selected prototypes of S-GRFs. For each of them, we list the values of E_{iso} and z used in order to evaluate their rate.

7. THE SHORT GRBs

7.1. General Properties

The observational features of short bursts with energy above $\approx 10^{52}$ erg are listed below and summarized in Figure 5. These bursts are interpreted within the theoretical framework of the NS–NS merger paradigm in the fireshell model as a new class that we indicate as S-GRBs.

The lower limit on the energetics of the S-GRBs is $(2.44 \pm 0.22) \times 10^{52}$ erg as measured in GRB 081024B.

The isotropic energies are in the range $(2.44 \pm 0.22) \times 10^{52} \lesssim E_{\text{iso}} \lesssim (2.83 \pm 0.15) \times 10^{53}$ erg (see

Figure 1 and Zhang et al. 2012; Muccino et al. 2013; Calderone et al. 2015; Ruffini et al. 2015b).

The spectral peak energies are in the range $2 \lesssim E_{\text{p,i}} \lesssim 8$ MeV (see Figure 1 and Zhang et al. 2012; Muccino et al. 2013; Calderone et al. 2015; Ruffini et al. 2015b) and increase monotonically with E_{iso} .

The cosmological redshifts are in the range $0.903 \leq z \leq 5.52$, with an average value of ≈ 2.48 (see Table 5).

The P-GRB and the prompt emission components have a total duration of a few seconds, which is expected to crucially be a function of the masses of the binary NSs (see Figures 5(a) and (b)).

Only in the case of GRB 090510 has an X-ray afterglow been observed not conforming to any known afterglow (see Figure 5(c)).

For all S-GRBs no SN association is expected or observed.

In all S-GRBs an extremely high energy GeV emission has been observed (see Figure 5(d)). It is interesting that even in one case, which was outside the nominal *Fermi*-LAT field of view, evidence for high-energy emission has been found (Ackermann et al. 2013; R. Ruffini & Y. Wang 2016, in preparation).

Table 4

List of the S-GRFs Considered in This Work up to the End of 2014

GRB	z	$E_{\text{iso}}/(10^{50} \text{ erg})$	GRB	z	$E_{\text{iso}}/(10^{50} \text{ erg})$
050509B	0.225	0.085 ± 0.022	090927	1.37	27.6 ± 3.5
050709	0.161	0.80 ± 0.08	100117A	0.915	78 ± 10
051221A	0.546	26.3 ± 3.3	100206A	0.408	4.67 ± 0.61
060502B	0.287	4.33 ± 0.53	100625A	0.453	7.50 ± 0.30
061201	0.111	1.51 ± 0.73	100724A	1.288	16.4 ± 2.4
061217	0.827	42.3 ± 7.2	101219A	0.718	48.8 ± 6.8
070429B	0.902	4.75 ± 0.71	111117A	1.3	34 ± 13
070724A	0.457	0.60 ± 0.14	120804A	1.3	70 ± 15
070729	0.8	11.3 ± 4.4	130603B	0.356	21.2 ± 2.3
070809	0.473	2.76 ± 0.37	131004A	0.717	12.7 ± 0.9
080123	0.495	11.7 ± 3.9	140622A	0.959	0.70 ± 0.13
080905A	0.122	6.58 ± 0.96	140903A	0.351	1.41 ± 0.11
090426	2.609	44.5 ± 6.6	141004A	0.573	21.0 ± 1.9
090515	0.403	0.094 ± 0.014			

Note. For each source (first and fourth columns) the values of z and E_{iso} (second, third, fifth, and sixth columns) are listed.

7.2. Theoretical Interpretation of S-GRBs within the NS–NS Merger Paradigm in the Fireshell Model

S-GRBs originate from NS–NS mergers with initial total mass $m_1 + m_2$ leading to a merged core with mass larger than M_{crit} so that a BH is formed (Ruffini et al. 2015b). In order to conserve energy and momentum, the outcome of such S-GRBs is a KNBH with additional orbiting material, or a binary companion (Bildsten & Cutler 1992; Ruffini et al. 2015b). If we compare and contrast the different episodes encountered in the description of the BdHNe (see Section 5) with those of S-GRBs, we find some remarkable analogies but also some differences in view of the simplicity of the underlying physical system of S-GRBs, which, unlike the BdHNe, do not exhibit any of the extremely complex activities related to the SN (see Section 5).

Episode 1 corresponds here to the activity of the NS–NS merger before the gravitational collapse into a BH. Because of the compactness of the systems, this process at times is not observable, or it possibly corresponds to faint precursors observed in some short bursts (see, e.g., Troja et al. 2010 and Ruffini et al. 2016).

Episode 2 corresponds to the GRB emission stemming from the NS–NS merger. It is described within the fireshell model as composed of two components (see Section 2): the P-GRB emission, with a mainly thermal spectrum (see Figure 5(a)), and the prompt emission, with a characteristic nonthermal spectrum (see Figure 5(b)). Typically in all S-GRBs so far analyzed (see, e.g., GRB 090227B, Muccino et al. 2013; GRB 140619B, Ruffini et al. 2015b) the baryon load is standard, e.g., $B \approx 10^{-5}$, and is consistent with the crustal masses of NS–NS mergers (Belvedere et al. 2014; Ruffini et al. 2015b). The average densities of the CBM where S-GRBs occur are $\langle n_{\text{CBM}} \rangle \approx 10^{-5} \text{ cm}^{-3}$, typical of the halos of GRB host galaxies (see, e.g., Muccino et al. 2013; Ruffini et al. 2015b). Most remarkable is that this model gives the theoretical explanation for the fulfillment of the $E_{\text{p},i}-E_{\text{iso}}$ relation for the short bursts (see Figure 1 and Zhang et al. 2012; Calderone et al. 2015; Ruffini et al. 2015b).

Episode 3, which corresponds to the traditional X-ray afterglow, is missing here in view of the absence of the SN and of all the characteristic processes originating from the

interaction between the GRB and the SN ejecta, as in the case of BdHNe (see Section 5). At times S-GRBs have nonprominent X-ray or optical emissions (see Figure 5(c)).

Episode 4, identified with the optical emission of an SN, is here missing.

Episode 5 coincides with the long-lived GeV emission. All S-GRBs consistently exhibit this emission, which appears to be strictly correlated to the one observed in the BdHNe. By analogy with BdHNe, we assume that the GeV emission originates from the activity of the newly born KNBH produced in the merger (Ruffini et al. 2015b). Indeed, the presence of a BH is the only commonality between BdHNe and S-GRBs. By comparing and contrasting Figures 3(d) and 5(d), we see that the turn-on of the GeV emission in S-GRBs occurs earlier and is energetically more prominent than the corresponding one of the BdHNe. To emphasize this point in Figure 5(d) we have represented by a dashed line the minimal turn-on time of the GeV emission of BdHNe (see Ruffini et al. 2016; R. Ruffini et al. 2016, in preparation). The very high angular momentum, expected to occur in NS–NS mergers, and the very high luminosities of the S-GRBs, originating in the corresponding BH formation, offer a great opportunity to analyze some of the features expected in a KNBH.

7.3. Prototypes

In Table 5 we list all the S-GRBs identified so far.

The first identified S-GRB, GRB 090227B, has been analyzed by Muccino et al. (2013). The analysis of its P-GRB emission has found a baryon load $B = 4.13 \times 10^{-5}$ and a Lorentz factor at the transparency condition $\Gamma = 1.44 \times 10^4$. The fit of the light curve of the prompt emission allowed the determination of the average number density of the CBM, i.e., $\langle n_{\text{CBM}} \rangle = 1.9 \times 10^{-5} \text{ cm}^{-3}$, which is typical of galactic halos where NS–NS mergers migrate, owing to natal kicks imparted to the binaries at birth (see, e.g., Berger 2014). These values are strikingly similar to those inferred for other S-GRBs: GRB 081024B ($B = 4.80 \times 10^{-5}$, $\Gamma = 1.07 \times 10^4$, and $\langle n_{\text{CBM}} \rangle = 5.0 \times 10^{-6} \text{ cm}^{-3}$; Y. Aimurov et al. 2016, in preparation), GRB 090510 ($B = 5.54 \times 10^{-5}$, $\Gamma = 1.04 \times 10^4$, and $\langle n_{\text{CBM}} \rangle = 8.7 \times 10^{-6} \text{ cm}^{-3}$; Ruffini et al. 2016), and GRB 140619B ($B = 5.52 \times 10^{-5}$, $\Gamma = 1.08 \times 10^4$, and $\langle n_{\text{CBM}} \rangle = 4.7 \times 10^{-5} \text{ cm}^{-3}$; Ruffini et al. 2015b).

With the exception of GRB 090227B, which was outside the nominal *Fermi*-LAT field of view (Ackermann et al. 2013), the GeV luminosity light curves of the above four S-GRBs and that of the additional example recently identified, GRB 140402A (R. Ruffini et al. 2016, in preparation), follow a common behavior when computed in the source rest frame (see Figure 5(d)).

8. ULTRASHORT GRBs

As pointed out in the Introduction, U-GRBs originate from the NS–BH binaries produced in the BdHNe, and nearly 100% of these binaries remain bound (Fryer et al. 2015). The lack of any observed source to date is mainly due to the extremely short duration of these systems (Fryer et al. 2015).

Interesting considerations, which may be of relevance for describing the U-GRB subclass, can be found in Popham et al. (1999).

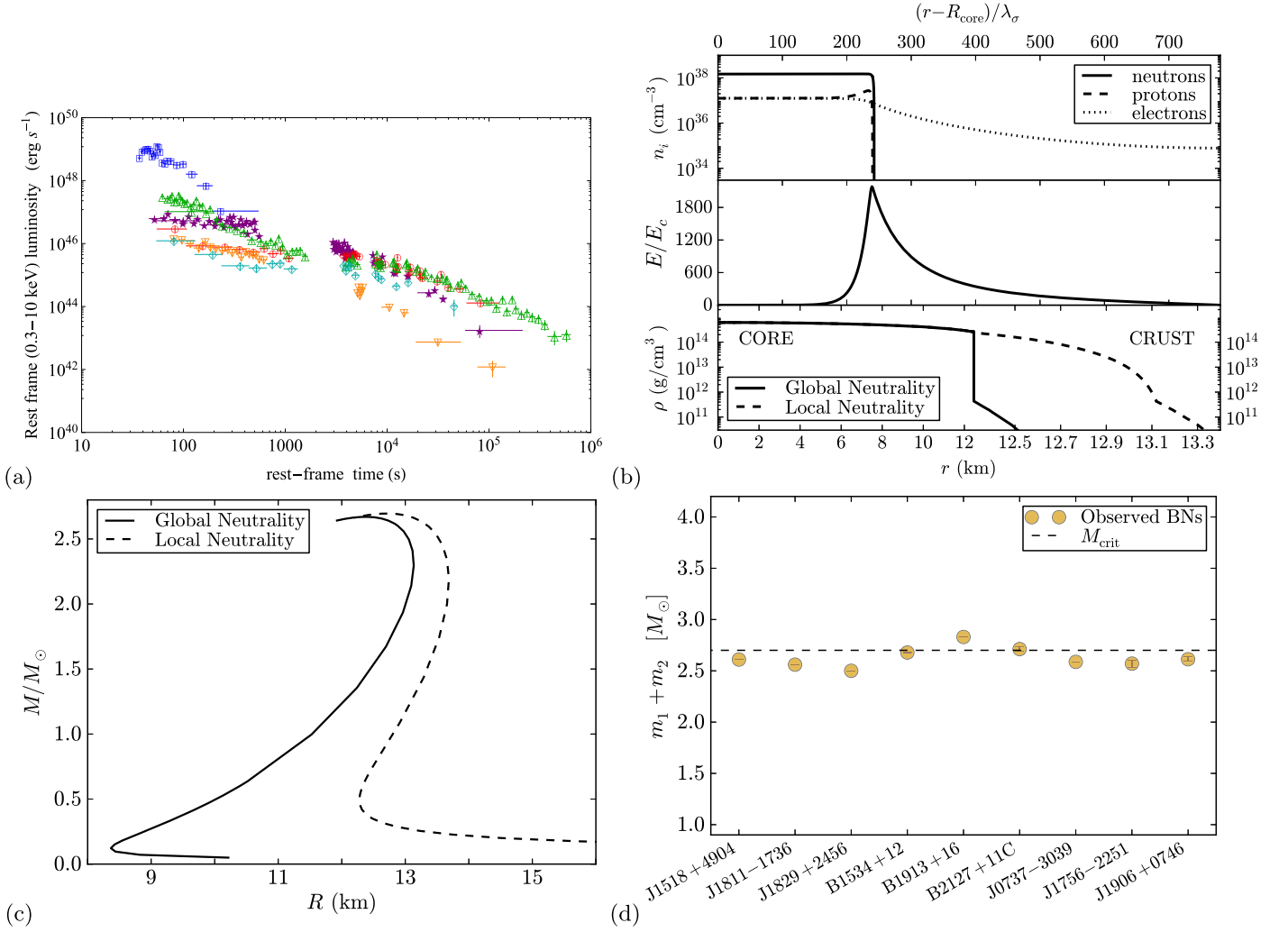


Figure 4. (a) Rest-frame 0.3–10 keV luminosity light curves of some selected S-GRFs: GRB 051210 (blue squares), GRB 051221 (green triangles), GRB 061201 (orange downward-pointing triangles), GRB 070809 (light-blue diamonds), GRB 130603B (purple stars), and GRB 140903A (red circles). See Table 4 for details on the sources. (b) Upper panel: particle density profiles in the NS core–crust boundary interface. Middle panel: electric field in the core–crust transition layer in units of E_c . Lower panel: density profile inside an NS with central density $\rho \sim 5\rho_{\text{nuc}}$, where ρ_{nuc} is the nuclear density, from the solution of the Tolman–Oppenheimer–Volkoff (TOV) equations (locally neutral case) and the globally neutral solution presented in Belvedere et al. (2012). Here the density at the edge of the crust is the neutron drip density $\rho_{\text{drip}} = 4.3 \times 10^{11} \text{ g cm}^{-3}$, and $\lambda_\sigma = \hbar/(m_\sigma c) \sim 0.4 \text{ fm}$ denotes the σ -meson Compton wavelength. Reproduced from Oliveira et al. (2014) with their kind permission. (c) Mass–radius relation obtained with the local and the new global neutrality equilibrium configurations, by applying the NL3 nuclear model, with a critical mass of $2.67 M_\odot$ for nonrotating NSs (Belvedere et al. 2012). Figure reproduced from Belvedere et al. (2012). (d) Plot of the galactic binary NSs with known total masses ($m_1 + m_2$, in solar masses). The horizontal dashed line marks the NS critical mass: systems beyond this value lead to BH formation. Reproduced from Ruffini et al. (2015b).

Table 5

List of the S-GRBs Considered in This Work up to the End of 2014

GRB	z	$E_{\text{iso}}/(10^{52} \text{ erg})$	GRB	z	$E_{\text{iso}}/(10^{52} \text{ erg})$
060801	1.13	3.27 ± 0.49	090510	0.903	3.95 ± 0.21
081024B	3.05	2.44 ± 0.22	140402A	5.52	4.7 ± 1.1
090227B	1.61	28.3 ± 1.5	140619B	2.67	6.03 ± 0.79

Note. For each source (first and fourth columns) the values of z and E_{iso} (second, third, fifth, and sixth columns) are listed.

9. THE GAMMA-RAY FLASHES

9.1. General Properties

The observational features of short bursts followed by an extended emission with energy below $\approx 10^{52} \text{ erg}$ are listed below and summarized in Figure 6. These bursts are interpreted

within the theoretical framework of a binary merger of an NS and a massive WD (della Valle et al. 1992, 1994) in the fireshell model as a new class that we indicate as GRFs.

The upper limit on the energetics of the GRFs is $(9.8 \pm 2.4) \times 10^{51} \text{ erg}$, as measured in GRB 070714B.

The isotropic energies are in the range $(8.9 \pm 1.6) \times 10^{49} \lesssim E_{\text{iso}} \lesssim (9.8 \pm 2.4) \times 10^{51} \text{ erg}$.

The spectral peak energies are in the range $0.2 \lesssim E_{\text{p,i}} \lesssim 2 \text{ MeV}$.

The cosmological redshifts are in the range $0.089 \leq z \leq 2.31$, with an average value of ≈ 0.54 (see Table 6).

The γ -ray emission is composed of (1) an initial spike-like harder emission and (2) a prolonged softer emission observed for up to 100 s (see Figure 6(a)).

The long-lasting X-ray afterglow does not exhibit any specific common late power-law behavior (see Figure 6(b)).

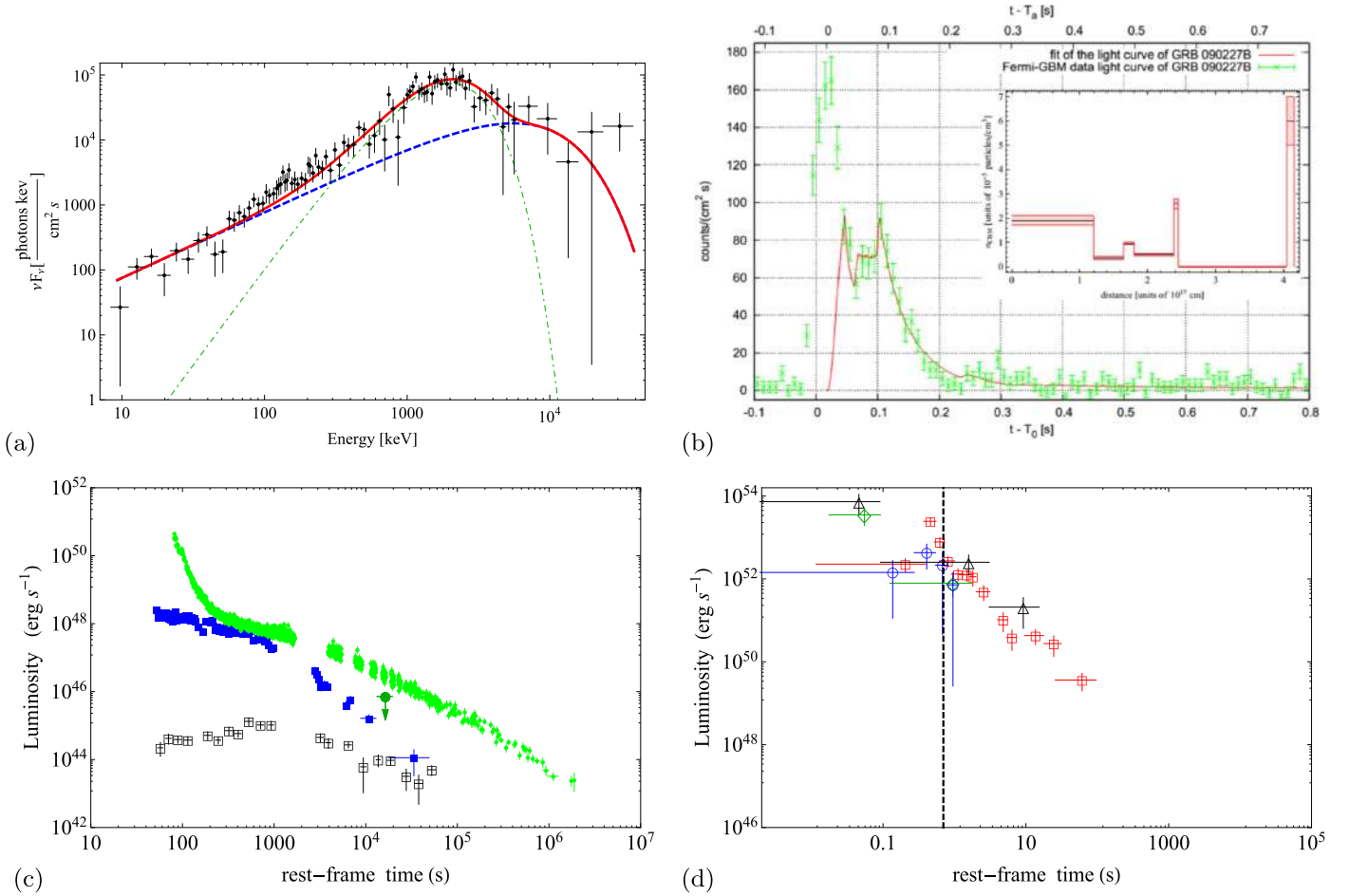


Figure 5. (a) Simulation of the observed P-GRB spectrum of the prototypical S-GRB 090227B: the dot-dashed green line represents the BB emission, and the dashed blue line corresponds to the early onset of the prompt emission within the P-GRB computed from the fireshell simulation in the energy band 8–40,000 keV; the sum of the two components is shown as a solid red line. Reproduced from Muccino et al. (2013). (b) NaI-n2 light curve of the prompt emission of the S-GRB 090227B (green data) and the simulation within the fireshell model (red curve). The inset reproduces the CBM profile required for the simulation. Reproduced from Muccino et al. (2013). (c) Available X-ray and optical luminosities of S-GRBs: the X-ray rest-frame 0.3–10 keV (blue filled squares) and the optical rest-frame 2–7 eV (black open squares, taken from De Pasquale et al. 2010) luminosity light curves of GRB 090510, and the X-ray rest-frame 0.3–10 keV upper limit of GRB 140619B (green filled circle; see, e.g., Ruffini et al. 2015b). For comparison the rest-frame 0.3–10 keV luminosity light curve of one of the prototypes of BdHNe, GRB 090618 (green circles), is shown. (d) Rest-frame 0.1–100 GeV luminosity light curves of the S-GRBs 081024B (green diamonds), 090510 (red squares), 140402A (black triangles), and 140619B (blue circles). The dashed vertical line marks the minimal turn-on time of the GeV emission of BdHNe. It is clear that in the case of S-GRBs the GeV emission turns on at shorter timescales and exhibits larger luminosities.

No SN association is expected or observed also in the case of nearby sources (Della Valle et al. 2006).

No high-energy GeV emission is expected or observed in the absence of BH formation.

9.2. Theoretical Interpretation of GRFs within the NS–WD Merger Paradigm in the Fireshell Model

As we mentioned, the mergers of NS–WD binaries, notoriously very common astrophysical systems (Cadelano et al. 2015), can be the progenitors of another GRB subclass: the GRFs. Possible evolutionary scenarios leading to NS–WD mergers have been envisaged, e.g., in Lazarus et al. (2014) and Tauris et al. (2000). Another less likely but possible scenario is the merger of an NS–WD binary produced, as recalled in Section 6.2, from an S-GRF, namely, the merger of a mass-asymmetric NS–NS binary with total mass $m_1 + m_2$ smaller than M_{crit} , which produces an MNS with a low-mass WD companion (see, e.g., Bildsten & Cutler 1992, and references therein), due to the energy and momentum conservation laws (Ruffini et al. 2015b).

With the term GRFs we dubbed a class of L-GRBs occurring in a CBM environment with low density, e.g., $\sim 10^{-3} \text{ cm}^{-3}$, with a light curve in γ -rays composed of an initial spike-like hard emission, identified with the P-GRB, and prolonged softer emission, explained as the prompt emission (see Figure 6(a) and Caito et al. 2009, 2010). No associated SN has ever been observed, although in the case of the low value of the cosmological redshift its detection would not have been precluded (Della Valle 2006). The prototype of such systems is GRB 060614 (Caito et al. 2009).

Apart from the absence of any SN associated with a GRF, the identification of NS–WD binaries as progenitor systems of the GRFs comes from the following observational and theoretical evidence: (a) the initial spike-like emission fulfills the $E_{\text{p},i} - E_{\text{iso}}$ relation for S-GRFs and S-GRBs (Zhang et al. 2012; Calderone et al. 2015; Ruffini et al. 2015b), both originating in NS–NS mergers (Ruffini et al. 2015b); (b) the value of the baryon load, $B \approx 10^{-3}$ (Caito et al. 2009, 2010) points to a system more baryon contaminated than the simpler and more compact NS–NS merger ($B \approx 10^{-5}$, see, e.g., Ruffini

Table 6
List of the GRFs Considered in This Work up to the End of 2014

GRB	z	$E_{\text{iso}}/(10^{50} \text{ erg})$	GRB	z	$E_{\text{iso}}/(10^{50} \text{ erg})$
050724	0.257	6.19 ± 0.74	061021	0.3462	50 ± 11
050911	0.165	0.89 ± 0.16	061210	0.409	0.24 ± 0.06
060505	0.089	2.35 ± 0.42	070506	2.31	51.3 ± 5.4
060614	0.125	21.7 ± 8.7	070714B	0.923	98 ± 24
061006	0.438	17.9 ± 5.6	071227	0.381	8.0 ± 1.0

Note. For each source (first and fourth columns) the values of z and E_{iso} (second, third, fifth, and sixth columns) are listed.

et al. 2015b); (c) the fit of the prompt emission within the fireshell model provides the CBM with low density, e.g., $\sim 10^{-3} \text{ cm}^{-3}$, typical of the halos of the GRB host galaxies (Caito et al. 2009, 2010); (d) the presence of a macronova emission in the optical afterglow of the prototype GRF 060614 (Jin et al. 2015).

In summary, we list below the different episodes observed (or not) in GRFs.

Episode 1 does not exist due to the compactness of the NS–WD merger.

Episode 2 corresponds to the γ -ray emission stemming from the NS–WD merger. The fireshell theory still applies to these systems in view of the considerations presented in Section 2. Also in this case a viable mechanism consists in the pair creation via $\nu\bar{\nu} \leftarrow e^+e^-$ during an NS–WD merger (see, e.g., Paschalidis et al. 2011). This is in line with an upper limit to the energetics of these systems in γ -rays of $E_{\text{iso}} \approx 10^{52} \text{ erg}$.

Episode 3 in GRFs, like in the cases of XRFs and S-GRFs, does not exhibit either a late common power-law behavior or the nesting discovered in the rest-frame 0.3–10 keV luminosity light curves of BdHNe (see Figure 6(b)). Also for GRFs, possible candidates for the explanation of the late X-ray afterglow emission are (a) the accelerated baryons interacting with the CBM after the P-GRB emission or (b) the possible radioactive decay of heavy elements synthesized in the ejecta of a compact binary merger (Li & Paczyński 1998).

Episode 4 is missing in view of the absence of the SN.

Episode 5, namely, the GeV emission, does not occur for NS–WD mergers. This fact, together with the energetics of these systems, $E_{\text{iso}} < 10^{52} \text{ erg}$, implies that both of these necessary and sufficient conditions for the BH formation are not fulfilled. Therefore, in an NS–WD merger, in view of the limited mass of the WD component, the NS critical mass is never reached in the accretion process during the merger.

9.3. Prototypes

In Table 6 we list all the GRFs identified so far.

The prototype of GRFs is GRB 060614 and has been analyzed by Caito et al. (2009). From the analysis of its P-GRB emission a baryon load $B = 2.8 \times 10^{-3}$ and a Lorentz factor at the transparency condition $\Gamma = 346$ have been found. From the fit of the light curve of the prompt emission it has been inferred that this burst occurred in a CBM with density $n_{\text{CBM}} = 2.3 \times 10^{-5} - 4.8 \times 10^{-3} \text{ cm}^{-3}$, which is typical of galactic halos where NS–NS and NS–WD mergers occur (see, e.g., Berger 2014). Analogous results were obtained for the GRF 071227: $B = 2.0 \times 10^{-4}$ and $n_{\text{CBM}} = 1.0 \times 10^{-4} - 1.0 \times 10^{-2} \text{ cm}^{-3}$ (Caito et al. 2010).

Further analyses on other GRF examples will be presented elsewhere.

10. THE OBSERVED RATES OF SHORT AND LONG BURSTS

The observed GRB occurrence rate is defined by the convolution of both (likely redshift-dependent) luminosity function, which describes the fraction of bursts with isotropic equivalent luminosities in the interval $\log L$ and $\log L + d \log L$, and cosmic GRB occurrence rate, which gives the number of sources at different redshifts. The definition of both of these functions is still an open issue and depends on a priori assumptions, and some investigations have been carried out in the literature (see, e.g., Soderberg et al. 2006; Guetta & Della Valle 2007; Liang et al. 2007; Virgili et al. 2009; Rangel Lemos et al. 2010; Wanderman & Piran 2010; Guetta et al. 2011; Kovacevic et al. 2014, for long bursts; Virgili et al. 2011; Wanderman & Piran 2015, for short bursts; and Sun et al. 2015, for both long and short bursts). To complicate the matter, also the instrumental sensitivity threshold, the field of view Ω_i , and the operational time T_i of the various detectors i observing GRBs introduce additional uncertainties to the problem.

In the following we ignore the possible redshift evolution of the luminosity function. Thus, if ΔN_i events are detected by various detectors in a finite logarithmic luminosity bin from $\log L$ to $\log L + \Delta \log L$, the total local event rate density of bursts between observed minimum and maximum luminosities, L_{min} and L_{max} , respectively, is defined as (see Sun et al. 2015)

$$\rho_0 \simeq \sum_i \sum_{\log L_{\text{min}}}^{\log L_{\text{max}}} \frac{4\pi}{\Omega_i T_i} \frac{1}{\ln 10} \frac{1}{g(L)} \frac{\Delta N_i}{\Delta \log L} \frac{\Delta L}{L}, \quad (2)$$

where

$$g(L) = \int_0^{z_{\text{max}}(L)} \frac{f(z)}{1+z} \frac{dV(z)}{dz} dz, \quad (3)$$

and the comoving volume is given by

$$\frac{dV(z)}{dz} = \frac{c}{H_0} \frac{4\pi d_L^2}{(1+z)^2 [\Omega_M(1+z)^3 + \Omega_\Lambda]^{1/2}}, \quad (4)$$

where d_L is the luminosity distance. The dimensionless function $f(z)$ describes the GRB cosmic redshift-dependent event rate density. In the following we assume no redshift dependency; therefore, we set $f(z) = 1$. The maximum redshift $z_{\text{max}}(L)$ in Equation (3) defines the maximum volume inside which an event with luminosity L can be detected. This redshift can be computed from the 1 s bolometric peak luminosity L , k -corrected from the observed detector energy band into the burst cosmological rest-frame energy band 1–10⁴ keV (Schaefer 2007), and the corresponding 1 s threshold peak flux f_{th} , which is the limiting peak flux to allow the burst detection (see Band 2003, for details). Therefore, z_{max} can be defined via (see, e.g., Zhang et al. 2009; Ruffini et al. 2014a)

$$f_{\text{th}} = \frac{L}{4\pi d_L^2(z_{\text{max}})k}, \quad (5)$$

where we duly account for the k -correction.

Within the assumptions that the GRB luminosity function does not evolve with redshift and that $f(z) = 1$, we investigate the evolution with the redshift of the GRB rates by separating the bursts into several redshift bins. As suggested in Sun et al. (2015), this can be done in each redshift interval $z_j \leq z \leq z_{j+1}$ by changing the integration limits of Equation (3) into z_j and $\min[z_{j+1}, z_{\max,j}(L)]$, where $z_{\max,j}(L)$ is the maximum redshift for the j th redshift bin. Finally, from Equation (2) we derive an event rate ρ_0^z in each redshift bin around z .

In the following we adopt the following fields of view and operational times for various detectors: *BeppoSAX*, $\Omega_{BS} = 0.25$ sr, $T_{BS} = 7$ yr; *BATSE*, $\Omega_B = \pi$ sr, $T_B = 10$ yr; *HETE-2*, $\Omega_H = 0.8$ sr, $T_H = 7$ yr; *Swift-BAT*, $\Omega_S = 1.33$ sr, $T_S = 10$ yr; *Fermi-GBM*, $\Omega_F = 9.6$ sr, $T_F = 7$ yr. We assume no beaming correction in computing the rates of the GRB subclasses.

10.1. Rate of S-GRFs

The local rate of S-GRFs, obtained from the sample of sources listed in Table 4, is $\rho_0 = 3.6_{-1.0}^{+1.4} \text{ Gpc}^{-3} \text{ yr}^{-1}$, and it is in agreement with the estimates obtained from the whole short-burst population detected by the *Swift-BAT* detector (and, therefore, including also S-GRBs and GRFs) and reported in the literature ($1\text{--}10 \text{ Gpc}^{-3} \text{ yr}^{-1}$; see, e.g., Clark et al. 2015, and references therein). In particular, our local rates with $f(z) = 1$ agree with recent more precise estimates: (a) $4.1_{-1.9}^{+2.3} \text{ Gpc}^{-3} \text{ yr}^{-1}$ for $L_{\min} = 5 \times 10^{49} \text{ erg s}^{-1}$ and for $f(z)$ described by a power-law merger delay model (Wanderman & Piran 2015); (b) $4.2_{-1.0}^{+1.3}$, $3.9_{-0.9}^{+1.2}$, and $7.1_{-1.7}^{+2.2} \text{ Gpc}^{-3} \text{ yr}^{-1}$ for $L_{\min} = 7 \times 10^{49} \text{ erg s}^{-1}$ and $f(z)$ described as Gaussian, lognormal, and power-law merger delay models, respectively (Sun et al. 2015).

The evolution of the S-GRF rate in various redshift bins is shown in Figure 7(c). This rate decreases as a power law from the local value in the interval $0.1 \leq z \leq 0.4$ to a value of $0.042_{-0.025}^{+0.046} \text{ Gpc}^{-3} \text{ yr}^{-1}$ in the interval $1.0 \leq z \leq 2.7$. Also in the case of S-GRFs the increasing sampled comoving universe volume and the threshold of the detectors play a fundamental role in the observed decrease of their rate at larger distances.

10.2. Rate of S-GRBs

Previously we have identified and described four S-GRBs in Ruffini et al. (2015b): GRB 081024B, GRB 090227B, GRB 090510, and GRB 140619B. Here we present two additional new members of this class: GRB 060801 (at $z \approx 1.13$ and with $z_{\max} \approx 2.04$, in this work) and GRB 140402A (at $z \approx 5.52$ and with $z_{\max} \approx 7.16$; R. Ruffini et al. 2016, in preparation). From these six S-GRBs detected by the *Fermi* and *Swift* satellites, we obtain via Equations (2)–(3) a local rate $\rho_0 = (1.9_{-1.1}^{+1.8}) \times 10^{-3} \text{ Gpc}^{-3} \text{ yr}^{-1}$.

With only six sources, we could not build the evolution with the redshift of such systems.

10.3. Rate of XRFs

In Kovacevic et al. (2014), we have estimated an updated observed rate for the XRFs at $z < 0.1$ based on the method outlined in Soderberg et al. (2006) and Guetta & Della Valle (2007). In this work, we consider the complete list of XRFs shown in Table 2 and the method outlined in Sun et al. (2015). From Equations (2)–(3) the local rate of XRFs is $\rho_0 = 100_{-34}^{+45} \text{ Gpc}^{-3} \text{ yr}^{-1}$, where the attached errors are determined from the

95% confidence level of the Poisson statistic (Gehrels 1986). Within the extent of our different classification criteria and different choices for $f(z)$, our estimate is in agreement with those reported for low-luminosity L-GRBs in Liang et al. (2007) and Virgili et al. (2009), and in particular with the value of $164_{-65}^{+98} \text{ Gpc}^{-3} \text{ yr}^{-1}$, obtained by Sun et al. (2015) with the same method.

In the IGC scenario the XRF out-states are NS–NS binary systems. For a reasonable set of binary initial conditions, population synthesis simulations performed by Fryer et al. (1999) provide an NS–NS formation rate of $0.2\text{--}1600 \text{ Gpc}^{-3} \text{ yr}^{-1}$. The NS–NS formation rate accounts for other possible channels in the population synthesis models, in addition to the one we considered from the XRFs. It is interesting, nevertheless, that our predicted rate is consistent with that obtained by Fryer et al. (1999).

For the same reason, our rate of XFRs can also be compared with the NS–NS merger rate proposed by Eichler et al. (1989). In this historical paper, the NS–NS merger rate is derived from the strong assumption that each merger ejects always the same amount of material r -process classified and the heavy r -process material. Eichler et al. (1989) obtain a rough estimate of $140\text{--}14,000 \text{ Gpc}^{-3} \text{ yr}^{-1}$, which is marginally consistent with the upper value of the local XRF rate.

The evolution of the XRF rate in various redshift bins is shown in Figure 7(a). It decreases from a value of $95_{-63}^{+123} \text{ Gpc}^{-3} \text{ yr}^{-1}$ in the interval $0 \leq z \leq 0.1$ to a value of $0.8_{-0.5}^{+1.1} \text{ Gpc}^{-3} \text{ yr}^{-1}$ in the interval $0.7 \leq z \leq 1.1$. This effect is mainly due to the intrinsic low luminosities of the bulk of the XRF population ($10^{46}\text{--}10^{48} \text{ erg s}^{-1}$; see, e.g., Bromberg et al. 2011) and to the threshold of the detectors: at increasing sampled universe comoving volumes, these low-luminosity XRFs become undetectable; therefore, at higher redshifts the total XRF rate decreases.

10.4. Rate of BdHNe

We proceed now in estimating the rate of BdHNe from the total sample of 233 sources (see Table 3). From Equations (2)–(3) the local rate of BdHNe is $\rho_0 = 0.77_{-0.08}^{+0.09} \text{ Gpc}^{-3} \text{ yr}^{-1}$. Our estimate is in agreement with two recent estimates obtained from long bursts with $L \geq 10^{50} \text{ erg s}^{-1}$ and by assuming $f(z) \neq 1$: (a) the value of $1.3_{-0.7}^{+0.6} \text{ Gpc}^{-3} \text{ yr}^{-1}$ obtained by Wanderman & Piran (2010), even though limited to the *Swift* long bursts and including some long bursts with $E_{\text{iso}} < 10^{52} \text{ erg}$, obtained from a GRB-inferred cosmic rate independent of the star formation rate; (b) the value of $0.8_{-0.1}^{+0.1} \text{ Gpc}^{-3} \text{ yr}^{-1}$ obtained by Sun et al. (2015) with the same method and including the star formation rate dependence.

In the IGC scenario the BdHNe out-states are NS–BH binary systems. Following again the work by Fryer et al. (1999), population synthesis simulations (which also accounts for alternative scenarios to that of the IGC model) provide an NS–BH formation rate of $0.02\text{--}1000 \text{ Gpc}^{-3} \text{ yr}^{-1}$. Also in this case, even though a straightforward comparison is not possible, the BdHN rate is consistent with the NS–BH formation rate obtained by Fryer et al. (1999).

The evolution of the BdHN rate in various redshift bins is shown in Figure 7(b). It slightly decreases from the local value in the interval $0.1 \leq z \leq 0.4$ to a value of $0.17_{-0.04}^{+0.05} \text{ Gpc}^{-3} \text{ yr}^{-1}$ in the interval $3.6 \leq z \leq 9.3$. As stated for the case of XRFs, this effect occurs because for increasing sampled universe comoving volumes, only the most luminous BdHNe are

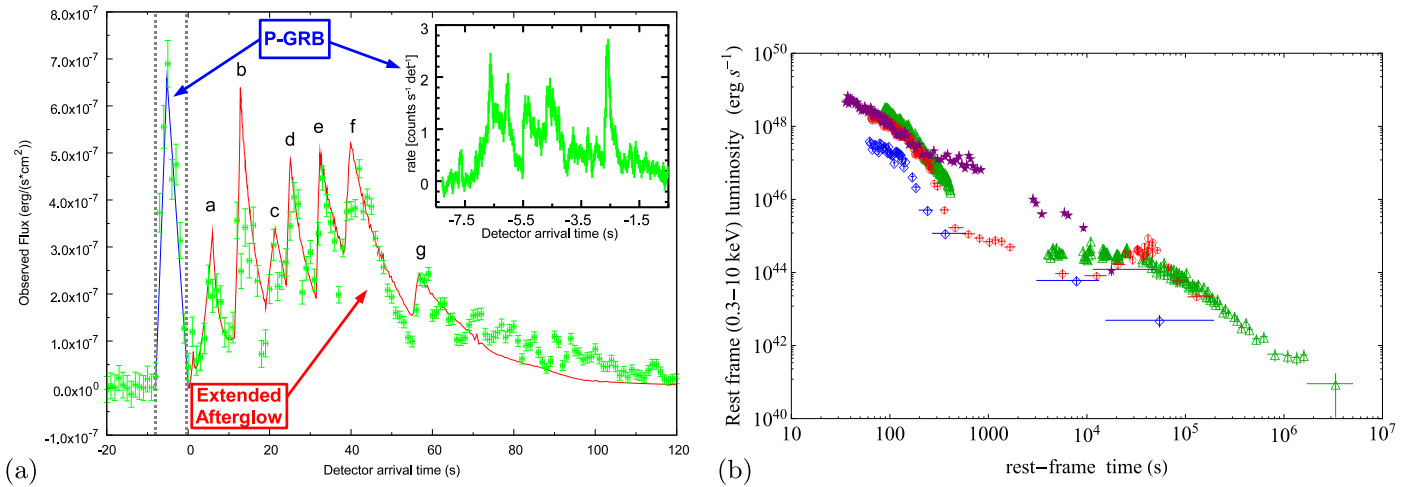


Figure 6. (a) Fireshell simulation of the *Swift*-BAT prompt emission of GRB 060614 (taken from Caito et al. 2009). (b) Rest-frame 0.3–10 keV luminosity light curves of selected GRFs: GRB 050724 (red circles), GRB 060614 (green triangles), GRB 070714B (purple stars), and GRB 071227 (blue diamonds).

detectable, even though in a less marked way than the case of the XRFs.

10.5. Rate of U-GRBs

As pointed out in Section 8, nearly 100% of the BdHNe lead to bound NS–BH binaries, which are the progenitor systems of U-GRBs (Fryer et al. 2015). If we include the possibility of other channels of formation for these NS–BH binaries, we can safely assume the BdHN local rate as a lower limit for these U-GRBs, e.g., $\rho_0 = 0.77^{+0.09}_{-0.08} \text{ Gpc}^{-3} \text{ yr}^{-1}$. From this consideration, it appears that the U-GRBs have the second higher rate among the short bursts after the S-GRFs.

10.6. Rate of GRFs

We proceed now in estimating the rate of GRFs from the total sample of 10 sources (see Table 6). From Equations (2)–(3) we obtain a local rate $\rho_0 = 1.02^{+0.71}_{-0.46} \text{ Gpc}^{-3} \text{ yr}^{-1}$ and represent the first estimate for these kinds of bursts originating from NS–WD mergers.

Due to the limited number of sources in our sample, we limited the study of the GRF rate evolution to two redshift bins, as shown in Figure 7(d). The rate ranges from a value consistent with the above local rate, in the redshift interval $0 \leq z \leq 0.35$, to a value of $0.080^{+0.088}_{-0.048} \text{ Gpc}^{-3} \text{ yr}^{-1}$, in the interval $0.35 \leq z \leq 2.31$. Also for GRFs, the cutoff in the rate at higher redshift occurs because for increasing sampled universe comoving volumes only the most luminous sources are detectable. However, this effect, as in the case of S-GRFs, is more pronounced due to their intrinsically weaker luminosities, when compared to those of S-GRBs.

11. CONCLUSIONS

The remarkable progress reached in understanding the GRB phenomenon has been made possible by the outstanding spectral and temporal information acquired from X-rays, γ -rays, and high-energy observatories, as well as from optical and radio data obtained by telescopes all over the planet. At the same time, this result has been fostered by a novel deeper theoretical understanding in the physics and astrophysics of WDs (see, e.g., Boshkayev et al. 2013), NSs (see, e.g., Belvedere et al. 2014; Cipolletta et al. 2015), and BHs (see,

e.g., Ruffini et al. 2010). Consequently, the understanding of the GRB phenomenon has evolved from an elementary paradigm based on a single jetted emission process as postulated in the fireball model (see, e.g., Sari et al. 1998; Piran 2005; Meszaros 2006; Gehrels et al. 2009, and references therein) to an authentic astrophysical laboratory involving many-body interactions between different astrophysical systems encountering previously unexplored regimes and observational evidence.

In the Introduction we reviewed the increasing number of GRB observations that have likewise led to the theoretical progress in the understanding of the GRB phenomena. While the role of NS–NS (or NS–BH) binaries as “in-states” of S-GRBs has been widely accepted and confirmed by strong observational and theoretical evidence (see, e.g., Goodman 1986; Paczynski 1986; Eichler et al. 1989; Narayan et al. 1991, 1992; Meszaros & Rees 1997; Rosswog et al. 2003; Lee et al. 2004; Berger 2014; Ruffini et al. 2015b, and figure 8), the identification of the progenitor systems for L-GRBs followed a more difficult path. Initially, theoretical models based on a single progenitor were proposed: a *collapsar* (Woosley 1993) or a *magnetar* (see, e.g., Zhang & Mészáros 2001). Then, the role of binary progenitor systems composed of two very massive stars for L-GRBs was recognized by Fryer et al. (1999), where several different scenarios were there envisaged leading to a *collapsar* (Woosley 1993), as well as a few leading, alternatively, to a variety of binary compact systems. These considerations were addressed by our group in a set of papers assuming that the birth of an SN and the occurrence of a GRB were qualitatively and quantitatively different astrophysical events in space and time. This led to the necessity of introducing the IGC paradigm (see, e.g., Ruffini et al. 2001c, 2006b, 2007, 2008, 2015c; Izzo et al. 2012b; Rueda & Ruffini 2012; Fryer et al. 2014). In the IGC paradigm the L-GRB–SN coincidence originates from CO_{core}–NS binary progenitor systems (see Figure 8). This approach differs from alternative descriptions, e.g., the *magnetar* and the *collapsar* models, where the two events are coming from a single progenitor star.

In Section 2 we reviewed the fireshell model for GRBs (see, e.g., Ruffini et al. 2001a, 2001b, 2001c) and its general description, which can be applied to any source of an optically

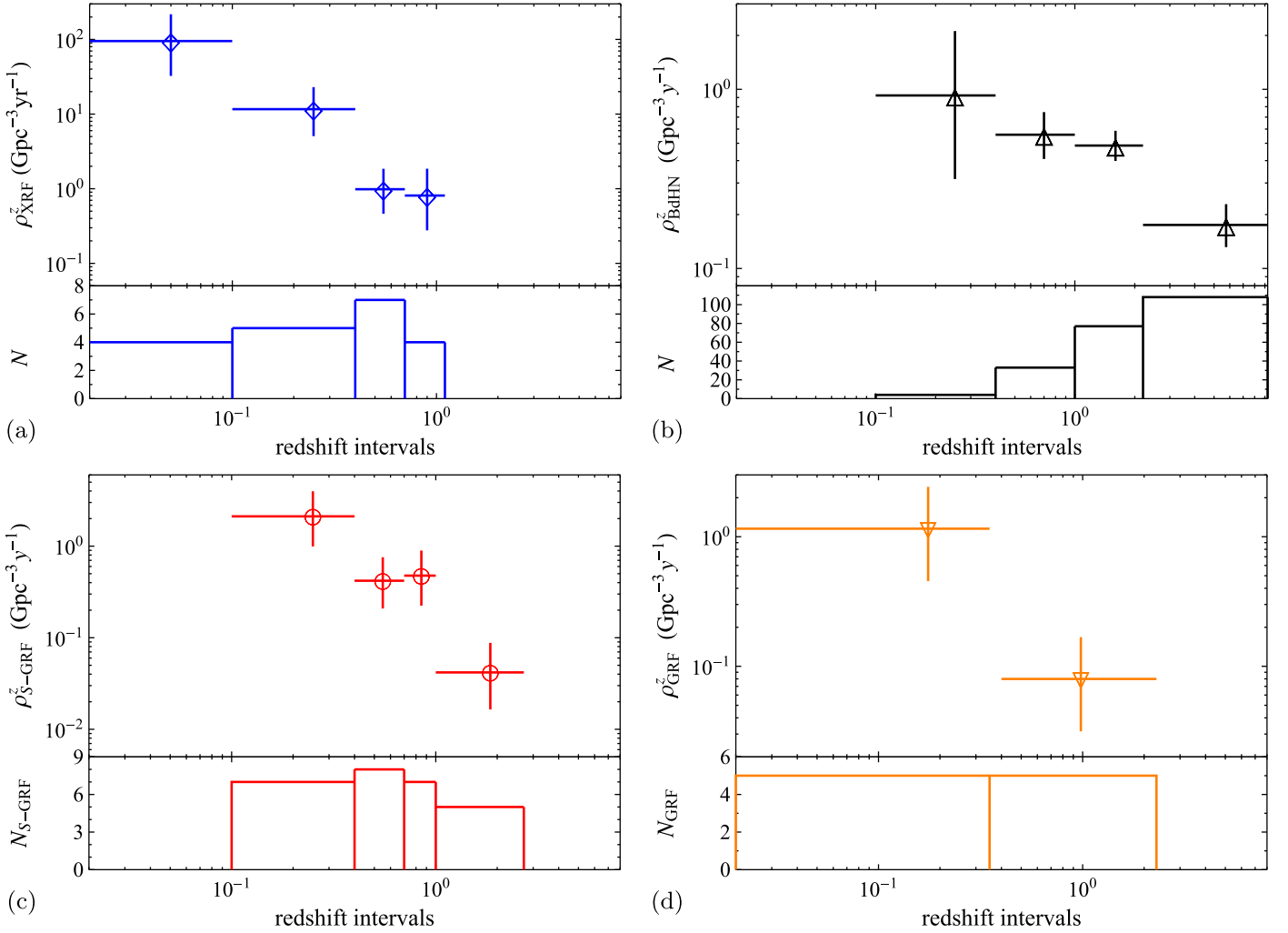


Figure 7. Evolution of the rate with redshift for the considered GRB subclasses: (a) the XRFs, (b) the BdHNe, (c) the S-GRFs, and (d) the GRFs. In each plot the upper panel shows the evolution rate with redshift, while the lower panel displays the number of observed sources in each redshift bin. Because of the limited amount of sources, for S-GRBs no redshift bin evolution is shown. In the case of U-GRBs, there are no current detections.

thick baryon-loaded e^+e^- plasma, i.e., in the quantum electrodynamical process expected in the formation of a BH (see, e.g., Preparata et al. 1998; Ruffini et al. 2000, 1999 Cherubini et al. 2009; Ruffini 2009), as well as in the case of a pair plasma created via $\nu\bar{\nu} \leftrightarrow e^+e^-$ mechanism in an NS–NS merger (Narayan et al. 1992; Salmonson & Wilson 2002; Rosswog et al. 2003), or in the hyperaccretion disks around BHs (Woosley 1993; Zalamea & Beloborodov 2011).

In Section 3 we discussed the role of the 10^{52} erg energy critical value introduced to discriminate between binary systems leading to the formation of an MNS (XRFs, S-GRFs, and GRFs), with energy lower than the above critical value, and those leading to the formation of a BH (BdHNe, S-GRBs, and U-GRBs), with energy larger than the above critical value. The value of 10^{52} erg is derived by considering the hypercritical accretion process onto an NS leading to an energy release in the form of neutrinos and photons, given by the gain of gravitational potential energy of the matter accreted in the NS. This includes the change of binding energy of the NS while accreting both matter and angular momentum (Becerra et al. 2016). A typical NS mass of $\approx 1.4 M_{\odot}$ has been assumed, as observed in galactic NS binaries (Zhang et al. 2011; Antoniadis 2015). An NS critical mass in the range from 2.2 up

to $3.4 M_{\odot}$, depending on the equations of state and angular momentum (see Cipolletta et al. 2015; Becerra et al. 2016, 2015, for details), has been assumed.

In Section 4 we described the properties of XRFs (see Figure 1). In these systems the distance between the CO_{core} and the NS companion is $a > 10^{11}$ cm. The hypercritical accretion process is not sufficient to push the NS beyond its M_{crit} , and an MNS is formed (see, e.g., Becerra et al. 2015, 2016). In Table 2 we list the XRFs considered in this work, as well as the spectral, temporal, and luminosity analysis of a selected prototype, e.g., GRB 060218. The complete theoretical simulation of this prototype is presented in Becerra et al. (2016).

In Section 5 we considered the BdHNe, for which the binary separation between the CO_{core} and the NS binary companion is $a < 10^{11}$ cm and the hypercritical accretion process triggers the gravitational collapse of the NS into a BH (see, e.g., Becerra et al. 2015, 2016). We show here an updated list of BdHNe (see Table 3), as well as a diagram summarizing some of the key properties and prototypes (see Figure 1), analyzed within the IGC paradigm and the fireshell model (see, e.g., GRB 090618 and GRB 130427A).

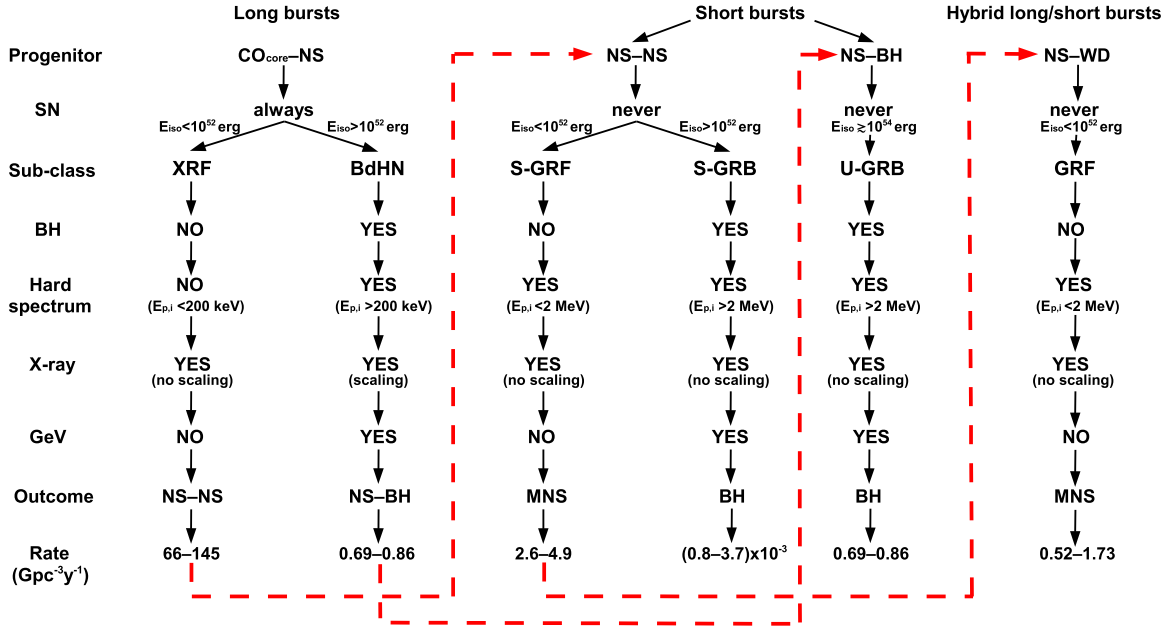


Figure 8. Summary of the properties of long, short, and hybrid long/short burst subclasses discussed in the Introduction. The red dashed lines indicate the evolutionary tracks linking the out-states and the in-states of some of the subclasses considered in this work.

In Section 6 we outlined the properties of S-GRFs listed in Table 4 and shown in Figure 1. These systems coincide with the short bursts considered in Berger (2014). They originate in NS-NS mergers leading to the formation of an MNS and possibly a binary companion, in order to fulfill the conservation of energy and momentum (Ruffini et al. 2015b).

In Section 7 we presented S-GRBs originating in NS-NS mergers leading to the formation of a BH (see Figure 1). We give, in Table 5, their updated list. We then described their prototypes, analyzed within the fireshell model (see, e.g., GRB 090227B and GRB 140619B), and outlined the key role of the P-GRB identification for their description, as well as the analysis of the GeV emission.

In Section 8, motivated by the results obtained by Fryer et al. (2015), where it was shown that nearly 100% of the NS-BH binaries, namely, the out-states of the BdHNe, remain bound, we added the description of this not yet observed but theoretically predicted subclass of U-GRBs, unaccounted for in current standard population synthesis analyses.

In Section 9 we reviewed the properties of the GRFs listed in Table 6 and shown in Figure 1. We recall and describe the results obtained from the sources analyzed within the fireshell model (see, e.g., GRB 060614, Caito et al. 2009; GRB 071227, Caito et al. 2010).

The most important result of the present article is the estimate of the rates of occurrence of the XRFs, BdHNe, S-GRFs, S-GRBs, U-GRBs, and GRFs. In Section 10 we introduced the procedure outlined in Sun et al. (2015) for estimating the local rates and their evolution with the redshift of the above subclasses of long and short bursts, assuming no beaming (note: the recent observation of the absence of GeV emission associated with a BdHN may limit this assumption). By ignoring possible redshift evolution of the GRB subclasses' luminosity functions and assuming that the GRB cosmic event rate density is redshift independent (e.g., $f(z) = 1$), the above method duly takes into account observational constraints, i.e., the detector solid angle coverage of the sky Ω and sensitivities,

which in turn define a maximum volume of observation depending on the intrinsic luminosity of the sources (see Section 10 and Soderberg et al. 2006; Guetta & Della Valle 2007; Liang et al. 2007; Virgili et al. 2009, 2011; Rangel Lemos et al. 2010; Wanderman & Piran 2010, 2015; Kovacevic et al. 2014; Sun et al. 2015, for details). We obtain

- an S-GRF local rate of $\rho_0 = 3.6_{-1.0}^{+1.4} \text{ Gpc}^{-3} \text{ yr}^{-1}$ (see Section 10.1);
- an S-GRB local rate of $\rho_0 = (1.9_{-1.1}^{+1.8}) \times 10^{-3} \text{ Gpc}^{-3} \text{ yr}^{-1}$ (see Section 10.2);
- an XRF local rate of $\rho_0 = 100_{-34}^{+45} \text{ Gpc}^{-3} \text{ yr}^{-1}$ (see Section 10.3);
- a BdHN local rate of $\rho_0 = 0.77_{-0.08}^{+0.09} \text{ Gpc}^{-3} \text{ yr}^{-1}$ (see Section 10.4; for the above reason this rate coincides with that of the U-GRBs; see Section 10.5);
- a GRF local rate of $\rho_0 = 1.02_{-0.46}^{+0.71} \text{ Gpc}^{-3} \text{ yr}^{-1}$ (see Section 10.6).

The local rates of S-GRFs, XRFs, and BdHNe are in agreement, within the extent of the different classification criteria, with those reported in the literature. The local rates of S-GRBs and GRFs are, instead, new ones following from the classification proposed in this work. The evolution with redshift of the rates of XRFs, BdHNe, S-GRFs, and GRFs is shown in Figure 7. It is certainly of interest to compare and contrast these results obtained from the direct observations of the sources in our new classification with the results computed from population synthesis models. Any possible disagreement will give the opportunity to identify possible missing links in the evolutionary phases within population synthesis analysis.

We are now in a position to apply the above rates of S-GRFs, S-GRBs, and U-GRBs to assess the detectability and the expected number of gravitational wave detections by LIGO from NS-NS and NS-BH binaries (Ruffini et al. 2016). We are also ready to apply the above BdHN rate to give an estimate of the contribution of GRBs to cosmic rays (R. Ruffini et al. 2016, in preparation).

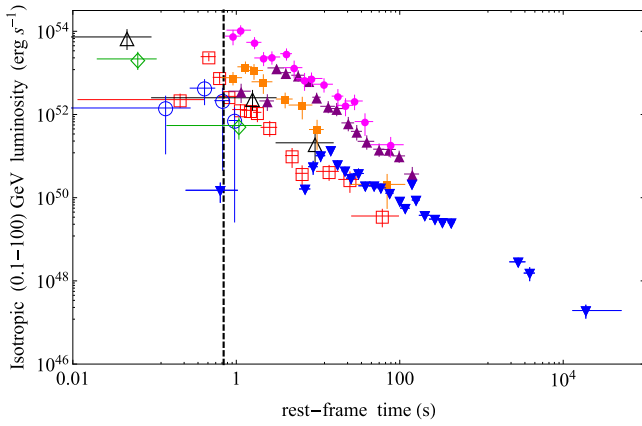


Figure 9. Rest-frame 0.1–100 GeV isotropic luminosity light curves of selected BdHNe (filled symbols) and all S-GRBs with available LAT data (open symbols). BdHNe: GRB 080916C (magenta circles), GRB 090902B (purple triangles), GRB 110731A (orange squares), GRB 130427A (blue downward-pointing triangles). S-GRBs: GRB 081024B (green diamonds), GRB 090510 (red squares), GRB 140402A (black triangles), GRB 140619B (blue circles). Also in this case the dashed vertical line marks the minimal turn-on time of the GeV emission of BdHNe.

Before concluding, in support of the classification proposed in this article, we recall that the luminosity light curves of the GeV emission are uniquely observed in both BdHNe and S-GRBs. In both cases it follows a precise power-law behavior with time $\propto t^{-1.2}$ (see Nava et al. 2014; Ruffini et al. 2016; see also Figure 9). An outstanding conclusion of this paper is that in both BdHNe and S-GRBs, where the presence of the BH is predicted, the turn-on of this GeV emission occurs after the P-GRB emission and at the beginning of the prompt emission phase (see Figures 3(d) and 5(d)). This commonality, in such different systems, and their energy requirements (see Table 7 and Figure 9) are naturally explained if we assume, as indicated in Ruffini et al. (2015c, 2015b), that this GeV emission originates by accretion processes in the newly born BH. We have pointed out in Ruffini et al. (2016) how the total energy of the GeV emission can be expressed in terms of the gravitational binding energy of matter accretion into Kerr BHs (see Ruffini & Wheeler 1969, in problem 2 of Section 104 in Landau & Lifshitz 2003). This energetics requirement could not be fulfilled in the case of accretion onto an NS, in view of the much smaller value of the gravitational binding energy when compared to the case of a rotating BH (see, e.g., Sibgatullin & Sunyaev 2000). On the general issue of the origin of the jetted GeV emission, and not just of its energetics, we refer to the last paragraph of the conclusions of Ruffini et al. (2016).

We have added a Table 7 with the values of the GeV emission for the case of both S-GRBs and BdHNe. These energy releases up to $\approx 10^{54}$ erg can be explained by the occurrence of accretion onto a rotating BH with mass in the range of 3–10 M_{\odot} . It is also clear from Figure 9 that S-GRBs and BdHNe have GeV emission sharing a common luminosity pattern and originating, in both cases, from a newly born Kerr BH (Ruffini et al. 2015c, 2015b). This picture includes also the first scenario of an IGC considered in Ruffini et al. (2001c) where an exploding CO_{core} is in a close binary system with an already formed BH companion. In view of the hypercritical accretion process of the SN ejecta onto an already formed BH, these systems have $E_{\text{iso}} \gtrsim 10^{54}$ erg and $E_{p,i} \gtrsim 2$ MeV. Their “out-states” are a binary composed of a more massive BH and a

Table 7
List of the Prompt and GeV Emission Properties of Selected BdHNe and S-GRBs

Source	z	$E_{p,i}$ (MeV)	E_{iso} (10^{52} erg)	E_{LAT} (10^{52} erg)
S-GRBs				
081024B	2.6 ± 1.6	8.7 ± 4.9	2.44 ± 0.22	2.70 ± 0.93
090510	0.903	7.89 ± 0.76	3.95 ± 0.21	5.78 ± 0.60
140402A	5.52 ± 0.93	6.1 ± 1.6	4.7 ± 1.1	16.6 ± 5.3
140619B	2.67 ± 0.37	5.34 ± 0.79	6.03 ± 0.79	2.34 ± 0.91
BdHNe				
080916C	4.35	2.76 ± 0.37	407 ± 86	440 ± 47
090902B	1.822	2.19 ± 0.22	292 ± 29	110 ± 5
110731A	2.83	1.16 ± 0.12	49.5 ± 4.9	42.5 ± 7.4
130427A	0.3399	1.25 ± 0.15	92 ± 13	19.9 ± 2.9

Note. We listed z , $E_{p,i}$, E_{iso} (in the rest-frame energy band 1–10,000 keV), and E_{LAT} (in the rest-frame energy band 0.1–100 GeV).

ν NS. Such systems, which we refer to as BH-SNe, are expected to be the late evolutionary stages of X-ray binaries such as Cyg X-1 or Cyg X-3 (see, e.g., Giacconi & Ruffini 1978).

In conclusion, we have computed the occurrence rate of short and long bursts following a new classification and obtaining figures in good agreement with the ones derived from population synthesis models. Essential to the classification have been the following new considerations:

- (1) the binary nature of the progenitors and their separation;
- (2) the essential role of the hypercritical accretion process onto an NS member of a close binary system, and the possible reaching of M_{crit} by the accretion process and the formation of a BH;
- (3) the activity of the newly born BHs originating the energetic prominent GeV emission, which can be explained in terms of the gravitational energy release by accreting matter onto a Kerr BH.

This classification is now open to a verification by the addition of new GRB sources and offers new possibilities of theoretical and observational activities, including:

- (1) the reaching of new observational constraints on the value of the NS critical mass M_{crit} and the minimum mass of a BH, which play a fundamental role in defining the separatrix among the different classes of our classification.
- (2) having elucidated the role of the activities of the newly born BH in explaining the energetics of the GeV emission, in order to identify its microphysical process, the study of fundamental issues of general relativistic quantum electrodynamical processes appears to be open to further lines of inquiry (see, e.g., Ruffini et al. 2010, and references therein);
- (3) it is conceivable that the sizable enlargement of the database of GRBs and of their spectral and luminosity time variability may open the possibility of further enlarging the above classification.

We thank the editor and the referee for their comments, which helped to improve the presentation and the

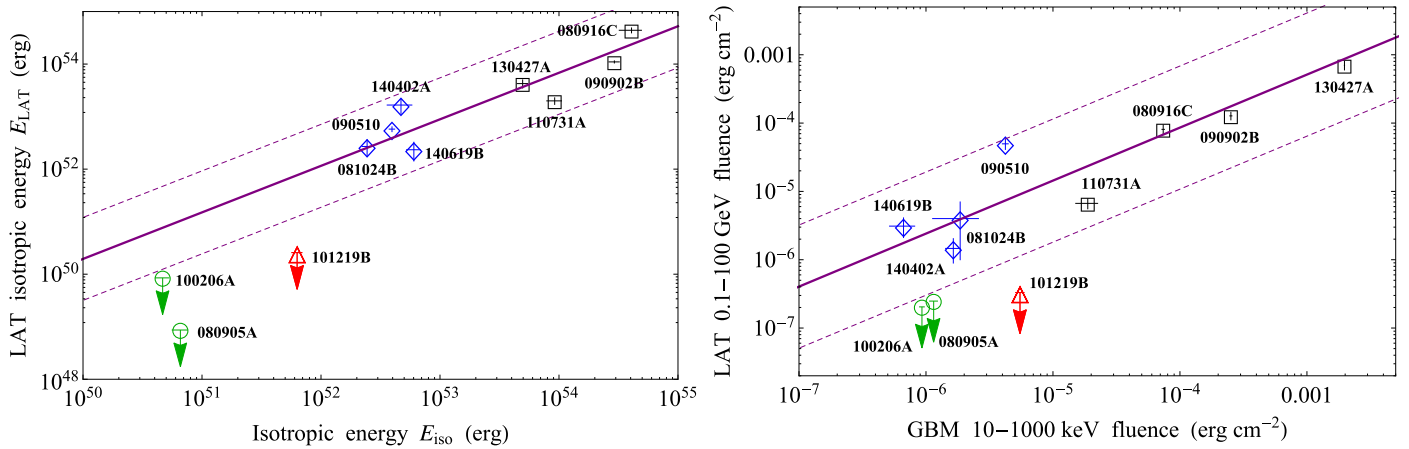


Figure 10. For the sources in Table 7 (BdHNe as black squares and S-GRBs as blue diamonds), as well as for two S-GRFs (green circles) and one XRF (red triangle) that did not exhibit GeV emission although they were in the optimal position ($<65^\circ$ from the LAT boresight) for its detection, we plot (left) the relation between E_{iso} of the prompt emission observed by the *Fermi*-GBM instrument and the total isotropic energy in the 0.1–100 GeV energy band observed by the *Fermi*-LAT instrument (or the corresponding upper limit if not detected) and (right) the relation between the 10–1000 keV fluence observed by the *Fermi*-GBM instrument and the total 0.1–100 GeV fluence observed by the *Fermi*-LAT instrument (or the corresponding upper limit if not detected). The purple solid line is the relation between the plotted quantities of BdHNe and S-GRBs, and the dashed lines are the corresponding dispersion.

contextualization of our results. This work made use of data supplied by the UK Swift Science Data Center at the University of Leicester. J.A.R. acknowledges the support by the International Cooperation Program CAPES-ICRANet financed by the CAPES-Brazilian Federal Agency for Support and Evaluation of Graduate Education within the Ministry of Education of Brazil. M.K. and Y.A. are supported by the Erasmus Mundus Joint Doctorate Program Grant N. 2013–1471 and 2014–0707, respectively, from EACEA of the European Commission. M. M. acknowledges the partial support of the project N 3101/GF4 IPC-11 and the target program F.0679 of the Ministry of Education and Science of the Republic of Kazakhstan.

APPENDIX

ON THE NONOBSERVED GEV EMISSION IN S-GRFs AND XRFs

In Figure 10 we compare and contrast the sources in Table 7, all exhibiting a GeV emission, with two S-GRFs and one XRF that, as theoretically expected within the fireshell model, do not exhibit any GeV emission. All these sources were in the optimal position ($<65^\circ$ from the LAT boresight) for the detection of the GeV emission.

In the left panel we plot the values of E_{iso} and of the isotropic energy in the *Fermi*-LAT energy band, or the corresponding upper limits if not observed. These upper limits were obtained by using the unbinned likelihood analysis that was performed assuming an integration time of 100 s after the flash trigger, a radius of the source region of 10° , and a zenith angle cut of 100° . This plot observationally supports the theoretical expectation, made in Ruffini et al. (2016) and quoted in Section 6.2 above, that S-GRFs have, if any, GeV fluxes necessarily 10^5 – 10^6 times weaker than those of S-GRBs, although their E_{iso} is only a factor of 10^2 smaller.

Motivated by a request of the referee, we also plotted, in the right panel, the values of the fluence observed by *Fermi*-GBM and by *Fermi*-LAT, or the corresponding upper limits if not observed (computed as above).

From both plots it is clear that the upper limits to the GeV emission of S-GRFs and XRFs are much lower than what one may expect from the extrapolation to lower energies of the one

observed in BdHNe and S-GRBs. This is a further clear observational support to the absence, theoretically implied by the fireshell model, of any GeV emission associated with S-GRFs and XRFs (see Sections 4.2 and 6.2).

REFERENCES

- Ackermann, M., Ajello, M., Asano, K., et al. 2013, *ApJS*, **209**, 11
Aksenov, A. G., Ruffini, R., & Vereshchagin, G. V. 2007, *PhRvL*, **99**, 125003
Aksenov, A. G., Ruffini, R., & Vereshchagin, G. V. 2009, *PhRvD*, **79**, 043008
Amati, L., & Della Valle, M. 2013, *IJMPD*, **22**, 30028
Amati, L., Frontera, F., in't Zand, J. J. M., et al. 2004, *A&A*, **426**, 415
Antoniadis, J. 2015, *ASSP*, **40**, 1
Atwood, W. B., Abdo, A. A., Ackermann, M., et al. 2009, *ApJ*, **697**, 1071
Band, D. L. 2003, *ApJ*, **588**, 945
Becerra, L., Bianco, C. L., Fryer, C. L., Rueda, J. A., & Ruffini, R. 2016, *arXiv:1606.02523*
Becerra, L., Cipolletta, F., Fryer, C. L., Rueda, J. A., & Ruffini, R. 2015, *ApJ*, **812**, 100
Belvedere, R., Boshkayev, K., Rueda, J. A., & Ruffini, R. 2014, *NuPhA*, **921**, 33
Belvedere, R., Pugliese, D., Rueda, J. A., Ruffini, R., & Xue, S.-S. 2012, *NuPhA*, **883**, 1
Berger, E. 2014, *ARA&A*, **52**, 43
Berger, E., Fong, W., & Chornock, R. 2013, *ApJL*, **774**, L23
Bianco, C. L., & Ruffini, R. 2004, *ApJL*, **605**, L1
Bianco, C. L., & Ruffini, R. 2005a, *ApJL*, **620**, L23
Bianco, C. L., & Ruffini, R. 2005b, *ApJL*, **633**, L13
Bianco, C. L., & Ruffini, R. 2006, *ApJL*, **644**, L105
Bildsten, L., & Cutler, C. 1992, *ApJ*, **400**, 175
Boër, M., Gendre, B., & Stratta, G. 2015, *ApJ*, **800**, 16
Boshkayev, K., Rueda, J. A., Ruffini, R., & Siutsou, I. 2013, *ApJ*, **762**, 117
Bromberg, O., Nakar, E., & Piran, T. 2011, *ApJL*, **739**, L55
Bucciantini, N., Metzger, B. D., Thompson, T. A., & Quataert, E. 2012, *MNRAS*, **419**, 1537
Bufano, F., Pian, E., Sollerman, J., et al. 2012, *ApJ*, **753**, 67
Cadelano, M., Pallanca, C., Ferraro, F. R., et al. 2015, *ApJ*, **812**, 63
Caito, L., Amati, L., Bernardini, M. G., et al. 2010, *A&A*, **521**, A80
Caito, L., Bernardini, M. G., Bianco, C. L., et al. 2009, *A&A*, **498**, 501
Calderone, G., Ghirlanda, G., Ghisellini, G., et al. 2015, *MNRAS*, **448**, 403
Campana, S., Mangano, V., Blustin, A. J., et al. 2006, *Natur*, **442**, 1008
Cano, Z., Bersier, D., Guidorzi, C., et al. 2011, *MNRAS*, **413**, 669
Cavallo, G., & Rees, M. J. 1978, *MNRAS*, **183**, 359
Cherubini, C., Geralico, A., Rueda, J. A., & Ruffini, R. 2009, *PhRvD*, **79**, 124002
Chiang, J., & Dermer, C. D. 1999, *ApJ*, **512**, 699
Cipolletta, F., Cherubini, C., Filippi, S., Rueda, J. A., & Ruffini, R. 2015, *PhRvD*, **92**, 023007

- Clark, J., Evans, H., Fairhurst, S., et al. 2015, *ApJ*, **809**, 53
- Cobb, B. E., Bloom, J. S., Perley, D. A., et al. 2010, *ApJL*, **718**, L150
- Costa, E., Frontera, F., Heise, J., et al. 1997, *Natur*, **387**, 783
- Dai, Z. G., & Lu, T. 1998a, *A&A*, **333**, L87
- Dai, Z. G., & Lu, T. 1998b, *PhRvL*, **81**, 4301
- Dai, Z. G., Wang, X. Y., Wu, X. F., & Zhang, B. 2006, *Sci*, **311**, 1127
- Damour, T., & Ruffini, R. 1975, *PhRvL*, **35**, 463
- D'Avanzo, P., Melandri, A., Palazzi, E., et al. 2012, GCN, 13069, 1
- Della Valle, M. 2006, in AIP Conf. Ser. 836, Gamma-Ray Bursts in the Swift Era, ed. S. S. Holt, N. Gehrels, & J. A. Nousek (Melville, NY: AIP), 367
- della Valle, M., Bianchini, A., Livio, M., & Orio, M. 1992, *A&A*, **266**, 232
- Della Valle, M., Chincarini, G., Panagia, N., et al. 2006, *Natur*, **444**, 1050
- della Valle, M., Rosino, L., Bianchini, A., & Livio, M. 1994, *A&A*, **287**, 403
- De Pasquale, M., Schady, P., Kuin, N. P. M., et al. 2010, *ApJL*, **709**, L146
- de Ugarte Postigo, A., Xu, D., Leloudas, G., et al. 2013, GCN, 14646, 1
- Dezalay, J.-P., Barat, C., Talon, R., et al. 1992, in AIP Conf. Ser. 265, Gamma-ray Bursts, Proc. of the Workshop, ed. W. S. Paciesas & G. J. Fishman (Huntsville: Univ. Alabama), 304
- Eichler, D., Livio, M., Piran, T., & Schramm, D. N. 1989, *Natur*, **340**, 126
- Evans, P. A., Beardmore, A. P., Page, K. L., et al. 2007, *A&A*, **469**, 379
- Evans, P. A., Beardmore, A. P., Page, K. L., et al. 2009, *MNRAS*, **397**, 1177
- Fryer, C. L., Oliveira, F. G., Rueda, J. A., & Ruffini, R. 2015, *PhRvL*, **115**, 231102
- Fryer, C. L., Rueda, J. A., & Ruffini, R. 2014, *ApJL*, **793**, L36
- Fryer, C. L., Woosley, S. E., & Hartmann, D. H. 1999, *ApJ*, **526**, 152
- Galama, T. J., Vreeswijk, P. M., van Paradijs, J., et al. 1998, *Natur*, **395**, 670
- Gehrels, N. 1986, *ApJ*, **303**, 336
- Gehrels, N., Ramirez-Ruiz, E., & Fox, D. B. 2009, *ARA&A*, **47**, 567
- Giacomazzo, B., & Perna, R. 2013, *ApJL*, **771**, L26
- Giacconi, R., & Ruffini, R. 1978, Physics and Astrophysics of Neutron Stars and Black Holes (Amsterdam: North Holland)
- Goodman, J. 1986, *ApJL*, **308**, L47
- Granot, J., Piran, T., & Sari, R. 1999, *ApJ*, **513**, 679
- Guetta, D., & Della Valle, M. 2007, *ApJL*, **657**, L73
- Guetta, D., Pian, E., & Waxman, E. 2011, *A&A*, **525**, A53
- Gursky, H., & Ruffini, R. (ed.) 1975, in Proc. Annual Meeting, Astrophysics and Space Science Library, Vol. 48, Neutron Stars, Black Holes and Binary X-ray Sources (Dordrecht: Reidel)
- Heise, J. 2003, in AIP Conf. Ser. 662, Gamma-Ray Burst and Afterglow Astronomy 2001: A Workshop Celebrating the First Year of the HETE Mission, ed. G. R. Ricker & R. K. Vanderspek (Melville, NY: AIP), 229
- Hill, J., Garnavich, P., Kuhn, O., et al. 2007, GCN, 6486, 1
- Izzo, L., Pisani, G. B., Muccino, M., et al. 2012a, arXiv:1210.8034
- Izzo, L., Rueda, J. A., & Ruffini, R. 2012b, *A&A*, **548**, L5
- Izzo, L., Ruffini, R., Penacchioni, A. V., et al. 2012c, *A&A*, **543**, A10
- Jin, Z.-P., Li, X., Cano, Z., et al. 2015, *ApJL*, **811**, L22
- Kann, D. A., Schulze, S., & Updike, A. C. 2008, GCN, 7627, 1
- Klebesadel, R. W. 1992, in Gamma-Ray Bursts—Observations, Analyses and Theories, ed. C. Theories, R. I. Ho, & E. E. Epstein (Cambridge: Cambridge Univ. Press)
- Kluźniak, W., & Ruderman, M. 1998, *ApJL*, **505**, L113
- Kouveliotou, C., Meegan, C. A., Fishman, G. J., et al. 1993, *ApJL*, **413**, L101
- Kouveliotou, C., Woosley, S. E., Patel, S. K., et al. 2004, *ApJ*, **608**, 872
- Kovacevic, M., Izzo, L., Wang, Y., et al. 2014, *A&A*, **569**, A108
- Landau, L. D., & Lifshitz, E. M. 2003, The Classical Theory of Fields (4th Engl. ed.; Oxford: Butterworth-Heinemann)
- Lazarus, P., Tauris, T. M., Knispel, B., et al. 2014, *MNRAS*, **437**, 1485
- Lee, W. H., Ramirez-Ruiz, E., & Page, D. 2004, *ApJL*, **608**, L5
- Levan, A. J., Fruchter, A. S., Graham, J., et al. 2013, GCN, 14686, 1
- Levan, A. J., Tanvir, N. R., Starling, R. L. C., et al. 2014, *ApJ*, **781**, 13
- Li, L.-X., & Paczyński, B. 1998, *ApJL*, **507**, L59
- Liang, E., Zhang, B., Virgili, F., & Dai, Z. G. 2007, *ApJ*, **662**, 1111
- Lü, H.-J., & Zhang, B. 2014, *ApJ*, **785**, 74
- MacFadyen, A. I., & Woosley, S. E. 1999, *ApJ*, **524**, 262
- MacFadyen, A. I., Woosley, S. E., & Heger, A. 2001, *ApJ*, **550**, 410
- Maeda, K., & Nomoto, K. 2003, *ApJ*, **598**, 1163
- Meegan, C. A., Fishman, G. J., Wilson, R. B., et al. 1992, *Natur*, **355**, 143
- Melandri, A., Pian, E., D'Elia, V., et al. 2014, *A&A*, **567**, A29
- Meszáros, P. 2006, *RPPh*, **69**, 2259
- Meszáros, P., & Rees, M. J. 1997, *ApJL*, **482**, L29
- Metzger, B. D., Giannios, D., Thompson, T. A., Bucciantini, N., & Quataert, E. 2011, *MNRAS*, **413**, 2031
- Metzger, M. R., Djorgovski, S. G., Kulkarni, S. R., et al. 1997, *Natur*, **387**, 878
- Muccino, M., Ruffini, R., Bianco, C. L., Izzo, L., & Penacchioni, A. V. 2013, *ApJ*, **763**, 125
- Narayan, R., Paczynski, B., & Piran, T. 1992, *ApJL*, **395**, L83
- Narayan, R., Piran, T., & Shemi, A. 1991, *ApJL*, **379**, L17
- Nava, L., Vianello, G., Omodei, N., et al. 2014, arXiv:1406.6693
- Nomoto, K., Yamaoka, H., Pols, O. R., et al. 1994, *Natur*, **371**, 227
- Nomoto, K. I., Iwamoto, K., & Suzuki, T. 1995, *PhR*, **256**, 173
- Nousek, J. A., Kouveliotou, C., Grupe, D., et al. 2006, *ApJ*, **642**, 389
- Oliveira, F. G., Rueda, J. A., & Ruffini, R. 2014, *ApJ*, **787**, 150
- Paczynski, B. 1986, *ApJL*, **308**, L43
- Panaiteescu, A., & Meszaros, P. 1998, *ApJL*, **493**, L31
- Panaiteescu, A., & Mészáros, P. 1999, *ApJ*, **526**, 707
- Paschalidis, V., Liu, Y. T., Etienne, Z., & Shapiro, S. L. 2011, *PhRvD*, **84**, 104032
- Patricelli, B., Bernardini, M. G., Bianco, C. L., et al. 2012, *ApJ*, **756**, 16
- Penacchioni, A. V., Ruffini, R., Bianco, C. L., et al. 2013, *A&A*, **551**, A133
- Penacchioni, A. V., Ruffini, R., Izzo, L., et al. 2012, *A&A*, **538**, A58
- Pian, E., Amati, L., Antonelli, L. A., et al. 2000, *ApJ*, **536**, 778
- Pian, E., Giommi, P., Amati, L., et al. 2004, *AdSpR*, **34**, 2711
- Piran, T. 2005, *RvMP*, **76**, 1143
- Pisani, G. B., Izzo, L., Ruffini, R., et al. 2013, *A&A*, **552**, L5
- Pisani, G. B., Ruffini, R., Aimuratov, Y., et al. 2016, arXiv:1610.05619
- Popham, R., Woosley, S. E., & Fryer, C. 1999, *ApJ*, **518**, 356
- Preparata, G., Ruffini, R., & Xue, S. 1998, *A&A*, **338**, L87
- Rangel Lemos, L. J., Bianco, C. L., Mosquera Cuesta, H. J., Rueda, J. A., & Ruffini, R. 2010, in XXV Texas Symp. Relativistic Astrophysics, ed. F. M. Rieger, C. van Eldik, & W. Hofmann, 204
- Rasio, F. A., & Shapiro, S. L. 1999, *CQGra*, **16**, R1
- Rees, M. J., & Meszaros, P. 1998, *ApJL*, **496**, L1
- Rhoades, C. E., & Ruffini, R. 1974, *PhRvL*, **32**, 324
- Rosswog, S., Ramirez-Ruiz, E., & Davies, M. B. 2003, *MNRAS*, **345**, 1077
- Rueda, J. A., & Ruffini, R. 2012, *ApJL*, **758**, L7
- Ruffini, R. 2009, in The Ergosphere and Dyadosphere of Black Holes, ed. D. L. Wiltshire, M. Visser, & S. Scott. (Cambridge: Cambridge Univ. Press), 161
- Ruffini, R. 2015, *AREp*, **59**, 591
- Ruffini, R., Bernardini, M. G., Bianco, C. L., et al. 2005, in AIP Conf. Ser. 782, XIth Brazilian School of Cosmology and Gravitation, ed. M. Novello & S. E. Perez Bergliaffa (Melville, NY: AIP), 42
- Ruffini, R., Bernardini, M. G., Bianco, C. L., et al. 2006a, *AdSpR*, **38**, 1291
- Ruffini, R., Bernardini, M. G., Bianco, C. L., et al. 2006b, in The Tenth Marcel Grossmann Meeting, ed. M. Novello, S. Perez Bergliaffa, & R. Ruffini (Singapore: World Scientific), 369
- Ruffini, R., Bernardini, M. G., Bianco, C. L., et al. 2007, in Proc. VI INTEGRAL Workshop, ESA SP-622, The Obscured Universe, ed. S. Grebenev, R. Sunyaev, & C. Winkler (Noordwijk: ESA), 561
- Ruffini, R., Bernardini, M. G., Bianco, C. L., et al. 2008, in Proc. MG11 Meeting on General Relativity, The Eleventh Marcel Grossmann Meeting, ed. H. Kleinert, R. T. Jantzen, & R. Ruffini (Singapore: World Scientific), 368
- Ruffini, R., Bianco, C. L., Chardonnet, P., Frascchetti, F., & Xue, S. 2002, *ApJL*, **581**, L19
- Ruffini, R., Bianco, C. L., Enderli, M., et al. 2013, GCN, 14526, 1
- Ruffini, R., Bianco, C. L., Frascchetti, F., Xue, S.-S., & Chardonnet, P. 2001a, *ApJL*, **555**, L107
- Ruffini, R., Bianco, C. L., Frascchetti, F., Xue, S.-S., & Chardonnet, P. 2001b, *ApJL*, **555**, L113
- Ruffini, R., Bianco, C. L., Frascchetti, F., Xue, S.-S., & Chardonnet, P. 2001c, *ApJL*, **555**, L117
- Ruffini, R., Bianco, C. L., Xue, S.-S., et al. 2004, *IJMPD*, **13**, 843
- Ruffini, R., Izzo, L., Bianco, C. L., et al. 2015a, *AREp*, **59**, 626
- Ruffini, R., Izzo, L., Muccino, M., et al. 2014a, *A&A*, **569**, A39
- Ruffini, R., Muccino, M., Aimuratov, Y., et al. 2016, *ApJ*, in press (arXiv:1607.02400v2)
- Ruffini, R., Muccino, M., Bianco, C. L., et al. 2014b, *A&A*, **565**, L10
- Ruffini, R., Muccino, M., Kovacevic, M., et al. 2015b, *ApJ*, **808**, 190
- Ruffini, R., Rodriguez, J., Muccino, M., et al. 2016, *ApJ*, arXiv:1602.03545
- Ruffini, R., Salmonson, J. D., Wilson, J. R., & Xue, S. 2000, *A&A*, **359**, 855
- Ruffini, R., Salmonson, J. D., Wilson, J. R., & Xue, S.-S. 1999, *A&A*, **350**, 334
- Ruffini, R., Vereshchagin, G., & Xue, S. 2010, *PhR*, **487**, 1
- Ruffini, R., Wang, Y., Enderli, M., et al. 2015c, *ApJ*, **798**, 10
- Ruffini, R., & Wheeler, J. A. 1969, in Significance of Space Research for Fundamental Physics, Proc. of the ESRO Collaboration, ed. A. F. Moore & V. Hardy, 52, 45
- Ruffini, R., & Wilson, J. 1973, *PhRvL*, **31**, 1362
- Ruffini, R., & Wilson, J. R. 1975, *PhRvD*, **12**, 2959
- Ryde, F. 2004, *ApJ*, **614**, 827
- Ryde, F. 2005, *ApJL*, **625**, L95

- Sakamoto, T., Lamb, D. Q., Kawai, N., et al. 2005, *ApJ*, 629, 311
- Salmonson, J. D., & Wilson, J. R. 2002, *ApJ*, 578, 310
- Sari, R. 1997, *ApJL*, 489, L37
- Sari, R. 1998, *ApJL*, 494, L49
- Sari, R., Piran, T., & Narayan, R. 1998, *ApJL*, 497, L17
- Schaefer, B. E. 2007, *ApJ*, 660, 16
- Sibgatullin, N. R., & Sunyaev, R. A. 2000, *AstL*, 26, 772
- Smartt, S. J. 2009, *ARA&A*, 47, 63
- Soderberg, A. M., Kulkarni, S. R., Nakar, E., et al. 2006, *Natur*, 442, 1014
- Sparre, M., Sollerman, J., Fynbo, J. P. U., et al. 2011, *ApJL*, 735, L24
- Starling, R. L. C., Wiersema, K., Levan, A. J., et al. 2010, arXiv:1004.2919
- Strong, I. B., Klebesadel, R. W., & Evans, W. D. 1975, in Seventh Texas Symp. Relativistic Astrophysics 262, Annals of the New York Academy of Sciences 262, ed. P. G. Bergman, E. J. Fenyves, & L. Motz 145
- Sun, H., Zhang, B., & Li, Z. 2015, *ApJ*, 812, 33
- Tanvir, N. R., Levan, A. J., Fruchter, A. S., et al. 2013, *Natur*, 500, 547
- Tauris, T. M., van den Heuvel, E. P. J., & Savonije, G. J. 2000, *ApJL*, 530, L93
- Tavani, M. 1998, *ApJL*, 497, L21
- Troja, E., Rosswog, S., & Gehrels, N. 2010, *ApJ*, 723, 1711
- Usov, V. V. 1992, *Natur*, 357, 472
- van Paradijs, J., Groot, P. J., Galama, T., et al. 1997, *Natur*, 386, 686
- Virgili, F. J., Liang, E.-W., & Zhang, B. 2009, *MNRAS*, 392, 91
- Virgili, F. J., Zhang, B., O'Brien, P., & Troja, E. 2011, *ApJ*, 727, 109
- Wanderman, D., & Piran, T. 2010, *MNRAS*, 406, 1944
- Wanderman, D., & Piran, T. 2015, *MNRAS*, 448, 3026
- Watson, A. M., Butler, N., Kuttyrev, A., et al. 2013, GCN, 14666, 1
- Waxman, E. 1997, *ApJL*, 491, L19
- Woosley, S. E. 1993, *ApJ*, 405, 273
- Woosley, S. E., & Bloom, J. S. 2006, *ARA&A*, 44, 507
- Xu, D., de Ugarte Postigo, A., Kruehler, T., et al. 2013, GCN, 14597, 1
- Zalamea, I., & Beloborodov, A. M. 2011, *MNRAS*, 410, 2302
- Zel'dovich, Y. B., Ivanova, L. N., & Nadezhin, D. K. 1972, *SvA*, 16, 209
- Zhang, B., Fan, Y. Z., Dyks, J., et al. 2006, *ApJ*, 642, 354
- Zhang, B., & Mészáros, P. 2001, *ApJL*, 552, L35
- Zhang, B., Zhang, B., Virgili, F. J., et al. 2009, *ApJ*, 703, 1696
- Zhang, C. M., Wang, J., Zhao, Y. H., et al. 2011, *A&A*, 527, A83
- Zhang, F.-W., Shao, L., Yan, J.-Z., & Wei, D.-M. 2012, *ApJ*, 750, 88



GRB 090510: A GENUINE SHORT GRB FROM A BINARY NEUTRON STAR COALESCING INTO A KERR–NEWMAN BLACK HOLE

R. RUFFINI^{1,2,3,4}, M. MUCCINO^{1,2}, Y. AIMURATOV^{1,3}, C. L. BIANCO^{1,2}, C. CHERUBINI⁵, M. ENDERLI^{1,3}, M. KOVACEVIC^{1,3},
R. MORADI^{1,2}, A. V. PENACCHIONI^{6,7}, G. B. PISANI^{1,2}, J. A. RUEDA^{1,2,4}, AND Y. WANG^{1,2}

¹ Dipartimento di Fisica, Sapienza Università di Roma and ICRA, Piazzale Aldo Moro 5, I-00185 Roma, Italy

² ICRANet, Piazza della Repubblica 10, I-65122 Pescara, Italy

³ Université de Nice Sophia-Antipolis, Grand Château Parc Valrose, Nice, CEDEX 2, France

⁴ ICRANet-Rio, Centro Brasileiro de Pesquisas Físicas, Rua Dr. Xavier Sigaud 150, Rio de Janeiro, RJ, 22290-180, Brazil

⁵ ICRA and Unit of Nonlinear Physics and Mathematical Modeling, Department of Engineering, Università Campus Bio-Medico di Roma, Via Alvaro del Portillo 21, I-00128, Rome, Italy

⁶ University of Siena, Department of Physical Sciences, Earth and Environment, Via Roma 56, I-53100 Siena, Italy

⁷ ASI Science Data Center, via del Politecnico s.n.c., I-00133 Rome Italy

Received 2015 October 9; revised 2016 September 1; accepted 2016 September 3; published 2016 November 7

ABSTRACT

In a new classification of merging binary neutron stars (NSs) we separate short gamma-ray bursts (GRBs) into two subclasses. The ones with $E_{\text{iso}} \lesssim 10^{52}$ erg coalesce to form a massive NS and are indicated as short gamma-ray flashes (S-GRFs). The hardest, with $E_{\text{iso}} \gtrsim 10^{52}$ erg, coalesce to form a black hole (BH) and are indicated as genuine short GRBs (S-GRBs). Within the fireshell model, S-GRBs exhibit three different components: the proper GRB (P-GRB) emission, observed at the transparency of a self-accelerating baryon- e^+e^- plasma; the prompt emission, originating from the interaction of the accelerated baryons with the circumburst medium; and the high-energy (GeV) emission, observed after the P-GRB and indicating the formation of a BH. GRB 090510 gives the first evidence for the formation of a Kerr BH or, possibly, a Kerr–Newman BH. Its P-GRB spectrum can be fitted by a convolution of thermal spectra whose origin can be traced back to an axially symmetric dyadotorus. A large value of the angular momentum of the newborn BH is consistent with the large energetics of this S-GRB, which reach in the 1–10,000 keV range $E_{\text{iso}} = (3.95 \pm 0.21) \times 10^{52}$ erg and in the 0.1–100 GeV range $E_{\text{LAT}} = (5.78 \pm 0.60) \times 10^{52}$ erg, the most energetic GeV emission ever observed in S-GRBs. The theoretical redshift $z_{\text{th}} = 0.75 \pm 0.17$ that we derive from the fireshell theory is consistent with the spectroscopic measurement $z = 0.903 \pm 0.003$, showing the self-consistency of the theoretical approach. All S-GRBs exhibit GeV emission, when inside the *Fermi*-LAT field of view, unlike S-GRFs, which never evidence it. The GeV emission appears to be the discriminant for the formation of a BH in GRBs, confirmed by their observed overall energetics.

Key words: gamma-ray burst: general – gamma-ray burst: individual (GRB 090510)

1. INTRODUCTION

Thanks to a fortunate coincidence of observations by *AGILE*, *Fermi*, and *Swift* satellites, together with the optical observations by the Very Large Telescope (VLT)/FORS2 and the Nordic Optical Telescope, it has been possible to obtain an unprecedented set of data, extending from the optical–UV, through the X-rays, all the way up to the high-energy (GeV) emission, which allowed detailed temporal/spectral analyses of GRB 090510 (De Pasquale et al. 2010).

In contrast with this outstanding campaign of observations, a theoretical analysis of the broadband emission of GRB 090510 has been advanced within the synchrotron/self-synchrotron Compton and traditional afterglow models (see, e.g., Sections 5.2.1 and 5.2.2 in Ackermann et al. 2010). Paradoxically, this same methodology has been applied in the description of markedly different types of sources: e.g., Soderberg et al. (2006b) for the low energetic long gamma-ray burst (GRB) 060218, Perley et al. (2014) for the high energetic long GRB 130427A, and Soderberg et al. (2006a) for the short gamma-ray flash (S-GRF) 051221A (see also Curran et al. 2008, and references therein).

In the meantime, it has become evident that GRBs can be subdivided into a variety of classes and subclasses (Ruffini et al. 2015b, 2015c, 2016), each of them characterized by specific different progenitors, which deserve specific theoretical

treatments and understanding. In addition, every subclass shows different episodes corresponding to specifically different astrophysical processes, which can be identified thanks to specific theoretical treatments and data analysis. In this article, we take GRB 090510 as a prototype for S-GRBs and perform a new time-resolved spectral analysis, in excellent agreement with the above temporal and spectral analysis performed by, e.g., the *Fermi* team. Now this analysis, guided by a theoretical approach successfully tested in this new family of short GRBs (S-GRBs; Muccino et al. 2013a; Ruffini et al. 2015b), is directed to identify a precise sequence of different events made possible by the exceptional quality of the data of GRB 090510. This includes a new structure in the thermal emission of the proper GRB (P-GRB) emission, followed by the onset of the GeV emission linked to the black hole (BH) formation, allowing us, as well, to derive the structure of the circumburst medium (CBM) from the spiky structure of the prompt emission. This sequence, for the first time, illustrates the formation process of a BH.

Already in 1974 February, soon after the public announcement of the GRB discovery (Strong et al. 1975), Damour & Ruffini (1975) presented the possible relation of GRBs to the vacuum polarization process around a Kerr–Newman BH. There, evidence was given for (a) the formation of a vast amount of e^+e^- -baryon plasma; (b) the energetics of GRBs to be of the order of $E_{\text{max}} \approx 10^{54} M_{\text{BH}}/M_{\odot}$ erg, where M_{BH} is the

BH mass; and (c) additional ultra-high-energy cosmic rays with energy up to $\sim 10^{20}$ eV originating from such extreme processes. A few years later, the role of an e^+e^- plasma of comparable energetics for the origin of GRBs was considered by Cavallo & Rees (1978), and it took almost 30 yr to clarify some of the analogies and differences between these two processes, leading, respectively, to the alternative concepts of “fireball” and “fireshell” (Aksenov et al. 2007, 2009). In this article we give the first evidence for the formation of a Kerr–Newman BH, in GRB 090510, from the merger of two massive neutron stars (NSs) in a binary system.

GRBs are usually separated into two categories, based on their duration properties (e.g., Mazets et al. 1981; Dezalay et al. 1992; Klebesadel 1992, pp. 161–68; Kouveliotou et al. 1993; Tavani 1998). S-GRBs have a duration $T_{90} \lesssim 2$ s, while the remaining ones with $T_{90} \gtrsim 2$ s are traditionally classified as long GRBs.

S-GRBs are often associated with NS–NS mergers (see, e.g., Goodman 1986; Paczynski 1986; Eichler et al. 1989; Narayan et al. 1991; Meszaros & Rees 1997; Rosswog et al. 2003; Lee et al. 2004; Nakar 2007; Endrizzi et al. 2016; Ruiz et al. 2016; see also Berger 2014 for a recent review); their host galaxies are of both early and late type, their localization with respect to the host galaxy often indicates a large offset (Sahu et al. 1997; van Paradijs et al. 1997; Bloom et al. 2006; Troja et al. 2008; Fong et al. 2010; Berger 2011; Kopač et al. 2012) or a location of minimal star-forming activity with typical CBM densities of $\sim 10^{-5}$ – 10^{-4} cm $^{-3}$, and no supernovae (SNe) have ever been associated with them.

The progenitors of long GRBs, on the other hand, have been related to massive stars (Woosley & Bloom 2006). However, in spite of the fact that most massive stars are found in binary systems (Smith 2014), that most Type Ib/c SNe occur in binary systems (Smith et al. 2011), and that SNe associated with long GRBs are indeed of Type Ib/c (Della Valle 2011), the effects of binarity on long GRBs have been for a long time largely ignored in the literature. Indeed, until recently, long GRBs have been interpreted as single events in the jetted *collapsar* fireball model (see, e.g., Rees & Meszaros 1992; Woosley 1993; Kobayashi et al. 1997; Piran 2005; Gehrels et al. 2009; Kumar & Zhang 2015 and references therein).

Multiple components evidencing the presence of a precise sequence of different astrophysical processes have been found in several long GRBs (e.g., Izzo et al. 2012; Penacchioni et al. 2012). Following this discovery, further results led to the introduction of a new paradigm explicating the role of binary sources as progenitors of the long GRB–SN connection. New developments have led to the formulation of the induced gravitational collapse (IGC) paradigm (Ruffini et al. 2001a, 2007, 2015c; Rueda & Ruffini 2012). The IGC paradigm explains the GRB–SN connection in terms of the interactions between an evolved carbon–oxygen core (CO_{core}) undergoing an SN explosion and its hypercritical accretion on a binary NS companion (Ruffini 2015). A large majority of long bursts are related to SNe and are spatially correlated with bright star-forming regions in their host galaxies (Fruchter et al. 2006; Svensson et al. 2010), with a typical CBM density of ~ 1 cm $^{-3}$ (Izzo et al. 2012; Penacchioni et al. 2012).

A new situation has occurred with the observation of the high-energy GeV emission by the *Fermi*-LAT instrument and its correlation with both long and short bursts with isotropic energy $E_{\text{iso}} \gtrsim 10^{52}$ erg, which has been evidenced in Ruffini

et al. (2015b, 2015c), respectively. On the basis of this correlation, the occurrence of such prolonged GeV emission has been identified with the onset of the formation of a BH (Ruffini et al. 2015b, 2015c).

As recalled above, the long GRBs associated with SNe have been linked to the hypercritical accretion process occurring in a tight binary system when the ejecta of an exploding CO_{core} accrete onto an NS binary companion (see, e.g., Rueda & Ruffini 2012; Fryer et al. 2014; Becerra et al. 2015). When the hypercritical accretion occurs in a widely separated system with an orbital separation $> 10^{11}$ cm (Becerra et al. 2015), the accretion is not sufficient to form a BH. For these softer systems with rest-frame spectral peak energy $E_{\text{peak}} < 200$ keV the upper limit of their observed energy is $E_{\text{iso}} \approx 10^{52}$ erg, which corresponds to the maximum energy attainable in the accretion onto an NS (Ruffini et al. 2015c). Such a long burst corresponds to an X-ray flash (XRF). The associated X-ray afterglow is also explainable in terms of the interaction of the prompt emission with the SN ejecta (C. L. Fryer et al. 2016, in preparation). In these systems no GeV emission is expected in our theory and, indeed, is not observed. Interestingly, pioneering evidence for such an XRF had already been given in a different context by Heise (2003), Amati et al. (2004), and Soderberg et al. (2006b). For tighter binaries ($< 10^{11}$ cm; Becerra et al. 2015), the hypercritical accretion onto the companion NS leads to the formation of a BH. For these harder systems with $E_{\text{peak}} > 200$ keV the lower limit of their observed energy is $E_{\text{iso}} \approx 10^{52}$ erg, which necessarily needs the accretion process into a BH. An associated prolonged GeV emission occurs after the P-GRB emission and at the beginning of the prompt emission and originates at the onset of the BH formation (Ruffini et al. 2015c). These more energetic events are referred to as binary-driven hypernovae (BdHNe). Specific constant power-law behaviors are observed in their high-energy GeV, X-rays, and optical luminosity light curves (Pisani et al. 2013; Ruffini et al. 2014, 2015c).

In total analogy, the formation of a BH can occur in short bursts, depending on the mass of the merged core of the binary system. When the two NS masses are large enough, the merged core can exceed the NS critical mass and BH formation is possible. In the opposite case, a massive NS (MNS) is created, possibly, with some additional orbiting material to guarantee the angular momentum conservation. We then naturally expect the existence of two short-burst subclasses: authentic S-GRBs, characterized by the formation of a BH (Ruffini et al. 2015b), with $E_{\text{iso}} \gtrsim 10^{52}$ erg, a harder spectrum (see Section 5.2), and associated with a prolonged GeV emission (see Section 6.5); and S-GRFs, producing an MNS (Ruffini et al. 2015b), with $E_{\text{iso}} \lesssim 10^{52}$ erg. In this second subclass, of course, the GeV emission should not occur and, indeed, is never observed.

Following the discovery of the first prototype of this S-GRB class, namely, GRB 090227B (Muccino et al. 2013a), the first detailed analysis of such a genuine S-GRB originating from a binary NS merger leading to a BH was done for GRB 140619B by Ruffini et al. (2015b), determining as well the estimated emission of gravitational waves. The latter has been estimated following the method applied by Oliveira et al. (2014) for GRB 090227B. From the spectral analysis of the early ~ 0.2 s, they inferred an observed temperature $kT = (324 \pm 33)$ keV of the e^+e^- plasma at transparency (P-GRB), a theoretically derived redshift $z = 2.67 \pm 0.37$, a total burst energy $E_{e^+e^-}^{\text{tot}} = (6.03 \pm 0.79) \times 10^{52}$ erg, a rest-frame peak energy

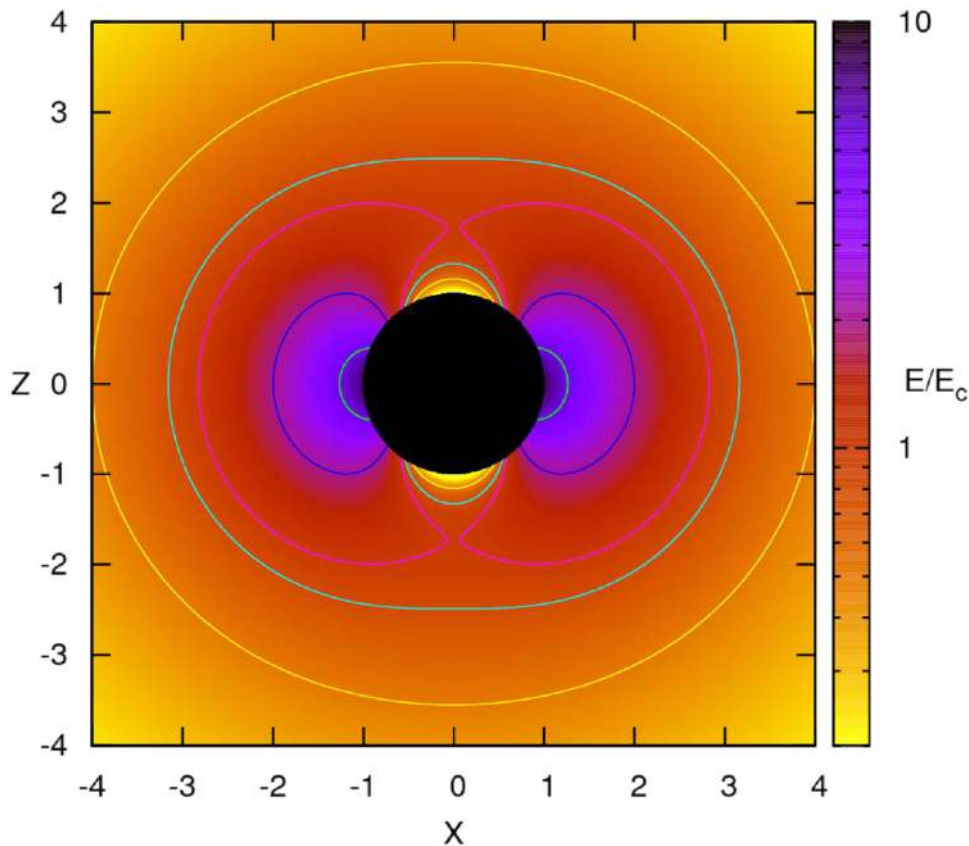


Figure 1. Projection of the dyadotorus of a Kerr–Newman BH corresponding to selected values of the ratio E/E_c , where E_c is the critical value for vacuum polarization and E is the electric field strength. The plot assumes a black hole mass energy $\mu = M_{\text{BH}}/M_\odot = 10$. This figure is reproduced from Cherubini et al. (2009), with their kind permission.

$E_{p,i} = 4.7$ MeV, a baryon load $B = (5.52 \pm 0.73) \times 10^{-5}$, and an average CBM density $n_{\text{CBM}} = (4.7 \pm 1.2) \times 10^{-5} \text{ cm}^{-3}$.

We turn in this article to the most interesting case of GRB 090510, which has, in addition to very similar properties of the members of this new class of S-GRB sources, a spectroscopically determined value of redshift and represents one of the most energetic sources of this family both in the γ -ray and in the GeV ranges. Actually, a first attempt to analyze GRB 090510 was made by interpreting this source as a long GRB (Muccino et al. 2013b). An unusually large value of the CBM density was needed in order to fit the data: this interpretation was soon abandoned when it was noticed that GRB 090510 did not fulfill the nesting conditions of the late X-ray emission typical of long GRBs (Ruffini et al. 2014); see also Section 5.1 and Figure 5.

In light of the recent progress in the understanding of the fireshell theory, we address the interpretation of GRB 090510 as the merging of a binary NS. We give clear evidence for the validity of this interpretation. In view of the good quality of the data both in γ -rays and in the GeV range, we have performed a more accurate description of the P-GRB, best fitted by a convolution of thermal spectra. This novel feature gives the first indication for the existence of an axially symmetric configuration of the dyadotorus emitting the e^+e^- plasma, which had been previously theoretically considered and attentively searched for. This gives the first indication that indeed the angular momentum plays a role and a dyadotorus is formed, as theoretically predicted in a series of papers (see Cherubini et al. 2009; Ruffini 2009; see also Figure 1). This naturally leads to the evidence for the formation of a rotating

BH as the outcome of the gravitational collapse. We turn then to the main new feature of GRB 090510, which is the high-energy 0.1–100 GeV emission (see Figure 10). The direct comparison of the GeV emission in this source and in the BdHN 130427A shows the remarkable similarities of these two GeV components (see Figure 10). The fact that the S-GRB 090510 originates from a binary NS merger and the BdHN 130427A originates from the IGC of an SN hypercritical accretion process onto a companion NS clearly points to the BH as originating this GeV emission, the reason being that these two astrophysical systems are different in their progenitors and physical processes and have in the formation of a BH their unique commonality.

This paper is structured as follows: in Section 2 we summarize the relevant aspects of the fireshell theory and compare and contrast it with alternative approaches. In Section 3 we discuss the recent progress on the NS equilibrium configuration relevant for S-GRBs and BdHNe. In Section 4 we move on to describe the observations of GRB 090510 and their analysis. The S-GRB nature of GRB 090510 is justified in Section 5, and we offer an interpretation of our results in Section 6. Section 7 concludes this work.

A standard flat Λ CDM cosmological model with $\Omega_m = 0.27$ and $H_0 = 71 \text{ km s}^{-1} \text{ Mpc}^{-1}$ is adopted throughout the paper.

2. SUMMARY OF THE FIRESHELL MODEL

The fireshell scenario (Ruffini et al. 2001a, 2001b, 2001c) has been initially introduced to describe a GRB originating in a gravitational collapse leading to the formation of a

Kerr–Newman BH. A distinct sequence of physical and astrophysical events are taken into account:

- (1) An optically thick pair plasma—the fireshell of total energy $E_{e^+e^-}^{\text{tot}}$ —is considered. As a result, it starts to expand and accelerate under its own internal pressure (Ruffini et al. 1999). The baryonic remnant of the collapsed object is engulfed by the fireshell—the baryonic contamination is quantified by the baryon load $B = M_B c^2 / E_{e^+e^-}^{\text{tot}}$, where M_B is the mass of the baryonic remnant (Ruffini et al. 2000; Aksenov et al. 2007, 2009).
- (2) After the engulfment, the fireshell is still optically thick and continues to self-accelerate until it becomes transparent. When the fireshell reaches transparency, a flash of thermal radiation termed proper-GRB (P-GRB) is emitted (Ruffini et al. 1999, 2000).
- (3) In GRBs, the e^+e^- -baryon plasma expands with ultra-relativistic velocities from the ultrarelativistic region near the BH to large distances. To describe such a dynamics that deals with unprecedentedly large Lorentz factors and also regimes sharply varying with time, Ruffini et al. (2001c) introduced the appropriate relative spacetime transformation paradigm. This paradigm gives particular attention to the constitutive equations relating four time variables: the comoving time, the laboratory time, the arrival time, and the arrival time at the detector corrected by the cosmological effects. This paradigm is essential for the interpretation of the GRB data: the absence of adopting such a relativistic paradigm in some current works has led to a serious misinterpretation of the GRB phenomenon.
- (4) In compliance with the previous paradigm, the interactions between the ultrarelativistic shell of accelerated baryons left over after transparency and the CBM have been considered. They lead to a modified blackbody spectrum in the comoving frame (Patricelli et al. 2012). The observed spectrum is, however, nonthermal in general; this is due to the fact that, once the constant arrival time effect is taken into account in the equitemporal surfaces (EQTSs; see Bianco & Ruffini 2005a, 2005b), the observed spectral shape results from the convolution of a large number of modified thermal spectra with different Lorentz factors and temperatures.
- (5) All the above relativistic effects, after the P-GRB emission, are necessary for the description of the prompt emission of GRBs, as outlined in Ruffini et al. (2001b). The prompt emission originates in the collisions of the accelerated baryons, moving at Lorentz factor $\gamma \approx 100$ –1000, with interstellar clouds of CBM with masses of $\sim 10^{22}$ – 10^{24} g, densities of ~ 0.1 – 1 cm^{-3} , and size of $\sim 10^{15}$ – 10^{16} cm, at typical distances from the BH of $\sim 10^{16}$ – 10^{17} cm (see, e.g., Izzo et al. 2012 for long bursts). Our approach differs from alternative treatments purporting late activities from the central engine (see, e.g., the collapsar model in Woosley 1993; Popham et al. 1999; Woosley & Bloom 2006, and references therein; and the magnetar model in Zhang & Mészáros 2001; Dai et al. 2006; Metzger et al. 2011; Bucciantini et al. 2012; Lü & Zhang 2014, and references therein).
- (6) $E_{e^+e^-}^{\text{tot}}$ and B are the only two parameters that are needed in a spherically symmetric fireshell model to determine the physics of the fireshell evolution until the

transparency condition is fulfilled. Three additional parameters, all related to the properties of the CBM, are needed to reproduce a GRB light curve and its spectrum: the CBM density profile n_{CBM} , the filling factor \mathcal{R} that accounts for the size of the effective emitting area, and an index α that accounts for the modification of the low-energy part of the thermal spectrum (Patricelli et al. 2012). They are obtained by running a trial-and-error simulation of the observed light curves and spectra that starts at the fireshell transparency.

- (7) A more detailed analysis of the pair creation process around a Kerr–Newman BH has led to the concept of dyadotorus (Cherubini et al. 2009). There, the axially symmetric configuration with a specific distribution of the e^+e^- , as well as its electromagnetic field, has been presented as a function of the polar angle. The total spectrum at the transparency of the e^+e^- plasma is a convolution of thermal spectra at different angles.

This formalism describing the evolution of a baryon-loaded pair plasma is describable in terms of only three intrinsic parameters: the e^+e^- plasma energy $E_{e^+e^-}^{\text{tot}}$, the baryon load B , and the specific angular momentum a of the incipient newly formed BH. It is, therefore, independent of the way the pair plasma is created.

In addition to the specific case, developed for the sake of example, of the dyadotorus created by a vacuum polarization process in an already-formed Kerr–Newman BH, more possibilities have been envisaged in the meantime:

- (a) The concept of dyadotorus can be applied as well in the case of a pair plasma created via the $\bar{\nu} \leftrightarrow e^+e^-$ mechanism in an NS merger as described in Narayan et al. (1992), Salmonson & Wilson (2002), Rosswog et al. (2003), and Zalamea & Beloborodov (2011), assuming that the created pair plasma is optically thick. The relative role of neutrino and weak interactions vs. the electromagnetic interactions in building the dyadotorus is currently topic of intense research.
- (b) Equally important is the relativistic magnetohydrodynamical process leading to a dyadotorus, indicated in the general treatment of Ruffini & Wilson (1975), and leading to the birth of a Kerr–Newman BH, surrounded by an oppositely-charged magnetosphere in a system endowed with global charge neutrality. Active research is ongoing.
- (c) Progress in understanding the NS equilibrium configuration imposing the global charge neutrality condition, as opposed to the local charge neutrality usually assumed (Rotondo et al. 2011a, 2011b; Rueda et al. 2011, 2014; Rueda & Ruffini 2013). A critical mass for a nonrotating NS of $M_{\text{crit}}^{\text{NS}} \approx 2.67 M_{\odot}$ has been found for the NL3 nuclear equation of state (Belvedere et al. 2012). The effects of rotation and of the nuclear equation of state on the critical mass are presented in Belvedere et al. (2014, 2015) and Cipolletta et al. (2015). The existence of electromagnetic fields close to the critical value has been evidenced in the interface between the core and the crust in the above global neutrality model, as well as very different density distributions in the crust and in the core, which could play an important role during the NS–NS mergers (see Figure 2 and Oliveira et al. 2014).

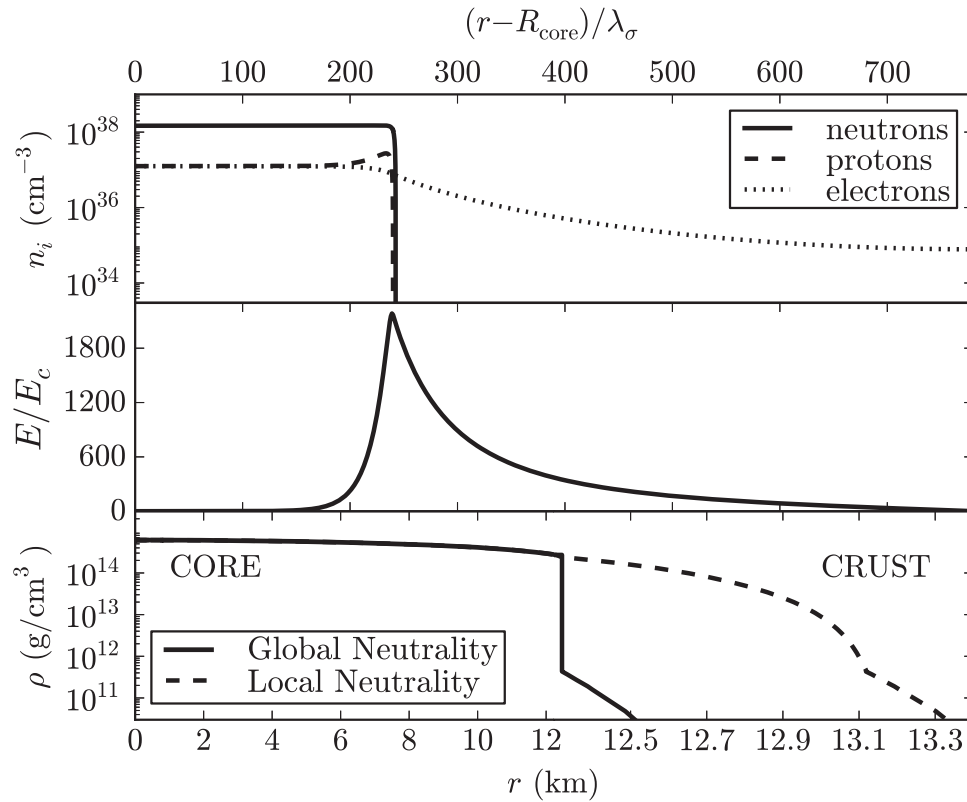


Figure 2. Particle density profiles (top panel) and the electric field in units of E_c (middle panel) in the core-crust transition layer normalized to the σ -meson Compton wavelength $\lambda_\sigma = \hbar/(m_\sigma c) \sim 0.4$ fm. Bottom panel: density profile inside an NS star with central density $\rho \sim 5\rho_{\text{nuc}}$, where ρ_{nuc} is the nuclear density, from the solution of the Tolman–Oppenheimer–Volkoff (TOV) equations (locally neutral case) and the globally neutral solution presented in Belvedere et al. (2012). The density at the edge of the crust is the neutron drip density $\rho_{\text{drip}} = 4.3 \times 10^{11} \text{ g cm}^{-3}$. This figure is reproduced from Belvedere et al. (2012), with their kind permission.

The above three possibilities have been developed in recent years, but they do not have to be considered exhaustive for the formation of a dyadotorus endowed by the above three parameters.

In conclusion, the evolution in the understanding of the GRB phenomenon, occurring under very different initial conditions, has evidenced the possibility of using the dyadotorus concept for describing sources of an optically thick baryon-loaded e^+e^- plasma within the fireshell treatment in total generality.

3. ON THE ROLE OF THE $\approx 10^{52}$ ERG LIMIT FOR S-GRBs AND BdHNe

The key role of neutrino emission in the hypercritical accretion process onto an NS has been already examined in the literature (see, e.g., Zel’dovich et al. 1972; Ruffini & Wilson 1973). The problem of hypercritical accretion in a binary system composed of a CO_{core} and a companion NS has been studied in Becerra et al. (2015, 2016) (see also references therein). The energy released during the process, in the form of neutrinos and photons, is given by the gain of gravitational potential energy of the matter being accreted by the NS and depends also on the change of binding energy of the NS while accreting matter and on the angular momentum carried by the accreting material (see, e.g., Becerra et al. 2016 and Ruffini et al. 2016). For a typical NS mass of $\approx 1.4 M_\odot$, a value observed in galactic NS binaries (Zhang et al. 2011; Antoniadis 2015), and an NS critical mass $M_{\text{crit}}^{\text{NS}}$ in the range from $2.2 M_\odot$ up to $3.4 M_\odot$ depending on the equations of state and angular momentum (see Becerra et al. 2015, 2016; Cipolletta et al. 2015, for details), the accretion luminosity can be as high as $L_{\text{acc}} \sim 0.1 \dot{M}_b c^2 \sim 10^{47} - 10^{51} \text{ erg s}^{-1}$ for accretion rates $\dot{M}_b \sim 10^{-6} - 10^{-2} M_\odot \text{ s}^{-1}$ (see Becerra et al. 2015, 2016, for

details). For binary systems with a separation of $\sim 10^{10} \text{ cm}$ ($P \sim 5$ minutes), our numerical simulations indicate that (a) the accretion process duration lasts $\Delta t_{\text{acc}} \sim 10^2 \text{ s}$ (see, e.g., Becerra et al. 2015, 2016), (b) the NS collapses to a BH, and (c) a total energy larger than $\approx 10^{52} \text{ erg}$ is released during the hypercritical accretion process. These systems correspond to the BdHNe (Becerra et al. 2016). For systems with larger separations the hypercritical accretion is not sufficient to induce the collapse of the NS into a BH and the value of $\approx 10^{52} \text{ erg}$ represents a theoretical estimate of the upper limit to the energy emitted by the norm in the hypercritical accretion process. This subclass of sources corresponds to the XRFs (Becerra et al. 2016).

The same energetic considerations do apply in the analysis of the hypercritical accretion occurring in a close binary NS system undergoing merging (Ruffini 2015). Therefore, in total generality, we can conclude that the energy emitted during an NS–NS merger leading to the formation of a BH should be larger than $\approx 10^{52} \text{ erg}$ (see Figure 3).

The limit of $\approx 10^{52} \text{ erg}$ clearly depends on the initial NS mass undergoing accretion, by norm assumed to be $\approx 1.4 M_\odot$, and on the yet-unknown value of $M_{\text{crit}}^{\text{NS}}$, for which only an absolute upper limit of $3.2 M_\odot$ has been established for the nonrotating case (Rhoades & Ruffini 1974). As already pointed out in Ruffini (2015), for NS–NS mergers, the direct determination of the energy threshold of $\approx 10^{52} \text{ erg}$ dividing S-GRFs and S-GRBs, as well as XRFs and BdHNe, provides fundamental information for the determination of the actual value of $M_{\text{crit}}^{\text{NS}}$, for the minimum mass of the newly born BH, and for the mass of the accreting NS.

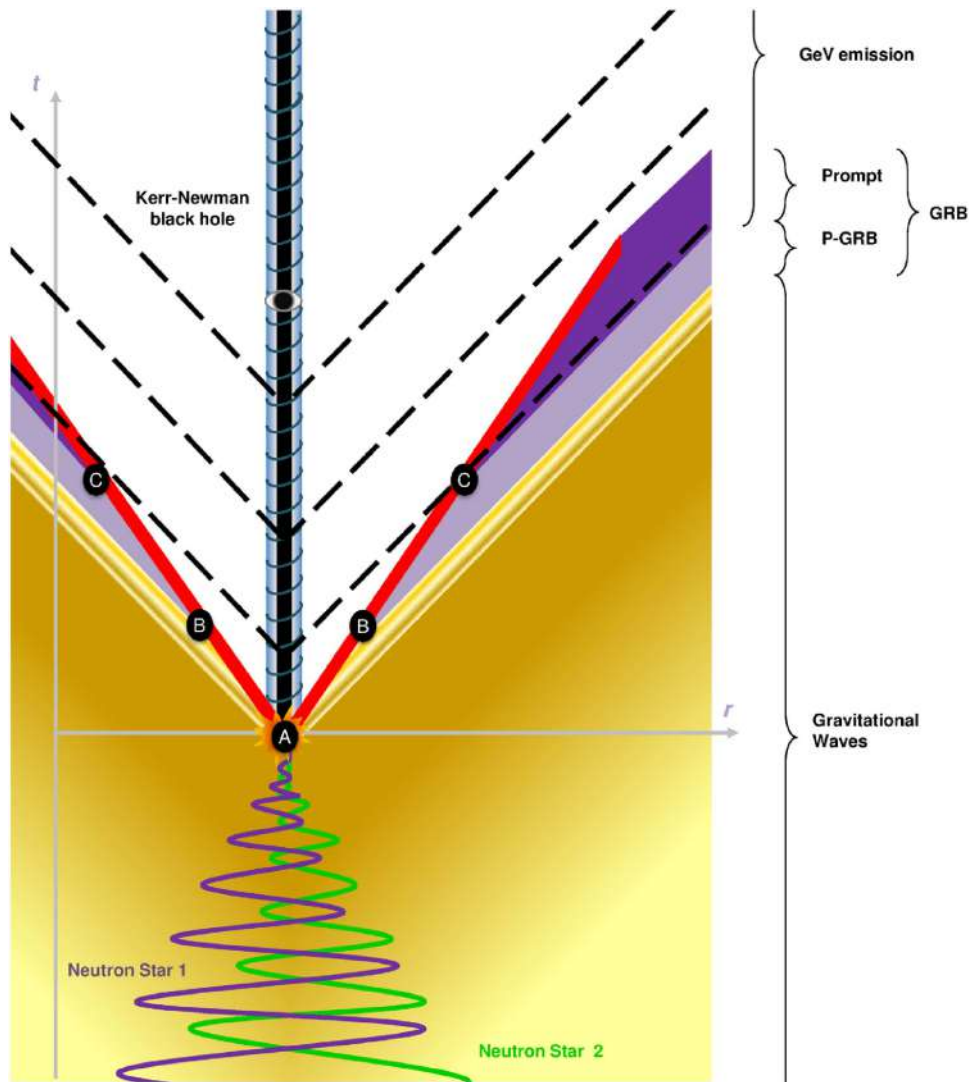


Figure 3. Spacetime diagram of an S-GRB, a binary NS merger leading to BH formation (taken from Enderli et al. 2015, with their kind permission). The binary orbit gradually shrinks due to energy loss through gravitational-wave emission (yellow–brown). At point A, the merger occurs: the fireshell (in red) is created and starts its expansion. It reaches transparency at point B, emitting the P-GRB (light purple). The prompt emission (deep purple) then follows at point C. The dashed lines represent the GeV emission (delayed relative to the start of the GRB) originating in the newly born BH. This spacetime diagram well illustrates how the GeV emission originates in the newly born BH and follows a different spacetime path from the prompt emission, contrary to what is stated in Ackermann et al. (2010). The prompt emission originates from the interactions of the baryons, accelerated to ultrarelativistic Lorentz factors during the pair-baryon electromagnetic pulse, with the clumpy CBM (see Section 2). The analysis of the spiky structure of the prompt emission allows us to infer the structure of the CBM (see Figure 9). There is the distinct possibility that the GeV emission prior to 0.6 s in the arrival time may interact with the prompt emission. In this sense the work by Zou et al. (2011) may become of interest.

4. ANALYSIS OF GRB 090510

In this section, we summarize the observations of GRB 090510, as well as the data analysis. We used *Fermi* (GBM and LAT) and *Swift*/XRT data for the purposes of this work.

4.1. Observations

The *Fermi*/GBM instrument (Meegan et al. 2009) was triggered at $T_0 = 00:22:59.97$ UT on 2009 May 10 by the short and bright burst GRB 090510 (Guiriec et al. 2009, trigger 263607781/090510016). The trigger was set off by a precursor emission of duration 30 ms, followed ~ 0.4 s later by a hard episode lasting ~ 1 s. This GRB was also detected by *Swift* (Hoversten et al. 2009), *Fermi*/LAT (Ohno & Pelassa 2009), *AGILE* (Longo et al. 2009), *Konus-Wind* (Golenetskii et al. 2009), and *Suzaku*-WAM (Ohmori et al. 2009). The

position given by the GBM is consistent with that deduced from *Swift* and LAT observations.

During the first second after LAT trigger at 00:23:01.22 UT, *Fermi*/LAT detected over 50 (over 10) events with an energy above 100 MeV (1 GeV) up to the GeV range, and more than 150 (20) within the first minute (Omodei et al. 2009). This makes GRB 090510 the first bright S-GRB with an emission detected from the keV to the GeV range.

Observations of the host galaxy of GRB 090510, located by VLT/FORS2, provided a measurement of spectral emission lines. This led to the determination of a redshift $z = 0.903 \pm 0.003$ (Rau et al. 2009). The refined position of GRB 090510 obtained from the Nordic Optical Telescope (Olofsson et al. 2009) is offset by $0''.7$ relative to the center of the host galaxy in the VLT/FORS2 image. At $z = 0.903$, this corresponds to a projected distance of 5.5 kpc. The identified host galaxy is a late-type galaxy

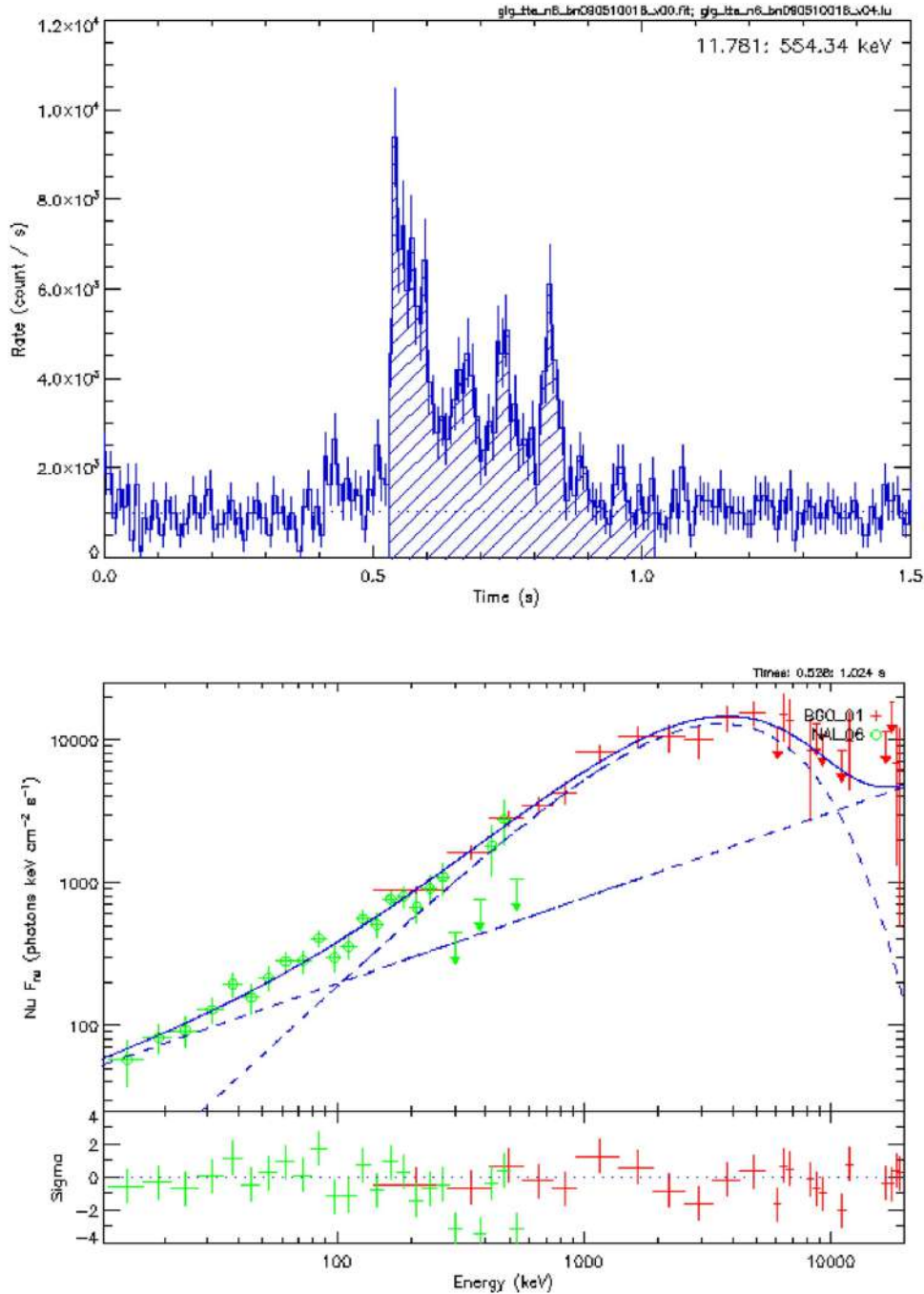


Figure 4. Top panel: GBM NaI-n6 light curve of GRB 090510 and interval considered to compute E_{iso} . Bottom panel: Comptonized+power-law best fit of the corresponding spectrum (from $T_0 + 0.528$ to $T_0 + 1.024$ s).

of stellar mass $5 \times 10^9 M_{\odot}$, with a rather low star formation rate $\text{SFR} = 0.3 M_{\odot} \text{ yr}^{-1}$ (Berger 2014, and references therein).

4.2. Data Analysis

Our analysis focused on *Fermi* (GBM and LAT) and *Swift*/XRT data. The *Fermi*/GBM signal is the most luminous in the NaI-n6 (8–900 keV, dropping the overflow high-energy channels and cutting out the K edge between ~ 30 and ~ 40 keV) and BGO-b1 (260 keV–40 MeV, again dropping the overflow high-energy channels) detectors. We additionally considered *Fermi*/LAT data in the 100 MeV–100 GeV energy range. We made use of standard software in our analysis: GBM time-tagged data—suitable in particular for S-GRBs—were

analyzed with the *rmfit* package⁸; LAT data were analyzed with the *Fermi* Science tools.⁹ The data were retrieved from the *Fermi* science support center.¹⁰ *Swift*/XRT data were retrieved from the UK *Swift* Data Centre at the University of Leicester,¹¹ and they have been reduced and analyzed using XSPEC.

Using GBM time-tagged event data binned in 16 ms intervals, the best fit in the interval $T_0 + 0.528$ s to $T_0 + 1.024$ s is a Comptonized+power-law model (see

⁸ http://fermi.gsfc.nasa.gov/ssc/data/analysis/rmfit/vc_rmfit_tutorial.pdf

⁹ <http://fermi.gsfc.nasa.gov/ssc/data/analysis/documentation/Cicerone/>

¹⁰ <http://fermi.gsfc.nasa.gov/ssc/data/access/>

¹¹ <http://www.swift.ac.uk/archive/index.php>

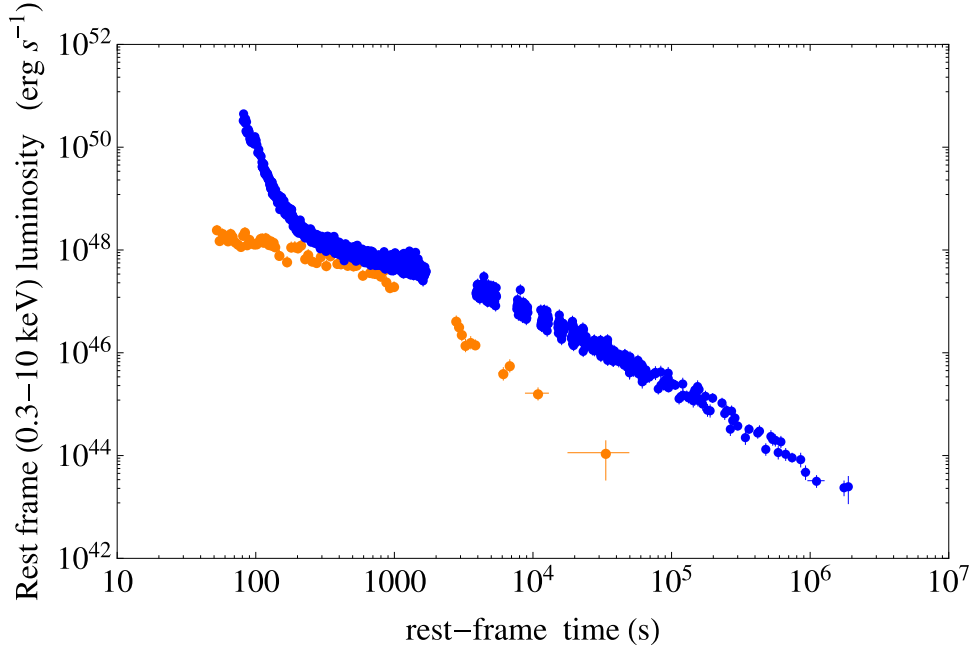


Figure 5. Rest-frame 0.3–10 keV luminosity light curves of GRB 090510 (in orange) and GRB 090618 (in blue), the prototypical IGC source. An overlapping pattern has been observed in IGC sources (Pisani et al. 2013), as well as a nesting behavior (Ruffini et al. 2014); it is clear from the deviation between the two light curves that GRB 090510 does not follow this characteristic pattern, thereby confirming its non-IGC nature.

Table 1
Spectral Analysis of the P-GRB of GRB 090510 in the Time Interval $T_0 + 0.528$ s to $T_0 + 0.640$ s.

Model	$C - \text{STAT}/\text{dof}$	E_{peak} (keV)	α	β	γ	kT (keV)
Band	221.46/237	2987 ± 343	-0.64 ± 0.05	-3.13 ± 0.42
Comp	392.65/238	3020 ± 246	-0.64 ± 0.05
Comp+PL	209.26/236	2552 ± 233	-0.26 ± 0.14	...	-1.45 ± 0.07	...
PL	492.83/239	-1.20 ± 0.02	...
BB+PL	250.09/237	-1.38 ± 0.04	477.5 ± 24.9

Note. The Columns List the Model, its C-STAT Over the Number of Degrees of Freedom (dof), the Peak Energy E_{peak} is the Peak Energy of the Comp or Band Component, the Low-energy Index α of the Comp or Band Component, the High-energy Index β of the Band Component, the Power-law Index γ , and the Temperature kT of the Blackbody Component.

Figure 4). Using this spectral model, we find an isotropic energy $E_{\text{iso}} = (3.95 \pm 0.21) \times 10^{52}$ erg. The observed peak energy of the best-fit Band model of the time-integrated GBM data is 4.1 ± 0.4 MeV, which corresponds to a rest-frame value of 7.89 ± 0.76 MeV.

The best-fit model during the first pulse (from $T_0 + 0.528$ s to $T_0 + 0.640$ s) in the 8 keV–40 MeV range is also a Comptonized+power-law model, preferred over a power law (PL, $\Delta C - \text{STAT} = 100$), a blackbody plus PL (BB + PL, $\Delta C - \text{STAT} = 41$), or a Band model ($\Delta C - \text{STAT} = 12$). The fitting statistics are summarized in Table 1. The peak energy E_{peak} of the Comptonized component is 2.6 MeV. The total isotropic energy contained in this time interval is $\sim 1.77 \times 10^{52}$ erg, while the isotropic energy contained in the Comptonized part reaches $\sim 1.66 \times 10^{52}$ erg.

5. GRB 090510 AS AN S-GRB

We here justify the interpretation of GRB 090510 as an S-GRB event. In addition to the duration and hardness properties that are similar to other GRBs interpreted as binary NS mergers, the

pattern of the late X-ray emission and the position of GRB 090510 in the $E_{\text{peak}} - E_{\text{iso}}$ plane favor this interpretation.

5.1. Late X-Ray Emission (Episode 3)

An important feature of BdHNe is the existence of a pattern in the behavior of their 0.3–10 keV late X-ray luminosity light curves, which we refer to as Episode 3 (see, e.g., Ruffini et al. 2015c). This emission is observationally characterized by the overlapping of the common late power-law behavior (Pisani et al. 2013), as well as by the nesting, namely, an inverse (direct) proportionality relation between the duration (the luminosity) of the plateau phase and the energy of the GRB emission: the more energetic the source, the smaller (higher) the duration (the luminosity) of the plateau (Ruffini et al. 2014).

If GRB 090510 were to be an IGC event exploding in a high-density environment, this characteristic Episode 3 would be expected and should be seen. Thanks to adequate coverage by the *Swift*/XRT instrument, the late X-ray (0.3–10 keV) emission of GRB 090510 has been well sampled. We computed its rest-frame 0.3–10 keV luminosity light curve, using a simple power-law

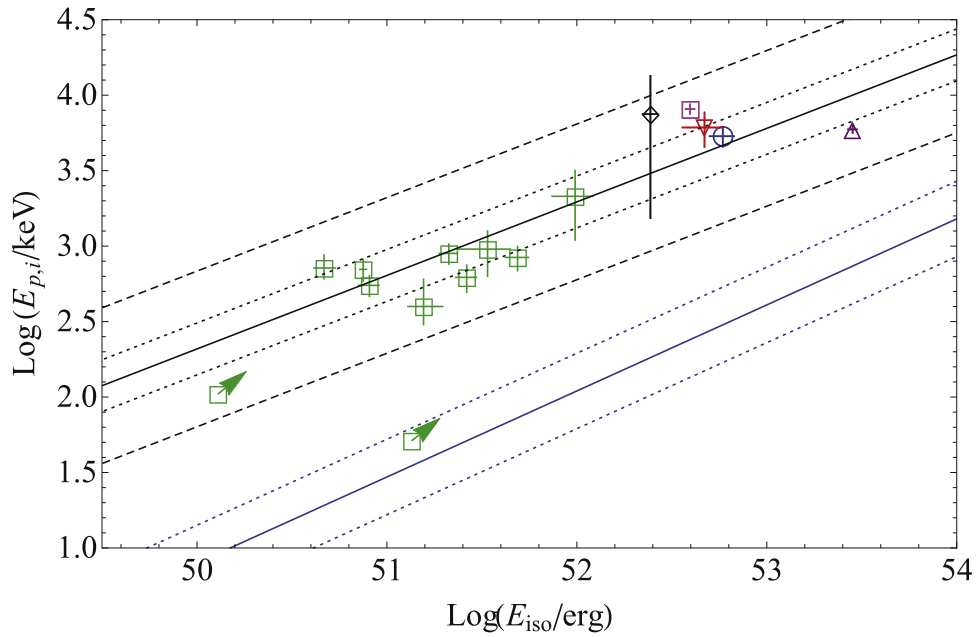


Figure 6. $E_{\text{peak}}-E_{\text{iso}}$ plot of all short bursts with redshift. The black line marks the relation for S-GRBs (which includes the theoretical redshifts we obtained for four GRBs). This relation takes the form $\log E_{\text{peak}} = A + \gamma (\log E_{\text{iso}})$, where $A = -22.0 \pm 3.2$, $\gamma = 0.49 \pm 0.06$, and E_{peak} and E_{iso} are respectively given in keV and erg. The dotted and dashed lines represent the 1σ and 3σ scatter of the relation, respectively ($\sigma_{\text{sc}} = 0.17 \pm 0.04$ dex). Green boxes indicate S-GRFs with a measured redshift; only lower limits are available for the two S-GRFs singled out by an arrow. GRB 090510 is marked by the pink square. The other four symbols indicate S-GRBs with a redshift derived from the fireshell analysis. The black diamond indicates GRB 081024B, the red inverted triangle GRB 140402A, the blue square GRB 140619B, and the purple triangle GRB 090227B. For comparison, the blue line marks the relation for long GRBs given in Calderone et al. (2015), $\log E_{\text{peak}} = A + \gamma (\log E_{\text{iso}} - B)$, where $A = 2.73$, $B = 53.21$, and $\gamma = 0.57 \pm 0.06$. The dotted lines represent the 1σ scatter of the relation ($\sigma_{\text{sc}} = 0.25$ dex).

spectral fit and taking care of the K -correction as follows:

$$L_{\text{rf}} = 4\pi d_l^2(z) f_{\text{obs}} \frac{\int_{0.3/(1+z)}^{10/(1+z)} \text{keV} E^{-\gamma} dE}{\int_{0.3}^{10} \text{keV} E^{-\gamma} dE}, \quad (1)$$

where f_{obs} is the XRT flux (in $\text{erg s}^{-1} \text{cm}^{-2}$) in the observed 0.3–10 keV range, d_l is the luminosity distance, γ is the photon index of the XRT spectrum, and $E^{-\gamma}$ is the spectral model (here, a simple power law) fitting the observed XRT flux.

The rest-frame 0.3–10 keV luminosity light curve is plotted in Figure 5: the comparison with the prototypical IGC source GRB 090618 shows a clear deviation from the overlapping and nesting patterns. Indeed, the late X-ray emission of GRB 090510 is much weaker than that of typical IGC sources and does not follow the typical power-law behavior as a function of time, which has a slope $-1.7 \leq \alpha_X \leq -1.3$. As a consequence, this result is inconsistent with the hypothesis of GRB 090510 being a BdHN disguised as a short burst. Instead, the interpretation as an S-GRB is in full agreement with the theory and the data (see below).

5.2. $E_{\text{peak}}-E_{\text{iso}}$ Relation

Although the sample of short bursts with a measured redshift and an estimate of E_{peak} is of modest size in comparison to that of long GRBs, it has been noted that a relation similar to the Amati one (Amati et al. 2002; Amati & Della Valle 2013) exists for short bursts (see, e.g., Zhang et al. 2012; Calderone et al. 2015). Plotted in Figure 6, this $E_{\text{peak}}-E_{\text{iso}}$ relation has almost the same slope as the Amati relation, but they drastically differ in their amplitudes.

While Zhang et al. (2012) extended this analysis to the above-defined S-GRFs, we have recently added four S-GRBs in this $E_{\text{peak}}-E_{\text{iso}}$ relation, which we have called the MuRuWaZha relation (Ruffini et al. 2015a).

With the parameters $E_{\text{peak}} = (7.89 \pm 0.76)$ MeV and $E_{\text{iso}} = (3.95 \pm 0.21) \times 10^{52}$ erg obtained in the previous sections, GRB 090510 falls right on the relation fulfilled by S-GRBs, and far from that of long GRBs (see Figure 6). This point further strengthens the identification of GRB 090510 as an S-GRB.

5.3. The Offset from the Host Galaxy

Long bursts are known to trace star formation (e.g., Bloom et al. 2002). They explode mainly in low-mass galaxies with high specific star formation rates. On the other hand, short bursts occur in a wider range of host galaxies, including old, elliptical galaxies with little star formation and young galaxies. Their median projected offset from the center of their host, about 5 kpc, is also known to be four times larger than that of long bursts (Bloom et al. 2002). With a projected offset of 5.5 kpc, as detailed previously, GRB 090510 falls in the typical short-burst range. Its host galaxy is a late-type one.

The results of the fireshell analysis summarized in the next section also support this conclusion. The average CBM density of GRB 090510 is indeed evaluated at $\langle n_{\text{CBM}} \rangle = 8.7 \times 10^{-6} \text{ cm}^{-3}$ (see next section), a low value that is typical of galactic halos.

6. INTERPRETATION

GRB 090510 exhibits several peculiar features: the spectrum of the P-GRB is not purely thermal, a weak precursor emission is clearly seen, and a GeV emission is observed—which never occurs in S-GRFs but appears to be a general property of the S-GRBs. This section is devoted to the analysis and interpretation of these features.

Ruffini et al. (2015b) establish theoretical predictions concerning S-GRBs that originate in a binary NS merger, with and without BH formation. We find that these predictions are fulfilled and that

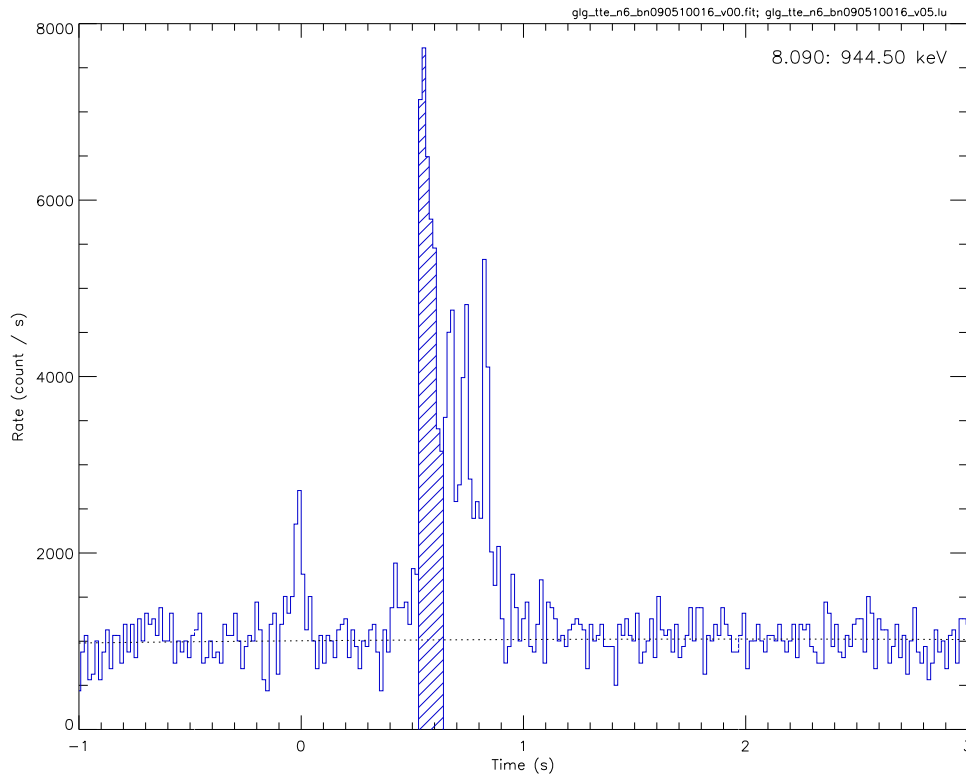


Figure 7. Counts light curve of GRB 090510 as seen by the NaI-n6 detector of *Fermi*/GBM with a 16 ms binning. The dashed area represents the interval in which the P-GRB is identified.

all features are consistent with GRB 090510 resulting from an NS merger, leading to the formation of a Kerr–Newman BH.

6.1. P-GRB

The identification of the P-GRB is especially relevant to the fireshell analysis, since it marks the reaching of the transparency of the fireshell. The P-GRB is followed by the prompt emission (Ruffini et al. 2001a). It is suggested in Ruffini et al. (2015b) that the GeV emission is produced by the newborn BH and starts only after the P-GRB is emitted, at the beginning of the prompt emission. Here, the bulk of the GeV emission is detected after the first main spike is over. Therefore, we identify the first main spike (from $T_0 + 0.528$ to $T_0 + 0.644$ s; see Figure 7) with the P-GRB. The results of the analysis within the fireshell theory (presented hereafter) also offer an a posteriori confirmation of this identification of the P-GRB.

The best-fit model of the P-GRB spectrum consists of a Comptonized+power-law model. We note that a Comptonized component may be viewed as a convolution of blackbodies (see Figure 8 and Table 2, for details).

The geometry of the fireshell is dictated by the geometry of the pair-creation region. It is in general assumed to be a spherically symmetric dyadosphere, which leads to a P-GRB spectrum generally described by a single thermal component in good agreement with the spectral data. Cherubini et al. (2009) found that the region of pair creation in a Kerr–Newman geometry becomes axially symmetric, thus effectively becoming a dyadotorus. Qualitatively, one expects a pure thermal spectrum resulting from the dyadosphere, while a convolution of thermal spectra of different temperatures is expected for a dyadotorus (see Figure 1).

In the present case of GRB 090510, also in view of the good quality of the γ -ray data, the P-GRB is best fitted by a

convolution of thermal spectra. The theoretically expected temperatures of the thermal components in the dyadotorus are a function of the polar angle. Knowing that the final spectrum at the transparency condition is a convolution of such thermal spectra at different angles, we adopted for simplicity a discrete number of thermal components (see Table 2). The number of such thermal components, leading in principle to a continuum, is a function of the quality of the data. This provides the first indication that indeed the angular momentum plays a role in the merging of the two NSs and that the dyadotorus is formed as theoretically predicted in a series of papers (Cherubini et al. 2009; Ruffini 2009). This opens a new area of research that is not going to be addressed in the present article. Previous identifications of pure thermal components in the P-GRB of other GRBs (e.g., Izzo et al. 2012; Ruffini et al. 2015b) nevertheless evidence that the angular momentum of the BH formed by GRB 090510 must be substantially large in order to affect the P-GRB spectrum.

Finally, the extra power-law component observed in the P-GRB spectrum is very likely related to a mildly jetted component necessary to fulfill the conservation of the energy and angular momentum of the system.

6.2. Prompt Emission

In order to simulate the light curve and spectrum of the prompt emission of GRB 090510, we assume that the initial fireshell energy $E_{e^+e^-}^{\text{tot}}$ is equal to E_{iso} . Since the P-GRB spectrum is not purely thermal, we derive an effective blackbody temperature from the peak energy of the Comptonized component. We obtain a temperature $kT_{\text{obs}} = (633 \pm 62)$ keV.

The fireshell theory allows the determination of all essential quantities of the model from the total pair plasma energy $E_{e^+e^-}^{\text{tot}}$

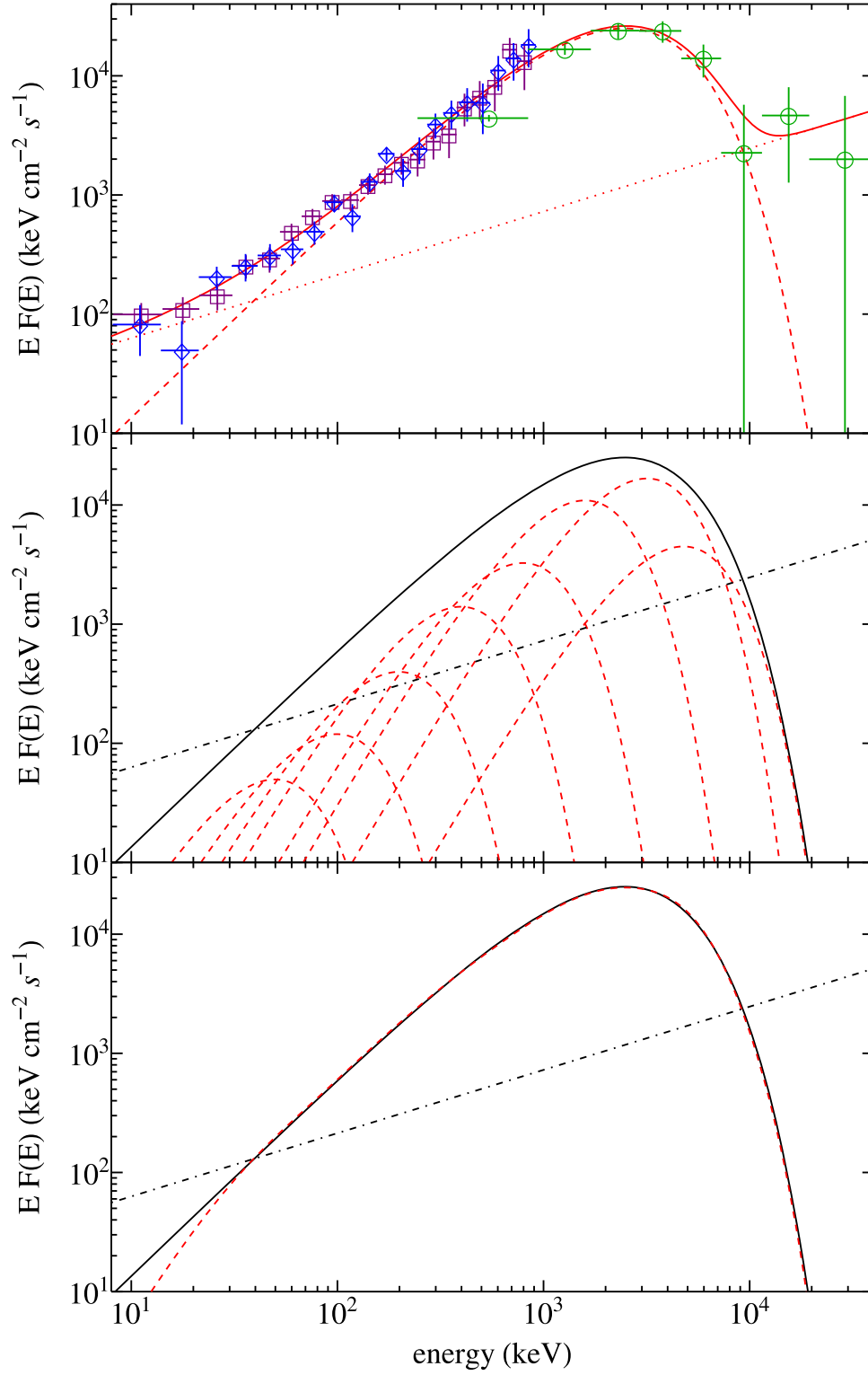


Figure 8. Top panel: P-GRB spectrum of GRB 090510 from the *Fermi*-GBM NaI-n6 (purple squares) and n7 (blue diamonds) and the BGO-b1 (green circles) detectors, in the time interval from $T_0 + 0.528$ to $T_0 + 0.644$ s. The best fit (solid red line) is composed of a power-law model (dotted red line) and a Comptonized model (dashed red curve). Middle panel: above Comptonized model (here the solid black line), viewed as a convolution of thermal components (dashed red curves). The convolution of blackbodies produces the result plotted in the bottom panel, namely, a dashed red curve reproducing the Comptonized model. The power-law component (dot-dashed black line in the middle and bottom panels) is very likely related to a mildly jetted component necessary to fulfill the conservation of the energy and angular momentum of the system.

and from the ratio of the energy contained in the P-GRB to $E_{e^+e^-}^{\text{tot}}$. This ratio directly leads to the baryon load B , which, in conjunction with $E_{e^+e^-}^{\text{tot}}$ and the relation between the predicted and observed temperatures, gives the Lorentz factor at

transparency, the temperature of the fireshell at transparency, and the radius at transparency.

Given $E_{\text{iso}} = 3.95 \times 10^{52}$ erg and $E_{\text{P-GRB}} = (42.1 \pm 3.8)\%$ $E_{e^+e^-}^{\text{tot}}$, we deduce a baryon load $B = 5.54 \times 10^{-5}$, a Lorentz

Table 2

The Parameters of the Blackbody (BB) Spectra Used in the Convolution Shown in Figure 8

BB	kT (keV)	$E_{\text{BB}}/E_{\text{P-GRB}}$ (%)
1	1216	8.8
2	811	43.6
3	405	31.8
4	203	9.6
5	101	4.4
6	51	1.2
7	25	0.4
8	13	0.2

Note. The columns list the number of BBs, their temperatures, and their energy content with respect to the P-GRB energy computed from the Comptonized model.

Table 3

Parameters Derived from the Fireshell Analysis of GRB 090510

Parameter	Value
B	$(5.54 \pm 0.70) \times 10^{-5}$
γ_{tr}	$(1.04 \pm 0.07) \times 10^4$
r_{tr}	$(7.60 \pm 0.50) \times 10^{12}$ cm
$E_{e^+e^-}^{\text{tot}}$	$(3.95 \pm 0.21) \times 10^{52}$ erg
kT_{blue}	$(1.20 \pm 0.11) \times 10^3$ keV
$\langle n \rangle$	$(8.7 \pm 2.1) \times 10^{-6}$ cm $^{-3}$

Note. Shown in the table are the baryon load B , the Lorentz factor at transparency γ_{tr} , the fireshell radius at transparency r_{tr} , the total energy of the electron-pair plasma $E_{e^+e^-}^{\text{tot}}$, the blueshifted temperature of the fireshell at transparency kT_{blue} , and the CBM average density $\langle n \rangle$

factor $\gamma = 1.04 \times 10^4$, a temperature at transparency $kT = 1.2$ MeV, and a radius at transparency $r_{\text{tr}} = 7.60 \times 10^{12}$ cm (see Table 3).

In order to determine the profile of the CBM, a simulation of the prompt emission following the P-GRB has been performed. The simulation starts at the transparency of the fireshell with the parameters that we determined above. A trial-and-error procedure is undertaken, guided by the necessity to fit the light curve of GRB 090510. The results of this simulation (reproduction of the light curve and spectrum, in the time interval from $T_0 + 0.644$ to $T_0 + 0.864$ s, and CBM profile) are shown in Figure 9. The average CBM density is found to be $\langle n_{\text{CBM}} \rangle = 8.7 \times 10^{-6}$ cm $^{-3}$. This low value, typical of galactic halo environments, is consistent with the large offset from the center of the host and further justifies the interpretation of GRB 090510 as an S-GRB originating in a binary NS merger.

Our theoretical fit of the prompt emission (see red line in the middle panel of Figure 9) predicts a cutoff at ~ 10 MeV. The spectrum at energy $\gtrsim 10$ MeV could be affected by the onset of the high-energy power-law component manifested both in the data of the Mini-Calorimeter on board *AGILE* (see top panel of Figure 4 in Giuliani et al. 2010) and in the data points from the *Fermi*-GBM BGO-b1 detector.

6.3. Precursor Emission

There is a weak precursor emission about 0.4 s before the P-GRB (or ~ 0.21 s in the cosmological rest frame). Two GeV

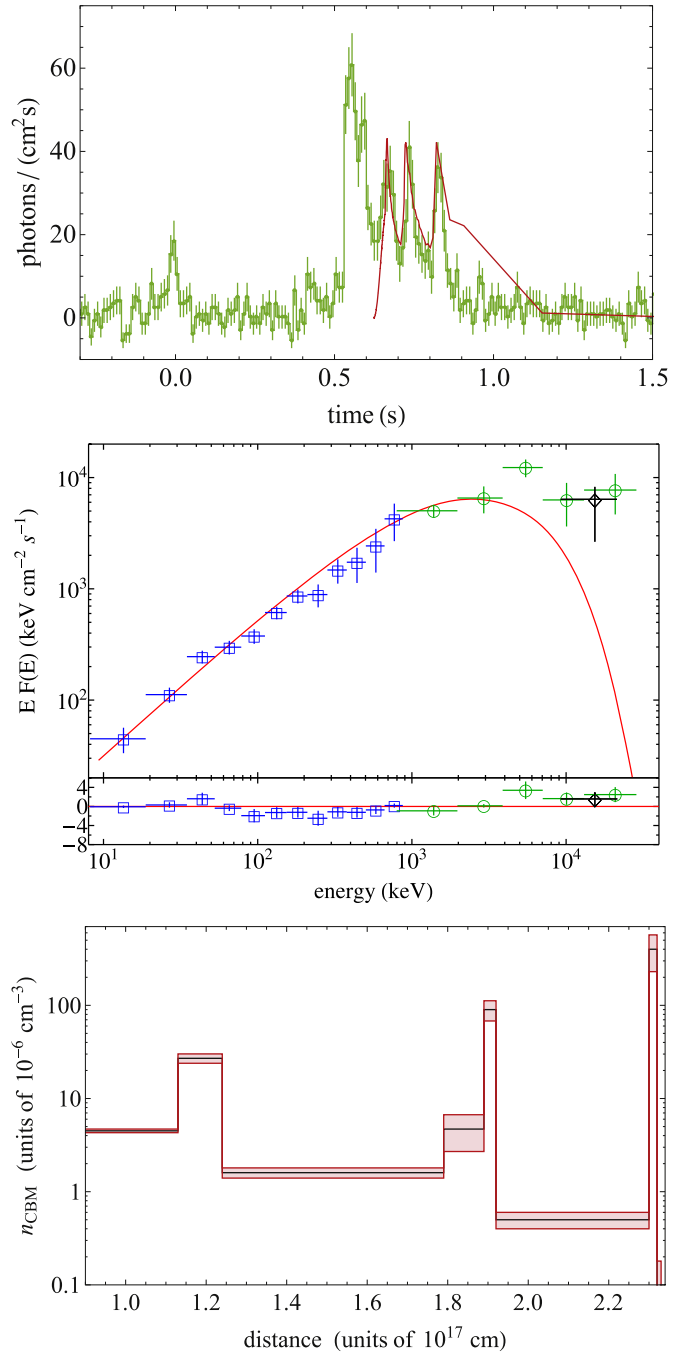


Figure 9. Results of the fireshell simulation of GRB 090510. Top panel: fit of the prompt emission *Fermi*-GBM NaI-n6 light curve. Middle panel: fit of the corresponding spectrum including the *Fermi*-NaI-6 (blue squares) and BGO-b1 (green circles) data in the time interval from $T_0 + 0.644$ to $T_0 + 0.864$ s. A single data point obtained from the Mini-Calorimeter on board *AGILE*, in the range 10–20 MeV and in the first 0.2 s of the *AGILE* light curve (from $T_0 + 0.5$ to $T_0 + 0.7$ s in the *Fermi* light curve), is shown for comparison (reproduced from Figure 4 in Giuliani et al. 2010). Bottom panel: density profile of the CBM inferred from the simulation of CBM clouds of $\sim 10^{22}$ g.

photons have been detected during the precursor emission. Precursors are commonly seen in long bursts: Lazzati (2005) found that $\sim 20\%$ of them show evidence of an emission preceding the main emission by tens of seconds. Short bursts are less frequently associated with precursors.

No significant emission from the GRB itself is expected prior to the P-GRB—since it marks the transparency of the fireshell

—but the precursor may be explainable in the context of a binary NS merger by invoking the effects of the interaction between the two NSs just prior to merger. Indeed, it has been suggested that precursor emission in short bursts may be caused by resonant fragmentation of the crusts (Tsang et al. 2012) or by the interaction of the NS magnetospheres (Hansen & Lyutikov 2001).

The timescale (~ 0.21 s between the precursor and the P-GRB) is consistent with a pre-merger origin of the precursor emission. From its formation to its transparency, the fireshell undergoes a swift evolution. The thermalization of the pair plasma is achieved almost instantaneously ($\sim 10^{-13}$ s; Aksenov et al. 2007), and the e^+e^- plasma of GRB 090510 reaches the ultrarelativistic regime (i.e., a Lorentz factor $\gamma > 10$) in a matter of 4.2×10^{-2} s, according to the numerical simulation. The radius of the fireshell at transparency, $r_{tr} = 7.60 \times 10^{12}$ cm, corresponds to more than 100 lt-s; however, relativistic motion in the direction of the observer squeezes the light curve by a factor of $\sim 2\gamma^2$, which makes the fireshell capable of traveling that distance under the observed timescale.

The spectral analysis of this precursor is limited by the low number of counts. Muccino et al. (2013b) interpreted the spectrum with a blackbody plus power-law model. This leads to a blackbody temperature of 34.2 ± 7.5 keV. The isotropic energy contained in the precursor amounts to $(2.28 \pm 0.39) \times 10^{51}$ erg.

6.4. Redshift Estimate

An interesting feature of the fireshell model is the possibility to infer a theoretical redshift from the observations of the P-GRB and the prompt emission. In the case of GRB 090510, a comparison is therefore possible between the measured redshift $z = 0.903 \pm 0.003$ and its theoretical derivation. An agreement between the two values would in particular strengthen the validity of our P-GRB choice, which would in turn strengthen our results obtained with this P-GRB.

The feature of the redshift estimate stems from the relations, engraved in the fireshell theory, between different quantities computed at the transparency point: the radius in the laboratory frame, the comoving frame and blueshifted temperatures of the plasma, the Lorentz factor, and the fraction of energy radiated in the P-GRB and in the prompt emission as functions of B (see Figure 4 in Ruffini et al. 2015b). Thus, the ratio $E_{P-GRB}/E_{e^+e^-}^{\text{tot}}$ implies a finite range for the coupled parameters $E_{e^+e^-}^{\text{tot}}$ and B (last panel of Figure 4 in Ruffini et al. 2015b). Assuming $E_{e^+e^-}^{\text{tot}} = E_{\text{iso}}$, this ratio is known since it is equal to the ratio between the observed fluences of the respective quantities:

$$\frac{E_{P-GRB}}{E_{e^+e^-}^{\text{tot}}} \approx \frac{4\pi S_{P-GRB} d_l^2(z)/(1+z)}{4\pi S_{e^+e^-}^{\text{tot}} d_l^2(z)/(1+z)} = \frac{S_{P-GRB}}{S_{e^+e^-}^{\text{tot}}}. \quad (2)$$

With the measured values $S_{P-GRB} = (9.31 \pm 0.76) \times 10^{-6}$ erg cm $^{-2}$ and $S_{e^+e^-}^{\text{tot}} = (2.19 \pm 0.18) \times 10^{-5}$ erg cm $^{-2}$, we find $E_{P-GRB}/E_{e^+e^-}^{\text{tot}} = (42.1 \pm 3.8)\%$.

In addition, knowing the couple $[E_{e^+e^-}^{\text{tot}}, B]$ gives the (blueshifted toward the observer) temperature of the fireshell at transparency kT_{blue} (Figure 4 in Ruffini et al. 2015b, second panel). But we also have the following relation between kT_{blue} and the observed temperature at transparency kT_{obs} , linking

their ratio to the redshift:

$$\frac{kT_{\text{blue}}}{kT_{\text{obs}}} = 1 + z. \quad (3)$$

Finally, since we assume that $E_{e^+e^-}^{\text{tot}} = E_{\text{iso}}$, we also have an expression of $E_{e^+e^-}^{\text{tot}}$ as a function of z using the formula of the K -corrected isotropic energy:

$$E_{\text{iso}} = 4\pi d_l^2(z) \frac{S_{\text{tot}}}{1+z} \frac{\int_{1/(1+z) \text{ keV}}^{10000/(1+z) \text{ keV}} EN(E) dE}{\int_{8 \text{ keV}}^{40000 \text{ keV}} EN(E) dE} \quad (4)$$

where $N(E)$ is the photon spectrum of the GRB and the fluence S_{tot} is obtained in the full GBM energy range 8–40,000 keV.

The use of all these relations allows a redshift to be determined by an iterative procedure, testing at every step the value of the parameters $E_{e^+e^-}^{\text{tot}}(z)$ and kT_{blue} . The procedure successfully ends when both values are consistent according to the relations described above. In the case of GRB 090510, we find $z = 0.75 \pm 0.17$, which provides a satisfactory agreement with the measured value $z = 0.903 \pm 0.003$.

6.5. GeV Emission

GRB 090510 is associated with a high-energy emission, consistently with all other observed S-GRBs, i.e., energetic events with $E_{\text{iso}} \gtrsim 10^{52}$ erg. The only case of an S-GRB without GeV emission, namely, GRB 090227B, has been explained by the absence of alignment between the LAT and the source at the time of the GRB emission. Nevertheless, evidence of some GeV emission in this source has been recently obtained (R. Ruffini et al. 2016, in preparation).

The GeV light curve of GRB 090510 is plotted in Figure 10, together with other S-GRB light curves and showing a common power-law behavior, which goes as $t^{-1.32}$, similar to the clustering of the GeV light curves found by Nava et al. (2014). These S-GRBs are compared with that of the BdHN 130427A, which shares a similar behavior. Ruffini et al. (2015b) suggest and argue that the GeV emission is related to the presence of a BH and its activity. This view is supported by the fact that the GeV emission is delayed with respect to the γ -ray emission: it starts only after the P-GRB is over.

The GeV emission of GRB 090510 is particularly intense, reaching $E_{\text{LAT}} = (5.78 \pm 0.60) \times 10^{52}$ erg. Such a large value, one of the largest observed among S-GRBs, is consistent with the large angular momentum of the newborn BH. This energetic cannot be explained in terms of NSs in view of the lower value of the gravitational binding energy.

The absence of GeV emission in S-GRBs is also confirmed from the strong upper limit to the GeV emission for S-GRBs imposed by the *Fermi*-LAT sensitivity. We assume for a moment that the GeV emission of an S-GRF is similar to that of S-GRBs. We then compute the observed GeV flux light curve of S-GRB 090510 at different redshifts, e.g., $z = 2.67$ and 5.52 , which correspond to the redshifts of the S-GRB 081024B and of the S-GRB 140402A, respectively (Y. Aimuratov et al. 2016, in preparation). The result is that if we compare these computed flux light curves with the *Fermi*-LAT sensitivity of the Pass 8 Release 2 Version 6 Instrument Response Functions,¹² which is approximately 10^{-11} erg cm $^{-2}$ s $^{-1}$, all

¹² http://www.slac.stanford.edu/exp/glast/groups/canda/lat_Performance_files/broadband_flux_sensitivity_p8r2_source_v6_all_10yr_zmax100_n03.0_e1.50_ts25.png

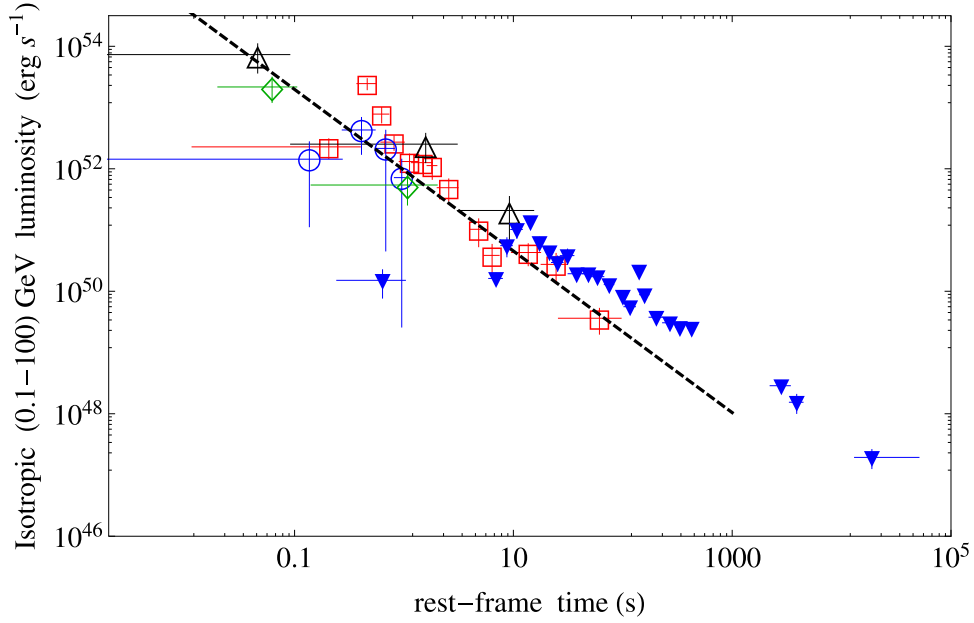


Figure 10. Isotropic rest-frame 0.1–100 GeV luminosity light curves of the S-GRBs 090510 (red squares), 081024B (green diamonds), 140402A (black triangles), and 140619B (blue circles) compared to that of the BdHN 130427A (blue downward-pointing triangles). The dashed black line marks the common behavior of all the S-GRB light curves, which goes as $t^{-1.32}$. In our approach this communality follows straightforwardly from the equality of the masses of the emerging extreme BH.

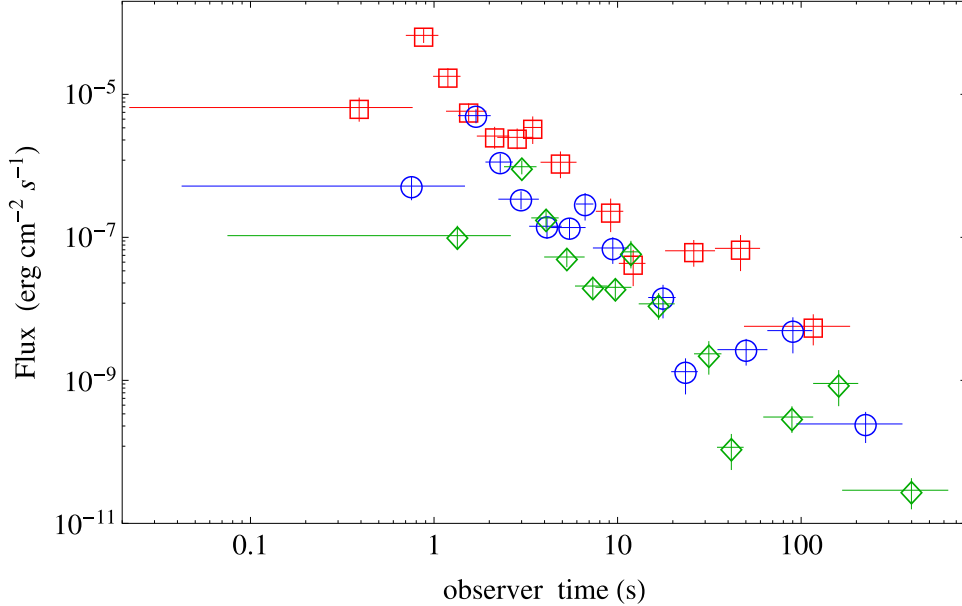


Figure 11. Observed 0.1–100 GeV flux light curve of the S-GRB 090510 (red squares) and the corresponding ones obtained by translating this S-GRB at $z = 2.67$ (blue circles) and at $z = 5.52$ (green diamonds).

of them are always well above the LAT broadband sensitivity by a factor of $\sim 10^5$ (see Figure 11). This result does not depend on the choice of the source. In their rest frame all the S-GRB GeV light curves follow a similar behavior. Therefore, the GeV emission of S-GRB 090510 is always above $\sim 10^5$ times the LAT sensitivity, even at higher redshifts. If we now assume that S-GRFs do conform to the same behavior of S-GRBs, the absence of detection of GeV emission implies that the S-GRFs necessarily have fluxes at least 10^5 – 10^6 times smaller than those of S-GRBs.

6.6. On the Energy Requirement of the GeV Emission

In order to estimate the energy requirement of the 0.1–100 GeV emission of Figure 10, we consider the accretion of mass M_{acc} onto a Kerr–Newman BH, dominated by its angular momentum and endowed with electromagnetic fields not influencing the geometry, which remains approximately that of a Kerr BH. We recall that if the infalling accreted material is in an orbit co-rotating with the BH spin, up to $\eta_+ = 42.3\%$ of the initial mass is converted into radiation, for a maximally rotating Kerr BH, while this efficiency drops to

$\eta_- = 3.8\%$ when the infalling material is on a counter-rotating orbit (see Ruffini & Wheeler 1969, in problem 2 of Section 104 in Landau & Lifshitz 2003). Therefore, the GeV emission can be expressed as

$$E_{\text{LAT}} = f_b^{-1} \eta_{\pm} M_{\text{acc}} c^2, \quad (5)$$

and depends not only on the efficiency η_{\pm} in the accretion process of matter M_{acc} but also on the geometry of the emission described by the beaming factor $f_b \equiv 1 - \cos \theta$ (here θ is the half-opening angle of jet-like emission).

Depending on the assumptions we introduce in Equation (5), we can give constraints on the amount of accreted matter or on the geometry of the system.

For an isotropic emission, $f_b \equiv 1$, the accretion of $M_{\text{acc}} \gtrsim 0.08 M_{\odot}$, for the co-rotating case, and of $M_{\text{acc}} \gtrsim 0.86 M_{\odot}$, for the counter-rotating case, is required.

Alternatively, we can assume that the accreted matter comes from the crustal material from a $1.6 + 1.6 M_{\odot}$ NS–NS binary progenitor. The crustal mass from the NL3 nuclear model for each of these NSs is $M_c = 4.30 \times 10^{-5} M_{\odot}$ (see, e.g., Belvedere et al. 2012, and Figure 2). Assuming that crustal material accounts also for the baryon load mass, e.g., $M_B \equiv E_{e^+e^-}^{\text{tot}}/c^2 = 1.22 \times 10^{-6} M_{\odot}$, the total available mass for accretion is $M_{\text{acc}} \equiv 2M_c - M_B = 8.48 \times 10^{-5} M_{\odot}$. Then, the presence of a beaming is necessary: from Equation (5), a half-opening beaming angle $\theta \gtrsim 2^\circ.70$, for the co-rotating case, and $\theta \gtrsim 0^\circ.81$, for the counter-rotating case, would be required.

The above considerations are clearly independent from the relativistic beaming angle $\theta_r = \gamma_{\text{LAT}}^{-1} \approx 0^\circ.1$, where the lower limit on the Lorentz factor $\gamma_{\text{LAT}} \approx 550$ has been derived, in a different context, by Lithwick & Sari (2001) to the GeV luminosity light curve (see Figure 10).

Further consequences on these results for the estimate of the rate of these S-GRBs will be presented elsewhere (R. Ruffini et al. 2016, in preparation).

7. CONCLUSIONS

It is interesting to recall some of the main novelties introduced in this paper with respect to previous works on GRB 090510. Particularly noteworthy are the differences from the previous review of short bursts by Nakar (2007), made possible by the discovery of the high-energy emission by the *Fermi* team in this specific source (Ackermann et al. 2010). A new family of short bursts characterized by the presence of a BH and associated high-energy emission with LAT data now available comprises GRBs 081024B, 090227B, 090510, 140402A, and 140619B (see, e.g., Figure 10). The excellent data obtained by the *Fermi* team and interpreted within the fireshell model have allowed us to relate in this paper the starting point of the high-energy emission to the birth of a BH.

Our fireshell analysis assumes that the γ -ray and the GeV components originate from different physical processes. First, the interpretation of the prompt emission differs from the standard synchrotron model: we model the collisions of the baryon accelerated by the GRB outflow with the ambient medium following a fully relativistic approach (see Section 2). Second, we assume that the GeV emission originates from the matter accretion onto the newly born BH, and we show that indeed the energy requirement is fulfilled. This approach explains also the delayed onset of the GeV emission, i.e., it is

observable only after the transparency condition, namely, after the P-GRB emission.

The joint utilization of the excellent data from the *Fermi*-GBM NaI-n6 and n7 and the BGO-b1 detectors and from the Mini-Calorimeter on board *AGILE* (Giuliani et al. 2010) has given strong observational support to our theoretical work. GRB 090510 has been analyzed in light of the recent progress achieved in the fireshell theory and the resulting new classification of GRBs. We show that GRB 090510 is an S-GRB, originating in a binary NS merger (see Figure 3). Such systems, by the absence of the associated SN events, are by far the simplest GRBs to be analyzed. Our analysis indicates the presence of three distinct episodes in S-GRBs: the P-GRB, the prompt emission, and the GeV emission. By following the precise identification of successive events predicted by the fireshell theory, we show evidence for the first indication of a Kerr BH or, possibly, a Kerr–Newman BH formation:

1. The P-GRB spectrum of GRB 090510, in the time interval from $T_0 + 0.528$ to $T_0 + 0.644$ s, is best fitted by a Comptonized component (see Figures 7 and 8 and Table 1), which is interpreted as a convolution of thermal spectra originating in a dyadotorus (see Cherubini et al. 2009; Ruffini 2009; see also Figure 1 and Section 2).
2. The prompt emission follows at the end of the P-GRB (see Figure 4). The analysis of the prompt emission within the fireshell model allows us to determine the inhomogeneities in the CBM giving rise to the spiky structure of the prompt emission and to estimate as well an averaged CBM density of $\langle n_{\text{CBM}} \rangle = 8.7 \times 10^{-6} \text{ cm}^{-3}$ obtained from a few CBM clouds of mass $\sim 10^{22}$ g and typical dimensions of $\sim 10^{16}$ cm (see Figure 9). Such a density is typical of galactic halos where binary NSs are expected to migrate due to large natal kicks.
3. The late X-ray emission of GRB 090510 does not follow the characteristic patterns expected in BdHN events (see Figure 5 and Pisani et al. 2013).
4. The GeV emission occurs at the end of the P-GRB emission and is initially concurrent with the prompt emission. This sequence occurs in both S-GRBs (Ruffini et al. 2015b) and BdHNe (Ruffini et al. 2015c). This delayed long-lasting (≈ 200 s) GeV emission in GRB 090510 is one of the most intense ever observed in any GRB (see Figure 10; see also Ackermann et al. 2013; Ruffini et al. 2016).
5. We then consider accretion on co-rotating and counter-rotating orbits (see Ruffini & Wheeler 1969, in problem 2 of Section 104 in Landau & Lifshitz 2003) around an extreme Kerr BH. Assuming the accretion of the crustal mass $2M_c = 8.60 \times 10^{-5} M_{\odot}$ from a $1.6 + 1.6 M_{\odot}$ NS–NS binary, fulfilling global charge neutrality (see Figure 2), geometrical beaming angles of $\theta \gtrsim 0^\circ.81$, for the co-rotating case, and $\theta \gtrsim 2^\circ.70$, for the counter-rotating case, are inferred. In order to fulfill the transparency condition, the initial Lorentz factor of the jetted material has to be $\gamma \gtrsim 550$ (see Section 6.6).
6. While there is evidence that the GeV emission must be jetted, no beaming appears to be present in the P-GRB and in the prompt emission, with important consequences for the estimate of the rate of such events (Ruffini et al. 2016).

7. The energetic and the possible beaming of the GeV emission requires the presence of a Kerr BH, or a Kerr–Newman BH dominated by its angular momentum and with electromagnetic fields not influencing the geometry (see also Section 6.5).
8. The self-consistency of the entire procedure has been verified by estimating, on the ground of the fireshell theory, the cosmological redshift of the source. The theoretical redshift is $z = 0.75 \pm 0.17$ (see Section 6.4), close to and consistent with the spectroscopically measured value $z = 0.903 \pm 0.003$ (Rau et al. 2009).
9. The values of E_{peak} and E_{iso} of GRB 090510 fulfill with excellent agreement the MuRuWaZha relation (see Section 5.2 and Figure 6; see also Ruffini et al. 2015a).

The main result of this article is that the dyadoturus manifests itself by the P-GRB emission and clearly precedes the prompt emission phase, as well as the GeV emission originating from the newly formed BH. This contrasts with the usual assumption made in almost the totality of works relating BHs and GRBs in which the BH precedes the GRB emission. In conclusion, in this article, we take GRB 090510 as the prototype of S-GRBs and perform a new time-resolved spectral analysis, in excellent agreement with that performed by the *AGILE* and the *Fermi* teams. Now this analysis, guided by a theoretical approach successfully tested in this new family of S-GRBs, is directed to identify a precise sequence of different events made possible by the exceptional quality of the data of GRB 090510. This includes a new structure in the thermal emission of the P-GRB emission, followed by the onset of the GeV emission linked to the BH formation, allowing us, as well, to derive the structure of the CBM from the spiky structure of the prompt emission. This sequence, for the first time, illustrates the formation process of a BH.

It is expected that this very unique condition of generating a jetted GeV emission in such a well-defined scenario of a newly born BH will possibly lead to a deeper understanding of the equally jetted GeV emission observed, but not yet explained, in a variety of systems harboring a Kerr BH. Among these systems we recall binary X-ray sources (see, e.g., Giacconi & Ruffini 1978, and references therein), microquasars (see, e.g., Chaty et al. 2015, and references therein), and, at larger scale, active galactic nuclei (see, e.g., Arsioli et al. 2015, and references therein).

We thank the editor and the referee for their comments, which helped to improve the presentation and the contextualization of our results. We are indebted to Marco Tavani for very interesting comments, as well as for giving us observational supporting evidence. This work made use of data supplied by the UK *Swift* Data Center at the University of Leicester. M.E., M.K., and Y.A. are supported by the Erasmus Mundus Joint Doctorate Program by Grant Numbers 2012-1710, 2013-1471, and 2014-0707, respectively, from the EACEA of the European Commission. C.C. acknowledges INdAM-GNFM for support. M.M. acknowledges the partial support of the project N 3101/GF4 IPC-11 and the target program F.0679 of the Ministry of Education and Science of the Republic of Kazakhstan.

REFERENCES

- Ackermann, M., Ajello, M., Asano, K., et al. 2013, *ApJS*, **209**, 11
- Ackermann, M., Asano, K., Atwood, W. B., et al. 2010, *ApJ*, **716**, 1178
- Aksenov, A. G., Ruffini, R., & Vereshchagin, G. V. 2007, *PhRvL*, **99**, 125003
- Aksenov, A. G., Ruffini, R., & Vereshchagin, G. V. 2009, *PhRvD*, **79**, 043008
- Amati, L., & Della Valle, M. 2013, *IJMPD*, **22**, 30028
- Amati, L., Frontera, F., in't Zand, J. J. M., et al. 2004, *A&A*, **426**, 415
- Amati, L., Frontera, F., Tavani, M., et al. 2002, *A&A*, **390**, 81
- Antoniadis, J. 2015, *ASSP*, **40**, 1
- Arsioli, B., Fraga, B., Giommi, P., Padovani, P., & Marrese, P. M. 2015, *A&A*, **579**, A34
- Becerra, L., Bianco, C. L., Fryer, C. L., Rueda, J. A., & Ruffini, R. 2016, arXiv:1606.02523
- Becerra, L., Cipolletta, F., Fryer, C. L., Rueda, J. A., & Ruffini, R. 2015, *ApJ*, **812**, 100
- Belvedere, R., Pugliese, D., Rueda, J. A., Ruffini, R., & Xue, S.-S. 2012, *NuPhA*, **883**, 1
- Belvedere, R., Rueda, J. A., & Ruffini, R. 2014, *JKPS*, **65**, 897
- Belvedere, R., Rueda, J. A., & Ruffini, R. 2015, *ApJ*, **799**, 23
- Berger, E. 2011, *NewAR*, **55**, 1
- Berger, E. 2014, *ARA&A*, **52**, 43
- Bianco, C. L., & Ruffini, R. 2005a, *ApJL*, **620**, L23
- Bianco, C. L., & Ruffini, R. 2005b, *ApJL*, **633**, L13
- Bloom, J. S., Kulkarni, S. R., & Djorgovski, S. G. 2002, *AJ*, **123**, 1111
- Bloom, J. S., Prochaska, J. X., Pooley, D., et al. 2006, *ApJ*, **638**, 354
- Bucciantini, N., Metzger, B. D., Thompson, T. A., & Quataert, E. 2012, *MNRAS*, **419**, 1537
- Calderone, G., Ghirlanda, G., Ghisellini, G., et al. 2015, *MNRAS*, **448**, 403
- Cavallo, G., & Rees, M. J. 1978, *MNRAS*, **183**, 359
- Cherubini, C., Giallardo, A. J. A., Rueda, H., & Ruffini, R. 2009, *PhRvD*, **79**, 124002
- Cipolletta, F., Cherubini, C., Filippi, S., Rueda, J. A., & Ruffini, R. 2015, *PhRvD*, **92**, 023007
- Curran, P. A., Starling, R. L. C., O'Brien, P. T., et al. 2008, *A&A*, **487**, 533
- Dai, Z. G., Wang, X. Y., Wu, X. F., & Zhang, B. 2006, *Sci*, **311**, 1127
- Damour, T., & Ruffini, R. 1975, *PhRvL*, **35**, 463
- Della Valle, M. 2011, *IJMPD*, **20**, 1745
- De Pasquale, M., Schady, P., Kuin, N. P. M., et al. 2010, *ApJL*, **709**, L146
- Dezalay, J.-P., Barat, C., Talon, R., et al. 1992, in *Gamma-ray bursts*, Proc. of the Workshop, AIP Conf. Ser. 265, ed. W. S. Paciesas & G. J. Fishman (Melville, NY: AIP), 304
- Eichler, D., Livio, M., Piran, T., & Schramm, D. N. 1989, *Natur*, **340**, 126
- Enderli, M., Bianco, C. L., Izzo, L., et al. 2014, in *Proceedings of Swift: 10 Years of Discovery (SWIFT 10)* (Trieste: SISSA) (pos.sissa.it/archive/conferences/233/073/SWIFT%2010_073.pdf)
- Endrizzi, A., Ciolfi, R., Giacomazzo, B., Kastaun, W., & Kawamura, T. 2016, arXiv:1604.03445
- Fong, W., Berger, E., & Fox, D. B. 2010, *ApJ*, **708**, 9
- Fruchter, A. S., Levan, A. J., Strolger, L., et al. 2006, *Natur*, **441**, 463
- Fryer, C. L., Rueda, J. A., & Ruffini, R. 2014, *ApJL*, **793**, L36
- Gehrels, N., Ramirez-Ruiz, E., & Fox, D. B. 2009, *ARA&A*, **47**, 567
- Giacconi, R., & Ruffini, R. (ed.) 1978, *Physics and Astrophysics of Neutron Stars and Black Holes* (Amsterdam: North Holland Publishing Company), 907
- Giuliani, A., Fuschino, F., Vianello, G., et al. 2010, *ApJL*, **708**, L84
- Golenetskii, S., Aptekar, R., Mazets, E., et al. 2009, *GCN*, **9344**, 1
- Goodman, J. 1986, *ApJL*, **308**, L47
- Guiriec, S., Connaughton, V., & Briggs, M. 2009, *GCN*, **9336**, 1
- Hansen, B. M. S., & Lyutikov, M. 2001, *MNRAS*, **322**, 695
- Heise, J. 2003, in *AIP Conf. Ser. 662, Gamma-Ray Burst and Afterglow Astronomy 2001: A Workshop Celebrating the First Year of the HETE Mission*, ed. G. R. Ricker & R. K. Vanderspek (Melville, NY: AIP), 229
- Hoversten, E. A., Barthelmy, S. D., Burrows, D. N., et al. 2009, *GCN*, **9331**, 1
- Izzo, L., Ruffini, R., Penacchioni, A. V., et al. 2012, *A&A*, **543**, A10
- Klebesadel, R. W. 1992, in *Gamma-Ray Bursts—Observations, Analyses and Theories*, ed. C. Ho, R. I. Epstein, & E. E. Fenimore (Cambridge: Cambridge Univ. Press)
- Kobayashi, S., Piran, T., & Sari, R. 1997, *ApJ*, **490**, 92
- Kopač, D., D'Avanzo, P., Melandri, A., et al. 2012, *MNRAS*, **424**, 2392
- Kouveliotou, C., Meegan, C. A., Fishman, G. J., et al. 1993, *ApJL*, **413**, L101
- Kumar, P., & Zhang, B. 2015, *PhR*, **561**, 1
- Landau, L. D., & Lifshitz, E. M. 2003, *The Classical Theory of Fields* (Oxford: Butterworth-Heinemann) IV rev. Engl. ed.
- Lazzati, D. 2005, *MNRAS*, **357**, 722
- Lee, W. H., Ramirez-Ruiz, E., & Page, D. 2004, *ApJL*, **608**, L5
- Lithwick, Y., & Sari, R. 2001, *ApJ*, **555**, 540
- Longo, F., Moretti, E., Barbiellini, G., et al. 2009, *GCN*, **9343**, 1
- Lü, H.-J., & Zhang, B. 2014, *ApJ*, **785**, 74
- Mazets, E. P., Golenetskii, S. V., Ilinskii, V. N., et al. 1981, *Ap&SS*, **80**, 3

- Meegan, C., Lichti, G., Bhat, P. N., et al. 2009, *ApJ*, **702**, 791
- Meszáros, P., & Rees, M. J. 1997, *ApJL*, **482**, L29
- Metzger, B. D., Giannios, D., Thompson, T. A., Bucciantini, N., & Quataert, E. 2011, *MNRAS*, **413**, 2031
- Mirabel, I. F., Chaty, S., Rodríguez, L. F., & Sauvage, M. M. 2015, in IAU Symp. 313, *Extragalactic Jets from Every Angle* (Paris: IAU), 370
- Muccino, M., Ruffini, R., Bianco, C. L., Izzo, L., & Penacchioni, A. V. 2013a, *ApJ*, **763**, 125
- Muccino, M., Ruffini, R., Bianco, C. L., et al. 2013b, *ApJ*, **772**, 62
- Nakar, E. 2007, *PhR*, **442**, 166
- Narayan, R., Paczynski, B., & Piran, T. 1992, *ApJL*, **395**, L83
- Narayan, R., Piran, T., & Shemi, A. 1991, *ApJL*, **379**, L17
- Nava, L., Vianello, G., Omodei, N., et al. 2014, *MNRAS*, **443**, 3578
- Ohmori, N., Noda, K., Sonoda, E., et al. 2009, GCN, **9355**, 1
- Ohno, M., & Pelassa, V. 2009, GCN, **9334**, 1
- Oliveira, F. G., Rueda, J. A., & Ruffini, R. 2014, *ApJ*, **787**, 150
- Olofsson, G., Ergon, M., Malesani, D., et al. 2009, GCN, **9338**, 1
- Omodei, N., Granot, J., Meszáros, P., et al. 2009, GCN, **9350**, 1
- Paczynski, B. 1986, *ApJL*, **308**, L43
- Patricelli, B., Bernardini, M. G., Bianco, C. L., et al. 2012, *ApJ*, **756**, 16
- Penacchioni, A. V., Ruffini, R., Izzo, L., et al. 2012, *A&A*, **538**, A58
- Perley, D. A., Cenko, S. B., Corsi, A., et al. 2014, *ApJ*, **781**, 37
- Piran, T. 2005, *RvMP*, **76**, 1143
- Pisani, G. B., Izzo, L., Ruffini, R., et al. 2013, *A&A*, **552**, L5
- Popham, R., Woosley, S. E., & Fryer, C. 1999, *ApJ*, **518**, 356
- Rau, A., McBreen, S., & Kruehler, T. 2009, GCN, **9353**, 1
- Rees, M. J., & Meszáros, P. 1992, *MNRAS*, **258**, 41
- Rhoades, C. E., & Ruffini, R. 1974, *PhRvL*, **32**, 324
- Rosswog, S., Ramirez-Ruiz, E., & Davies, M. B. 2003, *MNRAS*, **345**, 1077
- Rotondo, M., Rueda, J. A., Ruffini, R., & Xue, S.-S. 2011a, *PhLB*, **701**, 667
- Rotondo, M., Rueda, J. A., Ruffini, R., & Xue, S.-S. 2011b, *PhRvC*, **83**, 045805
- Rueda, J. A., & Ruffini, R. 2012, *ApJ*, **758**, L7
- Rueda, J. A., & Ruffini, R. 2013, *IJMPD*, **22**, 1360007
- Rueda, J. A., Ruffini, R., Wu, Y.-B., & Xue, S.-S. 2014, *PhRvC*, **89**, 035804
- Rueda, J. A., Ruffini, R., & Xue, S.-S. 2011, *NuPhA*, **872**, 286
- Ruffini, R. 2009, in *The Ergosphere and Dyadosphere of Black Holes*, ed. D. L. Wiltshire, M. Visser, & S. Scott (Cambridge: Cambridge Univ. Press), 161
- Ruffini, R. 2015, in *Thirteenth Marcel Grossmann Meeting: On Recent Developments in Theoretical and Experimental General Relativity, Astrophysics and Relativistic Field Theories*, Proc. of the MG13 Meeting on General Relativity, ed. K. Rosquist (Singapore: World Scientific Publishing), 242
- Ruffini, R., Bernardini, M. G., Bianco, C. L., et al. 2007, in *The Obscured Universe*, Proc. of the VI INTEGRAL Workshop, ESA SP-622, ed. S. Grebenev, R. Sunyaev, & C. Winkler (Noordwijk: ESA Publication Division), 561
- Ruffini, R., Bianco, C. L., Enderli, M., et al. 2015a, GCN, **18296**, 1
- Ruffini, R., Bianco, C. L., Frascchetti, F., Xue, S.-S., & Chardonnet, P. 2001a, *ApJL*, **555**, L107
- Ruffini, R., Bianco, C. L., Frascchetti, F., Xue, S.-S., & Chardonnet, P. 2001b, *ApJL*, **555**, L113
- Ruffini, R., Bianco, C. L., Frascchetti, F., Xue, S.-S., & Chardonnet, P. 2001c, *ApJL*, **555**, L117
- Ruffini, R., Muccino, M., Bianco, C. L., et al. 2014, *A&A*, **565**, L10
- Ruffini, R., Muccino, M., Kovacevic, M., et al. 2015b, *ApJ*, **808**, 190
- Ruffini, R., Rueda, J. A., Muccino, M., et al. 2016, arXiv:1602.02732
- Ruffini, R., Salmonson, J. D., Wilson, J. R., & Xue, S. 2000, *A&A*, **359**, 855
- Ruffini, R., Salmonson, J. D., Wilson, J. R., & Xue, S.-S. 1999, *A&A*, **350**, 334
- Ruffini, R., Wang, Y., Enderli, M., et al. 2015c, *ApJ*, **798**, 10
- Ruffini, R., & Wilson, J. 1973, *PhRvL*, **31**, 1362
- Ruffini, R., & Wilson, J. R. 1975, *PhRvD*, **12**, 2959
- Ruffini, R., & Wheeler, J. A. 1969, in *Significance of Space Research for Fundamental Physics*, Proc. of the ESRO Collaboration, ed. A. F. Moore & V. Hardy (Paris: European Space Research Organization), 45
- Ruiz, M., Lang, R. N., Paschalidis, V., & Shapiro, S. L. 2016, *ApJL*, **824**, L6
- Sahu, K. C., Livio, M., Petro, L., et al. 1997, *Natur*, **387**, 476
- Salmonson, J. D., & Wilson, J. R. 2002, *ApJ*, **578**, 310
- Smith, N. 2014, *ARA&A*, **52**, 487
- Smith, N., Li, W., Filippenko, A. V., & Chornock, R. 2011, *MNRAS*, **412**, 1522
- Soderberg, A. M., Berger, E., Kasliwal, M., et al. 2006a, *ApJ*, **650**, 261
- Soderberg, A. M., Kulkarni, S. R., Nakar, E., et al. 2006b, *Natur*, **442**, 1014
- Strong, I. B., Klebesadel, R. W., & Evans, W. D. 1975, in *Annals of the New York Academy of Sciences 262, Seventh Texas Symp. on Relativistic Astrophysics*, ed. P. G. Bergman, E. J. Fenyves, & L. Motz (New York: New York Academy of Sciences), 145
- Svensson, K. M., Levan, A. J., Tanvir, N. R., Fruchter, A. S., & Strolger, L.-G. 2010, *MNRAS*, **405**, 57
- Tavani, M. 1998, *ApJL*, **497**, L21
- Troja, E., King, A. R., O'Brien, P. T., Lyons, N., & Cusumano, G. 2008, *MNRAS*, **385**, L10
- Tsang, D., Read, J. S., Hinderer, T., Piro, A. L., & Bondarescu, R. 2012, *PhRvL*, **108**, 011102
- van Paradijs, J., Groot, P. J., Galama, T., et al. 1997, *Natur*, **386**, 686
- Woosley, S. E. 1993, *ApJ*, **405**, 273
- Woosley, S. E., & Bloom, J. S. 2006, *ARA&A*, **44**, 507
- Zalamea, I., & Beloborodov, A. M. 2011, *MNRAS*, **410**, 2302
- Zel'dovich, Y. B., Ivanova, L. N., & Nadezhin, D. K. 1972, *SvA*, **16**, 209
- Zhang, B., & Mészáros, P. 2001, *ApJL*, **552**, L35
- Zhang, C. M., Wang, J., Zhao, Y. H., et al. 2011, *A&A*, **527**, A83
- Zhang, F.-W., Shao, L., Yan, J.-Z., & Wei, D.-M. 2012, *ApJ*, **750**, 88
- Zou, Y.-C., Fan, Y.-Z., & Piran, T. 2011, *ApJL*, **726**, L2

GRB 140619B: A SHORT GRB FROM A BINARY NEUTRON STAR MERGER LEADING TO BLACK HOLE FORMATION

R. RUFFINI^{1,2,3,4}, M. MUCCINO^{1,2}, M. KOVACEVIC^{1,3}, F. G. OLIVEIRA^{1,3}, J. A. RUEDA^{1,2,4}, C. L. BIANCO^{1,2}, M. ENDERLI^{1,3}, A. V. PENACCHIONI^{4,5}, G. B. PISANI^{1,2}, Y. WANG^{1,2}, AND E. ZANINONI⁴¹ Dip. di Fisica and ICRA, Sapienza Università di Roma, Piazzale Aldo Moro 5, I-00185 Rome, Italy; ruffini@icra.it² ICRANet, Piazza della Repubblica 10, I-65122 Pescara, Italy³ Université de Nice Sophia Antipolis, CEDEX 2, Grand Château Parc Valrose, Nice, France⁴ ICRANet-Rio, Centro Brasileiro de Pesquisas Físicas, Rua Dr. Xavier Sigaud 150, Rio de Janeiro, RJ, 22290-180, Brazil⁵ Instituto Nacional de Pesquisas Espaciais, Av. dos Astronautas, 1758, São José dos Campos, SP, 12227-010, Brazil

Received 2014 November 30; accepted 2015 June 15; published 2015 August 4

ABSTRACT

We show the existence of two families of short gamma-ray bursts (GRBs), both originating from the merger of binary neutron stars (NSs): family-1 with $E_{\text{iso}} < 10^{52}$ erg, leading to a massive NS as the merged core, and family-2 with $E_{\text{iso}} > 10^{52}$ erg, leading to a black hole (BH). Following the identification of the prototype GRB 090227B, we present the details of a new example of family-2 short burst: GRB 140619B. From the spectral analysis of the early ~ 0.2 s, we infer an observed temperature $kT = (324 \pm 33)$ keV of the e^+e^- -plasma at transparency (P-GRB), a theoretically derived redshift $z = 2.67 \pm 0.37$, a total burst energy $E_{e^+e^-}^{\text{tot}} = (6.03 \pm 0.79) \times 10^{52}$ erg, a rest-frame peak energy $E_{p,i} = 4.7$ MeV, and a baryon load $B = (5.52 \pm 0.73) \times 10^{-5}$. We also estimate the corresponding emission of gravitational waves. Two additional examples of family-2 short bursts are identified: GRB 081024B and GRB 090510, remarkable for its well determined cosmological distance. We show that marked differences exist in the nature of the afterglows of these two families of short bursts: family-2 bursts, leading to BH formation, consistently exhibit high energy emission following the proper-GRB emission; family-1 bursts, leading to the formation of a massive NS, should never exhibit high energy emission. We also show that both the families fulfill an $E_{p,i}$ - E_{iso} relation with slope $\gamma = 0.59 \pm 0.07$ and a normalization constant incompatible with the one for long GRBs. The observed rate of such family-2 events is $\rho_0 = (2.1_{-1.4}^{+2.8}) \times 10^{-4} \text{ Gpc}^{-3} \text{ yr}^{-1}$.

Key words: gamma-ray burst: general

1. INTRODUCTION

The phenomenological classification of gamma-ray bursts (GRBs) based on their prompt emission observed T_{90} durations defines “long” and “short” bursts which are, respectively, longer or shorter than $T_{90} = 2$ s (Dezalay et al. 1992; Klebesadel 1992, pp. 161–168; Kouveliotou et al. 1993; Tavani 1998). Short GRBs have been often indicated as originating from binary neutron star (NS) mergers (see, e.g., Goodman 1986; Paczynski 1986; Eichler et al. 1989; Narayan et al. 1991; Meszaros & Rees 1997; Rosswog et al. 2003; Lee et al. 2004; Berger 2014).

An ample literature exists of short GRBs with a measured redshift, isotropic burst energy $E_{\text{iso}} < 10^{52}$ erg and rest-frame spectral peak energy $E_{p,i} < 2$ MeV (see, e.g., Berger 2014 and references therein). Thanks to extensive data provided by the *Swift*-XRT instrument (Burrows et al. 2005), it is possible to observe the long lasting X-ray afterglow of these short bursts to identify their host galaxies and to compute their cosmological redshifts. They have been observed in both early- and late-type galaxies with older stellar population ages (see, e.g., Berger 2014 for details), and at systematically larger radial offsets from their host galaxies than long GRBs (Sahu et al. 1997; van Paradijs et al. 1997; Bloom et al. 2006; Troja et al. 2008; Fong et al. 2010; Berger 2011; Kopač et al. 2012). None of these afterglows appears to have the specific power law signature in the X-ray luminosity when computed in the source rest-frame, as found in some long GRBs (see, e.g., Ruffini et al. 2014).

In the meantime, considerable progress has been obtained in the theoretical understanding of the equilibrium configuration of NSs, in their mass–radius relation (see Figure 2 in Section 2), and especially in the theoretical determination of the value of the NS critical mass for gravitational collapse $M_{\text{crit}}^{\text{NS}}$ (Rotondo et al. 2011; Rueda et al. 2011; Belvedere et al. 2012). This has led to a theoretical value $M_{\text{crit}}^{\text{NS}} = 2.67 M_{\odot}$ (Belvedere et al. 2012). Particularly relevant to this determination has been the conceptual change of paradigm of imposing global charge neutrality (Belvedere et al. 2012) instead of the traditional local charge neutrality (LCN) still applied in the current literature (see, e.g., Haensel et al. 2007 and references therein).

Similarly, noteworthy progress has been achieved in the determination of the masses of galactic binary pulsars. Of the greatest relevance has been the direct observation of NS masses larger than $2 M_{\odot}$ (see Antoniadis et al. 2013 and Section 2). In the majority of the observed cases of binary NSs the sum of the NS masses, $M_1 + M_2$, is indeed smaller than $M_{\text{crit}}^{\text{NS}}$ and, given the above determination of the NS critical mass, their coalescence will never lead to a black hole (BH) formation (see Figure 3 in Section 2). This of course offers a clear challenge to the traditional assumption that all short GRBs originate from BH formation (see, e.g., Berger 2014 and references therein).

Motivated by the above considerations, we propose in this article the existence of two families of short GRBs, both originating from NS mergers: the difference between these two families depends on whether the total mass of the merged core

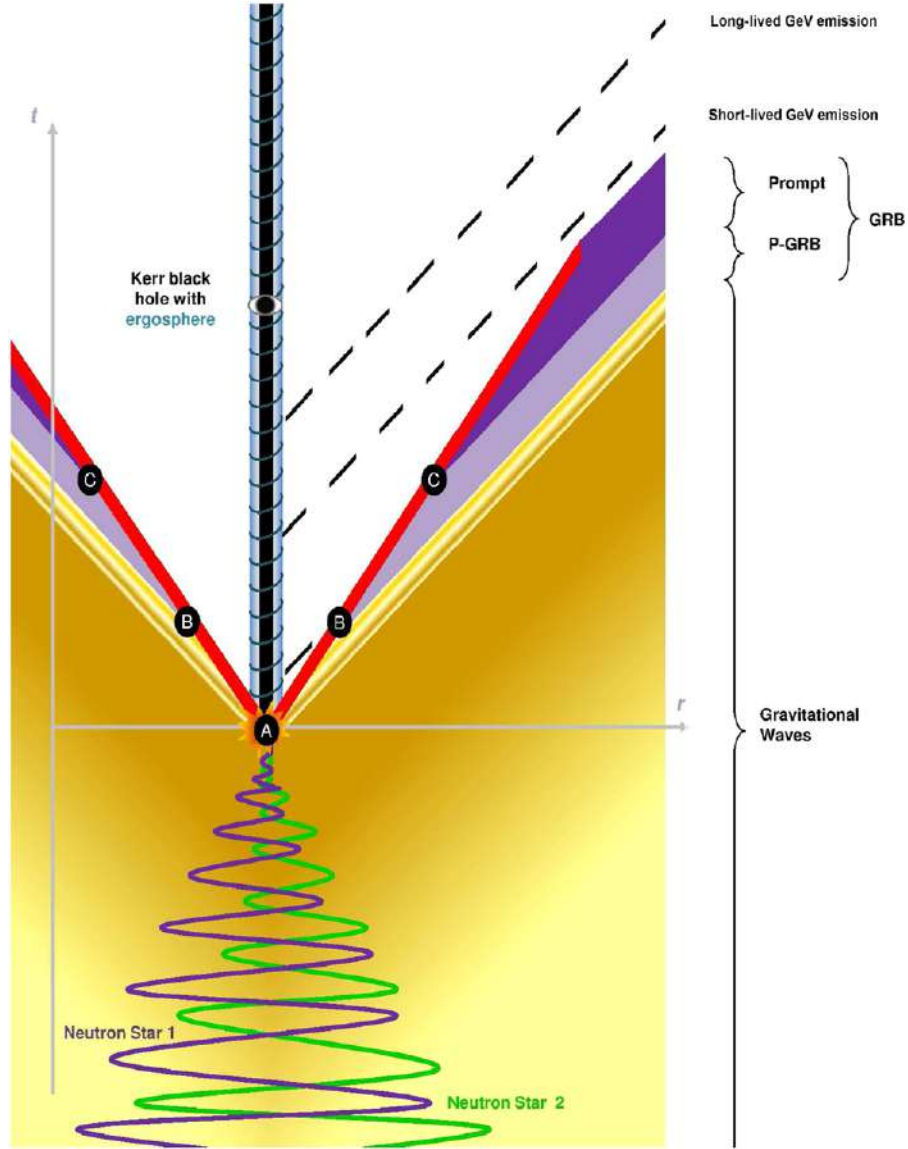


Figure 1. Space–time diagram of family-2 short GRBs. The orbital separation between the two NSs decreases due to the emission of GWs, until the merging occurs and a family-2 short GRB is emitted. Following the fireshell model (see Section 3): (A) vacuum polarization occurs while the event horizon is formed and a fireshell of e^+e^- plasma self-accelerates radially outwards; (B) the fireshell, after engulfing the baryons, keeps self-accelerating and reaches the transparency when the P-GRB is emitted; (C) the accelerated baryons interact with the local CBM giving rise to the prompt emission. The remnant of the merger is a Kerr BH. The accretion of a small (large) amount of orbiting matter onto the BH can lead to the short lived but very energetic 0.1–100 GeV emission observed in GRB 081024B, GRB 090510, and GRB 140619B. The absence of such an emission in GRB 090227B is due to the absence of observations of *Fermi*-LAT.

is smaller or larger than $M_{\text{crit}}^{\text{NS}}$. We assume that family-1 coincides with the above mentioned less energetic short GRBs with $E_{\text{iso}} < 10^{52}$ erg and the coalescence of the merging NSs leads to a massive NS as the merged core. We assume that family-2 short bursts with $E_{\text{iso}} > 10^{52}$ erg originate from a merger process leading to a BH as the merged core. The presence of the BH allows us to address the GRB nature within the fireshell model (Ruffini et al. 2001a, 2001b, 2001c) leading to specific signatures in the luminosity, spectra and time variability observed in two very different components: the proper-GRB (P-GRB) and the prompt emission (see Section 3). The prototype is GRB 090227B, which we already analyzed within the fireshell model in Muccino et al. (2013). We also assume that the BH gives rise to the short-lived ($\lesssim 10^2$ s in the observer frame) and very energetic GeV emission which has been found to be present in all these family-2 short GRBs,

when *Fermi*-LAT data are available. This article is mainly dedicated to giving the theoretical predictions and the observational diagnostics to support the above picture.

In Section 4 we recall the results obtained in the case of the prototype of family-2 short GRBs: GRB 090227B (Muccino et al. 2013). The analysis of its P-GRB emission led to a particularly low value of the baryon load, $B \sim 10^{-5}$, as well as to the prediction of the distance corresponding to a redshift $z = 1.61$, and consequently to $E_{e^+e^-}^{\text{tot}} = 2.83 \times 10^{53}$ erg. From the analysis of the spectrum and the light curve of the prompt emission we inferred an average circumburst medium (CBM) density $\langle n_{\text{CBM}} \rangle \sim 10^{-5} \text{ cm}^{-3}$ typical of galactic halos of GRB host galaxies.

In Section 5 we summarize the observations of a second example of such family-2 short bursts, GRB 140619B, and our data analysis from 8 keV up to 100 GeV. We also point out the

lack of any observed X-ray afterglow following the prompt emission (Maselli & D’Avanzo 2014).

In Section 6 we address GRB 140619B within the fireshell model and compare and contrast the results with those of the prototype, GRB 090227B (Muccino et al. 2013). In Section 6.1, from the fireshell equations of motion, we theoretically estimate and predict the value of the redshift of the source, $z = 2.67 \pm 0.37$. Consequently, we derive the burst energy $E_{\text{iso}} > 10^{52}$ erg and the value of the baryon load $B \sim 10^{-5}$. In Section 6.2 we infer an average density of the CBM $\langle n_{\text{CBM}} \rangle \sim 10^{-5} \text{ cm}^{-3}$ from fitting the prompt emission light curve and spectra. This parameter is typical of the galactic halo environment and further confirms a NS–NS merger as the progenitor for GRB 140619B (see Section 6.3 and Figure 1).

In Section 7 we discuss the possibility for Advanced LIGO to detect the emission of gravitational waves (GWs) from such a binary NS progenitor. From the dynamics of the above system, the total energy emitted in GW radiation corresponds to $E_{\text{GW}}^T = 7.42 \times 10^{52}$ erg, computed during the entire inspiral phase all the way up to the merger. This gives a signal below the sensitivity of the Advanced LIGO interferometer.

In Section 8 we focus on the short-lived ($\Delta t \approx 4$ s) but significant 0.1–100 GeV emission (see Figure 1). We first address the issue of whether this is a peculiarity of GRB 140619B, or whether the GeV emission can be considered to be a common feature of all these family-2 short GRBs. We first return to GRB 090227B to see how to explain the absence of observations of the GeV emission from this source, and we find a simple reason: GRB 090227B was outside the nominal LAT field of view (FOV, see Ackermann et al. 2013, and Section 4). We then turn our attention to another source, GRB 090510, which presents many of the common features of the family-2 short GRBs. Especially noteworthy is the presence of a high energy GeV emission lasting $\sim 10^2$ s, much longer than the one of GRB 140619B. The presence of an X-ray afterglow in GRB 090510 is fortunate and particularly important, though lacking a scaling law behavior (Ruffini et al. 2014), since it has allowed the optical identification of the source and the determination of its distance and its cosmological redshift $z = 0.903$. The corresponding isotropic energy and intrinsic peak spectral energy are, respectively, $E_{\text{iso}} > 10^{52}$ erg and $E_{p,i} = (7.89 \pm 0.76)$ MeV, typical again of family-2 short bursts. We then compare and contrast this high energy emission and their corresponding X-ray emissions in the family-2 short GRB 140619B and GRB 090510 with the afterglow of the family-1 short GRBs (see Figure 13 and Berger 2014).

In Section 9 we give an estimate for the rate of the family-2 short GRBs.

In Section 10 we discuss the existence of the new $E_{p,i}$ – E_{iso} relation for all short GRBs introduced by Zhang et al. (2012) and Calderone et al. (2015), with a power-law similar to the one of the Amati relation (Amati et al. 2008) for long GRBs, but with a different amplitude. Finally we draw our conclusions.

2. MOTIVATION FROM GALACTIC BINARY NS AND NS THEORY

Recent theoretical progress has been achieved in the understanding of the NS equation of state and equilibrium configuration and of the value of its critical mass $M_{\text{crit}}^{\text{NS}}$. In Rotondo et al. (2011) it has been shown to be impossible to

impose the LCN condition on a self-gravitating system of degenerate neutrons, protons, and electrons in β -equilibrium within the framework of relativistic quantum statistics and the Einstein–Maxwell equations. The equations of equilibrium of NSs, taking into account strong, weak, electromagnetic, and gravitational interactions in general relativity and the equilibrium conditions based on the Einstein–Maxwell–Thomas–Fermi equations along with the constancy of the general relativistic Fermi energies of particles, the “Klein potentials,” throughout the configuration have been presented in Rueda et al. (2011) and Belvedere et al. (2012), where a theoretical estimate of $M_{\text{crit}}^{\text{NS}} \approx 2.67 M_{\odot}$ has been obtained. The implementations of the above results by considering the equilibrium configurations of slowly rotating NSs by using the Hartle formalism has been presented in Belvedere et al. (2014a). Then in Rueda et al. (2014) a detailed study was made of the transition layer between the core and crust of NSs at the nuclear saturation density, and its surface tension and Coulomb energy have been calculated. A comprehensive summary of these results for both static and uniformly rotating NSs is discussed in Belvedere et al. (2014b). The absolute upper limit on the angular momentum of a rotating NS fulfilling the above microscopical conditions has been obtained in Cipolletta et al. (2015).

A vast number of tests have been performed in fitting the data of pulsars (Deneva et al. 2012; Lattimer 2012; Antoniadis et al. 2013; Kramer 2014). In particular, the high value of the recently measured mass of PSR J0348+0432, $M = (2.01 \pm 0.04) M_{\odot}$ (Antoniadis et al. 2013), favors stiff nuclear equations of state, like the one adopted in Belvedere et al. (2012) based on relativistic nuclear mean field theory à la Boguta & Bodmer (1977), which leads to the above theoretical estimate of $M_{\text{crit}}^{\text{NS}}$ (see also Figure 2). This value is supported by the above observational constraints, and in any case, is well below the absolute upper limit of $3.2 M_{\odot}$ for a non-rotating NS (Rhoades & Ruffini 1974).

If we turn to the binary NSs within our Galaxy (see Figure 3) we notice that only in a subset of them is the total mass of the components larger than $M_{\text{crit}}^{\text{NS}}$ and can lead to a BH in their merging process.⁶

Given this general understanding, we have identified the characteristic properties of family-2 short bursts, whose prototype was identified in GRB 090227B (Muccino et al. 2013). Equally important has been the identification of the observed characteristic features of family-1 short GRBs which will be discussed in the following sections.

⁶ During the refereeing process, an approach by Fryer et al. (2015) based on a combination of binary NS merger nuclear physics models and population synthesis appeared. They infer that for a maximum nonrotating NS mass of $M_{\text{crit}}^{\text{NS}}$ above 2.3–2.4 M_{\odot} , less than 4% of the NS mergers produces short GRBs by gravitational collapse to a BH. Here we go one step further by indicating the theoretical predictions characterizing short GRBs originating from the massive NS formation (family-1) and the ones originating from BH formation (family-2). We indicate: (a) the specific spectral features, (b) the presence of the GeV emission originating from the BH, and (c) the fulfillment of the $E_{p,i}$ – E_{iso} relation (see Zhang et al. 2012; Calderone et al. 2015, and Section 10). The paper by Fryer et al. (2015) was followed by Lawrence et al. (2015) where the authors examine the value of $M_{\text{crit}}^{\text{NS}}$ for a family of equations of state and concluded that a reasonable fraction of double NS mergers may produce neither short GRBs nor BHs. Here we again go one step further by indicating that in the case of a merged core with a mass smaller than $M_{\text{crit}}^{\text{NS}}$ leading to a massive NS, a less energetic short GRB with a softer emission tail indeed occurs (family-1 short bursts). We show also that these short GRBs fulfill the above $E_{p,i}$ – E_{iso} relation (see Section 10).

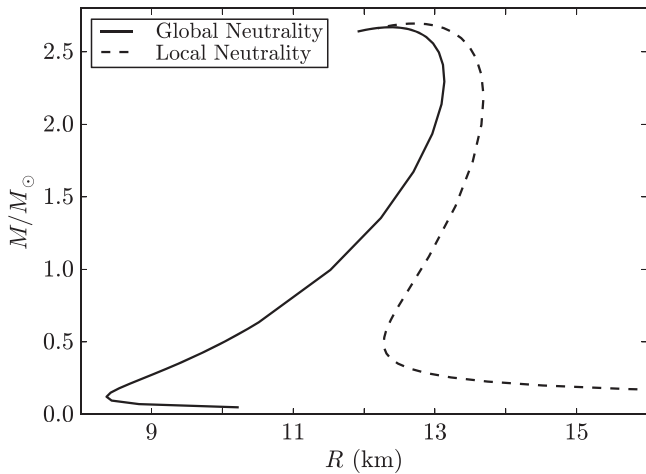


Figure 2. Mass–radius relation obtained with the local and the new global neutrality equilibrium configurations, by applying the NL3 nuclear model. Figure reproduced from Belvedere et al. (2012).

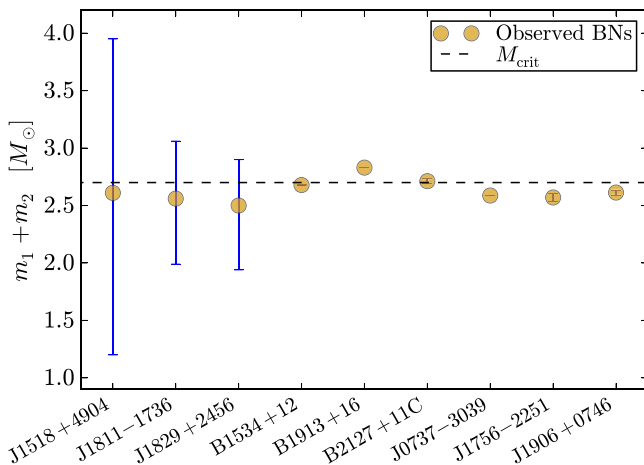


Figure 3. Plot of the binary NSs with known total masses ($M_1 + M_2$, in solar masses) and the corresponding uncertainties. The horizontal dashed line marks the critical NS mass of $2.67 M_\odot$ (Belvedere et al. 2012). Systems beyond this value lead to BH formation. Masses taken from Zhang et al. (2011) and Antoniadis (2014).

The crucial role of $M_{\text{crit}}^{\text{NS}}$ has been also shown in the corresponding analysis of long GRBs in distinguishing between the two different families (Ruffini et al. 2015) in the induced gravitational collapse paradigm (Izzo et al. 2012a; Rueda & Ruffini 2012; Fryer et al. 2014).

3. THE FIRESHELL MODEL

It is well known that the majority of the astrophysical community working on GRBs envisages the spectral and temporal analysis of both short and long GRBs considering their whole emission as a single event (see, e.g., Ackermann et al. 2013). This picture follows the conceptual framework of the “fireball model” (see, e.g., Sari et al. 1998; Piran 2005; Meszaros 2006, and reference therein).

The “fireshell model” (Ruffini et al. 2001a, 2001b, 2001c) has instead addressed a specific time-resolved spectral analysis leading to distinct signatures and to the identification of different astrophysical regimes within the same GRB (see, e.g., Izzo et al. 2010; Izzo et al. 2012b; Muccino et al. 2013; Ruffini et al. 2013 and references therein). This has led to introduction

of the concept of binary mergers of NS–NS and of FeCO–NS together with a set of new paradigms in order to describe the complexity of GRB phenomena within a “Cosmic-Matrix” approach (Ruffini 2015a).

In the fireshell model (Ruffini et al. 2001a, 2001b, 2001c) GRBs originate from an optically thick e^+e^- plasma (Damour & Ruffini 1975; Ruffini & Xue 2008; Ruffini et al. 2010) during the gravitational collapse to a BH. Such an e^+e^- plasma is confined to an expanding shell and reaches thermal equilibrium almost instantaneously (Aksenov et al. 2007). The annihilation of these pairs occurs gradually, while the expanding shell, called the *fireshell*, self-accelerates up to ultra relativistic velocities (Ruffini et al. 1999) and engulfs the baryonic matter (of mass M_B) left over in the process of collapse. The baryon load thermalizes with the pairs due to the large optical depth (Ruffini et al. 2000).

Assuming spherical symmetry of the system, the dynamics in the optically thick phase is fully described by only two free initial parameters: the total energy of the plasma $E_{e^+e^-}^{\text{tot}}$ and the baryon load B (Ruffini et al. 2000). Only solutions with $B \leq 10^{-2}$ are characterized by regular relativistic expansion; for $B \geq 10^{-2}$ turbulence and instabilities occur (Ruffini et al. 2000). The fireshell continues to self-accelerate until it reaches the transparency condition and a first flash of thermal radiation, the P-GRB, is emitted (Ruffini et al. 2001b). The radius r_{tr} at which the transparency occurs, the theoretical temperature (blueshifted toward the observer kT_{blue}), the Lorentz factor Γ_{tr} , as well as the amount of the energy emitted in the P-GRB are functions of $E_{e^+e^-}^{\text{tot}}$ and B (see, e.g., Ruffini et al. 2001b; Ruffini et al. 2009, and Figure 4).

After transparency, the residual expanding plasma of leptons and baryons collides with the CBM giving rise to multi-wavelength emission: the prompt emission. Assuming the fully radiative condition, the structures observed in the prompt emission of a GRB are described by two quantities associated with the environment: the CBM density profile n_{CBM} , which determines the temporal behavior of the light curve, and the fireshell surface filling factor $\mathcal{R} = A_{\text{eff}}/A_{\text{vis}}$, in which A_{eff} is the effective emitting area of the fireshell, and A_{vis} is its total visible area (Ruffini et al. 2002, 2005). This second parameter takes into account the inhomogeneities in the CBM and its filamentary structure (Ruffini et al. 2004).

The emission process of the collision between the baryons and the CBM is described in the comoving frame of the shell as a modified blackbody (BB) spectrum. This spectrum is obtained by the introduction of an additional phenomenological parameter α which characterizes the departure of the slope of the low energy part of the comoving spectrum from the purely thermal one (see Patricelli et al. 2012, for details). The nonthermal spectral shape of the observed GRB is then produced by the convolution of a very large number of modified thermal spectra with different temperatures and different Lorentz and Doppler factors. This convolution is performed over the surfaces of constant arrival time for photons at the detector (EQuiTemporal Surfaces, EQTS, Bianco & Ruffini 2005a, 2005b), encompassing the total observation time. The observed hard-to-soft spectral variation comes out naturally from the decrease with time of the comoving temperature and of the bulk Lorentz Γ factor. This effect is amplified by the curvature effect due to the EQTS which produces the observed time lag in the majority of the GRBs.

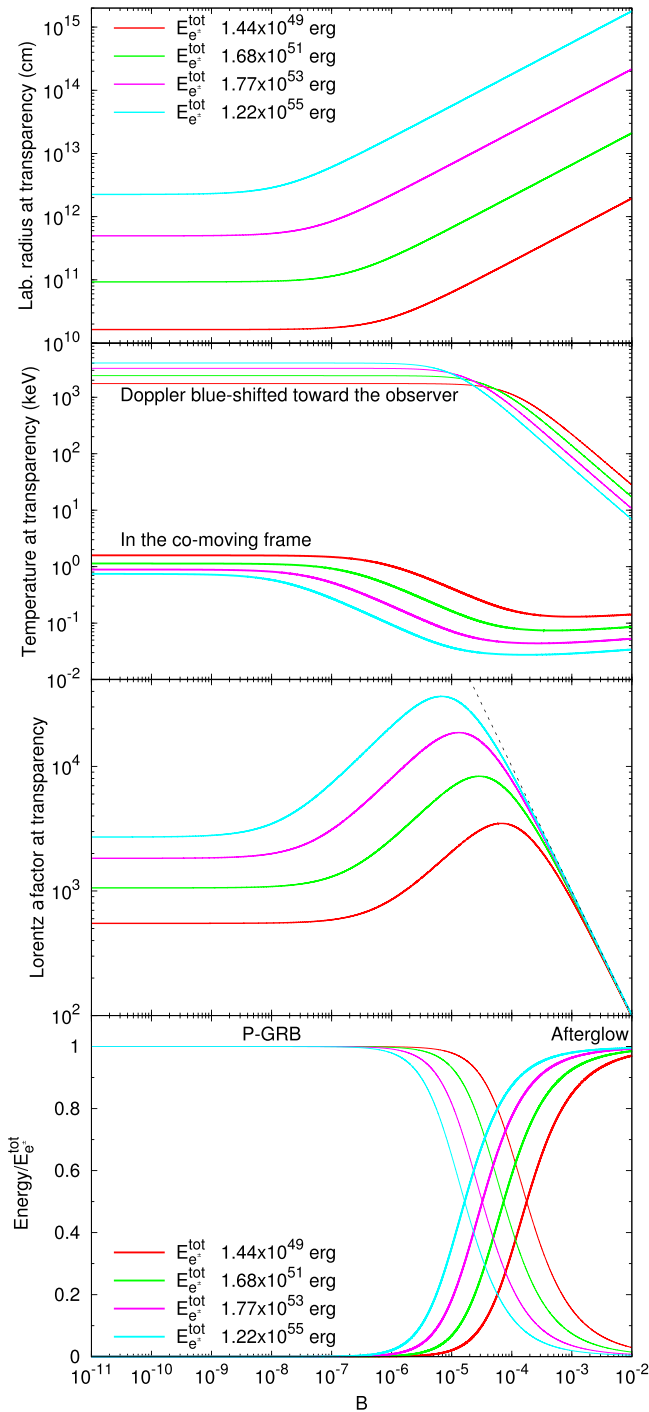


Figure 4. Main quantities of the fireshell model at transparency for selected values of $E_{e^+e^-}^{\text{tot}}$: the radius in the laboratory frame, the temperatures of the plasma in the co-moving frame and blueshifted toward the observer, the Lorentz Γ factor, and the fraction of energy radiated in the P-GRB and in the prompt emission as functions of B .

The canonical GRB light curve within the fireshell model is then characterized by a first (mainly thermal) emission due to the transparency of the e^+e^- -photon-baryon plasma, the P-GRB. A multi-wavelength emission, the prompt emission, follows due to the collisions between the accelerated baryons and the CBM.

The fireshell model has originally described the process of vacuum polarization due to the overcritical electromagnetic

field occurring at the moment of BH formation (Damour & Ruffini 1975). The formalism has been developed by considering a large number of relativistic quantum effects in the electrodynamics proposed for the NS crust (Belvedere et al. 2012, 2014a; Rueda et al. 2014), as well as on quantum-electrodynamics processes ongoing in the gravitational collapse (Han et al. 2012; Ruffini & Xue 2013). This has led to the results summarized in Figure 4.

The first description of the e^+e^- plasma within the fireshell model was performed under the simplified assumption of spherical symmetry (the dyadosphere; see, e.g., Preparata et al. 1998). The corresponding structure in the axially symmetric Kerr-Newman geometry has been considered (the dyadotorus; see, e.g., Cherubini et al. 2009; Ruffini 2009) and could possibly be tested.

The general formalism of the fireshell model can also be applied to any optically thick e^+e^- plasma in the presence of a baryon load, like the one created during the merging of binary NSs from $\nu\bar{\nu} \rightarrow e^+e^-$ (see, e.g., Salmonson & Wilson 2002 and references therein).

The P-GRB addresses the fully relativistic fundamental physics aspects of the model, in particular the acceleration process of the e^+e^- -baryon plasma, the collapsing NS quantum-electrodynamics, and the BH physics. The prompt emission addresses the conceptually simpler problem of the interaction of the accelerated baryons with the CBM, which does not allow nor require, by its own nature, a detailed description.

4. SUMMARY OF THE RESULTS FOR GRB 090227B: THE PROTOTYPE OF THE FAMILY-2 SHORT GRBS

GRB 090227B is a bright short burst with an overall emission lasting ~ 0.9 s and total fluence of 3.79×10^{-5} erg cm $^{-2}$ in the energy range 8 keV–40 MeV. This burst was significantly detected only in the LAT Low Energy (LLE) data since it was outside the nominal LAT FOV (Ackermann et al. 2013). However, only one transient-class event with energy above 100 MeV has been associated with the GRB (Ackermann et al. 2013).

The time-resolved spectral analysis on the time scale as short as 16 ms, made possible by the *Fermi*-GBM (Meegan et al. 2009), has allowed the identification of the P-GRB in the early 96 ms of emission. The corresponding thermal component has a temperature $kT = (517 \pm 28)$ keV (see the upper plots of Figure 9 in Muccino et al. 2013). The subsequent emission, fit by a Band function (see lower plots of Figure 9 in Muccino et al. 2013), has been identified with the prompt emission.

Due to the absence of an optical identification, a direct measurement of the cosmological redshift was not possible. From the temperature and flux of the P-GRB thermal component it was possible to derive (see Figure 4) a theoretical cosmological redshift $z = 1.61 \pm 0.14$, as well as the baryon load $B = (4.13 \pm 0.05) \times 10^{-5}$, the total plasma energy $E_{e^+e^-}^{\text{tot}} = (2.83 \pm 0.15) \times 10^{53}$ erg, and the extremely high Lorentz Γ factor at transparency $\Gamma_{\text{tr}} = (1.44 \pm 0.01) \times 10^4$ (see Section 4.1 in Muccino et al. 2013). Consequently, an average CBM number density $\langle n_{\text{CBM}} \rangle = (1.90 \pm 0.20) \times 10^{-5}$ cm $^{-3}$ has been determined which is typical of galactic halos where NS–NS mergers migrate, owing to natal kicks imparted to the binaries at birth (see, e.g., Narayan et al. 1992; Bloom et al. 1999; Fryer et al. 1999; Belczynski et al. 2006; Berger 2014).

In Muccino et al. (2013) it was concluded that the progenitor of GRB 090227B is a binary NS. For simplicity and as a lower limit, the masses of the two NS have been assumed to be the same, e.g., $M_1 = M_2 = 1.34 M_\odot$, so that the total merged core mass is $> M_{\text{crit}}^{\text{NS}}$ and therefore a BH is formed. This conclusion was drawn in view of the large total energy, $E_{\text{e}^+ \text{e}^-}^{\text{tot}} = 2.83 \times 10^{53}$ erg. Correspondingly, the energy emitted via GWs, $\sim 9.7 \times 10^{52}$ erg, has been estimated in Oliveira et al. (2014).

5. OBSERVATIONS AND DATA ANALYSIS OF GRB 140619B

At 11:24:40.52 UT on 2014 June 19, the *Fermi*-GBM detector (Connaughton et al. 2014) triggered and located the short and hard burst GRB 140619B (trigger 424869883/140619475). The on-ground calculated location, using the GBM trigger data, was R.A.(J2000) = 08^h54^m and decl. (J2000) = $-3^\circ 42'$, with an uncertainty of 5° (statistical only). The location of this burst was 32° from the LAT boresight at the time of the trigger, and the data from the *Fermi*-LAT showed a significant increase in the event rate (Kocevski et al. 2014). The burst was also detected by *Suzaku*-WAM (Iwakiri et al. 2014), showing a single pulse with a duration of ~ 0.7 s (50 keV–5 MeV). The analysis from 48.7 to 71.6 ks after the GBM trigger by the *Swift*-XRT instrument in the FOV of the *Fermi*-GBM and LAT, was completely in Photon Counting mode (Maselli & D’Avanzo 2014). No bright X-ray afterglow was detected within the LAT error circle. This set an upper limit on the energy flux in the observed 0.3–10 keV energy band of $\approx 9.24 \times 10^{-14}$ erg/(cm² s), assuming a photon index $\gamma = 2.2$. Therefore, no optical follow-up was possible and thus the redshift of the source is unknown.

We have analyzed the *Fermi*-GBM and LAT data in the energy range 8 keV–40 MeV and 20 MeV–100 GeV, respectively. We have downloaded the GBM TTE (Time-Tagged Events) files,⁷ suitable for short or highly structured events, and analyzed them by using the RMFIT package.⁸ The LLE data⁹, between 20–100 MeV, and the high energy data¹⁰, between 100 MeV–100 GeV, were analyzed by using the Fermi-science tools.¹¹ In Figure 5 we have reproduced the 64 ms binned GBM light curves corresponding to detectors NaI-n6 (8–260 keV, top panel) and BGO-b1 (260 keV–20 MeV, second panel), the 64 ms binned LLE light curve (20–100 MeV, third panel) and the 192 ms binned high-energy channel light curve (0.1–100 GeV, bottom panel). All the light curves are background subtracted. The NaI-n6 light curve shows a very weak signal, almost at the background level, while the BGO-b1 signal is represented by a short hard pulse, possibly composed by two sub-structures, with a total duration of $T_{90} \approx 0.7$ s. The vertical dashed line in Figure 5 represents the on-set of both LAT light curves, i.e., ~ 0.2 s after the GBM trigger. In principle, this allows us to determine the time interval within which the P-GRB emission takes place.

We have subsequently performed the time-integrated and time-resolved spectral analyses focused on the GBM data in the energy range 8 keV–40 MeV.

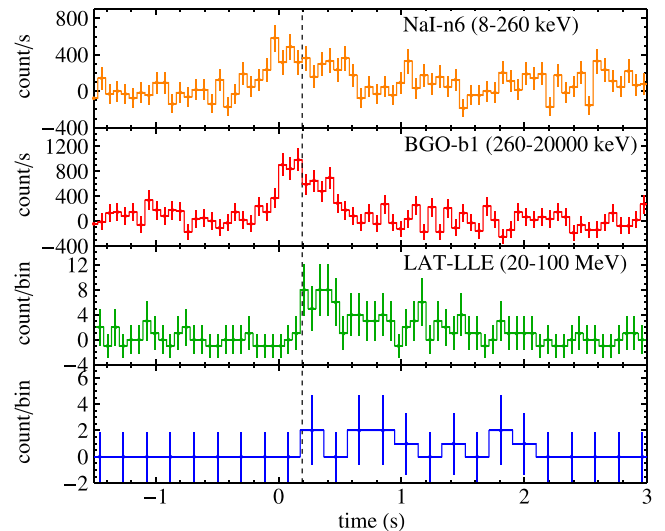


Figure 5. Background subtracted light curves of GRB 140619B from various detectors in various energy bands. From the top to the bottom panel: the 64 ms binned light curves from the NaI-n6 (8–260 keV, top panel) and BGO-b1 (260 keV–20 MeV, second panel) detectors, the 64 ms binned LLE light curve (20–100 MeV, third panel), and the 192 ms binned high-energy channel light curve (100 MeV–100 GeV, bottom panel).

5.1. Time-integrated Spectral Analysis

We have performed a time-integrated spectral analysis in the time interval from $T_0 - 0.064$ s to $T_0 + 0.640$ s, which corresponds to the T_{90} duration of the burst. We have indicated the trigger time by T_0 and have considered the following spectral models: Comptonization (Compt) and a Band function (Band et al. 1993). The corresponding plots are shown in Figure 6 and the results of the fits are listed in Table 1. From a statistical point of view, the Compt model provides the best fit to the data. In fact the Band function, which has an additional parameter with respect to the Compt model, improves the fit by only $\Delta\text{C-STAT} = 2.53$, where $\Delta\text{C-STAT}$ is the difference between the two C-STAT values of the Compt and Band models. If we consider $\Delta\text{C-STAT}$ as a χ^2 variable for the change in the number of the model parameters Δn (in this case $\Delta n = 1$), and assuming that the Compt model is nested within the Band model,¹² we conclude that the Band model improves the fit only at the 89% significance level, and anyway less than 2σ . Therefore it is not enough to reject the Compt model. The most interesting feature of the Compt model consists of its low-energy index, which is consistent with $\alpha \sim 0$. We proceed now to a time-resolved analysis to investigate the possibility that in the early phases of the prompt emission the spectrum is consistent with a BB spectrum, i.e., $\alpha \approx 1$, which corresponds to the signature of P-GRB emission.

5.2. Time-resolved Spectral Analysis

We performed the time-resolved spectral analysis by selecting time intervals with fluences larger than $\approx 10^{-6}$ erg cm⁻² in order to collect enough photons. Consequently, we have selected two time intervals that correspond to the main spike and the less intense structure (see the BGO-b1 light curve in Figure 6). The first time interval, from T_0 to

⁷ <ftp://legacy.gsfc.nasa.gov/fermi/data/gbm/bursts>

⁸ http://Fermi.gsfc.nasa.gov/ssc/data/analysis/rmfit/vc_rmfit_tutorial.pdf

⁹ http://fermi.gsfc.nasa.gov/ssc/observations/types/grbs/lat_grbs/

¹⁰ <http://fermi.gsfc.nasa.gov/cgi-bin/ssc/LAT/LATDataQuery.cgi>

¹¹ <http://fermi.gsfc.nasa.gov/ssc/data/analysis/documentation/Cicerone/>

¹² The Compt model can be considered a particular case of the Band model with $\beta \rightarrow -\infty$.

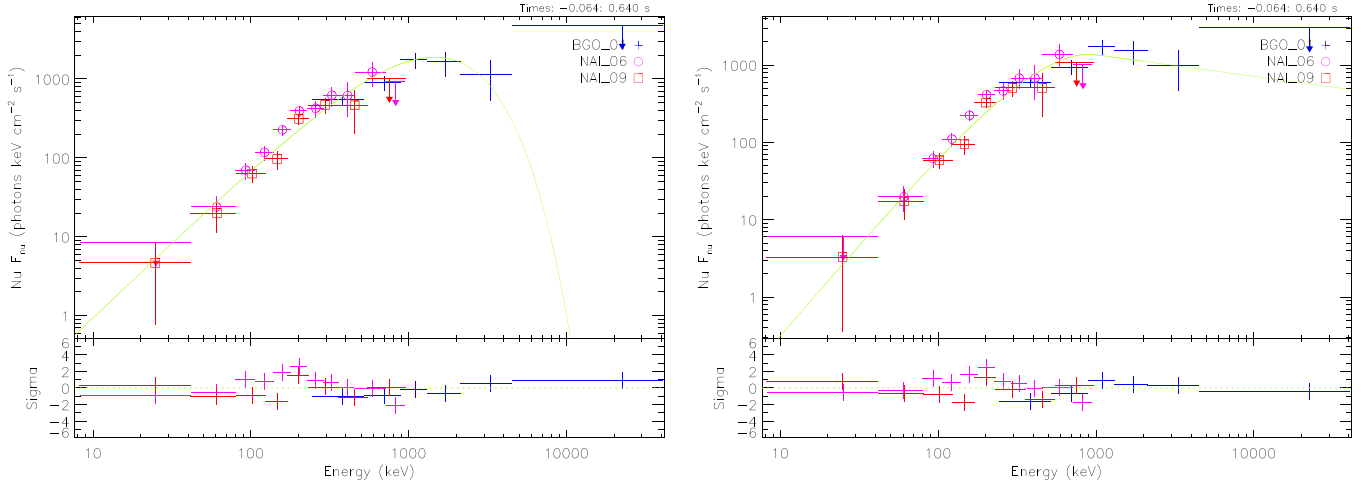


Figure 6. Combined NaI-n6, n9+BGO-b1 νF_ν spectra of GRB 140619B in the T_{90} time interval. The fit using the Compt spectral model is shown on the left, while the Band model fit is on the right.

Table 1
Summary of the Time-integrated (T_{90}) and Time-resolved (ΔT_1 and ΔT_2) Spectral Analyses

ΔT	Model	K (ph keV $^{-1}$ cm $^{-2}$ s $^{-1}$)	kT (keV)	E_p (keV)	α	β	F_{tot} (erg cm $^{-2}$ s $^{-1}$)	C-STAT/DOF
T_{90}	Compt	$(7.7 \pm 1.1) \times 10^{-3}$...	1456 ± 216	-0.09 ± 0.18	...	$(5.75 \pm 0.75) \times 10^{-6}$	365.09/346
	Band	$(7.8 \pm 1.3) \times 10^{-3}$...	908 ± 199	-0.38 ± 0.37	-2.28 ± 0.31	$(7.4 \pm 1.8) \times 10^{-6}$	362.56/345
ΔT_1	Compt	$(6.3 \pm 2.0) \times 10^{-3}$...	1601 ± 287	0.26 ± 0.32	...	$(9.4 \pm 1.6) \times 10^{-6}$	318.92/346
	BB	$(7.5 \pm 2.2) \times 10^{-8}$	324 ± 33	$(8.5 \pm 1.2) \times 10^{-6}$	323.86/347
ΔT_2	Compt	$(7.2 \pm 1.4) \times 10^{-3}$...	1283 ± 297	-0.11 ± 0.26	...	$(4.38 \pm 0.89) \times 10^{-6}$	391.65/346
	BB	$(3.8 \pm 1.1) \times 10^{-7}$	156 ± 15	$(2.33 \pm 0.28) \times 10^{-6}$	392.23/347

Note. In each column are listed, respectively, the time interval ΔT , the adopted spectral model, the normalization constant K of the fitting function, the BB temperature kT , the peak energy E_p , the low-energy α and high-energy β photon indexes, the total energy flux F_{tot} in the range 8 keV–40 MeV, and the value of the C-STAT over the number of degrees of freedom (dof).

$T_0 + 0.192$ s, is hereafter referred to as ΔT_1 , while the subsequent emission, from $T_0 + 0.192$ s to $T_0 + 0.640$ s, is designated by ΔT_2 .

In the ΔT_1 time interval, to identify the P-GRB, we have performed a spectral analysis by considering the BB and Compt spectral models. The spectra and the corresponding fits are shown in Figure 7 and the best fit parameters are listed in Table 1. As reported in Table 1, the Compt and the BB models are both viable. However, the value of the low-energy index of the Compt model in the ΔT_1 time interval, $\alpha = 0.26 \pm 0.32$, is consistent within three σ with $\alpha = 1$, which is the low energy index of a BB. We conclude that the BB model is an acceptable fit to the data and the best “physical model” of the ΔT_1 time interval and therefore identify it with the P-GRB emission. The corresponding observed temperature is $kT = (324 \pm 33)$ keV (see Table 1).

We then performed a spectral analysis on the time interval ΔT_2 to identify the prompt emission. We have again considered the Compt and BB spectral models (see Figure 8 and Table 1). By looking at Figure 8, it is immediately clear that the BB model does not adequately fit the data at energies larger than 1 MeV. Therefore the Compt model is favored. Its low-energy index, $\alpha = -0.11 \pm 0.26$, indicates that the spectral energy distribution in the ΔT_2 time interval is broader than that of the BB model. The Compt model is consistent with the spectral model adopted in the fireshell model and described in Patricelli et al. (2012) for the prompt emission.

In the next section we interpret the above data within the fireshell theoretical framework.

6. APPLICATION OF THE FIRESHELL MODEL TO GRB 140619B

After the P-GRB and the prompt emission identification, we have followed the same analysis described in Muccino et al. (2013) to determine the cosmological redshift, the baryon load and all the other physical quantities characterizing the plasma at the transparency point (see Figure 4). It is appropriate to underline that a remarkable difference between the long and the short GRBs is considered: the P-GRB emission in long GRBs represents on average the 1%–5% of the overall emission (see, e.g., the cases of GRB 970828, Ruffini et al. 2013, and GRB 090618, Izzo et al. 2012b), while in the cases of the short GRBs 090227B and 140619B (see Section 6.1), the P-GRB emissions represent $\sim 40\%$ of the overall observed fluence.

6.1. Redshift Estimate in Fireshell Model

From the observed P-GRB and total fluences, respectively, $S_{\text{BB}} = F_{\text{tot}}(\Delta T_1)\Delta T_1$ and $S_{\text{tot}} = F_{\text{tot}}(T_{90})T_{90}$ (see values in Table 1), we have estimated the ratio

$$\frac{E_{\text{P-GRB}}}{E_{e^+e^-}^{\text{tot}}} \approx \frac{4\pi d_l^2 S_{\text{BB}}/(1+z)}{4\pi d_l^2 S_{\text{tot}}/(1+z)} = \frac{S_{\text{BB}}}{S_{\text{tot}}} = (40.4 \pm 7.8)\%, \quad (1)$$

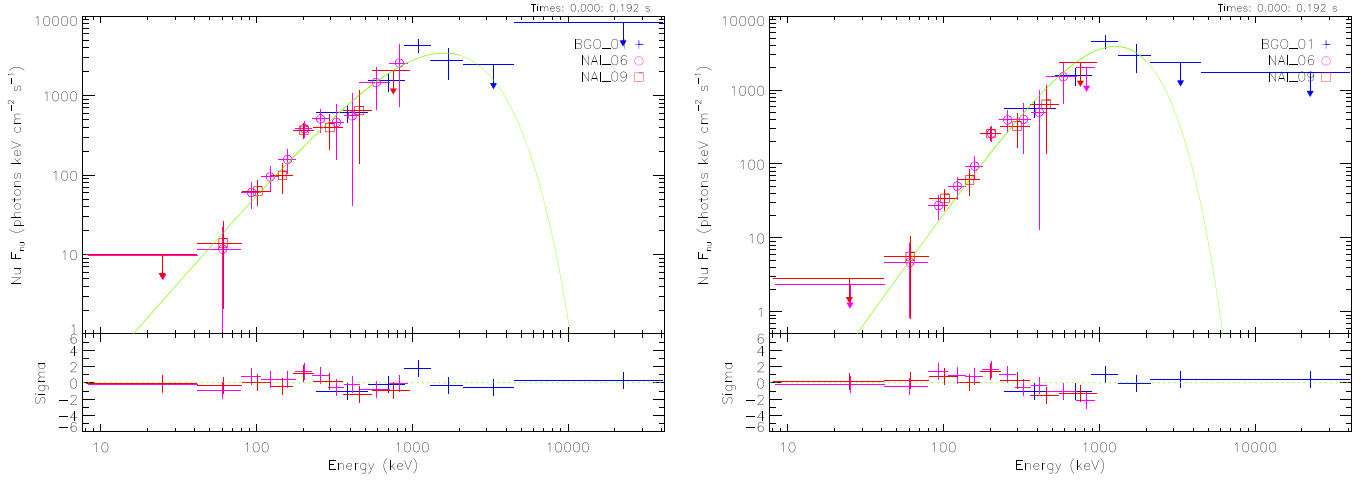


Figure 7. Same considerations as in Figure 6, in the ΔT_1 time interval, comparing Compt (left panel) and BB (right panel) models.

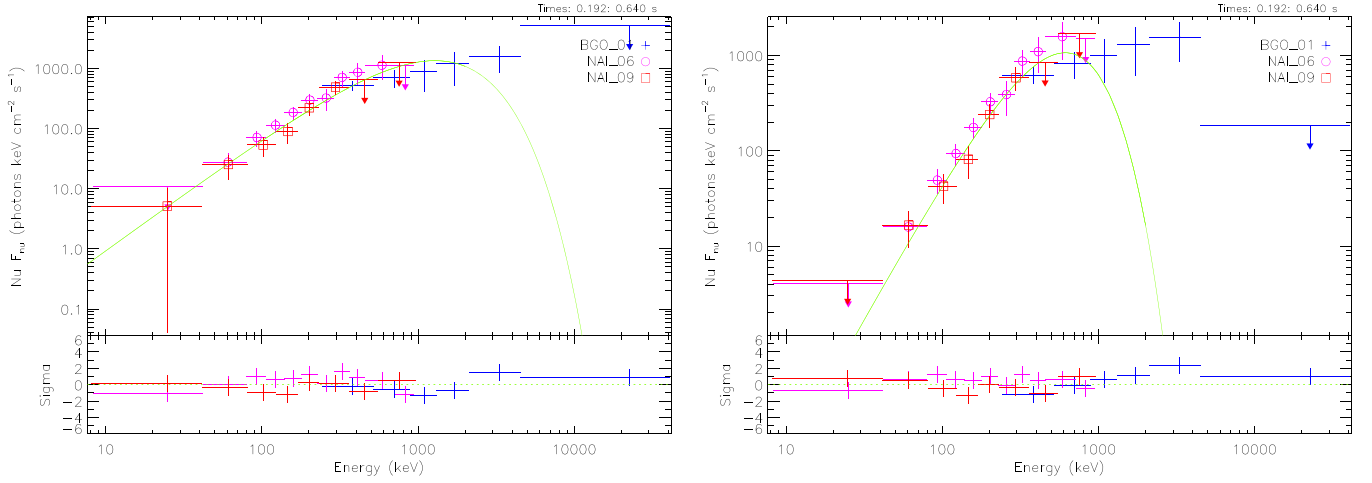


Figure 8. Same considerations as in Figure 6, in the ΔT_2 time interval, comparing Compt (left panel) and BB (right panel) models.

where the theoretically computed energy of the P-GRB, $E_{\text{P-GRB}}$, has been constrained by the observed thermal emission, E_{BB} , and we have imposed $E_{e^+e^-}^{\text{tot}} \equiv E_{\text{iso}}$. In Equation (1) the luminosity distance d_l and the redshift z of the source do not enter into the final computation.

From the last diagram in Figure 4, it is clear that for the value in Equation (1), we have different possible parameters ($E_{e^+e^-}^{\text{tot}}$, B) and for each of them we can determine the corresponding kT_{blue} (see the top diagram in Figure 4). Finally, from the ratio between kT_{blue} and the observed P-GRB temperature kT , we can estimate the redshift, i.e., $kT_{\text{blue}}/kT = (1 + z)$. To obtain the correct value of z and then the right parameters $[E_{e^+e^-}^{\text{tot}}(z), B(z)]$, we have made use of the isotropic energy formula

$$E_{\text{iso}} = 4\pi d_l^2 \frac{S_{\text{tot}}}{(1+z)} \frac{\int_{1/(1+z)}^{10000/(1+z)} E N(E) dE}{\int_8^{40000} E N(E) dE}, \quad (2)$$

in which $N(E)$ is the photon spectrum of the burst and the integrals are due to the K -correction on S_{tot} (Schaefer 2007). From the initial constraint $E_{\text{iso}} \equiv E_{e^+e^-}^{\text{tot}}$, we have found $z = 2.67 \pm 0.37$, which leads to $B = (5.52 \pm 0.73) \times 10^{-5}$

and $E_{e^+e^-}^{\text{tot}} = (6.03 \pm 0.79) \times 10^{52}$ erg. All the quantities so determined are summarized in Table 2. The analogy with the prototypical source GRB 090227B, for which we have $E_{\text{P-GRB}} = (40.67 \pm 0.12)\% E_{e^+e^-}^{\text{tot}}$ and $B = (4.13 \pm 0.05) \times 10^{-5}$, is very striking (Muccino et al. 2013).

We now proceed with the analysis of the subsequent emission to derive the properties of the surrounding CBM.

6.2. Analysis of the Prompt Emission

Having determined the initial conditions for the fireshell, i.e., $E_{e^+e^-}^{\text{tot}} = 6.03 \times 10^{52}$ erg and $B = 5.52 \times 10^{-5}$, the dynamics of the system is uniquely established. In particular, we obtain the Lorentz factor at transparency, $\Gamma_{\text{tr}} = 1.08 \times 10^4$, and we can simulate the light curve and the spectrum of the prompt emission. To reproduce the pulses observed especially in the BGO-b1 light curve (see Figure 5) we have derived the radial distributions of the CBM number density and of the filling factor \mathcal{R} around the burst site (see Table 3 and Figure 9). The errors in the CBM number density and in \mathcal{R} are defined as the maximum possible variation of the parameters to guarantee agreement between the simulated light curve and the observed data. The final simulation of the BGO-b1 light curve (260 keV–40 MeV) is shown in Figure 10.

Table 2

The Results of the Simulation of GRB 090227B in the Fireshell Model

Fireshell Parameter	Value
$E_{e^+e^-}^{\text{tot}}$ (erg)	$(6.03 \pm 0.79) \times 10^{52}$
B	$(5.52 \pm 0.73) \times 10^{-5}$
Γ_{tr}	$(1.08 \pm 0.08) \times 10^4$
$r_{\text{tr}}(\text{cm})$	$(9.36 \pm 0.42) \times 10^{12}$
kT_{blue} (keV)	$(1.08 \pm 0.08) \times 10^3$
z	2.67 ± 0.37
$\langle n_{\text{CBM}} \rangle (\text{cm}^{-3})$	$(4.7 \pm 1.2) \times 10^{-5}$

Interestingly, the average CBM number density in GRB 140619B, $\langle n_{\text{CBM}} \rangle = (4.7 \pm 1.2) \times 10^{-5} \text{ cm}^{-3}$ (see Table 3), is very similar to that of the prototype GRB 090227B, $\langle n_{\text{CBM}} \rangle = (1.90 \pm 0.20) \times 10^{-5} \text{ cm}^{-3}$. In both the cases the CBM densities are typical of the galactic halo environment.

We turn now to the spectrum of the prompt emission using the spectral model described in Patricelli et al. (2012) with a phenomenological parameter $\alpha = -1.11$. From fitting the light curve in the energy range 260 keV–40 MeV, we have extended the simulation of the corresponding spectrum down to 8 keV to check overall agreement with the observed data. The final result is plotted in Figure 11, where the rebinned NaI-n6 and n9 and BGO-b1 data in the ΔT_2 time interval show their agreement with the simulation; the lower panel in Figure 11 shows the residuals of the data around the fireshell simulated spectrum.

The fireshell approach is different from the fireball one, where the sharp luminosity variations observed in the prompt emission are attributed to the prolonged and variable activity of the “inner engine” (see, e.g., Rees & Meszaros 1994; Ramirez-Ruiz & Fenimore 2000; Piran 2004).

In the fireshell model, the observed time variability of the prompt emission is produced by the interaction of the accelerated baryons of the fireshell with the CBM “clumps” (see, e.g., Ruffini et al. 2002, 2006; Patricelli et al. 2012). The issue of the time variability in GRB light curves has been long debated. Zhang et al. (2006) and Nakar & Granot (2007) indicated difficulties in producing short time variability from CBM inhomogeneities. The opposite point of view has been expressed by Dermer & Mitman (1999) and Dermer (2006, 2008). In the fireshell model it has been shown that, from the correct computation of the equations of motion of the shell, of the EQTS, and of the Lorentz factor (Bianco & Ruffini 2005a, 2005b, and Section 3), the short time scale variability of GRB light curves occurs in regimes with the larger values of the Lorentz factor, when the total visible area of the emission region is very small and “dispersion” in arrival time of the luminosity peaks is negligible. Therefore the short time scale variability indeed can be produced by the CBM inhomogeneities (see Section 3 in Patricelli et al. 2012). This has been verified in the present case of GRB 140619B, where the values of the Lorentz factor Γ and the total transversal size of the fireshell visible area d_v at the initial radius of the CBM cloud are explicitly indicated in Table 3. These values of d_v are smaller than the thickness of the inhomogeneities ($\Delta r \approx 10^{16}$ – 10^{17} cm) and fully justify the adopted spherical symmetry approximation (Ruffini et al. 2002, 2006; Patricelli et al. 2012). Consequently, a finer description of each substructure in the spikes observed in the light curve is not necessary and does not

change the substantial agreement of the model with the observational data, which is provided by the average densities and the filling factors in Table 3.

6.3. The Progenitor System

In analogy with the case of GRB 090227B (see, e.g., Muccino et al. 2013; Oliveira et al. 2014), we conclude that the progenitor of GRB 140619B is a NS–NS merger. As a lower limit, we have considered the simplest case by assuming two NSs with the same mass M_{NS} such that the total mass would be larger than the NS critical mass $M_{\text{crit}}^{\text{NS}}$, e.g., $2M_{\text{NS}} \gtrsim M_{\text{crit}}^{\text{NS}}$. This condition is clearly necessary for the formation of a BH and the consequent application of the fireshell model. It is also appropriate here to recall that only a subset of binary NSs mergers can fulfill this stringent requirement (see Figure 3). This will strongly affect the estimate of the rate of these family-2 short GRBs, when compared with the usual expected binary NS rate (see Section 9 and Conclusions).

Referring to the work of Belvedere et al. (2012) on nonrotating NSs in the global charge neutrality treatment with all the fundamental interactions taken into account properly, we have considered two NSs with mass $M_{\text{NS}} = 1.34 M_{\odot} = 0.5M_{\text{crit}}^{\text{NS}}$ and corresponding radius $R = 12.24$ km. As a working hypothesis we assume that in the NS merger the crustal material from both NSs contributes to the GRB baryon load, while the NS cores collapse to a BH. For each NS the crustal mass from the NL3 nuclear model is $M_c = 3.63 \times 10^{-5} M_{\odot}$, so the total NS merger crustal mass is $M_{2c} = 2M_c = 7.26 \times 10^{-5} M_{\odot}$. On the other hand, the baryonic mass engulfed by the e^+e^- plasma before transparency is $M_B = E_{e^+e^-}^{\text{tot}} B/c^2 = (1.86 \pm 0.35) \times 10^{-6} M_{\odot}$, so we can conclude that only a small fraction of the crustal mass contributes to the baryon load, namely $M_B = (2.56 \pm 0.48)\% M_{2c}$. This value is consistent with the global charge neutrality condition adopted in Belvedere et al. (2012). The usually adopted LCN condition leads instead to a crustal mass $M_c^{\text{LCN}} \sim 0.2 M_{\odot}$ (see, e.g., Belvedere et al. 2012; Oliveira et al. 2014), which would be inconsistent with the small value of the baryon load inferred above.

7. ON THE GWS EMISSION AND THE DETECTABILITY OR ABSENCE THEREOF

Following the previous work on GRB 090227B (Oliveira et al. 2014), we now estimate the emission of GWs of the binary NS progenitor of the short GRB 140619B using the effective-one-body (EOB) formalism (Buonanno & Damour 1999, 2000; Damour et al. 2000; Damour 2001; Damour & Nagar 2010) and assess the detectability of the emission by the Advanced LIGO interferometer.¹³ The EOB formalism maps the conservative dynamics of a binary system of nonspinning objects onto the geodesic dynamics of a single body of reduced mass $\mu = M_1 M_2 / M$, with total binary mass $M = M_1 + M_2$. The effective metric is a modified Schwarzschild metric with a rescaled radial coordinate, $r = c^2 \eta_2 / (GM)$, where r_{12} is the distance between the two stars. The binary binding energy as a function of the orbital frequency Ω is given by $E_b(\Omega) = Mc^2 [\sqrt{1 + 2\nu(\hat{H}_{\text{eff}} - 1)} - 1]$, where the effective Hamiltonian $\hat{H}_{\text{eff}}^2 = A(u) + p_{\phi}^2 B(u)$ depends on the radial

¹³ <http://www.advancedligo.mit.edu>

Table 3
The Density and Filling Factor Masks of GRB 140619B

Cloud	Distance (cm)	n_{CBM} (cm^{-3})	\mathcal{R}	Γ	d_v (cm)
1th	1.50×10^{15}	$(1.2 \pm 0.2) \times 10^{-5}$	$(2.8 \pm 0.3) \times 10^{-11}$	1.08×10^4	2.76×10^{11}
2nd	1.20×10^{17}	$(9.2 \pm 1.1) \times 10^{-6}$...	2.07×10^3	1.16×10^{14}
3rd	1.70×10^{17}	$(2.5 \pm 0.5) \times 10^{-4}$	$(3.5 \pm 0.6) \times 10^{-10}$	1.84×10^3	1.85×10^{14}

Note. In each column are listed, respectively, the CBM cloud, the corresponding initial radius away from the BH, the number density, the filling factor, the Lorentz factor, and the total transversal size of the fireshell visible area.

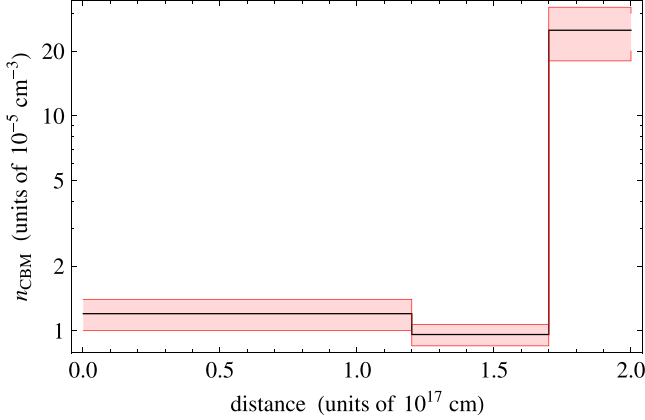


Figure 9. Radial CBM number density distribution of GRB 140619B (black line) and its range of validity (red shaded region).

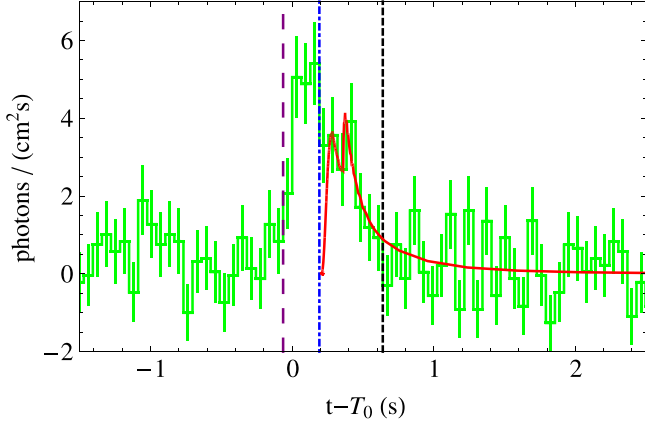


Figure 10. BGO-b1 (260 keV–40 MeV) simulated light curve of the prompt emission of GRB 140619B (solid red line). Each spike corresponds to the CBM number density profile described in Table 2 and Figure 9. The blue dotted–dashed vertical line marks the end of the P-GRB emission. The purple long-dashed and the black dashed vertical lines indicate, respectively, the starting and the ending times of the T_{90} time interval. Clearly visible outside of this time interval is the background noise level. The continuation of the simulation after T_{90} is due to the residual large angle emission of the EQTS (Bianco & Ruffini 2005a, 2005b) due to the density profile indicated in Table 3.

potential $A(u)$ of the variable $u = 1/r$ and $B(u) = u^2 A(u)$, while the angular momentum for the circular orbit is given by $p_\phi^2 = -A'(u)/[u^2 A(u)]'$, where a prime stands for the derivative with respect to u (see, e.g., Bini & Damour 2013 for further details). In order to obtain the derivative of the effective Hamiltonian \hat{H}_{eff} as a function of Ω , we must use the chain rule together with the relation $\Omega = \Omega(u)$ following from the angular

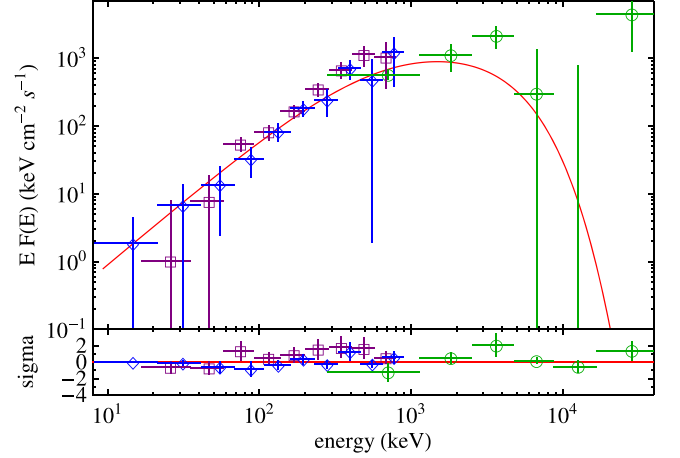


Figure 11. Top panel: comparison between the 8–900 keV data from the NaI-n6 (purple squares) and n9 (blue diamonds) detectors, and the 260 keV–40 MeV data from the BGO-b1 detector (green circles), and the simulation within the fireshell model (solid red curve) in the time interval ΔT_2 . Bottom panel: the residuals of the above mentioned data with the simulation.

Hamilton equation of motion in the circular case $GM\Omega(u) = (1/u)\partial H/\partial p_\phi = MA(u)p_\phi(u)u^2/(H\hat{H}_{\text{eff}})$, where G is the gravitational constant. Finally we obtain the rate of orbital energy loss through emission of GWs from the related derivative $dE_b/d\Omega$.

Using the well known matched filtering technique, we compute the signal-to-noise ratio (S/N) from the Fourier transform of the signal $h(t) = h_+ F_+ + h_\times F_\times$, where $h_{+, \times}$ are functions that depend on the direction and polarization of the source and $F_{+, \times}$ depend on the direction of the detector. By making an rms average over all possible source directions and wave polarizations, i.e., $\langle F_+^2 \rangle = \langle F_\times^2 \rangle = 1/5$, we obtain (see Flanagan & Hughes 1998 for details)

$$\langle S/N^2 \rangle = \int_{f_{\min}}^{f_{\max}} df_d \frac{h_c^2(f_d)}{5f_d^2 S_h^2(f_d)}, \quad (3)$$

where $S_h(f)$ is the strain noise spectral density (in units $1/\sqrt{\text{Hz}}$) of the interferometer. We have also introduced the characteristic GW amplitude, h_c , defined using the Fourier transform of the GW form $h(t)$, $h_c(f) = f|\hat{h}(f)|$, and it is given by

$$h_c^2(f) = \frac{2(1+z)^2}{\pi^2 d_L^2} \frac{dE_b}{df} [(1+z)f_d], \quad (4)$$

with z the cosmological redshift, $f_d = f/(1+z)$ the GW frequency at the detector, $f = \Omega/\pi$ the frequency in the source frame, f_{\min} the minimal bandwidth frequency of the detector, and $f_{\max} = f_c/(1+z)$ the maximal bandwidth frequency,

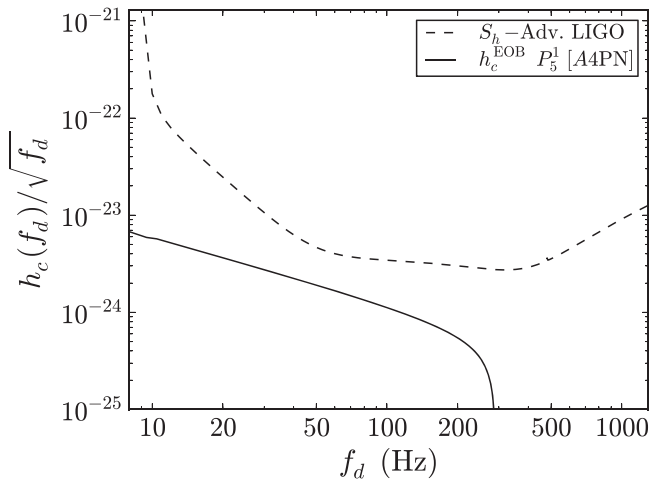


Figure 12. Sensitivity curve of Advanced LIGO $S_h(f)$ (dashed black curve) and the characteristic gravitational amplitude $h_c(f_d)/\sqrt{f_d}$ (solid black curve) of the binary NS progenitor of GRB 140619B, as a function of the frequency at the detector f_d . The EOB radial potential $A(u)$ was calculated using values for the coefficients in the 4th order post-Newtonian (PN) approximation and P_5^1 is the Padé approximant of order (1, 5).

where $f_c = \Omega_c/\pi$ is the binary contact frequency and d_L is the luminosity distance. In Figure 12 we show the strain-noise sensitivity of Advanced LIGO, $S_h(f)$, and the characteristic gravitational amplitude per square root frequency, $h_c(f_d)/\sqrt{f_d}$, both plotted as functions of the frequency at the detector f_d .

Following the above procedure we obtained for the short GRB 140619B a very low value $\langle S/N \rangle \approx 0.21$ compared to the value $S/N = 8$ needed for an optimal positive detection. The low value of the S/N is clearly due to the large cosmological distance to the source, $d \approx 21$ Gpc. Although the rms-averaged S/N we have computed might improve by a factor $\approx 5/2$ for an optimally located and polarized source (e.g. $\langle F_+^2 \rangle = 1$ and $\langle F_\times^2 \rangle = 0$) with an optimal face-on orbit ($\cos i = 1$), in the case of GRB 140619B it would increase only to a maximal value $S/N(\text{opt}) \approx 0.5$. From the dynamics of the system, we also find that this binary emits a total energy of $E_{\text{GW}}^T = 7.42 \times 10^{52}$ erg in gravitational radiation during the entire inspiral phase all the way up to the merger.

8. CONSIDERATIONS ON THE GEV EMISSION OF GRB 140619B

In addition to the analogies with GRB 090227B, GRB 140619B presents a novelty of special interest: a short-lived emission (~ 4 s) observed at energies $\gtrsim 0.1$ GeV. The light curve of this emission shows a rising part which peaks at ~ 2 s, followed by a decaying tail emission lasting another ~ 2 s in the observer frame (see Figure 13(b)). Since GRB 140619B was in the LAT FoV during the entire observational period, the absence of emission after ~ 4 s has been attributed to a cut-off intrinsic to the source. We divided the overall emission into four time intervals (see Figure 13(b)), each of them lasting 1 s. The corresponding spectra are best fit by power-law models. The total isotropic energy of the 0.1–100 GeV emission is $E_{\text{LAT}} = (2.34 \pm 0.91) \times 10^{52}$ erg.

In complete analogy with the GeV emission emitted in the binary-driven hypernovae (BdHNe), we attribute this high energy radiation to the newly formed BH. This identification is clearer here in view of the absence of a supernova (SN) and the

related constant power-law emission in X-rays, when measured in the cosmological rest-frame of the BdHN (Ruffini et al. 2014, 2015; Ruffini 2015b).

The presence of this GeV emission is not a peculiarity of GRB 140619B, but is a common feature of all these family-2 short GRBs. In line with this, the apparent absence of the GeV emission in GRB 090227B has already been discussed in Section 5: it can be explained simply by the fact that this source was outside the nominal LAT FoV. The significant detection in the LLE channel and the presence of only one transient-class event with energy above 100 MeV associated with the GRB (Ackermann et al. 2013) confirms that in optimal conditions the GeV emission from GRB 090227B should have been detected.

Now consider GRB 090510, which has the characteristics of the family-2 short GRBs ($E_{\text{iso}} > 10^{52}$ erg and $E_{p,i} > 2$ MeV), including the presence of a high energy GeV emission lasting $\sim 10^2$ s. This high energy emission continues up to the signal goes below the LAT threshold (Ackermann et al. 2013). The new feature of GRB 090510, among the family-2 short GRBs, is a well determined cosmological redshift inferred from the optical observations. The corresponding distance indeed coincides with the one theoretically predicted in the fireshell binary merger model (M. Muccino et al. 2015, in preparation).

In Figure 13(a) we compare and contrast the afterglows of the traditional low energetic short GRBs (see Berger 2014, for a review) with those of the family-2 short GRB 140619B (see Figure 13(b)) and GRB 090510 (see Figure 13(c)). In Figure 1 we show the evolution of the NS–NS merger generating a family-2 short GRB. In this system the conservation laws for total energy and the total angular momentum have to be satisfied during and following the binary NS merger (J. A. Rueda et al. 2015, in preparation). One of the most important issues is the determination of the dimensionless angular momentum $c J/(GM^2)$ of the newly born BH (where J and M are, respectively, the BH spin angular momentum and mass). These considerations have been applied to GRB 090510 (M. Muccino et al. 2015, in preparation).

Before closing, we call attention to GRB 081024B, which we are currently addressing within the fireshell model (Y. Aimuratov et al. 2015, in preparation), and which shows all the typical features of the family-2 short GRBs, including a distinctive GeV emission. In conclusion, we can safely assert that all family-2 short GRBs, when the observational requirements are fulfilled, present a short-lived but very intense GeV emission, which in our interpretation originates from the newly formed BH.

In Table 4 we listed the redshift, $E_{p,i}$, E_{iso} , and the GeV isotropic emission energy E_{LAT} in the rest-frame energy band 0.1–100 GeV of the three family-2 short GRBs discussed here. In computing E_{iso} we have inserted the energy computed in the rest-frame energy band 1–10000 keV.

9. THE RATE OF FAMILY-2 SHORT GRBS

With the identification of three family-2 short GRBs, namely GRB 090227B and GRB 140619B, with theoretically inferred redshifts, and GRB 090510 with a measured redshift, all of them detected by the *Fermi* satellite, we are now in a position to give an estimate of the expected rate ρ_0 of such events. Following Soderberg et al. (2006) and Guetta & Della Valle (2007), for these sources we have computed the 1 s peak photon flux f_p in the energy band 1–1000 keV, which is 16.98

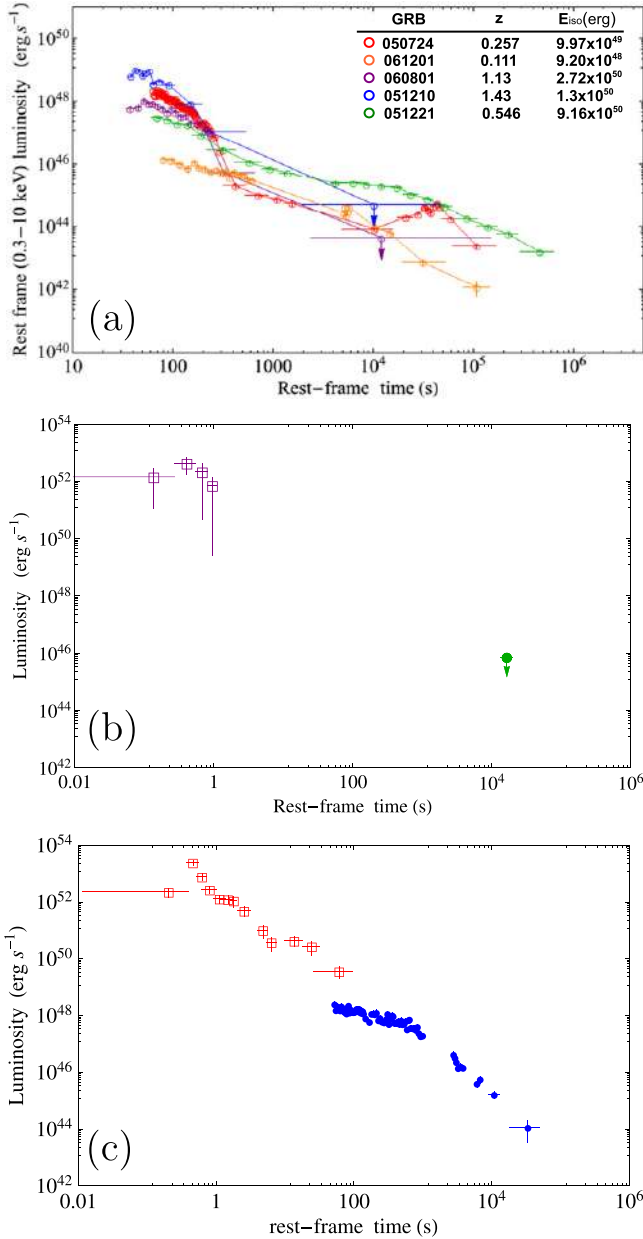


Figure 13. Top panel (a): the rebinned rest-frame 0.3–10 keV X-ray luminosities of weak short GRBs leading to massive NSs; the corresponding bursts, redshifts and energies are indicated in the legend. In their afterglows there is no regular power-law behavior at late times and no nesting (Ruffini et al. 2014). Middle panel (b): the short lived rest-frame 0.1–100 GeV isotropic luminosity light curve (purple squares) and the rest-frame 0.3–10 keV upper limit, as set from the analysis of GRB 140619B outlined in Section 3 (green circle). Bottom panel (c): the long lived rest-frame 0.1–100 GeV (red squares) and the rest-frame 0.3–10 keV (blue circles) isotropic luminosity light curves of GRB 090510.

photons $\text{cm}^{-2} \text{s}^{-1}$ for GRB 090227B, 9.10 photons $\text{cm}^{-2} \text{s}^{-1}$ for GRB 090510, and 4.97 photons $\text{cm}^{-2} \text{s}^{-1}$ for GRB 140619B. From the spectral parameters for each source, we have computed f_p for various redshifts until it coincided with the corresponding threshold peak flux f_T which is the limiting peak photon flux allowing burst detection (see the analysis in Band 2003 for details). In this way we have evaluated for each source the maximum redshift z_{max} at which the burst would have been detected and, then, the corresponding maximum comoving volume V_{max} . For GRB 140619B we

Table 4

The Redshift, the Rest-frame Peak Spectral Energy, the Isotropic Energy E_{iso} in the Rest-frame Energy Band 1–10000 keV, and the GeV Isotropic Emission energy E_{LAT} in the Rest-frame Energy Band 0.1–100 GeV of the Four family-2 Short GRBs Discussed Here

GRB	z	$E_{p,i}$ (MeV)	E_{iso} (10^{52} erg)	E_{LAT} (10^{52} erg)
081024B	>3.0	>8.2	>2.4	>2.7
090227B	1.61 ± 0.14	5.89 ± 0.30	28.3 ± 1.5	...
090510	0.903 ± 0.003	7.89 ± 0.76	3.95 ± 0.21	5.78 ± 0.60
140619B	2.67 ± 0.37	5.34 ± 0.79	6.03 ± 0.79	2.34 ± 0.91

Note. The values indicated for GRB 081024B will be Discussed in Y. Aimuravov et al. (2015, in preparation).

obtain $f_p \equiv f_T = 1.03 \text{ photons cm}^{-2} \text{s}^{-1}$ at maximum redshift $z_{140619B}^{\text{max}} = 5.49$; for GRB 090227B, which is the brightest one, we find $f_p \equiv f_T = 1.68 \text{ photons cm}^{-2} \text{s}^{-1}$ at a maximum redshift $z_{090227B}^{\text{max}} = 5.78$; finally, for GRB 090510, we get $f_p \equiv f_T = 1.96 \text{ photons cm}^{-2} \text{s}^{-1}$ at a maximum redshift $z_{090510}^{\text{max}} = 2.25$. Correspondingly we have computed V_{max} .

The empirical rate can be evaluated as

$$\rho_0 = \left(\frac{\Omega_F}{4\pi} \right)^{-1} \frac{N}{V_{\text{max}} T_F}, \quad (5)$$

where $N = 3$ is the number of identified energetic NS–NS short bursts, $\Omega_F \approx 9.6 \text{ sr}$ is the average Fermi solid angle, and $T = 6$ years is the Fermi observational period. We infer a local rate of $\rho_0 = (2.6^{+4.1}_{-1.9}) \times 10^{-4} \text{ Gpc}^{-3} \text{yr}^{-1}$, where the attached errors are determined from the 95% confidence level of the Poisson statistic (Gehrels 1986). At $z \geq 0.9$, the above inferred rate provides an expected number of events $N_{\geq} = 4^{+6}_{-3}$, which is consistent with the above three observed events during the Fermi observational period. Also at $z \leq 0.9$ our estimate $N_{<} = 0.2^{+0.31}_{-0.14}$ is consistent with the absence of any family-2 short GRB detection.

With the inclusion of GRB 081024B, with a theoretically estimated redshift $z > 3$ (more details will appear in Y. Aimuravov et al. 2015, in preparation), the above rate remains stable with smaller error bars, i.e., $\rho_0 = (2.1^{+2.8}_{-1.4}) \times 10^{-4} \text{ Gpc}^{-3} \text{yr}^{-1}$. This inferred rate is different from that of the long GRBs, recently estimated to be $\rho_{\text{L-GRB}} = 1.3^{+0.7}_{-0.6} \text{ Gpc}^{-3} \text{yr}^{-1}$ (Wanderman & Piran 2010), and also from the estimates of the family-1 short GRBs given in the literature (without a beaming correction $\rho_{\text{short}} = 1\text{--}10 \text{ Gpc}^{-3} \text{yr}^{-1}$; see e.g., Berger 2014 and Clark et al. 2014).

Such a low rate can be explained based upon the existing data of binary NSs within our Galaxy (see Section 2). From Figure 3 we notice that only a subset of them has the sum of the masses of the components larger than the critical NS mass and can collapse to a BH in their merger process. Only this subset can lead to a family-2 short GRB.

10. THE FAMILY-2 SHORT GRBS AND THE $E_{p,i}$ – E_{ISO} RELATION FOR SHORT GRBS

Now we discuss some general considerations for the new $E_{p,i}$ – E_{iso} relation for short GRBs (Zhang et al. 2012; Calderone et al. 2015), with a power law similar to the one of the Amati

relation for long GRBs (Amati et al. 2008), but different amplitude. This yet unexplained difference discourages the use of the Amati relation as an astronomical tool. All four family-2 short GRBs satisfy this new $E_{p,i}-E_{\text{iso}}$ relation (see the quantities listed in Table 4). We call attention to the need to investigate the physical reasons for the validity of this universal $E_{p,i}-E_{\text{iso}}$ relation, which appears to be satisfied by family-1 short bursts, where the binary NS merger does not lead to BH formation, and also the family-2 short bursts, where BHs are formed and reveal their presence by giving rise to the short-lived but significant GeV emission.

11. CONCLUSIONS

In this article we have predicted the occurrence of two different kinds of short GRBs originating from binary NS mergers, based on

- (a) the analysis of GRB 090227B, the prototype of short bursts originating from a binary NS leading to BH formation (Muccino et al. 2013),
- (b) the recent progress in the determination of the mass–radius relation of NSs and the determination of their critical mass $M_{\text{crit}}^{\text{NS}} \approx 2.67 M_{\odot}$ (Rotondo et al. 2011; Rueda et al. 2011, 2014; Belvedere et al. 2012, 2014a, 2014b), and
- (c) the recently measured mass of PSR J0348+0432, $M = (2.01 \pm 0.04) M_{\odot}$ (Antoniadis et al. 2013), establishing an absolute lower limit on $M_{\text{crit}}^{\text{NS}}$, and the remarkable information gained from radio observations of binary NS systems in our own Galaxy (Zhang et al. 2011; Antoniadis 2014).

The first kind of short GRBs, which we call family-1, are the most common ones with $E_{\text{iso}} < 10^{52}$ erg and rest-frame spectral peak energy $E_{p,i} < 2$ MeV, originating from binary NS mergers with merged core mass smaller than $M_{\text{crit}}^{\text{NS}}$ and leading, therefore, to a massive NS, possibly with a companion. We identify these family-1 short bursts with the ones extensively quoted in literature (see, e.g., Berger 2014 for a review).

The second kind of short GRBs, which we call family-2, are those with $E_{\text{iso}} > 10^{52}$ erg and harder spectra with $E_{p,i} > 2$ MeV, originating from binary NS mergers with merged core mass larger than $M_{\text{crit}}^{\text{NS}}$. These family-2 short bursts satisfy the necessary condition to form a BH, following the example of the prototype GRB 090227B (Muccino et al. 2013).

The application of the fireshell model (Ruffini et al. 2001a, 2001b, 2001c) to the family-2 short GRB 140619B analyzed here has allowed the determination of the physical parameters of this source: the identification of the P-GRB emission in the early ~ 0.2 s of its light curve, the theoretical cosmological redshift of $z = 2.67 \pm 0.37$ and consequently the total burst energy $E_{e^+e^-}^{\text{tot}} = (6.03 \pm 0.79) \times 10^{52}$ erg, the baryon load $B = (5.52 \pm 0.73) \times 10^{-5}$, and a Lorentz Γ factor at transparency $\Gamma_{\text{tr}} = (1.08 \pm 0.08) \times 10^4$. The analysis of the prompt emission has also led to the determination of the CBM density, $\langle n_{\text{CBM}} \rangle = (4.7 \pm 1.2) \times 10^{-5} \text{ cm}^{-3}$, typical of the galactic halo environment, where NS–NS binaries migrate to, due to natal kicks imparted to them at birth (see, e.g., Narayan et al. 1992; Bloom et al. 1999; Fryer et al. 1999; Belczynski et al. 2006; Berger 2014), clearly supporting the binary NS merger hypothesis of this source. Unexpectedly, we have found the existence of a short-lived and

very intense GeV emission, just after the P-GRB occurrence and during and after the prompt emission phase, which has led us to conclude that this high energy emission originates from the newly formed BH.

While this article was being refereed, we have discovered three additional examples of these family-2 short bursts: GRB 081024B, GRB 090510, and GRB 090227B. These have given evidence that all these family-2 short bursts indeed show the existence of high energy emission, with the sole exception of GRB 090227B, which at the time of the observation was outside the nominal LAT FOV.

In summary we formulate some norms and theoretical predictions.

- (1) All family-1 short GRBs have an extended X-ray afterglow (see, e.g., Figure 13(a) and Berger 2014). When computed in the rest-frame 0.3–10 keV energy band they do not show any specific power-law behavior (Pisani et al. 2013) or the “nesting” properties (Ruffini et al. 2014) which have been discovered in some long GRBs. We predict that family-1 short GRBs, originating from a binary merger to a massive NS, should never exhibit high energy emission. The upper limit of 10^{52} erg can be simply understood in terms of a merger leading to a massive NS.
- (2) All family-2 short GRBs have been observed not to have prominent X-ray or optical afterglows. They all have short-lived but very energetic GeV emissions (see, e.g., Figures 13(b) and (c)), when LAT data are available. The upper limit of 10^{54} erg can be also simply understood in terms of a merger leading to BH formation.
- (3) The high energy emission episode in family-2 short GRBs always occurs at the end of the P-GRB emission, during and after the prompt emission phase. This fact uniquely links the high energy emission to the occurrence of the newly born BH. The prompt emission phase studied within the fireshell model has also allowed the determination of a large number of essential astrophysical parameters, both of the source (e.g., $E_{e^+e^-}^{\text{tot}}$ and B) and of the CBM (e.g., α , n_{CBM} , and \mathcal{R}).

It is interesting that the very simplified conditions encountered in the short GRBs in the absence of a SN event, which characterize the long GRBs (Ruffini et al. 2015), have allowed definite progress in understanding some fundamental GRB properties, e.g., the correlation of high energy emission to the BH formation. They can be adapted to the case of long GRBs. The points summarized above go a long way toward reaching a better understanding of family-1 and family-2 long GRBs (Ruffini et al. 2015), as well as of the BdHNe (Ruffini et al. 2014). We are confident that GRB 140619B is one of the best examples of short GRBs obtained with the current space technology. We sincerely hope that the results of our research will lead to new missions with greater collecting area and time resolution in X- and gamma-rays.

We thank the referee for requesting additional observational support for our theoretical fireshell binary merger model. This has motivated us to improve the connection of our theoretical work with the observations, resulting in this new version of the manuscript. We are especially grateful to S. Campana and C. L. Fryer for useful suggestions in improving some conceptual and observational arguments, and to L. Izzo for the detailed analysis of the high energy emission. M.E., M.K. and F.G.O.

are supported by the Erasmus Mundus Joint Doctorate Program by grant Nos. 2012-1710, 2013-1471, and 2012-1710, respectively, from the EACEA of the European Commission. A.V.P. and E.Z. acknowledge the support by the International Cooperation Program CAPES-ICRANet financed by CAPES-Brazilian Federal Agency for Support and Evaluation of Graduate Education within the Ministry of Education of Brazil. This work made use of data supplied by the UK *Swift* Science Data Centre at the University of Leicester.

REFERENCES

- Ackermann, M., Ajello, M., Asano, K., et al. 2013, *ApJS*, **209**, 11
- Aksenov, A. G., Ruffini, R., & Vereshchagin, G. V. 2007, *PhRvL*, **99**, 125003
- Amati, L., Guidorzi, C., Frontera, F., et al. 2008, *MNRAS*, **391**, 577
- Antoniadis, J. 2015, in *Gravitational Wave Astrophysics*, ed. C. F. Sopuerta (Cham, Switzerland: Springer International Publishing), 1
- Antoniadis, J., Freire, P. C. C., Wex, N., et al. 2013, *Sci*, **340**, 448
- Band, D., Mateson, J., Ford, L., et al. 1993, *ApJ*, **413**, 281
- Band, D. L. 2003, *ApJ*, **588**, 945
- Belczynski, K., Perna, R., Bulik, T., et al. 2006, *ApJ*, **648**, 1110
- Belvedere, R., Boshkayev, K., Rueda, J. A., & Ruffini, R. 2014a, *NuPhA*, **921**, 33
- Belvedere, R., Pugliese, D., Rueda, J. A., Ruffini, R., & Xue, S.-S. 2012, *NuPhA*, **883**, 1
- Belvedere, R., Rueda, J. A., & Ruffini, R. 2014b, *JKPS*, **65**, 897
- Berger, E. 2011, *NewAR*, **55**, 1
- Berger, E. 2014, *ARA&A*, **52**, 43
- Bianco, C. L., & Ruffini, R. 2005a, *ApJL*, **633**, L13
- Bianco, C. L., & Ruffini, R. 2005b, *ApJL*, **620**, L23
- Bini, D., & Damour, T. 2013, *PhRvD*, **87**, 121501
- Bloom, J. S., Prochaska, J. X., Pooley, D., et al. 2006, *ApJ*, **638**, 354
- Bloom, J. S., Sigurdsson, S., & Pols, O. R. 1999, *MNRAS*, **305**, 763
- Boguta, J., & Bodmer, A. R. 1977, *NuPhA*, **292**, 413
- Buonanno, A., & Damour, T. 1999, *PhRvD*, **59**, 084006
- Buonanno, A., & Damour, T. 2000, *PhRvD*, **62**, 064015
- Burrows, D., Hill, J., Nousek, J., et al. 2005, *SSRv*, **120**, 165
- Calderone, G., Ghirlanda, G., Ghisellini, G., et al. 2015, *MNRAS*, **448**, 403
- Cherubini, C., Gericcio, A., J. A. Rueda, H., & Ruffini, R. 2009, *PhRvD*, **79**, 124002
- Cipolletta, F., Cherubini, C., Filippi, S., Rueda, J. A., & Ruffini, R. 2015, *PhRvD*, submitted (arXiv:1506.05926)
- Clark, J., Evans, H., Fairhurst, S., et al. 2014, arXiv:1409.8149
- Connaughton, V., Zhang, B.-B., Fitzpatrick, G., & Roberts, O. 2014, GCN, 16419, 1
- Damour, T. 2001, *PhRvD*, **64**, 124013
- Damour, T., Jaranowski, P., & Schäfer, G. 2000, *PhRvD*, **62**, 084011
- Damour, T., & Nagar, A. 2010, *PhRvD*, **81**, 084016
- Damour, T., & Ruffini, R. 1975, *PhRvL*, **35**, 463
- Deneva, J. S., Freire, P. C. C., Cordes, J. M., et al. 2012, *ApJ*, **757**, 89
- Dermer, C. D. 2006, *NCimB*, **121**, 1331
- Dermer, C. D. 2008, *ApJ*, **684**, 430
- Dermer, C. D., & Mitman, K. E. 1999, *ApJL*, **513**, L5
- Dezalay, J.-P., Barat, C., Talon, R., et al. 1992, AIP Conf. Ser. 265, ed. W. S. Paciesas & G. J. Fishman (Melville, NY: AIP), 304
- Eichler, D., Livio, M., Piran, T., & Schramm, D. N. 1989, *Natur*, **340**, 126
- Flanagan, E. E., & Hughes, S. A. 1998, *PhRvD*, **57**, 4535
- Fong, W., Berger, E., & Fox, D. B. 2010, *ApJ*, **708**, 9
- Fryer, C. L., Belczynski, K., Ramirez-Ruiz, E., et al. 2015, *ApJ*, submitted (arXiv:1504.07605)
- Fryer, C. L., Rueda, J. A., & Ruffini, R. 2014, *ApJL*, **793**, L36
- Fryer, C. L., Woosley, S. E., & Hartmann, D. H. 1999, *ApJ*, **526**, 152
- Gehrels, N. 1986, *ApJ*, **303**, 336
- Goodman, J. 1986, *ApJL*, **308**, L47
- Guetta, D., & Della Valle, M. 2007, *ApJL*, **657**, L73
- Haensel, P., Potekhin, A. Y., & Yakovlev, D. G. (ed.) 2007, *Astrophysics and Space Science Library* 326, *Neutron Stars 1: Equation of State and Structure* (New York: Springer)
- Han, W.-B., Ruffini, R., & Xue, S.-S. 2012, *PhRvD*, **86**, 084004
- Iwakiri, W., Tashiro, M., Terada, Y., et al. 2014, GCN, 16457, 1
- Izzo, L., Bernardini, M. G., Bianco, C. L., et al. 2010, *JKPS*, **57–3**, 551
- Izzo, L., Rueda, J. A., & Ruffini, R. 2012a, *A&A*, **548**, L5
- Izzo, L., Ruffini, R., Penacchioni, A. V., et al. 2012b, *A&A*, **543**, A10
- Klebesadel, R. W. 1992, in *Gamma-Ray Bursts—Observations, Analyses and Theories*, ed. C. Ho, R. I. Epstein, & E. E. Fenimore (Cambridge: Cambridge Univ. Press)
- Kocevski, D., Longo, F., Vianello, G., et al. 2014, GCN, 16421, 1
- Kopač, D., D’Avanzo, P., Melandri, A., et al. 2012, *MNRAS*, **424**, 2392
- Kouveliotou, C., Meegan, C. A., Fishman, G. J., et al. 1993, *ApJL*, **413**, L101
- Kramer, M. 2014, *IJMPD*, **23**, 30004
- Lattimer, J. M. 2012, *ARNPS*, **62**, 485
- Lawrence, S., Tervala, J. G., Bedaque, P. F., & Miller, M. C. 2015, *ApJ*, in press (arXiv:1505.00231)
- Lee, W. H., Ramirez-Ruiz, E., & Page, D. 2004, *ApJL*, **608**, L5
- Maselli, A., & D’Avanzo, P. 2014, GCN, 16424, 1
- Meegan, C., Lichti, G., Bhat, P. N., et al. 2009, *ApJ*, **702**, 791
- Meszáros, P. 2006, *RPPH*, **69**, 2259
- Meszáros, P., & Rees, M. J. 1997, *ApJL*, **482**, L29
- Muccino, M., Ruffini, R., Bianco, C. L., Izzo, L., & Penacchioni, A. V. 2013, *ApJ*, **763**, 125
- Nakar, E., & Granot, J. 2007, *MNRAS*, **380**, 1744
- Narayan, R., Paczynski, B., & Piran, T. 1992, *ApJL*, **395**, L83
- Narayan, R., Piran, T., & Shemi, A. 1991, *ApJL*, **379**, L17
- Oliveira, F. G., Rueda, J. A., & Ruffini, R. 2014, *ApJ*, **787**, 150
- Paczynski, B. 1986, *ApJL*, **308**, L43
- Patricelli, B., Bernardini, M. G., Bianco, C. L., et al. 2012, *ApJ*, **756**, 16
- Piran, T. 2004, *RvMP*, **76**, 1143
- Piran, T. 2005, *RvMP*, **76**, 1143
- Pisani, G. B., Izzo, L., Ruffini, R., et al. 2013, *A&A*, **552**, L5
- Preparata, G., Ruffini, R., & Xue, S. 1998, *A&A*, **338**, L87
- Ramirez-Ruiz, E., & Fenimore, E. E. 2000, *ApJ*, **539**, 712
- Rees, M. J., & Meszáros, P. 1994, *ApJL*, **430**, L93
- Rhoades, C. E., & Ruffini, R. 1974, *PhRvL*, **32**, 324
- Rosswog, S., Ramirez-Ruiz, E., & Davies, M. B. 2003, *MNRAS*, **345**, 1077
- Rotondo, M., Rueda, J. A., Ruffini, R., & Xue, S.-S. 2011, *PhLB*, **701**, 667
- Rueda, J. A., & Ruffini, R. 2012, *ApJL*, **758**, L7
- Rueda, J. A., Ruffini, R., Wu, Y.-B., & Xue, S.-S. 2014, *PhRvC*, **89**, 035804
- Rueda, J. A., Ruffini, R., & Xue, S.-S. 2011, *NuPhA*, **872**, 286
- Ruffini, R. 2009, in *The Kerr Spacetime*, ed. D. L. Wiltshire, M. Visser, & S. Scott (Cambridge: Cambridge Univ. Press)
- Ruffini, R. 2015a, ARep, in press
- Ruffini, R. 2015b, Proc. of the 2nd Cesar Lattes Meeting, ed. U. Barres de Almeida et al., in press
- Ruffini, R., Aksenov, A. G., Bernardini, M. G., et al. 2009, AIP Conf. Ser. 1132, ed. M. Novello & S. Perez (Melville, NY: AIP), 199
- Ruffini, R., Bernardini, M. G., Bianco, C. L., et al. 2005, AIP Conf. Ser. 782, Xth Brazilian School of Cosmology and Gravitation, ed. M. Novello & S. E. Perez Bergliaffa (Melville, NY: AIP), 42
- Ruffini, R., Bernardini, M. G., Bianco, C. L., et al. 2006, AIP Conf. Ser. 836, Gamma-Ray Bursts in the Swift Era, ed. S. S. Holt, N. Gehrels & J. A. Nousek (Melville, NY: AIP), 103
- Ruffini, R., Bianco, C. L., Chardonnet, P., Frascchetti, F., & Xue, S. 2002, *ApJL*, **581**, L19
- Ruffini, R., Bianco, C. L., Frascchetti, F., Xue, S.-S., & Chardonnet, P. 2001a, *ApJL*, **555**, L117
- Ruffini, R., Bianco, C. L., Frascchetti, F., Xue, S.-S., & Chardonnet, P. 2001b, *ApJL*, **555**, L113
- Ruffini, R., Bianco, C. L., Frascchetti, F., Xue, S.-S., & Chardonnet, P. 2001c, *ApJL*, **555**, L107
- Ruffini, R., Bianco, C. L., Xue, S.-S., et al. 2004, *IJMPD*, **13**, 843
- Ruffini, R., Izzo, L., Muccino, M., et al. 2013, ARep, submitted (arXiv:1311.7432)
- Ruffini, R., Muccino, M., Bianco, C. L., et al. 2014, *A&A*, **565**, L10
- Ruffini, R., Salmonson, J. D., Wilson, J. R., & Xue, S. 2000, *A&A*, **359**, 855
- Ruffini, R., Salmonson, J. D., Wilson, J. R., & Xue, S.-S. 1999, *A&A*, **350**, 334
- Ruffini, R., Vereshchagin, G., & Xue, S.-S. 2010, *PhR*, **487**, 1
- Ruffini, R., Wang, Y., Enderli, M., et al. 2015, *ApJ*, **798**, 10
- Ruffini, R., & Xue, S.-S. 2008, AIP Conf. Ser. 1059, ed. D.-S. Lee & W. Lee (Melville, NY: AIP), 72
- Ruffini, R., & Xue, S.-S. 2013, *PhLA*, **377**, 2450
- Sahu, K. C., Livio, M., Petro, L., et al. 1997, *Natur*, **387**, 476
- Salmonson, J. D., & Wilson, J. R. 2002, *ApJ*, **578**, 310
- Sari, R., Piran, T., & Narayan, R. 1998, *ApJL*, **497**, L17
- Schaefer, B. E. 2007, *ApJ*, **660**, 16
- Soderberg, A. M., Kulkarni, S. R., Nakar, E., et al. 2006, *Natur*, **442**, 1014
- Tavani, M. 1998, *ApJL*, **497**, L21
- Troja, E., King, A. R., O’Brien, P. T., Lyons, N., & Cusumano, G. 2008, *MNRAS*, **385**, L10
- van Paradijs, J., Groot, P. J., Galama, T., et al. 1997, *Natur*, **386**, 686
- Wanderman, D., & Piran, T. 2010, *MNRAS*, **406**, 1944
- Zhang, B., Fan, Y. Z., Dyks, J., et al. 2006, *ApJ*, **642**, 354
- Zhang, C. M., Wang, J., Zhao, Y. H., et al. 2011, *A&A*, **527**, A83
- Zhang, F.-W., Shao, L., Yan, J.-Z., & Wei, D.-M. 2012, *ApJ*, **750**, 88

GRB 130427A AND SN 2013cq: A MULTI-WAVELENGTH ANALYSIS
OF AN INDUCED GRAVITATIONAL COLLAPSE EVENTR. RUFFINI^{1,2,3,4}, Y. WANG^{1,2}, M. ENDERLI^{1,3}, M. MUCCINO^{1,2}, M. KOVACEVIC^{1,3}, C. L. BIANCO^{1,2},
A. V. PENACCHIONI⁴, G. B. PISANI^{1,3}, AND J. A. RUEDA^{1,2,4}¹ Dip. di Fisica and ICRA, Sapienza Università di Roma, Piazzale Aldo Moro 5, I-00185 Rome, Italy² ICRA Net, Piazza della Repubblica 10, I-65122 Pescara, Italy; yu.wang@icranet.org³ Université de Nice Sophia Antipolis, CEDEX 2, Grand Château Parc Valrose, Nice, France⁴ ICRA Net-Rio, Centro Brasileiro de Pesquisas Físicas, Rua Dr. Xavier Sigaud 150, Rio de Janeiro, RJ 22290-180, Brazil

Received 2014 March 7; accepted 2014 October 17; published 2014 December 11

ABSTRACT

We performed a data analysis of the observations by the *Swift*, *NuStar*, and *Fermi* satellites in order to probe the induced gravitational collapse (IGC) paradigm for gamma-ray bursts (GRBs) associated with supernovae (SNe) in the terra incognita of GRB 130427A. We compare our data analysis with those in the literature. We have verified that GRB 130427A conforms to the IGC paradigm by examining the power law behavior of the luminosity in the early 10^4 s of the XRT observations. This has led to the identification of the four different episodes of the binary driven hypernovae (BdHNe) and to the prediction, on 2013 May 2, of the occurrence of SN 2013cq, which was also observed in the optical band on 2013 May 13. The exceptional quality of the data has allowed the identification of novel features in *Episode 3* including: (1) the confirmation and the extension of the existence of the recently discovered nested structure in the late X-ray luminosity in GRB 130427A, as well as the identification of a spiky structure at 10^2 s in the cosmological rest-frame of the source; (2) a power law emission of the GeV luminosity light curve and its onset at the end of *Episode 2*; and (3) different Lorentz Γ factors for the emitting regions of the X-ray and GeV emissions in this *Episode 3*. These results make it possible to test the details of the physical and astrophysical regimes at work in the BdHNe: (1) a newly born neutron star and the supernova ejecta, originating in *Episode 1*; (2) a newly formed black hole originating in *Episode 2*; and (3) the possible interaction among these components, observable in the standard features of *Episode 3*.

Key words: black hole physics – gamma-ray burst: general – nuclear reactions, nucleosynthesis, abundances – stars: neutron – supernovae: general

1. INTRODUCTION AND SUMMARY
OF PREVIOUS RESULTS

That some long gamma-ray bursts (GRBs) and supernovae (SNe) can occur almost simultaneously has been known since the early observations of GRB 980425/SN 1998bw (Galama et al. 1998; Pian et al. 2000). This association of a GRB and an SN occurs most commonly in a family of less energetic long GRBs with the following characteristics: (1) isotropic energies E_{iso} in the range of 10^{49} – 10^{52} erg (Guetta & Della Valle 2007); (2) a soft spectrum with rest-frame peak energy $E_{p,i} < 100$ keV, although the instruments are sensitive up to GeV; and (3) supernova emissions observable up to a cosmological distance $z < 1$. Hereafter we will refer to this family as *family 1*. This is well recognized in the literature; see, e.g., (Maselli et al. 2014).

An alternative family of highly energetic long GRBs that are associated with SNe and that has a much more complex structure exists. Their characteristics are: (1) E_{iso} is in the range 10^{52} – 10^{54} erg; (2) they present multiple components in their spectra and in their overall luminosity distribution, ranging from X-ray to γ -ray all the way to GeV emission. They have peak energies from 100 keV to some MeV; (3) in view of their large energetics, their observation extends to the entire universe all the way up to $z = 8.2$ (Ruffini et al. 2014b). Hereafter we will refer to this family as *family 2*.

There was some doubt that SNe may be associated with very bright long GRBs. Naïve energetic arguments said it was unlikely for an SN to be in a powerful GRB within the single star collapse model (see e.g., Maselli et al. 2014).

For some years the issue of the coincidence of very energetic GRBs with SN has represented an authentic terra incognita. It is critical to clarify whether this association of GRBs and SNe is only accidental or if it is necessary, independent of their energetics. Of the 104 long GRBs with known redshift $z < 1$, 19 GRBs associated with SNe belonging to the *family 2* were observed (Kovacevic et al. 2014) before 2014 June, and GRB 130427A, with isotropic energy $E_{\text{iso}} \simeq 10^{54}$ erg, is the most energetic one so far.

In Ruffini et al. (2001, 2008) we introduced the paradigm of induced gravitational collapse (IGC) to explain the astrophysical reasons for the association of GRBs with supernovae. This paradigm indicates that all long GRBs, by norm, must be associated with SNe. The IGC paradigm differs from the traditional collapsar–fireball paradigm (see, e.g., Piran 2005 and references therein). In the collapsar–fireball model, the GRB process is described by a single episode: (1) it is assumed to originate in a “collapsar” (Woosley 1993), (2) the spectral and luminosity analysis is typically time integrated over the entire T_{90} (see e.g., Tavani 1998), and (3) the description of the afterglow is dominated by a single ultra-relativistic jetted emission (see, e.g., in Rhoads 1999; van Eerten et al. 2010; van Eerten & MacFadyen 2012; Nava et al. 2013). In contrast, the IGC paradigm considers a multi-component system, similar to those described by *S*-matrix in particle physics, as shown in Figure 1: (1) the in-states are represented by a binary system formed by an FeCO core, which is very close to the onset of an SN event and a tightly bound companion neutron star (NS; Ruffini et al. 2008; Rueda & Ruffini 2012; Izzo et al. 2012). The out-states are the creation of a new NS (ν -NS) and black hole

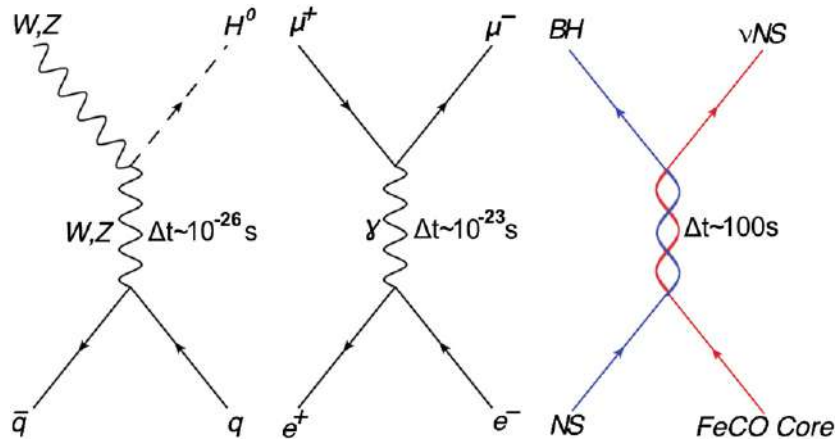


Figure 1. Three different matrices in fundamental physics. The first is the quark matrix leading to a Higgs boson. The middle is the classical electron–positron pair matrix, generating a muon and anti-muon pair. The third matrix is the most recent and it is considered in the present work. Δt is the duration of the intermediate state.

(BH). In the case of particle physics, the S -matrix describes a virtual phenomenon occurring on timescales of 10^{-26} s (Aad et al. 2012, $q\bar{q} \rightarrow WZH^0$) and 10^{-23} s (Bernardini 2004, $e^+e^- \rightarrow \mu^+\mu^-$). In the astrophysical case considered here, the cosmic matrix (C -matrix) describes a real event occurring on timescale ~ 200 s, which is still a very short time when compared to traditional astrophysical timescales. Following the accretion of the SN ejecta onto the companion NS binary, a BH is expected to be created, giving rise to the GRB. (2) Special attention is given to the analysis of the instantaneous spectra in the optical, X-ray, γ -ray, and GeV energy range (as exemplified in this article). (3) Four different episodes are identifiable in the overall emission, each with marked differences in the values of their Lorentz Γ factors (Ruffini et al. 2014c). The possible relevance of a binary system in the explanation of GRBs was already mentioned by Fryer et al. (1999) and Broderick (2005), but the binaries were a trigger to the traditional collapsar model.

The opportunity to probe the IGC paradigm (Izzo et al. 2012) comes from the prototypical source GRB 090618, which is a member of *family 2*. This source has extremely high energetics (i.e., $E_{\text{iso}} = 2.7 \times 10^{53}$ erg), is at a relatively close distance (i.e., $z = 0.54$), and has coverage in all existing γ , X-ray, and optical observatories.

The following results have been obtained (see visualized spacetime diagram in Figure 2):

1. *Episode 1*, which corresponds to the onset of the SN and the accretion process onto the companion NS, was identified in the early 1950 s, with a thermal plus power law component in the spectra (see Izzo et al. 2012, Figure 16), as well as a temporal evolution of the radius of the emitting region expanding from 10^9 cm to 7×10^9 cm (see Izzo et al. 2012, Figure 18). This leads to a precise determination of its overall energetics of 4×10^{52} erg.
2. *Episode 2*, with the GRB emission, follows the onset of gravitational collapse and the BH formation. It was also clearly identified with the following characteristic parameters: an isotropic energy $E_{\text{iso}} = 2.49 \times 10^{53}$, baryon loading $B = 1.98 \times 10^{-3}$, Lorentz factor $\Gamma = 495$ (see Izzo et al. 2012, Figure 4), and peak energy $E_{p,i} = 193$ keV. The average number density of the circumburst medium (CBM) is $(n_{\text{CBM}}) = 0.6 \text{ cm}^{-3}$. The characteristic masses of each CBM cloud are of the order $\sim 10^{22} - 10^{24}$ g, at 10^{16} cm in radii (see Izzo et al. 2012, Figure 10).
3. *Episode 3* of GRB 090618, detected by *Swift*-XRT, starts at 150 s after the burst trigger and continues all the way

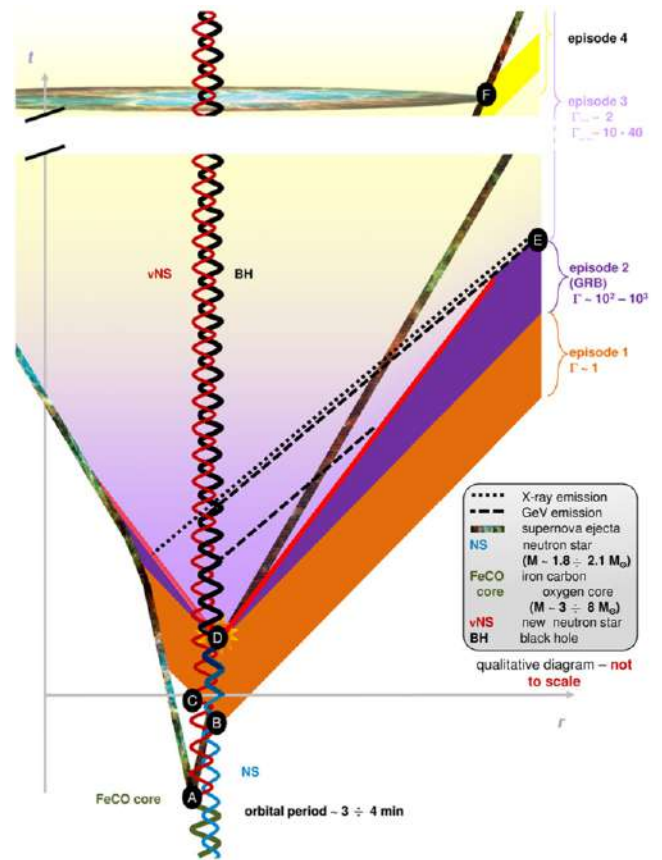


Figure 2. IGC spacetime diagram (not in scale) illustrates four episodes of the IGC paradigm: the nonrelativistic *Episode 1* ($\Gamma \approx 1$), the relativistic motion of *Episode 2* ($\Gamma \approx 10^2 \sim 10^3$), the mildly relativistic *Episode 3* ($\Gamma \approx 2$), and nonrelativistic *Episode 4* ($\Gamma \approx 1$). There is initially a binary system composed of a massive star (yellow thick line) and a neutron star (blue line). The massive star evolves and explodes as an SN at point A, forming a ν NS (red line). The companion NS accretes the supernova ejecta starting from point B, interacts with the ν NS starting from point C, and collapses into a black hole (black line) at point D; this period from point B to point D is defined as *Episode 1*. Point D is the beginning of *Episode 2*, which is caused by the collision of GRB outflow and interstellar filaments. At point E, *Episode 2* ends and *Episode 3* starts, lasting until the optical signal of the supernova emerges at point F, where *Episode 4* starts. (Credit to M. Enderli for drawing this visualized spacetime diagram.)

up to 10^6 s. It consists of three different parts (Nousek et al. 2006): a first very steep decay; a shallower decay, the plateau; and a final steeper decay with a fixed power law index. It soon became clear that *Episode 3*, which was

previously interpreted in the traditional approach as part of the GRB afterglow (Piran 2005; Rhoads 1999; van Eerten et al. 2010; van Eerten & MacFadyen 2012; Nava et al. 2013), appeared to be the seat of a set of novel independent processes occurring after the end of the GRB emission and preceding the optical observation of the SN, which we indicated as *Episode 4*.

Progress has recently been made in the analysis of *Episode 1*. It is characterized by the explosion of the FeCO core, followed by the hypercritical accretion onto the NS, which leads to the NS reaching critical mass and consequently its induced gravitational collapse to a BH. The hypercritical accretion of the SN ejecta onto the NS has been estimated using the Bondi–Hoyle–Lyttleton formalism to be $10^{-2} M_{\odot} \text{ s}^{-1}$; here M_{\odot} is the solar mass (Bondi & Hoyle 1944; Bondi 1952) (see, e.g., in Rueda & Ruffini 2012). The inflowing material shocks as it piles up onto the NS, producing a compressed layer on top of the NS (see, e.g., Fryer et al. 1996). As this compressed layer becomes sufficiently hot, it triggers the emission of neutrinos that cool the infalling material, allowing it to be accreted into the NS (Zel’dovich et al. 1972; Ruffini & Wilson 1975; Ruffini et al. 1999, 2000; Fryer et al. 1996, 1999). Recently Fryer et al. (2014) presented significant progress in understanding the underlying physical phenomena in the aforementioned hypercritical accretion process of the supernova ejecta into the binary companion neutron star (Ruffini et al. 2008; Rueda & Ruffini 2012). The new treatment, based on the two-dimensional cylindrical geometry smooth particle hydrodynamics code, has numerically simulated the process of hypercritical accretion—the classical Bondi–Hoyle regimes—in the specific case of the IGC paradigm, and led to the first astrophysical application of the neutrino production process considered in Zel’dovich et al. (1972) and in Ruffini & Wilson (1975; see e.g., in R. Ruffini et al., presentation in the Zeldovich-100 meeting)⁵. Indeed the fundamental role of neutrinos’ emission allows the accretion rate process to increase the mass of the binary companion star to its critical value, which leads to the black hole formation giving rise to the GRB in *Episode 2*. These results confirm and quantify the general considerations presented in Rueda & Ruffini (2012).

In *Episode 2* all technical, numerical, and basic physical processes have been tested in the literature, and the fireshell model is now routinely applied to all GRBs (see, e.g., GRB 101023 in Penacchioni et al. 2012 and GRB 110709B in Penacchioni et al. 2013).

The main aim of this paper is dedicated to a deeper understanding of the physical and astrophysical process present in *Episode 3*:

1. to give evidence of the universal properties of *Episode 3* observed in additional sources belonging to *family 2*, as compared to the very high variability of *Episode 1* and *Episode 2* components;
2. to present observations of GRB130427A leading to identification of new physical regimes encountered in *Episode 3* and their interpretation within the IGC paradigm;
3. to give evidence of the predictive power of the observations of *Episode 3* and outline the underlying physical process leading to the characterization of the two aforementioned families of GRBs.

To start we will summarize in the next paragraph some qualifying new features generally observed in *Episode 3* of selected GRBs of *Family 2* and proceed in the following paragraphs to the specific new information acquired about *Episode 3* from GRB 130427A. We will then proceed to the general conclusions.

2. THE QUALIFYING FEATURES OF EPISODE 3

As observations of additional sources fulfilling the IGC paradigm were performed, some precise qualifying features for characterizing *Episode 3* have been found.

1. In some GRBs with known redshift belonging to *family 2* the late X-ray luminosities at times larger than 10^4 s appeared to overlap when duly scaled in the proper rest frame of the GRB source (Penacchioni et al. 2012). This was soon confirmed for a sample of six GRBs (i.e., GRB 060729, GRB 061007, GRB 080319B, GRB090618, GRB 091127, and GRB 111228), which we call the golden sample (*GS*; Pisani et al. 2013); see Figure 3. This unexpected result led to the adoption of the universal luminosity versus time relation in the late X-ray emission of *Episode 3* as a distance indicator. For some GRBs without a known cosmological redshift and exhibiting the general features of the four episodes, we imposed the overlapping of the late power law X-ray emission in *Episode 3* with those of the *GS*, and consequently we inferred the value of the cosmological redshift of the source. This led to inferring the overall energetics of the source and a consistent description of each episode following our theoretical model. This was the case with GRB 101023, which has an inferred redshift $z = 0.9$ and $E_{\text{iso}} = 4.03 \times 10^{53}$ erg (Penacchioni et al. 2012), and GRB 110709B, with inferred redshift $z = 0.75$ and $E_{\text{iso}} = 2.43 \times 10^{52}$ erg (Penacchioni et al. 2013).

The above analysis initially addressed sources with $z < 1$, where the associated SNe are observable. However, there is no reason to doubt that the IGC paradigm also applies to sources for $z > 1$. In this case the SN is not observable with the current optical telescopes, but the existence of all the above episodes, with the exception of *Episode 4* related to the optical observation of the SN, can be verified in principle if they are above the observational threshold, and the members of the *GS* are correspondingly further increased. Indeed, significant results have been reached by observing the fulfillment of the above scaling laws in *Episode 3* of GRB 090423, at $z = 8.2$ (Ruffini et al. 2014b). The occurrence of this overlapping in the late X-ray emission observed by XRT is considered a necessary and sufficient condition to assert that a GRB fulfills the IGC paradigm.

2. The identification of a thermal emission occurring in the initial very steep decay of *Swift*-XRT data of *Episode 3* in GRB 090618 (Ruffini et al. 2014c). We are currently examining other GRBs with this feature, e.g., 060729, 061007, 061121 (Page et al. 2011; Starling et al. 2012; Friis & Watson 2013). From these thermal emissions it is possible to infer the dimensions of the X-ray emitting regions, as well as their Lorentz Γ factors, in this earliest part of *Episode 3* (Ruffini et al. 2014c). A typical mildly relativistic expansion regime with $\Gamma \lesssim 2$ and characteristic radii $R \sim 10^{13}$ cm has been identified (Ruffini et al. 2014c). These observational facts lead to a novel approach to the theoretical understanding of the X-ray emission

⁵ http://www.icranet.org/index.php?option=com_content&task=view&id=747&Itemid=880

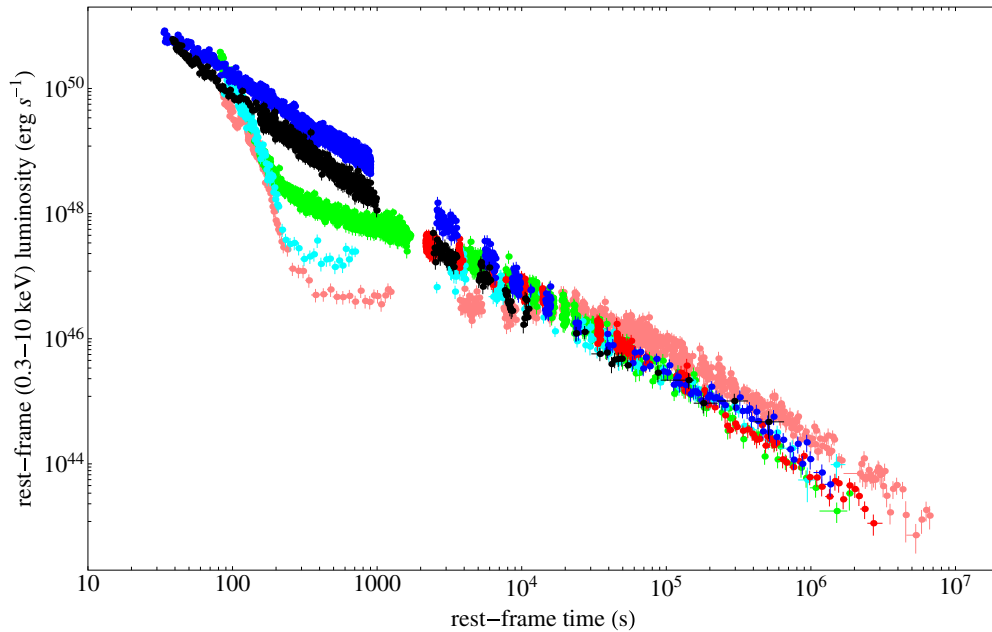


Figure 3. Golden sample scaling law (Pisani et al. 2013). X-ray luminosity light curves of the six GRBs with measured redshift in the 0.310 keV rest-frame energy range: in pink GRB 060729, $z = 0.54$; black GRB 061007, $z = 1.261$; blue GRB 080319B, $z = 0.937$; green GRB 090618, $z = 0.54$; red GRB 091127, $z = 0.49$; and in cyan GRB 111228, $z = 0.713$.

process of *Episode 3*, which is profoundly different from the ultra-relativistic one in the traditional jet afterglow collapsar paradigm model (Piran 2005; Mészáros 2006). We concluded that this emission is not only mildly relativistic, but also linked to a wide-angle emission from the SN ejecta in the absence of any sign of collimation (Ruffini et al. 2014c).

3. From the direct comparison of the late X-ray emission of the *GS* sources, we recently identified the appearance of a nested structure, which we illustrate in Figure 4, comparing the corresponding behavior of GRB 130427A with that of *GS* GRB 060729 (Ruffini et al. 2014c). The occurrence of these nested structures shows, among others, that in the case of the most intense sources, the common power law observed for the X-ray luminosities for times larger than 10^4 s does extend to earlier times; see Figure 4. Indeed, for the most intense sources, the common power law behavior is attained at an earlier time and at higher X-ray luminosities than the characteristic timescale indicated in (Pisani et al. 2013); see Figure 3. As we are going to show, in the highly energetic GRB 130427A, this behavior starts at much earlier times around 400 s.

Some of these results were presented by one of the authors in the 2013 Texas Symposium on Relativistic Astrophysics.⁶ There, the sources originating in a tight binary system composed of a FeCO core at the onset of an SN event and a companion NS were named binary driven hypernovae (BdHNe; Ruffini et al. 2014c), in order to distinguish them from the traditional hypernovae (HN).

The occurrence of the three features of *Episode 3* listed previously as obtained by our data analysis are becoming crucial to the theoretical understanding of the GRB–SN phenomenon. They have never been envisaged to exist or predicted in the traditional collapsar–fireball paradigm (Nava et al. 2013; van Eerten & MacFadyen 2012; van Eerten et al. 2010). The IGC

paradigm motivated an attentive data analysis of *Episode 3* and the discovery of its universality has been a by-product.

3. EPISODE 3 IN THE CASE OF GRB 130427A

In what follows we will show how GRB 130427A, which is associated with SN 2013cq and is the most luminous GRB observed in the past 40 yr, offers the longest multi-wavelength observations of *Episode 3* so far. It confirms and extends the above understanding and corresponding scaling laws already observed in X-rays to lower and higher energies. It also allows for the exploration of the occurrence of similar constant power law emission in the high-energy emission (GeV) and in the optical domain. We proceed with our data analysis of the ultra high GeV energy observations (*Fermi*-LAT), those in soft and hard X-rays (*Swift*-XRT and *NuStar*, respectively), as well as of optical observations (*Swift*-UVOT and ground based satellites). Our results are compared to those in the current literature. These observational facts set very specific limits on the Lorentz Γ factor of each component; the corresponding mechanism of emission; and the clear independence of any prolongation of the GRB emission of *Episode 2* to the emission process of *Episode 3*.

The observation of the scaling law in the first 2×10^4 s alone has allowed us to verify the BdHN nature of this source, which necessarily implies the presence of a SN. Consequently, we recall in Section 3.1 that we made the successful prediction of the occurrence of a supernova, which was observed in the optical band, as predicted on 2013 May 2.

In Section 3.2, we summarize our own data reduction of the *Fermi* and *Swift* satellites, and we compare them with those in the current literature.

In Section 3.3, we discuss the finding of a thermal component in the early part of the X-ray emission of *Episode 3*. This is crucial for identifying the existence of the X-ray emission of a regime with low Lorentz factor and small radius, which is typical for supernova ejecta.

⁶ <http://nsm.utdallas.edu/texas2013/proceedings/3/1/Ruffini.pdf>

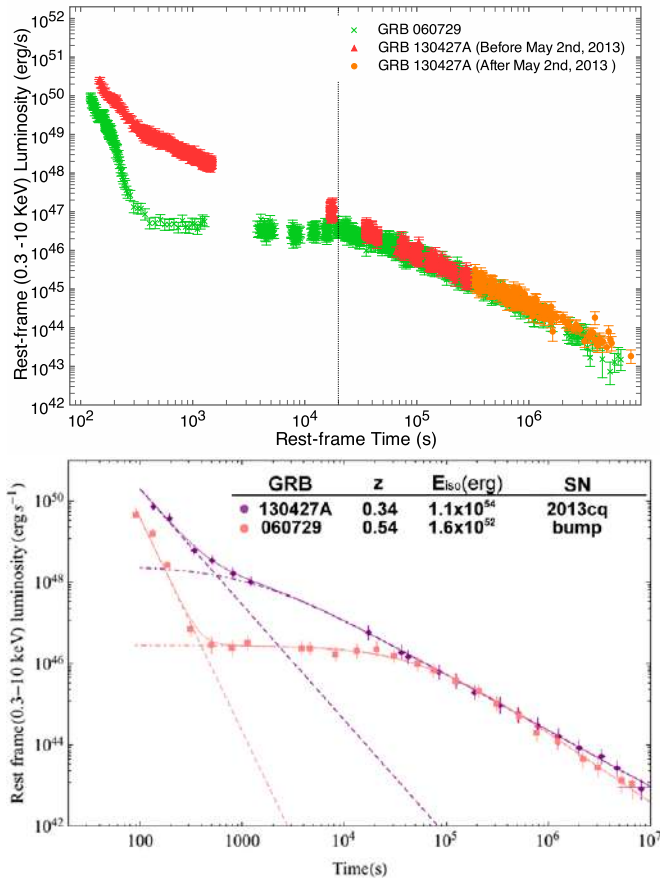


Figure 4. Top: overlapping of GRB 130427A and GRB 060729. The green crosses represent the light curve of GRB 060729. The red triangle and orange dots represent the light curve of GRB 130427A before and after 2013 May 2, respectively. The vertical line marks the time of 2×10^4 s, which is the lower limit for the domain of validity of the Pisani relation prior to GRB 130427A. Bottom: this figure shows that GRB 060729 and GRB 130427A have different magnitudes of the isotropic energy, but exhibit a common scaling law after 2×10^4 s. It also shows that the low isotropic energy GRB 060729 has a longer plateau, while the high isotropic energy GRB 130427A does not display an obvious plateau.

In Section 3.4 we compare the broadband (optical, X-ray, γ -ray, all the way up to GeV) light curves and spectra of *Episode 3*.

In Section 3.5 we point out the crucial difference between the X-, γ -ray, and GeV emission in *Episode-3*.

In Section 3.6 we proceed to a few general considerations on ongoing theoretical activities.

Sections 4 is the summary and conclusions.

3.1. Identification and Prediction

With the appearance of GRB 130427A, we decided to explore the applicability of the IGC paradigm in the terra incognita of GRB energies up to $\sim 10^{54}$ erg. In fact, prior to GRB 130427A, the only known case of an equally energetic source, GRB 080319B, had some evidence of an optical bump (Bloom et al. 2009; Tanvir et al. 2010), but in no way gave detailed information about the SN spectrum or type. We noticed in GRB 130427A the characteristic overlapping of the late X-ray decay in the cosmological rest frame of the source with that of GRB 060729, a member of the golden sample (in red in Figure 4), and from the overlapping we deduced a redshift that was consistent with the observational value $z = 0.34$ (Levan et al. 2013a).

Therefore from the observations of the first 2×10^4 s, GRB 130427A fulfilled the IGC paradigm, and we conclude, solely on this ground, that an SN should be observed under these circumstances. We sent the GCN circular 14526⁷ (Ruffini et al. 2013b) on 2013 May 2 predicting that the optical *R*-band of an SN will reach its peak magnitude in about 10 days in the cosmological rest frame on the basis of the IGC paradigm. Starting from 2013 May 13 the telescopes GTC, Skynet, and HST discovered the signals from the type Ic supernova SN 2013cq (de Ugarte Postigo et al. 2013; Trotter et al. 2013; Levan et al. 2013b, 2014; Xu et al. 2013). We kept updating the X-ray *Swift* data for weeks and confirmed the complete overlapping of the late X-ray luminosities, in the respective cosmological rest frames, of GRB 130427A and GRB 060729 (in orange in Figure 4). From these data it became clear that the power law behavior of the late-time X-ray luminosity with index $\alpha \sim 1.3$ indicated in Pisani et al. (2013)—leading to the new concept of the nesting of the light curves—started in this very energetic source at $\sim 10^2$ s following an initial phase of steeper decay (Ruffini et al. 2014c).

Contrary to the traditional approach that generally considers a GRB to be composed of the prompt emission followed by the afterglow, both of which vary from source to source, the IGC paradigm for *family 2* introduced *Episode 3*, which shows regularities and standard late-time light curves that are largely independent of the GRB energy. It soon became clear that, with *Episode 3*, we were starting to test the details of the physics and astrophysics of as yet unexplored regimes implied by the IGC paradigm: (1) a ν -NS and the SN ejecta, originating in *Episode 1*, (2) a newly formed BH originating in *Episode 2*, and (3) the possible interaction among these components observable in the standard features of *Episode 3*.

The joint observations of the *Swift*, *NuStar*, and *Fermi* satellites have offered the unprecedented possibility of clarifying these new regimes with the addition of crucial observations in the optical, X-ray, and high energy radiation for *Episode 3* of GRB 130427A, leading to equally unexpected results. The remainder of this paper is dedicated to understanding *Episode 3* of this remarkable event.

3.2. Data Analysis of Episode 3 in GRB 130427A

GRB 130427A was first observed by the *Fermi*-GBM at 07:47:06.42 UT on 2013 April 27 (von Kienlin 2013), which we set as the starting time t_0 throughout the entire analysis. After 51.1 s, the Burst Alert Telescope (BAT) on board *Swift* was triggered. The *Swift* Ultra Violet Optical Telescope (UVOT) and the *Swift* X-ray Telescope (XRT) began observing at 181 s and 195 s after the GBM trigger, respectively (Maselli et al. 2013). Because this was an extremely bright burst, successively more telescopes pointed at the source: the Gemini North telescope in Hawaii (Levan et al. 2013a), the Nordic Optical Telescope (NOT) (Xu et al. 2013), and the VLT/X-shooter (Flores et al. 2013), which confirmed the redshift $z = 0.34$.

⁷ GCN 14526: the late X-ray observations of GRB 130427A by *Swift*-XRT clearly show a pattern typical of a family of GRBs associated with supernovae (SNe), following the Induced Gravitational Collapse (IGC) paradigm (Rueda & Ruffini 2012; Pisani et al. 2013). We assume that the luminosity of the possible SN associated with GRB 130427A would be that of 1998bw, as was found in the IGC sample described in Pisani et al. (2013). Assuming the intergalactic absorption in the *I* band (which corresponds to the *R*-band rest frame) and the intrinsic one, with a Milky Way type for the host galaxy, we obtain a magnitude expected for the peak of the SN of $I = 22-23$ occurring 13–15 days after the GRB trigger, namely between the 10th and the 12th of 2013 May. Further optical and radio observations are encouraged.

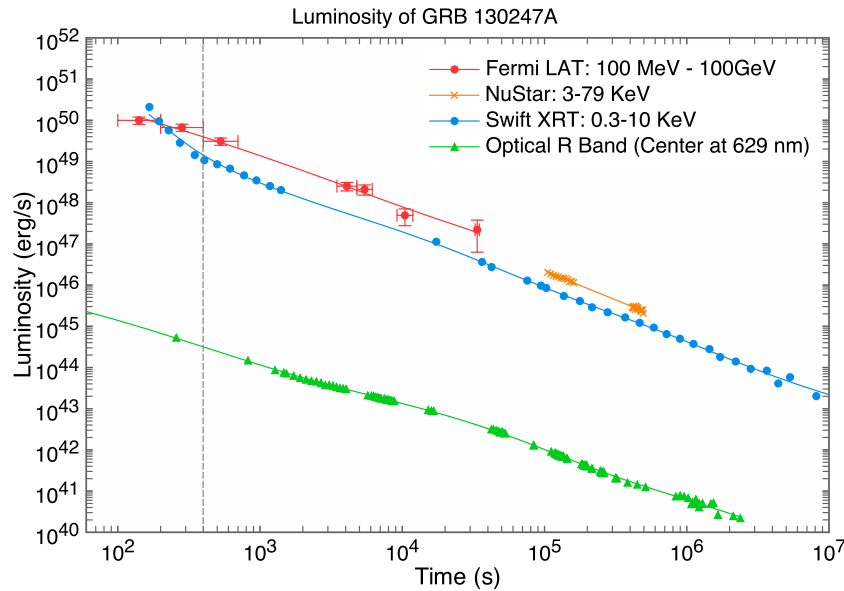


Figure 5. Multi-wavelength light curve of GRB 130427A. The high energy (100 MeV–100 GeV) emission detected by *Fermi*-LAT marked in red, and soft X-ray (0.3–10 keV) data from *Swift*-XRT marked in blue, are deduced from the original data. *NuStar* data (3–79 keV) marked in orange comes from (Kouveliotou et al. 2013). The optical (*R*-band, center at 629 nm) data marked in green comes from ground-based instruments (Perley et al. 2013). The error bars are too small with respect to the data points except for *Fermi*-LAT data. The horizontal error bars of *Fermi*-LAT represent the time bin in which the flux is calculated and vertical bars are statistical 1σ errors on the flux (the systematic error of 10% is ignored). The details in the first tens of seconds are ignored because we are interested in the behavior of the high energy light curve on a longer time scale. The vertical gray dashed line at (~ 400 s) indicates when the constant decaying slope starts. It is clear that all the energy bands have almost the same slope after 400 s in *Episode 3*.

GRB 130427A is one of the few GRBs with an observed adequate fluence in the optical, X-ray, and GeV bands simultaneously for hundreds of seconds. In particular it remained continuously in the LAT field of view until 750 s after the trigger of *Fermi*-GBM (Ackermann et al. 2013), which gives us the best opportunity so far to compare the light curves and spectra in different energy bands, and to verify our IGC paradigm. We did the data reduction of *Fermi* and *Swift* satellites using the following methods.

Fermi. Data were obtained from the Fermi Science Support Center,⁸ and were analyzed using an unbinned likelihood method with Fermi Science Tools v9r27p1.⁹ Event selections *P7SOURCE_V6* and *P7CLEAN_V6* were used, depending on which one gave more stable results. Recommended data cuts were used (e.g., $z_{\max} = 100$ degree). The background is composed of the galactic diffuse emission template and the isotropic emission template, as well as about 60 point sources that are within the 15° radius of the GRB (however, their contribution was found to be negligible). The parameters for the background templates were held fixed during the fit. Luminosity light curve in Figure 5 corresponds to the energy range of 100 MeV to 100 GeV, a circle radius of 15° , with a power law spectra assumption. Because the data points up to the last two give a photon index of ~ 2.1 with small errors, we set the photon index for the last two points to the value 2.1 during the fitting procedure in order to obtain more stable results. The light curve can be obtained with great temporal detail before 750 s. However, because we are interested in the general behavior of *Episode 3*, for simplicity we neglected such a fine temporal structure and rebinned the light curve. Therefore there are only three data points up to 750 s. The spectrum is plotted in Figure 6.

Swift. XRT data were retrieved from UKSSDC¹⁰ and were analyzed by the standard *Swift* analysis software included in the NASA’s Heasoft 6.14 with relevant calibration files.¹¹ In the first 750 s only Windows Timing (WT) data exists and the average count rate exceeds $300 \text{ counts s}^{-1}$; the highest count rate reaches up to $1000 \text{ counts s}^{-1}$, which is far beyond the value of $150 \text{ counts s}^{-1}$ that is suggested for the WT mode as a threshold of considering pile-up effects (Evans et al. 2007). Pile-up effects cause the detector to misrecognize two or more low energy photons as a single high energy photon, which softens the spectrum. We adopted the method proposed by Romano et al. (2006), fitting dozens of spectra from different inner sizes of box annulus selections in order to determine the extent of the distorted region. Taking the time interval 461–750 s as an example, the deviation comes from where the inner size is smaller than six pixels, as shown in Figure 6. Then we applied the standard XRT data analyzing process (Evans et al. 2007, 2009) to obtain the spectrum, as plotted in Figure 6. For the luminosity light curve we split XRT observations in the nominal 0.3–10 keV energy range to several slices with a fixed count number, followed the standard procedure (Evans et al. 2007, 2009), and considered the pile-up correction. The XRT light curves of different bands are shown in Figure 5.

3.3. The X-Ray Qualification of GRB 130427A as a BdHN

Here we first focus on the extended X-ray emission of *Episode 3*, which, as shown, gives the qualifying features for the identification of GRB 130427A as a BdHN. We first identify the power law component of the light curve after the steep decay and the end of the plateau. This power law component of GRB 130427A has a power law index $\alpha = -(1.31 \pm 0.01)$ and extends from 400 s to $\sim 10^7$ s without jet breaks. These results are consistent with previous papers (see, e.g., in Perley

⁸ <http://Fermi.gsfc.nasa.gov>

⁹ <http://Fermi.gsfc.nasa.gov/ssc/data/analysis/software/>

¹⁰ <http://www.Swift.ac.uk>

¹¹ <http://heasarc.gsfc.nasa.gov/heasoft/>

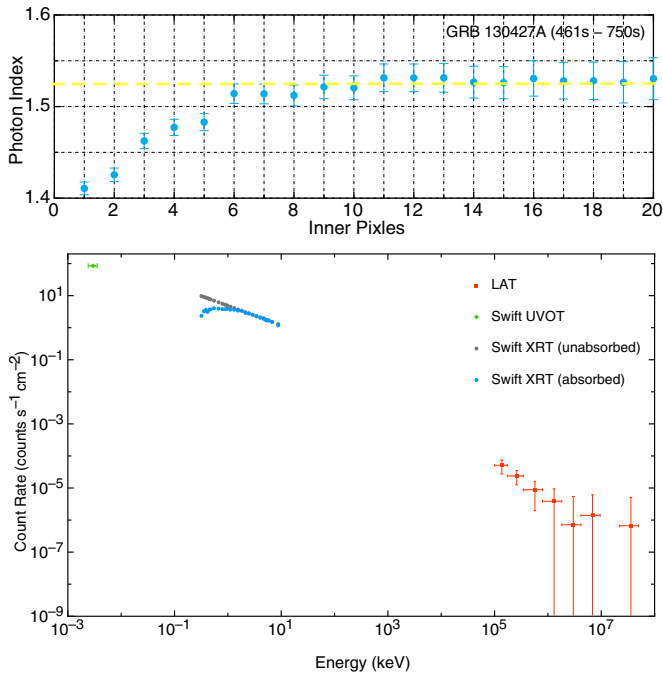


Figure 6. Top: data from the *Swift*-XRT (0.3–10 keV) in the time range of 461–750 s for GRB 130427A. The data shows the photon index for different region selections after considering the pile-up effect. After six inner pixels, the photon index approaches an almost constant value of 1.52. Bottom: spectra of GRB 130427A in the time range of 461–750 s. The green data points are from *Swift*-UVOT (Perley et al. 2013), the blue and gray points come from *Swift*-XRT, and red data correspond to *Fermi*-LAT. The horizontal error bars are energy bins in which the flux is integrated and the vertical ones are 1σ statistical errors on the count rate. The gray data points correspond to unabsorbed *Swift*-XRT data, while the blue ones are obtained with the assumption of absorption.

et al. 2013; Laskar et al. 2013) that find no jet break, but differs from Maselli et al. (2014), who claim a break of the later time light curve.

We turn to an additional crucial point: to confirm that the X-ray emission of *Episode 3* belongs to the SN ejecta and not the GRB. To do this it is crucial, as already done for other sources (Ruffini et al. 2014c), to determine the presence of a thermal component in the early time of *Episode 3* and infer the

temperature and the size of its emitter. By analyzing the XRT data, we find that adding a blackbody component efficiently improves the fit with respect to a single power law from 196 s to 461 s. The corresponding blackbody temperature decreases in that time duration, from 0.5 keV to 0.1 keV, in the observed frame. Figure 7 shows the evolution of the power law plus blackbody spectra in three time intervals. Clearly the flux of the thermal component drops with time, and the temperature corresponding to the peak flux energy decreases. Kouveliotou et al. (2013) found that a single power law is enough to fit the *NuStar* data in the *NuStar* epochs, and the reason could be that the thermal component has faded away or exceeded the observational capacity of the *Swift* satellite in the *NuStar* epochs, which start later than 10^5 s.

By assuming that the blackbody radiation is isotropic in the rest frame, the emitter radius along the line of sight increases from $\sim 0.7 \times 10^{13}$ cm at 196 s to $\sim 2.8 \times 10^{13}$ cm at 461 s in the observed frame. This is orders of magnitude smaller than the emission radius of the GRB, which is larger than 10^{15} cm in the traditional GRB collapsar afterglow model. The size of 10^{13} cm at hundreds of seconds is consistent with the observation of supernova ejecta. After considering the cosmological and the relativistic corrections, $t_a^d \simeq t(1+z)/2\Gamma^2$, where t and t_a^d are the time in the laboratory and observed frame, respectively, and Γ is the Lorentz factor of the emitter, we get an expansion speed of $\sim 0.8c$, corresponding to Lorentz factor $\Gamma = 1.67$. These results contradict the considerations inferred in Maselli et al. (2014) $\Gamma \sim 500$, which invoke a value of the Lorentz factor in the traditional collapsar afterglow model (see, e.g., Mészáros 2006). Again, in the prototypical GRB 090618, the Lorentz factors ($1.5 \leq \Gamma \leq 2.19$) and emission radii ($\sim 10^{13}$ cm) are very similar to those of GRB 130427A presented in Ruffini et al. (2014c). It is interesting that such a thermal component has been also found in the early parts of *Episode 3* of GRB 060729 (adopted in Figure 4) and many other SN associated GRBs (see Ruffini et al. 2014c; Grupe et al. 2007; Starling et al. 2012).

3.4. Discussion of Multi-Wavelength Observations in Episode 3

Now we turn to the most unexpected feature in the analysis of the optical, X-ray, γ -ray, and very high energy emission

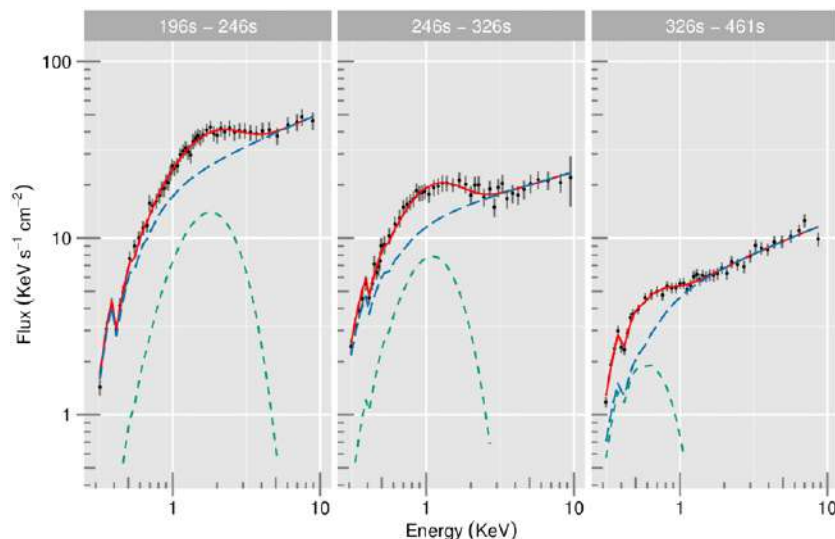


Figure 7. Spectral fitting of three time intervals (196 s–246 s, 246 s–326 s, and 326 s–461 s) in *Episode 3*; the data come from *Swift*-XRT (0.3 KeV–10 KeV, without pile-up area). Black points are the deduced data, the green dashed line presents the thermal component, the blue long-dashed line is the power law component, and the red line shows the combination of these two components. Clearly the flux of thermal component drops and the temperature decreases with time.

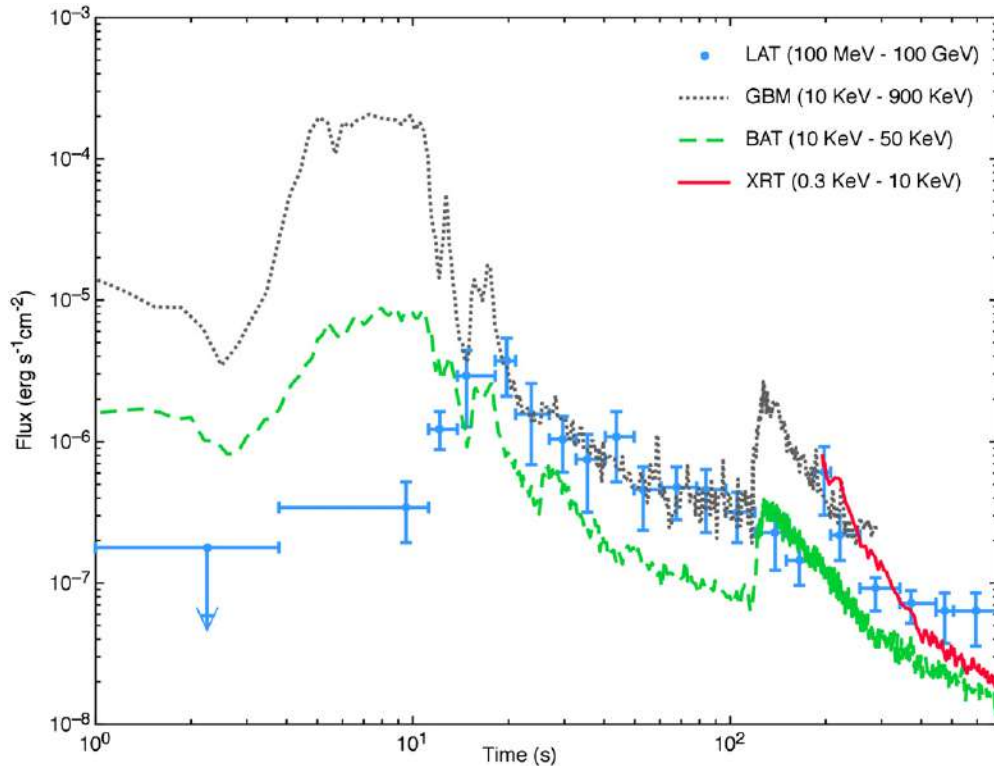


Figure 8. Flux of first 700 s. Blue points are the *Fermi*-LAT high energy emission from 100 MeV until 100 GeV (Ackermann et al. 2013), the gray dotted line represents the *Fermi*-GBM from 10 keV to 900 keV, the green dashed line represents the photons detected by *Swift* BAT from 10 keV to 50 keV, and the red solid line is the soft X-ray *Swift*-XRT detection in the range of 0.3–10 keV. This figure clearly shows that the *Fermi*-LAT emission reaches highest fluence at about 20 s, while the gamma-ray detected by *Fermi*-GBM releases most of the energy within the first 10 s.

in *Episode 3* of GRB 130427A. The optical emission was observed by *Swift*-UVOT and many ground-based telescopes (the *R*-band as an example for the optical observation). The soft X-ray radiation was observed by *Swift*-XRT (0.3–10 keV). Similarly, the hard X-ray radiation was observed by *Swift*-BAT (15–150 keV) and *NuStar* (3–79 keV). The γ -ray radiation was observed by *Fermi*-GBM (8 KeV–40 MeV), and the high energy radiation by *Fermi*-LAT (100 MeV–100 GeV). The main result is that strong analogies are found in the late emission at all wavelengths in *Episode 3*. After 400 s these luminosities show a common power law behavior with the same constant index as in the X-ray (and clearly with different normalizations), so by fitting multi-wavelength light curves together we have a power law index $\alpha = -(1.3 \pm 0.1)$.

Turning now to the spectrum, integrated between 461 s and 750 s, the energy range covers 10 orders of magnitude, and the best fit is a broken power law (see Figure 6). In addition to the traditional requirements for the optical supernova emission in *Episode 4*, and the much more energetically demanding requirement for the general multi-wavelength emission of *Episode 3* has to be addressed.

3.5. The Onset of Episode 3

In the previous sections we emphasized the clear evidence of GeV emission and its analogy in the late power law luminosities as functions of the arrival time for the X-ray, optical, and GeV emissions. Equally important in this section is to emphasize some differences between the X-ray, γ -ray, and the high energy GeV emission, especially with respect to the onset of *Episode 3* at the end of prompt emission in *Episode 2* (see Figure 8). We observe:

1. The γ -ray light curves observed by *Fermi*-GBM and hard X-ray observed by *Swift*-BAT have similar shapes. They reach the highest luminosity between 4 s and 10 s during the prompt emission phase of *Episode 2*.
2. The high energy (>100 MeV) GeV emission gradually rises, just after the γ - and X-ray prompt emissions drop down at the end of *Episode 2*: the high energy GeV emission raises to its peak luminosity at about 20 s. The turn on of the GeV emission coincides, therefore, with the onset of our *Episode 3*. These considerations were recently confirmed and extended by the earliest high energy observations in GRB 090510 (Ruffini et al. 2014, in preparation).
3. At about 100 s, the *Swift*-XRT starts to observe the soft X-ray and a sharp spike appears in the hard X-ray and gamma ray bands (see Figure 8). Only at this point does the *Swift*-XRT start to observe soft X-ray. We are currently addressing the occurrence of the spike to the thermal emission observed to follow in the sharp decay of the X-ray luminosity prior to the plateau and the above mentioned common power law decay (Ruffini et al. 2014b).

The detailed analysis of the prolonged emission observed by *Fermi*-LAT in GeV enables us to set specific limits on the Lorentz factor of this high energy emission. We analyzed the GeV emission from ~ 300 s to 2.5×10^4 s, dividing the time interval into seven sub-intervals and in each of them collecting the corresponding maximum photon energy and photon index of the spectral energy distribution, as shown in Ackermann et al. (2013, Figure 2). We focused our attention on the estimate of the Lorentz factor for this high energy component from the usual optical depth formula for pair creation $\tau_{\gamma\gamma}$ (see, e.g., Lithwick & Sari 2001; Gupta & Zhang 2008). We computed, for

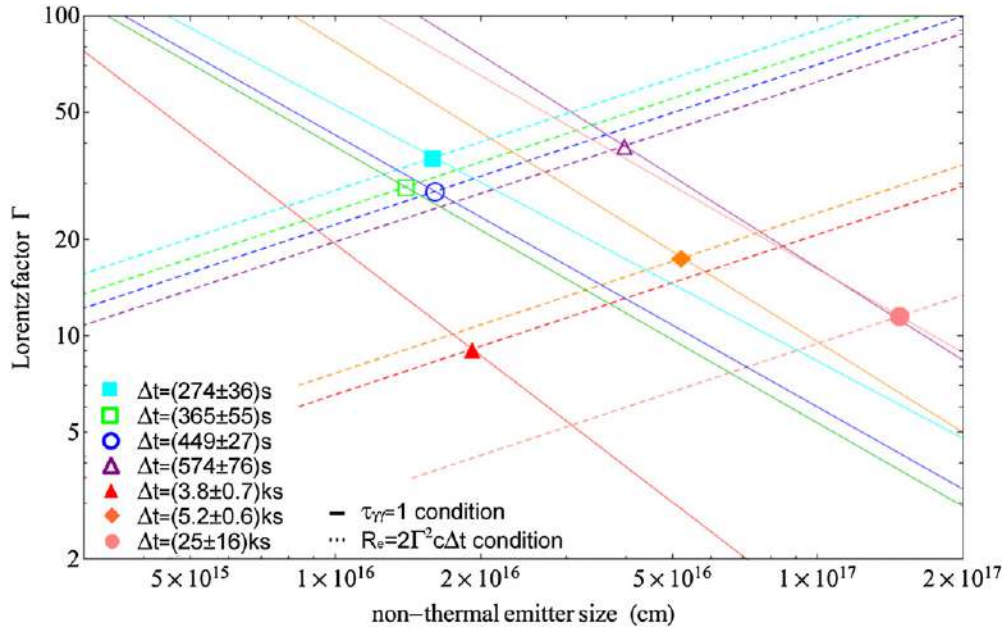


Figure 9. Constraints on the Lorentz factors and the size of the GeV emitting region at the transparency point. Solid curves represent the curves defined by varying the emitting region size from the $\tau_{\gamma\gamma} = 1$ condition; dot-dashed curves represent the radius of the emitter obtained from causality in the ultrarelativistic regime (i.e., $R_{em} = 2\Gamma^2 c \Delta t$). Filled circles correspond to the solutions of both limits. The different colors refer to the time intervals from ~ 273 s to 24887 s, in the order cyan, green, blue, purple, red, orange, and pink, respectively.

different values of radii of the emitter, the corresponding Lorentz factors at the transparency condition (i.e., $\tau_{\gamma\gamma} = 1$; see the solid curves in Figure 9). The constraints on the size of the emitting regions come from causality in the ultrarelativistic regime (i.e., $R_{em} = 2\Gamma^2 c \Delta t$), where Δt corresponds to the duration of the time intervals under consideration (see the dot-dashed curves in Figure 9). The values of the Lorentz factor range between ~ 10 and ~ 40 , and correspondingly, the radii of the emitting region at the transparency point are located between $\sim 10^{16}$ cm and $\sim 2 \times 10^{17}$ cm (see the filled circles in Figure 9).

3.6. General Considerations on Recent Theoretical Progress on BdHD

The concurrence of the above well-defined scaling laws and power law of the observed luminosities both in the X-ray and/or in the optical domains in *Episode 3* of GRB 130427A have been considered arguments in favor of looking to the r -process and to heavy nuclei radioactive decay as the energy sources (Ruffini et al. 2014c; see the pioneering work of Li & Paczynski 1998). The extended interaction of the ν -NS and its binary NS companion in the SN ejecta provides an environment for r -processes to create the needed neutron-rich very heavy elements to attribute some of the electromagnetic energy in *Episode 3* to nuclear decay, $\approx 10^{52}$ erg. Alternatively, we are considering emission originating from type-I and type-II Fermi acceleration mechanisms, which are introduced by Fermi precisely to explain the radiation process in the SN remnants (Fermi 1949). In addition these processes can lead to a power law spectrum (Aharonian 2004) that is similar to that presented in this paper and our recent letter (Ruffini et al. 2014c). The GRB emission of *Episode 2* interacting with the SNe ejecta could represent the energy injection long sought by Fermi for the onset of his acceleration mechanism (Fermi 1949).

Both of these processes can operate as energy sources for the mildly relativistic X-ray component and the relativistic GeV emission of *Episode 3*.

We are currently examining additional BdHN sources and giving particular attention to understanding the highest GeV energy emission, which is unexpected in the traditional r -process. The inferred Γ Lorentz factor for the GeV emission points to the possibility of a direct role of the two remaining components in the IGC paradigm: the newly born neutron star (ν NS) and the just born black hole (see Figure 1). There is also the distinct possibility that these two systems have become members of a newly born binary system¹² (Rueda & Ruffini 2012).

4. CONCLUSION

We recall that GRB 130427A is one of the most energetic GRBs ever observed ($E_{iso} \simeq 10^{54}$ erg), with the largest γ -ray fluence and the longest lasting simultaneous optical, X-ray, γ -ray, and GeV observations of the past 40 yr. For this reason we performed our own data analysis of the *Swift* and *Fermi* satellites (see Sections 3) in order to probe the BdHN nature of this source (see Section 3.3) and infer new perspectives for the IGC paradigm and the physical and astrophysical understanding of GRB.

We summarize the main results by showing how the analysis of GRB 130427A should be inserted in a wider context with three different areas: (1) the formulation and the observational consequences of the IGC paradigm; (2) the comprehension induced by the multi-wavelength observations of GRB 130427A; and (3) the BDHN versus HN properties. BDHN is relevant in establishing a new alternative distance indicator in astrophysics, which will be summarized in the following.

With reference to the formulation and observational consequences of the IGC paradigm:

1. The IGC paradigm introduces a new experience in astrophysics that has been successfully applied in particle

¹² Presentation of R. Ruffini in Yerevan: <http://www.icranet.org/images/stories/Meetings/meetingArmenia2014/talks/ruffini-1.pdf>

physics: to understand that a system traditionally considered elementary is actually a composed system, and that new components in the system can appear from the influence of collisions or decay. Well-known physical examples are represented by the introduction of the quark (Aad et al. 2012), or the creation of new particles in a decay or collision of elementary particle system: the Fermi theory of beta decay or the mesons production in electron positron collision in storage rings are classical examples. These facts are routinely accepted in particle physics, although Fermi had to explain them at the time (Fermi 1934). In astrophysics this situation is new. To see that a process until recently considered elementary, such as the GRB, does contain four different astrophysical systems, and that the interaction between two of them (i.e., the FeCO core undergoing SN and the companion NS binary) give rise to two different new systems, a ν NS and a BH, and that the entire process occurs in less than 200 s, is a totally new condition. To understand it, a new technical and conceptual approach is needed. The new style of research is more similar to that adopted in particle physics than in classical astronomy; see Figure 1.

2. Possibly the most profound novelty in this approach, for the understanding of GRBs, is the introduction of the four episodes that are summarized in Section 1. The traditional GRB description corresponds to *Episode 2*. *Episode 1* corresponds to the dynamical accretion of the SN ejecta onto the companion NS. We are now considering an enormous rate of accretion of 10^{31} g s^{-1} , which is 10^{15} times larger than that usually considered in the binary X-ray source in systems like Centaurus X-3 or Cygnus X-1 (see e.g., in Giacconi & Ruffini 1975). This process opened a new field of research by presenting the first realization of the hypercritical accretion introduced by Bondi–Hoyle–Littleton, as well as the testing ground of the neutrinos emission pioneered in the Zel’dovich et al. (1972) and Ruffini & Wilson (1975) (see Section 1). The pure analytic simplified solutions in Rueda & Ruffini (2012) are now supported by direct numerical simulation in Fryer et al. (2014, and Figure 1 therein).
3. The main revolution of the IGC paradigm for GRBs comes from the discovery of the universal laws discovered in *Episode 3*, which compare the explosive, irregular phases, varying from source to source in all observed GRBs in *Episode 1* and *Episode 2*. The universality of *Episode 3*, as well as the precise power laws and scaling laws discovered, changes the field of GRB analysis by making it one of time-resolved, high-precision, and reproducible measurements. Additional unexplored physical phenomena occurs in *Episode 3*, adding to the new ultrarelativistic regimes already observed in the *Episode 2* in previous years,¹³ see Figure 3 and Figure 4 as well as Figure 5.

With reference to the comprehension induced by the multi-wavelength observations of GRB130427:

1. Following the work on the GS (Pisani et al. 2013) and the more recent work on the nested structures (Ruffini et al. 2014c), we have first verified that the soft X-ray emission of GRB 130427A follows for time $t \simeq 10^4$ s the power law decay described in Pisani et al. (2013). Surprisingly, this most energetic GRB unveils that such power law behavior as already exists at the early time as $t \sim 100$ s (details in

Ruffini et al. 2014c). From the X-ray thermal component observed at the beginning of *Episode 3* following a spiked emission at ~ 100 s, a small Lorentz factor of the emitter is inferred ($\Gamma < 2$). This X-ray emission appears to originate in a mildly relativistic regime with a velocity $v \sim 0.8c$, does not appear to have substantial beaming, and appears to be relatively symmetric with no jet break; see Figure 5 and Ruffini et al. (2014c, Figure 2).

2. We made a multi-wavelength analysis of *Episode 3* where we compared optical data from *Swift*-UVOT and ground-based telescopes, X-ray data from *Swift*-XRT, γ -ray data from *Fermi*-GBM, and very high energy data in the GeV from *Fermi*-LAT. The high energy emission appears to be detectable at the end of the prompt radiation phase in *Episode 2*, when the fluence of the X-ray and γ -ray of the prompt exponentially decreases and becomes transparent for the very high energy photons in the *Fermi*-LAT regime. From the transparency condition of the GeV emission, a Lorentz Gamma factor of 10–40 is deduced. In principle this radiation, although no brake is observed in its power law, could be in principle beamed; see Figure 9.
3. Although the light curves of X-ray and GeV emission appear to be very similar, sharing similar power law decay index, their Lorentz Γ factors appear to be very different, and their physical origins are necessarily different. Within the IGC model, the X-ray and high energy can originate from the interaction of some of the physical components (e.g., neutron star and black hole) that were newly created in the C-matrix: the interaction of the GRBs with the SN ejecta (Ruffini et al. 2014b) may well generate the X-ray emission and the associated thermal component. The high energy should be related to the novel three components (i.e., the BH, the ν NS, and the SN ejecta). From the dynamics it is likely that the ν NS and the BH form a binary system (see e.g., Rueda & Ruffini 2012 and the presentation by one of the authors).¹⁴

With reference to the BDHN versus HN properties:

1. The verification of the BdHN paradigm in GRB 130427A has confirmed that for sources with isotropic energy approximately 10^{54} erg, the common power law behavior is attained at earlier times (i.e., $\sim 10^3$ s) and higher X-ray luminosities than the characteristic timescale indicated in (Pisani et al. 2013) (see Figure 3). From the observation of the constant-index power law behavior in the first 2×10^4 s of the X-ray luminosity light curve, which overlap with the known BdHNe, it is possible to estimate the redshift of the source, the isotropic energy of the GRB, and the fulfillment of the necessary and sufficient condition for predicting the occurrence of the SN after ~ 10 days in the rest frame of the source (see, e.g., GCN 14526). This procedure has been successfully applied to GRB 140512A (R. Ruffini et al., in preparation).
2. The overlap with the GS members of the late X-ray emission observed by the *Swift* XRT, referred to as the rest frame of the source, introduces a method to establish an independent distance estimator of the GRBs. Although this method has been amply applied (e.g., GRBs 060729, 061007, 080319, 090618, 091127, 111228A), we also declare that there are some clear outliers to this phenomenon, such as GRB 060614 (Ruffini et al. 2013a), 131202A (Ruffini et al.

¹³ Presentation of R. Ruffini in the 13th Marcel Grossmann Meeting: <http://www.icra.it/mg/mg13>

¹⁴ Presentation of R. Ruffini in Yerevan: <http://www.icranet.org/images/stories/Meetings/meetingArmenia2014/talks/ruffini-1.pdf>

2013c), and 140206A (Ruffini et al. 2014a). These are all cases of great interest and the solution of this contradiction may be of particular astrophysical significance. Particularly interesting is the case of GRB 060614 because the cosmological redshift has not been directly measured and there can be a misidentification of the host galaxy (Cobb et al. 2006).

3. As first pointed out in Rueda & Ruffini (2012) and Ruffini et al. (2014c), and further evidenced in Fryer et al. (2014), the crucial factor that may explain the difference between *family 1* and *family 2* GRBs is the initial distance between the FeCO core and its binary NS companion. The accretion from the SN ejecta onto the companion NS, and the consequent emission process decrease, by increasing this distance has consequently hampered the possibility for the binary companion NS to reach its critical mass (see Figures 3 and 4 in Izzo et al. 2012, and the discuss therein). Unlike *family 2*, in *family 1* no BH is formed, no GRB is emitted, and neither *Episode 2* nor *Episode 3* exists—only a softer and less energetic radiation from the accretion onto the neutron star will be observed in these sources. The problem of explaining the coincidence between the GRB and supernova in the case of *family 1* is just a tautology: no GRB in this family exists, only a hypernova (Ruffini et al. 2014c).

This paper addresses recent results on the IGC paradigm applied to long GRBs. The IGC paradigm and the merging of binary neutron stars has also been considered for short GRBs (see e.g., Muccino et al. 2013a, 2013b, 2014; Ruffini et al. 2014c) and is now being further developed.

We acknowledge the use of public data from the *Swift* and *Fermi* data archive. We thank Robert Jantzen for his careful reading and valuable advice. We also thank the editor and the referee for their constant attention and beneficial suggestions, which largely improve this paper. M.E., M.K., and G.B.P. are supported by the Erasmus Mundus Joint Doctorate Program by Grant Numbers 2012-1710, 2013-1471, and 2011-1640, respectively, from the EACEA of the European Commission.

REFERENCES

- Aad, G., Abajyan, T., Abbott, B., et al. 2012, *PhLB*, **716**, 1
- Ackermann, M., Ajello, M., Asano, K., et al. 2013, *Sci*, **343**, 42
- Aharonian, F. A. 2004, *Very High Energy Cosmic Gamma Radiation: A Crucial Window on the Extreme Universe* (Singapore: World Scientific Publishing)
- Bernardini, C. 2004, *PhP*, **6**, 156
- Bloom, J. S., Perley, D. A., Li, W., et al. 2009, *ApJ*, **691**, 723
- Bondi, H. 1952, *MNRAS*, **112**, 195
- Bondi, H., & Hoyle, F. 1944, *MNRAS*, **104**, 273
- Broderick, A. E. 2005, *MNRAS*, **361**, 955
- Cobb, B. E., Bailyn, C. D., van Dokkum, P. G., & Natarajan, P. 2006, *ApJL*, **651**, L85
- de Ugarte Postigo, A., Xu, D., Leloudas, G., et al. 2013, *GCN Circ.*, **14646**
- Evans, P. A., Beardmore, A. P., Page, K. L., et al. 2007, *A&A*, **469**, 379
- Evans, P. A., Beardmore, A. P., Page, K. L., et al. 2009, *MNRAS*, **397**, 1177
- Fermi, E. 1934, *Il Nuovo Cimento*, **11**, 1
- Fermi, E. 1949, *PhRv*, **75**, 1169
- Flores, H., Covino, S., Xu, D., et al. 2013, *GCN Circ.*, **14491**
- Friis, M., & Watson, D. 2013, *ApJ*, **771**, 15
- Fryer, C. L., Benz, W., & Herant, M. 1996, *ApJ*, **460**, 801
- Fryer, C. L., Rueda, J. A., & Ruffini, R. 2014, *ApJ*, **793**, L36
- Fryer, C. L., Woosley, S. E., & Hartmann, D. H. 1999, *ApJ*, **526**, 152
- Galama, T. J., Vreeswijk, P. M., van Paradijs, J., et al. 1998, *Natur*, **395**, 670
- Giacconi, R., & Ruffini, R. 1975, *Physics and Astrophysics of Neutron Stars and Black Holes* (Amsterdam: North Holland Publishing Co.)
- Grupe, D., Gronwall, C., Wang, X.-Y., et al. 2007, *ApJ*, **662**, 443
- Guetta, D., & Della Valle, M. 2007, *ApJL*, **657**, L73
- Gupta, N., & Zhang, B. 2008, *MNRAS*, **384**, L11
- Izzo, L., Rueda, J. A., & Ruffini, R. 2012, *A&A*, **548**, L5
- Kouveliotou, C., Granot, J., Racusin, J. L., et al. 2013, *ApJL*, **779**, L1
- Kovacevic, M., Izzo, L., Wang, Y., et al. 2014, *A&A*, **569**, A108
- Laskar, T., Berger, E., Zauderer, B. A., et al. 2013, *ApJ*, **776**, 119
- Levan, A. J., Cenko, S. B., Perley, D. A., & Tanvir, N. R. 2013a, *GCN Circ.*, **14455**
- Levan, A. J., Fruchter, A. S., Graham, J., et al. 2013b, *GCN Circ.*, **1468**
- Levan, A. J., Tanvir, N. R., Fruchter, A. S., et al. 2014, *ApJ*, **792**, 115
- Li, L.-X., & Paczynski, B. 1998, *ApJL*, **507**, L59
- Lithwick, Y., & Sari, R. 2001, *ApJ*, **555**, 540
- Maselli, A., Beardmore, A. P., Lien, A. Y., et al. 2013, *GCN Circ.*, **14448**
- Maselli, A., Melandri, A., Nava, L., et al. 2014, *Sci*, **343**, 48
- Mészáros, P. 2006, *RPPh*, **69**, 2259
- Muccino, M., Ruffini, R., Bianco, C. L., Izzo, L., & Penacchioni, A. V. 2013a, *ApJ*, **763**, 125
- Muccino, M., Ruffini, R., Bianco, C. L., et al. 2013b, *ApJ*, **772**, 62
- Muccino, M., Bianco, C. L., Izzo, L., et al. 2014, *GrCo*, **20**, 197
- Nava, L., Sironi, L., Ghisellini, G., Celotti, A., & Ghirlanda, G. 2013, *MNRAS*, **433**, 2107
- Nousek, J. A., Kouveliotou, C., Grupe, D., et al. 2006, *ApJ*, **642**, 389
- Page, K. L., Starling, R. L. C., Fitzpatrick, G., et al. 2011, *MNRAS*, **416**, 2078
- Penacchioni, A. V., Ruffini, R., Bianco, C. L., et al. 2013, *A&A*, **551**, A133
- Penacchioni, A. V., Ruffini, R., Izzo, L., et al. 2012, *A&A*, **538**, 58
- Perley, D. A., Cenko, S. B., Corsi, A., et al. 2013, *ApJ*, **781**, 37
- Pian, E., Amati, L., Antonelli, L. A., et al. 2000, *ApJ*, **536**, 778
- Piran, T. 2005, *RMP*, **76**, 1143
- Pisani, G. B., Izzo, L., Ruffini, R., et al. 2013, *A&A*, **552**, L5
- Rhoads, J. E. 1999, *ApJ*, **525**, 737
- Romano, P., Campana, S., Chincarini, G., et al. 2006, *A&A*, **456**, 917
- Rueda, J. A., & Ruffini, R. 2012, *ApJL*, **758**, L7
- Ruffini, R., Bernardini, M. G., Bianco, C. L., et al. 2008, in *11th Proc. Marcel Grossmann Meeting* (Singapore: World Scientific Publishing), **368**
- Ruffini, R., Bianco, C. L., Enderli, M., et al. 2013a, *GCN Circ.*, **15560**, 1
- Ruffini, R., Bianco, C. L., Enderli, M., et al. 2013b, *GCN Circ.*, **14526**
- Ruffini, R., Bianco, C. L., Enderli, M., et al. 2013c, *GCN Circ.*, **15576**, 1
- Ruffini, R., Bianco, C. L., Enderli, M., et al. 2014a, *GCN Circ.*, **15794**, 1
- Ruffini, R., Bianco, C. L., Frascchetti, F., Xue, S.-S., & Chardonnet, P. 2001, *ApJ*, **555**, L117
- Ruffini, R., Izzo, L., Muccino, M., et al. 2014b, *A&A*, **569**, A39
- Ruffini, R., Muccino, M., Bianco, C. L., et al. 2014c, *A&A*, **565**, L10
- Ruffini, R., Salmonson, J. D., Wilson, J. R., & Xue, S.-S. 1999, *A&A*, **350**, 334
- Ruffini, R., Salmonson, J. D., Wilson, J. R., & Xue, S.-S. 2000, *A&A*, **359**, 855
- Ruffini, R., & Wilson, J. R. 1975, *PhRvD*, **12**, 2959
- Starling, R. L. C., Page, K. L., Pe'er, A., Beardmore, A. P., & Osborne, J. P. 2012, *MNRAS*, **427**, 2950
- Tanvir, N. R., Rol, E., Levan, A. J., et al. 2010, *ApJ*, **725**, 625
- Tavani, M. 1998, *ApJL*, **497**, L21
- Trotter, A., Reichart, D., Haislip, J., et al. 2013, *GCN Circ.*, **1466**
- van Eerten, H. J., & MacFadyen, A. I. 2012, *ApJ*, **751**, 155
- van Eerten, H. J., Zhang, W., & MacFadyen, A. 2010, *ApJ*, **722**, 235
- von Kienlin, A. 2013, *GCN Circ.*, **14473**
- Woosley, S. E. 1993, *ApJ*, **405**, 273
- Xu, D., de Ugarte Postigo, A., Leloudas, G., et al. 2013, *ApJ*, **776**, 98
- Xu, D., de Ugarte Postigo, A., Schulze, S., et al. 2013, *GCN Circ.*, **14478**
- Zel'dovich, Y. B., Ivanova, L. N., & Nadezhin, D. K. 1972, *SvA*, **16**, 209

Induced gravitational collapse at extreme cosmological distances: the case of GRB 090423

R. Ruffini^{1,2,3,4}, L. Izzo^{1,2}, M. Muccino¹, G. B. Pisani^{1,3}, J. A. Rueda^{1,2,4}, Y. Wang¹, C. Barbarino^{1,5}, C. L. Bianco^{1,2},
 M. Enderli^{1,3}, and M. Kovacevic^{1,3}

¹ Dip. di Fisica and ICRA, Sapienza Università di Roma, P.le Aldo Moro 5, 00185 Rome, Italy
 e-mail: Ruffini@icra.it

² ICRANet, Piazza della Repubblica 10, 65122 Pescara, Italy

³ Université de Nice-Sophia Antipolis, Cedex 2, Grand Château Parc Valrose, Nice, France

⁴ ICRANet-Rio, Centro Brasileiro de Pesquisas Físicas, Rua Dr. Xavier Sigaud 150, 22290-180 Rio de Janeiro, RJ, Brazil

⁵ INAF-Napoli, Osservatorio Astronomico di Capodimonte, Salita Moiarriello 16, 80131 Napoli, Italy

Received 17 January 2014 / Accepted 25 May 2014

ABSTRACT

Context. The induced gravitational collapse (IGC) scenario has been introduced in order to explain the most energetic gamma ray bursts (GRBs), $E_{\text{iso}} = 10^{52} - 10^{54}$ erg, associated with type Ib/c supernovae (SNe). It has led to the concept of binary-driven hypernovae (BdHNe) originating in a tight binary system composed by a FeCO core on the verge of a SN explosion and a companion neutron star (NS). Their evolution is characterized by a rapid sequence of events: 1) the SN explodes, giving birth to a new NS (ν NS). The accretion of SN ejecta onto the companion NS increases its mass up to the critical value; 2) the consequent gravitational collapse is triggered, leading to the formation of a black hole (BH) with GRB emission; 3) a novel feature responsible for the emission in the GeV, X-ray, and optical energy range occurs and is characterized by specific power-law behavior in their luminosity evolution and total spectrum; 4) the optical observations of the SN then occurs.

Aims. We investigate whether GRB 090423, one of the farthest observed GRB at $z = 8.2$, is a member of the BdHN family.

Methods. We compare and contrast the spectra, the luminosity evolution, and the detectability in the observations by *Swift* of GRB 090423 with the corresponding ones of the best known BdHN case, GRB 090618.

Results. Identification of constant slope power-law behavior in the late X-ray emission of GRB 090423 and its overlapping with the corresponding one in GRB 090618, measured in a common rest frame, represents the main result of this article. This result represents a very significant step on the way to using the scaling law properties, proven in Episode 3 of this BdHN family, as a cosmological standard candle.

Conclusions. Having identified GRB 090423 as a member of the BdHN family, we can conclude that SN events, leading to NS formation, can already occur, namely at 650 Myr after the Big Bang. It is then possible that these BdHNe stem from 40–60 M_{\odot} binaries. They are probing the Population II stars after the completion and possible disappearance of Population III stars.

Key words. gamma-ray burst: general – gamma-ray burst: individual: GRB 090423 – black hole physics

1. Introduction

The induced gravitational collapse (IGC) paradigm (Ruffini 2011; Rueda & Ruffini 2012; Izzo et al. 2012b) has been proposed to explain a class of very energetic ($E_{\text{iso}} \sim 10^{52} - 10^{54}$ erg) long gamma ray bursts (GRBs) associated with supernovae (SNe). A new class of systems, with progenitor a tight binary composed by a FeCO core and a companion neutron star (NS), has been considered. These systems evolve in a very rapid sequence lasting a few hundred seconds in their rest frame: 1) the SN explodes giving birth to a new NS (ν NS); 2) the accretion of the SN ejecta onto the companion NS increases its mass, reaching the critical value; 3) the gravitational collapse is triggered, leading to the formation of a black hole (BH) with GRB emission. Such systems have been called binary-driven hypernovae (BdHN Ruffini et al. 2014a).

Observationally, this authentic cosmic matrix is characterized by four distinct episodes, with the “in” state represented

by a FeCO core and a NS and the “out” state by a ν NS and a BH. Each episode contains specific signatures in its spectrum and luminosity evolution. Up to now, the IGC paradigm has been verified in a dozen GRBs, all with redshift up to $z \sim 1$ (Izzo et al. 2012a; Penacchioni et al. 2012, 2013; Pisani et al. 2013; Ruffini et al. 2013).

Various approaches have been followed to reach an understanding of long GRBs. One of these has been the use of statistical tools to obtain general results that examine the most complete source catalog (see, e.g., Nousek et al. 2006; Kann et al. 2011; Salvaterra et al. 2012; Margutti et al. 2013, and references therein).

We follow a different approach here. We first identified the specific class of BdHNe of GRBs related to SNe, as mentioned above, widely tested at $z \approx 1$. We furthermore explore the members of this class by extending our analysis to higher values of the cosmological redshifts. We do that by taking the scaling laws for the cosmological transformations into account, as well as the

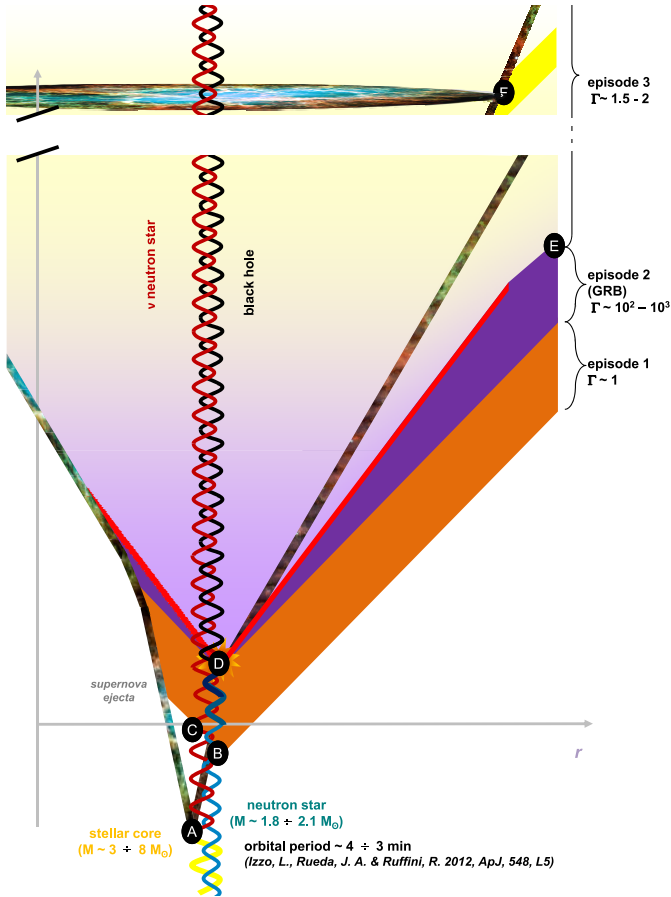


Fig. 1. Space-time diagram of the induced gravitational collapse applied to GRB 090618 (Enderli 2013; Ruffini 2013). The sequence is summarized as follows: A) the explosion as a SN of the evolved FeCO core which creates a ν -NS and its remnant; B) the beginning of the accretion of the SN ejecta onto the companion NS, emitting Episode 1; C) a prolonged interaction between the ν -NS and the NS binary companion; D) the companion NS reaches its critical mass by accretion, and a BH is formed with the consequent emission of a GRB; E) the arrival time at the separatrix between Episodes 2 and 3; F) the optical emission of the SN due to the decay of ^{56}Ni after $t_a^d \sim 10(1+z)$ days in the observer frame (Episode 4).

specific sensitivities of the GRB detectors (in this case *Swift*, Gehrels et al. 2005; and *Fermi*, Meegan et al. 2009).

Our aim is to verify that such BdHNe, originating in a SN and a companion NS, did form in the earliest phases of the universe. If this is confirmed, we go on to examine the possibility that all GRBs with $E_{\text{iso}} \sim 10^{52} - 10^{54}$ erg are indeed associated to SN and belong to the BdHN family independently of their space and time location.

2. The four episodes of BdHNe sources

In order to achieve this goal, we recall the four above-mentioned episodes, present in the most general BdHN (see Fig. 1):

Episode 1 has the imprint of the onset of a SN in the tight binary system with the companion neutron star (NS; see Fig. 2). It stemmed from the hyper-critical accretion of the SN matter ejecta ($\sim 10^{-2} M_{\odot} \text{ s}^{-1}$) (Rueda & Ruffini 2012). Decades of conceptual progress have passed from the original work of Bondi & Hoyle (1944) and Bondi (1952) to the problem of a “hypercritical” accretion rate. This problem has acquired growing scientific interest as it moved from the classical astronomical field to the

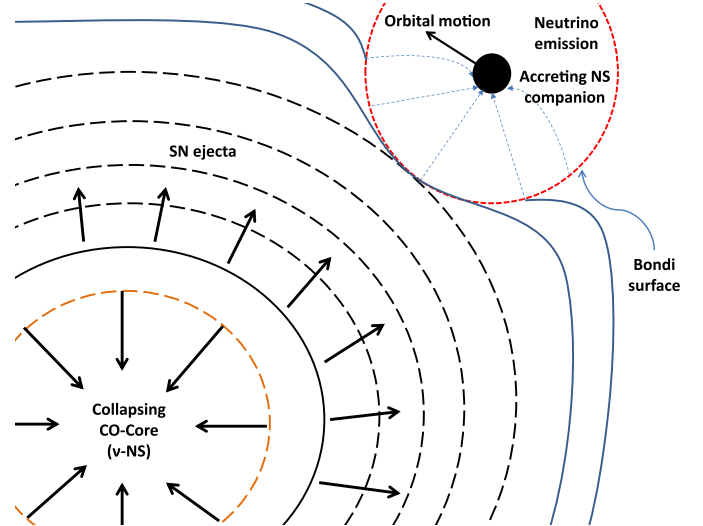


Fig. 2. Sketch (not in scale) of the accretion induced gravitational collapse (IGC) scenario.

domain of the relativistic astrophysics. The crucial role of neutrino cooling, earlier considered by Zel’dovich et al. (1972) and later on by Bisnovatyi-Kogan & Lamzin (1984) in SN fallback, has been recognized to play a crucial role in describing binary common envelope systems by Chevalier (1989, 1993). In the work by Fryer et al. (1996), and more recently in Fryer (2009), it was clearly shown that an accretion rate $\dot{M} \sim 10^{-2} M_{\odot} \text{ s}^{-1}$ onto a neutron star (NS) could lead in a few seconds to the formation of a black hole (BH), when neutrino physics in the description of the accreting NS is taken into due account. The data acquired in Episode 1 of GRB 090618 (Izzo et al. 2012a), as well as the one in GRB 101023 (Penacchioni et al. 2012), GRB 110709B (Penacchioni et al. 2013), and GRB 970828 (Ruffini et al. 2013), give for the first time the possibility to probe the Bondi-Hoyle hypercritical accretion and possibly the associated neutrino emission, which was theoretically considered by Zel’dovich et al. (1972); Chevalier (1993); Fryer et al. (1996), and Fryer (2009).

Episode 2 is the canonical GRB emission, which originated in the collapse of the companion NS, which reached its critical mass by accretion of the SN ejecta and then collapsed to a black hole (BH), indeed emitting the GRB.

Episode 3 observed in X-rays by *Swift*-XRT, shows very precise behavior consisting of steep decay, starting at the end point of the prompt emission, and then a plateau phase followed by a late power-law decay (see Pisani et al. 2013 and also Fig. 3). The late X-ray luminosities of BdHNe, in their rest-frame energy band 0.3–10 keV, show a common power-law behavior with a constant decay index clustering around $\alpha = -1.5 \pm 0.2$. The occurrence of such a constant afterglow decay has been observed in all the BdHN sources examined. For example, see in Fig. 4 the data for GRB 130427A, GRB 061121, GRB 060729, respectively. It appears an authentic nested structure, in the late X-ray emission of GRBs associated to SNe, and it has indeed to be indicated as the qualifying feature for a GRB to be a member of the BdHNe family (Ruffini et al. 2014a). It is clear that such a phenomenon offers a strong challenge for explaining by any GRB model.

In addition to these X-ray features, the observations of GRB 130427A by the *Swift*, *Fermi*, and Konus-WIND satellites and a large number of optical telescopes have led to the evidence of such power laws at very high energies, in γ -rays and

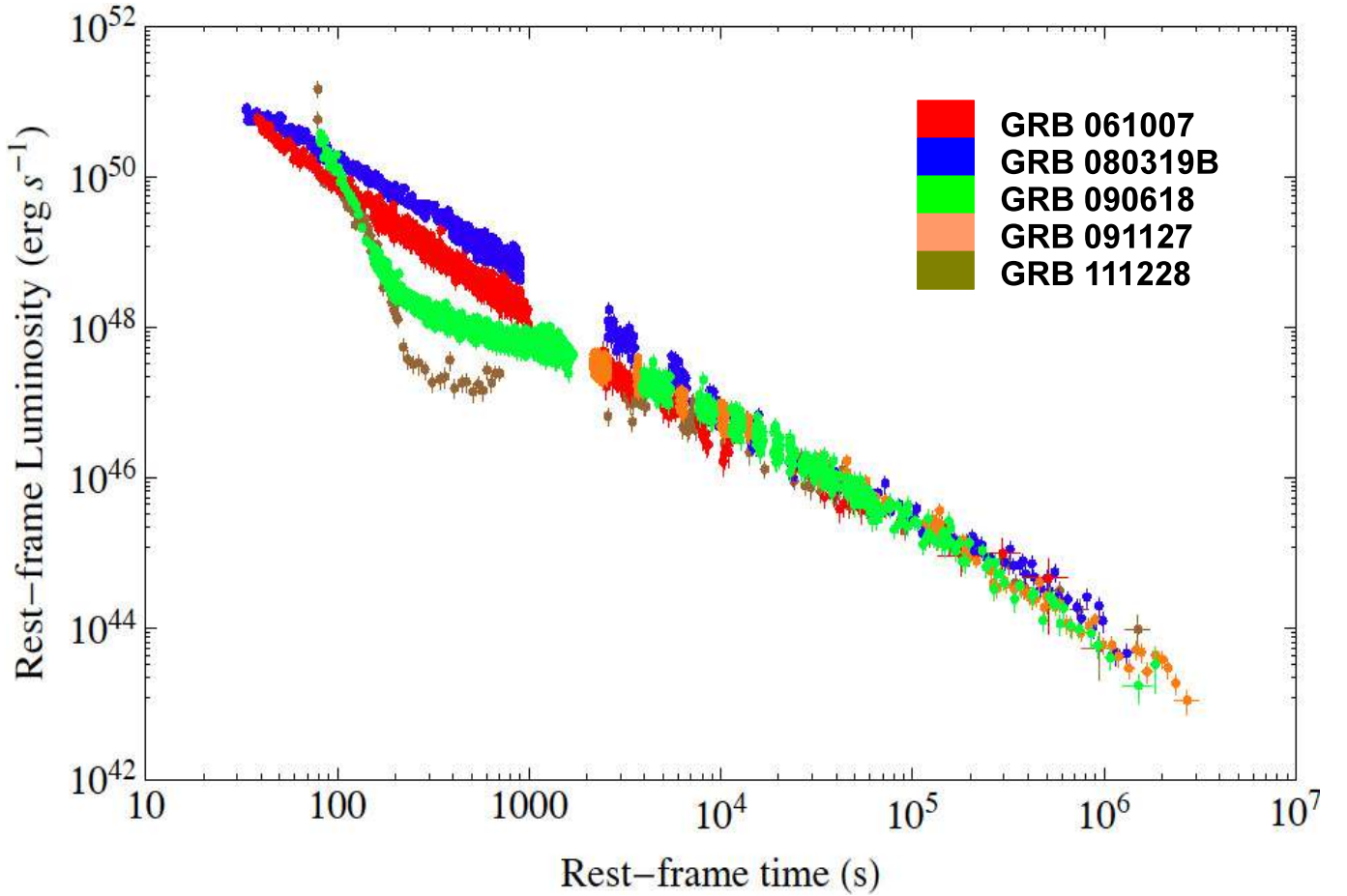


Fig. 3. Rest-frame, X-ray afterglow, luminosity light curves of some IGC GRBs-SNe belonging to the “golden sample” described in Pisani et al. (2013). The overlapping after 10^4 s is clearly evident, confirming the presence of an Episode 3 in this GRB.

at the optical wavelengths (Fermi-LAT collaboration & Fermi-GBM collaboration 2014; Melandri et al. 2014; see also Ruffini et al. 2014b).

Episode 4 is characterized by the emergence of the SN emission after about 10–15 days from the occurrence of the GRB in the rest frame of the source, which has been observed for almost all the sources fulfilling the IGC paradigm with $z \sim 1$.

3. GRB 090423 compared and contrasted with GRB 090618

We first consider the data of GRB 090423, one of the farthest GRB ever observed at $z = 8.2$ (Salvaterra et al. 2009; Tanvir et al. 2009), with the prototypical member of the BdHNe class, namely GRB 090618, and its associated SN (Izzo et al. 2012a). In other words we proceed with a specific ansatz: we verify that GRB 090423, at $z = 8.2$, presents analogous intrinsic features to GRB 090618, which was observed at $z = 0.54$.

We proceed by examining (see Sect. 4) each one of the above episodes for both sources, by a detailed spectral analysis and simulations. We first verify that Episode 1 of GRB 090618 transposed at redshift $z = 8.2$ should not have triggered the *Swift*-BAT detector. Indeed, no precursor in the light curve of GRB 090423 was detected. Consequently, we do not address any theoretical considerations of the hypercritical accretion in Episode 1 of GRB 090423, since it is not observable in this source (see Sect. 5). We also notice that the distance of

GRB 090423 prevents any possible detection of a SN associated with this GRB, and therefore Episode 4 cannot be observed in GRB 090423.

For Episode 2, we have found that indeed the transposed emission of GRB 090618 should provide a positive trigger: we show in Sect. 6 that the duration, the observed luminosity and the spectral emission of Episode 2 in GRB 090423 present analogous intrinsic features to the transposed ones of GRB 090618 and differ only in the spectral energy distribution due to different circumburst medium properties.

For Episode 3, the crucial result, probing the validity of the above ansatz, is that the late X-ray emission in GRB 090423, computed in the rest frame of the burst at $z = 8.2$, precisely coincides (overlaps) with the corresponding late X-ray emission in GRB 090618, as evaluated in the rest frame of the source at $z = 0.54$, see Sect. 7. The occurrence of this extraordinary coincidence in Episode 3 proves that GRB 090423 is indeed a member of the BdHN family. This in particular opens the possibility of elaborating a role for the late X-ray emission in BdHNe as a standard candle.

4. The data

GRB 090423 was discovered on 23 April 2009, 07:55:19 UT, T_0 from here, by the *Swift* Burst Alert Telescope (BAT; Krimm et al. 2009), at coordinates RA = 09^h 55^m 35^s, Dec = +18° 09' 37'' (J2000.0; 3' at 90% containment radius). The

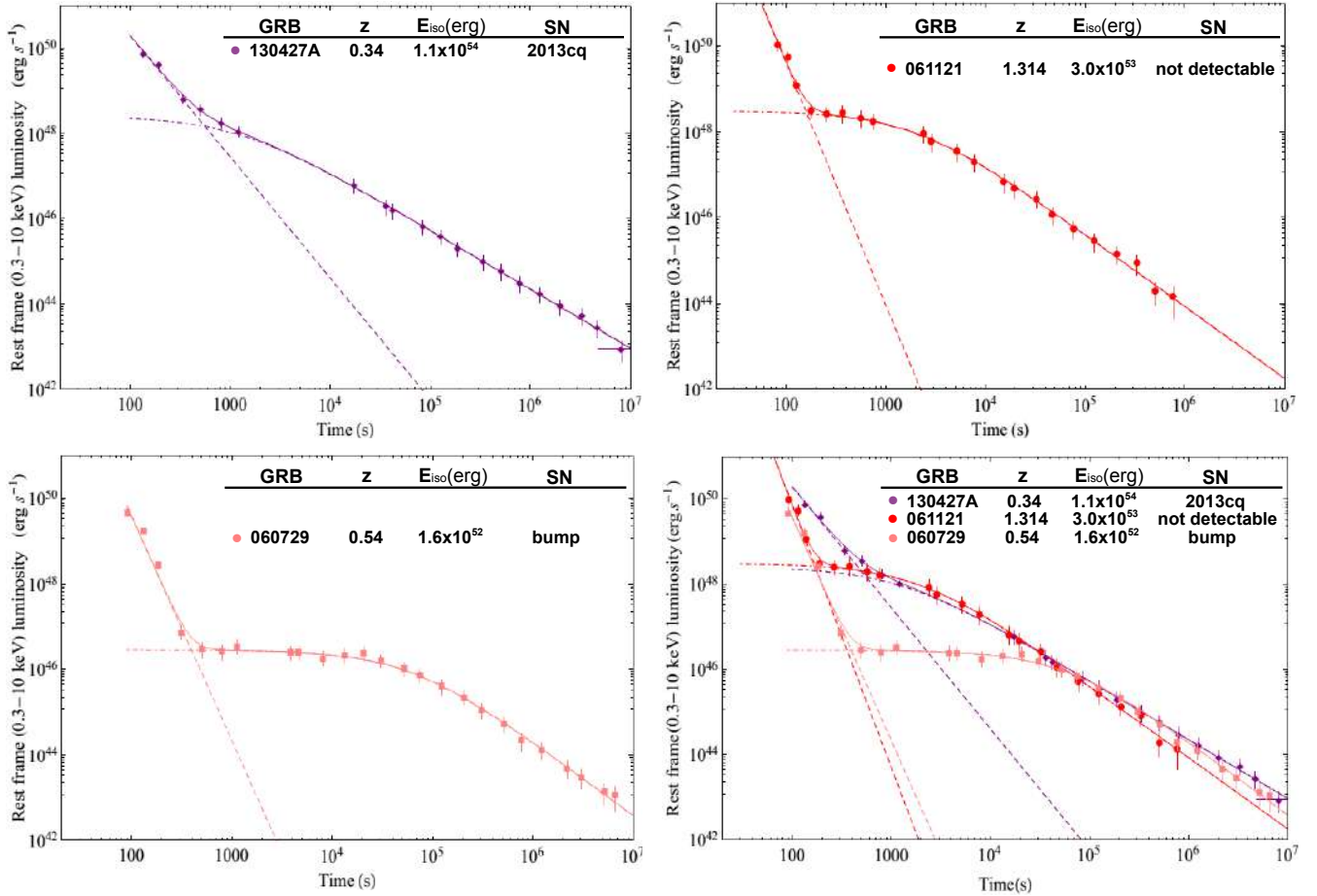


Fig. 4. Rest-frame, (0.3–10) keV, and re-binned luminosity light curves of GRB 130427A (*upper left*), GRB 061121 (*upper right*), GRB 060729 (*lower left*) and a combined picture (*lower right*). The fits to their emission is done using a power-law function for the early steep decay and a phenomenological function for the following emission, which is described well in [Ruffini et al. \(2014a\)](#).

Swift-BAT light curve showed a double-peaked structure with a duration of about 20 s. The X-ray Telescope (XRT; [Burrows et al. 2005](#)) on board the same spacecraft started to observe GRB 090423 72.5 s after the initial trigger, finding a fading source and providing enhanced coordinates for the follow-up by on-ground telescopes that have allowed the discovery of its redshift ($z = 8.2$, [Salvaterra et al. 2009](#); [Tanvir et al. 2009](#)). The light curve is characterized by an intense and long flare peaking at about $T_0 + 180$, followed by a power-law decay, observed from the second orbit of *Swift* ([Stratta & Perri 2009](#)). The prompt emission from GRB 090423 was also detected by the *Fermi* Gamma-Ray Burst Monitor (GBM, trigger 262166127/090423330; [von Kienlin 2009a](#)), whose on-ground location was consistent with the *Swift* position. The Large Area Telescope (LAT) on-board the *Fermi* satellite did not detect any signal from GRB 090423. The GBM light curve showed a single-structured peak with a duration of about 12 s, whose spectral energy distribution was best fit with a power law with an exponential cut-off energy, parameterized as $E_{\text{peak}} = (82 \pm 15)$ keV. The observed fluence was computed from *Fermi* data to be $S_\gamma = 1.1 \times 10^{-6}$ ergs/cm² that, considering the standard Λ CDM cosmological model, corresponds to an isotropic energy emitted of $E_{\text{iso}} = 1.1 \times 10^{53}$ ergs for the spectroscopic redshift $z = 8.2$ ([von Kienlin 2009b](#)). With these values for E_{peak} and E_{iso} , GRB 090423 satisfies the Amati relation, which is only valid for long GRBs ([Amati et al. 2002](#)).

5. The impossibility of detecting Episode 1

It has become natural to ask if observations of Episodes 1 and 2 in the hard X-ray energy range could be addressed for the case of GRB 090423. We have first analyzed a possible signature of Episode 1 in GRB 090423. Since the *Swift*-BAT, (15–150) keV, light curve is a single-structured peak with duration of ~ 19 s, as detected by *Swift*-BAT, with no thermal emission in its spectrum and no detection of any emission from a precursor in the *Swift* and *Fermi* data, we have considered the definite possibility that Episode 1 was not observed at all. In this light, the best way to check this possibility consists in verifying that the Episode 1 emission is below the threshold of the *Swift*-BAT detector, consequently, it could have not triggered the *Swift*-BAT. We have considered the prototype of Episode 1 as the one observed in GRB 090618 ([Izzo et al. 2012b](#)), which is at redshift $z = 0.54$, and then we transposed it at redshift $z = 8.2$, simulating the observed emission of GRB 090618 as if it had been observed at this large distance. Then, we performed a time-resolved spectral analysis of Episode 1 in GRB 090618, using a Band function as spectral model, and finally we translated the specific photon spectra obtained from the analysis at the redshift of GRB 090423. This last operation consists in two transformations, concerning the peak energy E_{peak} of the Band function and the normalization value K_{Band} . The new value of the peak energy is simply given by $E_{\text{peak},8} = E_{\text{peak}} (1 + 0.54)/(1 + 8.2)$, while the

normalization, which corresponds to the specific photon flux at 1 keV, requires knowledge of the luminosity distances of the two bursts, $d_l(z)$:

$$K_{\text{Band},8} = K_{\text{Band}} \left(\frac{1 + 8.2}{1 + 0.54} \right)^2 \left(\frac{d_l(0.54)}{d_l(8.2)} \right)^2. \quad (1)$$

Another transformation concerns the observational time of Episode 1 of GRB 090618 at redshift $z = 8.2$. At large distances, any astrophysical event will be dilated in time by the cosmological redshift effect, which in the current case modifies the time interval by a quantity $(1 + 8.2)/(1 + 0.54) = 5.97$. The knowledge of this time interval is fundamental since it represents the exposure of a simulated spectrum translated at $z = 8.2$. We considered Fermi GBM data for analyzing the time-resolved spectra of GRB 090618, as described by Izzo et al. (2012b). The wide energy range of Fermi GBM NaI detectors, (8–1000) keV, allows a more accurate determination of the Band parameters, which are used as input values for the simulated spectra. We also rebinned the Fermi data considering a signal-to-noise ratio (SNR) = 10, and finally performed our spectral analysis. The next step consisted in transforming the peak energy of the Band function and of the normalization of all these time-resolved photon spectra $N(E)$, as described above.

Following the work of Band (2003), the sensitivity of an instrument to detect a burst depends on its burst trigger algorithm. The *Swift*-BAT trigger algorithm, in particular, looks for excesses in the detector count rate above expected background and constant sources. There are several criteria for determining the correct BAT threshold significance σ_0 for a single GRB (Barthelmy et al. 2005), but in this work we have considered the treatment given in Band (2003). Recently, the threshold of *Swift*-BAT has been modified to allow detecting of subthreshold events, but since GRB 090423 was detected before, the Band (2003) analysis is still valid for our purposes. The preset threshold significance for *Swift*-BAT can be expressed by the following formula:

$$\sigma_0 = \frac{A_{\text{eff}} f_{\text{det}} f_{\text{mask}} \Delta t \int_{15}^{150} \epsilon(E) N(E) dE}{\sqrt{A_{\text{eff}} f_{\text{det}} \Delta t \int_{15}^{150} B(E) dE}}, \quad (2)$$

where A_{eff} is the effective area of the detector, f_{det} the fraction of the detector plane that is active, f_{mask} the fraction of the coded mask that is open, Δt the exposure of the photon spectrum $N(E)$, $\epsilon(E)$ the efficiency of the detector, and $B(E)$ the background. We considered the values for these parameters as the ones given in the Band work (with the exception of the detecting area, assumed to be $A_{\text{eff}} = 5200 \text{ cm}^2$), while the efficiency and the background were obtained from the *Swift*-BAT integrated spectrum of GRB 090423 using the XSPEC fitting package. Then we considered as input photon spectra $N(E)$ the ones obtained from the Fermi GBM analysis of Episode 1 of GRB 090618 and translated for the redshift $z = 8.2$. It is appropriate to note that the transformations of spectra presented above are the correct ones: since the sensitivity of *Swift*-BAT strongly depends on the peak energy of the photon flux of the single spectra of the GRB (for the *Swift*-BAT case, see e.g. Fig. 7 of Band 2003), we find that at $z = 8.2$ the observed peak energies of any spectrum will be lowered by a factor $(1 + 0.54)/(1 + 8.2)$. Our procedure also takes this further effect of the cosmological redshift into account.

Since the threshold significance of *Swift*-BAT is variable from a minimum value of $\sigma_0 = 5.5$ up to a maximum value of 11¹, with an average value of $\sigma_0 = 6.7$, the results of this

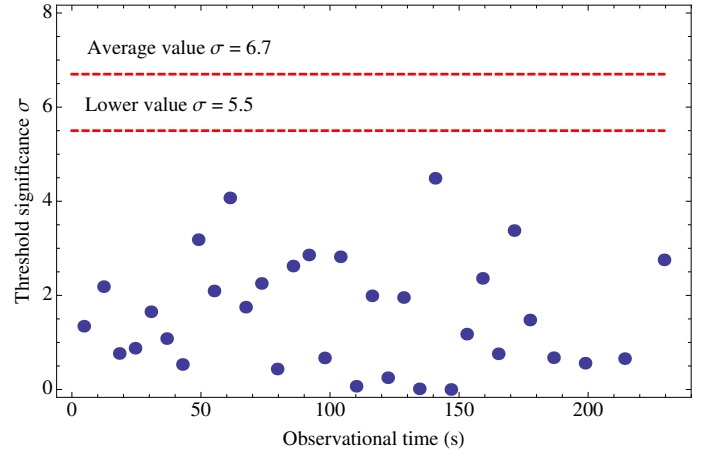


Fig. 5. Threshold significance σ_0 computed using the treatment of Band (2003) for any single time-resolved spectra of the first emission episode in GRB 090618, as if they were emitted at redshift 8.2. The dashed lines correspond to the values for the threshold significance of $\sigma_0 = 5.5$ and $\sigma_0 = 6.7$.

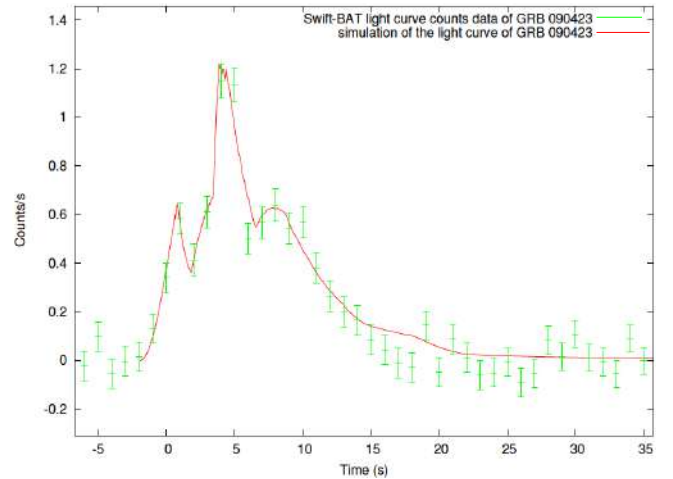


Fig. 6. *Swift*-BAT (15–150 keV) light curve emission of GRB 090423. The red line corresponds to the simulation of the GRB emission in the fireshell scenario (Izzo et al. 2010).

first analysis suggest that an Episode 1 similar to the one of GRB 090618 would not have been detected in GRB 090423 (see Fig. 5).

6. Detection of Episode 2 and its analysis

Episode 2 emission of GRB 090423, detected by *Swift*-BAT, was examined in the context of the fireshell scenario (Izzo et al. 2010; Ruffini 2011). A Lorentz Gamma factor of $\Gamma \sim 1100$ and a baryon load $B = 8 \times 10^{-4}$ were obtained. The simulations of the observed spikes in the observed time interval (0–440) s lead to homogeneous circumburst medium ($R = 10^{-8}$, see Bianco & Ruffini 2005 for a complete description), and an average density of 10^{-1} particles cm^{-3} . The simulation of the GRB 090423 emission is shown in Fig. 6.

We can now compare and contrast the emission observed in GRB 090423, expressed at $z = 8.2$ (see Fig. 6, Izzo et al. 2010), and the portion of the emission of GRB 090618 if observed at $z = 8.2$, (see Fig. 7, Izzo et al. 2012a). In view of the *Swift*-BAT threshold, only the dashed region in Fig. 8, lasting 6 s, would be

¹ http://swift.gsfc.nasa.gov/about_swift/bat_desc.html

Table 1. Results of the spectral fits of the T90 duration of GRB 090423 and of the $\Delta t_{A,obs}$ time interval for GRB 090618.

	α	β (keV)	$E_{p,i}$ (keV)	norm. (ph/cm ² /s/keV)	χ^2	Δt_{obs} (s)
090618	-0.66 ± 0.57	-1.99 ± 0.05	284.57 ± 172.10	0.3566 ± 0.16	0.924	6.1
090423	-0.78 ± 0.34	-3.5 ± 0.5	433.6 ± 133.5	0.015 ± 0.010	0.856	10.4

Notes. The latter is computed in a time interval corresponding to the one expected to be observed if GRB 090618 is transposed at the redshift $z = 8.2$, and in the observed energy range (89.6–896) keV.

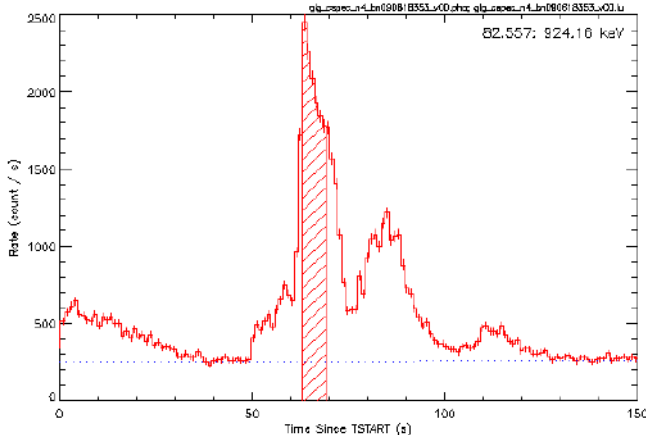


Fig. 7. Light curve of Episode 2 in GRB 090618, ranging from 50 to 150 s. The dashed region represents the portion which would have triggered the *Swift*-BAT if this GRB had been at the redshift $z = 8.2$. The observed duration of that interval is approximately $\Delta t \approx 6$ s. The results obtained in Fig. 6, when scaled to $z = 0.54$, provide $\Delta T \approx 3$ s.

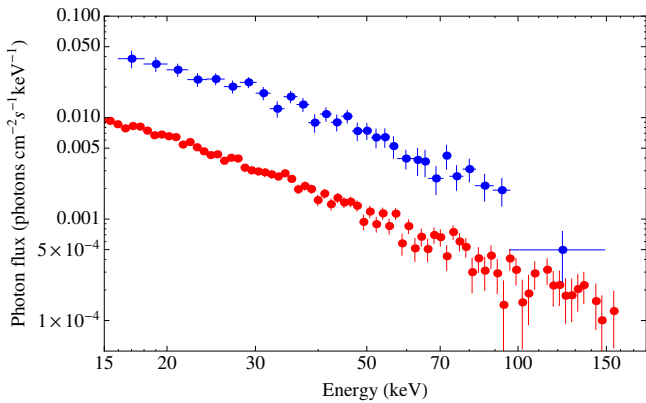


Fig. 8. Spectra of GRB 090423 (blue data) and of the spectrum of the emission of GRB 090618 considered as possible Episode 2 if GRB 090618 had been observed at $z = 8.2$. The low-energy photon index is ≈ -0.8 , which corresponds to the expectations from the Fireshell scenario (Ruffini 2011; Patricelli et al. 2012).

detectable. The observed flux in Fig. 6 and the one of the dashed region in Fig. 8 will be similar when compared in a common frame.

For the above considerations, the analysis presented in the previous section can be applied to Episode 2 of GRB 090618. Assuming a detector threshold for *Swift*-BAT of $\sigma_0 = 6.7$, see Eq. (2), only the dashed region in Fig. 7 is detectable when transposing GRB 090618 at $z = 8.2$. In the observer frame, this emission corresponds to the time interval ($T_{0,G} + 63.0$, $T_{0,G} + 69.1$) s, with $T_{0,G}$ the trigger time of Fermi GBM data

of GRB 090618. This time interval, at $z = 8.2$, has a duration $\Delta t_{A,obs} = \Delta t_{obs} \times 5.97 = 36.4$ s, owing to the time dilation by the cosmological redshift z (see Fig. 6). The remaining emission of GRB 090618 is unobservable, since below the threshold of the *Swift*-BAT detector. We note that $\Delta t_{A,obs}$ is quite comparable to the observed duration of GRB 090423 (see Fig. 6).

We turn now to comparing and contrasting the spectral energy distributions in the rest frame of the two GRBs. We consider the spectrum of GRB 090618 in the energy range (89.6–896) keV, which corresponds to the *Swift*-BAT band (15–150) keV in the rest frame of GRB 090423. As for the time interval in GRB 090423, we consider the observational time interval (63.0–69.1) s, determined from applying Eq. (2) to the entire Episode 2 of GRB 090618 (see the dashed region in Fig. 7). We fitted the spectral emission observed in GRB 090423 with a Band function (Band et al. 1993), and the results provide an intrinsic peak energy $E_{p,i} = (284.57 \pm 172.10)$ keV (see Table 1). The same model provides for the spectral emission of GRB 090423, in the T90 time duration, an intrinsic peak energy of $E_{p,i} = (433.6 \pm 133.5)$ keV. However, the break in GRB 090423 is steeper, while in GRB 090618 it is more shallow. This is clear in Fig. 8, where we show the spectra of both GRBs that are transformed to a common frame, which is the one at redshift $z = 8.2$. Very likely, the difference in the steepening at high energies is related to the structure of the circumburst medium (CBM): the more fragmented the CBM, the larger the cutoff energy of the fireshell spectrum (Bianco & Ruffini 2005). Another important result is that the low energy index α is quite similar in both GRBs. This agrees with the expectation from the fireshell scenario, where a photon index of ≈ -0.8 is expected in the early emission of a GRB (Patricelli et al. 2012).

The isotropic energy emitted in the time interval delineated by the dashed region in Fig. 7 has been computed to be $E_{iso} = 3.49 \times 10^{52}$ erg, which is very similar to the one computed for the T90 duration, in the same energy range, for GRB 090423, $E_{iso} = 4.99 \times 10^{52}$ erg.

7. Striking observations of Episode 3

That in long GRBs the X-ray emission, observed by *Swift*-XRT in energy range 0.3–10 keV, presents a typical structure composed of a steep decay, a plateau phase and a late power-law decay, was clearly expressed by Nousek, Zhang and their collaborators (Nousek et al. 2006; Zhang et al. 2006). This structure acquires a special meaning when examined in the most energetic sources, $E_{iso} = 10^{52}$ – 10^{54} erg, and leads to the fundamental proof that GRB 090423 is a BdHN source.

It has only been after applying the IGC paradigm to the most energetic long GRBs associated to SNe that we noticed the most unique characterizing property of the BdHN sources: while the steep decay and the plateau phase can be very different from source to source, the late X-ray power-law component overlaps,

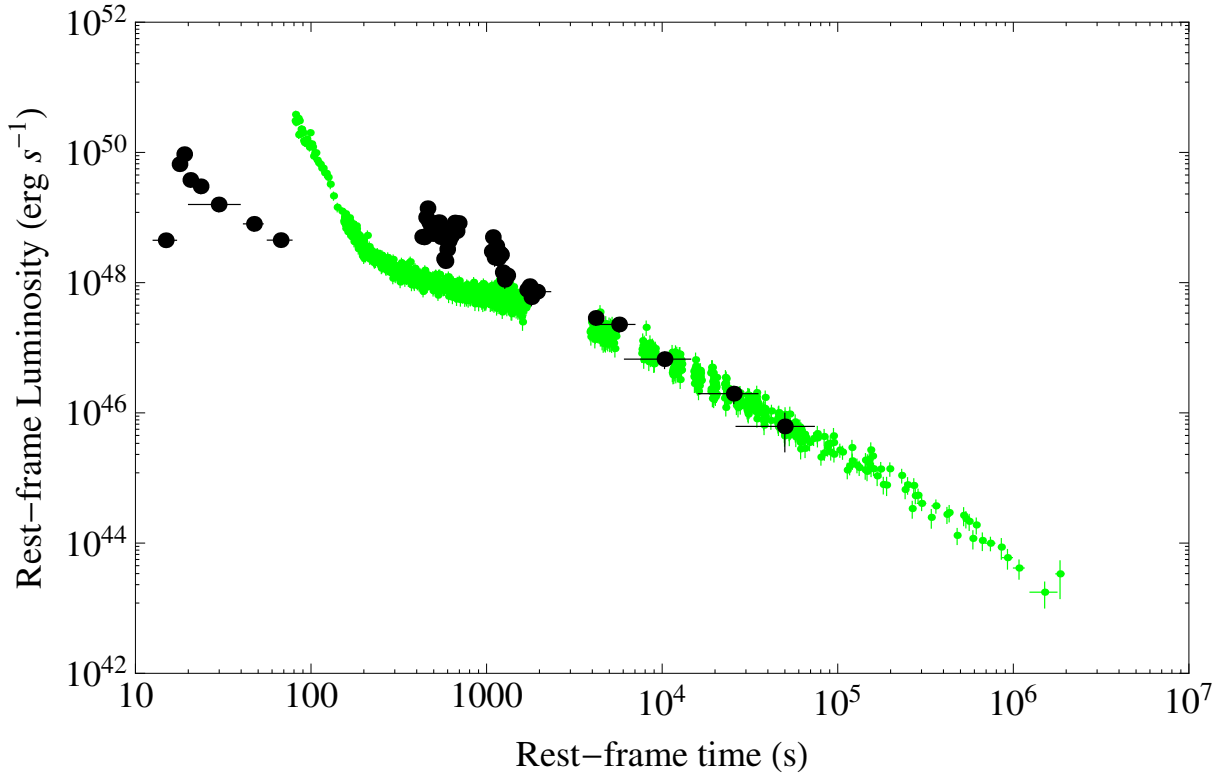


Fig. 9. Behavior of the Episode 3 luminosity of GRB 090423 (black dots) compared with the prototype case of GRB 090618 (green data).

when computed in the cosmological rest-frame (see [Pisani et al. 2013](#) and [Fig. 3](#)). This has become the crucial criterion for asserting membership of a GRB in the BdHN family. Indeed, when we report the late X-ray emission of Episode 3 in GRB 090423 at $z = 8.2$, and GRB 090618 at $z = 0.54$, we observe a complete overlapping at times longer than 10^4 s, see [Fig. 9](#).

7.1. Recent progress in understanding the nature of Episode 3

We recall:

- that the X-ray luminosity of Episode 3 in all BdHN sources presents precise scaling laws (see, e.g., [Fig. 3](#));
- that the very high energy emission all the way, up to 100 GeV, in GRB 130427A, as well as the optical one, follows a power-law behavior similar to the one in the X-ray emission described above. The corresponding spectral energy distribution is also described by a power-law function ([Kouveliotou et al. 2013](#); [Ruffini et al. 2014b](#)). These results clearly require a common origin for this emission process in Episode 3;
- that an X-ray thermal component has been observed in the early phases of Episode 3 of GRB 060202, 060218, 060418, 060729, 061007, 061121, 081007, 090424, 100316D, 100418A, 100621A, 101219B, and 120422A ([Page et al. 2011](#); [Starling et al. 2012](#); [Friis & Watson 2013](#)). In particular, this feature has been clearly observed in GRB 090618 and GRB 130427A ([Ruffini et al. 2014b](#)). This implies an emission region size of 10^{12-13} cm in these early phases of Episode 3, with an expansion velocity of $0.1 < v/c < 0.9$, with a bulk Lorentz Γ factor $\lesssim 2$ ([Ruffini et al. 2014a](#)).

The simultaneous occurrence of these three features imposes very stringent constraints on any possible theoretical models. In

particular, the traditional synchrotron ultra-relativistic scenario of the Collapsar jet model ([Woosley 1993](#); [Meszaros & Rees 2000](#)) does not appear suitable for explaining these observational facts.

In [Ruffini et al. \(2014a\)](#), we have recently pointed out the possibility of using the nuclear decay of ultra-heavy nuclei originally produced in the close binary phase of Episode 1 by r-process as an energy source of Episode 3. There is the remarkable coincidence that this set of processes leads to the value of the power-law emission with decay index α , similar to the one observed and reported in [Metzger et al. \(2010\)](#). The total energy emitted in the decay of these ultra-heavy elements agrees with the observations in Episode 3 of BdHN sources ([Ruffini et al. 2014a](#)). An additional possibility of process-generating a scale-invariant power law in the luminosity evolution and spectrum are the ones expected from type-I and type-II Fermi acceleration mechanisms ([Fermi 1949](#)). The application of these acceleration mechanisms to the BdHN remnant has two clear advantages: 1) for us, to fulfill the above-mentioned power laws, both for the luminosity and the spectrum; and 2) for Fermi, to solve the long-standing problem, formulated by Fermi in his classic paper, of identifying the injection source to make his acceleration mechanism operational on an astrophysical level.

8. Conclusions

The ansatz that GRB 090423 is the transposed of GRB 090618 at $z = 8.2$ has passed scrutiny. It is viable with respect to Episodes 1 and 4 and has obtained important positive results from the analysis of Episodes 2 and 3:

- Episodes 1 and 4 have not been detected in GRB 090423. This is consistent with the fact that the flux of Episodes 1 and 4 of GRB 090618 should not be observed by the

Swift-BAT detector or by the optical telescopes, owing to the very high redshift of the source and the current sensitivities of X-ray and optical detectors;

- Episode 2 of GRB 090423 has definitely been observed by Swift-BAT: its observed emission is comparable 1) to energy emitted (3.49×10^{52} erg for GRB 090618 and 4.99×10^{52} erg for GRB 090423); 2) to the observed time duration (34 s for the observable part of GRB 090618 when transposed to $z = 8.2$ and 19 s for GRB 090423); and 3) to the spectral energy distribution: the low energy part of the spectra of both GRBs is consistent with the expectation of the fireshell model (Patricelli et al. 2012). There is a significant difference only in the high energy part of the spectrum of GRB 090423, where a cutoff is observed at lower energy than the one in GRB 090618. This can be explained, in the fireshell scenario, by the existence of a dense and homogeneous CBM (Bianco & Ruffini 2005), which is expected for bursts at high redshifts;
- Episode 3 shows the striking feature of the overlapping of the late X-ray luminosities of Episode 3 in GRB 090618 and GRB 090423, when compared in their cosmological rest frames (see Fig. 9). This result confirms the extension of the relation presented in Pisani et al. (2013) for $z \leq 1$, all the way up to $z = 8.2$.

From an astrophysical point of view, all the above results clearly indicate that

- a) GRB 090423 is fully consistent with being a member of the BdHN family, and the associated SN did occur already at $z = 8.2$: the possibility of having an evolved binary system about 650 Myr after the Big Bang is not surprising, since the lifetime of massive stars with a mass up to $30 M_{\odot}$ is ~ 10 Myr (Woosley et al. 2002), which is similar to expectations from normal Population II binary stars also at $z = 8.2$, as pointed out by Belczynski et al. (2010);
- b) the FeCO core and the NS companion occurring at $z = 8.2$ also implies the existence, as the progenitor, of a massive binary $\sim 40\text{--}60 M_{\odot}$. Such massive binaries have recently been identified in η Carinae (Damineli et al. 2000). The very rapid evolution of such very massive stars will lead first to a binary X-ray source, like Cen-X3 (see, e.g., Gursky & Ruffini 1975) and Giacconi & Ruffini (1978), which will further evolve in the FeCO with the binary NS companion. A similar evolution starting from a progenitor of two very massive stars was considered by Fryer et al. (1999) and by Bethe & Brown (1998), leading to the formation of binary NSs or postulating the occurrence of GRBs. They significantly differ from the IGC model and also differ in their final outcomes;
- c) the results presented in this article open the way to considering the late X-ray power-law behavior in Episode 3 as a distance indicator and represents a significant step toward formulating a cosmological standard candle based on Episode 3 of these BdHN sources.

We turn now to fundamental issues in physics.

- 1) The traditional fireball jet model (Meszaros 2006) describes GRBs as a single phenomenon, originating in a collapsar (Woosley 1993) and characterized by jet emission moving at Lorentz Γ factor in the range $\approx 200\text{--}2000$. This contrasts with the BdHN model where the GRB is actually composed

of three different episodes that are conceptually very different among each other (see Fig. 1): Episode 1 is non-relativistic, and Episode 2 is ultra-relativistic with Lorentz Γ factor $\approx 200\text{--}2000$, Episode 3 is mildly relativistic, with $\Gamma \approx 2$.

- 2) The description of Episode 1, see Fig. 2, proposes the crucial role of the Bondi-Hoyle hypercritical accretion process of the SN ejecta onto the NS companion. This requires an urgent analysis of the neutrino emission pioneered in the classic papers of Zel'dovich et al. (1972); Chevalier (1993); Fryer et al. (1996), and (Fryer 2009).
- 3) The binary nature of the progenitors in the BdHN model and the presence of the specific scaling power laws in the luminosity in Episode 3 of GRB 090423, as well as in all the other sources of the “golden sample” (see Fig. 3; Pisani et al. 2013), has led us to consider the decay of heavy nuclear material originating in r -processes (Ruffini et al. 2014a), as well as type-I and type-II Fermi acceleration mechanism as possible energy sources of the mildly relativistic Episode 3 (Ruffini et al. 2014b).

Acknowledgements. We are very grateful to the referee for the very thoughtful considerations and advices which greatly improved the presentation of our manuscript. We thank David W. Arnett for fruitful discussions and support. We are also grateful to Elena Zaninoni and Gennaro De Tommaso for their comments on the manuscript. This work made use of data supplied by the UK Swift Science Data Centre at the University of Leicester. G.B.P., M.E., and M.K. are supported by the Erasmus Mundus Joint Doctorate Program by grant Nos. 2011-1640, 2012-1710, and 2013-1471, respectively, from the EACEA of the European Commission.

References

- Amati, L., Frontera, F., Tavani, M., et al. 2002, *A&A*, 390, 81
 Band, D. L. 2003, *ApJ*, 588, 945
 Band, D., Matteson, J., Ford, L., et al. 1993, *ApJ*, 413, 281
 Barthelmy, S. D., Barbier, L. M., Cummings, J. R., et al. 2005, *Space Sci. Rev.*, 120, 143
 Belczynski, K., Holz, D. E., Fryer, C. L., et al. 2010, *ApJ*, 708, 117
 Bethe, H. A., & Brown, G. E. 1998, *ApJ*, 506, 780
 Bianco, C. L., & Ruffini, R. 2005, *ApJ*, 620, L23
 Bisnovatyi-Kogan, G. S., & Lamzin, S. A. 1984, *Sov. Astron.*, 28, 187
 Bondi, H. 1952, *MNRAS*, 112, 195
 Bondi, H., & Hoyle, F. 1944, *MNRAS*, 104, 273
 Burrows, D., Hill, J., Nousek, J., et al. 2005, *Space Sci. Rev.*, 120, 165
 Chevalier, R. A. 1989, *ApJ*, 346, 847
 Chevalier, R. A. 1993, *ApJ*, 411, L33
 Damineli, A., Kaufer, A., Wolf, B., et al. 2000, *ApJ*, 528, L101
 Enderli, M. 2013, 27th Texas Symp. on Relativistic Astrophysics, Dallas, TX (USA), December 8–13
 Fermi, E. 1949, *Phys. Rev.*, 75, 1169
 Fermi-LAT collaboration, & Fermi-GBM collaboration. 2014, *Science*, 343, 42
 Friis, M., & Watson, D. 2013, *ApJ*, 771, 15
 Fryer, C. L. 2009, *ApJ*, 699, 409
 Fryer, C. L., Benz, W., & Herant, M. 1996, *ApJ*, 460, 801
 Fryer, C. L., Woosley, S. E., & Hartmann, D. H. 1999, *ApJ*, 526, 152
 Gehrels, N., Sarazin, C. L., O’Brien, P. T., et al. 2005, *Nature*, 437, 851
 Giacconi, R., & Ruffini, R. 1978, *Physics and astrophysics of neutron stars and black holes* (Amsterdam: North Holland Publishing)
 Gursky, H., & Ruffini, R. 1975, *Neutron stars, black holes and binary X-ray sources*; Proceedings of the Annual Meeting, San Francisco, Calif., February 28, 1974, (Dordrecht: D. Reidel Publishing), *Astrophys. Space Sci. Lib.* 48
 Izzo, L., Bernardini, M. G., Bianco, C. L., et al. 2010, *JKPS*, 57-3, 551
 Izzo, L., Rueda, J. A., & Ruffini, R. 2012a, *A&A*, 548, L5
 Izzo, L., Ruffini, R., Penacchioni, A. V., et al. 2012b, *A&A*, 543, A10
 Kann, D. A., Klose, S., Zhang, B., et al. 2011, *ApJ*, 734, 96
 Kouveliotou, C., Granot, J., Racusin, J. L., et al. 2013, *ApJ*, 779, L1
 Krimm, H. A., Beardmore, A. P., Evans, P. A., et al. 2009, *GRB Coordinates Network*, 9198, 1
 Margutti, R., Zaninoni, E., Bernardini, M. G., et al. 2013, *MNRAS*, 428, 729

² <http://nsm.utdallas.edu/texas2013/proceedings/3/1/Ruffini.pdf>

- Meegan, C., Lichti, G., Bhat, P. N., et al. 2009, *ApJ*, 702, 791
- Melandri, A., Pian, E., D'Elia, V., et al. 2014, *A&A*, 567, A29
- Meszáros, P. 2006, *Rep. Prog. Phys.*, 69, 2259
- Meszáros, P., & Rees, M. J. 2000, *ApJ*, 530, 292
- Metzger, B. D., Martínez-Pinedo, G., Darbha, S., et al. 2010, *MNRAS*, 406, 2650
- Nousek, J. A., Kouveliotou, C., Grupe, D., et al. 2006, *ApJ*, 642, 389
- Page, K. L., Starling, R. L. C., Fitzpatrick, G., et al. 2011, *MNRAS*, 416, 2078
- Patricelli, B., Bernardini, M. G., Bianco, C. L., et al. 2012, *ApJ*, 756, 16
- Penacchioni, A. V., Ruffini, R., Izzo, L., et al. 2012, *A&A*, 538, A58
- Penacchioni, A. V., Ruffini, R., Bianco, C. L., et al. 2013, *A&A*, 551, A133
- Pisani, G. B., Izzo, L., Ruffini, R., et al. 2013, *A&A*, 552, L5
- Rueda, J. A., & Ruffini, R. 2012, *ApJ*, 758, L7
- Ruffini, R. 2011, *Int. J. Mod. Phys. D*, 20, 1797
- Ruffini, R. 2013, 27th Texas Symposium on Relativistic Astrophysics, Dallas, TX (USA), December 8–13
- Ruffini, R., Izzo, L., Muccino, M., et al. 2013, [[arXiv:1311.7432](#)]
- Ruffini, R., Muccino, M., Bianco, C. L., et al. 2014a, *A&A*, 565, L10
- Ruffini, R., Wang, Y., Kovacevic, M., et al. 2014b, *ApJ*, submitted [[arXiv:1405.5723](#)]
- Salvaterra, R., Della Valle, M., Campana, S., et al. 2009, *Nature*, 461, 1258
- Salvaterra, R., Campana, S., Vergani, S. D., et al. 2012, *ApJ*, 749, 68
- Starling, R. L. C., Page, K. L., Pe'Er, A., Beardmore, A. P., & Osborne, J. P. 2012, *MNRAS*, 427, 2950
- Stratta, G., & Perri, M. 2009, *GRB Coordinates Network*, 9212, 1
- Tanvir, N. R., Fox, D. B., Levan, A. J., et al. 2009, *Nature*, 461, 1254
- von Kienlin, A. 2009a, *GRB Coordinates Network*, 9229, 1
- von Kienlin, A. 2009b, *GRB Coordinates Network*, 9251, 1
- Woosley, S. E. 1993, *ApJ*, 405, 273
- Woosley, S. E., Heger, A., & Weaver, T. A. 2002, *Rev. Mod. Phys.*, 74, 1015
- Zel'dovich, Y. B., Ivanova, L. N., & Nadezhin, D. K. 1972, *Sov. Astron.*, 16, 209
- Zhang, B., Fan, Y. Z., Dyks, J., et al. 2006, *ApJ*, 642, 354

LETTER TO THE EDITOR

On binary-driven hypernovae and their nested late X-ray emission

R. Ruffini^{1,2,3,4}, M. Muccino^{1,2}, C. L. Bianco^{1,2}, M. Enderli^{1,3}, L. Izzo^{1,2}, M. Kovacevic^{1,3}, A. V. Penacchioni⁴,
 G. B. Pisani^{1,3}, J. A. Rueda^{1,2,4}, and Y. Wang^{1,2}

¹ Dip. di Fisica and ICRA, Sapienza Università di Roma, piazzale Aldo Moro 5, 00185 Rome, Italy
 e-mail: marco.muccino@icra.it

² ICRANet, piazza della Repubblica 10, 65122 Pescara, Italy

³ Université de Nice Sophia Antipolis, CEDEX 2, Grand Château Parc Valrose, BP 2135, 06103 Nice, France

⁴ ICRANet-Rio, Centro Brasileiro de Pesquisas Físicas, rua Dr. Xavier Sigaud 150, 22290-180 Rio de Janeiro, Brazil

Received 14 March 2014 / Accepted 28 April 2014

ABSTRACT

Context. The induced gravitational collapse (IGC) paradigm addresses the very energetic (10^{52} – 10^{54} erg) long gamma-ray bursts (GRBs) associated to supernovae (SNe). Unlike the traditional “collapsar” model, an evolved FeCO core with a companion neutron star (NS) in a tight binary system is considered as the progenitor. This special class of sources, here named “binary-driven hypernovae” (BdHNe), presents a composite sequence composed of four different episodes with precise spectral and luminosity features.

Aims. We first compare and contrast the steep decay, the plateau, and the power-law decay of the X-ray luminosities of three selected BdHNe (GRB 060729, GRB 061121, and GRB 130427A). Second, to explain the different sizes and Lorentz factors of the emitting regions of the four episodes, for definiteness, we use the most complete set of data of GRB 090618. Finally, we show the possible role of r-process, which originates in the binary system of the progenitor.

Methods. We compare and contrast the late X-ray luminosity of the above three BdHNe. We examine correlations between the time at the starting point of the constant late power-law decay t_a^* , the average prompt luminosity (L_{iso}), and the luminosity at the end of the plateau L_a . We analyze a thermal emission (~ 0.97 – 0.29 keV), observed during the X-ray steep decay phase of GRB 090618.

Results. The late X-ray luminosities of the three BdHNe, in the rest-frame energy band 0.3–10 keV, show a precisely constrained “nested” structure. In a space–time diagram, we illustrate the different sizes and Lorentz factors of the emitting regions of the three episodes. For GRB 090618, we infer an initial dimension of the thermal emitter of $\sim 7 \times 10^{12}$ cm, expanding at $\Gamma \approx 2$. We find tighter correlations than the Daiotti–Willingale ones.

Conclusions. We confirm a constant slope power-law behavior for the late X-ray luminosity in the source rest frame, which may lead to a new distance indicator for BdHNe. These results, as well as the emitter size and Lorentz factor, appear to be inconsistent with the traditional afterglow model based on synchrotron emission from an ultra-relativistic ($\Gamma \sim 10^2$ – 10^3) collimated jet outflow. We argue, instead, for the possible role of r-process, originating in the binary system, to power the mildly relativistic X-ray source.

Key words. supernovae: general – binaries: general – gamma-ray burst: general – black hole physics – stars: neutron – nuclear reactions, nucleosynthesis, abundances

1. Introduction

The induced gravitational collapse (IGC) paradigm has been widely illustrated (Ruffini et al. 2006, 2007, 2008; Rueda & Ruffini 2012; Izzo et al. 2012a). It assumes that long, energetic (10^{52} – 10^{54} erg) gamma-ray bursts (GRBs) associated to supernovae (SNe) originate in a close binary system composed of an evolved massive star (likely a FeCO core) in the latest phases of its thermonuclear evolution and a neutron star (NS) companion. From an observational point of view, the complete time sequence of the IGC paradigm binary system has been identified in GRB 090618 (Izzo et al. 2012b), GRB 101023 (Penacchioni et al. 2012), GRB 110907B (Penacchioni et al. 2013), and GRB 970828 (Ruffini et al. 2013). We name these especially energetic systems, here, fulfilling the IGC paradigm, “binary-driven hypernovae” (BdHNe), to differentiate them from the traditional less energetic hypernovae.

In this Letter we introduce the IGC paradigm space-time diagram for the four distinct emission episodes (see Fig. 1): *Episode 1* corresponds to the onset of the FeCO core SN explosion, creating a new-NS (ν -NS, see A). Part of the SN ejecta triggers an accretion process onto the NS companion (see Rueda & Ruffini 2012; Izzo et al. 2012a, and B in Fig. 1), and a prolonged

interaction between the ν -NS and the NS binary companion occurs (C). This leads to a spectrum with an expanding thermal component plus an extra power law (see Fig. 16 in Izzo et al. 2012b, and Fig. 4 in Ruffini et al. 2013).

Episode 2 occurs when the companion NS reaches its critical mass and collapses to a black hole (BH), emitting the GRB (D) with Lorentz factors $\Gamma \approx 10^2$ – 10^3 (for details, see e.g. Ruffini et al. 2010; Izzo et al. 2012b; Ruffini et al. 2013).

Episode 3, observed in the X-rays, shows very precise behavior consisting of a steep decay, starting at the end point of the prompt emission (see E), and then a plateau phase, followed by a late constant power-law decay (see, e.g., Izzo et al. 2012b; Penacchioni et al. 2012; Ruffini et al. 2013).

Episode 4, not shown in Fig. 1, corresponds to the optical SN emission due to the ^{56}Ni decay (see Arnett 1996) occurring after ~ 10 – 15 days in the cosmological rest frame. In all BdHNe, the SN appears to have the same luminosity as in the case of SN 1998bw (Amati et al. 2007). Although the presence of the SN is implicit in all the sources fulfilling the IGC paradigm, it is only detectable for GRBs at $z \lesssim 1$, in view of the limitations of the current optical telescopes.

We are going to see in this Letter that Episodes 1 and 2 can differ greatly in luminosity and timescale from source to source,

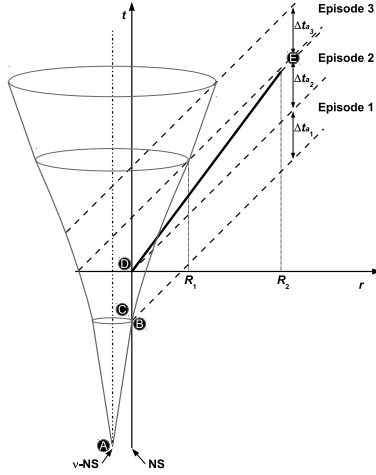


Fig. 1. IGC space-time diagram (not in scale) illustrates the relativistic motion of Episode 2 ($\Gamma \approx 500$, thick line) and the non-relativistic Episode 1 ($\Gamma \approx 1$) and Episode 3 ($\Gamma \approx 2$). Emissions from different radii, R_1 ($\sim 10^{13}$ cm) and R_2 ($\sim 10^{16}$ – 10^{17} cm), contribute to the transition point (E). Clearly, the X-ray luminosity originates in the SN remnant or in the newly-born BH, but not in the GRB.

while we confirm that in Episode 3, the late X-ray luminosities overlap: they follow a common power-law behavior with a constant slope in the source rest frame (Pisani et al. 2013). We point out here that the starting point of this power-law component is a function of the GRB isotropic energy E_{iso} .

The main goals of this Letter consist in a) comparing and contrasting the steep decay, the plateau, and the power-law decay of the X-ray luminosities as functions of E_{iso} by considering three selected GRBs (060729, 061121, and 130427A); b) pointing out the difference in the size and the Lorentz factors of the emitting regions of Episodes 1, 2, and 3 (for definiteness we use as prototype the source with the most complete dataset, GRB 090618); c) drawing attention to the possible role of the r-process, originating in the binary system of the progenitor, to power the mildly relativistic X-ray emission in the late phases of Episode 3.

2. The case of GRB 090618

We illustrate the difference in the emitting region sizes in the three episodes and their corresponding Lorentz factors:

Episode 1 has a thermal component expanding from $\sim 10^9$ cm to $\sim 10^{10}$ cm on a rest-frame timescale of ~ 30 s with an average velocity of $\sim 4 \times 10^8$ cm s $^{-1}$ (see Izzo et al. 2012b). The total energy is 4.1×10^{52} erg, well above the traditional kinetic energy expected in the early phases of a SN, and it originates in the accretion of the material of the SN ejecta on the companion NS in the binary system (Rueda & Ruffini 2012; Ruffini et al. 2013).

Episode 2 has been shown to be the ultra-relativistic prompt emission episode (e.g., the actual GRB) stemming from the collapse of the NS to a BH. Its isotropic energy is 2.5×10^{53} erg. The characteristic Lorentz factor at the transparency of the fireshell has been found to be $\Gamma = 490$ for GRB 090618. The characteristic spatial extension goes all the way up to $\sim 10^{16}$ – 10^{17} cm, reached at the end of Episode 2 (see Fig. 10 in Izzo et al. 2012b).

Episode 3 has an isotropic energy of $\approx 6 \times 10^{51}$ erg. A striking feature occurs during its steep decay phase: in the early observed 150 s, Page et al. (2011) have found a thermal component with a decreasing temperature from ~ 0.97 keV to ~ 0.29 keV (see also Starling et al. 2012). The surface radius

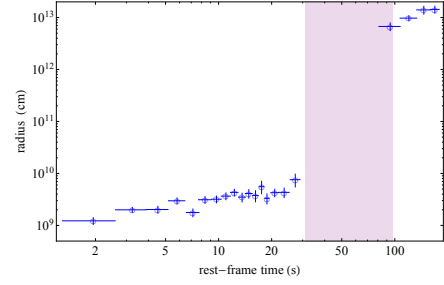


Fig. 2. Radii (open blue circles) of the emitting regions, measured in the cosmological rest frame. Episode 1 radius ranges from $\sim 10^9$ cm to $\sim 10^{10}$ and expands at $\Gamma \approx 1$ (Izzo et al. 2012b). The Episode 3 radius, in the early phases of the steep decay, starts from a value of $\sim 7 \times 10^{12}$ cm and expands at $\Gamma \approx 2$. The Episode 2 rest-frame duration is indicated by the shaded purple region. The expansion velocity at late times is expected to approach the asymptotic value of $0.1c$ observed in the optical spectra (Della Valle 2011), in the absence of any further acceleration process.

of the emitter can be inferred from the observed temperature T_0 and flux F_{BB} of the thermal component. We have, in fact (Izzo et al. 2012b),

$$r \approx \Gamma d_l (1+z)^{-2} \sqrt{F_{BB} / (\sigma T_0^4)}, \quad (1)$$

where d_l is the luminosity distance in the Λ CDM cosmological model and σ the Stefan-Boltzmann constant. As usual, $\Gamma = 1/\sqrt{1-\beta^2}$, where $\beta = v/c$ is the expansion velocity in units of the speed of light c .

In parallel, the relation between the detector arrival time t_a^d , the cosmological rest-frame arrival time t_a and the laboratory time t , is given by $t_a^d \equiv t_a(1+z) = t(1-\beta \cos \theta)(1+z)$, where θ is the displacement angle of the considered photon emission point from the line of sight (see, e.g., Bianco et al. 2001). We can then deduce the expansion velocity β , assumed to be constant, from the ratio between the variation of the emitter radius Δr and the emission duration in laboratory frame Δt , i.e. $\beta = \Delta r / (c \Delta t)$. Using the condition $\beta \leq \cos \theta \leq 1$ (Bianco et al. 2001), we obtain $0.75 \leq \beta \leq 0.89$ and, correspondingly, $1.50 \leq \Gamma \leq 2.19$ and radii $r \sim 10^{13}$ cm (see Fig. 2).

As is clear from Fig. 1, a sharp transition occurs between the end of Episode 2, where the characteristic dimensions reached by the GRB are $\sim 10^{16}$ – 10^{17} cm, and the emission at the beginning of X-ray luminosity, with an initial size of $\sim 7 \times 10^{12}$ cm. This leads to the conclusion that the X-ray emission of Episode 3 originates in the SN ejecta or in the accretion on the newly born BH and, anyway, not from the GRB.

3. The “nested” structure of Episode 3

We now turn to show the “nested” structure of the late X-ray luminosity. Pisani et al. (2013) have shown that the X-ray rest-frame 0.3–10 keV luminosity light curves present a constant decreasing power-law behavior, at $t_a \gtrsim 10^4$ s, with typical slopes of $-1.7 \lesssim \alpha_X \lesssim -1.3$. This has been proven in a sample of six BdHNe: GRBs 060729, 061007, 080319B, 090618, 091127, and 111228, hereafter *golden sample* (GS, see, e.g., Izzo et al. 2013; Pisani et al. 2013). That the late X-ray emission could play a fundamental role as a distance indicator has been explored inferring the redshifts of GRBs 101023 and 110709B (Penacchioni et al. 2012, 2013). The IGC paradigm also allowed predicting ~ 10 – 15 days in the cosmological rest frame before its discovery, the occurrence of the SN associated to GRB 130427A, the most luminous source ever observed in γ rays with $E_{\text{iso}} \approx 10^{54}$ erg

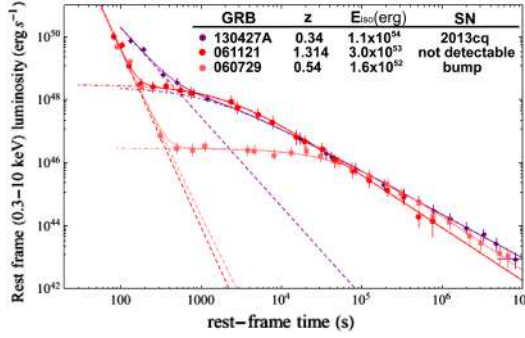


Fig. 3. Rest-frame 0.3–10 keV re-binned luminosity light curves of GRB 130427A (purple), GRB 061121 (red, shifted by 50 s in rest frame), and GRB 060729 (pink). The light curves are fitted by using a power-law for the steep decay phase (dashed lines) and the function in Eq. (2) for the plateau and the late decay phases (dot-dashed curves).

and $z = 0.34$ (Xu et al. 2013b; Flores et al. 2013). This was later confirmed by the observations (de Ugarte Postigo et al. 2013; Levan et al. 2013; Watson et al. 2013; Xu et al. 2013a).

We compare and contrast GRB 130427A X-ray data with GRB 060729, a member of the GS, and GRB 061121, which shows the general behavior of BdHNe. GRB 060729, at $z = 0.54$, has $E_{\text{iso}} = 1.6 \times 10^{52}$ erg (Grupe et al. 2007) and a SN bump in its optical afterglow (Cano et al. 2011). GRB 061121, at $z = 1.314$ (Bloom et al. 2006), has $E_{\text{iso}} = 3.0 \times 10^{53}$ erg, and its Episode 4 is clearly missing in view of the high cosmological redshift.

In Fig. 3 we have plotted the rebinned rest-frame 0.3–10 keV luminosity light curves of GRBs 130427A, 060729, and 061121. Their steep decay is modeled by a power-law function, i.e. $L_p(t_a/100)^{-\alpha_p}$, where L_p and α_p are the power-law parameters. The plateau and the late power-law decay are instead modeled by using the following phenomenological function

$$L(t_a) = L_X (1 + t_a/\tau)^{-\alpha_X}, \quad (2)$$

where L_X , α_X , and τ , respectively, are the plateau luminosity, the late power-law decay index, and the characteristic timescale of the end of the plateau. From Eq. (2), we have defined the end of the plateau at the rest-frame time $t_a^* = \tau[(1/2)^{1/\alpha_X} - 1]$, when the luminosity of the plateau is half of the initial one, $L_a(t_a^*) = L_X/2$.

From this fitting procedure, we can conclude that the three BdHN systems considered here share the following properties:

- a) the power-law decay for the more energetic sources starts directly from the steep decay, well before the $t_a \approx 2 \times 10^4$ s, as indicated in Pisani et al. (2013); consequently, the plateau shrinks as a function of the increasing E_{iso} (see Fig. 3);
- b) the luminosities in the power-law decay are uniquely functions of the cosmological rest-frame arrival time t_a independently on the E_{iso} of each source (see Fig. 3);
- c) most remarkably, the overlapping of the X-ray light curves reveals a “nested” structure of BdHN Episodes 3.

In our sample of BdHNe, we verify the applicability of the Dainotti-Willingale relations $\langle L_{\text{iso}} \rangle - t_a^*$ and $L_a - t_a^*$ (Dainotti et al. 2008, 2011b; Willingale et al. 2007), where $\langle L_{\text{iso}} \rangle = E_{\text{iso}}/t_{a,90}$ is the averaged luminosity of the prompt and $t_{a,90}$ is the rest-frame t_{90} duration of the burst. The resulting correlations, $\log_{10} Y_i = m_i \log_{10} X_i + q_i$, are shown in Fig. 4. The parameters of each BdHN and the best fit parameters, m_i and q_i (where $i = 1, 2$), are summarized in Table 1. As is clear from the extra scatter values σ_i , our total BdHN sample provides tighter correlations. The extra scatter of the $L_a - t_a^*$, $\sigma = 0.26$, is less than the Dainotti et al. (2011a) ones, i.e., $\sigma = 0.76$ for the whole sample of 62 bursts and

$\sigma = 0.40$ for the best subsample of eight bursts (*U0095*). The Dainotti-Willingale correlations consider X-ray afterglows characterized by a steep decay, a plateau phase, and a late power-law decay (Nousek et al. 2006; Zhang et al. 2006), independently of their energetics. In our BdHN sample we limit the attention to a) the most energetic sources, 10^{52} – 10^{54} erg, b) the presence of four emission episodes (neglecting Episode 4 for $z > 1$), and c) sources with determined redshift and complete data at $t_a = 10^4$ – 10^6 s. All these conditions appear to be necessary to fulfill the nested structure in Fig. 3 and the tighter correlations between the astrophysical parameters $\langle L_{\text{iso}} \rangle$, L_a , and t_a^* in Fig. 4.

To explain the above nested power-law decay and constrained correlations, we consider the decay of heavy elements produced in the r-process as a viable energy source (Burbidge et al. 1957), originating in binary NS mergers (see, e.g., Li & Paczyński 1998; Janka et al. 1999; Rosswog et al. 2004; Oechslin et al. 2007; Goriely et al. 2011; Piran et al. 2014).

Li & Paczyński (1998) have shown that the emission from the surface of an optically thick expanding ejecta in an adiabatic regime provides a flat light curve (see also Arnett 1982). This can explain, in principle, the observed steep decay and plateau phase of Episode 3 (see Fig. 3). After the ejecta becomes transparent, the heating source term due to the nuclear decays of the heavy nuclei, generated via r-process, becomes directly observable and dominates. The avalanche of decays with different lifetimes then provides the total energy release per unit mass per time that follows a power-law distribution, whose decay index has been estimated to be $-1.4 \lesssim \alpha \lesssim -1.1$ (Metzger et al. 2010). These values are strikingly similar to the ones we have found in the late X-ray luminosity.

This power-law behavior is different from the exponential decay observed in the optical light curves of traditional SN, powered by the decay of a single element ($^{56}\text{Ni} \rightarrow ^{56}\text{Co} \rightarrow ^{56}\text{Fe}$), which is not produced in the avalanche of many decays as in the r-process.

4. Conclusions

To summarize, short GRBs have been shown to come from binary NS mergers (see, e.g., Goodman 1986; Paczynski 1986; Eichler et al. 1989; Meszaros & Rees 1997; Rosswog et al. 2003; Lee et al. 2004; and more recently Muccino et al. 2013). Our subclass of long, extremely energetic (10^{52} – 10^{54} erg) sources is also initially driven by a tight binary system, formed by a ν -NS and a companion NS, surrounded by the SN ejecta (see Fig. 1). Then we denoted these most energetic GRBs by “BdHNe”. This is clearly different from the gravitational collapse of a single massive progenitor star described by the collapsar model (Woosley 1993; MacFadyen & Woosley 1999; Woosley & Bloom 2006).

We compared and contrasted the late X-ray luminosities of three BdHNe with different E_{iso} , finding a nested structure. We showed tight correlations between $\langle L_{\text{iso}} \rangle$, L_a and t_a^* (see Fig. 4 and Table 1) in agreement with the Dainotti-Willingale ones.

The above scaling laws, the nesting, and the initial dimension of $\sim 7 \times 10^{12}$ cm and Lorentz factor of $\Gamma \approx 2$ obtained from the steep decay of the X-ray luminosity put stringent limits on alternative theoretical models. They do not appear to be explainable within the traditional fireball jetted model, originating in the synchrotron radiation emitted by a decelerating relativistic shell with $\Gamma \sim 10^2$ and colliding with the circumburst medium at distances $\sim 10^{16}$ cm (see, e.g., Sari et al. 1998; Piran 2005; Meszaros 2006; Gehrels et al. 2009, and reference therein). In this Letter we alternatively proposed that the late X-ray luminosity comes from the wide angle emission of the SN ejecta or

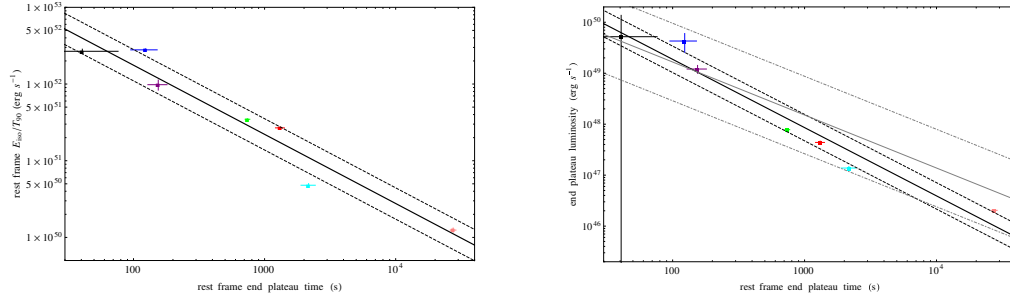


Fig. 4. The $\langle L_{\text{iso}} \rangle - t_a^*$ (left) and the $L_a - t_a^*$ (right) correlations (solid black lines) and the corresponding 1σ confidence levels (dashed black lines). The sources considered are GRB 060729 (pink), GRB 061007 (black), GRB 080319B (blue), GRB 090618 (green), GRB 091127 (red), GRB 111228A (cyan), and GRB 130427A (purple). The tighter BdHNe $L_a - t_a^*$ correlation is compared to the one in Dainotti et al. (2011a), corresponding to $m = -1.04$ and $q = 51.30$ (solid gray line) and $\sigma = 0.76$ (dot-dashed gray lines).

Table 1. List of the quantities of the sources considered and best fit parameters of the correlations in Fig. 4.

GRB	$\langle L_{\text{iso}} \rangle$ (10^{50} erg/s)	t_a^* (ks)	L_a (10^{47} erg/s)
060729	1.25 ± 0.08	27.4 ± 1.4	0.20 ± 0.01
061007	267 ± 18	0.041 ± 0.036	$521 \pm \text{unc}$
080319B	279 ± 7	0.12 ± 0.03	430 ± 170
090618	34.7 ± 0.3	0.74 ± 0.03	7.81 ± 0.17
091127	26.8 ± 0.3	1.31 ± 0.10	4.39 ± 0.26
111228A	4.79 ± 0.24	2.17 ± 0.27	1.38 ± 0.10
130427A	98 ± 15	0.16 ± 0.03	121 ± 21
Correlation	m_i	q_i	σ_i
$\langle L_{\text{iso}} \rangle - t_a^*$	$-(0.90 \pm 0.09)$	54.0 ± 0.3	0.20 ± 0.05
$L_a - t_a^*$	$-(1.34 \pm 0.14)$	52.0 ± 0.4	0.26 ± 0.08

in the accretion on the newly born BH. We call the attention on the role of the energy release in the SN ejecta from the decay of very heavy nuclei generated by r-process in binary NSs (Li & Paczyński 1998). This heavy nuclei avalanche decay (see, e.g., Metzger et al. 2010) may well explain the late X-ray luminosity of Episode 3. This emission follows the steep decay and plateau phase of the adiabatic optically thick expansion, prior to reaching transparency (see Fig. 3).

In the case of binary systems with longer periods and/or a lower accretion rate, which do not allow the NS companion to reach its critical mass and to form a BH, Episode 2 is missing. The presence of the companion NS will nevertheless strip the H and He envelopes of the core progenitor star. These sources have low energetic bursts ($E_{\text{iso}} < 10^{52}$ erg), such as GRB 060218 and GRB 980425, and their X-ray luminosity light curves do not overlap with the ones of our more energetic sample of BdHNe. These systems do not conform to the IGC paradigm and are traditional hypernovae¹.

Acknowledgements. This work made use of data supplied by the UK Swift Science Data Center at the University of Leicester. M.E., M.K., and G.B.P. are supported by the Erasmus Mundus Joint Doctorate Program by grant Nos. 2012-1710, 2013-1471, and 2011-1640, respectively, from the EACEA of the European Commission. We warmly thank the anonymous referee for very constructive suggestions that improved the presentation of this Letter.

References

Amati, L., Della Valle, M., Frontera, F., et al. 2007, A&A, 463, 913
 Arnett, D. 1996, Space Sci. Rev., 78, 559
 Arnett, W. D. 1982, ApJ, 253, 785
 Bianco, C. L., Ruffini, R., & Xue, S.-S. 2001, A&A, 368, 377
 Bloom, J. S., Perley, D. A., & Chen, H. W. 2006, GCN Circ., 5826
 Burbidge, E. M., Burbidge, G. R., Fowler, W. A., & Hoyle, F. 1957, Rev. Mod. Phys., 29, 547
 Cano, Z., Bersier, D., Guidorzi, C., et al. 2011, MNRAS, 413, 669
 Dainotti, M. G., Cardone, V. F., & Capozziello, S. 2008, MNRAS, 391, L79

¹ <http://nsm.utdallas.edu/texas2013/proceedings/3/1/Ruffini.pdf>

Dainotti, M. G., Fabrizio Cardone, V., Capozziello, S., Ostrowski, M., & Willingale, R. 2011a, ApJ, 730, 135
 Dainotti, M. G., Ostrowski, M., & Willingale, R. 2011b, MNRAS, 418, 2202
 de Ugarte Postigo, A., Xu, D., Leloudas, G., et al. 2013, GCN Circ., 14646, 1
 Della Valle, M. 2011, International Journal of Modern Physics D, 20, 1745
 Eichler, D., Livio, M., Piran, T., & Schramm, D. N. 1989, Nature, 340, 126
 Flores, H., Covino, S., Xu, D., et al. 2013, GRB Coordinates Network, Circular Service, 14491, 1
 Gehrels, N., Ramirez-Ruiz, E., & Fox, D. B. 2009, ARA&A, 47, 567
 Goodman, J. 1986, ApJ, 308, L47
 Goriely, S., Bauswein, A., & Janka, H.-T. 2011, ApJ, 738, L32
 Grupe, D., Gronwall, C., Wang, X.-Y., et al. 2007, ApJ, 662, 443
 Izzo, L., Rueda, J. A., & Ruffini, R. 2012a, A&A, 548, L5
 Izzo, L., Ruffini, R., Penacchioni, A. V., et al. 2012b, A&A, 543, A10
 Izzo, L., Pisani, G. B., Muccino, M., et al. 2013, EAS Pub. Ser., 61, 595
 Janka, H.-T., Eberl, T., Ruffert, M., & Fryer, C. L. 1999, ApJ, 527, L39
 Lee, W. H., Ramirez-Ruiz, E., & Page, D. 2004, ApJ, 608, L5
 Levan, A. J., Fruchter, A. S., Graham, J., et al. 2013, GRB Coordinates Network, Circular Service, 14686, 1
 Li, L.-X., & Paczyński, B. 1998, ApJ, 507, L59
 MacFadyen, A. I., & Woosley, S. E. 1999, ApJ, 524, 262
 Meszaros, P. 2006, Rep. Prog. Phys., 69, 2259
 Meszaros, P., & Rees, M. J. 1997, ApJ, 482, L29
 Metzger, B. D., Martínez-Pinedo, G., Darbha, S., et al. 2010, MNRAS, 406, 2650
 Muccino, M., Ruffini, R., Bianco, C. L., Izzo, L., & Penacchioni, A. V. 2013, ApJ, 763, 125
 Nousek, J. A., Kouveliotou, C., Grupe, D., et al. 2006, ApJ, 642, 389
 Oechslin, R., Janka, H.-T., & Marek, A. 2007, A&A, 467, 395
 Paczyński, B. 1986, ApJ, 308, L43
 Page, K. L., Starling, R. L. C., Fitzpatrick, G., et al. 2011, MNRAS, 416, 2078
 Penacchioni, A. V., Ruffini, R., Izzo, L., et al. 2012, A&A, 538, A58
 Penacchioni, A. V., Ruffini, R., Bianco, C. L., et al. 2013, A&A, 551, A133
 Piran, T. 2005, Rev. Mod. Phys., 76, 1143
 Piran, T., Korobkin, O., & Rosswog, S. 2014 [arXiv:1401.2166]
 Pisani, G. B., Izzo, L., Ruffini, R., et al. 2013, A&A, 552, L5
 Rosswog, S., Ramirez-Ruiz, E., & Davies, M. B. 2003, MNRAS, 345, 1077
 Rosswog, S., Speith, R., & Wynn, G. A. 2004, MNRAS, 351, 1121
 Rueda, J. A., & Ruffini, R. 2012, ApJ, 758, L7
 Ruffini, R., Bernardini, M. G., Bianco, C. L., et al. 2008, in The Eleventh Marcel Grossmann Meeting, eds. H. Kleinert, R. T. Jantzen, & R. Ruffini (Singapore: World Scientific), 368
 Ruffini, R., Bernardini, M. G., Bianco, C. L., et al. 2006, in The Tenth Marcel Grossmann Meeting., eds. M. Novello, S. Perez Bergliaffa, & R. Ruffini (Singapore: World Scientific), 369
 Ruffini, R., Bernardini, M. G., Bianco, C. L., et al. 2007, ESA SP, 622, 561
 Ruffini, R., Vereshchagin, G., & Xue, S.-S. 2010, Phys. Rep., 487, 1
 Ruffini, R., Izzo, L., Muccino, M., et al. 2013, A&A, submitted [arXiv:1311.7432]
 Sari, R., Piran, T., & Narayan, R. 1998, ApJ, 497, L17
 Starling, R. L. C., Page, K. L., Pe'er, A., Beardmore, A. P., & Osborne, J. P. 2012, MNRAS, 427, 2950
 Watson, A. M., Butler, N., Kutyrev, A., et al. 2013, GCN Circ., 14666, 1
 Willingale, R., O'Brien, P. T., Osborne, J. P., et al. 2007, ApJ, 662, 1093
 Woosley, S. E. 1993, ApJ, 405, 273
 Woosley, S. E., & Bloom, J. S. 2006, ARA&A, 44, 507
 Xu, D., de Ugarte Postigo, A., Kruehler, T., et al. 2013a, GCN Circ., 14597, 1
 Xu, D., de Ugarte Postigo, A., Schulze, S., et al. 2013b, GCN Circ., 14478, 1
 Zhang, B., Fan, Y. Z., Dyks, J., et al. 2006, ApJ, 642, 354

The cosmic matrix in the 50th anniversary of relativistic astrophysics*

R. Ruffini^{†,‡,§,‡‡}, Y. Aimuratov^{†,‡,¶}, L. Becerra^{†,‡}, C. L. Bianco^{†,‡},
 M. Karlica^{†,‡,¶}, M. Kovacevic^{†,‡,¶}, J. D. Melon Fuksman^{†,‡}, R. Moradi^{†,‡},
 M. Muccino^{†,‡}, A. V. Penacchioni^{||,**}, G. B. Pisani^{†,‡}, D. Primorac^{†,‡},
 J. A. Rueda^{†,‡,§}, S. Shakeri^{†,‡‡}, G. V. Vereshchagin[†], Y. Wang^{†,‡} and S.-S. Xue[†]

[†]*ICRANet, Piazza della Repubblica 10, I-65122 Pescara, Italy*

[‡]*Dip. di Fisica and ICRA, Sapienza Università di Roma,
 P.le Aldo Moro 5, I-00185 Rome, Italy*

[§]*ICRANet-Rio, Centro Brasileiro de Pesquisas Físicas,
 Rua Dr. Xavier Sigaud 150, 22290-180 Rio de Janeiro, Brazil*

[¶]*Université de Nice Sophia Antipolis, CEDEX 2,
 Grand Château Parc Valrose, Nice, France*

^{||}*ASI Science Data Center, Via del Politecnico s.n.c., I-00133 Rome, Italy*

^{**}*Department of Physical Sciences, Earth and Environment,
 University of Siena, Via Roma 56, I-53100 Siena, Italy*

^{††}*Department of Physics, Isfahan University of Technology,
 84156-83111, Iran
^{‡‡}ruffini@icra.it*

Received 24 March 2017

Accepted 28 March 2017

Published 11 May 2017

Our concept of induced gravitational collapse (IGC paradigm) starting from a supernova occurring with a companion neutron star, has unlocked the understanding of seven different families of gamma ray bursts (GRBs), indicating a path for the formation of black holes in the universe. An authentic laboratory of relativistic astrophysics has been unveiled in which new paradigms have been introduced in order to advance knowledge of the most energetic, distant and complex systems in our universe. A novel cosmic matrix paradigm has been introduced at a relativistic cosmic level, which parallels the concept of an S-matrix introduced by Feynmann, Wheeler and Heisenberg in the quantum world of microphysics. Here the “in” states are represented by a neutron star and a supernova, while the “out” states, generated within less than a second, are a new neutron star and a black hole. This novel field of research needs very powerful technological observations in all wavelengths ranging from radio through optical, X-ray and gamma ray radiation all the way up to ultra-high-energy cosmic rays.

Keywords: Binaries; black hole physics; gamma-ray bursts; neutron stars; supernovae; white dwarfs.

PACS Number(s): 04.70.-s, 98.70.Rz, 97.60.Bw, 97.80.-d, 97.60.Jd, 97.20.Rp

*Based on talks presented at the Fourteenth Marcel Grossmann Meeting on General Relativity, Rome, July 2015.

1. Introduction and the First Paradigm

We begin with a personal historical overview by the lead author.

Supernovae (SNe) have been known and studied for a long time, from 1054 A.D. to the classic work of Baade and Zwicky in 1934^{1,2} and of Oppenheimer and his students in 1939, and to the 1968 detection of the first pulsar, first in radio and then in optical wavelengths, located at the center of the Crab Nebula. The explanation of the energetics of pulsars as originating from the rotational energy of neutron stars (NSs) gave the first clear evidence for the existence of NSs through this discovery and led to the conclusion that the Crab supernova originated from gravitational collapse to a NS.

The next fundamental discovery came from the pioneering work of Riccardo Giacconi and his group with the X-ray astronomy detection of Sco X-1.³ In 1967, this X-ray source was theoretically interpreted by Shklovskii⁴ as originating from a binary system containing a NS. This was followed by the launch of the UHURU satellite on December 12, 1970. The coordination of the X-ray observations with ground-based optical telescope observations has since led to the discovery of a large number of binary X-ray sources in our galaxy.⁵ These systems give evidence for: (a) an X-ray emission due to accretion in a binary system composed of a massive star and a gravitational collapsed star, with X-ray luminosities originating from gravitational energy a million times more intense than those expected from the star's thermonuclear evolution; (b) the first determination of NS masses well above the value of the critical mass expected by Oppenheimer and Volkoff, see e.g. Fig. 1 on Cen X-3 and (c) the first identification of a black hole in Cygnus X-1.⁶⁻⁸

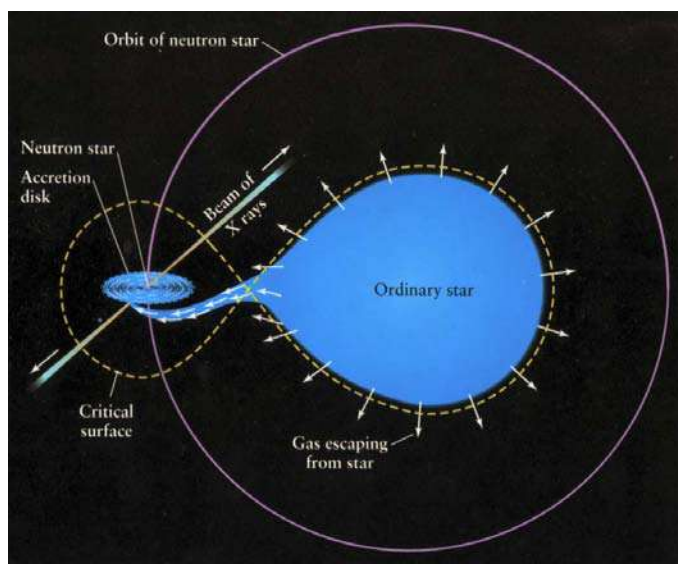


Fig. 1. X-ray binary Centaurus X3 detected by UHURU satellite. The pulse period is 4.84 s. A binary motion signature was found with a 1.7 day orbital period, thanks to UHURU.

Observations of GRBs only date back to their detection by the Vela satellites in the early 1970s, see e.g. Ref. 9 and references therein. It was only after the observations in 1997 by the BeppoSAX satellite¹⁰ which allowed the optical identification of GRBs. From the estimates of their cosmological distances, their enormous energetics is 10^3 – 10^4 times larger than those of supernovas, were able to be determined: energies of the order of 10^{54} erg, equivalent to the release of $\sim M_{\odot}c^2$ in few tens of seconds. This result had been predicted already in 1975 on purely theoretical grounds assuming that GRBs originated from an electron–positron plasma in the gravitational collapse to a Kerr–Newman black hole, see Ruffini, “Physics outside the horizon of a black hole” in Refs. 5 and 11. From these experiences, I had formulated a basic paradigm to serve as a guideline to interpret unitarily and consistently the occurrence of supernovae, the existence of binary X-ray sources and also possibly the nature of GRBs^{12–14}:

First paradigm

- *Supernovae originate from gravitational collapse to a neutron star.*
- *GRBs originate during the gravitational collapse to a black hole (BH).*
- *In studying a massive star, its binary nature and possibly the multiple systems involved in its behavior should of necessity be properly taken into account.*

We will see that the enforcement of this minimal set of assumptions has been extremely valuable. As the knowledge of these systems has evolved, I introduced two new and more specific paradigms narrowing in on the nature of the sources — each new paradigm being in clear agreement with the previous ones. I was well aware of a vast literature contemplating the possibility of relating different supernovae types to black holes over an extremely wide range of masses but I was very doubtful about these considerations since they violated more than one principle of my paradigm, they neglected a wealth of observational data, and they were based on a somewhat restrictive property related to metallicity in the thermonuclear evolution expected in a single star system (see e.g. Ref. 15). Moreover, after the splendid observations of the Hubble Space Telescope,¹⁶ today we begin to understand that even Eta Carinae is a binary system^{17,18} and that massive single stars are very likely a set of measure zero: massiveness implies multiplicity.

This situation has become even more interesting since the unexpected observation of a temporal and spatial coincidence between the occurrence of a GRB and a SN explosion, see e.g. GRB 980425¹⁹ and SN 1998bw,^{20,21} see Fig. 2. The explanation of this coincidence has led our group to introduce the induced gravitational collapse (IGC) paradigm (paradigm 1), a many-cosmic-body-interaction, and consequently we introduced a cosmic matrix: a C-matrix; see Fig. 3. The many-particle interaction in the S-matrix is confronted with this new concept of C-matrix involving a many-body interaction among astrophysical systems. This unprecedented situation has led to a series of new conceptual paradigms and the opening up of a new

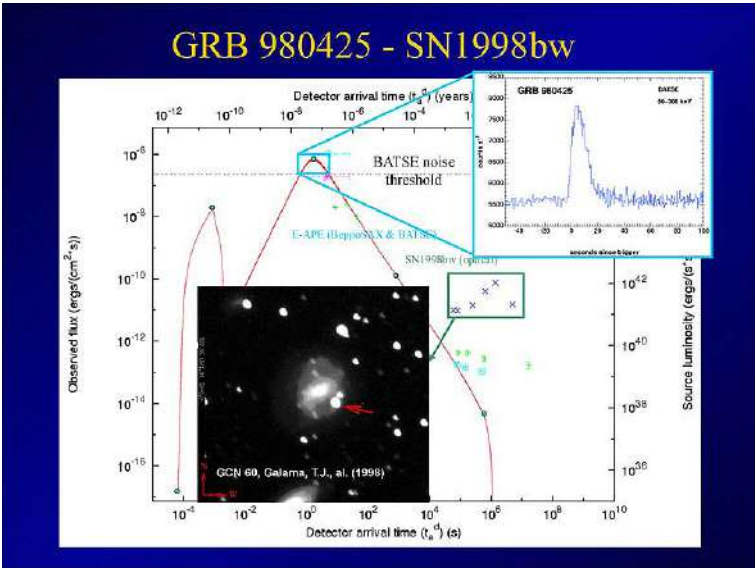


Fig. 2. GRB980425 and supernova SN 1998bw.

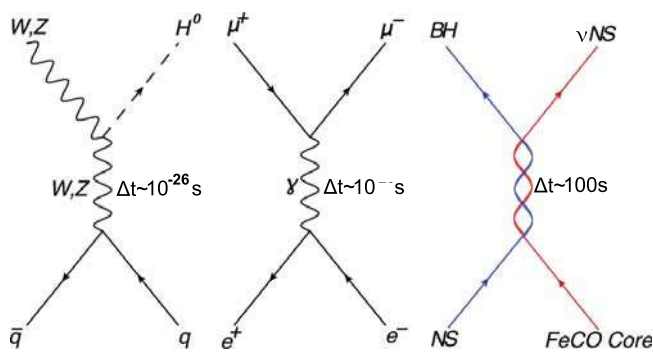


Fig. 3. The new concept of “C-matrix”, compared with the usual S-matrix. From Ref. 23.

understanding of a vast number of previously unknown domains within physics and astrophysics, see e.g. Ref. 22 and references therein.

1.1. Crab pulsar: A neutron star and a black hole

That NSs exist in nature has been proven by the discovery of pulsars. The year 1967 marked the discovery of the first pulsar, observed at radio wavelengths in November 28, 1967 by Jocelyn Bell Burnell and Antony Hewish.²⁴ Just a few months later, the pulsar NP0532 was found in the center of the Crab Nebula and observed first at radio wavelengths and soon after at optical wavelengths, see Fig. 4.

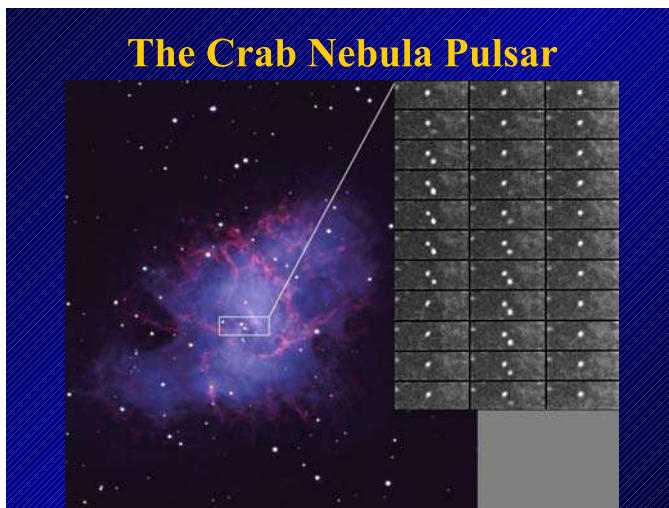


Fig. 4. The sequence of black and white images on the right is separated by one ms intervals, from which it is clear that the left star is a pulsar with a period of $P = 33$ ms. This period changes with a rate dP/dt of 12.5 ms per year. The fact that the loss of rotational energy of a NS with moment of inertia I is given by $dE/dt \propto -I(1/P^3)dP/dt$ explains precisely the energetics of the pulsar and proves at once the existence of NSs.²⁷

The discovery of NSs led our small group working around John Wheeler in Princeton to direct our main attention to go further and address the study of continuous gravitational collapse to a black hole as first introduced by Oppenheimer and his students (see Fig. 5). The work in Princeton addressed the topic of black holes, gravitational waves (GWs) and cosmology. A summary of that work can be found in Refs. 25 and 26, where a wide range of topics in relativistic astrophysics was reconsidered, including the possible sources of GWs, the cross-sections of GW detectors, and especially, an entirely new family of astrophysical phenomena occurring around NSs and black holes and in cosmology.

One of the most important results in the physics and astrophysics of BHs has been the BH mass-energy formula (see Fig. 6). From this, indeed, it became clear that up to 50% of the mass-energy of a BH could be extracted by using reversible transformations.²⁸ It then followed that during the formation of a BH, some of the most energetic processes in the universe should exist, releasing an energy of the order of $\sim 10^{54}$ erg for a $1 M_{\odot}$ BH (see Fig. 6).

1.2. The Vela and CGRO satellites and GRBs

In Ref. 29, I described how the observations of the Vela satellites were fundamental in discovering GRBs, see Fig. 7. Just a few months after the public announcement of their discovery,⁹ I formulated a theoretical model with T. Damour, a collaborator in Princeton, based on the extractable energy of a Kerr–Newmann black hole through a vacuum polarization process giving rise to GRBs, see Fig. 8. In our paper,¹¹

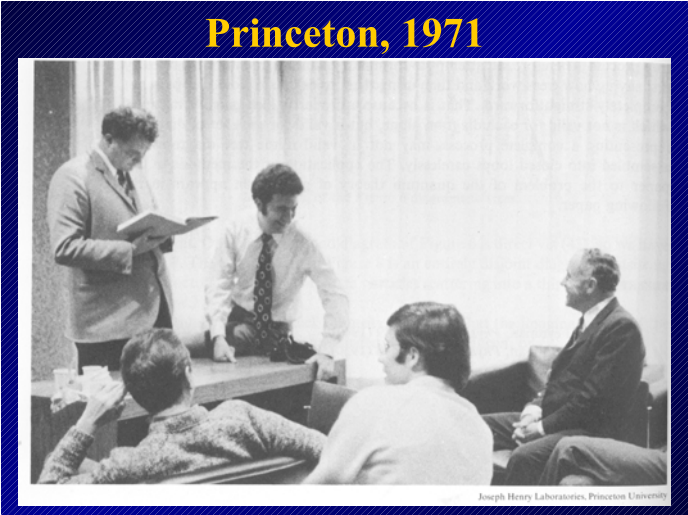


Fig. 5. Standing to the left Tullio Regge, sitting on the desk myself and sitting on the chair John Wheeler.

The Black Hole Mass-Energy formula

$$m^2 = \left(m_{ir} + \frac{e^2}{4m_{ir}} \right)^2 + \frac{L^2}{4m_{ir}^3},$$
$$S = 16\pi m_{ir}^2,$$
$$\frac{L^2}{4m_{ir}^4} + \frac{e^4}{16m_{ir}^4} \leq 1,$$
$$\delta S = 32\pi m_{ir} \delta m_{ir} \geq 0$$

Christodoulou,
Ruffini, 1971

5th Texas Symposium, 1970

A photograph of three men standing together in front of a wall with framed pictures.

Fig. 6. The black hole mass-energy formula. From Ref. 28.

we pointed out that vacuum polarization occurring in the field of electromagnetic BHs could release an enormous e^+e^- plasma which self-accelerates and gives origin to the GRB phenomenon. Energetics for GRBs all the way up to $\sim 10^{55}$ ergs was theoretically predicted for a $10 M_\odot$ BH.¹² The dynamics of this e^-e^+ plasma was first studied by J. R. Wilson and myself with the collaboration of Xue and Salmonson.^{30,31}

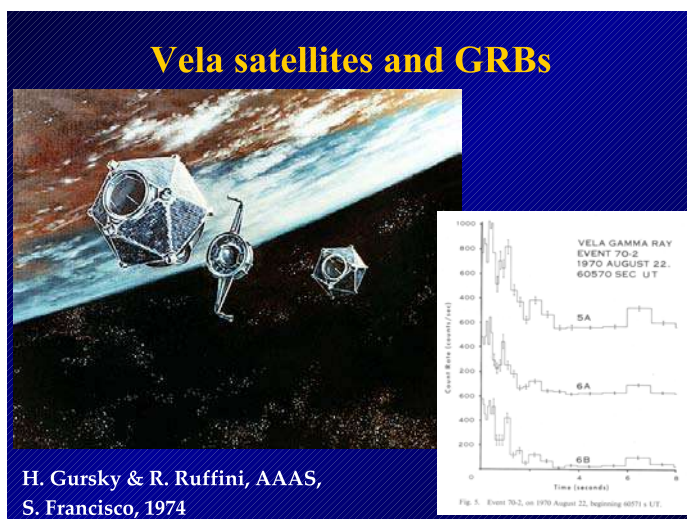


Fig. 7. The Vela satellites, see e.g. the Ian Strong chapter in Ref. 9.

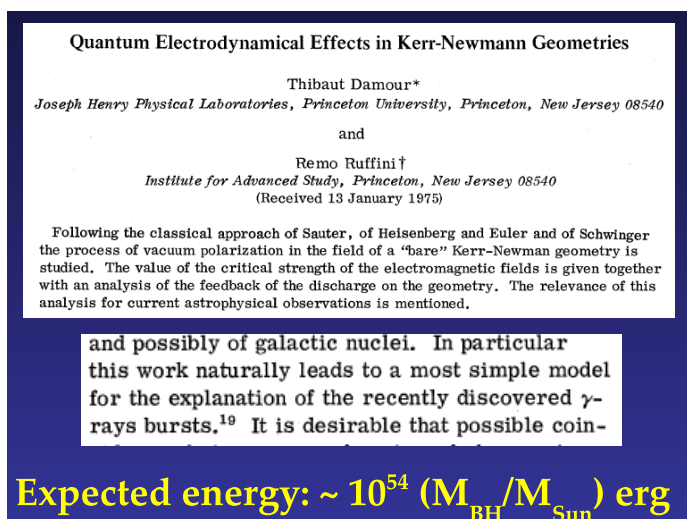


Fig. 8. The classic paper Ref. 11 on the extractable energy of a Kerr–Newmann black hole through vacuum polarization.

Initially it was difficult to model GRBs to understand their nature since their distances from the Earth were unknown, and thousands of models were presented³² attempting to explain the mystery they presented. The launching of the Compton Gamma Ray Observatory (CGRO) with the BATSE detectors on-board (see Fig. 9) led to the following important discoveries:

- (1) there is a homogeneous distribution of GRBs in the universe,

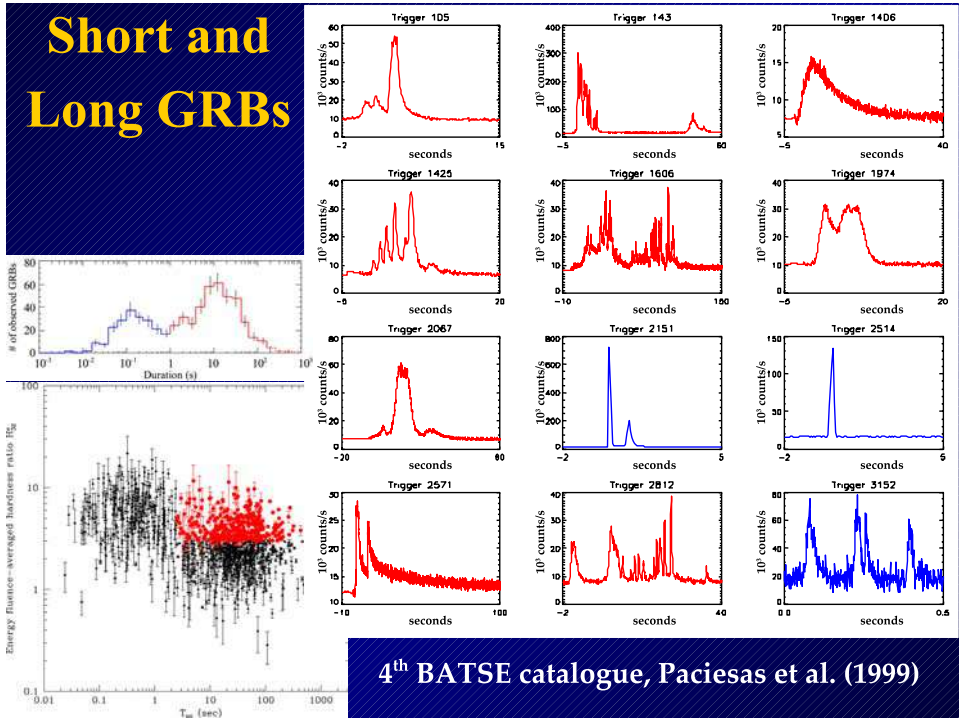
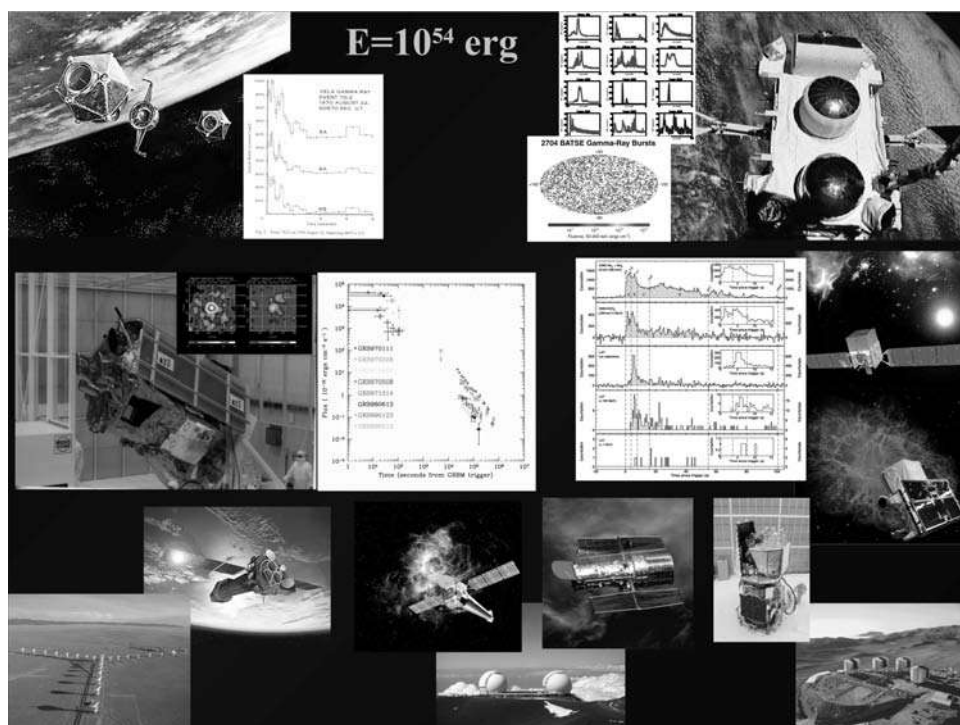


Fig. 9. Short and long GRB light curves and their temporal distribution from the 4th BATSE catalog, Ref. 33.

- (2) short GRBs exist lasting less than a second, and
- (3) long GRBs exist lasting more than one second.

The crucial contribution to interpreting GRBs came from the Italian-Dutch BeppoSAX satellite, see Fig. 10 (e.g. Ref. 34) which led to a much more precise definition of their position in the sky obtained using a wide field X-ray camera and narrow field instrumentation. This enabled the optical identification of GRBs and the determination of their cosmological redshift, and consequently of their energetics, which turned out to be up to $\sim 10^{55}$ erg, previously predicted in Ref. 11. Since that time no fewer than 10 different X- and γ -ray observatory missions and numerous observations at optical and radio wavelengths have allowed us to reach a deeper understanding of the nature of GRBs, see Fig. 10.

After reviewing below the basic differences between the most quoted “fireball model” of GRBs and our “fireshell model”, we will describe the IGC paradigm (the “second paradigm”) and the analysis of the GRB 090618 in the fireshell scenario.³⁵ This will show the first application of the IGC paradigm to it.³⁶ We will then indicate some recent results on a possible distance indicator inferred from a GRB-SN correlation within the IGC paradigm,³⁷ and then give some additional evidence coming from the identification of the NS created by the supernova and its use as a



cosmological distance candle. Next we will turn to the first example of the genuine short GRB 090227B³⁸ leading to black hole formation. Finally, we will illustrate a brand new paradigm dealing with the two families of short and long GRBs and a special role of the formation or not of a black hole.

A variety of models have been developed to theoretically explain the observational properties of GRBs, among which the fireball model³⁹ is one of those most often used. In Refs. 40–43, it was proposed that the sudden release of a large quantity of energy in a compact region can lead to an optically thick photon–lepton plasma and to the production of e^+e^- pairs. The sudden initial total annihilation of the e^+e^- plasma was assumed by Cavallo and Rees,⁴⁰ leading to an enormous release of energy pushing on the circumburst medium (CBM): the “fireball”, see e.g. Ref. 43 and references therein.

An alternative approach originating from the gravitational collapse to a black hole is the fireshell model, see e.g. Refs. 22 and 44. Here the GRB originates from an optically thick e^+e^- plasma in thermal equilibrium, with a total energy of E_{tot}^{\pm} . This plasma is initially confined between the radius r_h of a black hole and its dyadosphere^{45,46} radius

$$r_{ds} = r_h \left[2\alpha \frac{E_{\text{tot}}^{e^+e^-}}{m_e c^2} \left(\frac{\hbar}{\frac{m_e c}{r_h}} \right)^3 \right]^{1/4}, \quad (1)$$

where α is the usual fine structure constant, \hbar is the Planck's constant, c is the speed of light, and m_e is the mass of the electron. The lower limit of E_{tot}^{\pm} is assumed to coincide with the observed isotropic energy E_{iso} emitted in X-rays and gamma rays alone in the GRB. The condition of thermal equilibrium assumed in this model⁴⁷ distinguishes it from alternative ones, e.g. Ref. 40.

1.3.1. The fireball model

In the fireball model, the prompt emission, including the sharp luminosity variations,⁴⁸ is caused by the prolonged and variable activity of the “inner engine”.^{39,49} The conversion of the fireball energy to radiation is made by shocks, either internally (when faster moving matter overtakes a slower moving shell, see Ref. 49) or externally (when the moving matter is slowed down by the external medium surrounding the burst, see Ref. 50).

Synchrotron emission from relativistic electrons in the CBM has been given much attention, possibly accompanied by self-synchrotron Compton (SSC) emission, in order to explain the observed GRB spectra. These processes were purported to be consistent with the observational data of some GRBs.^{51,52} However, several limitations have been reported in relation to the low-energy spectral slopes of time-integrated spectra^{53–56} and the time-resolved spectra.⁵⁶ Additional limitations on SSC emission have also been pointed out in Refs. 57 and 58.

The latest phases of the afterglow are described in the fireball model by a single ultrarelativistic jetted emission assuming an equation of motion given by the Blandford-McKee self-similar power-law solution.⁵⁹ The maximum Lorentz factor of the fireball is estimated from the temporal occurrence of the peak of the optical emission, which is identified with the peak of the forward external shock emission^{60,61} in the thin shell approximation.⁶²

Several partly alternative and/or complementary scenarios have been developed independent of the fireball model, e.g. based on quasi-thermal Comptonization,⁶³ Compton drag emission,^{64,65} synchrotron emission from a decaying magnetic field,⁶⁶ jitter radiation,⁶⁷ Compton scattering of synchrotron self-absorbed photons,^{68,69} and photospheric emission.^{70–76} In particular, it was pointed out in Ref. 75 that photospheric emission overcomes some of the difficulties of purely nonthermal emission models. The collapsar model, leading to the astrophysical framework of the

“fireball” model characterized by a jetted ultrarelativistic (Lorentz gamma factor 100–500) emission, was then introduced.

1.3.2. The fireshell model

Let us turn to the fireshell model. The rate equation for the e^+e^- pair plasma and its dynamics (the pair-electromagnetic pulse or PEM pulse for short) have been described in Refs. 30 and 31. This equation applies to any electron–positron plasma giving rise to the GRB phenomena, independent of whether it is generated by vacuum polarization around a Kerr–Newman black hole¹¹ or other mechanisms, e.g. electron–positron pairs from a neutrino–antineutrino annihilation mechanism. This plasma engulfs the baryonic material of mass M_B left over from the process of gravitational collapse, while still maintaining thermal equilibrium between electrons, positrons and baryons.

The baryon load is measured by the dimensionless parameter $B = M_B c^2 / E_{\text{tot}}^{e^+e^-}$. References 31 and 77 showed that no relativistic expansion of the plasma exists for $B > 10^{-2}$, see Fig. 11. The fireshell is still optically thick and self-accelerates to ultrarelativistic velocities (the pair-electromagnetic-baryonic pulse or PEMB pulse for short.^{31,77}) Then the fireshell becomes transparent and the “proper GRB” (P-GRB) is emitted.⁷⁸ The final Lorentz gamma factor reached at transparency can vary over a wide range between 10^2 and 10^4 as a function of $E_{\text{tot}}^{e^+e^-}$ and B . To determine this final value, it is necessary to integrate explicitly the rate equation

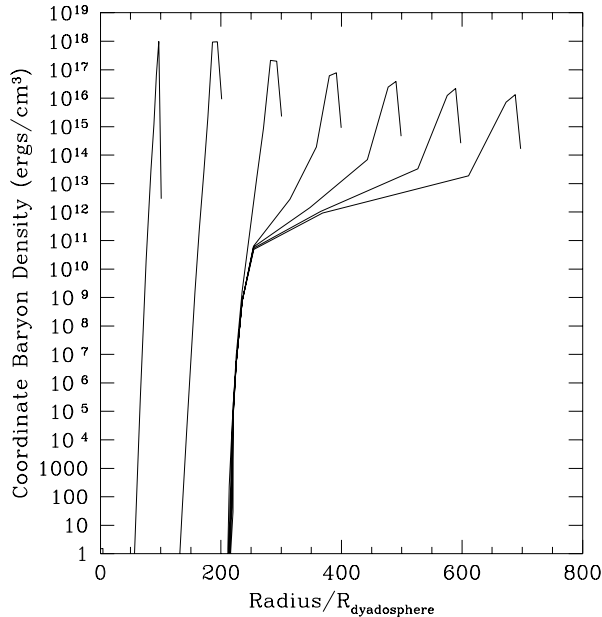


Fig. 11. The turbulent expansion for $B = 10^{-2}$. See details in Ref. 31.

for the e^+e^- annihilation process and evaluate, for a given black hole mass and given e^+e^- plasma radius, at what point the transparency condition is reached.³¹

The fireshell scenario does not require any prolonged activity of the inner engine and applies in generality to any confined amount of e^+e^- in a dyadosphere. After transparency, the remaining accelerated baryonic matter still expands ballistically and starts to slow down from collisions with the CBM of average density n_{CBM} . In the standard fireball scenario,⁴³ the spiky light curve is assumed instead to be caused by internal shocks.

In the fireshell model, the entire extended prompt emission is assumed to originate from an expanding thin baryonic shell, which maintains energy and momentum conservation during its collision with the CBM. The condition of a fully radiative regime is assumed.⁷⁸ This in turn allows one to estimate the characteristic inhomogeneities of the CBM, as well as its average density. It is appropriate to point out another difference between our treatment and others in the current literature. The complete analytic solution of the equations of motion of the baryonic shell were developed in Refs. 79 and 80, while elsewhere the Blandford–McKee self-similar approximate solution is almost always adopted without justification.^{72,81–89} The analogies and differences between the two approaches have been explicitly explained in Ref. 90.

In our general approach, a canonical GRB bolometric light curve is composed of two different parts: the P-GRB and the prompt radiation phase. The relative energetics of these two components and the observed temporal separation between the corresponding peaks is a function of the above three parameters $E_{\text{tot}}^{e^+e^-}$, B , and the average value of the CBM density n_{CBM} . The first two parameters are inherent to the accelerator mechanism characterizing the GRB, i.e. the optically thick phase, while the third parameter is inherent to the environment surrounding the GRB which gives rise to the prompt radiation phase by colliding with the baryonic fireshell.

For the observational properties of a relativistically expanding fireshell model, a crucial concept has been the introduction of the equi-temporal surfaces (EQTS). Here too our model differs from those in the literature by having derived an analytic expression for the EQTS obtained from the solutions to the equations of motion.^{80,90}

Details of the P-GRB and GRB prompt radiation are given in Ref. 13. Before closing it is appropriate to recall the fundamental diagram comparing and contrasting the P-GRB and the prompt radiation, see Fig. 12, characterizing the difference between short and long GRBs in the fireshell model as a function of the baryon load.

2. Unveiling the GRB-SN Connection: The Second Paradigm

2.1. Introduction

Until 1998 the study of GRBs and supernovae continued in parallel but disjoint from one another. Conceptually we have adopted the first paradigm mentioned

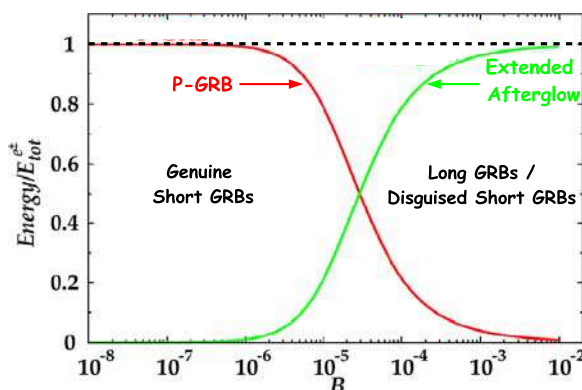


Fig. 12. (Color online) The energy emitted in the extended afterglow (solid green curve) and in the P-GRB (solid red curve) in units of $E_{e^+e^-}^{\text{tot}} = 1.77 \times 10^{53}$ erg (dashed horizontal line), as functions of B . The crossing point, corresponding to the condition $E_{\text{P-GRB}} \equiv 50\% E_{e^+e^-}^{\text{tot}}$, marks the division between the genuine short GRB region and the disguised short and long GRB region. The upper limit for B of 10^{-2} is determined by the onset of instabilities as shown in Fig. 11. From Ref. 38.

above: that supernovae originate from the formation of a NS and that GRBs are generated by the formation of a black hole. Something totally unexpected happened on April 25, 1998: the occurrence of GRB 980425 and the simultaneous observation of SN 1998bw, see Refs. 19–21. This coincidence has become extremely common for all long GRBs at values of the cosmological redshift less than 1.

While the collapsar proponents and other groups started to attempt hybrid models of NSs and black holes, supernovae creating black holes and similar ideas, we maintained our first paradigm and introduced a new “second paradigm”:

Second paradigm

- All long GRBs are necessarily associated with supernovae of type **SN Ic** and are components of a “**cosmic matrix**”.
- They originate from a massive binary system, which evolves through a binary X-ray source, and finally leads to a binary system composed of an **FeCO** core $> 2.8 M_{\odot}$ and a **NS** companion separated by $b_{\text{crit}} \sim 10^{11}$ cm. For $b < b_{\text{crit}}$ hypercritical accretion of the SN ejecta onto the NS leads to **BH** formation and to the consequent emission of a GRB. For $b > b_{\text{crit}}$ no **BH** is formed.
- For $b < b_{\text{crit}}$ a binary-driven hypernova (**BdHN**) occurs characterized by: **Episode 1** the hypercritical accretion, **Episode 2** the GRB, **Episode 3** the universal behavior, and **Episode 4** the optical SN observed. For $b > b_{\text{crit}}$ only **Episode 1** and **Episode 4** exist, and an **X-ray Flash** occurs”.

Our present paradigm has recently evolved from an earlier formulation,⁹¹ see Fig. 14. All these theoretical works and their observational feedback have recently

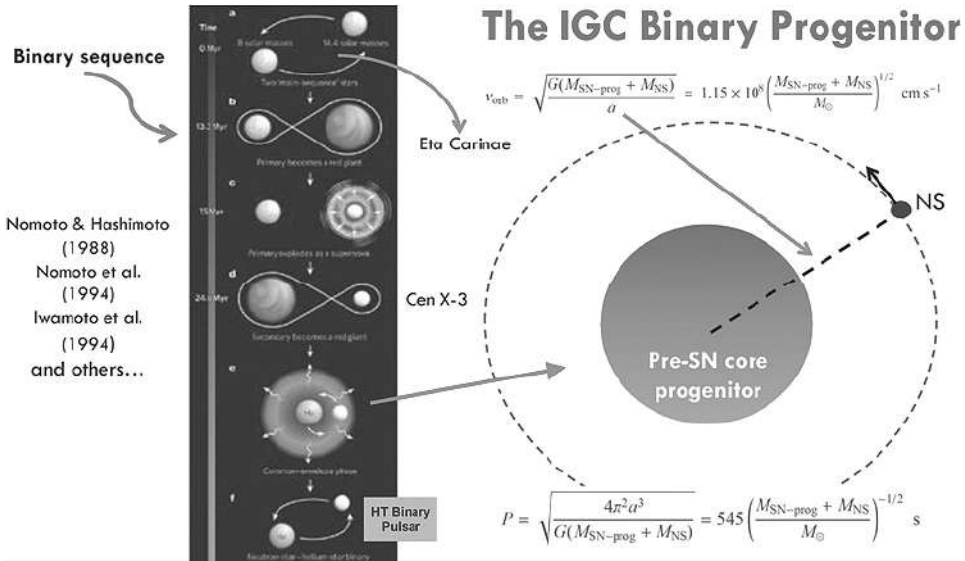


Fig. 13. The IGC binary progenitor. For details see Refs. 36 and 94.

led to the binary-driven hypernova model (BdHN).^{92,93} Contrary to the collapsar model which envisions a single object and a single event characterizing the GRB-supernova association, the IGC paradigm assumes as its progenitor a binary system containing an evolved Fe-Co core and a tightly bound neutron star binary companion, see Fig. 13. What was previously conceived for the GRB as a single ultra-relativistic event characterized by jetted emission appears to be a much more complex and rich system composed generally of four different episodes distinctively different in their astrophysical nature and with very specific signatures in their spectral and time varying luminosity emissions in selected wavelengths.

In conclusion, the IGC binary scenario applied here to the specific case of GRB 090618 naturally leads to understanding the energetics and the temporal coincidence of SNs and GRBs, as well as their astrophysical scenario and makes their correlation a direct consequence of the binary nature of the progenitor. In summary, we present in Figs. 15 and 16 the full interpretation of GRB 090618 observations as the four different episodes of the IGC paradigm.

Let us identify these four events in GRB 090618, the prototype of this most energetic family of GRBs, with an E_{iso} energy larger than 10^{52} erg, associated with supernovae. We describe a few key moments in the recent evolution of our understanding of this system which is very unique within physics and astrophysics. Some 20 additional examples of such a GRBs associated with supernovae have been identified by our group leading to the concept of binary driven-hypernovae.

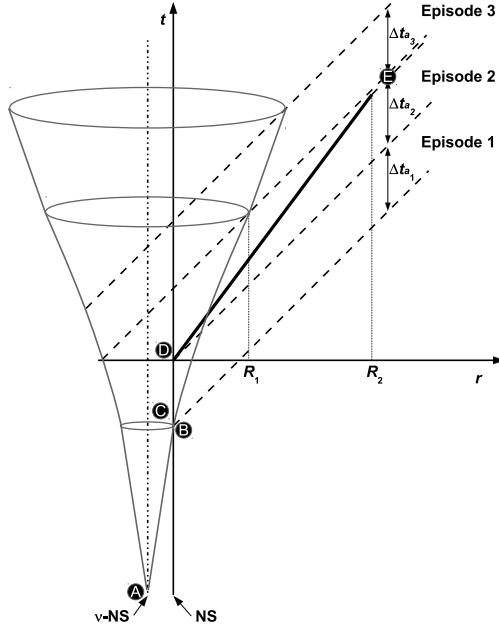


Fig. 14. The initial IGC spacetime diagram (not to scale), from Ref. 92. *Episode 1* corresponds to the onset of the FeCO core SN explosion, creating a new NS (ν -NS, see A). Part of the SN ejecta triggers an accretion process onto the NS companion (see B and Refs. 36 and 94), and a prolonged interaction between the ν -NS and the NS binary companion occurs (see C). This leads to a spectrum with an expanding thermal component plus an extra power law component (see Fig. 16 in Ref. 35). *Episode 2* occurs when the companion NS reaches its critical mass and collapses to a BH, emitting the GRB (D) with Lorentz factors $\Gamma \approx 10^2\text{--}10^3$ (for details, see e.g. Refs. 22 and 35). *Episode 3*, observed in the X-rays, shows very precise behavior consisting of a steep decay, starting at the end point of the prompt emission (see E), and then a plateau phase, followed by a late constant power-law decay (see Refs. 35 and 95). The figure illustrates the relativistic motion of Episode 2 ($\Gamma \approx 500$, thick line) and the nonrelativistic Episode 1 ($\Gamma \approx 1$) and Episode 3 ($\Gamma \approx 2$). Emissions from different radii, R_1 ($\sim 10^{13}$ cm) and R_2 ($\sim 10^{16}\text{--}10^{17}$ cm), contribute to the transition point (E). Clearly, the X-ray luminosity originates from the SN remnant or in the newly born BH, but not from the GRB.

2.2. The case of GRB 090618

The GRB 090618 discovered by the Swift satellite⁹⁸ represents the prototype of a class of energetic ($10^{52} \leq E_{\text{iso}} \leq 10^{55}$ erg) GRBs, characterized by the presence of a supernova observed 10 ($1+z$) days after the trigger time, and the observation of four distinct emission episodes in their GeV emission, hard X-ray light curve, soft X-ray and optical emission (see details in Ref. 35). The BAT light curve shows a multi-peak structure, whose total estimated duration is ~ 320 s and whose T_{90} duration in the (15–350) keV range was 113 s.⁹⁹ The first 50 s of the light curve shows a smooth decay trend followed by a spiky emission, with three prominent peaks at 62, 80 and 112 s after the trigger time, respectively, and each has the typical appearance of a

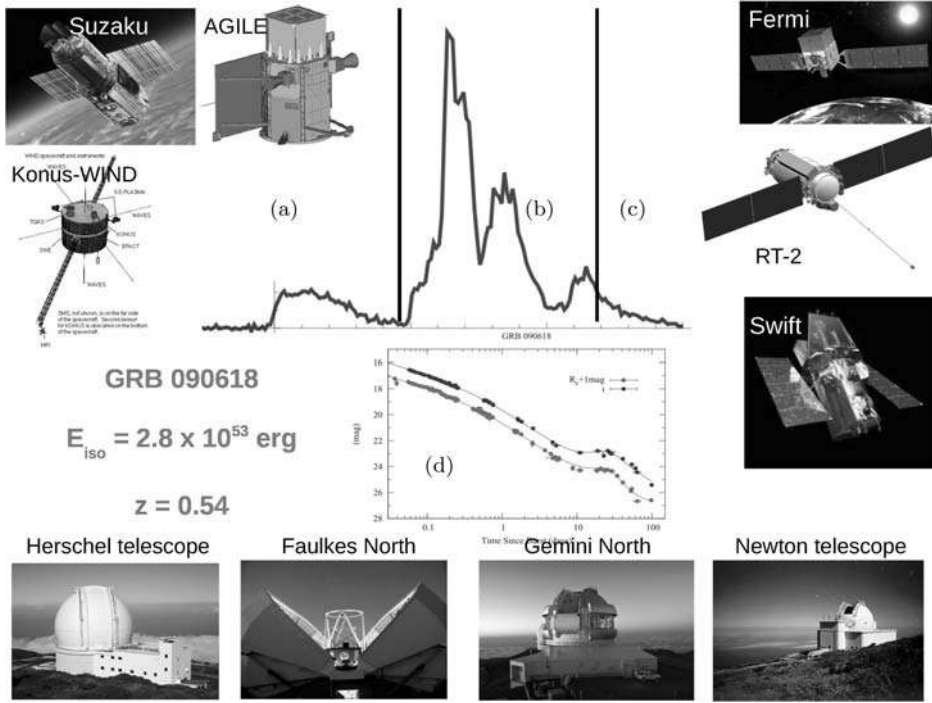


Fig. 15. GRB 090618 observations as the four different episodes implied by the IGC paradigm: (a) Episode 1, (b) Episode 2, (c) Episode 3 and (d) Episode 4 (i.e. the optical observations of the associated SN). Above are the satellites that participated in the observations: (in clockwise order) Fermi/GBM (8–1000 keV), Coronas-Photon/RT-2 (15–1000 keV), Swift/BAT (15–150 keV), Swift/XRT (0.3–10 keV), Swift/UVOT (optical band), AGILE/Super-AGILE (18–60 keV), AGILE/MCAL (350–10⁵ keV), Suzaku/WAM (50–5000 keV), Konus/WIND (20–2000 keV). Below are the ground based observatories that participated in the optical observations. Details in Refs. 35, 36 and 97.

fast-rise-exponential-decay (FRED) pulse.¹⁰⁰ The XRT observations started 125s after the BAT trigger time and lasted ~ 25.6 ks¹⁰¹ and reported an initially bright uncatalogued source, identified as the afterglow of GRB 090618. Its early decay is very steep, ending at 310s after the trigger time, when it starts a shallower phase, the plateau. Then the light curve breaks into a steeper late phase.

The GRB 090618 was also observed by the gamma ray burst (GBM) monitor on board the Fermi satellite.¹⁰² From an initial analysis, the time-integrated spectrum, ($t_0, t_0 + 140$)s in the (8–1000) keV range, was fit by a band spectral model¹⁰³ with a peak energy $E_{\text{peak}} = 155.5$ keV, $\alpha = -1.26$ and $\beta = -2.50$,¹⁰⁴ but with strong spectral variations within that time interval. The redshift of the source $z = 0.54$ was determined thanks to the identification of the MgII, MgI and FeII absorption lines using the KAST spectrograph mounted at the 3m Shane telescope at the Lick observatory.¹⁰⁵ Given the redshift and the distance of the source, we computed the emitted isotropic energy in the 8–10,000 keV energy range with the Schaefer

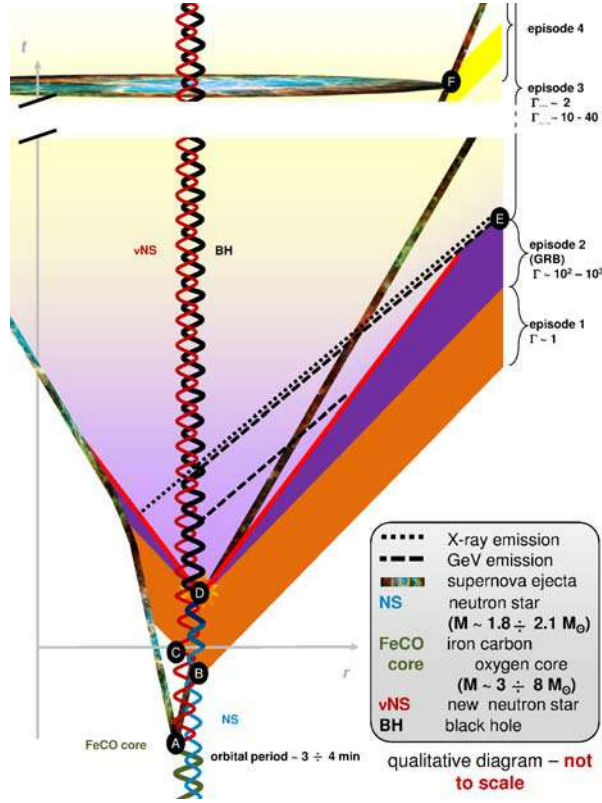


Fig. 16. (Color online) The further evolution of the IGC spacetime diagram (not to scale) illustrates 4 episodes of IGC paradigm: the nonrelativistic *Episode 1* ($\Gamma \simeq 1$), the relativistic motion of *Episode 2* ($\Gamma \simeq 10^2 \sim 10^3$), the mildly relativistic *Episode 3* ($\Gamma \simeq 2$), and nonrelativistic *Episode 4* ($\Gamma \simeq 1$). Initially there is a binary system composed of a massive star (yellow thick line) and a NS (blue line). The massive star evolves and explodes as a SN at point A, forms a ν NS (red line). The companion NS accretes the supernova ejecta starting from point B, interacts with the ν NS starting from point C, and collapses into a black hole (black line) at point D, this period from point B to point D we define as *Episode 1*. Point D is the starting of *Episode 2*, with two different components: one impacting on the SN filaments and one due to the collision of GRB outflow and interstellar filaments. At point E, *Episode 2* ends and *Episode 3* starts, *Episode 3* lasts till the optical signal of supernova emerges at point F, where the *Episode 4* starts. (Credit to M. Enderli for drawing this visualized spacetime diagram.)

formula¹⁰⁶: using the fluence in the range (8–1000 keV) as observed by the Fermi GBM, $S_{\text{obs}} = 2.7 \times 10^{-4}$,¹⁰⁴ and the Λ CDM (Λ cold dark matter) cosmological standard model $H_0 = 70$ km/s/Mpc, $\Omega_m = 0.27$, $\Omega_\Lambda = 0.73$, we obtain the value $E_{\text{iso}} = 2.90 \times 10^{53}$ erg for the emitted isotropic energy.

This GRB was observed also by Konus-WIND,¹⁰⁷ Suzaku-WAM¹⁰⁸ and by the AGILE satellite,¹⁰⁹ which detected emission in the (18–60) keV range and in the MCAL instrument, operating at energies greater than 350 keV, but it did not observe high-energy photons above 30 MeV. GRB 090618 was the first GRB

observed by the Indian payloads RT-2 on board the Russian satellite CORONAS-PHOTON.^{110–112} Thanks to the complete data coverage of the optical afterglow of GRB 090618, the presence of a supernova underlying the emission of its optical afterglow was reported.¹¹³ The evidence of a supernova emission came from the presence of several bumps in the light curve and by the change in R_c-i color index over time: in the early phases, the blue color is dominant, typical of the GRB afterglow, but then the color index increases, suggesting a core-collapse SN. At late times, the contribution from the host galaxy was dominant. We have analyzed the GRB 090618 with L. Izzo and other ICRANet researchers and Ph.D. students considering the BAT and XRT data of the Swift satellite together with the Fermi GBM and RT2 data of the Coronas-PHOTON satellite (see Fig. 15). The data reduction was made with the Heasoft v6.10 packages^a for BAT and XRT, and the Fermi-Science tools for GBM. The details of the data reduction and analysis are given in Ref. 35.

2.3. The emission process in Episode 1

2.3.1. The time-resolved spectra and temperature variation

A significant outcome of the multi-year work of Felix Ryde and his collaborators¹¹⁴ has been the identification of thermal plus power-law features observed in time-limited intervals in selected BATSE GRBs. Similar features have also been observed in the data acquired by the Fermi satellite.^{114,115} These emissions have been shown to present a thermal plus power-law(s) feature, with a temperature changing in time following a precise power-law behavior. Our aim has been to see if the first 50 s of emission of GRB 090618 conform to this feature. We made a detailed time-resolved analysis, considering different time bin durations to obtain good statistics in the spectra and to take into account the sub-structures in the light curve. We then used two different spectral models to fit the observed data, a classic band spectrum,¹⁰³ and a blackbody with a power-law component. To obtain more accurate constraints on the spectral parameters, we made a joint fit considering the observations from both the n4 NaI and the b0 BGO detectors, covering a wider energy range in this way, from 8 keV to 40 MeV. To avoid some bias from low-photon statistics, we considered an energy upper limit of the value of 10 MeV. Our analysis is summarized in Figs. 17–19.

2.3.2. The power-law decay of the black body temperature

Particularly interesting is the clear evolution in the time-resolved spectra, which corresponds to the blackbody and power-law component, see Fig. 17. In particular the kT parameter of the blackbody shows a strong decay, with a temporal behavior well described by a double broken power-law function, see the upper panel in Fig. 18.

^a<http://heasarc.gsfc.nasa.gov/lheasoft/>.

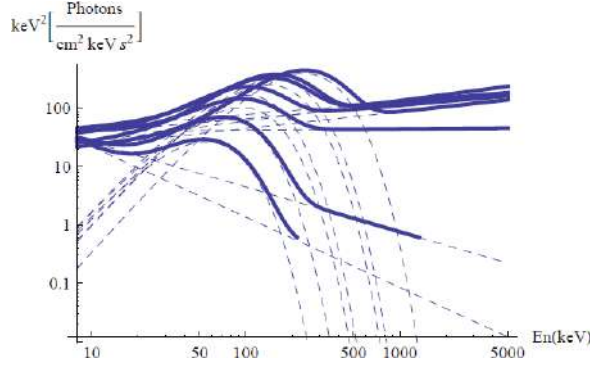


Fig. 17. Evolution of the BB+power-law spectral model in the $\nu F(\nu)$ spectrum of the first emission of GRB 090618. It shows the cooling of the blackbody and associated nonthermal components in time. We only plot the fitting functions for clarity. From Ref. 35.

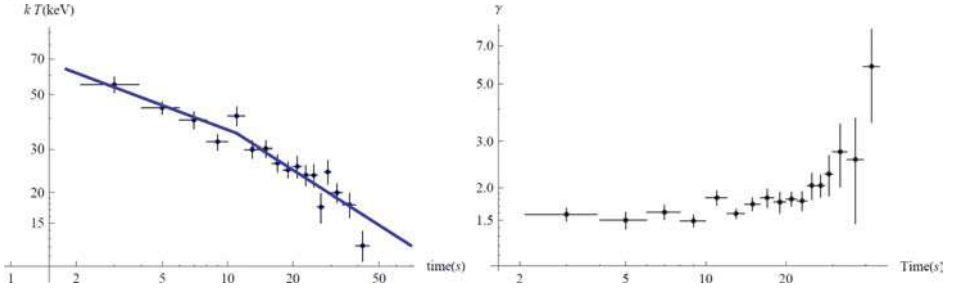


Fig. 18. (Color online) Evolution of the observed temperature kT of the blackbody component and the corresponding evolution of the power-law photon index. The blue line in the upper panel corresponds to the fit of the time evolution of the temperature with a broken power-law function. It shows a break time t_b around 11 s after the trigger time, as obtained from the fitting procedure. From Ref. 35.

From a fitting procedure we find that the best fit (R^2 -statistic = 0.992) for the two decay indexes for the temperature variation are $a_{kT} = -0.33 \pm 0.07$ and $b_{kT} = -0.57 \pm 0.11$. In Ref. 75, an average value for these parameters is given for a set of 49 GRBs: $\langle a_{kT} \rangle = -0.07 \pm 0.19$ and $\langle b_{kT} \rangle = -0.68 \pm 0.24$. The results presented in Figs. 17 and 18 point to a rapid cooling of the thermal emission with time of the first episode. The evolution of the corresponding power-law spectral component also appears to be strictly related to the change of the temperature kT . The power-law γ index falls, or softens, with temperature, see Fig. 17. An interesting feature appears to occur at the transition of the two power-laws describing the observed decrease of the temperature.

2.3.3. The radius of the emitting region

We turn now to estimate an additional crucial parameter for identifying the nature of the blackbody component: the radius r_{em} of the emitter. We proved

that the first episode is not part of a GRB. We can therefore provide the estimate of the emitter radius from nonrelativistic considerations, just corrected for the cosmological redshift z . In fact we find that the temperature $T_{\text{em}} = T_{\text{obs}}(1+z)$ of the emitter and that the luminosity of the emitter due to blackbody emission is

$$L = 4\pi r_{\text{em}}^2 \sigma T_{\text{em}}^4 = 4\pi r_{\text{em}}^2 \sigma T_{\text{obs}}^4 (1+z)^4, \quad (2)$$

where r_{em} is the emitter radius and σ is the Stefan–Boltzmann constant. From the luminosity distance definition, we also have that the observed flux ϕ_{obs} given by

$$\phi_{\text{obs}} = \frac{L}{4\pi D^2} = \frac{r_{\text{em}}^2 \sigma T_{\text{obs}}^4 (1+z)^4}{D^2}. \quad (3)$$

We then obtain

$$r_{\text{em}} = \left(\frac{\phi_{\text{obs}}}{\sigma T_{\text{obs}}^4} \right)^{1/2} \frac{D}{(1+z)^2}. \quad (4)$$

The above radius differs from the radius r_{ph} given in Eq. (1) of Ref. 75, which was also clearly obtained by interpreting the early evolution of GRB 970828 as belonging to the photospheric emission of a GRB and assuming a relativistic expansion with a Lorentz gamma factor Γ satisfying

$$r_{ph} = \hat{\mathcal{R}} D \left(\frac{\Gamma}{(1.06)(1+z)^2} \right), \quad (5)$$

where $\hat{\mathcal{R}} = (\phi_{\text{obs}}/(\sigma T_{\text{obs}}^4))^{1/2}$ and the prefactor 1.06 arises from the dependence of r_{ph} on the angle of the line of sight.¹¹⁶ Typical values of r_{ph} are at least two orders of magnitude higher than our radius r_{em} . Assuming a standard cosmological model ($H_0 = 70$ km/s/Mpc, $\Omega_m = 0.27$ and $\Omega_\Lambda = 0.73$) for estimating the luminosity distance D , and using the values for the observed flux ϕ_{obs} and the temperature kT_{obs} , we give in Fig. 19 the evolution of the surface radius that emits the blackbody r_{em} as a function of time. Assuming an exponential evolution with time t^δ of the radius in the comoving frame, we obtain the value $\delta = 0.59 \pm 0.11$ from a fitting procedure, which is well compatible with $\delta = 0.5$. We also notice a steeper behavior for the variation of the radius with time corresponding to the first 10s, which corresponds to the emission before the break of the double power-law behavior of the temperature. We estimate an average velocity of $\bar{v} = 4067 \pm 918$ km/s, $R^2 = 0.91$ in these first 10s of emission. In episode 1, the observations lead to a core of an initial radius of $\sim 12,000$ km expanding in the early phase with a higher initial velocity of ~ 4000 km/s. The effective Lorentz Γ factor is very low, $\Gamma - 1 \sim 10^{-5}$. I proposed to identify this first episode as the early phases of the accretion onto the companion NS which the SN ejects in the IGC scenario, later confirmed by the simulation.⁹⁶

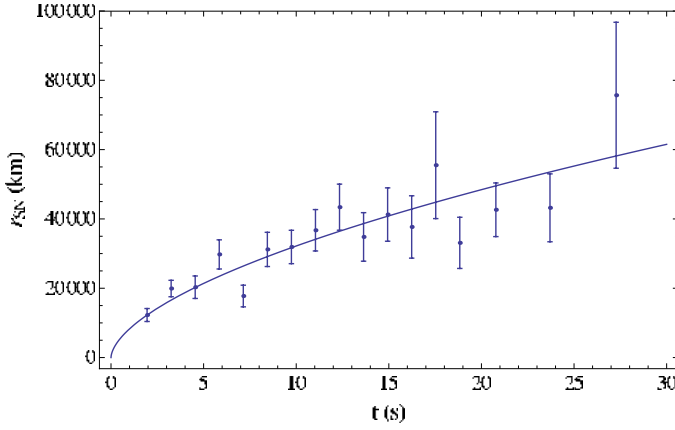


Fig. 19. Evolution of the Episode 1 emitter radius given by Eq. (4). From Ref. 35.

2.4. The emission process in Episode 2

2.4.1. The identification of the P-GRB

We have proceeded to the analysis of the data between 50 and 150 s after the trigger time as a canonical GRB in the fireshell scenario, namely Episode 2.⁹⁷ We proceed to identify the P-GRB within the emission between 50 s and 59 s, since we find a blackbody signature in this early second-episode emission. Considerations based on the time variability of the thermal component bring us to conclude that the first 4 s of this time interval due to the P-GRB emission. The corresponding spectrum (8–440 keV) is well fit ($\chi^2 = d1.15$) with a blackbody of temperature $kT = 29.22 \pm 2.21$ keV (norm = 3.51 ± 0.49), and an extra power-law component with photon index $\gamma = 1.85 \pm 0.06$, (norm = 46.25 ± 10.21). The fit with the band model is also acceptable ($\tilde{\chi}^2 = 1.25$), which gives a low-energy power-law index $\alpha = -1.22 \pm 0.08$, a high-energy index $\beta = -2.32 \pm 0.21$ and a break energy $E_0 = 193.2 \pm 50.8$. In view of the theoretical understanding of the thermal component in the P-GRB (see Sec. 3.2), we focus below on the blackbody+power-law spectral model. The isotropic energy of the second episode is $E_{\text{iso}} = (2.49 \pm 0.02) \times 10^{53}$ ergs. The simulation within the fireshell scenario is made assuming $E_{\text{tot}}^{e^+e^-} \equiv E_{\text{iso}}$. From the observed temperature, we can then derive the corresponding value of the baryon load. The observed temperature of the blackbody component is $kT = 29.22 \pm 2.21$, so that we can determine a value of the baryon load of $B = 1.98 \pm 0.15 \times 10^{-3}$, and deduce the energy of the P-GRB as a fraction of the total $E_{\text{tot}}^{e^+e^-}$. We therefore obtain a value of the P-GRB energy of $4.33_{-0.28}^{+0.25} \times 10^{51}$ erg. Next we can derive the radius of the transparency condition, to occur at $r_{\text{tr}} = 1.46 \times 10^{14}$ cm. We derive the bulk Lorentz factor of $\Gamma_{\text{th}} = 495$ and compare this value with the energy measured only in the blackbody component of $E_{\text{BB}} = 9.24_{-0.58}^{+0.50} \times 10^{50}$ erg, and with the energy in the blackbody plus the power-law component of $E_{\text{BB}+po} = 5.43_{-0.11}^{+0.07} \times 10^{51}$ erg,

and verify that the theoretical value is in between these observed energies. We have found this result to be quite satisfactory: it represents the first attempt to relate the GRB properties to the details of the BH responsible for the overall GRB energetics. The above theoretical estimates were based on a nonrotating BH of $10 M_{\odot}$, a total energy of $E_{\text{tot}}^{e^+e^-} = 2.49 \times 10^{53}$ erg and a mean temperature of the initial e^+e^- plasma of 2.4 MeV, derived from the expression for the dyadosphere radius, Eq. (1).

2.4.2. The refinement of the P-GRB nature

Standing the excellent results obtained in the e^+e^- spectra and the dynamics of the refinement and the direct comparison between theory and observations will have to address a variety of fundamental problems such as (1) the possible effect of rotation of the BH, leading to a more complex dyadotorus structure,²² (2) an analysis of the general relativistic, electrodynamical and strong interaction descriptions of the gravitational core collapse leading to BH formation,^{77,117,118} (3) a possible role of hypercritical accretion process in creating the electron–positron plasma out of neutrino–antineutrino annihilation.^{96,119,120} All these processes could alternatively lead to a dyadosphere near the Kerr–Newmann black hole with an efficiency (42%) similar to the electrodynamical case (50%).

2.4.3. The prompt emission and the CBM cloud structure

The prompt emission starts at the above given radius of the transparency, with an initial value of the Lorentz Γ factor of $\Gamma_0 = 495$. To simulate the extended-afterglow emission, we need to determine the radial distribution of the CBM around the burst site, which we assume for simplicity to be spherically symmetric, from which we infer a characteristic size of $\Delta R = 10^{15}–10^{16}$ cm. We already described above how the simulation of the spectra and of the observed multi-band light curves have to be performed together and need to be jointly optimized, leading to the determination of the fundamental parameters characterizing the CBM medium.¹²¹ This radial distribution is shown in Fig. 20 and is characterized by a mean value of $\langle n \rangle = 0.6$ part/cm³ and an average density contrast with a $\langle \delta n/n \rangle \approx 2$, see Fig. 20 and Tables 1 and 2. The data up to 8.5×10^{16} cm are simulated with a value for the filling factor $\mathcal{R} = 3 \times 10^{-9}$, while the data from this value on with $\mathcal{R} = 9 \times 10^{-9}$. From the radial distribution of the CBM density, and considering the $1/\Gamma$ effect on the fireshell visible area, we found that the CBM clumps causing the spikes in the extended afterglow emission have masses on the order of $10^{22}–10^{24}$ g. The value of the α parameter was found to be -1.8 along the total duration of the GRB. In Fig. 21, we show the simulated light curve (8–1000 keV) of the GRB and the corresponding spectrum, using the spectral model described in Refs. 79 and 122. The Episode 2, lasting from 50 s to 151 s, agrees with a canonical GRB in the fireshell scenario.

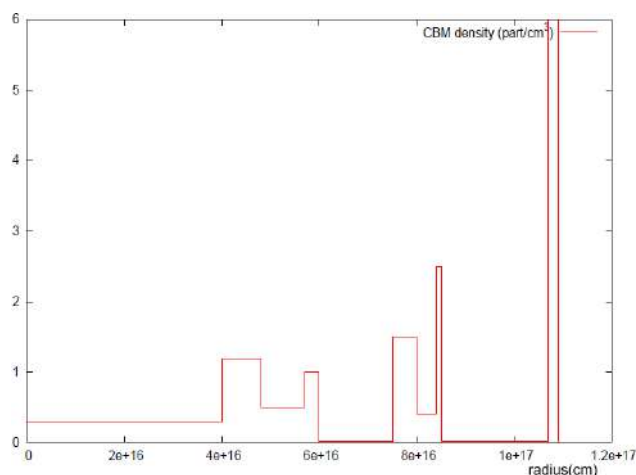


Fig. 20. Radial CBM density distribution for GRB 090618. The characteristic masses of each cloud are on the order of $\sim 10^{22-24}$ g and 10^{16} cm in radii. From Ref. 35.

Table 1. Final results of the simulation of GRB 090618 in the fireshell scenario. From Ref. 35.

Parameter	Value
$E_{\text{tot}}^{+e^{-}}$	$2.49 \pm 0.02 \times 10^{53}$ ergs
B	$1.98 \pm 0.15 \times 10^{-3}$
Γ_0	495 ± 40
kT_{th}	29.22 ± 2.21 keV
$E_{P\text{-GRB},th}$	$4.33 \pm 0.28 \times 10^{51}$ ergs
$\langle n \rangle$	0.6 part/cm^3
$\langle \delta n/n \rangle$	2 part/cm^3

Table 2. Physical properties of the three clouds surrounding the burst site: the distance from the burst site (column 2), the radius r of the cloud (column 3), the particle density ρ (column 4), and the mass M (the last column). From Ref. 35.

Cloud	Distance (cm)	r (cm)	ρ ($\#/\text{cm}^3$)	M (g)
First	4.0×10^{16}	1×10^{16}	1	2.5×10^{24}
Second	7.4×10^{16}	5×10^{15}	1	3.1×10^{23}
Third	1.1×10^{17}	2×10^{15}	4	2.0×10^{22}

2.5. The emission process of Episode 3

2.5.1. The late X-ray emission observed by swift/XRT

We now turn to the most important feature which has appeared in the analysis of Episode 3 of GRB 090618: the presence of a steep decay, followed by a plateau and a power law steep decay, see Fig. 22. This feature has unexpectedly become a common feature of all GRBs with energy larger than 10^{52} erg and even more striking, all the X-ray emissions at late times, when computed in the rest frame of the source

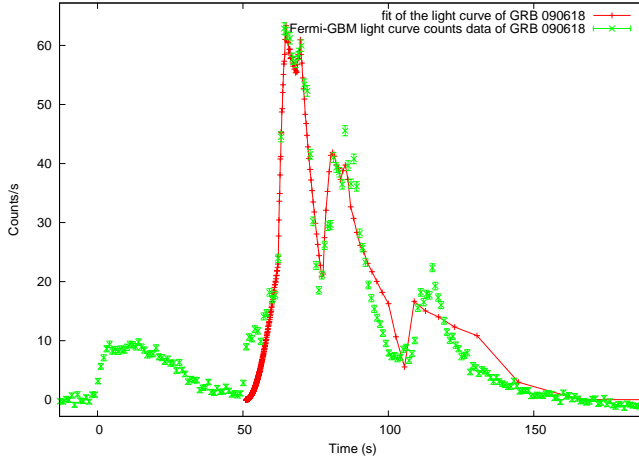


Fig. 21. Simulated light curve of the extended-afterglow of GRB 090618. From Ref. 35.

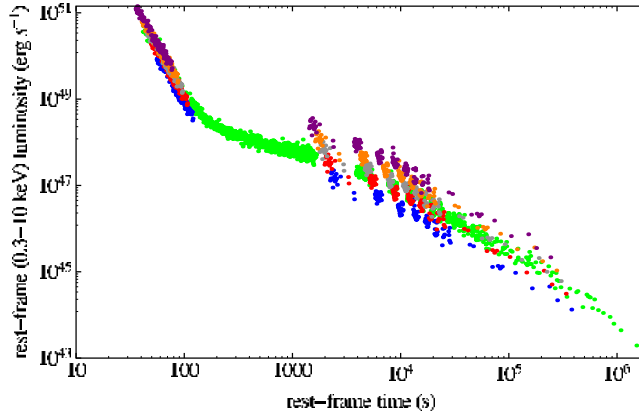


Fig. 22. (Color online) In green we show the rest frame X-ray luminosity light curve of GRB 090618 in the 0.3–10 keV energy range in comparison with the one of GRB 101023, computed for different hypothetical redshifts: respectively, from blue to purple: $z = 0.6, 0.8, 1.0, 1.2, 1.5$. The overlapping at late time of the two X-ray luminosity light curves is obtained for a redshift of $z = 0.9$. For further details see Refs. 95 and 123.

they overlap, see Fig. 23. This feature has become a most powerful method to estimate the cosmological redshift of the source, when not directly observed. We have focused our attention on the analysis of all the available XRT data of these sources.³⁷ Characteristically, XRT follow-up starts only about 100s after the BAT trigger (typical repointing time of Swift after the BAT trigger). Since the behavior was similar in all the sources, we have performed an analysis to compare the XRT luminosity light curve L_{rf} , where “rf” stands for rest frame, for the six GRBs with measured redshift z in the common rest frame energy range 0.3–10 KeV. To perform this computation, the first step is to convert the observed XRT flux f_{obs} to the one

in the 0.3–10 KeV rest frame energy range. In the detector frame, the 0.3–10 KeV rest frame energy range becomes $[0.3/(1+z)] - [10/(1+z)]$ KeV where z is the redshift of the GRB. We assume a simple power-law function as the best-fit for the spectral energy distribution of the XRT data^b:

$$\frac{dN}{dA dt dE} \propto E^{-\gamma}. \quad (6)$$

We can then write the flux light curve f_{rf} in the 0.3–10 KeV rest frame energy range as:

$$f_{\text{rf}} = f_{\text{obs}} \frac{\int_{\frac{0.3 \text{ keV}}{1+z}}^{\frac{10 \text{ keV}}{1+z}} E^{-\gamma} dE}{\int_{0.3 \text{ keV}}^{10 \text{ keV}} E^{-\gamma} dE} = f_{\text{obs}} (1+z)^{\gamma-1}. \quad (7)$$

Then we have to multiply f_{rf} by the luminosity distance to get L_{rf} :

$$L_{\text{rf}} = 4\pi d_L^2(z) f_{\text{rf}}, \quad (8)$$

where we assume a standard cosmological model Λ CDM with $\Omega_m = 0.27$ and $\Omega_\Lambda = 0.73$. Clearly, this luminosity must be plotted as a function of the rest frame time t_{rf} , namely:

$$t_{\text{rf}} = \frac{t_{\text{obs}}}{1+z}. \quad (9)$$

2.5.2. “The golden sample”

The X-ray luminosity light curves of the six GRBs with measured redshift in the 0.3–10 KeV rest frame energy band are plotted together in Fig. 23 and Table 3.

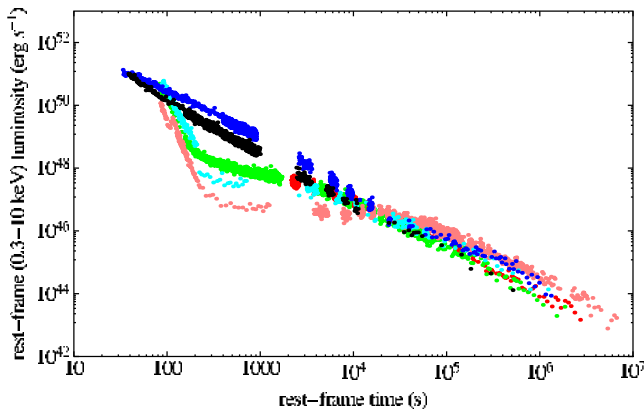


Fig. 23. (Color online) The X-ray luminosity light curves of the six GRBs with measured redshift in the 0.3–10 keV rest frame energy range: in pink GRB 060729, $z = 0.54$; in black GRB 061007, $z = 1.261$; in blue GRB 080319B, $z = 0.937$; in green GRB 090618, $z = 0.54$, in red GRB 091127, $z = 0.49$, in cyan GRB 111228, $z = 0.713$. From Ref. 37.

^b<http://www.swift.ac.uk/>.

Table 3. The GRB sample considered in this work. The redshifts of GRB 101023 and GRB 110709B, which are marked by an asterisk, were deduced theoretically by using the method outlined in Ref. 95 and the corresponding isotropic energy computed by assuming these redshifts. From Ref. 37.

GRB	z	E_{iso} (erg)
GRB 060729	0.54	1.6×10^{52}
GRB 061007	1.261	1.2×10^{54}
GRB 080319B	0.937	1.4×10^{54}
GRB 090618	0.54	2.7×10^{53}
GRB 091127	0.49	1.4×10^{52}
GRB 111228	0.713	2.3×10^{52}
GRB 101023	0.9*	1.3×10^{53}
GRB 110709B	0.75*	2.72×10^{53}

What is most striking is that these six GRBs, with redshift in the range 0.49–1.261, show a remarkably common behavior of the late X-ray afterglow luminosity light curves (Episode 3) despite that their prompt emissions (Episodes 1 and 2) are very different and that their energetics spans more than two orders of magnitude, see Table 3. Such a common behavior starts between 10^4 and 10^5 s after the trigger and continues up to when the emission falls below the XRT threshold. This universal behavior of Episode 3 represents strong evidence of very low or even the absence of beaming in this particular phase of the X-ray afterglow emission process. I proposed in the presentation that this late time X-ray emission in Episode 3 is related to the process of the SN explosion within the IGC scenario, possibly emitted by the newly born NS and BH and by the supernovae ejecta shocked by the GRB, and not by the GRB itself, see Fig. 16.

2.5.3. Episode 3 as a standard candle

As an example, we present in Fig. 22 the rest frame X-ray luminosity (0.3–10 KeV) light curve of GRB 090618 (considered as a prototype for the common behavior shown in Fig. 23) with the rest frame X-ray luminosity light curves of GRB 110709B estimated for selected values of its redshifts, $z = 0.4, 0.6, 0.8, 1.0, 1.2$ and similarly the correspondent analysis for GRB 101023 for selected values of the redshift, $z = 0.6, 0.8, 1.0, 1.2, 1.5$. We then find, with A.V. Penacchioni and other ICRANet researchers and Ph.D. students, that GRB 101023 should have been located at $z \sim 0.9$ and GRB 110709B at $z \sim 0.75$. These redshift estimations are within the range expected using the Amati relation as shown in Refs. 95 and 123. This is an important independent confirmation of validity for this new redshift estimator we propose for the family of IGC GRB-SN systems. It should be stressed, however, that the determination of the redshift is done assuming the validity of the standard Λ CDM cosmological model for sources with redshift in the range $z = 0.49$ –1.216. We are currently testing the validity of this assumption for sources at larger cosmological redshifts.

3. The GRB-SN and the IGC: The Second Paradigm

3.1. *IGC of a NS to a blackhole by a type Ib/c SN*

The systematic and spectroscopic analysis of GRB-SN events, following the pioneering discovery of the temporal coincidence of GRB 980425¹⁹ and SN 1998bw,²¹ has revealed evidence for the association of other nearby GRBs with Type Ib/c SNe (see Ref. 124 for a recent review of all the GRB-SN systems). It has also been clearly understood that SN Ib/c lack Hydrogen (H) and Helium (He) in their spectra, and the most likely explanation is that the SN progenitor star is in a binary system with a compact companion, a NS (see e.g. Refs. 125–127, for details). In the current literature there has been an attempt to explain both the SN and the GRB as two aspects of the same astrophysical phenomenon: the collapsar model. Hence, GRBs have been assumed to originate from a specially violent SN process, a hypernova or a collapsar (see e.g. Ref. 128 and references therein). Both of these possibilities imply a very dense and strong wind-like CBM structure. Such a dense medium appears to be in contrast with the CBM density found in most GRBs within our fireshell model (see e.g. Fig. 10 in Ref. 36). In fact, the average CBM density, inferred from the analysis of the afterglow, has been shown to be in most of the cases of the order of 1 particle cm^{-3} (see e.g. Ref. 44). The only significant contribution to the baryonic matter component in the GRB process is the one represented by the baryon load.³¹ In a GRB, the electron–positron plasma, loaded with a certain amount of baryonic matter, is expected to expand at ultra-relativistic velocities with Lorentz factors $\Gamma \gtrsim 100$.^{81,129,130} Such an ultra-relativistic expansion can actually occur if the amount of baryonic matter, quantifiable through the baryon load parameter, does not exceed the critical value $B \sim 10^{-2}$ (see Ref. 31, for details). For $B > 10^{-2}$ the electron–positron plasma loses its laminar motion and the turbulence occurs, see Fig. 11.

In our approach, following the first paradigm, we have consistently assumed that the GRB has to originate from the gravitational collapse to a BH. The SN follows, instead, the complicated pattern of the final evolution of a massive star, possibly leading to a NS or to a complete explosion but never to a BH. There is a further general argument in favor of our explanation, namely the extremely different energetics of SNe and GRBs. While the SN energy range is 10^{49} – 10^{51} erg, the GRBs are in a larger and wider range of energies 10^{49} – 10^{54} erg. It is clear that in no way a GRB, being energetically dominant, can originate from the SN. We explain the temporal coincidence of the two phenomena, the SN explosion and the GRB, using the concept of *IGC*.^{91,131}

In recent years, we have outlined two different possible scenarios for the GRB-SN connection. In the first version,⁹¹ we have considered the possibility that GRBs may have caused the trigger of the SN event. For this scenario to occur, the companion star has to be in a very special phase of its thermonuclear evolution (see Ref. 91 for details). More recently in Refs. 121, 131 and 132 I have proposed a different possibility occurring at the final stages of the evolution of a close binary system: the explosion in such a system of a Ib/c SN leads to an accretion process onto

the NS companion. The full spacetime diagram is represented in Fig. 14. Again, in order for this process to occur, a very fine tuning must exist in the thermonuclear evolution of the SN core and in the circular orbit of the companion NS. The NS will reach the critical mass value, undergoing gravitational collapse to a BH. The process of gravitational collapse to a BH leads to the emission of the GRB (see Figs. 24 and 25). Here we evaluate the accretion rate onto the NS and give the explicit expression of the accreted mass as a function of the nature of the components and the binary parameters following Ref. 94. The full spacetime diagram is represented in Fig. 14.

3.2. The accretion process of the SN ejecta onto the companion NS

We turn now to the details of the recent work with Jorge Rueda⁹⁴ and collaborators, of the accretion process of the SN material onto the NS. In a spherically symmetric accretion process, the magnetospheric radius is¹³³

$$R_m = \left(\frac{B^2 R^6}{\dot{M} \sqrt{2GM_{\text{NS}}}} \right)^{2/7}, \quad (10)$$

where B , M_{NS} , R are the NS magnetic field, mass, radius, and $\dot{M} \equiv dM/dt$ is the mass-accretion rate onto the NS. It can be seen that for high accretion rates the influence of the magnetosphere will be negligible. The NS captures the material ejected from the core collapse of the companion star in a region delimited by the

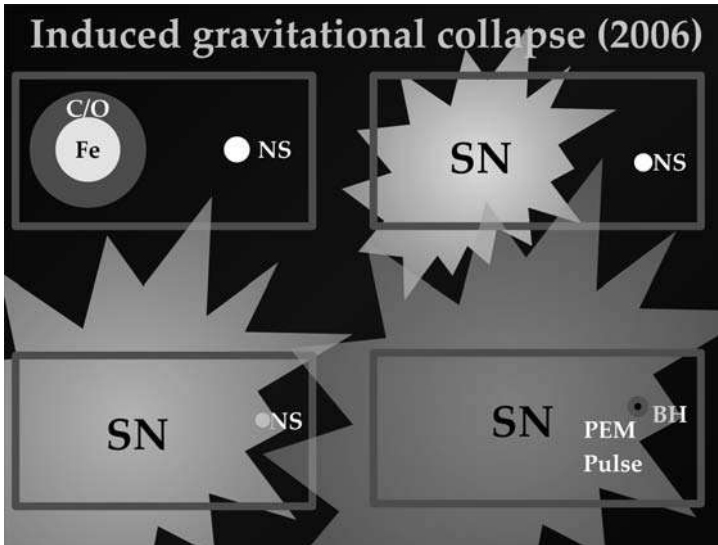


Fig. 24. Process of gravitational collapse to a BH induced by the type Ib/c SN on a companion NS in a close binary system. Figure reproduced from Ref. 131.

Hypercritical Accretion, Binary-Driven HNe, and IGC

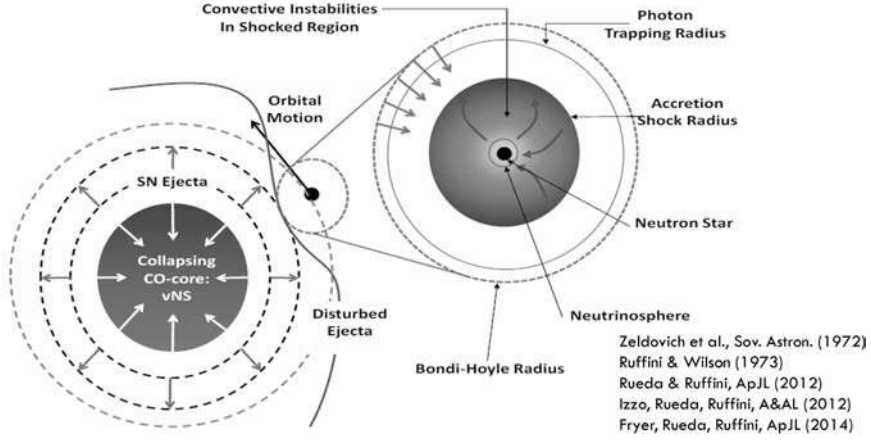


Fig. 25. Hypercritical accretion, binary-driven HNe and IGC.

radius R_{cap} from the NS center

$$R_{\text{cap}} = \frac{2GM_{\text{NS}}}{v_{\text{rel,ej}}^2}, \quad (11)$$

where M_{NS} is the initial NS mass and $v_{\text{rel,ej}}$ is the velocity of the ejecta relative to the orbital motion of the NS around the supernova progenitor star

$$v_{\text{rel,ej}} = \sqrt{v_{\text{orb}}^2 + v_{\text{ej}}^2}, \quad (12)$$

with v_{ej} the ejecta velocity in the frame of the supernova progenitor star with mass $M_{\text{SN-prog}}$ and v_{orb} is the orbital velocity of the NS, given by

$$v_{\text{orb}} = \sqrt{\frac{G(M_{\text{SN-prog}} + M_{\text{NS}})}{a}}, \quad (13)$$

where a is the binary separation, and thus the orbital period of the binary system is

$$P = \sqrt{\frac{4\pi^2 a^3}{G(M_{\text{SN-prog}} + M_{\text{NS}})}}. \quad (14)$$

The NS accretes the material that enters into its capture region defined by Eq. (11). The mass-accretion rate is given by¹³⁴

$$\dot{M} = \xi \pi \rho_{\text{ej}} R_{\text{cap}}^2 v_{\text{ej}} = \xi \pi \rho_{\text{ej}} \frac{(2GM_{\text{NS}})^2}{(v_{\text{orb}}^2 + v_{\text{ej}}^2)^{3/2}}, \quad (15)$$

where the parameter ξ lies in the range $1/2 \leq \xi \leq 1$, ρ_{ej} is the density of the accreted material, and in the last equality we have used Eqs. (11) and (12). The upper value $\xi = 1$ corresponds to the Hoyle–Lyttleton accretion rate.¹³⁵ The actual value of ξ depends on the properties of the medium in which the accretion process

occurs, e.g. vacuum or wind. The velocity of the SN ejecta v_{ej} will be much larger than the sound speed c_s of the already existing material between the C+O star and the NS due to the prior mass transfer, namely the Mach number of the SN ejecta will certainly satisfy $\mathcal{M} = v_{\text{ej}}/c_s \gg 1$. Thus, in practical calculations we can assume the value $\xi = 1$ in Eq. (15) and the relative velocity $v_{\text{rel, ej}}$ of the SN ejecta with respect to the NS companion is given only by the NS orbital velocity and the ejecta velocity as given by Eq. (12). In Fig. 25, we have sketched the accreting process of the supernova ejected material onto the NS. The density of the ejected material can be assumed to decrease in time following the simple power-law¹³⁶

$$\rho_{\text{ej}} = \frac{3M_{\text{ej}}}{4\pi r^3} = \frac{3M_{\text{ej}}}{4\pi\sigma^3 t^{3n}}, \quad (16)$$

where without loss of generality we have assumed that the radius of the SN ejecta expands as $r_{\text{ej}} = \sigma t^n$, with σ and n constants. Therefore, the velocity of the ejecta obeys $v_{\text{ej}} = nr_{\text{ej}}/t$. Equation (15) can be integrated analytically and the accreted mass in a given time interval is given by⁹⁴

$$\Delta M(t) = \int \dot{M} dt = \pi(2GM_{\text{NS}})^2 \frac{3M_{\text{ej}}}{4\pi n^3 \sigma^6} \mathcal{F} + \text{const.}, \quad (17)$$

where

$$\begin{aligned} \mathcal{F} = t^{-3(n+1)} & \left[-4n(2n-1)t^{4n} \sqrt{kt^{2-2n} + 1} {}_2F_1 \left(\frac{1}{2}, \frac{1}{n-1}; \frac{n}{n-1}; -kt^{2-2n} \right) \right. \\ & \left. - k^2(n^2-1)t^4 + 2k(n-1)(2n-1)t^{2n+2} + 4n(2n-1)t^{4n} \right] \\ & \times [k^3(n-1)(n+1)(3n-1)\sqrt{k+t^{2n-2}}]^{-1}, \end{aligned} \quad (18)$$

with $k = v_{\text{orb}}^2/(n\sigma)^2$ and ${}_2F_1(a, b; c; z)$ is the hypergeometric function. The integration constant is computed with the condition $\Delta M(t) = 0$ for $t \leq t_0^{\text{acc}}$, where t_0^{acc} is the time at which the accretion process starts, namely the time at which the SN ejecta reaches the NS capture region (see Fig. 25).

3.3. Reaching the critical mass of the accreting companion NS

We discuss now the problem of the maximum stable mass of a NS. Nonrotating NS equilibrium configurations have been recently constructed by M. Rotondo, J. Rueda, myself and many students, taking into proper account the strong, weak, electromagnetic and gravitational interactions within general relativity. The equilibrium equations are given by the general relativistic Thomas–Fermi equations coupled with the Einstein–Maxwell equations to form the Einstein–Maxwell–Thomas–Fermi system of equations, which must be solved under the condition of global charge neutrality.¹³⁷ These equations supersede the traditional Tolman–Oppenheimer–Volkoff ones that impose the condition of local charge neutrality throughout the configuration. The maximum stable mass $M_{\text{crit}} = 2.67 M_{\odot}$ of nonrotating NSs has been obtained in Ref. 137.

The high and rapid accretion rate of the SN material can lead the NS mass to reach the critical value $M_{\text{crit}} = 2.67 M_{\odot}$. This system will undergo gravitational collapse to a BH, producing a GRB. The initial NS mass is likely to be rather high due to the highly nonconservative mass transfer during the previous history of the evolution of the binary system (see e.g. Refs. 125–127, for details). Thus, the NS could reach the critical mass in just a few seconds. Indeed we can see from Eq. (15) that for an ejecta density 10^6 g cm^{-3} and velocity 10^9 cm s^{-1} , the accretion rate might be as large as $\dot{M} \sim 0.1 M_{\odot} \text{ s}^{-1}$. The occurrence of a GRB-SN event in the scenario depends on some specific conditions satisfied by the binary progenitor system, such as a short binary separation and an orbital period $< 1 \text{ h}$. This is indeed the case with GRB 090618 and 110709B that we have already analyzed within the context of this scenario in Refs. 36 and 123, respectively (see below in the next subsections). In addition to offering an explanation for the GRB-SN temporal coincidence, the considerations presented here lead to an astrophysical implementation of the concept of proto-BH, generically introduced in our previous works on GRBs 090618, 970828 and 101023 (see Refs. 36, 95 and 138). The proto-BH represents the first stage $20 \lesssim t \lesssim 200 \text{ s}$ of the SN evolution.

It is appropriate now to discuss the possible progenitors of such binary systems. A viable progenitor is represented by X-ray binaries such as Cen X-3 and Her X-1.^{6,9,139–143} The binary system is expected to follow an evolutionary track^{125–127}: the initial binary system is composed of main-sequence stars 1 and 2 with a mass ratio $M_2/M_1 \gtrsim 0.4$. The initial mass of the star 1 is likely $M_1 \gtrsim 11 M_{\odot}$, leaving a NS through a core-collapse event. The star 2, now with $M_2 \gtrsim 11 M_{\odot}$ after some almost conservative mass transfer, evolves filling its Roche lobe. It then starts a spiraling in of the NS into the envelope of the star 2. If the binary system does not merge, it will be composed of a helium star and a NS in close orbit. The helium star expands filling its Roche lobe and a nonconservative mass transfer to the NS takes place. This scenario naturally leads to a binary system composed of a C+O star and a massive NS, as the one considered here, see Fig. 25. It is clear that after the occurrence of the SN and the GRB emission, the outcome is represented, respectively, by a NS and a BH. If the NS and the BH are gravitationally bound they give rise to a new kind of binary system, which can lead itself to the merging of the NS and the BH and consequently to a new process of gravitational collapse of the NS into the BH. In this case the system could originate yet another process of GRB emission and possibly a predominant emission in gravitational waves.

4. The Application of the IGC Scenario to GRB 090618

4.1. The SN ejecta accretion onto the companion NS

We recall that the blackbody-emitting surface in Episode 1 evolves during the first $\sim 32 \text{ s}$, as observed in the rest frame, following a power-law behavior

$$r_{\text{em}} = \sigma t^n, \quad v_{\text{em}} = n \frac{r_{\text{em}}}{t} = n \sigma t^{n-1}, \quad (19)$$

where $\sigma = 8.048 \times 10^8 \text{ cm s}^{-n}$, $n \approx 3/5$ as shown in Fig. 19, and $v_{\text{em}} = dr_{\text{em}}/dt \sim 4 \times 10^8 \text{ cm s}^{-1}$ at the beginning of the expansion.

When the mass accreted onto the NS triggers the gravitational collapse of the NS into a BH, the authentic GRB emission is observed in the subsequent episode at $t - t_0 \gtrsim 50 \text{ s}$ (observer frame). The characteristics of GRB 090618 are shown in Table 3 of Ref. 35 and we refer to that reference for more details on the GRB light curve and spectrum simulation. We now turn to the details of the accretion process of the SN material onto the NS. We have initially assumed, as an order of magnitude estimate,³⁶ $r_{\text{SN}} = r_{\text{em}}$ and $v_{\text{SN}} = v_{\text{em}}$. The NS of initial mass M_{NS} accretes mass from the SN ejecta at a rate given by⁹⁴

$$\dot{M}_{\text{acc}}(t) = \pi \rho_{\text{ej}}(t) \frac{(2GM_{\text{NS}})^2}{v_{\text{rel, ej}}^3}, \quad \rho_{\text{ej}}(t) = \frac{3M_{\text{ej}}(t)}{4\pi r_{\text{SN}}^3(t)}, \quad (20)$$

where $r_{\text{SN}}^3(t)$ given by Eq. (19) and $M_{\text{ej}}(t) = M_{\text{ej},0} - M_{\text{acc}}(t)$ is the available mass to be accreted by the NS as a function of time, with $M_{\text{ej},0}$ the mass ejected in the SN. $v_{\text{rel, ej}} = \sqrt{v_{\text{orb}}^2 + v_{\text{SN}}^2}$ is the velocity of the ejecta relative to the NS, where v_{SN} is the SN ejecta velocity given by Eq. (19) and $v_{\text{orb}} = \sqrt{G(M_{\text{core}} + M_{\text{NS}})/a}$ is the orbital velocity of the NS. Here M_{core} is the mass of the SN core progenitor and a the binary separation. Hereafter we assume $a = 9 \times 10^9 \text{ cm}$, a value higher than the maximum distance traveled by the SN material during the total time interval of Episode 1, $\Delta t \simeq 32 \text{ s}$, $\Delta r \sim 7 \times 10^9 \text{ cm}$ (see Fig. 19). If the accreted mass onto the NS is much smaller than the initial mass of the ejecta, i.e. $M_{\text{acc}}/M_{\text{ej},0} \ll 1$, the total accreted mass can be obtained from the formula given by Eq. (8) of Ref. 94, which for GRB 090618 leads to

$$M_{\text{acc}}(t) = \int_{t_0^{\text{acc}}}^t \dot{M}_{\text{acc}}(t) dt \approx (2GM_{\text{NS}})^2 \frac{15M_{\text{ej},0}t^{2/5}}{8n^3\sigma^6\sqrt{1+kt^{4/5}}} \Big|_{t_0^{\text{acc}}}^t, \quad (21)$$

where $k = v_{\text{orb}}^2/(n\sigma)^2$ and t_0^{acc} is the time at which the accretion process starts, namely the time at which the SN ejecta reaches the NS capture region, $R_{\text{cap}} = 2GM_{\text{NS}}/v_{\text{rel, ej}}^2$, so for $t \leq t_0^{\text{acc}}$ we have $M_{\text{acc}}(t) = 0$. The accretion process leads to the gravitational collapse of the NS onto a BH when it reaches the critical mass value. Here we adopt the critical mass $M_{\text{crit}} = 2.67 M_{\odot}$ computed recently in Ref. 137. Equation (21) is more accurate for massive NSs since the amount of mass needed to reach the critical mass by accretion is much smaller than $M_{\text{ej},0}$. In general, the total accreted mass must be computed from the numerical integration of Eq. (20), which we present below for GRB 090618.

4.2. Inferences on the binary period

The occurrence of a GRB-SN event in the accretion induced collapse scenario is subject to some specific conditions of the binary progenitor system such as a short binary separation and orbital period. The orbital period in the present

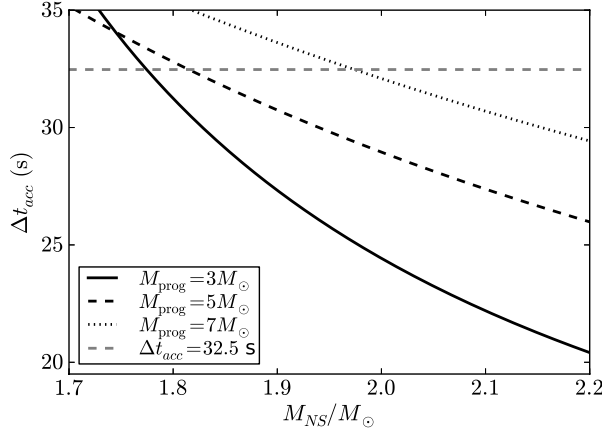


Fig. 26. Time interval Δt_{acc} of the accretion process onto the NS as a function of initial NS mass M_{NS} for selected values of the SN core progenitor mass M_{core} . The horizontal dashed line is the duration $\Delta t = 32.5$ s of the first episode of GRB 090618, which constrains the duration of the time needed by the NS to reach the critical mass. The crossing points between the dashed horizontal line and the solid curves give the NSs with M_{NS} that reach the critical mass in the time Δt . From Ref. 36.

case is

$$P = \sqrt{\frac{4\pi^2 a^3}{G(M_{\text{core}} + M_{\text{NS}})}} = 9.1 \left(\frac{M_{\text{core}} + M_{\text{NS}}}{M_{\odot}} \right)^{-1/2} \text{ min.} \quad (22)$$

We denote by Δt_{acc} the total time interval since the beginning of the SN ejecta expansion all the way up to the instant where the NS reaches the critical mass. In Fig. 26, we plot Δt_{acc} as a function of the initial NS mass and for different masses of the SN core progenitor mass. The mass of the SN ejecta is assumed to be $M_{\text{ej},0} = M_{\text{core}} - M_{\text{rem}}$, where M_{rem} is the mass of the central compact remnant (NS) left by the SN explosion. Here we assumed $M_{\text{core}} = (3-8)M_{\odot}$ at the epoch of the SN explosion, and $M_{\text{rem}} = 1.3 M_{\odot}$, following some of the type Ic SN progenitors studied in Refs. 125–127.

We can see from Fig. 26 that, for GRB 090618, the mass of the NS companion that collapses onto a BH should be in the range $1.8 \lesssim M_{\text{NS}}/M_{\odot} \lesssim 2.1$ corresponding to the SN Ic progenitors $3 \leq M_{\text{core}}/M_{\odot} \leq 8$. The massive NS companion of the evolved star is in line with the binary scenario proposed in Ref. 131. These results also agree with the well-understood Ib/c nature of the SN associated with GRBs. The most likely explanation for SN Ib/c, which lack H and He in their spectra, is that the SN progenitor star is in a binary system with an NS; see also Refs. 125, 126, 127 and also 144 and 145.

It is also interesting to compare the results on the IGC of an NS to a BH by a type Ib/c SN⁹⁴ with the results of Chevalier¹³⁶ on the accretion of supernova material by the central NS generated by the supernova. A total accreted mass of up to $0.1 M_{\odot}$ in a time of a few hours was obtained there for a normal type II SN.

Thus, a similar amount of mass can be accreted in the two cases, but in the latter the accretion occurs over a longer time. To reach a high accretion rate of the inner SN material onto the central NS, a mechanism is needed that helps to increase the density of the NS surrounding layers, which is decreasing due to the expansion after being unbound by the SN explosion. Reference 136 analyzed the possibility of having a reverse shock wave as this mechanism while it moves back through the SN core. The reverse shock is formed in the interaction of the mantle gas with the low-density envelope. The time scale of the accretion process is thus determined by the time it takes the reverse shock to reach the vicinity of the central newly born NS, which is a few hours in the case of SN II progenitors. However, the existence of a low-density outer envelope, e.g. H and He outer layers, is essential for the strength of the reverse shock. Fall-back accretion onto the central NS is expected to be relevant only in SN II but not in SN Ic like those associated to GRBs, where H and He are absent.

4.3. *The collapse time and the role of neutrinos*

The argument presented in Ref. 94 naturally explains the sequence of events: SN explosion — IGC-BH formation — GRB emission. Correspondingly, the accretion of the material ejected by the SN into the nearby NS of the IGC model presented here occurs almost instantaneously. Indeed for the SN expansion parameters obtained from the observations of Episode 1 in GRB 090618 (see Eq. (19), the accretion of the SN material onto the nearby NS occurs in a few seconds (see Fig. 26). The binary parameters are such that the ejecta density does not decrease too much (from 10^6 g cm^{-3} to $\sim 10^4 \text{ g cm}^{-3}$) before reaching the capture region of the NS, leading to a high accretion rate. As pointed out in Ref. 136, radiative diffusion will lower the accretion rate up to the Eddington limit (and then to even lower rates) when the trapping radius of the radiation in the flow $r_{\text{tr}} = \kappa \dot{M}_{\text{acc}} / (4\pi c)$,¹³⁶ where κ is the opacity, is equal to the Bondi radius $r_B = GM_{\text{NS}} / v_{\text{rel,ej}}^2$, the gravitational capture radius. The radius r_{tr} is located where the outward diffusion luminosity is equal to the inward convective luminosity. It can be checked that for the parameters of our system given by Eqs. (19)–(21), the equality $r_{\text{tr}} = r_B$ occurs in a characteristic time ~ 200 days, where we used $\kappa = 0.2 \text{ cm}^2 \text{ g}^{-1}$. Thus, this regime is not reached in the present case since the NS is brought to its critical mass just in a few seconds. In the case analyzed by Ref. 136, it happens in a time ~ 8 days. Only recently we have returned to the previously mentioned papers of Zel’dovich and collaborators¹¹⁹ and Ruffini and Wilson,¹²⁰ since it is clear that the role of neutrino emission is essential in the understanding of the accretion process of the SN ejecta into the companion of NS binary.

It is also a pleasure to show here in Fig. 27 the closest collaborators working at ICRANet headquarters in Pescara and at ICRA at the University of Rome “la Sapienza”.



Fig. 27. Group picture. Standing: Carlo Luciano Bianco, Marco Muccino, Wang Yu. Sitting: Remo Ruffini, Giovanni Pisani, Jorge Rueda, Milos Kovacevic, Luca Izzo.

5. Recent Highlights and the “Third Paradigm”

Some most recent results have appeared in Refs. 23, 38, 92, 96 and 147 and are summarized in a “third paradigm”, see Figs. 28 and 29.

Third paradigm

- *Long GRBs occur in a “cosmic matrix” composed of up to 4 different **Episodes**, each one characterized by specific astrophysical processes and Lorentz Γ factors (from $\Gamma \sim 1$ up to $\Gamma \sim 10^3$).*
- *Both short and long GRBs with $E_{\text{iso}} > 10^{52}$ erg originate from a gravitational collapse to a BH ($M > M_{\text{crit}} \sim 2.6 M_{\odot}$) and can have GeV emission:*
 - Long GRBs \rightarrow BdHNe \rightarrow BH + NS binaries \rightarrow “the” long GRBs.
 - Short GRBs \rightarrow massive BNS mergers \rightarrow BH \rightarrow “the” short GRBs.
- *Both short and long GRBs with $E_{\text{iso}} < 10^{52}$ erg do not form BH and have no GeV emission.*
 - Long GRBs \rightarrow binary NSs \rightarrow X-ray flashes \rightarrow XRFs.
 - Short GRBs \rightarrow short gamma ray flashes \rightarrow massive NS \rightarrow S-GRFs.

The progenitor systems of short bursts are traditionally identified with (NS) binary mergers, see, e.g. Refs. 148–157. This theoretical prediction

R. Ruffini et al.

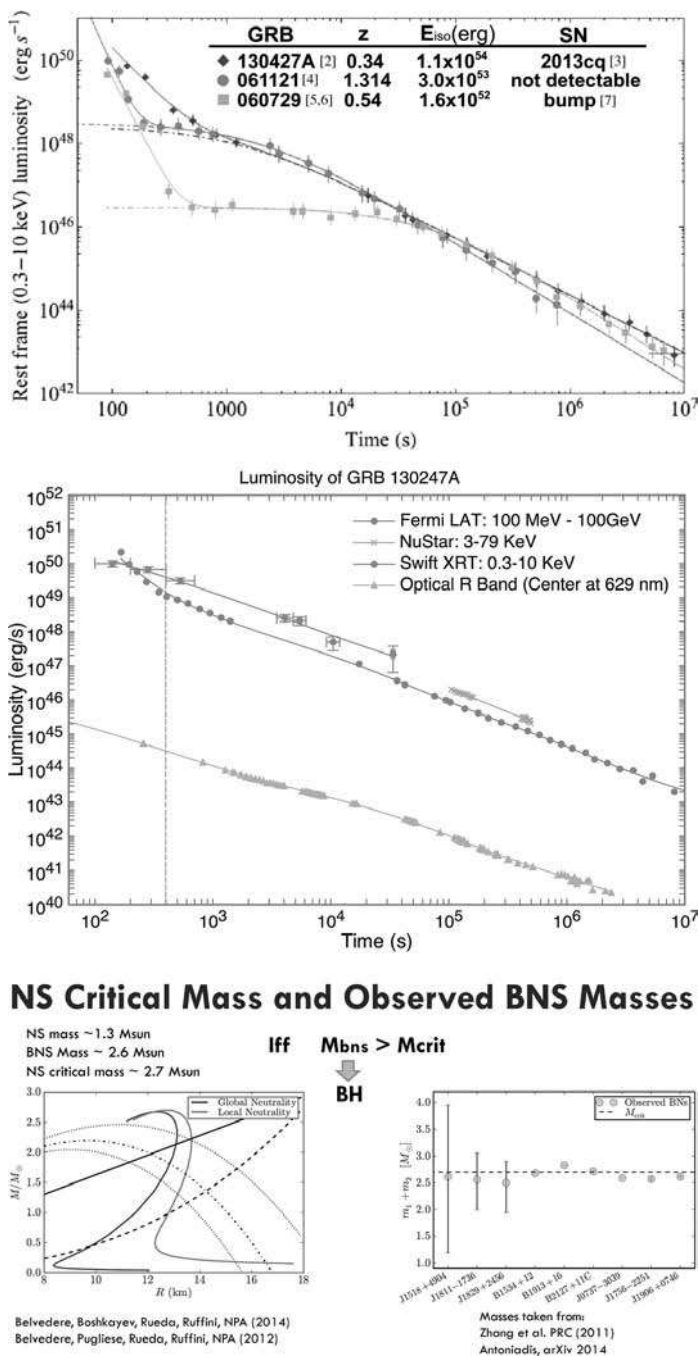


Fig. 28. Top: Episode 3 nesting.⁹² Middle: Episode 3 of GRB 130427A, see Ref. 93. Bottom: NS critical mass and observed BNS masses.

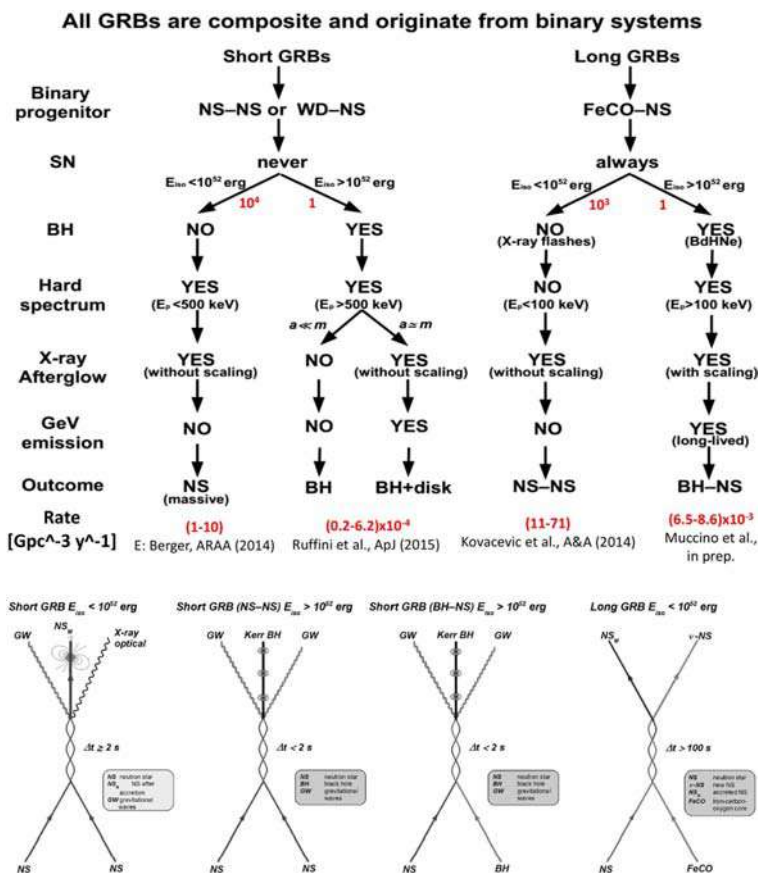


Fig. 29. Top: All GRBs are composite and originate from binary systems, see Refs. 93 and 146. Bottom: the five independent “cosmic matrix” relating SN and GRBs to their constituent NS and BH.

received further observational supports by the successful localization of some short burst afterglows with large off-sets from their hosts galaxies, both late and early type galaxies with no apparent association with star formation, see, e.g. Refs. 157–159.

Reference 148 proposed that the short bursts must be further sub-divided into two different sub-classes, depending on whether or not the NS–NS merger leads to a core with mass larger than the NS critical mass $M_{\text{crit}}^{\text{NS}167}$ which gravitationally collapses to a BH. The first class of short bursts is characterized by isotropic energies $E_{\text{iso}} \lesssim 10^{52}$ erg and rest-frame spectral peak energies $E_{p,i} \lesssim 2$ MeV^{148,168,169} and have as outcome a massive NS (MNS) with additional orbiting material, or even a binary companion (NS or white dwarf, WD), to conserve energy and momentum. We dubbed these moderately hard short bursts as short gamma-ray flashes (S-GRFs). The second class of authentic short GRBs (S-GRBs) has $E_{\text{iso}} \gtrsim 10^{52}$ erg

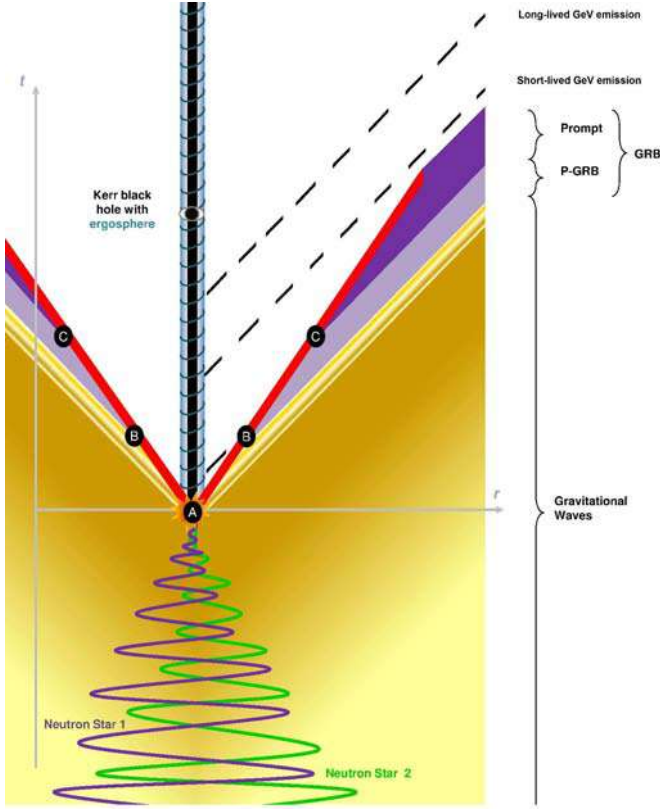


Fig. 30. The spacetime diagram of “the” short GRBs. The orbital separation between the two NSs decreases due to the emission of GWs, until the merging occurs and a family-2 short GRB is emitted. Following the fireshell model: (A) vacuum polarization occurs while the event horizon is formed and a fireshell of e^+e^- plasma self-accelerates radially outward; (B) the fireshell, after engulfing the baryons, keeps self-accelerating and reaches the transparency when the P-GRB is emitted; (C) the accelerated baryons interact with the local CBM giving rise to the prompt emission. The remnant of the merger is a Kerr BH. The accretion of a small (large) amount of orbiting matter onto the BH can lead to the short lived but very energetic 0.1–100 GeV emission observed in GRB 081024B, GRB 090510 and GRB 140619B. The absence of such an emission in GRB 090227B is due to the absence of observations of *Fermi*-LAT. From Ref. 148.

and $E_{p,i} \gtrsim 2 \text{ MeV}^{148,168,169}$ and lead to the formation of a Kerr BH with additional orbiting material, see Fig. 30. Differently from the case of S-GRFs, they exhibit the systematical presence of the 0.1–100 GeV emission, which is related to the activity of the newly-born BH. The relative rate of these two classes of short bursts has been discussed and presented in Ref. 148. There, it has been proved that the S-GRFs are the more frequent events among the short bursts, see also Ref. 170, as also pointed out from the analogy with NS–NS binaries within our Galaxy, for which only in a subset of them the total mass of the components is larger than M_{crit}^{NS} and can lead to a BH in their merging process. Similar conclusions have been also independently reached in Refs. 171 and 172.

A family-2 short: the case of GRB 140619B

Ruffini, R., Muccino, M., Kovacevic, M. et al. 2015 ApJ (in press); arXiv:1412.1018

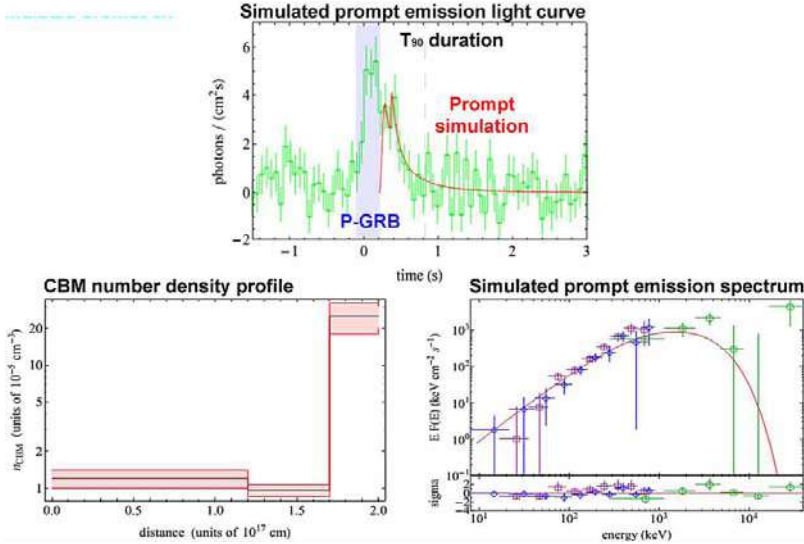


Fig. 31. (Color online) Top: The BGO-b1 (260 keV–40 MeV) simulated light curve of the prompt emission of GRB 140619B (solid red line). Each spike corresponds to the CBM number density profile shown in the figure below. The blue dot-dashed vertical line marks the end of the P-GRB emission. The purple long-dashed and the black dashed vertical lines indicate, respectively, the starting and the ending times of the T_{90} time interval. Clearly visible outside of this time interval is the background noise level. The continuation of the simulation after T_{90} is due to the residual large angle emission of the EQTS due to the density profile. Bottom left: The radial CBM number density distribution of GRB 140619B (black line) and its range of validity (red shaded region). Bottom right: Top panel: comparison between the 8–900 keV data from the NaI-n6 (purple squares) and n9 (blue diamonds) detectors, and the 260 keV–40 MeV data from the BGO-b1 detector (green circles), and the simulation within the fireshell model (solid red curve) in the time interval ΔT_2 . Bottom panel: the residuals of the above-mentioned data with the simulation. From Ref. 148.

Recently, within the fireshell model for GRBs, see, e.g. for a review Ref. 22, we have identified three examples of such authentic S-GRBs: 090227B,¹⁷³ 090510,¹⁷⁴ and 140619B,¹⁴⁸ see Fig. 31. All of them populate the high energy part of the $E_{p,i} - E_{\text{iso}}$ relation for short bursts^{168,169,174} and consistently exhibit, when they fall within the Fermi-LAT field of view (FoV), $a \lesssim 10^2$ s (in the observer frame) and very energetic GeV emission, starting soon after the transparency emission of the e^+e^- plasma. The apparent absence of the GeV emission in GRB 090227B has already been discussed in Ref. 148 and can be explained simply by the fact that this source was outside the nominal LAT FoV, though significant detection in the LAT low energy (LLE) channel and only one transient-class event with energy above 100 MeV were associated with this GRB.¹⁶⁰

Much of the current work has been dedicated to extract the maximum amount of information for the building of theoretical model of GRB 130427A, see Figs. 32 and 33, which in the meantime have appeared in the literature.⁹³

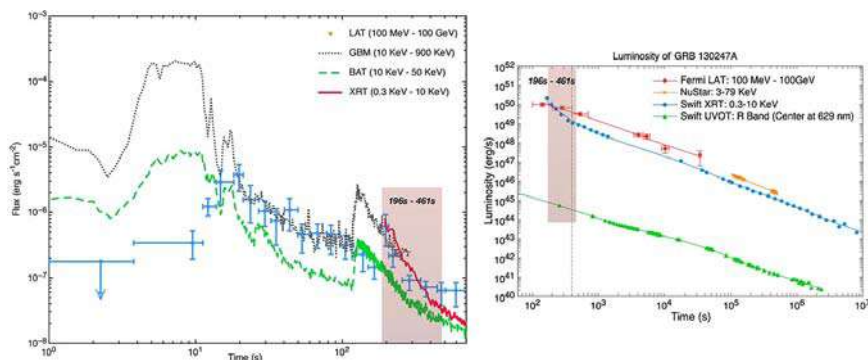


Fig. 32. (Color online) Left: Flux of first 700 s. Blue points are the Fermi-LAT high energy emission from 100 MeV till 100 GeV,¹⁶⁰ gray dotted line represents the Fermi-GBM, from 10 keV to 900 keV, green dashed line represents the photons detected by Swift BAT from 10 keV to 50 keV, and red solid line is the soft X-ray Swift-XRT detection, in the range of 0.3 KeV to 10 KeV. From this figure, clearly the Fermi-LAT emission reaches highest fluence at about 20 s while the gamma-ray detected by Fermi-GBM releases most of the energy within the first 10 s. Right: The multi-wavelength light curve of GRB 130427A. The high energy (100 MeV–100 GeV) emission detected by Fermi-LAT marked with red and soft X-ray (0.3–10 keV) data from Swift-XRT marked with blue are deduced from the original data. NuStar data (3–79 keV) marked with orange comes from Ref. 161. The optical (R band, center at 629 nm) data marked with green comes from ground based satellites.¹⁶² The error bars are too small with respect to the data points except for Fermi-LAT data. The horizontal error bars of Fermi-LAT represent the time bin in which the flux is calculated and vertical bars are statistical $1 - \sigma$ errors on the flux (the systematic error of 10% is ignored). The details in the first tens of seconds are ignored as we are interested in the behavior of the high energy light curve on a longer time scale. The vertical gray dashed line at (~ 400 s) indicates when the constant decaying slope starts. It is clear that all the energy bands have almost the same slope after 400 s in Episode 3. From Ref. 93.

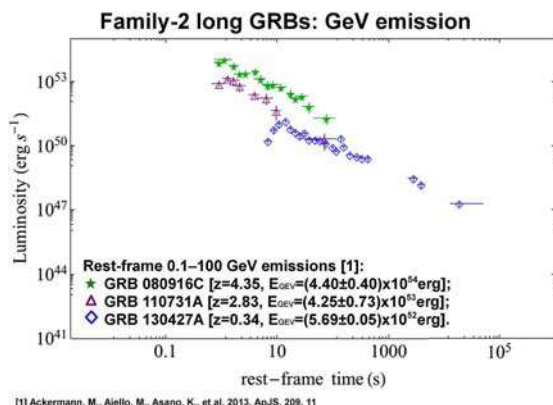


Fig. 33. (Color online) The common power-law behavior of the rest-frame 0.1–100 GeV isotropic luminosity light curves of selected BdHNe: GRB 080916C with green stars,^{163,164} GRB 110731A with purple triangles¹⁶⁵ and Primorac D. *et al.* in preparation, and GRB 130427A with blue diamonds.^{93,166} For each source the redshift and the total isotropic GeV emitted energy are also indicated. The GeV emission onset occurs soon after the P-GRB emission and during the prompt emission. Within the fireshell model, the GeV emission represents clear signature for a Kerr–Newman BH formation.

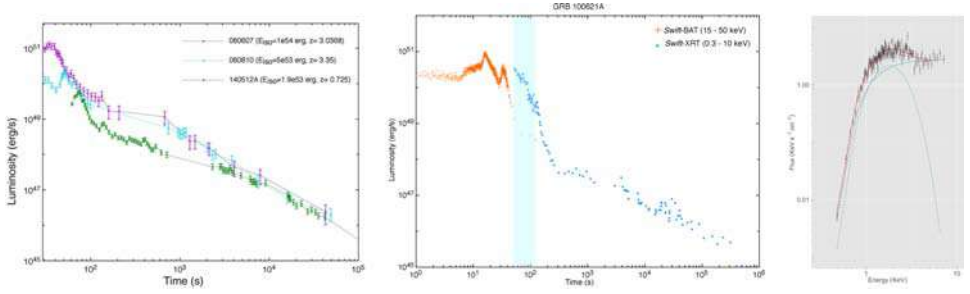


Fig. 34. (Color online) Left: Demonstration of X-ray flares in BdHN: the soft X-ray light-curves (0.3–10 keV) of GRB 080607, 080810, 140512 are transferred to their cosmological rest frame, clearly flares occur before 100 s, and the GBB with lower isotropic energy has a later and less luminous flare. Then comes the plateau, lower isotropic energy GRB has a longer duration plateau. At time later than 10^4 s, three light-curves overlap and decay following a similar power-law behavior. Middle: luminosity light-curve of GRB 100621A. The red crosses and the blue points are the data deduced from Swift-BAT in the energy band 15–50 keV and Swift-XRT in the energy band 0.3–10 keV respectively. The blue shadow indicates a time interval during which thermal component is determined. Light-curve is presented in its cosmological rest frame. Right: the spectrum from 51 s to 130 s and model fitting. Black crosses are the data with uncertainties. Short-dashed line presents the blackbody component with temperature 0.39 keV emitted from a radius of 5.13×10^{12} cm. Long-dashed line corresponds to the nonthermal power-law component. Solid line is the combination of the total two components. Spectrum is shown and fitted in the observers frame.

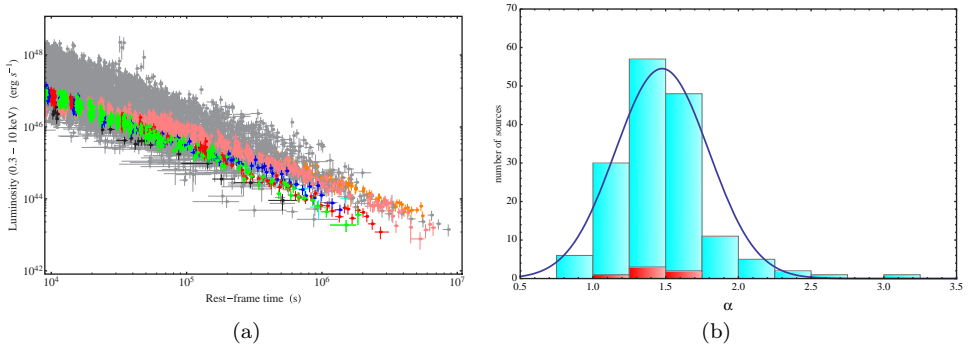


Fig. 35. (Color online) Panel (a): Late X-Ray Emission (LXRE) luminosity light curves of all 161 sources of the ES (gray) compared with the ones of the GS: GRB 060729 (pink), GRB 061007 (black), GRB 080913B (blue), GRB 090618 (green), GRB 091127 (red), and GRB 111228 (cyan), plus GRB 130427A.^{93,175} Panel (b): Distribution of the LXRE power law indexes α within the ES (cyan) compared to the one of the GS (red). Such a distribution follows a Gaussian behavior (blue line) with a mean value of $\mu_\alpha = 1.48$ and a standard deviation of $\sigma_\alpha = 0.32$.

In addition, the main current interest in our group is to probe the impact of the newly formed GRB, originating in the BH formation, on the SN ejecta. There are data on the flares and on the thermal emission in BdHN, which we are currently examining, see Fig. 34. Concurrently, we are considering the LXRE all the way to the afterglow and evidence for asymmetric emission, see Fig. 35.

6. Conclusions

This celebration of the 50th Anniversary of Relativistic Astrophysics comes after 17 years of research addressing the temporal and spatial coincidence of two of the most powerful events in the cosmos: the explosion of a supernova and the emission of a GBM. The first example of such a coincidence occurred with the GRB 980425 and the SN 1998bw. The pioneering results of BeppoSAX were soon followed by many observations from X-ray and gamma ray space observatories (the AGILE, FERMI, KONUS WIND and SWIFT satellites), as well as from ground-based optical telescopes. This has given clear evidence that far from being an exception such a coincidence is quite common: it pervades the occurrence of all most powerful hypernovae and long GRBs. We have followed in this presentation a historical approach explaining how the solution of this enigma has also lead to the unveiling of the basic astrophysical process occurring in long and short GRBs as well as in the occurrence of hypernovae.

The concept of GRB initially envisaged as a single-ultrarelativistic-jetted emission occurring in a “collapsar-fireball” has been superseded by a far reaching scenario (see Fig. 36). Progress has been slow but steady: it has required the introduction of new paradigms, the extension of known relativistic field theories to unexplored regimes, and strong observational support from space and ground observatories. We have outlined in this presentation some crucial moments of these developments. Our new outlook indicates the existence of seven subclasses of GRBs,

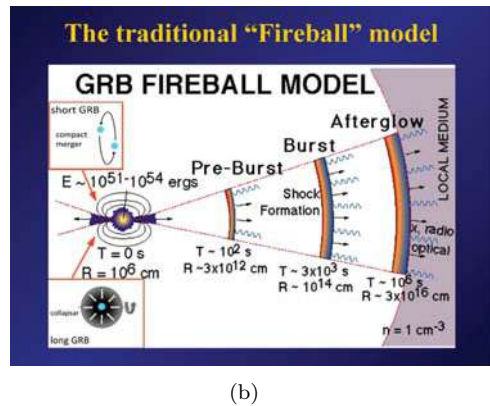
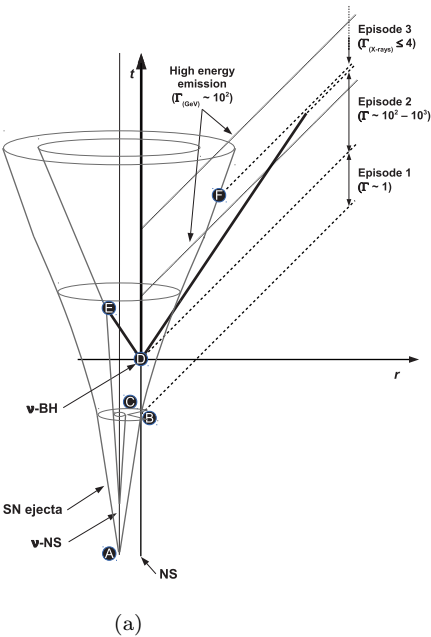


Fig. 36. Panel (a): Fireshell model. Panel (b): Fireball model.

many more than the initial division into short and long GRBs. The fireball model has been superseded by a more detailed “fireshell” model modulated on the IGC paradigm. The concept of a “cosmic matrix” brings to the attention of the astronomical community a new approach necessary to rationalize a sequence of astrophysical events occurring over a 3 h time scale, when measured in the cosmological rest frame of the GRB. It is as far from describing a single process as it can possibly be. The sequence of events instead encompasses (1) the matter accretion in a tight binary system composed of an Fe-CO core undergoing a SN explosion onto a tight companion NS, (2) the creation of a black hole by the gravitational collapse of the NS, following the accretion process and the emission of the GRB, (3) the concurrent emission of the jetted GeV emission, (4) the interaction of the GRB emission with the SN ejected (first presented here), (5) the final appearance of the optical SN emission after 10 days. It is expected that this celebration of the 50th Anniversary coincides with the opening of new era in relativistic astrophysics.

References

1. W. Baade and F. Zwicky, *Proc. US Nat. Acad. Sci.* **20** (1934) 254.
2. W. Baade and F. Zwicky, *Proc. Nat. Acad. Sci.* **20** (1934) 259.
3. R. Giacconi, H. Gursky, F. R. Paolini and B. B. Rossi, *Phys. Rev. Lett.* **9** (1962) 439.
4. I. S. Shklovsky, *Astrophys. J.* **148** (1967) 1.
5. R. Giacconi and R. Ruffini (eds.), *Physics and Astrophysics of Neutron Stars and Black Holes* (Amsterdam, North Holland Publishing Co., 1978).
6. R. W. Leach and R. Ruffini, *Astrophys. J.* **180** (1973) L15.
7. C. E. Rhoades and R. Ruffini, *Phys. Rev. Lett.* **32** (1974) 324.
8. R. Ruffini, Astrophysics and gravitation, in *Proc. Sixteenth Solvay Conf. Physics*, University of Brussels (September 1973).
9. H. Gursky and R. Ruffini (eds.), Neutron Stars, Black Holes and Binary X-Ray Sources, in *Proc. Annual Meeting*, San Francisco, Calif., 28 February 1974, Vol. 48 (Astrophysics and Space Science Library, 1975).
10. E. Costa, F. Frontera, J. Heise *et al.*, *Nature* **387** (1997) 783.
11. T. Damour and R. Ruffini, *Phys. Rev. Lett.* **35** (1975) 463.
12. R. Ruffini, Fundamental physics from black holes, neutron stars and gamma ray bursts, in *The Twelfth Marcel Grossmann Meeting*, eds. T. Damour, R. Jantzen and R. Ruffini (2012), pp. 286–367.
13. R. Ruffini, Black holes, supernovae and gamma ray bursts, in *The Thirteenth Marcel Grossmann Meeting*, eds. K. Rosquist, R. T. Jantzen and R. Ruffini (World Scientific Publishing Co. Pte. Ltd., 2015), pp. 242–314.
14. R. Ruffini, A. G. Aksenov, M. G. Bernardini *et al.*, *Am. Inst. Phys. Conf. Ser.* **1132** (2009).
15. A. Heger, C. L. Fryer, S. E. Woosley *et al.*, *Astrophys. J.* **591** (2003) 288.
16. E. Verner, F. Bruhweiler and T. Gull, *Astrophys. J.* **624** (2005) 973.
17. A. Damineli, A. Kaufer, B. Wolf *et al.*, *Astrophys. J.* **528** (2000) L101.
18. R. C. Iping, G. Sonneborn, T. R. Gull *et al.*, *Astrophys. J.* **633** (2005) L37.
19. E. Pian, L. Amati, L. A. Antonelli *et al.*, *Astrophys. J.* **536** (2000) 778.
20. S. R. Kulkarni, D. A. Frail, M. H. Wieringa *et al.*, *Nature* **395** (1998) 663.
21. T. J. Galama, P. M. Vreeswijk, J. van Paradijs *et al.*, *Nature* **395** (1998) 670.

22. R. Ruffini, G. Vereshchagin and S. Xue, *Phys. Rep.* **487** (2010) 1.
23. R. Ruffini, Y. Wang, M. Kovacevic et al., GRB 130427A and SN 2013cq: A multi-wavelength analysis of an induced gravitational collapse event, arXiv:1405.5723 (2014).
24. A. Hewish, S. J. Bell, J. D. H. Pilkington et al., *Nature* **217** (1968) 709.
25. W. Arnett, in *From Nuclei to White Dwarfs and Neutron Stars*, eds. A. Mezzacappa and R. Ruffini (World Scientific, Singapore), in press.
26. M. Rees, R. Ruffini and J. A. Wheeler, *Black Holes, Gravitational Waves and Cosmology: An Introduction to Current Research*, Topics in Astrophysics and Space Physics, Vol. 10 (Gordon and Breach, Science Publishers, Inc., New York, 1974).
27. A. Finzi and R. A. Wolf, *Astrophys. J.* **153** (1968) 865.
28. D. Christodoulou and R. Ruffini, *Phys. Rev. D* **4** (1971) 3552.
29. R. Ruffini, The ergosphere and dyadosphere of black holes, in *The Kerr Spacetime*, eds. D. L. Wiltshire, M. Visser and S. Scott (eds.) (Cambridge University Press, 2009).
30. R. Ruffini, J. D. Salmonson, J. R. Wilson and S.-S. Xue, *Astron. Astrophys.* **350** (1999) 334.
31. R. Ruffini, J. D. Salmonson, J. R. Wilson and S.-S. Xue, *Astron. Astrophys.* **359** (2000) 855.
32. R. Ruffini, Analogies, new paradigms and observational data as growing factors of relativistic astrophysics, in *Fluctuating Paths and Fields*, eds. W. Janke, A. Pelster, H. J. Schmidt and M. Bachmann (World Scientific, Singapore, 2001).
33. W. S. Paciesas, C. A. Meegan, G. N. Pendleton et al., *Astrophys. J. SS* **122** (1999) 465.
34. F. Frontera, GRB Afterglow Discovery with BeppoSax: Its Story 15 Years Later, in *The Thirteenth Marcel Grossmann Meeting*, eds. K. Rosquist, R. T. Jantzen and R. Ruffini (World Scientific Publishing Co. Pte. Ltd., 2015), pp. 33–53.
35. L. Izzo, R. Ruffini, A. V. Penacchioni et al., *Astron. Astrophys.* **543** (2012) A10.
36. L. Izzo, J. A. Rueda and R. Ruffini, *Astron. Astrophys.* **548** (2012) L5.
37. G. B. Pisani, L. Izzo, R. Ruffini et al., *Astron. Astrophys.* **552** (2013) L5.
38. M. Muccino, R. Ruffini, C. L. Bianco et al., *Astrophys. J.* **763** (2013) 125.
39. T. Piran, *Rev. Mod. Phys.* **76** (2004) 1143.
40. G. Cavallo and M. J. Rees, *Mon. Not. R. Astron. Soc.* **183** (1978) 359.
41. J. Goodman, Are gamma-ray bursts optically thick?, *Astrophys. J.* **308** (1986) L47.
42. B. Paczynski, *Astrophys. J.* **308** (1986) L43.
43. P. Meszaros, *Rep. Prog. Phys.* **69** (2006) 2259.
44. R. Ruffini, *Int. J. Mod. Phys. D* **20** (2011) 1797.
45. R. Ruffini, Beyond the critical mass: The dyadosphere of black holes, in *Frontiers Science Series 23: Black Holes and High Energy Astrophysics*, eds. H. Sato and N. Sugiyama (Universal Academic Press, 1998).
46. G. Preparata, R. Ruffini and S.-S. Xue, *Astron. Astrophys.* **338** (1998) L87.
47. A. Aksenov, R. Ruffini and G. Vereshchagin, *Phys. Rev. Lett.* **99** (2007) 125003.
48. E. Ramirez-Ruiz and E. E. Fenimore, *Astrophys. J.* **539** (2000) 712.
49. M. J. Rees and P. Meszaros, *Astrophys. J.* **430** (1994) L93.
50. M. J. Rees and P. Meszaros, *Mon. Not. R. Astron. Soc.* **258** (1992) 41P.
51. M. Tavani, *Astrophys. J.* **466** (1996) 768.
52. F. Frontera, L. Amati, E. Costa et al., *Astrophys. J. Suppl.* **127** (2000) 59.
53. A. Crider, E. P. Liang, I. A. Smith et al., *Astrophys. J.* **479** (1997) L39.
54. R. D. Preece, M. S. Briggs, T. W. Giblin et al., *Astrophys. J.* **581** (2002) 1248.
55. G. Ghirlanda, A. Celotti and G. Ghisellini, *Astron. Astrophys.* **393** (2002) 409.

56. G. Ghirlanda, A. Celotti and G. Ghisellini, *Astron. Astrophys.* **406** (2003) 879.
57. P. Kumar and E. McMahon, *Mon. Not. R. Astron. Soc.* **384** (2008) 33.
58. T. Piran, R. Sari and Y. Zou, *Mon. Not. R. Astron. Soc.* **393** (2009) 1107.
59. R. D. Blandford and C. F. McKee, *Phys. Fluids* **19** (1976) 1130.
60. E. Molinari, S. D. Vergani, D. Malesani *et al.*, *Astron. Astrophys.* **469** (2007) L13.
61. E. S. Rykoff, F. Aharonian, C. W. Akerlof *et al.*, *Astrophys. J.* **702** (2009) 489.
62. R. Sari and T. Piran, *Astrophys. J.* **520** (1999) 641.
63. G. Ghisellini and A. Celotti, *Astron. Astrophys. Suppl.* **138** (1999) 527.
64. A. A. Zdziarski, R. Svensson and B. Paczynski, *Astrophys. J.* **366** (1991) 343.
65. A. Shemi, *Mon. Not. R. Astron. Soc.* **269** (1994) 1112.
66. A. Pe'er and B. Zhang, *Astrophys. J.* **653** (2006) 454.
67. M. V. Medvedev, *Astrophys. J.* **540** (2000) 704.
68. A. Panaitescu and P. Mészáros, *Astrophys. J.* **544** (2000) L17.
69. B. E. Stern and J. Poutanen, *Mon. Not. R. Astron. Soc.* **352** (2004) L35.
70. D. Eichler and A. Levinson, *Astrophys. J.* **529** (2000) 146.
71. P. Mészáros and M. J. Rees, *Astrophys. J.* **530** (2000) 292.
72. P. Mészáros, *Annu. Rev. Astron. Astrophys.* **40** (2002) 137.
73. F. Daigne and R. Mochkovitch, *Mon. Not. R. Astron. Soc.* **336** (2002) 1271.
74. D. Giannios, *Astron. Astrophys.* **457** (2006) 763.
75. F. Ryde and A. Pe'er, *Astrophys. J.* **702** (2009) 1211.
76. D. Lazzati and M. C. Begelman, *Astrophys. J.* **725** (2010) 1137.
77. R. Ruffini, *Astron. Astrophys. Suppl.* **138** (1999) 513.
78. R. Ruffini, C. L. Bianco, P. Chardonnet *et al.*, *Astrophys. J.* **555** (2001) L113.
79. C. L. Bianco and R. Ruffini, *Astrophys. J.* **605** (2004) L1.
80. C. L. Bianco and R. Ruffini, *Astrophys. J.* **620** (2005) L23.
81. P. Meszaros, P. Laguna and M. J. Rees, *Astrophys. J.* **415** (1993) 181.
82. R. Sari, *Astrophys. J.* **489** (1997) L37.
83. R. Sari, *Astrophys. J.* **494** (1998) L49.
84. E. Waxman, *Astrophys. J.* **491** (1997) L19.
85. M. J. Rees and P. Meszaros, *Astrophys. J.* **496** (1998) L1.
86. J. Granot, T. Piran and R. Sari, *Astrophys. J.* **513** (1999) 679.
87. A. Panaitescu and P. Meszaros, *Astrophys. J.* **493** (1998) L31.
88. A. Gruzinov and E. Waxman, *Astrophys. J.* **511** (1999) 852.
89. J. van Paradijs, C. Kouveliotou and R. A. M. J. Wijers, *Annu. Rev. Astron. Astrophys.* **38** (2000) 379.
90. C. L. Bianco and R. Ruffini, *Astrophys. J.* **633** (2005) L13.
91. R. Ruffini, C. L. Bianco, P. Chardonnet *et al.*, *Astrophys. J.* **555** (2001) L117.
92. R. Ruffini, M. Muccino, C. L. Bianco *et al.*, *Astron. Astrophys.* **565** (2014) L10.
93. R. Ruffini, Y. Wang, M. Enderli *et al.*, *Astrophys. J.* **798** (2015) 10.
94. J. A. Rueda and R. Ruffini, *Astrophys. J.* **758** (2012) L7.
95. A. V. Penacchioni, R. Ruffini, L. Izzo *et al.*, *Astron. Astrophys.* **538** (2012) A58.
96. C. L. Fryer, J. A. Rueda and R. Ruffini, *Astrophys. J.* **793** (2014) L36.
97. R. Ruffini, L. Izzo, A. V. Penacchioni *et al.*, *PoS (Texas2010)* (2011) 101.
98. P. Schady, W. H. Baumgartner, A. P. Beardmore *et al.*, *GCN Circ.* **9512** (2009).
99. W. H. Baumgartner, S. D. Barthelmy, J. R. Cummings *et al.*, *GCN Circ.* **9530** (2009) 1.
100. G. J. Fishman, C. A. Meegan, R. B. Wilson *et al.*, *Astrophys. J. Suppl.* **92** (1994) 229.
101. A. P. Beardmore and P. Schady, *GCN Circ.* **9528** (2009) 1.
102. C. Meegan, G. Lichti, P. N. Bhat *et al.*, *Astrophys. J.* **702** (2009) 791.
103. D. Band, J. Matteson, L. Ford *et al.*, *Astrophys. J.* **413** (1993) 281.

104. S. McBreen, *GCN Circ.* **9535** (2009).
105. S. B. Cenko, D. A. Perley, V. Junkkarinen et al., *GCN Circ.* **9518** (2009).
106. B. E. Schaefer, *Astrophys. J.* **660** (2007) 16.
107. S. Golenetskii, R. Aptekar, E. Mazets et al., *GCN Circ.* **9553** (2009) 1.
108. K. Kono, A. Daikyuji, E. Sonoda et al., *GCN Circ.* **9568** (2009) 1.
109. F. Longo, E. Moretti, G. Barbiellini et al., *GCN Circ.* **9524** (2009).
110. Y. Kotov, A. Kochemasov, S. Kuzin et al., in *37th COSPAR Scientific Assembly* (Montréal, Canada, 13–20 July 2008), p. 1596.
111. A. Nandi, A. R. Rao, S. K. Chakrabarti et al., Indian Payloads (RT-2 Experiment) Onboard CORONAS-PHOTON Mission, arXiv:0912.4126 (December 2009).
112. A. R. Rao, J. P. Malkar, M. K. Hingar et al., *Astrophys. J.* **728** (2011) 42.
113. Z. Cano, D. Bersier, C. Guidorzi et al., *Mon. Not. R. Astron. Soc.* **413** (2011) 669.
114. F. Ryde, M. Axelsson, B. B. Zhang et al., *Astrophys. J.* **709** (2010) L172.
115. S. Guiriec, V. Connaughton, M. S. Briggs et al., *Astrophys. J.* **727** (2011) L33.
116. A. Pe’er, *Astrophys. J.* **682** (2008) 463.
117. C. Cherubini, A. Geralico, H. J. A. Rueda and R. Ruffini, *Phys. Rev. D* **79** (2009) 124002.
118. R. Ruffini, C. L. Bianco, P. Chardonnet et al., New perspectives in physics and astrophysics from the theoretical understanding of gamma-ray bursts, in *Cosmology and Gravitation*, eds. M. Novello and S. E. Perez Bergliaffa, American Institute of Physics Conference Series, Vol. 668 (American Institute of Physics, 2003).
119. Y. B. Zel’dovich, L. N. Ivanova and D. K. Nadezhin, *Soviet Astron.* **16** (1972) 209.
120. R. Ruffini and J. Wilson, *Phys. Rev. Lett.* **31** (1973) 1362.
121. R. Ruffini, M. G. Bernardini, C. L. Bianco et al., The role of grb 031203 in clarifying the astrophysical grb scenario, in *The 6th Integral Workshop — The Obscured Universe*, eds. S. Grebenev, R. Sunyaev, C. Winkler, A. Parmar and L. Ouweland, Vol. SP-622 (ESA Special Publication, 2007), p. 561.
122. B. Patricelli, M. G. Bernardini, C. L. Bianco et al., *Int. J. Mod. Phys. D* **20** (2011) 1983.
123. A. V. Penacchioni, R. Ruffini, C. L. Bianco et al., *Astron. Astrophys.* **551** (2013) A133.
124. J. Hjorth and J. S. Bloom, *The Gamma-Ray Burst — Supernova Connection*, in *Gamma-Ray Bursts*, eds. C. Kouveliotou, R. A. M. J. Wijers and S. Woosley, Cambridge Astrophysics Series, Vol. 51 (Cambridge University Press, Cambridge, 2012), pp. 169–190.
125. K. Nomoto and M. Hashimoto, *Phys. Rep.* **163** (1988) 13.
126. K. Nomoto, H. Yamaoka, O. R. Pols et al., *Nature* **371** (1994) 227.
127. K. Iwamoto, K. Nomoto, P. Höflich et al., *Astrophys. J.* **437** (1994) L115.
128. S. E. Woosley and J. S. Bloom, *Annu. Rev. Astron. Astrophys.* **44** (2006) 507.
129. A. Shemi and T. Piran, *Astrophys. J.* **365** (1990) L55.
130. T. Piran, A. Shemi and R. Narayan, *Mon. Not. R. Astron. Soc.* **263** (1993) 861.
131. R. Ruffini, M. G. Bernardini, C. L. Bianco et al., On gamma-ray bursts, in *The Eleventh Marcel Grossmann Meeting*, eds. H. Kleinert, R. T. Jantzen and R. Ruffini (World Scientific, Singapore, 2008).
132. R. Ruffini, M. G. Bernardini, C. L. Bianco et al., Black hole physics and astrophysics: The grb-supernova connection and urca-1 — urca-2, in *The Tenth Marcel Grossmann Meeting*, eds. M. Novello, S. Perez Bergliaffa and R. Ruffini (World Scientific, Singapore, 2006).
133. O. D. Toropina, M. M. Romanova and R. V. E. Lovelace, *Mon. Not. R. Astron. Soc.* **420** (2012) 810.
134. H. Bondi and F. Hoyle, *Mon. Not. R. Astron. Soc.* **104** (1944) 273.

135. F. Hoyle and R. A. Lyttleton, *Proc. Cambridge Philos. Soc.* **35** (1939) 405.
136. R. A. Chevalier, *Astrophys. J.* **346** (1989) 847.
137. R. Belvedere, D. Pugliese, J. A. Rueda *et al.*, *Nucl. Phys. A* **883** (2012) 1.
138. L. Izzo, R. Ruffini, C. L. Bianco *et al.*, On the thermal and double episode emissions in GRB 970828, arXiv:1205.6651 (2012).
139. E. Schreier, R. Levinson, H. Gursky *et al.*, *Astrophys. J.* **172** (1972) L79.
140. R. E. Wilson, *Astrophys. J.* **174** (1972) L27.
141. H. Tananbaum, H. Gursky, E. M. Kellogg *et al.*, *Astrophys. J.* **174** (1972) L143.
142. K. Davidson and J. P. Ostriker, *Astrophys. J.* **179** (1973) 585.
143. M. L. Rawls, J. A. Orosz, J. E. McClintock *et al.*, *Astrophys. J.* **730** (2011) 25.
144. A. V. Tutukov and A. V. Fedorova, *Astron. Rep.* **51** (2007) 291.
145. R. A. Chevalier, *Astrophys. J.* **752** (2012) L2.
146. M. Muccino, R. Ruffini, M. Kovacevic *et al.*, GRB 140619B: A short GRB from a binary neutron stars merger leading to the black hole formation, (2014) arXiv e-prints.
147. R. Ruffini, L. Izzo, M. Muccino *et al.*, *Astron. Astrophys.* **569** (2014) A39.
148. R. Ruffini, M. Muccino, M. Kovacevic *et al.*, *Astrophys. J.* **808** (2015) 190.
149. J. Goodman, *Astrophys. J.* **308** (1986) L47.
150. B. Paczynski, *Astrophys. J.* **308** (1986) L43.
151. D. Eichler, M. Livio, T. Piran and D. N. Schramm, *Nature* **340** (1989) 126.
152. R. Narayan, T. Piran and A. Shemi, *Astrophys. J.* **379** (1991) L17.
153. P. Meszaros and M. J. Rees, *Astrophys. J.* **482** (1997) L29.
154. S. Rosswog, E. Ramirez-Ruiz and M. B. Davies, *Mon. Not. R. Astron. Soc.* **345** (2003) 1077.
155. W. H. Lee, E. Ramirez-Ruiz and D. Page, *Astrophys. J.* **608** (2004) L5.
156. K. Belczynski, R. Perna, T. Bulik *et al.*, *Astrophys. J.* **648** (2006) 1110.
157. E. Berger, *Annu. Rev. Astron. Astrophys.* **52** (2014) 43.
158. D. B. Fox, D. A. Frail, P. A. Price *et al.*, *Nature* **437** (2005) 845.
159. N. Gehrels, C. L. Sarazin, P. T. O'Brien *et al.*, *Nature* **437** (2005) 851.
160. M. Ackermann, M. Ajello, K. Asano *et al.*, *Astrophys. J. Suppl.* **209** (2013) 11.
161. C. Kouveliotou, J. Granot, J. L. Racusin *et al.*, *Astrophys. J.* **779** (2013) L1.
162. D. A. Perley, S. B. Cenko, A. Corsi *et al.*, *Astrophys. J.* **781** (2014) 37.
163. A. A. Abdo, M. Ackermann, M. Arimoto *et al.*, *Science* **323** (2009) 1688.
164. L. Izzo, M. G. Bernardini, C. L. Bianco *et al.*, *Int. J. Mod. Phys. D* **20** (2011) 1949.
165. M. Ackermann, M. Ajello, K. Asano *et al.*, *Astrophys. J.* **763** (2013) 71.
166. M. Ackermann, M. Ajello, K. Asano *et al.*, *Science* **343** (2014) 42.
167. R. Belvedere, D. Pugliese, J. A. Rueda *et al.*, *Nucl. Phys. A* **883** (2012) 1.
168. F.-W. Zhang, L. Shao, J.-Z. Yan and D.-M. Wei, *Astrophys. J.* **750** (2012) 88.
169. G. Calderone, G. Ghirlanda, G. Ghisellini *et al.*, *Mon. Not. R. Astron. Soc.* **448** (2015) 403.
170. R. Ruffini, J. A. Rueda, M. Muccino *et al.*, *Astrophys. J.* **832** (2016) 136.
171. C. L. Fryer, K. Belczynski, E. Ramirez-Ruiz *et al.*, The Fate of the Compact Remnant in Neutron Star Mergers, arXiv e-prints (2015).
172. S. Lawrence, J. G. Tervala, P. F. Bedaque and M. C. Miller, *Astrophys. J.* **808** (2015) 186.
173. M. Muccino, R. Ruffini, C. L. Bianco *et al.*, *Astrophys. J.* **763** (2013) 125.
174. R. Ruffini, M. Muccino, Y. Aimuratov *et al.*, *Astrophys. J.* **831** (2016) 178.
175. G. B. Pisani, L. Izzo, R. Ruffini *et al.*, *Astron. Astrophys.* **552** (2013) L5.

The binary systems associated with short and long gamma-ray bursts and their detectability*

Jorge A. Rueda^{†,‡,§,***}, Y. Aimuratov^{†,‡,¶}, U. Barres de Almeida^{||},
 L. Becerra^{†,‡}, C. L. Bianco^{†,‡}, C. Cherubini^{**,††}, S. Filippi^{**,††}, M. Karlica^{†,‡,¶},
 M. Kovacevic^{†,‡,¶}, J. D. Melon Fuksman^{†,‡}, R. Moradi^{†,‡}, M. Muccino^{†,‡},
 A. V. Penacchioni^{†,‡,§§}, G. B. Pisani^{†,‡}, D. Primorac^{†,‡}, R. Ruffini^{†,‡,§},
 N. Sahakyan[¶], S. Shakeri^{†,|||} and Y. Wang^{†,‡}

[†]*ICRANet, Piazza Della Repubblica 10, I-65122 Pescara, Italy*

[‡]*Dip. di Fisica and ICRA, Sapienza Università di Roma,
 P.le Aldo Moro 5, I-00185 Rome, Italy*

[§]*ICRANet-Rio, Centro Brasileiro de Pesquisas Físicas,
 Rua Dr. Xavier Sigaud 150, 22290-180 Rio de Janeiro, Brazil*

[¶]*Université de Nice Sophia Antipolis, CEDEX 2,
 Grand Château Parc Valrose, Nice, France*

^{||}*Centro Brasileiro de Pesquisas Físicas,
 Rua Dr. Xavier Sigaud 150, 22290-180 Rio de Janeiro, Brazil*

^{**}*Unit of Nonlinear Physics and Mathematical Modeling,
 Università Campus Bio-Medico di Roma,
 Via A. del Portillo 21, I-00128 Rome, Italy*

^{††}*ICRA, Università Campus Bio-Medico di Roma,
 Via A. del Portillo 21, I-00128 Rome, Italy*

^{‡‡}*ASI Science Data Center,
 Via del Politecnico s.n.c., I-00133 Rome, Italy*

^{§§}*Dept. of Physical Sciences, Earth and Environment,
 University of Siena, Via Roma 56, I-53100 Siena, Italy*

^{¶¶}*ICRANet-Yerevan, Marshall Baghramian Avenue 24a,
 Yerevan 0019, Republic of Armenia*

^{|||}*Department of Physics,
 Isfahan University of Technology, 84156-83111, Iran*

^{***}*jorge.rueda@icra.it*

Received 2 March 2017

Accepted 3 March 2017

Published 13 April 2017

Short and long-duration gamma-ray bursts (GRBs) have been recently sub-classified into seven families according to the binary nature of their progenitors. For short GRBs, mergers of neutron star binaries (NS–NS) or neutron star-black hole binaries (NS–BH) are proposed. For long GRBs, the induced gravitational collapse (IGC) paradigm proposes

*Based on a talks presented at the Fourteenth Marcel Grossmann Meeting on General Relativity, Rome, July 2015.

a tight binary system composed of a carbon–oxygen core (CO_{core}) and a NS companion. The explosion of the CO_{core} as supernova (SN) triggers a hypercritical accretion process onto the NS companion which might reach the critical mass for the gravitational collapse to a BH. Thus, this process can lead either to a NS–BH or to NS–NS depending on whether or not the accretion is sufficient to induce the collapse of the NS into a BH. We shall discuss for the above compact object binaries: (1) the role of the NS structure and the equation-of-state on their final fate; (2) their occurrence rates as inferred from the X and gamma-ray observations; (3) the expected number of detections of their gravitational wave (GW) emission by the Advanced LIGO interferometer.

Keywords: Gamma-ray bursts; neutron stars; black holes.

PACS Number(s): 04.30.Tv, 04.40.Dg, 97.60.Bw, 97.60.Jd, 97.60.Lf, 98.62.Mw

1. Introduction

There has been a traditional phenomenological classification of GRBs based on the observed prompt duration, T_{90} : long GRBs for $T_{90} > 2$ s and short GRBs for $T_{90} < 2$ s. [1, 5] In this paper, we shall review the recent progress reached in the understanding of the nature of long and short GRBs that has led to a physical GRB classification, proposed in Refs. [6–8]. Such a classification, as we will see below, is based on the possible outcomes in the final stages of the evolution of the progenitor systems.

1.1. Long GRBs

The induced gravitational collapse (IGC) scenario introduces, as the progenitor of the long GRBs associated with SNe Ib/c, binaries composed of a carbon–oxygen core (CO_{core}) on the verge of supernova with a NS companion. [9, 11, 15] The explosion of the CO_{core} as SN, forming at its center a newly-born NS called hereafter νNS , triggers an accretion process onto the NS binary companion. Depending on the parameters of the *in-state*, i.e. of CO_{core} –NS binary, two sub-classes of long GRBs with corresponding *out-states* are envisaged. [6]

- *X-ray flashes (XRFs)*. Long bursts with $E_{\text{iso}} \lesssim 10^{52}$ erg are produced by CO_{core} –NS binaries with relatively large binary separations ($a \gtrsim 10^{11}$ cm). The accretion rate of the SN ejecta onto the NS in these systems is not high enough to bring the NS mass to the critical value M_{crit} , hence no BH is formed. The out-state of this GRB sub-class can be either a νNS –NS binary if the system keeps bound after the SN explosion, or two runaway NSs if the binary system is disrupted.
- *Binary driven hypernovae (BdHNe)*. Long bursts with $E_{\text{iso}} \gtrsim 10^{52}$ erg are instead produced by more compact CO_{core} –NS binaries ($a \lesssim 10^{11}$ cm, see e.g. Refs. [13] and [15]). In this case, the SN triggers a larger accretion rate onto the NS companion, e.g. $\gtrsim 10^{-2}$ – $10^{-1} M_{\odot} \text{ s}^{-1}$, bringing the NS to its critical mass M_{crit} , [11, 13] namely to the point of gravitational collapse with consequent formation of a BH. Remarkably, in Ref. [14], it was recently shown that the large majority of BdHNe leads naturally to NS–BH binaries owing to the high compactness of the binary that avoids the disruption of it even in cases of very high mass loss exceeding 50% of the total mass of the initial CO_{core} –NS binary.

In addition, it exists the possibility of BH-SNe.^[6] Long burst with $E_{\text{iso}} \gtrsim 10^{54}$ erg occurring in close CO_{core}-BH binaries in which the hypercritical accretion produces, as *out-states*, a more massive BH and a ν NS. These systems have been considered in Ref. [6] as a subset of the BdHNe but no specific example have been yet observationally identified.

1.2. Short GRBs

There is the consensus within the GRB community that the progenitors of short GRBs are mergers of NS-NS and/or NS-BH binaries (see, e.g. Refs. [16–20] for a recent review). Similarly to the case of long GRBs, in Ref. [6] short GRBs have been split into different sub-classes:

- *Short gamma-ray flashes (S-GRFs)*. Short bursts with energies $E_{\text{iso}} \lesssim 10^{52}$ erg, produced when the post-merger core do not surpass the NS critical mass M_{crit} , hence there is no BH formation. Thus, these systems left as byproduct a massive NS and possibly, due to the energy and angular momentum conservation, orbiting material in a disk-like structure or a low-mass binary companion.
- *Authentic short gamma-ray bursts (S-GRBs)*. Short bursts with $E_{\text{iso}} \gtrsim 10^{52}$ erg, produced when the post-merger core reaches or overcome M_{crit} , hence forming a Kerr or Kerr–Newman BH,^[8] and also in this case possibly orbiting material.
- *Ultra-short GRBs (U-GRBs)*. A new sub-class of short bursts originating from ν NS-BH merging binaries. They can originate from BdHNe (see Ref. [14]) or from BH-SNe.

In addition, it exists the possibility of *gamma-ray flashes (GRFs)*. These are bursts with hybrid properties between short and long, they have $10^{51} \lesssim E_{\text{iso}} \lesssim 10^{52}$ erg. This sub-class of sources originates in NS-WD mergers.^[6]

Table 1 summarized some observational aspects of the GRB sub-classes including the occurrence rate calculated in Ref. [6].

Table 1. Some observational aspects of the GRB sub-classes. In the first three columns, we indicate the GRB sub-class and their corresponding *in-states* and the *out-states*. In column 4, we list the E_{iso} (rest-frame 1–10⁴ keV), columns 5–6 list, for each GRB sub-class, the maximum observed redshift and the local occurrence rate computed in Ref. [6].

GRB sub-class	In-state	Out-state	E_{iso} (erg)	z_{max}	ρ_{GRB} (Gpc ^{−3} yr ^{−1})
XRFs	CO _{core} -NS	ν NS-NS	$10^{48}–10^{52}$	1.096	100^{+45}_{-34}
BdHNe	CO _{core} -NS	ν NS-BH	$10^{52}–10^{54}$	9.3	$0.77^{+0.09}_{-0.08}$
BH-SN	CO _{core} -BH	ν NS-BH	$>10^{54}$	9.3	$\lesssim 0.77^{+0.09}_{-0.08}$
S-GRFs	NS-NS	MNS	$10^{49}–10^{52}$	2.609	$3.6^{+1.4}_{-1.0}$
S-GRBs	NS-NS	BH	$10^{52}–10^{53}$	5.52	$(1.9^{+1.8}_{-1.1}) \times 10^{-3}$
U-GRBs	ν NS-BH	BH	$>10^{52}$	—	$\gtrsim 0.77^{+0.09}_{-0.08}$
GRFs	NS-WD	MNS	$10^{51}–10^{52}$	2.31	$1.02^{+0.71}_{-0.46}$

We focus here on the physical properties of the above progenitors, as well as on the main properties of NSs that play a relevant role in the dynamics of these systems and that lead to the above different GRB sub-classes. We shall discuss as well recent estimates of the rates of occurrence on all the above subclasses based on X and gamma-ray observations, and also elaborate on the possibility of detecting the gravitational wave (GW) emission originated in these systems.

2. IGC, Hypercritical Accretion, and Long GRBs

We turn now to the details of the accretion process within the IGC scenario. Realistic simulations of the IGC process were performed in Ref. [12], including: (1) detailed SN explosions of the CO_{core}; (2) the hydrodynamic details of the hypercritical accretion process; (3) the evolution of the SN ejecta material entering the Bondi–Hoyle region all the way up to its incorporation into the NS. Here, the concept of hypercritical accretion refers to the fact the accretion rates are highly super-Eddington. The accretion process in the IGC scenario is allowed to exceed the Eddington limit mainly for two reasons: (i) the photons are trapped within the infalling material impeding them to transfer momentum; (ii) the accreting material creates a very hot NS atmosphere ($T \sim 10^{10}$ K) that triggers a very efficient neutrino emission which become the main energy sink of these systems unlike photons.

The hypercritical accretion process in the above simulations was computed within a spherically symmetric approximation. A further step was given in Ref. [13] by estimating the angular momentum that the SN ejecta carries and transfer to the NS via accretion, and how it affects the evolution and fate of the system. The calculations are as follows: first the accretion rate onto the NS is computed adopting an homologous expansion of the SN ejecta and introducing the pre-SN density profile of the CO_{core} envelope from numerical simulations. Then, it is estimated the angular momentum that the SN material might transfer to the NS: it comes out that the ejecta have enough angular momentum to circularize for a short time and form a disc around the NS. Finally, the evolution of the NS central density and rotation angular velocity (spin-up) is followed computing the equilibrium configurations from the numerical solution of the axisymmetric Einstein equations in full rotation, until the critical point of collapse of the NS to a BH taking into due account the equilibrium limits given by mass-shedding and the secular axisymmetric instability.

Now we enter into the details of each of the above steps. The accretion rate of the SN ejecta onto the NS can be estimated via the Bondi–Hoyle–Lyttleton accretion formula:

$$\dot{M}_B(t) = \pi \rho_{\text{ej}} R_{\text{cap}}^2 \sqrt{v_{\text{rel}}^2 + c_{\text{s, ej}}^2}, \quad R_{\text{cap}}(t) = \frac{2GM_{\text{NS}}(t)}{v_{\text{rel}}^2 + c_{\text{s, ej}}^2}, \quad (1)$$

where G is the gravitational constant, ρ_{ej} and $c_{\text{s, ej}}$ are the density and sound speed of the SN ejecta, R_{cap} is the NS gravitational capture radius (Bondi–Hoyle radius), M_{NS} , the NS mass, and v_{rel} the ejecta velocity relative to the NS: $\mathbf{v}_{\text{rel}} = \mathbf{v}_{\text{orb}} - \mathbf{v}_{\text{ej}}$,

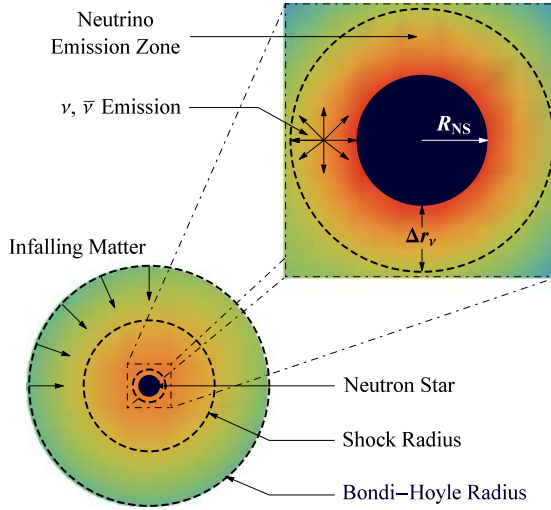


Fig. 1. Scheme of the IGC scenario: the CO_{core} undergoes SN explosion, the NS accretes part of the SN ejecta and then reaches the critical mass for gravitational collapse to a BH, with consequent emission of a GRB. The SN ejecta reach the NS Bondi-Hoyle radius and fall toward the NS surface. The material shocks and decelerates as it piles over the NS surface. At the neutrino emission zone, neutrinos take away most of the infalling matter gravitational energy gain. The neutrinos are emitted above the NS surface in a region of thickness Δr_ν about half the NS radius that allow the material to reduce its entropy to be finally incorporated to the NS. The image is not to scale. For further details and numerical simulations of the above process, see Refs. [12,15]

with $|\mathbf{v}_{\text{orb}}| = \sqrt{G(M_{\text{core}} + M_{\text{NS}})/a}$, the module of the NS orbital velocity around the CO_{core} , and \mathbf{v}_{ej} the velocity of the supernova ejecta (see Fig. 1).

Extrapolating the results for the accretion process from stellar wind accretion in binary systems, the angular momentum per unit time that crosses the NS capture region can be approximated by: $\dot{L}_{\text{cap}} = (\pi/2)(\epsilon_\rho/2 - 3\epsilon_\nu)\rho_{\text{ej}}(a, t)v_{\text{rel}}^2(a, t)R_{\text{cap}}^4(a, t)$, where ϵ_ρ and ϵ_ν are parameters measuring the inhomogeneity of the flow (see Ref. [13 for details).

In order to simulate the hypercritical accretion, it is adopted an homologous expansion of the SN ejecta, i.e. the ejecta velocity evolves as $v_{\text{ej}}(r, t) = nr/t$, where r is the position of every ejecta layer from the SN center and n is called expansion parameter. The ejecta density is given by $\rho_{\text{ej}}(r, t) = \rho_{\text{ej}}^0(r/R_{\text{star}}(t), t_0) \frac{M_{\text{env}}(t)}{M_{\text{env}}(0)} \left(\frac{R_{\text{star}}(0)}{R_{\text{star}}(t)}\right)^3$, where $M_{\text{env}}(t)$ the mass of the CO_{core} envelope, namely the mass of the ejected material in the SN explosion and available to be accreted by the NS, $R_{\text{star}}(t)$ is the position of the outermost layer of the ejected material, and ρ_{ej}^0 is the pre-SN density profile. The latter can be approximated with a power law: $\rho_{\text{ej}}(r, t_0) = \rho_{\text{core}}(R_{\text{core}}/r)^m$, where ρ_{core} , R_{core} and m are the profile parameters which are fixed by fitting the pre-SN profiles obtained from numerical simulations.

For the typical parameters of pre-SN CO_{core} and assuming a velocity of the outermost SN layer $v_{\text{sn}}(R_{\text{star}}, t_0) \sim 10^9 \text{ cm s}^{-1}$ and a free expansion $n = 1$ (for details

We consider the NS companion of the CO_{core} initially as nonrotating, thus at the beginning, the NS exterior spacetime is described by the Schwarzschild metric. The SN ejecta approach the NS with specific angular momentum, $l_{\text{acc}} = \dot{L}_{\text{cap}}/\dot{M}_B$ thus they will circularize at a radius r_{st} if they have enough angular momentum. What does the word “enough” means here? The last stable circular orbit (LSO) around a nonrotating NS is located at a distance $r_{\text{lso}} = 6GM_{\text{NS}}/c^2$ and has an angular momentum per unit mass $l_{\text{lso}} = 2\sqrt{3}GM_{\text{NS}}/c$. The radius r_{lso} is larger than the NS radius for masses larger than $1.67 M_{\odot}$, $1.71 M_{\odot}$, and $1.78 M_{\odot}$ for the GM1, TM1, and NL3 nuclear equation-of-state (EOS) [13]. If $l_{\text{acc}} \geq l_{\text{lso}}$, the material circularizes around the NS at locations $r_{\text{st}} \geq r_{\text{lso}}$. For the values of the IGC systems under discussion here, $r_{\text{st}}/r_{\text{lso}} \sim 10 - 10^3$, thus the SN ejecta have enough angular momentum to form a sort of disc around the NS. Even in this case, the viscous forces and other angular momentum losses that act on the disk will allow the matter in the disk to reach the inner boundary at $r_{\text{in}} \sim r_{\text{lso}}$, to then be accreted by the NS.

$$\dot{M}_{\text{NS}} = \left(\frac{\partial M_{\text{NS}}}{\partial M_b} \right)_{J_{\text{NS}}} \dot{M}_b + \left(\frac{\partial M_{\text{NS}}}{\partial J_{\text{NS}}} \right)_{M_b} \dot{J}_{\text{NS}}, \quad \dot{J}_{\text{NS}} = \xi l(r_{\text{in}}) \dot{M}_{\text{B}}, \quad (2)$$

In order to integrate Eqs. (1) and (2), we have to supply the two above partial derivatives which are obtained from the relation of the NS gravitational mass with M_b and J_{NS} , namely from the NS binding energy. The general relativistic calculations of rotating NSs in Ref. [21] show that, independent on the nuclear EOS, this relation is well approximated by the formula

where $j_{\text{NS}} \equiv cJ_{\text{NS}}/(GM_{\odot}^2)$. In addition, since the NS will spin up with accretion, we need information of the dependence of the specific angular momentum of the LSO as a function of both the NS mass and angular momentum. For corotating orbits, the following relation is valid for all the aforementioned EOS [\[13\]](#):

The NS accretes mass until it reaches a region of instability. There are two main instability limits for rotating NSs: mass-shedding or Keplerian limit and the secular

Table 2. Critical NS mass in the nonrotating case and constants k and p needed to compute the NS critical mass in the nonrotating case given by Eq. (5). The values are given for the NL3, GM1 and TM1 EOS.

EOS	$M_{\text{crit}}^{J=0} (M_{\odot})$	p	k
NL3	2.81	1.68	0.006
GM1	2.39	1.69	0.011
TM1	2.20	1.61	0.017

axisymmetric instability. The critical NS mass along the secular instability line is approximately given by [21](#):

$$M_{\text{NS}}^{\text{crit}} = M_{\text{NS}}^{J=0} (1 + k j_{\text{NS}}^p), \quad (5)$$

where the parameters k and p depends of the nuclear EOS (see Table 2). These formulas fit the numerical results with a maximum error of 0.45%.

Along the mass-shedding sequence, the NS has the maximum possible angular momentum [21](#): $J_{\text{NS,max}} \approx 0.7 GM_{\text{NS}}^2/c$. Figure 2 shows the evolution of the NS dimensionless angular momentum, $cJ_{\text{NS}}/(GM_{\text{NS}}^2)$, as a function of the NS mass for $\xi = 0.5$ and for selected values of the initial NS mass. The NS fate depends of the NS initial mass and the efficiency parameter ξ . The less massive initial configurations reach the mass-shedding limit with a maximum dimensionless angular momentum value while the initially more massive configurations reach the secular axisymmetric instability. It is interesting to note that the total angular momentum of the SN ejecta entering the Bondi–Hoyle region, L_{cap} , is much larger than the

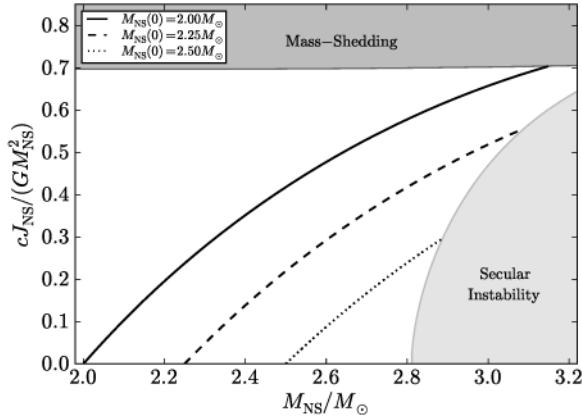


Fig. 2. Evolution of NSs of different initial masses $M_{\text{NS}} = 2.0, 2.25$ and $2.5 M_{\odot}$ during the hypercritical accretion in a BdHN. [13](#) It is shown the dimensionless angular momentum as a function of the NS mass. The binary parameters are: CO_{core} of a $M_{\text{ZAMS}} = 30 M_{\odot}$ progenitor star ($m = 2.801$, $M_{\text{env}} = 7.94 M_{\odot}$, $\rho_{\text{core}} = 3.08 \times 10^8 \text{ g cm}^{-3}$ and $R_{0\text{star}} = 7.65 \times 10^9 \text{ cm}$), a free expansion ($n = 1$) and a SN outermost ejecta velocity $v_{0\text{star}} = 2 \times 10^9 \text{ cm s}^{-1}$. The orbital period is of approximately 5 min.

maximum angular momentum that a uniformly rotating NS can support, $J_{\text{NS,max}}$. The numerical simulations in Ref. [13] indicate $L_{\text{cap}} \sim 10J_{\text{NS,max}}$. Thus, part of this angular momentum must be lost or redistributed before the material can reach the NS surface. This result leads to a clear prediction: the BHs produced through the IGC mechanism, namely those formed in BdHNe, have initial dimensionless spin ~ 0.7 and the excess of angular momentum could lead to a jetted emission with possible high-energy signatures and/or to the presence of a disk-like structure first around the NS as shown above and possibly also around the BH originated from the gravitational collapse of the NS.

2.1. Most recent simulations of the IGC process

Additional details and improvements of the hypercritical accretion process leading to XRFs and BdHNe have been recently presented in Ref. [15]. In particular:

- (1) It was there improved the accretion rate estimate including the density profile finite size/thickness and additional CO_{core} progenitors leading to different SN ejecta masses were also considered.
- (2) It was shown in Ref. [13], the existence of a maximum orbital period, P_{max} , over which the accretion onto NS companion is not high enough to bring it to the critical mass for gravitational collapse to a BH. Therefore, CO_{core} -NS binaries with $P > P_{\text{max}}$ lead to XRFs while the ones with $P \lesssim P_{\text{max}}$ lead to BdHNe. In Ref. [15] the determination of P_{max} was extended to all the possible initial values of the mass of the NS companion and the angular momentum transfer efficiency parameter was also allowed to vary.
- (3) It was computed the expected luminosity during the hypercritical accretion process for a wide range of binary periods covering XRFs and BdHNe.
- (4) It was there shown that the presence of the NS companion originates large asymmetries (see, e.g. simulation in Fig. 3) in the SN ejecta leading to observable signatures in the X-rays.

Figure 3 shows a simulation of an IGC process presented in Ref. [15]. We considered the effects of the gravitational field of the NS on the SN ejecta including the orbital motion as well as the changes in the NS gravitational mass owing to the accretion process via the Bondi formalism. The supernova matter was described as formed by point-like particles whose trajectory was computed by solving the Newtonian equation of motion. The initial conditions of the SN ejecta are computed assuming an homologous velocity distribution in free expansion. The initial power-law density profile of the CO envelope is simulated by populating the inner layers with more particles. For the $M_{\text{ZAMS}} = 30 M_{\odot}$ progenitor which gives a CO_{core} with envelope profile $\rho_{\text{ej}}^0 \approx 3.1 \times 10^8 (8.3 \times 10^7 / r)^{2.8} \text{ g cm}^{-3}$, we adopt for the simulation a total number of $N = 10^6$ particles. We assume that particles crossing the Bondi–Hoyle radius are captured and accreted by the NS so we removed them from the system as they reach that region. We removed these particles according to the

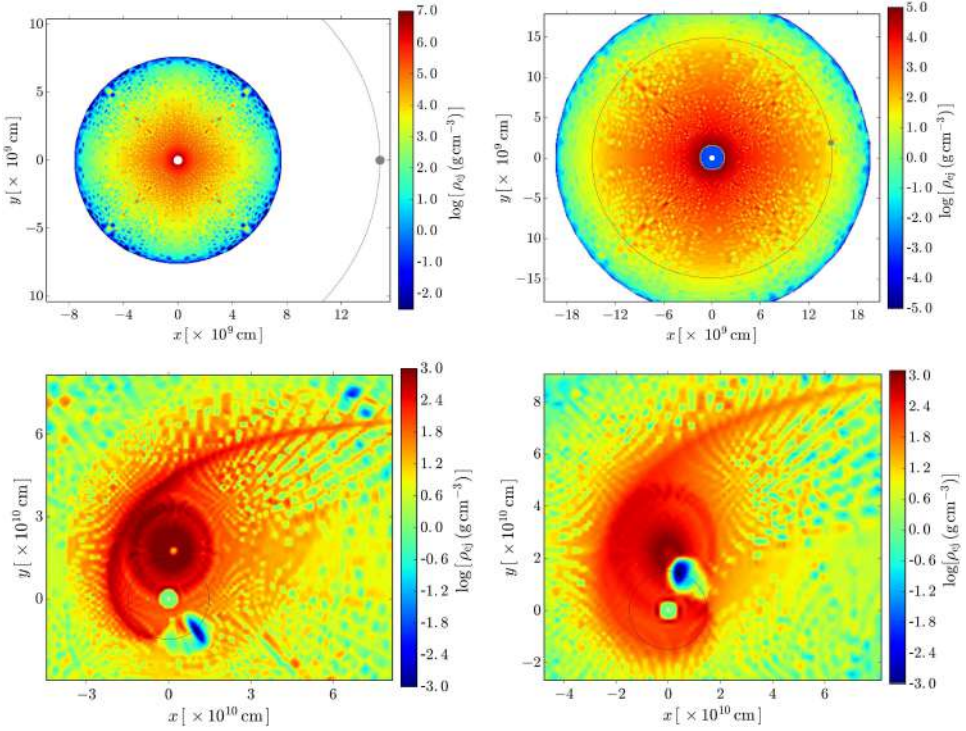


Fig. 3. Hypercritical accretion process in the IGC binary system at selected evolution times. In this example, the CO_{core} has a total mass of $9.44 M_{\odot}$ divided in an ejecta mass of $7.94 M_{\odot}$ and a νNS of $1.5 M_{\odot}$ formed by the collapsed high density core. The supernova ejecta evolve homologously with outermost layer velocity $v_{0,\text{star}} = 2 \times 10^9 \text{ cm s}^{-1}$. The NS binary companion has an initial mass of $2.0 M_{\odot}$. The binary period is $P \approx 5 \text{ min}$, which corresponds to a binary separation $a \approx 1.5 \times 10^{10} \text{ cm}$. The system of coordinates is centered on the νNS represented by the white-filled circle at $(0, 0)$. The NS binary companion, represented by the gray-filled circle, orbits counterclockwise following the thin-dashed circular trajectory. The colorbar indicates values of ejecta density in logarithmic scale. *Left upper panel*: initial time of the process. The supernova ejecta expand radially outward and the NS binary companion is at $(a, 0)$. *Right upper panel*: the accretion process starts when the first supernova layers reach the Bondi-Hoyle region. This happens at $t = t_{\text{acc},0} \approx a/v_{0,\text{star}} \approx 7.7 \text{ s}$. *Left lower panel*: the NS binary companion reaches the critical mass by accreting matter from the SN with consequent collapse to a BH. This happens at $t = t_{\text{coll}} \approx 254 \text{ s} \approx 0.85 P$. The newly-formed BH of mass $M_{\text{BH}} = M_{\text{crit}} \approx 3 M_{\odot}$ is represented by the black-filled circle. It is here evident the asymmetry of the supernova ejecta induced by the presence of the accreting NS companion at close distance. *Right lower panel*: $t = t_{\text{coll}} + 100 \text{ s} = 354 \text{ s} \approx 1.2 P$, namely 100 s after the BH formation. It appears here the new binary system composed of the νNS and the newly-formed BH.

results obtained from the numerical integration explained above. Figure 3 shows the orbital plane of an IGC binary at selected times of its evolution. The NS has an initial mass of $2.0 M_{\odot}$; the CO_{core} leads to a total ejecta mass $7.94 M_{\odot}$ and a νNS of $1.5 M_{\odot}$. The orbital period of the binary is $P \approx 5 \text{ min}$, i.e. a binary separation $a \approx 1.5 \times 10^{10} \text{ cm}$. For these parameters, the NS reaches the critical mass and collapses to form a BH.

2.2. Hydrodynamics and neutrino inside the accretion region

We turn now to give some details on the properties of the system inside the Bondi–Hoyle accretion region. We have seen that the accretion rate onto the NS can be as high as $\sim 10^{-2} - 10^{-1} M_{\odot} \text{ s}^{-1}$. For these accretion rates:

- (1) We can neglect the effect of the NS magnetic field since the magnetic pressure remains much smaller than the random pressure of the infalling material. [\[11, 22\]](#)
- (2) The photons are trapped in the accretion flow. The trapping radius, defined at which the photons emitted diffuse outward at a slower velocity than the one of the infalling material, is [\[23\]](#): $r_{\text{trapping}} = \min\{\dot{M}_B \kappa / (4\pi c), R_{\text{cap}}\}$, where κ is the opacity. For the CO_{core} , in Ref. [\[12\]](#) a Rosseland mean opacity roughly $5 \times 10^3 \text{ cm}^2 \text{ g}^{-1}$ was estimated. For the range of accretion rates, we obtain that $\dot{M}_B \kappa / (4\pi c) \sim 10^{13} - 10^{19} \text{ cm}$, a radius much bigger than the NS capture radius which is in our simulations at most 1/3 of the binary separation. Thus, in our systems, the trapping radius extends all the way to the Bondi–Hoyle region, hence the Eddington limit does not apply and hypercritical accretion onto the NS occurs.
- (3) Under these conditions, the gain of gravitational energy of the accreted material is mainly radiated via neutrino emission (see below). [\[11, 12, 22, 24, 25\]](#)

2.2.1. Convective instabilities

As the material piles onto the NS and the atmosphere radius, the accretion shock moves outward. The post-shock entropy is a decreasing function of the shock radius position which creates an atmosphere unstable to Rayleigh–Taylor convection during the initial phase of the accretion process. These instabilities can accelerate above the escape velocity driving outflows from the accreting NS with final velocities approaching the speed of light. [\[26, 27\]](#) Assuming that radiation dominates, the entropy of the material at the base of the atmosphere is [\[22\]](#): $S_{\text{bubble}} \approx 16(1.4 M_{\odot} / M_{\text{NS}})^{-7/8} (M_{\odot} \text{ s}^{-1} / \dot{M}_B)^{1/4} (10^6 \text{ cm} / r)^{3/8}$, in units of k_B per nucleon. This material will rise and expand, cooling adiabatically, i.e. $T^3 / \rho = \text{constant}$, for radiation dominated gas. If we assume a spherically symmetric expansion, then $\rho \propto 1/r^3$ and we obtain $k_B T_{\text{bubble}} = 195 S_{\text{bubble}}^{-1} (10^6 \text{ cm} / r) \text{ MeV}$. However, it is more likely that the bubbles expand in the lateral but not in the radial direction, [\[27\]](#) thus we have $\rho \propto 1/r^2$, i.e. $T_{\text{bubble}} = T_0(S_{\text{bubble}})(r_0/r)^{2/3}$, where $T_0(S_{\text{bubble}})$ is given by the above equation evaluated at $r = r_0 \approx R_{\text{NS}}$. This temperature implies a bolometric blackbody flux at the source from the bubbles

$$F_{\text{bubble}} \approx 2 \times 10^{40} \left(\frac{M_{\text{NS}}}{1.4 M_{\odot}} \right)^{-7/2} \left(\frac{\dot{M}_B}{M_{\odot} \text{ s}^{-1}} \right) \left(\frac{R_{\text{NS}}}{10^6 \text{ cm}} \right)^{3/2} \times \left(\frac{r_0}{r} \right)^{8/3} \text{ erg s}^{-1} \text{ cm}^{-2}, \quad (6)$$

where σ is the Stefan–Boltzmann constant.

In Ref. [12] it was shown that the above thermal emission from the rising bubbles produced during the hypercritical accretion process can explain the early ($t \lesssim 50$ s) thermal X-ray emission observed in GRB 090618. [10, 28] In that case, T_{bubble} drops from 50 keV to 15 keV expanding from $r \approx 10^9$ cm to 6×10^9 cm, for an accretion rate $10^{-2} M_{\odot} \text{ s}^{-1}$.

It is interesting that also r-process nucleosynthesis can occur in these outflows. [26] This implies that long GRBs can be also r-process sites with specific signatures from the decay of the produced heavy elements, possibly similar as in the case of the *kilonova* emission in short GRBs. [29] The signatures of this phenomenon in XRFs and BdHNe, and its comparison with kilonovae, deserves to be explored.

2.2.2. Neutrino emission

Most of the energy from the accretion is lost through neutrino emission. For the accretion rate conditions characteristic of our models $\sim 10^{-4} - 10^{-2} M_{\odot} \text{ s}^{-1}$, e^+e^- pair annihilation dominates the neutrino emission and electron neutrinos remove the bulk of the energy. The temperature of these neutrinos can be roughly approximated by assuming that the inflowing material generally flows near to the NS surface before shocking and emitting neutrinos. For accretion rates $\sim 10^{-4} - 10^{-2} M_{\odot} \text{ s}^{-1}$, neutrino energies $\sim 5 - 20$ MeV are obtained. [15] A detailed study of the neutrino emission will be presented elsewhere.

For the developed temperatures (say $k_B T \sim 1 - 10$ MeV) near the NS surface, the dominant neutrino emission process is the e^+e^- annihilation leading to $\nu\bar{\nu}$. This process produces a neutrino emissivity proportional to the ninth power of the temperature. The accretion atmosphere near the NS surface is characterized by a temperature gradient with a typical scale height $\Delta r_{\nu} \approx 0.7 R_{\text{NS}}$. [15] Owing to the aforementioned strong dependence of the neutrino emission on temperature, most of the neutrino emission occurs in the region Δr_{ν} above the NS surface.

These conditions lead to the neutrinos to be efficient in balancing the gravitational potential energy gain allowing the hypercritical accretion rates. The effective accretion onto the NS can be estimated as [22]: $\dot{M}_{\text{eff}} \approx \Delta M_{\nu} (L_{\nu} / E_{\nu})$, where ΔM_{ν} and L_{ν} are the mass and neutrino luminosity in the emission region (i.e. Δr_{ν}). E_{ν} is half the gravitational potential energy gained by the material falling from infinity to the $R_{\text{NS}} + \Delta r_{\nu}$. Since $L_{\nu} \approx 2\pi R_{\text{NS}}^2 \Delta r_{\nu} \epsilon_{e^-e^+}$ with $\epsilon_{e^-e^+}$ the e^+e^- pair annihilation process emissivity, and $E_{\nu} = (1/2)GM_{\text{NS}}\Delta M_{\nu}/(R_{\text{NS}} + \Delta r_{\nu})$, it can be checked that for $M_{\text{NS}} = 1.4 M_{\odot}$ this accretion rate leads to values $\dot{M}_{\text{eff}} \approx 10^{-9} - 10^{-1} M_{\odot} \text{ s}^{-1}$ for temperatures $k_B T = 1 - 10$ MeV.

2.3. Accretion luminosity

The gain of gravitational potential energy in the accretion process is the total one available to be released, e.g. by neutrinos and photons. The total energy released in the star in a time-interval dt during the accretion of an amount of mass dM_b with

angular momentum $l\dot{M}_b$, is given by [13–30](#)

$$L_{\text{acc}} = (\dot{M}_b - \dot{M}_{\text{NS}})c^2 = \dot{M}_b c^2 \left[1 - \left(\frac{\partial M_{\text{NS}}}{\partial J_{\text{NS}}} \right)_{M_b} l - \left(\frac{\partial M_{\text{NS}}}{\partial M_b} \right)_{J_{\text{NS}}} \right]. \quad (7)$$

This upper limit to the energy released is just the amount of gravitational energy gained by the accreted matter by falling to the NS surface and which is not spent in changing the gravitational binding energy of the NS. The total energy releasable during the accretion process, say $\Delta E_{\text{acc}} \equiv \int L_{\text{acc}} dt$, is given by the difference in binding energies of the initial and final NS configurations. The typical luminosity will be $L_{\text{acc}} \approx \Delta E_{\text{acc}} / \Delta t_{\text{acc}}$ where Δt_{acc} is the duration of the accretion process.

The duration of the accretion process is given approximately by the flow time of the slowest layers of the supernova ejecta to the NS. If the velocity of these layers is v_{inner} , then $\Delta t_{\text{acc}} \sim a/v_{\text{inner}}$, where a is the binary separation. For $a \sim 10^{11}$ cm and $v_{\text{inner}} \sim 10^8$ cm s $^{-1}$, we obtain $\Delta t_{\text{acc}} \sim 10^3$ s, while for shorter binary separation, e.g. $a \sim 10^{10}$ cm ($P \sim 5$ min), $\Delta t_{\text{acc}} \sim 10^2$ s, as validated by the results of our numerical integrations.

For instance, the NS in the system with $P = 5$ min accretes $\approx 1 M_{\odot}$ in $\Delta t_{\text{acc}} \approx 100$ s. With the aid of Eq. [\(3\)](#), we estimate a difference in binding energies between a $2 M_{\odot}$ and a $3 M_{\odot}$ NS, i.e. $\Delta E_{\text{acc}} \approx 13/200(3^2 - 2^2) M_{\odot} c^2 \approx 0.32 M_{\odot} c^2$ leading to a maximum luminosity $L_{\text{acc}} \approx 3 \times 10^{-3} M_{\odot} c^2 \approx 0.1 \dot{M}_b c^2$. This accretion power, which could be as high as $L_{\text{acc}} \sim 0.1 \dot{M}_b c^2 \sim 10^{47} - 10^{51}$ erg s $^{-1}$ for accretion rates in the range $\dot{M}_b \sim 10^{-6} - 10^{-2} M_{\odot} \text{ s}^{-1}$, necessarily leads to signatures observable in long GRBs (see, e.g. Refs. [110](#) and [112](#)).

2.4. Post-explosion orbits and formation of NS-BH binaries

We turn now to discuss the out-states of the IGC process. The SN explosion of the CO $_{\text{core}}$ leaves as a central remnant, the ν NS, while the IGC process triggered by the hypercritical accretion of the SN ejecta onto the NS companion leads to the formation of a BH. Thus, the question arises if BdHNe are natural sites for the formation of NS-BH binaries or if these binaries become disrupted during the SN explosion and the consequent IGC process. The answer to this question was recently given in Ref. [114](#), where it was shown that indeed most of BdHN form NS-BH binaries since the high compactness of the orbit avoids the unbinding of the orbit.

In typical systems, most of the binaries become unbound during the SN explosion because of the ejected mass and momentum imparted (kick) on the newly formed compact object in the explosion of the massive star. Under the instantaneous explosion assumption, if half of the binary system's mass is lost in the SN explosion, the system is disrupted. In general, the fraction of massive binaries that can produce double compact object binaries is thought to be low: $\sim 0.001 - 1\%$ [31–33](#)

The mass ejected during the SN alters the binary orbit, causing it to become wider and more eccentric. Assuming that the mass is ejected instantaneously, the

post-explosion semi-major axis is $a/a_0 = (M_0 - \Delta M)/(M_0 - 2a_0\Delta M/r)$, where a_0 and a are the initial and final semi-major axes respectively, M_0 is the total initial mass of the binary system, ΔM is the change of mass (equal to the amount of mass ejected in the SN), and r is the orbital separation at the time of explosion.^[32] For circular orbits, the system is unbound if it loses half of its mass. However, for very tight binaries as the one proposed in the IGC scenario, a number of additional effects can alter the fate of the binary.

The time it takes for the ejecta to flow past a companion in a SN is roughly 10–1000 s. Although the shock front is moving above 10^4 km s^{-1} , the denser, lower-velocity ejecta can be moving at 10^3 km s^{-1} .^[12] The broad range of times arises because the SN ejecta velocities varies from 10^2 – 10^4 km s^{-1} . The accretion peaks as the slow-moving (inner) ejecta flows past the NS companion. For normal (wide) binaries, this time is a small fraction of the orbital period and the “instantaneous” mass-loss assumption is perfectly valid. However, in the compact binary systems considered in the IGC scenario, the orbital period ranges from only 100–1000 s, and the mass loss from the SN explosion can no longer be assumed to be instantaneous.

We have seen how in BdHNe, the accretion process can lead to BH formation in a time-interval as short as the orbital period. We here deepen this analysis to study the effect of the SN explosion in such a scenario with a specific example of Ref. [14]. Figure 4 shows as the ejecta timescale becomes just a fraction of the orbital timescale, the fate of the post-explosion binary is altered. For these models, we assumed very close binaries with an initial orbital separation of $7 \times 10^9 \text{ cm}$ in circular orbits. With CO_{core} radii of 1 – $4 \times 10^9 \text{ cm}$, such a separation is small, but achievable. We assume the binary consists of a CO_{core} and a $2.0 M_{\odot}$ NS companion. When the CO_{core} collapses, it forms a $1.5 M_{\odot}$ NS, ejecting the rest of the core. We then vary the ejecta mass and time required for most of the ejected matter to move out of the binary. Note that even if 70% of the mass is lost from the system (the $8 M_{\odot}$ ejecta case), the system remains bound as long as the explosion time is just above the orbital time ($T_{\text{orbit}} = 180 \text{ s}$) with semi-major axes of less than 10^{11} cm .

The short orbits (on ejecta timescales) are not the only feature of these binaries that alters the post-explosion orbit. The NS companion accretes both matter and momentum from the SN ejecta, reducing the mass lost from the system with respect to typical binaries with larger orbital separations and much less accretion. In addition, as with common envelope scenarios, the bow shock produced by the accreting NS transfers orbital energy into the SN ejecta. Figure 4 shows the final orbital separation of our same three binaries, including the effects of mass accretion (we assume $0.5 M_{\odot}$ is accreted with the momentum of the SN material) and orbit coupling (30% of the orbital velocity is lost per orbit). With these effects, not only do the systems remain bound even for explosion times greater than 1/2 the orbital period but, if the explosion time is long, the final semi-major axis can be on par with the initial orbital separation.

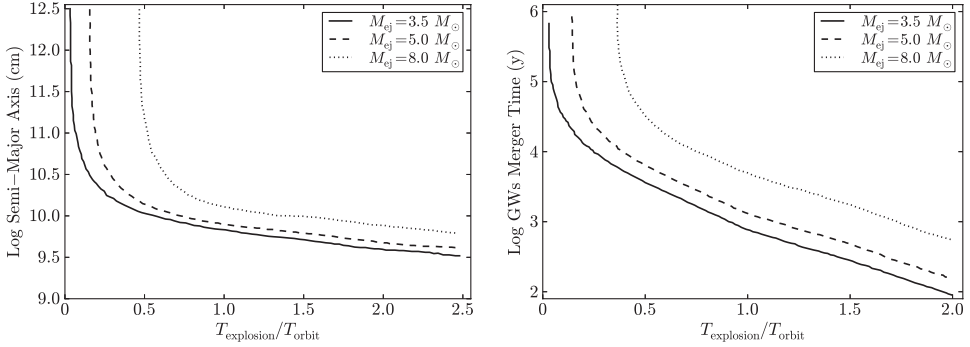


Fig. 4. Left panel: semi-major axis versus explosion time for three binary systems including mass accretion and momentum effects. Including these effects, all systems with explosion times above 0.7 times the orbital time are bound and the final separations are on par with the initial separations. Right panel: merger time due to GW emission as a function of explosion time. Beyond a critical explosion time (0.1–0.6 T_{orbit} depending on the system), the merger time is less than roughly 10,000 yr. For most of our systems, the explosion time is above this limit and we expect most of these systems to merge quickly.

The tight compact binaries produced in these explosions will emit GW emission, ultimately causing the system to merge. For typical massive star binaries, the merger time is many Myr. For BdHNe, the merger time is typically 10,000 yr, or less, as shown in the right panel of Fig. 4. Since the merger should occur within the radius swept clean by the BdHN, we expect a small baryonic contamination around the merger site which might lead to a new family of events which we term ultrashort GRBs, U-GRBs, to this new family of events.

3. NS–NS/NS–BH Mergers and Short GRBs

Let us turn to short GRBs. We have mentioned that the most viable progenitors of short GRBs appear to be mergers of NS–NS and/or NS–BH binaries. Specifically, in the case of NS–NS mergers, the value of the critical mass of the NS, which crucially depends on the nuclear EOS, has been also found to be a most relevant parameter since it defines the fate of the post-merger object.^[8] In this section, we discuss the conditions that determine the fate of the NS–NS binary merger by estimating the mass and angular momentum of the post-merger object. Once we know these values, we can compare the mass of the merged core with the value of the NS critical mass obtained for uniformly rotating NSs. Based on this, we can assess whether a massive NS or a BH is formed from the merger.

We proceed to estimate the mass and the angular momentum of the post-merger core via baryonic mass and angular momentum conservation of the system. We adopt for simplicity that nonrotating binary components. We first compute the total baryonic mass of the NS–NS binary $M_b = M_{b1} + M_{b2}$ using the relation between the gravitational mass M_i and the baryonic mass M_{b_i} ($i = 1, 2$) recently obtained in Ref. [21] and given in Eq. (3) assuming $j_{\text{NS}} = cJ_{\text{NS}}/(GM_{\odot}^2) = 0$. The

post-merger core will have approximately the entire baryonic mass of the initial binary, i.e. $M_{b,\text{core}} \approx M_b$, since little mass is expected to be ejected during the coalescence process. However, the gravitational mass of the post-merger core cannot be estimated using again the above formula since, even assuming nonrotating binary components, the post-merger core will necessarily acquire a fraction $\eta \leq 1$ of the binary angular momentum at the merger point. One expects a value of η smaller than unity since, during the coalesce, angular momentum is lost, e.g. by gravitational wave emission and it can be also redistributed, e.g. into a surrounding disk.

To obtain the gravitational mass of the post-merger core, we can use again Eq. (3) relating the baryonic mass $M_{b,\text{NS}}$ and the gravitational mass M_{NS} in this case with $j_{\text{NS}} \neq 0$. The mass and angular momentum of the post-merger core, respectively M_{core} and J_{core} , are therefore obtained from baryon mass and angular momentum conservation, i.e.

$$M_{\text{core}} = M_{\text{NS}}, \quad M_{b,\text{core}} = M_{b,\text{NS}} = M_{b_1} + M_{b_2}, \quad J_{\text{core}} = J_{\text{NS}} = \eta J_{\text{merger}}, \quad (8)$$

where J_{merger} is the system angular momentum at the merger point. The value of J_{merger} is approximately given by $J_{\text{merger}} = \mu r_{\text{merger}}^2 \Omega_{\text{merger}}$, where $\mu = M_1 M_2 / M$ is the binary reduced mass, $M = M_1 + M_2$ is the total binary mass, and r_{merger} and Ω_{merger} are the binary separation and angular velocity at the merger point. If we adopt the merger point where the two stars enter into contact we have $r_{\text{merger}} = R_1 + R_2$, where R_i is the radius (which depend on the EOS) of the i -component of the binary.

Given the parameters of the merging binary, the above equations lead to the merged core properties M_{core} and J_{core} (or j_{core}). These values can be therefore confronted with the values of uniformly rotating, stable NSs to check if such a merger will lead either to a new massive NS or to an unstable merged core collapsing to a BH.

For the sake of exemplifying, let us assume a mass-symmetric binary, $M_1 = M_2 = M/2$. In this case, Eq. (8) together with the above estimate of J_{merger} lead to the angular momentum of the merged core $J_{\text{core}} = (\eta/4)(GM^2/c)\mathcal{C}^{-1/2}$, where $\mathcal{C} \equiv GM_1/(c^2 R_1) = GM_2/(c^2 R_2)$ is the compactness of the merging binary components. Therefore, if we adopt $M_1 = 1.4 M_{\odot}$ and $\mathcal{C} = 0.15$ the above equations imply a merged core mass $M_{\text{core}} = (2.61, 2.65) M_{\odot}$ for $\eta = (0, 1)$, i.e. for a dimensionless angular momentum of the merged core $j_{\text{core}} = (0, 5.06)$. Whether or not these pairs $(M_{\text{core}}, j_{\text{core}})$ correspond to stable NSs depend on the nuclear EOS. A similar analysis can be done for any other pair of binary masses.

4. Detectability of GWs Produced by the GRB Progenitors

Having established the nature of the progenitors of each GRB sub-class, we turn now to briefly discuss the detectability of their associated GW emission. The minimum GW frequency detectable by the broadband aLIGO interferometer is

$f_{\min}^{\text{aLIGO}} \approx 10 \text{ Hz}$.^[35] Since during the binary inspiral, the GW frequency is twice the orbital one, this implies that a binary enters the aLIGO band for orbital periods $P_{\text{orb}} \lesssim 0.2 \text{ s}$. Thus, $\text{CO}_{\text{core}}\text{-NS}$ binaries, *in-states* of XRFs and BdHNe, and $\text{CO}_{\text{core}}\text{-BH}$ binaries, *in-states* of BH-SN, are not detectable by aLIGO since they have orbital periods $P_{\text{orb}} \gtrsim 5 \text{ min} \gg 0.2 \text{ s}$. Concerning their *out-states* after the corresponding hypercritical accretion processes, namely $\nu\text{NS-NS}$, *out-states* of XRFs, and $\nu\text{NS-BH}$, *out-states* of BdHNe and BH-SNe, they are not detectable by aLIGO at their birth but only when approaching the merger. Clearly, the analysis of the $\nu\text{NS-NS}$ mergers is included in the analysis of the S-GRFs and S-GRBs and, likewise, the merger of $\nu\text{NS-BH}$ binaries is included in the analysis of U-GRBs. In the case of NS-WD binaries, the WD is tidally disrupted by the NS making their GW emission hard to be detected (see, e.g. Ref. [36]).

A coalescing binary evolves first through the *inspiral regime* to then pass over a *merger regime*, the latter composed by the plunge leading to the merger itself and by the ringdown (oscillations) of the newly formed object. During the inspiral regime, the system evolves through quasi-circular orbits and is well described by the traditional point-like quadrupole approximation.^[37-39] The GW frequency is twice the orbital frequency ($f_s = 2f_{\text{orb}}$) and grows monotonically. The energy spectrum during the inspiral regime is: $dE/df_s = (1/3)(\pi G)^{2/3} M_c^{5/3} f_s^{-1/3}$, where $M_c = \mu^{3/5} M^{2/5} = \nu^{3/5} M$ is the so-called *chirp mass* and $\nu \equiv \mu/M$ is the symmetric mass-ratio parameter. A symmetric binary ($m_1 = m_2$) corresponds to $\nu = 1/4$ and the test-particle limit is $\nu \rightarrow 0$. The GW spectrum of the merger regime is characterized by a GW burst.^[40] Thus, one can estimate the contribution of this regime to the signal-to-noise ratio with the knowledge of the location of the GW burst in the frequency domain and of the energy content. The frequency range spanned by the GW burst is $\Delta f = f_{\text{qnm}} - f_{\text{merger}}$, where f_{merger} is the frequency at which the merger starts and f_{qnm} is the frequency of the ringing modes of the newly formed object after the merger, and the energy emitted is ΔE_{merger} . With these quantities defined, one can estimate the typical value of the merger regime spectrum as: $dE/df_s \approx \Delta E_{\text{merger}}/\Delta f$. Unfortunately, the frequencies and energy content of the merger regime of the above merging binaries are such that it is undetectable by LIGO.^[41]

Since the GW signal is deep inside the detector noise, the signal-to-noise ratio (ρ) is usually estimated using the matched filter technique.^[42] The exact position of the binary relative to the detector and the orientation of the binary rotation plane are usually unknown, thus it is a common practice to average over all the possible locations and orientations, i.e.^[42] $\langle \rho^2 \rangle = 4 \int_0^\infty \langle |\tilde{h}(f)|^2 \rangle / S_n(f) df = 4 \int_0^\infty h_c^2(f) / [f^2 S_n(f)] df$, where f is the GW frequency in the detector frame, $\tilde{h}(f)$ is the Fourier transform of $h(t)$, and $\sqrt{S_n(f)}$ is the one-sided amplitude spectral density of the detector noise, and $h_c(f)$ is the characteristic strain, $h_c = (1+z)/(\pi d_l) \sqrt{(1/10)(G/c^3)(dE/df_s)}$. We recall that in the detector frame, the GW frequency is redshifted by a factor $1+z$ with respect to the one in the source frame,

f_s , i.e. $f = f_s/(1+z)$ and d_l is the luminosity distance to the source. We adopt a Λ CDM cosmology with $H_0 = 71 \text{ km s}^{-1} \text{ Mpc}^{-1}$, $\Omega_M = 0.27$ and $\Omega_\Lambda = 0.73$.^[43]

A threshold $\rho_0 = 8$ in a single detector is adopted by LIGO.^[44] This minimum ρ_0 defines a maximum detection distance or GW horizon distance, say d_{GW} , that corresponds to the most optimistic case when the binary is just above the detector and the binary plane is parallel to the detector plane. In order to give an estimate, the annual number of merging binaries associated with the above GRB sub-classes detectable by aLIGO, we can use the lower and upper values of the aLIGO *search volume* defined by $\mathcal{V}_s = V_{\text{max}}^{\text{GW}} \mathcal{T}$, where $V_{\text{max}}^{\text{GW}} = (4\pi/3)\mathcal{R}^3$, where \mathcal{T} is the observing time and \mathcal{R} is the so-called *detector range* defined by $\mathcal{R} = \mathcal{F}d_{\text{GW}}$, with $\mathcal{F}^{-1} = 2.2627$ (see, Refs. [44] and [45] for details). For a $(1.4 + 1.4) M_\odot$ NS binary and the three following different observational campaigns we have^[44]: 2015/2016 (O1; $\mathcal{T} = 3$ months) $\mathcal{V}_S = (0.5-4) \times 10^5 \text{ Mpc}^3 \text{ yr}$, 2017/2018 (O3; $\mathcal{T} = 9$ months) $\mathcal{V}_S = (3-10) \times 10^6 \text{ Mpc}^3 \text{ yr}$, and the entire network including LIGO-India at design sensitivity (2022+; $\mathcal{T} = 1$ yr) $\mathcal{V}_S = 2 \times 10^7 \text{ Mpc}^3 \text{ yr}$. The maximum possible sensitivity reachable in 2022+ leads to $d_{\text{GW}} \approx 0.2 \text{ Gpc}$, hence $V_{\text{max}}^{\text{GW}} \approx 0.033 \text{ Gpc}^3$, for such a binary. One can use this information for other binaries with different masses taking advantage of the fact that d_{GW} scales with the binary chirp mass as $M_c^{5/6}$. The expected GW detection rate by aLIGO can be thus estimated as: $\dot{N}_{\text{GW}} \equiv \rho_{\text{GRB}} V_{\text{max}}^{\text{GRB}}$, where ρ_{GRB} is the inferred occurrence rate of GRBs shown in Table 1 computed in Ref. [6]. Bearing the above in mind, it is easy to check that there is a low probability for aLIGO to detect the GW signals associated with the GRB binary progenitors: indeed in the best case of the 2022+ observing rung one obtains, respectively, ~ 1 detection every 3 and 5 yr for U-GRBs and S-GRFs.

5. Conclusions

There is accumulated evidence on the binary nature of long and short GRBs. Such binaries are composed of CO_{cores}, NSs, BHs and WDs in different combinations. We have here focused on the salient aspects of the NS physics relevant for the understanding of these binaries and their implications in GRB astrophysics, including their associated GW emission. We have discussed the crucial role of the NS critical mass in discriminating the GRB sub-classes. Therefore, we expect that the increasing amount of GRB high-quality data will help in constraining the NS critical mass with high accuracy with the most welcome result of constraining the NS matter content and the corresponding nuclear EOS.

Acknowledgments

M. Karlica, M. Kovacevic and Y. A. are supported by the Erasmus Mundus Joint Doctorate Program Grant Nos. 2013–1471, 2013–1471 and 2014–0707, respectively, from EACEA of the European Commission. M. M. and J. A. R. acknowledge the partial support of the Project No. 3101/GF4 IPC-11, and the target program F.0679

of the Ministry of Education and Science of the Republic of Kazakhstan. C. C. and S. F. acknowledge INdAM-GNFM for support.

References

1. E. P. Mazets, S. V. Golenetskii, V. N. Ilinskii, V. N. Panov, R. L. Aptekar, I. A. Gurian, M. P. Proskura, I. A. Sokolov, Z. I. Sokolova and T. V. Kharitonova, *Astrophys. Space Sci.* **80** (1981) 3.
2. R. W. Klebesadel, The durations of gamma-ray bursts, in *Gamma-Ray Bursts — Observations, Analyses and Theories*, eds. C. Ho, R. I. Epstein and E. E. Fenimore (Cambridge University Press, 1992).
3. J.-P. Dezalay, C. Barat, R. Talon, R. Syunyaev, O. Terekhov and A. Kuznetsov, *AIP Conference Proceedings* **265** (1991) 304–309.
4. C. Kouveliotou, C. A. Meegan, G. J. Fishman, N. P. Bhat, M. S. Briggs, T. M. Koshut, W. S. Paciesas and G. N. Pendleton, *Astrophys. J.* **413** (1993) L101.
5. M. Tavani, *Astrophys. J.* **497** (1998) L21.
6. R. Ruffini, J. A. Rueda, M. Muccino, Y. Aimuratov, L. M. Becerra, C. L. Bianco, M. Kovacevic, R. Moradi, F. G. Oliveira, G. B. Pisani and Y. Wang, *Astrophys. J.* **832** (2016) 136.
7. R. Ruffini, Y. Wang, M. Enderli, M. Muccino, M. Kovacevic, C. L. Bianco, A. V. Penacchioni, G. B. Pisani and J. A. Rueda, *Astrophys. J.* **798** (2015) 10.
8. R. Ruffini, M. Muccino, M. Kovacevic, F. G. Oliveira, J. A. Rueda, C. L. Bianco, M. Enderli, A. V. Penacchioni, G. B. Pisani, Y. Wang and E. Zaninoni, *Astrophys. J.* **808** (2015) 190.
9. R. Ruffini, M. G. Bernardini, C. L. Bianco, L. Vitagliano, S.-S. Xue, P. Chardonnet, F. Fraschetti and V. Gurzadyan, Black hole physics and astrophysics: The GRB-Supernova connection and URCA-1–URCA-2, in *The Tenth Marcel Grossmann Meeting*, eds. M. Novello, S. Perez Bergliaffa and R. Ruffini (World Scientific, Singapore, 2006).
10. L. Izzo, J. A. Rueda and R. Ruffini, *Astron. Astrophys.* **548** (2012) L5.
11. J. A. Rueda and R. Ruffini, *Astrophys. J.* **758** (2012) L7.
12. C. L. Fryer, J. A. Rueda and R. Ruffini, *Astrophys. J.* **793** (2014) L36.
13. L. Becerra, F. Cipolletta, C. L. Fryer, J. A. Rueda and R. Ruffini, *Astrophys. J.* **812** (2015) 100.
14. C. L. Fryer, F. G. Oliveira, J. A. Rueda and R. Ruffini, *Phys. Rev. Lett.* **115** (2015) 231102.
15. L. Becerra, C. L. Bianco, C. L. Fryer, J. A. Rueda and R. Ruffini, *Astrophys. J.* **833** (2016) 107.
16. J. Goodman, *Astrophys. J.* **308** (1986) L47.
17. B. Paczynski, *Astrophys. J.* **308** (1986) L43.
18. D. Eichler, M. Livio, T. Piran and D. N. Schramm, *Nature* **340** (1989) 126.
19. R. Narayan, T. Piran and A. Shemi, *Astrophys. J.* **379** (1991) L17.
20. E. Berger, *Annu. Rev. Astron. Astrophys.* **52** (2014) 43.
21. F. Cipolletta, C. Cherubini, S. Filippi, J. A. Rueda and R. Ruffini, *Phys. Rev. D* **92** (2015) 023007.
22. C. L. Fryer, W. Benz and M. Herant, *Astrophys. J.* **460** (1996) 801.
23. R. A. Chevalier, *Astrophys. J.* **346** (1989) 847.
24. Y. B. Zel'dovich, L. N. Ivanova and D. K. Nadezhin, *Sov. Astron.* **16** (1972) 209.
25. R. Ruffini and J. Wilson, *Phys. Rev. Lett.* **31** (1973) 1362.

26. C. L. Fryer, F. Herwig, A. Hungerford and F. X. Timmes, *Astrophys. J.* **646** (2006) L131.
27. C. L. Fryer, *Astrophys. J.* **699** (2009) 409.
28. L. Izzo, R. Ruffini, A. V. Penacchioni, C. L. Bianco, L. Caito, S. K. Chakrabarti, J. A. Rueda, A. Nandi and B. Patricelli, *Astron. Astrophys.* **543** (2012) A10.
29. N. R. Tanvir, A. J. Levan, A. S. Fruchter, J. Hjorth, R. A. Hounsell, K. Wiersema and R. L. Tunnicliffe, *Nature* **500** (2013) 547.
30. N. R. Sibgatullin and R. A. Sunyaev, *Astron. Lett.* **26** (2000) 772.
31. C. L. Fryer, S. E. Woosley and D. H. Hartmann, *Astrophys. J.* **526** (1999) 152.
32. M. Dominik, K. Belczynski, C. Fryer, D. E. Holz, E. Berti, T. Bulik, I. Mandel and R. O'Shaughnessy, *Astrophys. J.* **759** (2012) 52.
33. K. A. Postnov and L. R. Yungelson, *Living Rev. Rel.* **17** (2014) 3.
34. J. G. Hills, *Astrophys. J.* **267** (1983) 322.
35. LIGO Scientific Collab. (J. Aasi *et al.*), *Class. Quantum Grav.* **32** (2015) 074001.
36. V. Paschalidis, M. MacLeod, T. W. Baumgarte and S. L. Shapiro, *Phys. Rev. D* **80** (2009) 024006.
37. P. C. Peters and J. Mathews, *Phys. Rev.* **131** (1963) 435.
38. P. C. Peters, *Phys. Rev.* **136** (1964) 1224.
39. M. Rees, R. Ruffini and J. A. Wheeler, *Black Holes, Gravitational Waves and Cosmology* (Gordon and Breach Science Publishers, New York, 1974).
40. M. Davis, R. Ruffini, W. H. Press and R. H. Price, *Phys. Rev. Lett.* **27** (1971) 1466.
41. R. Ruffini, J. Rodriguez, M. Muccino, J. A. Rueda, Y. Aimuratov, U. Barres de Almeida, L. Becerra, C. L. Bianco, C. Cherubini, S. Filippi, D. Gizzi, M. Kovacevic, R. Moradi, F. G. Oliveira, G. B. Pisani and Y. Wang, arXiv:1602.03545.
42. É. É. Flanagan and S. A. Hughes, *Phys. Rev. D* **57** (1998) 4535.
43. M. Rigault, G. Aldering, M. Kowalski, Y. Copin, P. Antilogus, C. Aragon, S. Bailey, C. Baltay, D. Baugh, S. Bongard, K. Boone, C. Buton, J. Chen, N. Chotard, H. K. Fakhouri, U. Feindt, P. Fagrelus, M. Fleury, D. Fouchez, E. Gangler, B. Hayden, A. G. Kim, P.-F. Leget, S. Lombardo, J. Nordin, R. Pain, E. Pecontal, R. Pereira, S. Perlmutter, D. Rabinowitz, K. Runge, D. Rubin, C. Saunders, G. Smadja, C. Sofiatti, N. Suzuki, C. Tao and B. A. Weaver, *Astrophys. J.* **802** (2015) 20.
44. B. P. Abbott *et al.*, *Living Rev. Rel.* **19** (2016) 1.
45. L. S. Finn and D. F. Chernoff, *Phys. Rev. D* **47** (1993) 2198.

Induced gravitational collapse in FeCO Core–Neutron star binaries and Neutron star–Neutron star binary mergers

R. Ruffini,^{1,2,3,4,5,*} Y. Aimuratov,^{1,5} C. L. Bianco,^{1,2} M. Enderli,^{1,5}
 M. Kovacevic,^{1,5} R. Moradi,^{1,5} M. Muccino,¹ A. V. Penacchioni,^{3,4}
 G. B. Pisani,¹ J. A. Rueda^{1,2} and Y. Wang^{1,2,†}

¹*Dip. di Fisica, Sapienza University of Rome and ICRA,
 Piazzale Aldo Moro 5, I-00185, Rome, Italy*

²*ICRANet, Piazzale della Repubblica 10, I-65122 Pescara, Italy*

³*ICRANet, Centro Brasileiro de Pesquisas Fisicas,*

rua Dr. Xavier Sigaud 150, 22290-180, Rio de Janeiro, Brazil

⁴*ICRANet, Av dos Astronautas 1758 Jd. Granja BR S José dos Campos,
 SP 12227-010, Brazil*

⁵*Université de Nice Sophie Antipolis, Nice,
 CEDEX 2 Grand Château Parc Valrose, France*

**ruffini@icra.it*

†yu.wang@icranet.org

Published 19 October 2015

We review the recent progress in understanding the nature of gamma-ray bursts (GRBs). The occurrence of GRB is explained by the Induced Gravitational Collapse (IGC) in FeCO Core–Neutron star binaries and Neutron star–Neutron star binary mergers, both processes occur within binary system progenitors. Making use of this most unexpected new paradigm, with the fundamental implications by the neutron star (NS) critical mass, we find that different initial configurations of binary systems lead to different GRB families with specific new physical predictions confirmed by observations.

Keywords: Black hole; supernova; gamma ray burst.

1. Introduction

Supernovae (SNe) have been known and studied for a long time, from 1054 A.D. to the classic work of Baade and Zwicky in 1934,^{1–3} to the discovery of pulsar in 1967,⁴ leading the identification of the first NS in the Crab nebula originated from the SN phenomenon. It has become clear that a NS has harbored for thousands of years inside that SN remnant, and the main energetics of the SN is from the loss of NS rotational energy.

Observations of GRBs date from the detection by the Vela satellites in the early 1970s, see e.g. in Ref. 5. Just after the announcement of GRBs, out of first principle, we indicated in Ref. 6 that GRBs could originate in the process of gravitational

collapse, leading to the birth of a black hole (BH), and we theoretically predicted consequently have energetics of the order of $10^{54} (M_{BH}/M_{\odot})$ erg, namely equivalent to the release of $\sim M_{\odot}c^2$ in few tens of seconds, here M_{BH} is the mass of BH and M_{\odot} is the solar mass.

It has only been after the observations by the Beppo-Sax satellite and the optical identification of GRBs that their enormous energetics, 10^3 – 10^4 times larger than those of SNe, have been confirmed and they coincide the theoretical prediction made on the ground of the BH mass-energy formula.⁶

From these premises, it was introduced the basic paradigm, see e.g. in Ref. 7 and the references there in, that the SN originated from the formation of a NS, and a GRB originated from the formation of a BH. These two astrophysical systems conceptually have consequently been assumed to be member of two conceptually distinct families.

This situation has become even more intricate and interesting after the unexpected observation of a temporal coincidence between the emission of a GRB and a SN, see e.g. GRB 980425⁸ and SN 1998bw.⁹ The explanation of this coincidence has gradually led from GRBs and SNe been traditionally considered as a single star event to a much more rich and complex comic many-body interaction and therefore to the introduction of a cosmic matrix: C-matrix. This totally unprecedented situation has led to the opening of a new understanding of a vast number of unknown domains of physics and astrophysics.

1.1. Crab nebula — Supernova as prove of the existence of neutron star

Of all the objects in the sky, none has been richer than the Crab nebula in results for physics, astronomy and astrophysics. Although a result of the 1054 A.D. SN observed by Chinese, Japanese and Korean astronomers, the nebula itself was not identified till 1731, and not associated with that SN until the last century, but it has been of interest to astronomers, and later astrophysicists and theoretical physicists ever since, even very recently, see e.g. the discovery by Agile of the giant flare discovered in September 2010.¹⁰ It was only in 1968 that a rotational pulsar was discovered at its center following the predicted existence of rapidly rotating NSs by John Wheeler. This is a absolutely first for the field for astronomy and astrophysics: in that decade hundreds of neutron stars observed as pulsars.

Independently from these successes, there still remains to explain an outstanding physical process needed to model this object: the expulsion of the shell of the SN remnant during the process of gravitational collapse to a NS. We are currently gaining some understanding of the physical processes governing NSs, motivated by the research on GRBs and BH formation which is being fully exploited to this end at the present time. The understanding of BH formation and consequently of the emission of GRBs is likely to lead, in this Faustian effort to learn the laws of nature, to the understanding of the process of NS formation and the expulsion of the remnant in the SN explosion.

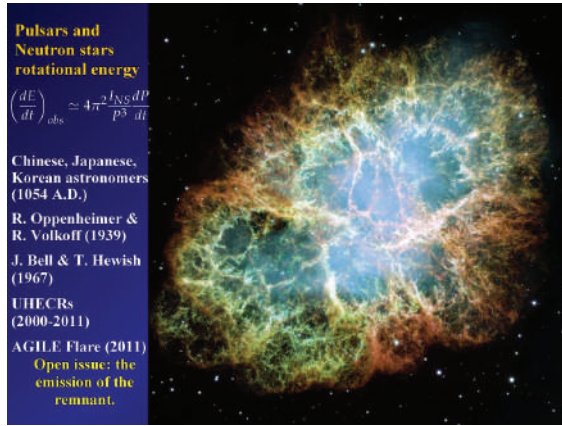


Fig. 1. Hubble Space Telescope photograph (2005) of the Crab Nebula.

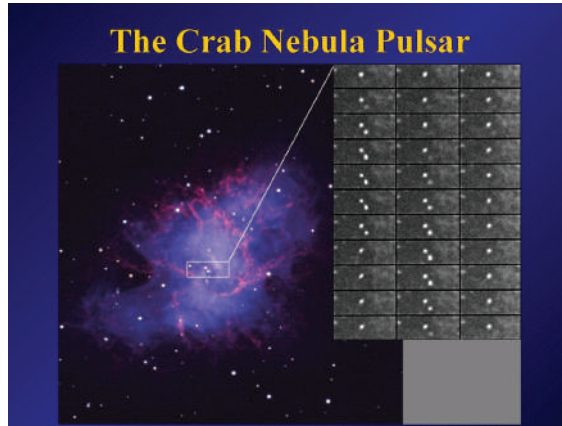


Fig. 2. The sequence of black and white images on the right is separated by one millisecond intervals, from which it is clear that the left star is a pulsar with a period of $P = 33$ milliseconds. This period changes with a rate dP/dt of 12.5 microseconds per year. The fact that the loss of rotational energy of a NS star with moment of inertia I is given by $dE/dt \propto -I(1/P^3)dP/dt$ explains precisely the energetics of the pulsar and proves at once the existence of NSs.¹¹

That NSs exist in nature has been proven by the direct observation of pulsars. The year 1967 marked the discovery of the first pulsar, observed at radio wavelengths in November 28, 1967 by Jocelyn Bell Burnell and Antony Hewish.⁴ Just a few months later, the pulsar NP0532 was found in the Crab Nebula (see Fig. 1) and observed first at radio wavelengths and soon after at optical wavelengths (see Fig. 2).

The discovery of NSs led our small group working around John Wheeler in Princeton (see Fig. 3), to go one step further and to direct our main attention to the study of a even more extreme phenomenon: the continuous gravitational collapse of a core with mass later than the critical NS mass introduced by Oppenheimer

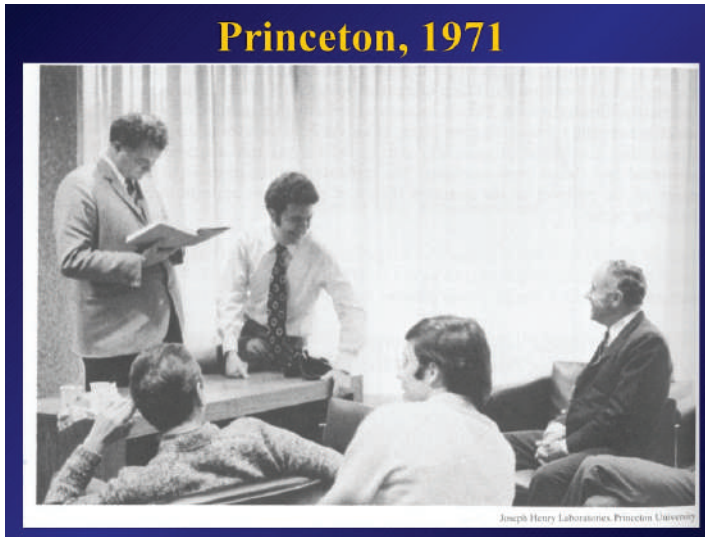


Fig. 3. Standing to the left T. Regge, sitting on the desk R. Ruffini and sitting on the chair J. A. Wheeler.

and his students. This soon led to the celebrated articles “Introducing the Black Hole” by J. A. Wheeler and R. Ruffini.¹² The work in Princeton addressed the topic of BHs, gravitational waves (GWs) and cosmology. A summary of that work can be found in Ref. 13, where a vast number of topics considered for the first time of relativistic astrophysics was reconsidered, including the cross-sections of GW detectors, the possible sources of GWs and especially, an entirely new family of phenomena occurring around BHs.

1.2. The BH mass-energy formula

A most important result in understanding the physics and astrophysics of BHs has been the formulation of the BH mass-energy formula. From this formula, indeed, it became clear that up to 50% of the mass-energy of a BH could be extracted by using reversible transformations.¹⁴ It then followed that during the formation of a BH, some of the most energetic processes in the universe could exist, releasing an energy of the order of $\sim 10^{54}$ erg for a few solar masses BH.

1.3. VELA satellites and GRBs

In Ref. 15 I described how the observations of the Vela satellites were fundamental in discovering GRBs, see Fig. 4. Initially it was difficult to model GRBs to understand their nature since their distance from the earth was unknown, and their energetics is consequently undefined. Thousands of models were presented, see e.g. in Ref. 16, attempting to explain their nature which was a profound mystery. Just a few months after the public announcement of their discovery,⁵ T. Damour, a collaborator at

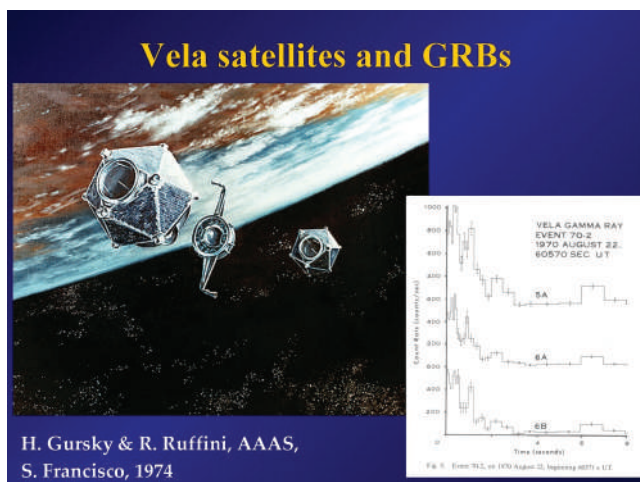


Fig. 4. The Vela satellites, see e.g. the I. Strong's chapter in Ref. 5.

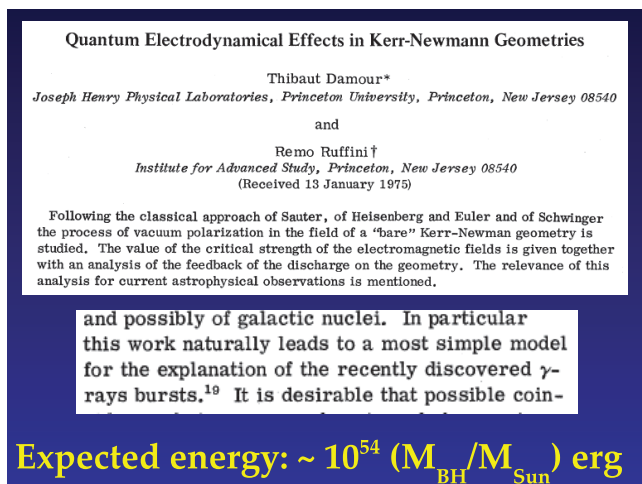


Fig. 5. The classic paper Ref. 6 by Damour and Ruffini on the extractable energy of a Kerr-Newman BH through vacuum polarization.

Princeton, and I formulated a theoretical model based on the extractable energy of a Kerr-Newmann BH through a vacuum polarization process as the origin of GRBs, see Fig. 5. In our paper,⁶ we pointed out that vacuum polarization occurring in the field of electromagnetic in Kerr-Newman BHs could release a vast e^+e^- plasma which self-accelerates and gives origin to the GRB phenomenon. Energetics for GRBs all the way up to $\sim 10^{55}$ ergs where theoretically predicted for a $10M_{\odot}$ BH. The dynamics of this e^-e^+ plasma was first studied by J. R. Wilson and myself with the collaboration of S.-S. Xue and J. D. Salmonson.^{17,18}

2. Classification of Short and Long GRBs

The launching of the Compton satellite with the BATSE detectors on-board led to important discoveries: the homogeneous distribution of GRBs in the universe and the classification of short-duration GRB with $T_{90} < 2$ second and long-duration GRB with $T_{90} > 2$ second, T_{90} means the duration containing 90% of total energy in the observer's frame.

The crucial contribution to understand the nature of GRBs came from the Beppo-Sax satellite which led to a more precise definition of their positions in the sky obtained using a wide field X-ray camera and a narrow field instrumentation. This enabled the optical identification of GRBs and the determination of their cosmological redshift, and consequently of their energetics, which turned out to be up to $\sim 10^{55}$ erg, precisely the value predicted by Damour and Ruffini in Ref. 6. Since that time no fewer than ten different X- and γ -ray observatory missions and numerous observations at optical and radio wavelengths on the ground have allowed us to reach unprecedented amount of high quality observational data and consequently a deeper understanding of the nature of GRBs.

The observational classification based on T_{90} reflects the GRB's central engine. In the single core collapse model, the progenitor of long GRB is a massive star which collapses to a black hole. The short GRB is due to the merger of two compact objects (NS-NS or NS-black hole). In the IGC model of long GRBs, the progenitor is a very special binary system. We will also show that both long and short GRBs have two distinct binary progenitors, see Sec. 3.

Many previous articles, e.g. Refs. 19–21, simply plot the histograms of T_{90} using the observed T_{90} . Two Gaussian distributions depicting short and long GRBs are obtained. We here plot our T_{90} histogram, shown in Fig. 6, with three improvements:

- (1) If one wants to compare the physics of GRBs, observer's frame cannot tell the

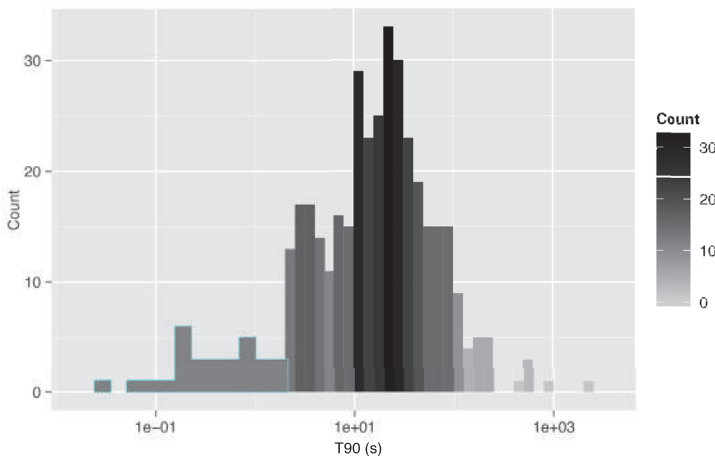


Fig. 6. T_{90} of GRBs with known redshift, blue frame contains short bursts with $T_{90} < 2$.

real T_{90} duration since GRBs are cosmological events with different redshift, we only consider those GRBs with known redshift and we transfer them to their rest frame. Duration decreases in GRB's rest frame, consequently more GRBs with $T_{90} < 2s$; (2) satellites are limited when GRB's flux is not adequate, it brings the effect that for some distant GRBs, T_{90} only contains the brightest part of the prompt emission, long GRBs are mis-classified as short ones, for example, GRB 090423, one of the farthest observed GRB at $z = 8.2$, has been discussed in detail in Ref. 22; (3) currently none of the satellite has a full energy coverage, each one observes a different energy band, as a result, the T_{90} from these satellites are different, we normalize T_{90} to the energy band of *Swift*-BAT, from 15 keV to ~ 150 keV.

3. Induced Gravitational Collapse Model

In Refs. 23 and 24, we have introduced the IGC paradigm in order to explain the astrophysical reasons for the conceptually unexpected association of GRBs with SNe. This IGC paradigm indicates that all long GRBs, by norm, have to be associated with a SN occurring in a binary system with a NS. The IGC paradigm differs from the traditional single star core collapsar model. In the collapsar-fireball model the GRB process is described by a single episode^{25–27} and references therein: (1) it is assumed to originate in a “collapsar”;²⁸ (2) the description of the late X-ray emission is dominated by a single ultra-relativistic jetted emission,^{29–33} shown in Fig. 7. There is a very fundamental different between the particle S-Matrix and cosmic C-Matrix, the in-state and the out-state in S-Matrix is reversible, oppositely the C-Matrix is not reversible. This is conceptually profound in the nature of general relativity which is not invariant for time reversal.

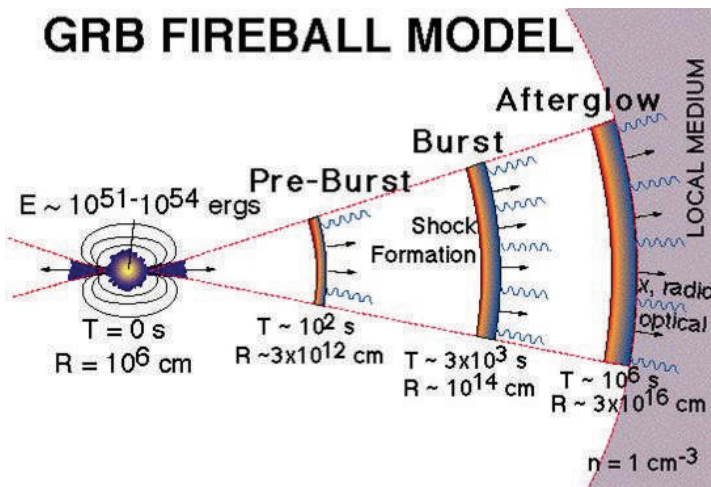


Fig. 7. Demonstration of fireball model, the central engine, the burst, the afterglow and the ISM (Figure is from Swift UK website).

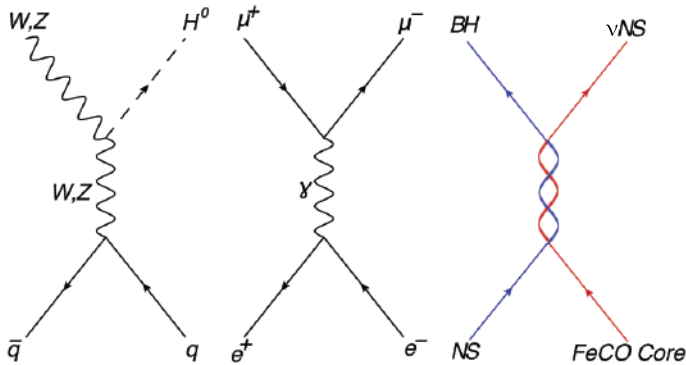


Fig. 8. Three different matrixes in the fundamental physics, first one is the quark matrix leading to Higgs boson. In the middle is the classical electron-positron pair matrix, generating muon and anti-muon pair. And the third matrix is the most recent one, which is considered in the present work, see e.g. in Ref. 7.

In contrast, the IGC paradigm considers a multi-component system, similar to the ones described by S -matrix in particle physics. For example, Fig. 8, the cosmic matrix of long GRBs: (1) the “in-states” are represented by a binary system formed by a FeCO core, very close to the onset of a SN event, and a tightly bound companion NS.^{24,34,35} The “out-states” are the creation of a new NS (ν -NS) and a black hole (BH). In the case of particle physics the S -matrix describes virtual phenomena occurring on time scales of 10^{-26} s for $q\bar{q} \rightarrow WZH^0$ ³⁶ and 10^{-23} s for $e^+e^- \rightarrow \mu^+\mu^-$.³⁷ In the astrophysical case, the cosmic matrix (C -matrix) describes real event occurring on timescale ~ 200 s, still a very short time when compared to traditional astrophysical time scales. Following the accretion of the SN ejecta onto the companion NS, a BH is created when the critical mass of a NS is reached, giving origin to the GRB; (2) special attention is given to the analysis of the instantaneous spectra in optical, X-ray, γ -ray and GeV energy range (as exemplified in this article); (3) four different episodes are identifiable in the overall emission, each with marked differences in the values of their Lorentz Γ factors.³⁸ Actually the possible relevance of a binary system in the explanation of GRBs was already mentioned in a pioneering work of Refs. 39 and 40, but the binaries in their case are triggers to the traditional collapsar model.

3.1. Families and episodes of GRBs

We here divide both long and short GRBs into two families respectively, namely family-1 and family-2, by a simple but fundamental threshold $E_{\text{iso}} \sim 10^{52}$ erg. This value corresponds to the minimal release of binding energy during the process that a NS, in a binary system as the initial state of IGC scenario, accretes enough matter to reach its critical mass and collapses to a black hole. This crucial result was obtained during many discussions I had with J. A. Rueda and Y. Wang in the preparation of the paper Ref. 41, such a distinction was first proposed for the long GRBs.

3.1.1. Families of long GRBs

Continued observations of massive stars have demonstrated that most, if not all, massive stars are in binary systems.^{42–44} A large fraction (50–75%) of these systems are in tight binaries that interact during the evolution (e.g. mass transfer, common envelope phase). The high binary fraction has led to a growing consensus that most type Ib/Ic SN progenitors are produced in interacting binary systems.^{45–49} Since the type of SNe associated to long-duration GRBs are of type Ic,⁵⁰ it is not surprising that binaries, often involving interactions of a massive star with a compact companion, have been invoked to produce GRB-SNe to remove the hydrogen envelope, spin up the star, or both.^{39,48,51–54} For the long GRBs, the IGC model requires a tight binary (produced in a common envelope phase) between a massive CO star (a star that has lost its hydrogen envelope and helium shell) and a NS companion.³⁴ Due to different configurations of binary system, especially the separation between two stars, two families of long GRBs are produced depending on whether or not a black hole formed.

The IGC paradigm is composed of four episodes, we delineate the family-2 long GRBs ($E_{\text{iso}} > 10^{52}$ erg, $T_{90} > 2$ s) which includes the most complete process, see Fig. 9.

Episode 1 originates in a unstable FeCO core leading to a SN event and the accretion onto the companion NS via the Bondi–Hoyle hypercritical accretion process.^{55,56} At the end of this episode, as the NS reaches its critical mass, it collapses to a BH.³⁴ It has become evident that the energetics of episode 1 is markedly different from the one of an isolated FeCO core that undergoes a SN and it is very sensitive to its binary nature and to the distance a between the SN and the NS: the tighter the binary system, the more energetic is episode 1. In GRB 130427A, a good prototype of such an extremely energetic emission occurs. The discovery of episode 1 offers the possibility of probing some of the pioneering works on “hypercritical accretion” by Refs. 57–59 which can in principle be tested with the possible observation of associated neutrino emission process.

In episode 2, along the direction of observer, a cavity is formed due to the accretion. In the vicinity of a black hole, the quantum electro-dynamical process occurring in the formation of the black hole leads to e^+e^- plasma which expands to ultra-relativistic velocity, a part of the plasma passes the cavity and interacts with the circumburst medium giving rise to a part of the prompt emission (see Refs. 61, 62 and references therein). The continuous accretion from SN ejecta on the newly formed black hole also contributes to the prompt emission. The physical picture in this episode is fundamentally important, it connects episode 1 and affects episodes 3, we propose an educative mimic as a simplification, the Chinese fortune cookie, shown in Fig. 11, which I developed with Y. Wang and our group in many conceptual discussions. The SN locates at the center, the cookie itself represents the SN ejecta, and the companion NS, which later becomes a black hole, locates inside the cavity that is carved by the effect of accretion onto the NS.

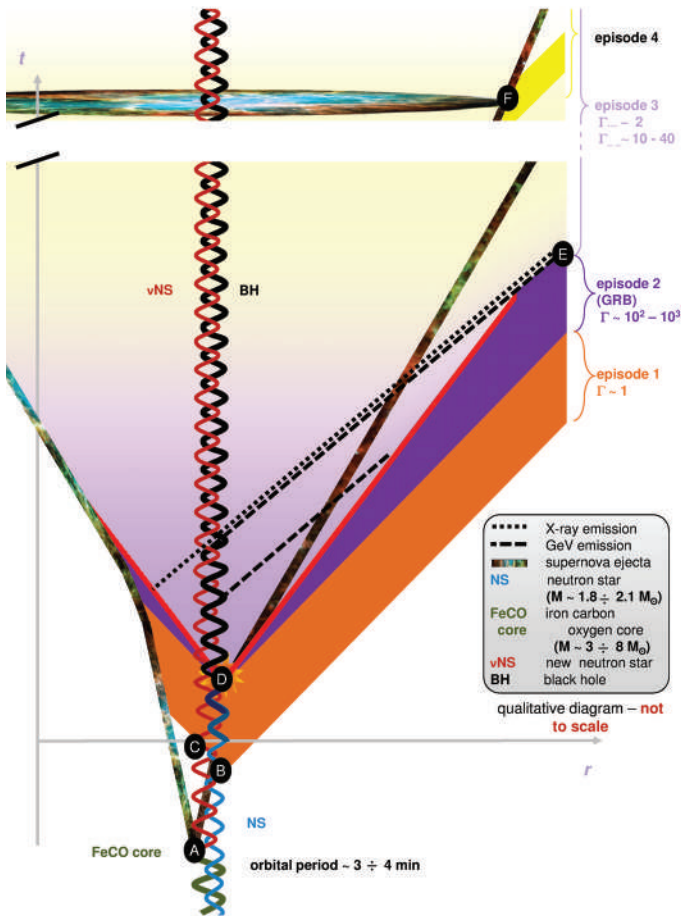


Fig. 9. The initial configuration is composed of an evolved, likely FeCO stellar core and a companion NS. (a) The core undergoes a SN and creates a new NS and its remnant; (b) beginning of the accretion of SN ejecta onto the companion NS, emitting episode 1; (c) the new NS interacts with mission from the episode 1; (d) accretion of the SN ejecta on the companion NS induces he black hole formation and the emission of e^+e^- plasma fireshell; (e) transition point between episode 2 and episode 3 which originates from the collision between the GRB ingoing to the SN remnant and collides with the ejecta originating binary driven hypernova (BdHN); (f) the SN optical signal peaks after tens of days.

Episode 3 is in our view mainly related to the SN ejecta. At this moment, we assume a novel idea which is quite different from the traditional approach, relating the so-called afterglow to the GRB phenomena, it is my opinion that the afterglow which clearly follows the prompt emission of the GRB is actually originating not in the GRB but is related to the SN ejecta. The SNe indeed are heated and accelerated as the collision of a portion of the e^+e^- plasma does not escape form the cavity indicated in Fig. 11. This concept can be visualized in the qualitative picture shown in Fig. 9, we compare and contrast that two cases of the long and short GRBs, only

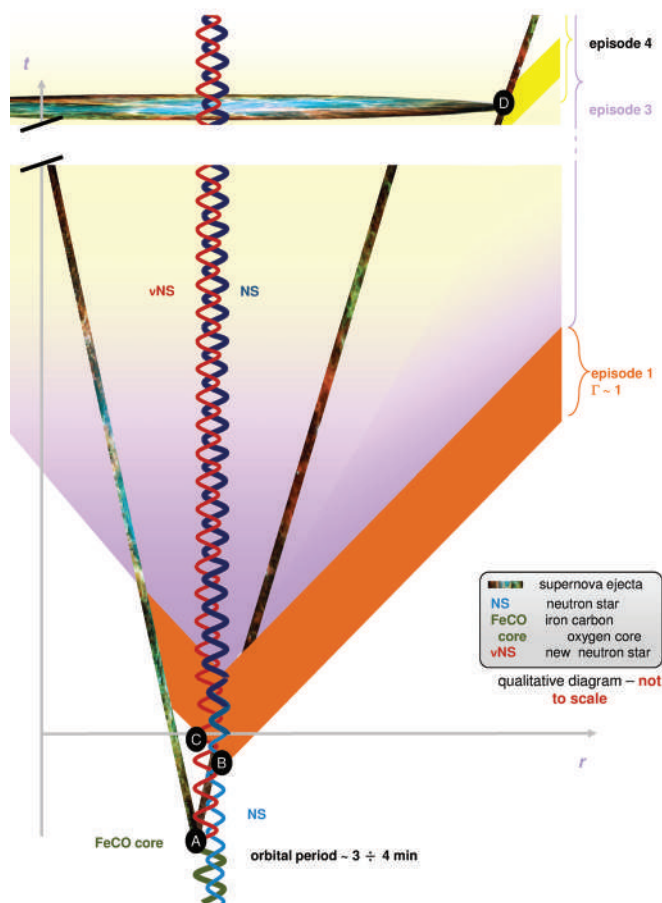


Fig. 10. The initial configuration is composed of an evolved, likely FeCO stellar core and a companion NS. (a) The core undergoes a SN and creates a new NS and its remnant; (b) beginning of the accretion of SN ejecta onto the companion NS, emitting episode 1; (c) the new NS interacts with mission from the episode 1, but the companion NS does not accrete enough matter to induce a black hole formation, no episode 2; (d) the SN optical signal peaks after tens of days.

in the long GBBs, episode 3 starts with a steeper decay of the X-ray light curve, in the 0.3–10 keV energy range, is followed by a plateau and then by a power-law decay with a almost constant index $-1.3 \lesssim \alpha \lesssim -1.7$. The overlapping of this late power-law decay which is measured in the rest-frame of the source, originally observed at times larger than 2×10^4 s,⁶³ has been considered the qualifying test for assuring the GRB to follow the IGC paradigm: a necessary and sufficient condition for the appearance of a SN at a later time, after 10 days in cosmological rest frame. The overlapping has also been used to probe the cosmological redshift of GRBs⁶⁴ and has led to consider the episode 3 as a “cosmic distance indicator”.⁶³ It is by now clear that the energy of the episode 3 is a standard feature, which is largely independent from the energy of the GRB.⁶³

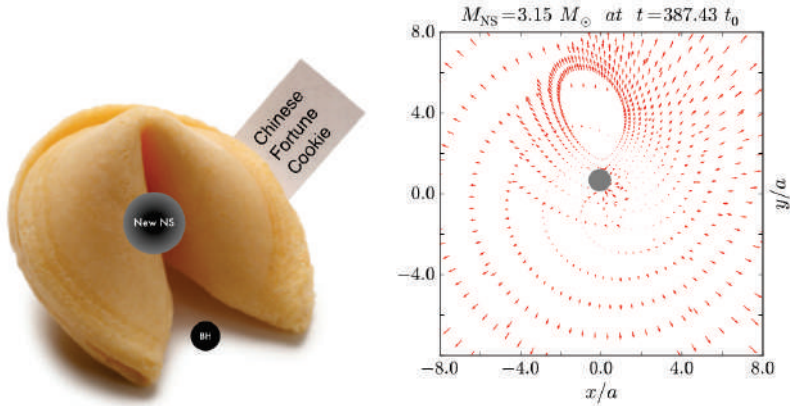


Fig. 11. Left: The shape of IGC episode 2 is similar to the Chinese fortune cookie. Right: Two dimensional simulation of the SN ejecta velocity field at $387.43 t_0$, $t_0 = 3.82$ s, a is the initial separation of two stars, the NS has been accreted to 3.15 solar masses.⁶⁰

Episode 4 is related to the optical appearance of the SN. This observational fact may very well be the consequence of a standard mass of the initial FeCO core.

Family 1 long GRB with $E_{\text{iso}} < 10^{52}$ erg, see Fig. 10, initially has a similar picture as the family-2 long GRB, a massive FeCO core collapse to a SN and the companion star accretes its ejecta, the difference is the binary components are too separated that the companion NS cannot accrete enough mass to form a black hole. As the result, there is no episode 2, because the formation of e^+e^- plasma relies on the BH, which absents in this family. Its episode 3 is simply an outcome of a hyper-nova, different from family-2 which goes through the heating and acceleration process, consequently, the nested and overlapped features do not appear in this family, and its luminosity of late X-ray emission is generally lower than Family-2 long GRB. In episode 4, a type Ib/c SN appears in the optical band in 10 – 20 days after the trigger of GRB, the same as Family-2. Most of energy of family-1 GRB is in X-ray, we call family-1 long GRB as X-ray flash (XRF).

3.1.2. Families of short GRBs

Progress has been obtained in the theoretical understanding of the equilibrium configuration of NSs, in their mass–radius relation, and especially in the theoretical determination of the value of the NS critical mass for gravitational collapse M_{crit}^{NS} .^{65,66} This has led to a theoretical value $M_{\text{crit}}^{NS} = 2.67M_{\odot}$, for instance for the NL3 equation of state.⁶⁷ Particularly relevant to this determination has been the conceptual change of paradigm of imposing global charge neutrality⁶⁷ instead of the traditional local charge neutrality still applied in the current literature, see, e.g. Ref. 68 and references therein. Similarly, noteworthy progress has been achieved in the determination of the masses of Galactic binary pulsars. Of the greatest relevance has been the direct observation of NS masses larger than $2M_{\odot}$,⁶⁹ pointing to

a very stiff nuclear equation of state hence to a large value of the NS critical mass, as pointed out above. In the majority of the observed cases of Galactic binary NSs, the sum of the NS masses, $M_1 + M_2$, is indeed smaller than M_{crit}^{NS} and, given the above determination of the NS critical mass, their coalescence will never lead to a BH formation. This of course offers a clear challenge to the traditional assumption that all short GRBs originate from BH formation, see e.g., Refs. 70, 71 and references therein.

Two families of short GRBs, both originating from NS mergers exist, and the difference between these two families depends on whether the total mass of the merged core is smaller or larger than M_{crit}^{NS} . This point has been clarified in many discussions with M. Muccino and J. A. Rueda and published in Ref. 71. The first family corresponding to the above mentioned less energetic short GRBs with $E_{\text{iso}} < 10^{52}$ erg, in which coalescence of the merging NSs leads to a massive NS as the merged core. In view of their relatively low value energetics, and the attributes of their hard X-ray spectra in the gamma-rays, we indicate them as short gamma flashes (S-GRFs). Paradoxically all the short bursts published in Ref. 70 belong to this class, and S-GRFs do not originate from the a process of the BH formation. The second family of short bursts with $E_{\text{iso}} > 10^{52}$ erg originate instead from a merger process leading to a BH as the merged core, in view of the hardness of the spectra and the high energetics of this class of short bursts, these sources deserve the name of short GRBs (S-GRBs). It is appropriate to remind that both long GRBs and short GRBs with $E_{\text{iso}} > 10^{52}$ lead to a BH formation, and both of them appear to have prominent GeV emission.

4. The IGC Paradigm for Long GRBs and Five Physical and Astrophysical Processes

The IGC paradigm integrates many physical and astrophysical processes:

- (1) The hypercritical accretion in episode 1.
- (2) The GRB emission in episode 2 composed by the P-GRB and the prompt emission, and possibly additional phase of hypercritical accretion.
- (3) The overlapping and nesting of the late X-ray emission in episode 3. item The GeV emission.
- (4) The SN observations.

4.1. The Hypercritical accretion in episode 1

In episode 1 of IGC paradigm, the SN explosion and the GRB occur following a precise time sequence as depicted in Fig. 9: explosion of the CO core \rightarrow hypercritical accretion onto the NS \rightarrow the critical mass is reached \rightarrow gravitational collapse to a BH is induced \rightarrow emission of the GRB. In episode 2, a part of the ejecta can continue the accretion onto the black hole producing significant emission in the most energetic GRBs. The theoretical framework and the first estimates of the hypercritical accretion onto the NS as a function of the nature of the binary parameters were

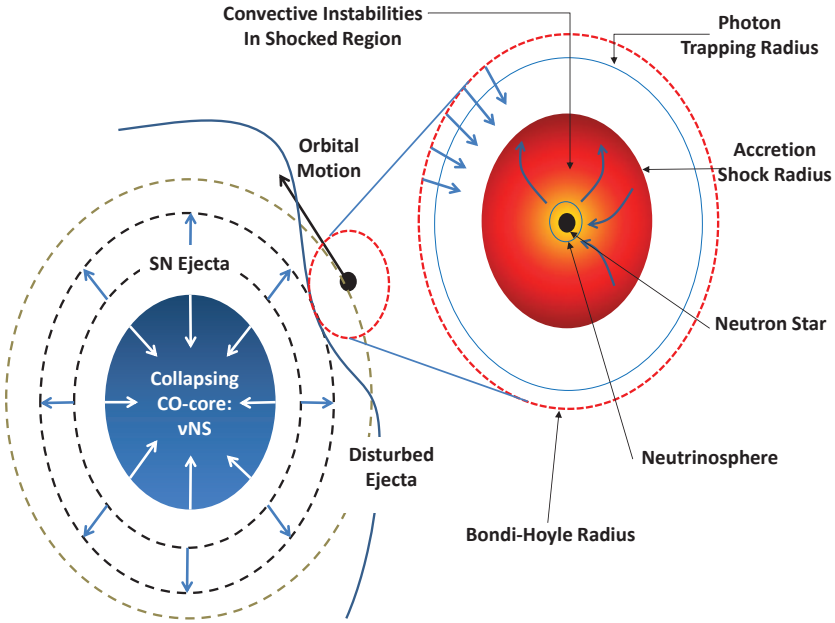


Fig. 12. Induced gravitational collapse scenario.

first presented in Ref. 34, see Fig. 12. The first more realistic numerical simulations of the IGC is performed by using more detailed SN explosions coupled to hypercritical accretion models from previous simulations of SN fallback in Refs. 59, 72, 73, and more recently Ref. 60 present the first estimates of the angular momentum transported by the SN ejecta, and perform numerical simulations of the angular momentum transfer to the NS during the hyper-accretion process in full general relativity.

For a wide variety of X-ray binaries, see e.g. in Ref. 74, the Eddington limit places a very fundamental role. In the present case of hypercritical accretion from the SN ejecta onto the companion NS within the IGC scenario, the Eddington limit plays no role since the photons are trapped in the flow. The trapping radius of photons emitted diffuse outward at a slower velocity than infalling material flows inward.⁷⁵

$$r_{\text{trapping}} = \min[(\dot{M}_{\text{BHL}}\kappa)/(4\pi c), r_{\text{BHL}}], \quad (1)$$

where κ is the opacity (in $\text{cm}^2 \text{g}^{-1}$) and c is the speed of light. If the trapping radius is larger or equal to the Bondi-Hoyle radius, the photons are trapped in the flow and the Eddington limit does not apply. The inflowing material shocks as it piles up onto the NS, producing an atmosphere on top of the NS, for details, see Refs. 57, 59, 75, 76. As the atmosphere compresses, it becomes sufficiently hot to emit neutrinos which cool the infalling material, allowing it to be incorporated into the NS. For details of the simulation of this process, we refer the reader to Refs. 59, 73, 77.

As material piles onto the NS and the atmosphere radius, the accretion shock moves outward. The accretion shock weakens as it moves out and the entropy jump (derived from the shock jump conditions) becomes smaller. This creates an atmosphere that is unstable to Rayleigh–Taylor convection. Simulations of these accretion atmospheres show that these instabilities can accelerate above the escape velocity driving outflows from the accreting NS with final velocities approaching the speed of light, ejecting up to 25% of the accreting material.^{73,78}

For the typical hypercritical accretion conditions of the ICG, the temperature of the bubble when it begins to rise is $T_{\text{bubble}} \sim 5$ MeV. If it rises adiabatically, expanding in all dimensions, its temperature drops to 5 keV at a radius of 10^9 cm, far too cool to observe. However, if it is ejected in a preferred direction due to the presence of angular momentum, as simulated by Ref. 73, it may expand in the lateral direction but not in the radial direction, so $\rho \propto r^2$ and $T \propto r^{-2/3}$. In this scenario, the bubble outflow would have $T_{\text{bubble}} \sim 50$ keV at 10^9 cm and $T_{\text{bubble}} \sim 15$ keV at 6×10^9 cm. This could explain the temperature and size evolution of the blackbody emitter observed in the episode 1 of several GRBs, see, e.g., in Refs. 63, 64, 79–81. We are currently deepening our analysis of the possible explanation of the thermal emission observed in episode 1 as due to the convective instabilities in the accretion process.

GRB 090618, as a typical example, its episode 1 lasts from 0 to 50 s and the episode 2 is from 50 s to 151 s after the trigger time, shown in Fig. 14. The blackbody emission observed in episode 1 of GRB 090618⁷⁹ evolves as $T \propto r^{-m}$ with $m = 0.75 \pm 0.09$, whose lower value is in striking agreement with the above simplified theoretical estimate.⁷⁹ The spectrum of episode 1 is shown in Fig. 13.

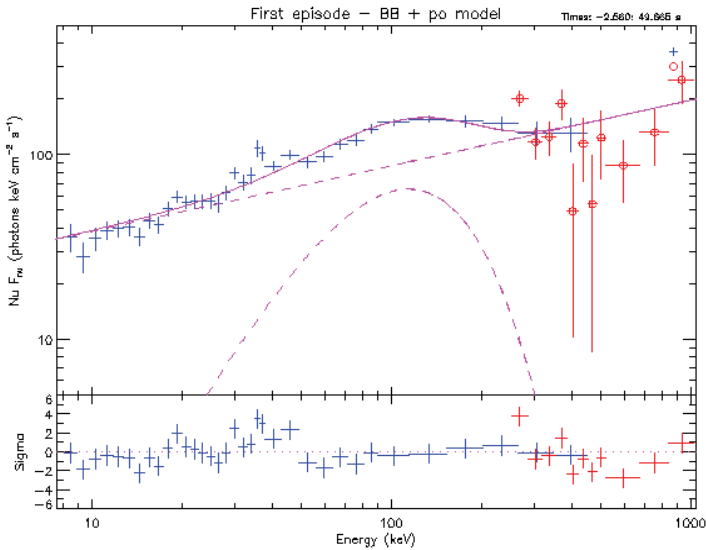


Fig. 13. Time-integrated spectra for the first episode (from 0 to 50 s) of GRB 090618 fitted blackbody + power-law (right) models with temperature $T = 32.07 \pm 1.85$ keV.

4.2. The GRB emission in episode 2: P-GRB and the prompt emission

According to the uniqueness theorem for stationary, the process of gravitational collapse of a core whose mass is larger than the NS critical mass will generally lead to a black hole. The creation of critical electric fields and consequent process of pair creation by vacuum polarization are expected to occur in the late phases of gravitational collapse when the gravitational energy of the collapsing core is transformed into an electromagnetic energy and eventually in e^+e^- pairs. Episode 2 starts from such an optically thick e^+e^- plasma in thermal equilibrium, with a total energy of $E_{\text{tot}}^{e^\pm}$. We call the evolution of this plasma shell as the fireshell model.

This plasma is initially confined between the radius r_h of a BH and the dyadosphere radius

$$r_{ds} = r_h \left[2\alpha \frac{E_{\text{tot}}^{e^+e^-}}{m_e c^2} \left(\frac{\hbar/m_e c}{r_h} \right)^3 \right]^{1/4}, \quad (2)$$

where α is the usual fine structure constant, \hbar the Planck constant, c the speed of light, and m_e the mass of the electron. The lower limit of $E_{\text{tot}}^{e^\pm}$ is assumed to coincide with the observed isotropic energy E_{iso} emitted in X-rays and gamma rays alone in the GRB.

The rate equation for the e^+e^- pair plasma and its dynamics have been described in Ref. 18. This plasma engulfs the baryonic material left over from the process of gravitational collapse having a mass M_B , still maintaining thermal equilibrium between electrons, positrons, and baryons. The baryon load is measured by the dimensionless parameter $B = M_B c^2 / E_{\text{tot}}^{e^+e^-}$. Reference 77 showed that no relativistic expansion of the plasma exists for $B > 10^{-2}$. The fireshell is still optically thick and self-accelerates to ultra-relativistic velocities.⁸² Then the fireshell becomes transparent and the P-GRB is emitted.⁸³ The final Lorentz gamma factor at transparency can vary over a wide range between 10^2 and 10^4 as a function of $E_{\text{tot}}^{e^+e^-}$ and B . For its final determination it is necessary to explicitly integrate the rate equation for the e^+e^- annihilation process and evaluate, for a given BH mass and a given e^+e^- plasma radius, at what point the transparency condition is reached.¹⁸ After transparency, along the direction pointing to the observer, the remaining accelerated baryonic matter still expands ballistically and starts to slow down from collisions with the CBM and filaments, producing a big amount of gamma-ray and X-ray photons in the GRB prompt emission.

We adopted a pragmatic approach in our fireshell model by making full use of the knowledge of the equations of motion, of the EQTS formulations,⁸⁴ and of the correct relativistic transformations between the comoving frame of the fireshell and the observer frame. Figure 14 shows an example of our simulation, the light curve of GRB 090618 in episode 2 starting from about 50s.

As discussed in Subsec. 3.1.1 and shown in Fig. 11, that e^+e^- dyadosphere can only be generated when the accretion reaches a critical mass, which means such

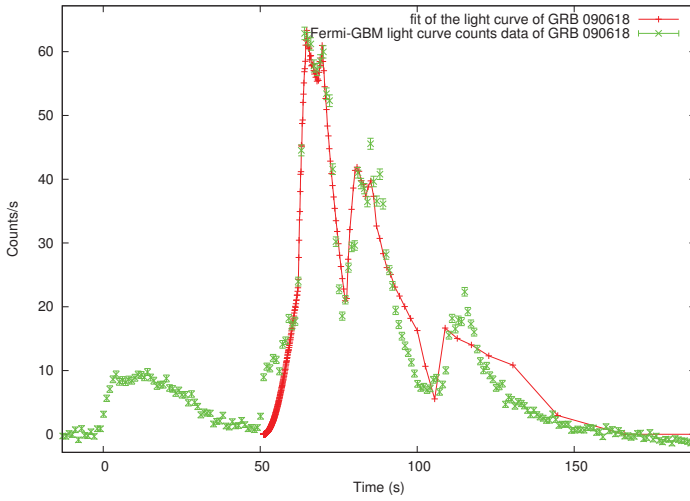


Fig. 14. Simulated light curve of the episode 2 of GRB 090618, from 58 s to 150 s, in the energy band 8–440 keV.

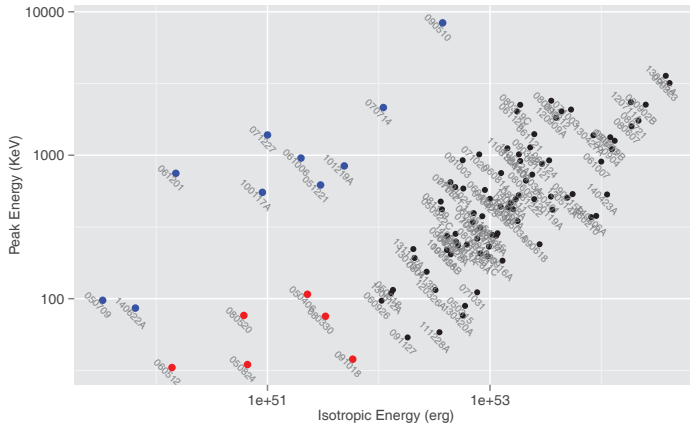


Fig. 15. The relation of isotropic energy and peak energy. Blue points are short GRBs, red and black points are long GRBs.

fireshell of plasma appears just in family-2 GRBs. As a result, the prompt emission of family-2 GRBs is a combination of outcome from the fireshell and the accretion onto black hole, while for the family-1 GRBs, solely accretion provides the energy. From the theory and simulation of hypercritical accretion, we already know that accretion generates X-ray photons with tens of keV, that photon's energy could peak at hundreds of keV, even some MeV since the accretion onto the newly formed BH, not just a NS. More over, the presence of angular momentum jets high Lorentz factor material, which generates high energy spectrum. In the observational aspect, shown in Fig. 15, confirms our simulations.

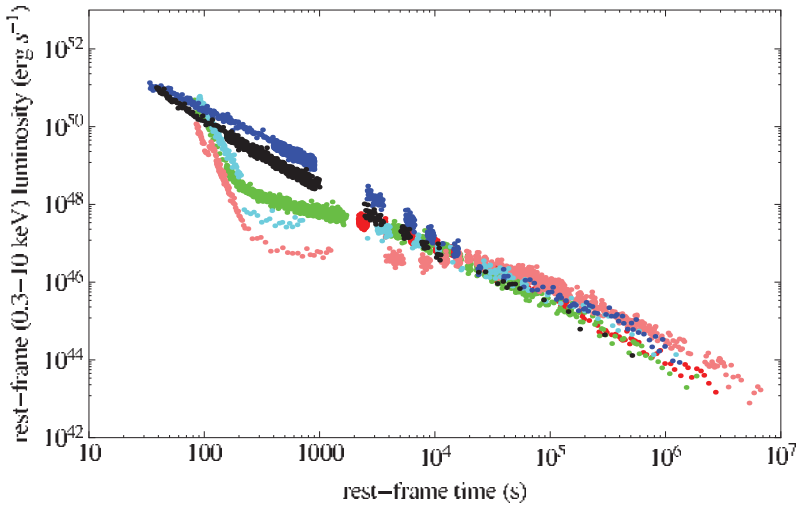


Fig. 16. (Color online) The X-ray luminosity light curves of the BdHNe members of the Golden Sample: GRB 060729, $z = 0.54$ (pink diamonds); GRB 061007, $z = 1.261$ (black stars); GRB 080319B, $z = 0.937$ (blue crosses); GRB 090618, $z = 0.54$ (green circles); GRB 091127, $z = 0.49$ (red squares); GRB 111228, $z = 0.713$ (cyan triangles).⁶³

4.3. The overlapping and nested of the late x-ray emission in episode 3

The photons in episode 3 have two origins, one is the heated SN ejecta, which contributes photons in the X-ray and lower energy, and the second is GeV photons originated from the interaction of black hole with newly born NS from the SN and the SN ejecta.⁷² This section we mainly focus on the X-ray emission from the SN ejecta.

It has been shown that the X-ray rest-frame 0.3–10 keV luminosity light curves present a constant decreasing power-law behavior, at times $\gtrsim 10^4$ s, with a typical value of the slope of $-1.7 \lesssim \alpha_X \lesssim -1.3$. This feature has been evidenced in a best sample of six GRBs, namely GRB 060729, 061007, 080319B, 090618, 091127, and 111228, hereafter *Golden Sample*, see e.g. in Ref. 63 and Fig. 16, and has been used also to infer the redshifts of GRBs 101023 and 110709B.^{80,85}

In Fig. 17, we compare the rebinned rest-frame 0.3–10 keV luminosity light curves of GRBs 130427A (purple), 060729 (pink) and 061121 (red). Their episode 3 emissions, are modeled by using the following phenomenological function of the rest-frame arrival time t_a ,

$$L(t_a) = L_p \left(\frac{t_a}{100} \right)^{\alpha_p} + L_X \left(1 + \frac{t_a}{\tau} \right)^{\alpha_X}, \quad (3)$$

where L_p and α_p are the steep decay luminosity (at $t_a = 100$ s) and index, and L_X , α_X and τ , respectively, are the plateau luminosity, the late power-law decay index and the characteristic time-scale of the end of the plateau.

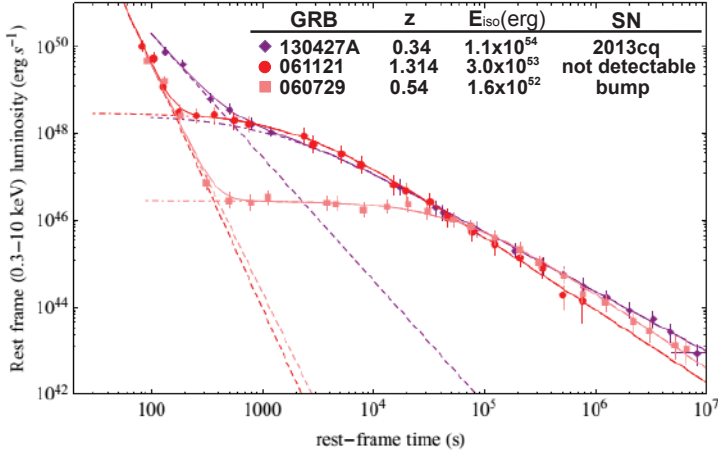


Fig. 17. (Color online) The rest-frame 0.3–10 keV re-binned luminosity light curves of GRB 130427A (purple diamonds), GRB 061121 (red circles) and GRB 060729 (pink squares). The light curves are fitted by using a power-law for the steep decay phase (dashed lines) and the function in Eq. (3) for the plateau and the late decay phases (dot-dashed curves).³⁸

From this fitting procedure, we conclude that the IGC GRBs exemplified in Fig. 17 share the following properties:

- (a) the power-law decay, for the more energetic sources, starts directly from the steep decay, well before the $t_a \approx 2 \times 10^4$ s as indicated in Ref. 63. Consequently the plateau shrinks for increasing E_{iso} (see Fig. 17);
- (b) the luminosities in the power-law decay are uniquely functions of the cosmological rest-frame arrival time t_a , independently on the E_{iso} of each source (see Fig. 17);
- (c) most remarkably, the overlapping of the X-ray light curves reveals a “nested” structure of episodes 3.

In GRB 130427A, the precise power-law decay of episode 3 in the X-rays is also observed in other wavelengths. In Fig. 18 are compared the data by the Fermi-LAT (100 MeV–100 GeV, red), the Swift-XRT (0.3–10 keV, blue), the NuStar⁸⁶ (3–79 keV, orange) and the Swift-UVOT⁸⁷ (optical R-band, green). Details are given in Ref. 41.

4.4. The GeV emission

It has always been a challenging topic of explaining GeV photons since the launch of Fermi satellite and the observation by Fermi-LAT. In the traditional collapse-fireball model, GeV photons originate from the same plasma outflow as lower energy ones, though the radiation mechanism participated varies. In the IGC paradigm, as we described, photons from optical to gamma-ray have many different origins in each one of the four episodes. The GeV photons instead have a different origin

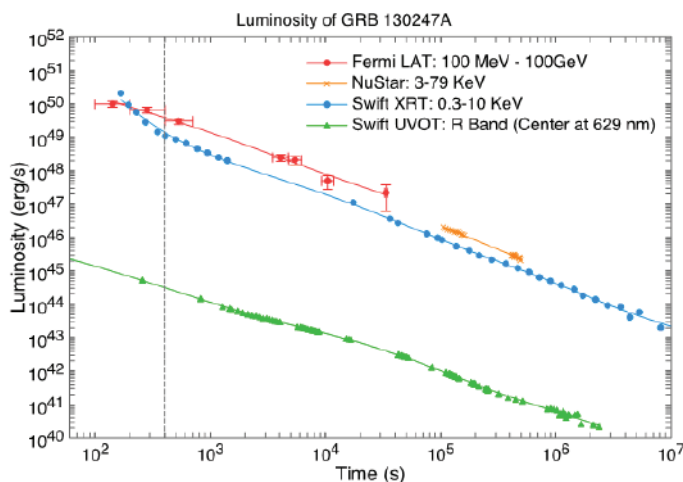


Fig. 18. (Color online) Multi-wavelength light curve of GRB 130427A from the data by the Fermi-LAT (100 MeV–100 GeV, red circles with errors), the Swift-XRT (0.3–10 keV, blue circles), the NuStar⁸⁶ (3–79 keV, orange crosses) and the R-band optical from Swift-UVOT⁸⁷ (green triangles).⁴¹

from all the others: they originate from the interaction of newly born black hole with the NS from the SN and the SN ejecta. The most significant factor for the identification of being originating from the black hole is the observation that the high GeV emission occurs after the emission of the P-GRB, which coincides with the moment of the formation of the blackhole.^{60,72} In this sense, GeV photons only exist in family-2 GRBs which possess a black hole, see Fig. 19 for family-2 long GRBs.

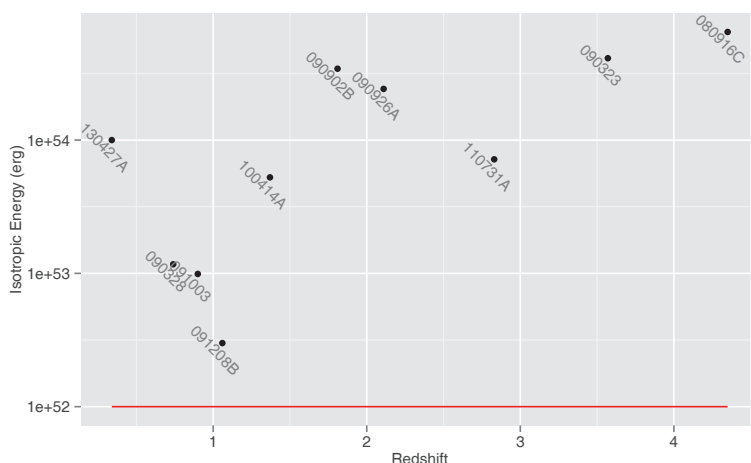


Fig. 19. GRBs with observed > 1 GeV photons, the horizontal redline indicates isotropic energy equals to 10^{52} erg, GRBs above this line are belong to family-2.

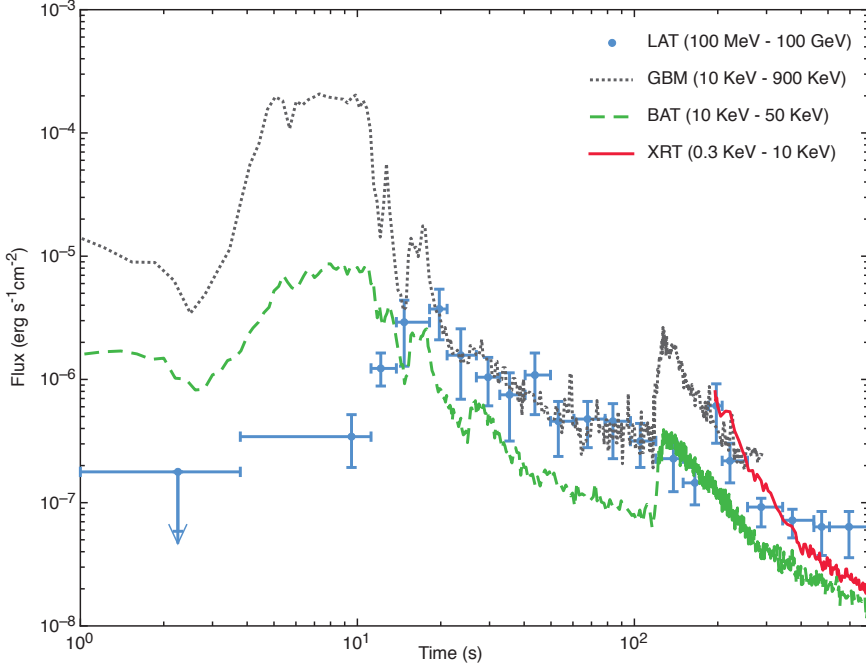


Fig. 20. Flux of first 700 s. Blue points are the *Fermi*-LAT high energy emission from 100 MeV till 100 GeV,⁸⁸ grey dotted line represents the *Fermi*-GBM, from 10 keV to 900 keV, green dashed line represents the photons detected by *Swift* BAT from 10 keV to 50 keV, and red solid line is the soft X-ray *Swift*-XRT detection, in the range of 0.3 KeV to 10 KeV. From this figure, clearly the *Fermi*-LAT emission reaches highest fluence at about 20 s while the gamma-ray detected by *Fermi*-GBM releases most of the energy within the first 10 s.⁴¹

GRB 130427A is one of the few GRBs with an observed adequate fluence in the optical, X-ray and GeV bands simultaneously for hundreds of seconds. In particular it remained continuously in the LAT field of view until 750 s after the trigger of *Fermi*-GBM,⁸⁸ which gives us the best opportunity so far to investigate different energy bands together, especially for the GeV photons. The first 700 s light curve is shown in Fig. 20, obviously, The GeV emission is quite dim in the first 10 s when gamma- and X-ray dominate the emission, then the GeV emission raises up coincidentally with the gamma and hard X-ray prompt emissions dropping down, the reason is at the beginning the intensive X-ray and gamma-ray photos block the GeV photons which are produced in the center. Such phenomena are common in many GRBs, shown in Fig. 21.

4.5. Supernova appearance

In the IGC, the occurrence of all the long GRBs require the explosion of SN. Normally the confirmation of SN is by detecting its optical emission from the nuclear decay of the ejecta at about 10 to 20 days after the GRB trigger. There are many

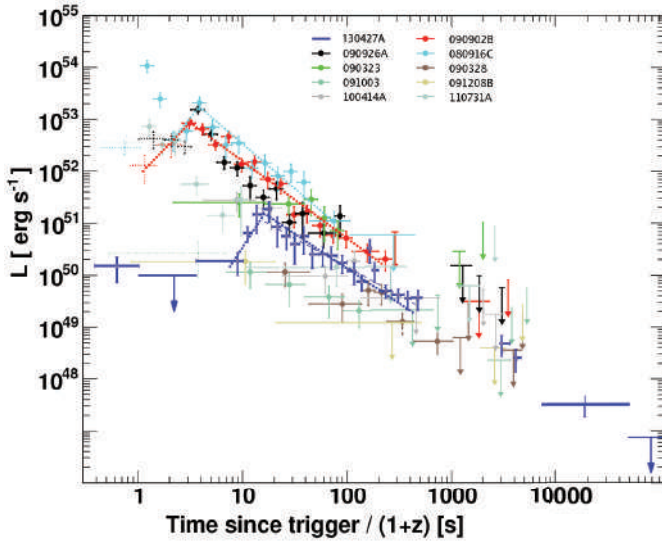


Fig. 21. Light curves of Fermi-LAT emission (100 MeV to 100 GeV), figure is from the first Fermi-LAT gamma-Ray burst catalog,⁸⁹ complemented.

reasons obstruct the optical detection, for instance, Poor localizations of bursts, contamination from host galaxy, and most important that GRB is a cosmological event with high redshift, but due to metal absorption, photons below ~ 400 nm are especially difficult to be detected, essentially no optical flux from GRB-SNe at $z > 1.2$.⁵⁴ Table 1 from Ref. 90 contains all the 35 confirmed GRB-SN connections updated to the 31 May 2014. Clearly, their isotropic energy vary many magnitudes from 10^{48} erg till 10^{54} erg, containing both family-1 and family-2 GRBs.

We had a successful prediction of SN appearance for GRB 130427A/SN2013cq. From the observations of the episode 3, GRB 130427A has been confirmed to fulfill the IGC paradigm, and we conclude, solely on this ground, that a SN should necessarily be observed under these circumstances. We sent the GCN circular 14526^{a91} on May 2, 2013 predicting that the optical R-band of a SN will reach its peak magnitude in about 10 days in the cosmological rest-frame on the basis of the IGC paradigm, and we encouraged the further observation. Indeed, starting from May 13, 2013, the telescopes GTC, Skynet and HST discovered the signals from the type Ic SN SN 2013cq.^{92–96}

^aGCN 14526: The late X-ray observations of GRB 130427A by *Swift*-XRT clearly evidence a pattern typical of a family of GRBs associated to SN following the IGC paradigm.^{34,63} We assume that the luminosity of the possible SN associated to GRB 130427A would be the one of 1998bw, as found in the IGC sample described in Ref. 63. Assuming the intergalactic absorption in the I-band (which corresponds to the R-band rest-frame) and the intrinsic one, assuming a Milky Way type for the host galaxy, we obtain a magnitude expected for the peak of the SN of $I = 22–23$ occurring 13–15 days after the GRB trigger, namely between the 10th and the 12th of May 2013. Further optical and radio observations are encouraged.

Table 1. The sample of the 35 confirmed GRB-SN connections updated to the 31 May 2014, from Ref. 90.

GRB	E_{iso} (erg)	Discovered by	z	SN identification	SN name
970228	1.86×10^{52}	BATSE/SAX	0.695	bump	
980326	5.60×10^{51}	BATSE/SAX	1(?)	bump	
980425	6.38×10^{47}	BATSE	0.0085	spec.	SN1998bw
990712	7.80×10^{51}	SAX	0.434	bump	
991208	2.59×10^{53}	SAX	0.706	bump	
000911	7.80×10^{53}	Konus-WIND	1.058	bump	
010921	1.10×10^{52}	HETE	0.45	bump	
011121	9.90×10^{52}	Ulysses	0.36	bump	SN 2001ke
020305	$0.7\text{--}4.6 \times 10^{51}$	Ulysses	0.2-0.5	bump	
020405	1.28×10^{53}	Ulysses	0.695	bump	
020410	2.20×10^{52}	Konus-WIND	~ 0.5	bump	
021211	1.30×10^{52}	HETE	1.006	spec.	SN 2002lt
030329	1.70×10^{52}	Konus-WIND	0.168	spec.	SN 2003dh
030723	1.60×10^{53}	HETE	< 1	bump	
031203	9.99×10^{49}	INTEGRAL	0.105	spec.	SN 2003lw
040924	1.10×10^{52}	HETE	0.86	bump	
041006	3.50×10^{52}	HETE	0.716	bump	
050525A	3.39×10^{52}	Konus-WIND	0.606	spec.	SN 2005nc
060218	1.66×10^{49}	Swift	0.033	spec.	SN 2006aj
060729	1.60×10^{52}	Swift	0.54	bump	
070419	7.90×10^{51}	Swift	0.97	bump	
080319B	1.30×10^{54}	Swift	0.937	bump	
081007	2.50×10^{51}	Swift	0.5295	bump	SN2008hw
090618	2.90×10^{53}	Fermi-GBM	0.54	bump	
091127	1.60×10^{52}	Fermi-GBM	0.49	bump	SN 2009nz
100316D	9.81×10^{48}	Swift	0.059	spec.	SN 2010bh
101219B	4.39×10^{51}	Fermi-GBM	0.55	spec.	SN 2010ma
111228A	7.52×10^{52}	Fermi-GBM	0.714	bump	
120422A	1.28×10^{51}	Swift	0.283	spec.	SN 2012bz
120714B	4.51×10^{51}	Swift	0.3984	spec.	SN 2012eb
120729A	2.30×10^{52}	Swift	0.80	bump	
130215A	3.10×10^{52}	Fermi-GBM	0.597	spec.	SN 2013ez
130427A	9.57×10^{53}	Fermi-GBM	0.3399	spec.	SN 2013cq
130702A	7.80×10^{50}	Fermi-GBM	0.145	spec.	SN 2013dx
130831A	4.56×10^{51}	Konus-WIND	0.4791	spec.	SN 2013fu

5. Conclusions

The nature of GRBs is presenting itself as one of the richest diagnostics ever encountered within physics and astrophysics. It is clear that phenomena never before explored in this domain can now be submitted to theoretical and observational scrutiny. In analogy with the S-matrix of particle physics, for long GRBs a cosmic matrix (C-matrix), in which the in-states are a NS and an evolved core undergoing

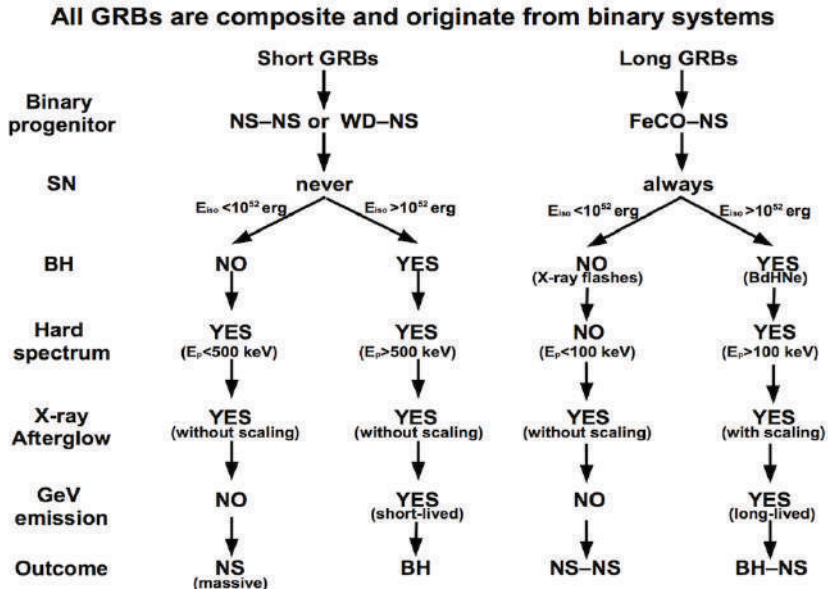


Fig. 22. All GRBs are composited and originated from binary systems, they follow four different routes of evolution. For long GRBs, the in-states are a NS and an evolved core undergoing a SN explosion in a binary system, and the out-states are a BH and a newly-born NS.⁴¹ For short GRBs, the in-states are two compact stars in a binary system, and the out-states is a BH or a NS.³⁸

a SN explosion in a binary system, and the out-states are a BH and a newly-born NS. For short GRBs, the in-states are two compact stars in a binary system, and the out-states is a BH or a NS. Fig. 22 shows that all GRBs are composited and originated from binary systems, they follow four different routes of evolution. In the induced gravitational collapse we have introduced, GRBs are classified to two families depending on the formation of black hole. We discussed several physical processes and phenomena in these families, namely the hypercritical accretion which initials the occurrence of GRB, the formation of e^-e^+ plasma as the causation of non-thermal emission in the prompt phase and the heating of SN ejecta, this heated and accelerated SN ejecta afterwards lead to the observation of spikes in the X-ray emission, as well as the overlapped and nested structures of late X-ray emissions. We also discussed GeV photons have a unique origination of the interaction between the black hole and newly born NS. And in the last section we show the connection of GRB and SN, and our successful prediction of SN 2013cq associated to GRB 130427A.

The cosmic matrix is at the basis of this new physics and relativistic astrophysics. Until now we have emphasized the action around the black hole, or the absence of it. Much work is still ahead in covering all possible interactions between the massive neutron star, the newly born neutron star, the supernova ejecta, and the newly born black hole.

Acknowledgments

I am very thankful to the president of the Chinese Academy of Sciences, Prof. Chunli Bai, to have promoted the 4th Galileo-Xu Guangqi meeting held in China, with the participation of so many young and distinguished scientists. Thanks to the presence of Prof. Frank C.N. Yang and his noble words expressed remembering Fermi will be a standing memory for all the participants to the 14th Marcel Grossmann meeting. My gratitude to Prof. Ronggen Cai, Prof. Yueliang Wu, and Prof. Yaping Zhang, for their work of preparing this splendid meeting and its publication. To many Chinese participants I confirm my usual happiness for their thought-provoking questions and discussion.

References

1. W. Baade and F. Zwicky, *Proc. Natl. Acad. Sci.* **20**, 254 (1934), doi:10.1073/pnas.20.5.254.
2. W. Baade and F. Zwicky, *Proc. Natl. Acad. Sci.* **20**, 259 (1934), doi:10.1073/pnas.20.5.259.
3. W. Baade and F. Zwicky, *Phys. Rev.* **46**, 76 (1934), doi:10.1103/PhysRev.46.76.2.
4. A. Hewish, S. J. Bell, J. D. H. Pilkington, P. F. Scott and R. A. Collins, *Nature* **217**, 709 (1968), doi:10.1038/217709a0.
5. H. Gursky and R. Ruffini (eds.), Neutron stars, black holes and binary X-ray sources, in *Proceedings of the Annual Meeting*, San Francisco, Calif., February 28, 1974, Astrophysics and Space Science Library, Vol. 48 (1975).
6. T. Damour and R. Ruffini, *Phys. Rev. Lett.* **35**, 463 (1975), doi:10.1103/PhysRevLett.35.463.
7. R. Ruffini, *Int. J. Mod. Phys. D* **20**, 1797 (2011), arXiv:1107.0862 [astro-ph.HE], doi:10.1142/S0218271811019876.
8. E. Pian *et al.*, *Astrophys. J.* **536**, 778 (2000), astro-ph/9910235, doi:10.1086/308978.
9. T. J. Galama *et al.*, *Nature* **395**, 670 (1998), astro-ph/9806175, doi:10.1038/27150.
10. M. Tavani *et al.*, *Science* **331**, 736 (2011), arXiv:1101.2311 [astro-ph.HE], doi:10.1126/science.1200083.
11. A. Finzi and R. A. Wolf, *Astrophys. J.* **153**, 865 (1968), doi:10.1086/149711.
12. R. Ruffini and J. A. Wheeler, *Phys. Today* **24**, 30 (1971), doi:10.1063/1.3022513.
13. M. Rees, R. Ruffini and J. A. Wheeler, Black holes, gravitational waves and cosmology: An introduction to current research (1974).
14. D. Christodoulou and R. Ruffini, *Phys. Rev. D* **4**, 3552 (1971), doi:10.1103/PhysRevD.4.3552.
15. D. L. Wiltshire, M. Visser and S. Scott (eds.), The ergosphere and dyadosphere of black holes, in *The Kerr Spacetime* (2009).
16. W. Janke, W. A. Pelster, H. J. Schmidt and M. Bachmann (eds.), Analogies, new paradigms and observational data as growing factors of relativistic astrophysics (2011).
17. R. Ruffini, J. D. Salmonson, J. R. Wilson and S.-S. Xue, *Astron. Astrophys.* **350**, 334 (1999), arXiv:astro-ph/9907030.
18. R. Ruffini, J. D. Salmonson, J. R. Wilson and S.-S. Xue, *Astron. Astrophys.* **359**, 855 (2000), arXiv:astro-ph/0004257.
19. J. P. Norris, T. L. Cline, U. D. Desai and B. J. Teegarden, Frequency of fast, narrow gamma-ray bursts and burst classification, in *American Institute of Physics Conference Series*, Vol. 115, ed. S. E. Woosley (AIP, 1984), pp. 367–372.

20. J.-P. Dezalay, C. Barat, R. Talon, R. Syunyaev, O. Terekhov and A. Kuznetsov, Short cosmic events — A subset of classical GRBs?, in *American Institute of Physics Conference Series*, Vol. 265, eds. W. S. Paciesas and G. J. Fishman (AIP, 1992), pp. 304–309.
21. C. Kouveliotou et al., *Astrophys. J. Lett.* **413**, L101 (1993), doi:10.1086/186969.
22. R. Ruffini et al., *Astron. Astrophys.* **569**, A39 (2014), arXiv:1404.1840 [astro-ph.HE], doi:10.1051/0004-6361/201423457.
23. R. Ruffini, C. L. Bianco, F. Frascchetti, S.-S. Xue and P. Chardonnet, *Astrophys. J. Lett.* **555**, L117 (2001), arXiv:astro-ph/0106534, doi:10.1086/323177.
24. R. Ruffini, On gamma-ray bursts, in *The Eleventh Marcel Grossmann Meeting on Recent Developments in Theoretical and Experimental General Relativity, Gravitation and Relativistic Field Theories*, eds. H. Kleinert, R. T. Jantzen and R. Ruffini (2008), pp. 368–505, arXiv:0804.2837.
25. P. Mészáros, *Rep. Prog. Phys.* **69**, 2259 (2006), arXiv:astro-ph/0605208, doi:10.1088/0034-4885/69/8/R01.
26. T. Piran, *Rev. Mod. Phys.* **76**, 1143 (2005), doi:10.1103/RevModPhys.76.1143.
27. P. Kumar and B. Zhang, *Phys. Rep.* **561**, 1 (2015), arXiv:1410.0679 [astro-ph.HE], doi:10.1016/j.physrep.2014.09.008.
28. S. E. Woosley, *Astrophys. J.* **405**, 273 (1993), doi:10.1086/172359.
29. J. E. Rhoads, *Astrophys. J.* **525**, 737 (1999), arXiv:astro-ph/9903399, doi:10.1086/307907.
30. Y. Z. Fan, D. M. Wei and C. F. Wang, *Astron. Astrophys.* **424**, 477 (2004), arXiv:astro-ph/0405392, doi:10.1051/0004-6361:20041115.
31. B. Zhang et al., *Astrophys. J.* **642**, 354 (2006), arXiv:astro-ph/0508321, doi:10.1086/500723.
32. H. van Eerten, W. Zhang and A. MacFadyen, *Astrophys. J.* **722**, 235 (2010), arXiv:1006.5125 [astro-ph.HE], doi:10.1088/0004-637X/722/1/235.
33. L. Nava, L. Sironi, G. Ghisellini, A. Celotti and G. Ghirlanda, *Mon. Not. R. Astron. Soc.* **433**, 2107 (2013), arXiv:1211.2806 [astro-ph.HE], doi:10.1093/Monthly Notices of the Royal Astronomical Society/stt872.
34. J. A. Rueda and R. Ruffini, *The Astrophys. J. Lett.* **758**, L7 (2012), arXiv:1206.1684 [astro-ph.HE], doi:10.1088/2041-8205/758/1/L7.
35. L. Izzo, J. A. Rueda and R. Ruffini, *Astron. Astrophys.* **548**, L5 (2012), arXiv:1206.2887 [astro-ph.HE], doi:10.1051/0004-6361/201219813.
36. G. Aad et al., *Phys. Lett. B* **716**, 1 (2012), arXiv:1207.7214 [hep-ex], doi:10.1016/j.physletb.2012.08.020.
37. C. Bernardini, *Phys. Perspec.* **6**, 156 (2004), doi:10.1007/s00016-003-0202-y.
38. R. Ruffini et al., *Astron. Astrophys.* **565**, L10 (2014), arXiv:1404.3946 [astro-ph.HE], doi:10.1051/0004-6361/201423812.
39. C. L. Fryer, S. E. Woosley and D. H. Hartmann, *Astrophys. J.* **526**, 152 (1999), arXiv:astro-ph/9904122, doi:10.1086/307992.
40. A. E. Broderick, *Mon. Not. R. Astron. Soc.* **361**, 955 (2005), arXiv:astro-ph/0411778, doi:10.1111/j.1365-2966.2005.09220.x.
41. R. Ruffini et al., *Astrophys. J.* **798**, 10 (2015), arXiv:1405.5723 [astro-ph.HE], doi:10.1088/0004-637X/798/1/10.
42. N. Smith, J. A. Morse, N. R. Collins and T. R. Gull, *Astrophys. J. Lett.* **610**, L105 (2004), arXiv:astro-ph/0406408, doi:10.1086/423341.
43. H. A. Kobulnicky and C. L. Fryer, *Astrophys. J.* **670**, 747 (2007), doi:10.1086/522073.

44. H. Sana *et al.*, *Science* **337**, 444 (2012), arXiv:1207.6397 [astro-ph.SR], doi:10.1126/science.1223344.
45. K. Nomoto and M. Hashimoto, *Phys. Rep.* **163**, 13 (1988), doi:10.1016/0370-1573(88)90032-4.
46. P. Podsiadlowski, P. C. Joss and J. J. L. Hsu, *Astrophys. J.* **391**, 246 (1992), doi:10.1086/171341.
47. E. De Donder and D. Vanbeveren, *Astron. Astrophys.* **333**, 557 (1998).
48. C. L. Fryer *et al.*, *Publ. Astron. Soc. Pac.* **119**, 1211 (2007), arXiv:astro-ph/0702338, doi:10.1086/523768.
49. S.-C. Yoon, S. E. Woosley and N. Langer, *Astrophys. J.* **725**, 940 (2010), arXiv:1004.0843 [astro-ph.SR], doi:10.1088/0004-637X/725/1/940.
50. M. Della Valle, *Int. J. Mod. Phys. D* **20**, 1745 (2011), doi:10.1142/S0218271811019827.
51. C. L. Fryer and S. E. Woosley, *Astrophys. J. Lett.* **502**, L9 (1998), arXiv:astro-ph/9804167, doi:10.1086/311493.
52. C. L. Fryer and A. Heger, *Astrophys. J.* **623**, 302 (2005), arXiv:astro-ph/0412024, doi:10.1086/428379.
53. E. P. J. van den Heuvel and S.-C. Yoon, *Astrophys. Space Sci.* **311**, 177 (2007), arXiv:0704.0659, doi:10.1007/s10509-007-9583-8.
54. S. E. Woosley and J. S. Bloom, *Annu. Rev. Astron. Astrophys.* **44**, 507 (2006), arXiv:astro-ph/0609142, doi:10.1146/annurev.astro.43.072103.150558.
55. H. Bondi and F. Hoyle, *Mon. Not. R. Astron. Soc.* **104**, 273 (1944).
56. H. Bondi, *Mon. Not. R. Astron. Soc.* **112**, 195 (1952).
57. Y. B. Zel'dovich, L. N. Ivanova and D. K. Nadezhin, *Sov. Astron.* **16**, 209 (1972).
58. G. S. Bisnovaty-Kogan and S. A. Lamzin, *Sov. Astron.* **28**, 187 (1984).
59. C. L. Fryer, W. Benz and M. Herant, *Astrophys. J.* **460**, 801 (1996), arXiv:astro-ph/9509144, doi:10.1086/177011.
60. L. Becerra, F. Cipolletta, C. L. Fryer, J. A. Rueda and R. Ruffini, arXiv:1505.07580 [astro-ph.HE].
61. R. Ruffini *et al.*, The blackholic energy and the canonical gamma-ray burst IV: The “long,” “genuine short” and “fake-disguised short” GRBs, in *American Institute of Physics Conference Series*, Vol. 1132, eds. M. Novello and S. Perez (AIP, 2009), pp. 199–266, arXiv:0907.5517 [astro-ph.HE].
62. R. Ruffini, G. Vereshchagin and S.-S. Xue, *Phys. Rep.* **487**, 1 (2010), arXiv:0910.0974 [astro-ph.HE], doi:10.1016/j.physrep.2009.10.004.
63. G. B. Pisani *et al.*, *Astron. Astrophys.* **552**, L5 (2013), arXiv:1304.1764 [astro-ph.HE], doi:10.1051/0004-6361/201220829.
64. A. V. Penacchioni *et al.*, *Astron. Astrophys.* **538**, A58 (2012), arXiv:1112.2970 [astro-ph.HE], doi:10.1051/0004-6361/201118403.
65. M. Rotondo, J. A. Rueda, R. Ruffini and S.-S. Xue, *Phys. Lett. B* **701**, 667 (2011), arXiv:1106.4911 [gr-qc], doi:10.1016/j.physletb.2011.06.041.
66. J. A. Rueda, R. Ruffini and S.-S. Xue, *Nucl. Phys. A* **872**, 286 (2011), arXiv:1104.4062 [gr-qc], doi:10.1016/j.nuclphysa.2011.09.005.
67. R. Belvedere, D. Pugliese, J. A. Rueda, R. Ruffini and S.-S. Xue, *Nucl. Phys. A* **883**, 1 (2012), arXiv:1202.6500 [astro-ph.SR], doi:10.1016/j.nuclphysa.2012.02.018.
68. P. Haensel, A. Y. Potekhin and D. G. Yakovlev (eds.), *Neutron Stars 1: Equation of State and Structure*, Astrophysics and Space Science Library, Vol. 326 (2007).
69. J. Antoniadis *et al.*, *Science* **340**, 448 (2013), arXiv:1304.6875 [astro-ph.HE], doi:10.1126/science.1233232.

70. E. Berger, *Annu. Rev. Astron. Astrophys.* **52**, 43 (2014), arXiv:1311.2603 [astro-ph.HE], doi:10.1146/annurev-astro-081913-035926.
71. R. Ruffini et al., *Astrophys. J.* **808**, 190 (2015), arXiv:1412.1018 [astro-ph.HE], doi:10.1088/0004-637X/808/2/190.
72. C. L. Fryer, J. A. Rueda and R. Ruffini, *Astrophys. J. Lett.* **793**, L36 (2014), arXiv:1409.1473 [astro-ph.HE], doi:10.1088/2041-8205/793/2/L36.
73. C. L. Fryer, *Astrophys. J.* **699**, 409 (2009), arXiv:0711.0551, doi:10.1088/0004-637X/699/1/409.
74. R. Giacconi and R. Ruffini (eds.), *Physics and astrophysics of neutron stars and black holes* (1978).
75. R. A. Chevalier, *Astrophys. J.* **346**, 847 (1989), doi:10.1086/168066.
76. J. C. Houck and R. A. Chevalier, *Astrophys. J.* **376**, 234 (1991), doi:10.1086/170272.
77. R. Ruffini and J. Wilson, *Phys. Rev. Lett.* **31**, 1362 (1973), doi:10.1103/PhysRevLett.31.1362.
78. C. L. Fryer, F. Herwig, A. Hungerford and F. X. Timmes, *Astrophys. J. Lett.* **646**, L131 (2006), arXiv:astro-ph/0606450, doi:10.1086/507071.
79. L. Izzo et al., *Astron. Astrophys.* **543**, A10 (2012), arXiv:1202.4374 [astro-ph.HE], doi:10.1051/0004-6361/201117436.
80. A. V. Penacchioni et al., *Astron. Astrophys.* **551**, A133 (2013), arXiv:1301.6014 [astro-ph.HE], doi:10.1051/0004-6361/201220679.
81. R. Ruffini et al., *Astron. Rep.* **59**, 626 (2015), doi:10.1134/S1063772915070094.
82. R. Ruffini, *Astron. Astrophys. Suppl. Ser.* **138**, 513 (1999), arXiv:astro-ph/9905072, doi:10.1051/aas:1999331.
83. R. Ruffini, C. L. Bianco, F. Frascchetti, S.-S. Xue and P. Chardonnet, *Astrophys. J. Lett.* **555**, L113 (2001), arXiv:astro-ph/0106532, doi:10.1086/323176.
84. C. L. Bianco and R. Ruffini, *Astrophys. J. Lett.* **620**, L23 (2005), arXiv:astro-ph/0501390, doi:10.1086/428500.
85. A. V. Penacchioni et al., *Int. J. Mod. Phys. Conf. Ser.* **23**, 254 (2013), doi:10.1142/S2010194513011409.
86. C. Kouveliotou et al., *Astrophys. J. Lett.* **779**, L1 (2013), arXiv:1311.5245 [astro-ph.HE], doi:10.1088/2041-8205/779/1/L1.
87. D. A. Perley et al., *Astrophys. J.* **781**, 37 (2014), arXiv:1307.4401 [astro-ph.HE], doi:10.1088/0004-637X/781/1/37.
88. M. Ackermann et al., *Science* **343**, 42 (2014), doi:10.1126/science.1242353.
89. M. Ackermann et al., *Astrophys. J.* **209**, 11 (2013), arXiv:1303.2908 [astro-ph.HE], doi:10.1088/0067-0049/209/1/11.
90. M. Kovacevic et al., *Astron. Astrophys.* **569**, A108 (2014), arXiv:1408.6227 [astro-ph.HE], doi:10.1051/0004-6361/201424700.
91. R. Ruffini et al., *GRB Coordinates Network* **14526**, 1 (2013).
92. A. de Ugarte Postigo et al., *GRB Coordinates Network* **14646**, 1 (2013).
93. A. Trotter et al., *GRB Coordinates Network* **1466** (2013).
94. A. J. Levan et al., *GRB Coordinates Network* **14686**, 1 (2013).
95. A. J. Levan et al., *Astrophys. J.* **792**, 115 (2014), arXiv:1307.5338 [astro-ph.HE], doi:10.1088/0004-637X/792/2/115.
96. D. Xu et al., *Astrophys. J.* **776**, 98 (2013), arXiv:1305.6832 [astro-ph.HE], doi:10.1088/0004-637X/776/2/98.

Predicting Supernova Associated to Gamma-Ray Burst 130427A*

Y. Wang^{1,2}, R. Ruffini^{1,2,3,4**}, M. Kovacevic^{1,2}, C. L. Bianco^{1,2}, M. Enderli^{1,2},
M. Muccino^{1,2}, A. V. Penacchioni⁴, G. B. Pisani^{1,2}, and J. A. Rueda⁴

¹*Dip. di Fisica and ICRA, Sapienza Università di Roma,
Piazzale Aldo Moro 5, I-00185 Rome, Italy*

²*ICRANet, Piazza della Repubblica 10, I-65122 Pescara, Italy*

³*Université de Nice Sophia Antipolis, CEDEX 2, Grand Château Parc Valrose, Nice, France*

⁴*ICRANet-Rio, Centro Brasileiro de Pesquisas Fisicas,
Rua Dr. Xavier Sigaud 150, Rio de Janeiro, RJ, 22290-180 Brazil*

Received January 26, 2015

Abstract—Binary systems constituted by a neutron star and a massive star are not rare in the universe. The Induced Gravitational Gamma-ray Burst (IGC) paradigm interprets Gamma-ray bursts as the outcome of a neutron star that collapses into a black hole due to the accretion of the ejecta coming from its companion massive star that underwent a supernova event. GRB 130427A is one of the most luminous GRBs ever observed, of which isotropic energy exceeds 10^{54} erg. And it is within one of the few GRBs obtained optical, X-ray and GeV spectra simultaneously for hundreds of seconds, which provides an unique opportunity so far to understand the multi-wavelength observation within the IGC paradigm, our data analysis found low Lorentz factor blackbody emission in the Episode 3 and its X-ray light curve overlaps typical IGC Golden Sample, which comply to the IGC mechanisms. We consider these findings as clues of GRB 130427A belonging to the IGC GRBs. We predicted on GCN the emergence of a supernova on May 2, 2013, which was later successfully detected on May 13, 2013.

DOI: 10.1134/S1063772915070148

1. INTRODUCTION: IGC PARADIGM

The Induced Gravitational Collapse (IGC) GRB paradigm describes a naturally evolutionary consequence of a binary system composed by a massive star and a neutron star, and includes four episodes corresponding to (1) Neutron star collapses into a black hole due to the accretion of the ejecta coming from its companion massive star that undergoes a supernova [1]. (2) The electron–positron pairs generated from the dyadosphere ballistically expands and engulfs baryonic matter, later collides at ultra-relativistic velocities with the ISM and filaments, which gives origin to the GRB [2]. (3) The starting of final steeper decay of the lightcurve, usually follows a plateau or a power-law with a constant decay index [3]. (4) The emergence of supernova in

optical band, normally nearly 10 days after the GRB trigger in its rest frame.

2. PREDICTION

The IGC paradigm demands special characteristics for the GRBs generated in the aforementioned binary system, such as the thermal radiation from accretion and supernova remnant, the overlapping of late afterglow and so on [4, 5]. In [3] we list some GRBs complying to the IGC paradigm, we call these GRBs the golden sample. After the first days' observation of the GRB 130427A, we found this new GRB exhibited similar features of the golden sample, especially the overlapping of the late decay with the golden sample, shown in Figure 1, which makes us consider this new GRB as a member of the IGC GRBs, immediately we send a letter to GCN on May 2, 2013, predicting that a supernova would appear in about 10 days [6]. Indeed, starting from May 13, 2013, the telescopes GTC, VLT and HST observed the signals of this supernova.

In this presentation, we will mainly discuss some evidences making GRB 130427A belong to the IGC

*The text was submitted by the authors in English.

**E-mail: Ruffini@icra.it

Paper was presented at the international conference in honor of Ya.B. Zeldovich 100th Anniversary “Subatomic Particles, Nucleons, Atoms, Universe: Processes and Structure” held in Minsk, Belarus, in March 10–14, 2014. Published by the recommendation of the special Editors: S.Ya. Kilin, R. Ruffini, and G.V. Vereshchagin.

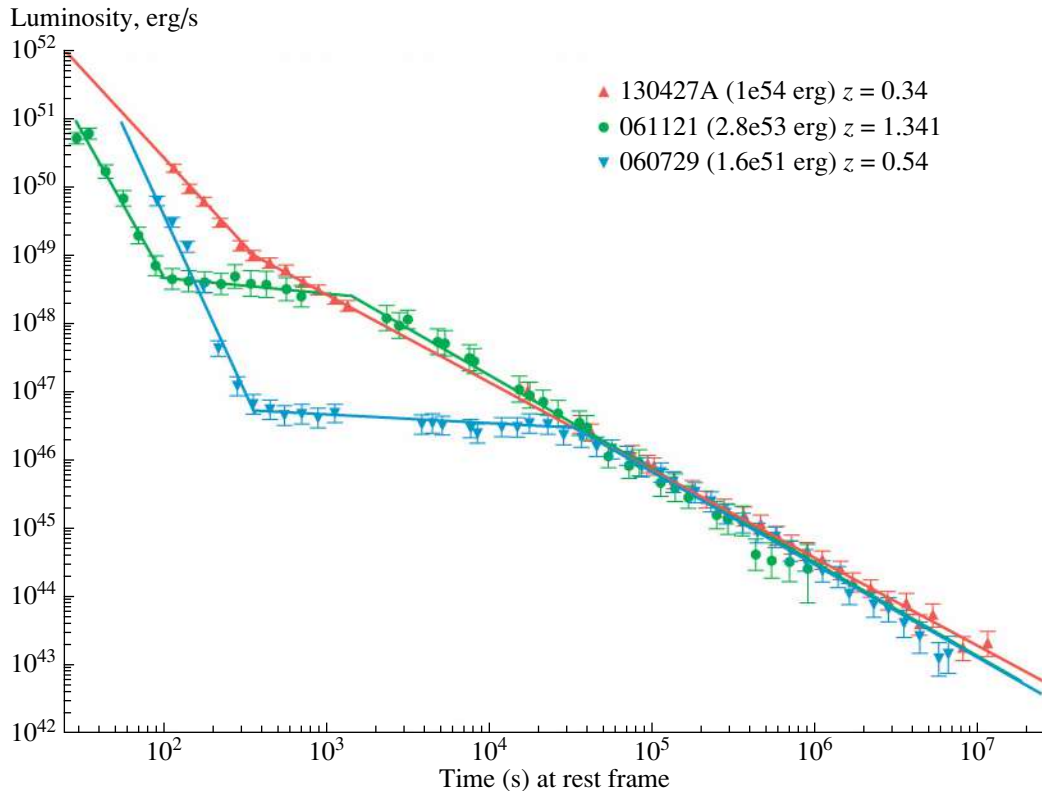


Fig. 1. An example of GRB 130427A overlaps two GBBs with different magnitude of isotropic energy from Golden Sample. GRBs' name, isotropic energy, and redshift are shown on the figure.

GRBs, specially the low Lorentz factor thermal radiator, and the multi-wave length observation in the Episode 3 of the GRB 130427A.

3. OBSERVATION AND DATA ANALYSIS

GRB 130427A was triggered by the *Fermi*-GBM at 07:47:06.42 UT on April 27, 2013 [7]. And the *Swift* Burst Alert Telescope (BAT) was triggered 51.1 s later. The *Swift* X-ray Telescope (XRT) and the *Swift* Ultra Violet Optical Telescope (UVOT) began observing 195 s and 181 s after the GBM trigger respectively [8]. On the ground, the Gemini North telescope at Hawaii [9], the Nordic Optical Telescope (NOT) [10] and the VLT/X-shooter [11] also took part in the observation and detected the redshift $z = 0.34$.

GRB 130427A is one of the few GRBs which has hundreds of seconds simultaneous data in the optical, x-ray and GeV emission [12], especially precious is its GeV emission, due to the long duration, high intensity and containing the highest energy photon (95.3 GeV) ever observed [13].

Following the standard procedure [14–16], we did the data reduction of Fermi and Swift satellite, using an unbinned likelihood method with Fermi Science

Tools v9r27p1 and NASA's Heasoft 6.14 with relevant calibration files. Data were obtained from Fermi Science Support Center,¹ and UKSSDC² light curve and spectrum are shown in Figs. 2 and 4. For the spectrum, we select 196–461 s because Swift XRT started observation at 195 s (Maselli et al. 2013), and the thermal component, which we are especially interested in, gradually fades away after 461 s.

4. THERMAL RADIATION IN EPISODE 3

By analyzing the X-ray data from 195 s to 461 s, we found that adding a blackbody component could efficiently improve the fitting solely by a single power law, the obtained blackbody temperature is in the range of 0.3 keV to 0.5 keV, if the blackbody radiation is isotropic, the radiation radius can be deduced from about 7×10^{12} cm to 2.8×10^{13} cm, with the expansion speed at $0.8c$, c is the speed of light. By analyzing the optical absorption lines of GRB associated supernovae, normally the speed of supernovae at about 10 days after the GRB trigger is around $0.1c$, the classical supernova theory holds the opinion that before the supernova appearing in optical band,

¹ <http://fermi.gsfc.nasa.gov>

² <http://www.swift.ac.uk>

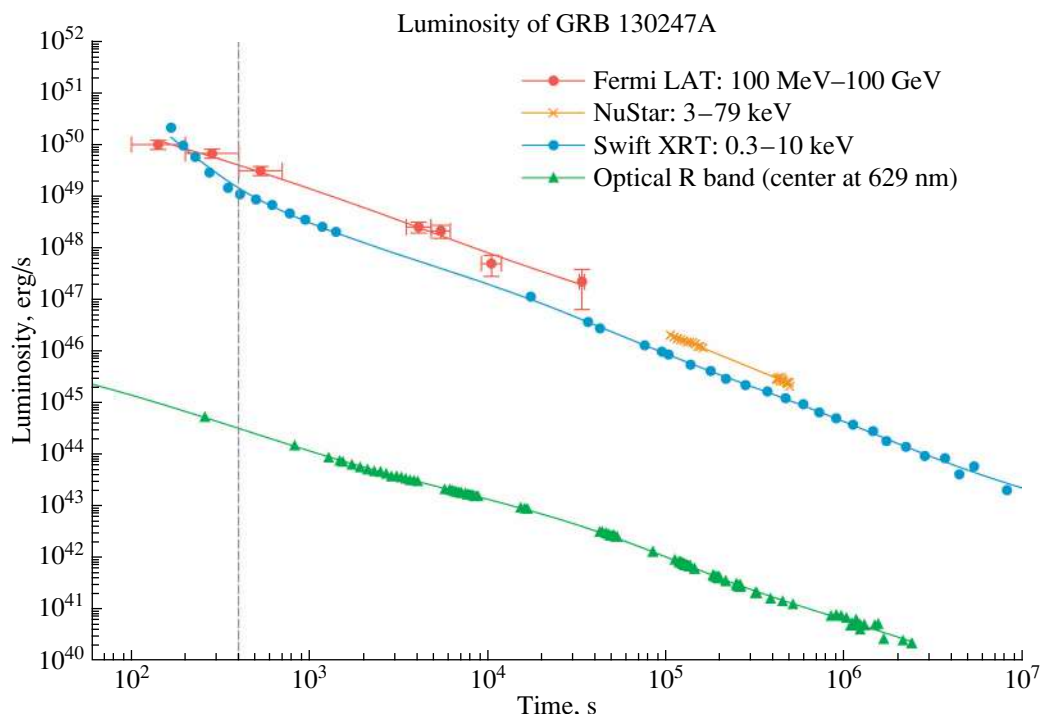


Fig. 2. The Multi-wavelength lightcurve of GRB 130427A. The GeV emission from Fermi LAT (red) and soft X-ray from Swift XRT (blue) are deduced from the original data. NuStar [17] provides higher energy X-ray than Swift XRT. The optical R band data comes from ground based telescopes [18]. The vertical dash line splits Episode 2 and Episode 3.

it undergoes a period of deceleration, from which we legitimately infer that the blackbody with the speed of $0.8c$ in the GRB 130427A probably is the supernova ejecta that IGC paradigm searches. For the GRB 130427A, or the broader IGC GRBs, the discovery of the supernova ejecta obviously is a key clue for predicting the emergence of supernova in the optical band.

5. MULTI-WAVELENGTH ANALYSIS

In the IGC paradigm, we separate Episode 2 and Episode 3 by the ending time of the prompt emission. Figure 3 demonstrates the light curve of the first 2 episodes, and Fig. 2 shows the light curve of Episode 3. The very high energy (100 MeV–100 GeV) emission is quite dim in the first 10 s when gamma and X-ray dominate the emission, then the very high energy emission raises up coincidentally with the gamma and hard X-ray prompt emissions dropping down. There is no soft X-ray observation during the first prompt emission, *Swift*-XRT starts to observe soft X-ray from 195 s, and the soft X-ray fluence is higher than the γ -ray observed by *Fermi*-GBM. Soft X-ray may have a flare between 100 s and 200 s, if it shares similar evolution as hard X-ray observed by *Swift*-BAT. In Fig. 2, clearly, the light curves of multi-wavelength from optical, X-ray to GeV follow power law decay,

and share similar decaying slope after the bending point around 400 s. We are currently attempting to link the mechanism of the possible soft X-ray flare to the thermal emission inside it, a direct and reasonable explanation is the existence of an extra process.

In the Episode 3, light curves have similar slope, but the spectra which extends 10 magnitudes of orders, from optical to GeV emission, can not be fitted by a single power law very well, instead the broken power-law gives a better fitting, the X-ray part has a photon index 1.6 ± 0.2 , and the GeV part has a softer photon index 1.9 ± 0.1 , shown in Fig. 4. As far as we know, this is the only relatively explicit multi-wavelength spectrum including GeV emission lasts for hundreds of seconds.

The IGC paradigm considers GeV emission originated from the interaction of neutron star and black hole, and the gamma-ray is described by fireshell model [2], the intensive X-ray and gamma-ray photons block the GeV photons at the beginning of the GRB, which could explain the behavior of GeV emission in Fig. 2. Also in the IGC paradigm, the collision between GRB outflow and supernova remnant is inevitable, which always happens around 100 s [19], and consequently emits thermal photons at the radius about 10^{12} cm, this collision may explain the flare and the associated thermal component.

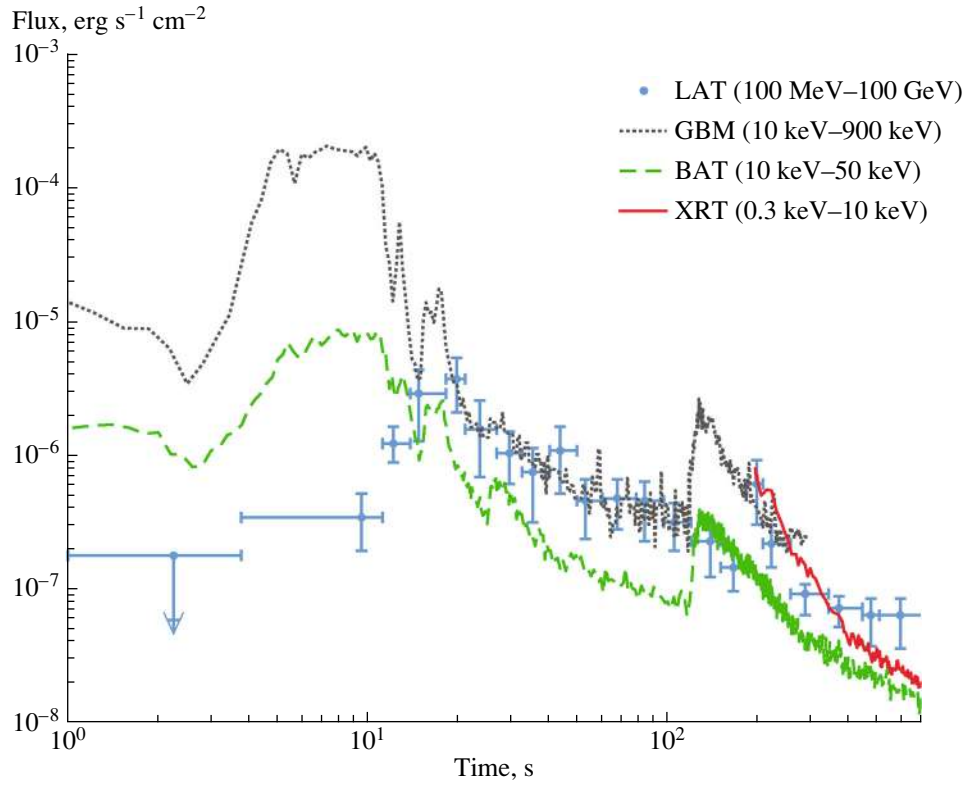


Fig. 3. Flux of first 700 s. Blue points are the *Fermi*-LAT high energy emission from 100 MeV till 100 GeV, grey dotted line represents the *Fermi*-GBM, from 10 keV to 900 keV, green dashed line represents the photons detected by *Swift* BAT from 10 keV to 50 keV, and red solid line is the soft X-ray *Swift*-XRT detection, in the range of 0.3 keV to 10 keV. From this figure, clearly the *Fermi*-LAT emission reaches highest fluence at about 20 s while the gamma-ray detected by *Fermi*-GBM releases most of the energy within the first 10 s.

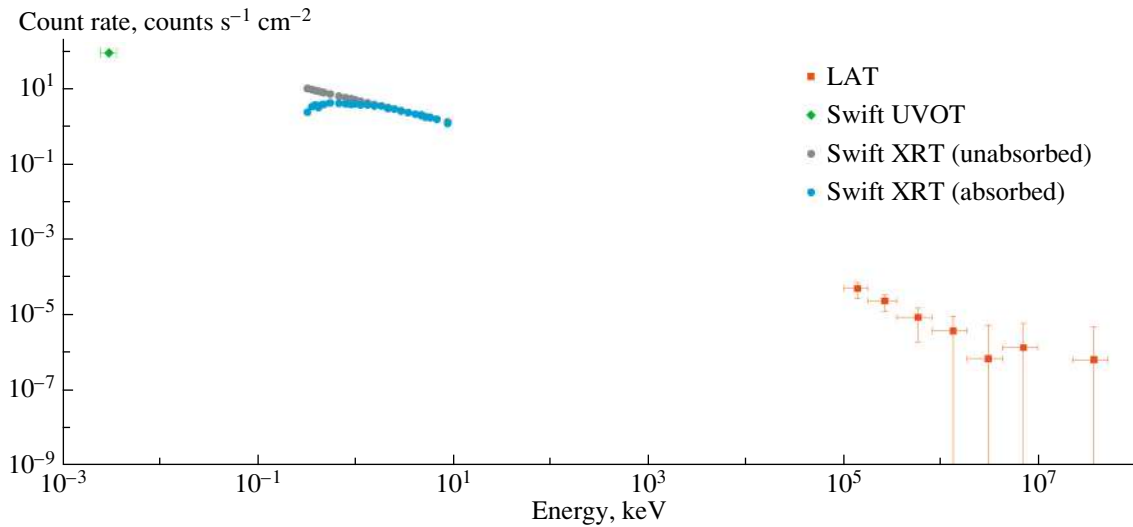


Fig. 4. Spectrum of GRB 130427A between 195 s and 461 s: Swift UVOT (green), Swift XRT (blue), and Fermi LAT (red).

6. CONCLUSION

In conclusion, first of all, the Pisani relation of the power-law overlapping [3], which is independent of energy and observed in all the golden sample,

this energetic GRB 130427A unveils such typical power-law behavior already exists at the early time as $t \sim 100$ s. Secondly, the thermal emission coming from the GRB outflow and SN remnant collision in

the early seconds of Episode 3 confirms the supernova event. Finally the multi-wavelength behavior occurs in optical, X-ray and GeV emissions conform to the IGC paradigm.

REFERENCES

1. J. A. Rueda and R. Ruffini, *Astrophys. J. Lett.* **758**, L7 (2012).
2. R. Ruffini, G. Vereshchagin, and S.-S. Xue, *Phys. Rep.* **487**, 1 (2010).
3. G. B. Pisani, L. Izzo, R. Ruffini, C. L. Bianco, M. Muccino, A. V. Penacchioni, J. A. Rueda, and Y. Wang, *Astron. Astrophys.* **552**, L5 (2013).
4. L. Izzo, J. A. Rueda, and R. Ruffini, *Astron. Astrophys.* **548**, L5 (2012).
5. A. V. Penacchioni, R. Ruffini, L. Izzo, M. Muccino, C. L. Bianco, L. Caito, B. Patricelli, and L. Amati, *Astron. Astrophys.* **538**, 58 (2012).
6. R. Ruffini, C. L. Bianco, M. Enderli, M. Muccino, A. V. Penacchioni, G. B. Pisani, J. A. Rueda, N. Sahakyan, Y. Wang, and L. Izzo, *GCN Circ.* **14526** (2013).
7. A. von Kienlin, *GCN Circ.* **14473** (2013).
8. A. Maselli, A. P. Beardmore, A. Y. Lien, V. Mangano, C. J. Mountford, K. L. Page, D. M. Palmer, and M. H. Siegel, *GCN Circ.* **14448** (2013).
9. A. J. Levan, S. B. Cenko, D. A. Perley, and N. R. Tanvir, *GCN Circ.* **14455** (2013).
10. D. Xu, A. de Ugarte Postigo, S. Schulze, J. Jessen-Hansen, G. Leloudas, T. Kruehler, J. P. U. Fynbo, and P. Jakobsson, *GCN Circ.* **14478** (2013).
11. H. Flores, S. Covino, D. Xu, T. Kruehler, J. Fynbo, B. Milvang-Jensen, A. de Ugarte Postigo, L. Kaper, and K. Wiersema, *GCN Circ.* **14491** (2013).
12. M. Ackermann, M. Ajello, K. Asano, W. B. Atwood, M. Axelsson, L. Baldini, J. Ballet, G. Barbiellini, M. G. Baring, D. Bastieri, et al., *Science* **343**, 42 (2013).
13. Y.-Z. Fan, P. H. T. Tam, F.-W. Zhang, Y.-F. Liang, H.-N. He, B. Zhou, R.-Z. Yang, Z.-P. Jin, and D.-M. Wei, *Astrophys. J.* **776**, 95 (2013).
14. P. Romano, S. Campana, G. Chincarini, J. Cummings, G. Cusumano, S. T. Holland, V. Mangano, T. Mineo, K. L. Page, V. Pal'shin, et al., *Astron. Astrophys.* **456**, 917 (2006).
15. P. A. Evans, A. P. Beardmore, K. L. Page, L. G. Tyler, J. P. Osborne, M. R. Goad, P. T. O'Brien, L. Vetere, J. Racusin, D. Morris, et al., *Astron. Astrophys.* **469**, 379 (2007).
16. P. A. Evans, A. P. Beardmore, K. L. Page, J. P. Osborne, P. T. O'Brien, R. Willingale, R. L. C. Starling, D. N. Burrows, O. Godet, L. Vetere, et al., *Mon. Not. R. Astron. Soc.* **397**, 1177 (2009).
17. C. Kouveliotou, J. Granot, J. L. Racusin, E. Bellm, G. Vianello, S. Oates, C. L. Fryer, S. E. Boggs, F. E. Christensen, W. W. Craig, et al., *Astrophys. J.* **779**, L1 (2013).
18. D. A. Perley, S. B. Cenko, A. Corsi, N. R. Tanvir, A. J. Levan, D. A. Kann, E. Sonbas, K. Wiersema, W. Zheng, X. H. Zhao, et al., *Astrophys. J.* **781**, 37 (2013).
19. R. Ruffini, G. V. Vereshchagin, and Y. Wang (2014, in preparation).

The Genuine Short GRB 090227B and the Disguised by Excess GRB 090510[‡]

Marco Muccino^{1,2*}, Carlo Luciano Bianco^{1,2}, Luca Izzo^{1,2},
Yu Wang^{1,2}, Maxime Enderli^{1,3}, Milos Kovacevic^{1,3},
Giovanni Battista Pisani^{1,3}, Ana Virginia Penacchioni⁴, and Remo Ruffini^{1,2,3,4}

¹Dipartimento di Fisica and ICRA, Sapienza Università di Roma, Piazzale Aldo Moro 5, I-00185 Rome, Italy

²ICRANet, Piazza della Repubblica 10, I-65122 Pescara, Italy

³Université de Nice Sophia Antipolis, Nice, CEDEX 2, Grand Château Parc Valrose, Nice, France

⁴ICRANet-Rio, CBPF, Rua Dr. Xavier Sigaud 150, Rio de Janeiro, RJ, 22290-180, Brazil

Received April 15, 2014

Abstract—GRB 090227B and GRB 090510, traditionally classified as short gamma-ray Bursts (GRBs), indeed originate from different systems. For GRB 090227B we inferred a total energy of the e^+e^- plasma $E_{e^+e^-}^{\text{tot}} = (2.83 \pm 0.15) \times 10^{53}$ erg, a baryon load of $B = (4.1 \pm 0.05) \times 10^{-5}$, and a CircumBurst Medium (CBM) average density $\langle n_{\text{CBM}} \rangle = (1.90 \pm 0.20) \times 10^{-5} \text{ cm}^{-3}$. From these results we have assumed the progenitor of this burst to be a symmetric neutron stars (NSs) merger with masses $m = 1.34 M_{\odot}$, radii $R = 12.24 \text{ km}$. GRB 090510, instead, has $E_{e^+e^-}^{\text{tot}} = (1.10 \pm 0.06) \times 10^{53}$ erg, $B = (1.45 \pm 0.28) \times 10^{-3}$, implying a Lorentz factor at transparency of $\Gamma = (6.7 \pm 1.7) \times 10^2$, which are characteristic of the long GRB class, and a very high CBM density, $\langle n_{\text{CBM}} \rangle = (1.85 \pm 0.14) \times 10^3 \text{ cm}^{-3}$. The joint effect of the high values of Γ and of $\langle n_{\text{CBM}} \rangle$ compresses in time and “inflates” in intensity in an extended afterglow, making appear GRB 090510 as a short burst, which we here define as “disguised short GRB by excess” occurring an overdense region with 10^3 cm^{-3} .

DOI: 10.1134/S0202289314030116

1. INTRODUCTION

After the initial BATSE classification of Gamma-Ray Bursts (GRBs) into “long” and “short” ones [1–4], in the recent years, owing to the observations by the *Swift* satellite [5], a third class of bursts with hybrid properties between short and long ones has been discovered: “short GRBs with extended emission” [6].

In the Fireshell model [7, 9], GRBs originate from an optically thick e^+e^- plasma in thermal equilibrium [10], formed around a Kerr-Newman black hole. This shell of plasma expands and engulfs a baryonic remnant, keeping its thermal equilibrium [11]. The engulfed baryonic mass M_B is described by the Baryon load $B = M_B c^2 / E_{e^\pm}^{\text{tot}}$, where $E_{e^\pm}^{\text{tot}}$ is the total plasma energy. The canonical GRB is composed of

emission at the transparency, the Proper-GRB (P-GRB), and an extended afterglow, due to collisions of accelerated baryons with the CircumBurst Medium (CBM) with density n_{CBM} . In this scenario the “short GRBs with extended emission” [6] have been successfully interpreted as “disguised short bursts” [12–14]: canonical long bursts with $3 \times 10^{-4} \leq B \leq 10^{-2}$, exploding in halos of their host galaxies, with $\langle n_{\text{CBM}} \rangle \approx 10^{-3} \text{ cm}^{-3}$. “Genuine short” GRBs [8, 15], instead, are characterized by smaller baryon loads, $B \lesssim 10^{-5}$ (see Fig. 1, right plot), therefore the energy emitted in their P-GRB is predominant, and an additional nonthermal component originating from the extended afterglow is expected.

We present our results on two short bursts: GRB 090227B, the first genuine short GRB, originating from a symmetric binary NSs merger [16], and GRB 090510, a *disguised short GRBs by excess* occurring in a medium with $\langle n_{\text{CBM}} \rangle \approx 10^3 \text{ cm}^{-3}$ [17].

2. THE GENUINE SHORT GRB 090227B

GRB 090227B has been detected by the *Fermi*-GBM [18] and the *Konus*-Wind [19] detectors. Due

*E-mail: marco.muccino@cra.it

[‡]Based on a plenary talk given at the 11th International Conference on Gravitation, Astrophysics and Cosmology of Asia-Pacific Countries (ICGAC-11), October 1–5, 2013, Almaty, Kazakhstan.

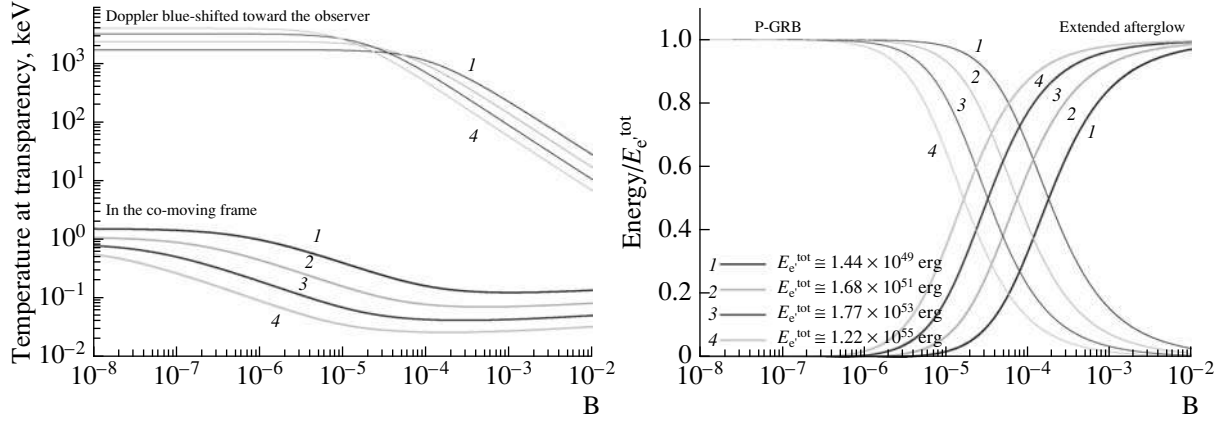


Fig. 1. The comoving and blueshifted temperatures of a plasma at the transparency, and the fraction of energy radiated in the P-GRB and in the extended afterglow as functions of B for selected values of $E_{e^+e^-}^{\text{tot}}$.

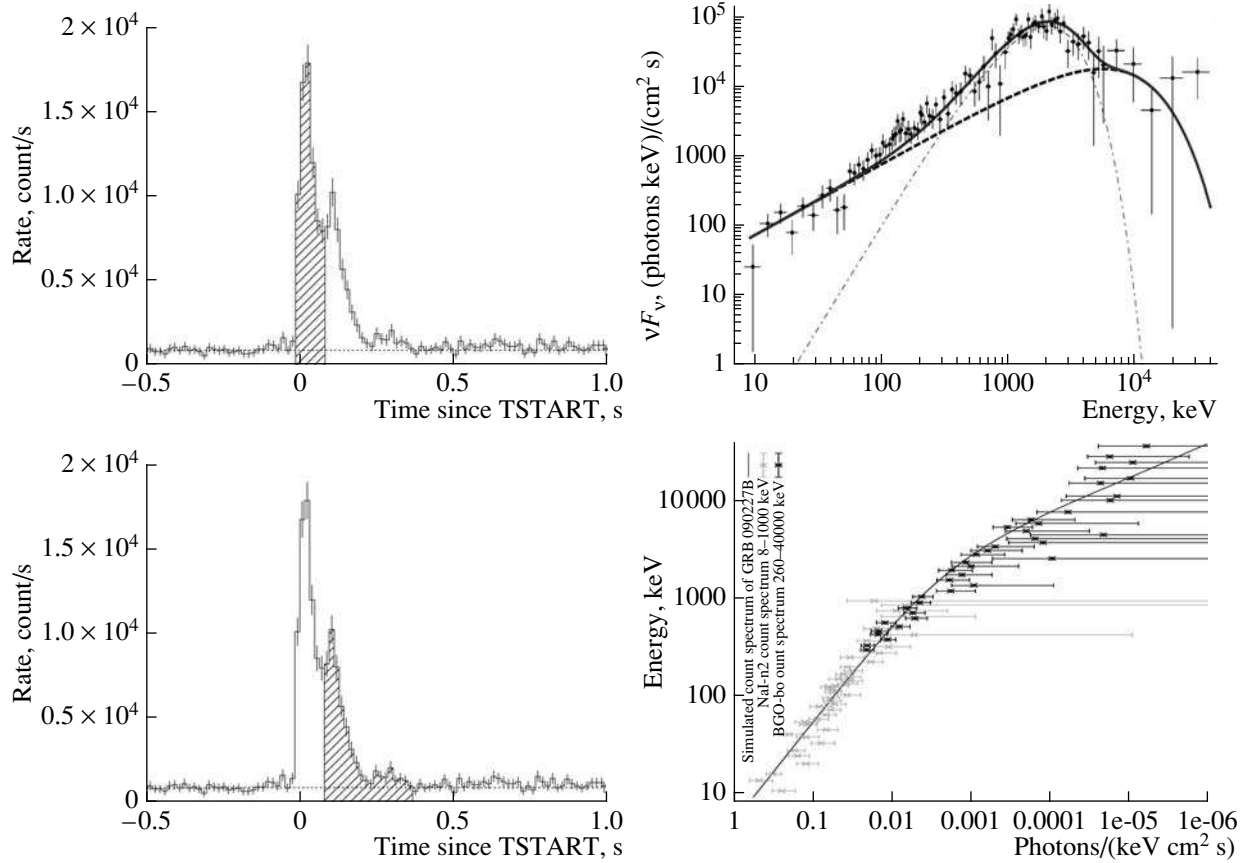


Fig. 2. Left: the NaI-n2 light curves of the P-GRB (upper panel) and the extended afterglow (lower panel). Right: the simulated νF_ν spectrum of a P-GRB (upper panel, solid red curve) as a sum of the onset of the extended afterglow (8 keV–40 MeV, dashed blue line) and of the BB emission of the P-GRB (dashed-dotted green line), compared to the observed data; (lower panel) the simulated photon spectrum of the extended-afterglow (8 keV–40 MeV) compared to the NaI-n2 (green) and the BGO-b0 (blue) data in the time interval from $T_0 + 0.015$ s to $T_0 + 0.385$ s.

to the lack of X-rays and optical follow-up, its redshift is unknown.

We have analyzed the *Fermi*-GBM data from the

NaI-n2 (8–900 keV) and the BGO-b0 (250 keV–40 MeV) detectors. The NaI-n2 light curve (see Fig. 2, left panels) shows two spike-like structures.

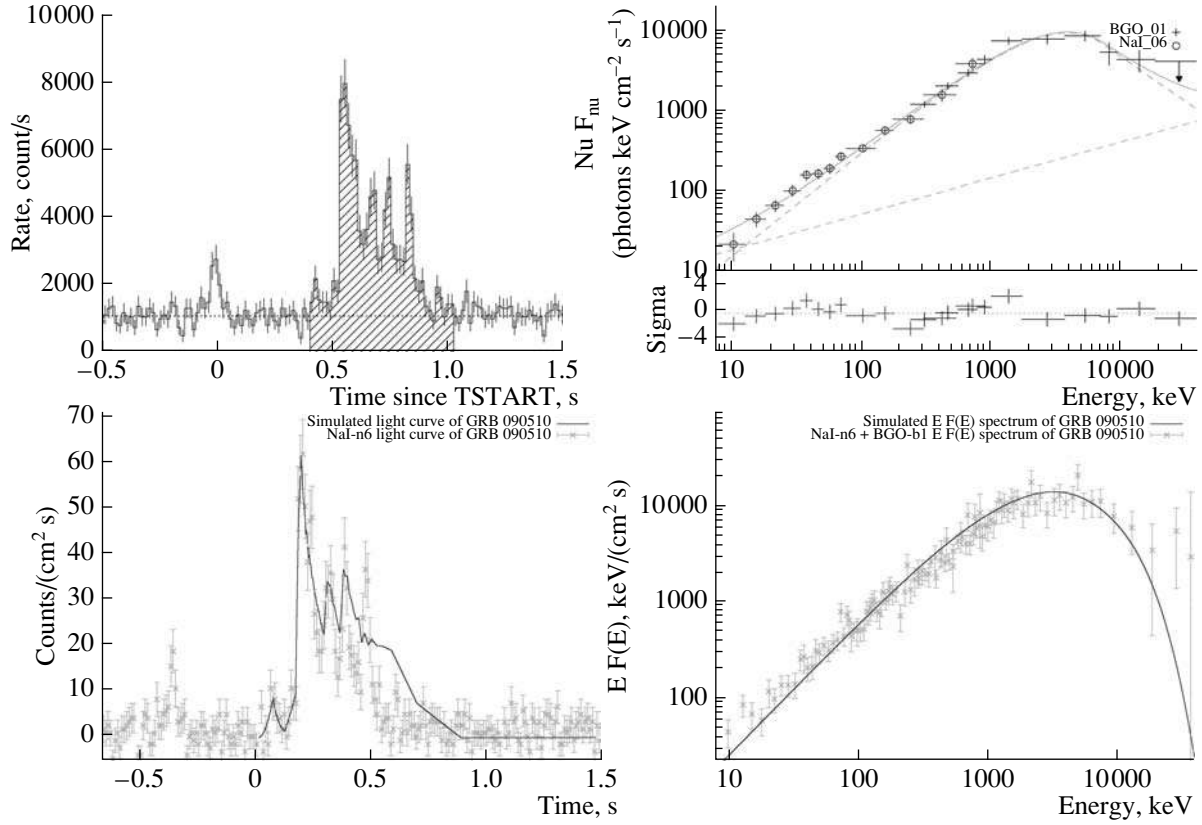


Fig. 3. Upper panels: the NaI-n6 light curve (left) and the NaI+BGO νF_ν spectrum in the ΔT_2 time interval. Lower panels: (left) the simulated light curve and spectrum (8 keV–40 MeV) of the early ~ 0.4 s of the extended afterglow (right).

We indicate the trigger time by T_0 . The spectrum of the first spike (from $T_0 - 0.016$ s to $T_0 + 0.080$ s) is best fitted by black body (BB) plus Band [20] model (see Table 1). The best fit of the second spike (from $T_0 + 0.080$ s to $T_0 + 0.368$ s) is a Band model (see Table 1). Consequently, we have interpreted the first spike, where a thermal spectrum is present, as a P-GRB and the second one as an extended afterglow.

Having identified the P-GRB, the correct value of B is determined when the theoretical energy and temperature of the P-GRB match the observed ones of thermal emission, namely, E_{BB} and kT_{obs} . Since the redshift z of GRB 090227B is unknown, we have estimated the ratio $E_{\text{P-GRB}}/E_{e^+e^-}^{\text{tot}}$ from the ratio of the observed fluences $S_{\text{BB}}/S_{\text{tot}}$. The fluence of the BB component of the P-GRB (see Table 1, first interval) is $S_{\text{BB}} = (1.54 \pm 0.45) \times 10^{-5}$ erg/cm². The total fluence of the burst is $S_{\text{tot}} = (3.79 \pm 0.20) \times 10^{-5}$ erg/cm² and has been evaluated in the time interval from $T_0 - 0.016$ s to $T_0 + 0.896$ s. Therefore we have $E_{\text{P-GRB}}/E_{e^+e^-}^{\text{tot}} = (40.67 \pm 0.12)\%$. From the right plot in Fig. 1, for each energy ratio we have a possible range for B and $E_{e^+e^-}^{\text{tot}}$. In turn, for each couple of B and $E_{e^+e^-}^{\text{tot}}$ we can determine the blueshifted

temperature kT_{blue} (Fig. 1, left plot) and, correspondingly, the redshift by the ratio $kT_{\text{blue}}/kT_{\text{obs}} = 1 + z$. We have computed the isotropic energy E_{iso} for each value of z , searching for the correct value fulfilling the condition $E_{\text{iso}} \equiv E_{e^+e^-}^{\text{tot}}$. We have found the equality at $z = 1.61 \pm 0.14$ for $B = (4.13 \pm 0.05) \times 10^{-5}$ and $E_{e^+e^-}^{\text{tot}} = (2.83 \pm 0.15) \times 10^{53}$ erg. The corresponding Lorentz factor at the transparency is $\Gamma_{\text{tr}} = (1.44 \pm 0.01) \times 10^4$. From a simulation of the extended afterglow light curve and spectrum [29, 30], we have derived the average CBM density $\langle n_{\text{CBM}} \rangle = (1.90 \pm 0.20) \times 10^{-5}$ cm⁻³, typical of the galactic halos environment. In Fig. 2, lower right panel, we have plotted the simulated spectrum of early ~ 0.4 s of emission. In the upper right panel, we have reproduced the total observed spectrum of the first spike (8–40000 keV) as a sum of the thermal spectrum of the P-GRB and of the early extended afterglow onset (from $T_0 + 0.015$ s to $T_0 + 0.080$ s).

3. THE DISGUISED SHORT BY EXCESS GRB 090510

GRB 090510 has been detected by the *Fermi*-GBM [21], *Fermi*-LAT [22], *Swift*-BAT [23], *AGILE* [24], *Konus-Wind* [25], and *Suzaku*-WAM [26]

Table 1. Results of spectral analysis of the P-GRB (best fit BB + Band model) and of the extended afterglow (EA, best fit Band model) in the energy range 8 keV–40 MeV

	kT (keV)	α	β	E_p (keV) (erg cm ⁻² s ⁻¹)	$F_{\text{tot}}/10^{-5}$ (erg cm ⁻² s ⁻¹)	$F_{BB}/10^{-5}$	C-STAT/DOF
P-GRB	517 ± 28	-0.80 ± 0.05	-2.14 ± 0.17	952 ± 251	31.3 ± 1.3	16.1 ± 4.7	263.51/239
EA		-0.79 ± 0.06	-2.01 ± 0.10	1048 ± 178	2.66 ± 0.26		276.50/241

Table 2. The ΔT_1 time interval: parameters of BB + PL and Compt models in the energy range 8–7000 keV. The ΔT_2 time interval: parameters of the best fits (Band + PL) in the energy ranges 8 keV–30 GeV (GBM + LAT)

Int	Model	$kT-E_p$ (keV)	α	β	γ	$F_{\text{tot}}/10^{-6}$ (erg cm ⁻² s ⁻¹)	C-STAT/DOF
ΔT_1	BB + PL	34.2 ± 7.5	-1.10 ± 0.14	7.6 ± 1.3	188.60/193
	Compt	990 ± 554	-0.81 ± 0.22	4.4 ± 1.6	189.97/194
ΔT_2	Band + PL	3941 ± 346	-0.71 ± 0.07	-2.97 ± 0.26	-1.62 ± 0.05	83.3 ± 6.8	199.20/256

detectors. Optical observations by VLT/FORS2 located its host galaxy at redshift $z = 0.903 \pm 0.003$ [27].

We have analyzed the *Fermi*-GBM data from NaI-n6 (8–900 keV) and BGO-b1 (260 keV–40 MeV) detectors and the LAT data in the energy range 100 MeV–30 GeV. The light curve of GRB 090510 is composed of two episodes, 0.5 s apart (see Fig. 3, upper left plot). From the analysis of the first episode, from $T_0 - 0.064$ s to $T_0 + 0.016$ s (in the following ΔT_1), we have found that BB+PL and Compt are the viable best fits (see Table 2). From our theoretical interpretation, the BB+PL, being equally probable as the Compt model, is adopted for its physical meaning. Therefore, the interval ΔT_1 has

been identified as the P-GRB. The total energy of the first episode is $E_1 = (2.28 \pm 0.39) \times 10^{51}$ erg.

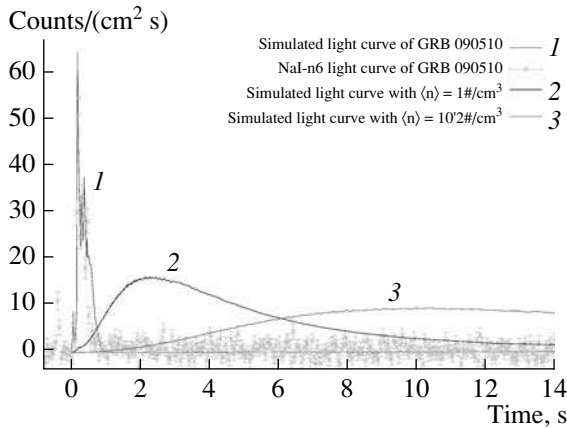
The second episode, from $T_0 + 0.400$ s to $T_0 + 1.024$ s (in the following ΔT_2), is interpreted as the extended afterglow. Combining the GBM (8 keV–40 MeV) and the LAT data up to 30 GeV [28], the best fit of this episode is Band+PL, and its total energy is $E_2 = (1.08 \pm 0.06) \times 10^{53}$ erg. The results are shown in Fig. 3 and Table 2.

We have started a simulation using as input parameters $E_{e^+e^-}^{\text{tot}}$, constrained to the isotropic energy of the burst, $E_{\text{iso}} = (1.10 \pm 0.06) \times 10^{53}$ erg, and the Baryon load $B = (1.45 \pm 0.28) \times 10^{-3}$, determined as illustrated in Section 2. This implies a Lorentz factor at transparency $\Gamma_{\text{tr}} = (6.7 \pm 1.6) \times 10^2$. From simulation of the extended afterglow light curve (see Fig. 3, lower left panel) and of the corresponding spectrum (8 keV–40 MeV) of the early ~ 0.4 s of the emission (lower right panel), we have inferred a very high CBM average density, $\langle n_{\text{CBM}} \rangle = (1.85 \pm 0.14) \times 10^3$ cm⁻³.

4. CONCLUSIONS

Although their intrinsic duration is $T_{90} < 2$ s, a detailed time-resolved spectral analysis has allowed for shedding light on the astrophysical origin of GRB 090227B and GRB 090510, proving that the GRBs classification is indeed much more complex.

GRB 090227B represents a real genuine short burst with $B = (4.13 \pm 0.05) \times 10^{-5}$. This implies that the P-GRB energy is comparable to the one of the extended afterglow. Within the Fireshell scenario, we have determined its cosmological redshift, $z =$

**Fig. 4.** The NaI-n6 light curve (crosses) and the extended afterglow simulations corresponding to $\langle n_{\text{CBM}} \rangle \approx 10^3$ cm⁻³ (1), 1 cm⁻³ (2), and 10^{-2} cm⁻³ (3).

1.61 ± 0.14 , as well as the energy, $E_{e^+e^-}^{\text{tot}} = (2.83 \pm 0.15) \times 10^{53}$ erg, and the Lorentz factor at the transparency, $\Gamma_{\text{tr}} = (1.44 \pm 0.01) \times 10^4$. From the average density of the CBM, $\sim 10^{-5} \text{ cm}^{-3}$, typical of the galactic halo of host galaxies [12–14], we infer that the progenitor of GRB 090227B is a merger of two NSs. In fact, the inferred baryon load is consistent with the mass of the crusts of a symmetric binary system of two neutron stars (NSs), with masses $m = 1.34 M_{\odot}$ and radii $R = 12.24 \text{ km}$, as described by the new model of NS fulfilling the global charge neutrality condition [31]. In this picture, assuming the NL3 nuclear model parameters, the NS critical mass is $M_{\text{cr}} = 2.67 M_{\odot}$. From the above characteristics of the binary NSs, we inferred an absolute upper limit on the energy emitted via gravitational waves, $\sim 9.6 \times 10^{52}$ ergs [32]. More details are given in the published paper [16].

In the case of GRB 090510, we point out that the inferred baryon of $B = 1.45 \times 10^{-3}$, is typical of long GRBs, and not consistent with the values inferred for genuine short bursts, see, e.g., GRB 090227B. Also the CBM density of $\sim 10^3 \text{ cm}^{-3}$, typical of dense clouds in the inner galactic regions, points at a different origin than the merger scenario for real short GRBs, see, e.g., [16, 33, 34]. The short nature of GRB 090510 is a by-product of the relativistic motion of the burst, $\Gamma_{\text{tr}} = (6.7 \pm 1.6) \times 10^2$, and of the high-density environment. Therefore its extended afterglow emission is compressed in time and “inflated” in intensity with respect to the canonical one (see Fig. 4), making it apparently closer to the genuine short class of GRBs [16]. More details are given in the published paper [17].

Within the Fireshell model, three different possible structures of the canonical GRB, supported by observational evidences, are derived.

(1) Long GRBs have $3.0 \times 10^{-4} \lesssim B \leq 10^{-2}$ and explode in environments with densities of $\langle n_{\text{CBM}} \rangle \approx 1 \text{ cm}^{-3}$, which are typical of the inner galactic regions and in agreement with the observational evidence of their occurrence close to star-forming regions.

(2) Disguised short GRBs have the same Baryon load as the long ones, but they occur in different environments. (a) *Disguised short GRBs by excess* occur in overdense media, e.g., $\langle n_{\text{CBM}} \rangle \approx 10^3 \text{ cm}^{-3}$, as in the present case of GRB 090510 [17], therefore the bulk of γ -ray emission occurs at short time-scale as for the genuine short GRBs. (b) *Disguised short GRBs by defect* occur in a CBM with $\langle n_{\text{CBM}} \rangle \approx 10^{-3} \text{ cm}^{-3}$, typical of galactic halos [12–14] as confirmed by the observed offset from the center of their

host galaxies [35, 36]. Therefore, their γ -ray emission is deflated in intensity and characterized by an extended emission, see, e.g., [6, 12–14].

(3) Genuine short GRBs occur for $B \lesssim 10^{-5}$ and $\langle n_{\text{CBM}} \rangle \approx 10^{-5} \text{ cm}^{-3}$, typical again of galactic halos. In these bursts the P-GRB emission is large as the extended afterglow one, and no X-ray emission and, consequently, no redshift determination are expected, as in the case GRB 090227B. Their progenitors are NSs mergers [16].

REFERENCES

1. R. W. Klebesadel, in *Gamma-Ray Bursts—Observations, Analyses and Theories*, ed. C. Ho, R. I. Epstein, and E. E. Fenimore (Cambridge University Press, 1992), p. 161–168.
2. J.-P. Dezalay et al., in *American Institute of Physics Conference Series*, ed. W. S. Paciesas and G. J. Fishman, **265**, 304 (1992).
3. C. Kouveliotou et al., *ApJ Lett.* **413**, L101 (1993).
4. M. Tavani, *ApJ Lett.* **497**, L21 (1998), astro-ph/9802192.
5. N. Gehrels et al., *Nature (London)* **437**, 851 (2005), astro-ph/0505630.
6. J. P. Norris and J. T. Bonnell, *ApJ* **643**, 266 (2006), astro-ph/0601190.
7. R. Ruffini et al., *ApJ Lett.* **555**, L117 (2001), astro-ph/0106534.
8. R. Ruffini et al., *ApJ Lett.* **555**, L113 (2001), astro-ph/0106532.
9. R. Ruffini et al., *ApJ Lett.* **555**, L107 (2001), astro-ph/0106531.
10. A. G. Aksenov, R. Ruffini, and G. V. Vereshchagin, *Phys. Rev. Lett.* **99**, 125003 (2007), arXiv: 0707.3250.
11. R. Ruffini, J. D. Salmonson, J. R. Wilson, and S. Xue, *A&A* **359**, 855 (2000), astro-ph/0004257.
12. M. G. Bernardini et al., *A&A* **474**, L13 (2007).
13. L. Caito et al., *A&A* **521**, A80+ (2010), arXiv: 1006.4842.
14. G. de Barros et al., *A&A* **529**, A130 (2011), arXiv: 1101.5612.
15. R. Ruffini et al., *ApJ Lett.* **581**, L19 (2002), astro-ph/0210648.
16. M. Muccino et al., *ApJ* **763**, 125 (2013), arXiv: 1205.6600.
17. M. Muccino et al., *ApJ* **772**, 62 (2013), arXiv: 1306.3467.
18. S. Guiriec, *GCN* **8921**, 1 (2009).
19. S. Golenetskii et al., *GCN* **8926**, 1 (2009).
20. D. Band et al., *ApJ* **413**, 281 (1993).
21. S. Guiriec, V. Connaughton, and M. Briggs, *GCN* **9336**, 1 (2009).
22. M. Ohno and V. Pelassa, *GCN* **9334**, 1 (2009).
23. E. A. Hovesteen et al., *GCN* **9331**, 1 (2009).
24. F. Longo et al., *GCN* **9343**, 1 (2009).
25. S. Golenetskii et al., *GCN* **9344**, 1 (2009).
26. N. Ohmori et al., *GCN* **9355**, 1 (2009).

27. A. Rau, S. McBreen, and T. Kruehler, GCN **9353**, 1 (2009).
28. M. Ackermann et al., ApJ **716**, 1178 (2010), arXiv: 1005.2141.
29. C. L. Bianco and R. Ruffini, ApJ Lett. **605**, L1 (2004), astro-ph/0403379.
30. B. Patricelli et al., ApJ **756**, 16 (2012), arXiv: 1206.5605.
31. R. Belvedere et al., Nucl. Phys. A **883**, 1 (2012); <http://www.sciencedirect.com/science/article/pii/S0375947412001029>.
32. J. A. Rueda and R. Ruffini, arXiv: 1205.6915.
33. S. I. Blinnikov, I. D. Novikov, T. V. Perevodchikova, and A. G. Polnarev, Sov. Astron. Lett. **10**, 177 (1984).
34. B. Paczynski, ApJ Lett. **494**, L45 (1998), astro-ph/9710086.
35. W. Fong, E. Berger, and D. B. Fox, ApJ **708**, 9 (2010), arXiv: 0909.1804.
36. E. Berger, New Astron. Rev. **55**, 1 (2011), arXiv: 1005.1068.

Analysis of the GRB 081024B

Yerlan Aimuratov,^{1,2} Remo Ruffini,^{1,2,3} Carlo L. Bianco,^{1,2} Maxime Enderli,^{1,2} Luca Izzo,^{1,2}
 Milos Kovacevic,^{1,2} Rahim Moradi,¹ Marco Muccino,¹ Anna V. Penacchioni,^{1,3}
 Giovanni B. Pisani,¹; Jorge A. Rueda,^{1,2} Yu Wang,¹ Elena Zaninoni^{1,3}

¹ *Dip. di Fisica and ICRA, Sapienza Università di Roma,
 Piazzale Aldo Moro 5, I-00185 Roma, Italia.*

² *Université de Nice Sophia Antipolis,
 Grand Château Parc Valrose, Nice, CEDEX 2, France.*

³ *ICRANet-Rio, Centro Brasileiro de Pesquisas Físicas,
 Rua Dr. Xavier Sigaud 150, 22290-180 Rio de Janeiro, Brazil.*

Recently we proposed the existence of two families of short GRBs, both originating from neutron star mergers: family-1 short bursts with $E_{iso} < 10^{52}$ erg and rest-frame spectral peak energy $E_{peak} < 2$ MeV, leading to a massive neutron star as the merged core; family-2 short bursts with $E_{iso} > 10^{52}$ erg and $E_{peak} > 2$ MeV, leading to a black hole as merged core. After the identification of the prototype GRB 090227B and GRB 140619B, we present the results of the analysis of GRB 081024B within the theoretical fireshell model. The presence of a short-lived high energy emission, which is expected to originate from the newly-born black hole, thus places this GRB 081024B among the family-2 short GRBs. From the detailed analysis we derived the redshift of the source $z = 2.56 \pm 1.63$, its isotropic energy $E_{iso} = (1.38 \pm 0.78) \times 10^{52}$ erg, and baryon load $B = (5.885 \pm 0.42) \times 10^{-5}$. These values are consistent with the ones found in GRBs 090227B, 090510 and 140619B.

Keywords: Gamma-ray burst; GRB 081024B; fireshell model.

1. Introduction

Since its discovery in 1967 and to the date, constantly improving space missions *BATSE*,¹ *Beppo-SAX*,² *SWIFT*,³ *FERMI*⁴ for observational studies of gamma-ray bursts (hereafter GRBs) reveal the growing variety of such type extragalactic events, exposing strict verification of existing theoretical models.^{5–11}

To the moment it occurred, GRB 081024B was the first clear detected short burst with GeV emission.^{12,13} Together with longer lasting high-energy bursts, reported by previous experiments, it shows new features allowing us to propose different gamma-ray emission processes between low and high-energy photons.

The previously done analysis on the GRB 081024B searched¹⁴ for differences and similarities in a spectra between short-hard and long lasting bursts. For the spectral lags in the hard-to-soft spectra evolution there is not an energy-dependent delay. They also noted that emission at high energy is greater than one from the lower range, and suggested that short GRBs may have greater efficiency in emitting gamma-rays.

Mostly delayed and relatively extended high-energy photons let suppose different mechanisms in acceleration or emission processes compared with the low-energetic episode.¹⁵ It was also noted that delayed onset and long-lived high-energy photons could have the form of general feature for the GRBs.

In this article we report on a detailed analysis of the high-energy emission from the short GRB 081024B within a theoretical fireshell model.

2. Fireshell Model

Customary to think that mergers of compact objects as black holes (BH) and neutron stars (NS) mostly lead to short-duration hard-spectrum bursts in galaxies and regions with low rate of star-formation. It was initially proposed in a way that binary NS mergers should lead to the gamma-ray emission with energy of an order $\gtrsim 10^{52}$ erg, and typically be on cosmological distances.^{17,18}

Alternative progenitor models such as NS-NS, NS-BH, a core-collapse supernovae (the collapsar model) were carried out with an aim to precisely estimate the properties and population of the GRBs. The discovery of a long-awaited afterglow from the long bursts evidenced for a relativistic expansion, source size 10^{17} cm (see Ref. 19), and a circumburst density ranged between $1\text{--}10\text{ cm}^{-3}$ (see Ref. 20). As regards of short bursts, then it was expected that they should have lower energy scale and potentially lower circumburst densities, because first shallow observational attempts to detect the afterglow were unsuccessful.

According to the fireshell model, all the GRBs originate from mergers of binary systems²¹ and this is a basic principle of the model. Corroborated by observations a proposed set of progenitors looks as follows: NS-NS, NS-BH, $\text{FeCO}_{\text{core}}\text{-NS}$, $\text{FeCO}_{\text{core}}\text{-BH}$. The classification is in agreement with temporal distribution of the GRBs, and depending on initial parameters of progenitors there are different families of short and long bursts. A binary NS-NS merger with total mass below the critical refers to family-1 short bursts with $E_{\text{iso}} < 10^{52}$ erg and rest-frame spectral peak energy $E_{\text{peak}} < 2$ MeV, leading to a massive neutron star as the merged core; the binary NS-NS merger with total mass exceeding the critical refers to family-2 short bursts with $E_{\text{iso}} > 10^{52}$ erg and $E_{\text{peak}} > 2$ MeV, leading to a black hole as merged core. In analogy, the merger of $\text{FeCO}_{\text{core}}\text{-NS}$ system refers to the family-1 long bursts with $E_{\text{iso}} < 10^{52}$ erg and the rest-frame spectral peak-energy $E_{\text{peak}} < 200$ keV, having SN explosion and leading to the NS-NS binary; the $\text{FeCO}_{\text{core}}\text{-NS}$ (and recently proposed $\text{FeCO}_{\text{core}}\text{-BH}$ for extremely high energies) merger refers to the family-2 long bursts with $E_{\text{iso}} > 10^{52}$ erg and $E_{\text{peak}} > 200$ keV with SN explosion leading to NS-BH binary.

A crucial point in division by families here is also whether or not the critical mass is reached and the black hole is formed. There are examples and observational signatures of these four sub-classes and their rate of occurrence.²¹

For the sake of clarity we consider hereafter a case of the family-2 short burst, and will concentrate mainly on this scenario also because analyzed GRB 081024B fits its main conditions.

We have the merger of NS-NS binary, and it is generally assumed that in this scenario the black hole is rapidly formed, powering the short gamma-ray burst. Damour & Ruffini²² proposed to interpret nature of GRB in terms of e^-e^+ pairs

plasma arises in the process of vacuum polarization during the formation of electrically charged and rotating black hole (Kerr-Newman BH). Expected total energy is approximately 10^{54} erg for the $10 M_{\text{solar}}$ black hole. Such a plasma of electrons and positrons is confined to an expanding shell — the fireshell, which is optically thick, and due to internal pressure it starts to expand and self-accelerates up to ultra-relativistic velocities,^{23,24} and thereby engulfs the baryonic matter (of mass M_B) left over in the process of collapse. A remnant matter of baryons is described by expression $B = M_B \times c^2 / E_{e^-e^+}^{\text{tot}}$ and called Baryon Load.²⁵ Due to large optical depth baryons are thermalized by pairs.

The fireshell continues to expand until it reaches transparency condition at some distance and the first flash of high-energy radiation is emitted.²⁶ The canonical gamma-ray burst is composed of Proper-GRB (P-GRB) — emission due to the transparency of the fireshell, and Prompt emission due to collisions between accelerated baryons and Circum-Burst Medium (CBM), having density n_{CBM} .

It was proposed that P-GRB should demonstrate thermal origin, and indeed, the presence of thermal component in early phases of the Prompt emission clearly evidenced a blackbody component in the spectra. There are two types of such component: a significant thermal emission lasting usually 20–50 seconds^{27,28} and a specific one lasting at most few seconds.^{29–31} It should be noted that the first component, varying with time and occurring at $\Gamma \sim 1$ has been associated with a Proto Black Hole, while the last mentioned is product of the e^-e^+ recombination, occurring at ultra-relativistic regimes with $\Gamma \gtrsim 10^2$, has been identified as P-GRB emission of the fireshell model.^{29–31}

In the matter of extended afterglow, known as Prompt emission one should follow the conception that residual expanding shell of baryons and leptons collides with the CBM, decreasing kinetic energy, and hence giving a rise to the multi-wavelength emission. Parameters affecting on behavior of such output are the CBM density profile n_{CBM} and the fireshell surface filling factor R .

To generalize the GRB scenario within the fireshell model one needs three parameters: $E_{e^-e^+}^{\text{tot}}$, M_B and n_{CBM} , while the radius r_{tr} at which the transparency occurs, the theoretical blue-shifted temperature kT_{blue} , the Lorentz factor Γ_{tr} , as well as amount of energy emitted in the P-GRB phase are all functions of total energy and Baryon Load. Using them it is possible to determine the physics of the fireshell evolution, P-GRB emission at the moment of transparency and its characteristics. The Prompt structure is well described by using the CBM density profile n_{CBM} , which determines temporal behavior of a light curve, and the surface filling factor $R = A_{\text{eff}}/A_{\text{vis}}$, where A_{eff} is an effective emitting area of shell and A_{vis} its total visible area, taking into account inhomogeneities of medium.³²

3. Data Analysis of the GRB 081024B

Our analysis of the GRB 081024B is concentrated on data obtained from the Fermi-GBM and the Fermi-LAT where detectors with the most luminous signal are NaI-n6,

NaI-n9 (8 keV:900 keV) and BGO-b1 (250 keV:40 MeV). The 64 ms light curves show one narrow spike of about 0.1 s followed by a longer pulse around 0.7 s. After 0.8 s there is no evidence of emission in the NaI and BGO detectors. To obtain GBM light curves and spectrum we used the **RMFIT**^a package. Time-Taged Event (TTE) files are suitable in particular for short GRBs because of high temporal resolution. After required data reduction we have proceeded with time-integrated and time-resolved analyses.

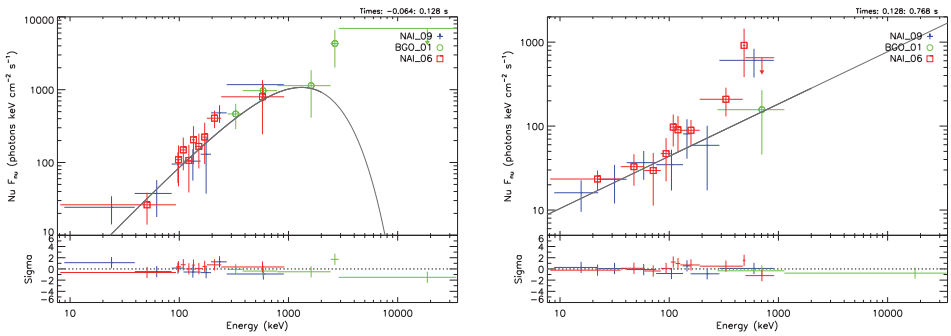


Fig. 1. Best-fit Comp (left) and Power Law (right) models for “a” and “b” time intervals.

The time-integrated analysis was performed in a time interval from $T_0 - 0.064$ s to $T_0 + 0.768$ s which corresponds to T_{90} duration of the burst. We have fitted the spectrum within this interval with different models and their combinations. The Figure 1 shows the best fit — Comptonized model (known as power law with exponential cutoff). The observed peak energy of the best fit is $E_{peak} = 1990 \pm 1190$ keV and $\gamma = -1.005 \pm 0.134$.

We have also performed the time-resolved analysis with data binned in 16 ms intervals by dividing burst event into two shorter episodes from $T_0 - 0.064$ s to $T_0 + 0.128$ s and from $T_0 + 0.128$ s to $T_0 + 0.768$ s, marked as intervals “a” and “b” respectively. It should be noted that for small photon fluxes the count statistics (C-Stat) is preferred. Within the first interval “a” the Comptonized model with $E_{peak} = 1317 \pm 598$ keV shows the best fit in comparison with Band and combination of Power Law+Blackbody models. In this time range observed blackbody temperature is $kT = 151.7 \pm 20.9$ keV. For the rest — “b” interval from $T_0 + 0.128$ s to $T_0 + 0.768$ s — the Power Law model is the best fit with photon index $\gamma = -1.377 \pm 0.075$ keV. The observed temperature here is $kT = 36.07 \pm 4.96$ keV and one sees a reduction of thermal deposit. Figure 1 illustrates the time-resolved fitting and the results of integrated and resolved analyses are summarized in Table 1.

^ahttp://fermi.gsfc.nasa.gov/ssc/data/analysis/rmfit/vc_rmfit_tutorial.pdf

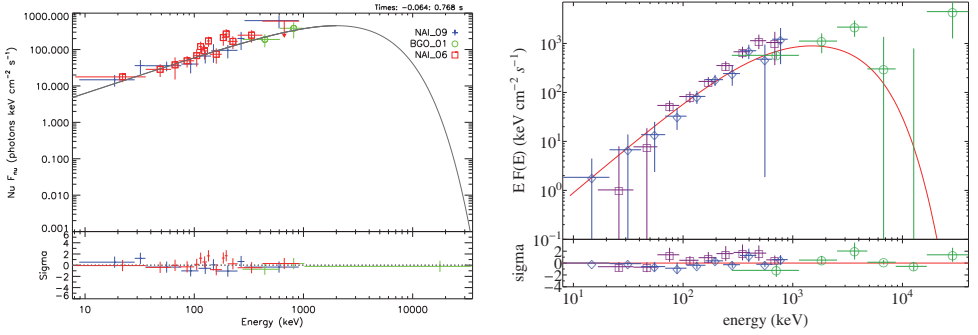


Fig. 2. On left panel: Best-fit Comptonized model for T_{90} time interval. On right panel: GRB 081024B simulated spectra within energy range 8 keV:40 MeV.

Table 1. Fitresults of time-integrated and time-resolved spectral analysis.

Fit	Interval (s)	Model	E_{peak} (keV)	γ	C-Stat/DOF
1	“a”+“b”, $-0.064 : +0.768$	Comp	1990 ± 1190	-1.005 ± 0.134	369.98/356
2	“a”+“b”, $-0.064 : +0.768$	BB+BB	—	—	370.14/350
3	“a”+“b”, $-0.064 : +0.768$	PL	—	-1.329 ± 0.052	373.52/352
4	“a”, $-0.064 : +0.128$	Comp	1317 ± 598	-0.4674 ± 0.289	327.52/353
5	“b”, $-0.128 : +0.768$	PL	—	-1.377 ± 0.075	376.09/352

4. Interpretation

We used a code for expanding shell simulation and on the basis of Baryon Load and energy ratio of the first pulse (P-GRB) with respect to total duration (T_{90}) derived the values of isotropic energy $E_{iso} = (1.83 \pm 0.78) \times 10^{52}$ and a redshift $z = 2.56 \pm 1.63$ (see Table 2).

Table 2. Summary on GRB 081024B analysis within fireshell model.

GBR name	Classification	Redshift z	E_{iso} (erg)	Baryon Load
081024B	Short-hard	2.56 ± 1.63	$(1.83 \pm 0.78) \times 10^{52}$	$(5.885 \pm 0.42) \times 10^{-5}$

After light curve simulation of the Prompt emission we obtained density profile of the circumburst medium next to the transparency and this allowed to perform the spectra simulation for entire energy range from 8 keV to 40 MeV (Fig. 2). Obtained values of E_{peak} and E_{iso} place this GRB 081024B among ones of the family-2 short bursts according to the fireshell model.

Acknowledgments

Y.A., M.E. and M.K. are supported by EMJD Program with Grant Numbers 2014–0707, 2012–1740, 2013–1471, from the agency EACEA of the European Commission.

References

1. G.J. Fishman, C.A. Meegan, R.B. Wilson et al., *BAAS*, **21**, 860F (1989).
2. S.L. Piro, L. Scarsi, R. Butler, *SPIE Proceedings*, **2517**, 169 (1995).
3. N. Gehrels, G. Chincarini, P. Giommi et al., *ApJ*, **611**, 1005 (2004).
4. C. Meegan, G. Lichti, P.N. Bhat, E. Bissaldi, et al., *ApJ*, **702**, 791 (2009).
5. S. Mao, B. Paczynski, *ApJ*, **388**, L45 (1992).
6. C. Kouveliotou, C. A. Meegan, G. J. Fishman et al., *ApJ*, **413**, L101 (1993).
7. E. Costa, F. Frontera, J. Heise, M. Feroci et al., *Nature*, **387**, 783 (1997).
8. J. van Paradijs, P.J. Groot, T. Galama et al., *Nature*, **386**, 686 (1997).
9. J.S. Bloom, S.G. Djorgovski, S.R. Kulkarni, *ApJ*, **554**, 678 (2001).
10. L. Amati, F. Frontera, M. Tavani et al. *A&A*, **390**, 81 (2002).
11. F.-W. Zhang, L. Shao, J.-Z. Yan, D.-M. Wei, *ApJ*, **750**, 88 (2012).
12. N. Omodei, *GCN*, 8407 (2008).
13. V. Connaughton, M. Briggs, *GCN*, 8408 (2008)
14. A.A. Abdo, M. Ackermann, M. Ajello et al., *ApJ*, **712**, 558 (2010).
15. M. Ohno, *Fermi Symposium, eConf Proceedings C091122* (2009).
16. A. Corsi, D. Guetta, L. Piro et al., *A&A*, **524**, A92 (2010).
17. D. Eichler, M. Livio, T. Piran, D.N. Schramm, *Nature*, **340**, L126 (1989).
18. B. Paczynski, *ApJ*, **308**, L43 (1986).
19. E. Waxman, S.R. Kulkarni, D.A. Frail, *ApJ*, **497**, 288 (1998).
20. A. Panaitescu, P. Kumar, *ApJ*, **571**, 779 (2002).
21. R. Ruffini, J.A. Rueda, M. Muccino, G.B. Pisani et al., 2016 in preparation.
22. T. Damour, R. Ruffini, *Phys.Review Letters*, **35**, 463 (1975).
23. R. Ruffini, J.D. Salmonson, J.R. Wilson, S.-S. Xue, *A&A*, **350**, 334 (1999).
24. R. Ruffini, J.D. Salmonson, J.R. Wilson, S.-S. Xue, *A&A*, **359**, 855 (2000).
25. R. Ruffini, C.L. Bianco, F. Fraschetti et al., *ApJ*, **555**, L117 (2001a).
26. R. Ruffini, C.L. Bianco, F. Fraschetti et al., *ApJ*, **555**, L113 (2001b).
27. F. Ryde, *ApJ*, **614**, 827 (2004).
28. F. Ryde, A. Pe'er, *ApJ*, **702**, 1211 (2009).
29. L. Izzo, R. Ruffini, C.L. Bianco et al., *arXiv:1205.6651* (2012a).
30. L. Izzo, R. Ruffini, A.V. Penacchioni et al., *A&A*, **543**, A10 (2012b).
31. A.V. Penacchioni, R. Ruffini, L. Izzo et al., *A&A*, **538**, A58 (2012).
32. R. Ruffini, C.L. Bianco, S.-S. Xue et al., *IJMPD*, **13**, 843 (2004).

GRB 140619B: A short GRB from a binary neutron star merger leading to black hole formation

Marco Muccino,^{1,2,*} R. Ruffini,^{1,2,3,4} Milos Kovacevic,^{1,3} Fernanda G. Oliveira,^{1,3} Jorge A. Rueda,^{1,2,4} Yerlan Aimuratov,^{1,3} Carlo L. Bianco,^{1,2} Maxime Enderli,^{1,3} Rahim Moradi,^{1,2} A. V. Penacchioni,^{4,5} Giovanni B. Pisani,^{1,2} and Yu Wang,^{1,2} E. Zaninoni⁴

¹*Dip. di Fisica, Sapienza Università di Roma and ICRA, Piazzale Aldo Moro 5, I-00185 Roma, Italy.*

** E-mail: marco.muccino@icra.it*

²*ICRANet, Piazzale della Repubblica 10, I-65122 Pescara, Italy.*

³*Erasmus Mundus Joint Doctorate IRAP Ph.D. Student. Université de Nice Sophia Antipolis, Nice, CEDEX 2, Grand Chateau Parc Valrose, France.*

⁴*ICRANet-Rio, CBPF, Rua Dr. Xavier Sigaud 150, Rio de Janeiro, RJ, 22290-180, Brazil.*

⁵*Instituto Nacional de Pesquisas Espaciais, Av. dos Astronautas, 1758, São José dos Campos, SP, 12227-010, Brazil.*

For short gamma-ray bursts (GRBs), double neutron star (NS) mergers are traditionally adopted as progenitors. We propose a classification of short bursts into two sub-classes: short gamma-ray flashes (S-GRFs) with isotropic energy $E_{\text{iso}} \lesssim 10^{52}$ erg and rest-frame spectral peak energy $E_{p,i} \lesssim 2$ MeV, when the merger leads to a very massive NS (MNS), and the authentic short GRBs (S-GRBs) with $E_{\text{iso}} \gtrsim 10^{52}$ erg and $E_{p,i} \gtrsim 2$ MeV, when a black hole (BH) is formed. Evidences for the BH formation in S-GRBs are provided by the observed high energy 0.1–100 GeV emission after the GRB emission from the e^+e^- -plasma transparency (P-GRB); in S-GRFs, leading to MNS, this emission is never observed. Both these sub-classes fulfill the $E_{p,i}-E_{\text{iso}}$ relation for short GRBs. We present here the recently identified S-GRB 140619B. From the spectral analysis of the early ~ 0.2 s, we infer an observed P-GRB temperature $kT = (324 \pm 33)$ keV, a theoretically derived redshift $z = 2.67 \pm 0.37$, a total burst energy $E_{e^+e^-}^{\text{tot}} = (6.03 \pm 0.79) \times 10^{52}$ erg, and a baryon load $B = (5.52 \pm 0.73) \times 10^{-5}$. We also estimate the emission of gravitational waves (GWs) of the progenitor NS–NS merger. Including all the S-GRBs so far identified, the observed rate of these sources is $\rho_0 = (3.5_{-2.0}^{+3.4}) \times 10^{-4} \text{ Gpc}^{-3} \text{ yr}^{-1}$.

Keywords: Gamma-ray burst: short GRBs; neutron stars; black holes.

1. Introduction

An ample literature indicates that short bursts, with observed durations $T_{90} < 2$ s, originate from NS–NS mergers (see Ref. 1, for a review). Recently we proposed² a classification for short bursts based on the total mass of the NS–NS merged core, which can be smaller or larger than the NS critical mass ($M_{\text{crit}}^{\text{NS}} = 2.67 M_{\odot}$, see Ref. 3). S-GRFs originate from NS–NS mergers leading to a merged core mass $\lesssim M_{\text{crit}}$. These sources have $E_{\text{iso}} \lesssim 10^{52}$ erg and $E_{p,i} \lesssim 2$ MeV^{2,4,5} (see Fig. 1). In order to conserve energy and momentum, the outcome of such S-GRFs is a MNS with additional orbiting material, or a binary companion. Since no BH is formed, no high energy emission is neither expected, nor observed, while ample emission in the X-ray and optical are observed¹, although without the regularity or nesting

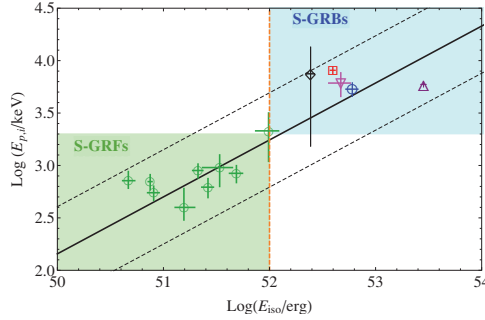


Fig. 1. The $E_{p,i}$ – E_{iso} relation^{2,4,5} (black solid line) with its uncertainty (black dashed lines) for S-GRFs (green circles in the green region) and S-GRBs (GRBs 081024B, black diamond, 090227B, purple triangle, 090510, red square, 140402A, magenta reversed square, and 140619B, blue circle, in the blue area). The orange vertical line marks the value $E_{iso} \equiv 10^{52}$ erg.

properties observed in long GRBs with $E_{iso} > 10^{52}$ erg^{6,7}. S-GRBs originate from NS–NS merger leading to a merged core with mass $> M_{crit}$. These sources have $E_{iso} \gtrsim 10^{52}$ erg and $E_{p,i} \gtrsim 2$ MeV^{2,4,5} (see Fig. 1). In order to conserve energy and momentum, the outcome of such S-GRBs is a Kerr–Newmann BH (KNBH) with additional orbiting material, or a binary companion. The BH formation is accompanied by the emission of a very energetic 0.1–100 GeV emission. At times, X-ray emission is also observed in these S-GRBs.

After the identification of GRBs 090227B⁸, 081024B (Aimuratov et al., in preparation), and 090510 (Enderli et al., ApJ submitted) we summarize here the result presented in Ref. 2 for another S-GRB: 140619B. In Sec. 2 we present our data analysis, from 8 keV up to 40 MeV. In Sec. 3 within the fireshell model we theoretically derive the redshift, $z = 2.67 \pm 0.37$, the burst energy, $E_{iso} > 10^{52}$ erg, and the value of the baryon load, $B \sim 10^{-5}$. In Sec. 4, assuming a symmetric NS–NS merger as the progenitor of GRB 140619B, we discuss the GW detectability by the Advanced LIGO. In Sec. 5 we address the origin of the 0.1–100 GeV emission. In Sec. 6 we estimate the observed rate of such S-GRBs. Finally we draw our conclusions.

2. Observations and Data Analysis

The short hard GRB 140619B was triggered and located by the *Fermi*-GBM⁹ and also by the *Suzaku*-WAM¹¹. The *Fermi*-LAT showed a significant increase in the event rate¹⁰. No bright X-ray afterglow was detected by the *Swift*-XRT instrument in the field of view of the *Fermi*¹². Consequently, no optical follow-up was possible and, thus, the redshift of the source is unknown.

We perform the spectral analysis on the GBM data (8 keV–40 MeV) by using black body (BB) and Comptonized (Compt) spectral models. In the time interval from T_0 to $T_0 + 0.192$ s (hereafter ΔT_1), the small difference between the C-STAT (see Tab. 1) suggests that the above spectral models are equally viable. However the Compt model α index is consistent with that of a BB within three σ , therefore,

Table 1. Results of the spectral analysis. Column content: time intervals ΔT , spectral models, BB temperatures kT or peak energies E_p , low-energy indices α , 8 keV–40 MeV energy fluxes F_{tot} , and the C-STAT values over the degrees of freedom (DOF).

ΔT	Model	kT or E_p (MeV)	α	F_{tot} (erg cm $^{-2}$ s $^{-1}$)	C-STAT/DOF
ΔT_1	Compt	1.60 ± 0.29	0.26 ± 0.32	$(9.4 \pm 1.6) \times 10^{-6}$	318.92/346
	BB	0.32 ± 0.03		$(8.5 \pm 1.2) \times 10^{-6}$	323.86/347
ΔT_2	Compt	1.28 ± 0.30	-0.11 ± 0.26	$(4.38 \pm 0.89) \times 10^{-6}$	391.65/346
	BB	0.16 ± 0.02		$(2.33 \pm 0.28) \times 10^{-6}$	392.23/347

we assume the BB model as the best fit. In the time interval from $T_0 + 0.192$ s to $T_0 + 0.640$ s (hereafter ΔT_2), both models are again equally probable. However, the BB model does not adequately fit the data at energies $\gtrsim 1$ MeV. Therefore, we adopt the Compt model. More details can be found in Ref. 2.

3. Theoretical Interpretation within the Fireshell Model

In the GRB fireshell model¹³, the ΔT_1 time interval, with its spectrum consistent with a BB, represents the P-GRB. The ΔT_2 time interval, instead, is identified with the prompt emission, a non-thermal emission due to the collisions between the accelerated baryons, after the transparency, and the circum-burst medium (CBM).

The ratio between the P-GRB energy and E_{iso} can be estimated, independently to the redshift z , from the ratio of P-GRB and the total observed fluences, e.g. $S_{BB}/S_{tot} = (40.4 \pm 7.8)\%$ (see Tab. 1). Following the analysis described in Refs. 2 and 8, from the above ratio, by applying the fireshell equations of motion, we obtained the redshift $z = 2.67 \pm 0.37$, the baryon load $B = (5.52 \pm 0.73) \times 10^{-5}$, and the total e^+e^- plasma energy $E_{e^+e^-}^{tot} = (6.03 \pm 0.79) \times 10^{52}$ ergs (details in Ref. 2).

The BGO-b1 (0.26–40 MeV) prompt emission light curve in Fig. 2 (left panel) has been simulated by using a CBM number density distribution with an average value of $\langle n_{CBM} \rangle = (4.7 \pm 1.2) \times 10^{-5}$ cm $^{-3}$. The corresponding spectrum¹⁴, is plotted in Fig. 2 (right panel).

4. The Progenitor System and the GW Emission

We assume a symmetric NS–NS merger as the progenitor of GRB 140619B and that the total crustal mass from both NSs contributes to the GRB baryon load. For non-rotating NSs in the global charge neutrality treatment³, the critical NS mass inferred from the NL3 nuclear model is $M_{crit}^{NS} = 2.67 M_\odot$. For NS masses $M_{NS} = 1.34 M_\odot$, so that $2M_{NS} > M_{crit}^{NS}$, the total NS crustal mass is $M_{2c} = 7.26 \times 10^{-5} M_\odot$. The baryonic mass engulfed by the e^+e^- plasma is $M_B = E_{e^+e^-}^{tot} B/c^2 = (1.86 \pm 0.35) \times 10^{-6} M_\odot$, therefore only $\approx 3\% M_{2c}$ contributes to the baryon load.

If the above NS binary is optimally located and polarized with optimal face-on orbit, the corresponding GW emission gives a signal-to-noise ratio of $\langle \text{SNR} \rangle \approx 0.5$, which is lower than the optimal value $\text{SNR} = 8$ for detection by the Advanced LIGO interferometer¹⁵, and therefore undetectable. The total gravitational radia-

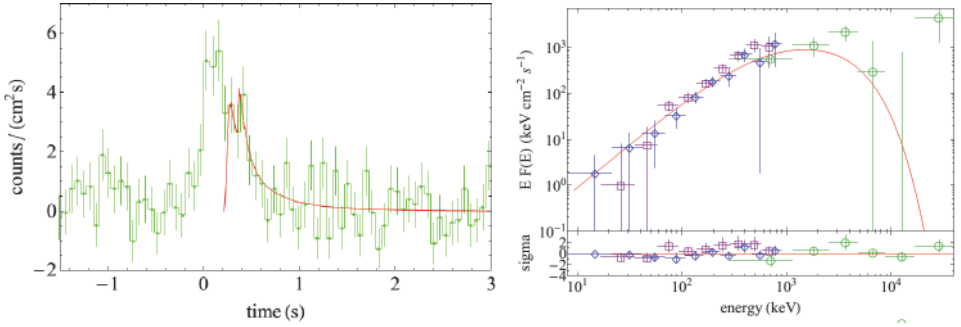


Fig. 2. Left: the BGO-b1 (0.26–40 MeV) simulated light curve of the prompt emission of GRB 140619B. Right: the 8–900 keV data from the NaI-n6 (purple squares) and n9 (blue diamonds) detectors, and the 260 keV–40 MeV data from the BGO-b1 detector (green circles), compared to the fireshell simulation (solid red curve) in the time interval ΔT_2 .

tion energy emitted during the entire inspiral-in phase all the way up to the merger, computed via the effective-one-body (EOB) formalism¹⁶, is $E_{\text{GW}}^T = 7.42 \times 10^{52}$ erg.

5. Considerations on the GeV Emission

The light curve of this emission in GRB 140619B shows a rising part which peaks at ~ 2 s (see Fig. 3). The absence of emission after ~ 4 s has been attributed to a cut-off intrinsic to the source. The spectrum of the observed 0.1–100 GeV emission of GRB 140619B is best fitted by a power-law with a photon index $\gamma = -1.9$. Its isotropic energy is $E_{\text{LAT}} = (2.34 \pm 0.91) \times 10^{52}$ erg.

All S-GRBs consistently exhibit GeV emission, when LAT data are available (see Fig. 3). Its turn-on occurs after the P-GRB emission and during the prompt emission. This GeV emission originate from the activity of the newly-born KNBH produced in the NS–NS merger and its very high angular momentum explains the large rest-frame 0.1–100 GeV luminosities of the S-GRBs².

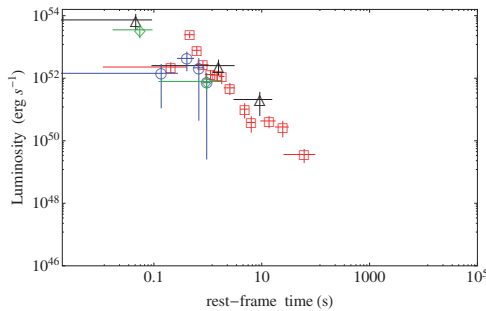


Fig. 3. The rest-frame 0.1–100 GeV luminosity light curves of the S-GRBs 081024B (green diamonds), 090510 (red squares), 140402A (black triangles), 140619B (blue circles).

6. The Rate of S-GRBs

To date, we have identified and described four S-GRBs, e.g., GRBs 081024B, 090227B, 090510, and 140619B². Here we present two additional new members: GRB 060801 and GRB 140402A. Following Refs. 17, 18, from these six S-GRBs ($N = 6$) we estimate their observed rate, $\rho_0 = \sum_{i=S,F} (4\pi/\Omega_i) N / (V_{\max,i} T_i)$, by evaluating for each source the maximum comoving volume $V_{\max,i}$ at which it would have been detected, by using the *Fermi* (F) and the *Swift* (S) solid angles and observational periods ($\Omega_F = 9.6$ sr and $T_F = 7$ y, and $\Omega_S = 2$ sr and $T_S = 10$ y, respectively). We infer $\rho_0 = (3.5^{+3.4}_{-2.0}) \times 10^{-4} \text{ Gpc}^{-3} \text{ y}^{-1}$.

7. Conclusions

We classified short bursts into two sub-classes, depending whether or not a BH is formed out of the NS–NS merger. S-GRFs, with $E_{iso} \lesssim 10^{52}$ erg and $E_{p,i} \lesssim 2$ MeV, lead to the formation of a MNS. S-GRBs, with $E_{iso} \gtrsim 10^{52}$ erg and $E_{p,i} \gtrsim 2$ MeV, lead to the formation of a KNBH, which explains the observed 0.1–100 GeV emission in S-GRBs and its lack in S-GRFs.

From our theoretical analysis, we inferred the astrophysical setting of the S-GRB 140619B. 1) Within the fireshell model, we derived a CBM density $\langle n_{CBM} \rangle \approx 10^{-5} \text{ cm}^{-3}$ typical of galactic halos where NS–NS mergers migrate¹. 2) Assuming NS masses $M_{NS} = 1.34 M_\odot$, we assessed that, in view of the large z , the corresponding GW signal cannot be detected by the Advanced LIGO. 3) The observed rate of S-GRBs, $\rho_0 = (3.5^{+3.4}_{-2.0}) \times 10^{-4} \text{ Gpc}^{-3} \text{ y}^{-1}$, which represents, at the moment, a lower limit, can be explained by the existing data of the galactic binary NSs. In fact, the total mass of the majority of these systems is $< M_{crit}^{NS}$ and, therefore, they will lead to S-GRFs². The relative rates of S-GRFs and S-GRBs can give, in principle, an indirect determination of M_{crit}^{NS} (Ruffini et al., in preparation).

Acknowledgments

JAR, AVP and EZ acknowledge the support by the International Cooperation Program CAPES-ICRANet financed by CAPES-Brazilian Federal Agency for Support and Evaluation of Graduate Education within the Ministry of Education of Brazil. MK and FGO acknowledge the support given by the International Relativistic Astrophysics Erasmus Mundus Joint Doctorate Program by the Grants 2013–1471 and 2012–1710, respectively, from EACEA of the European Commission. MM acknowledges the partial support of the project N 3101/GF4 IPC-11/2015, and the target program of the Ministry of Education and Science of the Republic of Kazakhstan.

References

1. E. Berger, *ARA&A* **52** (2014) 43 [arXiv:astro-ph/1311.2603].
2. R. Ruffini, M. Muccino, M. Kovacevic, F. G. Oliveira, J. A. Rueda, C. L. Bianco, M. Enderli, A. V. Penacchioni, G. B. Pisani, Y. Wang E. Zaninoni, *ApJ*, **808** (2015) 190 [arXiv:astro-ph/1412.1018].

3. R. Belvedere, D. Pugliese, J. A. Rueda, R. Ruffini and S. S. Xue, *Nuclear Physics A* **883** (2012) 1.
4. G. Calderone, G. Ghirlanda, G. Ghisellini, M. G. Bernardini, S. Campana, S. Covino, P. D'Avanzo, V. D'Elia, A. Melandri, R. Salvaterra, B. Sbarufatti and G. Tagliaferri, *MNRAS*, **448** (2015) 403 [arXiv:1408.1608].
5. F.-W. Zhang, L. Shao, J.-Z. Yan and D.-M. Wei, *ApJ* **750** (2012) 88 [arXiv:astro-ph/1201.1549].
6. R. Ruffini, Y. Wang, M. Kovacevic, C. L. Bianco, M. Enderli, M. Muccino, A. V. Penacchioni, G. B. Pisani and J. A. Rueda, *ApJ* **798** (2015) 10 [arXiv:astro-ph/1405.5723].
7. R. Ruffini, M. Muccino, C. L. Bianco, M. Enderli, L. Izzo, M. Kovacevic, A. V. Penacchioni, G. B. Pisani, J. A. Rueda, Y. Wang, *A&A Letter* **565** (2014) L10 [arXiv:astro-ph/1404.3946].
8. M. Muccino, R. Ruffini, C. L. Bianco, L. Izzo and A. V. Penacchioni, *ApJ* **763** (2013) 125 [arXiv:astro-ph/1205.6600].
9. V. Connaughton, B.-B. Zhang, G. Fitzpatrick and O. Roberts, *GRB Coordinates Network* **16419** (2014) 1.
10. D. Kocevski, F. Longo, G. Vianello, V. Connaughton, J. McEnery and E. Sonbas, *GRB Coordinates Network* **16421** (2014) 1.
11. W. Iwakiri, M. Tashiro, Y. Terada, T. Yasuda, S. Koyama, S. Takeda, T. Nagayoshi, J. Enomoto, S. Nakaya, T. Fujinuma, S. Matsuoka, M. Yamauchi, N. Ohmori, R. Kinoshita, M. Ohno, T. Kawano, S. Furui, Y. Fukazawa, K. Yamaoka, S. Sugita, U. Ehime, Y. Hanabata, Y. E. Nakagawa, M. Kokubun, T. Takahashi, Y. Urata, K. Nakazawa and K. Makishima, *GRB Coordinates Network* **16457** (2014) 1.
12. A. Maselli and P. D'Avanzo, *GRB Coordinates Network* **16424** (2014) 1.
13. R. Ruffini, G. Vereshchagin and S.-S. Xue *Phys. Rep.*, **487** (2010) 1.
14. B. Patricelli, M. G. Bernardini, C. L. Bianco, L. Caito, G. de Barros, L. Izzo, R. Ruffini and G. V. Vereshchagin, *ApJ* **756** (2012) 16 [arXiv:astro-ph/1206.5605].
15. Advanced LIGO interferometer <http://www.advancedligo.mit.edu>
16. T. Damour and A. Nagar, *Physical Review D* **81** (2012) 084016 [arXiv:astro-ph/0911.5041].
17. A. M. Soderberg, S. R. Kulkarni, E. Nakar, E. Berger, P. B. Cameron, D. B. Fox, D. Frail, A. Gal-Yam, R. Sari, S. B. Cenko, M. Kasliwal, R. A. Chevalier, T. Piran, P. A. Price, B. P. Schmidt, G. Pooley, D.-S. Moon, B. E. Penprase, E. Ofek, A. Rau, N. Gehrels, J. A. Nousek, D. N. Burrows, S. E. Persson, P. J. McCarthy, *Nature* **442** (2006) 1014 [arXiv:astro-ph/0604389].
18. D. Guetta, M. Della Valle, *ApJ Letter* **657** (2007) L73 [arXiv:astro-ph/0612194].

The binary systems associated with short and long gamma-ray bursts and their detectability*

Jorge A. Rueda^{†,‡,§,***}, Y. Aimuratov^{†,‡,¶}, U. Barres de Almeida^{||},
L. Becerra^{†,‡}, C. L. Bianco^{†,‡}, C. Cherubini^{**,††}, S. Filippi^{**,††}, M. Karlica^{†,‡,¶},
M. Kovacevic^{†,‡,¶}, J. D. Melon Fuksman^{†,‡}, R. Moradi^{†,‡}, M. Muccino^{†,‡},
A. V. Penacchioni^{‡,§,§§}, G. B. Pisani^{†,‡}, D. Primorac^{†,‡}, R. Ruffini^{†,‡,§},
N. Sahakyan^{¶¶}, S. Shakeri^{†,|||} and Y. Wang^{†,‡}

[†]ICRANet, Piazza Della Repubblica 10, I-65122 Pescara, Italy

[‡]Dip. di Fisica and ICRA, Sapienza Università di Roma,
P.le Aldo Moro 5, I-00185 Rome, Italy

[§]ICRANet-Rio, Centro Brasileiro de Pesquisas Físicas,
Rua Dr. Xavier Sigaud 150, 22290-180 Rio de Janeiro, Brazil

[¶]Université de Nice Sophia Antipolis, CEDEX 2,
Grand Château Parc Valrose, Nice, France

^{||}Centro Brasileiro de Pesquisas Físicas,
Rua Dr. Xavier Sigaud 150, 22290-180 Rio de Janeiro, Brazil

^{**}Unit of Nonlinear Physics and Mathematical Modeling,
Università Campus Bio-Medico di Roma,
Via A. del Portillo 21, I-00128 Rome, Italy

^{††}ICRA, Università Campus Bio-Medico di Roma,
Via A. del Portillo 21, I-00128 Rome, Italy

^{‡‡}ASI Science Data Center,
Via del Politecnico s.n.c., I-00133 Rome, Italy

^{§§}Dept. of Physical Sciences, Earth and Environment,
University of Siena, Via Roma 56, I-53100 Siena, Italy

^{¶¶}ICRANet-Yerevan, Marshall Baghramian Avenue 24a,
Yerevan 0019, Republic of Armenia

^{|||}Department of Physics,
Isfahan University of Technology, 84156-83111, Iran
***jorge.rueda@icra.it

Short and long-duration gamma-ray bursts (GRBs) have been recently sub-classified into seven families according to the binary nature of their progenitors. For short GRBs, mergers of neutron star binaries (NS–NS) or neutron star-black hole binaries (NS–BH) are proposed. For long GRBs, the induced gravitational collapse (IGC) paradigm proposes a tight binary system composed of a carbon–oxygen core (CO_{core}) and a NS companion. The explosion of the CO_{core} as supernova (SN) triggers a hypercritical accretion process onto the NS companion which might reach the critical mass for the gravitational collapse to a BH. Thus, this process can lead either to a NS–BH or to NS–NS depending on whether or not the accretion is sufficient to induce the collapse of the NS into a BH. We shall discuss for the above compact object binaries: (1) the role of the NS structure and the equation-of-state on their final fate; (2) their occurrence rates as inferred from the X and gamma-ray observations; (3) the expected number of detections of their gravitational wave (GW) emission by the Advanced LIGO interferometer.

Keywords: Gamma-ray bursts; neutron stars; black holes.

1. Introduction

There has been a traditional phenomenological classification of GRBs based on the observed prompt duration, T_{90} : long GRBs for $T_{90} > 2$ s and short GRBs for $T_{90} < 2$ s.^{1–5} In this paper, we shall review the recent progress reached in the understanding of the nature of long and short GRBs that has led to a physical GRB classification, proposed in Refs. 6–8. Such a classification, as we will see below, is based on the possible outcomes in the final stages of the evolution of the progenitor systems.

1.1. Long GRBs

The induced gravitational collapse (IGC) scenario introduces, as the progenitor of the long GRBs associated with SNe Ib/c, binaries composed of a carbon–oxygen core (CO_{core}) on the verge of supernova with a NS companion.^{9–15} The explosion of the CO_{core} as SN, forming at its center a newly-born NS called hereafter νNS , triggers an accretion process onto the NS binary companion. Depending on the parameters of the *in-state*, i.e. of CO_{core} -NS binary, two sub-classes of long GRBs with corresponding *out-states* are envisaged⁶:

- *X-ray flashes (XRFs)*. Long bursts with $E_{\text{iso}} \lesssim 10^{52}$ erg are produced by CO_{core} -NS binaries with relatively large binary separations ($a \gtrsim 10^{11}$ cm). The accretion rate of the SN ejecta onto the NS in these systems is not high enough to bring the NS mass to the critical value M_{crit} , hence no BH is formed. The out-state of this GRB sub-class can be either a νNS -NS binary if the system keeps bound after the SN explosion, or two runaway NSs if the binary system is disrupted.
- *Binary driven hypernovae (BdHNe)*. Long bursts with $E_{\text{iso}} \gtrsim 10^{52}$ erg are instead produced by more compact CO_{core} -NS binaries ($a \lesssim 10^{11}$ cm, see e.g. Refs. 13 and 15). In this case, the SN triggers a larger accretion rate onto the NS companion, e.g. $\gtrsim 10^{-2}$ – $10^{-1} M_{\odot} \text{ s}^{-1}$, bringing the NS to its critical mass M_{crit} ,^{11–13} namely to the point of gravitational collapse with consequent formation of a BH. Remarkably, in Ref. 14, it was recently shown that the large majority of BdHNe leads naturally to NS-BH binaries owing to the high compactness of the binary that avoids the disruption of it even in cases of very high mass loss exceeding 50% of the total mass of the initial CO_{core} -NS binary.

In addition, it exists the possibility of BH-SNe.⁶ Long burst with $E_{\text{iso}} \gtrsim 10^{54}$ erg occurring in close CO_{core} -BH binaries in which the hypercritical accretion produces, as *out-states*, a more massive BH and a νNS . These systems have been considered in Ref. 6 as a subset of the BdHNe but no specific example have been yet observationally identified.

1.2. Short GRBs

There is the consensus within the GRB community that the progenitors of short GRBs are mergers of NS-NS and/or NS-BH binaries (see, e.g. Refs. 16–20 for a

recent review). Similarly to the case of long GRBs, in Ref. 6 short GRBs have been split into different sub-classes:

- *Short gamma-ray flashes (S-GRFs)*. Short bursts with energies $E_{\text{iso}} \lesssim 10^{52}$ erg, produced when the post-merger core do not surpass the NS critical mass M_{crit} , hence there is no BH formation. Thus, these systems left as byproduct a massive NS and possibly, due to the energy and angular momentum conservation, orbiting material in a disk-like structure or a low-mass binary companion.
- *Authentic short gamma-ray bursts (S-GRBs)*. Short bursts with $E_{\text{iso}} \gtrsim 10^{52}$ erg, produced when the post-merger core reaches or overcome M_{crit} , hence forming a Kerr or Kerr–Newman BH,⁸ and also in this case possibly orbiting material.
- *Ultra-short GRBs (U-GRBs)*. A new sub-class of short bursts originating from ν NS-BH merging binaries. They can originate from BdHNe (see Ref. 14) or from BH-SNe.

In addition, it exists the possibility of *gamma-ray flashes (GRFs)*. These are bursts with hybrid properties between short and long, they have $10^{51} \lesssim E_{\text{iso}} \lesssim 10^{52}$ erg. This sub-class of sources originates in NS-WD mergers.⁶

Table 1 summarized some observational aspects of the GRB sub-classes including the occurrence rate calculated in Ref. 6.

We focus here on the physical properties of the above progenitors, as well as on the main properties of NSs that play a relevant role in the dynamics of these systems and that lead to the above different GRB sub-classes. We shall discuss as well recent estimates of the rates of occurrence on all the above subclasses based on X and gamma-ray observations, and also elaborate on the possibility of detecting the gravitational wave (GW) emission originated in these systems.

Table 1. Some observational aspects of the GRB sub-classes. In the first three columns, we indicate the GRB sub-class and their corresponding *in-states* and the *out-states*. In column 4, we list the E_{iso} (rest-frame 1–10⁴ keV), columns 5–6 list, for each GRB sub-class, the maximum observed redshift and the local occurrence rate computed in Ref. 6.

GRB sub-class	In-state	Out-state	E_{iso} (erg)	z_{max}	ρ_{GRB} (Gpc ⁻³ yr ⁻¹)
XRFs	CO _{core} -NS	ν NS-NS	10 ⁴⁸ –10 ⁵²	1.096	100 ⁺⁴⁵ ₋₃₄
BdHNe	CO _{core} -NS	ν NS-BH	10 ⁵² –10 ⁵⁴	9.3	0.77 ^{+0.09} _{-0.08}
BH-SN	CO _{core} -BH	ν NS-BH	>10 ⁵⁴	9.3	$\lesssim 0.77^{+0.09}_{-0.08}$
S-GRFs	NS-NS	MNS	10 ⁴⁹ –10 ⁵²	2.609	3.6 ^{+1.4} _{-1.0}
S-GRBs	NS-NS	BH	10 ⁵² –10 ⁵³	5.52	(1.9 ^{+1.8} _{-1.1}) × 10 ⁻³
U-GRBs	ν NS-BH	BH	>10 ⁵²	—	$\gtrsim 0.77^{+0.09}_{-0.08}$
GRFs	NS-WD	MNS	10 ⁵¹ –10 ⁵²	2.31	1.02 ^{+0.71} _{-0.46}

2. IGC, Hypercritical Accretion, and Long GRBs

We turn now to the details of the accretion process within the IGC scenario. Realistic simulations of the IGC process were performed in Ref. 12, including: (1) detailed SN explosions of the CO_{core} ; (2) the hydrodynamic details of the hypercritical accretion process; (3) the evolution of the SN ejecta material entering the Bondi–Hoyle region all the way up to its incorporation into the NS. Here, the concept of hypercritical accretion refers to the fact the accretion rates are highly super-Eddington. The accretion process in the IGC scenario is allowed to exceed the Eddington limit mainly for two reasons: (i) the photons are trapped within the infalling material impeding them to transfer momentum; (ii) the accreting material creates a very hot NS atmosphere ($T \sim 10^{10}$ K) that triggers a very efficient neutrino emission which become the main energy sink of these systems unlike photons.

The hypercritical accretion process in the above simulations was computed within a spherically symmetric approximation. A further step was given in Ref. 13 by estimating the angular momentum that the SN ejecta carries and transfer to the NS via accretion, and how it affects the evolution and fate of the system. The calculations are as follows: first the accretion rate onto the NS is computed adopting an homologous expansion of the SN ejecta and introducing the pre-SN density profile of the CO_{core} envelope from numerical simulations. Then, it is estimated the angular momentum that the SN material might transfer to the NS: it comes out that the ejecta have enough angular momentum to circularize for a short time and form a disc around the NS. Finally, the evolution of the NS central density and rotation angular velocity (spin-up) is followed computing the equilibrium configurations from the numerical solution of the axisymmetric Einstein equations in full rotation, until the critical point of collapse of the NS to a BH taking into due account the equilibrium limits given by mass-shedding and the secular axisymmetric instability.

Now we enter into the details of each of the above steps. The accretion rate of the SN ejecta onto the NS can be estimated via the Bondi–Hoyle–Lyttleton accretion formula:

$$\dot{M}_B(t) = \pi \rho_{\text{ej}} R_{\text{cap}}^2 \sqrt{v_{\text{rel}}^2 + c_{\text{s, ej}}^2}, \quad R_{\text{cap}}(t) = \frac{2GM_{\text{NS}}(t)}{v_{\text{rel}}^2 + c_{\text{s, ej}}^2}, \quad (1)$$

where G is the gravitational constant, ρ_{ej} and $c_{\text{s, ej}}$ are the density and sound speed of the SN ejecta, R_{cap} is the NS gravitational capture radius (Bondi–Hoyle radius), M_{NS} , the NS mass, and v_{rel} the ejecta velocity relative to the NS: $\mathbf{v}_{\text{rel}} = \mathbf{v}_{\text{orb}} - \mathbf{v}_{\text{ej}}$, with $|\mathbf{v}_{\text{orb}}| = \sqrt{G(M_{\text{core}} + M_{\text{NS}})/a}$, the module of the NS orbital velocity around the CO_{core} , and \mathbf{v}_{ej} the velocity of the supernova ejecta (see Fig. 1).

Extrapolating the results for the accretion process from stellar wind accretion in binary systems, the angular momentum per unit time that crosses the NS capture region can be approximated by: $\dot{L}_{\text{cap}} = (\pi/2)(\epsilon_\rho/2 - 3\epsilon_\nu)\rho_{\text{ej}}(a, t)v_{\text{rel}}^2(a, t)R_{\text{cap}}^4(a, t)$, where ϵ_ρ and ϵ_ν are parameters measuring the inhomogeneity of the flow (see Ref. 13 for details).

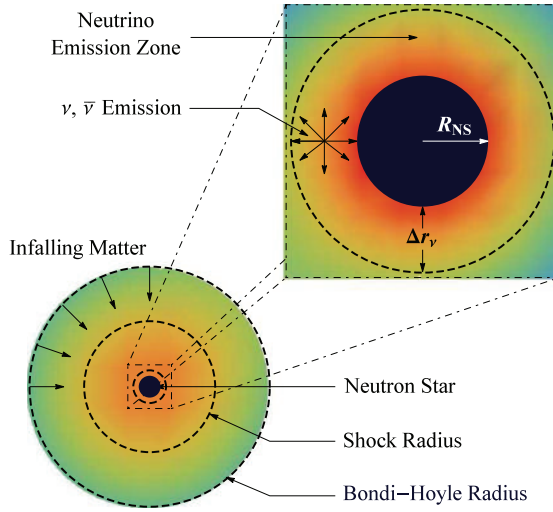


Fig. 1. Scheme of the IGC scenario: the CO_{core} undergoes SN explosion, the NS accretes part of the SN ejecta and then reaches the critical mass for gravitational collapse to a BH, with consequent emission of a GRB. The SN ejecta reach the NS Bondi-Hoyle radius and fall toward the NS surface. The material shocks and decelerates as it piles over the NS surface. At the neutrino emission zone, neutrinos take away most of the infalling matter gravitational energy gain. The neutrinos are emitted above the NS surface in a region of thickness Δr_ν about half the NS radius that allow the material to reduce its entropy to be finally incorporated to the NS. The image is not to scale. For further details and numerical simulations of the above process, see Refs. 12–15.

In order to simulate the hypercritical accretion, it is adopted an homologous expansion of the SN ejecta, i.e. the ejecta velocity evolves as $v_{\text{ej}}(r, t) = nr/t$, where r is the position of every ejecta layer from the SN center and n is called expansion parameter. The ejecta density is given by $\rho_{\text{ej}}(r, t) = \rho_{\text{ej}}^0(r/R_{\text{star}}(t), t_0) \frac{M_{\text{env}}(t)}{M_{\text{env}}(0)} \left(\frac{R_{\text{star}}(0)}{R_{\text{star}}(t)}\right)^3$, where $M_{\text{env}}(t)$ the mass of the CO_{core} envelope, namely the mass of the ejected material in the SN explosion and available to be accreted by the NS, $R_{\text{star}}(t)$ is the position of the outermost layer of the ejected material, and ρ_{ej}^0 is the pre-SN density profile. The latter can be approximated with a power law: $\rho_{\text{ej}}(r, t_0) = \rho_{\text{core}}(R_{\text{core}}/r)^m$, where ρ_{core} , R_{core} and m are the profile parameters which are fixed by fitting the pre-SN profiles obtained from numerical simulations.

For the typical parameters of pre-SN CO_{core} and assuming a velocity of the outermost SN layer $v_{\text{sn}}(R_{\text{star}}, t_0) \sim 10^9 \text{ cm s}^{-1}$ and a free expansion $n = 1$ (for details of typical initial conditions of the binary system see Refs. 12 and 13), Eq. (1) gives accretion rates around the order of $10^{-4} - 10^{-2} M_\odot \text{ s}^{-1}$, and an angular momentum per unit time crossing the capture region $\dot{L}_{\text{cap}} \sim 10^{46} - 10^{49} \text{ g cm}^2 \text{ s}^{-2}$.

We consider the NS companion of the CO_{core} initially as nonrotating, thus at the beginning, the NS exterior spacetime is described by the Schwarzschild metric. The SN ejecta approach the NS with specific angular momentum, $l_{\text{acc}} = \dot{L}_{\text{cap}}/\dot{M}_B$, thus they will circularize at a radius r_{st} if they have enough angular momentum. What does the word “enough” means here? The last stable circular orbit (LSO)

around a nonrotating NS is located at a distance $r_{\text{lso}} = 6GM_{\text{NS}}/c^2$ and has an angular momentum per unit mass $l_{\text{lso}} = 2\sqrt{3}GM_{\text{NS}}/c$. The radius r_{lso} is larger than the NS radius for masses larger than $1.67 M_{\odot}$, $1.71 M_{\odot}$, and $1.78 M_{\odot}$ for the GM1, TM1, and NL3 nuclear equation-of-state (EOS).¹³ If $l_{\text{acc}} \geq l_{\text{lso}}$, the material circularizes around the NS at locations $r_{\text{st}} \geq r_{\text{lso}}$. For the values of the IGC systems under discussion here, $r_{\text{st}}/r_{\text{lso}} \sim 10 - 10^3$, thus the SN ejecta have enough angular momentum to form a sort of disc around the NS. Even in this case, the viscous forces and other angular momentum losses that act on the disk will allow the matter in the disk to reach the inner boundary at $r_{\text{in}} \sim r_{\text{lso}}$, to then be accreted by the NS.

Within this picture, the NS accretes the material from r_{in} and the NS mass and angular momentum evolve as:

$$\dot{M}_{\text{NS}} = \left(\frac{\partial M_{\text{NS}}}{\partial M_b} \right)_{J_{\text{NS}}} \dot{M}_b + \left(\frac{\partial M_{\text{NS}}}{\partial J_{\text{NS}}} \right)_{M_b} \dot{J}_{\text{NS}}, \quad \dot{J}_{\text{NS}} = \xi l(r_{\text{in}}) \dot{M}_b, \quad (2)$$

where M_b is the NS baryonic mass, $l(r_{\text{in}})$ is the specific angular momentum of the accreted material at r_{in} , which corresponds to the angular momentum of the LSO, and $\xi \leq 1$ is a parameter that measures the efficiency of angular momentum transfer. We assume in our simulations $\dot{M}_b = \dot{M}_B$.

In order to integrate Eqs. (1) and (2), we have to supply the two above partial derivatives which are obtained from the relation of the NS gravitational mass with M_b and J_{NS} , namely from the NS binding energy. The general relativistic calculations of rotating NSs in Ref. 21 show that, independent on the nuclear EOS, this relation is well approximated by the formula

$$\frac{M_b}{M_{\odot}} = \frac{M_{\text{NS}}}{M_{\odot}} + \frac{13}{200} \left(\frac{M_{\text{NS}}}{M_{\odot}} \right)^2 \left(1 - \frac{1}{137} j_{\text{NS}}^{1.7} \right), \quad (3)$$

where $j_{\text{NS}} \equiv cJ_{\text{NS}}/(GM_{\odot}^2)$. In addition, since the NS will spin up with accretion, we need information of the dependence of the specific angular momentum of the LSO as a function of both the NS mass and angular momentum. For corotating orbits, the following relation is valid for all the aforementioned EOS¹³:

$$l_{\text{lso}} = \frac{GM_{\text{NS}}}{c} \left[2\sqrt{3} - 0.37 \left(\frac{j_{\text{NS}}}{\frac{M_{\text{NS}}}{M_{\odot}}} \right)^{0.85} \right]. \quad (4)$$

The NS accretes mass until it reaches a region of instability. There are two main instability limits for rotating NSs: mass-shedding or Keplerian limit and the secular

Table 2. Critical NS mass in the nonrotating case and constants k and p needed to compute the NS critical mass in the nonrotating case given by Eq. (5). The values are given for the NL3, GM1 and TM1 EOS.

EOS	$M_{\text{crit}}^{J=0} (M_{\odot})$	p	k
NL3	2.81	1.68	0.006
GM1	2.39	1.69	0.011
TM1	2.20	1.61	0.017

axisymmetric instability. The critical NS mass along the secular instability line is approximately given by²¹:

$$M_{\text{NS}}^{\text{crit}} = M_{\text{NS}}^{J=0} (1 + k j_{\text{NS}}^p), \quad (5)$$

where the parameters k and p depends of the nuclear EOS (see Table 2). These formulas fit the numerical results with a maximum error of 0.45%.

Along the mass-shedding sequence, the NS has the maximum possible angular momentum²¹: $J_{\text{NS,max}} \approx 0.7 G M_{\text{NS}}^2 / c$. Figure 2 shows the evolution of the NS dimensionless angular momentum, $c J_{\text{NS}} / (G M_{\text{NS}}^2)$, as a function of the NS mass for $\xi = 0.5$ and for selected values of the initial NS mass. The NS fate depends of the NS initial mass and the efficiency parameter ξ . The less massive initial configurations reach the mass-shedding limit with a maximum dimensionless angular momentum value while the initially more massive configurations reach the secular axisymmetric instability. It is interesting to note that the total angular momentum of the SN ejecta entering the Bondi–Hoyle region, L_{cap} , is much larger than the

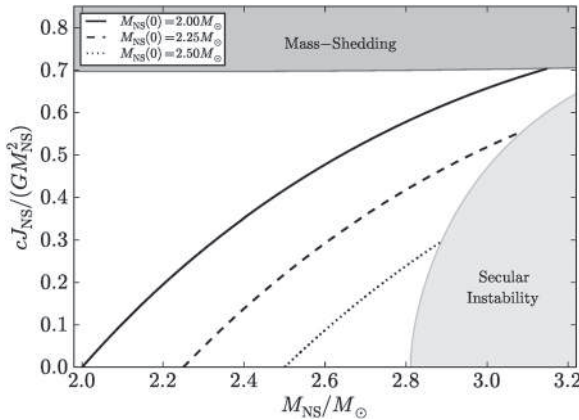


Fig. 2. Evolution of NSs of different initial masses $M_{\text{NS}} = 2.0, 2.25$ and $2.5 M_{\odot}$ during the hypercritical accretion in a BdHN.¹³ It is shown the dimensionless angular momentum as a function of the NS mass. The binary parameters are: CO_{core} of a $M_{\text{ZAMS}} = 30 M_{\odot}$ progenitor star ($m = 2.801$, $M_{\text{env}} = 7.94 M_{\odot}$, $\rho_{\text{core}} = 3.08 \times 10^8 \text{ g cm}^{-3}$ and $R_{0\text{star}} = 7.65 \times 10^9 \text{ cm}$), a free expansion ($n = 1$) and a SN outermost ejecta velocity $v_{0\text{star}} = 2 \times 10^9 \text{ cm s}^{-1}$. The orbital period is of approximately 5 min.

maximum angular momentum that a uniformly rotating NS can support, $J_{\text{NS,max}}$. The numerical simulations in Ref. 13 indicate $L_{\text{cap}} \sim 10J_{\text{NS,max}}$. Thus, part of this angular momentum must be lost or redistributed before the material can reach the NS surface. This result leads to a clear prediction: the BHs produced through the IGC mechanism, namely those formed in BdHNe, have initial dimensionless spin ~ 0.7 and the excess of angular momentum could lead to a jetted emission with possible high-energy signatures and/or to the presence of a disk-like structure first around the NS as shown above and possibly also around the BH originated from the gravitational collapse of the NS.

2.1. Most recent simulations of the IGC process

Additional details and improvements of the hypercritical accretion process leading to XRFs and BdHNe have been recently presented in Ref. 15. In particular:

- (1) It was there improved the accretion rate estimate including the density profile finite size/thickness and additional CO_{core} progenitors leading to different SN ejecta masses were also considered.
- (2) It was shown in Ref. 13, the existence of a maximum orbital period, P_{max} , over which the accretion onto NS companion is not high enough to bring it to the critical mass for gravitational collapse to a BH. Therefore, CO_{core} -NS binaries with $P > P_{\text{max}}$ lead to XRFs while the ones with $P \lesssim P_{\text{max}}$ lead to BdHNe. In Ref. 15, the determination of P_{max} was extended to all the possible initial values of the mass of the NS companion and the angular momentum transfer efficiency parameter was also allowed to vary.
- (3) It was computed the expected luminosity during the hypercritical accretion process for a wide range of binary periods covering XRFs and BdHNe.
- (4) It was there shown that the presence of the NS companion originates large asymmetries (see, e.g. simulation in Fig. 3) in the SN ejecta leading to observable signatures in the X-rays.

Figure 3 shows a simulation of an IGC process presented in Ref. 15. We considered the effects of the gravitational field of the NS on the SN ejecta including the orbital motion as well as the changes in the NS gravitational mass owing to the accretion process via the Bondi formalism. The supernova matter was described as formed by point-like particles whose trajectory was computed by solving the Newtonian equation of motion. The initial conditions of the SN ejecta are computed assuming an homologous velocity distribution in free expansion. The initial power-law density profile of the CO envelope is simulated by populating the inner layers with more particles. For the $M_{\text{ZAMS}} = 30 M_{\odot}$ progenitor which gives a CO_{core} with envelope profile $\rho_{\text{ej}}^0 \approx 3.1 \times 10^8 (8.3 \times 10^7 / r)^{2.8} \text{ g cm}^{-3}$, we adopt for the simulation a total number of $N = 10^6$ particles. We assume that particles crossing the Bondi-Hoyle radius are captured and accreted by the NS so we removed them from the system as they reach that region. We removed these particles according

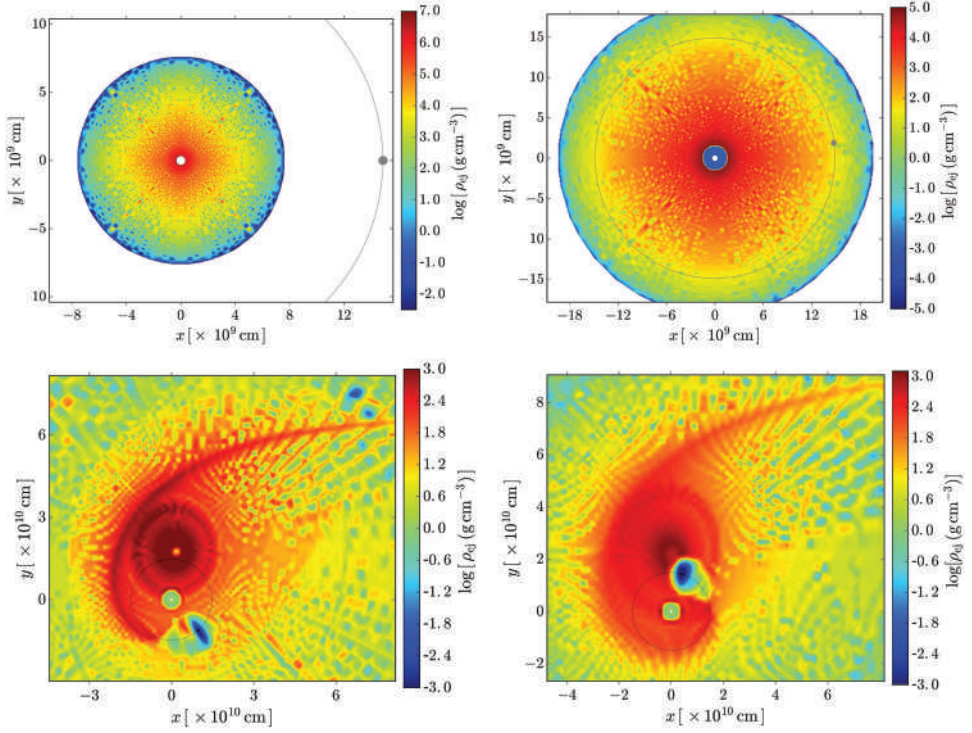


Fig. 3. Hypercritical accretion process in the IGC binary system at selected evolution times. In this example, the CO_{core} has a total mass of $9.44 M_{\odot}$ divided in an ejecta mass of $7.94 M_{\odot}$ and a νNS of $1.5 M_{\odot}$ formed by the collapsed high density core. The supernova ejecta evolve homologously with outermost layer velocity $v_{0,\text{star}} = 2 \times 10^9 \text{ cm s}^{-1}$. The NS binary companion has an initial mass of $2.0 M_{\odot}$. The binary period is $P \approx 5 \text{ min}$, which corresponds to a binary separation $a \approx 1.5 \times 10^{10} \text{ cm}$. The system of coordinates is centered on the νNS represented by the white-filled circle at $(0, 0)$. The NS binary companion, represented by the gray-filled circle, orbits counterclockwise following the thin-dashed circular trajectory. The colorbar indicates values of ejecta density in logarithmic scale. *Left upper panel*: initial time of the process. The supernova ejecta expand radially outward and the NS binary companion is at $(a, 0)$. *Right upper panel*: the accretion process starts when the first supernova layers reach the Bondi-Hoyle region. This happens at $t = t_{\text{acc},0} \approx a/v_{0,\text{star}} \approx 7.7 \text{ s}$. *Left lower panel*: the NS binary companion reaches the critical mass by accreting matter from the SN with consequent collapse to a BH. This happens at $t = t_{\text{coll}} \approx 254 \text{ s} \approx 0.85 P$. The newly-formed BH of mass $M_{\text{BH}} = M_{\text{crit}} \approx 3 M_{\odot}$ is represented by the black-filled circle. It is here evident the asymmetry of the supernova ejecta induced by the presence of the accreting NS companion at close distance. *Right lower panel*: $t = t_{\text{coll}} + 100 \text{ s} = 354 \text{ s} \approx 1.2 P$, namely 100 s after the BH formation. It appears here the new binary system composed of the νNS and the newly-formed BH.

to the results obtained from the numerical integration explained above. Figure 3 shows the orbital plane of an IGC binary at selected times of its evolution. The NS has an initial mass of $2.0 M_{\odot}$; the CO_{core} leads to a total ejecta mass $7.94 M_{\odot}$ and a νNS of $1.5 M_{\odot}$. The orbital period of the binary is $P \approx 5 \text{ min}$, i.e. a binary separation $a \approx 1.5 \times 10^{10} \text{ cm}$. For these parameters, the NS reaches the critical mass and collapses to form a BH.

2.2. Hydrodynamics and neutrino inside the accretion region

We turn now to give some details on the properties of the system inside the Bondi–Hoyle accretion region. We have seen that the accretion rate onto the NS can be as high as $\sim 10^{-2} - 10^{-1} M_{\odot} \text{ s}^{-1}$. For these accretion rates:

- (1) We can neglect the effect of the NS magnetic field since the magnetic pressure remains much smaller than the random pressure of the infalling material.^{11,22}
- (2) The photons are trapped in the accretion flow. The trapping radius, defined at which the photons emitted diffuse outward at a slower velocity than the one of the infalling material, is²³: $r_{\text{trapping}} = \min\{\dot{M}_B \kappa / (4\pi c), R_{\text{cap}}\}$, where κ is the opacity. For the CO_{core} , in Ref. 12, a Rosseland mean opacity roughly $5 \times 10^3 \text{ cm}^2 \text{ g}^{-1}$ was estimated. For the range of accretion rates, we obtain that $\dot{M}_B \kappa / (4\pi c) \sim 10^{13} - 10^{19} \text{ cm}$, a radius much bigger than the NS capture radius which is in our simulations at most 1/3 of the binary separation. Thus, in our systems, the trapping radius extends all the way to the Bondi–Hoyle region, hence the Eddington limit does not apply and hypercritical accretion onto the NS occurs.
- (3) Under these conditions, the gain of gravitational energy of the accreted material is mainly radiated via neutrino emission (see below).^{11,12,22,24,25}

2.2.1. Convective instabilities

As the material piles onto the NS and the atmosphere radius, the accretion shock moves outward. The post-shock entropy is a decreasing function of the shock radius position which creates an atmosphere unstable to Rayleigh–Taylor convection during the initial phase of the accretion process. These instabilities can accelerate above the escape velocity driving outflows from the accreting NS with final velocities approaching the speed of light.^{26,27} Assuming that radiation dominates, the entropy of the material at the base of the atmosphere is²²: $S_{\text{bubble}} \approx 16(1.4 M_{\odot}/M_{\text{NS}})^{-7/8} (M_{\odot} \text{ s}^{-1}/\dot{M}_B)^{1/4} (10^6 \text{ cm}/r)^{3/8}$, in units of k_B per nucleon. This material will rise and expand, cooling adiabatically, i.e. $T^3/\rho = \text{constant}$, for radiation dominated gas. If we assume a spherically symmetric expansion, then $\rho \propto 1/r^3$ and we obtain $k_B T_{\text{bubble}} = 195 S_{\text{bubble}}^{-1} (10^6 \text{ cm}/r) \text{ MeV}$. However, it is more likely that the bubbles expand in the lateral but not in the radial direction,²⁷ thus we have $\rho \propto 1/r^2$, i.e. $T_{\text{bubble}} = T_0(S_{\text{bubble}})(r_0/r)^{2/3}$, where $T_0(S_{\text{bubble}})$ is given by the above equation evaluated at $r = r_0 \approx R_{\text{NS}}$. This temperature implies a bolometric blackbody flux at the source from the bubbles

$$F_{\text{bubble}} \approx 2 \times 10^{40} \left(\frac{M_{\text{NS}}}{1.4 M_{\odot}} \right)^{-7/2} \left(\frac{\dot{M}_B}{M_{\odot} \text{ s}^{-1}} \right) \left(\frac{R_{\text{NS}}}{10^6 \text{ cm}} \right)^{3/2} \times \left(\frac{r_0}{r} \right)^{8/3} \text{ erg s}^{-1} \text{ cm}^{-2}, \quad (6)$$

where σ is the Stefan–Boltzmann constant.

In Ref. 12, it was shown that the above thermal emission from the rising bubbles produced during the hypercritical accretion process can explain the early ($t \lesssim 50$ s) thermal X-ray emission observed in GRB 090618.^{10,28} In that case, T_{bubble} drops from 50 keV to 15 keV expanding from $r \approx 10^9$ cm to 6×10^9 cm, for an accretion rate $10^{-2} M_{\odot} \text{ s}^{-1}$.

It is interesting that also r-process nucleosynthesis can occur in these outflows.²⁶ This implies that long GRBs can be also r-process sites with specific signatures from the decay of the produced heavy elements, possibly similar as in the case of the *kilonova* emission in short GRBs.²⁹ The signatures of this phenomenon in XRFs and BdHNe, and its comparison with kilonovae, deserves to be explored.

2.2.2. Neutrino emission

Most of the energy from the accretion is lost through neutrino emission. For the accretion rate conditions characteristic of our models $\sim 10^{-4} - 10^{-2} M_{\odot} \text{ s}^{-1}$, e^+e^- pair annihilation dominates the neutrino emission and electron neutrinos remove the bulk of the energy. The temperature of these neutrinos can be roughly approximated by assuming that the inflowing material generally flows near to the NS surface before shocking and emitting neutrinos. For accretion rates $\sim 10^{-4} - 10^{-2} M_{\odot} \text{ s}^{-1}$, neutrino energies $\sim 5 - 20$ MeV are obtained.¹⁵ A detailed study of the neutrino emission will be presented elsewhere.

For the developed temperatures (say $k_B T \sim 1 - 10$ MeV) near the NS surface, the dominant neutrino emission process is the e^+e^- annihilation leading to $\nu\bar{\nu}$. This process produces a neutrino emissivity proportional to the ninth power of the temperature. The accretion atmosphere near the NS surface is characterized by a temperature gradient with a typical scale height $\Delta r_{\nu} \approx 0.7 R_{\text{NS}}$.¹⁵ Owing to the aforementioned strong dependence of the neutrino emission on temperature, most of the neutrino emission occurs in the region Δr_{ν} above the NS surface.

These conditions lead to the neutrinos to be efficient in balancing the gravitational potential energy gain allowing the hypercritical accretion rates. The effective accretion onto the NS can be estimated as²²: $\dot{M}_{\text{eff}} \approx \Delta M_{\nu} (L_{\nu}/E_{\nu})$, where ΔM_{ν} and L_{ν} are the mass and neutrino luminosity in the emission region (i.e. Δr_{ν}). E_{ν} is half the gravitational potential energy gained by the material falling from infinity to the $R_{\text{NS}} + \Delta r_{\nu}$. Since $L_{\nu} \approx 2\pi R_{\text{NS}}^2 \Delta r_{\nu} \epsilon_{e^-e^+}$ with $\epsilon_{e^-e^+}$ the e^+e^- pair annihilation process emissivity, and $E_{\nu} = (1/2)GM_{\text{NS}}\Delta M_{\nu}/(R_{\text{NS}} + \Delta r_{\nu})$, it can be checked that for $M_{\text{NS}} = 1.4 M_{\odot}$ this accretion rate leads to values $\dot{M}_{\text{eff}} \approx 10^{-9} - 10^{-1} M_{\odot} \text{ s}^{-1}$ for temperatures $k_B T = 1 - 10$ MeV.

2.3. Accretion luminosity

The gain of gravitational potential energy in the accretion process is the total one available to be released, e.g. by neutrinos and photons. The total energy released in the star in a time-interval dt during the accretion of an amount of mass dM_b

with angular momentum $l\dot{M}_b$, is given by^{13,30}

$$L_{\text{acc}} = (\dot{M}_b - \dot{M}_{\text{NS}})c^2 = \dot{M}_b c^2 \left[1 - \left(\frac{\partial M_{\text{NS}}}{\partial J_{\text{NS}}} \right)_{M_b} l - \left(\frac{\partial M_{\text{NS}}}{\partial M_b} \right)_{J_{\text{NS}}} \right]. \quad (7)$$

This upper limit to the energy released is just the amount of gravitational energy gained by the accreted matter by falling to the NS surface and which is not spent in changing the gravitational binding energy of the NS. The total energy releasable during the accretion process, say $\Delta E_{\text{acc}} \equiv \int L_{\text{acc}} dt$, is given by the difference in binding energies of the initial and final NS configurations. The typical luminosity will be $L_{\text{acc}} \approx \Delta E_{\text{acc}} / \Delta t_{\text{acc}}$ where Δt_{acc} is the duration of the accretion process.

The duration of the accretion process is given approximately by the flow time of the slowest layers of the supernova ejecta to the NS. If the velocity of these layers is v_{inner} , then $\Delta t_{\text{acc}} \sim a/v_{\text{inner}}$, where a is the binary separation. For $a \sim 10^{11}$ cm and $v_{\text{inner}} \sim 10^8$ cm s⁻¹, we obtain $\Delta t_{\text{acc}} \sim 10^3$ s, while for shorter binary separation, e.g. $a \sim 10^{10}$ cm ($P \sim 5$ min), $\Delta t_{\text{acc}} \sim 10^2$ s, as validated by the results of our numerical integrations.

For instance, the NS in the system with $P = 5$ min accretes $\approx 1 M_{\odot}$ in $\Delta t_{\text{acc}} \approx 100$ s. With the aid of Eq. (3), we estimate a difference in binding energies between a $2 M_{\odot}$ and a $3 M_{\odot}$ NS, i.e. $\Delta E_{\text{acc}} \approx 13/200(3^2 - 2^2) M_{\odot} c^2 \approx 0.32 M_{\odot} c^2$ leading to a maximum luminosity $L_{\text{acc}} \approx 3 \times 10^{-3} M_{\odot} c^2 \approx 0.1 \dot{M}_b c^2$. This accretion power, which could be as high as $L_{\text{acc}} \sim 0.1 \dot{M}_b c^2 \sim 10^{47-51}$ erg s⁻¹ for accretion rates in the range $\dot{M}_b \sim 10^{-6-10^{-2}} M_{\odot} \text{ s}^{-1}$, necessarily leads to signatures observable in long GRBs (see, e.g. Refs. 10 and 12).

2.4. Post-explosion orbits and formation of NS-BH binaries

We turn now to discuss the out-states of the IGC process. The SN explosion of the CO_{core} leaves as a central remnant, the ν NS, while the IGC process triggered by the hypercritical accretion of the SN ejecta onto the NS companion leads to the formation of a BH. Thus, the question arises if BdHNe are natural sites for the formation of NS-BH binaries or if these binaries become disrupted during the SN explosion and the consequent IGC process. The answer to this question was recently given in Ref. 14, where it was shown that indeed most of BdHN form NS-BH binaries since the high compactness of the orbit avoids the unbinding of the orbit.

In typical systems, most of the binaries become unbound during the SN explosion because of the ejected mass and momentum imparted (kick) on the newly formed compact object in the explosion of the massive star. Under the instantaneous explosion assumption, if half of the binary system's mass is lost in the SN explosion, the system is disrupted. In general, the fraction of massive binaries that can produce double compact object binaries is thought to be low: $\sim 0.001-1\%$.³¹⁻³³

The mass ejected during the SN alters the binary orbit, causing it to become wider and more eccentric. Assuming that the mass is ejected instantaneously, the

post-explosion semi-major axis is $a/a_0 = (M_0 - \Delta M)/(M_0 - 2a_0\Delta M/r)$, where a_0 and a are the initial and final semi-major axes respectively, M_0 is the total initial mass of the binary system, ΔM is the change of mass (equal to the amount of mass ejected in the SN), and r is the orbital separation at the time of explosion.³⁴ For circular orbits, the system is unbound if it loses half of its mass. However, for very tight binaries as the one proposed in the IGC scenario, a number of additional effects can alter the fate of the binary.

The time it takes for the ejecta to flow past a companion in a SN is roughly 10–1000 s. Although the shock front is moving above 10^4 km s^{-1} , the denser, lower-velocity ejecta can be moving at 10^3 km s^{-1} .¹² The broad range of times arises because the SN ejecta velocities varies from 10^2 – 10^4 km s^{-1} . The accretion peaks as the slow-moving (inner) ejecta flows past the NS companion. For normal (wide) binaries, this time is a small fraction of the orbital period and the “instantaneous” mass-loss assumption is perfectly valid. However, in the compact binary systems considered in the IGC scenario, the orbital period ranges from only 100–1000 s, and the mass loss from the SN explosion can no longer be assumed to be instantaneous.

We have seen how in BdHNe, the accretion process can lead to BH formation in a time-interval as short as the orbital period. We here deepen this analysis to study the effect of the SN explosion in such a scenario with a specific example of Ref. 14. Figure 4 shows as the ejecta timescale becomes just a fraction of the orbital timescale, the fate of the post-explosion binary is altered. For these models, we assumed very close binaries with an initial orbital separation of $7 \times 10^9 \text{ cm}$ in circular orbits. With CO_{core} radii of 1 – $4 \times 10^9 \text{ cm}$, such a separation is small, but achievable. We assume the binary consists of a CO_{core} and a $2.0 M_{\odot}$ NS companion. When the CO_{core} collapses, it forms a $1.5 M_{\odot}$ NS, ejecting the rest of the core. We then vary the ejecta mass and time required for most of the ejected matter to move out of the binary. Note that even if 70% of the mass is lost from the system (the $8 M_{\odot}$ ejecta case), the system remains bound as long as the explosion time is just above the orbital time ($T_{\text{orbit}} = 180 \text{ s}$) with semi-major axes of less than 10^{11} cm .

The short orbits (on ejecta timescales) are not the only feature of these binaries that alters the post-explosion orbit. The NS companion accretes both matter and momentum from the SN ejecta, reducing the mass lost from the system with respect to typical binaries with larger orbital separations and much less accretion. In addition, as with common envelope scenarios, the bow shock produced by the accreting NS transfers orbital energy into the SN ejecta. Figure 4 shows the final orbital separation of our same three binaries, including the effects of mass accretion (we assume $0.5 M_{\odot}$ is accreted with the momentum of the SN material) and orbit coupling (30% of the orbital velocity is lost per orbit). With these effects, not only do the systems remain bound even for explosion times greater than 1/2 the orbital period but, if the explosion time is long, the final semi-major axis can be on par with the initial orbital separation.

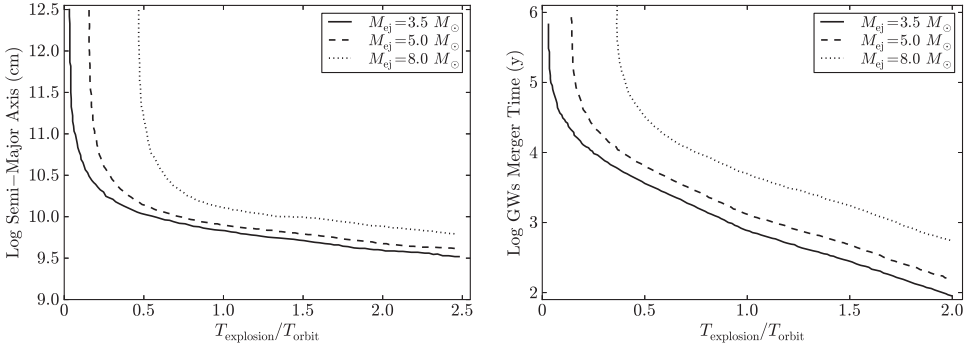


Fig. 4. Left panel: semi-major axis versus explosion time for three binary systems including mass accretion and momentum effects. Including these effects, all systems with explosion times above 0.7 times the orbital time are bound and the final separations are on par with the initial separations. Right panel: merger time due to GW emission as a function of explosion time. Beyond a critical explosion time (0.1–0.6 T_{orbit} depending on the system), the merger time is less than roughly 10,000 yr. For most of our systems, the explosion time is above this limit and we expect most of these systems to merge quickly.

The tight compact binaries produced in these explosions will emit GW emission, ultimately causing the system to merge. For typical massive star binaries, the merger time is many Myr. For BdHNe, the merger time is typically 10,000 yr, or less, as shown in the right panel of Fig. 4. Since the merger should occur within the radius swept clean by the BdHN, we expect a small baryonic contamination around the merger site which might lead to a new family of events which we term ultrashort GRBs, U-GRBs, to this new family of events.

3. NS–NS/NS–BH Mergers and Short GRBs

Let us turn to short GRBs. We have mentioned that the most viable progenitors of short GRBs appear to be mergers of NS–NS and/or NS–BH binaries. Specifically, in the case of NS–NS mergers, the value of the critical mass of the NS, which crucially depends on the nuclear EOS, has been also found to be a most relevant parameter since it defines the fate of the post-merger object.⁸ In this section, we discuss the conditions that determine the fate of the NS–NS binary merger by estimating the mass and angular momentum of the post-merger object. Once we know these values, we can compare the mass of the merged core with the value of the NS critical mass obtained for uniformly rotating NSs. Based on this, we can assess whether a massive NS or a BH is formed from the merger.

We proceed to estimate the mass and the angular momentum of the post-merger core via baryonic mass and angular momentum conservation of the system. We adopt for simplicity that nonrotating binary components. We first compute the total baryonic mass of the NS–NS binary $M_b = M_{b_1} + M_{b_2}$ using the relation between the gravitational mass M_i and the baryonic mass M_{b_i} ($i = 1, 2$) recently obtained in Ref. 21 and given in Eq. (3) assuming $j_{\text{NS}} = cJ_{\text{NS}}/(GM_{\odot}^2) = 0$. The

post-merger core will have approximately the entire baryonic mass of the initial binary, i.e. $M_{b,\text{core}} \approx M_b$, since little mass is expected to be ejected during the coalescence process. However, the gravitational mass of the post-merger core cannot be estimated using again the above formula since, even assuming nonrotating binary components, the post-merger core will necessarily acquire a fraction $\eta \leq 1$ of the binary angular momentum at the merger point. One expects a value of η smaller than unity since, during the coalesce, angular momentum is lost, e.g. by gravitational wave emission and it can be also redistributed, e.g. into a surrounding disk.

To obtain the gravitational mass of the post-merger core, we can use again Eq. (3) relating the baryonic mass $M_{b,\text{NS}}$ and the gravitational mass M_{NS} in this case with $j_{\text{NS}} \neq 0$. The mass and angular momentum of the post-merger core, respectively M_{core} and J_{core} , are therefore obtained from baryon mass and angular momentum conservation, i.e.

$$M_{\text{core}} = M_{\text{NS}}, \quad M_{b,\text{core}} = M_{b,\text{NS}} = M_{b_1} + M_{b_2}, \quad J_{\text{core}} = J_{\text{NS}} = \eta J_{\text{merger}}, \quad (8)$$

where J_{merger} is the system angular momentum at the merger point. The value of J_{merger} is approximately given by $J_{\text{merger}} = \mu r_{\text{merger}}^2 \Omega_{\text{merger}}$, where $\mu = M_1 M_2 / M$ is the binary reduced mass, $M = M_1 + M_2$ is the total binary mass, and r_{merger} and Ω_{merger} are the binary separation and angular velocity at the merger point. If we adopt the merger point where the two stars enter into contact we have $r_{\text{merger}} = R_1 + R_2$, where R_i is the radius (which depend on the EOS) of the i -component of the binary.

Given the parameters of the merging binary, the above equations lead to the merged core properties M_{core} and J_{core} (or j_{core}). These values can be therefore confronted with the values of uniformly rotating, stable NSs to check if such a merger will lead either to a new massive NS or to an unstable merged core collapsing to a BH.

For the sake of exemplifying, let us assume a mass-symmetric binary, $M_1 = M_2 = M/2$. In this case, Eq. (8) together with the above estimate of J_{merger} lead to the angular momentum of the merged core $J_{\text{core}} = (\eta/4)(GM^2/c)\mathcal{C}^{-1/2}$, where $\mathcal{C} \equiv GM_1/(c^2 R_1) = GM_2/(c^2 R_2)$ is the compactness of the merging binary components. Therefore, if we adopt $M_1 = 1.4 M_\odot$ and $\mathcal{C} = 0.15$ the above equations imply a merged core mass $M_{\text{core}} = (2.61, 2.65) M_\odot$ for $\eta = (0, 1)$, i.e. for a dimensionless angular momentum of the merged core $j_{\text{core}} = (0, 5.06)$. Whether or not these pairs $(M_{\text{core}}, j_{\text{core}})$ correspond to stable NSs depend on the nuclear EOS. A similar analysis can be done for any other pair of binary masses.

4. Detectability of GWs Produced by the GRB Progenitors

Having established the nature of the progenitors of each GRB sub-class, we turn now to briefly discuss the detectability of their associated GW emission. The minimum GW frequency detectable by the broadband aLIGO interferometer is

$f_{\min}^{\text{aLIGO}} \approx 10 \text{ Hz}$.³⁵ Since during the binary inspiral, the GW frequency is twice the orbital one, this implies that a binary enters the aLIGO band for orbital periods $P_{\text{orb}} \lesssim 0.2 \text{ s}$. Thus, $\text{CO}_{\text{core}}\text{-NS}$ binaries, *in-states* of XRFs and BdHNe, and $\text{CO}_{\text{core}}\text{-BH}$ binaries, *in-states* of BH-SN, are not detectable by aLIGO since they have orbital periods $P_{\text{orb}} \gtrsim 5 \text{ min} \gg 0.2 \text{ s}$. Concerning their *out-states* after the corresponding hypercritical accretion processes, namely $\nu\text{NS-NS}$, *out-states* of XRFs, and $\nu\text{NS-BH}$, *out-states* of BdHNe and BH-SNe, they are not detectable by aLIGO at their birth but only when approaching the merger. Clearly, the analysis of the $\nu\text{NS-NS}$ mergers is included in the analysis of the S-GRFs and S-GRBs and, likewise, the merger of $\nu\text{NS-BH}$ binaries is included in the analysis of U-GRBs. In the case of NS-WD binaries, the WD is tidally disrupted by the NS making their GW emission hard to be detected (see, e.g. Ref. 36).

A coalescing binary evolves first through the *inspiral regime* to then pass over a *merger regime*, the latter composed by the plunge leading to the merger itself and by the ringdown (oscillations) of the newly formed object. During the inspiral regime, the system evolves through quasi-circular orbits and is well described by the traditional point-like quadrupole approximation.^{37–39} The GW frequency is twice the orbital frequency ($f_s = 2f_{\text{orb}}$) and grows monotonically. The energy spectrum during the inspiral regime is: $dE/df_s = (1/3)(\pi G)^{2/3} M_c^{5/3} f_s^{-1/3}$, where $M_c = \mu^{3/5} M^{2/5} = \nu^{3/5} M$ is the so-called *chirp mass* and $\nu \equiv \mu/M$ is the symmetric mass-ratio parameter. A symmetric binary ($m_1 = m_2$) corresponds to $\nu = 1/4$ and the test-particle limit is $\nu \rightarrow 0$. The GW spectrum of the merger regime is characterized by a GW burst.⁴⁰ Thus, one can estimate the contribution of this regime to the signal-to-noise ratio with the knowledge of the location of the GW burst in the frequency domain and of the energy content. The frequency range spanned by the GW burst is $\Delta f = f_{\text{qnm}} - f_{\text{merger}}$, where f_{merger} is the frequency at which the merger starts and f_{qnm} is the frequency of the ringing modes of the newly formed object after the merger, and the energy emitted is ΔE_{merger} . With these quantities defined, one can estimate the typical value of the merger regime spectrum as: $dE/df_s \approx \Delta E_{\text{merger}}/\Delta f$. Unfortunately, the frequencies and energy content of the merger regime of the above merging binaries are such that it is undetectable by LIGO⁴¹.

Since the GW signal is deep inside the detector noise, the signal-to-noise ratio (ρ) is usually estimated using the matched filter technique.⁴² The exact position of the binary relative to the detector and the orientation of the binary rotation plane are usually unknown, thus it is a common practice to average over all the possible locations and orientations, i.e.⁴²: $\langle \rho^2 \rangle = 4 \int_0^\infty \langle |\tilde{h}(f)|^2 \rangle / S_n(f) df = 4 \int_0^\infty h_c^2(f) / [f^2 S_n(f)] df$, where f is the GW frequency in the detector frame, $\tilde{h}(f)$ is the Fourier transform of $h(t)$, and $\sqrt{S_n(f)}$ is the one-sided amplitude spectral density of the detector noise, and $h_c(f)$ is the characteristic strain, $h_c = (1+z)/(\pi d_l) \sqrt{(1/10)(G/c^3)(dE/df_s)}$. We recall that in the detector frame, the GW frequency is redshifted by a factor $1+z$ with respect to the one in the source frame,

f_s , i.e. $f = f_s/(1+z)$ and d_l is the luminosity distance to the source. We adopt a Λ CDM cosmology with $H_0 = 71 \text{ km s}^{-1} \text{ Mpc}^{-1}$, $\Omega_M = 0.27$ and $\Omega_\Lambda = 0.73$.⁴³

A threshold $\rho_0 = 8$ in a single detector is adopted by LIGO.⁴⁴ This minimum ρ_0 defines a maximum detection distance or GW horizon distance, say d_{GW} , that corresponds to the most optimistic case when the binary is just above the detector and the binary plane is parallel to the detector plane. In order to give an estimate, the annual number of merging binaries associated with the above GRB sub-classes detectable by aLIGO, we can use the lower and upper values of the aLIGO *search volume* defined by $\mathcal{V}_s = V_{\text{max}}^{\text{GW}} \mathcal{T}$, where $V_{\text{max}}^{\text{GW}} = (4\pi/3)\mathcal{R}^3$, where \mathcal{T} is the observing time and \mathcal{R} is the so-called *detector range* defined by $\mathcal{R} = \mathcal{F}d_{\text{GW}}$, with $\mathcal{F}^{-1} = 2.2627$ (see, Refs. 44 and 45, for details). For a $(1.4 + 1.4) M_\odot$ NS binary and the three following different observational campaigns we have⁴⁴: 2015/2016 (O1; $\mathcal{T} = 3$ months) $\mathcal{V}_s = (0.5\text{--}4) \times 10^5 \text{ Mpc}^3 \text{ yr}$, 2017/2018 (O3; $\mathcal{T} = 9$ months) $\mathcal{V}_s = (3\text{--}10) \times 10^6 \text{ Mpc}^3 \text{ yr}$, and the entire network including LIGO-India at design sensitivity (2022+; $\mathcal{T} = 1$ yr) $\mathcal{V}_s = 2 \times 10^7 \text{ Mpc}^3 \text{ yr}$. The maximum possible sensitivity reachable in 2022+ leads to $d_{\text{GW}} \approx 0.2 \text{ Gpc}$, hence $V_{\text{max}}^{\text{GW}} \approx 0.033 \text{ Gpc}^3$, for such a binary. One can use this information for other binaries with different masses taking advantage of the fact that d_{GW} scales with the binary chirp mass as $M_c^{5/6}$. The expected GW detection rate by aLIGO can be thus estimated as: $\dot{N}_{\text{GW}} \equiv \rho_{\text{GRB}} V_{\text{max}}^{\text{GRB}}$, where ρ_{GRB} is the inferred occurrence rate of GRBs shown in Table 1 computed in Ref. 6. Bearing the above in mind, it is easy to check that there is a low probability for aLIGO to detect the GW signals associated with the GRB binary progenitors: indeed in the best case of the 2022+ observing rung one obtains, respectively, ~ 1 detection every 3 and 5 yr for U-GRBs and S-GRFs.

5. Conclusions

There is accumulated evidence on the binary nature of long and short GRBs. Such binaries are composed of CO_{cores} , NSs, BHs and WDs in different combinations. We have here focused on the salient aspects of the NS physics relevant for the understanding of these binaries and their implications in GRB astrophysics, including their associated GW emission. We have discussed the crucial role of the NS critical mass in discriminating the GRB sub-classes. Therefore, we expect that the increasing amount of GRB high-quality data will help in constraining the NS critical mass with high accuracy with the most welcome result of constraining the NS matter content and the corresponding nuclear EOS.

Acknowledgments

M. Karlica, M. Kovacevic and Y. A. are supported by the Erasmus Mundus Joint Doctorate Program Grant Nos. 2013–1471, 2013–1471 and 2014–0707, respectively, from EACEA of the European Commission. M. M. and J. A. R. acknowledge the partial support of the Project No. 3101/GF4 IPC-11, and the target program

F.0679 of the Ministry of Education and Science of the Republic of Kazakhstan. C. C. and S. F. acknowledge INdAM-GNFM for support.

References

1. E. P. Mazets, S. V. Golenetskii, V. N. Ilinskii, V. N. Panov, R. L. Aptekar, I. A. Gurian, M. P. Proskura, I. A. Sokolov, Z. I. Sokolova and T. V. Kharitonova, *Astrophys. Space Sci.* **80** (1981) 3.
2. R. W. Klebesadel, The durations of gamma-ray bursts, in *Gamma-Ray Bursts — Observations, Analyses and Theories*, eds. C. Ho, R. I. Epstein and E. E. Fenimore (Cambridge University Press, 1992).
3. J.-P. Dezalay, C. Barat, R. Talon, R. Syunyaev, O. Terekhov and A. Kuznetsov, *AIP Conference Proceedings* **265** (1991) 304–309.
4. C. Kouveliotou, C. A. Meegan, G. J. Fishman, N. P. Bhat, M. S. Briggs, T. M. Koshut, W. S. Paciesas and G. N. Pendleton, *Astrophys. J.* **413** (1993) L101.
5. M. Tavani, *Astrophys. J.* **497** (1998) L21.
6. R. Ruffini, J. A. Rueda, M. Muccino, Y. Aimuratov, L. M. Becerra, C. L. Bianco, M. Kovacevic, R. Moradi, F. G. Oliveira, G. B. Pisani and Y. Wang, *Astrophys. J.* **832** (2016) 136.
7. R. Ruffini, Y. Wang, M. Enderli, M. Muccino, M. Kovacevic, C. L. Bianco, A. V. Penacchioni, G. B. Pisani and J. A. Rueda, *Astrophys. J.* **798** (2015) 10.
8. R. Ruffini, M. Muccino, M. Kovacevic, F. G. Oliveira, J. A. Rueda, C. L. Bianco, M. Enderli, A. V. Penacchioni, G. B. Pisani, Y. Wang and E. Zaninoni, *Astrophys. J.* **808** (2015) 190.
9. R. Ruffini, M. G. Bernardini, C. L. Bianco, L. Vitagliano, S.-S. Xue, P. Chardonnet, F. Fraschetti and V. Gurzadyan, Black hole physics and astrophysics: The GRB-Supernova connection and URCA-1–URCA-2, in *The Tenth Marcel Grossmann Meeting*, eds. M. Novello, S. Perez Bergliaffa and R. Ruffini (World Scientific, Singapore, 2006).
10. L. Izzo, J. A. Rueda and R. Ruffini, *Astron. Astrophys.* **548** (2012) L5.
11. J. A. Rueda and R. Ruffini, *Astrophys. J.* **758** (2012) L7.
12. C. L. Fryer, J. A. Rueda and R. Ruffini, *Astrophys. J.* **793** (2014) L36.
13. L. Becerra, F. Cipolletta, C. L. Fryer, J. A. Rueda and R. Ruffini, *Astrophys. J.* **812** (2015) 100.
14. C. L. Fryer, F. G. Oliveira, J. A. Rueda and R. Ruffini, *Phys. Rev. Lett.* **115** (2015) 231102.
15. L. Becerra, C. L. Bianco, C. L. Fryer, J. A. Rueda and R. Ruffini, *Astrophys. J.* **833** (2016) 107.
16. J. Goodman, *Astrophys. J.* **308** (1986) L47.
17. B. Paczynski, *Astrophys. J.* **308** (1986) L43.
18. D. Eichler, M. Livio, T. Piran and D. N. Schramm, *Nature* **340** (1989) 126.
19. R. Narayan, T. Piran and A. Shemi, *Astrophys. J.* **379** (1991) L17.
20. E. Berger, *Annu. Rev. Astron. Astrophys.* **52** (2014) 43.
21. F. Cipolletta, C. Cherubini, S. Filippi, J. A. Rueda and R. Ruffini, *Phys. Rev. D* **92** (2015) 023007.
22. C. L. Fryer, W. Benz and M. Herant, *Astrophys. J.* **460** (1996) 801.
23. R. A. Chevalier, *Astrophys. J.* **346** (1989) 847.
24. Y. B. Zel’dovich, L. N. Ivanova and D. K. Nadezhin, *Sov. Astron.* **16** (1972) 209.

25. R. Ruffini and J. Wilson, *Phys. Rev. Lett.* **31** (1973) 1362.
26. C. L. Fryer, F. Herwig, A. Hungerford and F. X. Timmes, *Astrophys. J.* **646** (2006) L131.
27. C. L. Fryer, *Astrophys. J.* **699** (2009) 409.
28. L. Izzo, R. Ruffini, A. V. Penacchioni, C. L. Bianco, L. Caito, S. K. Chakrabarti, J. A. Rueda, A. Nandi and B. Patricelli, *Astron. Astrophys.* **543** (2012) A10.
29. N. R. Tanvir, A. J. Levan, A. S. Fruchter, J. Hjorth, R. A. Hounsell, K. Wiersema and R. L. Tunnicliffe, *Nature* **500** (2013) 547.
30. N. R. Sibgatullin and R. A. Sunyaev, *Astron. Lett.* **26** (2000) 772.
31. C. L. Fryer, S. E. Woosley and D. H. Hartmann, *Astrophys. J.* **526** (1999) 152.
32. M. Dominik, K. Belczynski, C. Fryer, D. E. Holz, E. Berti, T. Bulik, I. Mandel and R. O'Shaughnessy, *Astrophys. J.* **759** (2012) 52.
33. K. A. Postnov and L. R. Yungelson, *Living Rev. Rel.* **17** (2014) 3.
34. J. G. Hills, *Astrophys. J.* **267** (1983) 322.
35. LIGO Scientific Collab. (J. Aasi *et al.*), *Class. Quantum Grav.* **32** (2015) 074001.
36. V. Paschalidis, M. MacLeod, T. W. Baumgarte and S. L. Shapiro, *Phys. Rev. D* **80** (2009) 024006.
37. P. C. Peters and J. Mathews, *Phys. Rev.* **131** (1963) 435.
38. P. C. Peters, *Phys. Rev.* **136** (1964) 1224.
39. M. Rees, R. Ruffini and J. A. Wheeler, *Black Holes, Gravitational Waves and Cosmology* (Gordon and Breach Science Publishers, New York, 1974).
40. M. Davis, R. Ruffini, W. H. Press and R. H. Price, *Phys. Rev. Lett.* **27** (1971) 1466.
41. R. Ruffini, J. Rodriguez, M. Muccino, J. A. Rueda, Y. Aimuratov, U. Barres de Almeida, L. Becerra, C. L. Bianco, C. Cherubini, S. Filippi, D. Gizzi, M. Kovacevic, R. Moradi, F. G. Oliveira, G. B. Pisani and Y. Wang, arXiv:1602.03545.
42. É. É. Flanagan and S. A. Hughes, *Phys. Rev. D* **57** (1998) 4535.
43. M. Rigault, G. Aldering, M. Kowalski, Y. Copin, P. Antilogus, C. Aragon, S. Bailey, C. Baltay, D. Baugh, S. Bongard, K. Boone, C. Buton, J. Chen, N. Chotard, H. K. Fakhouri, U. Feindt, P. Fagrelus, M. Fleury, D. Fouchez, E. Gangler, B. Hayden, A. G. Kim, P.-F. Leget, S. Lombardo, J. Nordin, R. Pain, E. Pecontal, R. Pereira, S. Perlmutter, D. Rabinowitz, K. Runge, D. Rubin, C. Saunders, G. Smadja, C. Sofiatti, N. Suzuki, C. Tao and B. A. Weaver, *Astrophys. J.* **802** (2015) 20.
44. B. P. Abbott *et al.*, *Living Rev. Rel.* **19** (2016) 1.
45. L. S. Finn and D. F. Chernoff, *Phys. Rev. D* **47** (1993) 2198.

The cosmic matrix in the 50th anniversary of relativistic astrophysics

R. Ruffini^{†,‡,§,‡‡}, Y. Aimuratov^{†,‡,¶}, L. Becerra^{†,‡}, C. L. Bianco^{†,‡},
M. Karlica^{†,‡,¶}, M. Kovacevic^{†,‡,¶}, J. D. Melon Fuksman^{†,‡}, R. Moradi^{†,‡},
M. Muccino^{†,‡}, A. V. Penacchioni^{||,**}, G. B. Pisani^{†,‡}, D. Primorac^{†,‡},
J. A. Rueda^{†,‡,§}, S. Shakeri^{†,‡‡}, G. V. Vereshchagin[†], Y. Wang^{†,‡} and S.-S. Xue[†]

[†]*ICRANet, Piazza della Repubblica 10, I-65122 Pescara, Italy*

[‡]*Dip. di Fisica and ICRA, Sapienza Università di Roma,
P.le Aldo Moro 5, I-00185 Rome, Italy*

[§]*ICRANet-Rio, Centro Brasileiro de Pesquisas Físicas,
Rua Dr. Xavier Sigaud 150, 22290-180 Rio de Janeiro, Brazil*

[¶]*Université de Nice Sophia Antipolis, CEDEX 2,
Grand Château Parc Valrose, Nice, France*

^{||}*ASI Science Data Center, Via del Politecnico s.n.c., I-00133 Rome, Italy*

^{**}*Department of Physical Sciences, Earth and Environment,
University of Siena, Via Roma 56, I-53100 Siena, Italy*

^{††}*Department of Physics, Isfahan University of Technology,
84156-83111, Iran*

^{‡‡}*ruffini@icra.it*

Our concept of induced gravitational collapse (IGC paradigm) starting from a supernova occurring with a companion neutron star, has unlocked the understanding of seven different families of gamma ray bursts (GRBs), indicating a path for the formation of black holes in the universe. An authentic laboratory of relativistic astrophysics has been unveiled in which new paradigms have been introduced in order to advance knowledge of the most energetic, distant and complex systems in our universe. A novel cosmic matrix paradigm has been introduced at a relativistic cosmic level, which parallels the concept of an S-matrix introduced by Feynmann, Wheeler and Heisenberg in the quantum world of microphysics. Here the “in” states are represented by a neutron star and a supernova, while the “out” states, generated within less than a second, are a new neutron star and a black hole. This novel field of research needs very powerful technological observations in all wavelengths ranging from radio through optical, X-ray and gamma ray radiation all the way up to ultra-high-energy cosmic rays.

Keywords: Binaries; black hole physics; gamma-ray bursts; neutron stars; supernovae; white dwarfs.

1. Introduction and the First Paradigm

We begin with a personal historical overview by the lead author.

Supernovae (SNe) have been known and studied for a long time, from 1054 A.D. to the classic work of Baade and Zwicky in 1934^{1,2} and of Oppenheimer and his students in 1939, and to the 1968 detection of the first pulsar, first in radio and then in optical wavelengths, located at the center of the Crab Nebula. The explanation of the energetics of pulsars as originating from the rotational energy of neutron stars (NSs) gave the first clear evidence for the existence of NSs through this discovery and led to the conclusion that the Crab supernova originated from gravitational collapse to a NS.

The next fundamental discovery came from the pioneering work of Riccardo Giacconi and his group with the X-ray astronomy detection of Sco X-1.³ In 1967, this X-ray source was theoretically interpreted by Shklovskii⁴ as originating from a binary system containing a NS. This was followed by the launch of the UHURU satellite on December 12, 1970. The coordination of the X-ray observations with ground-based optical telescope observations has since led to the discovery of a large number of binary X-ray sources in our galaxy.⁵ These systems give evidence for: (a) an X-ray emission due to accretion in a binary system composed of a massive star and a gravitational collapsed star, with X-ray luminosities originating from gravitational energy a million times more intense than those expected from the star's thermonuclear evolution; (b) the first determination of NS masses well above the value of the critical mass expected by Oppenheimer and Volkoff, see e.g. Fig. 1 on Cen X-3 and (c) the first identification of a black hole in Cygnus X-1.⁶⁻⁸

Observations of GRBs only date back to their detection by the Vela satellites in the early 1970s, see e.g. Ref. 9 and references therein. It was only after the observations in 1997 by the BeppoSAX satellite¹⁰ which allowed the optical identification of GRBs. From the estimates of their cosmological distances, their enormous energetics is 10^3 – 10^4 times larger than those of supernovas, were able to be determined: energies of the order of 10^{54} erg, equivalent to the release of $\sim M_{\odot}c^2$ in few tens of seconds. This result had been predicted already in 1975 on purely theoretical grounds assuming that GRBs originated from an electron–positron plasma in the gravitational collapse to a Kerr–Newman black hole, see Ruffini, “Physics outside the horizon of a black hole” in Refs. 5 and 11. From these experiences, I had

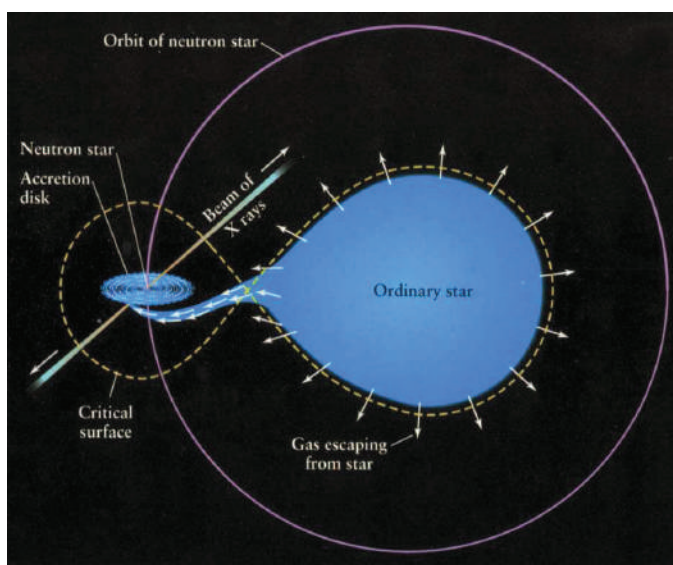


Fig. 1. X-ray binary Centaurus X3 detected by UHURU satellite. The pulse period is 4.84s. A binary motion signature was found with a 1.7 day orbital period, thanks to UHURU.

formulated a basic paradigm to serve as a guideline to interpret unitarily and consistently the occurrence of supernovae, the existence of binary X-ray sources and also possibly the nature of GRBs^{12–14}:

First paradigm

- *Supernovae originate from gravitational collapse to a neutron star.*
- *GRBs originate during the gravitational collapse to a black hole (BH).*
- *In studying a massive star, its binary nature and possibly the multiple systems involved in its behavior should of necessity be properly taken into account.*

We will see that the enforcement of this minimal set of assumptions has been extremely valuable. As the knowledge of these systems has evolved, I introduced two new and more specific paradigms narrowing in on the nature of the sources — each new paradigm being in clear agreement with the previous ones. I was well aware of a vast literature contemplating the possibility of relating different supernovae types to black holes over an extremely wide range of masses but I was very doubtful about these considerations since they violated more than one principle of my paradigm, they neglected a wealth of observational data, and they were based on a somewhat restrictive property related to metallicity in the thermonuclear evolution expected in a single star system (see e.g. Ref. 15). Moreover, after the splendid observations of the Hubble Space Telescope,¹⁶ today we begin to understand that even Eta Carinae is a binary system^{17,18} and that massive single stars are very likely a set of measure zero: massiveness implies multiplicity.

This situation has become even more interesting since the unexpected observation of a temporal and spatial coincidence between the occurrence of a GRB and a SN explosion, see e.g. GRB 980425¹⁹ and SN 1998bw,^{20,21} see Fig. 2. The explanation of this coincidence has led our group to introduce the induced gravitational collapse (IGC) paradigm (paradigm 1), a many-cosmic-body-interaction, and consequently we introduced a cosmic matrix: a C-matrix; see Fig. 3. The many-particle interaction in the S-matrix is confronted with this new concept of C-matrix involving a many-body interaction among astrophysical systems. This unprecedented situation has led to a series of new conceptual paradigms and the opening up of a new understanding of a vast number of previously unknown domains within physics and astrophysics, see e.g. Ref. 22 and references therein.

1.1. *Crab pulsar: A neutron star and a black hole*

That NSs exist in nature has been proven by the discovery of pulsars. The year 1967 marked the discovery of the first pulsar, observed at radio wavelengths in November 28, 1967 by Jocelyn Bell Burnell and Antony Hewish.²⁴ Just a few months later, the pulsar NP0532 was found in the center of the Crab Nebula and observed first at radio wavelengths and soon after at optical wavelengths, see Fig. 4.

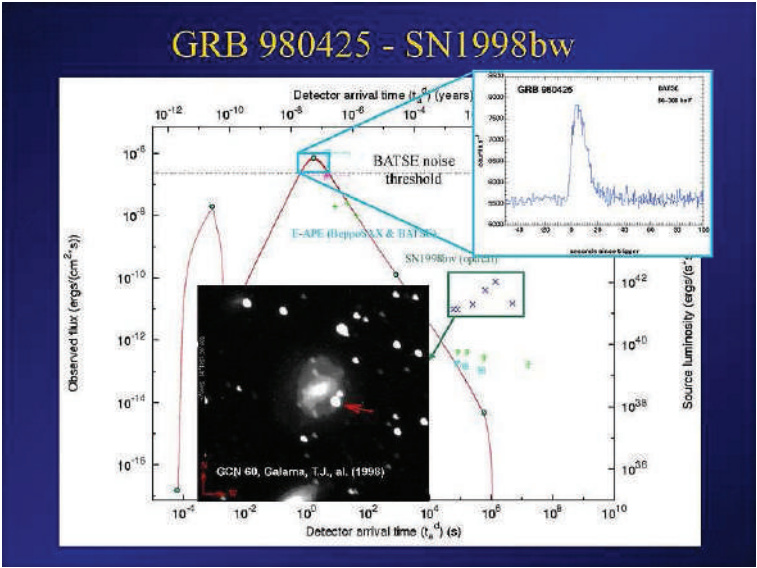


Fig. 2. GRB980425 and supernova SN 1998bw.

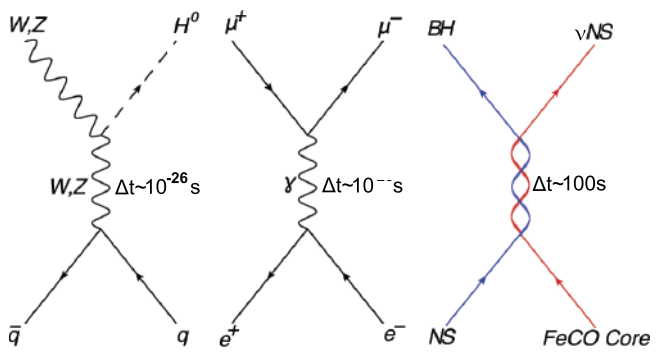


Fig. 3. The new concept of “C-matrix”, compared with the usual S-matrix. From Ref. 23.

The discovery of NSs led our small group working around John Wheeler in Princeton to direct our main attention to go further and address the study of continuous gravitational collapse to a black hole as first introduced by Oppenheimer and his students (see Fig. 5). The work in Princeton addressed the topic of black holes, gravitational waves (GWs) and cosmology. A summary of that work can be found in Refs. 25 and 26, where a wide range of topics in relativistic astrophysics was reconsidered, including the possible sources of GWs, the cross-sections of GW detectors, and especially, an entirely new family of astrophysical phenomena occurring around NSs and black holes and in cosmology.

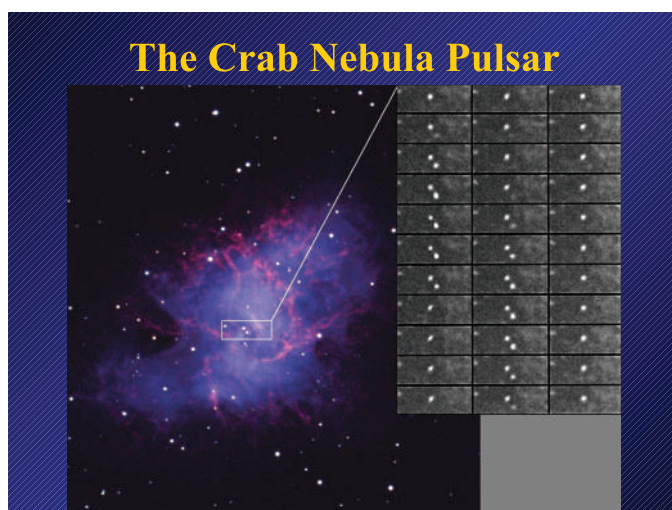


Fig. 4. The sequence of black and white images on the right is separated by one ms intervals, from which it is clear that the left star is a pulsar with a period of $P = 33$ ms. This period changes with a rate dP/dt of 12.5 ms per year. The fact that the loss of rotational energy of a NS with moment of inertia I is given by $dE/dt \propto -I(1/P^3)dP/dt$ explains precisely the energetics of the pulsar and proves at once the existence of NSs.²⁷

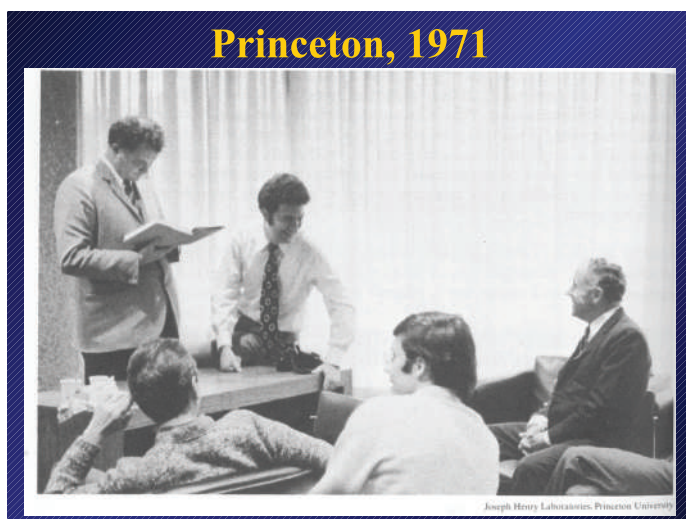


Fig. 5. Standing to the left Tullio Regge, sitting on the desk myself and sitting on the chair John Wheeler.

One of the most important results in the physics and astrophysics of BHs has been the BH mass-energy formula (see Fig. 6). From this, indeed, it became clear that up to 50% of the mass-energy of a BH could be extracted by using reversible transformations.²⁸ It then followed that during the formation of a BH, some of the

most energetic processes in the universe should exist, releasing an energy of the order of $\sim 10^{54}$ erg for a $1 M_{\odot}$ BH (see Fig. 6).

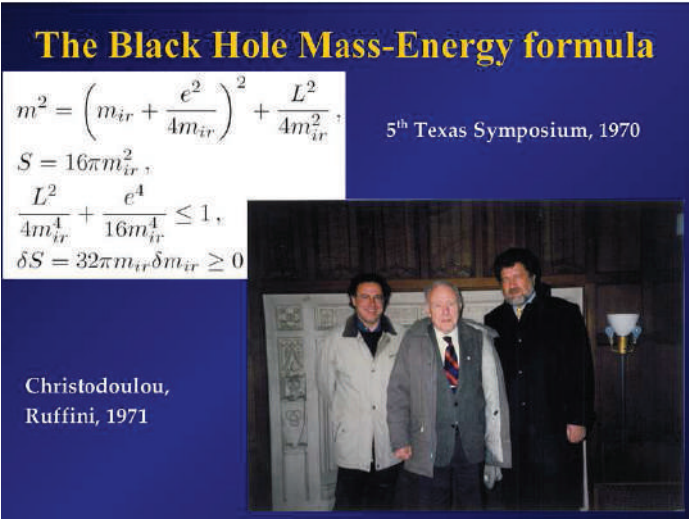


Fig. 6. The black hole mass-energy formula. From Ref. 28.

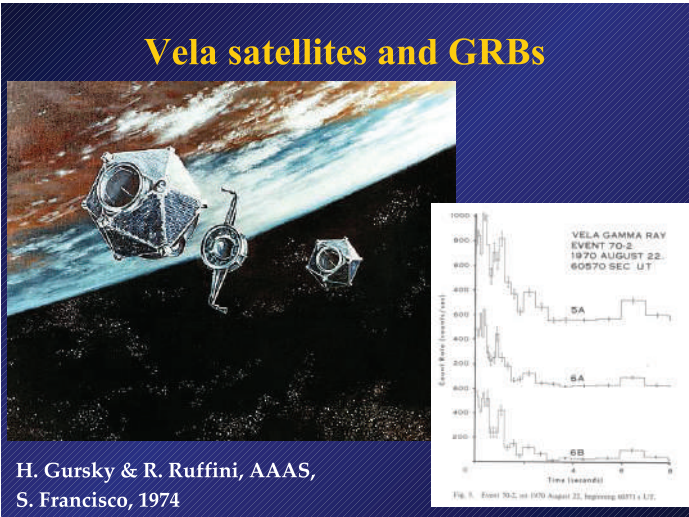


Fig. 7. The Vela satellites, see e.g. the Ian Strong chapter in Ref. 9.

1.2. The Vela and CGRO satellites and GRBs

In Ref. 29, I described how the observations of the Vela satellites were fundamental in discovering GRBs, see Fig. 7. Just a few months after the public announcement of their discovery,⁹ I formulated a theoretical model with T. Damour, a collaborator in Princeton, based on the extractable energy of a Kerr–Newmann black hole through a vacuum polarization process giving rise to GRBs, see Fig. 8. In our paper,¹¹ we pointed out that vacuum polarization occurring in the field of electromagnetic BHs could release an enormous e^+e^- plasma which self-accelerates and gives origin to the GRB phenomenon. Energetics for GRBs all the way up to $\sim 10^{55}$ ergs was theoretically predicted for a $10 M_\odot$ BH¹². The dynamics of this e^-e^+ plasma was first studied by J. R. Wilson and myself with the collaboration of Xue and Salmonson.^{30,31}

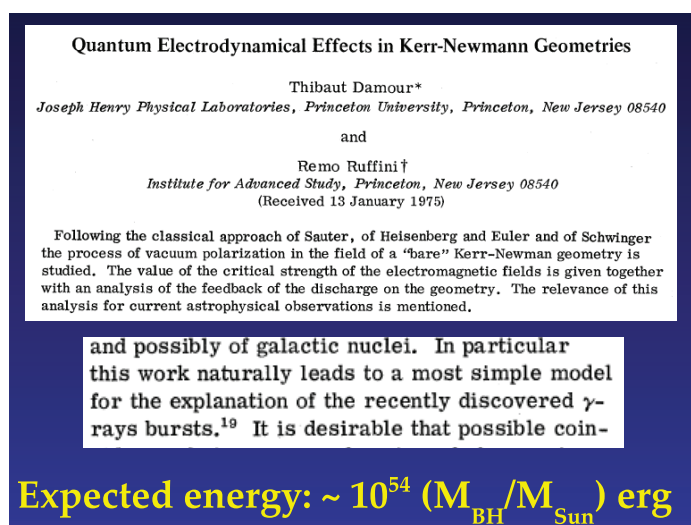


Fig. 8. The classic paper Ref. 11 on the extractable energy of a Kerr–Newmann black hole through vacuum polarization.

Initially it was difficult to model GRBs to understand their nature since their distances from the Earth were unknown, and thousands of models were presented³² attempting to explain the mystery they presented. The launching of the Compton Gamma Ray Observatory (CGRO) with the BATSE detectors on-board (see Fig. 9) led to the following important discoveries:

- (1) there is a homogeneous distribution of GRBs in the universe,
- (2) short GRBs exist lasting less than a second, and
- (3) long GRBs exist lasting more than one second.

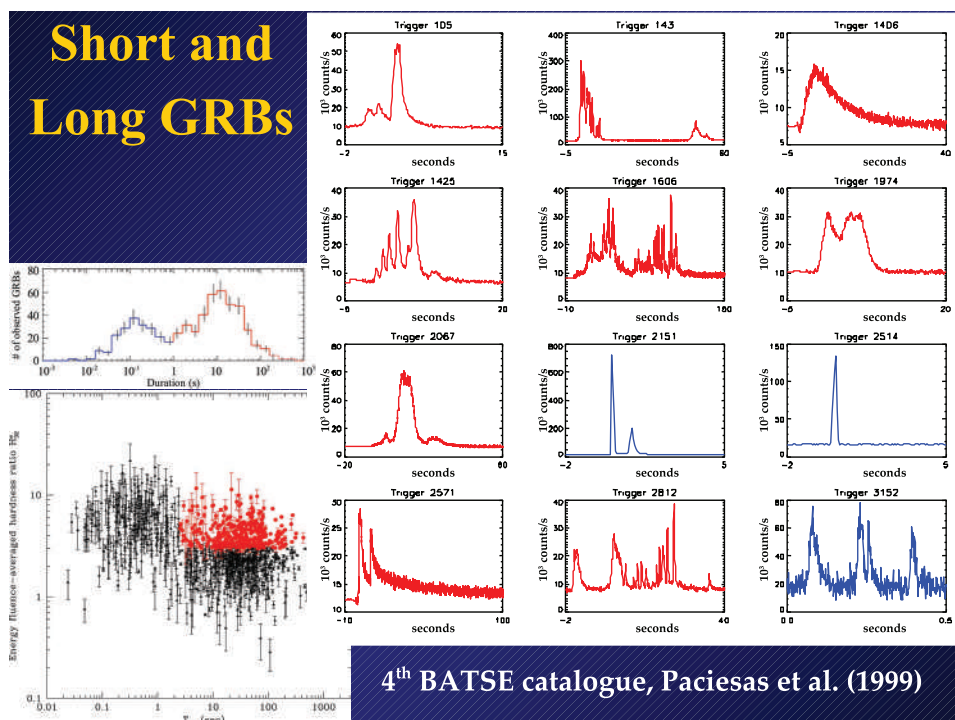


Fig. 9. Short and long GRB light curves and their temporal distribution from the 4th BATSE catalog, Ref. 33.

The crucial contribution to interpreting GRBs came from the Italian-Dutch BeppoSAX satellite, see Fig. 10 (e.g. Ref. 34) which led to a much more precise definition of their position in the sky obtained using a wide field X-ray camera and narrow field instrumentation. This enabled the optical identification of GRBs and the determination of their cosmological redshift, and consequently of their energetics, which turned out to be up to $\sim 10^{55}$ erg, previously predicted in Ref. 11. Since that time no fewer than 10 different X- and γ -ray observatory missions and numerous observations at optical and radio wavelengths have allowed us to reach a deeper understanding of the nature of GRBs, see Fig. 10.

After reviewing below the basic differences between the most quoted “fireball model” of GRBs and our “fireshell model”, we will describe the IGC paradigm (the “second paradigm”) and the analysis of the GRB 090618 in the fireshell scenario.³⁵ This will show the first application of the IGC paradigm to it.³⁶ We will then indicate some recent results on a possible distance indicator inferred from a GRB-SN correlation within the IGC paradigm,³⁷ and then give some additional evidence coming from the identification of the NS created by the supernova and its use as a cosmological distance candle. Next we will turn to the first example of the genuine short GRB 090227B³⁸ leading to black hole formation. Finally, we will illustrate a

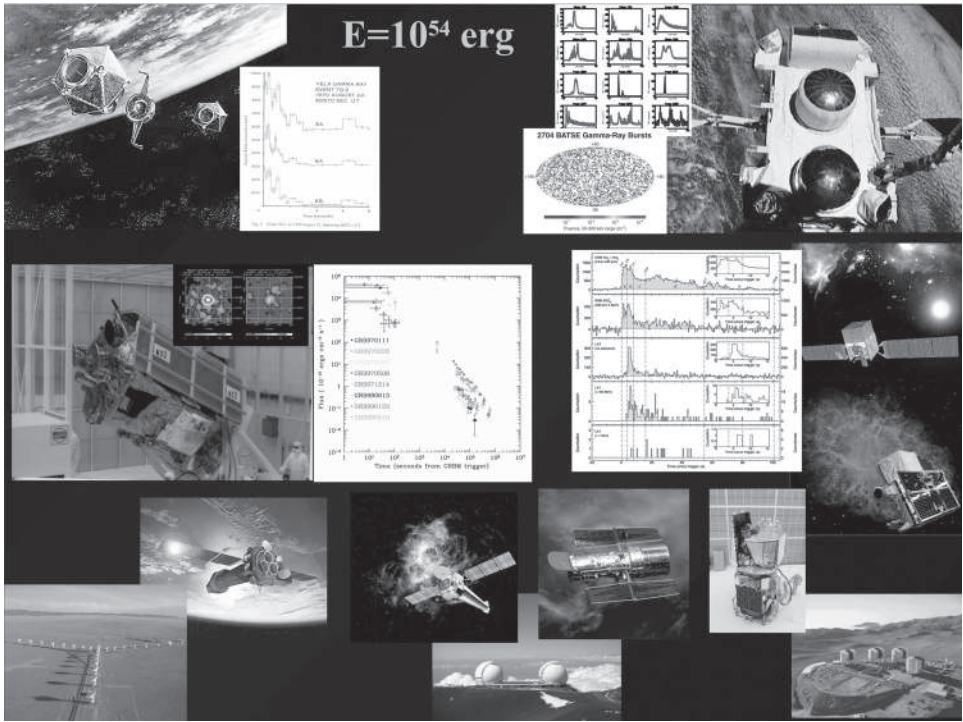


Fig. 10. The flotilla of space missions and the principal optical and radio astronomical observatories which participated in establishing the cosmological distances and energetics of GRBs extending up to the limit of 10^{55} Erg predicted in 1975, see Fig. 8. Most significant has been the central role played by the BeppoSAX mission through its coordinate observations of the narrow high energy field instruments and the wide field X-ray cameras, which led to the discovery of prolonged GRB emission and consequently to the optical identification of the GRB sources.

brand new paradigm dealing with the two families of short and long GRBs and a special role of the formation or not of a black hole.

1.3. *The fireball model compared and contrasted with the fireshell model*

A variety of models have been developed to theoretically explain the observational properties of GRBs, among which the fireball model³⁹ is one of those most often used. In Refs. 40–43, it was proposed that the sudden release of a large quantity of energy in a compact region can lead to an optically thick photon–lepton plasma and to the production of e^+e^- pairs. The sudden initial total annihilation of the e^+e^- plasma was assumed by Cavallo and Rees,⁴⁰ leading to an enormous release of energy pushing on the circumburst medium (CBM): the “fireball”, see e.g. Ref. 43 and references therein.

An alternative approach originating from the gravitational collapse to a black hole is the fireshell model, see e.g. Refs. 22 and 44. Here the GRB originates

from an optically thick e^+e^- plasma in thermal equilibrium, with a total energy of $E_{\text{tot}}^{e^\pm}$. This plasma is initially confined between the radius r_h of a black hole and its dyadosphere^{45,46} radius

$$r_{ds} = r_h \left[2\alpha \frac{E_{\text{tot}}^{e^+e^-}}{m_e c^2} \left(\frac{\hbar}{\frac{m_e c}{r_h}} \right)^3 \right]^{1/4}, \quad (1)$$

where α is the usual fine structure constant, \hbar is the Planck's constant, c is the speed of light, and m_e is the mass of the electron. The lower limit of $E_{\text{tot}}^{e^\pm}$ is assumed to coincide with the observed isotropic energy E_{iso} emitted in X-rays and gamma rays alone in the GRB. The condition of thermal equilibrium assumed in this model⁴⁷ distinguishes it from alternative ones, e.g. Ref. 40.

1.3.1. The fireball model

In the fireball model, the prompt emission, including the sharp luminosity variations,⁴⁸ is caused by the prolonged and variable activity of the “inner engine”.^{39,49} The conversion of the fireball energy to radiation is made by shocks, either internally (when faster moving matter overtakes a slower moving shell, see Ref. 49) or externally (when the moving matter is slowed down by the external medium surrounding the burst, see Ref. 50).

Synchrotron emission from relativistic electrons in the CBM has been given much attention, possibly accompanied by self-synchrotron Compton (SSC) emission, in order to explain the observed GRB spectra. These processes were purported to be consistent with the observational data of some GRBs.^{51,52} However, several limitations have been reported in relation to the low-energy spectral slopes of time-integrated spectra^{53–56} and the time-resolved spectra.⁵⁶ Additional limitations on SSC emission have also been pointed out in Refs. 57 and 58.

The latest phases of the afterglow are described in the fireball model by a single ultrarelativistic jetted emission assuming an equation of motion given by the Blandford-McKee self-similar power-law solution.⁵⁹ The maximum Lorentz factor of the fireball is estimated from the temporal occurrence of the peak of the optical emission, which is identified with the peak of the forward external shock emission^{60,61} in the thin shell approximation.⁶²

Several partly alternative and/or complementary scenarios have been developed independent of the fireball model, e.g. based on quasi-thermal Comptonization,⁶³ Compton drag emission,^{64,65} synchrotron emission from a decaying magnetic field,⁶⁶ jitter radiation,⁶⁷ Compton scattering of synchrotron self-absorbed photons,^{68,69} and photospheric emission.^{70–76} In particular, it was pointed out in Ref. 75 that photospheric emission overcomes some of the difficulties of purely nonthermal emission models. The collapsar model, leading to the astrophysical framework of the “fireball” model characterized by a jetted ultrarelativistic (Lorentz gamma factor 100–500) emission, was then introduced.

1.3.2. The fireshell model

Let us turn to the fireshell model. The rate equation for the e^+e^- pair plasma and its dynamics (the pair-electromagnetic pulse or PEM pulse for short) have been described in Refs. 30 and 31. This equation applies to any electron–positron plasma giving rise to the GRB phenomena, independent of whether it is generated by vacuum polarization around a Kerr–Newman black hole¹¹ or other mechanisms, e.g. electron–positron pairs from a neutrino–antineutrino annihilation mechanism. This plasma engulfs the baryonic material of mass M_B left over from the process of gravitational collapse, while still maintaining thermal equilibrium between electrons, positrons and baryons.

The baryon load is measured by the dimensionless parameter $B = M_B c^2 / E_{\text{tot}}^{e^+e^-}$. References 31 and 77 showed that no relativistic expansion of the plasma exists for $B > 10^{-2}$, see Fig. 11. The fireshell is still optically thick and self-accelerates to ultrarelativistic velocities (the pair-electromagnetic-baryonic pulse or PEMB pulse for short.^{31,77}) Then the fireshell becomes transparent and the “proper GRB” (P-GRB) is emitted.⁷⁸ The final Lorentz gamma factor reached at transparency can vary over a wide range between 10^2 and 10^4 as a function of $E_{\text{tot}}^{e^+e^-}$ and B . To determine this final value, it is necessary to integrate explicitly the rate equation for the e^+e^- annihilation process and evaluate, for a given black hole mass and given e^+e^- plasma radius, at what point the transparency condition is reached.³¹

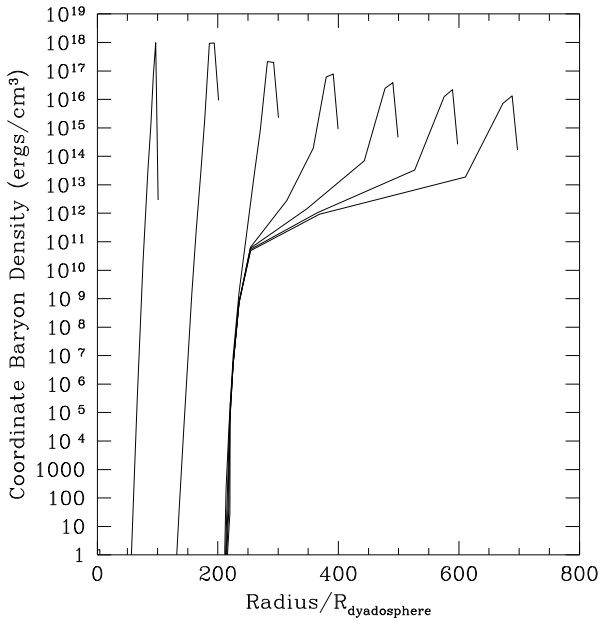


Fig. 11. The turbulent expansion for $B = 10^{-2}$. See details in Ref. 31.

The fireshell scenario does not require any prolonged activity of the inner engine and applies in generality to any confined amount of e^+e^- in a dyadosphere. After transparency, the remaining accelerated baryonic matter still expands ballistically and starts to slow down from collisions with the CBM of average density n_{CBM} . In the standard fireball scenario,⁴³ the spiky light curve is assumed instead to be caused by internal shocks.

In the fireshell model, the entire extended prompt emission is assumed to originate from an expanding thin baryonic shell, which maintains energy and momentum conservation during its collision with the CBM. The condition of a fully radiative regime is assumed.⁷⁸ This in turn allows one to estimate the characteristic inhomogeneities of the CBM, as well as its average density. It is appropriate to point out another difference between our treatment and others in the current literature. The complete analytic solution of the equations of motion of the baryonic shell were developed in Refs. 79 and 80, while elsewhere the Blandford–McKee self-similar approximate solution is almost always adopted without justification.^{72,81–89} The analogies and differences between the two approaches have been explicitly explained in Ref. 90.

In our general approach, a canonical GRB bolometric light curve is composed of two different parts: the P-GRB and the prompt radiation phase. The relative energetics of these two components and the observed temporal separation between the corresponding peaks is a function of the above three parameters $E_{\text{tot}}^{e^+e^-}$, B , and the average value of the CBM density n_{CBM} . The first two parameters are inherent to the accelerator mechanism characterizing the GRB, i.e. the optically thick phase, while the third parameter is inherent to the environment surrounding

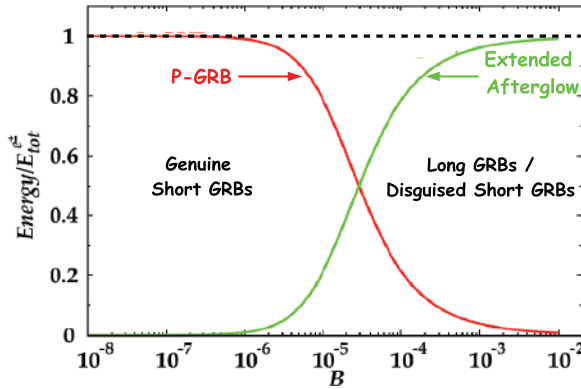


Fig. 12. (Color online) The energy emitted in the extended afterglow (solid green curve) and in the P-GRB (solid red curve) in units of $E_{\text{tot}}^{e^+e^-} = 1.77 \times 10^{53}$ erg (dashed horizontal line), as functions of B . The crossing point, corresponding to the condition $E_{\text{P-GRB}} \equiv 50\% E_{\text{tot}}^{e^+e^-}$, marks the division between the genuine short GRB region and the disguised short and long GRB region. The upper limit for B of 10^{-2} is determined by the onset of instabilities as shown in Fig. 11. From Ref. 38.

the GRB which gives rise to the prompt radiation phase by colliding with the baryonic fireshell.

For the observational properties of a relativistically expanding fireshell model, a crucial concept has been the introduction of the equi-temporal surfaces (EQTS). Here too our model differs from those in the literature by having derived an analytic expression for the EQTS obtained from the solutions to the equations of motion.^{80,90}

Details of the P-GRB and GRB prompt radiation are given in Ref. 13. Before closing it is appropriate to recall the fundamental diagram comparing and contrasting the P-GRB and the prompt radiation, see Fig. 12, characterizing the difference between short and long GRBs in the fireshell model as a function of the baryon load.

2. Unveiling the GRB-SN Connection: The Second Paradigm

2.1. Introduction

Until 1998 the study of GRBs and supernovae continued in parallel but disjoint from one another. Conceptually we have adopted the first paradigm mentioned above: that supernovae originate from the formation of a NS and that GRBs are generated by the formation of a black hole. Something totally unexpected happened on April 25, 1998: the occurrence of GRB 980425 and the simultaneous observation of SN 1998bw, see Refs. 19–21. This coincidence has become extremely common for all long GRBs at values of the cosmological redshift less than 1.

While the collapsar proponents and other groups started to attempt hybrid models of NSs and black holes, supernovae creating black holes and similar ideas, we maintained our first paradigm and introduced a new “second paradigm”:

Second paradigm

- All long GRBs are necessarily associated with supernovas of type **SN Ic** and are components of a “**cosmic matrix**”.
- They originate from a massive binary system, which evolves through a binary X-ray source, and finally leads to a binary system composed of an **FeCO** core $> 2.8 M_{\odot}$ and a **NS** companion separated by $b_{\text{crit}} \sim 10^{11}$ cm. For $b < b_{\text{crit}}$ hypercritical accretion of the SN ejecta onto the NS leads to **BH** formation and to the consequent emission of a GRB. For $b > b_{\text{crit}}$ no **BH** is formed.
- For $b < b_{\text{crit}}$ a binary-driven hypernova (**BdHN**) occurs characterized by: **Episode 1** the hypercritical accretion, **Episode 2** the GRB, **Episode 3** the universal behavior, and **Episode 4** the optical SN observed. For $b > b_{\text{crit}}$ only **Episode 1** and **Episode 4** exist, and an **X-ray Flash** occurs”.

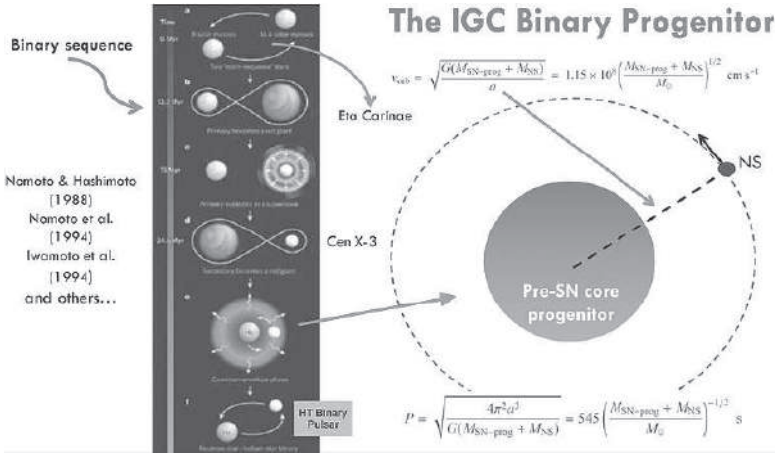


Fig. 13. The IGC binary progenitor. For details see Refs. 36 and 94.

Our present paradigm has recently evolved from an earlier formulation,⁹¹ see Fig. 14. All these theoretical works and their observational feedback have recently led to the binary-driven hypernova model (BdHN).^{92,93} Contrary to the collapse model which envisions a single object and a single event characterizing the GRB-supernova association, the IGC paradigm assumes as its progenitor a binary system containing an evolved Fe-Co core and a tightly bound neutron star binary companion, see Fig. 13. What was previously conceived for the GRB as a single ultra-relativistic event characterized by jetted emission appears to be a much more complex and rich system composed generally of four different episodes distinctively different in their astrophysical nature and with very specific signatures in their spectral and time varying luminosity emissions in selected wavelengths.

In conclusion, the IGC binary scenario applied here to the specific case of GRB 090618 naturally leads to understanding the energetics and the temporal coincidence of SNs and GRBs, as well as their astrophysical scenario and makes their correlation a direct consequence of the binary nature of the progenitor. In summary, we present in Figs. 15 and 16 the full interpretation of GRB 090618 observations as the four different episodes of the IGC paradigm.

Let us identify these four events in GRB 090618, the prototype of this most energetic family of GRBs, with an E_{iso} energy larger than 10^{52} erg, associated with supernovae. We describe a few key moments in the recent evolution of our understanding of this system which is very unique within physics and astrophysics. Some 20 additional examples of such a GRBs associated with supernovae have been identified by our group leading to the concept of binary driven-hypernovae.

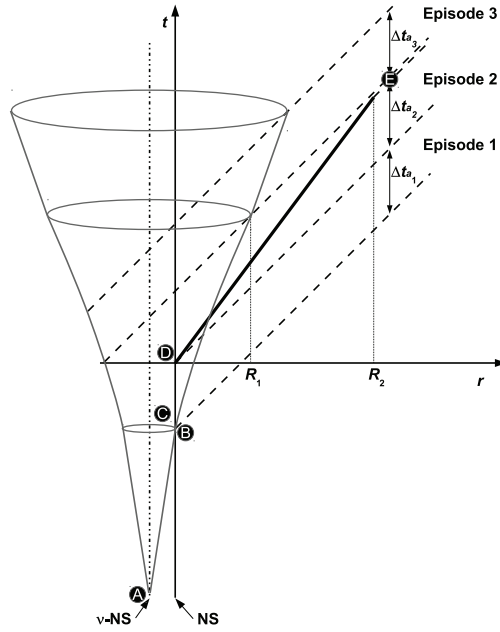


Fig. 14. The initial IGC spacetime diagram (not to scale), from Ref. 92. *Episode 1* corresponds to the onset of the FeCO core SN explosion, creating a new NS (ν -NS, see A). Part of the SN ejecta triggers an accretion process onto the NS companion (see B and Refs. 36 and 94), and a prolonged interaction between the ν -NS and the NS binary companion occurs (see C). This leads to a spectrum with an expanding thermal component plus an extra power law component (see Fig. 16 in Ref. 35). *Episode 2* occurs when the companion NS reaches its critical mass and collapses to a BH, emitting the GRB (D) with Lorentz factors $\Gamma \approx 10^2$ – 10^3 (for details, see e.g. Refs. 22 and 35). *Episode 3*, observed in the X-rays, shows very precise behavior consisting of a steep decay, starting at the end point of the prompt emission (see E), and then a plateau phase, followed by a late constant power-law decay (see Refs. 35 and 95). The figure illustrates the relativistic motion of Episode 2 ($\Gamma \approx 500$, thick line) and the nonrelativistic Episode 1 ($\Gamma \approx 1$) and Episode 3 ($\Gamma \approx 2$). Emissions from different radii, R_1 ($\sim 10^{13}$ cm) and R_2 ($\sim 10^{16}$ – 10^{17} cm), contribute to the transition point (E). Clearly, the X-ray luminosity originates from the SN remnant or in the newly born BH, but not from the GRB.

2.2. The case of GRB 090618

The GRB 090618 discovered by the Swift satellite⁹⁸ represents the prototype of a class of energetic ($10^{52} \leq E_{\text{iso}} \leq 10^{55}$ erg) GRBs, characterized by the presence of a supernova observed 10 ($1+z$) days after the trigger time, and the observation of four distinct emission episodes in their GeV emission, hard X-ray light curve, soft X-ray and optical emission (see details in Ref. 35). The BAT light curve shows a multi-peak structure, whose total estimated duration is ~ 320 s and whose T_{90} duration in the (15–350) keV range was 113 s.⁹⁹ The first 50 s of the light curve shows a smooth decay trend followed by a spiky emission, with three prominent peaks at 62, 80 and 112 s after the trigger time, respectively, and each has the typical appearance of a

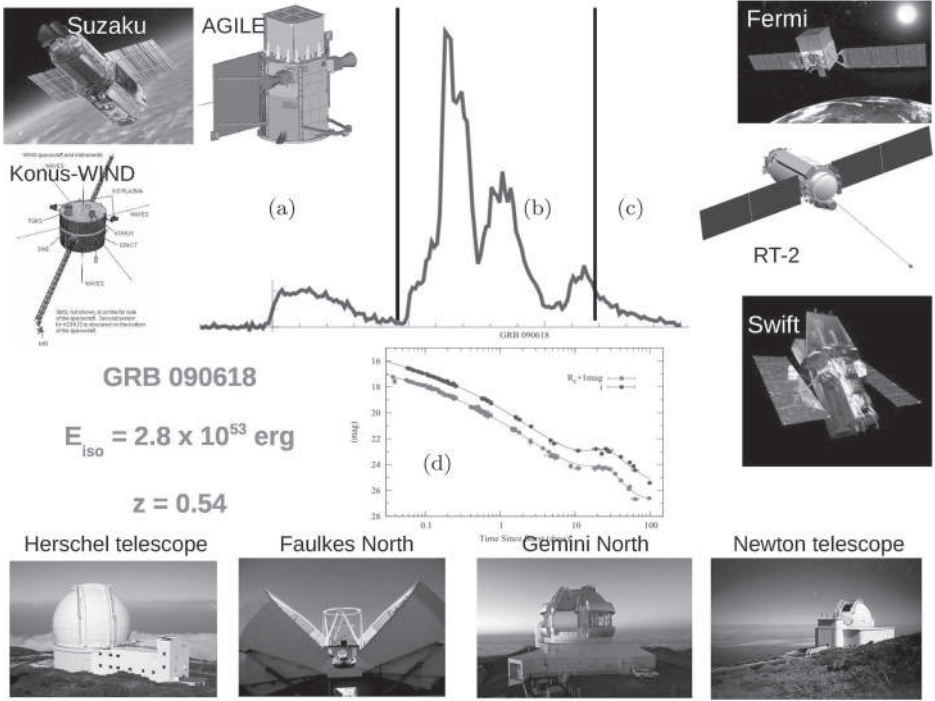


Fig. 15. GRB 090618 observations as the four different episodes implied by the IGC paradigm: (a) Episode 1, (b) Episode 2, (c) Episode 3 and (d) Episode 4 (i.e. the optical observations of the associated SN). Above are the satellites that participated in the observations: (in clockwise order) Fermi/GBM (8–1000 keV), Coronas-Photon/RT-2 (15–1000 keV), Swift/BAT (15–150 keV), Swift/XRT (0.3–10 keV), Swift/UVOT (optical band), AGILE/Super-AGILE (18–60 keV), AGILE/MCAL (350–10⁵ keV), Suzaku/WAM (50–5000 keV), Konus/WIND (20–2000 keV). Below are the ground based observatories that participated in the optical observations. Details in Refs. 35, 36 and 97.

fast-rise-exponential-decay (FRED) pulse.¹⁰⁰ The XRT observations started 125 s after the BAT trigger time and lasted ~ 25.6 ks¹⁰¹ and reported an initially bright uncatalogued source, identified as the afterglow of GRB 090618. Its early decay is very steep, ending at 310 s after the trigger time, when it starts a shallower phase, the plateau. Then the light curve breaks into a steeper late phase.

The GRB 090618 was also observed by the gamma ray burst (GBM) monitor on board the Fermi satellite.¹⁰² From an initial analysis, the time-integrated spectrum, ($t_0, t_0 + 140$) s in the (8–1000) keV range, was fit by a band spectral model¹⁰³ with a peak energy $E_{\text{peak}} = 155.5$ keV, $\alpha = -1.26$ and $\beta = -2.50$,¹⁰⁴ but with strong spectral variations within that time interval. The redshift of the source $z = 0.54$ was determined thanks to the identification of the MgII, MgI and FeII absorption lines using the KAST spectrograph mounted at the 3 m Shane telescope at the Lick observatory.¹⁰⁵ Given the redshift and the distance of the source, we computed the emitted isotropic energy in the 8–10,000 keV energy range with the Schaefer

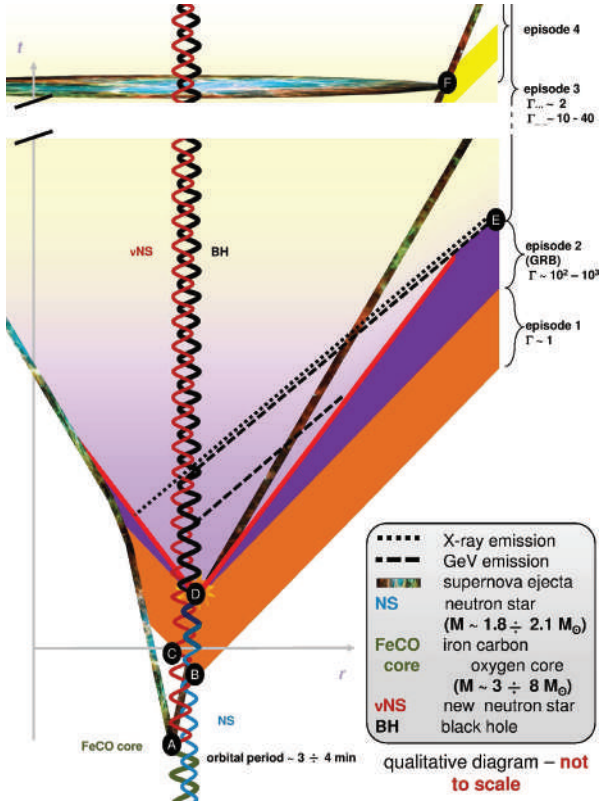


Fig. 16. (Color online) The further evolution of the IGC spacetime diagram (not to scale) illustrates 4 episodes of IGC paradigm: the nonrelativistic *Episode 1* ($\Gamma \simeq 1$), the relativistic motion of *Episode 2* ($\Gamma \simeq 10^2 \sim 10^3$), the mildly relativistic *Episode 3* ($\Gamma \simeq 2$), and nonrelativistic *Episode 4* ($\Gamma \simeq 1$). Initially there is a binary system composed of a massive star (yellow thick line) and a NS (blue line). The massive star evolves and explodes as a SN at point A, forms a ν NS (red line). The companion NS accretes the supernova ejecta starting from point B, interacts with the ν NS starting from point C, and collapses into a black hole (black line) at point D, this period from point B to point D we define as *Episode 1*. Point D is the starting of *Episode 2*, with two different components: one impacting on the SN filaments and one due to the collision of GRB outflow and interstellar filaments. At point E, *Episode 2* ends and *Episode 3* starts, *Episode 3* lasts till the optical signal of supernova emerges at point F, where the *Episode 4* starts. (Credit to M. Enderli for drawing this visualized spacetime diagram.)

formula¹⁰⁶: using the fluence in the range (8–1000 keV) as observed by the Fermi GBM, $S_{\text{obs}} = 2.7 \times 10^{-4}$,¹⁰⁴ and the Λ CDM (Λ cold dark matter) cosmological standard model $H_0 = 70 \text{ km/s/Mpc}$, $\Omega_m = 0.27$, $\Omega_\Lambda = 0.73$, we obtain the value $E_{\text{iso}} = 2.90 \times 10^{53} \text{ erg}$ for the emitted isotropic energy.

This GRB was observed also by Konus-WIND,¹⁰⁷ Suzaku-WAM¹⁰⁸ and by the AGILE satellite,¹⁰⁹ which detected emission in the (18–60) keV range and in the MCAL instrument, operating at energies greater than 350 keV, but it did not observe high-energy photons above 30 MeV. GRB 090618 was the first GRB ob-

served by the Indian payloads RT-2 on board the Russian satellite CORONAS-PHOTON.^{110–112} Thanks to the complete data coverage of the optical afterglow of GRB 090618, the presence of a supernova underlying the emission of its optical afterglow was reported.¹¹³ The evidence of a supernova emission came from the presence of several bumps in the light curve and by the change in R_c-i color index over time: in the early phases, the blue color is dominant, typical of the GRB afterglow, but then the color index increases, suggesting a core-collapse SN. At late times, the contribution from the host galaxy was dominant. We have analyzed the GRB 090618 with L. Izzo and other ICRANet researchers and Ph.D. students considering the BAT and XRT data of the Swift satellite together with the Fermi GBM and RT2 data of the Coronas-PHOTON satellite (see Fig. 15). The data reduction was made with the Heasoft v6.10 packages* for BAT and XRT, and the Fermi-Science tools for GBM. The details of the data reduction and analysis are given in Ref. 35.

2.3. *The emission process in Episode 1*

2.3.1. *The time-resolved spectra and temperature variation*

A significant outcome of the multi-year work of Felix Ryde and his collaborators¹¹⁴ has been the identification of thermal plus power-law features observed in time-limited intervals in selected BATSE GRBs. Similar features have also been observed in the data acquired by the Fermi satellite.^{114,115} These emissions have been shown to present a thermal plus power-law(s) feature, with a temperature changing in time following a precise power-law behavior. Our aim has been to see if the first 50 s of emission of GRB 090618 conform to this feature. We made a detailed time-resolved analysis, considering different time bin durations to obtain good statistics in the spectra and to take into account the sub-structures in the light curve. We then used two different spectral models to fit the observed data, a classic band spectrum,¹⁰³ and a blackbody with a power-law component. To obtain more accurate constraints on the spectral parameters, we made a joint fit considering the observations from both the n4 NaI and the b0 BGO detectors, covering a wider energy range in this way, from 8 keV to 40 MeV. To avoid some bias from low-photon statistics, we considered an energy upper limit of the value of 10 MeV. Our analysis is summarized in Figs. 17–19.

2.3.2. *The power-law decay of the black body temperature*

Particularly interesting is the clear evolution in the time-resolved spectra, which corresponds to the blackbody and power-law component, see Fig. 17. In particular the kT parameter of the blackbody shows a strong decay, with a temporal behavior well described by a double broken power-law function, see the upper panel in Fig. 18.

*<http://heasarc.gsfc.nasa.gov/lheasoft/>.

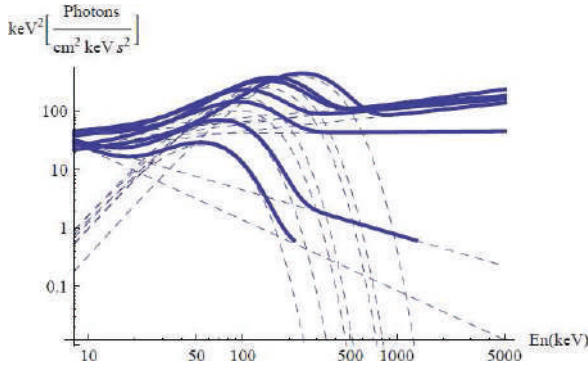


Fig. 17. Evolution of the BB+power-law spectral model in the $\nu F(\nu)$ spectrum of the first emission of GRB 090618. It shows the cooling of the blackbody and associated nonthermal components in time. We only plot the fitting functions for clarity. From Ref. 35.

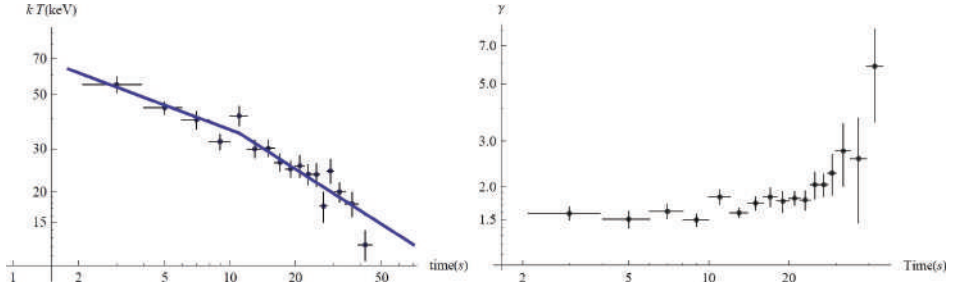


Fig. 18. (Color online) Evolution of the observed temperature kT of the blackbody component and the corresponding evolution of the power-law photon index. The blue line in the upper panel corresponds to the fit of the time evolution of the temperature with a broken power-law function. It shows a break time t_b around 11 s after the trigger time, as obtained from the fitting procedure. From Ref. 35.

From a fitting procedure we find that the best fit (R^2 -statistic = 0.992) for the two decay indexes for the temperature variation are $a_{kT} = -0.33 \pm 0.07$ and $b_{kT} = -0.57 \pm 0.11$. In Ref. 75, an average value for these parameters is given for a set of 49 GRBs: $\langle a_{kT} \rangle = -0.07 \pm 0.19$ and $\langle b_{kT} \rangle = -0.68 \pm 0.24$. The results presented in Figs. 17 and 18 point to a rapid cooling of the thermal emission with time of the first episode. The evolution of the corresponding power-law spectral component also appears to be strictly related to the change of the temperature kT . The power-law γ index falls, or softens, with temperature, see Fig. 17. An interesting feature appears to occur at the transition of the two power-laws describing the observed decrease of the temperature.

2.3.3. The radius of the emitting region

We turn now to estimate an additional crucial parameter for identifying the nature of the blackbody component: the radius r_{em} of the emitter. We proved

that the first episode is not part of a GRB. We can therefore provide the estimate of the emitter radius from nonrelativistic considerations, just corrected for the cosmological redshift z . In fact we find that the temperature $T_{\text{em}} = T_{\text{obs}}(1+z)$ of the emitter and that the luminosity of the emitter due to blackbody emission is

$$L = 4\pi r_{\text{em}}^2 \sigma T_{\text{em}}^4 = 4\pi r_{\text{em}}^2 \sigma T_{\text{obs}}^4 (1+z)^4, \quad (2)$$

where r_{em} is the emitter radius and σ is the Stefan–Boltzmann constant. From the luminosity distance definition, we also have that the observed flux ϕ_{obs} given by

$$\phi_{\text{obs}} = \frac{L}{4\pi D^2} = \frac{r_{\text{em}}^2 \sigma T_{\text{obs}}^4 (1+z)^4}{D^2}. \quad (3)$$

We then obtain

$$r_{\text{em}} = \left(\frac{\phi_{\text{obs}}}{\sigma T_{\text{obs}}^4} \right)^{1/2} \frac{D}{(1+z)^2}. \quad (4)$$

The above radius differs from the radius r_{ph} given in Eq. (1) of Ref. 75, which was also clearly obtained by interpreting the early evolution of GRB 970828 as belonging to the photospheric emission of a GRB and assuming a relativistic expansion with a Lorentz gamma factor Γ satisfying

$$r_{ph} = \hat{\mathcal{R}} D \left(\frac{\Gamma}{(1.06)(1+z)^2} \right), \quad (5)$$

where $\hat{\mathcal{R}} = (\phi_{\text{obs}}/(\sigma T_{\text{obs}}^4))^{1/2}$ and the prefactor 1.06 arises from the dependence of r_{ph} on the angle of the line of sight.¹¹⁶ Typical values of r_{ph} are at least two orders of magnitude higher than our radius r_{em} . Assuming a standard cosmological model ($H_0 = 70$ km/s/Mpc, $\Omega_m = 0.27$ and $\Omega_\Lambda = 0.73$) for estimating the luminosity distance D , and using the values for the observed flux ϕ_{obs} and the temperature kT_{obs} , we give in Fig. 19 the evolution of the surface radius that emits the blackbody r_{em} as a function of time. Assuming an exponential evolution with time t^δ of the radius in the comoving frame, we obtain the value $\delta = 0.59 \pm 0.11$ from a fitting procedure, which is well compatible with $\delta = 0.5$. We also notice a steeper behavior for the variation of the radius with time corresponding to the first 10 s, which corresponds to the emission before the break of the double power-law behavior of the temperature. We estimate an average velocity of $\bar{v} = 4067 \pm 918$ km/s, $R^2 = 0.91$ in these first 10 s of emission. In episode 1, the observations lead to a core of an initial radius of $\sim 12,000$ km expanding in the early phase with a higher initial velocity of ~ 4000 km/s. The effective Lorentz Γ factor is very low, $\Gamma - 1 \sim 10^{-5}$. I proposed to identify this first episode as the early phases of the accretion onto the companion NS which the SN ejects in the IGC scenario, later confirmed by the simulation⁹⁶.

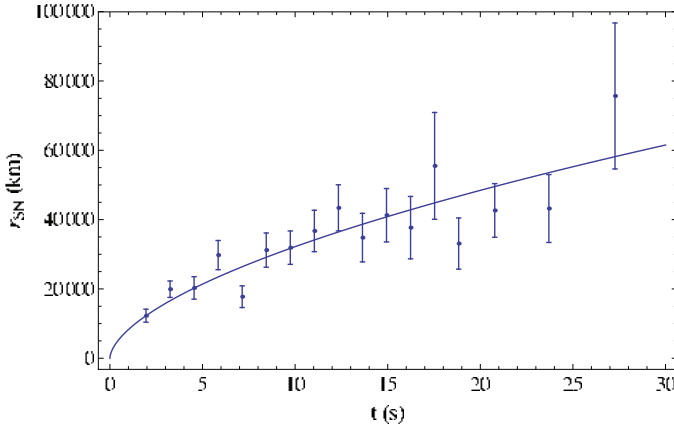


Fig. 19. Evolution of the Episode 1 emitter radius given by Eq. (4). From Ref. 35.

2.4. The emission process in Episode 2

2.4.1. The identification of the P-GRB

We have proceeded to the analysis of the data between 50 and 150 s after the trigger time as a canonical GRB in the fireshell scenario, namely Episode 2.⁹⁷ We proceed to identify the P-GRB within the emission between 50 s and 59 s, since we find a blackbody signature in this early second-episode emission. Considerations based on the time variability of the thermal component bring us to conclude that the first 4 s of this time interval due to the P-GRB emission. The corresponding spectrum (8–440 keV) is well fit ($\tilde{\chi}^2 = d1.15$) with a blackbody of temperature $kT = 29.22 \pm 2.21$ keV (norm = 3.51 ± 0.49), and an extra power-law component with photon index $\gamma = 1.85 \pm 0.06$, (norm = 46.25 ± 10.21). The fit with the band model is also acceptable ($\tilde{\chi}^2 = 1.25$), which gives a low-energy power-law index $\alpha = -1.22 \pm 0.08$, a high-energy index $\beta = -2.32 \pm 0.21$ and a break energy $E_0 = 193.2 \pm 50.8$. In view of the theoretical understanding of the thermal component in the P-GRB (see Sec. 3.2), we focus below on the blackbody + power-law spectral model. The isotropic energy of the second episode is $E_{\text{iso}} = (2.49 \pm 0.02) \times 10^{53}$ ergs. The simulation within the fireshell scenario is made assuming $E_{\text{tot}}^{e^+e^-} \equiv E_{\text{iso}}$. From the observed temperature, we can then derive the corresponding value of the baryon load. The observed temperature of the blackbody component is $kT = 29.22 \pm 2.21$, so that we can determine a value of the baryon load of $B = 1.98 \pm 0.15 \times 10^{-3}$, and deduce the energy of the P-GRB as a fraction of the total $E_{\text{tot}}^{e^+e^-}$. We therefore obtain a value of the P-GRB energy of $4.33_{-0.28}^{+0.25} \times 10^{51}$ erg. Next we can derive the radius of the transparency condition, to occur at $r_{\text{tr}} = 1.46 \times 10^{14}$ cm. We derive the bulk Lorentz factor of $\Gamma_{\text{th}} = 495$ and compare this value with the energy measured only in the blackbody component of $E_{\text{BB}} = 9.24_{-0.58}^{+0.50} \times 10^{50}$ erg, and with the energy in the blackbody plus the power-law component of $E_{\text{BB}+po} = 5.43_{-0.11}^{+0.07} \times 10^{51}$ erg,

and verify that the theoretical value is in between these observed energies. We have found this result to be quite satisfactory: it represents the first attempt to relate the GRB properties to the details of the BH responsible for the overall GRB energetics. The above theoretical estimates were based on a nonrotating BH of $10 M_{\odot}$, a total energy of $E_{\text{tot}}^{e^+e^-} = 2.49 \times 10^{53}$ erg and a mean temperature of the initial e^+e^- plasma of 2.4 MeV, derived from the expression for the dyadosphere radius, Eq. (1).

2.4.2. *The refinement of the P-GRB nature*

Standing the excellent results obtained in the e^+e^- spectra and the dynamics of the refinement and the direct comparison between theory and observations will have to address a variety of fundamental problems such as (1) the possible effect of rotation of the BH, leading to a more complex dyadotorus structure,²² (2) an analysis of the general relativistic, electrodynamical and strong interaction descriptions of the gravitational core collapse leading to BH formation,^{77,117,118} (3) a possible role of hypercritical accretion process in creating the electron–positron plasma out of neutrino–antineutrino annihilation.^{96,119,120} All these processes could alternatively lead to a dyadosphere near the Kerr–Newmann black hole with an efficiency (42%) similar to the electrodynamical case (50%).

2.4.3. *The prompt emission and the CBM cloud structure*

The prompt emission starts at the above given radius of the transparency, with an initial value of the Lorentz Γ factor of $\Gamma_0 = 495$. To simulate the extended–afterglow emission, we need to determine the radial distribution of the CBM around the burst site, which we assume for simplicity to be spherically symmetric, from which we infer a characteristic size of $\Delta R = 10^{15}$ – 10^{16} cm. We already described above how the simulation of the spectra and of the observed multi-band light curves have to be performed together and need to be jointly optimized, leading to the determination of the fundamental parameters characterizing the CBM medium.¹²¹ This radial distribution is shown in Fig. 20 and is characterized by a mean value of $\langle n \rangle = 0.6$ part/cm³ and an average density contrast with a $\langle \delta n/n \rangle \approx 2$, see Fig. 20 and Tables 1 and 2. The data up to 8.5×10^{16} cm are simulated with a value for the filling factor $\mathcal{R} = 3 \times 10^{-9}$, while the data from this value on with $\mathcal{R} = 9 \times 10^{-9}$. From the radial distribution of the CBM density, and considering the $1/\Gamma$ effect on the fireshell visible area, we found that the CBM clumps causing the spikes in the extended afterglow emission have masses on the order of 10^{22} – 10^{24} g. The value of the α parameter was found to be -1.8 along the total duration of the GRB. In Fig. 21, we show the simulated light curve (8–1000 keV) of the GRB and the corresponding spectrum, using the spectral model described in Refs. 79 and 122. The Episode 2, lasting from 50 s to 151 s, agrees with a canonical GRB in the fireshell scenario.

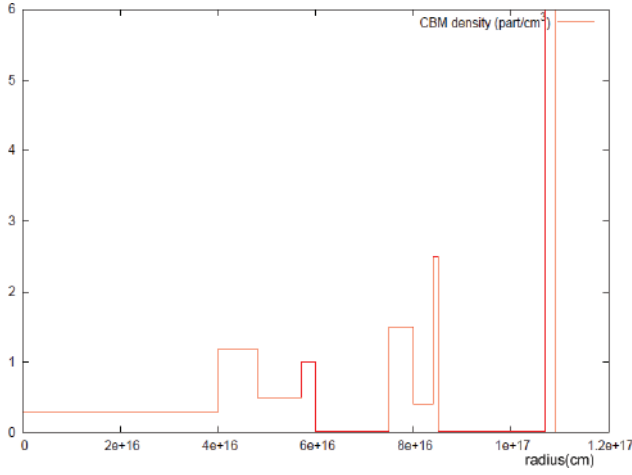


Fig. 20. Radial CBM density distribution for GRB 090618. The characteristic masses of each cloud are on the order of $\sim 10^{22-24}$ g and 10^{16} cm in radii. From Ref. 35.

Table 1. Final results of the simulation of GRB 090618 in the fireshell scenario. From Ref. 35.

Parameter	Value
$E_{\text{tot}}^{e^+e^-}$	$2.49 \pm 0.02 \times 10^{53}$ ergs
B	$1.98 \pm 0.15 \times 10^{-3}$
Γ_0	495 ± 40
kT_{th}	29.22 ± 2.21 keV
$E_{P\text{-GRB},th}$	$4.33 \pm 0.28 \times 10^{51}$ ergs
$\langle n \rangle$	0.6 part/cm^3
$\langle \delta n/n \rangle$	2 part/cm^3

Table 2. Physical properties of the three clouds surrounding the burst site: the distance from the burst site (column 2), the radius r of the cloud (column 3), the particle density ρ (column 4), and the mass M (the last column). From Ref. 35.

Cloud	Distance (cm)	r (cm)	ρ ($\#/\text{cm}^3$)	M (g)
First	4.0×10^{16}	1×10^{16}	1	2.5×10^{24}
Second	7.4×10^{16}	5×10^{15}	1	3.1×10^{23}
Third	1.1×10^{17}	2×10^{15}	4	2.0×10^{22}

2.5. The emission process of Episode 3

2.5.1. The late X-ray emission observed by swift/XRT

We now turn to the most important feature which has appeared in the analysis of Episode 3 of GRB 090618: the presence of a steep decay, followed by a plateau and a power law steep decay, see Fig. 22. This feature has unexpectedly become a common feature of all GRBs with energy larger than 10^{52} erg and even more striking, all

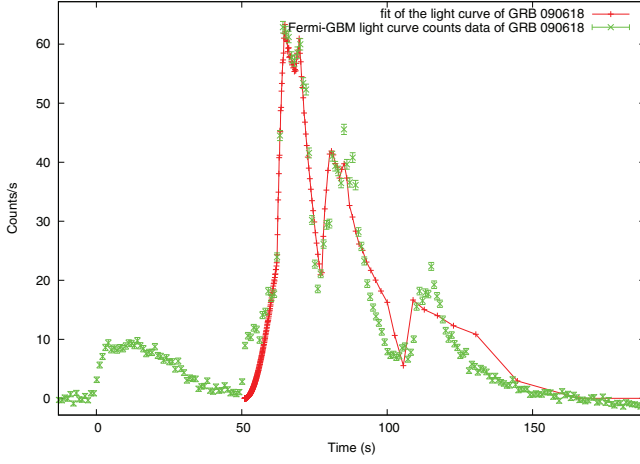


Fig. 21. Simulated light curve of the extended-afterglow of GRB 090618. From Ref. 35.

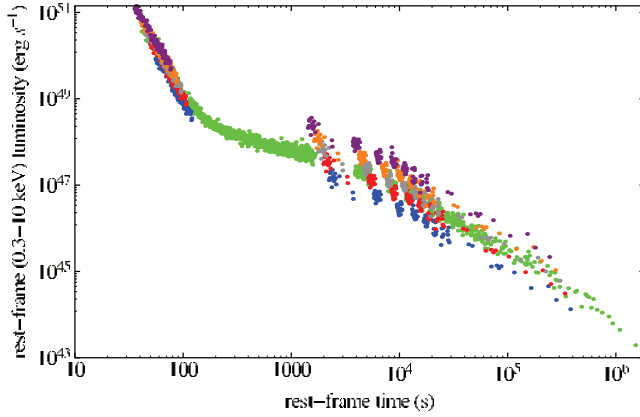


Fig. 22. (Color online) In green we show the rest frame X-ray luminosity light curve of GRB 090618 in the 0.3–10 keV energy range in comparison with the one of GRB 101023, computed for different hypothetical redshifts: respectively, from blue to purple: $z = 0.6, 0.8, 1.0, 1.2, 1.5$. The overlapping at late time of the two X-ray luminosity light curves is obtained for a redshift of $z = 0.9$. For further details see Refs. 95 and 123.

the X-ray emissions at late times, when computed in the rest frame of the source they overlap, see Fig. 23. This feature has become a most powerful method to estimate the cosmological redshift of the source, when not directly observed. We have focused our attention on the analysis of all the available XRT data of these sources.³⁷ Characteristically, XRT follow-up starts only about 100 s after the BAT trigger (typical repointing time of Swift after the BAT trigger). Since the behavior was similar in all the sources, we have performed an analysis to compare the XRT luminosity light curve L_{rf} , where “rf” stands for rest frame, for the six GRBs with measured redshift z in the common rest frame energy range 0.3–10 KeV. To perform

this computation, the first step is to convert the observed XRT flux f_{obs} to the one in the 0.3–10 KeV rest frame energy range. In the detector frame, the 0.3–10 KeV rest frame energy range becomes $[0.3/(1+z)] - [10/(1+z)]$ KeV where z is the redshift of the GRB. We assume a simple power-law function as the best-fit for the spectral energy distribution of the XRT data[†]:

$$\frac{dN}{dA dt dE} \propto E^{-\gamma}. \quad (6)$$

We can then write the flux light curve f_{rf} in the 0.3–10 KeV rest frame energy range as:

$$f_{\text{rf}} = f_{\text{obs}} \frac{\int_{\frac{0.3 \text{ keV}}{1+z}}^{\frac{10 \text{ keV}}{1+z}} E^{-\gamma} dE}{\int_{0.3 \text{ keV}}^{10 \text{ keV}} E^{-\gamma} dE} = f_{\text{obs}} (1+z)^{\gamma-1}. \quad (7)$$

Then we have to multiply f_{rf} by the luminosity distance to get L_{rf} :

$$L_{\text{rf}} = 4\pi d_l^2(z) f_{\text{rf}}, \quad (8)$$

where we assume a standard cosmological model Λ CDM with $\Omega_m = 0.27$ and $\Omega_\Lambda = 0.73$. Clearly, this luminosity must be plotted as a function of the rest frame time t_{rf} , namely:

$$t_{\text{rf}} = \frac{t_{\text{obs}}}{1+z}. \quad (9)$$

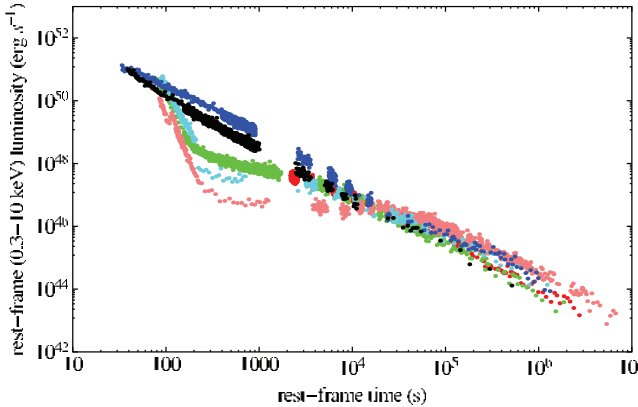


Fig. 23. (Color online) The X-ray luminosity light curves of the six GRBs with measured redshift in the 0.3–10 keV rest frame energy range: in pink GRB 060729, $z = 0.54$; in black GRB 061007, $z = 1.261$; in blue GRB 080319B, $z = 0.937$; in green GRB 090618, $z = 0.54$, in red GRB 091127, $z = 0.49$, in cyan GRB 111228, $z = 0.713$. From Ref. 37.

[†]<http://www.swift.ac.uk/>.

Table 3. The GRB sample considered in this work. The redshifts of GRB 101023 and GRB 110709B, which are marked by an asterisk, were deduced theoretically by using the method outlined in Ref. 95 and the corresponding isotropic energy computed by assuming these redshifts. From Ref. 37.

GRB	z	E_{iso} (erg)
GRB 060729	0.54	1.6×10^{52}
GRB 061007	1.261	1.2×10^{54}
GRB 080319B	0.937	1.4×10^{54}
GRB 090618	0.54	2.7×10^{53}
GRB 091127	0.49	1.4×10^{52}
GRB 111228	0.713	2.3×10^{52}
GRB 101023	0.9*	1.3×10^{53}
GRB 110709B	0.75*	2.72×10^{53}

2.5.2. “The golden sample”

The X-ray luminosity light curves of the six GRBs with measured redshift in the 0.3–10 KeV rest frame energy band are plotted together in Fig. 23 and Table 3. What is most striking is that these six GRBs, with redshift in the range 0.49–1.261, show a remarkably common behavior of the late X-ray afterglow luminosity light curves (Episode 3) despite that their prompt emissions (Episodes 1 and 2) are very different and that their energetics spans more than two orders of magnitude, see Table 3. Such a common behavior starts between 10^4 and 10^5 s after the trigger and continues up to when the emission falls below the XRT threshold. This universal behavior of Episode 3 represents strong evidence of very low or even the absence of beaming in this particular phase of the X-ray afterglow emission process. I proposed in the presentation that this late time X-ray emission in Episode 3 is related to the process of the SN explosion within the IGC scenario, possibly emitted by the newly born NS and BH and by the supernovae ejecta shocked by the GRB, and not by the GRB itself, see Fig. 16.

2.5.3. Episode 3 as a standard candle

As an example, we present in Fig. 22 the rest frame X-ray luminosity (0.3–10 KeV) light curve of GRB 090618 (considered as a prototype for the common behavior shown in Fig. 23) with the rest frame X-ray luminosity light curves of GRB 110709B estimated for selected values of its redshifts, $z = 0.4, 0.6, 0.8, 1.0, 1.2$ and similarly the correspondent analysis for GRB 101023 for selected values of the redshift, $z = 0.6, 0.8, 1.0, 1.2, 1.5$. We then find, with A.V. Penacchioni and other ICRA.Net researchers and Ph.D. students, that GRB 101023 should have been located at $z \sim 0.9$ and GRB 110709B at $z \sim 0.75$. These redshift estimations are within the range expected using the Amati relation as shown in Refs. 95 and 123. This is an important independent confirmation of validity for this new redshift estimator we propose for the family of IGC GRB-SN systems. It should be stressed,

however, that the determination of the redshift is done assuming the validity of the standard Λ CDM cosmological model for sources with redshift in the range $z = 0.49$ – 1.216 . We are currently testing the validity of this assumption for sources at larger cosmological redshifts.

3. The GRB-SN and the IGC: The Second Paradigm

3.1. *IGC of a NS to a blackhole by a type Ib/c SN*

The systematic and spectroscopic analysis of GRB-SN events, following the pioneering discovery of the temporal coincidence of GRB 980425¹⁹ and SN 1998bw,²¹ has revealed evidence for the association of other nearby GRBs with Type Ib/c SNe (see Ref. 124 for a recent review of all the GRB-SN systems). It has also been clearly understood that SN Ib/c lack Hydrogen (H) and Helium (He) in their spectra, and the most likely explanation is that the SN progenitor star is in a binary system with a compact companion, a NS (see e.g. Refs. 125–127, for details). In the current literature there has been an attempt to explain both the SN and the GRB as two aspects of the same astrophysical phenomenon: the collapsar model. Hence, GRBs have been assumed to originate from a specially violent SN process, a hypernova or a collapsar (see e.g. Ref. 128 and references therein). Both of these possibilities imply a very dense and strong wind-like CBM structure. Such a dense medium appears to be in contrast with the CBM density found in most GRBs within our fireshell model (see e.g. Fig. 10 in Ref. 36). In fact, the average CBM density, inferred from the analysis of the afterglow, has been shown to be in most of the cases of the order of $1 \text{ particle cm}^{-3}$ (see e.g. Ref. 44). The only significant contribution to the baryonic matter component in the GRB process is the one represented by the baryon load.³¹ In a GRB, the electron–positron plasma, loaded with a certain amount of baryonic matter, is expected to expand at ultra-relativistic velocities with Lorentz factors $\Gamma \gtrsim 100$.^{81,129,130} Such an ultra-relativistic expansion can actually occur if the amount of baryonic matter, quantifiable through the baryon load parameter, does not exceed the critical value $B \sim 10^{-2}$ (see Ref. 31, for details). For $B > 10^{-2}$ the electron–positron plasma loses its laminar motion and the turbulence occurs, see Fig. 11.

In our approach, following the first paradigm, we have consistently assumed that the GRB has to originate from the gravitational collapse to a BH. The SN follows, instead, the complicated pattern of the final evolution of a massive star, possibly leading to a NS or to a complete explosion but never to a BH. There is a further general argument in favor of our explanation, namely the extremely different energetics of SNe and GRBs. While the SN energy range is 10^{49} – 10^{51} erg, the GRBs are in a larger and wider range of energies 10^{49} – 10^{54} erg. It is clear that in no way a GRB, being energetically dominant, can originate from the SN. We explain the temporal coincidence of the two phenomena, the SN explosion and the GRB, using the concept of *IGC*.^{91,131}

In recent years, we have outlined two different possible scenarios for the GRB-SN connection. In the first version,⁹¹ we have considered the possibility that GRBs may have caused the trigger of the SN event. For this scenario to occur, the companion star has to be in a very special phase of its thermonuclear evolution (see Ref. 91 for details). More recently in Refs. 121, 131 and 132 I have proposed a different possibility occurring at the final stages of the evolution of a close binary system: the explosion in such a system of a Ib/c SN leads to an accretion process onto the NS companion. The full spacetime diagram is represented in Fig. 14. Again, in order for this process to occur, a very fine tuning must exist in the thermonuclear evolution of the SN core and in the circular orbit of the companion NS. The NS will reach the critical mass value, undergoing gravitational collapse to a BH. The process of gravitational collapse to a BH leads to the emission of the GRB (see Figs. 24 and 25). Here we evaluate the accretion rate onto the NS and give the explicit expression of the accreted mass as a function of the nature of the components and the binary parameters following Ref. 94. The full spacetime diagram is represented in Fig. 14.

3.2. *The accretion process of the SN ejecta onto the companion NS*

We turn now to the details of the recent work with Jorge Rueda⁹⁴ and collaborators, of the accretion process of the SN material onto the NS. In a spherically symmetric

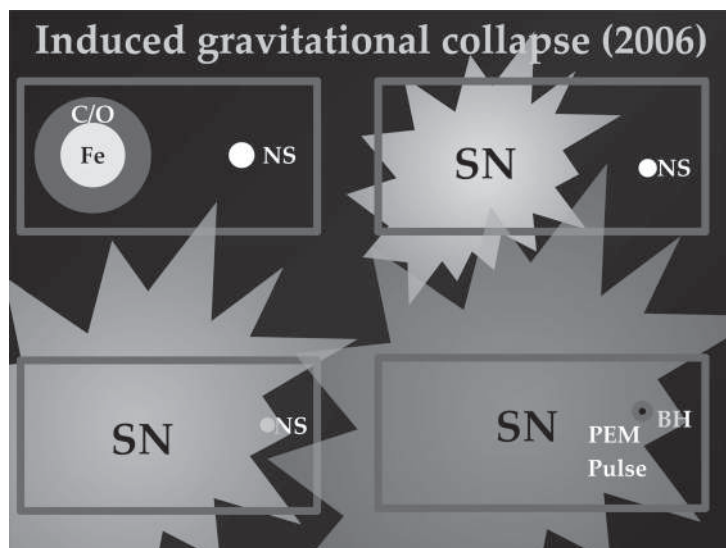


Fig. 24. Process of gravitational collapse to a BH induced by the type Ib/c SN on a companion NS in a close binary system. Figure reproduced from Ref. 131.

Hypercritical Accretion, Binary-Driven HNe, and IGC

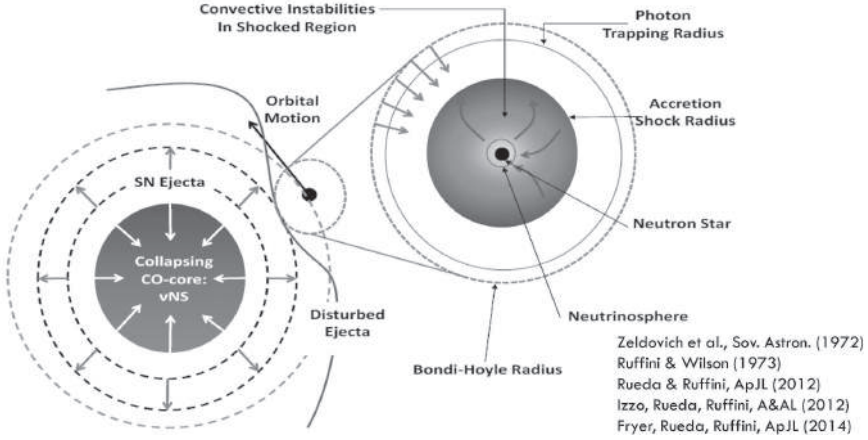


Fig. 25. Hypercritical accretion, binary-driven HNe and IGC.

accretion process, the magnetospheric radius is¹³³

$$R_m = \left(\frac{B^2 R^6}{\dot{M} \sqrt{2GM_{\text{NS}}}} \right)^{2/7}, \quad (10)$$

where B , M_{NS} , R are the NS magnetic field, mass, radius, and $\dot{M} \equiv dM/dt$ is the mass-accretion rate onto the NS. It can be seen that for high accretion rates the influence of the magnetosphere will be negligible. The NS captures the material ejected from the core collapse of the companion star in a region delimited by the radius R_{cap} from the NS center

$$R_{\text{cap}} = \frac{2GM_{\text{NS}}}{v_{\text{rel, ej}}^2}, \quad (11)$$

where M_{NS} is the initial NS mass and $v_{\text{rel, ej}}$ is the velocity of the ejecta relative to the orbital motion of the NS around the supernova progenitor star

$$v_{\text{rel, ej}} = \sqrt{v_{\text{orb}}^2 + v_{\text{ej}}^2}, \quad (12)$$

with v_{ej} the ejecta velocity in the frame of the supernova progenitor star with mass $M_{\text{SN-prog}}$ and v_{orb} is the orbital velocity of the NS, given by

$$v_{\text{orb}} = \sqrt{\frac{G(M_{\text{SN-prog}} + M_{\text{NS}})}{a}}, \quad (13)$$

where a is the binary separation, and thus the orbital period of the binary system is

$$P = \sqrt{\frac{4\pi^2 a^3}{G(M_{\text{SN-prog}} + M_{\text{NS}})}}. \quad (14)$$

The NS accretes the material that enters into its capture region defined by Eq. (11). The mass-accretion rate is given by¹³⁴

$$\dot{M} = \xi \pi \rho_{\text{ej}} R_{\text{cap}}^2 v_{\text{ej}} = \xi \pi \rho_{\text{ej}} \frac{(2GM_{\text{NS}})^2}{(v_{\text{orb}}^2 + v_{\text{ej}}^2)^{3/2}}, \quad (15)$$

where the parameter ξ lies in the range $1/2 \leq \xi \leq 1$, ρ_{ej} is the density of the accreted material, and in the last equality we have used Eqs. (11) and (12). The upper value $\xi = 1$ corresponds to the Hoyle–Lyttleton accretion rate.¹³⁵ The actual value of ξ depends on the properties of the medium in which the accretion process occurs, e.g. vacuum or wind. The velocity of the SN ejecta v_{ej} will be much larger than the sound speed c_s of the already existing material between the C+O star and the NS due to the prior mass transfer, namely the Mach number of the SN ejecta will certainly satisfy $\mathcal{M} = v_{\text{ej}}/c_s \gg 1$. Thus, in practical calculations we can assume the value $\xi = 1$ in Eq. (15) and the relative velocity $v_{\text{rel,ej}}$ of the SN ejecta with respect to the NS companion is given only by the NS orbital velocity and the ejecta velocity as given by Eq. (12). In Fig. 25, we have sketched the accreting process of the supernova ejected material onto the NS. The density of the ejected material can be assumed to decrease in time following the simple power-law¹³⁶

$$\rho_{\text{ej}} = \frac{3M_{\text{ej}}}{4\pi r^3} = \frac{3M_{\text{ej}}}{4\pi \sigma^3 t^{3n}}, \quad (16)$$

where without loss of generality we have assumed that the radius of the SN ejecta expands as $r_{\text{ej}} = \sigma t^n$, with σ and n constants. Therefore, the velocity of the ejecta obeys $v_{\text{ej}} = nr_{\text{ej}}/t$. Equation (15) can be integrated analytically and the accreted mass in a given time interval is given by⁹⁴

$$\Delta M(t) = \int \dot{M} dt = \pi (2GM_{\text{NS}})^2 \frac{3M_{\text{ej}}}{4\pi n^3 \sigma^6} \mathcal{F} + \text{const.}, \quad (17)$$

where

$$\begin{aligned} \mathcal{F} = t^{-3(n+1)} & \left[-4n(2n-1)t^{4n} \sqrt{kt^{2-2n} + 1} {}_2F_1 \left(\frac{1}{2}, \frac{1}{n-1}; \frac{n}{n-1}; -kt^{2-2n} \right) \right. \\ & \left. - k^2(n^2-1)t^4 + 2k(n-1)(2n-1)t^{2n+2} + 4n(2n-1)t^{4n} \right] \\ & \times [k^3(n-1)(n+1)(3n-1)\sqrt{k+t^{2n-2}}]^{-1}, \end{aligned} \quad (18)$$

with $k = v_{\text{orb}}^2/(n\sigma)^2$ and ${}_2F_1(a, b; c; z)$ is the hypergeometric function. The integration constant is computed with the condition $\Delta M(t) = 0$ for $t \leq t_0^{\text{acc}}$, where t_0^{acc} is the time at which the accretion process starts, namely the time at which the SN ejecta reaches the NS capture region (see Fig. 25).

3.3. Reaching the critical mass of the accreting companion NS

We discuss now the problem of the maximum stable mass of a NS. Nonrotating NS equilibrium configurations have been recently constructed by M. Rotondo, J. Rueda, myself and many students, taking into proper account the strong, weak, electromagnetic and gravitational interactions within general relativity. The equilibrium equations are given by the general relativistic Thomas–Fermi equations coupled with the Einstein–Maxwell equations to form the Einstein–Maxwell–Thomas–Fermi system of equations, which must be solved under the condition of global charge neutrality.¹³⁷ These equations supersede the traditional Tolman–Oppenheimer–Volkoff ones that impose the condition of local charge neutrality throughout the configuration. The maximum stable mass $M_{\text{crit}} = 2.67 M_{\odot}$ of nonrotating NSs has been obtained in Ref. 137.

The high and rapid accretion rate of the SN material can lead the NS mass to reach the critical value $M_{\text{crit}} = 2.67 M_{\odot}$. This system will undergo gravitational collapse to a BH, producing a GRB. The initial NS mass is likely to be rather high due to the highly nonconservative mass transfer during the previous history of the evolution of the binary system (see e.g. Refs. 125–127, for details). Thus, the NS could reach the critical mass in just a few seconds. Indeed we can see from Eq. (15) that for an ejecta density 10^6 g cm^{-3} and velocity 10^9 cm s^{-1} , the accretion rate might be as large as $\dot{M} \sim 0.1 M_{\odot} \text{ s}^{-1}$. The occurrence of a GRB–SN event in the scenario depends on some specific conditions satisfied by the binary progenitor system, such as a short binary separation and an orbital period $< 1 \text{ h}$. This is indeed the case with GRB 090618 and 110709B that we have already analyzed within the context of this scenario in Refs. 36 and 123, respectively (see below in the next subsections). In addition to offering an explanation for the GRB–SN temporal coincidence, the considerations presented here lead to an astrophysical implementation of the concept of proto-BH, generically introduced in our previous works on GRBs 090618, 970828 and 101023 (see Refs. 36, 95 and 138). The proto-BH represents the first stage $20 \lesssim t \lesssim 200 \text{ s}$ of the SN evolution.

It is appropriate now to discuss the possible progenitors of such binary systems. A viable progenitor is represented by X-ray binaries such as Cen X-3 and Her X-1.^{6,9,139–143} The binary system is expected to follow an evolutionary track^{125–127}: the initial binary system is composed of main-sequence stars 1 and 2 with a mass ratio $M_2/M_1 \gtrsim 0.4$. The initial mass of the star 1 is likely $M_1 \gtrsim 11 M_{\odot}$, leaving a NS through a core-collapse event. The star 2, now with $M_2 \gtrsim 11 M_{\odot}$ after some almost conservative mass transfer, evolves filling its Roche lobe. It then starts a spiraling in of the NS into the envelope of the star 2. If the binary system does not merge, it will be composed of a helium star and a NS in close orbit. The helium star expands filling its Roche lobe and a nonconservative mass transfer to the NS takes place. This scenario naturally leads to a binary system composed of a C+O star and a massive NS, as the one considered here, see Fig. 25. It is clear that after the occurrence of the SN and the GRB emission, the outcome is represented,

respectively, by a NS and a BH. If the NS and the BH are gravitationally bound they give rise to a new kind of binary system, which can lead itself to the merging of the NS and the BH and consequently to a new process of gravitational collapse of the NS into the BH. In this case the system could originate yet another process of GRB emission and possibly a predominant emission in gravitational waves.

4. The Application of the IGC Scenario to GRB 090618

4.1. The SN ejecta accretion onto the companion NS

We recall that the blackbody-emitting surface in Episode 1 evolves during the first ~ 32 s, as observed in the rest frame, following a power-law behavior

$$r_{\text{em}} = \sigma t^n, \quad v_{\text{em}} = n \frac{r_{\text{em}}}{t} = n \sigma t^{n-1}, \quad (19)$$

where $\sigma = 8.048 \times 10^8 \text{ cm s}^{-n}$, $n \approx 3/5$ as shown in Fig. 19, and $v_{\text{em}} = dr_{\text{em}}/dt \sim 4 \times 10^8 \text{ cm s}^{-1}$ at the beginning of the expansion.

When the mass accreted onto the NS triggers the gravitational collapse of the NS into a BH, the authentic GRB emission is observed in the subsequent episode at $t - t_0 \gtrsim 50$ s (observer frame). The characteristics of GRB 090618 are shown in Table 3 of Ref. 35 and we refer to that reference for more details on the GRB light curve and spectrum simulation. We now turn to the details of the accretion process of the SN material onto the NS. We have initially assumed, as an order of magnitude estimate,³⁶ $r_{\text{SN}} = r_{\text{em}}$ and $v_{\text{SN}} = v_{\text{em}}$. The NS of initial mass M_{NS} accretes mass from the SN ejecta at a rate given by⁹⁴

$$\dot{M}_{\text{acc}}(t) = \pi \rho_{\text{ej}}(t) \frac{(2GM_{\text{NS}})^2}{v_{\text{rel, ej}}^3}, \quad \rho_{\text{ej}}(t) = \frac{3M_{\text{ej}}(t)}{4\pi r_{\text{SN}}^3(t)}, \quad (20)$$

where $r_{\text{SN}}^3(t)$ given by Eq. (19) and $M_{\text{ej}}(t) = M_{\text{ej},0} - M_{\text{acc}}(t)$ is the available mass to be accreted by the NS as a function of time, with $M_{\text{ej},0}$ the mass ejected in the SN. $v_{\text{rel, ej}} = \sqrt{v_{\text{orb}}^2 + v_{\text{SN}}^2}$ is the velocity of the ejecta relative to the NS, where v_{SN} is the SN ejecta velocity given by Eq. (19) and $v_{\text{orb}} = \sqrt{G(M_{\text{core}} + M_{\text{NS}})/a}$ is the orbital velocity of the NS. Here M_{core} is the mass of the SN core progenitor and a the binary separation. Hereafter we assume $a = 9 \times 10^9 \text{ cm}$, a value higher than the maximum distance traveled by the SN material during the total time interval of Episode 1, $\Delta t \simeq 32$ s, $\Delta r \sim 7 \times 10^9 \text{ cm}$ (see Fig. 19). If the accreted mass onto the NS is much smaller than the initial mass of the ejecta, i.e. $M_{\text{acc}}/M_{\text{ej},0} \ll 1$, the total accreted mass can be obtained from the formula given by Eq. (8) of Ref. 94, which for GRB 090618 leads to

$$M_{\text{acc}}(t) = \int_{t_0^{\text{acc}}}^t \dot{M}_{\text{acc}}(t) dt \approx (2GM_{\text{NS}})^2 \frac{15M_{\text{ej},0} t^{2/5}}{8n^3 \sigma^6 \sqrt{1 + kt^{4/5}}} \bigg|_{t_0^{\text{acc}}}^t, \quad (21)$$

where $k = v_{\text{orb}}^2/(n\sigma)^2$ and t_0^{acc} is the time at which the accretion process starts, namely the time at which the SN ejecta reaches the NS capture region, $R_{\text{cap}} =$

$2GM_{\text{NS}}/v_{\text{rel,ej}}^2$, so for $t \leq t_0^{\text{acc}}$ we have $M_{\text{acc}}(t) = 0$. The accretion process leads to the gravitational collapse of the NS onto a BH when it reaches the critical mass value. Here we adopt the critical mass $M_{\text{crit}} = 2.67 M_{\odot}$ computed recently in Ref. 137. Equation (21) is more accurate for massive NSs since the amount of mass needed to reach the critical mass by accretion is much smaller than $M_{\text{ej},0}$. In general, the total accreted mass must be computed from the numerical integration of Eq. (20), which we present below for GRB 090618.

4.2. Inferences on the binary period

The occurrence of a GRB-SN event in the accretion induced collapse scenario is subject to some specific conditions of the binary progenitor system such as a short binary separation and orbital period. The orbital period in the present case is

$$P = \sqrt{\frac{4\pi^2 a^3}{G(M_{\text{core}} + M_{\text{NS}})}} = 9.1 \left(\frac{M_{\text{core}} + M_{\text{NS}}}{M_{\odot}} \right)^{-1/2} \text{ min.} \quad (22)$$

We denote by Δt_{acc} the total time interval since the beginning of the SN ejecta expansion all the way up to the instant where the NS reaches the critical mass. In Fig. 26, we plot Δt_{acc} as a function of the initial NS mass and for different masses of the SN core progenitor mass. The mass of the SN ejecta is assumed to be $M_{\text{ej},0} = M_{\text{core}} - M_{\text{rem}}$, where M_{rem} is the mass of the central compact remnant (NS) left by the SN explosion. Here we assumed $M_{\text{core}} = (3-8)M_{\odot}$ at the epoch of the SN explosion, and $M_{\text{rem}} = 1.3 M_{\odot}$, following some of the type Ic SN progenitors studied in Refs. 125–127.

We can see from Fig. 26 that, for GRB 090618, the mass of the NS companion that collapses onto a BH should be in the range $1.8 \lesssim M_{\text{NS}}/M_{\odot} \lesssim 2.1$ corresponding to the SN Ic progenitors $3 \leq M_{\text{core}}/M_{\odot} \leq 8$. The massive NS companion of the evolved star is in line with the binary scenario proposed in Ref. 131. These results also agree with the well-understood Ib/c nature of the SN associated with GRBs. The most likely explanation for SN Ib/c, which lack H and He in their spectra, is that the SN progenitor star is in a binary system with an NS; see also Refs. 125, 126, 127 and also 144 and 145.

It is also interesting to compare the results on the IGC of an NS to a BH by a type Ib/c SN⁹⁴ with the results of Chevalier¹³⁶ on the accretion of supernova material by the central NS generated by the supernova. A total accreted mass of up to $0.1 M_{\odot}$ in a time of a few hours was obtained there for a normal type II SN. Thus, a similar amount of mass can be accreted in the two cases, but in the latter the accretion occurs over a longer time. To reach a high accretion rate of the inner SN material onto the central NS, a mechanism is needed that helps to increase the density of the NS surrounding layers, which is decreasing due to the expansion after being unbound by the SN explosion. Reference 136 analyzed the possibility of having a reverse shock wave as this mechanism while it moves back through the

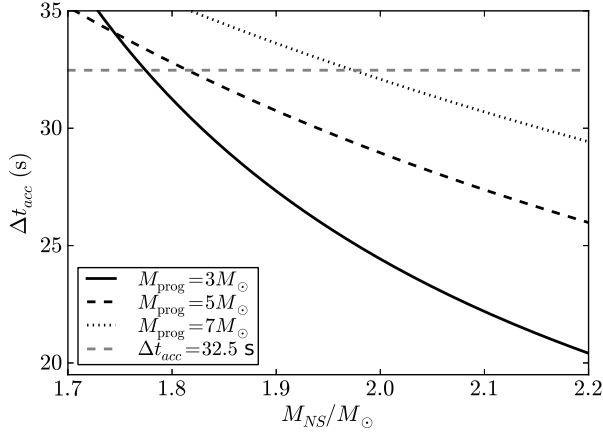


Fig. 26. Time interval Δt_{acc} of the accretion process onto the NS as a function of initial NS mass M_{NS} for selected values of the SN core progenitor mass M_{core} . The horizontal dashed line is the duration $\Delta t = 32.5$ s of the first episode of GRB 090618, which constrains the duration of the time needed by the NS to reach the critical mass. The crossing points between the dashed horizontal line and the solid curves give the NSs with M_{NS} that reach the critical mass in the time Δt . From Ref. 36.

SN core. The reverse shock is formed in the interaction of the mantle gas with the low-density envelope. The time scale of the accretion process is thus determined by the time it takes the reverse shock to reach the vicinity of the central newly born NS, which is a few hours in the case of SN II progenitors. However, the existence of a low-density outer envelope, e.g. H and He outer layers, is essential for the strength of the reverse shock. Fall-back accretion onto the central NS is expected to be relevant only in SN II but not in SN Ic like those associated to GRBs, where H and He are absent.

4.3. The collapse time and the role of neutrinos

The argument presented in Ref. 94 naturally explains the sequence of events: SN explosion — IGC-BH formation — GRB emission. Correspondingly, the accretion of the material ejected by the SN into the nearby NS of the IGC model presented here occurs almost instantaneously. Indeed for the SN expansion parameters obtained from the observations of Episode 1 in GRB 090618 (see Eq. (19), the accretion of the SN material onto the nearby NS occurs in a few seconds (see Fig. 26). The binary parameters are such that the ejecta density does not decrease too much (from 10^6 g cm^{-3} to $\sim 10^4$ g cm^{-3}) before reaching the capture region of the NS, leading to a high accretion rate. As pointed out in Ref. 136, radiative diffusion will lower the accretion rate up to the Eddington limit (and then to even lower rates) when the trapping radius of the radiation in the flow $r_{tr} = \kappa \dot{M}_{acc} / (4\pi c)$,¹³⁶ where κ is the opacity, is equal to the Bondi radius $r_B = GM_{NS} / v_{rel, ej}^2$, the gravitational capture radius. The radius r_{tr} is located where the outward diffusion luminosity is equal to

the inward convective luminosity. It can be checked that for the parameters of our system given by Eqs. (19)–(21), the equality $r_{\text{tr}} = r_B$ occurs in a characteristic time ~ 200 days, where we used $\kappa = 0.2 \text{ cm}^2 \text{ g}^{-1}$. Thus, this regime is not reached in the present case since the NS is brought to its critical mass just in a few seconds. In the case analyzed by Ref. 136, it happens in a time ~ 8 days. Only recently we have returned to the previously mentioned papers of Zel’dovich and collaborators¹¹⁹ and Ruffini and Wilson,¹²⁰ since it is clear that the role of neutrino emission is essential in the understanding of the accretion process of the SN ejecta into the companion of NS binary.



Fig. 27. Group picture. Standing: Carlo Luciano Bianco, Marco Muccino, Wang Yu. Sitting: Remo Ruffini, Giovanni Pisani, Jorge Rueda, Milos Kovacevic, Luca Izzo.

It is also a pleasure to show here in Fig. 27 the closest collaborators working at ICRANet headquarters in Pescara and at ICRA at the University of Rome “la Sapienza”.

5. Recent Highlights and the “Third Paradigm”

Some most recent results have appeared in Refs. 23, 38, 92, 96 and 147 and are summarized in a “third paradigm”, see Figs. 28 and 29.

The progenitor systems of short bursts are traditionally identified with (NS) binary mergers, see, e.g. Refs. 148–157. This theoretical prediction received further observational supports by the successful localization of some short burst afterglows with large off-sets from their hosts galaxies, both late and

early type galaxies with no apparent association with star formation, see, e.g. Refs. 157–159.

Third paradigm

- *Long GRBs occur in a “cosmic matrix” composed of up to 4 different Episodes, each one characterized by specific astrophysical processes and Lorentz Γ factors (from $\Gamma \sim 1$ up to $\Gamma \sim 10^3$).*
- *Both short and long GRBs with $E_{\text{iso}} > 10^{52}$ erg originate from a gravitational collapse to a BH ($M > M_{\text{crit}} \sim 2.6 M_{\odot}$) and can have GeV emission:*
 - Long GRBs \rightarrow BdHNe \rightarrow BH + NS binaries \rightarrow “the” long GRBs.
 - Short GRBs \rightarrow massive BNS mergers \rightarrow BH \rightarrow “the” short GRBs.
- *Both short and long GRBs with $E_{\text{iso}} < 10^{52}$ erg do not form BH and have no GeV emission.*
 - Long GRBs \rightarrow binary NSs \rightarrow X-ray flashes \rightarrow XRFs.
 - Short GRBs \rightarrow short gamma ray flashes \rightarrow massive NS \rightarrow S-GRFs.

Reference 148 proposed that the short bursts must be further sub-divided into two different sub-classes, depending on whether or not the NS–NS merger leads to a core with mass larger than the NS critical mass $M_{\text{crit}}^{\text{NS}}$ ¹⁶⁷ which gravitationally collapses to a BH. The first class of short bursts is characterized by isotropic energies $E_{\text{iso}} \lesssim 10^{52}$ erg and rest-frame spectral peak energies $E_{p,i} \lesssim 2 \text{ MeV}$ ^{148,168,169} and have as outcome a massive NS (MNS) with additional orbiting material, or even a binary companion (NS or white dwarf, WD), to conserve energy and momentum. We dubbed these moderately hard short bursts as short gamma-ray flashes (S-GRFs). The second class of authentic short GRBs (S-GRBs) has $E_{\text{iso}} \gtrsim 10^{52}$ erg and $E_{p,i} \gtrsim 2 \text{ MeV}$ ^{148,168,169} and lead to the formation of a Kerr BH with additional orbiting material, see Fig. 30. Differently from the case of S-GRFs, they exhibit the systematical presence of the 0.1–100 GeV emission, which is related to the activity of the newly-born BH. The relative rate of these two classes of short bursts has been discussed and presented in Ref. 148. There, it has been proved that the S-GRFs are the more frequent events among the short bursts, see also Ref. 170, as also pointed out from the analogy with NS–NS binaries within our Galaxy, for which only in a subset of them the total mass of the components is larger than $M_{\text{crit}}^{\text{NS}}$ and can lead to a BH in their merging process. Similar conclusions have been also independently reached in Refs. 171 and 172.

Recently, within the fireshell model for GRBs, see, e.g. for a review Ref. 22, we have identified three examples of such authentic S-GRBs: 090227B¹⁷³, 090510¹⁷⁴, and 140619B,¹⁴⁸ see Fig. 31. All of them populate the high energy part of the $E_{p,i} - E_{\text{iso}}$ relation for short bursts^{168,169,174} and consistently exhibit, when they fall within the Fermi-LAT field of view (FoV), $a \lesssim 10^2 \text{ s}$ (in the observer frame) and very energetic GeV emission, starting soon after the transparency emission of

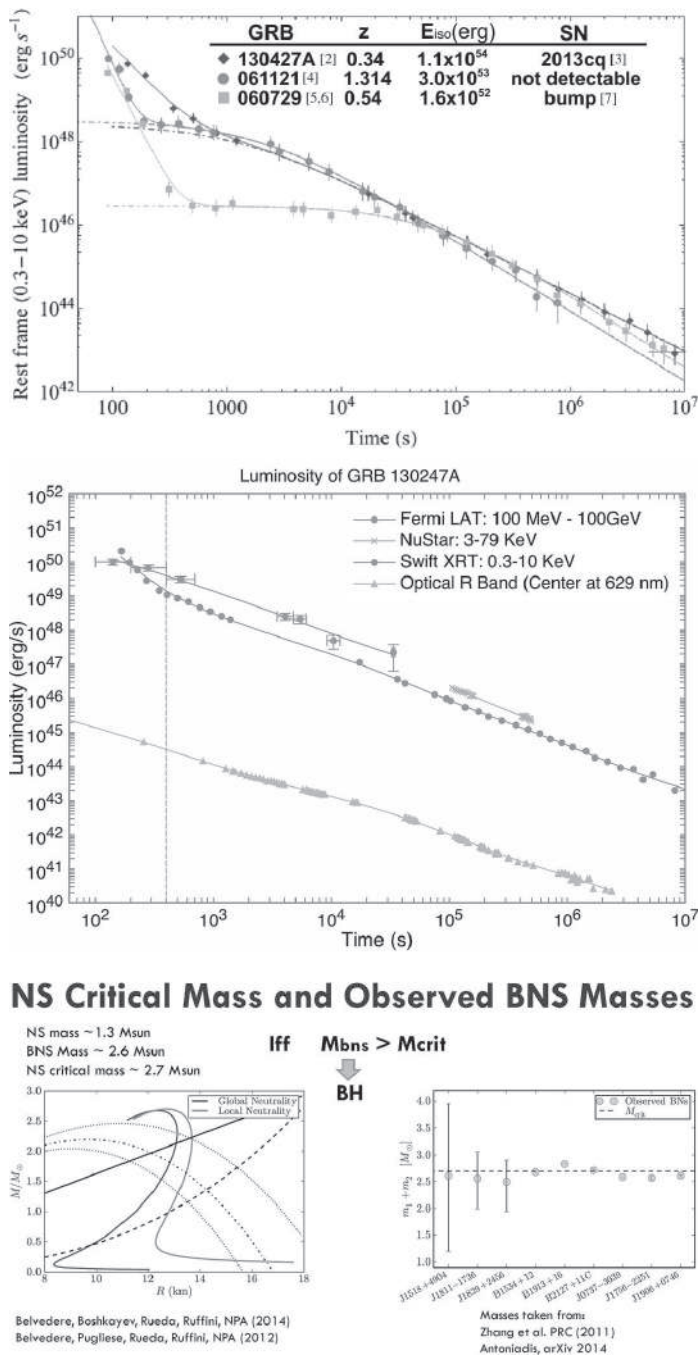


Fig. 28. Top: Episode 3 nesting.⁹² Middle: Episode 3 of GRB 130427A, see Ref. 93. Bottom: NS critical mass and observed BNS masses.

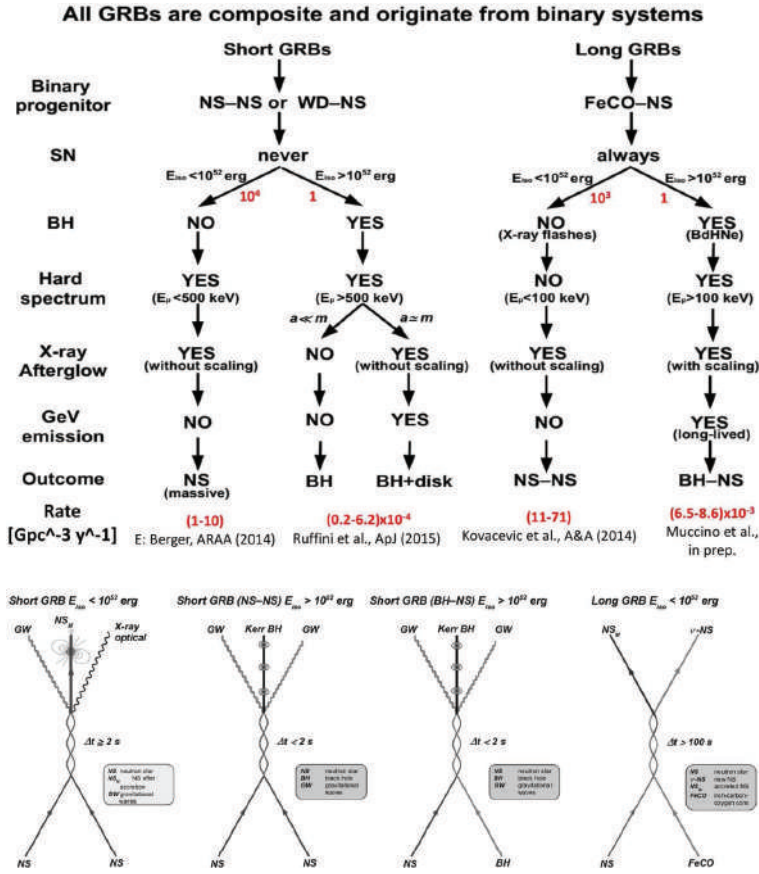


Fig. 29. Top: All GRBs are composite and originate from binary systems, see Refs. 93 and 146. Bottom: the five independent “cosmic matrix” relating SN and GRBs to their constituent NS and BH.

the e^+e^- plasma. The apparent absence of the GeV emission in GRB 090227B has already been discussed in Ref. 148 and can be explained simply by the fact that this source was outside the nominal LAT FoV, though significant detection in the LAT low energy (LLE) channel and only one transient-class event with energy above 100 MeV were associated with this GRB.¹⁶⁰

Much of the current work has been dedicated to extract the maximum amount of information for the building of theoretical model of GRB 130427A, see Figs. 32 and 33, which in the meantime have appeared in the literature.⁹³

In addition, the main current interest in our group is to probe the impact of the newly formed GRB, originating in the BH formation, on the SN ejecta. There are data on the flares and on the thermal emission in BdHN, which we are currently examining, see Fig. 34. Concurrently, we are considering the LXRE all the way to the afterglow and evidence for asymmetric emission, see Fig. 35.

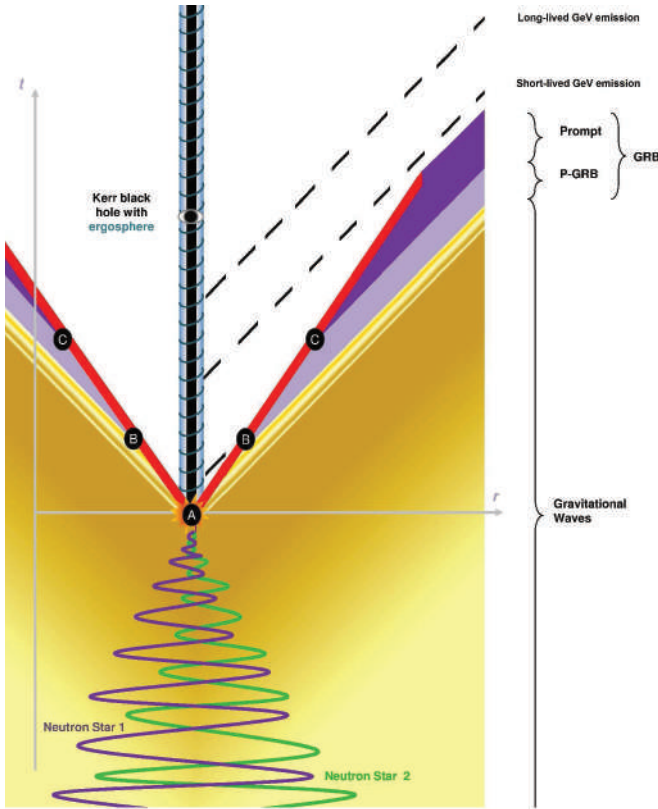


Fig. 30. The spacetime diagram of “the” short GRBs. The orbital separation between the two NSs decreases due to the emission of GWs, until the merging occurs and a family-2 short GRB is emitted. Following the fireshell model: (A) vacuum polarization occurs while the event horizon is formed and a fireshell of e^+e^- plasma self-accelerates radially outward; (B) the fireshell, after engulfing the baryons, keeps self-accelerating and reaches the transparency when the P-GRB is emitted; (C) the accelerated baryons interact with the local CBM giving rise to the prompt emission. The remnant of the merger is a Kerr BH. The accretion of a small (large) amount of orbiting matter onto the BH can lead to the short lived but very energetic 0.1–100 GeV emission observed in GRB 081024B, GRB 090510 and GRB 140619B. The absence of such an emission in GRB 090227B is due to the absence of observations of *Fermi*-LAT. From Ref. 148.

6. Conclusions

This celebration of the 50th Anniversary of Relativistic Astrophysics comes after 17 years of research addressing the temporal and spatial coincidence of two of the most powerful events in the cosmos: the explosion of a supernova and the emission of a GBM. The first example of such a coincidence occurred with the GRB 980425 and the SN 1998bw. The pioneering results of BeppoSAX were soon followed by many observations from X-ray and gamma ray space observatories (the AGILE, FERMI, KONUS WIND and SWIFT satellites), as well as from ground-based optical telescopes. This has given clear evidence that far from being an exception

A family-2 short: the case of GRB 140619B

Ruffini, R., Muccino, M., Kovacevic, M. et al. 2015 ApJ (in press); arXiv:1412.1018

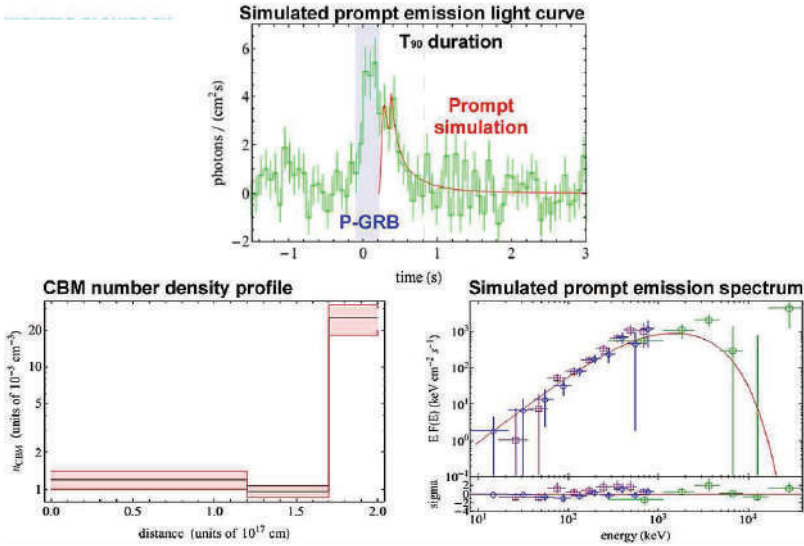


Fig. 31. (Color online) Top: The BGO-b1 (260 keV–40 MeV) simulated light curve of the prompt emission of GRB 140619B (solid red line). Each spike corresponds to the CBM number density profile shown in the figure below. The blue dot-dashed vertical line marks the end of the P-GRB emission. The purple long-dashed and the black dashed vertical lines indicate, respectively, the starting and the ending times of the T_{90} time interval. Clearly visible outside of this time interval is the background noise level. The continuation of the simulation after T_{90} is due to the residual large angle emission of the EQTS due to the density profile. Bottom left: The radial CBM number density distribution of GRB 140619B (black line) and its range of validity (red shaded region). Bottom right: Top panel: comparison between the 8–900 keV data from the NaI-n6 (purple squares) and n9 (blue diamonds) detectors, and the 260 keV–40 MeV data from the BGO-b1 detector (green circles), and the simulation within the fireball model (solid red curve) in the time interval ΔT_2 . Bottom panel: the residuals of the above-mentioned data with the simulation. From Ref. 148.

such a coincidence is quite common: it pervades the occurrence of all most powerful hypernovae and long GRBs. We have followed in this presentation a historical approach explaining how the solution of this enigma has also lead to the unveiling of the basic astrophysical process occurring in long and short GRBs as well as in the occurrence of hypernovae.

The concept of GRB initially envisaged as a single-ultrarelativistic-jetted emission occurring in a “collapsar-fireball” has been superseded by a far reaching scenario (see Fig. 36). Progress has been slow but steady: it has required the introduction of new paradigms, the extension of known relativistic field theories to unexplored regimes, and strong observational support from space and ground observatories. We have outlined in this presentation some crucial moments of these developments. Our new outlook indicates the existence of seven subclasses of GRBs, many more than the initial division into short and long GRBs. The fireball model

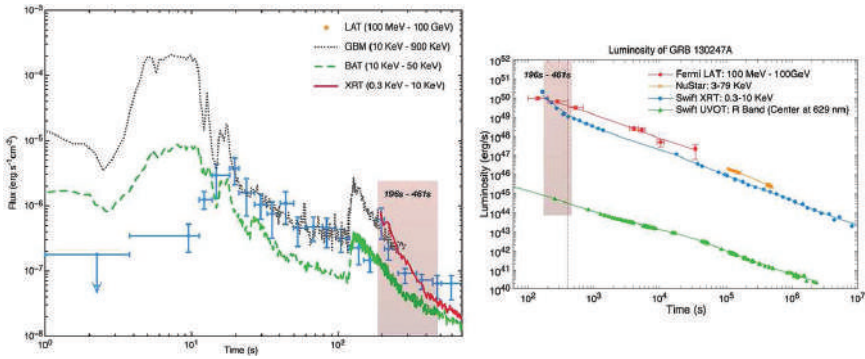


Fig. 32. (Color online) Left: Flux of first 700 s. Blue points are the Fermi-LAT high energy emission from 100 MeV till 100 GeV,¹⁶⁰ gray dotted line represents the Fermi-GBM, from 10 keV to 900 keV, green dashed line represents the photons detected by Swift BAT from 10 keV to 50 keV, and red solid line is the soft X-ray Swift-XRT detection, in the range of 0.3 KeV to 10 KeV. From this figure, clearly the Fermi-LAT emission reaches highest fluence at about 20 s while the gamma-ray detected by Fermi-GBM releases most of the energy within the first 10 s. Right: The multi-wavelength light curve of GRB 130427A. The high energy (100 MeV–100 GeV) emission detected by Fermi-LAT marked with red and soft X-ray (0.3–10 keV) data from Swift-XRT marked with blue are deduced from the original data. NuStar data (3–79 keV) marked with orange comes from Ref. 161. The optical (R band, center at 629 nm) data marked with green comes from ground based satellites.¹⁶² The error bars are too small with respect to the data points except for Fermi-LAT data. The horizontal error bars of Fermi-LAT represent the time bin in which the flux is calculated and vertical bars are statistical $1 - \sigma$ errors on the flux (the systematic error of 10% is ignored). The details in the first tens of seconds are ignored as we are interested in the behavior of the high energy light curve on a longer time scale. The vertical gray dashed line at (~ 400 s) indicates when the constant decaying slope starts. It is clear that all the energy bands have almost the same slope after 400 s in Episode 3. From Ref. 93.

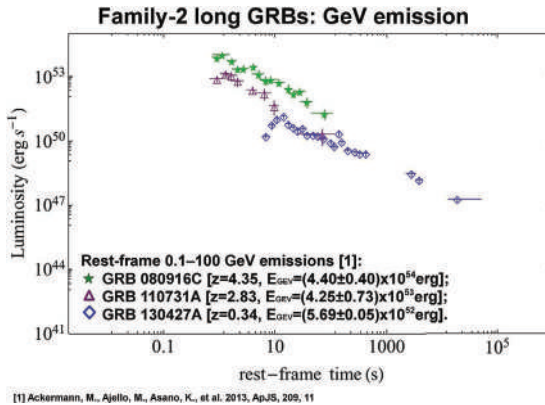


Fig. 33. (Color online) The common power-law behavior of the rest-frame 0.1–100 GeV isotropic luminosity light curves of selected BdHNe: GRB 080916C with green stars^{163,164}, GRB 110731A with purple triangles¹⁶⁵ and Primorac D. *et al.* in preparation, and GRB 130427A with blue diamonds.^{93,166} For each source the redshift and the total isotropic GeV emitted energy are also indicated. The GeV emission onset occurs soon after the P-GRB emission and during the prompt emission. Within the fireshell model, the GeV emission represents clear signature for a Kerr–Newman BH formation.

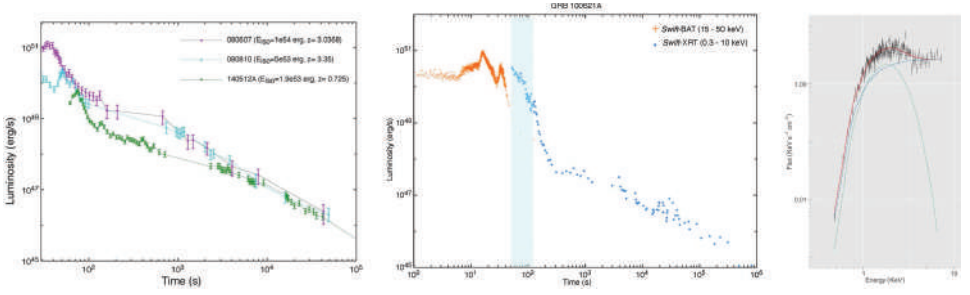


Fig. 34. (Color online) Left: Demonstration of X-ray flares in BdHN: the soft X-ray light-curves (0.3–10 keV) of GRB 080607, 080810, 140512 are transferred to their cosmological rest frame, clearly flares occur before 100 s, and the GBB with lower isotropic energy has a later and less luminous flare. Then comes the plateau, lower isotropic energy GRB has a longer duration plateau. At time later than 10^4 s, three light-curves overlap and decay following a similar power-law behavior. Middle: luminosity light-curve of GRB 100621A. The red crosses and the blue points are the data deduced from Swift-BAT in the energy band 15–50 keV and Swift-XRT in the energy band 0.3–10 keV respectively. The blue shadow indicates a time interval during which thermal component is determined. Light-curve is presented in its cosmological rest frame. Right: the spectrum from 51 s to 130 s and model fitting. Black crosses are the data with uncertainties. Short-dashed line presents the blackbody component with temperature 0.39 keV emitted from a radius of 5.13×10^{12} cm. Long-dashed line corresponds to the nonthermal power-law component. Solid line is the combination of the total two components. Spectrum is shown and fitted in the observers frame.

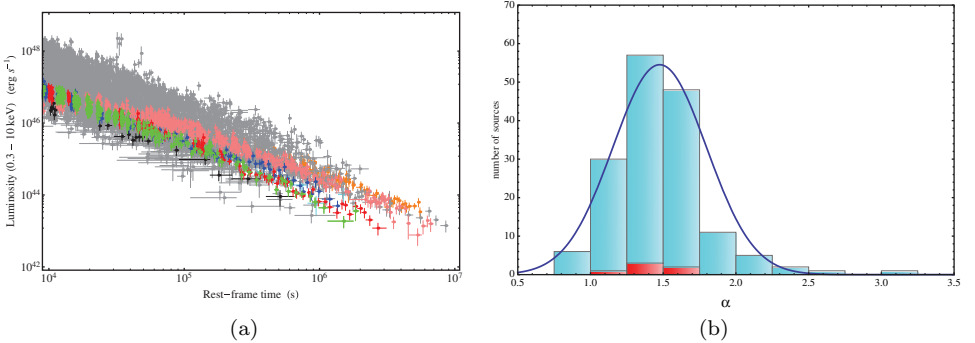


Fig. 35. (Color online) Panel (a): Late X-Ray Emission (LXRE) luminosity light curves of all 161 sources of the ES (gray) compared with the ones of the GS: GRB 060729 (pink), GRB 061007 (black), GRB 080913B (blue), GRB 090618 (green), GRB 091127 (red), and GRB 111228 (cyan), plus GRB 130427A.^{93,175} Panel (b): Distribution of the LXRE power law indexes α within the ES (cyan) compared to the one of the GS (red). Such a distribution follows a Gaussian behavior (blue line) with a mean value of $\mu_\alpha = 1.48$ and a standard deviation of $\sigma_\alpha = 0.32$.

has been superseded by a more detailed “fireshell” model modulated on the IGC paradigm. The concept of a “cosmic matrix” brings to the attention of the astronomical community a new approach necessary to rationalize a sequence of astrophysical events occurring over a 3 h time scale, when measured in the cosmological rest frame of the GRB. It is as far from describing a single process as it can possibly

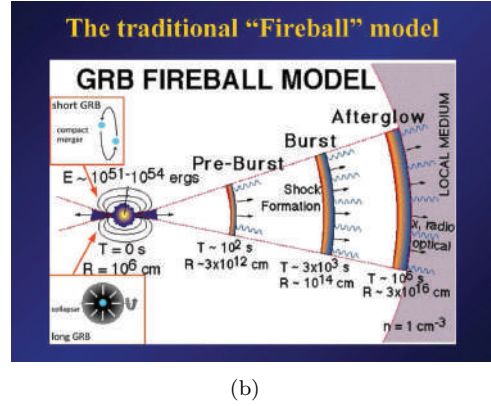
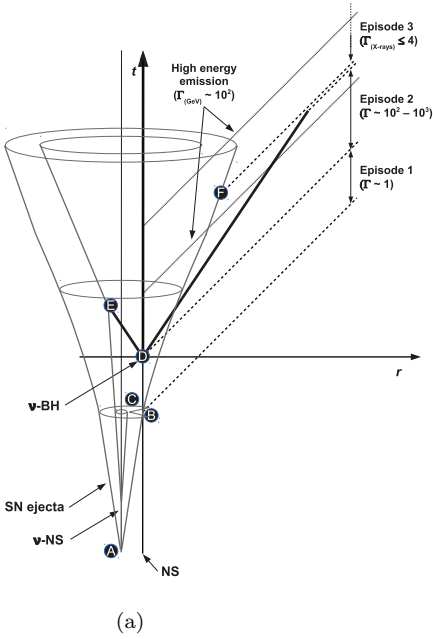


Fig. 36. Panel (a): Fireshell model. Panel (b): Fireball model.

be. The sequence of events instead encompasses (1) the matter accretion in a tight binary system composed of an Fe-CO core undergoing a SN explosion onto a tight companion NS, (2) the creation of a black hole by the gravitational collapse of the NS, following the accretion process and the emission of the GRB, (3) the concurrent emission of the jetted GeV emission, (4) the interaction of the GRB emission with the SN ejected (first presented here), (5) the final appearance of the optical SN emission after 10 days. It is expected that this celebration of the 50th Anniversary coincides with the opening of new era in relativistic astrophysics.

References

1. W. Baade and F. Zwicky, *Proc. US Nat. Acad. Sci.* **20** (1934) 254.
2. W. Baade and F. Zwicky, *Proc. Nat. Acad. Sci.* **20** (1934) 259.
3. R. Giacconi, H. Gursky, F. R. Paolini and B. B. Rossi, *Phys. Rev. Lett.* **9** (1962) 439.
4. I. S. Shklovsky, *Astrophys. J.* **148** (1967) 1.
5. R. Giacconi and R. Ruffini (eds.), *Physics and Astrophysics of Neutron Stars and Black Holes* (Amsterdam, North Holland Publishing Co., 1978).
6. R. W. Leach and R. Ruffini, *Astrophys. J.* **180** (1973) L15.
7. C. E. Rhoades and R. Ruffini, *Phys. Rev. Lett.* **32** (1974) 324.
8. R. Ruffini, Astrophysics and gravitation, in *Proc. Sixteenth Solvay Conf. Physics*, University of Brussels (September 1973).
9. H. Gursky and R. Ruffini (eds.), *Neutron Stars, Black Holes and Binary X-Ray*

- Sources, in *Proc. Annual Meeting*, San Francisco, Calif., 28 February 1974, Vol. 48 (Astrophysics and Space Science Library, 1975).
10. E. Costa, F. Frontera, J. Heise *et al.*, *Nature* **387** (1997) 783.
 11. T. Damour and R. Ruffini, *Phys. Rev. Lett.* **35** (1975) 463.
 12. R. Ruffini, Fundamental physics from black holes, neutron stars and gamma ray bursts, in *The Twelfth Marcel Grossmann Meeting*, eds. T. Damour, R. Jantzen and R. Ruffini (2012), pp. 286–367.
 13. R. Ruffini, Black holes, supernovae and gamma ray bursts, in *The Thirteenth Marcel Grossmann Meeting*, eds. K. Rosquist, R. T. Jantzen and R. Ruffini (World Scientific Publishing Co. Pte. Ltd., 2015), pp. 242–314.
 14. R. Ruffini, A. G. Aksenov, M. G. Bernardini *et al.*, *Am. Inst. Phys. Conf. Ser.* **1132** (2009).
 15. A. Heger, C. L. Fryer, S. E. Woosley *et al.*, *Astrophys. J.* **591** (2003) 288.
 16. E. Verner, F. Bruhweiler and T. Gull, *Astrophys. J.* **624** (2005) 973.
 17. A. Damineli, A. Kaufer, B. Wolf *et al.*, *Astrophys. J.* **528** (2000) L101.
 18. R. C. Iping, G. Sonneborn, T. R. Gull *et al.*, *Astrophys. J.* **633** (2005) L37.
 19. E. Pian, L. Amati, L. A. Antonelli *et al.*, *Astrophys. J.* **536** (2000) 778.
 20. S. R. Kulkarni, D. A. Frail, M. H. Wieringa *et al.*, *Nature* **395** (1998) 663.
 21. T. J. Galama, P. M. Vreeswijk, J. van Paradijs *et al.*, *Nature* **395** (1998) 670.
 22. R. Ruffini, G. Vereshchagin and S. Xue, *Phys. Rep.* **487** (2010) 1.
 23. R. Ruffini, Y. Wang, M. Kovacevic *et al.*, GRB 130427A and SN 2013cq: A multi-wavelength analysis of an induced gravitational collapse event, arXiv:1405.5723 (2014).
 24. A. Hewish, S. J. Bell, J. D. H. Pilkington *et al.*, *Nature* **217** (1968) 709.
 25. W. Arnett, in *From Nuclei to White Dwarfs and Neutron Stars*, eds. A. Mezzacappa and R. Ruffini (World Scientific, Singapore), in press.
 26. M. Rees, R. Ruffini and J. A. Wheeler, *Black Holes, Gravitational Waves and Cosmology: An Introduction to Current Research*, Topics in Astrophysics and Space Physics, Vol. 10 (Gordon and Breach, Science Publishers, Inc., New York, 1974).
 27. A. Finzi and R. A. Wolf, *Astrophys. J.* **153** (1968) 865.
 28. D. Christodoulou and R. Ruffini, *Phys. Rev. D* **4** (1971) 3552.
 29. R. Ruffini, The ergosphere and dyadosphere of black holes, in *The Kerr Spacetime*, eds. D. L. Wiltshire, M. Visser and S. Scott (eds.) (Cambridge University Press, 2009).
 30. R. Ruffini, J. D. Salmonson, J. R. Wilson and S.-S. Xue, *Astron. Astrophys.* **350** (1999) 334.
 31. R. Ruffini, J. D. Salmonson, J. R. Wilson and S.-S. Xue, *Astron. Astrophys.* **359** (2000) 855.
 32. R. Ruffini, Analogies, new paradigms and observational data as growing factors of relativistic astrophysics, in *Fluctuating Paths and Fields*, eds. W. Janke, A. Pelster, H. J. Schmidt and M. Bachmann (World Scientific, Singapore, 2001).
 33. W. S. Paciesas, C. A. Meegan, G. N. Pendleton *et al.*, *Astrophys. J. SS* **122** (1999) 465.
 34. F. Frontera, GRB Afterglow Discovery with Bepposax: Its Story 15 Years Later, in *The Thirteenth Marcel Grossmann Meeting*, eds. K. Rosquist, R. T. Jantzen and R. Ruffini (World Scientific Publishing Co. Pte. Ltd., 2015), pp. 33–53.
 35. L. Izzo, R. Ruffini, A. V. Penacchioni *et al.*, *Astron. Astrophys.* **543** (2012) A10.
 36. L. Izzo, J. A. Rueda and R. Ruffini, *Astron. Astrophys.* **548** (2012) L5.

37. G. B. Pisani, L. Izzo, R. Ruffini *et al.*, *Astron. Astrophys.* **552** (2013) L5.
38. M. Muccino, R. Ruffini, C. L. Bianco *et al.*, *Astrophys. J.* **763** (2013) 125.
39. T. Piran, *Rev. Mod. Phys.* **76** (2004) 1143.
40. G. Cavallo and M. J. Rees, *Mon. Not. R. Astron. Soc.* **183** (1978) 359.
41. J. Goodman, Are gamma-ray bursts optically thick?, *Astrophys. J.* **308** (1986) L47.
42. B. Paczynski, *Astrophys. J.* **308** (1986) L43.
43. P. Meszaros, *Rep. Prog. Phys.* **69** (2006) 2259.
44. R. Ruffini, *Int. J. Mod. Phys. D* **20** (2011) 1797.
45. R. Ruffini, Beyond the critical mass: The dyadosphere of black holes, in *Frontiers Science Series 23: Black Holes and High Energy Astrophysics*, eds. H. Sato and N. Sugiyama (Universal Academic Press, 1998).
46. G. Preparata, R. Ruffini and S.-S. Xue, *Astron. Astrophys.* **338** (1998) L87.
47. A. Aksenov, R. Ruffini and G. Vereshchagin, *Phys. Rev. Lett.* **99** (2007) 125003.
48. E. Ramirez-Ruiz and E. E. Fenimore, *Astrophys. J.* **539** (2000) 712.
49. M. J. Rees and P. Meszaros, *Astrophys. J.* **430** (1994) L93.
50. M. J. Rees and P. Meszaros, *Mon. Not. R. Astron. Soc.* **258** (1992) 41P.
51. M. Tavani, *Astrophys. J.* **466** (1996) 768.
52. F. Frontera, L. Amati, E. Costa *et al.*, *Astrophys. J. Suppl.* **127** (2000) 59.
53. A. Crider, E. P. Liang, I. A. Smith *et al.*, *Astrophys. J.* **479** (1997) L39.
54. R. D. Preece, M. S. Briggs, T. W. Giblin *et al.*, *Astrophys. J.* **581** (2002) 1248.
55. G. Ghirlanda, A. Celotti and G. Ghisellini, *Astron. Astrophys.* **393** (2002) 409.
56. G. Ghirlanda, A. Celotti and G. Ghisellini, *Astron. Astrophys.* **406** (2003) 879.
57. P. Kumar and E. McMahon, *Mon. Not. R. Astron. Soc.* **384** (2008) 33.
58. T. Piran, R. Sari and Y. Zou, *Mon. Not. R. Astron. Soc.* **393** (2009) 1107.
59. R. D. Blandford and C. F. McKee, *Phys. Fluids* **19** (1976) 1130.
60. E. Molinari, S. D. Vergani, D. Malesani *et al.*, *Astron. Astrophys.* **469** (2007) L13.
61. E. S. Rykoff, F. Aharonian, C. W. Akerlof *et al.*, *Astrophys. J.* **702** (2009) 489.
62. R. Sari and T. Piran, *Astrophys. J.* **520** (1999) 641.
63. G. Ghisellini and A. Celotti, *Astron. Astrophys. Suppl.* **138** (1999) 527.
64. A. A. Zdziarski, R. Svensson and B. Paczynski, *Astrophys. J.* **366** (1991) 343.
65. A. Shemi, *Mon. Not. R. Astron. Soc.* **269** (1994) 1112.
66. A. Pe'er and B. Zhang, *Astrophys. J.* **653** (2006) 454.
67. M. V. Medvedev, *Astrophys. J.* **540** (2000) 704.
68. A. Panaitescu and P. Mészáros, *Astrophys. J.* **544** (2000) L17.
69. B. E. Stern and J. Poutanen, *Mon. Not. R. Astron. Soc.* **352** (2004) L35.
70. D. Eichler and A. Levinson, *Astrophys. J.* **529** (2000) 146.
71. P. Mészáros and M. J. Rees, *Astrophys. J.* **530** (2000) 292.
72. P. Mészáros, *Annu. Rev. Astron. Astrophys.* **40** (2002) 137.
73. F. Daigne and R. Mochkovitch, *Mon. Not. R. Astron. Soc.* **336** (2002) 1271.
74. D. Giannios, *Astron. Astrophys.* **457** (2006) 763.
75. F. Ryde and A. Pe'er, *Astrophys. J.* **702** (2009) 1211.
76. D. Lazzati and M. C. Begelman, *Astrophys. J.* **725** (2010) 1137.
77. R. Ruffini, *Astron. Astrophys. Suppl.* **138** (1999) 513.
78. R. Ruffini, C. L. Bianco, P. Chardonnet *et al.*, *Astrophys. J.* **555** (2001) L113.
79. C. L. Bianco and R. Ruffini, *Astrophys. J.* **605** (2004) L1.
80. C. L. Bianco and R. Ruffini, *Astrophys. J.* **620** (2005) L23.
81. P. Meszaros, P. Laguna and M. J. Rees, *Astrophys. J.* **415** (1993) 181.
82. R. Sari, *Astrophys. J.* **489** (1997) L37.

83. R. Sari, *Astrophys. J.* **494** (1998) L49.
84. E. Waxman, *Astrophys. J.* **491** (1997) L19.
85. M. J. Rees and P. Meszaros, *Astrophys. J.* **496** (1998) L1.
86. J. Granot, T. Piran and R. Sari, *Astrophys. J.* **513** (1999) 679.
87. A. Panaitescu and P. Meszaros, *Astrophys. J.* **493** (1998) L31.
88. A. Gruzinov and E. Waxman, *Astrophys. J.* **511** (1999) 852.
89. J. van Paradijs, C. Kouveliotou and R. A. M. J. Wijers, *Annu. Rev. Astron. Astrophys.* **38** (2000) 379.
90. C. L. Bianco and R. Ruffini, *Astrophys. J.* **633** (2005) L13.
91. R. Ruffini, C. L. Bianco, P. Chardonnet *et al.*, *Astrophys. J.* **555** (2001) L117.
92. R. Ruffini, M. Muccino, C. L. Bianco *et al.*, *Astron. Astrophys.* **565** (2014) L10.
93. R. Ruffini, Y. Wang, M. Enderli *et al.*, *Astrophys. J.* **798** (2015) 10.
94. J. A. Rueda and R. Ruffini, *Astrophys. J.* **758** (2012) L7.
95. A. V. Penacchioni, R. Ruffini, L. Izzo *et al.*, *Astron. Astrophys.* **538** (2012) A58.
96. C. L. Fryer, J. A. Rueda and R. Ruffini, *Astrophys. J.* **793** (2014) L36.
97. R. Ruffini, L. Izzo, A. V. Penacchioni *et al.*, *PoS (Texas2010)* (2011) 101.
98. P. Schady, W. H. Baumgartner, A. P. Beardmore *et al.*, *GCN Circ.* **9512** (2009).
99. W. H. Baumgartner, S. D. Barthelmy, J. R. Cummings *et al.*, *GCN Circ.* **9530** (2009) 1.
100. G. J. Fishman, C. A. Meegan, R. B. Wilson *et al.*, *Astrophys. J. Suppl.* **92** (1994) 229.
101. A. P. Beardmore and P. Schady, *GCN Circ.* **9528** (2009) 1.
102. C. Meegan, G. Lichti, P. N. Bhat *et al.*, *Astrophys. J.* **702** (2009) 791.
103. D. Band, J. Matteson, L. Ford *et al.*, *Astrophys. J.* **413** (1993) 281.
104. S. McBreen, *GCN Circ.* **9535** (2009).
105. S. B. Cenko, D. A. Perley, V. Junkkarinen *et al.*, *GCN Circ.* **9518** (2009).
106. B. E. Schaefer, *Astrophys. J.* **660** (2007) 16.
107. S. Golenetskii, R. Aptekar, E. Mazets *et al.*, *GCN Circ.* **9553** (2009) 1.
108. K. Kono, A. Daikyuji, E. Sonoda *et al.*, *GCN Circ.* **9568** (2009) 1.
109. F. Longo, E. Moretti, G. Barbiellini *et al.*, *GCN Circ.* **9524** (2009).
110. Y. Kotov, A. Kochemasev, S. Kuzin *et al.*, in *37th COSPAR Scientific Assembly* (Montréal, Canada, 13–20 July 2008), p. 1596.
111. A. Nandi, A. R. Rao, S. K. Chakrabarti *et al.*, Indian Payloads (RT-2 Experiment) Onboard CORONAS-PHOTON Mission, arXiv:0912.4126 (December 2009).
112. A. R. Rao, J. P. Malkar, M. K. Hingar *et al.*, *Astrophys. J.* **728** (2011) 42.
113. Z. Cano, D. Bersier, C. Guidorzi *et al.*, *Mon. Not. R. Astron. Soc.* **413** (2011) 669.
114. F. Ryde, M. Axelsson, B. B. Zhang *et al.*, *Astrophys. J.* **709** (2010) L172.
115. S. Guiriec, V. Connaughton, M. S. Briggs *et al.*, *Astrophys. J.* **727** (2011) L33.
116. A. Pe'er, *Astrophys. J.* **682** (2008) 463.
117. C. Cherubini, A. Geralico, H. J. A. Rueda and R. Ruffini, *Phys. Rev. D* **79** (2009) 124002.
118. R. Ruffini, C. L. Bianco, P. Chardonnet *et al.*, New perspectives in physics and astrophysics from the theoretical understanding of gamma-ray bursts, in *Cosmology and Gravitation*, eds. M. Novello and S. E. Perez Bergliaffa, American Institute of Physics Conference Series, Vol. 668 (American Institute of Physics, 2003).
119. Y. B. Zel'dovich, L. N. Ivanova and D. K. Nadezhin, *Soviet Astron.* **16** (1972) 209.
120. R. Ruffini and J. Wilson, *Phys. Rev. Lett.* **31** (1973) 1362.
121. R. Ruffini, M. G. Bernardini, C. L. Bianco *et al.*, The role of grb 031203 in clarify-

- ing the astrophysical grb scenario, in *The 6th Integral Workshop — The Obscured Universe*, eds. S. Grebenev, R. Sunyaev, C. Winkler, A. Parmar and L. Ouwehand, Vol. SP-622 (ESA Special Publication, 2007), p. 561.
122. B. Patricelli, M. G. Bernardini, C. L. Bianco *et al.*, *Int. J. Mod. Phys. D* **20** (2011) 1983.
 123. A. V. Penacchioni, R. Ruffini, C. L. Bianco *et al.*, *Astron. Astrophys.* **551** (2013) A133.
 124. J. Hjorth and J. S. Bloom, *The Gamma-Ray Burst — Supernova Connection*, in *Gamma-Ray Bursts*, eds. C. Kouveliotou, R. A. M. J. Wijers and S. Woosley, Cambridge Astrophysics Series, Vol. 51 (Cambridge University Press, Cambridge, 2012), pp. 169–190.
 125. K. Nomoto and M. Hashimoto, *Phys. Rep.* **163** (1988) 13.
 126. K. Nomoto, H. Yamaoka, O. R. Pols *et al.*, *Nature* **371** (1994) 227.
 127. K. Iwamoto, K. Nomoto, P. Höflich *et al.*, *Astrophys. J.* **437** (1994) L115.
 128. S. E. Woosley and J. S. Bloom, *Annu. Rev. Astron. Astrophys.* **44** (2006) 507.
 129. A. Shemi and T. Piran, *Astrophys. J.* **365** (1990) L55.
 130. T. Piran, A. Shemi and R. Narayan, *Mon. Not. R. Astron. Soc.* **263** (1993) 861.
 131. R. Ruffini, M. G. Bernardini, C. L. Bianco *et al.*, On gamma-ray bursts, in *The Eleventh Marcel Grossmann Meeting*, eds. H. Kleinert, R. T. Jantzen and R. Ruffini (World Scientific, Singapore, 2008).
 132. R. Ruffini, M. G. Bernardini, C. L. Bianco *et al.*, Black hole physics and astrophysics: The grb-supernova connection and urca-1 — urca-2, in *The Tenth Marcel Grossmann Meeting*, eds. M. Novello, S. Perez Bergliaffa and R. Ruffini (World Scientific, Singapore, 2006).
 133. O. D. Toropina, M. M. Romanova and R. V. E. Lovelace, *Mon. Not. R. Astron. Soc.* **420** (2012) 810.
 134. H. Bondi and F. Hoyle, *Mon. Not. R. Astron. Soc.* **104** (1944) 273.
 135. F. Hoyle and R. A. Lyttleton, *Proc. Cambridge Philos. Soc.* **35** (1939) 405.
 136. R. A. Chevalier, *Astrophys. J.* **346** (1989) 847.
 137. R. Belvedere, D. Pugliese, J. A. Rueda *et al.*, *Nucl. Phys. A* **883** (2012) 1.
 138. L. Izzo, R. Ruffini, C. L. Bianco *et al.*, On the thermal and double episode emissions in GRB 970828, arXiv:1205.6651 (2012).
 139. E. Schreier, R. Levinson, H. Gursky *et al.*, *Astrophys. J.* **172** (1972) L79.
 140. R. E. Wilson, *Astrophys. J.* **174** (1972) L27.
 141. H. Tananbaum, H. Gursky, E. M. Kellogg *et al.*, *Astrophys. J.* **174** (1972) L143.
 142. K. Davidson and J. P. Ostriker, *Astrophys. J.* **179** (1973) 585.
 143. M. L. Rawls, J. A. Orosz, J. E. McClintock *et al.*, *Astrophys. J.* **730** (2011) 25.
 144. A. V. Tutukov and A. V. Fedorova, *Astron. Rep.* **51** (2007) 291.
 145. R. A. Chevalier, *Astrophys. J.* **752** (2012) L2.
 146. M. Muccino, R. Ruffini, M. Kovacevic *et al.*, GRB 140619B: A short GRB from a binary neutron stars merger leading to the black hole formation, (2014) arXiv e-prints.
 147. R. Ruffini, L. Izzo, M. Muccino *et al.*, *Astron. Astrophys.* **569** (2014) A39.
 148. R. Ruffini, M. Muccino, M. Kovacevic *et al.*, *Astrophys. J.* **808** (2015) 190.
 149. J. Goodman, *Astrophys. J.* **308** (1986) L47.
 150. B. Paczynski, *Astrophys. J.* **308** (1986) L43.
 151. D. Eichler, M. Livio, T. Piran and D. N. Schramm, *Nature* **340** (1989) 126.
 152. R. Narayan, T. Piran and A. Shemi, *Astrophys. J.* **379** (1991) L17.

153. P. Meszaros and M. J. Rees, *Astrophys. J.* **482** (1997) L29.
154. S. Rosswog, E. Ramirez-Ruiz and M. B. Davies, *Mon. Not. R. Astron. Soc.* **345** (2003) 1077.
155. W. H. Lee, E. Ramirez-Ruiz and D. Page, *Astrophys. J.* **608** (2004) L5.
156. K. Belczynski, R. Perna, T. Bulik *et al.*, *Astrophys. J.* **648** (2006) 1110.
157. E. Berger, *Annu. Rev. Astron. Astrophys.* **52** (2014) 43.
158. D. B. Fox, D. A. Frail, P. A. Price *et al.*, *Nature* **437** (2005) 845.
159. N. Gehrels, C. L. Sarazin, P. T. O'Brien *et al.*, *Nature* **437** (2005) 851.
160. M. Ackermann, M. Ajello, K. Asano *et al.*, *Astrophys. J. Suppl.* **209** (2013) 11.
161. C. Kouveliotou, J. Granot, J. L. Racusin *et al.*, *Astrophys. J.* **779** (2013) L1.
162. D. A. Perley, S. B. Cenko, A. Corsi *et al.*, *Astrophys. J.* **781** (2014) 37.
163. A. A. Abdo, M. Ackermann, M. Arimoto *et al.*, *Science* **323** (2009) 1688.
164. L. Izzo, M. G. Bernardini, C. L. Bianco *et al.*, *Int. J. Mod. Phys. D* **20** (2011) 1949.
165. M. Ackermann, M. Ajello, K. Asano *et al.*, *Astrophys. J.* **763** (2013) 71.
166. M. Ackermann, M. Ajello, K. Asano *et al.*, *Science* **343** (2014) 42.
167. R. Belvedere, D. Pugliese, J. A. Rueda *et al.*, *Nucl. Phys. A* **883** (2012) 1.
168. F.-W. Zhang, L. Shao, J.-Z. Yan and D.-M. Wei, *Astrophys. J.* **750** (2012) 88.
169. G. Calderone, G. Ghirlanda, G. Ghisellini *et al.*, *Mon. Not. R. Astron. Soc.* **448** (2015) 403.
170. R. Ruffini, J. A. Rueda, M. Muccino *et al.*, *Astrophys. J.* **832** (2016) 136.
171. C. L. Fryer, K. Belczynski, E. Ramirez-Ruiz *et al.*, The Fate of the Compact Remnant in Neutron Star Mergers, arXiv e-prints (2015).
172. S. Lawrence, J. G. Tervala, P. F. Bedaque and M. C. Miller, *Astrophys. J.* **808** (2015) 186.
173. M. Muccino, R. Ruffini, C. L. Bianco *et al.*, *Astrophys. J.* **763** (2013) 125.
174. R. Ruffini, M. Muccino, Y. Aimuratov *et al.*, *Astrophys. J.* **831** (2016) 178.
175. G. B. Pisani, L. Izzo, R. Ruffini *et al.*, *Astron. Astrophys.* **552** (2013) L5.

Evolution of an electron-positron plasma produced by induced gravitational collapse in binary-driven hypernovae

J. D. Melon Fuksman^{1,2,*}, L. Becerra^{1,2}, C. L. Bianco^{1,2}, M. Karlica^{1,2,3}, M. Kovacevic^{1,2,3}, R. Moradi^{1,2}, M. Muccino^{1,2}, G. B. Pisani^{1,2}, D. Primorac^{1,2}, J. A. Rueda^{1,2,4}, R. Ruffini^{1,2,3,4}, G. V. Vereshchagin^{1,2}, and Y. Wang^{1,2}

¹Dipartimento di Fisica, Sapienza Università di Roma, Piazzale Aldo Moro 5, 00185 Rome, Italy

²ICRANet, Piazza della Repubblica 10, 65122 Pescara, Italy

³Université de Nice Sophia Antipolis, CEDEX 2, Grand Château Parc Valrose, Nice, France

⁴ICRANet-Rio, Centro Brasileiro de Pesquisas Físicas, Rua Dr. Xavier Sigaud 150, 22290-180 Rio de Janeiro, Brazil

Abstract. The binary-driven hypernova (BdHN) model has been introduced in the past years, to explain a subfamily of gamma-ray bursts (GRBs) with energies $E_{\text{iso}} \geq 10^{52}$ erg associated with type Ic supernovae. Such BdHNe have as progenitor a tight binary system composed of a carbon-oxygen (CO) core and a neutron star undergoing an induced gravitational collapse to a black hole, triggered by the CO core explosion as a supernova (SN). This collapse produces an optically-thick e^+e^- plasma, which expands and impacts onto the SN ejecta. This process is here considered as a candidate for the production of X-ray flares, which are frequently observed following the prompt emission of GRBs. In this work we follow the evolution of the e^+e^- plasma as it interacts with the SN ejecta, by solving the equations of relativistic hydrodynamics numerically. Our results are compatible with the Lorentz factors estimated for the sources that produce the flares, of typically $\Gamma \lesssim 4$.

1 Introduction

The *induced gravitational collapse* (IGC) (see, e.g., [1], [2], [3]) has been proposed in the past years, as a way to explain a sub-class of long gamma-ray bursts (GRBs) called binary-driven hypernovae (BdHNe), characterised by an isotropic energy $E_{\text{iso}} \geq 10^{52}$ erg and a rest-frame spectral peak energy between 0.2 and 2 MeV. The model considers a binary system formed by a carbon-oxygen (CO) core and a neutron star (NS), which undergo a tight orbit. If the core-collapse of the CO star produces a supernova explosion, the ejected material may trigger an hypercritical accretion process onto the NS, due to a copious neutrino emission and the trapping of photons within the accretion flow. This process can cause the NS to collapse as well, thus forming a black hole (BH). It has been proposed in [4] and, e.g., [5], that such collapse can lead to the formation of an e^+e^- plasma, that later expands and interacts with the SN ejecta, finally producing a GRB.

In this scenario, the major portion of the optically thick e^+e^- -baryon plasma originating from the collapse expands away from the supernova (SN), giving rise to the canonical GRB *prompt emission*. This emission occurs at approximately 10^{15} - 10^{17} cm from the BH, and is measured to come from material that expands at Lorentz factors $\Gamma \sim 10^2$ - 10^3 (see e.g. [5]). Right after this first stage, that can last up to ~ 100 s, *X-ray flares* are frequently observed, followed by the so-called “plateau” and finally by the late decay of the X-ray afterglow [6]. By studying

the time evolution of the thermal component of the X-ray flares, it can be inferred that they originate from regions which move at roughly $\Gamma \lesssim 4$, as pointed out in [6].

These differences in the features of the prompt emission and the flares can be explained in terms of the IGC model. In it, the prompt emission is produced after the interaction of the e^+e^- with the SN ejecta, in a direction that corresponds to lower overall densities along the line of sight of an external observer (see [7] and Fig. 1). On the other hand, as the binary system keeps spinning, the mass density profile along that line changes. If a bigger amount of mass gets between the BH and the observer (see [8] and Fig. 1), an X-ray flare is emitted at the moment the plasma escapes the outermost regions of the SN ejecta, namely, at the shock *breakout*. Due to the deceleration of the shock by its interaction with the surrounding material, the Lorentz factors measured for the flares will be smaller than for the prompt emission.

In this work we describe numerically the evolution of the plasma along different directions, and study the compatibility of the IGC model with some of the above-mentioned observational features.

2 Equations and numerical scheme

We have modeled the evolution of the e^+e^- plasma and the SN ejecta following a single-fluid approach, where all the involved particle species, in this case baryons, photons, electrons and positrons, coming either from the plasma or the SN, are in *local thermodynamic equilibrium* (LTE).

*e-mail: david.melon@icranet.org

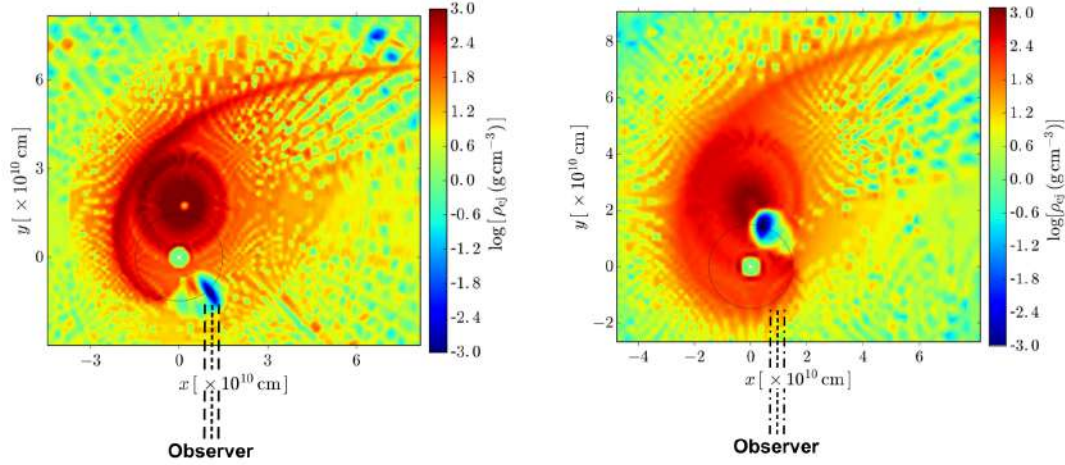


Figure 1. Density profiles calculated in [8] corresponding to the SN ejecta at (left) the moment of the collapse and (right) 100 s later. The line of sight of an observer that sees the initial prompt emission is indicated, to point out the change of the mass profile along it.

Under this assumption, the dynamics of the resulting fluid is governed by the equations of relativistic hydrodynamics (RHD). Throughout this work, we have numerically solved the one-dimensional RHD equations with the additional assumption of spherical symmetry, considering only a dependence of the intensive variables on the radial spherical coordinate. This allows us to study the evolution of the plasma along one selected radial direction at a time, thus to consider the different density distributions as seen through each direction. In the absence of gravity, the resulting equations of motion can be written as follows:

$$\frac{\partial(\rho\Gamma)}{\partial t} + \nabla \cdot (\rho\Gamma\mathbf{v}) = 0, \quad (1)$$

$$\frac{\partial m_r}{\partial t} + \nabla \cdot (m_r\mathbf{v}) + \frac{\partial p}{\partial r} = 0, \quad (2)$$

$$\frac{\partial \mathcal{E}}{\partial t} + \nabla \cdot (\mathbf{m} - \rho\Gamma\mathbf{v}) = 0, \quad (3)$$

where ρ is the comoving mass density, \mathbf{v} is the fluid velocity (natural units where $c = 1$ are used), $\Gamma = (1 - \mathbf{v}^2)^{-\frac{1}{2}}$ is the Lorentz factor, \mathbf{m} the total momentum density, and the subscript r indicates the radial component of a vector. The momentum density \mathbf{m} is defined as $\mathbf{m} = h\Gamma^2\mathbf{v}$, where h is the comoving enthalpy density, given by $h = \rho + \epsilon + p$, where p is the gas pressure and ϵ its internal energy density, both measured in the comoving frame. Finally, we denote by \mathcal{E} the value of ϵ in the laboratory (or coordinate) frame. In the above formulation of these equations, we compute this energy density by subtracting the coordinate mass density $\rho\Gamma$ to the $(0, 0)$ component of the fluid's energy-momentum tensor $T^{\mu\nu}$, as

$$\begin{aligned} \mathcal{E} &= T^{00} - \rho\Gamma \\ &= h\Gamma^2 - p - \rho\Gamma. \end{aligned} \quad (4)$$

Whenever the LTE condition holds, an equation of state relating ϵ , p and ρ can be obtained, thus closing the system defined by equations (1) to (4). In this work, we have used the equation of state of an ideal relativistic gas, which can

be expressed in terms of its enthalpy as:

$$h = \rho + \frac{\gamma p}{\gamma - 1}, \quad (5)$$

with $\gamma = 4/3$. Considering the contributions of all the involved particles to the total density, mass and energy, we have verified that equation (5) holds in the full range of parameters used in our simulations, with a value of γ that deviates from $4/3$ with a maximum error of 0.2%. The details of this calculation can be found in [6].

To integrate the above-defined system of equations, we have used the one-dimensional RHD module included in the PLUTO code [9]. The code works by making use of Godunov-type Riemann solvers, of which we have chosen an extension of the HLLC scheme to the equations of RHD (see [10] for the complete details). Among the possible configurations included in PLUTO, we have used a second-order total variation diminishing scheme for spatial reconstruction, and second-order Runge Kutta integration for time evolution. On each time step, the grid was updated in order to better follow total energy density gradients, by means of an adaptive mesh refinement algorithm provided by the CHOMBO library [11].

3 Simulations

3.1 Low density directions

As a verification of this scheme's applicability to our system, we have performed similar simulations to those in [7], which account for the evolution of the plasma in the lower density regions (see Fig. 1). To be more precise about this, we define the *baryon load* as $B = M_B c^2 / E_{e^+e^-}$, where M_B is the total integrated mass considering the assumed spherically symmetric distribution, and $E_{e^+e^-}$ is the initial internal energy of the plasma. Namely, B works as an indicator of the mass-to-energy ratio along each direction.

In this part, we will only consider density distributions such that $B < 10^{-2}$. As it is explained in detail in [7], in that case the plasma forms a slab that expands while

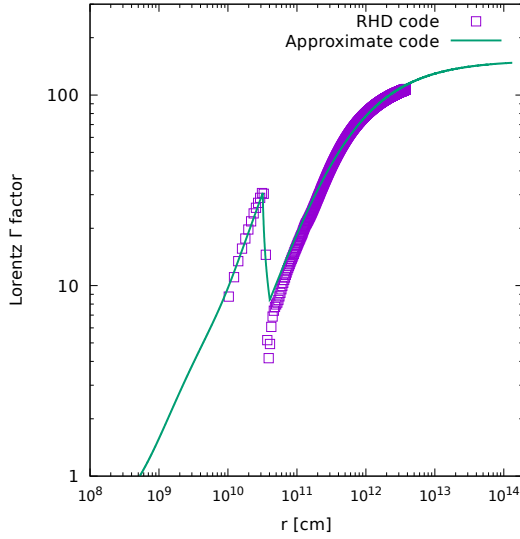


Figure 2. Lorentz factor Γ computed in with the PLUTO code, compared with the one computed with the semi-analytic approximate code. For this plot, the values $E_{e^+e^-} = 1.0 \times 10^{53}$ erg and $B = 6.61 \times 10^{-3}$ have been chosen. Similar good agreement is found for other values of $E_{e^+e^-}$ and B as long as $B < 10^{-2}$. Reproduced from [6].

accelerating, until it reaches a constant Lorentz factor of roughly $\Gamma \sim 1/B$. During its evolution, and still under the condition $B < 10^{-2}$, the slab's width remains constant when measured in the laboratory frame. This process is studied in [7] using an approximate semi-analytic code that assumes this feature, and allows to predict average intensive quantities by means of conservation equations.

In Fig. 2 we show the comparison between the Lorentz factors computed with both the semi-analytic code and PLUTO, for one particular value of $E_{e^+e^-}$ and B . The simulations run with PLUTO show the formation of a slab of constant width, that accelerates accordingly to what is expected from the semi-analytic code. This is in turn consistent with the treatment done in [7], and therefore, the analysis done so far for the prompt emission remains unchanged.

3.2 High density directions

Having applied the current scheme to the already-known region of the parameter space, we proceed to study the case $B > 10^{-2}$, which corresponds to the interaction of the e^+e^- plasma with the SN remnant along the higher density directions, and the subsequent emission of the flares. To this end, we have chosen for each simulation an initial density profile that matches the ones obtained in [8] (see Fig. 1). Hence, all the considered profiles were set in the following way:

$$\rho \propto (R_0 - r)^\alpha, \quad (6)$$

where R_0 and α , with $2 < \alpha < 3$, are fitting parameters. Each profile of this kind has a single baryon load, that corresponds to the evolution of the fluid along one particular direction. Similarly, we have taken the velocity to depend

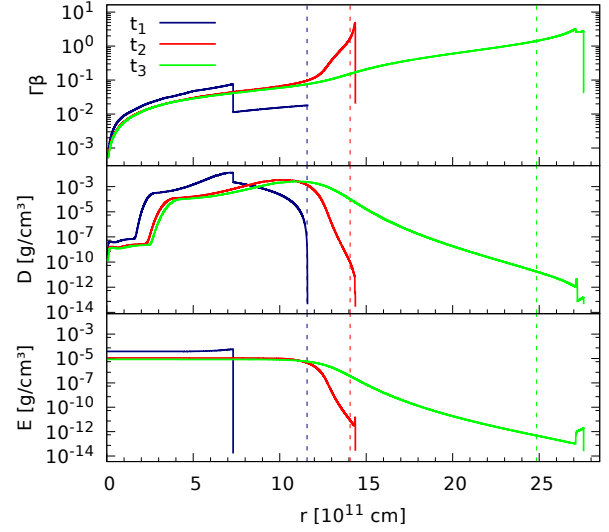


Figure 3. Profiles of $\Gamma v/c$ (up), $D = \rho\Gamma$ (center) and plasma internal energy \mathcal{E} (down) for $B = 200$ at three different times, labeled as t_1 (before the breakout), t_2 (at the breakout) and t_3 (after the breakout). The factor $\Gamma v/c$ is approximately equal to v/c when $v \ll c$, and to Γ when $v \sim c$. Contributions to \mathcal{E} due to the density have been neglected, in order to subtract the baryon's kinetic energy, and show the position of the shock. The vertical dashed lines indicate the position of R_{ph} at each time. See also [6].

on the radius as $v_r \propto r$, in order to set an initial profile that corresponds to the homologous expansion of the SN ejecta. Lastly, the plasma is initially contained within a radius of order $10^8 - 10^9$ cm, and has an uniform energy density.

Once the system is let to evolve from these initial conditions, the plasma expands and forms a shock that reaches the outermost part of the SN ejecta. Instead of forming a thin shell with an almost uniform Lorentz factor, the plasma evolves in such a way that the shock is followed by smooth energy and velocity distributions, where the module of the last may differ in several orders of magnitude from one point to another, as it is shown in Fig. 3.

After an initial expansion where Γ may reach values of several tenths, the shock rapidly elgulfs enough mass to decelerate and reach a non relativistic velocity distribution, typically in $t < 1$ s. This is maintained through the whole time the plasma is contained within the SN ejecta, until the breakout, in which the sudden decrease of the density causes the closest areas to the shock to reach relativistic velocities, as it can be seen in Fig. 3. From then on, the matter pushed by the shock -and no longer in homologous expansion- keeps expanding while cooling down.

As the shock propagates inside of the SN ejecta, photons are trapped inside the region occupied by the plasma, since their diffusion timescale is much longer than the dynamical times. Since characteristic equilibrium times are much shorter than both scales (see e.g. [12]), LTE is maintained during the whole evolution of the plasma within the SN material. However, at the breakout, the plasma reaches

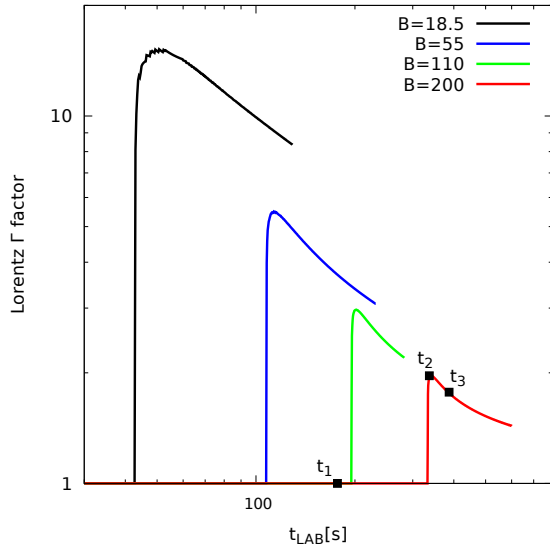


Figure 4. Lorentz gamma at the photospheric radius, calculated for different values of the baryon load, corresponding to different considered directions along the SN ejecta. The three times considered for $B = 200$ in Fig. 3 are indicated. Reproduced from [6].

the *photosphere*, which is an optically thin area located in the outermost regions of the SN ejecta. When this happens, photons begin to escape, and produce what is later observed as a flare.

To perform a comparison between these results and the observed Γ factors, we firstly recall from [13] that, before reaching an external observer, most of the photons are lastly scattered from a region peaked at $\tau \sim 1$, where τ is the optical depth calculated from the observer's line of sight. We hence define the transparency- or photospheric-radius R_{ph} as the value of the r coordinate that satisfies $\tau(R_{ph}) = 1$. Finally, we can give an estimation of the observed Γ by computing its value at $r = R_{ph}$.

Since τ is a Lorentz invariant when the total photon cross section is constant, which we assume as a first approximation, it can be calculated in laboratory coordinates as

$$\tau = \int_{R_{ph}}^{\infty} dr \sigma_T n_{e^-}(r), \quad (7)$$

where we set the cross section to $\sigma_T = 6.65 \times 10^{-25} \text{ cm}^2$, i.e., the one corresponding to Thomson scattering by electrons. Moreover, we compute the electron density as $n_{e^-} = \rho \Gamma / m_p$, where m_p is the proton mass. In doing so, we neglect the mass of the electrons, and we assume to have an average of one electron per nucleon.

Fig. 4, already shown in [6], shows the time evolution of $\Gamma(R_{ph})$, calculated for four different baryon loads that correspond to four different high-density directions along

the SN ejecta. For a high enough B , it can be seen that, indeed, $\Gamma(R_{ph}) \lesssim 4$.

4 Final remarks and future work

The performed simulations of the evolution of an e^+e^- plasma inside of a SN ejecta show as a result the formation, expansion and breakout of a shock. Within the IGC model's parameters, the Lorentz factor at the photospheric radius verifies $\Gamma \lesssim 4$ for a high enough integrated mass across the observer's line of sight. This is consistent with the existence of a thermal emitter expanding at such a Lorentz factor, as it is inferred from the thermal component observed in the X-ray flares.

We have said that RHD holds as long as LTE is granted. However, this is not the case for the thin region close to the shock, from where photons can escape. If this is taken into account, the pressure radiation, which is the dominant one, should be actually smaller, and consequently we should expect the actual Lorentz factors to be even smaller. Therefore, the results of this work must be taken as a superior limit for Γ . To take this effect into account, we are currently working on a scheme that evolves radiation and massive particles separately, which would allow to compute the emitted luminosity as well.

References

- [1] Rueda, J. A., & Ruffini, R., *ApJL*, **758**, L7 (2012)
- [2] Izzo, L., Rueda, J. A., & Ruffini, R., *A&A*, **548**, L5 (2012)
- [3] Fryer, C. L., Rueda, J. A., & Ruffini, R., *ApJL*, **793**, L36 (2014)
- [4] Damour, T., Ruffini, R., *APS*, **35**, 7, 463 (1975)
- [5] Ruffini, R., Rueda, J. A., Muccino, M., et al., **832**, 136 (2016)
- [6] Ruffini, R., Wang Y. et al, <https://arxiv.org/abs/1704.03821>, submitted to *ApJ* (2017)
- [7] Ruffini, R., Salmonson, J. D., Wilson, J. R., Xue, S., *A&A*, **359**, 855 (2000)
- [8] Becerra L., Bianco C. L., Fryer C. L., Rueda J. A., Ruffini R., *ApJ* **833**, 107 (2016)
- [9] Mignone, A., Zanni, C., Tzeferacos, P., et al., *The Astrophysical Journal Supplement Series*, **198**, 7 (2011)
- [10] Mignone, A., Bodo, G., *Mon. Not. R. Astron. Soc.*, **364**, 126 (2005)
- [11] Colella, P., Graves, D. T., Johnson, J. N., et al., *Chombo software package for AMR applications design document*, Tech. Rep. LBNL-6615E (2003)
- [12] Aksenov A. G. , Ruffini R., Vereshchagin G. V., *Phys. Rev. D* **79**, 043008 (2009)
- [13] Pe'er A., *ApJ*, **682**, 463 (2008)

THE FIRST ICRANET CATALOG OF BINARY-DRIVEN HYPERNOVAE

G. B. PISANI^{1,2}, R. RUFFINI^{1,2,3,4}, Y. AIMURATOV^{1,2,3}, C. L. BIANCO^{1,2}, M. KARLICA^{1,2,3}, M. KOVACEVIC^{1,2,3}, R. MORADI^{1,2}, M. MUCCINO^{1,2}, A. V. PENACCHIONI^{5,6}, D. PRIMORAC^{1,2}, J. A. RUEDA^{1,2,4}, Y. WANG^{1,2}

Draft version September 18, 2017

ABSTRACT

In a series of recent publications, scientists from ICRANet, led by professor Remo Ruffini, have reached a novel comprehensive picture of gamma-ray bursts (GRBs) thanks to their development of a series of new theoretical approaches. Among those, the induced gravitational collapse (IGC) paradigm explains a class of energetic, long-duration GRBs associated with Ib/c supernovae (SN), recently named binary-driven hypernovae (BdHNe).

BdHNe have a well defined set of observational features which allow to identify them. Among them, the main two are: 1) long duration of the GRB explosion, namely larger than 2 s in the rest frame; 2) a total energy, released in all directions by the GRB explosion, larger than 10^{52} ergs.

A striking result is the observation, in the BdHNe sources, of a universal late time power-law decay in the X-rays luminosity after 10^4 s, with typical decaying slope of ~ 1.5 . This leads to the possible establishment of a new distance indicator having redshift up to $z \sim 8$.

Thanks to this novel theoretical and observational understanding, it was possible for ICRANet scientists to build the first BdHNe catalog, composed by the 345 BdHNe identified up to the end of 2016.

Keywords: supernovae: general — binaries: general — gamma-ray burst: general — stars: neutron

1. TOWARDS A FIRST CATALOG OF BINARY-DRIVEN HYPERNOVAE

The first observations by the BATSE instrument on board the Compton γ -ray Observatory satellite have evidenced what has later become known as the prompt radiation of GRBs. On the basis of their hardness as well as their duration, GRBs were initially classified into short and long in an epoch when their cosmological nature was still being debated (Mazets et al. 1981; Klebesadel 1992; Dezalay et al. 1992; Kouveliotou et al. 1993; Tavani 1998).

The advent of the *BeppoSAX* satellite (Boella et al. 1997) introduced a new approach to GRBs by introducing joint observations in the X-rays and γ -rays thanks to its instruments: the Gamma-ray Burst Monitor (40–700 keV), the Wide Field Cameras (2–26 keV), and the Narrow Field Instruments (2–10 keV). The unexpected discovery of a well separate component in the GRB soon appeared: the afterglow, namely a radiation lasting up to 10^5 – 10^6 s after the emission of the prompt radiation (see Costa et al. 1997a,b; Frontera et al. 1998, 2000; de Pasquale et al. 2006). *BeppoSAX* clearly indicated the existence of a power law behavior in the late X-ray emission (LXRE).

The coming of the *Swift* satellite (Gehrels et al. 2004; Evans et al. 2007, 2010), significantly extending the ob-

servation energy band to the X-ray band thanks to its X-ray Telescope (XRT band: 0.3–10 keV), has allowed us for the first time to uncover the unexplored region between the end of the prompt radiation and the power-law late X-ray behavior discovered by *BeppoSAX*: in some long GRBs, a steep decay phase was observed leading to a plateau followed then by a typical LXRE power law behavior (Evans et al. 2007, 2010).

Recently, Pisani et al. (2013) noticed the unexpected result that the LXREs of a “golden sample” (GS) of six long, closeby ($z \lesssim 1$), energetic ($E_{iso} > 10^{52}$ erg) GRBs, when moved in the rest-frame of the sources, were showing a common power-law behavior (see Fig. 1), independently from the isotropic energy E_{iso} coming from the GRB prompt radiation (see Fig 2). More unexpected was the fact that the plateau luminosity and duration before merging in the common LXRE power-law behavior were clearly functions of the E_{iso} (see Fig. 2, and Ruffini et al. 2014c), while the late power-law remains independent from the E_{iso} of the prompt emission (see Fig. 1–2, and Pisani et al. 2013; Ruffini et al. 2014c). For this reason, this striking scaling law has been used as a distance indicator to independently estimate the cosmological redshift of some long GRBs by imposing the overlap of their LXRE (see, e.g., Penacchioni et al. 2012, 2013; Ruffini et al. 2013b,c, 2014a), and also to predict, ten days in advance, the observation of the typical optical signature of the supernova SN 2013cq, associated with GRB 130427A (Ruffini et al. 2015, 2013a; de Ugarte Postigo et al. 2013; Levan et al. 2013).

All these analyses are based on the paradigms introduced in Ruffini et al. (2001a) for the space-time parametrization of the GRB phenomena, in Ruffini et al. (2001b) for the interpretation of the structure of the GRB prompt radiation, and in Ruffini et al. (2001c) for the induced gravitational collapse (IGC) mechanism, further

¹ Dipartimento di Fisica, Sapienza Università di Roma and ICRA, Piazzale Aldo Moro 5, I-00185 Roma, Italy

² International Center for Relativistic Astrophysics Network (ICRANet), Piazza della Repubblica 10, I-65122 Pescara, Italy

³ Université de Nice Sophia-Antipolis, Grand Château Parc Valrose, Nice, CEDEX 2, France

⁴ ICRANet-Rio, Centro Brasileiro de Pesquisas Físicas, Rua Dr. Xavier Sigaud 150, Rio de Janeiro, RJ, 22290-180, Brazil

⁵ University of Siena, Department of Physical Sciences, Earth and Environment, Via Roma 56, I-53100 Siena, Italy

⁶ ASI Science Data Center, via del Politecnico s.n.c., I-00133 Rome Italy

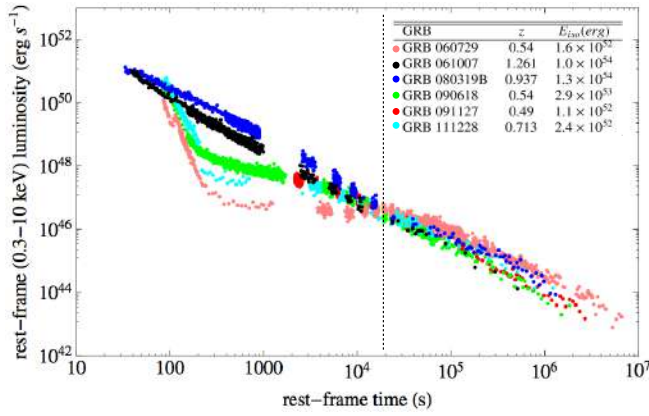


Figure 1. Scaling law found in the isotropic X-ray late times luminosity within the GS by Pisani et al. (2013). Despite the different early behavior, the different light curves join all together the same power law after a rest-frame time of $t_{rf} \sim 2 \times 10^4$ s.

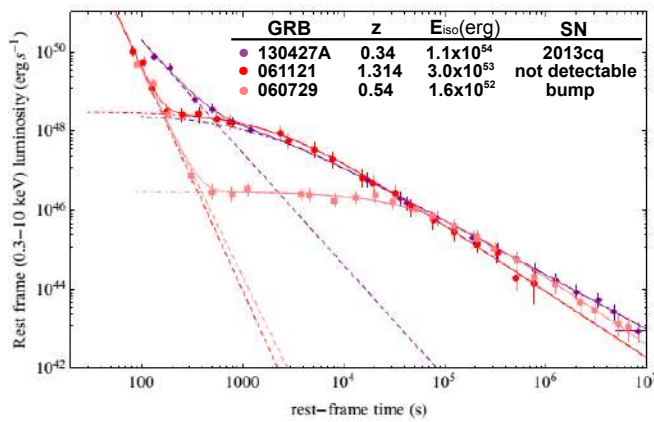


Figure 2. Nested structure of the isotropic X-ray luminosity of the BdHNe. This includes the previously mentioned scaling law of the late power law and leads to an inverse proportionality between the luminosity of the plateau and the rest-frame time delimiting its end and the beginning of the late power law decay Ruffini et al. (2014c).

developed in Ruffini et al. (2007), Rueda & Ruffini (2012), Fryer et al. (2014), and Ruffini et al. (2016). In the present case, the phenomenon points to an IGC occurring when a tight binary system composed of a carbon-oxygen core (CO_{core}) undergoes a supernova (SN) explosion in the presence of a binary neutron star (NS) companion (Ruffini et al. 2001b, 2007; Izzo et al. 2012; Rueda & Ruffini 2012; Fryer et al. 2014; Ruffini et al. 2015). When the IGC leads the NS to accrete enough matter and therefore to collapse to a black hole (BH), the GRB shows a long duration, and its prompt emission overtakes the threshold value of 10^{52} ergs. The overall observed phenomenon is called binary-driven hypernova (BdHN; Fryer et al. 2014; Ruffini et al. 2015, 2016).

A decisive further step has been the identification as a BdHN of GRB 090423 (Ruffini et al. 2014b) at the extremely high redshift of $z = 8.2$ (Salvaterra et al. 2009; Tanvir et al. 2009). On top of that, the LXRE of GRB 090423 overlaps entirely with the ones of the GS (see Fig. 3), extending such a scaling law up to extreme cosmological distances. This result led to the necessity of checking such a common behavior of the LXREs in BdHNe at redshifts larger than $z \sim 1$.

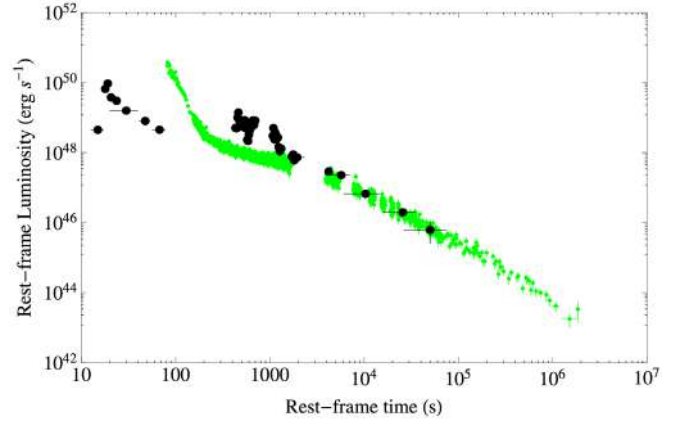


Figure 3. X-ray luminosity of GRB 090423 (black points) compared with the one of GRB 090618 (green points), the prototype BdHN, by Ruffini et al. (2014b).

In Pisani et al. (2016), we present an “enlarged sample” (ES) of 161 BdHNe observed up to the end of 2015. In this work we analysed the signatures contained in the LXREs at $t_{rf} \gtrsim 10^4$ s, where t_{rf} is the rest-frame time after the initial GRB explosion. In particular, we probed a further improvement for the presence of such an LXRE universal behavior of BdHNe by the introduction of a collimation effect within the emission mechanism.

In our recent work (Ruffini et al. 2017), we focused on analyzing the early X-Ray Flares in the GRB flare-plateau-afterglow (FPA) phase observed by Swift/XRT. The FPA occurs only in the BdHNe while is not present in the other subclasses of GRBs, for details see Ruffini et al. (2016). The sample presented in Table 9 of Ruffini et al. (2017), namely an updated version of the ES up to the end of 2016, together with the BdHNe lacking LXRE data and the ones from the pre-Swift-era, counts 345 BdHNe in total. This represents the current BdHNe catalog from ICRANet.

In the following, we present various insightful results which ICRANet scientists gained from this catalog: in Sections 2, 3, and 4, we describe how we built the ES and we study the LXRE features within it; finally, in Section 5 we refer to our up-to-date catalog of BdHNe and we draw our perspectives.

2. THE FIRST ENLARGED SAMPLE OF BDHN

Starting from the GS originally presented in Pisani et al. (2013), in Pisani et al. (2016) we have built a new sample of BdHNe, which we called “enlarged sample” (ES), under the following selection criteria:

- measured redshift z ;
- GRB rest-frame duration larger than 2 s;
- isotropic energy E_{iso} larger than 10^{52} erg; and
- presence of associated *Swift*/XRT data lasting at least up to $t_{rf} = 10^4$ s.

We collected 161 sources, satisfying our criteria, which cover 11 years of *Swift*/XRT observations, up to the end of 2015, see Table 2 of Pisani et al. (2016). The E_{iso} of each source has been estimated using the observed redshift z together with the best-fit parameters of the

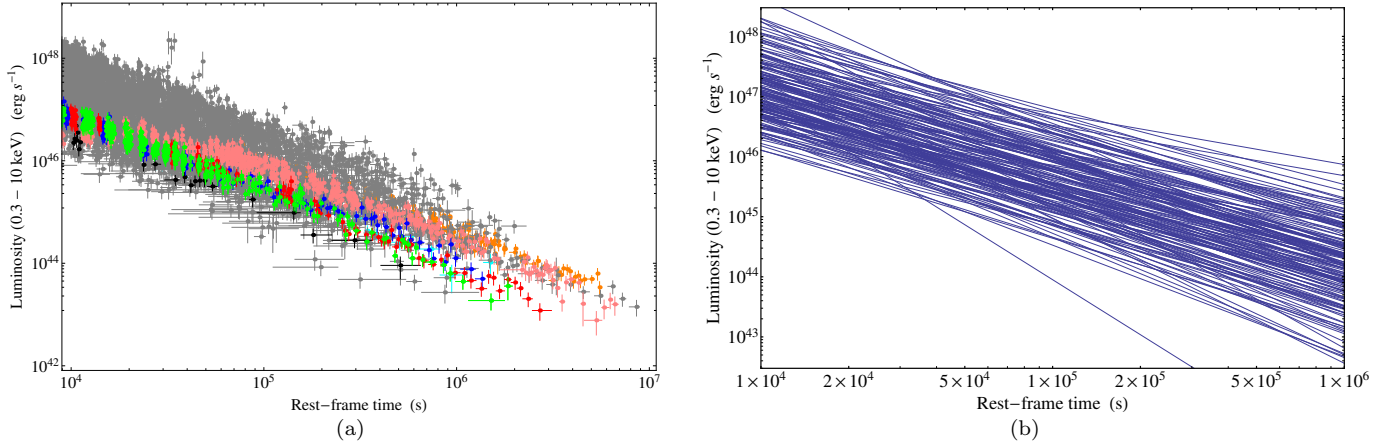


Figure 4. Panel (a): LXRE luminosity light curves of all 161 sources of the ES (gray) compared with the ones of the GS: GRB 060729 (pink), GRB 061007 (black), GRB 080913B (blue), GRB 090618 (green), GRB 091127 (red), and GRB 111228 (cyan), plus GRB 130427A (orange; from Pisani et al. 2016). Panel (b): power laws which best fit the luminosity light curves of the X-ray emissions of all 161 sources of the ES (from Pisani et al. 2016).

γ -ray spectrum published in the GCN circular archive⁷. Most of the ES sources, 102 out of 161, have γ -ray data observed by *Fermi*/GBM and Konus-WIND, which, with their energy bands being 10–1000 keV and 20–2000 keV, respectively, lead to a solid estimate of the E_{iso} , computed in the “bolometric” 1–10⁴ keV band (Bloom et al. 2001). The remaining sources of the ES have had their γ -ray emission provided by *Swift*/BAT only, with the unique exception of one source observed by HETE. The energy bands of these two detectors, being 15–150 keV and 8–400 keV, respectively, lead to an estimate of E_{iso} by extrapolation in the “bolometric” 1–10⁴ keV band (Bloom et al. 2001).

3. GOING TO THE REST-FRAME

We compare the *Swift*/XRT isotropic luminosity light curve $L_{iso}(t_{rf})$ for 161 GRBs of the ES in the common rest-frame energy range of 0.3–10 keV. We initially adjust the observed *Swift*/XRT flux f_{obs} as if it had been observed in the 0.3–10 keV rest-frame energy range. In the detector frame, the 0.3–10 keV rest-frame energy band becomes $[0.3/(1+z)] - [10/(1+z)]$ keV, where z is the measured redshift of the GRB. We assume a simple power-law as the best fit for the spectral energy distribution of the *Swift*/XRT data⁸:

$$\frac{dN}{dA dt dE} \propto E^{-\gamma}. \quad (1)$$

Hence, we can calculate the flux light curve in the 0.3–10 keV rest-frame energy band, f_{rf} , multiplying the observed one, f_{obs} , by the k-correction:

$$f_{rf} = f_{obs} \frac{\int_{0.3 \text{ keV}}^{10 \text{ keV}} \frac{1+z}{1+z} E^{1-\gamma} dE}{\int_{0.3 \text{ keV}}^{10 \text{ keV}} E^{1-\gamma} dE} = f_{obs} (1+z)^{\gamma-2}. \quad (2)$$

Then, to calculate the isotropic X-ray luminosity L_{iso} , we need to multiply f_{rf} by the spherical surface having the luminosity distance as radius

$$L_{iso} = 4\pi d_L^2(z) f_{rf}, \quad (3)$$

where we assume a standard cosmological Λ CDM model, namely $\Omega_m = 0.27$ and $\Omega_\Lambda = 0.73$. In the end, we convert the observed times into rest-frame times t_{rf} :

$$t_{rf} = \frac{t_{obs}}{1+z}. \quad (4)$$

After, we fit the isotropic luminosity light-curve late phase with a decaying power-law function defined as:

$$L_{iso}(t_{rf}) = L_0 t_{rf}^{-\alpha}, \quad (5)$$

where α , the power law index, is a positive number, and L_0 is the luminosity at a fixed time $t_{rf} = t_0$ after the GRB initial explosion in the rest-frame of the source. All the power-laws are shown in Fig. 4b. Fig. 5a shows the distribution of the α indexes within the ES. This distribution follows a Gaussian behavior having a mean value of $\mu_\alpha = 1.48$ and a standard deviation of $\sigma_\alpha = 0.32$. The LXRE luminosity light curves of the ES in the 0.3–10 keV rest-frame energy range are plotted in Fig. 4a, together with the curves of the GS. Fig. 4a shows that the power-laws within the ES span around two orders of magnitude in luminosity. The spread of the LXRE light curves in the ES is better shown off by Fig. 5b which display the distribution within the ES of the LXRE integrated energies E_{LT} defined as:

$$E_{LT} \equiv \int_{10^4 s}^{10^6 s} L_{iso}(t_{rf}) dt_{rf}. \quad (6)$$

The solid red line in Fig. 5b is the Gaussian function that best fits the late integrated energies E_{LT} in logarithmic scale. Its mean value is $\mu_{\text{Log}_{10}(E_{LT})} = 51.40$, and its standard deviation is $\sigma_{\text{Log}_{10}(E_{LT})} = 0.47$.

The LXRE power-law spread, given approximately by $2\sigma_{\text{Log}_{10}(E_{LT})} = 0.94$, is larger than the one of the previous work of Pisani et al. (2013), which results as $2\sigma_{\text{Log}_{10}(E_{LT})} = 0.56$. This is certainly due to the important growth of the number of BdHNe composing the ES (161) in respect to the ones of the GS (6).

Moreover, there is no evidence for a correlation between the LXRE power-law behavior and the isotropic energy radiated by the source during the GRB prompt radiation (for details, see Pisani et al. 2016).

⁷ http://gcn.gsfc.nasa.gov/gcn3_archive.html

⁸ <http://www.swift.ac.uk/>

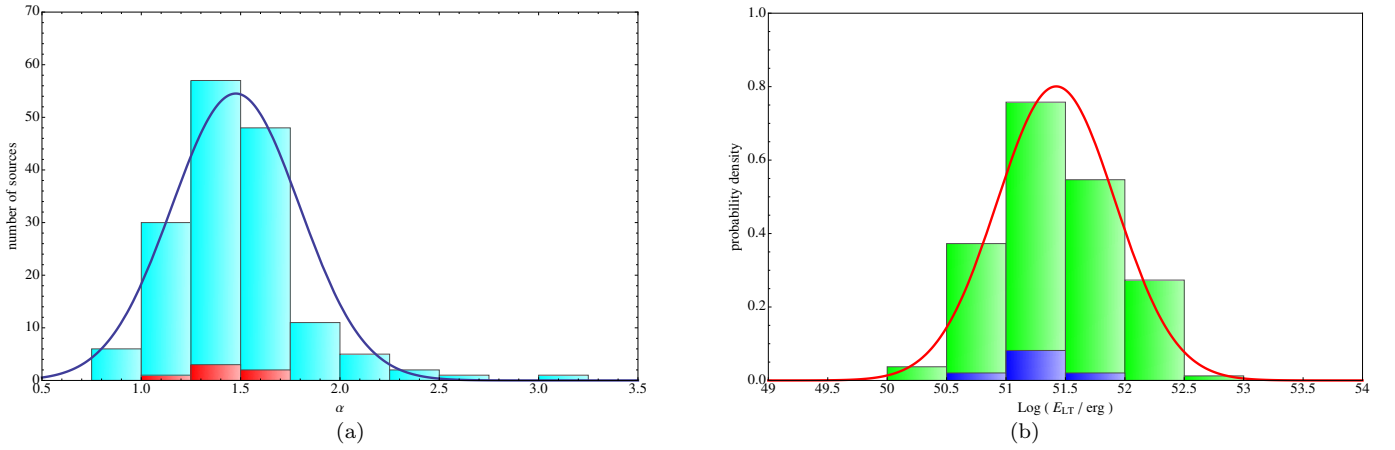


Figure 5. Panel (a): distribution of the LXRE power law indexes α within the ES (cyan) compared to the one of the GS (red). Such a distribution follows a Gaussian behavior (blue line) with a mean value of $\mu_\alpha = 1.48$ and a standard deviation of $\sigma_\alpha = 0.32$ (from Pisani et al. 2016). Panel (b): probability distribution of the LXRE integrated energies within the time interval 10^4 – 10^6 s in the rest-frame after the initial GRB trigger for all the sources of the ES (in green) compared with the GS (in blue). The solid red line represents the Gaussian function which best fits the ES data in logarithmic scale. Its mean value is $\mu_{\text{Log}_{10}(E_{LT})} = 51.40$, while its standard deviation is $\sigma_{\text{Log}_{10}(E_{LT})} = 0.47$ (from Pisani et al. 2016).

4. COLLIMATION

In Pisani et al. (2016), we also proposed to reduce the spread of the LXRE power laws within the ES by introducing a collimation effect in the emission mechanism. In fact, if such a process is not isotropic, our estimates for the LXRE luminosities are actually overestimations of the intrinsic ones. By introducing a collimation effect, namely assuming that the LXREs are not radiated isotropically but inside a double-cone region having half-opening angle θ , we can compute the intrinsic LXRE luminosity $L_{\text{intr}}(t_{rf})$ from the isotropic $L_{\text{iso}}(t_{rf})$:

$$L_{\text{intr}}(t_{rf}) = L_{\text{iso}}(t_{rf}) (1 - \cos \theta). \quad (7)$$

From Eq. 7, an angle θ can be computed for each source of the ES if an intrinsic universal LXRE light curve $L_{\text{intr}}(t_{rf})$ is given. By assuming GRB 050525A, which has the lowest luminosity within the ES, as our sole “isotropic” LXRE source, we obtain the probability distribution of the half-opening angle θ within the ES showed in Fig. 6a. The blue solid line represents a logarithmic normal distribution, which best fits the data. This distribution has a mode of $Mo_\theta = 17.62^\circ$, a mean of $\mu_\theta = 30.05^\circ$, a median of $Me_\theta = 25.15^\circ$, and a standard deviation of $\sigma_\theta = 19.65^\circ$. In addition, it is possible to verify that, by adjusting the $L_{\text{iso}}(t_{rf})$ light curve of each ES source for its corresponding θ , an overlap of the LXRE luminosity light curves as good as the one seen in the GS by Pisani et al. (2013) shown in Fig. 1 is obtained. Since the LXRE follows a power-law behavior, we can evaluate the tightness of the LXREs overlap estimating the correlation coefficient ρ between all the luminosity light-curve data points of the ES sources in log-log scale. Considering the data points of the LXRE power laws within the 10^4 – 10^6 s time interval (the time interval where we defined E_{LT}), we obtain $\rho = -0.94$ for the GS, $\rho = -0.84$ for the ES before the collimation effect correction, and $\rho = -0.97$ after the collimation correction. Therefore, assuming the collimation not only let the spread of the LXREs within the ES decrease, but makes the LXREs overlap even tighter than the one previously observed in the GS. This leads to the possible establishment of a new

distance indicator, eventually useful to test the standard cosmological Λ CDM model.

5. THE CURRENT BDHNE CATALOG

Thanks to the tremendous amount of work from ICRANet scientists in the past years (Ruffini et al. 2001a,b,c, 2007; Rueda & Ruffini 2012; Izzo et al. 2012; Fryer et al. 2014; Ruffini et al. 2015, 2016), today we know that all the observed GRBs having long duration and isotropic energy E_{iso} larger than 10^{52} erg are the observational result of a BdHN phenomenon. Therefore, these two signatures are necessary and sufficient to identify a BdHN source. This holds also in the case it was not possible to observe the other typical features of the BdHNe following the GRB explosion, like: the FPA structure in the X-rays; the LXRE in the X-rays; and the associated Ib/c SN in the optical rays. In our recent work (Ruffini et al. 2017), in order to focus our analysis on the early X-Ray Flares in the FPA phase, we collected all the BdHNe ever observed till the end of 2016, collecting all the GRBs which satisfies the following criteria:

- measured redshift z ;
- GRB rest-frame duration larger than 2 s;
- isotropic energy E_{iso} larger than 10^{52} erg.

The updated list presented in Table 9 of (Ruffini et al. 2017) is composed by 345 BdHNe, and represents the current ICRANet catalog of BdHNe. The ES, updated to the end of 2016, counts 182 BdHNe having *Swift*/XRT data up to at least 10^4 s in the rest-frame after the initial GRB explosion. It composes $\sim 53\%$ of the total BdHNe catalog. Since the *Swift* satellite is operating since 2005, we have an average of ~ 15 BdHNe per year having good LXRE observations. Consequently, this represents the expected rate of BdHNe which, in the near future, will be useful to test the standard cosmological Λ CDM model at redshifts up to $z \sim 8$.

This work made use of data supplied by the UK Swift Science Data Center at the University of Leices-

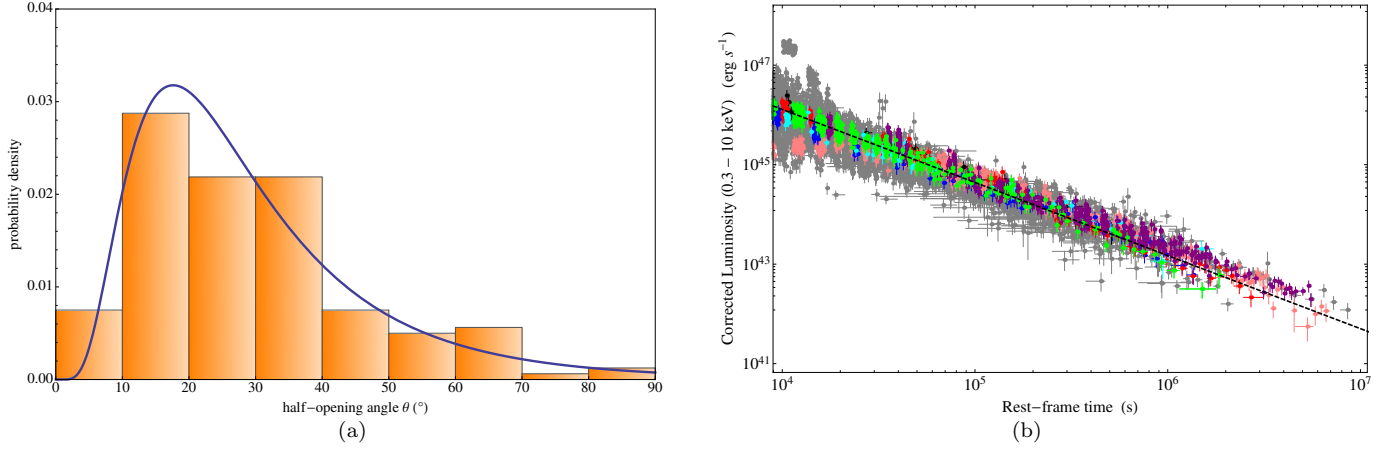


Figure 6. Left panel (a): probability distribution of the half-opening angle θ within the ES. The blue solid line represents a logarithmic normal distribution, which best fits the data. This distribution has a mode of $Mo_\theta = 17.62^\circ$, a mean of $\mu_\theta = 30.05^\circ$, a median of $Me_\theta = 25.15^\circ$, and a standard deviation of $\sigma_\theta = 19.65^\circ$ (from Pisani et al. 2016). Right panel (b): corrected LXRE luminosity light curves of all 161 sources of the ES (gray) compared to the ones of the GS: GRB 060729 (pink), GRB 061007 (black), GRB 080913B (blue), GRB 090618 (green), GRB 091127 (red), and GRB 111228 (cyan), plus GRB 130427A (purple; Pisani et al. 2013; Ruffini et al. 2015). The black dotted line represents the universal LXRE power law, namely the linear fit of the late emission of GRB 050525A (from Pisani et al. 2016).

ter. J. A. R. acknowledges the support by the International Cooperation Program CAPES-ICRANet financed by CAPES-Brazilian Federal Agency for Support and Evaluation of Graduate Education within the Ministry of Education of Brazil. M. M. acknowledges the partial support of the project No. 3101/GF4 IPC-11/2015, and the target program of the Ministry of Education and Science of the Republic of Kazakhstan.

REFERENCES

- Bloom, J. S., Frail, D. A., & Sari, R. 2001, *AJ*, 121, 2879
- Boella, G., Butler, R. C., Perola, G. C., et al. 1997, *A&AS*, 122, 299
- Costa, E., Frontera, F., Heise, J., et al. 1997a, *Nature*, 387, 783
- Costa, E., Feroci, M., Piro, L., et al. 1997b, *IAU Circ.*, 6576
- de Pasquale, M., Piro, L., Gendre, B., et al. 2006, *A&A*, 455, 813
- de Ugarte Postigo, A., Xu, D., Leloudas, G., et al. 2013, *GCN Circ.*, 14646, 1
- Dezalay, J.-P., Barat, C., Talon, R., et al. 1992, in *American Institute of Physics Conference Series*, Vol. 265, American Institute of Physics Conference Series, ed. W. S. Paciesas & G. J. Fishman, 304–309
- Evans, P. A., Beardmore, A. P., Page, K. L., et al. 2007, *A&A*, 469, 379
- Evans, P. A., Willingale, R., Osborne, J. P., et al. 2010, *A&A*, 519, A102
- Frontera, F., Costa, E., Piro, L., et al. 1998, *ApJ*, 493, L67
- Frontera, F., Amati, L., Costa, E., et al. 2000, *ApJSS*, 127, 59
- Fryer, C. L., Rueda, J. A., & Ruffini, R. 2014, *ApJ*, 793, L36
- Gehrels, N., Chincarini, G., Giommi, P., et al. 2004, *ApJ*, 611, 1005
- Izzo, L., Rueda, J. A., & Ruffini, R. 2012, *A&A*, 548, L5
- Klebesadel, R. W. 1992, in *Gamma-Ray Bursts - Observations, Analyses and Theories*, ed. C. Ho, R. I. Epstein, & E. E. Fenimore (Cambridge University Press), 161–168
- Kouveliotou, C., Meegan, C. A., Fishman, G. J., et al. 1993, *ApJ*, 413, L101
- Levan, A. J., Fruchter, A. S., Graham, J., et al. 2013, *GCN Circ.*, 14686, 1
- Mazets, E. P., Golenetskii, S. V., Ilinskii, V. N., et al. 1981, *Ap&SS*, 80, 3
- Penacchioni, A. V., Ruffini, R., Bianco, C. L., et al. 2013, *A&A*, 551, A133
- Penacchioni, A. V., Ruffini, R., Izzo, L., et al. 2012, *A&A*, 538, A58
- Pisani, G. B., Izzo, L., Ruffini, R., et al. 2013, *A&A*, 552, L5
- Pisani, G. B., Ruffini, R., Aimuratov, Y., et al. 2016, *ApJ*, 833, 159
- Rueda, J. A., & Ruffini, R. 2012, *ApJ*, 758, L7
- Ruffini, R., Bianco, C. L., Chardonnet, P., Frascchetti, F., & Xue, S.-S. 2001a, *ApJ*, 555, L107
- . 2001b, *ApJ*, 555, L113
- . 2001c, *ApJ*, 555, L117
- Ruffini, R., Bernardini, M. G., Bianco, C. L., et al. 2007, *ESA SP*, 622, 561
- Ruffini, R., Bianco, C. L., Enderli, M., et al. 2013a, *GCN Circ.*, 14526, 1
- . 2013b, *GRB Coordinates Network*, 14888
- . 2013c, *GRB Coordinates Network*, 15576
- . 2014a, *GRB Coordinates Network*, 15707
- Ruffini, R., Izzo, L., Muccino, M., et al. 2014b, *A&A*, 569, A39
- Ruffini, R., Muccino, M., Bianco, C. L., et al. 2014c, *A&A*, 565, L10
- Ruffini, R., Wang, Y., Enderli, M., et al. 2015, *ApJ*, 798, 10
- Ruffini, R., Rueda, J. A., Muccino, M., et al. 2016, *ApJ*, 832, 136
- Ruffini, R., Wang, Y., Aimuratov, Y., et al. 2017, *ArXiv e-prints*
- Salvaterra, R., Della Valle, M., Campana, S., et al. 2009, *Nature*, 461, 1258
- Tanvir, N. R., Fox, D. B., Levan, A. J., et al. 2009, *Nature*, 461, 1254
- Tavani, M. 1998, *ApJ*, 497, L21

What can we learn from GRBs?

Marco Muccino^{1,2,*}, Remo Ruffini^{1,2,3,4}, Yerlan Aimuratov^{1,3}, Laura M. Becerra^{1,2}, Carlo L. Bianco^{1,2}, Mile Karlica^{1,3}, Milos Kovacevic^{1,3}, Julio D. Melon Fuksman^{1,2}, Rahim Moradi^{1,2}, Ana V. Penacchioni^{5,6}, Giovanni B. Pisani^{1,2}, Daria Primorac^{1,2}, Jorge A. Rueda^{1,2,4}, Soroush Shakeri^{2,7}, Gregory V. Vereshchagin^{1,2}, She-Sheng Xue^{1,2}, and Yu Wang^{1,2}

¹Dip. di Fisica, Sapienza Università di Roma, Piazzale Aldo Moro 5, I-00185 Rome, Italy

²ICRANet-Pescara, Piazza della Repubblica 10, I-65122 Pescara, Italy

³Université de Nice Sophia-Antipolis, Grand Château Parc Valrose, Nice, CEDEX 2, France

⁴ICRANet-Rio, Centro Brasileiro de Pesquisas Físicas, Rua Dr. Xavier Sigaud 150, Rio de Janeiro, RJ, 22290-180, Brazil

⁵University of Siena, Dept. of Physical Sciences, Earth and Environment, Via Roma 56, I-53100 Siena, Italy

⁶ASI Science Data Center, via del Politecnico s.n.c., I-00133 Rome Italy

⁷Department of Physics, Isfahan University of Technology, 84156-83111, Iran

Abstract. We review our recent results on the classification of long and short gamma-ray bursts (GRBs) in different subclasses. We provide observational evidences for the binary nature of GRB progenitors. For long bursts the induced gravitational collapse (IGC) paradigm proposes as progenitor a tight binary system composed of a carbon-oxygen core (CO_{core}) and a neutron star (NS) companion; the supernova (SN) explosion of the CO_{core} triggers a hypercritical accretion process onto the companion NS. For short bursts a NS–NS merger is traditionally adopted as the progenitor. We also indicate additional sub-classes originating from different progenitors: (CO_{core})–black hole (BH), BH–NS, and white dwarf–NS binaries. We also show how the outcomes of the further evolution of some of these sub-classes may become the progenitor systems of other sub-classes.

1 Introduction

Gamma-ray bursts (GRBs) are traditionally classified based on their duration [1–5]: short GRBs last $\lesssim 2$ s, while long GRBs last $\gtrsim 2$ s.

Thanks to the extensive data collected by γ -ray telescopes, such as AGILE, BATSE, BeppoSAX, *Fermi*, *HETE-II*, *INTEGRAL*, Konus/WIND and *Swift*, to more sophisticated time-resolved spectral analyses, and to the theoretical treatment of the *fireshell* model [6–8] it has become evident that both long and short bursts originate from binary progenitors and that they can be further subdivided into a variety of sub-classes, depending on the evolution of these binary systems [9–11].

Short bursts are associated to NS–NS or BH–NS mergers [12–22]: their host galaxies are of both early- and late-type, their localization with respect to the host galaxy often indicates a large offset [23–29] or a location of minimal star-forming activity with typical circumburst medium (CBM) densities of $\sim 10^{-5}$ – 10^{-4} cm^{-3} , and no supernovae (SNe) have ever been associated to them.

Long bursts have been traditionally associated to the death of single massive stars [30]. The large majority of long bursts is related to SNe and are spatially correlated with bright star-forming regions in their host galaxies [31, 32] with a typical CBM density of $\sim 1 \text{ cm}^{-3}$ [33, 34]. However, the above single progenitor model contrasts with

the fact that most massive stars are found in binary systems [35], that most type Ib/c SNe occur in binary systems [36] and that SNe associated to long GRBs are indeed of type Ib/c [37]. Indeed, recently we have found evidence for multiple components in long GRB emissions evidencing the presence of a precise sequence of different astrophysical processes [33, 34], which led to the formulation of the Induced Gravitational Collapse (IGC) paradigm [6, 38–40] expliciting the role of binary systems as progenitors of the long GRBs. The IGC paradigm explains the GRB–SN connection by proposing as progenitors (or *in-state*) a tight binary system composed of a carbon-oxygen core (CO_{core}) undergoing a SN explosion and a companion neutron star (NS) [39–41]. The SN explosion triggers hypercritical accretion onto the companion NS [39, 40, 42].

Recent observations of a prolonged 0.1–100 GeV high energy emission by the *Fermi*–LAT instrument evidenced its correlation with both long [9] and short bursts [10] with isotropic energy $E_{\text{iso}} \gtrsim 10^{52} \text{ erg}$. On the basis of this correlation in such systems with different progenitors, we have identified the onset of the GeV emission with the moment of the formation of a black hole (BH) [9, 10]. This implies that systems with energy $E_{\text{iso}} \lesssim 10^{52} \text{ erg}$, which do not exhibit GeV emission, do not form BHs.

Indeed, we proposed the following classification scheme. Long GRBs, according to the IGC paradigm [9], are classified into two sub-classes [42]:

*e-mail: marco.muccino@icranet.it

- X-ray flashes (XRFs) with $E_{\text{iso}} \lesssim 10^{52}$ erg and rest-frame spectral peak energy $E_{p,i} \lesssim 200$ keV. These systems, already pioneered in a different context [43–45], originate in widely separated CO_{core}–NS binaries with an orbital separation $a > 10^{11}$ cm [41], therefore the hypercritical accretion onto the NS companion is insufficient to induce gravitational collapse to a BH [39–41] and, therefore, as expected in our theory no GeV emission is observed. The outcomes (or *out-states*) of XRFs are binaries composed of a new NS (ν NS) produced from the SN explosion, and a massive NS (MNS) which accreted matter from the SN ejecta. Their occurrence rate is $\rho_{\text{XRF}} = 100^{+45}_{-34} \text{ Gpc}^{-3} \text{ yr}^{-1}$ [42] (see figure 1).
- Binary-driven hypernovae (BdHNe) with $E_{\text{iso}} \gtrsim 10^{52}$ erg and $E_{p,i} \gtrsim 200$ keV. BdHNe occur in tighter binaries ($a < 10^{11}$ cm), where the hypercritical accretion onto the companion NS leads to the formation of a BH [41] and, therefore, to the emission of the associated prolonged GeV emission (observable when inside the LAT field of view). Specific constant power-law behaviors are observed in their high energy GeV and X-rays luminosity light curves [9, 46, 47]. The out-states of BdHNe are ν NS–BH binaries [41, 42, 48, 49]. The BdHN occurrence rate is $\rho_{\text{BdHN}} = 0.77^{+0.09}_{-0.08} \text{ Gpc}^{-3} \text{ yr}^{-1}$ [42] (see figure 1).

For progenitor system composed of a CO_{core} in binary with an already formed BH [8, 42], leading to bursts with $E_{\text{iso}} \gtrsim 10^{54}$ erg and $E_{p,i} \gtrsim 2$ MeV, the observational identification is still pending. In these systems, which correspond to the late evolutionary stages of X-ray binaries as Cyg X-1 and Cyg X-3 [50], or microquasars [51], the hypercritical accretion produces, as *out-states*, a more massive BH and a ν NS. Their occurrence rate can contribute to that of BdHNe, being CO_{core}–BH a particular case of BdHN progenitors (see figure 1).

In total analogy, the formation of a BH can occur in short bursts, depending whether or not the mass of the merged core of the binary system exceeds the NS critical mass. For NS–NS binaries, which are the outcomes of XRFs, we have [10, 42, 48]:

- Short gamma-ray flashes (S-GRFs), with $E_{\text{iso}} \lesssim 10^{52}$ erg and $E_{p,i} \lesssim 2$ MeV. They occur when the merged core does not exceed the NS critical mass and does not collapse into a BH, but still remains as a MNS with some additional orbiting material to guarantee the angular momentum conservation. As a consequence, no GeV emission is expected from these systems and, indeed, is not observed. The S-GRF occurrence rate is $\rho_{\text{S-GRF}} = 3.6^{+1.4}_{-1.0} \text{ Gpc}^{-3} \text{ yr}^{-1}$ [42] (see figure 1).
- Authentic short GRBs (S-GRBs) with $E_{\text{iso}} \gtrsim 10^{52}$ erg and $E_{p,i} \gtrsim 2$ MeV. They occur when a BH is formed in the NS–NS merger. Thus, these systems exhibit GeV emission. Their occurrence rate is $\rho_{\text{S-GRB}} = (1.9^{+1.8}_{-1.1}) \times 10^{-3} \text{ Gpc}^{-3} \text{ yr}^{-1}$ [42] (see figure 1).

We have recently proposed the existence of ultra-short GRBs (U-GRBs), a new hybrid sub-class of (yet unobserved) short bursts originating from the BdHNe out-states (ν NS–BH binaries), which remain bound nearly in 100%

of the cases [48]. These systems represent a yet unaccounted family of merging NS–BH binaries in the current standard population synthesis analyses [48], therefore, including other possible channels of formation for NS–BH binaries, the lower limit of the U-GRB occurrence rate can be assumed equal to the BdHN rate, i.e., $\rho_{\text{U-GRB}} \gtrsim 0.77^{+0.09}_{-0.08} \text{ Gpc}^{-3} \text{ yr}^{-1}$ [42] (see figure 1).

Finally, we proposed another sub-class of sources originating in NS–WD mergers: gamma-ray flashes (GRFs), a class of long GRBs occurring in a CBM environment with low density, e.g., $\sim 10^{-3} \text{ cm}^{-3}$, typical of the halos of the GRB host galaxies [42, 52, 53], not associated with SNe [54], and characterized by the presence of a macronova emission in the optical afterglow [55]. GRFs have $10^{51} \lesssim E_{\text{iso}} \lesssim 10^{52}$ erg and $0.2 \lesssim E_{p,i} \lesssim 2$ MeV and, therefore, the NS–WD merger forms a MNS and not a BH [42]. NS–WD binaries, are notoriously very common astrophysical systems [56] and their possible formation channels have been studied [57, 58]; as proposed in Ref. [42], another less likely but yet possible channel of formation is the merger of a NS–WD binary produced from an S-GRF. The GRF rate of occurrence is $\rho_{\text{GRF}} = 1.02^{+0.71}_{-0.46} \text{ Gpc}^{-3} \text{ yr}^{-1}$ [42] (see figure 1).

In all the above systems, the 10^{52} erg limit is clearly a function of the yet unknown precise value of the NS critical mass. As already pointed out in Ref. [42] the direct observation of the separatrix energy between S-GRFs and S-GRBs, and also between BdHNe and XRFs, gives fundamental informations for the determination of the actual value of maximum NS mass and for the minimum mass of the newly-formed BH.

In this paper we review the latest observational and theoretical results which led to above burst classification scheme. In Section 2, we briefly summarize the fireshell model. In Section 3, we describe the observational properties of XRFs and BdHNe and their interpretation within the IGC paradigm. In Section 4, we focus on the S-GRBs and specially on the theoretical interpretation of their GeV emission. In Section 4, we summarize our Conclusions.

2 The fireshell model

Before going into details in the observational and theoretical description of XRFs, BdHNe, S-GRFs and S-GRBs, we briefly summarize the fireshell model which is at the basis for the above classification of all bursts.

In the fireshell model [6–8], the GRB emission originates from an optically thick e^+e^- plasma of total energy $E_{e^+e^-}^{\text{tot}}$ – the fireshell. Its expansion and self-acceleration is due to the gradual e^+e^- annihilation [59]. Even after engulfing the baryonic mass M_B left over by the progenitor system, quantified by the baryon load $B = M_B c^2 / E_{e^+e^-}^{\text{tot}}$ [60], the fireshell remains still optically thick and continues its self-acceleration up to ultrarelativistic velocities [61, 62]. When the fireshell reaches the transparency condition, a first flash of radiation, the P-GRB, is emitted [7, 59, 60]. The spectrum of the P-GRB is determined by the geometry of the pair-creation region: in the case of the spherically symmetric dyadosphere, the P-GRB spectrum is generally described by a single thermal component

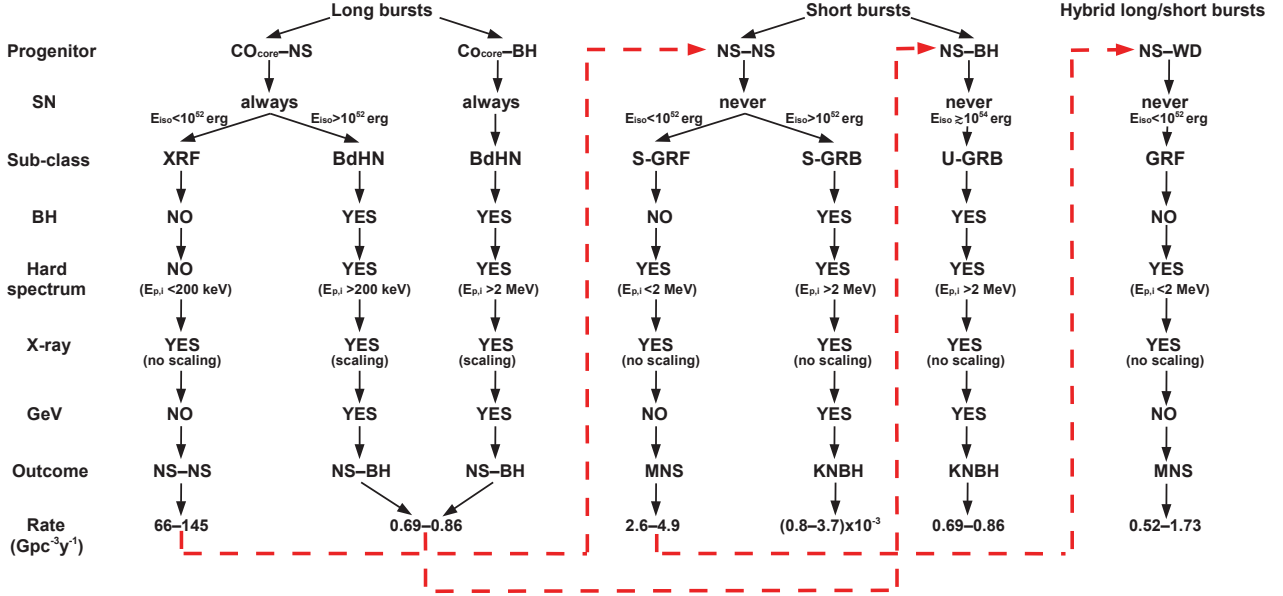


Figure 1. Summary of the properties of the burst sub-classes discussed in the Introduction. The red dashed lines indicate the evolutionary tracks linking out-states and in-states of some of the sub-classes. Additional details can be found in Ref. [42].

[10, 63]; in the case of an axially symmetric dyadotorus, the resulting P-GRB spectrum is a convolution of thermal spectra of different temperatures which resembles more a power-law spectral energy distribution with an exponential cutoff [64, 65].

After transparency, the accelerated baryons propagate through and interact in fully radiative regime with the CBM, giving rise to the prompt emission [7]. The structures observed in the prompt emission of a GRB depend on the CBM density n_{CBM} and its inhomogeneities [66–68]. In both long and short bursts the CBM clouds have similar masses (10^{22} – 10^{24} g), sizes ($\approx 10^{15}$ – 10^{16} cm), and typical distances from the BH ($\approx 10^{16}$ – 10^{17} cm) [10, 33]. The observed prompt emission spectrum results from the convolution of a large number of comoving spectra with decreasing temperatures and Lorentz and Doppler factors, due to each collision with the CBM, over the surfaces of constant arrival time for photons at the detector [69, 70] over the entire observation time.

To conclude, the evolution of an optically thick baryon-loaded pair plasma, is generally described in terms of $E_{e^+e^-}^{\text{tot}}$ and B and it is independent of the way the pair plasma is created. This general formalism can also be applied to any optically thick e^+e^- plasma, like the one created via $\nu\bar{\nu} \leftrightarrow e^+e^-$ mechanism in a NS merger as described in [17, 71, 72].

3 XRFs and BdHNe in the IGC paradigm

We here focus on the comparison between XRF and BdHN sub-classes within the IGC paradigm, giving a special attention to the latest theoretical results on the BdHNe.

In the IGC scenario, both XRFs and BdHNe originate in the hypercritical accretion process of the SN ejecta onto the NS binary companion. In this phenomenon pho-

tons are trapped in the accreting material and the accretion energy is lost through a large associated neutrino emission [39, 40, 73, 74]. In the XRFs, the CO_{core}-NS binary is widely separated ($a \gtrsim 10^{11}$ cm), thus the accretion rate $< 10^{-2} M_{\odot} \text{ s}^{-1}$ can only push the binary companion NS to become a MNS. The resulting emission, dubbed *Episode 1*, lasts $\sim 10^2$ – 10^4 s. Its spectrum is characterized by: 1) a thermal component spectrum with temperatures in the range of 0.1–2 keV and corresponding radii of 10^{10} – 10^{12} cm (see figure 2, left-panel), possibly originating from the outflow within the NS atmosphere driven out by Rayleigh-Taylor convection instabilities [40], and 2) a power-law component, possibly related to the excess of angular momentum of the system which necessarily leads to a jetted emission [41]. The long lasting X-ray emission does not exhibit any specific common late power-law behavior (see figure 2, right panel) and can be explained by the emission of the SN ejecta shocked by the hypercritical accretion emission of the XRF. This energy injection into the SN ejecta leads to the occurrence of a broad-lined SN Ic [75] with a kinetic energy larger than that of the traditional SNe Ic [42]. The absence of GeV emissions is implicit in the nature of the hypercritical accretion process not leading to a BH. Of course, all XRFs at redshift $z \lesssim 1$ exhibit an optical SN with a luminosity similar to the one of SN 1998bw [76], which occurs after 10–15 days in the source cosmological rest-frame.

In the IGC paradigm, the shorter the CO_{core}-NS binary period, the larger the accretion rate and the values of E_{iso} and $E_{p,i}$, and correspondingly the shorter the prompt emission duration [41]. Indeed, in BdHNe the CO_{core}-NS binary is more tightly bound ($a \lesssim 10^{11}$ cm) and the accretion rates of the SN ejecta can be $\gtrsim 10^{-2}$ – $10^{-1} M_{\odot} \text{ s}^{-1}$, leading the companion NS to collapse to a BH [40, 41]. For

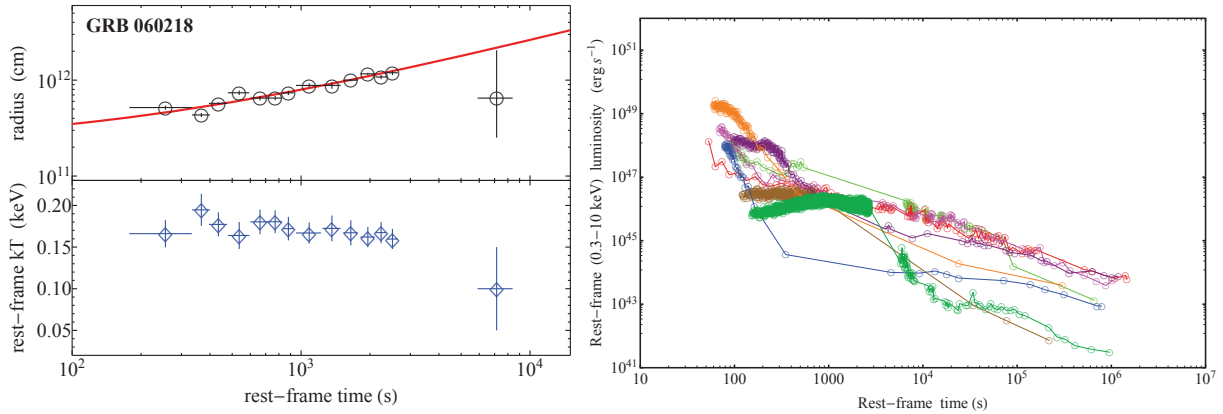


Figure 2. Left panel: the evolution of the radius of the thermal component detected in GRB 060218 (black circles) and its linear fit (solid red curve) and of the corresponding rest-frame temperature (blue diamonds). Reproduced from Ref. [77]. Right panel: rest-frame X-ray 0.3–10 keV luminosity light curves of selected XRFs: 050416A (red), 060218 (dark green), 070419A (orange), 081007 (magenta), 100316D (brown), 101219B (purple), and 130831A (green).

this reason BdHNe exhibit a more complex structure than XRFs composed of distinct Episodes.

- *Episode 1* in BdHNe, like in the case of XRFs, also originates in the hypercritical accretion process. The corresponding spectrum again exhibits: 1) an expanding thermal component with a decreasing temperature, typical radii of 10^9 – 10^{10} cm and an average expansion speed of $\sim 10^8$ – 10^9 cm s $^{-1}$ (see figure 3 (a)), and b) a power-law function [33, 34, 78].
- *Episode 2* corresponds to the γ -ray prompt emission of an authentic long GRB (see figure 3 (b)), stemming from the collapse of the companion NS to a BH and leading to the vacuum polarization process and the creation of an e^+e^- plasma. The analysis of the P-GRB emission indicates that BdHNe have a baryon load of $B \approx 10^{-4}$ – 10^{-2} and at transparency they reach a Lorentz factor of $\Gamma = 10^2$ – 10^3 . The prompt emission is produced by the interaction of the fireshell with the CBM clouds located at $\sim 10^{16}$ – 10^{17} cm from the burst site with average number density of ~ 1 cm $^{-3}$ [33, 78].
- *Episode 3* occurs after the prompt emission in the X-rays. It composed of a steep decay characterized by the presence of an early X-ray flare, a plateau and a late power-law decay which we refer as to the afterglow. These three components are dubbed flare-plateau-afterglow (FPA) phase [79]. During the early X-ray flare phase (typically at a rest-frame time of $\sim 10^2$ s) an expanding thermal component has been observed in its spectrum [9, 47, 79]. The inferred radii are typically $\sim 10^{12}$ – 10^{13} cm and they expand at mildly relativistic speed with $\Gamma \lesssim 4$ [9, 47, 78, 79]. The size of the corresponding emitting region is clearly incompatible with the radii inferred from Episodes 1 and 2. When computed in the source cosmological rest-frame, the plateau and the late power-law decay exhibit new features (see figure 3 (c)): 1) the overlapping of the afterglow phases, which have typical slopes of $-1.7 \lesssim \alpha \lesssim -1.3$ and show a characteristic common power-law behavior [46]; the nested property, which shows that the duration (the lu-

minosity) of the plateau phase is inversely (directly) proportional to the energy of the GRB emission, i.e., the more energetic the source, the smaller (higher) the duration (the luminosity) of the plateau [47]. The use of the overlapping of the afterglows as a distance indicator has been explored by inferring the redshifts of GRB 101023 [34], and has been applied to predict the occurrence of the SN associated to GRB 130427A before its discovery [80], later confirmed by the observations [81–84]. In the IGC scenario, the FPA originates from the SN ejecta [9, 79]. In BdHNe the SN ejecta experiences an energy injection from GRB emission leading to the occurrence of a broad-lined SN Ic [75] with a kinetic energy larger than that of the traditional SNe Ic. This energy injection results in an isotropic energy emission of 10^{51} – 10^{52} erg for the FPA phase. In particular, the X-ray flare can be modeled by considering the impact of the GRB on the SN ejecta and the propagation of the optically thick e^+e^- plasma into a medium largely baryon-contaminated ($B \approx 10$ – 10^2). A numerical integration starting at 10^{10} cm all the way to 10^{12} cm, where the transparency is reached, gives a perfect agreement between the radius of the emitter at transparency and the observations, as well a coincidence of the observed time of the peak emission of the flare [79]. The plateau and the afterglow phases are still under study (M. Karlica et al., in preparation).

- *Episode 4* corresponds to the optical SN emission observable in all BdHNe at $z \lesssim 1$ after ≈ 10 – 15 days in the cosmological rest-frame. All these SNe have a standard luminosity similar to the one of SN 1998bw [76].
- *Episode 5* is identified with the distinctive long-lived GeV emission, observed in the majority of BdHNe when within the LAT field of view. Though this emission follows a precise power-law behavior with index ≈ -1.2 [42, 85] (see figure 3 (d)), this emission is conceptually distinct in its underlying physical process from that of Episode 3: it originates, in facts, in the further accretion of matter onto the newly-formed BH and it is ob-

servable only after the transparency emission, i.e., the P-GRB [42].

4 The S-GRBs in the NS–NS merger paradigm

In Section 1 we discussed the rates of S-GRFs and S-GRBs, showing that S-GRFs are the most frequent events among the short bursts. This result is also in good agreement with the NS–NS binaries observed within our Galaxy: only a subset of them has a total mass larger than the NS critical mass $M_{\text{crit}}^{\text{NS}}$ and can form a BH in their merging process [10] if we assume that $M_{\text{crit}}^{\text{NS}} = 2.67M_{\odot}$ for a non-rotating, globally neutral NS within the NL3 nuclear model [87]. In this light S-GRBs are very important for inferring constraints on $M_{\text{crit}}^{\text{NS}}$, on the NS equation of state, and on the minimum mass of the newly-formed BH.

To date, within the fireshell model we have analyzed five authentic S-GRBs: 090227B [63], 140619B [10], GRB 090510 [64], 081024B and 140402A [65]. The analyses of the P-GRB emission and the correlation between the spikes of the prompt emission and CBM inhomogeneities gave the most successful test for the fireshell model. S-GRBs share some remarkable analogies but also some differences with BdHNe in view of the simplicity of the underlying physical system of S-GRBs, which unlike the BdHNe, do not exhibit any of the extremely complex activities related to the SN (see Section 3).

- *Episode 1* here is related to the NS–NS merger activity before the gravitational collapse into a BH and possibly corresponds to faint precursors observed in some short bursts [64, 88]. Because of the compactness of the systems this process at times is not observable.
- *Episode 2* corresponds to the GRB emission from the NS–NS merger. Within the fireshell model it is composed of the P-GRB, which occur before the onset of the GeV emission, and the prompt emission (see figure 4, left panel). From the analysis of their P-GRB emission, all S-GRBs have a standard values of the baryon load ($B \approx 5 \times 10^{-5}$), which is consistent with the crustal masses of NS–NS mergers [10, 89], and of the Lorentz factors at the transparency $\Gamma \approx 10^4$ [10, 63–65]. From the fit of the prompt emission (see figure 4, right panel), it came out that S-GRBs occur in a standard CBM with average density $\langle n_{\text{CBM}} \rangle \approx 10^{-5} \text{ cm}^{-3}$ [10, 63–65], which is typical of galactic halos where NS–NS mergers migrate, owing to natal kicks imparted to the binaries at birth [22].
- *Episode 3*, which corresponds to the traditional X-ray afterglow, differs from that of BdHNe which results from the interaction between the GRB and the SN ejecta. Work on this topic is still ongoing.
- *Episode 4*, identified with the optical emission of a SN, is here missing.
- *Episode 5* coincides with the GeV emission turning on soon after the P-GRB and being coeval with the prompt emission. With the exception of GRB 090227B, which was outside the nominal *Fermi*-LAT field of view [86],

all S-GRBs consistently exhibit this emission, which appears to be strictly correlated to that observed in the BdHNe. Since the presence of a BH is the only commonality between BdHNe and S-GRBs, by analogy we assume that the GeV emission originate from the activity of the newly-born BH produced in the merger [10]. The rest-frame 0.1–100 GeV luminosity light curves of all S-GRBs with LAT data follow a common power-law behavior with the rest-frame time which goes as $t^{-1.29 \pm 0.06}$ (see dashed black line in figure 5).

Table 1 lists the redshift, $E_{p,i}$, E_{iso} (in the rest-frame energy band 1–10000 keV), and the GeV isotropic emission energy E_{LAT} (in the rest-frame energy band 0.1–100 GeV) of all S-GRBs. The values of E_{LAT} represent lower limits to the actual GeV isotropic emission energies, since at late times the observations of GeV emission could be prevented due to instrumental threshold of the LAT. Using the maximum GeV photon observed energy $E_{\text{GeV}}^{\text{max}}$ listed in table 1, we derive a lower limit on the Lorentz factor of the GeV emission $\Gamma_{\text{GeV}}^{\text{min}}$ by requiring the optically thin condition to the high energy photons [90]. For each S-GRB we estimate lower limits in each time interval of the GeV luminosity light curves in figure 5. Then, $\Gamma_{\text{GeV}}^{\text{min}}$ for each S-GRB has been then determined as the largest among the inferred lower limits. It follows that the GeV emission is produced by an ultrarelativistic outflows with $\Gamma_{\text{GeV}}^{\text{min}} \gtrsim 300$ (see table 1).

We propose that the GeV emission in S-GRBs is produced by accretion onto the new-born BH of a certain amount of mass that remains bound to it because of the conservation of energy and angular momentum from the merger moment to the BH birth [64]. Lower limits on the amount of accreted mass can be attained by considering the accretion process onto a maximally rotating Kerr BH. Depending whether the infalling material is in co- or counter-rotating orbit with the spinning BH, the maximum efficiency of the conversion of gravitational energy into radiation is $\eta_+ = 42.3\%$ or $\eta_- = 3.8\%$, respectively [91] and, therefore, E_{LAT} can be expressed as

$$E_{\text{LAT}} = f_b^{-1} \eta_{\pm} M_{\text{acc}}^{\eta_{\pm}} c^2, \quad (1)$$

where f_b is the beaming factor which depends on the geometry of the GeV emission, and $M_{\text{acc}}^{\eta_{\pm}}$ is the amount of accreted mass depending on the choice of the efficiency. The observational evidence that the totality of S-GRBs exhibit GeV emission and that its absence is due instrumental absence of alignment between the LAT and the source at the time of the GRB emission suggest no significant beaming. Therefore, in the following we set $f_b \equiv 1$. The corresponding estimates of $M_{\text{acc}}^{\eta_{\pm}}$ in our sample of S-GRBs are listed in table 1.

5 Conclusions

Remarkable progresses in the understanding of GRBs have been made possible thanks to the great amount X- and γ -rays and high energy data and to a deeper theoretical understanding of WD [92], NS [87, 89] and BH [93], leading to a new paradigm purporting the role of binary systems as progenitors of GRBs: CO_{core}–NS binaries for long

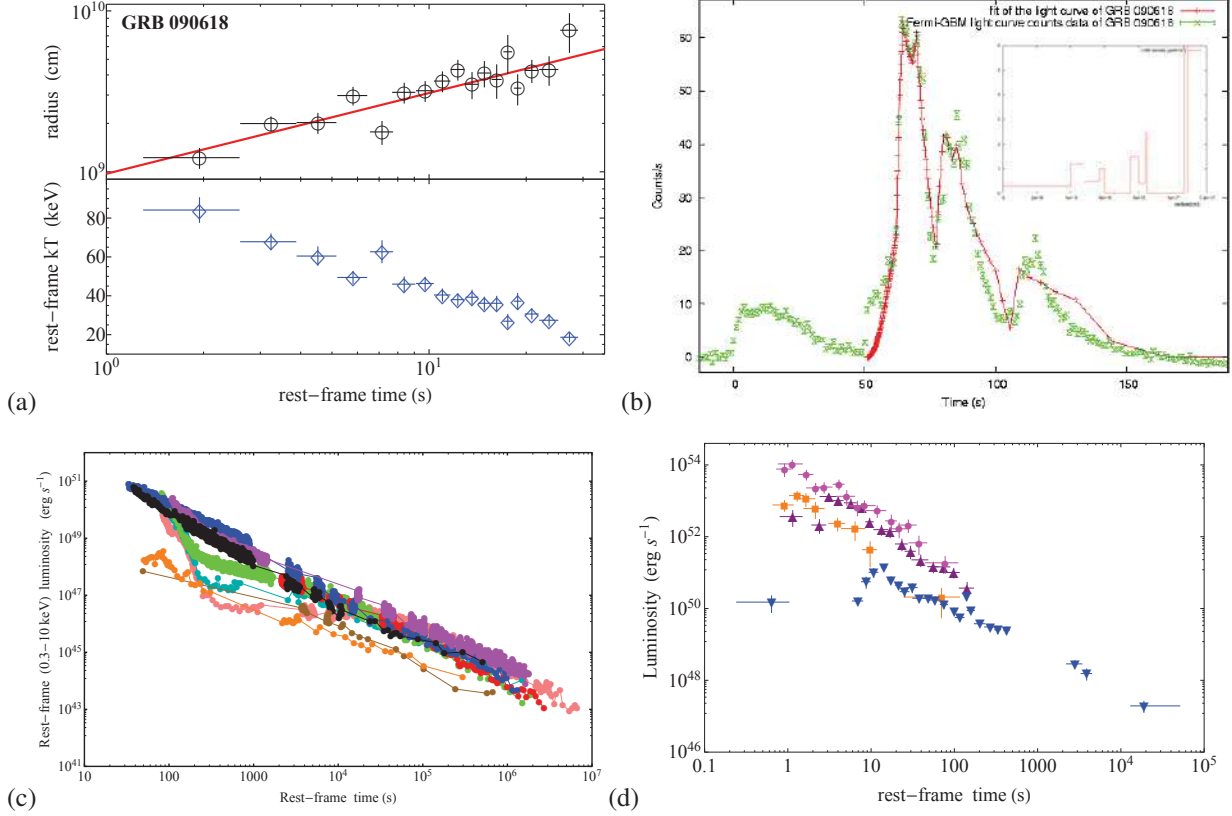


Figure 3. (a) The evolution of the radius of the thermal component detected in the Episode 1 of GRB 090618 (black circles) and its linear fit (solid red curve), and the decay of the corresponding rest-frame temperature (blue diamonds). (b) The fireshell simulation (red line) of the light curve of Episode 2 of the prototype GRB 090618 (green data). The small inset reproduces the CBM profile required for the simulation. Reproduced from Ref. [33]. (c) The rest-frame 0.3–10 keV luminosity light curves of selected BdHNe: 050525 (brown), 060729 (pink), 061007 (black), 080319B (blue), 090618 (green), 091127 (red), 100816A (orange), 111228A (light blue), and 130427A (purple) [79]. (d) The rest-frame 0.1–100 GeV luminosity light curves [86] of selected BdHNe: GRB 080916C (magenta circles), GRB 090902B (purple triangles), GRB 110731A (orange squares), GRB 130427A (blue reversed triangles).

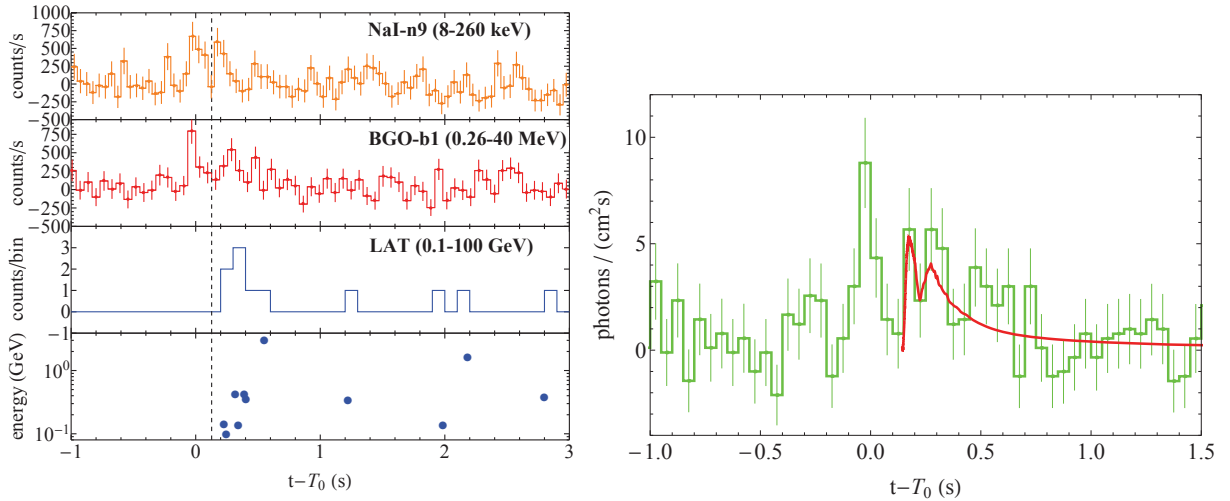


Figure 4. Left panel: background subtracted 50 ms binned data from the NaI-n9 (8–260 keV, top panel) and BGO-b1 (0.26–40 MeV, second panel) detectors, the 100 ms binned high energy data (0.1–100 GeV, third panel), and the high energy photons detected by the *Fermi*-LAT (bottom panel) for the S-GRB 081024B; the vertical dashed line marks the on-set of the LAT light curve. Right panel: the NaI-n9 light curve of the prompt emission of the S-GRB 081024B (green data) and the simulation within the fireshell model (red curve). All plots are reproduced from Ref. [65].

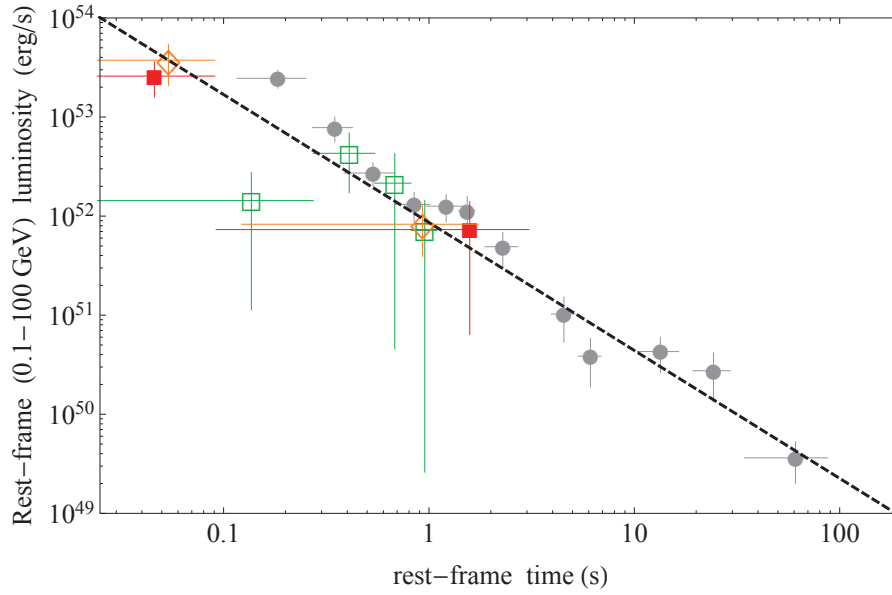


Figure 5. The rest-frame 0.1–100 GeV isotropic luminosities of the S-GRBs: 081024B (orange empty diamonds), 090510 (gray filled circles), 140402A (red filled squares), and 140619B (green empty squares). All the light curves start after the P-GRB emission. The dashed black line marks the common behavior of all the S-GRB light curves which goes as $t^{-1.29\pm0.06}$. Reproduced from Ref. [65].

GRB	z	$E_{p,i}$ (MeV)	E_{iso} (10^{52} erg)	E_{GeV}^{max} (GeV)	Γ_{GeV}^{min}	E_{LAT} (10^{52} erg)	$M_{acc}^{\eta+}$ (M_{\odot})	$M_{acc}^{\eta-}$ (M_{\odot})
081024B	3.12 ± 1.82	9.56 ± 4.94	2.64 ± 1.00	3	$\gtrsim 779$	$\gtrsim 2.79 \pm 0.98$	$\gtrsim 0.04$	$\gtrsim 0.41$
090227B	1.61 ± 0.14	5.89 ± 0.30	28.3 ± 1.5	—	—	—	—	—
090510	0.903 ± 0.003	7.89 ± 0.76	3.95 ± 0.21	31	$\gtrsim 551$	$\gtrsim 5.78 \pm 0.60$	$\gtrsim 0.08$	$\gtrsim 0.86$
140402A	5.52 ± 0.93	6.1 ± 1.6	4.7 ± 1.1	3.7	$\gtrsim 354$	$\gtrsim 4.5 \pm 2.2$	$\gtrsim 0.06$	$\gtrsim 0.66$
140619B	2.67 ± 0.37	5.34 ± 0.79	6.03 ± 0.79	24	$\gtrsim 471$	$\gtrsim 2.34 \pm 0.91$	$\gtrsim 0.03$	$\gtrsim 0.35$

Table 1. S-GRB properties: z , $E_{p,i}$, the maximum GeV photon observed energy E_{GeV}^{max} , the minimum Lorentz factor of the GeV emission Γ_{GeV}^{min} , E_{iso} , E_{LAT} , and the amount of infalling accreting mass co-rotating (counter-rotating) with the BH $M_{acc}^{\eta+}$ ($M_{acc}^{\eta-}$), needed to explaining E_{LAT} .

bursts within the IGC paradigm [6, 38–40], and NS–NS (or NS–BH) binaries for short bursts, as widely accepted and confirmed by strong observational and theoretical evidences [12–22]. These paradigms have led to the classification of GRBs in seven different sub-classes (see figure 1). We here focus our attention on the sub-classes of XRFS, BdHNe, S-GRFs and S-GRBs.

In Section 2, we review the fireshell model for GRBs [6–8] and its essential role in order to disentangle the various emission episodes characterizing each of the above sub-classes.

In Section 3, we summarize the commonalities and the differences between the observational properties of XRFs and BdHNe and provide their theoretical interpretation within the IGC paradigm, namely, whether or not the hypercritical accretion process leads to the formation of a BH.

In Section 4, we outline the properties S-GRFs and S-GRBs originating in NS–NS mergers leading to a MNS and the formation of a BH, respectively. Then, we focus on S-GRBs and on the key role of the P-GRB identification for their description, as well as the analysis of

the GeV emission. We finally discuss in details the GeV emission uniquely observed in both BdHNe and S-GRBs, when within the Fermi-LAT FoV. In both cases it starts after the P-GRB emission and it is coeval with the occurrence of the prompt emission [42]. Moreover, the rest-frame 0.1–100 GeV luminosities in BdHNe and S-GRBs share a common luminosity pattern, a precise power-law behavior with time $\propto t^{-1.2}$ [9, 10, 42, 65, 85]. These commonalities, in such different systems, as well as their energy requirements are naturally explained if we assume that the GeV emission originates by accretion processes in the newly-born BH [9, 10]. In all the identified S-GRBs, within the Fermi-LAT FoV, GeV photons are always observed [42, 64]. This implies that no intrinsic beaming is necessary to explain the S-GRB GeV emission. Within the hypothesis of isotropic emission, in the case of S-GRBs we point out how the total energy of the GeV emission can be attained from the gravitational binding energy of mass accretion of $M \gtrsim 0.03\text{--}0.08M_{\odot}$ or $M \gtrsim 0.35\text{--}0.86M_{\odot}$ for co- or counter-rotating orbits with a maximally rotating BH, respectively (see table 1). A lower limit on the Lorentz factor of the GeV emission of $\Gamma_{GeV}^{min} \gtrsim 300$ can be obtained

by requiring the optically thin condition to the high energy photons [90].

From the above consideration and the proposed classification scheme some considerations follow.

- The knowledge of the separatrix energy of 10^{52} erg, which discriminates between systems forming or not BHs and on which our classification scheme of GRBs is based, represents an observational constraints on the value of the NS critical mass M_{crit} , certainly in the range of $2.2\text{--}2.7 M_{\odot}$ for a non-rotating NS depending on the equations of state [87], and the minimum mass of a BH. This value is consistent and can be derived in BdHNe by considering the hypercritical accretion process onto a NS leading to an energy release in form of neutrinos and photons, given by the gain of gravitational potential energy of the matter accreted in the NS. This includes the change of binding energy of the NS while accreting both matter and angular momentum [42].
- Most noteworthy, the existence of a precise common power-law behavior in the rest-frame $0.1\text{--}100$ GeV luminosities of S-GRBs (see figure 5), following the BH formation, points to a commonality in the mass and spin of the newly-formed BH. This result is explainable with the expected mass of the merging NSs, each one of mass $M \approx 1.3\text{--}1.5 M_{\odot}$ [94], and the above expected range of the non-rotating NS critical mass, leading to a standard value of the BH mass and of its Kerr parameter [10].
- Finally, we discuss the gravitational wave (GW) detectability by advanced LIGO (aLIGO) from S-GRBs. We have already shown that binaries in which each NS has a mass $M_{\text{NS}} = 1.34 M_{\odot} = 0.5 M_{\text{crit}}^{\text{NS}}$ produce GW signals which are well below the signal to noise ratio $S/N = 8$ needed for a positive detection by aLIGO: a positive GW detection may occur only for sources located at $z \lesssim 0.14$ for the aLIGO 2022+ run, a redshift well above that of GRB 090510, to date the closest S-GRB located at $z = 0.903$ [10, 95, 96].

M. M. and J. A. R. acknowledge the partial support of the project N 3101/GF4 IPC-11, and the target program F.0679 0073-6/PTsF of the Ministry of Education and Science of the Republic of Kazakhstan.

References

- [1] E.P. Mazets, S.V. Golenetskii, V.N. Ilinskii, V.N. Panov, R.L. Aptekar, I.A. Gurian, M.P. Proskura, I.A. Sokolov, Z.I. Sokolova, T.V. Kharitonova, *Astrophysics and Space Science* **80**, 3 (1981)
- [2] J.P. Dezalay, C. Barat, R. Talon, R. Syunyaev, O. Terekhov, A. Kuznetsov, *Short cosmic events - A subset of classical GRBs?*, in *American Institute of Physics Conference Series*, edited by W. S. Paciesas & G. J. Fishman (1992), Vol. 265 of *American Institute of Physics Conference Series*, pp. 304–309
- [3] R.W. Klebesadel, *The durations of gamma-ray bursts*, in *Gamma-Ray Bursts - Observations, Analyses and Theories*, edited by C. Ho, R.I. Epstein, E.E. Fenimore (Cambridge University Press, 1992), pp. 161–168
- [4] C. Kouveliotou, C.A. Meegan, G.J. Fishman, N.P. Bhat, M.S. Briggs, T.M. Koshut, W.S. Paciesas, G.N. Pendleton, *ApJ Letters* **413**, L101 (1993)
- [5] M. Tavani, *ApJ Letters* **497**, L21 (1998), [arXiv:astro-ph/9802192](https://arxiv.org/abs/astro-ph/9802192)
- [6] R. Ruffini, C.L. Bianco, F. Fraschetti, S.S. Xue, P. Chardonnet, *ApJ Letters* **555**, L117 (2001), [arXiv:astro-ph/0106534](https://arxiv.org/abs/astro-ph/0106534)
- [7] R. Ruffini, C.L. Bianco, F. Fraschetti, S.S. Xue, P. Chardonnet, *ApJ Letters* **555**, L113 (2001), [arXiv:astro-ph/0106532](https://arxiv.org/abs/astro-ph/0106532)
- [8] R. Ruffini, C.L. Bianco, F. Fraschetti, S.S. Xue, P. Chardonnet, *ApJ Letters* **555**, L107 (2001), [arXiv:astro-ph/0106531](https://arxiv.org/abs/astro-ph/0106531)
- [9] R. Ruffini, Y. Wang, M. Enderli, M. Muccino, M. Kovacevic, C.L. Bianco, A.V. Penacchioni, G.B. Pisani, J.A. Rueda, *ApJ* **798**, 10 (2015), 1405.5723
- [10] R. Ruffini, M. Muccino, M. Kovacevic, F.G. Oliveira, J.A. Rueda, C.L. Bianco, M. Enderli, A.V. Penacchioni, G.B. Pisani, Y. Wang et al., *ApJ* **808**, 190 (2015), 1412.1018
- [11] R. Ruffini, J.A. Rueda, M. Muccino, G.B. Pisani, Y. Wang, L.M. Becerra, M. Kovacevic, F.G. Oliveira, Y. Aimuratov, C.L. Bianco et al., *ArXiv e-prints* (2016), 1602.02732
- [12] J. Goodman, *ApJ Letters* **308**, L47 (1986)
- [13] B. Paczynski, *ApJ Letters* **308**, L43 (1986)
- [14] D. Eichler, M. Livio, T. Piran, D.N. Schramm, *Nature* **340**, 126 (1989)
- [15] R. Narayan, T. Piran, A. Shemi, *ApJ Letters* **379**, L17 (1991)
- [16] P. Meszaros, M.J. Rees, *ApJ Letters* **482**, L29 (1997), [astro-ph/9609065](https://arxiv.org/abs/astro-ph/9609065)
- [17] S. Rosswog, E. Ramirez-Ruiz, M.B. Davies, *MNRAS* **345**, 1077 (2003), [astro-ph/0110180](https://arxiv.org/abs/astro-ph/0110180)
- [18] W.H. Lee, E. Ramirez-Ruiz, D. Page, *ApJ Letters* **608**, L5 (2004), [astro-ph/0404566](https://arxiv.org/abs/astro-ph/0404566)
- [19] E. Nakar, *Physics Reports* **442**, 166 (2007), [astro-ph/0701748](https://arxiv.org/abs/astro-ph/0701748)
- [20] A. Endrizzi, R. Ciolfi, B. Giacomazzo, W. Kastaun, T. Kawamura, *ArXiv e-prints* (2016), 1604.03445
- [21] M. Ruiz, R.N. Lang, V. Paschalidis, S.L. Shapiro, *ApJ Letters* **824**, L6 (2016), 1604.02455
- [22] E. Berger, *Annual Review of A&A* **52**, 43 (2014), 1311.2603
- [23] K.C. Sahu, M. Livio, L. Petro, F.D. Macchetto, J. van Paradijs, C. Kouveliotou, G.J. Fishman, C.A. Meegan, P.J. Groot, T. Galama, *Nature* **387**, 476 (1997), [arXiv:astro-ph/9705184](https://arxiv.org/abs/astro-ph/9705184)
- [24] J. van Paradijs, P.J. Groot, T. Galama, C. Kouveliotou, R.G. Strom, J. Telting, R.G.M. Rutten, G.J. Fishman, C.A. Meegan, M. Pettini et al., *Nature* **386**, 686 (1997)
- [25] J.S. Bloom, J.X. Prochaska, D. Pooley, C.H. Blake, R.J. Foley, S. Jha, E. Ramirez-Ruiz, J. Granot, A.V. Filippenko, S. Sigurdsson et al., *ApJ* **638**, 354 (2006), [arXiv:astro-ph/0505480](https://arxiv.org/abs/astro-ph/0505480)

- [26] E. Troja, A.R. King, P.T. O'Brien, N. Lyons, G. Cusumano, *MNRAS* **385**, L10 (2008), 0711.3034
- [27] W. Fong, E. Berger, D.B. Fox, *ApJ* **708**, 9 (2010), 0909.1804
- [28] E. Berger, *New Astron. Rev.* **55**, 1 (2011), 1005.1068
- [29] D. Kopač, P. D'Avanzo, A. Melandri, S. Campana, A. Gomboc, J. Japelj, M.G. Bernardini, S. Covino, S.D. Vergani, R. Salvaterra et al., *MNRAS* **424**, 2392 (2012), 1203.1864
- [30] S.E. Woosley, J.S. Bloom, *Annual Review of A&A* **44**, 507 (2006), astro-ph/0609142
- [31] A.S. Fruchter, A.J. Levan, L. Strolger, P.M. Vreeswijk, S.E. Thorsett, D. Bersier, I. Burud, J.M. Castro Cerón, A.J. Castro-Tirado, C. Conselice et al., *Nature* **441**, 463 (2006), arXiv:astro-ph/0603537
- [32] K.M. Svensson, A.J. Levan, N.R. Tanvir, A.S. Fruchter, L.G. Strolger, *MNRAS* **405**, 57 (2010), 1001.5042
- [33] L. Izzo, R. Ruffini, A.V. Penacchioni, C.L. Bianco, L. Caito, S.K. Chakrabarti, J.A. Rueda, A. Nandi, B. Patricelli, *A&A* **543**, A10 (2012), 1202.4374
- [34] A.V. Penacchioni, R. Ruffini, L. Izzo, M. Muccino, C.L. Bianco, L. Caito, B. Patricelli, L. Amati, *A&A* **538**, A58 (2012), 1112.2970
- [35] N. Smith, *Annual Review of A&A* **52**, 487 (2014), 1402.1237
- [36] N. Smith, W. Li, A.V. Filippenko, R. Chornock, *MNRAS* **412**, 1522 (2011), 1006.3899
- [37] M. Della Valle, *International Journal of Modern Physics D* **20**, 1745 (2011)
- [38] R. Ruffini, M.G. Bernardini, C.L. Bianco, L. Caito, P. Chardonnet, M.G. Dainotti, R. Fraschetti, R. Guida, G. Vereshchagin, S. Xue, *The Role of GRB 031203 in Clarifying the Astrophysical GRB Scenario*, in *ESA Special Publication* (2007), Vol. 622 of *ESA Special Publication*, p. 561, 0705.2456
- [39] J.A. Rueda, R. Ruffini, *ApJ* **758**, L7 (2012)
- [40] C.L. Fryer, J.A. Rueda, R. Ruffini, *ApJ Letters* **793**, L36 (2014), 1409.1473
- [41] L. Becerra, F. Cipolletta, C.L. Fryer, J.A. Rueda, R. Ruffini, *ApJ* **812**, 100 (2015), 1505.07580
- [42] R. Ruffini, J.A. Rueda, M. Muccino, Y. Aimuratov, L.M. Becerra, C.L. Bianco, M. Kovacevic, R. Moradi, F.G. Oliveira, G.B. Pisani et al., *ApJ* **832**, 136 (2016), 1602.02732
- [43] J. Heise, *X-Ray Flashes and X-Ray Counterparts of Gamma-Ray Bursts*, in *Gamma-Ray Burst and Afterglow Astronomy 2001: A Workshop Celebrating the First Year of the HETE Mission*, edited by G.R. Ricker, R.K. Vanderspek (2003), Vol. 662 of *American Institute of Physics Conference Series*, pp. 229–236, astro-ph/0111246
- [44] L. Amati, F. Frontera, J.J.M. in't Zand, M. Capalbi, R. Landi, P. Soffitta, L. Vetere, L.A. Antonelli, E. Costa, S. Del Sordo et al., *A&A* **426**, 415 (2004), astro-ph/0407166
- [45] A.M. Soderberg, S.R. Kulkarni, E. Nakar, E. Berger, P.B. Cameron, D.B. Fox, D. Frail, A. Gal-Yam, R. Sari, S.B. Cenko et al., *Nature* **442**, 1014 (2006), astro-ph/0604389
- [46] G.B. Pisani, L. Izzo, R. Ruffini, C.L. Bianco, M. Muccino, A.V. Penacchioni, J.A. Rueda, Y. Wang, *A&A* **552**, L5 (2013), 1304.1764
- [47] R. Ruffini, M. Muccino, C.L. Bianco, M. Enderli, L. Izzo, M. Kovacevic, A.V. Penacchioni, G.B. Pisani, J.A. Rueda, Y. Wang, *A&A* **565**, L10 (2014), 1404.3946
- [48] C.L. Fryer, F.G. Oliveira, J.A. Rueda, R. Ruffini, *Physical Review Letters* **115**, 231102 (2015), 1505.02809
- [49] L. Becerra, C.L. Bianco, C.L. Fryer, J.A. Rueda, R. Ruffini, *ApJ* **833**, 107 (2016), 1606.02523
- [50] R. Giacconi, R. Ruffini, *Physics and astrophysics of neutron stars and black holes* (1978)
- [51] I.F. Mirabel, L.F. Rodríguez, *Nature* **392**, 673 (1998)
- [52] L. Caito, M.G. Bernardini, C.L. Bianco, M.G. Dainotti, R. Guida, R. Ruffini, *A&A* **498**, 501 (2009), 0810.4855
- [53] L. Caito, L. Amati, M.G. Bernardini, C.L. Bianco, G. de Barros, L. Izzo, B. Patricelli, R. Ruffini, *A&A* **521**, A80+ (2010), 1006.4842
- [54] M. Della Valle, G. Chincarini, N. Panagia, G. Tagliaferri, D. Malesani, V. Testa, D. Fugazza, S. Campana, S. Covino, V. Mangano et al., *Nature* **444**, 1050 (2006), arXiv:astro-ph/0608322
- [55] Z.P. Jin, X. Li, Z. Cano, S. Covino, Y.Z. Fan, D.M. Wei, *ApJ Letters* **811**, L22 (2015), 1507.07206
- [56] M. Cadelano, C. Pallanca, F.R. Ferraro, M. Salaris, E. Dalessandro, B. Lanzoni, P.C.C. Freire, *ApJ* **812**, 63 (2015), 1509.01397
- [57] T.M. Tauris, E.P.J. van den Heuvel, G.J. Savonije, *ApJ Letters* **530**, L93 (2000), astro-ph/0001013
- [58] P. Lazarus, T.M. Tauris, B. Knispel, P.C.C. Freire, J.S. Deneva, V.M. Kaspi, B. Allen, S. Bogdanov, S. Chatterjee, I.H. Stairs et al., *MNRAS* **437**, 1485 (2014), 1310.5857
- [59] R. Ruffini, J.D. Salmonson, J.R. Wilson, S.S. Xue, *A&A* **350**, 334 (1999), arXiv:astro-ph/9907030
- [60] R. Ruffini, J.D. Salmonson, J.R. Wilson, S. Xue, *A&A* **359**, 855 (2000), arXiv:astro-ph/0004257
- [61] A.G. Aksenov, R. Ruffini, G.V. Vereshchagin, *Physical Review Letters* **99**, 125003 (2007), 0707.3250
- [62] A.G. Aksenov, R. Ruffini, G.V. Vereshchagin, *Physical Review D* **79**, 043008 (2009), 0901.4837
- [63] M. Muccino, R. Ruffini, C.L. Bianco, L. Izzo, A.V. Penacchioni, *ApJ* **763**, 125 (2013), 1205.6600
- [64] R. Ruffini, M. Muccino, Y. Aimuratov, C.L. Bianco, C. Cherubini, M. Enderli, M. Kovacevic, R. Moradi, A.V. Penacchioni, G.B. Pisani et al., *ApJ* **831**, 178 (2016), 1607.02400
- [65] Y. Aimuratov, R. Ruffini, M. Muccino, C.L. Bianco, A.V. Penacchioni, G.B. Pisani, D. Primorac, J.A. Rueda, Y. Wang, *ApJ* **844**, 83 (2017), 1704.08179

- [66] R. Ruffini, C.L. Bianco, P. Chardonnet, F. Fraschetti, S. Xue, *ApJ Letters* **581**, L19 (2002), [arXiv:astro-ph/0210648](#)
- [67] R. Ruffini, C.L. Bianco, S.S. Xue, P. Chardonnet, F. Fraschetti, V. Gurzadyan, *International Journal of Modern Physics D* **13**, 843 (2004), [arXiv:astro-ph/0405284](#)
- [68] R. Ruffini, M.G. Bernardini, C.L. Bianco, P. Chardonnet, F. Fraschetti, V. Gurzadyan, L. Vitagliano, S.S. Xue, *The Blackholic energy: long and short Gamma-Ray Bursts (New perspectives in physics and astrophysics from the theoretical understanding of Gamma-Ray Bursts, II)*, in *XIth Brazilian School of Cosmology and Gravitation*, edited by M. Novello & S. E. Perez Bergliaffa (2005), Vol. 782 of *American Institute of Physics Conference Series*, p. 42, [arXiv:astro-ph/0503476](#)
- [69] C.L. Bianco, R. Ruffini, *ApJ Letters* **633**, L13 (2005), [arXiv:astro-ph/0509621](#)
- [70] C.L. Bianco, R. Ruffini, *ApJ Letters* **620**, L23 (2005), [arXiv:astro-ph/0501390](#)
- [71] R. Narayan, B. Paczynski, T. Piran, *ApJ Letters* **395**, L83 (1992), [arXiv:astro-ph/9204001](#)
- [72] J.D. Salmonson, J.R. Wilson, *ApJ* **578**, 310 (2002), [astro-ph/0203349](#)
- [73] Y.B. Zel'dovich, L.N. Ivanova, D.K. Nadezhin, *Soviet Astronomy* **16**, 209 (1972)
- [74] R. Ruffini, J. Wilson, *Physical Review Letters* **31**, 1362 (1973)
- [75] K. Maeda, K. Nomoto, *ApJ* **598**, 1163 (2003), [astro-ph/0304172](#)
- [76] T.J. Galama, P.M. Vreeswijk, J. van Paradijs et al., *Nature* **395**, 670 (1998)
- [77] S. Campana, V. Mangano, A.J. Blustin, P. Brown, D.N. Burrows, G. Chincarini, J.R. Cummings, G. Cusumano, M. Della Valle, D. Malesani et al., *Nature* **442**, 1008 (2006), [arXiv:astro-ph/0603279](#)
- [78] R. Ruffini, *Black Holes, Supernovae and Gamma Ray Bursts*, in *Thirteenth Marcel Grossmann Meeting: On Recent Developments in Theoretical and Experimental General Relativity, Astrophysics and Relativistic Field Theories*, edited by K. Rosquist (2015), pp. 242–314
- [79] R. Ruffini, Y. Wang, Y. Aimuratov, L. Becerra, C.L. Bianco, M. Karlica, M. Kovacevic, L. Li, J.D. Melon Fuksman, R. Moradi et al., *ArXiv e-prints* (2017), [1704.03821](#)
- [80] R. Ruffini, C.L. Bianco, M. Enderli, M. Muccino, A.V. Penacchioni, G.B. Pisani, J.A. Rueda, N. Sahakyan, Y. Wang, L. Izzo, *GRB Coordinates Network* **14526**, 1 (2013)
- [81] A. de Ugarte Postigo, D. Xu, G. Leloudas, T. Kruehler, D. Malesani, J. Gorosabel, C.C. Thöne, R. Sanchez-Ramirez, S. Schulze, J.P. Fynbo et al., *GRB Coordinates Network* **14646**, 1 (2013)
- [82] A.J. Levan, A.S. Fruchter, J. Graham, N.R. Tanvir, J. Hjorth, J. Fynbo, D. Perley, S.B. Cenko, E. Pian, Z. Cano et al., *GRB Coordinates Network* **14686**, 1 (2013)
- [83] A.M. Watson, N. Butler, A. Kutyrev, W.H. Lee, M.G. Richer, C. Klein, O. Fox, J.X. Prochaska, J. Bloom, A. Cucchiara et al., *GRB Coordinates Network* **14666**, 1 (2013)
- [84] D. Xu, A. de Ugarte Postigo, T. Kruehler, D. Malesani, G. Leloudas, J.P.U. Fynbo, J. Hjorth, S. Schulze, P. Jakobsson, Z. Cano et al., *GRB Coordinates Network* **14597**, 1 (2013)
- [85] L. Nava, G. Vianello, N. Omodei, G. Ghisellini, G. Ghirlanda, A. Celotti, F. Longo, R. Desiante, R. Barniol Duran, *MNRAS* **443**, 3578 (2014), [1406.6693](#)
- [86] M. Ackermann, M. Ajello, K. Asano, M. Axelson, L. Baldini, J. Ballet, G. Barbiellini, D. Bastieri, K. Bechtol, R. Bellazzini et al., *ApJ Supplement* **209**, 11 (2013), [1303.2908](#)
- [87] F. Cipolletta, C. Cherubini, S. Filippi, J.A. Rueda, R. Ruffini, *Physical Review D* **92**, 023007 (2015), [1506.05926](#)
- [88] E. Troja, S. Rosswog, N. Gehrels, *ApJ* **723**, 1711 (2010), [1009.1385](#)
- [89] R. Belvedere, J.A. Rueda, R. Ruffini, *Journal of Korean Physical Society* **65**, 897 (2014)
- [90] Y. Lithwick, R. Sari, *ApJ* **555**, 540 (2001)
- [91] L.D. Landau, E.M. Lifshitz, *The classical theory of fields* (Course of theoretical physics - Pergamon International Library of Science, Technology, Engineering and Social Studies, Oxford: Pergamon Press, 4th rev.engl.ed., 1975)
- [92] K. Boshkayev, J.A. Rueda, R. Ruffini, I. Siutsou, *ApJ* **762**, 117 (2013), [1204.2070](#)
- [93] R. Ruffini, G. Vereshchagin, S. Xue, *Physics Reports* **487**, 1 (2010), [0910.0974](#)
- [94] F. Özel, P. Freire, *Annual Review of A&A* **54**, 401 (2016), [1603.02698](#)
- [95] F.G. Oliveira, J.A. Rueda, R. Ruffini, *ApJ* **787**, 150 (2014)
- [96] R. Ruffini, J. Rodriguez, M. Muccino, J.A. Rueda, Y. Aimuratov, U. Barres de Almeida, L. Becerra, C.L. Bianco, C. Cherubini, S. Filippi et al., *ArXiv e-prints* (2016), [1602.03545](#)

The binary progenitors of short and long GRBs and their gravitational-wave emission

J. A. Rueda^{1,2,3,*}, R. Ruffini^{1,2,3,4}, J. F. Rodriguez^{1,2}, M. Muccino^{1,2}, Y. Aimuratov^{1,2}, U. Barres de Almeida³, L. Becerra^{1,2}, C. L. Bianco^{1,2}, C. Cherubini^{5,6}, S. Filippi^{5,6}, M. Kovacevic^{1,2}, R. Moradi^{1,2}, G. B. Pisani^{1,2}, and Y. Wang^{1,2}

¹ *Dipartimento di Fisica and ICRA, Sapienza Università di Roma, P.le Aldo Moro 5, I-00185 Rome, Italy*

² *ICRANet, P.zza della Repubblica 10, I-65122 Pescara, Italy*

³ *ICRANet-Rio, Centro Brasileiro de Pesquisas Físicas, Rua Dr. Xavier Sigaud 150, 22290-180 Rio de Janeiro, Brazil*

⁴ *Université de Nice Sophia Antipolis, CEDEX 2, Grand Château Parc Valrose, Nice,*

⁵ *Unit of Nonlinear Physics and Mathematical Modeling, Università Campus Bio-Medico di Roma, Via A. del Portillo 21, I-00128 Rome, Italy*

⁶ *ICRA, Università Campus Bio-Medico di Roma, Via A. del Portillo 21, I-00128 Rome, Italy*

Abstract. We have sub-classified short and long-duration gamma-ray bursts (GRBs) into seven families according to the binary nature of their progenitors. Short GRBs are produced in mergers of neutron-star binaries (NS-NS) or neutron star-black hole binaries (NS-BH). Long GRBs are produced via the induced gravitational collapse (IGC) scenario occurring in a tight binary system composed of a carbon-oxygen core (CO_{core}) and a NS companion. The CO_{core} explodes as type Ic supernova (SN) leading to a hypercritical accretion process onto the NS: if the accretion is sufficiently high the NS reaches the critical mass and collapses forming a BH, otherwise a massive NS is formed. Therefore long GRBs can lead either to NS-BH or to NS-NS binaries depending on the entity of the accretion. We discuss for the above compact-object binaries: 1) the role of the NS structure and the nuclear equation of state; 2) the occurrence rates obtained from X and gamma-rays observations; 3) the predicted annual number of detections by the Advanced LIGO interferometer of their gravitational-wave emission.

1 Introduction

There has been a traditional phenomenological classification of gamma-ray bursts (GRBs) based on the observed prompt duration, T_{90} : long GRBs for $T_{90} > 2$ s and short GRBs for $T_{90} < 2$ s [1–5]. Progress has been made in the meantime in the understanding of the nature of both long and short GRBs leading to a physical, instead of empirical, classification of GRBs based on the progenitor systems [6–8].

*e-mail: jorge.rueda@icra.it

1.1 Long GRBs

In the case of long GRBs we stand on the induced gravitational collapse (IGC) scenario that introduces as their progenitors short-period binaries composed of a carbon-oxygen core (CO_{core}) with a NS companion [9–15]. The core-collapse of the CO_{core} , which forms a NS as central remnant (hereafter νNS), leads also to a SN explosion that triggers a massive, hypercritical accretion process onto the NS companion. The parameters of the *in-state*, i.e. of the CO_{core} -NS binary, lead to two sub-classes of long GRBs with corresponding *out-states* [6]:

- *X-ray flashes (XRFs)*. Long bursts with $E_{\text{iso}} \lesssim 10^{52}$ erg are produced by CO_{core} -NS binaries with relatively large binary separations ($a \gtrsim 10^{11}$ cm). The accretion rate of the SN ejecta onto the NS in these systems is not high enough to bring the NS mass to the critical value M_{crit} , hence no BH is formed. The out-state of this GRB sub-class can be either a νNS -NS binary if the system keeps bound after the SN explosion, or two runaway NSs if the binary system is disrupted.
- *Binary driven hypernovae (BdHNe)*. Long bursts with $E_{\text{iso}} \gtrsim 10^{52}$ erg are instead produced by more compact CO_{core} -NS binaries ($a \lesssim 10^{11}$ cm, see e.g., Refs. [13, 15]). In this case the SN triggers a larger accretion rate onto the NS companion, e.g. $\gtrsim 10^{-2}$ – $10^{-1} M_{\odot} \text{ s}^{-1}$, bringing the NS to its critical mass M_{crit} , [11–13] namely to the point of gravitational collapse with consequent formation of a BH. Remarkably, in Ref. [14] it was recently shown that the large majority of BdHNe leads naturally to NS-BH binaries owing to the high compactness of the binary that avoids the disruption of it even in cases of very high mass loss exceeding 50% of the total mass of the initial CO_{core} -NS binary.

In addition, it exists the possibility of *BH-SNe*. [6] Long burst with $E_{\text{iso}} \gtrsim 10^{54}$ erg occurring in close CO_{core} -BH binaries in which the hypercritical accretion produces, as *out-states*, a more massive BH and a νNS . These systems have been considered in Ref. [6] as a subset of the BdHNe but no specific example have been yet observationally identified.

1.2 Short GRBs

There is the consensus within the GRB community that the progenitors of short GRBs are mergers of NS-NS and/or NS-BH binaries (see, e.g., Refs. [16–19], and Ref. [20], for a recent review). Similarly to the case of long GRBs, in Ref. [6] short GRBs have been split into different sub-classes:

- *Short gamma-ray flashes (S-GRFs)*. Short bursts with energies $E_{\text{iso}} \lesssim 10^{52}$ erg, produced when the post-merger core do not surpass the NS critical mass M_{crit} , hence there is no BH formation. Thus these systems left as byproduct a massive NS and possibly, due to the energy and angular momentum conservation, orbiting material in a disk-like structure or a low-mass binary companion.
- *Authentic short gamma-ray bursts (S-GRBs)*. Short bursts with $E_{\text{iso}} \gtrsim 10^{52}$ erg, produced when the post-merger core reaches or overcome M_{crit} , hence forming a Kerr or Kerr-Newman BH, [8] and also in this case possibly orbiting material.
- *Ultra-short GRBs (U-GRBs)*. A new sub-class of short bursts originating from νNS -BH merging binaries. They can originate from BdHNe (see Ref. [14]) or from BH-SNe.

In addition, it exists the possibility of *gamma-ray flashes (GRFs)*. These are bursts with hybrid properties between short and long, they have $10^{51} \lesssim E_{\text{iso}} \lesssim 10^{52}$ erg. This sub-class of sources originates in NS-WD mergers. [6]

We focus here on the physical properties of the above progenitors, as well as on the main properties of NSs that play a relevant role in the dynamics of these systems and that lead to the above different GRB sub-classes. We shall discuss as well recent estimates of the rates of occurrence on all the above

subclasses based on X and gamma-ray observations, and also elaborate on the possibility of detecting the gravitational wave (GW) emission originated in these systems.

2 IGC, Hypercritical Accretion, and Long GRBs

We turn now to the details of the accretion process within the IGC scenario. Realistic simulations of the IGC process were performed in Ref. [12], including: 1) detailed SN explosions of the CO_{core} ; 2) the hydrodynamic details of the hypercritical accretion process; 3) the evolution of the SN ejecta material entering the Bondi-Hoyle region all the way up to its incorporation into the NS. Here the concept of hypercritical accretion refers to the fact the accretion rates are highly super-Eddington. The accretion process in the IGC scenario is allowed to exceed the Eddington limit mainly for two reasons: i) the photons are trapped within the infalling material impeding them to transfer momentum; ii) the accreting material creates a very hot NS atmosphere ($T \sim 10^{10}$ K) that triggers a very efficient neutrino emission which become the main energy sink of these systems unlike photons.

The hypercritical accretion process in the above simulations was computed within a spherically symmetric approximation. A further step was given in Ref. [13] by estimating the angular momentum that the SN ejecta carries and transfer to the NS via accretion, and how it affects the evolution and fate of the system. The calculations are as follows: first the accretion rate onto the NS is computed adopting an homologous expansion of the SN ejecta and introducing the pre-SN density profile of the CO_{core} envelope from numerical simulations. Then, it is estimated the angular momentum that the SN material might transfer to the NS: it comes out that the ejecta have enough angular momentum to circularize for a short time and form a disc around the NS. Finally, the evolution of the NS central density and rotation angular velocity (spin-up) is followed computing the equilibrium configurations from the numerical solution of the axisymmetric Einstein equations in full rotation, until the critical point of collapse of the NS to a BH taking into due account the equilibrium limits given by mass-shedding and the secular axisymmetric instability.

Now we enter into the details of each of the above steps. The accretion rate of the SN ejecta onto the NS can be estimated via the Bondi-Hoyle-Lyttleton accretion formula:

$$\dot{M}_B(t) = \pi \rho_{\text{ej}} R_{\text{cap}}^2 \sqrt{v_{\text{rel}}^2 + c_{\text{s, ej}}^2}, \quad R_{\text{cap}}(t) = \frac{2GM_{\text{NS}}(t)}{v_{\text{rel}}^2 + c_{\text{s, ej}}^2}, \quad (1)$$

where G is the gravitational constant, ρ_{ej} and $c_{\text{s, ej}}$ are the density and sound speed of the SN ejecta, R_{cap} is the NS gravitational capture radius (Bondi-Hoyle radius), M_{NS} , the NS mass, and v_{rel} the ejecta velocity relative to the NS: $\vec{v}_{\text{rel}} = \vec{v}_{\text{orb}} - \vec{v}_{\text{ej}}$, with $|\vec{v}_{\text{orb}}| = \sqrt{G(M_{\text{core}} + M_{\text{NS}})/a}$, the module of the NS orbital velocity around the CO_{core} , and \vec{v}_{ej} the velocity of the supernova ejecta (see Fig. 1).

Extrapolating the results for the accretion process from stellar wind accretion in binary systems, the angular momentum per unit time that crosses the NS capture region can be approximated by: $\dot{L}_{\text{cap}} = (\pi/2) (\epsilon_p/2 - 3\epsilon_v) \rho_{\text{ej}}(a, t) v_{\text{rel}}^2(a, t) R_{\text{cap}}^4(a, t)$, where ϵ_p and ϵ_v are parameters measuring the inhomogeneity of the flow (see Ref. [13] for details).

In order to simulate the hypercritical accretion it is adopted an homologous expansion of the SN ejecta, i.e. the ejecta velocity evolves as $v_{\text{ej}}(r, t) = nr/t$, where r is the position of every ejecta layer from the SN center and n is called expansion parameter. The ejecta density is given by $\rho_{\text{ej}}(r, t) = \rho_{\text{ej}}^0(r/R_{\text{star}}(t), t_0) \frac{M_{\text{env}}(t)}{M_{\text{env}}(0)} \left(\frac{R_{\text{star}}(0)}{R_{\text{star}}(t)} \right)^3$, where $M_{\text{env}}(t)$ the mass of the CO_{core} envelope, namely the mass of the ejected material in the SN explosion and available to be accreted by the NS, $R_{\text{star}}(t)$ is the position of the outermost layer of the ejected material, and ρ_{ej}^0 is the pre-SN density profile. The latter can be approximated with a power law: $\rho_{\text{ej}}(r, t_0) = \rho_{\text{core}}(R_{\text{core}}/r)^m$, where ρ_{core} , R_{core} and m are the profile parameters which are fixed by fitting the pre-SN profiles obtained from numerical simulations.

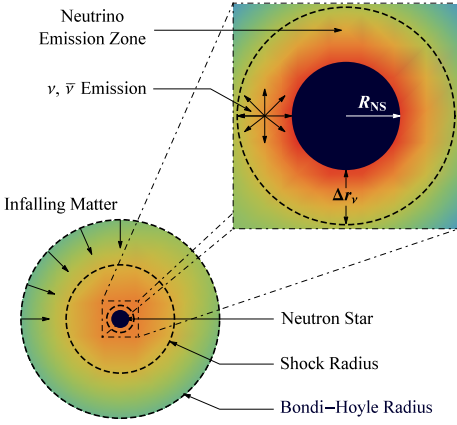


Figure 1. Scheme of the IGC scenario: the CO_{core} undergoes SN explosion, the NS accretes part of the SN ejecta and then reaches the critical mass for gravitational collapse to a BH, with consequent emission of a GRB. The SN ejecta reach the NS Bondi-Hoyle radius and fall toward the NS surface. The material shocks and decelerates as it piles over the NS surface. At the neutrino emission zone, neutrinos take away most of the infalling matter gravitational energy gain. The neutrinos are emitted above the NS surface in a region of thickness Δr_v about half the NS radius that allow the material to reduce its entropy to be finally incorporated to the NS. The image is not to scale. For further details and numerical simulations of the above process see Refs. [12, 13, 15].

For the typical parameters of pre-SN CO_{core} and assuming a velocity of the outermost SN layer $v_{\text{sn}}(R_{\text{star}}, t_0) \sim 10^9 \text{ cm s}^{-1}$ and a free expansion $n = 1$ (for details of typical initial conditions of the binary system see Refs. [12] and [13]), Eq. (1) gives accretion rates around the order of $10^{-4} - 10^{-2} M_{\odot} \text{ s}^{-1}$, and an angular momentum per unit time crossing the capture region $\dot{L}_{\text{cap}} \sim 10^{46} - 10^{49} \text{ g cm}^2 \text{ s}^{-2}$.

We consider the NS companion of the CO_{core} initially as non-rotating, thus at the beginning the NS exterior spacetime is described by the Schwarzschild metric. The SN ejecta approach the NS with specific angular momentum, $l_{\text{acc}} = \dot{L}_{\text{cap}}/\dot{M}_B$, thus they will circularize at a radius r_{st} if they have enough angular momentum. What does the word “enough” means here? The last stable circular orbit (LSO) around a non-rotating NS is located at a distance $r_{\text{iso}} = 6GM_{\text{NS}}/c^2$ and has an angular momentum per unit mass $l_{\text{iso}} = 2\sqrt{3}GM_{\text{NS}}/c$. The radius r_{iso} is larger than the NS radius for masses larger than $1.67 M_{\odot}$, $1.71 M_{\odot}$, and $1.78 M_{\odot}$ for the GM1, TM1, and NL3 nuclear equation of state (EOS).[13] If $l_{\text{acc}} \geq l_{\text{iso}}$ the material circularizes around the NS at locations $r_{\text{st}} \geq r_{\text{iso}}$. For the values of the IGC systems under discussion here, $r_{\text{st}}/r_{\text{iso}} \sim 10 - 10^3$, thus the SN ejecta have enough angular momentum to form a sort of disc around the NS. Even in this case, the viscous forces and other angular momentum losses that act on the disk will allow the matter in the disk to reach the inner boundary at $r_{\text{in}} \sim r_{\text{iso}}$, to then be accreted by the NS.

Within this picture, the NS accretes the material from r_{in} and the NS mass and angular angular momentum evolve as:

$$\dot{M}_{\text{NS}} = \left(\frac{\partial M_{\text{NS}}}{\partial M_b} \right)_{J_{\text{NS}}} \dot{M}_b + \left(\frac{\partial M_{\text{NS}}}{\partial J_{\text{NS}}} \right)_{M_b} \dot{J}_{\text{NS}}, \quad \dot{J}_{\text{NS}} = \xi l(r_{\text{in}}) \dot{M}_B, \quad (2)$$

where M_b is the NS baryonic mass, $l(r_{\text{in}})$ is the specific angular momentum of the accreted material at r_{in} , which corresponds to the angular momentum of the LSO, and $\xi \leq 1$ is a parameter that measures the efficiency of angular momentum transfer. We assume in our simulations $\dot{M}_b = \dot{M}_B$. The baryonic and gravitational mass are related by [21]:

$$\frac{M_b}{M_{\odot}} = \frac{M_{\text{NS}}}{M_{\odot}} + \frac{13}{200} \left(\frac{M_{\text{NS}}}{M_{\odot}} \right)^2 \left(1 - \frac{1}{137} j_{\text{NS}}^{1.7} \right), \quad (3)$$

where $j_{\text{NS}} \equiv cJ_{\text{NS}}/(GM_{\odot}^2)$. In addition, since the NS will spin up with accretion, we need information of the dependence of the specific angular momentum of the LSO as a function of both the NS mass

Table 1. Critical NS mass in the non-rotating case and constants k and p needed to compute the NS critical mass in the non-rotating case given by Eq. (5). The values are given for the NL3, GM1 and TM1 EOS.

EOS	$M_{\text{crit}}^{J=0} (M_{\odot})$	p	k
NL3	2.81	1.68	0.006
GM1	2.39	1.69	0.011
TM1	2.20	1.61	0.017

and angular momentum. For corotating orbits the following relation is valid for all the aforementioned EOS:[13]

$$l_{\text{iso}} = \frac{GM_{\text{NS}}}{c} \left[2\sqrt{3} - 0.37 \left(\frac{j_{\text{NS}}}{M_{\text{NS}}/M_{\odot}} \right)^{0.85} \right]. \quad (4)$$

The NS accretes mass until it reaches a region of instability. There are two main instability limits for rotating NSs: mass-shedding or Keplerian limit and the secular axisymmetric instability. The critical NS mass along the secular instability line is approximately given by:[21]

$$M_{\text{NS}}^{\text{crit}} = M_{\text{NS}}^{J=0} (1 + k j_{\text{NS}}^p), \quad (5)$$

where the parameters k and p depends of the nuclear EOS (see Table 1). These formulas fit the numerical results with a maximum error of 0.45%.

2.1 Most recent simulations of the IGC process

Additional details and improvements of the hypercritical accretion process leading to XRFs and BdHNe have been recently presented in Ref. [15]. In particular:

1. It was there improved the accretion rate estimate including the density profile finite size/thickness and additional CO_{core} progenitors leading to different SN ejecta masses were also considered.
2. It was shown in Ref. [13] the existence of a maximum orbital period, P_{max} , over which the accretion onto NS companion is not high enough to bring it to the critical mass for gravitational collapse to a BH. Therefore, CO_{core} -NS binaries with $P > P_{\text{max}}$ lead to XRFs while the ones with $P \lesssim P_{\text{max}}$ lead to BdHNe. In Ref. [15] the determination of P_{max} was extended to all the possible initial values of the mass of the NS companion and the angular momentum transfer efficiency parameter was also allowed to vary.
3. It was computed the expected luminosity during the hypercritical accretion process for a wide range of binary periods covering XRFs and BdHNe.
4. It was there shown that the presence of the NS companion originates large asymmetries (see, e.g., simulation in Fig. 2) in the SN ejecta leading to observable signatures in the X-rays.

Fig. 2 shows a simulation of an IGC process presented in Ref. [15]. We considered the effects of the gravitational field of the NS on the SN ejecta including the orbital motion as well as the changes in the NS gravitational mass owing to the accretion process via the Bondi formalism. The supernova matter was described as formed by point-like particles whose trajectory was computed by solving the Newtonian equation of motion. The initial conditions of the SN ejecta are computed assuming an homologous velocity distribution in free expansion. The initial power-law density profile of the CO

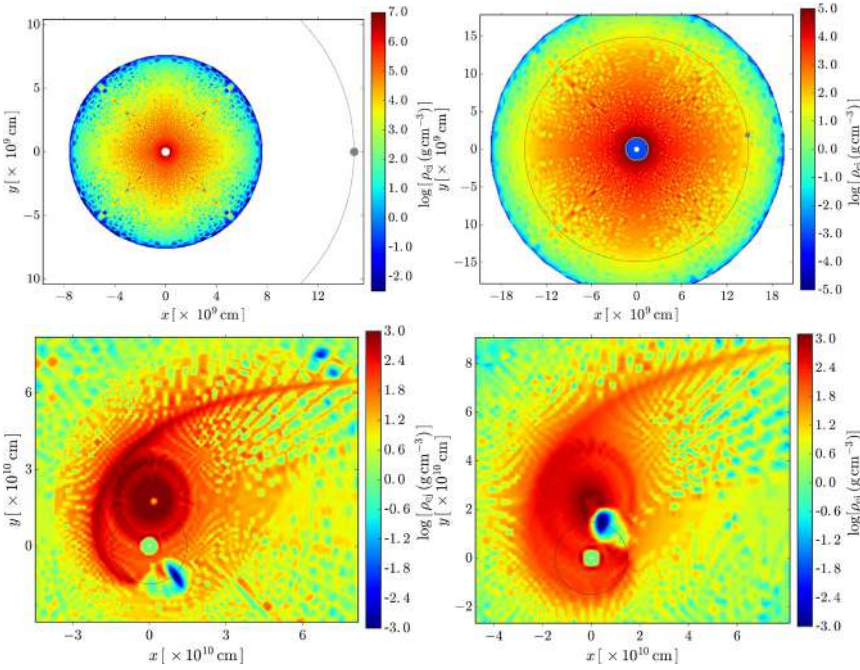


Figure 2. Hypercritical accretion process in the IGC binary system at selected evolution times. In this example the CO_{core} has a total mass of $9.44 M_{\odot}$ divided in an ejecta mass of $7.94 M_{\odot}$ and a νNS of $1.5 M_{\odot}$ formed by the collapsed high density core. The supernova ejecta evolve homologously with outermost layer velocity $v_{0,\text{star}} = 2 \times 10^9 \text{ cm s}^{-1}$. The NS binary companion has an initial mass of $2.0 M_{\odot}$. The binary period is $P \approx 5 \text{ min}$, which corresponds to a binary separation $a \approx 1.5 \times 10^{10} \text{ cm}$. The system of coordinates is centered on the νNS represented by the white-filled circle at $(0, 0)$. The NS binary companion, represented by the gray-filled circle, orbits counterclockwise following the thin-dashed circular trajectory. The colorbar indicates values of ejecta density in logarithmic scale. *Left upper panel:* initial time of the process. The supernova ejecta expand radially outward and the NS binary companion is at $(a, 0)$. *Right upper panel:* the accretion process starts when the first supernova layers reach the Bondi-Hoyle region. This happens at $t = t_{\text{acc},0} \approx a/v_{0,\text{star}} \approx 7.7 \text{ s}$. *Left lower panel:* the NS binary companion reaches the critical mass by accreting matter from the SN with consequent collapse to a BH. This happens at $t = t_{\text{coll}} \approx 254 \text{ s} \approx 0.85 P$. The newly-formed BH of mass $M_{\text{BH}} = M_{\text{crit}} \approx 3 M_{\odot}$ is represented by the black-filled circle. It is here evident the asymmetry of the supernova ejecta induced by the presence of the accreting NS companion at close distance. *Right lower panel:* $t = t_{\text{coll}} + 100 \text{ s} = 354 \text{ s} \approx 1.2 P$, namely 100 s after the BH formation. It appears here the new binary system composed of the νNS and the newly-formed BH.

envelope is simulated by populating the inner layers with more particles. For the $M_{\text{ZAMS}} = 30 M_{\odot}$ progenitor which gives a CO_{core} with envelope profile $\rho_{\text{ej}}^0 \approx 3.1 \times 10^8 (8.3 \times 10^7 / r)^{2.8} \text{ g cm}^{-3}$, we adopt for the simulation a total number of $N = 10^6$ particles. We assume that particles crossing the Bondi-Hoyle radius are captured and accreted by the NS so we removed them from the system as they reach that region. We removed these particles according to the results obtained from the numerical integration explained above. Fig. 2 shows the orbital plane of an IGC binary at selected times of its evolution. The NS has an initial mass of $2.0 M_{\odot}$; the CO_{core} leads to a total ejecta mass $7.94 M_{\odot}$ and a νNS of $1.5 M_{\odot}$. The orbital period of the binary is $P \approx 5 \text{ min}$, i.e. a binary separation $a \approx 1.5 \times 10^{10} \text{ cm}$. For these parameters the NS reaches the critical mass and collapses to form a BH.

2.2 Post-Explosion Orbits and Formation of NS-BH Binaries

We have seen how in BdHNe the accretion process can lead to BH formation in a time-interval as short as the orbital period. We here deepen this analysis to study the effect of the SN explosion in such a scenario following Ref. [14]. As the ejecta timescale becomes a fraction of the orbital one, the fate of the post-explosion binary is altered. For these models, we assumed tight binaries in circular orbit with an initial orbital separation of 7×10^9 cm. With CO_{core} radii of $1\text{--}4 \times 10^9$ cm, such a separation is small, but achievable. The binary consists of a CO_{core} and a $2.0 M_{\odot}$ NS companion. When the CO_{core} collapses, it forms a $1.5 M_{\odot}$ NS, ejecting the rest of the core. We then vary the ejecta mass and time required for most of the ejected matter to move out of the binary. Ref. [14] showed that even if 70% of the mass is lost from the system (in the $8 M_{\odot}$ ejecta case), the system remains bound as long as the explosion time is just above the orbital time ($T_{\text{orbit}} = 180$ s) with semi-major axes of less than 10^{11} cm.

The tight compact binaries produced in these explosions will emit GWs driving the system to merge. For typical massive star binaries, the merger time is many Myr. For BdHNe, the merger time is typically 10^4 yr, or less [14]. Since the merger should occur within the radius swept clean by the BdHN we expect a small baryonic contamination around the merger site which might lead to a new family of events which we term ultrashort GRBs, U-GRBs, to this new family of events.

3 NS-NS/NS-BH mergers and Short GRBs

Let us turn to short GRBs. We first proceed to estimate the mass and the angular momentum of the post-merger core via baryonic mass and angular momentum conservation of the system. We adopt for simplicity that non-rotating binary components. We first compute the total baryonic mass of the NS-NS binary $M_b = M_{b_1} + M_{b_2}$ using the relation between the gravitational mass M_i and the baryonic mass M_{b_i} ($i = 1, 2$) recently obtained in Ref. [21] and given in Eq. (3) assuming $j_{\text{NS}} = cJ_{\text{NS}}/(GM_{\odot}^2) = 0$. The post-merger core will have approximately the entire baryonic mass of the initial binary, i.e. $M_{b,\text{core}} \approx M_b$, since little mass is expected to be ejected during the coalescence process. However, the gravitational mass of the post-merger core cannot be estimated using again the above formula since, even assuming non-rotating binary components, the post-merger core will necessarily acquire a fraction $\eta \leq 1$ of the binary angular momentum at the merger point. One expects a value of η smaller than unity since, during the coalesce, angular momentum is loss e.g. by gravitational wave emission and it can be also redistributed e.g. into a surrounding disk.

To obtain the gravitational mass of the post-merger core, we can use again Eq. (3) relating the baryonic mass $M_{b,\text{NS}}$ and the gravitational mass M_{NS} in this case with $j_{\text{NS}} \neq 0$. The mass and angular momentum of the post-merger core, respectively M_{core} and J_{core} , are therefore obtained from baryon mass and angular momentum conservation, i.e.: $M_{\text{core}} = M_{\text{NS}}$, $M_{b,\text{core}} = M_{b,\text{NS}} = M_{b_1} + M_{b_2}$, $J_{\text{core}} = J_{\text{NS}} = \eta J_{\text{merger}}$, where J_{merger} is the system angular momentum at the merger point. The value of J_{merger} is approximately given by $J_{\text{merger}} = \mu r_{\text{merger}}^2 \Omega_{\text{merger}}$, where $\mu = M_1 M_2 / M$ is the binary reduced mass, $M = M_1 + M_2$ is the total binary mass, and r_{merger} and Ω_{merger} are the binary separation and angular velocity at the merger point. If we adopt the merger point where the two stars enter into contact we have $r_{\text{merger}} = R_1 + R_2$, where R_i is the radius (which depend on the EOS) of the i -component of the binary.

Given the parameters of the merging binary, the above equations lead to the merged core properties. For the sake of exemplifying, let us assume a mass-symmetric binary, $M_1 = M_2 = M/2$. In this case the above equations lead to the angular momentum of the merged core $J_{\text{core}} = (\eta/4)(GM^2/c)C^{-1/2}$, where $C \equiv GM_1/(c^2 R_1) = GM_2/(c^2 R_2)$ is the compactness of the merging binary components. Therefore, if we adopt $M_1 = 1.4 M_{\odot}$ and $C = 0.15$, $M_{\text{core}} = (2.61, 2.65) M_{\odot}$ for

$\eta = (0, 1)$, i.e. for a dimensionless angular momentum of the merged core $j_{\text{core}} = (0, 5.06)$. Whether or not these pairs $(M_{\text{core}}, j_{\text{core}})$ correspond to stable NSs depend on the nuclear EOS. A similar analysis can be done for any other pair of binary masses.

4 Detectability of GWs produced by the GRB progenitors

Having established the nature of the progenitors of each GRB sub-class, we turn now to briefly discuss the detectability of their associated GW emission. The minimum GW frequency detectable by the broadband aLIGO interferometer is $f_{\text{min}}^{\text{aLIGO}} \approx 10$ Hz.[35] Since during the binary inspiral the GW frequency is twice the orbital one, this implies that a binary enters the aLIGO band for orbital periods $P_{\text{orb}} \lesssim 0.2$ s. Thus, CO_{core}-NS binaries, *in-states* of XRFs and BdHNe, and CO_{core}-BH binaries, *in-states* of BH-SN, are not detectable by aLIGO since they have orbital periods $P_{\text{orb}} \gtrsim 5$ min $\gg 0.2$ s. Concerning their *out-states* after the corresponding hypercritical accretion processes, namely ν NS-NS, *out-states* of XRFs, and ν NS-BH, *out-states* of BdHNe and BH-SNe, they are not detectable by aLIGO at their birth but only when approaching the merger. Clearly, the analysis of the ν NS-NS mergers is included in the analysis of the S-GRFs and S-GRBs and, likewise, the merger of ν NS-BH binaries is included in the analysis of U-GRBs. In the case of NS-WD binaries the WD is tidally disrupted by the NS making their GW emission hard to be detected (see, e.g., Ref. [36]).

A coalescing binary evolves first through the *inspiral regime* to then pass over a *merger regime*, the latter composed by the plunge leading to the merger itself and by the ringdown (oscillations) of the newly formed object. During the inspiral regime the system evolves through quasi-circular orbits and is well described by the traditional point-like quadrupole approximation.[37–39] The GW frequency is twice the orbital frequency ($f_s = 2f_{\text{orb}}$) and grows monotonically. The energy spectrum during the inspiral regime is: $dE/df_s = (1/3)(\pi G)^{2/3} M_c^{5/3} f_s^{-1/3}$, where $M_c = \mu^{3/5} M^{2/5} = \nu^{3/5} M$ is the so-called *chirp mass* and $\nu \equiv \mu/M$ is the symmetric mass-ratio parameter. A symmetric binary ($m_1 = m_2$) corresponds to $\nu = 1/4$ and the test-particle limit is $\nu \rightarrow 0$. The GW spectrum of the merger regime is characterized by a GW burst.[40] Thus, one can estimate the contribution of this regime to the signal-to-noise ratio with the knowledge of the location of the GW burst in the frequency domain and of the energy content. The frequency range spanned by the GW burst is $\Delta f = f_{\text{qnm}} - f_{\text{merger}}$, where f_{merger} is the frequency at which the merger starts and f_{qnm} is the frequency of the ringing modes of the newly formed object after the merger, and the energy emitted is ΔE_{merger} . With these quantities defined, one can estimate the typical value of the merger regime spectrum as: $dE/df_s \approx \Delta E_{\text{merger}}/\Delta f$. Unfortunately, the frequencies and energy content of the merger regime of the above merging binaries are such that it is undetectable by LIGO.[41].

Since the GW signal is deep inside the detector noise, the signal-to-noise ratio (ρ) is usually estimated using the matched filter technique.[42] The exact position of the binary relative to the detector and the orientation of the binary rotation plane are usually unknown, thus it is a common practice to average over all the possible locations and orientations, i.e.: [42] $\langle \rho^2 \rangle = 4 \int_0^\infty \langle |\tilde{h}(f)|^2 \rangle / S_n(f) df = 4 \int_0^\infty h_c^2(f) / [f^2 S_n(f)] df$, where f is the GW frequency in the detector frame, $\tilde{h}(f)$ is the Fourier transform of $h(t)$, and $\sqrt{S_n(f)}$ is the one-sided amplitude spectral density of the detector noise, and $h_c(f)$ is the characteristic strain, $h_c = (1+z)/(\pi d_l) \sqrt{(1/10)(G/c^3)(dE/df_s)}$. We recall that in the detector frame the GW frequency is redshifted by a factor $1+z$ with respect to the one in the source frame, f_s , i.e. $f = f_s/(1+z)$ and d_l is the luminosity distance to the source. We adopt a Λ CDM cosmology with $H_0 = 71$ km s⁻¹ Mpc⁻¹, $\Omega_M = 0.27$ and $\Omega_\Lambda = 0.73$. [43]

A threshold $\rho_0 = 8$ in a single detector is adopted by LIGO.[44] This minimum ρ_0 defines a maximum detection distance or GW horizon distance, say d_{GW} , that corresponds to the most optimistic case when the binary is just above the detector and the binary plane is parallel to the detector plane.

In order to give an estimate the annual number of merging binaries associated with the above GRB sub-classes detectable by aLIGO we can use the lower and upper values of the aLIGO *search volume* defined by $\mathcal{V}_s = V_{\max}^{\text{GW}} \mathcal{T}$, where $V_{\max}^{\text{GW}} = (4\pi/3)\mathcal{R}^3$, where \mathcal{T} is the observing time and \mathcal{R} is the so-called *detector range* defined by $\mathcal{R} = \mathcal{F} d_{\text{GW}}$, with $\mathcal{F}^{-1} = 2.2627$ (see, Ref. [44, 45], for details). For a $(1.4+1.4) M_{\odot}$ NS binary and the three following different observational campaigns we have:[44] 2015/2016 (O1; $\mathcal{T} = 3$ months) $\mathcal{V}_s = (0.5-4) \times 10^5 \text{ Mpc}^3 \text{ yr}$, 2017/2018 (O3; $\mathcal{T} = 9$ months) $\mathcal{V}_s = (3-10) \times 10^6 \text{ Mpc}^3 \text{ yr}$, and the entire network including LIGO-India at design sensitivity (2022+; $\mathcal{T} = 1$ yr) $\mathcal{V}_s = 2 \times 10^7 \text{ Mpc}^3 \text{ yr}$. The maximum possible sensitivity reachable in 2022+ leads to $d_{\text{GW}} \approx 0.2 \text{ Gpc}$, hence $V_{\max}^{\text{GW}} \approx 0.033 \text{ Gpc}^3$, for such a binary. One can use this information for other binaries with different masses taking advantage of the fact that d_{GW} scales with the binary chirp mass as $M_c^{5/6}$. The expected GW detection rate by aLIGO can be thus estimated as: $\dot{N}_{\text{GW}} \equiv \rho_{\text{GRB}} V_{\max}^{\text{GRB}}$, where ρ_{GRB} is the inferred occurrence rate of GRBs computed in Ref. [6]. Bearing the above in mind it is easy to check that there is a low probability for aLIGO to detect the GW signals associated with the GRB binary progenitors: indeed in the best case of the 2022+ observing rung one obtains, respectively, ~ 1 detection every 3 and 5 yr for U-GRBs and S-GRFs.

References

- [1] E.P. Mazets, S.V. Golenetskii, V.N. Ilinskii, V.N. Panov, R.L. Aptekar, I.A. Gurian, M.P. Proskura, I.A. Sokolov, Z.I. Sokolova, T.V. Kharitonova, *Ap&SS***80**, 3 (1981)
- [2] R.W. Klebesadel, *The durations of gamma-ray bursts*, in *Gamma-Ray Bursts - Observations, Analyses and Theories*, edited by C. Ho, R.I. Epstein, E.E. Fenimore (Cambridge University Press, 1992), pp. 161–168
- [3] J.P. Dezalay, C. Barat, R. Talon, R. Syunyaev, O. Terekhov, A. Kuznetsov, *Short cosmic events - A subset of classical GRBs?*, in *American Institute of Physics Conference Series*, edited by W. S. Paciesas & G. J. Fishman (1992), Vol. 265 of *American Institute of Physics Conference Series*, pp. 304–309
- [4] C. Kouveliotou, C.A. Meegan, G.J. Fishman, N.P. Bhat, M.S. Briggs, T.M. Koshut, W.S. Paciesas, G.N. Pendleton, *ApJ***413**, L101 (1993)
- [5] M. Tavani, *ApJ***497**, L21 (1998), [arXiv:astro-ph/9802192](https://arxiv.org/abs/astro-ph/9802192)
- [6] R. Ruffini, J.A. Rueda, M. Muccino, Y. Aimuratov, L.M. Becerra, C.L. Bianco, M. Kovacevic, R. Moradi, F.G. Oliveira, G.B. Pisani et al., *ApJ***832**, 136 (2016), [1602.02732](https://arxiv.org/abs/1602.02732)
- [7] R. Ruffini, Y. Wang, M. Enderli, M. Muccino, M. Kovacevic, C.L. Bianco, A.V. Penacchioni, G.B. Pisani, J.A. Rueda, *ApJ***798**, 10 (2015), [1405.5723](https://arxiv.org/abs/1405.5723)
- [8] R. Ruffini, M. Muccino, M. Kovacevic, F.G. Oliveira, J.A. Rueda, C.L. Bianco, M. Enderli, A.V. Penacchioni, G.B. Pisani, Y. Wang et al., *ApJ***808**, 190 (2015), [1412.1018](https://arxiv.org/abs/1412.1018)
- [9] R. Ruffini, M.G. Bernardini, C.L. Bianco, L. Vitagliano, S.S. Xue, P. Chardonnet, F. Fraschetti, V. Gurzadyan, *Black Hole Physics and Astrophysics: The GRB-Supernova Connection and URCA-1 - URCA-2*, in *The Tenth Marcel Grossmann Meeting*, edited by M. Novello, S. Perez Bergliaffa, R. Ruffini (Singapore: World Scientific, 2006), p. 369, [astro-ph/0503475](https://arxiv.org/abs/astro-ph/0503475)
- [10] L. Izzo, J.A. Rueda, R. Ruffini, *A&A***548**, L5 (2012), [1206.2887](https://arxiv.org/abs/1206.2887)
- [11] J.A. Rueda, R. Ruffini, *ApJ***758**, L7 (2012), [1206.1684](https://arxiv.org/abs/1206.1684)
- [12] C.L. Fryer, J.A. Rueda, R. Ruffini, *ApJ***793**, L36 (2014), [1409.1473](https://arxiv.org/abs/1409.1473)
- [13] L. Becerra, F. Cipolletta, C.L. Fryer, J.A. Rueda, R. Ruffini, *ApJ***812**, 100 (2015), [1505.07580](https://arxiv.org/abs/1505.07580)
- [14] C.L. Fryer, F.G. Oliveira, J.A. Rueda, R. Ruffini, *Physical Review Letters* **115**, 231102 (2015), [1505.02809](https://arxiv.org/abs/1505.02809)
- [15] L. Becerra, C.L. Bianco, C.L. Fryer, J.A. Rueda, R. Ruffini, *ApJ***833**, 107 (2016), [1606.02523](https://arxiv.org/abs/1606.02523)

- [16] J. Goodman, *ApJ***308**, L47 (1986)
- [17] B. Paczynski, *ApJ***308**, L43 (1986)
- [18] D. Eichler, M. Livio, T. Piran, D.N. Schramm, *Nature***340**, 126 (1989)
- [19] R. Narayan, T. Piran, A. Shemi, *ApJ***379**, L17 (1991)
- [20] E. Berger, *ARAA***52**, 43 (2014), 1311.2603
- [21] F. Cipolletta, C. Cherubini, S. Filippi, J.A. Rueda, R. Ruffini, *Phys. Rev. D***92**, 023007 (2015), 1506.05926
- [22] C.L. Fryer, W. Benz, M. Herant, *ApJ***460**, 801 (1996), [astro-ph/9509144](#)
- [23] R.A. Chevalier, *ApJ***346**, 847 (1989)
- [24] Y.B. Zel'dovich, L.N. Ivanova, D.K. Nadezhin, *Soviet Astronomy* **16**, 209 (1972)
- [25] R. Ruffini, J. Wilson, *Physical Review Letters* **31**, 1362 (1973)
- [26] C.L. Fryer, F. Herwig, A. Hungerford, F.X. Timmes, *ApJ***646**, L131 (2006), [astro-ph/0606450](#)
- [27] C.L. Fryer, *ApJ***699**, 409 (2009), 0711.0551
- [28] L. Izzo, R. Ruffini, A.V. Penacchioni, C.L. Bianco, L. Caito, S.K. Chakrabarti, J.A. Rueda, A. Nandi, B. Patricelli, *A&A***543**, A10 (2012)
- [29] N.R. Tanvir, A.J. Levan, A.S. Fruchter, J. Hjorth, R.A. Hounsell, K. Wiersema, R.L. Tunnicliffe, *Nature***500**, 547 (2013), 1306.4971
- [30] N.R. Sibgatullin, R.A. Sunyaev, *Astronomy Letters* **26**, 772 (2000), [astro-ph/0011344](#)
- [31] C.L. Fryer, S.E. Woosley, D.H. Hartmann, *ApJ***526**, 152 (1999), [astro-ph/9904122](#)
- [32] M. Dominik, K. Belczynski, C. Fryer, D.E. Holz, E. Berti, T. Bulik, I. Mandel, R. O'Shaughnessy, *ApJ***759**, 52 (2012), 1202.4901
- [33] K.A. Postnov, L.R. Yungelson, *Living Reviews in Relativity* **17**, 3 (2014), 1403.4754
- [34] J.G. Hills, *ApJ***267**, 322 (1983)
- [35] LIGO Scientific Collaboration, J. Aasi, B.P. Abbott, R. Abbott, T. Abbott, M.R. Abernathy, K. Ackley, C. Adams, T. Adams, P. Addesso et al., *Classical and Quantum Gravity* **32**, 074001 (2015), 1411.4547
- [36] V. Paschalidis, M. MacLeod, T.W. Baumgarte, S.L. Shapiro, *Phys. Rev. D***80**, 024006 (2009)
- [37] P.C. Peters, J. Mathews, *Phys. Rev.* **131**, 435 (1963)
- [38] P.C. Peters, *Phys. Rev.* **136**, 1224 (1964)
- [39] M. Rees, R. Ruffini, J.A. Wheeler, *Black holes, gravitational waves and cosmology* (Gordon and Breach Science Publishers Inc., New York, 1974)
- [40] M. Davis, R. Ruffini, W.H. Press, R.H. Price, *Phys. Rev. Lett.* **27**, 1466 (1971)
- [41] R. Ruffini, J. Rodriguez, M. Muccino, J.A. Rueda, Y. Aimuratov, U. Barres de Almeida, L. Becerra, C.L. Bianco, C. Cherubini, S. Filippi et al., *ArXiv:1602.03545* (2016), 1602.03545
- [42] É.É. Flanagan, S.A. Hughes, *Phys. Rev. D***57**, 4535 (1998), [gr-qc/9701039](#)
- [43] M. Rigault, G. Aldering, M. Kowalski, Y. Copin, P. Antilogus, C. Aragon, S. Bailey, C. Baltay, D. Baugh, S. Bongard et al., *ApJ***802**, 20 (2015), 1412.6501
- [44] B.P. Abbott, R. Abbott, T.D. Abbott, M.R. Abernathy, F. Acernese, K. Ackley, C. Adams, T. Adams, P. Addesso, R.X. Adhikari et al., *Living Reviews in Relativity* **19** (2016), 1304.0670
- [45] L.S. Finn, D.F. Chernoff, *Phys. Rev. D***47**, 2198 (1993)

GRB 140619B: a short GRB from a neutron star merger leading to the black hole formation

Marco Muccino^{*,†ab} Remo Ruffini,^{abcd} Milos Kovacevic,^{ac} Luca Izzo,^{ab} Fernanda G. Oliveira,^{ac} Jorge A. Rueda,^{abd} Carlo L. Bianco,^{ab} Maxime Enderli,^{ac} Ana V. Penacchioni,^{de} Giovanni B. Pisani,^{ab} Yu Wang^{ab} and Elena Zaninoni^d.

^aDip. di Fisica, Sapienza Università di Roma, Piazzale Aldo Moro 5, I-00185 Rome, Italy.

^bICRANet, Piazza della Repubblica 10, I-65122 Pescara, Italy.

^cUniversité de Nice Sophia Antipolis, CEDEX 2, Grand Château Parc Valrose, Nice, France.

^dICRANet-Rio, CBPF, Rua Dr. Xavier Sigaud 150, Rio de Janeiro, RJ, 22290-180, Brazil.

^eINPE, Av. dos Astronautas, 1758, São José dos Campos, SP, 12227-010, Brazil.

E-mail: marco.muccino@icra.it

We propose a classification into two families for short GRBs, both originating from the merging of binary neutron stars (NSs): family-1 with $E_{iso} < 10^{52}$ erg, leading to a very massive NS and representing the large majority of the observed short bursts, and family-2 with $E_{iso} > 10^{52}$ erg, leading to a black hole (BH). Following the prototype GRB 090227B, we present here a new example of family-2 short burst: GRB 140619B. From the spectral analysis of the early ~ 0.2 s, we infer an observed temperature of the e^+e^- -plasma at transparency $kT = (324 \pm 33)$ keV, a theoretically derived redshift $z = 2.67 \pm 0.37$, a total burst energy $E_{e^+e^-}^{tot} = (6.03 \pm 0.79) \times 10^{52}$ erg, and a baryon load $B = (5.52 \pm 0.73) \times 10^{-5}$. We also estimate the corresponding emission of gravitational waves. The presence of the observed high energy emission ($\gtrsim 0.1$ GeV) is consistent with the accretion of $\approx 16\%$ of the NS–NS crustal masses onto the newly-formed BH. Depending on the amount of the total angular momentum of the merger, marked differences exist in the nature of the afterglows of these two families of short bursts. We also assert that both the families fulfill the recently proposed $E_{p,i}-E_{iso}$ relation for short GRBs. The observed rate of such family-2 events is $\rho_0 = (2.6^{+4.1}_{-1.9}) \times 10^{-4} \text{ Gpc}^{-3}\text{yr}^{-1}$.

Swift: 10 Years of Discovery,

2-5 December 2014

La Sapienza University, Rome, Italy

^{*}Speaker.

[†]We are especially grateful to S. Campana and C. L. Fryer for useful suggestions in improving some conceptual and observational arguments. ME, MK and FGO are supported by the Erasmus Mundus Joint Doctorate Program by grant Nos. 2012-1710, 2013-1471 and 2012-1710, respectively, from the EACEA of the European Commission. AVP and EZ acknowledge the support by the International Cooperation Program CAPES-ICRANet financed by CAPES-Brazilian Federal Agency for Support and Evaluation of Graduate Education within the Ministry of Education of Brazil.

1. Introduction

An ample literature indicates that short gamma-ray bursts (GRBs), with observed durations $T_{90} < 2$ s, originate from binary neutron star (NS) mergers (see [1], for a review). Recently we proposed a classification for short GRBs based on the total mass of the NS–NS merger, which can be smaller or larger than the NS critical mass ($M_{crit}^{NS} = 2.67 M_{\odot}$). Family-1 short bursts have $E_{iso} < 10^{52}$ erg and a total mass $< M_{crit}^{NS}$. The NSs coalescence leads to a massive NS and possibly a companion object, either a white dwarf or a less massive NS. Since no black hole (BH) is formed, no high energy emission is expected and, indeed, has not been observed, while ample emission in the X-ray and optical are observed [1], although without the regularity or nesting properties observed in family-2 long GRBs [2, 3]. Family-2 short bursts have $E_{iso} > 10^{52}$ erg and a total mass of the two NSs is $> M_{crit}^{NS}$. The merging leads to the BH formation and of some orbiting material or binary companion (see Fig. 1). For small values of the total angular momentum of the NS binary the formation of a single BH is expected and no X-ray, optical, and high-energy emission are observed; for larger values, some residual material and/or a binary companion is left orbiting and accreting onto the BH, leading to the presence of X-ray, optical, and high-energy emissions.

After the identification of GRB 090227B [4], we here present a second explicit example of a family-2 short burst: GRB 140619B. The redshift for both of these sources have been theoretically inferred by applying the fireshell model. A third example, GRB 090510, is only one with a measured redshift so far, e.g. $z = 0.903$. All of these family-2 short GRBs fulfill the $E_{p,i}$ – E_{iso} relation discovered for family-1 short GRBs [5, 6]. Here $E_{p,i}$ is the rest-frame spectral peak energy.

In Sec. 2 we present our data analysis of GRB 140619B, from 8 keV up to 100 GeV. Then by applying the fireshell model to the observed data, we theoretically derive the redshift, $z = 2.67 \pm 0.37$, the burst energy, $E_{iso} > 10^{52}$ erg, and the value of the baryon load, $B \sim 10^{-5}$. We assume a symmetric NS–NS merger as the progenitor for GRB 140619B and discuss the possibility for Advanced LIGO to detect the emission of gravitational waves (GWs, see Sec. 2.2). In Sec. 2.3 we address the origin of the short-lived ($\Delta t \approx 5$ s) but significant 0.1–100 GeV emission. In Sec. 2.4 we give an estimate on the rate of such family-2 short GRBs. Finally we draw our conclusions.

2. Observations and data analysis

At 11:24:40.52 UT on 19th June 2014, the *Fermi*-GBM detector [7] triggered the short GRB 140619B. The on-ground calculated location was RA(J2000) = 08^h54^m and Dec(J2000) = $-3^\circ42'$ (5° of statistical uncertainty), and was 32° from the LAT boresight. The *Fermi*-LAT showed a significant increase in the event rate [8]. The burst was also detected by *Suzaku*-WAM [9]. No bright X-ray afterglow was detected by the *Swift*-XRT instrument in the field of view of the *Fermi* [10]. Therefore, no optical follow-up was possible and, thus, the redshift of the source is unknown.

We analyzed the GBM data (8 keV–40 MeV). In a first time interval, from T_0 to $T_0 + 0.192$ s (hereafter ΔT_1), we performed a spectral analysis considering the black body (BB) and Compt spectral models. The small difference in the C-STAT values listed in Tab. 1 suggests that both spectral models are equally viable. However, the α index of the Compt model is consistent with that of a BB within three σ , and the BB model has one parameter less than the Compt model. Therefore, we assumed the BB model as the best fit. In the second time interval, from $T_0 + 0.192$

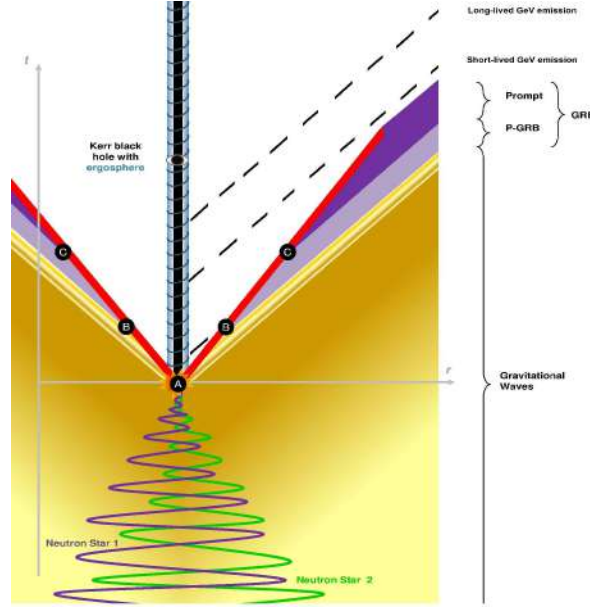


Figure 1: The space-time diagram of family-2 short GRBs. A) Vacuum polarization and self-acceleration of the fireshell; B) the transparency emission (P-GRB); C) interaction of the accelerated baryons with the local medium (prompt emission). The remnant of the merging is a Kerr BH. The accretion of a small (large) amount of orbiting matter onto the BH can give origin to the short (long) lived jetted 0.1–100 GeV.

ΔT	Model	K (ph keV $^{-1}$ cm $^{-2}$ s $^{-1}$)	kT (MeV)	E_p (MeV)	α	F_{tot} (erg cm $^{-2}$ s $^{-1}$)	C-STAT/DOF
ΔT_1	Compt	$(6.3 \pm 2.0) \times 10^{-3}$		1.60 ± 0.29	0.26 ± 0.32	$(9.4 \pm 1.6) \times 10^{-6}$	318.92/346
	BB	$(7.5 \pm 2.2) \times 10^{-8}$	0.32 ± 0.03			$(8.5 \pm 1.2) \times 10^{-6}$	323.86/347
ΔT_2	Compt	$(7.2 \pm 1.4) \times 10^{-3}$		1.28 ± 0.30	-0.11 ± 0.26	$(4.38 \pm 0.89) \times 10^{-6}$	391.65/346
	BB	$(3.8 \pm 1.1) \times 10^{-7}$	0.16 ± 0.02			$(2.33 \pm 0.28) \times 10^{-6}$	392.23/347

Table 1: Spectral analyses in the ΔT_1 and ΔT_2 time intervals. Column content: the time interval ΔT , the spectral model, the model normalization K , the BB temperature kT , the peak energy E_p , the low-energy index α , the 8 keV–40 MeV energy flux F_{tot} , and the C-STAT value over the degrees of freedom (DOF).

s to $T_0 + 0.640$ s (hereafter ΔT_2), we considered again the Compt and BB spectral models (see Tab. 1). As discussed above, also in this case both models are equally probable. However, the BB model does not adequately fit the data at energies larger than 1 MeV. Therefore, we adopted the Compt model. More details on the spectral analysis can be found in Ref. [11].

We interpret the above data within the fireshell model of GRBs [12, 13, 14]. The ΔT_1 time interval, where the spectrum is consistent with a BB, represents the P-GRB, namely the emission at the transparency of the expanding e^+e^- -photon-baryon plasma. The ΔT_2 time interval is identified with the prompt emission, a multi-wavelength emission due to the collisions between the accelerated baryons, after the transparency, and the circum-burst medium (CBM).

2.1 Redshift estimate and analysis of the prompt emission within fireshell model

The ratio between the P-GRB energy and total one can be estimated, independently to the redshift z , from the ratio of P-GRB and the total observed fluences, e.g. $S_{BB}/S_{tot} = (40.4 \pm 7.8)\%$ (see Tab. 1). Following the analysis described in Refs. [4, 11], from the above ratio, by applying

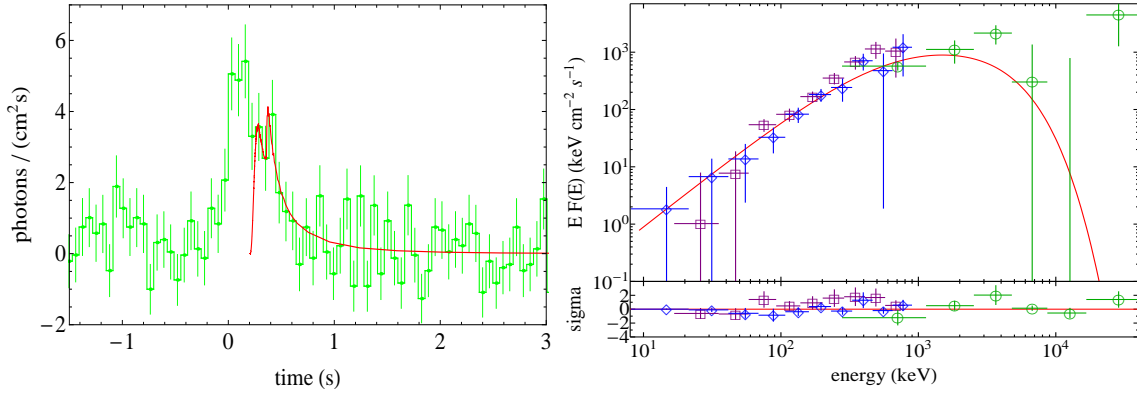


Figure 2: Left: the BGO-b1 (0.26–40 MeV) simulated light curve of the prompt emission of GRB 140619B. Right: comparison between the 8–900 keV data from the NaI-n6 (purple squares) and n9 (blue diamonds) detectors, and the 260 keV–40 MeV data from the BGO-b1 detector (green circles), and the simulation within the firshell model (solid red curve) in the time interval ΔT_2 (residuals are also shown).

the fireshell equations of motion, we obtained the redshift $z = 2.67 \pm 0.37$, the baryon load $B = (5.52 \pm 0.73) \times 10^{-5}$, and the total e^+e^- plasma energy $E_{e^+e^-}^{tot} = (6.03 \pm 0.79) \times 10^{52}$ ergs.

The BGO-b1 (0.26–40 MeV) prompt emission light curve in Fig. 2 (left panel) has been simulated by using a CBM number density distribution with an average value of $\langle n_{CBM} \rangle = (4.7 \pm 1.2) \times 10^{-5} \text{ cm}^{-3}$. The corresponding spectrum [15], is plotted in Fig. 2 (right panel).

2.2 The progenitor system and the GWs emission

We assume that the progenitor of GRB 140619B is a symmetric NS–NS merger and that the total crustal mass contributes to the GRB baryon load. For non-rotating NSs in the overall charge neutrality (OCN) treatment [16], the critical NS mass inferred from the NL3 nuclear model is $M_{crit}^{NS} = 2.67 M_\odot$. For NS masses $M_{NS} = 1.34 M_\odot$, so that $2M_{NS} > M_{crit}^{NS}$, the total NS crustal mass is $M_{2c} = 2M_c = 7.26 \times 10^{-5} M_\odot$. The baryonic mass engulfed by the e^+e^- plasma is $M_B = E_{e^+e^-}^{tot} B / c^2 = (1.86 \pm 0.35) \times 10^{-6} M_\odot$, therefore only $\approx 3\% M_{2c}$ contributes to the baryon load.

The GW emission from this binary NS gives a signal-to-noise ratio of $\langle \text{SNR} \rangle \approx 0.5$, for an optimally located and polarized source with optimal face-on orbit, and it is lower than the optimal value $\text{SNR} = 8$ for detection by the Advanced LIGO interferometer¹. The total gravitational radiation energy emitted during the entire inspiral-in phase all the way up to the merger, computed via the effective-one-body (EOB) formalism [17], is $E_{\text{GW}}^T = 7.42 \times 10^{52}$ erg.

2.3 Considerations on the GeV emission of GRB 140619B

The spectrum of the observed short-lived emission (~ 5 s) at energies $\gtrsim 0.1$ GeV of GRB 140619B is best fitted by a power-law with a photon index $\gamma = -1.9$. Its isotropic energy is $E_{\text{LAT}} = (2.02 \pm 0.52) \times 10^{53}$ erg. By applying the pair production optical depth $\tau_{\gamma\gamma}$ formula [18], we obtained an average lower limit on the Lorentz factor, e.g. $\langle \Gamma_{\text{LAT}} \rangle = 110.5 \pm 4.4$. The emitted energy can be explained by the accretion onto the BH of a fraction of the residual crustal mass $M_{\text{res}} = 2M_c - M_B$, occurring at the innermost stable circular orbit of an extreme Kerr BH,

¹<http://www.advancedligo.mit.edu>

in the co-rotating case. In fact, assuming a jetted outflow, we have an accretion energy $E_{acc} = \eta_{acc} \eta_M M_{res} c^2 \lesssim E_{LAT} / (2 \langle \Gamma_{LAT} \rangle^2)$, where η_{acc} is the accretion efficiency. From the above value of $\langle \Gamma_{LAT} \rangle$, the fraction of M_{res} which effectively accretes onto the BH is $\eta_M \lesssim (15.5 \pm 4.2)\%$.

2.4 The rate of family-2 short GRBs

Following Refs. [19, 20], with $N = 3$ family-2 short bursts, GRBs 090227B and 140619B with theoretically inferred redshifts and GRB 090510 with a measured one, we estimated their empirical rate $\rho_0 = (4\pi/\Omega_F)N/(V_{max}T_F)$, by evaluating for each source the maximum comoving volume V_{max} at which it would have been detected. Using the Fermi solid angle $\Omega_F \approx 9.6$ sr and observational period $T = 6$ years, we inferred $\rho_0 = (2.6^{+4.1}_{-1.9}) \times 10^{-4} \text{Gpc}^{-3} \text{yr}^{-1}$.

3. Conclusions

We here classified short GRBs into two families, both originating from NS–NS mergers, depending on the total NS masses $M_1 + M_2$, being $\geq M_{crit}^{NS}$. Family-1 short GRBs, with $E_{iso} < 10^{52}$ erg, we have $M_1 + M_2 < M_{crit}^{NS}$ and as a consequence no BH can be formed. Ample emission in the X-ray and optical are observed [1], although without any regularity or nesting properties, as observed in family-2 long GRBs [2, 3]. Family-2 short bursts, with $E_{iso} > 10^{52}$ erg, we have $M_1 + M_2 > M_{crit}^{NS}$ and a BH is formed. For small values of the total angular momentum we have the formation of a single BH; for larger values some residual matter orbits and accretes onto the BH. Within the second case we explained the short-lived 0.1–100 GeV emission of GRB 140619B as consistent with the accretion of $\approx 16\% M_{2c}$ onto an extreme Kerr BH, in the co-rotating case.

From our theoretical analysis, we inferred the astrophysical setting of GRB 140619B. 1) From the fit of the prompt emission light curve and spectrum, we derived a density $\langle n_{CBM} \rangle \approx 10^{-5} \text{cm}^{-3}$ typical of galactic halos where NS–NS mergers migrate [1]. 2) Assuming NS masses $M_1 = M_2 = 1.34 M_\odot$, the total energy emitted in gravitational waves corresponds to $E_{GW}^T = 7.42 \times 10^{52}$ erg; in view of the large z , the corresponding signal cannot be detected by the Advanced LIGO. 3) The empirical rate of family-2 short GRBs $\rho_0 = (2.6^{+4.1}_{-1.9}) \times 10^{-4} \text{Gpc}^{-3} \text{yr}^{-1}$, represents clearly a lower limit in view of the difficulties in doing detailed time-resolved spectral analyses, necessary to identify their P-GRB emissions, and can be explained by the existing data of the galactic binary NSs. Their majority has $M_1 + M_2 < M_{crit}^{NS}$ and, therefore, they will lead to family-1 short bursts, whose rate is $\rho \approx 1\text{--}10 \text{Gpc}^{-3} \text{yr}^{-1}$ [1]. The relative rates of family 1 and 2 short GRBs can lead, in principle, to an indirect determination of M_{crit}^{NS} (C. L. Fryer, private communication).

References

- [1] E. Berger, *Short-Duration Gamma-Ray Bursts*, *ARA&A* **52** (2014) 43 [arXiv:astro-ph/1311.2603].
- [2] R. Ruffini, Y. Wang, M. Kovacevic, C. L. Bianco, M. Enderli, M. Muccino, A. V. Penacchioni, G. B. Pisani and J. A. Rueda, *GRB 130427A and SN 2013cq: A Multi-wavelength Analysis of An Induced Gravitational Collapse Event*, *ApJ* **798** (2015) 10 [arXiv:astro-ph/1405.5723].
- [3] R. Ruffini, M. Muccino, C. L. Bianco, M. Enderli, L. Izzo, M. Kovacevic, A. V. Penacchioni, G. B. Pisani, J. A. Rueda, Y. Wang, *On binary-driven hypernovae and their nested late X-ray emission*, *A&A Letter* **565** (2014) L10 [arXiv:astro-ph/1404.3946].

- [4] M. Muccino, R. Ruffini, C. L. Bianco, L. Izzo and A. V. Penacchioni, *GRB 090227B: The Missing Link between the Genuine Short and Long Gamma-Ray Bursts*, *ApJ* **763** (2013) 125 [arXiv:astro-ph/1205.6600].
- [5] F.-W. Zhang, L. Shao, J.-Z. Yan and D.-M. Wei, *Revisiting the Long/Soft-Short/Hard Classification of Gamma-Ray Bursts in the Fermi Era*, *ApJ* **750** (2012) 88 [arXiv:astro-ph/1201.1549].
- [6] G. Calderone, G. Ghirlanda, G. Ghisellini, M. G. Bernardini, S. Campana, S. Covino, P. D'Avanzo, V. D'Elia, A. Melandri, R. Salvaterra, B. Sbarufatti and G. Tagliaferri, *There is a short gamma-ray burst prompt phase at the beginning of each long one*, [arXiv:1408.1608].
- [7] V. Connaughton, B.-B. Zhang, G. Fitzpatrick and O. Roberts, *GRB Coordinates Network* **16419** (2014) 1.
- [8] D. Kocevski, F. Longo, G. Vianello, V. Connaughton, J. McEnery and E. Sonbas, *GRB Coordinates Network* **16421** (2014) 1.
- [9] W. Iwakiri, M. Tashiro, Y. Terada, T. Yasuda, S. Koyama, S. Takeda, T. Nagayoshi, J. Enomoto, S. Nakaya, T. Fujinuma, S. Matsuoka, M. Yamauchi, N. Ohmori, R. Kinoshita, M. Ohno, T. Kawano, S. Furui, Y. Fukazawa, K. Yamaoka, S. Sugita, U. Ehime, Y. Hanabata, Y. E. Nakagawa, M. Kokubun, T. Takahashi, Y. Urata, K. Nakazawa and K. Makishima, *GRB Coordinates Network* **16457** (2014) 1.
- [10] A. Maselli and P. D'Avanzo, *GRB Coordinates Network* **16424** (2014) 1.
- [11] M. Muccino, R. Ruffini, M. Kovacevic, L. Izzo, F. G. Oliveira, J. A. Rueda, C. L. Bianco, M. Enderli, A. V. Penacchioni, G. B. Pisani, Y. Wang and E. Zaninoni, *GRB 140619B: a short GRB from a binary neutron stars merger leading to the black hole formation*, [arXiv:astro-ph/1412.1018].
- [12] R. Ruffini, C. L. Bianco, F. Frascchetti, S.-S. Xue and P. Chardonnet, *On a Possible Gamma-Ray Burst-Supernova Time Sequence*, *ApJ Letter* **555** (2001) L117 [arXiv:astro-ph/0106534].
- [13] R. Ruffini, C. L. Bianco, F. Frascchetti, S.-S. Xue and P. Chardonnet, *On the Interpretation of the Burst Structure of Gamma-Ray Bursts* *ApJ Letter* **555** (2001) L113 [arXiv:astro-ph/0106532].
- [14] R. Ruffini, C. L. Bianco, F. Frascchetti, S.-S. Xue and P. Chardonnet, *Relative Spacetime Transformations in Gamma-Ray Bursts* *ApJ Letter* **555** (2001) L107 [arXiv:astro-ph/0106531].
- [15] B. Patricelli, M. G. Bernardini, C. L. Bianco, L. Caito, G. de Barros, L. Izzo, R. Ruffini and G. V. Vereshchagin, *Analysis of GRB 080319B and GRB 050904 within the Fireshell Model: Evidence for a Broader Spectral Energy Distribution*, *ApJ* **756** (2012) 16 [arXiv:astro-ph/1206.5605].
- [16] R. Belvedere, D. Pugliese, J. A. Rueda, R. Ruffini and S. S. Xue, *Neutron star equilibrium configurations within a fully relativistic theory with strong, weak, electromagnetic, and gravitational interactions*, *Nuclear Physics A* **883** (2012) 1.
- [17] T. Damour and A. Nagar, *Effective one body description of tidal effects in inspiralling compact binaries*, *Physical Review D* **81** (2012) 084016 [arXiv:astro-ph/0911.5041].
- [18] T. Piran, *The physics of gamma-ray bursts*, *Rev. Mod. Phys.* **76** (2005) 1143.
- [19] A. M. Soderberg, S. R. Kulkarni, E. Nakar, E. Berger, P. B. Cameron, D. B. Fox, D. Frail, A. Gal-Yam, R. Sari, S. B. Cenko, M. Kasliwal, R. A. Chevalier, T. Piran, P. A. Price, B. P. Schmidt, G. Pooley, D.-S. Moon, B. E. Penprase, E. Ofek, A. Rau, N. Gehrels, J. A. Nousek, D. N. Burrows, S. E. Persson, P. J. McCarthy, *Relativistic ejecta from X-ray flash XRF 060218 and the rate of cosmic explosions*, *Nature* **442** (2006) 1014 [arXiv:astro-ph/0604389].
- [20] D. Guetta, M. Della Valle, *On the Rates of Gamma-Ray Bursts and Type Ib/c Supernovae*, *ApJ Letter* **657** (2007) L73 [arXiv:astro-ph/0612194].

Binary progenitors of GRBs within the fireshell model

M. Enderli^{*†ab}, C. L. Bianco^{bc}, L. Izzo^{bc}, M. Kovačević^{†ab}, M. Muccino^{bc}, G. B. Pisani^{†ab}, J. A. Rueda^{bc}, R. Ruffini^{bc}, Y. Wang^{bc}

^a *Université de Nice - Sophia Antipolis*

Cedex 2, Grand Château Parc Valrose, Nice, France

^b *Dip. di fisica & ICRA, Sapienza Università di Roma*

P.le Aldo Moro 5, I-00185 Roma, Italy

^c *ICRANet*

Piazza della Repubblica 10, I-65122, Pescara, Italy

E-mail: maxime.enderli@gmail.com

Recent results show that several distinct episodes may be individuated in some gamma-ray bursts (GRBs). Taking the effects of binarity into consideration - recalling in particular that type Ic supernovae (SNe) as well as most massive stars are indeed found in binary systems -, these results pave the way for a reinterpretation of GRBs as *composite events* in which binary interactions play a major role. It has been found that the observed diversity of GRBs may be accounted for by two main binary progenitor families: either a binary compact object merger, or the interaction between an evolved stellar core undergoing a SN and its companion neutron star. The energetics of a GRB is found to be largely determined by the presence or the absence of black hole formation. We present the different GRB families we obtain and we summarize their characteristics.

Swift: 10 Years of Discovery,

2-5 December 2014

La Sapienza University, Rome, Italy

^{*}Speaker.

[†]G.B. Pisani, M. Enderli, and M. Kovačević are supported by the Erasmus Mundus Joint Doctorate Program by Grant Numbers 2011-1640, 2012-1710, and 2013-1471 respectively, from the EACEA of the European Commission.

1. Introduction

It has been recognized for over 20 years that GRBs form (at least) two distinct groups, based on their duration and hardness properties [1, 2]. This dichotomy is thought to reveal an underlying difference in progenitor systems: long/soft GRBs are commonly interpreted as collapsar events, while circumstantial evidence points to a binary merger progenitor for short/hard bursts.

However, the fireshell model (reviewed e.g. in [3]) paints a different picture of the GRB phenomenon. In this framework, the collapse of an astronomical object to a black hole creates an overcritical electromagnetic field that powers the GRB through polarization of the vacuum. Indeed, the vacuum polarization leads to the production of an optically thick e^+/e^- pair plasma (the fireshell) that engulfs left-over baryons and expands and accelerates under its own pressure until it reaches transparency. A flash of thermal radiation, the Proper-GRB (P-GRB), is then emitted; the Lorentz factor of the plasma falls in the range $10^2 - 10^3$. Further interactions of the fireshell with the circumburst medium (CBM) produces the prompt emission.

Recent results (e.g. [4]) evidenced the fact that several episodes can be distinguished in a GRB. Since type Ic supernovae (those associated to GRBs) and massive stars are predominantly found in binary systems, it is a natural idea to study the consequences that binarity may have on a GRB event. It has been found that binary progenitors in the fireshell theory may be able to explain the diverse phenomenology of GRBs. A point of particular relevance is the presence or absence of black hole formation. The formation of a Kerr-Newman BH in the fireshell model may indeed deliver as much as $E_{iso} \sim 10^{55}$ erg for a $10 M_\odot$ BH [5]. Whether a BH forms or not is therefore of great importance regarding the energetics of the event.

Observational tests of the model include in particular: discrimination between the P-GRB (for which a blackbody component is expected) and the prompt emission, as well as spectral identification of the different *episodes* (defined below) as done in [4]; observation of the X-ray afterglow that exhibits a standard behavior for the BdHN family defined below [6]; theoretical determination of redshifts that may be compared to redshift measurements (if available), as in [7].

2. The GRB - SN connection

GRB - SN coincidental occurrences have been observed since 1998, with 35 spectroscopic or photometric associations up to the 31st of May 2014 [8]. The Induced Gravitational Collapse (IGC) paradigm has been formulated to explain the GRB - SN connection [9, 10, 11]. It promotes the idea that the GRB and the SN do not have the same origin: an evolved stellar core reaching the end of its main sequence life undergoes a SN, but the GRB is a consequence of the triggered gravitational collapse of its companion neutron star. The IGC paradigm predicts four episodes, each of them being characterized by a number of observables [12].

An isotropic energy above $\sim 10^{52}$ erg is expected to be compatible with the formation of a black hole [12]. Less energetic GRBs can however still be linked to binary progenitors, if the configuration of the binary does not allow the companion NS to accrete enough matter to collapse. The critical distance between the two bodies is found to be of the order of 10^{11} cm. We therefore obtain two sub-families within the IGC formalism, termed *traditional hypernovae* with $E_{iso} \lesssim 10^{52}$ erg, and *binary driven hypernovae* (BdHN, [12] and references therein) with $E_{iso} \gtrsim 10^{52}$ erg.

2.1 Binary driven hypernovae (BdHNe)

A BdHN event may be identified through the detection and the characterization of its episodes. We refer to Fig. 1 (right panel) for a space-time diagram describing the sequence of events occurring in a BdHN (e.g. [12]). The **first episode** is due to hypercritical accretion of the SN ejecta onto the companion NS. The (non relativistic) emission is characterized by a spectrum that includes an evolving thermal component superimposed on a power law component. The computed radius of the blackbody emitter typically evolves from $\sim 10^9$ cm to $\sim 10^{10}$ cm. An episode 1 has been clearly observed in GRB 090618 [4] in particular. Its energetics may reach up to $\sim 10^{52}$ erg. **Episode 2** is the signature of the fireshell created by the collapse of the companion NS after it accreted enough matter to exceed its critical mass. Its distinctive features include an ultra-relativistic nature (with Lorentz factor $\Gamma \sim 10^2 - 10^3$) and a relatively hard peak energy $E_p > 100$ keV. The energetics of episode 2 may reach a few 10^{53} erg. **Episode 3**, starting at the end of episode 2 (that is, typically $\sim 10^2$ s after trigger), is clearly visible in the X-ray domain. Its expansion velocity is only mildly relativistic. Three parts may be distinguished in the X-ray lightcurve: an initial steep decay, followed by a plateau phase (i.e. a shallow decay) and a final steeper decay. It has been found that this last part has a common behavior among BdHN events [6]. This peculiar feature may be used as a distance indicator. **Episode 4** simply consists in the SN peak optical emission, which occurs about 10 – 15 rest-frame days following the GRB itself. Optical detection may be successfully carried out as far as $z \sim 1$, with spectroscopic identification reasonably probable up to $z \sim 0.5$.

2.2 Classical hypernovae

In contrast to a BdHN event, a classical (in the sense not *binary driven*) hypernova lacks an episode 2 (see Fig. 1, left panel). This is understood as follows: if the distance between the stellar core and the companion NS is too large (and/or the companion NS is not massive enough), the latter may not accrete enough matter to undergo a gravitational collapse - which is the physical event at the origin of an episode 2. Episodes 1, 3, and 4 are still expected. Note that due to the lack of an episode 2, which is energetically the most prominent part of a BdHN, the total isotropic energy of a classical hypernova is not expected to exceed at most a few 10^{52} erg.

3. Binary compact object mergers

As pointed out in the literature (e.g. [13]), compact object mergers are prime candidates to explain short GRB events. There is indeed convincing circumstantial evidence pointing to this class of progenitors: the host galaxies of short GRBs (which are both early type and late type with old stellar populations), the absence to deep limits of associated SNe, and the offset from the associated host are important arguments. But just as BdHNe differ from classical hypernovae, we expect the merger of two compact objects to have markedly different energetics depending on whether a black hole is formed or not [12].

3.1 NS-NS or NS-WD merger leading to a NS remnant

Both NS – WD mergers and double NS mergers are likely candidates for the less energetic ($E_{iso} \lesssim 10^{52}$ erg) short GRBs (see Fig. 2, left panel). A detailed simulation of NS - WD mergers is

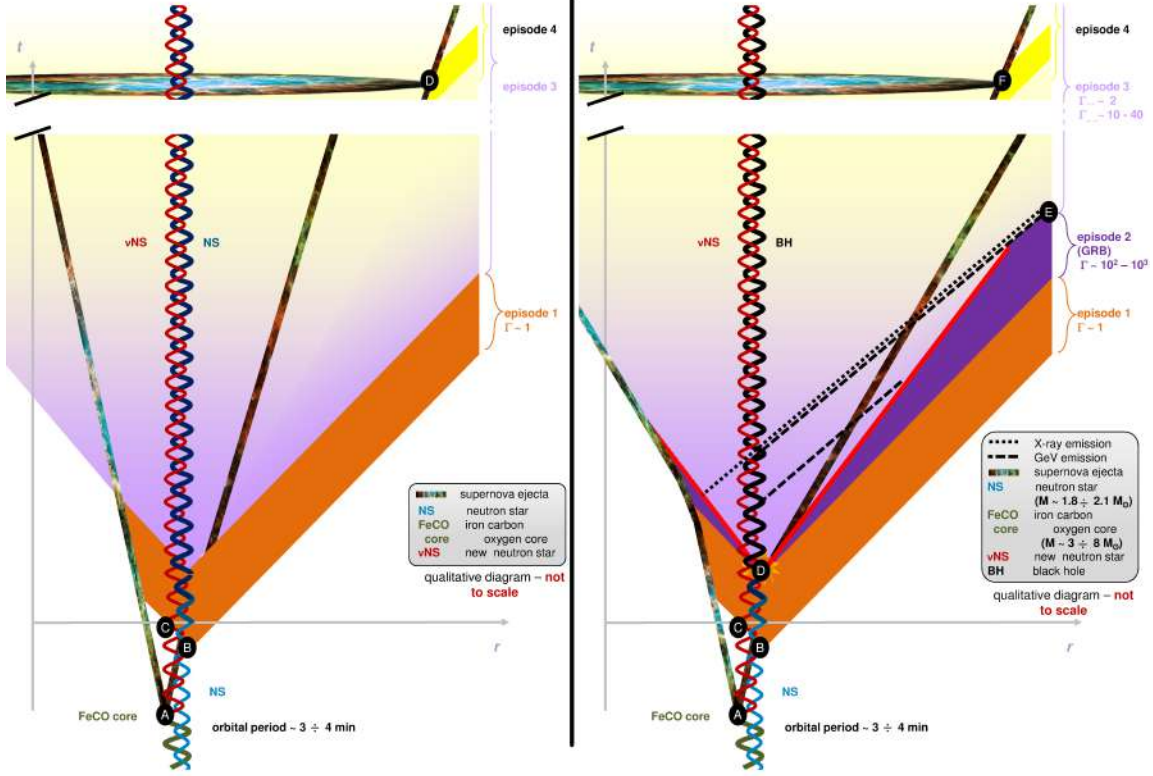


Figure 1: *Left panel:* Space-time diagram of an hypernova event. The initial configuration consists of an evolved (likely iron-carbon-oxygen) stellar core and its companion neutron star. At point A, the core undergoes a supernova and leaves a new neutron star (vNS) remnant. At point B, the companion neutron star starts to accrete matter from the supernova ejecta: this marks the beginning of Episode 1. Point C shows the beginning of the interaction of the vNS with Episode 1. The companion NS does not accrete enough matter to exceed its critical mass: no Episode 2 is emitted, on the contrary to a BdHN event (right panel). Finally, after $t \sim 10(1+z)$ days in observer frame, the supernova peaks in the optical due to ^{56}Ni decay (point D). *Right panel:* Space-time diagram of a binary driven hypernova event. The initial configuration is similar to the hypernova case - an evolved stellar core and a companion neutron star. At point A, the core undergoes a supernova and leaves a new neutron star (vNS) remnant. At point B, the companion neutron star starts to accrete matter from the supernova ejecta: this marks the beginning of Episode 1. Point C shows the beginning of the interaction of the vNS with Episode 1. When the companion NS has accreted enough matter to exceed its critical mass, it collapses to a black hole and emits a fireshell (point D). This is the start of Episode 2. Point E shows the transition between the ultra-relativistic Episode 2 and the mildly relativistic Episode 3. Finally, after $t \sim 10(1+z)$ days in observer frame, the supernova peaks in the optical due to ^{56}Ni decay (point F). Details in [12].

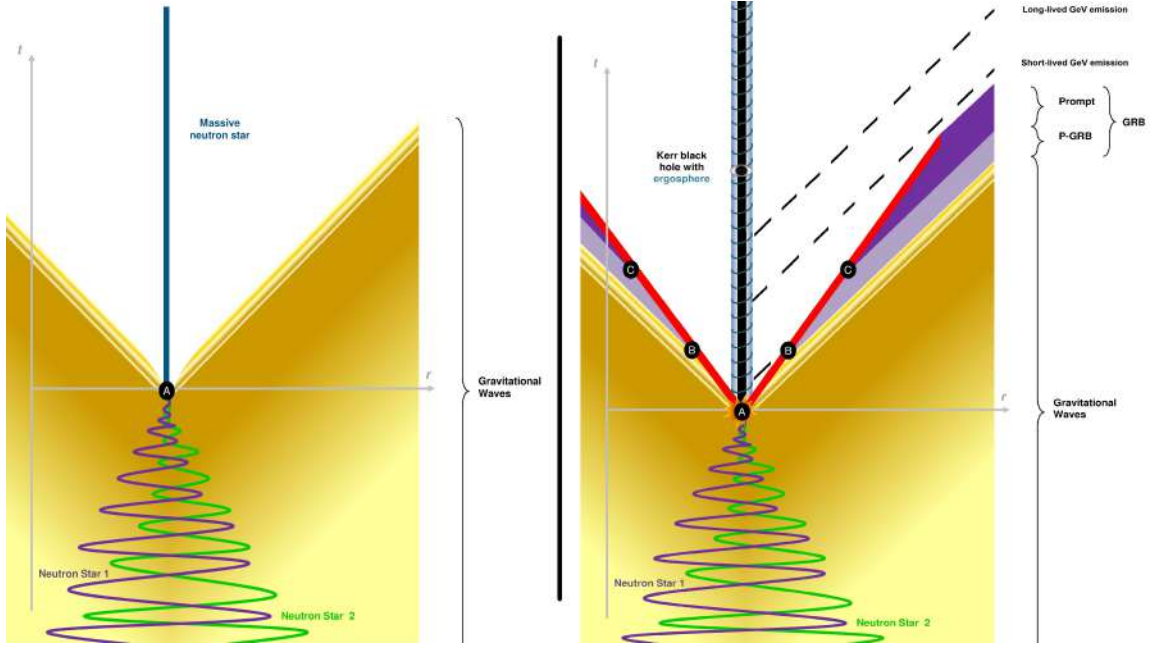


Figure 2: *Left panel:* Space-time diagram of an NS - NS merger leading to a NS remnant. The initial configuration consists of two neutron stars whose combined mass does *not* exceed the critical mass. The binary orbit shrinks due to gradually more intense gravitational wave emission, until merger finally occurs (point A). *Right panel:* Space-time diagram of an NS - NS merger leading to a BH remnant. The initial configuration consists of two neutron stars whose combined mass *exceeds* the critical mass. The binary orbit gradually until merger finally occurs (point A). The formation of a black hole implies the emission of a fireshell: a GRB event is observed (points B and C).

currently in preparation. NS – NS mergers have been explored more extensively in the literature. In particular, a set of papers ([14] and references therein) relevant to the present case develops the idea of the formation of an e^+/e^- self-accelerating plasma via neutrino - antineutrino annihilation during the merger. In this framework, the maximum energy budget is $< 10^{52}$ erg, in line with our expectations.

3.2 NS – NS merger leading to a BH remnant

If the combined mass of the two merging neutron stars exceeds the critical mass, a black hole is likely to form. As a result, following the predictions of the fireshell model, an energetic GRB should be emitted and would appear as a genuine short GRB (see Fig. 2, right panel). In particular, the genuine short GRB 090227B has been addressed in detail within the fireshell model, and has been found to be a likely outcome of an NS – NS merger [7]. Under overall charge neutrality condition, the NL3 nuclear model for a non-rotating NS critical mass gives a critical mass $M_{crit} = 2.67M_{\odot}$ [15].

4. Conclusion

We presented recent developments in the classification of GRBs within the fireshell model. Binarity is a key element, since it is expected that all GRBs originate in composite events - either

through compact object mergers or hypernovae. An important point lies in the fact that the energetics of a GRB are largely determined by the formation, or lack thereof, of a black hole. Ongoing work focuses on better characterization of the different progenitor families, and on reaching a more detailed understanding of the prominent observational features - among which the scaled X-ray afterglow and the GeV component.

References

- [1] C. Kouveliotou, C. A. Meegan, G. J. Fishman, N. P. Bhat, M. S. Briggs, et al., *Identification of two classes of gamma-ray bursts*, *ApJ*, **413** (1993) 101
- [2] M. Tavani, *Euclidean vs. non-Euclidean Gamma-Ray Bursts*, *ApJ*, **497** (1998) L21
- [3] Ruffini, R., *Proceedings of the Twelfth Marcel Grossmann Meeting on General Relativity*, World Scientific, Singapore (2011)
- [4] L. Izzo, R. Ruffini, A. V. Penacchioni, et al., *A double component in GRB 090618: a proto-black hole and a genuinely long gamma-ray burst*, *A&A*, **543** (2012) A10 [arXiv:1206.2887]
- [5] T. Damour, R. Ruffini, *Quantum Electrodynamical Effects in Kerr-Newmann Geometries*, *Physical Review Letters*, **35** (1975) 463.
- [6] G. B. Pisani, L. Izzo, R. Ruffini, C. L. Bianco, M. Muccino, A. V. Penacchioni, J. A. Rueda, Y. Wang, *Novel distance indicator for gamma-ray bursts associated with supernovae*, *A&A*, **552** (2103) L5 [arXiv:1304.1764]
- [7] M. Muccino, R. Ruffini, C. L. Bianco, L. Izzo, A. V. Penacchioni, *GRB 090227B: The Missing Link between the Genuine Short and Long Gamma-Ray Bursts*, *ApJ*, **763** (2013) 125 [arXiv:1205.6600]
- [8] M. Kovacevic, L. Izzo, Y. Wang, M. Muccino, M. Della Valle, L. Amati, C. Barbarino, M. Enderli, G. B. Pisani, L. Li, *A search for Fermi bursts associated to supernovae and their frequency of occurrence*, *A&A*, **569** (2014) A108 [arXiv:1408.6227]
- [9] R. Ruffini, C. L. Bianco, F. Frascchetti, S.-S. Xue, P. Chardonnet, *On a Possible Gamma-Ray Burst-Supernova Time Sequence*, *ApJ*, **555** (2001) L117 [arXiv:astro-ph/0106534]
- [10] R. Ruffini, M. G. Bernardini, C. L. Bianco, L. Caito, P. Chardonnet, M. G. Dainotti, R. Frascchetti, R. Guida, G. Vereshchagin, S.-S. Xue, *The Role of GRB 031203 in Clarifying the Astrophysical GRB Scenario*, *ESA-SP 622* (2007) 561 [arXiv:0705.2456]
- [11] R. Ruffini, M. G. Bernardini, C. L. Bianco, et al. *11th Proc. Marcel Grossmann Meeting*, World Scientific Publishing, Singapore (2008) 368
- [12] R. Ruffini, Y. Wang, M. Enderli, M. Muccino, M. Kovacevic, C.L. Bianco, A.V. Penacchioni, G.B. Pisani, J.A. Rueda, *GRB 130427A and SN 2013cq: a multi-wavelength analysis of an induced gravitational collapse event*, *ApJ*, **798** (2015) 10 [arXiv:1405.5723]
- [13] E. Berger, *Short-Duration Gamma-Ray Bursts*, *Annual Review of Astronomy and Astrophysics*, **52** (2014) 43 [arXiv:1311.2603]
- [14] J. D. Salmonson & J. R. Wilson, *A Model of Short Gamma-Ray Bursts: Heated Neutron Stars in Close Binary Systems*, *ApJ*, **578** (2002) 310
- [15] R. Belvedere, D. Pugliese, J. A. Rueda, R. Ruffini, & S.-S. Xue, *Neutron star equilibrium configurations within a fully relativistic theory with strong, weak, electromagnetic, and gravitational interactions*, *Nuclear Physics A*, **883** (2012) 1

DISSECTING THE GALACTIC TeV EXCESS

J. PETROVIĆ¹, T. PRODANOVIĆ¹ and M. KOVAČEVIĆ²

¹*Department of Physics, Faculty of Sciences, University of Novi Sad,
Trg Dositeja Obradovića 4, 21000 Novi Sad, Serbia
E-mail: jovana.petrovic@df.uns.ac.rs, prodanvc@df.uns.ac.rs*

²*Department of Physics and ICRA, Sapienza University of Rome,
Piazzale Aldo Moro 5, 00185 Rome, Italy
E-mail: Milos.Kovacevic@icranet.org*

Abstract. Diffuse gamma-ray emission has been studied in detail by the Fermi LAT telescope. Most of the emission comes from the interactions of galactic cosmic rays with the interstellar gas, as well as interactions with fields. However, at least a portion of the emission belongs to unresolved point sources. Another eye-on-the-sky in the past years, focusing on the high energy range (TeV), was the Milagro Cherenkov telescope and its last report of the diffuse Galactic disk emission for the region $30^\circ \leq l \leq 65^\circ, -2^\circ \leq b \leq 2^\circ$ states a gamma-ray differential flux of $F_{\gamma,\text{diff,MGO}} = 4.1 \pm 1.0 \times 10^{-12}$ photons $\text{TeV}^{-1} \text{cm}^{-2} \text{s}^{-1} \text{sr}^{-1}$ on 12 TeV, adopting a spectral index of 2.62. We compare this value to the Fermi LAT diffuse model and find an excess in gamma-rays dubbed the TeV excess. After removing all known point sources found in catalogues, such as the Fermi LAT and TeVCat catalogues, the TeV excess remains. Our goal was to give possible explanation of this excess by modeling point source candidates - pulsars and supernova remnants, that are still unresolved.

1. INTRODUCTION

Diffuse gamma emission from our galaxy - the Milky Way, has been measured in the recent years using several telescopes. Most of the measured emission above 1 GeV originates from cosmic ray interactions with the interstellar medium, resulting in neutral pion production and latter decay into two gamma rays. Another dominant source of gamma rays is from leptonic cosmic ray interactions via the inverse Compton scattering and Bremsstrahlung emission. Last guaranteed contributing source are the unresolved point sources. There are still open questions concerning the gamma-ray sky such as the galactic centre gamma-ray excess, as well as the high energy Milagro excess - still unexplained emission of gamma rays in the Milky Way.

Our goal was to give possible explanations for the unresolved excess measured at 12 TeV by the Milagro telescope, taking into account the newest diffuse gamma ray data from the Fermi LAT telescope, as well as all recorded point sources in the area of the sky that was observed by this Cherenkov telescope ($30^\circ \leq l \leq 65^\circ, -2^\circ \leq b \leq 2^\circ$) by modeling point source populations - supernova remnants and pulsars/pulsar wind nebulae.

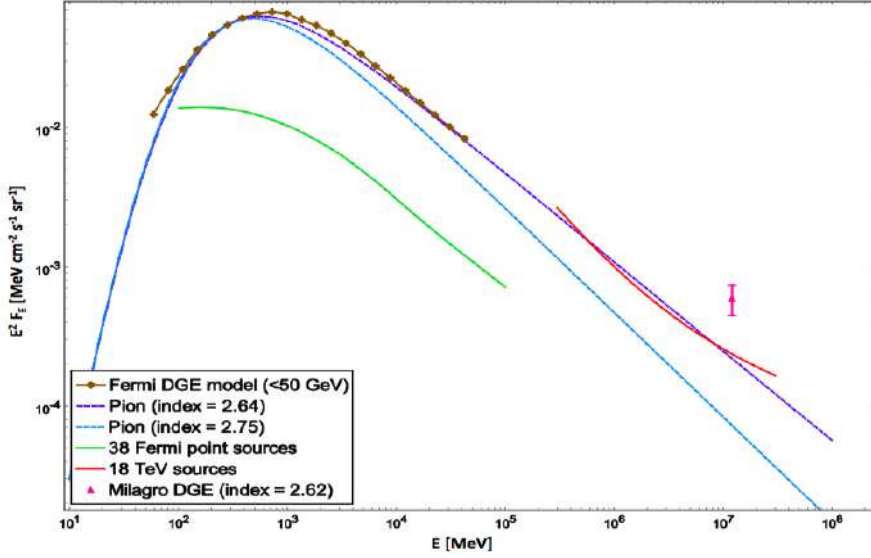


Figure 1: All selected data for the $30^\circ \leq l \leq 65^\circ$, $-2^\circ \leq b \leq 2^\circ$ sky region, including the Fermi LAT diffuse emission model, 38 Fermi point sources, 18 TeV TeVCat sources and the Milagro 12 TeV data point.

2. DIFFUSE AND POINT SOURCE GAMMA RAY DATA

In our analysis we have used the latest Milagro collaboration data for the Galactic region $30^\circ \leq l \leq 65^\circ$, $-2^\circ \leq b \leq 2^\circ$ observed above 12 TeV, from where the measured differential gamma ray flux at 12 TeV was derived to be $F_{\gamma, \text{diff, MGO}} = 4.1 \pm 1.0 \times 10^{-12}$ photons $\text{TeV}^{-1} \text{cm}^{-2} \text{s}^{-1} \text{sr}^{-1}$, assuming a spectral index of 2.62. Spectral indices we use are linked to the gamma-ray flux as $F_{\gamma, \text{diff, MGO}} \sim -\Gamma$, thus taking only positive values. The Fermi LAT Pass 7 Galactic Diffuse Model¹ has been adopted from the Fermi collaboration, and extrapolated over 50 GeV, selecting the data within the Milagro field of view and our region of interest.

From the measured diffuse flux, we subtract the smoothed contribution of all measured gamma ray point sources in our ROI from the Fermi LAT 4-year Point Source Catalog (3FGL)² and the eVcat catalog of TeV sources³.

In Figure 1, we plot all the data we selected - the Fermi LAT diffuse emission model, 38 Fermi point sources, 18 TeV TeVCat sources and the Milagro 12 TeV data point after subtracting all known point sources (the Milagro excess data point).

¹<http://fermi.gsfc.nasa.gov/ssc/data/access/lat/BackgroundModels.html>

²https://fermi.gsfc.nasa.gov/ssc/data/access/lat/4yr_catalog/

³<http://tevcat.uchicago.edu>

It can be concluded, that even after subtracting all known sources of gamma rays at high energies, the 12 TeV Milagro data point still stays well above all modeled gamma rays emission coming from diffuse and point source contributions, meaning it still stays unexplained.

3. SOURCE POPULATIONS AS TEV EXCESS EXPLANATIONS

We move to investigating the possibility that the explanation for this excess can be found in the population of unresolved galactic point sources. One of the most commonly identified sources in the Milky Way, that are a good candidate for the Milagro excess explanation, would be unresolved supernova remnants (see e.g. Wakely & Horan 2008).

For Galactic distribution of supernova remnants we take the distribution given in Green 2015, while for their fluxes we adopt a function from Pfrommer and Ensslin 2003, and their luminosity ($L_\gamma \sim -\Gamma + 1$) from the 3FGL Fermi LAT collaboration paper.

We do not at this stage assume any luminosity function but rather leave luminosity as a free parameter doing the analysis with maximal and minimal luminosity take for all sources, that we adopt from what has already been measured for Galactic supernova remnants by Fermi LAT in 3FGL. We also leave spectral index Γ as a free parameter.

We adopt their galactic distributions and luminosity functions, leaving the spectral indices in both cases as a free parameter in order to cover a larger range of potential sources.

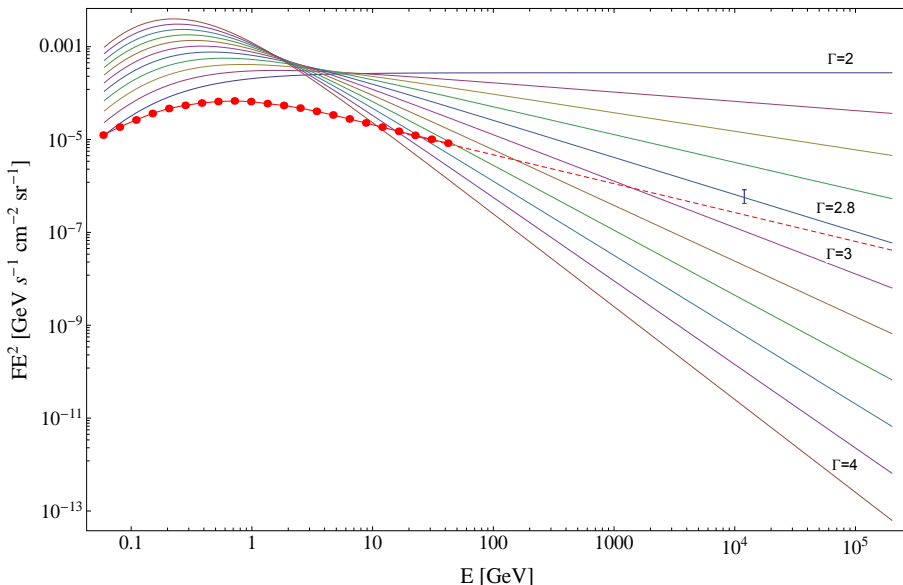


Figure 2: Modeled gamma ray flux for a population of supernova remnants with the maximal luminosity, where the spectral index takes values in the range $2 \leq \Gamma \leq 4$. Red points are the Pass 7 galactic diffuse emission measurement adopted from the Fermi LAT, and extrapolated to higher energies (dashed red), the blue data point is the Milagro 12 TeV excess.

In Figures 2. and 3. we present our results for supernova remnants where we implement the highest and lowest values for their luminosities that we adopt from the 3FGL catalogue of sources. We assume that the production of gamma rays from these sources is purely hadronic in nature and leave the spectral index Γ as a free parameter.

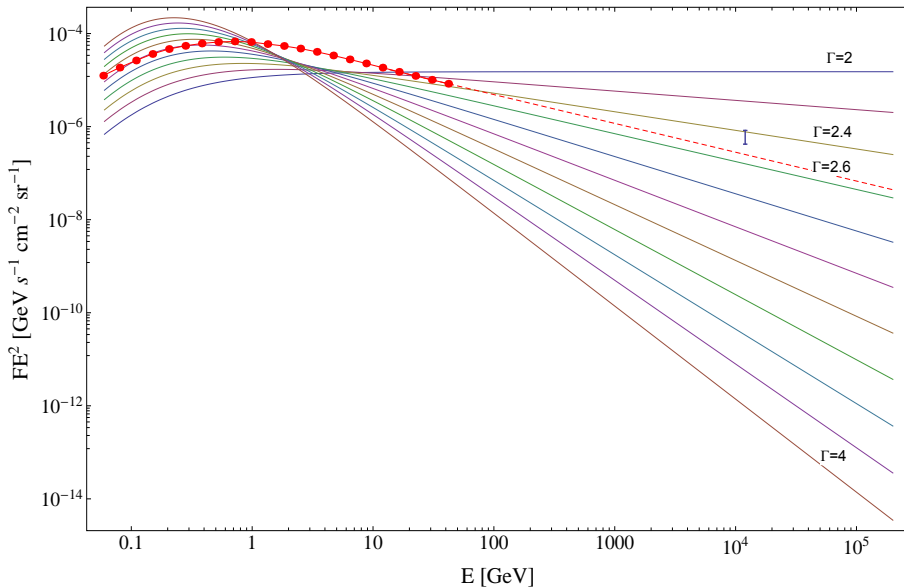


Figure 3: Modeled gamma ray flux for a population of supernova remnants with the minimal luminosity, where the spectral index takes values in the range $2 \leq \Gamma \leq 4$. Red points are the Pass 7 galactic diffuse emission measured by the Fermi LAT, and extrapolated to higher energies (dashed red), the blue data point is the Milagro 12 TeV excess.

As can be concluded from the Figures 2. and 3. above, for certain values of luminosity (minimal luminosity value) and spectral indices ($\Gamma = 2.4$ and $\Gamma = 2.6$), the Milagro excess data point (the Milagro derived flux at 12 TeV from which we subtract all known point sources) is reached by our modeled population of supernova remnants, while not overshooting the measured Fermi LAT diffuse foreground. Therefore we conclude that the Milagro excess could be explained by point sources - in this case supernova remnants, that remain undetected.

We have confirmed the existence of the Milagro gamma-ray TeV excess in the light of the most recent data from both the Milagro collaboration, the Fermi LAT Pass 7 diffuse galactic emission and 3FGL, as well as TeVcat point source data. We then modeled a population of sources that could potentially explain this excess in gamma rays - supernova remnants adopting their Galactic distribution and fluxes, varying the luminosity function value and spectral indices. We see that for some choices of the free parameters supernova remnants can indeed reach, and thus explain, the Milagro excess data point at 12 TeV.

References

- Abdo, A. A., Allen, B., Aune, T. et al.: 2008, *Astrophys. J.*, **688**, 1078-1083.
- Abeysekara, A. U., Alfaro, R., Alvarez, C. et al.: 2013, *Astroparticle Physics* **50**, 26.
- Acero, F., Ackermann, M., Ajello, M. et al.: 2015, *Astrophys. J. Supplement*, **218**, 23.
- Acero, F., Ackermann, M., Ajello, M. et al.: 2016, *Astrophys. J. Supplement*, **223**, 26.
- Ackermann, M., Ajello, M., Atwood, W. B. et al.: 2012, *Astrophys. J.*, **750**, 3.
- Atkins, R., Benbow, W., Berley, D. et al.: 2005, *Physical Review Letters*, **95**, 251103.
- Prodanović, T., Fields, B. D. & Beacom, J. F.: 2007, *Astroparticle Physics*, **27**, 10.
- Pfrommer, C., Ensslin, T. A.: 2003, *Astronomy and Astrophysics*, **407**, 73.
- Green, D. A.: 2015 *MNRAS*, **454**, 1517.

ERASMUS MUNDUS JOINT DOCTORATE
INTERNATIONAL RELATIVISTIC ASTROPHYSICS PH.D.



PH.D. THESIS

Application and Analysis of the Induced Gravitational Collapse in some Gamma-ray Bursts - Supernovae

PH.D. CANDIDATE
Miloš Kovačević

THESIS ADVISOR
Prof. Remo Ruffini

Sapienza Università di Roma
Université de Nice – Sophia-Antipolis

Rome
Submitted: September 2017
Defended: April 2018

Abstract

The title of the thesis is related to a larger study by a scientific group which I have been part of during the PhD course. The study of the group is related to developing Fireshell model in order to explain gamma-ray bursts; Induced Gravitational Collapse model in order to explain their connection to supernovae; and interpreting individual gamma-ray bursts, and groups of them, within these models. The thesis is a compilation of various work done by me during the duration of the PhD course related to the topic stated in the title. Not everything done during the PhD is presented in the thesis mainly due to time limitations. One of the non-included work consists of analysis of high-energy data from numerous gamma-ray bursts obtained by Fermi-LAT and Fermi-GBM space-based detectors, automating such analysis, looking for peculiarities and trying to find patterns in it, and trying to determine whether such features are intrinsic or due to instrumental effects.

The thesis is structured as follows: In Chapter 1 history of Gamma-ray burst discoveries and general conclusions which came from them will be presented. In Chapter 2 general information will be presented on the Fireball model, which is a mainstream model used to explain gamma-ray bursts. Then the general information on the Fireshell model will be presented. This will take a form of a short review of the work done by the group on the topic. In Chapter 3 the general information on the Induced Gravitational Collapse model will be presented. Again this will be a short review of the work done by the group. Since late 2013, I contributed in part to some of the analysis of high energy data and to lesser extent on statistics of gamma-ray burst observational properties.

In Chapter 4, I will present my work which started with systematic analysis of Swift-BAT and Swift-XRT data with the aims of detecting thermal black body emission in the late prompt phase of gamma-ray bursts. This involved close examination of data analysis techniques and writing Python scripts in order to automatize data analysis as much as possible. Then the results of several detected black bodies will be compared to each other in the rest-frame of gamma-ray burst host galaxy. Afterward the corrections due to relativistic expansion of the black body will be derived. Next a small simulation of spectrum from a black body with mildly relativistic expansion, and with varying velocity and temperature, will be done and the simulation applied to GRB 151027A. Finally the results will be compared to predictions of Induced Gravitational Collapse model. It was found that they are not in contradiction with the model.

In Chapter 5 the work which involved cross-correlation of gamma-ray burst and supernova catalogs in order to find potentially unnoticed connections up to mid 2014 will be presented. One probable such connection was found between Ic supernova and low-luminosity gamma-ray burst, and the rate of such events were calculated. It was found they overlap with previous estimates. I was one of the people leading the work. Next I will update the work with the same analysis up to year 2017 applying different statistical methods and involving more catalogs. The novel results indicate possible connection between short gamma-ray bursts and type II_n supernovae. The investigation of such possibility will

be carried out and its implications will be examined.

List of publications

- Kovacevic, M.; Izzo, L.; Wang, Y.; Muccino, M.; Della Valle, M.; Amati, L.; Barbarino, C.; Enderli, M.; Pisani, G. B.; Li, L.. (2014). A search for Fermi bursts associated to supernovae and their frequency of occurrence. *A&A*, 569, A108.
- Ruffini, R.; Wang, Y.; Enderli, M.; Kovacevic, M.; Bianco, C. L.; Muccino, M.; Penacchioni, A. V.; Pisani, G. B.; Rueda, J. A. (2015). GRB 130427A and SN 2013cq: A Multi-wavelength Analysis of an Induced Gravitational Collapse Event. *ApJ*, 798, 10.
- Ruffini, R.; Aimuratov, Y.; Becerra, L.; Bianco, C. L.; Chen, Y. C.; Karlica, M.; Kovacevic, M.; Melon Fuksman, J. D.; Moradi, R.; Muccino, M.; Pisani, G. B.; Primorac, D.; Rueda, J. A.; Wang, Y. (2017). On the nature of prompt emission, X and gamma ray flares and extended thermal emission in GRB 151027A. Submitted to *ApJ*.
- Ruffini, R.; Muccino, M.; Kovacevic, M.; Oliveira, F. G.; Rueda, J. A.; Bianco, C. L.; Enderli, M.; Penacchioni, A. V.; Pisani, G. B.; Wang, Y. (2015). GRB 140619B: a short GRB from a binary neutron star merger leading to black hole formation. *ApJ*, 808, 190.
- Ruffini, R.; Muccino, M.; Aimuratov, Y.; Bianco, C. L.; Cherubini, C.; Enderli, M.; Kovacevic, M.; Moradi, R.; Penacchioni, A. V.; Pisani, G. B.; Rueda, J. A.; Wang, Y. (2016). GRB 090510: A Genuine Short GRB from a Binary Neutron Star Coalescing into a Kerr-Newman Black Hole. *ApJ*, 831, 178.
- Ruffini, R.; Rueda, J. A.; Muccino, M.; Aimuratov, Y.; Becerra, L. M.; Bianco, C. L.; Kovacevic, M.; Moradi, R.; Oliveira, F. G.; Pisani, G. B.; Wang, Y. (2016). On the Classification of GRBs and Their Occurrence Rates. *ApJ*, 832, 136.
- Ruffini, R.; Muccino, M.; Bianco, C. L.; Enderli, M.; Izzo, L.; Kovacevic, M.; Penacchioni, A. V.; Pisani, G. B.; Rueda, J. A.; Wang, Y. (2014). On binary-driven hypernovae and their nested late X-ray emission. *A&A*, 565, L10.
- Ruffini, R.; Izzo, L.; Muccino, M.; Pisani, G. B.; Rueda, J. A.; Wang, Y.; Barbarino, C.; Bianco, C. L.; Enderli, M.; Kovacevic, M.. (2014). Induced gravitational collapse at extreme cosmological distances: the case of GRB 090423. *A&A*, 569, A39.
- Muccino, M.; Bianco, C. L.; Izzo, L.; Wang, Y.; Enderli, M.; Kovacevic, M.; Pisani, G. B.; Penacchioni, A. V.; Ruffini, R. (2014). The genuine short GRB 090227B and the disguised by excess GRB 090510. *GrCo*, 20, 3.
- Ruffini, R.; Aimuratov, Y.; Bianco, C. L.; Enderli, M.; Kovacevic, M.; Moradi, R.; Muccino, M.; Penacchioni, A. V.; Pisani, G. B.; Rueda, J. A.; Wang, Y. (2015). Induced

gravitational collapse in FeCO Core-Neutron star binaries and Neutron star-Neutron star binary mergers. *IJMPA*, 30, 28n29.

- Ruffini, R.; Rodriguez, J.; Muccino, M.; Rueda, J. A.; Aimuratov, Y.; Barres de Almeida, U.; Becerra, L.; Bianco, C. L.; Cherubini, C.; Filippi, S.; Gizzi, D.; Kovacevic, M.; Moradi, R.; Oliveira, F. G.; Pisani, G. B.; Wang, Y. (2016). On the rate and on the gravitational wave emission of short and long GRBs. *Arxiv*, 1602.03545.
- Pisani, G. B.; Ruffini, R.; Aimuratov, Y.; Bianco, C. L.; Kovacevic, M.; Moradi, R.; Muccino, M.; Penacchioni, A. V.; Rueda, J. A.; Shakeri, S.; Wang, Y. (2016). On the Universal Late X-Ray Emission of Binary-driven Hypernovae and Its Possible Collimation. *ApJ*, 833, 159.
- Rueda, Jorge A.; Aimuratov, Y.; de Almeida, U. Barres; Becerra, L.; Bianco, C. L.; Cherubini, C.; Filippi, S.; Karlica, M.; Kovacevic, M.; Fuksman, J. D. Melon; Moradi, R.; Muccino, M.; Penacchioni, A. V.; Pisani, G. B.; Primorac, D.; Ruffini, R.; Sahakyan, N.; Shakeri, S.; Wang, Y. (2017). The binary systems associated with short and long gamma-ray bursts and their detectability. *IJMPD*, 26, 9.
- Ruffini, R.; Aimuratov, Y.; Becerra, L.; Bianco, C. L.; Karlica, M.; Kovacevic, M.; Melon Fuksman, J. D.; Moradi, R.; Muccino, M.; Penacchioni, A. V.; Pisani, G. B.; Primorac, D.; Rueda, J. A.; Shakeri, S.; Vereshchagin, G. V.; Wang, Y.; Xue, S.-S. (2017). The cosmic matrix in the 50th anniversary of relativistic astrophysics. *IJMPD*, 26, 10.
- Ruffini, R.; Wang, Y.; Aimuratov, Y.; Barres de Almeida, U.; Becerra, L.; Bianco, C. L.; Chen, Y. C.; Karlica, M.; Kovacevic, M.; Li, L.; Melon Fuksman, J. D.; Moradi, R.; Muccino, M.; Penacchioni, A. V.; Pisani, G. B.; Primorac, D.; Rueda, J. A.; Shakeri, S.; Vereshchagin, G. V.; Xue, S.-S. (2018). Early X-Ray Flares in GRBs. *ApJ*, 852, 53R.

Acknowledgments

I acknowledge the support provided by the Erasmus Mundus Joint Doctorate program through grant 2013-1471, awarded by the EACEA of the European Commission; support and help provided by colleagues and friends at Erasmus program, Sapienza University of Rome and ICRANet.

Contents

Abstract	i
Contents	v
Introduction	1
1 Gamma-Ray Bursts	3
1.1 History of GRB discoveries	3
1.1.1 Vela	3
1.1.2 CGRO-BATSE	3
1.1.3 BeppoSAX	5
1.1.4 Swift	7
1.1.5 Fermi	9
1.1.6 Other satellites and detectors	10
1.2 Astrophysical conclusions and assumptions from observations	10
1.2.1 Isotropic energy, luminosity and energy source	10
1.2.2 Duration of a pulse and compactness problem	11
1.2.3 Locations of GRBs and their progenitors	12
2 Fireball and Fireshell Models	13
2.1 Fireball Model	13
2.1.1 Central engine	13
2.1.2 Fireball evolution	14
2.1.3 Shocks	14
2.1.4 Jets	16
2.1.5 Afterglow	16
2.2 Fireshell Model	17
2.2.1 Black holes	17
2.2.2 Central engine	18
2.2.3 Expansion of fireshell plasma	20
2.2.4 P-GRB	21
2.2.5 Extended afterglow	21
2.2.6 Fitting the GRB	23
2.2.7 Long and short GRBs in the fireshell model	25
3 Induced Gravitational Collapse	27
3.1 GRB-SN in the Fireball model	27
3.2 Different episodes in GRB light curve	28
3.3 The IGC	29
3.4 X-ray afterglows of IGC GRBs	33

3.4.1	Overlapping	33
3.4.2	Very energetic GRB 130427A	34
3.5	Binary systems and two families of GRBs	35
4	Thermal X-ray emission in the late prompt - early afterglow phases	37
4.1	Data Analysis	39
4.1.1	Swift BAT and XRT data	39
4.1.2	Software	40
4.1.3	Pile-up	42
4.1.4	Other difficulties	42
4.1.5	MCMC	44
4.2	Preliminary results	45
4.2.1	Two black bodies	49
4.3	GRB 151027A	51
4.3.1	Temperature from the first time interval	53
4.3.2	151027A in the IGC scenario	55
4.4	Thermal spectrum from relativistically expanding sphere	55
4.4.1	Basic equation	56
4.4.2	Non-expanding sphere	57
4.4.3	Relativistic movement of a surface element	58
4.4.4	Pulse from an expanding sphere	60
4.4.5	Continuous emission from an expanding sphere	63
4.4.6	Wave fronts from different velocities and temperatures	69
4.5	Simulation of spectrum	72
4.5.1	The code	72
4.5.2	151027A	76
4.5.3	Double black body	79
4.6	Concluding remarks	81
5	New GRB-SNe connections	83
5.1	Technical details	86
5.1.1	SN catalog	86
5.1.2	GRB catalogs	89
5.1.3	Program scripts	91
5.2	Analysis of long GRB - SN Ib/c connections, 2014	92
5.2.1	Statistics of potential connections	93
5.2.2	The sample of Ib/c connections	94
5.2.3	Discussion	96
5.3	New statistical approach	98
5.3.1	On randomness	98
5.3.2	Confidence level	99
5.3.3	Generating random positions and dates	103
5.3.4	Removing same GRBs	103
5.3.5	Time windows	104
5.3.6	Example of changes to distributions for long Fermi GRBs and Ia SNe	104
5.4	Analysis of long GRB - SN Ib/c connections, 2017	105
5.4.1	The sample of Ib/c connections	107
5.5	Analysis of short GRB - SN IIn connections	110

5.5.1	The sample of BATSE short GRBs – SN IIn connections	112
5.5.2	Fermi short GRB – SN IIn connections	114
5.5.3	Short GRBs – IIn SNe, no direct evidence	116
5.5.4	Rates	121
5.5.5	Properties of IIn-GRBs	123
5.5.6	Mechanisms behind IIn-GRBs	125
5.5.7	Future work	127

Bibliography

Introduction

Gamma-ray bursts were discovered in the 1970s. They are transient astronomical phenomena lasting from fraction of a second to several tens or hundreds of seconds. They emit most of the radiation as γ -rays, mainly in the keV range, but also in the MeV and even GeV. The discovery of their redshifts in the '90s, which can range from 0.01 up to 8, helped to classify them as cosmological astrophysical phenomena. With the known distance (calculated from the redshift) it was possible to calculate isotropic energy emitted which can range from 10^{48} to 10^{55} erg. This is an enormous amount of energy, especially when considering it is released in the interval of tens of seconds - luminosity can reach $10^{53} - 10^{54}$ erg/s. For comparison the total rest mass/energy of the Sun is about 2×10^{54} erg. Gamma-ray bursts are by far the most luminous objects on the stellar scale and consequently they are among the most distant observed objects. In the '90s a supernova was associated to a burst and since then many more associations were discovered. This means that gamma-ray bursts are a stellar phenomena, related to the "death" of a star, as opposed to, for example, active galactic nuclei which are galactic phenomena. Based on some basic astrophysical principals and observational evidence, gamma-ray burst emitting ejecta has to move at ultra-relativistic speed. In fact it is by far the fastest moving (known) object with velocities that can reach values of several hundred Lorentz factors. For comparison the jets of active galactic nuclei, the second most fastest objects, move with velocities on the order of 10 Lorentz factor.

The Collapsar model explains the central engine of gamma-ray bursts. Gamma-ray bursts happen when a massive star burns trough its nuclear fuel and the iron core of a star collapses into a black hole. The infalling material from the rest of the core and inner envelopes onto the black hole creates an ultrarelativistic jet along the rotation axes. The released gravitational potential energy is also responsible for supernova which accompanies gamma-ray burst. The rest of the scenario is explained within the Fireball model. The jet is composed of series of fireballs moving with ultrarelativistic but different velocities. The fireballs are thin shells within the jet cone consisting of photon-lepton plasma with small amount if baryons. The collision between these fireballs produces gamma-ray emission which is detected as gamma-ray burst. Collimated and boosted emission from an ultrarelativistic jet would explain enormous observed fluence.

Another way to explain gamma-ray burst dynamics is the Fireshell model and gamma-ray burst - supernova connection is explained by Induced Gravitational Collapse model. The basis for the latter is a close binary system composed of a Ic pre-supernova star and a neutron star. When the star explodes as supernova its ejecta accretes onto the companion neutron star. The neutron star then collapses into a black hole. The Fireshell model then states that gravitational energy of collapsing material into a black hole is completely converted, via process of vacuum polarization, into a relativistically expanding sphere of electrons, positrons and photons - the fireshell. When the fireshell sphere interacts with circum-burst medium, the emission occurs. The enormous isotropic energies of gamma-

ray bursts are explained by total conversion of gravitational potential energy to fireshell plasma, and by very high efficiency of fireshell emission.

Gamma-Ray Bursts

This chapter contains some basic information on Gamma-ray bursts (GRB). Firstly the history of main GRB discoveries and instruments which made them will be presented. Then some observational features will be presented and general astrophysical conclusions and assumptions which come out of them.

1.1 History of GRB discoveries

This section will present in chronological order mayor observational discoveries on GRBs and spacecrafts-instruments which made them.

1.1.1 Vela

Vela satellites were launched by the US in the 1960s in order to monitor nuclear bomb detonations, namely to assure compliance with the 1963 Partial Test Ban Treaty. Satellites were equipped with gamma-ray and X-ray detectors.

On July 2, 1967 a burst (~ 10 s) of gamma-rays was detected. This was the first ever observed GRB - GRB 670702¹. At the time it wasn't known where this GRB came from. After several more burst discoveries it was possible to crudely localize them based on different arrival time of bursts at different satellites. It was discovered that they didn't come from the Earth or the Sun. Therefore, they are of cosmic origin. Results from the Vela satellites were declassified in 1973 and astronomical community was introduced to a new phenomena. At that point nothing else was known about GRBs except their cosmic origin.

1.1.2 CGRO-BATSE

Next important discovery came from Burst And Transient Source Experiment, or BATSE for short. It was a gamma-ray detector on board of NASA's Compton Gamma-Ray Observatory (CGRO) satellite which operated from 1991 to 2000.

Thanks to the instrument capabilities BATSE detected about one GRB per day during its 9 year operation. BATSE also managed to localize most of them to within few degrees.

¹The GRB naming convention follows the format GRB YYMMDD. In the case of multiple detections on a single day, additional letters B, C, D... are added to successive bursts while the first burst has a letter A as suffix.

2704 BATSE Gamma-Ray Bursts

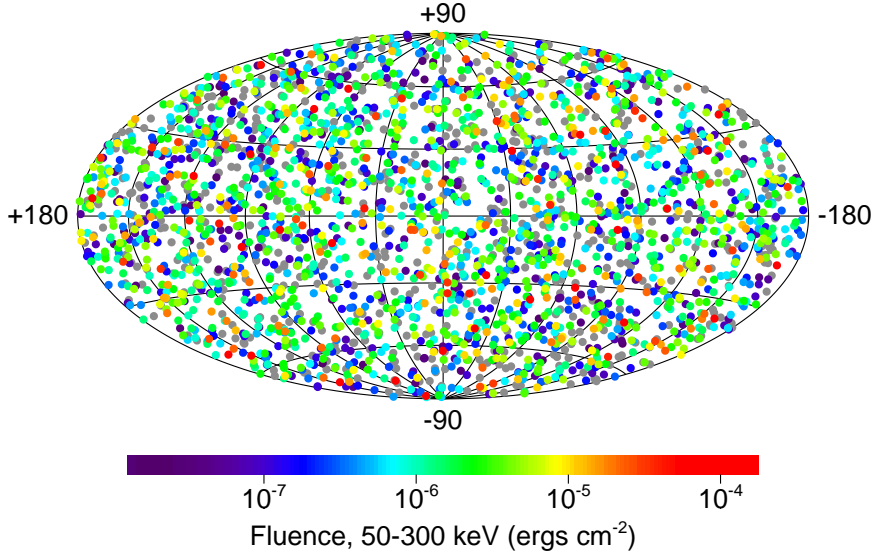


Figure 1.1: Galactic coordinates map of the 2704 GRBs detected by BATSE. The color code refers to the fluence of the bursts; gray dots indicate incomplete data. Credits: CGRO BATSE Team.

The map of GRB locations is given in Figure 1.1. The isotropic distribution was proof that they were not from the Milky Way galaxy. If they were, their distribution would not be isotropic but much more concentrated towards Milky Way plane. This strongly pointed towards cosmological origin although galactic halo and solar scenarios were not totally disregarded.

Another important discovery by the BATSE was GRB detailed temporal structure, i.e. the light curve.. The duration of a burst² can be from few milliseconds to several minutes. Light curves are composed of many pulses, usually with a fast rise and slow (exponential or power-law) decay, but can also be symmetrical. A single GRB can have pulses of different intensities and durations, which often overlap. Sometimes a GRB is composed of a single pulse. An example of several BATSE GRB light curves is given in Figure 1.2. Each GRB has a unique light curve.

Thanks to the BATSE and other gamma-ray detectors on board CGRO it was possible to observe the spectral shape of GRBs. It was discovered that the spectra of GRBs are non-thermal (no black body emission). The spectra can be described by the *Band* function (Eq. 1.1). This function represents two smoothly joined power-law functions.

$$N(E) = K \begin{cases} \left(\frac{E}{100} \right)^\alpha \exp \left[\frac{-E(2 + \alpha)}{E_p} \right] & , E \leq \left(\frac{\alpha - \beta}{2 + \alpha} \right) E_p \\ \left(\frac{E}{100} \right)^\beta \exp(\beta - \alpha) \left[\frac{(\alpha - \beta)E_p}{(2 + \alpha)} \right]^{\alpha - \beta} & , E > \left(\frac{\alpha - \beta}{2 + \alpha} \right) E_p \end{cases} \quad (1.1)$$

Here, N is the flux in units of: photons, per unit area, per unit time, per unit energy; α is the first power-law photon index (lower energy index); β is the second photon power-law index (high energy index); E_p is the peak energy. In most cases α parameter varies

²The duration of a burst is given by the T_{90} parameter. This parameter is the time interval in which 90% of energy is detected, starting from the point when 5% of energy is detected and ending at 95%.

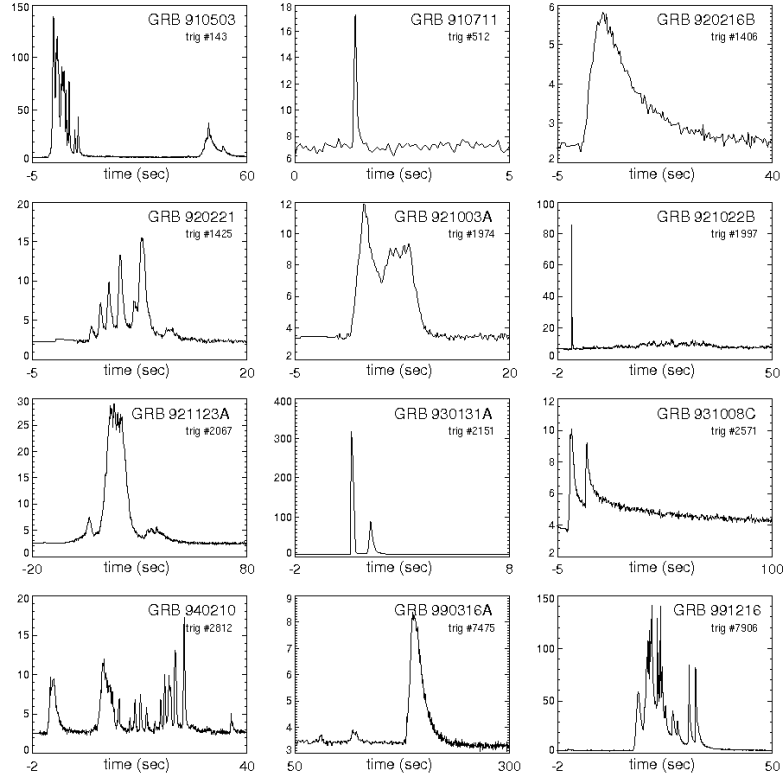


Figure 1.2: Twelve GRB light curves as seen by BATSE (in units of 10^3 counts/s) demonstrating their diversity in duration (milliseconds to tens of minutes), in temporal structure, and in pulse shape. Credits: BATSE Archive.

between $-1.5 \leq \alpha \leq 0.5$, β between $-2.5 \leq \beta \leq -2$, while the peak energy is in the range of $100 \text{ keV} \leq E_p \lesssim \text{MeV}$. An example of typical GRB spectrum (the Band function) is given in Figure 1.3.

It should be noted that this is referred to time integrated spectra (T_{90} time interval). In most cases there is a spectral evolution within each pulse, such that E_p evolves from higher energy to lower.

Plotting the number of bursts vs. their duration, a bimodal structure can be seen (Figure 1.4) with separation around 2 s. The first group is called *short* GRBs, and the second *long* GRBs. This division of GRBs was confirmed by subsequent detectors and it is the main division of GRBs to this day. The bimodal distribution follows the spectrum hardness³, which is related to E_p . Therefore, the two groups of GRBs can be divided into *short-hard* and *long-soft*.

1.1.3 BeppoSAX

BeppoSAX was a satellite equipped with gamma-ray and X-ray detectors and it operated from 1996 to 2002. It was a product of scientific collaboration based in Italy and contribution by Netherlands. The name *Beppo* comes from physicist Giuseppe Occhialini and *SAX* stands for *Satellite per Astronomia a raggi X*, Italian for *satellite for X-ray astronomy*.

³Harder spectra have a bigger ratio of high energy photons to low energy ones.

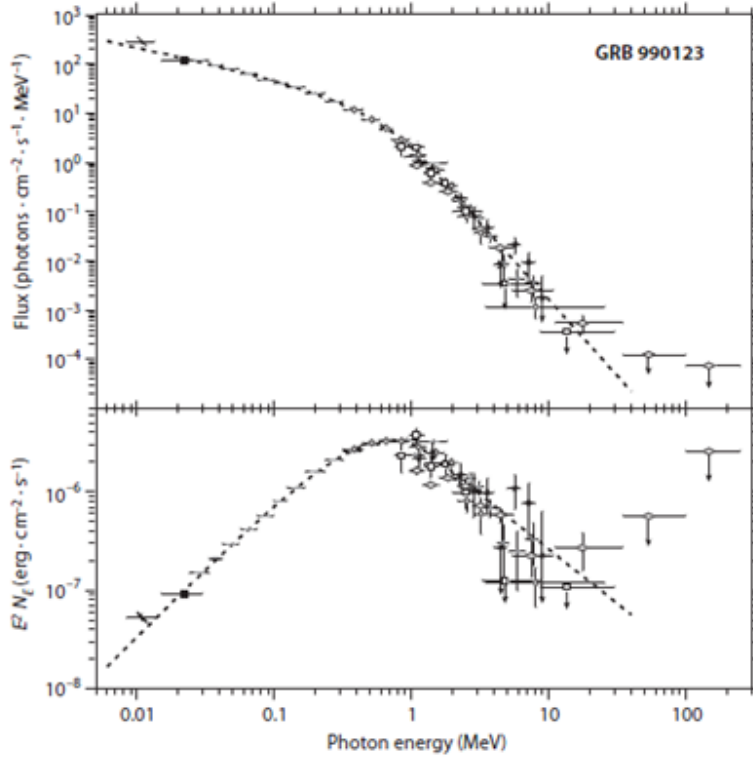


Figure 1.3: Flux spectrum (top) and spectral energy distribution (bottom) of GRB 990123, fitted with a Band function. Data points are from detectors on-board CGRO. Figure reproduced from (Briggs et al., 1999). Power-law functions on a log-log plot look like straight lines with power-law index being the slope. The plot $E^2 \times Flux$ vs. $\log E$ shows at which energy decade $d(\log E)$ most energy is released. Flux is multiplied by energy once since we are interested in energy, not number of photons, and the second time since we are interested in released energy per unit logarithm of energy $d(\log E)$, not per unit energy dE . On the lower plot the average slope of first power-law will be $\alpha + 2 \approx 1$, and the slope of second power-law will be $\beta + 2 \approx -0.5$. This means that there is a peak and it is at E_p energy. This is the reason why they are GRB, i.e. why most of the energy is released in gamma-ray domain, because the peak is in the gamma-ray domain.

At this point it was predicted that GRBs should emit an *afterglow* - softer (in the X-ray domain), longer, weaker and slowly fading emission which starts after the standard emission ends. Thanks to its capabilities BeppoSAX managed to observe first ever afterglow in the GRB 970228 (Frontera et al., 1998). The intensity of the afterglow had been reducing slowly and could be detected for couple of days in the X-ray domain. The localization of the afterglow was precise and fast enough to allow follow up by the optical telescopes which detected the optical counterpart of the afterglow. The localization by the optical telescopes allowed the detection of the host galaxy of the GRB. This in turn allowed the redshift of the galaxy, and by extension the redshift of the GRB, to be measured and it turned out to be cosmological $z = 0.695$ (Bloom et al., 2001). Soon after more GRB redshifts were measured and they were all cosmological. This definitely proved that GRBs are cosmological objects. Knowing distance⁴ it was possible to calculate the overall emitted energy⁵ and luminosity of GRBs. This was the moment when it was discovered that GRBs could release very large amounts of energy at very short time intervals.

Thanks to the good and fast localization of GRBs by BeppoSAX, many optical follow

⁴Distance is calculated from the redshift assuming standard cosmological model (Λ CDM model).

⁵Total electromagnetic/photon energy of GRB.

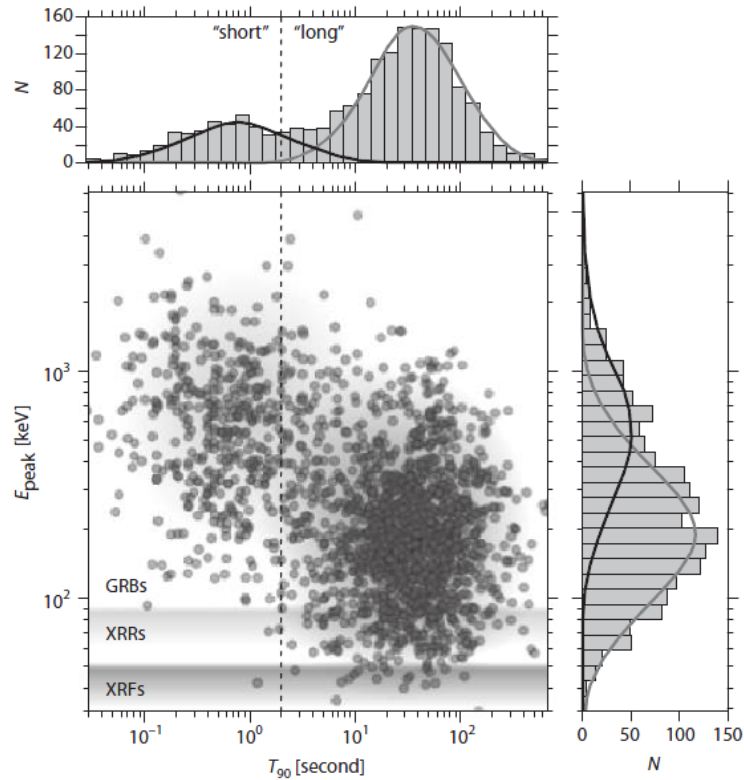


Figure 1.4: This diagram evidences the bimodal GRB distribution of BATSE events in terms of duration (horizontal axis) and spectral hardness (vertical axis), evaluated through the peak energy E_p of the spectral energy distribution. Two regions can clearly be distinguished, even if there is a significant overlap between them. Outset histograms show the number of events in appropriate time and energy bins.

ups were possible. This resulted in another important discovery. BeppoSAX detected long burst GRB 980425 and optical follow up showed a presence of a supernova about one day after GRB and at the same location. The supernova was a type Ic supernova, it was more luminous and had higher speed of expanding ejecta than typical core-collapse supernovae (Iwamoto et al., 1998). Although there were some hints of earlier GRB-supernova connection (Galama et al., 2000), this one is considered to be the first "good enough" evidence. GRB 980425 was a very low energy GRB $E_{iso} \sim 10^{48}$ erg and it wasn't certain at the time if all GRBs could be connected to supernovae or only low energy ones. In the coming years many more connections were discovered. Energy of GRBs varied from low to high and all the supernova were type Ic or Ib, very luminous, had high speed of expanding ejecta and were connected to long GRBs. At this point it was known that most of long GRBs are a stellar phenomena and connected to the "death" of a massive star, more precisely to the core collapse of a massive star without hydrogen envelope.

1.1.4 Swift

Swift is a satellite equipped with gamma-ray, X-ray and ultraviolet-optical detectors. It was launched in 2004 and is still operational. It is primarily NASA's project with strong participation from institutions in US, UK, Italy. The name *Swift* comes from the spacecraft's ability to rapidly slew.

One of the important discoveries by Swift is a detailed X-ray afterglow light curve

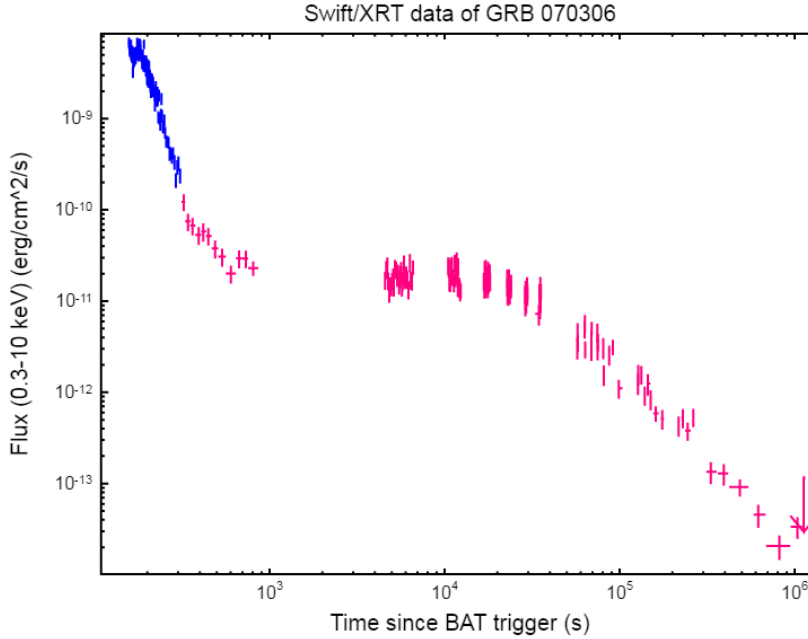


Figure 1.5: The afterglow of GRB 070306. The typical three phases can be seen - the steep decay, the plateau and the shallow decay. The light curve comes from XRT instrument (0.3 – 10 keV energy band) on board Swift. The flux is corrected for absorption which is present below 2 keV, i.e. the flux intensity is as if there is no absorption. The time is counted since the start of the GRB. Different colors correspond to different operation mode of XRT. The gaps are due to occultation of GRB by Earth since Swift satellite orbits Earth every 90 minutes. Credits: Swift Archive and University of Leicester.

(Figure 1.5). The typical structure of the afterglow is: it starts with a steep decay just after the main part (the *prompt* phase) of the GRB. After that there is a kind of *plateau* where intensity is almost constant. After that the emission continues to fade as a power-law with shallow decay. In some cases *flares* are present in the afterglow. They have a shape of the pulse similar to pulses in the prompt emission but last much longer and are softer and weaker. They are, however, spectrally harder and brighter than the underlying continuum afterglow emission. In other cases light curves don't follow standard shape, but have, for example, single power-law decay from the start.

Thanks to Swift's capabilities, especially to rapid and precise localization of GRB, many optical follow-ups were possible. This helped in discovering many GRB host galaxies and redshifts⁶. Up to the year 2016 Swift detected about 1000 GRBs and about 300 of them have a measured redshift (distance). Swift is by far the satellite most responsible for large number of GRB redshift measurements. Numerous optical follow-ups also allowed discoveries of many other connections between GRBs and supernovae.

Examination of the host galaxies helped to further define the long and short division of GRBs. Long GRBs tend to appear in spiral (young) galaxies, especially in the parts of significant star formation. Short GRBs tend not to have preference for galaxy type or a specific position within the galaxy.

Swift raw (and semi-processed) data are publicly available few hours after observation and there are publicly available software for the analysis of this data as well as detailed

⁶Redshift can be determined from the spectral lines in the optical afterglow of a GRB or the host galaxy.

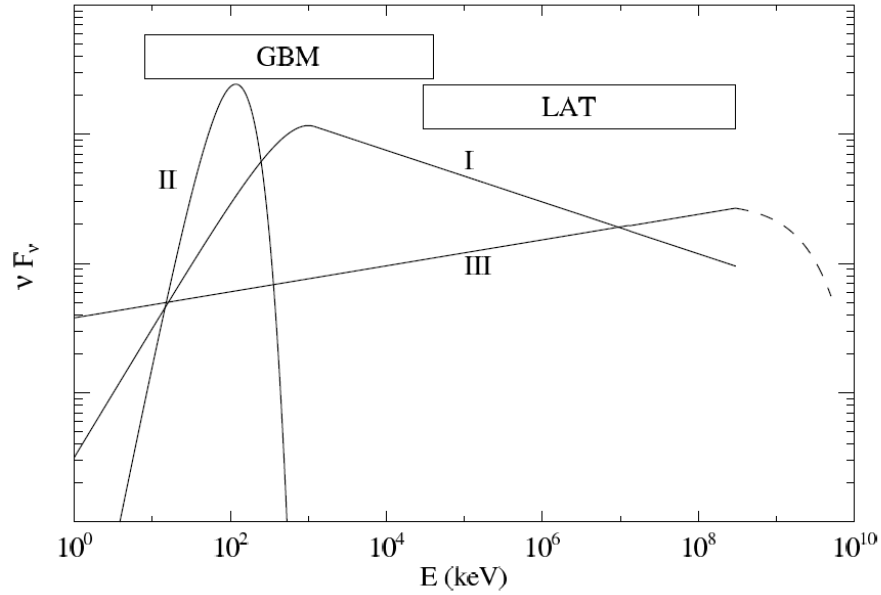


Figure 1.6: Three components in the prompt emission spectra found by Fermi: Band, underlying power-law and thermal.

explanation on their usage⁷.

1.1.5 Fermi

Fermi Gamma-ray Space Telescope, or just Fermi, is a satellite launched in 2008 and is still operational. It is NASA's project with participation from institutions in US, France, Germany, Italy, Japan, and Sweden. It carries gamma-ray instruments with a very wide range of energy coverage - from few keV up to several hundred GeV. Formally known as GLAST (Gamma-ray Large Area Space Telescope) it was renamed in honor of physicist Enrico Fermi.

Fermi capabilities helped to further discover properties of the prompt emission. Aside from the Band function, additional components were discovered (Figure 1.6). In some GRBs a black-body thermal component was found, usually at lower energies than the Band's E_p . Thermal component shows evolution such that temperature of the black body monotonically decreases. Another component was an underlying power-law which can start from few keV all the way up to GeV range.

Thanks to its wide field of view Fermi observed many bursts. Up to 2016 Fermi observed about 1600 GRBs, managed to capture their spectra and spectra evolution.

Fermi also managed to discover that afterglows can have a high energy component (GeV domain). In fact, the most energetic photons discovered were detected after the prompt emission, during the afterglow. The record breaking high energy photon came from GRB 130427A. It had an energy of 95 GeV (128 GeV in the rest frame of the burst). It was detected about 250 s after the beginning of the burst, significantly after the prompt emission (Ackermann et al., 2014).

Fermi raw (and semi-processed) data are publicly available few hours after observation and there are publicly available software for the analysis of this data as well as detailed

⁷<http://www.swift.ac.uk/>

explanation on their usage⁸.

1.1.6 Other satellites and detectors

The five mentioned missions were among the most crucial ones in GRB observations. The satellites and detectors on them were at the time most advanced in the field of GRB observations in the gamma-ray and X-ray domain. There were/are other satellites equipped with gamma-ray and X-ray detectors which complement the five mayor missions and help to improve statistics on GRB parameters such as host galaxy type, distance, duration, spectra, etc. These are: Wind-Konus, AGILE, INTEGRAL and XMM-Newton, Chandra, etc.

The most important energy interval for the study of Gamma-ray bursts is, of course, the gamma (and X-ray) domain. Optical detectors also played, and still do, important role. Sub arc-second localizations, position of GRB within the host galaxy, redshift measurement, etc. wouldn't be possible without optical observations. When it comes to GRBs, the more important optical (and near infra red) detectors today are: VLT, LBT, Keck Telescopes; GROND, PROMPT, ROTSE, and LT, Faulkes Telescopes, RATIR and others.

There are also radio telescopes observing the radio counterpart of the afterglow. These include VLBI, VLA, GMRT, ATCA, AMI, WSRT, etc. Radio afterglow can be detected for years after the GRB. Radio detectors can give the most precise localization (\sim milli-arcsecond). GRB 030329 was relatively close and had strong emission in the radio domain. Observations of the afterglow in the tens of days after it occurred made it possible, thanks to high precision of radio telescopes, to actually measure the angular size of a GRB emitting material. From there, knowing the redshift (distance), it was calculated that emitting ejecta in the afterglow phase was moving with relativistic speed⁹ (Taylor et al., 2004).

Up to now GRBs were not detected in the TeV range. The main detectors observing in this range are MAGIC, HESS, VERITAS, HAWC.

1.2 Astrophysical conclusions and assumptions from observations

In this section astrophysical conclusions and assumptions which come from GRB observations will be presented. These are not really models but some facts and assumptions which come from basic physical principles. These are basis for different models.

1.2.1 Isotropic energy, luminosity and energy source

With the observed fluence and known distance, it is possible to calculate released isotropic energy E_{iso} ¹⁰. This quantity can reach the values of $E_{iso} \sim 10^{54} - 10^{55}$ ergs. This is enormous amount of energy for a solar size source¹¹. For comparison, maximum energy emitted by some supernovae in the form of photons is $E_{iso} \sim 10^{52}$ erg (Dong et al., 2016). Moreover this amount of energy is released in a relatively short time period of tens of

⁸<http://fermi.gsfc.nasa.gov/ssc/>

⁹Lorentz factor $\gamma > 1$, but not $\gamma \gg 1$

¹⁰The term *isotropic energy/luminosity* is the amount of energy/luminosity calculated assuming isotropic emission of an object.

¹¹Weather one, two or more stars are involved, the system is stellar sized, unlike AGNs, for example, which is a system on the order of millions of stellar masses.

seconds, making GRBs the most luminous known objects in the universe with maximum $L_{iso} \sim 10^{53} - 10^{54}$ erg/s. This is the reason why it was possible to detect them all the way up to redshift 8. The most luminous ones could be detected even if they had been beyond redshift 10. The E_{iso} and L_{iso} refer to photons. The total released energy of GRB is even higher.

One of the objects that can produce this amount of energy is a black hole. The most energetic stellar phenomena, which are relatively understood, are core-collapse supernovae. Their energy comes directly from gravitational potential energy, i.e. from the kinetic energy of in-falling stellar material. This energy is later transformed into energy of the supernova (neutrinos, kinetic energy of ejecta, photons). It is reasonable to assume that a black hole is responsible for GRB energetics since the potential gravitational energy is even greater than the one neutron star has. All the supernova associated to GRBs were core-collapse SN and in vast majority of cases, when supernova could have been detected¹², it was detected. This further points to a scenario where a black hole is present and where GRBs are created when the inner core of the star collapses into a black hole.

Even with the black hole present it is hard to explain GRB enormous energies by conventional means and known astrophysical mechanisms. The amount of released energy can be few orders of magnitude smaller than E_{iso} if GRBs emit energy in the form of jets which are pointed towards the Earth. When there is a material falling onto a compact source - a super massive black hole in active galactic nuclei or stellar size black hole in X-ray binaries, the formation of jets occurs. It is reasonable to assume that jets also form in GRBs. Furthermore, it is reasonable to assume that a significant part of GRB total energy should be in the form of photons (gamma-ray photons), unlike standard core-collapse supernova where photons make up about 0.01 - 0.1 % of total supernova energy. This *efficiency* is important factor since if it is higher the total energy can be lower for a given E_{iso} .

There are also ideas in which energetics is explained by newly formed millisecond magnetars where rotational energy of the neutron star is transformed into GRB energy. The formation of the jet and high efficiency of conversion of total energy in to photons is also required.

1.2.2 Duration of a pulse and compactness problem

Thanks to the high temporal resolution of instruments the fine structure of the prompt light curve was observed. The shortest pulses have a duration on the order of $\delta t \approx 10$ ms. This can give information on the upper size of the emitting region. If an emitting region has a certain size and it emits an infinitesimally short pulse, the instrument far away would still detect a pulse with a duration of $\delta t \approx R/c$ where R is the radius of the source and c is speed of light. This means that an upper boundary on the GRB emitting region is $R \leq c\delta t \approx 3000$ km.

With typical values of E_{iso} , spectral shape, and R (volume), an average density of high energy photons can be calculated. From there the optical depth for electron-positron pair creation $2\gamma \rightarrow e^\pm$ can be estimated. This should be significant process since there are many photons with energies on the order of electron rest mass/energy (0.511 MeV) or higher. For typical GRB parameters it turns out that the value for this optical depth is very high, on the order of $\tau_{\gamma\gamma} \sim 10^{15}$. The process $2\gamma \leftrightarrow e^\pm$ would take place with very high rate and the higher energy photons would be trapped inside and with thermal

¹²With the current optical telescopes supernova can be detected up to redshift $z \approx 1$.

spectrum. Only small part from the surface would manage to escape and wouldn't produce the observed flux. Also, their spectrum should be thermal while observations show that higher energy photons have a power-law spectra (high energy part of the Band function). Another process that would take place with the presence of e^\pm is Compton scattering of lower energy photons onto e^\pm . This process would significantly increase optical depth for lower energy photons and their number should be smaller and spectrum thermal - which is clearly against observations. This problem is called *compactness problem*.

The solution to this problem is if assuming that emitting region expands towards the Earth with ultra-relativistic speed¹³. First: The energy of the photons is boosted by expanding emitting region¹⁴. Photons have smaller energy in the rest frame of the emitting region then observations suggests and there would be less high energy photons able to undergo electron-positron pair creation. Second: the observed duration of a pulse wouldn't imply such a compact source. With emitting region expanding towards the Earth, a large size one would produce much shorter pulses than if it were not expanding.

For typical values of GRB parameters, in order for opacity to be low enough $\tau \sim 1$ so that material is transparent, relativistic speed of the emitting region should be on the order of $\gamma \sim 100$ and in some GRBs $\gamma \sim 1000$. This makes GRBs objects with the fastest moving material in the universe. For comparison, active galactic nuclei jets are moving with Lorentz factor in the range of $\gamma \sim 2 - 20$ while the ones observed in our galaxy have speed $\gamma \sim 2$.

1.2.3 Locations of GRBs and their progenitors

With the arc-second and sub-arcsecond localizations of GRBs it was possible to determine their location within the host galaxy. Long GRBs tend to occur in the most luminous parts (high star formation) of star-forming galaxies. Together with their connection to Ib/c SNe and requirement for a black hole, this points to the conclusion that progenitors of long GRBs are massive stars. Short GRBs don't seem to have a preference for the galaxy type or a location within the galaxy. They can even be found at large distances from the host galaxy center. Also they are not connected to supernovae. This, coupled with their short duration, points towards merger of compact objects - two neutron stars or a neutron star and a black hole.

¹³Speed with Lorentz factor on the order of $\gamma \sim 10 - 100$ or higher.

¹⁴The energy is first boosted by expanding plasma and later lowered by expansion of the universe. The second process is much lesser than the first and not relevant here.

Fireball and Fireshell Models

In this chapter main properties of the Fireball and the Fireshell model will be presented.

2.1 Fireball Model

In this section main properties of the Fireball model will be presented. This model was developed during the '90s, after CGRO-BATSE data came in, and is generally accepted model. There are open questions and uncertainties, and some details in the model were added and modified as new data from GRBs arrived during the 2000s and 2010s. However, the underlying general picture still remains unchanged. The numerical values of certain important parameters in the model - such as Lorentz factor of the fireball, distance from central source, jet opening angle, peak energy of radiation, etc. - were derived taking typical values of parameters from GRB and other astronomical observations and applying them in the model. Since the model describes time evolution of GRB mechanism, the uncertainties in the model become more important as this time evolution progresses, and the model branches into several different scenarios later on. Which course is the most probable one can also depend on a specific GRB. This section presents the model as it describes time evolution of GRB mechanism and presents a typical course GRB takes (Figure 2.1). The main summary of the model can be found, for example, in (Piran, 1999), (Mészáros, 2006), (Kumar and Zhang, 2015).

2.1.1 Central engine

The fireball model doesn't go into details about the progenitors of GRB and the mechanism of creating large amounts of energy. It is probable that energy can be obtained from gravitational potential energy of collapse of a massive star core to a black hole (BH), merger of two compact objects into a BH, or, from rapid spin down of a magnetar. The scenario starts with large amount of energy $E_{tot} \sim 10^{54}$ erg being released in a relatively small volume (radius r_0). This energy will be in the form of gravitational waves, neutrinos and a *fireball* - a ball of electrons and positrons (e^\pm), gamma-rays (γ) and small amount of baryons. The amount of energy in the fireball is a fraction of total energy, on the order of $E_0 \sim 10^{50} - 10^{52}$ erg. The initial radius is $r_0 \sim 10^7$ cm which is several Schwarzschild radii of an ensuing BH. Gravitational waves and neutrinos will pass through the fireball almost

without interaction.

2.1.2 Fireball evolution

The fireball consists of electrons and positrons, gamma-rays and small amount of baryons - mostly protons with total mass of $M_0 \sim 10^{-5} M_\odot$. All these elements are coupled via electromagnetic interaction to each other and make up a single system. The amount of released energy is much greater than rest energy of baryons $E_0 \gg M_0 c^2$. A parameter to describe the amount of baryons is defined as $\eta \equiv E_0 / M_0 c^2$. Pair annihilation between e^\pm will create 2 γ photons and they will in turn create e^\pm pairs, etc. This process $e^\pm \leftrightarrow 2\gamma$, along with Compton scattering, will make the fireball optically thick and in thermal equilibrium. The initial temperature is on the order of $kT_0 \sim 1$ MeV.

Due to enormous internal pressure the fireball will expand outwards. Because the fireball is optically thick, only photons from the surface will escape while the majority of them will stay inside the fireball system, so the fireball expansion can be considered adiabatic. Since $E_0 \gg M_0 c^2$ the internal fireball pressure will be dominated by radiation which gives the adiabatic index of $\gamma_\alpha = 4/3$. Assuming radiation-dominated adiabatic expansion and considering relativistic dynamics gives the next picture:

The internal energy of the fireball will be transferred into bulk (outward) kinetic energy of baryons which are moving spherically outwards. The Lorentz factor Γ of baryons, and fireball as a whole, will increase linearly with radius r (distance from the BH) until it reaches value on the order of $\Gamma_{max} \sim \eta$ with numerical value on the order of $\Gamma \sim 10^2$. The (saturation) radius at which this happens is on the order of $r_s \sim r_0 \eta$ with numerical value of $r_s \sim 10^9$ cm. After this the Lorentz factor will remain constant and the fireball will continue expanding with constant speed. At this point most of the fireball energy will be in the bulk kinetic energy of protons.

With expansion the fireball will actually have the form of a spherical shell. The width of a shell is $\delta r_0 \sim r_0$ and the initial spreading of the shell due to internal pressure is negligible. The spreading of the shell will reach significant values well beyond saturation radius r_s .

When the rest-frame temperature inside the fireball drops to value of $kT \approx 20$ keV, the reaction $2\gamma \rightarrow e^\pm$ stops and the last of e^\pm annihilate. For typical values this happens before saturation radius r_s . However, there are still e^- which are associated to protons and, due to Compton scattering between photons and electrons, the fireball is still optically thick. The (photospheric) radius r_{ph} where the optical depth reaches value of $\tau \sim 1$, i.e. where the fireball becomes optically thin, is beyond the saturation radius r_s . Typical value is $r_{ph} \sim 10^{12}$ cm. At this point all the photons will escape and their spectrum will be thermal. This may explain thermal emission in some GRBs detected by Fermi. However, the spectra of most GRBs is highly non-thermal. Moreover, most of the fireball energy is in the form of bulk kinetic energy of the protons and only a small fraction is in the thermal-spectrum photons. This is highly inefficient way to produce radiation from the fireball energy. In order to have significant thermal emission, additional processes should take place that would boost the thermal spectrum photons to higher energies and intensity.

2.1.3 Shocks

In order to achieve higher efficiency the bulk kinetic energy of the protons needs to be transformed to radiation when the fireball is optically thin. The best assumption on how

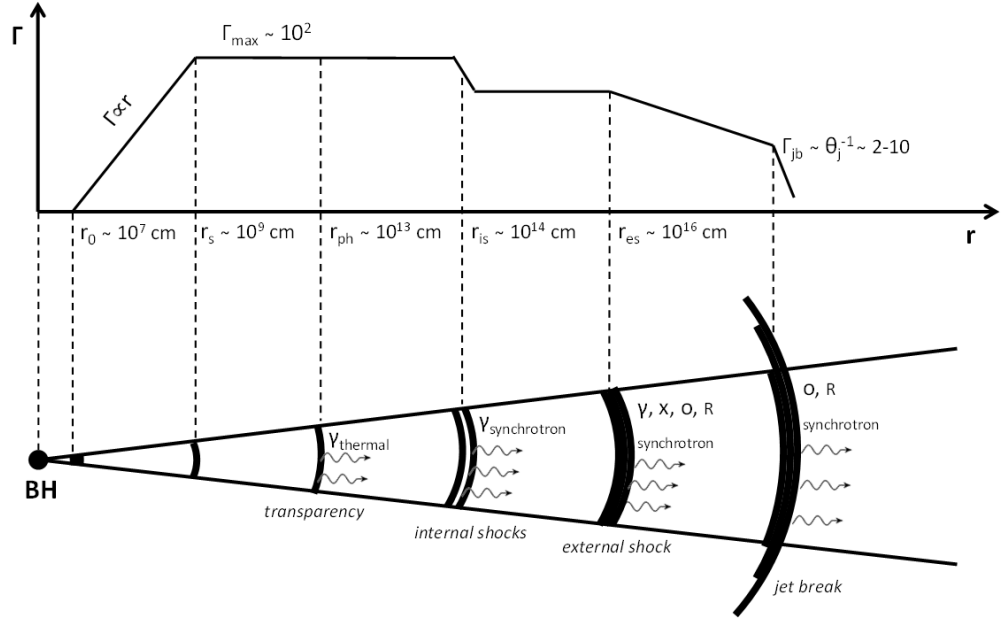


Figure 2.1: Evolution of fireball(s) and typical values for their Lorentz factor Γ and distance from the black hole r .

to do this is via shocks. When the fireball shell hits a standing or slower moving matter, a shock between two mediums will occur. The interaction between two mediums will happen via chaotic electric and magnetic fields (*collisionless shock*) and will increase internal energy (random kinetic energy) of particles (protons and electrons) in the mediums. Most of the energy in the fireball plasma is in the kinetic energy of protons but the shock will cause part of this energy to be transferred to electrons. The shock will also accelerate electrons via process *first order Fermi acceleration* to a power-law energy spectrum. Due to presence of magnetic fields a synchrotron emission from electrons is expected. The synchrotron emission from a power-law distributed electrons is a natural explanation for the GRB broken power-law spectrum. Photons produced by this emission are in the keV, MeV range. It is also possible that inverse Compton scattering of keV-photons onto accelerated electrons will occur as well as $2p \rightarrow 2p + \pi^0 \rightarrow 2p + 2\gamma$ interaction, both of which could produce photons in the MeV and GeV range.

At one point the fireball shell has to hit the external medium which has surrounded the star before collapse. If only this *external shock* is present it would produce only one peak in the light curve. This could be the case for single peak GRBs. In order to explain general multi-peak GRB light curve a series of shocks needs to happen. This is possible if the central engine produces several fireballs over some period of time and with different properties so they accelerate to different Lorentz factors. When the faster shell catches up with the slower one, a shock occurs. Each of these *internal shocks* would then be responsible for each peak in the GRB light curve. After the collision two shells merge into a single shell. For typical parameters of GRBs, the internal shocks can transform about 5-20% fireball energy to radiation. The internal shocks take place around $r_{is} \sim 10^{13}$ cm.

The afterglow is created when the shell(s), which have all merged together, hit the external medium, either interstellar medium or an ejected material (wind) from a progenitor star.

The shock, either internal or external, in the text above is the *forward shock*. In both

cases there will also be a *reverse shock*. When the two mediums collide, both of them will have shocked and unshocked zones. The forward shock is at the boundary of unshocked outer medium and shocked outer medium. The reverse shock is at the boundary of shocked and unshocked internal medium. The properties of reverse shocks are such that radiation produced by them will be synchrotron as well but the peak of emission should be at lower energies and the emission should be lower in intensity. Reverse shocks are used to explain optical flashes during the prompt emission in some GRBs.

2.1.4 Jets

Isotropic energy of GRBs can reach values of $E_{iso} \sim 10^{54} - 10^{55}$ erg and this is only the energy in the form of photons. The fireball energy is greater than this and the total energy even more so. In order to explain such high energies with a single star, a fireball, and the consequent radiation, is expected to be highly collimated, i.e. in the form of a narrow jet. Therefore, the fireball is actually a small part of a spherical shell moving with high Lorentz factor away from the BH.

In the non-jet/spherical case of a fireball which is moving with high Lorentz factor $\Gamma \gg 1$, an element of the shell only interacts with the surrounding elements if they are very close, within a light cone (interaction cone) of half angle of Γ^{-1} while it is decoupled from the rest of the fireball shell. Furthermore if the jet half angle is larger than the half angle of interaction $\theta_j > \Gamma^{-1}$, the element in the jet "doesn't know" whether it is in a jet or a sphere. This means that in the jet case of the fireball, the behavior will be similar as in the spherical case once $\Gamma \gg 1$. Also, while $\Gamma \gg 1$ the jet expands too rapidly in radial direction (away from the BH) and the sideways expansion of the jet is negligible. Therefore, main results derived from the spherical case then hold also for the jet case.

2.1.5 Afterglow

When the fireball(s) finally reach the external medium, either interstellar medium or a stellar wind, an afterglow is created. Just like in the internal shock case this *external shock* will accelerate electrons which will radiate via synchrotron process. The main difference is that this shock will happen on a longer time scale, Lorentz factor will decrease more slowly, electrons will radiate more in the soft X-ray domain (~ 10 keV) as well as in optical and radio, and the intensity will be lower and longer lasting. Typical value for distance at which external shock happens is $r_{es} \sim 10^{16}$ cm.

At some point in the afterglow phase Lorentz factor Γ of the fireball/jet will lower to value of $\Gamma \sim \theta_j^{-1}$, numerical value around $\theta_j \sim 5^\circ$ and $\Gamma_{jb} \sim 2 - 10$. Before this point most of the radiation came only from part of the jet $\theta \sim \Gamma^{-1}$ due to relativistic speed of the jet. After this point the entire jet is visible and the emitting surface will not continue to increase but will remain constant. Another important factor is that when $\Gamma \sim \theta_j^{-1}$ the jet will start to spread sideways significantly and accumulate much more medium matter which will cause Γ to decrease more rapidly. These two factors will cause rapid decrease in luminosity which is referred to as the *jet break*. Since the radiation across all the bands comes from the same mechanism in the afterglow phase, the jet break, which is caused by the geometrical effects of the jet, will cause the luminosity to decrease in all the bands at the same time, i.e. jet break should be achromatic.

Spreading of the jet after $\Gamma \sim \theta_j^{-1}$ will also cause the jet to become visible in the direction it wasn't visible before. The observer along this direction would miss the prompt

emission and the early phases of the afterglow but would see afterglow in the late phase, after jet brake. These kinds of afterglows are referred to as *orphan afterglows*. They haven't been discovered so far, probably due to observational difficulties.

2.2 Fireshell Model

In this section main properties of the Fireshell model will be presented. The basis of the model revolves around extracting large amounts of energy from a charged black hole (BH). This is done via process of electron-positron pair creation from strong electric field - a type of *vacuum polarization*. The model was being developed during the '70s focusing on BHs independently of GRBs. At the time little was known about GRBs, namely whether they are cosmological objects (large E_{iso}) or not. In the late '90s with the first measurements of GRB redshifts - which meant $E_{iso} \sim 10^{53}$ erg - the model received new attention in the contexts of GRBs. The model could naturally explain large values of E_{iso} without the need to assume jetted emission. The subsequent detection of some bursts with $E_{iso} \sim 10^{54}$ or even 10^{55} erg in the years and decades to follow, further strengthen this position. Central engine in the Fireshell model is the main aspect of the model. The fireshell model also directly explains the origin and gives precise dimensions for the ball/shell of electrons, positrons and subsequent gamma-rays, a system which is termed *fireball* in the Fireball model and *fireshell* in the Fireshell model. From this point on system evolves similarly like in the Fireball model although there are some key differences.

Review of the Fireshell model and associated topics can be found in (Ruffini et al., 2007a) which is a summary based on published papers, conference proceedings, workshops and other media prior to the end of 2007. Work revolving around black holes and energy extraction can be found in (Ruffini and Wheeler, 1971; Christodoulou and Ruffini, 1971; Damour and Ruffini, 1975; Preparata et al., 1998; Ruffini and Vitagliano, 2002; Cherubini et al., 2002; Ruffini et al., 2003b; Ruffini and Vitagliano, 2003; Cherubini et al., 2009; Ruffini and Xue, 2011; Han et al., 2012; Belvedere et al., 2012) and others. Physics of electron-positron pairs created from critical electric field is covered in (Ruffini et al., 2003c, 2007b; Aksenov et al., 2007; Kleinert et al., 2008; Aksenov et al., 2010; Han et al., 2010; Benedetti et al., 2011) and others. Initial evolution of the fireshell plasma, up to the point of reaching interstellar medium, and its radiation are described in (Ruffini et al., 1999, 2000; Bianco et al., 2001) and others. Interaction of fireshell with interstellar medium and its radiation are studied in (Ruffini et al., 2001a,b, 2002; Bianco and Ruffini, 2004; Ruffini et al., 2004b, 2005b; Bianco and Ruffini, 2005c,a, 2006) and others. Application of fireshell model to specific bursts can be found in (Ruffini et al., 2004a, 2005a; Bernardini et al., 2005; Ruffini et al., 2006; Bernardini et al., 2007; Caito et al., 2009, 2010; de Barros et al., 2011; Patricelli et al., 2012; Muccino et al., 2013a,b) and others.

This section will describe the Fireshell model as it describes time evolution of a GRB system (Figure 2.3) starting at energy extraction from black holes.

2.2.1 Black holes

Black holes (BH) can be divided into four categories based on rotation and electric charge. The simplest case is the non-rotating and non-charged BH - the Schwarzschild BH. Non-rotating but charged BH is called the Reissner–Nordström BH. Rotating but not charged BH is called Kerr BH. Black hole that is both rotating and charged is called Kerr–Newman BH.

The total energy of the BH system can be described as:

$$E^2 = \left(M_{ir} c^2 + \frac{Q^2}{4M_{ir}} \frac{c^2}{G} \right)^2 + \frac{L^2}{4M_{ir}^2} \frac{c^6}{G^2} \quad (2.1)$$

where G is gravitational constant, c is the speed of light and M_{ir} is *irreducible mass*. In CGS¹ units Coulomb's constant is set to $k_e \equiv 1$. This equation was derived from Einstein-Maxwell equations - general relativity in combination with Maxwell electromagnetic laws.

First term $M_{ir} c^2$ is the rest mass/energy of the BH. Second term related to charge Q is equal to energy of electric field. If the BH is not charged then this term is zero. Last term related to angular momentum L corresponds to rotational energy. If the BH is not rotating this term is zero. If a mass M of the BH system is defined as $E = M c^2$ than this energy/mass M incorporates also energy from electric field and rotation along with the "real" mass M_{ir} .

Einstein-Maxwell equations for the BH system also give limitation on the maximum angular momentum and maximum electric charge a BH can have for a given mass. This in turn gives maximum amount of rotational energy and electric (electromagnetic) energy for a given value of total energy of BH system. In the case of Kerr BH maximum amount of rotational energy BH can have is about 29% of the total energy E . In the case of Reissner–Nordström BH, maximum amount of electromagnetic energy is exactly 50% of the total energy E . For both rotating and/or charged BH it is theoretically possible to extract this energy.

Kerr BH "drags" the space around it in the direction of rotation. Because this effect is present outside the event horizon it is possible to interact with the BH system in such a way to extract its rotational energy. This can be done either by sending a particle in specific orbit around BH which then decays into two particles, or by use of magnetic fields. Theoretically all the rotational energy of a BH can be extracted in which case BH stops rotating and becomes a Schwarzschild BH.

Reissner–Nordström BH has an electric field which is present outside the event horizon. The field was created by charged progenitor star (or material surrounding it). When it fell inside the event horizon during a collapse to the BH, its electric field outside the horizon remained. Because of this it is possible to extract energy of the electric field. This can be done by a process of vacuum polarization of the field itself, or by the decay of outside particles into two oppositely charged particles. Theoretically all the electromagnetic energy of a BH can be extracted in which case BH stops being charged and becomes a Schwarzschild BH.

Schwarzschild BH has only a stationary gravitational field outside the event horizon and any interaction with it cannot decrease the BH mass/energy which is given by $E = M_{ir} c^2$. The precise definition of irreducible mass/energy (in any BH type) is that it is a part of the BH system energy that cannot be lowered, only increased².

2.2.2 Central engine

Extracting energy from a charged black hole via vacuum polarization is the key aspect of the fireshell model.

¹The centimetre–gram–second system of units.

²By means of processes within Einstein-Maxwell framework, not counting quantum processes such as Hawking radiation.

The model was fully developed for a non-rotating charged BH, i.e. Reissner–Nordström BH. It will be referred to as *electromagnetic black hole* (EMBH). The energy equation 2.1 for this system reduces to:

$$E = M_{ir}c^2 + \frac{Q^2}{4M_{ir}} \frac{c^2}{G} \quad (2.2)$$

Electric field \mathcal{E} of EMBH behaves almost as electric field of a charged particle $\mathcal{E} = Q/r^2$ (CGS units, $k_e \equiv 1$). This electric field extends from the event horizon r_+ out to infinity. As stated before maximum charged BH has an amount of electric energy of 50% of total BH system energy E .

Within the framework of quantum field theory (QFT), namely quantum electrodynamics (QED), vacuum is not simply "empty space" but has a certain energy associated to it. In the presence of electric field this energy reacts with it. One of the consequences is *vacuum polarization*. Much like in the ordinary polarization of dielectrics vacuum polarization reduces the initial electric field. Also, as dielectric breaks down when electric field reaches a certain critical value, vacuum also has a "breaking" point in which case an electron-positron pairs are created out of vacuum. The stronger the electric field more likely this process becomes. The process becomes significant when electric field reaches critical value of $\mathcal{E}_c = \frac{m_e^2 c^3}{e\hbar} \sim 10^{16}$ V/cm, where m_e is electron/positron mass, \hbar is reduced Planck constant. This is also the limit where other QED effects come into play. The value of \mathcal{E}_c is so large that it is beyond any contemporary experimental technique. However, electric field around EMBH can easily reach this value or much higher.

The volume around EMBH where electric field strength is larger than critical is called the *dyadosphere*. It extends from the event horizon r_+ out to r_{ds} which is the radius where \mathcal{E} drops to $\mathcal{E} = \mathcal{E}_c$ (Figure 2.2).

Electron-positron pair energy (rest mass/energy plus their kinetic energy) is created at the expense of EMBH electric field energy. Pairs will be created until electric field everywhere within the dyadosphere drops to $\mathcal{E} = \mathcal{E}_c$. To calculate number of pairs and their energy, as well as their distribution within the dyadosphere, EMBH electric field is imagined as being created by a series of thin spherical capacitors of thickness similar to electron Compton wavelength $\sim \lambda_e = \hbar/m_e c \sim 10^{-10}$ cm. Pairs in a single capacitor (at a given distance r) will be created until the "walls" of the capacitor are de-charged to the point when $\mathcal{E} = \mathcal{E}_c$. Energy of pairs in a certain capacitor (at a given distance r) will be equal to the difference between energies of initial \mathcal{E} and critical \mathcal{E}_c (final) electric field (Figure 2.2).

Main formula which comes from above arguments determines the amount of energy released in the form of e^\pm -pairs E_{e^\pm} :

$$E_{e^\pm} = \frac{Q^2}{4M_{ir}} \frac{c^2}{G} \left(1 - \frac{r_+}{r_{ds}}\right) \left(1 - \left(\frac{r_+}{r_{ds}}\right)^2\right) \quad (2.3)$$

Radius of event horizon r_+ and dyadosphere r_{ds} are determined by mass M_{ir} and charge Q of the EMBH. Therefore, the E_{e^\pm} is completely determined by these two parameters. For a maximally charged BH the relation is: $E_{e^\pm} \simeq \frac{M}{M_\odot} 0.9 \times 10^{54}$ erg where M is the total mass of the EMBH system. This is valid for a wide range of stellar BH masses $M \sim 1M_\odot - 100M_\odot$ and beyond. EMBHs with smaller charge will, of course, have less E_{e^\pm} . For EMBH to be maximally charged its progenitor star should have just one net elementary charge e per 10^{18} nucleons.

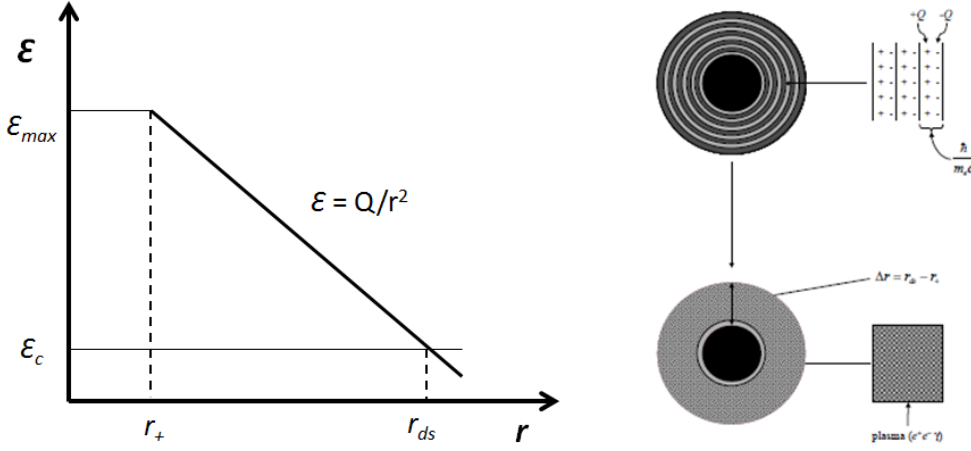


Figure 2.2: **Left:** Electric field \mathcal{E} as a function of radius r from the center of EMBH. Electric field will have maximum value at the horizon r_+ and will drop to critical value \mathcal{E}_c at r_{ds} . The volume between r_+ and r_{ds} , the dyadosphere, is place where electron-positron pairs are created. Coordinate r is from the reference system at infinity where space-time is flat, i.e. it is not affected by gravity of EMBH. **Right:** Modeling electric field in the dyadosphere as being made by a series of thin capacitors. The figure on the right was reproduced from (Ruffini and Vitagliano, 2002).

The processes of pair creation is completed on the order of $\sim \lambda_e/c = \hbar/m_e c^2 \sim 10^{-19}$ s. This means that there are no EMBH with electric fields larger then critical because they discharge instantly. The process of pair creation should happen when the EMBH is forming, during the collapse of the progenitor star. Charged progenitor core can exist in a neutron star. Neutron star will still have some protons and electrons. Heavier protons will concentrate towards the core while lighter electrons will be closer to the crust.

When formed electrons and positrons will begin to move in the electric filed and their own local field will cause resulting electric field to change which will effect the pairs, etc. The final result is an oscillation of electric field as well as concentration of pairs. Consequences of these processes are important when electric field is close to critical. However, for pair creation process around EMBH these effects are not relevant.

The final result is a shell of electron-positron pairs in the range $r_+ \lesssim r \lesssim r_{ds}$ with high amount of internal energy. Due to large optical depth for pair annihilation and consequent pair creation $e^\pm \leftrightarrow 2\gamma$, as well as other interactions, e^\pm - γ plasma is in thermal equilibrium. The plasma is termed *fireshell*. Dimensions and energy of the fireshell are uniquely determined by mass and charge of the EMBH. For a stellar size EMBH typical values are $r_+ \sim 10^6$ cm, $r_{ds} \sim 10^8$ cm, $kT \sim$ MeV.

2.2.3 Expansion of fireshell plasma

The fireshell plasma will start to expand due to enormous internal pressure. Fireshell is assumed not to have any baryon matter and expands as a pure e^\pm - γ plasma with radiation dominated internal pressure. Since the plasma is optically thick, most of the photons will remain trapped inside and expansion can be considered adiabatic. All the specifics of the plasma are known for a given EMBH mass and charge, and expansion can be precisely determined, i.e. exact dependence of plasma Lorentz factor on radius $\Gamma(r)$. This is done considering relativistic dynamics within general theory framework (curved space-time) as gravitational interaction of the BH is expected to affect the plasma expansion. The picture

that emerges is: The internal energy of the plasma is transferred into outward bulk kinetic energy of the electrons and positrons, i.e it cools as it expands with increasing intensity (Lorentz factor). The thickness of the fireshell remains the same³ during the expansion. The affect of the BH gravitational field on the plasma expansion is found to be marginal.

Fireshell theory assumes that remnants of the progenitor star are located beyond initial dyadosphere, at $r \sim 100r_{ds} \sim 10^{10}$ cm, with a width of about $\sim 10r_{ds} \sim 10^9$ cm, and that they form a spherical shell. New parameter B termed *baryon load* is defined as $B = \frac{M_B c^2}{E_{e\pm}}$ where M_B is mass of baryon remnant. As the e^\pm - γ plasma expands it will hit and engulf the baryon shell which will become part of the fireshell plasma. To model the collision next assumptions are used: collision is completely inelastic, geometry of the plasma shell doesn't change, baryon shell quickly comes in thermal equilibrium with plasma. This assumptions should hold if: $B < 10^{-2}$; number of fireshell electrons is much greater then that of baryons $> 10^6$; Lorentz factor of plasma is $\Gamma \gtrsim 100$ at the collision time. All of these factors are true for typical values of mass and charge of EMBH. After plasma hits and engulfs the baryon shell, system will heat up, Lorentz factor will suddenly drop, after that it will start to rise again as the internal energy is transferred to outward bulk kinetic energy of the baryons. When almost all of the internal energy is transferred to outward bulk kinetic energy of baryons, the final Lorentz factor will be $\Gamma = 1/B$.

2.2.4 P-GRB

However, before this asymptotic value is reached, plasma will cool enough for $2\gamma \rightarrow e^\pm$ reaction to stop and last of the e^\pm will annihilate; concentration of baryon-associated electrons will drop enough for plasma to become transparent and photons escape from the plasma carrying energy with them. After this *proper GRB* (P-GRB) emission, plasma will continue to expand with constant Lorentz factor, the one it had just before the P-GRB. This happens around $r \sim 10^{14}$ cm. Since photons were in thermal equilibrium, their spectrum will be thermal with temperature around $kT \sim 10$ keV and the duration of the P-GRB should be a fraction of a second. The P-GRB is emitted at the same time from a spherical surface with different Doppler boost towards the detector, and emitting surface has a certain thickness. These geometrical effects will cause the final spectrum of P-GRB to be quasi-thermal.

Initial energy of the fireshell $E_{e\pm}$ will be divided between energy of P-GRB and energy that remained in the fireshell. This ratio is determined mainly by baryon load B but also the initial energy $E_{e\pm}$ itself. If the baryon load is smaller, there will be less baryon-associated electrons, and transparency will be reached earlier, when more energy is in the form of internal energy and not bulk kinetic energy of baryons. Smaller the parameter B , P-GRB will be stronger with respect to fireshell kinetic energy.

2.2.5 Extended afterglow

As the fireshell baryons expand outwards they will reach the *circum-burst medium* (CBM) which starts at around $r \sim 10^{17}$ cm. This medium can be interstellar medium or material from a wind created by progenitor star. This interaction produces emission which is termed *extended afterglow*.

In modeling the interaction of fireshell with CBM next assumptions are used: geometry of the fireshell doesn't change; CBM is cold (marginal internal energy) and at rest; collision

³In the reference frame of the host galaxy, not in the co-moving frame of the plasma.

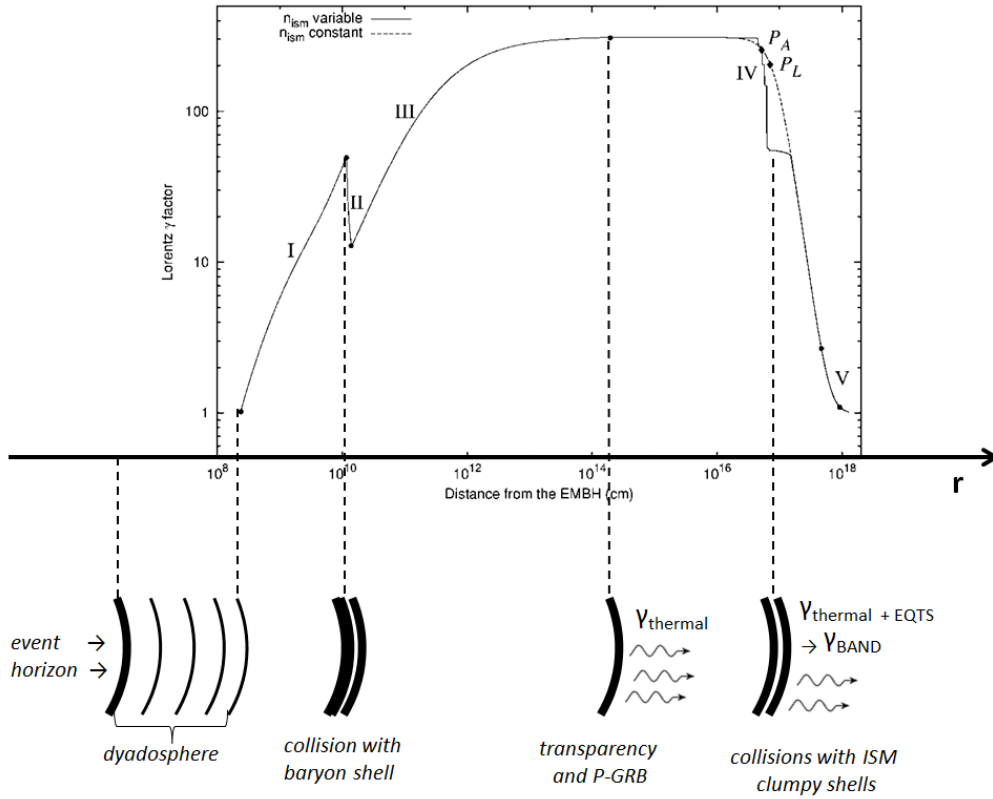


Figure 2.3: Evolution of the fireshell Lorentz factor with distance from BH as applied to GRB 991216. First faze corresponds to expansion of pure e^\pm - γ plasma. Second faze corresponds to interaction of fireshell plasma with baryon remnant. Third faze corresponds to expansion of e^\pm - γ -baryon plasma up to P-GRB. Fourth faze starts after P-GRB and involves also the interaction with ISM which gives rise to extended afterglow. Fifth faze corresponds to slowing down of plasma to relativistic speeds and onset of regular afterglow. Dashed line in faze 4 correspond to constant CBM density while solid line corresponds to ISM distributed in thin shells. Image reproduced from (Ruffini et al., 2002)

is inelastic; energy gained from collision is radiated immediately (fully radiative scenario). The model gives precise dependence of fireshell velocity on engulfed CBM mass M_{CBM} , initial Lorentz factor Γ_0 and baryon mass M_B - $\Gamma(M_{CBM}, M_B, \Gamma_0)$.

In order to determine light curve and spectrum as seen by detector, a concept of *Equi-temporal Surfaces* (EQTS) was introduced. Since the emitting region is expanding spherically at ultra-relativistic speed, photons arriving at the same time at the detector have been emitted at different times and at different places on the expanding fireshell sphere. The equitemporal surface is an imaginary surface such that photons emitted at intersections of the EQTS and fireshell as it expands, arrive at the same time at the detector. Then, from the precise evolution of the fireshell, a light curve can be modeled. If the CBM is assumed to be constant, extended afterglow would be seen as a single peak, following the P-GRB. At this point it should be noted that what is considered prompt emission, which is defined by the T_{90} parameter, in the fireshell model it is composed of P-GRB and the extended afterglow.

In order to explain general multi-peak structure of light curve, CBM is assumed to be distributed in thin shells such that thickness of each shell $\sim 10^{15}$ cm is greater than the distance between them $\sim 10^{16}$ cm. Interaction with each shell is responsible for each peak in the prompt light curve.

The resulting spectrum at each point in observational time will be a convolution of many different spectra over the corresponding EQTS. It is assumed that gained energy - which comes from interaction of the fireshell with CBM shell - is completely radiated away as thermal radiation. Then, from the known evolution of the fireshell and CBM distribution, it is possible to model resulting spectrum at each point of observational time. Because of convolution over EQTS, resulting spectrum will be non-thermal and similar to Band function. Observed reduction of peak of the Band function in the peaks of GRBs can naturally be explained in Fireshell model. Since each peak corresponds to a CBM shell, then first radiation from the front of the fireshell (direct Doppler boost) will come and later radiation from the edges of the fireshell (lesser Doppler boost) will come. In order to make such a model completely compatible with observed spectrum in several precisely observed GRBs, two new parameters were introduced.

First is the *surface filling factor* \mathcal{R} which is a function of distance $\mathcal{R}(r)$. It is a ratio between surface area of the fireshell that emits radiation to the total visible (from the detector point of view) surface area of the fireshell. The density and distribution of CBM determines the light curve and spectrum, and the parameter \mathcal{R} is related to spectrum, more precisely to the peak of the Band function. Physical interpretation of \mathcal{R} is that thin shells of CBM have a clumpy structure and as fireshell interacts with a certain CBM shell, only parts of the fireshell which hit these clumps will heat up and radiate. Since all the CBM shell is concentrated in the clumps, given parts of the fireshell will heat up more and the temperature, and the corresponding peak, will be higher. Increasing the \mathcal{R} increases the peak of the spectrum. Typical values are $10^{-12} \lesssim \mathcal{R} \lesssim 10^{-8}$ which implies very clumpy structure of the CBM shells.

Second parameter is related to the assumption of pure thermal spectrum in the co-moving frame of the fireshell. In order to explain spectra in some high energy GRBs, a new assumption had to be made. It introduced new parameter α such that spectrum in the co-moving fireshell frame is defined as: $(E/k_B T)^\alpha \times F_{BB}$ where F_{BB} is the pure thermal flux of the black body, E is the energy of the photon, $k_B T$ is temperature in units of energy. Parameter α changes the lower-energy slope of the black body spectrum. It is found that this parameter is in the range $\alpha \approx -1.8, -2.0$. This parameter remains constant throughout the burst. So far this parameter is only phenomenological, there is no physical explanation.

Mechanism for extended afterglow is also responsible for what is typically considered afterglow. When the fireshell expands to larger radii and Lorentz factor drops from ultra-relativistic to relativistic speeds, peaks in the light curve from interaction with CBM shells will be less intense, smoothed out and overlap with each other, peak of the spectrum will move to lower energies. This puts an end to prompt emission which is characterized with prominent gamma-ray peaks.

2.2.6 Fitting the GRB

The P-GRB is determined by two parameters: energy released in electron-positron pair creation $E_{e\pm}$ and baryon load B . Distance of baryon shell from BH is found not to be important. Since all the energy $E_{e\pm}$ is radiated away it is equated with isotropic energy of GRB E_{iso} . The next step is to determine the P-GRB emission in the prompt light curve by searching for a thermal (or quasi thermal) component. Usually the P-GRB also contains non-thermal component which might come from the early onset of the extended afterglow. When P-GRB is determined, the energy of the thermal component in P-GRB time interval

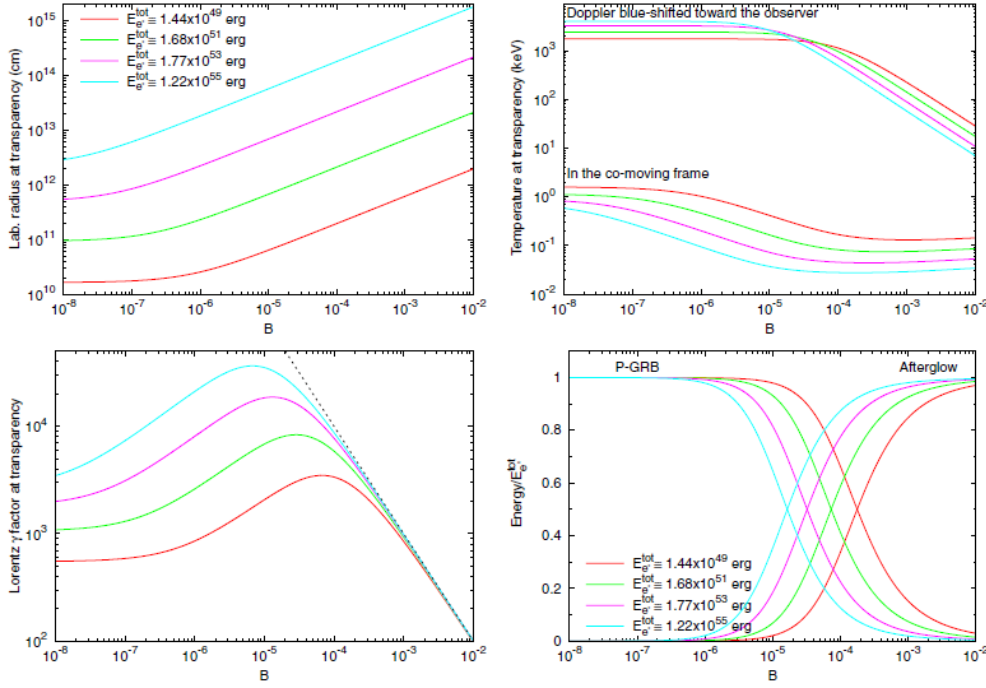


Figure 2.4: Properties of fireshell parameters at the point when transparency is reached and P-GRB is emitted. Dependence of fireshell radius (upper-left), temperature (upper-right), Lorentz factor (lower-left), ratio between energy in P-GRB and total energy, all on baryon load parameter B for four different values of total energy. Figure taken from (Muccino et al., 2013a).

as well as its temperature can be determined. From P-GRB thermal energy and E_{iso} the baryon load can be determined, and from there, all other parameters related to fireshell (Figure 2.4). Since the temperature is uniquely determined from parameters B and E_{iso} , it is possible to do a crosscheck with the temperature determined from observations. The previous cases assumed that redshift is known. If it is unknown it is also possible to determine it thanks to this "extra known parameter" connection between P-GRB parameters.

The $E_{e\pm}$ parameter is uniquely determined from EMBH mass and charge ratio. Knowing it offers a connection between these two EMBH parameters.

Extended afterglow (the rest of the T_{90} prompt emission), beside the $E_{e\pm}$ and B parameters, is also defined by CBM density distribution $n_{CBM}(r)$, filling factor distribution $\mathcal{R}(r)$ and black body spectral parameter α . The fitting of these parameters is done via the fireshell evolution simulation. First the distribution of parameters are determined and then simulated light curve and spectrum are compared to the observed one. Each step in the fireshell evolution doesn't depend only on the current CBM shell and filling factor, but also on all the previous ones. When simulating light curve and spectra the EQTS surfaces have to be taken into account. Therefore, a single peak in the prompt emission and its spectrum are dependent on the entire fireshell evolution. Because of this it is very difficult to produce correct CBM and filling factor distributions. Also, this is the reason why Fireshell model isn't simply "inventing" parameters and their evolution until the model fits the observation. All the parameters of the fireshell model have to be self-consistent to produce the exact light curve of GRB and its spectral evolution. For example, if an arbitrary GRB light curve and spectral evolution are given, the unique solution within fireshell model should not exist.

2.2.7 Long and short GRBs in the fireshell model

From observational point of view there are long ($T_{90} > 2$ s) and short ($T_{90} < 2$ s) GRBs. The first ones are thought to come from collapsing core of a massive star, and the second from mergers of two compact stars. There is also a third group. These GRBs have an initial short peak (< 2 s) and extended emission which looks more like a stronger afterglow then the typical prompt.

Within the Fireshell model these groups are explained based on baryon load B and average CBM density n_{CBM} .

The typical long GRBs are the ones with $B \gtrsim 10^{-4}$ and $n_{CBM} \sim 1 \text{ cm}^{-3}$ (typical for galaxy disk). For these values of B extended afterglow is much stronger then the P-GRB which sometimes is below detector threshold. For typical value of n_{CBM} most of the extended afterglow is contained within few tens of seconds. The entire T_{90} prompt emission is then basically just the extended afterglow.

If the baryon load is in the same range but CBM density is much lower $n_{CBM} \sim 10^{-3} \text{ cm}^{-3}$ (typical for galaxy halos), the extended afterglow still has more energy then P-GRB but is "deflated", i.e. its energy is spread over much longer time period and in the lower energy bands. In this case the P-GRB will have a more prominent peak then the peaks in the extended afterglow, which may even be below the detector threshold. This can explain the third observational group of GRBs where there is a short peak in the beginning and afterglow-like emission after it. The requirements for galactic halo CBM density points towards compact object mergers since orbiting compact objects are mostly thought to be in galactic halos. EMBH can be formed also from compact object mergers.

If the baryon load is very small $B \lesssim 10^{-5}$ most of the energy will be in the P-GRB and these would correspond to typical short ($T_{90} < 2$ s) GRBs. Density of CBM doesn't play a significant role here.

Induced Gravitational Collapse

Fireball and Fireshell model describe the Gamma-ray burst (GRB) event. The discovery of a first supernova (SN) associated to GRB in 1998, and many more other connection between long GRBs and SNe later on, related long GRBs to "death" of massive stars. This helped define the GRB models but the models also need to be incorporated into a wider picture which would explain the simultaneous occurrence of both phenomena.

The Induced gravitational collapse (IGC) idea was introduced in order to explain GRB-SN connection with the Fireshell model for GRBs. The center of the idea revolves around a binary star system in which one star is responsible for GRB and other for SN. Initially, at the beginning of 2000s, the binary model assumed that GRB triggers the other star to become a SN. About five years later the opposite scenario was considered in which a SN triggers the other star to become a GRB. Namely, a SN ejecta accretes onto the companion neutron star (NS) close to the maximum mass. As the material accretes the NS collapses into a black hole (BH) releasing gravitational potential energy in the form of an expanding fireshell. This version of events was termed *induced gravitational collapse*. From 2012 and on the IGC scenario received new attention as basic equations and details were laid down for accretion of SN ejecta onto NS. Also, GRBs fitted within the Fireshell model up to 2012 and later on showed additional features - features outside of fireshell model - that point to additional mechanisms, namely ones which could come from binary interaction of two stars. Furthermore, new observational features were discovered in these "IGC GRBs" that group them into a single class.

The IGC scenario was introduced as an expansion of the Fireshell model but it managed to get a life of its own. The binary scenario was expanded to include IGC-like events which would not lead to a BH formation and a GRB. The binary nature of the phenomena was further expanded to include also mergers of compact objects which produce short bursts. The new picture that emerged revolved around whether or not a BH was formed and consequently, whether the isotropic energy of burst is greater or lower than a limiting value of $\sim 10^{52}$ erg.

3.1 GRB-SN in the Fireball model

The Fireball scenario doesn't go into details about central engine. In order to explain the GRB-SN connection, a description of central engine and its ability to produce both GRB and SN must exist. Reviews on this topic can be found in (Woosley and Bloom, 2006),

(Hjorth and Bloom, 2012).

In standard model for normal (non-GRB) core-collapse SN, at the end of a star's life, the center of iron core collapses and forms a neutron star (NS). The gravitational potential energy released by the collapse ($\sim 10^{53}$ erg) is transformed to neutrinos (about 99% of energy) which then escape freely through the star, and partly transported to outer iron core and other outer layers which are then launched outwards as SN ejecta (about 1% of energy). In a sense the collapsing material of an inner iron core to a rigid NS "bounces off" the outer layers.

The standard central engine for a GRB Fireball model involves collapse of a center of iron core directly to a black hole (BH)¹. The rest of the in-falling core and, later on, outer layers create an accretion disk around a BH and gravitational potential energy of disk material is extracted as it finally falls into BH. Since the inner core was rotating before the collapse, the resulting BH will probably rotate. The rotational energy of a BH can also be extracted via the processes involving magnetic fields in the accretion disk. The energy extracted launches a fireball jet normal to the plane of disk much like in the case of active galactic nuclei or X-ray binaries.

In order to have a SN with a GRB, part of the extracted energy needs to be transported to outer layers of the star and launch them outwards as SN ejecta. The extracted energy from accretion disk will launch a "wind" made out of protons and neutrons outward with speed of about 0.1 c. This wind will then push out the outer layers of star which will become SN ejecta. Another scenario is for the central iron core to collapse initially to NS which will "bounce off" outer iron core and layers like in normal SN. However, this push will not give enough outward momentum for all SN layers and some of them will fall back to NS creating a BH and an accretion disk which will launch a fireball jet.

Previous two scenarios are part of the *collapsar* model and it can be considered as standard one. There is also *supernova* model in which initially a differentially rapidly-rotating super-massive NS is formed. Because of differential and rapid rotation (large centrifugal force) NS can have a much larger mass than typical NS and not collapse to a BH. The SN is, then, created in a usual way. As NS rotation slows down, the gravitational collapse to BH happens with the rest of the scenario playing out as in *collapsar* model. The delay between SN and a GRB can be from few seconds to years depending when the NS collapses. Another scenario involves a magnetar. If the central engine is assumed to be a magnetar instead of a BH, then SN ejecta can be launched like in normal type SNe and magnetar high rotational energy is transformed into a GRB jet.

3.2 Different episodes in GRB light curve

Fitting several GRBs within the Fireshell model showed that it is not possible to find a self-consistent set of parameters that would produce the light curve (LC). However, the "problem" seemed to be in the first parts of GRB LCs. If this part of the LC is excluded, the rest of the LC could be fitted within the Fireshell scenario. This first part also seems to be morphologically separate from the rest of the LC. Following these findings the GRB LC was divided into first part *episode 1* and second part *episode 2* with second part being interpreted as standard GRB. Spectral analysis of episode 1 also seems to show a common feature - a spectrum composed of thermal (black body) component and a power-law component. Time resolved spectral analysis of episode 1 seems to show peak of the black

¹In the long GRBs. Central engine for short bursts is merger of two compact objects

body emission decreasing to lower energies (black body cools) and decreasing spectral hardness of power-law component.

Detailed analysis within the Fireshell model of episode 2 and time resolved spectral analysis of episode 1 have been done for these GRBs: GRB 090618 (Izzo et al., 2012a), GRB 101023 (Penacchioni et al., 2012), GRB 110709B (Penacchioni et al., 2013) and GRB 970828 (Ruffini et al., 2015a).

An example of GRB 090618 will be presented here as a prototype for the mentioned class of GRBs. This GRB was strong and relatively near, and the data collected provide good statistics. Figure 3.1 and Figure 3.2.

Attempting to model the entire T_{90} prompt emission within the Fireshell model fails to give consistent parameters. The first broad peak (0 – 50 s) in the GRB LC has been recognized as episode 1. The rest of the prompt emission is episode 2 - the classical GRB which can be modeled within the Fireshell model. Time resolved spectral analysis of episode 1 has shown that it can be well fitted with a black body (BB) of decreasing temperature and a power-law component of decreasing hardness. Assuming a BB is a perfect and uniform sphere, and with known redshift (distance) to the burst, the radius of the BB can be calculated for every time step during episode 1. The radius of the BB increases from $r_{BB} \sim 10^9$ cm to $r_{BB} \sim 10^{10}$ cm during the observed 50 s which is about 30 s in the GRB host galaxy (redshift time correction). Results of analysis of episode 1 are shown in Figure 3.1.

Emission of the BB contributes significantly to the emission of episode 1. The radius of the BB emitter during these first 50 s observational time is much smaller than the radius at which typical GRB emission is released - whether the Fireshell or Fireball model are in question. Given how BB radius changes with time, the calculated speed is about 0.1 c which is non-relativistic speed. Speed of the emitting ejecta in both Fireball and Fireshell models are ultra-relativistic. These findings further point to the idea that the episode 1 is not part of the classical GRB emission.

The rest of the prompt emission, the episode 2, can be fitted within the Fireshell model. The first four seconds of episode 2 (50 – 54 s) are recognized as P-GRB emission. Total energy of electron-positron pairs is equated to isotropic energy of episode 2: $E_{e\pm} = 2.5 \times 10^{53}$ erg. Thermal emission in P-GRB is $E_{P-GRB,th} = 4.3 \times 10^{51}$ erg. From here the baryon load, Lorentz factor at transparency and temperature can be determined: $B = 1.98 \times 10^{-3}$, $\Gamma_0 = 495$, $kT = 29$ keV.

The rest of episode 2 is then extended afterglow. The density distribution of circum-burst medium (CBM) is modeled in order to produce given LC of episode 2 taking into account parameters from episode 1. The average density of CBM is $n_{CBM} = 0.6$ cm $^{-3}$. The filling factor varies in between $\mathcal{R} \approx 3 - 9 \times 10^{-9}$. The spectral parameter is $\alpha = -1.8$ for the entire duration of the extended afterglow. Results of analysis of episode 2 are shown in Figure 3.2.

Origin of the episode 1 within the IGC scenario is assumed to come from binary interaction between the SN ejecta and companion NS.

3.3 The IGC

The IGC scenario was created in order to explain connection between GRBs and SNe with the Fireshell model for GRBs. The scenario starts with a binary system composed of a massive star without its hydrogen and helium layers and a close orbiting NS. As

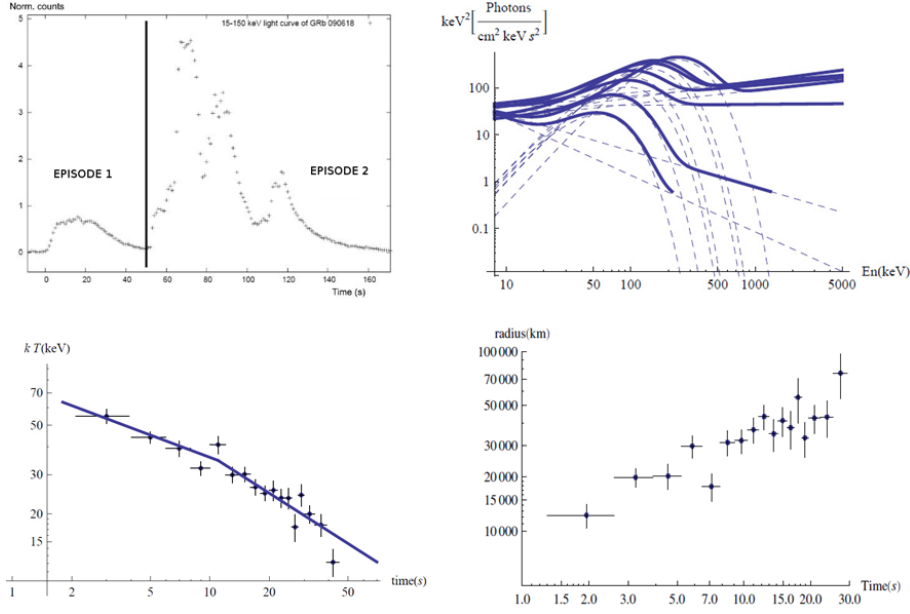


Figure 3.1: Episode 1 of GRB 090618. **Upper-left:** GRB 090618 light curve of its T_{90} prompt emission in the 15 – 150 keV energy range seen by Swift-BAT instrument. Emission of Episode 1 is well separated from the rest of the prompt emission. **Upper-right:** Time resolved analysis of Episode 1 using data from the Fermi-GBM detectors and fitting with power-law component plus a black body (BB). Decrease of the peak of the BB can be seen as well as decrease of power-law spectral index. Spectrum is in the spectrum energy distribution form. Due to clarity, data points are not shown, only the model. **Lower-left:** Temperature of the BB with respect to observer time. The best fit of the decreasing temperature is a broken power-law. **Lower-right:** Radius of the BB emitter calculated assuming a perfect BB uniform spherical surface. Time is in the frame of the GRB host galaxy. Figures taken from (Izzo et al., 2012a).

the massive star goes SN, the expanding SN ejecta accretes on to NS which then, under additional mass, collapses to a BH creating a GRB. The details of the process have been studied in (Rueda and Ruffini, 2012), (Fryer et al., 2014), (Fryer et al., 2015), (Becerra et al., 2015).

The initial conditions are: The pre-SN star lacks hydrogen and helium layer. This is required from observational and theoretical point of view. All SNe associated to GRBs were type Ic². Orbiting NS has to be close in order to accrete enough mass to collapse to BH. The radius of the pre-SN star is around $r \sim 10^9$ cm and with mass $M_{preSN} \sim 10 M_{\odot}$. The distance of NS with mass $M_{NS} \approx 2 M_{\odot}$ from the pre-SN should be around $a \sim 10^{10}$ cm with orbital period around $P \sim 10^2 - 10^3$ s. Hydrogen layer in a massive star is responsible for its enormous radius $R \gg a$. If a pre-SN star had a hydrogen envelope, the compact NS would orbit within it. The hydrogen envelope would be accreted onto NS or blown away by NS as it orbits the pre-SN star. Binary system with these kinds of stars and orbital parameters should be very rare, however, if each produces a GRB, then almost all of them will be detected.

The core of the pre-SN star collapses to a new NS and the ejecta is launched outwards. The initial speed of ejecta velocity is around $v_{ej} \sim 10^8$ cm/s. As the SN ejecta moves closer to the orbiting NS, a region around a NS where NS gravity is strong enough will capture parts of the moving SN ejecta and it will become gravitationally bound to NS. This

²Core-collapse SNe without hydrogen and helium in their spectra. Sometimes they were type Ib/c - without hydrogen but with traces of helium in their spectra.

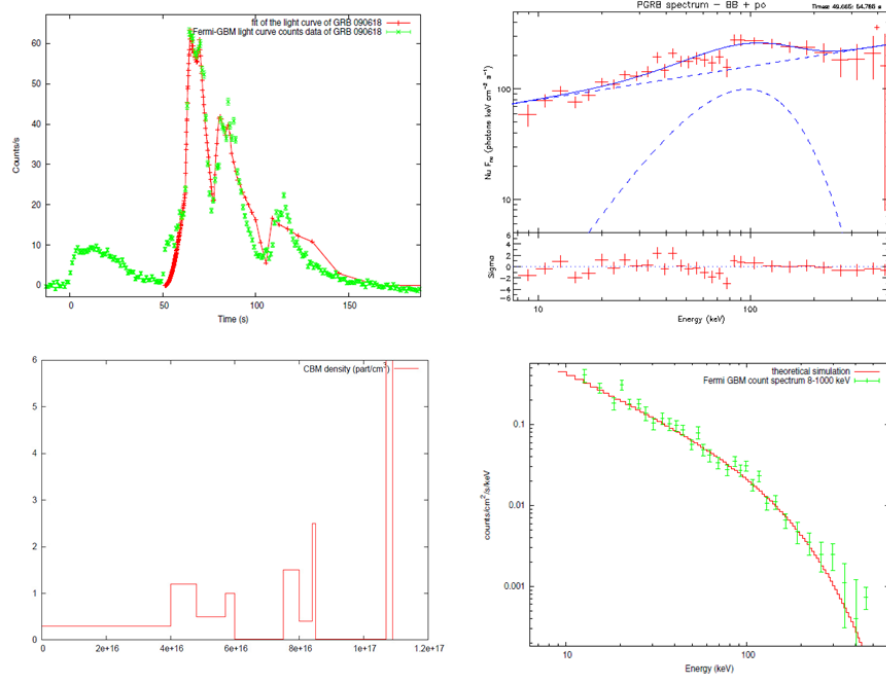


Figure 3.2: Episode 2 of GRB 090618. **Upper-left:** Entire T_{90} prompt emission in green, from the Fermi-GBM data. The red line represents simulated light curve of extended afterglow of episode 2 from the fireshell model. The P-GRB is small peak in the green data from time interval of 50 – 54 s. **Lower-left:** Distribution of CBM density into thick shells that are responsible of producing peaks in the simulated light curve. **Upper-right:** Spectrum of the P-GRB emission fitted with BB plus a power-law component. The data are from Fermi-GBM detectors. **Lower-right:** Spectrum in the time interval 58 – 150 s. Green points are data from the Fermi-GBM detector. The red line is simulated spectrum in this time interval from the Fireshell model. Figures taken from (Izzo et al., 2012a).

radius is *Bondi-Hoyle Radius* $r_{BH} \sim 10^8$ cm (Figure 3.3). The following accretion onto NS is very high (hypercritical) with $\dot{M} \gtrsim 10^{-3} M_{\odot} \text{ s}^{-1}$. This is well above the Eddington rate - the rate at which radiation pressure caused by accretion becomes strong enough to stop accretion becoming more stronger. However, if the optical opacity is very high, the photons push outwards with speed lesser than infilling speed of accreting material - the photons are "trapped in the flow" and accretion can be much higher. This is the case here and the radius at which photon trapping occurs is *photon trapping radius*. The inflowing material heats up as it piles up onto the NS, and produces an outgoing shock. Near the NS it is sufficiently hot to emit neutrinos that cool the in-falling material, allowing it to be incorporated into the NS. The shock moves outward as material piles up. At some point it will defragment and cause outflows which will accelerate to speed close to the speed of light. In this way about 25% of accreting material is ejected out. If the outflow moves out as a jet it would have a temperature of around 50 keV at radius of 10^9 cm, and as it cools and expands out, temperature of ~ 15 keV at 6×10^9 cm. This could be an explanation for the thermal emission in episode 1 as it coincides with observed temperature and radius evolution of the BB. The process of accretion onto NS before it collapses to BH lasts about $\sim 10^2$ s.

As the SN ejecta moves outwards and then is affected by orbiting NS gravity, it will have an angular momentum with respect to NS. Accreting matter will create a disk-like structure around NS. The angular momentum is much bigger than the maximum angular momentum NS can have before it starts to shed mass due to large centrifugal force. As the

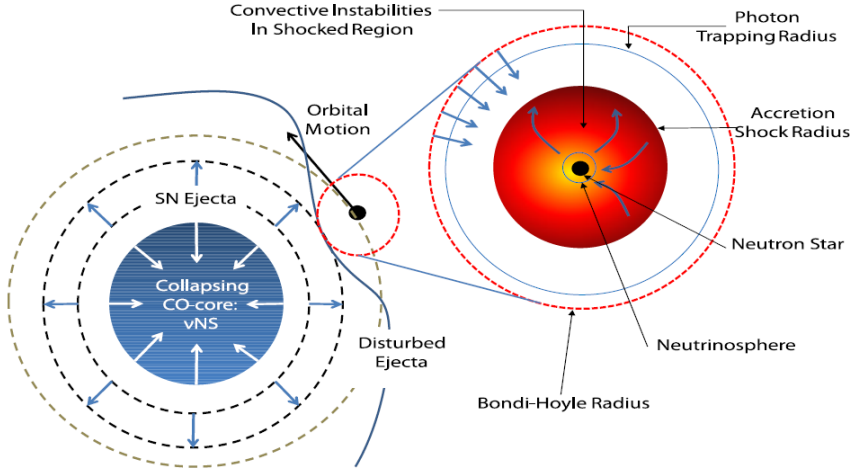


Figure 3.3: Interaction of SN ejecta with companion NS. Details are given in the text. Figure taken from (Fryer et al., 2015).

matter accretes it will spin up NS. In order for a mass to accrete on to NS, the accreting ejecta needs to lose angular momentum. The process in which angular momentum of an accreting disk gets decreased is by creation of a jet normal to the plane of accretion disk - similar process like in X-ray binaries. The jet could explain the power-law component seen in episode 1, or even high energy (GeV) emission if accretion continues after BH is formed.

For a wide range of pre-SN masses, orbiting periods, etc. the kick given to NS (later BH) by expanding SN ejecta isn't enough to unbound it from the new NS (previous pre-SN star). This is due to the fact that the system was very tightly bound (small distance between the stars) to begin with.

The rest of the SN ejecta (not accreted) will still be distorted by nearby orbiting NS and accreting matter. The SN ejecta will be significantly asymmetric. Radiation from accretion as well as highly expanding fireshell plasma (GRB ejecta) will interact with SN ejecta pumping energy into it and causing it to accelerate and radiate stronger. This is considered to be the explanation for the fact that SN associated to GRBs are faster and more luminous than non-GRB type Ic SNe. Specifically, the moment of interaction between GRB ejecta and SN ejecta is thought to be responsible for flares seen in the X-ray range after the prompt emission.

In principal, the IGC scenario can also be used with fireball model for GRBs. In both cases the NS can collapse to a BH. In the fireshell model the collapse creates a fireshell plasma while in the fireball model the collapse creates an accretion disk which then launches a fireball jet. The studding of binary systems and accretion of SN ejecta onto NS would be the same for both models since GRB doesn't yet happen in this time interval. The main difference arises when SN ejecta interacts with GRB ejecta - fireshell plasma in fireshell model or a fireball jet in fireball model. However, emission arising during the accretion is considered as possible explanation for features in episode 1 and episode 1 is a concept solely within the fireshell model.

3.4 X-ray afterglows of IGC GRBs

Although there are thousands of observed bursts, only few of them were strong and/or close enough to be well observed. Fewer still were observed by several space-based detectors in order to have good coverage of time and energy interval - which is important in order to do a detailed analysis. With recognition of distinct episodes in GRB T_{90} prompt LC, and their explanation within IGC theory, a group of *IGC GRBs* can be conceived. Apart from distinct episodes and SN associations³, another observational features regarding these bursts are: isotropic energy which is always above $E_{iso} \gtrsim 10^{52}$ erg; common features within the X-ray afterglow.

3.4.1 Overlapping

Another feature shared between IGC GRBs is their X-ray afterglow. In (Pisani et al., 2013) and (Ruffini et al., 2014b) this has been studied. Swift-XRT instrument (0.3 – 10 keV) is most important in measuring X-ray afterglows of GRBs. If a GRB has a redshift it is possible to calculate X-ray afterglow luminosity (in a fixed energy band) in the rest-frame of GRB host galaxy which is an intrinsic property of GRBs. The LC of the afterglow can then be plotted against the rest-frame time. The common feature of IGC GRBs is that their X-ray afterglows (the luminosity) - after about $\sim 10^4$ s when the plateau faze ends - decay in a common power-law slope which overlap, regardless of E_{iso} . Another feature regarding the X-ray afterglows of these bursts is: the more energetic the burst is (the larger the E_{iso}), the plateau faze lasts shorter and the common power-law part starts earlier. Figure 3.4.

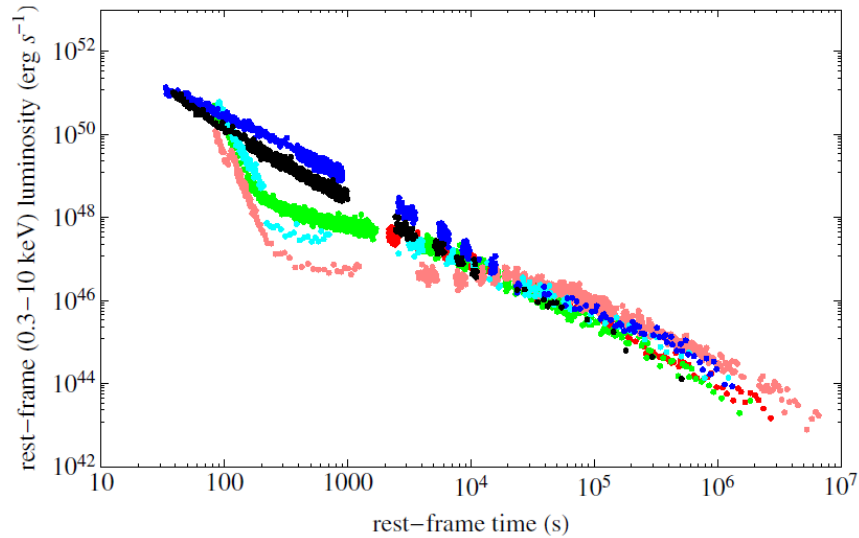


Figure 3.4: Rest frame luminosity of several GRB X-ray afterglows which were observed by Swift-XRT. The GRBs considered here were the ones with IGC characteristic: double episode in the prompt emission, SN association or a possibility of association if a GRB was closer then $z \lesssim 1$, $E_{iso} \gtrsim 10^{52}$; and well observed X-ray afterglow. The GRBs are: pink GRB 060729, $z = 0.54$; black GRB 061007, $z = 1.261$; blue GRB 080319B, $z = 0.937$; green GRB 090618, $z = 0.54$, red GRB 091127, $z = 0.49$, and in cyan GRB 111228, $z = 0.713$. Figure taken from (Pisani et al., 2013).

³Current optical detectors can observe SN if it is close enough, $z \lesssim 1$. If it is close enough, SN association can be certain or possible.

The overlapping feature gives a possibility to estimate the IGC GRB redshift if it is unknown.

Following the notion of episodes 1 and 2, the X-ray afterglow of IGC GRBs has been termed *episode 3*, and *episode 4* corresponds to optical SN emission 10-15 days after the start of GRB. It is not yet clear what is the physical reason behind the features of overlapping and nesting. It may have something to do with the emission of SN ejecta which has been affected by GRB ejecta, emission from a newly born NS, synchrotron emission of particles accelerated by Fermi mechanisms in the ejecta, or due to radiation from the heavy elements created in the r-process.

High redshift GRB 090423

This GRB is possibly the furthest one ever observed. Its redshift is at $z = 8.2$ which means it happened “just” 650 Myr after Big Bang⁴. In (Ruffini et al., 2014a) this burst has been analyzed within the IGC scenario. Its X-ray afterglow overlaps with other IGC GRBs and has an isotropic energy $E_{iso} \gtrsim 10^{52}$ erg. The SN couldn’t be observed due to high redshift and for the same reason episode 1 was below the detector threshold. Having confirmed that this GRB belongs to IGC class means that IGC scenario has been playing out since very early time in the universe.

3.4.2 Very energetic GRB 130427A

This GRB was very energetic $E_{iso} \sim 10^{54}$ erg, relatively nearby $z = 0.34$, and was observed by many instruments. This provided ample amount of data for analysis. This was also the first very energetic GRB to have an associated SN. From this point on the GRB-SN association was confirmed for all the range of GRBs isotropic energies. The GRB was studied within the IGC scenario in (Ruffini et al., 2015c).

The late X-ray afterglow overlaps with other IGC GRBs. In fact, the overlapping was evident early on and a notice on upcoming SN detection was sent since it should be easily detected given the low redshift of the GRB. Indeed, several days later a SN was detected. Also, the common power-law decay starts very early on for this very energetic burst which also fulfills the second feature of IGC GRB X-ray afterglows. The afterglow of this GRB was well observed from optical (eV) to very high energy (GeV) and the afterglow LC seems to decay with a common slope in all these energy bands. This implies that the same mechanism is responsible for the afterglow at all the energies.

Given this energetic GRB close proximity, it was very fluent - to fluent. The burst had overloaded Fermi-GBM detectors and a detailed analysis was hard to do. The distinction of episode 1 and 2 was hasn’t been done. There is also the possibility that the episodes overlap in time due to geometry of the IGC binary system and its position with respect to Earth.

The Swift-XRT instrument can deal with very high fluence and X-ray afterglow analysis can be done with ample amount of data. Analyzing first few hundred seconds of afterglow showed a spectrum consisting of a power-law (PL) component and a thermal (BB) component. The BB component temperature decreased from 0.5 keV to 0.1 keV in the time interval of about 250 s. The time interval where BB was detected corresponds to a soft peak in the X-ray and Gamma-ray energy band which happened about 100 s after the start of the main prompt emission.

⁴Within the framework of Standard cosmological model.

With the known BB fluence and redshift (distance), a BB radius can be calculated. The radius changed from about 1×10^{13} cm to 3×10^{13} cm in about 200 s. This gives an apparent superluminal⁵ velocity. After correcting for the relativistic expansion, a speed of $0.8 c$ is obtained. The radius of $\sim 10^{13}$ cm is much smaller than radius at which prompt GRB emission is emitted and even smaller than the one at which early afterglow is emitted - whether in fireshell or fireball model. This means that the BB emission cannot be from the GRB ejecta. It probably comes from the SN ejecta which expands slower than the GRB one. Also, the expansion speed (Lorentz factor) of the GRB ejecta at the time of the early afterglow is much higher than in this case. The radius and expansion speed of the BB emitter are also different than the ones derived from thermal emission in episode 1 - which comes from accreting SN ejecta onto companion NS. The possible detection of a similar BB component in the early stages of afterglow has been reported for several GRBs, including GRB 090618.

Another interesting feature is the light curve of the GeV emission. It seems to be anti-correlated with the keV-MeV emission. When this emission peaks, whether in the main part of the prompt or in the soft peak at 100 s, the GeV emission is absent. As soon as the keV-MeV emission lowers, the GeV emission emerges. So far there is no clear physical explanation for this within the IGC model.

3.5 Binary systems and two families of GRBs

In the work of (Ruffini et al., 2015b), (Ruffini et al., 2016c), (Ruffini et al., 2016b), (Ruffini et al., 2016a) and similar, a new concept was being introduced.

The standard division of GRBs is into long and short burst. Apart from the T_{90} duration of prompt emission, there are other observational features that support this division. These features point to the scenario where progenitors of long bursts are massive stars while progenitors of short bursts are mergers of two compact objects (BH, NS, white dwarf).

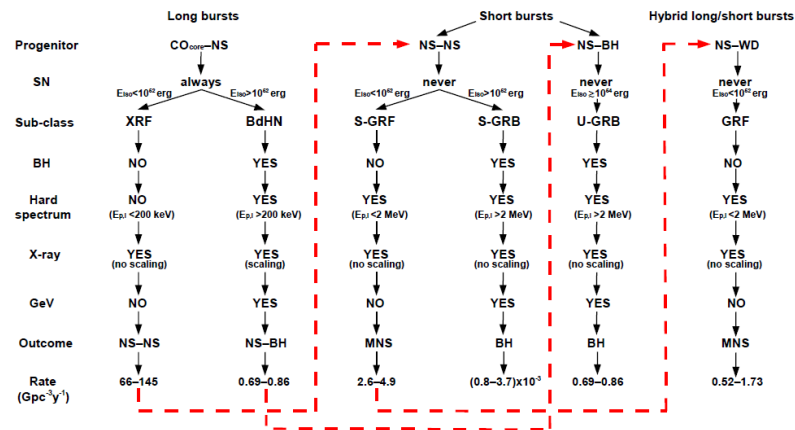


Figure 3.5: Characteristics, rates, progenitors and end results of binary systems producing GRBs. Details are given in the text. Figure taken from (Ruffini et al., 2016c).

The new picture that emerged from extending IGC scenario also differentiates between long and short bursts, and connects long to death of massive stars and short to mergers

⁵Due to (ultra)relativistic movement or expansion ($v \approx c$), the apparent speed may seem like larger than speed of light.

of compact objects. The difference is that progenitors of long are binary systems and not single stars. Apart from duration there is also a new parameter in extended-IGC scenario which further differentiates GRB classes - whether or not a BH is formed. This is a factor for both long and short types. Based on numerous observational features and basic energy evaluation, the minimum energy associated to BH formation is $\sim 10^{52}$ erg. This threshold energy is also the maximum energy that can be released without BH formation. Further differentiation of short GRBs comes from the type of compact objects that are merging.

Typical IGC GRBs are in the second column in Figure 3.5. They belong to the long class of GRBs when a BH is formed. If accretion onto the NS is not enough to collapse it into a BH, then only emission related to accretion on the NS is produced. The limiting value of $\sim 10^{52}$ erg was evaluated to correspond to energy threshold of creation of a BH. In the case a BH is not created then an X-ray flash (XRF) is emitted (first column in the figure). Short bursts are divided into three categories: Merger of two NSs with (fourth) or without BH creation (third), and a merger of a NS and a BH (fifth). The final class (sixth column) is made in a merger of NS and a white dwarf. The outcomes of some classes can be progenitors of others as can be seen in the Figure.

Thermal X-ray emission in the late prompt - early afterglow phases

Transition from the prompt emission to afterglow hasn't been well explored as prompt emission or the afterglow. The main reason for this lies in the instruments capabilities. From the start of the modern GRB astronomy in the 90s, many instruments were focused on observing prompt emission. The goal was to increase spectral and time resolution, as well as energy range. With the launch of Swift satellite at the end of 2004, the X-ray afterglow have been observed in detail and in great number for the first time. Still the late prompt and early afterglow emission remained elusive because Swift satellite needed about 100 seconds to point to GRB and start measuring with its narrow-view XRT (X-ray Telescope) in the soft X-rays. Meanwhile the wide-field BAT (Burst Alert Telescope) triggered on the burst and measured the prompt emission in hard X-rays which usually fades away by the time XRT begins observing. Few bursts detected by Swift have such a temporal and spectral structure that they are detected by both BAT and XRT at the same time. Usually these bursts have longer and stronger prompt emission, or have a hard flare at the start of the afterglow.

The analysis done so far in the literature - focusing on joint Swift BAT-XRT analysis or just XRT at the beginning of the afterglow - has found evidence for thermal emission (Nappo et al., 2017; Ruffini et al., 2017b; Basak and Rao, 2015b,a; Ruffini et al., 2015d; Larsson et al., 2015; Peng et al., 2014; Piro et al., 2014; Bellm et al., 2014; Friis and Watson, 2013; Sparre and Starling, 2012; Starling et al., 2012; Page et al., 2011; Starling et al., 2011; Campana et al., 2006; Liang et al., 2006).

In general this late thermal emission can be divided into two types. One has a relatively constant intensity and temperature of about ~ 0.1 keV (lower range of XRT band) over several hundreds of seconds. It was found mostly in close and weak Gamma-ray bursts (GRB) which have an accompanying supernova (SN). Often this thermal emission is assigned to SN shock break out, either from stellar envelope or dense wind medium. The weak GRB is often considered not to be "real" cosmological GRB but coming from a stronger SN. The second type of thermal emission has a varying intensity and temperature of order a magnitude in the period of tens of seconds. Temperature can reach $\sim 1 - 10$ keV. In most cases temperature starts from the highest value and then monotonically decreases. The intensity usually follows this path but there are more exceptions. These can be found in typical cosmological GRBs.

The interpretation of the second type can be found within fireball model. In it the thermal radiation is boosted by a Lorentz factor of $\Gamma \sim 10 - 100$, ultrarelativistic but smaller than during the prompt; however the process is practically the same as the one of thermal emission in the prompt phase within the fireball model. The speed $\Gamma \sim 10 - 100$ is not related to the speed of the photosphere. There is a relativistic jetted outflow and photosphere is the place where the transparency drops to around one. The photosphere may not move at all. The values of photosphere radius, Lorentz factor, comoving temperature, etc. are obtained within the fireball scenario (taking into account initial conditions and the fireball equations) in combination with observed values. Continues transparency/opacity changes in space and time have to be considered, i.e. the photosphere is not a sharp surface (where opacity suddenly drops from 'infinity' to zero) but photons come from a certain volume with different probability of emission. This then has to be coupled to (ultra)relativistic expansion in order to calculate thermal spectrum. Further effects such as different levels of thermalisation in the emitting volume and anisotropy of local photon fields, inverse-Compton scattering of thermal photons by electrons, radiative diffusion in the fireball wind before it reaches transparency radius, etc. may additionally affect the thermal emission. This has been studied in literature; for example (Mészáros and Rees, 2000; Daigne and Mochkovitch, 2002; Pe'er et al., 2007; Ruffini et al., 2013; Vereshchagin, 2014).

Similarly, with all the above considerations, thermal emission in the prompt phase is examined within the fireshell model starting from the dynamics of (ultra)relativistic plasma which then produces thermal emission. Literature concerning thermal emission in the prompt phase of the fireshell model: for example (Bianco et al., 2001; Ruffini et al., 2004b, 2005b; Bernardini et al., 2005; Bianco et al., 2011; Patricelli et al., 2012; Ruffini et al., 2014d).

Thermal emission in the late prompt - early afterglow phase in the fireshell model is explained within the wider IGC scenario. In it the late evolving thermal emission comes from the supernova ejecta expanding with mildly relativistic speeds $\Gamma \sim 2$ after it was hit by the fireshell plasma. Explaining thermal emission starting from the dynamics of the IGC system was done in (Ruffini et al., 2017b) where also comparisons were made with observations. Detailed modeling of motion of the plasma and transparency conditions is being presented in (Ruffini et al., 2018), however with no computation of spectrum.

Another approach to exploring late decaying thermal emission is the other way around, starting from observations and without assuming any model. The simplest case then is a perfect spherical black body with sharp surface and with uniform temperature. In this case if the black body is expanding then the velocity related to the boost of the spectrum is the same as the expansion speed of the photosphere. This assumption is considered to be valid enough when it comes to explaining thermal emission within the IGC scenario, i.e. explaining thermal emission as coming from the surface of the optically thick supernova ejecta. This method has been applied in (Izzo et al., 2012b) (although for thermal emission in Episode 1 - beginning of the burst) and in (Ruffini et al., 2014c, 2015d, 2018). From the simplest assumption of perfect spherical black body radius may be calculated and from there the expansion speed from time resolved analysis. If this expansion turns out to be superluminal then relativistic corrections should be applied.

Analysis in this chapter

Within systematic studies of thermal emission in Swift data, not much focus was given to searching for second type thermal emission with time resolved analysis in the joint Swift BAT-XRT data. This will be focus of the chapter. The spectrum of thermal emission looks like a bump, but a broad one and, unless it is well localized in the lower-middle XRT band, it doesn't really show in just XRT or just BAT band. Wider energy range is needed. Another factor to recognizing it is to find a decreasing temperature in time resolved analysis. Only bursts with redshift will be considered since then rest frame properties may be determined and potential thermal emissions compared.

Then thermal emission from a *spherically symmetric, expanding with constant velocity, sharp black body surface, with uniform and constant temperature* will be calculated starting from the very basis. Many of the results from this part are well known and might seem redundant. However, most of the equations from the literature are concerned with some assumptions of plasma dynamics which might be specific for those particular cases and usually they correspond to ultrarelativistic approximation. Some expressions from derivations will later be used in a code which computes observed spectrum from the above-mentioned thermal surface but with (inputted) varying velocity and temperature. It will be showed that just by changing velocity and temperature broader peaks or double peaks may appear in instantaneous spectrum.

4.1 Data Analysis

This section will be dedicated to instruments, data analysis software, methods and challenges.

4.1.1 Swift BAT and XRT data

Swift was launched at the end of year 2004 and is still operational in the year 2017. Instrument Swift-BAT energy range covers 15 – 150 keV while Swift-XRT covers 0.3 – 10 keV. The initial data (Level 0 data) after the burst are sent from the spacecraft to the ground where they are analyzed and Level 1 and Level 2 data are produced. Level 2 data are files which contain photons, their detection times, energy, etc. along with various instrument information. These data (photons) can be then binned in energy and time, along with other tasks, to produce files and responses for spectral fitting in software such as XSpec¹. Level 2 data start to be available few weeks after the burst. The Swift team provides means for users to analyze Level 1 data but this might be helpful if there is a specific burst of interest and not really for systematic analysis of many bursts. Swift team also produces automatic light curves and spectra. This is available on the website here² where other information in regards to instruments, data analysis, etc. may be found.

XRT modes

Instrument XRT has different modes of operation with two main being window timing mode (WT) and photon counting mode (PC). XRT is an imaging instrument which means it records direction of photons and can produce images. This option is available in PC

¹<https://heasarc.gsfc.nasa.gov/xanadu/xspec/>

²<http://www.swift.ac.uk/>

mode. PC mode is used when the intensity is below about one photon per second. Then there is time to read out each pixel in a square 600×600 pixel grid (24×24 arcminutes). When intensity is higher, then WT mode is used in which ten pixel rows are read out at the same time in order to be faster. Also the edges are truncated and this produces a semi one dimensional image (200×20 pixel grid). Data analysis of WT and PC modes are different in some respects. In this work only WT data will be used since the beginning of the afterglow or flares are intense and are recorded in WT mode. Also this means that background may be ignored (the intensity is almost always above 10 photons per second).

No mode distinctions exist for BAT data.

4.1.2 Software

Firstly the HEASoft software package ³ must be installed and access to calibration database CALDB⁴ available.

XRT

Level 2 data are analyzed by FTools⁵ which are a set of software meant for working with fits files.

General analysis of XRT data firstly involves *XSelect*⁶ which can filter photons based on energy, time, region, grade (quality/precision), etc. using other FTools. It creates typical spectral PHA file which is read in XSpec. It has many other applications but for this work the mentioned are enough. To run all the necessary commands in XSelect it has to happen within XSelect environment, or, all the commands may be typed in a text file (with .xco extension) and invoked when starting XSelect which will then execute them all one by one. By adding an exit command at the end the whole process may be completed with a single command line. Due to point spread function a point source will look like a line in WT data image, so, photons need to be filtered by position. During region selection a DS9⁷ program will be prompted showing WT image, then region may be selected and information saved as a text file with .reg extension. This file will be used during region filtering. Knowing the region information (position of center of circle, radius of circle and inner circle in the case of annulus), the same file may be written independently of DS9 and then used by XSelect.

The next step is to generate exposure map with *xrtexpomap* which takes the previously generated spectral file and instrument response files. All input parameters may be entered in a single command line when invoking the program.

Next step is to create an arf-response file with *xrtmkarf* with spectral file and exposure map. All input parameters may be entered in a single command line.

The final step may involve *grppha* which is mainly used to rebin the energy bins in order to have a minimum counts per bin. Since XRT data will be fitted with BAT data which can only be done with χ^2 statistics, the XRT data need to be bin to minimum of 20 counts per energy bin so they can be fitted based on χ^2 . All input parameters may be entered in a single command line. Also bad channels which fall outside range 0.3 – 10 keV should be marked.

³<https://heasarc.nasa.gov/lheasoft/>

⁴https://heasarc.gsfc.nasa.gov/docs/heasarc/caldb/caldb_intro.html

⁵https://heasarc.gsfc.nasa.gov/ftools/ftools_menu.html

⁶<https://heasarc.gsfc.nasa.gov/docs/software/lheasoft/ftools/xselect/xselect.html>

⁷<http://ds9.si.edu/site/Home.html>

The spectral file, the arf-response file, and RMF-response file (which is the same for all the burst in a given yearly periods) can now be loaded into XSpec and fitted.

XSpec has its own environment but similar to XSelect all the commands (including final "exit" command) may be written to a text file with *.xcm* and then invoked when starting XSpec which will run all the commands and exit.

Python:

All of these tasks are one-dimensional and can be run one by one within a programming language such as Python. There is no need for special Python packages from which these tools may be run and operated. It is possible to invoke them from Python the same way they would be started from operating system environment, and all the FTool tasks can be completed with a single command line.

User just needs to choose time period (with respect to GRB trigger), binning, region extension, model to fit, and run the Python script which has been written in the course of this work to simplify and speed up analysis. Since XSelect and XSpec have their own environments, text files with *.reg*, *.xco*, and *.xcm* extensions may be written by Python and invoked with the tools. With XSpec there is possibility to export results in a text file, or to log the XSpec output to a text file (*.log* extension). These text files may be read with Python and fitting information obtained. For XSpec there is also option to use Python package PyXspec which is specially design to operate XSpec from Python.

Information such as trigger time, burst position, trigger number, instrument information, etc. - which are needed in these FTool sequences - may be obtained from LEVEL 2 data files with Python package PyFITS which is used to manipulate FITS files. This is the basic chain. Additionally, some unnecessary files will be created during sequences and may be deleted at the end; plots from XSpec may be saved or imported into Python and from there make the plots, information from fitting saved or used for additional calculation; option to include background, option to run just XSpec with different model; folders created, deleted, files moved, etc.

All of this can be repeated for many time bins by running the process over and over again (in a single script), just with different time periods, or by using Python module for multiprocessing which then runs all different time bins at the same time on different processors and combines results in the end. This can be useful when using small computer cluster with relatively strong processors like the one at G9 at La Sapienza University. Good practice is to allow for few seconds before new process starts because some times running XSelect at the same time on many processors may result in crash. Similar Python script has been written to do this.

BAT

First FTool is *batbinevt* which has many purposes including to filter photons from Level 2 files based on energy and time, and to do energy binning thus producing a spectral PHA file. Next *batphasyserr* and *batupdatephakw* are used to account for systematic errors. Then *batdrngen* is run to produce response file. Then *grppha* to mark bad channels and other tasks. Finally XSpec may be run.

As in the XRT case all the commands with input parameters may be run on a single line and the processes are one dimensional. The Python script for BAT is similar to the one of XRT: inputs are time bin(s), binning, and other optional information such as light curve binning, mask weighing, checking the "fkey" parameter, etc. Again, for different time bins, jobs may be distributed to different processors and results combined in the end.

Joint XRT-BAT

Finally script which implements two previous procedures is made to do joint analysis of XRT and BAT. The input parameters for both XRT and BAT are as in individual cases and final results contain fit information (parameters and statistics) and plots. Again the jobs for different instruments or time bins may be distributed to different processors.

4.1.3 Pile-up

If the intensity of the burst (prompt, afterglow or flare) is stronger than about 100 photons per second, then pile up may occur in WT mode. The photons come in too rapidly and there is no time to read out pixels, even in fast WT mode. What happens is that two photons may be read as one photon with energy which is sum of the two. The end result is that spectrum looks harder than it is.

Central pixels (ones which are centered on the position of the burst) have the most counts. The central pixels should be excluded (by choosing annulus region selection instead of circle) until the pile-up effect is gone. To determine how much pixels should be excluded XRT spectrum may be fitted for each excluded pixel until it stops to change. Since this requires doing the same process just with different inner circle radius, Python scripts have been written that distribute the work to different processors and the results are combined in the end. When doing this only one exposure map may be generated since it doesn't depend on the selection region. This then can be done for different time bins.

In practice this can only give an estimate, and also depends if the spectrum is fitted with models other than power-law, which might be important if the intrinsic spectrum is not power-law (if the thermal emission is also there for example). With the estimation, when doing joint XRT-BAT analysis few pixels may be added or excluded to check if this changes the final spectrum and to what level. With excluding pixels the XRT statistics gets weaker, and the outer region radius may be expended to include more photons, but if it gets too big the question of background might become important.

Other methods for estimating pile-up includes checking the ratio of photons with different grades and how it changes with exclusion of pixels (excluding pixels until it more-or-less stops to change). This is also uncertain since even if there is no pile-up the ratio changes.

The pile-up effect, and how much pixels should be excluded, can really become an issue when intensity is above 1000 photons per second.

4.1.4 Other difficulties

Low energy spectral residuals in Windowed Timing Mode

If the source is very absorbed in the 0.3 – 2 keV range, spectrum may show an artificial bump in the 0.4 – 1 keV range and a turn-up at very low energy range. The bump may disappear if only grade 0 photons are used instead of typical grades 0-2. This option is implemented in scripts. The turn-up doesn't disappear and the energy where it starts changed over years. It is important to keep these effects in mind because the artifacts resemble thermal spectral component.

Position-dependent WT RMFs

The reason why WT image is compressed in one dimension is because 10 rows are read at a time. The merged "big" row where the source lies means that the source could be at any of the 10 rows which were merged. Depending where it is can produce different WT images (due to multiple pixel events being split between merged rows) and then spectra. So, position dependent RMFs may be used. There are 3 of them for each ordinary RMF. It cannot be precisely determined where the source actually lies and which one to use. So, one strategy is to use all of them and select the one where the fit statistics is best (lowest χ^2). Second strategy is to do fitting with all three and find an average value for 3 different sets of parameters, and combine all the confidence intervals of 3 sets of parameters (errors). In other words, treat it as an additional systematic error.

Burst position on the XRT detector

The position of the burst read in the header of the Level 2 data file doesn't always correspond to the brightest pixel in the WT image. Additionally, the brightest pixel may change during course of several seconds or tens of seconds. This is due to uncertainty of XRT pointing, so the same sky position (RA and Dec) may "drift" on the XRT detector plane as the satellite sways. The sky position should be chosen where the brightest pixel is.

Binning BAT data

By default BAT data are binned into 80 bins in the *batbinevt*, and later, bins corresponding to range below and above 15 – 150 keV are marked as bad in *grppha*. If the binning is custom and corresponds to 15 – 150 keV, then during fitting values corresponding to first 2 or 3 BAT bins will have unusual lower value. It is not clear what causes this and unlike previous problems it is not officially recognized. A way to overcome this is to have additional 3 bins from 10 – 15, 16 keV and then set them as bad in the *grppha*.

Additionally, default 80 bins are linearly equally spaced. It is more useful to have them logarithmically equally spaced and the number of such bins can be entered in the script (not counting first 3 bad bins).

Intrinsic column density

Intrinsic column density is an unknown factor. The value may be taken from Swift automatic analysis. Two values are from WT data and later PC data. Value from WT data is more precise but it may be wrong due to spectrum in XRT range being different than power-law (which was used to obtain column density) and varying. The PC data value is less precise but the spectrum in this later time is much more constant and powerlaw-like. Intrinsic column density may be left as a free parameter during fitting. Since it has to have the same value for different time bins, all the spectra may be fit simultaneously in XSpec with column density being the same parameter for all time bins. Value of intrinsic density is important if the thermal emission is in the lower band of the XRT range. Otherwise value(s) from automatic analysis may be taken and kept constant.

XRT-BAT normalization constant

These two instruments may have some unaccounted instrumental error so additional parameter during fitting may be a normalization constant. Since it has to be the same for all time bins (and at least very similar for other bursts), all the spectra may be fitted in XSpec with normalization parameter being the same for all time bins. Both instruments are on the same satellite, pointing in the same direction. In literature it was often found that normalization constant was close to one, and was kept as such during fitting. Ignoring it should not produce relevant effects.

Number of energy bins for XRT and BAT

XRT data should be binned minimum to 20 counts per bin. Depending on the intensity of the burst and excluded central pixels this may give different number of bins. BAT data should be binned in such a way to have at least half number of bins with errors smaller than the value. If XRT or BAT has many more bins than the other, then that one will affect χ^2 statistics much more and other instrument won't play much role. So, number of bins should be similar. This goes for the underlying component which can be power-law or cutoff-powerlaw, or Band function. If the thermal component is significantly in the range of one instrument, XRT for example, then XRT should have good resolution in order to follow the bump of the thermal component.

Another thing is as binning change within some expected intervals, the values obtained from the fit will change. In some cases this may produce significant differences in parameter values, errors, and comparisons between models.

Final remark

All the above mentioned should be kept in mind when reading results of from the fit. Small errors of the parameter may not mean it is likely close to that value. There may be underlying uncertainties which are beyond fitting in XSpec. Even if all the above uncertainties didn't exist, it is hard to claim detection of the thermal emission. Black body spectrum is distinguished by a steep index of +1 before the peak which then falls off exponentially. Even if thermal peak isn't deformed by mildly relativistic motion, or lack of complete thermalization, to detect it would require a black body peak to be significantly above underlying component. In vast majority of cases this is not true and at best adding a black body component is done to detect curvature of underlying component or a bump. Then, assuming it is a black body, the evolution of its temperature, luminosity and calculated radius may be followed. From there it may be discussed whether the results have physical sense. For example, radius should start from smaller value and only increase with time (also relativistic correction should be taken into account).

4.1.5 MCMC

When XSpec finds the best fit (minimum χ^2), the values correspond to that minimum. With the "error" command it is possible to find interval based on change of χ^2 . For example, changing the parameter where χ^2 changes by 2.706 corresponds to 90% confidence for that parameter. This then may give asymmetric errors. Similar may be done in whole parameter space to determine correlation between parameters and calculate error on flux for example. This statistical method would correspond to frequentist approach.

However, the parameter value corresponding to minimum χ^2 , although it may be the most probable value, it may not be the mean value. Difference is bigger if the probability distribution for the parameter is more asymmetric. Within XSpec there is a way to implement Markov Chain Monte Carlo (MCMC). The basic idea is that for a given data (and their errors) and model, the chain will "walk" through parameter space and eventually after some number of initial steps, it will start to trace the probability distribution in the parameter space. Then the more steps taken (10^4 , 10^5 , etc.), the better resolution of this probability function. The final output can be a fits or a text file with all the sets of parameters. The idea is that these sets of parameters are as if they were taken from the probability distribution. This statistical method corresponds to Bayesian approach. XSpec implements parallel processing when doing tasks such as MCMC.

Lets say there are 10^5 steps and parameter sets. The mean value of a parameter is then simply the average of all 10^5 generated parameters. The 90% confidence interval (for example) is found by sorting all 10^5 by value and then excluding the first and last 5%. This may be done within Python or within XSpec with "error" command which will then calculate errors based on MCMC results. XSpec offers a way to calculate flux with errors and will use MCMC results to do this. However, when trying to calculate unabsorbed flux (lower energy interval of 0.3 keV), or flux of just one component, with the command "cflux", there are some problems. Specific flux may be calculated within Python by taking all 10^5 parameter sets. Then, all the 10^5 unabsorbed fluxes for, say, black body and power-law are calculated, their values sorted, average value found, and 90% confidence interval found by excluding first and last 5%. These fluxes then take into account not just probability distribution of each parameter, but also the correlation between parameters since MCMC chain traced probability distribution in whole parameter space. This is also the way for calculating any other value and its errors based on parameters found in fit, such as radius of the black body, its apparent speed of expansion, etc. Python script has been written to do this.

The particular use of this method here is when the peak of the black body lies between XRT and BAT ranges (10 – 15 keV) and the temperature is not well constrained. In this case the value corresponding to minimum χ^2 and the main value may be different by a significant factor. This then translates to different values of radius since it depends much more on temperature ($R^2 \propto T^{-4}$) then on flux ($R^2 \propto F$). In this analysis the Goodman-Weare type of MCMC will be used.

4.2 Preliminary results

Taking into consideration details from previous section, the analysis of Swift GRBs with simultaneous data in XRT-BAT was done. Selected GRBs have strong intensity in XRT-BAT to allow time resolved analysis, and redshift to determine rest frame properties. When the work was being done, the selection was up to end of year 2015 / beginning of 2016. The MCMC method wasn't used. Values and errors from the best fit were taken, and errors of calculated values were determined by error propagation.

In many cases fit will improve if additional component is added such as black body. To select GRBs with probable black body, models were compared based on χ^2 , strength of the black body compared to the underling component, systematic residuals in *model minus data* when using only underlying component. For the underlying component, power-law and cutoff-powerlaw were used. Also Band function was used sometimes. Band function

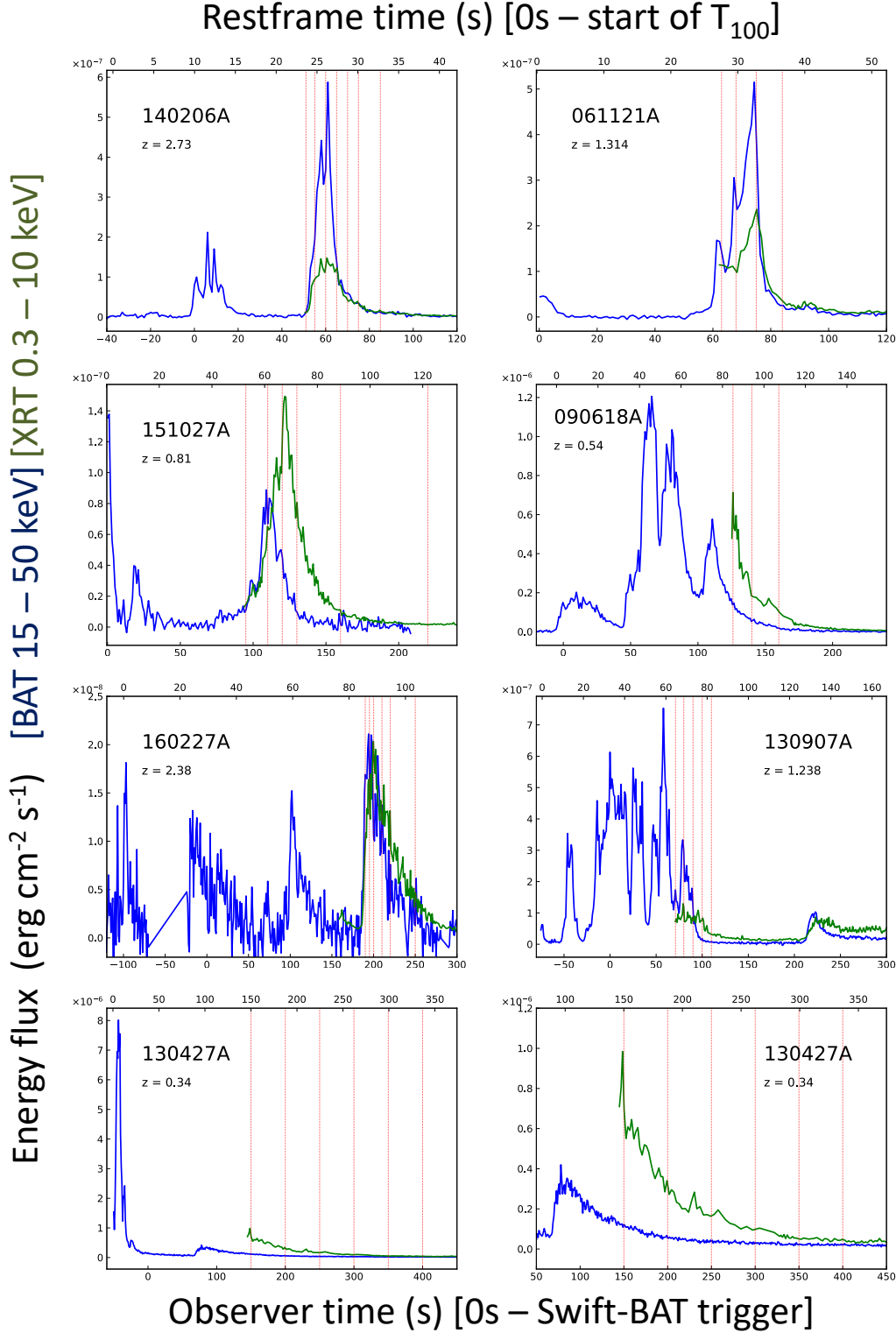


Figure 4.1: GRBs with time intervals where evidence for thermal component is relatively good. On each plot name of the burst and redshift z are shown. On the bottom axis is the observer time with respect to Swift-BAT trigger while on the upper axis is restframe time with respect to the very beginning of the burst which was determined as the start of the T_{100} interval which was obtained from automatic analysis on the Swift website. In some cases the start of this interval is much before the trigger. Blue lines are light curves of BAT detector while green correspond to XRT. Further details are in the text.

was also used to mimic power-law plus black body, and Band with exponential cutoff to mimic cutoff-powerlaw plus black body (with turnover at Band corresponding to peak of the black body). When the intensity was strong enough, fits with two black bodies were tried.

In the end these GRBs have relatively good evidence for a strongly evolving black body component: 140206A, 061121A, 151027A, 090618A, 160227A, 130907A, 130427A. On Figure 4.1 light curves of the XRT and BAT are presented along with time intervals where thermal emission was found. For GRB 140206A and 061121A, the time interval corresponds to the main part of the prompt emission. The XRT prompt detection is possible due to the fact that there was a precursors which triggered BAT so Swift had time to point XRT and catch the prompt. For 151027A thermal emission was in the second peak which was well separated from the first and has similar energy. For the rest the thermal emission was found in the slope of the last peak of the prompt emission, flare or in the extended emission.

In Figure 4.3 parameters of 7 bursts are shown. In the **upper-left** evolution of the temperature with time is shown. Time is in the rest frame of the burst as well as temperature, i.e. both are as if they were observed from the GRB host galaxy. Temperature is not the comoving temperature, i.e. no correction for relativistic motion is shown. It can be seen that temperature spans the range from 10 – 0.1 keV and for each burst starts from highest value and monotonically decreases up to an order of magnitude. In the **upper-right** is evolution of the luminosity of the black body with rest frame time. Unlike temperature, it seems there is detectable fast rise in luminosity and then slower decay about order of magnitude. Luminosity corresponds to whole black body luminosity calculated from black body formula, not just from specific energy range of detectors.

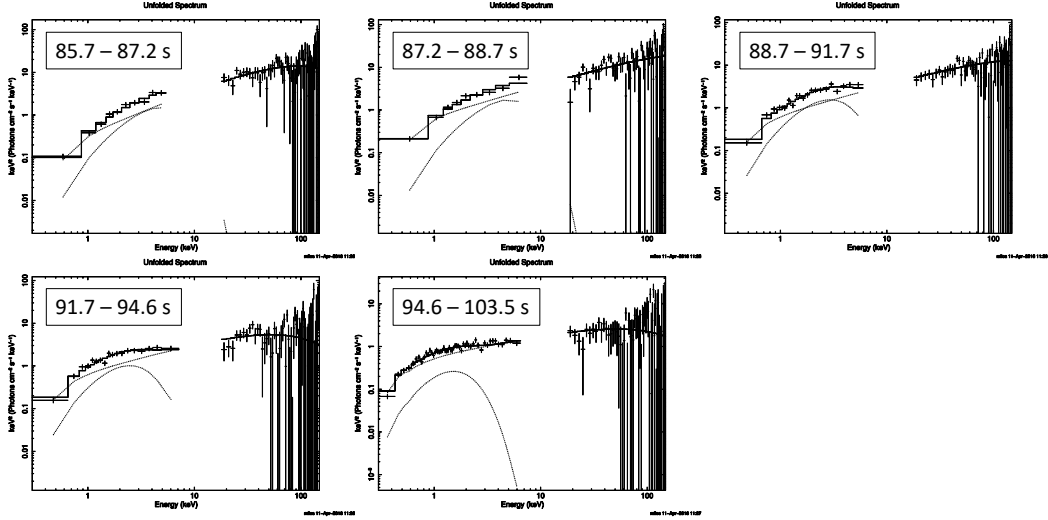
In the **lower-left** is shown radius for each burst with rest-frame time as calculated simply by $L = 4\pi R^2 \sigma T^4$ where L is luminosity (the one from previous case), T temperature as seen from the host galaxy and R the radius. No correction for relativistic motion has been applied. For all cases radius increases monotonically from lowest to highest value. This apparent radius may be used to see if the motion is relativistic or no. From evolution of radius with time, approximate velocities are: 130427A (2.5 c), 061121A (1.1 c), 090618A (0.9 c), 151027A (0.8 c), 130907A (0.7 c), 140206A (0.6 c), 160227A (0.5 c). Some bursts show superluminal velocities and clearly need correction. Other have non-negligible fraction of speed of light.

In the **lower-right** is crude comparison between black body isotropic energy calculated as integrated luminosity over time period where thermal emission was found, and, total energy of GRB. It can be seen that black body isotropic energy spans less than order of magnitude in range while isotropic energies of GRBs span about two orders of magnitude.

In Figures 4.4 and 4.2 spectral energy distribution of time resolved analysis is shown for bursts 140206A, 061121A, 151027A, 160227A and 130907A. Bursts 090618A and 130427A have an evidence for a second black body and will be shown later. The time intervals correspond to observation time since the GRB burst.

Bursts 160227A, 130907A, 130427A have started main part of emission before BAT trigger time. The $t = 0$ s in the Figure 4.3 for these bursts corresponds to actual start of the burst and not trigger time of BAT. For bursts 090618A and 130427A the XRT started observing after the peak of the extended emission. If it started observing earlier, it may be reasonably assumed that black body would exist and that evolution would be in similar matter as others. If data for these two bursts are extended to earlier times (espe-

160227A



130907A

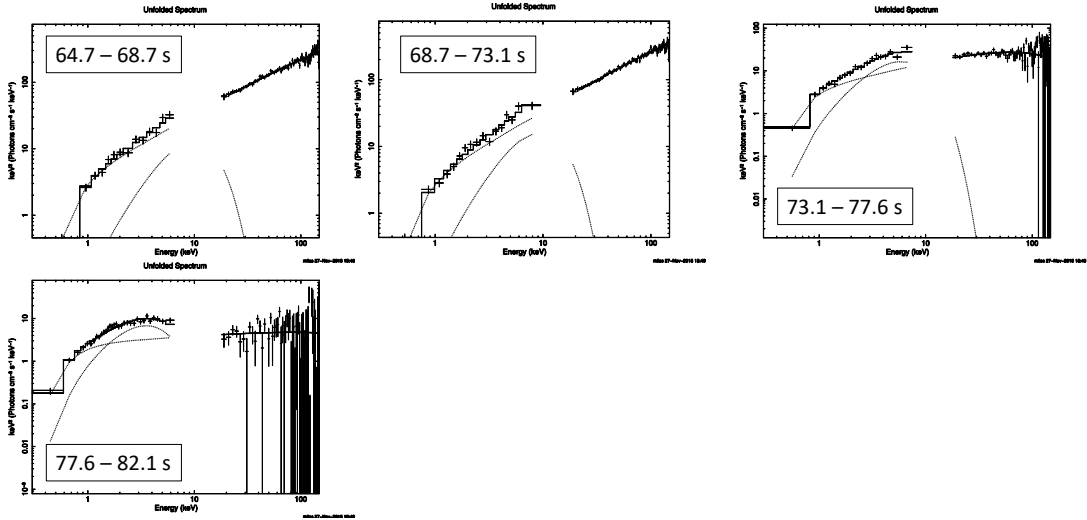


Figure 4.2: Spectral energy distribution of time resolved analysis of bursts 160227A and 130907A. First burst is fitted with cutoff-powerlaw and black body while the second is a combination of cutoff-powerlaw and just power-law. Time intervals correspond to restframe time centered on the start of T_{100} .

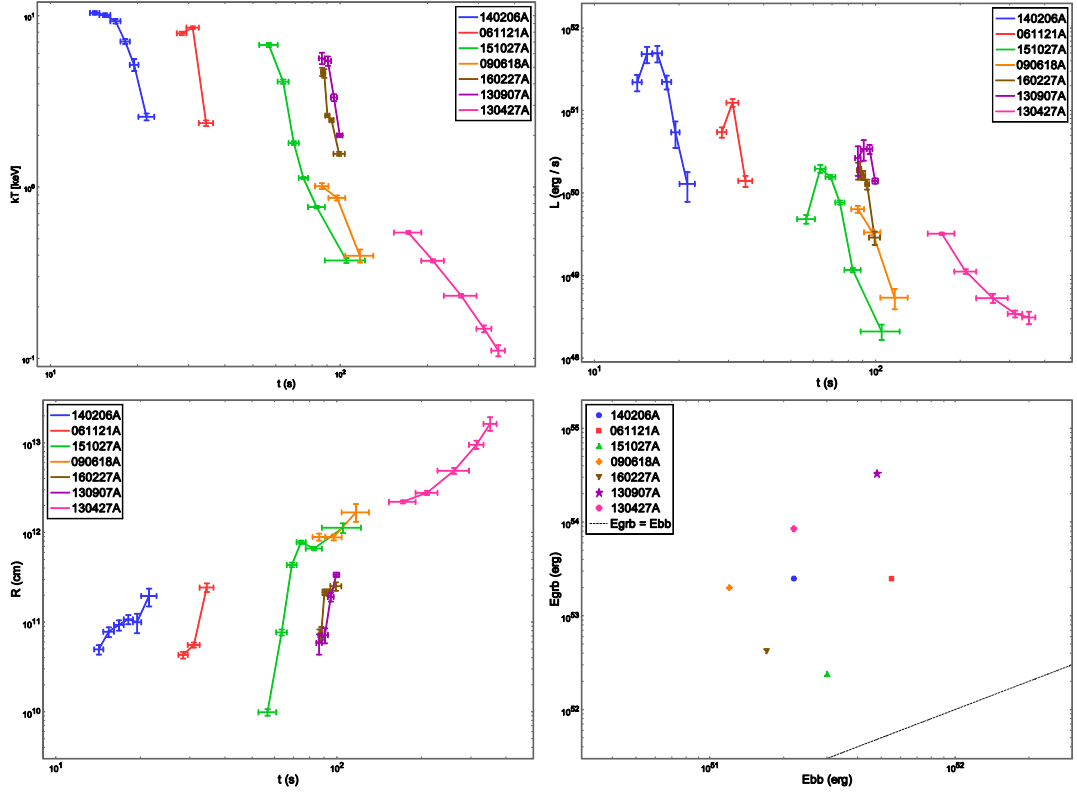


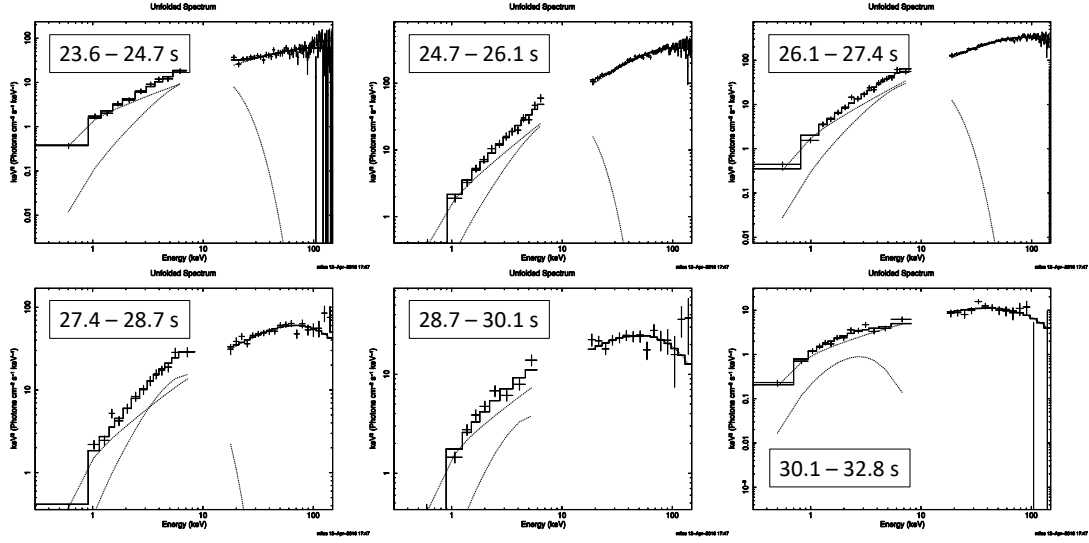
Figure 4.3: Parameters from the spectral fit versus rest frame time. Rest frame temperature, luminosity, calculated radius and approximate ratio of isotropic energy in thermal emission versus the entire burst. More details in the text.

cially 130427A), the parameters would be closer to the ones of bursts 151027A, 130907A and 160227A which show some clustering in parameter evolution. As mentioned before, thermal emission in bursts 140206A, 061121A happens during main part of the prompt emission. This may be reason why the parameters of their thermal emission seem to be outliers. Finally, the question might be asked do the detector sensitivity and limitations produce seemingly similar evolution of thermal emission. For example, it is known that within each pulse in the prompt emission, the peak evolves monotonically towards lower energies. Something similar might happen at the end of prompt emission where the spectra has a bump or curvature which is not due to thermal emission, and it evolves monotonically towards lower energies (which might be interpreted as black body cooling). Then the detectability of this bump/curvature may dictate intensity and change in luminosity (if it is assumed it comes from thermal emission). In the end these two may produce the calculated radius to only increase. This is something that should be kept in mind.

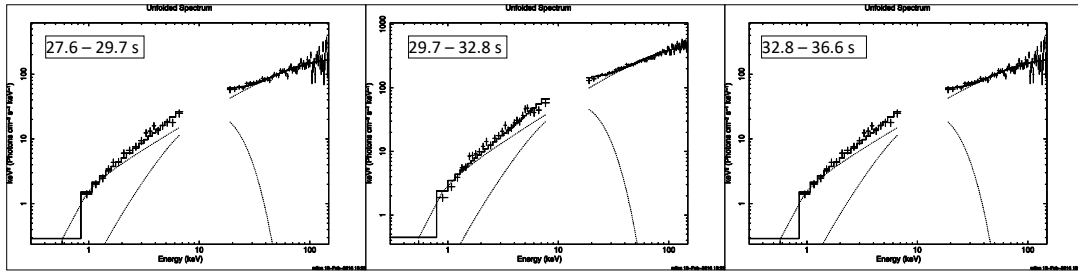
4.2.1 Two black bodies

In the bursts 090618A and 130427A relatively good evidence for two black bodies was found. In both cases the lower temperature black body is the one from the previous analysis, the one shown on the Figure 4.3 for these bursts, and it follows the pattern previously described. When fitting with just one black body the lower temperature one is recovered with similar parameters and evolution.

140206A



061121A



151027A

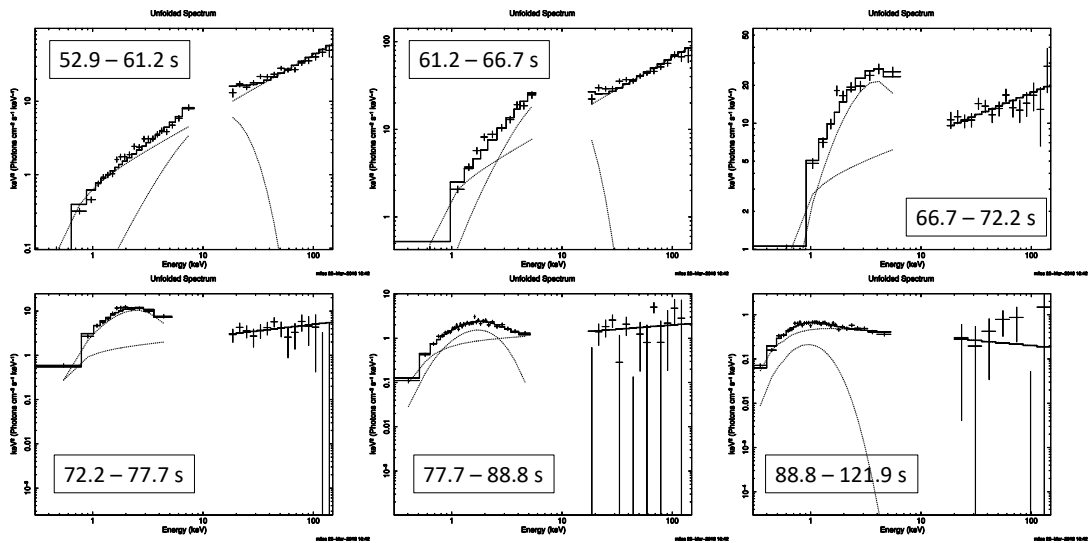


Figure 4.4: Spectral energy distribution of time resolved analysis of bursts 140206A, 061121A and 151027A. The first two bursts are fitted with cutoff-powerlaw and a black body while the last one is fitted with power-law with a black body. Time intervals correspond to restframe time centered on the start of T_{100} .

The second black body retains relatively constant temperature. In the case of 090618A, the temperature is around $kT_2 \approx 2.1$ keV. The luminosity in the first time bin is about 3 times higher than lower black body, and then drops more intensely about 3 times, while the lower black body drops about 2 times. For 130427A, the temperature of the higher black body relatively constant in the range of $kT_2 \approx 1.5 - 2$ keV. The luminosity in the first time bin is almost the same as the lower black body, but than it drops rapidly by about factor of 5, then 2, and than it remains the same, while the lower one drops more gradually and continuously without stooping. The parameters of the lower-temperature black body is in line with the one reported in (Ruffini et al., 2015d) which was found in the XRT data. In the Figure 4.5 time resolved analysis is shown.

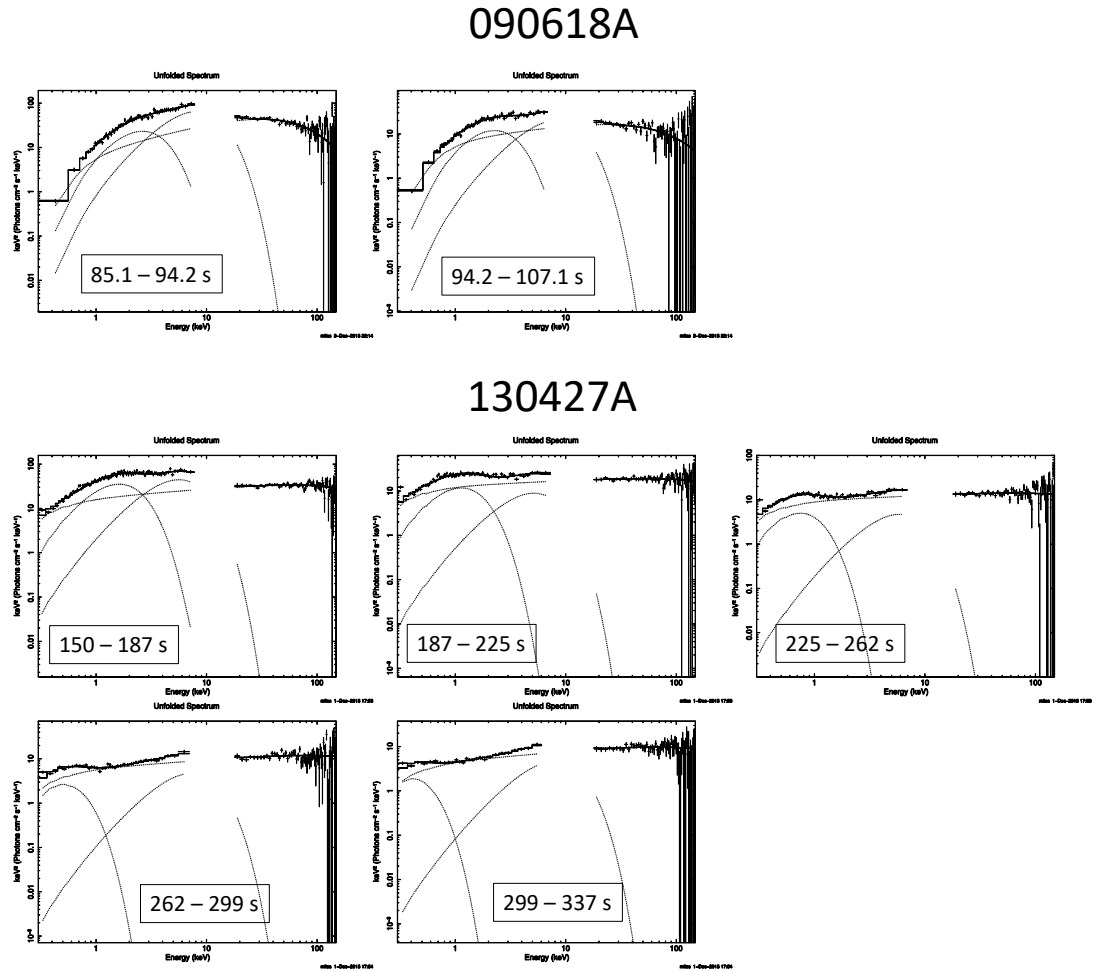


Figure 4.5: Spectral energy distribution of time resolved analysis of bursts 090618A and 130427A. Time intervals correspond to restframe time centered on the start of T_{100} . Both bursts are fitted with cutoff-powerlaw and a two black bodies. More details in the text.

4.3 GRB 151027A

This GRB has the strongest evidence for a black body and was analyzed in more detailed taking into account MCMC. The exclusion of central pixels was done in conservative way, i.e. for an interval, more were taken out rather than less. If, for example, less pixels

Time bin s	Model	α	L_u $\times 10^{49}$ erg/s	kT keV	L_{BB} $\times 10^{49}$ erg/s	R $\times 10^{10}$ cm	χ^2/DoF	Ftest
95 - 100	PL+BB	$1.349^{+0.024}_{-0.036}$	$20.4^{+1.5}_{-1.5}$	$2.2^{+1.1}_{-1.1}$	$1.34^{+1.1}_{-0.88}$	$6.4^{+14}_{-3.8}$	109/107	2×10^{-7}
100 - 110	PL+BB	$1.293^{+0.029}_{-0.031}$	$45.2^{+1.5}_{-1.6}$	$2.57^{+0.43}_{-0.50}$	$5.3^{+2.1}_{-2.2}$	$9.3^{+3.6}_{-2.9}$	66.9/77	1×10^{-5}
110 - 120	PL+BB	$1.392^{+0.028}_{-0.033}$	$63.0^{+1.9}_{-1.8}$	$2.17^{+0.22}_{-0.26}$	$15.8^{+3.6}_{-3.8}$	$22.6^{+4.5}_{-3.6}$	81.7/85	9×10^{-13}
120 - 130	PL+BB	$1.732^{+0.049}_{-0.057}$	$27.1^{+1.8}_{-1.9}$	$1.10^{+0.14}_{-0.12}$	$15.2^{+2.0}_{-1.9}$	87^{+19}_{-17}	101/103	9×10^{-27}
130 - 140	PL+BB	$1.82^{+0.11}_{-0.14}$	$9.0^{+1.6}_{-1.6}$	$0.617^{+0.046}_{-0.043}$	$6.3^{+1.0}_{-1.0}$	177^{+30}_{-28}	50.1/53	9×10^{-15}
140 - 150	CPL+BB	$1.65^{+0.15}_{-0.16}$	$5.3^{+1.4}_{-1.4}$	$0.469^{+0.065}_{-0.064}$	$2.61^{+0.70}_{-0.70}$	197^{+67}_{-52}	18.2/27	9×10^{-6}
150 - 160	PL+BB	$2.40^{+0.45}_{-0.34}$	$2.07^{+6.1}_{-6.1}$	$0.386^{+0.061}_{-0.061}$	$1.17^{+0.41}_{-0.38}$	195^{+81}_{-55}	23.4/27	2×10^{-5}
160 - 180	PL+BB	$2.15^{+0.29}_{-0.34}$	$1.43^{+0.38}_{-0.33}$	$0.193^{+0.032}_{-0.030}$	$0.52^{+0.29}_{-0.32}$	520^{+240}_{-250}	48.7/38	3×10^{-2}

Table 4.1: Time resolved analysis of GRB 151027A. Details are in the text.

are excluded, the temperature of thermal component gets higher in the first half of time bins.

In the Table 4.1 are results of the fit. First 6 intervals are fits from both BAT and XRT data while last 2 are just from XRT since emission in BAT range almost disappears. Models used are power-law and black body (PL+BB) or cutoff-powerlaw and black body (CPL+BB). Only in the sixth interval significant deviation from powerlaw is present and cutoff energy may be constrained within 90% significance. Parameter α corresponds to power-law or cutoff-powerlaw index. Parameter L_u is luminosity of the underlying component. If it is power-law, then the energy range used is 0.3 – 150 keV in the observer frame. For the last two intervals it is in 0.3 – 10 keV range. If it is cutoff-powerlaw, then it the range is from 0.3 keV to "infinity" since it converges because of the exponential cutoff. Parameter kT is temperature of the thermal component. Parameter L_{BB} is luminosity of the black body component corresponding to whole energy range. Parameter R is the apparent radius of thermal emission. The last two columns contain statistical information, with χ^2/DoF corresponding to best fit with thermal component, and Ftest corresponding to comparison between this statistic and the one with just underlying component (power-law or cutoff-powerlaw).

Values for fit parameter kT and calculated parameters L_u , L_{BB} , and R in the Table 4.1 are main values and their errors correspond to central 90% interval. This was obtained based on MCMC with 10^5 steps with exclusion of first 10^4 . Main values of kT and 90% interval are very similar to the ones corresponding to minimum χ^2 and 90% interval based on $\Delta\chi^2 = 2.706$. The only exception is for the first time bin.

In Figure 4.6 same time resolved analysis is shown. The time sequence is from left to right, up to down. First 8 plots correspond to XSpec command "ldata" which shows data as it is regardless of fitted model. The effective area correction has been applied so the data and model look like they are not convolved by instrument response. Additionally difference between data and model is shown in units of 1σ . The last 8 plot correspond to XSpec command "eeufspec" and present spectral energy distribution. Here the model is in the focus while the data may change if the model changes. In both cases the models correspond to best fit values, i.e. the values from minimum χ^2 and not the main values. However, both are very similar (except for the first interval).

In Figure 4.7 parameter evolution from Table 4.1 is shown. The time is rest frame time for all 4 plots. The temperature is rest frame temperature but not comoving temperature, i.e. as it would be seen from the host galaxy. The overall trend can be seen that temperature monotonically decreases, radius increases, luminosity increases and then more slowly decreases. The last plot corresponds to apparent velocity (in units of speed of light) based on evolution of apparent radius. This has also been calculated based on

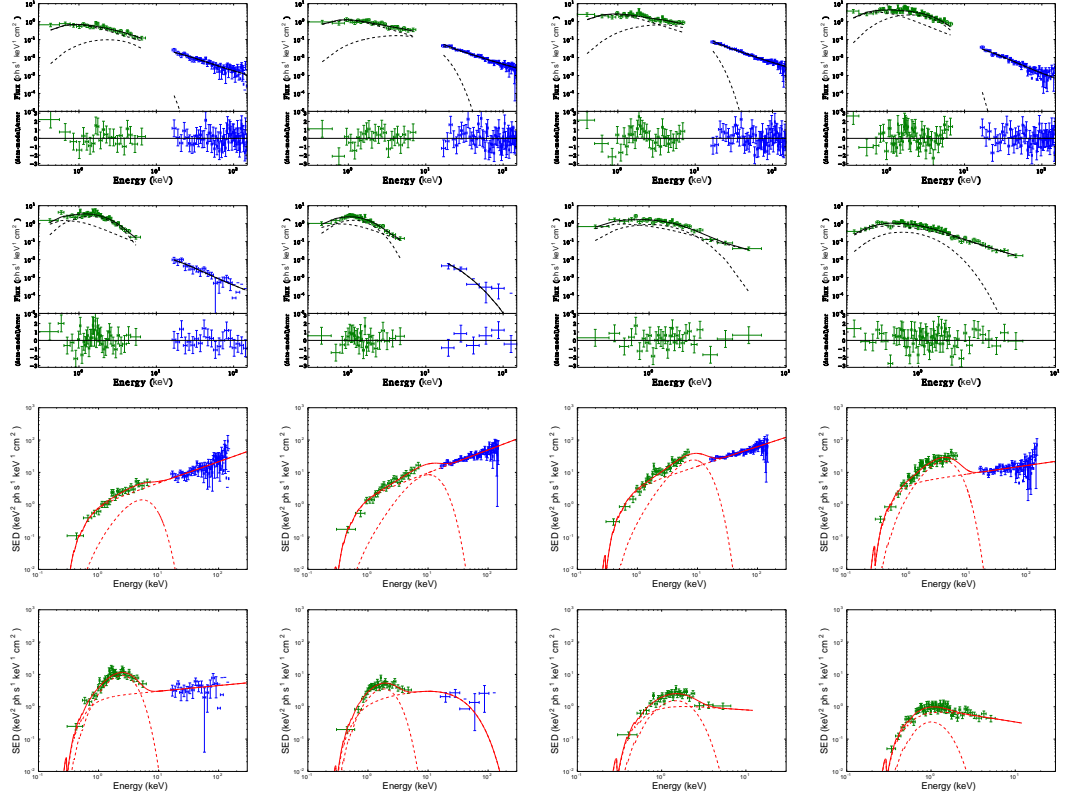


Figure 4.6: Plotted spectra from time resolved analysis of GRB 151027A. Details are in the text.

MCMC results from radii (two sets of radii for one set of speed). In principal this may give velocities which lower limit is negative. It seems that at first the speed increases and then decreases, and increases abruptly. However, when dealing with radii on the order of magnitude 10^{12} cm, small variation in fit results may give large absolute differences in radii, and hence velocity, than when dealing with radii of magnitude 10^{11} , 10^{12} cm for the same travel time. Also important to note that last two intervals have only XRT data and are less reliable.

4.3.1 Temperature from the first time interval

The parameters from first time interval diverge the most from a common trend, including the decreasing temperature trend. The temperature value and errors from minimum χ^2 is $kT = 1.33^{+0.61}_{-0.26}$ keV while from MCMC it is $kT = 2.2^{+1.1}_{-1.1}$ keV. This is a difference of almost factor of 2. In the first plot on Figure 4.8 are the results from MCMC for temperature. The 10^5 values are plotted against the χ^2 . Each empty circle is one value. With so many, they will outline the χ^2 "well" for the parameter. The minimum of χ^2 can be seen to indeed lie close to value of $kT = 1.3$ keV. However the whole distribution is skewed significantly to the higher values and the main value is very different. Even the large unsymmetry of errors from the χ^2_{min} results shows that distribution is skewed towards higher energies.

Additionally, there seems to be change in "slope of the well" near value of $kT = 2.5, 2.6$ keV. This might mean that temperature distribution is more complicated than just skewed, or it could mean that there is another thermal component at higher tempera-

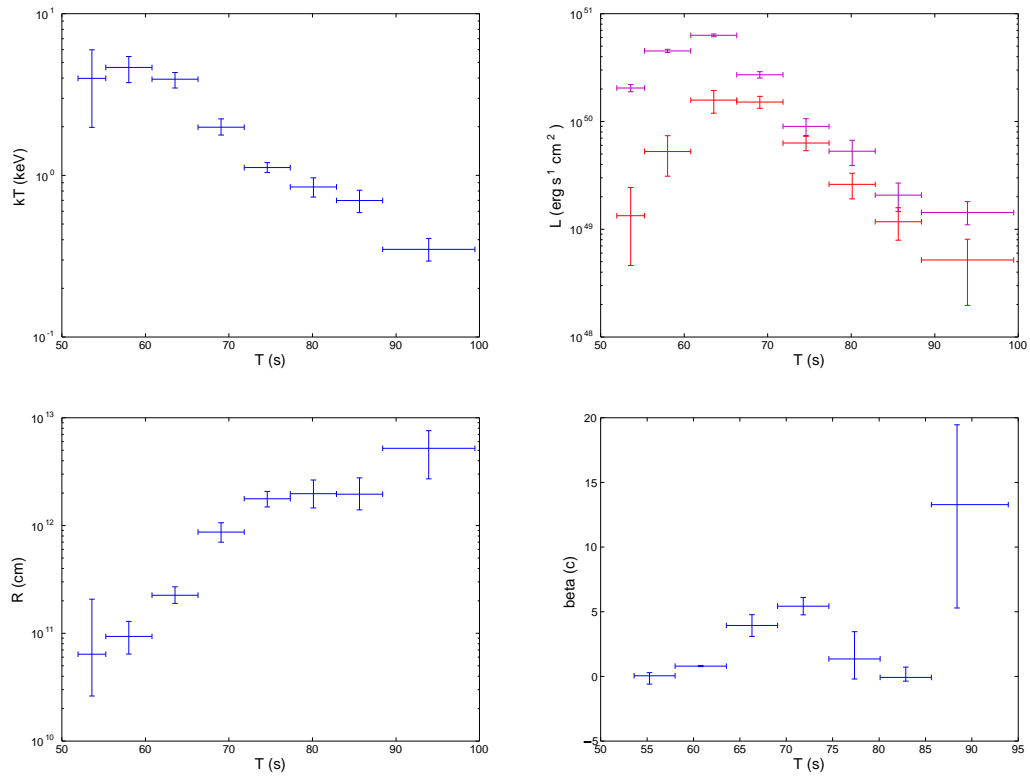


Figure 4.7: Evolution of parameters for 151027A. In the luminosity plot, red points correspond to black body while purple are from underlying component. Further details are in the text.

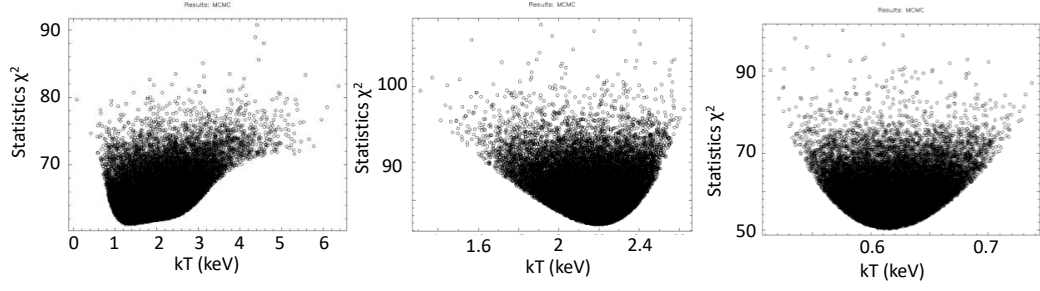


Figure 4.8: Results from MCMC related to temperature. From left to right, the first plot corresponds to first time interval 95 – 100 s, the second to 110 – 120 s time interval, and the last one to 130 – 140 s time interval.

ture, but cannot be detected due to non-existence of local χ^2 well (local minimum) due to influence of first black body. Then this higher black body may be the one which correspond to the one from all the other time intervals, and the one of $kT = 1.3$ keV (which would now have the main value closer to χ^2_{min} 1.3 keV value) is not related to it. The second plot on Figure 4.8 corresponds to temperature from third time interval. The distribution is skewed towards lower temperatures, but less and without "deformities". The third plot corresponds to fifth interval and χ^2 "well" is almost symmetric.

In any case, the main value and errors of the first-interval temperature are found considering MCMC results as coming from just one black body. The large errors reflect the wide distribution. With these error the temperature cannot be said to contradict the decreasing trend, however the main value is lower than the main value in the next time interval. The normalization constant may be read directly from luminosity since that is how it is defined in XSpec. From the plot the first point in luminosity fits well in the initially increasing trend. Finally the radius has large errors due to large errors of temperature. The main value of first radius is actually lower than the one of next and may be considered to fit well with monotonically increasing trend of radius, but the large asymmetric upper error has to be kept in mind.

4.3.2 151027A in the IGC scenario

Following the work (Ruffini et al., 2018), GRB 151027A was analyzed from the Induced Gravitational Collapse point of view in (Ruffini et al., 2017a) (Figure 4.9). The burst was interpreted as binary driven hypernova. The T_{90} prompt emission is made out of two peaks. The first one is identified as original GRB with the P-GRB component and extended afterglow. The second one is identified as *gamma-ray flare* which corresponds to interaction of fireshell plasma with supernova ejecta. Finally the flare in the afterglow (after T_{90} interval) is identified as *X-ray flare* which corresponds to late interaction of fireshell plasma with supernova ejecta.

4.4 Thermal spectrum from relativistically expanding sphere

Here the emission from *spherically symmetric, expanding with constant velocity, sharp black body surface, with uniform and constant temperature* will be derived. Although the focus is on mildly relativistic velocities, the derivations are valid for all values of Lorentz factor γ and for completeness the presented results will range from non-relativistic to ultra.

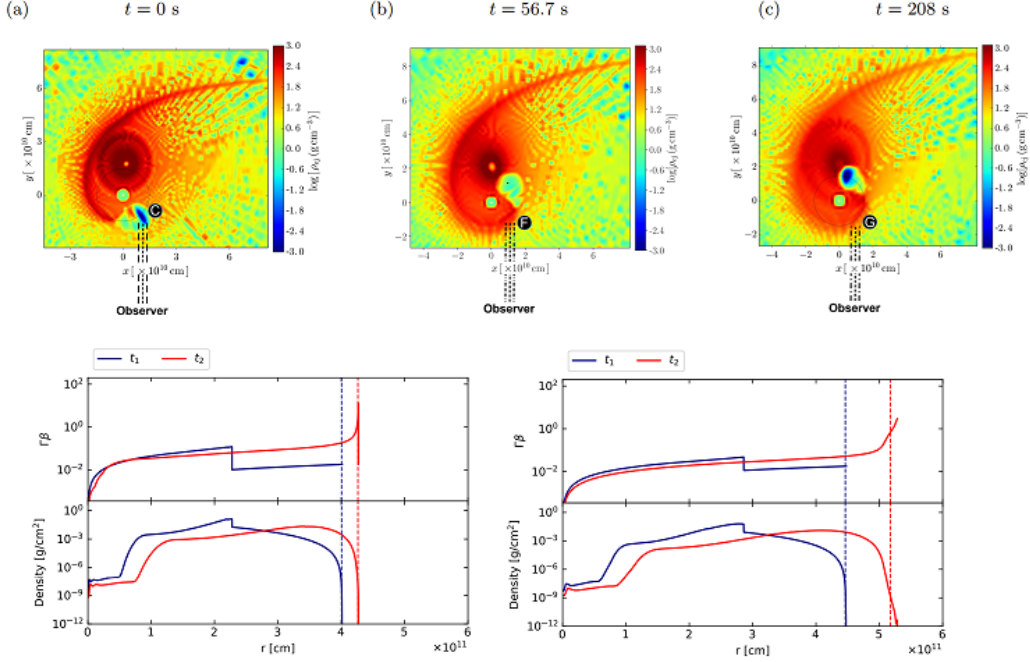


Figure 4.9: **The upper image** contains three snapshots of the density distribution of the SN ejecta in the equatorial plane of the progenitor binary system. The time $t = 0$ indicates the instant when the NS companion reaches, by accretion, the critical mass and leads to the formation of a BH (black dot). **The lower-left image:** Numerical simulation of the Gamma-ray flare. Above is the distribution of the velocity inside the SN ejecta at the two fixed values of the laboratory time t (before the plasma reaches the external surface of the ejecta) and t_2 (the moment at which the plasma, after having crossed the entire SN ejecta, reaches the external surface). Below is the corresponding distribution of the mass density of the SN ejecta in the laboratory frame. **The lower-right image:** The same as in the left, except for the X-ray flare. Images are taken from (Ruffini et al., 2017a).

4.4.1 Basic equation

Spectrum of a black body is described as:

$$N_{ES^2\Omega} = \frac{2}{h^3 c^2} \frac{E^2}{e^{\frac{E}{kT}} - 1} \cos \theta \quad (4.1)$$

where $N_{ES^2\Omega}$ are emitted photons in a unit of time, per unit of energy, from a unit of surface, in a unit of space angle. Subscript indexing will reflect these differential quantities. Only *per time* subscript is omitted since it will always be present and is implied. For the purposes of this section the units will be: photons / s keV cm² sr. Temperature (internal kinetic energy) kT is in units of keV, energy of photons (spectrum) E in keV. Constants such as speed of light in $c \approx 3 \times 10^{10}$ cm/s, Planck constant $h \approx 4.14 \times 10^{-18}$ keV s. Angle θ is an angle between the *normal* to surface element, and direction of space angle (photons direction).

Peak of the $N_{ES^2\Omega}$ spectrum is found by $\frac{d}{dE} [N_{ES^2\Omega}] = 0$. If $\frac{E}{kT} \equiv x$ then it gets to $\frac{x e^x}{e^x - 1} = 2$. The numerical (3-digit) solution is $x = 1.594 \approx 1.5$. So, the peak of $N_{ES^2\Omega}$ spectrum is at energy which is at $E_p \approx 1.5 \times kT$. Peak of the spectral energy distribution $E^2 \times N_{ES^2\Omega}$ is found in the same way and it comes down to $\frac{x e^x}{e^x - 1} = 4$. The numerical (3-digit) solution is $x = 3.921 \approx 4$. The peak of spectral energy distribution is at $E_p \approx 4 \times kT$. This is useful when looking at plots.

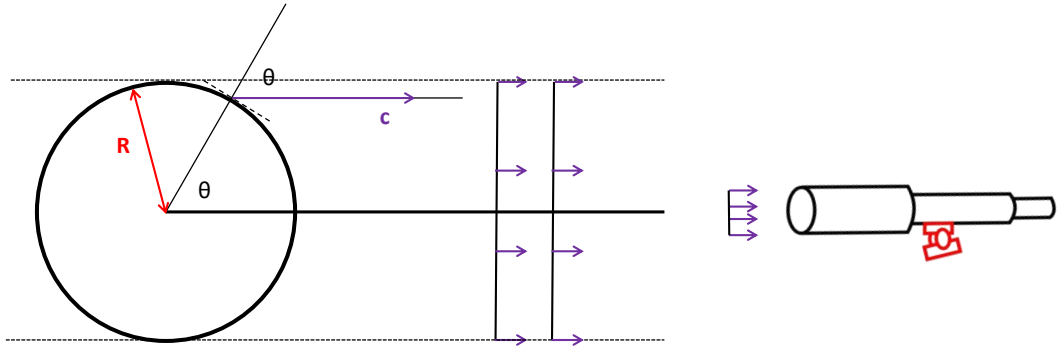


Figure 4.10:

The same quantity as $N_{ES^2\Omega}$ or any other $N_{...}$ but expressed as amount of energy, not number of photons, will be marked as F . In the basic case, $F_{ES^2\Omega} = E \times N_{ES^2\Omega}$ as well as any other case $F = E \times N$. The emitted energy is then in units of keV. The emitted energy over whole spectrum is obtained from integrating $F_{ES^2\Omega}$ over whole energy range. The final solution is $F_{S^2\Omega} = \frac{1}{\pi} \sigma T^4 \cos \theta$ where θ is the same angle as before and σ is the Stefan–Boltzmann constant. Integrating $F_{S^2\Omega}$ over half space angle: $F_{S^2} = \sigma T^4$. For unit consistency the σT^4 may be expressed as $\frac{2\pi^5}{15h^3c^2} (kT)^4$, with $\frac{2\pi^5}{15h^3c^2} \approx 6.416 \times 10^{33} \text{ s}^{-1} \text{ keV}^{-3} \text{ cm}^{-2}$.

4.4.2 Non-expanding sphere

First the method will be applied to still sphere (Figure 4.10) which will later be extended to expanding one.

Angle θ is between normal to the dS^2 surface and the direction of emission. It is also the angle between lines which connect center of the sphere to the surface element and the detector. Detector is far enough to have all the directions from each element reaching the area of detector - be practically parallel. This introduces wave fronts which are perpendicular to the main line connecting sphere with detector. Sphere has a temperature T , radius R and distance to detector d .

In order to get luminosity it can be done like:

$$L \equiv F = 4\pi R^2 F_{S^2} = 4\pi R^2 \sigma T^4$$

In order to get energy flux at detector:

$$F_{A^2} = \frac{L}{4\pi d^2} = \frac{R^2 \sigma T^4}{d^2}$$

It can also be done integrating each element of the sphere. It is needed to integrate these elements taking care of sphere shape and different direction of radiation for each element (with respect to surface of element) in order to have them all radiate in the same direction (towards detector). So, element of the sphere dS^2 is:

$$dS^2 = R \sin \theta d\varphi \times R d\theta = R^2 d\varphi \sin \theta d\theta$$

Each element will emit towards detector and it is described by the quantity $F_{S^2\Omega}$:

$$F_{S^2\Omega} = \frac{1}{\pi} \sigma T^4 \cos \theta \quad (4.2)$$

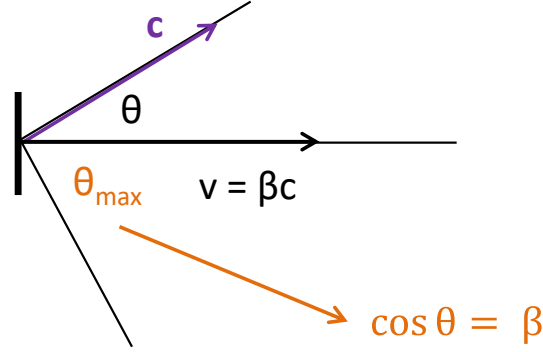


Figure 4.11:

Since it is axially symmetric with respect to φ it can be integrated over φ and this will give radiation from the line circle towards the detector:

$$F_{S\Omega} = \int_0^{2\pi} F_{S^2\Omega} R \sin \theta d\varphi = 2\pi R \sin \theta F_{S^2\Omega}$$

$$F_{S\Omega} = 2R\sigma T^4 \sin \theta \cos \theta$$

Now, to get F_Ω :

$$F_\Omega = \int_0^{\pi/2} F_{S\Omega} R d\theta = 2R^2\sigma T^4 \int_0^{\pi/2} \sin \theta \cos \theta d\theta$$

$$F_\Omega = R^2\sigma T^4$$

In order to get luminosity of the sphere it is needed to multiply by total solid angle:

$$L \equiv F = F_\Omega 4\pi = 4\pi R^2\sigma T^4$$

In order to get energy flux at detector:

$$F_{A^2} = \frac{F_\Omega}{d^2} = \frac{R^2\sigma T^4}{d^2}$$

4.4.3 Relativistic movement of a surface element

In this case the movement is in direction normal to its surface which is the case of the expanding sphere. In Figure 4.11 angle θ is between normal to the dS^2 surface and the direction of emission. It is also an angle from direction of movement and direction of emission. Speed is $\beta = \frac{v}{c}$, Lorentz factor is $\gamma = \frac{1}{\sqrt{1-\beta^2}}$, and relativistic Doppler factor is $D = \frac{1}{\gamma(1-\beta \cos \theta)}$, and when $\theta = 0$ ($\cos \theta = 1$), $D_{max} = \frac{1}{\gamma(1-\beta)}$. When $\beta \rightarrow 1$, $D_{max} \approx 2\gamma$.

The element won't radiate in half space angle but from $\theta = 0$ to θ such that $\cos \theta = \beta$. When considering comoving frame of the surface, the $\cos \theta = \beta$ angle corresponds to $\theta' = 90^\circ$. Even just considering simple motion, photons sent at angles beyond $\cos \theta = \beta$ will immediately get "swallowed up" by the moving surface. This is a well known effect, see for example (Bianco et al., 2001). The minimum relativistic Doppler factor is then $D_{min} = \gamma$.

β	0.1	0.3	0.9	0.99	0.999	0.9999	0.99999	0.999999
γ	1.005	1.048	2.294	7.089	22.37	70.70	223.5	702.5
D_{max}	1.106	1.363	4.359	14.11	44.71	141.4	446.9	1405

Table 4.2:

Some basic values of β , γ and D_{max} in Table 4.2 ranging from non-relativistic motion to ultra-relativistic seen in the prompt emission of few GRBs.

Change (boost) of thermal spectrum

How will the value $N_{ES^2\Omega}$ in the rest frame of BB surface change when it is boosted, i.e. what will detector which is in rest with respect to host galaxy see.

First, each photon's energy will be boosted by D . Spectrum will shift to higher energies. So, every E in $N_{ES^2\Omega}$ needs to be $\times \frac{1}{D}$ to account for the shift to higher energies. This will cause spectrum to "stretch", so each keV interval in the boosted spectrum will have $\frac{1}{D}$ less photons than the spectrum in the rest frame (just due to stretching). So, entire spectrum will go down by D , i.e. $N_{ES^2\Omega}$ should be also $\times \frac{1}{D}$.

Second, movement of the BB towards the detector will cause increase in intensity by a factor of $\frac{1}{1-\beta \cos \theta}$ (ordinary Doppler factor). And, since the BB was accelerated and is moving, the time will go slower in the rest frame of BB by a factor of γ and this will decrease the intensity of boosted spectrum. So, the $N_{ES^2\Omega}$ should be $\times \frac{1}{\gamma} \frac{1}{1-\beta \cos \theta}$, i.e. $N_{ES^2\Omega}$ should be $\times D$.

Third, beaming in the direction of movement will cause an increase in intensity. The solid angle $d\Omega'$ in the rest frame of BB will be "squeezed" to $d\Omega$ and this will cause an increase in intensity. Some basic equations are: $d\Omega' = \sin \theta' d\varphi' d\theta'$, $d\Omega = \sin \theta d\varphi d\theta$. Connection between θ' and θ can be presented as, for example, $\sin \theta' = \sin \theta D$. With basic trigonometric formula in both frames $\sin^2 \theta' + \cos^2 \theta' = 1$ and $\sin^2 \theta + \cos^2 \theta = 1$, any relation between $\sin \theta'$, $\sin \theta$, $\cos \theta'$, $\cos \theta$ can be found. It can also be found that $d\theta' = d\theta D$. Movement of BB is such that the beaming will happen only in line with θ and not in line with φ , so, $d\varphi' = d\varphi$. Finally, $d\Omega' = D^2 d\Omega$. So, $N_{ES^2\Omega}$ should be $\times D^2$.

Fourth the $\cos \theta$ factor in $N_{ES^2\Omega}$ is in the rest frame of BB. It should be transformed to $\cos \theta' = \frac{\cos \theta - \beta}{1 - \beta \cos \theta}$.

Finally,

$$\begin{aligned}
 N_{ES^2\Omega}^r &= \frac{2}{h^3 c^2} \frac{\left(\frac{E}{D}\right)^2}{e^{\frac{E/D}{kT}} - 1} \frac{1}{D} D D^2 \frac{\cos \theta - \beta}{1 - \beta \cos \theta} \\
 N_{ES^2\Omega}^r &= \frac{2}{h^3 c^2} \frac{E^2}{e^{\frac{E}{DkT}} - 1} \frac{\cos \theta - \beta}{1 - \beta \cos \theta}
 \end{aligned} \tag{4.3}$$

The $N_{ES^2\Omega}^r$ is boosted/relativistic spectrum, the one detector in the GRB host galaxy would see. Values E and θ are in the frame of host-galaxy/detector (laboratory frame). Temperature T is the "real" temperature, i.e. the comoving BB temperature. So, the boosted BB spectrum will be similar to normal BB spectrum but with different angle dependence and temperature boosted by factor D (which also depends on the angle).

In order to obtain $F_{ES^2\Omega}^r$, $N_{ES^2\Omega}^r$ should just be multiplied by $\times E$.

$$F_{ES^2\Omega}^r = \frac{2}{h^3 c^2} \frac{E^3}{e^{\frac{E}{DkT}} - 1} \frac{\cos \theta - \beta}{1 - \beta \cos \theta}$$

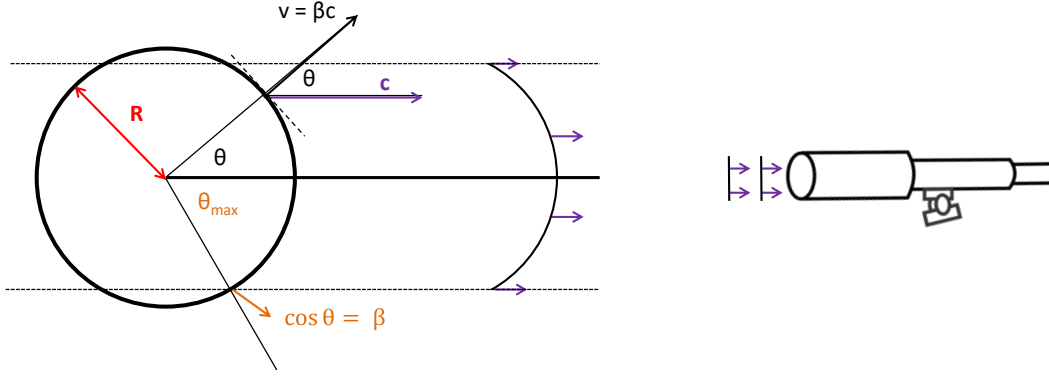


Figure 4.12:

In order to obtain $F_{S^2\Omega}^r$, $F_{ES^2\Omega}^r$ needs to be integrated over E , which is mathematically similar process as with normal (non-relativistic) BB.

$$F_{S^2\Omega}^r = \frac{1}{\pi} \sigma (DT)^4 \frac{\cos \theta - \beta}{1 - \beta \cos \theta} \quad (4.4)$$

Change of spectrum such that new temperature will increase by a factor of $\times D$ and flux from an element of surface be proportional to $(DT)^4$ is obtained in (Bianco et al., 2001).

4.4.4 Pulse from an expanding sphere

There is an infinitesimal short pulse from an expanding sphere. Sphere has a temperature T (BB rest frame) and radius R at the time of emission. Sphere expands uniformly in all directions with speed β . This pulse will be detected over time interval of $R(1 - \beta)/c$ but doesn't matter. Let's say we wait until detector measures everything and then examine the spectrum. In case of flux, since they are s^{-1} quantities, the obtained values would change in $R(1 - \beta)/c$ time interval. But let's say that we wait for all the photons/energy to collect, and then divide the photons/energy by the (infinitesimal) time the pulse was emitted in the rest frame of the galaxy. Similar goes for luminosity. The PEM pulse examined in the (Bianco et al., 2001), although lasts very short in the detector time range, is actually made for a certain time interval in the laboratory frame and is more similar to the case in the next subchapter.

Each part of the expanding sphere will behave just like the speeding element from the previous chapter. It necessary only to integrate these elements taking care of sphere shape and different direction of radiation for each element (with respect to surface of element) in order to have them all radiate in the same direction (towards detector). Angle θ for each element will be the same as in the previous chapter. Specifically, θ for each element will be the angle between normal to the element surface, and the direction of emission. Also, θ is angle between line center-element and line center-detector.

As before, element won't radiate in the half sphere solid angle but in the angle from $\theta = 0$ to angle where $\cos \theta = \beta$. This also means that detector will "see" only part of the sphere in the same angle range. So, there would be no difference for detector whether it's a sphere or a jet (sphere cut by the cone) with the same or bigger opening angle θ . Again, this is a well known effect (Bianco et al., 2001).

β	0.1	0.3	0.9	0.99	0.999	0.9999	0.99999	0.999999
γ	1.005	1.048	2.294	7.089	22.37	70.70	223.5	702.5
D_{max}	1.106	1.363	4.359	14.11	44.71	141.4	446.9	1405
B	1.07	1.25	3.60	11.3	36.0	115	360	1150

Table 4.3:

Spectrum

The spectrum of element surface is defined by equation 4.3.

$$N_{ES^2\Omega}^r = \frac{2}{h^3 c^2} \frac{E^2}{e^{\frac{E}{DkT}} - 1} \frac{\cos \theta - \beta}{1 - \beta \cos \theta}$$

Integrating over φ :

$$N_{ES\Omega}^r = 4\pi R \sin \theta N_{ES^2\Omega}^r = \frac{4\pi R}{h^3 c^2} \frac{E^2}{e^{\frac{E}{DkT}} - 1} \frac{\cos \theta - \beta}{1 - \beta \cos \theta} \sin \theta$$

and over θ :

$$N_{E\Omega}^r = \frac{4\pi R^2}{h^3 c^2} E^2 \int_0^{\arccos \beta} \frac{1}{e^{\frac{E\gamma}{kT}(1-\beta \cos \theta)} - 1} \frac{\cos \theta - \beta}{1 - \beta \cos \theta} \sin \theta d\theta$$

Integral will be marked I_e . To make the integral more simple $x \equiv \cos \theta$ and $dx = -\sin \theta d\theta$.

$$I_e = \int_{\beta}^1 \frac{1}{e^{\frac{E\gamma}{kT}(1-\beta x)} - 1} \frac{x - \beta}{1 - \beta x} dx$$

and:

$$N_{E\Omega}^r = \frac{4\pi R^2}{h^3 c^2} E^2 I_e$$

There is no analytical solution to I_e . Solving numerically for each E , the spectrum is very similar to black body spectrum with boosted temperature by a new value B , coming from sphere of radius R , and with additional constant A :

$$N_{E\Omega}^r \approx A \times \frac{2\pi R^2}{h^3 c^2} \frac{E^2}{e^{\frac{E}{B \times kT}} - 1}$$

The value B is defined by taking the peak energy E_p of the new spectrum and identifying new temperature as $B kT \approx E_p/1.59$. In the Table 4.3 are values for B for different β .

As expected value B is in between $D_{min} = \gamma$ which comes from the very edge and D_{max} which comes from the tip. The broadening of spectrum is little for any β . If β is low than there won't be much difference from normal BB. As β goes to 1, there will be more boosting but the part of the sphere which the detector "sees" gets less and less until it is only small part at the very tip which is going directly towards detector. So, as $\beta \rightarrow 1$, there will be more boosting but not much broadening of the spectrum.

Parameter A is found in the limit when $E \ll kT$ which makes $e^{\frac{E\gamma}{kT}(1-\beta x)} - 1 \rightarrow E\gamma(1-\beta x)/kT$ and I_e can be solved analytically. In this case:

$$A = \frac{2}{\gamma} \frac{1}{\beta^2} (\beta - \ln(1 + \beta))$$

β	0.1	0.3	0.9	0.99	0.999	0.9999	0.99999	0.999999
γ	1.005	1.048	2.294	7.089	22.37	70.70	223.5	702.5
D_{max}	1.106	1.363	4.359	14.11	44.71	141.4	446.9	1405
$f_{\beta 5}$	1.15	1.59	13.7	141	1.42×10^3	1.42×10^4	1.41×10^5	1.40×10^6
$f_{\beta 15}$	1.57	2.02	14.2	142	1.42×10^3	1.42×10^4	1.41×10^5	1.40×10^6

Table 4.4:

Flux & Luminosity

Energy flux $F_{S^2\Omega}$ from surface element is defined in equation 4.4:

$$F_{S^2\Omega}^r = \frac{1}{\pi} \sigma (DT)^4 \frac{\cos \theta - \beta}{1 - \beta \cos \theta}$$

$$F_{S^2\Omega}^r = \frac{1}{\pi} \sigma T^4 \frac{1}{\gamma^4} \frac{\cos \theta - \beta}{(1 - \beta \cos \theta)^5}$$

Similar to previous part integration goes over φ and then θ :

$$F_{\Omega}^r = 2R^2 \sigma T^4 \frac{1}{\gamma^4} \int_0^{\arccos \beta} \frac{\cos \theta - \beta}{(1 - \beta \cos \theta)^5} \sin \theta d\theta = 2R^2 \sigma T^4 \frac{1}{\gamma^4} I_5$$

Integral is I_5 . To make it more simple $x \equiv \cos \theta$ and $dx = -\sin \theta d\theta$.

$$I_5 = \int_{\beta}^1 \frac{x - \beta}{(1 - \beta x)^5} dx$$

The solution to the integral is:

$$I_5 = \frac{\beta(4 - 3\beta) - 1}{12\beta^2(1 - \beta)^4} + \frac{1 - \beta^2}{12\beta^2(1 - \beta^2)^4}$$

Now, to define the $f_{\beta 5}$ as $f_{\beta 5} \equiv 2 \frac{1}{\gamma^4} I_5$.

$$f_{\beta 5} = 2(1 - \beta^2)^2 \left(\frac{\beta(4 - 3\beta) - 1}{12\beta^2(1 - \beta)^4} + \frac{1 - \beta^2}{12\beta^2(1 - \beta^2)^4} \right)$$

When $\beta \rightarrow 1$:

$$f_{\beta 5} \approx \frac{17}{12} \frac{1}{1 - \beta} = f_{\beta 15}$$

$$F_{\Omega}^r = R^2 \sigma T^4 f_{\beta 5}$$

Values of $f_{\beta 5}$ for various β are given in Table 4.4:

Luminosity is:

$$L = L^r = 4\pi F_{\Omega}^r = 4\pi R^2 \sigma T^4 f_{\beta 5}$$

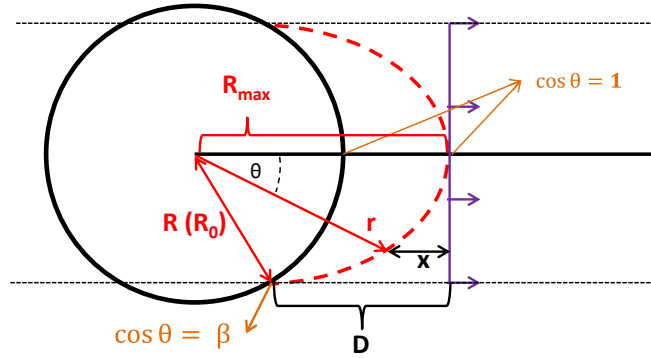


Figure 4.13:

4.4.5 Continuous emission from an expanding sphere

For the same reasons as in previous part, sphere will radiate from cone where θ goes from 0 to where $\cos \theta = \beta$. However, in this case wave fronts will be made from different parts of sphere emitting at different times and different radius. First, the edge of the cone will radiate at radius $R(R_0)$ and those photons will be “chasing” front part of the sphere. The last part to contribute to the wave front will be the front part at R_{max} (Figure 4.13).

From Figure 4.13 several independent equations come. First one involves time to create a wave front and is made up of time sphere expanded from R to r and time photons traveled to complete the wave front. So, 1) $\Delta t = \frac{r-R}{\beta c} + \frac{x}{c} = \text{const.}$ and for extreme cases it turns to: 2) $\Delta t = \frac{D}{c}$ and: 3) $\Delta t = \frac{R_{max}-R}{\beta c}$. From geometry of the picture: 4) $r \cos \theta + x = R_{max}$ which for extreme case(s) turns to: 5) $R\beta + D = R_{max}$. The equations 1, 2, 4 and 5 can be used to eliminate 4 parameters: D , Δt , x and R_{max} (this is generally not possible but here is because the special relation of the parameters and equations). The remaining parameters are connected:

$$r = \frac{R(1 - \beta^2)}{1 - \beta \cos \theta}$$

The equation describes an ellipse in polar coordinates. Value r is the “radius of this ellipse” as seen from the more distant focus (center of the sphere), β turns out to be eccentricity of the ellipse, R is radius when the edge of the cone has emitted photons and started creation of the wave front. R is also the a of the ellipse, i.e. the half of the longer width. When $\cos \theta = \beta$ the line of the tangent of the ellipse is normal to the line of the wave front. Of course, since everything is symmetric to angle φ the surface will be obtained by rotating ellipse across the φ angle.

This surface is the equitemporal surface (EQTS) explained in Chapter 2 when discussing the fireshell model, just for the constant velocity case which is a well known result (Rees, 1966). Literature concerning EQTS within the fireshell model - which were found starting from dynamics of the fireshell plasma, which gave dependence of velocity on time (or radius) - can be found in (Bianco et al., 2001; Bianco and Ruffini, 2004, 2005d,b, 2006). In it the EQTS are extremely elongated due to ultrarelativistic motion and are used to explain the prompt emission.

Additional useful equations:

$$R_{max} = R(1 + \beta)$$

with R_{max} being the radius when the tip of the sphere has emitted photons and completed creation of the wave front. This can be obtained from above ellipse equation for $\cos \theta = 1$ or from adding equation number 3 to other 4 equations. Also:

$$\Delta t = \frac{R}{c}$$

where Δt is time interval when the edge of the cone emitted photons and started to create the wave front, to when the tip of the sphere emitted photons and finished the creation of the wave front. This can be obtained from adding equation number 3 to other 4 equations. Even though this time interval is longer and longer for successive wave fronts (bigger and bigger R), the wave fronts will still be separated from each other by the same amount of distance/time. It just means that each successive wave front took longer time to be created.

Spectrum

The spectrum of element surface is defined by equation 4.3.

$$N_{ES^2\Omega}^r = \frac{2}{h^3 c^2} \frac{E^2}{e^{\frac{E}{BkT}} - 1} \frac{\cos \theta - \beta}{1 - \beta \cos \theta}$$

Integrating over φ and then θ :

$$N_{E\Omega}^r = \frac{4\pi}{h^3 c^2} E^2 \int_0^{\arccos \beta} r^2 \frac{1}{e^{\frac{E}{kT}(1-\beta \cos \theta)} - 1} \frac{\cos \theta - \beta}{1 - \beta \cos \theta} \sin \theta d\theta$$

The value of R will be different for each θ , so it was replaced with r and has to be inside the integral. Putting the ellipse equation in place:

$$N_{E\Omega}^r = \frac{4\pi R^2}{h^3 c^2} (1 - \beta^2)^2 E^2 \int_0^{\arccos \beta} \frac{1}{e^{\frac{E}{kT}(1-\beta \cos \theta)} - 1} \frac{\cos \theta - \beta}{(1 - \beta \cos \theta)^3} \sin \theta d\theta$$

Defining integral as I_{e3} and making integral more simpler $x \equiv \cos \theta$:

$$N_{E\Omega}^r = \frac{4\pi R^2}{h^3 c^2} (1 - \beta^2)^2 E^2 I_{e3}$$

with integral being:

$$I_{e3} = \int_{\beta}^1 \frac{1}{e^{\frac{E}{kT}(1-\beta x)} - 1} \frac{x - \beta}{(1 - \beta x)^3} dx$$

As in the previous case, there is no analytical solution to I_{e3} . Solving numerically for each E , the spectrum is very similar to black body spectrum with boosted temperature by a new value B , coming from sphere of radius R , and with additional constant A :

$$N_{E\Omega}^r \approx A \times \frac{2\pi R^2}{h^3 c^2} \frac{E^2}{e^{\frac{E}{B \times kT}} - 1} = N_{E\Omega}^{ab}$$

The value B is defined by taking the peak energy E_p of the new spectrum and identifying new temperature as $B kT \approx E_p/1.59$. In the Table 4.5 are values for B for different β .

Again, parameter A is found in the limit when $E \ll kT$ which makes also I_{e3} possible to be solved analytically. In this case:

β	0.1	0.3	0.9	0.99	0.999	0.9999	0.99999	0.999999
γ	1.005	1.048	2.294	7.089	22.37	70.70	223.5	702.5
D_{max}	1.106	1.363	4.359	14.11	44.71	141.4	446.9	1405
B	1.07	1.26	3.73	12.0	38.0	120	380	1200
$N_{E\Omega}^r/N_{E\Omega}^{ab} @10E_p$	1.02	1.30	2.39	2.54	2.53	2.54	2.53	2.55

Table 4.5:

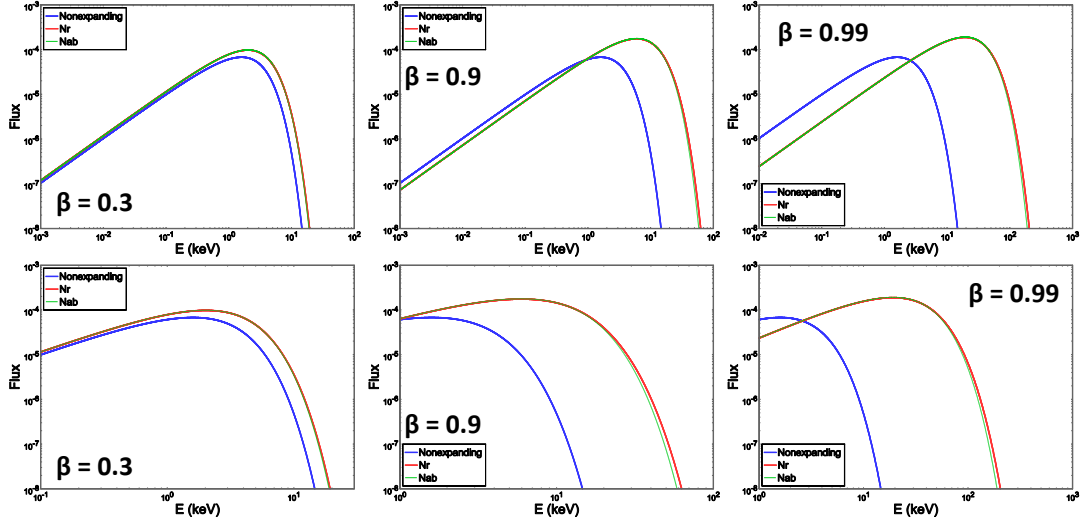


Figure 4.14: Thermal spectra for non-relativistic spectrum $N_{E\Omega}$ (blue), $N_{E\Omega}^r$ relativistic (red), and approximate $N_{E\Omega}^{ab}$ (green) are shown for three different expansion speeds. The (rest-frame) temperature of the BB is $kT = 1$ keV. The flux is in arbitrary units. Lower image is a zoomed in of upper one. Further details are in the text.

$$A = \frac{2}{\gamma}(1 - \beta^2)^2 \left(\frac{1}{6\beta^2(1 - \beta^2)^2} + \frac{2\beta - 1}{6\beta^2(1 - \beta)^2} \right)$$

In Figure 4.14 spectra are compared in order to estimate broadening. In the low-energy phase $N_{E\Omega}^r$ and $N_{E\Omega}^{ab}$ are exactly the same. The peak phase they are almost the same. The only difference (broadening) is seen after the peak. To quantify broadening of the spectrum, ratio of $N_{E\Omega}^r/N_{E\Omega}^{ab}$ is taken at 10 times the peak energy. Values are given in Table 4.5. As can be seen the broadening is small especially when considering that in BAT-XRT only the peak of BB is seen.

Noting again that R in $N_{E\Omega}^{ab}$ spectrum is the radius when the creation of the wave front started. Wave front was completed at radius of $R(1 + \beta)$. It is not possible to assign a single radius to the spectrum like in the case of non-expanding sphere or a pulse from an expanding sphere.

The spectrum in this case is very close to pure black body while in (Bianco et al., 2001) the spectrum is broadened due to the fact that expansion velocity changes drastically and that emission is coming from a certain volume and is defined by a "screening factor". Additionally case of inverse-Compton scattering of photons by electrons is examined.

Flux & Luminosity

Energy flux $F_{S^2\Omega}$ from surface element is defined in equation 4.4:

β	0.1	0.3	0.9	0.99	0.999	0.9999	0.99999	0.999999
γ	1.005	1.048	2.294	7.089	22.37	70.70	223.5	702.5
D_{max}	1.106	1.363	4.359	14.11	44.71	141.4	446.9	1405
$f_{\beta 7}$	1.31	2.33	38.0	425	4.30×10^3	4.30×10^4	4.30×10^5	4.24×10^6
$f_{\beta_{17}}$	4.78	6.14	43.0	430	4.30×10^3	4.30×10^4	4.29×10^5	4.24×10^6

Table 4.6:

$$F_{S^2\Omega}^r = \frac{1}{\pi} \sigma (DT)^4 \frac{\cos \theta - \beta}{1 - \beta \cos \theta}$$

$$F_{S^2\Omega}^r = \frac{1}{\pi} \sigma T^4 \frac{1}{\gamma^4} \frac{\cos \theta - \beta}{(1 - \beta \cos \theta)^5}$$

Integration goes over φ and then θ :

$$F_{\Omega}^r = 2\sigma T^4 \frac{1}{\gamma^4} \int_0^{\arccos \beta} r^2 \frac{\cos \theta - \beta}{(1 - \beta \cos \theta)^5} \sin \theta d\theta$$

As for the case of spectrum, the value of R will be different for each θ , so it was replaced with r and has to be inside the integral. Putting the ellipse equation in place:

$$F_{\Omega}^r = 2R^2 \sigma T^4 (1 - \beta^2)^4 \int_0^{\arccos \beta} \frac{\cos \theta - \beta}{(1 - \beta \cos \theta)^7} \sin \theta d\theta$$

$$F_{\Omega}^r = 2R^2 \sigma T^4 (1 - \beta^2)^4 I_7$$

Integral is I_7 . To make it more simple $x \equiv \cos \theta$.

$$I_7 = \int_{\beta}^1 \frac{x - \beta}{(1 - \beta x)^7} dx$$

Solution to the integral is:

$$I_7 = \frac{\beta(6 - 5\beta) - 1}{30\beta^2(1 - \beta)^6} + \frac{1 - \beta^2}{30\beta^2(1 - \beta^2)^6}$$

Now to define $f_{\beta 7}$ as:

$$f_{\beta 7} = 2(1 - \beta^2)^4 I_7$$

$$f_{\beta 7} = 2(1 - \beta^2)^4 \left(\frac{\beta(6 - 5\beta) - 1}{30\beta^2(1 - \beta)^6} + \frac{1 - \beta^2}{30\beta^2(1 - \beta^2)^6} \right)$$

When $\beta \rightarrow 1$ it can be simplified as:

$$f_{\beta 7} \approx f_{\beta_{17}} = \frac{43}{10} \frac{1}{1 - \beta}$$

Finally:

$$F_{\Omega}^r = R^2 \sigma T^4 f_{\beta 7}$$

with values for $f_{\beta 7}$ given in Table 4.6.

Luminosity is:

$$L = L^r = 4\pi F_{\Omega}^r = 4\pi R^2 \sigma T^4 f_{\beta 7}$$

Luminosity corresponds to wave fronts which were created from R to $R(1 + \beta)$ and sent in all directions. If detectors were put all around the BB at a big distance in host galaxy, they would detect this luminosity. The emitted energy per unit time corresponds to time in the host galaxy rest frame. This is not luminosity which corresponds to genuine luminosity (emitted energy per unit of host-galaxy time) at the point when radius was just R . This luminosity corresponds to the one from the pulse example:

$$L = 4\pi R^2 \sigma T^4 f_{\beta 5}$$

It is the luminosity which would be obtained if detectors would be around the black body almost touching it.

Apparent radius from observations

Radius from previous part R is real radius (for example, freezing the time and then measuring the radius in the host galaxy). Although it is the radius at which wave front has started. The temperature T is real temperature of BB, i.e. its rest-frame temperature. Question is the value of apparent radius calculated from observations. Since relativistic motion is the topic here, change of values due to expansion of the universe will be neglected. Quantities such as observed temperature T_o and observational time t_o are taken as if detector were in the host galaxy of BB. The observed luminosity is the luminosity from previous part $L_o = L$. All of these host-galaxy observational parameters may be calculated from real observation knowing the redshift.

The observed temperature will be connected to real one:

$$T_o = BT$$

Luminosity is

$$L = 4\pi R^2 \sigma T^4 f_{\beta 7}$$

and may also be expressed from observational parameters:

$$L = 4\pi R_o^2 \sigma T_o^4$$

where R_o is the apparent radius. Combining three equations:

$$R = R_o \times \frac{B^2}{\sqrt{f_7}}$$

Since $B \propto \frac{1}{\sqrt{1-\beta}}$, and $f_{\beta 7} \propto \frac{1}{1-\beta}$:

$$R \propto R_o \frac{1}{\sqrt{1-\beta}}$$

Precise values are given in Table 4.7. As can be seen they are very similar to γ so:

$$R \approx \gamma R_o$$

β	0.1	0.3	0.9	0.99	0.999	0.9999	0.99999	0.999999
γ	1.005	1.048	2.294	7.089	22.37	70.70	223.5	702.5
D_{max}	1.106	1.363	4.359	14.11	44.71	141.4	446.9	1405
$\frac{B^2}{\sqrt{F_{\beta 7}}}$	1.01	1.04	2.26	6.98	22.1	69.5	220	699

Table 4.7:

for any β .

Apparent radius R_o is calculated from observed temperature T_o and luminosity L (which is calculated from observed flux and known redshift). To obtain radius R , expansion speed β (γ) is needed.

Speed from observations

It's not possible to obtain speed from one wave front. Let's consider two wave fronts - front 1 and front 2.

$$R_1 = R_{1o} B^2 \frac{1}{\sqrt{F_{\beta 7}}}$$

$$R_2 = R_{2o} B^2 \frac{1}{\sqrt{F_{\beta 7}}}$$

These wave fronts will be detected over time period of Δt_o . This is the time between two wave fronts as they travel ($\Delta t_o c$ is the distance between them). The Δt_o won't be the same as Δt - time between when sphere went from R_1 and R_2 and started creation of the two wave fronts. The correct relation is:

$$\Delta t_o = \Delta t (1 - \beta^2)$$

Speed β is the real speed:

$$\beta = (R_2 - R_1) / \Delta t$$

and the apparent speed is:

$$\beta_o = (R_{2o} - R_{1o}) / \Delta t_o$$

Combining all equations:

$$\beta = (1 - \beta^2) \frac{B^2}{\sqrt{f_{\beta 7}}} \beta_o$$

and since $B^2 / \sqrt{f_{\beta 7}}$ is almost γ :

$$\beta \approx \frac{1}{\gamma} \beta_o$$

where γ is the real speed. Precise values of apparent velocity β_o are given for every real velocity β in Table 4.8.

Results obtained here assume that sphere has uniform and constant temperature and that expansion is constant. If there are several time bins from time resolved analysis,

β	0.1	0.2	0.3	0.4	0.5	0.6	0.7	0.8	0.9
β_0	0.100	0.204	0.316	0.438	0.581	0.758	0.990	1.35	2.10
β	0.93	0.96	0.99	0.993	0.996	0.999	0.9999	0.99999	0.999999
β_0	2.57	3.48	7.13	8.52	11.3	22.7	71.7	226	713

Table 4.8:

apparent velocity may be found for each two bins, and from there the real velocity and then radius. Approximation here is that for given time interval (between centers of two time bins) temperature and velocity may be considered as constant. Additional approximation, of course, is that values from time resolved analysis are averaged over time bin, but this is the case for every other analysis which involves time, energy, etc. bins, and has no special particularities here. The applicability of this approach is for the observed temperature-decaying thermal emission at the start of the afterglow phase.

4.4.6 Wave fronts from different velocities and temperatures

Temperature

The equation for spectrum of the wavefront:

$$N_{E\Omega}^r = \frac{4\pi R^2}{h^3 c^2} (1 - \beta^2)^2 E^2 I_{e3}$$

with integral being:

$$I_{e3} = \int_{\beta}^1 \frac{1}{e^{\frac{E\gamma}{kT}(1-\beta x)} - 1} \frac{x - \beta}{(1 - \beta x)^3} dx$$

and $x \equiv \cos \theta$. The temperature kT and speed β are constant in this case. If the temperature depends on time, and speed is the same, then again a single wavefront will be made from parts of a sphere which form an ellipse as it expands. The temperature for a wavefront may be expressed with respect to angle $kT = kT(\theta)$, i.e. $kT = kT(x)$:

$$I_{e3} = \int_{\beta}^1 \frac{1}{e^{\frac{E\gamma}{kT(x)}(1-\beta x)} - 1} \frac{x - \beta}{(1 - \beta x)^3} dx$$

and integral solution will depend on the function $kT(x)$. In most cases numerical integration will be needed and shape of the spectrum will depend on β as in previous section, and additionally on function $kT(x)$ parameters as well as initial value of kT for a given (initial) R . Depending on $kT(x)$ the spectrum may not be approximated as ordinary black body with different temperature and normalization.

The flux may be calculated with numerical integration of spectrum (since it was already calculated numerically) or following the equations from previous section:

$$F_{\Omega}^r = 2R^2 \sigma (1 - \beta^2)^4 I_{7,T}$$

In this case the temperature won't be constant but will have to go inside the integral with angle dependence for a given wavefront:

$$I_{7,T} = \int_{\beta}^1 T_{(x)}^4 \frac{x - \beta}{(1 - \beta x)^7} dx$$

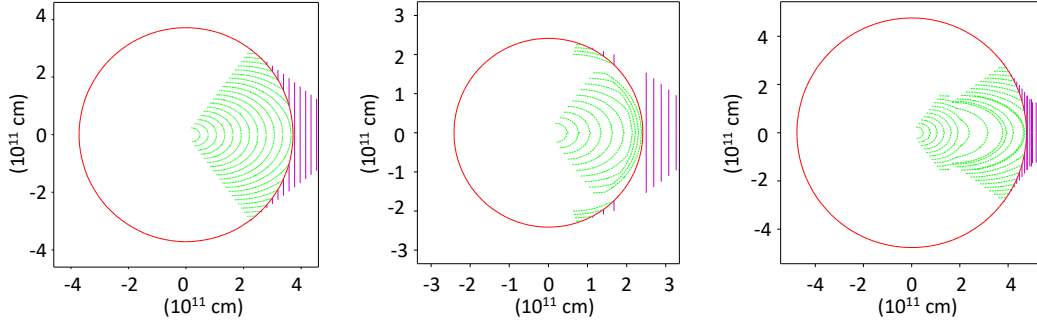


Figure 4.15: Wavefront surfaces from an expanding sphere. Green color corresponds to surfaces, red to the black body surface, and purple to wave fronts. Further details are in the text.

Speed

If velocity is also varying a single wavefront won't be made from an ellipse-shaped surface. In Figure 4.15 are presented three cases. The 2D plane corresponds to section of constant φ and is axially symmetric. All three start from initial radius of 3×10^{10} cm and to the time frame "captured" somewhere between 15 – 20 s. The first one (left) corresponds to constant expanding velocity of $0.6 c$. The surfaces are ellipses with eccentricity $\beta = 0.6$. The second (middle) corresponds to expanding velocity of $\beta_1 = 0.6$ which then drops to $\beta_2 = 0.3$ at 10 s. The wave fronts which were in the process of making during this shift have a "break". They are made out of two ellipses with eccentricities $\beta_1 = 0.6$ and $\beta_2 = 0.3$. If the first part is described by equation $r = R(1 - \beta_1^2)/(1 - \beta_1 \cos \theta)$ then the second part cannot be expressed with the same R and β_2 , it should have a different R . Starting of just- β_2 surfaces is also present in the plot. The third plot (right) corresponds to expanding velocity of $\beta_1 = 0.6$ which then jumps to $\beta_2 = 0.8$ at 10 s. Again, wave fronts which were in the process of making during this shift have a "break", but in the opposite direction. As in previous case, the second ellipse equation has a different R . Starting of just- β_2 surfaces is also present in the plot and some completed ones as well. For the last two cases the "different R " depends where/when the break in the speed occurs for a given wave front.

Velocity may change continuously. In Figure 4.16 are presented three cases. The first (left) corresponds to expanding velocity which changes linearly with time from $\beta_1 = 0.3$ to $\beta_2 = 0.8$. The second (middle) corresponds to expanding velocity which changes linearly from $\beta_1 = 0.8$ to $\beta_2 = 0.3$. The third (right) corresponds to expanding velocity which changes linearly from $\beta_1 = 0.3$ to $\beta_2 = 0.8$ and then back to $\beta_1 = 0.3$.

The surface equation may be considered as a continuously changing ellipse equation with $\beta(\theta)$ and $R_{(0)}(\theta)$. However to obtain the form it should be started from basics and (Figure 4.13) may be used. Time to create a wave front is $\Delta t = t + \frac{x}{c} = \text{const.}$ where t is time needed from black body to go from R_0 to r . Now, this time cannot be expressed as $t = (r - R_0)/(\beta c)$ since β isn't constant. For extreme cases equation turns to $\Delta t = \frac{D}{c}$. From geometry of the picture $r \cos \theta + x = R_{max}$ which for extreme case(s) turns to $R_0 \beta_0 + D = R_{max}$ where β_0 is initial value of β for the wave front. Combining them:

$$r \cos \theta = R_0 \beta_0 + tc$$

If β is expressed as function of t (which goes from $t = 0$ to $t = \Delta t$) for a given wave front,

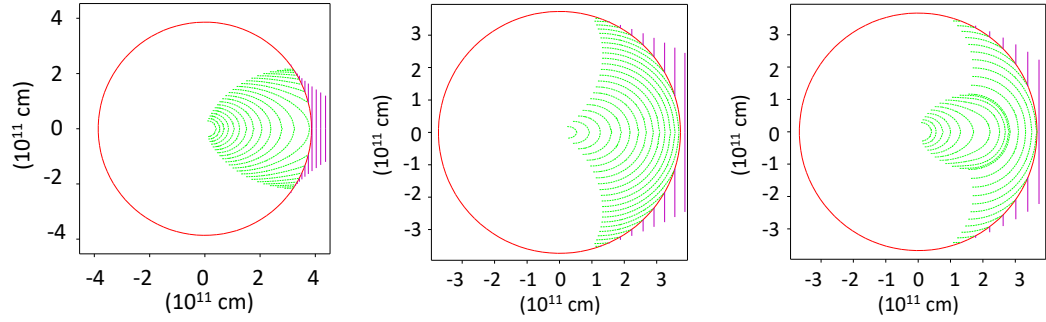


Figure 4.16: Wavefront surfaces from an expanding sphere. Green color corresponds to surfaces, red to the black body surface, and purple to wave fronts. Further details are in the text.

then r may be expressed as $r(t)$:

$$r = R_0 + \int_0^t \beta_{(t')} c dt'$$

This equation is the one obtained in (Bianco et al., 2001) for a general EQTS.

Then $\cos \theta$ may be expressed as $\cos \theta(t)$ and vice versa $t = t(\cos \theta)$. Then r may be expressed as function of $\cos \theta$ (and R_0 and β_0).

The spectrum of the wave front would be:

$$N_{E\Omega}^r = \frac{4\pi}{h^3 c^2} E^2 I_{e,r}$$

with integral being:

$$I_{e,r} = \int_{\beta_0}^1 r_{(x)}^2 \frac{1}{e^{\frac{E\gamma_{(x)}}{kT_{(x)}}(1-\beta_{(x)}x)} - 1} \frac{x - \beta_{(x)}}{(1 - \beta_{(x)}x)} dx$$

The flux would be:

$$F_{\Omega}^r = 2\sigma I_{5,T,r}$$

with integral:

$$I_{5,T,r} = \int_{\beta_0}^1 T_{(x)}^4 (1 - \beta_{(x)}^2)^2 r_{(x)}^2 \frac{x - \beta_{(x)}}{(1 - \beta_{(x)}x)^5} dx$$

Calculation of flux from a general EQTS was presented in chapters XXI - XXII in (Ruffini et al., 2003a) in which also integration over the EQTS with $\times D^4$ is the basis.

Absorbing back emitted photons

There is an additional complication when velocity increases, especially if it increases quickly and to a large value. In Figure 4.17 is shown example of an expanding sphere which starts from 3×10^{11} cm has initial velocity of $\beta_1 = 0.3$ and then jumps to $\beta_2 = 0.95$ at 10 s. Only the wave fronts which started when velocity was β_1 are shown in order to make it more clear.

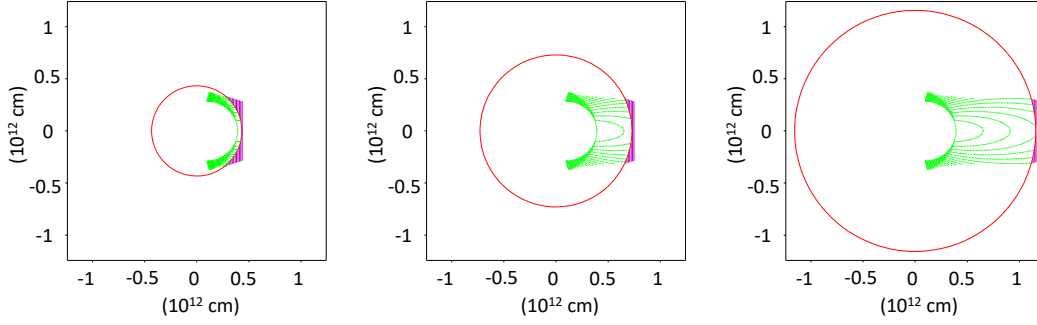


Figure 4.17: Wavefront surfaces from an expanding sphere. Green color corresponds to surfaces, red to the black body surface, and purple to wave fronts. Further details are in the text.

When the tangent to the surface is horizontal, it is the limiting case for the photons to exist. This is the case of the initial start of the wave front. It is also the limiting case when photons will be absorbed back to black body surface. If the tangent angle (with respect to horizontal axes) gets positive, then the photons will be absorbed back to black body and the wave front surface will decrease. In the first plot (left) the moment is shown just after the velocity jump. The drastic change of tangent angle (which gets positive) is seen. On the second plot (middle) open lines correspond to wave fronts which have been completely absorbed back and disappeared. The final plot (right) further shows this process as well as wave fronts that weren't completely absorbed, just have their surface decreased and then recompleted by black body during β_2 phase.

The previous analytical treatment, complicated as it is with varying velocity and temperature, is valid for wave fronts for which tangent to the surface has a negative angle (with respect to horizontal axis) all the way to completion of the front. The absorption of photons back further complicates matter. In order to obtain some useful resulting spectrum and flux with changing observer time, each wave front would have to be integrated numerically, and for each front parameters for integration would have to be different. Then possible decreasing of front because of absorption has to be taken into account. At this point it is easier to abandon the concept of wave fronts and simulate expansion and resulting spectrum directly. This will also make it easier to input changing speed and temperatures in tabular form if needed, not just analytical functions.

4.5 Simulation of spectrum

4.5.1 The code

Animation

Plots in Figures 4.15, 4.16 and 4.17 of surfaces which were traced by expanding black body as it created wave fronts, were frames from animation used to give simple visual inspection. It was made with Python animation module⁸. The main parameter is time t which goes from $t = 0$ to some value with certain resolution δt . Then velocity is given as a function of time $\beta(t)$. Then the radius R of the black body is calculated for each step. After

⁸https://matplotlib.org/api/_as_gen/matplotlib.animation.FuncAnimation

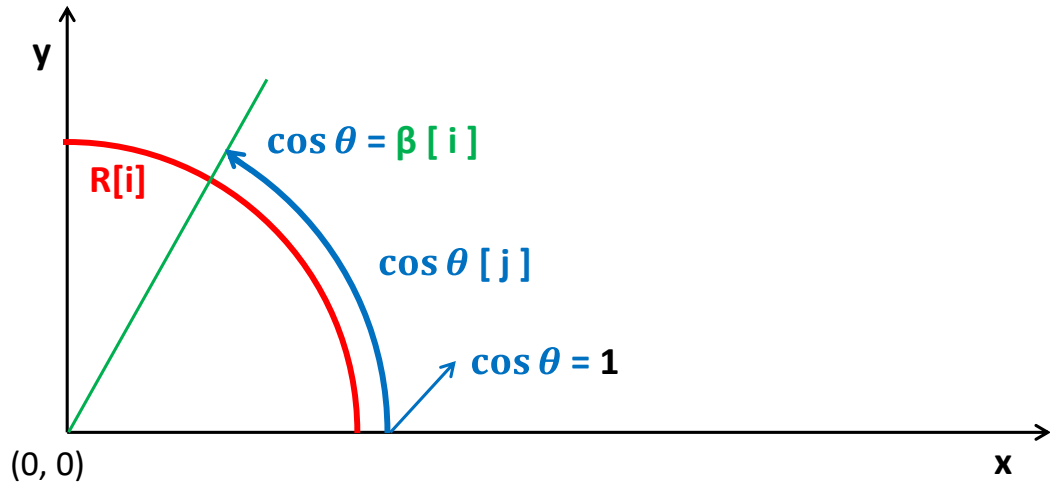


Figure 4.18: Plane in which simulation takes place.

that angle which traces full circle is defined with some resolution. Then the sets of $x(t)$ and $y(t)$ points for a black body may be expressed and black body expansion animated.

The wave fronts are defined to start at certain points in time. The initial value of coordinates x and y is defined from R and β at that time. Then the y coordinate remains the same while the x moves at the speed of light (this is the outer edge of the front). The intersection of wave front and black body is found by taking the same x and defining y from trigonometry of x and R . The two points are then connected with a line and wave front is defined. This intersection between wavefront and black body is also what defines the shape which black body traces as it expands.

In a nutshell this is how it was done, with additional details in regards to stopping animating shapes when they merge (wave front completion), or when they are completely absorbed by black body, and other details.

The concept

The idea is to abandon concept of wave fronts. Instead from taking observed quantities and calculating intrinsic ones based on some assumptions, the goal is to simulate black body expansion for a given velocity $\beta(t)$, simulate thermal emission based on $kT(t)$ and then simulate observed spectrum/flux and compare it to observations. So, the process goes from inputting $\beta(t)$ and $kT(t)$ in order to match observations.

The code is made in Python. The main parameter is time t which goes from $t = 0$ to some input value with certain input resolution δt (dt for simplicity). This is the first thing which determines resolution and will be indexed with i in arrays. So, $t[i]$. The velocity and temperatures are input parameters $\beta(t)$ and $kT(t)$ and have the same array length as t . So, $\beta[i]$ and $kT[i]$. From $t[i]$ and $\beta[i]$, $R[i]$ is calculated. The initial value of R is needed as input parameter.

The simulation takes place in an x-y plane which corresponds to cross section of constant φ (Figure 4.18). The center of the sphere is placed at coordinates $x=0$, and $y=0$. Only the upper-right quadrant is taken into account since lower part is symmetric to upper, and left part is of no interest as it is assumed that detector is far away on the right.

The second parameter which determines resolution is the angle θ . The plane corre-

sponds to $\theta = [0, \pi/2]$. However, since only the part of the sphere which goes to $\cos \theta = \beta$ will emit photons which will reach detector, the angle is defined $\cos \theta = [1, \beta[i]]$ for every step. The indexing with respect to angle will be marked by j in arrays. The number of angle steps is the same for each i -step, only the upper limit is different and is equal to $\beta[i]$. The number of elements is now $i_{max} \times j_{max}$.

The process of simulating expanding sphere emission by time steps and angle steps without considering wave fronts is similar to the one used to obtain the light curve in (Bianco et al., 2001) and chapter XXII in (Ruffini et al., 2003a).

Points

Instead of wave fronts each part of the sphere is considered as it emits. Since everything is symmetric with respect to φ one single part may be taken to be a φ -ring and is represented by single x and y coordinate on the plane. The parts will be different for different θ (index j) and t (index i). Additionally, the idea is to represent emission from these parts as it moves with speed of light. To define a *point*; it is a point on the plane which starts on the line of the black body and then moves along x -axis with the speed of light. So, additional indexing k is used for this movement. The point has 3 index - i , j and k . The i presents time when it was emitted. The j angle. Together i and j (with $R[i]$) presents starting point on the black body. They are the same for a single point. The k presents movement of the point with speed of light. The k has the same meaning as i , i.e. it represents elapsed time. So, k starts from the value of i and then increases with global time i . The y coordinate doesn't change with k for a point as the movement is along x -axis. Finally the x and y are 3D arrays (i, j, k) which represent x and y coordinates of all points on every step they take. The number of elements is $i_{max} \times j_{max} \times k_{max}$. The k may be considered as a third type of the resolution, but it is defined same as i , i.e. by dt . So, the resolution for crossed length of points/photons as they travel is $c dt$.

Excluding points which are absorbed back

Before calculating spectrum of each point, the absorbed points should be excluded. This is why it's important to mark position of a point for each step (with index k). Otherwise this wouldn't be necessary and is not necessary if speed is constant or monotonically decreases. In general case, for each point on each step the distance from center is compared to the current value of radius. If this value is lesser then one of radius, the point is excluded.

The question remains if the radius continues to expand beyond final time $t[i_{max}]$ with constant final speed $\beta[i_{max}]$ will it further absorb points. So, final time $t[i_{max}]$ needs to be extended enough and same process repeated. Since this will take more time then previous step, some points may be excluded from the start.

In Figure 4.19 plane is presented at $t[i_{max}]$. The points with x coordinate larger than $R[i_{max}]$ will never be absorbed. All of them may be excluded from checking. For the points with x coordinate lesser than $R[i_{max}]$, the ones below the $\cos \theta = \beta[i_{max}]$ line will never be absorbed. This is because the line $\cos \theta = \beta[i_{max}]$ (which is constant now) defines part of the sphere which emits photons and points already have a "head start". Points above this line and x coordinate lesser than $R[i_{max}]$ need to be checked for each step.

In principal for each point final coordinates, final values of R and β , equations may be put in place assuming sphere catches up to point. Then finding out if there is a solution

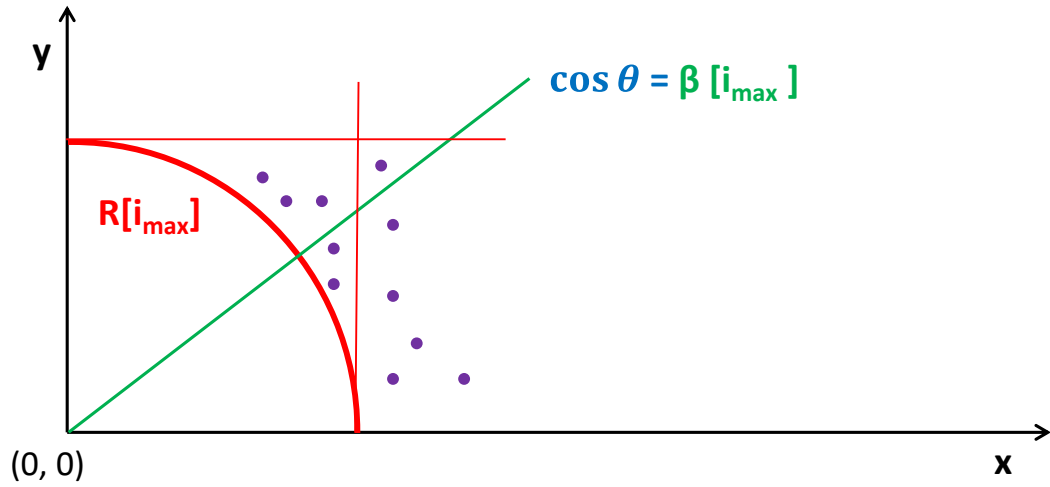


Figure 4.19: Plane in which simulation takes place at the last step. Purple dots represent points.

to this equation (in real numbers) it can be determined if point gets absorbed. However due to nature of the equations they would have to be solved numerically and possible nonexistence of solution (or a double solution if point enters and exits sphere during extended time) further complicates matter. In any way, for each point multiple calculations would have to take place.

Spectrum

Each point represents radiation from a φ -ring:

$$N_{ES\Omega}^r = \frac{4\pi R}{h^3 c^2} \frac{E^2}{e^{\frac{E\gamma}{kT}(1-\beta \cos \theta)} - 1} \frac{\cos \theta - \beta}{1 - \beta \cos \theta} \sin \theta$$

With dS being line element $R d\theta$:

$$N_{ES\Omega}^r R d\theta = dN_{E\Omega}^r = \frac{4\pi R^2}{h^3 c^2} \frac{E^2}{e^{\frac{E\gamma}{kT}(1-\beta \cos \theta)} - 1} \frac{\cos \theta - \beta}{1 - \beta \cos \theta} \sin \theta d\theta$$

Putting $x \equiv \cos \theta$:

$$dN_{E\Omega}^r = \frac{4\pi R^2}{h^3 c^2} \frac{E^2}{e^{\frac{E\gamma}{kT}(1-\beta x)} - 1} \frac{x - \beta}{1 - \beta x} dx$$

Since the ring has a certain thickness defined by j -resolution, the dx will be δx and equal to difference between $x[j]$ and $x[j+1]$. Putting other array values:

$$dN_{E\Omega}^r[i, j] = \frac{4\pi R_{[i]}^2}{h^3 c^2} \frac{E^2}{e^{\frac{E\gamma_{[i]}}{kT_{[i]}}(1-\beta_{[i]}x_{[j]})} - 1} \frac{x_{[j]} - \beta_{[i]}}{1 - \beta_{[i]}x_{[j]}} dx_{[j,j+1]}$$

Now, another index m has to be introduced to define energy resolution. Due to nature of black body spectra, steps should be placed equally logarithmic. So, $E = E[m]$ in the upper equation, and $dN_{E\Omega}^r = dN_{E\Omega}^r[i, j, m]$. The number of elements is $i_{max} \times j_{max} \times m_{max}$ minus the excluded pairs i, j from absorbed points. In order to reduce calculation time,

energy elements far away from the $kT_{[i]}$ peak (especially on the higher energy side) may be excluded from calculation and then equalized to zero.

In order to obtain observed quantities, $dN_{E\Omega}^r$ should be divided by comoving (in cosmological terms) distance squared d^2 calculated from the known redshift z . When the photon φ -ring reaches detector the value will drop by $z + 1$ because of stretching along x -axis but will also increase by $z + 1$ due to photons lowering of energy and more of them occupying keV interval. The values in array along m index should be shifted to lower energies. Since the energy intervals are in logarithmic equal spacing, all the elements should be shifted by same amount $z + 1$.

Arrival time

The points (which haven't been absorbed) all travel with the same velocity c and the distance/time between them along x -axis will be the same. The first point (the one most to the right and with $i = 0$) will be the first one to reach detector and it can be set as detector time zero. Then for each point starting position the distance/time can be determined as the distance from the first point. This time should be just multiplied by $\times(z + 1)$ in order to get detector time.

Then all of the point times need to be order along with points corresponding spectra. Then for a given (detector) time bin, the corresponding points are selected and their spectra summed. In this way, more points correspond to stronger emission, and the quantity $dN_{E\Omega}^r$ should also be multiplied by $\times dt$ to correct for this.

Finally, the summed spectrum is the observed one corresponding to detector time bin. In order to obtain energy flux the final spectrum should be multiplied by $\times E$, then by dE which is the difference between $E[m]$ and $E[m + 1]$, and then summed over all energy elements.

Turning on and off

Since there is a fixed time (from $t[i = 0]$ to $t[i_{max}]$) the black body in this simulation suddenly turns on and later off, and has a turn on and off period (with respect to x -axis and detector). The turn on period is time which start corresponds to the first point, and end to the point when the back of the sphere (at $t[i = 0]$) catches up to the tip of the sphere along x -axis. The turn off period is time which start corresponds to tip of the sphere (at $t[i_{max}]$), and end to the last point along x -axis.

To avoid this the time and other input parameters in the simulation can be set in such a way that: starting time of first (detector) time bin and ending time of detector last time bin do not correspond to turn on and off periods, but are in between. On the other hand the turn on or off period may have physical interpretation such as reaching suddenly transparency or previously transparent material suddenly becoming optically thick.

4.5.2 151027A

The simulation has been applied to this burst. From results of analysis of the burst in the previous section, it is clear that at some point it has relativistic expansion. If the expansion was not relativistic then apparent speed would be low for majority of time bins. The apparent speed seems to start as low. So, the initial values of radius and temperature can be taken as close to true, and initial speed as indeed relatively low. Then at maximum it reaches $\beta_a = 5$ which corresponds to $\beta \approx 0.97$ assuming uniform temperature

τ^s s	t^s s	kT^s keV	β^s	kT_o^s keV	L_o^s $\times 10^{49}$ erg/s	Time bin s	kT keV	L_{BB} $\times 10^{49}$ erg/s
	0 - 3	3.4	0.27	2.33	0.65	90 - 95		
3	4 - 7	3.4	0.27	2.33	1.78	95 - 100	$2.2^{+1.1}_{-1.1}$	$1.34^{+1.1}_{-0.88}$
6	8 - 14	3.4	0.30	2.39	5.31	100 - 110	$2.57^{+0.43}_{-0.50}$	$5.3^{+2.1}_{-2.2}$
12	15 - 23	3.2	0.35	2.33	13.0	110 - 120	$2.17^{+0.22}_{-0.26}$	$15.8^{+3.6}_{-3.8}$
18	24 - 75	0.55	0.895	1.14	14.2	120 - 130	$1.10^{+0.14}_{-0.12}$	$15.2^{+2.0}_{-1.9}$
48	76 - 128	0.24	0.895	0.600	6.77	130 - 140	$0.617^{+0.046}_{-0.043}$	$6.3^{+1.0}_{-1.0}$
76	129 - 181	0.2	0.895	0.434	3.20	140 - 150	$0.469^{+0.065}_{-0.064}$	$2.61^{+0.70}_{-0.70}$
103	182 - 233	0.13	0.895	0.329	2.25	150 - 160	$0.386^{+0.061}_{-0.061}$	$1.17^{+0.41}_{-0.38}$
131	234 - 338	0.07	0.895	0.194	0.58	160 - 180	$0.193^{+0.032}_{-0.030}$	$0.52^{+0.29}_{-0.32}$
187	339 - 444	0.02	0.895	0.120	0.10	180 - 200		
	445 - 499	0.02	0.895					

Table 4.9: Comparing results of simulation with observed values. Further details are in the text.

and velocity. This can be taken as a hint of maximum speed. Then the apparent speed decreases and again increases. Since radius is very big at this point, slight changes in its value correspond to large changes in apparent velocity. So, these values may be ignored. It was assumed that velocity monotonically increases to some value which then remains constant. Regarding the temperature it was assumed it monotonically decreases as is given by example of 151027A and other bursts in preliminary analysis. Although these temperatures are not comoving ones, in every case the temperature (as seen in host galaxy) goes down, so probably this reflects behavior of real (comoving) temperature.

Starting from these hints true values of temperature $kT(t)$ and velocity $\beta(t)$ were searched for by trying to match observed temperature and luminosity within 90% error for given observational time bins. It was also tried to place turn on and off periods around observational time bins. For a given true velocity distribution, times (true time) were calculated which approximately correspond to observational time bins. This was done by matching the points which come from tip of the sphere. Then velocities and temperatures were taken as constant within these periods and their values changed until they matched observations. The results are presented in Table 4.9.

The time t^s is the true time, i.e. the one which passes in the host galaxy as black body sphere expands. This is the global time of simulation. The kT^s are input values of comoving black body temperature, i.e. true temperature. The β^s is true input velocity of expansion. The kT_o^s and L_o^s are observed temperature and luminosity calculated from simulation for given observational time bins. These two quantities correspond to time periods which match exactly the given observational time bins. The time bins corresponding to t^s might not correspond exactly to observational time bins. Values kT and L_{BB} are observed quantities (luminosity is directly related to normalization constant as defined in XSpec) from previous section. First quantity τ is same as t^s and it shows time when back parts of the sphere emitted points/photons which ended up in the next observational time bin. This means that parameters in each t^s time bin affect also next observational time bin, or even the ones after.

First t^s time bin includes turn on time which is 1.3 s. It also follows the trend of non-increasing temperature and non-increasing speed, as well as initially increasing luminosity. The second-last t^s time bin is made to follow temperature and speed trends as well as having lower luminosity than the one from the previous bin. The last time bin just finishes with t^s time. Turn off time is 82 s. The observational time bins correspond to time elapsed

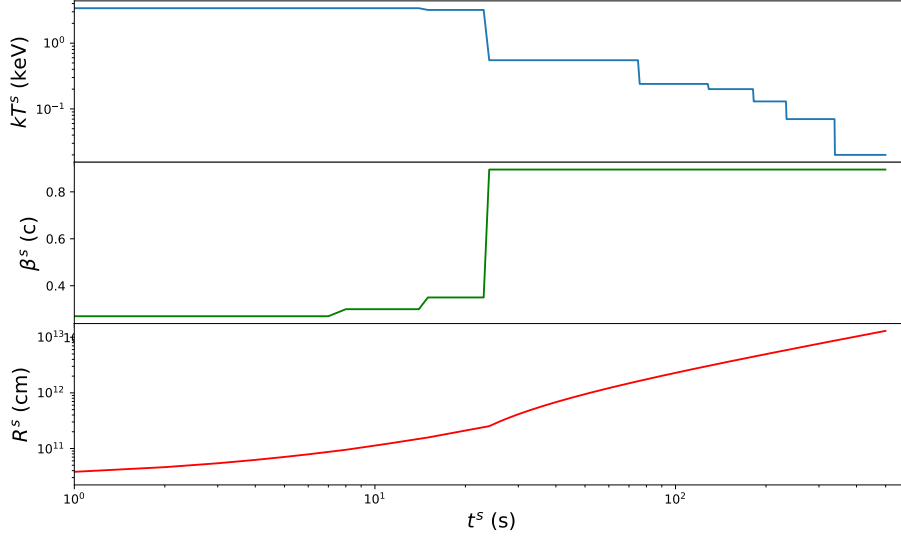


Figure 4.20: Input parameters in the simulation. Details are in the text.

since Swift trigger but this is just in order to be consistent with previous section. They may be considered to start from zero at 90 s.

Evolution of kT^s , β^s and radius R^s with time t^s is shown in Figure 4.20. The initial radius is chosen to be 3×10^{10} cm. The radius at $t = 338$ s which corresponds to ending of last observational time bin is $R = 8.7 \times 10^{12}$ cm.

Final temperature kT_o^s for a time bin was calculated based on the peak of the spectrum. This makes sense if the spectrum is close to that of a black body one. Given the varying velocity and temperature the final spectrum may be significantly distorted from black body one. So, visual inspection of spectra is needed and they are presented in Figure 4.21. The time bins correspond to observational ones with time zero corresponding to 90 s since Swift trigger. The first and last time bins don't have observational counterpart. As can be seen the spectra are blackbody-like and have a clear narrow peak.

In the Figure 4.22 are shown surfaces which were made by expanding black body as it created wave front for the velocity profile and initial radius of 151027A. The first plot (left) is focused on initial small velocity increase. The second (middle) on the final major velocity increase. Absorption of wave fronts happens during this phase. The final plot (right) focuses on part with final maximum constant velocity.

Discussion

The simulation matches nicely with observed values except for the luminosity of the second-last observational time bin where it is above 90 % interval. The input parameters were in a tabular form with sections matching closely the observational time bins. Sections may be selected differently or analytical function may be selected for input temperature and velocity. The time resolution was $dt = 1$ s starting from 0 s to 499 s. The resolution may be changed and it may have different values for different parts. It might be increased in the beginning when velocity profile is more complex and radius is smaller.

All in all, the observations were matched assuming expanding sphere with uniform

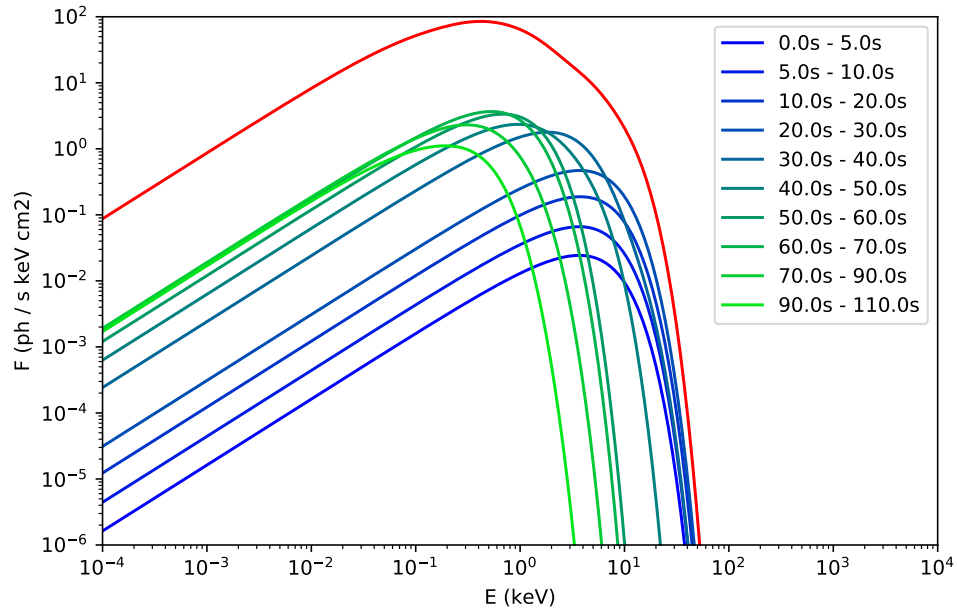


Figure 4.21: Final spectra from simulation. The red one is the cumulative one. Details are in the text.

temperature across its surface. The maximum velocity of $\beta^s = 0.895$ corresponds to Lorentz factor of $\gamma = 2.2$. Characteristic for this burst example is large velocity increase which coincides with sudden (absolute) temperature drop.

4.5.3 Double black body

With varying temperature, velocity, finite size of the emitter, it is possible to have a distorted black body spectrum. Instead of narrow peak of black body it is possible to have a broader peak or even a double peak. There is reasonable evidence for a double black body in some GRB (soft X-ray afterglow) spectra, so it might be produced by a single black body sphere with uniform but varying temperature and velocity.

The effect of having thermal spectrum in the co-moving frame of the emitting surface

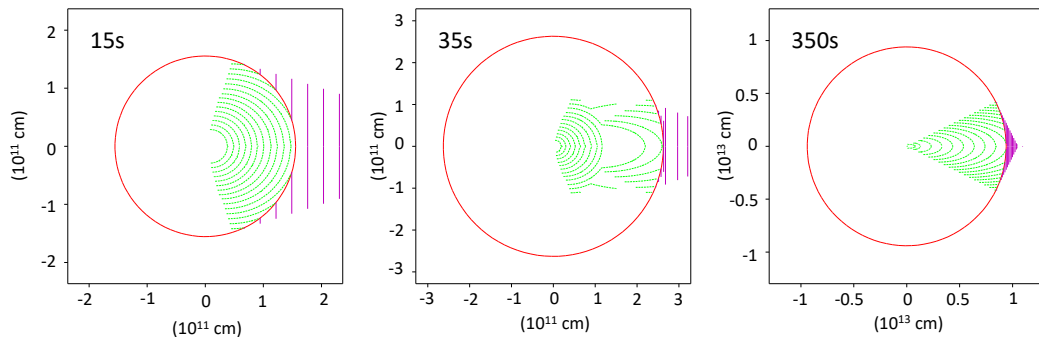


Figure 4.22: Wave front surfaces for velocity profile of 151027A. The time in the upper-right corner is simulation global time t^s .

which leads to an observed spectrum which is a convolution of thermal spectra over the EQTSs is a known effect and was presented in (Ruffini et al., 2004b; Bernardini et al., 2005). In it the EQTSs are obtained from fireshell dynamics and correspond to ultrarelativistic velocities $\Gamma \gtrsim 100$. It was shown that prompt non-thermal Band spectrum can be explained as convolution of different thermal spectra and it was applied to several GRBs. The changing of EQTSs to match the observation cannot be completely random but has to be done within the fireshell model by changing certain model parameters. In the case here the EQTSs, or the temperature change, are not determined by any model and can be in principal random. Focus is on mildly relativistic velocities $\Gamma \sim 2$ in order to explain spectra of temperature-decaying thermal emission in the beginning of the afterglow.

It is possible to produce a double peak even if the sphere doesn't expand. If the sphere is large enough, it will take time for wave front to be completed and if there is a sudden temperature change during creation of the front, the wave front will contain black body spectra with different temperatures. If the change of temperature is slower with respect to light crossing time of emitter, then the spectrum will have a single broader peak. If the change is shorter, then the spectrum might contain two bumps corresponding closely to initial and final temperature. On the left plot in Figure 4.23 are results of simulation of non-expanding sphere of radius 3×10^{12} cm which temperature drops instantly from 10 keV to 1 keV at about $t^s \approx 130$ s. As can be seen the change of temperature is recorded over several time bins with one of them showing clear double peak with same intensity.

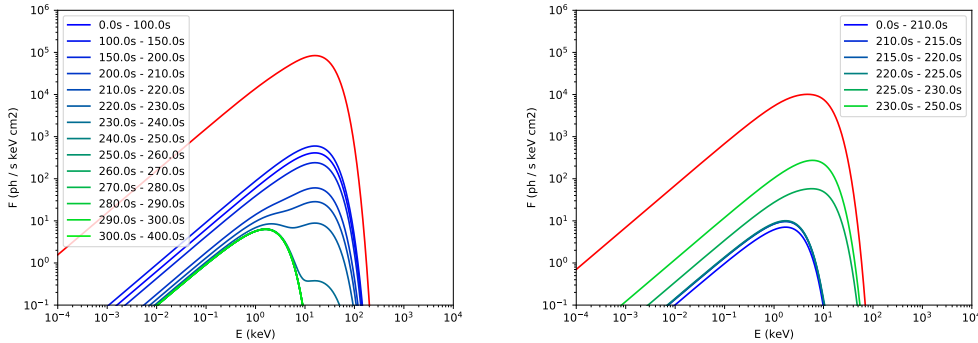


Figure 4.23: Examples of double or broaden black body peak. Details are in the text.

It is also possible to produce broaden or double peak just by change in velocity while comoving temperature remains the same. A single wave front would be composed of different β -ellipse surfaces and would contain blackbody spectra of all differently boosted temperatures. On the second plot of Figure 4.23 are results of simulation of expanding sphere which velocity changes suddenly from $0.1 c$ to $0.9 c$ at $t^s \approx 250$ s, with initial radius of 3×10^{12} cm and constant comoving temperature of 1 keV. At the point of change the resulting spectrum is broaden as it contains two black bodies with different boosted temperatures. If the temperature difference was greater the broaden peak would become double peak. In both plots redshift is zero and flux is in arbitrary units.

With both varying temperature and velocity, and different initial radius, many combinations can be made. In principal, double or broaden peak is more likely to happen if the radius is bigger, velocity and temperature changes more drastic.

In bursts 090618A and 130427A there is reasonable evidence for double peak. Based on preliminary analysis, the apparent radii of these bursts are relatively large even in the

first time bins $R_a \sim 10^{12}$ cm and for 130427A the radius goes beyond $R_a \sim 10^{13}$ cm. The apparent speed of ~ 1 c also points to relativistic expansion which implies real radius is actually bigger. Unlike 150127A where XRT data exists from the start of the peak in the light curve, in 130427A and 090618A the XRT data starts in the decaying part of the softer peak which came after the harder prompt emission. This means that probably the start of thermal emission, when temperatures should be higher, were missed. Given large radius (with respect to light crossing time) the higher temperature black body may show itself together with the lower one in the observed time bins. In a future work it would be interesting to examine data of both bursts in detail and do the simulation by trying to match both peaks in spectra by focusing also on period earlier than the first observed time bin.

4.6 Concluding remarks

In the Fireball model temperature-decaying emission in the late prompt - early afterglow phases is explained as coming from a late time central engine activity. The Lorentz factor is on the order of $\gamma \sim 10 - 100$, photosphere radius is at $R \sim 10^{13}$ cm. Double black body in Fireball model is often explained as coming from a cocoon surrounding the jet.

In the case of perfect spherical black body, Lorentz factor is about $\gamma \sim 2$ or nonrelativistic. Photosphere radius expands in the range $R \sim 10^{10} - 10^{13}$ cm. Double black body in the spectrum may come from the same black body with varying temperature and velocity.

Explaining this emission as coming from an expanding spherical perfect black body fits well into the IGC scenario. It is considered to come from interaction of fireshell plasma with supernova ejecta. The resulting Lorentz factor should be on the order of $\gamma \sim 2$ as is the case. From preliminary analysis all GRBs with reasonable evidence for a temperature-decaying thermal emission, have isotropic energies $E_{iso} > 10^{52}$ erg. The maximum luminosities and isotropic energies of black bodies are in a narrower range than GRB isotropic energies. GRB 151027A has a strong thermal emission which reaches luminosity of $L_{bb} \sim 10^{50}$ erg/s which is in line with maximum thermal luminosity of other bursts. This burst has total isotropic energy of 4×10^{52} erg (just above the 52-limit) while other burst can have above 10^{54} erg. This fits well within the IGC scenario in which strong thermal X-ray emission in the early afterglow comes from interaction of fireshell plasma with supernova ejecta, and only GRBs above the 52-limit produce fireshell plasma.

Often the spectrum is fitted with a perfect black body even if the parameters of the fit (temperature and flux) are later used in models which predict broaden black body. The progress should also occur in the observational part. The Swift has done a great job, but the black body, broaden or multi-peak black body, needs to be clearly identified and its evolution.

New GRB-SNe connections

Connections between Gamma-ray bursts (GRBs) and Supernovae (SNe) were discovered in the late '90s with the first GRB-SN connection of GRB 980425 and SN 1998bw¹. In the next couple of decades many more connections were discovered, mainly thanks to the fast and precise localization of GRBs by the Swift satellite. The GRB-SN connection is made by detection of SN signatures in the GRB afterglow by the optical telescopes.

The optical light curve (LC) of a SN consists of a rising part which lasts from few days to several tens of days, the maximum, and the decaying part. When the SN and a GRB occur from the same phenomena, then the optical LCs and spectra of - GRB afterglow, the SN and host galaxy - are superimposed. In the beginning the GRB afterglow is too strong compared to SN rising LC. Later on, as the GRB afterglow fades, and SN LC rises to maximum, SN features can be detected. The most reliable feature of a SN is its spectrum (determined mostly by the lines) which is superimposed on two spectral components: the continuous spectrum of GRB fading afterglow, and, continues spectrum of GRB host galaxy which is constant in shape and intensity. Another feature is a bump in the light curve (LC) of the GRB optical afterglow and its reddening², both of which are produced by the SN. The contribution by the host galaxy is usually smaller and easily subtracted since it is constant in time. Based on all these factors a SN detection can be made with different levels of certainty or it can be undetected even though it might be present. The basic differentiation of SN detection is whether it is based on a bump in optical LC or on a spectroscopic identification. The latter is considered in most cases a certain proof.

All GRBs connected to SNe were long GRBs ($T_{90} > 2$ s). Their isotropic energy spans entire range from $E_{iso} \sim 10^{48} - 10^{54}$ erg. SNe connected to GRBs were all type Ic or Ib (Ib/c) - core-collapse SNe with stripped hydrogen and, in most cases, stripped helium envelope. The speed of SN ejecta $v_{ej} \sim 0.03 - 0.1$ c was higher than non-GRB Ib/c SNe. They are more energetic and more luminous than non-GRB Ib/c SNe. Because of the last two factors these SNe are sometimes termed *hypernovae*. These GRB-SNe are, however, less luminous than special group of SNe called *superluminous supernovae* which are sometimes also termed hypernovae. The characteristics of most potentially detected

¹SN is named by the four digit number corresponding to the year of discovery. First 26 SNe of the year have a capital-letter suffix starting from A for the first SN, B for the second, etc. up to Z. Following SNe have a two letter suffix in small letters, again in alphabetical order, aa, ab... az, ba, bb, etc. Since 2016 a three letter suffix is used after all two letter combinations are "spent".

²Crude spectral analysis based on several filters in optical band. The intensity in lower-energy filters (red color) becomes stronger than in the higher-energy filters (blue color).

SNe also point to the type Ib/c with features of other GRB-SNe Ib/c (more luminous, etc.).

For a recent review on GRB-SN connections from observational point of view see (Cano et al., 2016).

In Table 5.1 confirmed and potential GRB-SN connections are listed. The table is an extension of one from (Kovacevic et al., 2014). Similar table in (Cano et al., 2016) has been of help in making the new one.

All the SNe which have a confirmed detection in a GRB afterglow were type Ib/c SNe and vast majority of possible SNe detections are also of this type. These SNe are typically discovered within 20 days of a GRB when their LCs reach maximum. Aside from these, there are a couple of interesting possible connections among which SN 1997cy and GRB 970514 (Germany et al., 2000) stand out. SN 1997cy was a type II SN – a core-collapse SN with hydrogen lines in the spectrum. Among other spectral lines, this SN also exhibits narrow Balmer³ emission lines in its spectrum which is typical of a subtype IIn SNe (*n* stands for narrow). Further investigation showed that this peculiar SN is actually a type Ia supernova which ejecta strongly interacts with a hydrogen-rich circum-stellar medium Ia-CSM (Silverman et al., 2013). This interaction gives rise to narrow hydrogen lines in the spectrum. Burst GRB 970514 was a short GRB with $T_{90} \approx 0.6$ s. SN 1997cy was discovered serendipitously two months after the GRB. Analysis showed that this SN was already in the decaying phase and it reached its maximum before. Given the small positional uncertainty of GRB position, its proximity to SN location, it seems this connection is real and not a coincidence (Germany et al., 2000). With the redshift of SN 1997cy $z = 0.063$, this would imply that GRB 970514 had an isotropic energy of $E_{iso} \approx 4 \times 10^{48}$ erg.

Except the previous special case all SNe connected to GRBs were discovered by observing the GRB afterglow with optical detectors. This in turn was made possible by relatively precise localization of GRB prompt emission. There are many cases when a GRB prompt emission wasn't precisely localized and no optical or soft X-ray follow-ups were possible. If a SN was physically connected to such a GRB then it might be possible that the SN was discovered serendipitously by optical telescopes. This is the main topic of this chapter. Are there any missed GRB-SN connections within the sample of detected GRBs and detected SNe?

Regarding SN types review on basic classification can be found, for example, in (Turatto, 2003; Pastorello, 2012). The classification is based on spectroscopic features which translate, with other observational evidence, into astrophysical features. In a nut-shell: basic division is on type I (SN progenitor doesn't have hydrogen envelope) and type II (has hydrogen envelope). Type Ia are thermonuclear SN without hydrogen envelope. Type Ib are core-collapse SN without hydrogen but with helium envelope. Type Ic are core-collapse SN without hydrogen and without helium envelope. Some broad-lined SNe Ib and Ic are known to be connected to GRBs and therefore put in one group Ib/c. Since they are similar from observational point of view, they are sometimes reported as Ib/c even without considering GRBs. Type II SNe are all core-collapse SNe. Type II can be divided based on the light curve shape into IIP and IIL. Type IIP exhibit a plateau in the LC after maximum while IIL have linear decay of LC after maximum. Type Iib are SNe in between type II and type Ib. They exhibit spectral features of type II (namely hydrogen lines) in the beginning and later on spectral features of type Ib. Type IIn are a special case and exhibit narrow hydrogen lines superimposed on medium and broader ones in the spectrum. This indicates interaction of SN energy (stored as kinetic energy of expanding

³Hydrogen lines corresponding to transition between orbit $n = 2$ and higher orbits.

GRB	E_{iso} (<i>erg</i>)	Discovered by	z	SN identification	SN name	Refs.
970228	1.86×10^{52}	SAX	0.695	bump		(Reichart, 1997)
980326	5.60×10^{51}	BATSE	1(?)	bump		(Bloom et al., 1999)
980425	6.38×10^{47}	BATSE	0.0085	spec.	SN 1998bw	(Galama et al., 1998)
990712	7.80×10^{51}	SAX	0.434	bump		(Zeh et al., 2004)
991208	2.59×10^{53}	Ulysses/Wind	0.706	bump		(Zeh et al., 2004)
000911	7.80×10^{53}	Ulysses/Wind	1.058	bump		(Lazzati et al., 2001)
010921	1.10×10^{52}	HETE	0.45	bump		(Zeh et al., 2004)
011121	9.90×10^{52}	SAX/Ulysses	0.36	bump	SN 2001ke	(Bloom et al., 2002)
020305	$0.7-4.6 \times 10^{51}$	HETE/Ulysses	0.2-0.5	bump		(Gorosabel et al., 2005)
020405	1.28×10^{53}	SAX/Ulysses	0.695	bump		(Masetti et al., 2003)
020410	2.20×10^{52}	SAX	~ 0.5	bump		(Levan et al., 2005)
020903	1.10×10^{49}	HETE	0.251	bump		(Bersier et al., 2006)
021211	1.30×10^{52}	HETE	1.006	spec.	SN 2002lt	(Della Valle et al., 2003)
030329	1.70×10^{52}	HETE/Wind	0.168	spec.	SN 2003dh	(Stanek et al., 2003)
030723	$< 1.6 \times 10^{53}$	HETE	< 1	bump		(Fynbo et al., 2004)
031203	9.99×10^{49}	INTEGRAL	0.105	spec.	SN 2003lw	(Malesani et al., 2004)
040924	1.10×10^{52}	HETE	0.86	bump		(Soderberg et al., 2006a)
041006	3.50×10^{52}	HETE	0.716	bump		(Soderberg et al., 2006a)
050416A	1.20×10^{51}	Swift	0.6528	bump		(Soderberg et al., 2007)
050525A	3.39×10^{52}	Wind/INTEGRAL	0.606	spec.	SN 2005nc	(Della Valle et al., 2006)
050824	$0.4-3 \times 10^{50}$	Swift	0.828	bump		(Soderberg et al., 2007)
060218	1.66×10^{49}	Swift	0.033	spec.	SN 2006aj	(Campana et al., 2006)
060729	1.60×10^{52}	Swift	0.54	bump		(Cano et al., 2011)
060904B	2.40×10^{52}	Swift	0.703	bump		(Cano, 2013)
070419	7.90×10^{51}	Swift	0.97	bump		(Hill et al., 2007)
080319B	1.30×10^{54}	Swift	0.937	bump		(Tanvir et al., 2010)
081007	2.50×10^{51}	Swift/Fermi	0.5295	bump	SN 2008hw	(Jin et al., 2013)
090618	2.90×10^{53}	Swift/Fermi	0.54	bump		(Cano et al., 2011)
091127	1.60×10^{52}	Swift/Fermi	0.49	bump	SN 2009nz	(Cobb et al., 2010)
100316D	9.81×10^{48}	Swift	0.059	spec.	SN 2010bh	(Chornock et al., 2010)
100418A	9.90×10^{50}	Swift	0.624	bump		(Holland et al., 2010)
101219B	4.39×10^{51}	Swift/Fermi	0.55	spec.	SN 2010ma	(Sparre et al., 2011)
101225A	1.20×10^{52}	Swift	0.847	bump		(Cano et al., 2016)
111209A	5.80×10^{53}	Swift	0.677	bump	SN 2011kl	(Kann et al., 2016)
111211A	5.70×10^{51}	Swift	0.478	bump		(de Ugarte Postigo et al., 2012)
111228A	7.52×10^{52}	Swift/Fermi	0.714	bump		(D'Avanzo et al., 2012)
120422A	1.28×10^{51}	Swift	0.283	spec.	SN 2012bz	(Melandri et al., 2012)
120714B	4.51×10^{51}	Swift	0.3984	spec.	SN 2012eb	(Klose et al., 2012)
120729A	2.30×10^{52}	Swift/Fermi	0.80	bump		(Cano et al., 2014)
130215A	3.10×10^{52}	Swift/Fermi	0.597	spec.	SN 2013ez	(Cano et al., 2014)
130427A	9.57×10^{53}	Fermi/Swift	0.3399	spec.	SN 2013cq	(Melandri et al., 2014)
130702A	7.80×10^{50}	Fermi	0.145	spec.	SN 2013dx	(Toy et al., 2016)
130831A	4.56×10^{51}	Swift	0.4791	spec.	SN 2013fu	(Cano et al., 2014)
140606B	3.50×10^{51}	Fermi	0.384	spec.	iPTF14bfu	(Cano et al., 2015)
150518	$> 5 \times 10^{49}$	Wind/MAXI	0.256	bump		(Pozanenko et al., 2015)
150818	1.00×10^{51}	Swift	0.282	spec.		(de Ugarte Postigo et al., 2015)
161219B	1.60×10^{50}	Swift	0.1475	spec.	SN 2016jca	(Ashall et al., 2017)

Table 5.1: The sample of 47 confirmed and possible GRB and SN Ib/c connections updated to 01 January, 2017. There are two potential GRB-SNe connections, based on the bump in the LC, prior to the first confirmed connection of GRB 980425 - SN 1998bw. The *PTF14bfu* is a SN, however it was not named by the standard SN convention. Isotropic energy is the one from the GRB prompt emission. References point to the SN discoveries (or potential discovery) and their connection to a GRB. It can be noted that all the redshifts are $z \leq 1$ which is a limit imposed by sensitivity of optical telescopes regarding detection of SNe. The satellites detecting GRBs: *SAX* stands for BeppoSAX satellite; *BATSE* is a detector on-board CGRO satellite; others are names of satellites. Often two or more satellites observed a GRB. Here focus is on the BATSE, Fermi and Swift. Their name is always shown if they detected a GRB. Names of other satellites are present if none of the three detected a GRB.

ejecta or radiation) with slow-moving pre-explosion ejected material from the progenitor. Such SNe can be type Ia-CSM (like SN 1997cy); they can be *supernova impostors* - stars which periodically eject large amounts of matter, and when the fresh ejected shell interacts with the older and slower moving one, energy is released and it gives rise to optical emission. This optical emission resembles a SN but is generally weaker; finally, they can be real type II SNe with SN energy interacting with slow-moving CSM which was ejected from the progenitor star prior to SN explosion. Short review of SNe IIn can be found (Habergham et al., 2014).

In the next section technical details regarding different SN and GRB catalogs, collecting information from them, and the computer script used to find all possible missed connections will be presented. Since new SNe and GRBs are discovered almost every day, the GRB and SN time limit for this work was chosen to be January 1, 2017. Then the search for missed connection between GRBs detected by Fermi and BATSE, and SNe Ib/c will be presented. This largely follows the work in (Kovacevic et al., 2014). Then the search for missed connection between short GRBs and SNe IIn will be presented.

5.1 Technical details

5.1.1 SN catalog

Sample of detected SNe was taken from two supernova catalogs.

Harvard catalog

One catalog is managed under *International Astronomical Union: Central Bureau for Astronomical Telegrams* (IAU: CBAT) with Harvard University⁴. The catalog itself can be found in the form of a text file on the website⁵. It lists all the SNe since 1885⁶ up to the end of 2015. Here the catalog stops probably due to large increase of SN detections and difficulty of categorizing them. There are about 6500 SNe in this catalog. For each SN there are information regarding position in the sky, date of detection and a type of SN - all which is needed for cross-correlation with GRBs.

The information from the website can be directly loaded from the web into a programming language (for example Python⁷) or copied into a text file and then loaded to a programming language.

The date of the detected SN, which is in YYYY-MM-DD format, are transformed into Modified Julian Day (MJD)⁸ format which is a 5 digit number for all the dates in the last hundred years or so, (and will be for the next century) and suitable for comparisons. In very few cases SN date is not listed. This happens for SNe which were initially named as SNe but for which there is a doubt whether the optical transient detected is SN at all or some other optical transient such as *luminous blue variable* star, *Eta Carinae* type star or even HII region. These “SNe” are, at this point, excluded. The date refers to date of discovery which can be before the maximum or after (more common).

SN positions have been determined with sub-arcsecond precision which is much smaller than typical prompt GRB positional uncertainty of Fermi and BATSE (several degrees or

⁴<http://www.cbat.eps.harvard.edu/iau/cbat.html>

⁵<http://www.cbat.eps.harvard.edu/lists/Supernovae.html>

⁶SN 1885A, first modern observation of a SN.

⁷<https://www.python.org/>

⁸For explanation see <http://tycho.usno.navy.mil/mjd.html>

tens of degrees). Therefore the SN positional errors can be neglected. In some cases the SN position is not given. Then the position of the host galaxy is used which is also listed in the catalog. The difference is, again, marginal (tens of arc-seconds) when compared to prompt GRB positional uncertainty.

Supernova types in the catalog follow typical classification: Ia, Ib, Ic, IIP, IIL, IIn, IIb. This is how SNe types are marked in the catalog. There are some specifications. For example, if a SN shows some peculiar characteristics, then an additional letter *p* is assigned to it. Or, if a classification is not certain, then a question mark ? is also added. Sometimes the type of a SN is determined just as a type I or II without sub-classification, and sometimes SN is not classified at all. In Table 5.2 is shown how SN types from the Harvard catalog are marked and to which general type they refer.

Asiago catalog

Second catalog which was used is *Asiago* catalog managed by Padova Observatory⁹ (Barbon et al., 2010). The online catalog can be found here¹⁰ as a text file, and on the NASA's HEASARC (High Energy Astrophysics Science Archive Research Center) server here¹² in numerous forms including a fits (Flexible Image Transport System) file. This catalog also contains all the necessary information for cross-correlation with GRBs along with many other. The information from the fits file catalog can be easily read into programming language. Like Harvard, this catalog contains all the SNe since 1885 up to the end of 2015 (with several more SNe in December 2015 than in Harvard). There are about 6500 SNe in this catalog.

The date which is in YYYY-MM-DD format is transformed into Modified Julian Day. The date can refer to the date of discovery, the date of determined maximum or date of an estimated maximum. Position is given as RA and Dec in decimal degrees.

The type of SN follows typical classification: Ia, Ib, Ic, IIP, IIL, IIn, IIb. If the classification is uncertain then : or ? is added and if SN shows peculiar features then *PEC* is added. The Asiago (HEASARC) catalog also differentiates type marked IIN?, which are supernova imposters, super-luminous supernova and some other specific types. There are SNe classified just as type I or II, and SNe which are not classified. In Table 5.2 it is shown how SN types from this catalog are marked and to which type they refer.

The naming convention in the Asiago (HEASARC) catalog is a little bit different than in Harvard - the double letters are all in capital and a “SN” is added in front. This needs to be transformed within a script to exactly match the names in Harvard catalog if SNe from both catalogs are to be compared.

Asiago catalogs 2014/15/16

Aside from the standard Asiago catalog of SNe recognized and named by the IAU convention, there are numerous more SNe detected by new wide field automatic optical telescopes. These are relatively new instruments and many SNe do not have an official IAU name. These SNe are named by the conventions corresponding to wide field telescopes transients.

⁹<http://graspa.oapd.inaf.it/about.html>

¹⁰<http://graspa.oapd.inaf.it/cgi-bin/sncat.php>

¹¹<http://graspa.oapd.inaf.it/asnc/cat.txt>

¹²<http://heasarc.gsfc.nasa.gov/w3browse/all/asiagosn.html>

SN group	SN type	Harvard		Asiago	
Ib/c	Ic	Ic, Ic?, Ic-p	N = 252	IC, IC?, IC:, IC PEC, IC PEC:	N = 305 (261)
	Ib	Ib, Ib?, Ib-p, Ibn	N = 128	IB, IB:, IB ?, IB PEC, IBN	N = 169 (140)
	Ib/c	Ib/c, Ib/c?, Ibc, Ibc?, Ic/b	N = 94	IB/C, IB/C:, IB/C PEC	N = 90 (75)
Ia	Ia	Ia, Ia?, Ia-p, Ia-p?, Iap	N = 3001	IA, IA:, IA?, IA ?, IA*, IA PEC	N = 4398 (3123)
none	I	I, I?, Ip, I-p	N = 62	I, I:, I*, I PEC	N = 90 (87)
IIn	IIn	IIn, IIn?	N = 201	IIN, IIN:, IIN?, II N, IIN ?, IIN PEC	N = 280 (228)
I Ib	I Ib	I Ib, I Ib?	N = 83	IIB, IIB:, IIB: PEC	N = 137 (102)
IIP	IIP	IIP, IIP?, II-P	N = 226	II P, II P:, II P PEC, II* P	N = 486 (372)
none	III	III, III?, II-L	N = 6	II L, II L:	N = 28 (24)
none	II	II, II?, II-p	N = 1010	II, II:, II?, II ?, II PEC	N = 1157 (955)

Table 5.2: Harvard catalog contains SNe up to the end of 2015. Asiago catalog contains SNe up to the end of 2016. This includes Asiago (HEASARC) catalog till the end of 2013, and Asiago catalogs 2014/15/16. Numbers in brackets correspond to Aaiago (HEASARC) catalog till the end of 2015. SNe with uncertain or peculiar types are included in that general type. Sometimes letters/symbols are interchanged or put differently. Many SNe are marked as in-between types Ib and Ic - type Ib/c. There are only few cases of double identification of types other than Ib/c and they are not included. SN group refers to how SNe types are grouped for the purpose of cross-correlation with GRBs. SNe that were determined just as type I or type II are not included in the analysis. Due to low number of III SNe they are also not included.

Asiago catalog contains special annual sections containing IAU and non-AIU SNe for years 2014¹³, 2015¹⁴, 2016¹⁵, etc. SNe in the annual sections for the previous years contain just IAU SNe as in the standard catalog. The wide-field optical telescopes have vastly increased the rate of SN detections. The number of non-IAU SNe has grown which has prompted IAU to introduce additional three-letter naming convention since 2016. Even so, there are still SNe in with non-IAU designations. For example, number of IAU SNe in the year 2014 is around 150 while Asiago catalog for 2015 (which contains IAU and non-IAU SNe) has around 950 SNe. The Asiago 2014/15/16 contain contain most of the important SNe but not all.

These catalogs are not on the HEASARC server and had to be copied from a web page to a text file and then loaded to a program.

Merging catalogs

The Harvard and standard Asiago catalogs are summary of all the observations and analysis of IAU SNe done by many optical telescopes and astronomers. They are practically the same. The Harvard catalog has two SNe not present in Asiago catalog, while Asiago has one not present in Harvard and several more SNe which are marked as LBV, eta-Car type stars, etc. in Harvard catalog.

The main difference is in the type of a SN. Often there are several observations and analysis of a single SN, and different analysis can make different classifications. In modern times SN classification is usually done by a computer program which compares SN spectrum to many different spectra and finds the closest match. There are also several different programs in use and they can produce different results. In most cases the type of a given SN in both catalogs is the same. However, in some cases it is different or is more precisely determined in one catalog (for example it is marked as type II? in one catalog and IIn in other). For the purposes of this work, selection of all the SNe of a given type is done in such a way to take into account also those SNe that have that type only in one

¹³http://graspa.oapd.inaf.it/cgi-bin/sncat_new.cgi?yr=2014

¹⁴http://graspa.oapd.inaf.it/cgi-bin/sncat_new.cgi?yr=2015

¹⁵http://graspa.oapd.inaf.it/cgi-bin/sncat_new.cgi?yr=2016

catalog. Taking all into account, this improves the statistics rather than diminishing it. Of course, if there are some particular SNe of interest (with high probability of belonging to a GRB) then their properties from both catalogs as well as other sources are checked.

The position and discovery dates of a given SN should be the same in both catalogs. To do a quick check to see if there are some errors in the catalogs, SNe from both catalogs are cross-correlated with each other. For some SNe there is a large discrepancy in position and discovery dates and these are further checked to see which catalog is “wrong” and afterwards it is corrected.

The IAU SNe from Harvard and Asiago catalog are taken up to the end of 2014. IAU and non-IAU SNe since the beginning of 2014 are taken from Asiago 2014/15/16 catalog(s).

Merging Harvard and standard Asiago catalog is important for SNe detected in the '90s - the period of time when CGRO-BATSE was detecting GRBs. Adding SNe from Asiago 2014/15/16 catalog is important for cross-correlation with GRBs detected by Fermi satellite which is still operational.

5.1.2 GRB catalogs

There were/are many GRB missions. In this work the GRB catalogs from the most important ones will be used such as CGRO-BATSE and Fermi-GBM. These two detectors have the largest number of detected GRBs and most precisely determined GRB parameters. The GRB catalog from the Swift-BAT instrument will not be used because the very precise localization of GRBs (few arc-minutes) made it possible for majority of them to be observed with optical telescopes, and if there was a SN connected to these GRBs then it was already discovered.

The main GRB parameters needed for cross-correlation with SNe are date, position and error of position. Another important parameter is the duration so difference between long and short GRBs can be studied. The GRB catalogs are not merged and are cross-correlated with SNe separately. This can be done because they contain different GRBs (different time periods).

CGRO-BATSE catalog

Burst And Transient Source Experiment (BATSE) is a wide field gamma-ray detector on board of NASA's Compton Gamma-Ray Observatory (CGRO) satellite which operated from 1991 to 2000. During this time it detected around 2700 GRBs with several degree localization accuracy. Field of view of BATSE is full sky, however due to proximity of Earth, it was something more than half of sky (with Earth blocking the other, smaller, half).

The official BATSE catalog can be found online here¹⁶; references (Meegan, 1997). The catalog is in the form of a text file. Due to the observational constraints, many GRBs out of 2700 don't have measured duration or fluence. So, the catalog is actually made out of several catalogs. The main catalog has 2702 GRBs and contains basic information such as date, position, etc; second catalog contains GRB durations and has 2135 GRBs; there are two catalogs for peak flux and fluence. In order to merge information from them into a single catalog, they all have to be read and same GRBs have to be matched by their trigger number which is the only parameter present in all the catalogs. Easier way is to

¹⁶<https://gammaray.nsstc.nasa.gov/batse/grb/catalog/current/index.html>

take the catalog from the NASA's HEASARC server¹⁷ which contains all the information in a single catalog. The catalog can be read as a fits file. The GRBs which don't have measured duration or fluence have a set value of zero for these parameters. The RA, Dec, position error are given in decimal degrees while date is in MJD. Numerous other information regarding each GRB is also present. If there are several GRBs during one day, the names of these GRBs all have a "-" suffix. In order to differentiate them they were selected within a script and named by the standard convention of adding B, C, D, etc. to successive burst detected on the same day. Out of 2702 GRBs, 1540 are long ($T_{90} \geq 2$ s), 497 are short ($T_{90} < 2$ s, and > 0 s), and 665 don't have a constrained duration.

The positional error represents spacial-averaged statistical 1σ (68%) error. There is an additional 1.6° systematic error. BATSE team adds these two values in quadrature to get 1σ confidence interval. The same is done with this work. Out of long GRBs with the highest error radius, the 4 with the highest error have a significantly higher radius than the rest, and are excluded by setting a limit of $er(max, long) \leq 16^\circ$, which makes a final of 1536 long GRBs. Out of short GRBs with the highest error radius, the 2 with the highest error have a significantly higher radius than the rest, and are excluded by setting a limit of $er(max, short) \leq 20^\circ$, which makes a final 495 short GRBs. The average value of positional error for long GRBs is $er(avg, long) = 3.7^\circ$ with standard deviation $\sigma(long) = 2.4^\circ$. The average value of positional error for short GRBs is $er(avg, short) = 7.0^\circ$ with standard deviation $\sigma(short) = 3.8^\circ$.

Fermi-GBM catalog

Gamma-ray Burst Monitor (GBM) is an instrument on board NASA's Fermi satellite which was launched in 2008 and is still operational. Fermi-GBM, up to 1 January 2017, detected about 2000 GRBs with several degrees to few tens of degrees localization accuracy. Field of view of GBM is full sky, however due to proximity of Earth, it was something more than half of sky.

The official Fermi-GBM can be found on NASA's HEASARC server¹⁸ in many forms including fits file; references (Gruber et al., 2014; von Kienlin et al., 2014; Bhat et al., 2016). The RA, Dec and positional error are given in decimal degrees while date is in MJD. Numerous other information regarding each GRB is also present including automatic spectrum. Out of 1980 GRBs, 1654 are long and 326 are short.

The positional error represents spacial-averaged statistical 1σ (68%) error. If a GRB was localized with arc-minute accuracy or more precisely by other satellites/instruments, then that position is given in the catalog and positional error is set to zero. If the Large Area Telescope (LAT) on-board Fermi detected a GRB with higher accuracy (several tens of arc-minutes), and there is no arc-minute localization by other instruments, then the LAT position and error are given. The error radius set to 50° means the GRB is not well localized, however only one GRB has this value. There is an additional 2-3 degrees (2.5°) systematic error associated to Fermi-GBM which is added in quadrature to statistical. For simplicity this is done for all GRBs, even the ones who were localized more precisely by other instruments. To exclude the tail of positional error distribution, the maximum error is set to $er(max, long) \leq 20^\circ$, which makes a final of 1640 long GRBs. For the short bursts this limit is set to $er(max, short) \leq 24^\circ$ which makes a final of 320 short bursts.

¹⁷<https://heasarc.gsfc.nasa.gov/W3Browse/all/batsegrb.html>

¹⁸<https://heasarc.gsfc.nasa.gov/W3Browse/fermi/fermigbrst.html>

The average value of error for long bursts is $er(avg, long) = 5.3^\circ$ with standard deviation $\sigma(long) = 3.5^\circ$. For short, $er(avg, short) = 8.7^\circ$ and standard deviation $\sigma(short) = 5.0^\circ$.

The GRB catalog is a subset of a larger trigger catalog¹⁹ which contains all the gamma-ray triggers, not just the ones that turned out to be GRBs. Most of the non-GRB triggers are identified as, for example, terrestrial flashes, solar flares, etc. and only small part of them are unidentified and may come from a SN. Majority of these unidentified triggers have very large error radius and are not suitable for cross-correlation.

5.1.3 Program scripts

SN scripts

For all three catalogs - Harvard, Asiago (HEASARC), Asiago 2014/15/16 - a *program script* was created which reads SNe parameters (Name, RA, Dec, type, etc.), either from fits or text files, into 1D-array *variables*. All three scripts are then read into a final SN script. SNe from Harvard and Asiago (Hea.) are taken till the end of 2014, and the rest are taken from Asiago 2014/15/16. SNe from Harvard and Asiago (H.) are by most part doubles (same ones), and of course only one is taken. However, a number of double SNe have a different type (or a type is more precisely determined), and if a certain type of SNe is needed then the SN is taken even if it is of that type only in one of the two catalogs.

SN double is found by matching its name, then the types are compared, and this is repeated for all SNe. Also in this way it is possible to double-check information regarding position in the sky, date, etc. For example, the distance of the doubles is calculated and it should be very close to zero or around 1 arc-second. If it is more than that it means that one of the catalogs has a wrong positional information. Then other sources of SN information can be checked to determine which of the two catalogs is in question. Often the problem is in a “typo”, a single digit in RA or Dec is entered wrong. This “typo” can give a rise to a huge or small discrepancy depending which digit is in question. The doubles with distances more or close to 1 degree were checked (about 10), while the rest were not (about 100 or more). Similar procedure has been done for dates which are more accurate in both catalogs.

The idea of the final SN script is to take all SNe from three catalogs into account and to easily select them based on type and/or date range (or any other parameter). The final SN script produces selected SNe parameters (RA, Dec, date, etc.) which can be used for cross-correlation with GRBs.

GRB scripts

For BATSE and Fermi a script has been created which reads the information from the fits file and creates variables as 1D arrays for all the GRB parameters - RA, Dec, error, date, T_{90} , etc. Within the script selection based on T_{90} , error radius or any other parameters can be done. The script with selected GRBs and their parameters can then be cross-correlated with SNe.

GRB-SN scripts

Final script uses the final SN script and a BATSE or a Fermi script. It then has all the SNe of a certain type and date range, and all the GRBs with a given T_{90} parameter. First,

¹⁹<https://heasarc.gsfc.nasa.gov/W3Browse/fermi/fermigtrig.html>

a time window (e.g. 30 days) is selected for a SN to happen after the GRB. Then, for a given SN, the script selects all the GRB with dates within time window of 30 days before the SN. Then, the distance of these GRBs from a SN position is calculated and compared to respective GRB positional errors. If a GRB error is larger than the distance to SN, that GRB is potentially connected to that SN. So, by this definition, potential connection between a GRB and a SN exists if a SN “happened” within a certain date range from a GRB and if it lies within GRB error radius. This is then done for all the SNe. In the end, all the potential GRB-SN connections are listed including their parameters. **Note:** The error 1σ radii encompass about 2/3 of GRB true positions, therefore this method is an approximation. This is related to other issues with the method which are discussed at the end of the chapter when considering future work.

Additionally:

- The time window can be given a series of values, and the script then automatically gives the number of potential connections for all the given time windows;
- If a time window is big enough, the same GRB might end up being connected to more than one SN. In this case the script can give the number of unique connections, i.e. exclude additional connections which have that GRB;
- Similar to the previous case it can also exclude connections which have the same SN but different GRBs, or, it can give the (maximum) number of GRBs any SN has associated to it for any time window;
- For GRBs, and/or SNe, random values of position and date can be selected instead of the real ones;
- In the case of random values, the script can, for example, be read into another script which can repeat the process any number of times and record connections for any number of random generated values and for all the time windows, and it can then compare it to the connections based on real positions and dates.
- The connections in different time windows are cumulative, i.e. connections in a bigger time window contain all the connections from the previous plus additional ones. In order to save time (computer resources), the script searches for connections in the first time window and then in the temporal range between the first and the second one, and so on. Then all connections are combined in the cumulative function. This is useful when repeating the process many times with different random values.
- Also, to save time, the job can be distributed to several cores in the processor. Each core can do the process for different temporal ranges or it can do entire cumulative function but for different random values. At the end all the results can be combined.
- Within the first or the second script, any other option-calculation can be implemented relatively simply.

5.2 Analysis of long GRB - SN Ib/c connections, 2014

This section describes work done in (Kovacevic et al., 2014). The goal was to find possible new physical connections between Ib/c SNe and long GRBs detected by Fermi-GBM. Most of the GRB connected to SNe were discovered by Swift-BAT since it can localize

Δt (days)	10	20	30	40	50	60	70	80	100	120	150	200	300	400	500	r_x (%)
$N_{Ib/c}(\Delta t)$	8	9	9	13	13	15	17	18	20	26	30	42	68	81	96	12
$N_{Ia}(\Delta t)$	10	23	30	42	51	64	77	85	108	131	164	213	338	440	519	66
$N_{Iip}(\Delta t)$	2	4	8	14	16	19	19	21	26	30	39	54	82	103	124	16
$N_{IIn}(\Delta t)$	1	2	4	6	8	9	9	9	11	11	14	21	30	38	51	6
$N_{tot}(\Delta t)$	31	67	98	136	166	209	240	260	314	378	471	627	893	1139	1399	100

Table 5.3: The cumulative number of each SN type associated within the error radius of Fermi long GRBs at different time intervals after the GRB date. In the first row the considered time intervals (in days) are listed. In the following rows the number of possible associations for each type of SN, respectively Ib/c, Ia, Iip and IIn, and the total number of SNe, for each considered time interval, are listed. In the last column the percentage r_x of the total number of each SN type over the total sample is shown. For brevity columns corresponding to time windows of 90 and 110 days are not shown in the table.

GRB precise enough to allow optical follow-ups. However, Swift-BAT has a practical field of view of 1.4 sr^{20} , which is about 6 times smaller then that of Fermi-GBM (FoV more than 8 sr^{21}). Since many Fermi bursts are not well localized, it is possible that there are real physical connections between long GRBs detected by Fermi (and not detected by Swift) and serendipitously detected SNe.

An estimation was made as to how many SN-GRBs Fermi should have detected based on number of detections made by Swift. For reasons of completeness analysis was made for events with redshift $z \leq 0.2$. Up to middle of 2014 Swift has detected two such events: GRB 060218 - SN 2006aj and GRB 100316D - SN 2010bh. So, Fermi should have detected $2^{+2.6}_{-1.3} \times N_{Fermi}/N_{Swift} \approx 1\text{-}7$ SNe-GRBs within $z \leq 0.2$ up to middle of 2014. Here, $N_{Fermi}/N_{Swift} \approx 1.5$ is simply the ratio of detected long GRBs by Fermi (during its 6 years of observation) and Swift (during its 10 years of observation). This takes into account different sky coverage of both detectors, their different sensitivities and different time period of operation. The 1σ error upper and lower limit attached to number of Swift observations ($2^{+2.6}_{-1.3}$) was derived from (Gehrels, 1986) assuming Poisson distribution in counting Swift's SN-GRBs. This error translates to interval of 1-7 SN-GRBs for Fermi. Confirmed number of SN-GRBs detected by Fermi ($z \leq 0.2$, up to middle of 2014) is just one (130702A - 2013dx), which means there are probably more connections which were missed.

5.2.1 Statistics of potential connections

The sample of 1147 long GRBs from Fermi catalog up to 31 May 2014 was considered. SNe from the Harvard catalog in the time period were considered. Then with the GRB-SN script potential connections were searched in a way that SN position should be within GRB error circle and occur a given period of time after the GRB. It is assumed that GRB and SN occur \approx simultaneously. Since discovery of SN might correspond to period before-during-after maximum (and maximum can happen at different times), in order to determine optimal period of time, the script was run for many time windows. This was done also to help differentiate real connections from coincidences. To further help resolve this, the same process was done for other types of SNe known not to be connected to GRBs, such as type Ia or II. In the Table 5.3 number of potential connections is listed for different SN types and different time windows.

In order to assign a probability to the numbers in Table 5.3, next steps are made:

²⁰https://swift.gsfc.nasa.gov/about_swift/bat_desc.html

²¹https://fermi.gsfc.nasa.gov/ssc/data/analysis/documentation/Cicerone/Cicerone_Introduction/GBM_overview.html

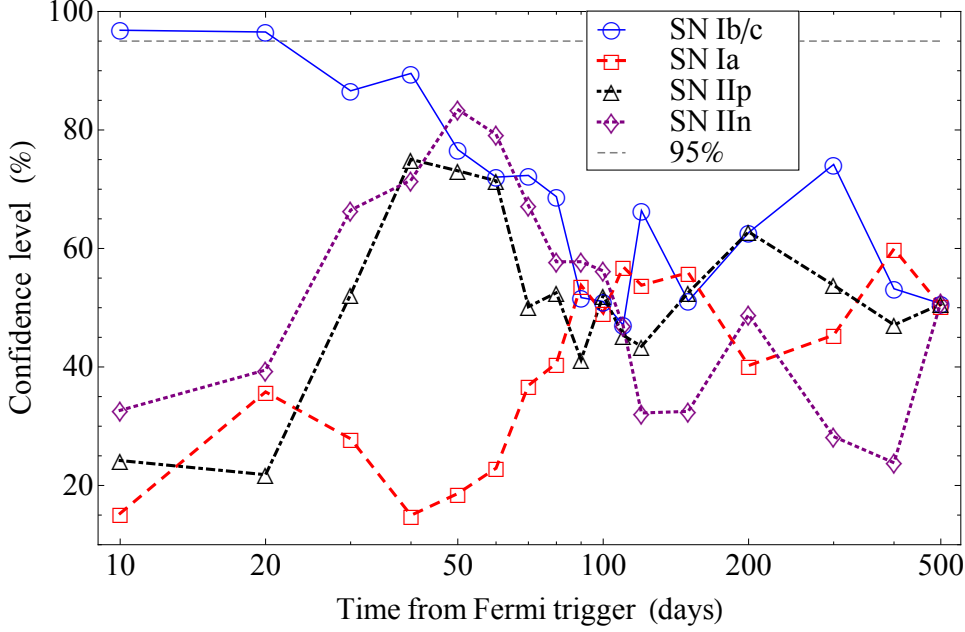


Figure 5.1: The statistical significance of the GRB-SN occurrence as a function of the temporal window. This plot shows the significance of the deviation of SNe Ib/c in the time interval $(T_0, T_0 + 20)$ days from the expected number of events assuming the relative proportion seen in the total SN sample.

Random distribution of SNe in the sky is assumed, and then spatial GRB-SN association follows the Poisson statistic, $e^{-\lambda} \lambda^n / n!$, where n is the number of observed associations and λ is the expected number of positive events, in a chosen temporal window Δt . The expected number of positive events can be evaluated from $N_{tot}(\Delta t)$ (last row in Table 5.3), times the percentage of each SN in the considered sample (see last column in Table 5.3). Therefore we have that $\lambda = N_{tot}(\Delta t) r_x$, where $x = \{\text{Ib/c, Ia, IIp, IIIn}\}$. It is then compared with the observations $N_x(\Delta t)$, and evaluated the corresponding confidence levels. In this way probability is based on comparing number of potential connections between different types. Also, in this way probability is normalized to number of connections of all the SNe (all types).

The results of the computation are shown in Fig. 5.1. A simple comparison of significance tracks reported in Fig. 5.1 between SNe Ib/c and other SN types shows that, as expected, only SNe Ib/c within $\sim 30 - 40$ days after the GRB triggers are suggestive of the existence of physical associations with GRBs. From a simple application of Poissonian statistic in regime of small numbers (Gehrels, 1986), a threshold was derived of $\geq 95\%$ confidence level, which corresponds to $\Delta t = 20$ days. In the following only associations between GRBs and SNe within 20 days from the GRB trigger are considered.

5.2.2 The sample of Ib/c connections

The list of GRB-SN Ib/c associations that the script has pinpointed is reported in Table 5.4, together with observational properties of the bursts and possibly related SNe. There are 9 cases. Five of them are known: GRB 130702A - SN 2013dx, GRB 091127 - SN 2009nz, GRB 101219B - SN 2010ma and GRB 130427A - SN 2013cq. Only the first known one has $z \leq 0.2$. For all SNe the redshift is determined from spectral observations

GRB	RA GBM (deg)	Dec GBM (deg)	Error radius (deg)	T_{90} (s)	Fluence (0.01 - 1) MeV (erg cm ⁻²)	Peak flux (0.01 - 1) MeV (photon cm ⁻²)	SN	date discovery	RA SN (deg)	Dec SN (deg)	z
090320B	183.4	49.8	9.5	29.2	1.67×10^{-6}	4.35 ± 0.25	2009di	2009 03 21	174.2411	45.0141	0.13
090426B	17.6	-19.2	18.1	16.1	6.77×10^{-7}	2.03 ± 0.18	2009em	2009 05 05	8.6855	-8.3993	0.006
110911A	258.58	-66.98	50.0*	8.96	5.94×10^{-7}	2.38 ± 0.41	2011gw	2011 09 15	112.0709	-62.3552	0.01
120121B	235.67	-39.34	7.9	18.4	1.95×10^{-6}	2.66 ± 0.21	2012ba	2012 01 21	230.6047	-38.2012	0.017
130702A	228.15	16.58	13.02	59	6.3×10^{-6}	7.03 ± 0.86	2013dx	2013 07 08	217.3116	15.7740	0.145

Table 5.4: Main parameters of the Fermi GRB sample presented here and of the supernovae associated with these bursts. Also are reported already known GRB-SN connection ($z \leq 0.2$) that were found with script in the last row of the table. * Nominal maximum value for the error radius of bursts detected by a single GBM detector.

GRB	α	β	E_{peak} (keV)	E_{iso} (erg)
090320B	-0.65 ± 0.35	-2.42 ± 0.30	62.6 ± 12.0	9.13×10^{49}
090426B	-0.50 ± 3.12	-1.65 ± 0.15	39.9 ± 76.9	1.94×10^{47}
110911A	-0.47 ± 0.50	-1.36 ± 0.18	44.8 ± 20.1	6.22×10^{47}
120121B	-0.73 ± 0.21	-2.95 ± 0.89	92.2 ± 12.2	1.39×10^{48}

Table 5.5: Results of the spectral fits of Fermi-GBM observations for the 4 GRBs with evidence of association with a SN Ic.

of the host galaxy.

The values of E_{iso} reported in Table 5.5 are derived from the spectral analysis of Fermi-GBM data of GRBs, using a Band function as spectral model and assuming SN redshift. Analysis was done with Time-Tagged Events (TTE) Fermi-GBM spectra which combine a high time resolution (up to $2\mu s$) with a good resolution in the spectral range. Spectra were fitted with RMfit package²².

GRB 090320B - SN 2009di

GRB 090320B was detected by the 10 and 11 Fermi-GBM detectors and also by Wind-KONUS. The T_{90} duration reported by Fermi is 29.2 s, while unfortunately there are no further information from Wind-KONUS for this trigger. The possibly associated SN is SN 2009di (Drake et al., 2009a), which was discovered on 21 March 2009, just one day after the GRB detection. At the moment of the discovery, the unfiltered magnitude of the SN was 18.6. Spectroscopy made with the 5.1m Palomar Hale telescope identified SN 2009di as a type Ic SN. The redshift of the SN was reported to be $z = 0.13$. The distance of the SN position and the Fermi one is 7.8 degree, while the Fermi error radius is about 9.5 degree.

GRB 110911A - SN 2011gw

GRB 090426B was observed by the detectors 3 and 5 of Fermi-GBM, with a T_{90} duration of 16.1 s. SN 2009em (Folatelli and Morrell, 2009; Navasardyan and Benetti, 2009a; Monard, 2009a), associated with this GRB, was discovered on 5 May 2009. Follow-up observations made 6 days late confirm the presence of an unfiltered magnitude 16.6 supernova. Further spectroscopic observations made around May 19 confirm the Ic nature of this SN, which corresponds to several known SNe Ic observed about one month from the maximum light, which plays against an association with GRB 090426B. The distance from the Fermi position is 13.8 degree, to be compared with an error radius of 18 degree.

²²<https://fermi.gsfc.nasa.gov/ssc/data/analysis/rmfit>

The redshift of this source was measured to be $z = 0.006$, which corresponds to a distance of 25.31 Mpc.

GRB 110911A - SN 2011gw

This GRB triggered Fermi detectors number 2 and 10. However, the signal from detector number 2 was dominated by noise, so only flux detected by number 10 is considered. This GRB was characterized by $T_{90} = 8.96$ s. SN 2011gw (Pignata et al., 2011) was discovered on 15 September by different observers, as an object of magnitude approximately 17.4. A spectrum obtained one month later, on 20 October, at NTT telescope revealed the Ib/c nature of this supernova, and a cross-check with the GELATO library found a match with other SNe at about two months post maximum. The redshift of this SN was reported to be 0.01 while the distance between the center of Fermi-GBM detectors and the SN was 48 degree, with an error radius of 50 degree. This large error box is due to the combination of two detectors that are located on the opposite sides of the Fermi spacecraft and increases the probability of a casual association for this GRB-SN event.

GRB 120121B - SN 2012ba

GRB 120121B was detected by Fermi detectors number 3 and 5 at 02h25m UTC. The T_{90} duration was 18.4 s. The best fit of the integrated spectrum of the GRB is a Band function with an intrinsic peak energy of $E_{p,i} = (92.2 \pm 12.2)$ keV. The SN associated to this GRB may be SN 2012ba (Pignata et al., 2012a). It was discovered on 21 January, the same day of the GRB trigger, as an object of unfiltered magnitude 16.6 still in rising phase. A spectrum obtained on 2 March (40 days after the discovery) with the 6.5-m Magellan II Clay telescope and then cross-correlated with the SNID libraries of SN spectra, showed a match with a type Ic SN more than 15 days after maximum. The redshift of the SN, $z = 0.017$ associated with the observed peak magnitude of 15.9, eleven days after the SN discovery, implied an absolute magnitude at maximum of -18.5, which is an upper limit to the intrinsic luminosity, considering the correction for dust extinction. This result suggests that SN 2012ba is a very luminous SN Ic, with an absolute magnitude similar to that of SN 2010bh, $R_{abs} \approx -18.5$ or even brighter, similarly to SN 1998bw $R_{abs} \approx -19$ (Bufano et al., 2012). The distance between the SN position and the Fermi center was of 4.1 degree, inside the Fermi error radius of 7.9 degree.

5.2.3 Discussion

Analysis discovered 5 GRB-SN connections within $z \leq 0.2$, and one of them was already known to be a physical association between GRB and SN: GRB 130702A - SN 2013dx. The optical afterglow of GRB 130702A (which was localized by Fermi and without Swift) was found by searching large 71 deg² area inside Fermi error circle (Singer et al., 2013). It could have easily been missed and with it, the emerging SN. The GRB was in between “cosmological” and underluminous, and had a relatively strong afterglow. The optical transient found showed signs of decreasing GRB optical afterglow (one of the reason it was identified with a GRB among numerous other optical sources in the area). Therefore, if a GRB-SN is serendipitously discovered before or close to maximum, it should show signs of decreasing GRB afterglow, unless the GRB is underluminous ($E_{iso} \sim 10^{48}$ erg) and its afterglow is week. So, the potential missed connections are most probably the ones that involve underluminous GRBs. That being said, it should be noted

that known GRB-SNe were observed with numerous and strongest optical instruments which were “staring” at a predefined position. Normal SNe are discovered by chance and observed by various instruments at various times, and even if a SN has a presence of an additional GRB-decaying-afterglow-like component, it might be missed.

After examination of the data, only SN 2012ba seems to be good candidate for being physical associated with a GRB (120121B). SN 2012ba was of type Ic and reached quickly a very bright maximum magnitude $R_{abs} \simeq -18.5$, about 11 days after the GRB trigger, which is very similar to the typical rising time and high luminosities of SNe associated with GRBs. To date there are only two other SNe associated with GRBs and classified as “Ic” (rather than “broad lines” Ic or Hypernovae): SN 2002lt, associated to GRB 021211, and SN 2013ez, associated to GRB 130215A. However, these observations do not imply that GRBs may be associated with “standard type Ic SNe”. We note that in all three cases, 2012ba, 2002lt and 2013ez, SN spectra were secured 20-40 days past maximum, therefore even if the pre-maximum spectra showed significantly broader lines, than observed in the post-maximum spectra, this difference shortly vanished after maximum (if the SN ejecta carry little mass) such that it is not easy to distinguish between the two types of SNe. The isotropic energy of this Fermi GRB-SN candidate is $E_{iso} = 1.39 \times 10^{48} \text{erg}$, which implies that this burst likely belongs to the low-luminosity subclass of GRBs.

Now, it is possible to independently estimate, admittedly on the very scanty statistic of one single object, the rate ρ_0 of local low-energetic long GRBs - type Ic SNe. For that a maximum distance of GRB 120121B for it to be detected by Fermi is needed. This can be estimated by examining count curve (in rmfit for example) of the burst in the most illuminated detector. The ratio of *unknown* peak of the curve (signal coming from maximum distance) to the square root of the *known* background (noise) is set to Fermi-GBM significance threshold of 4.5 (Band, 2003). From there the *calculated* peak (at maximum redshift/distance) is compared to the *known* actual peak (at $z = 0.017$), and the maximum redshift is calculated, and from there, the maximum (comoving) volume V_{max} . Background in Fermi-GBM oscillates at different points in orbit and orientation of the spacecraft, and the signal from GRB also depends on the orientation, etc. but the simplified approach is good enough for an estimation of z_{max} which will again be used for final estimation of rates. The maximum redshift for GRB 120121B to be detected by Fermi-GBM is $z_{max} \approx 0.021$.

The estimated rate can then be written as:

$$\rho_0 = \frac{N_{LE}}{V_{max} f_F T} , \quad (5.1)$$

where $N_{LE} = 1$ is the number of found physical connections, $f_F \approx 0.7$ the average ratio of Fermi-GBM solid angle over the total one, and $T = 6 \text{ y}$ the Fermi observational period. From there a local rate for this GRB - SN Ic events of $\rho_0 = 77^{+289}_{-73} \text{ Gpc}^{-3} \text{ yr}^{-1}$, where the errors are upper and lower limit determined from the 95% confidence level of the Poisson statistic for a single count (Gehrels, 1986). It is important to note here that Fermi might have detected more SN-GRBs that were missed, not just by direct observations, but also here, simply because the SN wasn't detected (directly or serendipitously). In other words, other GRBs in the Fermi GRB catalog might be SN-GRBs but the accompanying SN is not in the SN catalogs for the script to match it to the GRB as a potential pair. So, the $N_{LE} = 1$ in the formula is in a sense a minimum.

There is growing body of evidence that low luminosity GRBs are less beamed than high luminosity GRBs, indeed f_b^{-1} is of the order of 10, or less (Guetta and Della Valle, 2007).

After taking into account this correction derived value is $\rho_{0,b} \leq 770^{+2890}_{-730} \text{ Gpc}^{-3} \text{ yr}^{-1}$, which is consistent with $\rho_0 = 380^{+620}_{-225} \text{ Gpc}^{-3} \text{ yr}^{-1}$ in (Guetta and Della Valle, 2007), $325^{+352}_{-177} \text{ Gpc}^{-3} \text{ yr}^{-1}$ in (Liang et al., 2007), and $230^{+490}_{-190} \text{ Gpc}^{-3} \text{ yr}^{-1}$ in (Soderberg et al., 2006b). This analysis confirms the existence of a class of more frequent low-energetic GRBs - SNe Ic, whose rate is larger than the one obtained extrapolating at low redshifts the rate for high-energetic bursts, i.e., $\rho = 1.3^{+0.7}_{-0.6} \text{ Gpc}^{-3} \text{ yr}^{-1}$ (Wanderman and Piran, 2010).

5.3 New statistical approach

5.3.1 On randomness

Regarding the cataloged supernovae:

- Distribution of SNe in the sky is not isotropic. The area around galactic equator has almost no SNe due to dust extinction of the galactic plane. There are clusters of SNe in the sky due to nature of observational programs and constraints.
- SNe are not detected with a constant rate. Number of detected SNe increases over the years as optical instruments become more numerous and sensitive. This is especially the case when considering the sample of SNe used in this work, namely the Asiago catalogs for 2015 and 2016 which together have around 1800 SNe, while the total number of SNe in the sample (starting from SN 1885A) is around 8300.
- There is a correlation between SN positions in the sky and detection dates with annual periodicity due to orbit of Earth around the Sun. Again, clustering can occur here.
- All above mentioned is present to a different degree for different types of SNe.

This can be seen on Figures 5.2, 5.3 and 5.4. In the figures type Ia SNe were chosen since their large number shows best different biases. Additionally, another type was used (Ib/c) to show that these biases are to a different degree for different type. Of course intrinsically SNe are distributed isotropically in the sky and they occur at a constant rate. It is the observations that make detected SNe appear biased.

GRB sky positions and detection dates are approximated as uniformly random. Both CGRO-BATSE and Fermi-GBM are space-based detectors. Their detectors are composed of several smaller detectors which are oriented to cover all the sky simultaneously. Gamma-rays do not suffer from passage in interstellar medium as optical photons do. The only obvious bias and periodicity is due to orbit of satellites around the Earth - as Earth occults part of the sky, satellites pass through South Atlantic Anomaly (SAA)²³, and background rates (which affect sensitivity) vary. Orbits of both satellites are about 90 min which is much smaller than the smallest time period (10 days) used in the search for potential connections between GRBs and SNe and this periodicity bias is “smoothed out”. The main biases which are not smoothed out are the lesser exposure of equatorial plane due to blockage of Earth, and different degree of exposure between two poles exists due to SAA (Hakkila et al., 1998, 2003). The approximation is extended to the error radii of

²³Place above Earth, at the height of Fermi and CGRO orbits, where the Earth’s magnetic field is different so the radiation from the Sun can reach “below” and disrupt instruments on satellites.

GRBs, and duration, which are assumed not to be correlated to position in the sky and/or detection date. The issue with exposure maps will be addressed in more detail at the end of the chapter when discussing future work.

The biases in GRB position and dates are significantly less than those of SNe. The contrast regarding isotropy and detection rates between GRBs and SNe can be seen on Figures 5.2, 5.3 and 5.4.

5.3.2 Confidence level

To calculate the probability that potential GRB-SN connections are physical, i.e. to calculate confidence level (CL), information on random (non-physical) connections should be known. This can be estimated (like in the work of 2014) as comparing number of connections of different SNe types to each other and normalizing them all to number of connections for all types. Or, calculating expected number of random connections based on SNe rates, GRB rates, and GRB error radius and assigning certain distribution to it (like Poisson for example). However large non-uniformity of SNe makes this difficult.

To overcome this, only GRBs or SNe have to be uniformly random, not both. In this case uniform randomness of GRBs is assumed. The given GRB positions and dates (the original ones) can be imagined to be one set of infinite number of GRB sets with uniformly random positions and dates. To find distribution of number of coincident connections, GRB positions in the sky and dates should be randomized many times while keeping the original SN positions and dates the same. The original values of GRB error radii are used. Then, all the different obtained number of connections for each set of random GRBs (the frequency of these numbers), will show the distribution of random connection number. The more random sets of GRBs there are, the obtained distribution is closer to true distribution. This distribution is discrete as number of connections is a whole number. It is the specific non-randomness of SNe (coupled with given GRB error radii) that dictates this distribution. Then, the original number of connections (based on original GRB positions and dates) should be compared to this distribution.

With randomizing GRBs any physical connection that exist in the original GRB set, will be erased. So, if there are physical connections, the original number of connections (physical + random) should be higher than the number of connections obtained from random GRB sets. The percentage of different GRB sets that gives number of connections lower than the original one will then be the CL. So, for example, if a $CL = 95\%$ then it means that in 95% cases the random GRBs will give less connections than the original one. Then, the value of $1 - CL$ (5%) gives the probability that the given number of connections is due to randomness, i.e. that there is not a single physical connection. In a sense, physical connections are *signal* while random connections are *noise*. If number of original connections is zero, then, CL is set to zero.

This may be considered as a type of Monte Carlo simulations. In this way it really doesn't matter what is assumed for underlying distribution of random connection number - Poisson (λ), Log-normal (μ, σ), or if it can be approximated by analytical function - the distribution, and with it the CL, are obtained directly. Once more to note that the original GRB positions and dates have to be random for this to work, otherwise the obtained distribution wouldn't correspond to the real one.

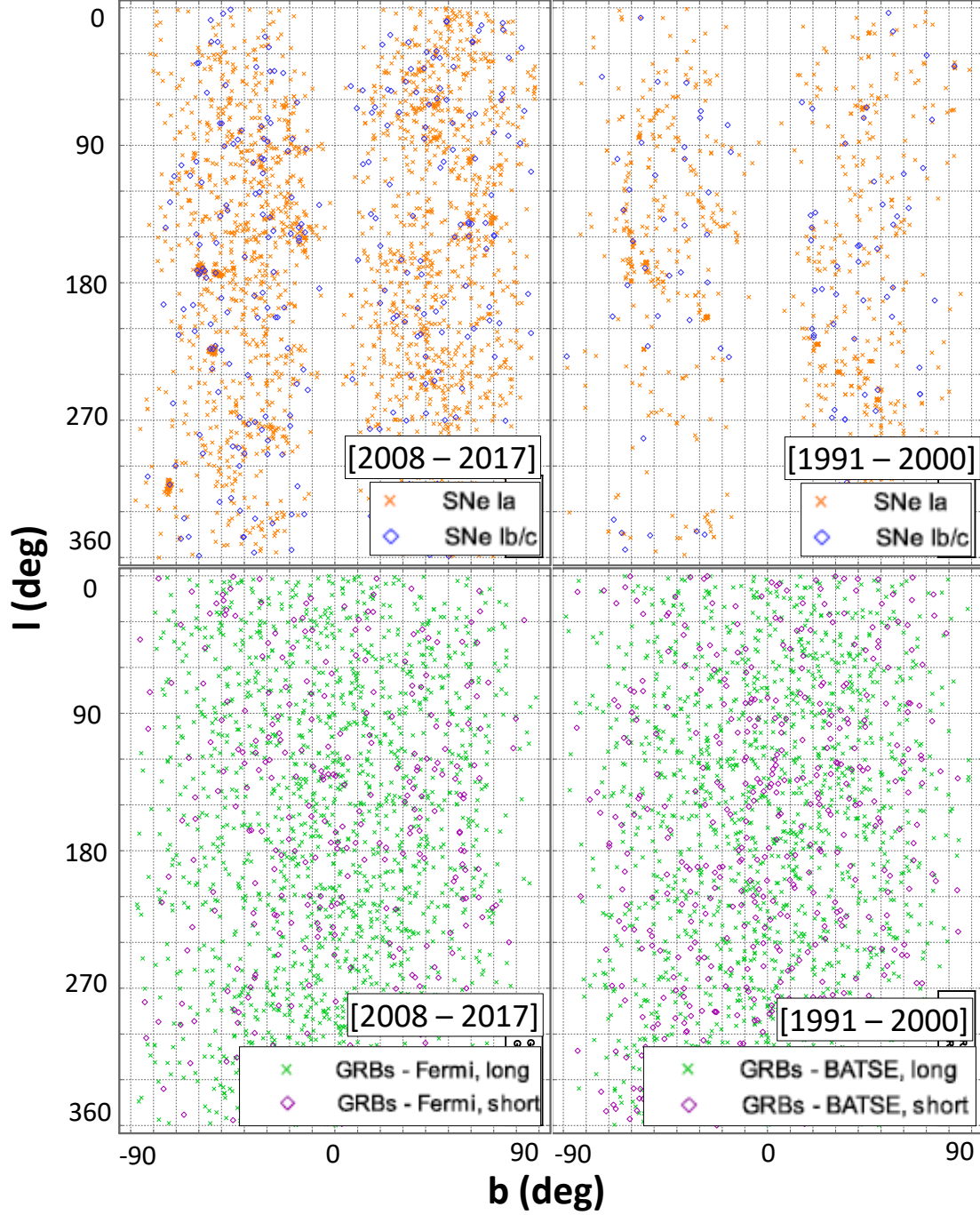


Figure 5.2: Positions of SNe and GRBs in the galactic coordinates - galactic longitude l and latitude b in degrees. **Upper-right:** SNe during the time interval of BATSE operation (1991 - 2000), plus couple of years more - around 750 Ia and 100 Ib/c. There are almost no SNe in the direction of galactic disk and there is a clustering in the shape of a large arc in the lower-left part. **Lower-right:** BATSE GRBs - about 1550 long and 500 short. Both long and short bursts are approximated as uniformly random. **Upper-left:** About 2200 Ia and 270 Ib/c SNe during the Fermi period (2008 - 2017). Again, absence of SNe in the galactic disk area, and clustering of SNe in certain patches of the sky. **Lower-left:** Fermi-GBM GRBs - about 1650 long and 320 short. Both long and short bursts are approximated as uniformly random. **Note:** Projection of the sky is on the flat rectangle surface. The area of the sky decreases and finally goes to zero as galactic latitude approaches $|b| \rightarrow 90^\circ$. Lesser number of bursts (and SNe) at higher/lower latitude is due to this.

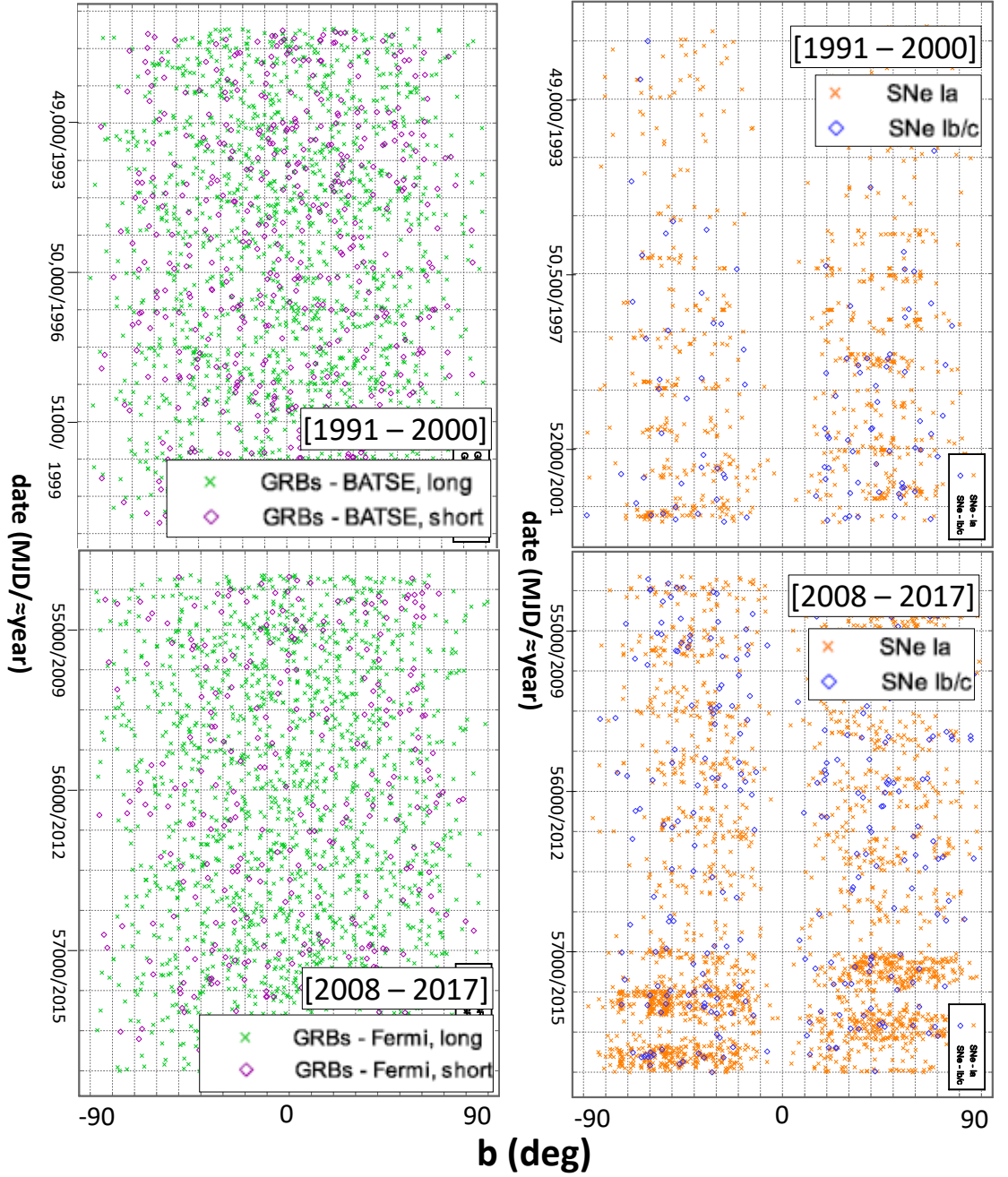


Figure 5.3: Correlation between SNe&GRBs dates with position (galactic latitude). Date is measured in Modified Julian Date, and galactic latitude b in degrees. The number and date intervals of GRBs and SNe is the same as in the previous figure. **Upper-right:** SNe during the time interval of BATSE operation (1991 - 2000), plus couple of years more. Number of detected SNe grows over passing years. Additionally, there is an annual periodicity in detection of SNe with respect to galactic latitude. SNe detections oscillate between upper and lower half of the (galactic) sky every year (switch happens every half a year). **Upper-left:** BATSE GRBs. Both long and short bursts are approximated as uniformly random on this plane, i. e. there is no correlation between position (latitude) and date. **Lower-right:** SNe during the Fermi period (2008 - 2017). Again, SNe detections increase over passing years and the same annual periodicity is present. Additionally, very large increase of SNe in the year 2015 (MJD \approx 57.000) and 2016 is present. Also, this large increase is mostly affecting SNe Ia while not so much SNe Ib/c. **Lower-left:** Fermi-GBM GRBs. Both long and short bursts are approximated as uniformly random on this plane. **Note:** Note on the projection of the sky is the same as in the previous figure.

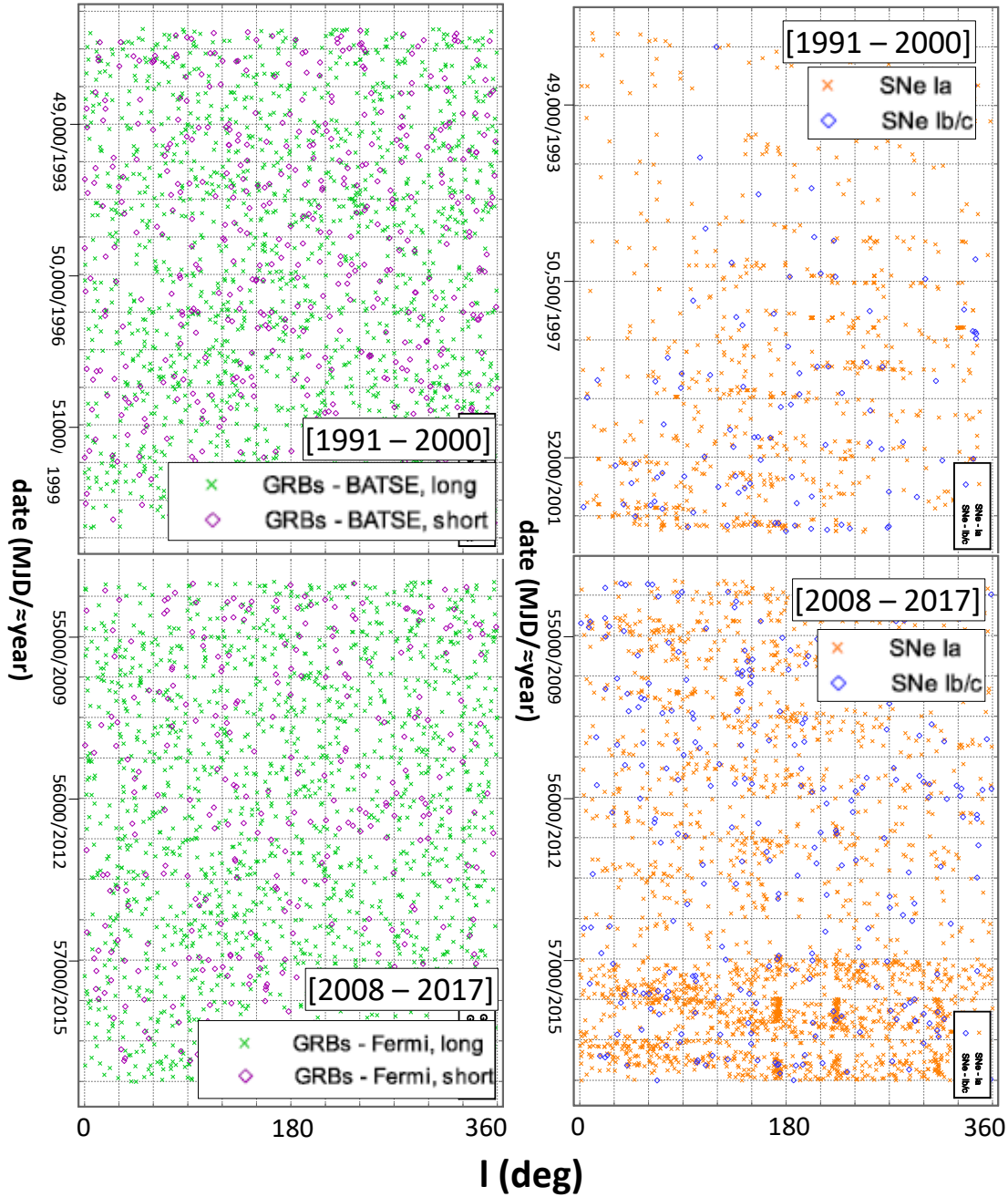


Figure 5.4: Correlation between SNe&GRBs dates with position (galactic longitude). Date is measured in Modified Julian Date, and galactic latitude l in degrees. The number and date intervals of GRBs and SNe is the same as in the previous figure. **Upper-right:** SNe during the time interval of BATSE operation (1991 - 2000), plus couple of years more. Similar to the case of date-latitude plot: Number of detected SNe grows over passing years; there is an annual periodicity in detection of SNe with respect to galactic latitude. **Upper-left:** BATSE GRBs. Both long and short bursts are approximated as uniformly random on this plane. **Lower-right:** SNe during the Fermi period (2008 - 2017). Similar to the previous cases: SNe detections increase over passing years and there is annual periodicity; very large increase of SNe in the year 2015 (MJD \approx 57.000) and 2016 is present and it is mostly due to SNe Ia while not so much SNe Ib/c. Additionally, there is clustering of Ia SNe in the plot as many have very similar latitude in a relatively short period of time (around years 2015, 2016). **Lower-left:** Fermi-GBM GRBs. Both long are approximated as uniformly random on this plane.

5.3.3 Generating random positions and dates

Random positions of GRBs in the sky are generated by generating random RA and Dec. RA is generated as a uniformly random number (with several digit decimal precision) between $0 \leq RA < 360$.

If Dec (δ) was generated as a uniformly random number, GRBs would be uniformly random on RA-Dec flat plane but on the sky they would concentrate toward the poles. To generate Dec it has to be taken into account that with $|\delta| \rightarrow 90^\circ$, the area of the sky shrinks as $\cos \delta$. So, δ should be generated as random numbers with $\cos \delta$ dependency. Since many random number generators generate uniformly random numbers (or non-uniform but corresponding to Poisson, Gauss, and other famous distributions), in order to generate random numbers in a range $x \in [x_{min}, x_{max}]$ with certain $f(x)$ dependency, it has to be obtained from uniform random numbers. To do this, an integral function $F(x) = \int f(x) dx$ is needed; then random uniform numbers in the range $x_u \in [F(x_{min}), F(x_{max})]$ should be generated; then each of these numbers should be transformed to $x = F^{-1}(x_u)$ (inverse function); then the random numbers x will be in the range $x \in [x_{min}, x_{max}]$ with $f(x)$ dependency. In the case of $\delta \in [-90, 90]$ with $\cos \delta$ dependency, random numbers in the range $[-1, 1]$ should be generated (with enough decimal precision), then they should be transformed as \arcsin . Or, with trigonometry equivalence, they can be transformed as \arccos and then subtracted with 90 .

GRB dates (as MJD) are generated as uniformly random numbers in the range from minimal GRB date to maximum (for the GRBs in question: Fermi or BATSE - long or short).

Of course, number of generated RA, Dec, and dates, matches the number of original GRBs in question.

5.3.4 Removing same GRBs

It can happen that some connections share the same GRB but different SNe, especially when time window gets large enough and/or SNe of the type are numerous. This is a physical impossibility. SNe are determined with arc-second precision which means they are definitely coming from different places, and for them to share an event which happens at the same time is not possible. So, the connections which have a GRB that is already in another connection with a different SN, are ignored by the script. This reduces the number of random connections and decreases the *noise* making physical connections stand out more.

It can happen (when finding connections with original GRB set) that a physical GRB-SN connection exists and that GRB is also randomly connected to other SN(e). Since the number of connections for different time windows is a cumulative function, it doesn't matter which connections are excluded. The number of connections vs. time will remain the same whether real connection remains or random one remains. Of course, if a closer examination of all GRB-SN connections is done in order to identify possible physical ones, then all the connections should be shown.

It can also happen that the same SN has more GRBs. Although there is no evidence of this, it is not a physical impossibility like the previous case. GRBs have a large error radius and some may come from the same source. For example, soft gamma repeaters, although not real GRB, are flashes of gamma-rays coming from the same source. So, these connections are not excluded.

Regarding exclusion of *different SNe - same GRB* connections (dSN-sGRB), it should

be noted that this also reflects on the distribution of number of random connections. For simplicity, if both (cataloged) SNe and GRBs were uniformly randomly distributed in the sky and occurred at a constant rate, the distribution of connections would follow Poisson statistics. From just statistical point of view, the dSN-sGRB connections are valid just as any other and they, with other connections, make all the connections which follow Poisson statistics. If dSN-sGRB connections are excluded, then the remaining connections would not follow Poisson statistic even if both GRBs and SNe are uniformly randomly distributed on the sky and time axis. The specific distribution with non uniformly random SNe is also changed by exclusion. This is taken care of by excluding the dSN-sGRB connections for all random sets of GRBs.

5.3.5 Time windows

The general assumption here is that GRBs and SNe go off approximately at the same time which is based on samples of known long GRB-SN Ib/c connections. Detection of SN happens after the explosion (usually one to several weeks). With detailed observation of the photometry and spectrum, explosion dates can be estimated but this is not certain and catalogs mostly contain dates of detection. So, in any case, SN detection should happen after the GRB and time window (TW) corresponds to the time after GRB(s) has happened. As the TW increases, more connections are added to existing ones. In this way a cumulative function of number of connections and CL is obtained.

SN dates are rounded up to the beginning of a certain day (MJD has no decimal points). GRB dates have a decimal point which points to the time of the day they occurred. So, SNe happening on the same day as GRBs will actually have a lower date by a fraction of a day. These SNe are also included in the TW - this is mainly done because most of SN dates of known GRB-SN have been fixed to the day their GRB happened although they might have been discovered after several days.

Based on known long GRB-SN Ib/c, physical connections are contained in the smaller TW and as the TW increases, they become outnumbered by random connections. So, as the TW increases CL should drop but it will not get smooth due to oscillation of random connections. Regarding the number of TWs, the more there are the higher the precision (after 100 days or more). However, the more there are the higher probability that one of them, due to simple chance, will reach very high CL and this might be mistaken for some new type of physical connection. TWs are chosen in the similar fashion as in the work of 2014: TW = [10days, 20d, 30d, 40d, 50d, 60d, 80d, 100d, 120d, 240d, 360d, 480d].

5.3.6 Example of changes to distributions for long Fermi GRBs and Ia SNe

To demonstrate how non uniform randomness of SNe and exclusion of dSN-sGRB connections affects the distribution of number of connections N (for all TW), 4 cases are considered (Table 5.6). SNe Ia were used in the time interval of Fermi GRBs, since it is clear for them. For each of 4 cases, $n = 1000$ random GRB sets were used. The $\langle N \rangle$ is average number of connections for a given TW; the $\sigma_N^2 = \sum_1^n (N - \langle N \rangle)^2 / (n - 1)$ is standard deviation²⁴ of the $n = 1000$ sample for a given TW.

In first case one uniformly random (u-random) set of SNe was generated and dSN-sGRB connections are included. Since SNe are u-random the N (for a given TW) should follow Poisson distribution. Poisson distribution approximates to Normal distribution for

²⁴Sample variance.

TW (days)	10	20	30	40	50	60	80	100	120	240	360	480
u-random SNe including dSN-sGRB connections												
$\langle N \rangle$	39.0	74.5	110.	145.	180.	215.	285.	354.	422.	822.	1206.	1573.
σ_N	6.13	8.47	10.5	12.1	13.2	14.5	16.7	18.4	20.4	28.3	34.6	40.8
$\sqrt{\langle N \rangle}$	6.25	8.63	10.5	12.1	13.4	14.7	16.9	18.8	20.6	28.7	34.7	39.7
u-random SNe excluding dSN-sGRB connections												
$\langle N \rangle$	37.6	69.5	99.4	127.	153.	179.	225.	267.	305.	477.	594.	679.
σ_N	5.79	7.70	9.11	10.2	10.8	11.4	12.5	13.3	13.9	14.8	15.5	15.9
$\sqrt{\langle N \rangle}$	6.13	8.34	9.97	11.3	12.4	13.4	15.0	16.3	17.5	21.8	24.4	26.1
Original SNe including dSN-sGRB connections												
$\langle N \rangle$	39.0	74.3	110.	145.	180.	215.	286.	356.	425.	837.	1234.	1623.
σ_N	7.61	11.6	15.3	18.1	21.4	24.4	30.4	35.7	40.4	65.7	88.1	110.
$\sqrt{\langle N \rangle}$	6.25	8.62	10.5	12.0	13.4	14.7	16.9	18.9	20.6	28.9	35.1	40.3
Original SNe excluding dSN-sGRB connections												
$\langle N \rangle$	32.0	55.9	77.1	96.1	114.	131.	162.	191.	218.	358.	456.	527.
σ_N	5.41	7.07	8.44	9.03	9.82	10.2	10.9	11.6	12.2	14.6	15.7	16.1
$\sqrt{\langle N \rangle}$	5.66	7.47	8.78	9.80	10.7	11.4	12.7	13.8	14.8	18.9	21.4	23.0

Table 5.6: Details are given in the text.

larger values of expected value²⁵. So, if the distribution is Poisson, the σ_N should be equal to $\sqrt{\langle N \rangle}$ which is the value of standard deviation for Poisson distribution. As can be seen in the first case, these values are very close.

In the second case, one u-random set of SNe was generated and dSN-sGRB connections are excluded. It can be seen that σ_N and $\sqrt{\langle N \rangle}$ have different values compared to previous case (especially for large TW when dSN-sGRB are more numerous). So, the distribution cannot be considered Poisson when excluding dSN-sGRB connections even though SNe (and GRBs) are u-random.

In the third case, original set of SNe was used and dSN-sGRB connections are included. It can be seen that σ_N is about twice larger than $\sqrt{\langle N \rangle}$.

In the fourth case, original set of SNe was used and dSN-sGRB are excluded. It can be seen that σ_N and $\sqrt{\langle N \rangle}$ have different values, and different proportions than in the previous case.

It can also be seen how for large number of Ia SNe, excluding dSN-sGRB drastically lowers number of connections, especially for larger TWs. The u-randomness of SNe and inclusion/exclusion of dSN-sGRB affects the number of connections, and at a different level for different TWs.

Note: Running simulation for any given case again, changes each of the values on the order of 1%.

For other types of SNe this differences are lesser because of their smaller number which makes their non-u-randomness less clear.

5.4 Analysis of long GRB - SN Ib/c connections, 2017

Here an analysis similar to the one of 2014 will be repeated with extended catalogs of GRBs and SNe (as defined in section 5.1) and new statistical approach (section 5.3). The confidence levels (CL) for long Fermi and BATSE bursts are presented in Table 5.7 and Figure 5.5.

The CLs in Figure 5.5 are also presented as $(1 - CL/100)^{-1}$. For example, increase of CL from 50 to 59 practically doesn't change anything, while the same amount of increase

²⁵Usually the limit in practice is set ≥ 20 .

TW (days)		10	20	30	40	50	60	80	100	120	240	360	480
Fermi													
Ib/c	N_0	10	12	17	20	22	26	34	43	52	95	138	157
	$\langle N \rangle$	4.77	9.04	13.14	17.13	21.10	25.01	32.62	39.97	47.16	87.98	123.8	154.1
Ib/c*	N_0	6	7	12	15	17	21	29	38	47	90	133	152
	$\langle N \rangle$	4.77	9.04	13.14	17.13	21.10	25.01	32.62	39.97	47.16	87.98	123.8	154.1
Ia	N_0	29	49	71	80	104	119	143	179	208	319	436	501
	$\langle N \rangle$	32.04	56.14	77.28	96.55	114.46	131.2	162.3	191.1	218.3	358.5	456.7	527.7
IIn	N_0	2	3	5	7	9	11	11	13	13	34	60	72
	$\langle N \rangle$	2.33	4.41	6.51	8.58	10.60	12.62	16.58	20.43	24.20	46.01	66.36	85.05
IIb	N_0	2	4	4	5	7	11	13	17	20	40	60	72
	$\langle N \rangle$	1.72	3.30	4.85	6.41	7.93	9.43	12.41	15.34	18.26	34.76	49.90	63.40
IIP	N_0	8	12	18	23	33	39	46	58	66	117	157	207
	$\langle N \rangle$	6.10	11.49	16.71	21.87	26.89	31.81	41.43	50.80	59.82	109.90	152.4	187.1
BATSE													
Ib/c	N_0	1	1	2	2	2	2	2	2	2	6	9	16
	$\langle N \rangle$	0.338	0.635	0.94	1.25	1.56	1.86	2.47	3.08	3.69	7.61	11.97	16.65
Ib/c*	N_0	0	0	1	1	1	1	1	1	1	5	8	15
	$\langle N \rangle$	0	0	39	29	21	15	7.9	4.2	2.3	12	8.6	30
Ia	N_0	3	9	9	10	15	17	22	27	29	58	76	101
	$\langle N \rangle$	2.80	5.27	7.65	9.89	12.19	14.43	18.78	23.05	27.27	53.22	77.54	98.79
IIn	N_0	0	0	0	0	1	2	2	2	2	6	8	12
	$\langle N \rangle$	0.289	0.565	0.841	1.11	1.37	1.63	2.17	2.69	3.22	6.46	9.78	13.02
IIb	N_0	0	0	0	0	0	1	1	1	2	2	3	4
	$\langle N \rangle$	0.039	0.074	0.111	0.145	0.183	0.214	0.283	0.349	0.417	0.830	1.29	1.86
IIP	N_0	1	1	1	1	1	1	1	1	1	3	5	7
	$\langle N \rangle$	0.142	0.278	0.396	0.528	0.656	0.780	1.04	1.30	1.57	3.10	4.72	6.54
		87	77	67	59	52	46	35	26	20	40	48	52

Table 5.7: Number of original connections N_0 , average number of connections $\langle N \rangle$ for $n = 10,000$ random GRB sets, Confidence level CL defined as percentage of times random GRB set gave number of connections N lesser then the original N_0 . The decimal places in $\langle N \rangle$ correspond to error estimated as σ_N/\sqrt{n} . Repeating the process for another $n = 10,000$ gives the $\langle N \rangle$ in the range of an estimated error and CL changes about $\pm 1\%$. The Ib/c* corresponds to original connections minus the known connections. **Fermi**: Number of Fermi long bursts is 1640. Number of SNe in the Fermi period: Ib/c - 273; Ia - 2203; IIn - 133; IIb - 97; IIP - 347. **BATSE**: Number of BATSE long bursts is 1536. Number of SNe in the BATSE period: Ib/c - 45 (62); Ia - 453 (575); IIn - 38 (45); IIb - 5 (7); IIP - 19 (26). Numbers in parentheses correspond to BATSE period of time plus 480 days, so that the last BATSE GRBs don't have a cutoff with for larger TWs.

from 90 to 99 means 10 times higher probability. The $(1 - CL/100)^{-1}$ value gives the right proportions between different TWs and types. It is actually the number of random GRB sets needed to expect to obtain value N_0 or higher - once.

Examining Figure 5.5 it can be seen that Fermi GRB and Ib/c SNe have a high significance for $TW = 10d$. This is due to 5 known connections, 4 of which have SN dates that have been set to the date of the corresponding GRB. The CL for Ib/c without known connections do not show high statistical significance. For BATSE the relatively high CL for $TW = 10d$ is due to single connection which is also the only known BATSE connection. Without it the CL falls even less. For BATSE different types for different TWs have a CL higher than Ib/c for $TW = 10d$. This is probably just a coincidence since there are many CLs with many TWs. It is interested to note, however, that types IIb and IIP have a relatively high significance for $TW \sim 10d - 500d$ for both Fermi and BATSE. It would be interesting to examine these connections in detail in some future work. Here the focus will be on Ib/c connections. Even though CLs without known connections do not show high significance doesn't mean there are no physical connections. In the coming text all connections with Ib/c SNe within $TW = 20d, 30d$ will be examined in detail.

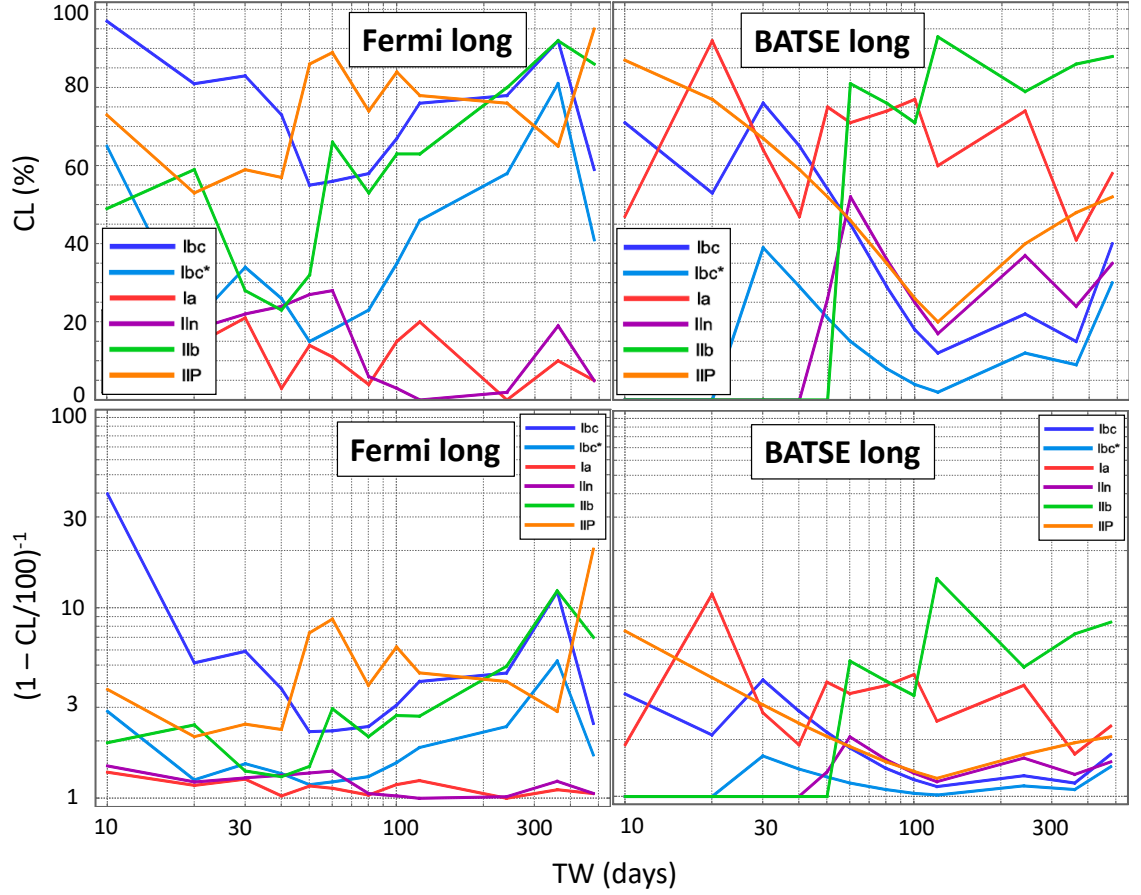


Figure 5.5: Confidence levels from the Table 5.7.

5.4.1 The sample of Ib/c connections

Unlike the case of 2014, the $TW = 30d$ was chosen, not based on CLs, but on the fact that SN may be discovered up to several weeks after maximum and maximum time occurs 10-15 days after the SN-explosion/GRB. To discriminate between coincidences and possible physical connections, SN will be examined further, mainly the time of the explosion and maximum, and absolute magnitude at these phases. The SN explosion should, of course, match the GRB date. Majority of known GRB-SNe have a higher luminosity (absolute magnitude) than ordinary Ib/c SNe, and a broader spectrum lines due to higher expansion velocity of the ejecta. SN 1998bw is taken as a typical representative of this class. Within $TW = 30d$ there are 17 connections, including 5 already known: GRB 091127 – SN 2009nz, GRB 101219B – SN 2010ma, GRB 130215A – SN 2013ez, GRB 130427A – SN 2013cq, GRB 130702A – SN 2013dx. The 12 new ones are presented in Table 5.8.

Note: In the Table 5.1 there are 7 known connections detected by Fermi. The two missing connections: SN iPTF14bfu (- GRB 140606B) is not present in the SNe catalogs used here, and GRB 081007 (- SN 2008hw) is not present in the Fermi GRB catalog although it was reported in GCN 8369 (Bissaldi et al., 2008). The SN iPTF14bfu can be taken into account in the statistics, however, there are also many other non-GRB-SNe which are not in the catalogs. Similar argument goes for the second case. The (random) GRB 110911A – SN 2011gw connection from 2014 work is not present here

GRB	ΔT (days)	SN	z	Phase	M (mag)	References
090320B	0.2	2009di	0.13		-20.1	(Drake et al., 2009b)
090426B	8.9	2009em	0.0058	max + 1m	-15.5	(Monard, 2009b; Folatelli and Morrell, 2009; Navasardyan and Benetti, 2009b)
100210	28.9	2010ak	0.037	max + 2w	-17.9	(Rex et al., 2010; Challis et al., 2010)
110307	27.0	2011bm	0.022	pre-max	-17.9	(Gall et al., 2011; Valenti et al., 2012)
120121B	0.2	2012ba	0.017	pre-max	-18.5*	(Pignata et al., 2012b)
130406	2.6	2013bv	0.06	max + 1w	-18.4	(Benitez et al., 2013; Kamble et al., 2013)
140831	23.6	2014dj	0.017	max + 2d	-17.4	(Tomasella et al., 2014)
150411	14.0	2015K	0.010	max + 1m	-16.9	(Andrews et al., 2015)
151003	21.3	OGLE15rb	0.028	max	-14.6	(Kangas et al., 2015)
160303	9.8	2016bau	0.0039	pre-max	-13	(Granata et al., 2016)
160308	22.3	2016bll	0.019	max	-16.7	(Rui et al., 2016)
160816	4.6	2016fhn	0.025	max + 1m	-15.6	(Terreran et al., 2016)

Table 5.8: Twelve potential Fermi long GRB – SN Ib/c connections within $TW = 30d$. The ΔT corresponds to time since GRB occurrence (up to 0.1d precision) to SN detection (which is rounded up to the beginning of the day of detection). Both dates are in MJD format. Only for the case of 120121B – 2012ba the exact times of the day were used since both occurred on the same day, otherwise ΔT would have been negative. The *Phase*: whether SN was in the rising, maximum, or post maximum phase at the time of detection. Day is marked by *d*, week by *w* and month by *m*. The *M* is absolute magnitude at the time of detection of SN, except for SN 2012ba where it corresponds to maximum. References correspond to information regarding SNe. The values *Phase* and *M* are approximate.

due to exclusion of GRB 110911A because of its huge error radius.

Based on SN phase, an explosion date can be estimated and compared to GRB date. In this way SN 2016fhn, SN 2015K, SN 2013bv, SN 2011bm, SN 2009em might be excluded since their estimated explosion date greatly differs from GRB date. Specifically: SN 2009em was also excluded in the previous work; SN 2013bv was recognized as a broad lined SN similar to SN 1998bw, however the estimated explosion date doesn't match the GRB one; SN 2011bm was studied in more detail and its explosion date was constrained between 19d and 22d after corresponding GRB; SN 2016fhn and SN 2015K are excluded.

Next, the absolute magnitude (luminosity) might be used. SN 2009di was detected no more than 2d after corresponding GRB. Absolute magnitude of -20 is very high, even higher than the one of SN 1998bw ($M \approx -18.5, -19$) at maximum (15d - 20d after GRB). If this SN was connected to GRB 090320B, it would imply that it was very young during detection and the magnitude would be too high for this phase. This SN was excluded also in the previous work. Supernova OGLE15rb had an absolute magnitude of -14 during maximum which makes it a weak SN and not a good candidate for GRB-SN. SN 2016bau has a very small magnitude, even for a young rising phase, and is excluded. SN 2016bll has a magnitude at maximum of -16.7, which is not in the range of more luminous GRB-SNe, and makes it an unlikely candidate.

SN 2012ba was analyzed in previous work and was considered as a good candidate for being physically connected to GRB 120121B.

GRB 100210 – SN 2010ak

Finally, only SN 2010ak is left. This SN was discovered on March 11, 2010 with apparent magnitude of 18.2. With the distance of $z = 0.037$, which makes absolute magnitude of -17.9. On March 12 (1 day later), cross-correlation with a library of supernova spectra indicated that 2010ak best matches a type-Ic supernova at a phase of roughly two weeks past maximum light. This would put its explosion date around the time of corresponding GRB 100210 (February 10, 2010). Also, absolute magnitude of -17.9 at two weeks past maximum would imply higher luminosity at maximum, similar to the one of SN 1998bw.

Although SN was classified as type Ic and not as broad lined type Ic, it should be noted that, like it was explained in the previous work, spectrum was obtained 2 weeks past maximum, and even if the pre-maximum spectra showed significantly broader lines, than observed in the post-maximum spectra, this difference might have vanished after maximum. Additionally, spectrum was obtained with low signal to noise ratio.

GRB 100210 was detected by the 2nd and 3rd NaI²⁶ detectors (n1 and n2)²⁷ of Fermi-GBM instrument. Emission in the BGO²⁸ detector is lost in the background noise. Software *rmfit* was used to view and examine the lightcurves. Due to low signal to noise ratio, it is hard to note whether or not lightcurve is a composed of a single peak or multiple peaks. The T_{90} duration in the catalog was reported to be 29s. The main emission is from $T_0 - 4s$ to $T_0 + 6s$ with T_0 being the burst trigger time. The TTE files of triggered detectors, as well as corresponding detector responses, were obtained. With various *ftool* software²⁹, TTE files were used to obtain spectrum (with background and responses) with these characteristics: time range in the main burst interval; energy channels were binned to provide enough signal to noise ratio for most of energy bins, lowest and highest energy channels were excluded as well as ones around *K-edge*³⁰ at 33 keV. The spectrum files were fit with *Xspec* software³¹. The results of the fit with power-law – exponential-cutoff model are: cutoff energy $E_c = 240^{+320}_{-100}$ keV and power-law index $\alpha = 1.25^{+0.18}_{-0.20}$ with 1σ errors. The fluence in the 10 keV – 1000 keV range for the given spectral result is 2.1×10^{-6} erg cm⁻² which corresponds to the value given in the catalog. Assuming $z = 0.037$ redshift for this burst, the isotropic energy would be $E_{iso} \approx 7 \times 10^{48}$ erg, and peak luminosity (at 1s interval) at $L_{iso}^p \approx 1 \times 10^{48}$ erg/s. This is higher than the one of GRB 980425 (SN 1998bw) $E_{iso} \approx 1 \times 10^{48}$ erg, but still in the low luminosity range.

The position of GRB 100210 (RA = 244.380°, Dec = 16.0800°) is 2.48° away from SN 2010ak (RA = 242.708°, Dec = 17.9767°) with error radius of 6.58°.

The evidence of physical connection GRB 100210 – SN 2010ak is strong as in the case of GRB 120121B – SN 2012ba, and it lies within $z \leq 0.2$ with E_{iso} significantly smaller than the ones for known connections. Like in the previous work, the rate can be estimated. The threshold redshift and volume for detection of GRB 100210 are $z_{max} = 0.052$ and $V_{max} = 0.047$ Gpc³. With period of observation of $T = 8$ years, the rate would be $\rho_0 = 3.8^{+14.2}_{-3.6}$ Gpc⁻¹ yr⁻¹ where the errors are upper and lower limit determined from the 95% statistic for a single count. This is very different than the one obtained in the previous work $\rho_0 = 77^{+289}_{-73}$ Gpc⁻¹ yr⁻¹ but the huge ranges do overlap. If the difference is real than it could mean that SN-GRB 100210 belongs to a different class of GRBs, i.e. that it is a low energetic end of classical GRBs and not in a special class of low energetic GRBs like SN-GRB 120121B was presumed to be. On the other hand, if SN-GRB 100210 does belong with SN-GRB 120121B, then the rate of occurrence may be estimated from both cases. Since the maximum volumes are different, the higher one will be taken into account, and the number of detections will be $N_{LE} = 1 + 1 \times (V_{max,2}/V_{max,1}) = 6.5$. The

²⁶Sodium iodide detectors with energy around 10 keV - 800 keV. There are 12 of them positioned on all sides of the detector. More information: https://fermi.gsfc.nasa.gov/ssc/data/analysis/documentation/Cicerone/Cicerone_Introduction/GBM_overview.html

²⁷The first detector is named n0.

²⁸Bismuth germanate detectors with energy around 500 keV - 40 MeV. There are 2 of them positioned on opposite sides of the detector.

²⁹https://heasarc.gsfc.nasa.gov/fertools/fertools_menu.html

³⁰https://fermi.gsfc.nasa.gov/ssc/data/analysis/GBM_caveats.html

³¹<https://heasarc.gsfc.nasa.gov/xanadu/xspec/>

corresponding rate is $\rho_0 = 25^{+54}_{-20} \text{ Gpc}^{-1} \text{ yr}^{-1}$ with errors same as before, but for a count of 2. Taking into account presumed beaming of $f_b^{-1} \sim 10$ the rate becomes $\rho_0 = 250^{+540}_{-200} \text{ Gpc}^{-1} \text{ yr}^{-1}$ which would put it even closer to the values of $\rho_0 = 380^{+620}_{-225} \text{ Gpc}^{-3} \text{ yr}^{-1}$ in (Guetta and Della Valle, 2007), $325^{+352}_{-177} \text{ Gpc}^{-3} \text{ yr}^{-1}$ in (Liang et al., 2007), and $230^{+490}_{-190} \text{ Gpc}^{-3} \text{ yr}^{-1}$ in (Soderberg et al., 2006b).

BATSE GRB – SNe connections

There are just two connection between BATSE GRBs and SNe in $TW = 30\text{d}$ (even up to $TW = 120\text{d}$). The one is a known and prototypical connection of GRB 980425 - SN 1998bw. The SN 1998bw (RA = 293.764° , Dec = -52.8458°) was detected, still in rising phase, around 2 days after GRB 980425 (RA = 291.910° , Dec = -53.1100°) which was 1.1° away from the SN and had an error radius of 2.3° .

The other connection is between GRB 961218A (RA = 97.7500° , Dec = -21.7300°) and SN 1997B (RA = 88.2624° , Dec = -17.8732°). GRB was 9.7° away from SN and had an error radius of 12.8° . SN 1997B (Gabrijelcic et al., 1997) was detected on January 13, 25 days after GRB. One day later inspection of a fully-reduced spectrum confirms SN 1997B to be like a type-Ic supernova, about 10 days past maximum. This would put its explosion date around the time of the GRB. The magnitude at this phase was around 16.5, and with redshift of $z = 0.010$ the absolute magnitude would be -16.7, which is a low value for a GRB-SN, 10 days after maximum. This connection is probably random.

5.5 Analysis of short GRB - SN IIn connections

Same analysis with CLs is applied to short GRBs. The CLs for short Fermi and BATSE bursts are presented in Table 5.9 and Figure 5.6.

TW (days)		10	20	30	40	50	60	80	100	120	240	360	480
		Fermi											
Ib/c	N_0	3	6	9	10	13	14	15	20	22	41	51	65
	$\langle N \rangle$	2.32	4.35	6.29	8.15	10.02	11.81	15.22	18.56	21.77	39.65	54.28	65.85
	CL (%)	59	73	82	70	80	70	43	60	49	57	27	42
Ia	N_0	11	25	32	42	50	56	68	77	91	131	152	170
	$\langle N \rangle$	14.48	24.41	32.77	40.01	46.52	52.44	63.16	72.82	81.78	124.16	148.85	164.37
	CL (%)	13	52	41	61	70	70	75	70	89	80	63	75
IIn	N_0	1	3	4	5	7	8	12	14	16	28	34	43
	$\langle N \rangle$	1.14	2.15	3.14	4.13	5.09	6.04	7.91	9.71	11.47	21.43	30.39	38.17
	CL (%)	32	63	61	60	75	74	90	89	88	91	74	79
IIb	N_0	0	0	0	1	3	4	5	8	9	20	32	34
	$\langle N \rangle$	0.848	1.62	2.37	3.11	3.84	4.56	5.99	7.36	8.70	16.30	23.15	29.14
	CL (%)	0	0	0	4.3	26	33	28	54	49	80	96	81
IIP	N_0	2	4	9	10	14	19	25	26	29	50	68	78
	$\langle N \rangle$	2.94	5.51	7.98	10.33	12.64	14.88	19.15	23.22	27.15	48.01	64.48	76.84
	CL (%)	20	19	59	42	62	84	90	71	63	61	68	54
		BATSE											
Ib/c	N_0	1	1	1	1	1	1	2	2	2	6	10	17
	$\langle N \rangle$	0.353	0.684	0.99	1.31	1.64	1.96	2.59	3.23	3.86	7.85	12.19	16.76
	CL (%)	70	51	37	27	19	14	27	16	10	20	23	49
Ia	N_0	0	5	6	6	7	8	11	12	17	42	62	76
	$\langle N \rangle$	2.81	5.22	7.53	9.72	11.83	13.92	17.93	21.82	25.63	48.37	68.09	83.80
	CL (%)	0	40	24	7.9	5.0	3.1	2.8	0.6	2.4	14	19	14
IIn	N_0	2	3	3	5	5	6	7	8	8	9	11	13
	$\langle N \rangle$	0.303	0.582	0.861	1.138	1.416	1.692	2.244	2.801	3.360	6.691	10.13	13.37
	CL (%)	96.3	97.9	94.4	99.4	98.6	99.3	99.3	99.2	97.9	77.2	56.7	41.9
IIb	N_0	0	0	0	0	0	0	0	0	0	1	1	1
	$\langle N \rangle$	0.043	0.080	0.117	0.149	0.187	0.222	0.289	0.362	0.431	0.865	1.35	1.95
	CL (%)	0	0	0	0	0	0	0	0	0	42	26	14
IIP	N_0	0	0	0	0	0	0	0	0	0	2	2	5
	$\langle N \rangle$	0.145	0.273	0.402	0.534	0.661	0.789	1.05	1.32	1.58	3.17	4.84	6.60
	CL (%)	0	0	0	0	0	0	0	0	0	17	4.7	21

Table 5.9: Same properties as in Table 5.7, only for short bursts. For BATSE IIn connections, $n = 100.000$ random GRB sets were used since CLs for some TWs exceed $CL \geq 99$.

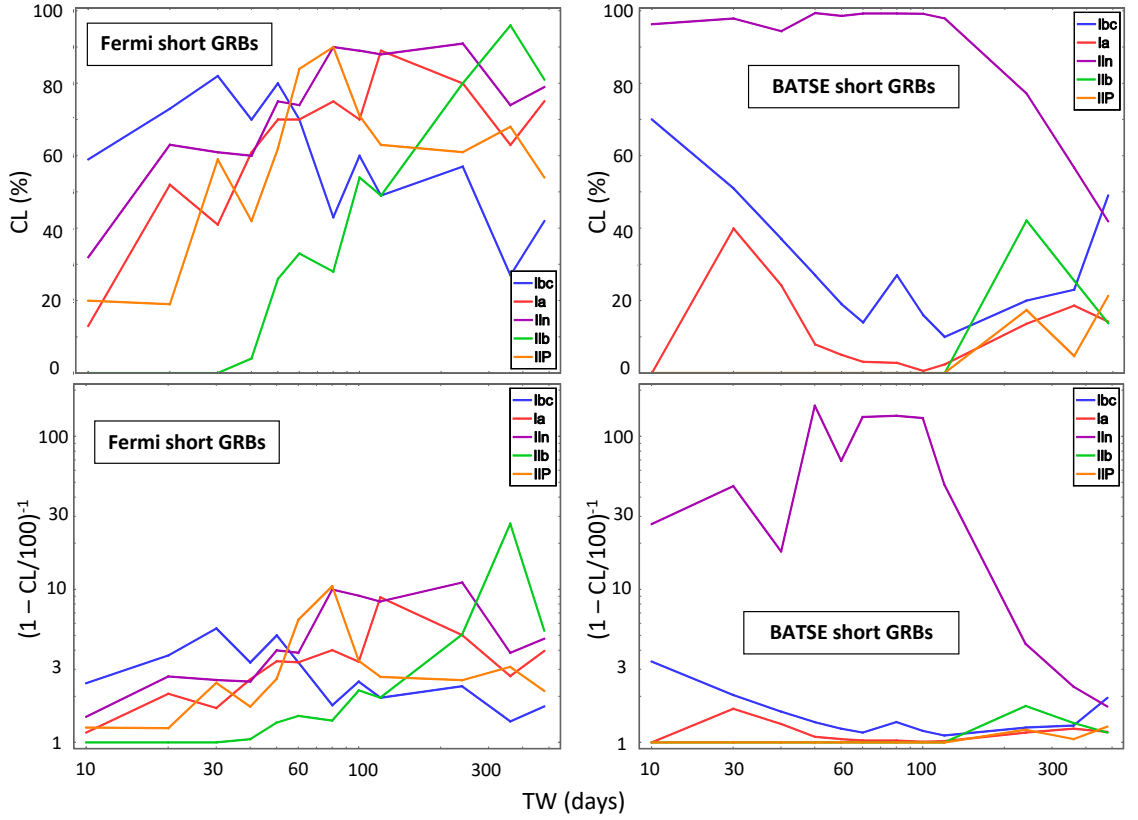


Figure 5.6: Confidence levels from the Table 5.9.

The striking feature of Table 5.9 and Figure 5.6 are very high CLs ($CL \geq 99$) for type IIn SNe and BATSE short GRBs. For Fermi bursts these SNe have a relatively high CLs in the similar TWs. Another interesting feature is relatively high CLs for IIb and IIP SNe for Fermi bursts. Since similar feature exists for the long bursts, it might imply connections which exist regardless of GRB duration. The relatively high CLs for these two types of SNe exist for BATSE long but not for BATSE short. Reason for this might be due to very low detected number of these types of SNe during BATSE period. Low CLs reflect the probability of physical connection regarding SNe in the catalog, not SNe in total. The possible connection between SNe IIb and IIP with GRBs (long and short) might be interesting to explore in a future work. Here, the possible connection between short GRB and SNe IIn will be further examined.

There are 5 CL cumulative curves for each GRB duration and space mission, which makes total of 20 CLs, each of which has 12 TWs. The BATSE short GRB – IIn is the only one that shows very high CLs but is that expected for 20 cumulative curves? To probe this a 12-point cumulative curve is generated from 48 independent Poisson distributed numbers with the same and large expected value $\lambda = 100$ and then adding them up, so that the ratio between points corresponds to ratios between TWs, i.e. the expected values in a cumulative curve are $[\lambda, 2\lambda, 3\lambda, 4\lambda, 5\lambda, 6\lambda, 8\lambda, 10\lambda, 12\lambda, 24\lambda, 36\lambda, 48\lambda]$. In order to obtain (expect) at least one point with $CL \geq 0.99$ about 20 cumulative curves are needed. In order to obtain a curve with at least 4 points having $CL \geq 0.99$ about 120 are needed. In order to obtain a curve with at least 4 points having $CL \gtrsim 0.993$ (like in the case of IIn CLs) about 200 are needed.

GRB	RA (deg)	Dec (deg)	T ₉₀ (s)	E _{iso} (erg)	Peak energy (keV)	Error radius (deg)	Distance (deg)	SN	ΔT (days)	RA (deg)	Dec (deg)	z
970308A	166.5	10.6	0.71	6.6×10^{45}	730±310	6.0	4.2	1997bs	37	170.059	12.9721	0.0024
970329B	169.7	8.8	0.46	4.7×10^{45}	400±88	4.9	4.2	1997bs	16	170.059	12.9721	0.0024
970408A	168.0	7.4	0.19	2.0×10^{45}	400±340	9.1	5.9	1997bs	6	170.059	12.9721	0.0024
970430A	259.7	44.9	0.64	3.5×10^{47}	710±260	10.5	10.4	1997cq	32	247.462	39.7556	0.032
970514A	67.6	-60.9	0.64	2.2×10^{48}	350±160	4.1	0.9	1997cy	62	68.228	-61.7160	0.064
971023B	191.4	-36.6	1.02	2.0×10^{46}	420±470	14.9	9.5	1998E	97	202.300	-33.1667	0.008
980501A	223.9	23.4	0.34	1.1×10^{47}	140±57	14.9	12.9	1998ct	59	237.799	21.9433	0.026
991002A	25.2	3.8	1.92	4.6×10^{47}	180±21	2.8	0.9	1999eb	-0.5	25.939	4.2239	0.018

Table 5.10: Sample of 8 BATSE short GRB – SNe IIn within TW = 100d. Column ΔT corresponds to time from GRB to SN detection. In the case of GRB 991002A – SN 1999eb, SN was actually discovered during the same day but before GRB. Peak energy corresponds to peak of the νF_ν spectrum. It was obtained from the BATSE spectral catalog for the power-law-exponential-cutoff model over whole burst duration. Column E_{iso} is calculated from fluence (20 keV – 2 MeV) reported in the spectral catalog for the same model and with assumption of SN redshift.

5.5.1 The sample of BATSE short GRBs – SN IIn connections

The CLs are (very) high from the beginning to the TW = 100d, 120d where $N_0 = 8$ and than it significantly drops in the next TW (TW = 240d) where $N_0 = 9$. The eight potential connections in the interval of TW = 100d are presented in Table 5.10.

SN 1997bs

The first thing to notice are 3 GRBs with similar E_{iso} (assuming the SN redshift) connected to this SN within time period of 40 days. This supernova has been an object of significant study (Van Dyk et al., 2000; Li et al., 2002; Kochanek et al., 2012; Adams and Kochanek, 2015). It is the prototypical supernova impostor - a star that ejects suddenly large amounts of material which interact with previously eject material and this causes optical emission. The optical emission is characterized by narrow Balmer lines superimposed on broader ones in the spectrum which classify them spectroscopically as IIn. The optical emission is generally weaker than standard SN. The nature of these events is such that they evolve on the order of tens of years. The most recent observations and analysis suggests that this SN might have been a real, but sub-luminous, SN (Adams and Kochanek, 2015). It is unclear at this point and more observations and time is needed.

If this SN is indeed a SN impostor, then CLs can be calculated specifically for IIn impostors. There are 38 IIn SNe during BATSE interval of 10 years (48 if additional 480 days are added). There is ambiguity also for other IIn impostor SNe, but if all the potential ones are taken into account (Kochanek et al., 2012; Habergham et al., 2014), then four of them 1997bs, 1999bw, 2000ch, (2001ac) are inside BATSE interval. This reduces number of original connections to just the one of 1997bs $N_0 = [1, 2, 2, 3, \dots 3]$ and greatly reduces connections from random GRB sets, so the CL $\gtrsim 0.9999$ for TW = 40d when the 3rd burst occurs ($\simeq 100$ more then for all IIn).

In order to probe an event of single IIn SN connected to 3 GRBs, another calculation might involve probability that a single IIn SN has more GRBs connected to it for each TW. The $N_0 = [1, 2, 2, 3, \dots 3]$ would be the maximum number of different GRBs a single SN has and so would N for all random GRB sets. In this way CL for TW = 40d is CL $\gtrsim 0.9995$ ($\simeq 50$ more then standard connection with IIn). This means that CL ≥ 0.99 for IIn doesn't imply that it probably has 3 GRBs connected to one SN, so, these 3-GRB – SN connection is an additional unique feature within very high CLs. In other words, if the CL ≥ 0.99 was due to pure randomness, than it is more likely that connections would be all single-GRB –

single-SN or maybe have one or more 2-GRB – single-SN connections.

The probability that this specific SN is connected to 3 short GRBs within 40 days can be calculated although question is what does it imply. For example, if there were many, many more SNe so that one would expect a random connection of one SN to 3 GRBs within 40 days, than that SN might be noticed and probability for chance coincidence would be extremely small for that specific SN. If all the SNe within BATSE time (including type I and II) are taken (957 in total), 1997bs still remains only one with triple connection, not just for $TW = 40$ days but for $TW = 480$ days as well. The CL for triple connection is $CL \geq 0.99$ for 40d, 50d, and 60d. This means that CL (regardless of very high CLs for IIn SNe) for having any SN connected to 3 short BATSE GRBs within $TW = 40$ days is also very high.

Looking at 3 GRBs they have E_{iso} (fluence) similar to each other. Also their $E_{\text{iso}} \sim 10^{45}$ erg is very low compared to others. This is due to very low redshift of this particular SN. This may be looked from an angle: if the triple connection is random than it is unlikely that it would be with a specific SN with very low redshift. The peak energy is typical of short GRBs. This would put these 3 GRBs in a separate group and away from the long and short GRBs in the $E_p - E_{\text{iso}}$ plane.

SN 1997cy

Another interesting case is GRB 970514A – SN 1997cy. SN 1997cy was examined in the literature (Germany et al., 2000; Turatto et al., 2000; Silverman et al., 2013; Inserra et al., 2016) while the first two references also covered its possible connection to GRB 970514A which occurred 62 days before. When it was discovered, this SN was the most luminous SN ever and was classified as type IIn. SN was in the post-maximum phase when it was discovered. Later it was understood that this SN is actually a type Ia-CSM SN, i.e. SN Ia which ejecta interacts with circum stellar medium (CSM) previously ejected by the star. The energy from the SN ejecta interacts with slow-moving CSM which causes narrow line from emission from CSM and spectral classification as IIn. The probability of physical connection to the GRB was found to be very likely if the extraordinary nature of the SN is taken into account, i.e. the probability was calculated for just that specific SN (not taking all other SNe into account) (Germany et al., 2000).

Like in the previous case CLs may be calculated only for Ia-CSM SNe. Only two such SNe during BATSE time are 1997cy and 1999E. The $N_0 = [0, 0, 0, 0, 0, 0, 1 \dots 1]$, i.e. only connection with 1997cy exists. The $CL_{80d} = 0.89$. If SN was discovered around maximum light, i.e. in the lower TW than the CL would be even higher. SN 1999E was found to be possibly connected to GRB 980910 (Rigon et al., 2003). Supernova was detected 125 days after GRB which would put it into $TW = 240d$. GRB was 4.8° from SN while its error radius was 6.6° . This connection was missed due to lack of T_{90} parameter for the GRB 980910 and this GRB wasn't included in the analysis. If all the durations are included (2695), than the peaking CLs are $CL_{80d} = 0.73$ and $CL_{240d} = 0.76$.

SN 1999eb

The corresponding burst GRB 991002 was observed also by Wind-Konus and BeppoSAX which allowed for a more accurate localization via Interplanetary Network (IPN) localization method. SN 1999eb lies outside 3σ GRB localization region (Pal'shin et al., 2013), therefore this connection is most probably a coincidence and can be excluded from

further examination. Other potential 7 GRBs were not localized by other IPN satellites for which examination has been carried out (Hurley et al., 2005a; Pal'shin et al., 2013; Hurley et al., 2010).

Although GRB 991002A – SN 1999eb is a coincidence connection, doesn't mean it should be excluded from potential connections when calculating CL , i.e. N_0 should not be set to one number lower for affected TWs. The potential connections also include coincidences. The original connection number N_0 was obtained using just BATSE GRB positions and error areas, and average number of random connections $\langle N \rangle$ was obtained from fake GRB sets using just BATSE error areas. During this process CL was obtained. If the given pair is to be excluded from N_0 then also fake GRB sets should be made with IPN-corrected BATSE error areas (for those BATSE GRBs which were detected by other IPN satellites). About quarter to a third of BATSE bursts were localized by IPN and on average reduction in error area was by a factor of 20 for one additional IPN satellite and factor of 87 for 2 satellites (Hurley et al., 2005a). This would produce lower values of $\langle N \rangle$ which would prompt rise in the CL , thereby countering reduction of CL by lower N_0 .

Of course that kind of analysis would be more accurate. It is one of the analysis discussed for future work at the end of this chapter.

Still it should be noted that this random connection is present since $TW = 10d$ and affects all the TWs. First random connection is expected to occur at $TW = 30d/40d$, therefore it can be stated that very high CLs are in part due to higher coincidence connections than would be expected.

Other SNe

For the rest of the SNe - SN 1997cq (Adams et al., 1997; Jha et al., 1997), SN 1997E (Nakano et al., 1997), SN 1998ct (Jha et al., 1998; Schwartz, 1998) - there is nothing in particular about them. They appear to be "ordinary" IIn SNe. Since the possible connection between IIn SNe and GRBs are not confirmed with many direct observations like it was done for Ibc SNe, nothing for certain can be said about explosion dates of possible pairs GRB – IIn SNe, namely do they occur simultaneously, one before the other and how much, and the brightness of SNe. At this point it is hard to further probe these 3 possible connections.

5.5.2 Fermi short GRB – SN IIn connections

From Table 5.9 and Figure 5.6 the IIn CLs are relatively high $CL \simeq 0.90$ for $TW = 80d, 100d, 120d, 240d$. Time window $TW = 240d$ has 28 unique pairs and 33 pairs in total. Several GRBs are connected to two or more SNe. There are also several connections with one SN and two GRBs, but this is expected given the sample of SNe and GRBs. Out of numerous connections 3 SNe stand out.

Supernova 2011A was studied in more detail (de Jaeger et al., 2015). It appears to be SN impostor but it cannot be determined for certain. It has special characteristics, such as double plateau in the LC, only observed before in SN 1997bs. Explosion date is estimated, with uncertainty, to be about 50 days before discovery. The corresponding GRB 101031 occurred 62 days before SN discovery. The position of GRB ($RA = 184.12^\circ$, $Dec = -7.47^\circ$) is 13.0° away from the SN ($RA = 195.255^\circ$, $Dec = -14.5263^\circ$) and GRB error radius is 16.1° . The burst had a duration of $T_{90} = 0.38$ s. Assuming SN redshift $z = 0.0089$ the GRB isotropic energy would be $E_{iso} \approx 4 \times 10^{46}$ erg and peak energy $E_p \sim 100$ keV.

Supernova 2011jb (Drake et al., 2011; Silverman et al., 2013) is a Ia-CSM. Discovery occurred about 40, 50 days after maximum. The corresponding GRB 110923 occurred 65 days before SN discovery. The position of GRB (RA = 181.4°, Dec = -1.6°) is 18.5° away from the SN (RA = 174.27°, Dec = 15.471°) and GRB error radius is 22.9°. The burst had a duration of $T_{90} = 1.66$ s. Assuming SN redshift $z = 0.084$ the GRB isotropic energy would be $E_{\text{iso}} \approx 2 \times 10^{48}$ erg and peak energy couldn't be estimated due to low fluence.

The CLs with just IIn impostors or just Ia-CSM subtypes doesn't change much with respect to CLs for all IIn SNe.

Supernova 2010mc was studied in more detail (Ofek et al., 2013; Smith et al., 2014). It is an "ordinary" IIn SN, however, it is a very interesting case because it had a pre-explosion episode which started to occur about 40 days before SN discovery (discovery date is the explosion date). If this episode existed even before, than its luminosity was smaller and couldn't be detected. The episode is defined by a month-long bump which emitted at least $E \sim 6 \times 10^{47}$ erg. The main explosion emitted $E \sim 3 \times 10^{49}$ erg. The analysis suggests that the pre-explosion episode, which occurred before SN explosion, was an outburst of material $\sim 10^{-2} M_{\odot}$ at a velocity of 2000 km s⁻¹. Shortly after the SN explosion, this ejected material was engulfed by the SN ejecta. The GRB 100706 occurred 44 days before SN detection/explosion (7 days before the pre-explosion bump). Another burst connected to this SN, GRB 100417, occurred 124 days before SN explosion, and another short one GRB 090118, 590 days before.

SNe IIn with pre-explosion activities

With improvements of optical instruments in the last decade, it became possible to detect pre-explosion activities from SNe, like SN 2010mc for example. There are still very few of these kinds of discoveries and they all involve SNe IIn. With the possible connection of GRB related to SN 2010mc and its pre-explosion episode, it is interesting to look for other possible bursts connected to such SNe (Table 5.11).

Some SNe don't have an IAU name. These are marked by the discoverer and their observational programs: "PTF" (Palomar Transient Factory), "LSQ" (La Silla Quest), "SNhunt" (Catalina Real-Time Transient Survey). The references for these transients are: 2010mc [a.k.a. PTF 10tel] (Ofek et al., 2013); PTF 10bjb, PTF 10weh, 2011ht, PTF 12cxj (Ofek et al., 2014); 2009ip (Margutti et al., 2014; Smith et al., 2016); LSQ13zm (Tartaglia et al., 2016); SNhunt248 (Mauerhan et al., 2015); 2015bh [a.k.a. SNhunt245] (Elias-Rosa et al., 2016; Thöne et al., 2017). The date column corresponds to start of the LC rise of the strongest peak which in most cases is considered as final SN explosion. For SN 2009ip this actually happened in the year 2012, i.e. SN 2009ip was a SN impostor. The column ΔT is the period of time before *date* when the pre-explosion activity started. The δt is the duration of this activity. The distance is the one between SN and GRB. The ΔT in the GRB part of the table is the period of time before *date* when the GRB occurred. The N_{exp} column is the expected random number of short Fermi GRBs within the δt period which encompass SN position with their error radius.

There are uncertainties in these parameters, especially ΔT and δt for SNe. These two depend on observation, binning of LCs, and other analysis procedures. In some cases it is also not clear whether or not the explosion corresponds to final explosion or to another SN impostor event. Some optical transients were always detectable due to their large star luminosity and they showed variations throughout the years, and in these cases it might not be clear whether an event was a pre-explosion outburst or a large variation in star

SN	Date	ΔT (days)	δt (days)	RA (deg)	Dec (deg)	Distance (deg)	GRB	RA (deg)	Dec (deg)	Error radius (deg)	ΔT [GRB] (days)	N_{exp}
PTF 10bjb	2010-05-10	100	100	192.4	-10.8							0.079
2010mc	2010-08-20	40	40	260.4	+48.1	3.7	100706	255.2	+46.9	12.5	45	0.032
PTF 10weh	2010-09-14	100	50	261.7	+58.9	8.5	100417	261.3	+50.4	9.5	150	0.12
2011ht	2011-09-26	200	200	152.0	+51.8							0.16
PTF 12cxj	2012-04-16	12	7	198.2	+46.5							0.0055
PTF 12cxj	2012-04-16	710	15	198.2	+46.5	8.6	100411	210.6	+47.9	31.7	736	0.056
2009ip	2012-09-23	60	60	335.8	-28.9	19.5	121014	320.4	-44.1	22.7	-12	0.095
LSQ13zm	2013-04-08	20	20	156.7	+19.9							0.016
SNhunt248	2014-06-05	60	60	225.0	+1.9							0.047
2015bh	2015-05-14	100	100	137.4	+33.1	5.8	150325	133.1	+37.8	10.5	50	0.079

Table 5.11: SNe with detected pre-explosion activity and corresponding GRBs. Details and explanations are given in the text.

SN	z	E_{pre} (erg)	E_{SN} (erg)	M_R (mag)	GRB	T_{90} (s)	E_{iso} (erg)	E_p (keV)
PTF 10bjb	0.026	2×10^{48}	2×10^{49}	-16.4				
2010mc	0.035	6×10^{47}	2×10^{49}	-18.5	100706	0.13	3×10^{47}	840 ± 330
PTF 10weh	0.138	5×10^{48}	7×10^{50}	-20.7	100417	0.19	2×10^{49}	250 ± 54
2011ht	0.0036	2×10^{47}	3×10^{49}	-16.8				
PTF 12cxj	0.036	9×10^{46}	8×10^{48}	-17.3				
PTF 12cxj	0.036	6×10^{46}	8×10^{48}	-17.3	100411	0.51	6×10^{47}	980 ± 2180
2009ip	0.0059	2×10^{48}	3×10^{49}	-18.5	121014	0.57	9×10^{47}	-
LSQ13zm	0.029	1×10^{48}	1×10^{50}	-18.5				
SNhunt248	0.0045	2×10^{48}	2×10^{49}	-15.0				
2015bh	0.0066	2×10^{48}	2×10^{49}	-17.6	150325	0.88	2×10^{47}	-

Table 5.12: Same rows as in Table 5.11. Column z is redshift of the SN. Column E_{pre} corresponds to radiated energy in the pre-explosion episode while E_{SN} is the energy radiated in the main SN event. Column M_R is absolute peak R magnitude of the main event. Parameter E_{iso} of GRB was calculated based on the fluence (10 keV – 1 MeV) reported in the catalog and assuming SN redshift. Parameter E_p is the peak energy for the power-law-cutoff model reported in the catalog.

luminosity. The detailed examination of the optical transients is not part of this analysis and references should be checked for more details. The N_{exp} is also an estimation and is not intended to precisely quantify the probability. If a GRB was close to the pre-explosion period but not within, then the δt was multiplied by 2, 3, etc. until it encompassed the burst. For 2009ip the focus was on its strongest period in 2012, and GRB occurred during the brightest peak (after start of its rise), but before another weaker peak which occurred about 30 days after, during the decay phase of the stronger one. For PTF 12cxj the conditions on error radius were relaxed which included GRB 100411. Since the specific SNe are in question, it should also be taken into account that if there were GRBs physically connected to them, they might have been missed if they were outside Fermi FoV (2/3 of the sky), and also, the GRB error is 1σ (2/3 of total) error. Even though it is an estimation, it seems unlikely that there would be so many random short Fermi GRBs for the selected optical transients and their periods of activity.

The physical parameters of SNe and GRBs are given in Table 5.12.

5.5.3 Short GRBs – IIn SNe, no direct evidence

Very high confidence levels (CLs) for BATSE short GRBs – IIn SNe coupled with triple GRB connection to supernova impostor SN 1997bs and previously examined connection of a GRB with exceptional Ia-CSM SN 1997cy; relatively high CLs for Fermi short GRB – IIn SNe and GRB occurrence in or close to periods of pre-explosion activity of other IIn SNe - all point to the physical connection between short GRBs and IIn SNe, i.e. SNe that can

Mission	short GRBs	long GRBs	ratio
BATSE	495	1536	$\approx 1:3$
Fermi	320	1640	$\approx 1:5$
Swift	102	948	$\approx 1:9$

Table 5.13: Long and short bursts for BATSE during entire mission period. Long and short bursts for Fermi and Swift up to 2017. For BATSE and Fermi the numbers correspond to the ones with cut on the high error radius but this doesn't change the ratio.

be of different physical origin but all have interaction with circum-stellar medium (CSM) in common. The question is then why these connections don't have any confirmed cases while long GRB – Ib/c SNe have many.

GRBs prompt emission needs to be precisely localized (arc-minute) and then soft X-ray and optical instruments may do follow-ups with arc-second or greater precision and discover GRB afterglow and later physical connection of a GRB and a SN (if there is one). For long GRBs this happened during the late 1990s and since the year 2005 Swift is responsible for majority of long GRB localizations that helped discoveries of a SN connection (Table 5.1). For short GRB the first afterglow discovery (and consequent redshift detection³²) came in the year 2005 - GRB 050509B (Berger, 2014), again thanks to Swift. Aside from two short GRBs detected by HETE-2 and one detected by INTEGRAL (which have a precise localization), all other short GRBs (about 70) were detected by Swift with at least arc-minute localization up to the beginning of 2013 (Berger, 2014) (about 100 up to the beginning of 2017). So, the question about non-detection of IIn SNe with short GRBs comes down to Swift-BAT. The online Swift catalog of GRBs is hosted here³³ where GRB information can be obtained as a text file and loaded into a program.

First thing to notice are different numbers and ratios of long GRBs to short ones for BATSE, Fermi-GBM and Swift-BAT (Table 5.13). Simply put BATSE is most suitable for detecting short GRBs, then Fermi and then Swift. In (Burns et al., 2016) it is argued that large ratio of long to short bursts for Swift (compared to Fermi) is due to larger Swift sensitivity to long bursts while the sensitivity for detecting short bursts is the same for both detectors, and that larger number of Fermi short burst is due to Fermi larger FoV. In any case, larger number of short bursts for BATSE and Fermi with respect to Swift remains. In (Bromberg et al., 2013) it is argued that division of long and short bursts for Swift should be at $T_{90} \approx 0.8$ s while for Fermi and BATSE the typical value $T_{90} \approx 2$ s is fine. This would further decrease number of Swift short bursts with respect to BATSE and Fermi. However (Burns et al., 2016) argue against such a division for Swift.

From the Tables 5.10 and 5.12, almost all good candidate short GRBs of BATSE and Fermi have isotropic energy in the range $E_{\text{iso}} \sim 10^{45} - 10^{48}$ erg, which is smaller than typical short GRB energies $E_{\text{iso}} \sim 10^{48} - 10^{53}$ erg, especially for SN 1997bs – GRB trio $E_{\text{iso}} \sim 10^{45} - 10^{46}$ erg. This is also the case for majority of Fermi GRBs within the CL_{240d} which were not selected as good candidates. However, the hardness of all these bursts (E_p) is in the range of typical short ones. Threshold for GRB detection varies on number of criteria, such as sensitivity of the detector, background rate which varies during an orbit, position of GRB with respect to detectors, trigger algorithms which may change during the course of the mission, etc; and on GRB properties itself with most important

³²Most redshift determinations for short GRBs come from identifying the host galaxy, not from afterglow spectrum.

³³https://swift.gsfc.nasa.gov/archive/grb_table/

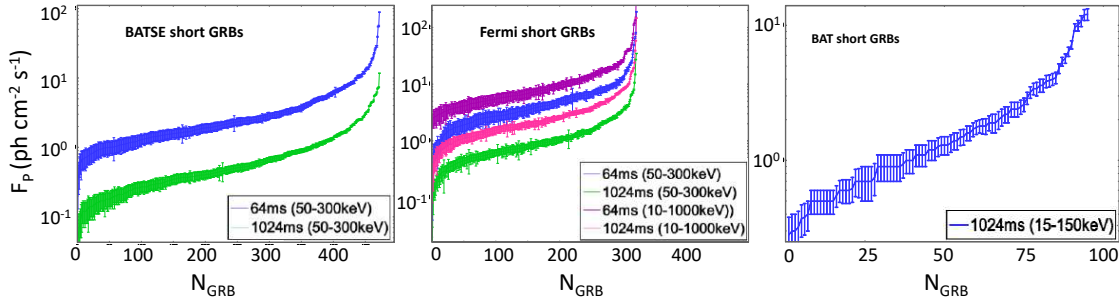


Figure 5.7: Peak fluxes of short GRBs for BATSE, Fermi and Swift with their 1σ errors. **BATSE:** F_p s for 64ms and 1024ms are presented. Due to the spiky nature of the light curve, the F_p s for longer integration time periods are, on average, less intense. Out of 495 short bursts, 472 have determined F_p s and are plotted. The plot for 256ms is not shown for clarity but is in between the two curves. **Fermi:** Same as in previous case with addition of different energy bands. As expected the F_p s for larger energy band are higher. Out of 320 short bursts, all have determined F_p s. **Swift:** Only the 1s F_p s are given. Out of 102 short bursts, 95 have determined F_p s. **Note:** Same place on the horizontal axis (N_{GRB}) for different time (ms) period curves may not correspond to the same GRB.

being the observational property *peak flux*, which depends on the E_{iso} and distance, but also on the shape of the light curve. Bursts with lower E_{iso} will *on average* give lower peak flux and these bursts will *on average* be harder to detect.

To compare the 3 instrument capabilities of detecting short GRBs, the peak fluxes (F_p) of the detected short bursts will be compared. For BATSE and Fermi F_p s are in the catalog for 64 millisecond (ms) period, 256 ms, and 1024 ms time range. Depending on the shape of the light curve, any of these (or all) may trigger the instrument. For Swift catalog, only the F_p for the period of 1s (1024 ms) is present. The energy range for F_p s are 50 – 300 keV for BATSE, 50 – 300 keV and 10 – 1000 keV for Fermi and 15 – 150 keV for Swift.

First to give an idea on the error of the F_p s, Figure 5.7 is presented. The bursts are sorted by their F_p and plotted for different instruments, different integration time ranges and energy bands.

The comparison of BATSE and Fermi F_p s is shown in Figure 5.8 with highlighted F_p s of 4 BATSE short GRBs in connection to SN 1997bs and SN1997cy. Comparing F_p s for both detectors in this way takes into account all the peculiarities of two detectors in regards of detecting short GRBs during the course of the mission times. Also, taking into account Fermi bursts till the year 2017 makes its mission time almost the same as the one of BATSE - about 9 years, so the F_p s curves can be read as sensitivity directly without considering difference in time periods. It can be seen that BATSE detected more short GRBs with lower F_p s than Fermi, and more short GRBs in total. It can also be seen that 4 GRBs in question have F_p s than are in lower part of Fermi F_p s distribution for all 3 time integration periods while for BATSE they are average. Especially the case of GRB 970408A (the lowest E_{iso}) which for all 3 time periods has F_p which is in the range where BATSE has many more detections than Fermi.

From instrument point of view this might explain the very high CLs $\text{CL} \geq 0.99$ for BATSE and not so high $\text{CL} \geq 0.90$ for Fermi. Additionally, Fermi short bursts have on average larger error radius (8.7°) then BATSE ones (7.0°). This doesn't increase the number of physical connections (if they exist) but does increase number of random connections (as er^2) which reduce CLs.

Finally the comparison of short GRBs from all 3 detectors is shown in Figure 5.9 with

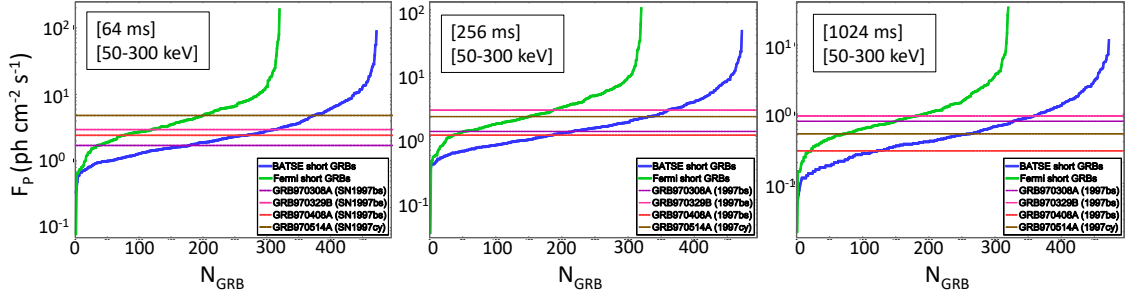


Figure 5.8: Peak fluxes of short GRBs for BATSE and Fermi and specifically the 4 good candidate BATSE GRBs, for 3 different integration time periods. Integration time periods and energy ranges are presented in the left-upper corners. Errors are not shown for clarity.

highlighted F_p s of all the BATSE and Fermi GRBs which are good candidates for physical connection. First thing to notice is significantly smaller number of detected short GRBs by Swift-BAT and higher F_p s for those bursts. The F_p s of good GRB candidates are average ones for BATSE, lower for Fermi and even lower for Swift. Additionally, good candidate GRBs have higher E_p , well above Swift energy range 15 – 150 keV which would make them even harder for Swift to detect.

If the number of physical connections for BATSE and Fermi is estimated as $N_0 - \langle N \rangle$ for CLs where it is high, than the number for BATSE would be around 5, and similar for Fermi. Given the ratio of detected short bursts for different missions, Swift should have detected one. If only the bursts with F_p s lower than the maximum $F_p \approx 1$ of a good GRB candidate are taken into account, then this number for Swift gets closer to zero, especially considering the case of GRB 970408A (lowest E_{iso}) which F_p is higher than that of just one Swift short GRB.

Detecting optical transient

Even if Swift observed some IIn-SN – GRBs, the optical transient might not have been detected by Swift-UVOT (Ultraviolet and Optical Telescope) and ground-based optical telescopes. Supernovae Ib/c connected to GRBs have by default high luminosity during maximum (which occurs regularly 10 - 15 rest-frame days after GRB) and are relatively easily detected (if they are there). For IIn SNe luminosity varies from high to low depending whether it is actually a SN (final explosion) or supernova impostor. The luminosity of final explosion may also vary and in some cases it is not clear whether an event is final SN explosion or SN impostor. Additional pre-explosion activity, which can occur tens of days or hundreds of days before final explosion, introduces even lower luminosities than those of SN impostors.

The good candidate SNe here are SN 1997bs, SN 1997cy (BATSE era) and SN 2011A, SN 2011jb, SN 2010mc, PTF 10weh, PTF 12cxj, SN 2009ip, SN 2015bh (Fermi era) (Figure 5.10).

SN 1997bs was detected around maximum phase and had an apparent V magnitude (which is close to R magnitude) of $m_V \sim 17$ and with $z = 0.0024$ gives absolute V magnitude of $M_V \sim -14$. It is unclear when was the explosion date. From most recent observations there is possibility that the event was a terminal SN explosion and not an impostor. GRB trio occurred 6, 16 and 37 days before the detection.

SN 1997cy was detected in post-maximum phase. It is unclear when was the maxi-

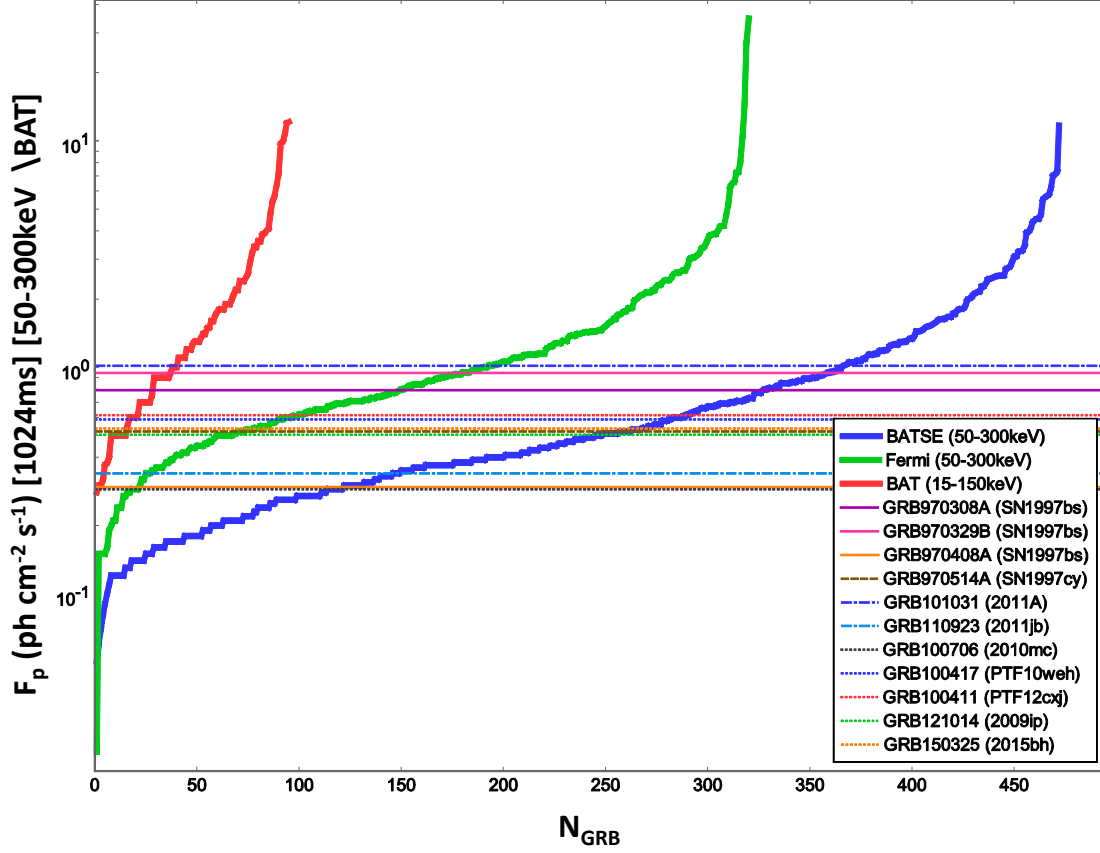


Figure 5.9: Peak fluxes of short GRBs for BATSE, Fermi, Swift and specifically the good candidate GRBs. The integration time for all the instruments is 1024 ms. The energy range for all is 50 – 300 keV except for Swift which is 15 – 150 keV.

imum and explosion date. The discovery apparent R magnitude was $m_R \sim 17$ and with $z = 0.064$ gives $M_R \sim -20$ and even more during maximum. This was a Ia-CSM supernova. The GRB was detected 62 days before SN detection.

SN 2011A was detected during maximum – post-maximum phase. It is unclear when was the explosion date. The discovery apparent R magnitude was $m_R \sim 18, 17$ and with $z = 0.0088$ gives $M_R \sim -15, -16$. The luminosity is in between normal IIn (terminal explosions) and impostors. The GRB was detected 62 days before SN discovery.

SN 2011jb was detected in post-maximum phase. It is unclear when was the maximum and explosion date. The discovery apparent R magnitude was $m_R \sim 18$ and with $z = 0.084$ gives $M_R \sim -20$ and even more during maximum. This was a Ia-CSM supernova. The GRB was detected 65 days before SN detection.

SN 2010mc was detected even before explosion. The apparent R magnitude during maximum was $m_R \sim 18, 17$ and with $z = 0.035$ gives $M_R \sim -18, -19$ at maximum. This was typical IIn SN and is considered to be final explosion. The apparent R magnitude of pre-explosion activity was $m_R \sim 22, 21$ which is $M_R \sim -14, -15$. The GRB was detected 45 days before SN explosion - several days before pre-explosion activity.

PTF 10weh was detected even before explosion. The apparent R magnitude during maximum was $m_R \sim 19, 18$ and with $z = 0.138$ gives $M_R \sim -21$ at maximum. This was typical IIn SN and is considered to be final explosion. The apparent R magnitude of pre-

explosion activity was $m_R \sim 22$ which is $M_R \sim -17$. The GRB was detected about 150 days before SN explosion - about 50 days before pre-explosion activity which itself lasted for 50 days and stopped 50 days before SN explosion.

PTF 12cxj was detected even before explosion. The apparent R magnitude during maximum was $m_R \sim 19, 18$ and with $z = 0.036$ gives $M_R \sim -17$ at maximum. This was typical IIn SN and is considered to be final explosion. The apparent R magnitude of pre-explosion activity which occurred around 700 days before SN explosion was $m_R \sim 23$ which is $M_R \sim -13$. The GRB was detected about 735 days before SN explosion - about 25 days before pre-explosion activity which itself lasted for about 15 days.

SN 2009ip was detected several times before final explosion which occurred in September 23, 2012. The apparent V magnitude during maximum was $m_V \sim 14$ and with $z = 0.0059$ gives $M_V \sim -17, -18$ at maximum. Most likely this was typical IIn SN and is considered to be final explosion, however there are some doubts. The second peak occurred 30 days after the main peak and had an $m_V \sim 15$. The GRB occurred 12 days after the main peak and about 20 days before the second.

SN 2015bh was detected before explosion. The apparent R magnitude during maximum was $m_R \sim 15$ and with $z = 0.0066$ gives $M_R \sim -17, -18$ at maximum. Most likely this was typical IIn SN and is considered to be final explosion. The apparent R magnitude of pre-explosion activity which started around 100 days before, and lasted till the SN explosion had an apparent R magnitude in the range of $m_R \sim 20 - 18$. The GRB occurred 50 days before SN explosion and in the middle of pre-explosion activity.

From the above examples it can be seen that GRB may occur several days before the main event or a minor event. In most cases optical follow-ups to Swift short bursts happen within a day or two and if there is no optical emission at that moment, it stops. In this way an optical transient might be missed if GRB occurred before it. Also, optical measurements might not have been sensitive enough to detect week pre-explosion activity if GRB occurred during it. In some cases an uncatalogued optical source was found in the error box of Swift but due to its non-fading characteristics, which is expected for GRB optical afterglows, it was dismissed as being connected to the GRB and optical observations stopped.

5.5.4 Rates

Possible physical connections are found by matching cataloged GRBs with cataloged SNe. While GRB instruments cover almost whole sky, optical ones cover very small part and many detectable SNe are missed. It is assumed that if number of catalog SNe where, for example, doubled, then on average there should be twice as more found physical connections and as many random, and the confidence levels remains similar. So the question is how many short GRBs in the catalog come from IIn SNe. To give a crude estimate the rate of IIn SNe is needed. In (Smartt et al., 2009) the estimated rate of core-collapse SNe is $9.6 \times 10^4 \text{ Gpc}^{-3} \text{ yr}^{-1}$ and percentage of IIn SNe of 3.8% in them, gives $\rho_{\text{IIn}} = 3.6 \times 10^3 \text{ Gpc}^{-3} \text{ yr}^{-1}$. In (Li et al., 2011) only general type II was considered which is $\rho_{\text{II}} = 4.5 \times 10^4 \text{ Gpc}^{-3} \text{ yr}^{-1}$ and is close to the general type II from previous work. In both works, however, it is stated that these are crude estimates.

Now, from Figure 5.10 it can be seen that most cataloged IIn SNe are in the $z \leq 0.1$ which corresponds to volume of $V \approx 0.25 \text{ Gpc}^3$. Both Fermi and BATSE operated for about $T \approx 10 \text{ y}$. So, the total number of SNe for the volume and time period should be $N_{\text{IIn}} \sim 10.000$. The number of cataloged IIn SNe during BATSE period is $N_{\text{IIn}}^b \approx 50$ and in

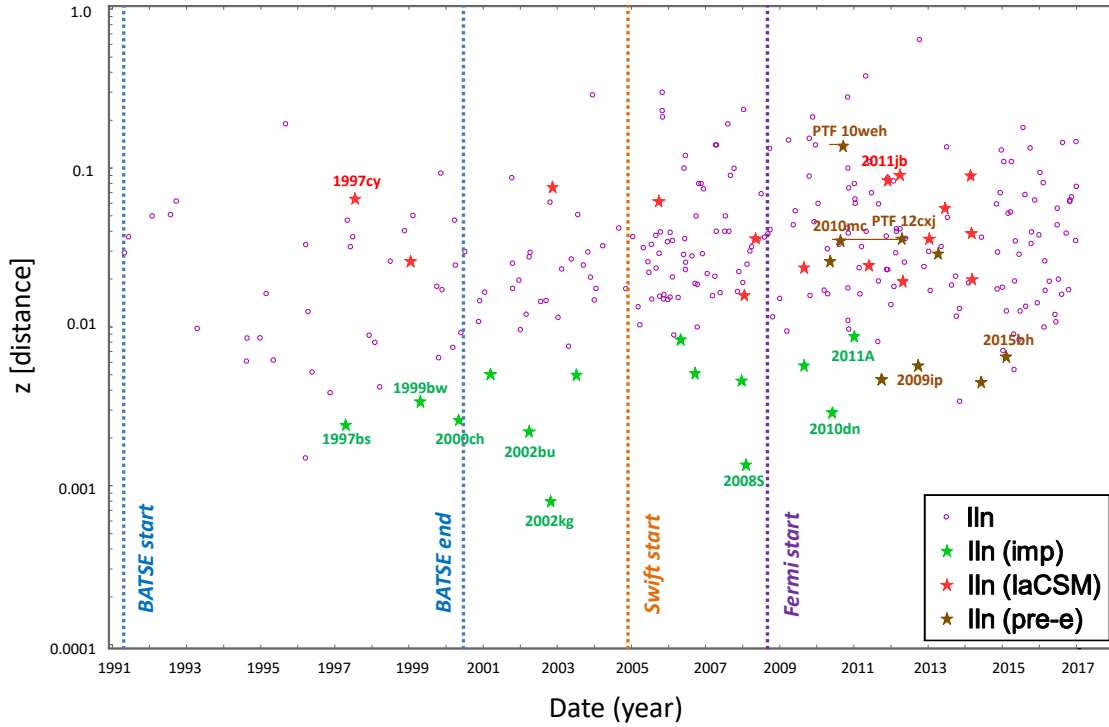


Figure 5.10: Supernovae IIn from the start of BATSE observations up to 2017. For smaller values $z \leq 0.005$ redshift corresponds to distance and not actual redshift which is affected by movement of Earth with respect to SN host galaxy. Marked SNe correspond to good candidates for physical connection to GRB. Also IIn impostors with very small distance, in the range of SN 1997bs, were marked. For SNe with pre-explosion activity (pre-e) the date corresponds to the date of the main peak. If the corresponding GRBs occurred much before than a line is added to the marker (PTF 10weh, PTF 12cxj).

Fermi $N_{\text{IIn}}^f \approx 150$. So, the catalog SNe in this volume are about ~ 100 times less in number than the entire IIn ones. Taking the number of physical connections for both instruments at ~ 5 (for both instruments they go all the way to $z \leq 0.1$), the total number of short bursts coming from all IIn SNe (not just cataloged ones) is around ~ 500 , basically the entire cataloged short GRBs. Again, these are very crude estimates.

If only GRB-trio for the close SN 1997bs ($z = 0.0024$) is considered as good candidate(s), then different results emerge. The maximum distance for detecting GRB in BATSE case is determined from the catalog parameter which corresponds to ratio of counts in second most illuminated detector, to, count threshold for that detector (for BATSE to register a GRB at least two detectors should be triggered). Only 2 out of 3 GRBs have this parameter in the catalog and maximum redshifts for them are $z = 0.0031$ and $z = 0.0047$. For simplicity the value of $z \approx 0.004$ was taken which corresponds to $V \approx 2 \times 10^{-5} \text{ Gpc}^3$. In that case the number of IIn SNe in the maximum volume and period of BATSE time would be $N_{\text{IIn}} \sim 1$ which is at order of magnitude of cataloged IIn SNe in $z \leq 0.004$. This would mean that not many more short GRBs come from IIn SNe. It is obvious from Figure 5.10 that IIn impostors (which are less luminous) are all very close since they are harder to detect at greater distances, and that they make majority of IIn SNe at lower redshifts, including SN 1997bs. Still, the general result matches order of magnitude regardless of IIn impostor special nature.

On the other hand taking into account Ia-CSM SN1997cy – GRB at $z \lesssim 0.1$ would give

the previous number of IIn SNe which is ~ 100 times larger than cataloged ones and would mean that many short GRBs in the catalog come from IIn SNe (or from Ia-CSM subtype of IIn SNe). For Fermi the good candidates span the range from very low distances to $z \approx 0.1$ and the same results apply.

If the number of IIn-short GRBs is indeed much larger, than again question might be asked regarding Swift non-detection. Even if all the previous arguments for Swift non-detection are taken into account - why out of 100 short GRBs, 30 of which have measured redshifts, all 30 of them are above $z \geq 0.1$. In Figure 5.9, the peak fluxes F_p s of good candidate GRBs correspond to 40% of Swift GRBs with lowest F_p and 8 of them have measured redshift. The uncertainty of these conclusions is large, but Swift short GRBs with measured redshifts suggest that IIn-GRBs are unlikely to make majority of short GRBs.

5.5.5 Properties of IIn-GRBs

The traditional division of GRBs to long and short comes from several observational missions. When GRBs are sorted by their duration, two peaks in the distribution can be seen with the division around $T_{90} \approx 2$ s. This division in duration is followed by the division in hardness in a way that short GRBs have higher peak energies E_p , and long bursts have smaller. There are additional features such as location in a galaxy, Ib/c SN association, etc. Two distributions are explained in literature as having different physical origin, namely the long ones are coming from death of a massive star while short ones are mergers of two compact objects. The IIn-GRBs should belong to neither of these.

Duration

The question then is why does the limit of $T_{90} = 2$ s seem also to be a limit on potential IIn-GRBs. The big difference between confidence levels (CLs) for short and long GRBs connected to IIn SNe is very clear for BATSE. For BATSE short bursts and IIn SNe, time windows of 40, 60, 80, 100 days have very high CLs and two final ones contain 8 short GRBs. Their duration of potential candidates takes the range from $T_{90} \approx 0.2$ s to $T_{90} \approx 1$ s. If all the long GRBs are taken into account (which number is 3 times higher than short), then only two additional GRBs appear in the 100d time window, one with $T_{90} \approx 10$ s and another one with $T_{90} \approx 130$ s. Changing T_{90} limit to 0.5s, 1.0s and 1.5s doesn't produce big difference, but the highest CLs are for the limit of $T_{90} \leq 2$ s.

For Fermi bursts the big difference in CLs between long and short is also clear although to a lesser extent because the CLs are not so high for the short as they are for BATSE. For Fermi short bursts, time windows of 80, 100, 120, 240 days have high CLs. The duration for given bursts also takes the range from $T_{90} \approx 0.2$ s to $T_{90} \approx 2$ s and the good candidate GRBs mostly have $T_{90} \leq 1.0$ s. Changing T_{90} limit to 0.5 s, 1.0 s and 1.5 s doesn't produce big difference, and adding long bursts to given time windows introduces several of them already at $T_{90} \leq 3$ s.

The limit of $T_{90} \approx 2$ s might be an argument for chance coincidence.

Peak energy and isotropic energy

Good candidate GRBs have higher peak energies which is typical for short GRBs. The isotropic energy is mostly in the $E_{iso} \sim 10^{45} - 10^{48}$ erg, especially the SN1997bs - GRB trio $E_{iso} \sim 10^{45} - 10^{46}$ erg while "normal" short GRBs have isotropic energies from $E_{iso} \sim 10^{48}, 10^{49}$ erg up to extreme cases of $E_{iso} \sim 10^{53}$ erg. Higher peak energies are expected

since the selected GRBs are actually short GRBs but again - if the IIn-GRBs are different than "standard" short, why do they also have peak energies similar as "normal" short as well as T_{90} . Again, this might be an argument against special class of IIn-GRBs. From the point of view that all connections are coincidences the lower isotropic energy might be explained due to fact that most cataloged SNe lie in the range $z \leq 0.1$; Lower peak flux and fluence are due to fact that coincidence connections prefer GRBs with bigger error radii and they have bigger errors due to lower peak flux and fluence.

On the other hand, IIn-GRBs with lower energies would produce such observational features.

Soft gamma repeaters and Giant flares

Soft gamma repeaters (SGR) are objects that periodically emit bursts of soft (lower energy) gamma radiation. They are much less energetic than GRBs and only several of them are known, all of which reside in Milky Way or its satellite galaxies. The SGR bursts are thought to come from the decay of magnetic field of magnetars. For reviews see (Woods and Thompson, 2006; Turolla et al., 2015).

In addition to "standard" bursts SGR-objects may emit flares and subtype of these flares are called *giant flares*. The flares are thought to originate in strong reconfiguration of magnetars magnetic field. Only three giant flares were observed - in 1979, 1998 and 2004. They have similar characteristics such as high energetics $E_{iso} > 10^{44}$ erg (in gamma-rays), hard-spectrum/peak-energy and they are composed of short initial spike which lasts about $\sim 0.1 - 1$ s, and, a lower intensity, decaying tail which lasts for hundreds of seconds and oscillates at the rotational frequency of the star. The strongest giant flare by far is the one from *SGR 1806-20* which occurred on December 2004 (hyper flare). The initial spike had an isotropic energy of $E_{iso} \approx 2 \times 10^{46}$ erg, had high peak energy of ~ 500 keV (and was detected up to 2 MeV) and lasted ~ 0.5 s.

It was noticed that if giant flares occurred further away than only the initial spike would be detected and it would seem like a short GRB. This is especially the case for 2004 flare and the topic was studied in (Hurley et al., 2005b; Palmer et al., 2005; Nakar et al., 2006). Such a burst could be detected up to 40, 50 Mpc ($z \approx 0.01$). Given the fact that the flare/burst occurred in the period of about 30 years (the time period when instruments existed that could detect it) and in one galaxy (Milky Way and satellites), implies that the rate of such events (which would be recognized as short GRBs) matches the rate of short GRBs detected by BATSE, i.e. almost all short GRBs in BATSE catalog should be hyper flares from SGR-objects. Trying to find other evidence to this such as clustering of short GRB positions toward Virgo cluster (since they are relatively close) or searching for close galaxies in data archives for reasonably localized short GRBs, came up with opposite results, i.e. that most short GRBs in BATSE catalog are not from SGR-objects. The discrepancy wasn't resolved and with the Swift precise localization of short GRBs in 2005 and detection of redshifts $z \geq 1$ the issue seems to be abandoned.

The case of hyper flares from SGR-objects relation to "standard" short GRBs is similar to the case of potential IIn-GRBs and "standard" short GRBs. The main difference is that the isotropic energy of IIn-GRBs may reach $E_{iso} \sim 10^{48}$ erg and hence, redshifts of $z \approx 0.1$, unless only GRB-trio of SN 1997bs ($z = 0.0024$) is taken as a good candidate. Now to come back to SGR-objects; the hyper flare of 2004 was about ~ 100 times more energetic than two previous giant flares and, although it would be very hard to explain it theoretically, in the future a new hyper flare might be detected with isotropic energy $E_{iso} \geq 10^{47}$ erg.

Finally, with introduction of SGR hyper flares as non-negligible portion of all short GRBs, does it mean that short GRBs may represent 3 different processes - "standard" short, SGR hyper flares, IIn-GRBs?

In any case SGR-objects show that there are phenomena which are similar to short GRBs, in terms of duration and spectrum (peak energy). On the other hand both of the phenomena, in all different theories, are considered to come from compact objects which doesn't seem to be the case for IIn-GRBs. Compact objects such as NSs produce wide range of electromagnetic (photon) phenomena depending on their age, mass, rotational period, magnetic field strength, on binary companion (if there is one), etc. These include systems, detected in Milky Way galaxy, such as radio pulsars, X-ray pulsars, high and low mass X-ray binaries, optical pulsars, gamma-ray pulsars, SGR-objects - which can have ordinary bursts, flares and giant (hyper) flares. Transient phenomena from SGR-objects most resemble properties of "normal" short GRBs with hyper flare matching it most and also having largest isotropic energy.

5.5.6 Mechanisms behind IIn-GRBs

Supernovae IIn

These SNe represent spectroscopic classification, and unlike other SNe types, it does not translate into a single pre-explosion stellar group. Narrow hydrogen lines indicate existence of slow moving, hydrogen-rich circum stellar medium (CSM) surrounding the star and this is the astrophysical aspect which binds all IIn SNe in a single group. Based on this definition SNe Ibn should also be in the *narrow* group but in this work they were grouped with Ib/c SNe due to the known connection with long GRBs. The recent works and reviews on SNe IIn: (Habergham et al., 2014; Smith, 2016). The main division of SNe IIn in this work was on "standard" IIn, impostors and Ia-CSM. However, the variety of stellar activity (which may or may not be the final "death" of a star) can be much greater. Additionally, the stars may be in a binary system and the companion can be a compact object star. The CSM is not simply a stellar wind but a much more massive shell of stellar material (in some cases even on the order of $\sim 10 M_{\odot}$). The interaction of released energy from stellar activity (usually SN ejecta, i.e. its kinetic energy) with the CSM (which can be aspherical) may define the evolution of the light curve and spectrum of the event more than characteristics of the stellar activity itself. If the star isn't in a binary system, the existence of a dense, massive CSM requires large mass ejections by the star. This means that star should be very massive, in some cases with initial masses more than $\sim 50 M_{\odot}$. The best candidates are Luminous Blue Variable (LBV) stars which can have relatively short periods of massive stellar eruptions (not the same as continues stellar winds). Massive stellar eruptions are also good explanation for SN impostors. One of the most famous, and best studied, LBVs is Eta Carinae star which resided in Milky Way. It has a mass of $\sim 100 M_{\odot}$, is part of a binary system with a similar but less intense star, and had a major eruption of $\sim 10 M_{\odot}$ about 150 years ago. While being good candidates LBVs are not the only ones, maybe not even the majority.

In most cases observations on the order of tens of years are needed to probe a IIn phenomenon correctly and determine the underlying stellar activity and whether it was terminal or no. So, many "normal" IIn SNe may be something else than an ordinary SN II explosion in a CSM, and also SNe IIn classified as impostors or Ia-CSM SNe may turn out to be some other types of IIn. The observations and science of IIn SNe is still in its young

stages.

Recently discovered class of SNe, *superluminous supernovae* (SLSN), are SNe which can have (radiated/photon) energies above $\sim 10^{51}$ erg and peak luminosities in the range $M_V \sim -21, -22.5$, as opposed to ordinary core-collapse SNe which usually have energies up to 2 - 3 orders of magnitude less and peak luminosities in the range $M_V \sim -15, -18$. They are also more energetic and luminous than thermonuclear type Ia or GRB-Ib/c SNe. They are further divided into more common SLSN I which do not show hydrogen in the spectrum and hence correspond to stars without hydrogen envelope; and to SLSN II which show hydrogen in the spectrum and almost all of them also show narrow hydrogen lines which means SLSN II are practically SLSN IIn (Inserra et al., 2018). The high luminosity and energetics of SLSN IIn is explained by interaction of SN ejecta with dense CSM. As in the case of normal-luminous IIn, SLSN IIn probably have a wide variety of underlying stellar activity/explosions.

It is interesting to note that IIb SNe may also have significant interaction with CSM, particularly at later times as exemplified by SN 1993J. The type IIb in this work have relatively high CLs ($\simeq 0.9$) for long BATSE and Fermi bursts at $TW \sim 100$ d. One of the BATSE candidates is SN 1993J (GRB 930203A), which probably has a binary B-type companion and resides in a nearby galaxy (≈ 3 Mpc).

Short GRBs

The purpose of this part is not to produce a model for IIn-GRBs but to explore some possibilities.

It is not uncommon to have gamma-rays (which can go all the way to GeV-TeV energies) from stellar activities such as novae, supernovae, eruptions and winds of massive stars, but these are continuous emissions with much lower luminosity than expected from IIn-GRBs $L_{IInGRB} \sim 10^{45} - 10^{48}$ erg/s. For example, Eta Carinae binary stars produce stellar winds which collide. It is considered that in the collision particles such as electrons are accelerated to high energies and then inverse Compton (IC) scattered of low-energy photons which gain energy and become gamma-rays. This was measured by INTEGRAL to have a luminosity of $L = 7 \times 10^{33}$ erg/s in the 20 – 100 keV band (Leyder et al., 2008).

Supernovae IIn are defined by existence of CSM and interaction of SN ejecta (or impostor ejecta) with it. The collision of the SN shell with slow moving CSM reminds of collisions of fireball shells in GRB scenario but these happen at ultra relativistic speed while SN ejecta moves at $v \sim 0.03 - 0.1$ c. However, in (Katz et al., 2012) the case of expansion of the SN ejecta into dense, optically thick CSM (dense wind) was studied. It was found that at one point a collisionless shock will form and energy will be radiated in hard X-rays/gamma-rays ($E \gtrsim 50$ keV) which can reach $E_{iso} \sim 10^{51}$ erg but the duration of the emission is on the order of 1 day which would make luminosity $L \sim 10^{46}$ erg/s. This is in the range of luminosity expected but would last longer than ~ 1 s and the peak energy should be an order of magnitude higher. The CSM in the model was wind-like, decaying with $1/r^2$ and starting from the stars surface. If the energy requirements are lower $E_{iso} \sim 10^{45} - 10^{48}$ erg and CSM is apshpherical with different density distribution, the resulting gamma emission might produce GRB within required parameters. Also, the emission might be longer but have a peak (detectable by GRB instruments) which last on the order of a 1 s.

The GRBs may be related to CSM but not come from the interaction with it. In (Chevalier, 2012) massive CSM in IIn systems is explained as originating from a common enve-

lope phase of a massive star and its binary compact object companion - neutron star (NS) or a black hole (BH). The compact object ejects the outer stellar envelope as it orbits the core of the star inside the star. The compact binary star may also explain large radiated SN energies in some IIn SNe when the CSM isn't too massive (which also implies the star isn't too massive). In the cited work it was found that rates of such binary systems and IIn SNe are different by order of magnitude but overlap within the large errors. Having a NS (which might be a magnetar) or a BH as a binary companion makes the possibility of a GRB occurring more probable and various mechanisms may be introduced. In fact the cited work suggested occurrence of GRBs related to IIn SNe but proposed it was suppressed by the CSM because of no known or possible observed connections except the possible one of IIn SN 1997cy – short GRB 970514 (Germany et al., 2000).

There are speculation on the existence of a *quark nova* which occurs when the neutron degeneracy in the NS cannot oppose the gravitational pressure and neutrons are dissolved into constituent quarks and a *quark star* is created. Released gravitational and nuclear energy create a quark nova (QN). In (Ouyed et al., 2013) it is argued that SN 2010mc and SN 2009ip, which have pre-explosion activity shortly before the main explosion, are a case of SN and a QN. The SN is responsible for the first peak and a QN for a second and more stronger peak (the main peak). Also in (Ouyed et al., 2011) it is argued that QNe may produce short GRBs, although this is speculated for low mass X-ray binaries when the massive NS goes QN and the QN ejecta interacts with dense circumbinary disk. With the right tuning of parameters in the model, as well as asymmetric CBM in IIn SNe, it might be possible to produce short GRBs with energetics lower than standard ones $E_{iso} < 10^{48}$ erg.

Finally, since SNe IIn represent significant number of different stellar activities the GRBs may be produced from different mechanisms in IIn SNe.

5.5.7 Future work

Statistical analysis

The basis of searching for connection in this work was whether a GRB encompasses SN with its 1σ statistical (plus systematic) error radius or not. This is an approximation. For example, if a GRB error radius is 10° and a SN is 1° from a GRB position (center of the error circle), second SN is 9° and a third one is 11° from it; then the first two SNe would be counted as *inside* with same probability and a third one would be *outside* and ignored. In reality the first one has the highest probability, the second and third have similar spacial probabilities of connection to GRB. Second, the connections with GRBs with smaller error radii should have more statistical weight. Third, GRB error surfaces were approximated as circles but are actually ellipses. Fourth, the GRB sky positions are not uniformly random.

In order to do everything properly map exposure of Fermi and BATSE should be taken into account when generating positions of random GRB sets. The exact error spread distribution for all GRBs should be known and more SNe (within 99% probability contour for example) should be taken into account for every single GRB. Also for each GRB detected by other satellites the combined error spread probability should be taken into account. This information is not available in the catalogs and has to be obtained, or approximated, in another way. The confidence levels for time windows should be obtained, again by randomizing GRB positions and dates, but taking above considerations into account.

Detailed analysis of GRBs

The good candidate GRBs should be checked in detailed, namely the morphology of the light curve and spectral analysis.

Search for nearby host galaxies of short GRBs localized by Swift

Since IIn-GRBs have lower energetics they should reside in nearby ($z \leq 0.1$) galaxies. The search for the galaxies in archival optical data may be performed at the position of error surface of short GRBs localized by Swift.

SNe type IIb and IIP

Since connections with these SNe show relatively high CLs it would be interesting to explore it further.

Final remarks

The purpose of this work isn't to claim existence of short GRB – IIn SN connections but to explore the possibility and its implications. The original idea was to look for well established connections between long GRBs and Ib/c SNe which might have been mist if only Fermi observed the GRB, and a SN was discovered serendipitously. Then the statistical approach was adopted in order to see if there is excess of these connections to random ones and in which time windows they reside in order to see from statistical point of view how many might have been mist and in which time windows to look for them. Other types of SNe were used as a comparison. Then the very high CLs were noted for short IIn SNe and BATSE short GRBs and the exploration into this possible connection started.

The majority of short GRB sample comes from BATSE (around 500) which has on average lower peak fluxes and fluences than the Swift sample, and to a lesser extent from Fermi (around 300 up to 2017). Detectors BATSE and Fermi are not suited for localizing bursts and hence, determination of the redshift. Up to year 2017 about 30 short GRBs have measured redshift and about 10 of those were also detected by Fermi. It seems there is room left for short GRBs with lower isotropic energies at distances $z \leq 0.1$. If this is the case then these could be giant flares from SGRs, IIn-GRBs, something else or combination of them.

In August, 2017 a gravitational wave GW 170817 was detected coinciding in sky-position and time with short GRB 170817A detected by Fermi-GBM (Abbott et al., 2017; Troja et al., 2017). The distance to the object is ~ 40 Mpc which implies isotropic energy of $E_{iso} \approx 5 \times 10^{46}$ erg. This is by far the closest short GRB and with lowest isotropic energy. General conclusion seems to be that this was regular short GRB detected off-axis. This event gives an example of, from observational point of view, short GRB occurring well below $z \approx 0.1$ and $E_{iso} < 10^{48}$ erg. Question now is how many of short GRBs detected by Fermi are "local" and how many are at cosmological distances; this question can also be extended to BATSE and other detector samples of short GRBs. Further events detected by both gravitational wave, gamma and optical detectors are needed to probe into the specific event of GW-GRB 170817 and population statistics of short GRBs.

Bibliography

- Abbott, B. et al. (2017). Gravitational Waves and Gamma-Rays from a Binary Neutron Star Merger: GW170817 and GRB 170817A. *ApJ*, 848:L13.
- Ackermann et al. (2014). Fermi-LAT Observations of the Gamma-Ray Burst GRB 130427A. *Science*, 343:42–47.
- Adams, M. T. et al. (1997). Supernova 1997cq in Anonymous Galaxy. *IAU Circ.*, 6674.
- Adams, S. M. and Kochanek, C. S. (2015). LOSS’s first supernova? New limits on the ‘impostor’ SN 1997bs. *MNRAS*, 452:2195–2207.
- Aksenov, A. G., Ruffini, R., and Vereshchagin, G. V. (2007). Thermalization of Nonequilibrium Electron-Positron-Photon Plasmas. *Physical Review Letters*, 99(12):125003.
- Aksenov, A. G., Ruffini, R., and Vereshchagin, G. V. (2010). Pair plasma relaxation time scales. *Phys. Rev. E*, 81(4):046401.
- Andrews, J. et al. (2015). ATel 7456: Spectroscopic classification of PSN J23355226+2336521 as a Type Ic. *The Astronomer’s Telegram*, 7456.
- Ashall, C. et al. (2017). GRB 161219B-SN 2016jca: a powerful stellar collapse. *ArXiv e-prints*.
- Band, D. L. (2003). Comparison of the Gamma-Ray Burst Sensitivity of Different Detectors. *ApJ*, 588:945–951.
- Barbon, R., Buondi, V., Cappellaro, E., and Turatto, M. (2010). VizieR Online Data Catalog: Asiago Supernova Catalogue (Barbon et al., 1999-). *VizieR Online Data Catalog*, 1.
- Basak, R. and Rao, A. R. (2015a). Discovery of Smoothly Evolving Blackbodies in the Early Afterglow of GRB 090618: Evidence for a Spine-Sheath Jet? *ApJ*, 812:156.
- Basak, R. and Rao, A. R. (2015b). Thermal Emissions Spanning the Prompt and the Afterglow Phases of the Ultra-long GRB 130925A. *ApJ*, 807:34.
- Becerra, L., Cipolletta, F., Fryer, C. L., Rueda, J. A., and Ruffini, R. (2015). Angular Momentum Role in the Hypercritical Accretion of Binary-driven Hypernovae. *ApJ*, 812:100.
- Bellm, E. C. et al. (2014). X-Ray Spectral Components Observed in the Afterglow of GRB 130925A. *ApJ*, 784:L19.
- Belvedere, R., Pugliese, D., Rueda, J. A., Ruffini, R., and Xue, S.-S. (2012). Neutron star equilibrium configurations within a fully relativistic theory with strong, weak, electromagnetic, and gravitational interactions. *Nuclear Physics A*, 883:1–24.
- Benedetti, A., Han, W.-B., Ruffini, R., and Vereshchagin, G. V. (2011). On the frequency of oscillations in the pair plasma generated by a strong electric field. *Physics Letters B*, 698:75–79.
- Benitez, S. et al. (2013). Nearby Supernova Factory II classification of Five Supernovae. *The Astronomer’s Telegram*, 4994.
- Berger, E. (2014). Short-Duration Gamma-Ray Bursts. *ARA&A*, 52:43–105.
- Bernardini, M. G., Bianco, C. L., Caito, L., Dainotti, M. G., Guida, R., and Ruffini, R. (2007). GRB 970228 and a class of GRBs with an initial spikelike emission. *A&A*, 474:L13–L16.
- Bernardini, M. G., Bianco, C. L., Chardonnet, P., Frascchetti, F., Ruffini, R., and Xue, S.-S. (2005). Theoretical Interpretation of the Luminosity and Spectral Properties of GRB 031203. *ApJ*, 634:L29–L32.
- Bersier, D. et al. (2006). Evidence for a Supernova Associated with the X-Ray Flash 020903. *ApJ*, 643:284–291.

- Bhat, P. N. et al. (2016). VizieR Online Data Catalog: The third Fermi/GBM GRB catalog (6yr) (Bhat+, 2016). *VizieR Online Data Catalog*, 222.
- Bianco, C. L., Massucci, F. A., and Ruffini, R. (2011). The Luminosity Evolution Over the Equitemporal Surfaces in the Prompt Emission of Gamma-Ray Bursts. *International Journal of Modern Physics D*, 20:1919–1929.
- Bianco, C. L. and Ruffini, R. (2004). Exact versus Approximate Equitemporal Surfaces in Gamma-Ray Burst Afterglows. *ApJ*, 605:L1–L4.
- Bianco, C. L. and Ruffini, R. (2005a). Exact versus Approximate Solutions in Gamma-Ray Burst Afterglows. *ApJ*, 633:L13–L16.
- Bianco, C. L. and Ruffini, R. (2005b). Exact versus Approximate Solutions in Gamma-Ray Burst Afterglows. *ApJ*, 633:L13–L16.
- Bianco, C. L. and Ruffini, R. (2005c). On the Exact Analytic Expressions for the Equitemporal Surfaces in Gamma-Ray Burst Afterglows. *ApJ*, 620:L23–L26.
- Bianco, C. L. and Ruffini, R. (2005d). On the Exact Analytic Expressions for the Equitemporal Surfaces in Gamma-Ray Burst Afterglows. *ApJ*, 620:L23–L26.
- Bianco, C. L. and Ruffini, R. (2006). Exact versus Approximate Beaming Formulae in Gamma-Ray Burst Afterglows. *ApJ*, 644:L105–L108.
- Bianco, C. L., Ruffini, R., and Xue, S.-S. (2001). The elementary spike produced by a pure e^+e^- pair-electromagnetic pulse from a Black Hole: The PEM Pulse. *A&A*, 368:377–390.
- Bissaldi, E. et al. (2008). GRB 081007 and GRB 081007B: Fermi GBM detection. *GRB Coordinates Network*, 8369.
- Bloom, J. S. et al. (1999). The unusual afterglow of the γ -ray burst of 26 March 1998 as evidence for a supernova connection. *Nature*, 401:453–456.
- Bloom, J. S. et al. (2001). The Redshift and the Ordinary Host Galaxy of GRB 970228. *ApJ*, 554:678–683.
- Bloom, J. S. et al. (2002). Detection of a Supernova Signature Associated with GRB 011121. *ApJ*, 572:L45–L49.
- Briggs, M. S. et al. (1999). Observations of GRB 990123 by the Compton Gamma Ray Observatory. *ApJ*, 524:82–91.
- Bromberg, O. et al. (2013). Short versus Long and Collapsars versus Non-collapsars: A Quantitative Classification of Gamma-Ray Bursts. *ApJ*, 764:179.
- Bufano, F., Pian, E., Sollerman, J., Benetti, S., Pignata, G., Valenti, S., Covino, S., D’Avanzo, P., Malesani, D., Cappellaro, E., Della Valle, M., Fynbo, J., Hjorth, J., Mazzali, P. A., Reichart, D. E., Starling, R. L. C., Turatto, M., Vergani, S. D., Wiersema, K., Amati, L., Bersier, D., Campana, S., Cano, Z., Castro-Tirado, A. J., Chincarini, G., D’Elia, V., de Ugarte Postigo, A., Deng, J., Ferrero, P., Filippenko, A. V., Goldoni, P., Gorosabel, J., Greiner, J., Hammer, F., Jakobsson, P., Kaper, L., Kawabata, K. S., Klose, S., Levan, A. J., Maeda, K., Masetti, N., Milvang-Jensen, B., Mirabel, F. I., Møller, P., Nomoto, K., Palazzi, E., Piranomonte, S., Salvaterra, R., Stratta, G., Tagliaferri, G., Tanaka, M., Tanvir, N. R., and Wijers, R. A. M. J. (2012). The Highly Energetic Expansion of SN 2010bh Associated with GRB 100316D. *ApJ*, 753:67.
- Burns, E. et al. (2016). Do the Fermi Gamma-Ray Burst Monitor and Swift Burst Alert Telescope see the Same Short Gamma-Ray Bursts? *ApJ*, 818:110.
- Caito, L., Amati, L., Bernardini, M. G., Bianco, C. L., de Barros, G., Izzo, L., Patricelli, B., and Ruffini, R. (2010). GRB 071227: an additional case of a disguised short burst. *A&A*, 521:A80.
- Caito, L., Bernardini, M. G., Bianco, C. L., Dainotti, M. G., Guida, R., and Ruffini, R. (2009). GRB060614: a “fake” short GRB from a merging binary system. *A&A*, 498:501–507.
- Campana, S., Mangano, V., Blustin, A. J., Brown, P., Burrows, D. N., Chincarini, G., Cummings, J. R., Cusumano, G., Della Valle, M., Malesani, D., Mészáros, P., Nousek, J. A., Page, M., Sakamoto, T., Waxman, E., Zhang, B., Dai, Z. G., Gehrels, N., Immler, S., Marshall, F. E., Mason, K. O., Moretti, A., O’Brien, P. T., Osborne, J. P., Page, K. L., Romano, P., Roming, P. W. A., Tagliaferri, G., Cominsky, L. R., Giommi, P., Godet, O., Kennea, J. A., Krimm, H., Angelini,

BIBLIOGRAPHY

- L., Barthelmy, S. D., Boyd, P. T., Palmer, D. M., Wells, A. A., and White, N. E. (2006). The association of GRB 060218 with a supernova and the evolution of the shock wave. *Nature*, 442:1008–1010.
- Cano, Z. (2013). A new method for estimating the bolometric properties of Ibc supernovae. *MNRAS*, 434:1098–1116.
- Cano, Z. et al. (2011). A tale of two GRB-SNe at a common redshift of $z=0.54$. *MNRAS*, 413:669–685.
- Cano, Z. et al. (2014). A trio of gamma-ray burst supernovae: GRB 120729A, GRB 130215A/SN 2013ez, and GRB 130831A/SN 2013fu. *A&A*, 568:A19.
- Cano, Z. et al. (2015). GRB 140606B/iPTF14bfu: detection of shock-breakout emission from a cosmological γ -ray burst? *MNRAS*, 452:1535–1552.
- Cano, Z. et al. (2016). The Observer’s Guide to the Gamma-Ray Burst-Supernova Connection. *LPI Contributions*, 1962:4116.
- Challis, P. et al. (2010). Supernova 2010ak in MCG +03-41-142. *Central Bureau Electronic Telegrams*, 2206.
- Cherubini, C., Geralico, A., Rueda, H. J. A., and Ruffini, R. (2009). e^-e^+ pair creation by vacuum polarization around electromagnetic black holes. *Phys. Rev. D*, 79(12):124002.
- Cherubini, C., Ruffini, R., and Vitagliano, L. (2002). On the electromagnetic field of a charged collapsing spherical shell in general relativity. *Physics Letters B*, 545:226–232.
- Chevalier, R. A. (2012). Common Envelope Evolution Leading to Supernovae with Dense Interaction. *ApJ*, 752:L2.
- Chornock, R. et al. (2010). Spectroscopic Discovery of the Broad-Lined Type Ic Supernova 2010bh Associated with the Low-Redshift GRB 100316D. *ArXiv e-prints*.
- Christodoulou, D. and Ruffini, R. (1971). Reversible Transformations of a Charged Black Hole. *Phys. Rev. D*, 4:3552–3555.
- Cobb, B. E. et al. (2010). Discovery of SN 2009nz Associated with GRB 091127. *ApJ*, 718:L150–L155.
- Daigne, F. and Mochkovitch, R. (2002). The expected thermal precursors of gamma-ray bursts in the internal shock model. *MNRAS*, 336:1271–1280.
- Damour, T. and Ruffini, R. (1975). Quantum Electrodynamical Effects in Kerr-Newmann Geometries. *Physical Review Letters*, 35:463–466.
- D’Avanzo, P., Melandri, A., Palazzi, E., Campana, S., Della Valle, M., Pian, E., Salvaterra, R., and Tagliaferri, G. (2012). GRB 111228A: possible detection of the SN with the TNG. *GRB Coordinates Network*, 13069.
- de Barros, G., Amati, L., Bernardini, M. G., Bianco, C. L., Caito, L., Izzo, L., Patricelli, B., and Ruffini, R. (2011). On the nature of GRB 050509b: a disguised short GRB. *A&A*, 529:A130.
- de Jaeger, T. et al. (2015). SN 2011A: A Low-luminosity Interacting Transient with a Double Plateau and Strong Sodium Absorption. *ApJ*, 807:63.
- de Ugarte Postigo, A. et al. (2012). GRB 111211A: detection of the SN with the 10.4m GTC. *GRB Coordinates Network*, 12802.
- de Ugarte Postigo, A. et al. (2015). GRB 150818A: Spectroscopic confirmation of the SN from GTC. *GRB Coordinates Network*, 18213.
- Della Valle, M. et al. (2003). Evidence for supernova signatures in the spectrum of the late-time bump of the optical afterglow of GRB 021211. *A&A*, 406:L33–L37.
- Della Valle, M. et al. (2006). Hypernova signatures in the late rebrightening of grb 050525a. *ApJ*, 642(2):L103.
- Dong, S. et al. (2016). ASASSN-15lh: A highly super-luminous supernova. *Science*, 351:257–260.
- Drake, A. J. et al. (2009a). Supernovae 2008iw, 2008ix, 2009bx, and 2009de-2009dk. *Central Bureau Electronic Telegrams*, 1766.

- Drake, A. J. et al. (2009b). Supernovae 2008iw, 2008ix, 2009bx, and 2009de-2009dk. *Central Bureau Electronic Telegrams*, 1766.
- Drake, A. J. et al. (2011). Supernova 2011jb. *Central Bureau Electronic Telegrams*, 2947.
- Elias-Rosa, N. et al. (2016). Dead or Alive? Long-term evolution of SN 2015bh (SNhunt275). *MNRAS*, 463:3894–3920.
- Folatelli, G. and Morrell, N. (2009). Supernovae 2009el and 2009em. *Central Bureau Electronic Telegrams*, 1807.
- Friis, M. and Watson, D. (2013). Thermal Emission in the Early X-Ray Afterglows of Gamma-Ray Bursts: Following the Prompt Phase to Late Times. *ApJ*, 771:15.
- Frontera, F. et al. (1998). High resolution imaging of the X-ray afterglow of GRB970228 with ROSAT. *A&A*, 334:L69–L72.
- Fryer, C. L., Oliveira, F. G., Rueda, J. A., and Ruffini, R. (2015). Neutron-Star-Black-Hole Binaries Produced by Binary-Driven Hypernovae. *Physical Review Letters*, 115(23):231102.
- Fryer, C. L., Rueda, J. A., and Ruffini, R. (2014). Hypercritical Accretion, Induced Gravitational Collapse, and Binary-Driven Hypernovae. *ApJ*, 793:L36.
- Fynbo, J. P. U. et al. (2004). On the Afterglow of the X-Ray Flash of 2003 July 23: Photometric Evidence for an Off-Axis Gamma-Ray Burst with an Associated Supernova? *ApJ*, 609:962–971.
- Gabrijelcic, A., Valles, P., Benetti, S., and Lidman, C. (1997). Supernova 1997B in IC 438. *IAU Circ.*, 6535.
- Galama, T. J. et al. (1998). An unusual supernova in the error box of the γ -ray burst of 25 April 1998. *Nature*, 395:670–672.
- Galama, T. J. et al. (2000). Evidence for a Supernova in Reanalyzed Optical and Near-Infrared Images of GRB 970228. *ApJ*, 536:185–194.
- Gall, E. et al. (2011). Supernova 2011bm in IC 3917 = PSN J12565389+2222282. *Central Bureau Electronic Telegrams*, 2695:2.
- Gehrels, N. (1986). Confidence limits for small numbers of events in astrophysical data. *ApJ*, 303:336–346.
- Germany, L. M. et al. (2000). SN 1997CY/GRB 970514: A New Piece in the Gamma-Ray Burst Puzzle? *ApJ*, 533:320–328.
- Gorosabel, J. et al. (2005). A possible bright blue supernova in the afterglow of GRB 020305. *A&A*, 437:411–418.
- Granata, V. et al. (2016). Asiago spectroscopic and photometric observations of AT2016bau. *The Astronomer’s Telegram*, 8818.
- Gruber, D. et al. (2014). The Fermi GBM Gamma-Ray Burst Spectral Catalog: Four Years of Data. *ApJS*, 211:12.
- Guetta, D. and Della Valle, M. (2007). On the Rates of Gamma-Ray Bursts and Type Ib/c Supernovae. *ApJ*, 657:L73–L76.
- Habergham, S. M. et al. (2014). Environments of interacting transients: impostors and Type II supernovae. *MNRAS*, 441:2230–2252.
- Hakkila, J. et al. (1998). BATSE sky exposure. In Meegan, C. A., Preece, R. D., and Koshut, T. M., editors, *Gamma-Ray Bursts, 4th Huntsville Symposium*, volume 428 of *American Institute of Physics Conference Series*, pages 144–148.
- Hakkila, J. et al. (2003). BATSE 5B Sky Exposure and Trigger Efficiency. In Ricker, G. R. and Vanderspek, R. K., editors, *Gamma-Ray Burst and Afterglow Astronomy 2001: A Workshop Celebrating the First Year of the HETE Mission*, volume 662 of *American Institute of Physics Conference Series*, pages 176–178.
- Han, W.-B., Ruffini, R., and Xue, S.-S. (2010). Electron-positron pair oscillation in spatially inhomogeneous electric fields and radiation. *Physics Letters B*, 691:99–104.
- Han, W.-B., Ruffini, R., and Xue, S.-S. (2012). Electron and positron pair production of compact stars. *Phys. Rev. D*, 86(8):084004.

BIBLIOGRAPHY

- Hill, J. et al. (2007). GRB 070419A, deep LBT photometry and possible supernova detection. *GRB Coordinates Network*, 6486.
- Hjorth, J. and Bloom, J. S. (2012). *The Gamma-Ray Burst - Supernova Connection*, pages 169–190.
- Holland, S. T. et al. (2010). GRB 100418A: possible evidence for a supernova. *GRB Coordinates Network*, 10661.
- Hurley, K., Briggs, M., Kippen, R. M., Kouveliotou, C., Fishman, C. M. G., Cline, T., Trombka, J., McClanahan, T., Stern, M. B. B., Kommers, J., Mazets, E., Golenetskii, S., Feroci, J. G. M., Frontera, F., Guidorzi, C., Montanari, E., Sinha, W. L. S., and Seetha, S. (2005a). The interplanetary network supplements to the BATSE 5B and untriggered burst catalogs. *Nuovo Cimento C Geophysics Space Physics C*, 28:299.
- Hurley, K. et al. (2005b). An exceptionally bright flare from SGR 1806-20 and the origins of short-duration γ -ray bursts. *Nature*, 434:1098–1103.
- Hurley, K., Guidorzi, C., Frontera, F., Montanari, E., Rossi, F., Feroci, M., Mazets, E., Golenetskii, S., Frederiks, D. D., Pal'shin, V. D., Aptekar, R. L., Cline, T., Trombka, J., McClanahan, T., Starr, R., Atteia, J.-L., Barraud, C., Pélangéon, A., Boër, M., Vanderspek, R., Ricker, G., Mitrofanov, I. G., Golovin, D. V., Kozyrev, A. S., Litvak, M. L., Sanin, A. B., Boynton, W., Fellows, C., Harshman, K., Goldsten, J., Gold, R., Smith, D. M., Wigger, C., and Hajdas, W. (2010). The Interplanetary Network Supplement to the BeppoSAX Gamma-ray Burst Catalogs. *ApJS*, 191:179–184.
- Inserra, C. et al. (2016). On Type II_n/Ia-CSM supernovae as exemplified by SN 2012ca*. *MNRAS*, 459:2721–2740.
- Inserra, C. et al. (2018). On the nature of hydrogen-rich superluminous supernovae. *MNRAS*, 475:1046–1072.
- Iwamoto, K. et al. (1998). A hypernova model for the supernova associated with the γ -ray burst of 25 April 1998. *Nature*, 395:672–674.
- Izzo, L., Ruffini, R., Penacchioni, A. V., Bianco, C. L., Caito, L., Chakrabarti, S. K., Rueda, J. A., Nandi, A., and Patricelli, B. (2012a). A double component in GRB 090618: a proto-black hole and a genuinely long gamma-ray burst. *A&A*, 543:A10.
- Izzo, L., Ruffini, R., Penacchioni, A. V., Bianco, C. L., Caito, L., Chakrabarti, S. K., Rueda, J. A., Nandi, A., and Patricelli, B. (2012b). A double component in GRB 090618: a proto-black hole and a genuinely long gamma-ray burst. *A&A*, 543:A10.
- Jha, S. et al. (1997). Supernova 1997cq in Anonymous Galaxy. *IAU Circ.*, 6675.
- Jha, S. et al. (1998). Supernova 1998ct in UGC 10062. *IAU Circ.*, 6964.
- Jin, Z.-P., Covino, S., Della Valle, M., Ferrero, P., Fugazza, D., Malesani, D., Melandri, A., Pian, E., Salvaterra, R., Bersier, D., Campana, S., Cano, Z., Castro-Tirado, A. J., D'Avanzo, P., Fynbo, J. P. U., Gomboc, A., Gorosabel, J., Guidorzi, C., Haislip, J. B., Hjorth, J., Kobayashi, S., LaCluyze, A. P., Marconi, G., Mazzali, P. A., Mundell, C. G., Piranomonte, S., Reichart, D. E., Sánchez-Ramírez, R., Smith, R. J., Steele, I. A., Tagliaferri, G., Tanvir, N. R., Valenti, S., Vergani, S. D., Vestrand, T., Walker, E. S., and Woźniak, P. (2013). Grb 081007 and grb 090424: The surrounding medium, outflows, and supernovae. *ApJ*, 774(2):114.
- Kamble, A. et al. (2013). JVL A observations of SN2013bv. *The Astronomer's Telegram*, 5034.
- Kangas, T. et al. (2015). PESSTO spectroscopic classification of optical transients. *The Astronomer's Telegram*, 8296.
- Kann, D. A. et al. (2016). Highly Luminous Supernovae associated with Gamma-Ray Bursts I.: GRB 111209A/SN 2011kl in the Context of Stripped-Envelope and Superluminous Supernovae. *ArXiv e-prints*.
- Katz, B. et al. (2012). X-rays, γ -rays and neutrinos from collisionless shocks in supernova wind breakouts. In Roming, P., Kawai, N., and Pian, E., editors, *Death of Massive Stars: Supernovae and Gamma-Ray Bursts*, volume 279 of *IAU Symposium*, pages 274–281.
- Kleinert, H., Ruffini, R., and Xue, S.-S. (2008). Electron-positron pair production in space- or time-dependent electric fields. *Phys. Rev. D*, 78(2):025011.
- Klose, S. et al. (2012). Supernova 2012eb = GRB 120714B. *Central Bureau Electronic Telegrams*,

3200.

- Kochanek, C. S. et al. (2012). Unmasking the Supernova Impostors. *ApJ*, 758:142.
- Kovacevic, M., Izzo, L., Wang, Y., Muccino, M., Della Valle, M., Amati, L., Barbarino, C., Enderli, M., Pisani, G. B., and Li, L. (2014). A search for Fermi bursts associated with supernovae and their frequency of occurrence. *A&A*, 569:A108.
- Kumar, P. and Zhang, B. (2015). The physics of gamma-ray bursts and relativistic jets. *Phys. Rep.*, 561:1–109.
- Larsson, J. et al. (2015). Evidence for Jet Launching Close to the Black Hole in GRB 101219b - A Fermi GRB Dominated by Thermal Emission. *ApJ*, 800:L34.
- Lazzati, D., Covino, S., Ghisellini, G., Fugazza, D., Campana, S., Saracco, P., Price, P. A., Berger, E., Kulkarni, S., Ramirez-Ruiz, E., Cimatti, A., Della Valle, M., di Serego Alighieri, S., Celotti, A., Haardt, F., Israel, G. L., and Stella, L. (2001). The optical afterglow of GRB 000911: Evidence for an associated supernova? *A&A*, 378:996–1002.
- Levan, A. et al. (2005). GRB 020410: A Gamma-Ray Burst Afterglow Discovered by Its Supernova Light. *ApJ*, 624:880–888.
- Leyder, J.-C. et al. (2008). Hard X-ray emission from η Carinae. *A&A*, 477:L29–L32.
- Li, W. et al. (2002). A Hubble Space Telescope Snapshot Survey of Nearby Supernovae. *PASP*, 114:403–415.
- Li, W. et al. (2011). Nearby supernova rates from the Lick Observatory Supernova Search - II. The observed luminosity functions and fractions of supernovae in a complete sample. *MNRAS*, 412:1441–1472.
- Liang, E. et al. (2006). Thermal Emission from a Hot Cocoon Surrounding the Jet of XRF 060218. *ArXiv Astrophysics e-prints*.
- Liang, E. et al. (2007). Low-Luminosity Gamma-Ray Bursts as a Unique Population: Luminosity Function, Local Rate, and Beaming Factor. *ApJ*, 662:1111–1118.
- Malesani, D., Tagliaferri, G., Chincarini, G., Covino, S., Della Valle, M., Fugazza, D., Mazzali, P. A., Zerbi, F. M., D’Avanzo, P., Kalogerakos, S., Simoncelli, A., Antonelli, L. A., Burderi, L., Campana, S., Cucchiara, A., Fiore, F., Ghirlanda, G., Goldoni, P., Götz, D., Mereghetti, S., Mirabel, I. F., Romano, P., Stella, L., Minezaki, T., Yoshii, Y., and Nomoto, K. (2004). SN 2003lw and GRB 031203: A Bright Supernova for a Faint Gamma-Ray Burst. *ApJ*, 609:L5–L8.
- Margutti, R. et al. (2014). A Panchromatic View of the Restless SN 2009ip Reveals the Explosive Ejection of a Massive Star Envelope. *ApJ*, 780:21.
- Masetti, N., Palazzi, E., Pian, E., Simoncelli, A., Hunt, L. K., Maiorano, E., Levan, A., Christensen, L., Rol, E., Savaglio, S., Falomo, R., Castro-Tirado, A. J., Hjorth, J., Delsanti, A., Pannella, M., Mohan, V., Pandey, S. B., Sagar, R., Amati, L., Burud, I., Castro Cerón, J. M., Frontera, F., Fruchter, A. S., Fynbo, J. P. U., Gorosabel, J., Kaper, L., Klose, S., Kouveliotou, C., Nicastro, L., Pedersen, H., Rhoads, J., Salamanca, I., Tanvir, N., Vreeswijk, P. M., Wijers, R. A. M. J., and van den Heuvel, E. P. J. (2003). Optical and near-infrared observations of the GRB020405 afterglow. *A&A*, 404:465–481.
- Mauerhan, J. C. et al. (2015). SN Hunt 248: a super-Eddington outburst from a massive cool hypergiant. *MNRAS*, 447:1922–1934.
- Meegan, C. A. (1997). The BATSE Catalog of Gamma-Ray Bursts. *NASA STI/Recon Technical Report N*, 1.
- Melandri, A., Pian, E., D’Elia, V., D’Avanzo, P., Della Valle, M., Mazzali, P. A., Tagliaferri, G., Cano, Z., Levan, A. J., Møller, P., Amati, L., Bernardini, M. G., Bersier, D., Bufano, F., Campana, S., Castro-Tirado, A. J., Covino, S., Ghirlanda, G., Hurley, K., Malesani, D., Masetti, N., Palazzi, E., Piranomonte, S., Rossi, A., Salvaterra, R., Starling, R. L. C., Tanaka, M., Tanvir, N. R., and Vergani, S. D. (2014). Diversity of gamma-ray burst energetics vs. supernova homogeneity: SN 2013cq associated with GRB 130427A. *A&A*, 567:A29.
- Melandri, A., Pian, E., Ferrero, P., D’Elia, V., Walker, E. S., Ghirlanda, G., Covino, S., Amati, L., D’Avanzo, P., Mazzali, P. A., Della Valle, M., Guidorzi, C., Antonelli, L. A., Bernardini, M. G.,

BIBLIOGRAPHY

- Bersier, D., Bufano, F., Campana, S., Castro-Tirado, A. J., Chincarini, G., Deng, J., Filippenko, A. V., Fugazza, D., Ghisellini, G., Kouveliotou, C., Maeda, K., Marconi, G., Masetti, N., Nomoto, K., Palazzi, E., Patat, F., Piranomonte, S., Salvaterra, R., Saviane, I., Starling, R. L. C., Tagliaferri, G., Tanaka, M., and Vergani, S. D. (2012). The optical SN 2012bz associated with the long GRB 120422A. *A&A*, 547:A82.
- Mészáros, P. (2006). Gamma-ray bursts. *Reports on Progress in Physics*, 69:2259–2321.
- Mészáros, P. and Rees, M. J. (2000). Steep Slopes and Preferred Breaks in Gamma-Ray Burst Spectra: The Role of Photospheres and Comptonization. *ApJ*, 530:292–298.
- Monard, L. A. G. (2009a). Supernova 2009em in NGC 157. *Central Bureau Electronic Telegrams*, 1798.
- Monard, L. A. G. (2009b). Supernova 2009em in NGC 157. *Central Bureau Electronic Telegrams*, 1798.
- Muccino, M., Ruffini, R., Bianco, C. L., Izzo, L., and Penacchioni, A. V. (2013a). GRB 090227B: The Missing Link between the Genuine Short and Long Gamma-Ray Bursts. *ApJ*, 763:125.
- Muccino, M., Ruffini, R., Bianco, C. L., Izzo, L., Penacchioni, A. V., and Pisani, G. B. (2013b). GRB 090510: A Disguised Short Gamma-Ray Burst with the Highest Lorentz Factor and Circumburst Medium. *ApJ*, 772:62.
- Nakano, S. et al. (1997). Supernova 1997E in NGC 2258. *IAU Circ.*, 6538.
- Nakar, E., Gal-Yam, A., Piran, T., and Fox, D. B. (2006). The Distances of Short-Hard Gamma-Ray Bursts and the Soft Gamma-Ray Repeater Connection. *ApJ*, 640:849–853.
- Nappo, F. et al. (2017). The 999th Swift gamma-ray burst: Some like it thermal. A multiwavelength study of GRB 151027A. *A&A*, 598:A23.
- Navasardyan, H. and Benetti, S. (2009a). Supernova 2009em in NGC 157. *Central Bureau Electronic Telegrams*, 1806.
- Navasardyan, H. and Benetti, S. (2009b). Supernova 2009em in NGC 157. *Central Bureau Electronic Telegrams*, 1806.
- Ofek, E. O. et al. (2013). An outburst from a massive star 40 days before a supernova explosion. *Nature*, 494:65–67.
- Ofek, E. O. et al. (2014). Precursors Prior to Type IIn Supernova Explosions are Common: Precursor Rates, Properties, and Correlations. *ApJ*, 789:104.
- Ouyed, R. et al. (2011). Quark-novae in Low-mass X-ray Binaries with Massive Neutron Stars: A Universal Model for Short-hard Gamma-ray Bursts. *ApJ*, 729:60.
- Ouyed, R. et al. (2013). SN 2009ip and SN 2010mc as dual-shock Quark-Novae. *Research in Astronomy and Astrophysics*, 13:1463–1470.
- Page, K. L. et al. (2011). GRB 090618: detection of thermal X-ray emission from a bright gamma-ray burst. *MNRAS*, 416:2078–2089.
- Palmer, D. M. et al. (2005). A giant γ -ray flare from the magnetar SGR 1806 - 20. *Nature*, 434:1107–1109.
- Pal'shin, V. D., Hurley, K., Svinkin, D. S., Aptekar, R. L., Golenetskii, S. V., Frederiks, D. D., Mazets, E. P., Oleynik, P. P., Ulanov, M. V., Cline, T., Mitrofanov, I. G., Golovin, D. V., Kozyrev, A. S., Litvak, M. L., Sanin, A. B., Boynton, W., Fellows, C., Harshman, K., Trombka, J., McClanahan, T., Starr, R., Goldsten, J., Gold, R., Rau, A., von Kienlin, A., Savchenko, V., Smith, D. M., Hajdas, W., Barthelmy, S. D., Cummings, J., Gehrels, N., Krimm, H., Palmer, D., Yamaoka, K., Ohno, M., Fukazawa, Y., Hanabata, Y., Takahashi, T., Tashiro, M., Terada, Y., Murakami, T., Makishima, K., Briggs, M. S., Kippen, R. M., Kouveliotou, C., Meegan, C., Fishman, G., Connaughton, V., Boër, M., Guidorzi, C., Frontera, F., Montanari, E., Rossi, F., Feroci, M., Amati, L., Nicastro, L., Orlandini, M., Del Monte, E., Costa, E., Donnarumma, I., Evangelista, Y., Lapshov, I., Lazzarotto, F., Pacciani, L., Rapisarda, M., Soffitta, P., Di Cocco, G., Fuschino, F., Galli, M., Labanti, C., Marisaldi, M., Atteia, J.-L., Vanderspek, R., and Ricker, G. (2013). Interplanetary Network Localizations of Konus Short Gamma-Ray Bursts. *ApJS*, 207:38.
- Pastorello, A. (2012). Supernova Taxonomy - New Types. *Memorie della Societa Astronomica*

- Italiana Supplementi*, 19:24.
- Patricelli, B., Bernardini, M. G., Bianco, C. L., Caito, L., de Barros, G., Izzo, L., Ruffini, R., and Vereshchagin, G. V. (2012). Analysis of GRB 080319B and GRB 050904 within the Fireshell Model: Evidence for a Broader Spectral Energy Distribution. *ApJ*, 756:16.
- Pe'er, A., Ryde, F., Wijers, R. A. M. J., Mészáros, P., and Rees, M. J. (2007). A New Method of Determining the Initial Size and Lorentz Factor of Gamma-Ray Burst Fireballs Using a Thermal Emission Component. *ApJ*, 664:L1–L4.
- Penacchioni, A. V., Ruffini, R., Bianco, C. L., Izzo, L., Muccino, M., Pisani, G. B., and Rueda, J. A. (2013). GRB 110709B in the induced gravitational collapse paradigm. *A&A*, 551:A133.
- Penacchioni, A. V., Ruffini, R., Izzo, L., Muccino, M., Bianco, C. L., Caito, L., Patricelli, B., and Amati, L. (2012). Evidence for a proto-black hole and a double astrophysical component in GRB 101023. *A&A*, 538:A58.
- Peng, F.-K. et al. (2014). Photosphere Emission in the X-Ray Flares of Swift Gamma-Ray Bursts and Implications for the Fireball Properties. *ApJ*, 795:155.
- Pignata, G. et al. (2011). Supernova 2011gw in IC 2200 = Psn J07281702-6221189. *Central Bureau Electronic Telegrams*, 2869.
- Pignata, G. et al. (2012a). Supernova 2012ba in ESO 328-46 = Psn J15222512-3812042. *Central Bureau Electronic Telegrams*, 3058.
- Pignata, G. et al. (2012b). Supernova 2012ba in ESO 328-46 = Psn J15222512-3812042. *Central Bureau Electronic Telegrams*, 3058.
- Piran, T. (1999). Gamma-ray bursts and the fireball model. *Phys. Rep.*, 314:575–667.
- Piro, L. et al. (2014). A Hot Cocoon in the Ultralong GRB 130925A: Hints of a POPIII-like Progenitor in a Low-Density Wind Environment. *ApJ*, 790:L15.
- Pisani, G. B., Izzo, L., Ruffini, R., Bianco, C. L., Muccino, M., Penacchioni, A. V., Rueda, J. A., and Wang, Y. (2013). Novel distance indicator for gamma-ray bursts associated with supernovae. *A&A*, 552:L5.
- Pozanenko, A. et al. (2015). GRB 150518A: possible SN observations. *GRB Coordinates Network*, 17903.
- Preparata, G., Ruffini, R., and Xue, S.-S. (1998). The dyadosphere of black holes and gamma-ray bursts. *A&A*, 338:L87–L90.
- Rees, M. J. (1966). Appearance of Relativistically Expanding Radio Sources. *Nature*, 211:468–470.
- Reichart, D. E. (1997). Observations and Theoretical Implications of GRB 970228. *ApJ*, 485:L57–L60.
- Rex, J. et al. (2010). Supernova 2010ak in MCG +03-41-142. *Central Bureau Electronic Telegrams*, 2203.
- Rigon, L. et al. (2003). SN 1999E: another piece in the supernova-gamma-ray burst connection puzzle. *MNRAS*, 340:191–196.
- Rueda, J. A. and Ruffini, R. (2012). On the Induced Gravitational Collapse of a Neutron Star to a Black Hole by a Type Ib/c Supernova. *ApJ*, 758:L7.
- Ruffini, R., Aimuratov, Y., Becerra, L., Bianco, C. L., Chen, Y. C., Karlica, M., Kovacevic, M., Melon Fuksman, J. D., Moradi, R., Muccino, M., Pisani, G. B., Primorac, D., Rueda, J. A., and Wang, Y. (2017a). On the nature of prompt emission, X and gamma ray flares and extended thermal emission in GRB 151027A. *ArXiv e-prints*.
- Ruffini, R., Bernardini, M. G., Bianco, C. L., Caito, L., Chardonnet, P., Dainotti, M. G., Frascchetti, F., Guida, R., Rotondo, M., Vereshchagin, G., Vitagliano, L., and Xue, S.-S. (2007a). The Blackholic energy and the canonical Gamma-Ray Burst. In Novello, M. and Perez Bergliaffa, S. E., editors, *XIIth Brazilian School of Cosmology and Gravitation*, volume 910 of *American Institute of Physics Conference Series*, pages 55–217.
- Ruffini, R., Bernardini, M. G., Bianco, C. L., Chardonnet, P., Frascchetti, F., Guida, R., and Xue, S.-S. (2006). GRB 050315: A Step toward Understanding the Uniqueness of the Overall Gamma-Ray

BIBLIOGRAPHY

- Burst Structure. *ApJ*, 645:L109–L112.
- Ruffini, R., Bernardini, M. G., Bianco, C. L., Chardonnet, P., Fraschetti, F., Gurzadyan, V., Lattanzi, M., Vitagliano, L., and Xue, S.-S. (2005a). Extracting energy from black holes: 'Long' and 'short' GRBs and their astrophysical settings. *Nuovo Cimento C Geophysics Space Physics C*, 28:589.
- Ruffini, R., Bernardini, M. G., Bianco, C. L., Chardonnet, P., Fraschetti, F., and Xue, S.-S. (2004a). GRB 980425, SN1998BW and the EMBH model. *Advances in Space Research*, 34:2715–2722.
- Ruffini, R., Bianco, C. L., Chardonnet, P., Fraschetti, F., Vitagliano, L., and Xue, S.-S. (2003a). New perspectives in physics and astrophysics from the theoretical understanding of Gamma-Ray Bursts. In Novello, M. and Perez Bergliaffa, S. E., editors, *Cosmology and Gravitation*, volume 668 of *American Institute of Physics Conference Series*, pages 16–107.
- Ruffini, R., Bianco, C. L., Chardonnet, P., Fraschetti, F., and Xue, S.-S. (2002). On the Structures in the Afterglow Peak Emission of Gamma-Ray Bursts. *ApJ*, 581:L19–L22.
- Ruffini, R., Bianco, C. L., Fraschetti, F., Xue, S.-S., and Chardonnet, P. (2001a). On the Interpretation of the Burst Structure of Gamma-Ray Bursts. *ApJ*, 555:L113–L116.
- Ruffini, R., Bianco, C. L., Fraschetti, F., Xue, S.-S., and Chardonnet, P. (2001b). Relative Spacetime Transformations in Gamma-Ray Bursts. *ApJ*, 555:L107–L111.
- Ruffini, R., Bianco, C. L., Xue, S.-S., Chardonnet, P., Fraschetti, F., and Gurzadyan, V. (2004b). On the Instantaneous Spectrum of Gamma-Ray Bursts. *International Journal of Modern Physics D*, 13:843–851.
- Ruffini, R., Bianco, C. L., Xue, S.-S., Chardonnet, P., Fraschetti, F., and Gurzadyan, V. (2005b). Emergence of a Filamentary Structure in the Fireball from GRB Spectra. *International Journal of Modern Physics D*, 14:97–105.
- Ruffini, R., Izzo, L., Bianco, C. L., Rueda, J. A., Barbarino, C., Dereli, H., Enderli, M., Muccino, M., Penacchioni, A. V., Pisani, G. B., and Wang, Y. (2015a). Induced gravitational collapse in the BATSE era: The case of GRB 970828. *Astronomy Reports*, 59:626–638.
- Ruffini, R., Izzo, L., Muccino, M., Pisani, G. B., Rueda, J. A., Wang, Y., Barbarino, C., Bianco, C. L., Enderli, M., and Kovacevic, M. (2014a). Induced gravitational collapse at extreme cosmological distances: the case of GRB 090423. *A&A*, 569:A39.
- Ruffini, R., Muccino, M., Aimuratov, Y., Bianco, C. L., Cherubini, C., Enderli, M., Kovacevic, M., Moradi, R., Penacchioni, A. V., Pisani, G. B., Rueda, J. A., and Wang, Y. (2016a). GRB 090510: a genuine short-GRB from a binary neutron star coalescing into a Kerr-Newman black hole. *ArXiv e-prints*.
- Ruffini, R., Muccino, M., Bianco, C. L., Enderli, M., Izzo, L., Kovacevic, M., Penacchioni, A. V., Pisani, G. B., Rueda, J. A., and Wang, Y. (2014b). On binary-driven hypernovae and their nested late X-ray emission. *A&A*, 565:L10.
- Ruffini, R., Muccino, M., Bianco, C. L., Enderli, M., Izzo, L., Kovacevic, M., Penacchioni, A. V., Pisani, G. B., Rueda, J. A., and Wang, Y. (2014c). On binary-driven hypernovae and their nested late X-ray emission. *A&A*, 565:L10.
- Ruffini, R., Muccino, M., Kovacevic, M., Oliveira, F. G., Rueda, J. A., Bianco, C. L., Enderli, M., Penacchioni, A. V., Pisani, G. B., Wang, Y., and Zaninoni, E. (2015b). GRB 140619B: a short GRB from a binary neutron star merger leading to black hole formation. *ApJ*, 808:190.
- Ruffini, R., Rodriguez, J., Muccino, M., Rueda, J. A., Aimuratov, Y., Barres de Almeida, U., Becerra, L., Bianco, C. L., Cherubini, C., Filippi, S., Gizzi, D., Kovacevic, M., Moradi, R., Oliveira, F. G., Pisani, G. B., and Wang, Y. (2016b). On the rate and on the gravitational wave emission of short and long GRBs. *ArXiv e-prints*.
- Ruffini, R., Rueda, J. A., Muccino, M., Aimuratov, Y., Becerra, L. M., Bianco, C. L., Kovacevic, M., Moradi, R., Oliveira, F. G., Pisani, G. B., and Wang, Y. (2016c). On the classification of GRBs and their occurrence rates. *ArXiv e-prints*.
- Ruffini, R., Salmonson, J. D., Wilson, J. R., and Xue, S.-S. (1999). On the pair electromagnetic pulse of a black hole with electromagnetic structure. *A&A*, 350:334–343.
- Ruffini, R., Salmonson, J. D., Wilson, J. R., and Xue, S.-S. (2000). On the pair-electromagnetic

- pulse from an electromagnetic black hole surrounded by a baryonic remnant. *A&A*, 359:855–864.
- Ruffini, R., Siutsou, I. A., and Vereshchagin, G. V. (2013). A Theory of Photospheric Emission from Relativistic Outflows. *ApJ*, 772:11.
- Ruffini, R., Siutsou, I. A., and Vereshchagin, G. V. (2014d). Spreading of ultrarelativistically expanding shell: An application to GRBs. *New A*, 27:30–33.
- Ruffini, R., Vereshchagin, G. V., and Wang, Y. (2017b). Thermal emission in the early afterglow of gamma-ray bursts from their interaction with supernova ejecta. *A&A*, 600:A131.
- Ruffini, R., Vereshchagin, G. V., and Xue, S.-S. (2007b). Vacuum polarization and plasma oscillations. *Physics Letters A*, 371:399–405.
- Ruffini, R. and Vitagliano, L. (2002). Irreducible mass and energetics of an electromagnetic black hole. *Physics Letters B*, 545:233–237.
- Ruffini, R. and Vitagliano, L. (2003). Energy Extraction from Gravitational Collapse to Static Black Holes. *International Journal of Modern Physics D*, 12:121–127.
- Ruffini, R., Vitagliano, L., and Xue, S.-S. (2003b). On a separatrix in the gravitational collapse to an overcritical electromagnetic black hole. *Physics Letters B*, 573:33–38.
- Ruffini, R., Vitagliano, L., and Xue, S.-S. (2003c). On plasma oscillations in strong electric fields. *Physics Letters B*, 559:12–19.
- Ruffini, R., Wang, Y., Aimuratov, Y., Barres de Almeida, U., Becerra, L., Bianco, C. L., Chen, Y. C., Karlica, M., Kovacevic, M., Li, L., Melon Fuksman, J. D., Moradi, R., Muccino, M., Penacchioni, A. V., Pisani, G. B., Primorac, D., Rueda, J. A., Shakeri, S., Vereshchagin, G. V., and Xue, S.-S. (2018). Early X-Ray Flares in GRBs. *ApJ*, 852:53.
- Ruffini, R., Wang, Y., Enderli, M., Muccino, M., Kovacevic, M., Bianco, C. L., Penacchioni, A. V., Pisani, G. B., and Rueda, J. A. (2015c). GRB 130427A and SN 2013cq: A Multi-wavelength Analysis of An Induced Gravitational Collapse Event. *ApJ*, 798:10.
- Ruffini, R., Wang, Y., Enderli, M., Muccino, M., Kovacevic, M., Bianco, C. L., Penacchioni, A. V., Pisani, G. B., and Rueda, J. A. (2015d). GRB 130427A and SN 2013cq: A Multi-wavelength Analysis of An Induced Gravitational Collapse Event. *ApJ*, 798:10.
- Ruffini, R. and Wheeler, J. A. (1971). Introducing the black hole. *Physics Today*, 24:30.
- Ruffini, R. and Xue, S.-S. (2011). Electron-positron pairs production in a macroscopic charged core. *Physics Letters B*, 696:416–421.
- Rui, L. et al. (2016). Spectroscopic Classification of SN 2016bll (=PTSS-16ckr) as a Type Ib Supernova. *The Astronomer's Telegram*, 8908.
- Schwartz, M. (1998). Supernova 1998ct in UGC 10062. *IAU Circ.*, 6957.
- Silverman, J. M. et al. (2013). Type Ia Supernovae Strongly Interacting with Their Circumstellar Medium. *ApJS*, 207:3.
- Singer, L. P. et al. (2013). Discovery and Redshift of an Optical Afterglow in 71 deg²: iPTF13bxi and GRB 130702A. *ApJ*, 776:L34.
- Smartt, S. J. et al. (2009). The death of massive stars - I. Observational constraints on the progenitors of Type II-P supernovae. *MNRAS*, 395:1409–1437.
- Smith, N. (2016). Interacting Supernovae: Types IIn and Ibn. *ArXiv e-prints*.
- Smith, N. et al. (2014). SN 2009ip and SN 2010mc: core-collapse Type IIn supernovae arising from blue supergiants. *MNRAS*, 438:1191–1207.
- Smith, N. et al. (2016). Massive stars dying alone: the extremely remote environment of SN 2009ip. *MNRAS*, 463:2904–2911.
- Soderberg, A. M. et al. (2006a). An HST Study of the Supernovae Accompanying GRB 040924 and GRB 041006. *ApJ*, 636:391–399.
- Soderberg, A. M. et al. (2007). A Spectacular Radio Flare from XRF 050416a at 40 Days and Implications for the Nature of X-Ray Flashes. *ApJ*, 661:982–994.

BIBLIOGRAPHY

- Soderberg, A. M., Kulkarni, S. R., Nakar, E., Berger, E., Cameron, P. B., Fox, D. B., Frail, D., Gal-Yam, A., Sari, R., Cenko, S. B., Kasliwal, M., Chevalier, R. A., Piran, T., Price, P. A., Schmidt, B. P., Pooley, G., Moon, D.-S., Penprase, B. E., Ofek, E., Rau, A., Gehrels, N., Nousek, J. A., Burrows, D. N., Persson, S. E., and McCarthy, P. J. (2006b). Relativistic ejecta from X-ray flash XRF 060218 and the rate of cosmic explosions. *Nature*, 442:1014–1017.
- Sparre, M. et al. (2011). Spectroscopic Evidence for SN 2010ma Associated with GRB 101219B. *ApJ*, 735:L24.
- Sparre, M. and Starling, R. L. C. (2012). A search for thermal X-ray signatures in gamma-ray bursts - II. The Swift sample. *MNRAS*, 427:2965–2974.
- Stanek, K. Z. et al. (2003). Spectroscopic Discovery of the Supernova 2003dh Associated with GRB 030329. *ApJ*, 591:L17–L20.
- Starling, R. L. C. et al. (2011). Discovery of the nearby long, soft GRB 100316D with an associated supernova. *MNRAS*, 411:2792–2803.
- Starling, R. L. C. et al. (2012). A search for thermal X-ray signatures in gamma-ray bursts - I. Swift bursts with optical supernovae. *MNRAS*, 427:2950–2964.
- Tanvir, N. R. et al. (2010). Late-time Observations of GRB 080319B: Jet Break, Host Galaxy, and Accompanying Supernova. *ApJ*, 725:625–632.
- Tartaglia, L. et al. (2016). Interacting supernovae and supernova impostors. LSQ13zm: an outburst heralds the death of a massive star. *MNRAS*, 459:1039–1059.
- Taylor, G. B. et al. (2004). The Angular Size and Proper Motion of the Afterglow of GRB 030329. *ApJ*, 609:L1–L4.
- Terreran, G. et al. (2016). Asiago spectroscopic classification of 5 supernovae. *The Astronomer's Telegram*, 9419.
- Thöne, C. C. et al. (2017). SN 2015bh: NGC 2770's 4th supernova or a luminous blue variable on its way to a Wolf-Rayet star? *A&A*, 599:A129.
- Tomasella, L. et al. (2014). Asiago spectroscopic classification of PSN J00574018+4347342 as a type-Ic SN. *The Astronomer's Telegram*, 6506.
- Toy, V. L. et al. (2016). Optical and Near-infrared Observations of SN 2013dx Associated with GRB 130702A. *ApJ*, 818:79.
- Troja, E. et al. (2017). The X-ray counterpart to the gravitational-wave event GW170817. *Nature*, 551:71–74.
- Turatto, M. (2003). Classification of Supernovae. In Weiler, K., editor, *Supernovae and Gamma-Ray Bursters*, volume 598 of *Lecture Notes in Physics*, Berlin Springer Verlag, pages 21–36.
- Turatto, M., Suzuki, T., Mazzali, P. A., Benetti, S., Cappellaro, E., Danziger, I. J., Nomoto, K., Nakamura, T., Young, T. R., and Patat, F. (2000). The Properties of Supernova 1997CY Associated with GRB 970514. *ApJ*, 534:L57–L61.
- Turolla, R. et al. (2015). Magnetars: the physics behind observations. A review. *Reports on Progress in Physics*, 78(11):116901.
- Valenti, S. et al. (2012). A Spectroscopically Normal Type Ic Supernova from a Very Massive Progenitor. *ApJ*, 749:L28.
- Van Dyk, S. D. et al. (2000). SN 1997bs in M66: Another Extragalactic η Carinae Analog? *PASP*, 112:1532–1541.
- Vereshchagin, G. V. (2014). Physics of Nondissipative Ultrarelativistic Photospheres. *International Journal of Modern Physics D*, 23:1430003–125.
- von Kienlin, A. et al. (2014). VizieR Online Data Catalog: The second Fermi/GBM GRB catalog (4yr) (von Kienlin+, 2014). *VizieR Online Data Catalog*, 221.
- Wanderman, D. and Piran, T. (2010). The luminosity function and the rate of Swift's gamma-ray bursts. *MNRAS*, 406:1944–1958.
- Woods, P. M. and Thompson, C. (2006). *Soft gamma repeaters and anomalous X-ray pulsars: magnetar candidates*, pages 547–586.

BIBLIOGRAPHY

- Woosley, S. E. and Bloom, J. S. (2006). The Supernova Gamma-Ray Burst Connection. *ARA&A*, 44:507–556.
- Zeh, A. et al. (2004). A Systematic Analysis of Supernova Light in Gamma-Ray Burst Afterglows. *ApJ*, 609:952–961.